

Advances in Structural and Multidisciplinary Optimization

**- Proceedings of the 11th World Congress of Structural and
Multidisciplinary Optimization (WCSMO-11)**

Edited by
Qing Li
Grant P Steven
Zhongpu (Leo) Zhang

Advances in Structural and Multidisciplinary Optimization

Proceedings of the 11th World Congress of Structural and
Multidisciplinary Optimisation
(WCSMO-11),
June 7-12, 2015, Sydney, Australia

Edited by

Qing Li, Grant P Steven, Zhongpu (Leo) Zhang

ISBN 13: 978-0-646-94394-7

Full text available online at <http://www.aeromech.usyd.edu.au/WCSMO2015/>

Preface

The present e-book contains the full-length papers from the 11th World Congress on Structural and Multidisciplinary Optimisation (WCSMO-11) held in Sydney, Australia on 7-12 June 2015, where the authors represented 35 different countries, from the Asian-Pacific, American, African and European regions. The conference is organized by The University of Sydney under the International Society for Structural and Multidisciplinary Optimization (ISSMO).

In WCSMO-11, 343 papers (167 in full-length) were presented in either verbal (317) or poster (26) form. All the abstracts submitted to WCSMO-11 were reviewed under a rigorous process by the International Papers Committee (IPC), who met in Sydney on 1-3 Feb 2015. All the full length papers published in this e-book were reviewed by the members from the local organizing committee, international scientific committee and expert invitees. As the editors of the e-book, we wish to acknowledge the authors who contributed the papers to WCSMO-11 and those who kindly participated in review of the papers within time constraint.

Scientifically, these collected full-length papers in this e-book well reflected the latest progress in some traditional and emerging areas of structural and multidisciplinary optimization, ranging from mathematical foundations to algorithmic development as well as advanced applications in multiscale, uncertainty, nonlinearity, additive manufacturing, multidisciplinary and multiphysics in metamaterials, phononics, photonics, plasmonics, piezoelectricity, electromagnetics, thermofluids, renewable energy, and acoustics for aerospace, automotive, biomedical, mechanical, civil and structural engineering.

This e-book is dedicated to the memory of ISSMO Founding President George Rozvany who passed away on July 31, 2015. George was a Professor of Structural Mechanics at Budapest University of Technology and Economics in Budapest, Hungary, the recipient of numerous honors and awards, a number of books and hundreds of technical publications and had an international reputation for his research activities. We will deeply miss George and the community has indeed suffered a deep loss.

We are also grateful to all of the contributors who made the organization of WCSMO-11 and publication of the e-book possible. Special thanks are also given to Bryant (Che-Cheng) Chang, Junning (John) Chen, Ali Entezari, Jianguang Fang, Salvatore Samuel Grasso, Zhipeng (Floyd) Liao, Andrian Sue, Guangyong Sun, Sriram Tammareddi, Scott Townsend, Phillip Tran, Paul Wong, Nobuhiro Yoda, Dequan (Darren) Zhang, Keke (Marco) Zheng for their tremendous secretarial and editing work.

Professor Qing Li, Co-Chair of WCSMO-11
Professor Grant Steven, Co-Chair of WCSMO-11
Dr Zhongpu (Leo) Zhang, Secretary of WCSMO-11

The University of Sydney
NSW 2006, Australia
August 2015

Conference Organizers

The International Society for Structural and Multidisciplinary Optimization (ISSMO)

The University of Sydney

Table of Contents

Improvement researches on involute tooth profile	p.1
<i>Jikai Fan, Youmin Hu, Yanlei Li, Xiong Jing, Xiaokun Duan</i>	
A level set method for the representation of multiple types of boundaries and its application in structural shape and topology optimization	p.7
<i>Qi Xia, Michael Yu Wang, Tielin Shi</i>	
A parallel optimization method based on kriging model	p.13
<i>Zhaojun Li, Xicheng Wang</i>	
Welded cellular cylindrical shell – a new structural solution for the optimum design of a cantilever column	p.19
<i>József Farkas, Károly Jármai</i>	
Topology optimization for coated structures	p.25
<i>Anders Clausen, Erik Andreassen, Ole Sigmund</i>	
Aerothermoelastic structural topology optimisation for a hypersonic transport aircraft wing	p.31
<i>David J. Munk, Gareth A. Vio, Grant P. Steven</i>	
Shape optimization method of shell structures concerned with material and geometrical nonlinearity	p.37
<i>Shintaro Kosaka, Masatoshi Shimoda</i>	
A sensitivity-based coordination method for optimization of product families	p.43
<i>Jun Zou, Wei-Xing Yao, Jun-Feng Zheng</i>	
Crash optimization of automobile frontal and side structures using equivalent static loads	p.49
<i>Youngmyung Lee, Jin-Seok Ahn, Gyung-Jin Park</i>	
A direct optimal control strategy for valves in heat exchanger networks and experimental validations	p.54
<i>Yi-Fei Wang, Qun Chen</i>	
Achieving minimum length scale in topology optimization by geometric constraints	p.60
<i>Mingdong Zhou, Boyan S. Lazarov, Fengwen Wang, Ole Sigmund</i>	
Adaptive multi-point sequential sampling methodology for highly nonlinear automotive crashworthiness design problems	p.65
<i>Siliang Zhang, Zhengchao Song, Guohong Shi, Rongying Qiu</i>	

Comparison of some commercial software systems for structural optimization	p.71
<i>Wook-han Choi, Cheng-guo Huang, Jong-moon Kim, Gyung-Jin Park</i>	
Novel approach in topology optimization of porous plate structures for phononic bandgaps of flexural waves	p.77
<i>Saeid Hedayatrasa, Kazem Abhary, Mohammad Uddin, Ching-Tai Ng</i>	
Topology optimization of continuum structures made of non-homogeneous materials of isotropic or cubic symmetry	p.83
<i>Sławomir Czarnecki, Radosław Czubacki, Tomasz Lewiński, Paweł Wawruch</i>	
A novel constraint handling strategy for expensive optimization problems .	p.89
<i>Kalyan Shankar Bhattacharjee, Tapabrata Ray</i>	
Experimental and numerical study of water impact investigations for aircraft crashworthiness application analysis	p.95
<i>Wang Yonghu, Shu Dongwei, Y. Fujii, A. Takita, R. Araki, Hu Wei</i>	
Weight minimization of trusses with natural frequency constraints	p.100
<i>Vu Truong Vu</i>	
Many-objective optimization in engineering design: case studies using a decomposition based evolutionary algorithm	p.106
<i>Hemant Kumar Singh, Tapabrata Ray</i>	
Lightweight design of vehicle structure with tailor rolled blank under crashworthiness	p.112
<i>Libin Duan, Guangyong Sun, Junjia Cui, Tao Chen, Guangyao Li</i>	
A flying wing UCAV design optimization using global variable fidelity modeling	p.121
<i>Maxim Tyan, Nhu Van Nguyen, Jae-Woo Lee</i>	
Gradient based structural optimization with fatigue constraints of jacket structures for offshore wind turbines	p.127
<i>Jacob Oest, Lars Chr. T. Overgaard, Erik Lund</i>	
Experience with several multi-fidelity surrogate frameworks	p.133
<i>Chanyoung Park, Raphael T. Haftka, Nam-Ho Kim</i>	
Speed dependent optimisation for variable stiffness vehicle suspension ..	p.139
<i>Xin Tang, Weihua Li, Haiping Du</i>	
Reliability-based microstructural topology design with respect to vibro-acoustic criteria	p.145
<i>Jianbin Du, Chuangchuang Sun</i>	

A new topology optimization algorithm for photonic band gap structures .	p.151
<i>Fei Meng, Xiaodong Huang, Baohua Jia</i>	
Topology optimization of 2D phononic band gap crystals based on BESO methods	p.157
<i>Yangfan Li, Xiaodong Huang, Fei Meng, Shiwei Zhou</i>	
Optimization of contact stress distribution in interference fit	p.162
<i>Niels Leergaard Pedersen</i>	
On the integration of tuned multi-mass dampers into a topology optimization method for machine tool structural dynamics	p.167
<i>Christian Brecher, Simo Schmidt, Marcel Fey</i>	
Fatigue life optimisation of damage tolerant structures using design space exploration	p.173
<i>Raj Das, Rhys Jones</i>	
Structural optimization of standardized trusses by dynamic grouping of modules	p.179
<i>Alexis Tugilimana, Rajan Filomeno Coelho, Ashley P. Thrall</i>	
A study of optimization for automotive parts and structures by using inertia relief	p.185
<i>Takanobu Saito, Jiro Hiramoto, Toshiaki Urabe</i>	
Design and optimization of billet structure about High-speed Rail bearing in cold rolling	p.191
<i>Xue-dao Shu, Ji-dong Ma, Jie He, Bao-shou Sun, Wen-fei Peng</i>	
Shape optimum design of graphene sheets	p.196
<i>Jin-Xing Shi, Masatoshi Shimoda</i>	
Life cycle vibration sensation rate evaluation model for the optimal human comfort design of super tall buildings	p.202
<i>Lilin Wang, Yimin Zheng, Tianyi Yu, Xin Zhao</i>	
Integrated optimal life cycle design of super tall buildings with viscous dampers	p.212
<i>Xin Zhao, Tao Shi</i>	
Parameter optimization for the integrated optimal design of super tall buildings with viscous damping walls	p.219
<i>Xi Zhan, Xin Zhao, Yimin Zheng</i>	
Optimization of wind-induced acceleration of super tall buildings by modal shape updating	p.225
<i>Xin Zhao, Xiang Jiang</i>	

Multi-objective free-form optimization for shape and thickness of shell structures with composite materials	p.231
<i>Kenichi Ikeya, Masatoshi Shimoda</i>	
Multi-level hierarchical MDO formulation with functional coupling satisfaction under uncertainty, application to sounding rocket design	p.237
<i>Loïc Brevault, Mathieu Balesdent, Nicolas Bérend, Rodolphe Le Riche</i>	
Multidisciplinary design optimization of an aero-engine fan blade with consideration of bypass and core performance	p.243
<i>Christopher Chahine, Tom Verstraete, Li He</i>	
Multi-objective optimization of material model parameters of an adhesive layer by using SPEA2	p.249
<i>Kaveh Amouzgar, Mirza Cenanovic, Kent Salomonsson</i>	
Large-scale robust topology optimization under load-uncertainty	p.255
<i>Carl-Johan Thore, Erik Holmberg, Anders Klarbring</i>	
Assessing sensitivities of maneuver load alleviation parameters on buckling reserve factors using surrogate model based extended Fourier amplitude sensitivity test	p.261
<i>Rahmetalla Nazzeri, Frank Lange, Matthias Haupt, Christophe Sebastien</i>	
Optimal design of a double coil magnetorheological fluid damper with various piston profiles	p.268
<i>Guoliang Hu, Zheng Xie, Weihua Li</i>	
Topology optimization considering the requirements of deep-drawn sheet metals	p.274
<i>Robert Dienemann, Axel Schumacher, Sierk Fiebig</i>	
Design optimization for multifunctional 3D printed structures with embedded functional systems	p.280
<i>A. Panesar, D. Brackett, I. Ashcroft, R. Wildman, R. Hague</i>	
Optimizing topology optimization with anisotropic mesh adaptation	p.286
<i>Kristian E. Jensen</i>	
Robust topology optimization of thin plate structure under concentrated load with uncertain load point	p.292
<i>Yoshiaki Nakazawa, Nozomu Kogiso, Takayuki Yamada, Shinji Nishiwaki</i>	
Structural and aerostructural design of aircraft wings with a matrix-free optimizer	p.298
<i>Andrew B. Lambe, Joaquim R. R. A. Martins</i>	

Topology optimization for heat conduction using generative design algorithms	p.304
<i>Danny J. Lohan, Ercan M. Dede, James T. Allison</i>	
Manufacture-oriented design optimisation of a flow diverter stent using lattice boltzmann method and simulated annealing	p.310
<i>Mingzi Zhang, Hitomi Anzai, Bastien Chopard, Makoto Ohta</i>	
Topology optimization of plate structures subject to initial excitations for minimum dynamic performance index	p.316
<i>Kun Yan, Gengdong Cheng</i>	
Structural approximations for composite optimisation	p.322
<i>Daniël M. J. Peeters, Mostafa M. Abdalla</i>	
Multi-parameter optimization study on the crashworthiness design of a vehicle by using global sensitivity analysis and dynamic meta-model	p.328
<i>ZHANG Weigang, ZHANG Yang, MA Tao, TANG Ting</i>	
Integrated multi-scale vibro-acoustic topology optimization of structure and material	p.335
<i>Xuan Liang, Jianbin Du</i>	
Efficient aerodynamic optimization using a multiobjective optimization based framework to balance the exploration and exploitation	p.342
<i>Zhiwei Feng, Tao Yang, Jianquan Ge, Qiangang Tang, Yang Ma</i>	
Optimization of process parameters for three-roll skew rolling based on design of experiment (DOE)	p.349
<i>Baoshou Sun, Guangxing Huang, Wenfei Peng, Xuedao Shu, Lu Wang</i>	
Reduced super beam based approach to finite element model updating of beam-type structures	p.354
<i>Wensheng Wang, Haojie Wei, Zhonghua Hou</i>	
Study on optimization for large structures using hybrid GA	p.360
<i>Ryota Nonami, Mitsuru Kitamura, Akihiro Takezawa</i>	
Tradeoff exploration in decomposition-based optimization	p.366
<i>Paolo Guarneri, Margaret M. Wiecek</i>	
Simulation study on the prediction of dangerous conditions for occupant in a running vehicle equipped with airbag	p.372
<i>Weigang Zhang, Ding Chen</i>	
Dual-mode operation of the finger-type manipulator based on distributed actuation mechanism	p.378
<i>Jong Ho Kim, Young June Shin, Sung-Hwan Kim, In Gwun Jang</i>	

Data based materials numerical modelling for FPSO safety and reliability optimization	p.384
<i>Robert E Melchers, Andrew E. Potts</i>	
Damage detection method in non-destructive testing based on topology optimization and eigenvalue analysis	p.390
<i>Takafumi Nishizu, Akihiro Takezawa, Mitsuru Kitamura</i>	
Multi-objective optimization using adaptive explicit non-dominated region sampling	p.396
<i>Anirban Basudhar</i>	
Simulation and optimization of MPV suspension system based on ADAMS	p.402
<i>Dongchen Qin, Junjie Yang, Qiang Zhu, Peng Du</i>	
A novel anti-optimization method for structural robust design under uncertain loads	p.407
<i>Zhifang Fu, Chunjie Wang, Junpeng Zhao</i>	
An improvement technique for Bi-directional Evolutionary Structural optimization (BESO) method	p.413
<i>Kazem Ghabraie</i>	
Optimal design and evaluation of cantilever probe for multifrequency atomic force microscopy	p.420
<i>Jiandong Cai, Qi Xia, Yangjun Luo, Michael Yu Wang, Li Zhang</i>	
Structural design of aircraft wing based on topology and global-local optimization	p.425
<i>Vasily Chedrik, Sergey Tuktarov</i>	
Geometric feature identification from topology optimization results	p.431
<i>Guilian Yi, Byeng D. Youn, Nam H. Kim</i>	
Cross sections and prestressing forces optimizations of prestressed concrete beams	p.437
<i>Yoyong Arfiadi, Alfian Wiranata Zebua</i>	
Research on integrated design and optimization for hypersonic-glide vehicle	p.443
<i>Jianquan Ge, Longyun Chen, Bin Zhang, Lei Wang</i>	
Shape optimization method for crashworthiness design based on equivalent static loads concept	p.449
<i>Laurent Genest, Louis Jézéquel¹, Frédéric Gillot¹, Frédéric Mercier</i>	
Optimizing snap-through structures by using gradient-only algorithms	p.455

Schalk Kok, Daniel N Wilke

Optimization of reinforced concrete frames by harmony search method ... p.460

Moacir Kripka, Deise Boito, Juliana Triches and Guilherme Fleith de Medeiros

A TIMP method for topology optimization with displacement and stress constraints in multiple loading cases p.465

Guilian Yi, Yunkang Sui, Byeng D. Youn

Interval buckling analysis of steel structures using mathematical programming approach p.471

Di Wu, Wei Gao, Francis Tin-Loi

Combining state of the art meta-models for predicting the behavior of non-linear crashworthiness structures for shape and sizing optimizations p.477

Axel Schumacher, Christopher Ortmann

Parameter optimisation design for a six-DOF heavy duty vehicle seat suspension p.483

Donghong Ning, Haiping Du, Weihua Li

Likelihood of buckling mode interaction in shape optimisation of manufacturable cold-formed steel columns p.489

Bin Wang, Benoit P. Gilbert, Hong Guan, Lip H. Teh

On the numerical optimization of multi-load spatial Michell trusses using a new adaptive ground structure approach p.494

Tomasz Sokół, George I. N. Rozvany

Topology optimization of members of dynamically loaded flexible multibody systems using integral type objective functions and exact gradients p.500

Alexander Held, Sven Knüfer, Robert Seifried

High-fidelity Structural optimization of a tow-steered composite wing p.506

Timothy R. Brooks, John T. Hwang, Graeme J. Kennedy, Joaquim R. R. A. Martins

Design optimization of multi-point constraints in structures p.512

Daniel N. Wilke, Schalk Kok

Distributed NSGA-II for seismic retrofitting optimization with multi-core PC cluster p.518

Keunhyoung Park, Hyo Seon Park

Enhanced second-order reliability method and stochastic sensitivity analysis using importance sampling..... p.524

Jongmin Lim, Byungchai Lee, Ikjin Lee

TV packaging optimization of the frontal drop impact using equivalent static loads	p.530
<i>Insik Han, Youngmyung Lee, and Gyung-Jin Park</i>	
Sensitivity analysis of structural response to external load position	p.535
<i>D. Wang</i>	
Topology and sizing optimisation of integral bus chassis with the use of a cooperative coevolutionary genetic algorithm with independent ground structures	p.541
<i>Wei Zhong, Ruiyi Su, Liangjin Gui, Zijie Fan</i>	
Reliability-based design optimization of wind turbine blades for fatigue life under wind load uncertainty	p.547
<i>Weifei Hu, K.K. Choi, Hyunkyoo Cho, Nicholas J. Gaul, Olesya I. Zhupanska</i>	
Multidisciplinary optimization of auto-body lightweight design using modified particle swarm optimizer	p.556
<i>Zhao Liu, Ping Zhu, Wei Chen, Ren-Jye Yang</i>	
Elastic moduli identification method for orthotropic structures based on vibration data	p.562
<i>Akira Saito, Yasunari Nishikawa, Shintaro Yamasaki, Kikuo Fujita, Atsushi Kawamoto, Masakatsu Kuroishi, Hideo Nakai</i>	
Accuracy improvement of MPP-based dimension reduction method using the eigenvectors of the hessian matrix	p.568
<i>Seongbin Kang, Ikjin Lee, Jongmin Lim</i>	
Utilization of gaussian kernel reliability analyses in the gradient-based transformed space for design optimization with arbitrarily distributed design uncertainties	p.574
<i>Po Ting Lin</i>	
Robust design and optimization of a radial turbine within a supercritical CO₂ solar Brayton cycle	p.580
<i>Rodney Persky, Emilie Sauret, Andrew Beath</i>	
Topology and size optimization of modular ribs in aircraft wings	p.586
<i>A.Rinku, G K Ananthasuresh</i>	
Design and optimization of a variable stiffness composite laminate	p.592
<i>Yan Zhang, Fenfen Xiong</i>	
Parameter estimation method using Bayesian statistics considering uncertainty of information for RBDO	p.598
<i>Makoto Ito, Nozomu Kogiso</i>	

A sequential optimization and mixed uncertainty analysis method based on Taylor series approximation	p.604
<i>Xiaoqian Chen, Wen Yao, Yiyong Huang, Yi Zhang</i>	
Zooming in surrogate optimization using convolute RBF	p.610
<i>Masao Arakawa</i>	
Surrogate models for data-inspired reliability design	p.616
<i>Norio Takeda, Tatsuya Kameyama</i>	
Optimal design of a parallel beam system with elastic supports to minimize flexural response to harmonic loading	p.622
<i>Bret R. Hauser, Bo P. Wang</i>	
Damage process sensitivity analysis using an XFEM-level set framework .	p.628
<i>L. Noël, P. Duysinx, K. Maute</i>	
A RBF neural network modeling method based on sensitivity analysis and pareto law	p.634
<i>Zongyu Wu, Yong Chen, Wen Yao, Xiaoqian Chen</i>	
A novative optimal shape design based on an isogeometric approach: application to optimization of surface shapes with discontinuous curvature	p.640
<i>Sarah Julisson, Christian Fourcade, Paul de Nazelle, Laurent Dumas</i>	
Optimization of structural topology using unstructured Cellular Automata	p.646
<i>Bogdan Bochenek, Katarzyna Tajs-Zielińska</i>	
Topology optimisation of passive coolers for light-emitting diode lamps ..	p.652
<i>Joe Alexandersen, Ole Sigmund, Niels Aage</i>	
Topology optimization considering design-dependent stokes flow loads ..	p.657
<i>Renato Picelli, William Martins Vicente, Renato Pavanello, Fred van Keulen</i>	
Blended composite optimization combining stacking sequence tables and a modified Shepard's method	p.663
<i>Yasser M. Meddaikar, Francis-Xavier Irisarri, Mostafa M. Abdalla</i>	
Parallel particle swarm optimization on GPU with application to trajectory optimization	p.669
<i>Qi Wu, Fenfen Xiong</i>	
Method of variable transformation for topology optimization with clear boundary shape.....	p.675
<i>Vladimir M. Uskov, Kirill A. Balunov</i>	
Gradient-based optimization of parameterized CAD geometries	p.681

Timothée Leblond, Pierre Froment, Paul de Nazelle, Reda Sellakh, Philippe Serré, Gaël Chevallier

Multidisciplinary design optimization of sound radiation from underwater double cylindrical shell structure p.686
Deqing Yang, Guilian Yi, Jiapeng Cheng

An explicit feature control approach in structural topology optimization ... p.692
Weisheng Zhang, Xu Guo, Wenliang Zhong

Structural dynamic topology optimisation of a direct-drive single bearing wind turbine generator..... p.698
M. Kirschnack, H. Polinder, R.A.J. van Ostayen, F.C.M. van Kempen, D.J. Rixen

Topology optimization of cellular materials for properties governed by nonlinear mechanics..... p.704
Josephine V. Carstensen, Reza Lotfi, James K. Guest

Applications of a consistent grayscale-free topology optimization method to industrial design problems p.710
Shintaro Yamasaki, Atsushi Kawamoto, Tsuyoshi Nomura, Kikuo Fujita

Solving multiple tour multiple traveling salesman problem with evolutionary programming p.716
László Kota, Károly Jármai

Level set-based topology optimization using the lattice Boltzmann method considering two-phase fluid flows..... p.722
Kentaro Yaji, Takayuki Yamada, Masato Yoshino, Toshiro Matsumoto, Kazuhiro Izui, Shinji Nishiwaki

Simultaneous optimization of topology and orientation of anisotropic material using isoparametric projection method..... p.728
Tsuyoshi Nomura, Ercan M. Dede, Tadayoshi Matsumori, Atushi Kawamoto

An efficient parallel coordination method for decomposition-based optimization using two duality theorems p.734
Meng Xu, Georges Fadel, Margaret M. Wiecek, Paolo Guarnieri

Electromagnetic levitation coil design using gradient-based optimization . p.744
Suzanne Roberts, Schalk Kok, Johan Zietsman, Helen Inglis

Reliability-based design optimization of nonlinear energy sinks p.750
Ethan Boroson, Samy Missoum

Multi-objective topology optimization of composite structures considering resin filling time p.758
Yuqing Zhou, Kazuhiro Saitou

Future challenges for topology optimization for the usage in automotive lightweight design technologies	p.766
<i>Sierk Fiebig, Jürgen Sellschopp, Holger Manz, Thomas Vietor, Joachim K. Axmann, Axel Schumacher</i>	
Tailored natural components – functional geometry and topology optimization of technical grown plants	p.774
<i>Anna-Lena Beger, Manuel Löwer, Jörg Feldhusen, Jürgen Prell, Alexandra Wormit, Björn Usadel, Christoph Kämpfer, Thomas-Benjamin Seiler, Henner Hollert, Franziska Moser, Martin Trautz</i>	
Topology optimization of a jacket structure for an offshore wind turbine with a genetic algorithm	p.780
<i>Johan Henrik Martens, Daniel Zwick, Michael Muskulus</i>	
Surrogate-based particle swarm optimization for large-scale wind farm layout design	p.786
<i>Ali Mehmani, Weiyang Tong, Souma Chowdhury, Achille Messac</i>	
One-dimensional function extrapolation using surrogates	p.792
<i>Yiming Zhang, Nam-Ho Kim, Chan-Young Park, Raphael T. Haftka</i>	
Fatigue sensitivity analysis of offshore wind turbine structures	p.798
<i>Kok-Hon Chew, Michael Muskulus, Srikanth Narasimalu, Kang Tai, E.Y.K. Ng</i>	
Optimization of laminated structures considering manufacturing efforts ...	p.804
<i>Markus Schatz, Horst Baier</i>	
A visually-informed decision-making platform for wind farm layout optimization	p.810
<i>Souma Chowdhury, Weiyang Tong, Ali Mehmani, Achille Messac</i>	
Shape optimisation of a gas injector	p.816
<i>Ruber Arley Ruiz-Mesa, Manuel Julio García</i>	
Simultaneous optimization of initial blank shape and blank holder force trajectory for square cup deep drawing using sequential approximate optimization	p.823
<i>Satoshi Kitayama, Marina Saikyo , Kiichiro Kawamoto, Ken Yamamichi</i>	
Robust shape optimization under vibroacoustic criteria and uncertain parameters	p.829
<i>Frédéric Gillot, Renata Troain, Koji Shimoyama, Sébastien Besset</i>	
Optimal design of wind farm layout and control strategy	p.834
<i>Longyan Wang, Md Rifat Shahriar, Andy Tan, Yuantong Gu</i>	
Reduced order simulation surrogate for wind turbine component design ..	p.840

Robert T. Rudolf

Adjoint methods of sensitivity analysis for Lyapunov equation..... p.845

Boping Wang, Kun Yan

**Structural damage identification by means of neural network
(evaluation of identification capability) p.851**

Kazuyuki Hanahara, Yukio Tada

Multiscale structural topology optimization p.857

Liang Xia, Piotr Breitkopf

Optimization of elastic plastic plates of piecewise constant thickness p.863

Jaan Lellep, Julia Polikarpus, Boriss Vlassov

**Form finding by shape optimization with the Vertex Morphing Method – About
the equivalence of sensitivity filtering and standard spline models p.869**

Kai-Uwe Bletzinger, Majid Hojjat, Electra Stavropoulou

**Stability-ensured topology optimization of boom structures with stress
constraints p.874**

Wenjun Li, Qicai Zhou, Zhen Jiang, Wei Chen

**Elimination of void element influence on optimization for nonlinear compliance
with a buckling constraint using moving iso-surface threshold method..... p.882**

Liyong Tong, Quantian Luo

**Optimization of pulsating blank holder force for deep drawing of cylindrical
cups p.888**

Jing Han, Shinji Natsume, Satoshi Kitayama, Koetsu Yamazaki, Hiroaki Uchida

**Acoustic radiation and sensitivity analysis of a randomly excited structure
based on FEM/IBEM combined with PEM p.894**

Baoshan Liu, Liyong Tong

**An immersed boundary approach for sensitivity analysis of fluid-structure
interactions p.900**

Ramana V. Grandhi, Koorosh Gopal

MIST topology optimization for bending plates under static loading..... p.906

Mahmoud Alfouneh, Liyong Tong

Structural optimization under complementarity constraints p.912

Sawekchai Tangaramvong, Francis Tin-Loi

**Conceptual design of box girder based on three-dimensional topology
optimization p.918**

Dongchen Qin, Peng Du, Qiang Zhu, Junjie Yang

Production-based multi-criteria design optimisation of an unconventional composite fuselage side panel by evolutionary strategies and a surrogate model of manufacturability analysis	p.924
<i>Onur Deniz, Peter Horst, Carsten Schmidt</i>	
Structural optimization for stabilized and stiffened structural system by tension members	p.930
<i>Yohei Yokosuka, Toshio Honma</i>	
Sizing optimization for industrial applications	p.936
<i>Miguel A.A.S. Matos, Peter M. Clausen, Claus B.W. Pedersen</i>	
A new method for maximum dynamic response topology optimization in the time domain.....	p.942
<i>Junpeng Zhao, Chunjie Wang</i>	
Convergence analysis of full elastic tensors to homogenization predictions in periodic composite material design	p.948
<i>P.G. Coelho, L.D. Amiano, J.M. Guedes, H.C. Rodrigues</i>	
Common automotive and aerospace requirements for commercial structural optimization software	p.954
<i>Steve Georgiadis, Vladimir Balabanov, Rodney Dreisbach, David Trop, Moritz Frenzel, Daniel Heiserer, David Keller, Markus Schemat</i>	
Multidisciplinary optimization and integration requirements for large-scale automotive and aerospace design work	p.961
<i>Moritz Frenzel, Daniel Heiserer, David Keller, Markus Schemat, Vladimir Balabanov, Rodney Dreisbach, Steve Georgiadis, David Trop</i>	
Topology optimization of a transient thermo-mechanical problem using material penalization.....	p.966
<i>Emiel van de Ven, Evert Hooijkamp, Matthijs Langelaar, Fred van Keulen</i>	
Robust shape optimization method for shell structures with unknown loadings	p.972
<i>Tomohiro Nagano, Masatoshi Shimoda</i>	
Optimal design of a wheelchair suspension based on a compliant mechanism	p.978
<i>Masakazu Kobayashi</i>	
Reliability-based design optimization of vehicle front-end structure for pedestrian lower extremity protection	p.983
<i>Guangyong Sun, Xiaojiang Lv, Jianguang Fang, Xianguang Gu, Qing Li</i>	

Optimization of bone tissue scaffolds fabricated by robocasting technique

..... p.989
Ali Entezari, Zhongpu Zhang, Junning Chen, Qing Li

Improvement researches on involute tooth profile

Jikai Fan^{1, a}, **Youmin Hu**^{1, 2, b}, **Yanlei Li**^{1, c}, **Xiong Jing**^{1, d}, **Xiaokun Duan**^{1, e}

¹State Key Laboratory of Digital Manufacturing Equipment and Technology, Huazhong University of Science and Technology, Wuhan, Hubei, China, 430074

²Wuxi institute, Huazhong University of Science and Technology, Wuxi, Jiangsu, China, 214174

^aemail:fan_ji_kai@163.com

^bemail:youmhwh@mail.hust.edu.cn

^cemial:liyanlei90@163.com

^demail:xjt513-1-34m@163.com,

^edxk2153@hust.edu.cn

1. Abstract

A kind of profile modification cubic curve of the involute spur gear is proposed in this paper using the geometric theory and the Curve fitting method. The derivation process of the key point coordinates and the curve equation is described in detail, the proposed modification curve tangents to both the involutes and the addendum circle. Using the modification curve to correct the flank shape of the driving and driven gears, the smooth transition between the cubic curve and involute can be ensured, as well as between the cubic curve and the addendum circle. Besides, the contact stress reduces obviously after modification using this method which can be verified with Hertz contact theory, finally, an example is adopted to illustrate how to implement this modification method. The goal of this article is to put forward a scheme for the optimization design and improvement of gears so as to improve the gears' working condition and prolong their service life.

2. Keywords: spur gears; profile modification; cubic curve; smooth transition

3. Introduction

It is common to see that the meshing impact, load mutation, speed fluctuation and other vibration with different formation because of the teeth deformation, manufacturing and installation errors and so on when the spur gear works[1, 2], consequently, modification was carried out on the gears in order to improve all sorts of undesirable phenomenon foregoing.

Tooth profile modification, refers to modifying the involute appropriately near the tip or root of the meshing teeth, which aims at compensating the machining error and elastic deformation of the teeth, and reducing the load impact during the gears enter and exit the mesh[3-5]. The pressure angle of the addendum of gear after modification is larger than unmodified; this means that the meshing angle of the start meshing point increases, that is the comprehensive radius of curvature of the start meshing point increases.

Height of modification, amount of modification and curve of modification are regarded as the three elements of gear modification. Amount of modification varies gradually from the maximum to zero, and its change rule is defined as the curve of modification, there are two types of modification curves: straight and curved[6], while neither straight line nor curve modification can guarantee that the modification curve not only tangent to the involute but also tangent to the addendum circle, in this case, when the gears enter the mesh, the addendum of driven gear contact with the root of driving gear tooth in terms of obtuse angle or chamfer, then sliding on the surface of the driving gear tooth, when the gears exit the mesh, the addendum of driving gear contact with the root of driven gear tooth in terms of obtuse angle or chamfer, then sliding on the surface of the driven gear tooth, In those cases mentioned above, the contact stress and contact deformation of gear teeth are very large, the transmission stability of gear is poor, so, the curve of modification proposed in this aims at improving all kinds of disadvantages stated above.

4.8. Tables and Figures

Tables and figures should be consecutively numbered. Place table caption above the table and figure caption below the figure. Table and figure captions should be centred. Allow one line space between the table and its caption and between the figure and its caption. Allow one line of space between the table or figure and the adjacent text.

4.The method of calculating the modification curve

The following part of this paper will detail the method of calculating the modification curve, In figure1, line

segment AE is the maximum amount of modification: $AE = \Delta_{\max}$, involute section AB is the length of the modification: $AB = L$, the gear tooth and the addendum circle intersect at point A . h_{\max} is the height of modification (mm) ;

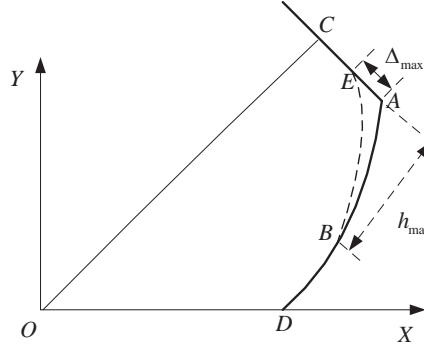


Fig.1.The three elements of gear modification

The modification curve put forward in this paper and addendum circle intersect at point E, and involute tooth surfaces intersect at point B, the modification curve tangent to the involute as well as the addendum circle at the both two points.

The specific steps of the modification curve are as follows:

4.1. Solution of point A coordinate

The parameters equation of the involute can be expressed as :

$$\begin{cases} x = r_b (\cos \alpha + \alpha \sin \alpha) \\ y = r_b (\sin \alpha - \alpha \cos \alpha) \end{cases} \quad (1)$$

where r_b is the radius of base circle (mm), The radius of addendum circle can be expressed as :

$$r_a = \frac{m(z+2)}{2} \quad (2)$$

where m is module (mm), z is the number of teeth, while the equation of addendum circle is

$$x^2 + y^2 = r_a^2 \quad (3)$$

from the involute equation and the equation of addendum circle, we can get that

$$r_b^2 (1 + \alpha^2) = r_a^2 \quad (4)$$

consequently,

$$\alpha_A = \sqrt{\left(\frac{r_a}{r_b}\right)^2 - 1} \quad (5)$$

the coordinate of point A is $[r_b (\cos \alpha_A + \alpha_A \sin \alpha_A), r_b (\sin \alpha_A - \alpha_A \cos \alpha_A)]$.

4.2. Solution of point B coordinate and the slope of involute

The length of arc BD is (from figure1 we know that $L_{AB} \approx \frac{h_{\max}}{\cos \theta}$)

$$L_{BD} = L_{DA} - L_{BA} = \int_0^{\alpha_A} \sqrt{\left(\frac{dx}{d\alpha}\right)^2 + \left(\frac{dy}{d\alpha}\right)^2} d\alpha - L_{BA} = \frac{r_a^2 - r_b^2}{2r_b} - \frac{h_{\max}}{\cos \theta} \quad (6)$$

while the length of arc BD is :

$$L_{BD} = \int_0^{\alpha_B} \sqrt{\left(\frac{dx}{d\alpha}\right)^2 + \left(\frac{dy}{d\alpha}\right)^2} d\alpha = \frac{r_b}{2} \alpha_B^2 \quad (7)$$

from equation (6) and (7), the α_B can be obtained. The coordinate of point B is $[r_b (\cos \alpha_B + \alpha_B \sin \alpha_B), r_b (\sin \alpha_B - \alpha_B \cos \alpha_B)]$, that is, (x_B, y_B) , the slope of involute of point B is

$$k_B = \frac{dy}{dx} = \tan \alpha_B \quad (8)$$

4.3. Solution of point E coordinate and the slope of addendum

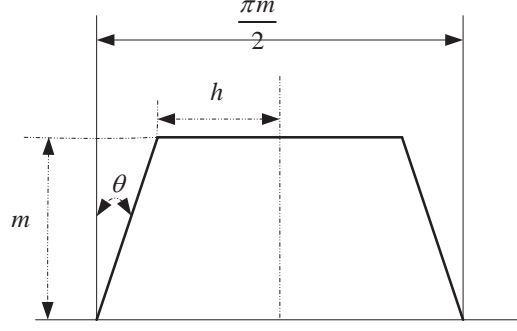


Fig.2. Gear parameter schematic diagram

As presented in figure2, the tooth surface of the addendum circle can be seen as a plane approximately, then AC is straight line, (AC perpendicular to OC and C is the pedal), we can easily get :

$$h = \frac{P}{4} - m \tan \theta = m \left(\frac{\pi}{4} - \tan \theta \right) \quad (9)$$

$\theta = 20^\circ$ is pressure angle. In figure2, assuming $\angle AOC = \beta$, then $\sin \beta = \frac{AC}{OA} = \frac{h}{r_a}$,

$$\beta = \arcsin \frac{h}{r_a} = \arcsin \frac{m \left(\frac{\pi}{4} - \tan \theta \right)}{r_a} \quad (10)$$

the slope of line segments OC is $k_{OC} = \tan(\beta + \alpha_A)$, and the slope of AC is

$$k_{AC} = k_E = \frac{-1}{k_{OC}} = \frac{-1}{\tan(\beta + \alpha_A)} \quad (11)$$

assuming the coordinate of point E is (x_E, y_E) , then $k_{AC} = k_E = \frac{y_E - y_A}{x_E - x_A}$, meanwhile, $|EA| = \Delta_{\max}$, that is

$\sqrt{(x_E - x_A)^2 + (y_E - y_A)^2} = \Delta_{\max}$, from above all we can get: $(x_E - x_A)^2 + k_E^2 (y_E - y_A)^2 = \Delta_{\max}^2$, that is $(1 + k_E^2)(x_E - x_A)^2 = \Delta_{\max}^2$, we can get fatherly :

$$\begin{cases} x_E = x_A - \frac{\Delta_{\max}}{\sqrt{1 + k_E^2}} \\ y_E = y_A - \frac{k_{AC} \Delta_{\max}}{\sqrt{1 + k_E^2}} \end{cases} \quad (12)$$

4.4. Comprehensive above solution, using the polynomial interpolation method, The cubic curve can be calculated that meet through points A and B, as well as tangent to the no modification curve at the both points is as follows:

$$y = ax^3 + bx^2 + cx + d, x \in [x_B, x_E] \quad (13)$$

various parameters are calculated as follows (the coordinate system of xOy is the coordinate system of involute):

$$\begin{bmatrix} a \\ b \\ c \\ d \end{bmatrix} = \begin{bmatrix} x_B^3 & x_B^2 & x_B & 1 \\ x_E^3 & x_E^2 & x_E & 1 \\ 3x_B^2 & 2x_B & 1 & 0 \\ 3x_E^2 & 2x_E & 1 & 0 \end{bmatrix}^{-1} \begin{bmatrix} y_B \\ y_E \\ k_B \\ k_E \end{bmatrix} \quad (14)$$

Where x_B 、 y_B 、 x_E 、 y_E 、 k_B 、 k_E are solved according to the steps mentioned above.

5.Theoretical bases

In this part of the paper, the gear contact stress decreases after modification is certified with Hertz contact theory [7].

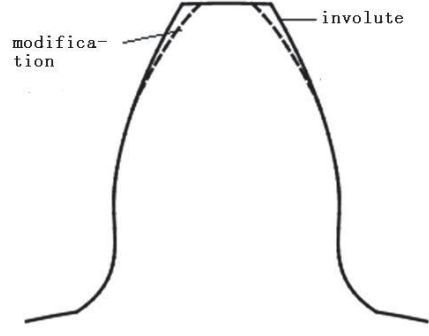


Fig.3.The modification curve diagram

In figure 3, the solid line represents the involute gear tooth profile, the dashed lines represent the tooth profile after modification using the proposed curve put forward in this paper. Based on Hertz contact theory, gear contact is approximately to regard as two cylindrical surfaces contact which have the parallel axis showed in figure 3, the driving tooth profile represented by the solid line contact with the driven gear surface in terms of obtuse angle, the obtuse angle can be regarded as a circular arc which radius is small enough, its radius is R_1 , the radius of the driven gear is R , according to the Hertz contact theory:

$$\left\{ \begin{array}{l} b_1 = \sqrt{\frac{4F}{\pi L} \left(\frac{1-\nu_1^2}{E_1} + \frac{1-\nu_2^2}{E_2} \right) \frac{R_1 R}{R_1 + R}} \\ \sigma_{1\max} = \sqrt{\frac{F}{\pi L} \frac{1}{\frac{1-\nu_1^2}{E_1} + \frac{1-\nu_2^2}{E_2}} \frac{R_1 + R}{R_1 R}} \\ \sigma_1 = \sqrt{\frac{F}{\pi L} \frac{1}{\frac{1-\nu_1^2}{E_1} + \frac{1-\nu_2^2}{E_2}} \frac{R_1 + R}{R_1 R}} \sqrt{b^2 - x^2}, (-b \leq x \leq b) \end{array} \right. \quad (15)$$

where b_1 is half of the contact width, $\sigma_{1\max}$ is the maximum contact stress, σ_1 is contact stress distribution along the direction of contact surface width. Similarly, the addendum of driving tooth after modification represent by dashed lines contact with the surface of driven gear in terms of circle arc with the radius of R_2 , the parameters are calculated as follows:

$$\left\{ \begin{array}{l} b_2 = \sqrt{\frac{4F}{\pi L} \left(\frac{1-\nu_1^2}{E_1} + \frac{1-\nu_2^2}{E_2} \right) \frac{R_2 R}{R_2 + R}} \\ \sigma_{2\max} = \sqrt{\frac{F}{\pi L} \frac{1}{\frac{1-\nu_1^2}{E_1} + \frac{1-\nu_2^2}{E_2}} \frac{R_2 + R}{R_2 R}} \\ \sigma_2 = \sqrt{\frac{F}{\pi L} \frac{1}{\frac{1-\nu_1^2}{E_1} + \frac{1-\nu_2^2}{E_2}} \frac{R_2 + R}{R_2 R}} \sqrt{b^2 - x^2} (-b \leq x \leq b) \end{array} \right. \quad (16)$$

where b_2 is half of the contact width, $\sigma_{2\max}$ is the maximum contact stress, σ_2 is contact stress distribution along the direction of contact surface width. F is the normal contact force (N), L is the length of contact line, it is gear

width here (mm), ν_1, ν_2 are the poisson's ratio of active and passive gear materials respectively, E_1, E_2 are the elasticity modulus of active and passive gear materials respectively (MP_a), Due to the tooth surface tangent to the addendum circle after modification, thus, $R_1 < R_2$, consequently $b_1 < b_2$, $\sigma_{1max} > \sigma_{2max}$, $\sigma_1 > \sigma_2$, so the driving gear teeth after modification according to this cubic curve have larger contact area and less contact stress during engaging-in, while the driven gear teeth after modification according to this cubic curve has larger contact area and less contact stress during engaging-out.

Example

To describe the steps of calculating this modification curve more clearly, the following part is a specified example using the method, A spur gear has the main parameters as shown in table 1.

Table 1: Gear parameters

<i>Number of teeth</i>	43
<i>Module/mm</i>	3
<i>Pressure angle/deg</i>	20
<i>Face width/mm</i>	82
<i>The addendum coefficient</i>	1
<i>Gear tip clearance coefficient</i>	0.25
<i>The maximum amount of modification/mm</i>	0.05
<i>The modification height/mm</i>	1.5

According to the mentioned method, the coordinate of points A , B and E are $(67.4553, 2.32)$, $(65.28, 1.31)$ and $(67.4, 2.32)$ respectively. The involute slope of point B is $k_B = \tan \alpha_B = 0.4228$. the addendum slope of point E is $k_E = -1.8$

$$\text{According to } y = ax^3 + bx^2 + cx + d, \{x \in [x_B, x_E]\}, \begin{bmatrix} a \\ b \\ c \\ d \end{bmatrix} = \begin{bmatrix} x_B^3 & x_B^2 & x_B & 1 \\ x_E^3 & x_E^2 & x_E & 1 \\ 3x_B^2 & 2x_B & 1 & 0 \\ 3x_E^2 & 2x_E & 1 & 0 \end{bmatrix}^{-1} \begin{bmatrix} y_B \\ y_E \\ k_B \\ k_E \end{bmatrix},$$

The coordinates of points B and E as well as the slope of the modification of these two points are substitute into the equation. The coefficients of cubic curve can be solved and the cubic curve of modification we obtain is :

$$y = -0.518367x^3 + 102.6712x^2 - 6773.383x + 148968.649 ; \{x \in [65.28, 67.4]\}$$

6. Conclusions

A modification curve of cubic curve is put forward in this paper, compared with the existing modification curve, the smooth transition between modification curve and involute has improved the stability of the transmission and reduce the vibration and noise, this is helpful for the improvement of the gear working conditions and increasing the service life. The smooth transition between modification curve and addendum has made the driven (driving) gear addendum contact the driving (driven) gear surface with circle arc instead of sharp corner during engaging-in (engaging-out, in this case according to Hertz contact theory, the driving and driven gear can be approximately regarded as the two cylinder with parallel axis, this increases the instantaneous contact area of the gear tooth surface, and decreases the contact stress of the gear teeth during both engaging-in and engaging-out, consequently, thus the instantaneous impact is reduced between teeth, besides, the cubic curve of modification is simple and suitable for parametric design and programming of numerical control machining.

7. Acknowledgements

The work here is supported by the National Natural Science Foundation of China (No. 51175208), the State Key Basic Research Program of China (NO.2011CB706803).

8. References

- [1] Mats Åkerblom, <GEAR NOISE AND VIBRATION—A LITERATURE SURVEY>. mats.akerblom@volvo.com Volvo Construction Equipment Components AB SE-631 85 Eskilstuna, Sweden
- [2] Bonori, G. and F. Pellicano, *Non-smooth dynamics of spur gears with manufacturing errors*. Journal of Sound and Vibration, 2007. 306(1-2): p. 271-283.
- [3] Bonori, G., M. Barbieri, and F. Pellicano, *Optimum profile modifications of spur gears by means of genetic*

- algorithms*. Journal of Sound and Vibration, 2008. 313(3-5): p. 603-616.
- [4] İmrek, H. and H. Düzcükoğlu, *Relation between wear and tooth width modification in spur gears*. Wear, 2007. 262(3-4): p. 390-394.
- [5] Zhang, J., et al., *The modified pitch cone design of the hypoid gear: Manufacture, stress analysis and experimental tests*. Mechanism and Machine Theory, 2007. 42(2): p. 147-158.
- [6] Li Runfang, *Stiffness analysis and the modification method of gear transmission*, ChongQing University Press, Chong Qing, China, 1998.
- [7] K.L.Johnson, *Contact mechanics*, Cambridge University Press, England, 1985.

A level set method for the representation of multiple types of boundaries and its application in structural shape and topology optimization

Qi Xia¹, Michael Yu Wang², Tielin Shi¹

¹ The State Key Laboratory of Digital Manufacturing Equipment and Technology, Huazhong University of Science and Technology, Wuhan, China, qxia,tlshi@mail.hust.edu.cn

² Department of Mechanical Engineering, National University of Singapore, Singapore, mpewmy@nus.edu.sg

1. Abstract

A level set method is developed for the representation of multiple types of boundaries, and it is applied in two structural shape and topology optimization problems. The first problem is the optimization of both structure and support, where both the homogeneous Neumann boundary and the Dirichlet boundary are optimized. The second problem is the optimization of structures subjected to pressure load, where both the non-homogeneous and homogeneous Neumann boundaries are optimized. In order to address the issue that how to represent different types of boundaries of a structure, a new scheme of representation is proposed. Two independent level set functions are used for the representation. The two types of boundaries are represented separately and are allowed to be continuously propagated during the optimization. The optimization problem of minimum compliance is considered.

2. Keywords: topology optimization, level set method, support, pressure load.

3. Introduction

A structure has several types of boundaries, for instance the Dirichlet boundary, the Neumann boundary, and the free boundary. Optimization of any one of them will be helpful to improve the performance of a structure, and there are engineering applications that require to simultaneously optimize two or more boundaries of a structure. For instance, in the optimization of structure with pressure load, both the free boundary and the Neumann boundary are required to be simultaneously optimized [1–11]. Also, it would be better if both the free boundary and the Dirichlet boundary (support) are simultaneously optimized [12–18].

In conventional level set method of structural shape and topology optimization [10, 19–22], usually only the traction free boundary of a structure is represented through a single level set function and is optimized, but the Dirichlet boundary and the Neumann boundary are specified before and fixed during the optimization. If multiple types of structure boundaries are to be simultaneously optimized, it seems that a natural extension of the conventional level set method is to use the zero level set of a single level set function to represent the multiple types of boundaries, and then impose different labels on the points of these boundaries, and track these points during the optimization. However, it is well known that such a tracking method is not able to deal with topological changes [10, 19–22]. Therefore, the conventional representation of a structure through a single level set function is not adequate for the simultaneous optimization of multiple types of boundaries.

Such a situation leads to a fundamental issue of the present study, i.e., how to represent multiple types of boundaries of a structure. In order to address this issue, a new scheme of representation through two level set functions is proposed, and it is applied in two structural shape and topology optimization problems.

4. Representation of structure and multiple types of boundaries

The scheme of representation is shown in Fig. 1. Two independent level set functions, denoted by Φ and Ψ , are used to represent a structure. The inside and outside regions with respect to the structure boundary are given by

$$\Omega = \{x \mid \Phi(x) < 0 \text{ and } \Psi(x) < 0, x \in \mathcal{D}\} \quad (1)$$

$$\mathcal{D} \setminus \overline{\Omega} = \{x \mid \Phi(x) > 0 \text{ or } \Psi(x) > 0, x \in \mathcal{D}\} \quad (2)$$

where \mathcal{D} is the reference domain. In other words, a structure is represented by the set of points where both of the two level set functions are negative. The level set function Φ or Ψ is constructed to be a signed distance function to a closed curve in 2D or a closed surface in 3D, and a rectilinear grid is used in the numerical implementation. With such a representation, the structure defined in Eq. (1) can be obtained through a boolean operation of the two level set functions

$$\Omega = \{x \mid \max\{\Phi(x), \Psi(x)\} < 0, x \in \mathcal{D}\} \quad (3)$$

In addition, many geometric properties including the unit outward normal n and the curvature κ can be readily expressed [23].

The free boundary to be optimized is represented by a portion of the zero-level set of Φ , i.e.,

$$\Gamma_H^\Phi = \{x | \Phi(x) = 0, \Psi(x) < 0, x \in \mathcal{D}\} \quad (4)$$

In the shape and topology optimization of both structure and support, the Dirichlet boundary to be optimized is represented by a portion of the zero-level set of Ψ , i.e.,

$$\Gamma_D = \{x | \Psi(x) = 0, \Phi(x) < 0, x \in \mathcal{D}\} \quad (5)$$

Similarly, in the shape and topology optimization of structures subjected to pressure load, the Neumann boundary Γ_N to be optimized is represented by a portion of the zero-level set of Ψ , i.e.,

$$\Gamma_N = \{x | \Psi(x) = 0, \Phi(x) < 0, x \in \mathcal{D}\} \quad (6)$$

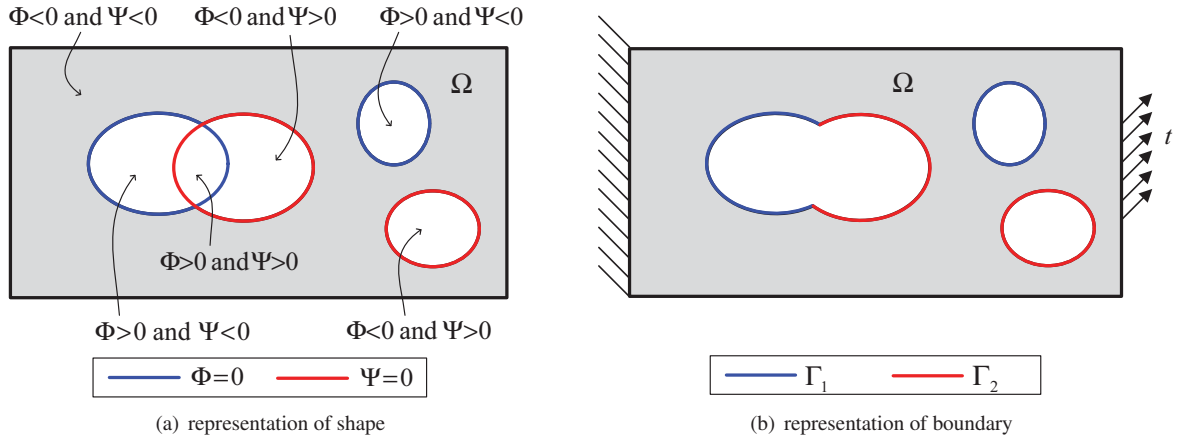


Figure 1: The scheme for the representation of shape and boundary.

During the optimization, the two types of boundaries are independently and continuously propagated. Propagation of the two boundaries is modeled separately by two independent Hamilton–Jacobi equations [10, 19–22]

$$\Phi_t + F^\Phi \cdot \nabla \Phi = b^\Phi \kappa |\nabla \Phi| \quad (7)$$

$$\Psi_t + F^\Psi \cdot \nabla \Psi = b^\Psi \kappa |\nabla \Psi| \quad (8)$$

where the velocity terms F^Φ , b^Φ , F^Ψ , b^Ψ are given by the shape derivatives of the optimization problem.

The concept of using multiple level set functions in the structural shape and topology optimization had been introduced in the design of structures that have several different materials [24, 25]. The idea is to use n level set functions to represent up to $2n$ different materials. In the present study, two level set functions are not used to represent multiple regions of different materials, but they are used to represent two different types of boundaries.

5. Shape and topology optimization of both structure and support

The effects of the support on a structure’s performance have been considered in optimization for a long time. In the early pioneering research work [26–30], the optimal position and stiffness of supports of discrete structures were considered. Recently, the optimization of support was extended for continuum structures. In these studies, the methods of optimization are divided into two categories. The first category is based on a field of background springs that represent potential supports [12–14]. A continuous design variable is given to each spring. When the value of a spring variable reaches the lower bound, the point where the spring is attached to the structure is considered as free. On the other hand, when the value of a spring variable reaches the upper bound, the attachment point is considered as fixed. Intermediate values of spring variables are penalized. The second category is based on continuous variation of support point or support boundary [15–18], which is similar to the shape optimization.

The optimization problem considered in the present study is the regularized minimum compliance problem

$$\inf_{\Omega \in \mathcal{U}_{ad}} J(\Omega) + \ell P(\Omega) \quad (9)$$

where J is the compliance; $\ell > 0$ is a fixed weighting parameter; $P(\Omega)$ is the perimeter of a structure. The set of admissible shapes is defined as $\mathcal{U}_{\text{ad}} = \{\Omega \subset \mathcal{D}, V(\Omega) \leq \bar{V}, C(\Gamma_D) \leq \bar{C}\}$ where $V(\Omega) \leq \bar{V}$ is a volume constraint; $C(\Gamma_D) \leq \bar{C}$ is a cost constraint of support given as

$$C(\Gamma_D) = \int_{\Gamma_D} c(x) ds \leq \bar{C} \quad (10)$$

where Γ_D is the Dirichlet boundary; $c(x)$ is a fixed scalar field that describes the cost of support at point x . The function $c(x)$ means that the cost of support depends on the position.

In the optimization, both the free boundary Γ_H and the Dirichlet boundary Γ_D are optimized. The results of shape derivative analysis are given by

$$\mathcal{L}'(\Omega)(\theta) = \int_{\Gamma_H} G_{\Gamma_H} \theta \cdot n ds + \int_{\Gamma_D} G_{\Gamma_D} \theta \cdot n ds \quad (11)$$

where \mathcal{L} is the Lagrangian; G_{Γ_H} and G_{Γ_D} are given by

$$G_{\Gamma_H} = -Ae(u) \cdot e(u) + \ell \kappa + \ell_1 \quad (12)$$

$$G_{\Gamma_D} = Ae(u) \cdot e(u) + \ell \kappa + \ell_1 + \ell_2 \left(\frac{\partial c}{\partial n} + \kappa c \right) \quad (13)$$

where f is the body force; u is the displacement; A is the elasticity tensor; $e(u)$ is the strain tensor; ℓ_1 and ℓ_2 are respectively the Lagrange multipliers for the volume constraint and the cost constraint of support; κ is the curvature of boundary.

The shape derivatives lead to the the velocity terms in Eq. (7) and (8) as

$$F^\Phi = (Ae(u) \cdot e(u) - \ell_1)n, \quad b^\Phi = \ell \quad (14)$$

$$F^\Psi = \left(-Ae(u) \cdot e(u) - \ell_1 - \ell_2 \frac{\partial c}{\partial n} \right) n, \quad b^\Psi = \ell + \ell_2 c \quad (15)$$

More details about the optimization problem and the shape derivative analysis are referred to [31].

6. Shape and topology optimization of structures subjected to pressure load

The problem of shape and topology optimization of structures subjected to pressure load is in most cases solved by using the SIMP method [32, 33]. Nevertheless, difficulties exist in the SIMP based solution, since one needs to find the pressure boundary from a smooth scalar field that represents the distribution of material in a reference domain. If the scalar field varies smoothly from 0 to 1 (unfortunately, this is true particularly in the early stage of optimization), the boundary of a structure and the pressure load is ambiguously defined. Several methods were proposed and integrated in the SIMP method to find the pressure boundary [1–5]. On the other hand, several creative approaches were proposed to mimic the effects of a pressure load by artificially incorporating another physical field into the optimization problem [6–9], hence circumventing the issue of pressure boundary. Nevertheless, the downside of these approaches is that some new numerical issues may arise [7, 8] and the optimization is more complex. The level set method was also used to solve the optimization with pressure load, for example the study by Allaire et al. [10] and by Guo et al. [11]. In these studies, the pressure boundary together with the free boundary are represented by the zero level set of a single level set function, then the pressure boundary is picked out from the zero level set by checking whether the normal vector is along a specified direction [10, 11]. Nevertheless, when the pressure load comes from several different directions, it will be much more complicated for these approaches to deal with the pressure boundary.

The optimization problem is also the regularized minimum compliance problem as given by Eq. (9), except that here is no constraint on the cost of Dirichlet boundary in the set of admissible shapes \mathcal{U}_{ad} , i.e., $\mathcal{U}_{\text{ad}} = \{\Omega \subset \mathcal{D}, V(\Omega) \leq \bar{V}\}$.

In the optimization, both the free boundary Γ_H and the Neumann boundary Γ_N are optimized. The results of shape derivative analysis are give by

$$\mathcal{L}' = \int_{\Gamma_H} G_{\Gamma_H} \theta \cdot n ds + \int_{\Gamma_N} G_{\Gamma_N} \theta \cdot n ds \quad (16)$$

where \mathcal{L} is the Lagrangian; G_{Γ_H} and G_{Γ_N} are given by

$$G_{\Gamma_H} = -Ae(u) \cdot e(u) + \ell \kappa + \ell_1 \quad (17)$$

$$G_{\Gamma_N} = -2\text{div}(p_0 u) - Ae(u) \cdot e(u) + \ell + \ell_1 \quad (18)$$

where p_0 is the constant magnitude of a pressure load, and in the present study, the magnitude of pressure load is assumed to be a constant, i.e., $p = -p_0 n$; ℓ_1 is the Lagrange multiplier for the volume constraint.

The shape derivatives lead to tentative velocity terms in Eq. (7) and (8) as

$$F^\Phi = (Ae(u) \cdot e(u) - \ell_1) n, \quad b^\Psi = \ell \quad (19)$$

$$F^\Psi = (2\text{div}(p_0 u) + Ae(u) \cdot e(u) - \ell_1) n, \quad b^\Phi = \ell \quad (20)$$

For most of the engineering applications considered in the literature, the pressure boundary Γ_N should not touch or cross the traction free boundary Γ_H . However, according to our experience of the present study, if the velocity terms are chosen according to Eqs. (19–20), the two boundaries may indeed touch or cross each other when the initial design is not so good or the size of descent steps of optimization is big. In order to address this issue, we modify the velocity vector F^Ψ on boundary Γ_N and modify F^Φ on boundary Γ_H , then we extend the modified velocities from the two boundaries to the entire reference domain by using a PDE based method [34]. More details about the shape derivative analysis and modification of velocity terms are referred to [35].

7. Numerical examples

7.1 Example 1: optimization of structure and support

The design problem is shown in Fig. 2(a). The shaded rectangular region at the middle is the admissible domain for the design of support. We do the finite element analysis by modifying a fixed background triangle mesh and do not use the artificial weak material, as proposed in our previous study [36]. The upper bound of volume is 0.35 m^3 , and the upper bound of the cost of support is 0.3. The initial design is shown in Fig. 2(b).

The optimal structure is shown in Fig. 2(c). The objective function of the optimal structure is 10.93; compliance is 10.74; the volume is 0.35; the cost of support of the optimal design is 0.29. It can be seen that the optimal support does not coincide with the two dash lines. In addition, it is interesting to see that in the design shown in Fig. 2(c) the three loads are connected and that the two loads at the bottom are effectively used to counteract the upper load, thus minimizing the compliance due to these loads. From this example, we see that for a structure that is subject to multiple loads, load path can be tailored by the support such that the loads are self-equilibrated. In such cases, the design of support is important.

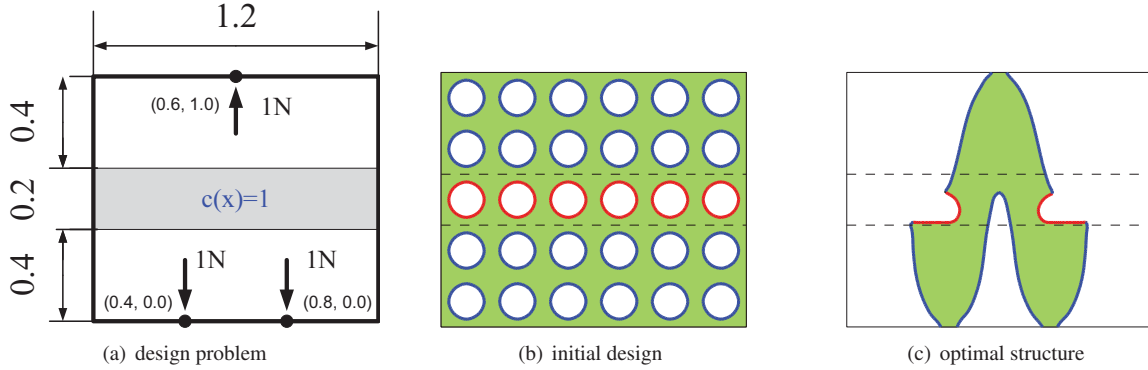


Figure 2: Design problem, initial design, and optimal structure.

7.2 Example 2: optimization of structure subject to pressure load

The optimal design problem of the third example is shown in Fig. 3(a). The pressure load is applied from the top of the structure. The reference domain is a rectangle of size $3 \text{ m} \times 1 \text{ m}$. The upper bound of volume is 0.9 m^3 . An Eulerian method employing a fixed mesh and ersatz material [10] is used for the finite element analysis. The pressure load is converted to a volume force as proposed in [10]. Only the left half is analyzed in this example. The initial design is shown in Fig. 3(b). The optimal structure is shown in Fig. 3(c).

8. Conclusions

A new scheme of representation is proposed to represent multiple types of boundaries of a structure. Two independent level set functions are used for the representation. The two types of boundaries are represented separately and are allowed to be continuously propagated during the optimization. The optimization problem of minimum compliance is considered. The numerical examples demonstrated that the proposed method is effective. In the future,

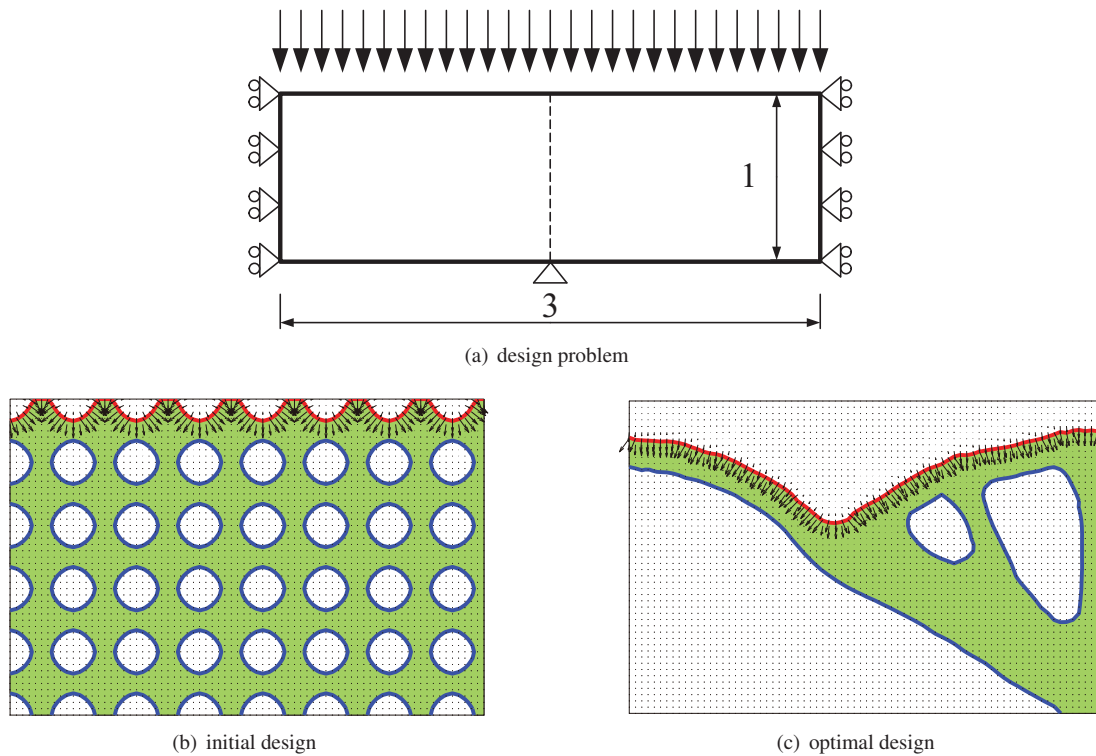


Figure 3: Design problem, initial design, and optimal design.

the proposed method will be applied to many optimization problems that involve with multiple type of boundaries.

9. References

- [1] V. B. Hammer, N. Olhoff, Topology optimization of continuum structures subjected to pressure loading, *Struct. Multidiscip. Optim.* 19 (2000) 85–92.
- [2] J. Du, N. Olhoff, Topological optimization of continuum structures with design-dependent surface loading - part I: new computational approach for 2D problems, *Struct. Multidiscip. Optim.* 27 (2004) 151–165.
- [3] J. Du, N. Olhoff, Topological optimization of continuum structures with design-dependent surface loading - part II: algorithm and examples for 3D problems, *Struct. Multidiscip. Optim.* 27 (2004) 166–177.
- [4] H. Zhang, X. Zhang, S. T. Liu, A new boundary search scheme for topology optimization of continuum structures with design-dependent loads, *Struct. Multidiscip. Optim.* 37 (2008) 121–129.
- [5] E. Lee, J. R. Martins, Structural topology optimization with design-dependent pressure loads, *Comput. Methods Appl. Mech. Eng.* 233–236 (2012) 40–48.
- [6] B. Chen, N. Kikuchi, Topology optimization with design-dependent loads, *Finite Elem. Anal. Des.* 37 (2001) 57–70.
- [7] O. Sigmund, P. M. Clausen, Topology optimization using a mixed formulation: an alternative way to solve pressure load problems, *Comput. Methods Appl. Mech. Eng.* 196 (2007) 1874–1889.
- [8] M. Bruggi, C. Cini, An alternative truly-mixed formulation to solve pressure load problems in topology optimization, *Comput. Methods Appl. Mech. Eng.* 198 (2009) 1500–1512.
- [9] B. Zheng, C. Chang, H. G. Gea, Topology optimization with design-dependent pressure loading, *Struct. Multidiscip. Optim.* 38 (2009) 535–543.
- [10] G. Allaire, F. Jouve, A. M. Toader, Structural optimization using sensitivity analysis and a level-set method, *J. Comput. Phys.* 194 (2004) 363–393.
- [11] X. Guo, K. Zhao, Y. X. Gu, Topology optimization with design-dependent loads by level set approach, in: 10th AIAA/ISSMO Multidisciplinary Analysis and Optimization Conference, Albany, New York, 2004.

- [12] T. Buhl, Simultaneous topology optimization of structure and supports, *Struct. Multidiscip. Optim.* 23 (2002) 336–346.
- [13] J. H. Zhu, W. H. Zhang, Maximization of structural natural frequency with optimal support layout, *Struct. Multidiscip. Optim.* 31 (2006) 462–469.
- [14] G. Jang, H. Shim, Y. Kim, Optimization of support locations of beam and plate structures under self-weight by using a sprung structure model, *J. Mech. Des.* 131 (2009) 021005–021005–11.
- [15] J. H. Son, B. M. Kwak, Optimization of boundary conditions for maximum fundamental frequency of vibrating structures, *AIAA J.* 31 (1993) 2351–2357.
- [16] S. Cox, P. Uhlig, Where best to hold a drum fast, *SIAM J. Optim.* 9 (1999) 948–964.
- [17] D. Wang, J. S. Jiang, W. H. Zhang, Optimization of support positions to maximize the fundamental frequency of structures, *Int. J. Numer. Meth. Eng.* 61 (2004) 1584–1602.
- [18] J. H. Zhu, W. H. Zhang, Integrated layout design of supports and structures, *Comput. Methods Appl. Mech. Eng.* 199 (2010) 557–569.
- [19] J. A. Sethian, A. Wiegmann, Structural boundary design via level set and immersed interface methods, *J. Comput. Phys.* 163 (2000) 489–528.
- [20] S. Osher, F. Santosa, Level-set methods for optimization problems involving geometry and constraints: Frequencies of a two-density inhomogeneous drum, *J. Comput. Phys.* 171 (2001) 272–288.
- [21] G. Allaire, F. Jouve, A. M. Toader, A level-set method for shape optimization, *C. R. Acad. Sci. Paris, Serie I*, 334 (2002) 1–6.
- [22] M. Y. Wang, X. M. Wang, D. M. Guo, A level set method for structural topology optimization, *Comput. Methods Appl. Mech. Eng.* 192 (2003) 227–246.
- [23] S. Osher, R. Fedkiw, *Level Set Methods and Dynamic Implicit Surfaces*, Springer-Verlag, New York, 2002.
- [24] M. Y. Wang, X. M. Wang, "Color" level sets: A multi-phase method for structural topology optimization with multiple materials, *Comput. Methods Appl. Mech. Eng.* 193 (2004) 469–496.
- [25] [2] M. Y. Wang, X. M. Wang, A level-set based variational method for design and optimization of heterogeneous objects, *Computer-Aided Design* 37 (2005) 321–337.
- [26] W. Prager, G. I. N. Rozvany, Plastic design of beams: optimal locations of supports and steps in yield moment, *Int. J. Mech. Sci.* 17 (1975) 627–631.
- [27] Z. Mróz, G. I. N. Rozvany, Optimal design of structures with variable support conditions, *J. Optim. Theory Appl.* 15 (1975) 85–101.
- [28] G. I. N. Rozvany, Z. Mróz, Column design: optimization of support conditions and segmentation, *J. Struct. Mech.* 5 (1977) 279–290.
- [29] N. Olhoff, J. E. Taylor, Designing continuous columns for minimum total cost of material and interior supports, *J. Struct. Mech.* 6 (1978) 367–382.
- [30] P. Pedersen, Topology optimization of 3d trusses with cost of supports, *Adv. Des. Autom.* 65 (1993) 761–768.
- [31] Q. Xia, M. Y. Wang, T. L. Shi, A level set method for shape and topology optimization of both structure and support of continuum structures, *Comput. Methods Appl. Mech. Eng.* 272 (2014) 340–353.
- [32] M. P. Bendsøe, Optimal shape design as a material distribution problem, *Struct. Optim.* 1 (1989) 193–202.
- [33] G. I. N. Rozvany, M. Zhou, T. Birker, Generalized shape optimization without homogenization, *Struct. Optim.* 4 (1992) 250–254.
- [34] D. P. Peng, B. Merriman, S. Osher, H. K. Zhao, M. Kang, A PDE-based fast local level set method, *J. Comput. Phys.* 155 (1999) 410–438.
- [35] Q. Xia, M. Y. Wang, T. Shi, Topology optimization with pressure load through a level set method, *Comput. Methods Appl. Mech. Eng.* 283 (2015) 177–195.
- [36] Q. Xia, T. Shi, S. Liu, M. Y. Wang, A level set solution to the stress-based structural shape and topology optimization, *Comput. Struct.* 90–91 (2012) 55–64.

A Parallel Optimization Method Based on Kriging Model

Zhaojun Li^{1,2}, Xicheng Wang²

¹ School of Computer Science and Technology, Dalian University of Technology, Dalian 116023, China,
lizhaojun@mail.dlut.edu.cn

² State Key Laboratory of Structural Analysis for Industrial Equipment, Dalian University of Technology, Dalian 116023,
China, guixum@dlut.edu.cn

1. Abstract

In many practical engineering designs, the forms of objective functions are not easily available in terms of the design variables. So as to obtain relatively accurate optimal solutions, a lot of computing iterations must be taken into account, which results in huge computational consumption. A parallel optimization method based on Kriging model is proposed in this paper: by developing entropy-based expected improvement algorithm on the Kriging model, this approach progressively provides a designer a rich and evenly distributed set of Pareto optimal points; meanwhile the implementation of the method proposed on a super-server is discussed, with speedup and efficiency described by statistical data. Two mathematical optimization problems and two engineering optimization problems are presented as testing cases, with the results showing that the proposed method can be effectively used for engineering optimization designs. The method developed in this paper could help the designers to search and compare near optimal design alternatives intelligently in the early design stages by utilizing high performance computing resources.

2. Keywords: expected improvement, engineering optimization, Kriging model

3. Introduction

Optimization refers to finding the values of decision variables, which correspond to and provide the maximum or minimum of one or more desired objectives. Problems may arise in engineering optimization at present: 1) The physical and mathematical models for multidiscipline field are complicated to be optimized directly, so that some general analysis programs, such as Ansys, Abaqus, Fluent, Moldflow, etc, have been used as black-box programs, how to develop the efficient optimization methods based on these black-box programs; 2) High performance computing that began to appear in the late 1970s and continue to undergo rapid development, how to solve a complex optimization problem by using advanced computing infrastructure efficiently [1-3]. Physical and mathematical models are hard to describe explicitly under normal engineering optimization situations, which makes “black-box optimization” a very effective way in solving these problems. This “only-use-function-values” optimization method is hailed as “the most useful algorithm” [4].

In this paper, a parallel optimization method based on Kriging model is developed. By weighted coefficient method of multi-objective optimization, an evenly and rich distributed set of Pareto solutions can be provided, in which a Pareto point obtained by optimizing weighted coefficient—with entropy-based expected improvement (EEI) algorithm. To make the method well performed within parallel computing environment, the parallel strategy is given. Test cases are developed, with numerical data showing that the proposed method not only effectively gives more precise optimal solutions through EEI algorithm but accelerates the whole optimization process using parallel strategy at the same time.

4. Related Work

4.1. “Black-box Optimization”

A typical “black-box optimization” process performed in this article is defined as: 1) Use sampling method (Latin hypercube sampling (LHS) [5], for example) to get a set of fairly well-distributed samples which are consistent with the limits of the design variables; 2) Compute the responses of all the samples using a black-box analysis program; 3) Try to set up a proximate model between the design variables and the responses so as to analyze the system features; 4) Calculate the optimal solution of the objective function under the approximation model established before with an appropriate sampling guidance function such as EI method; 5) Convergence analysis: if the optimal solution has met the given accuracy then stop; Otherwise, put the optimal solution into the sampling set as a new sample and go to step 2) [6].

4.2. Kriging Model

Samples mentioned above can be used as input data for “black-box optimization” and their responses would be acquired after necessary calculations performed by black-box analysis software. With samples $X = [X_1, X_2, \dots, X_n]$ and their responses y , Kriging model can be established as [7,8]:

$$\hat{y}(X) = f^T(X)\beta + z(X) \quad (1)$$

coefficient β is the regression ratio. Deterministic drift $f(X)$, provided the global approximation of simulation in the design domain, is often described as a polynomial of X . $z(X)$, known as fluctuation, offers the local approximation of simulation.

4.3. Expected Improvement

Expected Improvement (**EI**) criterion is a sampling guidance function which considers both the predicted value and the predicted variance while infilling a sample into the optimization models. To a new sample X , the Kriging model can predict its average value $\bar{y}(X)$ and its average variance σ^2 . Let y_{min} be the current minimum response value, therefore I (lets assume that it is a minimization problem and $y(X) = y_{min} - I$) will be the improvement of the response value at the given point. I is normally distributed with mean $\bar{y}(X)$ and variance σ^2 . The likelihood of this improvement is given by the normal density function [9]:

$$\frac{1}{\sqrt{2\pi}\sigma(X)} \exp \left[-\frac{(y_{min} - I - \bar{y}(X))^2}{2\sigma^2(X)} \right] \quad (2)$$

The expected improvement is simply the expected value of the improvement found by integrating over this density

$$E[I(X)] = \int_{I=0}^{I=\infty} I \left\{ \frac{1}{\sqrt{2\pi}\sigma(X)} \exp \left[-\frac{(y_{min} - I - \bar{y}(X))^2}{2\sigma^2(X)} \right] \right\} dI \quad (3)$$

using integration by parts, one can show that

$$E[I(X)] = \sigma(X) [v\Phi(v) + \phi(v)], v = \frac{y_{min} - \bar{y}(X)}{\sigma(X)} \quad (4)$$

where Φ and ϕ are the normal cumulative distribution function and density function, respectively.

5. Developed Methodology

5.1. Entropy-based Expected Improvement

In order to facilitate parallel computing, entropy-based expected improvement (**E EI**) is developed to optimize the infilling samples in the design space. The optimization of the weighted expected improvement (**WEI**) can be written as

$$\max E(I(X)) = \sum_{j=1}^2 \lambda_j E_j(I(X)) \quad (5)$$

and

$$\begin{cases} E_1(I(X)) = \Phi(v)(y_{min} - \bar{y}(X)), \\ E_2(I(X)) = \sigma(X)\phi(v), \\ \sum_{j=1}^2 \lambda_j = 1, \lambda_j \in [0, 1] \end{cases} \quad (6)$$

Shannon entropy can be introduced to measure the uncertainty about the searching range. If $\lambda_j \in [0, 1]$ are here defined as a probability that the optimal solution occurs in the local space and other space, respectively, then the Shannon entropy will be decreased during optimization process of Eq.5 and an entropy-based optimization model for the optimizing weighting coefficient can be constructed as

$$\begin{cases} \min - \sum_{j=1}^2 \lambda_j E(I) \\ \min H = - \sum_{j=1}^2 \lambda_j \ln(\lambda_j), \\ \sum_{j=1}^2 \lambda_j = 1, \lambda_j \in [0, 1] \end{cases} \quad (7)$$

where H is the information entropy. It can easily be proved that Eq.5 and Eq.7 having the same optimal solutions. By Lagrange multiplier method, an augmented function can be obtained as

$$\begin{cases} L(I, \eta, \mu) = -(1 - \eta) \sum_{j=1}^2 \lambda_j E_j - \eta \sum_{j=1}^2 \lambda_j \ln(\lambda_j) + \mu (\sum_{j=1}^2 \lambda_j - 1), \\ \eta \in (0, 1) \end{cases} \quad (8)$$

where η and μ are the weighting coefficient of multi-object optimization and Lagrange multiplier, respectively. Solving Kuhn-Tucker condition Eq.9 as follows

$$\frac{\partial L}{\partial \lambda_j} = 0, \frac{\partial L}{\partial \mu} = 0 \quad (9)$$

gives

$$\lambda_j^* = \frac{\exp[rE_j(I)]}{\sum_{j=1}^2 \exp[rE_j(I)]} \quad (10)$$

in which $r = (\eta - 1)/\eta$ is called as the quasi-weighting coefficient (here $\eta = 0.5$). λ_j^* is here called as the optimal weighting coefficient. Then a Pareto optimal sample can be obtained by solving Eq.5 with the optimal weight coefficient λ_j^* of Eq.10. For a specific weight coefficient $\lambda_j \in [0, 1]$, the optimization scheme stops when

$$\frac{E[I(X)]}{y_{max} - y_{min}} \leq \varepsilon_1 \quad (11)$$

where ε_1 is the stopping tolerance, y_{max} and y_{min} are the maximal and minimal function value in samples, respectively. Then considering the accuracies of both Kriging model and optimization simultaneously, besides Eq.11 the convergence condition of Eq.12

$$\frac{|f(X_n) - \hat{y}_n|}{f(X_n)} \leq \varepsilon_2 \quad (12)$$

should be satisfied too. Where, ε_1 and ε_2 are given errors (here take $\varepsilon_1 = \varepsilon_2 = 0.01$), \hat{y}_n is the approximate response value of the Kriging surrogate model.

5.2 A Parallel Strategy of EEI on Super Servers

It is assumed here that p cores can be used for the computation on super servers, and the parallel algorithm is described as follows

Step.1. Generate a set of N_s samples (each point corresponding to a group design variables) using LHS. Divide the N_s samples into p parts, which used as input data for black-box analysis programs, the first $p - 1$ cores get $\lceil N_s/p \rceil$ samples, the last core gets the remaining samples;

Step.2. Compute the responses of the samples using black-box program on each core respectively;

Step.3. Build a Kriging surrogate model between the sample sets and their corresponding output response values;

Step.4. Solve the maximizing problems of Eq.5 by the p cores, in which the weighted parameter of λ_1 is obtained by Eq.10 and $\lambda_i = (i - 1)/p, i = 2, 3, \dots, p$ for the rest of the computing cores;

Step.5. Compute the responses of the samples after step 4 is accomplished by using same black-box program;

Step.6. Check convergence. If the convergence criteria Eq.11 and Eq.12 are satisfied then stop, the optimization solution is obtained; Put new samples and their responses into the sampling set and the responding set respectively, redirect to step 3.

6. Test Cases

6.1 Math problems

In this section, the results for some classic mathematical problems are presented. For all of the problems, LHS is used and the number N_s of initial samples is 10, available computing cores p is 4.

6.1.1 Ackley Function

Ackley function is widely accepted by form of:

$$F(x_1, x_2) = -2 \exp(-0.2 \sqrt{x_1^2 + x_2^2}) - \exp((\cos(2\pi x_1) + \cos(2\pi x_2))) + 2 + \exp(2), (x_1, x_2) \in (-1.5, 1.5) \quad (13)$$

theoretically, the minimum value of Ackley function is 0 at (0,0). The iteration histories of Ackleys problem are shown in Fig. 1. The optimal value 0(0,0) is obtained after 33 iterations of WEI method and 10 iterations of EEI

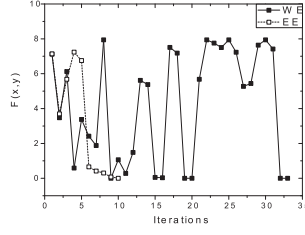


Figure 1: Iteration histories of Ackley problem

method, respectively.

6.1.2 Branin Function

Branin function is defined as:

$$F(x_1, x_2) = (x_2 - 5.1x_1^2/(4\pi^2) + 5x_1/\pi - 6)^2 + 10(1 - 0.125/\pi)\cos(x_1) + 10, \quad (14)$$

$$x_1 \in [-5, 10.0], x_2 \in [0, 15.0]$$

its optimal solution is 0.3979 at point (-3.1416, 12.28). Iteration histories of this problem is shown in Fig. 2. The optimization value 0.784(9.342, 3) is obtained by WEI method after 16 iterations and 0.5031(-3.271, 12.75)

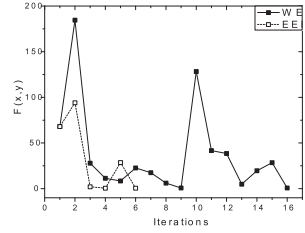


Figure 2: Iteration histories of Branin problem

obtained by EEI method after 6 iterations. Method of EEI has given a more precise solution which is closer to the optimal solution should be in theory.

6.2 Optimization Problem of Turbine Foundation

A turbine foundation is normally a concrete base for turbine generators. The turbine foundation optimization (TFO) problem can be described as:

$$\min F(X) = \min F(X_s, X_g)^T = \min f_l(X_s, X_g)^T$$

$$s.t. \begin{cases} u_q(X_s, X_g) \leq \bar{u}_q, q = 1, 2, \dots, Q \\ M\ddot{u}(t) + C\dot{u}(t) + Ku(t) = P(t) \\ \underline{x}_s^i \leq x_s^i \leq \bar{x}_s^i, \underline{x}_g^i \leq x_g^i \leq \bar{x}_g^i, \\ l = 1, 2, \dots, L, i = 1, 2, \dots, I, j = 1, 2, \dots, J \end{cases} \quad (15)$$

where, $X = (X_s, X_g)$ stands for design variables: X_s is a size design vector with I beam section areas, X_g is geometry design vector with J columns node coordinates, \underline{x}_s^i , \bar{x}_s^i and \underline{x}_g^i , \bar{x}_g^i represent section and geometry limits, i and j are defined as variable numbers; here $L = 2$, f_1 and f_2 are separately defined as amplitude computed by black-box analysis program (here Ansys software is used) dividing current average amplitude and construction weight (a linear function of the section areas) dividing current average weight of the foundation; $u_q(X)$ is the amplitude of the points concerned; Q is the number of points concerned; \bar{u}_q is the maximum amplitude of the foundation; $P(t)$ is disturbing force of the generator. TFO is a multi-objective engineering optimization problem. By means of the weighted coefficient method for solving multi-objective optimization, a weighted parameter ω to unify amplitude and weight to one objective function in order to reduce the complexity of modeling using Kriging method in

Table 1: Speedup and efficiency of test cases

Test Case	WEI		EEI	
	Speedup	Efficiency(%)	Speedup	Efficiency(%)
6.1.1	3.243	81.075	3.333	83.325
6.1.2	3.332	83.300	3.320	83.000
6.2.1	3.259	81.475	3.350	83.750
6.2.2	3.351	83.775	3.299	82.475

engineering practice. In this article, ω is defined as 0.5 for considering both structural weight and the amplitude at the same level. Therefore should $F(X)$ become $F(X) = 0.5f_1(X) + 0.5f_2(X)$ by now.

6.2.1 A 600MW Turbine Foundation Example

There are 15 size design variables and a geometry design variable for this example. The iteration histories are available in Fig. 3.

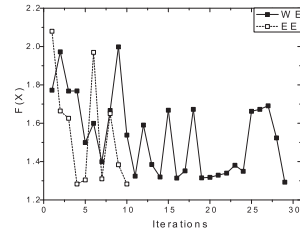


Figure 3: Iteration histories of the 600MW turbine foundation

Fig. 3 gives that iterations of EEI (10 optimization steps at optimal solution of $F(X) = 1.27$) is less than WEI (29 optimization steps at optimal solution of $F(X) = 1.28$).

6.2.2 A 300MW Turbine Foundation Example

There are 17 size design variables and two geometry design variables for this example. Fig. 4 and has described the iteration processes.

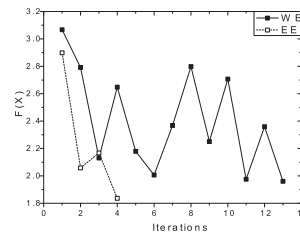


Figure 4: Iteration histories of the 300MW turbine foundation

According to Fig. 4, optimization iterations needed by EEI method (4 steps) is less than WEI method (13 steps); meanwhile WEI method has also got a not so good optimization result ($F(X) = 1.92$) than EEI ($F(X) = 1.83$), which is a very huge effort for this problem as a 0.1 more less of the objective function would gain nearly about $10^5 kg$ saving of the foundations construction of weight consume.

6.3 Speedup & efficiency statistic data for test cases

Table 1 has given the characteristics belonging to all the test cases including speedup and efficiency using the parallel strategy discussed in 5.2.

6.4 Results analysis & discussion

As can be seen from the above figures, the developed EEI method can normally calculate better optimization solutions and WEI method (and also EI method, obviously). This is a behavior caused by a reasonable weighted parameter is given while doing the optimization, which stands for a correct and direct way for searching final optimal solutions generally. A better solution always means better objective function values, which indicates great construction cost savings and better other related engineering technical indicators are obtained.

An ordinary way to save time cost while doing optimization must be making it into parallel pattern. Reading from Table 1, both WEI and EEI methods have expressed high speedup and efficiency for all test cases. This is very simple to comprehend that black-box optimization has established based on Kriging models: black-box programs are scheduled without too much correspondence to each other henceforth a much more considerable speedup could be made. Using the parallel strategy proposed above, engineering optimization problems can be estimated to be performed in a quicker mode.

7. Conclusion

This paper has developed an improved expected improvement method called entropy-based expected improvement (EEI) method, adapting to address computing-intensive optimization problems. It is based on black-box optimization method and global Kriging models. An optimal weighted parameter is calculated at each iteration, which is used for sampling guidance next iteration: it has similar process steps to normal WEI method but gives more accurate solutions under normal circumstances. A parallel strategy described as responses computed by different computing cores with black-box programs has been successfully implemented on a super server to deal with the problem encountered when EEI method needs to consider several samples and points at the same iteration, which could get large speedup and efficiency for engineering problems due to black-box optimizations manifest excellent character to be paralleled.

In order to verify the effectiveness of the proposed method, several examples consist of both math and engineering problems are developed. Numerical results have demonstrated that the raised method could get good speedup and better optimal solutions simultaneously, which surely gives an advance in parallel engineering optimization. We hope the method discussed may further be used in other related engineering optimization problems due to the common behaviors in black-box optimization as to ease the cost made by all of them.

8. Acknowledgements

The work proposed in this paper has sponsored by the following funds: the National Basic Research Program of China (No. 2012CB025905), the Fundamental Research Funds for the Central Universities of China (No. DUT14RC(3)060), the National Natural Science Funds of China (No. 11202049) and the 111 Project (No. B14013).

9. References

- [1] Rao S S and Rao S S, *Engineering optimization: theory and practice*, John Wiley & Sons, 2009.
- [2] Wang L, Ng A H C, Deb K, et al, *Multi-objective Optimisation Using Evolutionary Algorithms: An Introduction*, Springer London, 2011.
- [3] Prof Geng J, Prof Yan W, Dr. Xu W, et al, *Application of Commercial FEA Software*, Springer Berlin Heidelberg, 2008.
- [4] Powell M, Direct search algorithms for optimization calculations, *Acta Numerica*, 7, 287-336, 1998.
- [5] Iman R L, *Latin hypercube sampling*, Wiley Online Library, 2008.
- [6] Regis R G, Shoemaker C A, Constrained global optimization of expensive black box functions using radial basis functions, *Journal of Global Optimization*, 31(1), 153-171, 2005.
- [7] Oliver M A R, Kriging: A method of interpolation for geographical information systems, *Int. J. Geograph. Inf. Syst.*, 4, 313-332, 1990.
- [8] Shi H, Gao Y, Wang X, Optimization of injection molding process parameters using integrated artificial neural network model and expected improvement function method, *The International Journal of Advanced Manufacturing Technology*, 48(9-12), 955-962, 2010.
- [9] Vazquez E, Bect J, Convergence properties of the expected improvement algorithm with fixed mean and covariance functions, *Journal of Statistical Planning and inference*, 140(11), 3088-3095, 2010.

Welded cellular cylindrical shell – a new structural solution for the optimum design of a cantilever column

József Farkas¹, Károly Jármai²

¹ University of Miskolc, Hungary altfar@uni-miskolc.hu

² University of Miskolc, Hungary altjar@uni-miskolc.hu

1. Abstract

A cantilever column is loaded by compression and bending. The horizontal displacement of the column top as well as the outside diameter of the cylindrical shell are limited. The strengthening of the column is performed in the lower part of the column only.

Three structural versions of the column are optimized and compared to each other.

Firstly, the unstiffened circular shell is optimized. It is found that the required large thickness is unsuitable for fabrication.

Secondly, the stringer stiffened circular shell is optimized. The halved rolled UC section stringers are used only in the lower part of the column, the distance of the interruption of stiffeners is also optimized. It is found that the required shell thickness is unsuitable for fabrication.

Thirdly, a new structural version, the cellular shell is used. Cellular shells are constructed from two circular cylindrical shells and a grid of stiffeners welded between them. They have similar advantages than the cellular plates, namely they can produce a large stiffness with small structural height. Their smooth surface is suitable for corrosion protection and they are more aesthetic than the stringer stiffened shells.

The parts of the outer circular shell are welded to the stringers from outer side with longitudinal fillet welds. Halved circular hollow section (CHS) stringers enable the easy welding of the outer fillet welds.

The unknown variables to be optimized are as follows: thicknesses of the inner and outer shell, dimensions and number of the halved CHS stiffeners as well as the distance of the interruption of stiffeners.

The study shows a realistic case when the cellular shell can be used with smaller shell thicknesses and lower cost than the shell stiffened with outer side stringers.

The displacement constraint is so strict that the stress, shell buckling and beam-column buckling constraints are passive.

The cost function to be minimized contains the cost of material, welding and painting. The optimization is performed by a systematic search using a MathCAD algorithm.

2. Keywords: welded shell structures, structural optimization, cost calculation, cellular structures, cantilever columns

3. Introduction

Similar to cellular plates [1, 2, 3] the cellular shells are constructed from two circular cylindrical shells and a grid of stiffeners welded between them (Fig. 3). It is advantageous to use halved circular hollow section (CHS) stiffeners, since the parts of the outer circular shell can easily be welded to them.

The aim of present study is to show the advantages of cellular shells over the stringer stiffened ones. Their large stiffness and small structural height can be useful for a compressed and bent cantilever column in the case of a strict constraint on horizontal displacement of the top together with a constraint on maximum diameter.

The study compares three structural versions for the welded circular cylindrical shell as follows: (a) unstiffened, (b) stiffened with halved rolled I section stiffeners, and (c) stiffened by cellular shell.

The basis of the comparison is the cost, which contains the cost of material, welding and painting.

The base of the column is built-up, but the structural solution of the foundation and its cost is not treated.

Given data: column height $L = 15$ m, factored compression force $N_F = 2 \times 10^7$ [N], horizontal force $H_F = 0.1 N_F$, yield stress of steel $f_y = 355$ MPa, elastic modulus $E = 2.1 \times 10^5$ MPa. In the calculation of displacement the horizontal force is divided by the safety factor $\gamma_M = 1.5$.

Constraints: limitation of the horizontal displacement of the column top: $w_{\max} = L/\phi, \phi = 1000$ and limitation of the shell diameter: $D = 2R = 3000$ mm.

4. The unstiffened shell (Fig.1 without stiffeners)

It can be concluded that the solutions need very thick shell parts, not suitable for fabrication. It should be noted that the constraint on beam-column buckling is passive in this case.

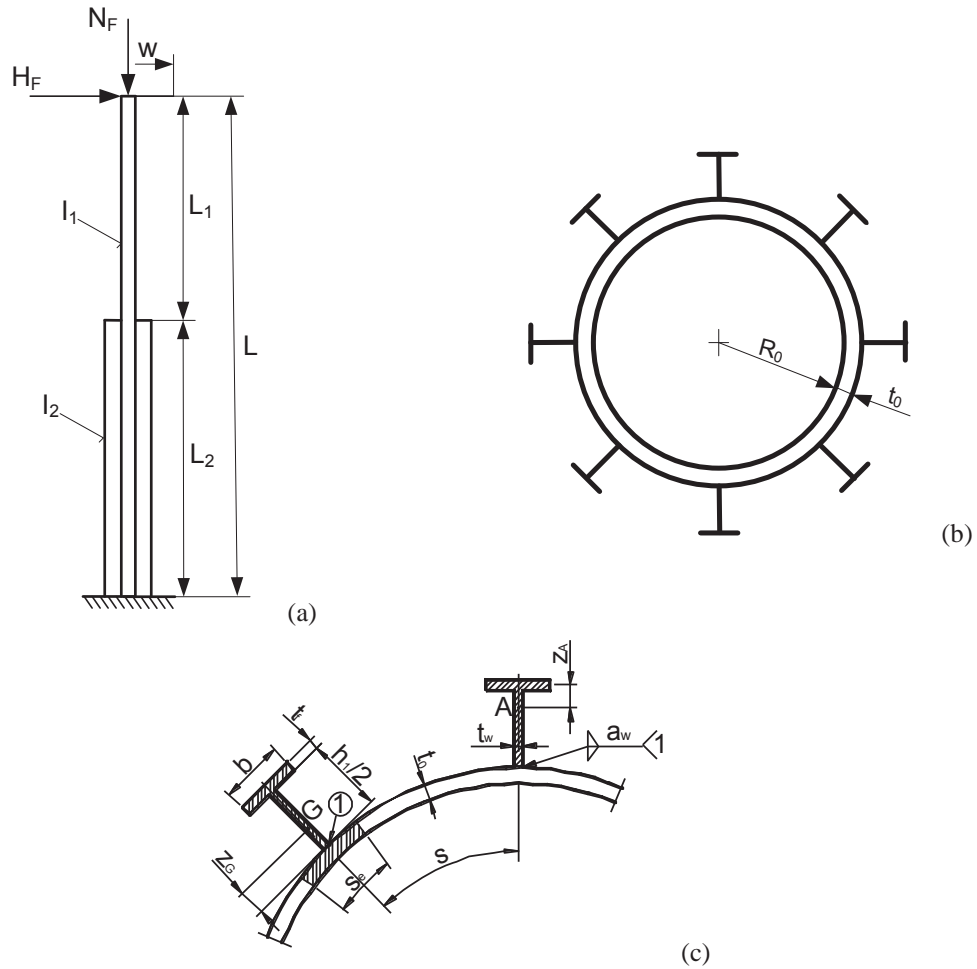


Figure 1: (a) Cantilever column loaded by a compressive and a horizontal force, the horizontal displacement w and the outside diameter are limited, (b) cross-section of the column, (c) dimensions of the stringer stiffeners

5. The shell stiffened with halved rolled I section stiffeners from outside (Fig.1)

Table 1: Some results of the optimization. Dimensions in mm, volume in mm^3 and costs in \$. The optima are marked by bolt letters

h	222.2	222.2	161.8	152.4
b	209.1	208.1	154.4	152.2
t_w	12.7	12.7	8	5.8
t_f	20.5	20.5	11.5	6.8
t	45	46	42	42
n_s	18	18	20	20
L_2	12000	9000	9500	9000
w	14.99	14.99	14.84	14.96
$10^{-9}V$	7.0130	6.847	6.666	6.545
K	96480	94850	88500	88010

The constraints on panel buckling and beam-column buckling (see section 3) are passive. It can be seen that the decrease of L_2 and the dimensions of stiffeners gives less volume and cost.

The main problem is the large shell thickness (over 40 mm), which is unsuitable for fabrication.

6. The column stiffened by cellular shell (Figs. 2, 3)

Halved circular hollow section (CHS) [4] stiffeners are used. This type of stiffeners have more advantages as follows: (a) they enable suitable welded joints for the cover shell elements, (b) their large torsional stiffness gives a large overall stiffness for the whole structure.

6.1 Geometric characteristics

The cross-sectional area of a half CHS is (Fig. 2)

$$A_s = \pi R_s t_s, \quad R_s = \frac{D_s - t_s}{2} \quad (1)$$

the distance of its gravity centre is

$$y_G = \frac{2R_s}{\pi} \quad (1a)$$

and its moment of inertia

$$I_s = \frac{R_s^3 \pi}{2} \left(1 - \frac{8}{\pi^2}\right) \quad (2)$$

The distance of its gravity centre to the shell centre

$$s = y_G + X, \quad X = \sqrt{R_0^2 - R_s^2}, \quad y_0 = R_0 - X \quad (3)$$

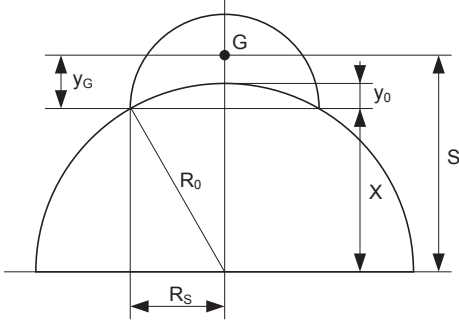


Figure 2: Geometry of the cellular shell

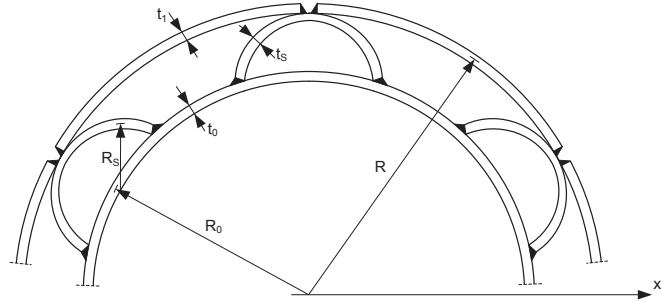


Figure 3: Dimensions of a cellular shell

The radius of the inner shell R_0 can be calculated from the following equation

$$R = s + \frac{t_s + t_1}{2} \quad (4)$$

(t_1 is the thickness of the outer shell)

$$R_0 = \sqrt{\left(R - \frac{2R_s}{\pi} - R_s - \frac{t_s + t_1}{2}\right)^2 + R_s^2} - \frac{t_0}{2} \quad (5)$$

The moment of inertia of n_s stiffeners about the centre of the shell

$$I_{xs} = \left(I_s + A_s s^2\right) \sum_{i=1}^{n_s} \cos^2\left(\frac{2\pi i}{n_s}\right) + \left(\frac{\pi R_s^3 t_s}{2}\right) \sum_{i=1}^{n_s} \sin^2\left(\frac{2\pi i}{n_s}\right) \quad (6)$$

The moment of inertia of the whole cellular shell (Fig.3)

$$I_x = \pi R_0^3 t_0 + \pi R^3 t_1 + I_{xs} \quad (7)$$

Fabrication constraint to enable the welding of the half CHS to the inner shell:
from

$$\frac{2R_0 \pi}{n_s} - 2R_s \geq 2t_s \quad (8)$$

the maximum allowable number of half CHS stiffeners

$$n_{s,\max} = \frac{\pi R_0}{R_s + t_s} \quad (9)$$

6.2 Constraint on horizontal displacement of the column top

$$w_{\max} = \frac{H_F}{EI_1 \gamma_M} \left[\frac{(L-L_2)^3}{3} + \mu \left(L - \frac{L_2}{2} \right) (L-L_2) L_2 + \mu \frac{L_2^2}{2} \left(L - \frac{L_2}{2} \right) \right] \leq \frac{L}{1000} \quad (10)$$

where

$$\mu = \frac{I_1}{I_2}, \gamma_M = 1.5, \quad I_1 = \pi R_0^3 t_1, I_2 = I_x \quad (11)$$

I_1 and I_2 are the moments of inertia of the upper and lower column part, respectively, γ_M is the safety factor.

6.3 Constraint on panel shell buckling of the outer shell parts between stiffeners

According to the Det Norske Veritas [5] design rules for shell buckling

$$\sigma_{\max} = \frac{N_F}{A} + \frac{H_F L}{W_x} \leq f_{ks} = \frac{f_y}{\sqrt{1 + \bar{\lambda}^4}}, \quad \bar{\lambda} = \sqrt{\frac{f_y}{f_E}} \quad (12)$$

$$f_E = C \frac{\pi^2 E}{12(1-\nu^2)} \left(\frac{t_1}{s_0} \right)^2, \quad C = \psi \sqrt{1 + \left(\frac{\rho_0 \xi}{\psi} \right)^2} \quad (13)$$

$$\psi = 4, \rho_0 = 0.5 \left(1 + \frac{R}{150 t_1} \right)^{-0.5}, \xi = 0.702 Z \quad (14)$$

$$Z = \frac{s_0^2}{R t_1} \sqrt{1 - \nu^2}, \nu = 0.3 \quad (15)$$

In the case of such a very strict displacement constraint the panel buckling constraint is not active. σ_{\max} is so small that the effective shell width is equal to the whole width s_0 .

Calculations show that this constraint is not active.

6.4 Constraint on beam-column buckling

The check should be performed by taking into account the overall buckling of the column [6]. For the calculation of the Euler critical stress the formula given by Timoshenko and Gere [7] is used.

$$\frac{N_F}{\chi_1 A f_y} + k_{yy1} \frac{H_F L}{W_x f_y} \leq 1 \quad (16)$$

$$\chi_1 = \frac{\phi_1 - \sqrt{\phi_1^2 - \lambda^2}}{2\lambda^2}, \quad \phi_1 = 1 + \alpha(\lambda - 0.2) + \lambda^2, \quad \lambda = \sqrt{\frac{f_y}{\sigma_E}}, \quad \sigma_E = \frac{\pi^2 E I_2}{4L^2 A C} \quad (17)$$

$$C = \frac{L_2}{L} + \frac{L_1 I_2}{L I_1} - \frac{1}{\pi} \left(\frac{I_2}{I_1} - 1 \right) \sin \frac{\pi L_2}{L} \quad (18)$$

$$\alpha = 0.34,$$

$$k_{yy1} = C_{my} \left(1 + 0.6 \lambda \frac{F}{\chi_1 A f_y} \right) \quad \text{for } \lambda < 1 \quad (19a)$$

$$k_{yy1} = C_{my} \left(1 + 0.6 \frac{F}{\chi_1 A f_y} \right) \quad \text{for } \lambda \geq 1 \quad (19b)$$

$$C_{my} = 0.6$$

6.5 The cost function

The cost of welding is formulated according to the fabrication sequence [8 - 11].

(1) Fabrication of 5 shell elements of length 3 m without stiffeners. For one shell element 2 axial butt welds are needed (GMAW-C) (K_{F1}). The cost of forming of a shell element into the cylindrical shape is also included (K_{F0}).

(2) Welding of the whole unstiffened shell from 5 elements with 4 circumferential butt welds (K_{F2}). Θ is the factor expressing the complexity of assembly

$$V_1 = 3000 \times 2R_0 \pi t_0, \rho = 7.86 \times 10^{-6} \text{ kgmm}^{-3}, k_F = 1.0 \text{ \$/min}, k_{M1} = 1.0 \text{ \$/kg.} \quad (20)$$

$$K_{F0} = k_F \Theta e^{\mu}, \mu = 6.8582513 - 4.527217 t_0^{-0.5} + 0.009541996 (2R_0)^{0.5} \quad (21)$$

$$K_{F1} = k_F \left[\Theta \sqrt{\kappa \rho V_1} + 1.3 \times 0.152 \times 10^{-3} t_0^{1.9358} (6000 + 2\pi R_0) \right] \quad (22)$$

$$\kappa = 4, V_1 = 2R_0 \pi t_0 \times 3000, \Theta = 2 \quad (23)$$

$$K_{F2} = k_F \left(\Theta \sqrt{25 \rho V_1} + 1.3 \times 0.152 \times 10^{-3} t_0^{1.9358} \times 4 \times 2R_0 \pi \right) \quad (24)$$

(3) Welding of the half CHS stiffeners to the base shell using SAW fillet welds

$$K_{F3} = k_F \left[\Theta \sqrt{(n_s + 1) \rho V_2} + 1.3 \times 0.2349 \times 10^{-3} a_w^2 2L_2 n_s \right] \quad (25)$$

$$V_2 = 5V_1 + n_s A_s L_2, \quad a_w = 0.3t_s \quad (a_{\min} = 3 \text{ mm}) \quad (26)$$

(4) Forming of the outer curved shell panels of length 3 m

$$K_{F4} = k_F \Theta e^{\mu_1}, \mu_1 = 6.8582513 - 4.527217 t_1^{-0.5} + 0.009541996 (2R)^{0.5} \quad (27)$$

(5) Welding of an outer curved shell panel of length L_2 using κ_3 shell parts of length 3 m by ($\kappa_{30}-1$) GMAW-C butt welds

$$K_{F5} = k_F \left(\Theta \sqrt{\kappa_{30} \rho V_3} + 1.3 \times 0.152 \times 10^{-3} t_1^{1.9358} \frac{2R\pi}{n_s} (\kappa_{30} - 1) \right) \quad (28)$$

$$V_3 = \frac{2R\pi L_2}{n_s} \quad (29)$$

$$\kappa_3 = \frac{L_2}{3000} \text{ round up to } \kappa_{30}$$

(6) Welding of the outer panels to the stiffened shell by SAW fillet welds of size $a_{w1} = 0.3t_s$

$$K_{F6} = k_F \left(\Theta \sqrt{(n_s + 1) \rho V_4} + 1.3 \times 0.2349 \times 10^{-3} a_{w1}^2 2n_s L_2 \right) \quad (30)$$

$$V_4 = V_2 + n_s V_3 \quad (31)$$

Painting cost

$$K_p = k_p S, S = 2\pi R_0 (2L - L_2) + 2R\pi L_2 \quad (32)$$

Material cost

$$K_M = k_M \rho V_4 \quad (33)$$

The total cost

$$K = K_M + 5(K_{F0} + K_{F1}) + K_{F2} + K_{F3} + \kappa_{30} K_{F4} + n_s K_{F5} + K_{F6} + K_p \quad (34)$$

The details of the search are shown in Table 2. For fabrication aspects the following limits are introduced: $t_{0\max} = 30$, $t_{1\max} = 30$, $t_{s\min} = 10$ mm.

Table 2: Details of the optimization. The maximal displacement in each case is near the allowable value of 15 mm. Dimensions in mm, volume V in mm^3 . The optimum is marked by bold letters

t_0	t_1	L_2	$V_4 \times 10^{-9}$	K (\$)
25	29	8900	5.768	78460
24	30	8900	5.720	77440
23	30	9300	5.705	79410
22	30	9800	5.719	78740
21	30	10300	5.733	78100
20	30	10900	5.776	77740
19	30	11700	5.876	77940
18	30	13200	6.1780	82920

The numerical values show the following results:

(a) The minimum volume and cost is found for the minimum number of stiffeners $n_s = 4$:

(b) The CHS stiffener profile of 101.6x10 gives the minimum volume and cost. The tendency is to minimize D_s to maximize R_0 , and to maximize t_s , thus, we select this profile.

7. Conclusions

A realistic numerical problem is investigated, in which the outer shell diameter and the horizontal displacement of the column top is limited. The numerical value of the compression force N_F is also given. Three structural solutions are optimized:

(1) the unstiffened circular cylindrical shell has the minimal volume $V = 5.316 \times 10^9 \text{ mm}^3$ but the shell thickness is 50 mm, which is unsuitable for fabrication,

(2) the circular shell stiffened with halved rolled UC sections has the structural volume $V = 6.545 \times 10^9 \text{ mm}^3$ and the cost $K = 88010$ \$, but the shell thickness is 42 mm, unsuitable for fabrication,

(3) the optimum solution of the column strengthened by cellular shell has values $V = 5.705 \times 10^9 \text{ mm}^3$ and $K = 77440$ \$, thickness 30 mm.

It can be concluded that in this case only the cellular shell version can fulfil all the requirements (horizontal displacement, maximum outer diameter, maximum thickness of 30 mm, minimum cost). In addition, the cellular shell can be more easily protected against corrosion and is much more aesthetic than the second version.

8. Acknowledgements

The research was supported by the TÁMOP-4.2.4B/2-11/1-2012-0001 project entitled ‘Campus Hungary’, supported by the European Union, co-financed by the European Social Fund. The research was supported also by the Hungarian Scientific Research Fund OTKA T 109860 projects and was partially carried out in the framework of the Center of Excellence of Innovative Engineering Design and Technologies at the University of Miskolc.

9. References

- [1] J. Farkas., Structural synthesis of welded cell-type plates. *Acta Techn. Hung.* 83 (1-2), 117-131, 1976.
- [2] J. Farkas., *Optimum design of metal structures*, Akadémiai Kiadó, Budapest, Ellis Horwood, Chichester, UK, 1984.
- [3] K. Jármai and J. Farkas, Comparison of rectangular and square box columns constructed from cellular plates with welded and rolled stiffeners. *Eng Struct*, 60, 199-205, 2014.
- [4] EN 10219-2. Cold formed circular hollow section profiles. CEN 2006.
- [5] Det Norske Veritas, *Buckling strength of shells*. Recommended practice RP-C202. Høvik, Norway, 2002.
- [6] EN 1993-1-1, Eurocode 3. Design of steel structures. Part 1-1. General rules and rules for buildings., 2009.
- [7] S.P. Timoshenko and J.M. Gere., *Theory of elastic stability*. McGraw Hill. New York-Toronto-London, 1961.
- [8] J. Farkas and K. Jármai, *Analysis and optimum design of metal structures*. Balkema, Rotterdam-Brookfield, 1997.
- [9] J. Farkas and K. Jármai, *Design and optimization of metal structures*,. Horwood, Chichester, UK, 2008.
- [10] J. Farkas and K. Jármai, *Optimum design of steel structures*, Springer, Heidelberg etc., 2013.
- [11] K. Jármai and J. Farkas, Cost calculation and optimization of welded steel structures, *J Constr Steel Res*, 50, 115-135, 1999.

Topology optimization for coated structures

Anders Clausen¹, Erik Andreassen², Ole Sigmund³

Technical University of Denmark, Lyngby, Denmark

¹ andcla@mek.dtu.dk

² erand@mek.dtu.dk

³ sigmund@mek.dtu.dk

1. Abstract

This paper presents new results within the design of three-dimensional (3D) coated structures using topology optimization. The work is an extension of a recently published two-dimensional (2D) method for including coated structures into the minimum compliance topology optimization problem. The high level of control over key parameters demonstrated for the 2D model can likewise be achieved in 3D. The effectiveness of the approach is demonstrated with numerical examples, which for the 3D problems have been solved using a parallel topology optimization implementation based on the PETSc toolkit.

2. Keywords: Topology optimization, Coating, 3D optimization.

3. Introduction

This study considers the design of coated structures in 3D using topology optimization. Metal coating of polymer structures can be used to enhance functional or visual properties. Many polymers are more easily processed into complex shapes than metals. By coating polymer structures with metal it is possible to combine the processing and cost advantages of polymers with the performance benefits of metal.

This work is based on a recently published paper [4], which introduced a novel method for modeling coated structures and material interface problems in relation to density based topology optimization. The original method was limited to 2D applications. In this paper the method is extended to 3D. As in the 2D version, the method assumes perfect bonding between the substrate and the coating material.

The paper considers minimum compliance problems. The approach is applicable for density based topology optimization and draws on the basic ideas of the SIMP approach (see e.g. [3]). As described in detail in the paper on 2D coating [4], the usual stiffness interpolation from SIMP is extended to include spatial gradients of the filtered design field. This allows to identify material interfaces and enforce coating. In order to control the spatial gradient field, and thereby assure a uniform coating thickness, a two-step filtering approach is applied.

The ability to accurately describe material interfaces is often mentioned as an advantage of level-set based approaches, for which interfaces are implicitly defined by iso-contours of a level-set function (for a review of level-set based topology optimization, see e.g. [9]). An example is [10], where a level-set based method for including material interface properties in the optimization of multi-phase elastic and thermoelastic structures is introduced. The method introduced in [4], and extended in this paper, shows that it is also possible to accurately capture material interfaces using a density based approach.

4. Problem formulation

This section recapitulates the optimization problem as defined in [4] with focus on conveying the main ideas of the approach. Furthermore, the relevant parameters chosen for the present study are described. The material model and characteristic properties are reported in the continuous versions of the design field and filters. Only when defining the optimization problem, the discretized version is introduced.

A coated structure is characterized by a base structure made of one material (referred to as the substrate in a process context) and a coating made of a different material. Initially, no limitations are put on the shape and dimensions of the base structure, whereas the coating is assumed to have a constant, predefined thickness, t_{ref} , at all surfaces of the base structure. Fig. 1 shows a sketch of a 3D coated structure. It is important to notice that the prescribed coating thickness, t_{ref} , is a fixed parameter which is defined as part of the design problem. For the optimization problem, it is convenient to define the coating based on the spatial gradient of the design field in order to assure sufficient design freedom. The modeled coating may be characterized by a thickness, t , which depends on the design field. This approach assures sufficient design freedom, but must be combined with a method to control the gradient field in order to end up with a design where $t = t_{\text{ref}}$.

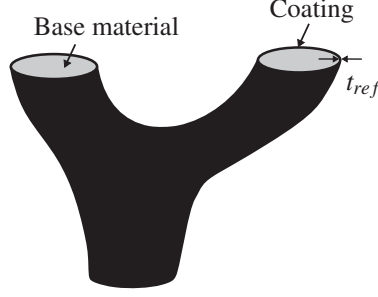


Figure 1: Illustrative sketch of a 3D coated structure with coating thickness t_{ref} .

To control the shape of the gradient a two-step filtering process is applied. First, the design field, μ , is smoothed (giving $\hat{\mu}$) and projected (giving $\varphi = \tilde{\hat{\mu}}$). This projection defines the base structure.

In order to identify the interface of the base structure, a second smoothing is applied (giving $\hat{\varphi}$). The norm of the spatial gradient, $\|\nabla\hat{\varphi}\|_{\alpha}$, in this second smoothed field is used to identify the interface (the index α means that the norm is normalized, such that its maximum value is one - see details in Section 4.4). The normalized norm is subsequently projected to model a sharp interface. This field, which is denoted $\overline{\|\nabla\hat{\varphi}\|_{\alpha}}$, defines the coating.

Thus, the desired coating thickness is defined indirectly by setting the filter radius used for the second smoothing (R_2), as this filter determines the width of the interface region.

4.1. Filters

In order to regularize the optimization problem a smoothing is performed using a so-called PDE-filter [6] with appropriate boundary conditions. The first smoothing (from μ to $\hat{\mu}$) is performed by solving the equation:

$$-\left(\frac{R_1}{2\sqrt{3}}\right)^2 \nabla^2 \hat{\mu} + \hat{\mu} = \mu \quad (1)$$

where the spatial neighborhood is defined by the magnitude of the scalar in front of the Laplacian. In the above form, R_1 corresponds to the filter radius in standard filtering techniques. Furthermore, a projection method ([5], [7]), in the form first proposed in [11], is applied as a means of obtaining black-and-white designs. The projection is determined by the step ‘‘sharpness’’ β and the threshold parameter $\eta \in [0; 1]$.

4.2. Interpolation function

The coating material has the mass density ρ^0 and elasticity modulus E^0 . The material properties of the base material are defined as ratios of the coating material’s properties. The mass density ratio is $\lambda_m \in]0, 1[$ and the stiffness ratio is $\lambda_E \in]0, 1[$. For simplicity, both materials are assumed to be isotropic with a Poisson’s ratio, ν^0 , independent of interpolation density.

The physical density, ρ , and stiffness, E , are defined as interpolations of φ and $\overline{\|\nabla\hat{\varphi}\|_{\alpha}}$:

$$\rho(\varphi, \overline{\|\nabla\hat{\varphi}\|_{\alpha}}) = \rho^0 \left[\lambda_m \varphi + (1 - \lambda_m \varphi) \overline{\|\nabla\hat{\varphi}\|_{\alpha}} \right] \quad (2)$$

$$E(\varphi, \overline{\|\nabla\hat{\varphi}\|_{\alpha}}) = E^0 \left[\lambda_E \varphi^p + (1 - \lambda_E \varphi^p) (\overline{\|\nabla\hat{\varphi}\|_{\alpha}})^{p_s} \right] \quad (3)$$

Opposite to the original paper [4] a distinction is made between the penalization parameters, p and p_g , penalizing φ and $\overline{\|\nabla\hat{\varphi}\|_{\alpha}}$, respectively.

Note that when the normalized gradient norm approaches its maximum value ($\overline{\|\nabla\hat{\varphi}\|_{\alpha}} = 1$), i.e. at the interface region, the physical density and stiffness approach ρ^0 and E^0 , respectively:

$$\begin{aligned} \rho_{coating}(\varphi, 1) &= \rho^0 [\lambda_m \varphi + (1 - \lambda_m \varphi)] = \rho^0 \\ E_{coating}(\varphi, 1) &= E^0 [\lambda_E \varphi^p + (1 - \lambda_E \varphi^p)] = E^0 \end{aligned} \quad (4)$$

Opposite, when the gradient norm approaches zero, i.e. when going away from the interface, the second term in Equation (2) and (3) vanishes. In these regions $\varphi = 1$ corresponds to base structure, whereas $\varphi = 0$ corresponds to void.

4.3. Optimization problem

The optimization problem is a standard minimum compliance problem with a constraint on the volume. For the discretized problem the continuous fields are replaced with vectors of element values (e.g. $\boldsymbol{\mu}$ instead of μ).

The global stiffness matrix, \mathbf{K} , is defined as:

$$\mathbf{K}(\boldsymbol{\mu}) = \sum_e \mathbf{k}_e(\boldsymbol{\mu}) = \sum_e E_e(\varphi_e(\boldsymbol{\mu}), \|\nabla \hat{\varphi}_e(\boldsymbol{\mu})\|_\alpha) \mathbf{k}_e^0 \quad (5)$$

where \mathbf{k}_e is the element stiffness matrix, and \mathbf{k}_e^0 is the element stiffness matrix for an element with unit elasticity modulus. To avoid a singular system in the numerical interpolation, the first term in Eq. (3), $\lambda_E \varphi_e^p$, is replaced with $\lambda_{E,\min} + (\lambda_E - \lambda_{E,\min}) \varphi_e^p$.

The optimization problem is defined in the following way:

$$\begin{aligned} \min_{\boldsymbol{\mu}}: \quad & c(\boldsymbol{\mu}) = \mathbf{U}^T \mathbf{K} \mathbf{U} \\ \text{subject to:} \quad & \mathbf{K} \mathbf{U} = \mathbf{F} \\ & g(\boldsymbol{\mu}) = V(\boldsymbol{\mu})/V^* - 1 \leq 0 \\ & 0 \leq \mu_e \leq 1, \quad \forall e \end{aligned} \quad (6)$$

Here c is the compliance, \mathbf{U} and \mathbf{F} are the global displacement and force vectors, respectively, g is the volume constraint, $V(\boldsymbol{\rho}(\boldsymbol{\mu})) = \sum v_i \rho_i(\boldsymbol{\mu})$ is the material volume and V^* is the maximum allowed volume.

Design updates are performed based on sensitivities using MMA ([8]). The sensitivity analysis is performed in a way analogous to the 2D version.

4.4. Parameters

In the second smoothing step, where the filter radius is set to R_2 , the filter radius is computed based on the specified coating thickness t_{ref} as $R_2 = 2.5t_{\text{ref}}$. This is independent on whether a 2D or 3D problem is considered. The same holds for the normalization factor α , which is defined as the inverse of the maximum possible gradient norm of the second smoothed field, $\hat{\varphi}$. It takes the value $\alpha = R_2/\sqrt{3}$.

As opposed to [4], the penalization factor on the gradient part is distinguished from the penalization on the design variable. This is done because in 3D it is usual to work with lower volume fractions. Thus, if the gradient field were to be penalized in the initial phase of the optimization, the corresponding sensitivities would be small. This can be circumvented by instead introducing the penalization on the gradient field gradually.

A continuation scheme is adopted for both the penalization parameters and the projection. The penalization for $\|\nabla \hat{\varphi}\|_\alpha$ is initialized as $p_g = 1$ and gradually increased to $p_{g,\max} = 3$. When $p_{g,\max}$ is achieved the penalization for φ is gradually increased from $p = 3$ to $p_{\max} = 4$. The two projections are performed with identical parameters. The threshold is $\eta = \eta_g = 0.5$. The sharpness parameter is initialized with $\beta = 16$. After reaching p_{\max} , β is gradually increased to 64 by doubling at convergence (or after 100 iterations since last update).

The parallel 3D implementation is based on the topology optimization framework [1] utilizing PETSc [2]. This allows solving problems with millions of design elements, which is necessary in order to have a fine enough discretization to capture the coating.

5. Results

The approach is demonstrated by solving the optimization problem in Eq. (6) on both a 2D domain and an equivalent 3D domain. The design problem for both cases consists of a distributed load applied at the entire top surface. The 2D domain is illustrated in Fig. 2. The full domain has the dimensions 200 by 50, however, by using a symmetry condition at the right edge only half of the domain is modeled. The center half of the bottom layer is clamped. The domain is discretized using bi-linear elements with two elements per unit length. The total load equals 10. The coating thickness is set to $t_{\text{ref}} = 1$.

The 3D design problem is similar to the 2D problem. Denote the vertical direction by z and the two horizontal directions by x and y . Again, a distributed load is applied at the entire top surface ($z = z_{\max}$). The load sums up to 0.25. The central area of the bottom layer ($z = 0$) is clamped. The *central area* here refers to points which are simultaneously in the central half in the x and y directions (see the optimized structure in Fig. 4 for visualization). Only a quarter of the domain is modeled, using symmetry constraints in both the x and y directions.

When discretizing the 3D problem the chosen domain decomposition approach from the parallelized PETSc code has to be taken into account. Using four decompositions, the number of elements in each direction should be a multiple of 16 (2^4). Simultaneously it is chosen to let the coating thickness $t_{\text{ref}} = 1$ correspond to an integer number of elements. This is not a requirement, but makes it easier to visually assess the results. Bearing these two choices in mind the full domain dimensions are defined as $192 \times 96 \times 48$ (a 4:2:1 length ratio), such that a

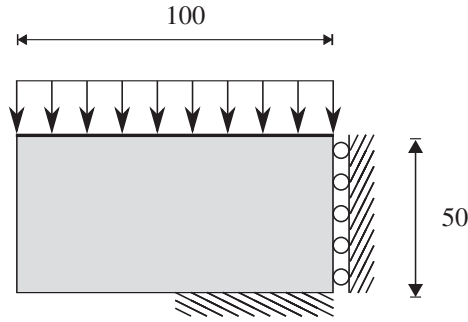


Figure 2: Design domain for the 2D problem, using a symmetry condition at the right edge.

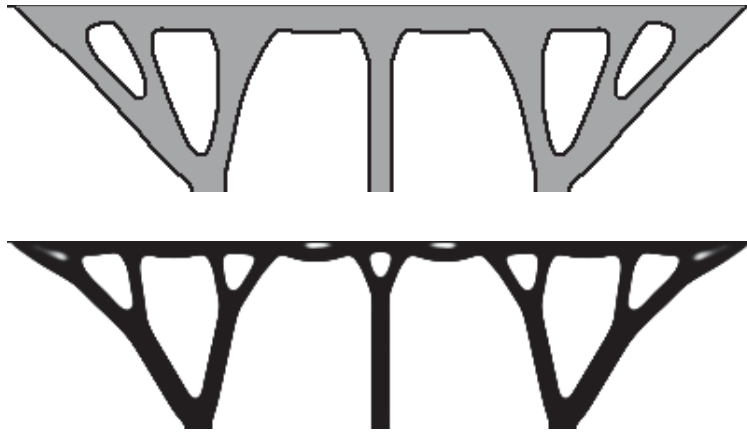


Figure 3: Optimized results in 2D. Top: Coated structure ($c = 814.9$). Bottom: Solid structure ($c = 636.0$).

quarter domain has the dimensions $96 \times 48 \times 48$ and can be resolved with $288 \times 144 \times 144$ tri-linear elements. This slight modification of dimensions compared to the modeled 2D domain (100×50) is justified by the easier interpretation of the results.

For both problems the material parameters of the coating and solid material are $\rho^0 = 1$ and $E^0 = 1$. The base material is defined by $\lambda_E = 0.35$ and $\lambda_m = 0.6$. The first filter radius is $R_1 = 10$. The elements in the topmost layer (at the loaded surface) are set as passive, solid elements. The boundary conditions for the PDE-filter are chosen as homogeneous Neumann conditions at all edges. For the 3D case, the projection sharpness, β , is initialized as 8 rather than 16 in order to stabilize the optimization.

The optimized results for the 2D problem are shown in Fig. 3 for both a coated structure and a solid structure (corresponding to $\lambda_E = \lambda_m = 1$). In the coated structure, the base material has a constant density and the coating is seen to be applied with a uniform thickness everywhere at the structure. The topology of the coated structure is simpler than for the solid structure, as the low density base material has a lower cost in the volume constraint than the solid material. The compliance for the coated structure is larger than for the solid structure, as the stiffness of the base material is disproportionately low with respect to its weight compared to the solid material.

Figure 4 shows the optimized coated structure for the full 3D problem viewed from below. The coating material is visualized in light blue at 35 % transparency, while the base material is light gray. Note that the clamped part of the bottom surface is clearly traced out by the structure. The coating material is again applied in a highly uniform manner at all visible interfaces.

The coated structure is compared with a solid structure optimized with the same parameters in Fig. 5. Only the modeled quarter part of each structure is shown. The structures are compared in full height and for two cross sections at 75 % and 50 % height. First consider the full height structures (a-b). The two structures show the same trend as their 2D equivalents in Fig. 3. The topology for the coated structure is simpler with a significantly lower number of holes. Again, the compliance for the coated structure is larger than for the solid structure due to the disproportionately low stiffness of the base material.

The cross sections in (c-f) further illustrate that the coating material is applied uniformly over the structure. In



Figure 4: Full 3D structure optimized using the coating approach. The coating material is rendered at 35% transparency to visualize the internal base structure.

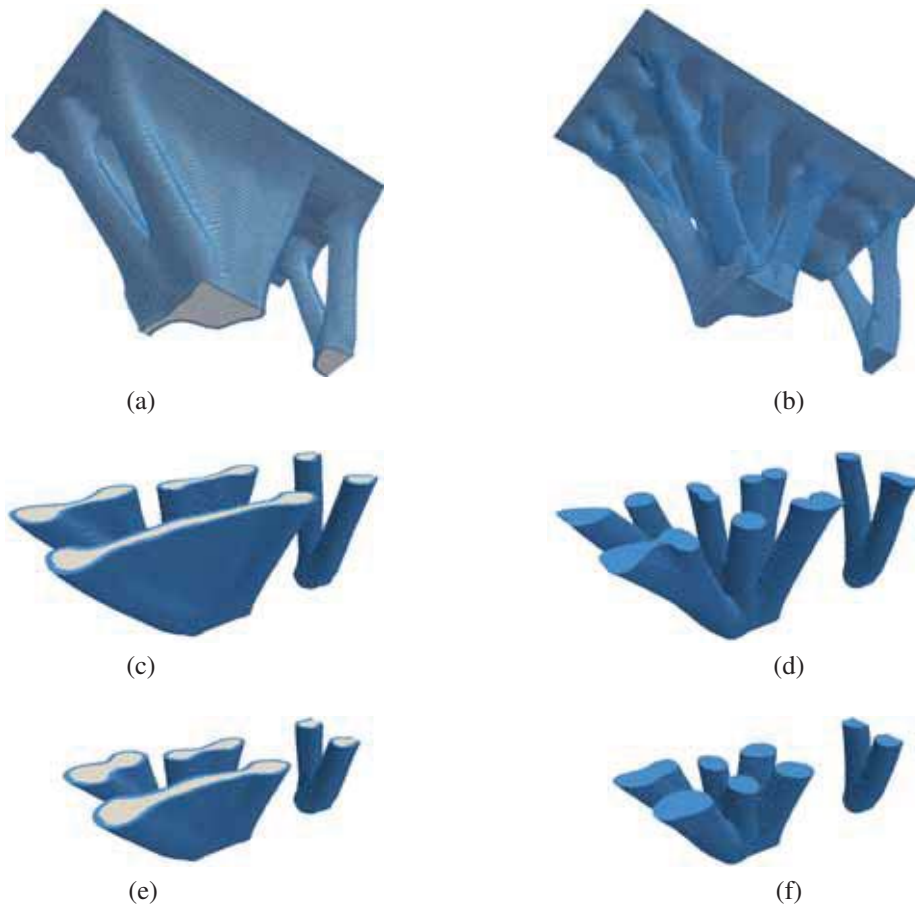


Figure 5: Optimized results in 3D (quarter domain). Left column: Coated structure ($c = 0.2742$). Right column: Solid structure ($c = 0.1420$). (a-b) View from below. Coating and solid material shown at 35% transparency. (c-d) Cross section at 75% height, view from above. (e-f) Cross section at 50% height, view from above.

addition, the figures very clearly show the difference in topology between the coated and solid structures. The pure solid structure continues to branch out in a higher number of members with increasing z -coordinate, whereas the coated structure consists of a few members which do not branch out but rather stay connected while adapting the cross sectional area.

6. Conclusion

It has been shown that coated structures in 3D can be designed using topology optimization. The approach is demonstrated on equivalent design problems in 2D and 3D. The high level of control over the modeled coating which is earlier demonstrated for the 2D model is likewise achieved in 3D.

7. Acknowledgments

The authors acknowledge financial support from the Villum Foundation (the NextTop project) and DTU Mechanical Engineering.

8. References

- [1] N. Aage, E. Andreassen, and B. S. Lazarov. Topology optimization using PETSc: An easy-to-use, fully parallel, open source topology optimization framework. *Structural and Multidisciplinary Optimization*, Published online:1–7, 2014.
- [2] S. Balay, S. Abhyankar, M. F. Adams, J. Brown, P. Brune, K. Buschelman, V. Eijkhout, W. D. Gropp, D. Kaushik, M. G. Knepley, L. C. McInnes, K. Rupp, B. F. Smith, and H. Zhang. PETSc Web page, 2014.
- [3] M. P. Bendsøe and O. Sigmund. *Topology Optimization. Theory, Methods and Applications*. Springer, 2003.
- [4] A. Clausen, N. Aage, and O. Sigmund. Topology optimization of coated structures and material interface problems. *Computer Methods in Applied Mechanics and Engineering*, Available online, 2015.
- [5] J. Guest, J. Prevost, and T. Belytschko. Achieving minimum length scale in topology optimization using nodal design variables and projection functions. *International Journal for Numerical Methods in Engineering*, 61(2):238–254, 2004.
- [6] B. S. Lazarov and O. Sigmund. Filters in topology optimization based on helmholtz-type differential equations. *International Journal for Numerical Methods in Engineering*, 86(6):765–781, 2011.
- [7] O. Sigmund. Morphology-based black and white filters for topology optimization. *Structural and Multidisciplinary Optimization*, 33(4-5):401–424, 2007.
- [8] K. Svanberg. Method of moving asymptotes - a new method for structural optimization. *International Journal for Numerical Methods in Engineering*, 24(2):359–373, 1987.
- [9] N. P. van Dijk, K. Maute, M. Langelaar, and F. Van Keulen. Level-set methods for structural topology optimization: a review. *Structural and Multidisciplinary Optimization*, 48(3):437–472, 2013.
- [10] N. Vermaak, G. Michailidis, G. Parry, R. Estevez, G. Allaire, and Y. Bréchet. Material interface effects on the topology optimization of multi-phase structures using a level set method. *Structural and Multidisciplinary Optimization*, Published online:1–22, 2014.
- [11] S. Xu, Y. Cai, and G. Cheng. Volume preserving nonlinear density filter based on heaviside functions. *Structural and Multidisciplinary Optimization*, 41(4):495–505, 2010.

Aerothermoelastic Structural Topology Optimisation for a Hypersonic Transport Aircraft Wing

David J. Munk¹, Gareth A. Vio², Grant P. Steven³

¹ School of AMME, The University of Sydney, NSW, Australia, david.munk@usyd.edu.au

² School of AMME, The University of Sydney, NSW, Australia, gareth.vio@usyd.edu.au

³ School of AMME, The University of Sydney, NSW, Australia, grant.steven@usyd.edu.au

1. Abstract

Aerothermoelasticity plays a vital role in the design of hypersonic aircraft as a strong coupling exists between the aerothermodynamic loads and the structural response. Fluid-thermal-structural interactions are one of the multi-disciplinary problems that must be solved for the design of hypersonic aircraft. Existing optimisation algorithms lack the capability to include these aerothermodynamic coupling effects. This article presents a novel bi-directional evolutionary structural topology optimisation algorithm that includes aerothermoelastic coupling effects. The time-varying temperature distribution is applied through an original formulation, solving for equilibrium of convective, radiative and through thickness conduction at each time step, with a time-marching unsteady conduction solution for time integration. The thermal solution is coupled with a high order aerodynamic solver and the structural finite element model. The results presented in this article show that the coupling between the thermal, structural and aerodynamic forces drive the optimisation of the design and must be taken into consideration to achieve a feasible working structure for the required environment.

2. Keywords: Hypersonic; Aerothermoelastic; Evolutionary; Aircraft.

3. Introduction

Hypersonic flight has been an active area of research for the past six decades, motivated by shorter flight times and reusable launch vehicles for affordable access to space [1]. In a recent review paper, McNamara and Friedmann [2] conclude that accurate modeling of the aerothermodynamics is crucial for the design of hypersonic vehicles. Furthermore the design of the airframe is crucial in order to survive the harsh environment [2]. Current high speed, high enthalpy tunnels are not suitable for the testing of scaled models of hypersonic vehicles [3]. Also, hypersonic aerothermoelastic scaling laws are not available at high Mach numbers [4]. Therefore, the development of accurate computational aerothermodynamic simulation capabilities is important for the design and analysis of hypersonic vehicles.

Aerothermodynamic applications to structural topology optimisation have not yet been considered for lightweight design. Eschenauer and Olhoff [5] and Krog *et al.* [6] both studied the internal design of wing ribs using topology optimisation methods. However, the aerodynamic load was prescribed and therefore not design dependent. Studies that have included aerodynamic loading feedback, to model aerodynamic-structure coupling, in the optimisation are shown in [7, 8]. These studies dealt with steady aerodynamic-structural coupling. Stanford and Beran [9] looked at dynamic aerodynamic-structural coupling. However, none of these studies had a temperature model included in the analysis. Stanford and Beran [10] recently added a thermal model, however a temperature profile is prescribed along the solid-fluid interface, therefore no aero-thermo coupling is present.

This paper extends the previous work by developing a structural topology optimisation algorithm with a strong coupling between the aerodynamics and thermodynamics. The article optimises the wing of a generic hypersonic cruise vehicle in its cruise condition for minimum weight. The importance of the aerothermodynamic coupling on the design of the structure is analysed.

4. Theoretical Analysis

The wing structure used in this article is the LAPCAT A2 [11]. A finite element mesh is generated from a series of node coordinates. The aerothermoelastic module is shown in Fig. 1.

The inertial and elastic modules make up the finite element analysis (Fig. 1 (left)). A strong coupling exists between the aerodynamic and structural modules, however the weak coupling between the thermal and aerodynamic module is ignored [12]. The weak feedback of the structural deformations on the thermal module is included in the analysis.

The inputs and outputs of the different modules are shown in Fig. 1 (right). MATLAB[®] is used to communicate between the different modules and check for convergence of optimisation.

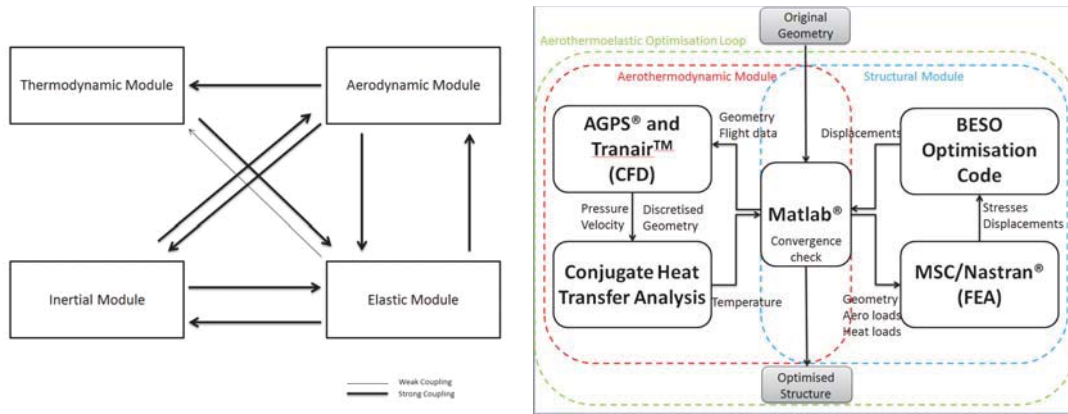


Figure 1: Degree of Coupling for the Aerothermoelastic Domain (left), Optimisation Network for Aerothermoelastic Coupling (right).

4.1. Structural Module

The structural deformation and stresses are calculated by performing a finite element analysis. The finite element software used is MSC/Nastran®. The initial structural model is shown in Fig. 2 (left).

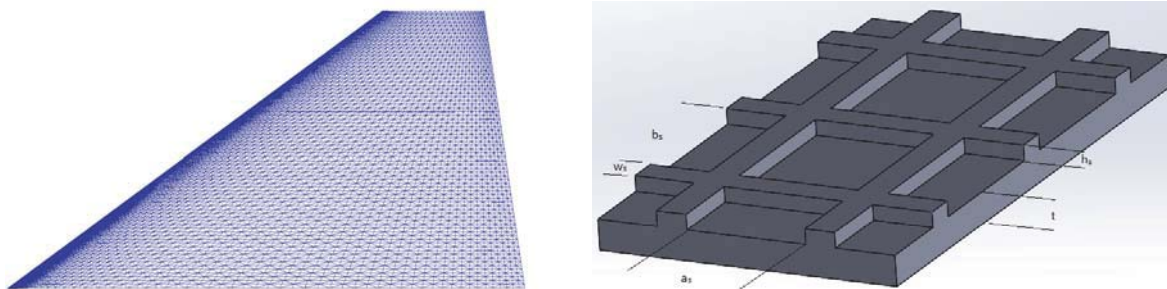


Figure 2: Initial Structural Model (left), Cross-Stiffened Skin (right).

The model uses four node shell elements (Fig. 2 (left)), since aircraft structures are built from metal plates. The initial model begins with all possible combinations of spars, ribs and cross-bars.

4.2. Aerodynamic Module

Two complementary software packages are used in the aerodynamic module, AGPS™ and Tranair®. AGPS™, the Aero Grid and Panelling System, takes the vehicles geometry and generates the grid points for an aerodynamic mesh. AGPS™ efficiently and accurately produces such a mesh, which can be updated from deformations in the structure, such that the structural module can update the aerodynamic module.

AGPS™ produces the input files for the aerodynamic solver Tranair®. The surface and wake meshes are written into a Tranair® input file, specifying the coordinates of each corner point of the mesh. Tranair® solves the non-linear, full potential equation for three-dimensional flow at subsonic, transonic and supersonic Mach numbers [13]. Tranair® uses an adaptive rectangular flow-field grid, which relieves the computational expense of generating a surface fitted flow-field grid for complex geometries by using a rectangular mesh that adapts to the vehicle surface. Tranair® has a boundary layer coupling incorporated into the code. The output of the aerodynamic module is the discretised geometry, used for all the other modules, the pressure loading on the wing, and the boundary layer edge properties, used to calculate the surface temperature in the thermal module.

4.3. Thermal Module

The temperature loading on the wing is determined by solving an equilibrium calculation at the solid-fluid interface. Heat is transferred by convection, due to aerodynamic heating, radiation of the skin to the environment and internal conduction. The solution is then stepped forward in time by solving the unsteady conduction equation.

At the fluid-solid interface the equilibrium condition states that:

$$q_{conv} - q_{rad} = q_{cond} \quad (1)$$

therefore, an expression for the temperature of the skin can be derived. The expression is solved for the wall temperature, T :

$$\sigma \varepsilon T^4 + \left(S_t \rho u C_w + \frac{k_w}{\Delta z} \right) T = S_t \rho u C_{aw} T_{aw} + \sigma \varepsilon T_e^4 + \frac{k_w T_{int}}{\Delta z} \quad (2)$$

where S_t is the Stanton number, C is the specific heat, ρ is the density, k_w is the conductivity coefficient, u is the local velocity at the edge of the boundary layer and Δz is the thickness of the wing skin. Eq. 3 calculates the surface temperature for a given flight condition at every location except in the stagnation region.

4.4. Topology Optimisation Algorithm

Structural failure occurs once a certain stress level is reached in a material, this is a case of under-design. Conversely, over-design is when low stress levels are present in a material. Ideally the stress in every part of a structure is near the same safe level. The evolutionary technique of this work begins with an over designed structure and slowly removes the unused material until a certain stress level is reached in the structure. The optimisation procedure also checks for material that is over-stressed and adds more material in these regions.

The algorithm used in this article is a hard-kill Bi-directional Evolutionary Structural Optimisation (BESO) method [14]. The algorithm is computationally far more efficient, compared to gradient methods, as the hard-killed elements are not involved in the finite element analysis. Furthermore, elements with intermediate densities, such as those found in soft-kill BESO and SIMP algorithms, may cause the global stiffness matrix to become ill-conditioned, particularly for a nonlinear structure. For these reasons the hard-kill BESO method is preferable, particularly for complex three-dimensional structures.

4.4.1. Sensitivity Number and Filter Schemes

When a continuum structure is discretised the sensitivity numbers can become discontinuous across the element boundaries. This leads to checkerboard patterns in the resulting topologies [15]. A secondary issue in topology optimisation is mesh dependency, this is when different topologies are obtained when using different finite element meshes. To overcome such problems nodal sensitivity numbers are defined by averaging the element sensitivity numbers as follows:

$$\alpha_j^n = \sum_{i=1}^M w_i \alpha_i^e \quad (3)$$

where M denotes the total number of elements connected to the j^{th} node. α_i^e is the element sensitivity number of the i^{th} element, for a fully stressed design the element sensitivities are defined as:

$$\alpha_i^e = \sigma_i^{ym} \quad (4)$$

w_i is the weight factor of the i^{th} element, defined by:

$$w_i = \frac{1}{M-1} \left(1 - \frac{r_{ij}}{\sum_{i=1}^M r_{ij}} \right) \quad (5)$$

where r_{ij} is the distance between the centre of the i^{th} element and the j^{th} node. The nodal sensitivity numbers are then converted into smoothed elemental sensitivity numbers. This is performed by a filter scheme that projects the nodal sensitivity numbers to the design domain. The filter has a length scale r_{min} that does not change with mesh refinement. The purpose of the scale parameter, r_{min} , is to identify the nodes that will influence the sensitivity of the i^{th} element. Where r_{min} must be large enough such that the sub-domain, Ω_i , covers more than one element. Nodes inside the sub-domain Ω_i contribute to the computation of the improved sensitivity number of the i^{th} element as:

$$\alpha_i = \frac{\sum_{j=1}^K w(r_{ij}) \alpha_j^n}{\sum_{j=1}^K w(r_{ij})} \quad (6)$$

where K is the total number of nodes in the sub-domain Ω_i , $w(r_{ij})$ is the linear weight factor defined as:

$$w(r_{ij}) = r_{min} - r_{ij} \quad (j = 1, 2, \dots, K) \quad (7)$$

The filter scheme smoothes the sensitivity numbers in the whole design domain. Therefore, the sensitivity numbers for void elements are automatically obtained. Void elements may have high sensitivity numbers due to high sensitivity numbers of solid elements within the sub-domain Ω_i . Therefore, void elements may be turned into solid elements in the next iterations.

This filter scheme is similar to the mesh-independency filter used by Sigmund and Petersson [16], except that node sensitivities are used in Eq. 10 instead of element sensitivities.

With ESO/BESO methods the sensitivity numbers of solid and void elements are based on discrete design variables of element presence (1) and absence (0). This results in convergence difficulties for the objective function and hence topology. Large oscillations are often observed in the evolution history of the objective function. Huang and Xie [17] found that by averaging the sensitivity number with its historical information is an effective way to solve this problem. The simple averaging scheme is given by:

$$\alpha_i = \frac{\alpha_i^k + \alpha_i^{k-1}}{2} \quad (8)$$

where k is the current iteration number. Therefore, the updated sensitivity number includes the whole history of the sensitivity information in the previous iterations.

4.4.2. Ensuring Connectivity

Aircraft structures usually consist of thin shell structures where the outer surface or skin of the shell is usually supported by longitudinal stiffening members and transverse frames to enable it to resist bending, compressive and torsional loads. The internal structure is a continuous frame structure, such that if the skin were removed the remaining structure would not fall apart. Such structures are known as semi-monocoque. Therefore, to ensure such a structure is output by the optimisation algorithm of this article a original connectivity filter has been developed. The connectivity filter ensures that all internal elements are connected. This is done by passing the internal solid elements through a filter that checks all nodes connected to the solid element are connected to another internal solid element.

4.4.3. Panel Buckling

Another consideration of the optimisation process is panel buckling, a common failure mode for high speed aircraft. Nonuniform stress distributions may result in panel buckling, while still having stress levels below the failure point. To prevent panel buckling a technique employed in the NASA developed structural sizing program HyperSizer[®] [18] is used for the optimisation of the skin.

The critical buckling stress for a plate is calculated by:

$$\sigma_{cr} = \frac{k\pi^2 E}{12(1-\nu^2)} \left(\frac{t}{b}\right)^2 \quad (9)$$

where $k = 4$ for simply supported panels, E is the modulus of elasticity of the plate, ν is the Poisson's ratio, t is the thickness and b is the characteristic length of the plate. The margin of safety of the panel can be calculated by:

$$MS_{buckling} = 1 - \frac{\sigma_{applied}}{\sigma_{cr}} \quad (10)$$

where $\sigma_{applied}$ is the applied buckling stress. For panels with a $MS_{buckling} < 0$ the thickness of the panel is increased. Cross-stiffened panels, see Fig. 2 (right), are used to model the skin of the wing. To reduce the computational space of the optimisation a smearing technique is employed to model the skin and stringers [19]. The smearing technique is employed by updating the thickness of the shells by:

$$t_e = t + h_s w_s \left(\frac{1}{a_s} + \frac{1}{b_s}\right) - \frac{h_s w_s^2}{a_s b_s} \quad (11)$$

where t is the thickness of the skin, t_s is the thickness of the stringers, w_s and h_s are the width and height of the stringers respectively and a_s and b_s are the spacing of the stringers in the chordwise and spanwise direction.

5. Results and Discussion

The LAPCAT A2 wing is optimised for its cruise condition. The aircraft is flying at Mach 5 with a 1° angle of attack, at an altitude of $25km$. Due to the brevity of this article only preliminary results are presented, further results will be shown in the presentation.

5. 1. Aerothermoelastic Coupling

The aerothermoelastic module couples the aerodynamic, thermal and structural module to determine the aerodynamic pressure and heating on the wing (see Section 4). The initial pressure and heat loading on the wing is given in Fig. 3.

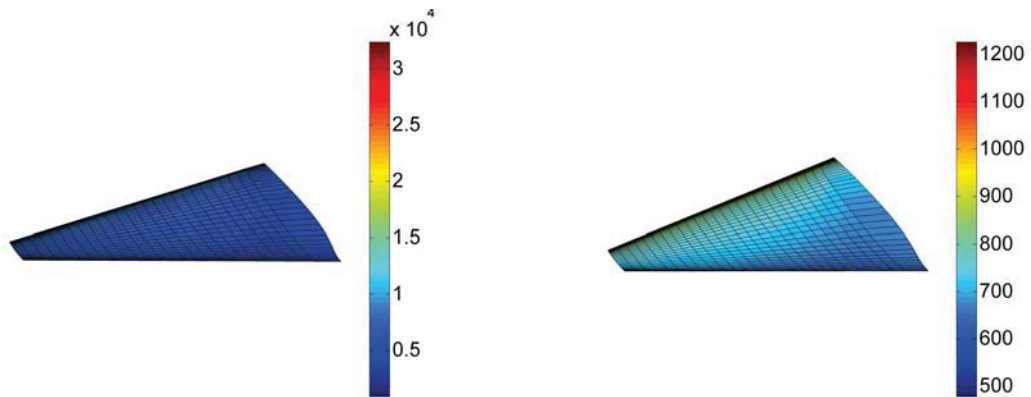


Figure 3: Initial Pressure Loading (left), Initial Thermal Loading (right).

5. 2. Optimisation

The internal structure of the A2 wing has been optimised for the load case defined in Section 5.1. The wing skin is kept unchanged, having a span varying thickness of $6mm$ at the root and $3mm$ at the tip. The internal structure has a constant thickness of $3mm$. The initial and final stress distribution can be seen in Fig. 4.

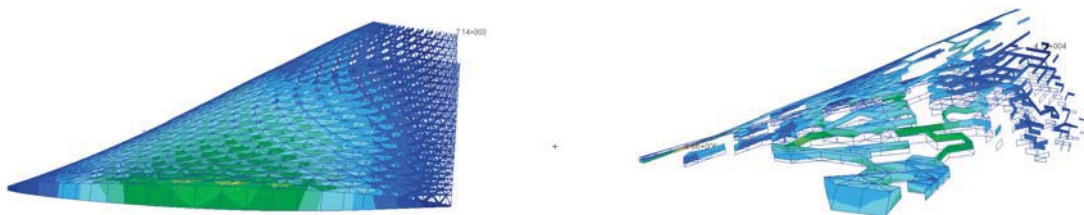


Figure 4: Initial Stress Distribution (left), Final Stress Distribution (right).

The final topology has kept the majority of its structure at the leading edge, since this coincides with the maximum temperature and therefore the region where the material is at its weakest. Furthermore, due to the low aspect ratio of the A2 wing large bending stresses at the root are not present. Therefore the wing is twisted, along the spanwise axis, causing torsion.

6. Conclusion

A novel bi-directional evolutionary optimisation technique with aerothermoelastic coupling has been demonstrated. The strong coupling between the aerodynamic and structural modules and the aerodynamic and thermal modules has been included. The aerodynamic loading is determined using Tranair[®]. The thermal loading is calculated by a novel conjugate method, with an unsteady conduction solver for time integration.

The optimisation algorithm was able to satisfy the weight constraint of $20tons$, without exceeding material limits or causing skin buckling. It was found that the deflections of the wing alter the loadcase significantly, indicating that there is a strong coupling present.

The optimisation algorithm allows multiple preliminary designs to be considered with the aerothermoelastic coupling present. This allows preliminary designs to be considered that have been optimised for a more realistic hypersonic environment.

References

- [1] A. A. Rodriguez, J. J. Dickeson, O. Cifdaloz, A. Kelkar, J. M. Vogel, and D. Soloway. Modeling and control of scramjet-powered hypersonic vehicles: Challenges, trends and tradeoffs. *AIAA Guidance, Navigation and Control Conference and Exhibit, AIAA Paper 2008-6793*, 2008.
- [2] J. J. McNamara and P. P. Friedmann. Aeroelastic and aerothermoelastic analysis of hypersonic vehicles: Current states and future trends. *AIAA Journal*, 2007.
- [3] N. Lamorte and P. P. Friedmann. Hypersonic aeroelastic and aerothermoelastic studies using computational fluid dynamics. *AIAA Journal*, 52:2062–2078, 2014.
- [4] J. Dugundji and J. M. Calligeros. Similarity laws for aerothermoelastic testing. *Journal of the Aerospace Sciences*, 29:935–950, 1962.
- [5] H. A. Eschenauer and N. Olhoff. Topology optimization of continuum structures: A review. *American Society of Mechanical Engineers*, 2001.
- [6] L. Krog, A. Tucker, M. Kemp, and R. Boyd. Topology optimisation of aircraft wing box ribs. *Altair Technology Conference*, 2004.
- [7] K. Maute and G. W. Reich. Integrated multidisciplinary topology optimisation approach to adaptive wing design. *Journal of Aircraft*, 43:253–263, 2006.
- [8] B. Stanford and P. Ifju. Aeroelastic topology optimization of membrane structures for micro air vehicles. *Struc. Multidisc. Optim.*, 38:301–316, 2009.
- [9] B. Stanford and P. Beran. Optimal structural topology of a plate-like wing for subsonic aeroelastic stability. *Journal of Aircraft*, 48:1193–1203, 2011.
- [10] B. Stanford and P. Beran. Aerothermoelastic topology optimization with flutter and buckling metrics. *Structural and Multidisciplinary Optimization*, 48:149–171, 2013.
- [11] R. Varvill and A. Bond. Lapcat ii a2 vehicle structure design specification. Technical report, Long Term Advanced Propulsion Concepts and Technologies II, 2008.
- [12] M. Rodgers. Aerothermoelasticity. *AeroSpace Engineering*, pages 34–43, 1958.
- [13] Boeing Company. *TRANAIR User's Manual*. Boeing Company, 2009.
- [14] X. Huang and Y. M. Xie. *Evolutionary Topology Optimization of Continuum Structures*. John Wiley and Sons, 2010.
- [15] C. S. Jog and R. B. Harber. Stability of finite element models for distributed-parameter optimization and topology design. *Comput. Meth. Appl. Mech. Engng.*, 130:1951–1965, 1996.
- [16] O. Sigmund and J. Petersson. Numerical instabilities in topology optimization: a survey on procedures dealing with checkerboards, mesh-dependencies and local minima. *Struct. Optim.*, 16:68–75, 1998.
- [17] X. Huang and Y. M. Xie. Convergent and mesh-independent solutions for the bidirectional evolutionary structural optimization method. *Finite Elem. and Des.*, 43:1039–1049, 2007.
- [18] M. D. Ardema. Structural sizing for buckling critical body structure of advanced aircraft. *J. Aircraft*, 40:1208–1211, 2003.
- [19] Y. Luan, M. Ohlrich, and F. Jacobsen. Smearing technique for vibration analysis of simply supported cross-stiffened and doubly curved thin rectangular shells. *J. Acoust. Soc. Am.*, 129:707–716, 2011.

Shape Optimization Method of Shell Structures Concerned with Material and Geometrical Nonlinearity

Shintaro Kosaka¹, Masatoshi Shimoda²

¹ Graduate school of engineering Toyota Technological Institute, Hisakata, Tenpaku-ku, Nagoya, Aichi, Japan, sd14409@toyota-ti.ac.jp

² Toyota Technological Institute, Hisakata, Tenpaku-ku, Nagoya, Aichi, Japan, shimoda@toyota-ti.ac.jp

1. Abstract

In this paper, we present a solution to a reaction force control problem of a shell structure based on the free-form optimization method for shells concerned with material nonlinearity and geometrical nonlinearity. The sum of squared error norms subjected to a specified force is minimized under a volume constraint. The shape optimum design problem is formulated as a distributed-parameter system under the assumptions that a shell is varied in the out-of-plane direction to the surface, whereas the thickness is not varied with respect to the shape change. The shape gradient function and the optimal conditions for this problem are theoretically derived using the material derivative method and the Lagrange multiplier method. The derived shape gradients are applied to the H^1 gradient method for shells, which was proposed one of the authors, to determine the optimal shape variation. The optimal shape of shell structures can be obtained without the shape parameterization, while maintaining the surface smoothness. The shape gradient function is calculated by a user sub-program which is developed using the result of non-linear FEM analysis based on a commercial solver. Several numerical examples are presented to verify the validity and practical utility of the proposed methodology and the developed system.

2. Keywords: FEM, Shape Optimization, Shell Structure, Material Nonlinear, Geometrical Nonlinear

3. Introduction

Shell structures have been widely utilized for automobile, train, airplane, architecture structure and so on. For instance, structures for energy absorption sometimes called crash box are attached to the end of an automobile or a train. Suspensions of automobiles are generally required to maximize the reaction force towards to an unexpected load. Moreover, structure dumpers are developed to absorb a seismic energy by the plastic deformation in the design of civil structures or buildings. Material nonlinearity and geometrical nonlinearity should be concerned in these design problem with large deformation and elasto-plasticity.

Some shape optimization methods concerning with material nonlinearity or geometrical nonlinearity have been published. Kaneko et al. [1] implement size optimization concerned with material non-linearity that is not path-dependent toward direct proportion load. And, Ryu et al. [2] showed sensibility analysis method for size optimization concerned with material non-linearity that is not path-dependent by the direct differentiation method. Thus, Ihara et al. [3] proposed a nonparametric design method for the compliance minimization problem concerned with material nonlinearity and the displacement control problem concerned with geometrical nonlinearity. Shintani et al. [4] proposed a solution method based on the H^1 gradient method for the mass minimization problem of 3D suspension parts subjected to the reaction force constraint.

In ours previous research, one of the authors proposed a shape optimization method for design of shell structures, and applied it to a linear stiffness problem and a linear frequency problem. In this work, we aim at developing a shape optimization method concerned with material nonlinearity and geometrical nonlinearity for controlling the reaction forces to equal to target values by applying the free-form optimization method for shells. We formulate the problem as a distributed parameter system, in which the squared error norm of the reaction forces to the target values is minimized under the volume constraint. The optimal shape variation is determined by the H^1 gradient method for shells.

In the following sections, domain variation for free-form design and the governing equation of the shell structure are described. Then, the formulation of the design problem and the derivation of the shape gradient function are presented. After introducing the free-form optimization method in detail, the validity and practical utility of this method are verified through several design examples at last.

4. Governing equation for a shell as a set of infinitesimal flat surfaces

As shown in Fig.1 (a) and (b) and Eqs.(1)-(3), consider that a shell having an initial bounded domain $\Omega \subset \mathbb{R}^3$ (boundary of $\partial\Omega$), mid-area A (boundary of ∂A) and side surface S undergoes domain variation in the

out-of-plane direction to the surface so that its domain, mid-area and side-surface become Ω_s , A_s and S_s , respectively. The notation dA expresses a small area. The subscript s indicates the iteration history of domain variation. It is assumed that the plate thickness h keeps a constant under the domain variation.

$$\Omega = \left\{ (x_1, x_2, x_3) \in \mathbb{R}^3 \mid (x_1, x_2) \in A \subset \mathbb{R}^2, x_3 \in \left(-\frac{h}{2}, \frac{h}{2}\right) \right\}, \quad \Omega = A \times \left(-\frac{h}{2}, \frac{h}{2}\right), \quad S = \partial A \times \left(-\frac{h}{2}, \frac{h}{2}\right) \quad (1)$$

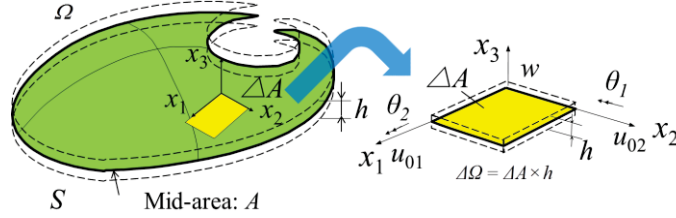


Figure 1: Shell as a set of infinitesimal flat surfaces.

The Mindlin-Reissner plate theory is used for concerning plate bending, whereas coupling of the membrane stiffness and bending stiffness is ignored. The displacement expressed by the local coordinates $\mathbf{u} = \{u_i\}_{i=1,2,3}$ are divided in the in-plane directions $\{u_\alpha\}_{\alpha=1,2}$ and the out-of-plane direction u_3 , given as

$$u_\alpha(x_1, x_2, x_3) = u_{0\alpha}(x_1, x_2) - x_3 \theta_\alpha(x_1, x_2) \quad (2)$$

$$u_3(x_1, x_2, x_3) = w(x_1, x_2) \quad (3)$$

where $\mathbf{u}_0 = \{u_{0\alpha}\}_{\alpha=1,2}$, w and $\boldsymbol{\theta} = \{\theta_\alpha\}_{\alpha=1,2}$ express the in-plane displacement, out-of-plane displacement and rotational angle of the mid-area of the plate, respectively. The tensor subscript notation with respect to $\alpha=1,2$ uses Einstein's summation convention and a partial differential notation for the spatial coordinates $(\cdot)_{,i} = \partial(\cdot)/\partial x_i$.

Then, the weak form of the equilibrium equation for $(\mathbf{u}_0, w, \boldsymbol{\theta}) \in U$ can be expressed as

$$a((\mathbf{u}_0, w, \boldsymbol{\theta}), (\bar{\mathbf{u}}_0, \bar{w}, \bar{\boldsymbol{\theta}})) = l(\bar{\mathbf{u}}_0, \bar{w}, \bar{\boldsymbol{\theta}}) - l_h(\bar{\mathbf{u}}_0, \bar{w}, \bar{\boldsymbol{\theta}}), \quad \forall (\bar{\mathbf{u}}_0, \bar{w}, \bar{\boldsymbol{\theta}}) \in U \quad (4)$$

where $(\bar{\cdot})$ expresses a variation. In addition, the bilinear symmetric form $a(\cdot, \cdot)$ and the linear form $l(\cdot)$ are defined as, respectively.

$$\begin{aligned} & a((\mathbf{u}_0, w, \boldsymbol{\theta}), (\bar{\mathbf{u}}_0, \bar{w}, \bar{\boldsymbol{\theta}})) \\ &= \int_{\Omega} \{S_{\alpha\beta}(u(\mathbf{u}_0, w, \boldsymbol{\theta})) \bar{E}_{\alpha\beta}(\bar{u}(\bar{\mathbf{u}}_0, \bar{w}, \bar{\boldsymbol{\theta}})) + 2S_{\alpha 3}(u(\mathbf{u}_0, w, \boldsymbol{\theta})) \bar{E}_{\alpha 3}(\bar{u}(\bar{\mathbf{u}}_0, \bar{w}, \bar{\boldsymbol{\theta}}))\} dx \end{aligned} \quad (5)$$

$$= \int_{\Omega} [C_{\alpha\beta\gamma\delta}(\mathbf{E}) \{u_{\gamma,\delta} + \frac{1}{2} u_{1,\gamma} u_{1,\delta}\} \{\bar{u}_{\alpha,\beta} + \frac{1}{2} \bar{u}_{1,\alpha} \bar{u}_{1,\beta}\} + C_{\alpha\beta}^S(\mathbf{E}) \{w_{,\beta} - \theta_\beta - u_{\eta,\beta} \theta_\eta\} \{\bar{w}_{,\alpha} - \bar{\theta}_\alpha - \bar{u}_{\eta,\alpha} \bar{\theta}_\eta\}] dx$$

$$l((\bar{\mathbf{u}}_0, \bar{w}, \bar{\boldsymbol{\theta}})) = - \int_A F w dA + \int_{S_g} (N_\alpha u_{0\alpha} + M_\alpha \theta_\alpha - Q w) dS \quad (6)$$

$$\begin{aligned} l_h((\bar{\mathbf{u}}_0, \bar{w}, \bar{\boldsymbol{\theta}})) &= \int_{\Omega} [C_{\alpha\beta\gamma\delta}(\mathbf{E}) \{h_{\gamma,\delta} + \frac{1}{2} (h_{\eta,\gamma} u_{\eta,\delta} + u_{\eta,\gamma} h_{\eta,\delta} + h_{\eta,\gamma} h_{\eta,\delta})\} \{\bar{u}_{\alpha,\beta} + \frac{1}{2} \bar{u}_{1,\alpha} \bar{u}_{1,\beta}\} \\ &\quad + C_{\alpha\beta}^S(\mathbf{E}) \{w_{,\beta}^h - \theta_\beta^h - h_{\eta,\beta} \theta_\eta^h - u_{\eta,\beta} \theta_\eta^h - h_{\eta,\beta} \theta_\eta^h\} \{\bar{w}_{,\alpha} - \bar{\theta}_\alpha - \bar{u}_{\eta,\alpha} \bar{\theta}_\eta\}] dx \end{aligned} \quad (7)$$

where S_{ij} and E_{ij} express the 2nd Piola-Kirchhoff stress and the Green-Lagrange strain tensor, respectively. In order to assume that the enforced displacement is a monotonous increasing function, $\{C_{\alpha\beta\gamma\delta}(\mathbf{E})\}_{\alpha,\beta,\gamma,\delta=1,2}$ and $\{C_{\alpha\beta}^S(\mathbf{E})\}_{\alpha,\beta=1,2}$ express an elastic tensor including bending and membrane components and an elastic tensor with respect to the shear component, which are functions of strain tensor in the total strain theory.

$\mathbf{f} = \{f_\alpha\}_{\alpha=1,2}$, $\mathbf{m} = \{m_\alpha\}_{\alpha=1,2}$ and q express the in-plane load, the out-of-plane bending moment and the out-of-plane load, respectively. $\mathbf{N} = \{N_\alpha\}_{\alpha=1,2}$, $\mathbf{M} = \{M_\alpha\}_{\alpha=1,2}$ and Q express the in-plane load, the bending moment and the shear force, respectively.

The enforced displacement $\mathbf{h} = \{h_i\}_{i=1,2,3}$ is divided into components in the in-plane direction $\{h_\alpha\}_{\alpha=1,2}$ and in the out-of-plane direction h_3 .

$$h_\alpha(x_1, x_2, x_3) = u_{0\alpha}^h(x_1, x_2) - x_3 \theta_\alpha^h(x_1, x_2) \quad (8)$$

$$h_3(x_1, x_2, x_3) = w^h(x_1, x_2) \quad (9)$$

where $\mathbf{u}_0^h = \{u_{0\alpha}^h\}_{\alpha=1,2}$, w^h and $\theta = \{\theta_\alpha^h\}_{\alpha=1,2}$ express the displacement vector in the in-plane direction, the flexure and the rotational angles of the mid-area of the plate, respectively. The subscripts of the Greek letters are expressed as $\alpha, \beta, \gamma, \delta, \eta = 1, 2$.

5. Formulation of the reaction forces control problem

The reaction forces control problem under a volume and the state equation (Eq. (4)) constraints is formulated as a distributed-parameter system. The design variable to be determined is the design velocity field \mathbf{V} .

When the NB control points are considered to a shell, the weak form of the equilibrium on p th control point can be expressed as Eq. (13) to control the reaction forces. $c^{(p)}$ indicates the weighting coefficient for the p th control point in Fig.2.

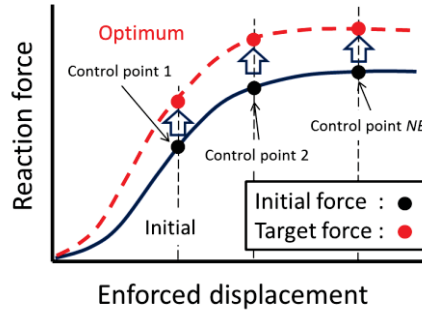


Figure 2: The reaction forces control problem

$$\text{Given } A, \hat{M}, \quad (10)$$

$$\text{Find } V, \quad (11)$$

$$\text{that minimize } \sum_{p=1}^{NB} c^{(p)} [I(\mathbf{r} \cdot \mathbf{T}^{(p)}) - \hat{T}^{(p)}]^2, \quad (12)$$

$$\text{subject to } a((\mathbf{u}_0^{(p)}, \mathbf{w}^{(p)}, \boldsymbol{\theta}^{(p)}), (\bar{\mathbf{u}}_0^{(p)}, \bar{\mathbf{w}}^{(p)}, \bar{\boldsymbol{\theta}}^{(p)})) = l(\bar{\mathbf{u}}_0^{(p)}, \bar{\mathbf{w}}^{(p)}, \bar{\boldsymbol{\theta}}^{(p)}) - l_h(\bar{\mathbf{u}}_0^{(p)}, \bar{\mathbf{w}}^{(p)}, \bar{\boldsymbol{\theta}}^{(p)}), \quad (13)$$

$$\forall (\bar{\mathbf{u}}_0^{(p)}, \bar{\mathbf{w}}^{(p)}, \bar{\boldsymbol{\theta}}^{(p)}) \in U, (\mathbf{u}_0^{(p)}, \mathbf{w}^{(p)}, \boldsymbol{\theta}^{(p)}) \in U, p = 1, \dots, NB$$

$$M (= \int_A h dA) \leq \hat{M} \quad (14)$$

where, $I(\mathbf{r} \cdot \mathbf{T}^{(p)})$ can be expressed as

$$I(\mathbf{r} \cdot \mathbf{T}^{(p)}) = \int_{A_p} r_i T_i^{(p)} dA = \int_{A_p} r_i S_{ij}^{(p)} n_j^{(p)} dA \quad (15)$$

where $\mathbf{r} = \{r_i\}_{i=1,2,3}$ expresses the unit vector of the enforced displacement direction. $\mathbf{T}^{(p)} = \{T_i\}_{i=1,2,3} = S_{ij}^{(p)} n_j^{(p)}$, $n_i^{(p)}$ and $\hat{T}^{(p)}$ express the stress vector, the normal vector to the surface and the target force, respectively. M and \hat{M} denote the volume and its constraint value, respectively. Letting $(\bar{\mathbf{u}}_0, \bar{w}, \bar{\boldsymbol{\theta}})$ and Λ denote the Lagrange multiplier for the state equation and the volume constraint, respectively, the Lagrange functional L associated with this problem can be expressed as

$$\begin{aligned} L = & \sum_{p=1}^{NB} c^{(p)} \left[I(\mathbf{r} \cdot \mathbf{T}^{(p)}) - \hat{T} \right]^2 \\ & + \sum_{p=1}^{NB} \left\{ l(\bar{\mathbf{u}}_0^{(p)}, \bar{w}^{(p)}, \bar{\boldsymbol{\theta}}^{(p)}) - l_h(\bar{\mathbf{u}}_0^{(p)}, \bar{w}^{(p)}, \bar{\boldsymbol{\theta}}^{(p)}) - a\left(\left(\mathbf{u}_0^{(p)}, w^{(p)}, \boldsymbol{\theta}^{(p)}\right), \left(\bar{\mathbf{u}}_0^{(p)}, \bar{w}^{(p)}, \bar{\boldsymbol{\theta}}^{(p)}\right)\right) \right\} \\ & + \Lambda (M - \hat{M}) \end{aligned} \quad (16)$$

For the sake of simplicity here, it is assumed that on the sub-boundaries, the non-zero boundary forces \mathbf{N} , \mathbf{Q} and \mathbf{M} and the surface forces \mathbf{f} , \mathbf{m} and q , do not vary with regard to the space (i.e., $\mathbf{f}' = \mathbf{m}' = q' = 0$). Then, using the design velocity field \mathbf{V} , the derivative \dot{L} of the domain variation of the Lagrange functional L can be expressed as

$$\begin{aligned} \dot{L} = & \sum_{p=1}^{NB} \left\{ c^{(p)} 2 \left[I(\mathbf{r} \cdot \mathbf{T}^{(p)}) - \hat{T}^{(p)} \right] I(\mathbf{r} \cdot \mathbf{T}'^{(p)}) - a\left(\left(\mathbf{u}_0'^{(p)}, w'^{(p)}, \boldsymbol{\theta}'^{(p)}\right), \left(\bar{\mathbf{u}}_0^{(p)}, \bar{w}^{(p)}, \bar{\boldsymbol{\theta}}^{(p)}\right)\right) \right\} \\ & + \sum_{p=1}^{NB} \left\{ l\left(\bar{\mathbf{u}}_0'^{(p)}, \bar{w}'^{(p)}, \bar{\boldsymbol{\theta}}'^{(p)}\right) - a\left(\left(\mathbf{u}_0^{(p)}, w^{(p)}, \boldsymbol{\theta}^{(p)}\right), \left(\bar{\mathbf{u}}_0'^{(p)}, \bar{w}'^{(p)}, \bar{\boldsymbol{\theta}}'^{(p)}\right)\right) - l_h\left(\bar{\mathbf{u}}_0'^{(p)}, \bar{w}'^{(p)}, \bar{\boldsymbol{\theta}}'^{(p)}\right) \right\} \\ & + \dot{\Lambda} (M - \hat{M}) + \langle \mathbf{G}\mathbf{n}, \mathbf{V} \rangle, \end{aligned} \quad (17)$$

where $\langle \mathbf{G}\mathbf{n}, \mathbf{V} \rangle = \int_A \mathbf{G}\mathbf{n} \cdot \mathbf{V} dA = \int_A G V_n dA$.

$$\begin{aligned} \mathbf{G} = & \sum_{p=1}^{NB} c^{(p)} (C_{\alpha\beta\gamma\delta}^B(\mathbf{E}^{(p)})) \\ & \times \left[(u_{0\gamma,\delta}^{(p)} - \frac{h}{2} \theta_{\gamma,\delta}^{(p)}) + \frac{1}{2} \{ (u_{0\eta,\gamma}^{(p)} - \frac{h}{2} \theta_{\eta,\gamma}^{(p)}) (u_{0\eta,\delta}^{(p)} - \frac{h}{2} \theta_{\eta,\delta}^{(p)}) + w_{,\gamma}^{(p)} w_{,\delta}^{(p)} \} \right] \\ & \times \left[(\bar{u}_{0\alpha,\beta}^{(p)} - \frac{h}{2} \bar{\theta}_{\alpha,\beta}^{(p)}) + \frac{1}{2} \{ (\bar{u}_{0\eta,\alpha}^{(p)} - \frac{h}{2} \bar{\theta}_{\eta,\alpha}^{(p)}) (\bar{u}_{0\eta,\beta}^{(p)} - \frac{h}{2} \bar{\theta}_{\eta,\beta}^{(p)}) + \bar{w}_{,\alpha}^{(p)} \bar{w}_{,\beta}^{(p)} \} \right] \\ & - C_{\alpha\beta\gamma\delta}^B(\mathbf{E}^{(p)}) \left[(u_{0\gamma,\delta}^{(p)} + \frac{h}{2} \theta_{\gamma,\delta}^{(p)}) + \frac{1}{2} \{ (u_{0\eta,\gamma}^{(p)} + \frac{h}{2} \theta_{\eta,\gamma}^{(p)}) (u_{0\eta,\delta}^{(p)} + \frac{h}{2} \theta_{\eta,\delta}^{(p)}) + w_{,\gamma}^{(p)} w_{,\delta}^{(p)} \} \right] \\ & \times \left[(\bar{u}_{0\alpha,\beta}^{(p)} + \frac{h}{2} \bar{\theta}_{\alpha,\beta}^{(p)}) + \frac{1}{2} \{ (\bar{u}_{0\eta,\alpha}^{(p)} - \frac{h}{2} \bar{\theta}_{\eta,\alpha}^{(p)}) (\bar{u}_{0\eta,\beta}^{(p)} - \frac{h}{2} \bar{\theta}_{\eta,\beta}^{(p)}) + \bar{w}_{,\alpha}^{(p)} \bar{w}_{,\beta}^{(p)} \} \right] \\ & - F^{(p)} (w_{,i}^{(p)} + \bar{w}_{,i}^{(p)}) n_i + \left\{ -F^{(p)} (w^{(p)} + \bar{w}^{(p)}) + \Lambda h \right\} H \end{aligned} \quad (18)$$

where $V_n = V_i n_i$ and $(\cdot)'$ expresses a shape derivative. H denotes twice the mean curvature of the mid-area. C_\circ is the suitably smooth function space that satisfies the constraints of the domain variation. The notations \mathbf{n}^{top} and \mathbf{n}^{bm} denote unit outward normal vectors at the top surface and the bottom surface, respectively, and a unit normal vector at the mid-area $\mathbf{n}^{mid} (\equiv \mathbf{n}) = \mathbf{n}^{top} = -\mathbf{n}^{bm}$ is assumed by Shimoda et al. [5].

The optimality conditions of the Lagrange functional L with respect to the state variables $(\mathbf{u}_0, w, \boldsymbol{\theta})$, the adjoint variables $(\bar{\mathbf{u}}_0, \bar{w}, \bar{\boldsymbol{\theta}})$ and Λ are expressed as

$$a\left(\left(\mathbf{u}_0^{(p)}, w^{(p)}, \boldsymbol{\theta}^{(p)}\right), \left(\bar{\mathbf{u}}_0'^{(p)}, \bar{w}'^{(p)}, \bar{\boldsymbol{\theta}}'^{(p)}\right)\right) = l\left(\bar{\mathbf{u}}_0'^{(p)}, \bar{w}'^{(p)}, \bar{\boldsymbol{\theta}}'^{(p)}\right) - l_h\left(\bar{\mathbf{u}}_0'^{(p)}, \bar{w}'^{(p)}, \bar{\boldsymbol{\theta}}'^{(p)}\right), \quad (19)$$

$$\left(\mathbf{u}_0^{(p)}, w^{(p)}, \boldsymbol{\theta}^{(p)}\right) \in U, \quad \forall \left(\bar{\mathbf{u}}_0'^{(p)}, \bar{w}'^{(p)}, \bar{\boldsymbol{\theta}}'^{(p)}\right) \in U, \quad p = 1, \dots, NB$$

$$a\left(\left(\mathbf{u}_0'^{(p)}, w'^{(p)}, \boldsymbol{\theta}'^{(p)}\right), \left(\bar{\mathbf{u}}_0^{(p)}, \bar{w}^{(p)}, \bar{\boldsymbol{\theta}}^{(p)}\right)\right) = c^{(p)} 2 \left[I(\mathbf{r} \cdot \mathbf{T}^{(p)}) - \hat{T}^{(p)} \right] I(\mathbf{r} \cdot \mathbf{T}^{(p)}), \quad (20)$$

$$\left(\bar{\mathbf{u}}_0^{(p)}, \bar{w}^{(p)}, \bar{\boldsymbol{\theta}}^{(p)}\right) \in U, \quad \forall \left(\mathbf{u}_0'^{(p)}, w'^{(p)}, \boldsymbol{\theta}'^{(p)}\right) \in U, \quad p = 1, \dots, NB$$

$$\dot{\Lambda}(M - \hat{M}) = 0, \quad \dot{\Lambda} \geq 0, \quad M - \hat{M} \leq 0. \quad (21)$$

where Eqs. (19) and (20) express the state equation for $(\mathbf{u}_0, w, \boldsymbol{\theta})$ and the adjoint equation for $(\bar{\mathbf{u}}_0, \bar{w}, \bar{\boldsymbol{\theta}})$, respectively. Eq. (21) denotes the governing equations for the volume constraint.

Substituting $(\mathbf{u}_0, w, \boldsymbol{\theta})$, $(\bar{\mathbf{u}}_0, \bar{w}, \bar{\boldsymbol{\theta}})$ and Λ determined by these equations into Eq. (17), the material derivative \dot{L} can be expressed as

$$\dot{L} = \langle G\mathbf{n}, \mathbf{V} \rangle \equiv \int_A G_i V_i d\Gamma \quad (22)$$

where coefficient function G_i expresses the shape gradient function, which is used in H^1 gradient method for shells.

6. H^1 gradient method for shells

The original traction method was proposed by Azegami in 1994 and developed for free-form shell optimization by Shimoda et al. [5]. It is a node-based shape optimization method that treats all nodes as design variables and does not require any design variable parameterization. The shape gradient function is not used directly while replaced by a distributed force to vary the shape. The governing equation is expressed by Eq. (23). α is introduced to control influence range of the shape gradient function.

$$\alpha \langle (\mathbf{V}_{0\alpha}, V_3, \boldsymbol{\theta}), (\bar{\mathbf{u}}_0, \bar{w}, \bar{\boldsymbol{\theta}}) \rangle + \alpha \langle (\mathbf{V} \cdot \mathbf{n})\mathbf{n}, (\bar{\mathbf{u}}_0, \bar{w}, \bar{\boldsymbol{\theta}}) \rangle = - \langle G\mathbf{n}, (\bar{\mathbf{u}}_0, \bar{w}, \bar{\boldsymbol{\theta}}) \rangle \quad (23)$$

$$(\mathbf{V}_{0\alpha}, V_3, \boldsymbol{\theta}) \in C_\Theta, \quad \forall (\bar{\mathbf{u}}_0, \bar{w}, \bar{\boldsymbol{\theta}}) \in C_\Theta$$

7. Result of numerical analysis

FE model consists of constant strain triangle elements. Initial barrel-shaped model is shown in Fig.3. The enforced displacement by 1mm is applied at the right edge in the positive X direction and the left edge is clamped in the state and adjoint analyses. The objective is to control the reaction force to 5000N at the enforced displacement 1mm. And, the volume constraint is set as 1.01 times of initial shape. Both edges of the barrel-shaped model are clamped in the velocity analysis.

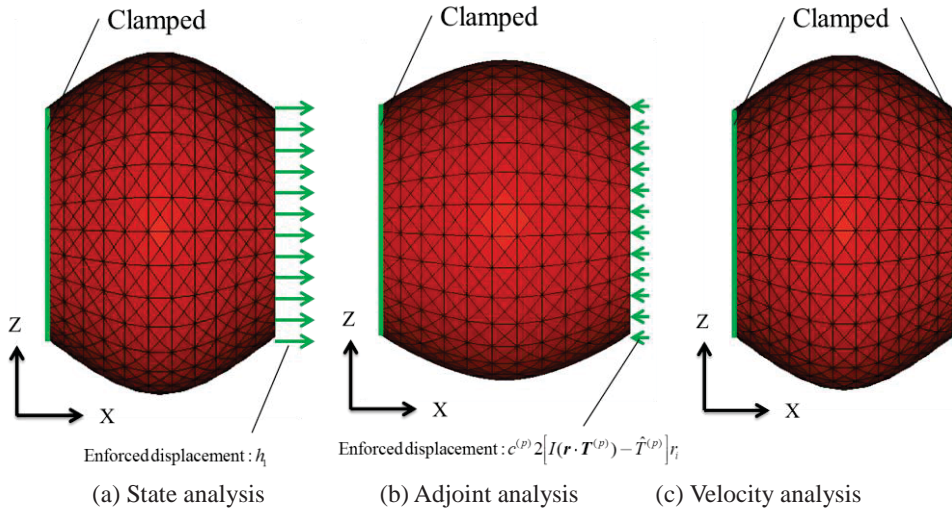


Figure 3: Boundary conditions

Fig.4 shows the iteration histories of objective and volume (a), and reaction force (b). It is clear that the reaction force is equal to 5000N at the enforced displacement 1mm. Fig.5 (a) shows the optimized shape at the 100th iteration and (b) shows the reaction force-enforced displacement curves. It is confirmed that the reaction force changes from 6481N to 5000N at the enforced displacement 1mm. Curvature of the middle part of barrel becomes bigger that owns lower stiffness, at which are valid results.

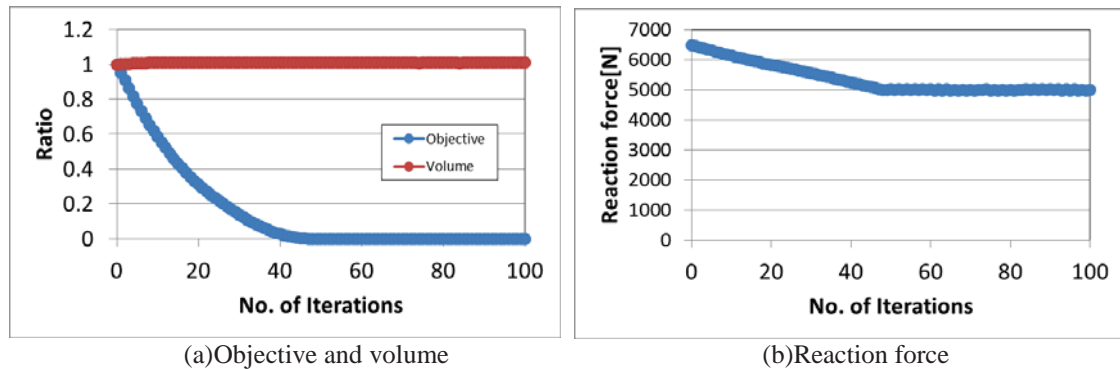


Figure 4: Iteration histories

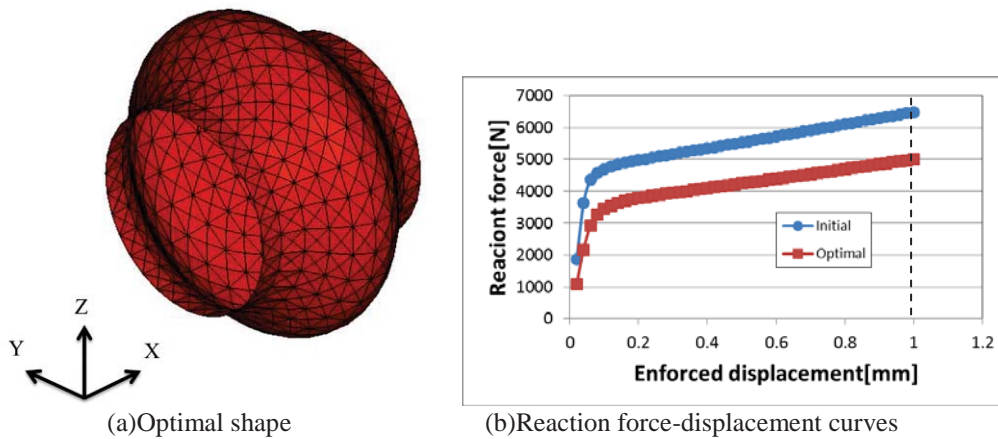


Figure 5: Optimization results

8. Conclusion

We presented a solution to a reaction force control problem of a shell structure based on the free-form optimization method for shells concerned with material nonlinearity and geometrical nonlinearity. With this method, the smooth out-of-plane domain variations for controlling the reaction forces to target values can be obtained. The results of a barrel-shaped model showed that the smooth optimal free-form shape and stable convergence histories were obtained.

With this method, it is easy to obtain the smooth optimal free-form shapes of shell structures without any shape design parameterization, and to control the reaction forces to target values.

9. References

- [1] I. Kaneko and G. Maier, Optimum design of plastic structures under displacement constraint, *Computer methods in applied mechanics and engineering*, 27, 369-391, 1981.
- [2] Y.S. Ryu, M. Hariman, C.C. Wu and J.S. Arora, Structural design sensitivity analysis of nonlinear response, *Computers & Structures*, 21, 245-255, 1985.
- [3] H. Ihara, H. Azegami, M. Shimoda and K. Watanabe, Solution to Shape Optimization Problem Considering Material Nonlinearity, *Transactions of the JSME, Series A*, 66(646), 1111-1118, 2000. (in Japanese)
- [4] K. Shintani, T. Nagatani, S. Ito and H. Azegami, Examination of Shape Optimization for the Nonlinear Buckling Phenomenon of Suspension Parts, *Transactions of the JSME, Series A*, 77(780), 1187-1198, 2011. (in Japanese)
- [5] M. Shimoda, Free-Form Optimization Method for Shell Structures, *Transactions of the JSME, Series A*, 79(797), 60-73, 2013. (in Japanese)

A Sensitivity-based Coordination Method for Optimization of Product Families

Jun Zou¹, Wei-Xing Yao², Jun-Feng Zheng³

¹ Nanjing University of Aeronautics and Astronautics, Nanjing, China, sc.zoujun@gmail.com

² Nanjing University of Aeronautics and Astronautics, Nanjing, China, wxyao@nuaa.edu.cn

³ Nanjing University of Aeronautics and Astronautics, Nanjing, China, zjfbest@nuaa.edu.cn

1. Abstract

This article discusses the bi-level decomposition approach for the optimization of product families with predefined platforms, and the challenge lies in providing an optimal compromise between the competing needs of all family members. To improve the efficiency of the optimization process, a new sensitivity-based coordination method (SCM) is proposed. The key idea in this approach is that the system coordinator not only provides consistent shared variables, but also makes tradeoff between all the products by using of sensitivity information. The coordinated shared variables are determined by minimizing performance deviation with respect to the optimal solution of subproblems and constraints violation. Each subproblem owns a significant degree of independence and can be solved in a simultaneous way. The numerical performance of the proposed method is investigated, and the results suggest that the new approach is robust and leads to a substantial reduction in computational effort compared with analytical target cascading (ATC) method. Then the proposed methodology is successfully applied to the structural optimization problem of wing structures for an unmanned aircraft family, which is more complicated and related to practical implementation issues.

2. Keywords: product family optimization; bi-level decomposition; sensitivity; system coordination; structural optimization

3. Introduction

Due to the highly competitive global marketplace, the contradiction between product variety and development and production costs is prominent. Under this backdrop, the product family design has received considerable attention from both industry [1] and academia [2, 3] in recent years.

In general terms, a product family is a group of related products that share a collection of the common elements, which called product platform, to satisfy a variety of market niches [4]. The core technology of product family design is product platform. Meyer and Lehnerd [5] defined the product platform as the set of parts, interfaces, and manufacturing processes that are shared among a set of products and allow the development of derivative products with cost and time savings. Jiao *et al.* [6] and Simpson *et al.* [7, 8] summarized the relevant terminology and applications in detail, respectively.

The challenge when optimizing a family of products with predefined platforms lies in providing an optimal compromise between the competing needs of all family members [9]. The product family problem can be solved by one-stage or multi-stage approach. When a product family problem is relatively small, the one-stage approach is preferred, as it can yield the best overall performance of the product family because the optimization is not partitioned into two or more stages [10]. The dimensionality of one-stage optimization problems is, however, considerably higher than in multi-stage approaches and often leads to computational difficulties. While for the decomposition-based multi-stage approach, in which the family design problem is partitioned into smaller subproblems, the complexity increases only linearly with the number of individual products and is more suitable for design of large and complex product families [11].

This article discusses the multi-stage approach for the optimization of product families with predefined platforms. Fellini *et al.* [12] pointed out that developing a rigorous global coordination strategy is necessary to increase the efficiency and robustness for product family design. Simpson *et al.* [13] adopted a two-stage approach that the product platform is designed during the first stage of the optimization, followed by instantiation of the individual products during the second stage. Allison *et al.* [14] decomposed the family design problem by individual variant, and the shared variables were coordinated at system level. Then he applied two decomposition-based method, collaborative optimization (CO) and ATC, to the aircraft family problem.

Some scholars have proposed some new methods to improve the computation efficiency of product family optimization. Kokkolaras *et al.* [15] presented an extended ATC methodology for product family problem. The ATC formulation for a single product was extended to a family of products to accommodate the presence of a shared product platform and local design targets. Roth and Kroo [16] presented a distributed optimization based on CO and ATC, named Enhanced Collaborative Optimization (ECO). The system level optimum is simply the average of the responses returned from the subspaces, and subspace's constraint set includes local constraints

and models of constraints from other subspaces. Öman and Nilsson [17] presented a multi-stage method named Critical Constraint Method (CCM) for structural optimization of product family problem, in which the problem reduction is performed by only considering the constraints that are critical in the optimal solution.

To improve the efficiency of the system coordinator and reduce the number of iterations needed for convergence, in this article a new SCM method is proposed. The key idea in this approach is that the system coordinator not only provides consistent shared variables, but also makes tradeoff between all individual products by using of sensitivity information to evaluate the performance deviation and constraint violation resulting from sharing. The new algorithm is described and tested by a numerical test case and a family of aircraft wing structures design example in this paper.

4. Problem formulation

The family design problem with predefined platforms is formulated as:

$$\begin{aligned} & \text{find } (\mathbf{x}_s, \mathbf{x}_{li}) \\ & \text{min } F(f_1(\mathbf{x}_s, \mathbf{x}_{l1}), \dots, f_n(\mathbf{x}_s, \mathbf{x}_{ln})) \\ & \text{s.t. } \mathbf{g}_i(\mathbf{x}_s, \mathbf{x}_{li}) \leq \mathbf{0} \quad (i = 1, 2, \dots, n) \end{aligned} \quad (1)$$

where \mathbf{x}_s is the vector of shared variables, which are the design variables of platform and shared between all the family members. \mathbf{x}_{li} is the vector of individual local variables for i th product. $f_i(\mathbf{x}_s, \mathbf{x}_{li})$ and $\mathbf{g}_i(\mathbf{x})$ is the design objective and set of constraints for i th product respectively. F is the design objective of the whole product family, which is the function of $f_i(\mathbf{x}_s, \mathbf{x}_{li})$. The product family includes n product variants.

5. Sensitivity-based coordination method

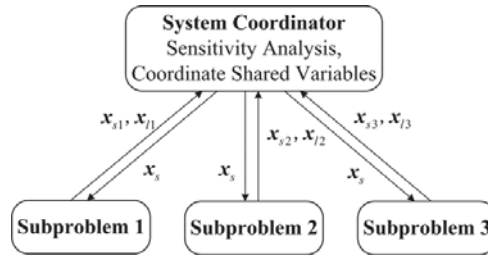


Figure 1: Schematic illustration of SCM

The basic idea of the new method is to provide an efficient system coordinator, so that the optimization process can converge with less number of iterations. This is done by decomposing the family problem into several subproblems and one system coordinator. Each subproblem is responsible for specifying the variables for one family member, and the task of the system level is to coordinate the different design of shared variables obtained from subproblems based on sensitivity information. The proposed SCM to solve the product family optimization problem defined in Eq. (1) is illustrated in Figure 1 and is here described in detail below.

5.1. System coordinator

The objective of system level is to ensure that all subsystems use the same values of shared variables \mathbf{x}_s . As each subsystem has very limited knowledge of the status and preferences of the other subsystems, a system coordinator with global sense will greatly improve the optimization efficiency. In general, sharing may cause deviations from the individually optimized design of subsystems, and inapposite consistency coordination may lead to infeasible design or large performance loss for the product variants [18]. The optimal value of coordinated shared variables \mathbf{x}_s is determined by minimizing the performance deviation with respect to the optimal solution of subproblems while remaining in feasible space.

Formally, the system level is defined as:

$$\begin{aligned} & \text{find } \mathbf{x}_s \\ & \text{min } \sum_{i=1}^n |F^{i,*} - F^{i,o}| + \sum_{i=1}^n \sum_{g_{ij} \in \mathbf{g}_i} \max(g_{ij}^*, 0) \end{aligned} \quad (2)$$

where $F^{i,o}$ corresponds to the value of F obtained from the solution of i th subproblem, as described in next part, while $F^{i,*}$ and g_{ij}^* ($g_{ij} \in \mathbf{g}_i$) is the value of F and constraint evaluated at a consistent shared variables \mathbf{x}_s .

It can be seen that the system level is an unconstrained minimization problem. A first order Taylor series approximation is introduced to evaluate the value of performance deviation and constraints. That is:

$$\begin{aligned}
F^{i,*} &\approx (\nabla F^{si,o})^T (\mathbf{x}_s - \mathbf{x}_{si}^o) + F^{i,o}(\mathbf{x}_{si}^o, \mathbf{x}_{li}^o) \\
\mathbf{g}_{ij}^* &\approx (\nabla \mathbf{g}_{ij}^{si,o})^T (\mathbf{x}_s - \mathbf{x}_{is}^o) + \mathbf{g}_{ij}^o(\mathbf{x}_{si}^o, \mathbf{x}_{li}^o)
\end{aligned} \tag{3}$$

where \mathbf{x}_s is the vector of shared variables after coordination, and $(\mathbf{x}_{si}^o, \mathbf{x}_{li}^o)$ is the optimal solution of i th subproblem. $\nabla F^{si,o}$ and $\nabla \mathbf{g}_{ij}^{si,o}$ is the gradient of F and \mathbf{g}_{ij} evaluated at the optimal design point of subproblem i . It easily to find out that the values of shared variables \mathbf{x}_s attempt to be closer to the solution of the subproblem that objective F and constraints are more sensitive to the change of shared variables.

5.2. Subproblem optimization

Each subspace optimization problem is responsible for the design of one individual product variant, which includes both shared variables \mathbf{x}_{si} and individual variables \mathbf{x}_{li} . The formulation of subsystem problem, as illustrated for the i th subproblem, is shown as follows:

$$\begin{aligned}
&\text{find } (\mathbf{x}_{si}, \mathbf{x}_{li}) \\
&\min F(f_1, \dots, f_i(\mathbf{x}_{si}, \mathbf{x}_{li}), \dots, f_n) + \|\mathbf{w}_i \circ (\mathbf{x}_s - \mathbf{x}_{si})\|_2^2 \\
&\text{s.t. } \mathbf{g}_i(\mathbf{x}_{si}, \mathbf{x}_{li}) \leq \mathbf{0}
\end{aligned} \tag{4}$$

where \mathbf{w}_i is the vector of penalty weights. The symbol \circ is used to indicate term-by-term multiplication of vectors. The sequence of \mathbf{w} is nondecreasing to guide the optimization process to convergence.

The system coordinator provides targets for shared variables \mathbf{x}_s and the objective value f_j ($j \neq i$) at the optimal solution of the other subproblems, which are treated as parameters. The objective of subproblem is a combination of the product family objective and a compatibility term.

5.3. Stopping criteria

The optimization is stopped based on two conditions: The change of the objective value and inconsistency of shared variables have to be smaller than defined corresponding critical values.

$$\left| \frac{F^{(k)} - F^{(k-1)}}{F^{(k-1)}} \right| \leq \varepsilon_F \quad \text{AND} \quad \max(\|\mathbf{x}_s - \mathbf{x}_{is}\|_2, i=1, \dots, n) \leq \varepsilon_x \tag{5}$$

where F is the value of objective function at the optimal point of subproblem optimizations, and ε_F is the corresponding stop criterion. \mathbf{x}_{is} refers to the optimal solution of shared variables at subproblem i , and \mathbf{x}_s refers to the vector of shared variables input from the system coordinator and ε_x is the corresponding stop criterion.

6. Numerical test

In this section, the numerical behaviour of the SCM is investigated through an analytic test problem. Results are compared with those obtained via the ATC approach. The test problem is Golinski's speed reducer problem [19]. The reason for selecting this problem is that each subsystem involves only local and global shared variables, and the global objective is a function of the objectives of each subsystem, which are the same as the formulation of product family problem defined in Eq. (1).

According to the design problem defined in [19], the weight, or local objective, of the gear subsystem is $f_1 = F_1$, and its local constraints are $\mathbf{g}_1 = \mathbf{g}_{\text{gear}}$. The weights for shaft 1 and 2 subsystem are $f_2 = F_2 + F_4 + F_6$ and $f_3 = F_3 + F_5 + F_7$, respectively. Similarly, the local constraints are $\mathbf{g}_2 = \mathbf{g}_{\text{shaft, 1}}$ for shaft 1 and $\mathbf{g}_3 = \mathbf{g}_{\text{shaft, 2}}$ for shaft 2. The optimal result of the original all-in-one problem is $F(\mathbf{z})=2994$ (rounded) [20].

6.1. Solve via ATC

The original design problem is decomposed into a two-level ATC formulation with three subproblems. The problem decomposition is shown below:

$$\begin{array}{ll}
\text{System Problem:} & \begin{aligned} &\text{find } \mathbf{x}_s = [x_1, x_2, x_3]^T \\ &\min f = F + \pi(\mathbf{c}) \\ &\text{s.t. No Constraints} \end{aligned} \\
& \text{where } \mathbf{c} = [\mathbf{x}_s; \mathbf{x}_s; \mathbf{x}_s] - [\mathbf{x}_{s1}; \mathbf{x}_{s2}; \mathbf{x}_{s3}] \\
& \text{Subproblem 1:} & \begin{aligned} &\text{find } \mathbf{x}_{s1} = [x_1^{(1)}, x_2^{(1)}, x_3^{(1)}]^T \\ &\min f_1 = F_1 + \pi(\mathbf{c}) \\ &\text{s.t. } \mathbf{g}_1 = \mathbf{g}_{\text{gear}} \leq \mathbf{0} \end{aligned} \\
& & \text{where } \mathbf{c} = \mathbf{x}_s - \mathbf{x}_{s1}
\end{array} \tag{6}$$

where the bracketed top-right index denotes the subsystem at which the shared variable copy is computed, and $\pi(\mathbf{c})$ is the penalty function with a quadratic form, that is $\pi(\mathbf{c}) = \|\mathbf{w} \circ \mathbf{c}\|_2^2$. The formulation of subproblem 2 and

3 are similar, thus the vector of shared variables is $\mathbf{x}_s = [x_1, x_2, x_3]^T$. Termination tolerances are set to $\varepsilon_F = 0.03\%$ and $\varepsilon_x = 0.01$. For all experiments, initial penalty parameters are $\mathbf{w}^{(1)} = \mathbf{0.1}$ and $\beta = 2$.

6.2. Solve via SCM

SCM uses the same problem decomposition strategy, yielding a system level problem and three subproblems. It is not difficult to find that the formulations of the three subproblems are exactly the same as the ATC method, while only the system level differs. This can be helpful for us to compare the efficiency of the system levels. The termination tolerances and initial penalty parameters are the same as that in the ATC method.

Convergence is achieved for the same four different starting points, which are shown in the Table 1. It can be seen that for the SCM, the convergence requires an average of 1226.5 function evaluations, which highlights an average computational saving about 25% over the ATC method. In addition, all the objective values converge to the global optimum, which are better and more stable compared with ATC approach. In summary, SCM robustly and efficiently solves this test problem.

Table 1: Solutions via ATC and SCM

Starting Point	Optimum Objective		System Iterations		Function Evaluations	
	ATC	SCM	ATC	SCM	ATC	SCM
$z=[3.10,0.75,21.50,7.80,7.80,3.40,5.25]^T$	2996	2994	25	17	1638	1268
$z=[2.60,0.70,17.00,7.30,7.30,2.90,5.00]^T$	2995	2994	25	17	1636	1192
$z=[3.60,0.80,28.00,8.30,8.30,3.90,5.50]^T$	2996	2994	25	17	1644	1253
$z=[3.60,0.80,17.00,7.30,8.30,2.90,5.00]^T$	2995	2994	25	17	1623	1193

7. Wing structures family

The second problem describes the approach for optimization of wing structures for an unmanned aircraft family with reconfigurable wing component, which is more complicated and related to practical implementation issues. The aircraft family consists of two variants, A and B, with different aspect ratio. Aircraft A mainly performs the dash mission with a low aspect ratio wing, while aircraft B mainly performs the surveillance mission with a high aspect ratio wing. The wing structure of aircraft A is adopted by aircraft B as inner wing section, which means it is a shared component in the aircraft family. The mission requirements and reference wing properties are summarized in Table 2 and Figure 2(a).

Table 2: Aircraft design parameters

Parameter	Aircraft A	Aircraft B
Maximum takeoff weight [kg]	3000	3000
Cruise altitude [m]	7000	12000
Cruise speed [Mach]	0.8	0.23
Wing span [m]	6.52	16.8
Leading edge sweep [deg.]	20	20
Aspect ratio	4	12
Max load factor [G]	12	2.5

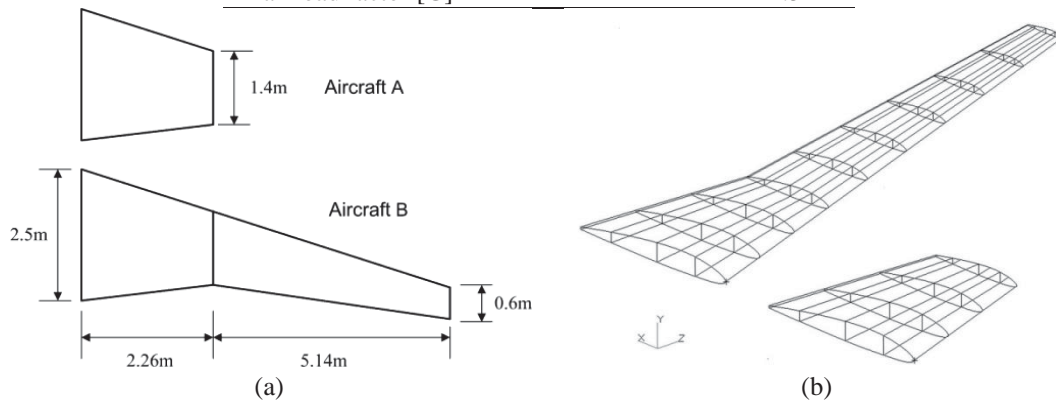


Figure 2: Planform and finite element models of the two aircraft wings

The wing structures are modeled consisting of spars, ribs, and skin panels, as showed in Figure 2(b). The skin panels, spar webs and the ribs are modeled as shear panels, and the spar caps as rod elements. All these elements can be designed, whereas the leading edge, trailing edge and ribs are not designed. The goal of the wing

structural optimization problem is to minimize the weight of the wing structure subject to stress and deflection constraints. The shape function linking method is adopted to reduce the number of design variables, and the value of linear function at a certain location determines the value of the property of that specific element. To simplify the computation, the span-wise distribution of the air load is based on Schrenk load distribution.

The upper and lower skin of wing box is subdivided into 2 regions by the spars, respectively. As the wing A is shared as the inner wing section of wing B, the shape function of wing B uses two independent linear functions to determine the size of each component, thus each component's shape function is determined by the property of elements at four locations, which means that there are 4 design variables for each component. As we can see from Table 3, there are 40 design variables in total for wing B, in which the Location 1 refers to wing root, Location 2 and 3 refer to the separation surface, and Location 4 located at wing tip. While for wing A, only the design variables at Location 1 and 2 are included, that is 20 variables in total. The individual optimal design problem for wing structure A and B is formulated as:

$$\begin{aligned}
 & \text{find } \mathbf{x}_A && \text{find } \mathbf{x}_B \\
 & \min m_A(\mathbf{x}_A) && \min m_B(\mathbf{x}_B) \\
 \text{A: s.t. } & \sigma_{\max} \leq 222 \text{ MPa} & \text{B: s.t. } & \sigma_{\max} \leq 267 \text{ MPa} \\
 & \sigma_{\min} \geq -167 \text{ MPa} & & \sigma_{\min} \geq -200 \text{ MPa} \\
 & \delta \leq 226 \text{ mm} & & \delta \leq 840 \text{ mm}
 \end{aligned} \tag{7}$$

where m is the weight of wing, and $\mathbf{x}_A = [x_{1A}, \dots, x_{20A}]^T$ and $\mathbf{x}_B = [x_{1B}, \dots, x_{40B}]^T$. σ_{\max} and σ_{\min} are the maximum tensile and minimum compression stresses, respectively. δ is the maximum deflection at wing tip. It is assumed that the structures are manufactured from aluminum with a density of 2.7 g/cm^3 and an elasticity modulus of $7.0 \times 10^4 \text{ MPa}$. The optima of individual design for wing A and B are 43.89 kg and 92.28 kg, respectively. The objective for the wing structures family is defined as the sum of normalized weight, that is:

$$F = m_A(\mathbf{x}_A)/43.89 + m_B(\mathbf{x}_B)/92.28 \tag{8}$$

As mentioned above, the vector of shared variables can be denoted as $\mathbf{x}_s = [x_{1A} \dots x_{20A}]^T = [x_{1B} \dots x_{20B}]^T$. Wing A has no individual variables, and the individual variables for wing B are $\mathbf{x}_{IB} = [x_{20B} \dots x_{40B}]^T$.

Implement the proposed methodology to solve this design problem. The optimization converged after 11 iterations with a value of 2.219. The design results are presented in Table 3.

Table 3: Wing structures design results of aircraft family

Components	Location & Variable Values					
	Wing Structure A		Wing Structure B			
	1	2	1	2	3	4
Front spar [mm ²]	171.68	135.40	171.68	135.40	148.50	50.00
Internal spar [mm ²]	198.77	122.69	198.77	122.69	121.37	50.00
Rear spar [mm ²]	71.79	56.57	71.79	56.57	50.00	50.00
Front upper skin [mm]	3.84	2.51	3.84	2.51	2.79	0.55
Front lower skin [mm]	2.37	2.44	2.37	2.44	3.00	0.50
Rear upper skin [mm]	3.10	1.75	3.1	1.75	2.30	0.50
Rear lower skin [mm]	2.06	0.83	2.06	0.83	1.59	0.50
Front web [mm]	1.92	1.09	1.92	1.09	1.00	1.00
Internal web [mm]	1.22	2.00	1.22	2.00	1.00	1.00
Rear web [mm]	1.77	1.08	1.77	1.08	1.00	1.00
Weight [kg]	51.66		96.13			

It can be seen that both wing A and B pay a price due to the commonality decision of sharing components. Compared with the individual design results, the increased weight for two wing structures are 7.77 kg and 3.85 kg, respectively. The weight of wing A increased more than that of wing B, this is due to the fact that the wing tip area for aircraft A needs to support the load on the outer wing section when it is used as inner wing section on aircraft B. In addition, for wing B, it is important to note that the designed property on the outer wing section is larger than the values on inner wing section for part of components. The reason is that the inner wing section is shared by the two family members, to satisfy the deflection constraint at wing tip for wing B, increasing the stiffness of outer wing section leads to less increment of design objective F than that of inner section.

8. Conclusions

This article discusses the bi-level decomposition approach for the optimization of product families with

predefined platforms. For decomposition-based method, a system coordinator with global sense will greatly improve the optimization efficiency. Based on this consideration, a new SCM is proposed in this article. The innovation of the new method is the system coordinator, which not only provides consistent shared variables to subsystems, but also does the tradeoff between the all subsystems by the use of sensitivity information. The shared variables are determined by minimizing the total performance deviation with respect to the optimal design of each subproblems and constraints violation incurred by sharing. The first order Taylor series approximation is introduced to evaluate the values of performance deviation and constraints violation. As many other decomposition-based methods, the family design problem is decomposed naturally by individual product. This decomposition by product variant provides many benefits, such as simplifying the analysis integration, reducing problem complexity, and enabling concurrent design of all product variants. Results from the numerical test problem suggest that SCM can robustly and efficiently solve the test problem, which performs better than the ATC method. In addition, both the formulations of SCM and numerical test suggest that the SCM is also suitable to the MDO problems that the subsystems are only linked through a number of shared variables. This article also illustrates the successful application of SCM to the structural optimization problem of wing structures for an unmanned aircraft family.

9. References

- [1] D. J. Pate, M. D. Patterson and B. J. German, Optimizing families of reconfigurable aircraft for multiple missions, *J Aircraft*, 49(6), 1988-2000, 2012.
- [2] M. Muffatto, Introducing a platform strategy in product development, *Int J Prod Econ*, 60-61, 145-153, 1999.
- [3] K. Fujita, H. Amaya and R. Aka, Mathematical model for simultaneous design of module commonalization and supply chain configuration toward global product family, *J Intell Manuf*, 24(5), 991-1004, 2013.
- [4] T. W. Simpson, Product platform design and customization: status and promise, *Ai Edam*, 18(1), 3-20, 2004.
- [5] M. H. Meyer and A. P. Lehnerd, *The Power of Product Platforms*, New York: Free Press, 1997.
- [6] J. R. Jiao, T. W. Simpson and Z. Siddique, Product family design and platform-based product development: a state-of-the-art review, *J Intell Manuf*, 18(1), 5-29, 2007.
- [7] T. W. Simpson, Z. Siddique and J. R. Jiao, *Product Platform and Product Family Design*, Springer, New York, 2006.
- [8] T. W. Simpson, J. R. Jiao, Z. Siddique et al, *Advances in Product Family and Product Platform Design*, Springer, New York, 2014.
- [9] S. A. Nelson, M. B. Parkinson and P. Y. Papalambros, Multicriteria optimization in product platform design, *J Mech Design*, 123, 199-204, 2001.
- [10] A. Messac, M. P. Martinez and T. W. Simpson, Effective product family design using physical programming, *Eng Optimiz*, 34(3), 245-261, 2002.
- [11] Z. H. Dai and M. J. Scott, Effective product family design using preference aggregation, *J Mech Design*, 128(4), 659-667, 2006.
- [12] R. Fellini, P. Panos, T. Weber et al, Application of a product platform design process to automotive powertrains, *Proceedings of the 8th AIAA/NASA/USAF/ISSMO Symposium on Multidisciplinary Analysis and Optimization*, Long Beach, CA, 6-8 September, 2000.
- [13] T. W. Simpson, J. Maier and F. Mistree, Product platform design: method and application, *Res Eng Des*, 13(1), 2-22, 2001.
- [14] J. Allison, B. Roth and M. Kokkolaras, Aircraft family design using decomposition-based methods, *Proceedings of the 11th AIAA/ISSMO Multidisciplinary Analysis and Optimization Conference*, Portsmouth, Virginia, 6-8 September, 2006.
- [15] M. Kokkolaras, R. Fellini, H. M. Kim et al, Extension of the target cascading formulation to the design of product families, *Struct Multidisc Optim*, 24(4), 293-301, 2002.
- [16] B. Roth and I. Kroo, Enhanced collaborative optimization, *12th AIAA/ISSMO Multidisciplinary Analysis and Optimization Conference*, Victoria, BC, 2008.
- [17] M. Öman and L. Nilsson, Structural optimization of product families subjected to multiple crash load cases, *Struct Multidisc Optim*, 41(5), 797-815, 2010.
- [18] R. Fellini, M. Kokkolaras, N. Michelena et al, A sensitivity-based commonality strategy for family products of mild variation, with application to automotive body structures, *Struct Multidisc Optim*, 27(1), 89-96, 2004.
- [19] J. Golinski, Optimal synthesis problems solved by means of nonlinear programming and random methods, *Journal of Mechanisms*, 5(3), 287-309, 1970.
- [20] S. Tosserams, L. F. P. Etman and J. E. Rooda, An augmented lagrangian decomposition method for quasi-separable problems in MDO, *Struct Multidisc Optim*, 34(3), 211-227, 2007.

Crash Optimization of Automobile Frontal and Side Structures Using Equivalent Static Loads

Youngmyung Lee¹, Jin-Seok Ahn², and Gyung-Jin Park³

¹Hanyang University, Seoul, Republic of Korea, lymkd@hanyang.ac.kr

²Hanyang University, Seoul, Republic of Korea, zombie0212@hanyang.ac.kr

³Hanyang University, Ansan, Republic of Korea, gjpark@hanyang.ac.kr

1. Abstract

Many commercial automobile industries are seeking to design the automobile structure for improvement of passenger safety as well as reduction of the mass of the automobile. Optimization can be employed to accommodate the crash environment. The automobile crash optimization problem has large nonlinearity in analysis while the analysis is carried out in the time domain. Although the performance of the computer has been significantly improved, automobile crash optimization still needs considerable computational cost. The equivalent static loads (ESLs) method has been developed for such nonlinear dynamic response structural optimization. The ESLs are static loads that generate the same displacement in the linear static analysis as those of the nonlinear dynamic analysis at a certain time step. The ESLs are generated at all the time steps and used as multiple external forces in linear static response structural optimization. Nonlinear analysis and linear static response optimization using ESLs are carried out sequentially until the convergence criteria are satisfied. A new ESLs method is proposed for automobile crash optimization and the proposed method is verified using two practical examples. Crash optimization under a frontal impact performed to minimize the mass, and the thicknesses of the structure are determined to satisfy the relative distance constraints. The side structure of an automobile is optimized under a side impact test. The mass is minimized while the regulation of Insurance Institute for Highway Safety (IIHS) is satisfied. The regulation is the limit of the maximum intrusion that is the relative distance between the B-pillar and the center line of the seat. The resultant designs are discussed from a practical viewpoint.

2. Keywords: Structural optimization, equivalent static loads (ESLs), frontal structure, side impact test, moving deformable barrier (MDB).

3. Introduction

Automobile safety regulations have become more stringent in the last decades. Many automobile industries are seeking to design the automobile structure for safety as well as reduction of the automobile mass. It is well-known that the mass of an automobile is one of the important factors for the fuel cost. Automobile structural optimization has been utilized to minimize an objective function such as mass while the conditions for safety are satisfied [1]. Automobile crash optimization generally uses nonlinear dynamic analysis that has large nonlinearity in the time domain. Therefore, optimization techniques for crash optimization should be able to address the nonlinearity in the time domain with an appropriate manner.

Automobile industries are trying to utilize a high-fidelity model in structural optimization. An intuitive design based on the designer's experience has been popularly utilized. The conventional optimization paradigm is difficult to use for crash optimization due to extremely high cost. Meta-models are actively used for optimization with approximated functions to save the cost [2-4]. The meta-model approaches vary depending on the sampling method, fitting function or interpolation function, and the optimum solution depends on the selection of a method. When the number of design variables is large, the number of sampling, i.e., the number of nonlinear dynamic analyses can be quite large. The equivalent static loads method (ESLM) has been utilized to save the computational cost as well as to use a gradient-based optimization process.

Since the ESLM was introduced by Choi and Park in 1999 [5], it has been applied to various practical examples [6-9]. Two domains such as the analysis domain and the design domain are defined. In the analysis domain, nonlinear dynamic analysis is performed, equivalent static loads (ESLs) are generated by using the displacement output of the analysis domain, and linear static structural optimization is carried out using the ESLs in the design domain. Generally, the finite element (FE) models of the two domains are the same. An FE model for crash analysis may not have boundary conditions; however, an FE model for linear static structural optimization requires boundary conditions. A novel method is proposed to solve this discrepancy by using the inertia relief technique [10] when using the ESLM. The proposed method is validated by solving two practical examples. The two examples are optimizations of a frontal structure and a side structure. Optimization of the frontal structure is carried out under the low speed impact test protocol of the Electronic Code of Federal Regulations (e-CFR) [11]

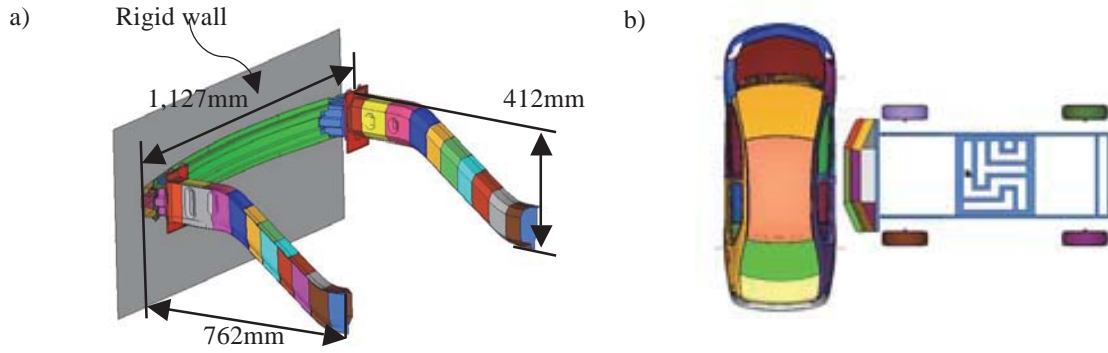


Figure 1: Finite element model: a) a frontal structure, and b) a side impact test

and side impact optimization is carried out based on the IIHS [12]. Nonlinear dynamic analysis is carried out using LS-DYNA 971 [13], linear static response structural optimization is conducted by using NASTRAN SOL 200, and calculation of ESLs is utilized using NASTRAN DMAP [14]. A computer program is developed for optimization with ESLM [15].

4. Test protocol of crash analysis

4.1. Frontal structure

An important function of an automobile frontal structure is to absorb impact energy. It reduces the physical injuries to passengers as well as damages to the interior of the engine room. There are two kinds of the low speed impact test of the e-CFR. One is the pendulum impact test and the other is the barrier impact test. In the pendulum impact test, a frontal structure is fixed at the rear end and the pendulum impacts the frontal structure. In the case of the barrier impact test, the frontal structure impacts a fixed rigid wall at a low velocity of 8 km/h. Jeong et al. performed crash optimization using the pendulum impact test [8]. In this research, the barrier impact test is utilized. Thus, the finite element model does not have any boundary conditions in nonlinear dynamic analysis. The finite element model is divided into 29 parts that has the 8,526 finite elements, and the total mass is 16.16 kg. The specific sizes of the frontal structure are illustrated in Figure 1 a).

4.1. Side structure

According to the side impact test protocol of the IIHS, the side impact test uses a motionless test automobile impacted by an IIHS moving deformable barrier (MDB). The mass of MDB is 1,500 kg, and the MBD impacts at a velocity of 50 km/h. In this research, the structural rating of IIHS is utilized. For example, it is evaluated as 'good', if the distance from the B-pillar point with maximum intrusion to a seat centerline is greater than 125mm. The finite element model is from the National Crash Analysis Center [16], which is the Yaris model from Toyota. The total number of finite elements is 974,445 and the total mass is 1,247 kg. The FE model of IIHS MDB is provided by the Livermore Software Technology Corporation [13]. Figure 1 b) shows the FE model with MBD. In the initial side impact simulation, the maximum distance between the deformed B-pillar and the seat centerline is 122.49 mm. In other words, the initial design would receive a nearly 'good' structural rating.

5. Equivalent static loads method for nonlinear dynamic response structural optimization

The schematic view of the two domains is presented in Figure 2. In the analysis domain, nonlinear dynamic response analysis is carried out. Then ESLs are generated. In the design domain, generated ESLs are applied as external loads in linear static response structural optimization. The process of ESLM is repeated until the convergence criterion is satisfied. The repeated process is called a design cycle.

The process of calculating ESLs is described in detail. Eq.(1) is the governing equation of nonlinear dynamic response analysis.

$$\mathbf{M}(\mathbf{b}, \mathbf{z}(t))\mathbf{z}_N(t) + \mathbf{K}_N(\mathbf{b}, \mathbf{z}(t))\mathbf{z}_N(t) = \mathbf{f}(t) \quad (t = 0, \dots, l) \quad (1)$$

where $\mathbf{b} \in R^n$ is the design variable vector, n is the number of design variables, \mathbf{M} is the mass matrix, $\mathbf{z}_N(t)$ is



Figure 2: Schematic view of the equivalent static loads method

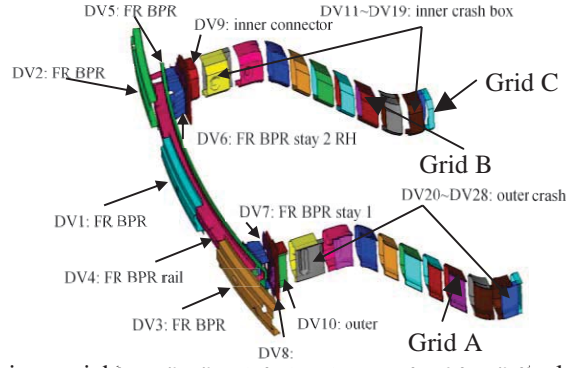


Figure 3: Design variables of a frontal structure and grids of displacement constraints

the acceleration vector, \mathbf{K} is the stiffness matrix, $\mathbf{z}_N(t)$ is the displacement vector, and $\mathbf{f}(t)$ the is dynamic load vector, subscript N means that it is from nonlinear analysis, t is time and l is the number of time steps.

The following equation is the governing equation of linear static analysis:

$$\mathbf{K}_L(\mathbf{b})\mathbf{z} = \mathbf{f} \quad (2)$$

where the subscript L means that it is from linear analysis, \mathbf{z} is the displacement vector and \mathbf{f} is the force vector. The displacement vector \mathbf{z} is replaced by $\mathbf{z}_N(t)$ to calculate ESLs in the following equation:

$$\mathbf{f}_{eq}(s) = \mathbf{K}_L(\mathbf{b})\mathbf{z}_N(t); \quad s = 1, \dots, l \quad (3)$$

Thus, the ESLs vector $\mathbf{f}_{eq}(s)$ is calculated as the product of linear stiffness matrix $\mathbf{K}_L(\mathbf{b})$ and the displacement vector $\mathbf{z}_N(t)$. Since the number of sets of ESLs is the same as that of time steps, the notations s and t exactly correspond. Finally, ESLs are applied as multiple loading conditions for linear static response structural optimization.

The overall process is as follows:

- Step 1. Set the initial design variables (cycle number: $k = 0$, design variables: $\mathbf{b}^{(k)} = \mathbf{b}^{(0)}$).
- Step 2. Perform nonlinear dynamic response analysis with $\mathbf{b}^{(k)}$.
- Step 3. Calculate the ESLs using Eq.(3).
- Step 4. Solve the linear static response structural optimization problem with ESLs using inertia relief analysis. Since the structures have no boundary conditions, the inertia relief technique is utilized [10].
- Step 5. When $k = 0$, go to Step 6. When $k > 0$, if the convergence criterion is satisfied then terminate the process. Otherwise, go to Step 6.
- Step 6. Update the design variables, set $k = k + 1$ and go to Step 2.

6. Automobile crash optimization using equivalent static loads

6.1. Frontal structure

Figure 3 shows the 28 design variables among 29 parts and three grids that are utilized for the displacement constraints. The objective function is the entire mass of the structure, and size optimization is carried out. The displacement constraints are defined using the distance from A to C and B to C. Using the displacement constraints, the bumper intrusion is constrained. The bound for the constraint is 140.5 mm that is the result of the initial nonlinear dynamic analysis.

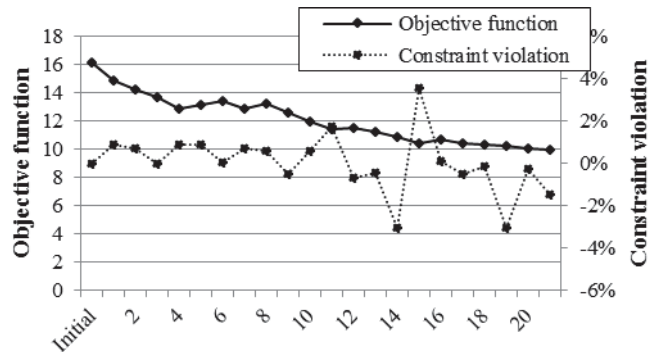


Figure 4: History of objective function and constraint violation of a frontal structure

a) ISO view

a) YZ Plane view

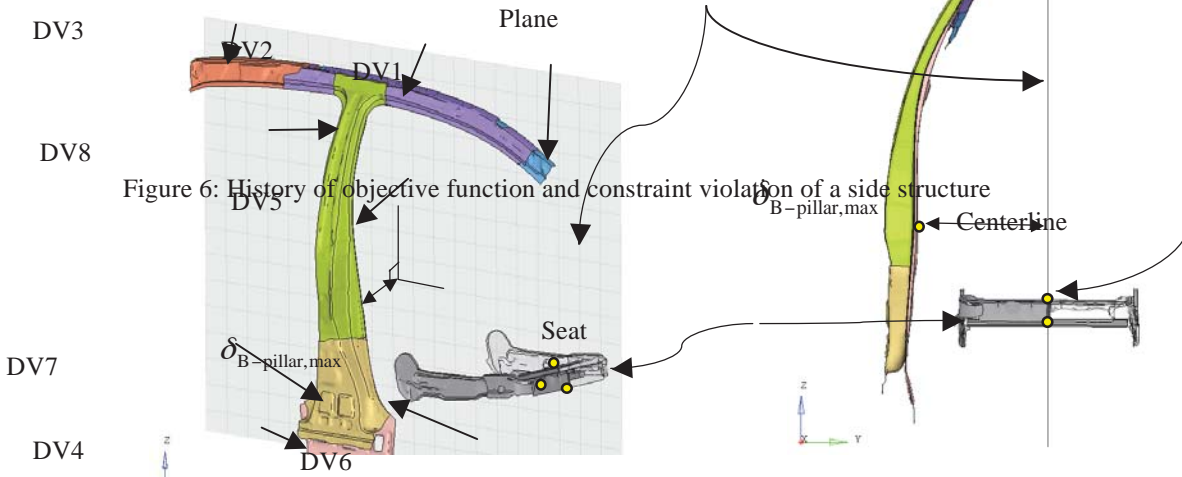


Figure 6: History of objective function and constraint violation of a side structure

Figure 5: Reference points of the displacement constraint for the side structure
Design formulation is as follows:

$$\text{Find } b_i \quad (i = 1, 2, \dots, 28) \quad (4)$$

$$\text{to minimize mass} \quad (5)$$

$$\text{subject to } |\delta_{x,A} - \delta_{x,C}| \geq 140.5 \text{ mm} \quad (6)$$

$$|\delta_{x,B} - \delta_{x,C}| \geq 140.5 \text{ mm} \quad (7)$$

$$0.7 \text{ mm} \leq b_i \leq 2.5 \text{ mm} \quad (8)$$

where b_i is the i th design variable that is thickness, and $\delta_{x,A}$, $\delta_{x,B}$, and $\delta_{x,C}$ are the displacements of grids A, B, and C, respectively.

Figure 4 shows the history of optimization. The process converges to the optimum solution in the 21st cycle. The mass is reduced by 38% from 16.16 kg to 9.98 kg while the displacement constraints are satisfied.

6.2. Side structure

The selected eight parts in Figure 5 are divided into the B-pillar and the roof rail. As shown in Figure 5, a plane is derived using three grids on the seat centerline. The design formulation is defined as follows:

$$\text{Find } b_i \quad (i = 1, 2, \dots, 8) \quad (9)$$

$$\text{to minimize mass} \quad (10)$$

$$\text{subject to } \delta_{B\text{-pillar,max}} \geq 125 \text{ mm} \quad (11)$$

As shown in Figure 6, the optimization process under the side impact test converges in the 6th cycle. The mass is decreased from 18.35 kg to 15.29 kg. Table 1 shows the history of eight design variables. The parts of roof-rail, DV1 to DV 3, do not have a significant effect on the side impact test.

7. Conclusions

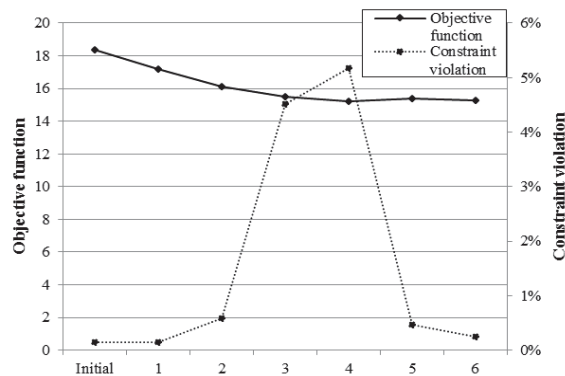


Table 1: Comparison of thickness of the initial and the optimum

Cycle No.	DV1	DV2	DV3	DV4	DV5	DV6	DV7	DV8
Initial	1.069	1.069	1.069	0.990	2.560	2.120	1.190	2.120
Optimum	0.500	0.500	0.500	0.606	2.016	1.589	1.288	1.577

Nonlinear dynamic response structural optimization of high-fidelity finite element model seems to be almost impossible in conventional gradient based optimization due to high nonlinearity and time-dependent behavior. In this research, crash optimization with the barrier impact test and the side impact test is carried out using ESLM. The inertia relief technique is utilized to avoid singularity that can occur in linear static response structural optimization. Practical examples are solved by the proposed method.

Crash optimization of a frontal structure is carried out to determine 28 design variables. The optimum thickness is derived by performing 22 nonlinear dynamic analyses. The displacement constraint is satisfied and the mass is reduced by 38%. Crash optimization of a side structure is also carried out for 8 design variables. The process converges in the 6th cycle while the displacement constraint of IIHS is satisfied. The mass is decreased by 17%. It is noted that the design variables of the roof-rail converge to the lower bound. If the roof crush test is considered, the optimum values can be different. In future research, considering various crash tests is necessary.

8. Acknowledgements

This research was supported by the Commercialization Promotion Agency for R&D Outcomes through the Ministry of Science (No. 2014K00042). The authors are thankful to Mrs. MiSun Park for her English correction of the manuscript.

9. References

- [1] A. Deb, M. S. Mahendrakumar, C. Chavan, J. Karve, D. Blankenburg and S. Storen, Design of an aluminum-based automobile platform for front impact safety, *International Journal of Impact Engineering*, 30 (8-9) 1055-1079, 2004.
- [2] X. Liao, Q. Li, X. Yang, W. Zhang and W. Li, Multiobjective optimization for crash safety design of automobiles using stepwise regression model, *Structural and Multidisciplinary Optimization*, 35 (6), 561-569, 2008.
- [3] R.N. Cadete, J.P. Dias and M.S. Pereira, Optimization in vehicle crashworthiness design using surrogate models, *6th World Congresses of Structural and Multidisciplinary Optimization*, Rio de Janeiro, Brazil, 2005.
- [4] J. Forsberg, L. Nilsson, Evaluation of response surface methodologies used in crashworthiness optimization, *International Journal of Impact Engineering*, 32, 759-777, 2006.
- [5] W.S. Choi and G.J. Park, Transformation of dynamic loads into equivalent static loads based on model analysis, *International Journal for Numerical Methods in Engineering*, 46 (1), 29-43, 1999.
- [6] P. Adduri, J.P. Leiva, G. Quinn and B. C. Watson, New approaches for shape and topology optimization for crashworthiness, *13th International LS-DYNA Users Conference*, Dearborn, Michigan, USA, 2013.
- [7] C.H. Chuang and R.J. Yang, Benchmark of topology optimization methods for crashworthiness design, *12th International LS-DYNA Users Conference*, Dearborn, Michigan, USA, 2012.
- [8] S.B. Jeong, S. Yoon, S. Xu and G.J. Park, Non-linear dynamic response structural optimization of an automobile frontal structure using equivalent static loads, *Proceedings of the Institution of Mechanical Engineers, Part D, Journal of Automobile Engineering*, 224 (4), 489-501, 2010.
- [9] S.I. Yi, J.Y. Lee and G.J. Park, Crashworthiness design optimization using equivalent static loads, *Proceeding of the Institution of Mechanical Engineers, Part D, Journal of Automobile Engineering*, 226 (1), 23-38, 2012.
- [10] L. Liao, A study of inertia relief analysis, *19th AIAA Structures, Structural Dynamics and Materials Conference*, Denver, Colorado, 2011.
- [11] Electronic Code of Federal Regulations, Title 49 –Transportation, Subtitle B – Other regulations relating to transportation, Chapter V – National Highway Traffic Safety Administration, Department of Transportation, Part 581– Bumper standard, 2009.
- [12] Side Impact Crashworthiness Evaluation Crash Test Protocol (Version VII), *Insurance Institute for Highway Safety (IIHS)*,
- [13] LS-DYNA 971 version user’s manual, *Livermore Software Technology Co.*, CA, 2007.
- [14] NASTRAN user’s guide, *MSC Software Co.*, Santa Ana, CA, 2013.
- [15] H.A. Lee and G.J. Park, A software development framework for structural optimization considering non linear static responses, *Structural and Multidisciplinary Optimization*, 10.1007/s00158-015-1228-x, 2015.
- [16] K.S. Opiela, Finite element model archive, <http://www.ncac.gwu.edu/vml/models.html>, 2014.

A Direct Optimal Control Strategy for Valves in Heat Exchanger Networks and Experimental Validations

Yi-Fei Wang, Qun Chen *

Tsinghua University, Beijing, China, chenqun@tsinghua.edu.cn

1. Abstract

Optimal operations of heat exchanger networks (HENs) are of great significance to energy conservation. As one of the most efficient methods to reduce the running costs of HENs, the pressure differential set points control strategy has been widely applied in practice, where the optimal pressure differentials of different sections are obtained by suitable empirical and mathematical models, and then the optimal pressure differentials are passed to control systems to guide the operations of each component. Most control systems in these methods are indirect control strategies. That is, it will take a long time to seek the operating parameters of each component due to the lack of direct operating parameters. Based on the newly proposed thermal resistance-based optimization method, we introduce a direct optimal control strategy for adjustable valves in HENs to obtain the optimal valve openings directly with the full awareness of HENs in physics. Finally, we take a variable water volume chiller system as an example to validate the proposed control strategy. Groups of experiments and the results illustrate the proposed direct valve control strategy of the HEN.

2. Keywords: heat exchanger networks; energy conservation; valve opening; control strategy.

3. Introduction

Heat exchanger networks (HENs) take the main components and cost large proportion of energy consumption in many engineering fields, such as power plant and chemical industries. Energy conservations demands the optimizations of HENs, where adjustable valve is an efficient way for HENs optimal control [1].

The main control method of adjustable valve focuses on the pressure differential set points control strategy. For instance, Wang et al. [2] proposed a pressure set point control method for an indirect water-cooled chilling system, and Lu et al. [3] raised a optimization method for a heat, ventilation and air condition (HVAC) system with the duct differential pressure set point. Besides, pressure differential of other set points also work in the optimal operating of HENS, such as the pressure differential of secondary VSP [4, 5], the fan static pressure [6], and the pressure drop through the heat exchanger [2].

However, the direct control parameters in a HEN are the opening of valves, rather than the set points of pressure differentials. With these optimal set points, it is unavoidable to control the valve openness by seeking the help of some control strategies, such as the PID controllers [3, 4, 7], the direct digital control (DDC) strategies [8], the online control strategies [9], and the feedback [10] or self-turning control strategies [11, 12].

Actually, the aforementioned methods with the optimal set points and the control strategies divide the optimization into two sequential steps virtually. One is to get the optimal set points to satisfy the requirements, and the other is to achieve these set points by regulating the valves through control strategies. However, these two sequential steps separate the influences of the valves and pipelines characteristics out of the global system performance, and consequently narrow down the range of the optimization results artificially. What's more, the control strategies require more or less setting time [13, 14]. The set points are only controlled close to but not indeed the optimal values, and incessantly varied within a range, which is influenced by the controller [15, 16].

In order to directly obtain the optimal valve openness for each pipeline, Chen et al. [17] provide a thermal resistance-based method for HEN optimization, which links the operating parameters, i.e. the valve openness, directly to the requirements, such as the required heat transfer rate and the surrounding temperature, and the performance of each component, including the heat exchanger thermal conductances, the pump characteristics, and the pipeline characteristics.

This paper provides an effort to obtain the direct optimal openness of the adjustable valves for HEN optimizations, avoiding the inconvenient control strategies with intermediate set points values. Based on the physical models of heat exchangers, pumps, and pipelines, we first fit the thermal conductances of heat exchangers and the characteristic parameters of pumps and pipelines in a VWV HEN by a series of experiments. With these fitted physical models, utilization of the thermal resistance-based optimization method directly offers different optimal valve openness under different operating conditions. Experimental measurements of the HEN performance illustrate that the optimized valve openness indeed lead to the lowest total energy consumptions of the HEN under different operating conditions.

4. Experiment facilities and measurement instruments

Fig.1 gives the sketch and the photo of an experimental HEN studied in this paper, consisting of two counter-flow plate heat exchangers, three adjustable valves (AV), three variable speed pumps (VSP), a thermostatic hot water tank, a chiller, and pipelines wrapped up with thermal insulating materials. The working fluids in Loop 1 and 3 are water, and that in Loop 2 is a refrigerant R142b. The pumps drive the working fluids to circulate in each loop, transferring heat in the thermostatic hot water tank through heat exchanger 1, heat exchanger 2, finally to the evaporator of the chiller. Three turbine volume flow-meters (VFM) with an accuracy $\pm 0.5\%$ of the full scale 20 L/min are utilized to measure the fluid flow rates in three loops. Three differential pressure transducers (DPT) with an accuracy $\pm 0.2\%$ of the full scale 350 kPa are employed to measure the pressure differentials of each VSP. A pressure gauge (PG) with the full scale 1.8 Mpa is equipped in Loop 2 to monitor the refrigerant absolute pressure. T type copper-constantan thermocouples (Produced by Omega Engineering) with an accuracy $\pm 0.2^\circ\text{C}$ serve to test the working fluid temperatures in each measurement points shown in Fig.1, where two thermocouples are placed in each point for accuracy. The subscript w and r represent water and refrigerant, i and o mean the inlet and the outlet of heat exchangers, and 1, 2 and e stand for heat exchanger 1, heat exchanger 2 and the evaporator, respectively. In addition to the measuring instruments, the experiment system also contains a data acquisition and control system (DACS) to log the measured data, including volume flow rates, pressure differentials and temperatures, and control the components, such as the openness of the AVs and the water temperature of the tank.

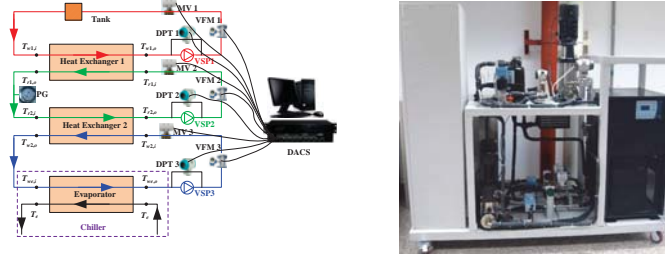


Fig.1 The sketch of a variable water volume heat exchanger network and the photo of the experiment facility

5. Physical models of each component

5.1 Physical models of heat exchangers

For the counter-flow heat exchangers, i.e. heat exchanger 1 and 2, the entransy dissipation-based thermal resistances are [18]

$$R_{hx1} = \frac{(T_{w1,i} + T_{w1,o}) - (T_{r1,i} + T_{r1,o})}{2Q} = \frac{\xi_1 \exp[(kA)_1 \xi_1] + 1}{2 \exp[(kA)_1 \xi_1] - 1}, \quad \xi_1 = \frac{1}{m_1 c_{p,1}} - \frac{1}{m_2 c_{p,2}}, \quad (1)$$

$$R_{hx2} = \frac{(T_{r2,i} + T_{r2,o}) - (T_{w2,i} + T_{w2,o})}{2Q} = \frac{\xi_2 \exp[(kA)_2 \xi_2] + 1}{2 \exp[(kA)_2 \xi_2] - 1}, \quad \xi_2 = \frac{1}{m_2 c_{p,2}} - \frac{1}{m_3 c_{p,3}}, \quad (2)$$

where R is the entransy dissipation-based thermal resistance, ξ is the flow arrangement factor of a heat exchanger, k is the heat transfer coefficient, A is the heat transfer area, m is the mass flow rate, and c_p is the constant pressure specific heat. The subscripts $hx1$ and $hx2$ represent heat exchangers 1 and 2, and the numbers 1, 2, and 3 represents the liquid driven by the pump₁, pump₂, and pump₃, respectively.

By assuming the evaporation temperature constant, the physical model of the evaporator is [18]

$$R_e = \frac{T_{we,i} + T_{we,o} - 2T_e}{2Q} = \frac{\xi_e \exp[(kA)_e \xi_e] + 1}{2 \exp[(kA)_e \xi_e] - 1}, \quad \xi_e = \frac{1}{m_3 c_{p,3}}, \quad (3)$$

where the subscript e stands for the evaporator.

Similarly, the entransy dissipation-based thermal resistance for the mixing process of the cooled hot water and the tank water gives [18]

$$R_m = \frac{T_{w1,i} - T_{w1,o}}{2Q} = \frac{1}{2m_1 c_{p,1}}, \quad (4)$$

where the subscript m means the mixing process.

5.2 Physical models of pumps

For a pump operating in a given speed, the mass flow rate m , and the head loss or the pressure drop H obey the following formula [19, 20]

$$H = a_0 + a_1 \frac{m}{\rho} + a_2 \frac{m^2}{\rho^2}, \quad (5)$$

where a_0, a_1, a_2 are the characteristic parameters of pump, which can be identified by experimental data, and ρ is the working fluid density.

Without considering the mechanical losses, the power consumption of the pump is represented as

$$P = mgH. \quad (6)$$

5.3 Physical models of pipelines with an adjustable valve in different openness

The head loss or the pressure drop of the pipelines with an adjustable valve in different openness, is calculated by [21]

$$H = H_s + H_d + H_v, \quad (7)$$

where H_s is the static head that the pump needs to lift, H_d is the dynamic head, and H_v is the head loss caused by the adjustable valve.

The dynamics head of the pump is expressed by [22]

$$H_d = dm^2, d = \frac{1}{2g\rho^2 S^2} \left(\frac{fL}{D} + \sum K_i \right), \quad (8)$$

where f is the Darcy friction-factor, L is the length of pipe, D is the pipe diameter, and K is the minor loss coefficient of the detail structure.

Assuming the valve openness in the given pipeline is c , the additional head loss caused by the valve, i.e. H_v , can be seen as a sudden contraction expressed as [22]

$$H_v = \left[b_1(1-c)^2 + b_2(1-c) \right] m^2. \quad (9)$$

where b_1 and b_2 are the coefficients, which are related to the size of the valve and the pipelines.

Then the pipeline head loss with a valve openness being c follows

$$H = H_s + \left[d + b_1(1-c)^2 + b_2(1-c) \right] m^2. \quad (10)$$

6. Determination of the characteristic parameters of each component

In order to identify the thermal conductances of heat exchangers, the characteristic parameters, a_0, a_1 and a_2 in Eq. (6), of pumps, and the characteristic parameters, H_s, b_1, b_2 , and d in Eq. (12), of pipelines, a group of experiments are conducted. In the experiments, the properties of water and R142b are assumed constant. The water average density is 1000 kg/m^3 , and the water constant pressure specific heats is 4196 J/(kg K) . The absolute pressure of Loop 2 is 0.47 MPa . In this condition, by referring to NIST-Refprop, the average density of R142b is 1100 kg/m^3 , and the constant pressure specific heat is 1304 J/(kg K) . ($300 \text{ K} \pm 10 \text{ K}$, saturated liquid).

6.1 Experiment to determine the thermal conductances of heat exchangers

We set the operating frequencies of pump₁, pump₂, and pump₃ at 30, 40 and 20 Hz, respectively, the temperature difference of the thermostatic hot water tank and the evaporating temperature is kept as $40 \text{ }^\circ\text{C}$. Under this working condition, we operate the experiment system at steady-state condition for 30 minutes, which are monitored by the DACS. Table 1 offers the thermal conductances of all heat exchangers in this operating condition.

Table 1 The thermal conductances of each heat exchanger

kA	$(kA)_1$	$(kA)_2$	$(kA)_3$
Value(W/K)	219.3	196.7	53.2

Because the thermal conductances are influenced by the fluid velocities, it is need to re-calculate the thermal conductances case by case with different working parameters.

6.2 Experiments to identify the characteristic parameters of pumps

The working point of each pump is determined by the mass flow rate and the head loss with the relation given in Eq. (5). We preform experiments with the three pumps at given rotation speeds, i.e. 30 Hz, 40 Hz and 20 Hz, respectively, and change the opening of the adjustable valves at 100%, 80%, 60%, 50%, 40%, 30% and 20%, sequentially. The average mass flow rates, the head losses of each pump and the fitted m - H curves are given in Fig.2. The points exp_1, exp_2 , and exp_3 represent the experiment data, and the dash lines fit_1, fit_2 , and fit_3 stand for the fitted m - H curves, respectively. Table 2 exhibits the characteristic parameters of the pumps and the maximum deviations between the experimental data and the fitted values, δ_{\max} .

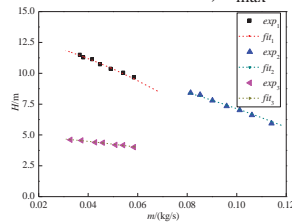


Fig. 2 The experiment data and the fitted curves of each pump at given speed

Table 2 The characteristic parameters of pump s and the maximum deviations

Pump	a_0	a_1	a_2	δ_{\max}
pump ₁	13.4	-32.6	-567.4	0.55%
pump ₂	5.1	-9.8	-141.5	3.73%
pump ₃	11.6	-18.5	-261.2	1.29%

The maximum deviations between the experiment data and the calculated values of pump₁, pump₂, and pump₃ are 5.31%, 4.95% and 5.17%, in sequence.

6.3 Experiments to identify the characteristic parameters of pipelines with different valve openness

For identifying the characteristic parameters, i.e. H_s , b_1 , b_2 , and d . We conduct experiments at 100 %, 50 %, 75 %, 25 % opening of the adjustable valve and with the valve openness of the VSPs at 50 Hz, 45 Hz, 40 Hz, 35 Hz, 30 Hz, 25 Hz and 20 Hz, sequentially. Fig.3 offers the averaged mass flow rates, the head losses of each pipeline and the fitted or calculated m - H curves of each pipeline, respectively, where the subscript *exp* means experimental values, *fit* represents the fitted values, and *cal* stands for the calculated values. Table 3 lists the characteristic parameters of the pipelines, and the maximum deviations between the experiment data and the fitted values.

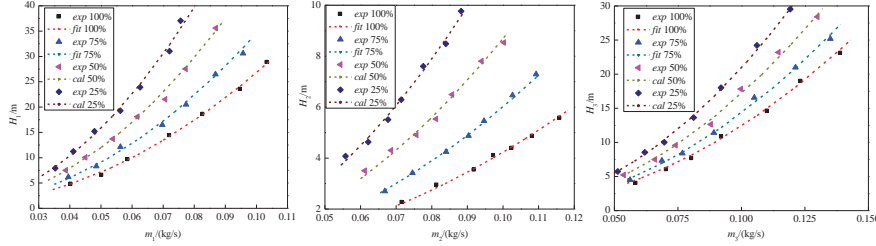


Fig. 3 The experiment data and the fitted curves of Loop 1 at different opening of the adjustable valve

Table 3 The characteristic parameters of pipelines and the maximum deviations

Parameter	H_s	d	b_1	b_2	δ_{\max}
Loop 1	0.569	2623.55	3099.3	2327.3	0.55%
Loop 2	0.358	1205.17	757.3	567.9	3.73%
Loop 3	0.1	413.04	711.4	536.0	1.29%

7. The thermal resistance-based method for HEN optimization

Based on the physical models of heat exchangers in Part 3.1, combining Eqs. (1) ~ (4) offers the inherent relation of the heat transfer processes in the entire experiment system [17, 18]:

$$T_h - T_e = Q(R_m + R_{hx1} + R_{hx2} + R_e). \quad (11)$$

For a VWV HEN with given pipeline structures, pumps, valves and heat exchangers, it is always needed to seek the optimal operating parameters of each valve for such objective as the minimum total power consumption of all pumps, at a fixed heat transfer rate, which is relevant to the running cost. With the power consumption of a pump given in Eq. (6), ignoring the mechanical losses, the total one of all pumps is

$$P_t = \sum P_i = \sum m_i g H_i. \quad (12)$$

The optimization for minimizing the total power consumption of all pumps, with the constraints expressed in Eqs. (5), (10) and (11), can be converted as a conditional extremum problem by the method of Lagrange multipliers, which provides a Lagrange function as

$$\begin{aligned} \Pi = & \sum P_i + \alpha [T_h - T_e - Q(R_m + R_{hx1} + R_{hx2} + R_e)] \\ & + \gamma_i [H_{s,i} + d_i m_i^2 + b_{1,i} (1 - c_i)^2 m_i^2 + b_{2,i} (1 - c_i) m_i^2 - H_i], \\ & + \beta_i \left(a_{0,i} + a_{1,i} \frac{m_i}{\rho_i} + a_{2,i} \frac{m_i^2}{\rho_i^2} - H_i \right) \quad i = 1, 2, 3 \end{aligned} \quad (13)$$

where α , β and γ are the Lagrange multipliers.

Making the partial derivations of the Lagrange function with respect to m_i , c_i , and H_i equal to zero offers the optimization equation set. Solving the equation set and Eqs. (5), (10), (11) simultaneously will get the optimal values of all the unknown parameters, including the openness of the adjustable valves, for the minimum total power consumption.

8. Experimental results and discussions

Based on the optimal openness of the adjustable valves for the given heat transfer rate and the referenced thermal conductances, we operate the experiment system at steady-state for 30 minutes. The DACS records temperatures and volume flow rates of each measurement point, and averaged values can be obtained. Since the thermal

conductance varies with different fluid velocities, it is necessary to compare the actual thermal conductances to the referenced ones during optimization, to ensure these valve openness being the optimal ones by eliminating the influences to the thermal conductances from different fluid velocities. If the thermal conductances deviations between experimental values and the referenced ones are within 5%, which is thought as the measurement uncertainties, experiment in that case is regarded as the one with optimal openness of the adjustable valves. Otherwise, optimization calculations should be made again with the newly experimental thermal conductances values, until deviations are within 5%. Obviously, the heat transfer rates by the experiment should be near the given heat transfer ones within the measurement uncertainties. To make it clear, the flowchart of this procedure is as below

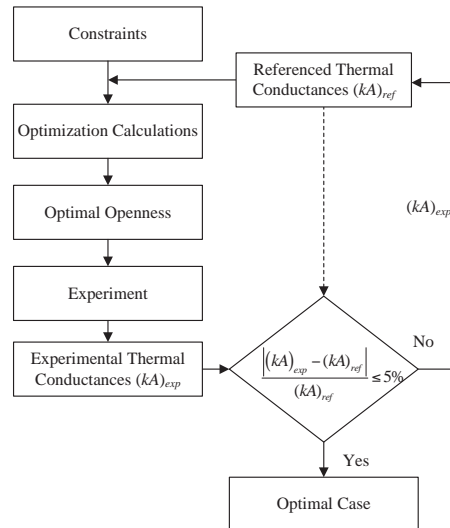


Fig.4 The flowchart of the optimization procedure used for finding actual optimal cases

8.1 Experiments with the optimal valve openness

When the heat transfer rate is fixed at 1000 W, and the temperature difference of the thermostatic hot water tank and the evaporating temperature is kept as 40 °C, solving Eqs. (5), (10), (11), and the equation set from the Lagrange function gives the optimal valve openness with the lowest total power consumption.. Table 4 exhibits the average temperatures at each measurement point, and the average volume flow rates and the corresponding mass flow rates in each loop with the optimal valve openness.

Table 4 The optimal valve openness of the adjustable valves

Openness	c_1	c_2	c_3
Value (100%)	53%	56%	45%

The average heat transfer rate is 1016 W. The maximum deviation to the average value is 1.28% from heat exchanger 1 (1003 W), and the maximum deviation to the target value 1000 W is 2.70% from evaporator, which are within the measurement uncertainties. Table 5 provides the experimental results of the head losses, the power consumptions of each pump and the corresponding total power consumption of all the pumps.

Table 5 The experimental results of the head losses, the power consumptions of each pump and the corresponding total power consumption of all the pumps

Parameter	H_1 (m)	H_2 (m)	H_3 (m)	P_1 (W)	P_2 (W)	P_3 (W)	P_t (W)
Experiment value (W/K)	10.57	7.38	4.36	4.95	6.98	1.89	13.82

8.2 Experiments with other alternative operating frequencies

Alternative experiments with the valve openness listed in Table 6 can also satisfy the same requirements, i.e. the heat transfer rate 1000 W, the temperature difference of the thermostatic hot water tank and the evaporating temperature 40 °C. Table 7 offers the energy consumptions of all the pumps in different alternative experiments.

Table 6 The valve openness of the adjustable valves in different alternative experiments

Openness (100%)	No.1	No.2	No.3	No.4	No.5	No.6	No.7
c_1	47%	48%	49%	50%	52%	51%	54%
c_2	60%	59%	57%	56%	55%	58%	56%
c_3	48%	52%	54%	55%	50%	54%	57%

Table 7 The energy consumptions of all the pumps in each alternative experiment

Case	No.0	No.1	No.2	No.3	No.4	No.5	No.6	No.7
Value(W)	13.82	15.50	14.99	15.03	15.04	14.87	15.29	15.47

It is shown in Table 7 that the power consumption of the optimized operating condition is lower than those of any other alternative ones, which validate our newly proposed optimal control strategy for HENs.

9. Conclusions

Based on the physical models of such components as heat exchangers, pumps and pipelines with adjustable valves in a HEN, we determined the characteristic parameters in these models for specific components experimentally. Combination of these physical models and the newly proposed thermal resistance-based optimization method for HENs offered a direct valve openness control strategy, which directly control the operation of a HEN with certain system requirements and constraints, such as prescribed heat transfer rates, fixed structures of heat exchangers and pipelines.

Further experimental results with the optimal valve openness and other alternative ones under the same system requirements showed that the total power consumption of all pumps in the optimal experiment was actually the lowest one, which validated our newly proposed direct optimal control strategy.

Acknowledgements

The present work is supported by the National Natural Science Foundation of China (Grant No. 51422603), the National Basic Research Program of China (Grant No. 2013CB228301), the Foundation for the Author of National Excellent Doctoral Dissertation of China (Grant No. 201150), and the Importation and Development of High-Caliber Talents Project of Beijing Municipal Institutions (Grant No. YETP0112).

Reference

- [1] M. Bojic, N. Trifunovic, Linear programming optimization of heat distribution in a district-heating system by valve adjustments and substation retrofit, *Build Environ*, **35** (2000) 151-159.
- [2] S.W. Wang, J. Burnett, Online adaptive control for optimizing variable-speed pumps of indirect water-cooled chilling systems, *Appl Therm Eng*, **21** (2001) 1083-1103.
- [3] L. Lu, W.J. Cai, L.H. Xie, S.J. Li, Y.C. Soh, HVAC system optimization - in-building section, *Energ Buildings*, **37** (2005) 11-22.
- [4] X.Q. Jin, Z.M. Du, X.K. Xiao, Energy evaluation of optimal control strategies for central VWV chiller systems, *Appl Therm Eng*, **27** (2007) 934-941.
- [5] Z.J. Ma, S.W. Wang, Energy efficient control of variable speed pumps in complex building central air-conditioning systems, *Energ Buildings*, **41** (2009) 197-205.
- [6] M. Ning, M. Zaheeruddin, Neuro-optimal operation of a variable air volume HVAC&R system, *Appl Therm Eng*, **30** (2010) 385-399.
- [7] J. Sun, A. Reddy, Optimal control of building HVAC&R systems using complete simulation-based sequential quadratic programming (CSB-SQP), *Build Environ*, **40** (2005) 657-669.
- [8] D.L. Loveday, G.S. Virk, Artificial-Intelligence for Buildings, *Appl Energy*, **41** (1992) 201-221.
- [9] Z.J. Ma, S.W. Wang, F. Xiao, Online performance evaluation of alternative control strategies for building cooling water systems prior to in situ implementation, *Appl Energy*, **86** (2009) 712-721.
- [10] X.Y. You, X. Xiao, Active control of laminar stability by feedback control strategy, *Int J Heat Mass Tran*, **43** (2000) 3529-3538.
- [11] H.B. Duan, Y. Fan, L. Zhu, What's the most cost-effective policy of CO₂ targeted reduction: An application of aggregated economic technological model with CCS?, *Appl Energy*, **112** (2013) 866-875.
- [12] H. Miki, A. Shimizu, Dynamic characteristics of phosphoric-acid fuel-cell stack cooling system, *Appl Energy*, **61** (1998) 41-56.
- [13] G.F. Franklin, J.D. Powell, A. Emami-Naeini, Feedback Control of Dynamic Systems, 4th ed., Addison Wesley, New Jersey, USA, 1993.
- [14] K. Ogata, Modern Control Engineering, 4th ed., Prentice Hall, New Jersey, USA, 2010.
- [15] B.C. Kuo, F. Golnaraghi, Automatic Control Systems, 8th ed., Wiley, New Jersey, USA, 2002.
- [16] G.F. Franklin, J.D. Powell, M.L. Workman, Digital Control of Dynamic Systems, 3rd ed., Prentice Hall, New Jersey, USA, 1997.
- [17] Q. Chen, Y.-F. Wang, Y.-C. Xu, A thermal resistance-based method for the optimal design of central variable water/air volume chiller systems, *Appl Energy*, **139** (2015) 119-130.
- [18] Q. Chen, Entropy dissipation-based thermal resistance method for heat exchanger performance design and optimization, *Int J Heat Mass Tran*, **60** (2013) 156-162.
- [19] Z.Y. Yang, H. Borsting, Energy Efficient Control of a Boosting System with Multiple Variable-Speed Pumps in Parallel, *Ieee Decis Contr P*, (2010) 2198-2203.
- [20] Z.Y. Yang, H. Borsting, Optimal Scheduling and Control of a Multi-Pump Boosting System, *Ieee Intl Conf Contr*, (2010) 2071-2076.
- [21] J.B. Rishel, HVAC pump handbook, McGraw-Hill, New York, USA, 1996.
- [22] W.F. M., Fluid mechanics, 4th ed., WCB/McGraw-Hill, Mass, USA, 1999.

Achieving Minimum Length Scale in Topology Optimization by Geometric Constraints

Mingdong Zhou^{1,2}, Boyan S. Lazarov¹, Fengwen Wang¹, Ole Sigmund¹

¹ Dept. of Mechanical Engineering, Technical University of Denmark, Kgs. Lyngby, Denmark, minzho@mek.dtu.dk

² Dassault Systèmes Deutschland GmbH, Simulia Office, Karlsruhe, Germany

1. Abstract

A topology optimization approach is presented to design structures with strict minimum length scale. The idea is inspired from the work on topology optimization with robust formulations [1, 2, 3], where the optimized nominal design possess minimum length scale if all the considered design realizations in the problem formulation share a consistent topology. However, the latter condition may not be satisfied depending on physical problems [2]. In the current study, two differentiable geometric constraints are formulated based on a filtering-threshold modeling scheme. Satisfying the constraints leads to designs with controllable minimum length scale on both solid and void phases. No additional finite element analysis is required for the constrained problem. Conventional topology optimization can be easily extended to impose minimum length scale on the final design with the proposed constraints. Numerical examples of designing a compliant mechanism and a slow-light waveguide are presented to show the effectiveness of this approach.

2. Keywords: topology optimization, minimum length scale, geometric constraint

3. Introduction

There has been tremendous interest in prototyping topologically optimized designs without the tedious post-processing in CAD softwares, thanks to the boosting macro- / micro- 3D printing technology. On the side of topology optimization, the optimized design must contain no single structural member whose size is below the resolution of a 3D printer in order to avoid prototype deficiency, such as holes or disconnected parts. One solution is to achieve minimum length scale in the topology optimization results. Another benefit of doing so is that, if a compliant mechanism is designed achieving minimum length scale helps guarantee a longer device life-time by preventing tiny-hinges appearing at structural joints (high-stress regions).

Previous attempts have been made to impose minimum length scale in topology optimization. Within the density-based approach [4], Poulsen proposed the so-called MOLE (MOnotonicity based minimum LEngth scale) method [5], which achieves minimum length scale larger than the size of a circular “looking glass”. Guest [6] suggested projection schemes by projecting the nodal density into the element space of a minimum feature size. However, it does not resolve the “one-node hinge” problem in designing compliant mechanisms and simple projection may result in grey scale for some design problems [1]. The robust formulations [1, 2, 3], which take the eroded, dilated and (one or several) intermediate design realizations into account at the same time, impose length scale on the intermediate blueprint design only if the considered design realizations share the same topology. However, as pointed out in [2], the robust formulation does not necessarily guarantee a consistent topology for the realizations in different physical problems and the length scale can only be checked a posteriori. Another drawback of using a robust formulation is the high computational cost, that finite analysis is basically required for each design realization in every iteration. A perturbation based technique [7] proposed by Lazarov et. al is a computationally efficient solution. However, due to the locality of the approximation, it cannot provide a clear length scale control for compliant mechanism problems. Recently, a skeleton-based idea, which is similar to that in [8] with the level set method, is implemented using a density based method in [9]. Both minimum and maximum length scale are considered in their works [8, 9]. However, the sensitivity regarding the change of the medial-zone is neglected in the sensitivity analysis. Possible shortcomings of this approach are discussed in detail in [10]. Within the level set based method [11], Chen et al. [13] applies a quadratical energy functional to design a thin elongated structural layout with length scale. However, there is no explicit way to define the exact length scale with this formulation. A rigorous mathematic approach for imposing minimum and maximum length scale in level set based topology optimization is proposed in [10, 12]. Besides the above approaches, predefined engineering features with length scale can be designed and optimized using a CSG based level set approach as discussed in [14]. Another option is to directly consider the manufacturing characteristics in the optimization process, which can always ensure manufacturable designs of optimized performance [15, 16].

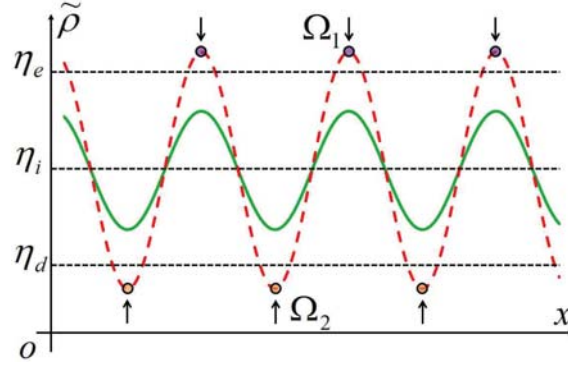


Figure 1: Re-designing a filtered field (from the solid to the dashed curve) to satisfy the conditions (i) – (ii) according to Eqs. (1) and (2). Minimum length scale is achieved on the physical field thresholded by η_i for the dashed curve.

In this study, a new approach is proposed based on a filtering-threshold topology optimization scheme [17], which utilizes a design field ρ ($0 \leq \rho \leq 1$), a filtered design field $\tilde{\rho}$ and a projected (physical) field $\bar{\rho}$. The idea is inspired from the work on topology optimization with robust formulations [1, 2, 3], where the optimized nominal design possess minimum length scale if all the considered design realizations $\bar{\rho}_\eta$ thresholded in a range $\eta \in (\eta_d, \eta_e)$ ($0 < \eta_d < \eta_i < \eta_e < 1$) share a consistent topology. One sufficient condition to the latter is as follows:

$$(i) \quad \tilde{\rho}(\mathbf{x}) \geq \eta_e, \quad \forall \mathbf{x} \in \Omega_1 = \{\mathbf{x} | \bar{\rho}_{\eta_i}(\mathbf{x}) = 1 \text{ and } \nabla \tilde{\rho} = 0\}; \quad (1)$$

$$(ii) \quad \tilde{\rho}(\mathbf{x}) \leq \eta_d, \quad \forall \mathbf{x} \in \Omega_2 = \{\mathbf{x} | \bar{\rho}_{\eta_i}(\mathbf{x}) = 0 \text{ and } \nabla \tilde{\rho} = 0\}; \quad (2)$$

where Ω_1 and Ω_2 represent the inflection region of the filtered field in the solid and void phase of the physical field, respectively. Fig. 1 illustrates this idea with a 1D example. The solid curve represents an initial filtered field, for which the physical fields thresholded at η_d, η_i, η_e possess different topologies. Re-designing it into the dashed curve as shown in the figure to satisfies (i) and (ii), a solid phase is ensured in Ω_1 for all the physical realizations thresholded by $\eta < \eta_e$ and a void phase remains in Ω_2 within $\eta > \eta_d$. As a result, all the physical realizations thresholded by $\eta \in (\eta_d, \eta_e)$ share a consistent topology and minimum length scale is expected on the blueprint design $\bar{\rho}_{\eta_i}$ for both solid and void phases. In this work, two geometric constraints are proposed to meet the above condition. By solving a constrained optimization problem, minimum length scale is realized without additional finite analysis, which alleviate the computational burden of using a robust formulation. This approach is purely geometrical and problem independent. Existing topology optimization framework can be easily extended to have minimum length scale in final optimized design by incorporating the proposed geometric constraints.

4. Geometric constraints for minimum length scale

The filtering-threshold topology optimization scheme [17] consists of a design field ρ , a filtered field $\tilde{\rho}$ and a physical field $\bar{\rho}$, whose relations are defined as follows:

$$\tilde{\rho}_i = \frac{\sum_{j \in \mathbf{N}_i} \omega(\mathbf{x}_j) v_j \rho_j}{\sum_{j \in \mathbf{N}_i} \omega(\mathbf{x}_j) v_j}, \quad \omega(\mathbf{x}_j) = R - |\mathbf{x}_i - \mathbf{x}_j|, \quad (3)$$

$$\bar{\rho}_i = \frac{\tanh(\beta \cdot \eta) + \tanh(\beta \cdot (\tilde{\rho}_i - \eta))}{\tanh(\beta \cdot \eta) + \tanh(\beta \cdot (1.0 - \eta))}. \quad (4)$$

where \mathbf{N}_i is the set of elements in the filter domain of the element i , R is the radius of the filter, v_j is the volume of the element j , β controls the steepness of the approximated Heaviside function and η is the threshold.

In order to fulfill the two requirements in Eqs. (1) and (2), two structural indicator functions are first defined to capture the inflection regions Ω_1, Ω_2 defined in Eqs. (1-2):

$$I^s = \bar{\rho} \cdot \exp(-c \cdot |\nabla \tilde{\rho}|^2), \quad (5)$$

$$I^v = (1 - \bar{\rho}) \cdot \exp(-c \cdot |\nabla \tilde{\rho}|^2), \quad (6)$$

where the subscripts s and v stand for the solid and void phase, respectively. The exponential term in Eqs. (5) and (6) annotates the inflection region of a filtered field ($|\nabla \tilde{\rho}| = 0$) with value 1, while the parameter c controls

the decay rate of I^s and I^v wherever $|\nabla\tilde{\rho}| \neq 0$. Because of numerical errors in calculating the gradient value ($\nabla\tilde{\rho}$), the parameter cannot be set arbitrarily large. Numerical experience implies that setting $c = r^4$ (where $r = R/h$ and h represents the element size) is effective in practice in capturing the inflection region during the optimization process. Based on the indicator functions, the geometric constraints are proposed as:

$$g^s = \frac{1}{n} \sum_{i \in \mathbf{N}} I_i^s \cdot [\min\{\tilde{\rho}_i - \eta_e, 0\}]^2 = 0, \quad (7)$$

$$g^v = \frac{1}{n} \sum_{i \in \mathbf{N}} I_i^v \cdot [\min\{\eta_d - \tilde{\rho}_i, 0\}]^2 = 0, \quad (8)$$

where n is the total number of elements. Satisfying these two constraints results in the value of the filtered field being larger than the threshold η_e at the inflection region Ω_1 and smaller than the threshold η_d at Ω_2 . Therefore, the sufficient condition is satisfied and minimal length scale is expected over the nominal design. The proposed geometric constraints are differentiable w.r.t. the design variable ρ and computationally cheap. They can be obtained from the value of the physical field $\tilde{\rho}$, the filtered field $\tilde{\rho}$ and its gradient $\nabla\tilde{\rho}$, which are directly available during the optimization process.

In practice, the equality constraints Eqs. (7-8) cannot be strictly satisfied due to numerical errors. It is pertinent to apply an relaxed version to a topology optimization problem:

$$\begin{aligned} \min : & \quad F(\mathbf{u}(\boldsymbol{\rho}), \boldsymbol{\rho}), \\ \text{s.t.} : & \quad g_j \leq 0, \quad j = 1 : m, \\ & \quad : \quad g^s \leq \varepsilon, \\ & \quad : \quad g^v \leq \varepsilon, \\ & \quad : \quad 0 \leq \boldsymbol{\rho} \leq 1. \end{aligned} \quad (9)$$

where F and g_j are the objective functional and constraints of the original problem respectively and ε is a small number. The minimum length scale on the final result is determined by the radius of the filter, the considered threshold range (η_d, η_e) and the threshold η_i for the blueprint design. Readers are referred to [2, 18] for predicting the minimum length scale using the linear-hat based filtering.

5. Numerical Examples

In this section, the proposed approach is applied to two benchmark examples. The constrained problem (9) is solved by the method of moving asymptotes (MMA) [19].

The first example is to design a compliant inverter with minimum length scale. The optimization problem is to maximize the output displacement, of which the direction is opposite to that of the external force. The detailed problem formulation and parameter definitions can be found in [2]. Fig. 2(a) shows a standard topologically optimized inverter containing tiny hinges at structural joints. The tiny hinges will cause high stress when the mechanism deforms and thus they shall be prevented in the blueprint design. Fig. 2(b,c) shows two such improved designs by applying the proposed geometric constraints. Different minimum length scales are achieved by adopting different threshold ranges $(\eta_d, \eta_e) = (0.4, 0.6)$ and $(0.3, 0.7)$, respectively. As the minimum length scale increases, the deforming capability (the absolute displacement) of the inverter reduces from $F = 3.81$ to 3.61. In this example, the design domain is discretized into 150×300 quadrilateral elements and the following parameters are implemented: $E_0 = 1$, $E_{min} = 10e-9$, $V^* = 0.2$, $k_{in} = 0.2$, $k_{out} = 0.005$ and $r = 10$ elements.

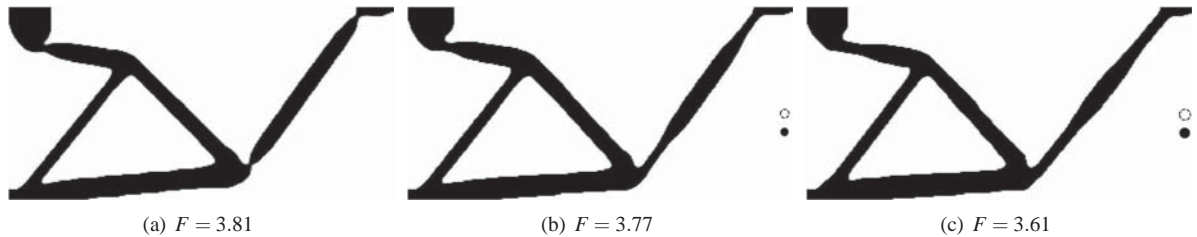


Figure 2: Optimized compliant mechanisms with different minimum length scale: (a) without length scale control, containing tiny hinges at structural joints; (b) with minimum length scale (equals to the size of the dashed and solid circles), considered threshold range $\eta \in (0.4, 0.6)$; (c) $\eta \in (0.3, 0.7)$.

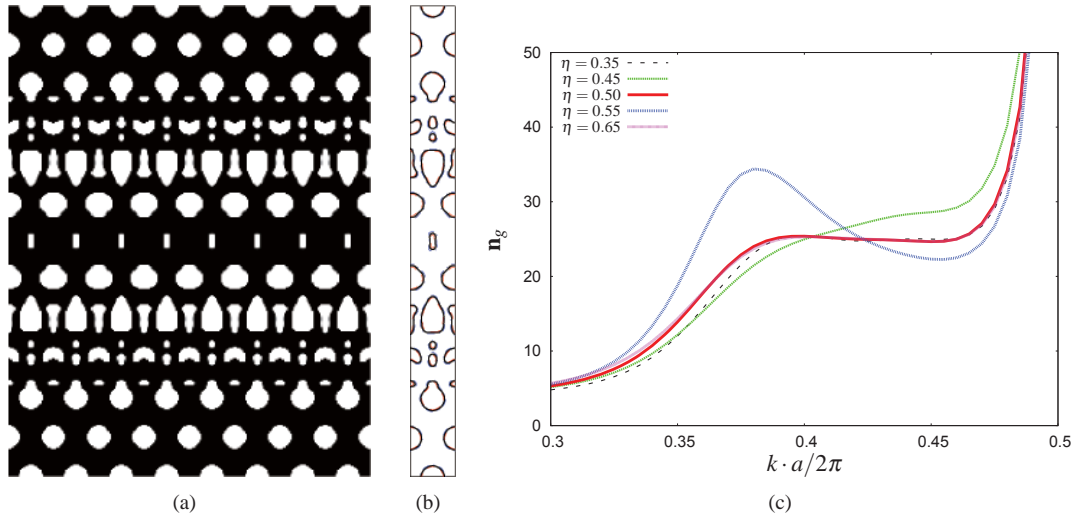


Figure 3: Optimized slow light waveguide by using both a robust formulation and geometric constraints. (a) the waveguide composed of 8 repeated cells; (b) contours in a single cell, the blueprint (in black bold lines), dilated (in blue dashed lines) and eroded design realization (in red dash-dotted lines); (c) performance of different realizations.

The second problem studies the design of a dispersion engineered slow light waveguide, which is obtained by minimizing the errors between actual group index n_g and a prescribed group index $n_g^* = 25$ in a given wavenumber range $k \in [0.3875, 0.4625] \cdot 2\pi/a$, where a is the width of the single cell shown in Fig. 3(b). The original problem formulation can be found in [20]. It is known that using a robust formulations cannot always guarantee the same topology for all the considered design realizations [20]. Here, by incorporating the proposed geometric constraints into the robust formulation, Fig. 3(a) shows the new optimized result containing 8 cells, in which minimum length scale in both solid and void phases are clearly identified. As shown in Fig. 3(b), the contours of the eroded, blueprint and dilated designs indicate a same topology. Equally optimized performance is achieved for the considered three designs as shown in Fig. 3(c). However, because the robust formulation here only takes three designs into account, the other intermediate realizations (e.g. $\eta = 0.45, 0.55$) still do not behave as well as the blueprint. This issue may be alleviated by including more realizations in the formulation. In this example, the design domain (one cell) is discretized into a 512×32 quad mesh. The following parameters are implemented: filter radius $r = 3.75$ elements, $\eta_d = 0.35$, $\eta_i = 0.5$ and $\eta_e = 0.65$, $\varepsilon = 10^{-6}$ and $\beta = 50$.

6. Conclusions

This paper introduces a novel approach to control minimum length scale in topology optimization results by using geometric constraints. Two numerical examples from different physical problems are presented to show the general applicability of this approach. Further investigations will be carried out on extending the current idea into maximum length scale control.

7. Acknowledgements

The authors acknowledge the financial support from the European Research Project “LaSciSO” (Grant No. 285782). A full length version of this paper including more theory, background and detailed examples has been submitted for publication in an international journal.

8. References

- [1] O. Sigmund, Morphology-based black and white filters for topology optimization, *Structural and Multidisciplinary Optimization*, 33, 401-424, 2007.
- [2] F. Wang, B. Lazarov, O. Sigmund, On projection methods, convergence and robust formulations in topology optimization, *Structural and Multidisciplinary Optimization*, 43, 767-784, 2011.
- [3] M. Schevenels, B.S. Lazarov, O. Sigmund, Robust topology optimization accounting for spatially varying manufacturing errors, *Computer Methods in Applied Mechanics and Engineering*, 200, 3613-3627, 2011.

- [4] M. Bendsøe, O. Sigmund, *Topology Optimization: Theory, Methods and Applications*, Springer-Verlag, Berlin, 2003.
- [5] T.A. Poulsen, A new scheme for imposing a minimum length scale in topology optimization, *International Journal for Numerical Methods in Engineering*, 57, 741-760, 2003.
- [6] J.K. Guest, J.H. Prévost, T. Belytschko, Achieving minimum length scale in topology optimization using nodal design variables and projection functions, *International Journal for Numerical Methods in Engineering*, 61, 238-254, 2004.
- [7] B.S. Lazarov, M. Schevenels, O. Sigmund, Topology optimization with geometric uncertainties by perturbation techniques, *International Journal for Numerical Methods in Engineering*, 90, 1321-1336, 2012.
- [8] X. Guo, W. Zhang, W. Zhong, Explicit feature control in structural topology optimization via level set method, *Computer Methods in Applied Mechanics and Engineering*, 272, 354-378, 2014.
- [9] W. Zhang, W. Zhong, X. Guo, An explicit length scale control approach in SIMP-based topology optimization, *Computer Methods in Applied Mechanics and Engineering*, 282, 71-86, 2014.
- [10] G. Allaire, F. Jouve, G. Michailidis, Thickness control in structural optimization via a level set method, (2014) < hal – 00985000 >, available at: <https://hal.archives-ouvertes.fr/hal-00985000>.
- [11] M.Y. Wang, X. Wang, D. Guo, A level set method for structural topology optimization, *Computer Methods in Applied Mechanics and Engineering*, 192, 227-246, 2003.
- [12] G. Michailidis, Manufacturing Constraints and Multi-Phase Shape and Topology Optimization via a Level-Set Method, Optimization and Control, *Ecole Polytechnique X*, (2014), available at: <https://tel.archives-ouvertes.fr/pastel-00937306>.
- [13] S. Chen, M.Y. Wang, A. Liu, Shape feature control in structural topology optimization, *Computer-Aided Design*, 40, 951-962, 2008.
- [14] M. Zhou, M.Y. Wang, Engineering feature design for level set based structural optimization, *Computer-Aided Design*, 45, 1524-1537, 2013.
- [15] M. Jansen, B.S. Lazarov, M. Schevenels, O. Sigmund, On the similarities between micro/nano lithography and topology optimization projection methods, *Structural and Multidisciplinary Optimization*, 48, 717-730, 2013.
- [16] M. Zhou, B.S. Lazarov, O. Sigmund, Topology optimization for optical projection lithography with manufacturing uncertainties, *Applied Optics*, 53, 2720-2729, 2014.
- [17] O. Sigmund, K. Maute, Topology optimization approaches, *Structural and Multidisciplinary Optimization*, 48, 1031-055, 2013.
- [18] X. Qian, O. Sigmund, Topological design of electromechanical actuators with robustness toward over- and under-etching, *Computer Methods in Applied Mechanics and Engineering*, 253, 237-251, 2013.
- [19] K. Svanberg, The method of moving asymptotes - a new method for structural optimization, *International Journal for Numerical Methods in Engineering*, 24, 359-397, 1987.
- [20] F. Wang, J.S. Jensen, O. Sigmund, Robust topology optimization of photonic crystal waveguides with tailored dispersion properties, *Journal of the Optical Society of America B*, 28, 387-397, 2011.

Adaptive multi-point sequential sampling methodology for highly nonlinear automotive crashworthiness design problems

Siliang Zhang*, Zhengchao Song, Guohong Shi, Rongying Qiu

Pan Asia Technical Automotive Center, Shanghai, P.R. China, zhangsiliangasn@163.com

1. Abstract

Automotive crashworthiness design is a highly expensive and non-linear problem. In metamodel-based crash design problem, the prediction error of the metamodel may induce a local or a wrong optimum. In the past few years, the multi-point objective-oriented sequential sampling methods have been demonstrated an efficient way to improve the fitting accuracy and find the true optimum. However existing infilling criteria are restricted to specify the number of the sequential samples obtained in each iteration. It is not practical for complex engineering design problems. In this paper, a new adaptive multi-point sequential sampling method is developed. The sequential sample size is determined by the prediction states of the fitting metamodels. To demonstrate the benefits, the new proposed method is applied to a highly nonlinear crashworthiness design problem. Results show that the proposed method can mitigate the effect of the prediction error, and more efficiently identify the crashworthiness design solution compared to the conventional approach.

2. Keywords: Metamodel-based optimization, objective-oriented sequential sampling method, adaptive multi-point strategy, crashworthiness design.

3. Introduction

Finite element (FE) simulations have been a useful tool for replacing the physical tests in crashworthiness design. However, high fidelity FE models are often computationally intensive, taking hours and even days to complete one computation cycle. A common approach to address this challenge is to employ metamodeling method predicting the simulation responses. The metamodel provides a cheap-to-run surrogate model to approximate the complex simulations [1]. The effectiveness of different metamodeling techniques vary based on the different modeling criteria, amount of available samples, and the behavior of the simulation responses [2].

However in complex engineering optimizations, the primal challenge is how to determine the number of samples required and how to allocate samples. Comparing to traditional one-stage DOE methods (Orthogonal experimental design, Uniform Design, Latin Hypercube Design et. al), sequential sampling methods have been identified as a more efficient strategy. In previous investigations, the sequential sampling criteria can be classified into two categories: model-oriented and objective-oriented. The model-oriented methods focus on the goal of creating a globally accurate metamodel, while the objective-oriented sequential sampling strategies have been demonstrated to have a higher efficiency of finding the global optimum [3]. The most widely used objective-oriented sequential sampling criteria, Efficient Global Optimization (EGO) algorithm, is first developed by Jones [4].

The EGO method only finds one point in one iteration, resulting in many sequential cycles before reaching convergence. To take advantage of the parallel computation capability and save the total amount of iterations, a multi-point sampling strategy is needed. Schonlau [5] defined the concept of multi-point sequential sampling method. Viana [6] extended the Probability of Improvement function to include multiple points at the same time. Zhu and Zhang [7] developed a new double-loop strategy to find q samples via Kriging Believer method.

However existing infilling criteria are restricted to specify the number of the sequential samples obtained in each iteration. It is not practical for complex engineering design problems. In this paper, a new adaptive multi-point sequential sampling method is developed. The following section reviews the concept of multi-point sequential sampling methods, and introduces the proposed adaptive strategy. A new infilling criterion is developed to determine whether there is a need to find one more sample. In Section 5, to demonstrate the effectiveness, the proposed adaptive multi-point sequential sampling method is applied to an automotive crashworthiness design problem. Finally, the discussions and conclusion are summarized in Section 6.

4: Adaptive multi-point sequential sampling methodology for complex engineering optimization

4.1. Multi-point Sequential sampling method for constrained optimization problem

For a constrained engineering optimization problem, the mathematical formulation can be defined as:

$$\begin{aligned} \min: & \quad y(\mathbf{x}) \\ \text{s.t:} & \quad g_i(\mathbf{x}) \leq \beta_i, \quad i = 1, 2, \dots, k \end{aligned} \quad (1)$$

where \mathbf{x} is the design variables; y and g_i represent the objective response and constraint responses; β_i is the i th constraint threshold. When the objective and constraint responses are replaced by metamodels ($\hat{y}(\mathbf{x})$ and $\hat{g}_i(\mathbf{x})$), considering the metamodeling imperfection, the prediction error affects the optimization accuracy and constraint feasibility, especially in high-dimensional and highly-nonlinear engineering problems.

The objective-oriented strategy can spread new samples to balance the optimization exploration and accuracy improvement. Evaluating the effects of prediction error on the objective responses $\hat{y}(\mathbf{x})$ and the constraints $\hat{g}_i(\mathbf{x})$, the generalized expected improvement function (GEI) of a constrained optimization problem can be defined as [7].

$$\max : \text{GEI}(\mathbf{x}) = \sqrt{\text{REI}(\mathbf{x}) \cdot \text{EV}(\mathbf{x})} \quad (2)$$

$$\text{where : REI}(\mathbf{x}) = (y_{\min} - \hat{y}(\mathbf{x})) \cdot \Phi\left(\frac{y_{\min} - \hat{y}(\mathbf{x})}{\sigma_y(\mathbf{x})}\right) + \sigma_y \cdot \phi\left(\frac{y_{\min} - \hat{y}(\mathbf{x})}{\sigma_y(\mathbf{x})}\right)$$

$$\text{EV}(\mathbf{x}) = \left[\prod_{i=1}^k \Phi\left(\frac{\beta_i - \hat{g}_i(\mathbf{x})}{\sigma_{g_i}(\mathbf{x})}\right) \right]^{1/k}$$

where k is the number of constraint responses; y_{\min} is the minimal objective response of the sampled points; $\hat{y}(\mathbf{x})$ and $\hat{g}_i(\mathbf{x})$ indicate the predicted value of the objective and constraint response respectively; $\phi(\mathbf{x})$ and $\Phi(\mathbf{x})$ represent the probability density function and cumulative density function of a standard normal distribution.

It is an efficient way to choose the global and quasi-local optimums of the GEI function as the sequential [8]. It should be noted that existing multi-points methods are developed to obtain a constant number q of sequential samples. But in real engineering problems, it is difficult to guess how many samples are needed in each cycle. A complex problem with a small q still needs many iterations, while with an over large q may induce intensive simulations. The following section will introduce a new adaptive multi-point sequential sampling method. The number q in each iteration is decided by the prediction states of the optimization problems adaptively.

4.2. Adaptive multi-point sequential sampling method for complex engineering optimization problem

The infilling criterion is the most important factor in sequential sampling process. In order to improve the sequential sampling efficiency, the weighted contribution of a new point is developed to replace the conventional generalized Expected Improvement function. The modified q GEI function is formulated as:

$$q\text{GEI} = \begin{cases} \text{GEI}, & q = 1 \\ \left(\frac{\text{GEI}}{q\text{GEI}_1}\right)^m, & q > 1 \end{cases} \quad (3)$$

where q is the number of the sequential samples obtained in each iteration; $q\text{GEI}_1$ represents the $q\text{GEI}$ value of the 1st sequential sample ($q = 1$); m is the power number. After the first point is found, the power function m of GEI downplays the relative contributions of the new points. As shown in Figure 1, when $m = 1$, the $q\text{GEI}$ function represents the relative GEI value. As the m value increases, the regions with small GEI will be diminished. If m is set to 2, the point where the GEI value is less than 10% of the $q\text{GEI}_1$ will be neglected. If m is set to 4, the point where the GEI value is less than 35% of the $q\text{GEI}_1$ will be neglected. Using the $q\text{GEI}$ function in the sequential sampling process, more efforts will be made in the regions with higher contribution.

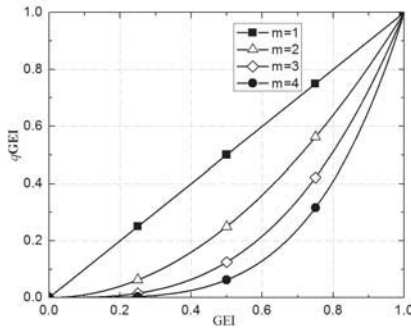


Figure 1: The influence of the m value in the $q\text{GEI}$ function

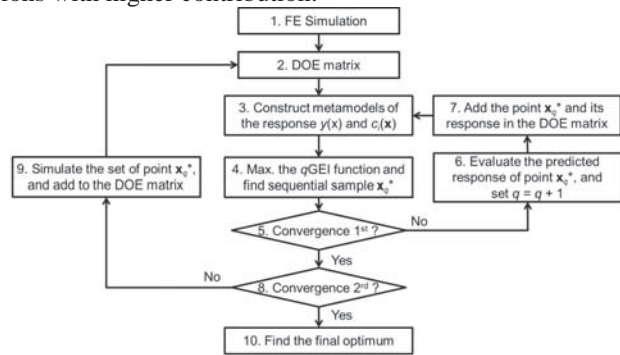


Figure 2: The flowchart of the proposed adaptive multi-point sequential sampling process

The true solution is likely to be near the inferior optimum of the infilling criterion, rather than the global optimum with the largest EI function. In this paper, the concept of the Kriging Believer strategy is adopted in the adaptive sequential sampling method. Different from any strategies in previous studies, the Kriging Believer strategy treats the predicted response as the true response during the sequential sampling process. The sequential samples obtained in each iteration are allocated to the global and quasi-local optimums.

The flowchart of the proposed method is shown in Figure 2.

Step 1: Generate a set of samples, and extract the simulated responses of these N training samples.

Step 2: Update the DOE matrix of the n samples (N initial DOE samples and all sequential samples).

Step 3: Based on the true observations at \mathbf{x}_n and predicted responses at \mathbf{x}_q , the Kriging models of the objective responses $\hat{y}(\mathbf{x})$ and constraint responses $\hat{c}_i(\mathbf{x})$ are constructed. \mathbf{x}_q is the sequential samples in the q^{th} iteration.

Step 4: Maximize the infilling criterion $q\text{GEI}$ and find the next sequential sample \mathbf{x}_q .

Step 5: Check the convergence. If the 1st stopping criterion is satisfied, go to **Step 8**.

Step 6: Evaluate the predicted response $\hat{y}(\mathbf{x})$ and $\hat{c}_i(\mathbf{x})$ of the newly added point \mathbf{x}_q , and set $q = q+1$.

Step 7: Add the sample \mathbf{x}_q into the training DOE samples.

Step 8: Check the convergence. If the 2nd stopping criterion is satisfied, the sequential sampling process is converged and goes to **Step 10**.

Step 9: Simulate the obtained samples \mathbf{x}_q by FE models, and add these points into the training samples n .

Step 10: After the sequential sampling process is terminated, the final design solution will be found.

5. Engineering application in a crashworthiness design problem

In this section, the benefits of the proposed adaptive sequential sampling method are demonstrated in a complex crashworthiness design example. Two different strategies are considered in this section:

- Conventional multi-point sequential sampling method with a constant q (GEI_cq): the sequential sampling method found q samples in each iteration. The sequential infilling criterion is defined by Eq. (2).
- Proposed adaptive multi-point sequential sampling method (GEI_aq): the sequential samples found in each iteration are determined by the prediction states, and the infilling criterion is defined by Eq. (3).

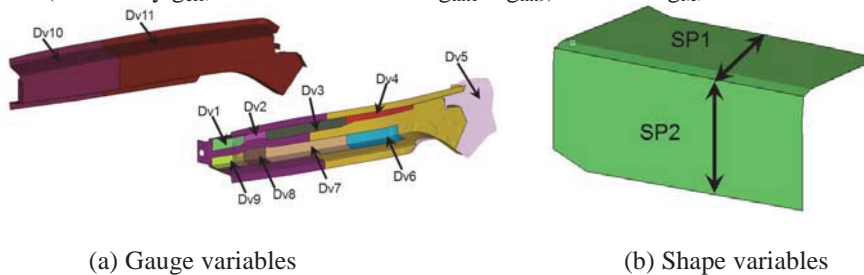
5.1. Crashworthiness design application

In the automotive crashworthiness design, FE simulations are used to predict crash performances. Since full size automotive simulation models are computationally expensive, metamodeling techniques are widely utilized to build surrogate models. In this section, a frontal impact design problem is utilized to demonstrate the effectiveness of the proposed adaptive multi-point sequential sampling method in real engineering design. The FE model is shown in Figure 3. The average mesh size is 5 mm. For the frontal impact investigation, the regulations and test configurations in the China National Crash Legislation of frontal impact (GB11551-2003) are followed. Considering the strain rate sensitivity of the sheets in high speed impact, stress versus plastic strain curves under different strain rates are defined in a load table. These curves are obtained from physical tension experiments.



Figure 3: Full-size finite element model of frontal impact simulation

The frontal side rail is the critical part in absorbing frontal impact, as shown in Figure 4. The sheet gauge and the component shape are important for absorbing the impact energy. Considering the symmetry of the rail structure, 11 sheet gauges and 16 shape variables are chosen as the design variables, as shown in Table 1. In this crashworthiness design problem, the Effective Acceleration f_{acc} is defined as the objective response, while ten crash performances (Efficiency g_{eff} , structural Intrusions $g_{\text{int}1} \sim g_{\text{int}9}$) and mass g_M , are treated as the constraints.



(a) Gauge variables

(b) Shape variables

Figure 4: Design variables of the crashworthiness design

Table 1: Design variables of the automotive crashworthiness design

	Component	Variables	DV	Original/mm	LB/mm	UB/mm
Gauge DV's	Upper Reinf. 1	Dv1	x1	1.20	0.60	1.60
	Upper Reinf. 2	Dv2	x2	1.20	0.60	1.60
	Upper Reinf. 3	Dv3	x3	1.20	0.60	1.60
	Upper Reinf. 4	Dv4	x4	1.20	0.60	1.60
	Frontal side rail outer	Dv5	x5	1.40	1.00	1.80
	Lower Reinf. 1	Dv6	x6	1.20	0.60	1.60
	Lower Reinf. 2	Dv7	x7	1.20	0.60	1.60
	Lower Reinf. 3	Dv8	x8	1.20	0.60	1.60
	Lower Reinf. 4	Dv9	x9	1.20	0.60	1.60
	Frontal side rail inner 1	Dv10	x10	1.40	1.00	1.80
	Frontal side rail inner 2	Dv11	x11	1.50	1.00	1.80
Shape DV's	Upper Reinf. 1 SP1	Dv12	x12	0.00	0.00	15.00
	Upper Reinf. 1 SP2	Dv13	x13	0.00	0.00	15.00
	Upper Reinf. 2 SP1	Dv14	x14	0.00	0.00	15.00
	Upper Reinf. 2 SP2	Dv15	x15	0.00	0.00	15.00
	Upper Reinf. 3 SP1	Dv16	x16	0.00	0.00	15.00
	Upper Reinf. 3 SP2	Dv17	x17	0.00	0.00	15.00
	Upper Reinf. 4 SP1	Dv18	x18	0.00	0.00	15.00
	Upper Reinf. 4 SP2	Dv19	x19	0.00	0.00	15.00
	Lower Reinf. 1 SP1	Dv20	x20	0.00	0.00	15.00
	Lower Reinf. 1 SP2	Dv21	x21	0.00	0.00	15.00
	Lower Reinf. 2 SP1	Dv22	x22	0.00	0.00	15.00
	Lower Reinf. 2 SP2	Dv23	x23	0.00	0.00	15.00
	Lower Reinf. 3 SP1	Dv24	x24	0.00	0.00	15.00
	Lower Reinf. 3 SP2	Dv25	x25	0.00	0.00	15.00
	Lower Reinf. 4 SP1	Dv26	x26	0.00	0.00	15.00
	Lower Reinf. 4 SP2	Dv27	x27	0.00	0.00	15.00

5.2. Sequential improvement and optimization results

All structural performances are interpolated by Kriging method. The optimization formulation is defined as:

$$\begin{aligned}
 \min: & \quad f_{acc} \\
 \text{s.t.} : & \quad c_1 = g_{int1} / \beta_1 \leq 1 \\
 & \quad c_9 = g_{in9} / \beta_9 \leq 1 \\
 & \quad c_{10} = 2 - g_{eff} / \beta_{10} \leq 1 \\
 & \quad c_{11} = g_M / \beta_{11} \leq 1
 \end{aligned} \tag{4}$$

where β_i represents the i th constraint target. Based on 180 samples generated by the Latin Hypercube method, the metamodel-based optimization results are shown in Table 2. But when the optimization solution is confirmed by the FE simulation model, there has a large discrepancy between predicted and simulated objective response f_{acc} . And two constraint responses (c_{10} , c_{11}) violate the design limits. The prediction error misleads to find an infeasible solution. In order to mitigate the prediction error, the multi-point sequential sampling method is used.

Table 2: The optimization results based on initial DOE samples

	Opt. Result	Target	Kriging-based	Simulation confirmation
Objective	f_{acc}	min.	0.91	1.04
	c_1		0.28	0.33
Constraints	c_2		0.35	0.48
	c_3		0.58	0.77
	c_4	≤ 1	0.18	0.25
	c_5		0.54	0.66
	c_6		0.75	0.81
	c_7		0.45	0.61
	c_8		0.70	0.62

c_9	0.82	0.88
c_{10}	0.99	1.15
c_{11}	0.95	1.01

To demonstrate the benefits of the proposed method, the conventional multi-point sequential sampling strategy GEI_cq with a constant q is also adopted in this example, formulated as:

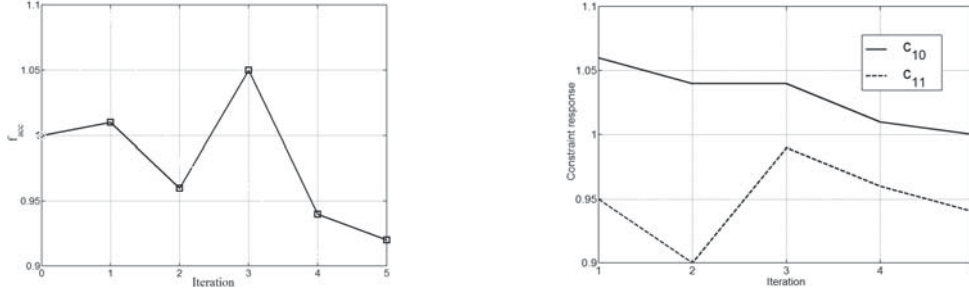
$$\max : \text{GEI}_{cq}(\mathbf{x}) = \sqrt{\text{REI}(\mathbf{x}) \cdot \text{EV}(\mathbf{x})} \quad (5)$$

$$\text{where : REI}(\mathbf{x}) = (f_{acc} - \hat{f}_{acc}(\mathbf{x})) \cdot \Phi\left(\frac{f_{acc}^{\min} - \hat{f}_{acc}(\mathbf{x})}{\sigma_f(\mathbf{x})}\right) + \sigma_f \cdot \phi\left(\frac{f_{acc}^{\min} - \hat{f}_{acc}(\mathbf{x})}{\sigma_f(\mathbf{x})}\right)$$

$$\text{EV}(\mathbf{x}) = \left[\prod_{i=1}^{11} \Phi\left(\frac{1 - \hat{c}_i(\mathbf{x})}{\sigma_{c_i}(\mathbf{x})}\right) \right]^{1/11}$$

In this infilling criterion, f_{acc}^{\min} represents the minimal objective response value of the sampled points, and $q = 5$ samples are newly added in each iteration. The limit criterion is utilized in this crashworthiness design problem: when GEI_{cq1} is less than 1%, the sequential sampling process will be terminated.

The GEI_cq method is converged after 5 iterations. The optimization solution is obtained based on initial training samples and the newly added samples. The solution is confirmed by FE simulation. Figure 5 illustrates the convergence history of the GEI_cq method. The objective response f_{acc} and two critical constraint responses c_{10}/c_{11} are monitored. The objective response f_{acc} reduced from 1.00 to 0.92, achieving 8% improvement, while two critical constraint response c_{10} and c_{11} are successively approaching to the design target 1. It demonstrates that the multi-point sequential sampling method GEI_cq can mitigate the prediction error in both objective response f_{acc} and all constraint responses, and ensure the accuracy and feasibility of the design solution.



(a) Objective response f_{acc}

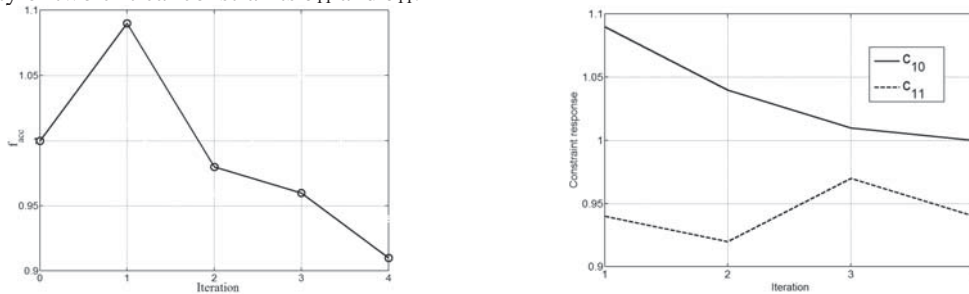
(b) Constraint responses c_{10} and c_{11}

Figure 5: Convergence history of the GEI_cq method

The newly proposed adaptive multi-point sequential sampling method GEI_aq do not need to define a number q , and can find a proper amount of sequential samples based on the prediction states of the fitting models. The infilling criterion of the proposed method is defined as:

$$\max : \text{GEI}_{aq} = \begin{cases} \text{GEI}_{cq}, & i = 1 \\ (\text{GEI}_{cq} / \text{GEI}_{aq1})^2, & i > 1 \end{cases} \quad (6)$$

Similar to the GEI_cq method, when the GEI_{aq1} value is less than 1%, the sequential improvement process terminates. The convergence histories of the proposed GEI_aq method are shown in Figure 6. The confirmed objective response reduced from 1.00 to 0.91, while two critical constraints satisfy the design requirements. The FE simulated results shows that the proposed GEI_aq can improve the objective response f_{acc} , and ensure the feasibility of two critical constraints c_{11} and c_{11} .



(a) Objective response f_{acc}

(b) Constraint responses c_{10} and c_{11}

Figure 6: Convergence history of the proposed GEI_aq method

The sequential samples obtained by these two methods are compared in Figure 7. In the 1st sequential iteration, the

GEI_cq with a constant q explored and found 5 new samples to improve the fitting states. But when the proposed adaptive method GEI_aq is used, 8 samples are allocated in the design space. It demonstrates that based on initial 180 training samples, the fitting responses of the crashworthiness design problem has large prediction error, and the number q used in the GEI_cq method is not enough. After the 1st iteration, the interpolation accuracy of the crash responses has been improved. Fewer points are needed in the next iterations. The conventional GEI_cq method with a constant q allocated more and more samples on the points with lower contribution. In summary, the proposed method is converged in the 4th iteration and 16 sequential samples are newly added. Comparing to the conventional GEI_cq method, the proposed strategy converge to the true crashworthiness solution faster. It demonstrates a higher efficiency in the complex engineering design problem.

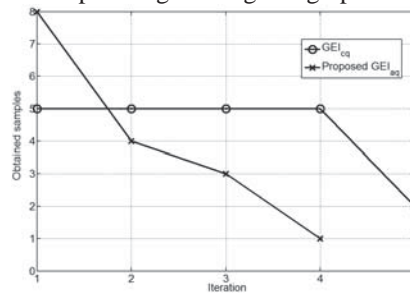


Figure 7: The samples obtained by two different sequential sampling methods

6. Discussions and conclusions

A few observations are made:

- The proposed adaptive multi-point sequential sampling method can decide the sample size by the prediction states of the design responses. It is beneficial for the problems where simulation models are computationally expensive and the parallel computing ability can be utilized to calculate many simulations at the same time.
- The crashworthiness design is a highly nonlinear problem. It is found that comparing to conventional sequential sampling method, the proposed adaptive strategy not only can improve the objective response (Effective Acceleration f_{acc}) and ensure the feasibility of ten crash constraint responses, but also can converge to the true solution in fewer iterations. It demonstrates the effectiveness and the efficiency of the newly proposed method.

7. References

- [1] G.G. Wang and S. Shan, Review of metamodeling techniques in support of engineering design optimization, *International Journal of Mechanical Design*, 129(4), 370-380, 2007.
- [2] R. Jin, W. Chen and T.W. Simpson, Comparative studies of metamodeling techniques under multiple modelling criteria. *Structural and Multidisciplinary Optimization*, 23(1), 1-13, 2001.
- [3] S.K. Chen, Y. Xiong and W. Chen, Multiresponse and multistage metamodeling approach for design optimization. *AIAA Journal*, 47(1), 206-218, 2009.
- [4] D.R. Jones, M. Schonlau and W.J. Welch, Efficient global optimization of expensive black-box functions. *Journal of Global Optimization*, 13(4), 455-462, 1998.
- [5] M. Schonlau, Computer experiments and global optimization. Ph.D. dissertation, University of Waterloo, Waterloo, 1997.
- [6] F.A.C. Viana and R.T. Haftka, Surrogate-based optimization with parallel simulations using the probability of Improvement, *13th AIAA/ISSMO Multidisciplinary Analysis and Optimization Conference*, Fort Worth, USA, September 13-15, 2010.
- [7] P. Zhu, S.L. Zhang and W. Chen, Multi-point objective-oriented sequential sampling strategy for constrained robust design, *Engineering Optimization*, 2014, DOI: 10.1080/0305215X.2014.887705.
- [8] W. Ponweiser, T. Wagner and M. Vincze, Clustered multiple generalized expected improvement: A novel infill sampling criterion for surrogate models, *IEEE Congress on Evolutionary Computation*, Hong Kong, P.R. China, 2008.

Comparison of some commercial software systems for structural optimization

Wook-han Choi¹, Cheng-guo Huang², Jong-moon Kim³, Gyung-Jin Park^{3*}

¹ Hanyang University, Seoul, Republic of Korea, dreamybird@hanyang.ac.kr

² Hanyang University, Seoul, Republic of Korea, huangcg@hanyang.ac.kr

³ Hanyang University, Seoul, Republic of Korea, thcbdie@hanyang.ac.kr

⁴ Hanyang University, Ansan, Republic of Korea, gjpark@hanyang.ac.kr

1. Abstract

Mathematical optimization theories are employed for the design of structures in structural optimization. These days, structural optimization is widely utilized for practical problems due to well-developed commercial software systems. Three representative general-purpose structural optimization systems such as Genesis, MSC.Nastran and OptiStruct are investigated and evaluated by solving various test examples in different scales. The performance of structural optimization depends on the quality of the optimum solution and the computational time, and these aspects are compared from the application viewpoint. For fair comparison, the same formulations are defined, and the same optimization methods are adopted for each example. Also, the same system environment is prepared, and the same optimization parameters are used. Linear static response size, shape and topology optimizations are applied to the examples and the results are compared. No system seems to be the best in all the cases and each system has advantages and drawbacks depending on the application. In general, Genesis is excellent in the computational time while OptiStruct gives excellent solutions, especially in topology optimization. Meanwhile, MSC.Nastran presents excellent solutions in shape optimization.

2. Keywords: Structural Optimization, Design Software, Performance comparison

3. Introduction

Optimization generally finds design variables to maximize/minimize an objective function, while design constraints are simultaneously satisfied. In structural optimization, the optimization problem is defined for the design of a structure. Nowadays, structural optimization is widely accepted due to the development of the finite element method (FEM) [1-3]. Structural analysis and optimization techniques have been continuously developed based on FEM. Recently, commercial design software systems are also well-developed to solve structural design problems, and they have their own FE analysis modules. They are MSC.Nastran [4], Genesis [5], OptiStruct [6], ANSYS [7], TOSCA [8], etc.

As the FE models become more complex and larger, designers are interested in the decision on the choice of a structural optimization software system. One of the reasons is that the systems give different performances. It is natural that a designer wants to use an appropriate system for her/his applications. However, there is no comparison study for the structural optimization systems. Some researches were performed with regard to the performance of structural optimization methods. Structural optimization is classified into the direct method and the approximation method. The direct method directly applies nonlinear programming (NLP) to a structural optimization problem; therefore, an NLP algorithm controls the overall process. On the other hand, the functions are approximated to explicit functions of design variables and an NLP algorithm is applied to the approximated problem. An approximation method is generally employed by commercial systems for structural optimization while the direct method is generally used in the academic sites. The performances of the direct method and the approximation method were compared [9]. The efficiency of an NLP algorithm is not very critical in the approximation method while it is crucial in the direct method. A comparative study of the optimization software systems, which have various NLP algorithms, was performed in [10].

In this research, three popularly used commercial structural optimization software systems such as Genesis, MSC.Nastran 2013.1 [4], Genesis 13.1 [5] and OptiStruct 13.0 [6] are investigated and evaluated. These software systems provide optimum solutions based on a gradient based optimization method and have their own FE analysis modules. Also, they have all the capabilities for size, shape, topology optimizations. The systems that do not have these conditions are excluded in this study. Linear static response size, shape and topology optimizations are explored and compared by various test examples. The examples cover small, medium and large scale problems. Evaluations of the systems are made for the quality of the optima and the computational cost.

4. Environment for comparison

Various factors can have influence on the performance of the structural optimization software system. They can be classified into the optimization environment and the system environment. The optimization environment consists of optimization formulation, convergence criteria, utilized optimization method, move limit strategy, constraint screening method, etc. Meanwhile, the system environment is determined by the performances of the computer such as the operating system, CPU, amount of memory usage, etc. It should be assured that the same conditions are used for a fair comparison. Some conditions are controllable in one software system but uncontrollable in another system. In that case, unification of the variables is made as much as possible. If the unification is impossible, default values of the software systems are used.

4.1 Optimization formulation

The formulation of linear static response structural optimization is represented as follows [11-12]:

$$\begin{aligned}
 &\text{Find} && \mathbf{b} \in R^n, \mathbf{z} \in R^l, \zeta \in R^1 \\
 &\text{to minimize} && f(\mathbf{b}, \mathbf{z}, \zeta) \\
 &\text{subject to} && \mathbf{K}(\mathbf{b})\mathbf{z} = \mathbf{f} \\
 &&& \mathbf{K}(\mathbf{b})\mathbf{y} - \zeta\mathbf{M}(\mathbf{b})\mathbf{y} = 0 \\
 &&& g_j(\mathbf{b}, \mathbf{z}, \zeta) \leq 0, j = 1, \dots, m \\
 &&& \mathbf{b}_L \leq \mathbf{b} \leq \mathbf{b}_U
 \end{aligned} \tag{1}$$

where \mathbf{b} is the design variable vector, \mathbf{z} are the state variable vector, and ξ and \mathbf{y} are the eigenvalue and eigenvector, respectively. n is the number of the design variables, l is the number of the state variables, and m is the number of the constraints, respectively. \mathbf{b}_L and \mathbf{b}_U are the lower bound and the upper bound of the design variable vector \mathbf{b} , respectively. f is the objective function and g_j is the j th constraint. \mathbf{K} is the stiffness matrix, \mathbf{M} can be either the mass matrix or geometry matrix, respectively. Each example uses an identical optimization formulation for all the software systems for a fair comparison.

4.2 Optimization method

An optimization algorithm has to be selected, but this selection is not very important because an approximation is used for the software systems. Modified method of feasible directions (MMFD), sequential linear programming (SLP) and sequential quadratic programming (SQP) are commonly supported by the three software systems. In MSC.Nastran, an optimization method can be automatically selected for a better performance. However, the utilized optimization method is unified by MMFD [13-14]. Each software system supports a separate optimizer for topology optimization and large scale problems. IPOPT [15], BIG-DOT [5] and Dual-Optimizer [16] are the optimizers in Genesis, MSC.Nastran and OptiStruct, respectively. These are based on the sequential unconstrained minimization technique (SUMT) [14].

4.3 Others

The convergence criteria of the optimization may affect the performance. In this research, the relative change of the objective function is used for a convergence criterion and the bound of the value is set by 0.001. Meanwhile, the normalized maximum constraint violation is used as another convergence criterion and set by 0.01. Because OptiStruct does not allow changing this criterion, the default value of OptiStruct is adopted. The move limit strategy is considered. A move limit is defined for the change of the design variables in an approximation problem. The value of the move limit can be defined in the three software systems. The lower and upper bounds of the move limit can be defined by a user in MSC.Nastran and Genesis; however, they cannot be defined by a user in OptiStruct. Therefore, the default values of the bounds are used. The same active set strategy for constraints is considered for large scale problems.

The system environments are also unified. The utilized operating system is MS Windows x64 Ultimate (version 6.1, Build 7601) that is commonly supported by the three software systems. The hardware system is 16.0GB Memory, 8 CPU and Intel core i7-3770 at 3.40GHz. The amount of memory usage has a significant impact on the performance of a software system. Three software systems support memory control options in different ways; however, the total amount of memory usage can be commonly determined. The amount of memory usage is unified as 8GB.

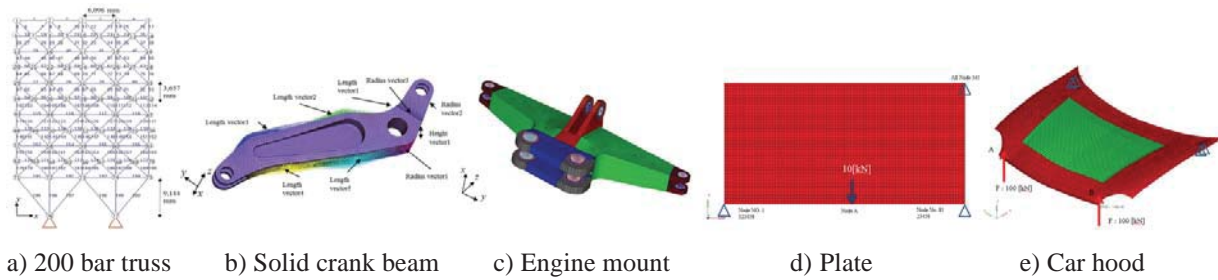


Figure 1: Finite element model of the structural optimization examples

5. Structural optimization

Structural optimization is classified into size, shape, topology, topometry and topography optimizations [4-6]. Size, shape and topology optimizations are classical optimization methods. On the other hand, topometry, topography optimizations are non-classical optimization methods. Structural optimization is classified based on the characteristics of the design variables [12]. The domain of FE analysis is not changed by design variables in size and topometry optimization. However, the domain of shape and topography optimization can be changed by the design variables. In the case of topology optimization, the distribution or existence of materials is determined by the design variables. In topometry optimization, each designable element has an independent design variable. Likewise, normal perturbation vectors are defined at all designable grids in topography optimization. Structural optimization examples are explored regarding each optimization.

5.1 Structural optimization examples

Many structural optimization examples are solved for the comparison of performance. However, only the representative examples, which show distinct characteristics of the software systems, are presented here. They are a 200 bar truss example [17], a solid crank example [18], an engine mount example [19], a plate example [20], and a car hood example [5] for size, shape, topology, topometry and topography optimization, respectively. The examples are illustrated in Figure 1. The detailed optimization formulation of each example is in [21]. The characteristics of each problem are summarized in Table 1.

5.2 Results of optimization

The optimization results for each example are shown in Table 2. The initial and final objective function values are compared. In topology optimization, the final objective function value, which is evaluated after an additional post-processing, is shown. The initial objective function values of the plate example are different for each software system, because the initial plate thickness is automatically determined by using the lower and upper bounds of the design variables. CPU time means the computational time for the optimization process and the elapsed time means the total time that includes the time for writing results and checking the license, etc.

Table 1: Structural optimization problems

Example	Design variables	Objective function	Constraints	Loading conditions	Remark
200 bar truss	96	Mass	Stress and displacement constraints	Multiple loading conditions	Size optimization
Solid crank beam	9	Mass	Stress constraints	A single loading condition	Shape optimization
Engine mount	57,280	Compliance	Fraction mass constraint	Multiple loading conditions	Topology optimization
Plate	3,200	Compliance	Volume constraint	A single loading condition	Topometry optimization
Car hood	2,069	Compliance	.	A single loading condition	Topography optimization

Table 2: Results of structural optimization problems

		Objective Function value		Iterations	Func. calls	CPU Time (s)	Elapsed time (s)
		Initial	Final [Final after post processing]				
200 bar truss	MSC.Nastran	5.082E+04	1.380E+04	18	18	10.84	31.20
	Genesis	5.082E+04	1.390E+04	13	13	0.82	1.00
	OptiStruct	5.082E+04	1.354E+04	25	25	1.40	21.56
Solid crank beam	MSC.Nastran	1.396E-02	1.439E-02	25	25	182.10	387.48
	Genesis	1.396E-02	1.440E-02	12	12	32.00	45.00
	OptiStruct	1.396E-02	1.448E-02	8	8	22.90	28.22
Engine mount	MSC.Nastran	3.560E+06	4.033E+05 [4.986E+05]	64	64	2232.00	4329.27
	Genesis	3.561E+06	4.839E+05 [3.517E+05]	21	21	1449.00	1869.00
	OptiStruct	3.561E+06	3.455E+05 [3.456E+05]	82	82	2304.01	3277.05
Plate	MSC.Nastran	1.229E+01	1.186E+01	16	16	8.47	23.65
	Genesis	1.096E+01	1.032E+01	11	11	4.76	5.00
	OptiStruct	1.799E+01	7.898E+00	17	17	6.46	14.57
Car hood	MSC.Nastran	3.6071E+04	2.822E+04	8	8	131.96	311.961
	Genesis	3.6054E+04	2.876E+04	15	15	15.00	24.00
	OptiStruct	3.5336E+04	2.975E+04	7	7	5.87	10.55

In size, topology and topometry optimizations, it seems that OptiStruct gives the best objective function value although more CPU time is necessary. Genesis gives solutions with the shortest CPU time. In shape and topography optimization, the optimum value from MSC.Nastran looks the best. However, the computational time is quite long compared to the other software systems. Figure 2 shows the results of shape, topology and topography optimization, respectively. There is no big difference in shape and topography optimization results among the three software systems. However, the final shapes from MSC.Nastran are different from those of other software systems, especially in topology optimization.

6. Structural optimization of a large scale structure

As the FE models of the structures become more complex and larger, the performance comparison of large scale structures is quite important. The scale of the problem depends on the size of the FE model and the number of design variables. The number of constraints is not considered in the decision of the scale if an active set strategy for constraints is used. Actually, topology, topometry and topography optimizations can be considered as large scale problems, because they are using many design variables. In this study, a large scale problem means an optimization problem with a large FE structure and many design variables.

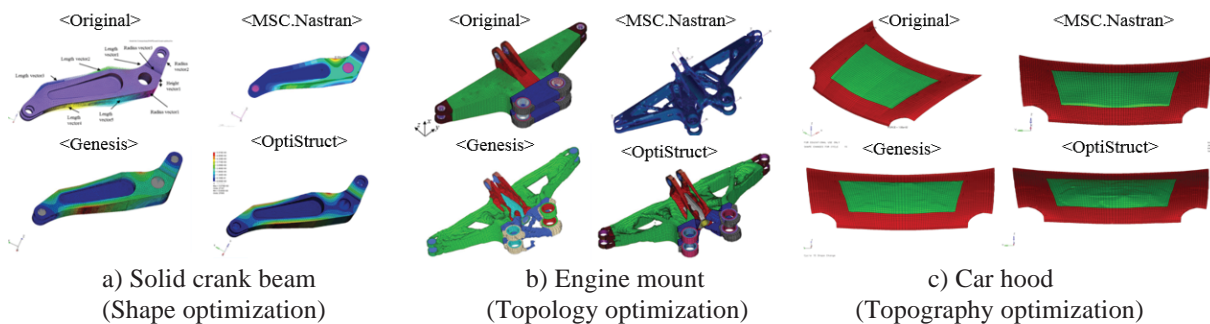


Figure 2: Results of optimization examples

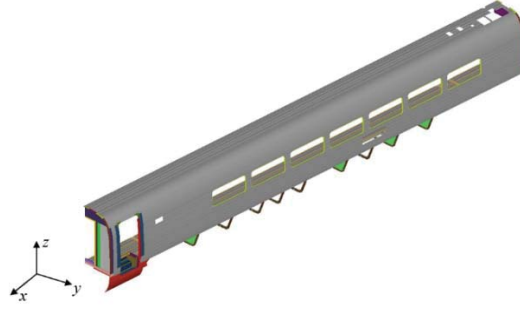


Figure 3: Finite element model of the passenger train

6.1 Structural optimization of a passenger train

An optimization of a passenger train is solved [22]. As illustrated in Fig. 3, the width, height and length are 1.5m, 3.0m, and 23.5m, respectively. The passenger train model consists of shell and solid elements. The total number of FE elements is 239,020 and the number of design variables is 3,410. Five loading conditions are applied as multiple loading conditions. The design formulation is as follows:

$$\begin{aligned}
 &\text{Find} && b_i, b_j \in R^n \\
 &\text{to minimize} && \text{Mass} \\
 &\text{subject to} && \sigma_{\text{von Mises}} \leq \sigma_{\text{allow}} \quad (2) \\
 &&& \delta_{z, \text{initial}} \leq \delta_{z, \text{current}} \\
 &&& b_{i, \text{lower}} \leq b_i \leq b_{i, \text{upper}}, \quad (i=1, \dots, 3398) \\
 &&& b_{j, \text{lower}} \leq b_j \leq b_{j, \text{upper}}, \quad (j=1, \dots, 12)
 \end{aligned}$$

where b_i is the i th size variable, b_j is j th the shape variable, and b_{lower} and b_{upper} are the lower bound and the upper bound of the design variable, respectively. $\sigma_{\text{von Mises}}$ is the von Mises stress, σ_{allow} is the allowable stress, $\delta_{z, \text{initial}}$ is the initial displacement in the z -axis, and $\delta_{z, \text{current}}$ is the displacement in the z -axis of the currently existing model, respectively. The objective function to be minimized is the mass of the structure while the displacement and stress constraints are satisfied. For this example, the amount of memory usage is extended to 64GB, because OptiStruct did not work with 16GB memory.

6.2 Results of the large scale example

The optimization results are shown in Table 2. In a large scale problem, the elapsed time is larger than the computational time, because there are many other processes in addition to the pure optimization process. It is noted that the optimum values are similar. That means the three systems can handle large scale optimization problems. OptiStruct is excellent in the computational time, even though it has a memory control issue. Genesis shows a good performance in the computational time. The computational time of MSC.Nastran is quite long compared to the other software systems. But it has no memory control issue. Actually, this example can be solved with 8GB memory by MSC.Nastran and Genesis.

Table 2: Results of the large scale example

		Objective Function value		Iterations	Func. Calls	CPU time	Elapsed time
		Initial	Final				
Passenger train	MSC.Nastran (IPOPT optimizer)	4.2739	3.5026	11	11	17h 39min	5d 9h 30min
	Genesis (BIGDOT optimizer)	4.2739	3.4972	11	11	1h 16min	3h 28min
	OptiStruct (Dual optimizer)	4.2739	3.4449	9	9	26min	46min

7. Conclusions

Linear static response optimizations are explored, and three commercial structural optimization systems are compared through various structural examples. Only representative examples are demonstrated here. We could see some performance distinctions out of the three software systems. No system is the best in all the cases and each system has advantages and disadvantages depending on the application. In general, Genesis is excellent in computational time while OptiStruct provides excellent solutions, especially in topology optimization. MSC.Nastran presents good solutions in shape optimization. In the case of a large scale example, the three systems give similar objective function values. OptiStruct is excellent in computational time; however, there is a memory control issue that is not found in Genesis and MSC.Nastran.

There can be various reasons for performance distinction, because performance is determined by a combination of many factors. The method for approximation is different in each of the three software systems. The move limit strategy is slightly different. Some parameters can be controllable in one system but uncontrollable in other system. This aspect should be theoretically investigated.

It is noted that the three systems never fail in any examples. That means that all of them are quite reliable. Also, even with one system, different results can be obtained when different decisions are made for the selection of the parameters. The authors hope that this paper helps practitioners in the decision of a structural optimization system.

8. Acknowledgements

This research was supported by the Commercialization Promotion Agency for R&D Outcomes through the Ministry of Science (No. 2014K00042). The authors are thankful to Mrs. MiSun Park for her English correction of the manuscript.

9. References

- [1] R.D. Cook, D.S. Malkus, M.E. Plesha, and R.J. Witt, *Concepts and applications of finite element analysis*, fourth edition, John Willy and Sons. Inc., NY, USA, 2001.
- [2] K.J. Bathe, *Finite element procedures in engineering analysis*, Prentice Hall, Englewood Cliffs, NJ, USA, 1996.
- [3] D.L. Logan, *A first course in the finite element method*, PWS Publishing Company, Boston, MA, USA, 1993.
- [4] MSC NASTRAN User's Guide, Ver. 2013.1, MSC Software Corporation, Santa Ana, CA, USA, 2013.
- [5] GENESIS User's Manual, Ver. 13.1, Vanderplaats Research and Development. Inc., Colorado Springs, CO, USA, 2014.
- [6] ALTAIR OPTISTRUCT User's Manual, Ver. 13.0, Altair Engineering. Inc., Troy, MI, 2014.
- [7] P. Kohnke, ANSYS theory reference manual, ANSYS. Inc., Canonsburg, PA, USA, 1994.
- [8] <http://www.3ds.com/products-services/simulia/products/tosca/>, Dassault systemes.
- [9] Y.S. Park, S.H. Lee and G.J. Park, A study of direct vs. approximation methods in structural optimization. *Structural Optimization*, Springer-Verlag, 10, 64-66, 1995.
- [10] U.P. Hong, K.H. Hwang and G.J. Park, A comparative study of software systems from the optimization viewpoint, *Structural and Multidisciplinary Optimization*, 27(6), 460-468, 2004.
- [11] R.T. Haftka and Z. Gurdal, *Elements of structural optimization*, Kluwer Academic Publishers, Dordrecht, Netherlands, 1992.
- [12] G.J. Park, *Analytical Methods in Design Practice*, Springer, Germany, 2007.
- [13] G.N. Vanderplaats, *Numerical optimization techniques for engineering design*, Vanderplaats Research & Dvelopment. Inc., Colorado Springs, CO, USA, 1999.
- [14] J.S. Arora, *Introduction to optimum design*, Elsevier, Waltham, MA, USA, 2012.
- [15] MSC NASTRAN Design Sensitivity and Optimization User's Guide, Ver. 2013.1, MSC Software Corporation, Santa Ana, CA, USA, 2013.
- [16] C. Fleury and V. Braibant, A new dual method using mixed variables, *International Journal for Numerical Methods in Engineering*, 23(3), 409-428, 1986.
- [17] E.J. Haug and J.S. Arora, *Applied Optimal Design*, New York, U.S.A, 1979.
- [18] ALTAIR HyperStrudy Tutorials, Ver. 13.0, Altair Engineering. Inc., Troy, U.S.A, 2014.
- [19] MD NASTRAN Demonstration Problems, Ver.2013.1, MSC Software Corporation, Santa Ana, CA, USA, 2013.
- [20] MSC NASTRAN Automated structural optimization in MSC Natran., MSC Software Corporation, Santa Ana, CA, USA, 2014.
- [21] C.G. Huang, A comparative study of performance of structural optimization software, Master's theses, Hanyang University, Korea, 2014. (In Korean)
- [22] Y.M. Lee, H.A. Lee, Y.W. Yoon and G.J. Park, Design of aluminium extrusion panels in a railway-car body using orthogonal arrays, *The seventh China-Japan-Korea joint symposium on optimization of structural and mechanical systems*, Huangshan, China, 2012.

Novel Approach in Topology Optimization of Porous Plate Structures for Phononic Bandgaps of Flexural Waves

Saeid Hedayatrasa¹, Kazem Abhary¹, Mohammad Uddin¹, Ching-Tai Ng²

¹ School of Engineering, University of South Australia, Mawson Lakes, SA 5095, Australia
saeid.hedayatrasa@mymail.unisa.edu.au

² School of Civil, Environmental and Mining Engineering, University of Adelaide, SA 5000, Australia

1. Abstract

This paper presents a novel multiobjective optimization strategy for topology optimization of single material phononic plates (PhPs), where the achieved topology can be produced by perforation of a uniform background plate. The primary objective of this optimization study is to exploit the widest relative bandgap of fundamental flexural guided wave modes for maximized phononic controllability. Principally, the optimum topology of such porous structure favors isolated scattering domains leading to maximized interfacial Bragg reflections. Hence, the widest achievable bandgap depends on assumed topology resolution and relevant topology generally has low structural worthiness. Therefore the homogenized in-plane stiffness of phononic unitcell is also incorporated in topology optimization as the second objective to explore the gradient of optimum bandgap topology with respect to its in-plane stiffness. Consequently, structurally worthy bandgap topologies with desired relative bandgap-stiffness performance could be taken from the obtained spread of optimized topologies. Moreover, functionally graded PhP with maximized bandgap efficiency and multiscale functionality could be designed through integration of optimized PhP unitcells of different stiffness. Nondominated sorting genetic algorithm (NSGA-II) is adopted for this multiobjective problem and fitness evaluation of topologies is performed through finite element method. Specific topology assessment is performed for convergence of the solution towards optimum feasible bandgap topology without penalizing the efficiency of genetic algorithm (GA). A set of Pareto topologies is selected and variation of bandgap width and in-plane stiffness across the two Pareto extremes is studied. Arbitrarily selected intermediate Pareto topology shows superior bandgap efficiency as compared with the relevant optimized topologies reported by other researchers. Moreover, the frequency response of a finite phononic plate structure of selected intermediate Pareto topology confirms high attenuation of flexural waves within its calculated bandgap frequency.

2. Keywords: Phononic; Bandgap; Plate; Topology Optimization

3. Introduction

Phononic crystals (PhCr) are heterogeneous acoustic meta-materials produced by periodic modulation of acoustic impedance in a lattice structure through either integration of two or more contrasting materials, or making porosities in a uniform background. The main feature of PhCr is the existence of frequency ranges over which propagation of vibroacoustic waves is prohibited. This phenomenon is caused by constructive reflection and superposition of waves at the interface of periodic heterogeneities i.e. Bragg and Mie resonant scatterings. Moreover, introducing any kind of defect in phononic lattice e.g. by altering the features of a few adjacent cells, leads to advent of local resonance modes within phononic bandgap frequency. This capability is used to trap and guide waves inside defects specially tuned for desired frequencies. Flat and concave wave fronts below bandgap frequency are other promising characteristics of PhCr applicable for self-collimation and steering of waves. Consequently, it is worthwhile to adjust the phononic properties so that the width and location of bandgap is optimized for application of interest. Essentially topology with maximum relative bandgap width (RBW) between subsequent modes of interest is desired [1]. RBW is the ratio of bandgap width over midgap frequency, and so seeking maximum RBW results in a topology which can provide widest bandgap at lowest frequency range for specific unitcell size. Consequently, the relevant topology supports phononic wave manipulation over the widest frequency range through miniature unitcells compared to wavelength.

The efficiency of PhCr is principally defined by the topology of its irreducible representative element (Unitcell). Most of topology optimization studies in relation to 2D periodic PhCr have been concerned with bandgaps of in-plane and/or anti-plane bulk waves while only few works have been devoted to bandgaps of guided waves through PhCr plate (PhP). Guided waves are structural waves confined by traction free surfaces of thin walled structures, so called plate waves when guided by parallel faces of plates. In-plane symmetric (S) and anti-plane asymmetric (A) Lamb waves as well as symmetric shear horizontal (SHS) and asymmetric shear horizontal (SHA) in-plane waves are the well-known guided wave modes generated in a plate structure. The plate wave energy is predominantly conveyed by the asymmetric (flexural) wave modes (S+SHA) under a general

lateral disturbance. Special characteristics of guided waves confined by finite thickness of such structures, make them ideal for non-destructive evaluation purposes [2] as well as production of low loss resonators, filters and waveguides [3].

Halkjær, Sigmund [4] studied the optimum topology of porous Polycarbonate PhP with rhombic unitcell for maximized RBW of first couple of flexural plate waves. The Mindlin plate theory was implemented for definition of band structure of bending waves and gradient based optimization was performed through method of moving asymptotes. The discontinuities of optimized topology were locally modified for satisfactory stiffness and manufacturability. In another investigation by Bilal and Hussein [5] the optimum topology of thin porous silicon PhPs for maximized RBW of basic flexural waves was studied. The Mindlin plate's theory was implemented and topology of square unitcell was optimized through genetic algorithm (GA) as an evolutionary based method.

Bandgaps of such porous materials are governed by wave reflection and scattering at the interface of inhomogeneities produced by perforation profile. Therefore the search for highest RBW naturally results in topologies with nearly isolated domains or in other words thin connectivity for strengthened interfacial reflections. The finer the topology resolution the thinner connectivity in the optimized topology for maximized bandgap. So largest achievable RBW is extremely dependent on assumed unitcell's resolution and relevant topology generally has low structural worthiness. Nevertheless, none of earlier works on topology optimization of porous PhCs [4-6] took into consideration the structural worthiness of achieved topologies.

Therefore, the focus of this paper is to investigate the contribution of this fact in optimum topology of PhP unitcell with 2D periodicity for maximized bandgap width of fundamental flexural waves (A_0+SHA_0). To serve this purpose, the homogenized in-plane stiffness of phononic unitcell is also incorporated in topology optimization as the second objective and structurally worthy bandgap topologies are explored. The gradient of optimum bandgap topology with respect to in-plane stiffness is also defined by which functionally graded PhP with maximized bandgap efficiency and multiscale functionality can be designed. Nondominated sorting genetic algorithm (NSGA-II) is adopted for this multiobjective problem and fitness evaluation of topologies is performed through finite element method. Relatively thin phononic unitcell of transversal aspect ratio (width to thickness) of 10 is modelled and square symmetric topology with no through thickness variation is assumed. Specialized filtering is applied to the topologies in order to incline the search space towards feasible bandgap topologies without compromising its diversity and randomness.

4. Modelling and analysis of PhP unitcell

2D PhP unitcell with square symmetry is assumed which is uniformly perforated through the thickness h (along z axis) to produce planar heterogeneity in x - y plane. The topology (i.e. perforation profile) of this porous PhP defines its bandgap efficiency caused by constructive reflections of wave at the interface of heterogeneities. Relatively thin plate unitcell with transversal aspect ratio (width over thickness) of $a/h=10$ is considered. 3D FEM model of the unitcell is constructed in ANSYS APDL (ANSYS® Academic Research, Release 14.5) using SOLSH190 elements, for fitness evaluation of individual topologies during optimization procedure. Polysilicon with elastic modulus $E_s = 169(GPa)$, Poisson's ratio $\nu_s = 0.22$ and density $\rho_s = 2330(kg/m^3)$ is taken as the base solid material of PhP widely used for fabrication of micro-devices like micro PhCs [7].

4.1. Modal band analysis and bandgap objective

The FEM notation of equation of motion for a loss free elastic medium in the absence of external forces is:

$$\mathbf{M}\ddot{\mathbf{q}} + \mathbf{K}\mathbf{q} = 0 \quad (1)$$

where \mathbf{K} is stiffness matrix and \mathbf{M} is mass matrix of FEM model. \mathbf{q} is vector of nodal displacements by which the displacement vector $\mathbf{U} = \{u, v, w\}$ is defined through matrix of shape functions \mathbf{N} :

$$\mathbf{U} = \mathbf{N}\mathbf{q} \quad (2)$$

Based on the Bloch-Floquet theory[8] the general solution for displacement filed \mathbf{U} in 2D PhP with infinite periodicity in x - y plane can be formulated by harmonic modulation of a periodic displacement filed as follows:

$$\mathbf{U}(\mathbf{X}, t) = \mathbf{U}_p(\mathbf{X})e^{i(\mathbf{k}\mathbf{x} - \omega t)} \quad (3)$$

where $\mathbf{X} = \{x, y, z\}$ is the location vector, \mathbf{U}_p is an a periodic function in x - y plane according to the PhP square lattice periodicity, $\omega = 2\pi f$ is circular frequency and $\mathbf{k} = \{k_x, k_y\}$ is the in-plane wave vector and $i = \sqrt{-1}$. After applying Bloch-Floquet periodic boundary condition on the plate unitcell with traction free upper and lower surfaces, we arrive at:

$$\mathbf{U}_{x+} = \mathbf{U}_{x-}e^{ik_x a}, \quad \mathbf{U}_{y+} = \mathbf{U}_{y-}e^{ik_y a} \quad (4)$$

where subscripts x+ and x- stand for corresponding points at two unitcell's faces parallel to y-z plane at $x = 0$ and $x = a$, respectively. Similarly subscripts y+ and y- stand for corresponding points at two unitcell's faces parallel to z-x plane at $y = 0$ and $y = a$. So the Bloch-Floquet boundary condition is in complex format and in order to handle it by ANSYS FEM solver two identical FEM models are superimposed so that one represents the real term and the other one imaginary term of complex displacement domain [9]. Due to the periodicity in Bloch-Floquet condition and the assumed square symmetry of topology the wave vector can be limited to irreducible Brillouin zone. However, according to the common practice searching only the border of irreducible Brillouin zone [1] suffices for evaluation of bandgap properties. By substituting the harmonic definition of nodal displacement $\mathbf{q} = \mathbf{q}_0 e^{i\omega t}$ in Eq.(1) and solving for nontrivial solutions, the modal frequencies of unitcell are calculated by Eigen value analysis of Eq.(5):

$$\mathbf{M}\omega^2 + \mathbf{K}(\mathbf{k}) = 0 \quad (5)$$

where stiffness matrix $\mathbf{K}(\mathbf{k})$ is a function of wave vector \mathbf{k} corresponding to applied Bloch-Floquet boundary conditions. In order to decouple the modal band structure of flexural plate waves, just half of unitcell through the thickness from midplane $z = 0$ to top plane $z = h/2$ is modelled and appropriate boundary conditions are applied to the mid-plane to enforce asymmetric modes [10].

Regarding bandgap efficiency of PhP unitcell, it is fundamentally desired to manipulate the largest wave length possible through specific unitcell size. Hence the first objective function of optimization F_1 to be maximized is defined as:

$$F_1 = \frac{\min_{i=1}^{n_k} \omega_{j+1}^2(k_i) - \max_{i=1}^{n_k} \omega_j^2(k_i)}{0.5(\min_{i=1}^{n_k} \omega_{j+1}^2(k_i) + \max_{i=1}^{n_k} \omega_j^2(k_i))} \quad (6)$$

Actually F_1 is the gap width over mean value of gap between Eigen values ω^2 of two subsequent modal branches j^{th} and $(j+1)^{\text{th}}$ of interest over the n_k discrete search points k_i on the border of irreducible Brillouin zone. Since the bandgap of fundamental flexural modes is desired, the first couple of modal branches are taken into account and so $j = 1$.

4.2. Numerical homogenization and stiffness objective

The strain energy compliance of PhP unitcell under particular loading condition is defined as the second objective function of optimization concerning the in-plane stiffness. It is well known that the strain energy of the unitcell under specified loading condition represents its relevant stiffness. Higher strain energy implies lower stiffness or higher compliance. The strain energy stored per volume of a finite element subjected to in-plane stress in x-y plane is theoretically defined as:

$$S = \frac{1}{2}(\sigma_x \varepsilon_x + \sigma_y \varepsilon_y + \tau_{xy} \gamma_{xy}) \quad (7)$$

where $\{\sigma_x, \sigma_y, \tau_{xy}\}$ and $\{\varepsilon_x, \varepsilon_y, \gamma_{xy}\}$ are corresponding in-plane stress and strain tensors, respectively. As for loading conditions the general stress state of $\sigma_x = \sigma_y = \tau_{xy} / \sqrt{2} = \sigma$ with shear and biaxial normal components is assumed uniformly throughout the unitcell. So with regard to linear elastic stress-strain relations, the Eq.(7) turns to:

$$S = \sigma^2 \left(\frac{1 - \nu_e}{E_e} + \frac{1}{G_e} \right) \quad (8)$$

where E_e , G_e and ν_e are the equivalent in-plane orthotropic elastic modulus, shear modulus and Poisson's ratio of assumed square symmetric PhP unitcell, respectively. Then the stiffness objective function F_2 , in order to attain maximum in-plane stiffness, is defined as strain energy compliance of unitcell based on its homogenized properties, to be minimized:

$$F_2 = \left(\frac{1 - \nu_e}{E_e} \right) + \left(\frac{1}{G_e} \right) \quad (9)$$

So the assumed relative magnitude of shear and normal stresses leads to an stiffness objective which equally accounts for normal and shear compliances (first and second terms of Eq.(9), respectively). However appropriate stress state could be assigned for any particular application. The numerical homogenization is employed and periodic boundary condition is applied to define the equivalent elastic properties of PhP unitcell and calculate F_2 .

An overall test strain is prescribed for the unitcell and the equivalent orthotropic stiffness is derived based on average stress field of elements over the entire unitcell. Detailed information regarding numerical homogenization of composite materials using FEM and periodic boundary condition can be found in Bendsoe and Sigmund [11].

5. Optimization approach

Non-dominated sorting Genetic algorithm (NSGA-II) [12] is employed for present multiobjective topology optimization problem. Basically a coded string of topology is processed by the algorithm to be mapped into the discretized design domain. Genetic algorithm (GA) mimics the process of natural selection: searches over a population of potential solutions, reproduces better generations using crossover and mutation functions and iteratively produces better and better approximations to the solution. Earlier works on topology optimization of PhCs through GA have proved its competency in this area [5, 13-19]. Multi-objective GA was implemented by the authors to study the optimum topology of 1D PhPs with respect to filling fraction of constituents and gradient 1D PhP structures were introduced [20]. NSGA-II sorts GA population based on non-dominated fitness and crowding distance. In this way the designs with the most dominated fitness are placed at the first rank (Pareto front) and among them those with highest crowding distance are preferred [12].

A binary bit-string design space is considered for defining the material type of any pixel of topology. For simplicity in FEM evaluation of topologies, the void elements corresponding to perforated region of unitcell are assigned a very compliant material. Following specialized topology initializing, filtering and modifications are applied to eliminate interrupting modes of disconnected segments and make optimized porous topologies converge towards feasible connected ones without disturbing the randomness and diversity of search domain. An identical fully solid population is randomly mutated with specified probability to deliver an initial population of likely connected topologies. All individual topologies are morphologically checked and the feasible connected segment only (if any) is delivered for analysis. The population is sorted and parent pool is created through tournament selection. Then the offspring population is defined by single point crossover and mutated with certain probability. The checkerboard problem is alleviated by the well-known technique of inverting randomly selected pixel (i.e. void to solid and vice versa) if surrounded by more than 2 dissimilar adjacent face to face pixels out of 4. Finally the idle disconnected segments of topology (where applicable) are faded out through a random-progressive manner. For this purpose a randomly selected disconnected segment is eliminated by specified probability which increases as the GA progresses. Due to rarity of perfectly connected topologies showing bandgap properties defined during population initialization and reproduction stages, the aforementioned algorithm is a robust approach for degrading invalid individuals while maintaining the diversity of search domain.

6. Results and discussion

PhP unitcell is modelled by element (i.e. topology) resolution of 32×32 in x-y plane leading to a design domain of 136 independent design variables for prescribed square symmetric topology. A population size of 200 is considered for this problem size, and from the total number of topologies delivered in Pareto front 12 topologies (Figure 1(a)) are selected and presented containing a variety of alternative optimized topology modes with different RBWs and in-plane stiffness.

Since RBW is defined as the gap width over midgap value of either Eigen values (F_1) or Eigen frequencies ($\Delta\omega/\bar{\omega}$) of desired mode branches in different works both quantities are obtained and included in the results. In order to evaluate the relative effective stiffness of optimized topologies with respect to stiffness of constitutive solid material, relative elastic modulus $E_r = E_e/E_s$ and relative shear modulus $G_r = G_e/G_s$ are calculated.

The gradient of RBW (both F_1 and $\Delta\omega/\bar{\omega}$) and logarithm of relative elastic modulus with respect to selected Pareto front topologies are given in Figure 1(b) and Figure 1(c), respectively. Accordingly, almost uniform reduction of RBW across the Pareto front is observed with simultaneous increase of both elastic and shear modulus by around 2 orders of magnitude. As expected, the stiffness of PhP unitcell penalizes its bandgap efficiency and the bandgap of extreme topology number 12 with highest stiffness is almost closed. Hence, the choice of optimum Pareto topology depends on desired relative bandgap-stiffness performance. In order to compare the performance of obtained topologies with preceding works on bandgaps of asymmetric waves, the intermediate Pareto topology number 6 (Figure 1(a)) is arbitrarily chosen and remodeled with Polycarbonate solid material of elastic modulus 2.3 GPa, density 1200 kg/m^3 and Poisson's ratio 0.35 and aspect ratio $r = 11$ as per work by Halkjær, Sigmund [4]. Accordingly the relevant frequency RBW of this topology is $\Delta\omega/\bar{\omega} = 0.328$ which is significantly higher than that of optimized connected topology reported by Halkjær, Sigmund [4] with $\Delta\omega/\bar{\omega} = 0.16$. Furthermore, the Eigen value RBW of topology number 6 remodeled with Polycarbonate solid material and $r = 11$ is $F_1 = 0.639$ which is around 13% higher than $F_1 = 0.5639$ reported for optimized topology obtained by Bilal and Hussein [5].

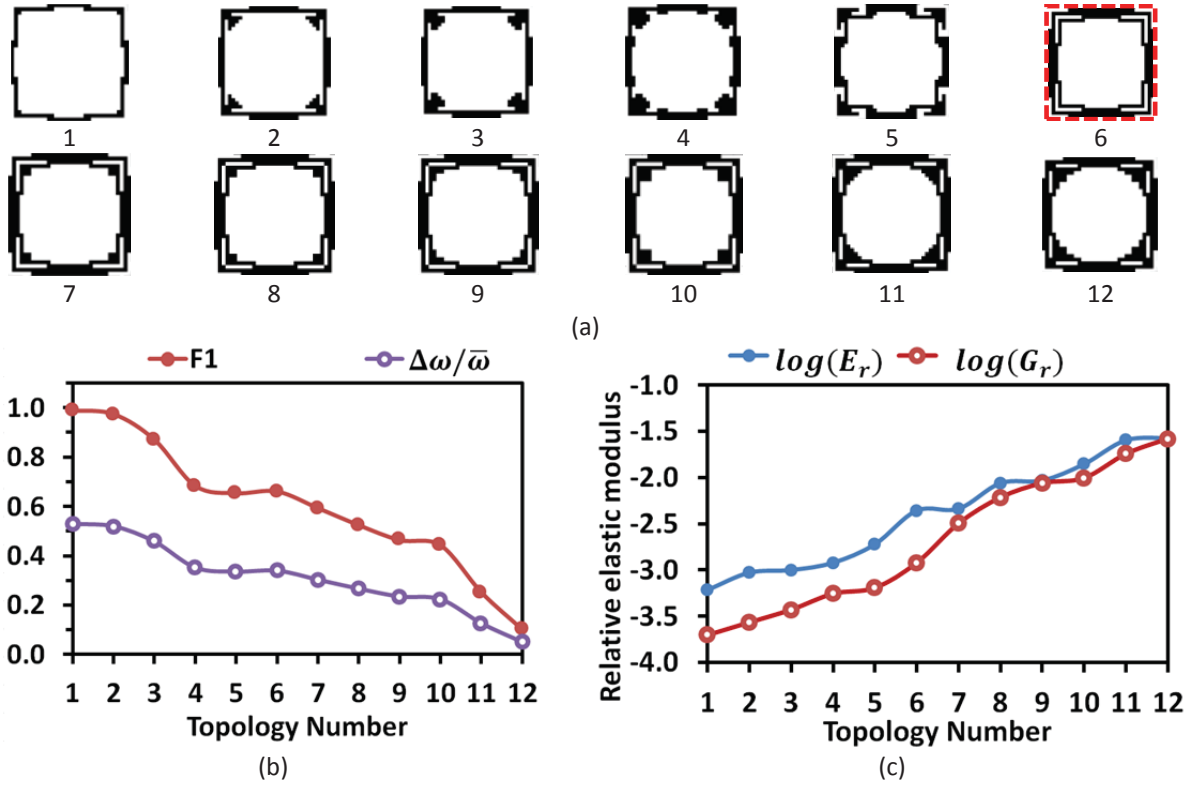


Figure 1: (a) Selected optimized topologies, and gradient of (b) RBW and (c) elastic properties across Pareto front

It is worth to emphasize that bandgap performance of an intermediate Pareto topology (Number 6), and even not the one with widest RBW (Number 1), was compared with results of other works aimed at topology with absolutely maximized RBW. Moreover, the topologies of present study are optimized based on marginally lower aspect ratio $r = 10 < 11$.

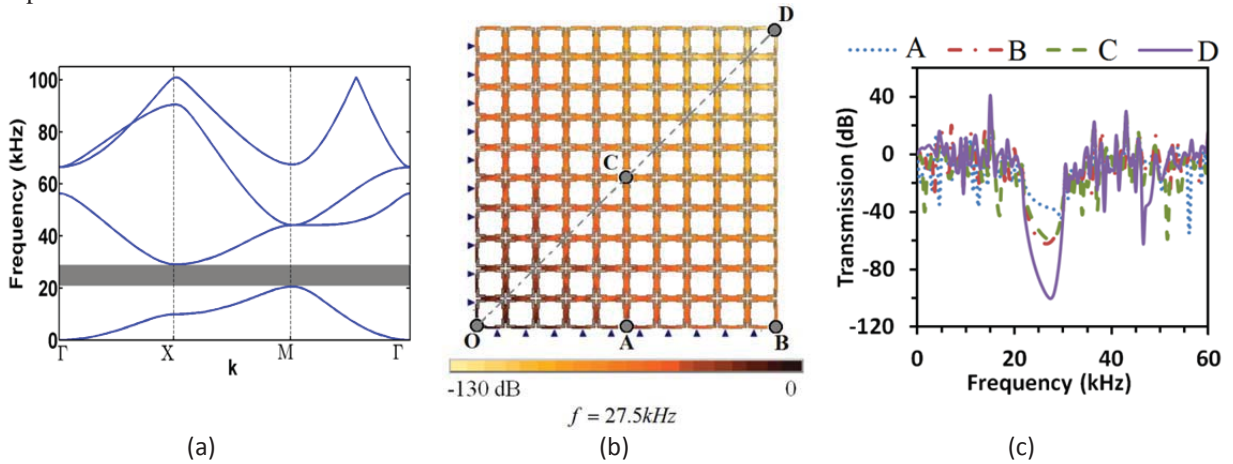


Figure 2: (a) Modal band structure of topology number 6 with 1 mm thickness, (a) harmonic response of its finite square PhP structure at bandgap frequency 27.5 kHz and (c) transmittance to selected measurement points

Finally the steady state harmonic response of a finite PhP structure of selected topology number 6 is defined in order to evaluate its bandgap performance compared with its modal band structure calculated for an infinitely periodic lattice. Unitcell of width $a = 10$ mm and thickness $h = 1$ mm is modeled and the corresponding modal band structure is shown in Figure 2(a). Accordingly, a bandgap is opened within first couple of flexural modes from just above 20 kHz to around 30 kHz. A square lattice of 20×20 unitcells with free boundaries is considered to be transversally loaded at the center for predominant excitation of asymmetric modes. Due to symmetry of the model, the top right quarter of plate is modelled only as shown in Figure 2(b). The plate is harmonically excited at central point O in the range 0-60 kHz corresponding to first two modal branches. Then the wave transmittance to the straight points A and B and diagonal ones C and D is measured as shown in Figure 2(c). It is evident that the transmittance of elastic wave is highly attenuated within bandgap frequency 20-30 kHz with highest damping of

around -100 dB at the most distant point D in 27.5 kHz and lowest damping of -40dB at closest point A in 30 kHz. The contour of wave transmittance corresponding to the bandgap frequency 27.5 kHz as presented in Figure 2(b) confirms the omnidirectional attenuation of wave up to -130 dB throughout the modelled finite PhP structure.

7. Conclusion

Topology optimization of porous phononic plates for widest bandgap of fundamental flexural waves was competently performed through specialized genetic algorithm. Multiobjective study was carried out and as a result the variation of bandgap performance with respect to effective in-plane stiffness of optimized topologies was explored. Specific topology processing was implemented to get feasible porous topologies without compromising the efficiency of genetic algorithm and diversity of design space. A broad range of Pareto topologies was delivered enabling the designer to select supreme topology based on required bandgap-stiffness performance. Arbitrarily chosen intermediate Pareto topology had excellent bandgap efficiency as compared with relevant results of other researchers, and omnidirectional attenuation of flexural waves through its finite square structure within calculated bandgap frequency was computationally observed.

6. References

- [1] Sigmund, O. and J.S. Jensen, Systematic design of phononic band-gap materials and structures by topology optimization, *Phil. Trans. R. Soc. Lond.*, **361**, 1001-1019, 2003.
- [2] Su, Z. and L. Ye, *Identification of damage using lamb waves: from fundamentals to applications*. Vol. 48. 2009: Springer.
- [3] Mohammadi, S., *Phononic band gap micro/nano-mechanical structures for communications and sensing applications*. 2010, Georgia Institute of Technology.
- [4] Halkjær, S., O. Sigmund, and J.S. Jensen, Maximizing band gaps in plate structures, *Structural and Multidisciplinary Optimization*, **32**(4), 263-275, 2006.
- [5] Bilal, O.R. and M.I. Hussein, *Topologically evolved phononic material: Breaking the world record in band gap size*, in *Photonic and Phononic Properties of Engineered Nanostructures*. 2012.
- [6] Dong, H.-W., X.-X. Su, and Y.-S. Wang, Multi-objective optimization of two-dimensional porous phononic crystals, *Journal of Physics D: Applied Physics*, **47**(15), 155301, 2014.
- [7] Olsson Iii, R. and I. El-Kady, Microfabricated phononic crystal devices and applications, *Measurement Science and Technology*, **20**(1), 012002, 2009.
- [8] Kittel, C., *Introduction to solid state physics*. Vol. 8. 1986: Wiley New York.
- [9] Aberg, M. and P. Gudmundson, The usage of standard finite element codes for computation of dispersion relations in materials with periodic microstructure, *The Journal of the Acoustical Society of America*, **102**, 2007, 1997.
- [10] Karmazin, A., *Time-Efficient Simulation of Surface-Excited Guided Lamb Wave Propagation in Composites*. Vol. 18. 2013: KIT Scientific Publishing.
- [11] Bendsoe, M.P. and O. Sigmund, *Topology optimization (Theory, methods and applications)*. 2003: Springer.
- [12] Pratap, A., S. Agarwal, and T. Meyarivan, A fast and elitist multiobjective genetic algorithm: NSGA-II, *IEEE transactions on evolutionary computation*, **6**(2), 182-197, 2002.
- [13] Gazonas, G.A., et al., Genetic algorithm optimization of phononic bandgap structures, *International Journal of Solids and Structures*, **43**(18-19), 5851-5866, 2006.
- [14] Dong, H.-W., et al., Topological optimization of two-dimensional phononic crystals based on the finite element method and genetic algorithm, *Structural and Multidisciplinary Optimization*, 1-12, 2014.
- [15] Dong, H.-W., et al., Topology optimization of two-dimensional asymmetrical phononic crystals, *Physics Letters A*, **378**(4), 434-441, 2014.
- [16] Hussein, M., et al., Multiobjective evolutionary optimization of periodic layered materials for desired wave dispersion characteristics, *Structural and Multidisciplinary Optimization*, **31**(1), 60-75, 2006.
- [17] Hussein, M.I., et al., Optimal synthesis of 2D phononic crystals for broadband frequency isolation, *Waves in Random and Complex Media*, **17**(4), 491-510, 2007.
- [18] Liu, Z.-f., B. Wu, and C.-f. He, Band-gap optimization of two-dimensional phononic crystals based on genetic algorithm and FPWE, *Waves in Random and Complex Media*, (ahead-of-print), 1-20, 2014.
- [19] Manktelow, K.L., M.J. Leamy, and M. Ruzzene, Topology Design and Optimization of Nonlinear Periodic Materials, *Journal of the Mechanics and Physics of Solids*, **61**(12), 2433-2453, 2013.
- [20] Hedayatrasa, S., K. Abhary, and M. Uddin, Numerical study and topology optimization of 1D periodic bimaterial phononic crystal plates for bandgaps of low order Lamb waves, *Ultrasonics*, **57**(0), 104-124, 2015.

Topology optimization of continuum structures made of non-homogeneous materials of isotropic or cubic symmetry

Sławomir Czarnecki, Radosław Czubacki, Tomasz Lewiński, Paweł Wawruch

Warsaw University of Technology, Faculty of Civil Engineering,
Department of Structural Mechanics and Computer Aided Engineering,
Armii Ludowej 16, 00-637 Warsaw, Poland
t.lewinski@il.pw.edu.pl

1. Abstract

The paper concerns optimum design of elastic moduli corresponding to: i) nonhomogeneous isotropy, or to ii) cubic symmetry, aimed at minimization of the total compliance. Similarly to the Free Material Design the cost of design is assumed as the integral of the trace of the elastic moduli tensor over the feasible domain. A proof is given that both the optimum design formulations discussed reduce to auxiliary problems being tensorial counterparts of the Monge-Kantorovich scalar problem. The paper comprises numerical analysis of the mentioned auxiliary problems and puts forward case studies concerning isotropy design. A characteristic feature of optimal isotropic designs is emergence of auxetic properties, where Poisson ratio attains negative values.

2. Keywords: Free material design, compliance minimization, anisotropy, cubic symmetry.

3. Introduction

The Free Material Design (FMD) of structures subjected to a single load case leads to optimal material designs being singular, viz. the optimal Hooke tensor occurs to have only one non-zero eigenvalue λ_1 . Thus in 3D case the eigenvalues (or Kelvin moduli) of the optimal Hooke tensor are $(\lambda_1, 0, 0, 0, 0, 0)$, while in 2D the optimal Kelvin moduli are $(\lambda_1, 0, 0)$, cf. [1, 4, 5, 8]. One of the methods to make the optimal Hooke tensor non-singular is to optimize the structure with respect to multiple loads, cf. [4, 5]. To arrive at positive values of all Kelvin moduli in the 3D case one should optimize the structure with respect to at least six independent load variants. For the 2D case three load cases suffice, see [4, 5].

A non-singular result can also be achieved by imposing isotropy, as shown recently by Czarnecki [6]. In this version of FMD -called IMD or the isotropic material design- the main unknowns are two scalar fields k and μ subjected to the isoperimetric condition expressed by the integral of the trace of Hooke tensor equal to $3k + 10\mu$. A less restrictive assumption, like cubic symmetry, leads to optimal values of the moduli among which one becomes zero, see [7]. This version of FMD will be called CSMD (cubic symmetry material design). The aim of the present paper is to publish these theoretical results and augment it with a numerical analysis. It occurs that the problems IMD and CSMD reduce to auxiliary problems similar to those known from the theory of materials with locking and having much in common with Monge-Kantorovich equation. The auxiliary minimization problems (in which test stress fields run through the set of statically admissible stresses corresponding to the given load) are solved, upon discretization, by representing the solutions via singular value decompositions (SVD) and then by performing minimization over free parameters; hence the numerical method developed is similar in spirit to the force method known from structural mechanics.

The paper puts emphasis on the links between FMD, IMD, CSMD and the minimum compliance problem as set by Bouchitté and Buttazzo [3].

4. The FMD problem revisited

Let us recall the stress-based setting of FMD, see [5]. Let the linear form $f(\mathbf{v})$ represent the work of given loads on the virtual displacement field $\mathbf{v} = (v_1, v_2, v_3)$ of the body occupying the domain Ω . Let Σ_f represent the set of statically admissible stress fields $\boldsymbol{\tau} = (\tau_{ij})$ such that

$$\int_{\Omega} \tau_{ij} \varepsilon_{ij}(\mathbf{v}) \, dx = f(\mathbf{v}) \quad \forall \mathbf{v} \in V \quad (1)$$

where V is the space of kinematically admissible displacements while $\varepsilon_{ij}(\mathbf{v}) = \frac{1}{2}(v_{i,j} + v_{j,i})$ where $(\cdot)_{,i} = \partial(\cdot)/\partial x_i$. Let $\|\boldsymbol{\tau}\|$ be the Euclidean norm or $\|\boldsymbol{\tau}\| = (\tau_{ij} \tau_{ij})^{1/2}$. The Hooke's law has the form $\tau_{ij} = C_{ijkl} \varepsilon_{kl}(\mathbf{u})$ with \mathbf{u} being the unknown displacement field. This field depends on the tensor field \mathbf{C} which will be indicated by $\mathbf{u} = \mathbf{u}(\mathbf{C})$.

Let $H_\Lambda^1(\Omega)$ be the set of positive semidefinite fields \mathbf{C} -which locally are elements of the set \mathbb{E}_s^4 of fourth rank tensors of appropriate symmetries - satisfying the isoperimetric condition which fixes the value Λ of the integral of $\text{tr}\mathbf{C} = C_{ijij}$ over the given design domain Ω . In its original setting [1] the FMD problem is formulated as

$$J = \min_{\mathbf{C} \in H_\Lambda^1(\Omega)} f(\mathbf{u}(\mathbf{C})) \quad (2)$$

By expressing \mathbf{C} by its spectral decomposition and performing minimization over the projectors, keeping the Kelvin moduli λ_i as fixed, one rearranges the problem (2) to the form

$$J = \min_{\boldsymbol{\tau} \in \Sigma_f} \min_{\substack{\lambda_1 \geq 0 \\ \int_\Omega \lambda_1 dx = \Lambda}} \int_\Omega \frac{1}{\lambda_1} \|\boldsymbol{\tau}\|^2 dx \quad (3)$$

Now the minimization over the Kelvin modulus λ_1 can be performed analytically, which leads to the formula

$$J = Z^2/\Lambda \quad , \quad Z = \min_{\boldsymbol{\tau} \in \Sigma_f} \int_\Omega \|\boldsymbol{\tau}\| dx \quad (4)$$

Thus the problem (2) is reduced to the above minimization problem with the integrand of linear growth. The result (4) has been found in an elementary way, hence needs mathematical justification. The main problem lies in the property of the integrand in problem in (4); its linear growth implies that the solutions cannot be, in general, sought in the class of functions; the solutions are measures.

The result (4) can be justified by the methods developed in [3], see Theorem 2.3, p.144 therein. It is worth showing here a complete proof of the estimate: $J \geq Z^2/\Lambda$. The Schwarz inequality is crucial, as seen below. Due to $\boldsymbol{\tau} \in \Sigma_f$ we have

$$f(\mathbf{v}) = \int_\Omega \left(\frac{1}{\sqrt{\lambda_1}} \boldsymbol{\tau} \right) \cdot \left(\sqrt{\lambda_1} \boldsymbol{\varepsilon}(\mathbf{v}) \right) dx \quad (5)$$

hence

$$f(\mathbf{v}) \leq \left(\int_\Omega \frac{1}{\lambda_1} \|\boldsymbol{\tau}\|^2 dx \right)^{1/2} \left(\int_\Omega \lambda_1 \|\boldsymbol{\varepsilon}(\mathbf{v})\|^2 dx \right)^{1/2} \quad (6)$$

Let $\|\boldsymbol{\varepsilon}(\mathbf{v})\| \leq 1$ a.e. on Ω . Then

$$f(\mathbf{v}) \leq \left(\int_\Omega \frac{1}{\lambda_1} \|\boldsymbol{\tau}\|^2 dx \right)^{1/2} \left(\int_\Omega \lambda_1 dx \right)^{1/2} = \left(\int_\Omega \frac{1}{\lambda_1} \|\boldsymbol{\tau}\|^2 dx \right)^{1/2} \Lambda^{1/2} \quad (7)$$

since now $\text{tr}\mathbf{C} = \lambda_1$. Thus we estimate

$$\int_\Omega \frac{1}{\lambda_1} \|\boldsymbol{\tau}\|^2 dx \geq \frac{1}{\Lambda} (f(\mathbf{v}))^2 \quad (8)$$

for \mathbf{v} such that $\|\boldsymbol{\varepsilon}(\mathbf{v})\| \leq 1$. Thus (8) implies

$$\inf_{\boldsymbol{\tau} \in \Sigma_f} \inf_{\substack{\lambda_1 \geq 0 \\ \int_\Omega \lambda_1 dx = \Lambda}} \int_\Omega \frac{1}{\lambda_1} \|\boldsymbol{\tau}\|^2 dx \geq \frac{1}{\Lambda} \left(\sup_{\substack{\|\boldsymbol{\varepsilon}(\mathbf{v})\| \leq 1 \\ \text{a.e. on } \Omega}} f(\mathbf{v}) \right)^2 \quad (9)$$

where the left hand side is equal to J , see (3); this ends the proof of the estimate discussed. In papers [4, 5] the following identity has been put forward

$$\sup\{f(\mathbf{v}) \mid \|\boldsymbol{\varepsilon}(\mathbf{v})\| \leq 1 \text{ a.e. on } \Omega\} = \inf \left\{ \int_\Omega \|\boldsymbol{\tau}\| dx \mid \boldsymbol{\tau} \in \Sigma_f \right\} \quad (10)$$

by invoking the arguments of Strang and Kohn [9] concerning the Michell truss problem. Just recently the present authors have noted that the identity (10) has been proved by Bouchitté and Valadier [2]. Denoting the value of (10) by Z one can rearrange (9) to the form

$$\inf_{\boldsymbol{\tau} \in \Sigma_f} \inf_{\substack{\lambda_1 \geq 0 \\ \int_{\Omega} \lambda_1 dx = \Lambda}} \int_{\Omega} \frac{1}{\lambda_1} \|\boldsymbol{\tau}\|^2 dx \geq \frac{1}{\Lambda} \left(\inf_{\boldsymbol{\tau} \in \Sigma_f} \int_{\Omega} \|\boldsymbol{\tau}\| dx \right)^2 \quad (11)$$

which proves $J \geq Z^2/\Lambda$.

Derivation (5) - (11) is inspired by some arguments used to prove Proposition 2.1 in [3]. This derivation is of vital importance, since it shows the passage from the functional (3) having the integrand of the quadratic growth to the functional with the integrand of linear growth at the right hand side of (11).

Much more subtle arguments are necessary to prove that $J \leq Z^2/\Lambda$ which would complete the proof of (4). In paper [3] and the papers cited therein one can find the equality (10) rearranged to the accurate form. The field \mathbf{v} should be a Lipschitz function from $\text{Lip}_{1,\rho}(\Omega)$ being the closure in the space of continuous functions on $\bar{\Omega}$ of the set of C^∞ functions with compact support vanishing on a given subset of Ω and such that $\rho(\nabla \mathbf{v}) \leq 1$ with $\rho(\nabla \mathbf{v}) = \|\boldsymbol{\varepsilon}(\mathbf{v})\|$.

Having solved problem (10) one can express the optimal λ_1 in terms of $\boldsymbol{\tau}^*$ being the minimizer of (4) or (10). The optimal body occupies the subdomain of Ω being the support of this measure, [4, 5].

5. The cubic symmetry material design (CSMD)

The set of admissible Hooke tensors will be restricted to the set of Hooke tensors of cubic symmetry at each point $x \in \Omega$. Thus we assign to each point x a triplet of unit vectors $(\mathbf{m}(x), \mathbf{n}(x), \mathbf{p}(x))$ and define the tensor

$$\mathbf{S} = \mathbf{n} \otimes \mathbf{n} \otimes \mathbf{n} \otimes \mathbf{n} + \mathbf{m} \otimes \mathbf{m} \otimes \mathbf{m} \otimes \mathbf{m} + \mathbf{p} \otimes \mathbf{p} \otimes \mathbf{p} \otimes \mathbf{p} \quad (12)$$

for each point of Ω . Let us recall the expression for components of the unit tensor in \mathbb{E}_s^4

$$I_{ijkl}^4 = \frac{1}{2} (\delta_{ik} \delta_{jl} + \delta_{il} \delta_{kj}) \quad (13)$$

and let $\mathbf{J} = \frac{1}{3} (\delta_{ij} \delta_{kl})$. Define $\mathbf{L} = \mathbf{I} - \mathbf{S}$, $\mathbf{M} = \mathbf{S} - \mathbf{J}$. All tensors \mathbf{C} of cubic symmetry are represented by Walpole's formula [10]

$$\mathbf{C} = a\mathbf{J} + b\mathbf{L} + c\mathbf{M} \quad (14)$$

with a, b, c being nonnegative moduli. The inverse of \mathbf{C} equals

$$\mathbf{C}^{-1} = \frac{1}{a}\mathbf{J} + \frac{1}{b}\mathbf{L} + \frac{1}{c}\mathbf{M} \quad (15)$$

provided that all the moduli are positive. The trace of \mathbf{C} equals $\text{tr}\mathbf{C} = a + 3b + 2c$. The cost of the design is defined as the integral of $\text{tr}\mathbf{C}$ over Ω and is assumed as equal Λ . The set of tensors \mathbf{C} in Ω represented by (14) and satisfying the mentioned cost constraint will be denoted by $H_\Lambda^2(\Omega)$.

The CSMD problem assumes the form (2) with H_Λ^1 replaced by H_Λ^2 . One can prove, see [7], that the compliance J is still given by (4) with $Z = Z_2$

$$Z_2 = \min_{\boldsymbol{\tau} \in \Sigma_f} \int_{\Omega} |||\boldsymbol{\tau}|||_2 dx \quad (16)$$

and

$$|||\boldsymbol{\tau}|||_2 = \frac{1}{\sqrt{3}} |\text{tr}\boldsymbol{\tau}| + \sqrt{2} \|\text{dev}\boldsymbol{\tau}\| \quad (17)$$

where $\text{tr}\boldsymbol{\tau} = \tau_{ii}$ and

$$\text{dev}\boldsymbol{\tau} = \boldsymbol{\tau} - \frac{1}{3} (\text{tr}\boldsymbol{\tau}) \mathbf{I} \quad , \quad \mathbf{I} = (\delta_{ij}) \quad (18)$$

One can prove that $|||\cdot|||_2$ is a norm in \mathbb{E}_s^2 . Let

$$|||\boldsymbol{\varepsilon}|||_2^* = \sup_{\boldsymbol{\tau} \neq 0} \frac{|\boldsymbol{\tau} \cdot \boldsymbol{\varepsilon}|}{|||\boldsymbol{\tau}|||_2} \quad (19)$$

be the norm dual to (17). The counterpart of the equality (10) reads

$$\sup\{f(\mathbf{v}) \mid \|\boldsymbol{\varepsilon}(\mathbf{v})\|_2^* \leq 1\} = \inf \left\{ \int_{\Omega} \|\boldsymbol{\tau}\|_2 \, dx \mid \boldsymbol{\tau} \in \Sigma_f \right\} \quad (20)$$

The trial fields \mathbf{v} are of Lipschitz class previously mentioned, where now $\rho(\nabla \mathbf{v}) = \|\boldsymbol{\varepsilon}(\mathbf{v})\|_2^*$

The norm $\|\cdot\|_2^*$ defined by (19) can be expressed explicitly. Appropriate computation gives

$$\|\boldsymbol{\varepsilon}\|_2^* = \max \left\{ \frac{\sqrt{3}}{3} |\text{tr}\boldsymbol{\varepsilon}|, \frac{\sqrt{2}}{2} \|\text{dev}\boldsymbol{\varepsilon}\| \right\} \quad (21)$$

Thus in the space of principal strains the ball $\|\boldsymbol{\varepsilon}\|_2^* \leq 1$ assumes the shape of a cylindrical domain of length 2 and radius $2\sqrt{3}/3$.

The problem at the left hand side of (20) is mathematically simpler than the right hand side, but its solution is of lesser importance. The maximizer \mathbf{v}^* does not determine the optimal moduli C_{ijkl}^* directly. To find them one cannot omit solving the problem (16).

Let $\boldsymbol{\tau}^*$ be the minimizer of (16). Then the optimal triplet $(\mathbf{m}^*, \mathbf{n}^*, \mathbf{p}^*)$ coincides with the triplet of eigenvectors of $\boldsymbol{\tau}^*$. Moreover, the optimal moduli are expressed by

$$\begin{aligned} a^*(x) &= \frac{\Lambda}{\sqrt{3}Z_2} |\text{tr}\boldsymbol{\tau}^*(x)| \\ b^*(x) &= 0 \\ c^*(x) &= \frac{\Lambda}{\sqrt{2}Z_2} \|\text{dev}\boldsymbol{\tau}^*(x)\| \end{aligned} \quad (22)$$

Note that $\text{tr}\mathbf{C}^*(x) = a^*(x) + 3b^*(x) + 2c^*(x) = \frac{\Lambda}{Z_2} \|\boldsymbol{\tau}^*(x)\|_2$ which shows that a^*, b^*, c^* satisfy the isoperimetric condition.

6. The isotropic material design (IMD)

The set H_{Λ}^3 corresponding to isotropy will replace the set H_{Λ}^1 in (2). The tensors \mathbf{C} are now represented by

$$\mathbf{C} = 3k\mathbf{J} + 2\mu\mathbf{K} \quad (23)$$

with $\mathbf{K} = \mathbf{I} - \mathbf{J}$ and $\text{tr}\mathbf{C} = 3k + 10\mu$. As proved by Czarnecki [6], the formula (4) holds good with Z given by (16) and with the integrand defined as below

$$\|\boldsymbol{\tau}\|_3 = \sqrt{10}|\text{tr}\boldsymbol{\tau}| + 5\sqrt{6}\|\text{dev}\boldsymbol{\tau}\| \quad (24)$$

Contrary to obvious discrepancies between isotropic materials and cubic crystals the problem (16) differs only in coefficients in (17) and (24). Assume $\boldsymbol{\tau} = \boldsymbol{\tau}^*$ is the minimizer of (4) with $\|\cdot\| = \|\cdot\|_3$.

The optimal moduli are expressed by

$$k^*(x) = \frac{\sqrt{10}}{3} \frac{\Lambda}{Z_3} |\text{tr}\boldsymbol{\tau}^*(x)|, \quad \mu^*(x) = \frac{\sqrt{3}}{2} \frac{\Lambda}{Z_3} \|\text{dev}\boldsymbol{\tau}^*(x)\| \quad (25)$$

Note that the integral of $\text{tr}\mathbf{C}^*$ is now equal to Λ . The support of $\boldsymbol{\tau}^*$ determines the optimal body. Having the bulk and shear moduli one can compute the optimal Poisson ratio ν^* . The interesting feature of many solutions is that in some large subdomains the optimal Poisson ratio approaches -1 and in other parts of the domain it approaches 1/2. Thus the optimal structures turn out to be of auxetic properties.

7. Construction of optimal solutions and exemplary results

The numerical method for constructing the optimal isotropic material and cubic material designs is based on solving problem (4) with integrands defined by appropriate norms for the trial stress fields. The numerical method has been developed in [4, 5, 6]; it is based on discretization of the set of statically admissible stresses. This linear affine set is represented by the solution of the discretized equilibrium equations with using the singular value decomposition technique (SVD). The free parameters of the representation are determined by performing minimization in the discretized counterpart of (4); for the details the reader is referred to [5]. The aim of the present section is to show only exemplary results: the optimal layouts of isotropic moduli found by the IMD technique outlined in Sec.6.

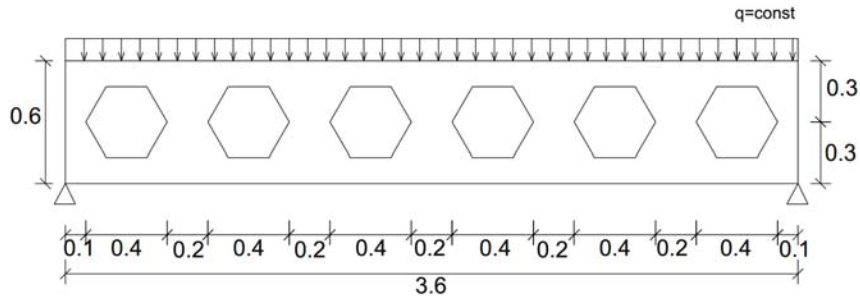


Figure 1: Dimensions of the girder considered

Consider the girder of dimensions 3.60×0.60 [m] lying on two non-sliding point supports, see Fig.1.

A uniformly distributed vertical load of intensity $q = 1.0$ [N/m] is applied along the upper edge. The design cost Λ , see (3), is assumed as equal to $E_0|\Omega|$, where Ω represents the area of the design domain. The modulus E_0 is assumed as equal 1.0 [N/m], the optimal values of the designed elastic moduli being proportional to E_0 , see (25). Two optimal designs are constructed: a) for the rectangular design domain without openings, and: b) for the design domain with six hexagonal openings, as shown in Fig.1. The scatter plots of the Young modulus E^* and

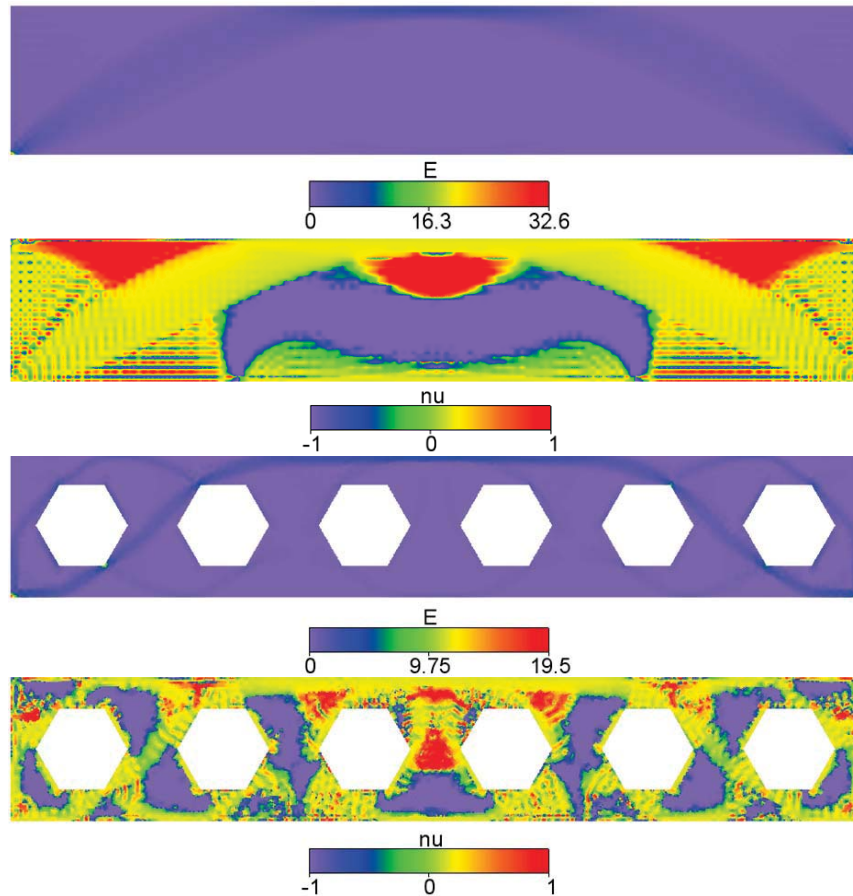


Figure 2: The layouts of Young modulus E^* and Poisson ratio ν^* in optimal isotropic girders: without openings (case a) and with openings (case b).

Poisson ratio ν^* of the optimal non-homogeneous isotropic material within the girder domain for both cases a) and b) are shown in Fig. 2. The results have been found with using the bilinear, isoparametric C2D4 finite elements, applied for the approximation of the stress fields. In case (a) the mesh of 5400 elements has been used, in case (b) the number of elements being equal 4555.

For the rectangular design domain the optimal material forms a characteristic arch. The presence of openings

brings about creation of stiffenings tangent to the openings, a characteristic feature of available optimal solutions to the scalar Monge-Kantorovich problem, see [3].

A characteristic property of the solution presented is emergence of the domains where the optimal Poisson ratio attains its lower and upper bounds. In the 2D setting these bounds are: -1 and 1, while in the 3D case they are tighter: -1, 1/2. In the 2D case considered we expect the former bounds. Note that in domains shown in the purple color the optimal layout of Poisson ratio reaches its lower bound equal to -1. In contrast, the red color indicates the domain where the Poisson ratio reaches its upper bound being equal to 1. Let us note lastly that in case of 3D optimal solutions constructed by the IMD method both the bounds : -1 and 1/2 are reached in typical optimal 3D designs [6]; selected 3D optimal solutions will be presented during the Conference.

8. Concluding remarks

The three versions of the material design considered come down to the problem (4) with different norms $\|\cdot\|$. To make this problem well posed one should sought the minimizer in the space of measures, as stressed in the paper [3] on shape optimization. The support of the minimizer determines the shape of the optimal body. Thus the material and shape optimizations are indissolubly bonded.

Optimum anisotropy becomes singular unless the strongest assumption of isotropy is imposed. The optimal isotropic bodies exhibit auxetic properties for majority of possible loads.

9. Acknowledgements

The present paper has been prepared within the Research Grant "Topology Optimization of Engineering Structures. A Synthesizing approach encompassing the methods of: free material design, multi-material design and Michell-like trusses", financed by the National Science Centre of Poland.

10. References

- [1] M.P. Bendsøe, J.M. Guedes, R.B. Haber, P. Pedersen and J.E. Taylor, An analytical model to predict optimal material properties in the context of optimal structural design, *Journal of Applied Mechanics*, 61, 930-937, 1994.
- [2] G. Bouchitté, M. Valadier, integral representation of convex functionals on a space of measures. *Journal of Functional Analysis* 80, 398-420, 1988.
- [3] G. Bouchitté, G. Buttazzo, Characterization of optimal shapes and masses through Monge-Kantorovich equation, *Journal of European Mathematical Society* 3, 139168, 2001.
- [4] S. Czarnecki, T. Lewiński, The Free material design in linear elasticity. pp 213-257, in: G.I.N. Rozvany, T.Lewiński (Eds.), *Topology Optimization in Structural and Continuum Mechanics*. Springer-Wien, 2014.
- [5] S.Czarnecki, T. Lewiński, A stress-based formulation of the free material design problem with the trace constraint and multiple load conditions. *Struct. Multidisc. Optim.*, 49, 707731, 2014.
- [6] S. Czarnecki, Isotropic material design, submitted 2015.
- [7] R. Czubacki, T. Lewiński, Topology optimization of spatial continuum structures made of non-homogeneous material of cubic symmetry, submitted 2015.
- [8] J. Haslinger, M. Kočvara, G. Leugering and M. Stingl, Multidisciplinary free material optimization, *SIAM Journal of Applied Mathematics* 70(7), 2709-2728, 2010.
- [9] G.Strang, R.V. Kohn, Hencky-Prandtl nets and constrained Michell trusses, *Computer Methods in Applied Mechanics and Engineering* 36(2), 207-222, 1983
- [10] L.J. Walpole, Fourth-rank tensors of the thirty-two crystal classes: multiplication tables. *Proceedings of the Royal Society of London*. A 391, pp. 149-179, 1984.

A Novel Constraint Handling Strategy for Expensive Optimization Problems

Kalyan Shankar Bhattacharjee¹, Tapabrata Ray²

¹ University of New South Wales, Canberra, ACT 2610, Australia, Kalyan.Bhattacharjee@adfa.edu.au

² University of New South Wales, Canberra, ACT 2610, Australia, T.Ray@adfa.edu.au

1. Abstract

Constraints are inherently present in any real world problem. In the context of multidisciplinary design optimization problems, such constraints arise out of physical laws, statutory requirements, user preferences etc. and are often computed using computationally expensive analysis e.g. FEM, CFD, CEM etc. While population based stochastic optimization algorithms are a preferred choice for the solution of such class of problems (often with the aid of approximations), they typically adopt a full evaluation policy i.e. all constraints and objective functions for all solutions are evaluated. Recent studies have highlighted the possibility of selected constraint evaluation (i.e. a subset of relevant constraints are only evaluated), although learning the sequence (or the subset) of constraints is far from trivial. In this paper, we introduce an approach for selective evaluation based on Support Vector Machine (SVM) models, wherein promising solutions are identified and evaluated based on the trade-off between need to learn and cost to learn. The performance of the proposed scheme is compared with other state-of-the-art constraint handling methods using a set of well-studied engineering design optimization problems. The aspect of selective evaluation has rarely been investigated in literature and the results clearly indicate the benefits selective evaluation which is of immense value in the context of computationally expensive optimization problems.

2. Keywords: Constraint Handling, Classifiers, Selective evaluation.

3. Introduction

Most real world optimization problems involve constraints and feasible solutions need to satisfy them. A generic constrained optimization problem can be expressed as:

$$\begin{aligned} & \underset{\mathbf{x}}{\text{minimize}} && f(\mathbf{x}) \\ & \text{subject to} && g_i(\mathbf{x}) \geq 0, \quad i = 1, 2, \dots, q \\ & && h_j(\mathbf{x}) = 0, \quad j = 1, 2, \dots, r \end{aligned}$$

where q represents the number of inequality constraints and r denotes the number of equality constraints. The equality constraints are replaced by a pair of inequalities. The vector $\mathbf{x} = [x_1 \ x_2 \ \dots \ x_n]$ denotes a solution represented using n design variables.

It is well known that the performance of all stochastic optimization algorithms are affected by the underlying mechanism of constraint handling. Constraint handling is an active area of research and existing methods can be classified into three categories i.e. (a) full evaluation policy with *feasibility first* principle: all constraints and objectives are evaluated for all solutions and feasible solutions are preferred over infeasible solutions (objective function value of infeasible solutions are essentially useless information) e.g. Non-dominated Sorting Genetic Algorithm(NSGA-II) [1] (b) full evaluation policy with marginally infeasible solutions preserved or stochastically preferred e.g. Infeasibility Driven Evolutionary Algorithm(IDEA) [5], Stochastic Ranking(SRES) [6], Epsilon Differential Evolution(eps-DEA) [7] (objective function values of infeasible solutions are used in ranking solutions) and (c) partial evaluation strategy e.g. *evaluate till you violate*[8] where constraints are evaluated in a sequence (DEACS) until a violation is encountered. In the context of computationally expensive optimization problems, partial evaluation policy offers the potential to reduce the number of function evaluations.

The evaluation cost can be further reduced if one can (a) screen potentially promising offsprings and (b) evaluate relevant constraints. In this paper, support vector machines (SVM) [9, 10] are used to identify promising offsprings and the relevant set of constraints. In the proposed approach, a SVM classifier is used to estimate the class label and the associated confidence about the quality of a solution. The use of a SVM classifier to identify promising solutions appeared in [11, 12]. In this study, we have used SVM ranking [10] models to predict the rank of a partially evaluated solution.

4. Proposed Approach

We adopt a generational model. The initial population is fully evaluated i.e. objective and all constraints for all the individuals are evaluated and the information is stored in an *Archive*. The first set of N parents are identified using roulette wheel selection, while the second set of N parents are identified using a random selection. A binary tournament between these N pairs of solutions result in N participating parents and offspring solutions are created

using simulated binary crossover (SBX) and polynomial mutation (PM). Offspring solutions are screened using a two-class SVM classifier, trained using the data from the *Archive* with its inputs being the variables of the optimization problem (\mathbf{x}) and the output being the final rank of the solutions. Offspring solutions predicted with a class label of 1 are considered as potential solutions.

For any given potential solution, the probability of satisfying its i^{th} constraint is given by $Feasibility_Index_i$. A value of 1 would indicate that it would satisfy the i^{th} constraint and 0 otherwise. Similarly, for a solution under consideration, $Rank_Index_i$ is computed for each constraint. The term $Rank_Index_i$ reflects the confidence that this solution is among the top 50% in a list based on the i^{th} constraint. To construct a list based on the i^{th} constraint, solutions are ordered based on the i^{th} constraint values i.e. feasible and furthest from the i^{th} constraint boundary at the top and infeasible and the furthest from the i^{th} constraint boundary at the bottom. In order to capture the local behavior, for each potential offspring solution, the classifiers (one for each constraint) are trained using k closest (in variable space) neighbors from the *Archive*. The inputs to these classifiers are the variable values and the outputs are the corresponding ranks based on that particular constraint under consideration. For a potential offspring, the constraint associated with least $Feasibility_Index$ and least $Rank_Index$ will be evaluated first. However, in the situation where $Feasibility_index$ of a solution is same in all its constraints, the sequence of evaluation is based on the following rule: (a) if all neighboring k solutions have all the constraints violated i.e. ($Feasibility_Index = 0$), the constraint having least $Rank_Index$ is evaluated first and (b) if all neighboring k solutions have all the constraints satisfied i.e. ($Feasibility_Index = 1$), the objective function for this solution is only evaluated since it is most likely a feasible solution. In the next step, SVM ranking model is utilized to predict rank of the potential offspring in all other constraints, where it has not been evaluated. In this ranking scheme, a regression model is created using actual ranks of all the solutions from the *Archive* based on the evaluated constraint as inputs and ranks based on other constraints or final rank as outputs. Hence, for any potential offspring solution, ranks based on all other constraints and its final rank in the population can be predicted. Rank prediction and insertion in the population are executed taking one offspring at a time instead of taking the whole set. Therefore insertion of one offspring might affect the position of the previous offsprings.

It is important for any learning based scheme to focus the region of interest and progressively improve its quality of prediction. To assist this, top solutions in a population undergo full evaluation (i.e. all constraints and objective function values for these solutions are evaluated). Please note that the final ranking of the population is based on *feasibility first* principle. The pseudo-code of the proposed approach is presented below: Classifier Guided Constraint Selection Mechanism (CGCSM).

5. Numerical Experiments

The success of a constraint handling strategy can be assessed from two different angles (a) ability of the approach to deliver the first feasible solution with minimal computational cost and (b) quality of the solution delivered for a fixed computational budget. While the second metric is largely used within the evolutionary computation community, such a metric does not solely assess the performance of constraint handling schemes. We objectively evaluate the performance of CGCSM and compare it with IDEA, NSGA-II, DEACS and SRES using 5 well studied benchmark engineering design problems: Belleville Spring [13], Helical Spring [13], Speed Reducer [14], and Step Cone Pulley [15]. The properties of the objective functions, nature of constraints, number of active constraints and the percentage of the feasible space are listed in Table 1.

Table 1: Properties of the Problems (Maximization Problem: max, Minimization Problem: min)

Problem	n	Obj	ρ %	LI	NE	NI	NA
Belleville Spring(min)	4	Quadratic	0.2595	7	0	0	-
Helical Spring(min)	3	Polynomial	0.0316	9	0	0	-
Speed Reducer(min)	7	Polynomial	0.0962	11	0	0	-
Step Cone Pulley(min)	5	Polynomial	0.0000	0	3	8	-

where n : number of variable, Obj: Objective function type, ρ : Percentage ratio of feasible space over entire search space, LI: number of linear inequalities, NE: number of equalities, NI: number of nonlinear inequalities and NA: number of active constraints.

The relative sizes of the feasible region (feasibility ratio) is based on random sampling of 1,000,000 random points. The results obtained using the proposed algorithm CGCSM are compared with those obtained using infeasibility driven evolutionary algorithm (IDEA) [5], non-dominated sorting genetic algorithm (NSGA-II) [1], Constraint sequencing (DEACS) [8], and Stochastic ranking (SRES) [6]. A one-to-one comparison of CGCSM with IDEA, NSGA-II, DEACS and SRES would offer insights on the actual utility of the classifier. Results, presented in Table 2, indicate the cost of evaluation till first feasible is obtained and Table 3 indicates the quality of the solution after 1000 function evaluations equivalent to evaluating 1000 solutions during the course of optimization using a full evaluation policy). As an example, for a problem involving 7 constraints, full evaluation of 1000 solutions would mean an evaluation budget of 8000. Each objective function evaluation or a constraint evaluation

Algorithm 1 CGCSM

SET: FE_{max} {Maximum evaluation budget}, N {Population size}, S_t {Confidence associated with SVM classifier (exponentially increases from 0 to 0.8 over FE_{max})}, $Popbin$ {Repository of ordered solutions evaluated so far (includes partial and fully evaluated solutions)}, $Archive$ {Repository of all fully evaluated solutions}

```
1: Initialize the population of  $N$  individuals using latin hypercube sampling
2: Evaluate  $Pop_{1:N, g_{1:q+2r}, f}$  and order them according to their final ranks (ordered based on feasibility first)
3:  $Popbin = Pop$ 
4: Update  $FE$ , Update  $Archive$ 
5: Update  $S_t$ 
6: while ( $FE \leq FE_{max}$ ) do
7:   Generate offspring solutions using BT, SBX and PM from  $Popbin_{1:N}$ 
8:   Construct a binary SVM classifier: Top  $100(1-S_t)$  percent solutions of the  $Archive$  is assigned a class label of 1
9:   Offspring solutions unique w.r.t  $Archive$  and with a predicted class label of 1 constitutes the set of  $C$  eligible offsprings ( $Childpop$ )
10:  for  $i = 1:C$  do
11:    For every member of  $Childpop$ , calculate the  $Feasibility\_Index_{i,1:q+2r}$  and  $Rank\_Index_{i,1:q+2r}$  based on its  $k$  neighbors from the
12:     $Archive$ 
13:    if  $Feasibility\_Index_{i,1:q+2r} = 1$  then
14:      Evaluate  $Childpop_{i,f}$ 
15:    else if  $Feasibility\_Index_{i,1:q+2r} = 0$  then
16:      [ $val, index$ ] =  $\min(Rank\_Index_{i, g_{1:q+2r}})$ ;  $g_{index}$  is the constraint to be evaluated
17:    else
18:      [ $val1, list1$ ] =  $\text{sort}(Feasibility\_Index_{i, g_{1:q+2r}})$ ; [ $val2, list2$ ] =  $\text{sort}(Rank\_Index_{i, g_{1:q+2r}})$ 
19:      Find  $index$ , where  $list1$  has a preference over  $list2$  and evaluate  $Childpop_{i, g_{index}}$ 
20:    end if
21:    Update  $FE$ 
22:    Construct SVM ranking model with inputs being rank of solutions in  $g_{index}$  and outputs being ranks in other constraints and final
23:    rank from  $Archive$ 
24:    Predict rank of  $Childpop_i$  in other constraints and its final rank based on the above SVM model
25:    if (Final rank of  $Childpop_i \leq (1 - S_t)|Popbin|$ ) then
26:      Evaluate  $Childpop_{i, g_{1:q+2r}}$  and place it in  $Popbin$  based on its actual final rank
27:      Update  $FE$ , Update  $Archive$ 
28:    else
29:      Place  $Childpop_i$  in  $Popbin$  according to its predicted final rank
30:    end if
31:  end for
32: end while
```

* FE denotes the evaluation cost i.e. 1 unit for each objective and 1 unit for each constraint evaluated

incurs a cost of 1 unit. Please take note that each equality constraints are imposed as two inequalities using all the algorithms except SRES (kept same as original formulation), however total evaluation budget is kept same for all the algorithms.

6. Results and discussion

The following parameters were used in this study: population size: 40; total evaluation budget is 1000 times the total number of constraints and objective for the problem; crossover probability: 0.9; mutation probability: 0.1; distribution index for crossover: 20; distribution index of mutation: 30; confidence in the classifier varied exponentially from 0 to 0.8 and the number of neighbors (k) was set to 12. We refer the readers to [9, 10] for the details on support vector machine classifiers. In our study, the standard SVM classifier of MATLAB toolbox was used with a Gaussian Radial Basis Function kernel with default settings and Karush-Kuhn-Tucker (KKT) violation level set as 0.05. Also for all the algorithms, same initial population has been used for a fair comparison.

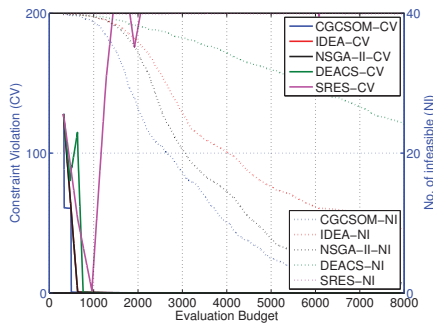
6.1. Performance on Problems

Convergence plots of mean sum of constraint violations (CV) and average number of infeasible individuals (NI) over the evaluation budget are shown in Figure 1a, Figure 2a, and Figure 3a for Belleville Spring, Speed Reducer, and Step Cone Pulley respectively. While, for the same problems the convergence plots of the mean objective function value (Obj) and average number of feasible individuals (NF) versus evaluation budget are shown in Figure 1b, Figure 2b, Figure 3b. In the context of partial evaluation policy (CGCSM and DEACS), solutions are evaluated offline to obtain the sum of constraint violation and objective function value for best individual in each generation. Hence, a fill up cost of 1 unit was assumed (i.e. to account for the case when a partially filled population is delivered).

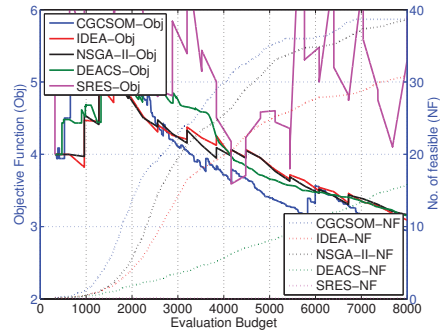
The best, mean, worst, median and standard deviation measures of the best solution across 30 independent runs obtained using *CGCSM*, *IDEA*, *NSGA-II*, *DEACS* and *SRES* are presented in Table 3.

The observations from the results can be summarized as follows:

(a) In Belleville Spring problem, Figure 1 indicates that CGCSM has the highest convergence rate when compared with other algorithms both in the contexts of mean sum of constraint violations and mean objective function value.

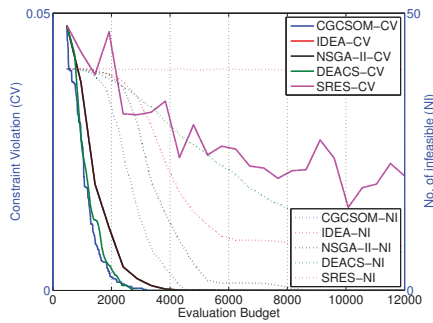


(a) Mean sum of CV and no. of infeasible individuals versus cost: Belleville Spring

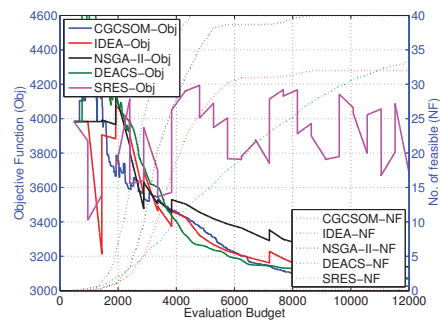


(b) Mean Obj and no. of feasible individuals versus cost: Belleville Spring

Figure 1: Convergence plot: Belleville Spring

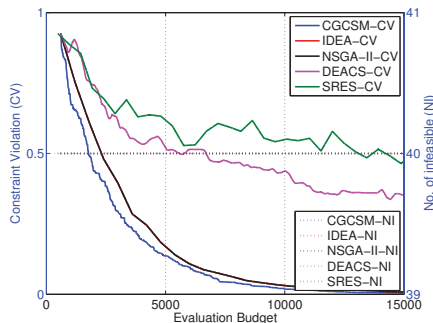


(a) Mean sum of CV and no. of infeasible individuals versus cost: Speed Reducer

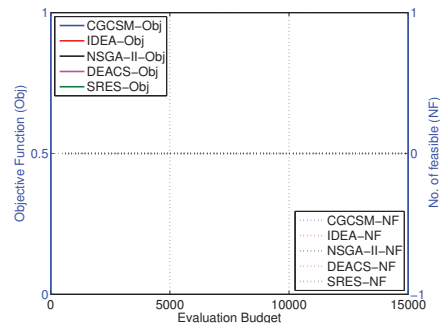


(b) Mean Obj and no. of feasible individuals versus cost: Speed Reducer

Figure 2: Convergence plot: Speed Reducer



(a) Mean sum of CV and no. of infeasible individuals versus cost: Step Cone Pulley



(b) Mean Obj and no. of feasible individuals versus cost: Step Cone Pulley

Figure 3: Convergence plot: Step Cone Pulley

This problem has relatively larger feasibility ration when compared to others. One can also observe from Table 3 that CGCSM outperforms other algorithms in the terms of the median optimal solution delivered. However, SRES is the best in terms of its ability to deliver the first feasible solution (Table 2 and Figures 1b). (b) CGCSM is able to deliver its first feasible solution at minimum cost for the Helical Spring design problem (Table 2). The design space for this problem is highly constrained. However quality of median optimal solution delivered by DEACS is best closely followed by CGCSM (Table 3). (c) Speed Reducer is also a highly constrained design problem which has highest number of linear inequalities among the problems discussed. The spread of the solutions is within 0.6% of the average objective value for DEACS, while it is 1.1% for CGCSM and much higher for others. This indicates better quality of convergence for the algorithms having partial evaluation policy in this problem. CGCSM performs better in terms of convergence (both mean CV and mean objective function value) than others. (d) Step Cone Pulley is an interesting problem as it has 8 non-linear inequality and 3 equality constraints which makes the problem highly constrained and difficult to solve. From Figure 3b, it can be observed that none of the algorithms could deliver feasible solutions within the fixed computational budget. However Figure 3a indicates better convergence of CGCSM and the final median violation values is also the lowest for CGCSM.

Table 2: Statistics of evaluation cost till first feasible for Problems

Problems	Algorithms	Best	Mean	Median	Worst	Std	Success
Belleville Spring	CGSCM	160.0000	1997.3793	1616.0000	5994.0000	1609.0422	29.0000
	IDEA	160.0000	2280.0000	1528.0000	6496.0000	1767.8565	29.0000
	NSGA-II	160.0000	2280.0000	1528.0000	6496.0000	1767.8565	29.0000
	DEACS	160.0000	1367.5000	1228.0000	3201.0000	792.5307	30.0000
	SRES	160.0000	1967.3600	1048.0000	7664.0000	2130.4546	25.0000
Helical Spring	CGSCM	920.0000	2314.8571	2130.0000	4780.0000	991.7325	21.0000
	IDEA	1450.0000	3317.0833	2730.0000	7610.0000	1583.5691	24.0000
	NSGA-II	1450.0000	3317.0833	2730.0000	7610.0000	1583.5691	24.0000
	DEACS	927.0000	3027.7000	2974.0000	6305.0000	1250.3888	30.0000
	SRES	530.0000	4978.4615	4740.0000	8760.0000	2762.9267	13.0000
Speed Reducer	CGSCM	336.0000	1622.0000	1428.0000	3204.0000	697.0129	30.0000
	IDEA	336.0000	2294.4000	2100.0000	6816.0000	1267.1713	30.0000
	NSGA-II	336.0000	2294.4000	2100.0000	6816.0000	1267.1713	30.0000
	DEACS	336.0000	1246.0333	1224.0000	2550.0000	601.8644	30.0000
	SRES	336.0000	4971.8571	5106.0000	9984.0000	2692.2567	28.0000
Step Cone Pulley	CGSCM	NaN	NaN	NaN	NaN	NaN	0.0000
	IDEA	NaN	NaN	NaN	NaN	NaN	0.0000
	NSGA-II	NaN	NaN	NaN	NaN	NaN	0.0000
	DEACS	NaN	NaN	NaN	NaN	NaN	0.0000
	SRES	NaN	NaN	NaN	NaN	NaN	0.0000

Table 3: Statistics for Problems

Problems	Algorithms	Feasibility	Best	Mean	Median	Worst	Std	Success
Belleville Spring	CGSCM	Feasible	2.2507	2.9440	2.6626	6.7106	0.9822	29.0000
		Infeasible	0.0000	0.0007	0.0000	0.0205	0.0037	1.0000
	IDEA	Feasible	2.4369	3.0897	2.8994	4.9255	0.5972	29.0000
		Infeasible	0.0000	0.0006	0.0000	0.0167	0.0030	1.0000
	NSGA-II	Feasible	2.2319	3.1649	2.9879	6.4377	0.8304	29.0000
		Infeasible	0.0000	0.0006	0.0000	0.0167	0.0030	1.0000
	DEACS	Feasible	2.4165	3.1518	3.1642	4.0260	0.4003	30.0000
		Infeasible	0.0000	0.0000	0.0000	0.0000	0.0000	0.0000
	SRES	Feasible	5.9192	5.9192	5.9192	5.9192	0.0000	1.0000
		Infeasible	0.0000	232.2841	1.0874	4625.5502	853.9785	29.0000
Helical Spring	CGSCM	Feasible	2.8223	4.0102	3.1356	6.9907	1.4696	21.0000
		Infeasible	0.0000	0.0659	0.0000	0.7494	0.1596	9.0000
	IDEA	Feasible	2.7684	3.9751	3.3809	7.1769	1.2899	24.0000
		Infeasible	0.0000	0.0438	0.0000	0.5380	0.1218	6.0000
	NSGA-II	Feasible	2.8068	4.1526	3.4674	7.3881	1.5122	24.0000
		Infeasible	0.0000	0.0438	0.0000	0.5380	0.1218	6.0000
	DEACS	Feasible	2.7434	2.9800	2.9937	3.1405	0.1057	30.0000
		Infeasible	0.0000	0.0000	0.0000	0.0000	0.0000	0.0000
	SRES	Feasible	3.7105	3.7105	3.7105	3.7105	0.0000	1.0000
		Infeasible	0.0000	0.5466	0.5863	1.4689	0.3452	29.0000
Speed Reducer	CGSCM	Feasible	3000.0118	3024.7515	3014.0820	3182.4136	33.0295	30.0000
		Infeasible	0.0000	0.0000	0.0000	0.0000	0.0000	0.0000
	IDEA	Feasible	3005.2093	3073.7129	3033.5242	3578.8939	116.8753	30.0000
		Infeasible	0.0000	0.0000	0.0000	0.0000	0.0000	0.0000
	NSGA-II	Feasible	3007.6698	3138.1983	3042.9740	4152.7143	249.6745	30.0000
		Infeasible	0.0000	0.0000	0.0000	0.0000	0.0000	0.0000
	DEACS	Feasible	3025.9020	3068.4133	3062.5951	3121.7496	18.5588	30.0000
		Infeasible	0.0000	0.0000	0.0000	0.0000	0.0000	0.0000
	SRES	Feasible	3259.1542	3684.9077	3684.9077	4110.6611	425.7534	2.0000
		Infeasible	0.0000	0.0207	0.0184	0.0636	0.0175	28.0000
Step Cone Pulley	CGSCM	Feasible	NaN	NaN	NaN	NaN	NaN	0.0000
		Infeasible	0.0005	0.0046	0.0040	0.0118	0.0028	30.0000
	IDEA	Feasible	NaN	NaN	NaN	NaN	NaN	0.0000
		Infeasible	0.0018	0.0083	0.0066	0.0304	0.0065	30.0000
	NSGA-II	Feasible	NaN	NaN	NaN	NaN	NaN	0.0000
		Infeasible	0.0018	0.0083	0.0066	0.0304	0.0065	30.0000
	DEACS	Feasible	NaN	NaN	NaN	NaN	NaN	0.0000
		Infeasible	0.0811	0.3527	0.3624	0.7589	0.1719	30.0000
	SRES	Feasible	NaN	NaN	NaN	NaN	NaN	0.0000
		Infeasible	0.2134	0.5110	0.4698	1.0447	0.1959	30.0000

Since only promising solutions are evaluated, use of classifiers would reduce the computational cost. However, the classifiers need to learn and their assessment needs to be reliable. The process of learning requires information from the evaluated solutions. Although use of poorly trained classifiers would save computational cost, the search outcome may not be satisfactory. To achieve this balance, the confidence associated with the classifier is varied from 0 to 0.8 exponentially during the course of search. In case of high confidence associated with the classifier, very few solutions would be evaluated and in turn the classifier would not have the opportunity to learn from diverse solutions. These observations seem to favor CGSCM for problems having highly constrained search space. In the context of evaluation cost associated with first feasible identification, performances of CGSCM and DEACS are nearly similar. However, in terms of convergence (both mean CV and mean objective function value) CGSCM performs better in 3 out of 4 problems.

7. Summary and Conclusions

Real life optimization problems often involve objective and constraint functions that are evaluated using computationally expensive numerical simulations e.g. computational fluid dynamics (CFD), finite element methods (FEM) etc. In order to solve such classes of problems, surrogate assisted optimization (SAO) methods are typically used, wherein computationally cheap and less accurate surrogates/approximation models of objectives/constraints are used during the course of search. In this paper, we explore an alternative path i.e. one where promising solutions are identified using support vector machine (SVM) based models. The key difference being, SVM models are used to identify promising solutions without explicitly attempting to approximate objective and constraint functions. Furthermore, for every promising solution, the approach identifies the constraints that are most likely to be violated and evaluates them first. In the event the constraints and objectives are evaluated using independent computationally expensive analysis (e.g. multi-disciplinary optimization), such an approach would only evaluate relevant constraints and/or objectives that are necessary to ascertain the rank of the solutions. The search behavior of CGSCM is compared with the following: NSGA-II (algorithm adopts a full evaluation policy), IDEA (algorithm maintains selected infeasible solutions), DEACS (algorithm evaluates selected set of constraints) and finally SRES (algorithm stochastically prefers infeasible solutions). The performance of the algorithm is further objectively assessed using a number of constrained engineering design optimization problems with limited computational budget. The rate of convergence of CGSCM is better for most of the problems and the final set of results are clearly better on all problems studied in this paper. We hope that this study would prompt design of efficient algorithms that selectively evaluate solutions and in particular selected set of constraints on the fly i.e. based on the trade-off between *need to learn/evaluate* and *cost to learn*.

8. References

- [1] K. Deb, A. Pratap, S. Agarwal, and T. Meyarivan, A fast and elitist multiobjective genetic algorithm: NSGA-II, *IEEE Transactions on Evolutionary Computation*, 6 (2), 182-197, 2002.
- [2] D. W. Coit, and A. E. Smith, Penalty guided genetic search for reliability design optimization, *Computers and Industrial Engineering*, Special Issue on Genetic Algorithms, 30 (4), 895-904, 1996.
- [3] S. Koziel and Z. Michalewicz, A decoder-based evolutionary algorithm for constrained parameter optimization problems, *Proceedings of the 5th Parallel Problem Solving from Nature – PPSN V*, Lecture Notes in Computer Science, T. Bäck, A. E. Eiben, M. Schoenauer, and H.-P. Schwefel, (Eds.), Springer, Heidelberg, Germany, 5199, 231-240, 1998.
- [4] A. Fitzgerald, and D. P. O'Donoghue, Genetic repair for optimization under constraints inspired by arabidopsis thaliana, *Parallel Problem Solving from Nature–PPSN X*, Lecture Notes in Computer Science, G. Rudolph, T. Jansen, S. Lucas, C. Poloni, and N. Beume, (Eds.), Springer, Dortmund, Germany, 5199, 399-408, 2008.
- [5] T. Ray, H. K. Singh, A. Isaacs, and W. Smith, Infeasibility driven evolutionary algorithm for constrained optimization, *Constraint-handling in evolutionary optimization*, Springer, 145-165, 2009.
- [6] T. P. Runarsson and X. Yao, Stochastic ranking for constrained evolutionary optimization, *IEEE Transactions on Evolutionary Computation*, 4 (3), 284-294, 2000.
- [7] T. Takahama and S. Sakai, Constrained optimization by the ϵ constrained differential evolution with gradient-based mutation and feasible elites, *IEEE Congress on Evolutionary Computation (CEC)*, 1-8, 2006.
- [8] M. Asafuddoula, T. Ray, and R. Sarker, Evaluate till you violate: A differential evolution algorithm based on partial evaluation of the constraint set, *IEEE Symposium on Differential Evolution (SDE)*, 31-37, 2013.
- [9] J. A. Suykens, T. Van Gestel, J. De Brabanter, B. De Moor, J. Vandewalle, *Least squares support vector machines*, 4, World Scientific, 2002.
- [10] O. Chapelle and S. S. Keerthi, Efficient algorithms for ranking with SVMs, *Information Retrieval*, 13 (3), 201-215, 2010.
- [11] I. Loshchilov, M. Schoenauer, and M. Sebag, A mono surrogate for multiobjective optimization, *Proceedings of the 12th annual conference on Genetic and evolutionary computation*, 471-478, ACM, 2010.
- [12] S. Bandaru, A. Ng, and K. Deb, On the performance of classification algorithms for learning pareto-dominance relations, *IEEE Congress on Evolutionary Computation (CEC)*, 1139-1146, 2014.
- [13] J. N. Siddall, *Optimal engineering design: principles and applications*, CRC Press, 1982.
- [14] J. Golinski, Optimal synthesis problems solved by means of nonlinear programming and random methods, *Journal of Mechanisms*, 5 (3), 287-309, 1970.
- [15] S. S. Rao, and S. S. Rao, *Engineering optimization: theory and practice*, John Wiley & Sons, 2009.

Experimental and numerical study of water impact investigations for aircraft crashworthiness application analysis

Wang Yonghu^{1,2,3}, Shu Dongwei³, Y. Fujii⁴, A. Takita⁴, R. Araki⁴, Hu Wei²

¹ School of Aeronautics, Northwestern Polytechnical University, Xi'an, 710072, P.R. China, wangyonghucn@163.com

² Civil Aviation Flight University of China, Guanghan, 618307, P.R. China

³ School of Mechanical and Aerospace Engineering, Nanyang Technological University, 50 Nanyang Avenue, Singapore 639798, Singapore, mdshu@ntu.edu.sg

⁴ School of Science and Technology, Gunma University, Kiryu, Tenjin-cho 1-5-1, 376-8515, Japan

1. Abstract

It is important for crashworthiness of an aircraft fuselage and its structural components to evaluate the aircraft airworthiness in crash-landing scenarios on different terrains (i.e. rigid, soil, and water). In this study, a new experimental method by Doppler shift is performed to measure the velocity and thus the water impact loads of a rigid sphere bottom structure dropping onto a water surface. Doppler Effect measurements are conducted to precisely obtain the water impact responses acting on the structure. And experimental results are validated and evaluated with the classical experimental data, as well as numerical simulation performed on the explicit FEM code LS-DYNA. A penalty coupling algorithm within the frame of multi-material Arbitrary Lagrangian Eulerian (ALE) model is utilized to numerically simulate the experimental cases. It concludes that the Doppler measurement is a reliable and effective method to not just obtain the water-impact responses and its great potential to be applied to aircraft crashworthiness analysis.

2. Keywords: Crashworthiness, Water impact; Drop tests; Doppler measurement; Finite element analysis

3. Introduction

There have been various research programs are conducted by NASA, IDRF and FAA to investigate fixed-wing aircraft and rotorcraft crashworthiness in order to improve survivability in the event of a crash [1]. During a crash onto ground, soil or water, the structures must be able to absorb the kinetic energy and limit the impact forces and deceleration that are transmitted to the occupants to tolerable levels. While considerable research has been performed on testing of aircraft impacting hard surfaces and soft soil, few studies have been focused on impacting onto water surface. There are some differences between impacting onto water and rigid surfaces. Water impact loads depend on the fluid-structure interaction and contrarily rigid surface impact loads depend only on structural characteristics. Due to the complex crash event, the wetted surfaces will strongly influence the loads path changes and the floating time for the damaged structure because of the water pressure. It is necessary to develop a reliable experimental method to measure the water impact responses and become a part of methodologies used to water crashworthiness analysis.

Recently some analytical, experimental, and finite element methods have been available to water impact domain, such as ship slamming, aircraft ditching, space capsule water landing, and torpedo water entry and so on [2, 3]. Th. von Karman and H. Wagner were the pioneers to theoretically study water impact problem for the purpose of estimating the impact forces and pressures based on the conservation of momentum [4, 5]. The history of crashworthiness studies can be traced back to the 1910s. Miloh [6] solved the displacement, velocity, and acceleration histories of a rigid sphere analytically, by employing the matched asymptotic method. Generalized Wagner Model (GWM) was created using the linearization analysis on the exact boundary condition around the intersection between the body and the free surface [7, 8] and can thus obtain satisfactory results.

4. Experiment methodology and verification

R. Araki, A. Takita, et al [9, 10] used the Doppler shift and the modifying Levitation Mass Method (LMM) [11] to conduct a water impact experiment analysis of a rigid sphere impact on water at School of Science and Technology, Gunma University, Japan. In the paper the experimental drop test is simply introduced and test data are certificated with some classical water impact data and a close correlation is observed through the numerical simulation.

4.1 Experimental setup

The impact of a stainless sphere on the clam water surface with initial downward velocity with variable water-entry height and then plunging into the water is tested in this study by the Doppler measurement. The experimental setup (Figure 1) divides into four systems, including water pool, the laser Doppler measurement module, quick-releasing facility, and high-speed camera.

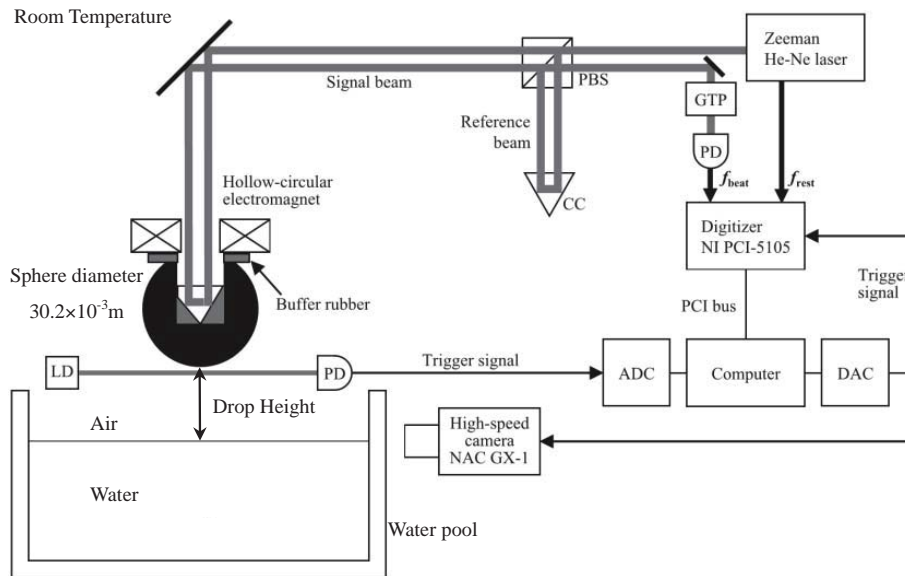


Figure 1 Experimental setup arrangement.

Code: CC=cube-corner prism, PBS=polarizing beam splitter, NPBS=non-polarizing beam splitter, GTP=Glan-Thompson prism, PD=photodiode, LD=laser diode, ADC=analogue-to-digital converter, DAC=digital-to-analogue converter.

Water pool is made of transparent acryl resin. During the test, it allows to adjust the variable dropping height which is between the bottom of the test article and water surface. The quick-releasing facility is equipped with a hollow-circular electromagnet to guarantee the test articles quick-release manually without any vibration. In this experiment, the test article is a tempered stainless sphere, which is punched a hole on the top and inlaid a cube corner prism. The total mass of the entire body is approximately 93.88 g. A high-speed camera (NAC Memrecam GX-1, NAC Image Technology, USA) is used to capture the images around the impact region with a resolution of 135 424 pixels and a frame rate of 15 000 fps. The digitizer and the high-speed camera are initiated by a sharp trigger signal generated using a digital-to-analogue converter (DAC). This signal is activated by means of a light switch, which is a combination of a laser diode and a photodiode.

The laser Doppler measurement module utilizes the laser Doppler interferometer to measure the velocity. A digitizer (NI PCI-5105, National Instruments Corp., USA) records the output signals of PD1 and PD2 with a sample number of 5M for each channel, a sampling rate of 30M samples per second, and a resolution of 8 bit. A Zeeman-type two-wavelength He-Ne laser in is used as the light source. Each beam has different frequency and orthogonal polarization. Differentiating the body's velocity which is calculated from the measured value of the Doppler shift frequency of the signal beam of the interferometer, the acceleration is calculated.

4.2 Experiment results and verification

Here only a test-run is conducted by the predetermined dropping position about 136mm from the water surface. In an effort to guarantee the reliability of measures and accuracy of test data, 7 drop measurements are taken in each set of measurements. The Levitation Mass Method (LMM) is developed to precisely measure the motion-induced time-varying beat frequency. Other water impact parameters, such as displacement, velocity and acceleration and impact force, are numerically calculated from the beat frequency. The results of the 7 drop measurements coincide well, indicating a high reproducibility of the measures [10]. In order to verify the experimental results, especially water impact force, the acquired water impacting acceleration is made to nondimensional impact drag coefficient as shown in Figure 2 in order to compare with some classical experimental data.

Comparing the new measures to the other classical experimental data, the repeatability and the reliability of the tests of impact accelerations are showed the effectiveness of the crashworthiness design for the sphere-bottom structures.

5. Numerical modelling and analysis

The main interest of the numerical simulations has been compared with the Doppler measure to estimate the efficiency of the nonlinear explicit codes to predict dynamic response of the structure. The fluid are defined as the ALE Multi Materials which is most versatile and widely using 1 point ALE multi-material element, the structure is modelled with the classical Lagrangian approach by the default Belytschko-Tsay element formulation.

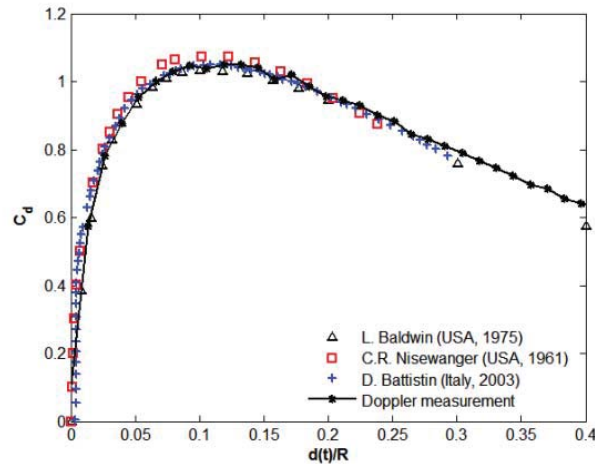


Figure 2 Comparison of Doppler measurement results with the experimental ones.

In order to reduce the computer time-consumption, only a quarter of the model is established with symmetric boundaries on XOY and YOZ planes, as shown in Figure 3. A cylindrical hole is embedded into the body in order to insert a cube corner prism. Meanwhile it demands the optical center coincide with the center of gravity of the sphere. For all the analysis cases the properties of the spherical body are taken as below. The mass of the impactor is 93.88 g, the density of the stainless steel body is 7650 kg/m^3 ; Young's modulus is $2.0 \times 10^{11} \text{ N/m}^2$; and Poisson's ratio is 0.3. The Poisson's ratio and Young's modulus of the material do not change the behavior of the sphere part because of its rigidity.

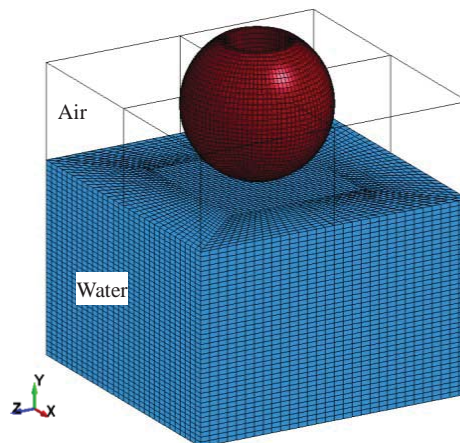


Figure 3 Three view of water impact model including air and water domain

The constitutive model and equation of state (EOS) model are simultaneously utilized to describe the nonlinear properties of a fluid or fluid-like deformation material in explicit dynamic codes LS-DYNA [12]. Material model *MAT_NULL and EOS model *EOS_LINEAR_POLYNOMIAL were contemporary used to model air. And then, the water was modeled using the Mie-Gruneisen EOS based on a cubic shock velocity-particle velocity. The penalty based coupling treats the FSI problem between a Lagrangian formulation modeling the structure and an ALE formulation modeling the fluid. The coupling mechanism between the MMALE and the structure is controlled by the keyword *CONSTRAINED_LAGRANGE_IN_SOLID (*CLIS). To get the proper numerical model and reach more correct solutions, convergence studies should be performed based on the convergence theorem, with respect to some parameters study. The selection of the contact stiffness based on the penalty coupling algorithm is required here. The coupling stiffness via the parameter PFAC, the penalty factor, in *CLIS should be analyzed in detail.

Numerical models of the experiment scenario are created and employed. Figure 4 show the comparison of the experimental, theoretical and numerical drag coefficient. The most concerned result is the maximum impact forces in the early-water entry. In the view of the acceleration peak and the overall shape of the curve, the prediction of nonlinear LS-DYNA codes coincides very well with one derived from the analytical MLM and shows a quite satisfactory agreement.

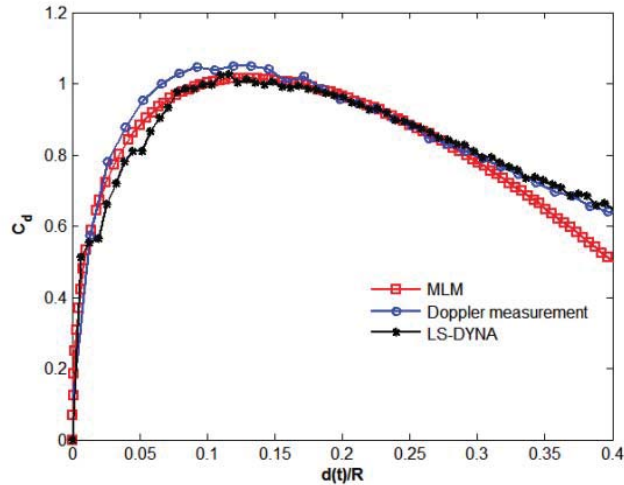


Figure 4 Numerical-analytical-experimental correlation for the impact drag coefficient

6. Conclusions

The present work is mainly to develop and verify a new suitable measurement of dynamic responses in water impact domain and its application is to be faced with aircraft crashworthiness analysis. The drop tests utilized by Doppler measurement are performed to precisely obtain acceleration, displacement and inertial impact force acting on the sphere bottom structure. The impact drag coefficient time histories are compared with other classical experimental results, together with the analytical method and numerical results. The results have been shown that Doppler measurement demonstrates the accuracy for predicting dynamic responses in water impact on a sphere. And it is feasible for other structures and it deserves further development for other crash-landing scenarios. The numerical simulation tests are efficiently carried out using a MMALE formulation and a penalty coupling algorithm to duplicate the experimental cases. And the verified numerical model can estimate the efficiency of the nonlinear explicit codes to predict the dynamic responses. They provide the opportunity to develop water impact analysis criteria for aircraft crashworthiness analysis.

7. Acknowledgements

The work has been done in the framework of the Joint Funds project of the National Natural Science Foundation of China (Grant No. U1333133). The activities have been partially funded by Grant No. F2013KF02 and Grant No. J2014-04 of CAFUC. And the strong support for the numerical research is greatly appreciated because of the offering of ANSYS/LS-DYNA from NPU and NTU. The work related to the experiment was supported in part by the Grant-in-Aid for Scientific Research (B) 18824360156 (KAKENHI 24360156).

References

- [1] K. Hughes, R. Vignjevic, et al. From aerospace to offshore: Bridging the numerical simulation gaps—Simulation advancements for fluid structure interaction problems. *International Journal of Impact Engineering*, 61(2013) 48-63.
- [2] Yong-hu Wang, Xiu-hua Shi. Review on research and development of water entry impact problem. *Explosion and Shock Waves*, 28(3), 276-282, 2008.
- [3] C. M. Seddon, and M. Moatamedi, Review of water entry with applications to aerospace structures, *International Journal of Impact Engineering*, 32(2006), 1045-1067.
- [4] Von Karman, T. The impact of seaplane floats during landing. *NACA TN 321*, National Advisory Committee for Aeronautics, Washington, USA, pp.1-16, 1929.
- [5] Wagner, H. Phenomena associated with impacts and sliding on liquid surfaces. *Mathematik und Mechanik*, 12(4), 193-215, 1932.
- [6] T. Miloh. On the initial-stage slamming of a rigid sphere in a vertical water entry. *Applied Ocean Research*. 13(1), 8–43, 1991.
- [7] O. M. Faltinsen. *Hydrodynamics of High-Speed Marine Vehicles*. Cambridge University Press. 2005.
- [8] A. Tassin, N. Jacques, El Malki Alaoui, et al. Assessment and comparison of several analytical models of water impact. *International Journal of Multiphysics*, 4(2010), 125–140.

- [9] R. Araki, A. Takita, et al. Impact force measurement of a spherical body dropping onto a water surface, *Review of Scientific Instruments*, 85, 075108 1-5, 2014.
- [10] R. Araki, A. Takita, et al. Impact force measurement of a spherical body dropping into a water surface from different height. *Journal of the Institute of Industrial Applications Engineers*, 2(4), 137-142, 2014.
- [11] H. S. Randhawa, H. M. Lankarani. Finite element analysis of impacts on water and its application to helicopter water landing and occupant safety. *International Journal of Crashworthiness*, 8:2, 189-200, 2003.
- [12] Livermore Software Technology Corporation. "LS-DYNA Keyword User's Manual", Livermore, California (USA), 2003.

Weight minimization of trusses with natural frequency constraints

Vu Truong Vu

Ho Chi Minh City University of Transport, Faculty of Civil Engineering, Ho Chi Minh City, Viet Nam,
vtruongvu@gmail.com

1. Abstract

The article presents the optimization of trusses subject to natural frequency constraints. Three planar trusses (10-bar, 37-bar and 200-bar structures) and three spatial trusses (52-bar, 72-bar and 120-bar structures) are surveyed. Differential Evolution method combined with finite element code is employed to find the optimal cross-section sizes and node coordinates. Constraint-handling technique is only based on a clear distinction between feasible solutions and infeasible solutions. The obtained results are equivalent to or better than solutions in literature.

2. Keywords: Truss optimization, natural frequency, differential evolution

3. Introduction

Truss optimization is one of the oldest developments of structural optimization. There were many publications on this field. However, except for simple problems that have been solved analytically, the search space and constraints are quite complex in most of actual structures. Consequently, there might not have explicit functions of constraints and closed-form solutions of stress, strain or natural frequency for these structures. In addition, due to the efficiency and capability of optimization methods, the so-called “optimum result” is often revised and improved with various approaches and algorithms. Structural optimization can be classified into three categories: cross-section size, geometry and topology. Depending on requirements, the study can include from one to all of the above types. This article only considers two types of optimization: the cross-section size and the geometry of trusses with natural frequency constraints. Six planar and spatial trusses are surveyed in this work. These structures are very common in literature and there are similar studies in [1-6]. However, the differences in this article are the quality of results and new groups of elements in 200-bar and 52-bar structures.

Although Differential Evolution (DE) has been proposed by Storn and Price [7] since 1997 and attracted many studies, there is not much application of DE to truss optimization with natural frequency constraints. Kaveh and Zolghadr [5] have compared nine algorithms but without DE. Recently, Pholdee and Bureerat [6] have considered DE in their comparison of various meta-heuristic algorithms for these problems.

4. Differential Evolution

Differential Evolution is a non-gradient optimization method which utilizes information within the vector population to adjust the search direction. Consider D -dimensional vectors $x_{i,G}$, $i = 1, 2, \dots, N$ as a population for each generation G , $x_{i,G+1}$ as a mutant vector in generation $(G + 1)$ and $u_{i,G+1}$ as a trial vector in generation $(G + 1)$. There are three operators in DE as follows.

- Mutation:

$$v_{i,G+1} = x_{r1,G} + FM(x_{r2,G} - x_{r3,G}) \quad i = 1, 2, \dots, N \quad (1a)$$

Another variant uses the best vector and two difference vectors for mutation. In this variant, Eq. (1a) becomes

$$v_{i,G+1} = x_{best,G} + FM(x_{r1,G} + x_{r2,G} - x_{r3,G} - x_{r4,G}) \quad (1b)$$

where r_1, r_2, r_3, r_4 are random numbers in $[1, N]$ and integer, which are mutually different and different from the running index i ; and FM is mutation constant in $[0, 2]$.

In this research, the variant with Eq. (1b) will be adopted.

- Crossover:

$$u_{i,G+1} = (u_{1i,G+1}, u_{2i,G+1}, \dots, u_{Di,G+1}) \quad (2)$$

$$\text{where } u_{ji,G+1} = \begin{cases} v_{ji,G+1} & \text{if } (r \leq CR) \text{ or } j = k \\ x_{ji,G} & \text{if } (r > CR) \text{ and } j \neq k \end{cases}, \quad j = 1, 2, \dots, D$$

where CR is the crossover constant in $[0, 1]$; r is random number in $(0, 1)$; and k is random integer number in $[1, D]$, which ensures that $u_{i,G+1}$ gets at least one component from $v_{i,G+1}$.

- Selection:

$$x_{i,G+1} = \begin{cases} u_{i,G+1} & \text{if } f(u_{i,G+1}) < f(x_{i,G}) \\ x_{i,G} & \text{otherwise} \end{cases} \quad (3)$$

where f is the objective function.

The DE was originally proposed for unconstrained optimization problems. For constrained optimization problems, a constraint-handling technique suggested by Jimenez et al [8] is supplemented. In this technique, the comparison of two solutions complies with the rule: (i) for two feasible solutions, the one with a better objective function value is chosen; (ii) for one feasible solution and one infeasible solution, the feasible solution is chosen; and (iii) for two infeasible solutions, the one with a smaller constraint violation is chosen. This technique requires no additional coefficient and gives a natural approach to the feasible zone from trials in the infeasible zone.

5. Problem Formulation and Results

Generally, the optimization problem can be defined as follows:

$$\begin{aligned} \text{Minimizing} \quad W &= \sum_{i=1}^N \rho_i L_i A_i & (4) \\ \text{Subject to:} \quad \omega_i &\geq \omega_{i,min} & i = 1..K \\ A_{i,min} &\leq A_i \leq A_{i,max} & i = 1..N \\ x_{i,min} &\leq x_i \leq x_{i,max} & i = 1..M \end{aligned}$$

where, W is the truss weight; ρ_i , L_i and A_i are the density, length and cross-section area of the i^{th} element, respectively; ω_i and $\omega_{i,min}$ are the i^{th} natural frequency and corresponding frequency limit; $A_{i,min}$ and $A_{i,max}$ are the lower bound and upper bound of the i^{th} cross-section area; $x_{i,min}$ and $x_{i,max}$ are the lower bound and upper bound of the i^{th} coordinate; N , K and M are the number of elements in the truss, number of frequencies subject to limits and number of nodes subject to coordinate constraints, respectively.

This study surveys three planar trusses (10-bar, 37-bar and 200-bar structures) and three spatial trusses (52-bar, 72-bar and 120-bar structures). For brevity, the basic parameters of problems and the optimal results compared with those in the literature are listed in table 1. Parameters of DE are as follows: population $N = 50$ (except $N = 150$ for 200-bar truss), crossover constant $CR = 0.9$, mutation constant $FM = 0.5$, number of iterations $I = 150$. Each problem is performed in 50 independent runs (except 100 runs for 200-bar truss). Other details are described in each problem.

Table 1: Parameters and the minimal weight of trusses

Parameters	Unit	Data of problems					
		10-bar	37-bar	200-bar	52-bar	72-bar	120-bar
Modulus of elasticity, E	N/m ²	6.98 × 10 ¹⁰	2.1 × 10 ¹¹	2.1 × 10 ¹¹	2.1 × 10 ¹¹	6.98 × 10 ¹⁰	2.1 × 10 ¹¹
Material density, ρ	kg/m ³	2770	7800	7860	7800	2770	7971.81
Frequencies constraints	Hz	ω ₁ ≥ 7 ω ₂ ≥ 15 ω ₃ ≥ 20	ω ₁ ≥ 20 ω ₂ ≥ 40 ω ₃ ≥ 60	ω ₁ ≥ 5 ω ₂ ≥ 10 ω ₃ ≥ 15	ω ₁ ≤ 15.916 ω ₂ ≥ 28.648	ω ₁ = 4 ω ₃ ≥ 6	ω ₁ ≥ 9 ω ₂ ≥ 11
Cross-section bounds	m ²	[0.645 × 10 ⁻⁴ , 40 × 10 ⁻⁴]	[10 ⁻⁴ , 10 ⁻³]	[0.1 × 10 ⁻⁴ , 30 × 10 ⁻⁴]	[10 ⁻⁴ , 10 ⁻³]	[0.645 × 10 ⁻⁴ , 30 × 10 ⁻⁴]	[10 ⁻⁴ , 129.3 × 10 ⁻⁴]
Nodes coordinate bounds	m	n/a	See details in 5.2	n/a	See details in 5.4	n/a	n/a
Minimal weight W _{min}	kg	524.56	359.45	2296.38	191.28	324.36	8710.90
W _{min} [1]	kg	529.09	n/a	2298.61	197.31	327.51	9046.34
W _{min} [2]	kg	535.61	n/a	n/a	n/a	326.67	n/a
W _{min} [3]	kg	524.88	364.72	n/a	193.36	324.50	n/a
W _{min} [4]	kg	535.14	363.03	n/a	207.27	n/a	n/a
W _{min} [5]	kg	532.34	360.56	n/a	195.62	334.66	8886.92
W _{min} [6]	kg	524.49	359.25	n/a	195.19	324.32	n/a

Table 2: Optimal results of planar trusses

10-bar truss		37-bar truss		200-bar truss	
Parameters	Results	Parameters	Results	Parameters	Results
A_1 (cm ²)	35.0930	Y_3, Y_{19} (m)	0.9736	A_1 (cm ²)	0.2789
A_2 (cm ²)	14.8802	Y_5, Y_{17} (m)	1.3372	A_2 (cm ²)	0.2725
A_3 (cm ²)	35.3906	Y_7, Y_{15} (m)	1.4965	A_3 (cm ²)	5.7222
A_4 (cm ²)	14.7917	Y_9, Y_{13} (m)	1.6024	A_4 (cm ²)	0.5423
A_5 (cm ²)	0.6450	Y_{11} (m)	1.6834	A_5 (cm ²)	1.4830
A_6 (cm ²)	4.5550	A_1, A_{27} (cm ²)	2.9844	A_6 (cm ²)	3.1676
A_7 (cm ²)	23.6841	A_2, A_{26} (cm ²)	1.0570	A_7 (cm ²)	4.8800
A_8 (cm ²)	23.5333	A_3, A_{24} (cm ²)	1.0806	A_8 (cm ²)	7.9840
A_9 (cm ²)	12.5161	A_4, A_{25} (cm ²)	2.6508	A_9 (cm ²)	18.7813
A_{10} (cm ²)	12.2117	A_5, A_{23} (cm ²)	1.3097	A_{10} (cm ²)	0.1000
ω_1 (Hz)	7.0002	A_6, A_{21} (cm ²)	1.0469	A_{11} (cm ²)	0.1000
ω_2 (Hz)	16.2058	A_7, A_{22} (cm ²)	2.6815	A_{12} (cm ²)	0.1000
ω_3 (Hz)	20.0003	A_8, A_{20} (cm ²)	1.3132	A_{13} (cm ²)	0.1000
W_{\min} (kg)	524.56	A_9, A_{18} (cm ²)	1.4278	A_{14} (cm ²)	0.2326
		A_{10}, A_{19} (cm ²)	2.6826	A_{15} (cm ²)	0.8481
		A_{11}, A_{17} (cm ²)	1.1798	A_{16} (cm ²)	1.2137
		A_{12}, A_{15} (cm ²)	1.2232	A_{17} (cm ²)	1.6352
		A_{13}, A_{16} (cm ²)	2.3931	A_{18} (cm ²)	2.0476
		A_{14} (cm ²)	1.0000	A_{19} (cm ²)	4.3721
		ω_1 (Hz)	20.0565	ω_1 (Hz)	5.0004
		ω_2 (Hz)	40.0129	ω_2 (Hz)	12.3446
		ω_3 (Hz)	60.0983	ω_3 (Hz)	15.0018
		W_{\min} (kg)	359.45	W_{\min} (kg)	2296.38

5.1 Planar 10-bar truss

The truss is shown in figure 1 where the added mass of 454 kg is attached at nodes 3– 6. Only cross-section sizes are optimized in this problem. The optimal weight is $W_{\min} = 524.56$ kg and converges after 150 iterations. Sizes of optimal cross-sections and natural frequencies are presented in table 2.

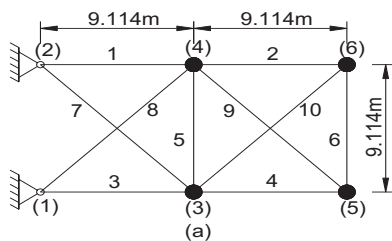
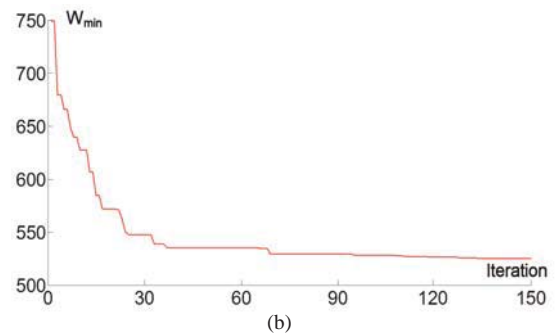


Figure 1: (a) Model of 10-bar truss
(b) Optimal cross-section sizes



5.2 Planar 37-bar truss

The truss is shown in figure 2 where the added mass of 10 kg is attached at lower nodes. The lower bars have a fixed cross-section area of 0.004m². For this problem, both cross-section sizes and y-coordinate of upper nodes are optimized. Upper nodes can move symmetrically in vertical direction. The optimal weight is $W_{\min} = 359.45$ kg and converges after 150 iterations. Sizes of optimal cross-sections and coordinates of nodes are listed in table 2.

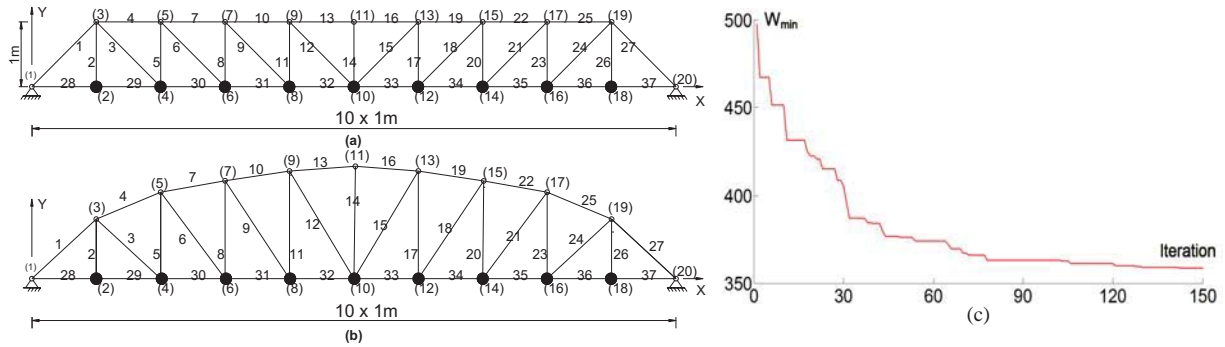


Figure 2: (a) Model of initial 37-bar truss, (b) Optimal shape, (c) Convergence of the optimal result

5.3 Planar 200-bar truss

The truss is shown in figure 3 where the added mass of 100 kg is attached at nodes 1–5. Only cross-section sizes are optimized. In comparison with the others, this problem has the high static indeterminacy, large number of element and wide range of cross-section size. This makes the optimization more difficult. Our approach is to use 19 groups of elements instead of 29 groups in [1]. Thus, the search space decreases one third.

For this structure, it notes generally that the lower storey, the bigger cross-section size. For example, the cross-section sizes gradually increase in groups of elements (1, 2, 3), (4, 5, 6, 7, 8, 9), (10, 11, 12, 13, 14), (15, 16, 17, 18, 19). In the article, we use this characteristic for the initialization of random values in DE algorithm. The optimal weight is $W_{\min} = 2296.38$ kg. Sizes of optimal cross-sections and natural frequencies are presented in table 2.

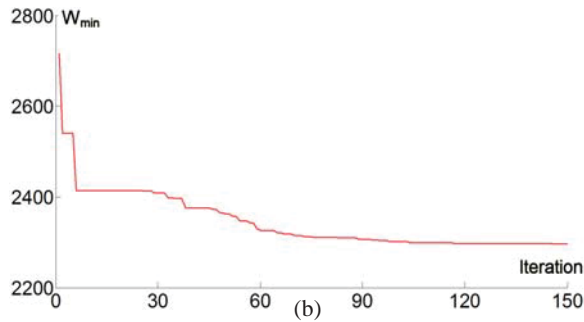
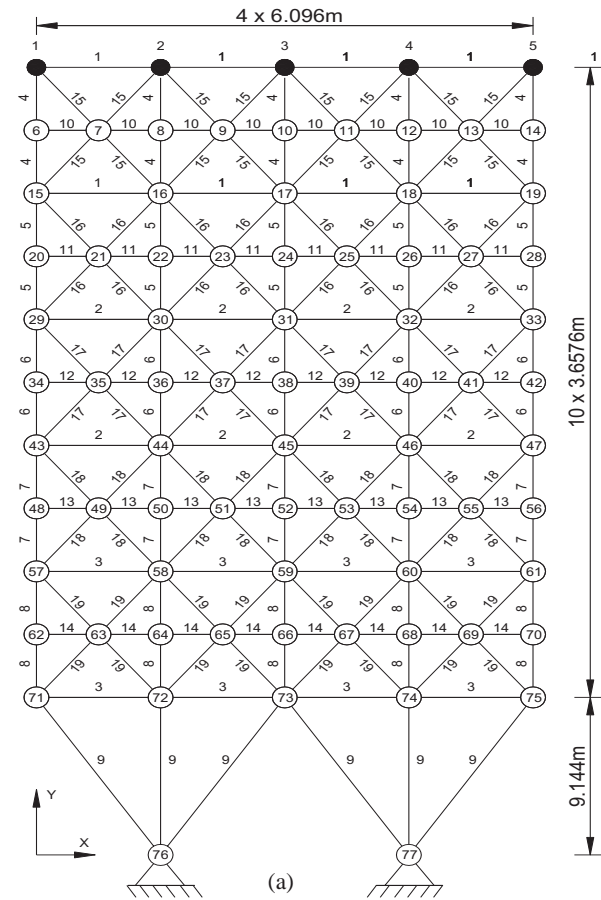


Figure 3: (a) Model of 200-bar truss (b) Convergence of the optimal result



5.4 Spatial 52-bar truss

The truss is shown in figure 4 where the added mass of 50kg is attached at free nodes 1–13. Both cross-section sizes and coordinate of nodes are optimized in this problem. Free nodes can move in range of $\pm 2m$ from their initial positions such that the symmetry is reserved. It notes that elements are divided to 9 groups which differs from 8 groups in [1]. The optimal weight is $W_{\min} = 191.28$ kg and converges after 150 iterations. Sizes of optimal cross-sections, coordinates of nodes and natural frequencies are listed in table 3.

5.5 Spatial 72-bar truss

The truss is shown in figure 5 where the added mass of 2270 kg is attached at nodes 17–20. Only cross-section sizes are optimized in this problem. Elements are divided to 16 groups, as seen in table 3. The optimal weight is $W_{\min} = 324.36$ kg and converges after 150 iterations. Sizes of optimal cross-sections and natural frequencies are listed in table 3.

5.6 Spatial 120-bar truss

The truss is shown in figure 6 where the added masses are attached at nodes as follows: 3000 kg at node 1, 500 kg at nodes 2–3, and 100 kg at nodes 14–37. Elements are divided to 7 groups, as seen in table 3. The optimal weight is $W_{\min} = 8710.90$ kg and converges after 150 iterations. Sizes of optimal cross-sections and natural frequencies are listed in table 3.

6. Conclusion

For six considered problems, Differential Evolution gives better or equivalent results compared with other methods in the literature. The convergence is rapid in round first 50 iterations. Especially, the different number of element groups in 52-bar truss and 200-bar truss also makes the minimum weights improved.

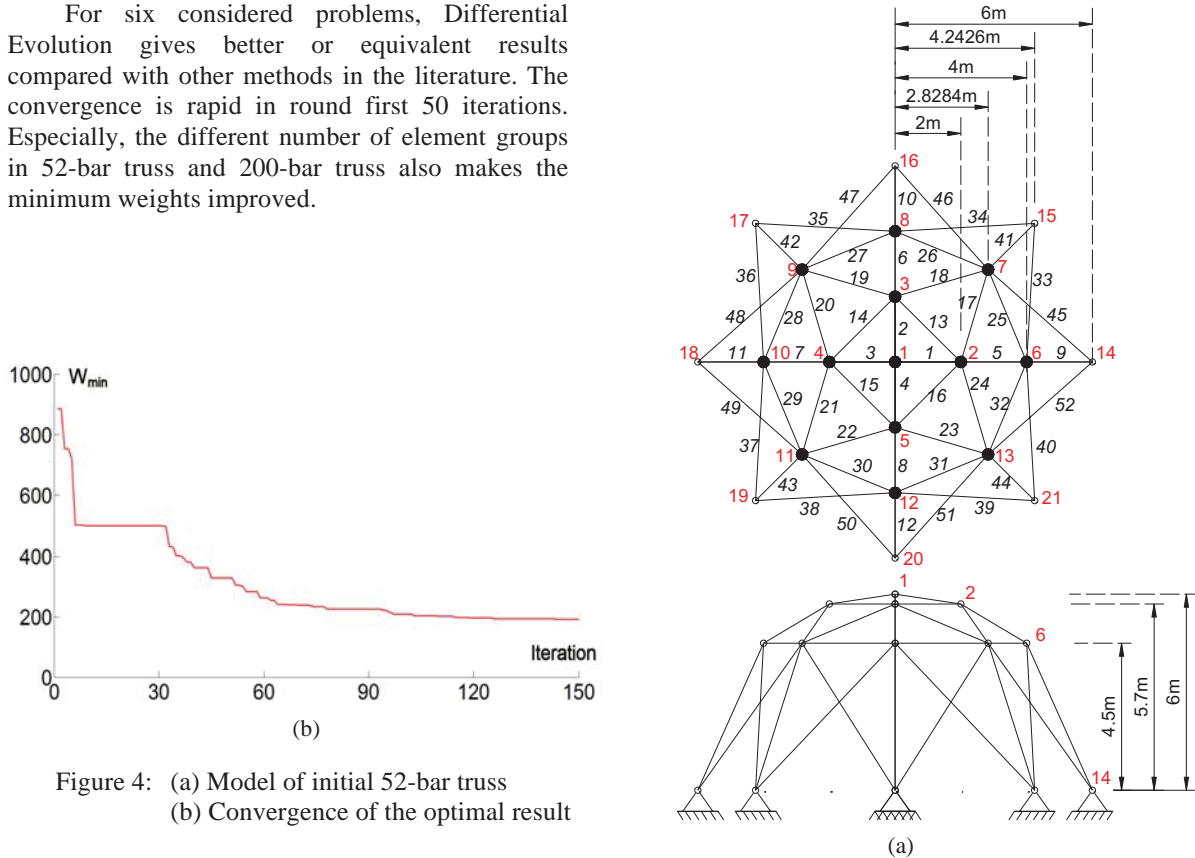


Figure 4: (a) Model of initial 52-bar truss
(b) Convergence of the optimal result

Table 3: Optimal results of spatial trusses

52-bar truss		72-bar truss		120-bar truss	
Parameters	Results	Parameters	Results	Parameters	Results
$A_1 - A_4$ (cm ²)	1.0000	$A_1 - A_4$ (cm ²)	16.9972	$A_1 - A_{12}$ (cm ²)	19.4686
$A_5 - A_8$ (cm ²)	1.5406	$A_5 - A_{12}$ (cm ²)	7.9173	$A_{13} - A_{24}$ (cm ²)	40.6526
$A_9 - A_{12}$ (cm ²)	1.0889	$A_{13} - A_{16}$ (cm ²)	0.6450	$A_{25} - A_{36}$ (cm ²)	10.7573
$A_{13} - A_{16}$ (cm ²)	1.2652	$A_{17} - A_{18}$ (cm ²)	0.6503	$A_{37} - A_{60}$ (cm ²)	21.0849
$A_{17} - A_{24}$ (cm ²)	1.0339	$A_{19} - A_{22}$ (cm ²)	12.5286	$A_{61} - A_{84}$ (cm ²)	9.7139
$A_{25} - A_{32}$ (cm ²)	1.2461	$A_{23} - A_{30}$ (cm ²)	8.0249	$A_{85} - A_{96}$ (cm ²)	11.6176
$A_{33} - A_{40}$ (cm ²)	1.3722	$A_{31} - A_{34}$ (cm ²)	0.6454	$A_{97} - A_{120}$ (cm ²)	14.8947
$A_{41} - A_{44}$ (cm ²)	1.0000	$A_{35} - A_{36}$ (cm ²)	0.6450	ω_1 (Hz)	9.0013
$A_{45} - A_{52}$ (cm ²)	1.6035	$A_{37} - A_{40}$ (cm ²)	7.9920	ω_2 (Hz)	11.0001
Z_1 (m)	6.0710	$A_{41} - A_{48}$ (cm ²)	8.0029	W_{\min} (kg)	8710.90
X_2 (m)	2.6047	$A_{49} - A_{52}$ (cm ²)	0.6450		
Z_2 (m)	3.7267	$A_{53} - A_{54}$ (cm ²)	0.6479		
X_6 (m)	4.1584	$A_{55} - A_{58}$ (cm ²)	3.6988		
Z_6 (m)	2.5000	$A_{59} - A_{66}$ (cm ²)	7.8182		
ω_1 (Hz)	15.2070	$A_{67} - A_{70}$ (cm ²)	0.6450		
ω_2 (Hz)	28.6487	$A_{71} - A_{72}$ (cm ²)	0.6450		
W_{\min} (kg)	191.28	ω_1 (Hz)	4.0002		
		ω_3 (Hz)	6.0008		
		W_{\min} (kg)	324.36		

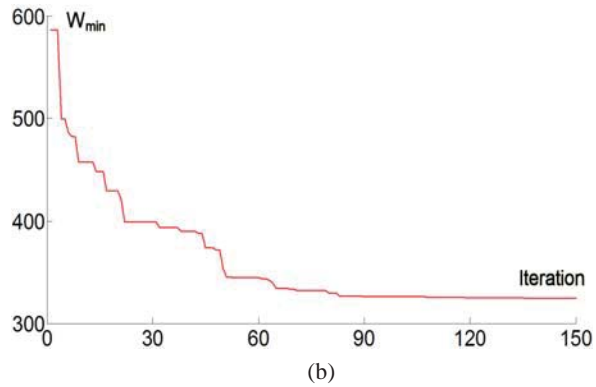
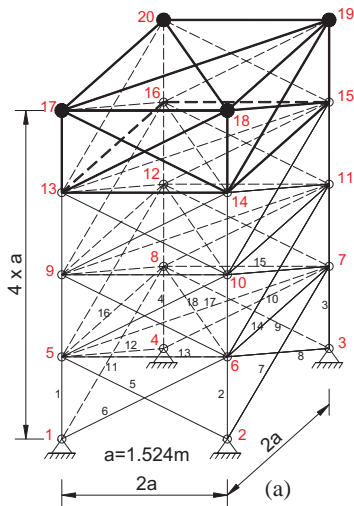


Figure 5: (a) Model of 72-bar truss
(b) Convergence of the optimal result

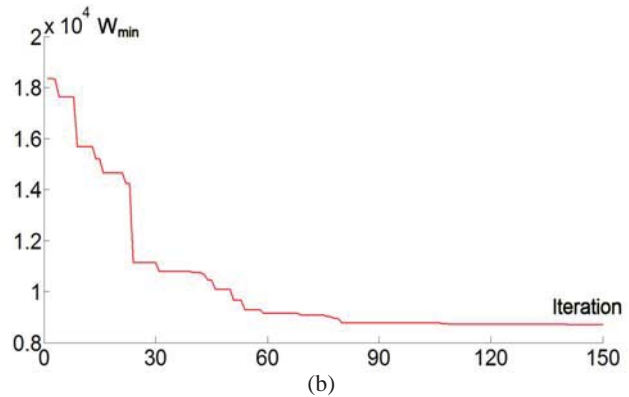
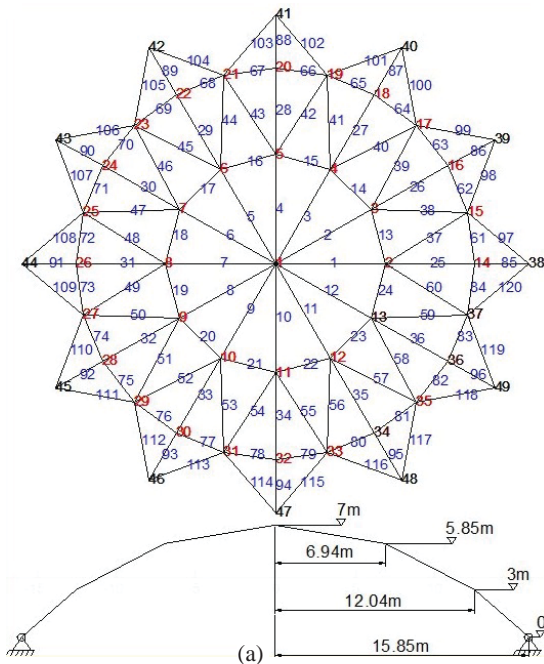


Figure 6: (a) Model of 120-bar truss,
(b) Convergence of the optimal result

7. References

- [1] A. Kaveh and A. Zolghadr, Truss optimization with natural frequency constraints using a hybridized CSS-BBBC algorithm with trap recognition capability, *Computers and Structures*, 102, 14–27, 2012.
- [2] W. Zuo, T. Xu, H. Zhang and T. Xu, Fast structural optimization with frequency constraints by genetic algorithm using adaptive eigenvalue reanalysis methods, *Structural Multidisciplinary Optimization*, 43, 799–810, , 2011
- [3] A. Kaveh and S.M. Javadi, Shape and size optimization of trusses with multiple frequency constraints using harmony search and ray optimizer for enhancing the particle swarm optimization algorithm, *Acta Mech*, 225, 1595–1605, 2014.
- [4] L. Wei, T. Tang, X. Xie and W. Shen, Truss optimization on shape and sizing with frequency constraints based on parallel genetic algorithm, *Structural Multidisciplinary Optimization*, 43, 665–682, 2011.
- [5] A. Kaveh and A. Zolghadr, Comparison of nine meta-heuristic algorithms for optimal design of truss structures with frequency constraints, *Advances in Engineering Software*, 76, 9-30, 2014.
- [6] N. Pholdee and S. Bureerat, Comparative performance of meta-heuristic algorithms for mass minimisation of trusses with dynamic constraints, *Advances in Engineering Software*, 75, 1-13, 2014.
- [7] R. Storn and K. Price, Differential Evolution - A Simple and Efficient Heuristic for Global Optimization over Continuous Spaces, *Journal of Global Optimization*, 11(4), 341-359, 1997.
- [8] F. Jimenez, J.L. Verdegay and A.F. Gomez-Skarmeta, Evolutionary techniques for constrained multiobjective optimization problems, *Proceedings of the workshop on multi-criterion optimization using evolutionary methods held at genetic and evolutionary computation conference*, 1999.

Many-objective Optimization in Engineering Design: Case Studies Using a Decomposition Based Evolutionary Algorithm

Hemant Kumar Singh, Tapabrata Ray

University of New South Wales, Canberra, Australia. Emails: {h.singh, t.ray}@adfa.edu.au

Abstract

Engineering design often involves simultaneous minimization/maximization of multiple conflicting objectives. The optimum solution of such problems comprises a set of designs representing best-tradeoff among objective values, known as Pareto optimal front (POF). It is well known that the existing multi-objective optimization algorithms can find POF for 2-3 objective problems successfully, but their performance deteriorates significantly for problems with 4 or more objectives, which are termed as “many-objective” optimization problems. There has been a significant recent interest in solving them. In this paper, we present a decomposition based approach for solving many-objective optimization problems. Further, we demonstrate that this improved capability can be exploited to solve various other intractable classes of problems. Two such classes presented are robust design optimization and “re-design” for robustness. In addition to the above, we also illustrate the benefits of multiobjective formulation for a special class of problems, where an user is interested in solving single objective optimization problems with different parameter values. We present numerical examples from various domains including mechanical, civil and aerospace industry to demonstrate the approaches and corresponding benefits.

1 Introduction

Optimization is an integral tool in engineering design used for pushing the boundaries of performance subject to several practical constraints. Multi-objective (MO) optimization algorithms are required where more than one conflicting objectives are simultaneously being optimized, for example, maximization of strength and minimization of weight of structural components, minimization of travel time and maximization of payload for space missions, maximization of engine efficiency and minimization of emissions etc. Optimum solutions of such problems is a set of designs representing best trade-off among the objectives, known as Pareto Optimal Front (POF). Population based methods such as Evolutionary Algorithms (EAs) [1] are commonly used to solve such problems, which “evolve” a population of solutions (designs) through a process similar to the Darwinian principle of natural selection. EAs simulate the evolution process through use of mathematical *crossover* and *mutation* (to generate new designs from “fitter parents”), *ranking* (to prioritize them based on performance) and *reduction* (to choose the designs to be retained for next generation). It is now well established in literature that the existing EAs can efficiently solve MO problems with 2-3 objectives but their performance deteriorates severely for problems with 4 or more objectives [2]. Such problems are referred to as “Many-objective” (MaO) optimization problems.

The poor performance of such algorithms for MaO problems is attributed to the ranking procedure based on Pareto-dominance. For MaO problems, most (or all) solutions in the population become *non-dominated* early in the search and hence there is no pressure to drive the solutions towards convergence. To deal with this challenge, a few different approaches have been reported in the literature. Some studies have focused on modifying the dominance relations [3] or adding a secondary ranking apart from Pareto dominance using various criteria such as sub-vector dominance, fuzzy dominance, ϵ -dominance etc. [4]. These methods may often result in reduced the diversity of solutions in POF in exchange for good convergence. Alternatively, the solutions can be ranked using an indicator such as hypervolume [5]. However, the calculation of hypervolume itself is computationally expensive. Interactive EAs [6, 7] have also been proposed, where a decision maker is asked to provide inputs/choices of preferred solutions during the search in an attempt to deliver designs in areas of interest. However, such user information may be hard to come by or at times misleading in absence of prior knowledge about the nature of the POF. For certain problems, reduction of original set of objectives to a manageable number has also been suggested [8]. Although each of these methods have their advantages and applicability, obtaining a well spread and converged POF for MaO problems still remains a challenge. In this regard, *decomposition* based methods [9, 10] have been most promising so far, which generate a set of diverse reference directions in the objective space and optimize linear combination of objectives along these directions to deliver diverse solutions on the POF.

It is to be noted that all the studies mentioned above have been presented in the context of deterministic optimization, *i.e.*, the original problem formulation itself had many objectives and no uncertainties in variables/objectives are considered. However, certain other useful classes of problems may also be modeled as MaO problems. For example, when a robust optimum is sought instead of deterministic optimum, the metrics for robustness could be added as additional objectives to the problem, resulting in an MaO problem. Similarly, one can also consider the problem of re-design for robustness of an existing product as an MaO problem. However, such extensions of many-objective optimization have only recently been proposed by the authors [11].

In this paper, an enhanced Decomposition Based Evolutionary Algorithm (DBEA) is presented for solving MaO problems in Section 2. Thereafter, its applications are demonstrated using three different classes of problems – deterministic, robust and re-design in Section 3. An additional special case is also illustrated in Section 3. Numerical experiments are presented on examples from civil, mechanical and aerospace engineering domain to highlight the benefits of the proposed approach. A summary of the work is given in Section 4.

2 Decomposition based Evolutionary Algorithm (DBEA)

The proposed algorithm is referred to as Decomposition Based Evolutionary Algorithm (DBEA). It generates a set of uniform reference direction through systematic sampling. The quality of solution a solution is measured by its distance from an associated direction and the distance from ideal point (in scaled objective space). While the first version of the algorithm [10] used a steady state model, it has been continually improved and the DBEA presented here uses generational model which is amenable to parallelization and has a number of enhancements over its first version. The pseudo-code of DBEA is presented in Algorithm 1 and the details of its key components are described below.

Generate: A structured set W reference points is generated spanning a hyperplane with unit intercepts in each objective axis using normal boundary intersection method (NBI) [12]. The approach generates W points on the hyperplane with a uniform spacing of $\delta = 1/s$ for any number of objectives M with s unique sampling locations along each objective axis. The reference directions are formed by constructing a straight line from the origin to each of these reference points. A population size equal to the number of reference points is used, generated using Latin Hypercube Sampling (LHS).

Scale: The objective values are scaled between between 0 and 1. If any coordinate of the ideal point matches with the corresponding coordinate of the Nadir point, the scaled value of the corresponding objective is set to 0.

Compute: Two measures d_1 and d_2 are computed for all feasible solutions. The

first measure d_1 is the Euclidean distance between origin and the foot of the normal drawn from the solution to the reference direction, while the second measure d_2 is the length of the normal. Mathematically, d_1 and d_2 are computed as $d_1 = \mathbf{w}^T \mathbf{f}(\mathbf{x})$; $d_2 = \|\mathbf{f}(\mathbf{x}) - \mathbf{w}^T \mathbf{f}(\mathbf{x}) \mathbf{w}\|$, where \mathbf{w} is a unit vector along any given reference direction. A value of $d_2 = 0$ implies that the solutions are perfectly aligned along the required reference directions ensuring good diversity, while a smaller value of d_1 indicates superior convergence.

Assign: If all solutions in the population are infeasible, solutions are randomly assigned to the reference directions. Since the population size is equal to the number of reference directions, every direction has an associated solution. If the population has one or more feasible solutions, the feasible set of solutions are randomly shuffled (to avoid any bias). Each solution is assigned to a reference direction for which its d_2 is minimum. The assigned direction is removed from the list of available reference directions and feasible solutions are sequentially assigned following the shuffled list. Subsequently, infeasible solutions are randomly assigned to the remaining directions.

Algorithm 1 Decomposition Based Evolutionary Algorithm (DBEA)

Require: Gen_{max} (maximum number of generations), W (number of reference points), p_c (probability of crossover), p_m (probability of mutation), η_c (crossover index), η_m (mutation index)

- 1: $i=1$;
 - 2: **Generate** W reference points using Normal Boundary Intersection (NBI)
 - 3: Construct W reference directions; Straight lines joining origin and W reference points
 - 4: Initialize the population using LHS sampling P^i ; $|P^i| = W$
 - 5: Evaluate P^i and compute the ideal point z^I and Nadir point z^N
 - 6: Scale the individuals of P^i using z^I and z^N
 - 7: **Compute** d_1 and d_2 for all individuals in P^i
 - 8: **Assign** individuals of P^i to the reference directions;
 - 9: **while** ($i \leq Gen_{max}$) **do**
 - 10: **Create** C offspring from P^i via recombination;
 - 11: Evaluate C and compute Ideal point (z^I) and Nadir point (z^N)
 - 12: **Scale** the individuals of P^i+C using z^I and z^N
 - 13: **Compute** d_1 and d_2 for all individuals in $C+P^i$
 - 14: **Replace** individuals in P^i using C
 - 15: $P^{i+1} = P^i$
 - 16: $i=i+1$
 - 17: **end while**
-

Create: The process of offspring creation involves two steps, *i.e.*, identification of participating parents for recombination and the recombination process itself. Two participating parents are recombined using simulated binary crossover (SBX) and polynomial mutation (PM). The first offspring (out of two) is considered as a member of C . Thus to generate W offspring solutions, W participating parents and their corresponding mating partners need to be identified. The selection of participating parents and their corresponding mating partner depends on the state of the population. If all the solutions in the parent population P are infeasible, the participating parents are identified via binary tournament, where their fitness measure is based on their sum of constraint violation. If all the solutions in the population are feasible, the first set of participating parents are the members of P itself, while their partners are identified using a roulette wheel selection. The use of roulette wheel induces a stochastic selection pressure to prefer partners that are close to a reference direction. In the event there is a mix of feasible and infeasible solutions in the population, mating partner selection for a feasible individual follows the schemes described above. To identify the rest of participating parents and their partners, the following strategy is adopted. The infeasible solutions in the population are first sorted based on their sum of constraint violation values and assigned to the set of weight directions (take note that these weight directions had infeasible solutions associated with them and this process alters the previous assignment). Following that, binary tournaments are conducted among all individuals in the population to identify the remaining participating parents and their mating partners. Such a process encourages the recombination between feasible and infeasible solutions.

Replace: The above **Create** process will result in C , *i.e.*, a set of W offspring. Since the individuals in P are already assigned to reference directions, such a process essentially looks through the list of C to identify potential candidates for replacement. In the event there are infeasible solutions in P , a sequential replacement scheme is adopted, wherein a solution from C with better fitness replaces the worst infeasible individual in P . Such a process will continue till all members of P become feasible. In the event all individuals in P are feasible, a sequential replacement scheme is once again adopted. In such a process, an individual from C replaces a dominated individual of P . In the event the offspring solution fails to dominate any individual in P , the replacement is carried out based on their fitness computed using the d_2 measure (smaller d_2 preferred). The process also adopts a single replacement policy, wherein an offspring can only replace one individual of P .

The constraint handling approach used in this work is based on an epsilon level comparison and has been reported earlier in [10]. The process adaptively controls an allowable constraint violation measure, which offers the marginally infeasible solutions to be selected as opposed to a feasibility first principle.

3 Numerical Experiments

In this section, numerical experiments are conducted using the proposed DBEA on a number of engineering problems. As mentioned previously, three different kind of problems are considered, namely deterministic, robust and re-design problems; along with an additional special case. These experiments are discussed next. For each of the experiments, the parameters chosen are: $Gen_{max} = 100$, $p_c = 1$, $p_m = 0.1$, $\eta_c = 30$, $\eta_m = 20$.

3.1 Deterministic optimization

For deterministic MaO optimization, two problems are chosen, which are discussed below.

The **water resource management (WRM)** problem was proposed in [13] in the context of urban planning and has emerged from the environmental engineering domain. The problem has three design variables: local detention storage capacity, maximum treatment rate and the maximum allowable overflow rate. The objective functions to be minimized are f_1 = drainage network cost, f_2 = storage facility cost, f_3 = treatment facility cost, f_4 = expected flood damage cost, and f_5 = expected economic loss due to flood.

The **general aviation aircraft (GAA)** is an example from aerospace engineering, first introduced by Simpson *et al.* [14]. The problem involves 9 design variables: cruise speed, aspect ratio, sweep angle, propeller diameter, wing loading, engine activity factor, seat width, tail length/ diameter ratio and taper ratio and the aim is to optimize 10 objectives: Minimize f_1 =takeoff noise, f_2 =empty weight, f_3 =direct operating cost, f_4 =ride roughness, f_5 =fuel weight, f_6 =purchase price, f_7 =product family dissimilarity and maximize f_8 = the flight range, f_9 =lift/drag ratio and f_{10} =cruise speed.

Thirty independent runs are conducted on the above two problems. Population sizes chosen for WRM and GAA are 210 and 715, respectively. Two standard metrics are used for measuring the quality of non-dominated set of solutions obtained by the algorithm, namely *Hypervolume* and *Inverse Generational Distance (IGD)*. Both of these measures provide a quantification of overall convergence and diversity of the solutions obtained and are hence commonly used for benchmarking MO algorithms [15]. A high value of hypervolume and low value of IGD indicates better quality of the POF obtained by an algorithm.

The results are compared with a well established decomposition based algorithm called MOEA/D (Multiobjective Evolutionary Algorithm Based on Decomposition) [9], shown in Table 1. It is observed that the best, mean and median metric values (both Hypervolume and IGD) across 30 runs achieved using DBEA are better than those obtained using MOEA/D. Furthermore, the standard deviations (Std.) obtained using DBEA is also lower than MOEA/D for all cases except Hypervolume for GAA, which reflects its consistency in obtaining the competitive results. For the case of Hypervolume of GAA, the reason for DBEA's standard deviation being higher is that the Hypervolume values themselves are significantly higher than those from MOEA/D. In terms of magnitude of Std. relative to mean values, DBEA performs much better.

Table 1: Performance metrics values for deterministic problems across 30 runs

Water resource management						
Algorithm	Metric	Best	Mean	Median	Worst	Std
DBEA	Hypervolume	0.43913	0.43628	0.43613	0.43378	0.00131
MOEA/D		0.35660	0.29864	0.29803	0.22559	0.03601
DBEA	IGD	0.08324	0.09417	0.09084	0.11909	0.01038
MOEA/D		0.07773	0.13413	0.13386	0.18848	0.02925
General aviation aircraft						
Algorithm	Metric	Best	Mean	Median	Worst	Std
DBEA	Hypervolume	0.03460	0.02583	0.02582	0.01647	0.00450
MOEA/D		0.01011	0.00303	0.002722	0.00094	0.00180
DBEA	IGD	0.28656	0.30918	0.30514	0.38737	0.02019
MOEA/D		0.30685	0.41841	0.41088	0.51788	0.05346

3.2 Robust design optimization

In the previous section (and in most literature), the optimization problems are considered *deterministic*, *i.e.*, it is assumed that performance estimates are exact and variable values can be achieved to an arbitrary precision. However, in practice, most engineering designs operate under uncertainties that may emerge from varying ambient conditions, material imperfections, inaccuracies in analyses/simulations, manufacturing precision etc. This work considers uncertainties in design variables only. For practical implementation, designs need to be robust, *i.e.*, less sensitive in the presence of uncertainties.

To obtain robust solutions, the deterministic problem needs to be transformed to a robust formulation by using *expected* values for performance and constraints instead of deterministic values. Two kinds of robustness measures need to be considered under uncertainty: *feasibility robustness* (the design should not become infeasible) and *performance robustness* (the performance should not deteriorate). They are quantified in terms of *sigma* levels, a terminology used in industry to judge the reliability of design [11]. Most of the past studies have either considered these measures as *constraints* rather than *objectives*, or have only considered one of these robustness measures instead of both. This has been partially motivated by lack of good techniques for solving MaO problems, because even if the original problem has only 2-3 objectives, the reformulated robust problem will become a MaO problem.

Using the robustness as constraints requires one to set the level of desired robustness level (say $> 4\sigma$) before optimization, which delivers only a partial solution set for the problems. Furthermore, it is not possible to predict the robustness levels expected from the optimization exercise without a priori knowledge about optimum solutions, in which case the optimization may not return any solutions (as there may not exist any 4σ designs). Only by considering the robustness measures as objectives can one obtain a full range of solutions with all possible trade-offs among the performance objectives, feasibility robustness and performance robustness. Towards this goal, in this paper, the deterministic problem is reformulated as an MaO problem as shown in Equation 1. This formulation is referred to as Feasibility and Performance Robust (FPR) formulation. For illustration of the concept, a mechanical design example from automotive industry is considered next.

$$\begin{aligned}
&\text{Minimize: } f'_i(\mathbf{x}) = \mu_{f_i(\mathbf{x})}, i = 1, 2, \dots, M \quad \{\text{expected performance objectives; } M = \text{no. of objectives}\} \\
&\text{Maximize: } f'_{M+1}(\mathbf{x}) = \text{Min}(\text{sigma}_g, R_c) \quad \{\text{feasibility robustness}\} \\
&\text{Maximize: } f'_{M+2}(\mathbf{x}) = \text{Min}(\text{sigma}_f, R_f) \quad \{\text{performance robustness}\} \\
&\text{Subject to: } \text{sigma}_g \geq 0 \\
&\text{where: } \text{sigma}_g \equiv \text{Min}(\mu_{g_j(\mathbf{x})}/\sigma_{g_j(\mathbf{x})}), j = 1 \dots K \text{ (no. of constraints)} \\
&\quad \text{sigma}_f \equiv \text{Min}(\sigma_{0,j}/\sigma_{f_j(\mathbf{x})}), j = 1 \dots M \text{ (no. of objectives)} \\
&\quad \sigma_{0,j}, j = 1 \dots M \text{ are allowable performance variations in each objective}
\end{aligned} \tag{1}$$

Vehicle Crash worthiness Optimization Problem (VCOP): VCOP has been studied in various works including Sun *et al.* [16]. A modified bi-objective formulation of the problem is studied in this paper which seeks to maximize the post-impact energy absorption (U) of the vehicle structure and aims to minimize the structural weight (M_s), subject to the constraint on peak deceleration (a). The calculations for U , M and a are done as suggested in [16]. A higher energy absorption lowers the risk to the occupants of the car. However, increase in energy absorption often leads to unwanted increase in the structural weight. To limit impact severity, a constraint on maximum deceleration is imposed in this formulation which is assumed to be 40 g ($g = 9.81 \text{ m/s}^2$). Part thicknesses of three key members – inner rail, outer rail and the cradle rails – of the vehicle front end structure have been chosen as design variables for the crash worthiness optimization problem. For each variable, the uncertainty is assumed to follow a Gaussian distribution with $\sigma = 0.05$. For each objective, maximum allowable $\sigma_{f,0}$ is set as 2.1. The results obtained using DBEA on the problem are shown in Figure 1. It can be clearly seen that the delivered set of designs span a range of sigma levels achievable, between 0 and 6σ . This gives the user a choice to select the design which is most suitable for the application.

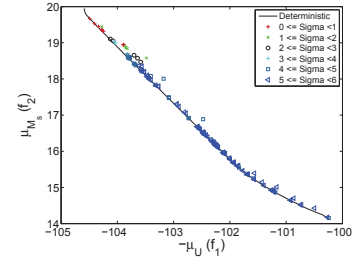


Figure 1: Robust solutions obtained for VCOP using DBEA. Here, Sigma is overall, *i.e.*, both feasibility and performance robustness achieve the indicated level

3.3 Re-design for robustness

Next, the applicability of presented DBEA is considered for “re-design for robustness (RDR)”. RDR is an endeavor to improve the robustness of an *existing* design by doing minimal changes to it. This need could arise, for example, in case operating conditions of the product have changed due to unforeseen circumstances. In such situations, instead of discarding all inventory of components for the product and re-designing it from scratch, it would be of great value to investigate whether only a few components could be replaced for making the product robust. In order to solve this problem, apart from the objectives considered in previous subsection, one more objective, f_{M+3} , is added for minimization, which is the number of components different from the base design. This formulation is referred to as FPRR formulation (FPR for Re-design), and contains $M + 3$ objectives, where M is the number of objectives in the deterministic formulation. To evaluate the objective f_{M+3} , a binary string is maintained in which 0 indicates the variable value is same as base design, whereas 1 indicates it’s different. This binary string is also evolved along with the variable vectors. For illustration of the concept, a mechanical design example from automotive industry is considered next where the objective is to reduce the weight of a car subject to constraints on satisfaction of several safety criteria in the event of side impact [17].

Car Side Impact Problem (CSIP): In CSIP, the uncertainties associated with 7 (out of 11) variables are modeled as Gaussian distribution with $\sigma_{x_i} = 0.0408, i = 1, 2 \dots 7$, and $\sigma_{f,0}$ is set as 2.5. The base design is taken from [18] as $\{1.0, 1.0, 1.0, 1.0, 1.0, 1.0, 1.0, 0.345, 0.192, 0, 0\}$, with a weight of 29.05 units; whereas the deterministic optimum for the problem is reported to be 23.59. The base design is actually *infeasible*, violating two of the constraints (lower rib deflection and pubic force criteria) marginally. The results obtained using DBEA on the FPRR formulation of CSIP are shown in Figure 2. It can be seen that by merely changing 2 variables out of 7, one can achieve *up to* 6σ designs, at the cost of corresponding weight values going up to 33.2 units. As the number of changed components increase, the same can be achieved with lower compromises in weight values.

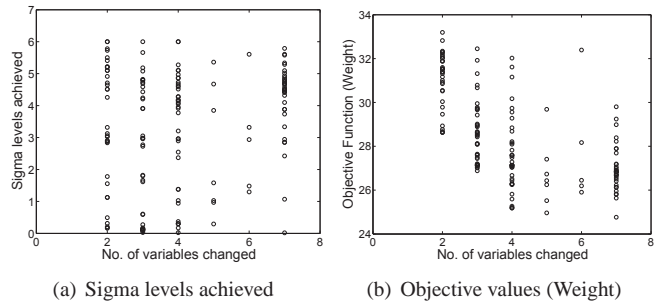


Figure 2: Solutions obtained for FPRR formulation of CSIP using DBEA.

3.4 Special class of single objective optimization problems with varying parameters

Lastly, we consider a special case where the original problem contains only single objective (SO), but this necessitates it being solved for several parameter settings according to the specific design case. Instead, it can be solved as multi-objective problem to get entire range of solutions for all parameter settings in one run. This is illustrated

using a reinforced beam design example.

The **reinforced concrete beam design problem (RCB)** has been studied as a constrained, single objective optimization problem in [19]. The problem was also solved for various values of a parameter a_6 (minimum allowable width)[19].

Instead of independent runs of SO optimization with different parameter values, we reformulate the problem and solve it as a bi-objective optimization problem, *i.e.*, minimize $-a_6$ (minimum allowable width) and minimize total cost. The results using DBEA for a single run are presented in Figure 3 for various values of the minimum allowable width parameter. The values are in agreement with those reported in [19] for minimum allowable width of 30. While most studies focus on the ability of MO formulations to deliver a set of trade-off solutions for problems involving conflicting set of objectives, the principle presented here can be exploited for problems such as above to deliver solutions spanning the region of interest (different parameter values) when objectives are not conflicting.

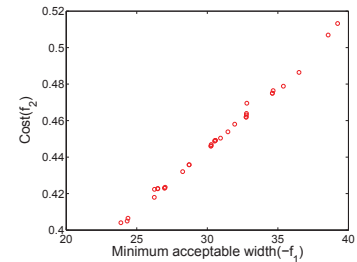


Figure 3: Optimal designs for RCB problem

4 Summary

In this paper, we have introduced an improved generational form of a decomposition based evolutionary algorithm for the solution of optimization problems involving many objectives. Apart from its ability to efficiently solve deterministic MaO problems, we have highlighted its extended use for two other important class of problems *i.e.* robust optimization and re-design for robustness. Numerical examples have been selected from various domains (mechanical, civil and aerospace) to highlight the benefits of proposed approach.

References

- [1] Deb, K., 2001. *Multi-objective optimization using evolutionary algorithms*. John Wiley & Sons.
- [2] Ishibuchi, H., Tsukamoto, N., and Nojima, Y., 2008. "Evolutionary many-objective optimization: A short review". In Proc. IEEE World Congress Computational Intelligence, pp. 2419–2426.
- [3] Sato, H., Aguirre, H., and Tanaka, K., 2007. "Controlling dominance area of solutions and its impact on the performance of moeas". In Lecture notes in Computer Science 4403: Evolutionary Multi-Criterion Optimization-EMO, Springer-Verlag, Berlin, pp. 5–20.
- [4] Koppen, M., and Yoshida, K., 2007. "Substitute distance assignments in NSGA-II for handling many-objective optimization problems". In Lecture notes in Computer Science 4403: Evolutionary Multi-Criterion Optimization, Springer Berlin/Heidelberg, pp. 727–741.
- [5] Zitzler, E., and Kunzli, S., 2004. "Indicator-based selection in multiobjective search". In Lecture notes in Computer Science 3242: Parallel Problem Solving from Nature - PPSN VIII, Springer Berlin/Heidelberg, pp. 832–842.
- [6] Deb, K., Sinha, A., Korhonen, P., and Wallenius, J., 2010. "An interactive evolutionary multiobjective optimization method based on progressively approximated value functions". *Evolutionary Computation, IEEE Transactions on*, **14**(5), Oct, pp. 723–739.
- [7] Thiele, L., Miettinen, K., Korhonen, P. J., and Molina, J., 2009. "A preference-based evolutionary algorithm for multi-objective optimization". *Evolutionary Computation*, **17**(3), pp. 411–436.
- [8] Singh, H. K., Isaacs, A., and Ray, T., 2011. "A Pareto corner search evolutionary algorithm and dimensionality reduction in many-objective optimization problems". *IEEE Transactions on Evolutionary Computation*, **15**(4), pp. 539–556.
- [9] Zhang, Q., and Li, H., 2007. "MOEA/D: A multiobjective evolutionary algorithm based on decomposition". *IEEE Transactions on Evolutionary Computation*, **11**, pp. 712–731.
- [10] Asafuddoula, M., Ray, T., and Sarker, R., 2013. "A decomposition based evolutionary algorithm for many objective optimization with systematic sampling and adaptive epsilon control". In Evolutionary Multi-Criterion Optimization, R. Purshouse, ed., Vol. 7811 of *Lecture Notes in Computer Science*, Springer Berlin Heidelberg, pp. 413–427.
- [11] Asafuddoula, M., Singh, H., and Ray, T., 2014. "Six-sigma robust design optimization using a many-objective decomposition based evolutionary algorithm". *IEEE Transactions on Evolutionary Computation*(99). Available online.
- [12] Das, I., and Dennis, J. E., August 1998. "Normal-boundary intersection: A new method for generating Pareto optimal points in multicriteria optimization problems". *SIAM J. Optim.*, **8**(3), pp. 631–657.
- [13] Musselman, K., and Talavage, J., 1980. "A trade-off cut approach lo multiple objective optimization". *Operations Research*, **28**(6), pp. 1424–1435.
- [14] Simpson, T. W., Chen, W., Allen, J. K., and Mistree, F., 1996. "Conceptual design of a family of products through the use of the robust concept exploration method". *AIAA/USAF/NASA/ISSMO Symposium on Multidisciplinary Analysis and Optimization*, **2**, pp. 1535–1545.
- [15] Singh, H., 2011. "Development of optimization methods to deal with current challenges in engineering design optimization". PhD thesis, School of Engineering and Information Technology, University of New South Wales Canberra, Australia.
- [16] Sun, G., Li, G., Zhou, S., Li, H., Hou, S., and Li, Q., 2011. "Crashworthiness design of vehicle by using multiobjective robust optimization". *Structural and Multidisciplinary Optimization*, **44**(1), pp. 99–110.
- [17] Saxena, D. K., and Deb, K., 2007. "Trading on infeasibility by exploiting constraints criticality through multi-objectivization: A system design perspective". In Evolutionary Computation, 2007. CEC 2007. IEEE Congress on, IEEE, pp. 919–926.
- [18] Gu, L., Yang, R., Tho, C., Makowskit, M., Faruquet, O., and Y. Li, Y. L., 2001. "Optimisation and robustness for crashworthiness of side impact". *International Journal of Vehicle Design*, **26**(4), pp. 348–360.
- [19] Coello, C. C., Christiansen, A. D., and Hernandez, F. S., 1997. "A simple genetic algorithm for the design of reinforced concrete beams". *Engineering with Computers*, **13**(4), pp. 185–196.

Lightweight design of vehicle structure with tailor rolled blank under crashworthiness

Libin Duan, Guangyong Sun, Junjia Cui, Tao Chen, Guangyao Li¹

State Key Laboratory of Advanced Design and Manufacturing for Vehicle Body,
Hunan University, Changsha, 410082, China, duanlibin_hnu@163.com

Abstract

Unlike existing uniform thickness structures, tailor rolled blank (TRB) which allows continuous metal thickness changes has been recently gaining comprehensive attention due to its excellent lightweight potential. The aim of this study is to combine the advantages of the TRB manufacturing technology with the structural optimization methodology to design the front longitudinal beam under impact load. First, a simplified frontal impact FE model was extracted from the full vehicle finite element model and experimentally verified. Then, the conventional uniform thickness inner panel was replaced with the TRB. Finally, the ε -SVR surrogate with artificial bee colony (ABC) algorithm was used to obtain the optimal thickness distribution of TRB. The results show that weight of TRB front longitudinal beam was reduced by 16.10%, while the crashworthiness was significantly improved.

Keywords: Tailor rolled blank (TRB); Front longitudinal beam (FLB); Crashworthiness optimization; Lightweight design

Introduction

Lightweight and crashworthiness design have being two challenges for automotive industry due to more and more strict safety regulations and environmental pressures. The conventional uniform thickness structures mainly use single material and uniform wall thickness. In fact, automotive components often bear very complex loading, implying that different regions should have different roles to maximize usage of materials. Obviously, potential of crashworthiness and lightweight of the conventional uniform thickness structures has not been fully exploited. In order to address the issue, some advanced manufacturing processes, such as tailor welded blank (TWB) and tailor rolled blank (TRB) have been presented and widely applied in automotive industry. For example, the inner door panel ^[1], B-pillar ^[2] and frontal side rail ^[3] are some typical examples for TWB structures adopted in vehicles. Compared with TWB, TRB varies the blank thickness with a continuous thickness transition, which leads to have better formability and greater weight reduction ^[4]. Due to the advantage of TRB, some researchers do some investigation to promote the application of TRB in vehicle industry. In this regards, Jeon et al. ^[5] developed a vehicle door inner panel using TRB. Sun and co-authors ^[6-7] studied the crashworthiness of TRB thin-walled structures under axial impact, and further compared comparatively the energy absorption characteristic between TRB columns and tapered tubes withstanding oblique impact load. Lately, Sun et al. ^[8] investigated the crashworthiness of TRB tubes under dynamic bending load. Though the TRB structures have excellent crashworthiness, it is by no mean easy to obtain the optimal thickness distribution. As an effective alternative, the structural optimization methodology is used to design the TRB parts. For example, Chuang et al. ^[9] adopted a multidisciplinary design optimization methodology to optimize the underbody parts considering multiple impact modes, seatbelt pull analysis and NVH.

It is well known that front longitudinal beam (FLB) is the most significant deformable part under vehicle frontal impact and its deformation pattern can greatly influence the vehicle safety ^[10]. To be authors' best knowledge, there have been very limited reports available on the crashworthiness design of front longitudinal beam with TRB (FLB-TRB). Therefore, the paper aims to performing the lightweight design of the FLB-TRB under crashworthiness criteria.

1. Frontal impact modeling and experimental verification

1.1 Proposed simplified frontal impact model

A single run of crashworthiness simulation for a full-scale vehicle often needs to spend more than 10 hours on some powerful computers ^[11]. Design optimization is an iterative process, which needs a lot of runs. Obviously, it is impractical to conduct design optimization using a finite element model of full-scale vehicle. Consequently, it is critical to construct an equivalent simplified FEM to largely reduce the expensively computational burden. Figure 1 shows these parts whose energy absorption (EA) ratios are large than 1% under 100% frontal impact.

¹ Corresponding Author: Telephone: +86-731-8882 1445; Email: gyli@hnu.edu.cn.

From which, it is easily found that the EA of FLB is more than half of energy dissipation of full-scale vehicle. From the perspective, the FLB is the most significant part under frontal impact. The other components such as roof, B-pillar, C-pillar, doors, rear frame, windscreen etc. have little effect on the crashworthiness, so these parts can be neglected to improve the computational efficiency. As we all known, the load transfer path has a significant effect on the deformation model and crashworthiness of parts. In order to maintain the original load transfer path after removing many unimportant parts, some equivalent square columns are added in the simplified frontal impact model. The full-scale vehicle and the corresponding simplified frontal impact model are impacted on a rigid wall with an initial velocity of 50 km/h, shown as in Figure 2.

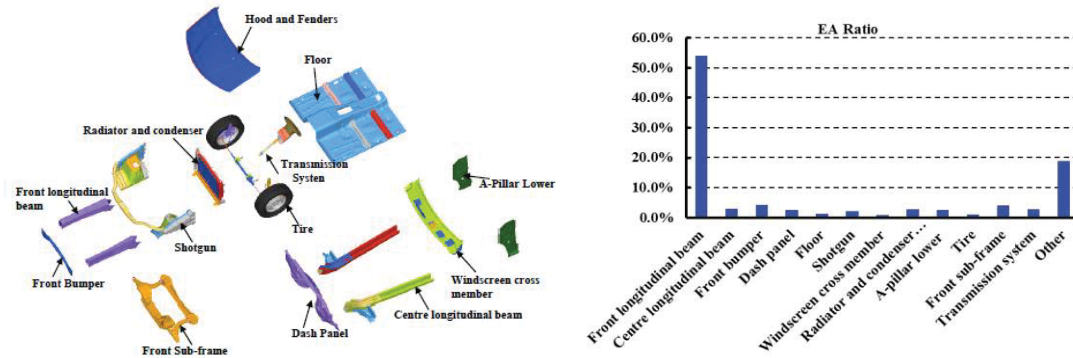


Figure 1: EA Ratio of key parts under frontal impact



Figure 2: Physical model and FE model under 100% frontal impact: (a) full-scale vehicle; (b) simplified frontal impact model

1.2 Experimental verification of numerical model

To conveniently describe the dynamic responses of the simulation and physical test, the following criteria are used: (1) the structural deformation; (2) the acceleration vs. time curve; and (3) the peak value and its corresponding time point. Figure 3 compares the structural deformations between the simulation and corresponding physical tests at $t=120\text{ms}$. The simulation results are agreed well with the results of physical tests regardless of the full-scale vehicle or the simplified frontal impact model. The deformation models of simulation and test for FLB are given in Figure 4. Figure 5 plots the deceleration histories of the numerical simulation and physical test at the left rocker of B-pillar. The pulses were filtered with CFC 60 Hz according to the standard of Society of Automotive Engineers (SAE) J211. It shows that the numerical simulations regardless of the full-scale vehicle or the simplified frontal impact model can very well capture the responses of test including the peak accelerations and the corresponding times. In addition, the results of the simplified frontal impact model are agreement with that of full-scale vehicle. According to the aforementioned analysis, the simplified frontal impact FEM can replace the full-scale vehicle FEM effectively to perform the subsequent design optimization.

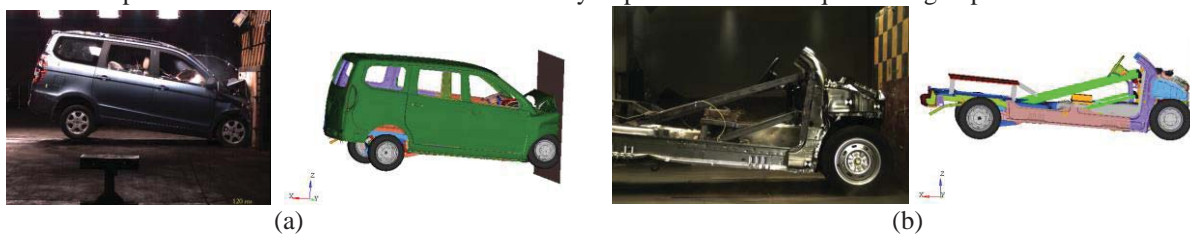


Figure 3: Comparison of deformation patterns between tests and numerical simulations at $t=120\text{ mm}$: (a) full-scale vehicle, (b) simplified frontal impact model.

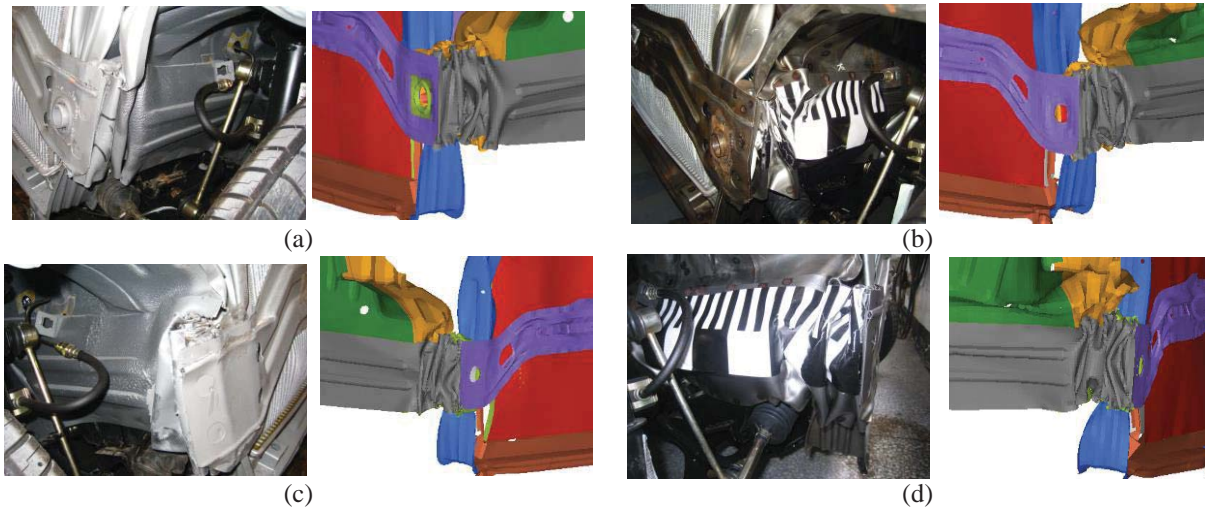


Figure 4: Comparison of FLB deformation patterns: (a) Left FLB of full-scale vehicle; (b) Left FLB of simplified frontal impact model; (c) Right FLB of full-scale vehicle; and (d) Right FLB of simplified frontal impact model

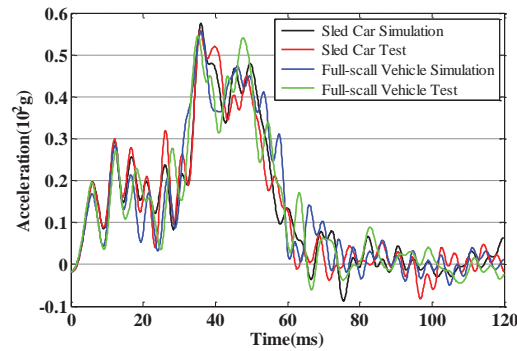


Figure 5: Acceleration history on the left sill of B-pillar

2. Finite element modeling of FLB-TRB

The deformation of the FLB has a mixed axial and bending mode under frontal impact. Compared with bending mode, the axial deformation will be a more appropriate mode for energy absorption and stability. According to the performance requirements, the FLB is divided into 4 different crush spaces (shown in Figure 6) in this study, where space A and space B are expected to generate a relatively uniform and progressive axial collapse, space C is defined by the dimensions of the engine compartment and space D expects high bending stiffness to resist bending deformation. Among these crush spaces, the spaces A, B and C belong to the crush zone, which are used to absorb kinetic energy, while the space D belongs to the transition zone, whose main aim is to transfer impact load.

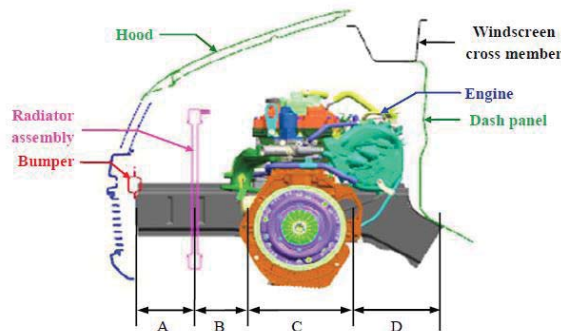


Figure 6: Crush spaces for front end structure

This work focuses on the lightweight design of FLB by combining the advantages of TRB manufacturing technology to maximize its weight reduction without compromising vehicle crashworthiness performances. Figure 7 show the schematic diagram of the whole manufacturing process of FLB-TRB, whose thickness customized can continuously vary along the rolling direction by adjusting the roll gap. The different roll spacing will produce different strain hardening, which directly results in different material properties. As a result, the variability of thicknesses and material properties in different local zones has to be considered in the numerical simulation of FLB-TRB. In order to address the issue, effective plastic stress-strain field should be constructed firstly. Then FE model of the FLB-TRB is modeled using 8-nodes thick shell elements (T-shell in LS-DYNA) [11].

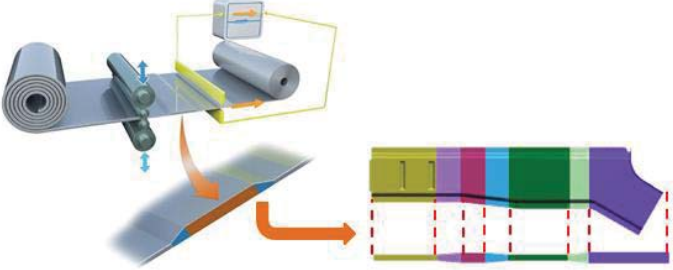


Figure 7: The schematic diagram of manufacturing process for FLB-TRB.

2.1 Material constitutive model for TRB

The material of FLB-TRB is HSLA340. Up to today, there is not material constitutive model for TRB available. In order to establish a relationship of strain vs. stress for the HSLA340 material of TRB, four specimens with thickness of 1.00, 1.17, 1.56 and 1.95mm are cut along the initial rolling direction to conduct uniaxial tensile tests on an INSTRON-5581 electronic universal testing machine. The effective stress-effective strain curves derived from test results are given in Figure 8. From which, it is easily found that the material properties of HSLA340 has a significant difference among the different thicknesses. Due to the expensive cost and time consuming of experimental tests, it is impractical to obtain the material characteristics of any thickness by experimental method. To address the issue, the piecewise linear interpolation method is used to interpolated the material performance of thickness from 1.0mm to 2.0mm.

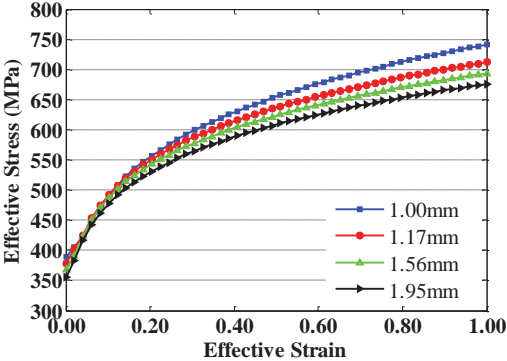


Figure 8: Effective stress-effective strain curves of HSLA340

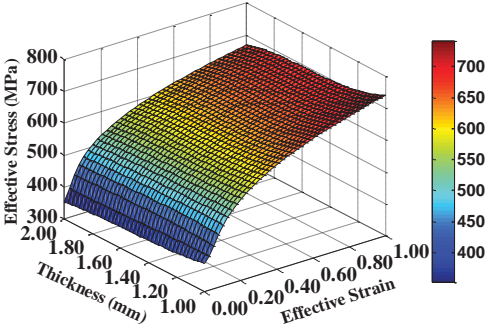


Figure 9: Effective stress-strain field of TRBs made of HSLA340

2.2 Finite element modeling of FLB-TRB

Figure 10(a) depicts the geometry model of the inner of TRB front longitudinal beam (TRB FLB-inner). To model the variable thickness of TRB, the 8-nodes thick shell element (T-shell in LS-DYNA) ^[11] was adopted. In which, the element of the constant thickness zone (CTZ) which has uniform mechanical property is organized into the same component, while the thickness transition zone (TTZ) needs to be divided into several components due to it has the non-uniform mechanical property, shown in Figure 10(b). The number of the components is decided by the modelling accuracy. In generally, the more the number of components are, the higher the modelling accuracy is. The material model used in the finite element modeling is piecewise linear plasticity material law (Mat 24 in LS-DYNA). The material performance of every component is calculated according to its thickness from Figure 9. The “automatic single surface” and “automatic surface to surface” contact are used in this model.

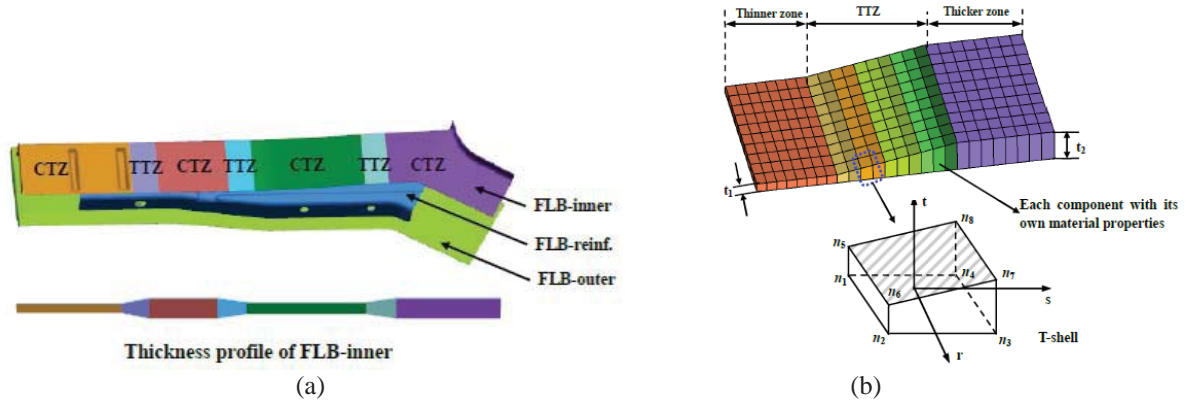


Figure 10: (a) Geometry model of TRB FLB-inner; and (b) FE model of TRB

3. Lightweight design of FLB-TRB under crashworthiness

Though the FLB-TRB has excellent potential of lightweight and crashworthiness, it is by no mean to obtain the optimal thickness distribution of FLB-TRB. Herein, structural optimization method was used to design the FLB-TRB. In the optimization progress, first, the conventional uniform thickness FLB panel is replaced with the TRB. Second, optimal Latin hypercube sampling (OLHS) ^[12] technique is used to generate sampling points and the objective and constraints function values are calculated using commercial software LS-DYNA. Following this the ϵ -SVR technique ^[13] is used to construct the surrogate models for the highly nonlinear impact responses. Finally, the Artificial Bee Colony (ABC) algorithm ^[14] is used to minimize the weight of TRB FLB-inner under the constraint of crashworthiness. The whole optimization procedure is shown in Figure 11.

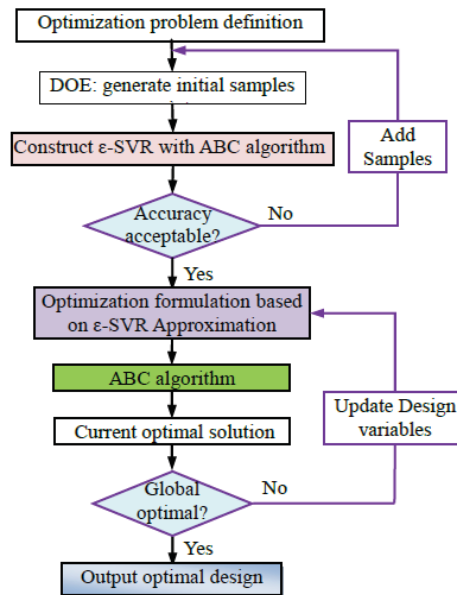


Figure 11: Flowchart of optimization process

3.1 Design responses and variables

In general, the crashworthiness of FLB can be evaluated by peak acceleration, energy absorption (FLB_EA), dash panel intrusion and FLB dynamic intrusion (Left and Right) [15, 16]. Hence, they are chosen as crashworthiness indicators of the simplified frontal impact model, represented by $A(x)$, $E(x)$, $S_1(x)$, $S_2(x)$ and $S_3(x)$, respectively. In addition, the weight of the TRB FLB-inner is regarded as the objective function, denoted by $M(x)$. The following three kinds of parameters are chosen as design variables: (a) thicknesses of constant thickness zone (CTZ), (b) length of thickness transition zone (TTZ) and (c) position of TTZ. Figure 12 shows the initial geometry parameters of the TRB FLB-inner with four different thickness segments. The design variables and their ranges are shown in Table 1.

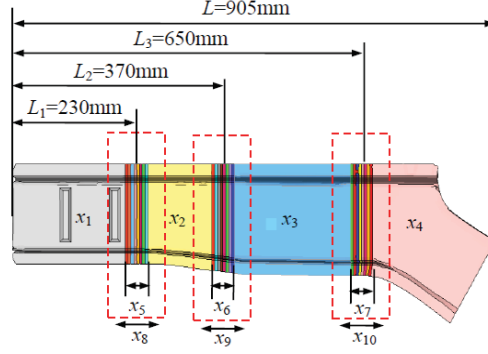


Figure 12: Geometry parameters of TRB FLB-inner

Table 1 Table 1 Geometry parameters of FLB-inner for dynamic impact (Unit: mm)

Variable	Description	Lower Bound	Upper Bound	Baseline Design
x_1	Thickness of CTZ	1.0	2.0	1.6
x_2	Thickness of CTZ	1.0	2.0	1.6
x_3	Thickness of CTZ	1.0	2.0	1.6
x_4	Thickness of CTZ	1.0	2.0	1.6
x_5	Length of TTZ	$Max(40, 100*(x_2-x_1))$	120.0	40.0
x_6	Length of TTZ	$Max(40, 100*(x_3-x_2))$	120.0	40.0
x_7	Length of TTZ	$Max(40, 100*(x_4-x_3))$	120.0	40.0
x_8	Position of TTZ	150.0	260.0	230.0
x_9	Position of TTZ	330.0	410.0	370.0
x_{10}	Position of TTZ	570.0	690.0	650.0

3.2 Optimization mathematical model

According to the description mentioned above, the optimization mathematical model can be written as:

$$\begin{cases} \min & M(x) \\ \text{s.t.} & A(x) \leq 57 \text{ g} \\ & E(x) \geq 63000 \text{ J} \\ & S_1(x) \leq 120 \text{ mm} \\ & S_2(x) \geq 210 \text{ mm} \\ & S_3(x) \geq 210 \text{ mm} \\ & \mathbf{x}^L \leq \mathbf{x} \leq \mathbf{x}^U, \quad \mathbf{x} = (x_1, x_2, x_3, x_4, x_5, x_6, x_7, x_8, x_9, x_{10})^T \end{cases} \quad (1)$$

where the constraint values are the responses of baseline design.

3.3 Optimization process

To establish high accuracy surrogates, OLHS technique is adopted to generate 300 sampling points and the output responses are calculated using commercial software LS-DYNA. Then, the ε support vector regression (ε -SVR) technique is used to construct the surrogate models for $M(x)$, $A(x)$, $E(x)$, $S_1(x)$, $S_2(x)$ and $S_3(x)$, respectively. The error measures applied for evaluating the model fitness, the squared correlation coefficient R_{CV-5}^2 and the root mean square error $RMSE_{CV-5}$ are calculated as follows:

$$R_{CV-5}^2 = \frac{1}{5} \sum_{j=1}^5 \left(1 - \frac{\sum_{i=1}^l (y_i - \hat{y}_i)^2}{\sum_{i=1}^l (y_i - \bar{y}_i)^2} \right) \quad (2)$$

$$RMSE_{CV-5} = \frac{1}{5} \sum_{j=1}^5 \sqrt{\frac{1}{l} \sum_{i=1}^l (y_i - \hat{y}_i)^2} \quad (3)$$

where l is the number of data points at each validation set, y_i is the observed response value, \hat{y}_i is the predicted value and \bar{y} is the mean value of y_i , respectively.

Table 2 lists the optimal parameters and the error results of the ε -SVRs. From which, it is easily found that the surrogates have a very high accuracy and can be used to the following design optimization.

Table 2 Optimal parameters and error results of ε -SVRs

Responses	C	ε	σ	R_{CV-5}^2	$RMSE_{CV-5}$
$M(x)$	23.4581	0.0986	2.2529	0.9929	0.0213
$A(x)$	0.6422	0.1961	1.5969	0.9688	0.0477
$E(x)$	34.7902	0.2438	1.4322	0.9728	0.0331
$S_1(x)$	1.5631	0.1331	1.9379	0.9810	0.0504
$S_2(x)$	2.9360	0.0436	3.3871	0.9631	0.0556
$S_3(x)$	18.1769	0.2322	1.4674	0.9867	0.0494

3.4 Optimization results and discussion

To obtain the optimal thickness profiles of FLB-inner without compromising vehicle crashworthiness, the ABC algorithm is used to solve the mathematical model. The iterative process of $M(x)$ is shown in Figure 13. From the Figure 13, it is easily found that the optimization progress was converges after 35 iterations. The optimal results are listed in Table 3 and the corresponding thickness profile of the TRB FLB-inner is shown in Figure 14.

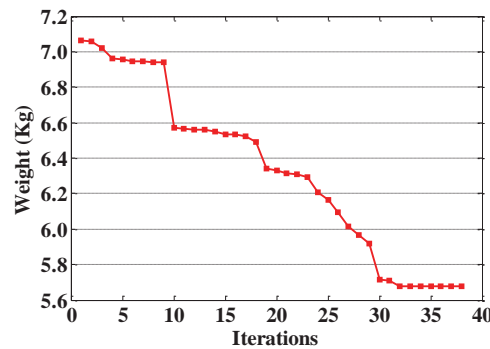


Figure 13: Iterative process of the weight of TRB FLB-inner

Table 3 Optimal results

Description	x_1	x_2	x_3	x_4	x_5	x_6	x_7	x_8	x_9	x_{10}
Baseline	1.60	1.60	1.60	1.60	40.0	40.0	40.0	230.0	370.0	650.0
Optimum	1.15	1.64	1.00	1.73	75.6	70.5	58.3	242.6	391.7	643.5

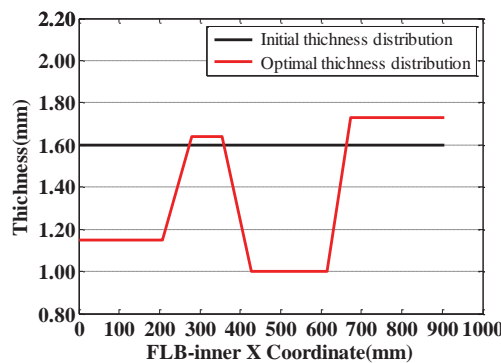


Figure 14: Thickness profile of TRB FLB-inner

Table 4 Improvements of vehicle performance for lightweight design optimization

Description	Baseline design	Optimal design	Improvement (%)
$M(x)$	6.77	5.68	-16.10%
$A(x)$	57.47	54.83	-4.59%
$E(x)$	61527.10	65846.79	7.02%
$S_1(x)$	136.24	106.81	-14.47%
$S_2(x)$	197.15	230.39	16.86%
$S_3(x)$	190.66	225.69	17.54%

Noted: Improvement = $\frac{\text{Optimal design}-\text{Baseline design}}{\text{Baseline design}} \times 100\%$

The Improvements of crashworthiness of TRB FLB-inner with respect to baseline design are listed in Table 4. Figure 15 compares the deformation patterns of the FLB before and after optimization. From which, it is easily found that the deformation patterns of the FLB can be greatly improved through the redistribution of thickness of the TRB FLB-inner. Figure 16 depicts the numerical results of crush pulses for the baseline and optimal design. In the baseline design, the space “B” of the front longitudinal beam buckled sideways and the space “D” happened sharp bending deformation, which greatly decrease the resistance load of the FLB. In the optimal design, the space “A” and space “B” occurred relatively uniform and progressive axial collapse and the previous sharp bending deformation disappeared in the space “D”, which leads to the reduction of peak acceleration. It is clearly shown from Table 4, Figure 15 and Figure 16 that optimal thickness distribution of the TRB FLB-inner can not only largely reduce its weight but also enhance vehicle crashworthiness.



Figure 15 Comparison of the numerical result before and after optimization: (a) Left FLB of baseline design; (b) Left FLB of optimal design; (c) Right FLB of baseline design; and (d) Right FLB of optimal design

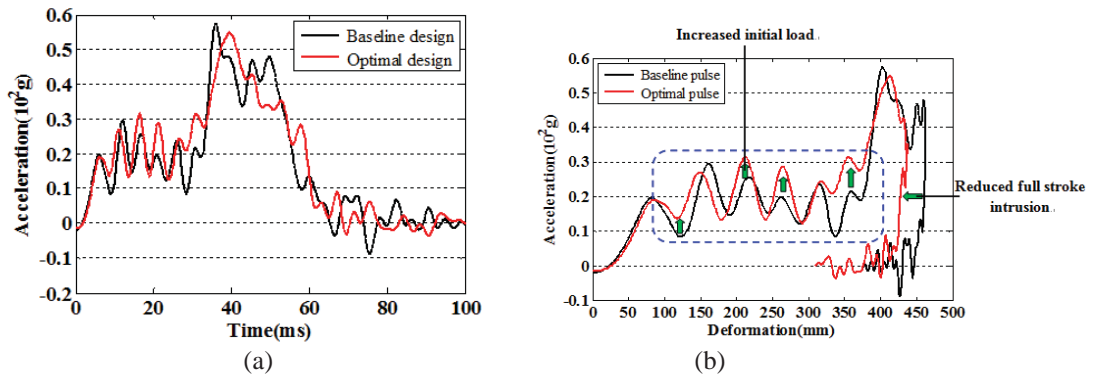


Figure 16 Comparison of crash pulses before and after optimization

4. Conclusions

In this work, the lightweight design of FLB-inner with TRB concept has been successfully performed under 100% frontal impact load case. The optimal solution shows that the weight of the FLB-inner can be reduced by 16.10%, while the crashworthiness is improved compared with the baseline design. It is clearly shown that the TRB technique has great potential to realize lightweight.

Acknowledgments

This work was supported from The National Natural Science Foundation of China (11202072, 61232014), The Doctoral Fund of Ministry of Education of China (20120161120005), National Natural Science Foundation of China (Grant No. 11202074), The Open Fund Program of the State Key Laboratory of Vehicle Lightweight Design, P. R. China (20130303), The Hunan Provincial Science Foundation of China (13JJ4036) and the Program of the Methodology Study on Designing Automotive Parts with Variable Thickness Blanks (QYT-KT-2013-003).

References

- [1] G.Y. Li, F.X. Xu, X.D. Huang and G.Y. Sun, Topology Optimization of an Automotive Tailor-Welded Blank Door, *Journal of Mechanical design*, 137(5), 055001 (May 01, 2015) (8 pages)
- [2] F. Pan, P. Zhu and Y. Zhang, Metamodel-based lightweight design of B-pillar with TWB structure via support vector regression, *Computers and Structures*, 88(1-2):36-44, 2010
- [3] Y.L. Shi, P. Zhu, L.B. Shen and Z.Q. Lin, Lightweight design of automotive front side rails with TWB concept, *Thin-Walled Structures*, 45(7):8-14, 2007
- [4] A. Meyer, B. Wietbrock and G. Hirt, Increasing of the drawing depth using tailor rolled blanks-Numerical and experimental analysis, *International Journal of Machine Tools & Manufacture*, 48, 522-531, 2008
- [5] S.J. Jeon, M.Y. Lee and B.M. Kim, Development of Automotive Door Inner Panel using AA 5J32 Tailor Rolled Blank, *Transactions of Materials Processing*, 20 (7): 512-517, 2011
- [6] G.Y. Sun, F.X. Xu, G.Y. Li and Q. Li, Crashing analysis and multiobjective optimization for thin-walled structures with functionally graded thickness, *International Journal of Impact Engineering*, 64, 62-67, 2014
- [7] G.Y. Li, F.X. Xu, G.Y. Sun and Q. Li, A comparative study on thin-walled structures with functionally graded thickness (FGT) and tapered tubes withstanding oblique impact loading, *International Journal of Impact Engineering*, 77, 68-83, 2015
- [8] G.Y. Sun, X. Tian, J. Fang, F. Xu, G. Li and X. Huang, Dynamical bending analysis and optimization design for functionally graded thickness (FGT) tube, *International Journal of Impact Engineering*, 78, 128-137, 2015
- [9] C.H. Chuang, R.J. Yang, G. Li, K. Mallela and P. Pothuraju, Multidisciplinary design optimization on vehicle tailor rolled blank design, *Structural and Multidisciplinary Optimization*, 35(6):551-560, 2008
- [10] G.X. Gu, G.Y. Sun, G.Y. Li, L.C. Mao and Q. Li, A Comparative study on multiobjective reliable and robust optimization for crashworthiness design of vehicle structure, *Structural and Multidisciplinary Optimization*, 48:669-684, 2013
- [11] J. Halquist, *LS-DYNA keyword user's manual version 971*. Livermore Software Technology Corporation, Livermore, CA, 2007
- [12] V.C.P. Chen, K.L. Tsui, R.R. Barton and M. Meckesheimer, A review on design, modeling and applications of computer experiments, *IIE Transactions*, 38(4): 273-291, 2006
- [13] V. Vapnik, *The nature of statistical learning theor*, Springer, Berlin, 1995
- [14] D. Karaboga and B. Basturk, A powerful and efficient algorithm for numerical function optimization: artificial bee colony (ABC) algorithm, *Journal of Global Optimization*, 39(3): 459-471, 2007
- [15] P. Zhu, Y. Zhang and G.L. Chen, Metamodel-Based Lightweight Design of Automotive Front Body Structure Using Robust Optimization, Proceedings of the Institution of Mechanical Engineers, Part D, *Journal of Automobile Engineering*, 223(9):1133-1147, 2009
- [16] F. Pan and P. Zhu, Lightweight design of vehicle front end structure: Contributions of multiple surrogates, *International Journal of Vehicle Design*, 57(2-3): 124-147, 2011

11th World Congress on Structural and Multidisciplinary Optimisation

07th - 12th, June 2015, Sydney Australia

A Flying Wing UCAV Design Optimization Using Global Variable Fidelity Modeling

Maxim Tyan¹, Nhu Van Nguyen² and Jae-Woo Lee³

¹ Post-doctoral fellow, Dept. of Aerospace Information Engineering, Konkuk University, Seoul, Korea, tyan.maxim@gmail.com

² Post-doctoral fellow, Dept. of Aerospace Information Engineering, Konkuk University, Seoul, Korea, nhuvan@gmail.com

³ Professor, Dept. of Aerospace Information Engineering, Konkuk University, Seoul, Korea, jwlee@konkuk.ac.kr

1. Abstract

This paper describes the multidisciplinary design optimization (MDO) process of a flying wing unmanned combat aerial vehicle (UCAV) using global variable fidelity modelling (GVFM) algorithm. A developed flying wing UCAV design framework combines aerodynamics, weight and balance, propulsion, performance, stability and control, and other disciplines. Analysis codes are based on low fidelity analysis and empirical equations. Design problem formulation focuses on features of a flying wing aircraft configuration that is known for its good aerodynamics, and poor stability and control (S&C). GVFM algorithm is implemented to increase prediction accuracy of analysis for important aerodynamic and S&C functions such as, lift-to-drag ratio, parasite drag coefficient, static margin etc. An automated high fidelity aerodynamic analysis (CFD) process is developed and integrated into GVFM model. Design optimization problems with low fidelity analysis and with implementation of GVFM model are successfully solved. The optimum solution obtained with low fidelity analysis shows 18.6% improvement of an objective function, while solution obtained with GVFM model about 15.9%. However CFD analysis of a low fidelity optimum solution indicates only 14.4% improvement, which means that low fidelity analysis underestimates the value of objective function by 4.2%. GVFM model converges to high fidelity value of a function by algorithm definition. The optimum UCAV configuration has longer operational range and improved stability and control characteristics comparing to the baseline.

2. Keywords

Unmanned Aerial Vehicle, Multidisciplinary Design Optimization, Variable Fidelity Optimization, Aircraft Conceptual Design, Computational Fluid Dynamics

3. Introduction

Unmanned aerial vehicle (UAV) systems are recently in a great interest. These days an application of UAV systems is narrowed down to military and special operations. But civil UAV market is also rapidly growing. Less strict design requirements for internal compartment of UAVs lead to development of unconventional configurations. These days one of the most promising aircraft schemes is a flying wing configuration. A clean flying wing is sometimes treating as theoretically ideal fixed wing aircraft. Lower parasite drag, lower radar cross section makes it fly further without risk to be discovered by radar. But stability issues inherent in this type of configuration were limiting it from being widely used. The current level of knowledge is high enough to efficiently solve stability and control problem by implementation of automatic control and special control devices. A flying wing configuration is becoming more popular nowadays.

Aircraft conceptual design is a complex problem that involves multiple disciplines. Multidisciplinary Design Optimization provides an efficient ways of treating all disciplines together. High accuracy of analysis methods at conceptual design stage narrows down the scope of preliminary and detailed design. Accuracy of analysis can be enhanced by implementation of computationally expensive high fidelity analysis methods. However, direct use of high fidelity analysis for design optimization faces number of problems. The main problem is huge computational time required to perform the analysis. Variable fidelity optimization algorithms tend to combine advantages of low and high fidelity analysis methods. Combination of both high and low fidelity algorithms makes it possible to achieve accuracy close to high fidelity one within lower computational time. This paper focuses on development of a flying wing UCAV conceptual design framework by expansion of existing GVFM algorithm for an MDO problem.

4. Integrated Design Framework

An integrated multidisciplinary design framework is developed [1] for a flying wing UAV conceptual design optimization.

Figure 1 shows the structure of the program. The analysis methods are based on textbook methods, empirical equations, and low fidelity aerodynamic analysis codes. Current analysis methods were validated using available information about existing aircraft configurations of current category (Flying wing UCAV). Prediction error of analysis results comparing to existing aircraft data is less than 10%. This level of accuracy is acceptable to be used at conceptual design stage. However analysis accuracy can be increased by implementation of variable fidelity algorithms. Increasing analysis accuracy at conceptual design stage may significantly reduce the scope of preliminary and detailed design stages and reduce the total cost of the development project.

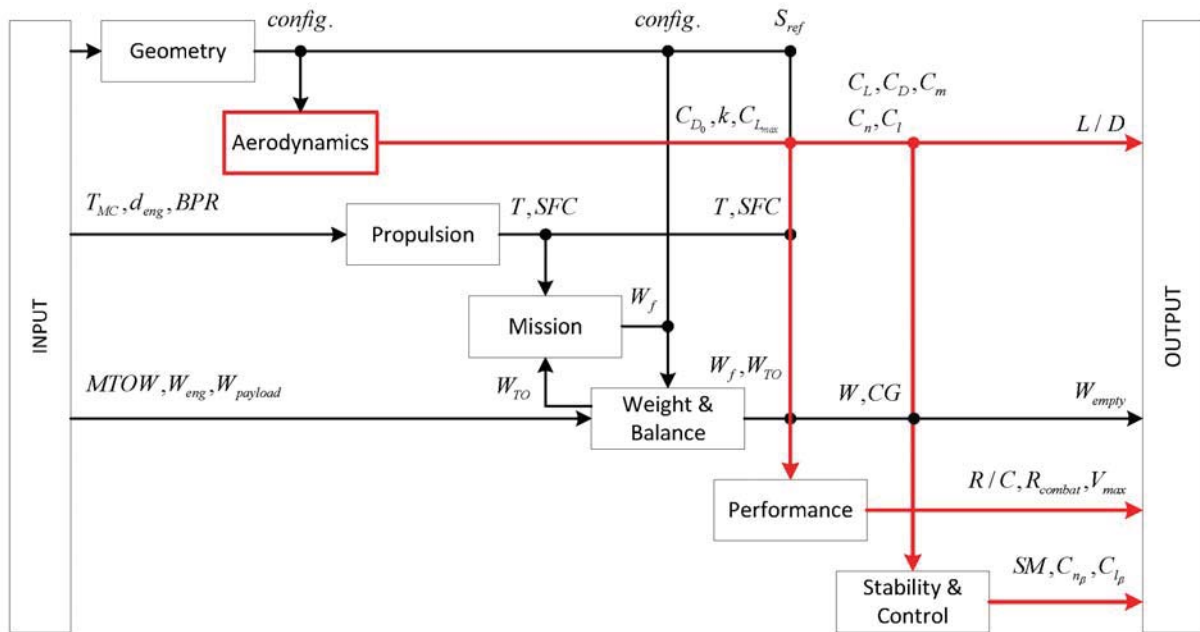


Figure 1: Integrated Design Framework Structure with Variable Fidelity Aerodynamic Module

5. Variable Fidelity Optimization Methodology

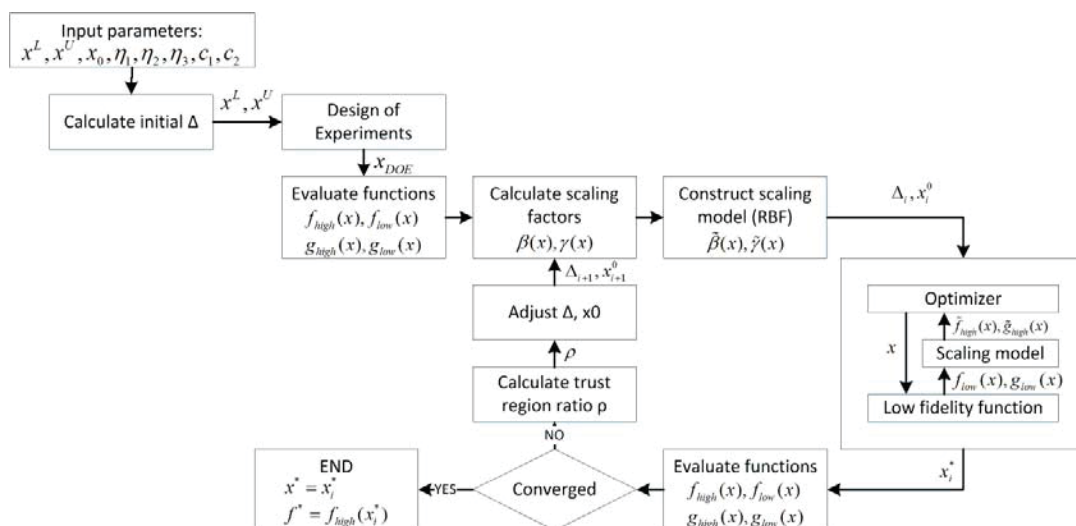


Figure 2: Global Variable Fidelity Modelling Process [2]

A variable fidelity optimization algorithm used in this study is the Global Variable Fidelity Modelling [ref] algorithm. The general idea of GVFM method is the initial sampling of high and low-fidelity functions over the design space and iterative refinement of a scaling model that represents the difference between high and low fidelity functions. The scaling model is a radial basis functions (RBF) network constructed using scaling factors at a given point x_i . Scaling factors are calculated as:

$$\beta(x_i) = f_{high}(x_i) - f_{low}(x_i) \quad (1)$$

And approximation of a high fidelity function can be reconstructed as:

$$\tilde{f}_{high}(x) = f_{low}(x) + \tilde{\beta}(x) \quad (2)$$

Where: $f_{high}(x)$ - High fidelity function
 $f_{low}(x)$ - Low fidelity function
 β - Scaling factor
 $\tilde{\beta}(x)$ - Scaling model
 $\tilde{f}_{high}(x)$ - Approximation of a high fidelity function

The sample points for scaling model initialization are uniformly distributed using design of experiments (DOE). The scaling model is then iteratively refined using points obtained at optimization. The detailed process of GVFM is presented in Figure 2.

5.1 Variable Fidelity Aerodynamic Analysis Module

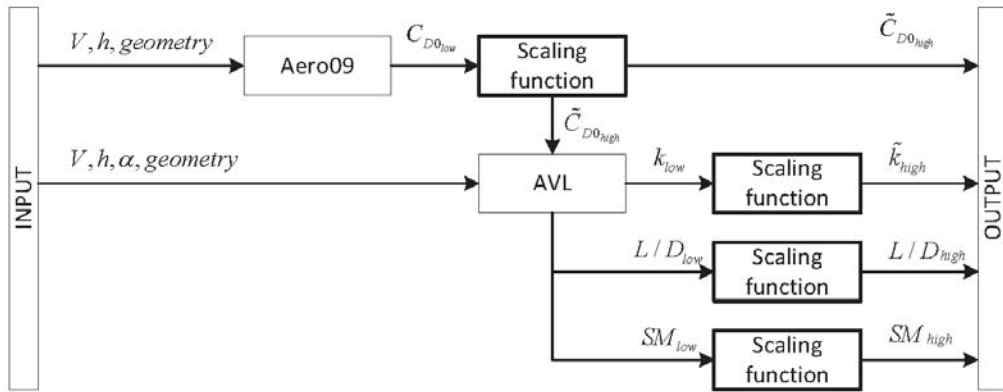


Figure 3: Variable Fidelity Aerodynamic Analysis

Aerodynamics, stability and control disciplines are extremely important for a flying wing aircraft configuration. This discipline supplies data for almost all other analysis disciplines as shown in

Figure 1 and it has a large effect on most characteristics of an aircraft. A high fidelity computational fluid dynamics (CFD) solver is added the aerodynamic analysis module to increase the accuracy of analysis. Automation of a high fidelity analysis process is a complex task. An automated framework for CFD analysis is developed that includes generation of a CAD model, generation of a structured computational grid, and pre and post processing of aerodynamic analysis results.

Figure 3 shows details about variable fidelity aerodynamic analysis module. Analysis estimates approximated values of high fidelity C_{D_0} , k , L/D , and SM for given aircraft configuration and flight condition. Module contains four scaling functions that are initialized and iteratively updated according to GVFM algorithm. Parameters such as lift-to-drag ratio and static margin are used directly as objective and constraint functions, while parasite drag coefficient and induced drag factor are supplied to performance analysis module.

6. Unmanned Combat Aerial Vehicle Design

6.1 Optimization formulation

Design formulation for a flying wing UCAV aircraft is mostly based on Nicolai [3] and Torenbeek [4] textbooks. An objective function of maximizing lift-to-drag ratio is quite common for different aircraft design optimization

formulations. Maximizing L/D parameter also leads to an increase of operational range that is constrained to be greater than 750 km for suppression of enemy air defenses (SEAD) [5] mission profile. Longitudinal stability of an aircraft is constrained by a static margin. It is decided to design aircraft with positive static margin between 5 and 15% that is slightly higher than static margin of a conventional fighter aircraft of similar size and weight. Low speed trim condition constraints elevator and wing area authority. Maximum trim angle of attack at landing speed of 65 m/s is set to 8 degrees with trim elevator deflection to be between -20 and 20 degrees. One of the main issues of a flying wing is a directional stability [6] [7] [8] [9]. Level of directional stability similar to that of conventional aircraft is not achievable without implementation of special control devices. It is decided to keep positive directional stability for clean configuration at level of $C_{n\beta} \geq 0.003$. By summarizing design requirements, optimization formulation can be written as shown in Table 1: UCAV Optimization Formulation.

Two design problems are solved in this study. The first one implements pure low fidelity optimization and the second one with GVFM aerodynamic model in an MDO loop. Table 1 shows that 6 of total 14 functions are affected by variable fidelity aerodynamics.

Table 1: UCAV Optimization Formulation

	Variable	Value	Function type
Maximize:	L/D		Variable Fidelity
Subject to:	SM	≤ 0.15	Variable Fidelity
	SM	≥ 0.05	Variable Fidelity
	R_{combat}	$\geq 750\text{km}$	Variable Fidelity
	R/C	$\geq 125\text{m/s}$	Variable Fidelity
	M_{max}	≥ 0.90	Variable Fidelity
	W_{empty}	$\leq 3500\text{kg}$	Low fidelity
	$C_{n\beta}$	≥ 0.003	Low fidelity
	$C_{l\beta}$	≤ -0.075	Low fidelity
	α_{trim}	$\leq 8\text{deg.}$	Low fidelity
	$\delta_{e_{trim}}$	$\leq 20\text{deg.}$	Low fidelity
	$\delta_{e_{trim}}$	$\geq -20\text{deg.}$	Low fidelity
	$l_{fuselage}$	$\geq 5.5\text{m}$	Exact
	Λ_{LE1}	$\geq \Lambda_{LE2}$	Exact

6.2 Baseline configuration

Boeing X45C UCAV is selected as a baseline configuration. The baseline is a typical low aspect ratio flying wing aircraft. The wing has two segments: central and outer. The central segment serves as a fuselage and stores a power plant, payload, and avionics. The planform shape of the wing can be parameterized with total 9 design variables. An internal space volume is secured by constraints that restrict the intersection of leading and trailing edges of central segment with the payload and engine. Longitudinal and lateral control device is joined and located on the outer segment of the wing. Elevon to chord ratio is 0.9, 0.85, and 0.8 at root, middle and tip chords respectively. The other components are GE F404 turbofan engine, fixed fuel weight of 3000 kg, 300 kg of uninstalled avionics, and 1132 kg of drop payload.

7. Results and Discussions

Table 2 shows results of MDO with implementation of low fidelity analysis only, and variable fidelity optimization using GVFM algorithm adopted for MDO use. In addition baseline and low fidelity optimum configurations were analyzed using high fidelity analysis. GVFM optimum is equal to high fidelity by algorithm definition. Figure 4 shows comparison of the baseline with optimum configurations of UCAV.

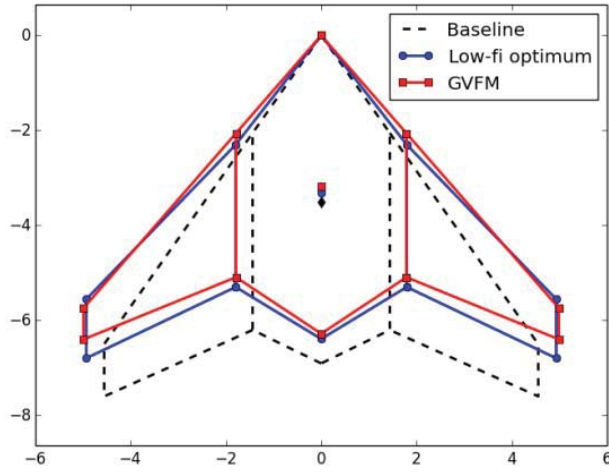


Figure 4: Baseline and Optimum UCAV Configuration

Results in Table 2 show that low fidelity analysis overpredicts the value of the objective function (lift-to-drag ratio at cruise flight condition). Low fidelity optimization shows 18.6% improvement of the objective function, however high-fidelity analysis of the low-fidelity optimum configuration shows only 14.4% improvement. MDO implementation of GVFM algorithm has terminated with the objective function value of 18.83 that is 15.9% higher than that of the baseline. Finally the combat radius of GVFM optimum configuration is 75 km longer than that of low-fidelity optimum. Overprediction of L/D and combat radius by low-fidelity analysis may lead to infeasible solution in case of more strict constraints, while variable fidelity model guarantees convergence to a high-fidelity result.

Table 2: UCAV Optimization Results

		LB	UB	Baseline		Low-fidelity		GVFM
				Low-fi	CFD	Low-fi	CFD	
	L/D			16.84	16.25	19.27	18.6	18.83
Constraints	SM	0.05	0.15	0.1182	0.1258	0.0501	0.0729	0.1123
	$C_{n\beta}$	0.003		0.0038		0.0030		0.0030
	$C_{l\beta}$		-0.075	-0.109		-0.09		-0.088
	α_{trim}		8	9.75		8.00		8.00
	$\delta_{e_{trim}}$	-20	20	-8.81		-4.92		4.75
	W_e		3500	3551		3500		3492
	R_{combat}	750		688.32	629.63	869.77	809.91	886.44
	R/C	125		139	138.7	143.7	142.9	146.4
	M_{max}	0.9		0.9372	0.9373	0.9439	0.9433	0.9398
Design Variables	Λ_{LE_1}	40	60	55		52.05		49.07
	Λ_{LE_2}	40	60	55		46.08		49.02
	c_1	6	7.5	6.91		6.39		6.28
	c_2	3	5.25	4.15		3		3.03
	c_3	0.5	1.8	1.1		1.24		0.66
	l_1	1	1.8	1.44		1.79		1.79
	l_2	3	3.2	3.11		3.13		3.20
	ϕ_1	-4	0	0		-1.2449		-0.87
ϕ_2	-4	0	-2		-0.6869		-1.08	

In terms of computational time, GVFM evaluated high fidelity function 31 times including 25 for scaling models initialization and 6 for their refinement. Single run of the high fidelity function takes about 18 hours, and about 1 hour for optimization loop. Total computational time required to get a converged solution is about 23 full days on a desktop computer. This value is quite high comparing to pure low fidelity optimization that converges in a couple of hours but also significantly lower than pure high fidelity optimization.

8. Acknowledgements

This work was supported by the National Research Foundation of Korea (NRF) [grant NRF-2014R1A2A2A01003833] funded by the Korean government (MSIP).

References

- [1] M. Tyan, "Global Variable Fidelity Methodology for Multidisciplinary Tailless UAV Design and Optimization," PhD Thesis, Konkuk University, Seoul, Korea, 2015.
- [2] M. Tyan, N. V. Nguyen and J.-W. Lee, "Improving variable fidelity modelling by exploring global design space and radial basis function networks for aerofoil design," *Engineering Optimization*, 2014.
- [3] L. M. Nicolai and G. E. Carichner, *Fundamentals of Aircraft and Airship Design*, Reston, Virginia: Americal Institute of Aeronautics and Astronautics Inc., 2010.
- [4] E. Torenbeek, *Advanced Aircraft Design*, Netherlands: A John Wiley & Sons, Ltd., 2013.
- [5] *MIL-STD 3013: Glossary of definitions, ground rules, and mission profiles to define air vehicle performance capability*, Department of defense, 2003.
- [6] J. Northrop, "The development of the all-wing aircraft," in *35th Wilbur Wright Memorial Lecture*, 1947.
- [7] R. T. Jones, "Notes on the stability and control of tailless airplanes," NASA, 1941.
- [8] I. K. Kostenko, *Flying wings*. 2nd edition. (in Russian), Moscow: Mashinostroeniye, 1988.
- [9] O. Lemko, *Flying wings history and ways of future development* (in Russian), Ukraine: Scientific center of Ukraine airforce, 2002.

Gradient based structural optimization with fatigue constraints of jacket structures for offshore wind turbines

Jacob Oest¹, Lars Chr. T. Overgaard², Erik Lund³

^{1,2,3} Department of Mechanical and Manufacturing Engineering, Aalborg University, Aalborg, Denmark,
¹ oest@m-tech.aau.dk, ² lcto@m-tech.aau.dk, ³ el@m-tech.aau.dk

1. Abstract

Investigating the fatigue life of support structures of offshore wind turbines is imperative to avoid unexpected failure. Therefore, in the context of structural optimization, including fatigue constraints is crucial, as the optimized design will meet the design criteria early in the design process without the need for extensive manual post-processing. Ultimately, the optimized design may be lighter and thus reduce both production and installation cost. The aim of this work is to present such a gradient based optimization method with fatigue constraints of jacket structures for the preliminary design phase. The key challenge is to efficiently deal with the very large number of non-linear fatigue constraints and the very large time-history loads that are used in the design of offshore support structures. In this paper main emphasis will be on the analytical design sensitivity analysis used in the optimization. Sensitivities determined by the direct differentiation method and by an aggregated adjoint method will be presented and evaluated.

2. Keywords: Structural optimization, fatigue constraints, sensitivity analysis

3. Introduction

In recent years a clear tendency in wind energy industry is to install larger wind turbines further away from the coast [4]. Being further away from the coast will, in most cases, mean favorable wind conditions but also deeper waters. This of course calls for larger and more complex support structures. The dominating type of support structure is the monopile. However, beyond shallow waters the jacket structure is often applied instead. Currently the support structures can account for as much as 20% of the total cost of the wind turbine [1, 9]. However, as the need for more complex jacket structures is inevitable, new and robust methods for designing lightweight and cost efficient support structures are required. Here, numerical optimization methods that can incorporate a wide range of design criteria can aid engineers during the design phase. In this work, we focus on developing fatigue constraints, which can be incorporated into the design optimization process. By including fatigue constraints in the early design phases, engineers may require less time for manual post-processing while also designing lighter structures.

Fatigue is already an integral part of the design of jacket structures from the conceptual phase to the final design. The offshore industry has a readily good statistically understanding of the environmental conditions and thus the fatigue loads during the expected lifetime. To further incorporate the operational conditions in the design of support structures for offshore wind turbines, we need rational, trustworthy, and efficient methods to evaluate and optimize for fatigue loading.

Although optimization with fatigue constraints can be a very powerful tool, it is a relatively unexplored domain. Some of the first who contributed to this area of research were Grunwald and Schnack [5], who formulated a shape optimization method to maximize the crack initiation phase of a simple test specimen. Their method was restricted to 2D problems under constant amplitude loading, using fatigue constraints based on equivalent stresses. Their findings were somewhat discouraging; they succeeded in their fatigue optimization but the results were similar if they applied the much simpler minimum equivalent stress optimization. In addition, their optimization for fatigue was computationally inefficient. Computational inefficiency is a key problem in optimization for fatigue that also applies today. Shortly after, Zeiler and Barkey [11] strongly suggested that optimization for fatigue was so well-developed that industry could start taking advantage of the method. They used a gradient based optimization method to optimize stiffness and damping of a greatly simplified six degree-of-freedom model of an automobile subjected to Formann crack-growth constraints. Their methods are also limited to proportional loading. More recently Martini and Tobias [7] applied non gradient based fatigue optimization on industrial components, gaining a better result when optimizing for fatigue than when optimizing for stress. The authors also made clear that fatigue optimization is now so well-established that it should be used in industry.

In this paper we present a method of gradient based 3D structural optimization with high-cycle fatigue constraints. The aim is to reduce the overall mass of a structure, having diameter and thickness of each member as design variables. The methods are intended for the preliminary design phase, that is, after the general topology of the structure has been determined. The constraints are based on Palmgren-Miners linear damage hypothesis. Computational efficiency is preserved through the use of gradient based optimization, where the design sensitivity analysis is performed using analytical expressions. The optimization is carried out using Sequential Linear Programming (SLP) with a global convergence filter [2].

The paper presents a brief insight into the theory behind the analytical design sensitivities. The implementation of these is later verified using central difference approximations of the presented constraint formulations. The optimization algorithm is developed for support structures of offshore wind turbines, but can easily be applied to many mechanical components under high-cycle fatigue. Lastly, a brief discussion of the method in its current state is given and ideas on how to elevate the current model are presented.

4. Fatigue Analysis

It is important to use an adequate cumulative damage theory when determining the fatigue damage in variable amplitude loading. The damage is defined as a fraction of the life of the structure. To predict the fatigue life, the fractions are summed using an accumulation rule. Even though many advanced and non-linear accumulation rules exist, none can fully represent the complicating aspects of variable amplitude loading [8]. Therefore, Palmgren-Miner's linear damage hypothesis is applied in this study. This rule does not take sequential effects and interaction of events into account, even though it can potentially have a large influence on the fatigue life of the structure. However, these shortcomings are deemed acceptable for the preliminary design-phase of jacket structures. Also, this is how the current recommended offshore practice [3] addresses fatigue. The material data for fatigue is given by Wöhler diagrams. A Wöhler diagram (S-N curves) represents the number of cycles to fatigue failure in high-cycle regime as a function of the stress amplitude.

4.1 Load Spectrum

Large time-history loads are used in the prescribed standards for design of fatigue life of wind turbine support structures [6]. This makes the fatigue investigation of support structures of offshore wind turbines very time consuming, even more so in design optimization, where all iterations may require a new simulation. Including large time-history loads and reducing the stress and displacement spectra through multiaxial Rainflow counting can be a good approach, because as a rule of thumb ten percent of the loads cause more than ninety percent of the damage [8]. However, multiaxial rainflow counting has not yet been implemented.

The current study only includes a load spectrum consisting of one minute of operational time. This is partly so because the aim of this work is to investigate design sensitivity analysis methods on fatigue constraints and not to present validated designs for jacket structures. As the time-history load is not reduced through methods such as Rainflow counting the time-history load is still sufficiently challenging for the problem at hand. One minute of operational time corresponds to 6,000 load combinations, resulting in 5,999 stress and displacement cycles as no reduction is done. Henceforth the total number of cycles are referred to as N_i .

The load spectrum in the authors possession does not include the torsional loads M_z and normal loads F_z , meaning that two shear loads, F_x and F_y , and two bending moments M_x and M_y represents the wind loads, see Figure 2. However, the developed design sensitivity analysis is capable of capturing the normal load and torsional moments if a more detailed time-history load is applied. It is believed that the normal and torsional loads will have a significant impact on the fatigue analysis, especially as the jacket is designed for large wind turbines in deep waters. Furthermore, hydrostatic wave loads may have a large impact on the fatigue on deep waters, but they are not included in this preliminary work.

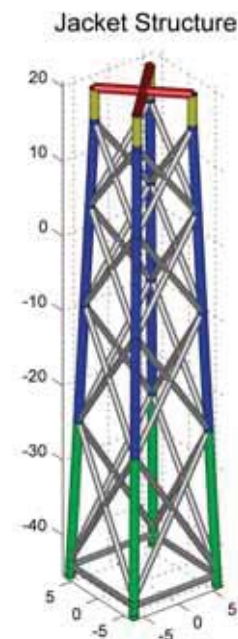


Figure 1: The OC4 reference jacket [10]. The five different colors represent five different sets of tube dimensions. Two shear forces and two bending moments are applied in the intersection of the red beams located at the jacket top. The dimensions shown on the figure are in meters.

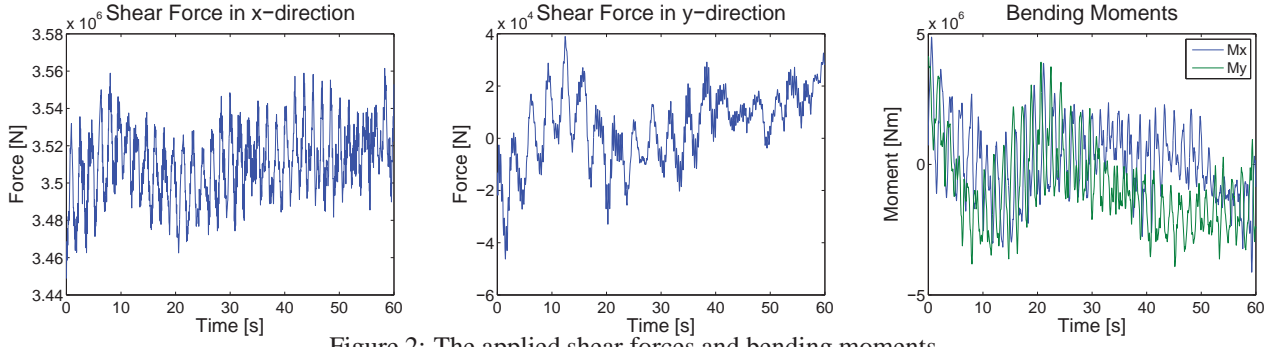


Figure 2: The applied shear forces and bending moments.

For every load time-history the displacements and stresses must be determined. In this work, the static stress analysis is conducted by use of the finite element method with linear assumptions. To apply the varying stresses and displacements in the fatigue analysis and the design sensitivity analysis, they must be reduced to a set of reversals.

4.2 Accumulated Damage

A log-log Wöhler diagram and the Basquin equation are utilized in order to determine the local damage caused by the loads:

$$\sigma_a(\mathbf{u}(\mathbf{x}), \mathbf{x}) = \sigma'_f (2N_{f\sigma})^{b_\sigma} \quad (1)$$

$$\tau_a(\mathbf{u}(\mathbf{x}), \mathbf{x}) = \tau'_f (2N_{f\tau})^{b_\tau} \quad (2)$$

σ_a and τ_a represent normal and shear stress amplitudes, respectively. \mathbf{u} is the global displacement vector and \mathbf{x} is the vector of all design variables v , that is $\mathbf{x} = [d_{grey}, d_{green}, d_{blue}, d_{yellow}, d_{red}, t_{grey}, t_{green}, t_{blue}, t_{yellow}, t_{red}]$. N_f is the number of cycles to failure, σ'_f is the fatigue strength for one reversal and b_σ is the regression slope, called the fatigue strength exponent, for normal stress. Since the loading conditions are multiaxial, it is very difficult to predict where the highest accumulated damage will occur. For this reason, the damage must be evaluated at many local points k for each stress cycle i . Accordingly, the local accumulated damage g_k can be calculated using Palmgren-Miners linear damage rule in combination with Eq. 1-2:

$$g_k(\mathbf{u}(\mathbf{x}), \mathbf{x}) = \sum_{i=1}^{N_i} \frac{n_i}{N_{fi}} = \sum_{i=1}^{N_i} \left(\frac{n_i}{\frac{1}{2} \exp\left(\frac{\ln(\sigma_{a_i}(\mathbf{u}(\mathbf{x}), \mathbf{x})/\sigma'_f)}{b_\sigma}\right)} + \frac{n_i}{\frac{1}{2} \exp\left(\frac{\ln(\tau_{a_i}(\mathbf{u}(\mathbf{x}), \mathbf{x})/\tau'_f)}{b_\tau}\right)} \right) \leq \bar{g} \quad (3)$$

Here n_i is the number of reversals the structure is subjected to with the corresponding stresses. Fatigue failure is expected to occur at $\bar{g} = 1$. The subscript k refers to the specific constraint number, as Eq. 3 constitutes the fatigue constraints.

5. Problem Formulation

The optimization problem under consideration is to reduce the overall mass m of a given preliminary design taking fatigue constraints into account. All other structural criteria are not included in this preliminary study. The requirements for the preliminary design are that the topology and choice of material are fixed during the entire optimization procedure. The design variables are tube diameter d and thickness t . As five symmetry conditions are enforced to produce a double symmetric jacket design for easy manufacturing, the number of design variables are kept low. The cost function is defined as:

$$f(\mathbf{x}) = \sum_{i=1}^{n_e} \rho A_i(\mathbf{x}) L_i = m \quad (4)$$

Here ρ is the material density and n_e is the number of elements. A_i and L_i are the cross sectional area and length of element i , respectively. The finite element mesh is set up such that each element represents a Bernoulli-Euler beam between two joints. Evaluating the fatigue in the cross section in each end of each element will thus approximate

the fatigue in the welds where failure is expected to occur. The optimization problem is defined as:

$$\underset{\mathbf{x}}{\text{minimize}} \quad f(\mathbf{x}) \quad (5)$$

$$\text{subject to} \quad g_k(\mathbf{u}(\mathbf{x}), \mathbf{x}) \leq \bar{g} \quad \forall k \quad (6)$$

$$\underline{d} \leq d_s \leq \bar{d} \quad \forall s \quad (7)$$

$$\underline{t} \leq t_s \leq \bar{t} \quad \forall s \quad (8)$$

The overline and underline represent the upper and lower limits and the subscript s represents the symmetry group, or element patch, in which the design variable belongs. As there is a very large number of highly nonlinear constraint functions, g_k , the optimization can be quite difficult to control. Moreover, as there are 6,000 different load combinations in the applied time-history load, it is imperative that the number of design iterations is kept to a minimum in order to reduce the computational demand.

6. Design Sensitivity Analysis

In order to use gradient based methods, design sensitivity analysis (DSA) needs to be performed, that is, the gradients of the cost function and the constraints with respect to the design variables must be determined. The DSA is performed analytically to ensure accurate and fast gradient evaluations.

6.1 Derivative of the cost function

As the cost function defined in Eq. 4 is an explicit function of a given design variable x_v , it is easily determined as:

$$\frac{df(\mathbf{x})}{dx_v} = \sum_{i=1}^{n_e} \left(\rho \frac{dA_i(\mathbf{x})}{dx_v} L_i \right) \quad (9)$$

6.2 Derivative of the constraint function

The constraint function defined in Eq. 3 is a function of the design variables, and also the displacements which are in itself a function of the design variables. This relationship will no longer be shown in the equations. Two different DSA methods will be presented; the direct differentiation method and an aggregated adjoint method. Using the direct differentiation method, the full derivative of the constraint with respect to a design variable x_v is given as:

$$\frac{dg_k}{dx_v} = \sum_{i=1}^{N_i} \left(\frac{\partial g_k}{\partial x_v} + \frac{\partial g_k}{\partial \mathbf{u}} \frac{d\mathbf{u}}{dx_v} \right) \quad (10)$$

The derivative of the displacement with respect to the design variables is the computational demanding part of this equation. This part is omitted when using the adjoint method. The partial derivatives are determined using the chain rule of differentiation:

$$\frac{\partial g_k}{\partial x_v} = \sum_{i=1}^{N_i} \left(\frac{\partial g_k}{\partial \sigma_a} \frac{\partial \sigma_a}{\partial x_v} + \frac{\partial g_k}{\partial \tau_a} \frac{\partial \tau_a}{\partial x_v} \right) \quad (11)$$

$$\frac{\partial g_k}{\partial \mathbf{u}} = \sum_{i=1}^{N_i} \left(\frac{\partial g_k}{\partial \sigma_a} \frac{\partial \sigma_a}{\partial \mathbf{u}} + \frac{\partial g_k}{\partial \tau_a} \frac{\partial \tau_a}{\partial \mathbf{u}} \right) \quad (12)$$

The stress sensitivities are found analytically. In the adjoint formulation, a Lagrange multiplier vector, λ , is introduced to omit the implicit and computational demanding $d\mathbf{u}/dx_v$. The full derivative using the adjoint method is given as:

$$\frac{dg_k}{dx_v} = \sum_{i=1}^{N_i} \left(\frac{\partial g_k}{\partial x_v} - \lambda \frac{d\mathbf{K}}{dx_v} \mathbf{u} \right) \quad (13)$$

\mathbf{K} is the global stiffness matrix. The Lagrange multiplier vector is solved as:

$$\mathbf{K}\lambda = \frac{\partial g_k}{\partial \mathbf{u}} \quad (14)$$

The calculation costs of the Lagrange multipliers are severely affected by the very large number of constraints. The amount of constraints can be reduced to one by aggregation functions, making the adjoint formulation very effective. The aggregation function sums all n_k constraints into a global constraint. The applied aggregation

functions are the Kreisselmeier-Steinhauser, the mean p-norm and the p-norm method. Depending on which aggregation method used, the global constraint is either an over or underestimate of the highest real constraint value. In the following, the formulation using the p-norm aggregation function is outlined. The single global constraint is then given as:

$$g^{p-norm} = \left(\sum_{k=1}^{n_k} (w_k (g_k - f^0))^p \right)^{1/p} \quad (15)$$

w_k is a weight factor, f^0 is an ideal value and p is a curve fitting factor. The constraint sensitivity using the adjoint method and p-norm aggregation is thus given as:

$$\frac{dg^{p-norm}}{dx_v} = \sum_{i=1}^{N_i} \left(\frac{\partial g^{p-norm}}{\partial x_v} - \lambda^{p-norm} \frac{dK}{dx_v} \mathbf{u} \right) \quad (16)$$

Where λ^{p-norm} is attained in a similar way as before.

7. Framework

The authors have established a framework for optimization of a 5 MW reference wind turbine jacket from UpWind [10] to demonstrate the proposed method. The highly idealized jacket is modeled as a Bernoulli-Euler 3D beam finite element model in MATLAB, see Figure 1. The initial design variables are seen on Table 1. The jacket is simplified as a fixed-free model and only include wind loads. The wind loads are based on very simplified dynamic multibody simulations of the wind-induced response of the turbine. These simulations present two shear forces and two bending moments at the jacket top. A total of 6,000 force and moment combinations are applied in the analysis. These loads represent a mean wind speed of 10 m/s applied in a constant direction, that is, orthogonal to the turbine blades.

Table 1: Initial beam dimensions of the jacket.

Symmetry Group	Red	Yellow	Blue	Green	Gray
Diameter	1.20m	1.20m	1.20m	1.20m	0.80m
Thickness	0.040m	0.040m	0.035m	0.050m	0.020m

7.1 Modeling Limitations

In its current form, the constraints do not take sequential effects, multiaxial effects, environmental effects, and non-proportionality effects into account. Moreover, the finite element formulation does not take material or geometric non-linearities into account. As the jacket is in high-cycle regime, the assumption of linear material behaviour is sound. The applied time-history loads determined by time-marching multibody simulations are very simplified. The largest errors are that the wind is applied in a constant angle and that the normal loads and torsional moments are not included. No hydrostatic loads are enforced on the submerged part of the jacket and the soil-structure interaction is simplified as fixed-free. Furthermore, the applied loads do not change when the design variables change. However, for proof-of-concept of the initial method, these assumptions are deemed acceptable.

8. Results

The design sensitivities are verified using central finite difference with a fixed perturbation of 1/100,000 of the original design variables. Results for two diameter and two thickness sensitivities are shown on Table 2 in root mean square percentage error. The remaining sensitivities have similar marginal deviations. The author's find the results very promising, especially since a fixed perturbation was applied. No optimization results are shown, as they will not reflect anything realistic until at least more representative time-history loads and the prescribed Det Norske Veritas design guidelines are applied.

Table 2: Root mean square percentage error compared to central difference approach.

DSA	dg/dx_1	dg/dx_2	dg/dx_6	dg/dx_7
Direct Differentiation Method	0.0004%	0.0018%	0.0007%	0.0022%
p-norm Adjoint Method	$6.5e^{-7}\%$	0.0004%	$6.8e^{-6}\%$	0.0004%

9. Discussion

Two different methods of performing the design sensitivity analysis have been presented. The suggested method depends entirely on the problem at hand. In the direct differentiation method accuracy is preserved. This method can, however, be time consuming when the optimization contains many design variables. The aggregated adjoint method is much faster at the cost of some accuracy. Both methods can, however, be applied for fatigue optimization of jacket structures for offshore wind turbines.

In its current state of development the algorithm will, to some extent, always favor a high moment of inertia. This means that the diameter will increase and the thickness will be lowered in each tube member in order to reduce mass. However, as no buckling constraints are included, poor choices of bounds on the design variables will result in buckling and ultimately total collapse of the structure. This fatigue optimization should not stand on its own; all analyses prescribed by Det Norske Veritas should still be carried out to ensure a reliable structure. Optimizations run by the authors indicate that the damage is currently underestimated. This can be explained by several observations: The simplified load time-history currently used does not include normal loads or the torsional moments induced by the wind. Furthermore, only one minute of a load time-history with a mean wind from a constant angle is used and then scaled to represent the desired lifetime. Including several load time-histories from different angles with different mean wind speeds will produce far more fatigue damage, and this will result in a better representation of the actual accumulated damage. Moreover, including hydrostatic loads and a complex soil-structure interaction model will also present a higher accumulated damage. Including offshore design guidelines will obviously also enforce a safety factor on the fatigue damage. Lastly, including additional constraints such as maximum displacement and eigenfrequency constraints will be very beneficial for the overall method. When the method is elevated to include some or all of the aforementioned, the authors believe that it can serve as a very powerful and efficient tool for optimizing a jacket structure under operational conditions. Furthermore, the method can easily be applied in other fatigue driven structural design problems such as aerospace and automobile industries.

10. Acknowledgements

The authors would like to thank the Danish Council for Strategic Research for funding the research project ABYSS (Advancing BeYond Shallow waterS).

11. References

- [1] Burton, T., Jenkins, N., Sharpe, D., and Bossanyi, E. *Wind Energy Handbook*. Wiley, 2011. ISBN 9781119993926.
- [2] Chin, C. M. and Fletcher, R. On the global convergence of an SLP filter algorithm that takes EQP steps. *Mathematical Programming*, 96(1):161–177, 2003. ISSN 0025-5610.
- [3] Det Norske Veritas. Fatigue design of offshore steel structures. Technical report, 2014.
- [4] European Wind Energy Association. Deep water - the next step for offshore wind energy. Technical report, 2013.
- [5] Grunwald, J. and Schnack, E. Modeling fatigue for shape optimization of dynamically loaded parts. *Advances in Engineering Software*, 29(1):63–67, 1998. ISSN 0965-9978.
- [6] International Electrotechnical Commission. Wind turbines - Part 1: Design requirements. Technical report, 2005.
- [7] Martini, K. and Tobias, C. Shape Optimization of a Steering System Based on Fatigue Analysis. *International Conference on Engineering Optimization*, 2010.
- [8] Stephens, R. I., Fatemi, A., Stephens, R. R., and Fuchs, H. O. *Metal Fatigue in Engineering*. John Wiley & Sons, 2000. ISBN 9780471510598.
- [9] The Carbon Trust. Offshore Wind Power: Big Challenge, Big Opportunity - maximising the Environmental, Economic and Security Benefits. Technical report, 2008.
- [10] Vorpahl, F., Kaufer, D., and Popko, W. Description of a basic model of the Upwind reference jacket” for code comparison in the OC4 project under IEA Wind Annex 30”. Technical report, Institute for Wind Energy and Energy Systems Technology, 2011.
- [11] Zeiler, T. A. and Barkey, M. E. Design sensitivities of fatigue performance and structural dynamic response in an automotive application. *Structural and Multidisciplinary Optimization*, 21(4):309–315, 2001. ISSN 1615-147X.

Experience with Several Multi-fidelity Surrogate Frameworks

Chanyoung Park¹, Raphael T. Haftka² and Nam-Ho Kim²

¹ University of Florida, Gainesville, FL, USA, cy.park@ufl.edu

² University of Florida, Gainesville, FL, USA, haftka@ufl.edu

³ University of Florida, Gainesville, FL, USA, nkim@ufl.edu

1. Abstract

In this paper, multi-fidelity surrogate (MFS) frameworks are investigated with the aid of an algebraic example for 100 different designs of experiments (DOEs). These include three Bayesian frameworks using 1) a model discrepancy function, 2) low fidelity model calibration and 3) a comprehensive approach. Two simple frameworks using 1) a discrepancy function and 2) low fidelity model calibration which are counterparts of the Bayesian frameworks 1) and 2) are also investigated. Their computational cost saving and accuracy improvement over a single fidelity surrogate model are investigated as a function of the ratio of the sampling costs of low and high fidelity simulations. The maximum cost saving was 85% and the maximum accuracy improvement was 40% when the number of low fidelity samples is about ten times larger than that of high fidelity samples for various computational costs. We found that the DOE can substantially change the relative standing of the different frameworks. Therefore, an important question is how to determine which model works best for a specific problem and DOE. The cross validation error appears to be a reasonable candidate for estimating which MFS models would perform poorly for a specific problem.

2. Keywords: Multi-fidelity surrogate framework, Comparison study, Discrepancy function, Calibration, Bayesian

3. Introduction

Surrogate models have been used as a cheap approximations, which can be built with several dozen data points. However, for sophisticated high fidelity models, the cost for obtaining sufficient data for achieving reasonable accuracy of a surrogate is high. Multi-fidelity surrogate (MFS) models have been developed to compensate for inadequate expensive high fidelity data with cheap low fidelity data by modelling the connection between two models. There are Gaussian process (GP) based Bayesian MFS frameworks and simple frameworks using the Kriging surrogate model which is a regular surrogate model based on GP, as well as other surrogates. However, the performance of different MFS frameworks with different complexities has been rarely compared.

Building an MFS using a model discrepancy function is a popular framework. An MFS is built by combining a low-fidelity surrogate based on low fidelity data set and a discrepancy surrogate based on low and high fidelity data sets. This multi-fidelity framework has been used in design optimization to alleviate computational burden. For example, non-Bayesian MFS models using linear regression were used by combining coarse and fine finite element models for aircraft structural optimization [1,3]. The same approach was used to combine aerodynamic prediction from cheap linear theory and expensive Euler solutions for aircraft aerodynamic optimization [2]. A Bayesian MFS model based on GP was later introduced by Kennedy and O'Hagan (2000). The Bayesian model allows to incorporate prior information [4,5]. Co-Kriging [9,10] provides an equivalent result for the Bayesian formulation with a non-informative prior and has good computational characteristics [6,7,8].

Model calibration is another MFS model based on tuning model parameters of a low fidelity model. A straight forward simple framework is to find parameters that minimize discrepancy between a calibrated low fidelity model and high fidelity data [14]. GP based Bayesian calibration frameworks were also introduced [11,12,13]. The Bayesian frameworks find best calibration parameters that is most statistically consistent with available information [11,15]. A general Bayesian MFS model that uses both calibration and a discrepancy function was proposed by Kennedy and O'Hagan (2001) offering greater flexibility.

The objectives of this paper are: (1) introduce characteristics of multi-fidelity surrogate frameworks, (2) investigate the performance of those surrogates in terms of accuracy (3) investigate the performance of the cross validation error as a surrogate performance estimator. This paper is organized as follows. Section 2 presents multi-fidelity surrogate models. Section 3 describes the methodology of the investigation. Section 4 presents results and discussion.

2. Multi-fidelity surrogate models with different frameworks

In this paper, we discuss three commonly used Bayesian MFS frameworks: using (1) a model discrepancy function, (2) a low fidelity model parameter calibration and (3) a combined approach. Two simpler MFS frameworks are

also discussed, which are simplified versions of the Bayesian MFS frameworks using the approach (1) and (2). The characteristics of frameworks and the differences between Bayesian and simple frameworks will be described in the following sections.

2.1 Simple MFS framework using a model discrepancy function

This framework provides a convenient way of fitting an MFS with regular surrogate models. In this framework the MFS is described with two surrogates $\hat{y}_{low}(\mathbf{x})$ and $\hat{\delta}(\mathbf{x})$ which represent a low fidelity function and a discrepancy function, respectively, as

$$\hat{y}_H(\mathbf{x}) = \rho \hat{y}_L(\mathbf{x}) + \hat{\delta}(\mathbf{x}) \quad (1)$$

where ρ is a regression scalar minimizing $(\rho \hat{y}_L(\mathbf{x}_H) - \mathbf{y}_H)^T (\rho \hat{y}_L(\mathbf{x}_H) - \mathbf{y}_H)$

Figure 1 illustrates an example with a high fidelity function $y_{HT}(x) = (6x - 2)^2 \sin(12x - 4)$ and a low fidelity function $y_{LT}(x) = (5.5x - 2.5)^2 \sin(12x - 4)$ and the corresponding data sets with 5 and 24 samples, respectively.

The high fidelity sampling point set is a subset of the low fidelity sampling point set.

Figure 2 (a) and (b) show fits by combining the simple MFS framework and the Kriging surrogate model that a low fidelity Kriging surrogate is fitted with the low fidelity data set and a Kriging surrogate of the discrepancy function is fitted using the difference at the common sampling points. To understand the effect of the regression scalar ρ , we fitted the surrogates with and without a condition $\rho=1$.

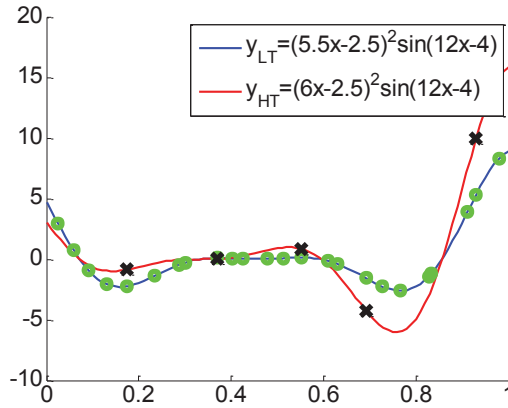


Figure 1: Low fidelity function and high fidelity function and low fidelity data (green circles) and high fidelity data (black crosses)

2.2 Bayesian MFS framework using a model discrepancy function

In the previous section, the simple framework was described. When the framework combined with a Kriging surrogate, it is a special case of the full Bayesian framework which was introduced [4,5]. The main differences between the simple framework and this Bayesian framework are: 1) the simple framework uses the low fidelity data set while the Bayesian framework uses high and low fidelity data sets to update the low fidelity response prior model and 2) whole low fidelity data is used to get the discrepancy function whereas the simplified framework use low fidelity data at the common points.

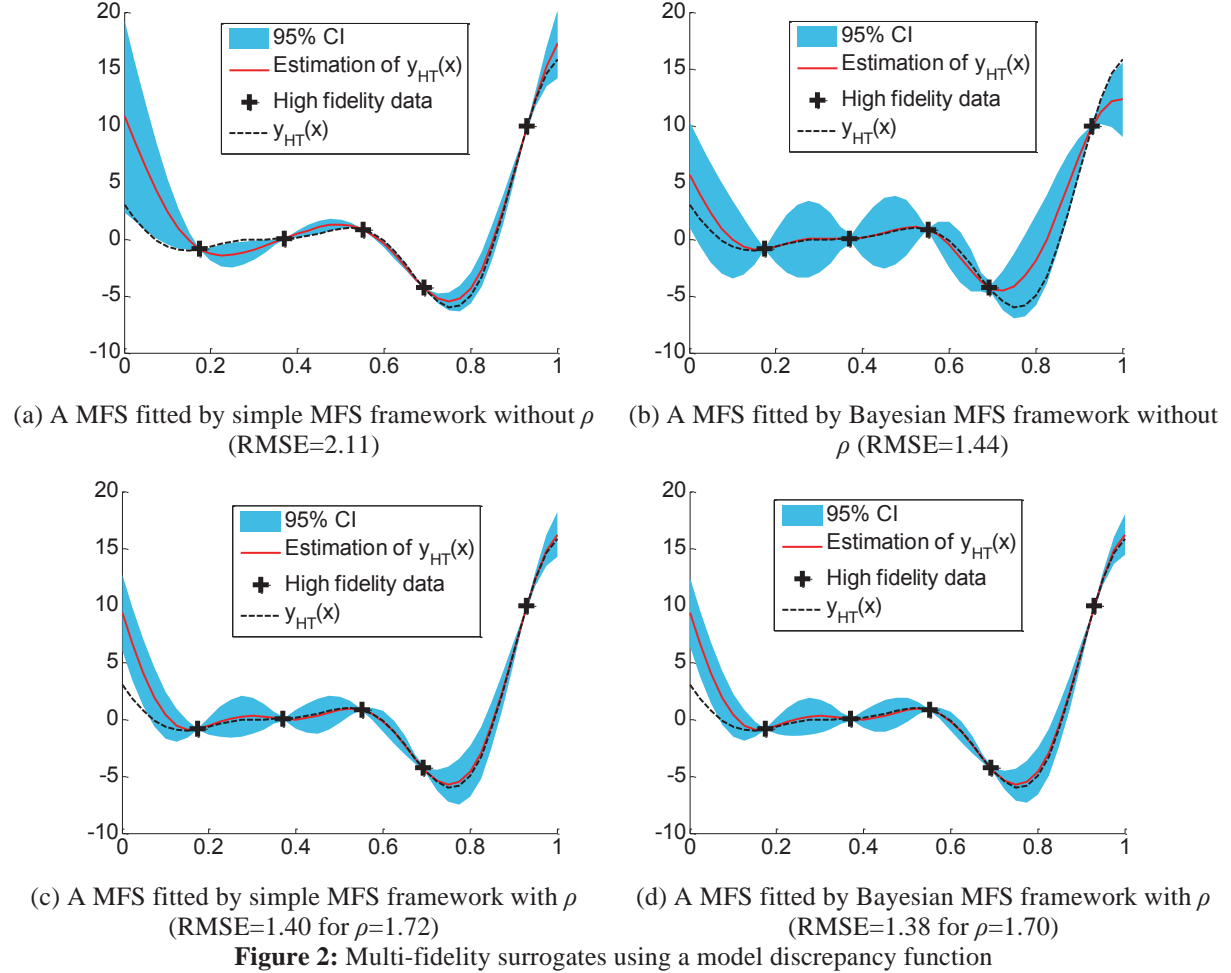
Figure 2 (c) and (d) present fits using the Bayesian MFS framework with and without the condition $\rho=1$ and the corresponding prediction uncertainties for 95% confidence. From a comparison between (a) to (d), the simple framework can provide a fit as good as Bayesian framework and the effect of the regression scalar is more important than applying the Bayesian framework for this example.

2.3 Simple MFS framework with model calibration

The previous two frameworks try to capture the discrepancy between high and low fidelity responses using a model discrepancy function. An widely used alternative framework is to tune parameters of a low fidelity model which is also known as model calibration. A simple calibration based framework is to build a surrogate of the low fidelity response $\hat{y}_L(\mathbf{x}, \mathbf{q})$ which is a function of the input variables \mathbf{x} and the model parameters \mathbf{q} to define the response as a function of model parameters. Then we can find optimal $\mathbf{q} = \boldsymbol{\theta}$ minimizing the discrepancy between the high fidelity data and the low fidelity prediction.

$$\hat{y}_H(\mathbf{x}) = \hat{y}_L(\mathbf{x}, \boldsymbol{\theta}) \quad (2)$$

Figure 3 (b) shows a fit using the Kriging surrogate model and the simple framework with the previous 1-D function example with the selection of calibration parameters as $y_{LT}(x, \{\theta_1, \theta_2\}) = (\theta_1 x - \theta_2)^2 \sin(12x - 4)$. Since the low fidelity function has the same function form with the high fidelity function, the calibrated parameters should be $\theta_1=6$, $\theta_2=-2$, and Fig. 3 (a) shows the sampling points to fit the surrogate.



2.4 Bayesian MFS framework with model calibration

The Bayesian MFS framework makes inference about $y_{HT}(\mathbf{x})$ by updating a high fidelity prior model based on low and high fidelity data sets [11,15]. A big difference from the previous simple framework is that the Bayesian framework captures the model inadequacy of a low fidelity function as well as calibrating the low fidelity model while the previous simple framework cannot capture the inadequacy. As Fig. 3 (c) shows, predictions at high fidelity data points perfectly match data even with the model inadequacy of the low fidelity model and the prediction uncertainties at those points are zero. In Fig. 3 (d), the comprehensive Bayesian framework calibrates parameters well but its fit is worse than the Bayesian framework without a model discrepancy function.

2.5 Comprehensive Bayesian MFS framework

A comprehensive MFS is a most flexible model that the model discrepancy between low and high fidelity model responses is captured by tuning low fidelity model parameters and a model discrepancy function [12,13].

2.6 Strategies for design of experiments

Building multi-fidelity surrogates requires a new sampling strategy since MFSs need low and high fidelity data sets and it is natural that the low fidelity data set is a super set of high fidelity data set to see the model discrepancy. A sampling strategy, which is called nested neighborhood design, is to generate low fidelity sampling points using LHS and to select high fidelity sampling points from the generated low fidelity sampling points having optimal

coverage [7]. All the examples in this paper use the nested neighborhood design.

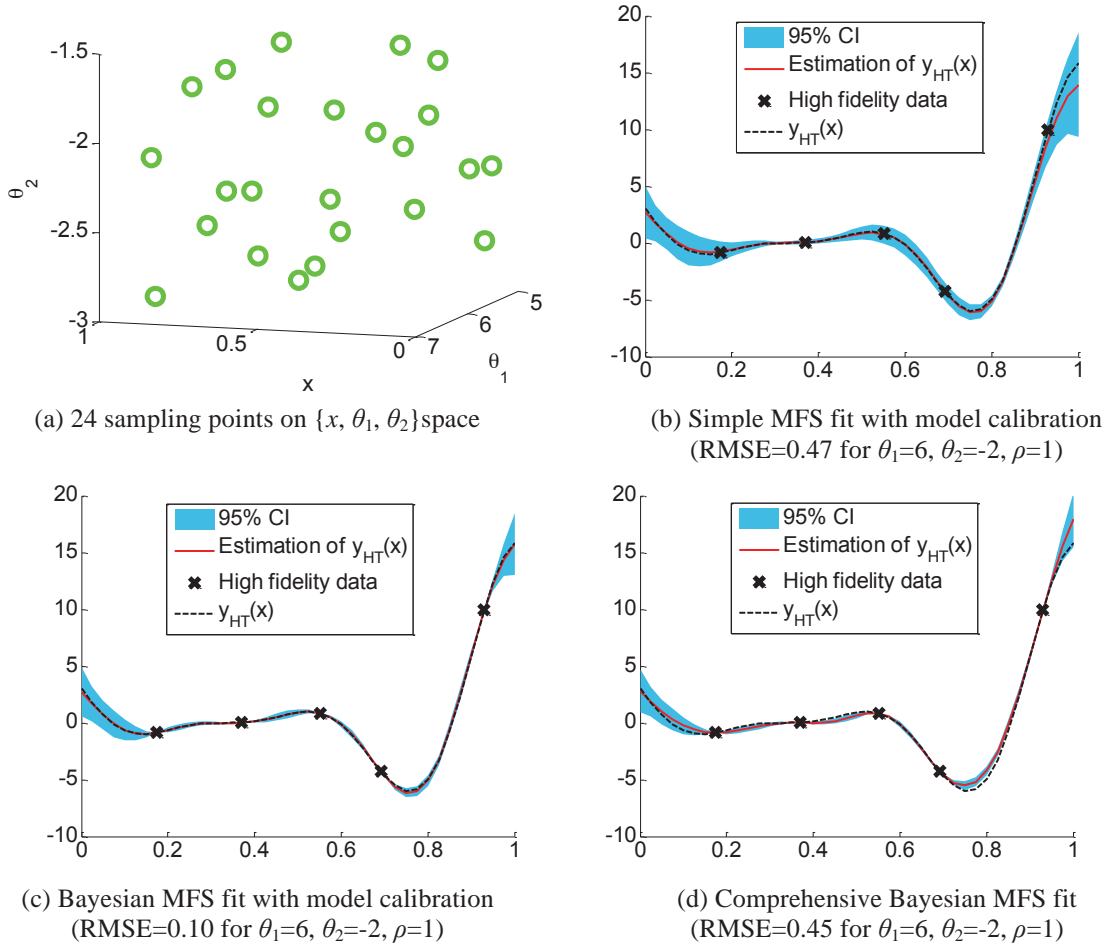


Figure 3: Multi-fidelity surrogates based on model calibration

3. Measurements of a surrogate model

In this section, we describe numerical experiments for assessing the robustness of prediction of the MFS frameworks. Since the performance of surrogates varies for different problems and design of experiments (DOE), cross validation error has been used as a measure to rank for surrogate models. We investigate whether the cross validation error can be employed to detect the worst MFS frameworks for a specific problem and specific DOE.

3.1 Assessing accuracy using root mean square error

MFS surrogates are fitted to function values at n points which are generated by the sampling strategy. We can measure the accuracy of an MFS using the RMSE which is the square root of square error integrated over the sampling domain. We use Monte Carlo integration at a large number of n_{test} test points as

$$\text{RMSE} = \sqrt{\frac{1}{n_{test}} \sum_{i=1}^{n_{test}} (y_i - \hat{y}_i)^2} \quad \text{for } i = 1, \dots, n_{test} \quad (3)$$

where \hat{y}_i and y_i are a prediction and a true function value at the i^{th} test point.

4. Numerical examples

We compare the previously described frameworks with the Hartmann 6 function example. Their accuracy was statistically assessed since their performances vary for different DOEs. 100 different DOEs were generated using nested neighborhood sampling and their accuracies were measured with the median RMSE of 100 RMSEs.

The computational cost saving for achieving a certain accuracy is main thrust of applying MFS frameworks for fitting a surrogate. In this section, we examine the described frameworks in that perspective. There are other factors that determine the efficiency of an MFS framework: 1) the ratio of high fidelity sample size to low fidelity sample size, 2) the ratio of the high fidelity data point evaluation cost to the low fidelity data point cost and 3) the

total computational budget. We also consider those three factors.

Table 1 shows cases for different factors that we discuss in this paper. The computational budget 56H means we have computational budget equivalent to evaluating 56 high fidelity samples. Here we use the high fidelity sample evaluation cost as a reference cost since typically we need to fit an MFS for a given high fidelity simulation that we have no choice but to choose a low fidelity simulation. Cost ratio 4 means 4 low fidelity samples can be evaluated with the budget for evaluating a single high fidelity sample. The cases show combinations of low and high fidelity samples for given total budget and cost ratio. For example, 36/80 of the budget of 56H and cost ratio 4 denotes a case with 36 high fidelity samples and 80 low fidelity samples for fitting an MFS. There are different cases for given computational budget and sample cost ratio. For example, the computational budget of 56H and a ratio of 4, leads to 36H+80/4H=56H.

Table 1: Computational budget and a data point evaluation ratio

Computational budget	LF sample cost ratio	Sample size ratio
56H	4	36/80, 26/120, 16/160, 6/200
	10	49/70, 46/100, 42/140, 35/210, 28/280, 21/350, 14/420, 7/490
	30	48/240, 46/300, 44/360, 42/420, 40/480, 38/540, 28/840, 18/1140
28H	4	18/40, 13/60, 8/80, 3/100
	10	22/60, 19/90, 16/120, 13/150, 10/180, 7/210, 4/240
	30	24/120, 22/180, 20/240, 18/300, 16/360, 14/420, 10/540, 6/660, 4/720

We use the Hartmann 6 function [16] over [0.1,1] as a high fidelity function and an approximated function of the Hartmann function as a low fidelity function. The approximated function uses a different alpha $\alpha_{approx} = \{0.5 \ 0.5 \ 2.0 \ 4.0\}^T$ and an approximated exponential function which is expressed as

$$f_{approx}^{exp}(x) = \left(\exp\left(\frac{-4}{9}\right) + \exp\left(\frac{-4}{9}\right) \frac{(x+4)}{9} \right)^9 \quad (4)$$

We generated 100 different DOEs using the nested neighborhood sampling to check the robustness of MFS frameworks. RMSE of each DOE was calculated for each framework based on the same 10,000 test points generated by LHS. The medians of 100 RMSEs were obtained for each framework and compared to one another. Table 2 shows the effect of cost saving for the best framework for different cases. The RMSEs of single fidelity surrogates show RMSE with the corresponding computational budget so that RMSE for the high fidelity fit remains the same for all cases. The cost saving is the computational cost saving by using the best MFS framework for the cost of the high fidelity fit which achieves the same level of RMSE with the corresponding MFS framework.

Table 2: The effect of cost saving for the best framework for the best sample size ratio

Computational budget	LF sample cost ratio	RMSEs of single fidelity surrogates	Best RMSE	Best sample size ratio	Cost saving
56H	4	RMSE _L =0.123 RMSE _H =0.132	0.095 (Bayesian disc.)	[26/120, 16/160]	50%
	10	RMSE _L =0.116 RMSE _H =0.132	0.072 (Bayesian disc.)	[28/280, 21/350]	75%
	30	RMSE _L =0.113 RMSE _H =0.132	0.06 (Bayesian disc.)	[44/360, 40/480]	83%
28H	4	RMSE _L =0.136 RMSE _H =0.166	0.125 (Bayesian disc.)	80/8	58%
	10	RMSE _L =0.122 RMSE _H =0.166	0.1 (Bayesian disc.)	[13/150, 7/210]	75%
	30	RMSE _L =0.114 RMSE _H =0.166	0.08 (Bayesian disc.)	[20/240, 14/420]	85%

5. Concluding Remarks

In this paper, we present a comparison study of five MFS building frameworks by combining low and high fidelity data sets using the 6D Hartmann 6 function: 1) a simple framework based on a discrepancy function approach using the Kriging surrogate model, 2) a Bayesian framework based on a discrepancy function, 3) a simple

framework based on model calibration using the Kriging surrogate model, 4) a Bayesian framework based on model calibration and 5) a comprehensive Bayesian framework.

We found that the MFS frameworks become useful as the cost of a low fidelity data point becomes cheaper than the cost of a high fidelity data point and the MFS frameworks become most beneficial for saving the computational cost. Based on the example, computational cost can be saved by 85% for the same accuracy with the single fidelity surrogate while the maximum accuracy improvement over the single fidelity surrogate is 60% improvement in terms of RMSE.

For the discrepancy function based frameworks, an interesting observation was that the simple framework could perform as well as the Bayesian framework and the use of the regression scalar ρ could be important. For the calibration based frameworks, the framework without a discrepancy function outperformed the comprehensive framework and the effect of the regression scalar ρ was not noticeable. In terms of accuracy, the discrepancy function based frameworks showed good performance generally. The calibration frameworks could show reliable performance with a few high fidelity samples whereas the performance of the discrepancy function based frameworks abruptly decreased for a few high fidelity samples but there were factors that might affect the results such as calibration parameter selection and calibration parameter bounds which were not seriously considered in this paper. There were optimal ratios maximizing the accuracy but the effect was not significant when sufficient number of low fidelity data points were obtained.

6. Acknowledgements

This work is supported by the U.S. Department of Energy, National Nuclear Security Administration, Advanced Simulation and Computing Program, as a Cooperative Agreement under the Predictive Science Academic Alliance Program, under Contract No. DE-NA0002378.

7. References

- [1] Balabanov, V., Haftka, R. T., Grossman, B., Mason, W. H., & Watson, L. T. (1998, September). Multifidelity response surface model for HSCT wing bending material weight. In *Proceedings of 7th AIAA/USAF/NASA/ISSMO Symposium on Multidisciplinary Analysis and Optimization* (pp. 778-788).
- [2] Knill, D. L., Giunta, A. A., Baker, C. A., Grossman, B., Mason, W. H., Haftka, R. T., & Watson, L. T. (1999). Response surface models combining linear and Euler aerodynamics for supersonic transport design. *Journal of Aircraft*, 36(1), 75-86.
- [3] Mason, B. H., Haftka, R. T., Johnson, E. R., & Farley, G. L. (1998). Variable complexity design of composite fuselage frames by response surface techniques. *Thin-walled structures*, 32(4), 235-261.
- [4] Kennedy, M. C., & O'Hagan, A. (2000). Predicting the output from a complex computer code when fast approximations are available. *Biometrika*, 87(1), 1-13.
- [5] Qian, P. Z., & Wu, C. J. (2008). Bayesian hierarchical modeling for integrating low-accuracy and high-accuracy experiments. *Technometrics*, 50(2), 192-204.
- [6] Forrester, A. I., Sobester, A., & Keane, A. J. (2007). Multi-fidelity optimization via surrogate modelling. *Proceedings of the royal society A: mathematical, physical and engineering science*, 463(2088), 3251-3269.
- [7] Le Gratiet, L. (2013). Multi-fidelity Gaussian process regression for computer experiments (Doctoral dissertation, Université Paris-Diderot-Paris VII).
- [8] Kuya, Y., Takeda, K., Zhang, X., & J. Forrester, A. I. (2011). Multifidelity surrogate modeling of experimental and computational aerodynamic data sets. *AIAA journal*, 49(2), 289-298.
- [9] Sacks, J., Welch, W. J., Mitchell, T. J., & Wynn, H. P. (1989). Design and analysis of computer experiments. *Statistical science*, 409-423.
- [10] Lophaven, S. N., Nielsen, H. B., & Søndergaard, J. (2002). *DACE-A Matlab Kriging toolbox, version 2.0*.
- [11] McFarland, J., Mahadevan, S., Romero, V., & Swiler, L. (2008). Calibration and uncertainty analysis for computer simulations with multivariate output. *AIAA journal*, 46(5), 1253-1265.
- [12] Kennedy, M. C., & O'Hagan, A. (2001). Bayesian calibration of computer models. *Journal of the Royal Statistical Society: Series B (Statistical Methodology)*, 63(3), 425-464.
- [13] Higdon, D., Kennedy, M., Cavendish, J. C., Cafo, J. A., & Ryne, R. D. (2004). Combining field data and computer simulations for calibration and prediction. *SIAM Journal on Scientific Computing*, 26(2), 448-466.
- [14] Zheng, L., Hedrick, T. L., & Mittal, R. (2013). A multi-fidelity modelling approach for evaluation and optimization of wing stroke aerodynamics in flapping flight. *Journal of Fluid Mechanics*, 721, 118-154.
- [15] Prudencio, E. E., & Schulz, K. W. (2012, January). The parallel C++ statistical library 'QUESO': Quantification of Uncertainty for Estimation, Simulation and Optimization. In *Euro-Par 2011: Parallel Processing Workshops* (pp. 398-407). Springer Berlin Heidelberg.
- [16] <http://www.sfu.ca/~ssurjano/hart6.html>

Speed dependent optimisation for variable stiffness vehicle suspension

Xin Tang¹, Weihua Li^{1*}, Haiping Du²

¹ School of Mechanical, Material and Mechatronics Engineering, University of Wollongong, NSW, Australia, xt955@uowmail.edu.au

² School of Electrical, Computer and Telecommunications Engineering, University of Wollongong, NSW, Australia
*Email: Weihuali@uow.edu.au

Abstract: In this research, an optimization of vehicle suspension performance under different vehicle speeds is studied. Besides finding optimal damping value to achieve a better suspension performance, changing the value of stiffness simultaneously and finding the optimal values in variable stiffness control can achieve the best suspension performance with utilizing the available information of speed. By optimizing the suspension stiffness parameter of quarter-car models subjected to random road excitation with different vehicle speeds, the proposed approach ensures the model to have an optimal operating performance. The optimization method applied in this paper is Genetic Algorithm, which increases the probability of finding the global optimum solution and avoids the convergence to a local minimum. A novel criterion for selecting the optimal suspension parameters is presented in terms of the sprung mass acceleration and the dynamic force degenerated between the wheel and the ground.

Keywords: quarter-car models, genetic algorithm, multi-objective, Magnetorheological damper.

1. Introduction

Suspension is one of the most important units to a vehicle. The parameters of suspension have a great effect to the performance of a car. For conventional passive vehicle suspension with constant parameter value, it is difficult to get good overall performance under different road conditions and speeds. With the development of auto industry and the increase of customer requirement, the research on optimizing vehicle suspension parameters is becoming more and more important. In the suspension parameter optimization progress of traditional vehicle design, the optimization goal, such as riding comfort, suspension deflection and tyre dynamic loading [1], is mostly considered separately.

In recent years, researchers [2, 3] have begun to consider the factors simultaneously, namely, multi-objective optimization. As these criteria mentioned above are conflicting, a suitable multi-objective method with weighting function should be chosen properly. In this case, a multi-objective optimization methodology is applied in this paper, an optimal solution is determined by using the Genetic Algorithm [4]. In order to conduct optimization progress for a vehicle suspension parameter, various suspension models were chosen to simulate, including linear quarter-car model [5], piecewise linear model [2] and sky-hook model [6], etc. In this paper, besides linear quarter-car model, a nonlinear model with Magnetorheological (MR) damper is also chosen to measure. Based on this nonlinear quarter-car model, special attention is paid to investigating the optimal suspension stiffness value under various vehicle horizontal speeds using Genetic Algorithm method.

This paper is organized as follows, the mechanical models employed and the corresponding equations are first presented. Then, the method to create road excitation [7] is introduced. The optimization criteria imposed are outlined and formulated. Next, some typical numerical results are presented. Quarter-car model with MR damper running over roads is also examined. The optimization results are presented under different vehicle speed.

2. Modelling and simulation of suspension under random road profile

2.1. Quarter-Car models

A vehicle suspension is a complex multi-degree freedom vibration system. In order to simplify the model applied, simultaneously, to simulate the running state of a car as realistic as possible, the following assumptions can be applied: (1) The vehicle suspension is a rigid body with a symmetrical structure. (2) The vehicle keeps running at a constant speed. The tyres always keep in contact with road surface. (3) Only vertical vibration should be considered in this case.

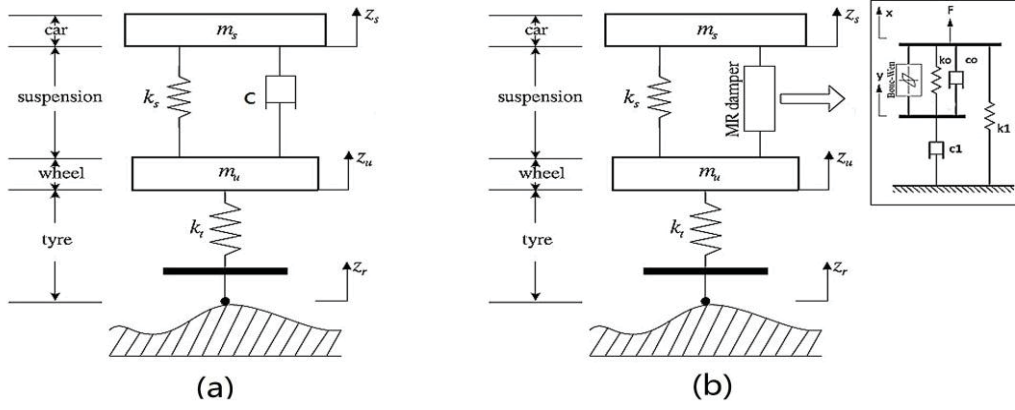


Figure 1: Vehicle model (a) linear model (b) nonlinear model [8]

Based on the assumptions shown above, the vehicle model can be simplified to a two Degree of Freedom (DOF) one. The two degrees of freedom are the sprung mass vertical vibration z_s and the unsprung mass vertical vibration z_u , respectively. The simulation in this article applies two quarter-car models [9], one is a linear model, and the other is a nonlinear model with MR damper. The models are shown in Figure 1. The linear quarter-car dynamic equations can be described by the following differential equations [8]:

$$m_s \ddot{z}_s + c(\dot{z}_s - \dot{z}_u) + k_s(z_s - z_u) = 0 \quad (1)$$

$$m_u \ddot{z}_u + k_t(z_u - z_r) - c(\dot{z}_s - \dot{z}_u) - k_s(z_s - z_u) = 0 \quad (2)$$

In this equation, m_s represents a body vehicle mass (sprung mass), m_u is a wheel vehicle mass (unsprung mass), k_s is the spring stiffness and k_t is the tire stiffness. In addition, z_s is the sprung mass displacement, and z_u represents the unsprung mass displacement. To better predict a MR damper response in model (b), a modified version of the Bouc-Wen model has been proposed by Spencer [10].

2.2. Random road excitation

Road roughness indicates the deflection between road surface and reference plane. Most studies have demonstrated that road roughness is a Gaussian probability distribution with zero mean value. It has smooth traversal characteristic if it is transferred to a stochastic process. The road roughness characteristics can be presented by power spectral density (PSD) function $S_q(\Omega)$. Qualitatively, a larger value of exponent n is defined to describe the roughness at longer wavelengths, while a smaller value at shorter wavelengths. For this reason, a spectra corresponding to the geometrical profile of typical roads can be represented by the following segmented function [6]

$$S_q(\Omega) = \begin{cases} S_q(\Omega_o)(\Omega/\Omega_o)^{-n_1}, & \text{if } \Omega \leq \Omega_o \\ S_q(\Omega_o)(\Omega/\Omega_o)^{-n_2}, & \text{if } \Omega \geq \Omega_o \end{cases} \quad (3)$$

Where, Ω is the spatial frequency, $\Omega_o = 1/2\pi$ is a reference spatial frequency, n is the frequency exponent; generally, $n_1 = 2$ and $n_2 = 1.5$ so that the resulting spectrum exhibits a slope discontinuity at $\Omega = \Omega_o$ in a log-log scale. Moreover, the value $S_q(\Omega_o)$ is a power spectral density value under the reference spatial frequencies. For a nonlinear quarter-car model, the road excitation can be generated by the spectral representation method [7, 11], as shown in Eq.(4). Using the harmonic superposition method, the harmonic component under different frequency are added together to generate random road roughness. Supposing that a car is traveling on a given road at a constant speed v , the road irregularities can be simulated by the following formula

$$z_r(t) = \sum_{i=1}^n \left(\sqrt{2S_q(i\Delta\Omega)\Delta\Omega} \right) \sin(i\omega_o t + \varphi_i) \quad (4)$$

In the previous equation, φ_i is the random numbers distributed uniformly among $[0, 2\pi]$, where $\Delta\Omega$ is the minimum spatial frequency value we considered, which equals $0.011m^{-1}$. In addition, the value of the fundamental temporal frequency ω_o can be determined by

$$\omega_o = 2\pi\Delta\Omega v \quad (5)$$

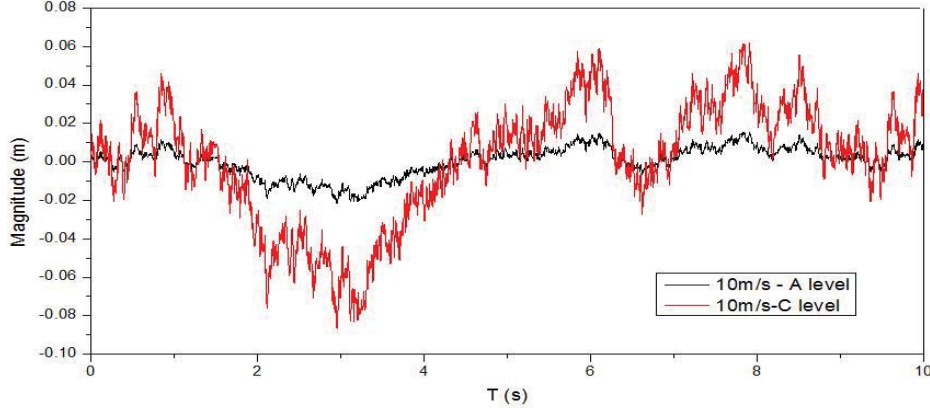


Figure 2: Variation of road roughness of Rank A & C vs time (specific speed:10 m/s)

The random road profile was simulated by Matlab[®] under different vehicle speeds, between 10 to 40 m/s. The consequence illustrates good-quality road (with $S_q(\Omega_o) = 16 \times 10^{-6} \text{ m}^3$) and bad-quality road (with $S_q(\Omega_o) = 256 \times 10^{-6} \text{ m}^3$) vs. time respectively, shown in Figure 2.

2.3. Suspension performance objective function

To optima the parameter of a vehicle suspension, two factors, riding comfort and tyre deflection, should be considered simultaneous. Particularly, riding comfort, which can be presented by J_1 , can be measured by Sprung Mass Acceleration (SMA). Note that in order to normalize the magnitude, SMA should be multiplied by the sprung mass to a force. In addition, another objective function J_2 can be represented by the force developed between the wheel and the ground, namely Tyre Dynamic Load (TDL). Then, the two sub-objective functions are combined into a unified objective function J , as defined by Eq.(6-8). Considering the random characteristic of the road excitation generated in time domain, the following performance index can be determined by expectations

$$J = w_1 J_1 + w_2 J_2 \quad (6)$$

$$J_1 = E \sqrt{\sum_{i=1}^N (m_s \ddot{z}_s)^2 / N} \quad (7)$$

$$J_2 = E \sqrt{\sum_{i=1}^N [k_t (z_u - z_r)]^2 / N} \quad (8)$$

where N is the total sampling points. The constants w_1 and w_2 denote the weighting coefficients balancing and adjusting the two performance indices, which include ride comfort and road holding. The proportion is determined by not only the contribution of the individual performance but also the normalized design. Depositing by the aforementioned progress, the weighting coefficients were determined as $w_1 = 0.15$ and $w_2 = 0.85$.

2.4. Simulation progress

In the simulation, the good-quality road profile was chosen as the road excitation. The length of the road is 100m. For the special case of vehicle model with linear properties, the response autospectral density of the linear dynamic system can be obtained easily in frequency domain by applying road profile spectral density under exact vehicle velocity and the stationary vehicle response matrix through the formula [12]

$$S_{XX}(\omega) = H_x(\omega)H_x(-\omega)S_{FF}(\omega) = |H_x(\omega)|^2 S_{FF}(\omega) \quad (9)$$

In the previous equation, $\omega = 2\pi\Delta\Omega v$ is the temporal frequency, $S_{XX}(\omega)$ and $S_{FF}(\omega)$ represent the spectral density of the response and the excitation, respectively. $H_x(\omega)$ is the frequency response functions of the system [13]. Except the linear suspension model presented before, the quarter-car model with MR damper system possesses strong nonlinearities. For this case, Genetic Algorithm (GA), in conjunction with appropriate integration methodologies developed for nonlinear systems [14], is applied to evaluate the suspension response with probabilistic characteristic.

Genetic Algorithms belong to the larger class of evolutionary algorithms (EA), which generate solutions to optimization problems using techniques inspired by natural evolution. This global optimization algorithm has a characteristic that it has less possibility to fall into partial optimal solution in the iterative process. For this reason, it has become a powerful tool to calculate complex optimization issues of a nonlinear system. More detailed discussion and description of Genetic Algorithm are available such as [4]. In the work presented in this article, GADS (Genetic Algorithm and Direct Search Toolbox) in MATLAB® was applied for optimizations. A fixed population size with string length of 50, the generations of 100 are used, crossover fraction is 0.8, and migration fraction is 0.2.

The parameter intending to optimize is the stiffness coefficient of the car suspension. The suspension reference parameter value is taken from the literature [6]. Moreover, the classic stiffness values for the specific method is taken from the literature [14]. The details can be seen in Table 1. More specific, the parameters for the MR damper in the nonlinear model (Figure 1b) were chosen to be $\alpha = 963 \text{ N/cm}$, $c_o = 53 \text{ N} \cdot \text{sec/cm}$, $k_o = 14 \text{ N/cm}$, $c_1 = 930 \text{ N} \cdot \text{sec/cm}$, $k_1 = 5.4 \text{ N/cm}$, $\gamma = 200 \text{ cm}^{-2}$, $\beta = 200 \text{ cm}^{-2}$, $n = 2$, $A = 207$, and $x_o = 18.9 \text{ cm}$.

Table 1: Suspension coefficients for special objective function

<i>Method</i>	$k_s(\text{Nm}^{-1})$	$k_t(\text{Nsm}^{-1})$	$c(\text{Nsm}^{-1})$	$m_s(\text{kg})$	$m_u(\text{kg})$
Mixed objective	16000				
SMA	8045	200000	1425	375	60
TD	15836				

3. Numerical results

In terms of a linear model, the suspension response with second moment characteristics in Eq.(4) is readily obtained by the digit sum of the corresponding response of the power spectral density function with specific ω . To compare the optimal stiffness values between linear model and nonlinear model, the results are depicted in Figure 3. A major phenomenon in linear model data can be observed that by increasing vehicle's speed, the changing trend of stiffness is getting smaller.

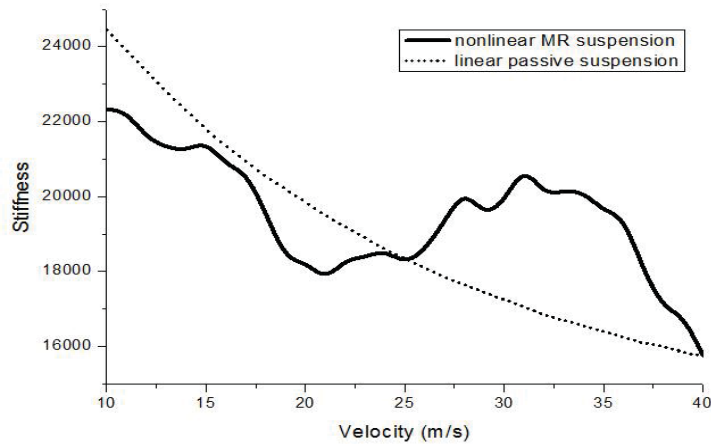


Figure 3: Linear and nonlinear system optimal stiffness values vs. velocity under mixed objective function

In Figure 3, the thick continuous curve illustrates the tendency of nonlinear model optimal parameter, and the thin dash line is obtained from the linear model as a reference. As a consequence, the trend is observed as the dependence of the linear suspension stiffness to the vehicle horizontal velocity, and the value of the nonlinear one demonstrates relative irregular trend within the velocity range considered. The result presented is attributed by the characteristic of MR damper, which has a strong nonlinearity in the relation between the output force and the cylinder's moving velocity.

In order to observe the effect of optimising stiffness value, verification of the result can be done by analysing the performance index of the system using optimal parameters. The normalized performance indexes aforementioned are drawn in Figure 4-6. It can be seen from the figures that, almost at the whole range of vehicle speed considered, the objective function values with optimal stiffness are smaller than the ones with the classic suspension parameter value. More specifically, Figure 4 demonstrates the overall performance of linear suspension.

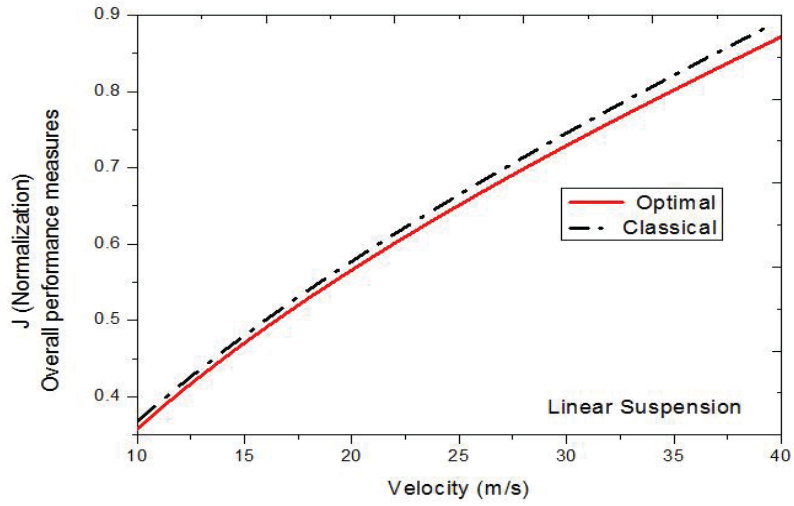


Figure 4: Overall performances for linear model

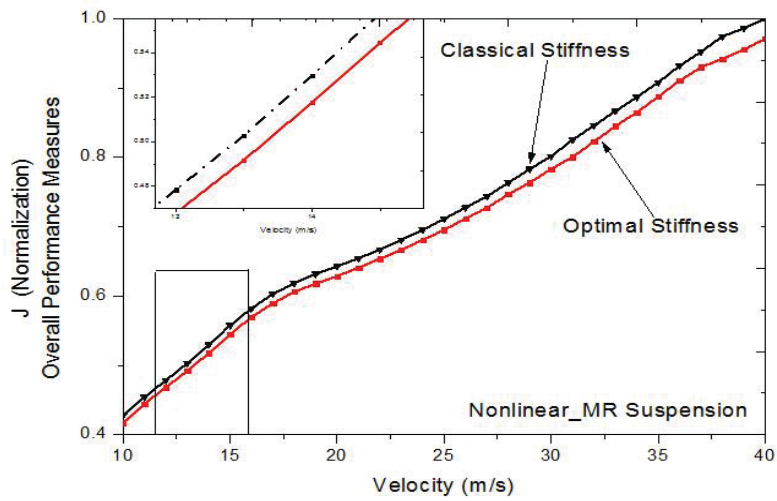


Figure 5: RMS overall performances for nonlinear model

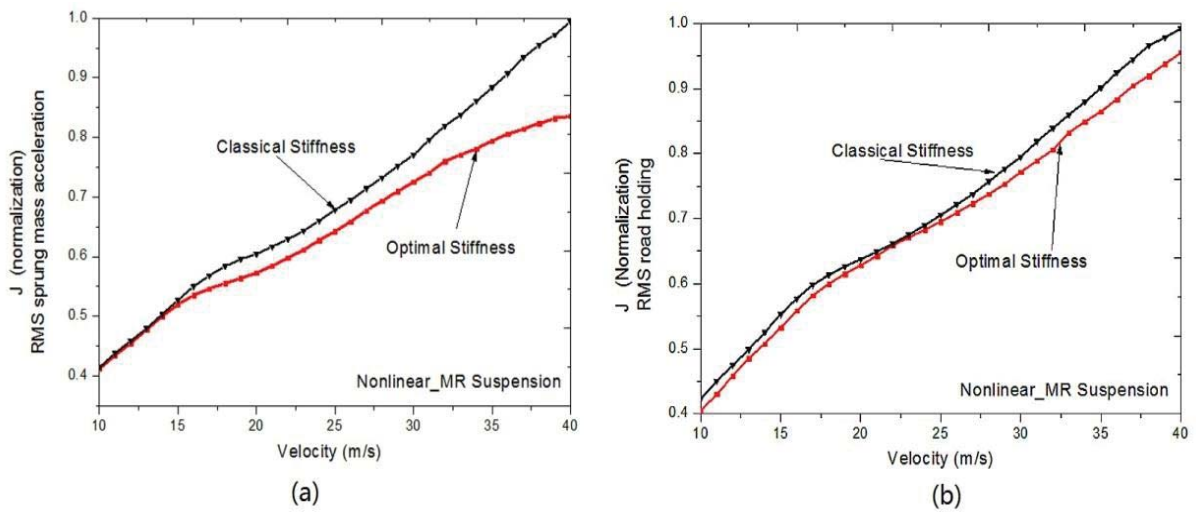


Figure 6: Single object performance of nonlinear model for (a) RMS sprung mass acceleration (b) RMS tyre dynamic loading

As a comparison, Figure 5 represents the nonlinear system overall performance. The associated nonlinear model performance value of sprung mass acceleration and tyre dynamic loading are depicted in Figure 6. For a single objective optimization shown in Figure 6, the overlap of optimal and classic data can be observed under specific vehicle speeds. The overlap effect can be explained after noting that the optimal stiffness value under specific vehicle speeds equals to the classic stiffness value as a reference coincidentally. More specifically, in terms of sprung mass acceleration, overlap is happened in the low vehicle speed region, while the overlap of tyre dynamic loading data can be observed in the medium vehicle speed area. Whether this phenomenon happens or not depends on the reference stiffness value we chosen. In general, after completing vehicle suspension stiffness optimization process, it can be predicted that the suspension performance can be improved in most traveling conditions.

4. Conclusion

Two major factors including improving vehicle comfort and reducing tire dynamic load were considered when optimizing the vehicle suspension. A two degree of freedom quarter-car model was established. Then, the analytical method was applied to solve the linear model problem. Simultaneously, the response of a quarter-car model with MR damper traveling the A level road with constant velocity is considered. The modified Bouc-Wen model is applied to evaluate the hysteretic behaviour of the MR damper. It can be seen from the simulation results that there is an obvious difference between the suspension performance under optimal stiffness value and the one under classic constant stiffness value. Therefore, changing stiffness based on different road profile conditions and the vehicle speeds is meaningful in practical application. Further study on real-time control of stiffness and damping based on the developed semi-active suspension will be considered and tested in the next step.

References

- [1] W.-Q. Ren, Y.-Q. Zhang, and G.-D. Jin, "Systematic research method for vehicle-generated road damage," *Zhongguo Gonglu Xuebao(China Journal of Highway and Transport)*, vol. 18, pp. 110-114, 2005.
- [2] G. Georgiou, G. Verros, and S. Natsiavas, "Multi-objective optimization of quarter-car models with a passive or semi-active suspension system," *Vehicle System Dynamics*, vol. 45, pp. 77-92, 2007.
- [3] B. J. Han, X. N. Gang, C. Y. Wan, W. Lu, and S. C. Zhi, "Multi-objective optimization design of passive suspension parameters based on collusion cooperation game theory," in *Intelligent Control and Automation (WCICA), 2010 8th World Congress on*, 2010, pp. 118-125.
- [4] Z. Michalewicz, *Genetic algorithms+ data structures= evolution programs*: Springer Science & Business Media, 1996.
- [5] T. Dahlberg, "An optimized speed-controlled suspension of a 2-DOF vehicle travelling on a randomly profiled road," *Journal of sound and vibration*, vol. 62, pp. 541-546, 1979.
- [6] G. Verros, S. Natsiavas, and C. Papadimitriou, "Design optimization of quarter-car models with passive and semi-active suspensions under random road excitation," *Journal of Vibration and Control*, vol. 11, pp. 581-606, 2005.
- [7] M. Shinozuka and G. Deodatis, "Simulation of stochastic processes by spectral representation," *Applied Mechanics Reviews*, vol. 44, pp. 191-204, 1991.
- [8] H. Du, J. Lam, K. Cheung, W. Li, and N. Zhang, "Direct voltage control of magnetorheological damper for vehicle suspensions," *Smart Materials and Structures*, vol. 22, p. 105016, 2013.
- [9] S. Türkyay and H. Akçay, "A study of random vibration characteristics of the quarter-car model," *Journal of sound and vibration*, vol. 282, pp. 111-124, 2005.
- [10] B. Spencer, S. Dyke, M. Sain, and J. Carlson, "Phenomenological model for magnetorheological dampers," *Journal of engineering mechanics*, vol. 123, pp. 230-238, 1997.
- [11] Y.-h. LIU, F. LI, and Y.-h. HUANG, "Numerical simulation methods of railway track irregularities," *Journal of Traffic and Transportation Engineering*, vol. 6, pp. 29-33, 2006.
- [12] L. D. Lutes, *Stochastic analysis of structural and mechanical vibrations*: Prentice Hall, 1997.
- [13] D. Karnopp, "How significant are transfer function relations and invariant points for a quarter car suspension model?," *Vehicle system dynamics*, vol. 47, pp. 457-464, 2009.
- [14] Ö. Gündoğdu, "Optimal seat and suspension design for a quarter car with driver model using genetic algorithms," *International Journal of Industrial Ergonomics*, vol. 37, pp. 327-332, 2007.

Reliability-Based Microstructural Topology Design with Respect to Vibro-Acoustic Criteria

Jianbin Du¹, Chuangchuang Sun²

¹ Tsinghua University, Beijing, China, dujb@tsinghua.edu.au

² Beihang University, Beijing, China, chuangchuang.sun@gmail.com

1. Abstract

A reliability-based vibro-acoustic microstructural topology optimization model taking into consideration the uncertainty of several selected design-independent parameters, such as the direction of the load, the frequency of the excitation, or their combinations is presented. The design objective is minimization of the sound power radiation from the macro vibrating composite structure that is assumed to be constructed by periodic micro unit cell filled up with two prescribed isotropic materials. A design process consisting of the serial execution of the uncertainty analysis and vibro-acoustic microstructural topology optimization is proposed. Numerical examples show that the uncertainty of the excitation frequency plays more important role in the vibro-acoustic microstructural design in comparison with the uncertainty of the loading direction. It is also shown that the optimum microstructural topology is not so sensitive to perturbation of the loading direction when the normalized variable corresponding to the excitation frequency takes the higher value, i.e. the optimum design is robust for perturbation of both the excitation frequency and the loading direction.

2. Keywords: Microstructural topology optimization; vibro-acoustic criteria; reliability index; uncertainty analysis; bi-material interpolation.

3. Introduction

During the past two decades, several important reliability-based models have been developed and applied to structural optimization, such as the (concurrent) RBDO model, RBSO model and RBTO model [1-4]. In the aspect of the RBTO model, Kharmanda et al. [4] considered the uncertainty of the material elasticity, structural thickness and loading in minimum compliance topology design, and their studies show that the RBTO model normally yields more reliable structures in comparison with the deterministic topology optimization model. Maute et al. [5] applied the first order reliability analysis method to the topology optimization of the compliant micro-electro-mechanical (MEMS) mechanism taking into account the uncertainty of the loading, boundary and material properties. Kang et al. [6] studied the non-probabilistic reliability-based topology optimization problem of the geometrically nonlinear structure. Applications of the RBTO model in thermal system and multi-physics system can be found in the Refs [7-8]. More introduction of the RBTO model may refer to the paper [9]. On the other hand, microstructural topology designs have also drawn a lot of attentions and have been applied to the fields of multi-physics and multi-scales [10-17]. However, up to now there are very few studies concerning the RBTO model combined with the microstructural designs, especially the vibro-acoustic microstructural designs.

The present paper aims at developing a reliability-based vibro-acoustic microstructural topology optimization model taking into account the uncertainty of the load direction, the excitation frequency or their combinations. The paper is organized as follows: Section 4 gives a brief introduction of the probabilistic reliability-based optimization model, and then the reliability-based vibro-acoustic microstructural topology optimization model and the corresponding solution method are presented and discussed in detail in Section 5. Several numerical examples are provided in Section 6 to validate the proposed method and some interesting features are discussed.

4. Optimization Considering Uncertainty

One way of considering the uncertainty of the model is introduction of the stochastic variables described by probability distribution function. A simple way to perform the uncertainty analysis is to introduce a reliability index β and meanwhile transform the random variable \mathbf{y} from the physical space to the normalized variable $\boldsymbol{\mu}$ in the standard space via probabilistic transformation [4, 18], i.e. $\boldsymbol{\mu} = T(\mathbf{x}, \mathbf{y})$, by which the optimization problem under uncertainty may be stated as a nested optimization problem:

$$\begin{aligned} & \min_{\mathbf{x}} \{f(\mathbf{x}, \mathbf{y})\} \\ & \text{s.t. } \beta(\boldsymbol{\mu}) = -\Phi^{-1}(P_f(\mathbf{y})) \geq \bar{\beta} \\ & \text{where } \beta = \min \|\boldsymbol{\mu}\|, \quad \text{s.t. } H(\mathbf{x}, \boldsymbol{\mu}) \leq 0 \end{aligned} \quad (1)$$

where Φ denotes the standard Gaussian cumulated function and $H(\mathbf{x}, \boldsymbol{\mu})$ corresponds to the limit state function in the standard space. If the random variables are dependent on the design variables, which imply that the limit state surface $H(\mathbf{x}, \mathbf{y}) = 0$ may change as the design variables change, solution of problem (1) requires alternating iterations between the reliability analysis of the inner layer and the optimization of the external layer.

5. Reliability-Based Vibro-Acoustic Bi-Material Microstructural Topology Optimization

5.1. Optimization Model

In this Section, the SIMP based vibro-acoustic bi-material microstructural topology optimization model including uncertainty parameters is established to implement the reliability-based zero-one design at the micro-scale. The element material volume density κ_i of the micro unit cell plays the role of the design variable. Each point of the macrostructure is assumed to be constructed by periodically arranged identical microstructure, and hereby the homogenization method may be used to calculate the equivalent material properties of the macrostructure.

Two classes of uncertainty parameters are considered and treated as random variables, i.e. the loading direction angle θ and the excitation frequency ω_p . It is noticed that the random variables here are design-independent (which is normally true in RBTO problem [4]), and thus the alternating iterations between the reliability analysis and the topology optimization may be avoided. Following the similar notations and assumptions as the Refs. [16, 19-21], the Reliability-Based Microstructural Topology Optimization (RBMTO) model for minimization of the sound power Π of the vibrating structure may be formulated in a discrete form as:

$$\begin{aligned} \min_{\boldsymbol{\kappa}} \left\{ \Pi(\boldsymbol{\kappa}, \mathbf{y}(\boldsymbol{\mu})) = \int_S \frac{1}{2} \operatorname{Re}(p_f v_n^*) dS = \frac{1}{2} \gamma_f c \omega_p^2 \mathbf{U}^* \mathbf{S}_n \mathbf{U} \right\} \\ \text{s.t. } \beta(\boldsymbol{\mu}) \geq \bar{\beta}, \\ (\mathbf{K} + i\omega_p \mathbf{C} - \omega_p^2 \mathbf{M}) \mathbf{U} = \mathbf{P}, \\ p_f = \gamma_f c v_n, \text{ (on S)} \\ \sum_{i=1}^{n_e} \kappa_i V_i - V^1 \leq 0, \quad (V^1 = \gamma V_0), \\ 0 \leq \kappa_i \leq 1, \quad (i = 1, \dots, n_e). \end{aligned} \quad (2)$$

where the symbol $\bar{\beta}$ is the prescribed target value of the reliability index, and the symbols \mathbf{y} and $\boldsymbol{\mu}$ are the vectors of the random variables and the corresponding normalized variables. The other symbols may refer to [16]. The extended bi-material SIMP model [16, 22-23] is applied to the micro unit cell to implement the zero-one microstructural design. The adjoint method is employed to perform the sensitivity analysis [16] and the MMA method [24] is used to solve the optimization model.

5.2. Reliability Analysis

Under the assumption that the random variables satisfy the Gaussian distribution, the reliability analysis may be performed in a straightforward way [4], where \mathbf{y} is calculated using the following transformation

$$y_j = E(y_j) + \sigma(y_j) \cdot \mu_j, \quad (j = 1, \dots, J) \quad (3)$$

and

$$\beta = \min_{\text{s.t. } \beta(\boldsymbol{\mu}) \geq \bar{\beta}} \left\{ d(\boldsymbol{\mu}) = \sqrt{\sum_{j=1}^J \mu_j^2} \right\}. \quad (4)$$

Here $E(y_j)$ and $\sigma(y_j)$ are the mean value and the standard deviation of the j th random variable y_j . For a prescribed target value $\bar{\beta}$ of the reliability index, the normalized variables may be calculated by Eq. (4), and then the random variable \mathbf{y} may be evaluated by Eq. (3). The normalized variable μ_j takes the same sign as the derivative of the objective function with respect to the mean value, i.e. $\frac{d\Pi}{dE(y_j)}$ in the present paper, which implies that the optimization will aim at improving the worst case.

5.3. Flow Chart of the Design Process

The design process of the reliability-based vibro-acoustic microstructural topology optimization is given in Fig. 1.

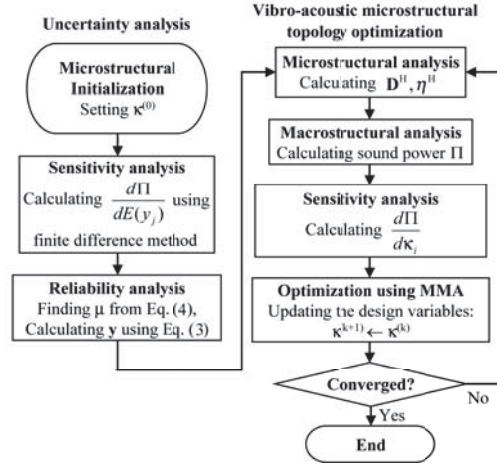


Figure 1: Flow chart of the reliability-based vibro-acoustic microstructural topology design

6. Numerical Examples

6.1. Example 1 - Minimization of the Sound Power Flow Considering Single Uncertainty Parameter

The first example concerns design of minimization of the sound power radiated from a simply supported vibrating composite beam-like structure subjected to the uniformly distributed harmonic pressure loading with the amplitude 1kN/m at the upper surface (see Fig. 2). The micro unit cell and the macrostructure are divided by 40×40 and 10×3 mesh using 8-node isoparametric elements respectively. The uncertainty parameter considered here is the excitation frequency ω_p . The mean value of the excitation frequency is $E(\omega_p) = 600 \text{ rad/s}$ and the standard deviation is $\sigma(\omega_p) = E(\omega_p)/10$. The Young's modulus, the Poisson's ratio and the mass density of the two prescribed solid materials are $E^1 = 210 \text{ GPa}$, $\nu^1 = 0.3$, $\eta^1 = 7800 \text{ kg/m}^3$, $E^2 = E^1/10$, $\nu^2 = \nu^1$ and $\eta^2 = \eta^1/10$. The upper limit of the material volume fraction γ of the stiffer material is set as 50%. The damping is ignored here.

Five different values of the reliability index β are tested and the corresponding optimum microstructural topologies are given in Table 1. The iteration histories of the objective function corresponding to different values of the reliability index β are shown in Fig. 3, where the unit of the sound power is transferred from "W" to "dB" by $10 \cdot \lg(\Pi/\Pi_0)$, and the reference value of the sound power $\Pi_0 = 10^{-12} \text{ W}$. It can be seen from Fig. 3 that the optimum value of the sound power becomes higher as the reliability of the design increases, i.e. the design of RBTO makes a balance between the performance and the reliability. The effect of the material volume fraction on the design is also studied. The optimum topologies corresponding to five different values of the material volume fraction α are shown in Table 2, where the reliability index takes the fixed value $\beta = 3$.

Another design case with different boundary and loading conditions (see Fig. 4) are studied. The configurations of the mesh, materials and uncertainty parameter are the same as Fig. 2. The optimum microstructural topologies corresponding to five different values of the reliability index β are given in Table 3.

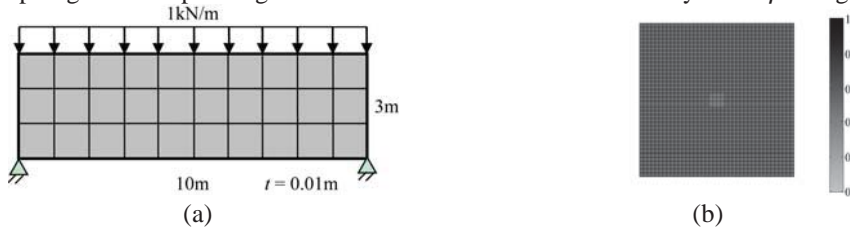


Figure 2: Simply supported beam. (a) Configuration, boundary and loading conditions of the macro beam; (b) Initial material distribution within the micro unit cell.

Table 1: Optimum microstructural topologies corresponding to five different values of reliability index ($\gamma = 0.5$) (Uncertainty parameter: excitation frequency, $E(\omega_p) = 600 \text{ rad/s}$, $\sigma(\omega_p) = E(\omega_p)/10$)

Optimum topology of the unit cell	$\beta = 0$ (deterministic design)	$\beta = 0.8$	$\beta = 1.5$	$\beta = 2.5$	$\beta = 3$
1 by 1 array					

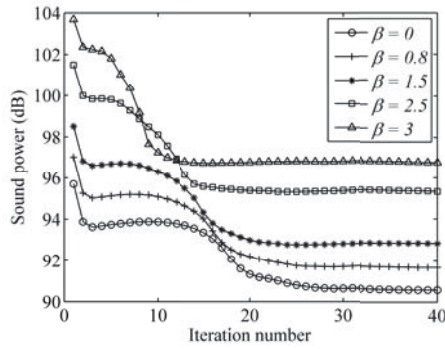


Figure 3: Iteration histories of the objective function corresponding to five different values of reliability index (Uncertainty parameter: excitation frequency, $E(\omega_p) = 600\text{rad/s}$, $\sigma(\omega_p) = E(\omega_p)/10$).

Table 2: Optimum microstructural topologies corresponding to different values of material volume fraction ($\beta = 3$) (Uncertainty parameter: excitation frequency ω_p , $E(\omega_p) = 600\text{rad/s}$, $\sigma(\omega_p) = E(\omega_p)/10$)

Optimum topology of the unit cell	$\gamma = 0.2$	$\gamma = 0.3$	$\gamma = 0.4$	$\gamma = 0.5$	$\gamma = 0.6$
1 by 1 array					
6 by 6 array					

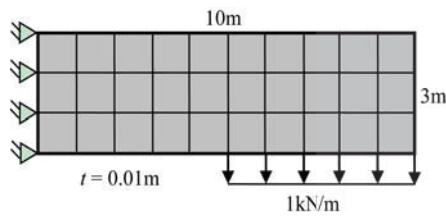


Figure 4: Cantilever beam subjected to bending loads.

Table 3: Optimum microstructural topologies corresponding to different values of reliability index ($\gamma = 0.5$) (Uncertainty parameter: excitation frequency ω_p , $E(\omega_p) = 600\text{rad/s}$, $\sigma(\omega_p) = E(\omega_p)/10$)

Optimum topology of the unit cell	$\beta = 0$ (deterministic design)	$\beta = 0.8$	$\beta = 2$	$\beta = 2.5$	$\beta = 3$
1 by 1 array					
6 by 6 array					

6.2. Example 2 - Minimization of the Sound Power Flow Considering Multiple Uncertainty Parameters

In this example, two uncertainty parameters, i.e. the excitation frequency ω_p and the loading direction angle θ are considered simultaneously in the design. The normalized variables denoted by μ_1 and μ_2 correspond to the two uncertainty parameters ω_p and θ . The reliability index takes the fixed value $\beta = 3$. The other parameter configurations are the same as those associated with Fig. 2 in the first example of Section 6.1.

The designs with respect to different combination values of the normalized variables but the fixed value 3 of the reliability index are performed, and the corresponding optimum microstructural topologies are shown in Fig. 5. It is seen that different optimum designs may have the same reliability (i.e. the same value of the reliability index) when more than one uncertainty parameters are considered. It can also be seen that when μ_1 takes a higher value, e.g. $\mu_1 > 2$, the change of the optimum microstructural topology is small since the change of the value of μ_1 gets smaller (from 2 to 3), while the interesting thing is, the change of the value of μ_2 is larger (from $\sqrt{5}$ to 0), which implies that the uncertainty design in the present stage is dominated by the excitation frequency and the design is not so sensitive to the uncertainty of the load. The optimum objective function values corresponding to different combination values of the normalized variables are given in Table 4. In order to get an overall sight, the interpolation surface of the optimum objective function with respect to (μ_1, μ_2) is also given in Table 4. It can be seen that the worst case happens at $(\mu_1=3, \mu_2=0)$. This implies that the uncertainty of the excitation frequency is more important than that of the loading direction for a given value 3 of the reliability index in the vibro-acoustic microstructural topology design.

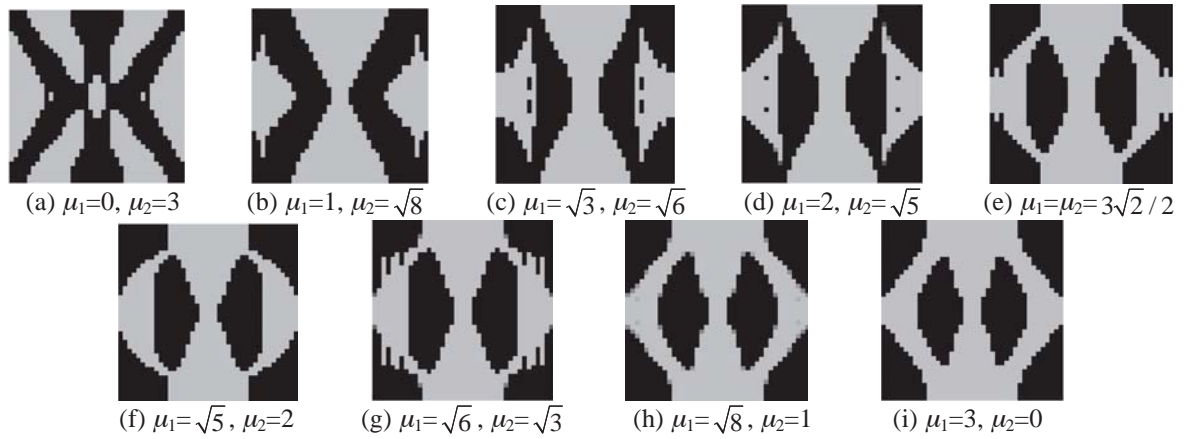


Figure 5: Optimum topologies of the unit cells corresponding to different combination values of normalized variables ($\beta = 3$; $\gamma = 0.5$); (Uncertainty parameter 1: ω_p , $E(\omega_p) = 600\text{rad/s}$, $\alpha(\omega_p) = E(\omega_p)/10$; normalized variable 1: μ_1); (Uncertainty parameter 2: θ , $E(\theta) = -90^\circ$, $\alpha(\theta) = E(\theta)/10$; normalized variable 2: μ_2)

Table 4: Optimum objective function values corresponding to different combination values of normalized variables ($\beta = 3$)

(μ_1, μ_2)	Π^{opt}/W	Interpolation surface of objective function: Π^{opt} vs. (μ_1, μ_2)
$(0, 3)$	0.1358×10^{-3}	
$(1, \sqrt{8})$	0.1779×10^{-3}	
$(\sqrt{3}, \sqrt{6})$	0.2227×10^{-3}	
$(2, \sqrt{5})$	0.2522×10^{-3}	
$(3\sqrt{2}/2, 3\sqrt{2}/2)$	0.2626×10^{-3}	
$(\sqrt{5}, 2)$	0.2857×10^{-3}	
$(\sqrt{6}, \sqrt{3})$	0.3277×10^{-3}	
$(\sqrt{8}, 1)$	0.4121×10^{-3}	
$(3, 0)$	4.7440×10^{-3}	

7. Conclusions

The reliability-based vibro-acoustic microstructural topology optimization model is developed and solved. The effects of single and multiple uncertainty parameters on the optimum microstructural topologies are studied in

detail and several interesting features are revealed. It is found that the uncertainty of the excitation frequency plays more important role in the vibro-acoustic microstructural design in comparison with the uncertainty of the loading direction.

8. Acknowledgements

The work is supported by National Natural Science Foundation of China (11372154)

9. References

- [1] G. Kharmanda, A. Mohamed and M. Lemaire, New hybrid formulation for reliability-based optimization of structures. In: *Proc. WCSMO-4*, Dalian, China, 2001.
- [2] G. Kharmanda, A. Mohamed and M. Lemaire, CAROD: Computer-aided reliable and optimal design as a concurrent system for real structures, *Int. J. CAN/CAM*, 2, 1-22, 2002.
- [3] G. Kharmanda, A. Mohamed and M. Lemaire, Efficient reliability-based design optimization using a hybrid space with application to finite element analysis, *Struct Multidisc Optim*, 24, 233-245, 2002.
- [4] G. Kharmanda, N. Olhoff, A. Mohamed, et al., Reliability-based topology optimization, *Struct Multidisc Optim*, 26, 295-307, 2004.
- [5] K. Maute and D.M. Frangopol, Reliability-based design of MEMS mechanisms by topology optimization, *Comput. Struct.*, 81, 813-824, 2003.
- [6] Z. Kang and Y. Luo, Non-probabilistic reliability-based topology optimization of geometrically nonlinear structures using convex models, *Comput Methods Appl Mech Engrg*, 198, 3228-3238, 2009.
- [7] H. Moon, C. Kim and S. Wang, Reliability-based topology optimization of thermal systems considering convection heat transfer, *10th AIAA/ISSMO Multidisciplinary Analysis and Optimization Conference*, Albany, New York, 2004.
- [8] S. Wang, H. Moon, C. Kim, J. Kang and K. Choi, Reliability-based topology optimization (RBTO), *IUTAM Symposium on Topological Design Optimization of Structures, Machines and Materials, Solid Mech. Appl.*, 137, 493-504, 2006.
- [9] X. Guo and G.D. Cheng, Recent development in structural design and optimization, *Struct Multidisc Optim*, 26(6), 807-823, 2010.
- [10] D. Fujii, B.C. Chen and N. Kikuchi, Composite material design of two-dimensional structures using the homogenization design method, *Int J Numer Methods Eng*, 50(9), 2031-2051, 2001.
- [11] H.C. Rodrigues, J.M. Guedes and M.P. Bendsoe, Hierarchical optimization of material and structure, *Struct Multidisc Optim*, 24(1), 1-10, 2002.
- [12] S.T. Liu, G.D. Cheng, Y. Gu and X.G. Zheng, Mapping method for sensitivity analysis of composite material property, *Struct Multidisc Optim*, 24(3), 212-217, 2002.
- [13] L. Liu, J. Yan and G.D. Cheng, Optimum structure with homogeneous optimum truss-like material, *Comput Struct*, 86(13-14), 1417-1425, 2008.
- [14] B. Niu, J. Yan and G.D. Cheng, Optimum structure with homogeneous optimum cellular material for maximum fundamental frequency, *Struct Multidisc Optim*, 39(2), 115-132, 2009.
- [15] S.L. Xu and G.D. Cheng, Optimum material design of minimum structural compliance under seepage constraint, *Struct Multidisc Optim*, 41(4), 575-587, 2010.
- [16] R.Z. Yang and J.B. Du, Microstructural topology optimization with respect to sound power radiation, *Struct Multidisc Optim*, 47(2), 191-206, 2013.
- [17] J.B. Du and R.Z. Yang, Vibro-acoustic design of plate using bi-material microstructural topology optimization, *Journal of Mechanical Science and Technology*, 29(4), 1-7, 2015.
- [18] A.M. Hasofer and N.C. Lind, An exact and invariant first order reliability format, *J. Eng. Mech., ASCE, EMI* 100, 111-121, 1974.
- [19] J.B. Du and N. Olhoff, Minimization of sound radiation from vibrating bi-material structures using topology optimization, *Struct Multidisc Optim*, 33(4-5), 305-321, 2007.
- [20] J.B. Du and N. Olhoff, Topological design of vibrating structures with respect to optimum sound pressure characteristics in a surrounding acoustic medium, *Struct Multidisc Optim*, 42(1), 43-54, 2010.
- [21] J.B. Du, X.K. Song and L.L. Dong, Design of material distribution of acoustic structure using topology optimization, *Chin J Theor Appl Mech*, 43(2), 306-315, 2011.
- [22] G.I.N. Rozvany, M. Zhou and T. Birker, Generalized shape optimization without homogenization, *Struct Optim*, 4(3-4), 250-252, 1992.
- [23] O. Sigmund, Materials with prescribed constitutive parameters: an inverse homogenization, *Int J Solids Struct*, 31(17), 2313-2329, 1994.
- [24] K. Svanberg, The method of moving asymptotes - a new method for structural optimization, *Int J Numer Methods Eng*, 24(2), 359-373, 1987.

A new topology optimization algorithm for photonic band gap structures

Fei Meng¹, Xiaodong Huang¹, Baohua Jia²

¹Centre of Innovative Structures and Materials, School of Civil, Environmental and Chemical Engineering, RMIT University, GPO Box 2476, Melbourne 3001, Australia Melbourne, Australia, huang.xiaodong@rmit.edu.au

²Centre for Micro-Photonics, Faculty of Engineering & Industrial Science, Swinburne University of Technology, GPO Box 218, Hawthorn, Victoria, 3122 Australia

1. Abstract

A new topology optimization algorithm is proposed based on bi-directional evolutionary structural optimization (BESO) method in order to design photonic crystals with maximum band gaps. The optimization process starts from a simple unit cell without band gap, and the photonic crystals are assumed to be periodically composed of two materials with different permittivity. Based on finite element analysis, the BESO algorithm gradually re-distributes dielectric materials within the unit cell until the resulting photonic crystals possess a maximal band gap at appointed position in the band diagram. Numerical results are presented to demonstrate the effectiveness of the proposed optimization algorithm.

2. Keywords: Topology optimization; photonic band gap; bi-directional evolutionary structural optimization (BESO).

3. Introduction

Photonic crystals are optical structures consist of dielectric materials with different refractive indexes. They have lattice constants and periodicity on the wavelength scale in one, two or three dimensions. Photonic crystals are also called photonic band gap (PBG) structures because of their ability of prohibiting the propagation of electromagnetic waves within certain frequency ranges [1]-[2]. In practice, a broader band gap means broader available bandwidth of electromagnetic signals, therefore it is of great significance to design photonic crystals with large band gap. The optical properties of photonic crystals depend not only on the properties of dielectric materials but also on their spatial distributions. For given materials, the design of photonic crystals becomes a typical topology optimization question: how to periodically distribute the materials to maximize the band gap. Due to the polarization of electromagnetic waves, both transverse magnetic polarization (TM modes) and transverse electric polarization (TE modes) should be considered, respectively or simultaneously.

The traditional design approach of photonic band gap structures is a trial-and-error process based on physical intuitions and parametric study. This process can be inefficient and time-consuming [3]. To get photonic crystals with larger band gaps, different topology optimization methods have been introduced, for example, level set method [4], genetic algorithm [5], evolutionary algorithm [6] and semidefinite programming method [7]. These methods have been proved to be useful and many interesting results have been obtained. However, the optimization method starts from an initial design with band gap [6] or a randomly generated initial topology, which makes the method less efficient.

In this paper a new approach based on bi-directional evolutionary structural optimization (BESO) method [9] is proposed to optimize the design of 2D photonic crystal. BESO and its former version evolutionary structural optimization (ESO) are structural optimization method based on finite element analysis. The basic concept of ESO [8] is to achieve the optimal structural topology by gradually removing inefficient materials from initial ground structure. In BESO, materials can not only be removed, but also added to the structure based on the sensitivity analysis. The BESO algorithm proposed by Huang and Xie [9] has been successfully applied to the optimization of mechanical structures, property of electromagnetic materials, and natural frequencies of vibrating structures.

To apply the BESO method, the unit cell of a photonic crystal is meshed into elements and represented by discrete design variables respectively. A simple initial topology without band gap is adopted. The ratio of band gap between two appointed adjacent bands and midgap value is maximized as the objective function. Then sensitivity analysis of the objective function is conducted and a mesh-independency filter is adopted to stabilize the sensitivity number. Based on sensitivity numbers, BESO algorithm gradually evolves the topology of the unit cell until the assigned band gap is successfully obtained and maximized.

4. Topology optimization problem

4.1 Finite element analysis for photonic crystals

Electromagnetic wave propagation in photonic crystals is governed by Maxwell's equations. In 2D cases, there are two possible polarizations of the magnetic and electric fields, namely TM (transverse magnetic) and TE (transverse electric) modes. In TM modes, the magnetic field is confined to the plane of wave propagation and the electric field $E = (0, 0, E)$ is perpendicular to this plane. In contrast, in TE modes, the electric field is confined to the plane of wave propagation and the magnetic field $H = (0, 0, H)$ is perpendicular to this plane. It is assumed that there are no point sources or sinks of electric displacement and magnetic fields in photonic crystal, the time-harmonic Maxwell equations can be decoupled and reduce to two independent equations:

$$-\nabla \cdot (\nabla E) = \varepsilon \left(\frac{\omega}{c} \right)^2 E \quad \text{for TM modes} \quad (1)$$

$$-\nabla \cdot \left(\frac{1}{\varepsilon} \nabla H \right) = \left(\frac{\omega}{c} \right)^2 H \quad \text{for TE modes} \quad (2)$$

where c is the speed of light, ω is the angular frequency of the electromagnetic wave and $\varepsilon(x)$ is the dielectric function. Due to the periodicity of the crystal, the dielectric function satisfies $\varepsilon(x) = \varepsilon(x+X)$, where X is the lattice translation vector.

According to Bloch-Floquet theory, the magnetic and electric fields can be represented as the product of a periodic function and an exponential factor as $H(x) = H_k(x)\exp(ikx)$ and $E(x) = E_k(x)\exp(ikx)$. The Maxwell equations can be converted to eigenvalue problems within a unit cell and only the wave vector k on the boundary of irreducible Brillouin zone needs to be considered for band diagram.

$$-(\nabla + ik) \cdot ((\nabla + ik)E_k) = \varepsilon \left(\frac{\omega}{c} \right)^2 E_k \quad \text{for TM modes} \quad (3)$$

$$-(\nabla + ik) \cdot \left(\frac{1}{\varepsilon} (\nabla + ik)H_k \right) = \left(\frac{\omega}{c} \right)^2 H_k \quad \text{for TE modes} \quad (4)$$

By discretizing the unit cell into square elements as in Fig.1, the above equations can be transformed into matrix format through the usual finite element method (FEM) procedure:

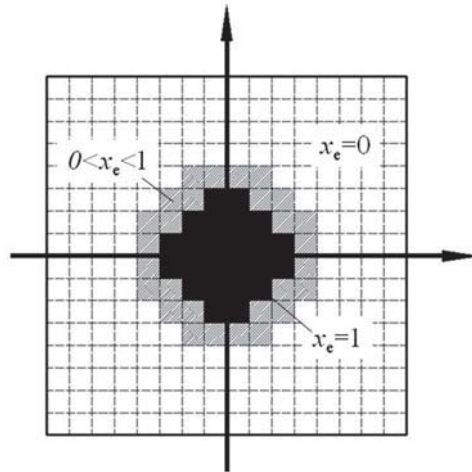


Figure 1: Discretization of a unit cell by square elements

$$\left(\sum_e K^e \right) E = \left(\frac{\omega}{c} \right)^2 \left(\sum_e \varepsilon_e M^e \right) E \quad \text{for TM modes} \quad (5)$$

$$\left(\sum_e \frac{1}{\varepsilon_e} K^e \right) H = \left(\frac{\omega}{c} \right)^2 \left(\sum_e M^e \right) H \quad \text{for TE modes} \quad (6)$$

where e denotes the number of element, and H and E are the eigenvectors for the magnetic and electric fields, respectively. K^e can be expressed by

$$K^e = K_1 + K_2 + K_3 + K_4 \quad (7)$$

where, $K_1 = \int_A \left(\frac{\partial N^T}{\partial x} \frac{\partial N}{\partial x} + \frac{\partial N^T}{\partial y} \frac{\partial N}{\partial y} \right) dA$

$$\mathbf{K}_2 = ik_x \int_A \left(\frac{\partial \mathbf{N}^T}{\partial x} \mathbf{N} - \mathbf{N}^T \frac{\partial \mathbf{N}}{\partial x} \right) dA$$

$$\mathbf{K}_3 = ik_y \int_A \left(\frac{\partial \mathbf{N}^T}{\partial y} \mathbf{N} - \mathbf{N}^T \frac{\partial \mathbf{N}}{\partial y} \right) dA$$

$$\mathbf{K}_4 = (k_x^2 + k_y^2) \int_A \mathbf{N}^T \mathbf{N} dA$$

\mathbf{M}^e is expressed by

$$\mathbf{M}^e = \int_A \mathbf{N}^T \mathbf{N} dA \quad (8)$$

where A denotes the total area of an element. The general form of Eqs. (5) and (6) can be expressed as

$$\mathbf{K} \mathbf{u} = \left(\frac{\omega}{c} \right)^2 \mathbf{M} \mathbf{u} \quad (9)$$

Where

$$\mathbf{K} = \left(\sum_e \mathbf{K}^e \right), \quad \mathbf{M} = \left(\sum_e \varepsilon_e \mathbf{M}^e \right) \quad \text{for TM modes} \quad (10)$$

$$\mathbf{K} = \left(\sum_e \frac{1}{\varepsilon_e} \mathbf{K}^e \right), \quad \mathbf{M} = \left(\sum_e \mathbf{M}^e \right) \quad \text{for TE modes} \quad (11)$$

Through sweeping wave vector (k_x , k_y) along the boundary of the first Brillouin zone, we can obtain the band diagram of a specific photonic crystal.

4.2 Objective function

Due to the lack of fundamental length scale in Maxwell's equation, the band gap-midgap ratio, which is independent of the lattice constant of the photonic crystal, is more useful than the absolute value of band gap. Therefore, the objective function in designing photonic structures is to maximize the band gap-midgap ratio between two adjacent bands (referred as band i and band $i+1$) as

$$f(\mathbf{X}) = 2 \frac{\min \omega_{i+1}(\mathbf{k}) - \max \omega_i(\mathbf{k})}{\min \omega_{i+1}(\mathbf{k}) + \max \omega_i(\mathbf{k})} \quad (12)$$

Where $\mathbf{X} = [x_1 \ x_2 \ \dots \ x_n]$ is the design variable, n is the total number of elements. For a bi-material photonic crystal optimization, the problem can be stated as

$$\text{Maximize: } f(\mathbf{X}) \quad (13)$$

$$\text{Subject to: } x_e = 0 \text{ or } 1$$

As shown in Fig.1, design variable $x_e = 0$ denotes material 1 with low permittivity and $x_e = 1$ denotes material 2 with high permittivity. In order to get a stable and reliable optimization process, x_e is a discrete value between 0 and 1 with a custom step size. The permittivity ε of element e is interpolated by following functions.

$$\varepsilon(x_e) = \varepsilon_1(1 - x_e) + \varepsilon_2 x_e \quad \text{for TM modes} \quad (14)$$

$$\varepsilon(x_e) = \frac{1}{(1 - x_e)/\varepsilon_1 + x_e/\varepsilon_2} \quad \text{for TE modes} \quad (15)$$

where ε_1 and ε_2 are the permittivity of materials 1 and 2 respectively.

4.3 sensitivity number

For objective function (12), the sensitivity number for element e can be expressed as

$$\alpha = \frac{\partial f(\mathbf{X})}{\partial x_e} = 4 \frac{\omega_{\text{bot}} \frac{\partial \omega_{\text{top}}}{\partial x_e} - \omega_{\text{top}} \frac{\partial \omega_{\text{bot}}}{\partial x_e}}{(\omega_{\text{top}} + \omega_{\text{bot}})^2} \quad (16)$$

where $\omega_{\text{top}} = \min_{\mathbf{k}} \omega_{i+1}(\mathbf{k})$, $\omega_{\text{bot}} = \max_{\mathbf{k}} \omega_i(\mathbf{k})$.

For a given frequency $\omega_i(\mathbf{k})$, and its corresponding eigenvector \mathbf{u}_i

$$\frac{\partial \omega_i(\mathbf{k})}{\partial x_e} = \frac{1}{2\omega_i(\mathbf{k})} \mathbf{u}_i^T \left(\frac{\partial \mathbf{K}}{\partial x_e} - (\omega_i(\mathbf{k}))^2 \frac{\partial \mathbf{M}}{\partial x_e} \right) \mathbf{u}_i \quad (17)$$

The derivatives of matrix \mathbf{K} and matrix \mathbf{M} for the finite element analysis can be calculated from the interpolation functions (14) and (15) of design variable

$$\frac{\partial \mathbf{K}}{\partial x_e} = 0, \quad \frac{\partial \mathbf{M}}{\partial x_e} = (\varepsilon_2 - \varepsilon_1) \mathbf{M}_1^e \quad \text{for TM modes} \quad (18)$$

$$\frac{\partial \mathbf{K}}{\partial x_e} = \left(\frac{1}{\varepsilon_2} - \frac{1}{\varepsilon_1} \right) (\mathbf{K}_1^e + \mathbf{K}_2^e + \mathbf{K}_3^e + \mathbf{K}_4^e), \quad \frac{\partial \mathbf{M}}{\partial x_e} = 0 \quad \text{for TE modes} \quad (19)$$

Based on the eigenfrequency and eigenvector calculated for finite element analysis, combining Eqs. (16)~(19), we can obtain the sensitivity number of each element, and then enhance existing topology by them.

5. Numerical implementation

5.1 Mesh-independency filter

Introducing a filtering scheme can effectively alleviate the numerical instabilities of the checkerboard pattern and mesh-dependency in the BESO method [11]. The modified sensitivity number of element e is

$$\hat{\alpha}_e = \frac{\sum_{i=1}^n w_i \alpha_i}{\sum_{i=1}^n w_i} \quad (20)$$

where the weight factor w_i is defined by

$$w_i = \begin{cases} r_{\min} - r_i^e, & \text{if } r_{\min} > r_i^e \\ 0, & \text{if } r_{\min} \leq r_i^e \end{cases} \quad (21)$$

where r_i^e denotes the distance between the center of element e and i . r_{\min} is the radius of the filter, defined to identify the neighboring elements that affect the sensitivity number of element i . r_{\min} is taken as 1/50 of lattice constant in this research.

In order to improve the stability and convergence of solution, elemental sensitivity numbers can be further averaged with their corresponding values in the previous iteration as

$$\tilde{\alpha}_e^k = \frac{1}{2} (\tilde{\alpha}_e^{k-1} + \hat{\alpha}_e^k) \quad (22)$$

where k is the current iteration number.

5.2 Topology evolution

The BESO process starts from an initial design filled up with material 2 which has a relative high permittivity with a pillar of material 1 in the center of the crystal lattice. The total volume of material 2, V , gradually decreases to a prescribed value V_0 , and then increases or decreases until the maximum band gap-midgap ratio is achieved. The volume of material 2 for the next iteration is calculated by

$$V_{k+1} = V_k (1 - \text{ER}) \quad \text{when } V > V_0 \quad (23)$$

$$V_{k+1} = V_k \left(1 + \frac{(f(\mathbf{X}_k) - f(\mathbf{X}_{k-1})) \cdot (V_k - V_{k-1})}{|f(\mathbf{X}_k) - f(\mathbf{X}_{k-1})| \cdot |V_k - V_{k-1}|} \text{ER} \right) \quad \text{after } V_0 \text{ is reached} \quad (24)$$

where ER is evolution rate, which is taken as 2% in this paper.

The design variables are modified according to the relative values of sensitivity numbers and target volume of material 2. Based on the relative ranking of the elemental sensitivity numbers $\tilde{\alpha}$, a threshold of the sensitivity number, α^* , is determined by using bi-section method so that the target volume of material w in the next iteration is equal to V_{k+1} . The design variable for each element is modified by comparing its sensitivity number with the threshold.

Different from other topology optimization methods with continuous design variable, BESO method uses discrete design variable. In each iteration, the variation of a design variable is a constant Δx ($\Delta x = 0.1$ is used in this paper). The design variable of element e is updated as:

$$x_e = \begin{cases} \min(x_e + \Delta x, 1), & \text{if } \tilde{\alpha}_e > \alpha^* \\ \max(x_e - \Delta x, 0), & \text{if } \tilde{\alpha}_e < \alpha^* \end{cases} \quad (25)$$

6. Numerical results and discussion

The 2D photonic crystal with a square lattice is considered in this paper. The photonic crystal consists of 2 materials: Vacuum background (relative permittivity $\varepsilon_1 = 1$) and GaAs (relative permittivity $\varepsilon_2 = 11.4$). The model is meshed with 64×64 bilinear square elements. The FE analysis is conducted by COMSOL Multiphysics, and the sensitivity analysis is handled in MATLAB.

The optimization process of the 7th band gap of TE modes is illustrated in Fig.2 as an example. The white color denotes air and the black color denotes GaAs. It can be seen that, at the first step, the band gap-midgap ratio is

-10.47%, which means there is no band gap at all. With the optimization continues, the band gap-midgap ratio gradually increases to a positive value and the filling ratio of GaAs gradually decreases from the initial value with almost 100%. At the end of optimization process, the band gap-midgap ratio and volume both tend to be stably convergent. The final band gap-midgap ratio is 44.27%, volume is 39.84%. The whole optimization process needs 60 iterations which demonstrate the high computational efficiency of the proposed optimization algorithm.

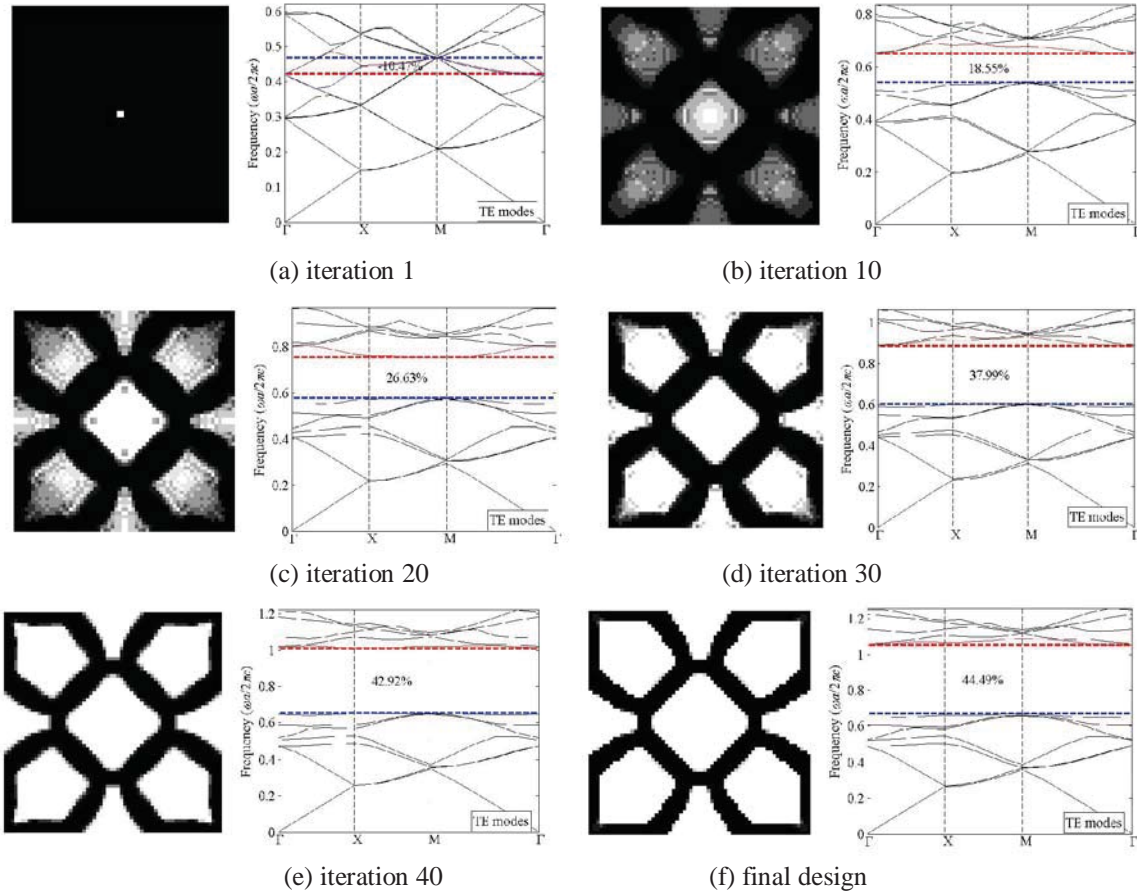
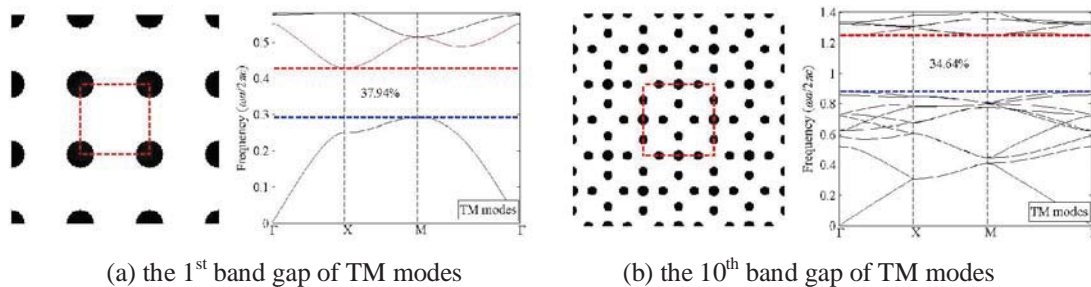


Figure 2: Evolution history of topology and band diagrams for the 7th band gap of TE modes

Figure 3 shows the optimized topologies and their corresponding diagrams for the 1st and 10th band gap of TM modes and the 1st and the 10th band gap of TE modes. From the same initial topology without band gap, the topology evolves and the band ratio increase to 37.94%, 34.64%, 28.40% and 29.56% respectively. It can be seen that the proposed BESO algorithm can robustly obtain the optimized results at both low frequency range and high frequency range.



(a) the 1st band gap of TM modes

(b) the 10th band gap of TM modes

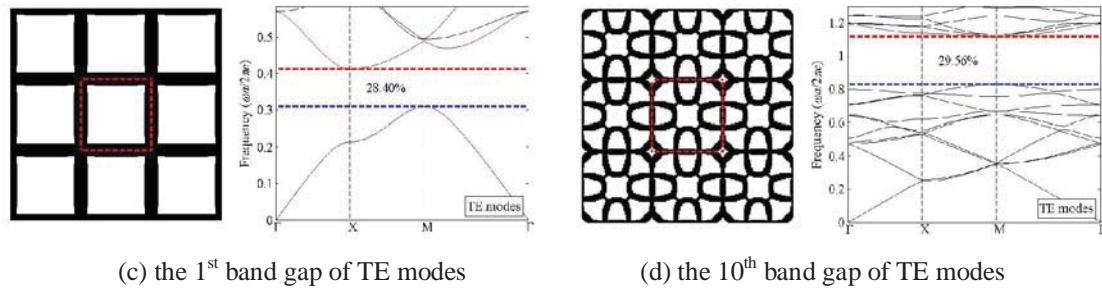


Figure 3: Optimized topologies of phononic crystals and their corresponding band diagrams

7. Conclusions

This paper investigates the topology optimization of 2D photonic crystals for both TM and TE modes. A new optimization method based on BESO is proposed to find the optimal design of photonic crystals with a maximum band gap. Based on the finite element analysis of photonic crystals, BESO gradually re-distributes the constituent material with the unit cell until the optimized band gap size is achieved. The numerical results indicate the effectiveness of the algorithm proposed in this paper for the design of photonic band gap structures. This algorithm can be further applied to other optimization problems of photonic crystals.

8. Acknowledgements

The second author is the recipient of an Australian Research Council Future Fellowship (FT130101094).

9. References

- [1] J.G. Fleming, S.Y. Lin, I. El-Kady, R. Biswas and K.M. Ho, All-metallic three-dimensional photonic crystals with a large infrared bandgap, *Nature*, 417(6884), 52-55, 2002.
- [2] J.D. Joannopoulos, S.G. Johnson, J.N. Winn and R.D. Meade, *Photonic Crystals: Molding the Flow of Light*, Princeton University Press, 2008.
- [3] M.M. Hossain, G. Chen, B. Jia, X.H. Wang and M. Gu, Optimization of enhanced absorption in 3D-woodpile metallic photonic crystals, *Optic Express*, 18(9), 9048-9054, 2010.
- [4] M.P. Bendsøe and N. Kikuchi, Generating optimal topologies in structural design using a homogenization method, *Computer Methods in Applied Mechanics and Engineering*, 71(2), 197-224, 1988.
- [5] M.P. Bendsøe, Optimal shape design as a material distribution problem, *Structural Optimization*, 1(4), 193-202 (1989).
- [6] M. Zhou and G.I.N. Rozvany, DCOC – an optimality criteria method for large systems, Part I: Theory, *Structural Optimization*, 5(1-2), 12-25, 1992.
- [7] H. Men, N.C. Nguyen, R.M. Freund, P.A. Parrilo and J. Peraire, Bandgap optimization of two-dimensional photonic crystals using semidefinite programming and subspace methods, *Journal of Computational Physics*, 229(10), 3706-3725, 2010.
- [8] Y.M. Xie and G.P. Steven, *Evolutionary Structural Optimization*, Springer, London, 1997.
- [9] X. Huang and Y.M. Xie, *Evolutionary Topology Optimization of Continuum Structures: Methods and Applications*, John Wiley & Sons, Chichester, 2010.
- [10] X. Huang, Z.H. Zuo and Y.M. Xie, Evolutionary topology optimization of vibrating continuum structures for natural frequencies, *Computers & Structures*, 88(5-6), 357-364, 2010.
- [11] X. Huang and Y.M. Xie, Bi-directional evolutionary topology optimization of continuum structures with one or multiple materials, *Computational Mechanics*, 43(6), 393-401, 2009.

Topology optimization of 2D phononic band gap crystals based on BESO methods

Yangfan Li¹, Xiaodong Huang¹, Fei Meng¹, Shiwei Zhou¹

¹Centre for Innovative Structures and Materials, School of Civil, Environmental and Chemical Engineering,
RMIT University, GPO Box 2476, Melbourne, VIC, 3001, Australia, huang.xiaodong@rmit.edu.au

1. Abstract:

Phononic band gap crystals, which could prohibit the propagations of elastic waves in certain frequency, are consisted of periodically distributed inclusions embedded in a matrix with high contrast in mechanical properties. In recent years, systematic design of phononic band gap crystals has attracted increasing attention due to their wide applications such as sound insulation, waveguides, or acoustic wave filtering. Toward an efficient and reliable optimization for phononic structures, we present a new topology optimization algorithm based on bi-directional evolutionary structural optimization (BESO) method and finite element analysis to maximize phononic band gaps. The optimization of maximizing the relative band gap size between two appointed neighbour bands starts from a unit cell without any band gap and then gradually adjusts the distribution of two materials in the following iteration steps based on the sensitivity analysis and BESO algorithm until the convergence criterions are satisfied. Various patterns of optimal phononic structures for both out-of-plane shear waves and in-plane mixed waves presented. Numerical results show that the proposed algorithm is very effective and efficient.

2. Keywords: Phononic Band Gap Crystals, Topology Optimization, Bi-directional Evolutionary Structural Optimization (BESO)

3. Introduction

Sparkled by the remarkable work on the photonic crystals (PnCs) with periodic constructions of two dielectrics composite materials, which offer control over the propagation of electromagnetic waves, the study of phononic band gap crystals was first carried out by Kushwaha in 1993 [1, 2]. In analogy to photonic crystals, phononic crystals (PnCs), which prohibit the propagation of mechanical waves in certain range of frequencies, are generally composed of periodically distributed inclusions embedded in a matrix with high contrast in elastic properties. Such novel property makes them desirable for a variety of applications, for instance, sound insulation, waveguides, acoustic wave filtering, negative refraction, shock isolations well as acoustic cloaking [3]. Thus, photonic/phononic crystals have attracted considerable interest during past few decades.

When PnCs are designed for sound insulation or shock isolation, usually it is best to have the band gap as wide as possible. Therefore, how to obtain the optimal band gap structure is of great interest here. A promising mean to achieve this goal is to utilize the topology optimization method for systematic and scientific approach of designing phononic structures. Topology optimization of phononic band gap structures was first performed by Sigmund and Jensen (2003) [4], using finite element method combined with the method of moving asymptotes (MMA) to maximize the band-gap sizes. This pioneering work only presented a few examples and lacked the analysis of coupled problem of in-plane and out-of-plane waves. Later a genetic algorithm (GA) in conjunction with finite element method was proposed for optimizing a two-dimensional phononic crystal for out-of-plane waves (Gazonas et. al) [5]. Hussein et al. [6, 7] used GA to conduct a series of optimization of both one-dimensional and two-dimensional phononic crystals. Rupp et al. [8] developed a gradient-based topology optimization to design two and three-dimensional phononic wave filters, including surface waveguides. Dong et al.[9] reported a more detailed work on topology optimization of two-dimensional phononic crystals using a two-stage GA and FEM for both out-of-plane waves and in-plane waves with and without volume constraint. Liu et al. [10] used a two-stage GA in conjunction with fast plane wave expansion method to optimize the band gap width of phononic crystals for in-plane coupled mode, out-of-plane acoustic mode and mixed mode. It should be noted that aforementioned algorithms often cost significant computations. Taking GA in combination with FEM for example, it usually would take more than several hundreds of steps before the optimal design was achieved [9, 10]. Though parallel computation could reduce the computational cost more easily than before, it is still lack of efficiencies.

Toward an efficient and reliable optimization for phononic structures, in this paper we propose a new topology optimization algorithm based on the bi-directional evolutionary structural optimization (BESO) method and finite element analysis to maximize phononic band gaps. The rest of the paper is organized as follows: governing equations and BESO optimization approach to optimize the band gap width between two adjacent bands are presented in section 4. In section 5, various patterns of optimal phononic band gap structures are presented for both out-of-plane shear waves and in-plane mixed waves. This is followed by conclusions.

4. Formulations

4.1 Analysis of phononic crystals

The propagation of mechanical waves in an elastic inhomogeneous medium is governed by

$$\rho \mathbf{u} = \nabla[\lambda(\mathbf{r}) + 2\mu(\mathbf{r})](\nabla \mathbf{u}) - \nabla \times [\mu(\mathbf{r})\nabla \times \mathbf{u}] \quad (1)$$

Where λ and μ are the Lamé's coefficients; ρ is the material density; $\mathbf{u}=\{\mathbf{u}_x, \mathbf{u}_y, \mathbf{u}_z\}$ is the displacement vector.

In this paper we only consider the elastic waves that propagate in the x-y plane, i.e. the wave field are independent of z so that $\partial \mathbf{u} / \partial z = 0$. Then Eq.(1) can be split into two coupled in-plane equations, which govern the longitudinal and transverse modes, and an out-of-plane equation that governs acoustic mode:

$$\rho \frac{\partial^2 u_x}{\partial t^2} = \frac{\partial}{\partial x} \left[(\lambda(\mathbf{r}) + 2\mu(\mathbf{r})) \frac{\partial u_x}{\partial x} + \frac{\partial u_y}{\partial y} \right] + \frac{\partial}{\partial y} \left[\mu(\mathbf{r}) \left(\frac{\partial u_x}{\partial y} + \frac{\partial u_y}{\partial x} \right) \right] \quad (2)$$

$$\rho \frac{\partial^2 u_y}{\partial t^2} = \frac{\partial}{\partial x} \left[\mu(\mathbf{r}) \left(\frac{\partial u_x}{\partial y} + \frac{\partial u_y}{\partial x} \right) \right] + \frac{\partial}{\partial y} \left[\frac{\partial u_x}{\partial x} + (\lambda(\mathbf{r}) + 2\mu(\mathbf{r})) \frac{\partial u_y}{\partial y} \right] \quad (3)$$

$$\rho \frac{\partial^2 u_z}{\partial t^2} = \frac{\partial}{\partial x} \left[\mu(\mathbf{r}) \frac{\partial u_z}{\partial x} \right] + \frac{\partial}{\partial y} \left[\mu(\mathbf{r}) \frac{\partial u_z}{\partial y} \right] \quad (4)$$

where $\mathbf{r}=(x,y)$ denotes the position vector.

According to the Floquet-Bloch wave theory, the displacement vector can be represented as the product of a periodic function and an exponential factor as:

$$\mathbf{u}(\mathbf{r}, \mathbf{k}) = \mathbf{u}_k(\mathbf{r}) e^{i(\mathbf{k} \cdot \mathbf{r})} \quad (5)$$

where $\mathbf{u}_k(\mathbf{r})$ is a periodic function of \mathbf{r} with the same periodicity as the structure; $\mathbf{k}=(\mathbf{k}_x, \mathbf{k}_y)$ is the Bloch wave vector.

Inserting Eq.(5) into either Eq.(2), Eq.(3) or Eq.(4), with $\lambda(\mathbf{r})=\lambda(x,y)$, $\mu(\mathbf{r})=\mu(x,y)$ and $\rho(\mathbf{r})=\rho(x,y)$; the elastic waves governing equations can be converted to eigenvalue problems within a unit cell. After discretized by finite element method (FEM), these equations can be written as:

$$\left(\mathbf{K}(k) - \omega^2 \mathbf{M} \right) \mathbf{u} = 0 \quad (6)$$

where $\mathbf{u}=\mathbf{u}_k$; \mathbf{K} and \mathbf{M} are stiffness matrix and mass matrix respectively. Due to the periodicity of the unit cell, only the wave vectors on the boundary of irreducible Brillouin zone are considered for the calculation of the band diagram.

4.2 Topology optimization problem

Our goal for the optimization of phononic crystals here is to maximize the relative band gap between two adjacent bands (referred as band n and band $n+1$). The objective function can be stated as follows:

$$\text{Max: } f(x_e) = 2 \frac{\min \omega_{n+1}(\mathbf{k}) - \max \omega_n(\mathbf{k})}{\min \omega_{n+1}(\mathbf{k}) + \max \omega_n(\mathbf{k})} \quad (7)$$

$$\text{Subjected to: } \sum_{e=1}^N x_e \times V_e = V$$

where x_e is the design variable which describes the material distribution in the unit cell. V_e and V are the elemental volume and the prescribed volume of the unit cell, respectively. It should be noted that the frequency is the function of the wave vector.

It is assumed that the phononic crystal is composed of two base materials. We use the linear material interpolation scheme, which has been applied successfully to the design of phononic crystals [4] as

$$\rho(x_e) = (1 - x_e) \rho_1 + x_e \rho_2 \quad (8)$$

$$\lambda(x_e) = (1 - x_e) \lambda_1 + x_e \lambda_2 \quad (9)$$

$$\mu(x_e) = (1 - x_e) \mu_1 + x_e \mu_2 \quad (10)$$

where subscripts '1' and '2' represent the matrix material and the inclusion material respectively. In the traditional BESO method [11-14], the discrete design variable is set $x_e=0$ or 1 only. However, numerical simulation shows that the optimization process of phononic crystals is very sensitive to the change of design variable. Thus, in this paper the variation of the design variable in each iteration step is limited to be $\Delta x_e=0.1$.

4.3 Sensitivity Analysis and BESO algorithm

For a given wave vector \mathbf{k} and assuming that eigenvectors are normalized to the global mass matrix, the sensitivities of eigenfrequencies $\omega_n(\mathbf{k})$ with respect to a change in an element design variable can be computed as:

$$\frac{\partial \omega_n(\mathbf{k})}{\partial x_e} = \frac{1}{2\omega_n} u(\mathbf{k})_n^T \left(\frac{\partial K}{\partial x_e} - \omega_n^2 \frac{\partial M}{\partial x_e} \right) u(\mathbf{k})_n \quad (11)$$

Thus, the sensitivity of the objective function can be written as:

$$\frac{\partial f(\mathbf{X})}{\partial x_e} = 4 \frac{\max \omega_n(\mathbf{k}) \frac{\partial \min \omega_{n+1}(\mathbf{k})}{\partial x_e} - \min \omega_{n+1}(\mathbf{k}) \frac{\partial \max \omega_n(\mathbf{k})}{\partial x_e}}{(\min \omega_{n+1}(\mathbf{k}) + \max \omega_n(\mathbf{k}))^2} \quad (12)$$

Originally proposed by Xie and Steven [15] in early 1990s, the essential idea of evolutionary structural optimization (ESO) method is by gradually deleting low efficient materials, remain topology of the structure evolves to an optimal design. Its later version, BESO allows adding materials while removing insufficient ones [16, 17]. Topology optimization of phononic band gap structures starts from a simple unit cell without any band gap. Then based on the sensitivity analysis and BESO algorithm, it will gradually modify the distribution of two materials in the following iteration steps by changing the value of the design variable of every element until the convergence criterions are satisfied. A filter scheme shown below is adopted to avoid checkerboard and mesh-dependency problems [11]:

$$\hat{\alpha}_i = \frac{\sum_{j=1}^M w(r_{ij}) \alpha_j}{\sum_{j=1}^M w(r_{ij})} \quad (13)$$

where r_{ij} denotes the distance between the centre of the element i and node j ; $w(r_{ij})$ is weight factor given as

$$w(r_{ij}) = \begin{cases} r_{\min} - r_{ij}, & \text{for } r_{ij} < r_{\min} \\ 0, & \text{for } r_{ij} \geq r_{\min} \end{cases} \quad (14)$$

with r_{\min} as the radius of the filter.

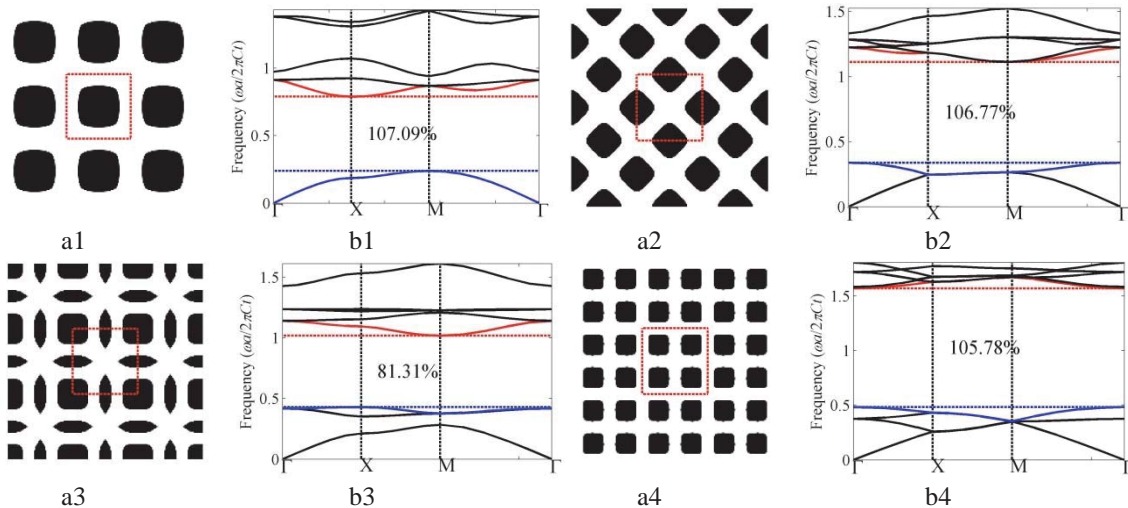
5 Numerical Results

In this example, our goal is to maximize the relative band gap between two neighbor bands of a 2D square unit cell for a prescribed material volume fraction. A solid-solid phononic structure design is considered with Epoxy as the matrix and Au as the inclusion material. The material parameters are: $\rho_{\text{epoxy}}=1200 \text{ kg/m}^3$, $\lambda_{\text{epoxy}}=6.38 \text{ GPa}$, $\mu_{\text{epoxy}}=1.61 \text{ GPa}$, $\rho_{\text{Au}}=19500 \text{ kg/m}^3$, $\lambda_{\text{Au}}=65.44 \text{ GPa}$ and $\mu_{\text{Au}}=29.94 \text{ GPa}$.

BESO starts from an initial design without band gap and gradually decreases the total volume of the unit cell using an evolutionary rate ER=2%. A mesh-independency filter is used to avoid tiny structures and the radius of the filter is 1/50 of the length of the lattice's diagonal line.

5.1 Out-of-Plane waves (Acoustic modes)

The optimal unit cells and the corresponding band diagrams for the first to eighth band gaps of the out-of-plane waves which propagate in the Au-Epoxy composite are demonstrated in figure 1 with the volume constraint of $V_f=0.38$. The optimized topologies show the distribution of 3×3 array of unit cells (the representative unit cell is shown within the red dashed box), in which black represents Au and white represents Epoxy. The optimal designs are very similar to those reported by Dong et al. [9] for the first and fifth band gap structures. It demonstrates the effectiveness of the proposed optimization method. It is also noted that the complexity of the optimal topologies increases when the appointed bands grow higher.



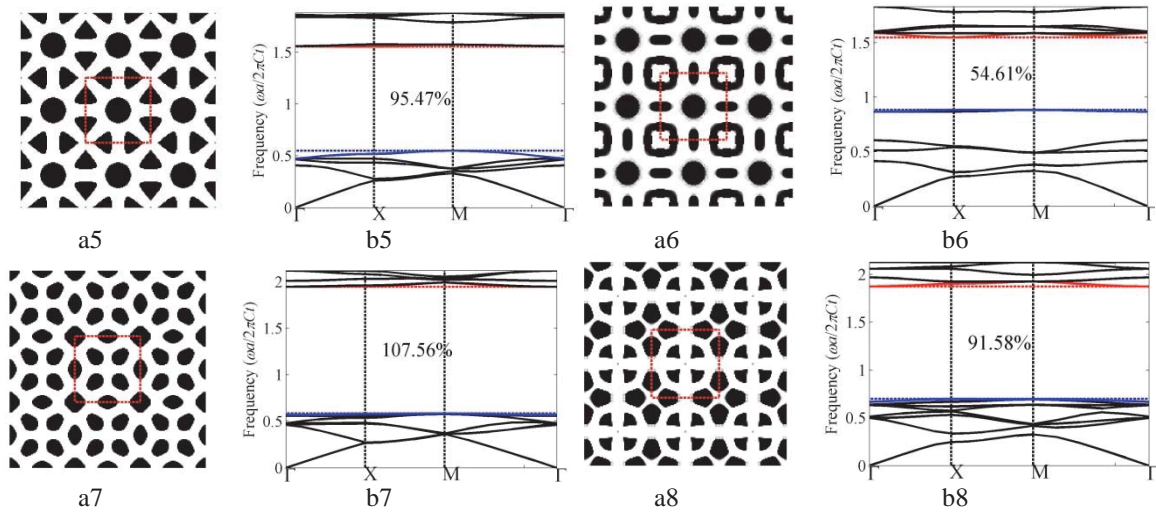


Figure 1: Optimized band gap structures and corresponding band diagrams from the first to eighth band for the out-of-plane mode. The black and white colours represent Au and Epoxy, respectively.

Figure 2 illustrates the evolution history of the first band gap optimization process for the out-of-plane mode. As shown in the figure, there is no initial gap between the first and second bands. The band gap occurs after several iterations and then the total volume of the unit cell gradually increases as the volume fraction decreases to the predefined value. Finally, the optimized gap size stably achieves its maximum value when the volume is kept to be the constraint value. It can also be concluded from figure 2 that the proposed algorithm is of high efficiency since the optimization process would converge in 70 iteration steps, which is much faster than present optimization methods, for instance GA would take nearly 1000 iterations [9].

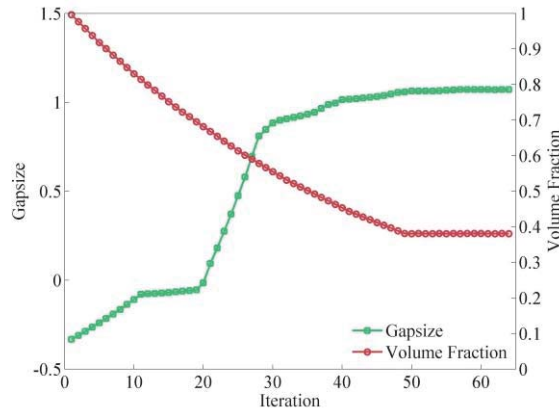


Figure 2: Evolution histories of the first band gap size and volume fraction.

5.2 In Plane waves (Coupled modes)

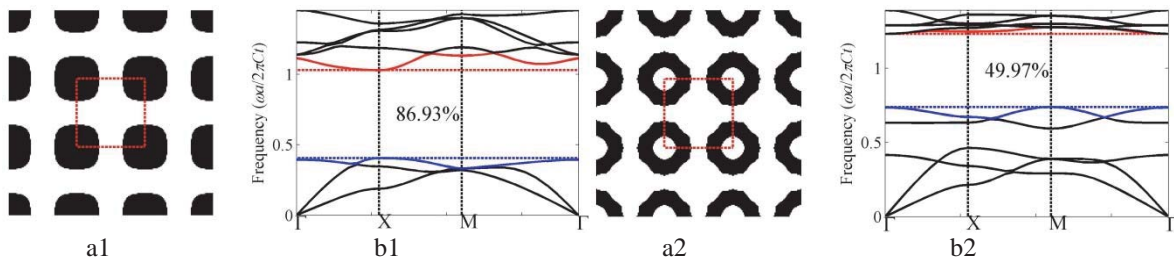


Figure 3: Optimized phononic band gap structures and corresponding band diagrams for third and fifth band gaps of in-plane mode.

The proposed optimization method can also be applied to the in-plane waves of phononic crystals. Using the same parameters for the previous examples, the optimization results for the third and fifth band gaps of the in-plane mode are shown in figure 3. The volume constraint is also set to be $V_f=0.38$. The optimized topology for the third band gap is analogous to the first band gap structure of the out-of-plane mode. The optimized topology for the fifth band gaps looks like a hollow diamond, which also has a small band gap between the third and fourth bands. It is observed that band gap between the third and fourth band can be easily obtained when optimizing for other band gaps.

6. Conclusions

This paper proposes a new optimization algorithm based on BESO in combination with FEM for the design of phononic band gap structures and systematically investigates the topology optimization of 2D phononic band gap crystals for both the out-of-plane and in-plane wave modes. Numerical results show that optimized topologies for various band gaps has been successfully achieved. The optimized band gap sizes well demonstrate the effectiveness of the proposed optimization algorithm. Moreover, the optimization method proposed in this paper is also efficient as the optimization usually converges within about 100 iterations.

7. Acknowledgements

The second author is the recipient of an Australian Research Council Future Fellowship (FT130101094).

8 References

- [1] M.S. Kushwaha, P. Halevi, L. Dobrzynski and B. Djafari-Rouhani, Acoustic band structure of periodic elastic composites. *Physical Review Letters*, 71(13), 2022-2025, 1993.
- [2] M.H. Lu, L. Feng and Y.F. Chen, Phononic crystals and acoustic metamaterials. *Materials Today*, 12(12), 34-42, 2009.
- [3] Y. Pennec, J.O. Vasseur, B. Djafari-Rouhani, L. Dobrzyński and P.A. Deymier, Two-dimensional phononic crystals: Examples and applications. *Surface Science Reports*, 65(8), 229-291, 2010.
- [4] O. Sigmund and J. Søndergaard Jensen, Systematic design of phononic band-gap materials and structures by topology optimization. *Philosophical Transactions of the Royal Society of London. Series A: Mathematical, Physical and Engineering Sciences*, 361(1806), 1001-19, 2003.
- [5] G.A. Gazonas, D.S. Weile, R. Wildman and A. Mohan, Genetic algorithm optimization of phononic bandgap structures. *International Journal of Solids and Structures*, 43(18-19), 5851-5866, 2006.
- [6] M.I. Hussein, K. Hamza, G.M. Hulbert, R.A. Scott and K. Saitou, Multiobjective evolutionary optimization of periodic layered materials for desired wave dispersion characteristics. *Structural and Multidisciplinary Optimization*, 31(1), 60-75, 2005.
- [7] M.I. Hussein, K. Hamza, G.M. Hulbert and K. Saitou, Optimal synthesis of 2D phononic crystals for broadband frequency isolation. *Waves in Random and Complex Media*, 17(4), 491-510, 2007.
- [8] O.R. Bilal and M.I. Hussein. Optimization of phononic crystals for the simultaneous attenuation of out-of-plane and in-plane waves, *ASME 2011 International Mechanical Engineering Congress and Exposition*, American Society of Mechanical Engineers, Denver, Colorado, USA, 969-972, 2011 (ISBN: 978-0-7918-5494-5)
- [9] H.W. Dong, X.X. Su, Y.S. Wang and C. Zhang, Topological optimization of two-dimensional phononic crystals based on the finite element method and genetic algorithm. *Structural and Multidisciplinary Optimization*, 50(4), 593-604, 2014.
- [10] Z. Liu, B. Wu and C. He, Band-gap optimization of two-dimensional phononic crystals based on genetic algorithm and FPWE. *Waves in Random and Complex Media*, 24(3), 286-305, 2014.
- [11] X. Huang and M. Xie. *Evolutionary topology optimization of continuum structures: methods and applications*, John Wiley & Sons, Chichester, 2010.
- [12] X. Huang and Y. Xie, Convergent and mesh-independent solutions for the bi-directional evolutionary structural optimization method. *Finite Elements in Analysis and Design*, 43(14), 1039-1049, 2007.
- [13] X. Huang and Y. Xie, Bi-directional evolutionary topology optimization of continuum structures with one or multiple materials. *Computational Mechanics*, 43(3), 393-401, 2009.
- [14] X. Huang, Z. Zuo and Y. Xie, Evolutionary topological optimization of vibrating continuum structures for natural frequencies. *Computers & structures*, 88(5), 357-364, 2010.
- [15] Y. Xie and G.P. Steven, A simple evolutionary procedure for structural optimization. *Computers & structures*, 49(5), 885-896, 1993.
- [16] O.M. Querin, V. Young, G.P. Steven and Y.M. Xie, Computational efficiency and validation of bi-directional evolutionary structural optimisation. *Computer Methods in Applied Mechanics and Engineering*, 189(2), 559-573, 2000.
- [17] X. Yang, Y. Xei, G. Steven and O. Querin, Bidirectional evolutionary method for stiffness optimization. *AIAA journal*, 37(11), 1483-1488, 1999.

Optimization of contact stress distribution in interference fit

Niels Leergaard Pedersen

Dept. of Mechanical Engineering, Solid Mechanics, Technical University of Denmark
Nils Koppels Allé, Building 404, DK-2800 Kgs. Lyngby, Denmark
email: nlp@mek.dtu.dk

1. Abstract

Assembly of shaft and hub by an interference fit is a classical connection with known advantages and disadvantages. The advantage being the level of possible torque transfer while the disadvantage is a possible fretting fatigue failure at the points of stress concentration. The pressure distribution in the contact is the source responsible for the fatigue failure. The distribution can be improved by design modification done directly on the contacting surfaces which however requires a very high production precision. Alternatively it is shown, how shape optimization of the hub side can improve the pressure distribution significantly.

2. Keywords: Interference fit, Contact, Optimization, Stress concentration.

3. Introduction

Interference fit or press fit is one of the most used assembly methods for shaft-hub connections. This type of assembly is superior with respect to possible torque transmission between two assembled parts. The disadvantage is that in the typical configuration disassembly is not possible. The limit to the use of an interference fit is typically dictated by the maximum heating or cooling of the parts during the assembly process. Once assembled the interference fit may fail due to fretting fatigue. Fretting fatigue is a type of fatigue where the parts due to relative movement between compressed parts fail. The failure is a gradual deterioration of the surface resulting in loss of contact pressure.

In a traditional design with straight assembly surfaces for shaft and hub, the result is a large stress concentration at the end of contact. The shaft is in the working condition typically loaded in both bending and torsion. The combination of the high stress and the relative motion result in the fretting fatigue. Results from roller bearings, see [1] and [2] indicate that for this case, although not directly comparable, is possible to achieve a constant contact pressure by special design of the rollers. Design changes to the interference fit contact surfaces should therefore also be possible. In the literature many different design changes have been proposed for improving the strength of the interference fit, different ways of changing the contact can be found in e.g. [3], [4], [5], [6], [7] and [8]. Improving the interference design by shape changes made to the hub can be found in [3] and [9]. For most of the papers the design improvement has been done without a focus directly on optimization but more by a trial and error method.

It might not be straight forward What the shape of an optimal contact pressure should be. If fretting fatigue is to be avoided then there should be no relative motion between the two parts in contact, the possibility for relative motion is controlled by the friction coefficient and the normal pressure, therefore one could argue that the contact pressure at the inlet to the contact should be high. This reasoning have lead to suggested design improvement where, e.g., there is a groove in the shaft and the hub has an overhang over part of this groove leading to an even higher stress concentration at the contact inlet. On the other hand if there is relative motion between two parts in contact then the contact pressure should be low in order not to result in fretting fatigue. As seen in the paper [10] the high stress values can result in deterioration of either the hub or the shaft or both due to the high stress. The interference fit should function in situations where the connection typically is loaded both in bending and torsion. The torsion only creates shear motion and therefore for a pure torsional load of an interference fit the way to design the contact pressure is one where the contact pressure is so high that relative motion is avoided and at the same time no deterioration of the surfaces takes place due to plasticity. For the interference fit in bending (rotating) it seems that even though the stresses are high at the inlet the stress will either be increased to a too high level or there will be inherently a relative motion between the two part. The design objective for the present work is therefore to have a constant contact pressure between the parts. The level of this contact pressure should be selected such that the fretting fatigue is avoided on one hand and on the other hand so high as possible to fully take advantage of the interference fit.

4. Stress singularity of standard design

To evaluate the size of the stress singularity a FE model with a mesh refinement is needed. Reducing the element size at the singularity will increase the maximum stress and the size of the stress will go to infinity as the element size goes towards zero.

The data for the shaft and hub connection used in the present work is

- Shaft: length $L_s = 0.6\text{m}$, diameter $D_f = 0.2\text{m}$
- Hub: Length $L_h = 0.3\text{m}$, thickness $t = 0.1\text{m}$, i.e., outer diameter of hub $D_h = 0.4\text{m}$

The interference is introduced in the finite element model by modeling a cooling of the hub by 100°C . The material properties of the hub and shaft are assumed identical and given by

$$E = 2.1 \cdot 10^5 \text{MPa}, \quad \nu = 0.3, \quad \alpha = 1.1 \cdot 10^{-5} / ^\circ\text{C}$$

where E is modulus of elasticity, ν is Poisson's ratio and α is the thermal expansion coefficient. A cooling of the hub by 100°C is used and this results in an interference fit of $\delta_d = 220\mu\text{m}$. The classical analytical pressure in the connection, under the assumption of rotational symmetry and infinitely long shaft and hub (plane model), is given by

$$p_f = \frac{E \delta_d}{2D_f} \left(1 - \left(\frac{D_f}{D_h} \right)^2 \right) \quad (1)$$

where $D_h = D_f + 2 \cdot t$ is the outer diameter of the hub. With the given data the pressure is $p_f = 86.6\text{MPa}$. The size of the singularity for the present design is estimated using the COMSOL program ([11]). The connection is modeled assuming axis symmetry as seen in Figure 2. In the contact modeling it is examined if the inclusion of friction is important for the evaluation of the pressure, from the computation it is found that the friction does have an influence but that it has a negligible influence on the contact pressure.

In order to evaluate the stress concentration factor it is here selected to identify the stress $10\mu\text{m}$ from the edge of the hub. The overall distribution of the stress is given in Figure 1a) and in Figure 1b) a zoom of the last 1mm is shown. The finite element model is highly refined with 30 FE nodes along the last $10\mu\text{m}$ of the contact in 1a) and in the shown zoom with 60 FE nodes along the last $10\mu\text{m}$. The stress converges to a level of 415MPa . From the computation we conclude that the theoretical stress concentration K_t for this case is

$$K_t \approx \frac{415}{86.6} = 4.8 \quad (2)$$

The exact value of the theoretical stress concentration factor can always be discussed. But it is clear that the stress concentration has a significant size.

5. Super element technique for contact analysis

An alternative to performing contact analysis by a traditional iterative finite element analysis (FEA) is to use the super element technique. The procedure involves no iterations see [12]. Application of the method for shrink fit analysis can be found in [13] and in relation to bolted connection see [14]. The primary advantage of the method is that no iterations are needed in the FE calculation. In Figure 2 an interference fit is shown. The axis symmetric model of half the connection is also shown together with the contact pressure distribution.

In the analysis the shaft and hub are separated. The super element FE model of the hub alone is given as

$$[S_{hp}]\{D_{hp}\} = \{F_{cp}\} \quad (3)$$

where $[S_{hp}]$ is the hub super element stiffness matrix. The order of this matrix equals the number of FE mesh nodes on the contact line. The resulting displacements of the contacting nodes are $\{D_{hp}\}$ and the corresponding nodal contact pressure forces are $\{F_{cp}\}$. The total contacting force is given as the sum of these nodal forces i.e.

$$F_p = \|\{F_{cp}\}\|_1 \quad (4)$$

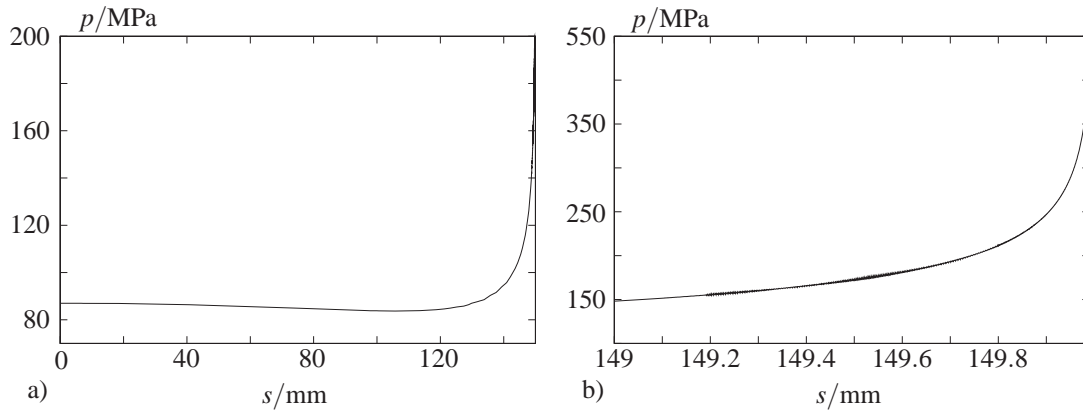


Figure 1: Contact pressure along interference fit. a) Full length of contact. b) Zoom of last 1mm of contact, the stress is not plotted for the last 10 μ m due to the singularity, the maximum stress 10 μ m from the edge is 415MPa.

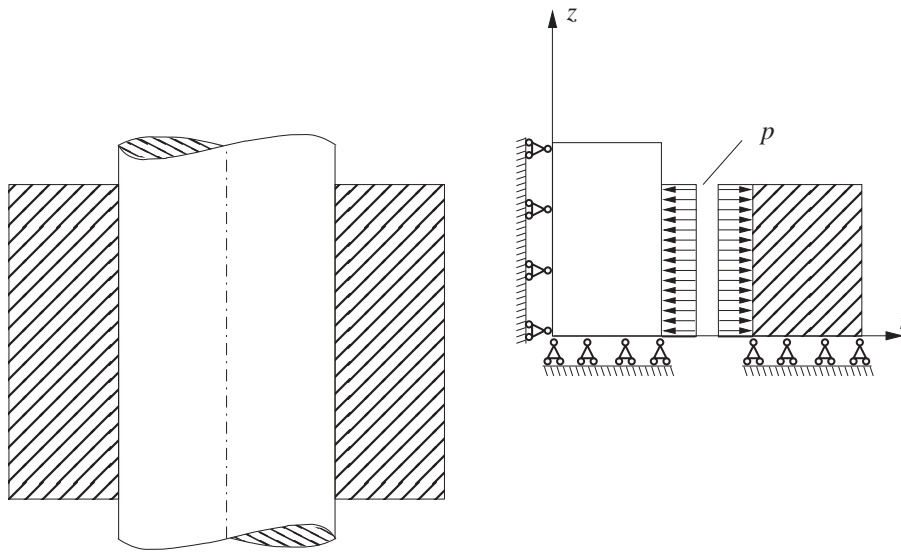


Figure 2: left: the interference fit. Right: of this an illustration of the axis symmetric model of half the shaft and hub used in the analysis. The contact pressure p is illustrated by a distribution that it is to be determined from the analysis.

With respect to the practical determination of the super element matrices see [12].

It is assumed that the contact line on the shaft has the same number of nodes (mutual corresponding) as the hub contact line. The analysis for the shaft can under this assumption be performed in a similar manner using the super finite element matrices for this part.

$$[S_{sp}]\{D_{sp}\} = -\{F_{cp}\} \quad (5)$$

where $[S_{sp}]$ is the shaft super element stiffness matrix. The order of this matrix also equals the number of FE mesh nodes on the contact line. The resulting displacements of the contacting nodes are $\{D_{sp}\}$ and the corresponding nodal contact pressure forces are $-\{F_{cp}\}$, i.e., a negative sign relative to the analysis of the hub, to express equilibrium with (3),

Before assembly the radial interference (negative gap) between the shaft and hub for the nodes on the line of contacts can be determined as

$$\{g\} = \{r_s\} - \{r_h\} \quad (6)$$

where $\{r_s\}$ and $\{r_h\}$ are the radial position of the nodes on the contact line for the shaft and hub respectively. After the two components are fitted together the nodes will be at the same point, i.e. we have that

$$\{r_s\} + \{D_{sp}\} = \{r_h\} + \{D_{sh}\} \Rightarrow \{g\} = \{D_{sh}\} - \{D_{sp}\} \quad (7)$$

The super element technique can be used in two different ways; either the contact force distribution, $\{F_{cp}\}$, is assumed known and from this the gap, $\{g\}$, can be found directly by

$$\{g\} = ([S_{hp}]^{-1} + [S_{sp}]^{-1})\{F_{cp}\} \quad (8)$$

alternatively the gap is assumed known and the contact force can be found from

$$\{F_{cp}\} = ([S_{hp}]^{-1} + [S_{sp}]^{-1})^{-1}\{g\} \quad (9)$$

The result we achieve is that under the given assumptions then contact force can be found directly without iterations from a given gap distribution. The analysis involved the determination of the inverse matrices for the two super finite element stiffness matrices, but the size of these is limited to the number of nodes on the contact line.

6. Design modification of contact zone

Under the assumption used in (8) we may find the gap $\delta(z)$, as a function of the position z , that will result in a constant stress. In Figure 3 the resulting gap for the shaft hub design used in the present work with a constant pressure of 86.6MPa is shown.

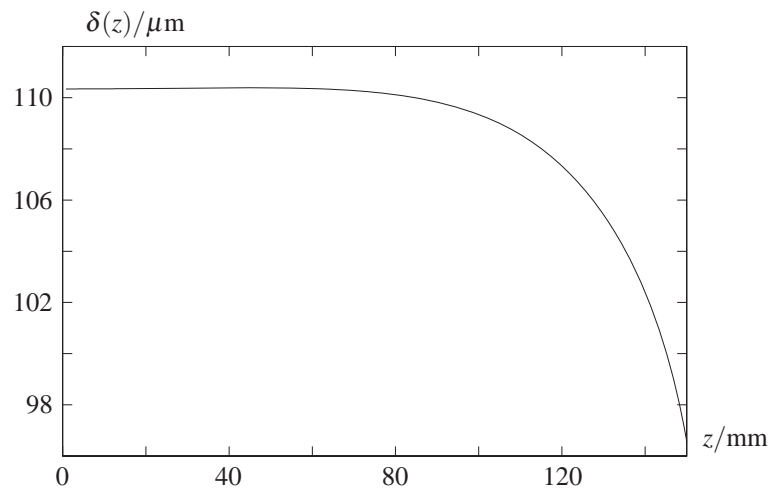


Figure 3: Gap as a function of axial position (see Figure 2) that result in a constant pressure, 86.6MPa, in the interference fit.

As can be seen in Figure 3 the variation in the gap is not very high as compared to the normal production methods where the interference is specified by tolerances, the variation lies in this case within $14\mu\text{m}$. Creating a shaft and hub with exactly the shown interference is therefore not desirable.

The results indicates that the connection for a constant interference is to stiff at the run-out of the hub relative to achieve a constant contact pressure. One way of changing this assuming that a constant interference is used is to make design changes to the hub side. A simple design change is to make a chamfer of the hub as seen in Figure 4a). The optimization problem can be stated as minimize the variation in the gap for a given constant pressure. The optimal design for this design change is shown in Figure 4b). The given simple design parameterization does not allow for a completely constant gap.

In Figure 4b) the optimal value of the chamfer is $a = 15.5\text{mm}$ which gives a total variation in the interference of $3.5\mu\text{m}$ to be compared to the original $14\mu\text{m}$ for no chamfer $a = 0\text{mm}$.

One disadvantage of the presented chamfer design is the reduction in the possible use of the hub, e.g., we can not use the whole length for a gear.

Alternative design change will be presented in the lecture. also the application of traditional contact analysis will be shown.

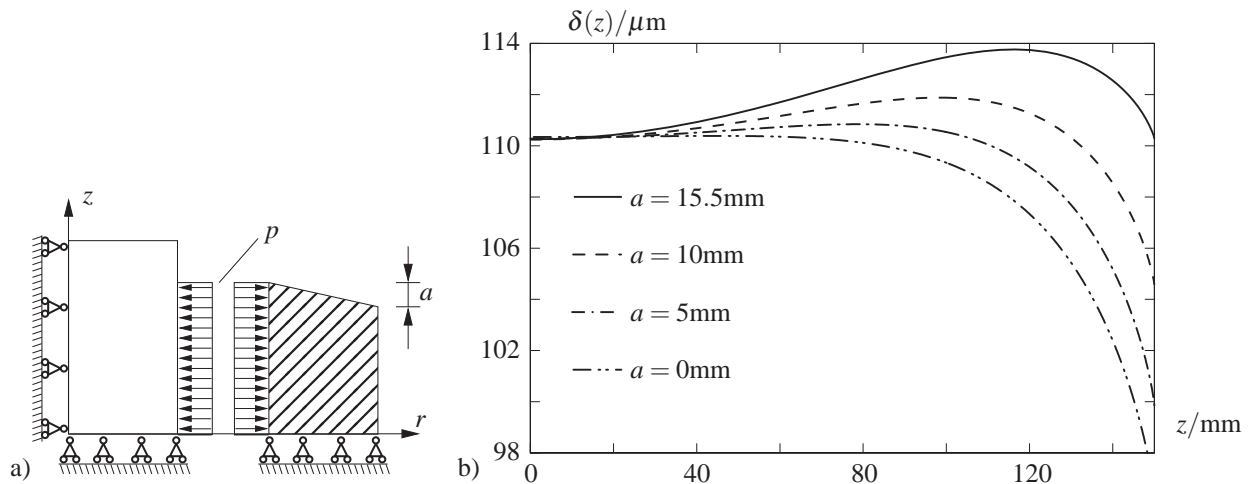


Figure 4: Gap as a function of axial position for different chamfer size that result in a constant pressure, 86.6MPa, in the interference fit.

7. References

- [1] H. Reusner. The logarithmic roller profile - the key to superior performance of cylindrical and taper roller bearings. *Ball bearing journal*, 230:2–10, 1987.
- [2] H. Fujiwara and T. Kawase. Logarithmic profiles of rollers in roller bearings and optimization of the profiles (reprint from the original paper (in Japanese) from the proceedings of the japan society of mechanical engineers part c, vol 72 (2006),3022-2029). *NTN Technical review*, 70:140–148, 2007.
- [3] K. Nishioka and H. Komatsu. Researches on increasing the fatigue strength of press-fitted shaft assembly. *Bulletin of the Japan Society of Mechanical Engineers*, 10(42):880–889, 1967.
- [4] D. J. White and J. Humpherson. Finite-element analysis of stresses in shafts due to interference-fit hubs. *Journal of Strain Analysis for Engineering Design*, 4(2):105–114, 1969.
- [5] Toshio Hattori, Suetoshi Kawai, Noriaki Okamoto, and Tadashi Sonobe. Torsional fatigue strength of a shrink fitted shaft. *Bulletin of the JSME*, 24(197):1893–1900, 1981.
- [6] Dong Hyong Lee, Seok Jin Kwon, Jeong Won Seo, and Won Hee You. Effects of hub contact shape on contact pressure and fatigue life in a press-fitted shaft. *Materials Science Forum, Mater. Sci. Forum*, 654-656:1638–1641, 2010.
- [7] Shunsuke Kataoka, Chu Sakae, Masanobu Kubota, and Yoshiyuki Kondo. Effect of stress relief groove shape on fretting fatigue strength. *Key Engineering Materials*, 353-358(PART 2):856–859, 2007.
- [8] Guillaume Biron, Aurelian Vadean, and Lucian Tudose. Optimal design of interference fit assemblies subjected to fatigue loads. *Structural and multidisciplinary optimization*, 47(3):441–451, 2013.
- [9] T. Juuma. Torsional fretting fatigue strength of a shrink-fitted shaft with a grooved hub. *Tribology international*, 33(8):537–543, 2000.
- [10] Masanobu Kubota, Shunsuke Kataoka, and Yoshiyuki Kondo. Effect of stress relief groove on fretting fatigue strength and index for the selection of optimal groove shape. *International journal of fatigue*, 31(3):439–446, 2009.
- [11] COMSOL AB. Stockholm, www.comsol.se, 1998-2009.
- [12] P. Pedersen. A direct analysis of elastic contact using super elements. *Computational mechanics*, 37(3):221–231, 2006.
- [13] Pauli Pedersen. On shrink fit analysis and design. *Computational Mechanics*, 37(2):121–130, 2006.
- [14] Niels Leergaard Pedersen and Pauli Pedersen. Bolt-plate contact assemblies with prestress and external loads: Solved with super element technique. *Computers and Structures*, 87(21-22):1374–1383, 2009.

On the integration of tuned multi-mass dampers into a topology optimization method for machine tool structural dynamics

Christian Brecher¹, Simo Schmidt², Marcel Fey³

¹ WZL of the RWTH Aachen University, Aachen, Germany, c.brecher@wzl.rwth-aachen.de

² WZL of the RWTH Aachen University, Aachen, Germany, simo.schmidt@wzl.rwth-aachen.de

³ WZL of the RWTH Aachen University, Aachen, Germany, m.fey@wzl.rwth-aachen.de

1. Abstract

Topology optimization is becoming an integral part of the design process in various industrial fields in order to keep up with the continuous drive to increase productivity and efficiency. In the field of machine tools, the dynamic behavior of a machine tool's structure is largely responsible for its overall performance. Thus, topology optimization methods targeting the optimization of Eigen frequencies are often used in industrial practice.

A machine tool's structural frequency response (e.g. to external excitation during cutting processes) is also dependent on its damping properties. Therefore, the dynamic behavior of machine tools can be significantly influenced by utilizing one or more vibration suppression systems like tuned mass dampers (hereinafter called TMDs) to target specific vibrations. Although TMDs are often used to solve problems during operation, they are in some cases utilized during the engineering phase, becoming an integral part of the machine design.

By combining both optimal utilization of vibration suppression systems and topology optimization within a structural optimization framework, potential synergetic effects of both approaches can be utilized.

In this paper, the recently started development of such an optimization framework including the automatic optimal positioning and analytic tuning of multi-mass dampers (hereinafter called MMDs) is described. The advantages of MMDs include robustness and easy implementation, as demonstrated by initial simulative results presented in this paper. The described framework in development addresses issues like manufacturing constraints for the topology optimization and restrictions on the MMDs physical properties. The paper concludes with a brief outlook on the consideration of constraints for additive manufacturing and the volumetric distribution of multiple MMDs embedded inside those structures.

2. Keywords: Machine tools, dynamics, tuned multi-mass dampers, topology optimization

3. Introduction

The application of topology optimization methods for structural dynamics problems has been discussed for many years. The optimization of dynamic behavior is a very general term. From a mechanical engineering standpoint, one can distinguish between indirect and direct methods. Indirect methods include those trying to maximize certain Eigen frequencies [1], achieve target (or shift specific) Eigen frequencies [2] or create a so-called band-gap behavior by maximizing the distance between distinct Eigen frequencies [3]. Many indirect methods include Eigen frequencies as optimization constraints rather than objective functions, e.g. [4, 5], a practice often applied in commercial products as well (see [6]). These methods can be called indirect, because the frequency-tuning is essentially achieved by optimizing the stiffness-to-mass ratio of a structure for certain Eigen frequencies and associated Eigen modes. The resulting dynamic behavior is indirectly affected by this optimization.

Direct methods on the other hand aim at influencing the dynamic behavior more directly, e.g. by synthesizing specific mode shapes [7] or minimizing the (maximum) frequency response at specific points or regions within the structure [8]. The latter is especially interesting in the field of machine tools, where the dynamic behavior at the tool center point (TCP) is often the most important point of interest.

The dynamic behavior of machine tools, and whether specific Eigen modes are potentially critical during operation, is in no small part also dependent on the damping properties of the structural parts and coupling components connecting them [9]. However, the topology optimization of the damping behavior of structural, load-bearing components has not been the focus of research. Instead, problems like an optimal material distribution within damping layers [10], especially regarding acoustics important in the automotive industry [11], were investigated.

Besides structural optimization techniques, a classic approach to reduce an existing machine's (or any vibrating structure's) peak response amplitude in one of its Eigen frequencies is to attach a vibration suppression system to it. Strategically positioned and tuned to absorb one response peak, the kinetic energy is either dissipated by different means of damping behavior or counteracted by opposing forces. Expensive, high-maintenance active systems (actors) can adapt to varying frequencies, passive systems like TMDs are only effective within a narrow frequency range. [9]

An extensive amount of research has been conducted into different types of TMDs. Regular ones consist of a single absorber mass connected to the main system with a specific attachment stiffness and optimal damping, see Eq.(1), Eq.(2). Many different approaches have emerged in the literature, using multiple degrees of freedom (DOF) for attachment [12] or distributing the damper mass over multiple masses [13-15]. They have in common, that the optimal tuning is usually achieved by using numeric optimization methods and significantly simplifying the system they are attached to. Also, available research is dominated by its application to buildings exposed to ground vibrations due to seismic activity, e.g. [16].

There is noticeably less research on the automatic optimum placement of such auxiliary systems, although [17] proposed a genetic algorithm approach to position damper systems (again in the field of civil engineering) across different floors of high-rise buildings, for example. Industrial applications of those optimized TMD systems in general and applications to machine tools in particular are rare, e.g. [18].

One aspect which all passive vibration suppression systems have in common is that their effectiveness depends on their mass in relation to the mass of the system they are attached to. By reducing the main system's mass, e.g. by topology optimization, the auxiliary system can be smaller. Yet, no research on a combined approach of topology optimization and integrated optimal tuning of TMD systems is available.

This lead to the research project presented in this paper, where a concept of integrating optimally tuned systems of MMDs into a topology optimization framework targeting the direct optimization of structural dynamics of machine tools is proposed. The general concept is summarized in Fig. 1. Either due to problems during operation or requirements during the design phase, the goal of optimizing structural dynamics can either be solved by damping critical vibrations or by optimizing one or more structural components w.r.t. static and especially dynamic considerations. The challenges and potentials of combining both approaches into an optimization framework are described in the following paragraphs. The motivational application example on the right side of the figure will be described in detail in the outlook of this paper.

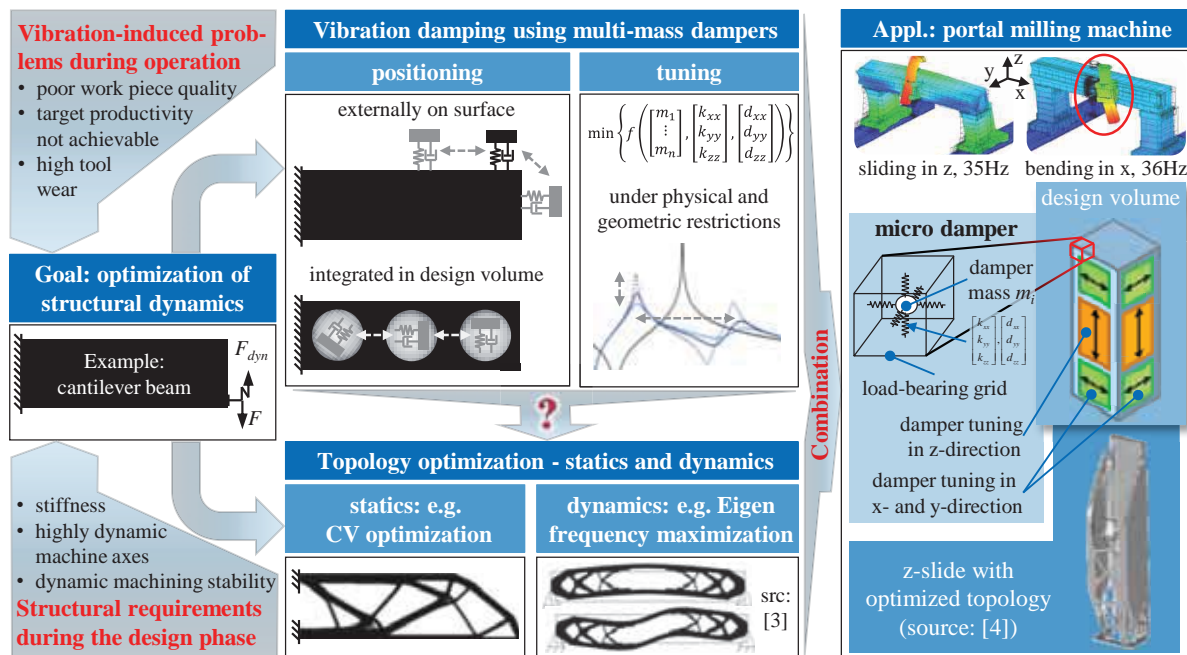


Figure 1: Schematic summary of the combined topology optimization and damping method concept

4. Analytically tuned MMDs

As mentioned above, the methods for optimal design of multi-mass or multi-DOF dampers presented in the literature focus on numerical optimization methods to optimize parameters like the number of masses, the mass fraction and the distribution of masses and attachment frequencies. Due to the computational effort of the combined optimization task, described in detail below, a fast analytic approach would be preferable.

Thus, the approach presented in this paper relies on analytic tuning methods of classical TMDs and applies them to a multi-stage design to broaden the effective frequency range and increase the robustness of the design.

4.1. Analytic tuning of multi-stage MMD units

When designing a regular TMD, the main system's dynamic behavior in the targeted Eigen mode is simplified to that of a single mass oscillator with an equivalent static stiffness and kinetic mass M . After defining the absorber mass m , the damper mass ratio $\mu = m/M$ is used throughout the optimal tuning. Using DEN HARTOGS [19] equations

to derive the optimal frequency ratio f_{opt} between the absorber's and the system's Eigen frequency (optimal detuning), the necessary attachment stiffness $k_{TMD,opt}$ can be calculated:

$$f_{opt} = \frac{\omega_{TMD}}{\omega_{sys}} = \frac{1}{1+\mu} \Rightarrow k_{TMD,opt} = m \left(\frac{\omega_{sys}}{1+\mu} \right)^2 \quad (1)$$

A TMDs performance relies on its optimal damping, which can be determined using BROCK'S [20] formula:

$$c_{TMD,opt} = 2m\omega_{sys} \sqrt{\frac{3\mu}{8(1+\mu)^3}} \quad (2)$$

Depending on the system's mass and the target frequency, it can be difficult to achieve the target damping value in practice, and deviations in $c_{TMD,opt}$ result in significantly reduced performance [16]. It is shown in several publications (e.g. [13,21]) that distributed mass dampers offer comparable performance to a single TMD with less damping, while being more robust to deviations in tuning (stiffness, damping or mass). Thus, distributing the single TMD mass represents the first design aspect of the MMD presented here as well (Fig. 2, left).

By attaching an absorber mass to a system, its resonance peak is split into two new resonance peaks. Neglecting any damping effects, the frequency spacing of those peaks can be calculated using Eq.(3) derived by [19]. The two solutions to this quadratic equation only depend on the mass fraction μ , where higher mass fractions increase the peak spreading effect of an absorber. A graphical representation of this formula is shown in Fig. 3 (top, middle).

$$\left(\frac{\omega}{\omega_{sys}} \right)^2 = \left(1 + \frac{\mu}{2} \right) \pm \sqrt{\mu + \frac{\mu^2}{4}} \quad (3)$$

Obviously, the distribution of the single TMD mass in an MMD reduces the peak spreading due to the decreasing individual mass fractions, narrowing the effective frequency range of a MMD system. To increase this frequency range, a multi-stage design is proposed, which calculates the newly created resonance peaks from the previous stage of absorbers using Eq.(3), and tunes additional masses to the lower- and uppermost peaks $\omega_{i,l}$ and $\omega_{i,u}$, respectively. This multi-stage design (as illustrated in Fig. 2, right) iteratively increases the effective frequency range of the proposed MMD system.

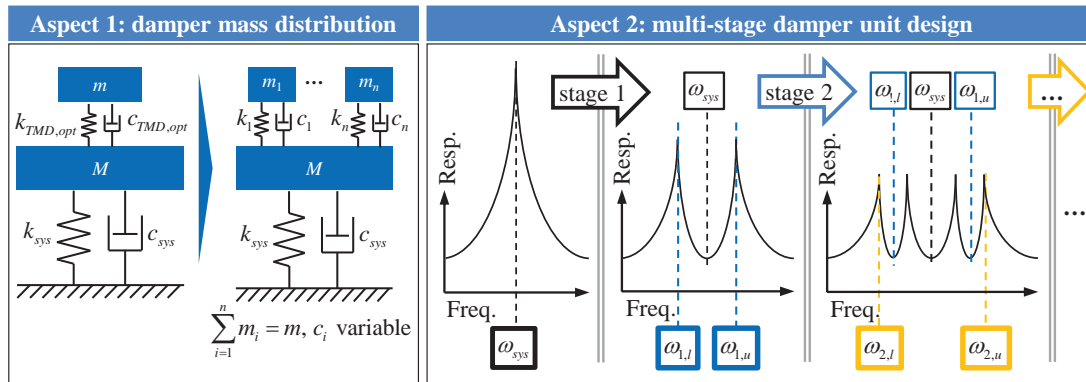


Figure 2: Design aspects of tuned multi-mass damper units

All MMD results presented in this paper are obtained from a FE simulation of a clamped, thick cantilever plate (steel, 20x100x500mm), where two MMDs are attached at different positions along the central axis and tuned to the 1st and 2nd bending mode (normal to the plate). The MMD attachment positions (as shown in Fig. 3, right) are chosen such that the mutual interference of both MMDs is low. The MMDs are idealized as point masses, individually connected via uniaxial springs/dashpots to the plate. A cantilever plate is chosen in order to validate the simulations on a test bench at a later stage. Also, the position of clamping can be moved along the longitudinal axis of the plate to detune the system and analyze the robustness of the MMD design.

An example of the multi-stage design and the spreading effect is demonstrated in Fig. 3 (bottom), where the overall damping of the MMD is kept constant and deliberately at a low level, such that the individual resonances can be clearly distinguished. Note that with an increase in stages, the maximum receptance is reduced, despite the constant damping.

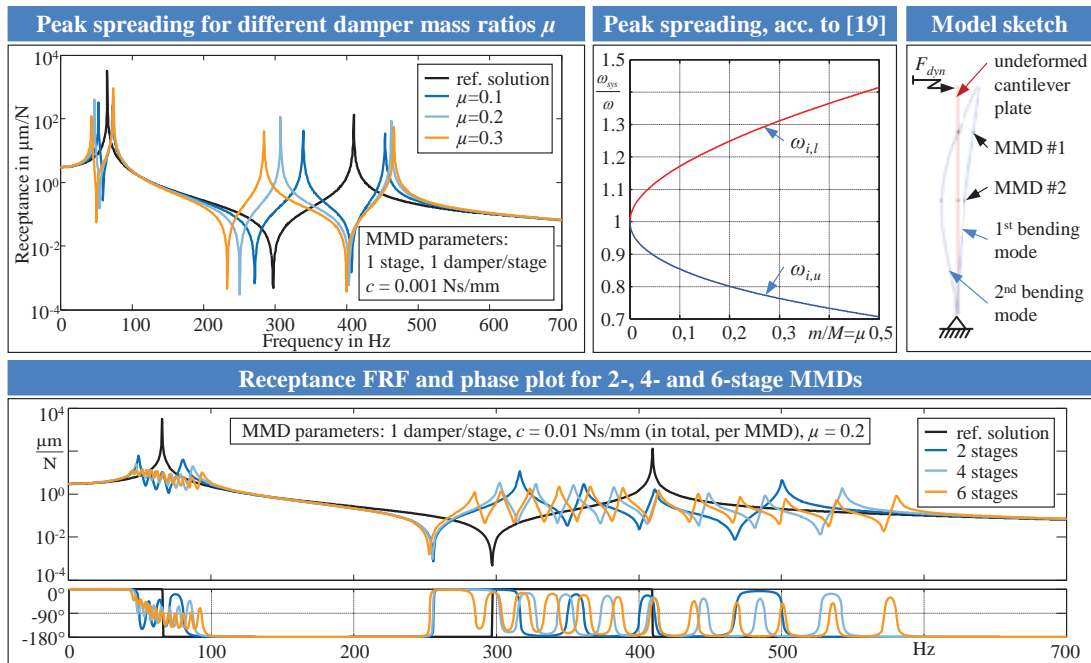


Figure 3: Utilizing the resonance peak spreading effect of adding absorbers to construct multi-stage MMDs

4.3. Robustness and manufacturing considerations

The premise of the presented MMD design is robustness both towards changing frequencies of the main system and towards variations and limitations in the stiffness and damping properties of available attachment devices for the individual dampers. Possible attachment devices include rubber attachment buffers in different configurations and shore hardness classes of rubber mixtures. An example of those buffers is shown in Fig. 4 (top, right).

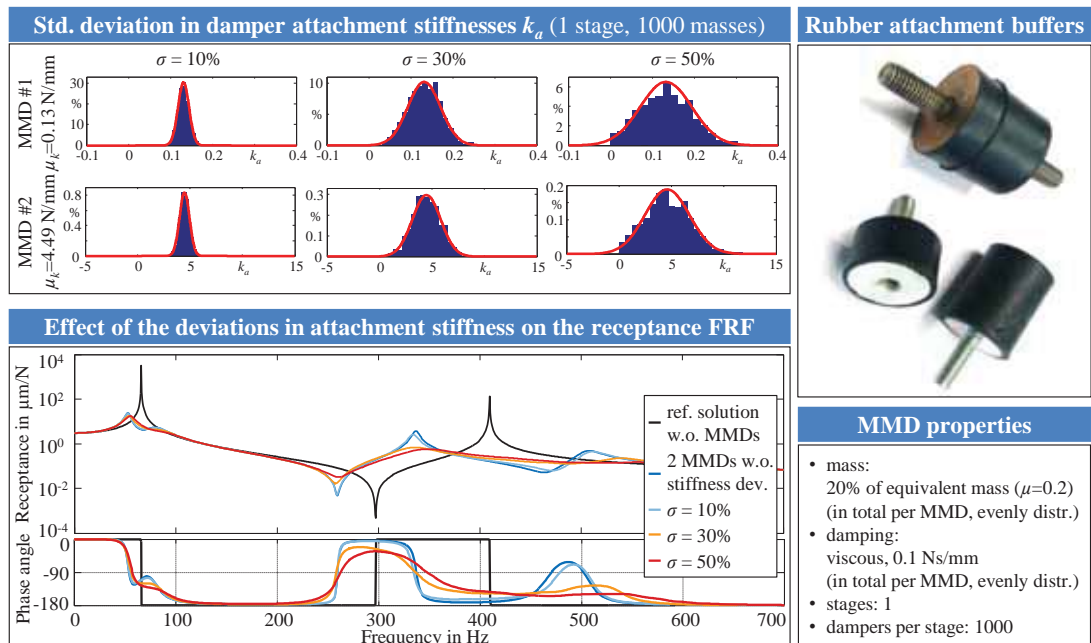


Figure 4: Effects of variations in the individual attachment stiffnesses on the MMD performance

Due to manufacturing and material property fluctuations, the stiffness of a single type of buffer and shore hardness can vary by more than 10%, the damping coefficients can vary even more. To consider those variations, the optimally tuned attachment stiffnesses, damping coefficients and masses of each individual damper are optionally subjected to a semi-truncated standard deviation to guarantee positive values, see Fig. 4 (top, left). Initial simulations for single- and multi-stage MMDs show a very beneficial effect of even large deviations, as can be seen in the example in Fig. 4 (bottom, left). Again, the sum total of viscous damping within each MMD

(0.1 Ns/mm) is very low compared to the optimum damping of a regular TMD with equal mass ($c_{TMD,opt} = 0.7262$ Ns/mm for the 2nd bending mode), obtainable from Eq.(2).

In contrast to the analytic tuning of regular TMDs, whose effectiveness relies heavily on optimal damping, the optimal tuning procedure presented here allows for the consideration of damping coefficients of available attachment devices. Available attachment stiffnesses are taken into account by scaling the number of masses per stage, thus changing the individual damper masses to achieve the same tuning frequency with different stiffnesses. Detailed results of this MMD design and practical validations on a test stand will be presented at a later stage.

4.3. Optimal positioning criteria

Any TMD needs to be in a position undergoing significant amplitudes within the targeted mode shape to be able to dissipate kinetic energy. Finding an optimal MMD position within a structure for a single targeted mode shape is straightforward. The nodal displacements of the considered mode shape, extracted from a FE modal analysis, yield optimal positions with high amplitudes. As soon as multiple MMDs are to be used to target multiple frequencies and mode shapes, the optimal positioning turns into a minimization problem, where optimal positions have high amplitudes at positions with low amplitudes in target modes of other MMDs. Even for a simple cantilever plate like the one used for demonstration in this paper, finding two optimal positions for both targeted Eigen modes cannot be realized without any mutual interference, see Fig.3 (top, right). The optimal positioning subproblem is further constrained by the necessity to have enough surface area at certain positions within the structure to attach MMDs to or to have enough local volume to integrate the MMDs into (see volumetric distribution in Ch. 6). Those constraints are imposed onto the positioning problem by the changing topology of the structure.

5. Topology optimization framework

5.1 Computational effort and technical challenges

The optimization framework under development is to be used for the optimization of real structural components of entire machine tools, which are often very large and complex structures containing a high number of DOFs. The FE dynamics analyses needed to calculate the system responses require a lot of computational effort. A modal analysis and subsequent frequency response calculation is necessary to determine the mode shapes and Eigen frequencies for tuning the MMDs and the frequency response behavior for the topology optimization module. Additionally, the tracking of Eigen modes (by using the MAC criterion, see e.g. [22]) will be considered, since mode shifting is likely to occur during the optimization process. To cope with the huge computational effort, a hybrid topology optimization scheme will be implemented to reduce the overall size of the system of equations by fully deleting Finite Elements in regular intervals (and adding some in critical areas, BESO-type approach). In between those reduction intervals, a localized topology optimization problem will be solved.

By adding, moving and retuning MMDs to and in the structure during the optimization process, the dynamic behavior of the structure is changed. The topology optimization in turn changes the dynamic behavior of the system, detuning the MMDs. A suitable coupling scheme has to be developed, while the achievable stability and convergence of the combined process and the topology optimization procedure in particular are critical but unknown. Due to this added complexity, the optimization core is kept modular to investigate the performance and suitability of different topology optimization approaches and coupling schemes (both implicit and explicit).

5.2 Applicability to real structures and manufacturing considerations

Structural components of machine tools are usually designed as welded steel or cast iron constructions. Welded steel constructions are comprised of mostly planar plates with relatively low wall thicknesses and are inherently ill-suited to be target designs of topology optimization methods. Thus, manufacturing constraints focus on improving the castability of the design proposals. A simple casting constraint would be to forbid the formation of undercuts in the designs w.r.t. a single cast removal direction. The framework in development operates on FE models discretized with a uniform Cartesian grid of hexahedra, allowing the definition of a casting direction along one of three principal axes of said grid. By allowing only the removal of surface material on the top and bottom projection of the structure w.r.t. the casting direction, undercuts are avoided, as proposed in [23], for example.

6. Outlook on additive manufacturing and the volumetric distribution of MMDs

The full potential of the combined optimization method can be exploited using additive manufacturing and distributing a large number of micro-dampers volumetrically within a load-bearing lightweight structure. A motivational, practical application is shown in Fig. 1 (top, right). Portal milling machines exhibit a dynamically challenging design component, namely the z-slide providing vertical movement of the main spindle. Typical mode shapes of this type of machine design include horizontal bending and sliding of said z-slide in the z-axis guides. Depending on the z-slide's vertical position, the Eigen frequencies change significantly, and surface area for the attachment of external TMDs is very limited. Volumetrically distributed MMDs which are tuned towards those typical Eigen modes and provide broadband performance due to their multi-stage design do not suffer from the

same spatial and frequency-related restrictions.

As mentioned above, the lighter the structure, the less damper mass is needed for vibration suppression. Also, the necessary individual damping associated with each mass increases with the number of dampers. By using additive manufacturing, it is conceivable that hundreds or thousands of masses can be integrated into a load-bearing truss structure derived by topology optimization and connected to it by parametrizable beams of material. Damping can be introduced into the masses for example by designing them as hollow spheres and retaining unmolten material within. These aspects will be the focus of research at a later stage of the ongoing framework development.

5. Acknowledgements

The authors would like to thank the German Research Foundation (DFG) for supporting this research under grant no. BR2905/57-1: "Optimale Positionierung und Auslegung von Mehrmassendämpfern innerhalb eines kombinierten Topologieoptimierungsverfahrens".

6. References

- [1] N.L. Pedersen, Maximization of eigenvalues using topology optimization, *Struct. Multidisc. Optim.*, 20(1), 2-11, 2000.
- [2] Z.D. Ma, H.C. Cheng and N. Kikuchi, Structural design for obtaining desired eigenfrequencies by using the topology and shape optimization method, *Comput. Syst. Eng.*, 5(1), 77-89, 1994.
- [3] J. Du and N. Olhoff, Topological design of freely vibrating continuum structures for maximum values of simple and multiple eigenfrequencies and frequency gaps, *Struct. Multidisc. Optim.*, 34(2), 91-110, 2007.
- [4] C. Hessel, *Integration der Topologieoptimierung in den CAD-gestützten Entwicklungsprozess*, Dissertation, Shaker, Aachen, 2003.
- [5] T.Y. Chen and C.B. Wang, Topological and sizing optimization of reinforced ribs for a machining centre, *Eng. Opt.*, 40(1), 33-45, 2008.
- [6] C. Pedersen, P. Allinger and J. Sauter, Topology optimization for static and dynamic properties in Machine Tools Designing, *final report for BMBF joint research project "SimCAT"*, PTKA-PFT, Karlsruhe, 2006.
- [7] T.D. Tsai and C.C. Cheng, Structural design for desired eigenfrequencies and mode shapes using topology optimization, *Struct. Multidisc. Optim.*, 47, 673-686, 2013.
- [8] L. Shu, M. Wang, Z. Fang, Z. Ma and P. Wei, Level set based structural topology optimization for minimizing frequency response, *J. Sound Vib.*, 330, 5820-5834, 2011.
- [9] M. Weck and C. Brecher, *Werkzeugmaschinen Fertigungssysteme 2: Konstruktion und Berchnung*, 8th Ed., Springer, Berlin, 2006.
- [10] Z. Kang, X. Zhang, S. Jiang and G. Cheng, On topology optimization of damping layer in shell structures under harmonic excitations, *Struct. Multidisc. Optim.*, 46, 51-67, 2012.
- [11] X. Zhang and Z. Kang, Topology optimization of damping layers for minimizing sound radiation of shell structures, *J. Sound Vib.*, 332, 2500-2519, 2013.
- [12] L. Zuo and S. Nayfeh, The Two-Degree-of-Freedom Tuned-Mass Damper for Suppression of Single-Mode Vibration Under Random and Harmonic Excitation, *Transactions of the ASME*, 128(Feb), 56-65, 2006.
- [13] A. Kareem and S. Kline, Performance of Multiple Mass Dampers under Random Loading, *J. Struct. Eng.*, 121(2), 348-361, 1995.
- [14] L. Zuo and S. Nayfeh, Optimization of the Individual Stiffness and Damping Parameters in Multiple-Tuned-Mass-Damper Systems, *J. Vib. Acoust.*, 127(Feb), 77-83, 2005.
- [15] T.P. Bandivadekar and R.S. Jangid, Mass distribution of multiple tuned mass dampers for vibration control of structures, *Int. J. Civil Struct. Eng.*, 3(1), 70-84, 2012.
- [16] J. Park and D. Reed, Analysis of uniformly and linearly distributed mass dampers under harmonic and earthquake excitation, *Eng. Struct.*, 23, 802-814, 2000.
- [17] Y. Arfiadi and M. Hadi, Optimum placement and properties of tuned mass dampers using hybrid genetic algorithms, *Int. J. Optim. Civil Eng.*, 1, 167-187, 2011.
- [18] Y. Yang, J. Munoa and Y. Altintas, Optimization of multiple tuned mass dampers to suppress machine tool chatter, *Int. J. Mach. Tool Manu.*, 50, 834-842, 2010.
- [19] J.P. Den Hartog, *Mechanical Vibrations*, Dover Publications, New York, 1985.
- [20] J. Brock, A Note on the Damped Vibration Absorber, *J. Appl. Mech.*, 13(4), A284, 1946.
- [21] A.S. Joshi and R.S. Jangid, Optimum parameters of multiple tuned mass dampers for base-excited damped systems, *J. Sound Vib.*, 202(5), 657-667, 1997.
- [22] T.S. Kim and Y.Y. Kim, Mac-based mode-tracking in structural topology optimization, *Comput. Struct.*, 74(3), 375-383, 2000.
- [23] S. Fiebig and J. Axmann, Combining nonlinear FEA simulations and manufacturing restrictions in a new discrete topology optimization method, *Proceedings of WCSMO-9*, June 13-17, Shizuoka, Japan, 2011.

Fatigue Life Optimisation of Damage Tolerant Structures using Design Space Exploration

Raj Das¹, Rhys Jones²

¹ University of Auckland, Auckland 1010, New Zealand, r.das@auckland.ac.nz

² Monash University, Wellington Road, Victoria 3168, Australia, rhys.jones@monash.edu

1. Abstract

In parametric design studies, the strength of a structure is often considered as the primary design criterion, and consequently the optimal (best) structural design is often chosen as the one that minimises the maximum stress generated. However, for structures whereby failure is governed by fracture or fatigue, residual strength and fatigue life, as distinct from stress, need to be considered as the explicit design objectives.

In this study, the design space for fatigue life for different structural configurations is evaluated to demonstrate the utilities of design space exploration for damage tolerance design optimisation. This was illustrated using the problem of the optimum design of a cutout shape with boundary cracks under biaxial load. The minimum fatigue life associated with the cracks was evaluated for each cutout geometry.

The design surface for fatigue life establishes that a design based on damage tolerance parameters poses a well-behaved optimisation problem with a well-defined minimum/maximum region. The design space was found to be flat for fatigue life, enabling the specification of design tolerances. The optimum values of the fatigue life obtained from the design space agreed well with those determined using various optimisation methods. It is shown that a design space exploration can provide a systematic way to reduce the weight of a structure by adopting a 'feasible non-optimal' solution that meets the design criteria, rather than aiming for the 'optimal' (best) solution.

2. Keywords: Design space; Shape optimisation; Damage tolerance; Fatigue life; Finite element analysis.

3. Introduction

The late twentieth century saw the development of sophisticated structural analysis methods, which led to the use of light weight structures with low design safety factors. This resulted in high operational stress levels. High service stresses increase the likelihood of crack initiation and propagation. Furthermore, structures are now being fabricated using high strength materials that have a relatively low resistance against crack propagation. This problem is of prime concern in the aerospace industry where weight reduction is an important consideration. This led to the inception of damage tolerance design philosophy in which the presence of cracks and defects in a structure is taken into account. To address this, we previously developed a range of damage tolerance optimisation techniques based on a heuristic algorithms [1-5], and applied it for maximising the residual strength and fatigue life of structures.

Design optimisation including damage tolerance parameters is an inherently iterative process. One challenge often faced by a designer is to automate the evaluation of several potential designs. Design space exploration can be of immense aid in obtaining a collection of 'preliminary' improved designs that (partially) meet the design specifications and can assist in further optimisation of structures. The aim of the present study is to demonstrate the advantages of design space exploration for durability based designs. The effectiveness and utilities of design space exploration in the context of damage tolerance optimisation are demonstrated. In particular, one purpose of this paper is to evaluate the characteristics of the design space fatigue life. The optimum solutions obtained via the design space study are compared with those predicted by different structural optimisation methods. The utility of design space exploration in designing light-weight structures is also emphasised.

A design space for structural designs is a collection of structural responses (i.e. the values of objective and constraint functions) for various structural geometries and/or configurations (expressed by combinations of design variables). One way to perform a detailed (iterative) design study is to visualise the partial or entire design space. The initial step for this is similar to that of optimisation. The 'design problem' is to be cast as an equivalent 'standard optimisation problem', in terms of a set of design variables and objective and constraint functions. The design space can then be determined by analysing the structure for each possible combination of the design variables (design point). Design space studies for multiple design criteria can aid in assessing the relative roles of multiple design objectives. For example, the variation of the minimum fatigue life and the maximum stress for different shapes provides the designer with an insight into the relative performance of these shapes. A designer has the option of choosing a design in the vicinity of an optimum solution rather than selecting the 'fatigue life optimum point' itself as the final design. This compromise may be necessary to meet a maximum strength

requirement, or to satisfy specific operational constraints. In this paper, we will evaluate the characteristics of the design space of one of the primary damage tolerance criteria, i.e. fatigue life of a structure via a simple example.

4. Example Problem

4.1 Problem Description

Design space exploration is illustrated through the simple problem of ‘the optimum design of a cylindrical (through-the-thickness) cutout located in a rectangular block under biaxial loading’. This specific problem was selected as it has been used in the previous optimisation studies by the present and other authors in the literature [3, 4, 6, 7]. Hence, this will enable us to correlate and compare the ‘optimum point(s)’ observed in the design space with those obtained using the different optimisation methods.

The problem geometry, loading and boundary conditions are shown in Figure 1. It is a three-dimensional rectangular block, 320 mm wide, 320 mm high, with a thickness of 20 mm, and has a circular through-the-thickness cutout at its centre. The diameter of the initial cutout was 20 mm. The material of the block was assumed to be an aluminium alloy (2219-T851) with a Young's modulus of 71 GPa and a Poisson's ratio of 0.3. A one-eighth model of the block along with the loads and constraints was considered, because the geometry, loading, and constraints are symmetric about the three planes (xy , yz , and xz), as shown in Figure 1. Symmetry boundary conditions were imposed on the planes (xz , yz and mid- xy planes) by constraining the appropriate displacements (u_x , u_y and u_z) and rotations (θ_x , θ_y and θ_z). All the planes (xy , yz and xz) mentioned in the rest of the paper refer to Figure 1.

A simple constant amplitude fatigue loading was assumed. The block was subjected to fluctuating (cyclic) stresses in the horizontal (x) and vertical (y) directions. The mean stresses for the present problem were 75 and 150 MPa, respectively, in the x and y direction, and the corresponding stress amplitudes were 25 and 50 MPa, respectively. The minimum fatigue life associated with the cracks was taken as the design criterion or objective function.

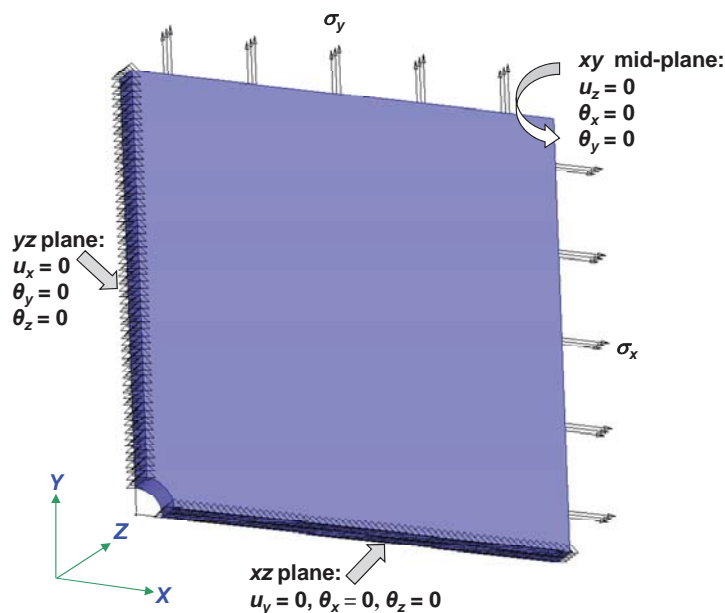


Figure 1: Schematic of the one-eighth model of a cylindrical cutout in a rectangular block under biaxial load (u_x , u_y , and u_z denote the displacements along the x , y and z axes, respectively, and θ_x , θ_y and θ_z denote the rotations about the respective axes).

4.2 Crack Modelling

A number of surface cracks were modelled on the hole boundary. All the cracks were assumed to be semi-elliptical flaws emanating from the hole surface with their major axes (c) parallel to the axis of the hole (z axis) and minor axes (a) normal to the hole surface, see Figure 2. An initial crack spacing approximately equal to the smallest crack size was used to achieve an effective modelling of the stress intensity factor and fatigue life variation along the structural boundary. Here we modelled 21 three-dimensional semi-elliptical cracks along the surface of the cylindrical hole (for one quarter) resulting in an initial crack spacing of ~ 0.75 mm. Each crack on the structural boundary was assumed to grow in the direction of the major and minor axes from an initial size of (c_i , a_i) to its final size of (c_f , a_f). The initial surface flaws were assumed to be of size, $c_i = 5$ mm, $a_i = 2$ mm, and the final acceptable

flaw size was taken as, $c_f = 8$ mm, $a_f = 4$ mm. These specific flaw cases were chosen, because these were the representative cases previously studied [3, 4]. All the cracks were grown simultaneously for fatigue life design space evaluation.

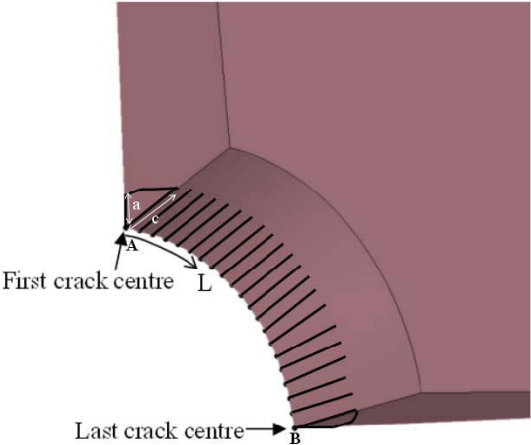


Figure 2: Locations of the three-dimensional semi-elliptical cracks along the hole surface (one-eighth model)

4.3 Geometry Representation

The geometric representation of the hole shape in the xy plane is given by:

$$\frac{x^p}{a^p} + \frac{y^p}{b^p} - 1 = 0 \tag{1}$$

where a , b , and p are the shape parameters. The shape of the hole is altered by varying these parameters. Any combination of them can be chosen as the design variables for optimisation. As such, this geometric description is ideally suited to the present problem of the optimum design of a cutout in a rectangular block under biaxial loading. Hence, in the present study, Equation 1 was used to generate the design points on the hole surface for a given combination of design variables (a , b , and p).

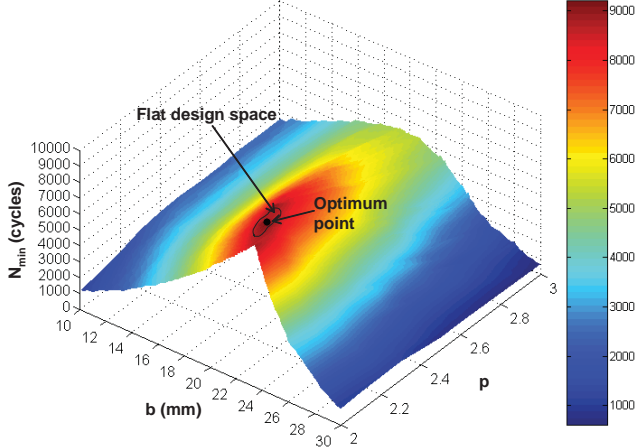


Figure 3: Fatigue life study: Design space plot of the objective function (the minimum fatigue life N_{min}) with hole geometric parameters, hole size (b) and curvature index (p)

5. Design Space Exploration

The design parameters, hole dimension (b) and curvature index/exponent (p), were varied to generate a set of design points to investigate the nature of variation of the minimum fatigue life associated with all the cracks on the boundary for different cutout shapes. The major axis b was varied from 10 to 30 mm, and the index p was varied from 2 to 3, generating a total of 1287 design points. This enabled a reasonably accurate representation of the design space, which was also used for validating the previous optimisation results. The design space for the

minimum fatigue life (N_{min}) is presented in Figure 3. As expected, the surface takes the shape of an ‘inverted ship hull’, which is intuitive. The maximum point (optimal hole) corresponds to a fatigue life of 9214 cycles. The size (b) and curvature (p) of the optimal hole shape are 22.8 mm and 2.1, respectively. The fatigue life optimal cutout is shown in Figure 4. It is noteworthy that for fatigue life, the optimal points exist on the plane $p = 2.1$, and the optimal shape represents a ‘super-ellipse’.

The design space of fatigue life of the cutout in Figure 3 is found to be flat for fatigue life. This ‘flat’ design space can be thought of as a set of local ‘optimums’ clustered in a small region. Since all of these optimum points have approximately the same value of the objective function (N_{min}), it is thus appropriate to conclude that this class of problems has a ‘global optimum region’ instead of a global optimum point. Furthermore, the flatness of the design space establishes that the design is robust in a Taguchi sense. The width of the flat region is within 10% of the average value of the design variables. So this is within the commonly adopted manufacturing tolerances. This insensitivity of the optimum point or flatness of the optimum region implies that it is feasible to extract the maximum fatigue life taking into account the variability in typical industrial manufacturing processes.

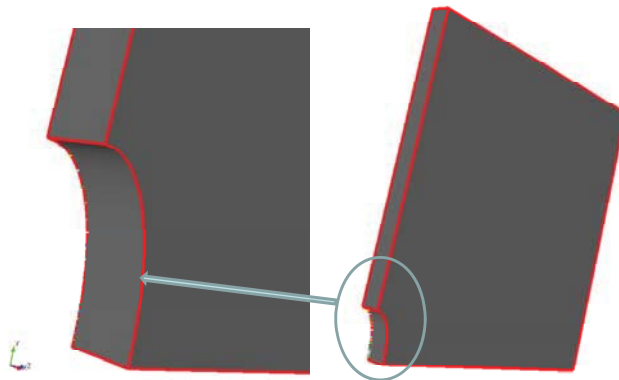


Figure 4: Fatigue life optimal shape with $b = 22.8$ mm and $p = 2.1$, with life optimised shape being larger than the initial cutout, leading to weight reduction

6. Relationship of Design Space Study with Structural Optimisation

Design space exploration and optimisation are closely related in that in structural optimisation we move through the design space using an algorithm to improve a current design, whereas in a design space study we attempt to obtain the overall variation in the design objective function with structural geometry/shape. Indeed, one of the earlier optimisation algorithms, known as the ‘random search method’, utilises a similar concept [8]. For many optimisation problems the optimum solution may not be unique and often depends on the initial (starting) shape, especially if multiple (local) optimum points exist. In such cases an initial examination of the nature of the design space can help set a starting solution that would (eventually) converge to an improved (local) optimum point. This can lead to a significant improvement in the structural performance in cases where there is a considerable variability among the objective functions associated with different local optimum shapes.

In contrast, for the present problem of the cutout shape design with fatigue life as the design objective, an initial design space evaluation can save computational time. The realisation that the design space around the optimum point is ‘flat’ means that once a design point is in the ‘near’ optimal zone, any solution in the neighbourhood could be taken as an acceptable design, because the fatigue life of the structure will not improve appreciably by further refining the solution to locate the ‘precise’ optimum point. In the context of practical structural designs, the extent of flatness in the design space can be used to specify the manufacturing tolerances during the design stage without compromising the fatigue life of the resultant structure.

Design space analysis can also be used for verifying the reliability and assessing the performance of optimisation algorithms before applying them to design optimisation of a relatively complex structure. In the previous studies, we performed the same damage tolerance based cutout optimisation problem using two ‘fundamentally’ different optimisation methods, a Biological method [3, 4] and nonlinear programming methods [6, 7]. The optimum results from the design space evaluations for fatigue life are compared with those obtained using the different optimisation methods [3, 4, 6, 7].

The hole dimensions and curvatures obtained using a heuristic and a gradient-based method are compared with those observed from the design spaces in Table 1. To compare the optimum point identified using the design space study for fatigue life, the hole shape optimisation was performed using the 3D Biological algorithm [4] and the nonlinear programming method [7]. The initial and final flaw sizes were the same as used in the design space study, i.e. $c_i = 5$ mm, $a_i = 2$ mm, and $c_f = 8$ mm, $a_f = 4$ mm. The fatigue life at the optimum point and the cutout geometry parameters are presented in Table 1. All the three approaches essentially predicted the same ‘near’

optimum solution.

Table 1: Comparison of the fatigue life optimisation results with the design space study

Methods	Hole major axis (b) (mm)	Hole curvature (p)	Objective function (N_{min}) (cycles)
Biological method [4]	22.909	-	9043
Nonlinear programming method [7]	22.876	2.132	9154
Design space study	22.8	2.1	9214

7. On Weight Reduction and Optimum Design

A design space plot can further help in lightening a shape by exploring alternative designs. There are cases when the design is deemed to be acceptable, but the structure is thought to be too heavy. This can be illustrated using the present example. Since in this example, a rectangular block supposedly from a generic structural component is used, the total weight of the structure is unknown. So the volume of the cutout shape is used instead to identify the weight savings. An increase in the cutout volume will lead to weight reduction of the resultant structure. Figure 5 presents the volume of the cutout (normalised relative to the volume of the initial circular cutout) for different shapes. By combining Figures 3 and 5, a non-optimal design point could be chosen that would have a lower weight, yet maintaining an adequate fatigue life.

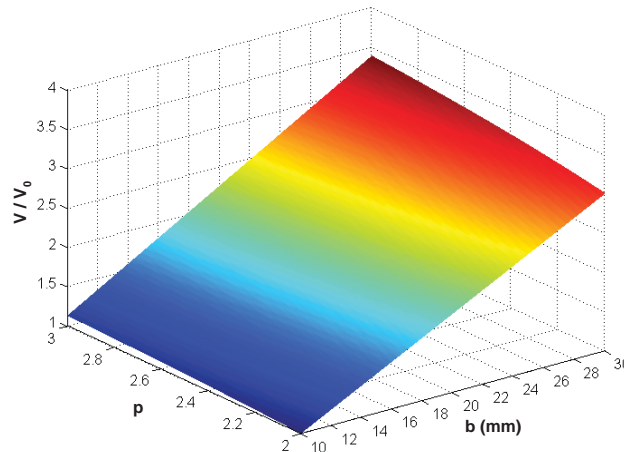


Figure 5: Volume (normalised) of the cutout at various design points

To illustrate this concept, let us consider a series of cutout shapes, all having the same (optimum) curvature index of $p = 2.1$. Figure 6 shows the variation of the (minimum) fatigue life with the cutout volume ratio (V/V_0) for the optimum curvature index ($p_{opt} = 2.1$). The fatigue life increases as the hole enlarges and it reaches a maximum value of 9,214 cycles at $V/V_0 = 2.322$. Beyond this optimum point the fatigue life reduces with an increase in the cutout volume. In this case an optimum shape leads to a weight saving of ~ 2.32 times the volume of a circular hole, in addition to a significant gain in the fatigue life (~ 7.9 times that of a circular hole).

However, the shape can be further lightened if the desired fatigue life (N_{design}) is lower than the maximum fatigue life that can be achieved by adopting an optimal shape. This is illustrated in Figure 6. For example, if the design life is $N_{design} = 7000$ cycles, then a line AB corresponding to $N_{min} = 7000$ cycles can be drawn in Figure 6. Any point above AB will constitute an acceptable design with a life $N_{min} > N_{design}$. In such a case the shape corresponding to point B ($V/V_0 = 2.474$) will provide the largest (acceptable) hole shape, or the lightest shape satisfying the fatigue life design limit. In this case, adopting a ‘non-optimal feasible’ design can lead to a further weight saving of $\sim 6.5\%$ over the fatigue life optimal shape. This weight reduction can be enhanced if the design fatigue life is further lowered, see Figure 6.

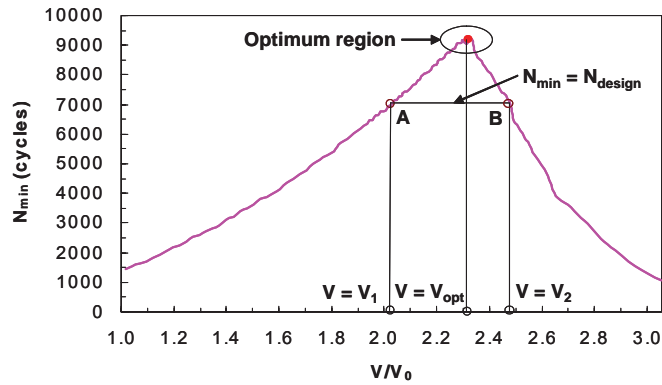


Figure 6: Variation of the minimum fatigue life with (normalised) volume for a super elliptical ('near' elliptical) hole with optimum curvature index ($p_{opt} = 2.1$)

8. Conclusions

In this paper, a design space exploration study has been undertaken to understand the nature and variation of the damage tolerance based objective functions with structural geometry and to illustrate the utility of design space exploration in the context of durability based design optimisation. The design space study was first demonstrated using the problem of the optimisation of a cutout shape under biaxial load with fatigue life as the design criteria. The shape of the cutout was parametrically represented using super ellipses. The minimum fatigue life associated with the flaws along the structural boundary was evaluated for various hole geometries to construct the design space.

The design surface for fatigue life it resembles an 'inverted ship hull'. These shapes confirm that the design based on fatigue life, indeed poses a well-behaved optimisation problem, i.e. a well-defined maximum region exists.

One benefit of a design space study is that it can provide an 'overall view' of the objective function distribution. From earlier studies it was concluded that for this category of problems multiple 'local' optimums can exist. The present study has shown that a set of 'local' optimum solutions can exist in a 'close' neighbourhood, rather than lying apart as found in many other classes of structural optimisation problems. It is therefore contended that this class of damage tolerance optimisation problems has a 'global' optimum region, rather than a single global optimum point. This feature of damage tolerance optimisation has not been previously reported.

It was found that the design space is flat, which supported the earlier findings using the various optimisation methods. This signifies that from an engineering design point of view, the structural responses of various geometries in the 'near' optimal region will not be considerably different. Thus, it may be sufficient to choose one of the shapes in the 'near' optimal region as the final design. This can immensely reduce optimisation effort and computational time, and also enable us to extract the optimum performance accounting for manufacturing tolerances, as there will not be any need to precisely locate the (local/global) optimum solution. We can also lighten a structure by removing material appropriately from a 'near' optimal geometry without significantly degrading its durability related structural performance.

9. References

- [1] R. Das, R. Jones and Y.M. Xie, Design of structures for optimal static strength using ESO, *Engineering Failure Analysis*, 12 (1), 61-80, 2005.
- [2] R. Das, R. Jones and S. Chandra, Damage tolerance based shape design of a stringer cutout using evolutionary structural optimisation, *Engineering Failure Analysis*, 14 (1), 118-137, 2007.
- [3] R. Das, R. Jones and D. Peng, Optimisation of damage tolerant structures using a 3D Biological algorithm, *Engineering Failure Analysis*, 13 (3), 362-379, 2006.
- [4] R. Das and R. Jones, Development of a 3D Biological Method for Fatigue Life based Optimisation and its Application to Structural Shape Design, *International Journal of Fatigue*, 31 (2), 309-321, 2009.
- [5] R. Das and R. Jones, Damage tolerance based design optimisation of a fuel flow vent hole in an aircraft structure, *Structural and Multidisciplinary Optimization*, 38 (3), 245-265, 2009.
- [6] R. Das and R. Jones, Designing cutouts for optimum residual strength in plane structural elements, *International Journal of Fracture*, 156 (2), 129-153, 2009.
- [7] R. Das and R. Jones, Fatigue life enhancement of structures using shape optimisation, *Theoretical and Applied Fracture Mechanics*, 52, 165-179, 2009.
- [8] G.N. Vanderplaats, Numerical Optimization Techniques for Engineering Design: with Application, McGraw-Hill, New York, 1984.

Structural optimization of standardized trusses by dynamic grouping of modules

Alexis Tugilimana¹, Rajan Filomeno Coelho², Ashley P. Thrall³

¹ Université Libre de Bruxelles, Bruxelles, Belgium, atugilim@ulb.ac.be

² Université Libre de Bruxelles, Bruxelles, Belgium, rfilomen@ulb.ac.be

³ University of Notre Dame, Notre Dame, USA, athrall@nd.edu

1. Abstract

Modular structures tend to be widely used in civil engineering since components can be mass-produced in high quality controlled facilities, leading to economy of construction and improved reliability. Existing research in optimization of modular structures has focused primarily on the notion of modularity where only the topology is repeated. This paper presents a novel approach for dynamic grouping and topology optimization of modular structures, including the spatial orientation of the modules as an additional design variable. This extends the standard notion of modularity by accounting for the topology invariance of the module under rigid body rotations. Group theory is used to handle the spatial rotations and gives a straightforward and efficient mathematical representation of the module properties in terms of a permutation matrix for the rotation and continuous variables for the topology. Further theoretical developments are proposed to couple the existing dynamic grouping techniques for module linking, which is coupled with the proposed method of optimization for modular structures. The proposed approach is illustrated through an academic modular truss bridge, where a memetic algorithm is used to optimize simultaneously the topology and the orientation of the modules.

2. Keywords: Structural optimization, modular structures, group theory.

3. Introduction

Stronger requirements on sustainability, safety, and cost push architects and engineers to develop new philosophies of design. Among them, modularity (i.e., dividing a complex structure into simpler subsystems that can be mass-produced in high quality-controlled facilities [8]) offers substantial advantages. First, the repeatability of the components together with their independence allows for an industrial manufacturing of the modules, leading to better quality controls of production, higher safety measures, and a reduced sensitivity to weather interferences. Secondly, prefabrication of the modules leads to a significant time saving during construction since several tasks can be carried out in parallel, i.e., the geotechnical phases and the manufacturing of modules [11]. While modularity in construction is not new, optimization of modular structures is still largely unexplored and can lead to improved sustainability, safety, and economy.

The coupling between modularity and optimization involves two scales that must be considered concurrently. On one hand, the module scale is defined by the topology and the shape variables identically repeated throughout the structure. On the other hand, the structure scale describes the way the whole system is assembled starting from the initial module. Topology optimization for modular structures has been carried out for continuous and discrete structures but is still restricted to the module scale, without the capability of changing the module orientation [6, 1]. In other words, the module topology is repeated throughout the whole structure using standard symmetry operations like translation, rotation, and reflection. On a different standpoint, authors in [12] focused on the optimal orientation of fixed-topology modules for architectural purposes, i.e., building communication networks for pedestrian traffic. Starting from a fixed topology, a genetic algorithm evaluated the optimal module assembly to minimize the walking distance between two terminals. Finally, considering a small number of identical modules, so-called a group, results in added flexibility in the design and improves the optimization process, while keeping the economical and functional advantages of modularity [1].

From these observations, it follows that the optimization focuses either on the module scale or on the assembly process to build the whole structure, but always through a decoupled methodology. Therefore, the present paper proposes a unified formulation for optimizing modular truss structures assuming a linear elastic behaviour, focusing simultaneously on the topology of the modules, their spatial orientations, and the way they are dynamically grouped. This problem, which includes different types of design variables, is solved using a memetic algorithm: a simultaneous analysis and design technique is used for the topology optimization (to handle a large number constraints and variables) while elements of group theory efficiently integrate the module rotations.

4. Group theory and rigid body rotations

Including module rotation in the optimization requires some care related to the structure assembly and the non-commutative character of the rigid body rotations. This section addresses the numerical approach for the latter problem. By denoting $d \in \{2, 3\}$ the spatial dimension and N_s the number of support reactions, the number of degrees of freedom is $N_d = dN_n - N_s$, with N_n being the number of nodes. The pin-jointed modular structure is made of N_m identical modules, each of them composed of N_{em} elements. Due to topological repetition, all modules can be expressed through a reduced number of variables for the cross sections and the bar lengths i.e., $\mathbf{a} \in \mathbb{R}_+^{N_{em}}$ and $\mathbf{l} \in \mathbb{R}_+^{N_{em}}$ respectively.

Accounting for spatial rotations in modular structures is of great interest, since fixing the way the modules are assembled before carrying out the topology optimization will inherently bias the process [6]. Group theory provides a rigorous mathematical background to systematically describe symmetry operations, i.e., the operations that map an object into coincidence with itself. Widely used in chemistry and physics [5], extensions to civil engineering applications have been carried out to reduce the computational effort using a particular group, so-called the point group, that leaves one point fixed under operations. For spatial rotations, the special orthogonal group $SO(3)$ is the most convenient set of symmetry operations to easily handle module orientation modifications while ensuring the topology invariance. Indeed, the latter corresponds to the group of all the rotations about the origin of a three-dimensional Euclidean space \mathbb{R}^3 .

In structural analysis, rotating the modules in space using $SO(3)$ requires some care: starting from an initial configuration, the module rotation leads to the dissociation between the forces and the nodes where they were initially applied, leading to unstable structures. Considering only a finite set, so-called admissible rotations, permits the circumvention of this problem of stability, by ensuring a perfect superposition between the initial and the final configurations for the boundary nodes only. Doing so, the symmetry operation will only consist of permuting the cross sections of the module elements in addition to continuously rotating the nodes inside the module. In group theory, any element of a symmetry group is associated a matrix representation. In the case of $SO(3)$ for module rotation, one defines the matrix representation \mathbf{P} such that, when rotating a module, a new topological configuration \mathbf{a}' is reached and expressed by $\mathbf{a}' = \mathbf{P}\mathbf{a}$ [10]. The latter formulation presents attractive outcomes since it allows for a perfect decoupling between the rotation \mathbf{P} and the topology \mathbf{a} , identical for all the modules. An illustration of the way the permutation matrices are acting on the structure is given in Fig. 1, where a rotation of 120 degrees is performed around the center c .

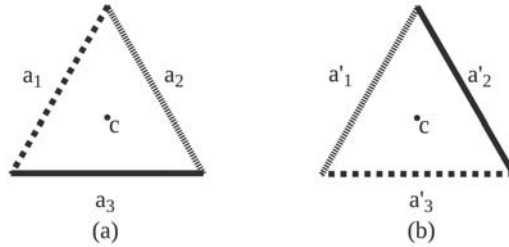


Figure 1: Effect of a permutation matrix on the topology of a triangular structure. The initial and final topologies, after a counter-clockwise rotation of 120 degrees around the point c , are depicted in (a) and (b) respectively. The final cross section vector \mathbf{a}' is obtained by a change in the topology between the bars and expressed by $\mathbf{a}' = \mathbf{P}_c \mathbf{a}$.

Building the set of admissible permutation matrices can be performed using Euler's theorem, stating that any rotation around some axis is composed of a combination of three orthogonal rotations. To do so, one starts from the rotations matrices \mathbf{P}_{nx} , \mathbf{P}_{ny} and \mathbf{P}_{nz} , corresponding to the matrix representations of the smallest admissible rotations of an angle $\alpha = 2\pi/n$ (with $n \in \mathbb{R}_0^+$), in the three orthogonal directions x , y and z respectively. Evaluating these three matrices is purely geometrical and consists of considering the module as a convex polygon that is rotated to ensure a perfect superposition between the initial and the final configuration. Such an operation can easily be carried out using a scalar measure, represented by the total square Euclidean distance e , that becomes zero for any admissible rotation:

$$e_n = \sum_{i=1}^{n_b} \min_j \|\mathbf{x}_{f,i}(n) - \mathbf{x}_j\|^2 \quad (1)$$

where n_b denotes the number of boundary nodes per module, $\mathbf{x}_{f,i}(n)$ and \mathbf{x}_j the i^{th} final and the j^{th} initial position of the boundary nodes respectively, for an angle of rotation $\alpha = 2\pi/n$. An example of the evolution of the total Euclidean distance with respect to α is illustrated in Fig. 2 for a hexagonal module, under a rotation around the c

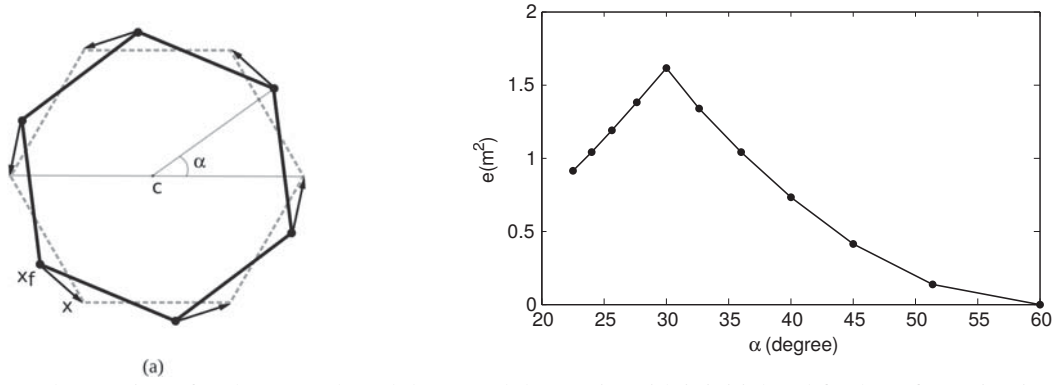


Figure 2: The rotation of an hexagonal module around the c axis, with its initial and final configuration in gray and black respectively (a). The total square Euclidean distance, obtained by summing the square of the norm of the black vectors, evolves towards zero for an angle of rotation ($\alpha = 2\pi/n$) of 60 degrees (b).

axis. Retaining the way the nodes are permuted when the total Euclidean distance is zero enables the building of the permutation matrix: \mathbf{P}_{kp} takes a unitary value if the k^{th} and the p^{th} bars are permuted.

The major problem when handling spatial rotations using $SO(3)$ relies on its non-commutative characteristic i.e., $\mathbf{P}_{nx}\mathbf{P}_{ny}\mathbf{P}_{nz} \neq \mathbf{P}_{ny}\mathbf{P}_{nz}\mathbf{P}_{nx}$ [5]. As a consequence, the order of the matrix multiplication matters for being able to explore all of the possible module orientations, which unfavourably impacts the size of the design space. Well known techniques have been developed to deal with combinatorial optimization and permutation-based problems without exploring the whole design space. However, most of them require sufficient information on the problem to enumerate the solutions in a clever way, by disregarding subsets of the design space that do not contain the solution [2]. In the present study, the non-commutative and discrete character of the design space for the admissible rotations forbids such an approach, leading to a standard complete enumeration procedure:

$$\mathbf{P}_{(L_\xi, L_\eta, L_\zeta)} = \mathbf{P}_{n_\xi}^{L_\xi} \mathbf{P}_{n_\eta}^{L_\eta} \mathbf{P}_{n_\zeta}^{L_\zeta} \begin{cases} L_\xi = 1, \dots, n_\xi - 1 \\ L_\eta = 1, \dots, n_\eta - 1 \\ L_\zeta = 1, \dots, n_\zeta - 1 \end{cases} \quad \forall \xi, \eta, \zeta \in \{x, y, z\} \quad (2)$$

where $\mathbf{P}_{n_\xi}^{L_\xi}$ corresponds to a rotation in the ξ^{th} direction with an angle of $2\pi L_\xi / n_\xi$. Since equation (2) generates the complete set of admissible rotations, the computational complexity becomes very high due to its exponential dependence with respect to the number of modules. Considering a structure made of N_m modules where each of them has, in average, n possibilities of rotation in each direction. The total number of possible combinations, accounting for the non-commutativity of the rotations, is exactly $3!n^{dN_m}$, leading to a time complexity $T(n, N_m) = \mathcal{O}(n^{N_m})$. Fortunately, in the case of module rotations, different combinations of permutation matrices lead to the same final configuration, thereby greatly reducing the complexity of the problem. In the hexagonal example in Fig. 2, a reduction of 12^{N_m} times the initial space of search can be performed, leading to a problem that is numerically tractable without extensive computational efforts.

5. Hybrid optimization algorithm for structural optimization of modular truss structures

The optimization problem addressed in the present paper consists of minimizing the compliance (the compliance is a measure of the energy stored in a structure undergoing deformation) of a modular truss structure under (i) the static and kinematic equilibrium conditions and (ii) a limitation on the allowable final volume and nodal displacements. First, modifications are made to the equilibrium equations to account for the permutation matrices and the topological repetition in the modular structures.

5.1. Equilibrium equations for modular truss structures

The module cross section vector \mathbf{a}_m can be expressed, according to group theory, by a permutation matrix \mathbf{P}^m and the fundamental cross section \mathbf{a} . Incorporating the latter formulation into the kinematic and static compatibility equations [9] enables the expression of the classical equilibrium equations for modular structures:

$$\sum_{m=1}^{N_m} \sum_{e=1}^{N_{em}} \frac{E a_{em}}{l_{em}} \gamma_{em}^T \gamma_{em} \mathbf{u} = \mathbf{f} \quad (3)$$

where a_{em} denotes the cross section of the e^{th} element in the m^{th} module, γ_{em} represents its direction cosines and

$\mathbf{u} \in \mathbb{R}^{N_d}$ and $\mathbf{f} \in \mathbb{R}^{N_d}$ denotes the displacement field and external force vector respectively. By introducing the permutation matrices \mathbf{P} and the cross section vector \mathbf{a} , the module cross section becomes

$$a_{em} = \sum_{r=1}^{N_{em}} \mathbf{P}_{er}^m a_r \quad (4)$$

where \mathbf{P}^m denotes the permutation matrix of the m^{th} module. Equations (3) and (4) can be coupled together to explicitly express the equilibrium equations in terms of a module orientation \mathbf{P}^m and the topology information \mathbf{a} (identical for all the modules) in the optimization problem.

5.2. Problem formulation for optimization of modular truss structures

Typically, the numerical optimization and analysis phases are considered distinct in a computational sense. Given a design domain, the structure is solved exactly through a finite element analysis, hence only the optimization is involved in the design space related to the cross section vector \mathbf{a} , distinct from the state space defined by the displacement field \mathbf{u} . This procedure, so-called nested analysis and design, is solved by an iterative procedure until the optimum is reached. Another paradigm, namely the simultaneous analysis and design, treats the design and state variables independently, so that equilibrium equations (3) are set as equality constraints and do not need to be solved at each iteration [4, 3]. Following the latter formulation, coupled with equations (3) and (4), the problem definition for compliance minimization of modular structures can be stated as

$$\begin{aligned} & \underset{\mathbf{P}, \mathbf{a}, \mathbf{u}}{\text{Minimize}} \quad \frac{1}{2} \mathbf{f}^T \mathbf{u} \\ & \text{s.t.} \quad \sum_{m=1}^{N_m} \sum_{e=1}^{N_{em}} \frac{E a_{em}}{l_{em}} \gamma_{em}^T \gamma_{em} \mathbf{u} = \mathbf{f} \\ & \quad |u_{e,m}| - u_{\text{lim}} \leq 0 \\ & \quad N_m \sum_{e=1}^{N_{em}} a_e l_e - v_{\text{lim}} = 0 \end{aligned} \quad (5)$$

with $\mathbf{a} \in \mathbb{R}_+^{N_{em}}$, $\mathbf{P} \in \mathbb{P}$, the set of admissible permutation matrices $\mathbb{P} \subset \mathbb{R}^{N_{em} \times N_{em}}$. In equation (5), u_{lim} and v_{lim} correspond to the allowable magnitudes for the displacements and the volume respectively. The major issue in solving equation (5) is the different nature of the design variables. Although simultaneous analysis and design topology optimization problem can be efficiently solved using mathematical programming, the discrete character of the permutation matrices makes the resolution of equation (5) difficult with a single algorithm.

Among algorithms that are able to manage multiple types of design variables, hybrid algorithms offer a great potential to efficiently solve equation (5). Indeed, combining global and a local search techniques provides the advantages of both methods, i.e., being able to explore the design space with non-continuous variables and easily handling large scale problems [7]. In this study, the Lamarckian approach is used, in which a genetic algorithm and a gradient-based method are employed together [7]. In such an approach, the design variables are divided into two parts, each of them are handled by one of the two algorithms. The genetic algorithm manages the discrete variables for the permutation matrices while the gradient-based method works only with the continuous variables, and both are coupled for the evaluation of the objective functions and constraints. The general functioning of the proposed memetic algorithm is depicted in Fig. 3: in one iteration of the algorithm, the genetic operators perform modifications to the permutation matrices before applying the interior-point algorithm, to drive the individuals to local optima for a fixed module orientation. The major advantage of the proposed approach relies in the use of a mathematical programming to solve equation (5) for fixed values of the permutation matrices, taking advantage of the inherent sparsity of the problem as well as the capability of providing analytically the Jacobian matrices [4].

6. Numerical application

To illustrate the proposed approach, an academic application of a simply supported bridge truss made of 4 identical modules is studied (Fig. 4). The design domain is made of a 13 x 3 grid regularly spaced by one meter while the ground structure at the module scale is composed of 66 bars. The bridge, made of steel (S235), has a span of 12 meters and is submitted to a single load acting at the upper node at midspan with a magnitude of 100 kN. The Young's modulus E and the limitations on the volume v_{lim} and the displacement u_{lim} are equal to 235 MPa, 10% of the initial volume of the ground structure, and 1/800 of the span respectively. To solve the non-linear problem (5), a genetic algorithm for integer programming handles the permutation matrices (using truncated Laplacian crossover and power mutation operators), while an interior-point algorithm with analytic Jacobian handles the cross sections

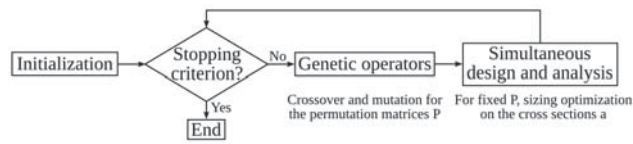


Figure 3: General flowchart of the memetic algorithm. The permutation matrices are managed by the genetic operators while the cross sections \mathbf{a} and the displacement field \mathbf{u} are handled by the local search algorithm

and the displacement field. A small population size of 20 individuals is sufficient to ensure a fast convergence of the algorithm since only the spatial orientation variables are handled by the genetic algorithm. The convergence criterion is based on the stable condition (10^{-8}) for the design variables and the objective function.

The proposed approach is compared with the optimization of periodic modular structures [6]. In the latter, the module orientation is a priori fixed, taking advantage of the structural symmetry; in the present example, this corresponds to a topology symmetry between the modules 1 and 4 and the modules 2 and 3. The results are depicted in Fig. 5, corresponding to the module topology and their spatial orientations to build the whole structure, where a final compliance of 25.74 J is reached. Fig. 6 gives the results obtained by the proposed approach, where a gain in efficiency is clearly demonstrated in comparison with the previous method: simultaneous module topology and spatial orientation decreases the objective function to 22.49 J. The cross sections as well as the module orientations are such that the whole structure presents strong elements to handle the flexural loads on the bridge. In addition, it can be noticed that the latter solid configuration exhibits similarities with those obtained from continuous optimization for a simply supported bridge [3].

From a computational viewpoint, 30 generations are sufficient to respect the stopping criterion. This fast convergence towards the solution can be explained by the simultaneous optimization of the module orientation and their topology. The same optimal configuration can be attained by different module topologies and spatial arrangements, representing the existence of multiple but equivalent local minima. In addition, the latter observation also explained the high robustness of the algorithm with respect to the genetic parameters, where variations on the results were only observed for a population size less than 10 individuals together with a convergence tolerance lower than 10^{-3} .

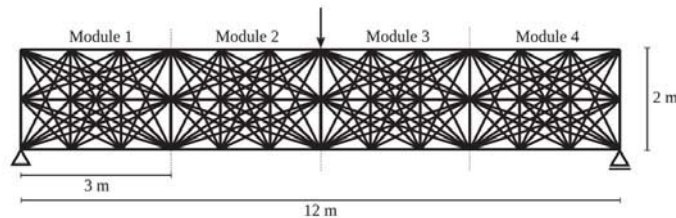


Figure 4: Ground structure

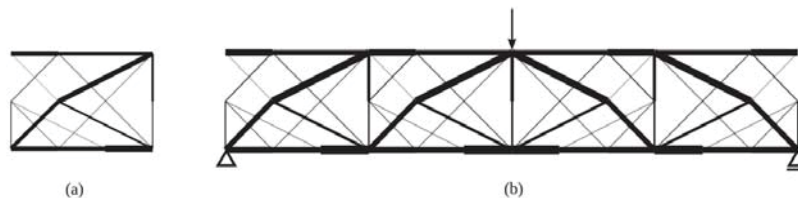


Figure 5: The results obtained when imposing the topology symmetry, with the module topology (a) and the final module distribution (b) (compliance = 25.74 J)

6. Conclusions

This paper describes a novel approach for the structural optimization of modular structures i.e., structures made of identical topological components. By coupling elements of group theory and mathematical programming techniques, the problem is properly addressed and solved through a memetic algorithm, allowing for a clear decoupling between design variables of different natures. A genetic algorithm handles the discrete variables using truncated

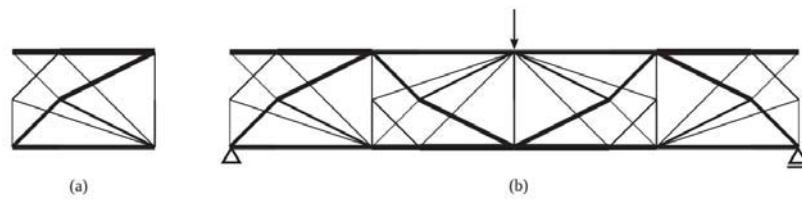


Figure 6: The results obtained by the proposed approach, with the module topology (a) and the final module distribution (b) (compliance = 22.49 J)

genetic operators while, for fixed module orientations, a simultaneous analysis and design manages the topology optimization at the module scale; the latter barrier problem is solved using an interior-point algorithm, which is well suited for problems involving a large number of design variables and constraints. With a limited computational effort, optimal configurations, in terms of module orientation and topology, are generated and provide better optimization results than applying standard optimization approaches for modular structures. For future works, extensions of the proposed method to manage partial modularity and dynamic grouping of modules will be investigated, in order to provide a complete unified framework.

6. Acknowledgement

The first author would like to thank the Fonds National de la Recherche Scientifique (FNRS, Belgium) for financial support of this research.

7. References

- [1] H. J. Barbarosa, A. C. Lemonge, and C. C. Borges. A genetic algorithm encoding for cardinality constraints and automatic variable linking in structural optimization. *Engineering Structures*, 30:3708–3723, 2008.
- [2] J. Bard F. *Practical Bilevel Optimization: Algorithms and Applications*. Kluwer Academic Publishers, 1998.
- [3] M. Bendsøe and O. Sigmund. *Topology Optimization: Theory, Methods and Applications*. Springer, Berlin, 2003.
- [4] B. Descamps and R. Filomeno Coelho. A lower-bound formulation for the geometry and topology optimization of truss structures under multiple loading. *Structural Multidisciplinary Optimization*, 48:49–58, 2013.
- [5] M. Hamermesh. *Group theory and its application to physical problems*. Dover, 1989.
- [6] X. Huang and Y. M. Xie. Optimization design of periodic structures using evolutionary topology optimization. *Structural and Multidisciplinary Optimization*, 36:597–606, 2008.
- [7] V. Kelner, F. Capitanescu, O. Léonard, and L. Wehenkel. A hybrid optimization technique coupling an evolutionary and a local search algorithm. *Journal of Computational and Applied Mathematics*, 215:448–456, 2008.
- [8] J. H. Mikkola and O. Gassmann. Managing modularity of product architectures: Toward an integrated theory. *IEEE Transactions on Engineering Management*, 50:1–15, 2003.
- [9] J. Petersson. On continuity of the design-to-state mappings for trusses with variable topology. *International Journal of Engineering Science*, 39:1119–1141, 2001.
- [10] J. N. Richardson, S. Adriaenssens, P. Bouillard, and R. Filomeno Coelho. Symmetry and asymmetry of solutions in discrete variable structural optimization. *Structural and Multidisciplinary Optimization*, 47:631–643, 2012.
- [11] R. E. Smith. *PREFAB Architecture: a guide to modular design and construction*. John Wiley & Sons, 2010.
- [12] M. Zawidzki and K. Nishinari. Modular truss-z system for self-supporting skeletal free-form pedestrian networks. *Advances in Engineering Software*, 47:147–159, 2012.

A study of optimization for automotive parts and structures by using inertia relief

Takanobu Saito¹, Jiro Hiramoto², Toshiaki Urabe²

¹ JFE Steel Corporation, Chiba, Japan, takan-saito@jfe-steel.co.jp

² JFE Steel Corporation, Chiba, Japan

1. Abstract

The topology analysis method was developed to optimize the part shape and configuration of automotive components [1]. The key point of the method is to embed solid elements in a model made of shell elements for topology optimization. Improvements of static stiffness were verified for a simple cylindrical model, automotive floor model and full vehicle model. However, in addition to static stiffness using constraints, stiffness while driving is required in the body stiffness of a full vehicle. Inertia relief is known as a method for the expression of behaviour while driving.

In this study, stiffness optimizations by using inertia relief were carried out for an automotive full vehicle model. Specifically, the optimized automotive components were the joints linking a side-member and a cross-member. These components are made of steel sheets and have rectangular cross sections.

The results show that the developed topology optimization method, in which solid elements are embedded in a model consisting of shell elements, is valuable in the optimization of automotive rectangular steel sheet components by using inertia relief. The points of difference and similarity between the static stiffness using constraints and the stiffness using inertia relief were clarified by the optimization results.

2. Keywords: Topology optimization, shape optimization, industrial applications, inertia relief

3. Introduction

Environmental issues are rapidly emphasizing the necessity of engineering measures for automobile weight reduction. One such measure is reducing the weight of the body-in-white by using high strength steels, which is effective for reducing the mass of automotive parts. However, thickness reduction by using high strength steels also reduces the stiffness of the part, and the decrease in the rigidity of the part decreases the rigidity of the entire vehicle. In general, topology optimization is known as a technology which improves stiffness without increasing weight [2] [3]. In topology optimization, a design area constructed of solid elements is used, and the effective elements are retained after deleting unnecessary elements during the topology optimization process for the required properties. In the conventional solid element method, the residual shape is commonly complicated, and as the name implies, only solid elements are ordinarily used in the topology optimization method for optimization of cast parts such as an engine block or a lower control arm. On the other hand, in automotive bodies consisting of metal sheets, conventional topology optimization is used as a temporary answer which provides a rough sketch [4], a guide for design from scratch and a method of searching for supersensitive areas of material density in the current shape by using shell elements for the body [5] [6].

Thus, conventional topology optimization by using shell elements is advantageous when searching for stiffened areas. However, the answer is limited to increasing the material thickness, and the effect is smaller than changing the shape. Topology optimization using solid elements is very effective for creating new shapes but is not used to make new shapes for automotive bodies. The reason for this limited range of use is the difficulty of applying conventional topology optimization to an automotive body, which is mainly composed of thin steel sheets and is normally modeled by using shell elements. For this problem, the topology analysis method was developed to optimize the part shape and configuration of automotive components [1]. The key point of the method is to embed solid elements in a model made of shell elements for topology optimization. Improvements of static stiffness have been verified for a simple cylindrical model, automotive floor model and full vehicle model.

On the other hand, static stiffness using constraint of nodes cannot express deformation while driving [7]. Figure 1 shows the boundary condition and deformation in the static stiffness method [1]. Here, torsional deformation occurred in all parts of the body in the mode in which one point of the front bilateral suspension parts was forced and the other three points were constrained. However, because the automotive body is mounted on the suspension and the displacement of the suspension is not constrained, there is a difference between static stiffness and the condition while driving. For this reason, simulation under the loading condition of driving is necessary. Inertia relief is known as a method for expressing behavior while driving [8]. Inertia relief can solve the deformation

while driving without constraint of the suspension parts because the deformation by loading force and the inertia of loading force are calculated in this method.

This paper describes stiffness optimizations for an automotive full vehicle model by using inertia relief, in which solid elements were embedded in the shell elements for topology optimization. Specifically, the optimized automotive components were the joints linking a side-member and a cross-member. These components are made of steel sheets and have rectangular cross sections.

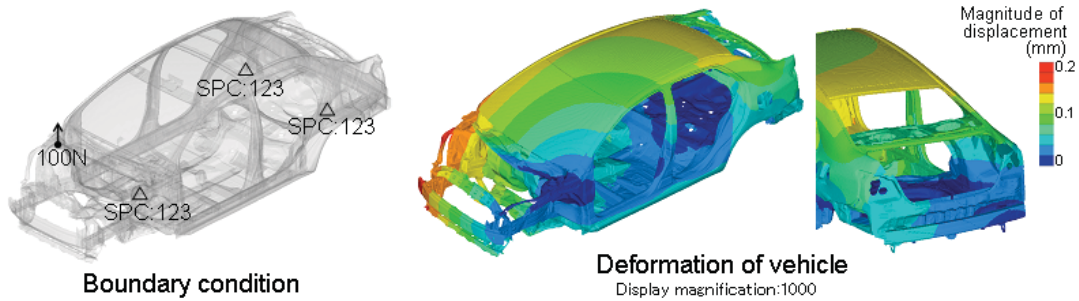


Figure 1: Boundary condition and deformation in static stiffness

4. Stiffness analysis and sensitivity analysis by using inertia relief

4.1. Boundary conditions and deformation of stiffness analysis

A full vehicle model, which is available to the public at the National Crash Analysis Center (NCAC), was used for the stiffness analysis. This model consists of shell elements [9]. Figure 2 shows the boundary conditions for the stiffness analysis compared with static torsion. In static torsion, one point of the suspension was forced by 1000N in the front or rear, and the other points were constrained. The loading conditions for inertia relief were vertical bending in the front or rear caused by passing over a gap, torsion by both sides in the front or rear by lane change, torsion by one side in the front or rear by running aground and horizontal bending in the front or rear by lane change. The solver of the stiffness analysis is NASTRAN2012.

Static torsion (Loading in front)	Inertia relief (Vertical bending in rear)	Inertia relief (Torsion by both sides in rear)	Inertia relief (Vertical bending in front)	Inertia relief (Torsion by both sides in front)
Static torsion (Loading in rear)	Inertia relief (Torsion by one side in rear)	Inertia relief (Horizontal bending in rear)	Inertia relief (Torsion by one side in front)	Inertia relief (Horizontal bending in front)

Figure 2: Boundary conditions for the stiffness analysis in this research

Figure 3 shows the deformations in several boundary conditions. The deformation of static torsion is displayed with the magnification of 1000, and that of inertia relief is displayed with the magnification of 300. The length of the vehicle is 4178mm. The results of static torsion in front loading or rear loading show deformation over the entire body. In inertia relief, only the area near the loading point is deformed. For example, under rear loading, the neighbourhood of the rear suspension is deformed and the front of the body is not deformed greatly. Similarly, under front loading, the neighbourhood of the front suspension is deformed and the rear of the body is not deformed greatly because the whole deformation occurs between the loading point and the constrained point in static torsion with constraints, but in inertia relief, the deformation in the neighbourhood of loading mainly occurs by the inertia of the force. It is assumed that the partial deformation of the body calculated by using inertia relief is close to the typical behaviour which occurs during a lane change while driving.

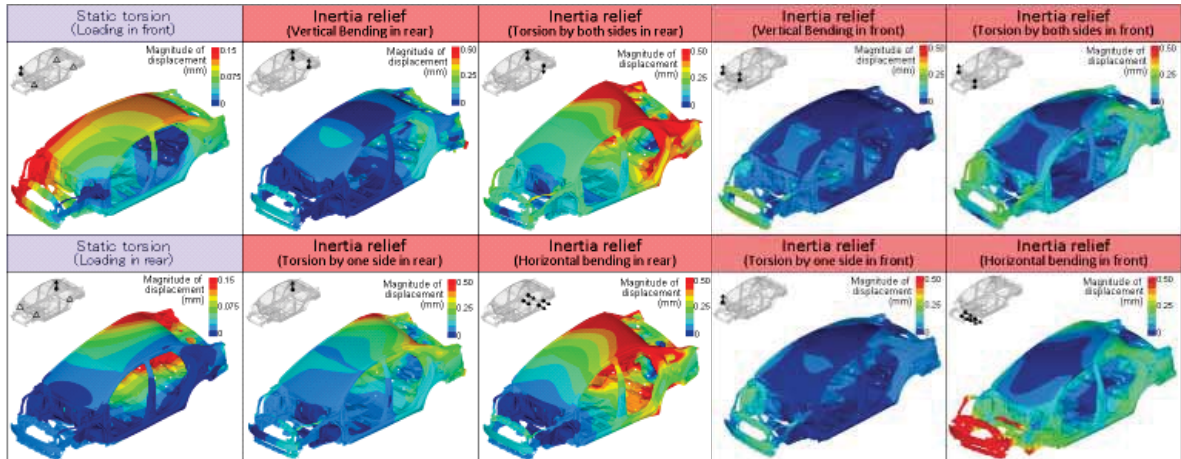


Figure 3: Deformations in several boundary conditions

4.2. Sensitivity analysis of automotive body

Sensitivity analysis of a full vehicle model consisting of shell elements was carried out by topology optimization for several boundary conditions. Figure 4 shows the results of static torsion in front loading, rear loading and complex loading in the front and rear. Figure 5 shows the results of vertical bending in the front and rear, torsion by both sides in the front and rear, torsion by one side in the front and rear and horizontal bending in the front and rear by inertia relief. Figure 6 shows the results of complex loading in the rear, complex loading in the front and rear by inertia relief. The objective response was a minimization of compliance, and the constraint function was lower than 25% of the residual volume fraction. In the case of complex loading, the weight of compliance was the same, the objective response was a minimization of the sum of the weighted compliance and the constraint function was lower than 25% of the residual volume fraction. The solver of the topology optimization analysis was Optistruct11. Side panels, roof-outers and window glass are not displayed.

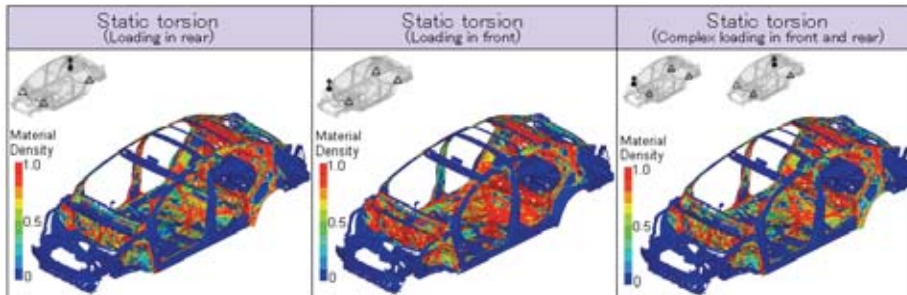


Figure 4: Sensitivity analysis of static torsion

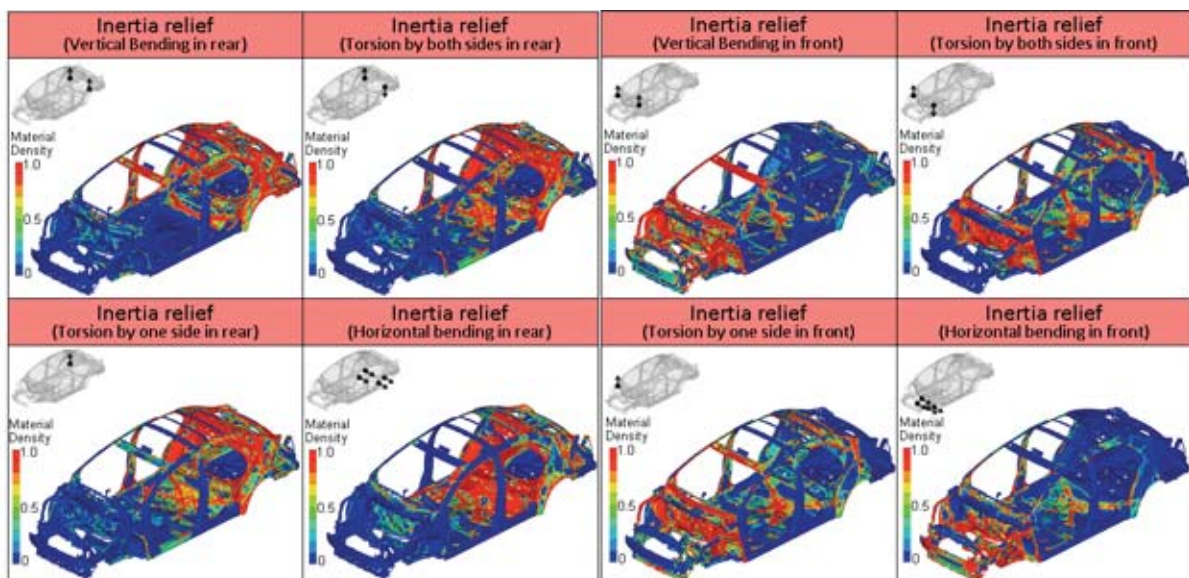


Figure 5: Sensitivity analysis of loading conditions by inertia relief

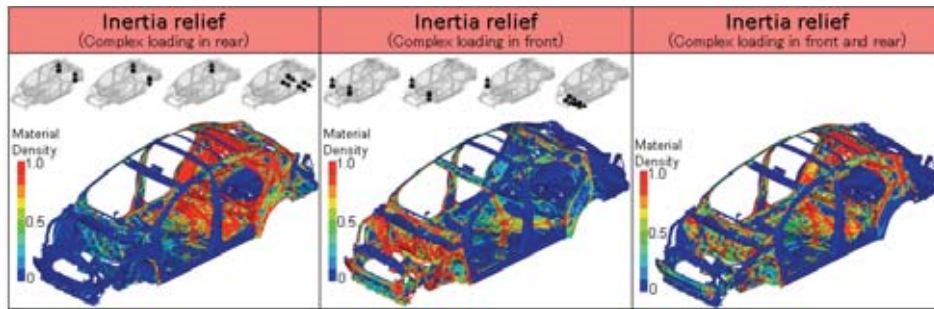


Figure 6: Sensitivity analysis of complex loading conditions by inertia relief

The contour is material density. A large material density area shows a large influence on the stiffness of the automotive body. The sensitivity of the entire body was high in all boundary conditions of static torsion, as shown by Figure 4, because deformation of the entire body occurs in static torsion independent of the loading position. With inertia relief, the sensitivity of the rear side of the body was high in the rear loading conditions, and the sensitivity of the front side of the body was high in the front loading conditions, as shown by Figure 5. This is because the deformation of the neighbourhood of the loading point is predominant in inertia relief. The sensitivity of the rear side of the body was high in the rear complex loading conditions of inertia relief, the sensitivity of the front side of the body was high in the front complex loading conditions of inertia relief and the sensitivity of the entire body was high in the front and rear complex loading conditions of inertia relief, as shown by Figure 6, because inputs from several areas of the body are added in complex loading in inertia relief.

Figure 7 shows the sensitivity analysis of the static torsion and inertia relief in the case of rear complex loading for the selection of the stiffened area. The result is focused in the rear side of the body and the contour is over 0.5. The high sensitivity areas of static torsion are the seat-back, wheel-house, rear suspension, rear side-member and rear cross-member. The high sensitivity areas of inertia relief are the rear floor-member, seat-back, wheel-house, speaker panel, rear suspension, rear side-member, rear cross-member and rear floor-side. The high sensitivity points of inertia relief are larger than those of static torsion because rear side loading was used in inertia relief. Thus, high sensitivity points can be found by using inertia relief, but there are cases in which high sensitivity points are overlooked when using static torsion.

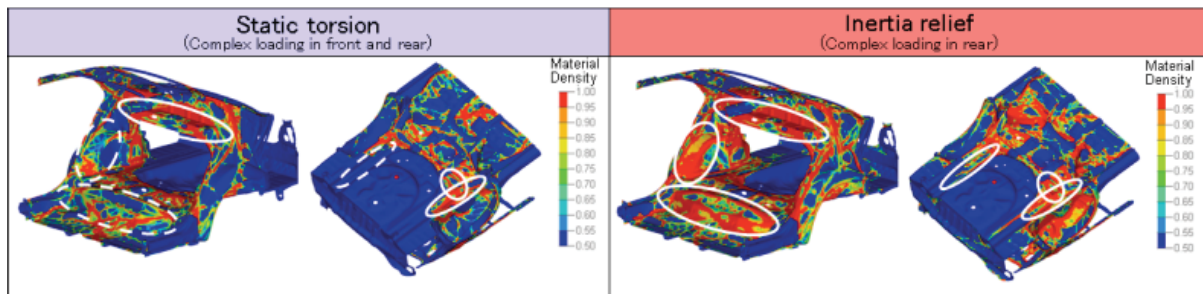


Figure 7: Comparison between static torsion and loading condition by inertia relief

5. Topology optimization by embedded method by using inertia relief

5.1. Difference of residual areas by loading condition of optimization

The validity of the method in which solid elements are embedded in an automotive model made of shell elements for topology optimization by using inertia relief was verified. Figure 8 shows the area where countermeasures are necessary indicated by the sensitivity analysis. Figure 9 shows the original shape with the target area of optimization. The target area was the neighbourhood of the rear cross-member connected with the rear side member, as shown in Figure 10. The end of the rear cross-member was deleted, and the cut edge of the rear cross-member consisting of shell elements was connected with the solid elements of the design area to transmit the load.

The loading conditions of the topology optimization were static torsion in complex loading in the front and rear, vertical bending in the front and rear, torsion by both sides in the front and rear, torsion by one side in the front and rear, horizontal bending in the front and rear by inertia relief and complex loading in the rear and complex loading in the front by inertia relief. The objective response of the optimization was a minimization of the sum of the weighted compliance with the same weight, and the constraint function was lower than 20% of the residual volume fraction. The solver of the topology optimization analysis was Optistruct11.

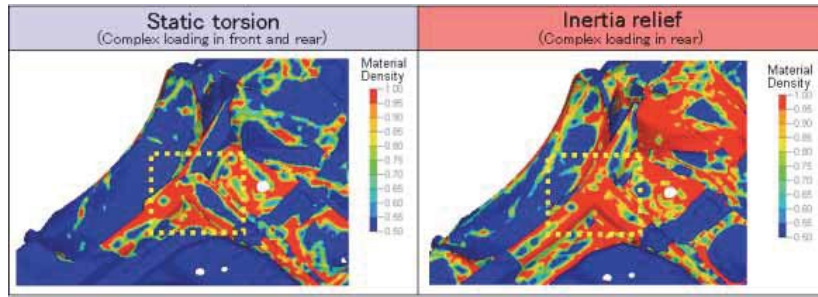


Figure 8: Target by sensitivity analysis

Figure 11 shows the results of the topology optimization for several loading conditions. The residual shape of static torsion was similar to the shape of horizontal bending in the rear by inertia relief. The residual area was the joint linking the cross-member and the side-member and the face of the ground side in the design area. These results show the load path from the loading point to the cross-member and floor by the side-member. The most important area was retained for this load path. The residual area was not only the joint linking the cross-member and the side-member, but also the joint linking the floor and the side-member, and its shape was complicated. This is because the automotive body has a monocoque structure which is made of steel sheets, and the load path is complex because each part of the body plays a role in transmitting loads. Moreover, the conventional material mechanics theory approach cannot solve this load path because the mode of stiffness is not a simple mode such as bending or torsion. On the other hand, the residual shapes for the other conditions were different from the static torsion and the horizontal bending in the rear by inertia relief. These results show that the required shape for stiffness differs depending on the mode of loading.

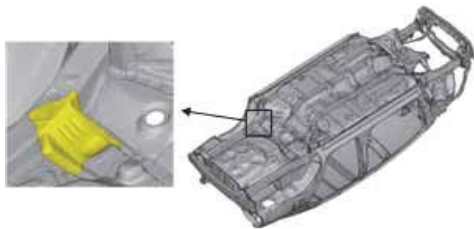


Figure 9: Target area of original shape

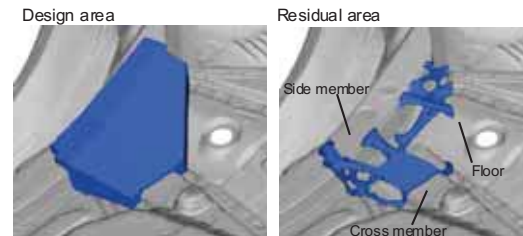


Figure 10: Full vehicle model with embedded solid elements

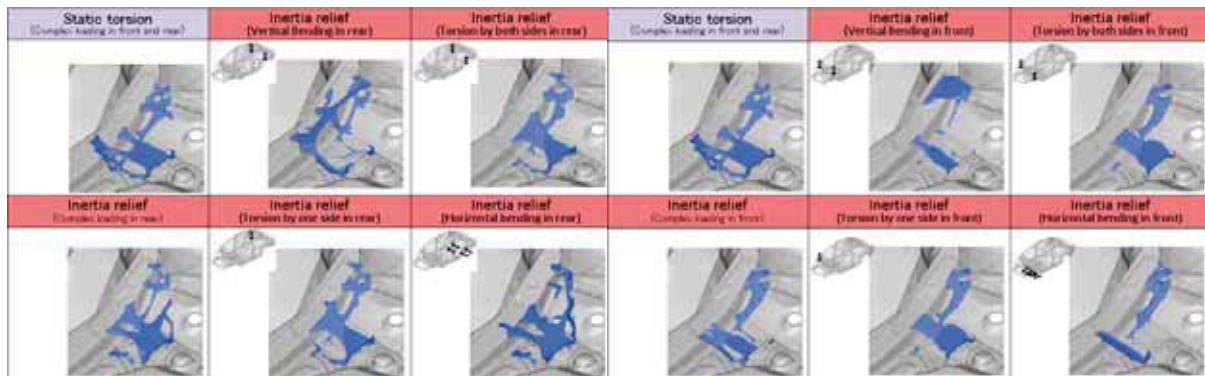


Figure 11: Residual areas of topology optimization for several loading conditions

5.2. Design by using residual shape and effect on mode of stiffness

The new shape designed based on the topology optimization of static torsion and horizontal bending in the rear by inertia relief is shown in Figure 12, together with the original shape. The parts were the joint linking the cross-member and the side-member, the floor and the side-member. The total weight increase in the full vehicle was only 0.1kg.

Figure 13 shows the improvement ratio of stiffness compared with the original shape in the loading condition of static torsion and several inertia relief conditions. Stiffness is calculated by the change of the displacements on the loading point. The solver of the stiffness analysis was NASTRAN2012. The improvement ratios of static torsion and horizontal bending in the rear by inertia relief are larger than those of the other conditions. Thus, the validity of the developed method, in which a design area consisting of solid elements is embedded in an automotive body consisting of shell elements, could be verified by using a full vehicle model. As the improvement ratios of the other conditions were small, these results show that the loading condition used in optimization is important.

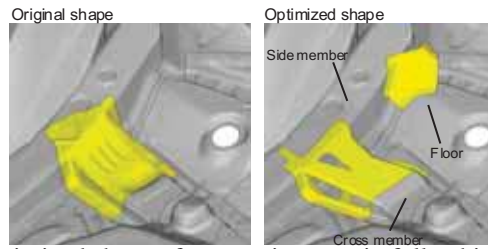


Figure 12: Optimized shape of connecting area in full vehicle model

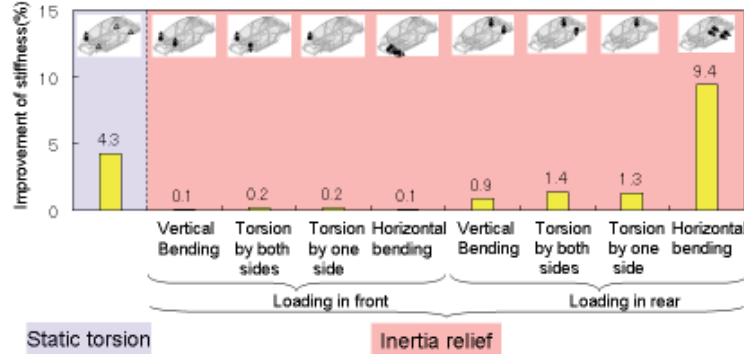


Figure 13: Improvement ratio of stiffness by optimal shape

6. Conclusions

It is clear that the topology optimization method in which solid elements are embedded in the shell elements of an automotive body is effective when using inertia relief for the driving condition.

There is a substantial difference between the static torsion method using constraints and the method of inertia relief. That is, in the static torsion method, deformation occurs over the entire automobile body, whereas in inertia relief, the area near the loading point is deformed.

With the static tension method, the sensitivity of the entire body was high, but with inertia relief, the sensitivity of the loading side of the body was high. Moreover, the sensitivity of the entire body was high in the complex loading conditions of inertia relief because inputs from several areas of the body are added in inertia relief.

The validity of the method in which a design area consisting of solid elements is embedded in an automotive body consisting of shell elements for topology optimization by using inertia relief was verified with a full vehicle model.

7. References

- [1] Saito, T., Hiramoto, J., and Urabe, T.: Development of Optimization Method for Automotive Parts and Structures, SAE Technical Paper 2014-01-0410, 2014.
- [2] Suzuki, K. and Kikuchi, N.: A homogenization method for shape and topology optimization, *Comput. Meths Appl. Mech. Eng.*, 93, pp. 291-318, 1991.
- [3] Azegami, H., Kaizu, S., Shimoda, M. and Katamine, E.: Irregularity of shape optimization problems and an improvement technique, *Computer Aided Optimization Design of Structures V*, edited by Hernandez, S. and Brebbia, C. A., Computational Mechanics Publications, Southampton, pp. 309-326, 1997.
- [4] Inazumi, T., Kuriyama, Y., Watanabe, K. and Fukui, K.: WorldAutoSteel Program, Future Steel Vehicle (Second Report) - Structural Design Aided by Computer Optimization Methods -, *JSAE Transactions*, Vol. 44, No. 2, pp. 517-522, 2013.
- [5] Nomura, A., Murakami, S., Tanaka, K. and Kuroda, Y.: Development of Lightweight Body with Improved Structural Dynamic Performances Using a Concurrent Design Optimization Approach, *Subaru Technical Review*, No. 31, pp. 161-166, 2004.
- [6] Niwa, T., Iizuka, N., Nakamura, G. and Yuge, K.: Application of Nonlinear Topology Optimization on Thin-Walled Steel Structure for Crashworthiness, *JSAE Transactions*, No. 86-12, pp. 5-8, 2012.
- [7] Anvari, M. and Beigi, B.: Automotive Body Fatigue Analysis – Inertia Relief or Transient Dynamics, SAE Technical Paper 1999-01-3149, 1999.
- [8] Nelson, M. and Wolf, J.: The Use of Inertia Relief to Estimate Impact Loads, SAE Technical Paper 770604, 1977.
- [9] NCAC Technical Summary: Development & Validation of Finite Element Model for the 2010 Toyota Yaris Passenger Sedan, November (2011).

Design and optimization of billet structure about High-speed Rail bearing in cold rolling

Xue-dao SHU¹, Ji-dong MA², Jie HE, Bao-shou SUN, Wen-fei PENG

¹ Faculty of Mechanical Engineering and Mechanics Ningbo University, Ningbo, China, shuxuedao@nbu.edu.cn

¹ Zhejiang Provincial Key Laboratory of Part Rolling Technology, Ningbo, China

² Faculty of Mechanical Engineering and Mechanics Ningbo University, Ningbo, China, 328885877@qq.com

Abstract: Bearing is one of the key parts in high-speed trains. To achieve the high-precision forming of outer ring in bearing for high trail, the paper analyses the sections of the outer ring and deduces the calculating formula for the volume. All of that is based on the basic theory of cold rolling and the principle of volume conversation by the application of the finite element software ABAQUS. According that, the paper designs four typical structure of blank of the outer ring in bearing and then analyses their defects and causing reasons in the process of cold rolling between different structure. Through the analysis, the paper eventually gets the best size of the symmetric blank about outer ring, which lays the theoretical foundation of implementing the high-precision forming of outer ring in bearing for high trail.

Keywords: cold rolling; High-speed Rail bearings; bearing blank; forming quality

1. Introduction

High-speed rail bearing is the key components of high-speed train in running mechanism and is the key material in the construction of the high-speed train. It supports the static and dynamic radial load from the train weight and vehicle load. Besides, it bears the additional unsteady force in axle direction[1-3]. Thus Its reliability has a great affect on the security of train operation.

The rational blank structure will directly determine the quality of high-speed rail and rolling stability of the cold forming[4-5]. Currently the working method for blank from experience not only has the high cost of production, and a long preparation time, but also can not get the Goods in high-precision. Thus structural design of the blank has important theoretical significance and applicable value for the study of parameters in cold rolling process. Based on the principle of constant volume, the paper simulate the rolling process of the billet in four different structures to get the best structure for the bear outer in the high-speed rail through the finite element software ABAQUS.

2 the structural design of blank and the set of program

The diameter of closed hole, formed by the driving roller and core roll in the cold rolling process, gradually expanded. So the unformed piece can be regarded as blank and the optimal shape is various. The outer ring in high-rail bear is symmetry in the axial direction, its size is shown in Fig.1

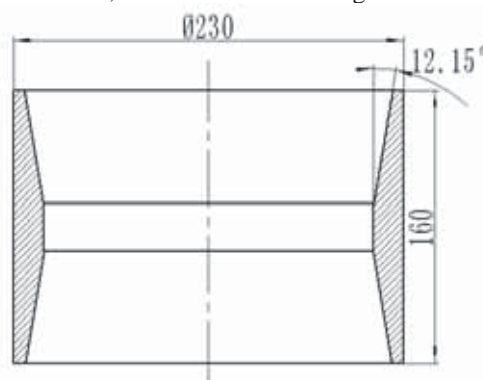


Figure.1 High-Speed Rail bearing outer ring structure size

Thus this paper uses the half model as shown in Fig.2.

$$V_{\text{outer}} = \pi \left(\frac{R}{2}\right)^2 B_1 - \frac{1}{3} \pi B_2 (r_1^2 + r_2^2 + r_1 r_2) - \pi r_2^2 B_3 \quad (1)$$

It can be obtained by the Pythagorean theorem from Eq.(1) that

$$r_1 = r_2 + \tan \alpha B_2 \quad (2)$$

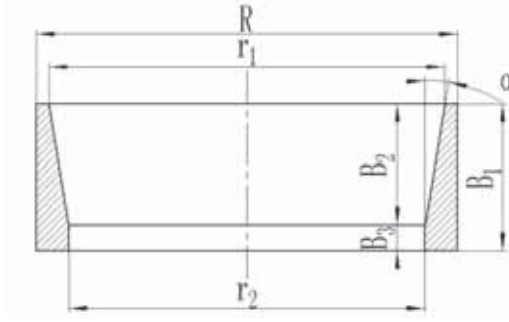


Figure.2 Symmetrical structure size

We can obtain the Eq.(3) from simplify the Eq. (1) and Eq.(2)

$$V_{outer} = \frac{1}{4} \pi R B_1 - \frac{1}{3} \pi B_2 (3r_2^2 + 3r_2 \tan \alpha B_2 + \tan^2 \alpha B_2^2) - \pi r_2^2 B_3 \quad (3)$$

Where R is the outer diameter of the outer ring; B_1 is the width of the outer ring; B_2 is the vertical width of the cant; B_3 is the width of the vertical surface; r_1 is the radius of the up surface; r_2 is the radius of the bottom surface and α is the bevel angle.

It can be obtained from the principle of constant volume

$$V_{outer} = V_{blank} \quad (4)$$

$$V_{blank} = \frac{1}{4} \pi R B_1 - \frac{1}{3} \pi B_2 (3r_2^2 + 3r_2 \tan \alpha B_2 + \tan^2 \alpha B_2^2) - \pi r_2^2 B_3 \quad (5)$$

Based on the analysis and principle, the paper designs four kinds structural shapes of blank to analyze and compare the finite element simulation of cold rolling about the outer ring of the high-speed rail bear.

The designed options of the blank are as follows:

Option one: the cross-section of blank is rectangular, whose the biggest advantage is convenient to machine and saving the cost. The paper ultimately draw the structure of option one, which is shown in the Fig.3.



Figure.3 Rectangular section blank

Option two and option three: the cross-sections of blank are both half-cone bevel. According to principle of constant volume and actual production experience, the upper part of the pre-formed of option two is the finished oblique cone, while the taper of option three is different with the finished oblique cone, where the rolling force makes the internal metal flow downward to complete the cold rolling. The structure of option two and option three are separately shown in Fig.4 and Fig.5.

Option four: the cross-section of the blank is identical for finished structure. During the cold rolling, the shape of cross-section don't change while the diameter of the outer ring increases because of the rolling force. The structure of option four is shown in Fig.6.

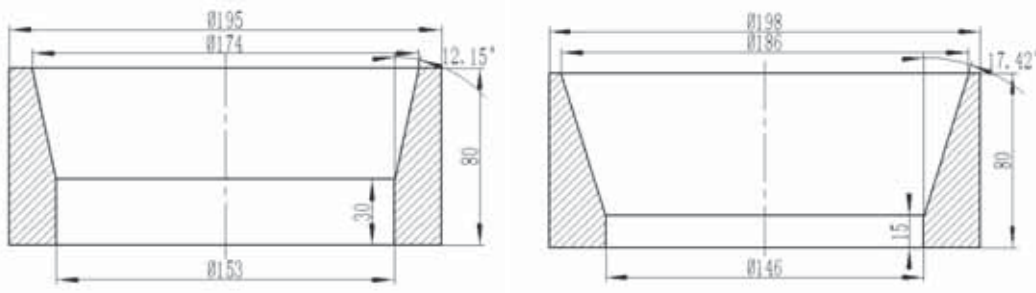


Figure.4 On the half-cone oblique section blank Figure.5 Under the half-cone oblique section blank

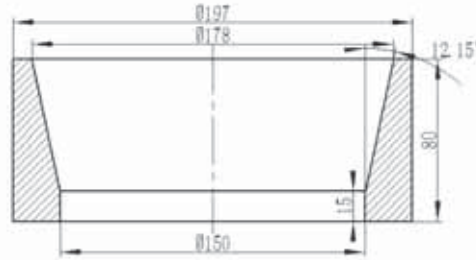
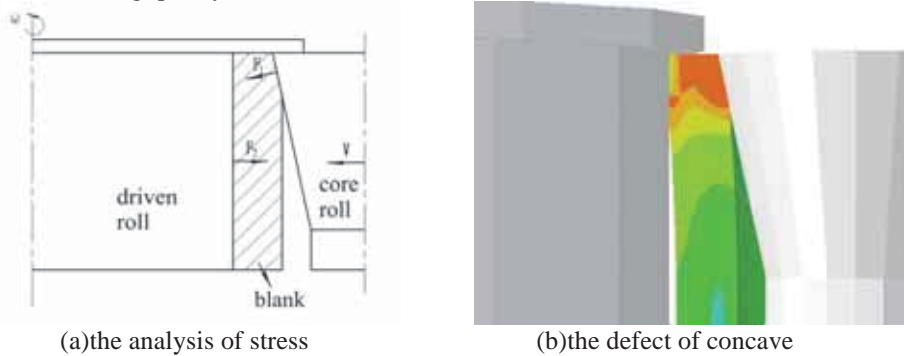


Figure.6 Cone oblique section blank

3 the finite element analysis results of cold rolling about the blank of outer ring in high-speed rail bear

The analysis result of option is shown in Fig.7, the forming quality of option one didn't meet the requirements of finished product. It will produce obviously defect of concave as shown in Fig.7(b) in the simulation of cold rolling, which makes rolling process unstable. It can be obtained that the blank deformed and gradually stick to the outer surface of the core roll by the feed force due to the upper surface of core roll firstly contacting with billets. As shown in Fig.7(a),the rolling force form core roll is perpendicular to oblique cone, which has the downward component in the vertical direction. Thus the internal metal is easily flowing to the place where has no constraints and can't form the shape as designed. The defect of concave resulting from that affects the stability of the cold rolling mill and the forming quality of blank.



(a)the analysis of stress

(b)the defect of concave

Figure.7 Option one

The analysis result of option two is shown in Fig.8, it describes the situation of the forming quality about the blank which owns the section of upper half cone shape. Although option two consume less material during billet machining, but its forming quality didn't meet expectations. It will generate the defect of concave and the defect of filling discontent in cone angle in the cold rolling, which are shown in Fig.8(b) and (c),and makes the rolling process instability. The forming mechanism of concave defects is similar with the option two. The roll of outer ring in high-speed rail bear belongs to cold working and don't have the high thermoplastic as the same as the hot cerclage. The Fig.8(c) shows the structure of blank at 100 step. It is the cone angle of core roller don't completely fit in the blank that leads to defects and affects the forming precision of the outer ring in high-speed rail bear.

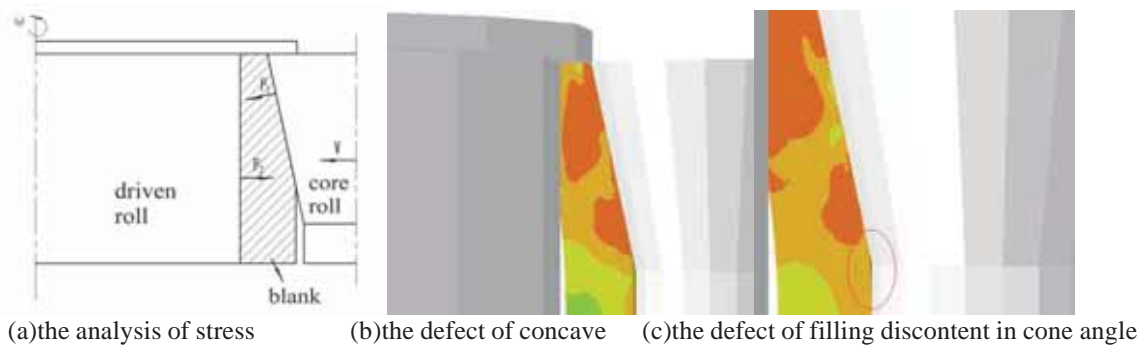


Figure.8 Option two

The analysis result of option is shown in Fig.9.

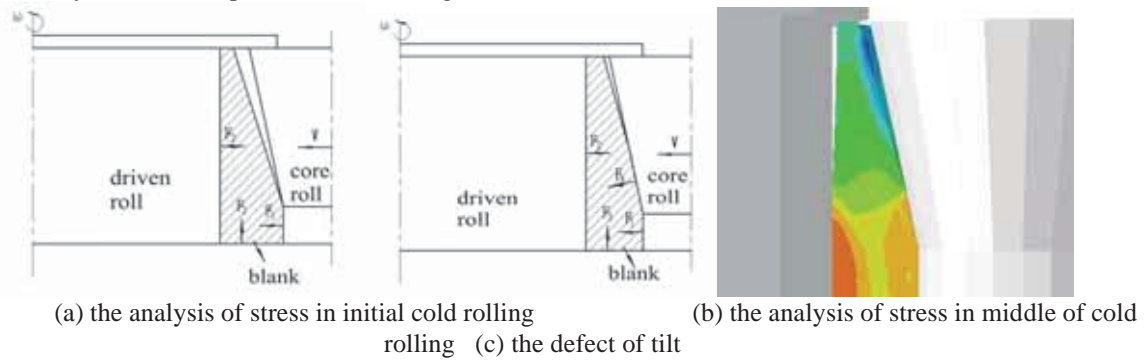
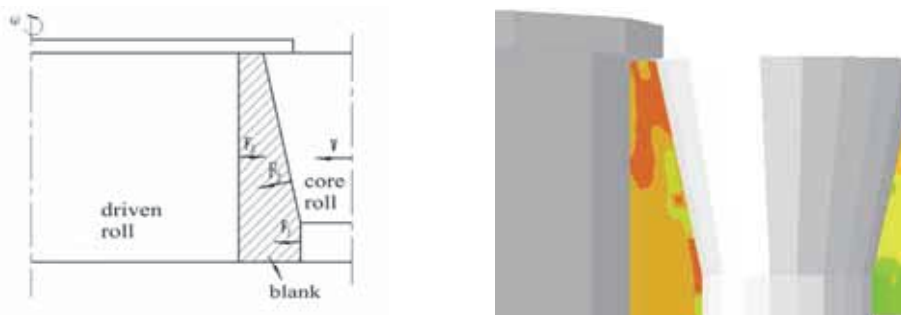


Figure.9 Option three

The Fig.9 shows the situation of forming quality about the option three. The angle of oblique cone in the blank is different from the angle in high-speed rail bear. The vertical plane of blank directly contact with the core roll. As shown in Fig.9(a), core roll firstly contacts with the vertical plane of blank and squeezes the blank in radial direction, which makes the diameter of the blank gradually larger. With cold rolling going on, as shown in the Fig.9(b), blank gradually forms the shape of oblique cone and fits in outer surface of the core roll. In the meanwhile, the situation of force is $F_1 + F_{4x} > F_2$ and The blank is under squeezing in the radial direction. The situation of force is $F_3 > F_{4y}$. In the axial direction, and internal metal accelerate flows to the upper end of the blank where the resistance is smaller. It leads the upper end of the blank to deform in advance and ultimately generates the defect of tilt.

The analysis result of option is shown in Fig.10, it shows the situation of forming quality about the blank with the cone bevel section. The structure is a viable option after considering of the defects of the three options. Fig.10(d) shows that the forming quality of the blank is better after cold rolling. Besides, the process of roll is stable. The inner surface of the preformed blank is identical to the outer surface of the core roll in option four. In the initial cold rolling, as shown in Fig.10(a), the stress is more even and balance than the previous options in radial and axial direction. It doesn't appear that the metal accelerate flow to some direction due to The blank is tightly suppressed by the core roll. Compared with the Fig. 10(b), Fig. 7(b), Fig. 8(c) and Fig. 9(c), the defect of concave, filling discontenent in cone angle and tilt don't appear in option four, and the forming effect achieves the requirement. Compared with Fig.10(c) and Fig.10(d), it is drawn that the structural size of option four is the best one in above options.



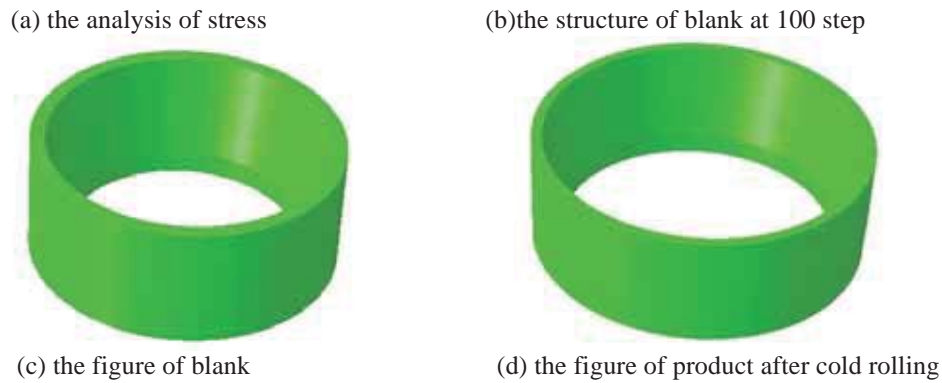


Figure.10 option four

5 conclusion

(1)According to the structure of finished outer ring,the paper analyses that the cross-section of outer ring in high-speed rail bear can be a rectangular or a oblique cone,and derives the volume calculating formula of the outer ring in high-speed rail bear.

(2)The paper designs four typical structure of the blank based on the principle of volume constant,and simulates each structure by applying ABAQUS.Then the paper analyze the various defects and causes in cold rolling through the stress and deformation in the process.As a result,the paper summarizes the advantages and disadvantages of the four structures of the blank,and eventually achieves the best structural size of the outer ring in high-speed rail bear.

5. Acknowledgements

The project was supported by following funds: the National Natural Science Foundation of China (Grant No.51475247).

6. References

- [1] SUN Zhen-hua,Research and analysis of the High Speed Bearings for Railway Passenger cars in our Country [J].Rolling Stock,2004,42(8):4-9.
- [2] HE Qiang,LI An-ling.The Development Trend of High-speed Railway Bearing[J].Journal of Xuzhou Institute of Technology(Natural Sciences Edition),2012,27(1),58-63.
- [3] Yang Xiao-wei.The profiles of high-speed railway bearing[J].Bearing,2010,(10),59-61.
- [4] SHU Xue-dao,XIAO Min. Blank design and process parameters optimization of high neck flange forming by closed ring rolling[J].Journal of University of Science and Technology Beijing,2012,34(11),1332-1337.
- [5] XIAO Min. Research on the Key Technologies of High Neck Flange Forming with Closed Ring rolling Technology[D].Ningbo:a master's degree thesis of Ningbo University,2011.
- [6] ZHAO Yu-min.Cold Rolling and Simulation for Step Inner Rings[J].Bearing,2006,(8):13-14.
- [7] HUA Lin.the design methods of blank and the forming rules in Ring Rolling [J].Transactions of The Chinese Society of Agricultural Machinery,1994,25(3):92-97.
- [8] LI Tian-SHUN.Numerical Simulation of the Concave-section Ring Rolling[D].Jinan:a master's degree thesis of shandong University,2013.
- [9] XIAO Min,SHU Xue-DAO.Influence of Blank Shape on Roll Forming of Long Neck Flange[J].Hot working Technology,2010,39(23),120-123.

Shape Optimum Design of Graphene Sheets

Jin-Xing Shi¹, Masatoshi Shimoda²

¹ Department of Advanced Science and Technology, Toyota Technological Institute, 2-12-1 Hisakata, Tenpaku-ku, Nagoya, Aichi 468-8511, Japan, shi@toyota-ti.ac.jp

² Department of Advanced Science and Technology, Toyota Technological Institute, 2-12-1 Hisakata, Tenpaku-ku, Nagoya, Aichi 468-8511, Japan, shimoda@toyota-ti.ac.jp

1. Abstract

Graphene sheet (GS) is a monolayer of carbon atoms arranged in a honeycomb lattice and is the strongest material ever measured and the thinnest material ever synthesized in the universe. Due to its unique mechanical, structural and electronic properties, GS is supposed to be a base material for nanoelectromechanical systems (NEMS), given that lightness and stiffness are the essential characteristics sought in NEMS for sensing applications. In this study, shape optimum design of GS is carried out to improve its stiffness for these applications. At first, we model C-C bond as an equivalent continuum beam by means of molecular mechanics (MM) method. So that GS can be adopted as a continuum frame structure. Then, we optimize the shape of the atomistic finite element model based on a free-form optimization method for frame structures. In the optimization process, we use the compliance as objective function and minimize it under the volume constraint. Each equivalent continuum beam is assumed to vary in the off-axis direction to the centroidal axis and we derive the shape gradient function for determination of the optimal design velocity field based on the free-form optimization method. Using the derived optimal design velocity field, the shape optimum design of GS can be carried out without shape parametrization. The numerical results show that, using the proposed shape optimization method, the compliance of GS can be significantly reduced that would be helpful for designing GS used in NEMS.

2. Keywords: Compliance; Free-form; Graphene sheets; Molecular mechanics; Shape optimum design.

3. Introduction

Due to its large specific surface area, high intrinsic mobility, high Young's modulus and thermal conductivity, Graphene sheet (GS), a one-atomic-thick monolayer of graphite, has been proposed to be used in nanoelectromechanical systems [1]. For a broad range of industrial applications of GSs, the prediction of mechanical properties for the perfect 2D nanostructure, such as the stiffness, vibration characteristics and buckling analysis, have been carried out by means of experiment [2], *ab initio* energy calculation [3] or molecular dynamics (MD) simulation [4], molecular mechanics (MM) method [5] and continuum mechanics [6]. Conduction experiments with nano-size systems are difficult and expensive, while MD methods are time consuming and have convergence problems. Thus, developing appropriate continuum mathematical models based on MM method and continuum mechanics for nanostructures is important for the development of GSs [7].

Here, we need to introduce MM method for modeling frame-like structure of GSs. For a GS can be treated as a large array of molecule consisting of C atoms, MM method has played important roles for modeling GSs. From the viewpoint of MM method using the equivalent atomistic based continuum mechanics, MM method depicts the forces between individual atoms as typical beam elements (shown as Fig. 1). According to the Tersoff-Brenner force field theory [8] and a link between molecular and solid mechanics of C-C bond, we assume the equivalent C-C beam with circular cross-section of diameter d and initial length 1.42 \AA , and get the proposed material constants are Young's modulus $E_b = 5.53 \text{ TPa}$, shear modulus $G_b = 0.871 \text{ TPa}$ and $d = 1.46 \text{ \AA}$ [9].

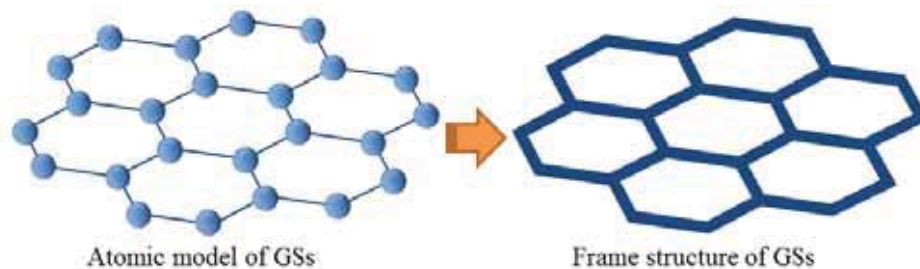


Figure 1 Molecular mechanics method for graphene sheets

Recently, the shape of GSs can be controlled by an external electric field [10] or chemically modifying the

adherence of GSs on metal [11]. Hence, shape optimum design of GSs can make an effective role to improve their mechanical behaviors.

Shape optimum design of traditional continuum structures such as shell, solid or frame structures have been carried out based on the free-form optimization method. The free-form optimization method is a gradient method with a P. D. E. (Partial Differential Equation) smoother in the Hilbert space for shape optimization of continua, which is also called H^1 gradient method or traction method and does not require any shape parameterization. This method was firstly proposed by Azegami [12] and Shimoda et al. developed this optimization method for designing frame [13], shell [14] and solid structures [15]. The free-form optimization method is a parameter-free or a node-based shape optimization method that treats all nodes in the body as design variables. The advantages of this method include efficiency for treating large-scale problems and the ability to obtain a smooth shape. Using the free-form optimization method, it is possible to obtain the optimized shapes of frame-like structures of GSs.

The present work is arranged as following. In section 4, we introduce the MM method for GSs and build the frame-like continuum model of GSs at first. Then, we use a developed free-form shape optimization method for the frame structure and build the shape optimization system for designing the shape of GSs. Using the shape optimization method, we carry out two examples to do shape optimum design of GSs in section 5. At last, conclusions are presented in section 6.

4. Shape optimum design of graphene sheets

Based on the MM method, we assemble the frame-like GS finite element models for shape optimization in the present work. Thus, shape optimum design of GSs can be simplified to a shape optimization problem of frame structures as shown in Fig. 2.

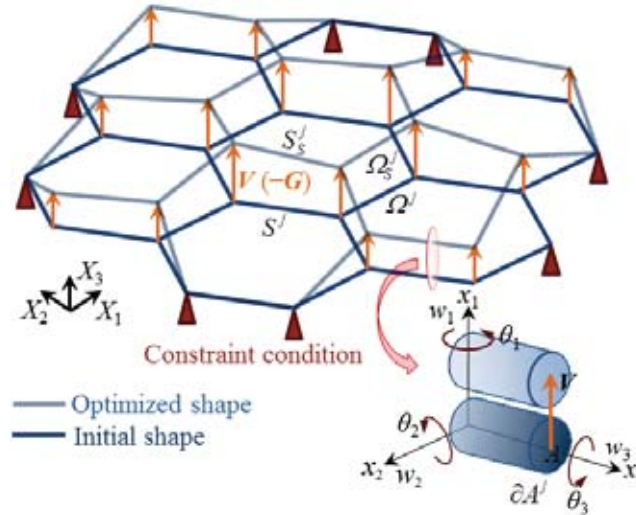


Figure 2 Shape variation of frame structure of graphene sheets

4.1. Domain variation of frame structure of graphene sheets

As shown in Fig. 2, members Ω^j , $j = 1, 2, \dots, N$ consisting of Timoshenko beams compose a frame structure of GSs that can be represented by a bounded domain $\Omega \subset \mathbb{R}^3$, where N is the number of beams and \mathbb{R} is a set of positive real numbers. The notations (x_1, x_2, x_3) and (X_1, X_2, X_3) indicate the local coordinate system with respect to the beam and the global coordinate system, respectively. Hence, we have

$$\Omega^j = \left\{ (x_1^j, x_2^j, x_3^j) \in \mathbb{R}^3 \mid (x_1^j, x_2^j) \in A^j \subset \mathbb{R}^2, x_3^j \in S^j \subset \mathbb{R} \right\}, \quad \Gamma^j = \partial A^j \times S^j \quad \Omega^j = A^j \times S^j \quad (1)$$

where S^j , Γ^j and Ω^j express the centroidal axis, circumference surface and whole domain of member j , respectively. A^j and ∂A^j express the cross section and its circumference of member j , respectively. The subscript j shall be frequently omitted to avoid the complexity of expression in the sequel. $\mathbf{w} = \{w_i\}_{i=1,2,3}$ and $\boldsymbol{\theta} = \{\theta_i\}_{i=1,2,3}$ express displacement vector and rotation vector in the x_1, x_2, x_3 directions of the local coordinate system, respectively. Then, The weak form governing equation in terms of $(\mathbf{w}, \boldsymbol{\theta})$ can be expressed as

$$a((\mathbf{w}, \boldsymbol{\theta}), (\bar{\mathbf{w}}, \bar{\boldsymbol{\theta}})) = l((\bar{\mathbf{w}}, \bar{\boldsymbol{\theta}})), \quad \forall (\bar{\mathbf{w}}, \bar{\boldsymbol{\theta}}) \in U, (\mathbf{w}, \boldsymbol{\theta}) \in U \quad (2)$$

where the notation $(\bar{\cdot})$ expresses a variation, and U expresses admissible function space in which the given

constraint conditions of $(\mathbf{w}, \boldsymbol{\theta})$ are satisfied. In the frame structure of GSs as shown in Fig. 2, due to the domain variation \mathbf{V} (design velocity field) in the out-of-plane direction to the centroidal axis, the initial domain Ω^j and a centroidal axis S^j of member j become Ω_s^j and S_s^j , respectively. The subscript s expresses the iteration history of the domain variation.

4.2. Compliance minimization problem

We utilize a free-form optimization method for frame structures to minimize the compliance of the frame structure of GSs, the shape optimization problem for finding the optimal design velocity field \mathbf{V} can be formulated as

$$\text{Given } \Omega \quad (3)$$

$$\text{Find } \mathbf{V} \text{ or } \Omega_s \quad (4)$$

$$\text{that minimizes } l(\mathbf{w}, \boldsymbol{\theta}) \quad (5)$$

$$\text{subject to Eq. (2) and } M \left(= \sum_{j=1}^N \int_{S^j} A dS \right) \leq \hat{M} \quad (6)$$

where M and \hat{M} denote the volume and its constraint value, respectively.

Letting $(\bar{\mathbf{w}}, \bar{\boldsymbol{\theta}})$ and Λ denote the Lagrange multipliers for the state equation and volume constraints, respectively, the Lagrange functional L associated with compliance minimization problem can be expressed as

$$L(\Omega, (\mathbf{w}, \boldsymbol{\theta}), (\bar{\mathbf{w}}, \bar{\boldsymbol{\theta}}), \Lambda) = l((\mathbf{w}, \boldsymbol{\theta})) + l((\bar{\mathbf{w}}, \bar{\boldsymbol{\theta}})) - a((\mathbf{w}, \boldsymbol{\theta}), (\bar{\mathbf{w}}, \bar{\boldsymbol{\theta}})) + \Lambda(M - \hat{M}) \quad (7)$$

The material derivative \dot{L} of the Lagrange functional can be derived as

$$\dot{L} = l((\bar{\mathbf{w}}', \bar{\boldsymbol{\theta}}')) + l((\mathbf{w}', \boldsymbol{\theta}')) - a((\mathbf{w}', \boldsymbol{\theta}'), (\bar{\mathbf{w}}, \bar{\boldsymbol{\theta}})) - a((\mathbf{w}, \boldsymbol{\theta}), (\bar{\mathbf{w}}', \bar{\boldsymbol{\theta}}')) + \dot{\Lambda}(M - \hat{M}) + \langle \mathbf{Gn}, \mathbf{V} \rangle, \quad \mathbf{V} \in C_{\Theta} \quad (8)$$

where \mathbf{Gn} ($\equiv \mathbf{G}$) expresses the shape gradient function (i.e., sensitivity function), which is a coefficient function in terms of \mathbf{V} . \mathbf{n} is defined as an outward unit normal vector on the circumference surface Γ or as a unit normal vector on the centroidal axis S . The notations $(\cdot)'$ and $\dot{(\cdot)}$ are the shape derivative and the material derivative with respect to the domain variation, respectively.

The optimum conditions of the Lagrange functional L with respect to $(\mathbf{w}, \boldsymbol{\theta})$, $(\bar{\mathbf{w}}, \bar{\boldsymbol{\theta}})$ and Λ are expressed as

$$a((\mathbf{w}, \boldsymbol{\theta}), (\bar{\mathbf{w}}', \bar{\boldsymbol{\theta}}')) = l((\bar{\mathbf{w}}', \bar{\boldsymbol{\theta}}')), \quad \forall (\bar{\mathbf{w}}', \bar{\boldsymbol{\theta}}') \in U \quad (9)$$

$$a((\mathbf{w}', \boldsymbol{\theta}'), (\bar{\mathbf{w}}, \bar{\boldsymbol{\theta}})) = l((\mathbf{w}', \boldsymbol{\theta}')), \quad \forall (\mathbf{w}', \boldsymbol{\theta}') \in U \quad (10)$$

$$\dot{\Lambda}(M - \hat{M}) = 0 \quad M - \hat{M} \leq 0 \quad \Lambda \geq 0 \quad (11)$$

When the optimality conditions are satisfied, Assuming that the external forces do not vary with regard to the space and the iteration history s and considering the self-adjoint relationship $(\mathbf{w}, \boldsymbol{\theta}) = (\bar{\mathbf{w}}, \bar{\boldsymbol{\theta}})$, which is obtained from Eqs. (9) and (10), we get

$$\dot{L} = \langle \mathbf{Gn}, \mathbf{V} \rangle = \sum_{j=1}^N \left\{ \int_{S^j} G_1 \mathbf{V} \cdot \mathbf{n} dS + \int_{S^j} G_0 \mathbf{V} \cdot \mathbf{n} dS \right\} \quad (12)$$

$$G_1 = 2h_1 h_2 \left\{ E w_{3,3} \theta_{2,3} - \mu \theta_{3,3} (w_{2,3} + \theta_1) \right\} \quad (13)$$

$$G_0 = \Lambda A H + \left\{ 2(F_i w_i + C_1 \theta_1 - C_2 \theta_2 + C_3 \theta_3) H \right\} \quad (14)$$

where $\mathbf{F} = \{F_i\}_{i=1,2,3}$ and $\mathbf{C} = \{C_i\}_{i=1,2,3}$ are the force and couple vectors per unit length applied to member j , respectively. The notation μ is the Lamé constant and E is the Young's modulus. H denotes the curvature of the centroidal axis. Moreover, the tensor subscript notation uses Einstein's summation convention and a partial differential notation for the spatial coordinates $(\cdot)_{,i} = \partial(\cdot) / \partial x_i$.

4.3. Free-form optimization method for frame structures of graphene sheets

The free-form optimization method described here was proposed by Shimoda for solving the shape optimization problem of frame structures [13]. In this method, the negative shape gradient function $-\mathbf{G}$ ($= -\mathbf{Gn}$) is applied as a distributed force to a pseudo-elastic frame structure in the normal direction to the centroidal axis (shown as Fig. 2). This makes it possible both to reduce the objective functional and to maintain smoothness, i.e., mesh regularity simultaneously. The optimal shape variation, or the optimal design velocity field \mathbf{V} is determined as the displacement field in this pseudo-elastic frame analysis, and the obtained \mathbf{V} is used to update the shape. We call

this analysis for \mathbf{V} velocity analysis. In other words, this method is a gradient method in a Hilbert space with Laplacian smoother. The stiffness tensor of the pseudo-elastic frame structure has a role of the positive definiteness tensor, which is needed in a gradient method in a function space. The governing equation of the velocity analysis is expressed as

$$a((\mathbf{V}, \boldsymbol{\theta}), (\bar{\mathbf{w}}, \bar{\boldsymbol{\theta}})) = -\langle \mathbf{Gn}, (\bar{\mathbf{w}}, \bar{\boldsymbol{\theta}}) \rangle, \forall (\bar{\mathbf{w}}, \bar{\boldsymbol{\theta}}) \in C_{\odot}, (\mathbf{V}, \boldsymbol{\theta}) \in C_{\odot} \quad (15)$$

$$C_{\odot} = \left\{ (V_1, V_2, V_3, \theta_1, \theta_2, \theta_3) \in (H^1(S))^6 \mid \text{satisfy Dirichlet condition for shape variation} \right\} \quad (16)$$

In problems where convexity is assured, this relationship definitely reduces the Lagrange functional in the process of updating the shape of GSs using the design velocity field \mathbf{V} determined from Eq. (16).

The shape optimization process for frame structure of GSs is built by repeating stiffness analysis, sensitivity analysis for calculating the shape gradient functions, velocity analysis and shape updating, in which stiffness analysis and velocity analysis are conducted using a standard commercial FEM code.

5. Results and discussion

In order to evaluate the shape optimization process for frame structure of GSs, we execute two examples to optimize the shape a rectangular GS and a circular GS. The volume constraint is set to be $M \leq \hat{M} = 1.05M_{\text{initial}}$, where M_{initial} is the initial volume of GSs. It should be noted that the constraint conditions utilized in the present work are expressed as 1 (x_1 direction), 2 (x_2 direction), 3 (x_3 direction), 4 (θ_1 direction), 5 (θ_2 direction) and 6 (θ_3 direction).

5.1. Example 1

In this example, we built a frame model of rectangular GS containing 2006 carbon atoms and 2946 equivalent C-C beams. In the structural analysis shown in Fig. 4 (a), three corner points are constrained in 123 and the remaining one point undergoes a concentrated force. In the velocity analysis shown in Fig. 4 (b), all of the four sides of the rectangular GS are constrained in 123 and all of the remained nodes are constrained in 12. The shape optimum design of the rectangular GS is carried out using the proposed shape optimization process. The optimized shape and the iteration history are expressed in Figs. 4 (c) and (d), respectively. The optimized shape of GS is smooth and the iteration history shows that the compliance ratio is reduced by 97.4% normalized to the initial shape. The optimization process converges according to the volume constraint.

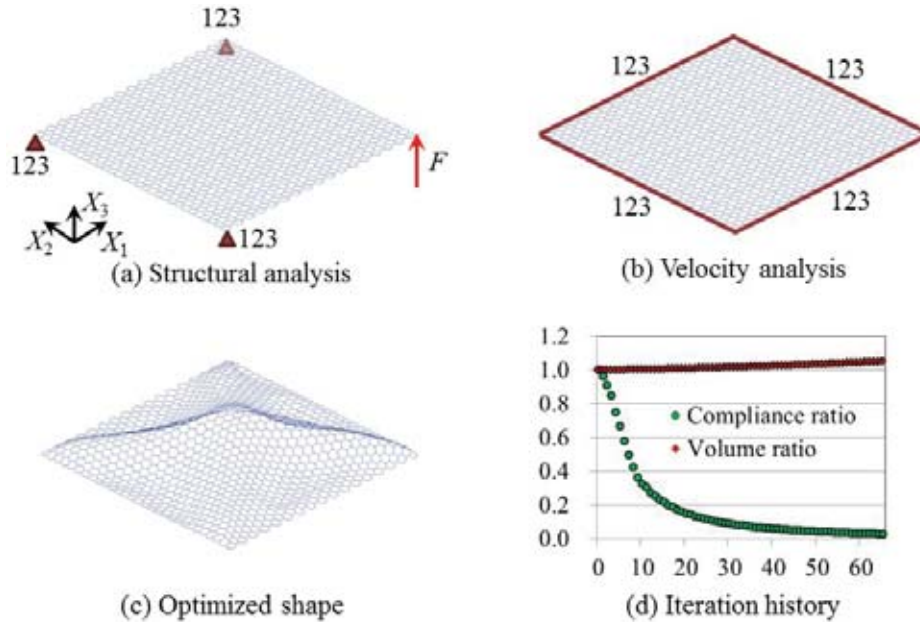


Figure 4 Shape optimization for a rectangular graphene sheet

5.1. Example 2

A frame model of circular GS containing 3120 carbon atoms and 4607 equivalent C-C beams is built in this example. In both of the structural analysis and the velocity analysis shown in Figs. 5 (a) and (b), the edge of the circular GS is constrained in 123. Moreover, all of the remained nodes are constrained in 12 in the velocity analysis. There is a linear nodal forces acting on the surface of the circular GS in the structural analysis. Using the proposed

shape optimization process, the shape optimum design of the circular GS is carried out. The optimized shape and the iteration history are shown in Figs. 5 (c) and (d), respectively. The optimization process converges according to the volume constraint, and we obtain a smooth optimized shape of the circular GS. In the iteration history expressed in Fig. 5 (d), the compliance ratio is reduced by 55.5% normalized to the initial shape and the volume ratio goes up to $1.05 M_{\text{initial}}$.

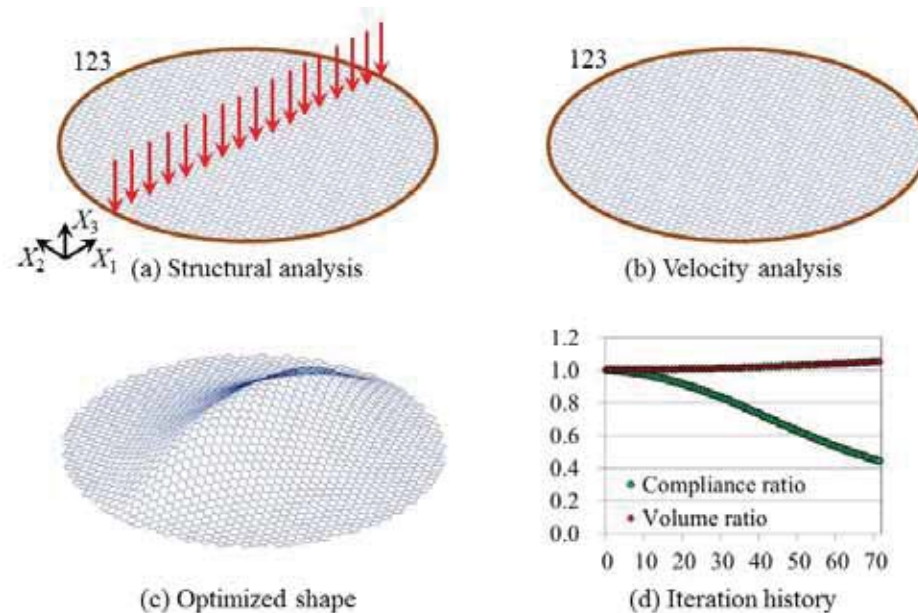


Figure 5 Shape optimization for a circular graphene sheet

6. Conclusions

In the present work, we built the frame-like continuum mechanical model of GSs based on the MM method at first. Then, we formulated the compliance minimization problem of the frame structure of GSs and adopted a shape optimization method that can be used in the optimum design of GSs. This method was developed based on the free-form optimization method, so that the optimized shape of GSs could be determined without re-mesh and requiring shape design parameterization. The objective of the developed optimization method was to minimize the compliance of GSs under the volume constrain. To confirm the effectiveness of the proposed shape optimization method, two examples were carried out using the developed free-form shape optimization method. The results showed that the obtained optimal shapes in both of the two design problems were smooth and the compliance of each case was reduced significantly.

7. Acknowledgements

This work is supported by a grant-in-aid from the Research Center of Smart and Tough Machines at the Toyota Technological Institute, and a grant-in-aid for Scientific Research, Grant Number 26420091, given by the Japan Society for the Promotion of Science.

8. References

- [1] A.K. Geim, Graphene: status and prospects, *Science*, 324, 1530-1534, 2009.
- [2] C. Lee, X. Wei, J.W. Kysar and J. Hone, Measurement of the elastic properties and intrinsic strength of monolayer graphene, *Science*, 321, 385-388, 2008.
- [3] L. Wang, Q. Zheng, J.Z. Liu and Q. Jiang, Size Dependence of the thin-shell model for carbon nanotubes, *Physical Review Letters*, 95, 105501, 2005.
- [4] Y.K. Shen and H.A. Wu, Interlayer shear effect on multilayer graphene subjected to bending, *Applied Physics Letters*, 100, 101909, 2012.
- [5] J.X Shi, T. Natsuki, X.W. Lei and Q.Q. Ni, Equivalent Young's modulus and thickness of graphene sheets for the continuum mechanical models, *Applied Physics Letters*, 104, 223101, 2014.
- [6] J.X Shi, Q.Q. Ni, X.W. Lei and T. Natsuki, Nonlocal vibration analysis of nanomechanical systems resonators using circular double-layer graphene sheets, *Applied Physics A*, 115, 213-219, 2014.
- [7] J.X Shi, Q.Q. Ni, X.W. Lei and T. Natsuki, Study on wave propagation characteristics of double-layer graphene sheets via nonlocal Mindlin-Reissner plate theory, *International Journal of Mechanical Sciences*, 84, 25-30, 2014.

- [8] A.K. Rappe, C.J. Casewit, K.S. Colwell, W.A. Goddard III and W.M. Skiff, UFF, a full periodic table force field for molecular mechanics and molecular dynamics simulations, *Journal of the American Chemical Society*, 114, 10024-10035, 1992.
- [9] X.W. Lei, T. Natsuki, J.X Shi and Q.Q. Ni, Analysis of carbon nanotubes on the mechanical properties at atomic scale, *Journal of Nanomaterials*, 2011, 805313, 2011.
- [10] T. Georgiou, L. Britnell, P. Blake, R.V. Gorbachev, A. Gholinia, A.K. Geim, C. Casiraghi and K.S. Novoselov, Graphene bubbles with controllable curvature, *Applied Physics Letters*, 99, 093103, 2011.
- [11] J. Lu, A.H. Castro Neto and K.P. Loh, Transforming moiré blisters into geometric graphene nano-bubbles, *Nature Communications*, 3, 823, 2012.
- [12] H. Azegami, Solution to domain optimization problems. *Transactions of the Japan Society of Mechanical Engineers Series A*, 60, 1479-1486, 1994. (in Japanese)
- [13] M. Shimoda, Y. Liu and T. Morimoto, Non-parametric free-form optimization method for frame structures, *Structural and Multidisciplinary Optimization*, 50, 129-146, 2014.
- [14] M. Shimoda and Y. Liu, A non-parametric free-form optimization method for shell structures, *Structural and Multidisciplinary Optimization*, 50, 409-423, 2014.
- [15] J.X Shi and M. Shimoda, Interface shape optimization of designing functionally graded sandwich structures, *Composite Structures*, 125, 88-95, 2015.

Life Cycle Vibration Sensation Rate Evaluation Model for the Optimal Human Comfort Design of Super Tall Buildings

Lilin Wang¹, Yimin Zheng^{1,2}, Tianyi Yu², Xin Zhao^{1,2}

¹ Department of Structural Engineering, Tongji University, Shanghai, China, 22zx@tjadri.com

² Tongji Architectural Design (Group) Co., Ltd., Shanghai, China, 22zx@tjadri.com

1. Abstract

The wind-induced vibrations of super tall buildings become excessive due to strong wind loads, super building height and high flexibility. In view of individual uncertainty and diversity of wind-induced vibration response, a life cycle vibration sensation rate model based on AIJES-V001-2004 was proposed to evaluate human comfort performance of super tall buildings under wind load. The maximum acceleration was adopted as the quantitative index of the performance. Pseudo excitation method was employed in the frequency domain analysis for the calculation of the vibration sensation rate of the super tall building under random wind load. The randomness of the wind speed being taken into consideration, the vibration sensation rate of human comfort was obtained for the whole life cycle. A cost model for the wind-induced human comfort of super tall buildings was derived based on the vibration sensation rate model. This model evaluated the life cycle cost of different design schemes, which could help make design choice based on the minimum life cycle cost criterion. The proposed method was applied to the human comfort design choice of a super tall building with and without tuned mass damper (TMD), tuned liquid column damper (TLCD) or combined tuned damper (CTD) device to illustrate its effectiveness and applicability.

2. Keywords: super tall building; AIJES-V001-2004; life cycle cost; human comfort performance; optimal design

3. Introduction

The design method widely adopted nowadays is strictly subjected to the design code criteria. However, it is hard for the house owner to master the specific performance of tall buildings under different wind pressures. For example, the engineer is aiming to meet safety usage, but the owner hopes to raise the human comfort significantly. Besides, as structural performance has no economic assessment, the owner cannot understand benefits from the initial investment to determine whether a damper and what kind of the damper to be installed to control the vibration of tall buildings. Most importantly, it is not only the subjective feeling of vibration but also the acceptable failure risk level of occupants that determines the goal of structural performance. [1] In all above, it is a key problem that both the owner and the engineer are needed to pursue for a balance or a reasonable design standard between economic benefits and comfort performance.

The performance based design methodology is a significantly useful approach to solve the above problem, which aims at guaranteeing the safety and comfort performance, implement specific different performance levels and lead to the minimum life cycle cost when suffering possible random wind [2]. Guoxiong Bo et al [3] carried out the beneficial exploration and perfection of the wind-resistant performance based design, in which the concept of benefit-cost ratio is taken to assess the economical efficiency. However, the authors did not consider the failure effect of the human comfort performance, which made the performance assessment for buildings with a TMD impossible. The author originally proposed a life cycle cost model to evaluate human comfort performance of tall buildings and to decide the human comfort design choice whether to install a TMD or not [4]. It is a pity that the failure effect of the TMD itself on the structural human comfort performance was not considered in that model.

In order to better serve real objects, a further study is investigated in this paper, in which the internationally adopted Japanese AIJES-V001-2004[5] is adopted. A vibration-sensation model is proposed to estimate the human comfort performance and a life cycle cost with the consideration of damper failure is explored. The proposed method is applied to the human comfort design choice of a super tall building with and without tuned mass damper (TMD), tuned liquid column damper (TLCD) or combined tuned damper (CTD) device [6] to illustrate its effectiveness and applicability.

4. Human Comfort Performance Based Life Cycle Cost Model

The existing vibration-induced human comfort performance criteria are closely relative to the acceleration limitation of the vibration environment. That is to say, according to the limitation given by the selected criterion, it is easy to judge whether a building performance meets the performance requirement or not with structural acceleration known. However, for convenience of mastering and utilizing these human comfort criteria, it is necessary to further understand these criteria [7]: (1) the allowed vibration limitation given by vibration comfort

standards is artificially divided by ensuring a certain significant level, the allowed vibration limitation itself also has kind of uncertainty; (2) nowadays there has been no effective method to evaluate the whole-system performance just according to vibration comfort performance of each part; (3) there is no criterion with the economic failure evaluation if the performance is beyond standard limitation and this no doubt has to be considered by engineers and designers. Therefore, it is essentially important to improve the existing standard.

4.1 Vibration-Sensation Rate Model

4.1.1 Wind-induced human comfort performance criterion

Nowadays Japanese wind-induced human comfort performance criterion of building structures (AIJES-V001-2004) [5] is generally recognized. The 10-minute peak acceleration of the structure under 1-year wind loads is taken as the evaluation index. Japanese criterion determines five levels (H-10~H-90) of comfort performance depending on the proportion of people who have the vibration sensation, in which H-10 represents 10% of people feeling vibration without discomfort, H-30 with a similar meaning and rest on. Most importantly, the each-level performance of Japanese comfort standard is associated with the vibration frequency.

$$\alpha_{\max} = af_1^b \quad (1)$$

Where α_{\max} = the maximum acceleration response (cm/s^2), f_1 = the vibration frequency, a and b are related coefficients which shows in figure 1.

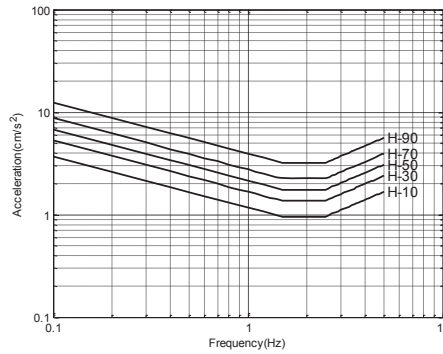


Figure 1: The building horizontal vibration performance evaluation curves under wind load

4.1.2 Vibration-sensation rate model under once random vibration

For the view of psychophysics, the uncertainty people reacting to vibration subjectively can be divided into two categories: (1) ambiguity due to the subjective reacting criteria not clear in the concept; (2) random caused by people's sensation differences in vibration stimulation. The ambiguity of uncertainty can be described by psychophysical Fechner law.

$$v(u) = c \ln(u) + d \quad (2)$$

Where u = the vibration acceleration, v = degree of membership of subjective response, c and d are undetermined coefficients which can be determined by the above Japanese criterion.

Besides, Griffin et al. [8] hold the view that the distribution of people's vibration feeling is subject to the normal or lognormal distribution and it has been proved in later studies that the variability of human ability to feel vibration can be approximately taken as the lognormal distribution:

$$f(x|u) = \frac{1}{\sqrt{2\pi}u\sigma} \exp\left(-\frac{(\ln(u) - \mu_{\ln(x)})^2}{2\sigma^2}\right) \quad (3)$$

Where $\sigma^2 = \ln(1 + \delta^2)$, $\mu_{\ln(x)} = \ln(x) - \sigma^2/2$, in which x and δ are respectively the expectation value of the variable μ and the coefficient of variation. Equation (9) means that for once random vibration with the acceleration x , people have different feelings due to differences of human sensibility. And people actually feel vibration stimulation with equivalent acceleration u , although these feelings are different from each other, they generally remain stable at an average equivalent stimulation x .

According to Japanese wind-induced human comfort performance criterion, taking the ambiguity and randomness of human sensation into account, a vibration-sensation rate model is proposed as follows:

$$A(x) = \int_{u_{\min}}^{\infty} \frac{1}{\sqrt{2\pi}u\sigma} \exp\left(-\frac{(\ln(u/x) + 0.5\sigma^2)^2}{2\sigma^2}\right) v(u) du \quad (4)$$

The physical meaning of the equation (4) is the rate of people that have feelings without discomfort under once random vibration.

4.1.3 Vibration-sensation rate model under one-year strong wind

Cao Hong et al. [9] believe that it is reasonable to utilize normal distribution to describe the distribution of wind-induced structural peak acceleration response.

$$f_{\ddot{x}_m}(x) = \sqrt{\frac{2}{\pi\sigma_x^2}} \exp\left(-\frac{x^2}{2\sigma_x^2}\right) \quad (5)$$

Therefore, the probability distribution function of peak acceleration response will be:

$$F_{\ddot{x}_m}(x) = \frac{2}{\sqrt{\pi}} \int_0^{\frac{x}{\sqrt{2}\sigma_x}} e^{-t^2} dt \quad (6)$$

Assuming that there are N structural peak acceleration responses during the period $(0, T)$ and these peak acceleration responses $\ddot{x}_m (m=1, 2, 3 \dots N)$ are mutual independent. So the distribution of $\ddot{z}_m = \max\{\ddot{x}_m\}$ can be showed in the following equation:

$$F_{\ddot{z}_m}(x) = \left[\frac{2}{\sqrt{\pi}} \int_0^{\frac{x}{\sqrt{2}\sigma_x}} e^{-t^2} dt \right]^N \quad (7)$$

$$f_{\ddot{z}_m}(x) = N [F_{\ddot{x}_m}(x)]^{N-1} \sqrt{\frac{2}{\pi\sigma_x^2}} \exp\left(-\frac{x^2}{2\sigma_x^2}\right) \quad (8)$$

Where $F_{\ddot{x}_m}(x)$ and $F_{\ddot{z}_m}(x)$ are the probability distribution functions of peak acceleration response \ddot{x}_m and the maximum of them \ddot{z}_m respectively, $f_{\ddot{x}_m}(x)$ and $f_{\ddot{z}_m}(x)$ are the probability distribution density functions of \ddot{x}_m and \ddot{z}_m respectively. T represents the time of gustiness which usually is 10 minutes.

From all above, the expectation of vibration-sensation rate, that is, the vibration-sensation rate with random acceleration distribution can be illustrated as:

$$E[A(x)] = \int_0^{\infty} f_{\ddot{z}_m}(x) A(x) dx = \int_0^{\infty} N \left[\frac{2}{\sqrt{\pi}} \int_0^{\frac{x}{\sqrt{2}\sigma_x}} e^{-t^2} dt \right]^{N-1} \sqrt{\frac{2}{\pi\sigma_x^2}} \exp\left(-\frac{x^2}{2\sigma_x^2}\right) A(x) dx \quad (9)$$

It is needed to note that the expectation of vibration-sensation rate showed in equation (9) is under a certain wind pressure w_0 [10]. Taking one-year wind pressure distribution into consideration, the expectation of vibration-sensation in one year is:

$$\bar{A}(x) = \int_0^{+\infty} E[A(x)|w = w_0] f(w_0) dw_0 \quad (10)$$

In order to simplify the calculation, equation (10) can be replaced by equation (11).

$$\bar{A}(x) = \sum_{i=1}^m E[A(x)|w = w_i] \times [F(w_i) - F(w_{i-1})] \quad (11)$$

Where $F(w_i)$ is the probability distribution function of the maximum average wind pressure during 10 minutes, m

is the number of wind pressure grades [22].

4.2 Failure Cost Model of Human Comfort Performance

It is well known that for different building usages, even the same vibration level can result in different failure costs. For example, hospitals, superior hotels and superior offices which need higher level human comfort performance suffer more than tour towers with low comfort performance requirement. Therefore, referring to estimating failure costs of human comfort performance, the building usage, the number of occupants, vibration-sensation rate and local economic level are needed to consider. For different building usages, the recommended failure cost model is shown as follow:

$$c(x) = n(\alpha C) [\chi \bar{A}(x)] \quad (12)$$

For the whole building, the failure cost can be shown in equation (13):

$$c_1 = \int_{x_{\min}}^{x_{\max}} c(x) dx \quad (13)$$

Where n = the number of people in the vibration environment; αC represents the economic evaluation index, C = the local average annual income, α = the coefficient which can be calculated by regression analysis; $\chi \bar{A}(x)$ represents the vibration-sensation rate of different structural usage, χ = the effect coefficient of building usage (e.g. 1.0 for superior hotels and superior offices and 0.8 for tour towers).

4.3 Life Cycle Cost Model

The discount rate of money is utilized to calculate the whole life cycle cost. For convenience, assuming that the structure is time-independent and the failure cost is the same in every year, the life cycle cost model is illustrated as follow [11-13]:

$$L_{CC} = C_0 + C_m + C_f = C_0 + C_m + \theta \sum_{i=1}^{T_{life}} c_1 \frac{1}{(1+r)^i} \quad (14)$$

Where C_0 = the initial investment cost, C_m = the maintenance cost, C_f = the failure cost, T_{life} = structural service life period (like 100 years for the super tall building), r = money discount rate, θ = the adjustment coefficient representing policy maker's attitude to risk (e.g. $\theta > 1$ for optimistic, $\theta < 1$ for pessimistic and $\theta = 1$ for intermediate, especially for research and consulting institutions [14]).

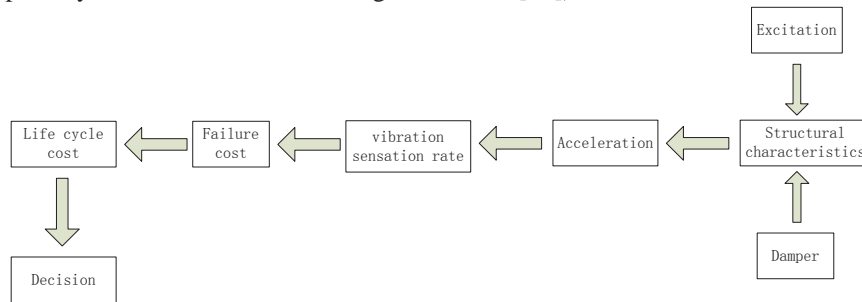


Figure 2: Process Diagram of Life Cycle Cost Calculation

4.4 Life Cycle Cost Model for the damper-structure system

4.4.1 Wind-induced Vibration Control Theory

In order to raise human comfort performance, dampers are usually installed in the structure to suppress the amplitude of vibration. The effectiveness of a damper can be illustrated by vibration control coefficient and finally result in the decrease of life cycle cost. The vibration control coefficient η is defined as follow:

$$\eta = \frac{\sigma_{\ddot{x}} - \sigma_{\ddot{x}}^{damper}}{\sigma_{\ddot{x}}} = 1 - \frac{\xi_{na}}{\xi_e} = \frac{\bar{A}_{\ddot{x}} - \bar{A}_{\ddot{x}}^{damper}}{\bar{A}_{\ddot{x}}} \quad (15)$$

Where σ_x and σ_x^{damper} are acceleration responses of the primary system and the damper-structure system respectively, ξ_{sa} =the sum of structural damping ratio and aerodynamic damping ratio, ξ_e =the equivalent damping ratio of the damper-structure system [15].

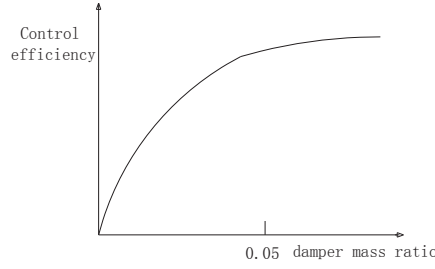


Figure 3: Vibration control coefficient and mass ratio [3].

4.4.2 Dynamic reliability of wind-resistant damper

The damper (e.g. a TMD) installed in the building to suppress the vibration response usually has large amplitude of vibration response itself, which may lead to itself or other surrounding structural damage. Therefore, it is necessary to install a snubbing system in the building to snub the damper to guarantee the damper's safety. Most importantly, even if it does not cause damage, the damper tends to be locked-in when the structure suffers a quite strong wind in some real objects, which no doubt causes the failure of damper. For a large given limitation b , the expectation of passage times that the relative displacement of the damper with respect to the main structure exceeds the limitation meets the Poisson distribution shown in the following equation:

$$v_b = \frac{\sigma_y}{2\pi\sigma_y} \exp\left(-\frac{b^2}{2\sigma_y^2}\right) \quad (16)$$

Based on first-passage failure criterion, the dynamic reliability of the damper which means the transcendence degree is equal to zero ($N=0$) is given as follow:

$$P_{s1}(b > y(t)) = \exp\left[-\frac{\sigma_y T}{2\pi\sigma_y} \exp\left(-\frac{b^2}{2\sigma_y^2}\right)\right] \quad (17)$$

For the dynamic reliability with both-side limitation:

$$P_{s2}(-b < y(t) < b) = \exp\left[-\frac{\sigma_y T}{\pi\sigma_y} \exp\left(-\frac{b^2}{2\sigma_y^2}\right)\right] \quad (18)$$

However, with a relatively small limitation b , the Poisson distribution is unreasonable. The Vanmarcke approach, which is based on the Markov model, is proposed as follow [9].

$$P_{s2}(-b < y(t) < b) = \exp\left[-\frac{\sigma_x T}{2\pi\sigma_x} \exp\left(-\frac{r^2}{2}\right) \frac{1 - \exp\left(-\frac{\sqrt{\pi}}{2} qr\right)}{1 - \exp\left(-\frac{r^2}{2}\right)}\right] \quad (19)$$

Taking the wind-field-environment random of the structural site into consideration, the failure probability of the damper under one-year wind is P_f which is shown in equation (26) and equation (21).

$$P_{f2} = 1 - P_{s2} \quad (20)$$

$$P_f = \int_0^{+\infty} P_{f2}(-b < y(t) < b | \omega = \omega_k) f(\omega) d\omega \quad (21)$$

Where $f(\omega)$ is the probability distribution density function of maximum wind pressure during 10 minutes of once

strong wind.

4.4.3 Life Cycle Cost Model of the structure-damper system

For different building usages, the human comfort performance based failure cost of the structure-damper system can be calculated by the following equation:

$$c(x) = \alpha \chi C \left[P_f \cdot \bar{A}(x) + (1 - P_f) \cdot \bar{A}(x)^{damper} \right] \quad (22)$$

And the life cycle cost model of the structure-damper system is the same as before:

$$c_1 = \int_{x_{min}}^{x_{max}} c(x) dx \quad (23)$$

$$L_{CC} = C_0 + C_m + C_f = C_0 + C_m + \theta \sum_{i=1}^{T_{life}} c_1 \frac{1}{(1+r)^i} \quad (24)$$

The parameters in the above equation are the same as before. It is needed to note that Guoxiong Bu et al. had studied the initial investment cost C_0 and the maintenance cost C_m of TMD [3]. Therefore, these data of other dampers (e.g. a TLCD or a CTD) can be studied in a similar manner to the analysis of a TMD.

4.5 Life Cycle Cost Model Based Optimal Design

4.5.1 Optimal Design Theory

As the damper is installed in the building, the initial investment and maintenance costs increase when the damper mass increases, however, the failure cost even decreases to a constant value (see figure 4). Therefore, there is a minimum value of life cycle cost which needs to be analyzed and calculated in detail.

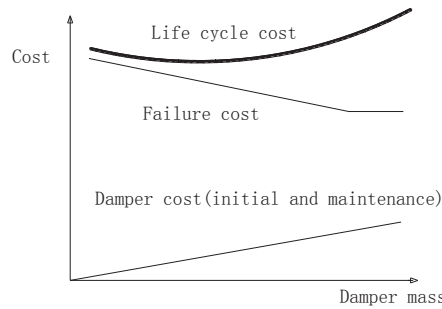


Figure 4: Diagram of optimal design theory

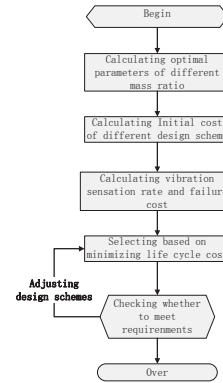


Figure 5: selection method of the damper

4.5.2 Process of Optimal Design

The optimal design process of wind-induced human comfort performance, which is based on minimizing life cycle cost, is shown as follows: (1) calculating the optimal parameters of different mass ratios to maximize the effectiveness of the dampers; (2) calculating the initial investment and maintenance costs according to different damper parameters; (3) calculating the acceleration response, the vibration-sensation rate and the performance-failure cost according to different damper parameters; (4) calculating the life cycle cost of the whole building and finding out the minimum value; (5) checking whether human comfort performance meets the criterion and the owner's requirement or not. If not, go back to step 4.

The main steps of damper selection are shown in figure 5.

5. Response Analysis

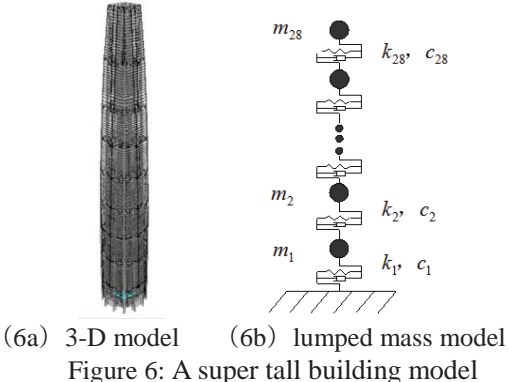
As the wind loads are usually describing as random processes, the analysis of random vibration response is the basis to calculate the vibration-sensation rate. For the random process characteristic of the wind load, the structural response under the wind load can be described with the response power density spectrum which can be calculated by load spectrum and frequency-response function. Also, the pseudo excitation method can be employed to help analyze the random process that has the dense vibration modes or the nonlinear damping [17]. The along-wind response is caused by the fluctuating wind and the fluctuating wind can be described by a Gaussian stationary random process with zero mean. Moreover, the spectrum of longitudinal turbulence proposed by Davenport (1961)

is adopted in this study. It is easy to calculate the acceleration response of the along-wind load. As is generally known, the cross-wind load is stronger and may be the chief control load for the wind-sensitive structure with the increasing building height. However, it is so complicated that the cross-wind load spectrum cannot be calculated similarly to that of the along-wind which is according to the quasi-steady theory and the strip assumption. Nowadays high frequency force balance test is widely used to simulate the cross-wind load spectrum based on an assumption that the first mode of vibration is linear [18]. Yong Quan and Ming Gu [19] had studied super tall buildings with four different kinds of wind environments and fifteen types of structural shapes and proposed a closed equation of the cross-wind load spectrum which can be used to calculate the standard deviation of the cross-wind acceleration response.

When the structural shape is unsymmetrical and changeable, there exists torsional vibration under the wind load. The structural torsional vibration is due to asymmetries of windward, leeward and lateral wind pressures associated with turbulence and wake excitation. That is to say, owing to the deviation between the structural mass centre and stiffness centre, the bending vibration mode and the torsional vibration mode couple with each other, in which case, the structural response is quite different from that of the single direction. Therefore, the torsional response needs to be considered for these asymmetry-shape buildings [20].

6. Case Study

A 729m high 69m wide 141-storey super building whose building function contains commercial shop, office, hotel and tourism is studied in this study. The 3-D model and lumped mass multi-degree-freedom model are showed in figure 6. The damping ratio is 2%, the local wind environment is C and the 50-year wind pressure is 0.45 kPa. The human comfort performance and the optimal design scheme are studied.



6.1 Response and Vibration Sense Rate of Structure

The possibility wind pressure in one year can be separated in 6 grades of 0.1, 0.3, 0.45, 0.5, 0.57, 0.67 Kpa, which is in consistent with the velocity grades of 10.62, 22.03, 26.54, 28.44, 30.34, 32.85 ms⁻¹ respectively. The fluctuating wind load spectrum can be calculated by the above spectrum function mentioned in section 4 and the structural response can be with the pseudo excitation method. Taking 26.54ms⁻¹ (0.45Kpa) for example, the structural response of standard deviation acceleration is shown in figure 7. It is concluded that the response under the cross-wind is larger than that under the along-wind. It is needed to point out that the cross-wind response is approximately linear because the structural generalized first-order power spectrum is based on the assumption that structural first mode of vibration is approximately linear according to the high frequency force balance test. However, all modes are involved and the structural first mode of vibration is a bending-shearing type. The vibration-sensation rates of the primary structure are calculated by taking all grades of one-year wind pressure into consideration showing in figure 8.

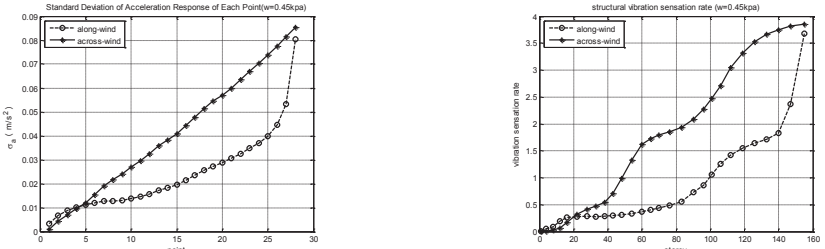


Figure 7: Root mean square of acceleration Figure 8: Vibration sense rate without damper

6.2 Optimal Parameters of Dampers

The optimal parameters of dampers can be calculated by maximizing the vibration control efficiency. Because the cross-wind response is dominant, the structural responses under the cross-wind are calculated. The relationships between parameters and vibration control efficiency of the TMD and the TLCD are shown in figure 9 and figure 10 respectively.

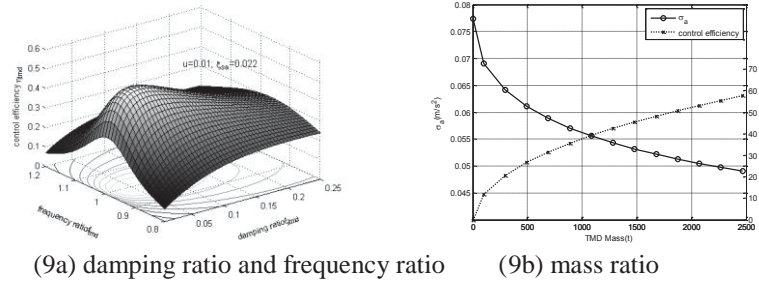


Figure 9: Relationship amongst parameters and vibration control efficiency of TMD

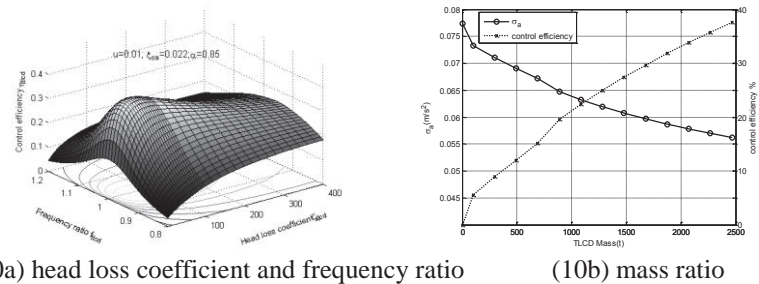


Figure 10: Relationship amongst parameters and vibration control efficiency of TLCD

6.3 Life Cycle Cost Evaluation and Design Choice

With the vibration-sensation rate of the structural human comfort performance known, it is available to evaluate the design schemes to minimize the life cycle cost. Assuming that the life cycle and the discount rate of money are 100 years and 3.5% respectively, the structural life cycle costs of different design schemes are shown in figure 11 and table 1.

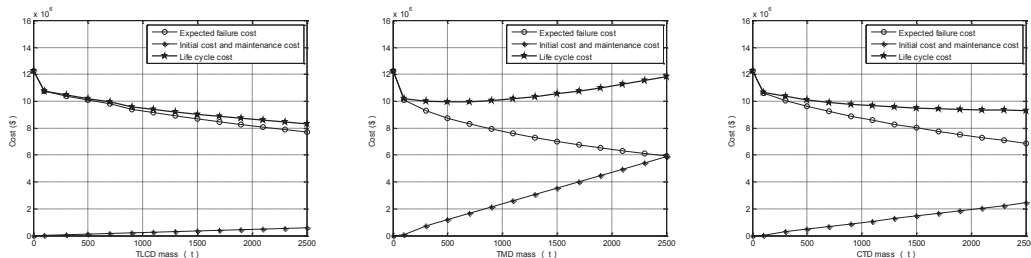


Figure 11: Relationship of life cycle cost and damper mass

Table 1 Expected life cycle cost

Structural scheme	Damper mass t	C_0 10 ⁶ \$	C_m 10 ⁶ \$	C_f 10 ⁶ \$	L_{CC} 10 ⁶ \$	
Primary structure	0	0	0	12.26	12.26	
TMD-structure system	500	1.12	0.056	8.76	9.94	
TLCD-structure system	1000	0.22	0.011	9.27	9.50	
TLCD-structure system	TLCD	650	0.15	0.008	8.74	9.73
	TMD	350	0.79	0.039		

It is highly efficient to improve the human comfort performance by installing a damper. Also, the total life cycle cost decreases. From the data in the table 1, it is easily concluded that in terms of life cycle cost, the design scheme with a TLCD-structure system is the best. After that, the design scheme with a CTD-structure system ranks second.

Then, the design scheme with a TMD-structure system follows and the primary structure system without any damper. It is worth being noted although the life cycle cost drops continuously with the mass rising, the damper mass of the TLCD or the CTD is decided twice as high as that of the TMD for the consideration that the volume of the TLCD filled with water is usually several times as large as that of the TMD.

6.4 Human comfort performance check

The selected design scheme based on the minimum life cycle cost should also meet the limitation requirements of Chinese code criterion and the owner's thoughts. For this study case, the structural peak-acceleration response can be obtained by calculating the structural root mean square under 10-year wind pressure and selecting the peak factor of 2.5 (99.3% for insurance) with assumption that the structural response meets Gaussian distribution with a zero-mean value.

Table 2 Check for human comfort performance

Structural scheme	10-year wind pressure	
	Root mean square (m/s ²)	Peak value (m/s ²)
Primary structure	0.0773	0.193
500t TMD-structure system	0.0584	0.146
1000t TLCD-structure system	0.0604	0.151
1000t CTD-structure system	0.0572	0.143

It is easily concluded that the human comfort performance of all different design schemes can meet limitation requirements of Chinese code for hotels and offices but exceed slightly that for apartments. Measurements such as selecting larger damper mass can be taken to obtain more optimal design schemes when the owner has higher requirements.

7. Conclusion

Due to strong wind loads, super building height and high flexibility, the wind-induced vibrations of super tall buildings become excessive. Aiming to assess the human comfort performance of super tall building conveniently and effectively, a brand-new life cycle cost model based on AIJES-V001-2004 is studied in this paper. The proposed method is also applied to the human comfort design choice of a super tall building with and without tuned mass damper (TMD), tuned liquid column damper (TLCD) or combined tuned damper (CTD) device to illustrate its effectiveness and applicability, which could help make design choice based on the minimum life cycle cost criterion. Some conclusions are drawn as follows:

- (1) The damper has high effectiveness to improve the human comfort performance of super tall buildings. And properly increasing the initial investment can help to reduce the total life cycle cost. These have great significance to the decision of damper installation, which can be used for the structural early optimal design and provide a quite efficient method to solve the later related problems.
- (2) The initial investment and vibration control performance are different among the TMD, the TLCD and the CTD, the life cycle cost of them are also different. The life cycle cost of the TLCD-structure system is much less than that of the TMD-structure system, but the volume of TLCD is several times as large as that of TMD with the same mass ratio, which is no doubt with larger space required. The life cycle cost of the CTD-structure is between that of the TMD-structure and that of the TLCD-structure. It is concluded that the CTD can fully utilize the high effectiveness of a TMD and economical advantage of a TLCD, which makes it a competitive option.
- (3) Due to the lack for data of initial investment and maintenance cost of a TLCD, the relative costs of a TLCD are calculated in a similar way to TMD in this study, which, of course, needs further research in real objects.
- (4) It is strongly noted that it is hard to evaluate the costs of human comfort failure accurately because of strong variability of human subjective feelings and economic factors. There is also a large amount of work to do before the proposed method to be widely used. However, the proposed method provides an innovative idea for the optimal design of wind-induced human comfort performance for super tall buildings.

8. Acknowledgement

The authors are grateful for the support from the Shanghai Excellent Discipline Leader Program (No.14XD1423900) and Key Technologies R & D Program of Shanghai (Grant No. 09dz1207704).

9. Reference

- [1] Griffin M. J., *Handbook of human vibration*. Academic press, 2012.
- [2] Petrini F., and Ciampoli M., Performance-Based Wind Design of Tall Buildings. *Structure and Infrastructure Engineering*, 2012, 8(10SI): 954-966.
- [3] Guoxiong Bu, Ping Tan, and Fulin Zhou, Optimal design of the TMD device based on cost-effectiveness

- criterion. *Journal of Civil Engineering*, 2011, 44(5): 24-31.
- [4] Xin Zhao, and Tianyi Yu, Human comfort performance-based life cycle cost model of high-rise structures under wind load. *Journal of Tongji University (natural science)*, 2013, 41(12): 1793-1798.
- [5] Aij A I O J, *Guidelines for the Evaluation of Habitability to Building Vibration*. Tokyo, 2004.
- [6] Tongji Architectural Design (Group) Co., Ltd. (China). *A combined tuned damper for wind-induced vibration control of super tall buildings*. CN, 20553346.X, 2015- 01-14.
- [7] *Bases for Design of Structures - Serviceability of Buildings and Walkways Against Vibrations*. ISO10137, 2007.
- [8] Griffin M. J., and Whitham E. M., Individual variability and its effect on subjective and biodynamic response to whole-body vibration. *Journal of Sound and Vibration*, 1978, 58(2): 239-250.
- [9] Hong Cao, Qiusheng Li, Guiqing Li, and Da Huo, Calculation of wind-resistant structure safety. *Journal of Civil Engineering*, 1994, 27(1): 40-48.
- [10] Naidong Luo, and Guofan Zhao, Analysis of dynamic reliability for resisting wind loading of high-rise building. *Journal of Dalian University of Technology*, 2002, 42(2): 208-212.
- [11] Frangopol D. M., and Lin K. Y., Estes A.C., Life-cycle cost design of deteriorating structures. *Journal of Structural Engineering*, 1997, 123(10): 1390-1401.
- [12] Wen Y. K., and Kang Y. J., Minimum building life-cycle cost design criteria. II: Applications. *Journal of Structural Engineering*, 2001, 127(3): 338-346.
- [13] Wen Y. K., Kang Y. J., Minimum building life-cycle cost design criteria. I: Methodology. *Journal of Structural Engineering*, 2001, 127(3): 330-337.
- [14] Blair A. N., Ayyub B. M., and Bender W.J., Fuzzy stochastic risk-based decision analysis with the mobile offshore base as a case study. *Marine structures*, 2001, 14(1): 69-88.
- [15] Weilian Qu, Muhua Tao, and C. C. Chang, Practical Design Method for Effect Kinds of Passive Dynamic Absorbers on Fluctuation Wind-induced Vibration Response Control of Tall Buildings. *Journal of Building Structures*, 2004 (2): 29-34.
- [16] Ping Tan, Guoxiong Bu, and Fulin Zhou, Study on wind-resistant dynamic reliability of TMD with limited spacing. *Journal of Vibration and Shock*, 2009, 28(6): 42-45.
- [17] Y.L. Xu, W.S. Zhang, J.M. Ko, and J.H. Lin, Pseudo-excitation method for vibration analysis of wind-excited structures. *Journal of Wind Engineering and Industrial Aerodynamics*, 1999, **83**(1-3): 443-454.
- [18] Yong Quan, Huilan Cao, and Ming GU, Cross-wind Effect of High-rise Buildings. *Journal of Tongji University (natural science)*, 2010, 38(6): 810-818.
- [19] Yong Quan, and Ming GU, Power Spectra of Across-wind Loads on Super High-rise Buildings. *Journal of Tongji University (natural science)*, 2002, 30(5): 627-632.
- [20] Yi Tang, Ming Gu, and Xinyang Jin, Research on Wind-induced Response of Structurally Asymmetric Tall buildings. *Journal of Tongji University (natural science)*, 2010, 38(2): 178-182.

Integrated Optimal Life Cycle Design of Super Tall Buildings with Viscous Dampers

Xin Zhao^{1,2}, Tao Shi¹

¹ Department of Structural Engineering, Tongji University, Shanghai, China, 22zx@tjadri.com

² Tongji Architectural Design (Group) Co., Ltd., Shanghai, China, 22zx@tjadri.com

1. Abstract

The life cycle of a super tall building has many stages such as design, construction, operation, maintenance and so on. The life cycle cost of the structure is mainly composed of the construction, maintenance and disaster lost costs. Viscous dampers can effectively improve the energy dissipation capacity of super tall building structures under earthquakes. The life cycle cost could be reduced by the introduction of viscous dampers due to two facts. One is that the structural members can be further optimized for considering the reduction of earthquake actions due to additional damping, and the other is that the structural damage could be alleviated with the viscous dampers to reduce the maintenance and disaster lost. The integrated optimal design of the life cycle cost about the main structural members using viscous dampers was addressed in this paper. Integrated optimal design was then applied to minimize the sizes of structural members. A life cycle cost assessment method was proposed to evaluate the whole life cycle cost of buildings which include construction, maintenance and disaster lost costs. A super tall building located in high seismicity area was applied in the final part of this paper to illustrate the effectiveness of the proposed optimal life cycle design method.

2. Keywords: super tall building; viscous dampers; life cycle cost; integrated optimal design.

3. Introduction

The past decade has witnessed the great development of super tall buildings in China. Especially for those buildings in seismic prone area, special measures are needed for improving the seismic performance of the super tall buildings. Energy dissipation system is widely applied in the design of high-rise buildings. Viscous dampers can effectively improve the energy dissipation capacity of super tall building structures under earthquakes. Viscous dampers can generate damping forces by velocity-dependent viscosity effects of the viscous liquid under different earthquake levels, and thus have been widely applied in engineering practices^[1].

According to previous study^[2,3], the damped outriggers are installed between service core and column and it will not occupy space. The structure will be safer with the reduction of response and internal forces due to increase of damping, furthermore the structural damage could be alleviated with the viscous dampers.

The optimal design of super tall building is usually equal to the optimization of construction cost. But the life cycle of a super tall building has many stages such as design, construction, operation, maintenance and etc. When engineers optimize the structure, they always neglect the damage cost under different levels of earthquake.

This paper developed an integrated optimal life cycle design method which can further optimize the additional redundancies introduced by the installation of viscous dampers in the outrigger trusses in super tall buildings. An optimal design process was applied to further optimize the structural members with high redundancies in iterative nature. A life cycle cost assessment method was proposed to evaluate the whole life cycle cost of buildings. A 250 meter high super high-rise building is adopted in the last part to show the effectiveness of the proposed method. The performance and cost of the optimized structure and primitive structure were compared at the end.

4. Optimal Design Process

Viscous dampers offer additional damping to the structure and dissipate the energy during different earthquake intensity. The seismic performance of structure can be improved with the energy dissipation capacity of the viscous dampers. The structural members can be further optimized for considering the reduction of earthquake actions. On the other hand, the damage lost could be much less than the original structure. To reduce the redundancies introduced by the viscous dampers, the following integrated optimal design process can be employed:

- (1) Assess the contribution of different outrigger trusses on the structural lateral stiffness;
- (2) Remove those outriggers which have small contribution on the lateral stiffness;
- (3) Install damped outriggers with viscous dampers, and calculate the addition damping ratios;
- (4) Determine the design constraints of components, such as story drift, period and stress ratio;
- (5) Conduct sensitivity analysis and indicate those members which need to be optimized;
- (6) Optimize those components of high redundancies, and check the design constraints to make sure they are

- below specified limits;
- (7) After the optimization of structural components, sensitivity analysis will be conducted using updated sizes of structural components. Those components of high redundancies will be optimized again like in step (6) until the margins of design constraints are as small as specified;
 - (8) Step (1) to (7) will be conducted for different structural schemes with different number of damped outrigger and stiff outrigger combinations;
 - (9) The overall life cycle costs of different structural schemes will be compared and the scheme with least cost will be the final scheme to be employed.

It is worth pointing out that in step (6), structural member sizes are commonly determined by multiple constraints. The multiple constraints are related with numerous design requirements, say global design criteria (such as period, story drift, shear weight ratio and etc.) and component design criteria (such as stability, bending strength, shearing strength, stress ratio, axial compression ratio and etc.).

The sensitivity analysis and optimization design of structure used in this paper is based on the virtual work principle. The virtual work principle indicates that when the system is given any geometric possible displacement and deformation, the sum of all the virtual work produced by external forces in the system is equal to the sum of all the virtual work produced by internal forces with micro deformation of each section in the system^[4].

Assuming d_i is the virtual work on real displacement about this component. The sensitivity index is shown in Eq.1:

$$\alpha_i = \frac{d_i}{\beta_i} \quad (1)$$

where d_i is the virtual work of component's displacement, β_i is generally chosen the component's weight or cost, etc.

According to the sensitivity indices, we can easily obtain one component's contribution to the monitoring parameter, and it is convenient to obtain the effectiveness of the structural system, the rationality of layout and the sensitivity of the components for several criteria.

5. Life Cycle Cost Assessment

With the rapid development of construction industry, engineers need comprehensive assessment method to evaluate the different schemes in preliminary design. Life cycle cost assessment, which is an effective assessment method, is being used more and more widely in the study of structural life cycle design. Life cycle cost assessment method is used to evaluate the cost in whole life cycle, and to guide engineers how to select a safer and more economical scheme.

The previous study has already put forward that the optimization objective is to minimize the life cycle cost^[5].

The scholars in China and other countries had a deep study on the theory and analysis model^[6]. The expression of analysis model is shown in Eq.2:

$$C_{tot} = C_b + C_m + C_f \quad (2)$$

where C_b is construction cost; C_m is maintenance cost; C_f is loss cost.

The significance of performance based design is to make a balance of economic and safety, and to minimize the life cycle cost. The life cycle cost refers to the construction cost, maintenance cost and lost cost. The lost cost may be caused by external force (such as wind load, earthquake, fire, explosion and etc.) or internal function (such as corrosion, aging and etc.). To super tall buildings, the main cause that we should consider in design is external force.

Different earthquake intensity has different probability of occurrence. The earthquake intensity and loss have a corresponding relation to the same structure. The expression of loss cost under the earthquake is shown in Eq.3:

$$C_f = \int_0^1 c_i dp_i \quad (3)$$

where p_i is the probability of earthquake of intensity i , c_i is the loss cost under earthquake of intensity i .

According to Eq.3, the loss cost can be expressed in Eq.4:

$$c_i = \sum_{j=1}^N \beta(B_j) \cdot n \cdot c_j \quad (4)$$

Where j is the component category, $\beta(B_j)$ is the loss coefficient of component, n is the number of damaged component, c_j is the lost cost of component.

The relation between peak acceleration of earthquake, earthquake intensity and probability of earthquake is given as Eq.5 and Eq.6^[7]:

$$A = 10^{(I \lg 2 - 2.11)} \quad (\text{m/s}^2) \quad (5)$$

$$p_i = 1 - F_{III}(x) = 1 - \exp\left(-\left(\frac{w-x}{w-\varepsilon}\right)^k\right) \quad (6)$$

where A is peak acceleration of earthquake; I is earthquake intensity; w is upper limit of earthquake intensity; k is shape function.

With Eq.6, we can easily get the relationship between the probability of earthquake and the peak acceleration. For example, when the peak acceleration is 0.15g, earthquake intensity I is 7.56, w is 6.14, and shape function K is 8.110, Eq.6 can be expressed in Eq.7.

$$p_i = 1 - F_{III}(x) = 1 - \exp\left[-\left(\frac{121g^2 - 2.11 - \lg A}{5.861g^2}\right)^{8.11}\right] \quad (7)$$

The lost coefficient can be gained from classification of earthquake damage to buildings and special structures. The damage state can be divided into 5 states, and every state has its own corresponding lost coefficient. As it is shown in Table.1, $\beta(B_i) = 0$ indicates that the component is undamaged, and $\beta(B_i) = 1$ indicates that the component cannot be repaired.

Fig.1 shows that most finite element analysis software judge the damage levels of components with performance level in FEMA 356. In FEMA 356, 'IO' is operational performance, 'LS' is life safety, and 'CP' is collapse prevention. Fig.2 is the relationship between the damage levels and performance levels. So we can easily obtain the performance level with finite element analysis software, then we can gain the lost coefficient.

To assess the life cycle cost, the following Life cycle cost assessment process can be employed:

- (1) To simplify the calculation, select several typical peak acceleration, such as the peak accelerations of frequent earthquake, moderate earthquake, and rare earthquake in *Code for Seismic Design of Buildings*.
- (2) Calculate the probability of different earthquake intensity (p_i).
- (3) Analyze the structure with different earthquake intensity.
- (4) Calculate every component's loss coefficient $\beta(B_i)$.
- (5) Obtain the lost cost with Eq.4.

Table.1 Definition of damage coefficient on different level for the reinforced concrete elements

Damage level	Description of classification	$\beta(B_i)$
Undamaged (B1)	No crack and no need to repair. (<0.5IO)	0.00
Slight damage (B2)	A little crack, and just need simple repair. (0.5IO)	0.05
Moderate damage (B3)	Concrete occur obvious crack, but the steel bars do not yield. (IO)	0.15
Severe damage (B4)	The concrete spalls severely, and the steel bars yield. The component should be repaired and reinforced. (LS)	0.90
Collapse (B5)	The component is absolutely damaged, and cannot be repaired. (CP)	1.00

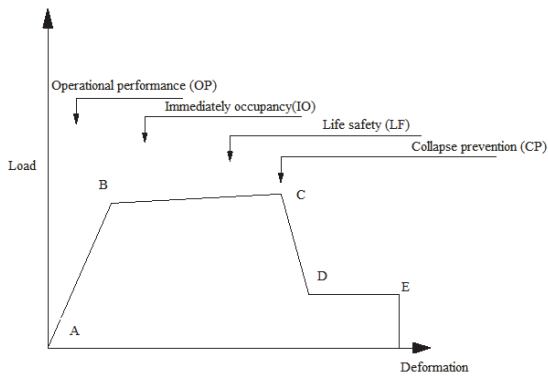


Fig.1 Performance levels of elements from FEMA



Fig.2 Damage levels and performance levels

6. Case Study

A 250-meter-high super high-rise building with 63 floors and 3 mechanical floors is adopted in this study. The structural system is frame-core wall structure. The plane of tower is 57.02m×35.62m, and the spacing of frame column is 10.2 meters along the long side and 5.6 meters along the short side. The core tube is in the middle with the size of 32.2m×13.7m. There are three belt trusses (16th floor, 32th floor, 48th floor) and two outriggers (32th floor, 48th floor). Fig.3 and Fig.4 show the structural system of tower. The outriggers are only installed in the X direction. Five ground motion records were used for nonlinear time history analysis. The acceleration amplitude is set to 35 gal and the duration is set to 40s. The damping ratio is 4% in frequent earthquake.



Fig.3. 250 meters high model

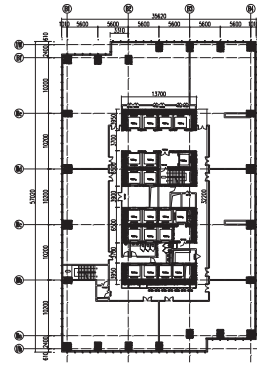


Fig. 4 Typical layout plan of tower

6.1 Remove Outriggers

As is shown in Table.2, the story drift about one outrigger in zone 3 is 1/545, and it is better to remove the outrigger in zone 2 because of the less stiffness loss. When two outriggers are removed, the story drift will be amplified too much, and the structural stiffness and stability are difficult to meet the requirements. So the damped outriggers should be installed on the outrigger in zone 3.

Table.2 Optimal position of outriggers

Number of outriggers	2	1	1	0
Location	Zone 2,3	Zone 2	Zone 3	--
Story drift in the X direction	1/674	1/571	1/545	1/496

6.2 Install Viscous Dampers

The structure will be safer with the reduction of response and internal forces due to increase of damping. Fig.5 shows that the dampers can be put in 8 grids, Fig.7 and 8 show the layout of damped outriggers. The parameters of dampers are as follows: the maximum damping force is 2000kN, the damping coefficient is $C=400 \text{ kN}/(\text{m/s})^{0.3}$, the damping exponent is $\alpha =0.3$ and the stiffness is $K=4.0 \times 10^5 \text{ kN/m}$. Fig.6 and Table.3 show that the story drift decreased, and the additional damping ratio increased with the increase of dampers. The calculation results about four various quantities of dampers are shown in following Table.3.

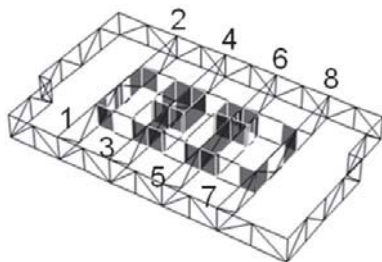


Fig.5 8 grids that can be installed viscous dampers

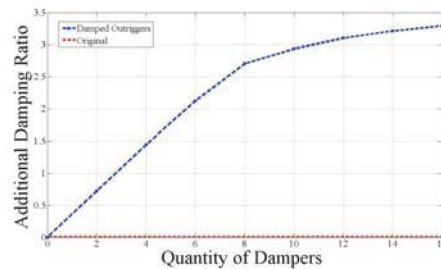


Fig.6 Additional damping ratio with different quantity of VDs

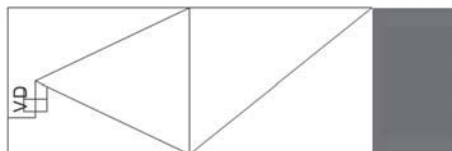


Fig.7 Damped outrigger with 1 VD

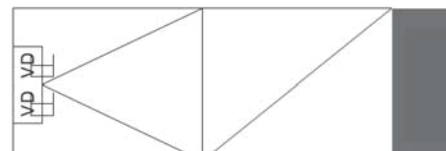


Figure.8 Damped outrigger with 2 VDs

Table.3 Calculation result of four schemes

Scheme	Location	Story Drift	Additional Damping Ratio
with 4 VDs	Grid 3,4,5,6 (one VD in one grid)	1/666	1.44%
with 8 VDs	Grid 3,4,5,6 (2VDs in every two grids)	1/706	2.70%
with 12 VDs	Grid 3,2,7,8 (one VD in one grid)	1/744	3.10%
with 16VDs	Grid 3,4,5,6 (2VDs in every two grids) Grid 1,2,3,4,5,6,7,8 (2VDs in every two grids)	1/769	3.29%

6.3 Sensitivity Analysis

Virtual couple and actual seismic force are put on the structure to conduct the sensitivity analysis for determining the optimization strategy. The virtual force is acted on the 49th floor where is the maximum story drift. Sensitivity index $\alpha_i = d_i / \beta_i$ of component is shown in following Table.4.

Table.4 shows that the diagonal members of belt trusses in Zone 3 and Zone 4 have the most contribution to maximum story drift and the second is chord members in Zone 3. To save the cost, the size of components that have small contribution to the story drift should be reduced, such as the belt trusses in Zone 1 and Zone 2.

Table.4 Sensitivity index of belt truss

	Zone1 (16F)	Zone2 (32F)	Zone 3 (48F)	Zone 4 (63F)
Chord Member	<5	<5	10-30	<5
Diagonal Member	<5	<5	50-80	50-100

6.4 Component Redundancy Analysis

This study chose belt trusses optimization as an example for the limits of paper. The design of outriggers usually needs to consider global design criteria and component design criteria. As is shown in Table.5, the stress ratio is about 0.6 to 0.9 which is under 0.9 that the Chinese code limits.

Table.5 Stress ratio of belt trusses (unit: mm)

Story	Member	Section Size	Stress Ratio
16F	Diagonal Member	500x500x50x50	0.760
	Chord Member	700x500x50x50	0.729
32F	Diagonal Member	500x500x50x50	0.850
	Chord Member	700x500x50x50	0.736
48F	Diagonal Member	500x500x50x50	0.666
	Chord Member	700x500x50x50	0.687
63F	Diagonal Member	500x500x50x50	0.732
	Chord Member	700x500x50x50	0.784

6.5 Member Optimization

The members of belt trusses whose sensitivity index to story drift is low will be the first to be optimized, when the seismic performance criteria is met. With the integrated optimal design method, the materials are distributed reasonably, and the economy of the structure is improved. Table.6 shows the section size of belt trusses which are optimized with the guidance of sensitivity analysis after several iterations.

Table.6 Optimization scheme comparison (unit: mm)

	Component	Original Structure	Scheme with 4VDs	Scheme with 8 VDs
Zone1	Diagonal Member	500x500x50x50	500x450x45x45	500x450x45x45
	Chord Member	700x500x50x50	600x500x40x40	600x450x40x40
Zone2	Diagonal Member	500x500x50x50	500x500x45x45	500x450x45x40
	Chord Member	700x500x50x50	600x500x40x40	550x450x40x40
Zone3	Diagonal Member	500x500x50x50	500x500x50x50	500x500x50x50
	Chord Member	700x500x50x50	700x500x45x45	700x450x45x45
Zone4	Diagonal Member	500x500x50x50	500x500x50x50	500x500x50x50
	Chord Member	700x500x50x50	700x500x45x45	700x450x45x45

		Scheme with 12VDs	Scheme with 16 VDs
Zone1	Diagonal Member	500x450x45x40	500x450x45x35
	Chord Member	600x400x40x40	600x400x40x40
Zone2	Diagonal Member	500x450x45x35	500x450x45x30
	Chord Member	550x450x40x35	550x450x40x30
Zone3	Diagonal Member	500x500x50x50	500x500x50x50
	Chord Member	700x450x45x45	700x450x45x45
Zone4	Diagonal Member	500x500x50x50	500x500x50x50
	Chord Member	700x450x45x45	700x450x45x45

6.6 Life Cycle Cost Assessment

The ground motion record will be used for nonlinear time history analysis. The acceleration amplitude is respectively set to 35 gal, 100gal and 220gal. And the duration is set to 30s. The frame beams and coupling beams are simulated with FEMA plastic twisted beam. The frame columns and shear walls are simulated with fiber units. Different components are assessed by failure condition with the plastic hinge rotation or strain.

This paper chose the steel bars in the shear walls as an example for the limits of paper. Fig.9 shows the failure condition under rare earthquake whose acceleration amplitude is 220 gal. The deeper color represents the greater damage. The steel bar about original scheme with no viscous damper damaged at the bottom and middle of structure. And the damage of integrated optimal structure is less with the additional damping ratio of the viscous dampers. The largest strain of reinforcement in the shear walls are under the condition of 'LS' which is Chinese code limits.

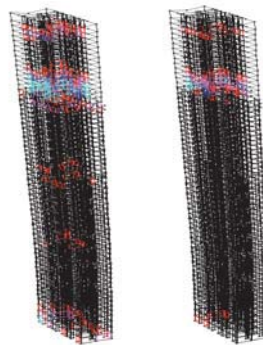


Fig.9 Damage condition of steel bars in shear walls

The lost cost of components under different earthquake intensity is shown in Table.7. The Lost cost of integrated optimal structure is much smaller than the cost of uncontrolled structure with the energy dissipation of viscous dampers. And the lost cost is smaller with the increase of viscous dampers. Every scheme is undamaged under the frequent earthquake.

Table.7 Lost Cost under different earthquake intensity (unit: RMB)

	Original Structure	Scheme with 4VDs	Scheme with 8VDs	Scheme with 12VDs	Scheme with 16 VDs
35gal (63%)	0	0	0	0	0
100ga(10%)	3,770,000	3,010,000	2,430,000	2,210,000	1,910,000
220gal (2%)	4,900,000	4,120,000	3,300,000	3,050,000	2,800,000
Sum	135,700	112,500	90,300	83,100	75,100

6.7 Optimization Result

Table.8 is the optimization comparison with different number of viscous dampers, in which it can be clearly observed that the damped outriggers can be removed the inner outriggers that cost 365 ton steels. The outer outriggers of the scheme with 12 and 16 VDs cost more steels than other schemes. The lost cost is smaller with the increase of viscous dampers. The optimal lost cost scheme with is the scheme with 16VDs. The price of every viscous damper is about 10,000 RMB. The price of steel is about 10,000RMB per ton. In Table 8, the economy of scheme with 8VDs is the best.

Table.9 shows the period and story drift about original structure and scheme with 8VDs. Period is a little larger than the previous scheme, and the story drift is reduced with the installation of viscous dampers.

Table.8 Optimization scheme comparison

	Original Structure	Scheme with 4VDs	Scheme with 8 VDs	Scheme with 12VDs	Scheme with 16 VDs
Outer Outrigger	149t	115t	115t	230t	230t
Inner Outrigger	365t	0	0	0	0
Belt Truss	1181t	1026t	976t	948t	934t
Viscous Damper	0	40,000RMB	80,000RMB	120,000RMB	160,000RMB
Lost Cost	135700 RMB	112500 RMB	90300 RMB	83100 RMB	75100 RMB
Total	17.0 million RMB	11.6 million RMB	11.0 million RMB	12.0 million RMB	11.9million RMB

Table.9 Optimization scheme comparison of global design criteria

	Original Structure	Scheme with 8 VDs
First period	5.83s	6.06s
Second Period	4.96s	5.00s
Third Period	3.96s	3.96s
Story Drift	1/674	1/692

7. Conclusion

This article discusses the optimization design method of viscous dampers for super high-rise building. This method is made use of sensitivity analysis, which is based on principle of virtual work. And the components can be optimized for the redundancies introduced by the viscous dampers. A 250-meter-high super high-rise building is addressed in this study, without reducing the safety of structure, the additional damping ratio is increased and the economy of the structure is improved.

We can draw the following conclusions:

1. The installation of the damped outriggers can increase additional damping ratio of structure, consume earthquake energy and reduce response under the earthquake. Meanwhile, there are some redundancies for component optimization.
2. In the process of integrated optimal design, sensitivity analysis, which is based on principle of virtual work, is used to judge the component's contribution to some criteria so that the optimal strategy can be obtained.
3. Life cycle cost assessment method is used to evaluate the cost in whole life cycle, and to guide engineers how to select a safer and more economical scheme.
4. Optimization calculation results show that the integrated optimal design of viscous dampers is reasonable and can be guidance to other designs of super tall buildings.

8. Acknowledgement

The authors are grateful for the support from the Shanghai Excellent Discipline Leader Program (No.14XD1423900) and Key Technologies R & D Program of Shanghai (Grant No. 09dz1207704).

9. Reference

- [1] Rob J. Smith and Michael R. Willford. The damped outrigger concept for tall building [J]. The Structural Design of Tall and Special Buildings, 2007, 16:501~517
- [2] Rob Smith, Michael Willford. Damped outriggers for tall buildings[J]. The Arup Journal, 2008, 3: 15~21
- [3] Zhengqing Chen and Zhihao Wang. A novel passive energy dissipation system for frame-core tube structure [A]. In: The Seventh Asia-Pacific Conference on Wind Engineering, Taipei: Taiwan, 2009.
- [4] Baker, W. F. Stiffness Optimization Methods for Lateral Systems of Buildings: A Theoretical Basis. Electronic Computation. Indianapolis, Indiana: American Society of Civil Engineers, 269278, 1991.
- [5] Frangopol D M, Liu M. Maintenance and management of civil infrastructure based on condition, safety, optimization, and life-cycle cost[J]. Structure and Infrastructure Engineering. 2007, 3(1): 29-41
- [6] Wen Y K, Kang Y J. Minimum building life-cycle cost design criteria. I: Methodology[J]. Journal of Structural Engineering-Asce. 2001, 127(3): 330-337.
- [7] Hongwei, Z. Integrated optimal structural design for super tall buildings with bucking-restrained braces: Tongji University, 2015

Parameter Optimization for the Integrated Optimal Design of Super Tall Buildings with Viscous Damping Walls

Xi Zhan¹, Xin Zhao^{1,2}, Yimin Zheng^{1,2}

¹ Department of Structural Engineering, Tongji University, Shanghai, China, 22zx@tjadri.com

² Tongji Architectural Design (Group) Co., Ltd., Shanghai, China, 22zx@tjadri.com

Abstract

Viscous damping walls can effectively suppress the vibration amplitude of the super tall building structures under both earthquake and wind. Comparing with other viscous dampers, viscous damping walls can dissipate more energy due to shear type mechanism and larger contacting areas. There are differences in economic cost and energy-dissipating capacity between viscous damping walls with different parameters and viscous damping walls with better parameters cost more. By the introduction of viscous damping walls in super tall buildings, the material consumption of main structures can be reduced by the reduction of earthquake action and an integrated optimal design of super tall buildings with viscous damping walls was adapted in this paper. A parameter optimization method of viscous damping walls was proposed in this paper to consider the overall costs of the structure including the cost of material consumption and the cost of viscous damping walls and optimal number of the viscous damping walls. A super tall building located in high seismicity area was applied in the last part of the paper to illustrate the proposed parameter optimization method. Numerical analysis results show that the proposed method is reasonable and effective.

Keywords: parameter optimization method; viscous damping walls; overall costs; super tall buildings

1. Introduction

The application of energy dissipation control for high-rise structure become more and more extensive for many areas of China in high intensity seismic zone. As a new innovative high efficient energy dissipation device in recent years, viscous damping wall was firstly proposed by M.Miyazkai and Aiima[1] in 1986 and firstly manufactured successfully by Sumitomo Construction company (Arima et al.1988) [2]. Viscous damping wall is mainly composed of steel plate hanging in the upper floor, thin steel box fixed on the lower floor and viscous liquid of high viscosity between the inner and outer plates, as depicted in Fig.1. When the structure is subjected to wind or earthquake, relative displacement and relative velocity between the floors will make the steel plate moving in the viscous liquid and thus generate the shear deformation of the viscous liquid. Viscous damping walls consume energy through the internal friction produced by the flowing of the liquid, thereby reducing the seismic response of the structure, as depicted in Fig.2.

As the energy dissipation device of the structure, viscous damping wall can work in frequent earthquake, moderate earthquake and rare earthquake and can be flexibly arranged according to the locations of partition walls in tall buildings. Comparing with the traditional rod type viscous damper, viscous damping wall has more energy dissipation capacity [3] due to the larger friction area between the surfaces of embedded steel plate and the viscous media. There are many practical cases in high-rise building nowadays [4][5].

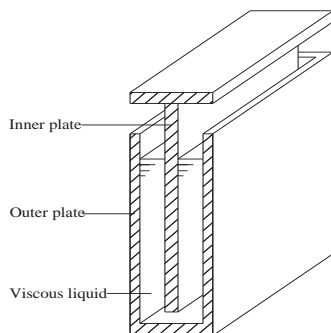


Figure 1: Viscous Damping Wall Unit

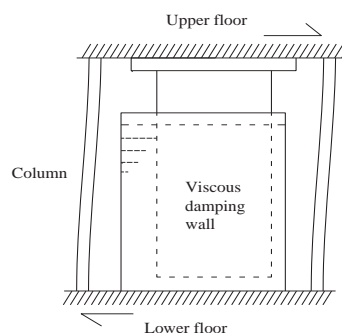


Fig 2: Work Status of Viscous Damping Walls

The research and application of viscous damping wall in China lags behind these in Japan [6] and other countries and specific system needs to be established and improved. Primary, the arrangement form of viscous damping

walls is based on engineering experience and there is short of more convenient optimal placement algorithm. Then, there is not much research on the optimization space by the introduction of energy dissipation device in the past. Thirdly, there is lack of deep research on the parameter and number optimization of viscous damping walls. Search the optimal parameter method based on the integrated optimal structural design for tall buildings with viscous damping walls [7] was proposed for parameter optimization to minimize the structure overall cost with the optimization variable of parameters provided by the manufacturer, and the optimal parameters of viscous damping wall and corresponding optimal additional damping ratio for the structure and optimal number of viscous damping walls will be derived.

2. Parameter optimization of viscous damping walls

Compared with the prototype design, the energy dissipation structure can be optimized since the response subjected to earthquake or wind is decreased due to the additional damping. The energy dissipation structure design with optimization based on the performance improvement design is called integrated optimization design. Integrated optimization design can not only ensure the performance of structure and reduce the failure cost due to the disasters, also reduce the cost of the main structure with optimization of the components. For the overall cost of structure, the integrated optimal design can indeed play advantage of the energy dissipation technology. The overall cost of integrated optimal structure C cover two parts as follows:

$$C=C_d + C_s \quad (1)$$

Where: C_s refers to main structure cost; C_d refers to equipment cost namely the cost of viscous damping walls. Compared with the prototype design structure, main structure cost C_s of integrated optimal structure decreased but the equipment cost C_d increased, and as the number of viscous damping wall added to structure grow, the additional damping increases and the optimization degree of the structure deepens, thus the main structure cost C_s get smaller and the equipment cost C_d become larger as depicted in Fig 3. The main structure cost and equipment cost are added up together to get overall cost of integrated optimal structure as depicted in Fig 3. The curve indicate that there is a lowest point in the overall cost curve and the lowest point namely the minimum cost corresponds to optimal additional damping ratio for the structure and and optimal number of viscous damping wall with certain parameter combinations.

The damping coefficient c and velocity exponent a are two main parameters of viscous damping wall and damping force $F=cv^a$. There is certain different damping force with different parameter combinations and unit price of viscous dampig wall largely depends upon damping force and additional damping ratio largely depends on the parameter combination, therefore parameter optimization with integrated optimal structure can both ensure the additional damping ratio and reduce the overall cost of integrated optimal structure. This is especially important for popularizing the use of viscous damping wall.

The main structure cost curve can get through the integrated optimal structural design for tall buildings with viscous damping walls and equipment cost curve can be gained in the Eq (2) using time history analysis method.

$$\varepsilon_a = \sum_j W_{ej} / (4\pi W_s) \quad (2)$$

Where: ε_a refers to additional damping ratio; W_{ej} refers to energy consumption in a reciprocating cycle with expected displacement of j -th energy dissipation equipment; W_s refers to total strain energy of structure with energy dissipation equipment.

There are different overall costs with different parameter combinations and minimum overall cost corresponds to the optimal parameter of viscous damping wall and the corresponding optimal additional damping ratio and optimal number of viscous damping wall. Search the optimal parameter method based on the integrated optimal structural design for tall buildings with viscous damping walls was proposed for parameter optimization to minimize the structure overall cost with the optimization variable of parameters provided by the manufacturer, and the optimal parameters of viscous damping wall and corresponding optimal additional damping ratio for the structure and optimal number of viscous damping walls will be derived.

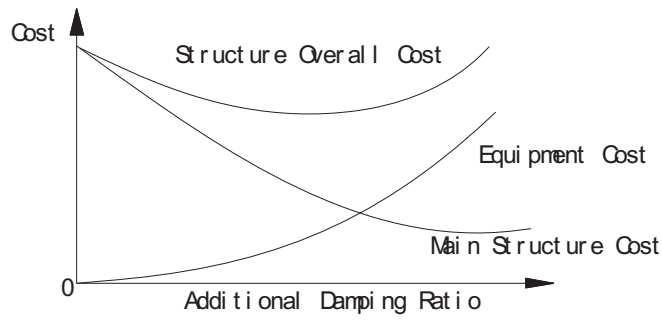


Fig 3: relation Curve

The specific process for the parameter optimization of viscous damping wall is: the first step is to gain the relationship between the optimized cost savings and additional damping ratio and the relation curve by the integrated optimal structural design; the second step is to get the relationship between the viscous damping wall cost and additional damping ratio and the relation curve by time-history analysis method with different parameter combinations; the third step is to get overall cost of integrated optimal structure with different parameter combinations; the fourth step is to compare the overall cost of integrated optimal structure with different parameter combinations to get minimum cost and corresponding optimal parameters of viscous damping wall, optimal additional damping ratio for the structure and optimal number of viscous damping wall.

3. Case study

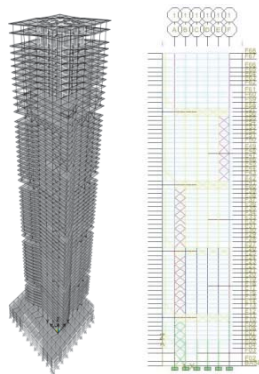


Fig.4: Three-Dimensional and Elevation Model

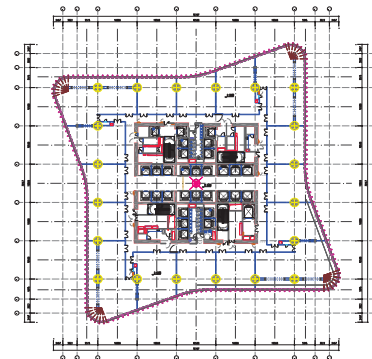


Fig.5: Plan View of Standard Story

As shown in Fig.6 and 7, belt truss frame core-wall structural system is applied a high-rise building with 300-meter and 68 floors. According to Chinese standard, the design characteristic period is 0.55s and the fortification intensity is 7 degree. The basic acceleration is 0.15g and Site class is III. The frame beams are made by sectional steel while the columns in the case are designed as SRC columns. The structure comprises of column braces on 1-58th floor and belt-trusses on the 11-12, 26-27, 41-42, and 57-58th floor. The damping ratio in the frequent earthquake is set to 4% and 5% for the moderate and rare earthquake.

Four parameters combinations provided by manufacturer were optimized in this paper and combinations are presented in table 1.

Table1: Four parameters combinations

Tonnage (t)	Parameters Combinations		Cost (10 ⁴ yuan)
	<i>C</i>	<i>a</i>	
100	2348	0.45	6
150	3522	0.45	8
200	4000	0.45	11
300	5871	0.45	20

The first step for the parameters optimization of viscous damping wall is to gain the relationship between the optimized cost savings and additional damping ratio and the relation curve by the integrated optimal structural design. The result of four integrated optimization for original structure is presented in table 2 and the curve fitting

of the results is depicted in Fig 6.

That optimized cost savings in table 2 is negative means this value is decreased cost relative to the original structure cost.

Table2: Results of Integrated Optimization for Original Structure

Additional Damping Ratio	Optimized Cost Savings
1.40%	-1307.41
4.20%	-2605.6
7.00%	-3648.67
11%	-4317.12

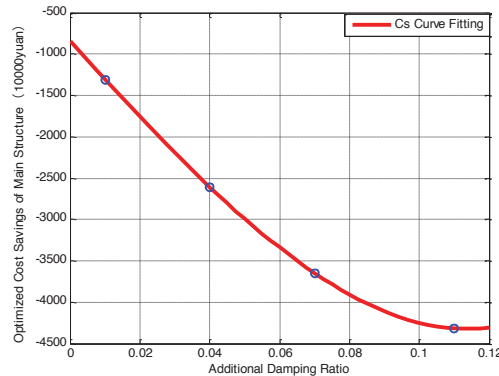


Fig.6: Relationship between the Optimized Cost Savings and Additional Damping Ratio

The second step is to get the relationship between the viscous damping wall cost and additional damping ratio and the relation curve by time-history analysis method with different parameter combinations. The additional damping ratio of structure with 66, 198, 264 and 396 viscous damping walls is respectively calculated as presented in table 3 and curve fitting of the data namely relation curve for the viscous damping wall cost and additional damping ratio is depicted in Fig 7.

Table3 Additional Damping Ratio

Additional Damping Ratio	Number	66	198	264	396
C=2348	Moderate Earthquake	1.63%	3.68%	5.62%	6.10%
	Frequent Earthquakes	2.69%	6.32%	9.42%	10.34%
C=3522	Moderate Earthquake	2.48%	5.72%	8.60%	9.38%
	Frequent Earthquakes	4.20%	9.58%	14.46%	15.94%
C=4000	Moderate Earthquake	2.85%	6.56%	9.72%	10.56%
	Frequent Earthquakes	4.82%	10.88%	16.66%	18.26%
C=5871	Moderate Earthquake	4.27%	9.68%	14.37%	15.71%
	Frequent Earthquakes	7.35%	16.51%	21.00%	21.74%

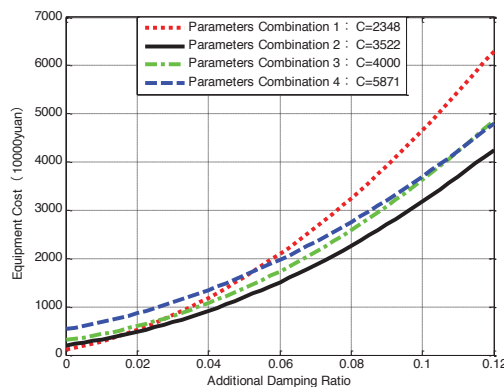


Fig.7: Relationship between Viscous Damping Wall Cost and Additional Damping Ratio

The third step is to get overall cost of integrated optimal structure with different parameter combinations, and the total cost curve will be plotted by adding the first two fitting curve together as depicted in Fig 8.

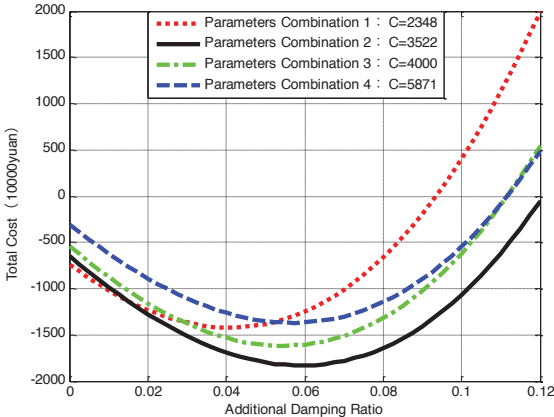


Fig.8: Total cost Curve under Four Parameter Combinations

The fourth step is to compare the overall cost of integrated optimal structure with different parameter combinations to get minimum cost and corresponding optimal parameters of viscous damping wall, optimal additional damping ratio for the structure and optimal number of viscous damping wall. The minimum value of the curve with four parameter combinations is calculated as presented in table4.

Table4: Minimum Value for the Curve under Four Parameter Combinations

Parameter C (a=0.45)	2348	3522	4000	5871
Single Equipment Cost (10000yuan)	6	8	11	20
Additional Damping Ratio	4.09%	5.91%	5.44%	5.70%
Minimum Total Cost (10000yuan)	-1420.5	-1830.4	-1617.1	-1368.6
Optimal Number	204	186	140	94

As presented in table4, when the damping coefficient $c=3522$ and velocity exponent $a=0.45$, the overall cost is minimal and corresponding optimal additional damping ratio for the structure is 5.91% and optimal number of viscous damping is 186.

4. Conclusion

Search the optimal parameter method based on the integrated optimal structural design for tall buildings with viscous damping walls was proposed for parameter optimization to minimize the structure overall cost with the optimization variable of parameters provided by the manufacturer, and the optimal parameters of viscous damping wall and corresponding optimal additional damping ratio for the structure and optimal number of viscous damping walls will be derived.

Main conclusions are as follows:

- (1) There are different overall costs with different parameter combinations and minimum overall cost corresponds to optimal parameters of viscous damping wall and the corresponding optimal additional damping ratio and optimal number of optimal damping wall. when the damping coefficient $c=3522$ and velocity exponent $a=0.45$, the overall cost is minimal and corresponding optimal additional damping ratio for the structure is 5.91% and optimal number of viscous damping is 186 in the case study.
- (2) Results show that the optimal parameters corresponding to the minimum total cost is not the biggest, and parameter or additional damping ratio is not the higher the better. Economy and effect should be taken into comprehensive consideration and parameter optimization can take a maximum of the economic effect viscous damping wall should have.
- (3) Parameter optimization with integrated optimal structure can both ensure the additional damping ratio and reduce the overall cost of integrated optimal structure. This is especially important for popularizing the use of viscous damping wall.
- (4) Parameter combinations provided by manufacturers are taken as optimization variables and the method proposed in this paper has high maneuverability which is practical and can promote the popularization and application of viscous damping wall.

5. Acknowledgements

The authors are grateful for the supports from the Shanghai Excellent Discipline Leader Program (No.14XD1423900) and Key Technologies R & D Program of Shanghai (Grant No. 09dz1207704).

6. References

- [1] Miyazaki, M., Arima, F., Kidata, Y., Hristov, I. Earthquake Response Control Design of Buildings Using Viscous Damping Walls. *Proceedings of First East Asia Pacific Conference, Bangkok*,1986. 1882~1891
- [2] Arima, F., Miyazaki, M., Tanaka, H., ect. A Study on Buildings with Large Damping Using Viscous Damping Walls. *9th World Conference on Earthquake Engineering*. Tokyo-Kyoto:1988. 821-826
- [3] M. Miyazaki, Y. Mitsusaka, Design of a building with 20% or greater damping, *Proc. 10th World Conf. on Earthquake Engineering*, Madrid, 1992, pp. 4143~4148
- [4] Fei, C., Weiqing, L., Shuguang, W., ect. The research of Energy dissipation design of Jin Bainian square with viscous damping walls. *Building Science*, 2008, 24(9):56-59.
- [5] Zhengcang Z., ect. Kagoshima airport terminal building a seismic reinforcement- three-dimensional elastoplastic analysis of structure adding viscous damping walls. *Building Structures*, 2000,(6) 20-23.
- [6] Dongsheng D., Shuguang W., Weiqing, L. etc. Research and application of fluid viscous damping wall in high-rise structure [J]. *Journal of Building Structures*, 2010,31(9): 87-94
- [7] Xi, Z., Xin, Z., and Yimin, Z. Optimal number of viscous damping walls for the seismic design of tall buildings [J]. *Building Structures*, 2014, 44(S2): 384-388.

Optimization of wind-induced acceleration of super tall buildings by modal shape updating

Xin Zhao^{1,2}, Xiang Jiang¹

¹ Department of Structural Engineering, Tongji University, Shanghai, China, 22zx@tjadri.com

² Tongji Architectural Design (Group) Co., Ltd., Shanghai, China, 22zx@tjadri.com

1. Abstract

With the increase of height and flexibility of modern super tall buildings, structural wind-induced vibrations become significant under wind loads. The structural acceleration is commonly requested to be below certain limit in design process to avoid occupant discomfort under wind loads. For slightly excessive wind-induced acceleration responses scenarios, say below 20% over the code limit, the computational optimization method is usually adopted due to the fact that it's more cost effective than the supplementary damping systems method. The wind induced acceleration of certain super tall building is determined by dynamic properties under given wind loadings. As all known that the wind-induced response of super tall buildings is commonly contributed by the first vibration mode, which is actually related to the building period and modal shape of first vibration mode. A straightforward method to reduce the building acceleration is to change the natural vibration period. The natural vibration period is not quite effective due to the fact that it is global quantity and the expense of changing vibration period is very high. A modal shape updating method is proposed in this paper to reduce the building acceleration by locally calibrating the modal shape near the floor where maximum building acceleration occurs. Due to its local impact nature, the expense of changing local curve of modal shape is lower comparing with that of changing vibration period. A real super tall building project is taken as an example in the last part of this paper to show the effectiveness and applicability of the proposed modal shape updating method. The results show that the modal shape updating method provides a powerful tool for wind-induced dynamic serviceability design of super tall building structures with slightly excessive wind-induced acceleration responses.

2. Keywords: Modal shape updating, wind-induced acceleration, computational optimization, super tall buildings

3. Introduction

With the increase of height and flexibility of modern super tall buildings, structural wind-induced vibrations under wind loads have been a problem of great concern. The structural acceleration is commonly requested to be below certain limit in design process to avoid occupant discomfort under wind loads.

There are two measures to reduce the wind-induced acceleration responses when they exceed the comfort criteria. One measure is to absorb dynamic energy by installing supplementary damping systems, and the other measure is to fine-tune design variables of structural members according to structural optimization principles. When the acceleration responses exceed the comfort criteria with large margins, it is cost-effective to use dampers to mitigate peak acceleration. There are however many cases in engineering practices that the margins over the comfort criteria are small, say below 20% over the code limit, the computational optimization method is usually adopted due to the fact that it's more cost effective than the supplementary damping systems method.

For schemes of additional supplementary damping systems, lots of research have been carried out on the usage of various structural damping devices^[1]. On the other hand, there are still few researches on optimization techniques for economical design of super tall buildings subject to wind-induced acceleration design requirements^[2] even though wind forces and wind-induced responses can be accurately predicted by aerodynamic wind-tunnel techniques.

The wind induced acceleration of certain super tall building is determined by dynamic properties under given wind loadings. As all known that the wind-induced response of super tall buildings is commonly contributed by the first vibration mode, which is actually related to the building period and modal shape of first vibration mode. A straightforward method to reduce the building acceleration is to change the natural vibration period. The natural vibration period is not quite effective due to the fact that it is global quantity and the expense of changing vibration period is very high. A modal shape updating method is proposed in this paper to reduce the building acceleration by locally calibrating the modal shape near the floor where maximum building acceleration occurs. Due to its local impact nature, the expense of changing local curve of modal shape is lower comparing with that of changing vibration period.

4. Theoretical Basis

4.1. Wind-induced Response Analysis

It has been recognized that for many super tall buildings the across wind responses may exceed the along wind responses in terms of wind-induced dynamic serviceability design. In view of the wind-induced response of super tall buildings is commonly contributed by the first vibration mode, practical methods of acceleration response of super tall buildings are developed based on the moment gust loading factor method and the curve fitted power spectra of across wind loads^[3]. By solving the equation of motion, the acceleration response equation is obtained through vibration analysis in the frequency domain as follows:

$$\sigma_{a_R(z)}^2 = \sigma_{y_R}^2 \approx \frac{\varphi_1^2(z)}{M_1^{*2}} \frac{\pi f_1 S_{F_1^*}(f_1)}{4(\xi_{s1} + \xi_{a1})} \quad (1)$$

where $\varphi_1(z)$ means the mode shape vector normalized with respect to the modal amplitude of the top floor, M_1^* means the first mode generalized mass, f_1 means the first modal frequency, ξ_{s1} means the damping ratio of the structure while ξ_{a1} for the aerodynamic damping and $S_{F_1^*}(f_1)$ means the first generalized across-wind force spectrum. The unified formula of the power spectra of across-wind loads can be expressed as:

$$S_M^*(f) = \frac{f S_M(f)}{(0.5 \rho U_H^2 B H^2)^2} = \frac{S_p \beta (n/f_p)^\alpha}{\{1 - (n/f_p)^2\}^2 + \beta (n/f_p)^2} \quad (2)$$

where B , H are width and height of the building respectively, $n = fB/U_H$, U_H is the mean wind speed at the top of the building with a 10-year return period; f_p is the location parameter, deciding the peak frequency of the spectrum; β is the band width parameter; S_p is the amplitude parameter; and α is the deflection parameter. All the four parameters, which are functions of the aspect ratio, height ratio and wind field condition, can be identified by curve fitting technique^[4].

The displacements ϕ of the story under modal conditions means the mode shape vector normalized with respect to the mass matrix^[5]. Thus, acceleration response of the top floor can be simplified as

$$\sigma_{a(H)} = \frac{\phi_1^2(H)}{\sum_{z=0}^H (m(z) \phi_1^2(z))} \sqrt{\frac{\pi f_1 S_{F_1^*}(f_1)}{4(\xi_{s1} + \xi_{a1})}} = \frac{\phi_1^2(H)}{4 \sum_{z=0}^H (m(z) \phi_1^2(z))} \rho H U_H^2 B \sqrt{\frac{\pi S_M^*(f_1)}{\xi_{s1} + \xi_{a1}}} \quad (3)$$

where $m(z)$ means the lumped mass of the story at the elevation z , ρ means the air density.

4.2. Modal Shape Updating Method

Through the wind-induced response analysis, we can obtain that the acceleration response of the top floor is determined by the period and modal shape of first vibration mode. In view of the natural vibration period is not quite effective when fine tuning sizes of structural members, the modal shape updating method is adopted to reduce the acceleration response by locally calibrating the modal shape near the floor where maximum building acceleration occurs. In each iteration of the modal shape updating process, the natural vibration period is assumed to remain unchanged. In this case, the constraints of acceleration response can be equally converted into the modal shape constraints.

$$a_H = c g_f \phi_1^2(H) \leq a_H^l \Leftrightarrow \phi_1(H) \leq \phi_1^U(H) \quad (4)$$

where g_f means the peak factor, c means the constant part in equation (3).

When the modal shape updates after an iteration, adverse impact of the natural vibration period on the acceleration response will be considered in the acceleration optimization process.

The mathematical model of modal shape updating method is introduced as follows:

$$\text{Minimize } V = \sum_{j=1}^m A_j \sum_{jk=1}^{jn} l_{jk}$$

subject to

$$\phi = \frac{L^{(m)}}{6Q_s} \sum_{m=1}^N \left(\begin{bmatrix} \mathbf{F}_i^{(m)} & \mathbf{F}_j^{(m)} \end{bmatrix} \begin{bmatrix} 2\mathbf{C}^{(m)} & \mathbf{C}^{(m)} \\ \mathbf{C}^{(m)} & 2\mathbf{C}^{(m)} \end{bmatrix} \begin{bmatrix} [\mathbf{f}_i^{(m)}]^T \\ [\mathbf{f}_j^{(m)}]^T \end{bmatrix} \right) \leq \phi^l$$

$$0.6m \leq b_j, h_j \leq 1.5m \quad (j = 1, 2 \dots m)$$

$$0.06m \leq t_j \leq 0.15m \quad (j = 1, 2 \dots m)$$

where V is the volume of the material consumption (as the objective function in the optimization process), ϕ and ϕ^l are the modal shape of the initial structure and the modal shape limitation (this inequality as the constraint in the optimization process), $L^{(m)}$ means the length of m_{th} component, Q_s means the virtual load acting on the top floor, $F_i^{(m)}$ and $F_j^{(m)}$ are forces of the m_{th} component due to the modal load conditions while $f_i^{(m)}$ and $f_j^{(m)}$ for forces due to virtual load conditions, the matrix $C^{(m)}$ means the diagonal matrix of the m_{th} component where the elements are $1/EA$, $1/GA_Y$, $1/GA_Z$, $1/GI_X$, $1/EI_Y$ and $1/EI_Z$ respectively, b_j , h_j and t_j are the width, height and thickness of the flange and web of the steel members (as the design variables in the optimization process).

By the modal shape updating method, the optimal section sizes for economical design of super tall buildings subject to wind-induced acceleration design requirements are obtained effectively.

5. Case Study

A real super tall building project is shown in this part to show the effectiveness and applicability of the proposed modal shape updating method. The structure parameters and wind environment parameters are shown in Table 1 and Table 2.

Table 1: Structure parameters

H / m	B / m	D / m	f_1 / Hz	$\zeta_s / \%$
598	68	68	0.107	1.5

Table 2: Wind field parameters

Wind field	$\omega_0 / (kN / m^2)$	α	H_T	$\omega_H / (kN / m^2)$	$U_H / (m / s)$
C	0.30	0.22	400	0.90	37.3

The structural material is a mixed use of structural steel and reinforced concrete. It includes a central reinforced concrete core wall, eight exterior composite mega-columns in the perimeter and four at the corner. The central core walls are connected to the perimeter mega-columns by 5 outrigger trusses in X direction and 4 outrigger trusses in Y direction. The eight perimeter mega-columns and the 4 corner mega-columns are connected by nine belt trusses. The structural system and layout of outriggers are shown in Figure 1.

Outriggers are selected as the optimization design variables due to the fact that outriggers are the most sensible per volume for the modal updating according to the sensitivity analysis results. The outrigger members are divided into 10 groups, namely group 1~5 for the diagonal members and group 6~10 for the flange members in zone 2,4,6,7,8 respectively. The initial member sizes of diagonal members and flange members are $1.1m \times 1.1m \times 0.1m \times 0.1m$ and $1m \times 1m \times 0.1m \times 0.1m$ respectively. The lower and upper boundary of the member sizes are $0.6m \sim 1.5m$ for width and height and $0.06m \sim 0.15m$ for thickness.

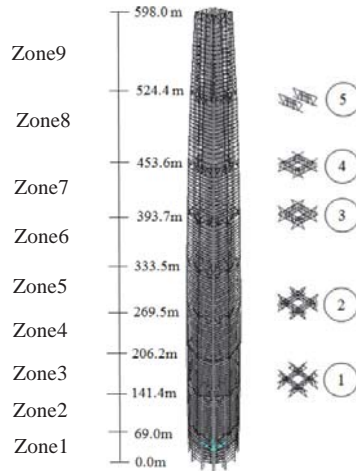


Figure 1: Structural system and layout of outriggers

According to the parameters in Table 1 and Table 2, the relationship between non-dimensional power spectra of across-wind loads and the reduced frequency as shown in Figure 2. The power spectrum value will stay constant in the modal shape updating process as the frequency is assumed to be unchanged.

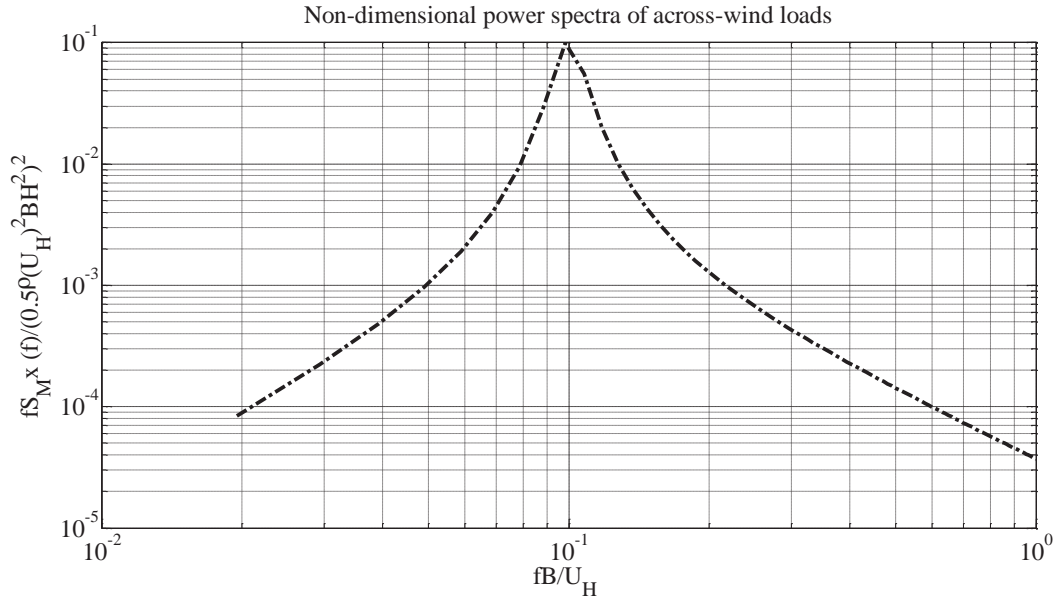


Figure 2: Non-dimensional power spectra of across-wind loads

The acceleration response of the top floor is 0.26 m/s^2 (4% over the 0.25 m/s^2 limitation in Chinese code). From equation (4), we can see clearly that the square of modal shape normalized with respect to the mass matrix value need to reduce by 4%, namely from 0.104 to 0.102, in the acceleration optimization process when the building period is assumed to be unchanged. When the modal shape updates after an iteration, the adverse impact of the natural vibration period on the acceleration response is taken into consideration to revise the modal shape variation range.

The member sizes of the outriggers before and after optimization are compared in Table 3.

Table 3: Comparison of member sizes of the outriggers before and after optimization

Members		α	h/m	t/m
Diagonal chords	Opti-1	1.1 (0.83)	1.1 (1.5)	0.1 (0.06)
	Opti-2	1.1 (1.2)	1.1 (1.5)	0.1 (0.06)
	Opti-3	1.1 (1.355)	1.1 (1.5)	0.1 (0.06)
	Opti-4	1.1 (1.5)	1.1 (1.5)	0.1 (0.15)
	Opti-5	1.1 (1.5)	1.1 (1.5)	0.1 (0.15)
Flange chords	Opti-6	1 (0.6)	1 (0.6)	0.1 (0.06)
	Opti-7	1 (0.6)	1 (1.5)	0.1 (0.06)
	Opti-8	1 (1.23)	1 (1.22)	0.1 (0.124)
	Opti-9	1 (1.36)	1 (1.42)	0.1 (0.136)
	Opti-10	1 (1.5)	1 (1.5)	0.1 (0.15)

From Table 3, we can come to the conclusion that heights of diagonal chords all increase to the upper boundary 1.5m while width of diagonal chords only in zone 7 and 8 comes to the upper boundary, increase a little in zone 2, decreased in zone 1. Heights and widths of the flange chords in zone 6, 7, and 8 all increased a lot. Flange chords in zone 2 and 4 decreased to the lower boundary. The outrigger members in higher zones and diagonal chords contribute more for the modal shape normalized with respect to the mass matrix of the top floor.

Figure 3 and Figure 4 compare the modal shape normalized with respect to the mass matrix and normalized with respect to the modal amplitude of the top floor before and after optimization. We can obtain that the modal shape normalized with respect to the mass matrix reduce to 0.1012 from Figure 3. Figure 4 shows that the modal shape normalized with respect to the modal amplitude of the top floor after optimization is mostly larger than the initial mode shape. The results indicate that the modal shape updating method brings a larger generalized mass of the structure from another perspective.

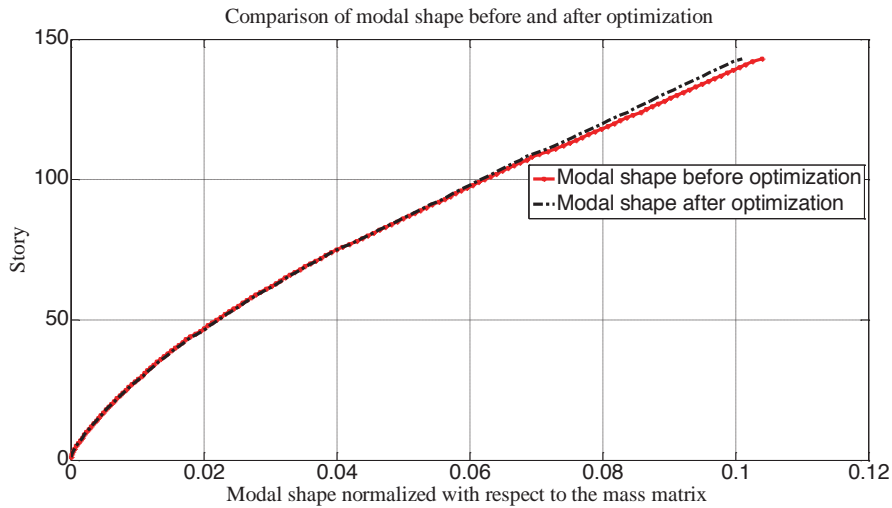


Figure 3: Comparison of modal shape normalized with respect to the mass matrix

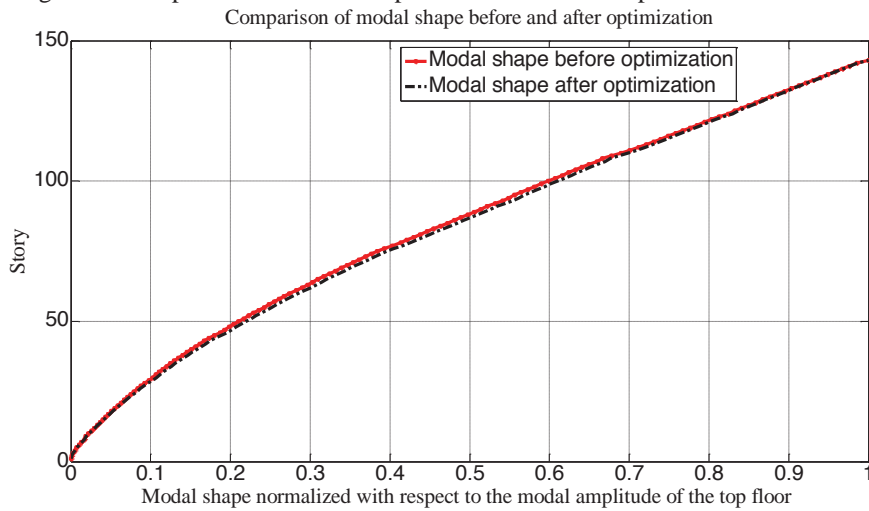


Figure 4: Comparison of modal shape normalized with respect to the modal amplitude of the top floor
 Change of modal shape normalized with respect to the mass matrix is shown in Figure 5. As we can see from equation (4), the optimization of modal shape (reducing by 2.7%) would bring a 5.3% reduction in the acceleration response when the building period is assumed to be unchanged. Since the acceleration exceeds the code limit by only 4%, the extra optimized 1.3% was for the compensation of the longer building period (from 9.29s to 9.36s).

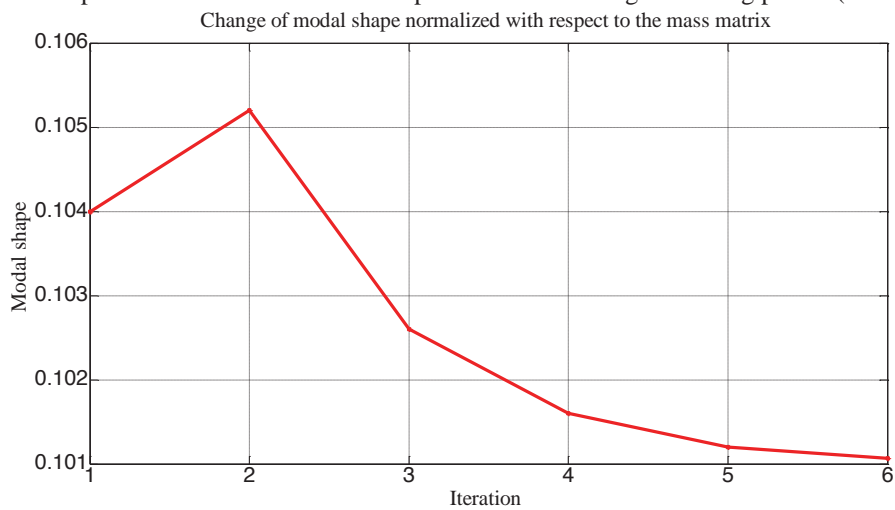


Figure 5 Change of modal shape normalized with respect to the mass matrix
 Change of volume of outrigger members is shown in Figure 6. 15% (54m³) additional steel is needed for the acceleration optimization by the modal shape updating method.

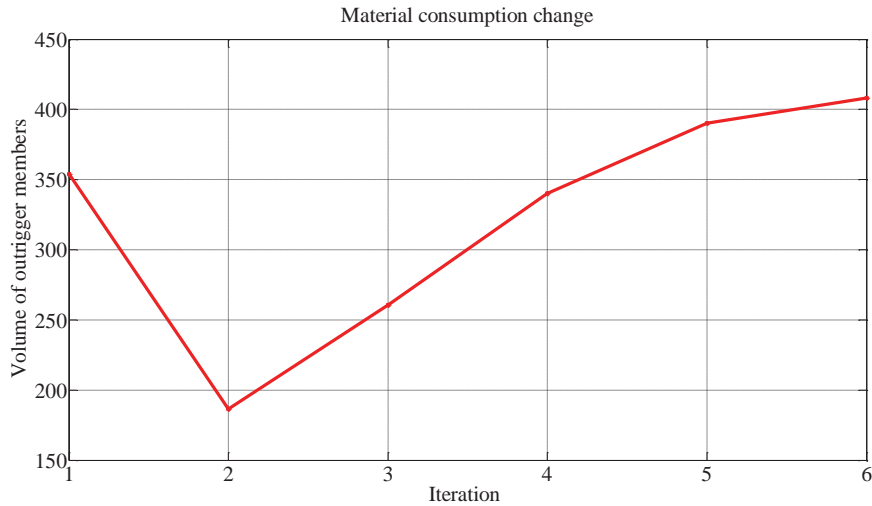


Figure 6 Change of volume of outrigger members

6. Conclusion

The modal shape updating method provides a powerful tool for wind-induced dynamic serviceability design of super tall building structures with slightly excessive wind-induced acceleration responses. Through the real super tall building project to show the effectiveness and applicability of the proposed modal shape updating method, we can come to the conclusion that:

- (1) Outriggers are selected as the optimization design variables due to the fact that outriggers are the most sensible per volume for the modal updating. The outrigger members in higher zones and diagonal chords contribute more for the modal shape normalized with respect to the mass matrix of the top floor;
- (2) The optimization of modal shape normalized with respect to the mass matrix (reducing by 2.7%) would bring a 5.3% reduction in the acceleration response when the building period is assumed to be unchanged. Since the acceleration exceeds the code limit by only 4%, the extra optimized 1.3% was for the compensation of the longer building period (from 9.29s to 9.36s);
- (3) The modal shape normalized with respect to the modal amplitude of the top floor after optimization is mostly larger than the initial mode shape, which indicates that the modal shape updating method brings a larger generalized mass of the structure from another perspective.
- (4) 15% (54m³) additional steel is needed for the acceleration optimization. The expense for the acceleration optimization is acceptable.

5. Acknowledgements

The authors are grateful for the support from the Shanghai excellent discipline leader program (No.14XD1423900) and Key Technologies R & D Program of Shanghai (Grant No. 09dz1207704).

6. References

- [1] Jr.B.F Spencer, S. Nagarajaiah, State of the art of structural control[J]. Journal of structural engineering, 129(7): 845-856, 2003.
- [2] C.M Chan, M.F Huang, K.C.S Kwok, Stiffness Optimization for Wind-Induced Dynamic Serviceability Design of Tall Buildings[J]. Journal of Structural Engineering, 135(8): 985-997, 2009.
- [3] M. Gu, Y. Quan, Across-wind loads of typical tall buildings, Journal of Wind Engineering and Industrial Aerodynamics, 92 (2004) 1147–1165, 2004.
- [4] Y. Quan, M. Gu, Power Spectra of Across -wind Loads on Super High -rise Buildings, Journal of Tongji University, 30(5): 627-632, 2002.
- [5] CSI SAP. CSi Analysis Reference Manual[J]. I: Berkeley (CA, USA): Computers and Structures INC, 2008.

Multi-objective Free-form Optimization for Shape and Thickness of Shell Structures with Composite Materials

Kenichi Ikeya¹, Masatoshi Shimoda²

¹ Graduated School of Engineering, Toyota Technological Institute, Aichi, Japan, ken.usa09@hotmail.co.jp

² Toyota Technological Institute, Aichi, Japan, shimoda@toyota-ti.ac.jp

1. Abstract

In this paper, we present a two-phase optimization method for designing the shape and thickness of a shell structure consisting of an orthotropic material. Compliance vector for multiple loadings is used as the objective functional. The objective functional is quantified by the weighted sum method and minimized under the volume and the state equation constraints. In 1st phase, the shape is optimized, in which it is assumed that a shell is varied in the out-of-plane direction to the surface to create the optimal free-form. In 2nd phase, thickness optimization is implemented following the shape optimization to decrease the compliance further. A parameter-free shape and thickness optimization problem is formulated in a distributed-parameter system based on the variational method. The shape and thickness sensitivities are theoretically derived and applied to the H^1 gradient method for shape and size optimization. The optimal multi-objective free-form of a shell structure with an orthotropic material can be determined using the proposal method, and the influence of orthotropic materials to the optimum shape and thickness distribution is fully investigated.

2. Keywords: Shell, Free-form, Shape optimization, Thickness optimization, Composite material

3. Introduction

Shell structures are widely used in various industrial products. From an economic point of view, weight reduction is strictly required in the structural design of cars, aircrafts and so on. The usage of composite materials in shell structures is one of the solutions to meet the requirement since they have higher material performances than metals. In especial, orthotropic materials can be used for making specific stiff directions of shell structures. Moreover, with design optimization, mechanical properties can be significantly improved.

In the case of optimizing the shell structures, shape optimization, including parametric and non-parametric methods, is an effective mean. The free-form optimization method for shells is one of the non-parametric methods for arbitrarily formed shells that can determine the optimal smooth and natural free-form without causing jagged surfaces and without requiring shape parameterization. This method was proposed [1] based on the traction method, or H^1 gradient method [3, 4]. However, there has seldom study of shape optimizations for shell structures consisting of anisotropic materials. In our previous work [1, 2], we developed a free-form optimization method for determining a dynamically natural and optimal shell form. However, this method has been only applied to the shell structures with isotropic material. In this work, the method is applied to a shell structure with an orthotropic material, and the influence of the difference of the materials is investigated. In addition, a non-parametric method for thickness distribution based on the gradient method is newly developed introducing Poisson's equation both to reduce the objective functional and to maintain thickness smoothness. The shape and the thickness optimization method is also integrated to obtain higher stiffness of shell structures, or to eliminate the waste of the thickness.

The key point of the integrated on the two-phase optimization of shell structures is determining the shape first, subsequently, reducing unnecessary thickness for lighting-weight. In addition, multi-objective shell structures with multi-boundary conditions are considered for actual applications. In the present work, we use the compliance vector for multi-loading as the objective functional. The compliance minimization problem is formulated in a distributed-parameter shape and thickness optimization system. The sensitivity functions, also called the shape and thickness gradient functions, or the optimal conditions, are theoretically derived using the material derivative method and the adjoint method. The derived shape gradient functions are applied to the proposed two-phase optimization method.

4. Governing Equation for a Shell with an Orthotropic Material

As shown in Fig. 1(a), we consider a shell having an initial bounded domain $\Omega \subset \mathbb{R}^3$ with the boundary $\partial\Omega$, mid-surface A with the boundary ∂A , side surface S and thickness t . It is assumed for simplicity that a shell structure occupying a bounded domain is a set of infinitesimal flat surfaces. The Mindlin-Reissner plate theory is applied concerning plate bending. Using the sign convention in Fig. 1-(b), the displacements expressed by the local

coordinates $\mathbf{u} = \{u_i\}_{i=1,2,3}$ are considered by dividing them into the displacements in the in-plane direction $\{u_\alpha\}_{\alpha=1,2}$ and in the out-of-plane direction u_3 .

When NB boundary conditions are independently applied to a shell, the weak form of the n th state equation with respect to $(\mathbf{u}_0^{(n)}, w^{(n)}, \boldsymbol{\theta}^{(n)}) \in U^{(n)}$, ($n = 1, \dots, NB$) can be expressed as Eq. (1).

$$a((\mathbf{u}_0^{(n)}, w^{(n)}, \boldsymbol{\theta}^{(n)}), (\bar{\mathbf{u}}_0^{(n)}, \bar{w}^{(n)}, \bar{\boldsymbol{\theta}}^{(n)})) = l((\bar{\mathbf{u}}_0^{(n)}, \bar{w}^{(n)}, \bar{\boldsymbol{\theta}}^{(n)})), \quad \forall (\bar{\mathbf{u}}_0^{(n)}, \bar{w}^{(n)}, \bar{\boldsymbol{\theta}}^{(n)}) \in U^{(n)}, \quad n = 1, \dots, NB, \quad (1)$$

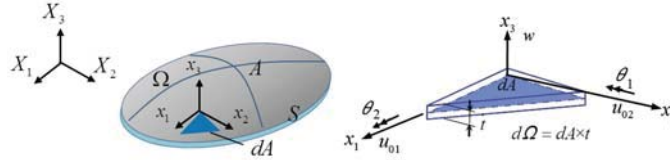
where the energy bilinear form $a(\cdot, \cdot)$ and the linear form $l(\cdot)$ for the n th state variables $(\mathbf{u}_0^{(n)}, w^{(n)}, \boldsymbol{\theta}^{(n)})$ are respectively defined as:

$$a((\mathbf{u}_0^{(n)}, w^{(n)}, \boldsymbol{\theta}^{(n)}), (\bar{\mathbf{u}}_0^{(n)}, \bar{w}^{(n)}, \bar{\boldsymbol{\theta}}^{(n)})) = \int_{\Omega} \{E_{\alpha\beta\gamma\delta} (u_{0\alpha}^{(n)} - x_3 \theta_{\alpha,\beta}^{(n)}) (\bar{u}_{0\gamma}^{(n)} - x_3 \bar{\theta}_{\gamma,\delta}^{(n)}) + E_{\alpha\beta}^S (w^{(n)} - \theta_\alpha^{(n)}) (\bar{w}^{(n)} - \bar{\theta}_\beta^{(n)})\} d\Omega, \quad (2)$$

$$= \int_A \{e_{\alpha\beta\gamma\delta}^B \kappa_{\gamma,\delta}^{(n)} \bar{\kappa}_{\alpha,\beta}^{(n)} + e_{\alpha\beta\gamma\delta}^M u_{0\gamma}^{(n)} \bar{u}_{0\alpha}^{(n)} + k e_{\alpha\beta}^S \gamma_\beta^{(n)} \bar{\gamma}_\alpha^{(n)}\} dA. \quad (3)$$

$$l((\bar{\mathbf{u}}_0^{(n)}, \bar{w}^{(n)}, \bar{\boldsymbol{\theta}}^{(n)})) = \int_{A_j^{(n)}} (f_\alpha^{(n)} \bar{u}_{0\alpha}^{(n)} - m_\alpha^{(n)} \bar{\theta}_\alpha^{(n)} + q^{(n)} \bar{w}^{(n)}) dA + \int_A t (b_\alpha^{(n)} \bar{u}_{0\alpha}^{(n)} + b_3^{(n)} \bar{w}^{(n)}) dA + \int_{\partial A_g^{(n)}} (N_\alpha^{(n)} \bar{u}_{0\alpha}^{(n)} ds - M_\alpha^{(n)} \bar{\theta}_\alpha^{(n)} + Q^{(n)} \bar{w}^{(n)}) ds, \quad (4)$$

where the notations $\{u_{0\alpha}\}_{\alpha=1,2}$, w and $\{\theta_\alpha\}_{\alpha=1,2}$ express the in-plane displacements, out-of-plane displacement and rotational angles of the mid-surface of the shell, respectively. In this paper, the subscripts of the Greek letters are expressed as $\alpha = 1, 2$, and the tensor subscript notation uses Einstein's summation convention and a partial differential notation for the spatial coordinates $(\cdot)_{,i} = \partial(\cdot) / \partial x_i$. $(\bar{\cdot})$ denotes a variation. Loads acting relative to the local coordinate system $(x_1, x_2, 0)$ are defined as: $q^{(n)}$, $\mathbf{f}^{(n)} = \{f_\alpha^{(n)}\}_{\alpha=1,2}$, $\mathbf{m}^{(n)} = \{m_\alpha^{(n)}\}_{\alpha=1,2}$, $\mathbf{N}^{(n)} = \{N_\alpha^{(n)}\}_{\alpha=1,2}$, $Q^{(n)}$, $\mathbf{M}^{(n)} = \{M_\alpha^{(n)}\}_{\alpha=1,2}$ and $hb^{(n)} = \{hb_i^{(n)}\}_{i=1,2,3}$ denote non-zero out-of-plane load, a non-zero in-plane loads, a non-zero out-of-plane moments, a non-zero in-plane loads, a non-zero shearing force, a non-zero bending moments and a body force, respectively. In addition, $\{E_{\alpha\beta\gamma\delta}\}_{\alpha,\beta,\gamma,\delta=1,2}$ and $\{E_{\alpha\beta}^S\}_{\alpha,\beta=1,2}$ express an orthotropic elastic tensor including bending and membrane stresses, and an orthotropic elastic tensor with respect to the shearing stress, respectively. $\{e_{\alpha\beta\gamma\delta}^B\}_{\alpha,\beta,\gamma,\delta=1,2}$, $\{e_{\alpha\beta}^S\}_{\alpha,\beta=1,2}$ and $\{e_{\alpha\beta\gamma\delta}^M\}_{\alpha,\beta,\gamma,\delta=1,2}$ express orthotropic elastic tensors with respect to bending, shear and membrane component, respectively. The constants k expresses a shear correction factor (assuming $k=5/6$).



(a) Geometry of shell and global coordinates (b) Local coordinates and DOF of flat surface

Figure 1: Shell as a set of infinitesimal flat surfaces.

The notations $\{\kappa_{\alpha\beta}^{(n)}\}_{\alpha,\beta=1,2}$ and $\{\gamma_\alpha^{(n)}\}_{\alpha=1,2}$ express the curvatures and the transverse shear strains. It should be noted that $U^{(n)}$ in Eq. (1) is given by:

$$U^{(n)} = \{(u_{01}^{(n)}, u_{02}^{(n)}, w^{(n)}, \theta_1^{(n)}, \theta_2^{(n)}) \in (H^1(A))^5 \mid \text{satisfy the given Dirichlet conditions on each subboundary}\}, \quad (5)$$

where H^1 is the Sobolev space of order 1.

5. Multi-objective Free-form Optimization for Shape-thickness Problem Considered Orthotropic Material

In this study, with the aim of maximizing the stiffness of a multi-objective shell structure, a compliance vector $\{l((\mathbf{u}_0^{(1)}, w^{(1)}, \boldsymbol{\theta}^{(1)})), l((\mathbf{u}_0^{(2)}, w^{(2)}, \boldsymbol{\theta}^{(2)})), \dots, l((\mathbf{u}_0^{(NB)}, w^{(NB)}, \boldsymbol{\theta}^{(NB)}))\}$ is used as an index of structural stiffness under multi-loading conditions. This objective functional is scalarized by the weighted sum method as follows:

$$\sum_{n=1}^{NB} c^{(n)} \frac{l((\mathbf{u}_0^{(n)}, w^{(n)}, \boldsymbol{\theta}^{(n)}))}{l_{init}^{(n)}}, \quad (6)$$

$$\sum_{n=1}^{NB} c^{(n)} = 1, \quad (7)$$

where $l_{init}^{(n)}$ indicates the compliance for the n th boundary condition of the initial shape, which is used for normalizing the compliances. $c^{(n)}$ indicates the weighting coefficient of the n th boundary condition, which has the relationship shown in Eq. (7).

Letting the volume and the state equations in Eq. (1) be the constraint conditions and the weighted sum compliance in Eq. (6) the objective functional to be minimized, a distributed-parameter shape optimization problem for finding the optimal design velocity field \mathbf{V} , or A_s can be formulated as:

$$\text{Given } A, t \quad (8)$$

$$\text{find } A_s \text{ (or } \mathbf{V}), t_s \quad (9)$$

$$\text{that minimizes } \sum_{n=1}^{NB} c^{(n)} \frac{l((\mathbf{u}_0^{(n)}, w^{(n)}, \boldsymbol{\theta}^{(n)}))}{l_{init}^{(n)}}, \quad (10)$$

$$\text{subject to } M (= \int_A t dA) \leq \hat{M} \text{ and Eq. (1)} \quad (11)$$

where M and \hat{M} denote the volume and its constraint value, respectively.

5.1. Derivation of gradient functions

Letting $(\bar{\mathbf{u}}_0^{(n)}, \bar{w}^{(n)}, \bar{\boldsymbol{\theta}}^{(n)})$ and Λ denote the Lagrange multipliers for the n th state equation and the volume constraint, respectively, the Lagrange functional L associated with this problem can be expressed as:

$$\begin{aligned} & L(\Omega, (\mathbf{u}_0^{(1)}, w^{(1)}, \boldsymbol{\theta}^{(1)}), (\bar{\mathbf{u}}_0^{(1)}, \bar{w}^{(1)}, \bar{\boldsymbol{\theta}}^{(1)}), (\mathbf{u}_0^{(2)}, w^{(2)}, \boldsymbol{\theta}^{(2)}), \dots, (\bar{\mathbf{u}}_0^{(NB)}, \bar{w}^{(NB)}, \bar{\boldsymbol{\theta}}^{(NB)}), \Lambda) \\ &= \sum_{n=1}^{NB} c^{(n)} \frac{l((\mathbf{u}_0^{(n)}, w^{(n)}, \boldsymbol{\theta}^{(n)}))}{l_{init}^{(n)}} + \sum_{n=1}^{NB} \{l((\bar{\mathbf{u}}_0^{(n)}, \bar{w}^{(n)}, \bar{\boldsymbol{\theta}}^{(n)}) - a((\mathbf{u}_0^{(n)}, w^{(n)}, \boldsymbol{\theta}^{(n)}), (\bar{\mathbf{u}}_0^{(n)}, \bar{w}^{(n)}, \bar{\boldsymbol{\theta}}^{(n)}))\} + \Lambda(M - \hat{M}). \end{aligned} \quad (12)$$

Using the design velocity field \mathbf{V} to represent the amount of domain variation, the material derivative \dot{L} [1, 5] of the Lagrange functional L can be expressed as:

$$\begin{aligned} \dot{L} &= \sum_{n=1}^{NB} c^{(n)} \frac{l((\mathbf{u}_0'^{(n)}, w'^{(n)}, \boldsymbol{\theta}'^{(n)}))}{l_{init}^{(n)}} + \sum_{n=1}^{NB} \{l((\bar{\mathbf{u}}_0'^{(n)}, \bar{w}'^{(n)}, \bar{\boldsymbol{\theta}}'^{(n)}) - a((\mathbf{u}_0^{(n)}, w^{(n)}, \boldsymbol{\theta}^{(n)}), (\bar{\mathbf{u}}_0'^{(n)}, \bar{w}'^{(n)}, \bar{\boldsymbol{\theta}}'^{(n)})) \\ &\quad - a((\mathbf{u}_0'^{(n)}, w'^{(n)}, \boldsymbol{\theta}'^{(n)}), (\bar{\mathbf{u}}_0^{(n)}, \bar{w}^{(n)}, \bar{\boldsymbol{\theta}}^{(n)}))\} + \Lambda'(M - \hat{M}) + \langle \mathbf{Gn}, \mathbf{V} \rangle_S + \langle G_t, t' \rangle_t, \quad \mathbf{V} \in C_\Theta \quad (13) \\ \langle \mathbf{Gn}, \mathbf{V} \rangle_S &= \int_A G_A V_n dA + \int_A G_f V_n dS \\ \langle G_t, t' \rangle_t &= \int_A G_t t' dA \end{aligned}$$

By using the KKT optimality conditions, the shape and thickness gradient functions G_A and G_t (i.e., sensitivity functions) for this problem are derived as

$$G_A = \left\{ \sum_{n=1}^{NB} \left[-\frac{c^{(n)}}{l_{init}^{(n)}} \left\{ E_{\alpha\beta\gamma\delta}(\mathbf{u}_{0\alpha,\beta}^{(n)} + \frac{t}{2} \boldsymbol{\theta}_{\alpha,\beta}^{(n)})(\mathbf{u}_{0\gamma,\beta}^{(n)} + \frac{t}{2} \boldsymbol{\theta}_{\gamma,\beta}^{(n)}) - E_{\alpha\beta\gamma\delta}(\mathbf{u}_{0\alpha,\beta}^{(n)} - \frac{t}{2} \boldsymbol{\theta}_{\alpha,\beta}^{(n)})(\mathbf{u}_{0\gamma,\beta}^{(n)} - \frac{t}{2} \boldsymbol{\theta}_{\gamma,\beta}^{(n)}) \right\} \right] + \Lambda t H \right\} \mathbf{n}, \quad (14)$$

$$G_t = \sum_{n=1}^{NB} \left\{ \frac{c^{(n)}}{l_{init}^{(n)}} \left(\frac{\partial E_{\alpha\beta\gamma\delta}^B}{\partial t} \boldsymbol{\theta}_{\gamma,\delta} \boldsymbol{\theta}_{\alpha,\beta} + \kappa_0 \frac{\partial E_{\alpha\beta}^S}{\partial t} \boldsymbol{\gamma}_\alpha \boldsymbol{\gamma}_\beta + \frac{\partial E_{\alpha\beta\gamma\delta}^M}{\partial t} \mathbf{u}_{0\gamma,\delta} \mathbf{u}_{0\alpha,\beta} \right) \right\} + \Lambda, \quad (15)$$

where H is calculated by the area strain, modifying the proposed method [1].

The shape gradient functions are applied to the H^1 gradient method to determine the optimal design velocity field \mathbf{V} and the optimal thickness variation field t' .

6. H^1 gradient method for shells

The free-form optimization method for shell was proposed by Shimoda et al. [1], which consists of main three processes; (1) Derivation of shape gradient function (2) Numerical calculation of shape gradient function (3) The H^1 gradient method for determining the optimal shape variation. The H^1 gradient method is a gradient method in a Hilbert space. The original H^1 gradient method was proposed by Azegami in 1994 [6] and also called the traction method. Shimoda modified the original method for free-form shell optimization. In the present paper, we newly propose a H^1 gradient method for determining the optimal thickness distribution and integrate it with the H^1 gradient method for shape optimization [1]. It is a node-based shape and thickness optimization method that can treat all nodes as design variables and does not require any design variable parameterization.

6.1. H^1 Gradient Method for Thickness Optimization of Shell

The H^1 gradient method for shells can be easily expanded to the thickness optimization. When the state equations and the adjoint equations are satisfied, the perturbation expansion of the Lagrange functional L can be written as:

$$\Delta L = \langle G_t, \Delta s t' \rangle + O(|\Delta s|^2) \quad (16)$$

where $\Delta s (> 0)$ is sufficiently small constant. To obtain the optimal thickness variation field t' , the following weak formed Poisson's equation, or the governing equation for t' is introduced.

$$a(t \zeta; v) + a_t \langle t \zeta - t_0, v \rangle = -\langle G_t, \Delta s t \zeta \rangle, \quad \forall n \in C_t, t \zeta \in C_t \quad (17)$$

$$a(t \zeta; v) = \int_A t_{,i} k_{ij} v_{,j} dA \quad (18)$$

where t' and t_0 denote thickness variation field and the reference thickness, respectively. It is assumed that $t' - t_0 > 0$. The notations α_t and k_{ij} are equivalent to the heat transfer coefficient and the thermal conductivity tensor in the steady heat transfer equation, respectively. Eq. (17) can be also easily solved with a standard commercial FEM code. The kinematic admissible function space C_t is defined as:

$$C_t = \{t \in H^1 \mid \text{satisfy Dirichlet condition for thickness variation}\} \quad (19)$$

Substituting Eq. (17) into Eq. (16), we obtain:

$$\Delta L; \langle G_t, \Delta s t' \rangle = -\langle a(t', v) + \alpha_t \langle t' - t_0, v \rangle \rangle \quad (20)$$

Furthermore, taking into account the positive definitiveness of the bilinear form $a_t \langle t', v \rangle > 0$, $\alpha_t \langle t' - t_0, v \rangle$ and $\Delta s > 0$ in Eq. (17),

$$\Delta L < 0 \quad (21)$$

In problems where convexity is assured, this relationship definitely reduces the Lagrange functional in the process of updating the shell thickness using the thickness variation field t' determined by Eq. (17). In this method, the negative thickness gradient function $-G_t$ is applied as a distributed internal heat generation to a pseudo-elastic shell to the design surface. The thickness variation field t' is calculated as the solution or the pseudo-temperature distribution of Poisson's equation and is used to update the original thickness.

6.2. Two-phases optimization method

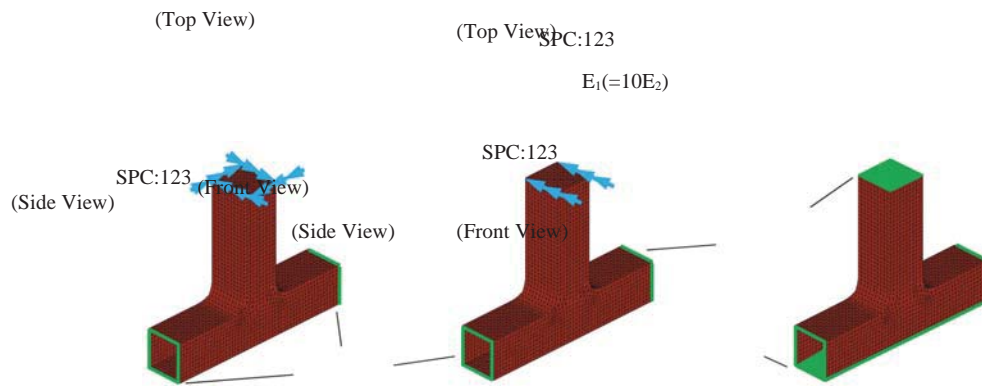
To minimize the compliance and mass of shell structures, both shape and thickness are treated as design variables in the optimization. In the present work, the shape optimization is applied firstly to shell structures composed of orthotropic materials. Then, the thickness optimization is carried out after shape convergence.

7. Calculated Results

The proposed method is applied to T-joint model. The initial shape and the problem definition are illustrated in Fig.2. In the stiffness analyses shown in Fig.2 (a) and (b), left and right side edges of T-joint are simply supported in both analyses. A coupling force is applied as load case 1 (i.e., torsional condition) at the top edge of T-joint and a distributed force to y direction is applied as load case 2 (i.e., bending condition). In the velocity analysis shown in Fig.2 (c), it is assumed that right, left side edges and top, bottom surfaces are simply supported. The volume constraints of both shape and thickness are set as 1.00 times the initial value. The material constants are used as $E_1 = 210000 \text{ Pa}$, $E_2 = 21000 \text{ Pa}$, $G_{12} = 65000 \text{ Pa}$ and $\nu = 0.3$. The optimization results of isotropic model and orthotropic model are expressed in 8.1 and 8.2, respectively.

7.1. Isotropic material

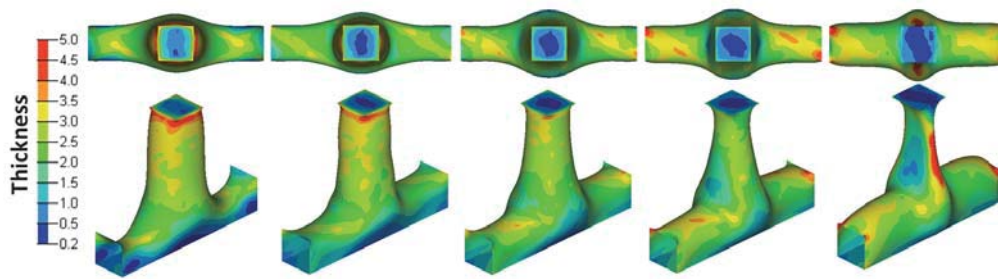
In this problem, an isotropic material is distributed as base material and the proposed two-phase optimization method is applied. Figure 3 shows the Pareto optimal shapes and thickness obtained, where the weighting coefficient $c^{(1)}$ is varied over 5 stages from 1.0 to 0.0. When $c^{(1)}$ is small, the shape and thickness distribution are strongly influenced by load case 2. As the value of the weighting coefficient $c^{(1)}$ is increased, the shape and thickness distribution gradually begin to show the influence of load case 1. As shown in Fig 3 (a)-(e), core part of T-joint is firstly expanded and the bead on a neck is gradually disappeared instead of the arms are gradually expanded while the value of the coefficient $c^{(1)}$ is decreased. In the thickness optimization, thickness is distributed on a neck and gradually disappeared instead of appearing thickness distributions on the side of arms. It is clear that



(a) Stiffness analysis (Load case 1) (b) Stiffness analysis (Load case 2) (c) Velocity analysis
 Figure 2: Boundary conditions for design problem 2

a set of Pareto optimal shapes and the thickness distributions (i.e., intermediate shapes and thickness distributions) can be obtained by varying the weighting coefficient.

In Fig 4, the compliance ratio of the results above having two objective functionals is shown. It is shown that the compliances for the two load cases involve a trade-off.



(a) $c^{(1)}=1.0$ (b) $c^{(1)}=0.8$ (c) $c^{(1)}=0.5$ (d) $c^{(1)}=0.2$ (e) $c^{(1)}=1.0$
 Figure 3: Pareto optimal shapes and thickness under multi-loading conditions of T-joint model

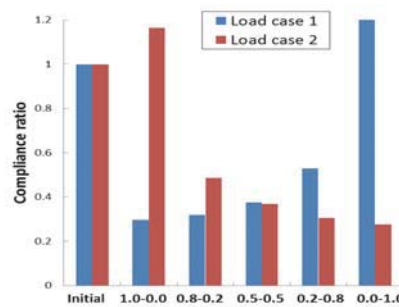


Figure 4: Comparison of compliance of T-joint model

7.2. Orthotropic material

The same optimization problems as 7.1 with orthotropic materials are solved to investigate the influence of material. Material distribution of E_1 is illustrated in Fig 5. The direction of E_2 is vertical to E_1 . Young's modulus ratio is set as $E_1 : E_2 = 10 : 1$.

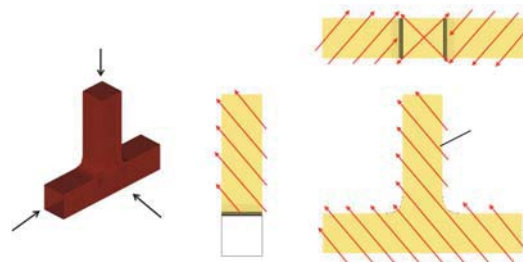


Figure 5: Material layout for orthotropic material of T-joint model

Figure 6 shows the Pareto optimal shapes and thickness obtained, where the weighting coefficient $c^{(1)}$ is varied over 5 stages from 1.0 to 0.0. As shown in Fig 6 (a)-(e), both shape and thickness show similar pattern as isotropic one however they are gradually twisted while the value of the coefficient $c^{(1)}$ is decreased. Compared with the isotropic material, the Pareto optimal shapes and thickness with orthotropic material are clearly different from those of the isotropic one.

In Fig 7, the compliance ratio of the results above having two objective functionals is shown. As isotropic material, it is showed that the compliances for the two load cases involve a trade-off as isotropic material.

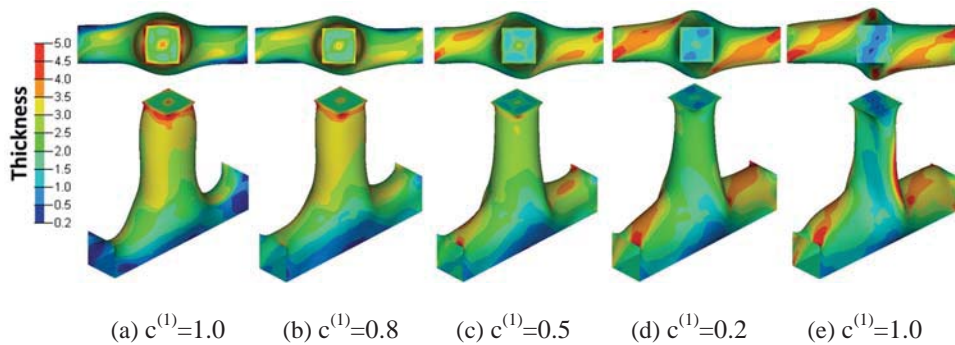


Figure 6: Pareto optimal shapes and thickness under multi-loading conditions of T-joint model

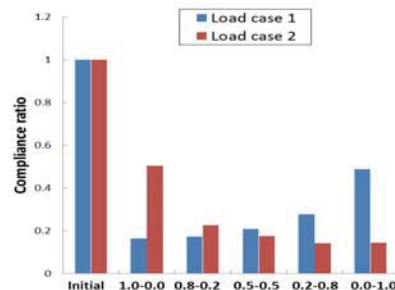


Figure 7: Comparison of compliance of T-joint model

8. Conclusion

This paper proposed a non-parametric multi-objective free-form optimization method for shape and thickness of shell structures consisting of orthotropic materials. We designed the Pareto optimal free-form shape and thickness of multi-objective shell structures under multi-boundary conditions. The shape and thickness gradient functions were derived and applied to this free-optimization method. A design example was presented to verify the effectiveness and practical utility of this method. The proposed method makes it possible to obtain the smooth and natural Pareto optimal shape and thickness while reducing the objective functional without shape and thickness parameterization. According to this method, a natural bead pattern and thickness can be obtained according to the boundary conditions. An orthotropic material was distributed to these design problems and the influence of material distributions to the optimal shape and thickness distributions of shell structures was also investigated in detail.

9. References

- [1] Shimoda, M, Yang, L, A non-parametric free-form optimization method for shell structures, *Struct Multidisc Optim*, 50, 409-423, 2014.
- [2] Shimoda, M, Optimal Free-form Design of Shell Structures Involving a Natural Frequency Problem, *EVOLUTIONARY AND DETERMINISTIC METHODS FOR DESIGN, OPTIMIZATION AND CONTROL*, edited by Poloni, C, Quagliarella, D et al., CIRA, Capua, 17-28, 2011.
- [3] Shimoda, M and Tstuji, J, Non-parametric Shape Optimization Method for Rigidity Design of Automotive Sheet Metal Structures, *SAE 2006 Transactions, Journal of Passenger Cars - Mechanical Systems*, 483-492, 2006(2006-01-0584).
- [4] Shimoda, M, Azegami, H and Sakurai, T, Traction Method Approach to Optimal Shape Design Problems, *SAE 1997 Transactions, Journal of Passenger Cars*, 106(6), 2355-2365, 1998.
- [5] Choi, K. K. and Kim, N. H, *Structural Sensitivity Analysis and Optimization 1*, Springer, New York, 243, 2005.
- [6] Azegami, H, A Solution to Domain Optimization Problems, *Trans. of Jpn. Soc. of Mech. Eng.*, Ser. A, 60, 1479-1486, 1994.

Multi-level hierarchical MDO formulation with functional coupling satisfaction under uncertainty, application to sounding rocket design.

Loïc Brevault^{1,2}, Mathieu Balesdent², Nicolas Bérend², Rodolphe Le Riche³

¹ CNES – Launcher directorate, Paris, France, loic.brevault@onera.fr

² Onera - The french aerospace lab, F-91123 Palaiseau, France

³ CNRS LIMOS and Ecole Nationale Supérieure des Mines de Saint-Etienne, Saint-Etienne

1. Abstract

At early design phases, taking into account uncertainty in the optimization of a multidisciplinary system is essential to assess its optimal performances. Uncertainty Multidisciplinary Design Optimization methods aim at organizing not only the different disciplinary analyses, the uncertainty propagation and the optimization, but also the handling of interdisciplinary couplings under uncertainty. A new multi-level hierarchical MDO formulation ensuring the coupling satisfaction for all the realizations of the uncertain variables is presented in this paper. Coupling satisfaction in realizations is essential to maintain the equivalence between the coupled and decoupled UMDO formulations and therefore to ensure the physical consistency of the obtained designs. The proposed approach relies on two levels of optimization and surrogate model in order to ensure, at the convergence of the optimization problem, the coupling functional relations between the disciplines. The proposed formulation is compared to a classical MDO formulation on the design of a two stage sounding rocket.

2. Keywords: MDO formulation, Stage-Wise Decomposition formulation, Uncertainty, rocket design.

3. Introduction

Multidisciplinary Design Optimization (MDO) is a set of engineering methodologies to optimize systems modeled as a set of coupled disciplinary analyses (also called subsystem analyses). For example, a launch vehicle is customarily decomposed into interacting submodels for propulsion, aerodynamics, trajectory, mass and structure. Taking into account the different disciplines requires to model and manage the interactions between them all along the design process. Using MDO in the early design phases may improve system performances and decrease design cycle cost [1]. At these steps, the determination of the optimal system architecture requires a complete design space exploration through repeated discipline simulations. To make the exploration computationally affordable, low fidelity disciplinary analyses are mostly employed, which introduce uncertainties. Handling the uncertainties at early design phases is thus essential to efficiently characterize the optimal system performances and its feasibility because it may reduce the duration and the cost of the next design phases. Uncertainty-based Multidisciplinary Design Optimization (UMDO) aims at solving MDO problems in the presence of uncertainty. This induces several new challenges compared to deterministic MDO: uncertainty modeling, uncertainty propagation, optimization under uncertainty and interdisciplinary coupling handling under uncertainty. In this paper, we focus on the interdisciplinary coupling satisfaction as it is essential to ensure the system physical consistency.

In deterministic MDO, the interactions between the disciplines are represented by coupling variables and the system multidisciplinary consistency is described as a set of interdisciplinary equations to be satisfied. Two types of coupling handling approaches may be distinguished: the **coupled** versus the **decoupled** methods depending if the couplings are found by MultiDisciplinary Analysis (MDA) or by the system optimizer at the MDO convergence. These methods may be used within single-level or multi-level UMDO formulations. Compared to single-level formulations (*e.g. Multi Discipline Feasible* (MDF) [2], *Individual Discipline Feasible* (IDF) [2]) multi-level formulations (*e.g. Collaborative Optimization* (CO), [4], *Analytical Target Cascading* (ATC) [3]) facilitate the system level optimization by introducing additional disciplinary optimizers in order to distribute the problem complexity over different dedicated disciplinary optimizations.

In the presence of uncertainty, the coupling variables are uncertain variables. Coupled single-level UMDO formulations (Fig.1) have been proposed [5,6] based on MDF combining Crude Monte Carlo (CMC) and MDA. Whereas in deterministic MDO, for a given design there is only one set of coupling variables that satisfies the interdisciplinary coupling equations, in UMDO, the uncertain coupling variables have to satisfy the system of interdisciplinary equations for each realization of the uncertain variables. The computational cost of the coupled single-level approaches becomes prohibitive due to the required number of discipline evaluations. In literature [7,8], decoupled single and multi-level UMDO formulations have therefore been investigated to overcome this computational burden. These approaches ensure the multidisciplinary system consistency for some particular realizations (*e.g. at the Most Probable failure Point*) or for the first statistical moments (*i.e. mean, standard*

deviation) of the uncertain coupling variables. Thus, it allows to limit the number of variables that have to be handled by the optimizer, however it does not ensure the multidisciplinary consistency of the system design for all the uncertain variable realizations.

The objective of this paper is to introduce a new multi-level UMDO formulation (named Multi-level Hierarchical Optimization under uncertainty - MHOU) with functional coupling satisfaction under uncertainty (*i.e.* in realizations). The rest of the paper is organized as follows. First (section 4), the existing coupled MDF formulation under uncertainty is introduced. In a second part (section 5), MHOU formulation is introduced by using subsystem optimizers in addition to the system level optimizer in order to distribute the UMDO problem complexity over different dedicated subsystem optimizations. The proposed formulation hierarchically optimizes the whole system. It relies on the iterative construction of Polynomial Chaos Expansions (PCE) in order to represent, at the convergence of the UMDO problem, the feedback couplings between the disciplines as would MDA do. PCEs allow one to remove the feedback couplings and to introduce multi-level optimization while ensuring the physical relevance of the obtained design at the convergence. Finally, in a third part (section 6), the proposed formulation is compared to MDF on the design of a two solid stage sounding rocket.

4. Coupled approach: *Multi Discipline Feasible* (MDF) under uncertainty

The most straightforward UMDO formulation is an adaptation of the single-level deterministic MDF formulation (Fig.1) which is a *coupled approach*. It consists in ensuring the coupling satisfaction by propagating uncertainty through the disciplines with CMC and to solve the system of interdisciplinary equations by MDA for each realization generated using CMC [5,6]. MDF under uncertainty can be formulated as follows:

$$\min_{\mathbf{z} \in \mathcal{Z}} \mathbb{E}[f(\mathbf{z}, \mathbf{Y}(\mathbf{z}, \mathbf{U}), \mathbf{U})] \quad (1)$$

$$\text{s. t. } \mathbb{K}[\mathbf{g}(\mathbf{z}, \mathbf{Y}(\mathbf{z}, \mathbf{U}), \mathbf{U})] \leq 0 \quad (2)$$

with, \mathbf{z} the design variable vector belonging to \mathcal{Z} , \mathbf{U} the uncertain variable vector defined by $\xi_{\mathbf{U}}(\cdot)$ the joint probability distribution function (PDF) on the sample space Ω , $f(\cdot)$ the performance function, $\mathbb{E}[\cdot]$ an uncertainty measure of the performance function (*e.g.* expected value), $\mathbf{g}(\cdot)$ the inequality constraint function vector and $\mathbb{K}[\cdot]$ an uncertainty measure of the inequality constraint (*e.g.* probability of failure). In the rest of the paper, an uncertain variable vector is noted \mathbf{U} and a realization of this vector \mathbf{u} . For a given design variable vector \mathbf{z}_0 , to evaluate the uncertainty measure $\mathbb{E}[f(\mathbf{z}_0, \mathbf{Y}(\mathbf{z}_0, \mathbf{U}), \mathbf{U})]$, it is necessary to propagate the uncertainty in the system models. CMC is used to estimate $\mathbb{E}[\cdot]$ and $\mathbb{K}[\cdot]$. To ensure multidisciplinary system consistency, the input coupling variable vector \mathbf{Y} , which depends of \mathbf{z} and \mathbf{U} , has to satisfy the following system of coupled equations:

$$\forall \mathbf{u} \in \Omega, \forall (i, j) \in \{1, \dots, N\}^2 \ i \neq j, \begin{cases} \mathbf{y}_{ij} = \mathbf{c}_{ij}(\mathbf{z}_i, \mathbf{y}_i, \mathbf{u}) \\ \mathbf{y}_{ji} = \mathbf{c}_{ji}(\mathbf{z}_j, \mathbf{y}_j, \mathbf{u}) \end{cases} \quad (3)$$

where N is the number of disciplines, \mathbf{y}_{ij} is the input coupling variable vector from discipline i to discipline j , \mathbf{y}_i is the input coupling vector composed of the input coupling coming from all disciplines (represented by the dot) to the discipline i , and $\mathbf{c}_{ij}(\cdot)$ is the output coupling vector from discipline i to discipline j . Eqs.(3) is a system of coupled equations which has to be solved for all the realizations of the uncertain variables in order to ensure that the input coupling variables and the corresponding output coupling variables are equal. For one realization of the uncertain variable vector, the solving of Eqs.(3) is called a MultiDisciplinary Analysis (MDA) and often involves Fixed Point Iteration method. To estimate $\mathbb{E}[\cdot]$ and $\mathbb{K}[\cdot]$, repeated MDAs are performed for a set of uncertain variable realizations sampled by CMC. The computational cost of MDA under uncertainty corresponds to that of one MDA multiplied by the number of uncertain variable realizations. For each iteration in \mathbf{z} of MDF under uncertainty, MDA is performed resulting in a prohibitive computational cost due to a large numbers of calls to the disciplines to solve Eqs.(1-2). In order to reduce the computational cost, a decoupled multi-level UMDO formulation is proposed in the following section.

5. Proposed decoupled multi-level formulation: Multi-level Hierarchical Optimization under Uncertainty

5.1. Interdisciplinary coupling satisfaction with a decoupled approach

In order to avoid the repeated MDAs, decoupled approaches aim at propagating uncertainty on decoupled disciplines allowing one to evaluate them in parallel and to ensure coupling satisfaction by introducing equality constraint in the UMDO formulation. However, two main challenges are faced to decouple the design process:

- Uncertain input coupling variable vector \mathbf{Y} has to be handled by the system level optimizer. However, an optimizer can only handle a finite number of parameters to represent these uncertain variables. It is necessary to find a technique to represent an infinite number of realizations of the input uncertain coupling variables with a finite number of parameters.
- Equality constraints between the input coupling variables \mathbf{Y} and the output coupling variables computed by $\mathbf{c}(\cdot)$, which are two uncertain variables, have to be imposed. Equality between two uncertain variables corresponds to an equality between two functions which is sometimes reduced to equality between parameters [7,8] (equality in statistical moments, in realizations, *etc.*).

In order to overcome these two issues, an approach has been proposed [9] based on a surrogate model of the

coupling functional relations. In deterministic decoupled MDO approaches, considering a scalar coupling y_{ij} from the discipline i to the discipline j , only one equality constraint in the MDO formulation is added between the input coupling variable y_{ij} and the output coupling variable $y_{ij} = c_{ij}(\mathbf{z}_i, y_i)$.

However, in the presence of uncertainty, coupling satisfaction involves an equality constraint between two uncertain variables. To ensure coupling satisfaction in realizations, an infinite number of equality constraints have to be imposed, one for each realization of the uncertain variables:

$$\forall \mathbf{u} \in \Omega, y_{ij} = c_{ij}(\mathbf{z}_i, y_i, \mathbf{u}) \quad (4)$$

To solve this problem, a new integral form for the interdisciplinary coupling constraint is introduced:

$$J_{ij} = \int_{\Omega} [c_{ij}(\mathbf{z}_i, y_i, \mathbf{u}) - y_{ij}]^2 \xi_U(\mathbf{u}) d\mathbf{u} = 0 \quad (5)$$

In order to have the integral in Eq.(5) equal to zero, the input coupling variables must be equal to the output coupling variables for each realization of the uncertain variables. Nevertheless, to decouple the disciplines, the uncertain input coupling variables y_{ij} have to be handled by the optimizer. In order to solve this second issue, a surrogate model of the coupling relation is introduced: $y_{ij} \rightarrow \hat{y}_{ij}(\mathbf{U}, \boldsymbol{\alpha}^{(ij)})$. The surrogate model, written $\hat{y}_{ij}(\mathbf{U}, \boldsymbol{\alpha}^{(ij)})$, provides a functional representation of the dependency between the uncertain variables \mathbf{U} and the input coupling variables with $\boldsymbol{\alpha}^{(ij)}$ the vector of the metamodel parameters. To decouple the disciplines, the surrogate model parameters $\boldsymbol{\alpha}^{(ij)}$ are handled by the system level optimizer. Note that, in order to keep \hat{y}_{ij} simple, the dependency between \hat{y}_{ij} and \mathbf{z} is not present here: \hat{y}_{ij} is not a function of \mathbf{z} , it is learned for a specific \mathbf{z}^* which is the unknown UMDO optimum. We propose to model the coupling functional relations with Polynomial Chaos Expansion (PCE) because this surrogate model presents advantages in terms of uncertainty analysis and propagation [10]. PCE allows one to approximate a function $h: \Omega \rightarrow \mathbb{R}$ according to:

$$h(\mathbf{U}) \simeq \sum_{k=1}^d \alpha_k \Psi_k(\mathbf{U}) = \hat{h}(\mathbf{U}, \boldsymbol{\alpha}) \quad (6)$$

with Ψ_1, \dots, Ψ_d a basis of orthogonal polynomials and d the truncation degree. The choice of the polynomial basis is made consistently with the distribution $\xi_U(\cdot)$ of the input random variables \mathbf{U} . The polynomial basis is orthogonal to the weighting function [10] of the input uncertain variable distributions. The difficulty in PCE is the estimation of the polynomial coefficients. Different techniques may be employed if black box functions are considered: the orthogonal spectral projection or the regression [10]. This approach may be easily generalized to coupling vector \mathbf{y}_{ij} . In the proposed formulation, PCE coefficients are determined with the regression method adapted to multi-level optimization. PCE is used to model the input coupling variables \mathbf{Y} and the PCE coefficients $\boldsymbol{\alpha}$ are handled by the system level optimizer. The proposed formulation is presented in the next section.

5.2. Multi-level Hierarchical Optimization under Uncertainty (MHO)

MHO formulation (Fig. 2) is inspired from SWORD formulation [11] modified for uncertainty handling. MHO is a semi-decoupled multi-level formulation ensuring interdisciplinary coupling satisfaction for all the realizations of the uncertain variables. It assumes that the system level objective $f(\cdot)$ is decomposable into a sum of the subsystem contributions. For instance, the Gross Lift-Off Weight (GLOW) of a launch vehicle is decomposable as the sum of the stage masses. In the proposed formulation, the optimization process is the following:

- At the system level:

$$\min_{\mathbf{z}_{sh} \in \mathcal{Z}_{sh}, \boldsymbol{\alpha}} \sum_{k=1}^N \mathbb{E}[f_k(\mathbf{z}_{sh}, \mathbf{z}_k^*, \hat{\mathbf{y}}(\mathbf{U}, \boldsymbol{\alpha}), \mathbf{U})] \quad (7)$$

$$\text{s. t. } \mathbb{K}[\mathbf{g}(\mathbf{z}_{sh}, \mathbf{z}_k^*, \hat{\mathbf{y}}(\mathbf{U}, \boldsymbol{\alpha}), \mathbf{U})] \leq 0 \quad (8)$$

$$\forall j \in \{1, \dots, N\}, J_j^* = \mathbf{0} \quad (9)$$

$$\forall k \in \{1, \dots, N\}, \mathbb{K}[\mathbf{g}_k(\mathbf{z}_{sh}, \mathbf{z}_k^*, \hat{\mathbf{y}}(\mathbf{U}, \boldsymbol{\alpha}), \mathbf{U})] \leq 0 \quad (10)$$

- At the subsystem level:

$k = N$

While $k > 0$

Given $\mathbf{y}_{Nk}, \dots, \mathbf{y}_{(k+1)k}$

For the k^{th} subsystem:

$$\mathbf{z}_k^* = \underset{\mathbf{z}_k \in \mathcal{Z}_k}{\operatorname{argmin}} \mathbb{E}[f_k(\mathbf{z}_{sh}, \mathbf{z}_k, \hat{\mathbf{y}}(\mathbf{U}, \boldsymbol{\alpha}), \mathbf{U})] \quad (11)$$

$$\text{s. t. } \mathbb{K}[\mathbf{g}_k(\mathbf{z}_{sh}, \mathbf{z}_k, \hat{\mathbf{y}}(\mathbf{U}, \boldsymbol{\alpha}), \mathbf{U})] \leq 0 \quad (12)$$

$$\forall j \in \{k+1, \dots, N\}, J_{kj} = \int_{\Omega} [c_{kj}(\mathbf{z}_{sh}, \mathbf{z}_k, \mathbf{y}_k(\mathbf{u}, \boldsymbol{\alpha}^{(k)}), \mathbf{u}_k) - \hat{y}_{kj}(\mathbf{u}, \boldsymbol{\alpha}^{(kj)})]^2 \xi_U(\mathbf{u}) d\mathbf{u} = 0 \quad (13)$$

$k \leftarrow k - 1$

where Eq. (13) is considered for $k \neq N$. \mathbf{z}_k is the local design variable vector of the k^{th} subsystem and \mathbf{z}_{sh} is the shared design variable vector between several subsystems. This formulation allows one to optimize each subsystem separately in a hierarchical process. The system level optimizer handles \mathbf{z}_{sh} and the PCE coefficients α of the feedback coupling variables. The handling of PCE coefficients at the system level allows one to remove the feedback couplings and to optimize the subsystems in sequence. The surrogate models of the functional feedback couplings provide the required input couplings to the different subsystems. The k^{th} subsystem level optimizer handles \mathbf{z}_k and the corresponding problem aims at minimizing the subsystem contribution to the system objective while satisfying the subsystem level constraints $\mathbf{g}_k(\cdot)$. The interdisciplinary coupling constraint Eq. (13) guarantees the couplings whatever the realization of the uncertain variables. This formulation is particularly suited for launch vehicle in order to decompose the design process into the different stage optimizations [11].

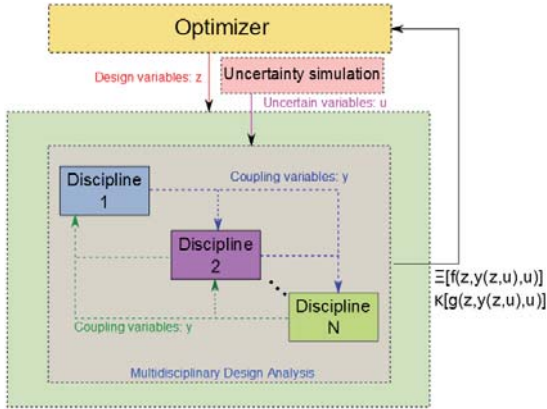


Figure 1 : MDF under uncertainty

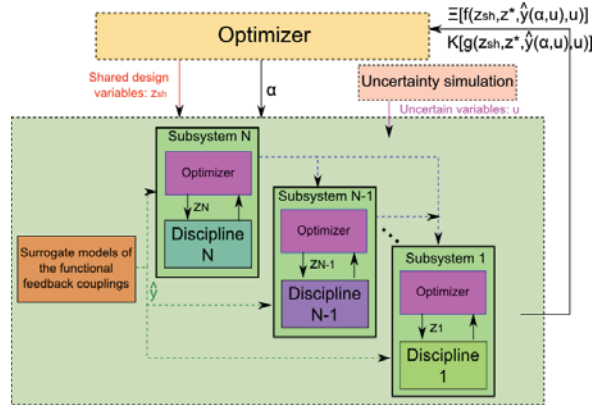


Figure 2 : MHOU formulation

6. Application: two stage sounding rocket design

The launch vehicle design test case consists of the design of a two solid stage sounding rocket for a payload of 800kg that has to reach an altitude of 300km. Four disciplines are involved: propulsion, mass budget and geometry design, aerodynamics and trajectory (Figure 3). The sounding rocket design is decomposed into two subsystems, one for each stage. MHOU formulation enables a hierarchical design process decomposed into two teams, one for each sounding rocket stage. The k^{th} subsystem objective is to minimize a function of the stage mass $\mathbb{E}(M_k(\cdot)) + 2\sigma(M_k(\cdot))$ (with σ the standard deviation). The system level objective is to minimize a function of the GLOW. The uncertainty measure for the constraints $\mathbf{g}_k(\cdot)$ is the probability measure $\mathbb{P}[\cdot]$. The required feedback couplings for the 2nd stage design are $\hat{\mathbf{y}}_{12} = [h_{f1}, v_{f1}]^T$ which are the separation altitude and velocity between the 1st and 2nd stages (Fig. 3). The design constraints for the 2nd stage are $\mathbf{g}_2 = [Pe_2, h_{f2}, Nf_2]^T$ which involve the avoidance of the breakaway of the jet in the divergent skirt (Pe_2), the apogee altitude (h_{f2}) and the maximal axial load factor (Nf_2). The same constraints are taken into account for the 1st stage expected for the apogee altitude. The proposed multi-level decoupled formulation and MDF under uncertainty are compared.

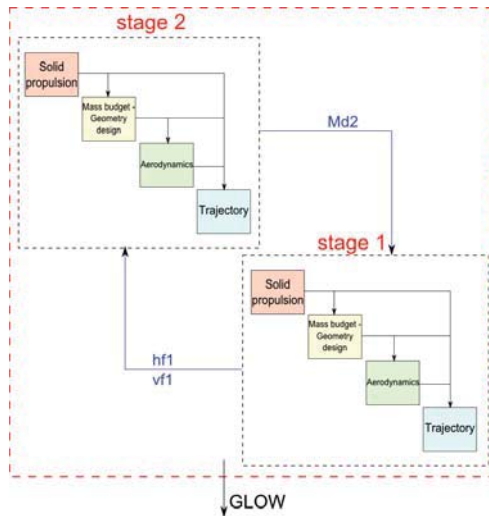


Figure 3: Design Structure Matrix of the sounding rocket

Table 1: Design variables

Design variables	Symbol	Min	Max
1 st stage diameter (m)	D_1	0.5	1.0
1 st stage propellant mass (kg)	Mp_1	1000	3000
1 st stage nozzle expansion ratio	ε_1	1.0	20.0
1 st stage grain relative length (%)	Rl_1	30	80
1 st stage combustion depth (%)	Wp_1	30	80
2 nd stage diameter (m)	D_2	0.5	1.0
2 nd stage propellant mass (kg)	Mp_2	2000	3000
2 nd stage nozzle expansion ratio	ε_2	1.0	20.0
2 nd stage grain relative length (%)	Rl_2	30	80
2 nd stage combustion depth (%)	Wp_2	30	80

The design variables are resumed in Table 1. The uncertain variables taken into account are the 1st stage combustion regression rate coefficient $\mathcal{N}(3.99,0.05)$ in cm/s/MPa^{0.3} and the 2nd stage dry mass error $\mathcal{N}(0,50)$ in kg. The mission has to ensure that the payload reaches at least an altitude of 300km (with a probability of failure of 3×10^{-2}). MDF under uncertainty and MHOu formulations use CMC to propagate uncertainty, to estimate $\mathbb{E}[\cdot]$, $\mathbb{P}[\cdot]$, and $J_{ij}(\cdot)$ based on a fixed set of 10^3 random samples. The FPI convergence criterion is set to a relative error of 1%. Both system level optimizers are stopped when 5.6×10^6 evaluations of the disciplines is reached.

Table 2: Sounding rocket problem results

	MDF under uncertainty	MHOu
Objective function	7.07 (t)	6.68 (t)
Design variables	$[2850, 0.75, 4.4, 69.4, 66, 2395.8, 0.76, 9.97, 69.5, 65.9]^T$	$[2659.5, 0.79, 9.24, 30.7, 43.5, 2287, 0.75, 17.4, 41.0, 63.9]^T$
$\mathbb{P}[h_{f2} \leq 300]$ apogee altitude	0.028	0.029

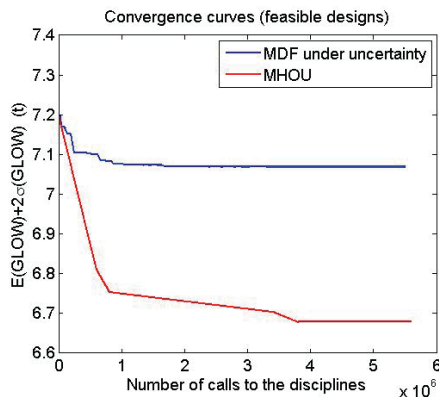


Figure 4: Convergence curves on the feasible designs w.r.t. the number of discipline evaluations

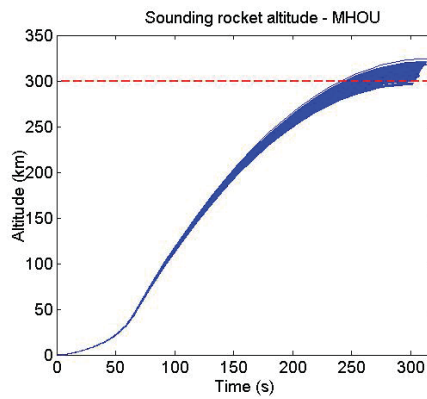


Figure 5: Sounding rocket altitude as a function of time for the optimal design - MHOu

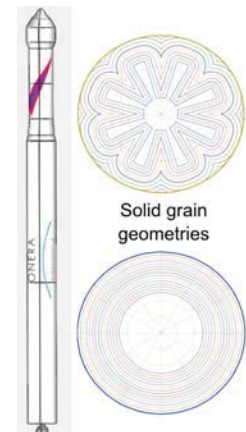


Figure 6: Optimal sounding rocket sizing and geometry

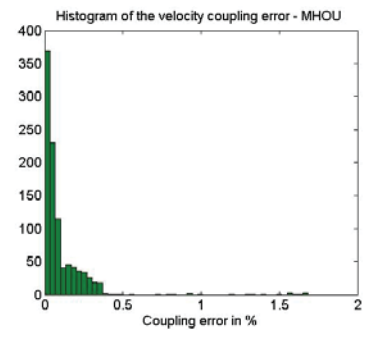
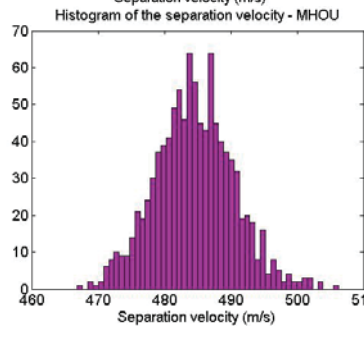
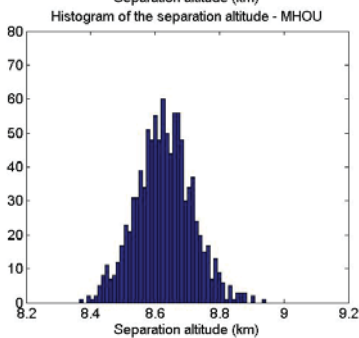
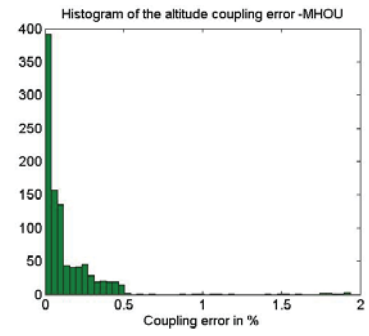
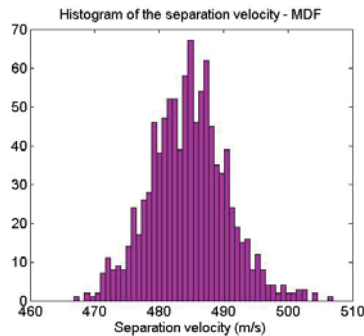
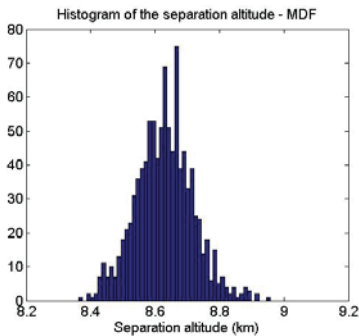


Figure 7: Altitude (blue) and velocity (pink) couplings in MDF and MHOu formulations + coupling error (green)

The discipline modeling (propulsion, sizing, aerodynamics and trajectory) is adapted from classical launch vehicle models at the early design phases [12, 13]. Gradient based optimizer (SQP) is used at the system level in both formulations. CMA-ES optimization algorithm [14] is used at the subsystem level for MHOu formulation. The two problems start from the same feasible baseline to be optimized. The results of the sounding rocket problem are resumed in Table 2. MHOu presents better characteristic in terms of quality of objective function (6.68t) than to MDF (7.07t) for a fixed discipline evaluation budget (Fig. 4). Both MDF and MHOu solutions satisfy the constraints especially the apogee altitude of 300km as illustrated in Figure 5. Only 2.9% of the trajectories do not reach the required altitude. Moreover, MHOu ensures interdisciplinary coupling satisfaction for the feedback couplings as illustrated by the comparison of the couplings for the optimal design found with MHOu with a coupled approach (MDA) and the decoupled approach (Fig. 7). The separation altitude and velocity distributions are similar with MDF (MDA on the optimal MHOu design) and MHOu (Fig. 7). Moreover, the interdisciplinary coupling error for the separation altitude and velocity are represented in Figure 7. The coupling error is always lower than 2% and concentrated between 0% and 0.5 %.

7. Conclusions: This paper provides a new multi-level hierarchical UMDO formulation that ensures the system multidisciplinary feasibility for all the realizations of the uncertain variables. The proposed formulation is based on the iterative construction of surrogate models (PCE) of the functional coupling relations. The PCE coefficients are handled by the system level optimizer and subsystem optimizers only handle local design variables. Numerical comparisons between MDF and the proposed formulation have been performed on the design of a sounding rocket highlighting the efficiency of MHOu in this test case. Additional research effort is needed to incorporate mixed aleatory and epistemic uncertainties in UMDO.

8. Acknowledgements: The work presented in this paper is part of a CNES/ONERA PhD thesis. The authors gratefully acknowledge T. Coquet for the solid rocket propulsion models used in this work.

9. References

- [1] J. RRA Martins and A. Lambe. Multidisciplinary design optimization: a survey of architectures. *AIAA Journal*, 51(9):2049-2075, 2013.
- [2] R. Balling and J. Sobieszcanski-Sobieski. Optimization of coupled systems-a critical overview of approaches. *AIAA Journal*, 34(1):6-17, 1996.
- [3] J. Allison, M. Kokkolaras, M. Zawislak, and P. Y Papalambros. On the use of analytical target cascading and collaborative optimization for complex system design. In 6th World Congress on Structural and Multidisciplinary Optimization, Rio de Janeiro, Brasil, May 2005
- [4] RD Braun, AA Moore, and IM Kroo. Use of the collaborative optimization architecture for launch vehicle design. In 6th Symposium on Multidisciplinary Analysis and Optimization, Bellevue, WA, USA, Sept. 1996
- [5] P. N Koch, B. Wujek, O. Golovidov, and T. W Simpson. Facilitating probabilistic multidisciplinary design optimization using kriging approximation models. In 9th AIAA Symposium on Multidisciplinary Analysis & Optimization, Atlanta, GA, USA, Sept. 2002.
- [6] L. Jaeger, C. Gogu, S. Segonds, and C. Bes. Aircraft multidisciplinary design optimization under both model and design variables uncertainty. *Journal of Aircraft*, 50(2):528-538, 2013.
- [7] C. D McAllister and T. W Simpson. Multidisciplinary robust design optimization of an internal combustion engine. *Journal of mechanical design*, 125:124, 2003.
- [8] X. Du, J. Guo, and H. Beeram. Sequential optimization and reliability assessment for multidisciplinary systems design. *Structural and Multidisciplinary Optimization*, 35(2):117-130, 2008.
- [9] L. Brevault, M. Balesdent, N. Bérend, R. Le Riche Decoupled UMDO formulation for interdisciplinary coupling satisfaction under uncertainty. 15th AIAA/ISSMO Multidisciplinary Analysis and Optimization Conference, Atlanta, GA, USA, June 2014
- [10] M. Eldred. Recent advances in non-intrusive polynomial chaos and stochastic collocation methods for uncertainty analysis and design. In 50th AIAA Structures, Structural Dynamics, and Materials Conference, Palm Springs, CA, USA, May 2009
- [11] M. Balesdent, N. Bérend and Ph. Dépincé. New multidisciplinary design optimization approaches for launch vehicle design, *Proceedings of the Institution of Mechanical Engineers, Part G: Journal of Aerospace Engineering*, 0954410012460013, SAGE Publications, 2012
- [12] F. Castellini. Multidisciplinary design optimization for expendable launch vehicles. PhD thesis, 2012.
- [13] A. Ricciardi. Generalized geometric analysis of right circular cylindrical star perforated and tapered grains. *Journal of Propulsion and Power* 8(1):51-58, 1992
- [14] N. Hansen, S. Müller, P. Koumoutsakos. Reducing the time complexity of the derandomized evolution strategy with covariance matrix adaptation (CMA-ES). *Evolutionary Computation* 11(1):1-18, 2003

Multidisciplinary Design Optimization of an Aero-Engine Fan Blade with Consideration of Bypass and Core Performance

Christopher Chahine^{1,2}, Tom Verstraete³, Li He⁴

¹ Von Karman Institute for Fluid Dynamics, Rhode-Saint-Genèse, Belgium, chahine@vki.ac.be

² University of Oxford, Department of Engineering Science, Oxford, United Kingdom

³ Von Karman Institute for Fluid Dynamics, Rhode-Saint-Genèse, Belgium, verstraete@vki.ac.be

⁴ University of Oxford, Department of Engineering Science, Oxford, United Kingdom, li.he@eng.ox.ac.uk

1. Abstract

A multidisciplinary and multiobjective optimization of a transonic fan blade for a high bypass ratio turbofan engine is presented including aerodynamic as well as structural static and dynamic performance criteria. The optimization strategy applied is based on a two-level approach consisting of a Differential Evolution algorithm coupled to a Kriging metamodel in order to speed up the optimization process. High-fidelity performance evaluations are carried out by means of 3D Computational Fluid Dynamics and Computational Structural Mechanics analysis tools. Multiple key operating points are considered in the optimization process; aerodynamic performance is evaluated at top-of-climb and cruise conditions, while maximum stresses are evaluated at take-off operation, taking into account centrifugal and gas loads. Blade vibration is furthermore assessed over the entire operating range. Aerodynamic performance is separately evaluated for core and bypass flows in order to match the requirements specified by the engine cycle design.

2. Keywords: Multidisciplinary Optimization, Fan Blade, Turbofan, Bypass Ratio, Aerostructural Optimization.

3. Introduction

High bypass ratio turbofan engines are today the almost exclusive powerplant of choice for medium and long haul commercial aircraft due to high obtainable thrust levels combined with good fuel efficiency. About 80% of a modern turbofan engine's thrust is generated by the fan. Low engine fuel consumption requires the fan blades to transfer mechanical shaft power into thrust with the lowest possible amount of aerodynamic losses (high propulsive efficiency). Although this goal can be formulated easily, in practice additional requirements such as stable operation under widely varying operating conditions, transonic relative inlet flows and structural integrity constraints significantly complexify the design problem. Structural loads occurring during operation include centrifugal forces, aerodynamic loads and periodic blade excitations from varying sources. As the fan blade is a safety critical component, all of the above aspects need to be considered in the design process.

In the aero-structural design process commonly applied by industry, the structural and aerodynamic design are mostly handled separately from each other and the design progresses iteratively from one discipline to another until a satisfactory solution is found. The result is a lengthy and expensive design process with the additional disadvantage that interactions between the involved disciplines are difficult to reveal.

In this paper the application of a multidisciplinary and multiobjective optimization system to the above stated design problem is presented. The optimization method enables the concurrent evaluation of aerodynamic and structural performance criteria, therefore facilitating the identification of the interaction of disciplines and allowing the design to progress towards global optimal solutions in a reduced design time.

4. Baseline design

Specified engine cycle requirements are the starting point for the fan blade design process. To enable a reasonable design space definition, a baseline design was generated using two-dimensional preliminary aerodynamic design tools based on first principles and correlations. The methods enable a reasonable estimation on required spanwise blade angle distributions and suitable profiles to be made. The obtained geometry was analyzed using CFD and slightly adjusted manually to meet the operating range requirements. However, not all aerodynamic specifications could be met at the end of this design stage.

5. Optimization system

The optimization system shown in Fig. 1 is the result of more than one and a half decades of research and development at the von Karman Institute [1],[2]. The core components of the system are a multiobjective Differential Evolution algorithm (DE) [3,4], a database, several metamodels, including Radial Basis Functions,

Artificial Neural Networks and Kriging, and a high fidelity evaluation chain including a fully automatic geometry and CAD generation, automatic meshing and high-fidelity performance evaluations by Computational Fluid Dynamics (CFD) and Computational Structural Mechanics (CSM). The optimization method is based on a two-level strategy coupling the evolutionary optimization to a sequentially updated metamodel. Prior to the optimization an initial design space sampling is performed using a fractional factorial Design of Experiments containing 128 samples plus the baseline and a design at the center of the design space. Each sample is evaluated by the high fidelity evaluation chain. The resulting relationships between optimization parameters and performance are stored in a database which serves to train the first metamodel. On the next level the optimization is performed using exclusively the metamodel for the performance evaluations. Since metamodel evaluations are computationally cheap, thousands of generations can be computed by the Differential Evolution algorithm within a few minutes. However, since the metamodel predictions at early stages of the process can be expected to be rather inaccurate, eight of the best performing designs of the Pareto front predicted by the metamodel are chosen for re-evaluation by the high-fidelity evaluation chain. The results are added to the database and used to re-train the metamodel, making it more accurate in the regions where it previously predicted optimal designs. In the remainder of this paper, one loop consisting of optimization, high-fidelity re-evaluation and metamodel generation is termed an iteration. Ordinary Kriging is used as metamodel. Each performance parameter is predicted with one dedicated metamodel, which reduces prediction error and training cost. Further implementation details of the system can be found in e.g. [4],[5].

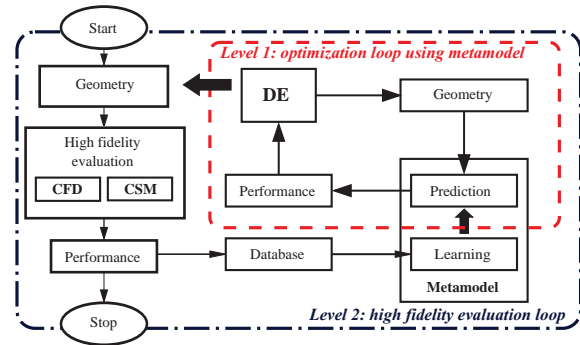


Figure 1: Flow chart of the optimization system.

6. Fan blade parametrization

The geometry of the fan blade is defined by parametric Bézier and B-Spline curves which specify the blade chord, blade angles, the thickness distributions at hub and tip sections and the profile stacking axis by lean and sweep, see Figs. 2 and 3. The blade metal angles at the leading edge, trailing edge and an intermediate point as well as the chord length are defined by spanwise B-Spline curves, as shown in Fig. 2. Control points for these distributions are defined on four spanwise positions which are being fixed for three of the points at 0, 50 and 100% span. The spanwise position of the fourth control point is added as an optimization parameter in order to allow additional control of the blade geometry close to the bypass splitter. Some of the control points are directly defined as optimization parameters and are indicated with arrows, while others are defined via geometric dependencies to other control points (e.g. angles and distances). The blade thicknesses at hub and tip sections are defined by B-Spline curves as

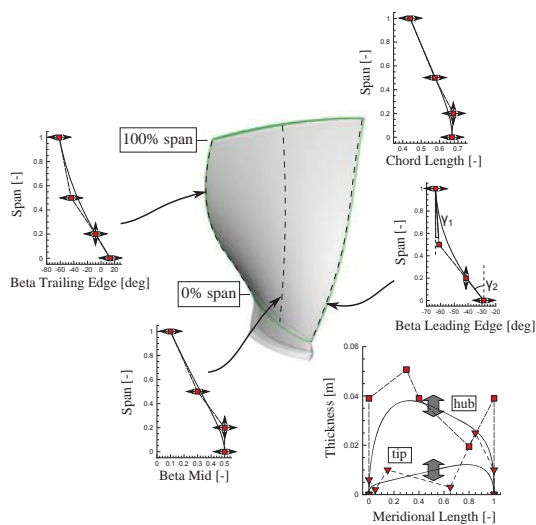


Figure 2: Parametrization of blade angles, chord length and thickness.

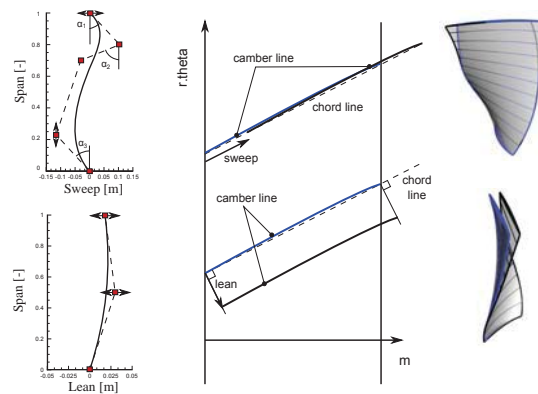


Figure 3: Lean and sweep definition and parametrization.

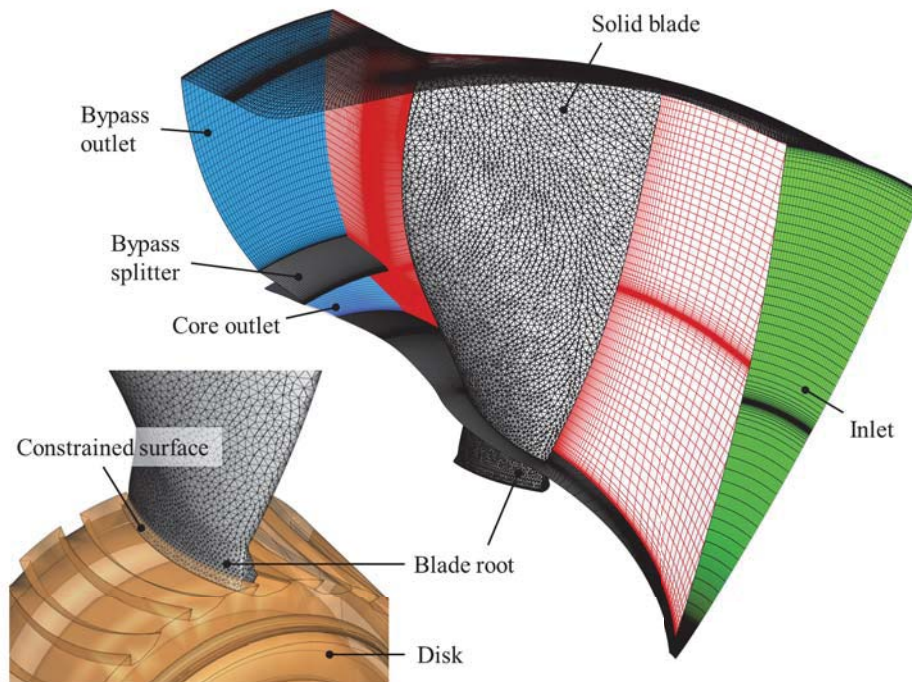


Figure 4: Computational domains of the baseline fan blade.

shown in Fig. 2 and are designed based on [6]. Both distributions can be scaled independently by a uniform scaling factor, therefore allowing thickness changes without altering the actual distributions. In addition, the number of blades is allowed to be modified resulting in a total of 26 optimization parameters.

7. High fidelity performance evaluations

The aerodynamic performance of the fan blade is assessed using the commercially available 3D Reynolds-Averaged Navier-Stokes solver FINE™/Turbo from Numeca. The solver is a structured, density based code using a finite volume method. The fluid domain is discretized using a multi-block structured mesh consisting of about 2 million grid points with a domain averaged non-dimensional height of the first cell near the wall (y^+) of about 3. Turbulence effects are taken into account with the one-equation Spalart-Allmaras turbulence model.

To meet the aerodynamic design and off-design targets of the fan blade, its performance is evaluated at two key flight conditions, namely top-of-climb (ToC) and cruise. In total nine operating points are computed for each design, including four points on the top-of-climb speedline and five points on the cruise speedline. An automatic convergence check is performed after each CFD computation, which assesses the mass flow error between domain inlet and outlet and the iteration errors of isentropic efficiency and total pressure ratio. Only converged cases are subsequently assessed by an automatic postprocessing step, which extracts the required performance parameters needed by the optimizer. Non-converged cases are considered as failed and are automatically excluded from the optimization process.

The computational domains of the baseline fan blade for both solid and fluid are shown in Fig. 4. The fluid domain comprises one periodic section of the full annulus with periodic boundary conditions being applied at each side of the domain. Total pressure, total temperature, absolute inflow angle and turbulent kinematic viscosity are imposed as boundary conditions at the inlet. The low hub-to-tip radius ratio of the blade results in a transonic flow at all considered operating conditions with the relative inlet flow to the blade being subsonic for the lower part of the blade extending to about 50 percent span and supersonic for the remaining part of the blade up to the blade tip. The flow at the subsonic root section (the portion of the blade feeding the engine core) is highly sensitive towards outlet pressure differences, requiring the mass flow to be imposed as the core outlet boundary condition in order to obtain a stable flow solution. In contrast the static pressure with the radial equilibrium law is defined as boundary condition for the bypass outlet. Performance curves are computed by changing the bypass outlet static pressure. The solid domain of the fan is discretized with an unstructured mesh consisting of quadratic tetrahedral elements. The computations are performed using the open-source finite element solver CalculiX [7]. Stresses in the blade

are computed by means of a static analysis at take-off conditions taking into account geometric non-linearities. The blade is subjected to centrifugal and gas loads whereas the gas loads are extracted from the converged take-off CFD computation of the baseline geometry and interpolated onto the FEM grid.

Additionally to the structural static evaluation, fan blade vibration is considered at all previously mentioned key operating points (take-off, top-of-climb and cruise) to assess the risk of possible high-cycle fatigue failure. Modal analysis is used to determine the natural frequencies of the fan blade while centrifugal stiffening is included in the computations in order to take into account the non-linear increase of blade stiffness with increasing rotational speed (an effect known as centrifugal stiffening). The margins between excitation frequencies and blade natural frequencies at the rotational speeds associated with the aforementioned operating points are evaluated using the Campbell diagram. Excitations from one-per-revolution and two-per-revolution disturbances are considered covering possible sources like unbalance and cross-wind. The fan blade is modelled using material properties of Ti-6Al-4V.

An important detail of the solid domain is the blade root and its restraint, which is the part of the solid extending out of the fluid domain as shown in Fig. 4. The root has important structural implications for both stresses and vibrations as it is the portion of the blade that connects to the fan disk and therefore defines the boundary conditions for the structural simulations. A typical blade-disk assembly is shown on the left bottom part of Fig. 4. In the structural computation all mesh nodes on the upper dovetail root surface are restrained in all degrees of freedom in order to simulate the disk assembly. In reality, these surfaces are in contact with the disk and small relative movements between disk and blade root are possible. Fixing the nodes will thus result in unrealistically high stress concentrations on the surface. These stresses are not taken into account in the postprocessing step.

8. Objectives and constraints

Two objectives and in total 12 aerodynamic and structural constraints are defined for the optimization problem. The objectives are defined to maximize peak efficiency at cruise rotational speed and maximize stall margin, defined as the non-dimensional mass flow difference between the cruise design point and the last converged CFD operating point towards low mass flows, see Fig. 5. The maximization problem is converted to an equivalent minimization problem, such that both objectives are stated as

$$\mathbf{minimize} = \begin{cases} -\eta_{cruise,peak} \\ -\left(\frac{\dot{m}_{cruise,design} - \dot{m}_{cruise,stall}}{\dot{m}_{cruise,stall}}\right) \end{cases} \quad (1)$$

The stall margin objective implies the assumption that numerical instabilities occurring at lower mass flows resemble the physical process of stall/surge in a real fan.

The constraints are defined as follows

$$\dot{m}_{cruise,stall} \leq \dot{m}_{cruise,design} \leq \dot{m}_{cruise,choke} \quad (2)$$

$$0.97 \cdot \dot{m}_{toc,design} < \dot{m}_{eval,toc} < 1.03 \cdot \dot{m}_{toc,design} \quad (3)$$

$$\Pi_{t-t,bypass,eval,toc} > 1.7 \quad (4)$$

$$\Pi_{t-t,core,eval,toc} > 1.4 \quad (5)$$

$$Ma_{max,bypass,eval,toc} < 0.9 \quad (6)$$

$$Ma_{max,core,eval,toc} < 0.9 \quad (7)$$

$$\alpha_{max,bypass,eval,toc} < 70 \text{ deg} \quad (8)$$

$$\alpha_{max,core,eval,toc} < 70 \text{ deg} \quad (9)$$

$$\sigma_{vM} < 800 \text{ MPa} \quad (10)$$

$$\Delta \hat{F}_{cruise} + \Delta \hat{F}_{ToC} + \Delta \hat{F}_{T/O} > 12 \quad (11)$$

Four constraints (Eq. (2) and (3)) are imposed to ensure that the operating range of the fan matches the engine cycle design requirements at cruise and top-of-climb defined as $\dot{m}_{cruise,design} = 541 \text{ kg/s}$ and $\dot{m}_{toc,design} = 699 \text{ kg/s}$. A top-of-climb evaluation point with a 6% stall margin with respect to the total pressure ratio is defined as shown in Fig. 5. This is the operating point where the required total pressure ratio is the highest throughout the mission. Two constraints are therefore defined to ensure that the pressure ratios for core

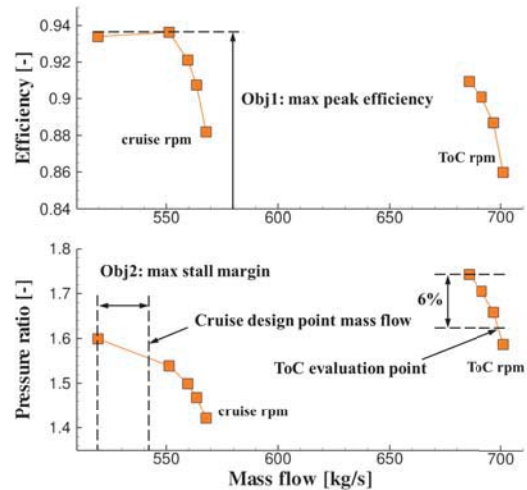


Figure 5: Definition of objectives and the top-of-climb evaluation point shown on the performance map of the baseline design.

and bypass flows are not lower than the design requirements, see Eq. (4) and (5). Additionally, Eq. (6)-(9) limit the maximum absolute inlet Mach numbers and the maximum absolute flow angles at the bypass and core inlet to ensure that the stators located further downstream (Outlet Guide Vane in the bypass and Engine Section Stator in the core) receive a healthy inlet flow and performance improvements of the fan blade are not obtained at the cost of overall stage performance. The absolute flow angle is measured with respect to the meridional plane. Equation (10) defines that the maximum von Mises stresses in the fan blade are required to be lower than 800 MPa, leaving a 130 MPa dynamic stress margin towards the yield stress of the titanium alloy. Blade vibration is assessed at cruise, top-of-climb and take-off. A minimum required frequency margin between the first bending mode of the blade and the first harmonic of a one and two per revolution excitation are defined as constraint (Eq. (11)).

9. Results

In Fig. 6 the objective space is shown after a total of 10 iterations. Each symbol in the plot represents a design which was evaluated by the high-fidelity evaluation chain. DOE samples are shown as circles while designs generated during the optimization appear as squares. Samples that are satisfying the constraints are shown in light blue. Improved performance is obtained towards the lower left corner of the objective space. An indication of all designs generated during the optimization is given in the upper right corner of Fig. 6. However, the designs which are satisfying all imposed constraints are located in the region marked with the red square. The main part of Fig. 6 shows a close up on this region.

As the optimization problem is highly constrained, only three designs in the DOE database initially satisfied all constraints. After nine iterations the Kriging metamodel became sufficiently accurate to guide the optimizer to the feasible region of the design space. Subsequently, all designs generated during the ninth and tenth iteration were feasible.

The best design found after 10 iterations is designated as IT010_IND001 in Fig. 6. The baseline design is shown as orange diamond to enable a performance comparison. It should again be emphasized that the baseline design violates a number of constraints and is therefore not part of the feasible set of designs. In contrast, design IT010_IND001 is satisfying all imposed constraints and at the same time shows improvements in both objectives.

A more detailed assessment of the aerodynamic performances of both designs is possible by comparing their performance maps, as shown in Fig. 7. The cruise design point mass flow is indicated by the dashed line. As shown in the lower part of Fig. 7, the pressure ratio of the fan was successfully increased over the entire operating range to meet the core and bypass pressure ratio requirements at top-of-climb. The baseline design generates overall a lower pressure ratio, which generally translates to higher obtainable efficiencies. However, with the increase in pressure ratio the optimized design still obtains a peak efficiency of 93.7%; an 0.05% improvement over the baseline design. The peak efficiency occurs at a mass flow of 561kg/s which is 0.037% above the design point mass flow. This can be deemed as reasonably close for a numerical prediction.

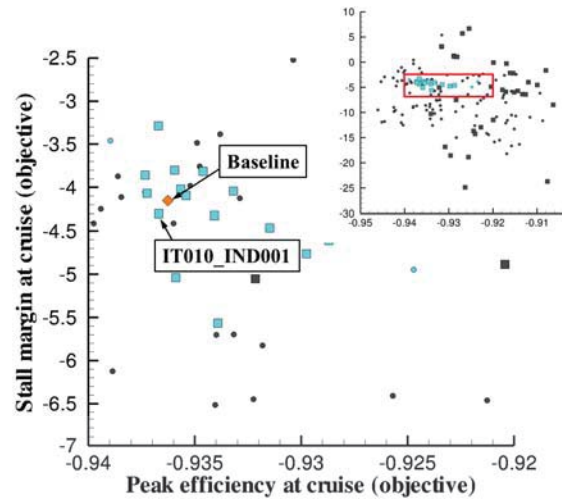


Figure 6: Objective space of the optimization after a total of 10 iterations.

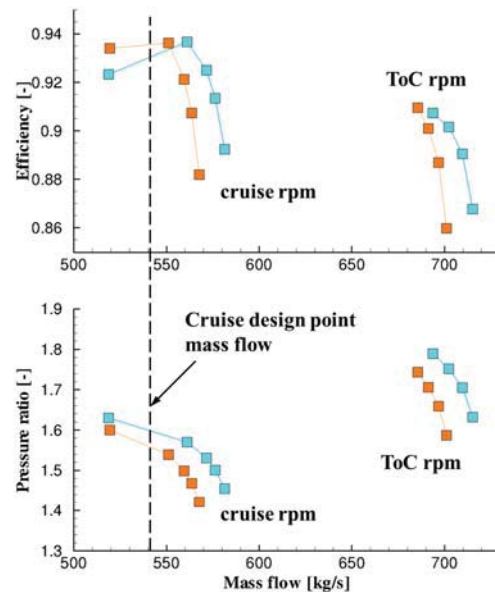


Figure 7: Comparison of performance maps of the baseline design (orange) and the optimized design (light blue).

An analysis of the optimization process reveals that the structural constraints were among the most difficult to satisfy. As the baseline design was generated purely based on aerodynamic considerations, it violated both the stress and the vibration constraints. A comparison of the von Mises stress distributions on the suction side surfaces of baseline and optimized design is shown in Fig. 8. Peak stresses exceeding the constraint value occur in the baseline design at the leading edge close to the transition to the dovetail root and on the suction side hub region close to the trailing edge (both regions are indicated by ellipses in Fig. 8). The stress levels in the critical regions were successfully lowered by the optimizer as shown on the right hand side of Fig. 8. As noted above, the high stresses in the dovetail root are not taken into account in the postprocessing step as these are artificially increased due to the boundary conditions applied in the structural computations.

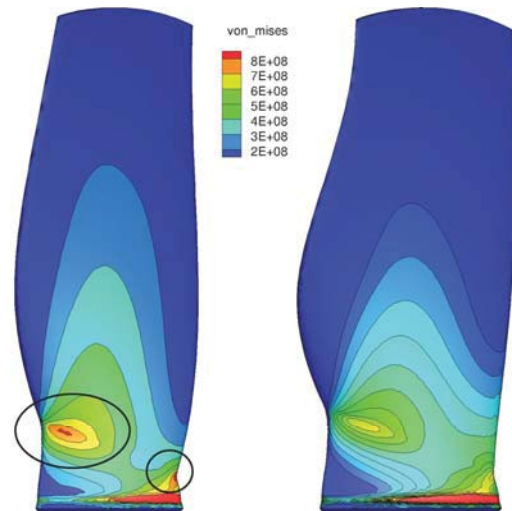


Figure 8: Von Mises stress distribution in the baseline (left) and the optimized design.

10. Conclusions

This paper presents the application of a two-level optimization system based on a Differential Evolution algorithm coupled to a sequentially updated Kriging metamodel to the multidisciplinary and multiobjective optimization of a transonic fan blade for a high-bypass ratio turbofan engine. Aerodynamic performance requirements for bypass and core sections are simultaneously taken into account in the optimization problem formulation. Stresses and vibrations are furthermore considered as structural constraints. The result is a problem with a total of 12 aerodynamic and structural constraints. The optimization system successfully identified the feasible region in the design space after 9 iterations. Subsequently, the objectives (efficiency and stall margin) were rapidly improved. The best design was found after 10 iterations, which showed an improvement of both objectives with respect to the baseline design; a significant improvement, as the baseline design did not satisfy all imposed constraints.

11. Acknowledgements

The research leading to these results has received funding from the European Union Seventh Framework Programme (FP7/2007-2013) under grant agreement no [316394].

12. References

- [1] S. Pierret, *Designing Turbomachinery Blades by Means of the Function Approximation Concept Based on Artificial Neural Network, Genetic Algorithm, and the Navier-Stokes Equations*, PhD thesis, Faculté Polytechnique de Mons/ von Karman Institute for Fluid Dynamics, 1999.
- [2] T. Verstraete, *Multidisciplinary Turbomachinery Component Optimization Considering Performance, Stress, and Internal Heat Transfer*, PhD thesis, University of Ghent/ von Karman Institute for Fluid Dynamics, 2008.
- [3] R. Storn and K. Price, Differential Evolution - A Simple and Efficient Heuristic for Global Optimization over Continuous Spaces, *Journal of Global Optimization*, 11(4), 341-359, 1997.
- [4] T. Verstraete, *Multidisciplinary Optimization of Turbomachinery Components using Differential Evolution*, VKI LS 2010-07 *Introduction to Optimization and Multidisciplinary Design in Aeronautics and Turbomachinery*, Rhode-Saint-Genèse, Belgium, 2010.
- [5] T. Verstraete, CADO : a Computer Aided Design and Optimization Tool for Turbomachinery Applications, *2nd International Conference on Engineering Optimization*, Lisbon, Portugal, 2010.
- [6] A. Wennerstrom, *Design of Highly Loaded Axial Flow Fans and Compressors*, Concepts ETI, 2001.
- [7] G. Dhondt and K. Wittig, A Free Software Three-Dimensional Structural Finite Element Program, www.calculix.de.

Multi-objective optimization of material model parameters of an adhesive layer by using SPEA2

Kaveh Amouzgar¹, Mirza Cenanovic², Kent Salomonsson³

¹ School of Engineering, Jönköping University, Jönköping, Sweden, kaveh.amouzgar@jth.hj.se

² School of Engineering, Jönköping University, Jönköping, Sweden, mirza.cenanovic@jth.hj.se

³ School of Engineering, Jönköping University, Jönköping, Sweden, kent.salomonsson@jth.hj.se

1. Abstract

The usage of multi material structures in industry, especially in the automotive industry are increasing. To overcome the difficulties in joining these structures, adhesives have several benefits over traditional joining methods. Therefore, accurate simulations of the entire process of fracture including the adhesive layer is crucial. In this paper, material parameters of a previously developed meso mechanical finite element (FE) model of a thin adhesive layer are optimized using the Strength Pareto Evolutionary Algorithm (SPEA2). Objective functions are defined as the error between experimental data and simulation data. The experimental data is provided by previously performed experiments where an adhesive layer was loaded in monotonically increasing peel and shear. Two objective functions are dependent on 9 model parameters (decision variables) in total and are evaluated by running two FE simulations, one is loading the adhesive layer in peel and the other in shear. The original study converted the two objective functions into one function that resulted in one optimal solution. In this study, however, a Pareto front is obtained by employing the SPEA2 algorithm. Thus, more insight into the material model, objective functions, optimal solutions and decision space is acquired using the Pareto front. We compare the results and show good agreement with the experimental data.

2. Keywords: Multi-objective optimization, parameter identification, micro mechanical model, adhesive, CZM

3. Introduction

Nowadays, adhesive joints are broadly used in industry due to providing galvanic insulation, vibration damping, and sealing capacity. In case adhesive joints are utilized to carry loads, finite element methods and constitutive laws are required to be developed in order to facilitate simulations in the product development process. The accuracy of the constitutive material model is highly dependent on the proper material parameters. Emphasis has to be put on accurately identifying these material parameters. Determination of material parameters have been done previously using inverse methods. Mahneken [1] introduces a unified strategy for identifying material parameters, by coupling a gradient based optimization algorithm with a FEM framework for inelastic material models. The constitutive model parameters of a thin walled tube in axial crushing were identified by Markiewicz [2]. Two identified parameters were optimized by using the BFGS algorithm. Traditionally only one objective, one load case, has been studied in literature. However, depending on the nature of the problem several load cases (ex. tensile and shear) might occur simultaneously. Optimizing parameters with consideration to only one load case, despite more cases being required, will result in an inaccurate numerical model. Accordingly, more than one objective is needed to be optimized, consequently it will require more experiments and simulations [3, 4]. Aguir et al. studied the behavior of an elasto-plastic material in a sheet metal forming process. They identified the material parameters of stainless steel based on shear and bulge experiments. The error between the experimental results and the FEM simulations were minimized by using surrogate base multi-objective optimization [4].

In optimization problems with more than one objective, one extreme solution would not satisfy both objective functions and the optimal solution of one objective will not necessarily be the best solution for the other objective(s). Thus, different solutions will produce a trade-off between different objectives and a set of solutions is required to represent the optimal solutions for all objectives. The characteristic of evolutionary methods which use a population of solutions that evolve in each generation is well suited for multi-objective optimization problems.

There are a number of significant studies comparing different MOEAs [5, 6, 7, 8, 9, 10, 11]. The most representative, discussed and compared evolutionary algorithms are Non-dominated Sorting GA (NSGA-II) [12], strength Pareto evolutionary algorithm (SPEA, SPEA2) [5, 13], Pareto archived evolution strategy (PAES)[14, 8], and Pareto enveloped based selection algorithm (PESA, PESA II) [15, 16]. Extensive comparison studies and numerical simulation on various test problems concludes to a better overall behavior of NSGA-II and SPEA2 compared to other algorithms.

Table 1: Parameter settings for the SPEA2 algorithm.

Init. pop.	Arch. pop.	Cross over prob.	Mutation prob.	SBX distr. index	Mutation distr. index
40	40	0.8	0.2	10	10

In this work, material parameters of an adhesive layer based on the previous work by Salomonsson and Andersson [17] are optimized by using SPEA2. The strength Pareto evolutionary algorithm has been applied on real world engineering applications previously [18]. The two objectives are defined as the error between the experiments and finite element simulations, to identify the optimal value of the material parameters. In the next section the material model and the original study are briefly introduced. The optimization process is outlined in section 5. Whereas section 6 presents the results and section 7 is devoted to the conclusions.

4. Problem definition

In adhesive material models, two deformation modes dominate; 1) peel deformation, and 2) shear deformation [19]. In research literature, a number of experimental methods have been developed to measure the stress elongation relations. An alternative approach is to develop a constitutive law for the adhesive layer, also referred as the cohesive zone model, that couples the peel and shear stresses in an integrated manner. Salomonsson and Andersson [17] developed a meso mechanical model in order to compare with experimental data [20, 21]. A representative volume element (RVE) of the adhesive layer was designed and the parameters for the interface elements in the FE-model were determined by calibrating the simulated peel and shear stress-elongation curves to the experimental curves.

The proposed model by Salomonsson and Andersson can to a sufficient extent simulate the stress-elongation relation in peel and shear. The study defined two objective functions as the fitness of the peel and shear simulations. They transformed the two objectives into one by using the product of the two. There is no prior knowledge about the objectives, whether they are conflicting or non-conflicting. In case of conflicting objectives, a set of Pareto optimal solutions would be needed while in non-conflicting objectives the optimization would result in one optimal solution. Therefore, their provided solution might have been one of the optimal solutions. The aim of this paper is to analyze the problem using a true multi-objective optimization method and generate a number of Pareto optimal points. Comparing the results of this paper and the previous research performed by Salomonsson and Andersson, either confirms global optimality of their solution or shows that there exist a set of trade-off solutions.

5. Procedure

The same mesomechanical model created by Salomonsson and Andersson [17] is used in this project. The model consists of a representative volume element (RVE) of an adhesive layer. The thickness of RVE is the same as the thickness of adhesive layer in the experiment which was 0.2 mm. Based on studies and preliminary simulations, the length of 0.8 mm for the RVE is chosen to be enough to capture the fracture process. A set of 9 parameters is chosen as the variables to be calibrated by the optimization study. The parameters with superscript I are related to the polymer blend and for the minerals the parameters are identified by superscript II. The set of nine variables are:

$$\kappa = [\sigma_Y^I, \lambda_2^I, \sigma_0^I, \delta_{nc}^I, \delta_{tc}^I, \lambda_2^{II}, \sigma_0^{II}, \delta_{nc}^{II}, \delta_{tc}^{II}] \quad (1)$$

See [17] for a detailed explanation.

The Young's modulus for the polymer blend is set to $E^I = 2\text{GPa}$ and the hardening modulus is $H^I = 200\text{MPa}$. Poisson's ratio for the polymer is set to $\nu^I = 0.35$. The Young's modulus and Poisson's ratio for mineral grains are set to $E^{II} = 70\text{GPa}$ and $\nu^{II} = 0.35$ and is considered elastic. The aforementioned parameters are fixed during all simulations. The two objective functions are defined by using FE simulations and the results from experiments. In this report, the case in pure peel load is denoted as MOD1 and the shear load is denoted as MOD2. The MOOP is defined by minimizing the two objectives.

The strength Pareto evolutionary algorithm (SPEA2) [13] is used to solve this optimization problem. Simulated binary crossover (SBX) and polynomial mutation are the operators employed in the SPEA2 algorithm. The parameter setting for the algorithm and the genetic operators are based on the recommendations in the literature and the author's experience which are presented in table 1.

The lower and upper limit for the all 9 variables are defined by Salomonsson, one of the authors of the original paper. The variables and their bounds are shown in table 2. The 40 initial sampling points known as design of experiment (DoE) are generated by using the Latin hypercube sampling method. The iterative Latin hypercube sampling method using maximin (maximize minimum distance between the point) with 20 iterations is the specific

Table 2: The upper and lower limits of the variables and the optimal solutions in the original study.

	σ_Y^I (MPa)	$\lambda_2^I(-)$	σ_0^I (MPa)	$\delta_{nc}^I(\mu\text{m})$	$\delta_{ic}^I(\mu\text{m})$	$\lambda_2^{II}(-)$	σ_0^{II} (MPa)	$\delta_{nc}^{II}(\mu\text{m})$	$\delta_{ic}^{II}(\mu\text{m})$
Range	[45, 55]	[0.1, 0.8]	[20, 25]	[45, 80]	[20, 60]	[0.1, 0.8]	[9, 11]	[10, 60]	[30, 100]
Optimal	50	0.31	23	53	38	0.39	10	21	49

method employed in this study. In order to reduce the convergence time and create better comparable results, one of the initial DoEs is replaced by the optimal solution obtained in the original study, listed in table 2. The objective function for peel and shear are defined as the L_2 -norm of the error between the experimental data and the simulation data.

$$f := \frac{1}{n} \gamma \|ED - SD\| \quad (2)$$

where ED and SD denote the experimental stress data and the simulated stress data and n denotes the number of simulation points. The objectives are penalized by γ in order to capture the crucial parts of the curves. This would also improve the accuracy of the comparison between the two curves.

In the simulation of the shear load case (MOD2) it is cumbersome to catch the descending part of the curve. The elements in the FE model become distorted and the analysis fails because of large deformation in some parts of the RVE when a large crack coalesce. Thus, in the simulation of the second objective only the stress values within the range of 0 to 70 μm of elongations are considered.

Each FE simulation of MOD1 varies between 30 min to approximately 2 hours, while MOD2 can take up to 8 hours. In every generation of the SPEA2 algorithm, 40 new fitness evaluations of both objectives are performed. Therefore, parallel computation across several work stations is beneficial.

In order to reduce the computation time of FE simulation one way could be to employ meta-modeling techniques. Employing meta-modeling methods to reduce the cost of FE simulations computational time is more or less mandatory. However, the ‘‘curse of dimensionality’’ is a known problem in surrogate modeling of high dimensional problems, that can affect the accuracy of the meta-models. Consequently the final non-dominated solutions can be affected. In this project, dealing with surrogate models generated from 9 variables for MOD1 and MOD2 can increase the error in computing the fitness functions. This approximation along with the definition of the objective functions, which are rough calculation of the errors between the two curves, will increase the error. This can lead the search direction of the MOO algorithm to an incorrect path. Thus, in this study it has been decided not to employ any surrogate modeling and compute the fitness functions by running the actual FE simulations. Despite that, the obtained results can be used to compare the accuracy of different meta-modeling methods.

Table 3: Original optimal parameters and optimal parameters of MOO

	σ_Y^I (MPa)	$\lambda_2^I(-)$	σ_0^I (MPa)	$\delta_{nc}^I(\mu\text{m})$	$\delta_{ic}^I(\mu\text{m})$	$\lambda_2^{II}(-)$	σ_0^{II} (MPa)	$\delta_{nc}^{II}(\mu\text{m})$	$\delta_{ic}^{II}(\mu\text{m})$
Orig. study	50	0.31	23	53	38	0.39	10	21	49
This study	49.67	0.29	22.88	52.6	38.51	0.36	10	20.39	52.39

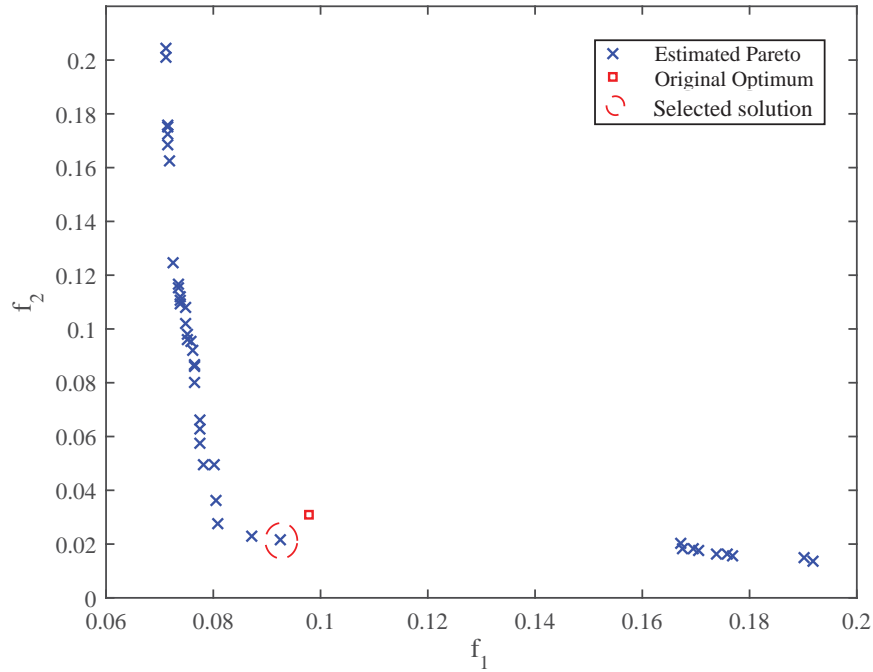


Figure 1: Pareto front (non-dominated solutions)

6. Results

The set of non-dominated solutions are illustrated in figure 1. It is clear that the objectives are conflicting and the original solution, indicated by the square, is not far off from the optimal set of solutions in the lower left corner. This can also be seen in both figures 2a and 2b, where the similarity between the curves is evident. On the other hand, a better fit to the experimental data is observed in figure 2d compared to figure 2c. The authors of the original study stated three reasons for not reaching a better fit to the peel curve: 1) A too narrow search space for the parameters, 2) the nature of conflicting objectives, 3) the inherit property of the cohesive model [17]. In this study the search space of the parameters is broadened. The conflicting nature of peel and shear can still be a reason for not reaching a better fit. The discrepancy between the MOD1 simulation curve and experimental curve is due to the nature of the cohesive zone model. As suggested by the original authors, using a different cohesive law with different fracture energies in peel and shear could improve the fitness.

Table 3 shows the decision variables generating the selected optimal solution. The similarity in the values of the parameters indicate a need for a sensitivity analysis in order to further map the dependencies of variable changes to the objectives. However, by comparing the parameters σ_0^I and σ_0^{II} during the evolutions in the original study and the optimal selected solution in this study, it can be concluded that these parameters are almost constant.

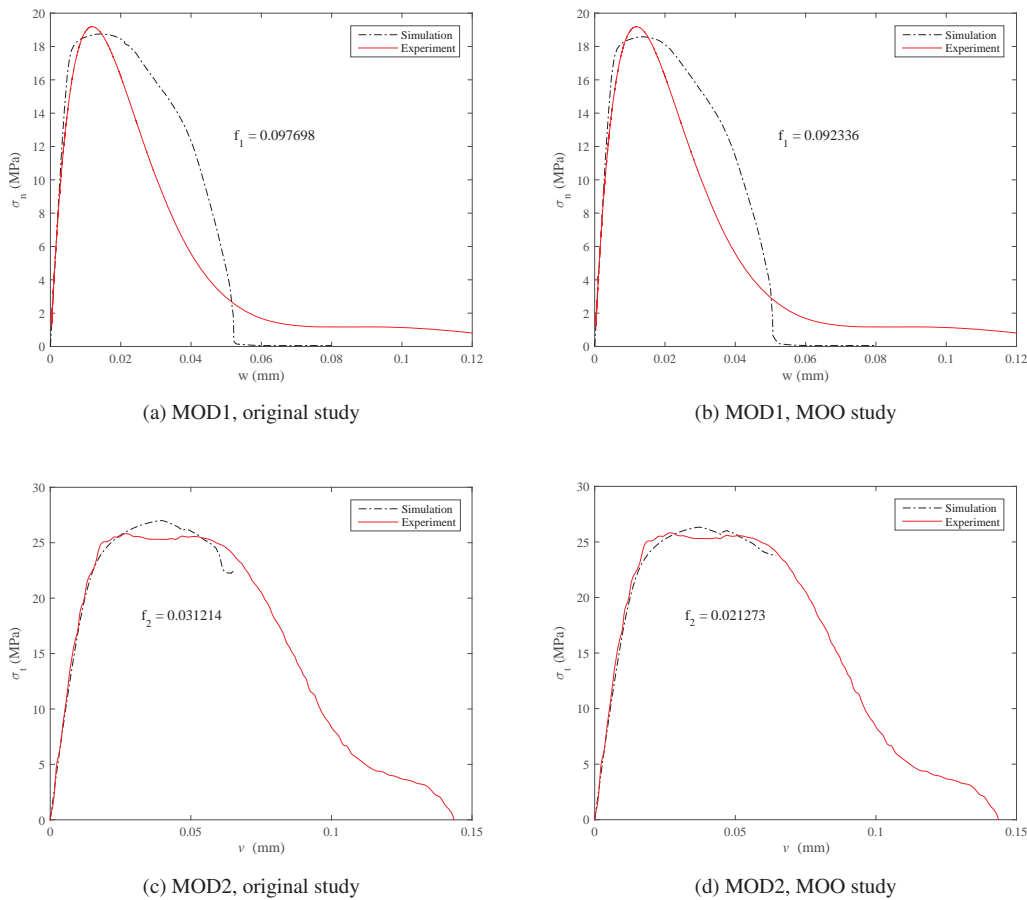


Figure 2: Stress-elongation curves.

7. Conclusion

In the future, the MOO of the adhesive layer can be further studied by performing sensitivity analysis in order to better understand the nature of the problem and provide a broad insight to the decision makers. Also, further studies on the parameter setting of the optimization algorithm for a faster convergence is useful. By obtaining the best set of non-dominated solutions, an interesting study can be carried out in employing or developing proper, accurate and fast meta models for these types of problems, including curve fitting and parameter identification. Another interesting study is to employ the guided evolutionary multi objective optimization method which focuses on finding more solutions in a user defined objective space.

References

- [1] Rolf Mahnken and Erwin Stein. A unified approach for parameter identification of inelastic material models in the frame of the finite element method. *Computer methods in applied mechanics and engineering*, 136(3):225–258, 1996.
- [2] Eric Markiewicz, Pierre Ducrocq, and Pascal Drazetic. An inverse approach to determine the constitutive model parameters from axial crushing of thin-walled square tubes. *International Journal of Impact Engineering*, 21(6):433–449, 1998.
- [3] Yang Liu and Fan Sun. Parameter estimation of a pressure swing adsorption model for air separation using multi-objective optimisation and support vector regression model. *Expert Systems with Applications*, 40(11):4496–4502, 2013.
- [4] Hamdi Aguir, Hédi BelHadjSalah, and Ridha Hambli. Parameter identification of an elasto-plastic behaviour using artificial neural networks–genetic algorithm method. *Materials & Design*, 32(1):48–53, 2011.

- [5] Eckart Zitzler and Lothar Thiele. *An evolutionary algorithm for multiobjective optimization: The strength Pareto approach*. Number 43. Citeseer, 1998.
- [6] Eckart Zitzler, Kalyanmoy Deb, and Lothar Thiele. Comparison of multiobjective evolutionary algorithms: Empirical results. *Evolutionary computation*, 8(2):173–195, 2000.
- [7] David A. Van Veldhuizen. *Multiobjective Evolutionary Algorithms: Classifications, Analyses, and New Innovations*. Technical report, Evolutionary Computation, 1999.
- [8] JD Knowles. Approximating the nondominated front using the Pareto archived evolution strategy. *Evolutionary computation*, pages 1–35, 2000.
- [9] Kalyanmoy Deb, Dhiraj Joshi, and Ashish Anand. *Real-Coded Evolutionary Algorithms with Parent-Centric Recombination*. 2001.
- [10] Kalyanmoy Deb and Tushar Goel. A hybrid multi-objective evolutionary approach to engineering shape design. *Lecture notes in computer science*, 2001.
- [11] a Konak, D Coit, and a Smith. Multi-objective optimization using genetic algorithms: A tutorial. *Reliability Engineering & System Safety*, 91(9):992–1007, September 2006.
- [12] Kalyanmoy Deb, Amrit Pratap, Sameer Agarwal, and T. Meyarivan. A Fast Elitist Multi-Objective Genetic Algorithm: NSGA-II. *IEEE Transactions on Evolutionary Computation*, 6:182–197, 2000.
- [13] Eckart Zitzler, Marco Laumanns, and Lothar Thiele. SPEA2: Improving the strength Pareto evolutionary algorithm. *Computer Engineering*, pages 1–21, 2001.
- [14] Joshua Knowles. The pareto archived evolution strategy: A new baseline algorithm for pareto multiobjective optimisation. *Evolutionary Computation*, 1999. *CEC*, 1999.
- [15] D Corne and J Knowles. The Pareto envelope-based selection algorithm for multiobjective optimization. *Problem Solving from Nature PPSN VI*, (Mcdm), 2000.
- [16] DW Corne, NR Jerram, and JD Knowles. PESA-II: Region-based selection in evolutionary multiobjective optimization. *Genetic and Evolutionary*, 2001.
- [17] Kent Salomonsson and Tobias Andersson. Modeling and parameter calibration of an adhesive layer at the meso level. *Mechanics of Materials*, 40(1):48–65, 2008.
- [18] N. Stromberg K. Amouzgar, A. Rashid. Multi-Objective Optimization of a Disc Brake System by using SPEA2 and RBFN. In *Proceedings of the ASME 2013 International Design Engineering Technical Conferences*, volume 3 B, Portland, OR, August 4-7 2013. American Society of Mechanical Engineers.
- [19] Anders Klarbring. Derivation of a model of adhesively bonded joints by the asymptotic expansion method. *International Journal of Engineering Science*, 29(4):493–512, 1991.
- [20] Tobias Andersson and Ulf Stigh. The stress–elongation relation for an adhesive layer loaded in peel using equilibrium of energetic forces. *International Journal of Solids and Structures*, 41(2):413–434, 2004.
- [21] KS Alfredsson, Anders Biel, and K Leffler. An experimental method to determine the complete stress-deformation relation for a structural adhesive layer loaded in shear. In *Proceedings of the 9th international conference on the mechanical behaviour of materials, Geneva, Switzerland*, 2002.

Large-scale robust topology optimization under load-uncertainty

Carl-Johan Thore¹, Erik Holmberg², Anders Klarbring³

¹ Division of Solid Mechanics, Linköping University, Linköping, Sweden, carl-johan.thore@liu.se

² Saab AB, Linköping, Sweden, erik.holmberg@saabgroup.com

³ Division of Solid Mechanics, Linköping University, Linköping, Sweden, anders.klarbring@liu.se

1. Abstract

Structures designed by topology optimization (TO) are frequently sensitive to loads different from the ones accounted for in the optimization. In extreme cases this means that loads differing ever so slightly from the ones it was designed to carry may cause a structure to collapse. It is therefore clear that handling uncertainty regarding the actual loadings is important. To address this issue in a systematic manner is one of the main goals in the field of robust TO. In this work we present a deterministic robust formulation of TO for maximum stiffness design which accounts for uncertain variations around a set of nominal loads. The idea is to find a design which minimizes the maximum compliance obtained as the loads vary in infinite, so-called uncertainty sets. This naturally gives rise to a semi-infinite optimization problem, which we here reformulate into a non-linear, semi-definite program. With appropriate numerical algorithms this optimization problem can be solved at a cost similar to that of solving a standard multiple load-case TO problem with the number of loads equal to the number of spatial dimensions plus one, times the number of nominal loads. In contrast to most previously suggested methods, which can only be applied to small-scale problems, the presented method is – as illustrated by a numerical example – well-suited for large-scale TO problems.

2. Keywords: Robust optimization, Topology optimization, Large-scale optimization, Non-linear semi-definite programming

3. Introduction

Robust problem formulations in structural optimization can be divided into two groups [3]: (i) *stochastic* and (ii) *deterministic*, or worst-case. The stochastic approach is perhaps the most common. It can essentially be divided into two classes: reliability-based methods [15], often based on an inner loop where the structure is optimized and an outer loop where the uncertainty parameters are modified, and "sampling-based" methods, where the stochastic problem is converted into a deterministic by sampling from a probability distribution [10]. A drawback of stochastic methods is their reliance on good statistical data, and, in certain applications more importantly [3], they only provide probabilistic guarantees of robustness.

In this paper we consider robust deterministic topology optimization of discretized continuum bodies governed by a linear equilibrium equation of the form

$$K\mathbf{u} = \mathbf{f}_0 + \mathbf{f}_{var}$$

where \mathbf{f}_0 is a given fixed load and \mathbf{f}_{var} is allowed to vary in some uncertainty set. The special case when $\mathbf{f}_0 = \mathbf{0}$ has been treated in both finite- and infinite-dimensional settings by several authors [2, 8, 17, 5, 13]. The general case with a non-zero \mathbf{f}_0 is however less explored. Ben-Tal et al. [3, p. 215] showed how to formulate the problem as a semi-definite program, which was however not suitable for large-scale problems (see also [7]). Kanno [14] proposed an optimization problem in the form of a mathematical program with equilibrium constraints (MPEC). That formulation resembles the so-called simultaneous formulation in traditional stiffness optimization [9] involving the equilibrium equation as an explicit constraint; consequently it may be difficult to solve large-scale instances of the MPEC-formulation. To the authors' knowledge, the only paper dealing with large-scale, deterministic robust structural optimization is [12]. Therein the authors propose a special algorithm to solve a generalized, inhomogeneous eigenvalue problem arising from the maximization of the compliance. That algorithm however requires up to 15 factorizations of a system matrix (involving the stiffness matrix) for each design, while the method we propose requires just one. In addition, the method proposed herein is readily implemented using standard linear solvers and software for non-linear programming.

In the following the space of symmetric $n \times n$ matrices with real entries is denoted \mathbb{S}^n . For \mathbf{A} and \mathbf{B} in \mathbb{S}^n , " $\mathbf{A} \succeq \mathbf{B}$ " (" $\mathbf{A} \succ \mathbf{B}$ ") means that $\mathbf{A} - \mathbf{B}$ is positive semi-definite (positive definite). The set of symmetric, positive

semi-definite matrices is denoted \mathbb{S}_+^n . The Euclidean vector norm is denoted $\|\cdot\|$, \mathbb{R}_+ is the set of non-negative real numbers, and \mathbf{I} denotes an identity matrix of appropriate size.

4. The model

We consider a linearly elastic continuum body divided into m elements. Associated with each element is a design variable x_i which determines whether there is material in the element or not. The design variables are collected in a vector \mathbf{x} of length m . To avoid numerical issues such as checkerboards and mesh dependency a different set of variables, referred to as physical variables, are used to compute the stiffness matrix (and mass). These variables are related to the design variables through a so-called filter [6], using which the i -th physical variable is written as

$$\rho_i(\mathbf{x}) = \sum_{j=1}^m \Psi_{ij} x_j, \quad \Psi_{ij} = \frac{\phi_{ij} v_j}{\sum_{k=1}^m \phi_{ik} v_k}, \quad \phi_{ij} = \max(0, R - \|\mathbf{e}_i - \mathbf{e}_j\|),$$

where v_j and \mathbf{e}_j denotes the volume and the position of the geometric center, respectively, of element j , and R is the filter radius.

The structure is assumed to be in quasi-static equilibrium undergoing small deformations when subject to a nodal load vector \mathbf{f}_r . By the standard displacement-based FEM the nodal displacement vector \mathbf{u} should therefore satisfy

$$\mathbf{K}(\mathbf{x})\mathbf{u} = \mathbf{f}_r, \quad (1)$$

where, following the SIMP-approach to TO, the stiffness matrix $\mathbf{K}(\mathbf{x}) = \sum_{i=1}^m \rho_i(\mathbf{x})^p \mathbf{K}_i$, in which p is a positive constant and $\mathbf{K}_i \in \mathbb{S}_+^n$ are element stiffness matrices. Here n denotes the number of degrees of freedom. We assume that rigid body motions are prevented, so $\mathbf{K}(\mathbf{1}) \succ \mathbf{0}$, where $\mathbf{1}$ is a vector of ones.

The load vector in (1) is defined as

$$\mathbf{f}_r = \mathbf{f}_0 + \mathbf{B}^\top \mathbf{r}, \quad (2)$$

where $\mathbf{r} \in T = \{\mathbf{r} \in \mathbb{R}^d \mid \|\mathbf{r}\| \leq 1\}$, with d the number of spatial dimensions. The vector \mathbf{f}_0 , the nominal load, is fixed during optimization, while $\mathbf{B}^\top \mathbf{r}$, where $\mathbf{B}^\top \in \mathbb{R}^{n \times d}$, is allowed to vary — it is through this variation that uncertainty is accounted for. The (fixed) matrix \mathbf{B} can be used to specify which nodes are subject to load-uncertainty, and in which direction the uncertainty (if any) is greatest.

5. Optimization problem

We begin by defining the worst-case compliance as

$$\max_{\mathbf{r} \in T} \mathbf{f}_r^\top \mathbf{u}_r(\mathbf{x}), \quad (3)$$

where $\mathbf{u}_r(\mathbf{x})$ solves (1). Assuming constant density, the problem of minimizing the worst-case compliance with an upper bound on the weight can now be written as

$$\min_{\mathbf{x} \in \mathcal{H}} \max_{\|\mathbf{r}\| \leq 1} \mathbf{f}_r^\top \mathbf{K}(\mathbf{x})^{-1} \mathbf{f}_r,$$

where $\mathcal{H} = \{\mathbf{x} \in \mathbb{R}^m \mid \varepsilon \leq x_i \leq 1, i = 1, \dots, m, \sum_{i=1}^m v_i \rho_i(\mathbf{x}) \leq v\}$, in which the positive constant v is the upper bound on the volume. The small positive constant ε ensures that the stiffness matrix is positive definite if the structure is appropriately supported.

A natural thing to do when confronted with a min-max problem is to reformulate it into a bound formulation:

$$\begin{aligned} & \min_{\mathbf{x} \in \mathcal{H}, z \in \mathbb{R}_+} z \\ & \text{subject to } \mathbf{f}_r^\top \mathbf{K}(\mathbf{x})^{-1} \mathbf{f}_r \leq z, \quad \forall \mathbf{r} \in \mathbb{R}^d : \|\mathbf{r}\| \leq 1, \end{aligned} \quad (4)$$

where z is an additional variable and ”:” should be read as ”such that”. Since there is now an infinite number of constraints it is not immediately clear that anything has been gained from this reformulation. However, the semi-infinite problem (4) can be reformulated as a non-linear semi-definite program using the following result.

Theorem 1. $\mathbf{f}_r^\top \mathbf{K}(\mathbf{x})^{-1} \mathbf{f}_r \leq z$ for all $\mathbf{r} \in \mathbb{R}^d : \|\mathbf{r}\| \leq 1$ if and only if there exists a $\lambda \in \mathbb{R}_+$ such that

$$\begin{pmatrix} \lambda \mathbf{I} & \mathbf{0} \\ \mathbf{0} & z - \lambda \end{pmatrix} - \begin{pmatrix} \mathbf{B} \\ \mathbf{f}_0^\top \end{pmatrix} \mathbf{K}(\mathbf{x})^{-1} \begin{pmatrix} \mathbf{B}^\top \mathbf{f}_0 \end{pmatrix} \succeq \mathbf{0}.$$

To prove Theorem 1 we use two lemmas:

Lemma 1. [S-lemma] (See [3, p. 483] for a proof.) For \mathbf{A}_1 and \mathbf{A}_2 in \mathbb{S}^n , with $\mathbf{y}_0^\top \mathbf{A}_1 \mathbf{y}_0 > 0$ for some \mathbf{y}_0 ,

$$\mathbf{y}^\top \mathbf{A}_1 \mathbf{y} \geq 0 \Rightarrow \mathbf{y}^\top \mathbf{A}_2 \mathbf{y} \geq 0 \Leftrightarrow \exists \lambda \in \mathbb{R}_+ : \mathbf{A}_2 \succeq \lambda \mathbf{A}_1.$$

Lemma 2. For $\mathbf{A} \in \mathbb{R}^{n \times n}$,

$$\begin{pmatrix} \mathbf{y} \\ 1 \end{pmatrix}^\top \begin{pmatrix} \mathbf{A} & \mathbf{b} \\ \mathbf{b}^\top & c \end{pmatrix} \begin{pmatrix} \mathbf{y} \\ 1 \end{pmatrix} \geq 0 \quad \forall \mathbf{y} : \|\mathbf{y}\|^2 \leq 1 \Leftrightarrow \begin{pmatrix} \mathbf{y} \\ w \end{pmatrix}^\top \begin{pmatrix} \mathbf{A} & \mathbf{b} \\ \mathbf{b}^\top & c \end{pmatrix} \begin{pmatrix} \mathbf{y} \\ w \end{pmatrix} \geq 0 \quad \forall (\mathbf{y}, w) : \|\mathbf{y}\|^2 \leq w^2.$$

Proof. The implication from right to left follows immediately by taking $w = 1$. Now consider going from left to right, beginning with

$$\begin{pmatrix} \mathbf{y} \\ 1 \end{pmatrix}^\top \begin{pmatrix} \mathbf{A} & \mathbf{b} \\ \mathbf{b}^\top & c \end{pmatrix} \begin{pmatrix} \mathbf{y} \\ 1 \end{pmatrix} = \mathbf{y}^\top \mathbf{A} \mathbf{y} + 2\mathbf{b}^\top \mathbf{y} + c \geq 0 \quad \forall \mathbf{y} : \|\mathbf{y}\|^2 \leq 1. \quad (5)$$

Let $\mathbf{y} = \mathbf{u}/w$, with $\|\mathbf{u}\|^2 \leq w^2$ and $w \neq 0$. Clearly $\|\mathbf{y}\|^2 = \|\mathbf{u}/w\|^2 = \|\mathbf{u}\|^2/w^2 \leq 1$. Substituting $\mathbf{y} = \mathbf{u}/w$ in (5) gives

$$\mathbf{u}^\top \mathbf{A} \mathbf{u} + 2\mathbf{b}^\top \mathbf{u} w + cw^2 \geq 0, \quad \forall (\mathbf{u}, w) : \|\mathbf{u}\|^2 \leq w^2, w \neq 0.$$

Going back to the statement of the lemma it is clear that $w = 0$ implies $\mathbf{y} = \mathbf{0}$, reducing the right side to the trivial inequality $0 \geq 0$. \square

Proof of Theorem 1. Straightforward algebraic manipulations show that (the argument "x" is omitted)

$$\begin{aligned} \mathbf{f}_r^\top \mathbf{K}^{-1} \mathbf{f}_r &\leq z, & \forall \mathbf{r} \in \mathbb{R}^d : \|\mathbf{r}\| \leq 1 &\Leftrightarrow \\ z - \mathbf{f}_0^\top \mathbf{K}^{-1} \mathbf{f}_0 - \mathbf{r}^\top \mathbf{B} \mathbf{K}^{-1} \mathbf{B}^\top \mathbf{r} - 2\mathbf{r}^\top \mathbf{B} \mathbf{K}^{-1} \mathbf{f}_0 &\geq 0 & \forall \mathbf{r} \in \mathbb{R}^d : \|\mathbf{r}\| \leq 1. \end{aligned}$$

By Lemma 2 the last statement is equivalent to

$$w^2(z - \mathbf{f}_0^\top \mathbf{K}^{-1} \mathbf{f}_0) - \mathbf{y}^\top \mathbf{B} \mathbf{K}^{-1} \mathbf{B}^\top \mathbf{y} - 2\mathbf{y}^\top \mathbf{B} \mathbf{K}^{-1} \mathbf{f}_0 w \geq 0, \quad \forall (\mathbf{y}, w) \in \mathbb{R}^{d+1} : \|\mathbf{y}\|^2 \leq w^2. \quad (6)$$

Since the condition $\|\mathbf{y}\|^2 \leq w^2$ can be written as

$$\begin{pmatrix} \mathbf{y} \\ w \end{pmatrix}^\top \mathbf{A}_1 \begin{pmatrix} \mathbf{y} \\ w \end{pmatrix} \geq 0, \quad \text{where } \mathbf{A}_1 = \begin{pmatrix} -\mathbf{I} & \mathbf{0} \\ \mathbf{0} & 1 \end{pmatrix},$$

Lemma 1 can be invoked to conclude that (6) is equivalent to

$$\exists \lambda \in \mathbb{R}_+ : \begin{pmatrix} \lambda \mathbf{I} & \mathbf{0} \\ \mathbf{0} & z - \lambda \end{pmatrix} - \begin{pmatrix} \mathbf{B} \\ \mathbf{f}_0^\top \end{pmatrix} \mathbf{K}^{-1} (\mathbf{B}^\top \mathbf{f}_0) \succeq \mathbf{0}.$$

\square

Remark. A different proof of Theorem 1 can be obtained by using Theorem 8.2.3 in [3] together with the Schur-complement theorem [3, Lemma 6.3.4]. By the former theorem one can also obtain a formulation where \mathbf{K} need not be invertible [7, Proposition 2],[3, p. 215]; the price to pay is a matrix inequality of large size, something which is, at present, difficult to handle numerically.

Using Theorem 1 we now replace (4) by the following problem:

$$\begin{aligned} \min_{\mathbf{x} \in \mathcal{H}, z \in \mathbb{R}_+, \lambda \in \mathbb{R}_+} \quad & z \\ \text{subject to} \quad & \begin{pmatrix} \lambda \mathbf{I} & \mathbf{0} \\ \mathbf{0} & z - \lambda \end{pmatrix} - \begin{pmatrix} \mathbf{B} \\ \mathbf{f}_0^\top \end{pmatrix} \mathbf{K}(\mathbf{x})^{-1} (\mathbf{B}^\top \mathbf{f}_0) \succeq \mathbf{0}. \end{aligned} \quad (7)$$

It can be shown [4, Prop. 5.72 (i)] that if \mathbf{K} is linear in \mathbf{x} , the matrix inequality defines a convex set, making (7) a convex problem. An extension to include multiple loads, each in the form of a nominal load plus an uncertainty, is straightforward, but for notational simplicity we have refrained from doing this here.

Theorem 2. The set of globally optimal solutions to (7) is non-empty and compact.

Proof. Take $\mathbf{x}_0 \in \mathcal{H}$ and let

$$\mathbf{A}(\mathbf{x}) = \begin{pmatrix} \mathbf{B} \\ \mathbf{f}_0^\top \end{pmatrix} \mathbf{K}(\mathbf{x})^{-1} (\mathbf{B}^\top \mathbf{f}_0), \quad (8)$$

and $\mathbf{A}_0 = \mathbf{A}(\mathbf{x}_0)$. Let $\lambda_0 = \lambda_{max}(\mathbf{A}_0) \geq 0$ and $z_0 = 2\lambda_{max}(\mathbf{A}_0) \geq 0$, where $\lambda_{max}(\cdot)$ denotes the maximum eigenvalue. The inequality

$$\mathbf{A}_0 \preceq \lambda_{max}(\mathbf{A}_0)\mathbf{I} = \begin{pmatrix} \lambda_0\mathbf{I} & \mathbf{0} \\ \mathbf{0} & z_0 - \lambda_0 \end{pmatrix},$$

then shows that the feasible set of (7) is non-empty.

The inequality $\mathbf{A}(\mathbf{x}) \succeq \mathbf{0}$ holds for all $\mathbf{x} \in \mathcal{H}$ and implies that $z \geq \lambda$ for any feasible (\mathbf{x}, z, λ) . The globally optimal solutions to (7) are thus contained in the set

$$\mathcal{F} = \{(\mathbf{x}, z, \lambda) \mid \mathbf{x} \in \mathcal{H}, 0 \leq z \leq z_0, 0 \leq \lambda \leq z_0, (\mathbf{x}, z, \lambda) \text{ satisfies the matrix inequality in (7)}\}.$$

We now consider the problem

$$\min_{(\mathbf{x}, z, \lambda) \in \mathcal{F}} z,$$

which has the same set of globally optimal solutions as (7). Since \mathcal{F} is the intersection of a compact and a closed set, hence compact, and the objective function is lower semi-continuous, existence of a non-empty, compact set of globally optimal solutions follows from Weierstrass' theorem [1, Theorem 4.7]. \square

The proof of Theorem 2 shows how a feasible initial point for (7) may be chosen, and provides upper bounds on z and λ .

Remark. The worst-case uncertainty vector, and therefore the worst-case load vector \mathbf{f}_r , depends on the design through

$$\mathbf{r}(\mathbf{x}) \in \arg \max_{\|\mathbf{r}\| \leq 1} (\mathbf{r}^\top \mathbf{B} + \mathbf{f}_0^\top) \mathbf{K}(\mathbf{x})^{-1} (\mathbf{f}_0 + \mathbf{B}^\top \mathbf{r}) = \arg \max_{\|\mathbf{r}\| \leq 1} \left[\mathbf{r}^\top \mathbf{H}(\mathbf{x}) \mathbf{r} + 2\mathbf{f}_0^\top \mathbf{K}(\mathbf{x})^{-1} \mathbf{B}^\top \mathbf{r} \right],$$

where $\mathbf{H}(\mathbf{x}) = \mathbf{B} \mathbf{K}(\mathbf{x})^{-1} \mathbf{B}^\top$. The first-order necessary optimality conditions for this problem read

$$\mathbf{H}(\mathbf{x}) \mathbf{r} - \mathbf{b}(\mathbf{x}) = \mu \mathbf{r}, \quad \|\mathbf{r}\| = 1, \quad (9)$$

where $\mathbf{b}(\mathbf{x}) = -2\mathbf{B} \mathbf{K}(\mathbf{x})^{-1} \mathbf{f}_0$ and $\mu \in \mathbb{R}_+$ is a Lagrange multiplier. (9) is an inhomogeneous eigenvalue problem [16]; $\mathbf{r}(\mathbf{x})$ is an eigenvector associated with the maximum eigenvalue. Since the multiplicity of the latter may be greater than one we do not expect $\mathbf{x} \rightarrow \mathbf{r}(\mathbf{x})$ to be smooth in general.

6. Numerical treatment

To evaluate the left-hand side of the matrix constraint, rather than forming $\mathbf{K}(\mathbf{x})^{-1}$ explicitly, we solve the linear system

$$\mathbf{K}(\mathbf{x}) \mathbf{U} = (\mathbf{B}^\top \mathbf{f}_0) \quad (10)$$

for $\mathbf{U} \in \mathbb{R}^{n \times (d+1)}$. The computational cost, which is dominated by the factorization of $\mathbf{K}(\mathbf{x})$, for this is the same as that of solving the equilibrium equations in a standard multiple-load case formulation with $d+1$ loads.

Scaling is important when solving optimization problems numerically. To this end, in view of the proof of Theorem 2, we introduce new variables $z := z/z_0$ and $\lambda := \lambda/z_0$, where $z_0 = 2\lambda_{max}(\mathbf{A}_0)$, with \mathbf{A}_0 defined in the proof of Theorem 2. Now (7) can be replaced by

$$\begin{aligned} & \min_{\mathbf{x} \in \mathcal{H}, z \in [0,1], \lambda \in [0,1]} z \\ & \text{subject to} \quad \begin{pmatrix} \lambda \mathbf{I} & \mathbf{0} \\ \mathbf{0} & z - \lambda \end{pmatrix} - \frac{1}{z_0} \begin{pmatrix} \mathbf{B} \\ \mathbf{f}_0^\top \end{pmatrix} \mathbf{U}(\mathbf{x}) \succeq \mathbf{0}. \end{aligned} \quad (11)$$

where $\mathbf{U}(\mathbf{x})$ denotes the solution to (10).

Problem (11) is converted into an ordinary non-linear optimization problem (NLP) by noting that $\mathbb{S}_+^q \ni \mathbf{A} \Leftrightarrow \exists \mathbf{L} \in \mathcal{L}^q : \mathbf{A} = \mathbf{L} \mathbf{L}^\top$, where \mathcal{L}^q denotes the set of lower triangular $q \times q$ -matrices with non-negative diagonal entries. This leads to the problem

$$\begin{aligned} & \min_{\mathbf{x} \in \mathcal{H}, z \in [0,1], \lambda \in [0,1], \mathbf{L} \in \mathcal{L}_{[-1,1]}^{d+1}} z \\ & \text{subject to} \quad \begin{pmatrix} \lambda \mathbf{I} & \mathbf{0} \\ \mathbf{0} & z - \lambda \end{pmatrix} - \frac{1}{z_0} \begin{pmatrix} \mathbf{B} \\ \mathbf{f}_0^\top \end{pmatrix} \mathbf{U}(\mathbf{x}) = \mathbf{L} \mathbf{L}^\top, \end{aligned} \quad (12)$$

where $\mathcal{L}_{[-1,1]}^{d+1}$ denotes the set of lower triangular $q \times q$ -matrices with each diagonal entry in $[0, 1]$ and each off-diagonal entry in $[-1, 1]$. These bounds are motivated by the fact that

$$\begin{pmatrix} \lambda \mathbf{I} & \mathbf{0} \\ \mathbf{0} & z - \lambda \end{pmatrix} - \frac{1}{z_0} \begin{pmatrix} \mathbf{B} \\ \mathbf{f}_0^\top \end{pmatrix} \mathbf{U}(\mathbf{x}) \preceq \mathbf{I},$$

which holds since $\lambda \leq 1$ and $z \leq 1$ and the second matrix to the left is positive semi-definite [recall (8)]. At a feasible point then, $\mathbf{L}\mathbf{L}^\top \preceq \mathbf{I}$, showing that the diagonal elements of $\mathbf{L}\mathbf{L}^\top - \mathbf{I}$ must be non-positive. The latter implies the aforementioned bounds on the entries of \mathbf{L} .

A theoretical drawback of the NLP-formulation (12) is that it might have stationary points not present in problem (11). In practise we have however never experienced convergence to such points, and this theoretical drawback therefore outweighs practical drawbacks of e.g. PENLAB [11] which requires evaluation of second-order derivatives.

7. Numerical example

Figure 1 shows a numerical example. The ground structure is a cylinder, meshed with $m = 14640$ 8-node hexahedral elements, resulting in a total of $n = 46800$ displacement degrees of freedom. Problem (12) is solved with the

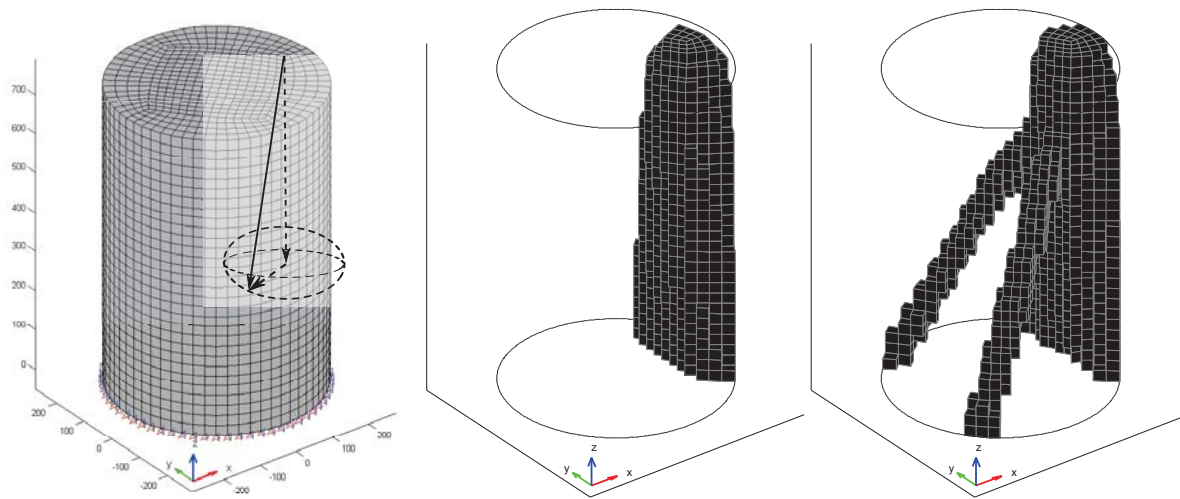


Figure 1: Numerical example. Left: Ground structure, with dimensions in [mm]. The figure shows the total load as the sum of a nominal load (dashed arrow in negative z -direction) and an uncertain part which varies in the sphere. Middle: Minimum compliance design for a single load case. Right: Worst-case compliance design.

code `fminsdp` for non-linear SDPs [18], using `Ipopt` [19] as NLP-solver. First-order derivatives of the non-linear part of the matrix constraint are computed using the adjoint method [9], and `Ipopt`'s limited-memory quasi-Newton approximation, with 90 correction pairs, is used for the Hessian of the Lagrangian. The update strategy for the barrier parameter is set to "adaptive", and default settings used otherwise.

A load of 1000 [N] applied at the top of the structure pointing in the negative z -direction is used as the nominal load, and in the robust formulation we allow for variations of up to 100 [N] in each coordinate direction, i.e. the matrix $\mathbf{B} \in \mathbb{R}^{3 \times 46800}$ in (2) is given by $\mathbf{B} = (\mathbf{0} \ 100\mathbf{I} \ \mathbf{0})$, where \mathbf{I} is a three-by-three identity matrix positioned at the degrees of freedoms associated with the loaded node.

The middle plot in Fig. 1 shows a design obtained when uncertainty is not accounted for; the result is a curved column. The right plot shows a designed obtained when taking load variations into account. Now the column is supported by two legs – intuitively a more robust design.

8. Concluding remarks

We have presented a problem formulation for deterministic worst-case compliance design in the form of a non-linear semi-definite program whose computational cost is similar to that of solving an ordinary minimum compliance problem with three (in 2D) or four (in 3D) load cases. The optimization problems are readily solved using software for ordinary NLPs.

9. Acknowledgements

This research was supported in part by the Swedish Foundation for Strategic Research, Grant No. AM13-0029, and NFFP Grant No. 2013-01221, which is funded by the Swedish Armed Forces, the Swedish Defence Materiel Administration and the Swedish Governmental Agency for Innovation Systems.

10. References

- [1] N Andréasson, A Evgrafov, and M Patriksson. *An Introduction to Continuous Optimization*. Studentlitteratur, 2005.
- [2] A Ben-Tal and A Nemirovski. Robust truss topology design via semidefinite programming. *SIAM Journal on Optimization*, 7:991–1016, 1997.
- [3] A Ben-Tal, L El Ghaoui, and AS Nemirovski. *Robust Optimization*. Princeton Series in Applied Mathematics. Princeton University Press, 2009.
- [4] JF Bonnans and A Shapiro. *Perturbation Analysis of Optimization Problems*. Springer, 2000.
- [5] K Brittain, M Silva, and DA Tortorelli. Minmax topology optimization. *Structural and Multidisciplinary Optimization*, 45(5):657–668, 2012.
- [6] TE Bruns and DA Tortorelli. Topology optimization of non-linear elastic structures and compliant mechanisms. *Computer Methods in Applied Mechanics and Engineering*, 190(26):3443–3459, 2001.
- [7] GC Calafiore and F Dabbene. Optimization under uncertainty with applications to design of truss structures. *Structural and Multidisciplinary Optimization*, 35(3):189–200, 2008.
- [8] E Cherkaev and A Cherkaev. Minimax optimization problem of structural design. *Computers & Structures*, 86(13):1426–1435, 2008.
- [9] PW Christensen and A Klarbring. *An Introduction to Structural Optimization*. Springer, 2009.
- [10] PD Dunning and HA Kim. Robust topology optimization: Minimization of expected and variance of compliance. *AIAA Journal*, 51(11):2656–2664, 2013.
- [11] J Fiala, M Kočvara, and M Stingl. PENLAB: A MATLAB solver for nonlinear semidefinite optimization. *pre-print*, 2013.
- [12] F Gournay, G Allaire, and F Jouve. Shape and topology optimization of the robust compliance via the level set method. *ESAIM Control, Optimisation and Calculus of Variations*, 14(01):43–70, 2008.
- [13] E Holmberg, C-J Thore, and A Klarbring. Worst-case topology optimization using semi-definite programming. In A Eriksson, A Kulachenko, M Mihaescu, and G Tibert, editors, *27th Nordic Seminar on Computational Mechanics*, pages 280–283, 2014.
- [14] Y Kanno. An implicit formulation of mathematical program with complementarity constraints for application to robust structural optimization. *Journal of the Operations Research Society of Japan*, 54(2):65, 2011.
- [15] G Kharmanda, N Olhoff, A Mohamed, and M Lemaire. Reliability-based topology optimization. *Structural and Multidisciplinary Optimization*, 26(5):295–307, 2004.
- [16] RMM Mattheij and G Söderlind. On inhomogeneous eigenvalue problems. i. *Linear Algebra and its Applications*, 88-89(0):507 – 531, 1987.
- [17] A Takezawa, S Nii, M Kitamura, and N Kogiso. Topology optimization for worst load conditions based on the eigenvalue analysis of an aggregated linear system. *Computer Methods in Applied Mechanics and Engineering*, 200(25):2268–2281, 2011.
- [18] C-J Thore. *Fminsdp – a code for solving optimization problems with matrix inequality constraints*, 2013. <http://www.mathworks.com/matlabcentral/fileexchange/43643-fminsdp>.
- [19] A Wächter and LT Biegler. On the implementation of a primal-dual interior point filter line search algorithm for large-scale nonlinear programming. *Mathematical programming*, 106:25–27, 2006.

Assessing sensitivities of maneuver load alleviation parameters on buckling reserve factors using surrogate model based extended Fourier amplitude sensitivity test

Rahmetalla Nazzeri¹, Frank Lange², Matthias Haupt³, Christophe Sebastien⁴

¹ Technical University of Braunschweig, Braunschweig, Germany, r.nazzeri@tu-bs.de

² Airbus Operations GmbH, Hamburg, Germany, frank.lange@airbus.com

³ Technical University of Braunschweig, Braunschweig, Germany, m.haupt@tu-bs.de

⁴ Airbus Operations S.A.S., Toulouse, France, christophe.sebastien@airbus.com

1. Abstract

To assess the impact of maneuver load alleviation parameter changes on the buckling reserve factor a multidisciplinary high fidelity analysis is necessary. To this end flight maneuver calculation, linear static analysis using a global Finite Element Model and a structural sizing need to be performed. The use of surrogate modeling techniques helps to avoid the time consuming high fidelity analysis but still provides accurate results. In the frame of global sensitivity analysis the surrogate model is used to apply variance based extended Fourier amplitude sensitivity test. The contribution of input parameter variation of the maneuver load alleviation system to the variance of the surrogate model output in terms of buckling reserve factors is measured. The sensitivity study is performed on the upper cover of a backward swept composite wing and the results are compared to those of the high fidelity analysis. Note that the variation of maneuver load alleviation parameters is nowadays assessed by external loads resulting from the flight maneuver calculation only. The presented approach includes reserve factors and hence provides an insight into the structural response. In this way those maneuver load alleviation parameters are found that affect the structure in terms of buckling reserve factors the most and can be used for future design changes and weight reductions.

2. Keywords: Surrogate model, sensitivity analysis, maneuver load alleviation, buckling, reserve factor

3. Introduction

Recent developments in the field of multidisciplinary analysis have led to an increased investigation of Maneuver Load Alleviation (MLA) effects on the aircraft wing [7]. Especially during early design phase of the aircraft the use of an active load alleviation system has a significant impact on the overall aircraft design and flight performance evaluation [8]. In this scope the present work demonstrates a surrogate model based sensitivity analysis on MLA parameters for the wing upper cover. The surrogate model is constructed using an already existing data basis which contains MLA parameter values and local skin buckling Reserve Factor (*RF*) values provided by the Airbus Operations GmbH. Note that the preparation of such a data basis takes in general several months and includes the work of different departments and disciplines. Figure 1 demonstrates how the high fidelity process looks like and in which way this long process is replaced by a surrogate model.

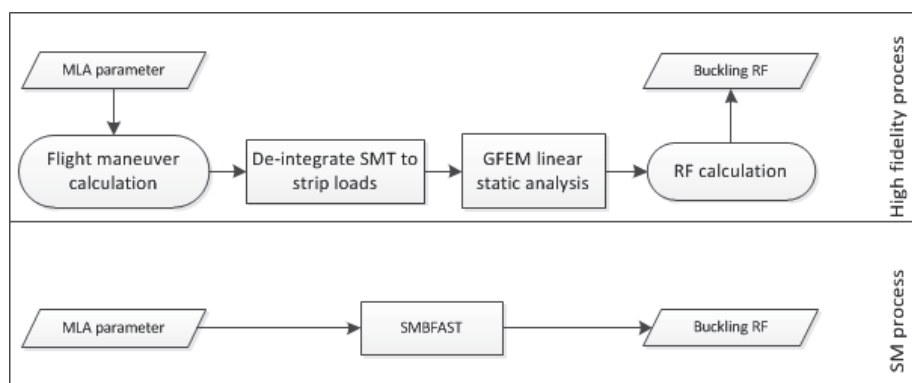


Figure 1: High fidelity versus surrogate model process overview

The surrogate model replaces the flight maneuver calculation, the de-integration of the Shear Moment Torque (SMT) values to strip loads along the wing and the linear static analysis using a Global Finite Element Model (GFEM), which consists of 1- and 2-dimensional elements, and finally the *RF* calculation.

High Dimensional Approximation (HDA) is used for the construction of the surrogate model and is based on the works of [5] and [6]. HDA uses a linear expansion of non-linear functions and works in a similar way as artificial neural networks. Internal validation of the surrogate model is performed using the concept of cross validation and the Root Mean Square (RMS) error as a failure index. The constructed surrogate model can be used to assess the effect of MLA parameter changes on the structure in terms of RF quickly. Previous works from [3] and [4] have shown a proper use of extended Fourier Amplitude Sensitivity Test (eFAST) applied on a surrogate model in order to perform sensitivity analysis. The combined use of both approximation and sensitivity analysis technique is called Surrogate Model Based Fourier Amplitude Sensitivity Test (SMBFAST).

4. Maneuver load alleviation vs local skin buckling reserve factor

The MLA is used for the reduction of the loads acting on the wing during flight maneuvers. For this purpose the vertical load factor n_z at center of gravity is measured by an accelerometer and is compared against a threshold value. If the threshold value is reached inner and outer ailerons are deflected upwards for positive n_z values. For negative n_z values the ailerons are deflected downwards. The aileron deflections lead to a redistribution of the lift along the wing with an additional reduction of the wing bending moment. This effect is shown on a simple example in Figure 2 for the left wing of a schematic passenger aircraft. Here the aileron upward deflections shift the center of pressure inboards which yield a reduction of the wing root bending moment. Note that the resulting pitching moments are compensated with additional deflections of the elevators included in the MLA law.

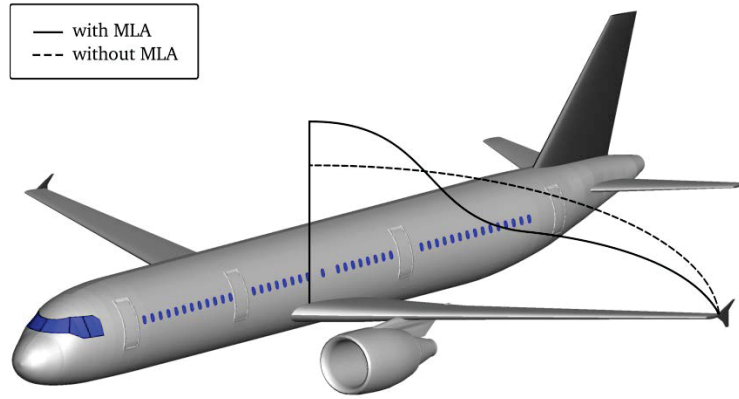


Figure 2: Schematic change of lift distribution with and without MLA

The MLA is integrated into the flight maneuver calculation software at Airbus and consists of different control laws depending on the flight condition. The load factor is the main driving parameter for the activation of the MLA and in addition positive/negative load factor values steer the upward/downward deflection of the ailerons. But still the available control laws prescribe aileron deflections based on the Mach number Ma and calibrated airspeed v_{cas} as well. Hence in the scope of this study the chosen MLA parameters for analysis are 3 of its steering quantities and the resulting deflection angles of the inner aileron ϑ_{in} and the outer aileron ϑ_{out} . Eq. (1) shows the relationship between the SMT values by which the change of lift distribution can be seen and the MLA as a function of previous 5 parameters. The same order of MLA parameters is used for the construction of the surrogate model.

$$SMT_{MLA} = MLA(\vartheta_{in}, \vartheta_{out}, n_z, Ma, v_{cas}) \quad (1)$$

The change of the lift distribution along the wing with an active MLA leads to different wing bending moments which again influence the wing torque due to the sweep angle. This combined bending and torque leads to compression and shear loads in the skin panels of the wing upper covers while the supporting stringers are axially loaded only. The RF value is an estimator in order to evaluate if the structure can sustain these loads. The RF value is the comparison of the allowable stress value against the stress values of the applied loads, cf. Eq. (2). The structure is statically sized if the value is higher than 1 and fails for values lower than 1.

$$RF = \frac{\sigma_{allowable}}{\sigma_{applied}} \gtrless 1 \quad (2)$$

After the internal loads are computed on GFEM level many ways exist to compute the RF values during the structural sizing. For local skin buckling an analytical approach based on energy method is used for the presented

study. The different stringer bays are computed individually for local skin buckling what reduces the region of analysis to 1 stringer and 2 skin panels. The idealized stiffened panel is shown in Figure 3. The skin panels are simply supported at all edges with the stringer itself providing simply support. The approach of Rayleigh-Ritz is used then to solve the energy equation. More about the solution of stability problems is found in [10].

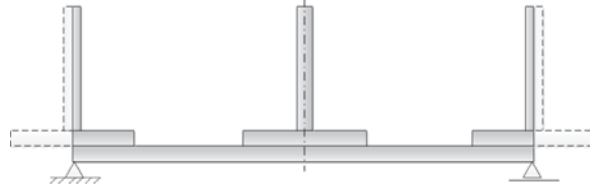


Figure 3: Schematic view of a stiffened panel

5. Surrogate model based extended Fourier amplitude sensitivity Test

In order to perform SMBFAST the software toolkit MACROS is used which is developed by the company DATADVANCE. The chosen method for the construction of the surrogate model is called HDA. Previous observations of [5] have shown superiority in time performance and accuracy compared to techniques like artificial neural networks, Kriging and radial basis functions. Unlike artificial neural networks which is based on a single type of basis functions HDA is based on linear expansion of different types of functions which are namely sigmoid, radial basis and linear functions. The linear expansion of the basis functions is done according to the approach shown in Eq. (3). Here the exact function $f(X)$ is approximated by a superimposition of mentioned basis functions φ_j and their weighting values α_j . The number of superimpositions p is estimated by a boosting algorithm until the accuracy is converging, cf. [6].

$$f(X) \approx \tilde{f}(X) = \sum_{j=1}^p \alpha_j \varphi_j(X) \quad (3)$$

For the purpose of linear expansion techniques like elastic net and regularization are used for parameter initialization and an additional hybrid learning algorithm is used to improve these initial parameters. The latter is based on regression analysis and gradient based optimization.

In order to check the accuracy of the surrogate model the data basis is partitioned into a training set n_{train} and a test set n_{test} following the principles of cross validation. The training set is used to build the model while the purpose of the latter is its validation. The RMS error is recommended by [9] for the cross validation of the surrogate model and takes into account the exact sample values y_i and the predicted values $\tilde{f}(x_i)$ as shown in Eq. (4).

$$RMS = \varepsilon(\tilde{f}(X)|X_{test}) = \sqrt{\frac{1}{n_{test}} \sum_{i=1}^{n_{test}} (y_i - \tilde{f}(x_i))^2} \quad (4)$$

eFAST is applied on the constructed surrogate model in order to assess the sensitivity of input parameter variations on the output values. eFAST is a variance decomposition method for global sensitivity analysis, cf. [3]. The presented core ideas are mainly based on the work of [1] with a proposal for computational implementation described in [2].

The variance value s^2 takes into account the model output y_i as well as its mean value \bar{y} and is an estimator for the change of the model output resulting by input changes. Eq. (5) shows the variance value in a general notation.

$$s^2 = \frac{\sum_{i=1}^n (y_i - \bar{y})^2}{n-1} \quad (5)$$

The idea using eFAST is to split the total variance value into partial variances according to the contribution of each input dimension. This variance splitting is performed in the frequency domain using a Fourier transformation of the surrogate model. The input parameters are then varied at frequencies according to [1] for which the Fourier coefficients are determined. If an input parameter has high influence on the model output the amplitude of the oscillation in the frequency domain is high. The surrogate model is expanded into a Fourier series in the frequency domain as follows:

$$\tilde{f}(s) = \sum_{k=-\infty}^{+\infty} \{A_k \cos(ks) + B_k \sin(ks)\} \quad (6)$$

Here the Fourier coefficients A_k and B_k are defined as:

$$A_k = \frac{1}{\pi} \int_{-\pi}^{\pi} \tilde{f}(s) \cos(ks) dx ; B_k = \frac{1}{\pi} \int_{-\pi}^{\pi} \tilde{f}(s) \sin(ks) dx \quad (7)$$

Using these Fourier coefficients the partial variance value s_i^2 for each input dimension is calculated in the following way:

$$s_i^2 = 2 \sum_{k=1}^{\infty} (A_k^2 + B_k^2) \quad (8)$$

Finally the main effect S_i is determined using the partial and total variance values:

$$S_i = \frac{s_i^2}{s^2} \quad (9)$$

The main effect can take values between 0 and 1 while higher values indicate more influence of the input parameter on the model output. For example a main effect value of 0.3 for an input parameter means that this parameter contributes by 30% to the total variance.

The main effect takes only the individual contribution of each input parameter variation on the model output into account. On the other hand the total effect S_{Ti} which is only available using the eFAST considers the interaction effects S_{ij} between the input parameters as well. Interaction effects quantify the impact on the output variance when multiple parameters are varied simultaneously. For instance the main effect of one input parameter can tend to zero whereas its total effect can reach high values due to its high effect on the model output in combination with another input parameter. Eq. (10) shows how the interaction effects are added to the main effect of each input dimension.

$$S_{Ti} = S_i + \sum_{j=1}^n S_{ij}, \text{ with } j \neq i \quad (10)$$

6. Available data basis for the construction of the surrogate model

The data basis for the construction of the surrogate model is provided by the Airbus Operations GmbH and consists of MLA parameter values and local skin buckling RF values. For the MLA parameters input as well as output quantities of the control law are chosen. The main input quantities that affect the results of the MLA are the load factor n_z , the Mach number Ma and the calibrated airspeed v_{cas} . The resulting inner and outer aileron deflections are taken into account as well. The RF values are computed for each skin panel of the wing upper cover but the minimum value for each load case overall skin panels is considered only.

1522 different steady longitudinal maneuvers are provided using different flight parameters and which correspond to EASA CS 25.331 requirements. The load cases are purely mechanical ones and don't consider any thermal or pressure contribution.

Table 1 summarizes the 5 different input dimensions and the output dimension with the range of their values. In this way the input matrix for the HDA has the size 1522x5 and the output vector 1522x1.

Table 1: Available data basis for surrogate model construction

RF	$\vartheta_{in} / \text{deg}$	$\vartheta_{out} / \text{deg}$	n_z	Ma	$v_{cas} / \text{m/s}$
$[RF_{min}; RF_{max}]$	$[0; -25]$	$[15; -30]$	$[-1; 2.5]$	$[0.4; 0.96]$	$[123; 193]$

While the input parameters are mentioned in their original scale the RF values are stated in form of RF_{min} and RF_{max} . Here RF_{min} and RF_{max} refer to the minimum and maximum values overall load cases which are already in the output vector.

7. Results using surrogate model based Fourier amplitude sensitivity test

For the interpretation of the results the surrogate model is discussed first and later on a conclusion on the main and total effects resulting from the eFAST follows. In order to construct the surrogate model the RMS error value is taken as an indicator for its reliability.

In the original data basis with 1522 load cases very high RF values exist which are like noise for the training set. Hence the data basis is reduced by the number of load cases using the RF values in order to minimize the RMS error. The HDA is run 4 times with a different threshold for the RF each. From the first to the second run all the load cases which yield a RF value that is higher than $1.77\% * RF_{max}$ are removed which reduces the number of

load cases in the data basis from 1522 to 783. At the same time the RMS error is reduced from 3.04 to 0.11. Further due to this load case selection all the negative load factors are removed and with this all the positive aileron deflections. One can conclude that the flight cases with negative load factors are not relevant for the structure in the scope of this study since these cases are noisy data in terms of very high RF s. The same principle of load case selection is applied to the following HDA runs, which is summarized in Table 2.

Table 2: Internal validation of surrogate model using data basis in original and reduced form

	HDA 1	HDA 2	HDA 3	HDA 4
Nr. Load Cases	1522	783	567	366
RF	RF_{max}	$1.77\% * RF_{max}$	$1.50\% * RF_{max}$	$1.33\% * RF_{max}$
RMS	3.04	0.11	0.08	0.05

The optimal solution is found in the third HDA run because here we have a RMS error below 0.10 and still have an adequate number of load cases for later SMBFAST (according to DATADVANCE sample size needs to be at least around 100 times dimensionality of input matrix).

Figure 4 shows the absolute error between real and predicted RF values using the different HDA runs as described in Eq. (11). Here the predicted RF values resulting from the constructed surrogate models are compared to the real RF values overall available load cases. One can see that the absolute error value decreases from the first until the last run with a reducing number of load cases.

$$err_{RF} = RF_{real} - RF_{predicted} \quad (11)$$

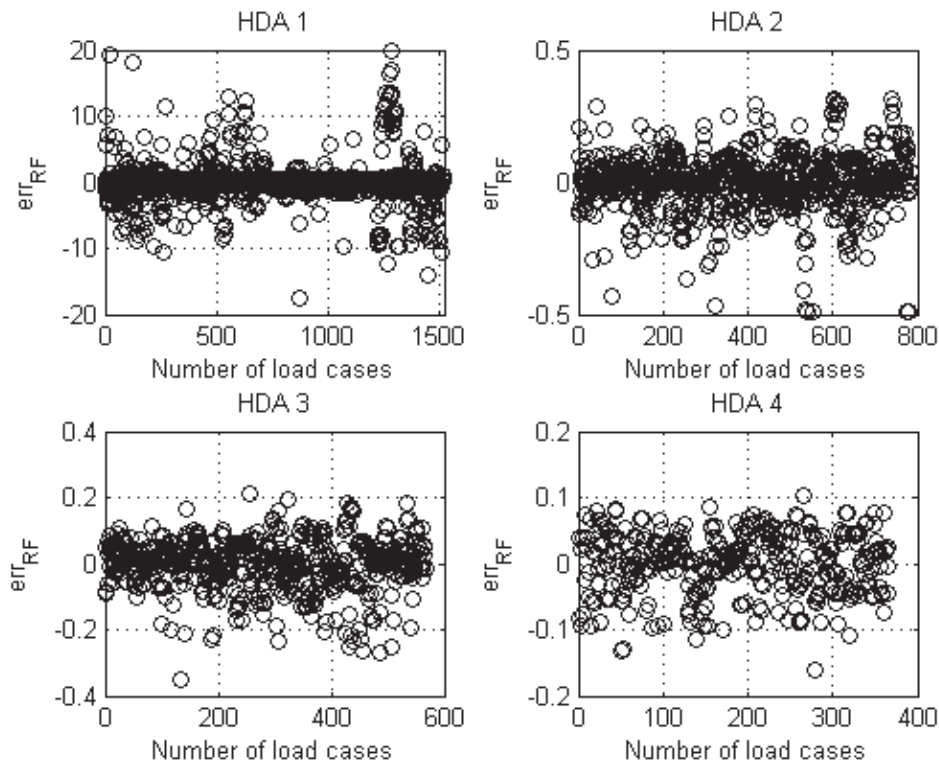


Figure 4: Comparison of HDA runs using err_{RF}

In addition Table 3 shows the change of the design space for each HDA run. The biggest change in the design space occurs from the first HDA run to the second one. In addition to the previously mentioned removal of positive aileron deflections and negative load factors here the smallest value for the calibrated airspeed has changed from 123 m/s to 141 m/s. The design space for the following HDA runs is still filled properly although the number of load cases is reduced by around 200 cases each.

Table 3: Change of the design space due to load case reduction by RF values

HDA loop	RF	ϑ_{in} / deg	ϑ_{out} / deg	n_z	Ma	v_{cas} / m/s
1	$[RF_{min}; RF_{max}]$	[0; -25]	[15; -30]	[-1; 2.5]	[0.4; 0.96]	[123; 193]
2	$[RF_{min}; 1.77\% * RF_{max}]$	[0; -25]	[0; -30]	[1.5; 2.5]	[0.4; 0.96]	[141; 193]
3	$[RF_{min}; 1.50\% * RF_{max}]$	[0; -25]	[0; -30]	[1.7; 2.5]	[0.4; 0.96]	[141; 193]
4	$[RF_{min}; 1.33\% * RF_{max}]$	[0; -25]	[0; -30]	[1.7; 2.5]	[0.4; 0.87]	[141; 193]

The third HDA run is used for the application of the eFAST. Figure 5 shows a comparison of the total and main effect values for the chosen MLA parameters. The diagram demonstrates that in terms of ranking both main and total effect are identical. In both cases changes of the load factor n_z result in the highest changes of RF values. The main effect value for the load factor is 0.037 which means that the load factor causes 3.7% of the total variance only. On the other hand the total effect value for the load factor is 0.73 which means that 73% of the total variance relates to this input parameter.

The Mach number and the calibrated airspeed are listed next in the ranking. One can conclude that the flight parameters itself which are more an input for the MLA law have much higher influence on the RF than the aileron deflections. Furthermore the total effects have much higher values than the main effects which yield high influence on the RF by varying the input parameters simultaneously. The combinational effect of the MLA parameters drives the RF value more than just changing one parameter and keeping the others constant. Hence the main effect contributions are negligible whereas the interaction effects are the main drivers.

Note that the shown behaviour of main and total effects is confirmed with results coming from high fidelity analysis inside Airbus Operations GmbH.

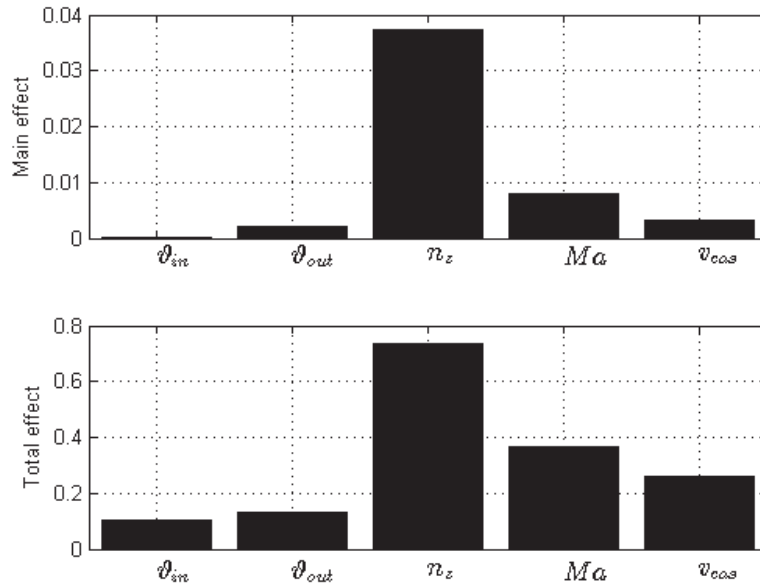


Figure 5: Main and total effects of MLA parameters on RF value

The application of eFAST on the constructed surrogate model from the first HDA run has shown different ranking and values for the total and main effects compared to the results shown in Figure 5. One can conclude that the results of the SMBFAST are strongly dependent on the quality of the sampled data basis and can lead in the worst case to conclusions which are not consistent with engineering judgment.

8. Summary and outlook

HDA is used in order to construct a cheap and fast to evaluate surrogate model compared to the overall industrial process. The application of eFAST yield in main and total effect values which are confirmed with high fidelity analysis inside Airbus Operations GmbH. The study has shown much higher influence of the flight parameters on the RF values compared to the aileron deflections for different flight points. But still for a given flight point the

load factor, the Mach number and the calibrated airspeed are constant while the aileron deflections can be modified. Hence the aileron deflections are the only parameters that can be varied in order to affect the RF values and thus to reach a reduction of the structural weight.

In future applications the constructed surrogate model can be used for instance for optimization of the aileron deflections as shown in Figure 6. Here the surrogate model of the third HDA run is used in order to plot the evolution of the RF value with the outer aileron deflection as the variable parameter and the other parameters hold on constant value. The RF values in the plot are normalized to 1. In Figure 6 the change of RF from its minimum to its maximum value is around 13% which can result in weight savings even if they are small. Hence in this way one can choose a certain flight condition and find the optimum value for the aileron deflections using surrogate model based optimization algorithms.

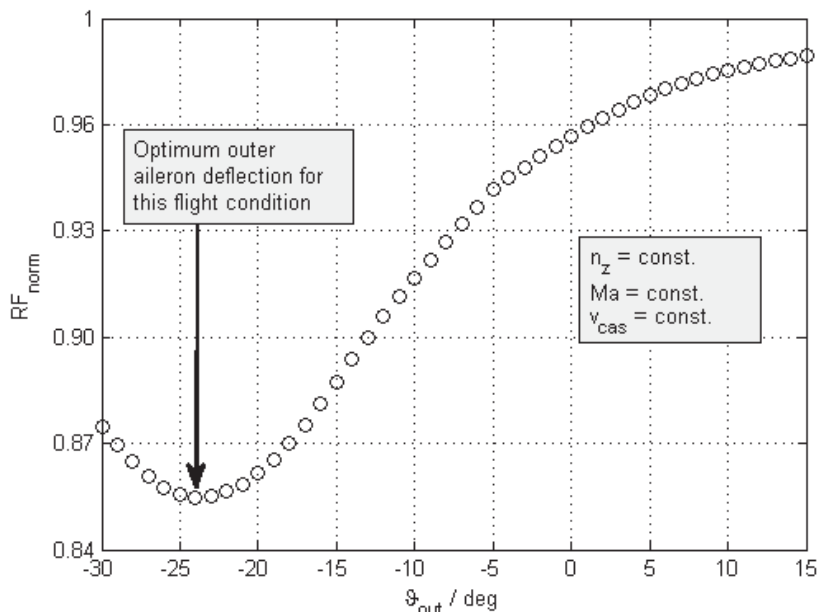


Figure 6: Evolution of normalized RF by outer aileron deflection changes for constant flight parameters

9. References

- [1] A. Saltelli, S. Tarantola, K. P.-S. Chan, A Quantitative Model-Independent Method for Global Sensitivity Analysis of Model Output, *Technometrics*, 41 (1), 39-56, 1999.
- [2] G. J. McRAE, J. W. Tilden, J. H. Seinfeld, Global sensitivity analysis - a computational implementation of the Fourier Amplitude Sensitivity Test (FAST), *Computers & Chemical Engineering*, 6 (1), 15-25, 1982.
- [3] S. Marino, I. B. Hogue, C. J. Ray, D. E. Kirschner, A methodology for performing global uncertainty and sensitivity analysis in systems biology, *Journal of Theoretical Biology*, 254 (2008), 178– 196, 2008.
- [4] D.W. Stephens, D. Gorissen, K. Crombecq, T. Dhaene, Surrogate based sensitivity analysis of process equipment, *Applied Mathematical Modelling*, 35 (2011), 1676–1687, 2010.
- [5] E. Burnaev, M. Belyaev, A. Lyubin, Construction of approximation based on linear expansion in heterogeneous nonlinear functions, *Proceedings of the conference Information Technology and Systems*, Gelendzhik, Russia, 2011, pp. 344-348.
- [6] S. Grihon, S. Alestra, D. Bettebghor, E. Burnaev, P. Prikhodko, Comparison of different techniques for surrogate modeling of stability constraints for composite structures, *DYNACOMP 2012 1st International Conference on Composite Dynamics*, Arcachon, France, 2012.
- [7] S. Haghghat, J. R. R. A. Martins, H. H. T. Liu, Aeroservoelastic Design Optimization of a Flexible Wing, *Journal of Aircraft*, 49 (2), 432-443, 2012.
- [8] N. Paletta, *Maneuver Load Controls, Analysis and Design for Flexible Aircraft*, Diss., Università degli Studi di Napoli Federico II, 2011.
- [9] A. Forrester, A. Sobester, A. Keane, *Engineering design via surrogate modelling - a practical guide*, John Wiley & Sons, West Sussex, 2008.
- [10] S. P. Timoshenko, J. M. Gere, *Theory of elastic stability*, McGraw-Hill, New York, 1961.

Optimal design of a double coil magnetorheological fluid damper with various piston profiles

Guoliang Hu^{1,2}, Zheng Xie¹, Weihua Li^{2,*}

¹School of Mechatronic Engineering, East China Jiaotong University, Nanchang City, Jiangxi Province, China, glhu@ecjtu.edu.cn

²School of Mechanical, Materials and Mechatronics Engineering, University of Wollongong, NSW, Australia, weihuali@uow.edu.au

Abstract

A magnetorheological (MR) damper is one of the most advanced devices used in a semi-active control system to mitigate unwanted vibration because the damping force can be controlled by changing the viscosity of the internal magnetorheological fluids (MRF). This study proposes a typical double coil MR damper where the damping force and dynamic range were derived from a quasi-static model based on the Bingham model of MR fluid. A finite element model was built to study the performance of this double coil MR damper by investigating seven different piston configurations, including the numbers and shapes of their chamfered ends. The objective function of an optimisation problem was proposed and then an optimisation procedure was constructed using the ANSYS parametric design language (APDL) to obtain the optimal value of a double coil MR damper. Furthermore, an experimental analysis was also carried out. These results were then compared with the optimised MR damper's simulation results, which clearly validated the simulated results. The relevant results of this analysis can easily be extended to other MR dampers.

Keywords: MRF, MR damper, Double coil, Finite element analysis, Optimal design

1. Introduction

The rheological properties of a magnetorheological fluid (MRF) can be continuously changed within several milliseconds by applying or removing external magnetic fields. These unique features have led to the development of many MRF-based devices such as the MR damper, MR valve, MR brake, MR clutch, and so on.

Recently, some studies in literature have focused on the geometric optimisation of an MR damper, with the results showing that their performance can be improved significantly by optimising the design of the magnetic circuit that controls these systems. Zhang et al. [1] proposed the use of finite elements to improve the magnetic design of an MR damper. Kham et al. [2] used finite element software to simulate nine different configurations of the pistons for an MR damper and investigate how these configurations would affect and influence the maximum pressure drop; the results showed that a single coil piston with chamfered ends was better than the other configurations for the same magnitude of input current and piston velocity. Ferdaus et al. [3] established 2D axi-symmetric and a 3D model of an MR damper that considered the shape of the piston, the MR fluid gap, the air gap, and the thickness of the damper's housing. All these models were simulated with different currents, different piston velocities, and different strokes. Parlak et al. [4] investigated the geometrical optimisation of an MR shock damper using the Taguchi experimental design approach by specifying four parameters (gap, flange thickness, radius of piston core, and current excitation) and by selecting the maximum dynamic range required as the target value; this analysis was carried out using analytical equations rather than experimental data. Parlak et al. [5] presented a method for optimising the design of the target damper force and maximum magnetic flux density of an MR damper; this new approach used an electromagnetic analysis of the magnetic field and a CFD analysis of MR flow together to obtain the optimal value of the design parameters. Nguyen and Choi [6] presented an optimal design of a passenger vehicle MR damper that was constrained in a specific cylindrical volume, and an advanced objective function that collectively included the damping force, the dynamic range, and an inductive time constant. Nguyen and Choi [7] also proposed two types of shear mode MR dampers for a front loader washing machine, where an optimisation methodology based on a finite element analysis integrated with an optimisation tool was used to obtain the optimal geometric dimensions of the MR dampers; the results showed that an MR damper with three coils and without a non-magnetic bobbin was the best configuration for this application.

In this study a double coil MR damper was developed and prototyped, and the damping force and dynamic range were also derived. A finite element model was built to investigate the performance of the double coil MR damper by considering seven pistons with different configurations. An optimisation procedure was then constructed with the ANSYS parametric design language (APDL) to obtain the optimal parameters of the double coil MR damper. Finally, a series of dynamic experimental tests were also carried out.

2. Design considerations for a double coil MR damper with an annular gap

Figure 1 shows a schematic for the proposed double coil MR damper under consideration. Two chambers in the cylinder are separated by a floating piston. The section with the piston head is filled with MR fluid and the accumulator that compensates for the changes in volume induced as the piston rod moves is filled with pressurised nitrogen gas. As the damper piston rod moves, the MR fluid flows through the annular gap to the other side of the piston. There is a double coil of wire inside the piston head used for winding is heat resistant and electrically insulated. When a direct current is applied to the double coil, a magnetic field occurs around the piston head. It is noted that the direction of the current applied onto the double coil can be the same or the reverse, and it can enlarge the maximum damping force or the dynamic range to some extent.

Figure 2 shows the magnetic circuit of the double coil MR damper with an annular gap at both ends of the flanges and in the middle of the flange, where the flux lines are perpendicular to the flow direction and caused a field-dependent resistance to the fluid flow. The double coil MR damper is shaped to guide the magnetic flux axially through the damper core, across the length of the core flange and the gap at one end, then on through the flux return and across the gap and core flange at the opposite end. The volume of fluid through which the magnetic field passes is defined as an active volume, and the MR effects only occur within the active volume. The most effective MR dampers have a high magnetic flux density passing through a large active volume, but a lot of magnetic coils are needed to produce large magnetic fields. An optimised circuit would maintain a balance between the field produced and power required by the magnetic coils.

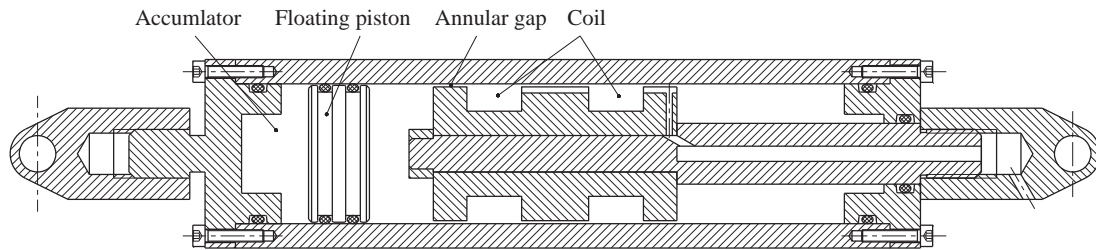


Figure 1: Schematic diagram of a double coil MR damper with annular gap

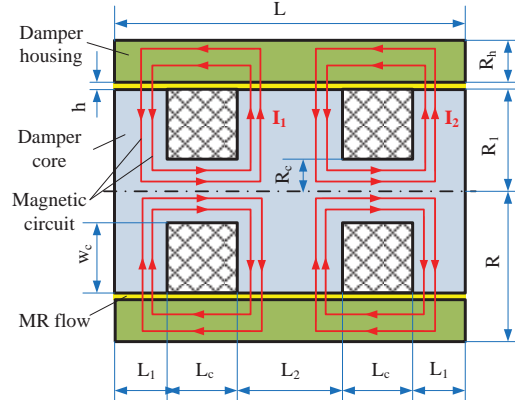


Figure 2: Magnetic circuit of the double coil MR damper with annular gap

Some of the important dimensions of double coil MR damper are also listed in Fig.2. Damper geometry is characterised by the length of the gap L , the length of the end flange L_1 , the length of the middle flange L_2 , the length of the coil L_c , the thickness of the piston head housing R_h , the width of the annular gap h , the radius of the piston head R , the internal radius of the piston core R_c , the external radius of the piston core R_1 , and the width of the coil W_c .

The total damping force F generated by the double coil MR damper consists of three components: the field-dependent force F_τ due to the magnetic field, the viscous force F_η due to the viscous effects, and the frictional force F_f .

$$F = F_\tau + F_\eta + F_f \quad (1)$$

where

$$F_{\eta} = \frac{6\eta LqA_p}{\pi(R_1 + 0.5h)h^3} \quad (2)$$

$$F_{\tau} = 2c_1 \frac{L_1}{h} A_p \tau_{y1} \text{sgn}(v_p) + c_2 \frac{L_2}{h} A_p \tau_{y2} \text{sgn}(v_p) \quad (3)$$

where A_p is the cross-sectional area of the piston head, and η is the plastic viscosity. q is the flow rate through the double coil MR damper, and it can be calculated from the velocity of the piston v_p . τ_{y1} and τ_{y2} are the yield stresses of the MR fluid in the end flange and middle flange, respectively. c_1 and c_2 are coefficients which depended on the flow velocity profile, and have a value ranging from a minimum value of 2.07 to a maximum value of 3.07.

As shown in Eq. (1), the first term is called the controllable force because it varies with the applied field, whereas the sum of the latter two terms is referred to as the uncontrollable force because they generate a constant force according to the velocity of the piston.

The dynamic range D is defined as the ratio of the total damping force to the uncontrollable force, and it is given by

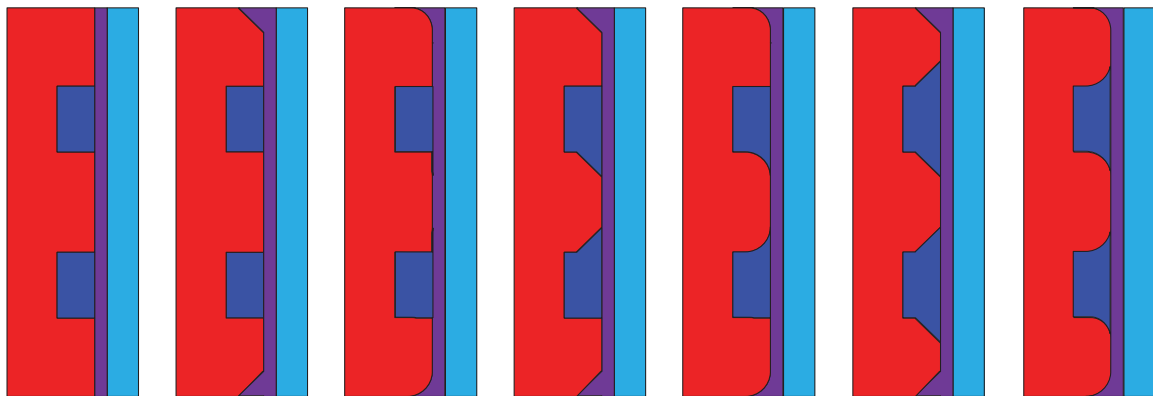
$$D = \frac{F_{\tau} + F_{\eta} + F_f}{F_{\eta} + F_f} = 1 + \frac{F_{\tau}}{F_{\eta} + F_f} \quad (6)$$

Here, the dynamic range D was introduced to evaluate the performance of the double coil MR damper. Normally, it is better to keep the dynamic range as large as possible to maximise the effectiveness of the MR damper. The dynamic range is proportional to the shear force and is a function of the size of the gap. The width of the annular gap h is inversely proportional to the controllable force, so a small gap width will increase the range of the controllable force, but when h is less than 0.5 mm, the viscous force F_{η} is much faster than the controllable force F_{τ} , this reduces the dynamic range. Again when the gap becomes wider both F_{τ} and F_{η} fall, so finding an optimal width gap that maximises the dynamic range is very important. Moreover, parameters such as the length of the flange L_1 and L_2 , the radius of the piston head R , the yield stress τ_{y1} and τ_{y2} , the thickness of the piston head housing R_h and the internal radius of the core of the piston R_c will also play an important role in searching for the right design.

3. Modelling an optimal design of a double coil MR damper using the finite element method

The magnetic field in an MR damper is produced by an electromagnet. Here in the ANSYS simulation model the excitation coil is considered to be the electromagnet, and the magnetic field provided by this excitation coil is needed to energise the MR fluid. By varying the current through the excitation coil the density of the magnetic flux can be varied and the MR fluid is energised accordingly.

To investigate how the shape of the piston affects the performance of a double coil MR damper, seven models with different shaped pistons were designed, as shown in Fig.3. The model 1 piston was defined as having a plain end, the model 2 piston was defined as have each end of the piston chamfered, the model 3 piston was defined as having a radius on each end, the model 4 piston was defined as having chamfers on the top, bottom, and in the middle, the model 5 piston was defined as having a radius on the top, bottom and in the middle, the model 6 piston was defined as having both ends chamfered, and the model 7 piston was defined as having a radius on every edge.



(a) Model 1 (b) Model 2 (c) Model 3 (d) Model 4 (e) Model 5 (f) Model 6 (g) Model 7

Figure 3: Simulation models with different piston shapes

Figure 4 shows the results of the magnetic flux densities between the different models when the current varied from 0.1A to 1.0A. Here the magnetic flux densities decreased with the number of chamfers on the damper piston,

the maximum density of magnetic flux appeared in Model 1, which means that this piston had the optimal geometrical shape. Moreover, density of magnetic flux in the model with a radius was greater than the chamfered model; the reason can be found in Figure 5 which shows that the distribution of magnetic flux lines along the resistance gap in model 1 were more even than in models 6 and 7. The damper piston with chamfers had larger reluctances at its core because the core was larger and the cross-sectional area through which the magnetic flux passed decreased, which in turn caused the magnetic flux densities in the fluid resistance gap to decrease as well.

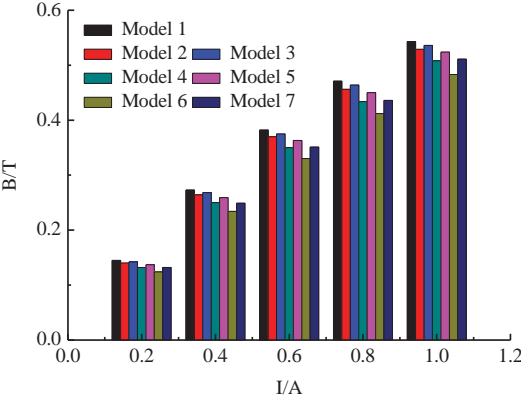
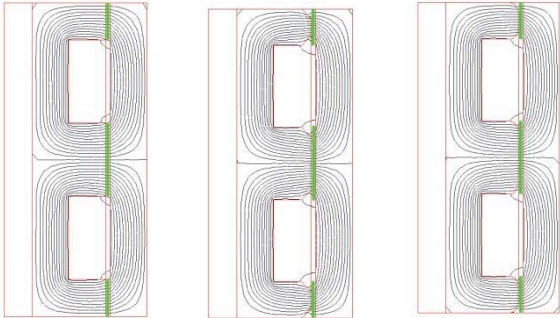


Figure 4: Magnetic flux density of different models



(a) Model 1 (b) Model 6 (c) Model 7

Figure 5: Distributions of magnetic flux lines of different models

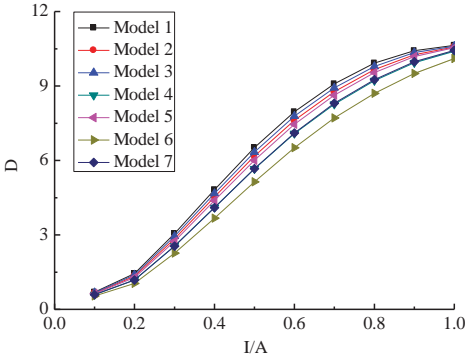


Figure 6: Dynamic range of MR damper under different currents

Figure 6 shows the dynamic range of the proposed MR damper under different piston configurations when the applied current varied from 0.1A to 1.0A. Here the dynamic range decreased as the number of chamfers on the pistons increased, and so too did the damping performance. Moreover, the dynamic range in the model with a radius on the edges was greater than the model with chamfered edges. When the current varied from 0.1A to 1.0A, the damping force steadily increased and then stabilised when the current was close to 1.0A due to the magnetic saturation of MRF in the resistance gap. From Figure 4 to Figure 6, model 1 with square ends had the maximum B value under different currents, while the damping force and dynamic range was also better in model 1 than in the

other models. So the piston with square ends was selected as the optimal geometry for the double coil MR damper.

To optimise the double coil MR damper using FEM, an analysis log file to solve the damper's magnetic circuit calculate the objective function was built using the ANSYS parametric design language (APDL). In the analytical log file, the length of resistance L_1 and the radius of the damper core r_1 were used as the design variables (DVs), and initial values were assigned to them, respectively. First, starting with the initial values of the DVs, the magnetic flux density, damping force and dynamic range were calculated by executing the log file. The ANSYS optimisation tool then transformed the optimisation problem with constrained DVs to an unconstrained one via penalty functions. The search direction of DVs was assumed to be the negative of the gradient of unconstrained objective function, and a combination of a golden-section algorithm and local quadratic fitting techniques were used to calculate new DVs. If convergence occurs, the DVs at this iteration would be the optimum, but if not then subsequent iterations would be carried out.

Figure 7 shows the results of the damping force between the initial design and optimal design, respectively. Here the damping force with an optimal design was greater than the initial design, although the difference between both of them improved significantly when the applied current exceeded 0.5A.

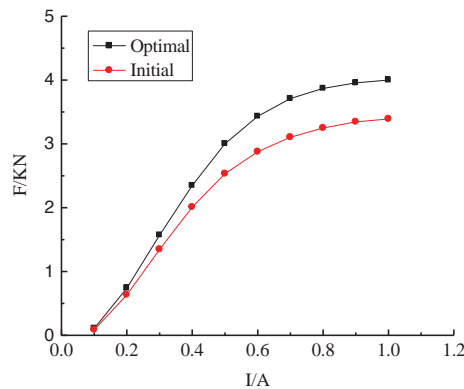


Figure 7: Comparison of damping force between initial design and optimal design

4. Experimental evaluation of double coil MR damper

Figure 8 shows the change in the damping force under different damper displacements and applied current directions. Here, the INSTRON 8801 test machine was set at sinusoidal loading with a frequency of 0.5Hz and displacement amplitude of 5mm and 7.5mm, respectively. The applied current I_1 and I_2 in the double coils were set to 0.5A with the same direction and reverse direction, respectively. The figure shows that the damping force with the currents in a reverse direction were much greater than currents in the same direction. Moreover, the damping force increased as the displacement amplitude increased, because the increased velocity of the damper led to an increase in the viscous force in Eq.(2), so the damping force also increased.

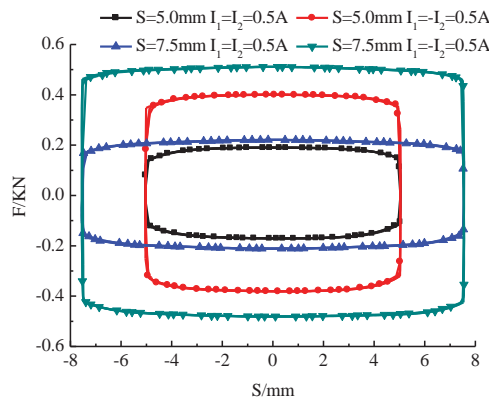


Figure 8: Damping forces under different displacements and different current directions

Figure 9 shows the damping force under the applied currents changed from 0A to 1.0A. Here, the INSTRON 8801 test machine was set at a sinusoidal loading with displacement amplitude of 10mm and a frequency of 1.0Hz, while the applied currents I_1 and I_2 in the double coils were applied the reverse direction. As expected, the damping

force increased from 0.33kN at 0A to 1.21kN at 1.0A, and the dynamic range nearly equal 4.

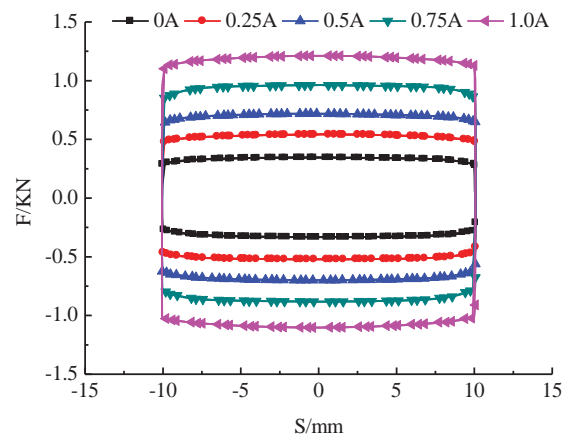


Figure 9: Damping force under different current

5. Conclusion

A double coil MR damper was proposed and the damping force and dynamic range were also derived. A finite element model was built to investigate the performance of a double coil MR damper while considering pistons with different configurations; the simulation results showed that the piston with square ends had a better damping performance. An optimisation procedure was constructed using the ANSYS APDL to obtain the optimal value of the double coil MR damper. Further, an experimental analysis was also carried out to verify the damping performance of the proposed MR damper.

6. Acknowledgements

This research was financially supported by the National Natural Science Foundation of China (No. 51475165, 51165005, 11462004) and the Australian Research Council Discovery Project (No. 1501002636).

7. References

- [1] H. H. Zhang, C. R. Liao and W. M. Chen, A magnetic design method of MR fluid dampers and FEM analysis on magnetic saturation, *Journal of intelligent material systems and structures*, 17(8-9), 813-818, 2006.
- [2] M. S. A. Khan, A. Suresh, N. S. Ramaiah, Analysis of magnetorheological fluid damper with various piston profiles. *International Journal of Engineering and Advanced Technology*, 2(2), 77-83, 2012.
- [3] M. M. Ferdaus, M. M. Rashid and M. H. Hasan, Optimal design of Magneto-Rheological damper comparing different configurations by finite element analysis, *Journal of mechanical science and technology*, 28(9), 3667-3677, 2014.
- [4] Z. Parlak, T. Engin and V. Ari. Geometrical optimisation of vehicle shock dampers with magnetorheological fluid, *International journal of vehicle design*, 54(4), 371-392, 2010.
- [5] Z. Parlak, T. Engin and İ Çallı, Optimal design of MR damper via finite element analyses of fluid dynamic and magnetic field, *Mechatronics*, 22(6), 890-903, 2012.
- [6] Q. H. Nguyen and S. B. Choi, Optimal design of a vehicle magnetorheological damper considering the damping force and dynamic range, *Smart Materials and Structures*, 18(1), 015013, 2009.
- [7] Q. H. Nguyen, S. B. Choi and J. K. Woo, Optimal design of magnetorheological fluid-based dampers for front-loaded washing machines, *Proceedings of the Institution of Mechanical Engineers, Part C: Journal of Mechanical Engineering Science*, 228(2), 294-306, 2014.

Topology optimization considering the requirements of deep-drawn sheet metals

Robert Dienemann¹, Axel Schumacher², Sierk Fiebig³

^{1,2} University of Wuppertal, Faculty D – Mechanical Engineering, Chair for Optimization of Mechanical Structures, Wuppertal, Germany

¹ dienemann@uni-wuppertal.de

² schumacher@uni-wuppertal.de

³ Volkswagen AG, Braunschweig, Germany, sierk.fiebig@volkswagen.de

1. Abstract

Topology-optimized designs for minimum compliance or minimum stress at minimum mass are often framework structures due to their homogeneous stress distribution over the cross section and therefore the best possible material utilization. From the manufacturing's point of view complex framework structures, which often develops during topology optimization, are difficult to manufacture because of possible undercuts. Manufacturing of these designs is often only possible by joining of numerous components or by 3D printing.

For mass production sheet metal parts manufactured by deep drawing are often more efficient concerning the costs in relation to their performance. Therefore we implemented a manufacturing constraint to the 3D topology optimization based on the density method ensuring that thin walled structure results. Thereby more flexibility for the mid surface design and also for cut-outs is reached compared to the optimization based on CAD-parameters. Also a variable thickness distribution for tailored blanks can be achieved.

Results for deep drawing structures with optimized topologies will be compared with optimized structures without manufacturing restriction due to their performance.

2. Keywords: topology optimization, sheet metals, deep drawing, manufacturing constraint, thin walled structures

3. Introduction

The optimization of shell structures is important in the field of mechanical engineering, but also in civil engineering and architecture (roof structures). In these fields a strengthened research has taken place in recent years.

Ansola et. al [1] propose a combination of CAD-parameters for the mid surface description and the SIMP-algorithm for the identification of optimal cut-outs. Thereby the optimization algorithm runs serially through the shape optimization of the mid surface and afterwards the topology optimization. This approach was taken up by Hassani et al. [2] and a simultaneous shape- and topology-optimization was introduced. The shape optimization takes place in the Finite Element Model, which shape can be modified by control points of splines. Both methods highly depend on the parametrization of the mid surface.

Zienkiewicz and Campbell [3] use the node coordinates as design variables instead of the CAD-parameters. Thereby a larger freedom of design is achieved. However by using sensitivities of coordinates of boundary nodes the finite element mesh becomes irregular. Yonekura et al. [4] keep the mesh regularity for small shape modifications.

In literature there are few attempts for the optimization of shells based on solid elements. Lochner-Aldinger and Schumacher [5] use the density method and extract isosurfaces of the element densities as mid surfaces.

4. The new approach for topology optimization for deep-drawn sheet metals

Our new approach uses the homogenisation method [6] on a linear voxel mesh. The derived method *Solid Isotropic Material with Penalisation* (SIMP) introduces material with the artificial density $0 < \rho_i \leq 1$ and Young's modulus E_i in element i (see equation 1). E_0 is the Young's modulus of the basic material. By increasing the penalty exponent s over 1.0 intermediate densities are penalized and thereby the optimized design rather converges to a black&white design.

$$E_i = \rho_i^s E_0 \quad (1)$$

Because of the use of sensitivities our approach is suitable for linear static load cases. All kinds of objective functions or constraints can be used, if their sensitivities are known.

4.1. Calculation of the mid surface

To allow the manufacturing by deep drawing in a single forming step, the optimized structure must have

- no undercuts.
- a constant wall thickness. Thereby the thinning during the forming process is neglected. By not considering the forming process also the material hardening and residual stresses are ignored.

These two manufacturing constraints can be achieved by modifying the sensitivities of the objective function. An increase of the element densities is only allowed near the current mid surface. Thus the mid surface can move according to the sensitivities. The mid surface can be found by calculating the average of the element coordinates in the punch direction weighted with the element densities. Figure 1 shows the procedure of deriving the mid surface from the volume mesh. Only a single cross section is displayed. Initially the user has to define the global punch direction. The mesh is divided into columns with the same width w , which is the element edge length. The midpoint of each column is calculated by equation 2.

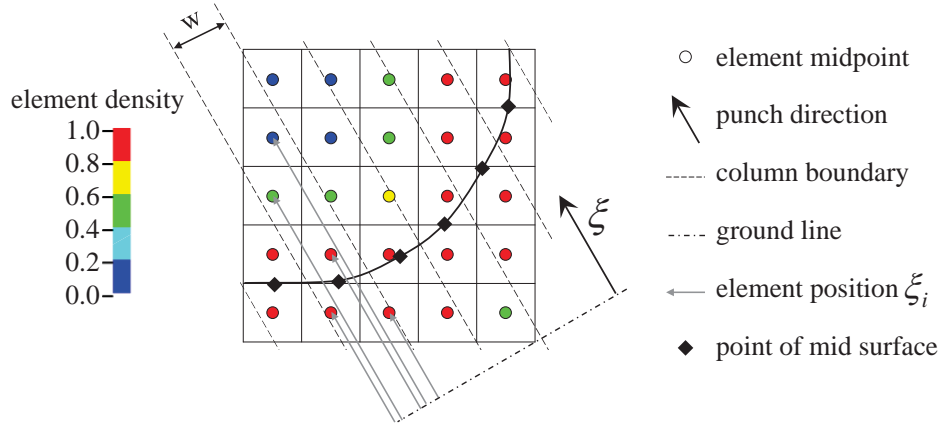


Figure 1: Calculation of mid surface

$$\xi_m = \frac{\sum \xi_i \cdot \rho_i}{\sum \rho_i} \quad (2)$$

ξ_i are the distances between the element midpoints from a ground line. For one exemplary column these distances are marked as grey arrows. The midpoint of each element decides to which column the element belongs. The connection of all midpoints with distance ξ_m present the mid surface.

4.2 Penalization of sensitivities

In order to get a shell structure sensitivities far away from the mid surface are penalized. The penalization factor P_i for the sensitivities of each element is calculated by equation 3.

$$P_i = \frac{1}{2} \left[1 - \frac{2}{\pi} \operatorname{atan} \left(\frac{a}{b} \left[d_i - \frac{b}{2} \right] \right) \right] \quad (3)$$

d_i is the minimum distances between the midpoint of element i and the mid surface. b is the user defined desired wall thickness, a/b describes the discreteness of the penalty function (see Figure 2). A larger quotient a/b ensures that the shell thickness does not exceed b , but slows down the convergence rate. The penalisation factor is normalized $P_i \in]0,1[$.

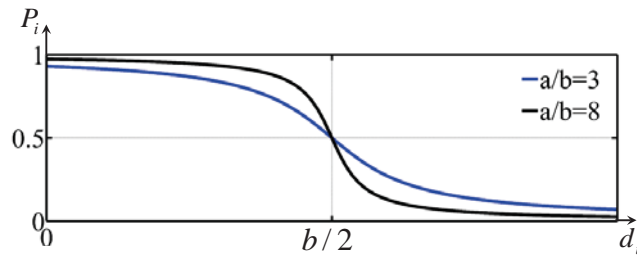


Figure 2: Graph of penalisation function for element sensitivities as a function of the distance from the mid surface

4.3. Convergence

The movement of the mid surface can stagnate, if the penalisation of the sensitivities is stronger than the improvement of the objective function. This problem is solved by alternating the desired wall thickness b . By increasing the desired wall thickness, elements are accumulated at the side of the shell, where the sensitivities are larger, by decreasing the desired wall thickness the shell's midface has moved to an improved design.

Also the penalisation of intermediate densities has an influence on the convergence. Figure 3 shows the movement of the mid surface. Only a single cross section is displayed. Even if a lower located mid surface would be better for the possible objective function compliance, the stiffness of the structure would temporarily decrease due to the lower stiffness of elements with penalized intermediate density (image at the right). That is the reason why the optimization starts without penalisation of intermediate densities (penalty exponent $s = 1$) until a convergence criterion is reached. Thereby at least the tensile/compressive stiffness remains the same between the images on the left and the right. After the increase of the penalty exponent this convergence problem is also solved by alternating the desired wall thickness.

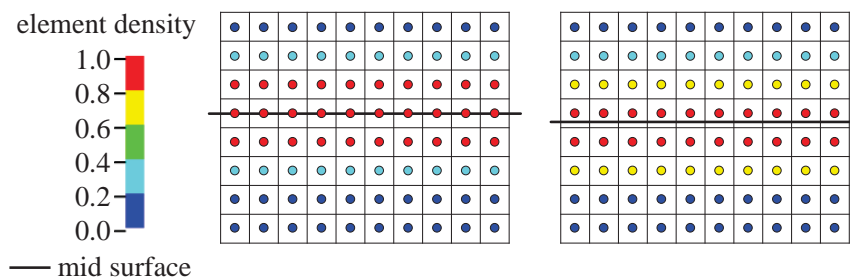


Figure 3: Movement of mid surface through change of elements densities

4.4 Optimization procedure

Figure 4 shows the optimization algorithm. Convergence criterion 1 can be the change of the objective function from one iteration to the next one or the maximum change of element densities. Convergence criterion 2 is the improvement of the objective function after the alternation of the desired wall thickness. During the alternation of the desired wall thickness and at the start of the optimization, the current desired wall thickness b_{curr} is larger than the desired wall thickness b .

5. Examples

In the following example topology optimizations of a cantilever beam (see Figure 5a) with and without manufacturing constraint are performed. The compliance is minimized considering a volume fraction constraint of 6.25 %. The design space is discretised by $120 \times 80 \times 48$ elements. One end of the structure is fixed, at one edge a line load of 200 N/mm is applied. The elements at the line load are defined as non-design space. A sensitivity filter with the radius of $r = (1.7 \text{ element edge lengths})$ and a penalty exponent $s = 3$ are used. The material is steel with Young's Modulus $E_0 = 210000MPa$ and Poisson's Ratio $\nu = 0.3$.

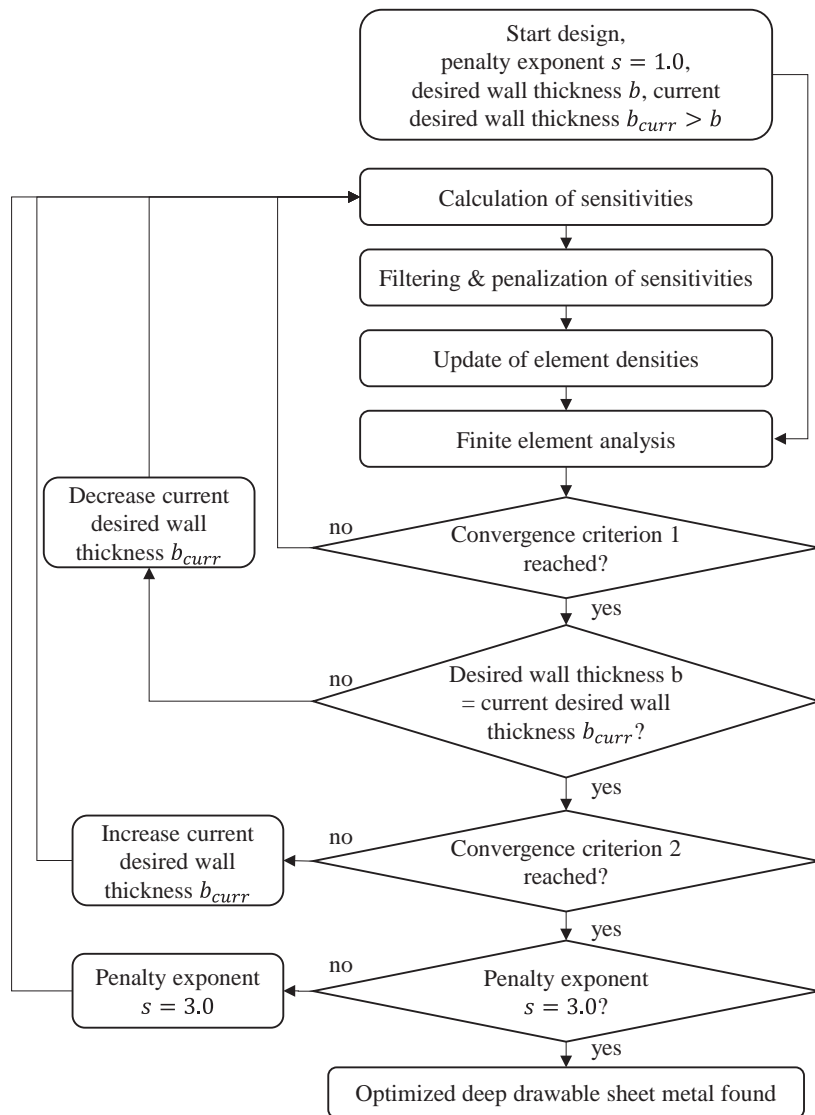


Figure 4: Optimization procedure

5.1 Cantilever Beam without manufacturing constraint

Without the manufacturing constraint a compliance of 32181.7 Nmm is achieved (see Figure 5b/c). 416 iterations were necessary followed by a final conversion to a black&white design. The convergence criterion is the improvement of the objective function per iteration of less than 0.01 % per iteration.

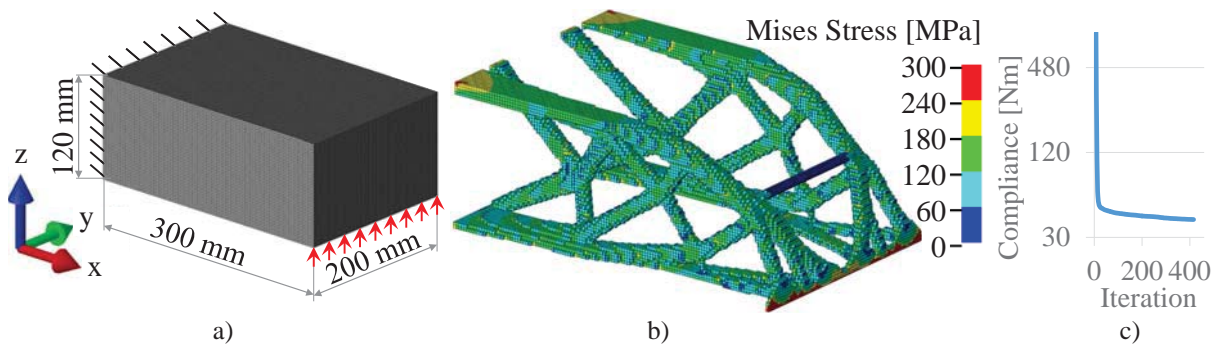


Figure 5: Cantilever Beam: a) FE-Model with loads and boundary condition, b) Stresses of final design (converted to black&white design) without manufacturing constraint, c) Compliance history

5.2 Cantilever Beam with manufacturing constraint

The same optimization task as in chapter 5.1 is performed by using the optimization procedure for thin walled structures described in chapter 4.4. The desired wall thickness is $b = (3 \text{ element edge lengths})$. This is the thinnest possible structure that ensures that a bending stress state can be represented with linear volume elements. The punch direction was chosen as z . The convergence criteria 1 and 2 were the improvement of the objective function per iteration of less than 0.1%. The penalisation parameter for the manufacturing restriction is chosen as $a = 25$. Figure 6a shows the compliance history of the topology optimization process. In Figure 6b) the success of the alternation of the desired wall thickness between intermediate result [3] and [4] can be seen. In Figure 7 the design changes during the optimization process are shown.

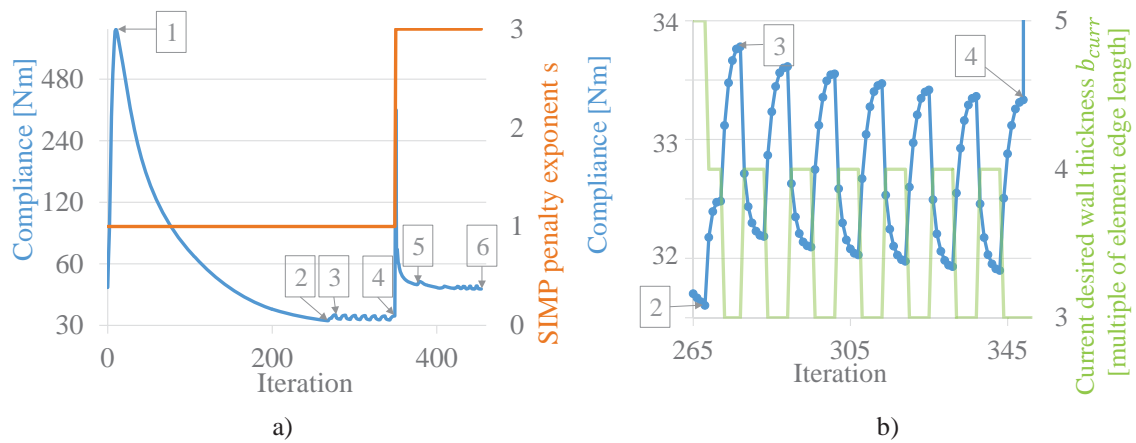


Figure 6: Compliance history: a) whole Optimization (logarithmic scale) with change of penalty exponent s , b) detail of convergence history with change of desired wall thickness

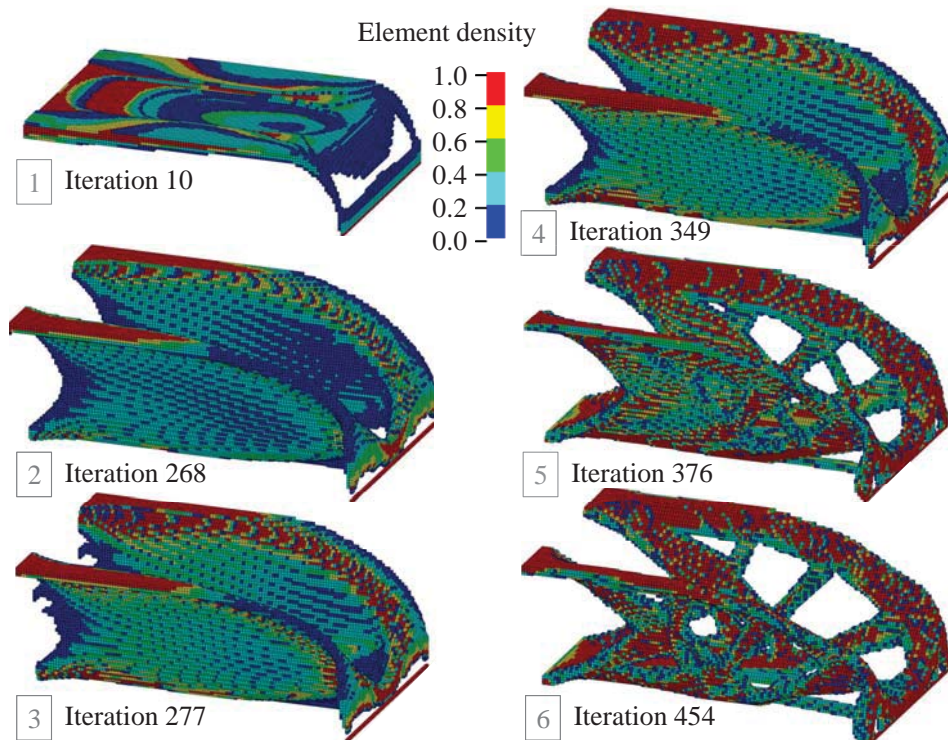


Figure 7: Element densities of intermediate results during the optimization (elements with density $x_i > 0.1$)

In Figure 8a the final black&white design of the shell structure is shown. This structure reaches a compliance of 40121.4 Nmm at a buckling safety of 5.98. In comparison to the optimization without manufacturing constraint the compliance is 24.7 % worse, whereby the manufacturing is much easier.

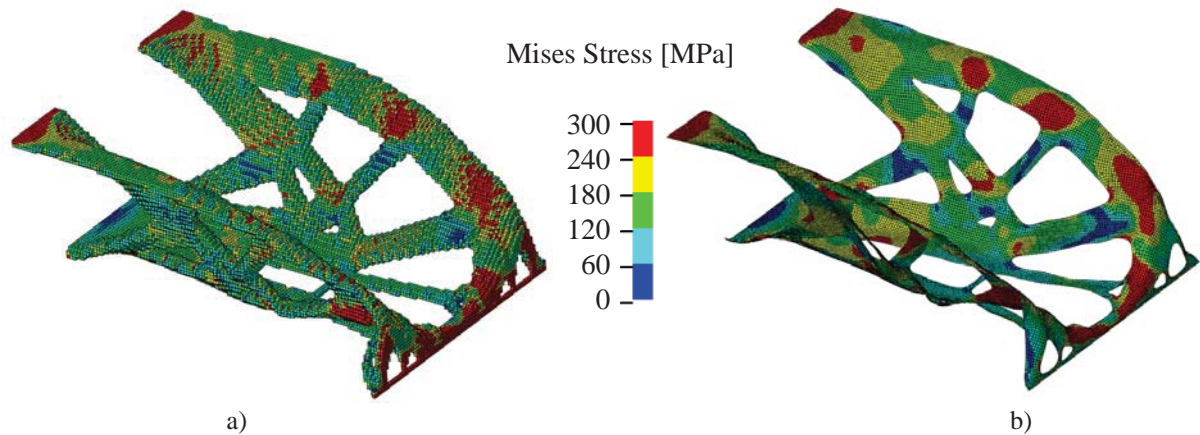


Figure 8: Stress a) of final design with manufacturing constraint (converted to black&white design), b) converted to surface model with shell elements

In order to check the quality of the finite element model with solid elements, a surface model of the optimized design with the same volume has been created. Thereby the compliance increases by 1.6 %. As to be seen in Figure 8, also the stresses are very similar, although the solid model is calculated with only three linear voxels across the sheet metal thickness.

6. Final remarks

Besides the shown application examples, the manufacturing constraint for the topology optimization of deep drawable sheet metals has been tested for several structures with multiple load cases. The results are promising, but we have to note that the gradient based optimization method will find most probably only local optima.

Compared to gradient based topology optimizations without manufacturing constraint the presented method needs more iterations and the objective function of the optimized designs is usually worse, but it can be guaranteed that the structures can be manufactured easily.

Further research activities will focus on the improvement of the computational efficiency, multishell structures, stress- and buckling constraints, the implementation of the deep drawing simulation in the optimization and automatization of the conversion to a surface model in order to perform a following shape optimization.

7. References

- [1] R. Ansola, J. Canales, J.A. Tarrago and J. Rasmussen, On simultaneous shape and material layout optimization of shell structures, *Structural and Multidisciplinary Optimization*, 24, 175-184, 2002.
- [2] B. Hassani, S.M. Tavakkoli and H. Ghasemnejad, Simultaneous shape and topology optimization of shell structures, *Structural and Multidisciplinary Optimization*, 48, 221-233, 2013.
- [3] O.C. Zienkiewicz and J.S. Campbell, Shape Optimization and sequential linear programming, In: R.H. Gallagher and O.C. Zienkiewicz, *Optimum Structural Design*, John Wiley & Sons, Chichester, 1973.
- [4] M. Yonekura, M. Shimoda and Y. Liu, Optimal Free-form Design of Shell Structure for Stress Minimization, *10th World Congress on Structural and Multidisciplinary Optimization*, Orlando, USA, 2013.
- [5] I. Lochner-Aldinger and A. Schumacher, Homogenization method, In: S. Adriaenssens, P. Block, D. Veenendaal, C. Williams, *Shell Structures for Architecture – Form Finding and Optimization*, Routledge, New York, 2014
- [6] M.P. Bendsøe, Optimal shape design as a material distribution problem, *Structural Optimization*, 1, 193-202, 1989

Design optimization for multifunctional 3D printed structures with embedded functional systems

A. Panesar¹, D. Brackett, I. Ashcroft, R. Wildman, R. Hague

Faculty of Engineering, The University of Nottingham, Nottingham, NG7 2RD, UK, ¹ajit.panesar@nottingham.ac.uk

1. Abstract

This paper presents an optimization based approach for the design of additively manufactured (AM), or 3D printed, multi-material parts with embedded functional systems (for example, a structural part with electronic/electrical components and associated conductive paths). The main contribution of this paper is the coupling strategy that enables the structural topology optimization (TO) of a part to be carried out in conjunction with the internal system design. This is achieved by accommodating the effects of system integration on the structural response of the part within TO. This work aims to demonstrate that the presented coupled optimization approach provides improved designs for 3D printed circuit volumes (PCVs) which provide benefits including: optimal system design, miniaturization, circuit encapsulation (protection) and tailored structure-system performance.

The coupled optimization strategy outlined in this work consists of: 1) a placement method used to determine suitable component locations (influenced by information extracted from the skeleton i.e. medial axis of the structure), 2) a routing method for optimal shortest distance connections between points (here, Dijkstra's algorithm is used to route between two fixed points by tracing skeletal members), and 3) integration into a TO routine taking account of the effect of routing on structure and vice-versa. This paper will report the developments made on the proposed coupled optimization strategy by detailing how the results from automatic placement and routing techniques are considered for the TO.

2. Keywords: additive manufacturing, 3D printing, multifunctional devices, topology optimization.

3. Introduction

A multifunctional part, by definition, has multiple uses, such as structural and electrical functions, for example, a structural health monitoring (SHM) part. Multifunctional designs could be physically realized using additive manufacturing (AM) or 3D printing multi-material processes which are still under development. A variety of techniques have been proposed, primarily using stereolithography and direct write/print technologies and the reader is directed to [1] for a history of work carried out in this area. The EPSRC Centre in Innovative Manufacturing in Additive Manufacturing at the University of Nottingham, UK, has the development of multi-functional 3D printing processes, specifically multi-material jetting, as one of its main aims. The Centre also focuses on developing design optimization strategies and methods to enable this multifunctional design paradigm. The motivation for this work lies in the realization of the ultimate aim which is to be able to intelligently optimize the design of a multifunctional part, such as the concepts included in Figure 1. Such multifunctional AM (MFAM) designs require coupling of the embedded system optimization (i.e. intelligent placement of system components and the associated routing) with a topology optimization (TO) routine (i.e. structural optimization technique that iteratively improves the material layout within a given design space, for a given set of loads and boundary conditions [2][3]). This coupling, in principle, should enable in a more compact, better integrated and capable design and is the focus of this paper.

The paper takes the following structure: firstly, the strategy for optimization of multifunctional design is outlined; secondly, the details of the coupling strategies are discussed; and thirdly, the appropriateness and effectiveness of the strategy is demonstrated by evaluating and discussing the results for an example test case.

4. Methodology

4.1 Coupling Strategy

Figure 2a shows a coupling between a TO routine (specifically, bi-directional evolutionary structural optimization (BESO) algorithm [3]) and a system optimization (specifically, placement of components and associated connection routing). This coupled optimization strategy is essential to fully exploit the design freedoms offered by MFAM. The main reason for the choice of BESO was the well-defined solid-void representation provided at every iteration within the TO which meant that the internal system optimization could be performed at every iteration of TO (if necessary). In previous works [4][5], the authors demonstrated a single direction coupling of the

aforementioned optimization strategy. This preliminary work looked at integrating the system optimization into a structural TO algorithm such that the finite element analysis (FEA) conducted as part of TO accounted for updated material properties for regions where the components were placed and the routes were identified. In this paper, the authors extend this work to benefit from a bi-directional coupling between the TO and internal system optimization. This is best illustrated by Figure 3 wherein we can observe the use of elemental sensitivities from both the structural and system aspect of our design to update the design variables for subsequent optimization runs.

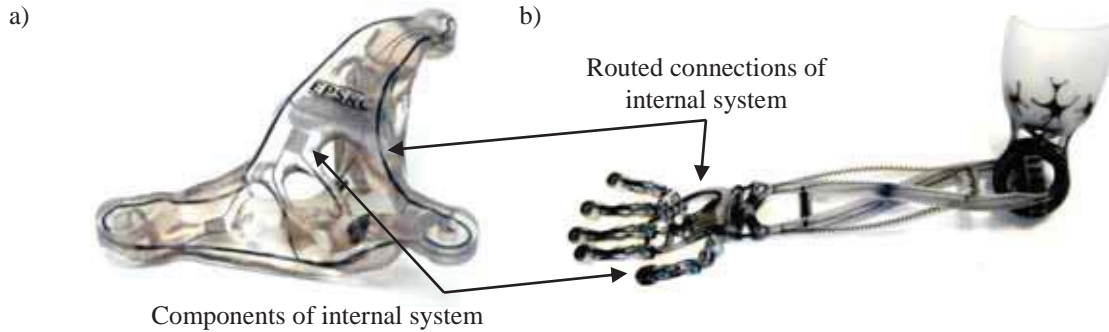


Figure 1: Multi-material jetted concept prototype - a) an example of a topologically optimized structural part with integrated internal system of placed components and the associated routing, b) a prosthetic arm with embedded systems and the associated connections between components [6].

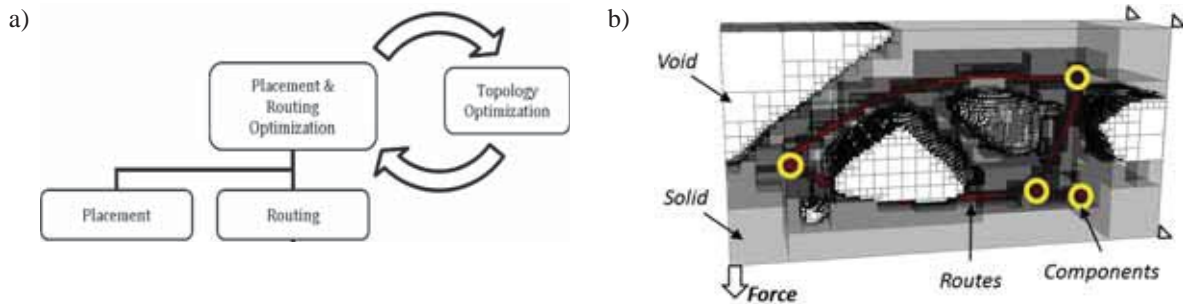


Figure 2: Coupling placement and routing optimization with structural topology optimization

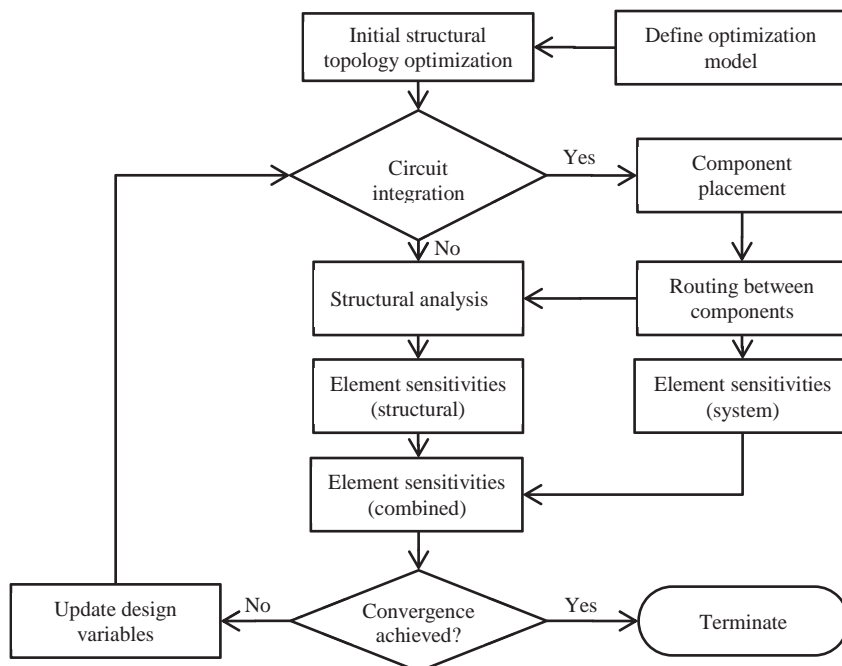


Figure 3: Flowchart showing the coupled optimization procedure

4.2 System Optimization: Placement and Routing Methodology

In this work, system design/optimization means the intelligent placement of components (based on some performance and/or geometry criterion) and the associated connection routing. A wide range of automated placement and/or routing techniques have been employed in numerous fields, including electronics, civil (buildings), aerospace, navigation systems, and artificial intelligence (robotics). The electronics community has benefited significantly from advancements in these techniques and this is evident from the highly miniaturized and optimized very large scale integration (VLSI) and printed circuit board (PCB) designs. Although in principle it would be best to perform placement and routing in one step as placement has significant repercussions on the routing but due to the nested dependencies these can be more efficiently (in terms of computational expense) tackled independently. The reader is directed to the authors previous works [4][5] for details on the placement and routing strategies/techniques within the context of MFAM design. Currently, PCBs within electronic devices are limited to a stacked 2D (i.e. 2.5D) paradigm [7], however, with the development of multi-material AM the design of functional devices in true 3D, termed printed circuit volumes (PCVs), can be considered. The 3D placement of internal components and the associated routing of connecting tracks should enable more compact, better integrated and capable MFAM systems.

One of the key enablers for MFAM system design is the skeletal information. This can be obtained through the process of skeletonization which is the general name given to a process which reduces the quantity of geometric information (i.e. dimensionality) required to represent a structure whilst preserving the essence of the topology. In 3D, this means a 2D medial surface and a 1D medial axis. A thinning algorithm, as detailed in [8][9], has been used to obtain the skeletal information of the part's topology. For this study, the medial axis is used to obtain appropriate orientations of placed components in accordance with the approach outlined in [5] and to identify the optimal routes.

With regards to the system design considered herein, placement of the component involves: identifying potential locations; identifying the orientation for the component under consideration; and finally assessing the location suitability for this component. Once the internal components have been placed, the next task is to generate the connections to form a circuit, commonly termed routing. The routing optimization aims to improve the circuit efficiency by lowering resistance, which is proportional to the conductive track length. This is, achieved by identifying the shortest paths between components subject to design rules and constraints. By doing so, we also minimize the utilization of the conductive track material.

In this study, a MATLAB [10] implementation utilizing the Dijkstra's algorithm [11] is employed to route between two points by tracing members on the medial axis. This approach is described by the following steps:

1. Obtain the medial axis for the current structural topology.
2. Compute the length of each medial axis member (i.e. branch point to branch point).
3. Identify the link and the points on it that are nearest to the placement location. Find the distance from the aforementioned points to the branch points of the link they lie on (see Figure 4).
4. Develop a graph (network) representing the path finding problem.
5. Solve the graph problem using Dijkstra's algorithm.

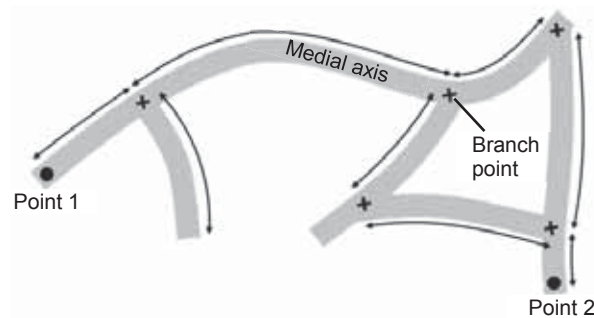


Figure 4: Routing method: shortest path identification based on the medial axis. Distances between points are represented by double ended arrows.

4.3 Coupled Optimization Procedure

The combined elemental sensitivity of an element within the design domain or ' $i\alpha$ ', as outlined in Figure 3, is computed using Eq.(1)

$$i\alpha = \frac{i\alpha_1 + \lambda i\alpha_2}{1 + \lambda} \quad (1)$$

where, α_1 represents the normalized structural elemental sensitivities (i.e. normalized strain energies) after thresholding the outliers (e.g. at the regions where the loads and boundary conditions are applied), α_2 represents

the normalized system elemental sensitivities, and λ is a weighting factor influencing the relative importance of the structural and system sensitivities.

For this study, a heuristic was defined (Eq.(2)) for the computation of internal system elemental sensitivities.

$$i\alpha_2 = \frac{1}{1 + d_i} \quad (2)$$

where, d_i is the Euclidian distance between ' i^{th} ' element within the design domain and the closest point from it on the routed paths. Doing so, assigns a value of '1' to those elements which form a route and a lower value for elements that are further away from the routed paths.

As combined elemental sensitivities ' α ' is used for updating the design variables in our modified BESO implementation, it can therefore be claimed that the objective function being minimized in this problem is $\sum i\alpha$.

5. Simulation, Results and Discussion

In order to assess the proposed coupling strategy, a test case with the problem definition of Figure 5, is considered. Herein, four pre-placed components (based on the static arbitrary performance map of Figure 5a – two components at maximum values and two at minimum values) are chosen with the component connection topology of Figure 5b. Table 1 details the parameters set for the coupled optimization formulation (modified BESO) for the considered test case of Figure 5.

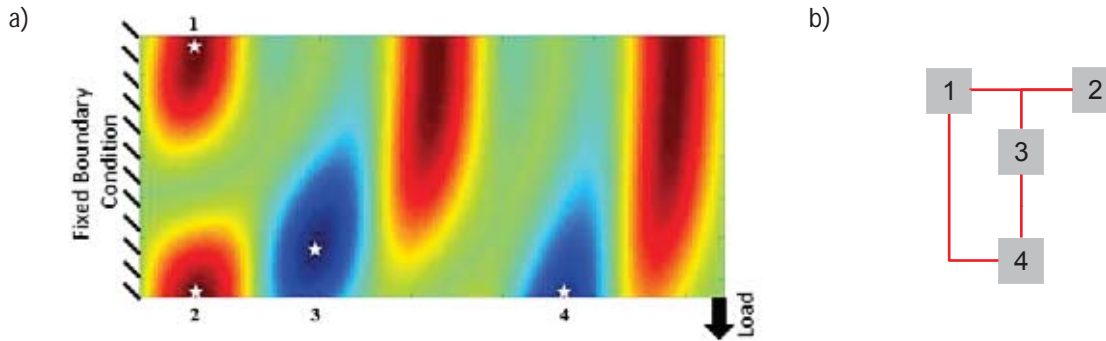


Figure 5: Problem definition a) four components placed within the design domain based on a static external performance map for the considered cantilever problem b) topology of the connected components defining the system configuration.

Table 1: Parameters used for the coupled optimization formulation

Parameter	Description	Value
λ	Parameter used for the single objective weighted sum formulation	1
$E_{Structure}$	Modulus of elasticity used for structure	1
E_{Void}	Modulus of elasticity used for the void region	1e-6
E_{System}	Modulus of elasticity used for system	1e-3
ν	Poisson's ratio used for all materials	0.3
R_{min}	Filter used to avoid checker-boarding	2
er	Evolution rate used for BESO	2%
Vol_{frac}	Target volume fraction used for optimization	40%
$Iter^{limit}$	Number of optimization iterations after which the process is terminated	60

Figure 6 shows the sensitivities of the structure and internal system as well as the combined sensitivities from which the design variables are updated (c), plus the optimized structure and system results (d) and the results from the TO with just structural sensitivities (e). Figure 7 shows the history of the artificial objective function calculated as a weighted sum of the structural and system sensitivities. Optimization progress was observed to be generally stable with only a few discontinuities over the history which correspond to sudden changes in the structural members selected for routing through.

In the coupled results (Figure 6d), the skeleton is shown with the red portions representing the actual routes used (overlapping routes are allowed at this stage in the design process). It was observed that the structural members that had routes within them had increased thickness that those that didn't and in comparison with the reference structure for which there are two contributing reasons. The first reason is that the routes affect the mechanical performance of the structure due to a lower Young's modulus being used for the material property of those

elements in the FEA and so the structure is thickened up to compensate. The second reason is that due to the heuristic nature of the internal system sensitivity definition where the sensitivities are linked to Euclidean distance from the medial axis (Eq.(2)), the combined sensitivities for those regions of the structural members are higher than they would be otherwise which affects the design variable update.

The differences in the evolution of the solutions between the coupled structure and system optimization problem, and the structure only TO can also be observed. It can be seen that the structural topology looks identical for the early stages in both optimization problems. This can be understood by examining the element removal criterion, i.e. lower $i\alpha$ values, and as medial axis is going to be well within the mostly solid structure, one can expect similar elements being chosen for removal. However, with removal of more material from the structure, the influence of system elemental sensitivities can be witnessed and it is evident that the coupled formulation has a significant effect on the material layout for the structure.

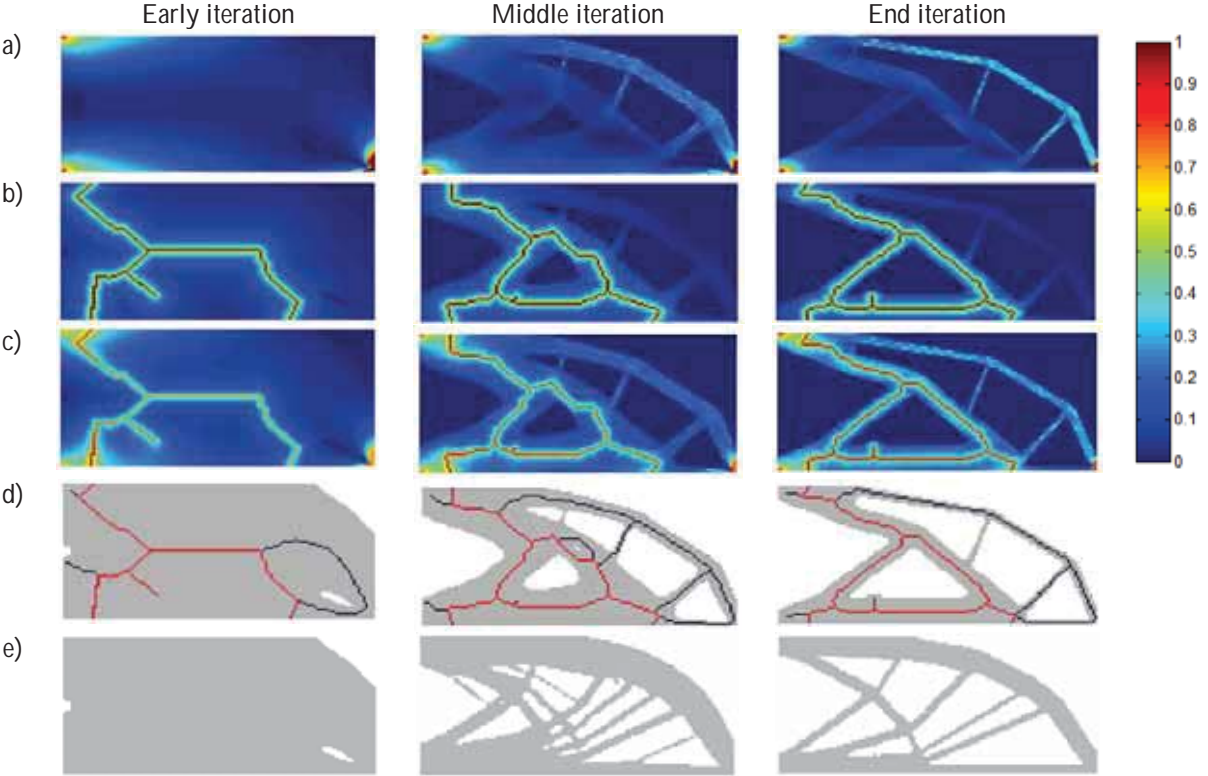


Figure 6 – a) Sensitivities for structure, b) sensitivities for internal system, c) combined sensitivities using Eq.(1), d) resulting coupled solution, and e) TO using just structural sensitivities for comparison.

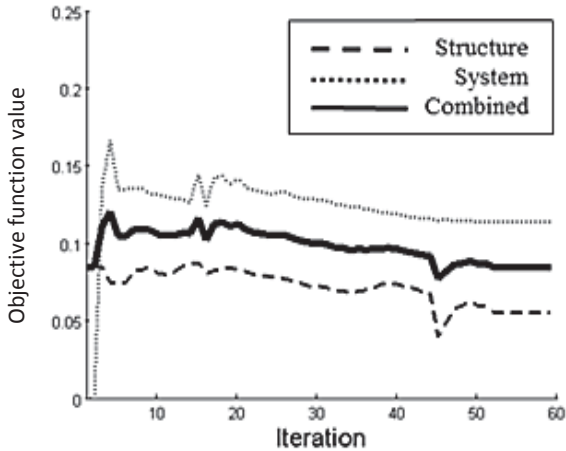


Figure 7 – Objective function formed as a weighted sum of the structure and system sensitivities.

6. Concluding Remarks

This paper has presented a coupled optimization formulation for the design of additively manufactured multi-material parts with embedded functional systems (e.g., a structural part with electronic/electrical components and associated conductive paths). This marks a significant step towards being able to exploit the design freedom offered by these manufacturing processes.

The main contribution of this paper is the coupling strategy that enables the structural TO of a part to be carried out in conjunction with the system design through the use of combined structural and internal system sensitivities, based on the routing between components placed based on a performance map. Following each structural optimization iteration, the placement of the components was determined, associated routing performed, and the design variables then updated for the next iteration of the TO phase.

The results have demonstrated that the method through the evaluation on a 2D cantilever test case for a simple connection topology. There is work to be done on tuning the heuristic internal system sensitivity definition to ensure it is not inappropriately biasing the structural member thickness through the use of the ‘distance from medial axis’ measure. The next steps are to evaluate this method on a non-static performance map that changes in response to changes in the structure.

7. Acknowledgements

The authors would like to thank the UK Engineering and Physical Sciences Research Council (EPSRC) for funding this work, grant number: EP/I033335/2.

8. References

- [1] A. J. Lopes, E. MacDonald, and R. B. Wicker, “Integrating stereolithography and direct print technologies for 3D structural electronics fabrication,” *Rapid Prototyp. J.*, vol. 18, no. 2, pp. 129–143, 2012.
- [2] M. P. Bendsoe and O. Sigmund, *Topology optimization: Theory, Methods and Applications*. 2003.
- [3] X. Huang and Y. M. Xie, *Evolutionary Topology Optimization of Continuum Structures*, First. Wiley, 2010.
- [4] D. Brackett, A. Panesar, I. Ashcroft, R. Wildman, and R. Hague, “An optimization based design framework for multi-functional 3D printing,” in *24th Annual International Solid Freeform Fabrication Symposium – An Additive Manufacturing Conference*, 2013.
- [5] A. Panesar, D. Brackett, I. Ashcroft, R. Wildman, and R. Hague, “Design Optimization Strategy for Multifunctional 3D Printing,” in *25th International Solid Freeform Fabrication Symposium*, 2014.
- [6] M. Amos and S. Cardell-Williams, Matthew Wimhurst, “3D Printed Prosthetic Arm,” 2013.
- [7] E. Beyne, “3D System Integration Technologies,” in *International Symposium on VLSI Technology, Systems, and Applications*, 2006, pp. 1–9.
- [8] T. Lee and R. Kashyap, “Building skeleton models via 3-D medial surface / axis thinning algorithms,” *Graph. Model. Image Process.*, vol. 56, no. 6, pp. 464–478, 1994.
- [9] M. Kerschnitzki, P. Kollmannsberger, M. Burghammer, G. N. Duda, R. Weinkamer, W. Wagermaier, and P. Fratzl, “Architecture of the osteocyte network correlates with bone material quality,” *J. Bone Miner. Res.*, vol. 28, no. 8, pp. 1837–1845, 2013.
- [10] “MATLAB R2013a.” Mathworks, Massachusetts, USA, 2013.
- [11] E. W. Dijkstra, “A Note on Two Problems in Connexion with Graphs,” *Numer. Math.*, vol. 1, pp. 269–271, 1959.

Optimizing Topology Optimization with Anisotropic Mesh Adaptation

Kristian E. Jensen¹

¹ Imperial College London, SW7 2AZ London, United Kingdom, kristianejlebjerger@gmail.com

1. Abstract

Mesh adaptation is rarely used in topology optimisation, with exceptions found in continuous methods such as phase field and some level-set techniques. Anisotropic mesh adaptation involve not only refinement and coarsening operations, but also smoothing and swapping, which allow for the appearance of elongated elements aligned with physical features, such as those found in structural optimisation. We use an anisotropic mesh generator based on local mesh modifications and an open source finite element engine (FEniCS) in combination with the method of moving asymptotes. Discrete sensitivities are calculated automatically and converted to continuous ones, such that they can drive the mesh adaptation and be interpolated between meshes. Results for stress and compliance constrained volume minimisation indicate that mesh independence is possible in a rounded 2D L-bracket geometry, the rounding fillet being 1 % of the characteristic length scale. Finally, the combination is tested for 3D compliance minimisation, where 50 is found to be a typical average element aspect ratio, indicative of the speed-up relative to isotropic mesh adaptation.

2. Keywords: Anisotropic; mesh; adaptation; topology; optimization

3. Introduction

Fixed structured meshes remain popular for topology optimisation due to ease of implementation and parallelisation [1, 2]. Adapted meshes have, however, also seen some use in the context of continuous sensitivities [3, 4] and recently also for discrete sensitivities [5], but we are not aware of any work employing mesh adaptation of the anisotropic kind, which is the aim of this work. The hypothesis is that stretching of elements to accommodate anisotropic features in the design and the physics will enable a more efficient use of computational resources compared to isotropic mesh adaptation.

4. Anisotropic Mesh Adaptation

We choose to apply a continuous framework [6] for anisotropic mesh adaptation. That is, we estimate the optimal local size and orientation of elements by means of a spatially varying symmetric positive definite tensor field, a metric tensor field, $\underline{\mathcal{M}}$. If one wishes to minimise the interpolation error of some scalar, $\tilde{\rho}$, then the metric is [7]

$$\underline{\mathcal{M}} = \frac{1}{\eta} \left(\det[\underline{\text{abs}}(\underline{\mathbf{H}}(\tilde{\rho}))] \right)^{-\frac{1}{2q+d}} \underline{\text{abs}}(\underline{\mathbf{H}}(\tilde{\rho})), \quad (1)$$

where $\det(\dots)$ returns the determinant, $\underline{\mathbf{H}}(\dots)$, returns the Hessian, $\underline{\text{abs}}(\dots)$ takes the absolute value of the tensor in the principal frame, q is the error norm to be minimised, d is the dimension and finally, η is a scaling factor used to control the number of elements. Several metrics can be combined using the inner ellipse method [8] illustrated in figure 1, where it can also be seen that the metric has units of inverse squared length. The metric can be used

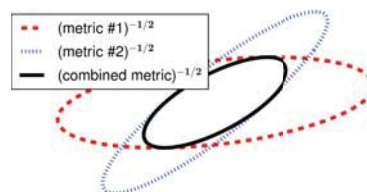


Figure 1: The process of combining two metrics using the inner ellipse method is shown for the case where there is an intersection and thus also a loss of anisotropy, but anisotropy is preserved whenever one ellipse is entirely within the other.

to map elements to metric space, where the ideal elements are regular triangles or tetrahedra. Various heuristic quality metrics exists to quantify the difference from the perfect element [9]. These metrics are generally invariant

under rotations in metric space, which can give rise to large angles in real space and thus also problems with iterative solvers. This is, however, mostly an issue for extreme aspect ratio elements, and it is possible to reduce the occurrence of large angles with advancing front techniques [10]. We use a popular technique [8, 11] based on the local mesh modifications shown in figure 2. The results presented here are based on an Octave/MATLAB implementation, which is fully vectorised. It is, however, still around an order of magnitude slower than an equivalent C++ implementation [12].

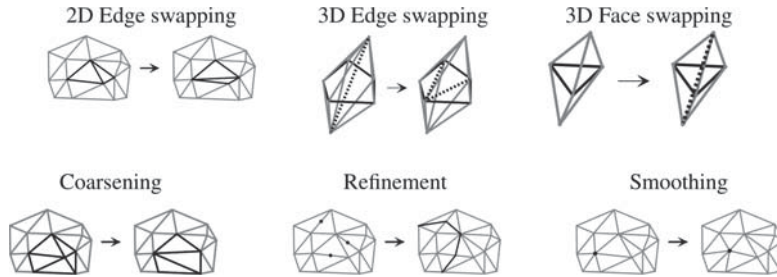


Figure 2: Local swapping mesh modification operations are illustrated in two and three dimensions (top row), while coarsening, refinement and smoothing are sketched for two dimensions. Smoothing and swapping operations are only allowed, when they improve the worst local element quality, and in three dimensions this is also true for the refinement.

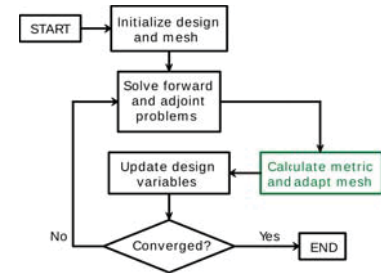


Figure 3: The flowchart for an optimisation is sketched with the mesh adaptation between the sensitivity analysis and the optimiser.

5. Topology Optimisation

We use the standard approach of Solid Isotropic Material with Penalisation (SIMP) [13] together with the method of moving asymptotes [14],

$$E = E_{\min} + (E_{\max} - E_{\min})\rho^{P_E}, \quad \text{where } 0 \leq \rho \leq 1, \quad (2)$$

where E is the Young's modulus, ρ is the design variable and P_E is the SIMP penalisation exponent. For compliance minimisation, $P_E = 1$ gives rise to a convex problem, which does not have a discrete solution. Its solution, however, constitutes a good initial guess for an optimisation with larger P_E , where the optimal solution is discrete. This kind of continuation approach is common for addressing problems with local minima within the field of structural optimisation [15].

We calculate the discrete sensitivity with respect to the design variables automatically [16], and then normalise the sensitivity with the design variable volumes to calculate an approximate continuous sensitivity, ∂_ρ . To this, we apply Helmholtz smoothing [17], such as to impose a minimum length scale, L_{\min} ,

$$\partial_\rho - \tilde{\partial}_\rho + L_{\min}^2 \nabla^2 \tilde{\partial}_\rho = 0. \quad (3)$$

The filter is also applied on the design variable and both scalar fields are then used to calculate metrics using equation (1). The metrics are combined using the inner ellipse method, and the result is passed to the mesh generator. The filtered continuous sensitivities, mma asymptotes as well as current, old and older design variables are interpolate on to the new mesh. The discrete sensitivity on the new mesh is estimate by multiplying with the new design variable volumes, and then design variables are optimised completing the optimisation loop sketched in figure 3.

We use an open source high level finite element package [18] (FEniCS) for solving the forward problem. Both displacements and design variable are represented with continuous linear basis functions. The Hessian calculation in equation (1) involves Galerkin projection and these are performed with an iterative solver, but a direct solver is applied for the forward, adjoint and filter problems.

6. Setup

We show results in the context of linear elasticity in three dimensions as well as for plane stress, but in both cases we use E_{\max} and a characteristic length, L_{char} to non-dimensionalise the problem,

$$\nu = 0.3, \quad E_{\min} = 10^{-3}E_{\max}, \quad L_1 = 0.1L_{\text{char}}, \quad \underline{\sigma}_{\text{load}} = E_{\max}/L_{\text{char}}, \quad q = 2 \quad \text{and} \quad c_{\text{MMA}} = 10^3,$$

where ν is the Poisson ratio, L_1 is a length scale associated with the load boundary condition and c_{MMA} is the MMA c parameter for controlling the enforcement of constraints. We also use move limits

$$\text{abs}(\rho_{i+1} - \rho_i) = \Delta\rho,$$

and we fix these at $\Delta\rho = 0.1$.

6.1 Stress and compliance constrained volume minimisation in two dimensions

This setup is specific to a L-bracket geometry with a rounded corner (fillet 1% of the characteristic length scale). For these optimisations, we use a stress penalisation scheme [19] to avoid problems with void stress, and we use a 10-norm to convert the local constraints to a single global one [20]. We also smooth the stress sensitivity with a Helmholtz filter based on the element metric calculated as Steiner ellipses and use a factor of four higher tolerance for the metric associated with the stress sensitivity. We scale the number of iterations with the mesh tolerance:

$$it_{\max} = \text{round}(600\sqrt{0.02/\eta\rho}), \quad C_{\max} = 2.5E_{\max}L_{\text{char}}^2, \quad \sigma_{\max} = 1.5E_{\max}, \quad P_E = 3 \quad \text{and} \quad L_{\min} = 5 \cdot 10^{-2}L_{\text{char}},$$

where C_{\max} and σ_{\max} is the maximum compliance and von misses stress, respectively.

6.2 Volume constrained compliance minimisation in three dimensions

The implementation is tested for a cantilever, stool and crank geometry, which correspond to bending, compression and torsion, respectively. The tests are described as part of another work [21]. We use volume fractions of 10 %, 20 % and 50 %, minimum length scales of $5 \cdot 10^{-3}$, $1 \cdot 10^{-2}$ and $1 \cdot 10^{-2}$, respectively. Convergence is investigated for the cantilever, but mesh tolerances for the stool and crank are fixed at 0.04 and 0.02. We use as much symmetry as possible and fix the maximum number of iterations at $it_{\max} = 300$. To reduce issues with local minima, the SIMP exponent is increased exponentially throughout the first 2/3rds of the optimisation

$$P_E^i = \min(4^{3i/(2it_{\max})}, 4).$$

7. Results

Due to the inconsistent formulation of our approach, we do not expect convergence in a strict sense and thus plot the best results satisfying the constraints to the tolerance of the MMA c parameter*.

The two dimensional results are shown in figure 4 with the volume throughout the optimisations plotted in figure 5(a). Both the topology and objective function seems to converge, which was not the case for a sharp corner. The maximum von misses stress is twice the allowed value underlining the need for post processing of designs obtained with stress constrained topology optimisation. We attribute the fact that the volume and compliance in figure 5 converge from above to the continuous design variables, that is the area of intermediate, and thus suboptimal design, is reduced with mesh refinement. The opposite behaviour would be expected, if the convergence of the forward problem was the dominating effect.

The compliance for the three dimensional results is plotted in figure 5(b) with the actual designs shown in figures 6 and 7 by means of $\rho = 0.5$ iso-surfaces and slices at constant x . Note that these representations can produce quadrilaterals from purely tetrahedral meshes, and that the blue wireframe represents the computational domain in which objective function and node count are calculated, see top of each design. All designs agree with a previous work [21] and in the case of the cantilever we get convergence of topology as well as objective function, but we did find a different topology, if the cantilever was optimised with $L_{\min} = 5 \cdot 10^{-2}$. The oscillations for the objective functions plotted in figure 5(b) seem stronger than for the two dimensional case, but the absence of a stress constraint seems to improve the ability to recover from infeasible designs.

7.1 Computational cost

The computational time in hours[†] is printed above the designs in figures 4, 6 and 7. An estimate for the aspect ratio (AR) is also printed for the three dimensional results. This is calculated by first computing the Steiner ellipsoid and then dividing the product of the radii with the cubed minimum radii. The aspect ratio can be used as an estimate of speed-up relative to isotropic adaptation and it seems to vary with mesh resolution, but values below 50 are rare. One can make an equivalent analysis for the two-dimensional results and arrive at 4-5, but as seen from figures 4, 6 and 7, it also depends on the problem.

The mesh adaptation takes up 20-30 % of the total computational time for the two dimensional results and 40-50 % in three dimensions. This is with single threaded computations, a direct solver and an Octave/MATLAB implementation for the mesh adaptation, so it might be possible to decrease the total computational time with an order of magnitude, by employing an optimised C++ mesh adaptation implementation [12] in combination with an iterative solver. In this regard, the influence of elements with large angles would be particularly interesting.

*In three dimensions we use $c_{\text{mma}} = 10^3$, but show designs satisfying the constraints to within 0.5%

[†]Using an Intel(R) Core(TM) i7 870 @ 2.93GHz, everything being run single threaded

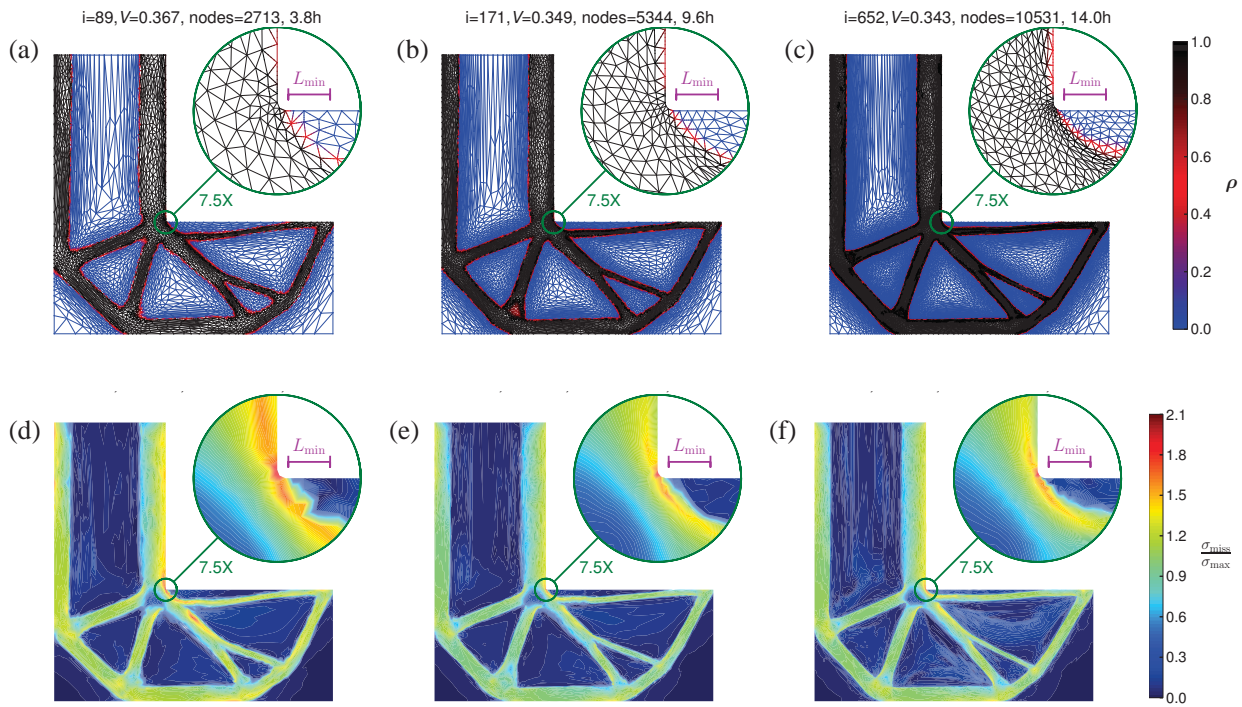


Figure 4: Optimisations with a rounded corner for $\eta_{\bar{\rho}}$ equal to 0.03 (left), 0.015 (middle) and 0.0075 (right). The design variables and mesh elements are shown for the iteration (i) at which the lowest volume fraction (V) occurs, while the stress and compliance constraints are satisfied. The designs are shown in the upper row (a-c) with the von misses stress below (d-e).

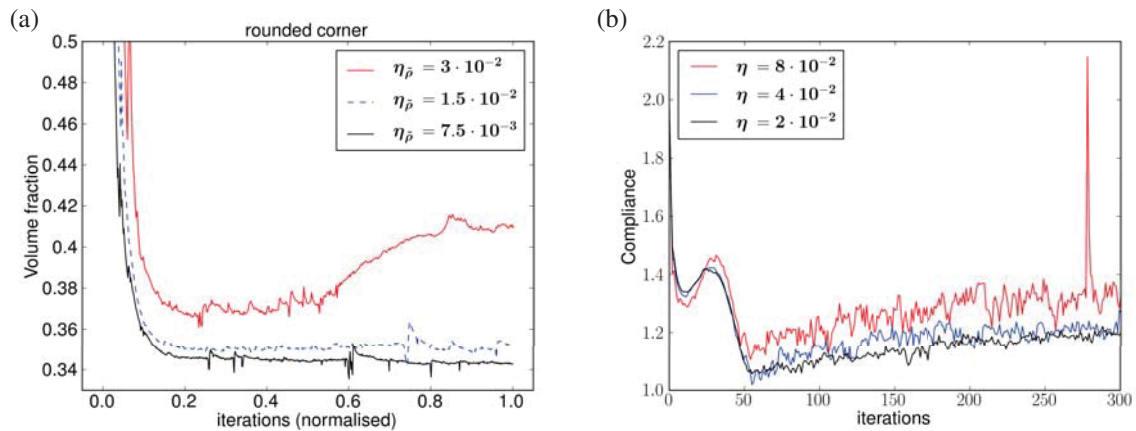


Figure 5: The volumes of optimisations for a stress and compliance constrained L-bracket problem is plotted to the left (a), while the compliance for a volume constrained three dimensional cantilever problem is plotted to the right (b). In both cases three different values for the tolerances of the mesh adaptation is shown. Note how the coarse stress constrained optimisation becomes infeasible and fails to recover. The spike of the coarse three dimensional could also be due to infeasible designs. For the three dimensional problems, the P_E parameter is smaller than 4 before iteration 200.

8. Conclusion

We have combined topology optimisation with anisotropic mesh adaptation and tested the implementation on stress and compliance constrained volume minimisation for the two dimensional L-bracket problem with a ever so slightly rounded corner as well as on volume constrained compliance minimisation in three dimensions. In both cases we are able to get mesh independence for the topology and convergence of the objective function.

9. Acknowledgement

This is work supported by the Villum Foundation.

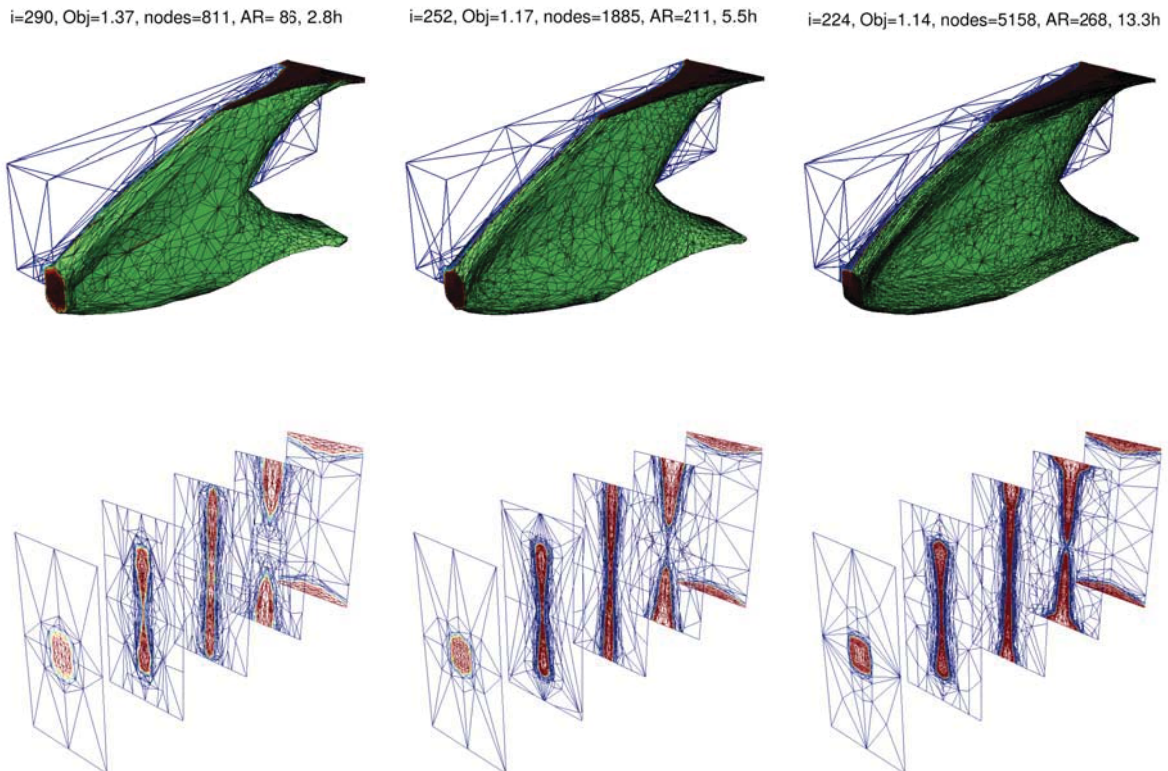


Figure 6: The best cantilever designs that satisfy the volume constraint to a relative tolerance of 0.5% are shown in terms of the $\rho = 0.5$ isosurfaces as well as slices at x/L_y equal to 0, 0.25, 0.5, 0.75 and 1. They all give the same topology, but the slice through $x = 0.25L_y$ shows significant variations.

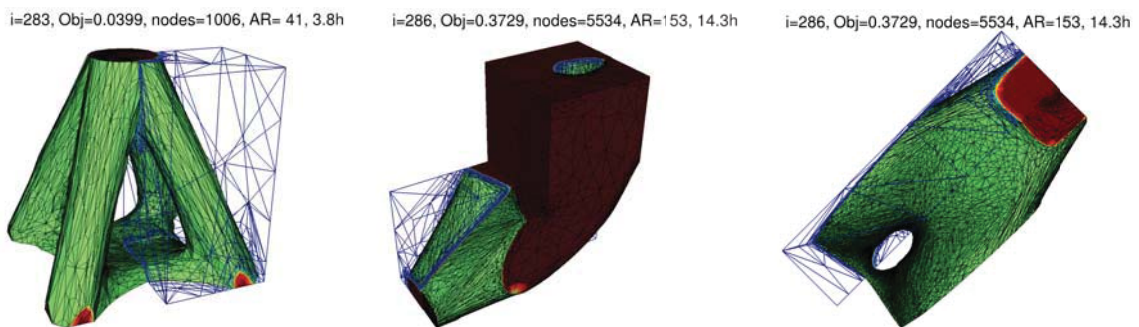


Figure 7: The best stool (left) and crank (center, right) designs are plotted in terms of their $\rho = 0.5$ isosurfaces. The crank shown from the side (center) with the support visible and from the bottom where the load is applied (right). Note that the title statistics pertain to the actual computational domain as illustrated with the blue wireframe.

10. References

- [1] Erik Andreassen, Anders Clausen, Mattias Schevenels, Boyan S Lazarov, and Ole Sigmund. Efficient topology optimization in matlab using 88 lines of code. *Structural and Multidisciplinary Optimization*, 43(1):1–16, 2011.

- [2] Niels Aage, Erik Andreassen, and Boyan Stefanov Lazarov. Topology optimization using petsc. *Structural and Multidisciplinary Optimization*, 2015.
- [3] Mathias Wallin, Matti Ristinmaa, and Henrik Askfelt. Optimal topologies derived from a phase-field method. *Structural and Multidisciplinary Optimization*, 45(2):171–183, 2012.
- [4] Samuel Amstutz and Antonio A Novotny. Topological optimization of structures subject to von mises stress constraints. *Structural and Multidisciplinary Optimization*, 41(3):407–420, 2010.
- [5] Asger Nyman Christiansen, J Andreas Bærentzen, Morten Nobel-Jørgensen, Niels Aage, and Ole Sigmund. Combined shape and topology optimization of 3d structures. *Computers & Graphics*, 46:25–35, 2015.
- [6] Adrien Loseille and Frédéric Alauzet. Continuous mesh framework part i: well-posed continuous interpolation error. *SIAM Journal on Numerical Analysis*, 49(1):38–60, 2011.
- [7] Long Chen, Pengtao Sun, and Jinchao Xu. Optimal anisotropic meshes for minimizing interpolation errors in \mathcal{L}^p -norm. *Mathematics of Computation*, 76(257):179–204, 2007.
- [8] CC Pain, AP Umpleby, CRE De Oliveira, and AJH Goddard. Tetrahedral mesh optimisation and adaptivity for steady-state and transient finite element calculations. *Computer Methods in Applied Mechanics and Engineering*, 190(29):3771–3796, 2001.
- [9] Yu V Vasilevski and KN Lipnikov. Error bounds for controllable adaptive algorithms based on a hessian recovery. *Computational Mathematics and Mathematical Physics*, 45(8):1374–1384, 2005.
- [10] Adrien Loseille. Metric-orthogonal anisotropic mesh generation. *Procedia Engineering*, 82:403–415, 2014.
- [11] Xiangrong Li, Mark S Shephard, and Mark W Beall. 3d anisotropic mesh adaptation by mesh modification. *Computer methods in applied mechanics and engineering*, 194(48):4915–4950, 2005.
- [12] Georgios Rokos, Gerard J Gorman, James Southern, and Paul HJ Kelly. A thread-parallel algorithm for anisotropic mesh adaptation. *arXiv preprint arXiv:1308.2480*, 2013.
- [13] Martin Philip Bendsoe and Ole Sigmund. *Topology optimization: theory, methods and applications*. Springer, 2003.
- [14] Krister Svanberg. The method of moving asymptotes a new method for structural optimization. *International journal for numerical methods in engineering*, 24(2):359–373, 1987.
- [15] Albert A Groenwold and LFP Etman. A quadratic approximation for structural topology optimization. *International Journal for Numerical Methods in Engineering*, 82(4):505–524, 2010.
- [16] Patrick E Farrell, David A Ham, Simon W Funke, and Marie E Rognes. Automated derivation of the adjoint of high-level transient finite element programs. *SIAM Journal on Scientific Computing*, 35(4):C369–C393, 2013.
- [17] Boyan Stefanov Lazarov and Ole Sigmund. Filters in topology optimization based on helmholtz-type differential equations. *International Journal for Numerical Methods in Engineering*, 86(6):765–781, 2011.
- [18] Anders Logg, Kent-Andre Mardal, Garth N. Wells, et al. *Automated Solution of Differential Equations by the Finite Element Method*. Springer, 2012.
- [19] GD Cheng and Xiao Guo. ϵ -relaxed approach in structural topology optimization. *Structural Optimization*, 13(4):258–266, 1997.
- [20] Pierre Duysinx and Ole Sigmund. New developments in handling stress constraints in optimal material distribution. In *Proc of the 7th AIAA/USAF/NASA/ISSMO Symp on Multidisciplinary Analysis and Optimization*, volume 1, pages 1501–1509, 1998.
- [21] Thomas Borrvall and Joakim Petersson. Large-scale topology optimization in 3d using parallel computing. *Computer methods in applied mechanics and engineering*, 190(46):6201–6229, 2001.

Robust Topology Optimization of Thin Plate Structure under Concentrated Load with Uncertain Load Point

Yoshiaki Nakazawa¹, Nozomu Kogiso², Takayuki Yamada³, Shinji Nishiwaki⁴

¹ Osaka Prefecture University, Sakai, Japan, su102024@edu.osakafu-u.ac.jp

² Osaka Prefecture University, Sakai, Japan, kogiso@aero.osakafu-u.ac.jp

³ Kyoto University, Kyoto, Japan, takayuki@me.kyoto-u.ac.jp

⁴ Kyoto University, Kyoto, Japan, shinji@prec.kyoto-u.ac.jp

1. Abstract

This study investigates the robust topology optimization of the thin plate under concentrated load with uncertain load point. Several researches investigated the effect of uncertain load direction, load magnitude or load distribution on the topology optimization. However, the robust topology optimization considering uncertainty of the load point has not been studied yet. In this study, the load point uncertainty is modelled through the convex hull model. The nominal concentrated load in out-of-plane direction is applied at the center of the plate modeled based on Reissner-Mindlin plate theory. The load point uncertainty is limited in a circle centered at the nominal load point. The worst load condition is defined as the applied load at the worst point in the convex hull that gives the worst value of the mean compliance. The worst point is easily obtained from the convex hull approach. Then, the robust objective function is formulated as a weighted sum of the mean compliance obtained from the mean load condition and the worst compliance obtained from the worst load condition. This robust topology optimization is constructed using the level set-based topology optimization method. Through numerical examples, the robust optimum configuration is compared with the deterministic optimum configuration. Then, validity of the proposed robust design method is discussed.

2. Keywords: Level Set-Based Topology Optimization, Robust Optimization, Thin Plate Structure, Convex Hull, Worst Load Case

3. Introduction

Recently, the robust optimum design is widely applied to the field of engineering design problems that consider uncertainties of design parameters such as material constants and applied load conditions [1, 2]. Integrating the topology optimization and the robust design is generally called the robust topology optimum design. Several studies have been conducted on the robust topology optimization. Takezawa *et al.* [3] introduced the worst load condition of the applied load direction or the load distribution in the topology optimization. Chen *et al.* [4] applied the random field process to evaluate the space-varied random parameters. We proposed the robust topology optimization method [5] that integrates the level set-based topology optimization [6] and the sensitivity based robust optimization method [7]. Then, we applied the stationary stochastic process to model spatially-variable uncertain parameters for the robust topology optimization [8]. On the research, uncertain design parameters such as Young's modulus and distributed load with spatial distribution are modeled by using the stationary stochastic process with a reduced set of random variables.

This study considers the robust topology optimization for the thin plate structure. On the authors' previous study [9], deterministic level set-based topology optimization method for the thin-plate structure was proposed, where the bending plate is modeled based on Reissner-Mindlin theory, This study extends it to the robust topology optimization in consideration of the applied load point uncertainty. Under actual situation, the applied load point may be varied. Therefore, the variation of the applied load point is modeled by using the convex hull modeling [10]. The convex hull is applied to obtain the worst case of uncertain parameters. By approximating the uncertainty parameter range in the convex hull, the worst case is easily obtained. Then, the objective function is formulated as a weighted sum of the mean compliance by the mean applied load and the worst compliance that is given by the worst load condition. Through numerical example, the validity of the robust topology design is discussed.

4. Topology Optimization

4.1 Level Set-Based Topology Optimization

This study uses the level set-based topology optimization method [6]. The method can create holes in the solid domain during optimization by introducing energy term derived from the phase field theory. Additionally, the

method allows qualitative control of the geometry complexity of optimal configurations.

The level set function $\phi(\mathbf{x})$ is introduced to represent a clear shape boundary $\partial\Omega$ between the material domain Ω and the void domain $D\setminus\Omega$ as $\phi(\mathbf{x}) = 0$ where \mathbf{x} indicates an arbitrary position in D . The level set function is defined to take a positive value in the material domain and negative in the void domain as follows:

$$\begin{cases} 0 < \phi(\mathbf{x}) \leq 1 & \forall \mathbf{x} \in \Omega \setminus \partial\Omega \\ \phi(\mathbf{x}) = 0 & \forall \mathbf{x} \in \partial\Omega \\ -1 \leq \phi(\mathbf{x}) < 0 & \forall \mathbf{x} \in D \setminus \Omega \end{cases} \quad (1)$$

The limit state function is bounded in $[-1, 1]$ for introducing a fictitious interface energy based on the concepts of phase field method to the objective functional.

The design optimization is formulated as following equation that contains an objective functional $F(\Omega(\phi))$.

$$\inf_{\phi} F(\Omega(\phi)) = \int_{\Omega} f(\mathbf{x}) d\Omega \quad (2)$$

where $f(\mathbf{x})$ is the integrand function.

Since the above formulation allows to have discontinuous at every point, the regularization term is introduced based on the concept of phase field method [6].

$$\inf_{\phi} F_R(\Omega(\phi)) = \int_{\Omega} f(\mathbf{x}) d\Omega + \int_D \frac{1}{2} \tau |\nabla\phi|^2 d\Omega \quad (3)$$

$$\text{subject to } G(\Omega) = \int_{\Omega} d\Omega - V_{\max} \leq 0 \quad (4)$$

where F_R is a regularized objective functional, τ is a regularization parameter that represents the ratio of the fictitious interface energy, and $G(\Omega)$ indicates the volume constraint with the upper limit V_{\max} .

Using Eq (3) and (4), Lagrangian \bar{F}_R is define as below:

$$\bar{F}_R(\Omega(\phi), \phi) = \int_{\Omega} f(\mathbf{x}) d\Omega + \lambda G(\Omega(\phi)) + \int_D \frac{1}{2} \tau |\nabla\phi|^2 d\Omega \quad (5)$$

The KKT conditions of the above optimization problem are derived as follows:

$$\bar{F}'_R = 0, \quad \lambda G = 0, \quad \lambda \geq 0, \quad G \leq 0 \quad (6)$$

where \bar{F}'_R and λ indicate the Lagrangian and the Lagrange multiplier, respectively.

4.2 Updating the Level Set Function

Level set function that satisfies the KKT conditions in Eq. (6) is candidate solutions of the optimization problem. Introducing a fictitious time t , and assuming that the variation of the level set function with respect to the time t is proportional to the gradient of Lagrangian, as follows:

$$\frac{\partial\phi}{\partial t} = -K(\phi)\bar{F}'_R \quad (7)$$

where $K(\phi) > 0$ is the positive proportionality coefficient.

Substitute Eq. (5) into Eq. (7) and applying Dirichlet boundary condition to the body domain boundary ∂D_N and Neumann boundary condition to the other boundary, the following time evolution equation is obtained:

$$\begin{aligned} \frac{\partial\phi}{\partial t} &= -K(\phi)(\bar{F}'_R - \tau\nabla^2\phi) \\ \frac{\partial\phi}{\partial n} &= 0 && \text{on } \partial D \setminus \partial D_N \\ \phi &= 1 && \text{on } \partial D_N \end{aligned} \quad (8)$$

where $H(\phi)$ is Heaviside function. Note that Eq. (8) is a reaction-diffusion equation, and the smoothness of the level set function is ensured. Further details are provided in [6].

5. Robust Topology Optimization

Robust optimum design considers the effect of uncertainty of design variables and parameters on the objective function and constraints. As shown in Fig. 1, the robust optimum design has smaller deterioration of the performance under variation of design parameters than that of the deterministic optimum design where z_0 and Δz denote nominal value and variation of design parameter, respectively.

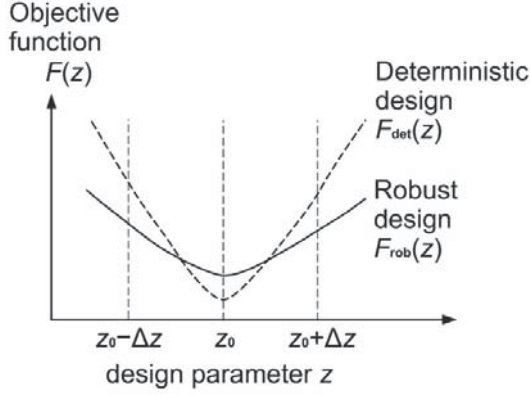


Figure 1: Concept of robust optimization

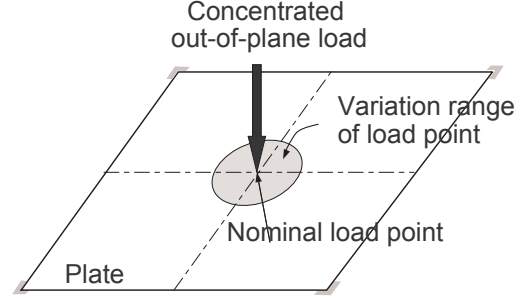


Figure 2: Variation range of applied load point on the plate

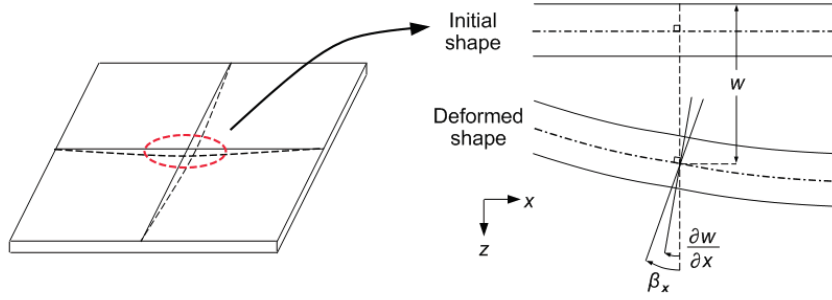


Figure 3: Reissner-Mindlin assumption

5.1 Design Problem of Thin Plate Structure

This study considers the variation of the load point of the applied concentrated load. As shown in Fig. 2, the square plate with fixed four vertices with applied the concentrated out-of-plane load is considered. The load point is modeled as uncertain parameter, where the nominal point is set at the center and the variation range is limited inside of the circle.

The conventional topology design problem is to minimize the mean compliance. That is, by using the strain energy $a(\mathbf{u}, \mathbf{v})$ and the mean compliance $l(\mathbf{u})$, the objective functional is defined as follows:

$$\inf_{\Omega} : F(\Omega) = l(\mathbf{u}) \quad (9)$$

$$\text{subject to} : a(\mathbf{u}, \mathbf{v}) = l(\mathbf{v}) \quad \text{for } \forall \mathbf{v}, \mathbf{u} \in U \quad (10)$$

where $a(\mathbf{u}, \mathbf{v})$ and $l(\mathbf{v})$ are defined as follows:

$$a(\mathbf{u}, \mathbf{v}) = \int_{\Omega} \boldsymbol{\varepsilon}(\mathbf{u}) : \mathbf{E} : \boldsymbol{\varepsilon}(\mathbf{v}) d\Omega \quad (11)$$

$$l(\mathbf{v}) = \int_{\Gamma_t} \mathbf{t} \cdot \mathbf{v} d\Gamma \quad (12)$$

where $\boldsymbol{\varepsilon}$ is the linearized strain tensor, \mathbf{E} is the elasticity tensor and the U is defined as follows:

$$U = \{ \mathbf{v} = v_i \mathbf{e}_i : v_i \in H^1(D) \} \text{ with } \mathbf{v} = 0 \text{ in } \Gamma_u \quad (13)$$

Based on Reissner-Mindlin theory, the strain energy for the thin plate structure is described as follows:

$$\frac{1}{2} a(\mathbf{u}, \mathbf{u}) = \frac{1}{2} \iint \left\{ M_x \frac{\partial \beta_x}{\partial x} + M_y \frac{\partial \beta_y}{\partial y} + M_{xy} \left(\frac{\partial \beta_y}{\partial x} + \frac{\partial \beta_x}{\partial y} \right) + Q_x \left(\frac{\partial w}{\partial x} + \beta_x \right) + Q_y \left(\frac{\partial w}{\partial y} + \beta_y \right) \right\} dx dy \quad (14)$$

where M_x, M_y, M_{xy} are the bending and the torsional moments, Q_x and Q_y are the shear force, β_x and β_y are the rotational angle, and h is the plate thickness as shown in Fig. 3.

The worst load case is defined as the load case that gives the worst value of the mean compliance in the given convex hull. In this study, the worst case is found to lie on the boundary on the convex hull by preliminary analysis. Therefore, the convex hull model is adopted. The worst case is easily obtained as solving the sub-optimization problem in each iteration of the topology optimization loop.

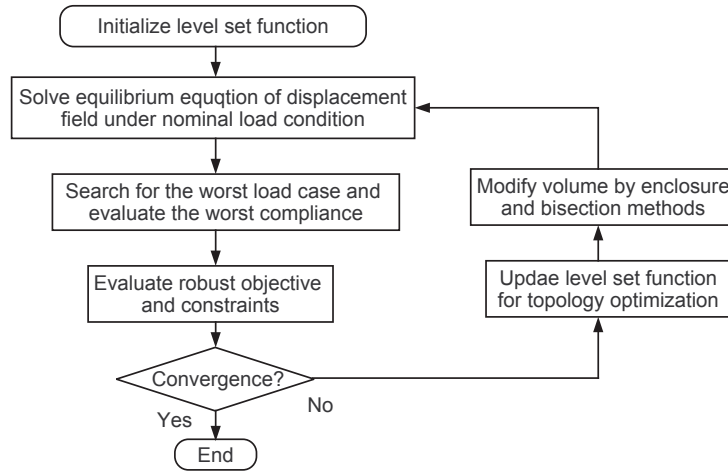


Figure 4: Flowchart of robust topology optimization

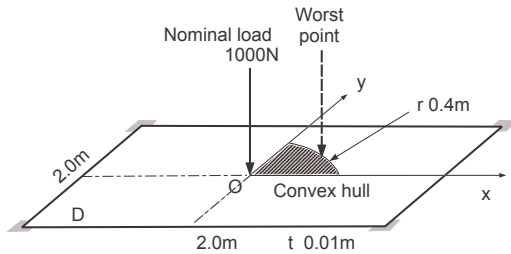


Figure 5: Plate model and convex hull for uncertain load point

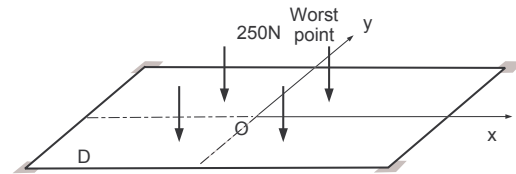


Figure 6: Plate model for robustness evaluation

5.2 Robust Topology Optimization

The objective of the robust topology optimization is defined as a weighted sum of the mean and the worst compliance as follows:

$$f_{\text{robust}}(\mathbf{x}) = (1 - \alpha)a_{\text{nom}}(\mathbf{u}, \mathbf{u}) + \alpha a_{\text{worst}}(\mathbf{u}, \mathbf{u}) \quad (15)$$

where $a_{\text{nom}}(\mathbf{u}, \mathbf{u})/2$ is the strain energy density under the deterministic nominal load, and $a_{\text{worst}}(\mathbf{u}, \mathbf{u})/2$ is the strain energy density under the worst load in the convex hull, and $0 < \alpha < 1$ is a positive weighting coefficient.

The computational flow of the proposed robust topology optimization method is shown in Fig. 4. Starting the initialization of the level set function, the equilibrium equation of the nominal load is solved using FEM to evaluate the mean compliance. Then, the worst load condition is searched in the convex hull and the robust objective function is evaluated. After the convergence check, the level set function is updated. Then, the volume is modified to fit the upper limit by the enclosure and bisection method [8]. The equilibrium equation is solved for the updated geometry and the process is repeated until convergence.

6. Numerical Examples

As a simple numerical example, the square plate with 2.0m on a side and 0.01m in thickness with the fixed four vertices as shown in Fig. 5 is considered as a fixed design domain D . Young's modulus and Poisson's ratio are set as 210GPa, and 0.33, respectively. The fixed design domain D is discretized to 21850 elements for evaluating the mean and the worst compliance. For the topology optimization, the regularization parameter τ and the volume constraint are set as 5.0×10^{-5} and 50%, respectively.

The concentrated out-of-plane load of 1000N is applied at the center of the plate as a nominal load point. As a random parameter, the load point is assumed to be varied in the circle centered at the nominal load point. The convex hull is set as the quarter sector shown in Fig. 5, because of considering the symmetry condition,

It is expected that the unsymmetric load condition for the worst case will yield the unsymmetric optimum configuration. However, since the uncertain point will be lie on the other sectors, the unsymmetric configuration is not suitable as the robust optimum configuration. Therefore, the other three symmetric points to the worst load point are also considered as the worst load points. For evaluating the worst compliance a_{worst} in Eq. (15), the plate model is arranged to apply the four concentrated loads of four divided magnitude of 250N at the worst points as shown in Fig. 6.

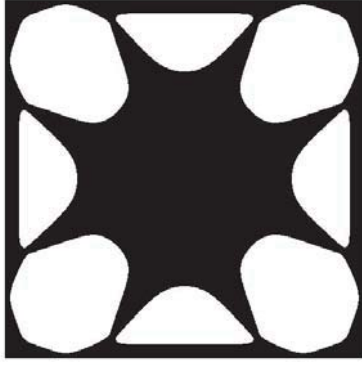


Figure 7: Deterministic optimum configuration

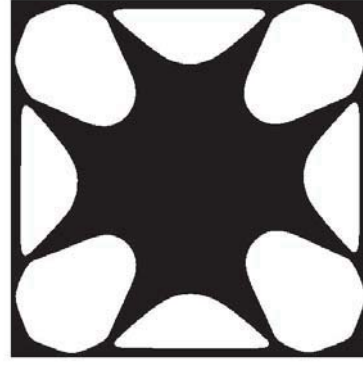


Figure 8: Robust optimum configuration ($\alpha = 0.70$)

Table 1: Mean compliance under deterministic load

Configuration	Load point [m]	Mean Compliance [J/m ³]
Deterministic	(0.0, 0.0)	7.606×10^4
Robust ($\alpha = 0.30$)	(0.0, 0.0)	7.572×10^4
Robust ($\alpha = 0.50$)	(0.0, 0.0)	7.559×10^4
Robust ($\alpha = 0.70$)	(0.0, 0.0)	7.545×10^4

Table 2: Mean compliance under worst load

Configuration	Load point [m]	Mean Compliance [J/m ³]	Increase rate [%]
Deterministic	(0.0, 0.40)	8.127×10^4	6.848
Robust ($\alpha = 0.30$)	(0.0, 0.40)	8.048×10^4	6.292
Robust ($\alpha = 0.50$)	(0.0, 0.40)	8.016×10^4	6.049
Robust ($\alpha = 0.70$)	(0.40, 0.0)	7.984×10^4	5.813
Deterministic	(0.40, 0.0)	8.126×10^4	6.832
Robust ($\alpha = 0.30$)	(0.40, 0.0)	8.047×10^4	6.284
Robust ($\alpha = 0.50$)	(0.40, 0.0)	8.008×10^4	5.951
Robust ($\alpha = 0.70$)	(0.0, 0.40)	7.974×10^4	5.680

The deterministic optimum configuration obtained under the nominal load condition is shown in Fig. 7. The robust optimum configuration under $\alpha = 0.7$ in Eq. (15) is shown in Fig. 8. These configurations are very similar with each other except for the hole shape closed to the vertices. Fig. 8 shows the robust design under the case of $\alpha = 0.7$. The other optimum configurations for the smaller values of the weighting factors are almost the same in Fig. 8.

Table 1 compares the mean compliance values under the deterministic load between the deterministic and the robust optimum configurations with $\alpha = 0.3, 0.5$ and 0.7 . It is found that the mean compliance of the robust configuration under the deterministic load is smaller than that of the deterministic configuration.

Then, Table 2 compares the mean compliance values under the worst load conditions. The load point shows the worst load point. The values of the mean compliance under the rotationally symmetric load point are also listed. The deterioration of the compliance value are almost the same between the deterministic and the robust configurations, though the deterioration rates of the robust configurations are smaller than that of the deterministic configuration. It means that the deterministic optimum configuration has higher robustness in this case. That's why the optimum configurations are the similar configurations.

It is expected that the research concerning the robust optimum design will expect to obtain the different design from the deterministic one. However, that is not always true. We must consider the effect of the random parameter on the deterministic optimum configuration first.

For the purpose, the out-of-plane deformation distributions for the deterministic optimum configuration are compared between the nominal and the worst load conditions in Fig. 9. The maximum displacement occurs at the load point under the nominal case. On the other hand, the maximum occurs not at the load point under the worst load case, at the righter position from the worst load point, at the edge of the hole. It is considered that the hole makes the maximum displacement position shift from the worst load point to the edge of the hole, that will make the deterioration of the worst compliance smaller. As a result, the deterministic optimum configuration happens to be

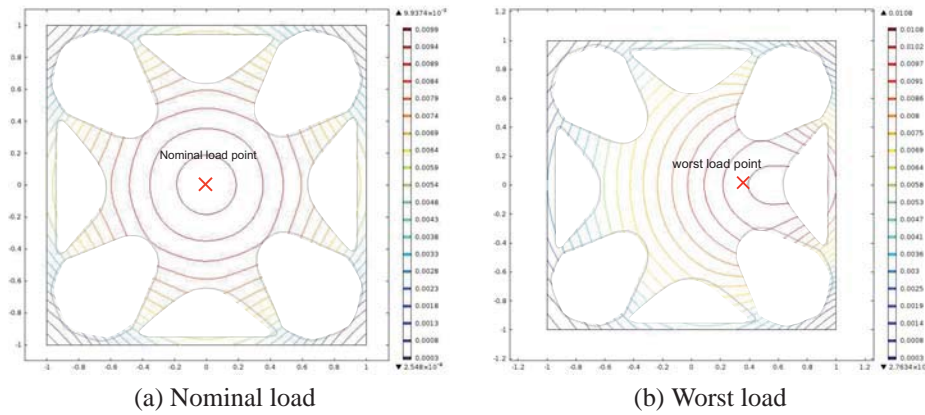


Figure 9: Out-of-plane deformation distribution for deterministic optimum configuration

robust for variations of the load point in this example.

7. Conclusion

This paper investigates the robust topology optimum design for the thin plate structure under the concentrated load with uncertain load point. The uncertainty is modeled by using the convex hull to find the worst load condition that yield the worst value of the mean compliance. The robust objective function is formulated as a weighted sum of the mean and the worst compliance. The optimum configuration is obtained by using the level set-based topology optimization.

Through the numerical examples, the robust configuration is almost similar to the deterministic configuration. It means that we must consider the effect of uncertainties of the design parameters on the deterministic optimum configuration at first.

We will investigate the effect of the other design parameters on the optimum configuration for the thin plate structure.

8. References

- [1] H. Beyer and B. Sendhoff, Robust optimization - a comprehensive survey, *Computer methods in Applied Mechanics and Engineering*, 196, 33-34 (2007), 3190-2281.
- [2] G. Park, T. Lee, K. Lee, and K. Hwang, Robust design: an overview *AIAA Journal*, 44, 1 (2006), 181-191.
- [3] A. Takezawa, S. Nii, M. Kitamura, and N. Kogiso, Topology optimization for worst load conditions based on the eigenvalue analysis of an aggregated linear system, *Computer methods in Applied Mechanics and Engineering*, 200, 25-28 (2011), 2268-2281.
- [4] S. Chen, W. Chen and S. Lee, Level set based robust shape and topology optimization under random field uncertainties, *Structural and Multidisciplinary Optimization*, 41, 4 (2010), 507-524.
- [5] Y. Hirano, T. Yamada, N. Kogiso, S. Nishiwaki, and A. Iga, Robust design using level-set based topology optimization for coupled thermal and structural problems, *13th AIAA/ISSMO Multidisciplinary Analysis Optimization Conference*, USA (2010) AIAA-2010-9357.
- [6] T. Yamada, K. Izui, S. Nishiwaki, and A. Takezawa, A topology optimization method based on the level set method incorporating a fictitious interface energy, *Computer methods in Applied Mechanics and Engineering*, 199, 45-48 (2010), 2876-2891.
- [7] S. Sundaresan, K. Ishii and D. R. Houser, A Robust Optimization Procedure with Variations on Design Variables and Constraints, *Engineering Optimization*, 24, 2 (1995), 101-117.
- [8] K. Ueda, M. Otomori, N. Kogiso, T. Yamada and S. Nishiwaki, Level Set-Based Robust Topology Design Considering Spatial Uncertainty *14th AIAA/ISSMO Multidisciplinary Analysis and Optimization Conference*, USA (2012), AIAA-2012-5565.
- [9] H. Horio, N. Kogiso, M. Otomori, T. Yamada, and S. Nishiwaki, Level set-based topology optimization of thin plate structure for maximizing stiffness under out-of-plane deformation, *Transaction of the JSME*, 80, 811 (2014), DSM0054 (in Japanese).
- [10] Y. Ben-Haim and I. Elishakof, *Convex Models of Uncertainty in Applied Mechanics*, Elsevier, (1990).

Structural and Aerostructural Design of Aircraft Wings with a Matrix-Free Optimizer

Andrew B. Lambe¹, Joaquim R. R. A. Martins²

¹ Institute for Aerospace Studies, University of Toronto, Toronto, Ontario, Canada, andrew.lambe@mail.utoronto.ca

² Department of Aerospace Engineering, University of Michigan, Ann Arbor, Michigan, USA, jrram@umich.edu

1. Abstract

In structural optimization subject to failure constraints, computing the gradients of a large number of functions with respect to a large number of design variables may not be computationally practical. Often, the number of constraints in these optimization problems is reduced using constraint aggregation at the expense of a higher mass of the optimal structural design. This work presents results of structural and coupled aerodynamic and structural design optimization of aircraft wings using a novel matrix-free augmented Lagrangian optimizer. By using a matrix-free optimizer, the computation of the full constraint Jacobian at each iteration is replaced by the computation of a small number of Jacobian-vector products. The low cost of the Jacobian-vector products allows optimization problems with thousands of failure constraints to be solved directly without resorting to constraint aggregation. The results indicate that the matrix-free optimizer reduces the computational work of solving the optimization problem by an order of magnitude compared to a traditional sequential quadratic programming optimizer. Furthermore, the use of a matrix-free optimizer makes the solution of large multidisciplinary design problems, in which gradient information must be obtained through iterative methods, computationally tractable.

2. Keywords: Matrix-free optimizer, multidisciplinary design optimization, structural optimization, constraint aggregation

3. Introduction

When solving structural optimization problems or multidisciplinary design optimization (MDO) [9] problems involving a structural analysis, we want to use failure constraints directly in our problem formulation. However, constraining the optimization problem in this way for complex structures like aircraft wings leads to a problem formulation with thousands of constraints. Often, constraint aggregation, such as Kreisselmeier–Steinhauser (KS) aggregation [7, 12], is employed to reduce the number of constraints in the problem yet still obtain a feasible final design. While this approach is effective in reducing the computational cost of the optimization, it compromises the quality of the final structural design. The KS parameter must be chosen to balance accuracy of the feasible design space with the conditioning of the optimization problem itself.

We propose to avoid excessive constraint aggregation by using a gradient-based optimizer that, instead of requiring the gradients explicitly, requires only matrix-vector products with the constraint Jacobian. When a structural or multidisciplinary analysis is solved at each optimizer iteration, the expression for the constraint Jacobian is

$$\left[\frac{dc}{dx} \right] = \left[\frac{\partial C}{\partial x} \right] - \left[\frac{\partial C}{\partial y} \right] \left[\frac{\partial R}{\partial y} \right]^{-1} \left[\frac{\partial R}{\partial x} \right] \quad (1)$$

where R are the governing equations of the analysis, y are the state variables, x are the design variables, and C are the design constraints. To form both forward and transpose matrix-vector products with (1), only a single linear system needs to be solved per product, thus avoiding the high cost of forming Jacobian. An optimizer that accesses gradient information through matrix-vector products alone is referred to as a matrix-free optimizer. The research discussed in this paper follows our previous work developing a matrix-free augmented Lagrangian algorithm [1, 8].

In this paper, we present the results of applying our matrix-free optimizer to a pair of aircraft wing design optimization problems. The first problem is a minimum-mass problem subject to failure constraints on the wing at two load conditions. The second problem is an MDO problem in which the take-off gross weight (TOGW) of an aircraft is minimized for a design mission considering both structural and aerodynamic characteristics of the wing.

4. Matrix-Free Augmented Lagrangian Method

We chose to modify the classical augmented Lagrangian algorithm [2] to create a matrix-free optimizer capable of solving optimization problems with nonlinear equality and inequality constraints. In the augmented Lagrangian

algorithm, the nonlinear constraints in the optimization problem

$$\begin{aligned}
& \text{minimize} && F(x) \\
& \text{with respect to} && x \\
& \text{subject to} && C(x) \geq 0 \\
& && x_L \leq x \leq x_U
\end{aligned} \tag{2}$$

are relaxed to yield

$$\begin{aligned}
& \text{minimize} && \Phi(x, t; \lambda, \rho) = F(x) - \lambda^T (C(x) - t) + \frac{\rho}{2} (C(x) - t)^T (C(x) - t) \\
& \text{with respect to} && x, t \\
& \text{subject to} && x_L \leq x \leq x_U \\
& && t \geq 0,
\end{aligned} \tag{3}$$

where Φ is the augmented Lagrangian function, λ is a vector of Lagrange multiplier estimates, ρ is a penalty parameter, and t is a vector of slack variables. Each major iteration of the augmented Lagrangian method consists in solving problem (3) and updating ρ and λ based on the constraint infeasibility at the optimal choice of x and t . We use the updating scheme proposed by Conn et al. [2] to solve problem (3) approximately.

Problem (3) is solved by an L_∞ trust-region approach. The trust region subproblem is given by

$$\begin{aligned}
& \text{minimize} && Q(p) = \frac{1}{2} p^T B p + g^T p \\
& \text{with respect to} && p \\
& \text{such that} && p_L \leq p \leq p_U,
\end{aligned} \tag{4}$$

where B is an estimate of the Hessian $\nabla^2 \Phi$, g is the gradient $\nabla \Phi$, and p is the search direction in both x and t . The choice of the L_∞ trust region makes handling the bound constraints in problem (3) easy. Subproblem (4) is solved by the algorithm of Moré and Toraldo [10], modified to account for the case where the approximate Hessian B is indefinite. Moré and Toraldo's algorithm needs only matrix-vector products with B to solve (4), so all that is needed to make the algorithm matrix-free is a suitable approximation to $\nabla^2 \Phi$.

In our optimization problems of interest, we do not have access to second derivatives of any of the functions. Therefore, we use quasi-Newton methods to approximate $\nabla^2 \Phi$ in the trust-region subproblem. To increase the accuracy of our model Hessian B , we use two quasi-Newton approximations within B instead of a single one. We have developed two approaches to approximating $\nabla^2 \Phi$ that balance a low cost of implementation with the ability to exploit the structure of $\nabla^2 \Phi$. Analytically, the true Hessian of the Lagrangian is given by

$$\nabla^2 \Phi = \begin{bmatrix} \nabla^2 F - \sum_{i=1}^m \lambda_i \nabla^2 C_i + \sum_{i=1}^m (\rho (C_i(x) - t_i)) \nabla^2 C_i + \rho J^T J & \rho J^T \\ \rho J & \rho I \end{bmatrix}, \tag{5}$$

where $J = [\nabla C(x)]^T$.

In the split-quasi-Newton approach, the augmented Lagrangian is broken up into Lagrangian and infeasibility functions and a separate quasi-Newton method is used to approximate the Hessian of each function. In particular,

$$\begin{aligned}
\Phi(x, t; \lambda, \rho) &= \mathcal{L}(x, t; \lambda) + \rho \mathcal{I}(x, t) \\
\mathcal{L}(x, t; \lambda) &= F(x) - \lambda^T (C(x) - t) \\
\mathcal{I}(x, t) &= \frac{1}{2} (C(x) - t)^T (C(x) - t).
\end{aligned} \tag{6}$$

We use a symmetric rank-one (SR1) [11] quasi-Newton approximation to $\nabla^2 \mathcal{L}$ and a Broyden–Fletcher–Goldfarb–Shanno (BFGS) [11] quasi-Newton approximation to $\nabla^2 \mathcal{I}$. These choices were made based on the fact that $\nabla^2 \mathcal{I}$ is positive-semidefinite near a local minimum, while $\nabla^2 \mathcal{L}$ could be indefinite. Both quasi-Newton approximations are of the limited-memory variety to allow us to solve large problems efficiently.

In the approximate-Jacobian approach, we directly approximate the Jacobian itself using a quasi-Newton method and truncate the term $\sum_{i=1}^m (\rho (C_i(x) - t_i)) \nabla^2 C_i$ in (5). This truncation is justified by the fact that $C(x) - t = 0$ at an optimal solution, so the term becomes negligible as optimality is approached. Again, we use a limited-memory SR1 approximation to $\nabla^2 \mathcal{L}$ for the Lagrangian Hessian, while the Jacobian is approximated by a full-memory adjoint Broyden method [13]. The adjoint Broyden update is given by

$$A^{k+1} = A^k + \frac{\sigma^k \sigma^{k,T}}{\sigma^{k,T} \sigma^k} (J^{k+1} - A^k), \tag{7}$$

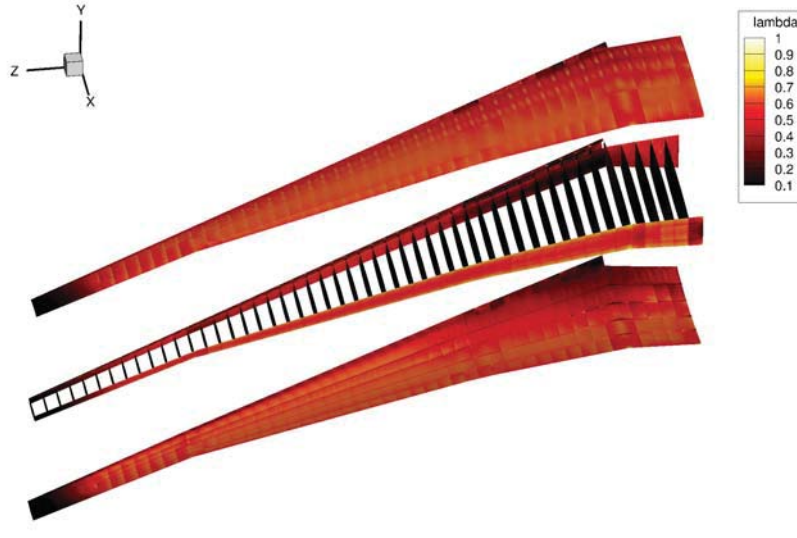


Figure 1: Exploded view of structure layout used in the test problems. The contours represent stress as a fraction of the yield stress for the optimal wing structure using a KS parameter value of 100.

where A^k is the approximate Jacobian at iteration k and

$$\sigma^k = (J^{k+1} - A^k)s^k. \quad (8)$$

In contrast to quasi-Newton methods for square matrices, there are no limited-memory variants of the adjoint Broyden method with a convergence guarantee, so we use the full memory version. To improve the computational performance of this method on large problems in a parallel computing environment, message passing interface (MPI) standard instructions are used to distribute the matrix approximation over multiple processors and form matrix-vector products with A .

5. Analysis Software

Our matrix-free optimizer, AUGLAG, is benchmarked against the SQP optimizer SNOPT [3]. SNOPT also uses a limited-memory quasi-Newton approximation to $\nabla^2 \mathcal{L}$ to solve a given optimization problem. However, SNOPT requires the full constraint Jacobian to be computed at each iteration, while AUGLAG needs only Jacobian-vector products. While we expect to see a difference in the results due to the difference in optimization algorithms, our aim is to show that AUGLAG is still competitive with SNOPT due to the low cost of the trust-region iterations in AUGLAG.

The wing structure used in our test problems is analyzed using the Toolkit for the Analysis of Composite Structures (TACS) [4], a finite-element analysis code. The wing aerodynamics were analyzed using the three-dimensional panel code TriPan [5]. All analysis and optimization codes were accessed through the MACH framework (MDO of aircraft configurations at high fidelity) [6]. The MACH framework includes modules for aerostructural analysis and geometry warping.

Prior to this project, both the TACS and TriPan codes and the MACH framework possessed modules for efficiently computing derivatives using the adjoint method. However, in order to enable the matrix-free approach to optimization, modules needed to be added to compute forward and transpose matrix-vector products with the partial derivative matrices shown in (1). We expect other researchers interested in using a matrix-free optimizer would need to undertake similar modifications to their solvers. However, if the direct and adjoint methods are already available, the implementation is relatively straightforward.

6. Structural Optimization Results

The first problem we study is the minimization of a wing box mass subject to failure constraints. The outer wing geometry is based on the Boeing 777-200ER civil transport. Figure 1 shows the structural layout used. The wing is 30.5 m from root to tip, and the assumed aircraft mass is 298 000 kg. The wing is analyzed at two load

Table 1: Average run times for specific computations in the wing structure optimization problem

Computation	Wall Time, 32 proc.
Objective and 2832 constraints	2.31 s
Jacobian of 2832 constraints	188.50 s
Objective gradient only	0.02 s
Jacobian-vector product with 2832 constraints	0.40 s
Transpose Jacobian-vector product with 2832 constraints	0.33 s

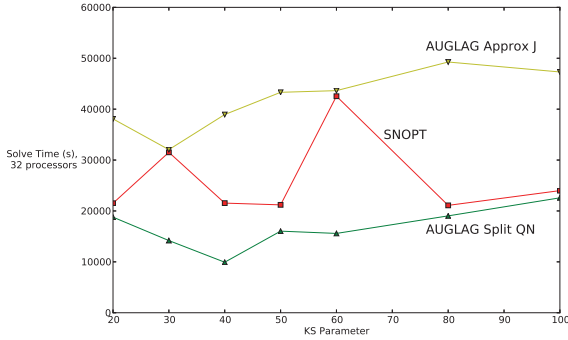


Figure 2: Run time to solve the wing structure optimization problem for a range of KS parameter values

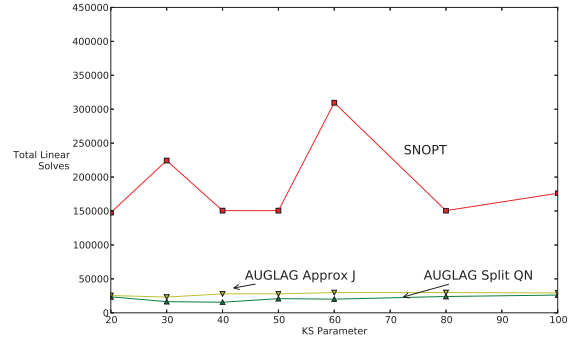


Figure 3: Number of linear solve operations to solve the wing structure optimization problem for a range of KS parameter values

cases: a 2.5g pull-up maneuver and a 1g push-over maneuver. The wing model itself contains nearly 46 000 finite elements and 250 000 degrees of freedom. Individual thickness design variables and yield stress failure constraints are assigned to consistent patches of elements. Note that KS aggregation is still used in the failure constraints of this problem, but only at the level of the element patches. The optimization problem has 1416 variables and 2832 constraints.

Figures 2 and 3 show the cost of the optimization using SNOPT and the two versions of AUGLAG over a range of KS parameters in terms of both run time and the number of linear solve operations. The latter metric treats one matrix-vector product as equivalent in cost to forming a single row or column of the constraint Jacobian. Because the linear solve operation is the most expensive in forming the Jacobian (1), the number of linear solves acts as a computational cost estimate. Figure 3 shows that AUGLAG is far more efficient than SNOPT at optimizing the wing design, in terms of the number of linear solves, for a range of KS parameter values. Reductions in the number of linear solves can be up to an order of magnitude. However, Figure 2 shows that AUGLAG is only more efficient in terms of run time when using the split-quasi-Newton Hessian approximation.

The variation in the results with the increasing KS parameter value shown in Figures 2 and 3 raises the question of whether or not this is a random phenomenon based on the starting point. The starting point used was a constant

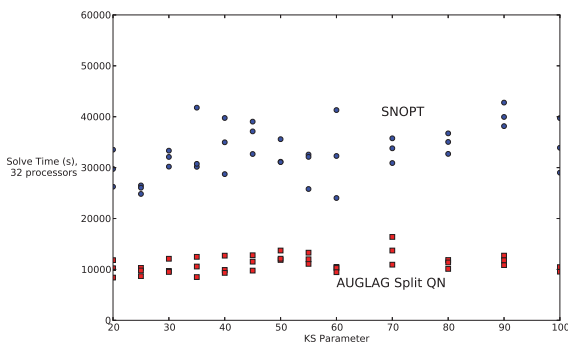


Figure 4: Run time to solve the wing structure optimization problem from a random starting point

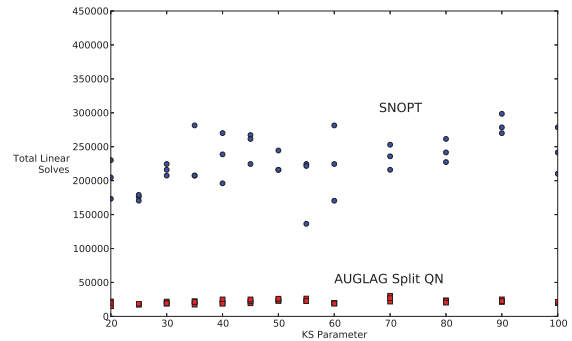


Figure 5: Number of linear solve operations to solve the wing structure optimization problem from a random starting point

Table 2: Average run times for specific computations in the aerostructural optimization problem

Computation	Wall Time, 32 proc.
Objective and 4251 constraints	16.82 s
Jacobian of 4251 constraints	26 926.00 s
Objective gradient only	3.86 s
Jacobian-vector product with 4251 constraints	14.36 s
Transpose Jacobian product with 4251 constraints	8.15 s

Table 3: Computational resources to solve the aerostructural optimization problem

Optimizer	Number of Linear Solves	Wall Time, 32 proc.
SNOPT (50 iteration estimate)	217107	382.5 hr
AUGLAG Split QN (average)	38481	38.0 hr

thickness in all elements. Figures 4 and 5 show results for SNOPT and the split-quasi-Newton version of AUGLAG using sets of randomly-generated thickness values as the starting points. The data in Figures 4 and 5 fall into a particular range for each optimizer, suggesting that the oscillations observed in Figures 2 and 3 are indeed a random occurrence.

The difference in the results between Figures 2 and 3 comes from the fact that the relative cost of computing the Jacobian in this problem is low compared to evaluating the constraints. Table 1 shows that, using 32 processors in parallel, obtaining the Jacobian requires only 90 times as much time as computing the objective and all the failure constraints. If all linear solves were near-equal effort, we would expect a factor closer to a thousand. However, TACS is designed to compute gradients very efficiently once the functions have been evaluated. As a result, the large number of iterations taken by AUGLAG hinders the performance more than the matrix-free interface helps. The results are further tempered by the fact that both versions of AUGLAG could only converge reliably to an optimality tolerance of 3×10^{-4} while SNOPT was able to converge to a tolerance of 10^{-5} . We believe this is caused by the inability of the augmented Lagrangian algorithm to update the Lagrange multipliers as frequently. Despite the different tolerances, AUGLAG computes optimal mass values that are within 1-3% of the mass predicted by SNOPT. Because of this similarity in solutions, we can say that AUGLAG provides a fast estimate of an optimal solution for problems with many design variables and many constraints.

7. Aerostructural Optimization Results

The wing design optimization problem is now expanded to include aerodynamic analysis and aerostructural coupling. The objective of the new problem is to minimize the TOGW of the aircraft for a 7725-nautical-mile design mission. TOGW includes the weight of the wing structure, the weight of the fuel burned, and fixed weights representing the payload and the rest of the aircraft structure. A third load case and another 1416 failure constraints are added to model the wing at cruise. An angle-of-attack design variable is introduced for each load case along with corresponding constraints to match the aircraft weight to the lift generated by the wing. Finally, five twist variables are introduced to allow the optimizer to twist the jig shape of the wing to alleviate high loads. The final design problem contains 1424 design variables and 4251 constraints.

The critical feature of this problem is the high cost of computing the Jacobian. Because the problem is multidisciplinary, the linear system that is solved in forming the Jacobian or Jacobian-vector products can only be solved iteratively, so the cost of the Jacobian is far higher than the cost of the objective and constraint functions. Our tests (see Table 2) suggest that computing the full Jacobian would take about 7.5 hours using 32 processors. Under this time constraint, an optimizer like SNOPT would only be able to complete five iterations in a typical two-day high-performance computing job. Given that the structural optimization problem shown in Section 6 required approximately 50 iterations to converge, this run time is estimated to be 16 days, which is too long.

Using the split-quasi-Newton version of AUGLAG and a convergence tolerance of 3×10^{-4} , we are able to compute optimal wing designs within the two-day limit. Table 3 shows the run time and number of linear solves required by AUGLAG, averaged over seven KS parameter values, compared with our estimate of the resources required for SNOPT to solve the same problem. In terms of both the number of linear solves and run time, AUGLAG is up to an order of magnitude faster than the estimated results of SNOPT.

8. Conclusions

We have presented results for the optimization of a wing structure using a new matrix-free optimizer. We deliberately avoided aggressive constraint aggregation and formulated problems with both thousands of variables and thousands of constraints. Our matrix-free optimizer is capable of solving these large optimization problems much more quickly than a traditional optimizer. Depending on the relative cost of the Jacobian evaluation, the total computational effort can be reduced by up to an order of magnitude. We expect that further gains are possible if more advanced optimization algorithms are adapted to be matrix-free.

9. Acknowledgements

Computations were performed on the GPC supercomputer at the SciNet HPC Consortium. SciNet is funded by: the Canada Foundation for Innovation under the auspices of Compute Canada; the Government of Ontario; Ontario Research Fund - Research Excellence; and the University of Toronto.

10. References

- [1] S. Arreckx, A. Lambe, J. R. R. A. Martins, and D. Orban. A matrix-free augmented Lagrangian algorithm with application to large-scale structural design optimization. *Optimization and Engineering*, 2015. (Accepted subject to revisions).
- [2] A. R. Conn, N. I. M. Gould, and P. L. Toint. A Globally Convergent Augmented Lagrangian Algorithm for Optimization with General Constraints and Simple Bounds. *SIAM Journal on Numerical Analysis*, 28(2): 545–572, 1991.
- [3] P. E. Gill, W. Murray, and M. A. Saunders. SNOPT: An SQP Algorithm for Large-Scale Constrained Optimization. *SIAM Journal on Optimization*, 12(4):979–1006, 2002.
- [4] G. J. Kennedy and J. R. R. A. Martins. A parallel finite-element framework for large-scale gradient-based design optimization of high-performance structures. *Finite Elements in Analysis and Design*, 87:56–73, Sept. 2014. ISSN 0168874X. doi: 10.1016/j.finel.2014.04.011. URL <http://linkinghub.elsevier.com/retrieve/pii/S0168874X14000730>.
- [5] G. J. Kennedy and J. R. R. A. Martins. A parallel aerostructural optimization framework for aircraft design studies. *Structural and Multidisciplinary Optimization*, 50(6):1079–1101, December 2014. doi: 10.1007/s00158-014-1108-9.
- [6] G. K. W. Kenway, G. J. Kennedy, and J. R. R. A. Martins. Scalable parallel approach for high-fidelity steady-state aeroelastic analysis and derivative computations. *AIAA Journal*, 52(5):935–951, May 2014. doi: 10.2514/1.J052255.
- [7] G. Kreisselmeier and R. Steinhauser. Systematic Control Design by Optimizing a Vector Performance Indicator. In *Symposium on Computer-Aided Design of Control Systems*, pages 113–117, Zurich, Switzerland, 1979. IFAC.
- [8] A. B. Lambe and J. R. R. A. Martins. A matrix-free approach to large-scale structural optimization. In *Proceedings of the 10th World Congress on Structural and Multidisciplinary Optimization*, Orlando, FL, May 2013.
- [9] J. R. R. A. Martins and A. B. Lambe. Multidisciplinary design optimization: A survey of architectures. *AIAA Journal*, 51(9):2049–2075, September 2013. doi: 10.2514/1.J051895.
- [10] J. J. Moré and G. Toraldo. On the Solution of Large Quadratic Programming Problems with Bound Constraints. *SIAM Journal on Optimization*, 1(1):93–113, 1991.
- [11] J. Nocedal and S. J. Wright. *Numerical Optimization*. Springer-Verlag, 2nd edition, 2006.
- [12] N. M. K. Poon and J. R. R. A. Martins. An adaptive approach to constraint aggregation using adjoint sensitivity analysis. *Structural and Multidisciplinary Optimization*, 34:61–73, 2007. doi: 10.1007/s00158-006-0061-7.
- [13] S. Schlenkrich, A. Griewank, and A. Walther. On the local convergence of adjoint Broyden methods. *Mathematical Programming*, 121:221–247, 2010. doi: 10.1007/s10107-008-0232-y.

Topology Optimization for Heat Conduction Using Generative Design Algorithms

Danny J. Lohan¹, Ercan M. Dede², James T. Allison³

¹ University of Illinois at Urbana-Champaign, USA, dlohan2@illinois.edu

² Toyota Research Institute of North America, Ann Arbor, USA, eric.dede@tema.toyota.com

³ University of Illinois at Urbana-Champaign, USA, jtalliso@illinois.edu

1. Abstract

In this article, generative design algorithms are investigated as a strategy for solving two-dimensional steady-state heat conduction topology optimization problems. The motivation for this study is to investigate alternative numerical strategies for the eventual solution of richer three-dimensional multidisciplinary electro-thermal design problems related to functional electrical power systems. The efficient solution of such problems is critical for future power-dense electronics, where the optimal layout of heat sources (e.g., electrical devices) and heat sinks in combination with heat flow control structures and devices is important. Thus, as a first step toward this greater goal, generative algorithms are explored for their possible benefits, which include enabling a broader variety of objective functions, design constraints, and design variables plus separation of the design description from the computational mesh. Specifically, a new design method based the Space Colonization Algorithm is investigated. The generative algorithm is implemented using two distinct techniques. The first method is to use the generative algorithm to produce a starting topology for the SIMP Method; this will be referred to here as the Hybrid Approach. The second technique is to use the generative algorithm to produce topologies that can be meshed directly and evaluated with a finite element solver; this will be referred to here as the Generative Design Approach. A two-dimensional case study is used to compare the effectiveness of the SIMP, Hybrid, and Generative Design approaches. These initial studies involve a homogeneously heated square design domain where the thermal compliance design objective and computational cost are assessed.

2. Keywords: Topology Optimization, Generative Algorithms, Conduction

3. Introduction

Topology optimization was first explored in structural design. Given a design domain, topology optimization algorithms determine the distribution of material within the domain to achieve the best structural performance. Numerous approaches have been developed to assign material distribution, from density to evolutionary approaches. A recent review describes existing topology optimization approaches in more detail [1]. Beyond structural design, topology optimization algorithms have been tailored to solve heat transfer problems, including two-dimensional heat conduction problems [2, 3, 4] and multiphysics thermo-fluid problems [5, 6]. Extensions to three-dimensional heat conduction problems [7] and transient heat transfer problems [8, 9] have been made.

Generative algorithms involve the iterative application of simple recursive rules to produce sophisticated algorithm outputs. These algorithms have gained popularity in generative art and architecture in recent decades [10]. More recently, they have been used in engineering design, both for their ability to explore novel designs, and for use as design abstractions that allow exploration of high-dimension system designs using a low-dimension set of generative algorithm parameters. More specifically, instead of adjusting system design variables directly, we adjust generative algorithm rule parameters to produce new designs. This indirect representation reduces problem dimension, and can support faster design space search when coupled with optimization algorithms. Applying an optimization algorithm on generative algorithm parameters is analogous to optimizing on a mapping. For some complex design problems, optimization of these indirect system representations have been found to produce meaningful and improved solutions, whereas conventional direct design representations can fail to produce useful designs [11].

In this work, we look to compare three different strategies with respect to their abilities to produce designs for effective heat extraction. The first strategy is the Solid Isotropic Material with Penalization (SIMP) approach, which is a mature topology optimization method that will be used as a comparison baseline. The second strategy is to use a generative algorithm to produce a topology that can be meshed and solved with a finite element solver. The third strategy utilizes the same generative algorithm to create a starting topology for the SIMP approach [12], which is then used to produce an optimal topology. A discussion of findings and suggestions for future work follow.

4. Problem Formulation

Consider a homogeneously heated design domain, as shown in Fig 1. The steady-state conductive heat transfer across the domain can be represented by the following governing equations:

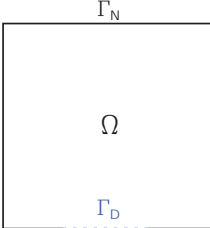
$$\begin{aligned} \nabla \cdot (k\nabla T) + f &= 0 \text{ on } \Omega \\ T &= 0 \text{ on } \Gamma_D \\ (k\nabla T) \cdot \mathbf{n} &= 0 \text{ on } \Gamma_N, \end{aligned} \quad (1)$$


Figure 1: Homogeneously heated design domain.

where T is the temperature state variable, f is the heat generated, and k is the thermal conductivity of the material in the domain, Ω . On the Dirichlet boundary, Γ_D , referred to from here on as the *heat sink*, the temperature is set to zero. The adiabatic Neumann boundary condition, Γ_N , restricts heat flux out of the domain. The thermal compliance of the system is given by the sum of the compliance across the design domain.

$$C = \int \nabla T \cdot \mathbf{q} \, dA = \int \nabla T (k\nabla T) \, dA \quad (2)$$

The initial design optimization problem considered here is:

$$\begin{aligned} \underset{\mathbf{x}}{\text{minimize}} \quad & C(\mathbf{x}) \\ \text{subject to} \quad & V(\mathbf{x}) = V_D \\ & R(\mathbf{x}) \geq R_{\min} \end{aligned} \quad (3)$$

where the amount of material, $V(\mathbf{x})$, is constrained to be V_D and the radius of a conductive path, $R(\mathbf{x})$, must be larger than R_{\min} . The design variable vector, \mathbf{x} , is a general representation of the topology. This representation will change between the different design approaches. The performance of the following three algorithms will be evaluated to assess the use of generative algorithms in topology design optimization for steady-state heat conduction.

4.1 SIMP Approach

The SIMP approach considers a design domain that is discretized into finite elements. Each element is assigned a material amount, γ , which is treated as the design variable. The algorithm is driven by a sensitivity filter that changes the material distribution from element to element. An ideal solution results in a domain consisting only of void, $\gamma = 0$, and fully-dense material, $\gamma = 1$. A detailed description of the implementation of this approach is outlined in [12].

4.2 Generative Design Approach

The generative design approach (GDA) is fundamentally different from SIMP. A gradient-free optimization method is used to adjust generative algorithm parameters to minimize the objective function [11]. Each design candidate considered in the search is represented using an abstract generative algorithm rule parameter vector. This vector is then used to generate a design topology, which is then evaluated via finite element analysis to determine $C(\mathbf{x})$. This vector is much lower in dimension than a design vector based on direct design representation (e.g., γ for each finite element, as in SIMP). Also, in SIMP and related approaches, the design domain discretization is used as the finite element mesh. This can limit the numerical efficiency of thermal analysis. In the generative algorithm approach, the design description is separate from the analysis mesh, allowing us to use a non-uniform mesh that is tailored for each topology, improving analysis accuracy and efficiency. A novel meshing technique is introduced here that is congruent with the unique properties of the GDA. A genetic algorithm (GA) is used here as the gradient-free optimization method.

4.3 Hybrid Approach

The final approach considered here combines the SIMP approach with a generative algorithm. These tools are used in a nested manner to search for an optimal topology. The outer loop GA adjusts generative algorithm parameters to produce a topology that serves as a starting point for the SIMP algorithm (inner loop). The generated topology is mapped to a discretized domain, and the SIMP algorithm uses gradient information to find a local minimum. Using a local improvement strategy for individual designs within a GA population is sometimes referred to as a

memetic algorithm [13].

5. Generative Algorithm

Optimal topologies for heat conduction problems typically resemble dendritic structures [2, 4, 5, 7]. Given this tendency, we predict a faster convergence to optimal designs if the search is restricted to dendritic topologies. To perform a targeted search of dendritic structures, a survey of prospective algorithms was completed. Dendritic structures have been a topic of research interest earliest cited in 1976 [14]. In computer graphics, researchers have attempted to efficiently and accurately reproduce dendritic structures [15, 16, 17]. In topology design, researchers have applied different generative algorithms to various heat transfer applications [18, 19, 20, 21, 22]. Table 1 summarizes the primary algorithms of interest, dividing them into three main groups. The L-System and constructal theory algorithms use rules to define components and guide their assembly. The next class of the algorithms may be considered “Interaction Based” where only the rules governing interactions are controlled. The Erosion Model and SIMP techniques can also be looked at as generative algorithms as they evolve designs over time. Where the SIMP procedure moves material, the Erosion Model adds material to the design domain. The algorithms were evaluated on their relative number of design variables, whether or not they have a tendency to create overlapping members, and whether or not the algorithm inherently stays within a prescribed design boundary.

Table 1: Generative algorithm assessment

Generative Algorithm		# Design Vars	Overlap	Boundary Adherence
Building Block Based	L-System (LinenMayer)	Med	Yes	No
	Constructal Theory (Bejan)	Med	Yes	No
Interaction Based	Reaction Diffusion	Low	No	Yes
	Particle System (Rodkaew)	Low	No	Yes
	Space Colonization (Runions)	Low	No	Yes
Sensitivity Based	Erosion Model (Bejan)	High	No	Yes
	SIMP (Sigmund)	High	No	Yes

The Reaction Diffusion, Particle System, and Space Colonization algorithms stand out as the best candidates due to their low dimension and ability to handle boundary constraints. The Space Colonization algorithm was ultimately chosen since it has been successfully scaled into three dimensions and its growth procedure intuitively translates to a heat transfer framework. Future work should include the exploration of other candidate generative algorithms.

5.1 Space Colonization Algorithm

The Space Colonization Algorithm (SCA) used here is an adaptation of an algorithm developed by Rodkaew et al. [15]. Hormone centers, called auxins, are strategically placed on the design domain. The algorithm begins from a source node and grows a dendritic structure towards the auxins. This procedure is similar to the accepted theory for vein growth in plant leaves called the *canalization hypothesis* [23]. This concept of growing a topology towards hormone sources may be easily translated to a heat transfer problem where conductive paths can be grown towards heat sources. A rigorous description of implementation in two- and three-dimensions can be followed in [16] and [17], respectively.

Our SCA modifications for conductive heat transfer paths were made to ensure each topology satisfied constraints present when using the SIMP approach (Fig. 2). This supports a direct comparison between the three algorithms presented here. The amount of conductive material is fixed, and the symmetry of boundary conditions is used to reduce the design space by half (Fig. 2a-b). In the SCA, the endpoints of each branch are set to the minimum radius, R_{\min} . Path width increases continuously closer to the heat sink (Fig. 2c). A discretized boundary is created to better illustrate the final topology (Fig. 2d).

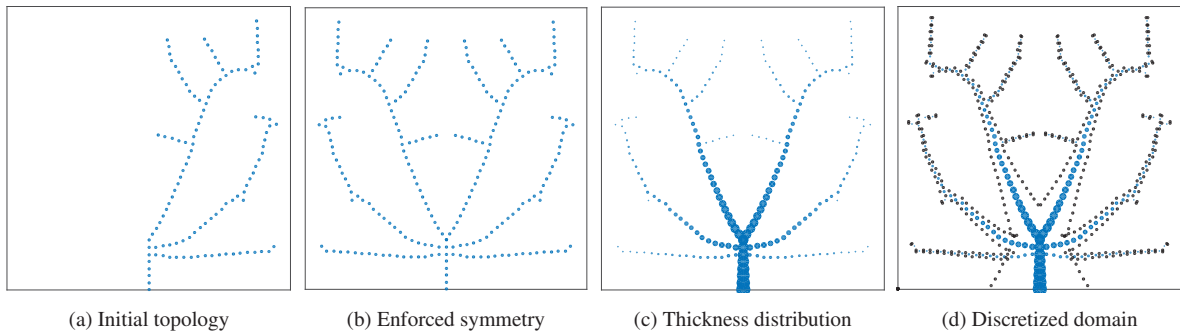


Figure 2: Space colonization modifications applied to a steady-state conductive heat transfer problem.

5.2 Application of Generative Design Approach

To use the generated topology with any of the desired approaches, the structure must be converted into a usable form. Given the intricate nature of the generated topologies, standard meshing approaches often result in non-conformal meshes. To handle this issue, a novel technique was developed to mesh the generated designs. This technique was inspired by force-directed graphs [24] and particle generators. An evenly distributed grid of points is generated on the design domain (Fig. 3a). Attractive forces are added between the discretized boundary nodes and the grid nodes. The system is then simulated for a given time to create a point cloud with a dense particle distribution near the boundaries (Fig. 3b). Additional particles can be introduced during the simulation to increase node density. At the final time step, the initial grid is regenerated on the domain to enforce a minimum accuracy for the finite element solver (Fig. 3c). Delaunay triangulation is then used to convert the point cloud into a mesh that can be used with a finite element solver, shown in Fig. 3d.

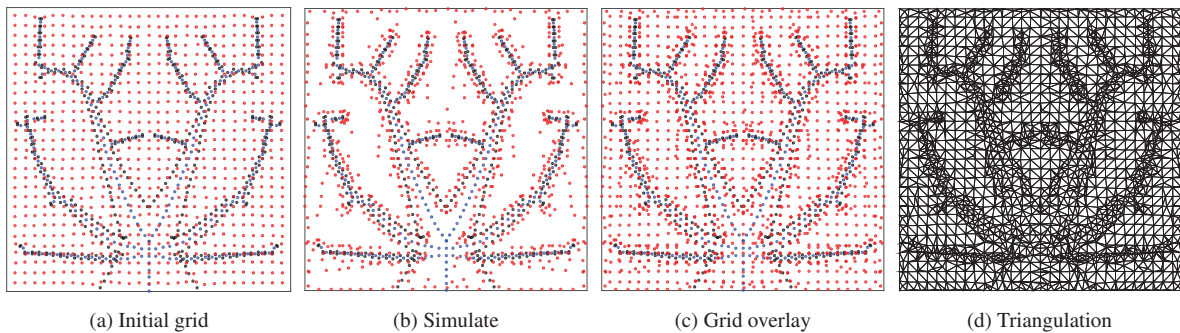


Figure 3: Automated meshing procedure based on force-directed particles and particle generation.

5.3 Application of Hybrid Approach

To use the generated topology with the SIMP approach it must be mapped on to a discretized domain. Starting with a void domain, the parameter γ is set to 1 for every element which contains a node. All of the elements within the minimum radius distance, R_{\min} , of each node are also set so $\gamma = 1$. The initial mapping can be seen in Fig. 4b and is used by the SIMP algorithm to produce the optimal topology Fig. 4c.

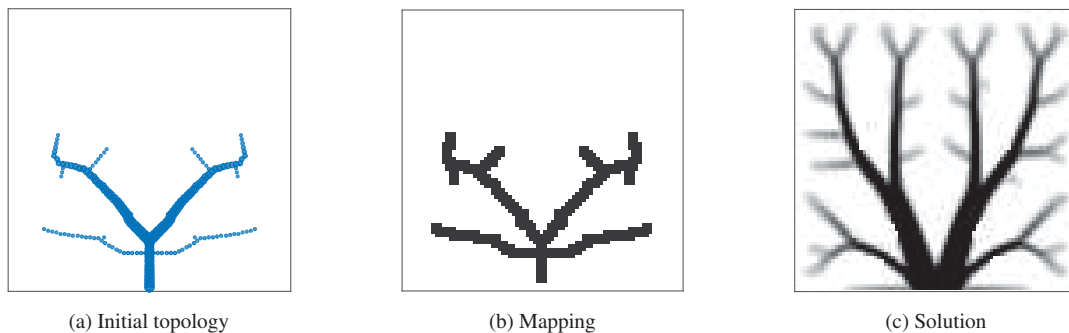


Figure 4: Discretized domain mapping for the hybrid optimization approach.

6. Results

The SIMP approach with a sensitivity filter and a homogeneous initial material distribution was used to develop a baseline topology for comparison. The chosen parameters follow: $ne1x = ne1y = 80$, $penal = 3$, $volfrac = 0.2$, $R_{min} = 2$, [25]. Equivalent parameters were enforced on the generative algorithm. A GA was implemented using the MATLAB[®] global optimization toolbox. A population size of 100 and 5 generations were used with parallel computing activated. The GA operates on each auxin location. Ten auxins were used to guide the growth of the generative algorithm. The following experimental results were performed using an Intel[®] Core[™]i5-4570 CPU @ 3.20 GHz with 8.00 GB (RAM) 64-bit Operating System running Windows 8.1. The results presented in Table 2 are the best of 10 trials.

Table 2: Numerical results

	SIMP	GDA	Hybrid
Objective Value	1709	1274	1528
# of Elements	6400	4710	6400
# of Design Variables	6400	40	6440
Total Time (s)	3.19	245.6	1574.0

Table 3: GA variation

	GDA	Hybrid
Best Objective	1274	1528
Worst Objective	1455	1598
Mean Objective	1373	1548
Std. Dev.	73 \approx 5%	32 \approx 2%
Mean Time (s)	220	1579

The SIMP approach was found to converge quickly to a local optimum. The GDA was found to produce the best objective value at an increase in computational cost. The hybrid approach only produces a small improvement in performance, but incurred significant computational expense. Table 3 presents the variation in the GA solutions between the 10 trials. The computational cost of evaluating a topology using the GDA is outlined in Table 4, where the amount of time to complete each task is presented.

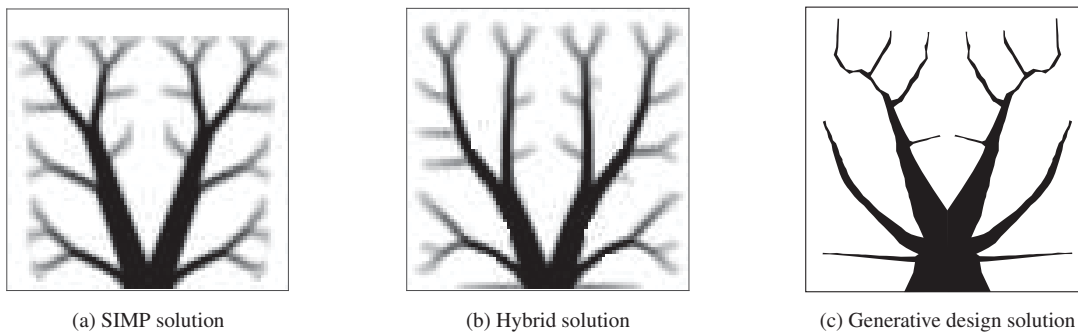


Figure 5: Best topologies obtained using the three optimization approaches.

Table 4: Generative design approach evaluation time

Section	Generation	Meshing	Finite Element Solver	Total
Time (s)	0.21	0.31	0.17	0.69

7. Conclusion

Given comparable resolution and topological structure, the generative design approach was found to converge on higher performance solutions. Benefits of this approach include the explicit representation of thermally conductive heat transfer paths, the binary assignment of material, and the low design problem dimension. While the GDA design abstraction limits design space coverage, the search is more targeted and finds better performing designs. It is important to note that there is a computational expense increase when comparing the generative design approach to SIMP, yet this increase may be worthwhile due to the improvement in objective value, and for the potential to solve more general problems.

The authors look to increase problem complexity to capitalize on the properties of generative algorithms. Several additional studies are in progress. A concurrent path and layout planning problem that designs the optimal placement of heat sources on a design domain, along with the best topology to extract heat, is being investigated. An alternate formulation to maximize power density with trade-offs between the amount of conductive material and computing elements is also being investigated. Future work will look to embed additional properties in generative algorithms that are important for multi-physics applications, as well extension to three-dimensional problems.

8. Acknowledgments

The work presented in this article was supported by the Toyota Research Institute of North America.

9. References

- [1] O. Sigmund and K. Maute, "Topology Optimization Approaches," *Structural and Multidisciplinary Optimization*, vol. 48, pp. 1031–1055, December 2013.
- [2] A. Gersborg-Hansen, M. P. Bendsoe, and O. Sigmund, "Topology Optimization of Heat Conduction Problems Using the Finite Volume Method," *Structural and Multidisciplinary Optimization*, vol. 31, pp. 251–259, March 2006.
- [3] V. Vishwakarma, A. Das, and K. D. P., "Steady State Conduction Through 2D Irregular Bodeis by Smooth Particle Hydrodynamics," *International Journal of Heat and Mass Transfer*, vol. 54, pp. 314–325, January 2013.
- [4] C. Zhuang, Z. Xiong, and H. Ding, "A Level Set Method for Topology Optimization of Heat Conduction Problems Under Multiple Loading Cases," *Computer Methods in Applied Mechanics and Engineering*, vol. 196, pp. 1074–1084, January 2007.
- [5] E. M. Dede, "Optimization and Design of a Multipass Branching Microchannel Heat Sink for Electronics Cooling," *ASME Journal of Electronic Packaging*, vol. 134, December 2012.
- [6] A. A. Koga, E. C. C. Lopes, H. F. Villa Nova, and C. R. de Lima, "Development of Heat Sink Device by Using Topology Optimization," *International Journal of Heat and Mass Transfer*, vol. 64, no. 0, pp. 759–772, 2013.
- [7] F. H. Burger, J. Dirker, and J. P. Meyer, "Three-Dimensional Conductive Heat Transfer Topology Optimization in a Cubic Domain for the Volume-To-Surface Problem," *International Journal of Heat and Mass Transfer*, vol. 67, pp. 214–224, December 2013.
- [8] H. D. Chungang Zhuang, Zhenhua Xiong, "Topology Optimization of Transient Heat Conduction Problem on a Traingular Mesh," *Numerical Heat Transfer*, vol. 64, pp. 239–262, June 2013.
- [9] C. Zhuang and Z. Xiong, "A Global Heat Compliance Measure Based on Topolgy Optimization for the Transient Heat Conduction Problem," *Numerical Heat Transfer, Part B: Fundamentals*, vol. 45, no. 5, pp. 445–471, 2014.
- [10] C. Reas and C. McWilliams, *Form+Code, Art, and Architecture*. Princeton Architectural Press, September 2010.
- [11] N. Cheney, R. MacCurdy, J. Clune, and H. Lipson, "Unshackling Evolution: Soft Robotics with Multiple Materials and a Powerful Generative Encoding," in *Proceedings of the 15th Annual Conference on Genetic and Evolutionary Computation Conference*, GECCO '13, pp. 167–179, ACM, July 2013.
- [12] M. P. Bensoe and O. Sigmund, *Topology Optimization - Theory, Methods, and Application*. Springer, 2nd ed., 2004.
- [13] A. E. Eiben and J. E. Smith, *Introduction to Evolutionary Computing*, ch. 10, pp. 173–188. Springer, 2003.
- [14] M. Meinhardt, "Morphogenesis of Lines and Nets," *Models and Hypothesis. Differentiation 6*, vol. 6, pp. 117–123, August 1976.
- [15] Y. Rodkaew, S. Siripant, C. Lursinsap, and P. Chongstitvatana, "An Algorithm for Generating Vein Images for Realistic Modeling of a Leaf," in *In Proceedings of the International Conference on Computational Mathematics and Modeling*, 2002.
- [16] A. Runions, M. Fuhrer, B. Lane, P. Federl, A.-G. Rolland-Lagan, and P. Prusinkiewicz, "Modeling and Visualization of Leaf Venation Patterns," in *ACM Transactions on Graphics*, vol. 24, pp. 702–711, 2005.
- [17] A. Runions, B. Lane, and P. Prusinkiewicz, "Modeling Trees with a Space Colonization Algorithm," in *Eurographics Workshop on National Phenomena*, pp. 63–70, 2007.
- [18] A. Bejan, I. Dincer, S. Lorente, A. F. Miguel, and A. H. Reis, *Porous and Complex Flow Structures in Modern Technology*. Springer Science, 2004.
- [19] A. Bejan and S. Lorente, "Constructal Theory of Generation of Configuration in Nature and Engineering," *Journal of Applied Physics*, vol. 100, no. 4, pp. –, 2006.
- [20] A. Bejan and S. Lorente, "Constructal Law of Design and Evolution: Physics, Biology, Technology, and Society," *Journal of Applied Physics*, vol. 113, no. 15, pp. –, 2013.
- [21] S. Salakij, J. A. Liburdy, D. V. Pence, and M. Apreotesi, "Modeling in Site Vapor Extraction During Convective Boiling in Fractal-Like Branching Microchannel Networks," *Interantional Journal of Heat and Mass Transfer*, vol. 60, pp. 700–712, May 2013.
- [22] D. Heymann, D. Pence, and V. Narayanan, "Optimization of Fractal-Like Branching Microchannel Heat Sink for Single-Phase Flows," *Internation Journal of Thermal Sciences*, vol. 49, no. 8, pp. 1383–1393, 2012.
- [23] T. Sachs, "The Control of Patterned Differentiation of Vascular Tissues," *Advances in Botonical Research*, vol. 6, pp. 152–262, 1981.
- [24] S. Bowmick and S. M. Shontz, "Towards High-Quality, Untangled Meshes via a Force-Direct Graph Embedding Approach," *Procedia Computer Science*, vol. 1, no. 1, pp. 357–366, 2010.
- [25] E. Andreassen, A. Clausen, M. Schevenels, B. S. Lazarov, and O. Sigmund, "Efficient Topology Optimization in MATLAB using 88 Lines of Code," *Structural and Multidisciplinary Optimization*, vol. 43, pp. 1–16, January 2011.

Manufacture-Oriented Design Optimisation of a Flow Diverter Stent Using Lattice Boltzmann Method and Simulated Annealing

Mingzi Zhang¹, Hitomi Anzai², Bastien Chopard³, Makoto Ohta⁴

¹ Graduate School of Engineering, Tohoku University, Sendai, Japan, mingzi.zhang@biofluid.ifs.tohoku.ac.jp

² FRIS, Tohoku University, Sendai, Japan, anzai@biofluid.ifs.tohoku.ac.jp

³ CUI, University of Geneva, Geneva, Switzerland, bastien.chopard@unigh.ch

⁴ IFS, Tohoku University, Sendai, Japan, ohta@biofluid.ifs.tohoku.ac.jp

1. Abstract

Background: Flow diverter (FD) intervention is becoming increasingly popular for treatment of cerebral aneurysms (CAs), but post-stenting complications such as delayed rupture and post-stenting stenosis are frequently reported.

Purpose: To reduce the risk of post-stenting complications, we designed an optimisation method for a practical FD composed of 3D helix-like wires using intra-aneurysmal maximum velocity (AMV) as the optimisation objective.

Method: Random modification was performed at each stage to assign a slight change to the starting phase of an arbitrarily selected sub-wire, followed by computational fluid dynamics simulation to model the corresponding haemodynamic behaviours. The optimisation process employed a combination of lattice Boltzmann fluid simulation and simulated annealing. The method was applied to two idealized aneurysm geometries: the straight (S) and curve (C) models.

Results: We evaluated the flow reduction R_f by measuring the AMVs before and after design optimisation with respect to the non-stented case. The R_f of the FD in the S model showed an improvement from 83.63 to 92.77%, and the R_f for the C model increased from 92.75 to 95.49%, both having reached a pre-defined convergence status. By visualizing the streamlines entering an aneurysm after optimisation, we found that an efficient FD design may be closely associated with the disruption of the bundle of inflow by strut placement inside inflow area.

Conclusions: The method improved the flow-diverting performance of an FD while maintaining its original porosity and helix-like structure. This study has provided a design optimisation method for the most commonly used helix-like FD devices.

2. Keywords: cerebral aneurysm, flow diverter, design optimisation, computational fluid dynamics.

3. Introduction

Flow diverter (FD) intervention as an emerging endovascular treatment for cerebral aneurysms (CAs) is attracting growing interest among both clinicians and medical engineers. By blocking aneurysmal inflow, FD intervention is intended to induce thrombotic occlusion inside aneurysms and eventually lead to local haemodynamic rehabilitation. However, clinical reports reveal that complications including post-stenting stenosis and delayed CA rupture frequently occur, and further studies suggest that such complications are closely associated with FD structure design [1–4].

Tominaga et al. observed that post-stenting in-stent stenosis was associated with a high metal-to-arterial tissue ratio of a stent [5], and Lieber et al. and Rhee et al. have shown that the porosity level of FD devices in modifying post-stenting haemodynamic is crucial [3,6]. These studies suggested that an FD design with high flow-diversion efficiency and proper porosity level could avert in-stent stenosis. As to delayed CA rupture, a previous study indicated that a concentrated inflow jet and small impingement regions may lead to rupture [7,8], whereas an increased maximum velocity inside the CA due to FD intervention may be a factor in impingement formation. Thus, an FD design reducing intra-aneurysmal maximum velocity (AMV) can likely contribute to the prognosis of FD intervention.

Recently, the technique of design optimisation has been introduced to achieve an optimally designed FD device for a given CA geometry. Srinivas et al. and Lee et al. performed FD optimisation studies using the exploration of design space approach [9,10], and Anzai et al. studied the optimal FD strut placement for different shapes of CAs using simulated annealing (SA) [11]. These studies have practically shown that optimisation of FD structure can effectively improve device performance from the viewpoint of hemodynamics. However, a manufacture-oriented optimisation strategy that could be applied to the commonly used FD composed of

helix-like woven wires has not yet been performed.

The purpose of this study is to develop an optimisation method for helix-like FD structures to reduce the AMV inside CAs. Based on the combination of LB fluid simulation and SA, this optimisation method automatically identifies optimal FD wire configurations corresponding to a given aneurysm geometry. In view of the correlation between device porosity and in-stent stenosis, we ensured that the porosity was maintained at the high level of 80% by appropriate design of the modification objective. The method can deal with FD devices composed of helical wires and can be flexibly integrated with modern FD manufacturing processes when patient-specific FD fabrication is desired.

4. Methods

4.1. Aneurysm and FD Models

Different vascular geometries produce different aneurysmal inflow characteristics. As suggested by our previous study [11], the intra-aneurysmal hemodynamics differs markedly when the same aneurysm geometry is coupled with different configurations of the parent artery. To investigate the feasibility of the proposed optimisation method under different haemodynamic conditions, two configurations of idealized vascular geometry were used: a straight (S) and curved (C) model. Both models used an aneurysmal diameter of 4.8 mm with a neck diameter of 2.8 mm. The diameter of the parent artery and the curvature radius of the C model were defined as 3.5 and 6.0 mm, respectively.

Each FD was assumed to comprise 8 helix-like woven wires: four clockwise and four anticlockwise wires with strut thickness and width both of 50 μm . The mathematical description of an FD helix trajectory was generated in accordance with the given vascular model and expressed as follows:

$$\text{Clockwise helix: } \begin{cases} x = [R + r * \sin(\omega_\alpha + \theta_n)] * \cos(\omega_\beta) \\ y = [R + r * \sin(\omega_\alpha + \theta_n)] * \sin(\omega_\beta) \\ z = r * \cos(\omega_\alpha + \theta_n) \end{cases}, \theta_n = 2(n - 1) \cdot \frac{\pi}{4} \quad (1)$$

$$\text{Anticlockwise helix: } \begin{cases} x = [R + r * \cos(\omega_\alpha + \theta_m)] * \cos(\omega_\beta) \\ y = [R + r * \cos(\omega_\alpha + \theta_m)] * \sin(\omega_\beta) \\ z = r * \sin(\omega_\alpha + \theta_m) \end{cases}, \theta_m = 2\left(m - \frac{1}{2}\right) \cdot \frac{\pi}{4} \quad (2)$$

where r and $\theta_{n \text{ or } m}$ denote the radius and starting phase of a helix, respectively, R represents the curvature radius of a helix and ω_α and ω_β are parameters associated with the length and pitch of the helix. To mimic the commonly applied FD stent with homogeneous wire configurations, we created an initial FD structure with uniform helix arrangements: $n \text{ or } m \in (1,2,3,4)$ indicates the sequence of either the four clockwise (n) or the four anticlockwise (m) helical subsets. The helix radius r was set as 1.7 mm. In this manner, a deployed FD stent with its struts clinging to the wall of the parent artery was created. As determined by the FD parameters described above, the porosity of the deployed FD was 80%.

4.2. Random Modification

The random modification was designed to alter slightly the relative positions of the eight helices without changing the device porosity. At each stage of optimisation, the random modification function was invoked once. It arbitrarily selected one of the eight helices and added a stochastic variable $\Delta\theta \in \left(-\frac{\pi}{8}, \frac{\pi}{8}\right)$ to the starting phase, the design variable, of the selected helix:

$$\theta_{n \text{ or } m, \text{current}} = \theta_{n \text{ or } m, \text{previous}} + \Delta\theta \quad (3)$$

In this manner, the one-step modification caused an axial displacement of the selected helix along the centre line of the parent artery. In this study, we just modified the starting phase $\theta_{n \text{ or } m}$ and left other parameters defining a helix unchanged.

4.3. Lattice Boltzmann (LB) Simulation

LB fluid simulation was used as the CFD solver in our study. LB is a mesoscopic approach that simulates the time and space evolution of kinetic quantities using a particle-distribution function $f_i(r, t)$. The index i denotes the possible lattice directions, running from zero to the lattice coordinate number of the chosen lattice topology; r and t represent discrete positions on a regular lattice and discretised time steps, respectively [12]. Fluid in LB simulation is described in terms of the density distribution of idealized fluid particles moving and colliding on a regular lattice. The collision-propagation dynamic process can be written as

$$f_i(r + \Delta t v_i, t + \Delta t) = f_i(r, t) + \frac{1}{\tau} (f_i^{eq} - f_i) \quad (4)$$

where f^{eq} and τ are the so-called local equilibrium distribution and relaxation time, respectively. Here we used D3Q19 lattice topology for 3D steady flow simulation. Bounceback rule was applied to define the non-slip boundary and FD wires. After sensitivity tests, the spatial discretization (Δr) was set at 0.05 mm, corresponding to fluid cell quantities of 3.57×10^6 and 3.01×10^6 for the S and C models, respectively. In a previous study [11], blood flow was assumed to be an incompressible Newtonian fluid and to have a constant velocity of 0.23 m/s at the inlet, giving the same Reynolds number (Re) of 200 for both cases. Velocity was defined with parabolic profiles at inlets and a constant pressure boundary was imposed at outlets. Constant density and kinematic viscosity were assumed to be 1040 kg/m^3 and $4.0 \times 10^{-6} \text{ m}^2/\text{s}$, respectively. Based on the above definition, the kinetic viscosity of the lattice (ν_{LB}) was chosen as 0.012, giving a relaxation time τ of $(6\nu_{LB} + 1)/2 = 0.536$. We used the open source LBM library Palabos version 1.4 [13] for its high flexibility and parallelism.

4.4. Simulated Annealing

The same cooling schedule of SA that we previously developed [11] was employed to control random modifications progressing towards the optimal solution. It was designed to identify the FD structure with the best flow diversion rate within a certain range of temperature drop. The AMV was selected as the objective function of SA.

Optimisation started with a uniform FD structure and ended on reaching the lower temperature limit. We assumed that optimisation experienced 50 temperature decrements and accordingly calculated the lower limits for all cases as shown in Table 1. During each stage of optimisation, stent structure was first modified and then CFD was performed to obtain the corresponding AMV. The LB simulation and the optimisation process were fully automated by building the two parts into one program. On a parallel computing system with 256 cores at the Institute of Fluid Science, Tohoku University, CFD simulations of the S and C models required approximately 30 min and 45 min, respectively.

Table 1: Initial temperature and lower temperature limits of SA for the S and C models.

	S model	C model
Initial temperature	2.414×10^{-3}	6.636×10^{-4}
Lower temperature limit	1.244×10^{-5}	3.420×10^{-6}

4.5. Flow reduction rate

To evaluate quantitatively the flow diversion efficiency of the FD device, we introduced a dimensionless index of flow reduction (FR) rate,

$$R_f = \frac{V_{w/o} - V_{current}}{V_{w/o}} \times 100\% \quad (5)$$

where $V_{w/o}$ is the AMV without FD intervention and $V_{current}$ is the AMV calculated after FD implantation of a given wire configuration.

5. Results

The optimisation procedure required 913 and 908 SA iterations for the S and C models, respectively, until the lower temperature limits were reached. No further FR improvement of AMV was obtained during the final 100 iterations for both cases. Compared with the initial uniform FD interventions, the R_f values of optimized FD interventions were improved by 9.12% and 2.74% for the S and C models, respectively. The AMV and R_f under non-stent, initial stent and optimized FD intervention for both models are shown in Table 2.

5.1. Optimisation Process

Figure 1 shows the SA processes of both cases. The R_f of the S model increased during the initial 400 iterations, rising from around 84% at iteration 0 to approximately 92% at iteration 400 before stabilizing at 92%. For the C model, the R_f fluctuated between 92% and 88% during the initial 200 iterations before the best R_f of 95.49% was finally achieved. The models showed a similar trend, by which R_f increased during the first hundreds of iterations and then stabilized.

5.2. FD Structures and Haemodynamic Differences

Figure 2 shows the FD structures and the haemodynamic differences between the initial and the optimized FDs. As can be observed in both cases, the FD wires had a tendency of concentrating at the inflow proximal end. The homogeneous wire structures were disrupted and large holes could be observed in the optimized FD structures. Compared with the initial FD intervention, the magnitude of velocity components perpendicular to the

aneurysmal orifice markedly decreased, particularly in the inflow area, after optimized FD intervention. The isovelocity surfaces, colour-coded by velocity magnitude, corresponded to 0.01 and 0.015 m/s for the S and C models, respectively. As visualized from the isovelocity surface in the optimized case, the flow region with high velocity magnitude was reduced in the aneurysmal orifice compared with that in the initial case.

Table 2: The AMV and the R_f under non-stent, initial stent and optimized FD conditions of S and C models, respectively.

	Non-stent	Initial stent placement		Optimal stent placement	
	$V_{w/o}$ ($10^{-3}m/s$)	$V_{initial}$ ($10^{-3}m/s$)	$R_f(\%)$	$V_{optimal}$ ($10^{-3}m/s$)	$R_f(\%)$
S model	36	6.131	83.63	2.610	92.77
C model	145.828	10.560	92.75	6.567	95.49

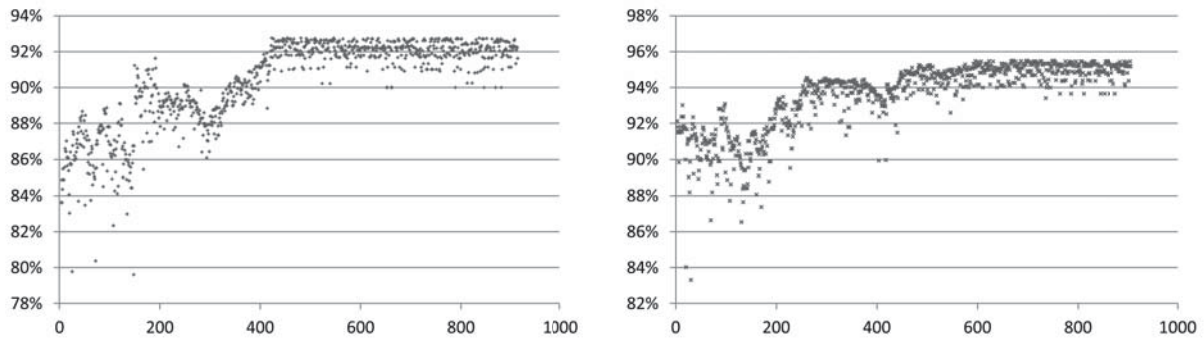


Figure 1: SA process for S and C models. (Left: S model, right: C model, horizontal coordinate: SA step and vertical coordinate: FR rate)

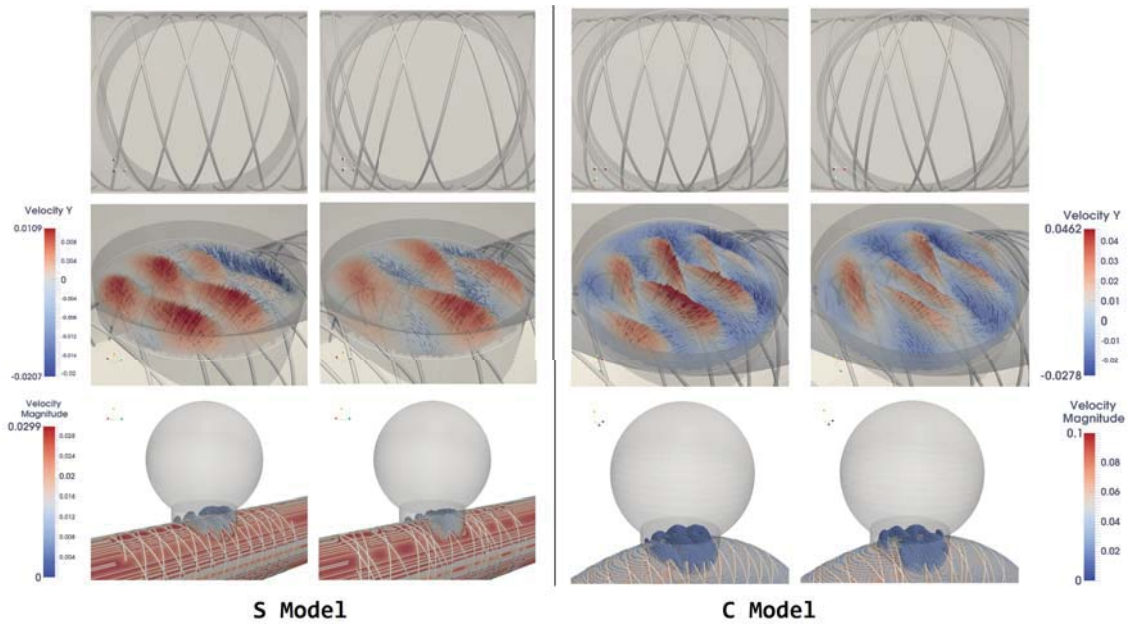


Figure 2: The initial/optimized FD structures (top), the visualization of velocity components perpendicular to the neck plane (middle) and the isovelocity surfaces (bottom) for S and C models. The left and right columns in the S/C models correspond to the initial and the optimized FD interventions, respectively.

5.3. Alteration of intra-aneurysmal average velocity (AAV) reduction rate

Figure 3 shows the alteration of AAV with respect to AMV during the optimisation process. As can be observed in the figure, an FR improvement of AMV did not accompany that of AAV. For the S model, the highest R_f of 92.77% was obtained, whereas the reduction rate of AAV was only around 93% at this point (refer to point A in Figure 3). The highest reduction rate of AAV was observed as point B (just over 94%), whereas the R_f of AMV

was only approximately 87%. For the C model, optimal solutions are observed to concentrate in region C (Figure 3); nonetheless, the maximum reductions of AMV (point D) and AAV (point E) are not at the same point.

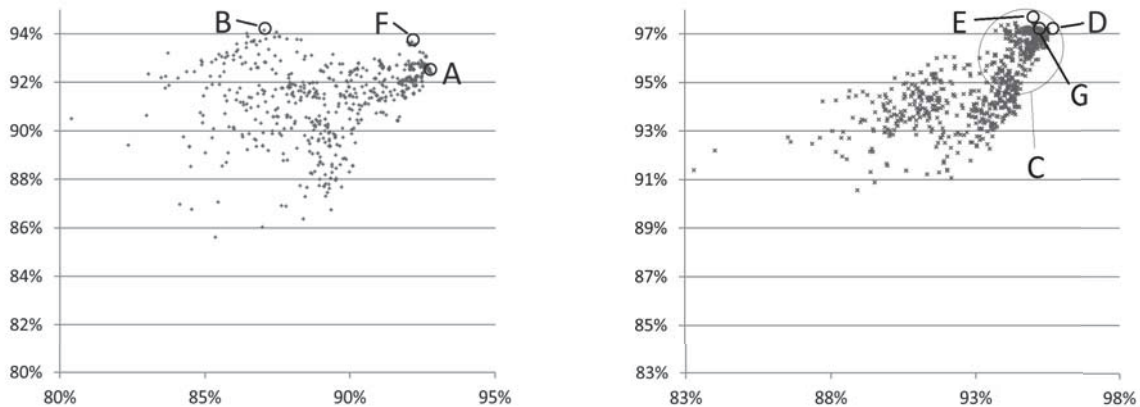


Figure 3: Reduction rates of AMV (horizontal coordinates) and AAV (vertical coordinates) of S model (left) and C model (right), respectively.

6. Discussion

In this study, we performed wire structure optimisation for an FD device composed of helix wires according to two idealized CA geometries. Results suggested that the optimized FD structures had flow-reducing capability superior to the initial uniform structures. The shape of each wire and the woven angle of two arbitrary wires were maintained over the optimisation period, following the intention of introducing minimal alterations to the FD's initial configuration.

6.1. Improving FR Rate by Disrupting the Bundle of Inflow (BOI)

First introduced by Anzai et al. [11,14], disrupting the BOI of a given CA geometry is crucial for increasing the FR rate. BOI refers to the inflow bundle of an aneurysm and can be visualized as the concentrated streamlines that enter an aneurysm. As shown in Figure 4, the width and magnitude of BOI after optimized FD intervention decreased in both S and C models compared with those after initial FD intervention; the FD wires became denser within the BOI zones (refer to the yellow circles with dotted lines in Figure 4). Anzai et al. used AAV as the objective function for optimisation [11], whereas we used AMV in this study. However, the same trend of wire struts concentrating inside the BOI zone after optimisation was observed, confirming the importance of disrupting BOI to obtaining an increased FR rate. Moreover, in the S model, the flow complexity, a flow characteristic associated with CA rupture [7], was observed to decrease after optimisation, with the flow pattern within the aneurysm showing no flow divisions or separations.

6.2. Selecting an Objective Function for Optimisation

Different objective functions lead to different optimisation solutions. Selecting a proper objective function(s) is important for optimisation to identify meaningful modifications. Here we used AMV as the objective function because of its possible correlation with CA ruptures. In addition to AMV, many other haemodynamic parameters (such as AAV, vorticity, wall shear stress and pressure) have been used for FD structure optimisation in previous studies. Performing optimisation for FD devices is driven by improving treatment prognosis, but no consensus on a critical parameter(s) that can clearly determine the prognosis has yet been reached.

We measured the AAV during the simulation because it is considered to be associated with post-stenting thrombotic occlusion. As observed in Figure 3, an advanced AMV reduction does not always accompany increased AAV reduction. Thus, to achieve an FD structure with both lower AMV and AAV, the FD structures corresponding to point F and G in Figure 3 may be considered as optimal compromise solutions for the S and C models, respectively. Alternatively, optimisation using multiple objective functions can be applied, provided that the critical parameters correlated with short-term thrombotic occlusion or delayed CA rupture can be identified.

7. Conclusion

In this paper, we developed an optimisation method for FD wires with helix-like structure. This method improved the flow-diverting performance of an FD while maintaining its original porosity and helix-like structure. In addition, this study has provided a design optimisation method for the most commonly used helix-like FD devices.

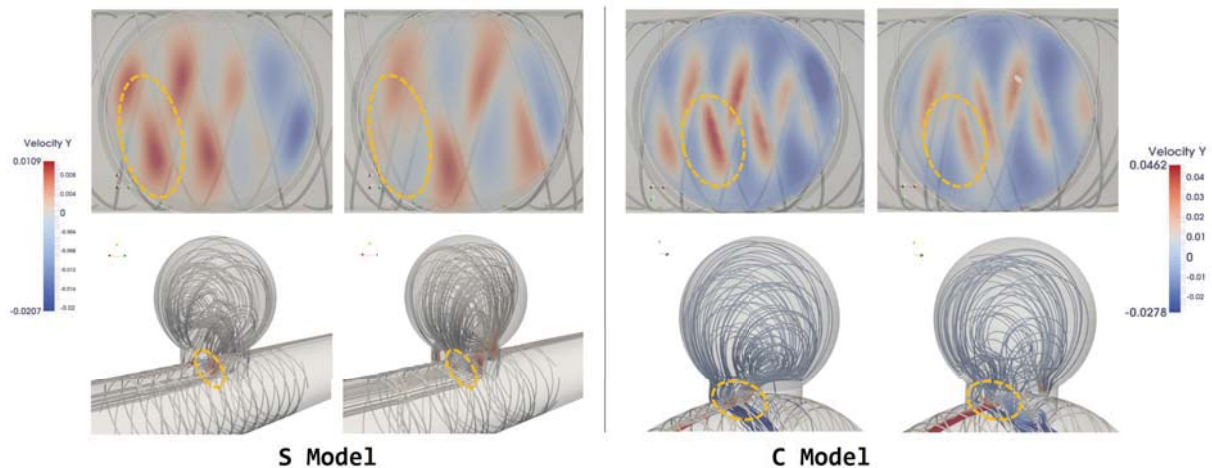


Figure 4: BOI zones (the yellow circles with dotted lines) alterations after FD structure optimisation. The left and right columns in S/C models correspond to initial and optimized FD interventions, respectively.

8. Acknowledgements

This study was supported by a Grant-in-Aid for Scientific Research (B), Japan Ministry of Education, Science, Sports and Culture, 2013–2015 (25282140, Makoto Ohta) and also in part by the Excellent Graduate Schools program and the JSPS Core-to-Core Program (A. Advanced Research Networks) at the Institute of Fluid Science, Tohoku University, Japan.

9. References

- [1] J.E. Cohen, J.M. Gomori, S. Moscovici, R.R. Leker and E. Itshayek, Delayed complications after flow-diverter stenting: reactive in-stent stenosis and creeping stents, *Journal of Clinical Neuroscience*, 21 (7), 1116-1122, 2014.
- [2] T. Mattingly, B. Van Adel, E. Dyer, P. Lopez-Ojeda, D.M. Pelz, S.P. Lownie, T. Marotta and M. Boulton, Failure of aneurysm occlusion by flow diverter: a role for surgical bypass and parent artery occlusion, *Journal of NeuroInterventional Surgery*, 7, e31, 2015.
- [3] B.B. Lieber, A.P. Stancampiano and A.K. Wakhloo, Alteration of hemodynamics in aneurysm models by stenting: influence of stent porosity, *Annals of Biomedical Engineering*, 25 (3), 460-469, 1997.
- [4] S. Appanaboyina, F. Mut, R. Löhner, C. Putman and J. Cebal, Simulation of intracranial aneurysm stenting: techniques and challenges, *Computer Methods in Applied Mechanics and Engineering*, 198 (45-46), 3567-3582, 2009.
- [5] R. Tominaga, H. Harasaki, C. Sutton, H. Emoto, H. Kambic and J. Hollman, Effects of stent design and serum cholesterol level on the restenosis rate in atherosclerotic rabbits, *American Heart Journal*, 126 (5), 1049-1058, 1993.
- [6] K. Rhee, M.H. Han and S.H. Cha, Changes of flow characteristics by stenting in aneurysm models: influence of aneurysm geometry and stent porosity, *Annals of Biomedical Engineering*, 30 (7): 894-904, 2002.
- [7] J.R. Cebal, F. Mut, J. Weir and C.M. Putman, Association of hemodynamic characteristics and cerebral aneurysm rupture, *American Journal of Neuroradiology*, 32 (2), 264-270, 2011.
- [8] J.R. Cebal, M.A. Castro, J.E. Burgess, R.S. Pergolizzi, M.J. Sheridan and C.M. Putman, Characterization of cerebral aneurysms for assessing risk of rupture by using patient-specific computational hemodynamics models, *American Journal of Neuroradiology*, 26 (10), 2550-2559, 2005.
- [9] K. Srinivas, S. Townsend, C.J. Lee, T. Nakayama, M. Ohta, S. Obayashi and T. Yamaguchi, Two-dimensional optimization of a stent for an aneurysm, *Journal of Medical Devices*, 4 (2), 021003, 2010.
- [10] C.J. Lee, K. Srinivas and Y. Qian, Three-dimensional hemodynamic design optimization of stents for cerebral aneurysms. *Proceedings of the Institution of Mechanical Engineers, Part H: Journal of Engineering in Medicine*, 228 (3), 213-224, 2014.
- [11] H. Anzai, J.L. Falcone, B. Chopard, T. Hayase and M. Ohta, Optimization of strut placement in flow diverter stents for four different aneurysm configurations. *Journal of Biomechanical Engineering*, 136 (6), 061006, 2014.
- [12] S. Succi, *The Lattice-Boltzmann Equation*, Oxford University Press, Oxford, 2001.
- [13] www.palabos.org.
- [14] H. Anzai, B. Chopard and M. Ohta, Combinational optimization of strut placement for intracranial stent using a realistic aneurysm, *Journal of Flow Control, Measurement & Visualization*, 2 (2), 67-77, 2014.

Topology optimization of plate structures subject to initial excitations for minimum dynamic performance index

Kun Yan, Gengdong Cheng

State Key Laboratory of Structural Analysis for Industrial Equipment, Faculty of Vehicle Engineering and Mechanics, Dalian University of Technology, Dalian 116023, P. R. China

1. Abstract

This paper studies optimal topology design of damped vibrating plate structures subject to initial excitation. The design objective is to minimize an integrated square performance measure, which is often used in optimal control theory. The artificial density of the plate element is the topology design variable. The Lyapunov's second method is applied to reduce the calculation of performance measure to the solution of the Lyapunov equation. An adjoint variable method is developed in our study, which only needs to solve the Lyapunov equation twice. However, when the problem has a large number of degrees of freedom, the solution process of Lyapunov equation is computational costly. Thus, the full model is transform to a reduced space by mode reduction method. And we propose a selection method to decrease the number of eigenmodes to further reduce the scale of reduced model. Numerical example of optimum topology design of bending plates is presented for illustrating validity and efficiency of our new algorithm.

2. Keywords: Adjoint method, vibration control, topology optimization

3. Introduction

Structural topology optimization and structural vibration control have called attention both in theoretical research and practical applications in engineering. Structural topology optimization provides a powerful automated tool for improving the structural performance in the initial conceptual design stage. Usually, optimization problems are formulated to minimize the material usage or to optimize the structural performance. Structural vibration control is a particularly important consideration in dynamic system design. Many control algorithms have been developed for passive and active control. Passive control systems that do not require any external power are widely used to reduce the response of structures.

In engineering applications, shell structures are widely used. Structural topology optimization and structural vibration control of shell structures has received an ever increasing attention. Several researchers have applied structural topology optimization techniques to structural vibration control problems. In most of existing works, structural topology optimization techniques are used to obtain the layout of piezoelectric or damping material on a main structure. Kang et al. investigate the optimal distribution of damping material in vibrating structures subject to harmonic excitations by using topology optimization method [1]. Chia et al. introduced cellular automata algorithms into the layout optimization of damping layers [2]. Zheng et al. dealt with topology optimization of plates with constrained layer damping treatment for maximizing the sum of the modal damping ratios, which are approximated with the modal strain energy method [3]. In this paper, the problem of a plate or shell just contains damping material will be considered.

Many performance indices have been considered in vibration control optimization problems, like H_2 or H_∞ norms. In time domain, there is a classic problem formulation of passive structural vibration control that deals with the dynamic system disturbed by initial conditions. The objective is to find design parameters of the damped vibration system that minimize the performance index in the form of time integral of the quadratic function of state variables (displacement and velocities, e.g. see equation (5)). This performance index can be evaluated by Lyapunov's second method [4]. Based on the Lyapunov equation, the evaluation of performance indices are simplified into matrix quadratic forms and do not require the time domain integration. Parameter optimization problems with a quadratic performance index have been solved by this method [5]. Wang et al. applied the Lyapunov equation to solve the transient response optimization problem of linear vibrating systems excited by initial conditions [6]. Du applied the Lyapunov equation to obtain the optimum configuration of dynamic vibration absorber (i.e., DVA) attached to an undamped or damped primary structure [7].

A well-known efficient solution technique for calculating the dynamic response of structures is to transform the model into a reduced space. Various methods for this requirement are available now, such as the Guyan reduction, mode superposition, modal acceleration and Ritz vector methods [8]. Among others, the mode superposition method is generally recognized as an efficient approach for dealing with large-scale proportionally damped structures. Generally, the structural response of reduced model is expressed as a linear combination of their first

dozens or hundreds eigenmodes. However, for some cases, the eigenmodes of low order may have no effect on the structural response of reduced model. In this paper, a selection method is used to find these eigenmodes to decrease the number of basis vectors to further reduce the scale of the reduced model.

In this paper, an approach is developed for topology optimization involving a quadratic performance index of linear elastic shell structure subject to initial excitations. Mode reduction method and eigenmode selection method are used to decrease the computing time of optimization process. At last, a cantilever plate example and several illustrative results are presented.

4. Topology optimization problem formulation

4.1 Governing equations

Consider a viscously damped linear vibration system governed by the equation:

$$\mathbf{M}\ddot{\mathbf{u}} + \mathbf{C}\dot{\mathbf{u}} + \mathbf{K}\mathbf{u} = \mathbf{0} \quad (1)$$

where $\mathbf{M}(N \times N)$ is the mass matrix, $\mathbf{C}(N \times N)$ is the damping matrix, $\mathbf{K}(N \times N)$ is the stiffness matrix, and $\mathbf{u}(N \times 1)$ is displacement vector. N is the structural degree of freedoms. Assume the system is excited by initial displacements or velocities. And the design problem is to find in \mathbf{M} , \mathbf{K} and \mathbf{C} matrices to minimize a performance matrix in the form

$$J = \int_0^T q(\mathbf{u}, \dot{\mathbf{u}}) dt \quad (2)$$

where, $q(\mathbf{u}, \dot{\mathbf{u}}) = \mathbf{u}^T \mathbf{Q}_u \mathbf{u} + \dot{\mathbf{u}}^T \mathbf{Q}_v \dot{\mathbf{u}}$ is a quadratic function of \mathbf{u} and $\dot{\mathbf{u}}$. Transient dynamic responses have to be performed to evaluate the objective function. Direct or adjoint methods can be applied to evaluate the response sensitivity required for evaluation sensitivity of the performance. Alternative, if we replace the upper bound of integration to infinite, we can use Lyapunov's second method to evaluate the performance without performing transient dynamic response analysis.

To apply Lyapunov's second method to this system, it is necessary to rewrite Eq.(1) in the state space form

$$\dot{\mathbf{X}} = \mathbf{A}\mathbf{X} \quad (3)$$

Where

$$\mathbf{A} = \begin{bmatrix} \mathbf{0} & \mathbf{I} \\ -\mathbf{M}^{-1}\mathbf{K} & -\mathbf{M}^{-1}\mathbf{C} \end{bmatrix} \quad \mathbf{X} = \begin{bmatrix} \mathbf{u} \\ \dot{\mathbf{u}} \end{bmatrix} \quad (4)$$

The matrix \mathbf{A} is $(2N \times 2N)$. The vector \mathbf{X} is $(2N \times 1)$. Structural design parameters such as mass density, damping ratio and spring stiffness are contained in the matrix \mathbf{A} . The optimization problem is to choose these parameters to minimize the performance measure J defined by

$$J = \int_0^\infty \mathbf{X}^T \mathbf{Q} \mathbf{X} dt \quad (5)$$

for a given initial excitation $\mathbf{X}(0)$. In Eq.(5), $\mathbf{Q}(2N \times 2N)$ is a positive semi-definite symmetric weighting matrix and t denotes time. According to Lyapunov theory of stability, for an asymptotically stable system, there exist a symmetric positive semi-definite matrix $\mathbf{P}(2N \times 2N)$ satisfying

$$\mathbf{A}^T \mathbf{P} + \mathbf{P} \mathbf{A} = -\mathbf{Q} \quad (6)$$

Eq.(6) is the well-known Lyapunov equation. Based on the Lyapunov's second equation, the Eq.(5) can be further simplified as

$$J = \mathbf{X}(0)^T \mathbf{P} \mathbf{X}(0) \quad (7)$$

That is to say, to minimize J in Eq.(5) is equivalent to minimize $\mathbf{X}(0)^T \mathbf{P} \mathbf{X}(0)$, where $\mathbf{X}(0)$ is the initial state vector and the unknown symmetric matrix \mathbf{P} can be obtained by solving Eq.(6).

4.2 Mathematical formulation of topology optimization problem

In this paper, the topology optimization problem for finding the optimal distribution of given material to minimize the quadratic integral form structural performance index of a vibrating structure excited by initial excitation is considered. The mathematical formulation of topology optimization problem is expressed as

$$\begin{aligned} & \text{find } (\rho_1, \rho_2, \dots, \rho_{N_e}) \\ & \min J = \int_0^\infty \mathbf{X}^T \mathbf{Q} \mathbf{X} dt \\ & \text{s.t. } \dot{\mathbf{X}} = \mathbf{A}\mathbf{X} \end{aligned}$$

$$\begin{aligned} \sum_{i=1}^{N_e} \rho_i V_i - V_{frac} \times \sum_{i=1}^{N_e} V_i^e &= 0 \\ 0 \leq \rho_{min} \leq \rho_i \leq 1, \quad i &= 1, 2, \dots, N_e \end{aligned} \quad (8)$$

where, ρ_i is the artificial density of i th element, ρ_{min} is lower bound of artificial density, V_i^e is the volume of i th element, V_{frac} is the specific volume fraction, and N_e is the number of elements in design domain.

An artificial damping material model that has a similar form as the SIMP approach is used and the artificial densities of elements are taken as design variables. The elemental mass matrix and stiffness matrix are expressed by

$$\mathbf{M}_i = \rho_i \tilde{\mathbf{M}}_i, \quad \mathbf{K}_i = \left[\frac{\rho_{min} - \rho_{min}^p}{1 - \rho_{min}^p} (1 - \rho_i^p) + \rho_i^p \right] \tilde{\mathbf{K}}_i \quad (9)$$

where, $\tilde{\mathbf{M}}_i$ and $\tilde{\mathbf{K}}_i$ are the elemental mass matrix and stiffness matrix of i th element with $\rho_i = 1$, respectively; p is the penalty parameter and it is set to be $p=3$ in this paper. The Rayleigh damping theory is employed, and the elemental damping matrix is obtained by

$$\mathbf{C}_i = \left[\frac{\rho_{min} - \rho_{min}^p}{1 - \rho_{min}^p} (1 - \rho_i^p) + \rho_i^p \right] (\alpha \tilde{\mathbf{M}}_i + \beta \tilde{\mathbf{K}}_i) \quad (9)$$

where, α and β are the damping parameters.

5. Sensitivity analysis scheme

The topology optimization problems always are solved by gradient-based mathematical programming algorithms, which need the sensitivity analysis of the objective function with respect to design variables. In this paper, a sensitivity analysis scheme derived by adjoint variable method is applied, which is more efficient than direct variable method in the problems involving a large number of design parameters. For the case, initial condition independent of design parameters, the sensitivity analysis scheme can be expressed as

$$\frac{\partial J}{\partial \rho_i} = \mathbf{X}(0)^T \frac{\partial \mathbf{P}}{\partial \rho_i} \mathbf{X}(0) = \sum_{k=1}^{2N} \sum_{l=1}^{2N} \lambda_{kl} D_{kl}^i \quad (10)$$

where, λ is the adjoint matrix. λ and \mathbf{D} can be obtained by

$$\mathbf{A}\lambda + \lambda\mathbf{A}^T + \mathbf{S} = 0 \quad (11)$$

where, $\mathbf{S} = \mathbf{X}(0)\mathbf{X}(0)^T$

$$\mathbf{D}^i = \frac{\partial \mathbf{Q}}{\partial \rho_i} + \frac{\partial \mathbf{A}^T}{\partial \rho_i} \mathbf{P} + \mathbf{P} \frac{\partial \mathbf{A}}{\partial \rho_i} \quad (12)$$

$$\text{where, } \frac{\partial \mathbf{A}}{\partial \rho_i} = \begin{bmatrix} 0 & 0 \\ -\frac{\partial(\mathbf{M}^{-1})}{\partial \rho_i} \mathbf{K} - \mathbf{M}^{-1} \frac{\partial \mathbf{K}}{\partial \rho_i} & -\frac{\partial(\mathbf{M}^{-1})}{\partial \rho_i} \mathbf{C} - \mathbf{M}^{-1} \frac{\partial \mathbf{C}}{\partial \rho_i} \end{bmatrix}$$

6. Transformation of equations to reduced space

When the analysis model has a large numbers of DOFs, the solution of Lyapunov matrix equation is computational costly, which will makes the computing time of optimization process increased significantly. For example, for a 1,000-dof system, the number of unknowns in \mathbf{P} is 2,001,000. Thus model reduction is necessary to implement the proposed approach. The mode reduction method and eigenmode selection method are used to decrease the computing time of optimization process.

6.1 mode reduction method

To use mode reduction method, a linear transformation is employed, which can be expressed as

$$\mathbf{u} = \mathbf{T}\mathbf{u}_m \quad (13)$$

where, \mathbf{u} and \mathbf{u}_m are the displacement vectors of full model and reduced model, respectively; \mathbf{T} is the transformation matrix. Generally, matrix \mathbf{T} contains the first several eigenmodes of full model. However, for some cases, the eigenmodes of lower order may have no effect on the structural response. A selection method is applied

to find these eigenmodes to decrease the number of basis vectors in transformation matrix to further reduce the scale of reduced model, and will be introduced in next section. The transformation matrix \mathbf{T} is expressed as

$$\mathbf{T} = \{\boldsymbol{\varphi}_{c_1}, \boldsymbol{\varphi}_{c_2}, \dots, \boldsymbol{\varphi}_{c_m}\} \quad (14)$$

where, c_1, c_2, c_m are the number of 1st, 2nd, m th reserved eigenmodes. The mass, damping, and stiffness matrices of reduced model are respectively obtained by

$$\mathbf{M}_{re} = \mathbf{T}^T \mathbf{M} \mathbf{T}, \mathbf{C}_{re} = \mathbf{T}^T \mathbf{C} \mathbf{T}, \mathbf{K}_{re} = \mathbf{T}^T \mathbf{K} \mathbf{T} \quad (15)$$

The initial conditions of reduced model are obtained by

$$\mathbf{u}_{re,0} = \mathbf{M}_{re}^{-1} \mathbf{T}^T \mathbf{M} \mathbf{u}_0, \mathbf{v}_{re,0} = \mathbf{M}_{re}^{-1} \mathbf{T}^T \mathbf{M} \mathbf{v}_0 \quad (16)$$

Include the sensitivity of matrix \mathbf{T} with respect to design parameters in sensitivity analysis scheme will make the analysis much complicated. Thus, in this paper, the sensitivity of matrix \mathbf{T} with respect to design parameters is ignored.

6.2 Eigenmode selection method

We use the model participation factor (MPF) to evaluate which eigenmode in first several eigenmodes of full model have no effect on the structural response. High value of MPF of i th eigenmode means that this eigenmode has large effect on structural response. Low MPF value means that this eigenmode has a little effect on structural response. The MPF value is obtained by

$$\text{MPF} = \frac{(\mathbf{u}_0^T \boldsymbol{\varphi}_i)^2}{(\mathbf{u}_0^T \mathbf{u}_0)(\boldsymbol{\varphi}_i^T \boldsymbol{\varphi}_i)}, \text{MPF} = \frac{(\mathbf{v}_0^T \boldsymbol{\varphi}_i)^2}{(\mathbf{v}_0^T \mathbf{v}_0)(\boldsymbol{\varphi}_i^T \boldsymbol{\varphi}_i)} \quad (17)$$

where, \mathbf{u}_0 and \mathbf{v}_0 are the initial displacement and velocity vector, respectively, and $\boldsymbol{\varphi}_i$ is the eigenvector of i th eigenmode. The MPF values of all eigenmodes are located between 0 and 1.

For the case an optimization problem has both initial velocity and displacement, the MPF values for initial velocity and displacement need to be calculated separately and weighted summed. The weighted coefficients are the objective function values from using the initial velocity and displacement as initial condition separately.

7. Numerical example

To avoid the checkerboard phenomenon, the sensitivity filter method is used, the filter radius is 1.5. For some cases, drastic change of the design may cause that the Lyapunov equation cannot be solved. Thus, the move limit of design parameter is set to be 0.02.

In this section, a numerical example is presented to verify the sensitivity analysis scheme and the proposed approach.

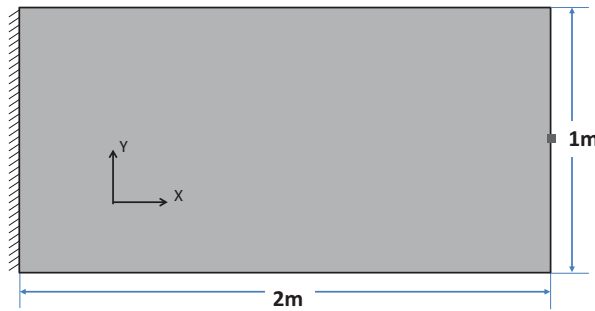


Figure 1: Geometry model

We consider a $2\text{m} \times 1\text{m} \times 0.1\text{m}$ rectangular plate. The left edge of the plate is clamped and other three edges are free as shown in figure 1. The material parameters is $E=69\text{GPa}$, $\nu=0.3$, $\rho_i = 2700\text{kg/m}^3$. A concentrate mass element locates at the middle of the right edge of the plate, and $m=50\text{kg}$. The initial condition is that the Z-direction velocity of mass element is 10m/s . The plate is uniform meshed by 4-nodes square element, 40×20 , as shown in Figure 2. The objective function is

$$J = \int_0^{\infty} u_{mass}^2 dt \quad (18)$$

where, u_{mass} is the Z direction displacement of mass element.

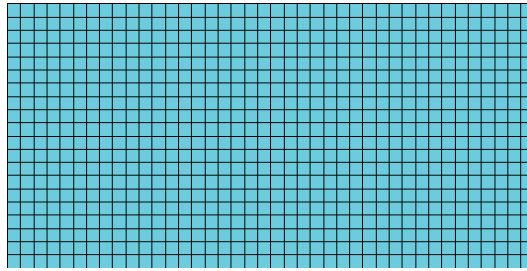


Figure 2: The finite model

Considering the symmetry of the finite element model, initial condition, and constraints, only the artificial densities of the elements in bottom half of the structure are considered in the optimization process. The artificial density of the element in the top half of structure is set to be same with that of the element at symmetrical position. Considering the accuracy of sensitivity results and efficiency of optimization process, in this example, the transformation matrix \mathbf{T} will contains 60 eigenmodes selected from first 300 eigenmodes of full model. To verify the accuracy of sensitivity results obtained by the proposed sensitivity analysis scheme, the finite difference method is also applied to obtain the sensitivity results. The sensitivity results of the purple element as shown in figure 3 by the finite difference method and adjoint method are both shown in figure 3. The damping parameters are $\alpha = 0.1$, $\beta = 0$, and the analysis model is a uniform design ($V_{frac} = 0.5$). Numerical results show that the relative error of the results obtained by two methods is small for most elements.

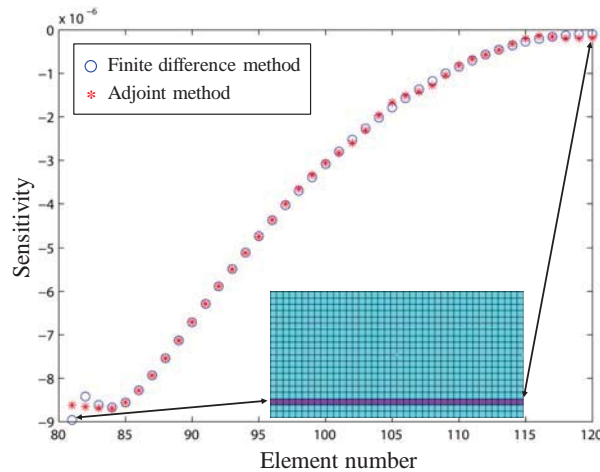


Figure 3: Sensitivity results of several elements from two methods

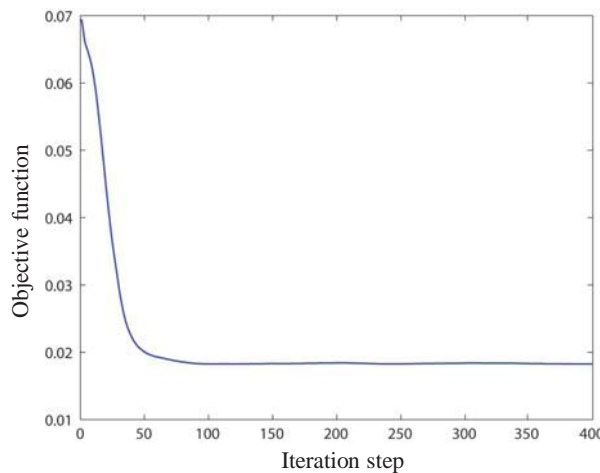


Figure 4: Iteration history of objective function

Firstly, perform a topology optimization with $\alpha = 0.1$, $\beta = 0$, $V_{frac} = 0.5$, and $\rho_{min} = 0.001$ by proposed approach. Figure 4 shows the iteration history of objective function and. From the results, a stable decrease of the objective function can be observed. Next, perform another topology optimization with $\alpha = 0$, $\beta = 0.1$, $V_{frac} = 0.5$, and $\rho_{min} = 0.001$ by proposed approach. The optimized designs are shown in figure 5. The results witness that the optimized designs under different damping parameters are such different. Thus, obtain the accurate damping parameters are important to whether the optimized design is reasonable.

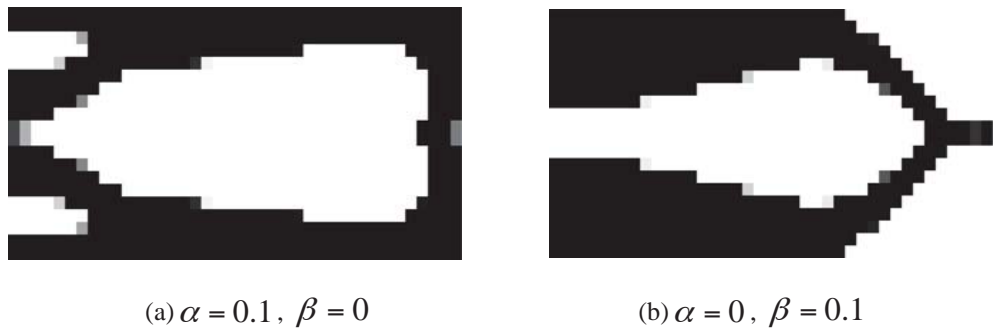


Figure 5: Optimized designs under different damping parameters

8. Conclusions

The problem of topology optimization with respect to vibration control of a shell structure subject to initial excitation is considered. The design objective is minimization of dynamic performance index in the form of time integral of the quadratic function of state variables. An approach is developed to handle this topology optimization problem. Mode reduction method and an eigenmode selection method are applied to decrease the scale of reduced model. The numerical example is presented to verify the sensitivity analysis scheme and the proposed approach for topology optimization problem considered in this paper. The results show that the sensitivity analysis scheme for reduced model can obtain accurate results, and also witness that the damping parameters have a great effect on the optimized design.

9. Acknowledgement

This work is supported by National Natural Science Foundation of China (91216201 and 11372062).

10. References

- [1] Kang Z, Zhang X, Jiang S, et al. On topology optimization of damping layer in shell structures under harmonic excitations[J]. *Structural and Multidisciplinary Optimization*, 46(1): 51-67, 2012.
- [2] Chia CM, Rongong JA, Woeden K, Strategies for using cellular automata to locate constrained layer damping on vibrating structures. *J Sound Vib* 319:119-139, 2009.
- [3] Zheng L, Xie RL, Wang Y, El-Sabbagh A, Topology optimization of constrained layer damping on plates using Method of Moving Asymptote (MMA) approach. *Shock Vib* 18:221-244, 2011.
- [4] Kalman RE, Bertram, JE, Control System Analysis and Design Via the "Second Method" of Lyapunov: I—Continuous-Time Systems. *Journal of Fluids Engineering*, 82(2), 371-393, 1960.
- [5] Ogata K, Yang Y, *Modern control engineering*, 1970.
- [6] Wang BP, Kitis L, Pilkey WD, Transient Response Optimization of Vibrating Structures by Liapunov's Second Method. *J. Sound Vib.*, 96, pp. 505-512, 1984.
- [7] Du D, Analytical solutions for DVA optimization based on the Lyapunov equation. *Journal of Vibration and Acoustics*, 130(5), 054501, 2008.
- [8] Bathe KJ, *Finite element procedures*. Prentice Hall, New Jersey, 1996.

Structural approximations for composite optimisation

Daniël M. J. Peeters¹, Mostafa M. Abdalla¹

¹ Delft University of Technology, The Netherlands, d.m.j.peeters@tudelft.nl

1 Abstract

A way to approximate the response of, variable stiffness, composites for optimisation is explained. A two-level approximation scheme is proposed inspired by traditional approximation concepts such as force approximations. First an approximation in terms of the in- and out-of-plane stiffness matrices is made. In the stiffness approximation a generalised convex linearisation approach is used: compliance, stress and inverse buckling load are approximated in terms of the linear and reciprocal stiffness matrices. Either the lamination parameters, or the nodal fibre angle distribution are used as design variables. A quadratic approximation is used to build the approximations in fibre angle space. Conservativeness is guaranteed by adding a convex damping function to the approximations. The method of conservative, convex separable approximations is used for the optimisation.

2 Keywords: Optimisation, variable stiffness, approximations, multi-level

3 Introduction

Composite materials are attractive due to their high stiffness- and strength-to-weight ratio. It has been shown that by spatially varying the stiffness of the composite, better performance can be obtained without adding extra weight. To optimise variable stiffness laminates, a three-step optimisation approach has been developed. [1, 2] In step one the optimal stiffness distribution is found, in step two the optimal fibre angles are obtained, and in step three the optimal fibre paths are retrieved. The critical numerical parts of this optimisation are the approximations used.

Response surfaces can be used as an approximation method to reduce the computational effort. This method is accurate, but choosing the response surfaces is problem-dependent. [3] The Rayleigh-Ritz method is often used to approximate eigenvalues, or buckling factors. It has been used to optimise buckling factors, but the shape functions need to be chosen, which is also problem-dependent. [4]

A generally applicable method is linearisation. Since stress and displacement are linear functions of the reciprocal sizing variables in a statically determinate structure, they are often reciprocally approximated. The 'convex linearisation' (ConLin) method introduced by Fleury and Braibant is a generalisation of linear or reciprocal approximations [5]. Whether a variable is approximated linearly or reciprocally depends on the derivative at the approximating point: linear if the derivative is positive, reciprocal if the derivative is negative. Vanderplaats recognised that approximating structural responses using the force in a member led to better approximations, called force approximations. [6] A two-level approximation is formulated. On level one, the stress is approximated as a function of the section properties. On level two, the section properties are approximated in terms of the physical properties. Once level two has converged, the stress is calculated based on the new properties, and a new level one approximation is made. This is repeated until the stress converges. [6, 7]

In this paper the ideas of force approximations and the ConLin method are combined. In level one approximations the structural responses are approximated in terms of the stiffness matrices, using a generalised version of the ConLin approximations. For level two approximation, a quadratic *approximation of approximation* is constructed along the lines of the Gauss-Newton method.

This paper is organised as follows: the approximations in terms of the stiffness are given in section 4. The lamination parameter and fibre angle approximation are discussed in sections 5 and 6. The way these approximations are used is explained in section 7 and this paper is concluded in section 8.

4 Approximations in stiffness space

The level one approximation, in stiffness space, is derived for three different structural responses. Compliance is discussed first since, as will be shown, it is the most straight-forward. Next, stress and buckling are discussed.

4.1 Compliance approximations

To clarify the rationale of the approximation, the derivation is first done for elastic trusses, then for general structures.

4.1.1 Elastic trusses

The strain energy of a truss made of an elastic material, with only A_e , the area of each element, as design variables is defined as:

$$U = \sum_e \frac{1}{2} \cdot E \cdot \varepsilon_e^2 \cdot A_e \cdot l_e \quad (1)$$

where E is the Young's modulus, l_e is the length and ε_e is the strain of element e . Using the standard strain-displacement equation, the principle of minimal total potential energy can be written as

$$\min_{\varepsilon, u} \sum_e \frac{1}{2} \cdot E \cdot \varepsilon_e^2 \cdot A_e \cdot l_e - f^t \cdot u \quad \text{s.t.} \quad \varepsilon_e - b_e^T \cdot u = 0 \quad (2)$$

The Lagrangian of this function can be formulated. Taking the Lagrange dual, and using the Young-Fenchel-Moreau transform leads to

$$\max_{\sigma} \left(- \left(\sum_e f^*(\sigma_e) A_e l_e \right) + \min_u \left(\sum_e \sigma_e A_e l_e b_e - f \right)^T \cdot u \right) \quad (3)$$

$$f^*(\sigma_e) = \sigma_e \cdot \varepsilon_e - g(\varepsilon) \quad \text{and} \quad \sigma_e = \frac{\partial g(\varepsilon)}{\partial \varepsilon} \quad (4)$$

Using the standard equation for stress and assuming that strong duality holds, equation (2) can be written as:

$$\min_F \sum_e f^* \left(\frac{F_e}{A_e} \right) \cdot A_e \cdot l_e \quad \text{s.t.} \quad \sum_e F_e \cdot b_e \cdot l_e = f \quad (5)$$

Implementing the correct expression for f^* , the minimal total potential energy and minimal compliance can be written as

$$C^* = \min_A \left(\min_F U^* \right) = \min_A \left(\min_F \left(\frac{1}{2} \sum_e \frac{F_e^2 \cdot l_e}{E \cdot A_e} \right) \right) \quad (6)$$

The minimisation over the, equilibrated, element forces corresponds to structural analysis, the minimisation with respect to the element areas corresponds to structural design. Since this is a min-min formulation convergence is guaranteed by alternating analysis and design.

Using the force F_e at iteration k in equation 6, the compliance is approximated in terms of A_e . This approximation has four desirable properties:

1. separable: each element area A_e only depends on properties of element e .
2. convex: the second derivative with respect to the element areas is larger than zero.
3. homogeneous: doubling A_e halves the compliance, hence the approximation is homogeneous of order -1.
4. conservative: the internal force F_e does not change as a function of the area, hence $F^{(k)}$ is always feasible, furthermore the compliance of $F^{(k+1)}$ is at least as good as the approximation based on $F^{(k)}$.

These four properties mean the optimisation using this approximation is numerically efficient (separable), a feasible solution can always be found (homogeneous), has a solution (convex) and is globally convergent (conservative). Ideally, a good structural approximation should retain as much as possible of these four properties.

4.1.2 General structures

Three equations need to be satisfied for a general structure:

1. equilibrium: $N_{\mu\nu, \nu} + b_\mu = 0$
2. strain-displacement: $\varepsilon_{\mu\nu}^0 = \frac{1}{2} (u_{\mu, \nu} + u_{\nu, \mu})$
3. material law: $N_{\mu\nu} = A_{\mu\nu\alpha\beta} \cdot \varepsilon_{\alpha\beta}$

where N is the generalised stress, ε^0 is the strain at mid-plane, and A is the generalised stiffness matrix.

Assuming the strain-displacement is satisfied in weak form, and denoting the test function as \tilde{N} :

$$\int_{\Omega} \tilde{N}_{\mu\nu} \cdot \varepsilon_{\mu\nu}^0 - \frac{1}{2} \cdot \tilde{N}_{\mu\nu} (u_{\mu, \nu} + u_{\nu, \mu}) d\Omega = 0 \quad (7)$$

Taking the symmetry of the second term into account, noting that $(\tilde{N}_{\mu\nu} \cdot u_\mu)_{, \nu} = \tilde{N}_{\mu\nu} \cdot u_{\mu, \nu} + \tilde{N}_{\mu\nu, \nu} \cdot u_\mu$, and using the Gauss theorem, equation 7 becomes:

$$\int_{\Omega} \tilde{N}_{\mu\nu} \cdot \varepsilon_{\mu\nu}^0 d\Omega + \int_{\Omega} \tilde{N}_{\mu\nu, \nu} \cdot u_\mu d\Omega - \oint_{\Gamma_t} \tilde{N}_{\mu\nu} \cdot u_\mu \cdot n_\nu dA = 0 \quad (8)$$

Defining $\tilde{N}_{\mu\nu}$ as a change in stress distribution that satisfies the equilibrium equation $\partial N_{\mu\nu}$, means the second term equals zero. Furthermore, the normal of $\partial N_{\mu\nu}$ is zero, thus the third term is zero as well. Hence

$$\int_{\Omega} \partial N_{\mu\nu} \cdot \varepsilon_{\mu\nu}^0 d\Omega = 0 \quad (9)$$

Noting that $\varepsilon_{\mu\nu}^0 = \frac{\partial U^*(N_{\mu\nu})}{\partial N_{\mu\nu}}$ and using the material law, the total strain energy and minimum compliance can be written as:

$$C^* = \min_A \min_N \int_{\Omega} U^*(N, A) d\Omega = \min_A \min_N \int_{\Omega} \frac{1}{2} \cdot A_{\alpha\beta\mu\nu}^{-1} N_{\mu\nu} N_{\alpha\beta} d\Omega \quad (10)$$

In the general case, the compliance is in terms of A^{-1} , thus the approximation should also be in this form. Defining the load and strain at mid-plane as:

$$N = [N_x \quad N_y \quad N_{xy}]^T \quad \varepsilon^0 = [\varepsilon_x^0 \quad \varepsilon_y^0 \quad \gamma_{xy}^0]^T \quad (11)$$

the compliance can be written as:

$$U^* = \frac{1}{2} N^T \cdot A^{-1} \cdot N = \frac{1}{2} (N \cdot N^T) : A^{-1} = \phi : A^{-1} \quad (12)$$

where $:$ denotes the Frobenius inner product, meaning $A : B = \text{trace}(A \cdot B^T)$

This approximation can be shown to be convex, in terms of A , the normalised stiffness matrix \hat{A} and the height h . The approximation in equation (10) is also separable: the normalised general stiffness matrix and height do not influence other elements. Conservativeness also still holds: the minimisation in terms of A is still done in a feasible space for N . Homogeneity of order -1 still holds, since the form of the approximation has not changed. Hence, the approximation still has the four desirable properties.

4.2 Stress approximations

Next, an approximation for stress is derived. This is often used since the (local) stress constraints are often a driving factor. The same approach as that for compliance is used: first develop approximations for elastic trusses, then general structures.

4.2.1 Elastic trusses

Stress is usually set as constraint, and is expressed as a failure index, which also normalises the stress:

$$r_e \approx \frac{F_e^{(k)}}{\sigma_{all} \cdot A_e} \quad (13)$$

where σ_{all} denotes the maximum allowable stress. However, a modification has to be added since F_e is not just dependent on the area of element e , it is also dependent on the other areas. Since we are interested in creating a homogeneous approximation, this modification should have two properties: one, for the current area, it should be zero, two, if all areas are scaled with the same factor, it should remain zero. The total approximation becomes a linear-reciprocal function:

$$r_e \approx \frac{F_e^{(k)}}{\sigma_{all} \cdot A_e} + \sum_e a_e \cdot A_e \quad (14)$$

Hence, the approximation is separable in terms of the areas. The function is convex: the second derivative with respect to the element area is positive. homogeneity also holds in a limited sense: scaling the area will scale the stress approximation. The approximation is not necessarily conservative. How this lack of conservativeness is handled is explained in section 7.

4.2.2 General structures

For a general structure, the failure index is a function of strain $r_e = r_e(\varepsilon_e)$ and may be locally approximated by [8]:

$$r = N^T A^{-1} g + s_i \cdot \Delta N \quad \text{with} \quad g^{(k)} = \left. \frac{\partial r}{\partial \varepsilon} \right|_{\varepsilon = \varepsilon^{(k)}} \quad (15)$$

Hence, the stress has both a local term, depending on A^{-1} , and a global term due to the load redistribution ΔN . The local approximation of r is given by

$$r = \phi : A^{-1} \quad \text{with} \quad \phi = \frac{1}{2} (Ng^T + gN^T) \quad (16)$$

Upon inspection, it was found ϕ is not positive semi-definite (psd), which is necessary for convexity. To guarantee convexity, the term ϕ is divided in a psd and a non-psd part. [8] The indefinite part is approximated using a linear expansion. The details are explained in Khani et. al. [8]

The load redistribution part is approximated in a linear way, similar to the force approximation introduced by Vanderplaats and Thomas [6]. The total approximation of the stress is linear-reciprocal:

$$r \approx \phi : A^{-1} + \psi : A \quad (17)$$

which is the same form as was found for trusses. This function is convex and homogeneous by construction, it is also separable even though the load redistribution is taken into account. The approximation, again, is not necessarily conservative.

4.3 Buckling optimisation

The buckling factor λ is calculated using [2]

$$(K^b - \lambda K^g) \cdot a = 0 \quad (18)$$

where K^b is the global bending stiffness matrix and K^g is the global geometric stiffness matrix. a is the mode shape normalised with respect to K^b . Deriving equation (18) with respect to a design variable A leads to

$$\frac{d\lambda}{dA} = \lambda a^T \cdot \left(\frac{dK^b}{dA} + \lambda \frac{dK^g}{dA} \right) \cdot a \quad (19)$$

The first term of this equation is the derivative of the bending stiffness, which is local. The second term is the derivative of the geometric stiffness, which is not local: it represents the load redistribution due to the stiffness change of a single element. It can be seen the buckling factor is homogeneous of order zero with respect to the in-plane stiffness matrices from the general FE equilibrium and material law. Hence, λ depends on the load redistribution. Furthermore, λ is homogeneous of order one with respect to the bending stiffness. The inverse buckling load $r = 1/\lambda$ is approximated since it behaves similarly to the compliance and stress responses. This has the same homogeneity: order zero in terms of the in-plane stiffness and order one in terms of the *inverse* bending stiffness. The approximation has the following form: [2]

$$r \approx \sum_n \psi : A + \phi : D^{-1} \quad (20)$$

where the sum over all nodes is taken and no constant is added since the first part is zero at the approximation point, and the second part is exactly the inverse buckling load at the approximation point. It is shown in IJsselmuiden et al. [2] that the approximation is convex. Looking at equation (20), separability is also satisfied, and homogeneity is satisfied by construction. Just as for stress, conservativeness is not guaranteed.

5 Approximations in lamination parameter space

In step one of the three-step optimisation approach, the stiffness is optimised in terms of the lamination parameters. This is not really a level two approximation since the lamination parameters describe the stiffness matrices exactly:

$$A = h \cdot (\Gamma_0 + \Gamma_1 \cdot V_1 + \Gamma_2 \cdot V_2 + \Gamma_3 \cdot V_3 + \Gamma_4 \cdot V_4) \quad (21)$$

$$D = \frac{h^3}{12} \cdot (\Gamma_0 + \Gamma_1 \cdot W_1 + \Gamma_2 \cdot W_2 + \Gamma_3 \cdot W_3 + \Gamma_4 \cdot W_4) \quad (22)$$

where h is the thickness of the laminate and Γ are the laminate invariant matrices.

The feasible region of either the in- or out-of-plane lamination parameters separate is defined as

$$\begin{aligned} 2 \cdot V_1^2 \cdot (1 - V_3) + 2 \cdot V_2^2 \cdot (1 + V_3) + V_3^2 + V_4^2 - 4 \cdot V_1 \cdot V_2 \cdot V_4 &\leq 1 \\ V_1^2 + V_2^2 &\leq 1 \\ -1 &\leq V_3 \leq 1 \end{aligned} \quad (23)$$

If balanced laminates are desired, V_2 and V_4 are set to zero. Note that although V is used, this also holds for the out-of-plane lamination parameters W . For the combination of in- and out-of-plane lamination parameters there is no easy relationship. The feasible region has been defined in earlier work. [9, 10] The design space has been shown to be convex in terms of the lamination parameters. [1]

6 Approximations in fibre angle space

In step two of the three-step optimisation approach, the lay-up at the different nodes is optimised. Based on the approximation in stiffness space, a Taylor expansion in terms of the change in fibre angles is made:

$$f^{(2)}(\theta) \approx f_0^{(1)} + g \cdot \Delta\theta + \Delta\theta^T \cdot H \cdot \Delta\theta = f^{(1)}(A(\theta)) \quad (24)$$

where $f_0^{(1)}$ denotes the value, g the gradient and H is an approximation of the Hessian of the first approximation in stiffness space at the approximation point; A contains the components of the stiffness matrices A and D . g_i can be found by deriving equation (24). Deriving a second time, the Hessian is found to be

$$H_{ij} = \frac{\partial^2 f^{(1)}}{\partial \theta_i \partial \theta_j} = \frac{\partial^2 f^{(1)}}{\partial s_\alpha \partial s_\beta} \cdot \frac{\partial s_\alpha}{\partial \theta_i} \cdot \frac{\partial s_\beta}{\partial \theta_j} + \frac{\partial f^{(1)}}{\partial s_\alpha} \cdot \frac{\partial^2 s_\alpha}{\partial \theta_i \partial \theta_j} \quad (25)$$

Convexity is guaranteed by omitting the underlined part of equation (25), which is not guaranteed to be psd, and using only the Gauss-Newton part which is always psd. Since an approximation has to have equal function and gradient at the approximation point as the approximated function, using only part of the Hessian gives a valid approximation which is convex and separable. Note that homogeneity is not relevant in fibre-angle space and is not discussed.

7 Using the approximations

The method of conservative convex separable approximations (CCSA) is used. [11] As shown in the previous sections, the approximations, either in terms of the stiffness or the fibre angles, are always convex and separable. To assure the approximation is conservative, a damping function d is added:

$$f \approx \hat{f}(x) + \rho \cdot d(x) \quad (26)$$

where \hat{f} is an approximation, and ρ is the damping factor. This was done for both levels of approximation: both for stiffness and fibre angle approximation a damping function was added. To make the notation clear: a 1 denotes the approximation in stiffness space a 2 indicates fibre angles, if no superscript is added, it holds for both approximations.

The functions need to satisfy the following conditions: [11]

- the functions are continuous and the gradient and Hessian with respect to x exist and are continuous
- at the approximation point $\hat{f}(x) = f(x)$ and $d(x) = 0$
- at the approximation point $\nabla_x \hat{f}(x) = \nabla_x f(x)$ and $\nabla_x d(x) = 0$
- $\nabla_{xx}^2 \hat{f}(x)$ is positive semi-definite
- $\nabla_{xx}^2 d(x)$ is positive definite

The solution procedure is explained in algorithm 1. This algorithm is used to optimise a curved plate for buckling, while constraining the compliance in another paper by the authors. [12]

Algorithm 1 Solution Procedure

- 1: start from an initial fibre angle distribution.
 - 2: perform an FEA and calculate the sensitivities for the first level approximation $f^{(1)}$.
 - 3: add the damping function $\rho^{(1)} \cdot d^{(1)}$ to the first level approximation.
 - 4: calculate the gradient and Hessian for the second level approximation $f^{(2)}$.
 - 5: add the damping function $\rho^{(2)} \cdot d^{(2)}$ to the second level approximation.
 - 6: apply the steering constraint, build the Lagrangian \mathcal{L} and solve the system.
 - 7: calculate first level approximation $f^{(1)}$ and update damping factor of level two $d^{(2)}$.
 - 8: if the first level approximation $f^{(1)}$ is improved, continue, else go back to step 5.
 - 9: if the first level approximation $f^{(1)}$ has converged, or the maximum number of iterations is reached, continue, else return to step 4.
 - 10: perform an FEA and update the damping factor of first level approximation $d^{(1)}$.
 - 11: if the FE response has improved, continue, else go back to step 3.
 - 12: if FEA has converged, the optimal fibre angle distribution is found, else return to step 2.
-

8 Conclusion

An approximation approach for the optimisation of, variable stiffness, composites is proposed. The three-step optimisation approach for variable stiffness composites is used as guideline. In step one the optimal stiffness distribution is found, in step two the optimal nodal fibre angle distribution is found, in step three the fibre paths are found. The approximations in this paper focus on step one and two.

Analogous to the force approximation a two-level approximation approach is proposed. In level one, a generalised ConLin method is used: the structural responses are approximated in terms of the in- and out-of-plane stiffness matrices and their inverse. In step one, lamination parameters are used to optimise the stiffness distribution. Since the stiffness matrices are perfectly described by the lamination parameters, this is not a level two approximation. In step two, a second-order Taylor approximation in terms of the change in fibre angles is made at the approximation point as a level two approximation.

The conservative, convex separable approximation method is used during the optimisation. Convexity and separability are guaranteed by construction of the approximations. Conservativeness is not guaranteed. A damping function and damping factor are added to the stiffness and fibre angle approximations to guarantee conservativeness and thus global convergence.

In this paper only compliance, stress and inverse buckling load have been approximated, but the method is more generally applicable. Other responses may be approximated in a similar manner.

9 Acknowledgements

This work is supported by the CANAL (CreAting Non-conventionAl Laminates) Project, part of the European Union Seventh Framework Program.

References

- [1] IJsselmuiden, S. T., *Optimal design of variable stiffness composite structures using lamination parameters*, Ph.D. thesis, Delft University of Technology, 2011.
- [2] IJsselmuiden, S. T., Abdalla, M. M., and Gürdal, Z., “Optimization of Variable-Stiffness Panels for Maximum Buckling Load Using Lamination Parameters,” *AIAA Journal*, Vol. 48, No. 1, 2010, pp. 134–143.
- [3] Venter, G., Haftka, R. T., and Starnes, J. H., “Construction of Response Surface Approximations for Design Optimization,” *AIAA Journal*, Vol. 36, No. 12, 2015/02/17 1998, pp. 2242–2249.
- [4] Wu, Z., Weaver, P. M., Raju, G., and Kim, B. C., “Buckling analysis and optimisation of variable angle tow composite plates,” *Thin-Walled Structures*, Vol. 60, No. 0, 2012, pp. 163 – 172.
- [5] Fleury, C., “CONLIN: An efficient dual optimizer based on convex approximation concepts,” *Structural optimization*, Vol. 1, No. 2, 1989, pp. 81–89.
- [6] Vanderplaats, G. and Thomas, H., “An improved approximation for stress constraints in plate structures,” *Structural optimization*, Vol. 6, No. 1, 1993, pp. 1–6.
- [7] Vanderplaats, G., Kodiyalam, S., and Long, M., *A two-level approximation method for stress constraints in structural optimization*, American Institute of Aeronautics and Astronautics, 2015/02/17 1989.
- [8] Khani, A., IJsselmuiden, S., Abdalla, M., and Gürdal, Z., “Design of variable stiffness panels for maximum strength using lamination parameters,” *Composites Part B: Engineering*, Vol. 42, No. 3, 2011, pp. 546 – 552.
- [9] Setoodeh, S., Abdalla, M., and Gürdal, Z., *Approximate Feasible Regions for Lamination Parameters*, American Institute of Aeronautics and Astronautics, 2015/02/18 2006.
- [10] Wu, Z., Raju, G., and Weaver, P., *Feasible Region of Lamination Parameters for optimization of Variable Angle Tow (VAT) Composite Plates*, American Institute of Aeronautics and Astronautics, 2015/02/18 2013.
- [11] Svanberg, K., “a class of globally convergent optimization methods based on conservative convex separable approximations,” *Siam J. optim.*, Vol. 2, 2002, pp. 555–573.
- [12] Peeters, D., Hesse, S., and Abdalla, M., “Stacking Sequence Optimisation of Variable Stiffness Laminates with Manufacturing Constraints,” *Composites Structures*, accepted.

Multi-Parameter Optimization Study on the Crashworthiness Design of a Vehicle by Using Global Sensitivity Analysis and Dynamic Meta-model

ZHANG Weigang¹ ZHANG Yang² MA Tao³ TANG Ting⁴

¹State Key Laboratory of Advanced Design & Manufacturing for Vehicle Body, Hunan University, Changsha, China,
zhangwg@hnu.edu.cn

²Hunan University, Changsha, China, zhangyanghndx@163.com

³Hunan University, Changsha, China, mataobetter@126.com

⁴Hunan University, Changsha, China, tangtingxyz@126.com

Abstract: In a vehicle's concept design stage, there are usually a lot of design parameters need to be defined and optimized. For such a complex and non-linear system of a vehicle, multi-parameter optimization not only has a great computation, but also face the difficulty to obtain optimum solutions. This paper aimed at an optimization problem of a vehicle's crashworthiness with 20 design parameters, and presented a new method which uses global sensitivity analysis and dynamic meta-model. First, vehicle crash simulation model was constructed and design parameters were simplified by using global sensitivity analysis, then, the sensitive parameters were used to construct an initial meta-model. During the optimization solving process, the design domain and meta-model were updated continually until the accuracy of the solutions met the requirement of the convergence criteria. Final results showed that the presented method in this paper could not only successfully solve the multi-parameter optimization problem, but also significantly reduce the computation time and cost.

Keywords: Multi-parameter Optimization, Vehicle Crashworthiness, Concept Design, Global Sensitivity Analysis, Dynamic Meta-model.

1. Introduction

Generally, to develop a totally new car, it has to go through three stages: concept design, detailed design and engineering modifying, among which concept design mainly involves in the defining of overall performance, overall parameters and structure forms, etc., which then become the basis for later design. During the whole process of the car development, concept design is so important because in this stage, the design space is very big and the defined results have great effect on the development^[1]. According to relative statistics, when concept design finishes, about 70% of the total cost for the car development can be estimated out^[2]. Therefore, it can be concluded that the success of a new car's development relies much on the concept design.

Concept design of a car involves in many aspects. In this paper, it is only going to discuss about the concept design of crashworthiness, i.e., the optimum matching design of body structure and occupant restraint system. Traditional way was that of defining body structure first and then occupant restraint system was matched by using computer simulation and optimization method. For example, references [3,4,5,6] introduced the similar work of optimization matching design of occupant restraint system on the basis of defined body frame structure. This kind of design usually involves few design parameters and can be classified as local optimization problem. Although it is simple, it is hard to make it optimum of the overall cost and overall performance at the same time. If the performance of the body structure is not so good, then great challenge will be there for the matching design of occupant restraint system, accompanied by rising cost. An improved method is to design body structure and occupant restraint system concurrently, however, this will make the design become more complex because the parameter numbers increase a lot, thus the computation cost grows fast, and optimization work becomes very difficult^[7]. Thus, it is necessary for researchers to find a way to solve the problem of optimization for high

nonlinear system with multi-parameters.

In this paper, in order to conduct concept design for the match of a new car's body structure and occupant restraint system, a simplified simulation model is established with 20 design parameters defined. Then, global sensitivity analysis method based on variance is used to find out and select important design parameters, which are used to establish meta-model. Finally, a new method is proposed to update meta-model and global optimum solution is obtained after 5 iterations. The method presented in this paper can be as a reference for solving the problem of the optimization design of high nonlinear system with multi-parameters.

2. Methodology

2.1 Establishment of simplified concept model for crash analysis

In the stage of a car's crashworthiness concept design, what is needed to consider is the match design of the performances of body structure and occupant restraint system. The body structure's performance can be described by an Equivalent Dual-Trapezium Wave(EDTW) as the broken line shown in Figure 1. EDTW is a simple curve, which is not only capable of replacing the complex curve(as the full line shown in Figure 1), but also reflects the important information of the crashworthiness, such as the first step acceleration a_1 , the second step acceleration a_2 , and also the important impact moments t_c , t_e , etc.

For EDTW In Figure 1, only the wave shape is assumed, while the parameters a_1 , a_2 , t_c , t_e , etc. are all unknown and need to be defined within a given design space.

For the occupant restraint system, Madymo software which is specialized for dynamic analysis of multi-rigid body is used to establish a simulation model which includes window shield, steering system, seatbelt, airbag, seat, floor and Hybrid III 50% male dummy, as shown in Figure 2. All the parameters for occupant restraint system design are included in this model.

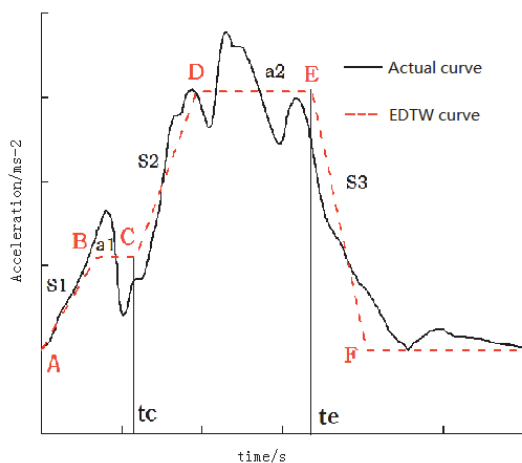


Figure 1: EDTW used in the concept design of crashworthiness

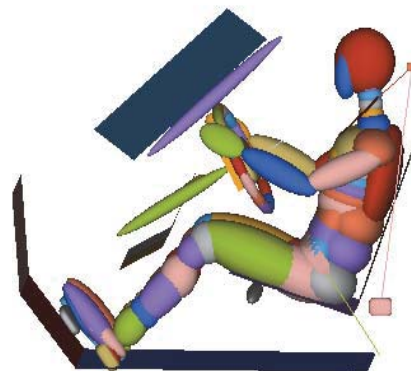


Figure 2: Simulation model for occupant restraint system

By now, a complex system is established. EDTW in Figure 1 is an input for the simulation model in Figure 2 when impact simulation begins. The goal of the concept design is to define all the parameters, which are a_1 , a_2 , slope s_1 , s_2 , s_3 and moment t_c included in Figure 1 and the force limit of seatbelt force limiter F_x , seatbelt preload l , preload time of the seatbelt pre-loader T_y , belt stiffness δ , height of the seatbelt D ring, the ignition time of the airbag t_i , vent hole area scale s , airbag volume v , air inflation portion p , coefficient of air

permeability c , steering wheel angle W_A , seat position S_p , seat back angle S_A and knee bolster stiffness k , etc. which are included in Figure 2. The initial values and varying spaces for all the parameters are assumed as shown in Table 1.

Table 1: All the design parameters, initial values and varying spaces

Design parameters/unit	Initial values	Varying spaces	Design parameters/unit	Initial values	Varying spaces
a_1/ms^{-2}	108	[90, 150]	δ	16%	[10%,20%]
a_2/ms^{-2}	304	[240,350]	v/L	30	[26,34]
S_1/ms^{-3}	7900	[6300,9400]	s	1.0	[0.8,1.2]
S_2/ms^{-3}	12900	[10300,15500]	t_i/ms	25	[20,30]
S_3/ms^{-3}	-18	[-20,-16]	p	1.0	[0.8,1.2]
t_c/ms	23	[20,26]	c	0.7	[0.6,0.8]
F_x/N	4000	[3000,5000]	K	1.0	[0.8,1.2]
l/mm	35	[30,80]	S_p/mm	258	[248,268]
H/m	1	[0.9,1.1]	S_A/deg	17	[10,25]
T_y/ms	15	[10,20]	W_A/deg	29	[27,31]

2.2 Optimization Model for the System Design

In order to conduct the concept design, an optimization model needs to be established. The objective of the optimization is to reduce the occupant injury by using computer simulation method. The occupant injury evaluation involves in head, chest and legs, and the corresponding index are Head Injury Criterion (HIC), chest acceleration within 3ms (C_{3ms}), chest depression(D), and leg axial force(F) respectively, which should not exceed the respective limits. In this paper, a Weighted Injury Criterion^[8](WIC) which combines HIC , C_{3ms} , D and F is used as described by Eq.(1):

$$WIC = 0.6\left(\frac{HIC}{1000}\right) + 0.35\left(\frac{C_{3ms}}{60} + \frac{D}{75}\right) / 2 + 0.05\left(\frac{F_{FL} + F_{FR}}{20}\right) \quad (1)$$

Where, F_{FL} and F_{FR} are the axial forces of left leg and right leg respectively.

Thus, the mathematical optimization model is established as follows:

Variables: $a_1, a_2, S_1, S_2, S_3, t_c, F_x, l, H, T_y, \delta, v, s, t_i, p, c, k, S_p, S_A, W_A$

Min WIC

S.t. $HIC \leq 1000, C_{3ms} \leq 60g, D \leq 75mm, F_{FL} \leq 10KN, F_{FR} \leq 10KN.$

How to resolve the above optimization problem? Traditional mathematical optimization methods are obviously unable to do so because of large computation involving in iterations. With the development of numerical meta-model method in recent years, optimization efficiency has been improved a lot. The most representative meta-models are Response Surface Model (RSM), Kriging model and Radial Basis Function (RBF) model. However, researches showed that each kind of meta-model has its adaptability. For example, RSM is easy to construct and has high efficiency of response prediction, but is unsuitable for high nonlinear system; Kriging model is suitable for high nonlinear system as long as the parameters' number is within 8; RBF

model has moderate accuracy and efficiency, and its local accuracy is hard to achieve when used for high nonlinear system with multi-parameters^[9]. Therefore, if parameters' number can be reduced for high nonlinear system, then it is more convenient to obtain the solution. Reference [10] presented a method named global sensitivity analysis based on variance which can be used to find out sensitive parameters, so those insensitive parameters can be removed and the total parameters number reduced.

2.3 Theory of Global Sensitivity Analysis Based on Variance

It is assumed that there is a system expressed as Eq.(2):

$$Y=f(X) \tag{2}$$

$$X = (X_1, X_2, \dots, X_k,)$$

Where X_i is independent with each other and uniformly distributed within [0,1].

By using Monte Carlo sampling method, two matrices A, B are generated as follows:

$$A = \begin{bmatrix} x_{11} & \dots & x_{1i} & \dots & x_{1k} \\ x_{21} & \dots & x_{2i} & \dots & x_{2k} \\ \dots & \dots & \dots & \dots & \dots \\ x_{n1} & \dots & x_{ni} & \dots & x_{nk} \end{bmatrix}, B = \begin{bmatrix} x'_{11} & \dots & x'_{1i} & \dots & x'_{1k} \\ x'_{21} & \dots & x'_{2i} & \dots & x'_{2k} \\ \dots & \dots & \dots & \dots & \dots \\ x'_{n1} & \dots & x'_{ni} & \dots & x'_{nk} \end{bmatrix}$$

Where k is the design parameters number and n is the sampling number.

If the i column of matrix B is replaced by the i column of matrix A, and the i column of matrix A is replaced by the i column of matrix B, then another two matrices C_i and C_{-i} are generated:

$$C_i = \begin{bmatrix} x_{11} & \dots & x'_{1i} & \dots & x_{1k} \\ x_{21} & \dots & x'_{2i} & \dots & x_{2k} \\ \dots & \dots & \dots & \dots & \dots \\ x_{n1} & \dots & x'_{ni} & \dots & x_{nk} \end{bmatrix}, C_{-i} = \begin{bmatrix} x'_{11} & \dots & x_{1i} & \dots & x'_{1k} \\ x'_{21} & \dots & x_{2i} & \dots & x'_{2k} \\ \dots & \dots & \dots & \dots & \dots \\ x'_{n1} & \dots & x_{ni} & \dots & x'_{nk} \end{bmatrix}$$

By substituting above matrices into Eq.(2), the corresponding outputs can be obtained. It is assumed that y_A , y_B and y_C are the output vectors corresponding to the input matrices A, B and C, then the estimated variance is calculated by Eq.(3):

$$\hat{V}(Y) = \frac{1}{n} y_A^T (y_A - y_B) \tag{3}$$

Where $\hat{V}(Y)$ is the total variance.

At the same time, followings are defined as Eq.(4), Eq.(5) and Eq.(6):

$$\hat{f}_0^2 = \frac{1}{n} y_A^T y_B \tag{4}$$

$$\hat{U}_i = \frac{1}{n} y_A^T y_{C_i} \tag{5}$$

$$\hat{U}_{-i} = \frac{1}{n} y_A^T y_{C_{-i}} \tag{6}$$

Then for the input parameter x_i , the main effect index \bar{S}_{x_i} is estimated by Eq.(7):

$$\bar{S}_{x_i} = \frac{\hat{U}_i - \hat{f}_0^2}{\hat{V}(Y)} \tag{7}$$

And the whole effect index $\bar{S}_{x_i}^T$ is estimated by Eq.(8):

$$\bar{S}_{x_i}^T = \frac{\hat{V}(Y) - (\hat{U}_{-i} - \hat{f}_0^2)}{\hat{V}(Y)} \tag{8}$$

The main effect index reflects the influence of single parameter on the system response, while the whole effect index not only reflects the single parameter’s influence on the system response, but also reflects the parameters’ interaction influence.

As to the system studied in this paper, by using the above method, the estimated main effect index and whole effect index of each parameter are calculated, and the results are shown in Table 2.

Table 2: Parameters, main effect and whole effect index

parameters	a ₁	a ₂	S ₁	S ₂	S ₃	t _c	F _x	l	H	T _y
Main effect	-0.0018	0.4371	-0.0006	0.0034	0.0193	0.0171	0.0693	0.0276	0.0081	0.003
Order	18	1	17	13	7	8	4	5	10	12
Whole effect	0.0274	0.4630	0.0465	0.0434	0.0268	0.0372	0.1013	0.0395	0.0133	0.008
Order	11	1	6	7	12	9	4	8	14	18

Table 2: (Continues)

parameters	δ	v	s	t _i	p	c	K	S _p	S _A	W _A
Main effect	-0.0200	0.0259	0.1606	-0.0018	0.1038	-0.4E-4	-0.0003	0.0056	0.0159	0.001
Order	20	6	2	19	3	15	16	11	9	14
Whole effect	0.0213	0.0707	0.2467	0.0274	0.1199	0.1E-4	0.0049	0.0090	0.0133	0.009
Order	13	5	2	10	3	20	19	17	15	16

According to the results in Table 2, 11 parameters with higher index values are selected. Although the parameters number is reduced from 20 to 11, it is still hard to construct a single meta-model which has expected local and overall accuracy. Thus, during the iteration process, meta-model needs to be updated again and again in order to be more and more accurate till the solution is obtained.

2.4 Technique of Dynamic Meta-model

Meta-model continuously changes, then dynamic meta-model emerges. i.e., during the process of each iteration, design space reduces continually, and a new meta-model is constructed to replace the old one. The theory and algorithm for constructing dynamic meta-model are introduced below.

(1) First step, Hypercube Latin method is used to sample within the given initial design space, thus the whole design space can be described by a few samples, correspondingly, the system responses are calculated and thus initial meta-model can be established;

(2) Second step, the initial meta-model is solved by using multi-island genetic algorithm, and the first

solution is obtained;

(3) Third step, updating design space. For the kth times iteration, a design space is defined by Eq.(9) based on the solution x'_{k-1} of the k-1th times iteration:

$$(S_k^{L'}, S_k^{U'}) = (x'_{k-1} - \frac{1}{10} L_{k-1}, x'_{k-1} + \frac{1}{10} L_{k-1}) \tag{9}$$

Where, $S_k^{L'}$ and $S_k^{U'}$ are the lower and upper limit of the design space respectively for the kth times iteration, and L_{k-1} is the design space size for the k-1th times iteration;

(4) Fourth step, by using global sensitivity analysis during the k-1th times iteration, another solution x''_{k-1} is obtained, thus for the kth times iteration, another design space is defined by Eq.(10) based on x''_{k-1} :

$$(S_k^{L''}, S_k^{U''}) = (x''_{k-1} - \frac{1}{10} L_{k-1}, x''_{k-1} + \frac{1}{10} L_{k-1}) \tag{10}$$

(5) Fifth step, the design space for the kth times iteration is updated by considering the above two defined spaces and also the initial design space, which can be expressed by Eq.(11):

$$(S_k^L, S_k^U) = (S_k^{L'}, S_k^{U'}) \cup (S_k^{L''}, S_k^{U''}) \cup S \tag{11}$$

(6) Sixth step, convergence criterion. New meta-model is constructed based on new samples sampled from the updated design space and iteration calculation is going on until solution is obtained. If the error between the two solutions of kth and k-1th time iteration is less than ξ (assigned value of 0.5%), also at the same time, the solutions between meta-model and simulation model is less than 5%, then the global optimization ends, otherwise, the iteration continues until the convergence criterion is satisfied.

2.5 Optimization results

By 5 times iteration, the results converged. All the parameter's initial values and the corresponding optimized results are shown in Table 3. Compared with initial injury values, *WIC* is reduced by 36.5% after optimization.

Table 3: Parameters, initial values and optimized results

Parameters (input and output)	Initial values	Optimized results	Parameters (input and output)	Initial values	Optimized results
a_1/ms^{-2}	108	112	s	1.0	1.01
a_2/ms^{-2}	304	243	p	1	1.08
S_1/ms^{-3}	7900	9368	t_i/ms	25	24.6
S_2/ms^{-3}	12900	13771	<i>HIC</i>	754	400
t_c/ms	23	25	C_{3ms}/g	56.3	43.6
F_x/N	4000	4458	<i>D/mm</i>	37	33
<i>l/mm</i>	35	66	<i>WIC</i>	0.717	0.455
<i>H/m</i>	1	0.973			

3. Conclusion

This paper studied the optimization design problem for a high nonlinear system with multi-parameters during a new car's crashworthiness concept design stage. A simplified concept simulation model was established first and then the methods of Global Sensitivity Analysis and dynamic meta-model were used to do research and optimization. The productive work of the research was that the number of design parameters was reduced effectively and system model was simplified, which in a great degree made the optimization computation cost reduced and the global optimum solution obtained. The research work done in this paper can be a good reference for other similar optimization problems in modern engineering.

4. Acknowledgements

This study is granted by National Nature Science Foundation of China, the granted number is 51275164.

5. References

- [1] CHANG Weibo. Study on Concept Design and Optimization of Car Body Based on Frontal Impact Crashworthiness[D]. Changsha: Hunan University, China, 2012.
- [2] CHENG Aiguo, SHEN Yang, YAO Zuoping. Advanced Methods and Procedures for Vehicle Body Design[M], *China Machine Press*, 2011.
- [3] GE Ruhai. Study on the Match Design of Occupant Restraint System in Frontal Crash[D]. Zhenjiang,: Jiangsu University, China, 2007.
- [4] X.G Gu, G.Y. Sun, G.Y.Li, et al. Multi-objective optimization design for vehicle occupant restraint system under frontal impact. *Structural and Multidisciplinary Optimization*[J], 47(3): 465-477,2013.
- [5] ZHANG Xuerong, SU Qingzu. Parameters Optimization and Robustness Analysis of Vehicle Occupant Restraint System[J]. *Automotive Engineering*, 32(12): 1053-1056, 2010.
- [6] ZHANG Junyuan. Study on the Parameters Optimization and Performance Robustness of Occupants Restraint System of a Mini-van [D]. Jilin: Jilin University, China, 2003.
- [7] LI Tiezhu, LI Guangyao, GAO Hui, et al. The Performance Improvement of Vehicle Occupant Restraint System Based on Reliability Optimization. *Chinese Mechanical Engineering*[J],21(8): 993-999, 2010.
- [8] Viano D C, Arepally S. Assessing the safety performance of occupant restraint systems[R]. *SAE Technical Paper*, 1990.
- [9] ZHANG Yang. The Study on Global Sensitivity Analysis and Dynamic Meta-model for Nonlinear System with Multi-parameters[D], Changsha: Hunan University, China, 2014.
- [10] Sobol I.M. Global Sensitivity Indices for Nonlinear Mathematical Models and Their Monte Carlo Estimates. *Mathematical Modelling & Computational Experiment*, 55(1-3):407-414, 1993.

Integrated multi-scale vibro-acoustic topology optimization of structure and material

Xuan Liang¹, Jianbin Du²

¹ Tsinghua University, Beijing, China, liangx13@mails.tsinghua.edu.cn

² Tsinghua University, Beijing, China, dujb@tsinghua.edu.cn

Abstract

The paper deals with the problem of the integrated layout design of macro and micro structure taking into consideration vibro-acoustic criteria. A multi-scale topology optimization model is presented for minimization of the sound power radiation from the vibrating composite structure with different designable periodic microstructures in different domains of the macrostructure. An extended multi-material interpolation model based on SIMP and PAMP is developed to implement the concurrent multi-scale topological design of the structure and material, and to achieve optimum distribution of the prescribed number of materials at both the micro and macro scale. The equivalent material properties of the macrostructure are calculated using homogenization method. The method of MMA is utilized to solve the multi-scale optimization model with respect to vibro-acoustic criteria. Numerical examples are given to validate the model and the method developed.

Keywords: structure and material; vibro-acoustic criteria; multi-scale; integrated method; topology optimization

1. Introduction

Vibration and noise attenuation is one of the most concerned problems in vibro-acoustic field, where structural topology optimization can act as a strong tool. Most of the present work concerning vibro-acoustic design generally focuses on topological optimization of the macrostructure including the distribution of the materials and damping [1-3]. A few works concerned topology optimization of the macrostructure or the microstructure of materials to achieve the optimum vibro-acoustic properties [4-5], which normally only involves single scale design. In recent years, some methods of concurrent topology optimization at structure and material scale have been proposed including the Hieratical topology optimization [6-7] and the PAMP model [8-9]. However, the former method may give rise to a large challenge in manufacturability for the microstructural configuration varies from point to point in the macro design domain. As for the latter, only single base material is taken into consideration to produce composite composed of porous microstructure. Moreover, design objectives of the above-mentioned methods generally involves extreme structural properties such static compliance or thermal elasticity [6-9] without respect to vibration and noise attenuation. In order to exert the potential of the structure and material to the largest extent, it is necessary to establish a multi-material and multi-scale model and further develop an effective and efficient method to combine the vibro-acoustic topology design of the macro and micro structure simultaneously. In this paper, section 2 will discuss the two scale multi-material interpolation model and optimization model with respect to vibro-acoustic criteria will be analysed in section 3. Then some numerical examples will be given to validate the viability of the presented method in section 4 and a brief conclusion is made in section 5.

2. Two-scale Multi-material Interpolation Model

The extended multi-material interpolation model at the micro scale based on the present SIMP [10] and PAMP model is illustrated as follows:

$$\mathbf{D}_e^{\text{MI}} = \kappa_n^p \left\{ \kappa_{n-1}^p [\kappa_{n-2}^p () + (1 - \kappa_{n-2}^p) \mathbf{D}_{n-2}^*] + (1 - \kappa_{n-1}^p) \mathbf{D}_{n-1}^* \right\} + (1 - \kappa_n^p) \mathbf{D}_n^* \quad (1)$$

$$\eta_e^{\text{MI}} = \kappa_n^q \left\{ \kappa_{n-1}^q [\kappa_{n-2}^q () + (1 - \kappa_{n-2}^q) \eta_{n-2}^*] + (1 - \kappa_{n-1}^q) \eta_{n-1}^* \right\} + (1 - \kappa_n^q) \eta_n^* \quad (2)$$

where \mathbf{D}_0^* , \mathbf{D}_1^* , ..., \mathbf{D}_{n-1}^* , \mathbf{D}_n^* and η_0^* , η_1^* , ..., η_{n-1}^* , η_n^* represent respectively the elasticity matrices and mass density of the multiple designate solid isotropic base materials numbered as 0, 1, ..., n-1 and n. The symbol P and Q are the penalty factors while P normally takes the value 3 or 4 and Q usually takes the value 1 or 2 in order to achieve the clear zero-one design.

Theoretically speaking, with the above-mentioned multi-material interpolation model, multiple microstructures can be formulated. For convenience of illustration, in this article two microstructures in macro scale with multiple designate base materials are involved to perform topology design and variables like μ_1 , μ_2 , ..., μ_{n-1} , μ_n to

formulate the other microstructure in a similar way, based on which the material interpolation model at the macro scale can be expressed with the following equations if the macrostructure is meshed into N_e finite elements:

$$\mathbf{D}^{\text{MA}} = \boldsymbol{\rho}^p \mathbf{D}^{\text{H1}} + (1 - \boldsymbol{\rho}^p) \mathbf{D}^{\text{H2}} \quad (3)$$

$$\boldsymbol{\eta}^{\text{MA}} = \boldsymbol{\rho}^q \boldsymbol{\eta}^{\text{H1}} + (1 - \boldsymbol{\rho}^q) \boldsymbol{\eta}^{\text{H2}}, \quad \boldsymbol{\rho} = [\rho_1, \rho_2, \dots, \rho_{N_e}]^T \quad (4)$$

where \mathbf{D}^{H1} , \mathbf{D}^{H2} and $\boldsymbol{\eta}^{\text{H1}}$, $\boldsymbol{\eta}^{\text{H2}}$ represent the equivalent stiffness matrices and mass density calculated via the homogenization method [11]. The symbol $\boldsymbol{\rho}$ denotes the relative volume density vector of the first microstructure in each element of the macrostructure, which may differ from point to point at macro scale, ranging from 0 to 1. Especially for the case where two designate solid base materials are taken into consideration, assuming the microstructure unit cell is discretized into n_e finite elements, the interpolation model at the micro scale above will be expressed as follows:

$${}_1\mathbf{D}^{\text{MI}} = \boldsymbol{\kappa}^p \mathbf{D}_1^* + (1 - \boldsymbol{\kappa}^p) \mathbf{D}_0^*, \quad {}_1\boldsymbol{\eta}^{\text{MI}} = \boldsymbol{\kappa}^q \boldsymbol{\eta}_1^* + (1 - \boldsymbol{\kappa}^q) \boldsymbol{\eta}_0^*, \quad \boldsymbol{\kappa} = [\kappa_1, \kappa_2, \dots, \kappa_{n_e}]^T \quad (5)$$

$${}_2\mathbf{D}^{\text{MI}} = \boldsymbol{\mu}^p \mathbf{D}_1^* + (1 - \boldsymbol{\mu}^p) \mathbf{D}_0^*, \quad {}_2\boldsymbol{\eta}^{\text{MI}} = \boldsymbol{\mu}^q \boldsymbol{\eta}_1^* + (1 - \boldsymbol{\mu}^q) \boldsymbol{\eta}_0^*, \quad \boldsymbol{\mu} = [\mu_1, \mu_2, \dots, \mu_{n_e}]^T \quad (6)$$

where \mathbf{D}_1^* and \mathbf{D}_0^* represent the constitutive matrices while $\boldsymbol{\eta}_1^*$ and $\boldsymbol{\eta}_0^*$ denote the mass density of the two designate solid isotropic base materials numbered as 1 and 0. In Eq. (5) and (6), the symbol $\boldsymbol{\kappa}$ and $\boldsymbol{\mu}$, varying from zero to unit vector, denote the relative volume density vector of the stiffer isotropic material (material 1) in one discretized micro unit cell of the first and second microstructure, which may differ from element to element. Clearly the elasticity matrix of the element becomes \mathbf{D}_1^* and \mathbf{D}_0^* when the material volume density κ_i and μ_j ($i, j = 1, 2, \dots, n_e$) take the values 1 and 0, respectively. Especially, if \mathbf{D}_0^* equals zero matrix, the above interpolation model indicates topology optimization model based on single base material and porous composites may be acquired for holes will appear when κ_i or μ_j takes the value 0 in the result, which may correspond to the topology optimization using PAMP model. When the dynamic properties such as sound radiation power, fundamental frequency and band gap between eigenfrequencies of the macrostructure are taken into consideration, similar interpolation formulation may be employed to deal with the inertia part of the dynamic equations.

3. Optimization model with respect to vibro-acoustic criteria

Given the example of bi-material model used at both macro and micro scale, the macrostructure is assumed to be composed by two different designable composite materials, each of which is constructed by periodically arranged identical micro unit cells. And the micro unit cell is filled up with two prescribed solid isotropic base materials. The topology optimization model aimed at the best mechanical performance of the macrostructure such as the static compliance and sound radiation power may be formulated as:

$$\begin{aligned} & \min_{\boldsymbol{\kappa}, \boldsymbol{\mu}, \boldsymbol{\rho}} \left\{ \Pi(\mathbf{u}, \boldsymbol{\kappa}, \boldsymbol{\mu}, \boldsymbol{\rho}) \right\} \\ & s.t. \\ & \mathbf{G}(\mathbf{u}, \mathbf{D}^{\text{H}}(\boldsymbol{\kappa}, \boldsymbol{\mu}, \boldsymbol{\rho})) = \mathbf{0}, \\ & \frac{1}{N_e} \frac{1}{n_e} \left\{ \left(\sum_{s=1}^{N_e} \rho_s \right) \left(\sum_{i=1}^{n_e} \kappa_i \right) + \left[\sum_{s=1}^{N_e} (1 - \rho_s) \right] \left(\sum_{j=1}^{n_e} \mu_j \right) \right\} - \gamma_1 \leq 0 \\ & \sum_{i=1}^{n_e} \kappa_i V_i - V^2 \leq 0, \quad (V^2 = \gamma_2 V^{\text{MI}}), \\ & \sum_{j=1}^{n_e} \mu_j V_j - V^3 \leq 0, \quad (V^3 = \gamma_3 V^{\text{MI}}), \\ & \sum_{s=1}^{N_e} \rho_s V_s - V^4 \leq 0, \quad (V^4 = \gamma_4 V^{\text{MA}}), \\ & 0 \leq \kappa_i, \mu_j, \rho_s \leq 1, \quad (i, j = 1, \dots, n_e; s = 1, \dots, N_e). \end{aligned} \quad (7)$$

The symbol Π represents the design objective which may be expressed as the function of the structural response (e.g. displacement) vector \mathbf{u} . The first constraint in Eq. (7) is a general form of the governing equations of the macrostructure, from which the structural response such displacement vector may be solved. The symbol \mathbf{D}^H indicates the equivalent macro elasticity matrices of the metamaterial, which will be calculated using homogenization analysis at both micro and macro scales, relying on the topology design variable κ , $\boldsymbol{\mu}$ and $\boldsymbol{\rho}$. The symbols $\gamma_1, \dots, \gamma_4$ denote the material volume fractions under different scales, and γ_1 is the upper limit of the total volume fraction of the strong material (i.e. material no. 1) in the whole structure. As further illustration for the volume constraint equations, V^{MI} and V^{MA} denote respectively volume of the micro unit cell and the admissible design domain of the macrostructure, while V_i (or V_j) and V_s represent respectively the volume of one element in the micro unit cell and the macrostructure. It is necessary to note that not all the constraints above are essential so that we can reduce some of the inequations according to practical design requirement. Meanwhile even extra constraints such as the lower limits of the volume fractions can be added to the optimization model. Given the model established above, sensitivity analysis is performed and the MMA method [12] is employed in the optimum search in this paper. As a complementary step, the technology of density filtering [13] is used to help avoid the Checkboard problem [14].

4. Numerical Examples

4.1. Benchmark Example 1 - Micro-scale design of microstructure

To verify the validity of the presented integrated method applied to topology design of the vibro-acoustic metamaterial, microstructural topology optimization of the four-edge-clamped $1\text{m} \times 1\text{m} \times 0.01\text{m}$ wall structure with a harmonic unit concentrated force working at its centre as shown in Figure 1. And the design objective is minimization of the sound radiation power caused by the vibration of the plate. Specially speaking, structural damping in this example is neglected. The macrostructure is assumed to consist of single composite material uniformly. Discretize the macrostructure and micro unit cell into 16×16 and 40×40 four-node Kirchhoff plate elements respectively. The micro unit cells will be filled with two designate isotropic base materials, of which the strong material (in dark color) has Young's modulus $E_1 = 2.1 \times 10^{11} \text{Pa}$, mass density $\eta_1 = 7800 \text{kg/m}^3$ and Poisson ratio $\nu_1 = 0.3$, while values of Young's modulus and mass density of the weak material (in light color) are tenth of those of the strong one except the identical Poisson ratio. Given volume constraint, volume fraction of the strong material is limited to not exceeding 50% of volume of the microstructure unit cell. The macro material volume density vector $\boldsymbol{\rho}$ is assigned to one mandatorily in each iteration step, and the micro material volume density vector $\boldsymbol{\mu}$ is initialized to zero to ensure the macrostructure is evenly composed by only identical microstructure. Comparison of the optimum topology (Table 1) of the bi-material microstructure (6×6 array of unit cells) under harmonic excitation with round frequency $\omega_p = 300 \text{rad/s}$ between utilizing the proposed integrated method and using only micro-scale design elucidates validity of the present work in this paper.

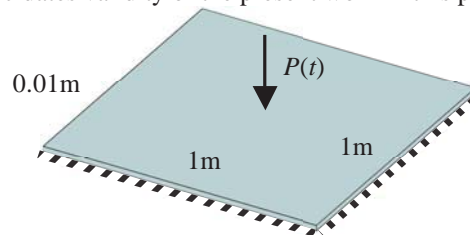

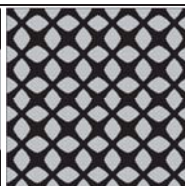


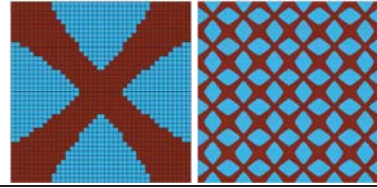
Figure 1: Four-edge-clamped plate loaded by harmonic concentrated force

Table 1: Comparison of microstructural design of vibro-acoustic metamaterial between using micro-scale optimization and using the presented method

$\gamma_1 = \gamma_2 = 0.5$	Sound power of the Optimum design/W	Microstructural topology	
Results in the reference [6]	3.238×10^{-6}		

Results using new integrated method

4.099×10^{-6}



4.2. Benchmark Example 2 - Simultaneous multi-scale design for minimization of structural static compliance
 The presented concurrent method of topology optimization is here employed to minimize the static compliance of the MBB beam (shown in Figure 2) as a comparison to the result demonstrated in a previous paper where the PAMP interpolation model was proposed, to validate the correctness of our innovative concurrent approach. According to the publication, all the variables involved in this example are non-dimensional. The concentrated vertical force working at the mid-point of the upper edge of the beam is $P = 1000$ and the length and the height of the beam are 4 and 1 respectively. Corresponding to original model, constitutive constants of the two base materials are as follows: Young's modulus $E_1 = 2.1 \times 10^5$ (in dark color) and $E_2 = 2.1 \times 10^{-5}$ (in light color), Poisson ratio $\nu_1 = \nu_2 = 0.3$. Given the axial symmetry condition, only the right half of the beam is taken as the macro design domain. Discretize the macrostructure and the micro unit cell respectively into 50×25 and 25×25 elements with two-dimensional four-node isoparametric element. Meanwhile the upper limit of total volume fraction of the base material is 0.25 for the macrostructure and 0.4 for the micro unit cell. The volume density vector $\boldsymbol{\mu}$ is initialized to zero, which helps to assure only the first microstructure contributes to the optimum configuration of the beam, to keep consistent with optimization using PAMP model. Optimum topologies of the macro and micro structure are shown in Table 2, where with comparison between our results and those using PAMP model, obviously good consistency can be confirmed. Hence the effectiveness and correctness of the proposed integrated method in this paper can be strongly validated.

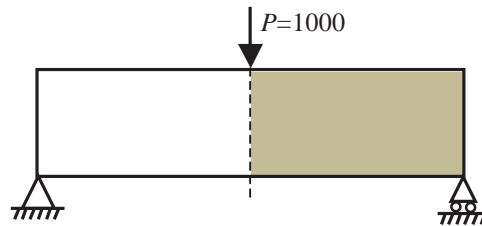


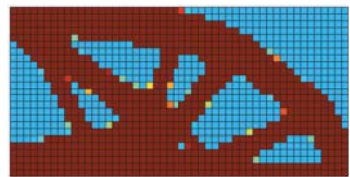
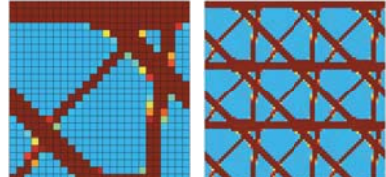


Figure 2: MBB beam

Table 2: Comparison of macrostructural and microstructural design of MBB beam for minimum static compliance between using micro-scale optimization and using the presented method

$\gamma_1 = 0.25, \gamma_2 = 0.4$	Optimum Compliance	Macrostructural topology	Microstructural topology
Results in the reference [10]	2234		
Results using new integrated method	703		

4.3. Example 3 - Simultaneous multi-scale design for minimization of sound radiation power
 Simultaneous topology optimization with respect to vibro-acoustic criteria of the macro and micro structure, that is, structure and material, of the four-edge-clamped $1.2\text{m} \times 1.2\text{m} \times 0.01\text{m}$ plate loaded by harmonic uniform pressure on its top surface as shown in Figure 3, which amounts to 100N at each node, is considered in this example. And the design objective is to minimize of the sound radiation power produced by the vibration. Similar to Example 4.1, structural damping is neglected. The macrostructure and the micro unit cell are discretized into 30×30 and

25×25 four-node Kirchhoff plate elements, respectively. The micro unit cell will be filled with two designate base materials: Aluminium Alloy (in dark color) and Epoxy Resin (in light color) with Young’s modulus $E_1 = 7.76 \times 10^{10} \text{ Pa}$, $E_2 = 4.35 \times 10^9 \text{ Pa}$, mass density $\eta_1 = 2.73 \times 10^3 \text{ kg/m}^3$, $\eta_2 = 1.18 \times 10^3 \text{ kg/m}^3$, Poisson ratio $\nu_1 = \nu_2 = 0.3$, respectively. Regarding the constraints, upper limit of total volume fraction of the strong material in the whole macrostructure is 0.5, while upper limits of volume fraction of the strong material in the first and second microstructure are 0.5 and 0.25 respectively. No constraint of the volume fraction of the first microstructure in the macro design domain is imposed. Optimum topologies and sound power of the bi-material macrostructure and microstructure (4×4 array of unit cells) under harmonic excitation of different round frequencies including $\omega_p = 100, 500, 800$ and 2500 rad/s are shown respectively in Table 3 and Table 4. Note that for the optimum macrostructural topology, elements in dark color represent the first optimum microstructure. Figure 3 shows the iteration history curve of the objective function under excitation frequency $\omega_p = 100 \text{ rad/s}$. Our tests indicate ideal numerical stability of the presented method in certain range of low frequencies including 500 and 800 rad/s. Numerical oscillation was observed in the iteration history curve of the objective function at high frequencies, e.g. 2500 rad/s, as a result of which it failed to acquire clear 0 or 1 macro and micro topology. Possible reason is that the presented material interpolation model is a stiffness-dominated one while stiffness may not be the most influential factor when high frequency excitation is considered. Hence some improvement to the material interpolation model should be further researched in the future.

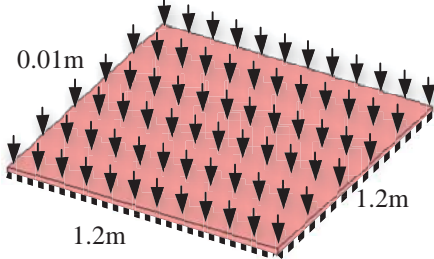


Figure 3: Four-edge-clamped plate with harmonic uniform pressure on top surface

Table 3: Optimum macrostructural and microstructural of the four-edge-clamped Kirchhoff plate under harmonic uniform on the surface

$\omega_p(\text{rad/s})$	Macrostructural topology	Microstructural topology			
		First Microstructure		Second Microstructure	
100					
500					
800					

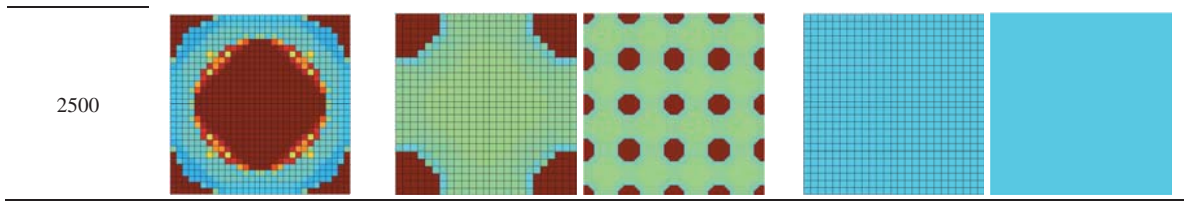
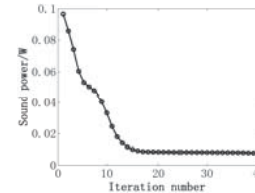


Table 4: Comparison of the sound power between the initial and the optimum topology design of the plate

ω_p (rad/s)	Sound Power/W	
	Initial design	Optimum design
100	0.100	0.008
500	3.316	0.226
800	16.332	2.426
2500	8.341	6.538

Figure 3: Iteration history curve of the objective function ($\omega_p = 100\text{rad/s}$)



5. Conclusions

This paper presents an integrated multi-scale topology optimization method of finding the optimum macro and micro topology configuration of the structure and material simultaneously based on a multi-material interpolation model, with respect to the vibro-acoustic criteria. Numerical examples validate the reliability of the new method through comparison with research results of some benchmark examples. Our study shows effectiveness of the presented method in designing optimum vibro-acoustic structure and metamaterial aiming at minimization of sound radiation power of the vibrating structure. The presented work may offer new ideas and relevant theoretical basis for conceptual design of the structural and material for vibration and noise attenuation.

Acknowledgements

The work is supported by National Natural Science Foundation of China (11372154).

References

- [1] J.B. Du and N. Olhoff, Topological Design of Vibrating Structures with Respect to Optimum Sound Pressure Characteristics in a Surrounding Acoustic Medium, *Structural and Multidisciplinary Optimization*, 42(1), 43-54, 2010.
- [2] J.B. Du and N. Olhoff, Minimization of Sound Radiation From Vibrating Bi-Material Structures Using Topology Optimization, *Structural and Multidisciplinary Optimization*, 33(4-5), 305-321, 2007.
- [3] J.B. Du, X.K. Song and L.L. Dong, Design on material distribution of acoustic structure using topology optimization, *Chinese Journal of Theoretical and Applied Mechanics*, 43(2), 306-315, 2011.
- [4] J.B. Du and R.Z. Yang, Vibro-acoustic design of plate using bi-material microstructural topology optimization, *Journal of Mechanical Science and Technology*, 29(4), 1-7, 2015.
- [5] R.Z. Yang and J.B. Du, Microstructural topology optimization with respect to sound power radiation, *Structural and Multidisciplinary Optimization*, 47(2), 191-206, 2013.
- [6] P.G. Coelho, P. Fernandes, J.M. Guedes and H.C. Rodrigues, A hierarchical model for concurrent material and topology optimization of three-dimensional structures, *Structural and Multidisciplinary Optimization*, 35(2), 107-115, 2008.
- [7] H. Rodrigues, J.M. Guedes and M.P. Bendsøe, Hierarchical Optimization of Material and Structure, *Structural and Multidisciplinary Optimization*, 24(1), 1-10, 2002.
- [8] L. Liu, J. Yan and G.D. Cheng, Optimum structure with homogeneous optimum truss-like material, *Computers and Structures*, 86, 1417-1425, 2008.
- [9] J. Deng, J. Yan and G.D. Cheng, Multi-objective concurrent topology optimization of thermoelastic structures composed of homogeneous porous material, *Structural and Multidisciplinary Optimization*, 47(4), 583-597, 2013.
- [10] G.I.N. Rozvany, M. Zhou and T. Birker, Generalized Shape Optimization without Homogenization, *Structural Optimization*, 4(3-4), 250-252, 1992.
- [11] M.P. Bendsøe and N. Kikuchi, Generating Optimal Topologies in Structural Design Using a Homogenization Method, *Computer Methods in Applied Mechanics and Engineering*, 71(2), 197-224, 1988.
- [12] K. Svanberg, The Method of Moving Asymptotes - A New Method for Structural Optimization, *International Journal for Numerical Methods in Engineering*, 24(2), 359-373, 1987.
- [13] T.E. Bruns and D.A. Tortorelli, Topology Optimization of Non-Linear Elastic Structures and Compliant

- Mechanisms, *Computer Methods in Applied Mechanics and Engineering*, 190(26-27), 3443-3459, 2001.
- [14] O. Sigmund and J. Petersson, Numerical Instabilities in Topology Optimization: A Survey on Procedures Dealing with Checkerboards, Mesh-Dependencies and Local Minima, *Structural Optimization*, 16(1), 68-75, 1998.

Efficient Aerodynamic Optimization Using a Multiobjective Optimization Based Framework to Balance the Exploration and Exploitation

Zhiwei Feng¹, Tao Yang¹, Jianquan Ge¹, Qiangang Tang¹, Yang Ma¹

¹ National University of Defense Technology, Changsha, China, fzwnudt@nudt.edu.cn

Abstract

In many aerospace engineering design problems, objective function evaluations can be extremely computationally expensive, such as the optimal design of the aerodynamic shape of an airfoil using high-fidelity computational fluid dynamics (CFD) simulation. A widely used approach for dealing with expensive optimization is to use cheap global surrogate (approximation) models to substitute expensive simulation. The effective global optimization (EGO) based on Kriging model is a widely used approach for dealing with the expensive optimization problems. In the standard EGO and most Kriging based aerodynamic optimization application, one sampling point is determined for expensive simulation. To make best use of parallel computing resources, multi-point infill sampling criteria is need to improve the efficiency of aerodynamic shape optimization. In this paper, a recently developed multiobjective optimization based framework balance the global exploration and local exploitation in EGO, called EGO-MO, is introduced. It can generate multiple test solutions simultaneously to take the advantage of parallel computing. The EGO-MO is applied for the aerodynamic shape design of a transonic airfoil to minimize drag maintaining the reference lift. The class/shape transformation (CST) method is employed for the parameterization of airfoil. The open source code SU² is adopted to perform the high-fidelity aerodynamic analysis of initial and infill sampling points. The comparison of EGO-MO and standard EGO for the transonic airfoil problem is presented. The investigation shows that the EGO-MO feature less iteration numbers and can give better optimal results.

Keywords: aerodynamic shape optimization; efficient global optimization; multi-point infill sampling criteria; multiobjective optimization; MOEA/D

Introduction

In the optimization design of aerodynamic shape of a flight vehicle ^[1, 2] or airfoil ^[3, 4], the objective function evaluation is done via high-fidelity and expensive computational fluid dynamics (CFD) simulation. In spite of great development of computing technology, such as the more accurate and faster simulation code and parallel computing, the efficient optimization method is still an open research area. Modern heuristics are not suitable since these methods often require an unbearable number of function evaluations.

Due to the importance of expensive optimization, much effort has been made for developing methods to produce a reasonably good solution within a given budget on computational cost or time ^[5, 6]. A widely used approach for dealing with expensive optimization utilizing high-fidelity analysis is to use cheap global surrogate (approximation) models to substitute expensive simulation. Kriging is have been widely applied to many expensive optimization problems ^[7-10], since it can approximate nonlinear and multi-modal functions, and produce unbiased prediction at untested points. Actually, Kriging has been. Efficient Global Optimization (EGO) is the most popular Kriging based expensive optimization method ^[5].

The infill sample selection criterion is an important issue for Kriging based optimization, such as EGO. In the original EGO or several aerodynamic optimization problems, one test points for evaluation is determined at each iteration. To make good use of parallel computing resources, a multiobjective optimization based framework has been proposed to balance the exploration and exploitation for expensive optimization problem, called EGO-MO ^[11]. It treats balancing the local exploitation and global exploration as a multiobjective optimization problem (MOP). Then, a multiobjective optimization algorithm can be used for obtaining the Pareto set, i.e., a set of best trade-off solutions for balancing exploitation and exploration. Several points can be selected from the Pareto set for evaluation in a parallel manner. In such a way, parallel computing techniques can be used for reducing the clock time for optimization. Additionally, the Multiobjective Evolutionary Algorithm based on Decomposition (MOEA/D) ^[12] is employed to solve the aforementioned MOP. Due to the population nature of MOEA/D, it is able to escape from local optimal solutions and give a set of high quality trade-off candidates for local exploitation and global exploration.

In this paper, the EGO-MO is applied to the aerodynamic shape optimization problem, more exactly the airfoil shape optimization. The remainder of this paper is organized as follows. Section 2 introduces the Kriging and the

EI criterion. Section 3 presents the basic idea and framework of EGO-MO. Section 4 presents the airfoil shape optimization result. The comparison between of original EGO and EGO-MO for airfoil shape optimization problem is also presented in this section. Finally, Section 5 concludes the paper.

1. Kriging and Expected Improvement

1.1 Gaussian Stochastic Process Modeling

Let

$$y = g(x), x \in R^n \quad (1)$$

be the objective to minimize. We assume that the function value evaluation of $g(x)$ is expensive. To construct a Gaussian stochastic process (Kriging) model for $g(x)$, K sample points $x^1, \dots, x^K \in R^n$ and their function values (responses) y^1, \dots, y^K are required. Suppose

$$y = \mu + \varepsilon(x) \quad (2)$$

where μ is a constant and $\varepsilon(x)$ is a Gaussian stochastic process with following properties:

$$E[\varepsilon(x)] = 0, \text{Var}[\varepsilon(x)] = \sigma^2, \text{Cov}[\varepsilon(x^i), \varepsilon(x^j)] = \sigma^2 [c_{ij}(x^i, x^j)] \quad (3)$$

where the correlation function $c(x^i, x^j)$ is assumed to depend only on x^i and x^j .

There are some different forms of correlation function such as the Gaussian function, exponential function, spherical function and spline function. The Gaussian function is used in this paper, which has the following form

$$c(x^i, x^j) = \exp[-d(x^i, x^j)] \quad (4)$$

where

$$d(x^i, x^j) = \sum_{k=1}^n \theta_k |x_k^i - x_k^j|^{p_k} \quad (5)$$

$\theta_i > 0$, and $1 \leq p_i \leq 2$.

The unknown hyperparameters in the above Gaussian stochastic process modeling are μ , σ , $\theta_i (i=1, \dots, n)$, and $p_i (i=1, \dots, n)$. Given K points $x^1, \dots, x^K \in R^n$ and their responses y^1, \dots, y^K , these hyperparameters can be estimated by maximizing the likelihood that $g(x)=y^i$ at sampled points $x = x^i (i=1, \dots, K)$. The details can be found in [5].

If the hyperparameter estimations $\hat{\mu}$, $\hat{\sigma}^2$, $\hat{\theta}_i$, and $\hat{p}_i (i=1, \dots, n)$ are given, one can predict $g(x)$ at any untested point x based on the response values y^i at x^i for $i=1, \dots, K$.

The best linear unbiased predictor of $g(x)$ is as follows

$$\hat{y}(x) = \hat{\mu} + r^T C^{-1} (y - \mathbf{1}\hat{\mu}) \quad (6)$$

and its mean squared error is

$$s^2(x) = \hat{\sigma}^2 \left[1 - r^T C^{-1} r + \frac{(1 - \mathbf{1}^T C^{-1} r)^2}{\mathbf{1}^T C^{-1} r} \right] \quad (7)$$

where $r = [c(x, x^1), \dots, c(x, x^K)]^T$. $N(\hat{y}(x), s^2(x))$ can be regarded as a predictive distribution for $g(x)$ given the response value y^i at x^i for $i=1, \dots, K$.

1.2 Expected Improvement

After building a predictive distribution model for the objective function, we then define a metric for measuring the merit of evaluating a new untested point for minimizing $g(x)$. The expected improvement [5] is introduced in the following.

Let $N(\hat{y}(x), s^2(x))$ is a predictive distribution model for $g(x)$, and the minimal value of $g(x)$ over all the evaluated points is g_{\min} , then the improvement of $g(x)$ at a untested point x is

$$I(x) = \max\{g_{\min} - g(x), 0\} \quad (8)$$

Thus, the expected improvement (EI) can be calculated as

$$E[I(x)] = \begin{cases} [(g_{\min} - \hat{y}(x))] \Phi\left(\frac{g_{\min} - \hat{y}}{\hat{s}(x)}\right) + \hat{s}(x) \phi\left(\frac{g_{\min} - \hat{y}}{\hat{s}(x)}\right) & \hat{s} > 0 \\ 0 & \hat{s} = 0 \end{cases} \quad (9)$$

The above formula has two terms. The first term prefers points whose prediction values are small and have low uncertainty. It reflects the local exploitation. The second term is the product of the error s multiplying the probability density function. It reflects the global exploration. Therefore, the EI can be considered as a balance between exploiting promising areas of the design space and exploring uncertain areas ^[13].

2. Algorithm Framework for EGO-MO

2.1 The Basic Idea

The basic idea of EGO-MO is to use a multiobjective optimization algorithm for finding a set of test points, which can balance exploitation and exploration in different ways. We set the first and second items of the EI as two objective functions. More specially, the MOP is:

$$\begin{aligned} \max F(x) &= (f_1(x), f_2(x))^T \\ \text{subject to } & x \in \Omega \end{aligned} \quad (10)$$

$$\text{where } f_1(x) = [(g_{\min} - \hat{y}(x))] \Phi\left(\frac{g_{\min} - \hat{y}}{\hat{s}(x)}\right), \quad f_2(x) = \hat{s}(x) \phi\left(\frac{g_{\min} - \hat{y}}{\hat{s}(x)}\right).$$

It should be pointed out that any other two metrics reflect global exploration and local exploitation can also be used as two objectives in our approach. The Pareto optimal solutions of the above problem should be good candidate points for evaluation. Due to its simplicity and efficient, the MOEA/D ^[12] is used to solve the above MOP. Let the objective to minimize is $g(x)$, our proposed EGO-MO works as follows.

Algorithm Parameters:

K_I : the number of initial points in **Initialization**;

K_E : the number of function evaluations at each generation.

Step 1 Initialization: Generate K_I points x^1, \dots, x^{K_I} from the search space by using an experiment design method and evaluate the function values of these K_I point. Set $P_{\text{eval}} = \{x^1, \dots, x^{K_I}\}$.

Step 2 Stopping Condition: If a predetermined stopping condition is met, output the minimum function value in P_{eval} as an approximation to the optimum and stop.

Step 3 Model Building: By using the function values of the points in P_{eval} , build a predictive distribution model for objective function $g(x)$.

Step 4 Locating Candidate Points: Using MOEA/D, solve Problem (10) and obtain the Pareto optimal solutions x^1, \dots, x^N .

Step 5 Selecting Points for Function Evaluation: Select K_E points from x^1, \dots, x^N using a selection scheme.

Step 6 Function Evaluation: Evaluate the function values of all the K_E selected points in **Step 5**, then add all these points to P_{eval} and go to **Step 2**.

In **Step 2**, the stopping condition is:

$$\max_{x \in \{x^1, \dots, x^N\}} E[I(x)] / (Y_{\max} - Y_{\min}) \leq \varepsilon_r \quad (11)$$

where Y_{\max} and Y_{\min} are the maximum and minimum of evaluated function values, $\max_{x \in \{x^1, \dots, x^N\}} E[I(x)]$ is the maximum of expected improvement of the Pareto optimal points x^1, \dots, x^N , ε_r is a predefined convergence threshold.

2.2 MOEA/D for Locating Candidate Points

To solve Problem (10), MOEA/D first decomposes it into N single objective optimization subproblems. The objective in each subproblem is a weighted linear or nonlinear aggregation function of f_1 and f_2 . Thus, each subproblem is associated with a weight and its optimal solution is a Pareto optimal solution to Problem (10). If the decomposition is done properly, then the optimal solutions to these subproblems will provide a good approximation to the Pareto front of (10). MOEA/D makes use of the neighbourhood relationship among these

subproblems and optimizes all the subproblems simultaneously.

2.3 Selecting Points for Function Evaluation

In order to select K_E points from N candidate solutions obtained by MOEA/D, we have the following considerations.

- 1) The point to be evaluated should be different from the points already evaluated.
- 2) The selected points should be evenly distributed on the PF. Therefore, if two solutions x^i and x^j whose weight vectors are close, they cannot both be selected.
- 3) The selected points should be uniformly filling the design space with the evaluated points. The points maximizing the minimum distance to the evaluated points are preferred.

3. Airfoil Shape Optimization

3.1 Optimization Problem

In the airfoil shape optimization problem, the drag is minimized while the lift is maintain the same level of the base airfoil (RAE2822^[14]).

$$\begin{aligned} & \text{minimize} && C_d \\ & \text{subject to} && C_l \geq C_{l_{\text{Base}}} \end{aligned} \quad (1.12)$$

The flight condition used for design optimization is set as follows: (1) The Mach number is 0.729; (2) The angle of attack of 2.31 degree; (3) The freestream temperature is 288.15K; (4) The Reynolds number is 6.5 million.

3.2 Design variable

The airfoil shape is deformed using the class/shape transformation (CST) method^[15]. In the CST method, the airfoil shape is represented by the combination of the class function and the shape function, as follows

$$\xi(\psi) = C_{N_1}^{N_2}(\psi)S(\psi) + \psi\Delta\xi_{te} \quad (1.13)$$

where $\xi = \frac{z}{c}$, $\psi = \frac{x}{c}$, $C_{N_1}^{N_2}(\psi) = \psi^{N_1}(1-\psi)^{N_2}$ is the class function, and $S(\psi) = \sum_{i=0}^N [A_i\psi^i]$ is the shape function,

$\Delta\xi_{te}$ is the trailing-edge thickness ratio. For general airfoils, the class parameters N_1 and N_2 are set to 0.5 and 1.0, respectively. The Bernstein polynomial is employed as the shape function to describe the detailed shape. The airfoil shape can be represented using the Bernstein polynomial with different weight coefficients. These weight coefficients are then employed as design variables in optimization.

Fourteen weights are used in this paper, i.e., seven weights are placed on each lower and upper surface. The weights are allowed to vary in range of not distorting or disturbing the grid deformation as described in Table 1. The slopes of airfoil described by the upper and lower bounds of variables are presented in Figure 1.

Table 1: The bound of design variable

No.		1	2	3	4	5	6	7
Lower surface	Upper	-0.10	-0.10	-0.10	-0.15	-0.01	-0.10	0.10
	Lower	-0.16	-0.16	-0.17	-0.30	-0.05	-0.20	-0.02
Upper surface	Upper	0.16	0.16	0.20	0.20	0.30	0.20	0.30
	Lower	0.10	0.10	0.10	0.15	0.16	0.12	0.18

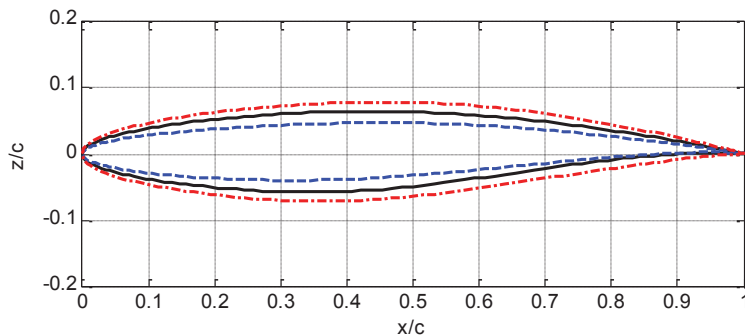


Figure 1: The bounds of the airfoil shape

3.3 Aerodynamic analysis

Although the expensive simulation is replaced with the Kriging model, the numerical experiments on sampling data are still required. The design condition is considered to be compressible flow. In the airfoil shape optimization problem, the Stanford University Unstructured (SU²) software suite [16] is employed as the high-fidelity computational fluid dynamics (CFD) simulation tools. The governing equation of viscous compressible flow is adopted for aerodynamic analysis. Spatial numerical flux is discretized using JST scheme. Viscous flux is discretized using the 1st upwind differencing method with SA turbulence modeling. The mesh used is an unstructured, O-grid that wraps around the RAE 2822 airfoil. It has 22,842 elements in total with 192 edges making up the airfoil boundary and 40 edges along the far-field boundary. The first grid point of the airfoil surface is at a distance of 1E-5 chords, and the far-field boundary is located approximately one hundred chord lengths away from the airfoil. The grid deformation module in SU² is used to deform the grid system, which employs the linear elasticity equations. The computational capacity of SU² for the viscous analysis of RAE2822 has been demonstrated in [14]. It is appropriate for being used in design procedure.

3.4 Settings for optimization

The first Kriging model is built on 105 initial sampling test points, which are generated using the optimized Latin hypercube sampling method [17]. The parameter for stopping condition is set as $\epsilon_r = 1 \times 10^{-6}$. The multiobjective evolutionary algorithm based on decomposition (MOEA/D) is employed to solve the multiobjective problem that balance exploitation and exploration and locate the candidate points. The number of function evaluation at each generation is 3. Parameters used in MOEA/D are set as follows: a) the number of subproblems N is 300; b) the number of generation is 300; c) the number of neighborhood is 20; d) Aggregation method: Tchebycheff approach.

3.5 Design Result

The initial Kriging model is built by using 105 initial points, the optimization stopped by 11 iterations for EGO-MO, and 23 iterations for standard EGO. Although the iteration number of EGO-MO is less than the standard EGO, its function evaluation number, 33, is larger than standard EGO.

The optimum geometry found by EGO-MO and standard EGO is depicted in Figure 2. The wall pressure distribution and pressure field contour is illustrated in Figure 3 and 4. As can be seen in Figure 3 and 4, airfoil obtained by standard EGO is optimized such that shape from the stagnation point to the maximum thickness point is changed gradually on the upper surface; and the maximum thickness point is moved toward the trailing edge. However, the EGO-MO found a more slender shape than the base.

The aerodynamic performance of optimum airfoil is presented in Table 2.

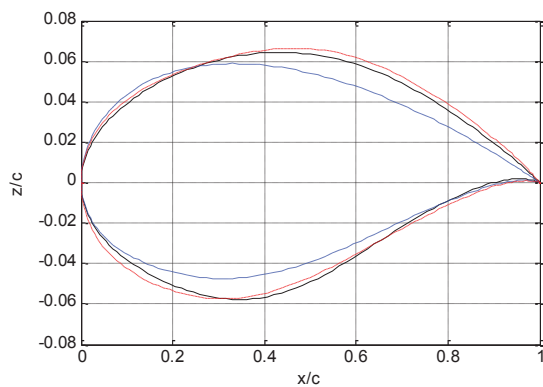


Figure 2: Optimum airfoil shape

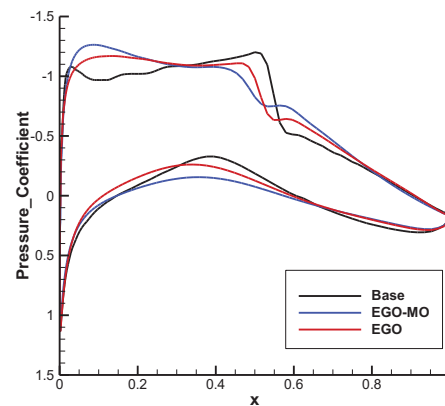


Figure 3: Wall pressure distribution

Table 2: The aerodynamic performance of optimum airfoil

		Lift Coefficient	Drag Coefficient	L/D
Base		0.72377	0.013453	53.8
EGO-MO	Optimum	0.784424	0.0114207	68.6843
	Improvement	+8.38%	-15.11%	+27.67%
Standard EGO	Optimum	0.735569	0.0118942	61.8425
	Improvement	+1.63%	-11.59%	+14.95%

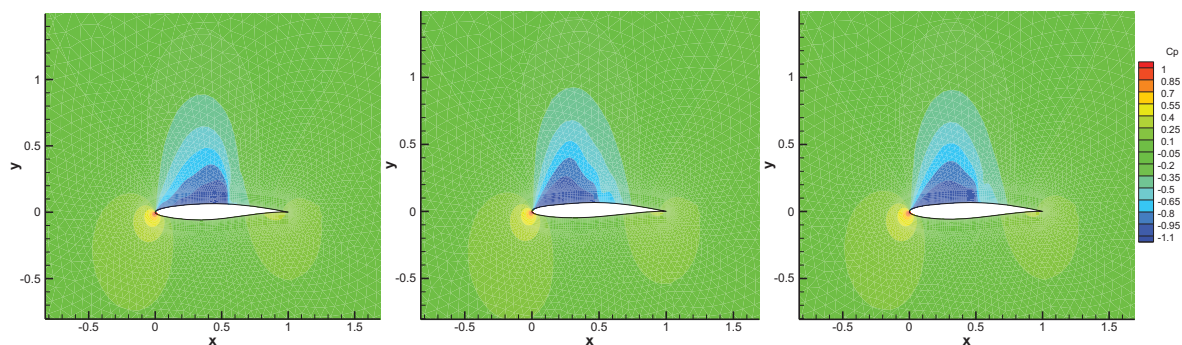


Figure 4: Pressure field comparison (left: baseline, middle: optimum of EGO-MO, right: optimum of standard EGO)

4. Conclusions

In the optimal design of the aerodynamic shape of an airfoil using high-fidelity computational fluid dynamics (CFD) simulation, objective function evaluations can be extremely computationally expensive. In this paper, a recently developed multi-point infill sampling criteria for EGO, called EGO-MO, is applied for the optimization of the transonic airfoil shape. In the EGO-MO, the multiobjective optimization based framework is employed for multi-point infill sampling criteria to enhance the efficiency of the standard EGO. The Kriging and EI infill sampling criteria is introduced firstly. Afterwards, the basic idea and the algorithm framework of EGO-MO are briefly presented. In the airfoil shape optimization problem, the objective is to minimize drag maintaining the reference lift for the transonic airfoil rae2822. The class/shape transformation (CST) function is employed for the parameterization of the airfoil. The open source code SU² is adopted to perform the high-fidelity aerodynamic analysis of initial and infill sampling points. The EGO-MO and standard EGO is applied to solve the aforementioned airfoil optimization problem. The two methods are compared for the function evaluation number and the iteration number. The optimum results are also analyzed for the mechanism of the drag reduction.

Acknowledgements

This research was supported by the National Natural Science Foundation of China under the grant of 51375486.

References

- [1] Sasaki D, Obayashi S, Sawada K, et al. Multiobjective aerodynamic optimization of supersonic wings using Navier-Stokes equations [C]. *Barcelona, Spain: European Congress on Computational Methods in Applied Sciences and Engineering*, 2000.
- [2] Jeong S, Suzuki K, Obayashi S, et al. Optimization of nonlinear lateral characteristic of lifting-body type reentry vehicle [J]. *Journal of Aerospace Computation, Information and Communication*, 6(3): 239–55, 2009.
- [3] Namgoong H, Crossley W A, Lyrantzis A S. Morphing Airfoil Design for Minimum Drag and Actuation Energy Including Aerodynamic Work [J]. *Journal of Aircraft*, 49(4): 981-90, 2012.
- [4] Vecchia P D, Daniele E, D'amato E. An airfoil shape optimization technique coupling PARSEC parameterization and evolutionary algorithm [J]. *Aerospace Science and Technology*, 32: 103-10, 2014.
- [5] Jones D R, Schonlau M, Welch W J. Efficient global optimization of expensive black-box functions [J]. *Journal of Global Optimization*, 13: 455-92, 1998.
- [6] Zhang Q, Liu W, Tsang E, et al. Expensive multiobjective optimization by MOEA/D with Gaussian process model [J]. *IEEE Transactions on Evolutionary Computation*, 14(3): 456-74, 2009.
- [7] Rumpfkeil M P. Optimizations under uncertainty using gradients, Hessians, and surrogate models [J]. *AIAA Journal*, 51(2): 444-51, 2013.
- [8] Koziel S, Leifsson L. Surrogate-based aerodynamic shape optimization by variable-resolution models [J]. *AIAA Journal*, 51(1): 94-106, 2013.
- [9] Keane A J. Cokriging for robust design optimization [J]. *AIAA Journal*, 50(11): 2351-64, 2012.
- [10] Han Z-H, Görtz S. Hierarchical Kriging model for variable-fidelity surrogate modeling [J]. *AIAA Journal*, 50(9): 1885-96, 2012.
- [11] Feng Z, Zhang Q, Zhang Q, et al. A multiobjective optimization based framework to balance the global exploration and local exploitation in expensive optimization [J]. *Journal of Global Optimization*, 61(4): 677-94, 2015.
- [12] Zhang Q, Li H. MOEA/D: a multiobjective evolutionary algorithm based on decomposition [J]. *IEEE Transactions on Evolutionary Computation*, 11: 712-31, 2007.

- [13] Sobester A, Leary S J, Keane A J. On the design of optimization strategies based on global response surface approximation models [J]. *Journal of Global Optimization*, 33: 31-59, 2005.
- [14] Palacios F, Economon T D, Aranake A C, et al. Stanford University Unstructured (SU²): open-source analysis and design technology for turbulent flows [C]. National Harbor, Maryland: *52nd Aerospace Sciences Meeting*, 2014.
- [15] Kulfan B M. Universal Parametric Geometry Representation Method [J]. *Journal of Aircraft*, 45(1): 142-58, 2008.
- [16] Palacios F, Colonno M R, Aranake A C, et al. Stanford University Unstructured (SU²): An open-source integrated computational environment for multi-physics simulation and design [C]. Grapevine , Texas: *51st AIAA Aerospace Sciences Meeting including the New Horizons Forum and Aerospace Exposition*, 2013.
- [17] Morris M D, Mitchell T J. Exploratory designs for computational experiments [J]. *Journal of Statistical Planning and Inference*, 43: 381-402, 1995.

Optimization of Process Parameters for Three-roll Skew Rolling Based on Design of Experiment(DOE)

Baoshou Sun¹, Guangxing Huang², Wenfei Peng, Xuedao Shu, Lu Wang

¹ College of Mechanical Engineering and Mechanics, Ningbo University, China, 315211

² Zhejiang Provincial Key Laboratory of Part Rolling Technology, Ningbo, 315211, aemail:695842684@qq.com

1. Abstract

Titanium alloy with high strength, corrosion resistance, heat resistance and many other advantages, has widely applications in aviation industry and the military-industrial complex. Three-roll rolling is one of mature methods in current production of titanium alloy bars. In this paper, we take the titanium alloy bars TC 4 as the model and adapt DEFORM-3D finite element software to simulate the three-roll skew rolling process. By this means the feasibility of titanium alloy bar used in three-roll skew rolling and the deformation mechanisms are analyzed. Additionally, experiment design method is applied to determine the critical process parameters impacting the forming quality of three-roll skew rolling. Range analysis and variance analysis methods show that the influencing parameters of average distance of swirl marks in decreasing sequence are as follows: deflection angle, initial temperature of rolled piece, angular velocity of rolled piece, and the optimal parameter combination are as follows: deflection angle = 8, initial temperature = 900°C, angular velocity = 10 rad/s.

2. Keywords: Titanium alloy bar, three-roll cross rolling, numerical simulation, orthogonal experiment

3. Introduction

Titanium alloy material has low density, high melting point, high specific strength, heat resistance, corrosion resistance, small linear expansion coefficient, as well as good bio-compatibility, and because of its meet the strict requirements for the materials, such as the aviation industry can work normally under high temperature, corrosive environment, so in the aerospace, Marine transportation, automobile manufacturing, chemical industry, metallurgy and other industries plays an important role^[1-2]. In recent years, China's aviation, aerospace, power and the rapid development of ocean engineering, all kinds of titanium products demand is growing, especially in the aircraft industry proportion is the largest, the application of titanium alloy in large passenger aircraft airbus A380 dosage of titanium alloy to 45 tons/frame, total weight of 10%; The same amount of titanium alloy material Boeing reached 15%. In the development of fighter jets, the requirement to have higher mobility, the fuselage as light as possible, the titanium alloy can better satisfy the use requirement. American F22 fighter, accounted for 39% of body weight, titanium alloy with titanium structure with 36 tons, two engines titanium 5 tons^[3-4]. Titanium alloy in aviation air also measures the development level of high and low dosage, the applications of titanium alloy to aviation industry in China started late, aviation parts on the proportion of titanium alloy dosage still exists a certain gap compared with abroad. For example, in the batch production of titanium in the aircraft engine usage is not high, and Europe and the United States in some developed countries have the titanium dosage proportion on the engine has reached more than 30%^[5-7]. Because of the expensive titanium alloy, in order to make full use of the titanium alloy bars, the application of three-roll skew rolling mill rolling into small diameter rod, effectively improve the material utilization rate. In addition, the three of three roll mill roll on bar uniform compressive stress, is more advantageous to the plastic deformation of metals.

4. The finite element model three-roll skew rolling

4.1. The determination of process parameters

Through a lot of three-roll skew rolling finite element simulation, combining with the actual production to determine a set of process parameters affecting the quality of skew rolling forming as shown in table 1.

Tab.1 Parameters of rolling process

Rolling temperature /°C	Roll angular velocity /rad/s	Deflection Angle /°	Tilt Angle /°
1000	10	8	5

4.2. Material model

Rolled piece material chosen as of TC4 titanium alloy, the plastic body. Material properties including material yield limit, ultimate strength, and the flow stress - strain relationship and so on, its deformation temperature at 800 ~ 800 °C, strain rate in 0.01 ~ 20 s⁻¹. TC4 material properties are shown in table 2.

Tab.2 Material property

Material parameters	Density (kg/m ³)	Elasticity modulus(Gpa)	Poisson's ratio	yield stress (Mpa)	shear modulus (Gpa)
rolling meta	4400	100	0.34	919	44

4.3. Three-roll skew rolling finite element modeling

According to three in the three-roll skew rolling mill roll space position relations, roll the geometry size of three-roll skew rolling titanium alloy rod finite element model is established, in order to coordinate the z axis as the direction of the rolling line, three roll around the z axis direction of 120 ° evenly distributed, roll line and the rolling line intersection, each roll around the axis of rotation, contact each other, rolled piece from the bite into the roll end, under the effect of rolling friction was into three roll pass, as the bar shaft forward, its diameter decreases continuously. Three-roll skew rolling in the process of the finite element model is established, Due to the complexity of three roll location in space coordinates, to accurately set the deflection Angle and tilt Angle, two important parameters to ensure the smooth progress of rolling.

In actual production, the three-roll skew rolling mill space geometric relation of deformation zone, and the metal flow conditions are relatively complex. The following assumptions: (1) bar as a plastic body, only plastic deformation; (2) roll as a rigid body, the rigid-plastic finite element model. Because of the hot rolling is a large deformation process therefore the friction between the roller and the rolled piece can be set to the shear friction. Bar front circular conical design, convenient its bite. As shown in Figure 1.

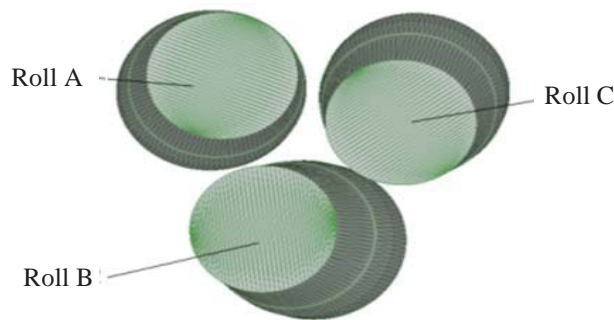
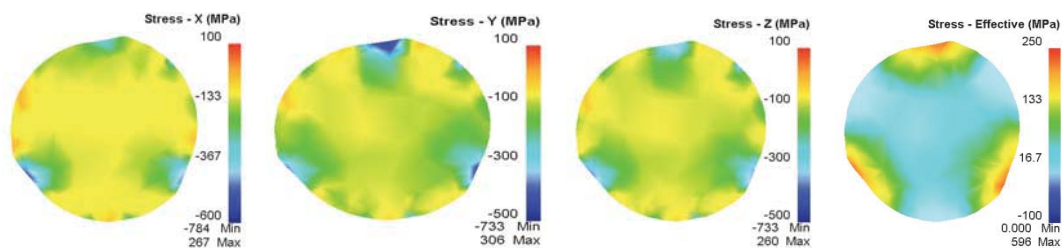


Fig.1 The finite element model of three-roll skew rolling

5. Titanium alloy rod three-roll skew rolling forming law



(a) Transverse stress σ_x (b) Longitudinal stress σ_y (c) Axial stress σ_z (d) Equivalent stress $\bar{\sigma}$

Fig.2 Stress field on cross section of stable rolling stage

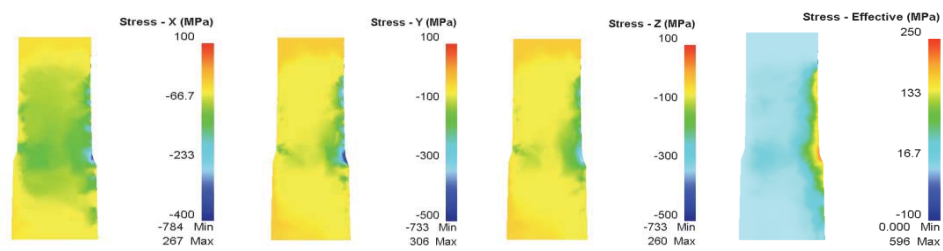
Fig. 2(a) shows the distribution of transverse stress σ_x in the cross section of the part. At the stable initial rolling stage, the circular cross section starts to transit to a polygon due to that the bar has been completely into the three roll pass. It is observed that the distribution of compressive stresses occur at the three contact zone. Maximum

value about - 425 MPa appears at the contact point. The compressive stress will become smaller if it is farther away from the contact area. However, the contact adjacent region will be affected by the tensile stress, which is quite common characteristics in three-roll skew rolling deformation.

Fig.2(b) shows the distribution of the stress σ_y in the cross-section of the part. As the process proceeds, the compressive stress in contact area is getting larger, which is ranged from - 500 MPa to - 700 MPa. It is also observed that tensile stress zone shrinks due to the spreading of compressive stress in the radial direction.

Fig.2(c) shows the distribution of axial stress σ_z in the cross-section of the part. Similar to Fig. 3(a) and (b), compressive stress occurs at the contact area, the most of the rest area is the distribution of tensile stress. The metal at the outer layer squeezed by roller will flow along axial direction, which has the small resistance to flow. This will result in tensile stress of the metal at the outer layer of the part and cause the axial flow of metal,.

The distribution of equivalent stress $\bar{\sigma}$ in the cross-section of the part is shown in Fig. 2(d). The equivalent stress intensity of part gradually decreases from outer surface to the center, and the maximum equivalent stress is 250 MPa, the minimum equivalent stress is at the center of rolled pieces for three-roll skew rolling. The forces generated by three-roll skew rolling act uniformly on the part, which is helpful to reduce the radial size and extend along axial direction. .



(a) Transverse stress σ_x (b) Longitudinal stress σ_y (c) Axial stress σ_z (d) Equivalent stress $\bar{\sigma}$

Fig.3 Stress field on longitudinal-section of stable rolling stage

Fig.3 (a) shows the distribution of transverse stress σ_x at the longitudinal cross section of the part. It is observed that the compressive stresses are distributed in the most portion of the longitudinal cross-section. The compressive stress has penetrated into the rolled piece, its value is ranged from -60 MPa to -100 MPa. In practical, the metal has fully filled into three roll passage during stable rolling stage. The rolled metal is acted by force in all directions. As the rolling proceeds, the compressive stress will permeate gradually into bar from outer to inner.

Fig. 3(b) shows the distribution of the radial stress σ_y at the longitudinal cross-section of the part. It is observed that the compressive stress at the roller entrance and roller shoulder is greater than that of other area. The maximum value of compressive stress -200MPa. The stress value gradually decreases inward to the smaller value of -100 MPa. This is because the effect of roller on bar is obvious at the roller shoulders and thus will result in the maximum compressive stress value.

Fig. 3(c) shows the distribution of the axial stress σ_z at the longitudinal section of the part. It is observed that the distributed compressive stress is obvious and gradually decreases inward. Its value in between -300 MPa and -100 MPa. This will result in metal deformation to extend along the axial direction.

Fig. 3(d) shows the distribution of the equivalent stress $\bar{\sigma}$ at the longitudinal section of the part. It is observed that the local contact stress value is the largest, up to 250 MPa, which is named as the largest stress intensity. It is, gradually weakened and finally reduced to zero. The distribution of the stress suggest that metal flow along axial direction will benefit to the axial extension of the part.

6.Three-roll skew rolling bar orthogonal experiment design

Orthogonal experimental design using orthogonal table to select the representative strong test conditions, use to analysis the comprehensive comparison on the test results.

6.1 Experimental determination of parameters

Bar spiral tracks in the three-roll skew rolling is a very common phenomenon. The finite element simulation of rolling screw rod surface marks as shown in figure 4, this is due to the action of three-roll skew rolling roll Angle, roll friction of bar bar axis at the same time also will be around its own axis forward movement, the metal

deformation area will generate additional axial shear deformation and torsion deformation, three roll is bound to be left in the surface of the bar under the pressure of the spiral tracks, this kind of thread trace can not disappear completely, but through the optimization of rolling technology and can effectively reduce the spiral tracks. Study on the average distance between rolling bar spiral mark as test index, spiral mark small average spacing optimization goal for this test. Applying bar placed, DEFORM-3D ruler in post-processing function measuring the distance between the two spiral mark, measuring average after multiple spiral mark spacing.

During three-roll skew rolling, the initial temperature, deflection Angle, roll angular velocity is the important process parameters affecting the quality of three roll skew rolling. In this paper, the author studies on titanium alloy bars the rolling forming process, the selected process parameters: the initial temperature (A), deflection Angle (B), roll angular velocity (C). In the range of factors should be in the actual production experience within the scope of each factor in three levels, the level of the three factors values shown in table 3.

Tab.3 Experimental factors and factor levels

Factor	Level 1	Level 2	Level 3
initial temperature (A) /°C	900	950	1000
deflection Angle (B) /°	8	9	10
roll angular velocity (C) /rad/s	5	10	15

6.2 Range analysis results

By range analysis can directly influence on process parameters of three roll cross rolling spiral mark on average spacing. The test data and range analysis are shown in Table 4.

Tab.4 Range analysis in orthogonal test

Number	Factor level settings			average distance
	(A) /°C	(B) /°	(C) /rad/s	
1	1(900)	1(8)	1(5)	30.4254
2	1	2(9)	2(10)	30.2457
3	1	3(10)	3(15)	31.5452
4	2 (950)	1	2	30.6178
5	2	2	3	31.7856
6	2	3	1	32.5547
7	3 (1000)	1	3	30.4572
8	3	2	1	32.3524
9	3	3	2	32.5247
T1	92.2163	91.5004	95.3325	
T2	94.9581	94.3837	93.3882	282.5078
T3	95.3343	96.6246	93.788	
t1	30.73	30.50	31.77	
t2	31.65	31.46	31.13	
t3	31.77	32.21	32.26	
Optimum level	1	1	2	
R	3.118	5.1242	1.9443	
Order	B、A、C (B>A>C)			

In this experiment, the average distance between spiral mark as a single index by the range analysis. T_i is a column corresponding to section i of the target value of factors and levels. The Range R value is greater, the greater the influence that the process parameters on the average pitch spiral mark, Influence of forming on the surface of the metal bar is also larger. Can be based on the test results of the poor to determine the size of the effect of technical parameters on the spiral mark average spacing progression, As can be seen from table 4 various technological parameters of extreme value $R_2 > R_1 > R_3$, so the effect of technical parameters on the screw marks the average distance between primary and secondary order to B, A, C. Explain the deflection angle change for adjusting spiral mark average spacing is the key. The best level combination resulting process parameters for three roll skew rolling: The initial temperature is 900°C, the deflection angle is 8°, the roll angular velocity is 10 rad/s.

By the process parameters and test index and T value change trend can be seen that the initial temperature of rolled pieces in spiral mark minimum average spacing, with the temperature increases, the spiral mark average spacing increases gradually, so the initial temperature of rolled pieces is unfavorable and exorbitant. With the increase of deflection angle, the more obvious the spiral traces, This is due to the deflection angle increases with the deformation zone is shortened, rolling force increases, roll in the horizontal direction velocity increase. Increase the amount of billet at every turn under pressure, this will make the bar in the rolling deformation in-homogeneity, cross section triangle effect, bar section roundness error increase. Effect of test indexes and change trend can be seen from the roll angular velocity, as the roll angular velocity changes, test index and T value first decreases then increases. When the roll angular velocity in 10 rad/s, spiral mark T value minimum average spacing, roll speed should be controlled within a certain range, should not be too big or too small.

7. Conclusion

(1) Finite element numerical simulation analysis of the titanium alloy rod three-roll skew rolling deformation zone distribution regularity of stress field, strain field and demonstrate the feasibility of titanium alloy rod three-roll skew rolling, by optimizing the rolling process parameters can improve the quality of three-roll skew rolling bar finished product;

(2) Through the analysis of range to determine the primary and secondary order effects of three parameters on the average spacing bar spiral mark for: Work-piece deflection angle, initial temperature, roll angular velocity. The best combination of the process parameters as the initial temperature of work-piece is 900°C, the deflection angle is 8°, the roll angular velocity is 10 rad/s.

8. Acknowledgements

The project was supported by following funds: the National Natural Science Foundation of China (Grant No. 51475247), the Natural Science Foundation of Zhejiang (Grant No. LY12E05008).

9. References

- [1] Lou Guantao. Study on the application status and development direction of [J]. titanium industry progress, titanium alloy, 2003, (2): 9-13.
- [2] Li Liang, Sun Jianke, Meng Xiangjun. The application status and development prospect of [J]. titanium industry progress, titanium alloy (2004, 5):19-24
- [3] Hu Qingxiong. The application and Prospect of titanium [J]. advances in titanium industry outlook, 2003,20 (4): 11-15.
- [4] Chun-xiao cao. Air China with titanium alloy is facing the challenges of the 21st century [J]. Journal of titanium industry progress, 1999, (5) : 1-5.
- [5] Yong-qing zhao, zheng-ping xi, heng-lei qu. China's aviation research status with titanium alloy materials [J]. Journal of aviation materials, 2003, 23 (z1) : 215-219.
- [6] Wang Naikun, Jiang Shuhua, Qu Zhi Cheng. Application of [J]. orthogonal experimental design method in the design of experiments of Heilongjiang traffic science and technology, 2003.26:89-90.
- [7] Wang Yan, Sui Si Lian. The experimental design and data analysis of MATLAB [M]. Beijing: Tsinghua University press, 2012.

Reduced super beam based approach to finite element model updating of beam-type structures

Wensheng Wang¹, Haojie Wei¹, Zhonghua Hou¹

¹ Department of Engineering Mechanics, Henan University of Science and Technology, Luoyang, China,
Email: wswang@live.cn

1. Abstract

A reduced super beam based finite element model updating technique for beam-type structures is proposed in this paper. The model reduction method is adopted to condense the entire beam-type structural model into a reduced super beam model with much less degree of freedom. And the eigensolutions and eigensensitivities are re-analyzed from the reduced eigenequation of the reduced super beam in the updating process, thus reducing the computational load of the traditional model updating methods which perform on the original structure. The modal dynamic property difference approach is adopted for updating the reduced super beam model and standard optimization techniques are used to find the optimal values of the structural parameters that minimize the difference. The effectiveness and efficiency of the proposed method are illustrated through a complicated stiffened cylindrical shell structure.

2. Keywords: Reduced super beam, model updating, beam-type structures, optimization

3. Introduction

Great progresses have been achieved in finite element method (FEM) modeling during the past decades. However, due to the uncertainties in the geometry, material properties and boundary conditions of the FEM model, the dynamic responses of a structure predicted by a highly idealized numerical model usually differ from the experimental results. For example, He et al. [1] reported that the differences between the experimental and numerical modal frequencies of an aircraft wing exceeded 10% for most modes and even reached 70% in some cases. Similarly, more than 60% difference was found between the analytical and measured frequencies of an aero-engine casing by Ma et al. [2]. Therefore, an effective model updating method is necessary to obtain a more accurate FEM model that are required in a large number of applications, such as optimization design, damage identification, structural control and so on[3].

In the past years, various FEM model updating methods have been developed and practically applied, which can be classified into two categories: one-step methods and iterative methods [4]. The former directly reconstruct the stiffness and mass matrices of the analytical model, and the symmetry, positive-definiteness and sparseness in the updated matrices cannot be preserved. The latter modify the physical parameters of the FEM model repeatedly to minimize the modal properties discrepancy between the analytical model and the measurement counterparts, which are becoming more popular. Optimization techniques are employed in most iterative model updating methods, the eigensolutions and sensitivity matrices of the analytical model must be calculated in each iteration [5]. As the analytical model of a practical structure in engineering usually comprises a large number of degrees of freedom (DOFs), it is very time-consuming to extract the eigensolutions and eigensensitivities from the large-size system matrices, especially for many uncertain parameters that need to be updated.

To address the computational difficulty, reduced model-based FEM model updating methods have been investigated. The substructure based model updating method has been studied [6-8], which is advantageous mainly in two aspects. Firstly, it is much easier and quicker to analyze the small system matrices for eigensolutions and eigensensitivities, as the original structure is replaced by smaller substructures. Secondly, the separated substructures are analyzed independently when applied to model updating. When the updating parameters are localized within parts of a structure, only one or more substructures containing the parameters are re-analyzed during model updating, and the other substructures are untouched. However, the construction of the reduced base needs a lot of intricate matrices calculation and the accuracy of the substructure based model updating method relies on the optimum selection of master modes in the substructures.

In this work, a reduced super beam based updating method for beam-type structure is presented. The reduced super beam method [9-10], based on the plane cross section assumption and displacement interpolation function of beam, is a new model reduction method for beam-type structure. This paper intends to develop the reduced super beam method and apply it to calculate the eigensolutions and eigensensitivities for the sensitivity based model updating process. The modal dynamic property (frequencies and mode shapes) difference approach is adopted for updating the reduced super beam model. In particular, Eigensensitivities with respect to an updating

parameter of the global structure is calculated from the derivative matrices of the reduced super beam, which can save a large amount of computational effort in the model updating process. A complicated stiffened cylindrical shell structure is employed to demonstrate the effectiveness and efficiency of the proposed method.

4. Reduced super beam method

The reduced super beam method is briefly introduced in this section for model updating purpose. Considering a complicated free-free beam-type structure shown schematically in Figure 1(left figure), Oxyz is the global coordinate system, in which the Ox axis is along the structural axis and Oy and Oz are in the cross section perpendicular to the structural axis.

As the first step of the new model reduction method, the structure is divided into several parts by a number of cross section which is perpendicular to the structural axis. The intersections of the cross sections with the structural axis are defined as the master nodes. The original FEM model, which may have hundreds of thousands DOFs, will be reduced to a super beam model with the master nodes. Each master node has six degrees of freedom, i.e., three translational and three rotational degrees of freedom.

To construct such a super beam, each structural part is modeled as a super beam element. That is, the nodal displacement field in each part is approximated by the generalized displacement of the two master nodes at its end through twice transformation (i.e., the first transformation is performed between the structural node and the projective node, while the second transformation is performed between the projective node and the master node as shown in Figure 1). The detail of the reduction method is as follows.

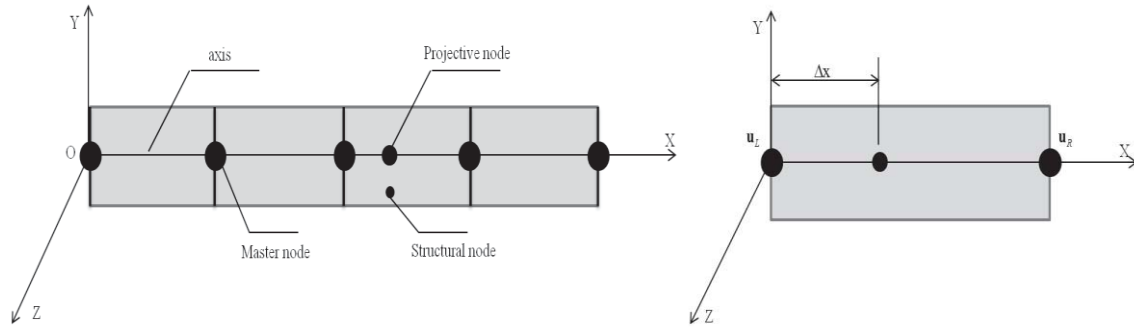


Figure 1: Principle of the model reduction method

In each part i , considering the deformation characteristics of beam-type structure, the well known plane cross-section assumption is applied to project the nodal displacements \mathbf{u}_j of each structural node j to the rigid body motion vector \mathbf{q}_{ji} of its corresponding projective nodes on the Ox axis. The relationship can be expressed as

$$\mathbf{u}_j = \mathbf{R}_j \mathbf{q}_{ji} \quad (1)$$

The expand form of Eq. (1) is

$$\begin{Bmatrix} u_{jx} \\ u_{jy} \\ u_{jz} \\ u_{j\theta_x} \\ u_{j\theta_y} \\ u_{j\theta_z} \end{Bmatrix} = \begin{bmatrix} 1 & 0 & 0 & 0 & z_{ej} & -y_{ej} \\ 0 & 1 & 0 & -z_{ej} & 0 & 0 \\ 0 & 0 & 1 & y_{ej} & 0 & 0 \\ 0 & 0 & 0 & 1 & 0 & 0 \\ 0 & 0 & 0 & 0 & 1 & 0 \\ 0 & 0 & 0 & 0 & 0 & 1 \end{bmatrix} \begin{Bmatrix} q_{jix} \\ q_{jiy} \\ q_{jiz} \\ q_{j\theta_x} \\ q_{j\theta_y} \\ q_{j\theta_z} \end{Bmatrix} \quad (2)$$

The six column of \mathbf{R}_j is denoted by $\mathbf{R}_{j1}, \mathbf{R}_{j2}, \mathbf{R}_{j3}, \mathbf{R}_{j4}, \mathbf{R}_{j5}, \mathbf{R}_{j6}$. The displacement vector \mathbf{q}_{ji} of the projective node between the two master nodes of each part i can be obtained through displacement interpolation function of beam. Suppose the displacement of the master nodes is $\mathbf{u}_L = (u_1, v_1, w_1, \theta_{x1}, \theta_{y1}, \theta_{z1})^T$ (left) and $\mathbf{u}_R = (u_2, v_2, w_2, \theta_{x2}, \theta_{y2}, \theta_{z2})^T$ (right) respectively, as shown in figure 1(right figure). According to the finite element theory of frame structure, displacement transformation between the projective node and the two master nodes can be approximated by the interpolation function of beam element as

$$\mathbf{q}_{ji} = \mathbf{N} \{ \mathbf{u}_L, \mathbf{u}_R \}^T \quad (3)$$

The expand form of interpolation functions N can be found in paper [10]. By Eq. (1) and (3), the transformation relationship matrices between the displacement of each structural node j and the two master nodes in each part i can be written as

$$\bar{\mathbf{R}}_j = \mathbf{R}_j N \quad (4)$$

The displacement of \tilde{m} nodes in each part i are all projected to the two assumed master nodes of the part i . Using the transformation (4), the transformation equation of the part i can be defined as:

$$\mathbf{U}_i = \bar{\mathbf{T}}_i \{ \mathbf{u}_L, \mathbf{u}_R \}^T \quad (5)$$

where $\mathbf{U}_i = (\mathbf{u}_1, \dots, \mathbf{u}_j, \dots, \mathbf{u}_m)^T$ is the nodal displacement vector of the \tilde{m} FEM nodes in part i , and the transformation matrices between the \tilde{m} FEM nodes and the two master nodes of the part i is $\bar{\mathbf{T}}_i = (\bar{\mathbf{R}}_1, \dots, \bar{\mathbf{R}}_j, \dots, \bar{\mathbf{R}}_m)^T$, with size of $6\tilde{m} \times 12$. Each column in the transformation matrices $\bar{\mathbf{T}}_i$, actually a reduced base vector with explicit and localized form, can be obtained with very low computational cost. With this transformation(5), the mass and stiffness matrices of the super beam element are defined as

$$\mathbf{m}_s = \bar{\mathbf{T}}_i^T \mathbf{m} \bar{\mathbf{T}}_i, \mathbf{k}_s = \bar{\mathbf{T}}_i^T \mathbf{k} \bar{\mathbf{T}}_i \quad (6)$$

where \mathbf{m}_s and \mathbf{k}_s has dimension 12×12 . Once the super beam element is constructed by Eq.(6), it could be assembled to obtain a free-free reduced super beam model. For a uniform beam type structure, it is only necessary to construct the super element once, otherwise, it is needed to construct several super beam elements for non-uniform general beam type structure. In this reduction process, the retained DOFs in the reduced model preserve its physical characteristics and provide the possibility for further necessary manipulation. The accuracy of the reduced super beam model is further improved by modifying the stiffness matrices of super beam element and considering the effect of shear deformation in a rational way, and the interested reader can refer to paper [10].

Suppose the whole beam-type structure with s nodes ($6s$ DOFs) was divided into p ($p \ll s$) parts, in other words, there are $p+1$ master nodes in all. A final reduced super beam model has DOFs ($6(p+1)$), which is much less than $6s$. The mass and stiffness matrices of the reduced super beam are defined as

$$\mathbf{K}_R = \sum_1^p \mathbf{k}_s, \quad \mathbf{M}_R = \sum_1^p \mathbf{m}_s \quad (7)$$

5. Model updating using modal property

Sensitivity-based FEM model updating method is the most frequently used updating method, and the general objective function combining the modal properties (frequencies and mode shapes) is usually represented as [6]

$$J(r) = \sum_i w_{\lambda_i}^2 \left[\lambda_i(r)^A - \lambda_i^E \right]^2 + \sum_i w_{\phi_i}^2 \sum_j \left[\phi_{ji}(r)^A - \phi_{ji}^E \right]^2 \quad (8)$$

where λ_i^E represents the eigenvalue corresponding to the i th experimental frequency, and ϕ_{ji}^E is the i th experimental mode shape at the j th experimental point. λ_i^A and ϕ_{ji}^A denote the corresponding eigenvalue and mode shape from the FE model, expressing as the function of the updating parameters r . w_{λ_i} and w_{ϕ_i} are the weight coefficients due to the different measurement accuracy of the frequencies and mode shapes. The objective function is minimized by continuously adjusting the parameters r of the initial FE model through optimization process.

5.1 Sensitivity analysis

To find the optimal searching direction, sensitivity analysis is usually conducted to compute the rate of the change of a particular response quantity with respect to the change in a physical parameter. For the objective function, a truncated Taylor series of $J(r)$ is defined as

$$Z(r) = J(r) + [\nabla J(r)]^T (\Delta r) + \frac{1}{2} (\Delta r)^T [\nabla^2 J(r)]^T (\Delta r) \quad (9)$$

where Δr denotes a step vector from the current r . $\nabla J(r)$ and $\nabla^2 J(r)$ are the gradient and the Hessian of $J(r)$, respectively. After an iterative process, the optimized r^* is reached with $\nabla J(r) \approx 0$. The gradient and Hessian of $J(r)$ can be expressed by the sensitivity matrices as

$$\nabla J(r) = [S(r)]^T \{ 2f(r) \} \quad \nabla^2 J(r) = S(r)^T S(r) \quad (10)$$

where $f(r)$ encloses the weighted residuals $w_{\lambda_i} (\lambda_i(r)^A - \lambda_i^E)$ and $w_{\phi_i} (\phi_{ji}(r)^A - \phi_{ji}^E)$. The sensitivity matrices of the

eigenvalues and mode shapes with respect to a parameter r can be expressed as

$$S_{\lambda}(r) = \frac{\partial \lambda(r)}{\partial r} \quad S_{\phi}(r) = \frac{\partial \phi(r)}{\partial r} \quad (11)$$

The sensitivity matrices $S(r)$ may be determined analytically or by using the finite difference method [11].

5.2 Eigensolutions with reduced super beam method

The eigensolutions and eigensensitivity matrices can be calculated based on the classical eigenequation

$$\mathbf{K}\phi_i = \lambda_i \mathbf{M}\phi_i \quad (12)$$

where \mathbf{K} and \mathbf{M} are the stiffness and mass matrices, λ_i and ϕ_i are the i th eigenvalue and eigenvector, respectively.

In traditional model updating methods, the eigensolutions and eigensensitivities analysis based on the large-size system matrices is expensive, updating the FEM model of a large-scale structure usually involves a heavy workload and many runs are usually required to achieve the convergence of the optimization.

In the present paper, a beam-type structure is condensed to a reduced super beam based on the aforementioned reduced method, aiming at reducing the sizes of the stiffness and mass matrices and eliminating the expensive reanalyses of eigenproblems due to the variations of the updating parameters. The reduced solutions are then transformed to obtain eigensolutions and eigensensitivity of the global structure by using transformation matrix, which is an assemblage of \bar{T}_i .

We also suppose that the stiffness and mass matrices depend linearly on the model parameter \mathbf{r} , which is often encountered in practical applications of model updating. Specifically, it is assumed that the mass and stiffness matrices of the original model take the form as

$$\mathbf{K}(\mathbf{r}) = \mathbf{K}_0 + \sum_i^{N_r} \mathbf{K}_i r_i \quad \mathbf{M}(\mathbf{r}) = \mathbf{M}_0 + \sum_i^{N_r} \mathbf{M}_i r_i \quad (13)$$

where $\mathbf{K}_0, \mathbf{M}_0, \mathbf{K}_i$ and \mathbf{M}_i are constant matrices, independent of \mathbf{r} , and N_r is the number of structural model parameters to be updated. Then the construction of the super beam element is guided by the linear dependence so that the stiffness and mass matrix for each beam element depend linearly on only one of the parameters to be updated. The mass and stiffness matrices at the reduced level admit a similar representation as (14),

$$\mathbf{K}_R(\mathbf{r}) = \mathbf{K}_{R0} + \sum_i^{N_r} \mathbf{K}_{Ri} r_i \quad \mathbf{M}_R(\mathbf{r}) = \mathbf{M}_{R0} + \sum_i^{N_r} \mathbf{M}_{Ri} r_i \quad (14)$$

In order to save computational time, the constant matrices are computed and assembled once and, therefore, there is no need for this computation to be repeated during the iterations in optimization for model updating.

6. Numerical example: a stiffened cylindrical shell structure

To illustrate the feasibility and computational efficiency of the proposed method, a uniform typical stiffened cylindrical shell structure in free-free boundary condition is employed here as shown in figure 2. Figure 3 gives its FEM model with 4530 elements, 3060 nodes and 18360 DOFs in total. The material of the structure is isotropic with Young's modulus $E = 7.0 \times 10^4 \text{ MPa}$, Poisson's ratio $\nu = 0.3$, and mass density $\rho = 2.7 \times 10^{-3} \text{ g/mm}^3$.

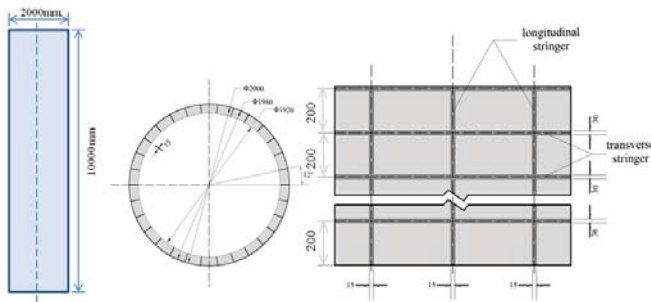


Figure 2: Typical stiffened cylindrical shell structure

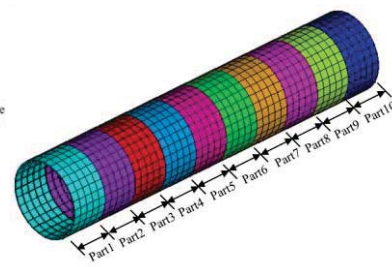


Figure 3: FEM model of the cylinder structure

The original full FEM model was reduce to a super beam model of 50 uniform super beam elements in this paper, and the reduced super beam model has 306 DOFs in total, which is much less than the original model. The first six overall natural frequencies and corresponding mode shapes are calculated using the reduced super beam model, and compared with the original model in Table 1. Some minor differences are found in Table 1, and the relative differences in frequencies are less than 3% for almost all modes. Modal assurance criterion (MAC) [9] values of all

mode shapes are above 0.88, which indicate the similarity between the reduced and original mode shapes.

Table 1: The frequencies and mode shapes of the cylinder structure using the proposed method

Frequency order	Original model (hz)	Reduced model(hz)	Difference (%)	MAC
1 st bending	89.53	84.32	5.82	0.88
1 st torsional	130.46	133.72	2.50	0.95
2 nd bending	186.59	183.16	1.84	0.90
1 st axial	220.86	227.45	2.98	0.91
2 nd torsional	261.07	267.59	2.50	0.94
3 rd bending	284.84	291.90	2.48	0.89

In model updating, the simulated ‘experimental’ modal data are usually obtained by intentionally introducing damages on some elements, and then the analytical model is updated to identify these damages. In this present paper, the simulated frequencies and mode shapes, which are treated as the ‘experimental’ data, are calculated from the FE model by intentionally reducing the bending rigidity, torsional rigidity and axial rigidity in some parts. The simulated reduction is listed in Table 2 and denoted in figure 3.

Table 2: Assumed rigidity reduction in some parts

	Case1	Case2
Assumed discrepancy	Part2/Part3 (-30%)	Part1 (-30%)
	Part6 (-20%)	Part4/Part5 (-20%)
	Part8 (-30%)	Part9 (-30%)

The eigensolutions and eigensensitivities of the analytical model are calculated using the proposed reduction method, and match the ‘experimental’ counterparts through an optimization process. The rigidity of all reduced super beam elements is assumed as unknown and chosen as the updating parameter. Accordingly, there are 50 updating parameters in total. The weight coefficients are set to 1.0 for the frequencies and 0.1 for the mode shapes. The Lanczos method is employed to calculate the eigensolutions and the analytical method is used for the eigensensitivities. To calculate the eigensensitivity of the global structure with respect to an updating parameter, the derivative matrices of only one super beam element that contains the parameter is required while those in other substructures are set to zero. The optimization is processed by using Method of Moving Asymptotes (MMA) [12], which stops until the objective change between two successive iterations is less than a specified tolerance 0.05%.

In the case1, the rigidity of randomly selected parts is assumed to be reduced by 30% and 20%, that is, the rigidity of part2, part3 and part8 are reduced by 30% and part6 is reduced by 20%, while the other parts remain unchanged. Then the damaged structure is used to obtain the ‘experimental’ frequencies and mode shapes. The model updating process is conducted to make the analytical model reproduce the ‘experimental’ frequencies and mode shapes. The frequencies and mode shapes before and after the updating are compared in Table 3. It demonstrates that the analytical modal datas closely match the simulated ‘experimental’ counterparts after the updating.

Table 3: The frequencies and mode shapes of the cylinder structure before and after updating (case1)

Frequency order	Experimental frequencies (hz)	Before updating			After updating		
		Analytical frequencies(hz)	Difference (%)	MAC	Analytical frequencies(hz)	Difference (%)	MAC
1 st bending	80.82	84.32	4.33	0.85	77.81	3.72	0.89
1 st torsional	124.56	133.72	7.35	0.79	119.87	3.76	0.88
2 nd bending	167.70	183.16	9.22	0.82	170.88	1.89	0.92
1 st axial	211.77	227.45	7.41	0.83	203.39	3.95	0.90
2 nd torsional	241.07	267.59	11.01	0.73	233.71	3.05	0.87
3 rd bending	264.46	291.90	10.38	0.75	275.46	4.15	0.85

Without losing generality, the rigidity of different parts is assumed to have some known discrepancy as well. In case2, the rigidity of part1, part9 are reduced by 30% and part4, part5 are reduced by 20% (see Table 2). The frequencies and mode shapes before and after the updating are compared in Table 4. In Table 4, the frequencies and mode shapes of the updated model better match the ‘experimental’ counterparts.

It should be noted that using the proposed reduced super beam method, the eigensolutions and eigensensitivities are calculated based on the reduced equation with size of 306×306 , rather than on the original global eigenequation with size of 18360×18360 . The eigensolutions based on the reduced super beam model takes only 0.25 second, while it takes about 5000 seconds based on the original model. As comparison, the proposed reduced super beam-based model updating method achieves higher efficiency.

Table 4: The frequencies and mode shapes of the cylinder structure before and after updating (case2)

Frequency order	Experimental frequencies (hz)	Before updating			After updating		
		Analytical frequencies(hz)	Difference (%)	MAC	Analytical frequencies(hz)	Difference (%)	MAC
1 st bending	82.13	84.32	2.67	0.80	80.07	2.51	0.90
1 st torsional	127.01	133.72	5.28	0.78	121.99	3.95	0.89
2 nd bending	173.74	183.16	5.42	0.85	176.99	1.87	0.93
1 st axial	215.93	227.45	5.34	0.82	207.06	4.11	0.89
2 nd torsional	254.11	267.59	5.31	0.83	245.07	3.56	0.91
3 rd bending	263.05	291.90	10.97	0.73	274.75	4.45	0.87

7. Conclusions

This paper has proposed a reduced super beam based model updating method for beam-type structure. The eigensolutions and eigensensitivities of the original structure are calculated from a greatly reduced super beam model, and calculation of the eigensensitivities with respect to an updating parameter only requires analysis of the super beam element that contains the parameter. The proposed model updating method is advantageous in improving the computational efficiency. The Application to a typical stiffened cylindrical shell structure demonstrates that the proposed model updating method is efficient to be applied to update large-scale structures with a large number of design parameters.

It is only an introduction of the proposed method in this paper. Although the examples given are simple, which have shown the effectiveness and efficiency. Great efforts will be made to apply the method to more complex practical problems in further research.

8. Acknowledgements

This research was supported by the Natural Science Foundation of China (11402077).

9. References

- [1] He Erming, Chen Yi, Li Yulong, et al. Dynamic modification and application of wing double-beam model, *Chinese Journal of Applied Mechanics*, 30(3), 367-372, 2013.
- [2] Ma Shuangchao, Zang Chaoping, Lan Haibo. Dynamic model updating of an aero-engine casing, *Journal of Aerospace Power*, 28(4), 878-884, 2013.
- [3] J. E. Mottershead, M. I. Friswell. Model updating in structural dynamics: a survey. *Journal of Sound and Vibration*, 167(2), 347-375, 1993.
- [4] J. M. W. Brownjohn, P. Q. Xia, H. Hao, et al. Civil structure condition assessment by FE model updating: methodology and case studies. *Finite Elements in Analysis and Design*, 37(10), 761-775, 2001.
- [5] P. G. Bakira, E. Reynders and G. D. Roeck. Sensitivity-based finite element model updating using constrained optimization with a trust region algorithm. *Journal of Sound and Vibration*, 305(1-2), 211-225, 2007.
- [6] Shun Weng, Yong Xia, Youlin Xu, et al. Substructure based approach to finite element model updating, *Computers and Structures*, 89(9-10), 772-782, 2011.
- [7] D. P Zhu, X. J Dong and Y. Wang. Substructure model updating through modal dynamic residual approach, *Proceedings of the 9th International Workshop on Structural Health Monitoring, Stanford, CA*. 2013.
- [8] C. Papadimitriou, D. C. Papadioti. Component mode synthesis techniques for finite element model updating, *Computers and Structures*, 126(15), 15-28, 2013.
- [9] W. S. Wang, G. D. Cheng and Q. H. Li. Fast dynamic performance optimization of complicated beam-type structures based on two new reduced physical models, *Engineering Optimization*, 45(7), 835-850, 2013.
- [10] G. D. Cheng, W. S. Wang. Fast dynamic analysis of complicated beam-type structure based on reduced super beam model, *AIAA Journal*, 52(5), 952-963, 2014.
- [11] J. E. Mottershead, M Link, M. Friswell. The sensitivity method in finite element model updating: A tutorial, *Mechanical Systems and Signal Processing*, 25(7), 2275-2296, 2011.
- [12] K. Svanber. The method of moving asymptotes—a new method for structural optimization, *International Journal for Numerical Methods in Engineering*, 24(2), 359-373, 1987.

Study on Optimization for Large Structures using Hybrid GA

Ryota Nonami¹, Mitsuru Kitamura², Akihiro Takezawa³

¹ Hiroshima University, Graduate School of Engineering, Department of Transportation and Environmental Systems

² Professor, Hiroshima University, Faculty of Engineering, Division of Mechanical Systems and Applied Mechanics

³ Associate Professor, Hiroshima University, Faculty of Engineering, Division of Mechanical Systems and Applied Mechanics

1. Abstract

A lot of stiffeners are attached large structures. The optimization of the structure with design valuable of number and position of stiffeners is difficult. Because there are problems with creating FEM model and optimization method. When the number of stiffener is changed, FEM model is recreated. As a result, the time for optimization is increase. Therefore, a calculation method for evaluation of the structure's strength without recreating FEM models by the change of the design is proposed. The optimization time is curtailed using this calculation method.

Also, this optimization is combinational optimization problem. Therefore, the genetic algorithm is used. However, when all design variable is expressed as strings, strings length becomes long. As a result, the convergence deteriorate and the calculation amount is increased. In order to solve this problem, the Hybrid GA which combined the genetic algorithm with the other optimization method is proposed. The structural optimization is performed using two proposed method.

2. Keywords: FEM, structural optimization, hybrid GA

3. Introduction

The optimization of large structures is important for the design. The optimization of the structure with design variable of the plate thickness and the shape of stiffener is popular study filed and many reported. A ship is one of large structures. A ship has a lot of number of stiffeners. As a result, in order to obtain the better optimal solution, the optimization of the structure with design valuable of number and position of stiffeners is required. However, there is a problem as creation time of FEM models.[1][2] The FEM model has to be defined nodes at the position of stiffeners as a characteristic of FEM. When new nodes are added, the adjustability of mesh is lost. It is necessary to recreate the FEM model, in order to maintain the adjustability of mesh. However, the optimization of the structure has to examine much number of propositions for design. Creating FEM models is required a long time. As a result, it is too difficult to create FEM models of all propositions for design. Therefore, a calculation method for evaluation of the structure's strength without recreating FEM models by the change of the design is proposed.

This optimization is combinational optimization problem. Therefore, the genetic algorithm is used. However, when all design variable is expressed as strings, strings length becomes long. When the optimization is performed using this strings, the convergence becomes aggravation. As a result, it is difficult to get the optimal solution. In order to solve this problem, a study about the hybrid GA is advanced. In this study, Hybrid GA which combined the genetic algorithm with the other optimization method is applied.

The structural optimization for large structures is performed using these two method in this study.

4. Research target

The research target is shown in Fig 1. The stiffeners are allocated in the plate. In this study, the model is optimized. The design valuables are plate thickness and the number of stiffeners, the position of stiffeners, the shape of stiffeners.

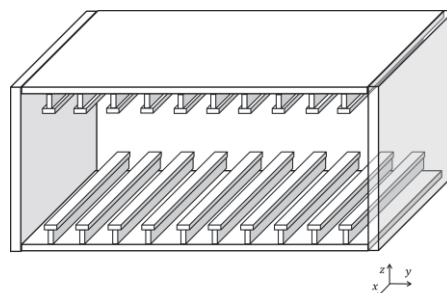


Figure 1: research target

4. Calculation method for FEM

The method of changing stiffness and degree of freedom is explained by this section.

The rigid matrix of target FEM model is divided into α and β . α is region of unchanged structure. β is region of changed structure. Next, the region of adding nodes are added. This region is γ . When stiffness equation is divided into three of region, the stiffness equation is expressed by Eq.(1). [3]

$$\begin{bmatrix} \mathbf{K}_{\alpha\alpha} & \mathbf{K}_{\alpha\beta} & 0 \\ \mathbf{K}_{\beta\alpha} & \mathbf{K}_{\beta\beta} + \Delta\mathbf{K}_{\beta\beta} & \Delta\mathbf{K}_{\beta\gamma} \\ 0 & \Delta\mathbf{K}_{\gamma\beta} & \Delta\mathbf{K}_{\gamma\gamma} \end{bmatrix} \begin{bmatrix} \mathbf{x}'_{\alpha} \\ \mathbf{x}'_{\beta} \\ \mathbf{x}'_{\gamma} \end{bmatrix} = \begin{bmatrix} \mathbf{f}_{\alpha} \\ \mathbf{f}_{\beta} \\ \mathbf{f}_{\gamma} \end{bmatrix} \quad (1)$$

\mathbf{x}'_{α} and $\mathbf{x}'_{\beta}, \mathbf{x}'_{\gamma}$ are expressed by the displacement of after changed structure. \mathbf{f}_{α} and $\mathbf{f}_{\beta}, \mathbf{f}_{\gamma}$ are expressed by the load vector of after changed structure. Also, $\mathbf{f}_{\gamma} = 0$ because adding nodes are nothing. When Eq.(1) is solved about \mathbf{x}'_{α} and $\mathbf{x}'_{\beta}, \mathbf{x}'_{\gamma}$, it gets Eq.(2).

$$\begin{bmatrix} \mathbf{G}_{\alpha\alpha} & \mathbf{G}_{\alpha\beta} & 0 \\ \mathbf{G}_{\beta\alpha} & \mathbf{G}_{\beta\beta} & 0 \\ 0 & 0 & \mathbf{I} \end{bmatrix} \begin{bmatrix} \mathbf{f}_{\alpha} \\ \mathbf{f}_{\beta} - \Delta\mathbf{K}_{\beta\beta}\mathbf{x}'_{\beta} - \Delta\mathbf{K}_{\beta\gamma}\mathbf{x}'_{\gamma} \\ -\Delta\mathbf{K}_{\gamma\beta}^{-1}\Delta\mathbf{K}_{\gamma\beta}\mathbf{x}'_{\beta} \end{bmatrix} = \begin{bmatrix} \mathbf{x}'_{\alpha} \\ \mathbf{x}'_{\beta} \\ \mathbf{x}'_{\gamma} \end{bmatrix} \quad (2)$$

The \mathbf{G} matrix of Eq.(2) is the inverse matrix of whole stiffness matrix shown in Eq.(3).

$$\begin{bmatrix} \mathbf{G}_{\alpha\alpha} & \mathbf{G}_{\alpha\beta} \\ \mathbf{G}_{\beta\alpha} & \mathbf{G}_{\beta\beta} \end{bmatrix} = \begin{bmatrix} \mathbf{K}_{\alpha\alpha} & \mathbf{K}_{\alpha\beta} \\ \mathbf{K}_{\beta\alpha} & \mathbf{K}_{\beta\beta} \end{bmatrix}^{-1} \quad (3)$$

When Eq.(2) is simplified, \mathbf{x}'_{β} and \mathbf{x}'_{γ} are expressed by Eq.(4).

$$\begin{bmatrix} \mathbf{x}'_{\beta} \\ \mathbf{x}'_{\gamma} \end{bmatrix} = \begin{bmatrix} \mathbf{G}_{\beta\alpha}\mathbf{f}_{\alpha} + \mathbf{G}_{\beta\beta}(\mathbf{f}_{\beta} - \Delta\mathbf{K}_{\beta\beta}\mathbf{x}'_{\beta} - \Delta\mathbf{K}_{\beta\gamma}\mathbf{x}'_{\gamma}) \\ \Delta\mathbf{K}_{\gamma\gamma}^{-1}\mathbf{f}_{\gamma} - \Delta\mathbf{K}_{\gamma\beta}^{-1}\Delta\mathbf{K}_{\gamma\beta}\mathbf{x}'_{\beta} \end{bmatrix} \quad (4)$$

$\mathbf{G}_{\beta\alpha}\mathbf{f}_{\alpha} + \mathbf{G}_{\beta\beta}\mathbf{f}_{\beta}$ is expressed by \mathbf{x}_{β} . Then, substituted $\mathbf{G}_{\beta\alpha}\mathbf{f}_{\alpha} + \mathbf{G}_{\beta\beta}\mathbf{f}_{\beta} = \mathbf{x}_{\beta}$ for Eq.(4) and solved \mathbf{x}'_{β} and \mathbf{x}'_{γ} . As a result, Eq.(5) is got.

$$\begin{bmatrix} \mathbf{x}'_{\beta} \\ \mathbf{x}'_{\gamma} \end{bmatrix} = \begin{bmatrix} \mathbf{I} & 0 \\ 0 & 0 \end{bmatrix} + \begin{bmatrix} \mathbf{G}_{\beta\beta} & 0 \\ 0 & \mathbf{I} \end{bmatrix} \begin{bmatrix} \Delta\mathbf{K}_{\beta\beta} & \Delta\mathbf{K}_{\beta\gamma} \\ \Delta\mathbf{K}_{\gamma\beta} & \Delta\mathbf{K}_{\gamma\gamma} \end{bmatrix}^{-1} \begin{bmatrix} \mathbf{x}_{\beta} \\ 0 \end{bmatrix} \quad (5)$$

In order to solve displacement after adding nodes, $\mathbf{G}_{\beta\beta}$ and $\Delta\mathbf{K}, \mathbf{x}_{\beta}$ are required. Also, when Eq.(2) is solved about \mathbf{x}'_{α} , Eq.(6) is got.

$$\mathbf{x}'_{\alpha} = \mathbf{x}_{\alpha} - \mathbf{G}_{\alpha\beta} (\Delta\mathbf{K}_{\beta\beta}\mathbf{x}'_{\beta} + \Delta\mathbf{K}_{\beta\gamma}\mathbf{x}'_{\gamma}) \quad (6)$$

It becomes possible to calculate the displacement after changed structures using Eq.(5) and Eq.(6). As a result, the number of stiffeners can be changed without recreating FEM model using this calculation method.

4. Hybrid GA

The hybrid GA is optimization method which combined GA with other optimization method. In this section, the design variables treated by GA and the other optimization method are explained. The flow of hybrid GA is shown in Fig. 2.

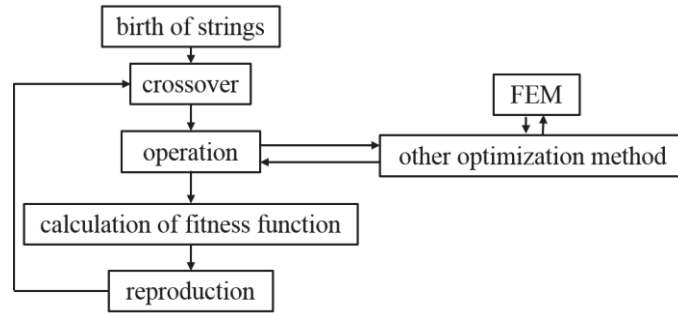
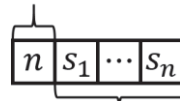


Figure 2: flow of hybrid GA

4.1 genetic algorithm

The design variables are plate thickness and the number of stiffeners, the position of stiffeners, the shape of stiffeners. The shape of stiffeners is chosen from select list. Then, discrete variables are the shape and number of stiffeners. The optimization with discrete variables can be performed using GA. Therefore, these two design variables are treated by GA. In order to perform optimization by GA, the design variables were expressed by strings as shown in Fig 3.

number of stiffeners



shape of stiffeners

Figure 3: strings

4.2 other optimization method

The plate thickness and the number of stiffeners are near the continuous variables. Then, the optimization with these two design variables is difficult to perform by GA. Therefore, the other optimization method is proposed. First, the updating method for design variables is explained. In plate bending theory, the bending stress of the plate is expressed by Eq.(7).

$$\sigma = \beta \frac{pl^2}{t^2} \quad (7)$$

σ : bending stress

p : uniformly varying load

l : plate length

t : plate thickness

β : correction coefficient with aspect ratio

When step a is the present design variable, t_a is expressed by Eq.(8)

$$t_a = \beta \frac{pl_a}{\sqrt{\sigma_a}} \quad (8)$$

If σ_a agrees with the constraint condition in step $a+1$, t_a is expressed by Eq.(9)

$$t_{a+1} = \beta \frac{pl_{a+1}}{\sqrt{\sigma_c}} \quad (9)$$

σ_c : constraint condition

Eq.(10) is got from Eq.(8) and Eq.(9).

$$t_{a+1} = \frac{t_a l_{a+1} \sqrt{\sigma_a}}{l_a \sqrt{\sigma_c}} \quad (10)$$

When span is changed, plate thickness is decided satisfactory to the constraint condition by Eq.(10).Also, when $l_{a+1}=l_a$, Eq.(11) is got.

$$t_{a+1} = t_a \frac{\sqrt{\sigma_a}}{\sqrt{\sigma_c}} \quad (11)$$

In this method, span and plate thickness are updated by Eq.(10) and Eq.(11). This optimization method of process is shown in Fig. 4.

- (1) The plate thickness is changed by Eq.(11).
- (2) Each span is extended unit length. The weight is calculated and the efficient vector of span is calculated.
- (3) When span is changed using calculated vector, plate thickness is changed by Eq.(10).
- (4) The weight after changed span and thickness is calculated. So, the weight is judged whether minimum weight or not.
- (5) The stress is analyzed using FEM.

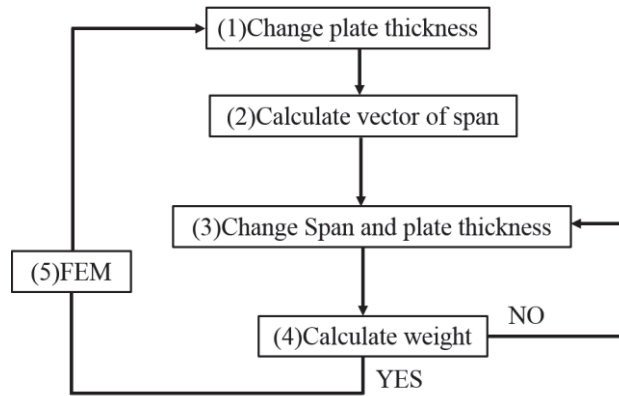


Figure 4: flow of optimization method

4.3 example problem

In this section, the hybrid GA is examined. The optimization target is shown in Fig.5. When optimization is performed using FEM, the optimization time becomes long. Therefore, the testing is performed without FEM. Eq.(12) is used instead of FEM. When span is extended, the rigid of stiffener is down and thickness is thinned, stress is upped.

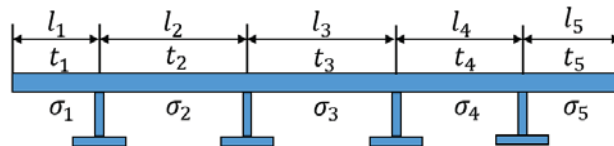


Figure 5: optimization target for example problem

$$\sigma_i = l_i + \frac{1}{t_i} + \frac{1}{I_i} \quad (12)$$

- σ_i : ith stress
 l_i : ith span
 t_i : ith thickness
 I_i : ith inertia of stiffener

The object function is expressed by Eq(13).The constraint condition is expressed by Eq(14).In this example problem, σ_c is 35. The augmented object functions using Eq.(13) and Eq(14) is expressed by Eq.(15).The design variables is the span and plate thickness.

$$f(X) = weight \quad (13)$$

$$g(X) = \sum_{i=1}^n \max[0, \frac{(\sigma_i - \sigma_c)}{\sigma_c}] \quad (14)$$

σ_i : stress of constraint condition

$$F(X) = f(X) + rg(X) \quad (15)$$

The result of optimization is shown in Fig.6. The stress of constraint condition to be satisfied. Stiffeners are allocated at regular intervals. As a result, attached stiffeners properly by this method are confirmed.

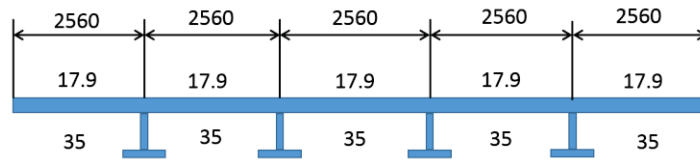


Figure 6: result of optimization

5. Structural optimization

In this section, The optimization is performed by eq (10). The FEM model for optimization is shown in Fig.7. The stiffener is allocated in the x-direction. The region of optimization is top plate. The object function is weight. The weight is minimized. The constraint condition is Eq(14). σ_c is 5. σ_i is the max stress of between stiffeners. The design variables is the span and plate thickness. The load condition is shown in Fig.8.

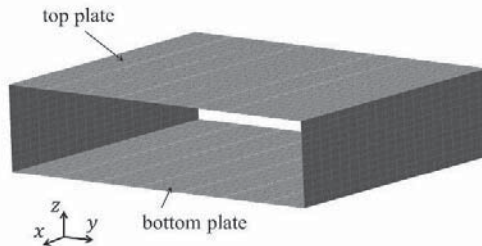


Figure 7: FEM model for optimization

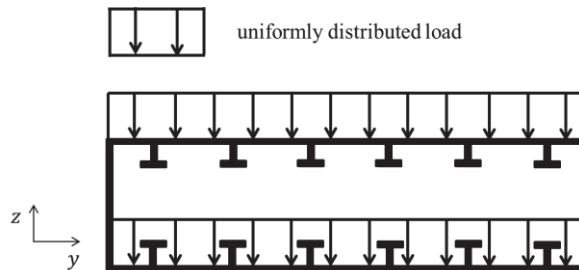


Figure 8: load condition

The result of optimization is shown in Fig.9. The stress of these plates are excepted from constraint condition. Stiffeners are allocated at bilateral symmetry. As a result, attached stiffeners properly by this method are confirmed.

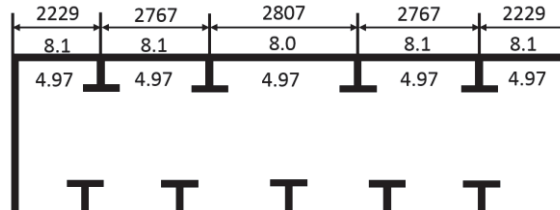


Figure 9: result of optimization

6. Conclusion

In this study, optimization of the ship structures with design valuable of the number and position of stiffeners is performed. The following two methods are proposed for optimization of the ship structures.

1. The calculation method for evaluation of the strength structures without recreating FEM models is proposed.
2. The hybrid GA which combined GA with proposed optimization method is proposed.

When optimization is performed using the three above mentioned method, stiffeners are allocated at proper positions and optimal solution can be got. As a result, the efficacy of proposed methods is confirmed.

7. References

- [1] Kitamura M Hamada K Takezawa A Uedera T: Shape Optimization System of the Bottom Structure of a Ship Incorporating Individual Mesh Sub-division and Multi-point Constraint: International Journal of Offshore and Polar Engineering, Vol. 21, No. 3, pp. 209-215, 2011.
- [2] Hirakawa S Kitamura Maki M: Application of Genetic Algorithm to Structural Design of 150KDWT Tanker using PrimeShip-HULL Rule Calculation Software: International Offshore and Polar Engineering Conference, 2011.
- [3] Furuya K Yoshimura T Suto A Saito K :Sensitivity Analysis of FRF using Eigenvalue and Eigenvector of Component Stiffness Matrix: Dynamics and design Conference, 2004.

Tradeoff exploration in decomposition-based optimization

Paolo Guarneri¹, Margaret M. Wiecek²

¹ Technical University of Cluj-Napoca, Cluj-Napoca, Romania, Paolo.Guarneri@emd.utcluj.ro

² Clemson University, Clemson, SC, USA, wmalgor@clemson.edu

1. Abstract

In multidisciplinary design, the approaches based on decomposition formally describe the design tasks by means of interconnected optimization (sub)problems, each presenting objective and constraint functions specific to different disciplines or subsystems. The presence of multiple objectives implies that tradeoffs must be taken into account during the design process, which, in engineering design, has been addressed through the concept of Pareto optimality. Although a number of numerical methods have been developed for computing Pareto solutions in applied fields, such a concept has not been extensively investigated when applied to decomposition schemes for large-scale problems.

This paper responds to the need of understanding the impact of multicriteria decision making techniques on distributed multidisciplinary optimization. To rely on Lagrangian duality, that proved to be effective for subproblem coordination in the single objective case, scalarization techniques such as the weighted-sum method, ϵ -constraint method, and Chebyshev-norm method, are considered in this paper. Scalarized optimization subproblems are properly formulated and a solution algorithm for computing Pareto designs, whose convergence is proven based on pre-existing results, is demonstrated on a numerical example, showing that subproblem negotiation is the mechanism that allows tradeoff exploration and the computation of Pareto designs for the overall system.

2. Keywords: Multidisciplinary optimization, multiobjective optimization, Lagrangian relaxation, Pareto design.

3. Introduction

Decomposition of optimization problems into subproblems, that has been widely used to reduce the size of the problem and exploit parallel computing, reflects from the design perspective the distribution of the tasks over different design groups according to their expertise in specific fields, that nowadays are more and more integrated in engineered systems. The integration of different disciplines underlies the presence of multiple criteria asking for negotiation mechanisms that drive the decision making process. Through negotiation it is in fact possible to reach a compromise solution that in the optimal design context is related to Pareto optimality.

Multiobjective extensions of algorithms developed for the single objective case include the Multiobjective Collaborative Optimization [1] and the Multiobjective Concurrent SubSpace Optimization [2]. The capability of genetic algorithms to converge towards Pareto (or, more appropriately, nondominated) solutions is exploited in [3, 4, 5].

A different school of thought, to which this paper belongs, relies on the previously-established results originated in the single objective scenario, in which subproblem coordination is achieved through Lagrangian relaxation. The subproblems that are identified in the MDO problem share engineering quantities that prevent separability. In order to decompose the problem, copies of the shared variables are introduced along with equality constraints between the original variables and their copies to guarantee the consistency with the original problem formulation. Decomposition becomes possible after relaxing such equality constraints into the objective function, which is unique in the single objective case. Examples of this type of approach in engineering optimization can be found in [6, 7, 8, 9]. To extend this decomposition and solving scheme based on Lagrangian relaxation to the multiobjective case, the scalarization of the multiobjective problem is necessary. While weighted-sum aggregations are proposed in [10, 11], this paper complements the previous works by discussing popular scalarization techniques other than the weighted-sum, namely the ϵ -constraint method and the Chebyshev-norm method.

The objective is to implement a coordination algorithm that is able to compute Pareto design making use of the negotiation mechanism that originates in the scalarization and in the subproblem communication enabled by Lagrangian relaxation. After introducing the multidisciplinary, multiobjective problem in Section 4, three scalarized, relaxed formulations are presented in Section 5. Some details about the coordination algorithm and the numerical results are reported in Section 6. A short discussion concludes the paper in Section 7.

4. Formulation of the design problem

A multidisciplinary multiobjective optimization problem is formulated as

$$\begin{aligned}
& \min_{\substack{\mathbf{x}_i, \mathbf{x}^i \\ i=1, \dots, N}} \begin{bmatrix} \vdots \\ \mathbf{f}_i(\mathbf{x}_i, \mathbf{p}_i(\mathbf{x}_i), \mathbf{q}_i(\mathbf{x}^i)) \\ \vdots \end{bmatrix} \\
& \text{s.t. } \mathbf{x}_i \in X_i, \mathbf{x}^i \in X^i \\
& \quad \mathbf{g}_i(\mathbf{x}_i, \mathbf{p}_i(\mathbf{x}_i), \mathbf{q}_i(\mathbf{x}^i)) \leq \mathbf{0} \\
& \quad i = 1, \dots, N
\end{aligned} \tag{1}$$

where \mathbf{f}_i and \mathbf{g}_i are the design criteria and constraints assigned to a specific team i that has control over the decision variable \mathbf{x}_i , and $\mathbf{p}_i(\mathbf{x}_i)$ and $\mathbf{q}_i(\mathbf{x}^i)$ are the linking variables that model the relationships between team i and the remaining teams that have control on variables $\mathbf{x}^i = [\mathbf{x}_j]_{\forall j \neq i}$ (i.e., all design variables except for those of team i), with $X^i = \prod_{j=1, j \neq i}^N X_j$. The linking variables collect all of the possible interactions between the teams, $\mathbf{p}_i(\mathbf{x}_i) = [\mathbf{p}_{ij}(\mathbf{x}_i)]_{\forall j \neq i}$ and $\mathbf{q}_i(\mathbf{x}^i) = [\mathbf{q}_{ij}(\mathbf{x}_j)]_{\forall j \neq i}$.

Problem (1) requires dedicated, distributed algorithms because of the dynamics involved among the design teams, which makes the problem unsuitable for centralized algorithms. The introduction of copies \mathbf{Q}_i and \mathbf{P}_i gives the teams the freedom to improve their respective objectives whereas the equality constraints, defined through the aggregations $\mathbf{P}_i = [\mathbf{P}_{ij}]_{\forall j \neq i}$ and $\mathbf{Q}_i = [\mathbf{Q}_{ij}]_{\forall j \neq i}$,

$$\begin{aligned}
\mathbf{P}_i - \mathbf{p}_i(\mathbf{x}_i) &= \mathbf{0} \\
\mathbf{Q}_i - \mathbf{q}_i(\mathbf{x}^i) &= \mathbf{0}
\end{aligned} \tag{2}$$

limit their freedom in the light of the decisions made by the others and, in the mathematical sense, guarantee the consistency with the original problem (1). The integration of the new variables \mathbf{P}_i and \mathbf{Q}_i and constraints (2) into (1) yields the following formulation

$$\begin{aligned}
& \min_{\substack{\mathbf{x}_i, \mathbf{x}^i, \mathbf{P}_i, \mathbf{Q}_i \\ i=1, \dots, N}} \begin{bmatrix} \vdots \\ \mathbf{f}_i(\mathbf{x}_i, \mathbf{p}_i(\mathbf{x}_i), \mathbf{Q}_i) \\ \vdots \end{bmatrix} \\
& \text{s.t. } \mathbf{x}_i \in X_i, \mathbf{x}^i \in X^i, \mathbf{P}_i \in Y_i, \mathbf{Q}_i \in Z_i \\
& \quad \mathbf{g}_i(\mathbf{x}_i, \mathbf{p}_i(\mathbf{x}_i), \mathbf{Q}_i) \leq \mathbf{0} \\
& \quad \mathbf{P}_i - \mathbf{p}_i(\mathbf{x}_i) = \mathbf{0} \\
& \quad \mathbf{Q}_i - \mathbf{q}_i(\mathbf{x}^i) = \mathbf{0} \\
& \quad i = 1, \dots, N
\end{aligned} \tag{3}$$

where $Y_i = \{\mathbf{p}_i(\mathbf{x}_i) : \mathbf{x}_i \in X_i\}$ and $Z_i = \{\mathbf{q}_i(\mathbf{x}^i) : \mathbf{x}^i \in X^i\}$, $i = 1, \dots, N$. Problem (3) is the starting point of the distribution procedure which includes three steps, scalarization, relaxation, and the actual decomposition into sub-problems. Note that this order cannot be changed since scalarization yields a single objective problem suitable for Lagrangian relaxation that makes the problem additively separable.

5. Decomposition of scalarized problems

5.1. Weighted-sum scalarization

The application of weighted-sum transforms problem (3) into a single-objective problem due to the introduction of positive weights, which in the spirit of MDO can be conveniently categorized into intra-subproblem weights \mathbf{w}_i that quantify the tradeoffs within each subproblem and the inter-subproblem weights b_i that balance the importance among the subproblems. The relaxation of the consistency constraints (2) in the single-objective problem yields

$$\begin{aligned}
& \min_{\substack{\mathbf{x}_i, \mathbf{x}^i, \mathbf{P}_i, \mathbf{Q}_i \\ i=1, \dots, N}} \sum_{i=1}^N b_i \mathbf{w}_i^T \mathbf{f}_i(\mathbf{x}_i, \mathbf{p}_i(\mathbf{x}_i), \mathbf{Q}_i) + \sum_{i=1}^N \mathbf{u}_i^T (\mathbf{P}_i - \mathbf{p}_i(\mathbf{x}_i)) + \sum_{i=1}^N \mathbf{v}_i^T (\mathbf{Q}_i - \mathbf{q}_i(\mathbf{x}^i)) \\
& \text{s.t. } \mathbf{x}_i \in X_i, \mathbf{x}^i \in X^i, \mathbf{P}_i \in Y_i, \mathbf{Q}_i \in Z_i \\
& \quad \mathbf{g}_i(\mathbf{x}_i, \mathbf{p}_i(\mathbf{x}_i), \mathbf{Q}_i) \leq \mathbf{0} \\
& \quad i = 1, \dots, N
\end{aligned} \tag{4}$$

which can be decomposed into N subproblems of the type

$$\begin{aligned} \min_{\mathbf{x}_i, \mathbf{Q}_i} & b_i \mathbf{w}_i^T \mathbf{f}_i(\mathbf{x}_i, \mathbf{p}_i(\mathbf{x}_i), \mathbf{Q}_i) - \mathbf{u}_i^T \mathbf{p}_i(\mathbf{x}_i) + \mathbf{v}_i^T \mathbf{Q}_i \\ \text{s.t.} & \mathbf{x}_i \in X_i, \mathbf{Q}_i \in Z_i \\ & \mathbf{g}_i(\mathbf{x}_i, \mathbf{p}_i(\mathbf{x}_i), \mathbf{Q}_i) \leq \mathbf{0} \end{aligned} \quad (5)$$

where $\mathbf{u}_i, \mathbf{v}_i, i = 1, \dots, N$, are the Lagrange multipliers associated with the relaxed constraints.

5.2. ε -constraint scalarization

When the ε -constraint method is applied, only one objective is optimized, arbitrarily, the s -th objective of the l -th subproblem. Tradeoffs are taken care of by bounding the remaining objectives that are placed in inequality constraints. The consistency constraints (2) are then relaxed to the optimized objective function giving the problem

$$\begin{aligned} \min_{\substack{\mathbf{x}_l, \mathbf{x}^l, \mathbf{P}_l, \mathbf{Q}_l \\ \mathbf{x}_i, \mathbf{x}^i, \mathbf{P}_i, \mathbf{Q}_i \\ i=1, \dots, N, i \neq l}} & f_l^s(\mathbf{x}_l, \mathbf{p}_l(\mathbf{x}_l), \mathbf{Q}_l) + \mathbf{u}_l^T (\mathbf{P}_l - \mathbf{p}_l(\mathbf{x}_l)) + \mathbf{v}_l^T (\mathbf{Q}_l - \mathbf{q}_l(\mathbf{x}^l)) + \\ & + \sum_{i=1, i \neq l}^N \mathbf{u}_i^T (\mathbf{P}_i - \mathbf{p}_i(\mathbf{x}_i)) + \sum_{i=1, i \neq l}^N \mathbf{v}_i^T (\mathbf{Q}_i - \mathbf{q}_i(\mathbf{x}^i)) \\ \text{s.t.} & \mathbf{x}_l \in X_l, \mathbf{x}^l \in X^l, \mathbf{P}_l \in Y_l, \mathbf{Q}_l \in Z_l \\ & \mathbf{x}_i \in X_i, \mathbf{x}^i \in X^i, \mathbf{P}_i \in Y_i, \mathbf{Q}_i \in Z_i \\ & f_l^r(\mathbf{x}_l, \mathbf{p}_l(\mathbf{x}_l), \mathbf{Q}_l) \leq \varepsilon_l^r, r \neq s \\ & \mathbf{f}_i(\mathbf{x}_i, \mathbf{p}_i(\mathbf{x}_i), \mathbf{Q}_i) \leq \varepsilon_i \\ & \mathbf{g}_l(\mathbf{x}_l, \mathbf{p}_l(\mathbf{x}_l), \mathbf{Q}_l) \leq \mathbf{0} \\ & \mathbf{g}_i(\mathbf{x}_i, \mathbf{p}_i(\mathbf{x}_i), \mathbf{Q}_i) \leq \mathbf{0} \\ & i = 1, \dots, N, i \neq l \end{aligned} \quad (6)$$

which is decomposable into a subproblem related to team l

$$\begin{aligned} \min_{\mathbf{x}_l, \mathbf{Q}_l} & f_l^s(\mathbf{x}_l, \mathbf{p}_l(\mathbf{x}_l), \mathbf{Q}_l) - \mathbf{u}_l^T \mathbf{p}_l(\mathbf{x}_l) + \mathbf{v}_l^T \mathbf{Q}_l \\ \text{s.t.} & \mathbf{x}_l \in X_l, \mathbf{Q}_l \in Z_l \\ & f_l^r(\mathbf{x}_l, \mathbf{p}_l(\mathbf{x}_l), \mathbf{Q}_l) \leq \varepsilon_l^r, r \neq s \\ & \mathbf{g}_l(\mathbf{x}_l, \mathbf{p}_l(\mathbf{x}_l), \mathbf{Q}_l) \leq \mathbf{0} \end{aligned} \quad (7a)$$

and a collection of $N - 1$ subproblems associated with the other teams $i = 1, \dots, N, i \neq l$

$$\begin{aligned} \min_{\mathbf{x}_i, \mathbf{Q}_i} & -\mathbf{u}_i^T \mathbf{p}_i(\mathbf{x}_i) + \mathbf{v}_i^T \mathbf{Q}_i \\ \text{s.t.} & \mathbf{x}_i \in X_i, \mathbf{Q}_i \in Z_i \\ & \mathbf{f}_i(\mathbf{x}_i, \mathbf{p}_i(\mathbf{x}_i), \mathbf{Q}_i) \leq \varepsilon_i \\ & \mathbf{g}_i(\mathbf{x}_i, \mathbf{p}_i(\mathbf{x}_i), \mathbf{Q}_i) \leq \mathbf{0} \end{aligned} \quad (7b)$$

5.3. Chebyshev-norm scalarization

To avoid nondifferentiability issues, the min-max formulation of the Chebyshev-norm method can be re-written by minimizing the upper bound α on the objective functions. To preserve the team independence, the auxiliary variable α must be copied and the consistency constraints of the type $\alpha - \alpha_i = 0, i = 1, \dots, N$, are introduced and relaxed along with consistency constraints (2), producing the following formulation

$$\begin{aligned} \min_{\substack{\alpha, \alpha_i \\ \mathbf{x}_i, \mathbf{x}^i, \mathbf{P}_i, \mathbf{Q}_i \\ i=1, \dots, N}} & \alpha + \sum_{i=1}^N m_i (\alpha - \alpha_i) + \sum_{i=1}^N \mathbf{u}_i^T (\mathbf{P}_i - \mathbf{p}_i(\mathbf{x}_i)) + \sum_{i=1}^N \mathbf{v}_i^T (\mathbf{Q}_i - \mathbf{q}_i(\mathbf{x}^i)) \\ \text{s.t.} & \mathbf{x}_i \in X_i, \mathbf{x}^i \in X^i, \mathbf{P}_i \in Y_i, \mathbf{Q}_i \in Z_i \\ & b_i \mathbf{w}_i^r f_i^r(\mathbf{x}_i, \mathbf{p}_i(\mathbf{x}_i), \mathbf{Q}_i) \leq \alpha_i \\ & \mathbf{g}_i(\mathbf{x}_i, \mathbf{p}_i(\mathbf{x}_i), \mathbf{Q}_i) \leq \mathbf{0} \\ & i = 1, \dots, N \end{aligned} \quad (8)$$

that decomposes into N subproblems for each design task, $i = 1, \dots, N$,

$$\begin{aligned}
& \min_{\alpha_i, \mathbf{x}_i, \mathbf{Q}_i} -m_i \alpha_i - \mathbf{u}_i^T \mathbf{p}_i(\mathbf{x}_i) + \mathbf{v}_i^T \mathbf{Q}_i \\
& \text{s.t. } \mathbf{x}_i \in X_i, \mathbf{Q}_i \in Z_i \\
& \quad b_i w_i^r f_i^r(\mathbf{x}_i, \mathbf{p}_i(\mathbf{x}_i), \mathbf{Q}_i) \leq \alpha_i \\
& \quad \mathbf{g}_i(\mathbf{x}_i, \mathbf{p}_i(\mathbf{x}_i), \mathbf{Q}_i) \leq \mathbf{0}
\end{aligned} \tag{9a}$$

and one additional subproblem for updating the value of the auxiliary variable α

$$\min_{\alpha} \alpha + \alpha \sum_{i=1}^N m_i \tag{9b}$$

where $m_i, i = 1, \dots, N$ are the Lagrange multipliers associated with the relaxed consistency constraint for α .

6. Numerical implementation of the coordination algorithm

The solution of the scalarized problems is obtained by an iterative procedure that is based on the duality theory. Under some mathematical conditions that are not discussed in this paper for sake of brevity (refer to [7, 9]), relaxed problems such as the ones presented in Section 5 can be solved with the following two-step iterative procedure:

1. In iteration t , solve the subproblems with respect to the so-called primal variables \mathbf{x}_i^t , \mathbf{Q}_i^t , \mathbf{x}^{it} , and \mathbf{P}_i^t (and α_i^t) for the fixed values of the Lagrange multipliers \mathbf{u}_i^t , \mathbf{v}_i^t (and m_i^t). In this step decomposition is exploited because the relaxed scalarized problems can be tackled by referring to subproblems, that can be independently undertaken by different teams.
2. Using the newly-computed values \mathbf{x}_i^t , \mathbf{Q}_i^t , \mathbf{x}^{it} , and \mathbf{P}_i^t , tune the multipliers (dual variables) for the dual function maximization using a subgradient update rule of the type $\mathbf{u}_i^{t+1} = \mathbf{u}_i^t + a_t (\mathbf{P}_i^t - \mathbf{p}_i(\mathbf{x}_i^t))$ (analogously for \mathbf{v}_i and m_i), where a_t is an appropriate scalar. This step represents the communication between the design teams.

These steps are iterated until convergence is reached, that is, the consistency is achieved within the desired tolerance, no objective function improvement is possible, or the maximum number of iterations is reached. Convergence issues may arise due to subproblem unboundedness specifically when subproblems do not have any objective but only constraints (only Lagrangian linear terms are then minimized). For this reason quadratic penalty terms of the type $\mu \|\mathbf{Q}_i - \bar{\mathbf{q}}_i\|_2^2$ and $\mu \|\bar{\mathbf{P}}_i - \mathbf{p}_i(\mathbf{x}_i)\|_2^2$ are added. Unbounded subproblem (9b) certainly requires the quadratic augmentation $\mu \sum_{i=1}^N (\alpha - \bar{\alpha}_i)^2$, which leads to the finite solution $\alpha^* = \frac{\sum_i \bar{\alpha}_i}{N} - \frac{(1 + \sum_i m_i)}{2\mu N}$.

This coordination algorithm has been implemented and demonstrated on an engineering problem in which the design of a suspension system for passenger vehicles is performed to optimize the ride comfort and the road holding while the team responsible for the spring design has to minimize its mass. The design team dedicated to the damper design does not have any specific objective to optimize but only design constraints to be satisfied. A representation of the problem is depicted in Fig. 1, in which the shared variables and the links between the subproblems are identified (refer to [9] for the detailed equations).

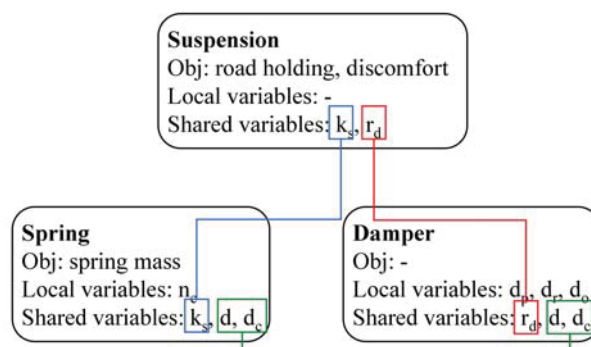


Figure 1: Model of the suspension system design problem

To verify the results of the numerical tests, the scalarized problems were solved using a centralized algorithm with different values of the scalarization parameters (weights and thresholds). The comparison showed good agreement

between the results obtained with the distributed and centralized algorithms, as depicted in Fig. 2, in which the results are shown for the weighted-sum scalarization (similar plots were obtained for the other two methods and are not reported here for sake of brevity).

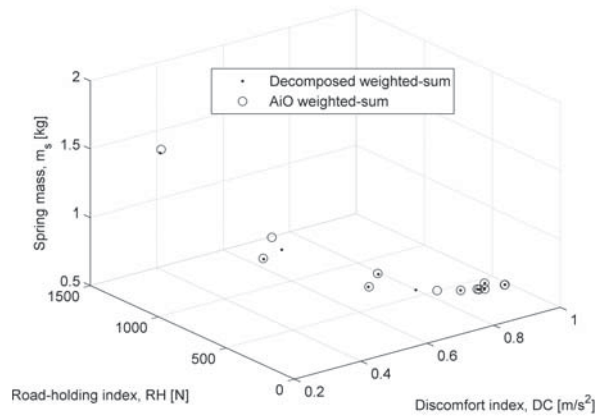


Figure 2: Pareto solutions computed with the weighted-sum method using the centralized (a.k.a., All in One, AiO) and the distributed formulations

7. Discussion

In multicriteria optimization, scalarization methods imply some sort of negotiation for setting the scalarization parameters, which allows for the computation of Pareto points as well as tradeoff exploration at those points. When these methods are applied to distributed multicriteria optimization, another layer of negotiation is added. In this paper, the distributed algorithm based on the relaxation models the communication among the design teams through the Lagrangian terms that balance the objective functions and the consistency constraints, and are intrinsically influenced by the scalarization parameters. The updating of the multipliers (and the penalty parameter in the case of quadratic augmentation), which requires the computation of new designs for each subproblem until convergence towards a (Pareto!) design that works for the whole system has been achieved, represents the inherent mechanism of negotiation in the distributed algorithm.

Relying on more advanced theory of vector-valued Lagrangian relaxation and multiobjective duality, the first layer of negotiation would be avoided, since the distributed algorithm would work on a sequence of solution sets that would be expected to converge to the Pareto set. Different formulations [12, 13] are available based on the way of relaxing the constraints over the vector of the objectives using matrices of Lagrangian multipliers U_i and V_i

$$\begin{aligned}
 \min_{\substack{\mathbf{x}_i, \mathbf{x}^i, \mathbf{P}_i, \mathbf{Q}_i \\ i=1, \dots, N}} & \begin{bmatrix} \vdots \\ \mathbf{f}_i(\mathbf{x}_i, \mathbf{p}_i(\mathbf{x}_i), \mathbf{Q}_i) \\ \vdots \end{bmatrix} + \sum_{i=1}^N U_i(\mathbf{P}_i - \mathbf{p}_i(\mathbf{x}_i)) + \sum_{i=1}^N V_i(\mathbf{Q}_i - \mathbf{q}_i(\mathbf{x}^i)) \\
 \text{s.t. } & \mathbf{x}_i \in X_i, \mathbf{x}^i \in X^i, \mathbf{P}_i \in Y_i, \mathbf{Q}_i \in Z_i \\
 & \mathbf{g}_i(\mathbf{x}_i, \mathbf{p}_i(\mathbf{x}_i), \mathbf{Q}_i) \leq \mathbf{0} \\
 & i = 1, \dots, N
 \end{aligned} \tag{10}$$

which may suggest additive separability of the type

$$\begin{aligned}
 \min_{\substack{\mathbf{x}_i, \mathbf{Q}_i \\ i=1, \dots, N}} & \sum_{i=1}^N \begin{bmatrix} \mathbf{0} \\ \mathbf{f}_i(\mathbf{x}_i, \mathbf{p}_i(\mathbf{x}_i), \mathbf{Q}_i) \\ \mathbf{0} \end{bmatrix} - U_i \mathbf{p}_i(\mathbf{x}_i) + V_i \mathbf{Q}_i \\
 \text{s.t. } & \mathbf{x}_i \in X_i, \mathbf{Q}_i \in Z_i \\
 & \mathbf{g}_i(\mathbf{x}_i, \mathbf{p}_i(\mathbf{x}_i), \mathbf{Q}_i) \leq \mathbf{0} \\
 & i = 1, \dots, N
 \end{aligned} \tag{11}$$

Although multiobjective duality theory has been investigated from a theoretical standpoint, it is not ready yet for practical applications and presents two research challenges in MDO. First, since Lagrangian matrix multipliers balance the objectives and the consistency constraints, they necessarily assume different values at each Pareto point

and hence result in a set of matrix multipliers U_i and V_i associated with the Pareto set; thus, a subgradient algorithm for dual vector problems is needed for tuning these matrices. Second, unlike the single-objective scenario in which $\min(\sum_i f_i) = \sum_i \min f_i$, the vector extension $\min(\sum_i \mathbf{f}_i) = \sum_i \min \mathbf{f}_i$ is not immediate because the optimal solutions are sets computed according to Pareto optimality; thus, a way to decompose (11) is required to build the Pareto set starting from the Pareto sets of subproblems (see [14] on the algebra of efficient sets) considering the associated sets of matrix multipliers.

8. Acknowledgements

P. Guarneri is sponsored by the European Commission under the DeMoTest-EV Marie Curie IAPP project, whose support is greatly appreciated. The views presented in this work do not necessarily represent the views of the European Commission, that is not liable for any use that may be made of the information contained herein.

M.M. Wiecek is supported by the National Science Foundation, grant number CMMI-1129969.

9. References

- [1] R. V. Tappeta and J. E. Renaud. Multiobjective collaborative optimization. *Journal of Mechanical Design*, 119(3):403–411, 1997.
- [2] C. H. Huang, J. Galuski, and C. L. Bloebaum. Multi-objective Pareto concurrent subspace optimization for multidisciplinary design. *AIAA Journal*, 45(8):1894–1906, 2007.
- [3] S. Gunawan, S. Azarm, J. Wu, and A. Boyars. Quality-assisted multi-objective multidisciplinary genetic algorithms. *AIAA Journal*, 41(9):1752–1762, 2003.
- [4] A. Khajavirad, J. J. Michalek, and T. W. Simpson. An efficient decomposed multiobjective genetic algorithm for solving the joint product platform selection and product family design problem with generalized commonality. *Structural and Multidisciplinary Optimization*, 39(2):187–201, 2009.
- [5] S. Parashar and C. L. Bloebaum. Multi-objective genetic algorithm concurrent subspace optimization (MO-GACSSO) for multidisciplinary design. In *47th AIAA/ASME/ASCE/AHS/ASC Structures, Structural Dynamics and Materials Conference*, Newport, RI, 2006.
- [6] H. M. Kim, N. F. Michelena, P. Y. Papalambros, and T. Jiang. Target cascading in optimal system design. *Journal of Mechanical Design*, 125:474–480, 2003.
- [7] J. B. Lassiter, M. M. Wiecek, and K. R. Andrighetti. Lagrangian coordination and analytical target cascading: Solving ATC-decomposed problems with lagrangian duality. *Optimization and Engineering*, 6(3):361–381, 2005.
- [8] S. Tosserams, M. Kokkolaras, L. F. P. Etman, and J. E. Rooda. A nonhierarchical formulation of analytical target cascading. *Journal of Mechanical Design*, 132(5):051002–051002–13, 2010.
- [9] P. Guarneri, J. T. Leverenz, M. M. Wiecek, and G. Fadel. Optimization of nonhierarchically decomposed problems. *Journal of Computational and Applied Mathematics*, 246:312–319, 2013.
- [10] N. Kang, M. Kokkolaras, and P. Y. Papalambros. Solving multiobjective optimization problems using quasi-separable MDO formulations and analytical target cascading. *Structural and Multidisciplinary Optimization*, 50(5):849–859, 2014.
- [11] B. Dandurand, P. Guarneri, G. M. Fadel, and M. M. Wiecek. Bilevel multiobjective packaging optimization for automotive design. *Structural and Multidisciplinary Optimization*, 50(4):663–682, 2014.
- [12] D. J. White. Vector maximisation and Lagrange multipliers. *Mathematical Programming*, 31(2):192–205, 1985.
- [13] K. Tarvainen. Duality theory for preferences in multiobjective decisionmaking. *Journal of Optimization Theory and Applications*, 88(1):237–245, 1996.
- [14] M. Gardenghi, T. Gómez, F. Miguel, and M. M. Wiecek. Algebra of efficient sets for multiobjective complex systems. *Journal of Optimization Theory and Applications*, 149(2):385–410, 2011.

Simulation Study on the Prediction of Dangerous Conditions for Occupant in a Running Vehicle Equipped with Airbag

Weigang ZHANG¹ Ding CHEN²

¹State Key Laboratory of Advanced Design and Manufacturing for Vehicle Body, Hunan University, Changsha, China,

zhangwg@hnu.edu.cn

²Hunan University, Changsha, China, 13787116236@163.com

Abstract: Generally, when a vehicle is equipped with an airbag, crash tests are conducted to check the performance of the airbag on certain defined conditions. Even if the performance of the airbag is perfect during the test, it may hurt vehicle occupant in reality traffic due to changed boundary conditions, such as the out-of-position occupant. This paper has built a simulation model for occupant and restraint system including an airbag by using MADYMO software, and conducted the crash simulation for a combination of different boundary conditions: different size dummies, different sitting positions, and different crash speed. According to the results of the MADYMO simulations, a metamodel was constructed and validated, through which all the dangerous conditions for vehicle occupant could be predicted by using NSGA-II genetic optimization algorithm. The results of this research will be useful in further intelligent airbag system development.

Keywords: Simulation Study, Prediction of Dangerous Conditions, Vehicle Occupant, Airbag, Metamodel

1. Introduction

Airbag is an important safety system for vehicle occupants when crash accident happens, and its protection effects have been widely approved^[1,2]. However, airbag can also be a potential dangerous object for occupants. Recently, occupant injury caused by airbag has happened frequently. For example, in a rear end collision accident which was not serious, a 10 years old child who sat in the front side seat was injured by the expanding airbag^[3]. That is to say, airbag is not absolutely safe. Then, it is necessary to know when the airbag is safe and when it is not^[4-6].

From laboratory tests and computer simulation^[7], it has been found that airbag's protection effect is affected by boundary conditions, such as vehicle crash speed, occupant size and sitting position, etc, that is to say, for a vehicle with very good crash test results, when it runs on road, it may not be safe for out-of-position occupant^[5]. Thus for a vehicle equipped with airbag, it is necessary to investigate the safe and unsafe conditions.

This paper established a vehicle's crash simulation model by using MADYMO software. In order to investigate the safe condition and unsafe condition, a series of simulations were conducted, based on which the metamodel was constructed and validated. By using NSGA-II genetic optimization algorithm^[8], Pareto solutions were obtained, which means that safe conditions and unsafe conditions were successfully predicted, which is useful for further intelligent restraint system development.

2. Methods

2.1 Establishing and Validating of Simulation Model

A car is taken as an investigation model. A MADYMO simulation model has established including the occupant compartment, restraint system and dummy. The restraint system includes seatbelt and airbag, and the dummy has three kinds of Hybrid III 50 percent male, 95 percent male, and 5 percent female^[9]. The established model is shown as Figure 1.

After the simulation model is established, it is necessary to validate the model. Full vehicle crash test data are used for the simulation model. B pillar acceleration curve, in the following Figure 2, is used for model input and the simulation results, such as the dummy’s head impact acceleration curve, chest acceleration curve and chest compression are utilized to compare with the test results.



Figure 1: Computer simulation model

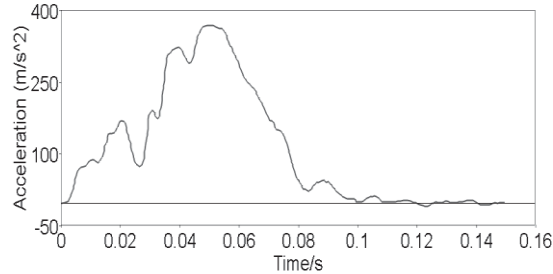


Figure 2: B pillar acceleration curve

The comparisons of simulation and test results are indicated in Figure 3, from which it can be seen that the curve shapes, peak values and the corresponding time are coincident, errors are within the range of 15%. Therefore, the established simulation model can be used to replace the real car for further study.

2.2 Boundary Conditions for Simulation

In this study, the seat fore-and-aft position, dip angle of seatback and vehicle running speed are chosen as the boundary elements, the values of the boundary conditions are listed in Table 1.

Table 1: Values of boundary conditions

condition	Lower limit	Upper limit
Seat position / mm	-180	+20
Dip angle of seatback/deg	-12	+12
Running speed/(km/h)	40	100

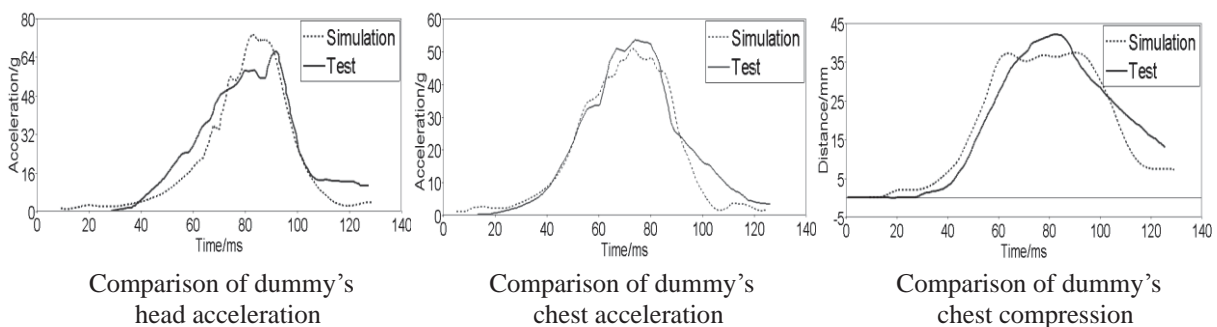


Figure 3: Comparison of model simulation and crash test

In Table 1, the values of seat position and seatback dip angle can be directly used as input data in the simulation model, while the values of running speed need to be transformed to a series of crash pulses in order to simulate collision in MADYMO^[10]. A small part of sample crash pulses are shown in Figure 4.

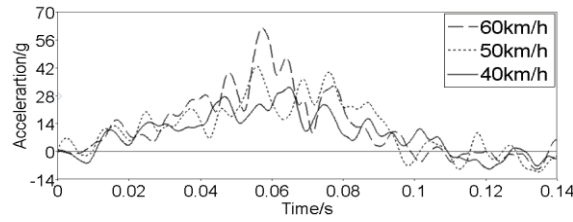


Figure 4: Simulated crash pulses

3. Metamodel

Since simulation model is incapable to predict all safe and unsafe conditions, metamodel is used to replace simulation model^[11-13]. In this paper, Kriging model and RBF model^[14] are constructed and the corresponding accuracies are compared, and RBF is proved to be the better one which used here to search for Pareto solutions.

However, static metamodel is difficult to get enough local accurate solution, thus, dynamic metamodel is proposed and constructed based on RBF model. The dynamic metamodel is used for the grey area which needs high accuracy^[15].

The method of constructing metamodel is as follows:

(1) After boundary conditions are defined, optimized Latin experimental design method is used to take samples, so that the studied parameters are divided uniformly, then the divided parameters are randomly combined, thus the whole design space can be described by using lesser samples. The least samples which are needed to construct metamodel is shown as Eq.(1):

$$N_1 = 2n + 1 \tag{1}$$

Where, N_1 is the least sample number, and n is the design parameter's number.

(2) After static metamodel is established, NSGA-II optimization algorithm is used to search for Pareto solutions and the boundary region. By updating the boundary region and grey area samples, metamodel is updated. The updated samples are defined as follows:

It is assumed that for the q times, sample space is shown as Eq.(2), Eq.(3), Eq.(4):

$$S_q^i = (S_q^{iL}, S_q^{iU}) \tag{2}$$

$$S_q^{iL} = x_{q-1}^{i*} - \frac{1}{N_{q-1}} L_{q-1} \tag{3}$$

$$S_q^{iU} = x_{q-1}^{i*} + \frac{1}{N_{q-1}} L_{q-1} \tag{4}$$

Where, S_q^{iL} is the lower limit of parameter i for the q times iteration, while S_q^{iU} is the upper limit; x_{q-1}^{i*} is the solution of parameter i for q-1 times iteration, and L_{q-1}^i is the design space of parameter i for q-1 times iteration.

(3) For each updated metamodel, validation is necessary. If the error is within 15%, then searching stops; if it is not, then searching continues until the model accuracy meets the requirement. The flow chart is shown as Figure 5.

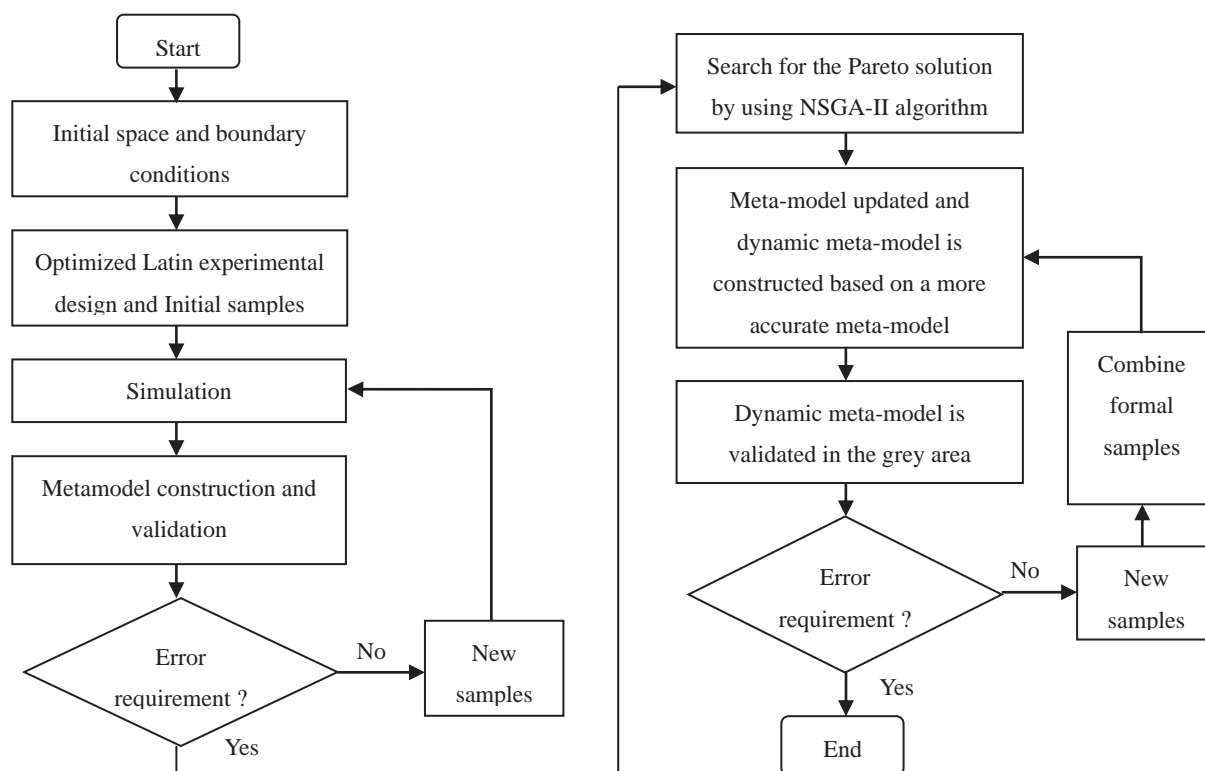


Figure 5: Flow chart of metamodel construction and solution

4. Prediction of Dangerous Conditions

Based on the constructed metamodel, dangerous conditions for the occupant in the running vehicle can be predicted. Head injury index ($HIC \leq 1000$), Chest 3ms acceleration value ($C_{3ms} \leq 60g$) and Chest compression ($D \leq 45mm$) are chosen for the evaluating indicator of risk of danger. If the injury values are within follows, then it is considered that the occupant is in safe condition, otherwise, it is dangerous.

As described above, first step, two static metamodels of Kriging and RBF are constructed. Then, metamodel updated. The accuracies of both static metamodel and dynamic metamodel are compared as shown in Table 2 and Table 3 respectively.

Table 2: Comparisons of static metamodel accuracies

Static Model	Kriging model			RBF model		
	HIC	C _{3ms}	D	HIC	C _{3ms}	D
Sample 1	10.59%	12.21%	0.71%	11.54%	5.72%	10.27%
Sample 2	14.13%	4.53%	0.43%	2.90%	2.21%	0.43%
Sample 3	12.37%	2.64%	14.51%	15.78%	9.11%	4.37%
Sample 4	21.91%	20.46%	4.43%	8.34%	8.13%	1.72%
Sample 5	9.33%	20.59%	3.50%	2.77%	3.26%	0.05%

Table 3: Comparisons of static metamodel and dynamic metamodel accuracies

Static Model	RBF model			Dynamic Model	RBF model		
	HIC	C _{3ms}	D		HIC	C _{3ms}	D
Sample 1	11.54%	5.72%	10.3%	Sample6	0.91%	1.2%	1.05%
Sample 2	2.90%	2.21%	0.43%	Sample7	3.24%	0.66%	0.68%
Sample 3	15.78%	9.11%	4.37%	Sample8	6.5%	2.42%	4.46%
Sample 4	8.34%	8.13%	1.72%	Sample9	4.66%	2.16%	2.28%
Sample 5	2.77%	3.26%	0.05%	Sample 10	5.91%	6.91%	0.86%

From Table 2 and Table 3, it can be seen that the local accuracy of dynamic metamodel is higher than that of static metamodel, RBF model is more accurate than Kriging model, and the dynamic metamodel gets high accuracy in grey area, therefore, RBF model is used for searching the Pareto solution.

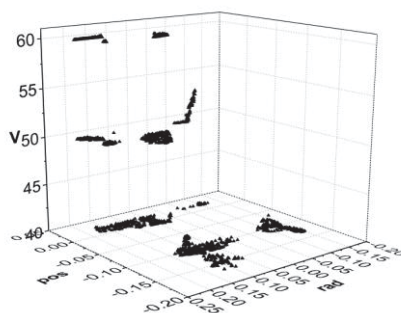


Figure 6: Pareto solution - Safe conditions

Figure 6 shows the Pareto solution, which means the shadow areas are the safe conditions. That is to say, for those areas that is out of the shadows, the occupant faces a high risk of danger if frontal crash happens.

From Figure 6, it can be seen that in most cases for the running vehicle, occupant will face a high risk of danger if frontal collision happens. Thus this study is important and meaningful for protecting occupant by warning based on the simulation data, and it can be sure that future intelligent restraint system is bound to have this function.

5. Conclusion

This paper conducted a study to predict dangerous conditions for occupant in a running vehicle by using computer simulation and metamodel techniques, the results can be a good reference for future further intelligent restraint system development.

6. Acknowledgements

This study is financially supported by National Nature Science Foundation of China, the project number is 51275164.

7. References

- [1] Crandall C S, Olson L M, Sklar D P. Mortality reduction with air bag and seat belt use in head-on passenger car collisions. *American journal of epidemiology*, 153(3): 219-224, 2001.
- [2] Iyota, Teru, and Toshihiro Ishikawa. The effect of occupant protection by controlling airbag and seatbelt. *Proceedings of the 18th International Technical Conference on the Enhanced Safety of Vehicles*, NHTSA, Nagoya, Japan. 2003.
- [3] Braver E R, Scerbo M, Kufera J A, et al. Deaths among drivers and right-front passengers in frontal collisions: redesigned air bags relative to first-generation air bags. *Traffic injury prevention*, 9(1): 48-58, 2008.
- [4] National Highway Traffic Safety Administration. Federal Motor Vehicle Safety Standards; Occupant Crash Protection. Washington, DC:National Highway Traffic Safety Administration, US Department of Transportation; 1997.
- [5] T. W. Kim and H. Y. Jeong, Stochastic analysis of the variation in injury numbers of automobile frontal crash tests, *Int. J. Autom. Technol.*, vol. 11, no. 4, pp. 481–488, Aug. 2010.
- [6] Yeh, Isheng, Brian Kachnowski, and Thiag Subbian. *An expert system for vehicle restraint system design*. No. 2005-01-1304. SAE Technical Paper, 2005.
- [7] Fu Yan, et al. *A multi-objective optimization and robustness assessment framework for passenger airbag shape design*. No. 2007-01-1505. SAE Technical Paper, 2007.
- [8] Deb, Kalyanmoy, et al. A fast elitist non-dominated sorting genetic algorithm for multi-objective optimization: NSGA-II. *Lecture notes in computer science*1917 (2000): 849-858.
- [9] Bai Z, Jiang B, Zhu F, et al. Optimizing the passenger air bag of an adaptive restraint system for multiple size occupants. *Traffic injury prevention*, 15(6): 556-563, 2014.
- [10] National Crash Analysis Center (NCAC). *Public finite element model archive*; 2001 <www.ncac.gwu.edu/archives/model/index.html>.
- [11] Seo Y D, Chung S H, Yoh J J. Automotive airbag inflator analysis using the measured properties of modern propellants. *Fuel*, 90(4): 1395-1401, 2011.
- [12] Abdel-Nasser Y A. Frontal crash simulation of vehicles against lighting columns using FEM. *Alexandria Engineering Journal*, 52(3): 295-299, 2013.
- [13] Teng T L, Chang F A, Liu Y S, et al. Analysis of dynamic response of vehicle occupant in frontal crash using multibody dynamics method. *Mathematical and Computer Modelling*, 48(11): 1724-1736, 2008.
- [14] Hou, S., Tan, W., Zheng, Y., Han, X., & Li, Q. Optimization design of corrugated beam guardrail based on RBF-MQ surrogate model and collision safety consideration. *Advances in Engineering Software*, 78, 28-40, 2014.
- [15] Peng, L., Liu, L., & Long, T. Optimization strategy using dynamic radial basis function metamodel. *Chinese Journal of Mechanical Engineering*, 47(7), 164-170, 2011.
- [16] ZHONG Zhihua, ZHANG Weigang. *Automobile collision safety technology*. Beijing:China Machine Press , 2003.

Dual-mode Operation of the Finger-type Manipulator Based on Distributed Actuation Mechanism

Jong Ho Kim¹, Young June Shin², Sung-Hwan Kim³, In Gwun Jang¹

¹ KAIST, Daejeon, Republic of Korea, jonghokim@kaist.ac.kr; igjang@kaist.edu

² Agency for Defense Development, Daejeon, Republic of Korea, yjshin@add.re.kr

³ Samsung Electronics, Suwon, Republic of Korea, murphy99@kaist.ac.kr

1. Abstract

Using the distributed actuation mechanism recently developed, this paper proposes the dual-mode operation of a finger-type manipulator that can switch between the force and velocity modes in order to achieve either the maximum force or the maximum velocity with the limited actuation power. The mathematical equations are derived for the fingertip force and velocity. Then, optimization scheme determines the maximum force and velocity that a finger-type manipulator can achieve at the given fingertip position along the given task direction. The numerical examples clearly demonstrate the effectiveness of the proposed dual-mode operation, which can enhance the operational efficiency of a manipulator in terms of velocity and/or force.

2. Keywords: dual-mode operation, distributed actuation mechanism, finger-type manipulator, design optimization, structural redundancy.

3. Introduction

For several decades, versatile manipulation systems have been applied to various fields such as military, service, and clinics. However, the performances of the state-of-the-art systems are not satisfactory because the performance of an actuator itself appears to be saturated (or slowly improve). A variety of researches have been investigated in order to provide an alternative solution for the current actuators, including the development of a new actuator such as artificial muscle [1]-[2], the enhancement of motor efficiency [3]-[4], and a new mechanism design [5]-[6]. They partially contribute to performance enhancement, but much remains to be improved.

In particular, the severe limitations in installation space and supplying power are an immense challenge to overcome in wearable robots. Considering that the actuating mechanism of a manipulator affects its system performance, the authors recently proposed the distributed actuation mechanism [7] that can provide additional degrees of freedom in actuation. The experiments validated the improvement of fingertip force through changing the posture angle and slider positions of the distributed actuation mechanism. Due to the increased complexity, however, more systematic approach is necessary to thoroughly analyse the distributed actuation mechanism.

This paper proposes the dual-mode operation of the distributed actuation mechanism in order to enhance the usability and efficiency during operation. The force and velocity of a finger-type manipulator were first derived in terms of control parameters (i.e. one posture angle, three slider positions, and three thrusting parameters). Then, design optimization for maximizing fingertip force and velocity determined the force and velocity modes, respectively, of the finger-type manipulator. Furthermore, the force and velocity octagons were obtained in order to effectively represent the allowable force and velocity, respectively, along the eight task directions at the given fingertip position. Based on these quantitative information, the appropriate trajectory and corresponding actuation control can be determined for the given tasks. Thus, the dual-mode distributed actuation mechanism can provide more efficient operation.

4. Mathematical Derivation of Dual-mode Distributed Actuation Mechanism

In [7], the distributed actuation mechanism, which is a multi-linked mechanism with sliding actuation, was proposed in order to implement the spatially distributed actuation of muscles, as illustrated in Figure 1. It was proven that this mechanism can provide a range of fingertip forces through relocating the slider positions at the given fingertip position. The goal of this paper is to propose the dual-mode operation of the distributed actuation mechanism for more efficient operation through maximizing either fingertip force or velocity.

In this section, mathematical equations for fingertip force and velocity were derived with the notations as follows:

l_j : length of the link j

c_j : length of the connecting rod at the joint j

θ_j : joint angle at the joint j

h : slider hinge offset

x_j and x_{hj} : positions of the front and back sliders at the joint j , respectively

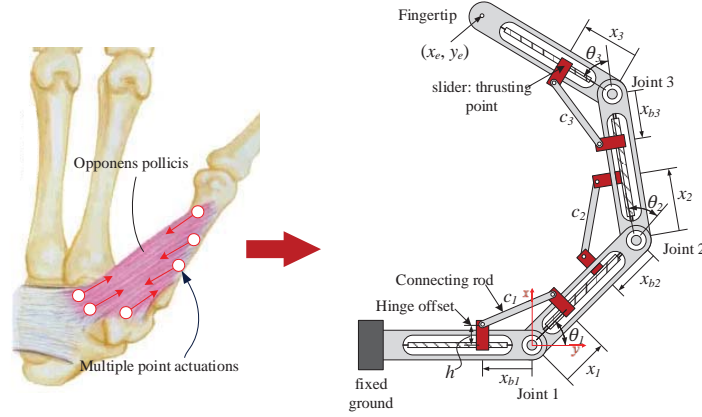


Figure 1: Concept of a distributed actuation mechanism for a robot finger using a sliding actuation [7]

4.1. Derivation of Fingertip Velocity

As illustrated in Figure 1, a robot finger with distributed actuation mechanism can be considered as a three-link planar manipulator, in which the fingertip at (x_e, y_e) has the generalized planar velocity, $\mathbf{v}_e = [x_e \quad y_e \quad \theta_e]^T$. At the fingertip position, θ_2 and θ_3 can be expressed in terms of θ_1 using the inverse kinematics. Figure 2 presents the trigonometric relationship of each joint as follows:

$$c_j^2 = x_j'^2 + x_{bj}'^2 + 2x_j'x_{bj}' \cos \theta_j \quad (1)$$

where $x_j' = x_j - h \tan(\theta_j/2)$ and $x_{bj}' = x_{bj} - h \tan(\theta_j/2)$. Through differentiating Eq. (1) with respect to time, the joint angular velocity was derived as follows:

$$\theta_j = \frac{\left(x_{bj} - h \tan \frac{\theta_j}{2}\right) \left(x_j \cos \theta_j + x_{bj}\right) + \left(x_j - h \tan \frac{\theta_j}{2}\right) \left(x_j + x_{bj} \cos \theta_j\right)}{\sin \theta_j \left(x_j - h \tan \frac{\theta_j}{2}\right) \left(x_{bj} - h \tan \frac{\theta_j}{2}\right) + \frac{1}{2} h \sec^2 \frac{\theta_j}{2} \left(1 + \cos \theta_j\right) \left\{ \left(x_j - h \tan \frac{\theta_j}{2}\right) + \left(x_{bj} - h \tan \frac{\theta_j}{2}\right) \right\}} \quad (2)$$

where $x_{bj} = \sqrt{c_j^2 - \left\{ \left(x_j - h \tan \frac{\theta_j}{2}\right) \sin \theta_j \right\}^2} - \left(x_j - h \tan \frac{\theta_j}{2}\right) \cos \theta_j + h \tan \frac{\theta_j}{2}$. Then, the fingertip velocity was determined through the differential kinematics as follows:

$$\mathbf{v}_e = \mathbf{J}(\boldsymbol{\theta})\boldsymbol{\theta} \quad (3)$$

where $\mathbf{J}(\boldsymbol{\theta})$ is a 3×3 Jacobian matrix.

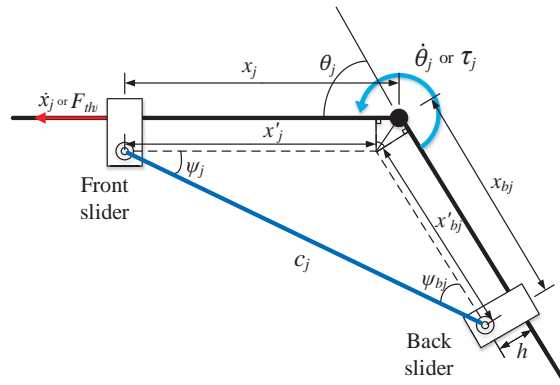


Figure 2: Schematic diagram of the joint j

4.2. Derivation of Fingertip Force

In order to derive the fingertip force of a kinematically redundant manipulator, the additional rotational degrees of freedom at the fingertip were provided as follows:

$$\mathbf{x}_e = [x_e \quad y_e \quad \theta_e]^T \text{ and } \mathbf{F}_e = [F_x \quad F_y \quad M_z]^T. \quad (4)$$

Through the procedure explained in [7], the joint torque was derived as follows:

$$\tau_j = F_{thj} \frac{x_j \tan \psi_j + h}{1 + \mu_j \tan \psi_j} \quad (5)$$

where $\psi_j = \cos^{-1} \left(c_j^2 + \left(x_j - h \tan \frac{\theta_j}{2} \right)^2 - \left(x_{bj} - h \tan \frac{\theta_j}{2} \right)^2 \right) / 2c_j \left(x_j - h \tan \frac{\theta_j}{2} \right)$; F_{thj} and μ_j are the thrusting force and the Coulomb friction coefficient at the joint j . Based on the static force equilibrium, the fingertip force was derived as follows:

$$\mathbf{F}_e = \mathbf{J}^{-T}(\boldsymbol{\theta}) \boldsymbol{\tau} \quad (6)$$

where $\mathbf{J}^T(\boldsymbol{\theta})$ means a transposed matrix of the inverse Jacobian.

6. Numerical Simulation for Dual-mode Distributed Actuation Mechanism

6.1. Optimization for the maximum fingertip force and velocity

To determine the maximum fingertip force and velocity, optimization formulations were expressed as follows:

1) Force mode

$$\begin{aligned} \text{Maximize} \quad & F_{d_j}(\theta_1, x_i, F_{thi}) = \mathbf{F}_e \cdot \mathbf{d}_j \quad i = 1, 2, 3; j = 1, \dots, 8 \\ \text{subject to} \quad & \theta_1^{(l)} \leq \theta_1 \leq \theta_1^{(u)} \\ & x_i^{(l)} \leq x_i \leq x_i^{(u)} \quad i = 1, 2, 3 \\ & -F_{thi}^{(u)} \leq F_{thi} \leq F_{thi}^{(u)} \quad i = 1, 2, 3 \\ & M_z \cdot \theta_e \geq 0 \\ & F_x \cdot x_e + F_y \cdot y_e \geq 0 \end{aligned} \quad (7)$$

2) Velocity mode

$$\begin{aligned} \text{Maximize} \quad & v_{d_j}(\theta_1, \dot{x}_i, \dot{x}_i) = \mathbf{v}_e \cdot \mathbf{d}_j \quad i = 1, 2, 3; j = 1, \dots, 8 \\ \text{subject to} \quad & \theta_1^{(l)} \leq \theta_1 \leq \theta_1^{(u)} \\ & \dot{x}_i^{(l)} \leq \dot{x}_i \leq \dot{x}_i^{(u)} \quad i = 1, 2, 3 \\ & -\dot{x}_i^{(u)} \leq \dot{x}_i \leq \dot{x}_i^{(u)} \quad i = 1, 2, 3 \\ & M_z \cdot \theta_e \geq 0 \\ & F_x \cdot x_e + F_y \cdot y_e \geq 0 \end{aligned} \quad (8)$$

where \mathbf{d}_j denotes a unit vector which forms a vertex of a regular octagon centered at the origin; F_{thi} and \dot{x}_i represent the thrusting force and velocity of a slider at the joint i , respectively. Design variables are one posture angle (θ_1), three slider positions (x_j), and three thrusting parameters (F_{thi} for the force mode or \dot{x}_i for the velocity mode). The lower and upper bounds for θ_1 were set to avoid the singular postures between 20° and 90° . The lower and upper bounds for x_i , \dot{x}_i , F_{thi} , and x_{bi} were also set considering the geometrical and physical limitations. Note that the lower bounds of thrusting force and velocity were set to be negative values of their upper bounds in order to represent movements in the opposite direction. Constraints for positive rotational and translational power at the fingertip were implemented to obtain physically meaningful results. Through the optimization formulated in Eqs. (7) and (8), the maximum fingertip force and velocity along the eight task directions (\mathbf{d}_j , $j=1, \dots, 8$) were determined. Design parameters used in optimization were listed in Table 1.

Table 1: Design parameters for the distributed actuation mechanism

	Joint 1	Joint 2	Joint 3
Link length [mm]	$l_1=114$	$l_2=114$	$l_3=109.6$
Connecting rod [mm]	$c_1=80$	$c_2=80$	$c_3=80$
Friction coefficient	$\mu_1=0$	$\mu_2=0$	$\mu_3=0$
Hinge offset [mm]	15.5		
Max. motor torque [gf·cm]	780		
Max. motor speed [rpm]	39		
Max. motor power [mW]	30.7		

Specifications for actuation were based on the electric motor, PGM12-1230E(3V), whose gear ratio is 1/256. Figure 3 depicts the workspace of a robot finger (grey area enclosed by black lines) and eight fingertip positions (red circles with their own numbers) to be analysed. The origin of the graph represents the base of a robot finger. In order to solve Eqs. (7) and (8), sequential quadratic programming method in MATLAB fmincon was used.

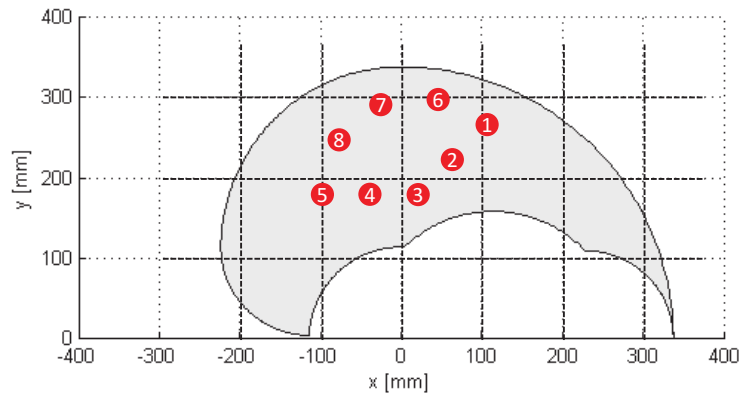


Figure 3: Target fingertip positions in workspace

6.2. Optimization results and discussion

To demonstrate the effectiveness of the proposed dual-mode operation, the maximum velocity and force were obtained. For Position 8 along the negative x direction, for example, the optimized posture angles and slider positions were illustrated as blue lines and green squares, respectively, for the force mode; red lines and orange squares for the velocity mode (Figure 4). Table 2 demonstrates that the difference of the control parameters between the force and velocity modes affects the performance at the same fingertip position.

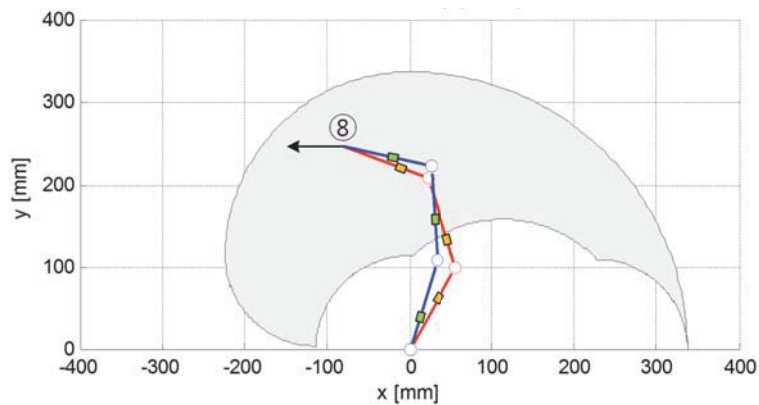


Figure 4: Optimized posture angle and slider positions for Position 8 (blue lines for the force mode and red lines for the velocity mode)

Table 2: Optimization results for Position 8 along the negative x direction

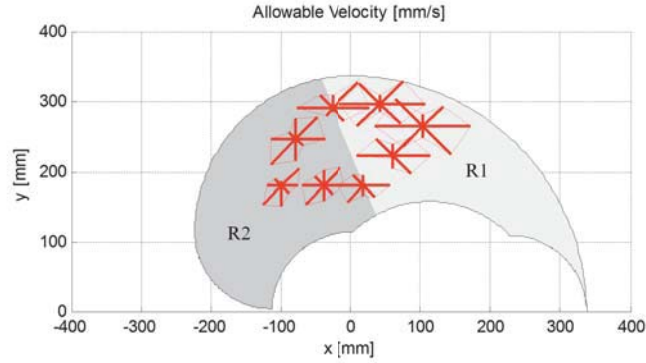
	θ_1 [°]	x_1 [mm]	x_2 [mm]	x_3 [mm]	Force	Velocity
Force mode	73.03	42.07	49.68	43.76	16.18 [N]	1.26 [mm/s]
Velocity mode	60.90	71.75	37.00	66.86	0.26 [N]	4.52 [mm/s]

As depicted in Figure 5, the velocity and force octagons (red-dotted lines and blue-dotted lines, respectively) represent the approximate, allowable values at the given fingertip position. Information on force and velocity octagons can be utilized in order to plan the optimal trajectory of a manipulator in the workspace. All the corresponding control parameters for operation can be obtained from the optimization. For example, suppose that a certain task starts at Position 1 and ends at Position 5. The task is also required to provide a fast motion in Region R1 and to generate a large force in Region R2. Then, the system performance during operation significantly depends on the trajectory as follows:

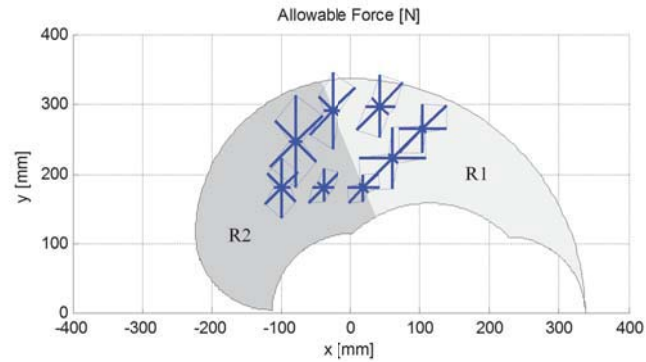
- 1) Path 1-6-7-8-5
Fast motion and large force are available in R1 and R2, respectively.
- 2) Path 1-2-3-4-5

Slower motion in R1 and smaller force in R2 are achieved although the maximum thrusting force and velocity of sliders are identical.

Table 3 indicates that the maximum value even at the same fingertip position significantly varies depending on the task direction (specifically, ranging from 2.61 to 8.22 for force or from 2.04 to 11.54 for velocity). Thus, more efficient operation will be possible for the given task if the trajectory and corresponding control parameters are appropriately determined.



(a) Velocity octagon



(b) Force octagon

Figure 5: Allowable velocity and force at various fingertip positions in workspace

Table 3: Summary of optimization results for dual-mode operation

	Point 1	Point 2	Point 3	Point 4
F_{max}/F_{min}	$F_{d6}/F_{d8}=8.22$	$F_{d6}/F_{d8}=7.56$	$F_{d6}/F_{d8}=3.28$	$F_{d6}/F_{d8}=2.61$
V_{max}/V_{min}	$V_{d5}/V_{d7}=4.11$	$V_{d5}/V_{d6}=11.54$	$V_{d5}/V_{d2}=9.51$	$V_{d6}/V_{d8}=2.04$
	Point 5	Point 6	Point 7	Point 8
F_{max}/F_{min}	$F_{d7}/F_{d1}=3.80$	$F_{d6}/F_{d8}=2.77$	$F_{d7}/F_{d8}=4.90$	$F_{d7}/F_{d1}=6.85$
V_{max}/V_{min}	$V_{d6}/V_{d3}=6.86$	$V_{d1}/V_{d3}=5.66$	$V_{d1}/V_{d7}=9.26$	$V_{d6}/V_{d8}=3.66$

7. Conclusion

In this paper, the dual-mode distributed actuation mechanism was proposed for the efficient operation of a finger-type manipulator. Through mathematically deriving fingertip force and velocity, and maximizing them, it was proven that the proposed dual-mode operation provides a mechanical duality which maximizes either a fingertip force or velocity of the manipulator, depending on the task. Numerical results discovered the force and velocity octagons that represent allowable force and velocity along the eight task directions at the given fingertip position in workspace. These information would be vital to optimally design a task-oriented trajectory, thus expending the proposed concept to the real-world robotic manipulators for delicate tasks. Future work will focus on the experimental validation of the proposed dual-mode mechanism.

8. References

- [1] J. D. W. Madden, N. A. Vandesteeg, P. A. Anquetil, P. G. A. Madden, A. Takshi, R. Z. Pytel, S. R. Lafontai

- ne, P. A. Wieringa, and I. W. Hunter, Artificial Muscle Technology: Physical Principles and Naval Prospects, *IEEE Journal of Oceanic Engineering*, 29 (3), 706-728, 2004.
- [2] S. Alfayada, F. B. Ouezdoua, F. Namounb, and G. Ghengc, High performance integrated electro-hydraulic actuator for robotics – Part I: Principle, prototype design and first experiments, *Sensors and Actuators A: Physical* 169 (1), 115– 123, 2011.
- [3] S. Seok, A. Wang, D. Otten, and S. Kim, Actuator Design for High Force Proprioceptive Control in Fast Legged Locomotion, in *Proceeding of IEEE/RSJ International Conference on Intelligent Robots and Systems*, 1970-1975, 2012.
- [4] J. Urata, T. Hirose, Y. Namiki, Y. Nakanishi, I. Mizuuchi and M. Inaba, Thermal Control of Electrical Motors for High-Power Humanoid Robots, in *Proceeding of IEEE/RSJ International Conference on Intelligent Robots and Systems*, 2047-2052, 2008.
- [5] T. Takaki and T. Omata, High-performance anthropomorphic robot hand with grasping-force-magnification mechanism, *IEEE/ASME Transactions on Mechatronics*, 16 (3), 583–591, 2011.
- [6] Y. J. Shin, H. J. Lee, K.-S. Kim, and S. Kim, A Robot Finger Design Using a Dual-Mode Twisting Mechanism to Achieve High-Speed Motion and Large Grasping Force, *IEEE Transactions on Robotics*, 28 (6), 1398-1405, 2012.
- [7] Y. J. Shin and K.-S. Kim, Distributed actuation mechanism for a finger-type manipulator: Theory and experiments, *IEEE Transactions on Robotics*, 26 (3), 569–575, 2010.

Data based materials numerical modelling for FPSO safety and reliability optimization**Robert E Melchers¹, Andrew E. Potts²**¹ The University of Newcastle, Australia, rob.melchers@newcastle.edu.au² AMOG Consulting, Melbourne, Australia & Houston, TX, USA, andrew_potts@amogconsulting.com**Abstract**

Adequate modelling of material behaviour is required for the optimal operation and structural-environmental system safety and reliability of complex structural-mechanical systems. Herein floating production storage and offloading (FPSO) vessels are considered. These are used for offshore oil and gas exploration and exploitation activities. Critical components are the mooring lines, usually 8-12 per vessel. Typically they consist of a wire (or non-metallic) rope (some 100mm diam.) with steel chains at the upper (FPSO) end and on the seafloor. They are meant to keep an FPSO 'on-station' within close limits. Failure may result in rupture of oil production pipelines (risers) with possibly extreme environmental effects and high costs to operators and to industry. Recently the industry has funded ground-breaking research to improve understanding of the fatigue, wear and corrosion particularly of the upper chains. The present paper outlines the new mathematical-probabilistic models developed for prediction of chain corrosion and pitting, using data collected by the industry world-wide and in a set of major field research projects in Australia. Both forms of corrosion are functions of seawater temperature and local seawater pollution. The unique full-scale experimental work for the wear of full-scale chain links is outlined together with the on-going development of numerical models that will ultimately include associated finite element modelling. The outcomes provide much improved basic knowledge, and numerical and probabilistic modelling to permit improved optimisation of FPSO operations and overall risk management.

Keywords: Materials, safety, reliability, modelling, optimization.

1. Introduction

Floating Production Storage and Offloading (FPSO) vessels increasingly are being used for oil and gas related operations offshore and in particular in deeper waters, currently up to 3 km deep. The FPSOs are moored on-station using a set of mooring lines consisting, for various operational conditions, at the upper end of chain, then wire or non-metallic rope and, at the base more chain (Fig. 1). The reliability of this system is crucial as failure can incur rupture of risers and subsequent environmental and other damage [1]. Field inspection of the system is difficult, costly and generally unreliable owing to the harsh operational conditions prevalent in most operational areas. Early design and operational protocols were based on cold-water North Sea experience. This is reflected in most current requirements defined by Classification Societies [1]. These offer design guidance usually in terms of expected life in years, mainly for uniform corrosion loss, with a nominal allowance for wear, but offer little guidance about the separate effects of corrosion and wear and of the influences of climatic, environmental and operational conditions. As oil and gas exploration and exploitation increasingly has moved to warmer waters in tropical climates, such as in West Africa and the Timor Sea it has become evident, including from field observations, that improved material characterization is required for robust prediction of likely safe life and thus of optimal operational protocols including timely mooring replacement. This paper gives an overview of recent efforts in that direction, using field full-scale laboratory observations over extended time periods and built on analytical tools for corrosion and wear.

2. Optimal structural reliability

The lifetime reliability of any system can be represented by the development with time of the stochastic loading $Q(t)$ acting on the system and the (deteriorating, monotonically decreasing) random variable capacity $R(t)$ of the system (Fig. 2). For known time dependency of $R(t)$ and with $Q(t)$ also known from local climatic information, the probability of failure at any time t as given by [2]:

$$p_f|t = \iint_{D_f} f_Q(x) \cdot f_R(x) dx \quad (1)$$

where $f_Q(x)|t$ is the (conditional) probability density function for the load Q and similarly for R at t . As conventional, D_f represents the failure domain defined by the performance function (or Limit State function) $G(\mathbf{X}) = G(R, Q) = R - Q < 0$. Each mooring line composed of a chain of many links and also of wire rope is a classic 'series' system – one for which failure of any one (or more) components means failure of the overall

system. It is therefore sufficient to consider only the simplest problem given by Eq. 1, without entering into ‘systems’ reliability considerations [2]. For the collection of mooring lines industry practice will not tolerate failure of more than one and thus the corresponding probability of a second mooring line failure given that one has occurred need not, to a first approximation, be considered.

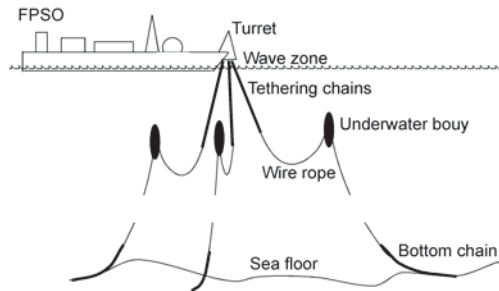


Figure 1: Schematic view of FPSO mooring system [3].

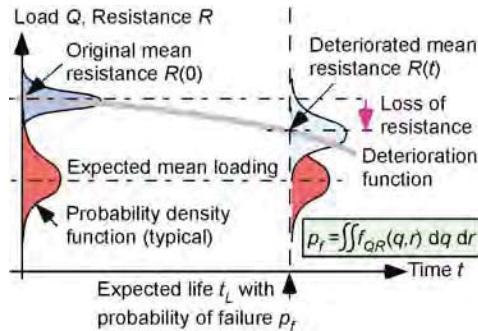


Figure 2: Development of structural deterioration with time, and the probability density functions for capacity and loading [3].

For an individual mooring line subject to corrosion the limit state function $G(\cdot)$ is a function of time:

$$G(\mathbf{X}, t) = R(t) - Q(t) < 0 = [A - a_p(t)] - Q(t) < 0 = [A - K(c(t))] - Q(t) < 0 \quad (2)$$

where A is the cross-sectional area of the chain link or rope and a_p the area loss of the cross-section caused by corrosion $c(t)$ and $K(\cdot)$ is the functional relationship between $a_p(t)$ and $c(t)$. It is clear that $c(t)$ is crucial to estimating the probability of failure at any time t .

Although it is common in the engineering literature to assume a constant ‘corrosion rate’ there is now much evidence that this is a misleading concept. The functional form for $c(t)$ is highly nonlinear, particularly in the earlier years of exposure, as shown in Fig. 3 for general corrosion loss as a function of exposure time [4]. The parameters that describe this form have been determined for clean coastal seawaters as a function mainly of water temperature but also other parameters and, more recently, also for the influence of water pollution. The main effect of water pollution is on microbiologically influenced corrosion (MIC) resulting from the involvement of bacteria on the corrosion processes [5]. For long-term corrosion the effect is shown schematically in Fig. 3. It is clear that the assumption of a corrosion rate, that is a linear function passing through the origin, is a very poor approximation for the actual development of corrosion with time and hence for optimization decisions based on it. The determination of the actual corrosion behavior at a particular operational offshore site is therefore critical to making optimal reliability-based decisions.

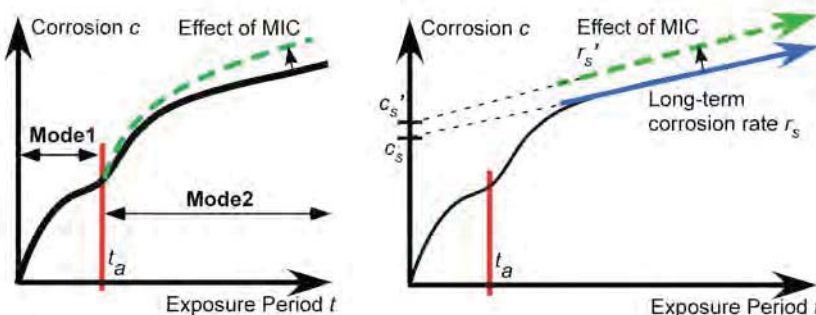


Figure 3: Typical bi-modal loss function for immersion corrosion in temperate waters, showing (some) model parameters and also idealized long-term trend and the effect of MIC [4, 5].



Figure 4: Field recovered chain links (76mm diam.) after surface cleaning showing highly varied local corrosion.

3. Field observations of mooring chain corrosion

Field experience in some geographical operational areas had shown that in some cases the mooring chains were found, during routine inspection, to show corrosion more severe than expected based on early, mainly North Sea, experience. In particular, in some cases of severe pitting corrosion were observed on mooring chain, with deep, elliptical pits of very considerable size on some chain links in the near-submerged splash zone (Fig. 4). It was

thought this could be caused by higher water temperatures. As a result, a joint industry project (SCORCH: seawater corrosion of rope and chain) was established to investigate the corrosion rates of mooring chains (and wire rope) in tropical waters. This was an unprecedented cooperative effort between most of the leading oil and gas producers (the so-called ‘majors’), contractors and materials suppliers.

The SCORCH JIP developed a data-base of worldwide corrosion measurements from in-service and retired mooring chain and wire rope from 18 FPSOs for chain and 13 FPSOs for wire rope from warm waters off South-East Asia, West Africa, the Gulf of Mexico, Brazil and the North West Shelf of Australia (Fig. 5) [6, 7]. Sample chain links taken from many of the chains recovered from industry operations were subjected to photogrammetric measurement, from which computer 3D images of chain links were constructed (Fig. 6). This allowed computer meshing, statistical analysis of the corroded surface and relatively simple estimation of maximum pit depth and also of pit size [7].



Figure 5: Locations of controlled tests or literature/in-kind data sites (★) and operational field data sites (★) [7].



Figure 6: Computer model of chain link constructed from photogrammetric data [7].

As shown in Figs. 4 and 6, the most severe corrosion was found, repeatedly, to be pitting corrosion, for example some 10-15 mm in depth and often 100-200mm or more in size after 7-8 years seawater exposure. In most cases the most severe corrosion occurred in the region around and just below the still water level. Such severe pitting was not observed in all cases. Where severe pitting corrosion was observed there was also evidence of black corrosion deposits within the pitted areas and strong hydrogen sulphide and other odours. Taken together, this suggests, but does not prove, the involvement of microbiologically influenced corrosion [8]. To investigate this possibility, water quality analyses were undertaken in the immediate vicinity of the chains showing severe pitting. This showed a high degree of correlation with the concentration of dissolved inorganic nitrogen (DIN) in the seawater and that has been strongly linked with MIC of steel in seawater [5]. This allowed estimation of the increase in long-term corrosion (cf. Fig. 3). It is noted that normal, natural, unpolluted ocean seawater has negligible DIN. Usually elevated DIN can be attributed to anthropological or industrial pollution, including that from oil drilling and recovery operations [9].

The observation that the most critical corrosion for chain links is that of pitting, permits simplification of the limit state function (Eq. 2) to represent the probability of the deepest pit $y(t)$ penetrating a given distance (d) into the chain link (or a wire rope):

$$p_f = P[G(\mathbf{X}) < 0] = P[d - y(t) < 0] \quad (3)$$

As visually evident from Fig. 6 and as also noted below, there is much variability in the maximum pit depth observed relative to all the other parameters involved, and this suggests that in addition to conventional reliability analysis the results also can be represented through application of Extreme Value theory. This is described in the next section.

For optimization, the key issue is the determination of the maximum acceptable probability of failure within an overall expected cost or expected cost-benefit analysis. Eqs. (1-3) provide the tools to determine the relationship between acceptable depth of pit penetration d and the corresponding probability of mooring line (and hence system) failure. This also will involve the probability of failure in axial tension for a given depth of pitting.

4. Site and laboratory corrosion tests

In addition to the examination of actual chains recovered from operations, a large series of controlled field tests was conducted over 3.5 years at selected sites around Australia. This program comprised some 388 chain coupon and chain link tests (and also 373 wire and wire rope tests), designed specifically to investigate the impact of sea temperature, depth, water velocity, oxygenation and steel grade. Also, laboratory tests were conducted to assess the effect of MIC, and the combined effect of corrosion and wear, of full-sized mooring chains. The details have

been described elsewhere [6, 7]. The results showed mainly uniform or general corrosion rather than pitting. The average corrosion rates for uniform corrosion were much lower than those for pitting, consistent with what has been found elsewhere.

These results added rigor to the field test results and confirmed that steel composition, location on a link and at the weld zone did not cause significant variations. The results also confirmed that corrosion of chains showed the bi-modal model characteristic (Fig. 3) and were consistent with the effect of seawater temperature, seawater oxygen content, water particle velocity, splash zone action and tidal zone wetting, all as expected from earlier work [4]. This is important as it indicates that other research results, for various steels, can be applied also for steel chains.

5. Extreme value analysis of corrosion pitting

For estimating the reliability of systems in which one random variable predominates, an extreme value analysis can be both useful and illustrative. There is a long history of applying it to pit depth data [10]. Usually, for pit depth, the so-called Gumbel extreme value distribution for the maximum pit depth measured on multiple areas or samples is used. The usual approach is to plot the pit depth data on a Gumbel plot [11]. It consists of one axis showing the reduced variate w that represents the cumulative probability, more formally given by the function $\phi(y_i)$, defining the probability that pit depth $y < y_i$ where y_i is a given value. If the data is truly Gumbel, a straight best-fit line can be constructed through the data. Typical pit depth data (85 pit depths across 25 chain links) are shown on the Gumbel plot in Fig. 7. It is evident immediately that the collected data does not all fit a straight line - only some of it does, as shown. In fact the deepest pits, those of most practical interest, are shown at the upper right and clearly do not fit the linear trend (or indeed any linear trend). This suggests strongly that they are part of a statistical population, with, most likely, a different probability distribution [2]. In turn this implies that the mechanism causing pitting is different in some way, a point noted earlier in a more general context [12]. In the present case it can be shown that this subset is more consistent with the Frechet extreme value distribution, as also found for other cases reported for a variety of exposure conditions [12]. The implication of this observation is that the random variable representation for pit depth y in Eq. (3) must be more complex than a simple random variable and must distinguish between deeper pits and shallower pits. This distinction has only recently been recognized [12] and the necessity to do so in reliability analysis has not been proposed previously.

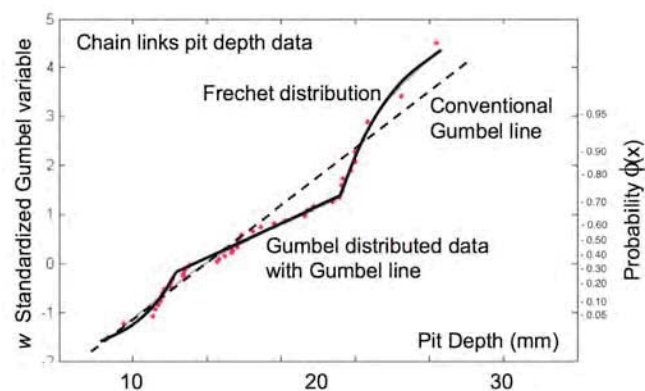


Figure 7: Gumbel extreme value plot showing typical data for pit depth. Data from [6].

6. Wear of mooring chains

Wear of mooring chains can, under certain circumstances, be the primary mechanism of degradation and potentially failure. The current level of codification regarding the analysis of wear on anchor chains is rudimentary [6, 7]. It uses an average annual loss of metal due to both corrosion and wear, without discrimination, and is based on empirical data and engineering experience. There is an extensive body of research for wear as caused by dry sliding and rolling contact [13], confined mainly to 'pin-on-disk' tests, but there is almost no information about the wear of chains in sea water.

It is known that wear can be the result of a number of different processes that can take place by themselves or in combination. Material is removed from the surfaces in contact through a complex combination of local shearing, ploughing, gouging, welding, tearing, and others [14]. Other major subcategories of wear include adhesive, abrasive, corrosive, surface fatigue, and deformation wear, as well as fretting, impact, erosion and cavitation. However, the modes of wear usually recognized for chain links are [6, 7, 15]:

- Adhesive (sliding) wear, in which interlink rotational motion cause wear at the crown of the chain (Fig. 8).
- Abrasive wear, where chain abrasion against objects including the seabed, ship hulls and other mooring components causes wear on the outer body of the chain link.



Figure 8: Adhesive (sliding) wear in the interlink zone.



Figure 9: Wear rig at The University of Newcastle, Australia, showing 5-link chain set under cantilever-applied static axial load and hydraulic oscillatory lateral loading system.

Of the various analytical models for wear, the Archard equation [14] is the best known and widely applied:

$$V = k/H \cdot N \cdot D \quad (4)$$

where V is the volume of material lost, N is the normal force between sliding contacts, D is the sliding distance, H is the hardness of the contacting materials and k is a dimensionless ‘wear coefficient.’ Laboratory test results show that typically k varies by several orders of magnitude [16] even with high metal compatibility and good lubrication conditions. This was found also in the results for wear tests on machined 0.5 inch diam. steel rods sometimes considered relevant to offshore chain wear [15] although these are known to substantially over-estimate wear compared with field observations. The changing topography of the contact surfaces in chains wear is a contributing factor (Fig. 8). In a desire to obtain data more relevant to actual mooring chains several wear tests were conducted as part of the SCORCH-JIP on full-scale stud-less chain links (76 mm nominal diam.) using the wear test rig shown in Fig. 9. It uses a static load for axial tension through a 1:10 ratio lever arm. The central link in the 5-link test specimen is displaced laterally by a hydraulic jack. The upper and lower links are held in place and are restrained from rotation. The angular changes are fixed by the lateral displacement.



Figure 10: Progression of wear on full-scale links as number of wear cycles increases (from left to right).

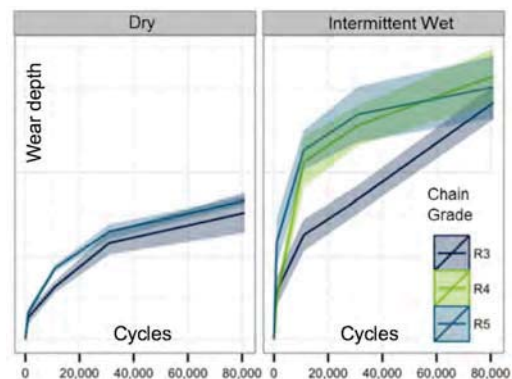


Figure 11: Wear as a function of number of cycles, steel grade and water lubrication [7].

Three grades of chain were tested under two lubrication conditions: dry and intermittent wet (simulating a ‘splash zone’ effect). Measurements of the interlink diameter at the crown of the chain link were taken at various times during the tests to monitor the progression of wear over time (Fig. 10). The bright metal is the worn contact surface of a chain link. A summary of wear test results is shown in Fig. 11. It is clear that wear is not a linear function of the number of cycles of loading as implied by Eq. 4, but it is consistent with earlier findings for small diameter bars [15]. The changing trend has been attributed to the effects of work hardening, the formation of patches of hard martensite, gradual accumulation of worn particles and the formation of protective films (mostly oxides) on the sliding surfaces [17]. Again, this departure from the usual assumption of linearity could have a major influence on prediction of likely service life and hence on the optimization of the strategies for safety management of FPSOs, particularly those operating in Tropical waters [18]. Similar differences are expected to arise in the wear of chains under other, relevant, conditions, including in the touch-down zone where abrasion from sands and rock could be significant, and in areas such as at the fairleads and in the splash-zone.

7. Optimization

Once improved understanding is reached of the mechanisms of corrosion and wear under the different conditions that may be involved, numerical modeling efforts based on much better theoretical and empirical foundations can commence in earnest, thereby opening up the possibility for robust optimization. For example, for structural optimization, say of chain possibly subject to long-term corrosion, one obvious choice for the objective function is minimization of Eqn. (1) subject to the constraints set by the requirement to meet the limit state function Eqn. (2) or, for the simplified problem, Eqn. (3). The design variables in this case would be terms such as the cross-sectional area A , with given random variables/processes for loading Q . Fundamentally this is an extremely simple optimization problem, however the accuracy with which it is solved depends much on the accurate representation of the applied mechanics 'within' it - in this case the evolution of corrosion with time and the associated uncertainties.

8. Conclusion

For the robust reliability optimisation of the design and the operation of infrastructure facilities it is necessary to have a sound understanding of the factors involved and their inter-relationship to form a sound basis for the development of analytical models. Such models are the essential backbone for robust optimization. It was shown that the processes and hence the models for time dependent corrosion and maximum pit depth are much more complex than conventionally assumed by a simple corrosion rate. Similarly, it was shown that for wear of chains the behaviour is not as simple as predicted by conventional wear models. The results obtained are considered ground-breaking for industry and expected to lead to revisions of design codes and optimal operational practices.

9. Acknowledgements

The authors acknowledge the support of the Australian Research Council and the SCORCH-JIP. The material presented herein is in the public domain and is not part of the privileged information available only to SCORCH-JIP participants. The opinions and analyses presented herein are those of the authors. More details about the SCORCH-JIP are available at www.amogconsulting.com/dev/index.php/scorch-jip

10. References

- [1] API, *Design and Analysis of Station-keeping Systems for Floating Structures*, Recommended Practice 2SK, 3rd Ed., American Petroleum Institute, Washington, DC, 2005.
- [2] R.E. Melchers, *Structural reliability analysis and prediction*, Chichester: John Wiley, 1998.
- [3] R.E. Melchers, Safety and reliability of FPSO mooring systems, *Proc ASRANet Working Conference*, 2-4 July, Croydon, London, 2012.
- [4] R.E. Melchers, Corrosion wastage in aged structures, (In) *Condition Assessment of Aged Structures*, (Eds) J.K. Paik and R.E. Melchers, Woodhead, Cambridge, 77-106, 2008.
- [5] R.E. Melchers, Long-term immersion corrosion of steels in seawaters with elevated nutrient concentration, *Corrosion Science*, 81: 110-116, (2014).
- [6] Fontaine, E., Armstrong, R., Potts, A.E., Melchers, R.E., Chaplin, C.R., François, M. Semi-Empirical Modelling for Seawater Corrosion of Wire Rope, *Proc. 19th International Offshore and Polar Engineering Conference*, Osaka, Japan, June 21-26, 2009.
- [7] J. Rosen, K. Jayasinghe, A.E. Potts, R.E. Melchers, R. Chaplin, SCORCH JIP - Findings from investigations into mooring chain and wire rope corrosion in warm waters, *Offshore Techn. Conf.* Houston, TX. Paper 26017, 2015.
- [8] B.J. Little and J.S. Lee, *Microbiologically Influenced Corrosion*, Hoboken, Wiley, 2007.
- [9] J.M. Odom, Industrial and environmental activities of sulfate-reducing bacteria, (In) *The sulfate-reducing bacteria: Contemporary perspectives*, (Ed) J.M. Odom & R. Singleton Jr., Springer, NY, 189-210, 1993.
- [10] P.M. Aziz, Application of the statistical theory of extreme values to the analysis of maximum pit depth data for aluminum, *Corrosion*, 12 (10), 495t-506t, 1956.
- [11] J. Galambos, *The asymptotic theory of extreme order statistics*, 2nd Ed., Krieger, Malabar, FL, 1987.
- [12] R.E. Melchers, Extreme value statistics and long-term marine pitting corrosion of steel, *Probabilistic Engineering Mechanics* 23: 482-488, 2008.
- [13] A.D. Sarkar and J. Halling, *Wear of Metals*, Elsevier Science, 1976.
- [14] J.F. Archard, Contact and Rubbing of Flat Surfaces, *Journal of Applied Physics*, 24 (8), 981-988, 1953.
- [15] G.J. Shoup and R.A. Mueller, Failure Analysis of a Calm Buoy Anchor Chain System. *Offshore Techn. Conf.*, Houston, TX, Paper 4764, 1984.
- [16] E. Rabinowicz, The Wear Coefficient – Magnitude, Scatter, Uses, *Journal of Tribology*, 103 (2), 188-193, 1981.
- [17] S.C. Lim, M.F. Ashby and J.H. Brunton, The Effects of Sliding Conditions on the Dry Friction of Metals, *Acta Metallurgica*, 37 (3), 767-772, 1989.
- [18] M. Wang and R. D'Souza, Mooring Chain Corrosion Design Considerations for an FPSO in Tropical Water, Paper No. 04-0046, *Proc. OMAE Specialty Symp. on FPSO Integrity*, Houston, TX, 2004.

Damage Detection Method in Non-Destructive Testing Based on Topology Optimization and Eigenvalue Analysis

Takafumi Nishizu¹, Akihiro Takezawa², Mitsuru Kitamura³

¹ Hiroshima University, Hiroshima, Japan, d145208@hiroshima-u.ac.jp

² Associate Professor, Hiroshima University, Hiroshima, Japan, akihiro@hiroshima-u.ac.jp

³ Professor, Hiroshima University, Hiroshima, Japan, kitamura@hiroshima-u.ac.jp

Abstract

Non-destructive testing detects damage according to a difference in a physical phenomenon between a normal structure and damaged structure. However, the accuracy of such damage detection typically depends on the skill of the engineer. As a solution, a numerical method of detecting damage to a structure based on a dynamical numerical model such as a finite element model was proposed. This method automatically derives a structure with a response that is equal to that of a damaged structure employing an optimization algorithm. The procedure can be applied to not only non-destructive testing but also automatic structural health monitoring. Among structural optimization methods, topology optimization can optimize the structure fundamentally by changing the topology and not just the shape of a structure. We thus employ topology optimization for structural optimization. Damage detection using topology optimization based on frequency response analysis has been suggested. However, the eigenvalue-based technique that is traditionally used in damage detection has not been integrated with topology optimization. The present study thus examines a damage detection method using topology optimization based on eigenvalue analysis. Our method derives a structure that has the same eigenvalues as a damaged structure employing topology optimization and can identify a damaged structure.

Keywords: topology optimization, eigenvalue analysis, non-destructive testing, sensitivity analysis

1 Introduction

Non-destructive testing is important for improving the life span of structures. Different non-destructive testing methods employ ultrasonic waves, eddy current, piezoelectric sensors, lightwave fibers and other phenomena and devices [1]. In non-destructive testing, damage is detected according to the difference between responses for a normal structure and damaged structure. Because the process of specifying damage is usually performed by an engineer, the accuracy of damage detection depends on the skill of the engineer. To establish an identification method that does not depend on the skill of the testing engineer, methods based on a database of damaged structures have been proposed. However, such methods cannot be applied to structures with an innovative shape or in cases of unexpected damage.

In contrast, analytical methods of damage specification have been proposed [2, 3]. Such methods specify a damaged structure by non-destructive testing employing a numerical calculation based on a dynamical model and optimization algorithm.

However, there has been a recent focus on topology optimization as a novel structural optimization method [4], which fundamentally optimizes the structural shape [5, 6, 7]. Moreover, two studies on topology optimization in terms of damage detection methods of non-destructive testing have been published. Lee et al. [8] developed a damage identification method based on the difference in the frequency response between damaged and undamaged structures. Niemann et al. [9] verified this approach experimentally in the damage detection of a composite. These methods derive the damaged structure by matching the frequency response of the optimized structure to that of the damaged structure corresponding to the detected response in actual non-destructive testing. However, only these two studies have reported an analytical damage detection method employing topology optimization. Other vibration characteristics such as the structural eigenfrequency, which is the most fundamental vibration characteristic, have not been used in such a way.

The present study establishes a damage detection method using eigenfrequency analysis and topology optimization. Specifically, this study derives an approximated shape of the damaged structure by matching the eigenfrequencies

of the optimized structure with those of the damaged structure corresponding to the detected eigenfrequency in actual non-destructive testing through a structural topology optimization procedure. In chapter 2, we formulate a topology optimization problem to minimize the difference in eigenvalues between a damaged structure and the current structure. In chapter 3, an optimization algorithm based on sensitivity analysis and a method of moving asymptotes (MMA)[10] is constructed. In chapter 4, we clarify the validity and utility of the proposed methodology using numerical examples.

2 Formulation

2.1 Eigenvalue Analysis Employing the Finite Element Method

This study employs the finite element method for the eigenvalue analysis of structures. A free vibration problem of a structure is first discretized by finite element analysis. A discretized vibration equation is obtained by assuming that the solution is a periodic displacement $\Phi e^{i\omega t}$:

$$(\mathbf{K} - \omega_n^2 \mathbf{M})\Phi = 0, \quad (1)$$

where \mathbf{K} is the stiffness matrix, \mathbf{M} is the mass matrix, ω_n denotes the natural angular frequencies and Φ is the amplitude vector. Φ is obtained as eigenvectors by solving the above equation as an eigenvalue problem.

2.2 Topology Optimization

A fundamental idea of topology optimization is the introduction of the design domain D and characteristic function χ_Ω . That is, the optimization problem is replaced with a material distribution problem of the characteristic function χ_Ω on the design domain D :

$$\chi_\Omega(\mathbf{x}) = \begin{cases} 1 & \text{if } \mathbf{x} \in \Omega_d \\ 0 & \text{if } \mathbf{x} \in D \setminus \Omega_d \end{cases} \quad (2)$$

Through this process, the set of χ_Ω in the fixed design domain D is regarded as an optimal structure.

However, optimization based on the above equation evaluates the discontinuous function χ_Ω in the fixed design domain D . This means that a discontinuous value is evaluated about an infinite design variable. Unfortunately, an optimum solution does not exist in this case. This issue is resolved by replacing the optimization problem with respect to a characteristic function with an optimization problem with respect to a continuous density function. As this relaxation method, a homogenization method and the solid isotropic material with penalization (SIMP) method have been proposed [11]. These methods regard the approximated optimization problem to be a problem of the volume fraction of a composite material comprising the host material and a very weak material that imitates a hole. A gray domain in which it is difficult to identify a structure or hole is often observed in this optimization problem. Because the SIMP method can adjust the nonlinearity of the relationship between the density function and physical property by penalization parameters, it is used for topology optimization in the present study. Young's modulus and material density are correlated with the density function $\mathbf{d} = [d_1, d_2, \dots, d_l]$, where l is the number of optimized elements:

$$E_i^* = d_i^3 E \text{ for } i = 1, \dots, l, \quad (3)$$

$$\rho_i^* = d_i \rho \text{ for } i = 1, \dots, l, \quad (4)$$

where E and ρ are Young's modulus and the mass density respectively. The superscript suffix * indicates a physical property that is expressed by the density function \mathbf{d} in optimization. The exponent of the design variable is freely set in the SIMP method. We use a Young's modulus of 3 and material density of 1, because these values have been effective in past work [5][6].

2.3 Objective Function and Optimization Problem

We premise that the eigenvalue and eigenmode of the damage structure are obtained, and we detect damage by deriving a structure that has the same eigenvalue employing optimization. This study supposes a simple structure that has non-repeating lower eigenvalues and eigenmodes. To avoid repeating eigenvalues during optimization, we set an objective function that is the square of the rate of change between the designated eigenvalue and current eigenvalue [5]:

$$J(\mathbf{d}) = \sum_{i=1}^m w_i \frac{(\lambda_{\text{target}i} - \lambda_i)^2}{\lambda_{\text{target}i}^2}, \quad (5)$$

where $\lambda = \omega_n^2$ is the eigenvalue, $\lambda_{\text{target}i}$ is the target of the i -th eigenvalue, λ_i is the i -th eigenvalue, m is the number of eigenvalues used in optimization and w_i denotes the weighting factor of each eigenvalue. The topology optimization problem in this study is then expressed as

$$\underset{\mathbf{d}}{\text{minimize}} J(\mathbf{d}) \quad (6)$$

Subject to

$$0 < d_i \leq 1 \text{ for } i = 1, \dots, l. \quad (7)$$

3 Optimization Procedure

3.1 Optimization Algorithm

Figure 1 is a flowchart of the optimization procedure used in the present study. This study first sets a damaged structure as the target structure and calculates the eigenvalue using the vibration equation. The obtained eigenvalues are then set as the target eigenvalues in the objective function of Eq.(5). These values imitate the eigenvalues of the damaged structure obtained in actual non-destructive testing. The optimization calculation is then repeated until the objective function converges. We calculate the eigenvalues and eigenvectors by solving the vibration equation of the optimized structure. This method needs to check whether the order and shapes of eigenmodes of the optimized structure correspond to those of the damaged structure. When the order of eigenvalues and eigenmodes of the optimized structure does not correspond to that of the damaged structure, eigenvalues of appropriate order are selected in the objective function. After calculating the objective function, the optimization finishes when the objective function converges. When the objective function does not converge, the method calculates the sensitivities of the objective function and updates the design variable using the MMA.

4 Numerical Examples

We demonstrate the utility and validity of the proposed method in numerical example. Example model is of structures that support a heavy load because their eigenvalues are readily affected by damage. The heavy load is modeled as a non-structural mass. Physical properties and size are handled as dimensionless quantities and all example models are of virtual material with Young's modulus $E = 1$ and mass density $\rho = 1$. The mechanical models of the example is two-dimensional plane stress model. We use the commercially available finite element analysis software Comsol Multiphysics for FEM. Each element is formulated using a first-order isoparametric element. Design variables are defined on each finite element.

This example is the optimization of a 2-by-1 rectangular plate supporting a distributed mass on the right side with in-plane stiffness. The left side is fixed and the distributed non-structural mass having total mass of 1 is set on the right side. The domain is discretized by square elements in an 80-by-40 configuration. The target damaged structure is set to have a semicircular hole at the center of the left side as shown in fig. 3.

After preliminary analysis and optimization of the target structure, we decided to include the first to fifth eigenvalues in the objective function because they are at least required for the smooth convergence of the optimization.

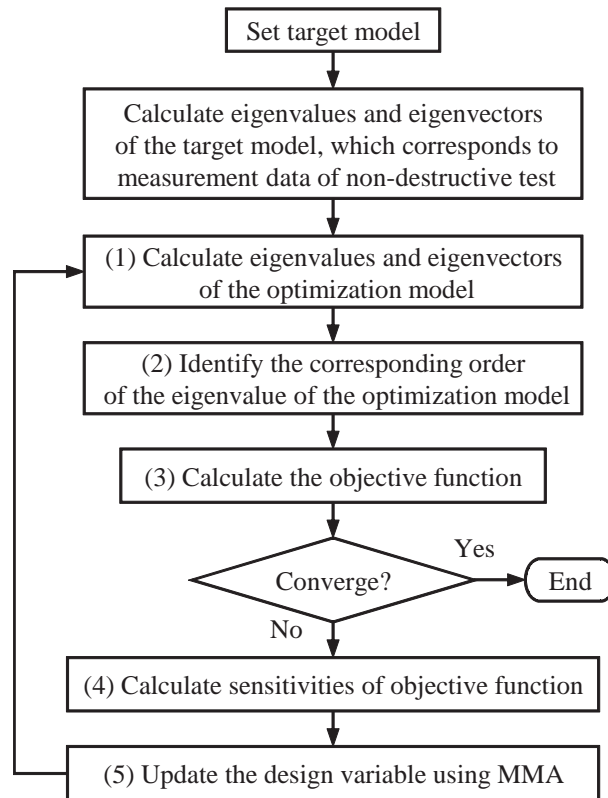


Figure 1: Flowchart of the optimization procedure.

Figure 4 shows the first to fifth eigenmode shapes. The damage at the center of the left side might affect tensile vibration more strongly than bending vibration. All weighting coefficients of eigenvalues in Eq.(5) are 1. Figure 5 shows the convergence history of optimization. We regard that the objective function has converged after 500 cycles . Figure 6 shows the resulting structure of optimization. The eigenvalues are given in Table 1. During optimization, there was no eigenmode switching and correspondence of the mode shape between the optimized and target structures were maintained. The optimal structure has a slit-like void at the center of the left side. Although the identification of the damage shape is not perfect, it can be said that the damage position was detected from Fig. 6. We confirm that the optimized and damaged structures have almost identical eigenvalues in Table 1 and can say the damage identification was achieved through eigenvalue matching.

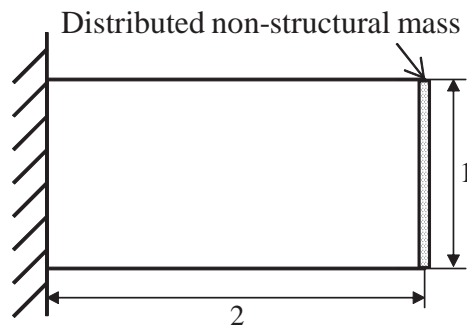


Figure 2: Analysis model of the cantilever example.



Figure 3: Damaged model of the cantilever example.

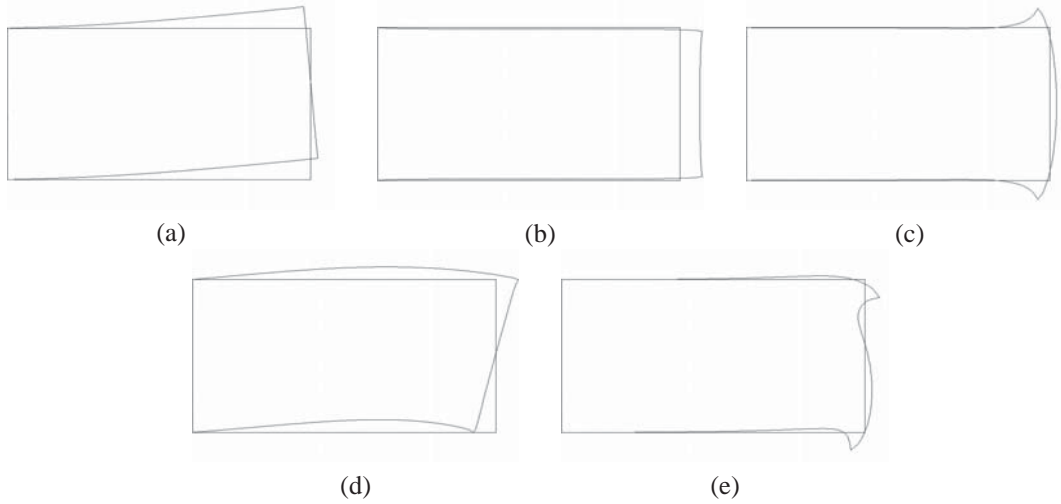


Figure 4: Eigenmode shapes of the damaged structure of the cantilever example. (a) First mode, (b) second mode, (c) third mode, (d) fourth mode, (e) fifth mode.

Table 1: Eigenfrequencies of optimal and damaged structures of the cantilever example (Hz).

Order	1st	2nd	3rd	4th	5th
Damaged structure	2.01×10^{-2}	4.20×10^{-2}	4.98×10^{-2}	5.39×10^{-2}	6.00×10^{-2}
Optimal structure	2.01×10^{-2}	4.20×10^{-2}	4.98×10^{-2}	5.39×10^{-2}	6.00×10^{-2}
Error(%)	0.08	0.01	0.01	0.01	0.01

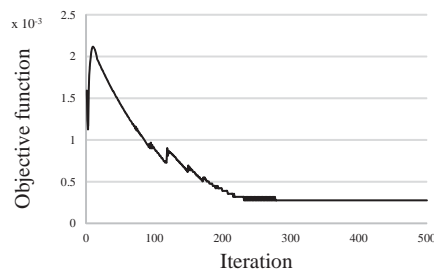


Figure 5: Convergence history of the cantilever example.

5 Conclusions

We developed a damage detection method that designates the eigenvalue of a damaged structure by non-destructive testing and derives a structure having eigenvalues identical to those of the damaged structure automatically through topology optimization. For this method, we set a minimization problem of the difference in eigenvalues between the damaged structure and optimized structure, and construct an optimization algorithm employing sensitivity anal-



Figure 6: Optimal configuration of the cantilever example.

ysis and the MMA. Although identification of the damage shape was not perfect, it was demonstrated that detection of the damage position using the proposed method is possible in several numerical example.

We believe that the application of the proposed method requires only the measuring of the eigenvalue by hammering when eigenmodes are the same for the damaged structure and undamaged structure as in the first example. However, when eigenmodes of the undamaged structure are different from those of the damaged structure, it is necessary to solve not only the eigenvalue but also the eigenmode. In that case, eigenmode optimization should be introduced in damage identification. This approach can contribute also to specification of the damage shape. Of course, effective methods of measuring the eigenmode shape must be studied for practical use in that case.

Because the proposed method is based on eigenvalue analysis, target structures are limited to simple examples. However, various techniques of non-destructive damage detection such as detection using ultrasonic waves or eddy current could be integrated with the topology optimization framework. We will investigate such an extension in future work.

References

- [1] Paul E. Mix, *Introduction to Nondestructive Testing: A Training Guide*, Wiley-Interscience, 2 edition, 2005.
- [2] R. D. Adams, P. Cawley, C. J. Pye, B. J. Stone, A vibration technique for non-destructively assessing the integrity of structures, *Journal of Mechanical Engineering Science*, 20, 93-100, 1978.
- [3] P. Cawley, R. D. Adams, The location of defects in structures from measurements of natural frequencies, *Journal of Strain Analysis for Engineering Design*, 14 (2), 49-57, 1979.
- [4] M. P. Bendsøe and O. Sigmund, *Topology Optimization: Theory, Methods, and Applications*, Springer-Verlag, Berlin, 2003.
- [5] Z. D. Ma, N. Kikuchi, H. C. Cheng, Topological design for vibrating structures, *Computer Methods in Applied Mechanics and Engineering*, 121 (1-4), 259-280, 1995.
- [6] N. L. Pedersen, Maximization of eigenvalues using topology optimization, *Structural and Multidisciplinary Optimization*, 20 (1), 2-11, 2000.
- [7] X. Yang, Y. Li, Topology optimization to minimize the dynamic compliance of a bi-material plate in a thermal environment, *Structural and Multidisciplinary Optimization*, 47 (3), 399-408, 2013.
- [8] J. S. Lee, J. E. Kim, and Y. Y. Kim, Damage detection by the topology design formulation using modal parameters, *International Journal for Numerical Methods in Engineering*, 69 (7), 1480-1498, 2007.
- [9] H. Niemann, J. Morlier, A. Shahdin, and Y. Gourinat, Damage localization using experimental modal parameters and topology optimization, *Mechanical Systems and Signal Processing*, 24 (3), 636-652, 2010.
- [10] K. Svanberg, The method of moving asymptotes- a new method for structural optimization, *International Journal for Numerical Methods in Engineering*, 24 (2), 359-373, 1987.
- [11] M. P. Bendsøe and O. Sigmund, Material interpolation schemes in topology optimization, *Archive of Applied Mechanics*, 69 (9), 635-654, 1999.

Multi-objective Optimization Using Adaptive Explicit Non-Dominated Region Sampling

Anirban Basudhar

Livermore Software Technology Corporation, Livermore, CA, USA, abasudhar@lstc.com

1. Abstract

A new method to efficiently perform multi-objective optimization (MOO), referred to as Adaptive Explicit Multi-objective Optimization (AEMOO), is presented. Unlike existing methods, it uses binary classification to explicitly define the decision boundary between dominated and non-dominated (ND) regions in the design space. An adaptively refined support vector machine (SVM) is used to define the boundary. AEMOO has several advantages that stem from the availability of the estimated explicit boundary bounding the ND design space, which represents Pareto-optimal (PO) designs at convergence. It allows for an effective adaptive sampling strategy that samples "important" regions in the design space. Additionally, explicit knowledge of the PO design space facilitates efficient real time Pareto-optimality decisions. AEMOO uses a hybrid approach that considers the distribution of samples in both design and objective spaces. Two variants of AEMOO are presented - one based purely on classification and the other based on both classification and metamodel approximation. The results are compared to the widely used NSGAI method and Pareto Domain Reduction (PDR) using test problems up to 30 variables. AEMOO shows significantly better efficiency and robustness compared to these existing methods.

2. Keywords: support vector machine, hybrid adaptive sampling, real time optimality decision, binary response.

3. Introduction

Multi-objective optimization (MOO) often involves locating a set of Pareto optimal points that are ND over the entire design space (x-space). The multiple objectives typically represent quantities with different units that are not comparable. Additionally, finding a solution set that can represent the complete Pareto front is more challenging than finding a single solution. Therefore, efficient and accurate solution of MOO problems is overall much more challenging compared to single-objective optimization (SOO), and is still an evolving research area.

Classical MOO approaches involve scalarization of the objectives to convert MOO into several SOO problems [1], but these approaches are not well suited to find a set of points that can represent the complete PO front. Evolutionary algorithms, e.g. SPEA and NSGAI, are extensively used to solve MOO problems in a true multi-objective sense [2,3]. These methods are applied in a direct optimization framework or in conjunction with metamodel approximations to alleviate the cost of potentially expensive evaluations (e.g. crashworthiness) [4]. The metamodel-based method is further classified based on sampling schemes. In some of these, sampling is based on direct optimization (e.g. genetic operators) [5]. The metamodel's accuracy estimate is used to determine which samples need to be evaluated using the expensive evaluator, and rest of the samples are evaluated using a metamodel. In other methods, sampling is directed to obtain accurate metamodels and a method like NSGAI is then applied on the metamodels to find PO points. A basic approach is to use sequential space-filling samples for metamodeling [4]. While this approach is global, filling the space is prohibitively expensive in higher dimensions. Another metamodel-based MOO algorithm is ParEGO [6], which is an extension of its SOO counterpart. ParEGO involves scalarization of objectives. Additionally, it was tested only up to eight variables in [6].

One major limitation of commonly used MOO methods is the lack of explicit definition of PO regions of design space. To determine whether a given sample is ND, one needs to evaluate the objective functions and constraints at not only that point but over the entire design space. ND points are determined using pairwise comparison in objective (f) space before mapping them back to the design space. For large sample sizes, these calculations can add significant overhead. Additionally, in the absence of an explicit definition of ND regions of the design space, it is difficult to adaptively add samples in those regions of particular interest. A sequential metamodel-based method known as Pareto Domain Reduction (PDR) was recently developed that focuses on sampling based on design space sparsity in the vicinity of predicted front [7]. Hyperboxes constructed around previous ND points were sampled. However, performance of PDR depended on the number and size of such hyperboxes.

This paper presents a novel classification-based adaptive explicit MOO approach (AEMOO) that mitigates aforementioned limitations of existing methods by providing an efficient sampling scheme. This is made possible by constructing an explicit definition of the boundary separating dominated and ND samples in the design space using a support vector machine (SVM) [8] and using a hybrid sampling scheme that accounts for sparsity in both spaces (x and f space). Treatment of MOO as a binary classification problem involves a paradigm shift in its solution approach. The goal in MOO is to determine whether a design is PO or not, and to find a set of such designs. Therefore, it is naturally suited for treatment as binary classification. Using the proposed approach, a

single evaluation of the trained classifier can determine if a design is ND. This makes it especially attractive for real time Pareto-optimality decisions. Explicit definition of ND regions also facilitates implementation of a proposed adaptive sampling scheme that selects samples in these regions. Restricting the sampling region using the decision boundary improves the PO front search efficiency. AEMOO can be implemented either as a classifier assisted direct method or in conjunction with metamodel approximations. It should be noted that in the latter approach, constraints can be handled using metamodel approximations or by approximating the zero level using a classifier. Classifier-based handling allows the handling of discontinuous and binary constraint functions [9].

4. Adaptive Explicit Multi-objective Optimization (AEMOO)

Two variants of the proposed AEMOO method are presented in this section. In Section 4.1 the basic idea of classification-based MOO is presented. In Section 4.2 a classifier-assisted direct optimization method is presented. A second method that utilizes classification as well metamodel approximation is presented in Section 4.3.

4.1. Classification Approach for MOO - Dynamic Classifier

Typically, solution of MOO is a set of PO points. Part of the design space is PO while other regions are dominated. Such a problem is ideal for applying classification methods, the two classes being dominated (-1 class) and ND (+1 class) (Fig. 1). Once a classifier separating dominated and ND samples is trained, Pareto-optimality of any design is determined using a single classifier evaluation, in contrast with existing methods.

SVM is used to construct the decision boundary in this work (Eq.(1)). It constructs the optimal boundary that maximizes the margin between two sample classes (± 1) in a feature space. A kernel K maps the design and feature spaces. In this work, a Gaussian kernel is used to construct SVM boundaries ($s(\mathbf{x}) = 0$). Spread of the kernel is assigned the largest value without any training misclassification. The SVM is defined as:

$$s(\mathbf{x}) = b + \sum_{i=1}^N \alpha_i y_i K(\mathbf{x}, \mathbf{x}_i) \quad (1)$$

Here, $y_i = \pm 1$ is class label, α_i is the Lagrange multiplier for i^{th} sample and b is bias. Each sample's class needs to be assigned prior to the construction of SVM boundary. An issue in using classification for MOO is that although it is known that dominated samples (class -1) cannot be PO, the opposite is not true; being ND among current samples isn't sufficient to be PO. However, +1 samples represent PO designs if the data is sufficient. A decision boundary obtained by assigning +1 class to the current ND samples represents an estimate of the PO front, and is refined adaptively. As points are added, samples may switch from +1 to -1 as ND samples may be dominated by newer samples until convergence. As class definition of existing samples can change during the course of AEMOO, the classifier is referred to as *dynamic*. The classification based AEMOO method has several advantages.

- Explicit definition of the ND region facilitates implementation of an efficient sampling scheme
- It facilitates efficient real time Pareto optimality decisions
- It uses information in both design and objective spaces to enhance its efficiency and robustness
- The classification approach allows the handling of binary and discontinuous constraint functions
- As ND region is explicitly defined in the design space, AEMOO is unaffected by number of objectives.

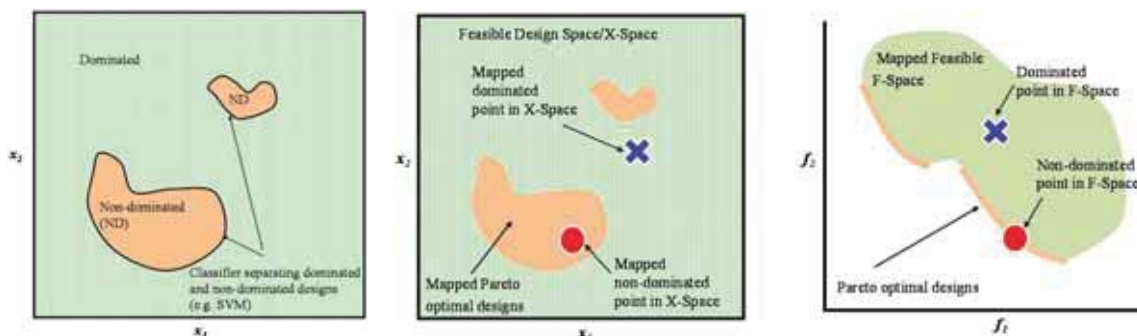


Figure 1: Boundary defining ND regions in design space (left). Design-Objective space Mapping (right).

4.2. Direct AEMOO Method

Direct AEMOO is based on SVM classification only and does not approximate function values. It evaluates more samples in the explicitly defined SVM-based ND regions to avoid waste of samples and increase efficiency. The sign of SVM value $s(\mathbf{x})$ determines whether a sample is ND or not, and is straightforward to determine.

A fraction of samples per iteration are selected within the $s(\mathbf{x}) > 0$ ND region of design space. Details are shown in

Fig. 2. Sampling important regions of the design space allows a faster increase in the SVM accuracy, as sampling based only on the objective space can lead to clustering of samples in design space, where the SVM is constructed. Maximizing the value of SVM, one of the sampling criteria, is equivalent to maximizing the probability of locating a ND sample [8,10]. Additionally, one generation of NSGAI is also used to select samples, first within the $s(\mathbf{x}) > 0$ regions and then using an unconstrained formulation. Using NSGAI-based samples, the algorithm ensures that the effects of sparsity in the objective function space and genetic operator-based evolution are also accounted for. In order to ensure a global search, a small fraction of samples is added based on maximum minimum distance in the entire unconstrained design space. Such samples are not expected to provide an efficient sampling scheme, and are therefore optional, but guarantee the location of the complete Pareto front when run for a sufficient time.

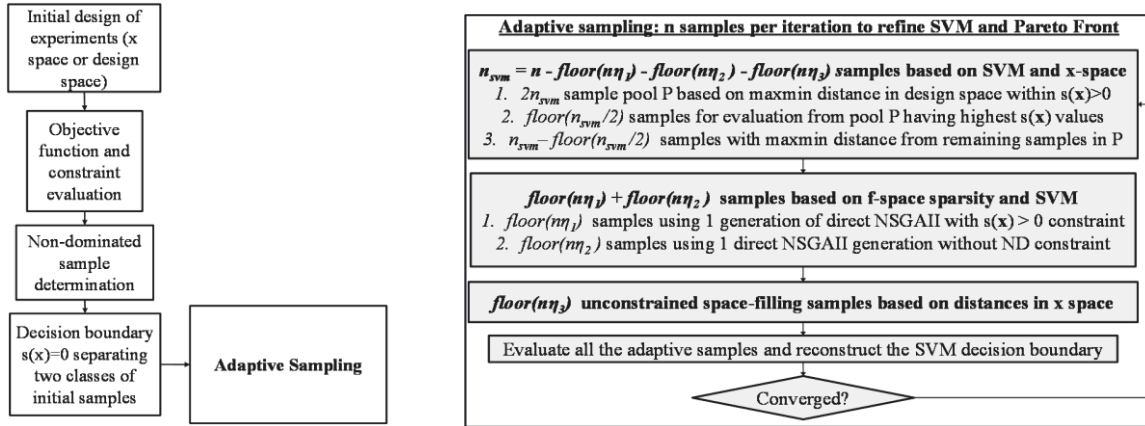


Figure 2: Summary of direct AEMOO method (left) and sampling scheme (right)

4.3. Metamodel-assisted AEMOO Method

In this approach, metamodel approximation and SVM are used together. Basic idea is same as direct AEMOO - to consider ND ranking along with sample sparsity in both x and f spaces. However, the single generation of direct NSGA-II samples is replaced with converged predicted PO samples obtained using metamodel-based NSGAI. Metamodel approximation and the SVM-based classification serve as complementary approaches that help in enhancing accuracy by accounting for distribution of samples in both spaces. The methodology is shown in Fig. 3.

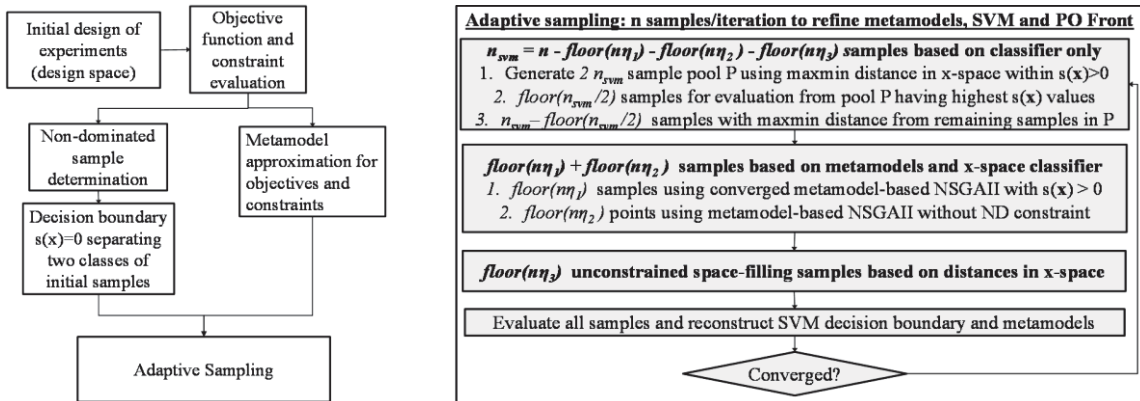


Figure 3: Summary of metamodel-assisted AEMOO method (left) and sampling scheme (right)

5. Results

Several examples are presented to validate the efficacy and efficiency of AEMOO. A 10 variable analytical example using direct AEMOO is presented, followed by three 30 variable examples using metamodel-assisted AEMOO. Efficiency is compared to existing methods PDR and NSGAI. Finally, AEMOO is used for tolerance based MOO of a Chevrolet truck [11]. The sample type fractions are $\eta_1 = \eta_2 = 0.2$ and $\eta_3 = 0.1$ (Fig. 2 and 3). Unless mentioned, $\text{floor}(1.5*(m+1))+1$ samples are used per iteration, m being the number of variables. AEMOO showed comparatively higher efficiency also when larger sample sizes were used, but those results haven't been shown. Radial basis function metamodels have been used for function approximations, but others can also be used. For examples 1-4, one of the objectives is $f_1 = x_1$. The second objective f_2 is provided with the individual examples.

5.1. Example 1. Analytical example with ten variables and two objectives - ZDT3 (Direct AEMOO)

This example has 10 variables ($m = 10$) and 2 objectives. The second objective f_2 is:

$$f_2 = r(\mathbf{x})h(f_1(\mathbf{x})r(\mathbf{x})), \text{ where } r(\mathbf{x}) = 1 + \frac{9}{m-1} \sum_{i=2}^m x_i, h(\mathbf{x}) = 1 - \sqrt{\frac{f_1(\mathbf{x})}{r(\mathbf{x})}} - \left(\frac{f_1(\mathbf{x})}{r(\mathbf{x})} \right) \sin(10\pi f_1(\mathbf{x})) \quad (2)$$

The Pareto fronts at successive iterations are plotted in Fig. 4. The front at iteration 125 (2250 points) is quite close to the actual one, and shows that AEMOO can locate disjoint PO fronts even when only classification is used. NSGAI found four of the disjoint regions on the front accurately, but completely missed one region. This can be attributed to sampling based on the f-space only without considering design space sparsity, unlike in AEMOO.

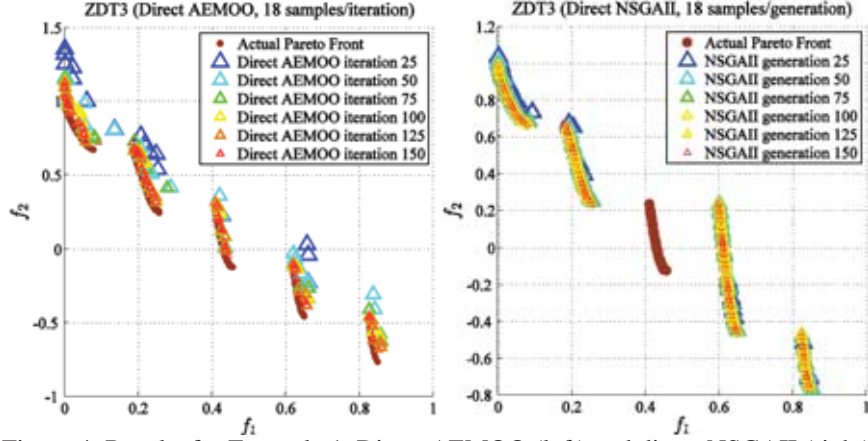


Figure 4: Results for Example 1. Direct AEMOO (left) and direct NSGAI (right).

5.2. Example 2. Analytical example with 30 variables and 2 objectives - ZDT1 (Metamodel-assisted AEMOO) This problem consists of two objectives f_1 and f_2 . The second objective is:

$$f_2 = r(\mathbf{x})h(f_1(\mathbf{x})r(\mathbf{x})), \text{ where } r(\mathbf{x}) = 1 + \frac{9}{m-1} \sum_{i=2}^m x_i, h(\mathbf{x}) = 1 - \sqrt{\frac{f_1(\mathbf{x})}{r(\mathbf{x})}} \quad (3)$$

Optimization results are shown in Fig. 5 using trade off plots at different iterations at intervals of 10. The results shown are the evaluated Pareto optimal points. The proposed AEMOO method is able to locate the entire spread of Pareto front at the 10th iteration itself (470 samples), after which it adds diversity. The samples on the front are very well diversified by the 20th iteration. In comparison, performance of direct NSGAI is much slower and it takes 40-50 generations (1920-2400 samples) to obtain a diversified front. Even at 50th generation, the Pareto front using NSGAI is not as accurate as the 10th iteration of AEMOO. PDR performs more efficiently than direct NSGAI, but still takes 20-30 iterations (940-1410 samples) to obtain a well diversified accurate front.

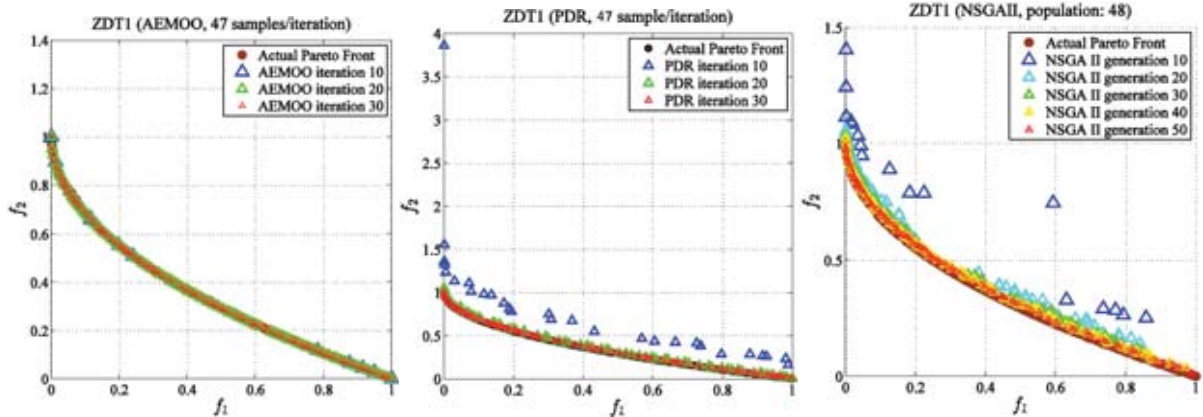


Figure 5: Example 2. Metamodel-assisted AEMOO (left), PDR (center) and direct NSGAI (right).

5.3. Example 3. Analytical example with 30 variables and 2 objectives - ZDT2 (Metamodel-assisted AEMOO) This problem consists of 30 variables ($m = 30$) and two objective functions. The second objective is:

$$f_2 = r(\mathbf{x})h(f_1(\mathbf{x})r(\mathbf{x})), \text{ where } r(\mathbf{x}) = 1 + \frac{9}{m-1} \sum_{i=2}^m x_i, h(\mathbf{x}) = 1 - \left(\frac{f_1(\mathbf{x})}{r(\mathbf{x})} \right)^2 \quad (4)$$

Optimization results are shown using computed trade off plots in Fig. 6. AEMOO is able to find a very well diversified and accurate front before the 10th iteration itself (470 samples). On the contrary, with a comparable population size of 48, direct NSGAI failed to obtain the Pareto front even after 50 generations. The population size for NSGAI had to be increased to find the actual front. PDR was able to locate the Pareto front with a sample

size of 47 per iteration, but was slower than AEMOO, as it took 30 iterations (1410 samples) to obtain a front of comparable (but not quite as good) accuracy and diversity.

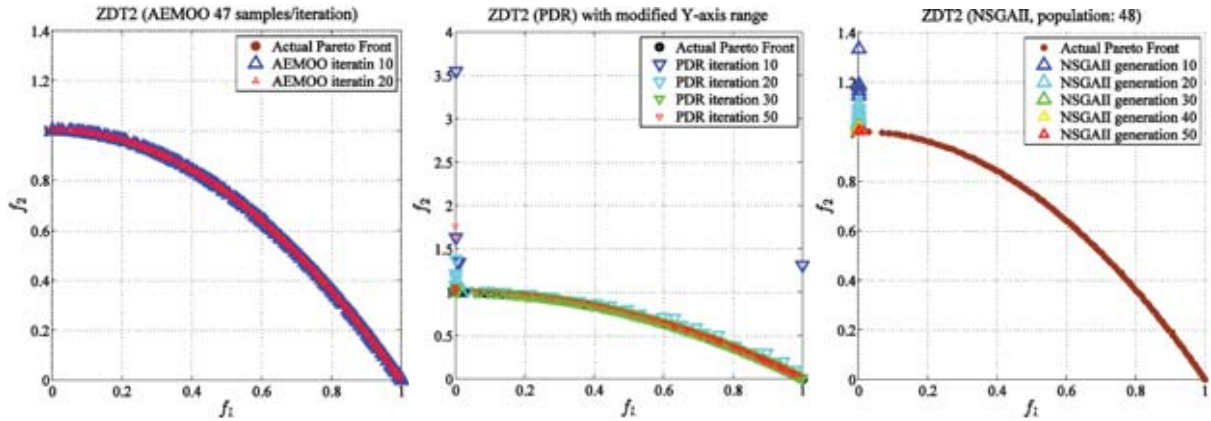


Figure 6: Example 3. Metamodel-assisted AEMOO (left), PDR (center) and direct NSGAI (right).

5.4. Example 4. Analytical example with 30 variables and 2 objectives - ZDT3 (Metamodel-assisted AEMOO)

This optimization problem is similar to Example 1 (Eq.(2)), except that it has 30 variables instead of 10. PO fronts using the three methods are shown in Fig. 7, along with the actual front. AEMOO located all five disjoint regions on the front within first 10 iterations, following which it further added samples on the front to increase diversity. Both NSGAI and PDR were significantly slower and had lower accuracy. Using population size of 48, direct NSGAI completely missed 2 out of 5 regions. PDR was able to sample 4 of the regions satisfactorily at 40-50 iterations (1880-2350 samples). It found one ND sample close to the fifth region, but not on it.

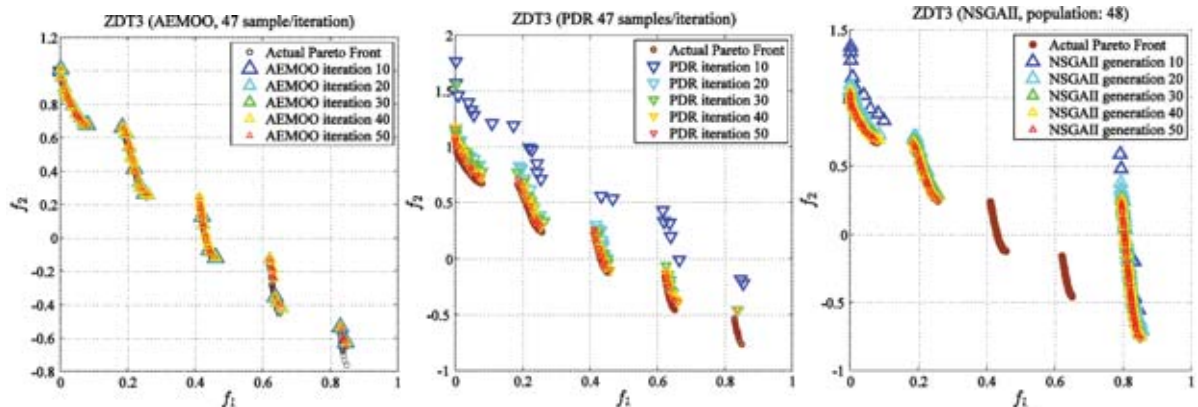


Figure 7: Example 4. Metamodel-assisted AEMOO (left), PDR (center) and direct NSGAI (right).

5.5. Example 5. 7 variable tolerance optimization of Chevrolet C2500 truck (Metamodel-assisted AEMOO)

AEMOO is used for multi-objective tolerance optimization of a Chevrolet truck. LS-OPT is used to build global metamodels, based on the truck's responses at 1500 samples (using LS-DYNA). MOO is run on the metamodels.. Mass is minimized while tolerance is maximized (Eq. (5)). Relative tolerance and 6 thicknesses x are the variables.

$$\begin{aligned}
 & \min_{\text{tolerance}, \bar{\mathbf{x}}} \{-\text{tolerance}, \text{scaled_mass}(\bar{\mathbf{x}})\} \\
 & \text{s.t.} \quad P(\text{scaled_mass}(\bar{\mathbf{x}}) > 0.9) \leq P_{\text{target}} \\
 & \quad \quad P(\text{scaled_stage1_pulse}(\bar{\mathbf{x}}) > 1) \leq P_{\text{target}} \\
 & \quad \quad P(\text{scaled_stage2_pulse}(\bar{\mathbf{x}}) > 1) \leq P_{\text{target}} \\
 & \quad \quad P(\text{scaled_disp}(\bar{\mathbf{x}}) > 1) \leq P_{\text{target}} \quad \text{where } P_{\text{target}} = 0 \text{ in this work}
 \end{aligned} \tag{5}$$

In figure 3, the vehicle parts to be optimized are shown along with the optimization results. The Pareto front obtained using AEMOO and NSGAI are shown. 100 samples per iteration are used to solve this example to ensure at least one sample of each class in the initial sampling. Other approaches to avoid this restriction are possible, but are outside the scope of this paper. AEMOO results are provided for 30 iterations that were completed at the time of writing this paper and compared to NSGAI is run up to 50 generations. The PO front using AEMOO has a better spread, and diversity compared to the NSGAI front even at the 50th generation, which shows its superior performance. At the same stage (30th iteration), the PO front using AEMOO is clearly better. The PO front consists of a knee at 6% tolerance suggesting it to be a good design, as there is rapid mass increase beyond it.

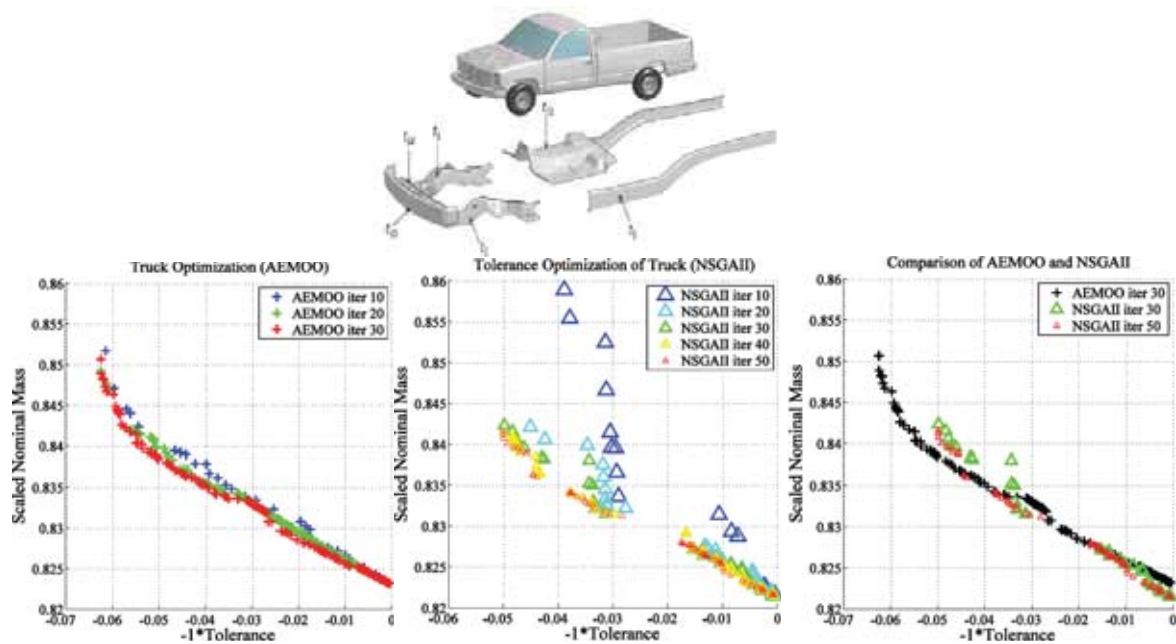


Figure 8: Truck to be optimized (top), AEMOO (left), PDR (center), NSGAI (center) and overlaid fronts (right).

5. Concluding Remarks

A new classification-based adaptive sampling approach to solve MOO problems is presented. The proposed AEMOO method has several advantages compared to existing methods due to this radically different approach. Two variations of the method are presented - direct and metamodel assisted. The method's efficacy is validated using standard examples of up to 30 variables. It has been shown to clearly outperform existing methods like NSGAI and PDR in terms of efficiency. Additionally, ability to locate disjoint Pareto fronts has been shown. Ability to solve constrained MOO has also been shown using a tolerance-based crashworthiness optimization example. As AEMOO explicitly defines the ND region boundaries in the design space, it also naturally facilitates real-time Pareto optimality decisions. This work is expected to open new avenues for research in the field of MOO. As the sampling scheme is partly based on design space classification, which discards significant regions of the space as dominated, it is expected to be affected by objective space dimensionality to a lesser extent. Future work is needed to validate this hypothesis. Additionally there is scope for further improvement in constraint handling.

6. Acknowledgements

The author is thankful to Dr. Nielen Stander and Mr. Imtiaz Gandikota of LSTC for their valuable feedback and for allowing the use of their machines for running some of the comparative studies.

7. References

- [1] Deb, K. (2001). Multi-objective optimization using evolutionary algorithms (Vol. 16). John Wiley & Sons.
- [2] Laumanns, M. (2001). SPEA2: Improving the strength Pareto evolutionary algorithm.
- [3] Deb, K., Pratap, A., Agarwal, S., & Meyarivan, T. A. M. T. (2002). A fast and elitist multiobjective genetic algorithm: NSGA-II. *Evolutionary Computation, IEEE Transactions on*, 6(2), 182-197.
- [4] Stander, N., Roux, W.J., Basudhar, A., Eggleston, T., Goel, T., Craig, K.J. LS-OPT User's Manual Version 5.0, April 2013.
- [5] Li, M., Li, G., & Azarm, S. (2008). A kriging metamodel assisted multi-objective genetic algorithm for design optimization. *Journal of Mechanical Design*, 130(3), 031401.
- [6] Knowles, J. ParEGO: A hybrid algorithm with on-line landscape approximation for expensive multiobjective optimization problems. Technical report TR-COMPSYSBIO-2004-01, September 2004.
- [7] Stander, N. An Adaptive Surrogate-Assisted Strategy for Multi-Objective Optimization. *10th World Congress on Structural and Multidisciplinary Optimization*, Orlando, Florida, USA, 2013
- [8] Vapnik, V.N., and Vapnik, V.. *Statistical learning theory*. Vol. 1. New York: Wiley, 1998.
- [9] Basudhar, A., and Missoum, S. Adaptive explicit decision functions for probabilistic design and optimization using support vector machines. *Computers & Structures* 86.19 (2008): 1904-1917.
- [10] Basudhar, A., Dribusch, C., Lacaze, S. and Missoum, S. Constrained efficient global optimization with support vector machines. *Structural and Multidisciplinary Optimization* 46, no. 2 (2012): 201-221.
- [11] National Crash Analysis Center. Finite element model archive, www.ncac.gwu.edu/vml/models.html. 2008.

Simulation and Optimization of MPV Suspension System Based on ADAMS

Dongchen Qin¹, Junjie Yang¹, Qiang Zhu¹, Peng Du¹

¹ Zhengzhou University, Zhengzhou, China, dcqin@zzu.edu.cn

1. Abstract

The suspension system is one of the key parts in vehicles, which can directly influence such performances as the steering stability and the ride comfort. The multi-body dynamics model of multi-purpose vehicles (MPV) front suspension is built with ADAMS/VIEW, and the location parameters of the front wheel are simulated. In order to improve the kinematics performance and steering stability, the sensitivity analysis and optimization design for the front suspension are carried out. The results can provide some guide and reference for the R&D of the MPV.

2. Keywords: Macpherson Suspension, Multi-body Dynamics, ADAMS/VIEW, Optimization Design

3. Introduction

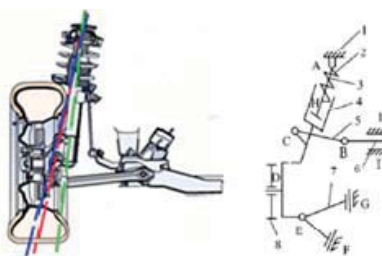
The most important assembly designs of the automobile are suspension, engine and transmission. The design of suspension system influences a variety of performances. Vehicle suspension is the important structure linked to the frame and tires. In the paper, the front McPherson independent suspension of a MPV was analysed for improving its performance. And the virtual prototype model for this suspension, the dynamic simulation models, parametric processing and the optimization of front independent suspension are established. The suspension set up and perfect virtual prototyping model, will upgrade this MPV's independent suspension design level, and also provide foundations for a new suspension design of similar models.

4. Multi-body dynamics model of MPV suspension

Utility of vehicle suspension system is to pass all forces and moments between the wheel and the frame (or body), and to ease the impact load coming from rough road, which can reduce the vibration of bearing system caused by the impact load. And also the suspension system can reduce the interior noise of vehicle and increase occupant comfortable, which can ensure the vehicle's ride comfort. As an important force transmission member connected the frame (or body) and the axle (or wheel), the vehicle suspension system is a key component to ensure the vehicle safety.

4.1 Composition and characteristic of McPherson independent suspension

The front suspension of this MPV uses McPherson independent suspension. Figure1 shows a typical configuration.



1-body;2-coil spring;3-shock absorber upper body;4-knuckle assembly;5-tie rod;6-steering rack;7-under the arm;8-wheel assembly

Figure1: McPherson suspension structure diagram

4.2 Coordinates of the key points of the model

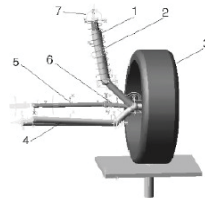
The spatial coordinates and parameters of the key points are important for establishing suspension model, which is the most important task before executing the kinematic simulation in ADAMS. This article uses the coordinate mapping instrument to get the space parameters of the left suspension under no-load conditions. The table1 shows the front suspension positional parameters.

Table1: The positional parameters of front McPherson independent suspension

Parameter name	The kingpin inclination angle	The caster angle	The toe angle	The camber of front wheel	The volume of wheel spin(mm)
Value of design	9°—11.5°	2.5°—3.5°	0°—4°	0°—0.95°	9

4.3 The simulation model

A drive was added on the test platform after building the model of the guiding mechanism. The figure2 shows the model and the test platform.



1-shock absorber; 2-coil spring; 3-wheel; 4-lower control arm; 5-tie rod; 6-knuckle assembly; 7-body

Figure2: The simulation model of the front McPherson suspension

5 The performance simulation and analysis of MPV suspension

The common analysis method of the kinematic characteristics of the suspension is that wheels beat with a wheel on one side or both sides up and down along the vertical directional, variation of wheel position parameters is calculated and analyzed. Based on full load, the range of the run out is at popular -50~+50mm for a vehicle of this study, while the characteristics of the toe angle of wheel, camber angle and wheel hop gauge changing are calculated.

The range of the front toe angle is $-0.77^{\circ}\sim 0.80^{\circ}$ in figure3, and which meets the requirements, that is, the change in angle of less than $\pm 1^{\circ}$. The jump has a positive camber angle, varied from $-0.38^{\circ}\sim 2.74^{\circ}$ in figure4. The range of variation is too large, and the straight running stability will deteriorate automobiles. The range of the caster angle is $2.77^{\circ}\sim 3.37^{\circ}$ in figure5. The amount of change is small, which meets the design requirements, and is favor of the vehicle load handing and stability. The range of kingpin inclination angle is $7.47^{\circ}\sim 11.16^{\circ}$ in the figure6. The amount of change is too large and is not conducive to vehicle handing and stability. The figure7 shows that the change range of the wheel tread is between $-22.844\text{ mm}/50\text{mm}$ and $12.723\text{ mm}/50\text{mm}$, which it's an important performance for a worn tiner.

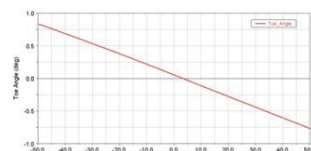


Figure3: the curve of toe angle

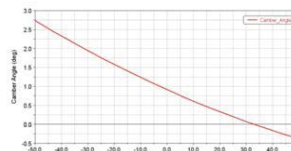


Figure4: the curve of the wheel camber angle

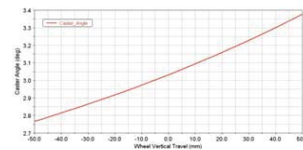


Figure5: the curve of the caster angle

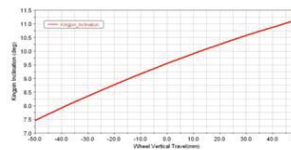


Figure6: the curve of the kingpin inclination angle

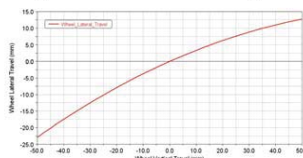


Figure7: the curve of the front wheel tread

The simulation model was builded in ADAMS/VIEW, and combined the date of the front McPherson suspension, and elected the method of left wheel jumping, and executed the kinematic simulation of the McPherson suspension. The curve of front toe angle, the camber angle, the kingpin inclination angle, the caster angle and wheel tread could be got. And the front toe angle of front wheel is too large, and the change range of the wheel tread is beyond the common. So these will increased tire wear.

6. Suspension performance sensitivity analysis

The performance of the vehicle front suspension for sensitivity analysis can get the properties of all the suspension components and installation location of vehicle suspension and provide a reference to the design of suspension. The model of suspension is built and the design parameters of suspension and the sensitivity of the performance of the vehicle are calculated with using the Insight module and CAR module in ADAMS. And the sensitivity of suspension performance is analyzed in VIEW. In this article, the ADAMS/VIEW is selected for analyzing the sensitivity of suspension performance. The main impact factors of operational stability can be found from this model.

6.1 Design variables

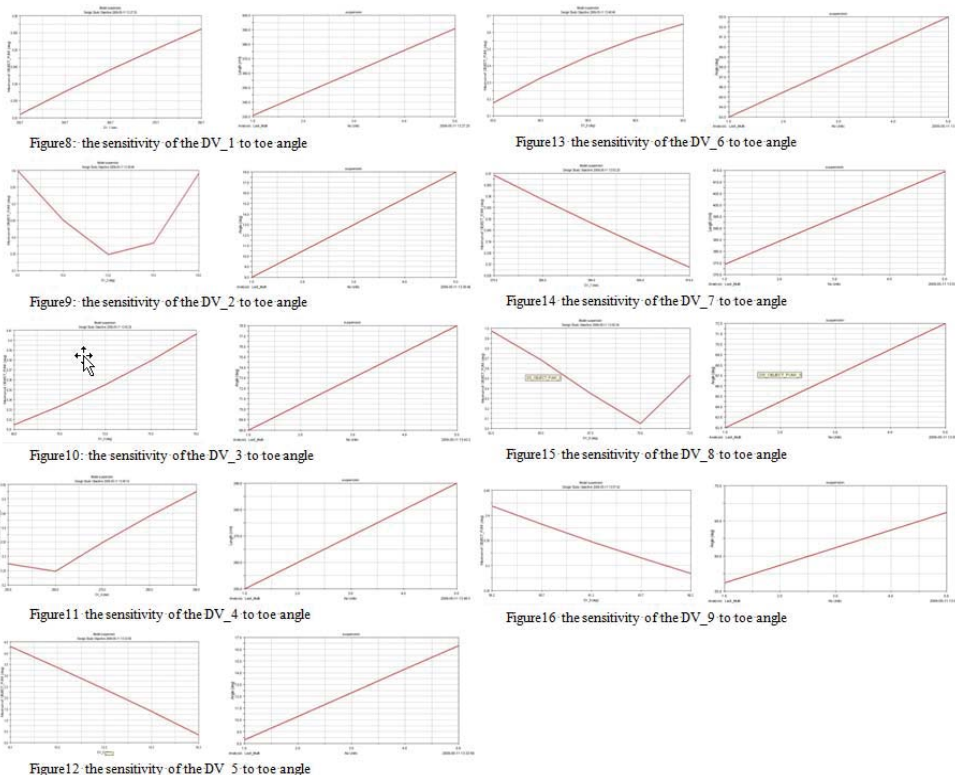
According to the front suspension structure and the position parameters of the front wheel, the length and position angle in space of links EG, EF, CB are elected as design variables sensitivity analysis. The table2 shows the symbol and the significance of 9 variables.

Table2: Definition of the design variable

Number	Design	Means	Code in ADAMS
1	x1	The length of EG	DV_1
2	x2	The angle between the EG and xy plane	DV_2
3	x3	The angle between EG projection in the xy plane and x-axis	DV_3
4	x4	The length of EF	DV_4
5	x5	The angle between EF and xy plane	DV_5
6	x6	The angle between EF projection in the xy plane and x-axis	DV_6
7	x7	The length of CB	DV_7
8	x8	The complement of the angle between CB and xy plane	DV_8
9	x9	The complement of the angle between CB projection in the xy plane and the y-axis	DV_9

6.2 Sensitivity analysis

This paper focuses on the front wheel alignment toe angle, the camber angle, and the volume of tire lateral slip, which was recorded with the initial values of the sensitivity. The conclusion can be got from the figures 8 to 16.



(1) On a larger camber factors followed as: angle between the link EF and xy plane(x5), and complementary angle of xy plane with connecting rod CB(x8), angle between the connecting rod EG and xy plane(x2), other factors less affected.

(2) The front wheel lateral amount greater factor in turn: the angle between the link rod CB and xy plane(x8), the link EF and xy plane angle(x5), EG and xy plane angle(x2), other factors less affected.

7. The optimization of the MPV suspension

The smallest amount of sideslip change is made in order to optimize the range direction. The simulation mode is executed in the ADAMS/View, with adjustments to the hard point coordinates of air spring independent suspension, and then the best hard point coordinate as the last optimization design point. Such parameters as angle between EF and xy plane, angle between EF projection in the xy plane and the x-axis, angle between complementary angle of CB and the xy plane, and angle between complementary angle of CB projection and y-axis are optimized, and the curve of experimental and results of optimization are obtained.

7.1 The objective function

In order to reduce tire wear, we select the front wheel lateral slip amount as the optimization of the objective function. Through optimizing such parameters as angle between EF and xy plane, angle between CB and xy plane, angle between complementary angle of CB projection and xy plane, angle between complementary angle of CB projection in the xy plane and y-axis, the value of the minimum lateral slip of the wheels is obtained.

7.2 The optimization model

The objective function in the optimization and design variables are set in the window of ADAMS. The design variables are DV_5, DV_6, DV_8 and DV_9. And the optimization goal is that the objective function takes the minimum value. For optimization of the front independent suspension performance, the sequential quadratic programming method of ADAMS/VIEW is used. Table3 shows the optimization result.

7.3 The optimization results

Table3 shows the different values of DV_5, DV_6, DV_8, DV_9 for the twice optimization iteration.

Table3: The result of suspension optimization

Iterations	Objective function(mm)	x5(deg)	x6(deg)	x8(mm)	x9(deg)
0	2.9869	61.20	73.085	270	73.085
1	0.33697	62.33	72.601	266.46	72.601
2	0.33712	64.60	72.601	266.46	72.601

7.4 Suspension characteristic curves comparing

The simulation curves of the optimized models are shown as following. The blue curve represents the simulation after optimization, and the red curve represents the simulation before optimization. Figures17~21 show the comparison results of the alignment parameters.

The range of variation optimized camber is $0.579^{\circ} \sim 1.769^{\circ}$ from the figure17. The changes of the toe angle of the front wheel are not large as that can be seen from figure18. The optimization result of the toe angle is acceptable when the wheels balanced and within the design limits. Figure19 shows that the kingpin inclination optimized range is $2.733^{\circ} \sim 3.412^{\circ}$, with expanding the scope of change little compared with optimization before. The change

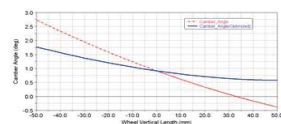


Figure17: the comparison of camber angle

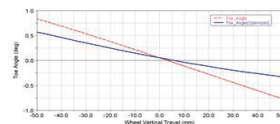


Figure18: the comparison of the toe angle

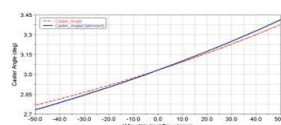


Figure19: the comparison of the caster angle

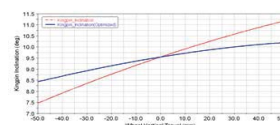


Figure20: comparison of the kingpin inclination angle

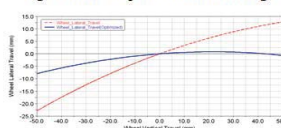


Figure21: the comparison of volume lateral slip of wheels

range of the kingpin inclination angle is $8.432^{\circ}\sim 10.193^{\circ}$ from the figure20. The volume of wheel lateral slip range is $-7.945\sim 0.79$ from the figure21. The curve of optimization is better than that of before.

The parameters of the internal connect position of the steering tie rod, the external position of the lower support arm change very large for this suspension model. By adjusting the parameters a greater response to the result of each change can be obtained. The camber angle of front wheel, the caster angle, and the volume of lateral slip will become better through the comparison of simulation curves, while the change of the toe angle is not obvious. We can get a new suspension layout scheme by optimizing design. The simulation results of the suspension performance are more reasonable. And the maneuverability and stability of the vehicle can be greatly improved.

8. Conclusions

In this paper, taking the front McPherson independent suspension of a MPV as the object, the structure of the suspension is analyzed briefly, and the dynamics model of the suspension combined with multi-body system dynamics theory is established in ADAMS/VIEW. And the curves of the vehicle performance are obtained, which include the toe angle, the camber angle, the kingpin inclination angle, the caster angle and the volume of lateral slip of the front wheel. On the basis of the suspension performance simulation, by using ADAMS/VIEW to set the variables of the suspension, the influence of the camber angle, the kingpin angle and the volume of lateral slip can be analyzed. Those results can provide data for improving the design of MPV suspension. The coordinates of two inner points and the tie rod inner point are changed through using optimized design parameters. The layout scheme is optimized and executed. Comparing with the previous design, the optimized simulation results are more reasonable.

9. References

- [1] Jiang Liu, Based on virtual prototype technology suspension system performance analysis and optimization, *Shanghai: Shanghai Jiao Tong University*,2007.
- [2] M. H. Kim, J. H. Oh, J. H. Lee, M. C. Jeon, Development of rollover criteria based on simple physical model of rollover event. *International Journal of Automotive Technology*, (1):51~59,2006.
- [3] N. Orlandea, M.A. Chace, Simulation of vehicle suspension with ADAMS computer program, *SAE Technical Paper 770053*.
- [4] Wenjie Yi, Vehicle Dynamics suspension kinematics analysis and parameter optimization, *Beijing :Beijing Institute of Technology*,2003.
- [5] Shaoqi Cen, Xiao Pan, Dongchen Qin, Application research on vehicle handling stability dynamics simulating using ADAMS, *Journal of Zhengzhou University(Engineering Science)*,27(3):55~58,2006.
- [5] Peng Ji, Zhenjun Sun, Guohua Cui, Application of ADAMS in vehicle handling stability evaluation, *Agricultural Equipment & Vehicle Engineering*,(5):32~34.2006.
- [6] Dongchen Qin, Modeling,simulation and optimization oriented to handling and stability of sport utility vehicle,*Wuhan: Huazhong University of Science and Technology*,2007.
- [7] Aihua Feng, Virtual Prototype technology-based vehicle ride comfort analysis and driving simulation, *Changchun:Jilin University*,2007.
- [8] Hailin Sun, The kinematics/elastokinematics simulation and analysis of the multi-link suspension system of the car, *Changchun:Jilin University*,2006.

A Novel Anti-optimization Method for Structural Robust Design under Uncertain Loads

Zhifang Fu¹, Chunjie Wang^{1,2}, Junpeng Zhao¹

¹School of Mechanical Engineering and Automation, Beihang University, Beijing 100191, China; zhifang_fu@buaa.edu.cn

²State Key Laboratory of Virtual Reality Technology and Systems, Beihang University, Beijing 100191, China;

1. Abstract

Robust design aims to find a configuration set in which the structural performance is least sensitive to uncertain parameters. The robust design method under loads uncertainty is a nested optimization. In each iteration process, the worst-case constraints can be achieved by the anti-optimization, and then the outer loop performs the optimization under the constraints. In this paper, a new anti-optimization technique is used to alleviate the computational burden with the help of the axial stress forces in members of the truss under each load respectively. The axial forces are the main information in the anti-optimization process which can be easily found by finite element analysis, and the sign of the forces decide the value of the loads in the corresponding constraints. The optimum of the structure is achieved by minimizing the value of the objective function subject to the worst-case constraints under uncertainty loads while the robustness is ensured by the anti-optimization process conducting the worst-case-scenario. The robust design of a 10-bar and a 25-bar truss under uncertain loads are carried out to demonstrate the effectiveness of the present method.

2. Keywords: robust design; uncertain loads; worst-case; anti-optimization;

3. Introduction

The optimization of structure is always performed under deterministic loading conditions. However, the loads are uncertain in most practical situations, and the designer must take the effects of the uncertainty into consideration. The existing popular approaches to describe uncertainties can be classified as probabilistic methods [1,2] and the convex model methods [3,4,5,]. The probabilistic methods require a detailed description of the uncertainties, which can hardly be used in practical engineering. In contrast, the convex model methods, which just require the knowledge of the bounds of the uncertain parameters, so it is well suited for cases where lack of information makes the implementation of probabilistic approaches very difficult.

The theory of convex models was investigated in detail by Ben-Haim and Elishako [6] and Elishako et al. [7], and it is implemented on the constraints by the use of an anti-optimization process, which finds the worst-case produced by the uncertain load condition. The anti-optimization is actually a two-level optimization problem. At the outer level, it obtains the best design by optimizing the design variables, while at the inner level it seeks the worst condition for a given design from anti-optimization.

After the anti-optimization method is proposed, many researchers have applied it to the theory and practice. Marco Lombardi et al.[8] described a technique for design under uncertainty based on the worst-case-scenario technique of anti-optimization, the method can alleviate the computational burden. Marco Lombardi [9] compared two different approaches which use anti-optimization, namely a nested optimization and a two steps optimization, where anti-optimization is solved once for all constraints before starting the optimization. Stewart McWilliam [10] present two new methods for solving constraint equations by anti-optimization method of uncertain structures using interval analysis. Zhiping Qiu [11] studied the anti-optimization problem of structures with uncertain design variables by combing the conventional optimization and interval analysis.

In this paper, a new anti-optimization technique is used to alleviate the computational burden with the help of the axial stress forces in members of the truss under each load respectively. The axial forces are the main information in the anti-optimization process which can be easily found by finite element analysis, and the signs of the forces decide the value of the loads in the corresponding constraints.

4. Problem formulation

In the deterministic formulation of structural optimization problems, the design variables and parameters are assumed deterministic and the objective function as well as the constraints is referred to their nominal values. The classical formulation of structural optimization problem can be mathematically expressed as:

$$\begin{aligned} & \text{find} && \mathbf{X} \\ & \text{minimize} && f(\mathbf{X}) \\ & \text{subject to} && g_i(\mathbf{X}) \leq 0 \quad (i = 1, 2, \dots, k) \end{aligned} \quad (1)$$

Where $\mathbf{X} = (x_1, \dots, x_n)^T$ is the n-dimensional vector of design variables, $f(\mathbf{X})$ the objective function, $g_i(\mathbf{X})$ the

inequality constraint functions, and k is the total number of constraints. For simplicity, the equality constraint functions are not described here.

However, one may observe that the objective function $f(\mathbf{X})$ and/or the constraints $g_i(\mathbf{X})$ may depend on some design parameters subject to uncertainty. In this paper, only loads uncertainty is concerned, and the stress and displacement are the constraints, and interval variables are referred to the loads that vary about their nominal values and the design variable are controllable design parameters that need to be determined by the designer, such as the area of truss elements. Considering for the sake of simplicity the case where the uncertainty is limited to the constraint functions $g_i(\mathbf{X})$, so Eq. (1) becomes:

$$\begin{aligned}
& \text{find} && \mathbf{X} \\
& \text{minimize} && f(\mathbf{X}) \\
& \text{subject to} && \underline{\sigma}_i^{allow} \leq \sigma_i(\mathbf{X}, \mathbf{P}) \leq \bar{\sigma}_i^{allow} \quad (i = 1, 2, \dots, k) \\
& && \underline{u}_j^{allow} \leq u_j(\mathbf{X}, \mathbf{P}) \leq \bar{u}_j^{allow} \quad (j = 1, 2, \dots, t) \\
& && \mathbf{P}^L \leq \mathbf{P} \leq \mathbf{P}^U
\end{aligned} \tag{2}$$

in where it is assumed that $\mathbf{P} = [P_1, P_2, \dots, P_n]$ is the loads uncertainty design parameter vector that only the bounds are known, \mathbf{P}^L and \mathbf{P}^U denote the lower and upper bound of \mathbf{P} , i.e. $\mathbf{P} \in \mathbf{P}^I = [\mathbf{P}^L, \mathbf{P}^U]$. $\sigma_i(\mathbf{X}, \mathbf{P})$ and $u_j(\mathbf{X}, \mathbf{P})$ are the implicit response variables: nodal displacement and element stress. $\underline{\sigma}_i^{allow}$ and $\bar{\sigma}_i^{allow}$ are the allowable stress of the i th element, k is the number of element. \underline{u}_j^{allow} and \bar{u}_j^{allow} are the maximum allowable displacement of the j th node, t is the number of node.

In formulation (2), we require that $\sigma_i(\mathbf{X}, \mathbf{P})$ and $u_j(\mathbf{X}, \mathbf{P})$ are satisfied for all the possible values of \mathbf{P} , and the structural robust optimization problem can be expressed as an alternative formulation is:

$$\begin{aligned}
& \text{find} && \mathbf{X} \\
& \text{minimize} && f(\mathbf{X}) \\
& \text{subject to} && \max_{\mathbf{P} \in \mathbf{P}^I} \sigma_i(\mathbf{X}, \mathbf{P}) - \bar{\sigma}_i^{allow} \leq 0 \quad (i = 1, 2, \dots, k) \\
& && \underline{\sigma}_i^{allow} - \min_{\mathbf{P} \in \mathbf{P}^I} \sigma_i(\mathbf{X}, \mathbf{P}) \leq 0 \quad (i = 1, 2, \dots, k) \\
& && \max_{\mathbf{P} \in \mathbf{P}^I} u_j(\mathbf{X}, \mathbf{P}) - \bar{u}_j^{allow} \leq 0 \quad (j = 1, 2, \dots, t) \\
& && \underline{u}_j^{allow} - \min_{\mathbf{P} \in \mathbf{P}^I} u_j(\mathbf{X}, \mathbf{P}) \leq 0 \quad (j = 1, 2, \dots, t) \\
& && \mathbf{P}^L \leq \mathbf{P} \leq \mathbf{P}^U
\end{aligned} \tag{3}$$

The maximization of $\sigma_i(\mathbf{X}, \mathbf{P})$ and $u_j(\mathbf{X}, \mathbf{P})$ over \mathbf{P}^I is a process of finding the worst value of \mathbf{P} for each constraint, and this is an anti-optimization process.

The worst-case set of parameters is searched at each optimization iteration process, and this can be very expensive to solve. The novel anti-optimization method proposed in the paper is to alleviate the computational burden which is a main difficulty that restricts the application of structural robust design optimization. The process is described as follows:

In the anti-optimization, the stress of each element $\sigma_i(\mathbf{X}, P_\gamma)$ and the displacement of each node $u_j(\mathbf{X}, P_\gamma)$ are obtained under the load P_γ . When $\sigma_i(\mathbf{X}, P_\gamma) \geq 0$, the force P_γ will be replaced by P_γ^U which is the upper bound of P_γ in the constraint $\max_{\mathbf{P} \in \mathbf{P}^I} \sigma_i(\mathbf{X}, P_\gamma) - \bar{\sigma}_i^{allow} \leq 0$, and the force P_γ will be replaced by P_γ^L which is the lower bound of P_γ in the constraint $\underline{\sigma}_i^{allow} - \min_{\mathbf{P} \in \mathbf{P}^I} \sigma_i(\mathbf{X}, P_\gamma) \leq 0$. Similarly, when $u_j(\mathbf{X}, P_\gamma) \geq 0$, the force P_γ will be replaced by P_γ^U which is the upper bound of P_γ in the constraint $\max_{\mathbf{P} \in \mathbf{P}^I} u_j(\mathbf{X}, P_\gamma) - \bar{u}_j^{allow} \leq 0$ the force P_γ will be instead with P_γ^L which is the lower bound of P_γ in the constraint $\underline{u}_j^{allow} - \min_{\mathbf{P} \in \mathbf{P}^I} u_j(\mathbf{X}, P_\gamma) \leq 0$. In the converse, when $\sigma_i(\mathbf{X}, P_\gamma) < 0$, the force P_γ will be replaced by P_γ^L in the constraint $\max_{\mathbf{P} \in \mathbf{P}^I} \sigma_i(\mathbf{X}, P_\gamma) - \bar{\sigma}_i^{allow} \leq 0$, and the force P_γ will be replaced by P_γ^U in the constraint $\underline{\sigma}_i^{allow} - \min_{\mathbf{P} \in \mathbf{P}^I} \sigma_i(\mathbf{X}, P_\gamma) \leq 0$. Similarly, when $u_j(\mathbf{X}, P_\gamma) < 0$, the

force P_γ will be replaced by P_γ^L in the constraint $\max_{\mathbf{P} \in \mathbf{P}^l} u_j(\mathbf{X}, P_\gamma) - u_j^{-allow} \leq 0$, the force P_γ will be replaced by P_γ^U in the constraint $u_j^{allow} - \min_{\mathbf{P} \in \mathbf{P}^u} u_j(\mathbf{X}, P_\gamma) \leq 0$. By the analysis of the anti-optimization process, the worst-case can be achieved easily. And then the robust optimization changed to a deterministic optimization problem. In order to improve the efficiency of convergence, the initial values of design parameters are inherited by the result of certainty optimization. The flow diagram of the optimization process is showed as Figure 1.

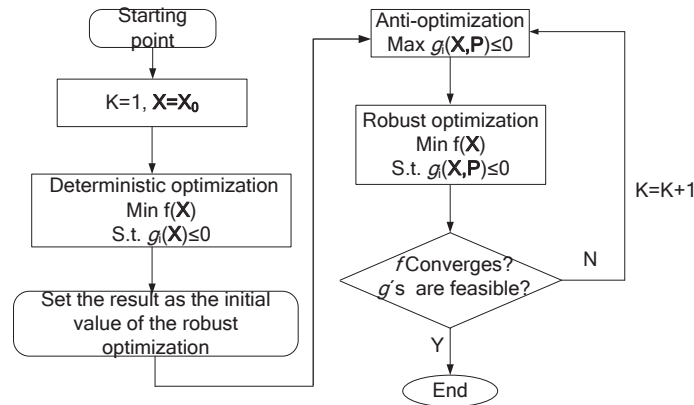


Figure 1: Optimization process

5. Numerical examples

5.1. Example 1: 10-bar aluminium truss

Consider the well-known 10-bar truss which is made of aluminum as shown in Fig. 2. The characteristics of the truss are as follows: the modulus of elasticity E is 68 948MPa(10 000ksi), the weight density ρ is 2768 kg/m³(0.1 lb/in.³) and the length L of each of the vertical and horizontal bars is 9.144 m (360 in.). The maximum allowable stress in each member is the same for tension and compression. The allowable stress $\sigma_{j,allowable}$ is 172.37MPa (25ksi) for all bars except bar 9, for which the allowable stress is 517.11MPa (75ksi). The maximum allowable vertical displacement $\delta_{2,allowable}$ at joint 2 is 0.1270 m (5in.). The cross-sectional area of member j is A_j and the minimum gauge constraint of each member A_{min} is 0.645cm²(0.1in.²). The joint 4 is subjected to a vertical load P_1 while the joint 2 is subjected to both a vertical load P_2 and a horizontal load P_3 as shown in Fig. 2. Their nominal values are $\bar{P}_1=444.8\text{kN}$ (100 kip), $\bar{P}_2=444.8\text{kN}$ (100 kip), and $\bar{P}_3=1779.2\text{kN}$ (400 kip) respectively.

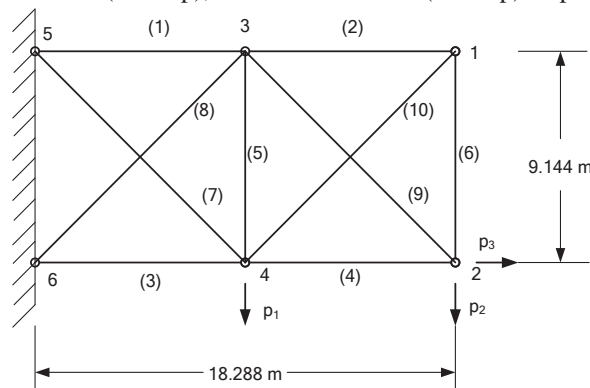


Figure 2: 10-bar truss

Following the equilibrium and compatibility equations, one may easily obtain the axial forces N_i ($i=1,2,\dots,10$) in the members and the vertical displacement δ_2 at joint 2 as follows:

$$N_1 = p_2 - \frac{\sqrt{2}}{2} N_8 \quad (4) \quad N_2 = -\frac{\sqrt{2}}{2} N_{10} \quad (5) \quad N_3 = -p_1 - 2p_2 + p_3 - \frac{\sqrt{2}}{2} N_8 \quad (6)$$

$$N_4 = -p_2 + p_3 - \frac{\sqrt{2}}{2} N_{10} \quad (7) \quad N_5 = -p_2 - \frac{\sqrt{2}}{2} N_8 - \frac{\sqrt{2}}{2} N_{10} \quad (8) \quad N_6 = -\frac{\sqrt{2}}{2} N_{10} \quad (9)$$

$$N_7 = \sqrt{2}(p_1 + p_2) + N_8 \quad (10) \quad N_8 = \frac{a_{22}b_1 - a_{12}b_2}{a_{11}a_{22} - a_{12}a_{21}} \quad (11) \quad N_9 = \sqrt{2}p_2 + N_{10} \quad (12)$$

$$N_{10} = \frac{a_{11}b_2 - a_{21}b_1}{a_{11}a_{22} - a_{12}a_{21}} \quad (13) \quad a_{11} = \left(\frac{1}{A_1} + \frac{1}{A_3} + \frac{1}{A_5} + \frac{2\sqrt{2}}{A_7} + \frac{2\sqrt{2}}{A_8}\right) \frac{L}{2E} \quad (14) \quad a_{12} = a_{21} = \frac{L}{2A_3E} \quad (15)$$

$$a_{22} = \left(\frac{1}{A_2} + \frac{1}{A_4} + \frac{1}{A_6} + \frac{2\sqrt{2}}{A_9} + \frac{2\sqrt{2}}{A_{10}}\right) \frac{L}{2E} \quad (16) \quad b_1 = \left(\frac{p_2}{A_1} + \frac{p_1 + 2p_2 - p_3}{A_3} - \frac{p_2}{A_5} + \frac{2\sqrt{2}(p_1 + p_2)}{A_7}\right) \frac{\sqrt{2}L}{2E} \quad (17)$$

$$b_2 = \left(\frac{\sqrt{2}(p_3 - p_2)}{A_4} - \frac{\sqrt{2}p_2}{A_5} - \frac{4p_2}{A_9}\right) \frac{L}{2E} \quad (18) \quad \delta_2 = \sum_{i=1}^{10} \frac{N_i^0 N_i L_i}{A_i E} \quad (19)$$

Where the values of N_i^0 are calculated from Eqs. (4)- (13) with a substitution $p_1 = p_3 = 0$ and $p_2 = 1$.

The optimal cross-sectional areas and weight are listed in Table 1 for comparison with its deterministic counterpart. They agree well with those of Lombardi [4] and Elishakoff et al. [7], which are also shown in Table 1. Stresses of all the elements and displacement of node 2 occurring at various load vertices in an optimal structure are shown in Table 2, they do not exceed the allowable stresses and/or displacement requirement, and some of them reached the allowable values in some load vertices. The anti-optimization technique is just used once in the optimization process, so the method alleviates the computational burden.

Table 1: Optimal cross-sectional areas of the 10-bar truss under different design conditions

Member no.	Cross-section area(cm ²)				
	Loads with no uncertainty			Loads with 10% uncertainty	
	Present	Ref.[4]	Present	Ref.[4]	Ref.[7]
1	26.033	26.019	28.797	28.799	28.799
2	0.645	0.645	0.645	0.645	0.645
3	26.033	26.045	44.016	44.019	44.019
4	78.060	78.064	90.584	90.587	90.589
5	24.932	24.912	27.782	27.783	27.783
6	0.645	0.645	0.645	0.645	0.645
7	72.665	72.716	79.851	79.858	79.855
8	0.645	0.645	0.645	0.645	0.645
9	17.791	17.817	29.841	29.841	29.843
10	0.912	0.912	0.645	0.645	0.645
Weight(Kg)	725.08	725.34	884.41	884.46	884.47

Table 2: Stresses and displacement of node 2 δ_2 occurring at various load vertices in an optimal structure

Loads vertices Member no.	UUU	UUL	ULU	ULL	LLU	LUL	LLU	LLL
1	1.718	1.7237	1.402	1.409	1.713	1.720	1.399	1.405
2	0.967	1.046	0.712	0.791	0.968	1.047	0.713	0.791
3	1.124	0.319	1.524	0.720	1.323	0.519	1.7237	0.919
4	1.627	1.235	1.7237	1.331	1.627	1.235	1.7237	1.331
5	-1.720	-1.711	-1.412	-1.403	-1.7237	-1.715	-1.415	-1.407
6	0.967	1.046	0.712	0.791	0.968	1.047	0.713	0.791
7	1.7237	1.721	1.569	1.566	1.568	1.565	1.413	1.410
8	-1.163	-1.555	-0.811	-1.203	-0.912	-1.303	-0.560	-0.951
9	2.289	2.287	1.875	1.873	2.289	2.287	1.875	1.873
10	-1.368	-1.479	-1.007	-1.118	-1.369	-1.480	-1.008	-1.119
δ_2	0.101	0.127	0.065	0.092	0.091	0.118	0.056	0.082

3.2. Example 2: 25-bar steel truss

The 25-bar steel truss as shown in Fig. 3 is considered here. The Young's modulus of the truss E is 199 949.2MPa (2.9e10⁴ksi). The length L of each of the vertical and horizontal bars is 15.24 m(600 in.). The joint 12 is

hinge-supported while Joints 6, 8 and 10 are roller-supported. Joints 11, 9 and 7 are subjected to vertical loads P_1 , P_2 and P_3 respectively while Joint 1 is subjected to a horizontal load P_4 as shown in Fig. 3. Their nominal values are $\bar{P}_1 = \bar{P}_3 = 1779.2\text{KN}(400\text{kip})$, $\bar{P}_2 = 2224\text{KN}(500\text{kip})$, and $\bar{P}_4 = 1334.4\text{KN}(300\text{kip})$ respectively. The maximum allowable stress in each member is the same whether in tension or compression. The allowable stress $\sigma_{j,\text{allowable}}$ is $172.37\text{MPa}(25\text{ksi})$ for all bars. Only the stress constraints are considered in the analysis. The axial forces N_j in members can be easily found by finite element analysis. The cross-sectional area of member j is A_j and the minimum gauge constraint of each member A_{min} is $0.645\text{cm}^2(0.1\text{ in.}^2)$.

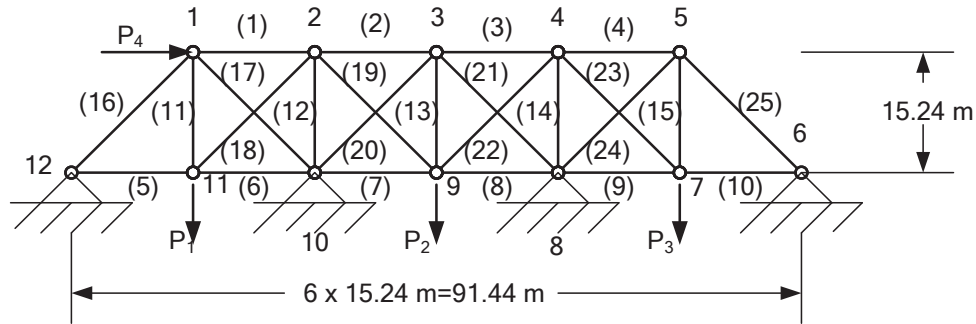


Figure 3: 25-bar truss

Similar to Example 1, this problem of minimum volume design is solved using the proposed model with the truss under nominal loads P_1 , P_2 and P_3 with 10% uncertainty and load P_4 with 20% uncertainty. The optimal cross-sectional areas and weight are listed in Table 1 for comparison with those of no uncertainty. They agree well with those of Lombardi [4] and Ganzerli, S. et al. [12] also shown in Table 3. Stresses of all the elements occurring at various load vertices in an optimal structure are computed also, they do not exceed the allowable stresses and/or displacement requirement, and some of them reached the allowable values in some load vertices.

Table 3: Optimal cross-sectional areas of the 25-bar truss under different design conditions

Member no.	Cross-section area(cm^2)				
	Minimum weight design				
	Loads with no uncertainty		Loads P_1 through P_3 with 10% uncertainty and load P_4 with 20% uncertainty		
	Present	Ref.[4]	Present	Ref.[4]	Ref.[12]
1	19.677	19.666	27.139	27.374	26.419
2	0.645	0.645	0.645	0.645	0.645
3	1.441	1.442	6.223	6.234	5.117
4	0.645	0.645	1.633	1.574	4.193
5	74.740	74.615	90.066	89.793	89.514
6	23.575	23.536	35.879	35.555	35.687
7	0.645	0.645	0.645	0.645	0.645
8	0.645	0.645	3.868	3.896	2.740
9	0.645	0.645	0.823	0.839	2.107
10	34.860	34.648	38.913	38.640	39.669
11	52.263	52.146	65.181	65.006	65.337
12	82.674	82.708	92.387	92.593	91.671
13	64.923	64.914	71.306	71.310	71.385
14	66.725	66.778	73.878	73.884	73.760
15	68.932	68.937	75.702	75.710	75.692
16	3.9713	3.965	25.670	25.644	25.340
17	77.749	77.711	93.160	92.897	93.371
18	72.191	72.237	78.817	79.097	78.347
19	44.736	44.730	52.087	52.077	51.580
20	44.719	44.730	52.008	52.035	51.518

21	47.061	47.073	51.965	51.989	52.049
22	45.953	45.946	50.977	50.961	50.772
23	48.557	48.492	53.574	53.530	53.535
24	48.421	48.492	53.560	53.611	53.412
25	48.930	48.999	54.571	54.645	56.101
Volume(cm ³)	1.791 x 10 ⁶	1.790 x 10 ⁶	2.111 x 10 ⁶	2.111 x 10 ⁶	2.111 x 10 ⁶

6. References

- [1] Lógó, J.. New type of optimality criteria method in case of probabilistic loading conditions. *Mechanics Based Design of Structures and Machines*,35(2):147–162, 2007.
- [2] Lógó, J., Ghaemi, M., Movahedi Rad, M.. Optimal topologies in case of probabilistic loading: The influence of load correlation.*Mechanics Based Design of Structures and Machines*,37(3):327–348, 2009.
- [3] Doltsinis I, Kang Z, Cheng G. Robust design of non-linear structures using optimization methods. *Computer methods in applied mechanics and engineering*, 194(12): 1779-1795, 2005.
- [4] Au F T K, Cheng Y S, Tham L G, et al. Robust design of structures using convex models. *Computers & structures*, 81(28): 2611-2619, 2003.
- [5] Sandgren E, Cameron T M. Robust design optimization of structures through consideration of variation. *Computers & structures*, 80(20): 1605-1613, 2002.
- [6] Ben-Haim Y, Elishakoff I. Convex models of uncertainty in applied mechanics[M]. Elsevier, 2013.
- [7] Elishakoff I, Haftka R T, Fang J. Structural design under bounded uncertainty—optimization with anti-optimization. *Computers & structures*, 53(6): 1401-1405, 1994.
- [8] Lombardi M, Haftka R T. Anti-optimization technique for structural design under load uncertainties. *Computer methods in applied mechanics and engineering*, 157(1): 19-31, 1998.
- [9] Lombardi M. Optimization of uncertain structures using non-probabilistic models. *Computers & structures*, 67(1): 99-103, 1998.
- [10] McWilliam S. Anti-optimisation of uncertain structures using interval analysis. *Computers & Structures*, 79(4): 421-430, 2001.
- [11] Qiu, Z., & Wang, X.. Structural anti-optimization with interval design parameters. *Structural and Multidisciplinary Optimization*, 41(3), 397-406,2010.
- [12] Ganzerli, S., & Pantelides, C. P.. Optimum structural design via convex model superposition. *Computers & Structures*, 74(6), 639-647,2000.

An improvement technique for Bi-directional Evolutionary Structural optimisation (BESO) method

Kazem Ghabraie¹

¹ School of Civil Engineering and Surveying, University of Southern Queensland, QLD, Australia,
kazem.ghabraie@usq.edu.au

1. Abstract

Bi-directional Evolutionary Structural optimisation (BESO) method is now a well-known and popular method in topology optimisation. A new interpretation of this method is presented in which the method is viewed as a two-step procedure. Based on this interpretation, a simple heuristic improvement technique is introduced to improve BESO results. The proposed improvement technique is tested and verified through numerical examples and its performance is compared with the averaging sensitivity stabilisation technique proposed in [1]. It is shown that the proposed improvement is robust than the averaging sensitivity technique.

2. Keywords: Topology optimisation, BESO, Conjugate gradient method, hard-kill, soft-kill

3. Introduction

The Bi-directional Evolutionary Structural optimisation (BESO) method was originally proposed in references [2, 3, 4] as an extension to the ESO (Evolutionary Structural optimisation) method introduced by Xie and Steven [5, 6]. In the ESO method, materials are gradually removed from the least efficient parts of the design domain. BESO has the capability of adding material to efficient parts as well as removing inefficient materials. Using a finite element discretisation of the design domain, BESO adds and removes materials through adding and removing elements.

There are two variations of the BESO method. In hard-kill BESO, the inefficient elements are completely removed from the finite element model while in the soft-kill variation, they are replaced by a considerably weaker material. Soft kill BESO can also be extended to solve multi-material distribution problems [7]. In all variations of BESO the elements can only assume the considered material or existence states, and thus the final topology has no elements with intermediate density (grey elements). Another advantage of the BESO method is its capability to be easily combined with any available Finite Element package. Despite these advantages, however, BESO is usually considered as an intuitive method with no solid mathematical background [8].

Usually the BESO method is said to be founded on the simple idea of gradually removing materials from the inefficient parts and adding them to the efficient parts of the structure. In this paper, we propose a different interpretation of this method. This interpretation helps us to propose a simple approach to improve this method.

The original BESO method was very sensitive to the selection of its algorithmic parameters and was not always stable. An improved version of this method was proposed by Huang and Xie [1]. The improving procedure proposed here can be considered as alternatives to the simple stabilising procedure introduced by Huang and Xie in section 2.4 of reference [1] (hereafter referred to as HX). We will demonstrate the application of these improving techniques and compare them with each other through some examples.

4. Design variables in BESO

In BESO, for each element we use one design variable. The design variable of element e is denoted by x_e which can typically assume discrete values of 0 or 1. The design variable vector is denoted by $\mathbf{x} = [x_1, x_2, \dots, x_n]^T$ where n is the number of elements.

Assuming a soft-kill approach, the following linear interpolation scheme can be used to relate the elastic modulus of element e to its design variable

$$E_e = E^{(0)} + (E^{(1)} - E^{(0)})x_e, \quad e = 1, \dots, n. \quad (1)$$

The hard-kill can be obtained if $E^{(0)} = 0$ is used in the above equation.

The equilibrium equation can be written as $\mathbf{K}(\mathbf{x})\mathbf{u} = \mathbf{f}$ in which \mathbf{u} and \mathbf{f} are nodal load and displacement vectors respectively, and \mathbf{K} is the global stiffness matrix derived by assembling element stiffness matrices as follows,

$$\mathbf{K}(\mathbf{x}) = \sum_{e \in \mathcal{E}} \mathbf{K}_e^g(x_e). \quad (2)$$

Here \mathbf{K}_e^g is the global level stiffness matrix of element e and \mathcal{E} represents all the elements which are present in the design domain and can be defined as $\mathcal{E} = \{e \in \{1, \dots, n\} | E_e > 0\}$.

5. Compliance minimisation problem

Defined as $c(\mathbf{u}, \mathbf{x}) = \mathbf{f}^T \mathbf{u}$, mean compliance is the most commonly used objective function in topology optimisation of structures. The compliance minimisation problem is usually considered with a volume constraint as follows,

$$P_d : \min_{\mathbf{x} \in \{0,1\}^n} \{c(\mathbf{u}, \mathbf{x}) | \mathbf{K}(\mathbf{x})\mathbf{u} = \mathbf{f}, V \leq \bar{V}\}, \quad (3)$$

where V is the total volume and \bar{V} is the maximum allowable volume of material in the structure.

Sensitivities of the mean compliance w.r.t. design variables take the form

$$\frac{\partial c}{\partial x_e} = -\mathbf{u}^T \frac{\partial \mathbf{K}}{\partial x_e} \mathbf{u} = -\mathbf{u}^T \frac{\partial \mathbf{K}_e^g}{\partial E_e} \frac{\partial E_e}{\partial x_e} \mathbf{u} = -(E^{(1)} - E^{(0)}) \mathbf{u}^T \frac{\mathbf{K}_e^g}{E_e} \mathbf{u} = -\frac{E^{(1)} - E^{(0)}}{E_e} \mathbf{u}_e^T \mathbf{K}_e \mathbf{u}_e, \quad e \in \mathcal{E}, \quad (4)$$

where \mathbf{u}_e and \mathbf{K}_e respectively denote the displacement vector and local stiffness matrix of element e . In a hard-kill approach, noting that $E^{(0)} = 0$ and $E_e = E^{(1)}$, $\forall e \in \mathcal{E}$, the above equation will reduce to $\frac{\partial c}{\partial x_e} = -\mathbf{u}_e^T \mathbf{K}_e \mathbf{u}_e$, $e \in \mathcal{E}$.

In BESO, the efficiency of the elements is measured using a parameter called *sensitivity number*. Denoting the sensitivity number of element e by α_e , we can write (see e.g. [9])

$$\alpha_e = -\frac{\partial c}{\partial x_e}, \quad e \in \mathcal{E}. \quad (5)$$

In hard-kill approach Eq.(5) can only be used to calculate sensitivity numbers of non-void elements. A filtering approach can be used in this case to extrapolate sensitivity numbers of void elements. In [1], Huang and Xie used a two-level filtering scheme which is also adopted here. In this approach firstly nodal sensitivities are derived by averaging sensitivities of the elements connecting to each node in the following form

$$\tilde{\alpha}_j = \frac{\sum_{e \in \mathcal{E}_j} v_e \alpha_e}{\sum_{e \in \mathcal{E}_j} v_e}. \quad (6)$$

Here, \mathcal{E}_j represents the set of elements connected to node j and v_e denotes the volume of element e . Filtered element sensitivities are then calculated through the following filtering scheme

$$\hat{\alpha}_e = \frac{\sum_{j=1}^N w_{ej} \tilde{\alpha}_j}{\sum_{j=1}^N w_{ej}}, \quad w_{ej} = \max\{0, r - r_{ej}\} \quad (7)$$

where $\hat{\alpha}_e$ is the filtered sensitivity of element e , N is the number of nodes in the design domain, w_{ej} is a linear weighting factor, r is the filtering radius and r_{ej} is the distance between the centroid of element e and node j . In [1], Huang and Xie showed that this filtering scheme is also useful in overcoming numerical instabilities such as checkerboard formation and mesh dependency [10].

Different algorithms have been proposed for adding and removing elements in BESO. In the examples solved here, we use the algorithm introduced by [11] and [1]. This algorithm uses two controlling parameters, namely, evolutionary volume ratio (R_v) and maximum allowable admission ratio (R_a). The first one controls the volume change and the second one controls the maximum amount of materials which can be added in each iteration. Once the volume of the design reaches the limit of \bar{V} , R_v will have no effect and all later iterations will have the same volume. In such cases, the number of adding and removing elements will be equal in each iteration, and R_a determines this number.

6. Reinterpretation of BESO procedure

Consider the following unconstrained continuous version of P_d in Eq.(3)

$$P_c : \min_{\mathbf{x} \in \mathbb{R}^n} \{c(\mathbf{u}, \mathbf{x}) | \mathbf{K}(\mathbf{x})\mathbf{u} = \mathbf{f}\} \quad (8)$$

The BESO algorithm firstly finds a descent (or search) direction based on P_c and then this direction is modified to satisfy the constraints defined in P_d .

In the first step, the BESO algorithm uses the *steepest descent vector* which is defined as $-\nabla f$ for a general objective function f [12]. Denoting the descent vector by $\mathbf{d} = [d_1, \dots, d_n]^T$ and the gradient vector by $\mathbf{g} = [g_1, \dots, g_n]^T$, in any iteration like k we have

$$\mathbf{d}^{[k]} = -\nabla c(\mathbf{x}^{[k]}) = -\mathbf{g}^{[k]}. \quad (9)$$

The superscripts in square brackets denote the iteration number. It is clear that $\alpha_e^{[k]} = d_e^{[k]} = -g_e^{[k]}$.

The second step involves modifying the descent vector to satisfy the constraints in P_a . The modified vector is denoted by $\hat{\mathbf{d}} = [\hat{d}_1, \dots, \hat{d}_n]^T$ and referred to as the *move vector* here. Using this notation, in any iteration k , updating of design variables could be expressed as $\mathbf{x}^{[k+1]} = \mathbf{x}^{[k]} + \hat{\mathbf{d}}^{[k]}$.

Noting the condition $x_e \in \{0, 1\}$, the only possible values for \hat{d}_e are $-1, 0$, and 1 corresponding to removing, not changing, and adding element e respectively. In each iteration, based on R_v and R_a we can determine two sensitivity number thresholds for adding and removing elements: α_{add} and α_{del} (see e.g. [1]). After finding these thresholds, the relationship between $\hat{\mathbf{d}}$ and \mathbf{d} in iteration k can be expressed as

$$\hat{d}_e^{[k]} = \text{sgn} \left(\text{sgn} \left(d_e^{[k]} - \alpha_{del}^{[k]} \right) + \text{sgn} \left(d_e^{[k]} - \alpha_{add}^{[k]} \right) \right), \quad e = 1, \dots, n. \quad (10)$$

Based on this interpretation, we propose an improvement technique to the first step of the BESO algorithm in the next section.

7. The proposed improvement technique

We propose a heuristic improvement technique by using nonlinear a Conjugate Gradient method [13] as an alternative solver for the first step of BESO. Nonlinear conjugate gradient methods converge faster than the steepest descent method and demand negligible amount of extra memory and computations which make them suitable for large-scale problems. In conjugate gradient methods the descent direction is defined as

$$\begin{cases} \mathbf{d}^{[1]} &= -\mathbf{g}^{[1]} \\ \mathbf{d}^{[k]} &= -\mathbf{g}^{[k]} + \beta^{[k]} \mathbf{d}^{[k-1]}, \quad k > 1 \end{cases} \quad (11)$$

where β is a scalar. Different formulae are suggested for β . For example the one proposed by Fletcher and Reeves [13], can be expressed as

$$\beta_{FR}^{[k]} = \frac{\mathbf{g}^{[k]} \cdot \mathbf{g}^{[k]}}{\mathbf{g}^{[k-1]} \cdot \mathbf{g}^{[k-1]}}, \quad k > 1. \quad (12)$$

To improve BESO, based on Eq.(11), we propose to use the following equation instead of Eq.(9) in each iteration,

$$\begin{cases} d_e^{[1]} &= \hat{\alpha}_e^{[1]} \\ d_e^{[k]} &= \hat{\alpha}_e^{[k]} + \beta_{FR}^{[k]} \hat{\alpha}_e^{[k-1]}, \quad k > 1 \end{cases} \quad (13)$$

where

$$\beta_{FR}^{[k]} = \frac{\sum_{e \in \mathcal{E}} (\hat{\alpha}_e^{[k]})^2}{\sum_{e \in \mathcal{E}} (\hat{\alpha}_e^{[k-1]})^2}. \quad (14)$$

The HX stabilising procedure involves averaging consecutive sensitivity numbers, i.e. setting $d_e^{[k]} = \frac{\hat{\alpha}_e^{[k]} + \hat{\alpha}_e^{[k-1]}}{2}$ for $k > 1$. Noting that in BESO only the direction of sensitivities vector is important, this stabilisation technique can also be expressed by replacing $\beta_{FR}^{[k]}$ in Eq.(13) with $\beta_{HX}^{[k]} = 1$. In the next section we test the proposed improvement technique (Eq. 13) and compare it with the HX technique.

8. Numerical examples

8.1. Example 1

A simply supported beam is considered in the first example. The size of the beam is 180×30 and only half of it is modelled due to symmetry. Four node bi-linear unit square elements are used to discretise the modelled domain. Design domain of the problem is depicted in Fig. 1a. The force p has the magnitude of 1. Base material has an elasticity modulus of $E = 1$ and a Poisson's ratio of $\nu = 0.3$. The filtering radius is selected as $r_f = 4.5$. All units are consistent. A hard-kill approach is adopted with $R_a = 4\%$ and $R_v = 1\%$. The problem starts with an initial full design domain and the target volume fraction is 50%. The solution was terminated after 200 iterations if convergence was not achieved.

The solutions obtained using no improvement (NO), The proposed improvement in Eqs. (13) and (14) (FR), and Huang and Xie stabilising procedure of averaging sensitivities (HX) are shown in Fig. 1c. The evolution histories of objective function values are shown in Fig. 1b. It can be seen that without using the improvements, the solution procedure is unstable. Both FR and HX stabilised the solution procedure and resulted in a considerable reduction (12%) in the final value of the objective function. The results obtained via FR and HX improvements are very similar in this case.

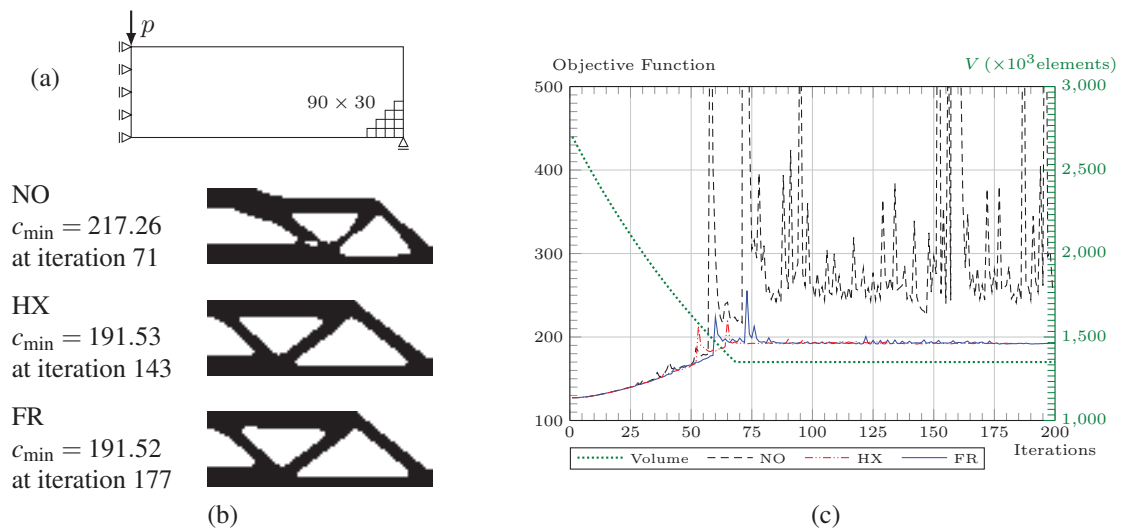


Figure 1: Design domain (a), optimum topologies obtained (b), and the evolution history of volume and objective function values (c) for the simply supported beam in example 1.

8.2. Example 2

For the second example a short cantilever beam loaded as shown in Fig. 2a is considered where $p = 1$. The domain size is 64×40 which is discretised into four node bi-linear unit square elements. The material is the same as the previous example. We start from a full design domain. The target volume fraction is 50%. The hard-kill approach with $R_a = 5\%$, $R_v = 1\%$, and $r_f = 4$ is used. All units are consistent.

The evolution history of the objective function values and the obtained topologies are shown in Fig. 3b and Fig. 3c respectively. Like the previous example, without using the improvements, the solution procedure is unstable. Both FR and HX stabilised the solution procedure and resulted in a considerable reduction (8%) in the final value of c . Again almost identical results are obtained from using FR and HX improvements.

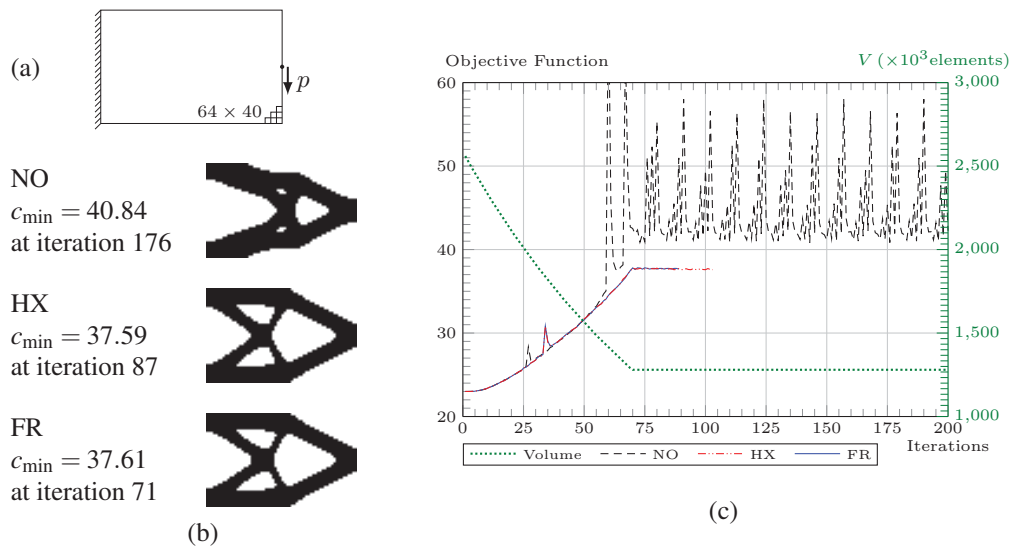


Figure 2: Design domain (a), optimum topologies obtained (b), and the evolution history of volume and objective function values (cb) for the short cantilever beam starting from full design domain.

To test the proposed approach in a slightly different situation, the same problem is reconsidered with the initial design depicted in Fig. 3a. As the initial design satisfies the volume constraint, the volume will not change during the solution making R_v redundant. The evolution history of the objective function values and the obtained topologies are shown in Fig. 3a and Fig. 3b respectively. It can be seen that without applying the stabilisation techniques the BESO algorithm is not stable. Although both improvements lead to better solutions, only the FR approach was successful in obtaining a stable solution in this case.

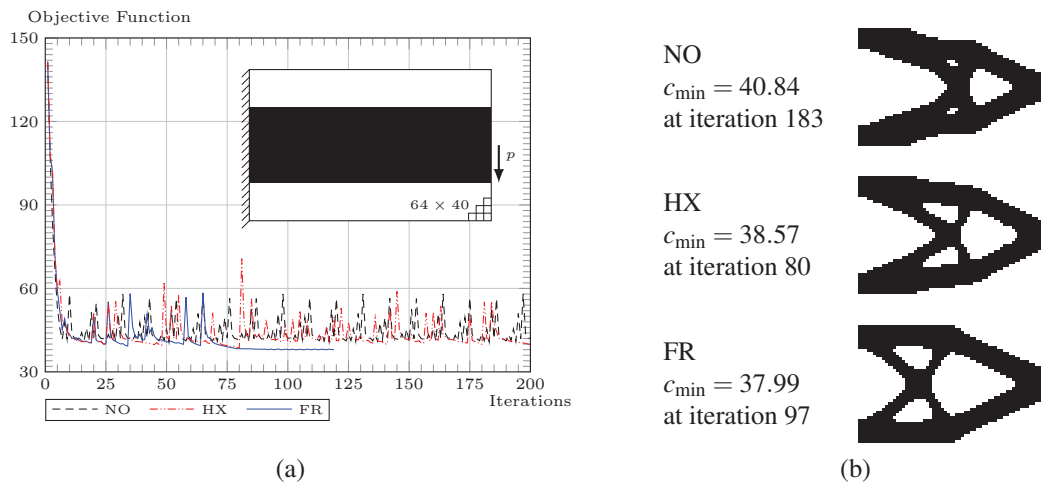


Figure 3: The initial design and the evolution history of objective function values (a), and optimum topologies obtained (b) for the short cantilever beam.

8.3. Example 3

In the third example, performance of the improvement techniques are compared in a two-material distribution problem in absence of filtering. In two material problems, if filtering technique is used, the E_e in the denominator of sensitivities in Eq.(4) will give more weight to sensitivity numbers of weaker elements. This will result in unclear topologies [9, 14]. This problem can be solved by using a nonlinear interpolation scheme instead of Eq.(1) (see e.g. [7, 15]), giving different weights to sensitivity numbers of different material phases [16, 17], modifying the filtering scheme [14], or simply by avoiding the filtering scheme (see e.g. [18]). The last approach is used here. Note that in a soft-kill BESO, filtering is not necessary for extrapolating sensitivity numbers. To control checkerboard formation, 9-node elements are used in this example which are known to improve the behaviour of topology optimisation methods with respect to checkerboard formation [10].

The short cantilever beam in example 2 is solved again by a soft-kill approach and with two materials with elastic moduli of $E^{(1)} = 1$ and $E^{(0)} = 0.2$ each filling 50% of the design domain. $R_a = 1\%$ is adopted in this example. Fig. 4 shows the obtained results for this example. Even without using any improvement the BESO procedure is stable in this case. However, it can be seen that in the absence of a filtering scheme, the HX approach didn't improve the solution and in fact resulted in a worse design where materials are scattered in the design domain. The evolution graph of objective function values reveals that the HX solution is unstable (Fig. 4a). The FR approach, on the other hand, worked well in this case as well and resulted in a slightly improved (0.4%) design compared to the case where no improvement approach was used.

9. Conclusion

The BESO method is studied and a new interpretation of this method is proposed. Two separate steps are identified in the BESO algorithm in each iteration. The first step involves finding a descent vector for the unconstrained optimisation problem. The second one involves adjusting the move direction to satisfy the constraints of the actual constrained optimisation problem. The current BESO algorithm uses the steepest descent method in its first step and a rounding off technique in its second step to find a feasible move vector.

A heuristic improvement technique is proposed which involves using a conjugate gradient method instead of the steepest descent method in the first step of BESO. The difference of the required computational time and effort for applying this approach is negligible in topology optimisation problems.

Through numerical examples, the usefulness of this approach is verified and its results are compared with the stabilisation procedure suggested by Huang and Xie [1]. It is shown that the proposed approach can improve and stabilise BESO solutions in both hard-kill and soft-kill variations. It is also shown that unlike the stabilisation procedure suggested by Huang and Xie, the proposed approach doesn't necessarily require using a filtering scheme.

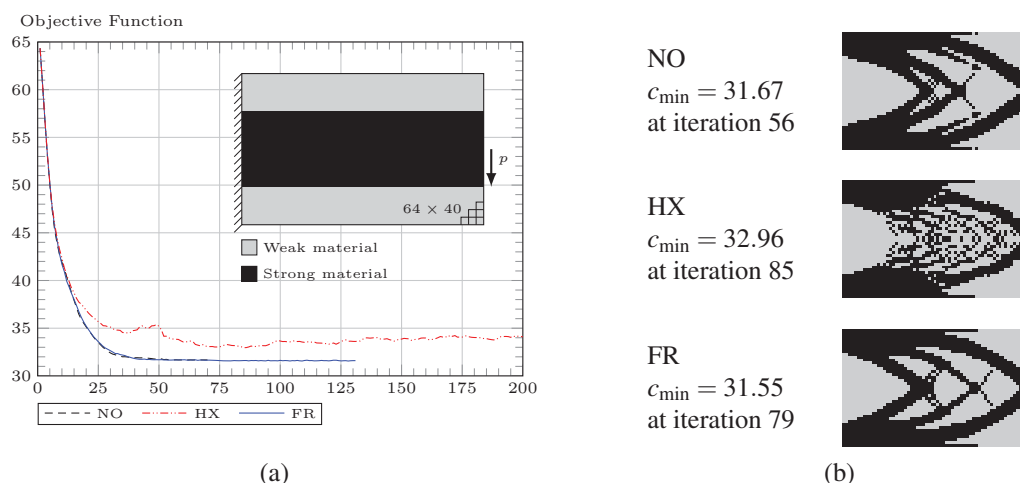


Figure 4: The initial design and the evolution history of objective function values (a), and optimum topologies obtained (b) for the third example.

References

- [1] X. Huang and Y. M. Xie. Convergent and mesh-independent solutions for the bi-directional evolutionary structural optimization method. *Finite Elements in Analysis and Design*, 43 (14), 1039–1049, 2007.
- [2] O. M. Querin, G. P. Steven, and Y. M. Xie. Evolutionary structural optimisation (ESO) using a bidirectional algorithm. *Engineering Computations*, 15 (8), 1031–1048, 1998.
- [3] X. Y. Yang, Y. M. Xie, G. P. Steven, and O. M. Querin. Bidirectional evolutionary method for stiffness optimization. *American Institute of Aeronautics and Astronautics Journal*, 37 (11), 1483–1488, 1999.
- [4] X. Huang and Y. M. Xie. *Evolutionary topology optimization of continuum structures*. John Wiley and Sons, 2010.
- [5] Y. M. Xie and G. P. Steven. A simple evolutionary procedure for structural optimization. *Computers & Structures*, 49 (5), 885–896, 1993.
- [6] Y. M. Xie and G. P. Steven. *Evolutionary structural optimization*. Springer, London, 1997.
- [7] X. Huang and Y. M. Xie. Bi-directional evolutionary topology optimization of continuum structures with one or multiple materials. *Computational Mechanics*, 43 (3), 393–401, February 2009.
- [8] G. I. N. Rozvany. A critical review of established methods of structural topology optimization. *Structural and Multidisciplinary Optimization*, 37 (3), 217–237, 2009.
- [9] K. Ghabraie. *Exploring Topology and Shape Optimisation Techniques in Underground Excavations*. PhD thesis, School of Civil, Environmental and Chemical Engineering Science, RMIT University, Melbourne, Australia, August 2009.
- [10] O. Sigmund and J. Petersson. Numerical instabilities in topology optimization: A survey on procedures dealing with checkerboards, mesh-dependencies and local minima. *Structural and Multidisciplinary Optimization*, 16 (1), 68–75, August 1998.
- [11] X. Huang, Y. M. Xie, and M. C. Burry. A new algorithm for bi-directional evolutionary structural optimization. *Japan Society of Mechanical Engineers International Journal Series C*, 49 (4), 1091–1099, 2006.
- [12] J. Herskovits. *Advances in Structural Optimization*, chapter A view on nonlinear optimization, pages 71–116. Kluwer Academic Publishers, Holland, 1995.
- [13] R. Fletcher and C. M. Reeves. Function minimization by conjugate gradients. *The Computer Journal*, 7 (2), 149–154, 1964.

- [14] K. Ghabraie. An improved soft-kill BESO algorithm for optimal distribution of single or multiple material phases. under review for publication in *Structural and Multidisciplinary Optimization*.
- [15] T. Nguyen, K. Ghabraie, and T. Tran-Cong. Applying bi-directional evolutionary structural optimisation method for tunnel reinforcement design considering nonlinear material behaviour. *Computers and Geotechnics*, 55, 57–66, January 2014.
- [16] K. Ghabraie, Y. M. Xie, X. Huang, and G. Ren. Shape and reinforcement optimization of underground tunnels. *Journal of Computational Science and Technology*, 4 (1), 51–63, 2010.
- [17] K. Ghabraie, Y. M. Xie, and X. Huang. Using BESO method to optimize the shape and reinforcement of underground openings. In N. Ghafoori, editor, *Challenges, Opportunities and Solutions in Structural Engineering and Construction: Proceedings of the 5th International Structural Engineering and Construction Conference (ISEC-5), 22-25 Sep. 2009, Las Vegas, USA*, pages 1001–1006, London, 2010. Taylor and Francis.
- [18] Y. Liu, F. Jin, Q. Li, and S. Zhou. A fixed-grid bidirectional evolutionary structural optimization method and its applications in tunnelling engineering. *International Journal for Numerical Methods in Engineering*, 73 (12), 1788–1810, 2008.

Optimal Design and Evaluation of Cantilever Probe for Multifrequency Atomic Force Microscopy

Jiandong Cai¹, Qi Xia², Yangjun Luo³, Michael Yu Wang⁴, Li Zhang¹

¹ The Chinese University of Hong Kong, Hong Kong, jdcai@mae.cuhk.edu.hk, lizhang@mae.cuhk.edu.hk

² Huazhong University of Science and Technology, Wuhan, China, qxia@mail.hust.edu.cn

³ Dalian University of Technology, Dalian, China, yangjunluo@dlut.edu.cn

⁴ National University of Singapore, Singapore, michael.wang@nus.edu.sg

1. Abstract

In multifrequency atomic force microscopy (AFM) to simultaneously measure topography and material properties of specimens, it is highly desirable that the higher order resonance frequencies of the cantilever probe are assigned to be integer harmonics of the excitation frequency. In this paper, a structural optimization technique is employed to design cantilever probes so that the ratios between one or more higher order resonance frequencies and the fundamental natural frequency are ensured to be equal to specified integers. A one-layer probe with variable width is optimally designed for assigning single and multiple resonance frequencies. Moreover, a three-layer model is proposed to provide more frequency choices. All the designs are verified by experiments, through the focused ion beam (FIB) milling based fabrication technique and AFM measurement.

2. Keywords: Multifrequency atomic force microscopy, Cantilever probe, Eigenfrequency, Structural optimization, Focused ion beam

3. Introduction

Among various atomic force microscopy (AFM) techniques, tapping mode is particularly attractive for imaging soft specimens because it does not suffer from lateral friction, hence having minimal damages to a soft specimen as well as to probe tip. In the tapping mode, a probe is excited at or near its fundamental resonance frequency, and its tip touches the sample surfaces once in every oscillation. A feedback controller is used to keep the vibration amplitude at a constant level by adjusting the height of probe base or sample table, to provide the topography of the specimen.

Conventional tapping mode AFM involves the excitation and detection at a single frequency component of the tip's motion, inevitably losing the information contained in other harmonic components. In recent years, tapping mode AFM is emerging to excite or/and detect at multiple frequencies to maximize the potential of AFM for characterization, defined as multi-frequency AFM [1].

Periodic tapping between the probe tip and the sample surface produces a periodic pulse-like tip-sample interaction force, and it was observed that the response of probe due to such a tip-sample force contains rich information about material properties of the sample, which can be observed in the higher harmonics of the response [2]. In practice, however, there exists a significant difficulty. Because the responses at higher harmonics are typically several orders smaller in magnitude than that at the excitation frequency, and also because applying a large tapping force is not suitable for high resolution imaging, a reasonable signal-to-noise ratio at the higher harmonics is not readily available [3].

According to the theory of vibration, if the frequency of a higher harmonic is equal to one of the resonance frequencies of the probe, the response of the probe at such a frequency can be greatly enhanced. However, in regards to the commonly used rectangular cantilever probe, their high order resonance frequencies do not naturally align with any one of the harmonics [1]. Therefore, the probe should be redesigned [4]. Sahin *et al.* [5] designed a cantilever probe with a notch whose third order flexural resonance frequency was equal to the 16th harmonic and the probe is called a harmonic cantilever. But this design has a limited capability and a general methodology is not available. Li *et al.* [6] attached a concentrated mass to the probe to tailor the second and the third order eigenfrequencies to be integer multiplies of the fundamental eigenfrequency. If large change of the frequencies is required, the mass needs to be heavy. As a consequence, this will lower the fundamental resonance frequency of the probe. Xia *et al.* [7] employed the level set based topological optimization method to design harmonic probe. But the result is not practical from manufacturing and structure stability issues, and also only one order eigenfrequency assignment is achieved.

For imaging material composition, several harmonics are required to accurately reconstruct the tip-sample interaction force, and they should lie in the frequency range with high sensitivity, typically in a low range for soft materials and a high range for hard samples. Therefore, a practical methodology is needed to design harmonic probes with pre-determined eigenfrequencies. Actually, this type of structural optimization problem with eigenfrequency requirement has been a subject of extensive interests and investigations in past decade. Maeda and Nishiwaki [8] designed the vibrating structures that targets desired eigenfrequencies and eigenmodes shapes. Meske *et al.* [9] introduced a new optimality criteria method to handle eigenfrequency problems. And Du and Olhoff [10] applied SIMP method and bound formulation to maximize eigenfrequencies and frequency gaps. Tsai and Cheng [11] utilized SIMP method and MAC to obtain desired eigenfrequencies and mode shape.

Here, this study proposes a design framework for developing a practical novel probe to meet the demands of multifrequency AFM. There are two types of design to demonstrate. The first design is one-layer design with variable beam width. Another design is three-layer design with symmetric top and bottom layers, whose width are the design variables, while the middle layer is kept constant.

4. Optimization design

With above defined cantilever design specification, the task now is to devise an optimal design to ensure that the set of M orders $I = \{I_1, I_2, \dots, I_M\}$ of cantilever resonance frequencies match the required set of M harmonics $J = \{J_1, J_2, \dots, J_M\}$ according to

$$\omega_{I_k} = \Omega_{J_k} = J_k \omega_1, \quad k = 1, 2, \dots, M \quad (1)$$

Optimization technique is employed here as a systematic approach. The design variable for one layer design is the cross-sectional width along the beam length. However, only the width of symmetric top and bottom layer is chosen as the design variable for three-layer design.

The major optimization goal is to satisfy the resonance harmonics assignment constraints. For nano-scale imaging, the effective spring constant K_I of the fundamental mode is also required to be high. Also higher excitation frequency brings higher scanning rate. Therefore, the objective is to maximize the fundamental resonance frequency, setting the function $\lambda_1 = \omega_1^2$. Thus the design optimization problem is described as follows with multiple frequency constraints:

$$\begin{aligned} \text{Max } \lambda_1 &= \omega_1^2 \\ \text{Such that: } \lambda_{I_k} - J_k^2 \lambda_1 &= 0, \quad k = 1, 2, \dots, M \end{aligned} \quad (2)$$

The weak form of the state equation for eigenvalue problem is given by

$$a(u, v) = \lambda b(u, v), \quad \forall v \in U \quad (3)$$

where $a(u, v) = \int_{\Omega} C_{ijkl} u_{kl} v_{ij} dV$ and $b(u, v) = \int_{\Omega} \rho u_i v_i dV$. Here, the displacement field u defines the mode shape of the eigenvalue problem in bilinear form for structure domain Ω . U denotes all kinematically admissible displacement fields and v is the test function. C and ρ denote the elasticity tensor and material density respectively.

In the present study, analysis of AFM cantilever probe with variable width and constant thickness distribution is modeled by the Bernoulli-Euler beam theory. The slenderness ratio of bending in vertical direction for most commercial probes is larger enough to justify the use of Bernoulli-Euler beam theory [12]. During practical tapping mode AFM detection process, the optical detection of the probe mainly involves the vertical bending mode. Vibration in other directions is neglected. For instance, torsional signal is filtered out at signal analysis step for this kind of measurement.

5. Evaluation

We started the design with a commercial probe stock (AppNano, FORTA). Nominal specifications of the silicon probe include: length 225 μm , width 27 μm , thickness 2.7 μm , spring constant 1.6 N/m, and fundamental frequency 61 kHz. Real dimensions of the probe were also measured, and they were used in the optimization. The material properties of silicon is 2330 kg/m^3 in density and 169 GPa for the Young's modulus of bending in $\langle 110 \rangle$ direction since the probe is made from standard (100) silicon wafer. In addition, mass of the probe tip was considered in the computation, and it was evaluated from scanning electronic microscopy (SEM) images, which approximately accounts for 3% of total mass. The picket-shape end of the probe remained unchanged in the design.

5.1 One-layer design

The first case of optimization was to achieve $\omega_2/\omega_1 = 6$, i.e., matching the second resonance frequency to the 6th

harmonic. Based on the optimized design shown in Fig. 1(a), the cantilever is fabricated from a commercial rectangular probe by modification of its width-profile using focused ion beam (FIB) milling (FEI Quanta 200 3D FIB). The ion beam energy and current were 30 kV and 5 nA, respectively. Fig. 1 (b) shows the SEM image of the probe obtained. The as-prepared probe was then installed on an AFM (Bruker Bioscope) to measure its resonance frequencies. In Fig. 1 (c), the first two resonance peaks f_1 (64.24 kHz) and f_2 (387.26 kHz) are shown. The ratio between f_2 and f_1 is 6.03, which is fairly close to our design expectation.

Another case of optimization was to simultaneously achieve two integer frequency ratios $\omega_2/\omega_1=6$ and $\omega_3/\omega_1=17$. Fig. 2 (a) shows the design result. After FIB milling, the as-prepared probe, shown in Fig. 2 (b), was measured for its resonance frequencies, which are shown in Fig. 2 (c). Here, we only concern with the peaks of flexural vibration. The first three resonance frequencies are 61.96 kHz, 369.35 kHz and 1056.3 kHz, respectively. The ratio values of f_2/f_1 and f_3/f_1 are 5.96 and 17.05, respectively.

It is worthy to note that the fabrication of the final probe was achieved through several rounds of local modifications, in consideration of the differences of the cross-section shape between the computational model and the real probe. The cross section of the real probe stock is not truly rectangular, but it is treated as rectangular in the computational model for convenience.

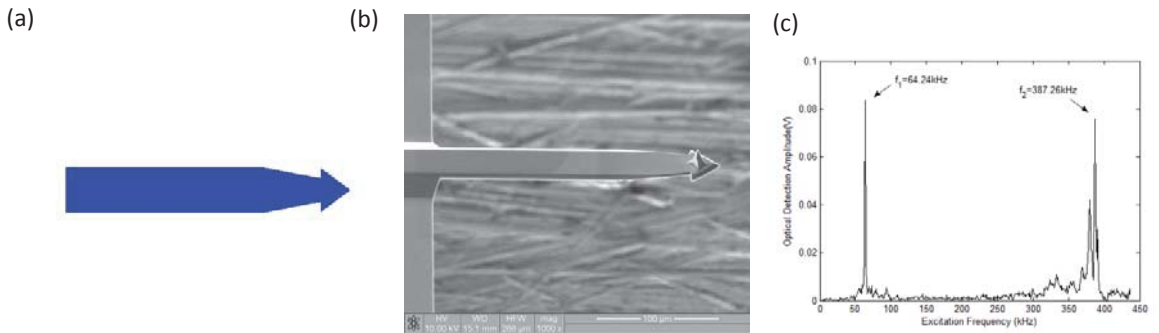


Figure.1 (a) Optimally designed result with frequency constraint $\omega_2/\omega_1=6$; (b) SEM image of probe after FIB milling; (c) Frequency spectrum of fabricated probe

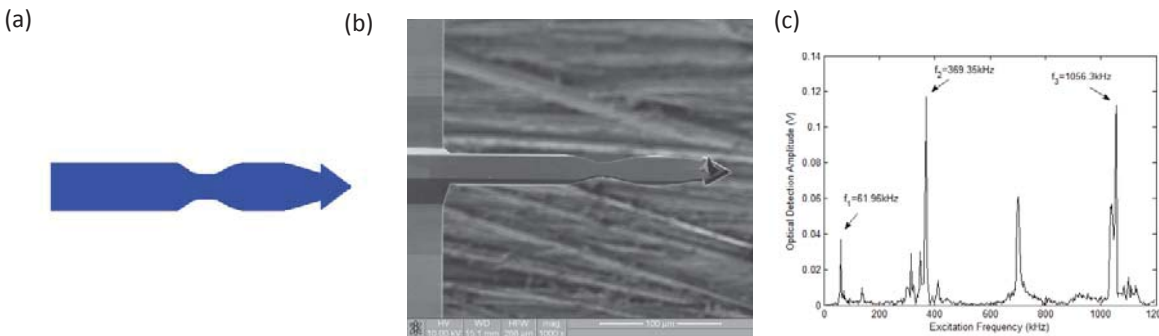


Figure.2 (a) Optimally designed result with frequency constraints $\omega_2/\omega_1=6$ and $\omega_3/\omega_1=17$; (b) SEM image of probe after FIB milling; (c) Frequency spectrum of fabricated probe

5.2 Three layer design

Three-layer design provides larger capability for tailoring frequencies. The design domain of three-layer design is broader than that of one-layer design, since the width of top and bottom layer can be zero, which is avoided in one-layer design. The real dimension of probe thickness is 2.8 μm . And we set the thickness of top and bottom layer as 0.7 μm . Thus the maintained middle layer has a thickness of 1.4 μm .

The first case of optimization is to achieve $\omega_2/\omega_1 = 4$. Fig. 3 (a) shows the pattern of top and bottom layer. Based on this design, we fabricate the probe using FIB milling. The ion beam energy and current were 30 kV and 3 nA,

respectively. Fig. 3 (b) and (c) demonstrated the probe from front and back view, respectively. Fabricated probe is then installed on AFM to measure its resonance frequencies. In Fig. 3 (d), the frequency peaks are 78.89 kHz and 320.79 kHz, which means that the ratio between f_2 and f_1 is 4.07.

The second case of optimization is to simultaneously achieve $\omega_2/\omega_1=6$ and $\omega_3/\omega_1=14$. Fig. 4 (a) shows the pattern of top and bottom layer. Fig. 4 (b) and (c) present the front and back view of the FIB milled probe, respectively. Fig. 4 (d) demonstrates the frequency spectrum obtained from AFM measurement. The first three flexural resonance frequencies are 77.34 kHz, 455.94 kHz and 1093.6 kHz, respectively. The ratio values of f_2/f_1 and f_3/f_1 are 5.90 and 14.14, respectively.

Precise depth control of FIB milling is difficult, such that the final milled depth of top and bottom layer are achieved by several rounds. Also, the final pattern is obtained after several local modifications.

6. Conclusion

In summary, a systematic structural optimization method is presented to design harmonic cantilever probes. The ratios between one or more higher order resonance frequencies and the fundamental natural frequency are made to be equal to specified integers, while the fundamental natural frequency is maximized. The approach is demonstrated with one-layer and three-layer designs. Examples of tailoring single and multiple frequencies are presented. The harmonic probes designed through the optimization approach were fabricated using the FIB technique. Their resonance frequencies were measured, and the results verified the effectiveness of the probes of our design.

7. Acknowledgements

Financial support from the Research Grants Council of Hong Kong S.A.R. (grant No. CUHK417213) for this work is gratefully acknowledged.

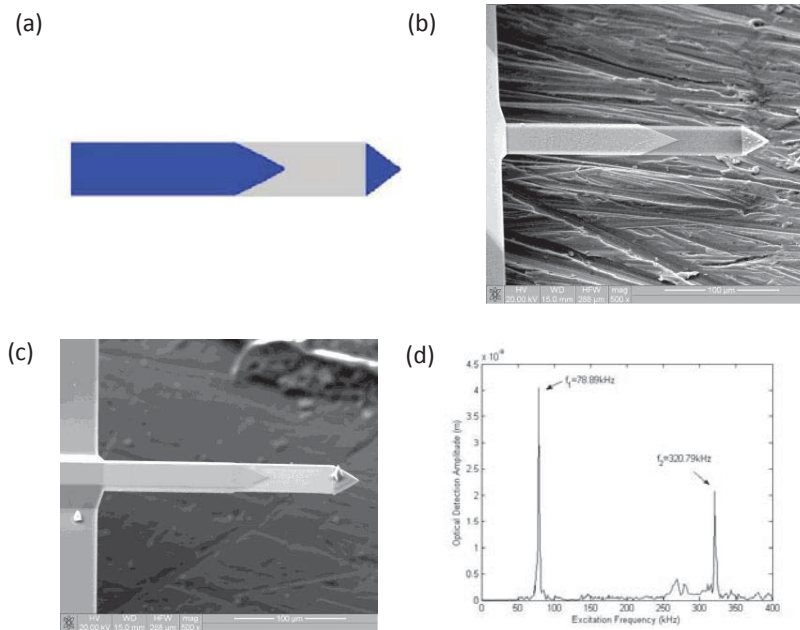


Figure. 3 (a) Optimally designed top and bottom layer pattern with frequency constraint $\omega_2/\omega_1=4$; (b) SEM image of probe's front side; (c) SEM image of probe's back side; (d) Frequency spectrum of fabricated probe

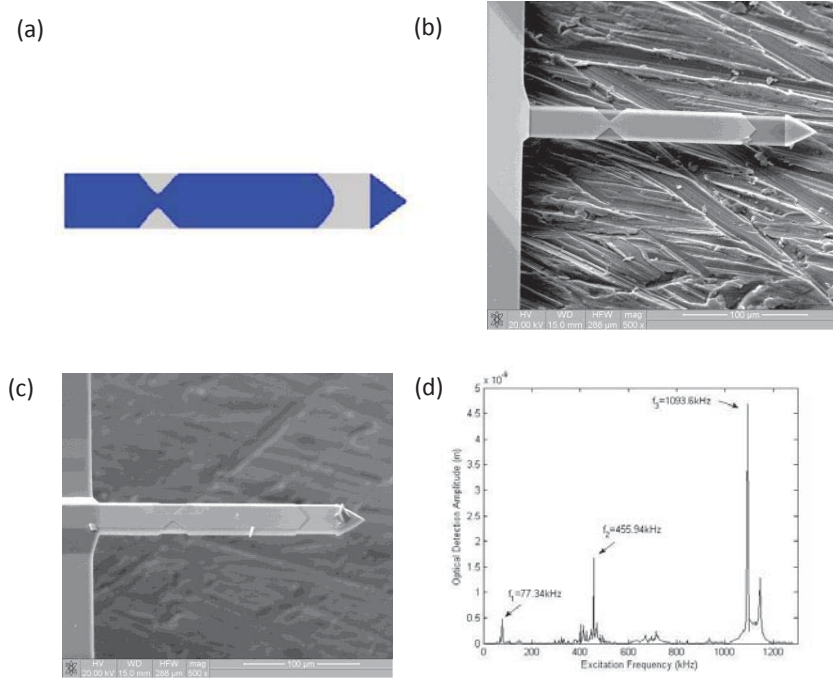


Figure. 4 (a) Optimally designed top and bottom layer pattern with frequency constraints $\omega_2/\omega_1=6$ and $\omega_3/\omega_1=14$; (b) SEM image of probe's front side; (c) SEM image of probe's back side; (d) Frequency spectrum of fabricated probe

8. References

- [1] R. Garcia and E. T. Herruzo, The emergency of multifrequency force microscopy, *Nature Nanotechnology*, 7, 217-226, 2012.
- [2] O. Sahin, C. F. Quate and O. Salgaard, Resonant harmonic response in tapping-mode atomic force microscopy, *Physical Review B*, 69, 165416, 2004.
- [3] T. R. Rodriguez and R. Garcia, Tip motion in amplitude modulation (tapping mode) atomic force microscopy: Comparison between continuous and point mass models, *Applied Physics Letters*, 80, 1646-1648, 2002.
- [4] J. Cai, Q. Xia, Y. Luo, L. Zhang and M. Y. Wang, A variable-width harmonic probe for multifrequency atomic force microscopy, *Applied Physics Letters*, 106 (7), 071901, 2015.
- [5] O. Sahin, G. Yaraliolu, R. Grow, S. F. Zappe, A. Atalar, C. F. Quate and O. Solgaard, Higher-resolution imaging of elastic properties using harmonics cantilevers, *Sensors and Actuators A: Physical*, 114, 183-190, 2004.
- [6] H. Li, Y. Chen and L. Dai, Concentrated-mass cantilever enhances multiple harmonics in tapping-mode atomic force microscopy, *Applied Physics Letters*, 92, 151903, 2008.
- [7] Q. Xia, T. Zhou, M. Y. Wang and T. Shi, Shape and topology optimization for tailoring the ratio between two flexural eigenfrequencies of atomic force microscopy cantilever probe, *Frontiers of Mechanical Engineering*, 9(1), 50-57, 2014.
- [8] Y. Maeda and S. Nishiwaki, Structural topology optimization of vibrating structures with specified eigenfrequencies and eigenmodes shape, *International Journal for Numerical Methods in Engineering*, 67, 597-628, 2006.
- [9] R. Meske, B. Lauber and E. Schinack, A new optimality criteria method for shape optimization for natural frequency problems, *Structural and Multidisciplinary Optimization*, 31, 295-310, 2006.
- [10] J. Du and N. Olhoff, Topological design of freely vibration continuum structures for maximum values of simple and multiple eigenfrequencies and frequency gaps, *Structural and Multidisciplinary Optimization*, 34, 91-110, 2007.
- [11] T. D. Tsai and C. C. Cheng, Structural design for desired eigenfrequencies and mode shapes using topology optimization, *Structural and Multidisciplinary Optimization*, 47, 673-686, 2013.
- [12] N. L. Pedersen, Design of cantilever probes for atomic force microscopy (AFM), *Engineering Optimization*, 32, 373-392, 2000.

Structural design of aircraft wing based on topology and global-local optimization

Vasily Chedrik¹, Sergey Tuktarov¹

¹ Central Aerohydrodynamic Institute, Zhukovsky, Moscow region, Russia, chedrik@yandex.ru

1. Abstract

An approach to structural design based on topology and global-local optimization is proposed. It exploits the mathematical models of different fidelity. Solid model is used for topology optimization, shell/beam model – for structural sizing on global level, refined panel model – for detailed sizing on local model, aerodynamic model – for loads and aeroelasticity analysis. Structural design procedure is described. Main features concerning the stated global-local optimization problem is discussed. A numerical example of wing optimization of an advanced helicopter with low aspect ratio is considered.

2. Keywords: Aircraft wing, strength, buckling, topology optimization, global-local approach.

3. Introduction

The aircraft structural design is very complicated problem. It is due to that many operating constraints arising from different technical disciplines, determining the performance of the aircraft, should be taken into account. Multidisciplinary design optimization approach is often used to solve this problem involving highly large number of design variables and constraints. This process is very time-consuming and, in practice, it is necessary to simplify the design problem by using mathematical structural models of different levels. In this case, structural optimization should be done both on models of global and local levels. Many technical papers [1–4] are devoted to the development of the multilevel methods for analysis and optimization. In the paper [4] authors presented a global-local approach for structural analysis and optimization with taking into account strength/buckling constraints.

The aim of this work is to combine the structural optimization based on the global-local approach with topology optimization to perform a complete design procedure of aircraft structures. Topology optimization of continuum structures is to find the optimal designs by determining the best locations and geometries of cavities in the design domains. Many numerical methods for topology optimization of continuum structures have been investigated extensively, for example [5–9]. Two heuristic methods of structure topology optimization are presented in the paper [8]. They are based on the application of the fully-stressed design criterion, used in practice to determine the structural rational parameters taking into account the strength constraints. In our context, the topology optimization allows to determine the principal load-carrying directions in which structural material should be located. These directions are strongly related with the way of load application and number of load cases. Usually various engineering interpretations of the topology optimization results can be proposed by designer. In this approach several structural layouts are generated, and the global-local structural optimization is performed for them.

The approach is demonstrated on the example of design of low-aspect-ratio wing of advanced helicopter.

4. Structural design procedure

The general process of structural synthesis includes the topology optimization stage directed on search of reasonable structural layouts under action of some extreme loads. Initial data for the topology optimization are geometric outlines of a structure. Flow-chart of structural optimization is shown in Figure 1.

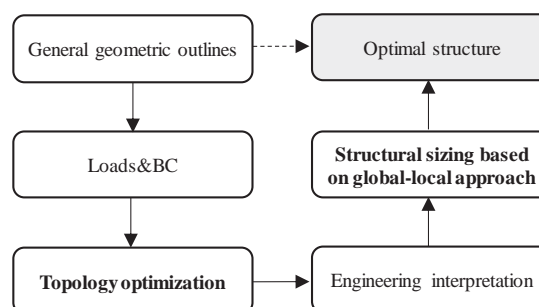


Figure 1: Flow-chart of structural optimization

The topology optimization results are interpreted by design engineers. The second stage is design of structural elements in the interpreted layouts. This stage includes shape optimization and determination of structural element sizes such as shell thicknesses, section dimensions of beam-type elements with taking into account the operative constraints of structure.

We consider that the geometric outlines of mechanical body are specified. They define the place of load-bearing structure (design domain). The structure is supposed to be fixed in some parts and is subjected by external loads of several load cases. The design domain is divided in detail on finite elements for analysis of displacements and stresses by using finite element (FE) method. The main aspects of applied topology optimization methods are discussed in the paper [8].

An engineering interpretation of topology results are performed intuitively based on the obtained distribution of material in solid finite element model. Therefore, several alternative layouts should be generated to make a choice of reasonable structural layout after structural sizing. Structural sizing is fulfilled by means of the global-local approach to optimization described below. The auxiliary optimization algorithms in this approach are based on optimality criteria and mathematical programming methods. Finally, the best structural layout is found by comparison of the obtained structural masses.

4.1. Topology optimization

The most popular approach for determining the optimal structural layout is to minimize the compliance function or the potential strain energy with taking into account a constraint to the given volume (weight) of the structure. Mathematically the statement of the structural optimization problem looks as follows

$$\text{Find } \min \mathbf{f}^T \mathbf{U} \text{ subject to } \int_{\Omega} \rho(x) d\Omega \leq M_0 \quad (1)$$

Here \mathbf{f} is a vector of external load, \mathbf{U} is a displacement vector, $\rho(x)$ is a material density in the considered design domain, Ω is a set of elements in the design domain, and M_0 is a value restricting the material mass. The solution of the optimization problem is based on the introduction of a design variable x in each finite element, which relates Young's modulus with the density of each finite element of the structure by means of the following expressions: $\rho(x) = \rho_0 x$ and $E(x) = E_0 x^p$; where ρ_0 and E_0 are the initial density and Young's modulus of material, and p is a penalty value used in algorithms for selection of the needed and unneeded structural elements [6, 9]. Note that the problem statement (1) supposes the only one load case. At the same time, the designed structure of aircraft must bear various loads, and the stresses in its elements must be less than the allowable values. To allow for many load cases the objective function in (1) is replaced by the weighted sum of compliances for all considered load cases. Two heuristic methods of topology optimization which consider stress constraints for many load cases are presented in the paper [8]. The developed algorithms based on the use of a simple fully-stressed design criterion. They allow obtaining reasonable structural layouts with taking into consideration of many load cases and different allowable stresses in the structural elements. The comparison of the resulting structures with the optimal topology, obtained by two approaches showed that they are in good agreement. Both these methods can be used in the structural design of aircraft wing based on topology and global-local optimization.

4.2. Global-local structural optimization method

Generally the finite element method is used for static and buckling analysis. These problems are usually solved with using different fidelity meshes. The high fidelity grid is not mandatory to perform stress analysis of regular aircraft structure but it is significantly required for computation of buckling load and shape of panels. Design engineers prepare several mathematical models which include both the full-scale structure under research and its separate parts. The global full-scale model includes only global structural parameters. The local model of a separate aircraft component should be created with more details to take into account the stress irregularities and to determine buckling loads and shapes if compressing forces are available.

Problems of interaction between the global and local models are discussed in [4]. The main idea is to interpolate the internal nodal forces computed on the global model into the nodal forces of the local model. In the optimization process on local model applied forces are considered as fixed. The initial elastic parameters of the local FE model have to be close to the elastic parameters of the global one. The possible difference between them is due to the holes and the stiffening structural elements. The accordance of the elastic material characteristics and the loads on the models is performed by their recalculations at the global and local levels of the approach.

The general optimization problem with using global and local models can be solved by using two-level approach described in [2, 3]. In this approach the initial optimization problem is decomposed into separate optimization problems of two levels. Consider such two-level approach when system problem is divided into a set of smaller subproblems with their own goal functions and constraints. The individual optimization of subsystem is performed independently on the first level and coordinate problem is solved on the second (system) level. Generally, the nonlinear programming problem is formulated by the following way:

Minimize $f(\mathbf{X})$ subject to constraints

$$\mathbf{g}_j(\mathbf{X}) \leq 0, \quad j = 1, 2, \dots, m; \quad \mathbf{h}_k(\mathbf{X}) = 0, \quad k = 1, 2, \dots, p; \quad x_i^l \leq x_i \leq x_i^u, \quad i = 1, 2, \dots, n, \quad (1)$$

where x_i^l и x_i^u denotes upper and lower limits of x_i , which are components of the vector of design variables

$\mathbf{X} = \{x_1, x_2, \dots, x_n\}^T$. The vector \mathbf{X} is subdivided into two subvectors \mathbf{Y} and \mathbf{Z} : $\mathbf{X} = \{\mathbf{Y}, \mathbf{Z}\}^T$. The vector \mathbf{Y} includes the interaction variables between subsystems and the vector \mathbf{Z} has the variables belonging only to subsystems. The vector \mathbf{Z} can be partitioned by following way: $\mathbf{Z} = \{\mathbf{Z}_1, \mathbf{Z}_2, \dots, \mathbf{Z}_k, \dots, \mathbf{Z}_K\}^T$, where \mathbf{Z}_k are the vectors with variables related with only k -th subsystem and K is number of subsystems.

The vector \mathbf{Y} may appear in all constraint functions while the vectors \mathbf{Z}_k appear only in the constraint sets: $\mathbf{g}^{(k)} \leq 0, \quad \mathbf{h}^{(k)} = 0$. The bound constraints can be written as $\mathbf{Y}^{(l)} \leq \mathbf{Y} \leq \mathbf{Y}^{(u)}, \quad \mathbf{Z}_k^{(l)} \leq \mathbf{Z}_k \leq \mathbf{Z}_k^{(u)}, \quad k = 1, 2, \dots, K$.

The goal function can be expressed as $f(\mathbf{X}) = \sum_{k=1}^K f^{(k)}(\mathbf{Y}, \mathbf{Z}_k)$, where $f^{(k)}(\mathbf{Y}, \mathbf{Z}_k)$ is the contribution of the k -th subsystem to the general goal function. The two-level method can be formulated as follows.

In the first level problem we tentatively fix the values of the vector \mathbf{Y} at values of vector \mathbf{Y}^* . The problem Eq.(1) is reformulated as K independent optimization problems as follows:

Find the vector \mathbf{Z}_k which minimizes function $f^{(k)}(\mathbf{Y}, \mathbf{Z}_k)$ at satisfying the constraints:

$$\mathbf{g}^{(k)}(\mathbf{Y}, \mathbf{Z}_k) \leq 0, \quad \mathbf{h}^{(k)}(\mathbf{Y}, \mathbf{Z}_k) = 0, \quad \mathbf{Z}_k^{(l)} \leq \mathbf{Z}_k \leq \mathbf{Z}_k^{(u)}, \quad k = 1, 2, \dots, K. \quad (2)$$

In the second level problem the following problem is solved:

Find new vector \mathbf{Y}^* which minimizes the function

$$f(\mathbf{Y}) = \sum_{k=1}^K f^{(k)}(\mathbf{Y}, \mathbf{Z}_k^*), \quad (3)$$

at satisfying the constraints $\mathbf{Y}^{(l)} \leq \mathbf{Y} \leq \mathbf{Y}^{(u)}$. Here \mathbf{Z}_k^* are the vectors of variables which are the optimal solution of the first level problems. The constraint on bounds of the vector \mathbf{Y} is added into the problem to provide a finite value of the goal function $f(\mathbf{Y}^*)$ at solving the second level problem.

The iterative algorithm can be represented in the following steps:

- 1) Start with an initial coordination vector \mathbf{Y}^* .
- 2) Solve the K first level problems Eq.(2) and find the optimal vectors $\mathbf{Z}_k, k = 1, 2, \dots, K$.
- 3) Solve the first level problem Eq.(3) and find new vector \mathbf{Y}^* .
- 4) Check for the convergence of goal function f and the vector \mathbf{Y}^* by comparison their values with those obtained earlier in iteration process.
- 5) If the process has not converged, go to step 2 and repeat the process until convergence.

Satisfying to buckling constraints at structural optimization is important requirement at aircraft design. Such constraints are prescribed to structural panel which generally consists of plate elements modeling a skin of the aircraft lifting surface and bar elements modeling stiffening stringers. Different buckling shapes can be encountered for the panel under compression/tension and shear loads. Stress constraints in panel and gauge constraints on panel design variables are also imposed. The design variables for local level (in the panel) are skin thickness, sizes of stringer elements and panel stringer step.

5. Numerical optimization example

A wing of an advanced helicopter with low aspect ratio is considered as an example for approval of the developed method. The research purpose is to find optimal wing structural parameters which provide minimum weight at satisfying to strength, buckling and aeroelasticity constraints. Obviously, the minimum of structural weight corresponds to some reasonable layout which can be found by topology optimization.

To determine aerodynamic forces in extreme load cases and to perform aeroelasticity analyses an aerodynamic model of the wing has been created. Also the wing outlines serve for generation of a solid finite element model which is used in topology optimization (Figure 2, left). It is important to correctly transfer pressure loads from aerodynamic to FE model. It was performed by interpolation of the obtained pressures with using polynomial function of nodal coordinates in outer surfaces of the FE model. Topology optimization was accomplished to minimize compliance at saving 30 percent of initial solid model weight in the final design. The obtained pattern where the load-bearing material should be distributed is shown in Figure 2, right.

In the pattern the lighter regions corresponds to low material densities and the darker regions – to high material densities which define the load-carrying regions. It is seen that some wing-box can be considered as structural layout together with a set of cross rib elements in the trailing part of the wing. However, it is difficult to choose explicitly one layout corresponding to this pattern. That is why it is worth to consider several possible layouts. The

following seven ones were proposed based on intuition. They are shown in Figure 3 with hidden upper skin of wing.

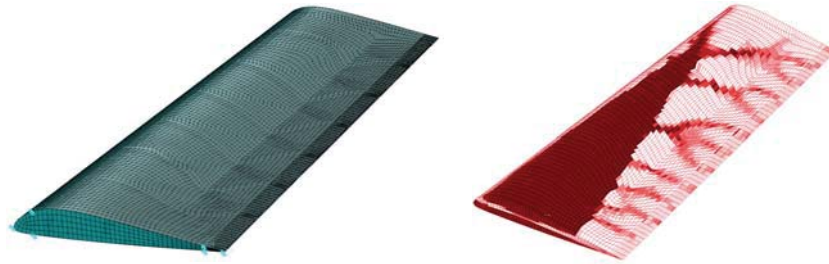


Figure 2: Initial solid FE model (left), topology result (right)

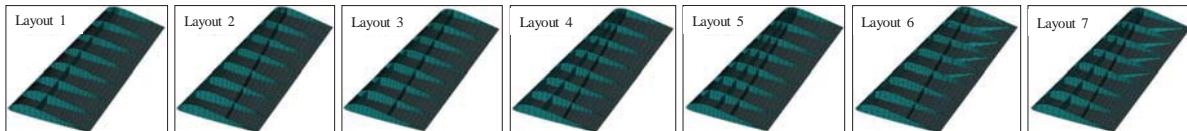


Figure 3: Alternative structural layouts

Description of these seven layouts is given in Table 1.

Table 1: Description of structural layouts

1	Single-spar layout in which the spar is in the centre of the maximum material concentration zone.
2	Two-spar layout in which spars are at the bounds of the maximum material concentration zone.
3	The same as <i>Layout 2</i> but the wing-box width is narrowed (front spar is along the maximum structural depths).
4	Three-spar layout with spars corresponding to <i>Layout 1</i> and <i>Layout 2</i> .
5	Three-spar layout with spars corresponding to <i>Layout 1</i> and <i>Layout 3</i> .
6	The same as <i>Layout 2</i> with additional ribs at the end part of the wing.
7	The same as <i>Layout 4</i> with additional ribs at the end part of the wing.

In the global optimization level the thicknesses of the panel skins, ribs and spars are considered as design variables (DV). Minimum thickness for all DV is 1.2 mm. The allowable stress in design researches chosen from strength and fatigue conditions is equal 240 MPa. The number of DV in layouts varies from 71 to 89. This difference is due to the number spars and additional ribs in these layouts.

The structural optimization under strength requirements for these seven layouts leads to the following optimal weight values: 35.5 kg, 31.6 kg, 31.7 kg, 32.2 kg, 32.3 kg, 32 kg and 32.5 kg, respectively. Therefore, the optimal structural layouts from the viewpoint of strength are two-spar configurations. However, buckling analysis showed that all of the considered layouts do not satisfy to buckling requirements.

Then the structural optimization with stress and buckling requirements were accomplished. The best layout here is three-spar wing with additional ribs (weight 42.4 kg). The second layout in weight rank is two-spar wing with additional ribs (weight 43.2 kg). They are slightly different in weight so these both are studied in further investigations. Comparison of all alternative structural layouts with optimal distribution of material showed that the weight benefit was about 10 percent owing to the choice of location of the primary elements.

Optimum thicknesses for design variables are shown in Figure 4. It is worth to mention that thicknesses in wing-box root part significantly change both in spanwise and chordwise directions.

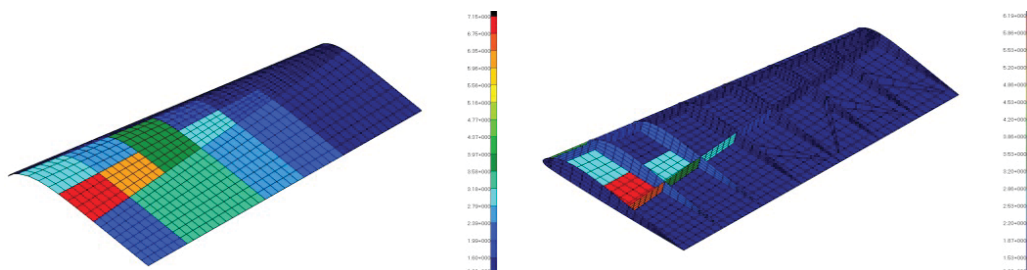


Figure 4: Optimum thicknesses after strength/buckling optimization on global level

For some wing upper panels the buckling constraints become active. This is due to the fact that upper panels have smooth skin (no stringers). Buckling shape for optimal wing is shown in Figure 5. The buckling load factor is equal 1. It is obvious that the stiffened panel is more effective to resist buckling. So addition of stringer elements is necessary to include. Addition of such elements in global finite element significantly increases both the number of degrees of freedom and the number of DV. Some of new design variables related with stringer elements are geometric and they define stringer shape. Therefore it is necessary to consider the design problem with using local models of panels. In the local optimization problem the design variables are the number of stringers, thicknesses of stringer elements, the stringer depth and skin thickness. In this research the shape of stringer section is rectangular, and we have four DV for each panel. Only upper wing panels are considered because they are under the action of compression loads. Figure 6 shows relation between global FE model and local one for a separate panel.

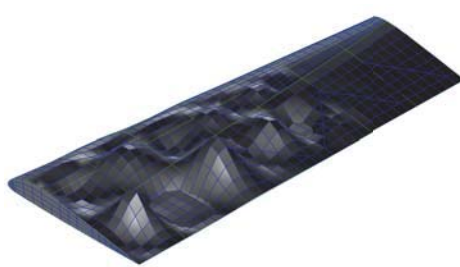


Figure 5: Buckling shape

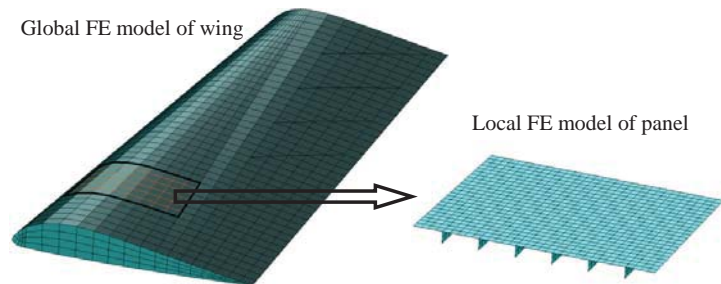


Figure 6: Extraction of local model from global model

Iterative global-local optimization was performed. The two-spar wing had the least weight (36.3 kg) while weight of three-spar wing was 38.1 kg. Note that panel smeared thicknesses are significantly reduced if compared with the results obtained for smooth thickness with optimization on global model. For example, thickness of root upper panel was 7.4 mm and after global-local optimization it became 3.14 mm. Optimum stringer parameters of this panels are following ones: the number of stringers is 6, its depth is 30 mm and its thickness is 1.86 mm. Note that different optimal solutions can be obtained during the optimization process at parametric change of stringer step and depth. More technological root panel structure was obtained with the stringer depth of 45 mm. In this case the skin thickness is 2.01 mm and stringer thickness is 3.45 mm. The global-local approach to optimization of wing with stiffened panels allowed reducing of structural weight by 16.8 percent.

Aeroelasticity analysis was performed for the chosen two-spar layout with additional ribs at the end part of wing. Note that the constraint on the divergence speed was satisfied. The obtained optimum parameters after global-local optimization do not provide flutter requirements. The flutter speed after analysis was 112 m/s but it must be greater than 145.2 m/s. The sensitivity analysis showed that it was necessary to increase minimum thicknesses of the lower panel skin up to 1.3 mm. In addition, the needed thickness of lower panel skin in the root part in the trailing edge was 1.5 mm. The damping coefficients versus flight speed are shown in Figure 7.

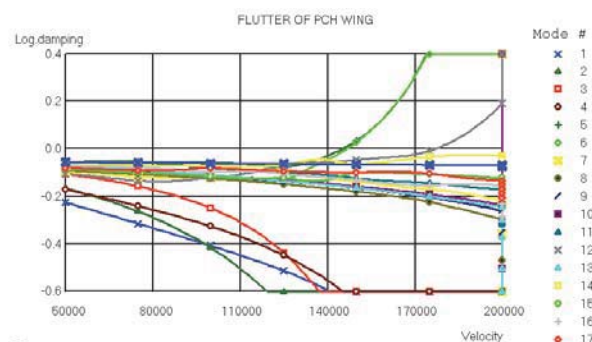


Figure 7: Damping coefficients versus flight speed

There three flutter forms with speeds 146 m/s, 147 m/s and 177 m/s. Note that change of panel skin thicknesses for taking into account flutter constraints leads to the increase in weight by 0.8 kg. Weight of optimum wing structure with satisfying all imposed constrains is 37.1 kg.

5. Conclusions

The paper has proposed an approach to structural design based on topology and global-local optimization. The approach was demonstrated on an example of the low aspect-ratio wing. Application of topology optimization

helped to determine several alternative layouts. Comparison of the chosen alternative structural layouts with optimal distribution of material showed that the weight benefit was about 10 percent owing to the choice of location of the primary elements. By means of structural optimization under strength/buckling requirements two reasonable layouts were obtained: the three-spar and the two-spar wing with additional ribs at the end part. It was shown that the additional significant reduction of weight could be reached by use of global-local optimization. This approach to optimization of wing with stiffened panels allowed additionally reducing of structural weight by 16.8 percent. It is concluded that the best structural layout from the viewpoint of strength, buckling and aeroelasticity is two-spar wing with additional ribs at the end part.

The developed approach is a very useful tool for the design process of complex aerospace structures. It gives reliable results and reduces computational costs compared to a traditional approach to optimization.

6. References

- [1] J. Sobieszczyński-Sobieski, B.B. James and M.F. Riley, Structural sizing by generalized, multilevel optimization, *AIAA Journal*, 1, Vol. 25, 139-145, 1987.
- [2] S.S. Rao, *Engineering Optimization: Theory and Practice*, Fourth Edition, John Wiley & Sons, Inc., 2009.
- [3] V.V. Chedrik, Two-level design optimization of aircraft structures under stress, buckling and aeroelasticity constraints. *10th World Congress on Structural and Multidisciplinary Optimization*, WCSMO-10, Orlando, USA, 2013.
- [4] V.V. Chedrik, S.A. Tuktarov, Optimization of Composite Structures Based on Global-Local Approach, *International Conference on Engineering and Applied Sciences Optimization (OPT-i)*, Kos, Greece, 2014 (ISBN:978-960-99994-5-8).
- [5] Y.M. Xie, G.P. Steven, A simple evolutionary procedure for structural optimization. *Computers & Structures*, 49 (5), 885-896, 1993.
- [6] M.P. Bendsøe and O. Sigmund, *Topology Optimization: Theory, Methods and Applications*, Springer-Verlag, Berlin, 2003.
- [7] Y.M. Xie, X. Huang, *Evolutionary topology optimization of continuum structures: methods and applications*. Wiley, 2010.
- [8] V. V. Sysoeva, V. V. Chedrik, Algorithms for structural topology optimization, *TsAGI Science Journal*, 42 (2), 259-274, 2011.
- [9] V.M. Uskov, K.A. Balunov, Method for topology optimization with clear boundary shape of structure, *International Conference on Engineering and Applied Sciences Optimization (OPT-i)*, Kos, Greece, 2014 (ISBN:978-960-99994-5-8).

Geometric Feature Identification from Topology Optimization Results

Guilian Yi¹, Byeng D. Youn², Nam H. Kim³

¹ Seoul National University, Seoul, Republic of Korea, flybirdyi@126.com

² Seoul National University, Seoul, Republic of Korea, bdyoun@snu.ac.kr

³ University of Florida, Florida, US, nkim@ufl.edu

1. Abstract

Topology optimization yields an overall layout of a structure in the form of discrete density (e.g., SIMP) or continuous boundary geometry (e.g., level-set method). One of important drawbacks, however, is that it leads to a geometry with zigzag boundaries and/or irregular shapes, which is difficult to be interpreted for manufacturability, as well as to be utilized in subsequent applications such as shape optimization. It is considered the most significant bottleneck to interpret topology optimization results and to produce a parametric CAD model that can be used for shape optimization. The objective of this paper is to interpret geometric features out of a topology design to minimize human intervention in producing a parametric CAD model. The active contour method is first used to extract boundary segments from the greyscale image of topology optimization. Using the information of roundness and curvature of segments, simple geometric features, such as lines, arcs, circles, fillets, extrusion and sweep, are then identified. An optimization method is used to find parameters of these geometric features by minimizing errors between the boundary of geometric features and that of actual segments. Lastly, using the parametric CAD model, surrogate-based shape optimization is employed to determine the optimal shape. The entire process is automated with MATLAB and Python scripts in Abaqus, while manual intervention is needed only when defining geometric constraints and design parameters. 2-D beam and plate structures are presented to demonstrate effectiveness of the proposed methods.

2. Keywords: geometric features identification, active contour method, topology optimization, shape optimization, section optimization

3. Introduction

As one of the most active research topics in the field of structural optimization, topology optimization yields a prediction of the structural type and overall layout of materials. It can obtain robust results based on well-developed numerical approaches, and has received more and more research attentions recently because of its great potential of application to many industrial areas. Since most topology optimization approaches are element-based, where the initial design space is discretized by uniform rectangular finite elements and the design variables are assumed to be constant within each finite element, it is efficient in computation and has been applied successfully for solutions of many industrial optimization problems. However, one of important drawbacks of topology optimization is that, it is difficult to interpret topological results in terms of geometric features for conventional manufacturability. The optimal topological results often come out as greyscale images with zigzag boundaries and irregular shapes. They are not only difficult to make in the perspective of manufacturability, but also cannot be used directly in subsequent applications such as section and shape optimization. These problems are due to the lack of geometric boundary features and model parameterization. Many engineering applications require a shape of parameterized and smooth geometry, especially for manufacturing. There is a gap in automated geometric information extraction techniques in order to seamlessly integrate topology optimization with section and shape optimization. Therefore, there are needs to identify geometric features out of topology design and to obtain simple and smooth shapes for achieving cost-efficient design and for manufacturing components economically.

In the literature, some conventional methods were proposed to identify geometric boundaries by using image interpretation [1-2], density contour [3-4], geometric templates [5-6] and B-spline curves [7-8]. However, drawbacks of these methods still exist and make it difficult to achieve an efficient way for geometric features identification from topology results. For example, too many manual interventions are required in image processing, no parameterized model or geometric features can be obtained from density contours, limited geometric features can be represented by templates, and B-spline is expensive in the perspective of manufacturing. All of those shortcomings of existing geometric boundary detection methods drove us to interpret geometric features out of a topology design to minimize human intervention in producing a parametric CAD model.

In this paper, the geometric features identification techniques are limited to two dimensional structures, and simple geometric components are used for geometric features interpretation. Once the parameterized CAD model

for the topology result is obtained, shape optimization and section optimization are employed to fine tune the identified geometry and make sure the structural performances in line with that of the topology result. The whole procedures yield a structural design framework of integrated topology and shape/section optimization.

4. Geometric features identification

It is important to identify the boundaries of geometric features from topology results. Although B-spline curves can provide nice shapes for a structure, and they are used commonly in daily life, it is very expensive, i.e. money and time, to manufacture them. On the other hand, more than 90% of machine parts are composed of simple geometric features, such as straight lines, fillets and circles. Therefore, straight lines, arcs, fillets, and circles are used as basic geometric features to interpret topology results and construct boundaries of geometry.

4.1. Active contour method

Normally, element-based topology results are greyscale images, or result text file for element density values. This research can start with either of them. The image functions in Matlab, “imread()” and “rgb2grey()”, can read images and transform them into image data. Then, the image data are processed by the active contour method [9-10] to yield smooth and closed boundary segment data, which are composed of coordinate values. Each of the closed segments represents an outer/inner boundary.

A Matlab code based on active contour method made by Su [11] is used here to extract geometry boundaries from topology greyscale images. Figure 1(a) shows the initial greyscale image, and Figure 1(b) shows the extracted boundaries (red lines). Actually, the boundaries are expressed by a sequence of points, which are the blue crossed points as shown in Figure 1(c).

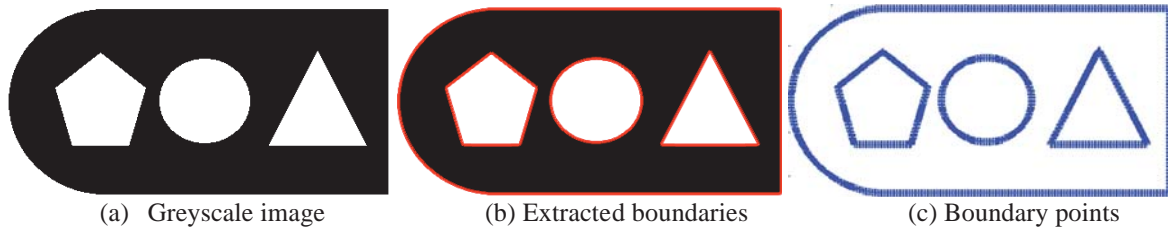


Figure 1: Image interpretation by using the active contour method

4.2. Circles detection

Among many geometric features, circle is a very common shape, and different from straight lines, arcs and fillets. In order to identify a circle, “roundness” is used to detect circles from other geometric features. With identified boundary points of a closed loop, the centroid of a geometric feature is expressed as

$$(x_0, y_0) = \left(\frac{1}{n} \sum_{i=1}^n x_i, \frac{1}{n} \sum_{i=1}^n y_i \right) \quad (1)$$

where i is the number of boundary point, and n is the total number of the boundary points of the geometric feature. x_i and y_i are the coordinates of the i -th boundary point, and x_0 and y_0 are the coordinates for the centroid point.

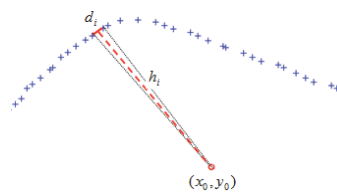


Figure 2: A portion of the boundary

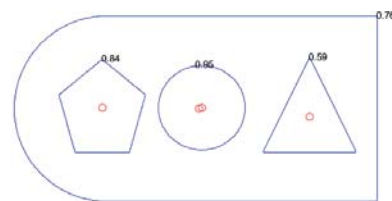


Figure 3: Roundness values

As shown in Figure 2, a small triangular is formed with two neighbored points and the centroid, whose base length and height can be expressed as

$$d_i = \sqrt{(x_i - x_{i+1})^2 + (y_i - y_{i+1})^2} \quad h_i = \frac{|k_i x_0 - y_0 + y_i - k_i x_i|}{\sqrt{1 + k_i^2}} \quad (2)$$

where $k_i = \frac{y_{i+1} - y_i}{x_{i+1} - x_i}$. Therefore, the perimeter and area of this geometric feature can be obtained as

$$P = \sum_{i=1}^{n-1} d_i \quad A = \sum_{i=1}^{n-1} \frac{1}{2} d_i h_i \quad (3)$$

where P and A denote the perimeter and area of a closed geometric feature, respectively.

The roundness of this geometric feature can then be defined by

$$m = 4\pi AP^{-2} \quad (4)$$

where m represents the roundness value of a closed geometric feature. A roundness value closer to 1.0 indicates that the object is approximately circle. Figure 3 shows the centroids (red circle points) and roundness values for the four geometric features. By setting the threshold of 0.9, circles can be identified first.

4.3. Straight lines and fillets identification

After identifying circles, it is assumed that other closed-loop boundaries are composed of straight lines and fillets between two lines. Since the boundaries are identified and described by points, it makes sense to interpret a straight boundary section as a line segment according to its curvature. Starting from the initial point, slopes of lines connecting following points with the initial point are calculated. If these slopes change beyond a threshold, it is considered that the current line ends and a new line starts from the ending point. A fillet tangent to the two straight lines is used to express corner boundaries.

Figure 4 shows the geometric relationship of a fillet and two straight lines (red lines) on a portion of a geometric feature (blue cross points), and the relationship is formulated in Eq. (5) to calculate fillet center coordinates and tangent points for a given fillet radius. In Figure 4, n_1 and n_2 are, respectively, the numbers of two tangent points' locations in a closed geometric feature. The points between the n_1 -th and n_2 -th points are used to approximate a fillet tangent to two straight lines.

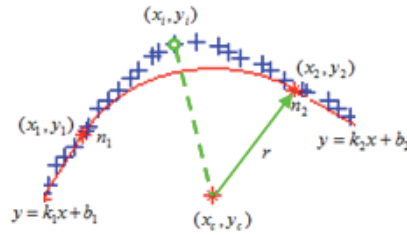


Figure 4: Geometric relationship of a fillet and a straight line

$$\begin{cases} \sqrt{(x_1 - x_c)^2 + (y_1 - y_c)^2} - r = 0 \\ \sqrt{(x_2 - x_c)^2 + (y_2 - y_c)^2} - r = 0 \\ (x_1 - x_c) + k_1(y_1 - y_c) = 0 \\ (x_2 - x_c) + k_2(y_2 - y_c) = 0 \\ k_1x_1 + b_1 - y_1 = 0 \\ k_2x_2 + b_2 - y_2 = 0 \end{cases} \quad (5)$$

where (x_c, y_c) denotes coordinates of the fillet center point, and r is the fillet radius. (x_1, y_1) and (x_2, y_2) are two tangent points at both ends of the fillet. k_1 and k_2 are the slopes, and b_1 and b_2 are the y-intercept of the two lines.

In order to estimate more accurate fillets, Eq. (6) is formulated to minimize the maximum distance from the initial boundary segment data points to the fillet.

Find r

$$\text{Min } f(r) = \max_{i \in \{n_1, n_2\}} \left| \sqrt{(x_i - x_c)^2 + (y_i - y_c)^2} - r \right| \quad (6)$$

s.t. $r > 0$

Once the optimal fillet radius is obtained from Eq. (6), the fillet center point and two tangent points can be determined by solving Eq. (5). Figure 5 shows a pentagon identified with 5 line segments and 5 fillets before and after fillet estimation. The blue lines are the initial boundaries, which are not smooth, and the red lines are the identified boundaries. The red star points on the red line are tangent points, and red star points inside of the boundaries are fillet center points. Arc can be detected in a same way as fillets.

The estimation process for fillets obviously alleviates the errors between final parameterized smooth shapes and initial topological shapes, and makes sure the shapes to be consistent with the geometric features. At last, the geometries will be output in forms of parameterized CAD model with straight lines, fillet, arcs and circles, and be

rebuilt in Abaqus.

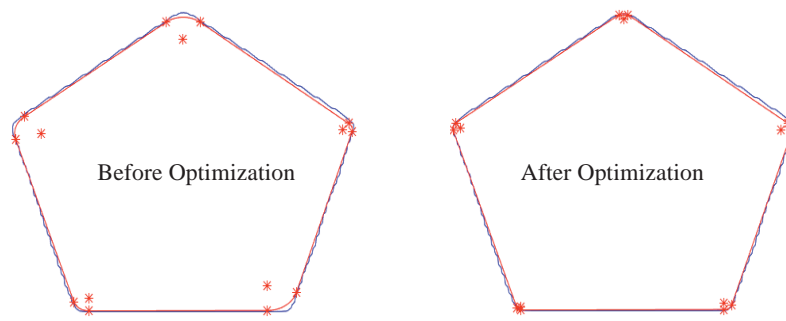


Figure 5: Before and after optimization for fillets

5. Section and shape optimization for identified structure

Although the boundary shapes are extracted from topology optimization results, the extracted geometry may not be considered an optimum geometry because the structural response can slightly be different from that of topology design. Therefore, a follow-up section or shape optimization is performed to fine tune the structural geometry for desired performances. The same optimization formulation used for topology optimization is better to be used for the section or shape optimization. During the follow-up optimization, no new geometry features will be introduced, but the initial features will be modified to find the optimum design.

In the follow-up optimization, there are a couple of things to be noted. Firstly, dimensions of the CAD model should be fully constrained so that the entire geometry can be regenerated after its parameters are changed. Secondly, since not all of the parameters are necessary for optimization, a limited number of dimensions can be selected as design variables, and their lower/upper bounds needs to be determined. The lower/upper bounds are selected such that the geometry can be well defined within these bounds. Since the selection totally depends on the experiences of designers, this parameterization process has to be done manually, and it is the only time that requires human intervention in the whole design procedure.

As the dimensions change, the structural shape and mesh change too. It causes numerical errors when we use finite difference method to calculate the sensitivities in optimization. In order to address the issue of mesh-related numerical errors, the surrogate model-based optimization approach is employed to perform the shape optimization. The optimization problems will be solved by the “fmincon” function in Matlab. The optimization for the CAD model is implemented automatically by using Matlab to execute Python scripts for Abaqus.

6. Numerical examples

In order to demonstrate the validity and capability of the proposed framework for geometric features identification, two numerical examples are tested here. The first example is topology result of a cantilever beam from Yi and Sui [12]. Section optimization is considered with beam elements. The second example is topology result of a clamped plate from Yi [13], and shape optimization is considered for the topology shape. The topology optimization of both structures was performed to minimize structural mass with a displacement constraint.

Example 1: Beam element identification and section optimization. It was required that the displacement at the loading point was no larger than 0.35mm. Figure 6 shows the grayscale image of the optimal topology result, where the minimum mass was 1990.17kg, and the displacement at the loading point was an active constraint.



Figure 6: Topology shape

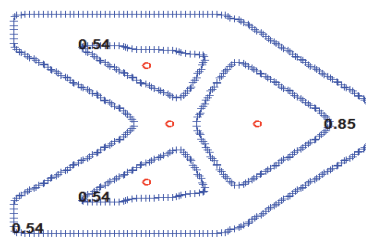


Figure 7: Boundaries and roundness

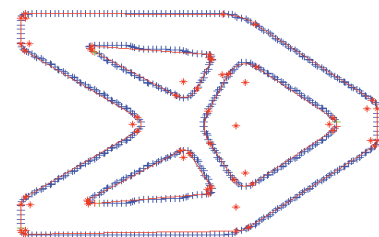


Figure 8: Straight lines and fillets

Figure 7 gives the boundary points and roundness values of closed boundary segments. By implementing the geometric features identification techniques on those boundary segments, the parameterized CAD model with straight lines and fillets is overlapped on top of the initial boundaries, which is shown in Figure 8. Although the fillets are determined by optimization, they are not used in section optimization, but used to determine the

approximations of straight lines. The middle lines of two closely parallel straight lines are determined one by one. They are crossed to each other and construct a beam element structure. As shown in Figure 9, the red lines are identified boundary line segments, and the green lines are beam elements of the cantilever beam.

Since the cantilever beam is symmetric, four section areas are selected as design objectives (shown in Figure 10). A rectangular profile is defined for each of them. Since the thickness of the beam is 1.0mm, the design variables are actually the heights of the rectangular sections of Sec1, Sec2, Sec3 and Sec4 separately. A lower bound of $lb = [0.1, 0.1, 0.1, 0.1]$ (mm) and an upper bound of $ub = [10, 15, 10, 15]$ (mm) are given for the design variables. Since the mesh on beam elements does not change during optimization, no surrogate model is required, and the section optimization is conducted directly. The optimum point is found at $\mathbf{x}^* = [6.12, 7.81, 3.71, 6.71]$ (mm). The structural mass is 1981.13kg, and the displacement at the loading point is 0.35mm. Displacement contour of the beam with optimal sections is shown in Figure 11.

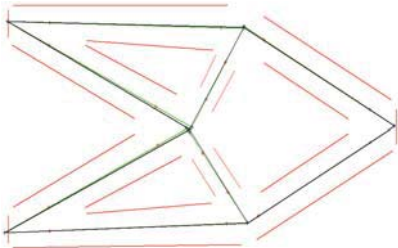


Figure 9: Beam element structure

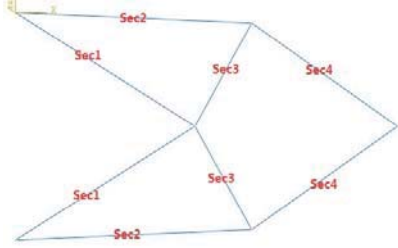


Figure 10: Design objectives

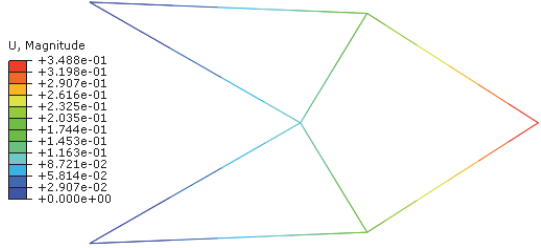


Figure 11: Optimal sections

Example 2: Plate shape identification and shape optimization. The displacement at the middle of the plate along the loading direction was required to be no larger than 0.74m. The result text file of the optimal density values is used for image interpretation. Figure 12 shows the topology shape (in black and grey) read by Matlab and boundaries (in red) detected by the active contour method. The total mass was 5.31kg, and the displacement at the middle was 0.74m. The exact boundaries are identified and shown in Figure 13, where the fillets and arcs are already optimized. The CAD model is rebuilt in Abaqus and the fully constrained geometry is shown in Figure 14.

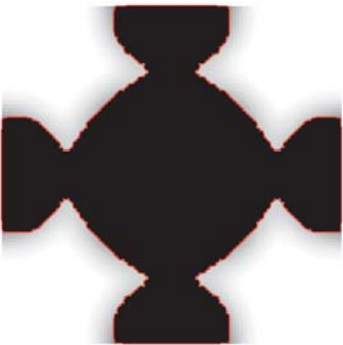


Figure 12: Topology shape

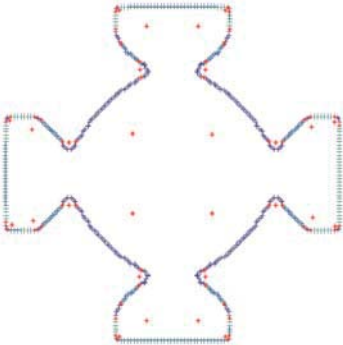


Figure 13: Identified boundaries

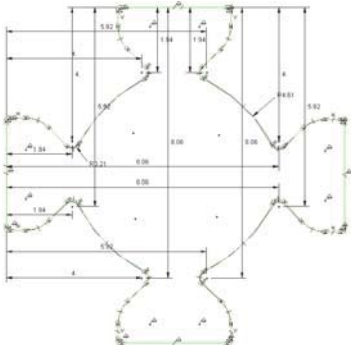


Figure 14: Fully constrained CAD model

Since the geometry is fully symmetric and the dimensions are related to each other, the dimensions for the short fillet, x-coordinate and y-coordinate of the fillet center point, and fillet radius, respectively, are considered as design variables x_1 , x_2 and x_3 , which are marked as pink lines in Figure 15. The shape optimization with a displacement constraint is performed on the identified geometry. The Kriging surrogate model is utilized to approximate the

relationship between three design variables and the displacement at the middle point of the plate. The optimal design is found at $\mathbf{x}^*=[2.01, 4.14, 0.1]$ (m), where the structural mass is 5.00kg, which is reduced by 5.84% compared to the topology result, and the displacement at the middle point is 0.74m. Figure 16 gives a full dimensions of the optimal shape of the identified geometry. The displacement contour of the optimal shape is shown in Figure 17.

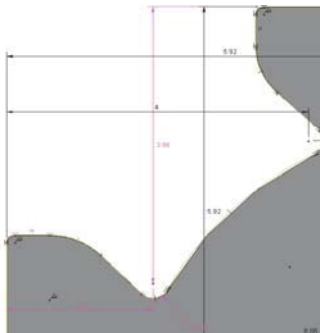


Figure 15: Design variables

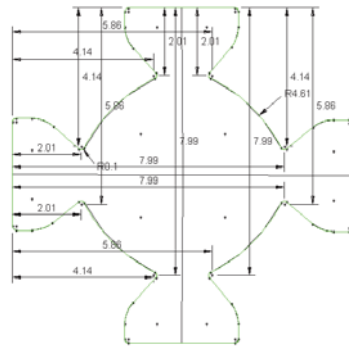


Figure 16: Optimal shape

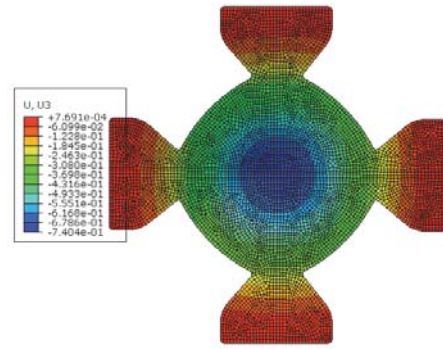


Figure 17: Displacement contour

7. Conclusions

In this paper, 2D geometry features are identified from topology optimization results, followed by section or shape optimization. Both numerical examples indicate that the proposed techniques for geometric features identification are valid and capable to interpret topology results. In addition, the proposed structure design framework shows that topology and shape/section optimization can be integrated to effectively obtain structural designs for manufacturing. However, some future work needs to be considered, for example, parameterizing boundary conditions to make process fully automatic, and applying this integration framework into 3 dimensional structures.

8. Acknowledgements

We gratefully acknowledge the financial assistance from the China Scholarship Council and the Brain Korea 21 Plus project in 2015.

9. References

- [1] N. Olhoff, M.P. Bendsøpe and J. Rasmussen, On CAD-Integrated Structural Topology and Design Optimization, *Computer Methods in Applied Mechanics and Engineering*, 89(1-3), 259-279, 1991.
- [2] M. Chirehdast, H-C. Gea, N. Kikuchi and P.Y. Papalambros, Structural Configuration Examples of an Integrated Optimal Design Process, *Journal of Mechanical Design*, 116(4), 997-1004, 1994.
- [3] A.V. Kumar and D.C. Gossard, Synthesis of Optimal Shape and Topology of Structures, *Journal of Mechanical Design*, 118(1), 68-74, 1996.
- [4] Y.L. Hsu, M.S. Hsu and C.T. Chen, Interpreting Results from Topology Optimization Using Density Contours, *Computers & Structures*, 79(10), 1049-1058, 2001.
- [5] C.Y. Lin and L.S. Chao, Automated image interpretation for integrated topology and shape optimization, *Structural and Multidisciplinary Optimization*, 20(2), 125-137, 2000.
- [6] A.R. Yildiz, N. Ozturk, N. Kaya and F. Ozturk, Integrated optimal topology design and shape optimization using neural networks, *Structural and Multidisciplinary Optimization*, 25(4), 251-260, 2003.
- [7] K.H. Change and P.S. Tang, Integration of design and manufacturing for structural shape optimization. *Advances in Engineering Software*, 32(7), 555-567, 2001.
- [8] P.S. Tang and K.H. Change, Integration of topology and shape optimization for design of structural components. *Structural and Multidisciplinary Optimization*, 22(1), 65-82, 2001.
- [9] T.F. Chan and L.A. Vese, Active contours without edges, *IEEE Transactions on Image Processing*, 10(2), 266-277, 2001.
- [10] C. Li, C.Y. Kao, and J. C. Gore et al., Minimizing of region-scalable fitting energy for image segmentation. *IEEE Transactions on Image Processing*, 17(10), 1940-1949, 2008.
- [11] D.C. Su, Codes for active contour without edge are available online, <http://www.mathworks.com/matlabcentral/fileexchange/34548-active-contour-without-edge>.
- [12] G.L. Yi and Y.K. Sui, Different effects of economic and structural performance indicators on model construction of structural topology optimization, *Acta Mechanica Sinica*, 2015.(DOI: 10.1007/s10409-015-0418-5)
- [13] G.L. Yi, Expanded SIMP method for structural topology optimization by transplanting ICM method, PhD dissertation, Beijing University of Technology Press, Beijing, 2014.

Cross Sections and Prestressing Forces Optimizations of Prestressed Concrete Beams

Yoyong Arfiadi¹, Alfian Wiranata Zebua²

¹ Atma Jaya Yogyakarta University, Yogyakarta, Indonesia, yoyong@mail.uajy.ac.id

² Atma Jaya Yogyakarta University, Yogyakarta, Indonesia, alfianzeb@yahoo.com

1. Abstract

In many cases prestressed concrete structures are more advantages than ordinary reinforced concrete structures. However, designing prestressed concrete structures that fulfil the optimum criteria is not an easy task. This is because there is an interaction between the size of cross sections and prestressing force that has to be given to the structures. Optimization of prestressed concrete structures becomes a challenging task for most structural designers. This paper considers optimization procedures for prestressed concrete beams. For obtaining prestressing force, the moment coefficient method, which is the ratio of moment due to prestressing force divided by prestressing force, is used in the computation. In statically determinate structures this coefficient exactly is the eccentricity between center of gravity of the section and the center of gravity of the prestressing steel. However, in statically indeterminate structures, this ratio is not the same as the eccentricity; due to the presence of the secondary moments. This leads to the concept of the moment coefficient- β . The optimization of both cross sections and prestressing force is carried out using real coded genetic algorithms (RCGAs), which has been successfully applied in many problems. One of the advantages of RCGAs is that it has the ability to explore the unknown domains that might be difficult to achieve by using binary coded. To show the effectiveness of the method, numerical examples are carried out using the proposed method. In the numerical examples, the optimization of cross sections and prestressing forces of both simple and continuous beams are considered. It can be shown that the method is effective to obtain the optimum cross section as well as prestressing force.

2. Keywords: prestressed concrete, optimization, real coded genetic algorithms, indeterminate prestressed structures.

3. Introduction

When the span of structures tends to be longer and longer, the needs of light structures becomes essential. Prestressed concrete is one of the solution to reduce the dimension of the members. With the simple concept, i.e., to reduce the tensile stress in concrete by applying the prestressing force, while maintaining the compressive force within the allowable stress, prestressed concrete has been receiving attention from designers. By using prestressed concrete it is possible to design longer structures compare to ordinary reinforced concrete. In another word, it is possible to achieve more efficient prestressed concrete members in contrast to ordinary reinforced concrete ones for the same loading. Other advantages of prestressed concrete are much less cracking, rapid construction and better quality control compared to ordinary reinforced concrete construction. Despite those advantages, designing prestressed concrete becomes more complex. This is due to the interaction between prestressing force and other requirements such as allowable stresses, which are also the function of the prestressing forces.

One method to design prestressed concrete members is by using the famous Lin's load balancing method [1], which is very simple, especially for one-span simple beams. For complex members, such as continuous beams, there will be a secondary moment due to the hyperstatic forces presence in statically indeterminate structures. In addition, for continuous beam the smooth transition of the cable profile should be maintained in the middle supports that render the application of the load balancing method. In order to alleviate this difficulty, the use of moment coefficient- β method has been proposed in [2-3]. This method has the ability also to avoid searching the concordant cable, which is usually very tedious. In statically determinate prestressed structures the coefficient- β turns to, exactly, the eccentricity of the tendon with respect to the center of gravity of concrete sections.

Recently optimization methods have also received a considerably attention from the structural designers [4-5]. These include size, shape and topology optimizations [6-7]. The algorithms used to optimize the problems include particle swarm optimizations, genetic algorithms, and ant colony methods [6-9]. In this paper real coded genetic algorithms (RCGAs) that have been used in control system [10] is used to optimize the cross sections and prestressing force of prestressed beams.

4. Design of Determinate and Indeterminate Prestressed Beams

The elastic design of prestressed concrete beams is to ensure that the stresses under service load conditions are

within the allowable stresses as follows:

$$\sigma_L \leq \sigma \leq \sigma_U \quad (1)$$

where σ_L = allowable compressive stress (lower limit), σ_U = allowable tensile stress (upper limit), and the stresses at the extreme fibers σ can be obtained as

$$\sigma = -\frac{F}{A_c} \pm \frac{M_F y_f}{I_c} \pm \frac{M y_f}{I_c} \quad (2)$$

in which F = prestressing force, A_c = cross section area, M_F = moment due to prestress, y_f = distance from the extreme fibers to the center of gravity of the concrete section, I_c = second moment area of the section, and M = moment due to external loads.

The moment due to prestress M_F can be obtained as:

$$M_F = \begin{cases} F \times e & \dots \dots \dots \text{for statically determinate structures} \\ F \times \beta & \dots \dots \dots \text{for statically indeterminate structures} \end{cases} \quad (3)$$

where e = the eccentricity of center of gravity of the steel (cgs) with respect to the center of gravity of the concrete section (cgc), and β = prestressing moment coefficient. Eq. (3) clearly indicates that for determinate structures $e = \beta$. The coefficient β can be obtained by dividing moment due to prestressing force (as the effect of the equivalent load from prestressing) by the magnitude of prestressing force in the tendons [2-3]. Throughout the paper, notation β will be used as a general case. Eq. (3) also means that here we have already considered the effect of the secondary moment due to the hyperstatic moment in the statically indeterminate prestressed concrete structures. Following [2-3], at transfer (initial condition), the stress at the top fiber can be obtained as follows:

$$\sigma_{ci} \leq -\frac{F_1}{A_c} - \frac{M_{F1} y_t}{I_c} - \frac{M_{DL} y_t}{I_c} \leq \sigma_{ti} \quad (4)$$

where F_1 = prestressing force at transfer, $M_{F1} = F_1 \times \beta$, y_t = neutral axis distance to top fiber, M_{DL} = moment due to dead load, σ_{ti} = allowable tensile stress in concrete at transfer, and σ_{ci} = allowable compressive stress in concrete at transfer.

Similarly, the stress at the bottom fiber has to follow:

$$\sigma_{ci} \leq -\frac{F_1}{A_c} + \frac{M_{F1} y_b}{I_c} + \frac{M_{DL} y_b}{I_c} \leq \sigma_{ti} \quad (5)$$

where y_b = neutral axis distance to top fiber

At the final condition, the stress at the top fiber has to follow:

$$\sigma_c \leq -\frac{F}{A_c} - \frac{M_F y_t}{I_c} - \frac{M_{TL} y_t}{I_c} \leq \sigma_t \quad (6)$$

where F = prestressing force at the final stage after loss of prestress, $M_F = F \times \beta$, M_{TL} = moment due to the total load, σ_t = allowable tensile stress at the final condition, and σ_c = allowable compressive stress at the final condition.

Similarly, the stress at the bottom fiber has to follow:

$$\sigma_c \leq -\frac{F}{A_c} + \frac{M_F y_b}{I_c} + \frac{M_{TL} y_b}{I_c} \leq \sigma_t \quad (7)$$

4.1. Prestressing Force Governed by Stress Conditions at Transfer

For simplicity, we take the notations:

$$r = \sqrt{\frac{I_c}{A_c}}, \quad Z_t = \frac{I_c}{y_t}, \quad Z_b = \frac{I_c}{y_b} \quad (8)-(10)$$

At transfer, when the stress at the top fiber is in tension, and considering Eqs. (8) and (9), after several manipulations one can obtain[2-3]:

$$F_1 \left(-\beta - \frac{r^2}{y_t} \right) < \sigma_{ti} Z_t + M_{DL} \quad (11)$$

Eq. (11) becomes

$$F_{i\max} = \frac{\sigma_{ti} Z_t + M_{DL}}{\left(-\beta - \frac{r^2}{y_t}\right)}, \quad \text{for } \left(-\beta - \frac{r^2}{y_t}\right) > 0 \quad (12a)$$

$$F_{i\min} = \frac{\sigma_{ti} Z_t + M_{DL}}{\left(-\beta - \frac{r^2}{y_t}\right)}, \quad \text{for } \left(-\beta - \frac{r^2}{y_t}\right) < 0 \quad (12b)$$

Similarly, when the resulting stress at the top fiber is a compressive stress, we can obtain as follows:

$$F_{i\min} = \frac{\sigma_{ci} Z_t + M_{DL}}{\left(-\beta - \frac{r^2}{y_t}\right)}, \quad \text{for } \left(-\beta - \frac{r^2}{y_t}\right) > 0 \quad (13a)$$

$$F_{i\max} = \frac{\sigma_{ci} Z_t + M_{DL}}{\left(-\beta - \frac{r^2}{y_t}\right)}, \quad \text{for } \left(-\beta - \frac{r^2}{y_t}\right) < 0 \quad (13b)$$

Eqs. (12)-(13) are the results to ensure that the stress at the top fiber is within the allowable stress.

Similarly, in order to make sure that the stress at the bottom fiber at transfer in Eq. (7) is within the allowable stress, considering Eq. (10) one obtains as follows.

When the resulting stress is tensile stress:

$$F_{i\max} = \frac{\sigma_{ti} Z_b - M_{DL}}{\left(\beta - \frac{r^2}{y_b}\right)}, \quad \text{for } \left(\beta - \frac{r^2}{y_b}\right) > 0 \quad (14a)$$

$$F_{i\min} = \frac{\sigma_{ti} Z_b - M_{DL}}{\left(\beta - \frac{r^2}{y_b}\right)}, \quad \text{for } \left(\beta - \frac{r^2}{y_b}\right) < 0 \quad (14b)$$

When the resulting stress is compressive stress:

$$F_{i\min} = \frac{\sigma_{ci} Z_b - M_{DL}}{\left(\beta - \frac{r^2}{y_b}\right)}, \quad \text{for } \left(\beta - \frac{r^2}{y_b}\right) > 0 \quad (15a)$$

$$F_{i\max} = \frac{\sigma_{ci} Z_b - M_{DL}}{\left(\beta - \frac{r^2}{y_b}\right)}, \quad \text{for } \left(\beta - \frac{r^2}{y_b}\right) < 0 \quad (15b)$$

Eqs. (14)-(15) will ensure that the stress at the bottom fiber is within the allowable stress.

4.2. Prestressing Force Governed by Stress Conditions at the Final Stage

By using similar steps, the resulting equations from the final stage condition, after loss of prestress can be obtained by considering:

$$F = \alpha F_i \quad (16)$$

where α = effective prestress coefficient after loss of prestress.

Following [2-3], when the resulting stress at the top fiber is governed by the allowable tensile stress:

$$F_{i\max} = \frac{\sigma_t Z_t + M_{TL}}{\alpha \left(-\beta - \frac{r^2}{y_t}\right)}, \quad \text{for } \left(-\beta - \frac{r^2}{y_t}\right) > 0 \quad (17a)$$

$$F_{i\min} = \frac{\sigma_t Z_t + M_{TL}}{\alpha \left(-\beta - \frac{r^2}{y_t}\right)}, \quad \text{for } \left(-\beta - \frac{r^2}{y_t}\right) < 0 \quad (17b)$$

When the resulting stress at the top fiber is governed by the allowable compressive stress:

$$F_{i\min} = \frac{\sigma_c Z_t + M_{TL}}{\alpha \left(-\beta - \frac{r^2}{y_t} \right)}, \quad \text{for} \left(-\beta - \frac{r^2}{y_t} \right) > 0 \quad (18a)$$

$$F_{i\max} = \frac{\sigma_c Z_t + M_{TL}}{\alpha \left(-\beta - \frac{r^2}{y_t} \right)}, \quad \text{for} \left(-\beta - \frac{r^2}{y_t} \right) < 0 \quad (18b)$$

When the stress at the bottom fiber is in tension:

$$F_{i\max} = \frac{\sigma_t Z_b - M_{TL}}{\alpha \left(\beta - \frac{r^2}{y_b} \right)}, \quad \text{for} \left(\beta - \frac{r^2}{y_b} \right) > 0 \quad (19a)$$

$$F_{i\min} = \frac{\sigma_t Z_b - M_{TL}}{\alpha \left(\beta - \frac{r^2}{y_b} \right)}, \quad \text{for} \left(\beta - \frac{r^2}{y_b} \right) < 0 \quad (19b)$$

Similarly, when the stress in the bottom fiber is in compression one can obtain:

$$F_{i\min} = \frac{\sigma_c Z_b - M_{TL}}{\alpha \left(\beta - \frac{r^2}{y_b} \right)}, \quad \text{for} \left(\beta - \frac{r^2}{y_b} \right) > 0 \quad (20a)$$

$$F_{i\max} = \frac{\sigma_c Z_b - M_{TL}}{\alpha \left(\beta - \frac{r^2}{y_b} \right)}, \quad \text{for} \left(\beta - \frac{r^2}{y_b} \right) < 0 \quad (20b)$$

Prestressing forces for indeterminate prestressed concrete beams can be obtained from Eqs. (12)-(20). For determinate structures, the coefficient $\beta = e$.

5. Optimization of Prestressing Force and Cross Sections

In this paper real coded genetic algorithms (RCGAs) which have been successfully applied in the control systems [10] are used to optimize the cross sections as well as the magnitude of the prestressing force. RCGAs have the advantages that they can explore the unknown domain of design variables [10]. This is due to mutation and crossover operators used in the RCGAs. The steps of GAs used in RCGAs are also slightly modified, where after crossover and mutation, a portion of new individuals are inserted in order to increase the variability in the population. In addition, elitist strategy [11] is also used in this paper. Flow chart of RCGAs used in this paper is depicted in Fig.1. The objective function J is taken as the cost of the material given by

$$J = C_f \times \frac{1}{W} \quad (21)$$

where C_f is coefficient to scale the objective function and W is the total cost of the material obtained from

$$W = W_c \times C_c + W_s \times C_s \quad (22)$$

in which C_c = unit cost of concrete, W_c = weight of concrete, C_s = unit cost of steel, and W_s = weight of steel.

5.1. Numerical Example 1

The first example is a simple beam having span = 15 m, $f'_c = 30$ MPa, $f'_{ci} = 25$ MPa, unit weight of concrete = 24 kN/m³, unit weight of steel = 7.85 kN/m³, unit cost of concrete = 1,500,000.00 unit/m³, unit cost of steel = 40,000.00 unit/kg, dead load = 9.1 kN/m, and live load = 5 kN/m. The cable profile is parabolic with no eccentricity at the end of the member. The cgs of the tendon at midspan is taken minimum 0.12 m from the bottom fiber. The minimum width of beam is set up to 0.4 m. The allowable stress is taken as follows: allowable tensile stress at initial $\sigma_{ti} = 0.25\sqrt{f'_{ci}}$, allowable compressive stress at initial $\sigma_{ci} = -0.60f'_{ci}$, allowable tensile stress at the final stage $\sigma_t = 0.50\sqrt{f'_c}$, and allowable compressive stress at the final stage $\sigma_c = -0.45f'_c$.

RCGAs are used to optimize the structures, where maximum generation is taken = 500, probability of crossover =

0.8, probability of mutation = 0.1, portion of inserted new individuals = 10% of the total population, population size = 15. The scale factor C_f is taken = 10^8 and the effective prestress coefficient $\alpha = 0.8$.

After 500 generations the resulting beam section is $b = 0.40$ m, and $h = 0.71$ m. The prestressing force at transfer F_1 is bounded between 1755.5 kN and 2693.6 kN. In this case the minimum force $F_1 = 1755.5$ kN is used, resulting in the objective function $J = 6.1518$.

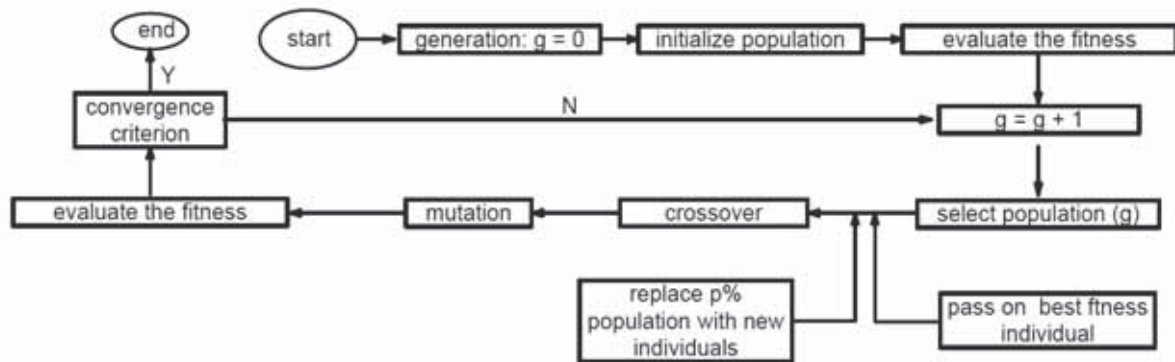


Fig.1. Flowchart for optimization

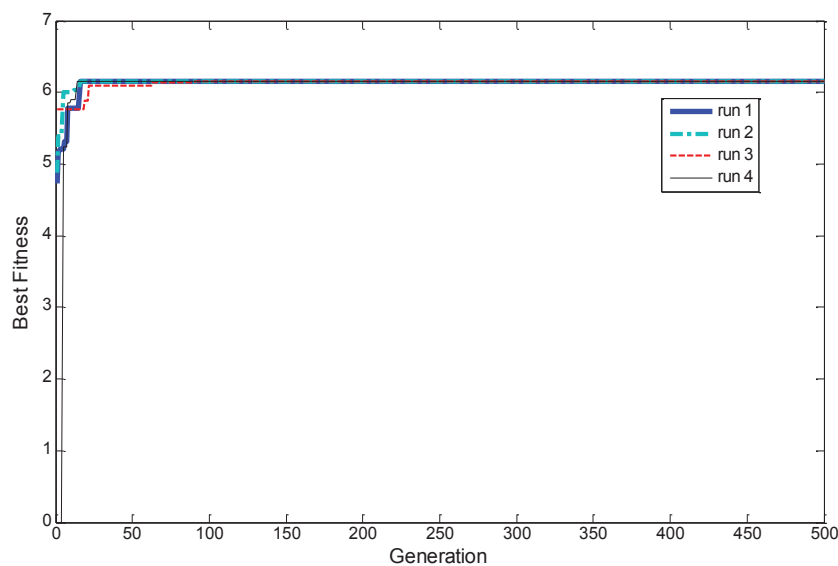


Fig. 2. Best fitness of example 1

5.2. Numerical Example 2

A three-span beam is designed as prestressed concrete member. Each span has 15 m in length. Other properties are the same as in numerical example 1. The same RCGAs are utilized, where four runs have been carried out to solve this problem. In this case C_f is taken = 10^8 . The evolving best fitness for this case is shown in Fig. 3. After 500 generations the resulting design is $b = 0.40$ m, $h = 1.28$ m, the prestressing force at initial $F_1 = 553.7$ kN to 685.1 kN. By using $F_1 = 553.7$ kN, the resulting objective function $J = 2.186$.

6. Conclusions

The optimization method for obtaining the cross sections and prestressing forces has been discussed in this paper. Determination of the prestressing force is utilizing the coefficient- β so that it is not necessary to compute the secondary moment that presence in the statically indeterminate structures. The optimization method is utilizing

real coded genetic algorithms. It is noted that for simple beams, the coefficient β is exactly equals to the eccentricity of the cable from the center of gravity of the sections. Two numerical examples have been carried out. The first is a one-span beam and the second is a three-span beam. It is demonstrated that the procedure is able to obtain the cross sections as well as the prestressing force that has to be given to the structures.

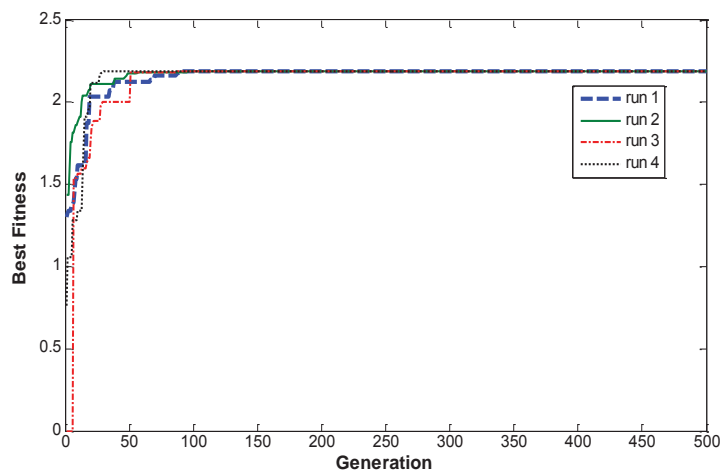


Fig. 3. Best fitness of example 2

7. Acknowledgements

The authors appreciate the financial assistance from Atma Jaya Yogyakarta University, Indonesia so that this research can be completed.

8. References

- [1] T.Y. Lin, Load balancing method for design and analysis of prestressed concrete structures. *J. Amer. Conc. Inst.* 60(6), 719–742, 1963
- [2] Y. Arfiadi, Determination of prestressing force in statically indeterminate structures (in Bahasa Indonesia), *Berita HAKI*, Oct-Nov. edition, 1986.
- [3] Y. Arfiadi and M.N.S. Hadi, Moment coefficients for statically indeterminate prestressed concrete structures, *Asian Journal of Civil Engineering*, 12 (1), 39-59, 2010.
- [4] M. Galante, Genetic Algorithms as an approach to optimize real-world trusses. *Int. J. Numerical Methods in Engrg.* 39(3), 361-382, 1996.
- [5] P. Kripakaran, A. Gupta, and J.W. Baugh Jr., A novel optimization approach for minimum cost design of trusses, *Comp. and Struct.* 85,(23- 24),1782-1794, 2007.
- [6] Rajan, S.D. Sizing, shape, and topology design optimization of trusses using genetic algorithm.” *J. of Struct. Engrg.*, 121(10), 1480-1487, 1995
- [7] R. Frans and Y. Arfiadi, Sizing, shape, and topology optimizations of roof trusses using hybrid genetic algorithms, *2nd Int. Conf. on Sustainable Civil Engrg. Struct. and Constr. Materials 2014, Procedia Engineering*, 95,185 – 195, 2014.
- [8] L. Li, Z. Huang, and F. Liu, An improved particle swarm optimizer for truss structure optimization, *Int. Conf. on Computational Intelligence and Security*, 1, 924-928., 2006.
- [9] M. Dorigo, M., V. Maniezzo, A. Colorni, Ant system: optimization by a colony of cooperating agents, *IEEE Transactions on Syst., Man, and Cybern., Part B: Cybernetics*, 26(29-41), 1996
- [10] Y. Arfiadi and MNS. Hadi, Optimal direct (static) feedback controller using real coded genetic algorithms, *Computer and Structures*, 79 (17), 1625-1634, 2006.
- [11] J.J. Grefenstette, Optimization of control parameters for genetic algorithms, *IEEE Transac. on Syst. Man and Cybern.* 1986; 16(1): 122-128.

Research on Integrated Design and Optimization for Hypersonic-Glide Vehicle

Jianquan Ge¹, Longyun Chen, Bin Zhang, Lei Wang

¹National University of Defense Technology, Changsha, China, jack_keh@sina.com

Abstract

The emergence of Hypersonic-Glide Vehicle (HGV) in the hypersonic regime brings a new series of technical challenges, such as strong system integration of parametric model, aerodynamics, thermal, trajectory, and problems about rapidly selecting acceptable conceptual designs. Traditionally, the subsystem of HGV models is designed and optimized separated without considering coupling, leading to losing the globally optimal solution. In this paper, the HGV Integrated Design Environment (HGVIDE) for HGV design and optimization will be presented, to improve the quality and efficiency of the traditional single solution optimization. First of all, a parametric design method based on class function/shape function transformation (CST) and power function was established as the starting step on which the engineering estimation models for aerodynamic force and flux were executed. Secondly, it assesses the effect of vehicle design variables on the maximum lift-drag ratio boost-glide trajectory. Finally, the performance optimization problem is presented, which demonstrate the application of optimization techniques to the multi-disciplinary and multi-objective design of HGV. The investigation shows that the methods feature higher efficient and further complete, thus can give better optimal results for HGV integrated design and optimization problems.

Keywords: Hypersonic-Glide Vehicle, Parametric Modeling, Integrated Design, Multi-objective Optimization

Introduction

Hypersonic vehicles employing high L/D body offer affordable commercial and military applications. The emergence of Hypersonic-Glide Vehicle (HGV) in the hypersonic regime brings a new series of technical challenges, such as strong system integration of parametric modeling, aerodynamics, thermal, trajectory, and problems about rapidly selecting acceptable conceptual designs. To address these challenges, a HGV Integrated Design Environment (HGVIDE) which is based on Multi-disciplinary Design Optimization (MDO) method and multi-disciplinary integration technology is designed and applied to HGV multidisciplinary design optimization. Many examples of MDO applications are presented in the literature^[1-4]. The need to improve the engineering design process is an endless challenge^[5]. For this purpose, system level optimization is needed to determine the most effective integrated concept. Whether the goals are to improve the quality of a design, or to reduce the amount of time required to do design, the desire to get better always exists. Traditionally, the subsystem of HGV models are designed and optimized separated without considering coupling. However the solution to the design problem does not reside within one discipline but will only be found by investigating the complex interactions between various disciplines. The objective of this paper was the development of integrated system approach to evaluate the best design to achieve overall performance. The HGVIDE is a tool used in research and development arena, focused on the design and optimization to improve the quality and efficiency of the traditional single solution optimization. The key idea is to use multi-disciplinary and multi-objective design and optimization aiming at aerodynamic performance and ballistic performance simultaneously to get more acceptable results. The reference design point for HGV was as shown in figure 2-3 with the evaluation of the unpowered skipping trajectory. The major blocks of the simulation are geometry module, aerodynamics force module, aerodynamics thermal module, trajectory simulation module, and optimization module. Example capabilities of the process are demonstrated followed by conclusions and future plans.

1 HGVIDE Multi-Disciplinary Module

There are five main modules which make up the HGVIDE system, such as the Geometry Module, the Aerodynamics Force Module, the Aerodynamics Thermal Module, the Trajectory Simulation Module, and optimization module. The execution of the HGVIDE system is shown in Figure 1, as a design structure matrix. In this figure, the HGVIDE analysis modules are shown on the diagonal of a matrix in their execution order. The data generated by a module is shown on the module's row of the matrix (with the exception of the left column, which is input by the user or the optimization system). The data that a module needs from the HGVIDE system is shown in Figure 1. This is a useful tool for visualizing the overall process, as "feedforward" interactions are shown in the upper right triangle of the matrix, and "feedback" interactions are shown in the lower left. It helps to make module

execution order decisions, as the desire is to minimize feedback interactions, which must be handled through iteration. Note that the HGVIDE system is far too complex to display in a single figure, so Figure 1 only shows the most significant interactions between modules. A system-level optimization layer is then added to the entire multidisciplinary analysis system .

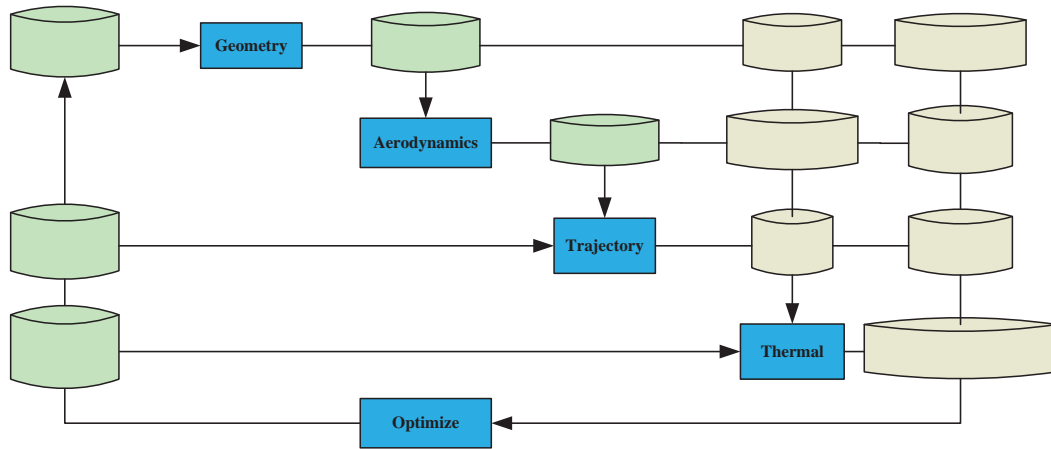


Figure 1: Main Modules of HGVIDE

1.1 Geometry Module

The HGVIDE Geometry Module is responsible for maintaining a geometric model of the configuration being analyzed, and for updating that model as system level design variables are being changed. This module based on class function/shape function transformation(CST)^[6], dividing geometry configuration into top view outline parameter, side-looking outline parameter and bottom view outline parameter.

1.1.1 Top View Outline Parameter

As figure 2 shows, the top view outline parameter consists of six parameter, but total length L and bottom width W are separately assigned to 4000mm and 2400mm. In addition, the length of the dome L_1 and width of the dome bottom W_1 are nearly constant, so only two parameters are needed, the length of precentrum L_2 and width of the precentrum bottom W_2 to describe the top view outline.

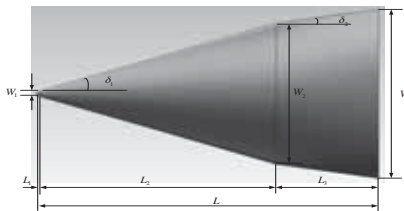


Figure 2: Top View Outline

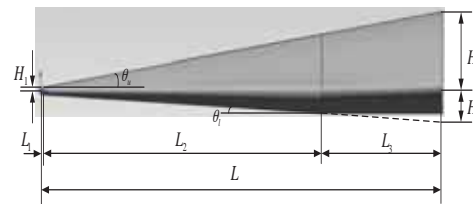


Figure 3: Side-looking Outline

1.1.2 Side-looking Outline Parameter

As figure 3 shows, the top view outline parameter consists of three parameters, but the thickness of the half dome H_1 are nearly constant, so only two parameters are needed, the thickness of back cone bottom H_u and H_l to describe the top view outline.

1.1.3 Bottom View Outline Parameter

Based on class function/ transformation (CST), the bottom view outline physical coordinate (x, y) is converted into parameterized coordinate (ψ, η) as Eq.(1), then the parameterized coordinate (ψ, η) can describe as multiply class function $C_{N_{c2}}^{N_{c1}}(\psi)$ by shape function $S_{N_{c2}}^{N_{c1}}(\psi)$ as follows:

$$\eta(\psi) = C(\psi) \cdot S(\psi) \quad (1)$$

)

Shape function is $S = 2^{2N_c}$ based on this mission. Class function is $C(\psi) = \psi^{N_{c1}}(1-\psi)^{N_{c2}}$, $\psi \in (0,1)$. Where N_{c1}, N_{c2} are class function index numbers, we can get $N_{c1} = N_{c2} = N_c$ for plane symmetry aircraft.

In conclusion, the HGVIDE geometry module just need $L_2, W_2, H_u, H_l, N_{cu}$ and N_{cl} all six parameters to

express the Hypersonic-Glide Vehicle (HGV) appearance geometry feature. These parameters based on CST are separately but definitely, to confirm this module. examples are showed as follows.

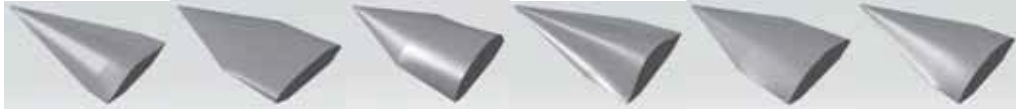


Figure 4: Examples based on CST method

The HGVIDE Geometry Module provides the structural subsystem data associated with the overall vehicle. The data includes a global surface mesh model and mass properties of the vehicle. A conceptual layout of the Geometry Module showing its three major components are shown graphically in Figure 5.

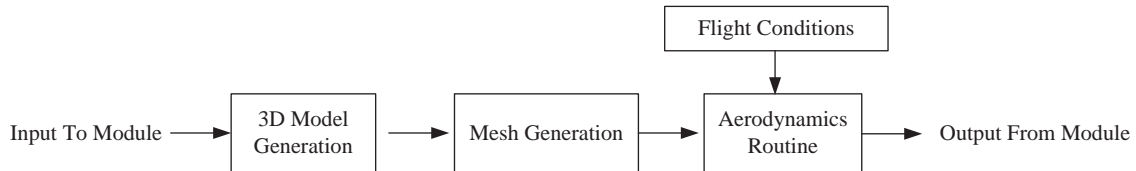


Figure 5: Architecture of the Aerodynamics Force Module

1.2 Aerodynamics Force Module

The HGVIDE Aerodynamics Force Module computes the aerodynamic performance of the vehicle over the expected flight envelope using a set of engineering estimation methods to aerodynamic analysis. This includes the modified Newton's formula as Eq.(2) based on Lees' contribution to complete pressure coefficient simulation of the windward side, and the Prandtl-Meyer's formula as Eq.(3) to complete the leeside. This approach combines the panel method code and the engineering estimation methods which described above to bias the low fidelity solution. This results in a good compromise between accuracy and solution time.

Modified Newton's formula:

$$C_p = C_{p_{max}} \sin^2 \theta, \quad C_{p_{max}} = \frac{2}{\gamma M_1^2} \left\{ \left[\frac{(\gamma+1)M_1^2}{4\gamma M_1^2 - 2(\gamma-1)} \right]^{\frac{\gamma}{\gamma-1}} \left(\frac{1-\gamma+2\gamma M_1^2}{\gamma+1} \right) - 1 \right\} \quad (2)$$

where C_p is the pressure coefficient, $C_{p_{max}}$ is the max pressure coefficient, θ is the inclination of the aircraft.

Prandtl-Meyer's formula:

$$C_p = -\frac{\gamma+1}{2} \delta^2 \left\{ \sqrt{1 + \left[\frac{4}{(\gamma+1) \text{Ma}_\infty \delta} \right]^2} - 1 \right\} \quad (3)$$

in which, δ is the impact angle.

1.3 Aerodynamics Thermal Module

The HGVIDE Aerodynamics Thermal Module computes the stagnation point aerodynamic heating environment, and simulates the stagnation heat flux as the main index of the whole vehicle aerodynamic heating. Based on the flight conditions, height and temperature of the wall, this module introduces Scala formula as Eq.(4) to compute the density of stagnation heat flux.

$$q_{ws} = \frac{12.488}{\sqrt{R_N}} (10.0)^a (3.281 \times 10^{-3} v_\infty)_b, \quad \begin{aligned} a &= -(0.9689 + 6.9984 \times 10^5 T_w)(5.626 + 3.2285 \times 10^{-5} h) \\ b &= (0.9793 + 4.6715 \times 10^{-5} T_w)(2.838 + 9.843 \times 10^{-7} h) \end{aligned} \quad (4)$$

where q_{ws} is the density of stagnation heat flux, R_N is the radius of curvature of stagnation, v_∞ is the flight velocity, T_w is the temperature of the wall, and h is the flight height.

1.4 Trajectory Simulation Module.
Based on boost – gliding trajectory, the trajectory simulation will consist of a three degree of freedom (3DOF) and a three section of process includes boost, free and reentry phase as Eq.(5~7), untrimmed analysis of the vehicle starting at time zero to the desired final statement.

Section 1: Boost Phase

$$\begin{cases} \dot{V} = \frac{P_c}{m} - \frac{1}{m} C_x q S_M + g \sin \theta \\ \dot{\theta} = \frac{1}{mV} (P_c + CV^\alpha) \alpha + \frac{g}{V} \cos \theta \\ y = V \sin \theta \\ x = V \cos \theta \\ \alpha = A_\varphi (\varphi_{pr} - \theta) \\ m = m_0 - mt \end{cases} \quad (5)$$

Section 2: Free Phase

$$\begin{cases} \dot{v}_x = \frac{P}{m} \cos \varphi(t) - \frac{fM}{r^3} x \\ \dot{v}_y = \frac{P}{m} \sin \varphi(t) - \frac{fM}{r^3} (y + R) \\ x = v_x \\ y = v_y \end{cases} \quad (6)$$

Section 3: Reentry Phase

$$\begin{cases} \dot{V} = -\frac{D}{m} - \frac{fM}{r^2} \sin \theta_r \\ \dot{\theta}_r = \frac{1}{V} \left[\frac{L \cos v}{m} - \left(\frac{fM}{r^2} - \frac{V^2}{r} \right) \cos \theta_r \right] \\ \dot{\sigma}_r = \frac{-L \sin v}{mV \cos \theta_r} + \frac{V \cos \theta_r \sin \sigma_r \tan \phi}{r} \\ \dot{\phi} = \frac{V \cos \theta_r \cos \sigma_r}{r} \\ \dot{\lambda} = \frac{-V \cos \theta_r \sin \sigma_r}{r \cos \phi} \\ r = V \sin \theta_r \end{cases} \quad (7)$$

For the sake of analysis efficiency, the attitude dynamics and other less important equations are neglected.

1.5 Multi-disciplinary integration

Each of these component modules has a clearly description above. The HGV Integrated Design Environment (HGVIDE) which based on multi-disciplinary integration technology is designed and applied to HGV multidisciplinary design optimization.

2 HGV Trajectory Performance Multidisciplinary optimization

The fundamental approach employed in this work included construction of a parametric configuration geometry model; development of physics models for aerodynamics, heat flux, and mass properties as functions of geometric variables; then use of trajectory analysis to assess vehicle performance and a numerical optimization algorithm to search the set of geometric variables that maximize overall performance. To demonstrate the application of optimization techniques to the multi-disciplinary and multi-objective design of HGV, overall performances optimization problems are established. In this section, six geometry parameters and mass (M) are set as design parameters, the trajectory performance design function presents maximal range trajectory R_f and minimal total heat adsorption capacity of stationary point Q , and the corresponding Pareto fronts are used for describing results.

2.1 Optimization Model

Now, there are all seven design parameters, therein six geometry parameters are not facility to complete optimization, so we take Latin-Hypercube experiment design (DOE) to acquire the sensitivity of each parameter about the R_f and Q . In our research, N_{cl} has the minimal effect on range trajectory (1%) and total heat adsorption capacity of stationary point (2%), as a result, we select other six parameters M , L_2 , N_{cu} , H_u , H_l , W_2 for optimization. On the other hand, during the parameters sensitivity analysis, it's easy to find that the tendency of maximal range trajectory R_f and minimal total heat adsorption capacity of stationary point Q response curve for six geometry parameters are opposite. In practice, the R_f and Q are important to HGV overall performance design, but the opposite tendency impose restrictions on the best optimization, so only aiming at R_f and Q meanwhile, can we realize multi-disciplinary trajectory optimization.

In order to endure the volume ratio and stability of the HGV, meanwhile considering the structural strength and thermal protection, it's reasonable to regard the volume V , the longitudinal pressure coefficient X_p , the dynamic pressure η and heat flux Q as constraint conditions. Optimization model as Eq.(8) follows:

$$\begin{aligned}
F &= \begin{cases} \max f_1(X) = R_f \\ \min f_2(X) = Q \end{cases} \\
X &= (M, L_2, W_2, H_u, H_l, N_{cu}) \\
s.t. & \begin{cases} V \geq 1.6 \\ V_e \geq 0.22 \\ X_p \geq 0.6 \\ \eta \leq 650kPa \\ Q \leq 1000kW/m^2 \end{cases}
\end{aligned} \tag{8}$$

Where F is Optimization objective, X is design space, and $s.t.$ are constraint conditions.

2.2 Multi-disciplinary Optimization Result

Based on Multi-Disciplinary Integration platform we created before, by calling genetic algorithm optimizer Darwin, it's not difficult to establish the optimization model for Multi-disciplinary Optimization. In the end, the corresponding Pareto front is obtained as figure 6 shows.

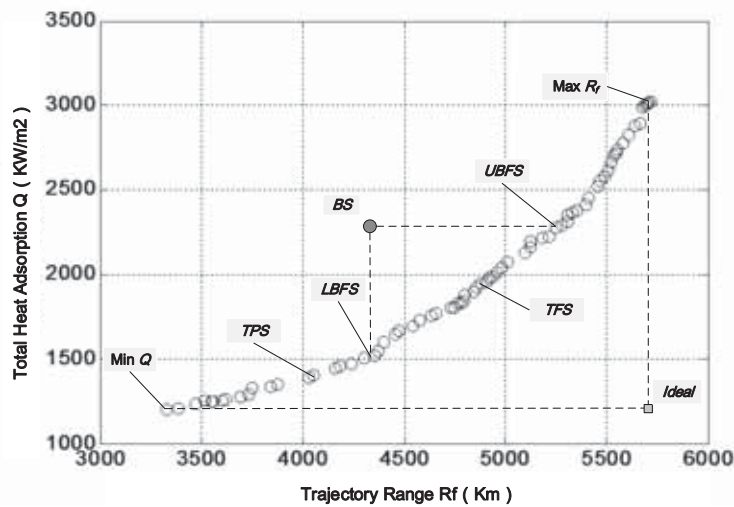


Figure 6: Multi-disciplinary optimization Pareto fronts

In figure 6, the based starting design (BS) and optimization Pareto fronts are separately marked as solid and hollow circles. More specifically, “Min Q” and “Max Rf” are maximal range trajectory R_f and minimal total heat adsorption capacity of stationary point Q , but the hollow-black (“Ideal”), which represents both maximal range trajectory and minimal total heat adsorption capacity of stationary point is conflicted, is impossible to reach. What's meaningful to feasible solution is Pareto fronts which within the range from “LBFS” to “UBFS”, such as “TFS”, can magnify trajectory range and decrease total heat adsorption capacity of stationary point. In addition, the Pareto fronts outside of this range, such as “TPS”, can only change just one of two optimization performance.

In conclusion, the BS and TFS project appearance of HGV are showed in Figure 6, and the comparison between BS and TFS is also presented in Table 1. What's more, trajectory performance multi-disciplinary optimization based on HGVIDE in this article have achieved outstanding improvement. The maximal range trajectory R_f increases from 4332.6km to 4874.5km rising 12.51%, at the same time, the minimal total heat adsorption capacity of stationary point Q decreases from 2284.1kW/m² to 1942.3kW/m² decreasing 14.92%. In practice, we can select the finest corresponding Pareto front on the basis of design demands.



(a) BS project appearance

(b) TFS project appearance

Figure 7: BS(a) and TFS(b) project appearance of HGV

Table 1: Comparison between BS and TFS

Index	BS	TFS	Difference(%)
R_f (km)	4332.6	4874.5	12.51
Q (kW/m ²)	2284.1	1942.3	-14.92

3 CONCLUSIONS

In this article, a HGV Integrated Design Environment (HGVIDE) which based on Multidisciplinary Design Optimization (MDO) method and multi-disciplinary integration technology is designed and applied to HGV multidisciplinary design optimization. To develop a reasonable goal requirement in pre-concept design phase of HGV, a probabilistic analysis is presented. The procedure consists of probabilistic model based CST, aerodynamics force, thermal, trajectory simulation module, and multi-objective optimization. The most influential variables are selected by design of experiment method to make approximate model in the initial step. The objective is minimizing flux and maximizing range, the use of genetic algorithms to select from discrete component choices has been proven valuable in selecting the Pareto front. The HGV design capabilities presented in this paper will allow engineers to make quick changes to conceptual aero-shape design and get accurate, integrated results.

Results of the system level optimization showed the HGV tends to accelerate to the optimization efficient. And the presented methodology is satisfied to establish the acceptable solution requirement in pre-concept design phase. The HGVIDE system provides a design, analysis, and optimization tool with extensive capabilities, the environment can be used for on HGV integrated design and optimization, which has a good reference value for HGV overall design. The present approach provides many benefits to conceptual designers. The approach offers a better method for comparing the viability of candidate designs. Further work will focus on increasing the fidelity of the example models and incorporating more discrete system selection choices for construction of more complex systems.

4 Acknowledgments

The authors wish to acknowledge the rest member of HGVIDE System team, whose contribution work is the base of this research.

5 References

- [1] Paul V. tartabini, Kathryn E. Wurster and J.J. Korte, Multidisciplinary analysis of a lifting body launch vehicle, *Journal of Spacecraft and Rockets*, 788-795, 2002.
- [2] Nosratollahi, Mortazavi, Adami and Hosseini, Multidisciplinary design optimization of a reentry vehicle using genetic algorithm, *Aircraft Engineering and Aerospace Technology*, 194-203, 2010
- [3] Takeshi Tsuchiya, Yoichi Takenaka and Hideyuki Taguchi, Multidisciplinary Design Optimization for Hypersonic Experimental Vehicle, *American Institute of Aeronautics and Astronautics*, 1655-1662, 2007.
- [4] Deog-jae Hur, Dong-chan Lee, Multidisciplinary Optimal Design Concept for Vehicle Body Structural Design, *Multidiscipline Modeling in Materials and Structures*, 73-85, 2005.
- [5] Feng Z, Zhang Q, Zhang Q, et al, A multiobjective optimization based framework to balance the global exploration and local exploitation in expensive optimization, *Journal of Global Optimization*, 61(4), 677-94, 2015.
- [6] Kulfan, B M and Bussoletti, J E, "Fundamental" parametric geometry representations for aircraft component shapes, *11th AIAA/ISSMO Multidisciplinary Analysis and Optimization Conference*, Portsmouth, Virginia, 1-45, 2006.

Shape optimization method for crashworthiness design based on Equivalent Static Loads concept

Laurent Genest^{1,2}, Louis Jézéquel¹, Frédéric Gillot¹, Frédéric Mercier²

¹ LTDS, École Centrale de Lyon, Ecully, France,

louis.jezequel@ec-lyon.fr, frederic.gillot@ec-lyon.fr

² CAE Models and Methods Department, Renault S.A.S., Guyancourt, France,

laurent.genest@renault.com, frederic.mercier@renault.com

1. Abstract

Shape optimization of parameterized thin shell structures is increasingly considered by automotive industry in order to face nonlinear dynamics problems like crashworthiness. Since the number of shape parameters is important, traditional multidisciplinary optimization methods such as metamodeling techniques become less efficient due to expensive calculation times. A way to get around the problem is to switch to gradient methods which are less sensitive to the number of parameters. However, shape sensitivities are often hard and costly to calculate for highly nonlinear problems.

Inspired by the Equivalent Static Loads Method, we defined linear static problems on which we perform a shape sensitivity analysis. After linking sensitivity maps with CAD parameters, gradients are used as descent directions for the nonlinear objective function. We applied successfully the method to two test cases: minimization of a nodal displacement and maximization of the absorbed energy. Because the calculation of this descent direction is inexpensive, this new optimization method allows performing crashworthiness optimization studies with a large number of parameters.

2. Keywords: Shape optimization, Crashworthiness, Equivalent Static Loads, Approximated gradient.

3. Introduction

Depending on the optimization variables that describe the shape of the domain to be optimized, shape optimization can be classified in three categories : topology, shape and parametric optimizations [3]. Automotive industry has a growing interest on parametric shape optimization since it directly takes into account the manufacturing process. Indeed, knowing more severe specifications and a will of mass reduction, this industry is enlarging the optimization design space to shape parameters.

Crashworthiness is one of the most dimensioning specifications of the body in white and is still problematic. Even if it is possible to calculate a descent direction with finite difference [5], this method has not been used due to the numerical noise, the high nonlinearity and the heavy calculation time (e.g. crashworthiness time calculation for a full vehicle: around 10h/16 processors) of this rapid dynamics problem. Instead, car designers used metamodeling techniques which have been successfully applied to optimization problems with thickness and materials parameters and also with a few number of shape parameters [6, 2].

However, the optimization cost of those methods dramatically increase with the number of shape parameters. A way to get around this issue is to switch to gradient methods where the number of parameters has a reduced effect on the optimization cost.

Recently, a new optimization algorithm for nonlinear problems, the *Equivalent Static Loads Method*, has been proposed by Park [7]. Inspired by this method, we have defined linear static problems equivalent to the rapid dynamic problem on which we calculate shape sensitivity. This gradient is then used as descent direction for the nonlinear problem. This method and its applications to two crashworthiness specifications are explained in following parts.

4. Calculation of the descent direction

In order to test our descent directions, we have applied the method to mono-objective crashworthiness problems. The rapid dynamic problem could be written as follow :

Optimization problem in rapid dynamic

Find the n shape parameters $P = \{P_i\}$, $i = 1..n$

To minimize $J_{NL}(P)$, the nonlinear objective function

Subject to constraints on the variation of the shape parameters $P_i^{min} \leq P_i \leq P_i^{max}$, $i = 1..n$

Where X_{NL} is the solution of the rapid dynamic equation (1).

$$M(P)\ddot{X}_{NL}(t,P) + K_T[X_{NL}(t,P),P]\Delta X_{NL}(t,P) = F_{NL}(t,P), \quad t = t_1..t_f \quad (1)$$

With M the mass matrix, K_T the tangent stiffness matrix, F_{NL} the external loading vector and X_{NL} the displacement vector.

4.1. Equivalent Static Loads concept

Park proposed the Equivalent Static Loads Method (ESLM) and successfully applied it to several nonlinear problems [7, 8]. As illustrated in Figure 1, ESLM consists in the creation of f linear static problems equivalent to the nonlinear problem at a time t_s and this for each time step $s = 1..f$. The optimization is performed on the *Design Domain* (linear static problems) and the result is used to update the *Analysis Domain* (nonlinear problem). A new nonlinear analysis is performed and new equivalent static problems are created. This process is repeated until convergence.

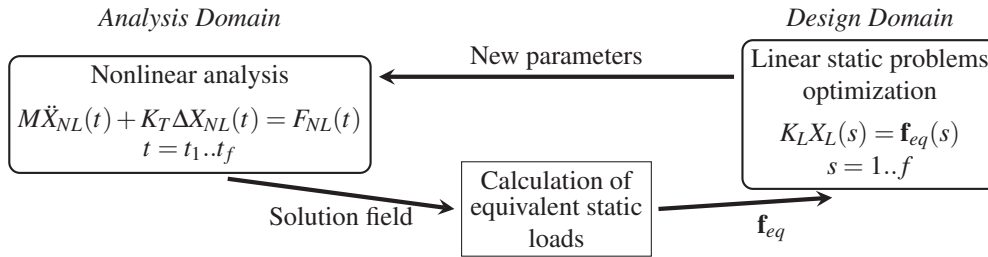


Figure 1: Optimization process of the Equivalent Static Loads Method

Linear static equations are defined in equation (2).

$$K_L(P)X_L(s,P) = \mathbf{f}_{eq}(s), \quad s = 1..f \quad (2)$$

where K_L is the static linear stiffness matrix of the initial (non-deformed) domain, X_L the linear displacement vector solution of the equation and $\mathbf{f}_{eq}(s)$ is the equivalent static load chosen to preserve the field at step time t_s we want to optimize in the linear static problem.

For example, if we want to optimize the displacement of a node, we have to preserve the non-linear displacement $X_{NL}(t_s)$ solution of (1) at t_s . Writing $\mathbf{f}_{eq}(s) = K_L X_{NL}(t_s)$, we preserve the nonlinear displacement field: $X_L(s) = X_{NL}(t_s)$.

4.2. Presentation of the method

Inspired by the Equivalent Static Loads Method, we propose to use the shape sensitivity calculated on equivalent linear static problems as a descent direction for the rapid dynamic problem. We studied two crashworthiness specifications. The first one is to minimize a nodal displacement. Then, we defined a static linear problem that preserve the displacement field. In the second study, we had to maximize the absorbed energy of a part of the domain. In this case, we had to preserve both strain and stress fields in a linear static problem.

Methods of calculation of the two descent directions are explained in this part. Shape sensitivities are first calculated on the nodes position of the CAE* model. The link between this sensitivity mapping and CAD† parameters is explained in the next section.

4.2.1. Descent direction calculation for the optimization of a nodal displacement

The objective function that we want to minimize is $J_{NL}(P) = u_{NL}(t_a, P)$ where $u_{NL}(t_a, P)$ is a nodal displacement at t_a fixed. Since the objective function is a displacement function, we need to preserve X_{NL} in the equivalent linear static equation (3).

$$K_L(P)X_L(P) = \mathbf{f}_{eq} \quad (3)$$

with K_L the linear stiffness matrix of the initial non-deformed domain and $\mathbf{f}_{eq} = K_L X_{NL}(t_a)$.

The shape sensitivity is issued from the linear model, that means that we approximate $d_P J_{NL}$ by $d_P J_L$. Because $\partial_P J_L = 0$, the descent direction used for the nonlinear objective function is $d_P J_L = \partial_Q J_L \cdot \partial_P Q$ where Q is the nodes

*Computer Aided Engineering

†Computer Aided Design

position of the CAE model. We have seen that, under quasi-static and quasi-proportionnal loadings (reversibility) hypotheses [4], we have $\langle dpJ_{NL}, dpJ_L \rangle \geq 0$ and then $-dpJ_L$ is well a descent direction of the rapid dynamic problem.

Since the explicit algorithm used to solve equation (1) is stable, quasi-static hypohese is validated. The following conditions are needed to validate the second hypohese:

- the initial state is the non-deformed and non-hardened state,
- the material law is a Prandtl-Reuss law,
- the hardening law is a power function,
- principal directions of stress tensor are quasi-constants,
- and elastic strains are negligible.

4.2.2. Descent direction calculation for the optimization of the absorbed energy

Another important crashworthiness specification is to ensure a good behavior of the crash scenario. Engineers have to control the energy absorbed by a component of the car. The nonlinear objective function is defined in equation (4).

$$J_{NL}(P) = \int_{\Omega(P)} \int_{t_1}^{t_f} \langle \sigma_{NL}(\mathbf{x}, t) \rangle \{ \dot{\epsilon}_{NL}(\mathbf{x}, t) \} dt dV \quad (4)$$

where σ_{NL} is the stress field and $\dot{\epsilon}_{NL}(\mathbf{x}, t) \approx \frac{1}{\Delta\tau} (\epsilon_{NL}(\mathbf{x}, t) - \epsilon_{NL}(\mathbf{x}, t - \Delta\tau))$ with ϵ_{NL} the strain field.

Doing a temporal discretization and writing $\Delta\tau = t_s - t_{s-1}$, we rewrite equation (4) to (5).

$$J_{NL}(P) = \sum_{s=1}^f \int_{\Omega(P)} \langle \sigma_{NL}(\mathbf{x}, t_s) \rangle \{ \epsilon_{NL}(\mathbf{x}, t_s) \} - \{ \epsilon_{NL}(\mathbf{x}, t_{s-1}) \} dV \quad (5)$$

With this kind of objective function, we need to preserve both stress and strain fields within the same linear static problem. To do so, we have to use the secant stiffness matrix $K_S(P, t_s)$ which is calculated by assembling the element secant stiffness matrices: $K_S(P, t_s) = \sum_{e=1}^{nb.elem.} [T^e(P)]^T [K_S^e(P, t_s)]_{loc} [T^e(P)]$ where $[T^e(P)]$ is the change of basis matrix and $[K_S^e(P, t_s)]_{loc}$ is calculated with the secant modulus of elasticity visible in Figure 2.

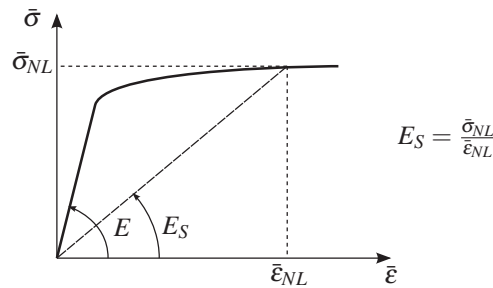


Figure 2: Definition of the secant modulus of elasticity E_S

By using the secant stiffness matrix, we can define linear static problems for each time step which preserve $\sigma_{NL}(\mathbf{x}, t_{s_1})$ and $\epsilon_{NL}(\mathbf{x}, t_{s_2})$ in the same equation (6). The equivalent static load is calculated to preserve the strain field.

$$K_S(P, s_1, s_2) X_L(P) = \mathbf{f}_{eq}^e \quad (6)$$

The equivalent linear objective function is then $J_L(P) = \sum_{s=1}^f \tilde{J}_L(P, s, s) - \tilde{J}_L(P, s, s-1)$, where $\tilde{J}_L(P, s_1, s_2)$, calculated with equation (6), is defined in equation (7).

$$\tilde{J}_L(P) = \int_{\Omega(P)} \langle \sigma_L(\mathbf{x}, s_1) \rangle \{ \epsilon_L(\mathbf{x}, s_2) \} dV \quad (7)$$

Since \tilde{J}_L is a compliance-like criteria, it is quite easy to assess a shape derivative. The descent direction used for the nonlinear problem is then defined in equation (8).

$$\partial_P J_L(P) = \sum_{s=1}^f \partial_P \tilde{J}_L(P, s, s) - \partial_P \tilde{J}_L(P, s, s-1) \quad (8)$$

4.3. Test algorithm

In order to test the descent directions calculated previously, we have used the algorithm illustrated in figure 3. By using an adaptative step-length, the test algorithm is closed to a line-search algorithm.

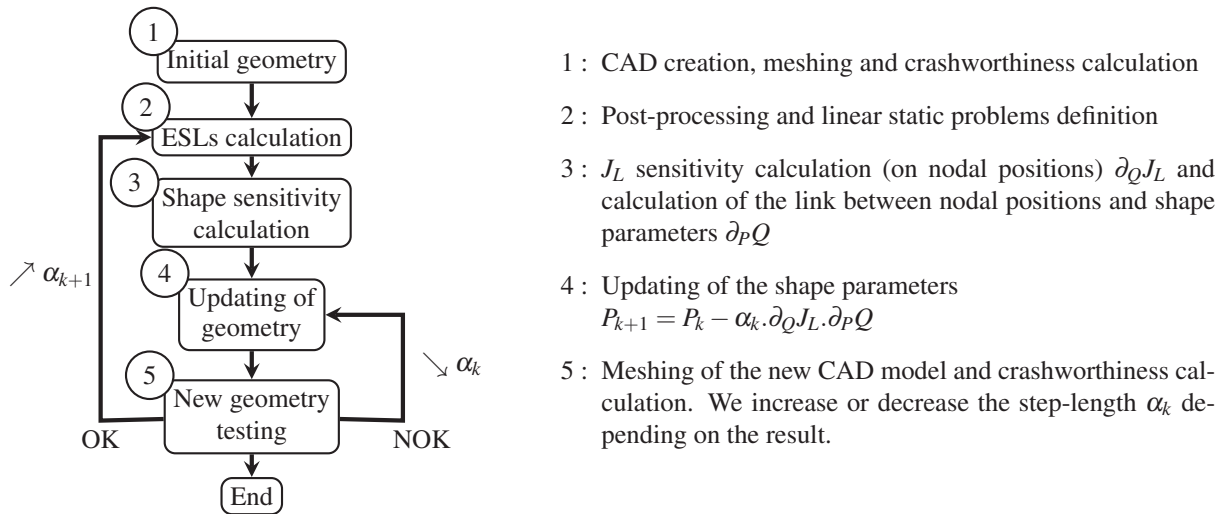


Figure 3: Algorithm used for testing the descent direction

Previously, we said that the shape sensitivity is calculated on the nodes position. We still have to link the sensitivity mapping to CAD parameters. In our case, we know the mathematical definition of the geometry : it is a B-spline surface S headed by its control points P . Because we know the mathematical definition of the parametric surface, we can easily link the nodal position of a node q and the position of the control point $p_{\alpha\beta}$.

$$\partial_{p_{\alpha\beta}} q = \frac{\partial S(\mathbf{u}_q, \mathbf{v}_q)}{\partial p_{\alpha\beta}} = b_{\alpha,l}(\mathbf{u}_q) b_{\beta,m}(\mathbf{v}_q) \quad (9)$$

where S is the B-spline surface of orders (l, m) , $b_{.,a}$ the B-spline function of order a and $(\mathbf{u}_q, \mathbf{v}_q)$ the parametric coordinates of the node q obtained by minimizing the distance $D(S, q)$ between the node and the surface by a Newton-Raphson method.

5. Applications

We have used our method on two industrial cases : the minimization of a crash-box crushing that is a nodal displacement minimization problem and the maximisation of the PEA[‡] that is an absorbed energy problem.

5.1. Minimization of a crash-box crushing

In this test case, we want to minimize the crushing of the 150mm length crash-box in steel defined in figure 4-a. This beam has a thickness of 1.5mm and is launched through a rigid wall with an initial velocity of $16\text{km}\cdot\text{h}^{-1}$ (pushing mass : 450kg). The geometry is defined with 3 sketches heading 16 control points illustrated in figure 4-b. Due to symetries, we defined 3 shape parameters on each sketch (9 shape parameters for the problem).

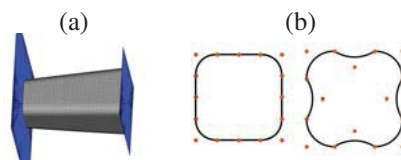


Figure 4: "Crash-box" test case (a) and its sketches (b)

Figure 5 represents the results of the optimization. The line-search of the first iteration, figure 5-a, shows that the problem is noisy and nonlinear. We have done several optimization studies in order to see the effect of the

[‡]Progressive Energy Absorbed

repeatability and of the mesh length. These results are visible in figure 5-b and show that a good CAE model quality is needed. We can also see in figure 5-c the crushing of the initial model and of the optimized one. The result which seems like a castle could be explained by the fact that the geometry is the one that have the greater second moment of area.

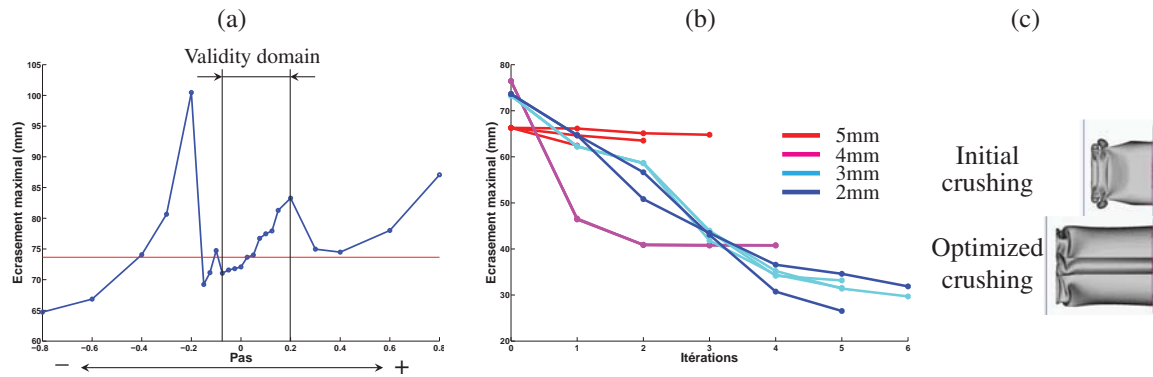


Figure 5: Results : line-search used for the first iteration (a), Effect of repeatability and mesh length on optimization process (b) (mesh length : 2-5mm), Initial and optimized models crushing (c)

5.2. Maximization of the Progressive Energy Absorbed of a front side member

Traditionnaly, the strategy chosen by engineers to absorb kinetic energy is a progressive crush of the front side member. Chase proposed a criterion called Progressive Energy Absorbed (PEA) in order to ensure a good behavior of the crushing process [1]. We choosed to maximize this objective function for our second test case. The S-beam visible in figure 6-a is defined with 120 CAD parameters and is launched onto a rigid wall with an initial velocity of $30\text{km}\cdot\text{h}^{-1}$ (pushing mass : 450kg, thickness : 1.5mm). We also defined 6 zones in order to calculate the PEA with equation (10).

$$PEA = \sum_{N=1}^5 (EA_N(U_N) - EA_N(U_{N-1})) - EA_6 \quad (10)$$

Where $EA_N(U_N)$ is the energy absorbed by zone N when the beam has crushed of U_N , EA_6 is the total energy absorbed by zone 6 and values of U_N can be seen in figure 6-b.

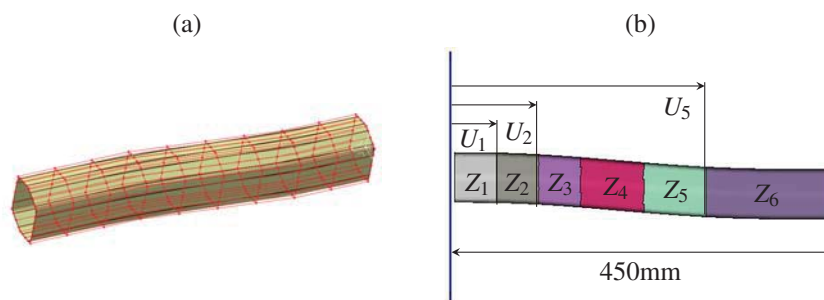


Figure 6: "S-Beam" test case, its control net (a) and zones for the PEA calculation (b)

Results are in figure 7. The initial geometry has a bad behavior: buckling. By maximizing the PEA, the rear part is reinforced and in 6 iterations, the front side member is crushing progressively.

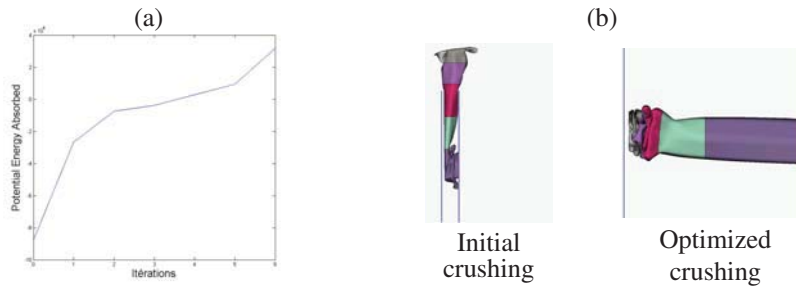


Figure 7: Results : PEA function of iterations (a),
Initial and optimized models crushing (b)

6. Conclusions

We have proposed a method that use linear static problems in order to calculate a descent direction for a nonlinear crashworthiness problem. Since the calculation of the shape sensitivity is really fast compared to the crashworthiness calculation, this descent direction can be used for crashworthiness problems with a high number of parameters without having a too expensive optimization cost. We still have to calculate a descent direction for other crashworthiness problems like pulses or the Occupant Load Criterion and use them for multi-objectives optimization problems.

7. Acknowledgements

We thank Marc Albertelli (Renault) for fruitfull discussion on the Equivalent Static Loads approach.

8. References

- [1] N. Chase, R. Averill and R. Sidhu, Design optimization of progressively crushing rails, *SAE Technical Paper*, 2009-01-0353, 2009.
- [2] F. Duddeck, Multidisciplinary optimization of car bodies, *Structural and Multidisciplinary Optimization*, 35, 375-389, 2008.
- [3] P. Froment, F. Gillot, Y. Tourbier and L. Jézéquel, CAD-based large scale shape optimization method with intensive simulations, *10th World Congress on Structural and Multidisciplinary Optimization*, Orlando, Florida, USA, 2013.
- [4] J. Lemaitre and J.-L. Chaboche, *Mechanics of Solid Materials*, Cambridge University Press, 1990.
- [5] P.O. Marklund and L. Nilsson, Optimization of a car body component subjected to side impact, *Structural and Multidisciplinary Optimization*, 21, 383-392, 2001.
- [6] F. Mercier, M. Guillon and S. Maillot, Deployment of optimization studies using Alternova : design of a hood inner panel for pedestrian safety performance, *Ingénieurs de l'Automobile*, 29-46, 2012.
- [7] G.-J. Park, Technical overview of the equivalent static loads method for non-linear static response structural optimization, *Structural and Multidisciplinary Optimization*, 43, 319-337, 2011.
- [8] S.-I. Yi, J.-Y. Lee and G.-J. Park, Crashworthiness design optimization using equivalent static loads, *Proceedings of the Institution of Mechanical Engineers, Part D : Journal of Automobile Engineering*, 226, 2012.

Optimizing snap-through structures by using gradient-only algorithms

Schalk Kok¹, Daniel N Wilke²

¹ Department of Mechanical and Aeronautical Engineering, University of Pretoria, South Africa, schalk.kok@up.ac.za

² Department of Mechanical and Aeronautical Engineering, University of Pretoria, South Africa, nico.wilke@up.ac.za

1. Abstract

This paper presents a robust technique to design snap-through structures. The structural analysis of the snap-through structure makes use of an arc length control algorithm. To ensure robustness, the prescribed arc length per increment is halved whenever complex roots are encountered in the arc length control algorithm, or when the required number of Newton-Raphson iterations exceeds five. The resulting structural analysis is robust, but now different analyses makes use of different increment sizes. The resulting optimization problem, which minimizes the error between a target load-deflection curve and the simulated curve, now contains numerical discontinuities. We demonstrate how gradient-only optimization algorithms can robustly optimize such problems.

2. Keywords: Snap-through, arc length control, gradient-only optimization.

3. Introduction

Analysis of snap-through structures usually requires the use of the arc length control method [1]. In this method, the usual equilibrium equations are augmented with parametrizing the prescribed loads, and then solving this free parameter by setting the computed arc length increment equal to some prescribed value. Usually this prescribed arc length is selected as constant for each load increment during the analysis.

Sometimes, the arc length control algorithm fails to find a solution for a specific load increment. This can manifest in two ways. First, the quadratic control equation may indicate a complex root. Secondly, the Newton-Raphson scheme used to solve the global equilibrium equations may need an excessive number of iterations to solve. Even in cases where the number of iterations are reasonable (<20), our experience indicates that the algorithm may then find solutions on other branches of the equilibrium path. Therefore, we halve the prescribed arc length increment whenever complex roots are encountered, or whenever the number of Newton-Raphson iterations exceeds five.

The automatic adjustment of the prescribed arc length increment presents a difficulty when attempting to design a snap-through structure to provide a specific load-displacement curve, using classical gradient-based optimization algorithms. The adjusting of the prescribed arc length has the same consequence as allowing automatic time increments for transient problems: the cost function of the resulting optimization problem contains discontinuities since the same problem is analyzed repeatedly, each time using different prescribed arc length values.

We have significant experience in solving optimization problems that uses non-constant discretization algorithms [2]. Here we demonstrate how classical gradient based algorithms struggle to solve this snap-through design problem, since these algorithms can get stuck at the numerical (non-physical) discontinuities. We also demonstrate how gradient-only algorithms, a family of algorithms that do not use function values at all, succeed in designing the snap-through structures.

4. Numerical example

We demonstrate our algorithm using a simple 1D optimization problem. The structure of interest is similar to the well known Lee frame, but here we use a geometrically nonlinear truss code for the analysis. The structure is depicted in Figure 1. Note that two vertical loads are applied, as well as a single horizontal force. The structure is analysed for the case $\lambda = 0.5$, i.e. the horizontal force is one quarter of the total vertical load.

We use our robust arc-length control algorithm to first demonstrate that the problem can be solved for a large range of ideal prescribed arc length increments \bar{L} . For this problem a total arc length of 70 units is prescribed. The analyses are performed for ideal arc length increments of $\bar{L} = 0.21875, 0.4375, 0.875, 1.75$ and 3.5 . If these ideal arc lengths can be used without modification throughout the analyses, this would translate to 320, 160, 80, 40 and 20 equal increments to analyse the problem. Figure 2 depicts the horizontal and vertical displacement of point C, using the two extreme choices for \bar{L} . Using $\bar{L} = 0.21875$ required 320 increments, while using $\bar{L} = 3.5$ required 26 increments (since some load steps required \bar{L} to be reduced). Figure 3 depicts the equilibrium path of point C in space. Note that at about 70% of the total arc length, the equilibrium path undergoes a sharp turn. It is this corner that is difficult to negotiate if we use a large ideal arc length increment.

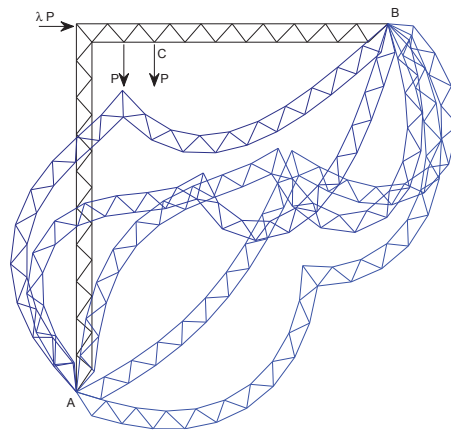


Figure 1: Undeformed and deformed truss, depicting 5 equal arc length increments

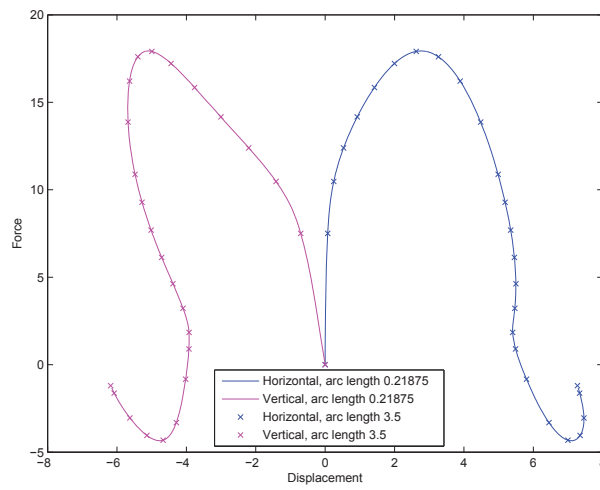


Figure 2: Undeformed and deformed truss, depicting 5 equal arc length increments

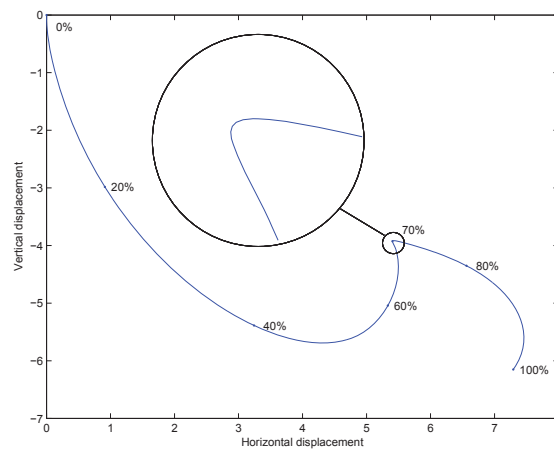


Figure 3: Displacement of Point C for a total arc length of 70 units.

Now that the analysis has been demonstrated to be robust, we can proceed to investigate an optimisation problem. We pose a 1D optimisation problem, using the horizontal force component $F_x = \lambda P$ as the single design variable. We use the horizontal and vertical force-deflection curves as target curves, for the case $\lambda = 0.5$ and $\bar{L} = 0.21875$ (visible as the solid lines in Figure 2). In cases where we use a larger value for \bar{L} , the analysis requires fewer increments. In order to compute a cost function (sum of square error for 320 increments) for these cases, we construct an interpolating spline between the total arc length and the quantity of interest (horizontal displacement, vertical displacement and load). This allows the computation of the cost function for any number of load steps available. Note however that this step does introduce discontinuities in the cost function as soon as one analysis requires a different number of increments as another. To demonstrate the nature of these discontinuities, we compute the cost function for various choices of \bar{L} . The cost function is computed for $\lambda \in [0.47; 0.53]$. Since the target curves were computed for $\bar{L} = 0.21875$ and $\lambda = 0.5$, we expect the cost function minimum to be at $\lambda = 0.5$.

Figure 4 depicts the cost function curves for various choices of \bar{L} . Note that as the ideal arc length is increased, the optimum of the cost function curve drifts from the correct solution ($\lambda = 0.5$), and some discontinuities occur. This behaviour is identical to the variable time-stepping problem in [2]. Classical gradient based algorithms may become trapped in the highlighted local minimizers, if a line search process happens to locate these local minimizers. These step discontinuities manifest as ridges in higher dimensional optimization problems, and in our experience are more likely to affect classical gradient based algorithms.

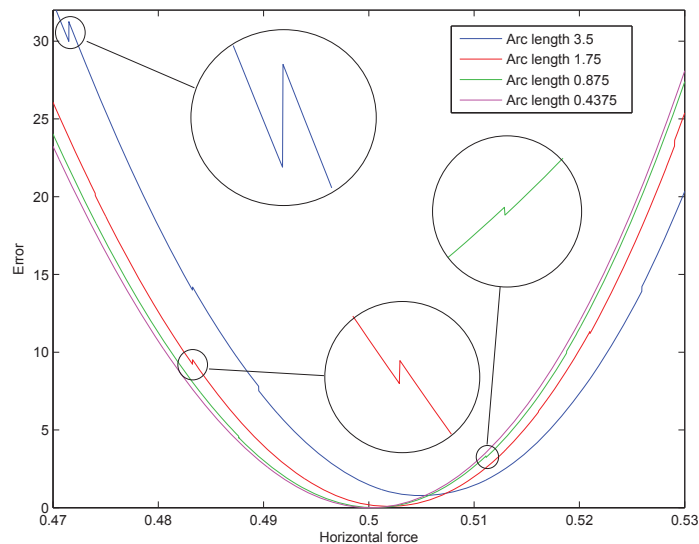


Figure 4: Cost function as the horizontal force varies

Figure 5 depicts the gradient of the cost function, using analytical derivatives. Although the cost function suggest discontinuities, any analysis is either to the left or the right of the discontinuity. For such an analysis, an analytical sensitivity analysis can be performed. Therefore, we have the gradient of the cost function available everywhere.

The suggested algorithm to solve this discontinuous optimization problem, is a gradient-only algorithm. For algorithmic details, refer to [3]. In essence, function values are ignored and we search for a sign change in the cost function gradient. Notice from Figure 5 that the function gradient also contains small discontinuities, but the information remains consistent (i.e. there is no sign change in the gradient over the discontinuity).

Note the drift in the optimum for the largest choice of $\bar{L} = 3.5$, from the actual solution $\lambda = 0.5$ to $\lambda = 0.5049$. The quality of the solution can only be judged by comparing the target curves to the solved load-displacement curves, as done in Figure 6. Notice that all the features of the target curves are captured.

Finally, to further motivate the use of varying arc-length increments, Table 1 summarizes the analyses times for various choices of \bar{L} . There is clear benefit in using large ideal arc-lengths, but this benefit diminishes gradually. If the ideal arc-length is chosen too large, almost every increment has to be re-run with a smaller arc-length, and this reduces the benefit of using large arc-lengths. Nevertheless, for this problem we can expect a speed increase of a factor 6 when we solve the optimization problem using $\bar{L} = 3.5$ rather than $\bar{L} = 0.21875$.

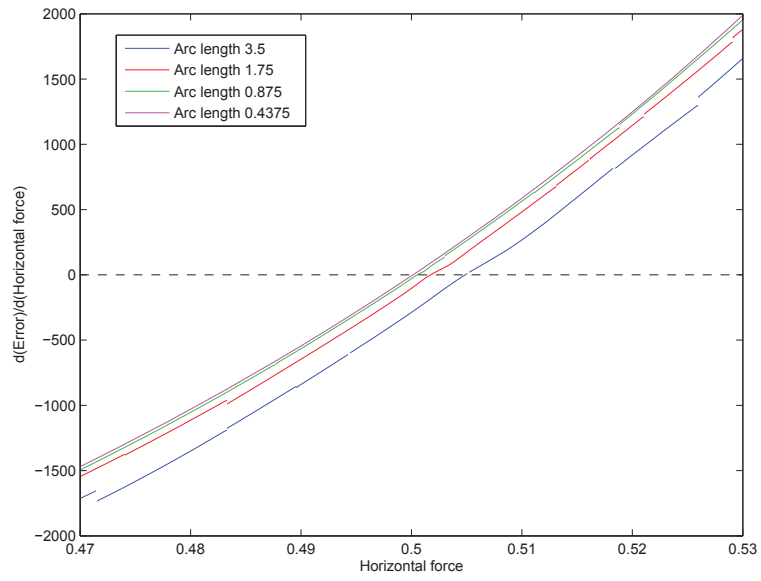


Figure 5: Cost function derivative as the horizontal force varies

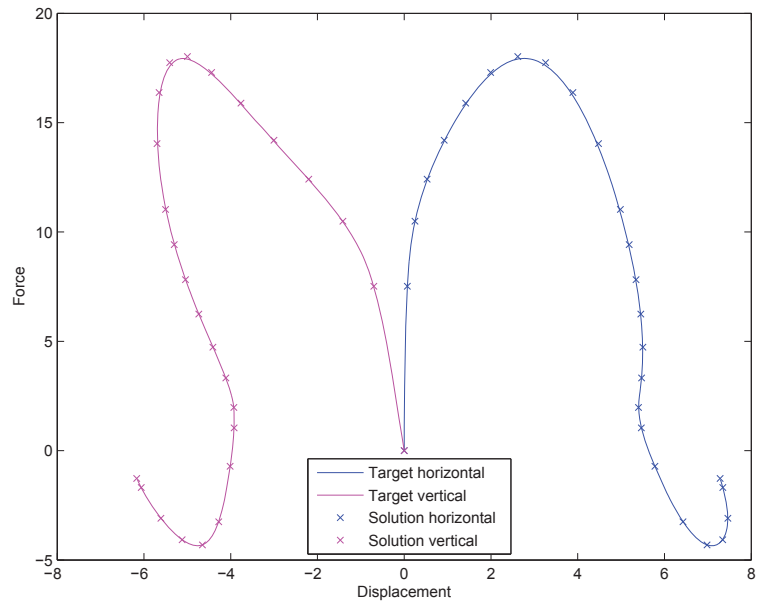


Figure 6: Optimal solution using ideal arc length $\bar{L} = 3.5$ versus the target load-displacement curves

Table 1: Analysis times for different choices of \bar{L}

\bar{L}	Time(s)
0.21875	8.83
0.43750	5.17
0.87500	2.76
1.75000	1.68
3.50000	1.46

5. Conclusions

We demonstrated that gradient-only algorithms can be used to solve optimization problems that use variable arc-length control methods in the analysis step. Although the analysis algorithm introduces numerical discontinuities into the cost function, gradient-only methods are insensitive to these discontinuities. We are currently working on higher dimensional problems, including shape design variables.

6. References

- [1] M. Ritto-Corrêa and D. Camotin, On the arc-length and other quadratic control methods: Established, less known and new implementation procedures, *Computers & Structures*, 86, 1353-1368, 2008.
- [2] D.N. Wilke, S. Kok and A.A. Groenwold, The application of gradient-only optimization methods for problems discretized using non-constant methods, *Structural and Multidisciplinary Optimization*, 40, 433-451, 2010.
- [3] D.N. Wilke, S. Kok, J.A. Snyman and A.A. Groenwold, Gradient-only approaches to avoid spurious local minima in unconstrained optimization, *Optimization and Engineering*, 14(2), 275-304, 2013.

Optimization of Reinforced Concrete Frames by Harmony Search Method

Moacir Kripka, Deise Boito, Juliana Triches and Guilherme Fleith de Medeiros

Engineering Graduate Program, University of Passo Fundo, Passo Fundo, Brazil. E-mail: mkripka@upf.br;
julianatriches@yahoo.com.br; dboito@uol.com.br; guifleith@upf.br.

Abstract

The aim of this work is to present a procedure developed in order to minimize the cost of reinforced concrete building frames. To achieve this objective the cross sections dimensions, the area of steel and the concrete strength of beams and columns were taken as design variables. The constraints related to dimensions and strength were based on the Brazilian standard ABNT NBR 6118 (2007). The total cost, composed by the costs of concrete, steel and formworks, was minimized by the usage of Harmony Search Algorithm (HS), an optimization method developed by Geem, Kim and Loganathan (2001), inspired by the observation that the aim of music is to search for a perfect state of harmony. The search process is compared to a musician's improvisation process. Some structures were analyzed, and the results were compared to those obtained from the conventional design procedure, in an attempt to identify the influence of factors such as resistance class, material costs and beams/columns costs on the optimal design of reinforced concrete building frames. This work is a sequence of former studies of the authors regarding optimization of grillages and columns sections by heuristics methods.

Keywords: Building. Frames. Optimization. Reinforced Concrete. Harmony Search Method.

1. Introduction

Structural analysis and design usually involve both highly complex procedures and a great number of variables. As a consequence, the solution has to be found iteratively while initial values are set to the variables based mainly on designer's sensitivity and experience. Also, the number of analysis steps is remarkably increased if optimum values are to be found among all possible alternatives. To mathematically describe the physical response of a structure, extreme function values can be found by using optimization techniques.

The great development of structural optimization took place in the early 60's, when programming techniques were used in the minimization of structures weight. From then on, a great diversity of general techniques has been developed and adapted to structural optimization. However, one of the reasons normally attributed to the little application of the optimization techniques to real structural engineering problems consists of the complexity of the mathematic model generated, normally described by non-linear behavior functions and producing a non-convex space of solutions (several points of optimum), problems for which the resolution by traditional mathematical programming methods have proved to be little efficient. For the resolution of these kind of problems the heuristic methods have played an important role, since they involve only values of functions in the process, regardless if there is unimodality or even continuity in their derivatives. Despite the great emphasis in the development of global optimization methods, researchers are even far from the attainment of a method that can be applied with the same efficiency to any class of problems.

This work presents the application of Harmony Search method to the optimization of reinforced concrete building frames. To achieve this objective the cross sections dimensions, the area of steel and the concrete strength of beams and columns were taken as design variables. The constraints related to dimensions and strength were based on the Brazilian standard ABNT NBR 6118/2007 [1]. This work is a sequence of former studies of the authors regarding optimization of grillages and columns sections by heuristics methods (e.g. [2] and [3]).

The next sections of this paper present a brief description of the optimization method, the developed formulation, simple application example and some preliminary conclusions.

2. Harmony Search Optimization Algorithm

Harmony Search Algorithm (HS) is a metaheuristic proposed by Geem, Kim and Loganathan in 2001 [4]. It consists in an analogy to musical improvisation of jazz, where musicians try to find, through repeated attempts, the perfect harmony (best solution to a problem). Iterations are called improvisations or practice. Variables correspond to musical instruments. Values for variables are the sounds of instruments. Each solution is called harmony, and the calculation of the objective function is called aesthetic estimation. The method can be summarized in five steps:

- Initialization of problem and algorithm parameters: definition of the objective function, the constraints and

parameters of the algorithm. Main parameters are Harmony Memory Size (HMS), Harmony Memory Considering Rate (HMCR), Pitch Adjusting Rate (PAR) and Maximum Improvisation (MI).

- Initialization of Harmony Memory: definition of first Harmony Memory (initial group of solutions). Harmony Memory (HM) is represented by a matrix, each line corresponding to a solution vector. The matrix has a number of rows equal to HMS and number of columns equal to the number of variables of the problem (N). Harmonies are generated randomly between a lower and upper range.

- Improvisation of a new harmony: from the initial solution, a new harmony is generated. This step is performed by using the parameters PAR and HMCR. For each variable of the new solution, a random number between 0 and 1 is generated. This number is compared to the value of HMCR (Harmony Memory Considering Rate). If the random number is lesser (probability equal to HMCR), the value of the respective variable in the new solution vector is retrieved from Harmony Memory existing. If the random number is greater (probability equal to 1-HMCR), a new value for the variable is generated. The choice of this new value can be done in two different ways. Again, a random number between 0 and 1 is generated and compared to the parameter PAR. If the number is less than the rate (probability equal to PAR), Harmony Memory is considered, but with little adjustment, defined by bw (maximum variation of tone) and a random number. If this is greater than PAR (probability equal to 1-PAR), the new value for the variable is randomly generated within the interval of possible solutions.

- Update of Harmony Memory: At each new harmony improvised, it is checked whether this is better than the worst harmony of Harmony Memory (HM), relative the objective function. If confirmed this condition, the new harmony replaces the worst harmony of HM.

- Check the stopping criterion: usually, the maximum number of improvisations MI. If it is not achieved, the algorithm returns to the third step (improvisation of a new harmony).

Regarding the original work of Geem, Kim and Loganathan, several improvements and variations of the method have been proposed by other authors. An extensive study regarding these variations can be found, e.g., in Ingram and Zhang [5], and in Fourie, Green and Geem [6].

Mahadavi, Fesanghary and Damangir [7], for example, refined the method by developing the Improved Harmony Search Algorithm (IHS). It was suggested in IHS the dynamic variation of parameters PAR and bw , according to the number of iterations, between minimum and maximum limits for each factor. PAR increases linearly, while the parameter bw decreases exponentially.

Along with the inclusion of the variable parameters of IHS, other variations in original algorithm were proposed and incorporated into present work:

- Instead of generating all initial solutions randomly, as usual, one predefined solution can be included in the Harmony Memory;

- To avoid premature convergence to local minimum, the Harmony Memory is restarted when all solutions achieve similar values. Only the best current solution is included in this new HM;

- As an additional stopping criterion to avoid unnecessary calculations, the algorithm developed in this work can terminate the search when the best solution found does not varies after successive NR restarts.

3. Problem formulation

Considering rectangular cross sections of a plane frame, the objective of optimum design is to obtain a configuration that is capable of producing internal forces (N_{rd} and M_{rd} to columns and M_{rd} and V_{rd} to beams) equal or higher than the applied external loadings (N_{sd} , M_{sd} , V_{sd}), with minimal cost. The verification is made according to Brazilian standard ABNT NBR-6118/07 [1], regarding strength and limitations of size, spacing, and steel ratio.

Regarding columns, the design variables are the values that represent the cross section dimensions and the steel bar diameters, as well as the concrete strength. To beams, the width is fixed, since its influence is not significant in relation to the height. In addition, the reinforcement section can be easily obtained from the height. Based on this fact, just the height of concrete section and the concrete strength were considered as design variables to beams. In this study, the dimensions of the cross section of beams and columns were considered as discrete, varying in steps of five centimeters. The diameters of the reinforcement bars of columns were limited to those available in commercial stores and the beams steel areas were considered as continuous. The concrete strength can vary in steps of 5MPa.

The cost function to be minimized in the optimization process considers the total cost of materials, being: cost of concrete per unit volume, cost of the reinforcement per unit mass and cost of formwork per unit area. All costs provide a relative value per unit length of the optimized element. This cost is multiplied by the total length of beams and columns, giving the total cost of the frame.

4. Preliminary Results

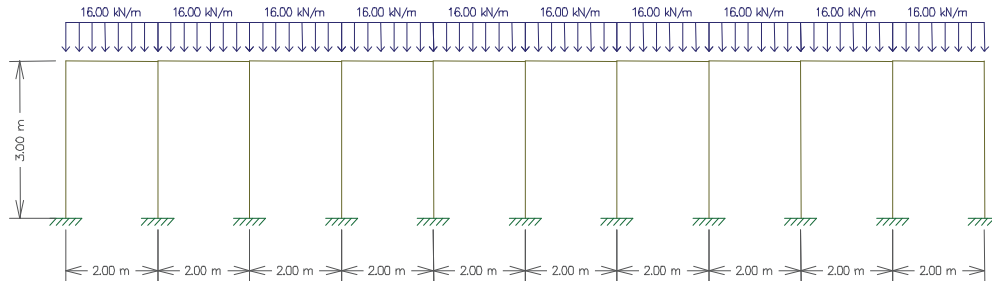
The formulation was implemented using the Fortran programming language, by the association of Harmony Search optimization method and frame analysis by the displacement method.

The input parameters used by the optimization software are: number of nodes, number of beams, number of columns, nodal coordinates, position of each element, cross sectional dimensions, support conditions, imposed loads, characteristic strength of steel, characteristic strength of concrete, unit cost of concrete, unit cost of steel and unit cost of formwork.

Some numerical simulations were performed in order to test the efficiency of the proposed procedure. For these simulations, several initial solutions were utilized, resulting in the convergence to a single optimal solution, regardless the cross sectional initially adopted to beams and columns.

Some preliminary results are presented in the sequence of this work. The example consists in a 20 meters frame, composed by a variable number of columns. The analysis started by considering 11 columns (spans of 2 m), according to Figure 1. Beams and columns width were set at 0.2 m, with columns height of 3 m. A load of 16 kN/m was applied to beams, with the self weight computed automatically, based on the specific weight of the material (25 KN/m³). The characteristic concrete strength (f_{ck}) was equivalent to 25 MPa, with the following unit costs, denominated in Brazilian currency (R\$): CA-50 steel bars = R\$ 3.97/kg; CA-50 steel bars = R\$ 3.89/kg; formworks = R\$ 8.68/m², and concrete = R\$ 233.55/m³.

Figure 1: example - original frame



To the original configuration, the optimized sizes of concrete section and the amount of gauges of the elements were achieved, and the corresponding total cost was computed. After each analysis, the number of columns was gradually reduced, in order to identify the optimal spacing. Figure 2 illustrates the results obtained, indicating that the optimal span was about 4 m to the example. It can be stressed that this result is quite similar to those suggested by practitioners. In this case, the optimal span corresponds to a relation beam height / span of 13.33.

Figure 2: example - cost versus span to variable number of columns

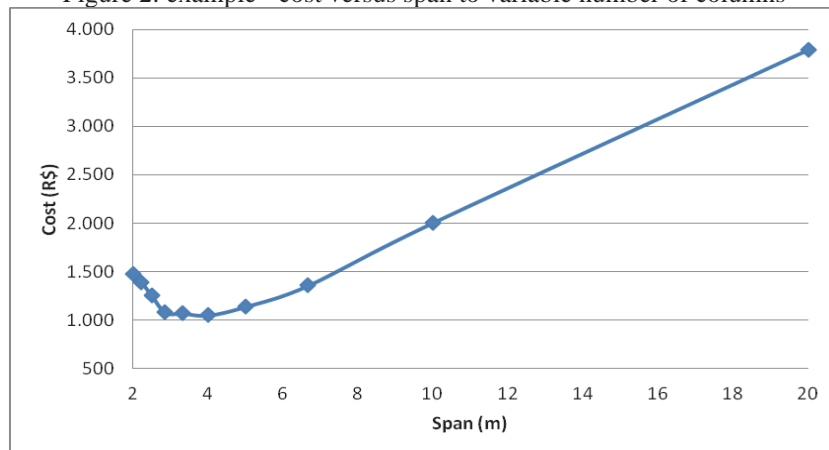


Figure 3 presents the relative cost of elements (beams and columns). It can be seen that the beams correspond to the major part of total cost to spans greater than 5 m. In addition, based in Figure 4 it can be observed that, despite the span considered, the main cost is due to the amount of steel, followed by concrete.

Figure 3: example – relative cost of elements

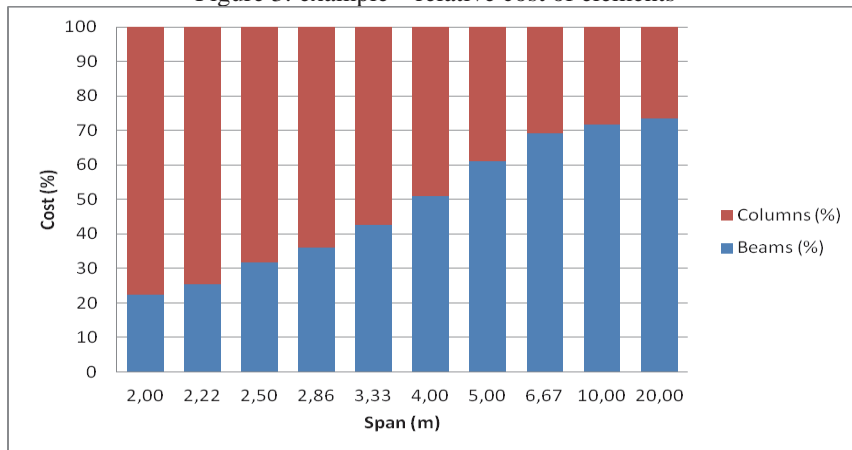
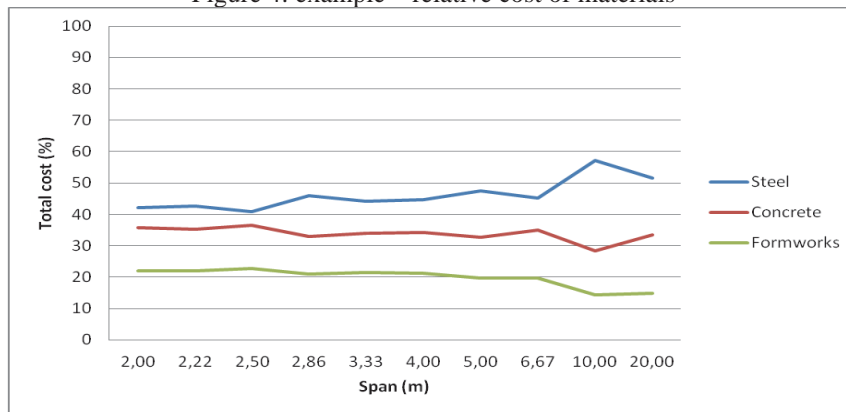


Figure 4: example – relative cost of materials



In order to assess the behavior of Harmony Search when compared to other heuristics, the optimization of isolated elements was performed with both Harmony Search and Simulated Annealing. Both methods led to similar results, but the number of function evaluations was much larger with Simulated Annealing. In addition, it was observed that optimal cost decreases rapidly to HS, when compared to SA.

5. Conclusions

This work dealt with the problem of optimization of reinforced concrete building frames, following the requirements of the Brazilian standard NBR 6118 (ABNT 2007), and using the Harmony Search optimization method. To the examples analyzed, the optimization method was quite efficient in minimizing structural cost. The software has been an important tool for pre-sizing of reinforced concrete elements. To the example presented in this work, the optimal span was about 4 m, coincident with the practice. As observed in former studies developed by the authors, the steel accounts for the biggest part of the overall cost of elements, followed by concrete and formworks.

Other structures with higher complexity are being studied in order to generalize the obtained results, as well as to obtain parameters to allow the designers to reduce the global cost of building structures.

6. Acknowledgements

To CNPq (first author) and CAPES (second author) for the financial support granted.

7. References

- [1] Brazilian Association of Technical Standards, Procedures for the design of reinforced concrete structures. NBR 6118, Rio de Janeiro. (in Portuguese), 2007.
- [2] R. Bordignon, M. Kripka, *Optimum Design of Reinforced Concrete Columns Subjected to Uniaxial Flexural Compression*, Computers and Concrete, 9(5), 345-358, 2012.
- [3] G.F. Medeiros, M. Kripka, *Structural optimization and proposition of pre-sizing parameters for beams in reinforced concrete buildings*. Computers and Concrete, v. 11, p. 253-270, 2013.
- [4] Z.W. Geem, J.H. Kim, G.V.A. Loganathan, *A New Heuristic Optimization Algorithm: Harmony Search*, Simulation, 76(2), 60-68, 2001.
- [5] G. Ingram, T. Zhang, *Overview of Applications and Developments in the Harmony Search Algorithm. From: Geem Z.W. "Music-Inspired Harmony Search Algorithm"*, Springer, SCI191, pp. 15-37, 2009.
- [6] J. Fourie, R. Green; Z.W. Geem, *Generalised Adaptive Harmony Search: A Comparative Analysis of Modern Harmony Search*, Journal of Applied Mathematics, Article ID 380985, 2013.
- [7] M. Mahadavi, M. Fesanghary, E. Damagir, *An Improved Harmony Search Algorithm for Solving Optimization Problems*, Applied Mathematics and Computation, vol. 188, n. 2, pp. 1567-1579, 2007.

A TIMP Method for Topology Optimization with Displacement and Stress Constraints in Multiple Loading Cases

Guilian Yi¹, Yunkang Sui², Byeng D. Youn³

¹ Seoul National University, Seoul, Republic of Korea, flybirdyi@126.com

² Beijing University of Technology, Beijing, China, ysui@bjut.edu.cn

³ Seoul National University, Seoul, Republic of Korea, bdyoun@snu.ac.kr

1. Abstract

A method of transplanting ICM (Independent Continuous and Mapping) ideas into material with penalization (TIMP) for continuum structural topology optimization is proposed in this paper. TIMP method is a development of SIMP (Solid Isotropic Material with Penalization) method, which is widely studied and used by internal and overseas researchers. Since the filter function in ICM and the penalty function in SIMP are observed regarding to their similar formulations, the mathematical connection between the two methods yields analogies. Thus, several progresses in ICM are transplanted into SIMP for further developments, which yield to the TIMP method. There are two basic perspectives in TIMP: (1) weight and allowable stress penalty functions are added into SIMP besides Young's modulus penalty function, and (2) design variables in TIMP are confined to the artificial material densities in SIMP. In order to demonstrate the validity and capability of TIMP, topology optimization models of minimizing weight with displacement/stress constraints under multiple loading cases are constructed. The unit virtual loading method is utilized to explicit displacement constraints, while the stress constraint globalization strategy is employed to convert enormous stress constraints into global structural distortion energy constraints. Three penalty functions in TIMP method play an important role to obtain sensitivities of constraints for free. The nonlinear programming algorithm is used for solutions, and the whole solution programming is implemented by Python scripts on ABAQUS software. Several numerical examples are presented for testing, and the effects of linear and nonlinear element weight penalty functions on the convergence speed are studied and discussed through numerical examples. It is demonstrated that, the proposed method is efficient and valid, and a nonlinear weight penalty function can yield higher convergence speed than a linear function.

2. Keywords: ICM method, SIMP method, TIMP method, displacement constraints, stress constraints

3. Introduction

The traditional structural topology optimization was early proposed by Maxwell at the end of the 19th century and further studied by Michell at the beginning of the 20th century. However, the modern structural topology optimization has been started since 1988, when Bendsøe and Kikuchi [1] proposed the Homogenization method (HM). The concept of continuum structural topology optimization was presented after that, as well as corresponding numerical methods. With the development of high performance computing science and technology, the research on numerical approaches for the continuum structural topology optimization has been made great progresses, and most of them are based on the "ground structure approach" [2]. Besides HM, the ground structure approach is represented with the Solid Isotropic Material with Penalization (SIMP) method [3], the Evolutionary Structural Optimization (ESO) method [4], the Independent Continuum and Mapping (ICM) method [5], the Level Set Method (LSM) [6] and so on.

Among these numerical approaches, the SIMP method is popular and has many practical applications because of its easy implementation. However, the development of SIMP method has stopped in a theory system with only one penalty function, which is the Young's modulus penalty function. While we thought about whether there was something we could do for its improvement, it's found out that the ICM method could be instructive. There are two reasons to do so. Firstly, the ICM method has made significant progresses over the decades. Its theory foundation is tamped and its modeling and solution approaches are tempered. Several numerical laws have been concluded within this method. Secondly, although the filter function in the ICM method has different definitions from the penalty function in the SIMP method, their mathematical formulations are similar. Therefore, it is possible to transplant progresses and ideas of the ICM method into the SIMP method. The transplanting work could achieve big developments of SIMP.

In SIMP method, the artificial relative density variables are defined between 0 and 1. The penalty function is formulated to put penalization on the Young's modulus of element with intermediate densities. The material used for an element yields to 0 or 1 by the penalization. Therefore, the core idea of SIMP is the concept of penalization. ICM method uses the independent continuous topological variables. The polish and filter functions are formulated to realize the higher-order approximations of the step function and its inverse function separately. The independent

topological variables, which are discrete as 0 or 1 in nature, are mapped as continuous variables in [0, 1]. The continuous topological variables will be inverted into discrete variables at the end of optimization. The core idea of ICM is the concept of approximation.

If the penalization of SIMP is analogized with the approximation of ICM, new penalty functions can be presented: element weight penalty function and allowable stress penalty function. In previous application of SIMP, elemental weight is a linear function of the artificial relative densities. However, in ICM, several filter functions, including the element weight filter function, are nonlinear functions. It implies that the element weight penalty function could be linear and nonlinear. Therefore, this paper proposes a method of transplanting ICM ideas into material with penalization for the continuum structural topology optimization, which is called TIMP. TI represents Transplanting ICM Ideas, and MP is the latter half part of Solid Isotropic Material with Penalization. Since ICM and SIMP methods have not been compared to each other on the perspective of “ideas” before, the proposed TIMP method will further the developments of SIMP, and solve topology optimization problems easier than the traditional SIMP method.

The validity and capability of TIMP method is going to be demonstrated through three concrete tasks in this paper: (1) to formulate optimization model of minimizing weight with displacement constraints under multiple loading cases by TIMP, and (2) to construct optimization model of minimizing weight with stress constraints under multiple loading cases by TIMP and convert enormous local stress constraints into global structural distortion energy constraint by utilizing the stress constraint globalization strategy; (3) to provide unified formulations and solutions for the two optimization models, and to develop the solution process into secondary development software by Python scripts in ABAQUS.

4. TIMP method

In SIMP method, the Young’s modulus penalty function is described as below,

$$E_i = \rho_i^{p_E} E_i^0 \quad (1)$$

where the subscript “*i*” is the number of the element, and ρ_i denotes the element relative density variable (the ratio of the actual material density to the artificial material density). p_E is called the penalty factor. E_i^0 and E_i are the element Young’s modulus for actual material and for artificial material separately.

With the idea of approximation in ICM method, different formulations of highly nonlinear and derivative filter functions are used to approximate inverse functions of the step functions [7]. Element weight, stiffness and allowable stress et al. are identified by them. This paper uses the method of analogy in the way that, the relative density variables and the penalty function in SIMP are, respectively, in analogy to the independent topology variables and the filter functions in ICM. Therefore, ideas of ICM method are transplanted into SIMP method, and two penalty functions in the form of power function similar to Eq.(1) are introduced as bellow,

$$w_i = \rho_i^{p_w} w_i^0 \quad (2)$$

$$\bar{\sigma}_i = \rho_i^{p_{\bar{\sigma}}} \bar{\sigma}_i^0 \quad (3)$$

where w_i and $\bar{\sigma}_i$ represent, respectively, the element weight and material allowable stress for elements with intermediate densities. w_i^0 and $\bar{\sigma}_i^0$ are, respectively, the initial element weight and initial material allowable stress for elements filled with actual material. p_w and $p_{\bar{\sigma}}$ are, respectively, the penalty factors of element weight and allowable stress. Obviously, Eq. (2) is linear when $p_w = 1.0$, and nonlinear when $p_w > 1.0$.

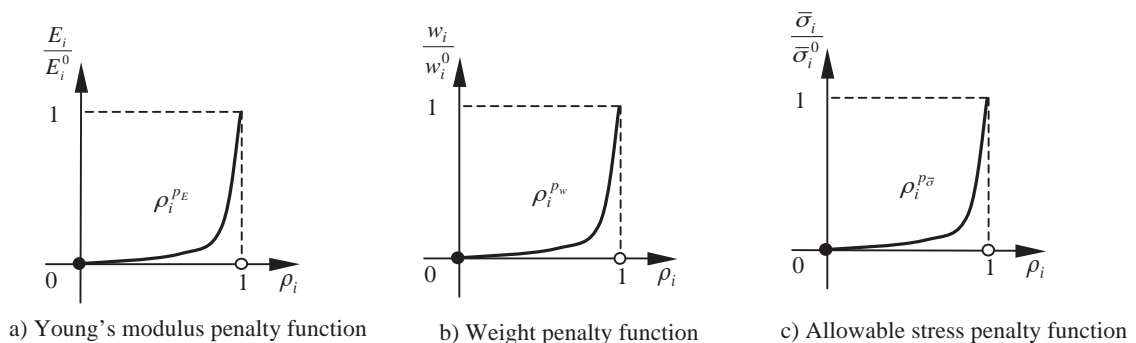


Figure 1: Curves for penalty functions in TIMP method

Based on the above analogies between ICM and SIMP methods, a new theory system on the basis of Eq. (1), Eq. (2) and Eq. (3) is proposed and called TIMP method. Their curves are plotted in Figure 1, where a) for the Young's modulus penalty function, b) for the element weight penalty function, and c) for the allowable stress penalty function.

Actually, Eq. (2) was usually used in a linear expression for researches by using SIMP method, but never presented in the name of penalty function. However, the TIMP method could have both linear and nonlinear expressions of the element weight penalty function. It is an expansion and development of the SIMP method.

5. Topology optimization problems with displacement constraints under multiple loading cases

The minimum-weight formulation for topology optimization with displacement constraints under multiple loading cases is usually expressed as below,

$$\begin{cases} \text{For } \boldsymbol{\rho} \\ \text{Min } W(\boldsymbol{\rho}) \\ \text{s.t. } u_{lr}(\boldsymbol{\rho}) \leq \bar{u}_r \quad (l=1, \dots, L; r=1, \dots, R) \\ \rho_{\min} \leq \rho_i \leq 1 \quad (i=1, \dots, N) \end{cases} \quad (4)$$

where $\boldsymbol{\rho}$ is the artificial relative density vector, and $W(\boldsymbol{\rho})$ is the total weight of the structure. “ l ” and “ r ” are, respectively, the number of loading case and number of point with displacement constraint in a loading case. $u_{lr}(\boldsymbol{\rho})$ represents the displacement function at the r -th point of interest in the l -th loading case, and \bar{u}_r is the allowable displacement at this point. “ L ” and “ R ” are, respectively, the total number of loading cases and total number of points with displacement constraints. “ N ” is the total number of elements. In order to avoid the singularity of the stiffness matrix, the minimum value of the artificial relative density is $\rho_{\min} = 0.001$.

Based on the TIMP method, element weights under different densities can be identified with Eq. (2), and the total weight of the structure can be expressed as below,

$$W(\boldsymbol{\rho}) = \sum_{i=1}^N w_i^0 \rho_i^{p_w} \quad (5)$$

According to the derivations in the paper [8], the displacement function was expressed explicitly with Eq. (1) by using the unit virtual loading method. Thus, the explicit expression for the displacement at the r -th point of interest in the l -th loading case can be stated as

$$u_{lr} = \sum_{i=1}^N u_{lri} = \sum_{i=1}^N \frac{D_{lri}^0}{\rho_i^{p_E}} \quad (6)$$

where u_{lri} represents the displacement contribution of the i -th element to the displacement at the r -th point of interest in the l -th loading case. D_{lri}^0 is the constant coefficient in the displacement contribution function of the i -th element to the displacement at the r -th point of interest in the l -th loading case.

6. Topology optimization problems with stress constraints under multiple loading cases

Topology optimization problems with stress constraints under multiple loading cases can be formulated as below,

$$\begin{cases} \text{For } \boldsymbol{\rho} \\ \text{Min } W(\boldsymbol{\rho}) \\ \text{s.t. } \sigma_{li} \leq \bar{\sigma} \quad (l=1, \dots, L) \\ \rho_{\min} \leq \rho_i \leq 1 \quad (i=1, \dots, N) \end{cases} \quad (7)$$

where σ_{li} is the von Mises stress of the i -th element in the l -th loading case, and $\bar{\sigma}$ is the allowable stress. The objective can be expressed in the same way as Eq. (5).

The stress constraints globalization strategy is based on the von Mises yield criterion, and deals with the local stress constraints into a single combined relationship. This globalization strategy has been applied effectively in ICM method [9]. Its main ideas can be transplanted and used in TIMP method too. According to the von Mises yield criterion, when the element distortion energy density is no less than a certain allowable value, the strength of the material is about to yield. On the contrary, it is safe only if a relationship exists as below,

$$U_{li}^d = \frac{1+\nu}{3E_i} (\sigma_{VMli})^2 \leq \bar{U}_i^d = \frac{1+\nu}{3E_i} (\sigma_Y)^2 \quad (8)$$

where U_{li}^d is structural distortion energy density of the i -th element in the l -th loading case, and \bar{U}_i^d is allowable

distortion energy density of the i -th element. ν denotes the Poisson's ratio. σ_Y is the yield stress of the material (allowable stress), and σ_{VMli} represents the equivalent von Mises stress of the i -th element in the l -th loading case. It should be noted that a safety factor is required in Eq. (8) for practical engineering problems.

By multiplying the element volume V_i on both sides of Eq. (8) and performing the summation of all elements, the structural total distortion energy constraints can be obtained and described as below,

$$\sum_{i=1}^N U_{li}^d V_i \leq \sum_{i=1}^N \bar{U}_i^d V_i \quad (9)$$

Thus, stress constraints are globalized into structural distortion energy constraints in Eq. (9), whose left side could be identified with Eq. (1) and right side could be identified with both Eq. (1) and Eq. (3). Their formulations are expressed as below,

$$\begin{aligned} V_i U_{li}^d &= \frac{(\rho_i^{(n-1)})^{p_E}}{\rho_i^{p_E}} (V_i U_{li}^d)^{(n-1)} \\ V_i \bar{U}_i^d &= \frac{1+\nu}{3E_i^0 \rho_i^{p_E}} V_i (\bar{\sigma}_i^0 \rho_i^{p_{\bar{\sigma}}})^2 = V_i \bar{U}_i^{d0} \rho_i^{2p_{\bar{\sigma}}-p_E} \end{aligned} \quad (10)$$

where “ n ” is the number of iteration. $\rho_i^{(n-1)}$ is the relative densities obtained from the $(n-1)$ -th iteration, and $(V_i U_{li}^d)^{(n-1)}$ represents the distortion energy of the i -th element in the l -th loading case obtained from the $(n-1)$ -th iteration, which can be computed by finite element analysis. $\bar{U}_i^{d0} = \frac{1+\nu}{3E_i^0} \bar{\sigma}_i^0$, and it represents the allowable distortion density for the element with solid material.

Eq. (9) could be also expressed in a different form as below,

$$\sum_{i=1}^N \frac{U_{li}^d}{\bar{U}_i^d} \leq N \quad (11)$$

One should be noticed that $\sigma_{VMli} \leq \sigma_{Yi}$ is a sufficient and unnecessary condition for Eq. (11). Therefore, the stress constraints in Eq. (7) can be replaced by the structural distortion energy constraints as below,

$$\sum_{i=1}^N \frac{(U_{li}^d)^{(n-1)} (\rho_i^{(n-1)})^{p_E}}{\bar{U}_i^{d0} \rho_i^{2p_{\bar{\sigma}}}} \leq N \xi_l \quad (12)$$

where ξ_l is the adjusting factor of the structural distortion energy for the l -th loading case, and $\xi_l = \left(\frac{\bar{\sigma}}{\sigma_{VMmax}}\right)^\theta$,

where σ_{VMmax} denotes the maximum von Mises stress and θ is a constant determined by tests.

7. Unified models and solutions

In order to reduce the unnecessary calculation caused by the inactive constraints, whose left side values are far less than the right side values, only the active constraints can be selected to construct the optimization models. Thus, the subscripts l and r in displacement /stress constraints are merged into a single sequential number j , and the total number of active constraints is denoted by L_a .

Assuming that $x_i = \rho_i^{-p_E}$, $\underline{x}_i = 1$, and $\bar{x}_i = 0.001^{-p_E}$, a unified formulation for Eq. (4) and Eq. (7) with explicit objective and constraints formulations can be described as below,

$$\left\{ \begin{array}{l} \text{For } x_i \quad (i = 1, \dots, N) \\ \text{Min } W = \sum_{i=1}^N w_i^0 x_i^{-\eta} \\ \text{s.t. } \sum_{i=1}^N A_{ji} x_i^\mu - B_j \leq 0 \quad (j = 1, \dots, L_a) \\ \underline{x}_i \leq x_i \leq \bar{x}_i \end{array} \right. \quad (13)$$

For Eq. (4), $\eta = \frac{p_w}{p_E}$, $A_{ji} = D_{ji}^0$, $\mu = 1$, and $B_j = \bar{u}_j$. For Eq. (7), $\eta = \frac{p_w}{p_E}$, $A_{ji} = \frac{(U_{li}^d)^{(n-1)} (\rho_i^{(n-1)})^{p_E}}{\bar{U}_i^{d0}}$,

$\mu = \frac{2P_{\bar{\sigma}}}{P_E}$, and $B_j = N\zeta_j$. Therefore, the sensitivities of objective and constraints are obtained for free by using methods and approached in Section 5 and Section 6.

The nonlinear programming algorithm, Dual Mapping Sequential Quadratic Programming (DMSQP), can be used for solutions of Eq. (13). Since the dual problem of Eq. (13) is formulated based on the dual theory, the number of design variables are reduced incredibly. Then, Sequential Quadratic Programming (SQP) is employed to address the dual problem based on its Kuhn-Tucker conditions. The whole solution programming is implemented by Python scripts on ABAQUS software, and results will be output automatically.

8. Numerical examples

In order to demonstrate the validity and capability of the TIMP method, a plate structure is studied here, and the influences of the linear element weight penalty function (LEWPF) and nonlinear element weight penalty function (NEWPF) on the convergence speed are observed specifically.

Figure 2 shows the dimensions of a rectangular plate. The concentrated loading is $P_1 = P_2 = 3600\text{N}$. Multiple loading cases are considered, and they are: Case 1 is to apply P_1 at the intersection of 1/3 horizontal and 1/2 vertical, Case 2 is to apply P_2 at the intersection of 2/3 horizontal length and 1/2 vertical, and Case 3 is to apply both P_1 and P_2 at the same time. The material properties are that, the Young's modulus $E = 210\text{GPa}$, Poisson's ratio $\nu = 0.3$, and density $\rho = 7800\text{kg/m}^3$. The allowable stress of the material is 100MPa . Filtering schemes are utilized to alleviate the mesh-dependency and checker-board issues.

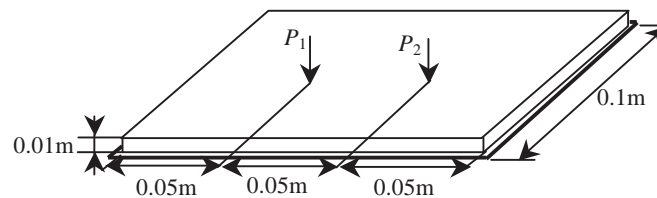


Figure 2: A rectangular plate with multiple loading cases

Firstly, topology optimizations with displacement constraints for the plate under different boundary conditions (BCs) are observed. It is required that the displacements along the loading direction at the loading points are no more than 0.028mm when the plate is clamped, and no more than 0.064mm when it is simply-supported. Both of LEWPF ($p_w = 1.0$) and LEWPF ($p_w > 1.0$) are used and optimization parameters are set by trial and errors. Figure 3 and Figure 4 show the optimum topologies of the clamped and simply-supported plates separately. The parameters and final results are presented in Table 1. It is found out that, the optimum topologies are similar while under the same BCs, and the utility of NEWPF yield less iterations and better satisfaction with stress constraints than the utility of LEWPF.

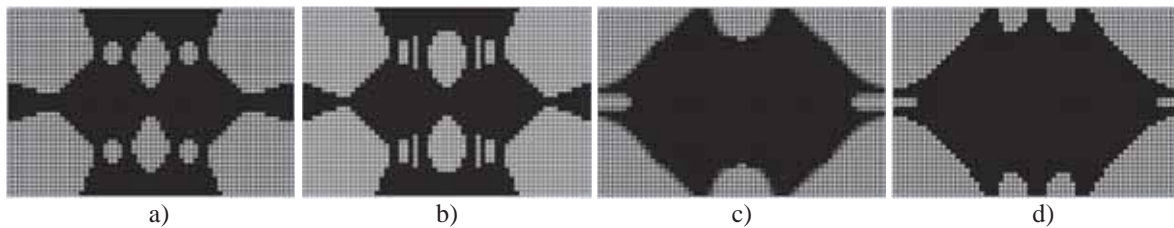


Figure 3: Topologies under displacement constraints: a) clamped plate with LEWPF, b) clamped plate with NEWPF, c) simply-supported plate with LEWPF, and d) simply-supported plate with NEWPF

Table 1: Optimization parameters and results for clamped plate with displacement constraints

BCs.	p_w	p_E	Iterations	Displacement / mm			Weight reduced by / %
				Case 1	Case 2	Case 3	
Clamped	1.0	3.0	30	0.023	0.023	[0.028, 0.028]	51.28
	1.5	4.5	20	0.024	0.024	[0.028, 0.028]	52.99
Simply-supported	1.0	3.0	36	0.042	0.043	[0.064, 0.064]	39.32
	1.5	4.5	31	0.042	0.042	[0.062, 0.062]	40.17

Secondly, topology optimizations with stress constraints for the plate under different BCs are studied too. Figure 5 and Figure 6 show the optimum topologies of the clamped and simply-supported plates separately. The parameters and final results are presented in Table 2.

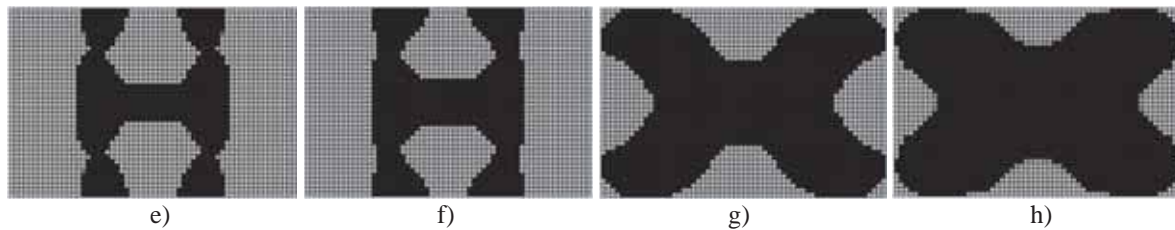


Figure 4: Topologies under stress constraints: e) clamped plate with LEWPF, f) clamped plate with NEWPF, g) simply-supported plate with LEWPF, and h) simply-supported plate with NEWPF

Table 2: Optimization parameters and results for clamped plate with displacement constraints

BCs.	p_w	p_E	$p_{\bar{\sigma}}$	θ	Iterations	Max von Mises Stress / MPa			Weight reduced by / %
						Case 1	Case 2	Case 3	
Clamped	1.0	3.5	1.7	0.5	26	97.34	97.34	103.68	68.12
	1.5	3.5	2.0	1.5	23	85.10	85.10	92.77	65.47
Simply-supported	1.0	3.0	2.0	3.0	13	78.52	78.52	101.86	30.78
	1.5	3.5	2.0	1.5	11	76.36	76.36	90.42	21.07

9. Conclusions

The proposed TIMP method is a development of the SIMP method, and its application in addressing topology optimization models with displacement and stress constraints under multiple loading cases are detailed discussed in this paper. Numerical examples of a rectangular plate under different boundary conditions demonstrate that using nonlinear element weight penalty function yields better results and higher convergence speed than using linear element weight penalty function. It is indicated that the TIMP method is valid and capable to address complicated topology optimization problems.

10. Acknowledgements

This research was supported by the Chinese National Natural Science Foundation under the grant No. 11172013 and a grant from the Brain Korea 21 Plus project in 2015.

11. References

- [1] M.P. Bendsøe and N. Kikuchi, Generating optimal Topologies in Structural Design Using a Homogenization Method, *Computer Methods in Applied Mechanics and Engineering*, 71(2), 197-224, 1988.
- [2] D.S. Ramrakhiani, M.I. Frecker and G. Lesieutre, Hinged Beam Elements for the Topology Design of Compliant Mechanisms Using the Ground Structure Approach, *Structural and Multidisciplinary Optimization*, 37(6), 557-567, 2009.
- [3] M.P. Bendsoe and O. Sigmund, *Topology Optimization: Theory, Methods and Applications*, Springer-Verlag, Berlin, 2003.
- [4] Y.K. Sui, *Modeling, Transformation and Optimization - New Developments of Structural Synthesis Method*, Dalian University of Technology Press, Dalian, 1996.
- [5] Y.M. Xie and G.P. Steven, A Simple Evolutionary Procedure for Structural Optimization, *Computers and Structures*, 49(5), 885-896, 1993.
- [6] G. Allaire, F. Jouve and A.M. Toader, Structural Optimization Using Sensitivity Analysis and A Level-set Method, *Journal of Computational Physics*, 194(1), 363-393, 2004.
- [7] Y.K. Sui and X.R. Peng, The ICM Method with Objective Function Transformed by Variable Discrete Condition for Continuum Structure, *Acta Mechanica Sinica*, 22(1), 68-75, 2006.
- [8] Y.K. Sui and G.L. Yi, A discussion about choosing an objective function and constraints in structural topology optimization, *10th World Congress on Structural and Multidisciplinary Optimization*, Orlando, Florida, USA. USB stick. ed. 2013. paper id = 5365.
- [9] Y.K. Sui and H.L. Ye, *Continuum topology optimization methods ICM* (Chinese Edition), Science Press, Beijing, 2013.

Interval buckling analysis of steel structures using mathematical programming approach

Di Wu¹, Wei Gao², Francis Tin-Loi³

¹ University of New South Wales, Sydney, Australia, di.wu@unsw.edu.au

² University of New South Wales, Sydney, Australia, w.gao@unsw.edu.au

³ University of New South Wales, Sydney, Australia, f.tinloi@unsw.edu.au

Abstract

A novel mathematical programming approach is proposed in this study to assess the linear buckling load of steel structure with uncertain system parameters. The considered uncertainties of system parameters are modelled by the interval approach such that only bounds of uncertain parameters are available. This particular uncertainty model is applicable for situations where probabilistic approach is inapplicable due to the insufficiency of the data of system parameters. By implementing an alternative finite element formulation for the two-dimensional beam element, the deterministic second order geometrically nonlinear problem is formulated into a mathematical programming problem. Furthermore, by treating all the interval uncertain system parameters as bounded mathematical programming variables, the integration of interval uncertainties in the deterministic linear buckling analysis becomes possible, such that the lower and upper bounds of the buckling load can be adequately obtained by solving two explicit nonlinear programs. The proposed computational scheme offers a single-phase interval buckling analysis for steel structures by combining the linear analysis of the structure at its reference configuration with the eigenvalue calculation. Such ability can well maintain the physical feasibility of the engineering structures for the purpose of uncertainty analysis, so the physically meaningful lower and upper bounds of the buckling load can be efficiently obtained. In addition, unlike traditional uncertain buckling analysis, the proposed method is able to thoroughly model the dependency between uncertain system parameters (i.e., the physical relationship between cross-sectional area and second moment of area of beam element must be compatible when cross-sectional area possesses uncertainty). One numerical example is presented to illustrate the accuracy and applicability of the proposed approach.

Keywords: interval analysis, buckling, steel structure, mathematical programming, dependency.

1. Introduction

Linear buckling analysis provides a computational framework which has been prevalently implemented for assessing the safety of engineering structures against large deformation. Due to its extensive applicability, computational efficiency and remarkable accuracy, linear buckling analysis has been extensively performed in modern engineering applications by integrating such analysis framework into front-edge engineering analysis software.

However, one practical issue often encountered among engineering application is the impact of uncertainties of system parameters. The existence of uncertainties of system parameters is inherent, and the impact upon the structural response is mercurial yet inevitable [1]. Such implications can influence structural performance [2], and consequently structural safety would be compromised if the impacts of uncertainties are not addressed appropriately [3].

In order to rigorously assess structural safety against large deformation, buckling analyses with considerations of uncertainties of system parameters have been proposed. Numbers of research works on the linear buckling analysis with stochastic uncertainties have been developed. However, types of uncertainties of system parameters are not unique. Such diversity of uncertainty stimulates further development of other forms of non-deterministic linear buckling analysis for various engineering situations.

This paper presents a mathematical programming based uncertain linear buckling analysis for assessing the buckling load of engineering frames which involve interval uncertain parameters. The presented method offers the worst and best case buckling loads of frames including both uncertain-but-bounded material properties and loading conditions in two explicit calculations. Uncertain linear buckling analysis is transformed into an eigenvalue problem with interval parameters within finite element (FE) framework. Furthermore, the proposed method is able to reformulate the interval eigenvalue problem into two explicit nonlinear mathematical programs (NLP), which individually depicts the feasible regions for the worst and best case buckling load. The applicability, accuracy, as well as the computational efficiency of the presented approach are illustrated through a practically motivated numerical example.

2. Deterministic linear buckling analysis

From traditional finite element method (FEM), by assuming constant axial force, the deterministic linear buckling analysis can be formulated into an eigenvalue problem as:

$$(\mathbf{K}_M + \lambda_b \mathbf{K}_G) \mathbf{z} = \mathbf{0} \quad (1)$$

where $\mathbf{K}_M, \mathbf{K}_G \in \mathfrak{R}^{d \times d}$ denote the conventional material and geometric stiffness matrices at reference configuration respectively; d denotes the total degree of freedom of the structure; λ_b denotes the structural buckling load which is the minimum positive eigenvalue of Eq.(1); $\mathbf{z} \in \mathfrak{R}^d$ is a non-zero vector which denotes the eigenvector corresponding to the buckling load or the eigenvalue. Since the eigenvalue analysis defined in Eq.(1) is indeterminate, the eigenvector \mathbf{z} denotes the shape of the buckling of engineering structure instead of actual buckled deformation [4].

In this study, an alternative FE formulation of the 2-dimensional beam is adopted. For i th element, the adopted FE model is illustrated in Figure 1.

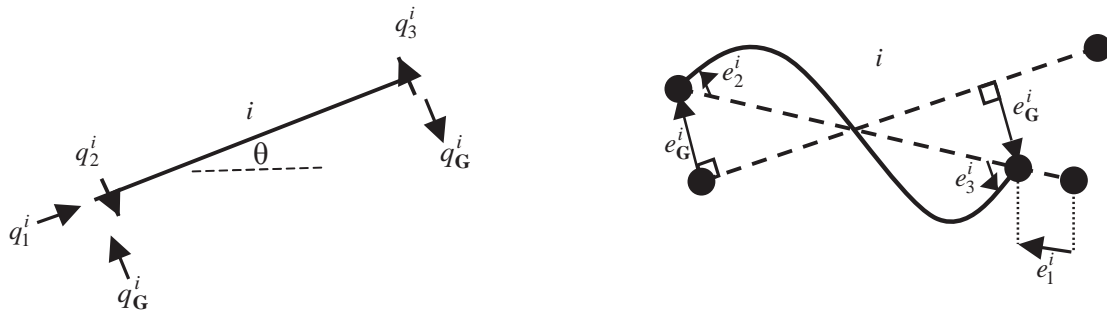


Figure 1: Generic 2D frame element i with second-order geometric nonlinearity (a) generalized stresses, (b) generalized strains

The adopted approach is based on the second-order geometric theory which assumes that displacements from undeformed configuration are geometrically small [5]. For a generic 2D frame element, there are four generalized stress/strain components involved in the second-order geometrically nonlinear 2D frame element. The axial and two end rotational components are adopted from linear analysis such that:

$$\mathbf{q}^i = [q_1^i \quad q_2^i \quad q_3^i]^T \in \mathfrak{R}^3 \quad (2)$$

$$\mathbf{e}^i = [e_1^i \quad e_2^i \quad e_3^i]^T \in \mathfrak{R}^3 \quad (3)$$

whereas the additional transverse component is employed for the purpose of the second-order geometrically nonlinear analysis [5], which takes the form of:

$$\mathbf{q}_G^i = [q_G^i] \in \mathfrak{R} \quad (4)$$

$$\mathbf{e}_G^i = [e_G^i] \in \mathfrak{R} \quad (5)$$

where, \mathbf{q}^i and \mathbf{q}_G^i denote the generalized stresses which are illustrated in Figure 1(a); \mathbf{e}^i and \mathbf{e}_G^i denote the generalized strain which are illustrated in Figure 1(b). Therefore, the equilibrium condition of the i th 2D frame element for the second-order geometrically nonlinear analysis is:

$$\begin{bmatrix} \cos \theta & -\sin \theta / L_i & -\sin \theta / L_i \\ \sin \theta & \cos \theta / L_i & \cos \theta / L_i \\ 0 & 1 & 0 \\ -\cos \theta & \sin \theta / L_i & \sin \theta / L_i \\ -\sin \theta & -\cos \theta / L_i & -\cos \theta / L_i \\ 0 & 0 & 1 \end{bmatrix} \begin{bmatrix} q_1^i \\ q_2^i \\ q_3^i \end{bmatrix} + \begin{bmatrix} -\sin \theta \\ \cos \theta \\ 0 \\ \sin \theta \\ -\cos \theta \\ 0 \end{bmatrix} q_G^i = \begin{bmatrix} F_1^i \\ F_2^i \\ F_3^i \\ F_4^i \\ F_5^i \\ F_6^i \end{bmatrix} \quad (6)$$

or

$$\mathbf{C}_0^{iT} \mathbf{q}^i + \mathbf{C}_G^{iT} \mathbf{q}_G^i = \mathbf{F}^i \quad (7)$$

where L_i is the length of the i th element. The elemental compatibility condition is defined as:

$$\begin{bmatrix} \cos \theta & \sin \theta & 0 & -\cos \theta & -\sin \theta & 0 \\ -\sin \theta / L^i & \cos \theta / L^i & 1 & \sin \theta / L^i & -\cos \theta / L^i & 0 \\ -\sin \theta / L^i & \cos \theta / L^i & 0 & \sin \theta / L^i & -\cos \theta / L^i & 1 \end{bmatrix} \begin{bmatrix} u_1^i \\ u_2^i \\ u_3^i \\ u_4^i \\ u_5^i \\ u_6^i \end{bmatrix} = \begin{bmatrix} e_1^i \\ e_2^i \\ e_3^i \end{bmatrix} \quad (8)$$

$$\begin{bmatrix} -\sin \theta & \cos \theta & 0 & \sin \theta & -\cos \theta & 0 \end{bmatrix} \begin{bmatrix} u_1^i \\ u_2^i \\ u_3^i \\ u_4^i \\ u_5^i \\ u_6^i \end{bmatrix} = e_G^i \quad (9)$$

or

$$\mathbf{C}_0^i \mathbf{u}^i = \mathbf{e}^i \quad (10)$$

$$\mathbf{C}_G^i \mathbf{u}^i = \mathbf{e}_G^i \quad (11)$$

and the constitutive condition is defined as:

$$\left\{ \begin{bmatrix} E_i A_i / L_i & 0 & 0 \\ 0 & 4E_i I_i / L_i & 2E_i I_i / L_i \\ 0 & 2E_i I_i / L_i & 4E_i I_i / L_i \end{bmatrix} + (-q_1^i) \begin{bmatrix} 0 & 0 & 0 \\ 0 & 2L_i / 15 & -L_i / 30 \\ 0 & -L_i / 30 & 2L_i / 15 \end{bmatrix} \right\} \begin{bmatrix} e_1^i \\ e_2^i \\ e_3^i \end{bmatrix} = \begin{bmatrix} q_1^i \\ q_2^i \\ q_3^i \end{bmatrix} \quad (12)$$

$$\left(\frac{-q_1^i}{L_i} \right) \mathbf{e}_G^i = \mathbf{q}_G^i \quad (13)$$

or

$$(\mathbf{S}_0^i + \mathbf{S}_G^i) \mathbf{e}^i = \mathbf{q}^i \quad (14)$$

$$\mathbf{S}_F^i \mathbf{e}_G^i = \mathbf{q}_G^i \quad (15)$$

where E_i, A_i, I_i are the Young's modulus, cross-sectional area and the second moment of area of the i th element, respectively. Eqs.(6)-(15) alternatively formulate the three governing equations for the second-order geometrically nonlinear 2D frame element. This unconventional formulation is equivalent to the governing equation formulated by the traditional FEM. For example, let $\theta = 0$ and substitute Eqs.(10), (11) (14) and (15) into Eq.(7), thus

$$\begin{aligned} \mathbf{F}^i &= \mathbf{C}_0^{iT} \mathbf{q}^i + \mathbf{C}_G^{iT} \mathbf{q}_G^i \\ &= \mathbf{C}_0^{iT} (\mathbf{S}_0^i + \mathbf{S}_G^i) \mathbf{e}^i + \mathbf{C}_G^{iT} \mathbf{S}_F^i \mathbf{e}_G^i \\ &= \mathbf{C}_0^{iT} (\mathbf{S}_0^i + \mathbf{S}_G^i) \mathbf{C}_0^i \mathbf{u}^i + \mathbf{C}_G^{iT} \mathbf{S}_F^i \mathbf{C}_G^i \mathbf{u}^i \\ &= \mathbf{C}_0^{iT} \mathbf{S}_0^i \mathbf{C}_0^i \mathbf{u}^i + (\mathbf{C}_0^{iT} \mathbf{S}_G^i \mathbf{C}_0^i + \mathbf{C}_G^{iT} \mathbf{S}_F^i \mathbf{C}_G^i) \mathbf{u}^i \\ &= (\mathbf{K}_M^i + \mathbf{K}_G^i) \mathbf{u}^i \end{aligned} \quad (16)$$

where $\mathbf{K}_M^i = \mathbf{C}_0^{iT} \mathbf{S}_0^i \mathbf{C}_0^i$, and $\mathbf{K}_G^i = \mathbf{C}_0^{iT} \mathbf{S}_G^i \mathbf{C}_0^i + \mathbf{C}_G^{iT} \mathbf{S}_F^i \mathbf{C}_G^i$. Eq.(16) coincides with the traditional FE formulation

for linear buckling analysis. Therefore, the eigenvalue problem of the linear buckling analysis of 2D frame with n elements can be alternatively expressed as:

$$(\mathbf{K}_M + \lambda_{cr} \mathbf{K}_G) \mathbf{z} = \mathbf{C}_0^T \mathbf{S}_0 \mathbf{C}_0 \mathbf{z} + \lambda_{cr} (\mathbf{C}_0^T \mathbf{S}_G \mathbf{C}_0 + \mathbf{C}_G^T \mathbf{S}_F \mathbf{C}_G) \mathbf{z} = 0 \quad (17)$$

where for a second-order geometrically nonlinear 2D frame, $\mathbf{C}_0 \in \mathfrak{R}^{3n \times d}$ and $\mathbf{C}_G \in \mathfrak{R}^{n \times d}$ are the two global compatibility matrices, and their transposes are the global equilibrium matrices; $\mathbf{S}_0, \mathbf{S}_G \in \mathfrak{R}^{3n \times 3n}$ and $\mathbf{S}_F \in \mathfrak{R}^{n \times n}$ are the global deterministic stiffness matrices calculated at reference configuration for 2D frames. Eq.(17) presents the alternative formulation for the deterministic linear buckling analysis which is beneficial for interval linear buckling analysis.

3. Solution algorithm of uncertain linear buckling analysis of frame structure

The uncertain parameters considered in this investigation are including the Young's modulus, cross-sectional area and second moment of inertia of each structural element, as well as the externally applied loadings at reference configuration.

Therefore, by considering uncertainties of parameters, the worst case buckling load can be calculated by solving:

$$\begin{aligned} & \min \lambda_b \\ & \text{subject to:} \\ & \left\{ \begin{array}{l} \mathbf{C}_0^T \mathbf{S}_0(\mathbf{E}, \mathbf{A}, \mathbf{I}) \mathbf{C}_0 \mathbf{z} + \lambda_b [\mathbf{C}_0^T \mathbf{S}_G(\mathbf{F}_{ref}) \mathbf{C}_0 + \mathbf{C}_G^T \mathbf{S}_F(\mathbf{F}_{ref}) \mathbf{C}_G] \mathbf{z} = 0 \\ \mathbf{E} \in \tilde{\mathbf{E}} := \{\mathbf{E} \in \mathfrak{R}^n \mid \underline{E}_i \leq E_i \leq \overline{E}_i, \text{ for } i = 1 \dots n\} \\ \mathbf{A} \in \tilde{\mathbf{A}} := \{\mathbf{A} \in \mathfrak{R}^n \mid \underline{A}_i \leq A_i \leq \overline{A}_i, \text{ for } i = 1 \dots n\} \\ \mathbf{F}_{ref} \in \tilde{\mathbf{F}} := \{\mathbf{F}_{ref} \in \mathfrak{R}^d \mid \underline{F}_{ref}^j \leq F_{ref}^j \leq \overline{F}_{ref}^j, \text{ for } j = 1 \dots d\} \\ \mathbf{I} = f(\mathbf{A}) \\ \|\mathbf{z}\|_2 = 1 \end{array} \right. \quad (18) \end{aligned}$$

and the best case solution can be determined as:

$$\begin{aligned} & \max \lambda_b \\ & \text{subject to:} \\ & \left\{ \begin{array}{l} \mathbf{C}_0^T \mathbf{S}_0(\mathbf{E}, \mathbf{A}, \mathbf{I}) \mathbf{C}_0 \mathbf{z} + \lambda_b [\mathbf{C}_0^T \mathbf{S}_G(\mathbf{F}_{ref}) \mathbf{C}_0 + \mathbf{C}_G^T \mathbf{S}_F(\mathbf{F}_{ref}) \mathbf{C}_G] \mathbf{z} = 0 \\ \mathbf{E} \in \tilde{\mathbf{E}} := \{\mathbf{E} \in \mathfrak{R}^n \mid \underline{E}_i \leq E_i \leq \overline{E}_i, \text{ for } i = 1 \dots n\} \\ \mathbf{A} \in \tilde{\mathbf{A}} := \{\mathbf{A} \in \mathfrak{R}^n \mid \underline{A}_i \leq A_i \leq \overline{A}_i, \text{ for } i = 1 \dots n\} \\ \mathbf{F}_{ref} \in \tilde{\mathbf{F}} := \{\mathbf{F}_{ref} \in \mathfrak{R}^d \mid \underline{F}_{ref}^j \leq F_{ref}^j \leq \overline{F}_{ref}^j, \text{ for } j = 1 \dots d\} \\ \mathbf{I} = f(\mathbf{A}) \\ \|\mathbf{z}\|_2 = 1 \\ z^i \cdot z_{b,det}^i \geq 0 \text{ for } i = 1 \dots d \end{array} \right. \quad (19) \end{aligned}$$

where $z_{b,det}^i$ denotes the i th component of the deterministic buckling mode vector, which is the eigenvector corresponding to $\lambda_{b,det}$. In addition, the constraint $\mathbf{I} = f(\mathbf{A})$ is introduced to model the dependency between the cross-sectional area and the second moment of area of the same structural element.

Eqs.(18) and (19) provide a mathematical programming based approach for calculating the worst and best case buckling loads for 2D frames. The proposed method transforms the uncertain linear buckling analysis, which in essence is an interval eigenvalue problem, into two explicit NLPs. By adopting the formulation of the generalized stress/strain with the unique structural characteristics of the stiffness matrices, the interval parameters are able to be extracted out from the stiffness matrices and explicitly modelled as mathematical programming variables. Unlike traditional interval analysis, the proposed method involves no interval arithmetic such that the sharpness of the worst and best buckling loads are not compromised due to the inveterate issue of dependency associated with

interval arithmetic [6].

4. Numerical example

In order to illustrate the applicability, accuracy, and efficiency of the presented computational approach, one practically motivated frame structure is investigated. The reference configuration of the structure is shown in Figure 2. The NLPs involved in both worst case and best case calculations are solved by a commercial NLP solver named CONOPT [7], which implemented within a sophisticated modelling environment named the general algebraic modelling system or GAMS [8].

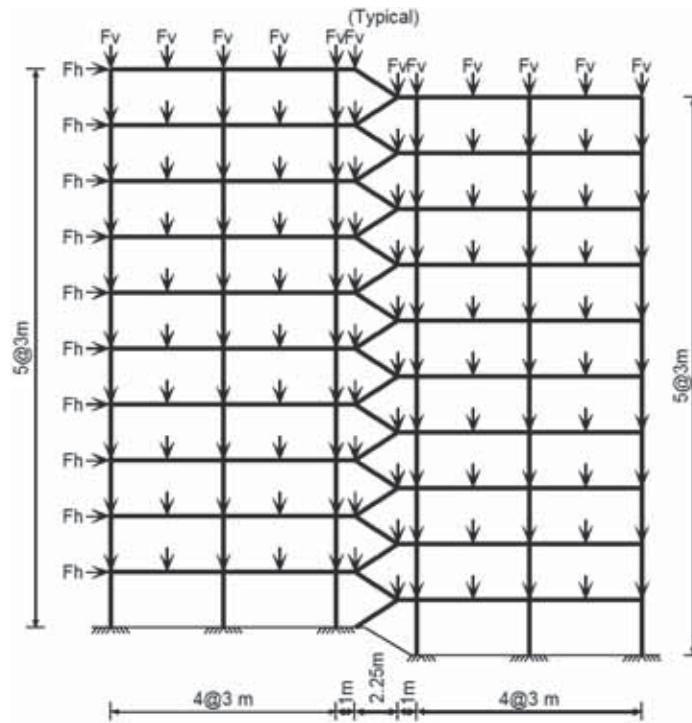


Figure 2: Ten-storey five-bay frame

The considered uncertain parameters are including the Young's modulus, cross-sectional area of beam and column, second moment of inertia of beam and column, as well as the applied loadings at reference configuration. All the information on the uncertain parameters has been presented in Table 1.

Table 1: Interval parameters of ten-storey five-bay frame

Interval Parameters	Lower bound	Upper bound
E	176 GPa	224 GPa
A_c	$326.8 \times 10^{-4} \text{ m}^2$	$361.2 \times 10^{-4} \text{ m}^2$
A_b	$56.34 \times 10^{-4} \text{ m}^2$	$62.26 \times 10^{-4} \text{ m}^2$
F_v	68kN	92kN
F_h	24kN	36kN

For the ten-storey frame shown in Figure 1, 400WC270 has been implemented to model all columns whereas beams are modelled by 310UB46.2 [9]. In order to maintain the physical feasibility between the cross-sectional area and second moment of inertia for the same element, the following compatibility conditions are introduced as:

$$I_c(A_c) = 0.1898A_c^2 + 0.0241A_c - 2 \times 10^{-5} \quad (20)$$

for all the 400WC270 columns, and

$$I_b(A_b) = -0.8876A_b^2 + 0.0288A_b - 4 \times 10^{-5} \quad (21)$$

for all the 310UB46.2 beams.

The worst and best structural buckling load calculated by the proposed NLP approach are $\lambda_{b,\text{worst}}^{\text{NLP}} = 27.81$ and $\lambda_{b,\text{best}}^{\text{NLP}} = 53.34$ respectively. Due to the unavailability of analytical solution for complex structure such as the one in current example, the Monte-Carlo simulation method with 100,000 simulations has been performed to partially verify the accuracy of the proposed method. The results reported by 100,000 simulations are $\lambda_{b,\text{worst}}^{\text{mcs}} = 36.01$ for the worst case, and $\lambda_{b,\text{best}}^{\text{mcs}} = 40.55$ for the best case. It is obvious that the performance of the Monte-Carlo simulation with 100,000 iterations provides enclosed solutions and the computational efficiency consumed is far more than the proposed NLP method.

5. Conclusion

Uncertain linear buckling analysis with interval parameters has been investigated. A mathematical programming founded approach is presented to assess the buckling loads of engineering frames against undesirably large displacement by calculating the worst and best case buckling loads.

All interval parameters considered in this study are able to be modelled as mathematical programming variables with upper and lower bounds through reformulations of the traditional FE approach. The advantage is that the interval dependence associated with interval arithmetic can be completely eliminated, so the sharpness of the extremity of the buckling loads can be enhanced.

For situations, such as eigen-buckling analyses of structures involving repeated eigenvalues, structures with closely spaced eigenvalues, as well as defective structural systems etc, have not been investigated in the present study.

6. Acknowledgements

This research work is supported by Australian Research Council through Discovery Grant Projects.

6. References

- [1] W. Gao, C. Song and F. Tin-Loi, Probabilistic interval analysis for structures with uncertainty, *Structural Safety*, 32 (3), 191-199, 2010.
- [2] W. Gao, D. Wu, C. Song, F. Tin-Loi and X. Li, Hybrid probabilistic interval analysis of bar structures with uncertainty using a mixed perturbation Monte-Carlo method, *Finite Elements in Analysis and Design*, 47, 643-652, 2011.
- [3] D. Wu, W. Gao, G. Li, S. Tangaramvong and F. Tin-Loi, A Robust assessment of collapse resistance of structures under uncertain loads based on Info-Gap model, *Computer Methods in Applied Mechanics and Engineering*, 285, 208-227, 2015.
- [4] J. S. Przemieniecki, *Theory of Matrix Structural Analysis*, Dover Publication Inc, New York, 1985.
- [5] G. Maier, A matrix structural theory of piecewise linear elastoplasticity with interacting yield planes, *Meccanica*, 5(1), 54-66, 1970.
- [6] R. L. Muhanna, H. Zhang, R. L. Mullen, Combined axial and bending stiffness in interval finite element methods, *ASCE Journal of Structural Engineering*, 133 (12), 1700-1709, 2007.
- [7] A. S. Drud, CONOPT-a large-scale GRG code, *ORSA Journal on Computing*, 6 (2), 207-216, 1994.
- [8] A. Brooke, D. Kendrick, A. Meeraus, R. Raman, GAMS: A User's Guide. GAMS Development Corporation, Washington, DC, 2014.
- [9] OneSteel Publications, *Hot-Rolled Structural & Welded Sections 5th Ed*, OneSteel Market Mills, 2000.

Combining state of the art meta-models for predicting the behavior of non-linear crashworthiness structures for shape and sizing optimizations

Axel Schumacher, Christopher Ortman

University of Wuppertal, Faculty D – Mechanical Engineering, Chair for Optimization of Mechanical Structures, Wuppertal, Germany, schumacher@uni-wuppertal.de, ortmann@uni-wuppertal.de

Abstract

In this contribution, we consider a shape optimization problem of a simple crashworthiness structure. The application example is an aluminum frame clamped on one side and impacted on the other side. The structural analysis is carried out with the finite element method using explicit time integration. Contact phenomena, buckling phenomena and non-linear material data are taken into account. With the aid of this example, a large number of different meta-models using radial basis functions, Kriging (Gaussian processes) and neural networks are generated.

The advantages and disadvantages of these different methods and the problems by relying on the common quality criterions “coefficient of determination R^2 ” and “leave-one-out-cross-validation R_{press}^2 ” are shown. The combination and superposition of the different meta-model techniques is investigated in order to enhance the meta-model prediction capability.

Keywords: meta-models, crashworthiness, Gaussian Processes, Kriging, neural networks, radial basis functions

1. Introduction

For a limited number of design variables, the use of meta-model techniques is very popular in structural optimization processes. Hereby, we get smooth and continuous descriptions of the structural responses. The quality of the meta-models can be scaled individually depending on the available time. After the creation of the meta-models, the optimization can be performed without further time-consuming finite element simulations using the responses of the meta-models.

When using meta-models for non-linear dynamic mechanical problems (e.g. crashworthiness problems), the nonlinearities and the limited amount of sampling points due to the high computational effort, can cause low prediction capabilities of the meta-models. Further difficulties can arise due to non-smooth behavior of the structural responses, insufficient material data, physical and numerical bifurcation points and finite element mesh dependency.

In commercial and scientific software codes there exist a large number of different meta-model-techniques. The question arises which one is the most suitable for the mechanical problem at hand and which quality criterions can be used for this decision.

In this contribution a large number of different meta-model techniques and some combinations and superpositions of the different meta-models is investigated in order to enhance the meta-model prediction capability.

2. Crashworthiness example

The considered application example shown in figure 1 is an aluminum frame (300 x 150 x 5 mm, wall thickness: 2 mm) clamped on one side and impacted by a rigid wall under an angle of 10 degree. The rigid wall has a mass of 2 kg and an initial velocity of 5 m/s. The design variable describes the y-position of the inner walls (symmetric, see figure 1b). Figure 2 shows the deformation and the reaction force of the frame depending on the value of the design variable.

3. Meta-model techniques

In this chapter the relevant meta-modelling techniques are described and applied to the crashworthiness example. For this purpose 7 sampling points are used, assuming that more sampling points are not available. The quality criterions R^2 and if possible R_{press}^2 are calculated. In order to evaluate these quality criterions and the prediction capabilities of the meta-models, 6 additional validation points are used. For this purpose the regression parameter R_{val}^2 is calculated for the validation points similarly as R^2 is calculated for the sampling points.

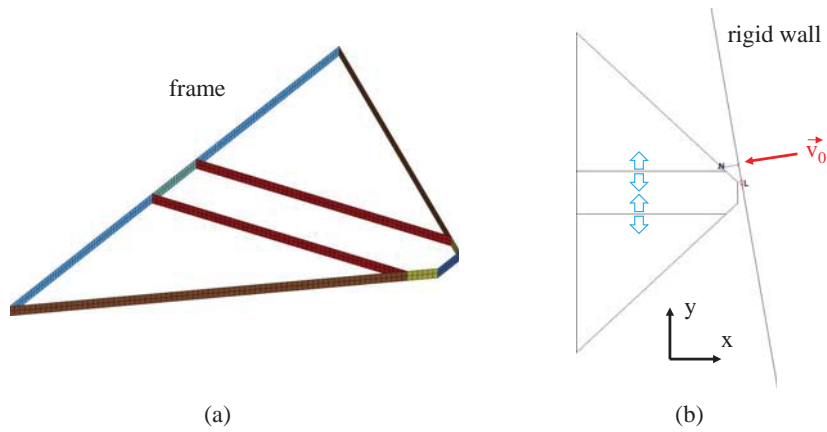


Figure 1: Aluminum frame [1]

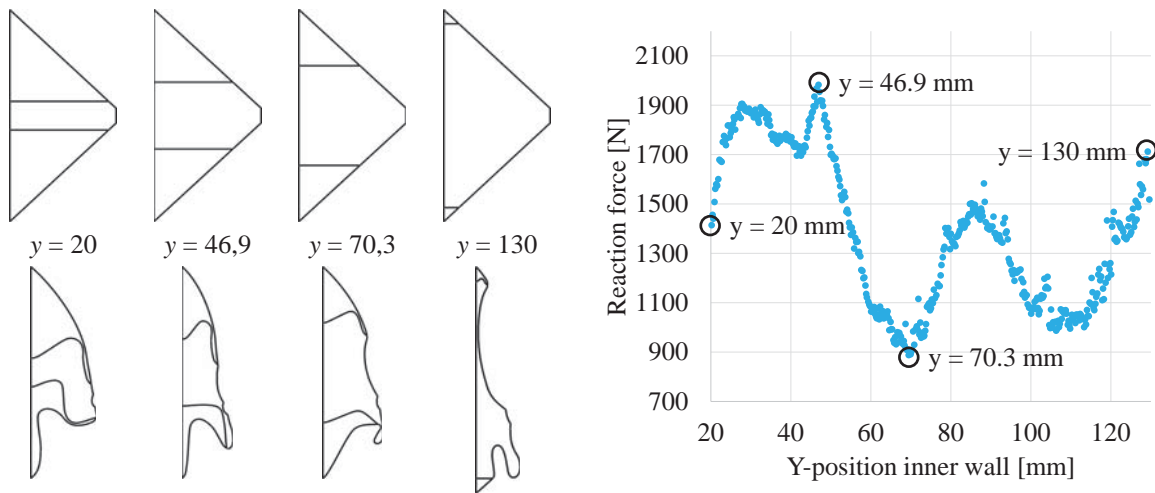


Figure 2: Deformation and reaction force of the frame depending on the value of the design variable [1]

3.1 Radial basis functions

The value of a radial basis function depends on the distance to a center point $C(x_n/y_n)$ called radius $r = \|\vec{x} - \vec{c}\|$. Some common types of radial basis functions are:

- Linear: $\varphi(r) = r$,
- Cubic: $\varphi(r) = r^3$,
- Multiquadric: $\sqrt{a + r^2}$ with the positive shape parameter a .

The interpolation is typically done by a linear combination of n (normalized) radial basis functions centered around the n sampling points:

$$f(\vec{x}) = \sum_{i=1}^n w_i \cdot \varphi(r) \quad (1)$$

The weights w_i can be determined by the following equation system:

$$\begin{bmatrix} \varphi(r_{11}) & \dots & \varphi(r_{1n}) \\ \dots & \dots & \dots \\ \varphi(r_{n1}) & \dots & \varphi(r_{nn}) \end{bmatrix} \cdot \begin{bmatrix} w_1 \\ \dots \\ w_n \end{bmatrix} = \begin{bmatrix} g_1 \\ \dots \\ g_n \end{bmatrix} \quad (2)$$

Figure 3 shows three meta-models with different kinds of radial basis functions for the crashworthiness example. The real (usually unknown) relation between the design variable and the structural response is indicated by blue dots. The training sampling points are pictured by red dots and the validation sampling points by purple dots.

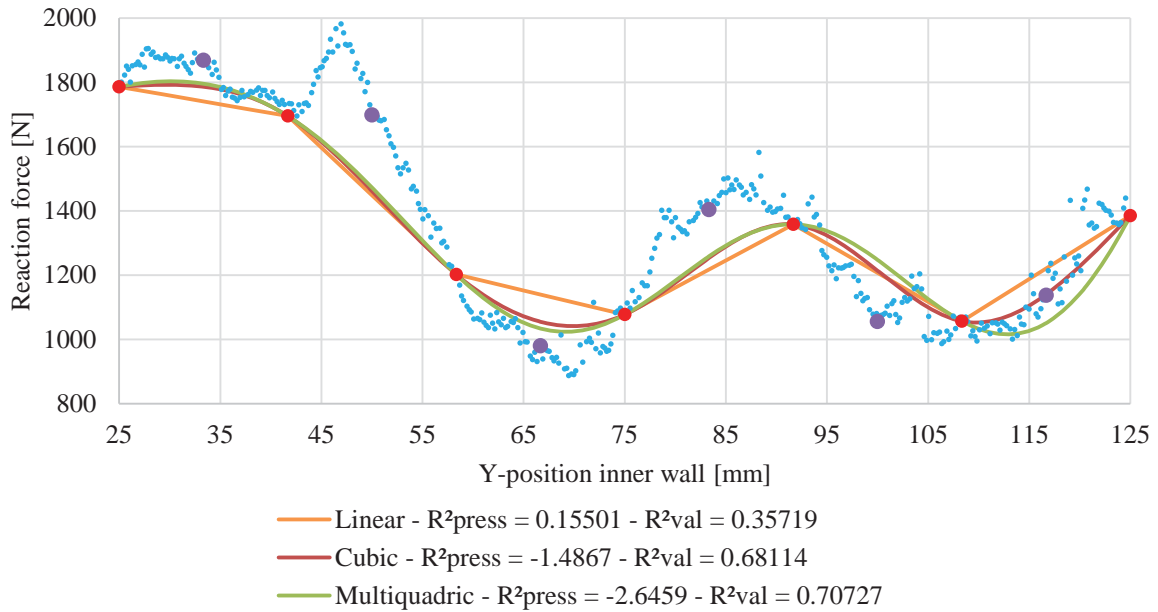


Figure 3: Meta-modeling example with radial basis functions [1]

3.2 Neural network

A neural network consists of three different kinds of neurons: the input neurons (process input data), the output neurons (process output data) and the hidden neurons (internal representation of the environment/problem). A common net type is a feed-forward multi-layer-perceptron net (figure 4).

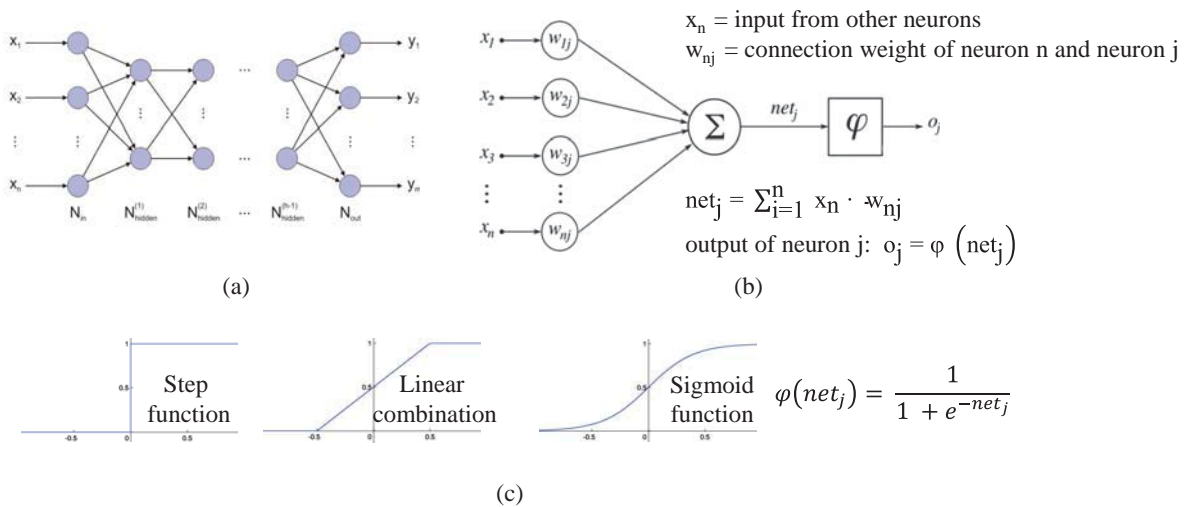


Figure 4: Meta-modeling with neural networks: multi-layer (a), neuron input/output (b), common neuron activation functions (c) [1, 2, 3]

The neural networks learn with training data (here: sampling points). The learning process is an optimization of the weights between the neurons to minimize the error between the neural network outputs and the given sampling points. A common approach for this is the supervised learning with backpropagation, which is a version of the method of steepest descent adapted for neural networks.

Figure 5 shows three different approximations with multi-layer-perceptron networks for the crashworthiness example. Each consists of a single input neuron, a single output neuron and two layers of hidden neurons. The number of hidden neurons in each hidden layer varies.

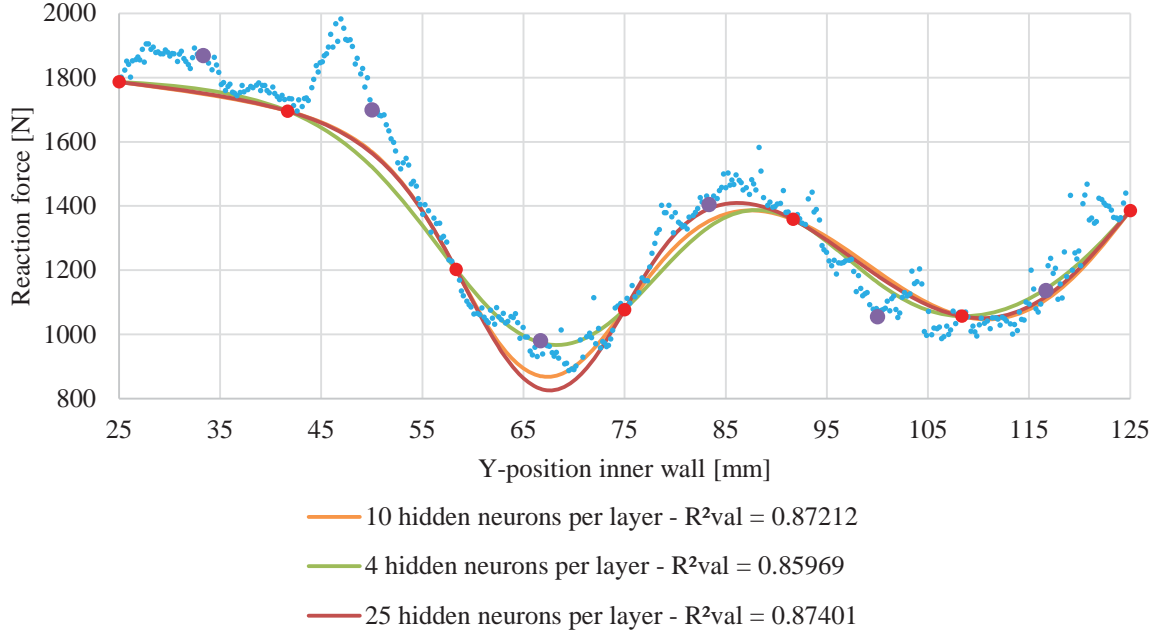


Figure 5: Meta-modeling example with neural networks [1]

3.3 Gaussian Processes (Kriging)

Gaussian processes are also known as Kriging. The similarity influence (figure 6) of a sampling point on an arbitrary point is defined with the covariance function. A common approach is the “squared exponential”:

$$Cov(x, x') = \sigma_f^2 \cdot e^{-(x-x')^2/(2l^2)} \quad (3)$$

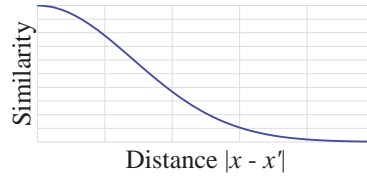


Figure 6: Similarity influence of a sampling point [1]

A covariance matrix between all sampling points with the x -value vector \vec{p}_x can be calculated as:

$$\underline{Cov}(\vec{p}_x) = \begin{bmatrix} Cov(x_1, x_1) & \dots & Cov(x_1, x_n) \\ \dots & \dots & \dots \\ Cov(x_n, x_1) & \dots & Cov(x_n, x_n) \end{bmatrix} \quad (4)$$

The covariance matrix between an arbitrary point and the sampling points can be determined as:

$$\underline{Cov}(x, \vec{p}_x) = [Cov(x, x_1) \quad \dots \quad Cov(x, x_n)] \quad (5)$$

The interpolation $\tilde{g}(x)$ can be defined as:

$$\tilde{g}(x) = \underline{Cov}(x, \vec{p}_x) \cdot \underline{Cov}(\vec{p}_x)^{-1} \cdot \vec{p}_g \quad (6)$$

Three different Kriging interpolations for the crashworthiness example are shown in figure 7. They differ in the choice of the parameter theta, which is similar but not identical to the length scale parameter l in (9). Theta = 8.8315 is optimized for a maximal value of R_{press}^2 .

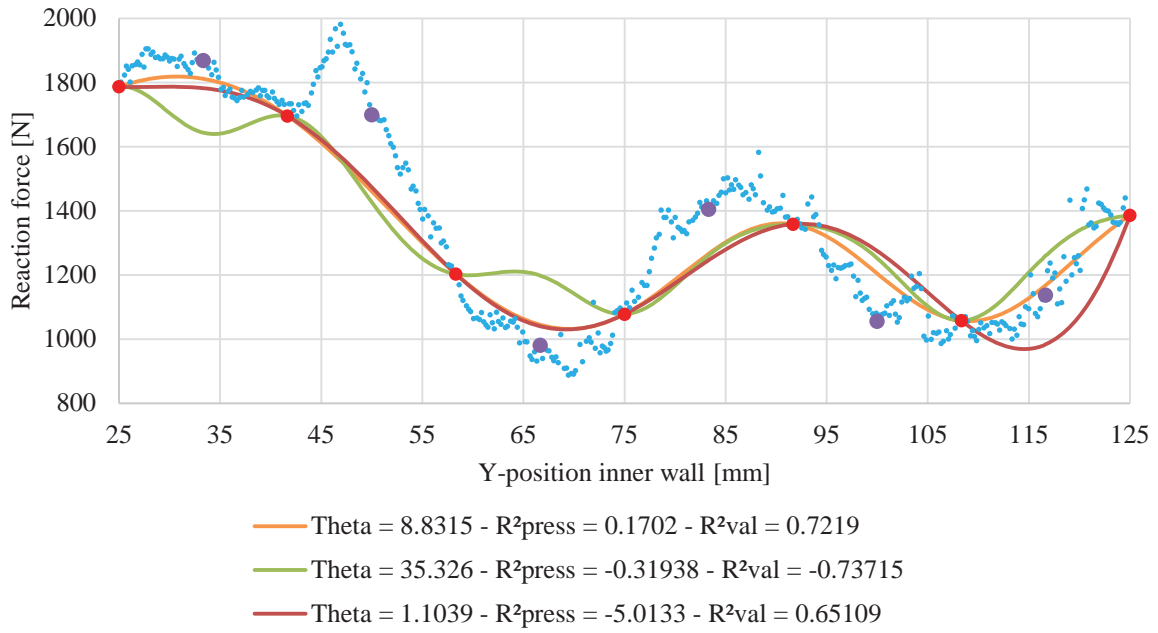


Figure 7: Meta-modeling example with Gaussian processes [1]

3.4 Typical characteristics of the different approaches

Typical characteristics of the three described approaches are summarized in table 1. There exist a lot of other meta-model techniques which are not considered in this contribution, e.g. support vector machine regression, random forest or fuzzy regression model.

Table 1: Typical characteristics of the described approaches for meta-modeling

Radial basis functions	Neural networks	Gaussian Processes (Kriging)
<ul style="list-style-type: none"> - Interpolation depends on the type of the radial basis function - Smooth transitions between the sampling points - This smoothness limits the versatility 	<ul style="list-style-type: none"> - “Black-box-systems” - Limited versatility due to the activation function - The higher the number of hidden neurons the better the versatility but the higher the risk of overlearning - The training can be computationally expensive - The approximation accuracy of the given sampling points can be poor - High resilience to outlier sampling points 	<ul style="list-style-type: none"> - Usually it is an interpolation - Very versatile and can even adapt to non-smoothness - The length scale parameter l controls the “frequency” - The determination of this parameter can be difficult, a common approach is an optimization of this parameter by the maximum likelihood principle

4. Superposition of the meta-models

The quality criterions R^2 and R^2_{press} , the average absolute error at the validation points $|\epsilon|_{ave}$ and the regression parameter for the validation points R^2_{val} for each meta-model of the crashworthiness example are summarized in table 2.

Table 2: Validation of the meta-models

Meta-model	R^2	R^2_{press}	$ \epsilon _{ave}$	R^2_{val}
Linear radial basis function	1	0.15501	159.984148	0.35718969
Cubic radial basis function	1	-1.4867	117.684404	0.68113786
Multiquadric radial basis function	1	-2.6459	129.308549	0.70727437
Neural network 10 hidden neurons	1	-	96.9827279	0.87212213
Neural network 4 hidden neurons	1	-	78.6433099	0.85968893
Neural network 25 hidden neurons	1	-	93.5231771	0.8740076
Kriging Theta = 8.8315	1	0.1702	112.8654049	0.7219
Kriging Theta = 1.1039	1	-5.0133	150.4035117	0.6510925
Kriging Theta = 35.326	1	-0.31938	196.3350898	-0.73714623

Often all available sampling points are used for the training of the meta-model in order to maximize its quality. This is especially true for crashworthiness problems, where due to the high computational effort of each crash simulation only a very limited number of sampling points is available. In these cases there is no validation data and usually R_{press}^2 is the main decision criterion for the evaluation of a meta-model.

Astonishingly, for the given crashworthiness example there is no correlation between R_{press}^2 and the real prediction capabilities of the meta-models (evaluated by R_{val}^2). For example the radial basis function meta-model with the highest value of R_{press}^2 (linear radial basis function) has the lowest value of R_{val}^2 of all radial basis function meta-models.

The question arises whether there exists a possibility to reduce the risk of choosing a meta-model with a low prediction capability by relying on common quality criterions like R_{val}^2 and R_{press}^2 .

In relation to the computational effort for the generation of the sampling points, the computational effort for the creation of meta-models is very low. The idea is to generate a lot of different meta-models and to find a suitable superposition of the models in order to enhance the overall prediction capability or at least to reduce the risk of choosing a meta-model with a low prediction capability.

Figure 9 shows four different meta-models which are based on the superposition of the meta-models shown in the previous chapter. For the superposition the meta-models are weighted equally.

The superposition of all meta-models has a value $|\varepsilon|_{ave}$ of 107.29. The average value of $|\varepsilon|_{ave}$ of all meta-models is 126.192258. This difference is quite surprising, because the superposition is just a simple averaging of the meta-models. Because of the lower average error the R_{val}^2 value of the superposition of all meta-models is with 0.73399 also significantly better than the average R_{val}^2 value of all meta-models with 0.55414.

This is also true for the $|\varepsilon|_{ave}$ values of all other superpositions compared to the average $|\varepsilon|_{ave}$ value of the meta-models which have been used for the superposition (radial basis functions: 126.1 to 135.66, neural networks: 89.118 to 89.716 and Kriging: 136.15 to 153.2). Whether this is a mere coincidence or a possible strategy for the enhancement of meta-modeling remains the topic of further research.

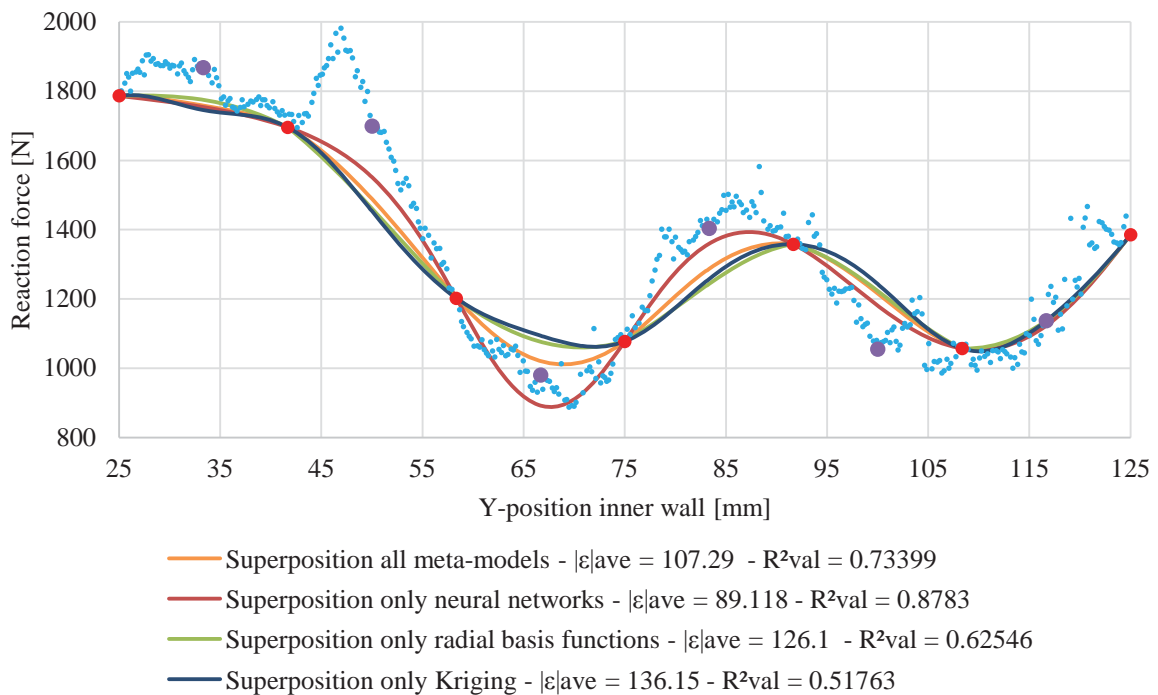


Figure 8: Superposition of the meta-models

7. References

- [1] C. Ortmann, A. Schumacher: Meta-models in structural optimization – techniques and strategies”, Proceedings of the Automotive CAE Grand Challenge 2014, 15th and 16th of April 2014 in Hanau
- [2] <http://pi.informatik.uni-siegen.de/Arbeitsgebiete/ci/knn/>, access March 26th, 2015
- [3] http://de.wikipedia.org/wiki/K%C3%BCnstliches_neuronales_Netz, access March 26th, 2015

Parameter optimisation design for a six-DOF heavy duty vehicle seat suspension

Donghong Ning, Haiping Du, Weihua Li

University of Wollongong, NSW, Australia, hdu@uow.edu.au

1. Abstract

In this paper, the stiffness and damping parameters of a six-degree-of-freedom (DOF) heavy duty vehicle seat suspension are optimised on the base of different vibration excitations with genetic algorithm (GA). Optimisations are implemented under two conditions, that is, all the legs have same stiffness and damping, and legs which are symmetric with x axis have same stiffness and damping. Swept sinusoidal vibrations are applied as excitations. Translational vibration along x and y axes and rotational vibration around x and y axes are carried out, respectively. The optimisation results show that a smaller weighted value of root mean square (RMS) acceleration in six DOFs according to ISO 2631-1 can be obtained under the second condition, which means the suspension can be more comfortable. But higher acceleration transmissibility from the vibration excitation to the same DOF acceleration output around the resonance frequency is also obtained under the second condition. These results indicate that when optimising multi-DOF heavy duty vehicle seat suspension, the dominant vibration DOF will cause vibrations in other DOFs due to the structural coupling. So the dominant vibration DOF and its related vibration DOFs should be considered at the same time.

2. Keywords: six-DOF, seat suspension, GA.

3. Introduction

Nowadays, the vehicle seat suspension has been an increasing demand because the exposure to vibration transferred from rough road has significant influence on drivers' safety, healthy and comfort[1], especially, for heavy duty vehicles which always work in severe environments. Generally, a one or two degrees of freedom (DOFs) vibrations are considered to design and optimise seat suspension[2, 3]. However, heavy duty vehicles always have special functions, such as digging, dumping and shovelling, and the vibrations will come from different sources besides rough road surface. Therefore, a multi-DOF seat suspension should be designed to satisfy the requirements of heavy duty vehicles.

The multi-DOF motion platform has been widely applied in many fields. Based on its parallel mechanism, a kind of six-DOF vehicle seat suspension is designed. The six-DOF suspension includes one base platform which is fixed on the vehicle cab floor, one top platform which is used for assembling vehicle seat, and six legs which are used to connect the base and top platform. There are springs and dampers in each leg.

As the suspension performance is closely related to the choices of the spring stiffness and the damper damping property, how to choose the optimal stiffness and damping will be critical for the seat suspension performance. Due to the complex structural configuration of the six-DOF seat suspension and because there are six springs and six dampers in the six-DOF seat suspension, conventional optimisation algorithms based on gradient calculation are hard to be applied. In this paper, the genetic algorithm (GA), which is a well-known stochastic search algorithm for global optimization of complex systems based Darwinian principle of "survival of the fittest" [4, 5], is used to search for the optimal stiffness and damping for six legs. The weighted value of root mean square (RMS) according to ISO 2631-1 in six-DOF of top platform and the relative displacement of top and base platform are considered when optimising the suspension. Numerical results are obtained and analysed in the paper.

4. Six-DOF heavy duty vehicle seat suspension

Vertical and horizontal vibrations are always involved for the design of passenger vehicles seat suspension. For heavy duty vehicles such as excavators and drill rigs which have special functions, vibrations come from multiple sources except road surfaces. Therefore, the drivers will suffer multi-DOF vibration.

4.1. Six-DOF suspension design

Multiple-DOF motion platform is a kind of parallel mechanism which has a six-DOF movable top platform. Based on the structure of multiple-DOF motion platform, the six-DOF vehicle seat suspension is designed as shown in Figure 1. The six-DOF suspension includes one base platform which is fixed on the vehicle cab floor, one top platform which is used for assembling vehicle seat, and six legs connecting the base and top platform. There are springs and dampers in each leg. The x axis points to the vehicle traveling direction, and the two sides of x axis are symmetric. When the base platform suffers a six-DOF vibration translating along x, y and z axis, and rotating around x, y and z axis, the suspension can attenuate it in six-DOF.

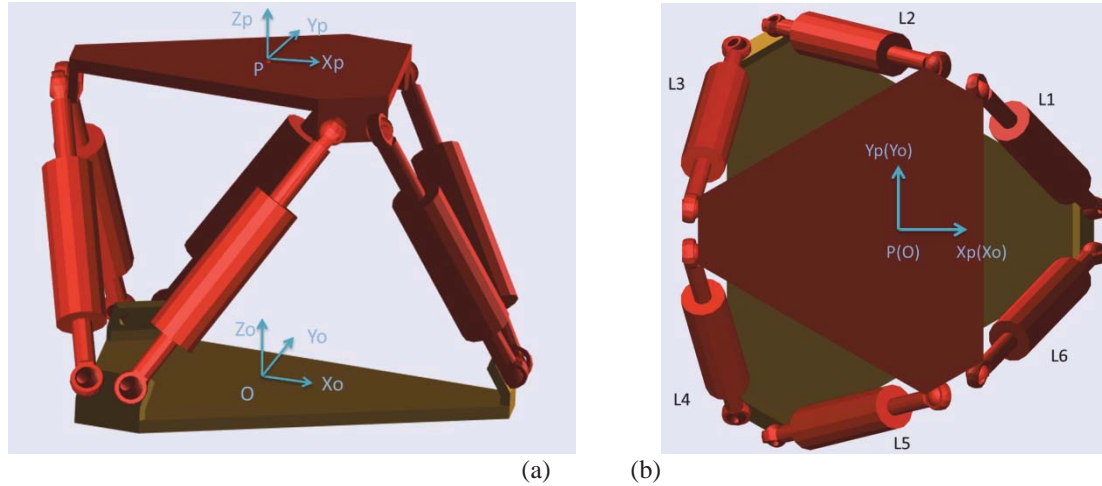


Figure 1: Six-DOF vehicle seat suspension. (a) Side view (b) Top View.

4.2. Six-DOF suspension model

The traditional modelling method used to compute dynamics and derive equations is error-prone and complicated. SimMechanics is a new way which can model 3D multibody system easily and accurately using blocks in Matlab/Simulink. In this paper, a 3D model is designed in PTC Creo firstly. Then the 3D model is transferred into SimMechanics. An 80kg load is added on the top platform to imitate the weight of seat and driver. The stiffness k and damping c of six legs can be set independently. The translation displacements and rotation angles of six-DOF vibration can be implemented on the base platform. Using sensor blocks in SimMechanics, we can get the vibration response of seat surface.

5. Optimisation method

Parameter optimisation of vehicle seat should involve two things, drivers' comfort and vehicle handling. Attenuating the vibration acceleration transmitting to seat surface can enhance drivers' comfort, which always need soft springs when the vibration frequency is higher than resonance frequency. And in low frequency band, hard springs can perform better in attenuating seat surface acceleration. The displacement between seat surface and cab floor is an important factor which influence vehicle handling. So the seat surface acceleration and relative displacement should be considered comprehensively when optimise suspension parameter.

5.1. Vibration evaluation

Root-mean-square (RMS) acceleration is always used to evaluate vibration. The six-DOF vibration total value of RMS acceleration can be determined as Eq. (1). The translational vibration RMS accelerations a_x , a_y and a_z are expressed in m/s^2 , and the rotational vibration rms accelerations a_{rx} , a_{ry} and a_{rz} are expressed in rad/s^2 . The multiplying factors k are given by ISO 2631-1 for seat surface vibration [6]. In Eq. (1), $k_x = 1$, $k_y = 1$, $k_z = 1$, $k_{rx} = 0.63 m/rad$, $k_{ry} = 0.4 m/rad$, $k_{rz} = 0.2 m/rad$. A small a_v implies the driver fell comfortable when operating a vehicle.

$$a_v = (k_x^2 a_x^2 + k_y^2 a_y^2 + k_z^2 a_z^2 + k_{rx}^2 a_{rx}^2 + k_{ry}^2 a_{ry}^2 + k_{rz}^2 a_{rz}^2)^{\frac{1}{2}} \quad (1)$$

5.2. GA optimization

GA is a well-known stochastic search algorithm for global optimization of complex systems. It applies Darwinian principle of "survival of the fittest" and uses selection, crossover, and mutation operators to breed good solutions. For optimizing the six-DOF seat suspension parameters of springs and dampers, GA is utilised to search the optimal stiffness and damping of suspension legs to obtain a minimal seat surface vibration total value a_v . The stiffness band of springs is set as 9000 to 30000 N/m , and the damping band of dampers is set as 50 to 1000 $N*s/m$. At the same time, the relative displacement between seat surface and cab floor is limited in $\pm 0.025m$ in three axes.

6. Optimisation results

To simplify the optimisation process and at the same time present more optimisation options, the optimisation is operated in two conditions. In the first condition, all the legs of the suspension are assumed to have the same

stiffness and damping. The second condition considers the symmetry of the suspension, so leg 1 and leg 6, leg 2 and leg 5, leg 3 and leg 4 share the same stiffness and damping respectively. In each condition, the suspension is optimised in four kinds of vibration excitations. Translational vibrations along x and y axis and rotational vibrations around x and y axis are respectively implemented on the base platform of the suspension. In this paper, the swept sinusoidal signal is applied as vibration sources. The amplitudes are $0.01m$ for translational vibration and 1 degree (about 0.0174 rad) for rotational vibration. And the vibration frequency band is between 0.5 to 10 Hz .

6.1. Optimised stiffness and damping

The GA optimisation results with two conditions are shown in Table 1. In the same legs condition, the optimisation results of translational vibration along x axis and rotational vibration around x and y axis have the same stiffness around the lowest value and different damping. This is because lower stiffness always leads to smaller acceleration, and proper damping can limit the biggest displacement around resonance frequency. Figure 2 shows the total value of RMS acceleration of the optimised suspension. It implies that when taking the symmetry of the suspension into account, we can get more comfortable optimisation parameters under these four kinds of vibration excitation.

Table 1: GA optimisation results

Vibration DOF	Symmetric Legs						Same Legs	
	L1 and L6		L2 and L5		L3 and L4		All Legs	
	$k(N/m)$	$c(N*s/m)$	$k(N/m)$	$c(N*s/m)$	$k(N/m)$	$c(N*s/m)$	$k(N/m)$	$c(N*s/m)$
x	17366.1	979.2	12643.7	703.6	12893.5	320.8	9000.3	682.6
y	9407.9	531.1	10436.5	785.8	13953.3	812.2	10148.5	782.3
rx	29111.6	830.1	11039.8	59.5	12414.8	621.9	9000.3	410.9
ry	9000.2	287.6	12597.7	499.4	9001.3	54.3	9000.3	511.9

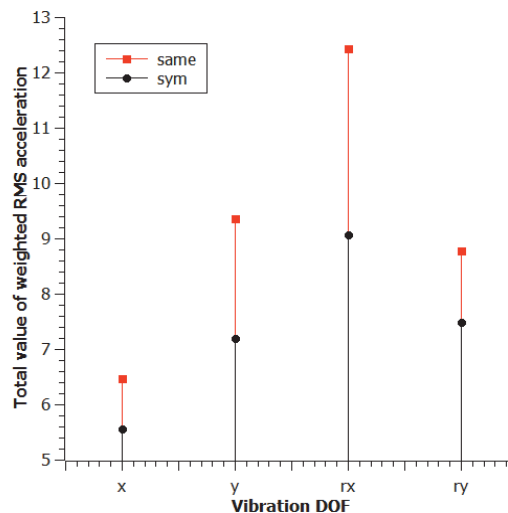


Figure 2: Total value of RMS acceleration

6.2. Comparison of optimisation results under two conditions

When only translational vibration along x axis is implemented on the base platform of the 6-DOF seat suspension, the optimisation result considered the symmetry property can get a lower total value of RMS acceleration. But it gets higher acceleration transmissibility along x axis in resonance frequency, as shown in Figure 3 (a). Figure 3 (b) shows the RMS acceleration in six-DOF respectively and the six-DOF total RMS acceleration. It notes that the condition with same legs has a bigger rotational acceleration around y axis. While in condition with symmetric legs has a third dominant acceleration along z axis.

Figure 4 shows that there is a similar result when only translational vibration along y axis is implemented.

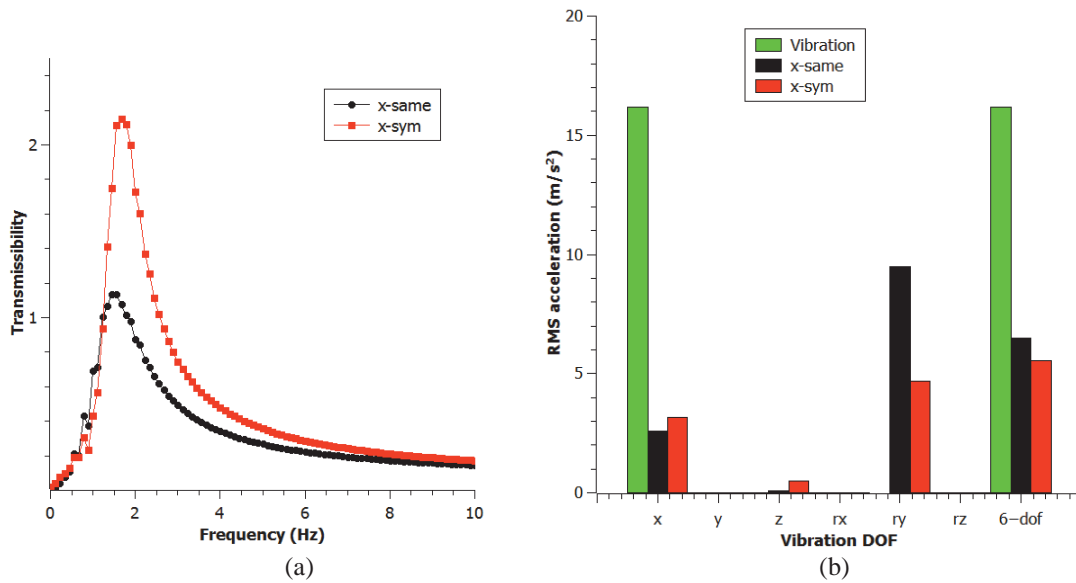


Figure 3: Vibration along x axis. (a) Transmissibility (b) RMS acceleration

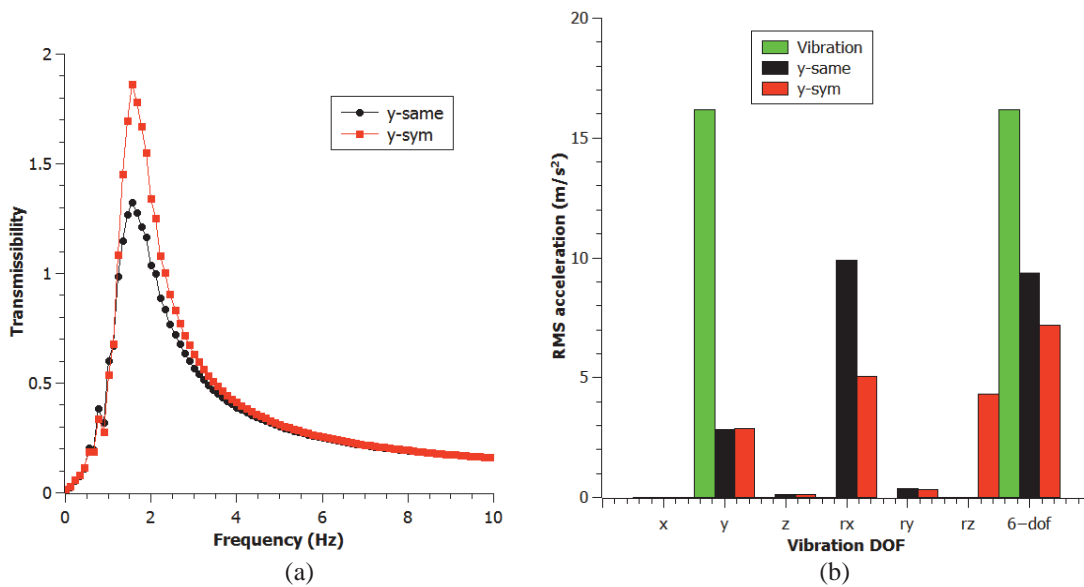


Figure 3: Vibration along y axis. (a) Transmissibility (b) RMS acceleration

When optimising the 6-DOF suspension under rotation vibration, in the vibration excitation DOF, the transmissibility of the one optimised based on symmetric property in resonance period is higher than the other one. But it will decline quickly unlike optimisation under translational vibration.

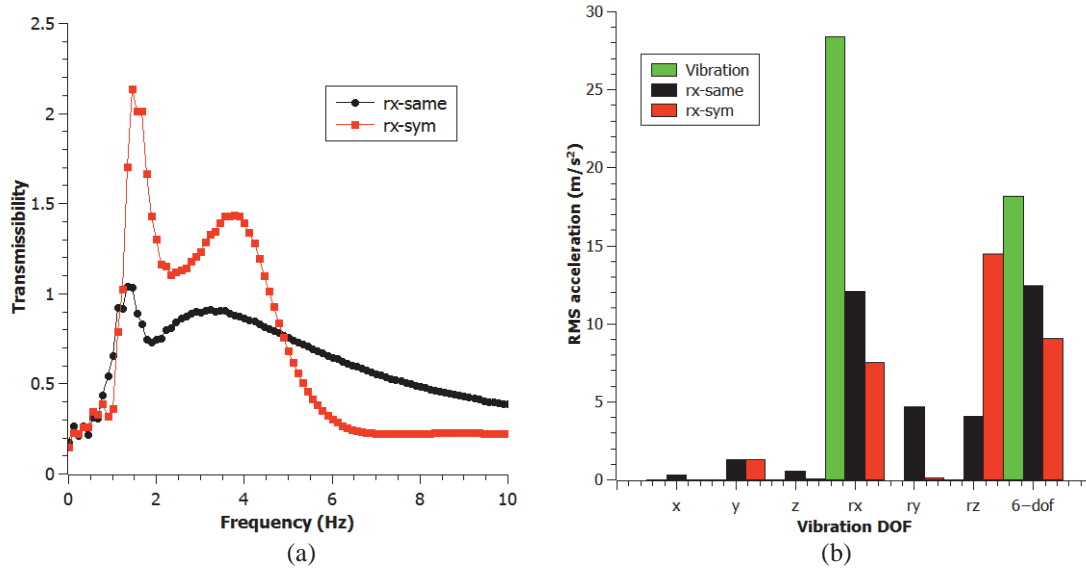


Figure 3: Vibration around x axis. (a)Transmissibility (b) RMS acceleration

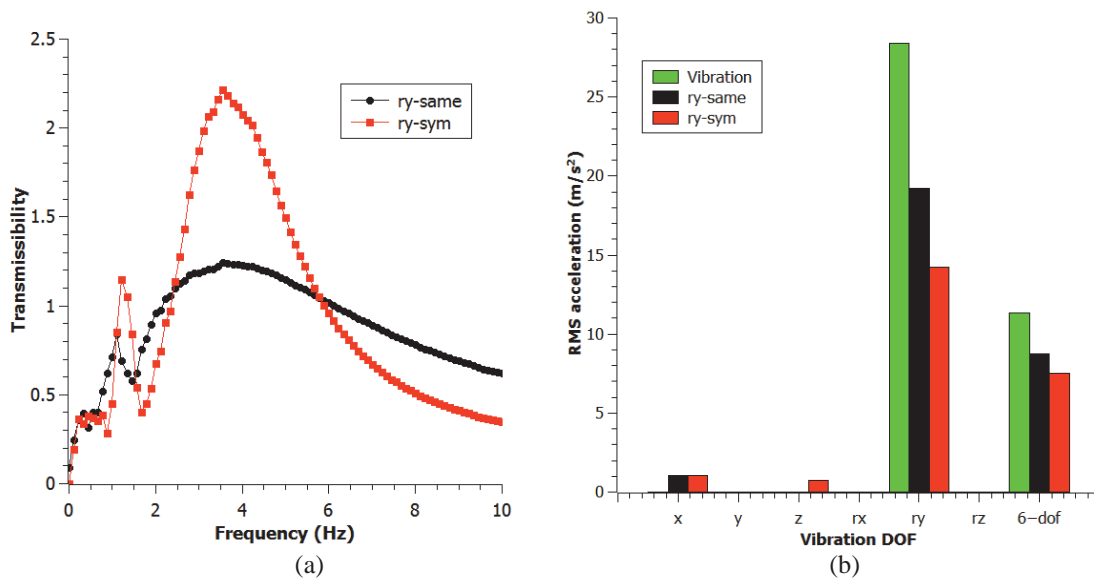


Figure 3: Vibration around y axis. (a)Transmissibility. (b) RMS acceleration

7. Conclusion

In this study, a 6-DOF heavy duty vehicle seat suspension is designed in PTC Creo, and modelled in SimMechanics. GA is applied to search the optimal stiffness and damping of suspension legs. The optimisation is implemented under two conditions which are taking the suspension symmetry into account and taking all the legs to have the same stiffness and damping. Swept sinusoidal vibration signals which including translational vibration along x and y axes, and rotational vibration around x and y axes, are carried out on base platform of the suspension respectively. Eight sets of optimisation results are compared and analysed. The condition considering symmetry can get smaller total value of RMS acceleration which means it can be more comfortable. But its transmissibility in vibration excitation DOF is always higher in resonance period. When taking multi-DOF vibration optimisation, the dominant vibration DOF will cause vibrations in other DOFs. Heavy duty vehicles always have special working environments in which the dominant vibration DOFs are different. Designing and optimising the multi-DOF heavy duty vehicle seat suspension should consider the dominant vibration DOF and other related DOFs vibration at the same time.

8. References

1. Paddan, G. and M. Griffin, *Effect of seating on exposures to whole-body vibration in vehicles*. Journal of Sound and Vibration, 2002. **253**(1): p. 215-241.

2. Du, H., W. Li, and N. Zhang, *Semi-active variable stiffness vibration control of vehicle seat suspension using an MR elastomer isolator*. *Smart materials and structures*, 2011. **20**(10): p. 105003.
3. Wu, J.-D. and R.-J. Chen, *Application of an active controller for reducing small-amplitude vertical vibration in a vehicle seat*. *Journal of Sound and Vibration*, 2004. **274**(3): p. 939-951.
4. Du, H., J. Lam, and K.Y. Sze, *Non-fragile output feedback H^∞ vehicle suspension control using genetic algorithm*. *Engineering Applications of Artificial Intelligence*, 2003. **16**(7): p. 667-680.
5. Bauml, A., J. McPhee, and P. Calamai, *Application of genetic algorithms to the design optimization of an active vehicle suspension system*. *Computer methods in applied mechanics and engineering*, 1998. **163**(1): p. 87-94.
6. International Organization for Standardization, *Mechanical vibration and shock—evaluation of human exposure to whole body vibration—part 1: general requirements*, ISO 2631-1:1997, 1997.

Likelihood of buckling mode interaction in shape optimisation of manufacturable cold-formed steel columns

Bin Wang¹, Benoit P. Gilbert¹, Hong Guan¹ and Lip H. Teh²

¹ Griffith University, QLD, Australia, b.wang@griffith.edu.au, b.gilbert@griffith.edu.au, h.guan@griffith.edu.au

² University of Wollongong, NSW, Australia, lteh@uow.edu.au

1. Abstract

This paper investigates the likelihood of buckling mode interaction in shape optimisation of manufacturable cold-formed steel columns. A literature review is carried out to examine local, distortional and global buckling mode interactions. Optimised columns available in the literature and the research outcomes previously carried out by the authors are discussed in some detail. The average elastic buckling stresses are reported herein and the need for incorporating the buckling mode interactions into shape optimisation algorithms is quantified.

2. Keywords: Shape optimisation; Cold-formed steel structures; Buckling mode interactions.

3. Introduction

Cold-formed steel (CFS) structures are widely used due to their advantages over hot-rolled steel, which include a high capacity to weight ratio, lightweight profiles, reduced installation time and manufacturing processes at room temperature [1]. The manufacturing processes, namely “roll-forming” and “brake-pressing”, allow the formation of any cross-sectional shape. Yet, CFS cross-sections used in practice are mainly limited to “Cee”, “Z” and “Σ” cross-sectional shapes, with or without intermediate stiffeners [2]. As the cross-sectional shape of the CFS profiles controls the fundamental buckling modes (local (L), distortional (D) (for open sections) and global (G)), discovering innovative and optimum cross-sectional shapes is a key element in saving material and enhancing the profitability of CFS members. The need is reinforced by the recent development of a new structural design method, the Direct Strength Method (DSM) [3], which allows designing any cross-sectional shape with the same degree of difficulty.

In the literature, shape optimisation of manufacturable CFS profiles has mainly been studied by Leng et. al. [4], Wang et. al. [5, 6] and Franco et. al. [7]. In these studies, different optimisation methods were used to achieve similar objectives. Nevertheless, the capacity of the optimised profiles was always calculated using the DSM as published in the North American [8] and Australian [9] design specifications. Therefore, only local-global (LG) buckling mode interaction was considered in the DSM equations [8, 9]. In all of the above studies, various column lengths and number of manufacturing folds per cross-section were investigated.

Results from the literature and the research performed by the authors show that, (i) the nominal member axial compressive capacity of short and intermediate columns is governed by local or distortional buckling [4], (ii) the nominal member axial compressive capacity of all columns is typically governed by global buckling [6] and (iii) the nominal distortional and global axial compressive capacities are close to each other [4, 6]. This indicates that global-distortional buckling mode interaction may occur. However, as the different buckling modes have different post-buckling reserves [10], similar level of local, distortional and global capacities does not necessarily involve interaction. The aim of this paper is to quantify if buckling mode interaction needs to be considered in the design equations in shape optimisation of CFS manufacturable columns.

In this paper, existing literature on local-distortional (LD), distortional-global (DG) and local-distortional-global (LDG) buckling mode interactions is reviewed. The corresponding DSM equations in compression are also reviewed. The average elastic buckling stresses of the optimised cross-sections available in the literature [4] and those of the authors' previous study [6] are summarised herein and the likelihood of the buckling mode interaction occurring in shape optimisation of manufacturable CFS columns is quantified.

4. Existing literature on buckling mode interaction

Buckling mode interaction was shown to significantly affect the post-buckling behaviour and ultimate strength of CFS members [11-13]. Yet, only LG buckling mode interaction is currently considered in design specifications [8, 9]. Numerical and experimental investigations, such as in [11-14], are currently performed to better understand LD, DG and LDG buckling mode interactions and new DSM buckling mode interaction equations are being developed.

However, as these new equations are usually conservative when no buckling mode interaction is considered, the domain of validity of these equations is currently unclear. A summary of the DSM equations can be found in [15] and in Sections 4.1 to 4.3.

CFS columns usually experience buckling mode interaction due to close values of elastic buckling stresses [15], i.e. $f_{ol} \approx f_{od}$ (for LD buckling mode interaction), $f_{od} \approx f_{oc}$ (for DG buckling mode interaction) and $f_{ol} \approx f_{od} \approx f_{oc}$ (for LDG buckling mode interaction), where f_{ol} , f_{od} and f_{oc} are the local, distortional and global elastic buckling stresses, respectively.

Silvestre et. al. [13, 16] numerically investigated the influence of LD buckling mode interaction on CFS lipped channels. The ratio between the distortional and local elastic buckling stresses (f_{od} / f_{ol}) was chosen between 0.9 and 1.1. The studies conclude that for columns that are not prone to distortional buckling (distortional slenderness ratio $\lambda_d \leq 1.5$) and the range of f_{od} / f_{ol} ratios considered, the LD interactive compressive strength is fairly accurately estimated by the DSM pure distortional nominal capacity in compression N_{cd} . For slender column against distortional buckling ($\lambda_d > 1.5$), the LD interactive compressive strength can be estimated by the modified DSM equations (Eqs. (3) and (4)) presented in Section 4.1. Young et. al. [14] and Kwon et. al. [17] experimentally tested CFS lipped channels that experienced LD buckling mode interaction despite large f_{od} / f_{ol} ratios, ranging between 1.1 and 2.7 in [14] and 1.4 and 3.2 in [17]. In these two studies, interaction was deemed to occur due to the high yield stress of the specimens that permits the development of elastic secondary bifurcation.

Dinis and Camotim [12] studied DG buckling mode interaction and the length of the columns was so selected that $f_{od} = f_{oc}$. To avoid LD buckling mode interaction, the columns were designed to have the distortional elastic buckling stress to be 20% lower than the local elastic buckling stress. This suggests that a ratio f_{od} / f_{ol} less than 0.8 is sufficient to prevent LD buckling mode interaction.

Dinis et. al. [11, 18] experimentally and numerically investigated LDG buckling mode interaction of CFS lipped channels and designed the profiles to ensure a strong interaction with the elastic buckling stresses, f_{ol} , f_{od} and f_{oc} , of no more than 3-4% apart.

4.1 DSM equations for LD buckling mode interaction

Schafer [10] estimated the nominal capacity of CFS columns against LD buckling mode interaction by replacing the nominal yield capacity N_y in the DSM equations for pure local buckling with the nominal distortional capacity N_{cd} . The nominal capacity in compression N_{cld} for LD buckling mode interaction is then given as,

$$\begin{cases} \text{For } \lambda_{ld} > 0.776: N_{cld} = \left[1 - 0.15 \left(\frac{N_{ol}}{N_{cd}} \right)^{0.4} \right] \left(\frac{N_{ol}}{N_{cd}} \right)^{0.4} N_{cd} \\ \text{For } \lambda_{ld} \leq 0.776: N_{cld} = N_{cd} \end{cases} \quad (1)$$

where N_{ol} is the elastic local buckling load and λ_{ld} is the LD non-dimensional slenderness ratio expressed as,

$$\lambda_{ld} = \sqrt{\frac{N_{cd}}{N_{ol}}} \quad (2)$$

Eq. (1) is referred to as an NLD approach. Yang and Hancock [19] adopted a similar method to Schafer [10] but replaced the nominal yield capacity N_y in the DSM equation for pure distortional buckling with the nominal local capacity N_{cl} . The nominal capacity in compression N_{cdl} for LD buckling mode interaction (referred to as the NDL approach) is then given as,

$$\begin{cases} \text{For } \lambda_{dl} > 0.561: N_{cdl} = \left[1 - 0.25 \left(\frac{N_{od}}{N_{cl}} \right)^{0.6} \right] \left(\frac{N_{od}}{N_{cl}} \right)^{0.6} N_{cl} \\ \text{For } \lambda_{dl} \leq 0.561: N_{cdl} = N_{cl} \end{cases} \quad (3)$$

where N_{od} is the elastic distortional buckling load and λ_{dl} is the distortional-local (DL) non-dimensional slenderness ratio expressed as,

$$\lambda_{dl} = \sqrt{\frac{N_{cl}}{N_{od}}} \quad (4)$$

4.2 DSM equation for DG buckling mode interaction

Silvestre et. al. [20] expressed the nominal capacity in compression N_{cde} for DG buckling mode interaction in a similar way to [19] and replaced the nominal local capacity N_{cl} in the DSM equation for pure distortional buckling with the nominal global capacity N_{ce} . N_{cde} is then expressed as,

$$\begin{cases} \text{For } \lambda_{de} > 0.561: N_{cde} = \left[1 - 0.25 \left(\frac{N_{od}}{N_{ce}} \right)^{0.6} \right] \left(\frac{N_{od}}{N_{ce}} \right)^{0.6} N_{ce} \\ \text{For } \lambda_{de} \leq 0.561: N_{cde} = N_{ce} \end{cases} \quad (5)$$

where λ_{de} is the DL non-dimensional slenderness ratio expressed as,

$$\lambda_{de} = \sqrt{\frac{N_{ce}}{N_{od}}} \quad (6)$$

4.3 DSM equation for LDG buckling mode interaction

Dinis et. al. [11] proposed a new DSM equation for LDG buckling mode interaction and assessed its accuracy. The nominal capacity N_{clde} in compression against LDG buckling mode interaction is given as,

$$\begin{cases} \text{For } \lambda_{lde} > 0.776: N_{clde} = \left[1 - 0.15 \left(\frac{N_{ol}}{N_{cde}} \right)^{0.4} \right] \left(\frac{N_{ol}}{N_{cde}} \right)^{0.4} N_{cde} \\ \text{For } \lambda_{lde} \leq 0.776: N_{clde} = N_{cde} \end{cases} \quad (7)$$

where N_{cde} is the nominal capacity for DG buckling mode interaction (Eq. (5)) and λ_{lde} is the LDG non-dimensional slenderness ratio expressed as,

$$\lambda_{lde} = \sqrt{\frac{N_{cde}}{N_{ol}}} \quad (8)$$

5. Results and discussion

Studies on shape optimisation of manufacturable CFS columns available in the literature [4] and that of the authors [6] are summarised in Table 1, which consists of a total of 22 studies cases. Note that the work presented in [7] is not considered herein as the elastic buckling stresses of the optimised sections are not reported. Note also that the study described in [4] includes both construction (for end-use purposes) and manufacturing constraints, and considers singly and point-symmetric cross-sections. The algorithm converges to ‘‘Cee’’ and ‘‘Σ’’ cross-sectional shapes for the 610 mm and 1,220 mm long columns, respectively, and to ‘‘Cee’’ and squashed ‘‘S’’ cross-sectional shapes for the 4,880 long columns. Although the algorithm presented in [6] considers singly-symmetric cross-sections only, it converges to closed or nearly closed ‘‘Cee’’ and ‘‘bean’’ cross-sectional shapes for all column lengths. Further the elastic buckling stresses in compression for the 4,880 mm long column in [4] are not presented and compared herein as they were not reported in [4].

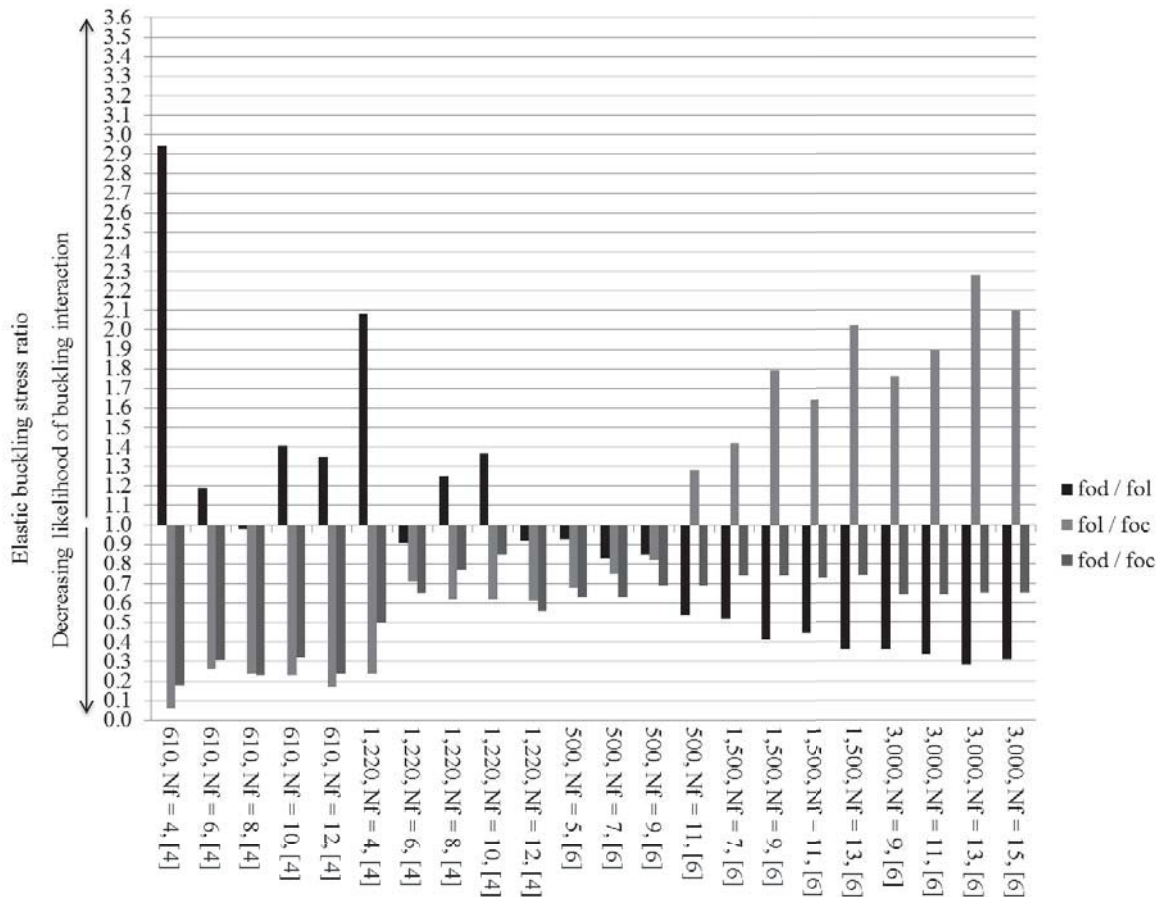
Fig. 1 plots the elastic buckling stress ratios f_{od}/f_{ol} , f_{ol}/f_{oc} and f_{od}/f_{oc} for the cases reported in Table 1. The 610 mm and 1,220 mm long columns in [4] and the 500 mm long columns in [6] usually show close local and distortional elastic buckling stresses, with f_{ol} and f_{od} within 20% of each other. LD buckling mode interaction is therefore likely to occur. However, for these columns, the distortional slenderness ratio is less than 1.5 and the DSM equation for pure distortional buckling is able to accurately predict the strength of the columns (see Section 4 and [9]). No DSM interaction equations therefore need to be considered for these columns. For the 1,500 mm and 3,000 mm long columns in [6], f_{ol} is in general at least twice greater than f_{od} and no LD buckling mode interactions is likely to occur.

In Fig. 1, the global elastic buckling stress is always greater than the distortional counterpart. For 5 out of 22 studied cases, the ratio f_{od} / f_{oc} is less than 0.5. Therefore DG buckling mode interaction is unlikely to occur for these cases. For the remaining cases, the f_{od} / f_{oc} ratio closer to unity (1.0) is 0.85 and the average f_{od} / f_{oc} ratio equals 0.68. Therefore, no close proximity of the global and distortional elastic buckling stresses exists for the remaining cases and the likelihood of DG buckling mode interaction is low.

Additionally, the elastic local, distortional and global buckling stresses are never close to each other, i.e. all within 15 % of each other, and LDG buckling mode interaction is therefore unlikely to be encountered.

Table 1: Summary of available studies in the literature

Study	Yield stress f_y (MPa)	Objective of algorithm	Number of folds N_f	Column length (mm)		
Leng et. al. [4]	228	Maximise the column capacity for a 279.4 mm wide and 1 mm thick steel sheet	4, 6, 8, 10 and 12	610	1220	4880
Wang et. al. [6]	450	Minimise the cross-section area of a 1.2 mm thick columns subjected to axial compressive load of 75 kN	5, 7, 9, 11, 13 and 15	500	1500	3000



Studied cases: Column length (mm), Number of folds N_f and Literature reference number

Fig. 1 Elastic buckling stress ratios for optimised columns reported in [4, 6]

7. Conclusions

The authors have investigated the likelihood of buckling mode interaction in shape-optimised manufacturable CFS columns. The literature on buckling mode interactions and the DSM equations proposed by various researchers to determine the nominal capacity of a column experiencing LD, DG and LDG buckling mode interaction were reviewed. Although, the nominal global and distortional capacities are close to each other, this paper shows that strong buckling mode interactions are unlikely to be encountered in the studied cases. As such, buckling mode interactions still need to be further assessed in future studies on shape-optimisation of CFS members.

8. References

- [1] Hancock GJ, *Design of cold-formed steel structures (to AS/NZ 4600:2007) - 4th Edition*, (Australian Steel Institute), North Sydney, Australia, 2007.
- [2] Gilbert BP, Teh LH, Guan H "Self-shape optimisation principles: Optimisation of section capacity for thin-walled profiles", *Thin-Walled Structures*, 60, 194-204, 2012a.
- [3] Schafer BW "Review: the direct strength method of cold-formed steel member design", *Journal of Constructional Steel Research*, 64, 766-778, 2008.
- [4] Leng J, Li Z, Guest JK, Schafer BW "Shape optimization of cold-formed steel columns with fabrication and geometric end-use constraints", *Thin-Walled Structures*, 85, 271-290, 2014.
- [5] Wang B, Gilbert BP, Molinier AM, Guan H, Teh LH, "Shape optimisation of manufacturable cold-formed steel columns for all buckling modes - Part I: Hough transform", *Proceedings of the Eight International Conference on Advances in Steel Structures*, Lisbon, Portugal, 2015a.
- [6] Wang B, Gilbert BP, Guan H, Teh LH, "Shape optimisation of manufacturable cold-formed steel columns for all buckling modes - Part II: Improved method", *Proceedings of the Eight International Conference on Advances in Steel Structures*, Lisbon, Portugal, 2015b.
- [7] Franco JMS, Duarte JP, Batista EdM, Landesmann A "Shape Grammar of steel cold-formed sections based on manufacturing rules", *Thin-Walled Structures*, 79, 218-232, 2014.
- [8] North American Specification for the Design of Cold-formed Steel Structural Members (AISI-S100-12), American Iron and Steel Institute (AISI), Washington DC, 2012.
- [9] AS/NZS 4600, Cold-formed steel structures, Standards Australia, Sydney, 2005.
- [10] Schafer B "Local, distortional, and Euler buckling of thin-walled columns", *Journal of Structural Engineering*, 128, 289-299, 2002.
- [11] Dinis PB, Batista EM, Camotim D, dos Santos ES "Local-distortional-global interaction in lipped channel columns: Experimental results, numerical simulations and design considerations", *Thin-Walled Structures*, 61, 2-13, 2012.
- [12] Dinis PB, Camotim D "Post-buckling behaviour and strength of cold-formed steel lipped channel columns experiencing distortional/global interaction", *Computers & structures*, 89, 422-434, 2011.
- [13] Silvestre N, Camotim D, Dinis PB "Post-buckling behaviour and direct strength design of lipped channel columns experiencing local/distortional interaction", *Journal of Constructional Steel Research*, 73, 12-30, 2012.
- [14] Young B, Silvestre N, Camotim D "Cold-formed steel lipped channel columns influenced by local-distortional interaction: strength and DSM design", *Journal of Structural Engineering*, 139, 1059-1074, 2013.
- [15] Souza dos Santos E, de Miranda Batista E, Camotim D "Cold-formed steel columns under L-D-G interaction", *Steel Construction*, 7, 193-198, 2014.
- [16] Silvestre N, Camotim D, Dinis P "Direct strength prediction of lipped channel columns experiencing local-plate/distortional interaction", *Advanced Steel Construction*, 5, 45-67, 2009.
- [17] Kwon YB, Kim BS, Hancock GJ "Compression tests of high strength cold-formed steel channels with buckling interaction", *Journal of Constructional Steel Research*, 65, 278-289, 2009.
- [18] Dinis PB, Camotim D, Batista EM, Santos E "Local/distortional/global mode coupling in fixed lipped channel columns: behaviour and strength", *International Journal of Advanced Steel Construction*, 7, 2011, 113-130, 2011.
- [19] Yang D, Hancock GJ "Compression tests of high strength steel channel columns with interaction between local and distortional buckling", *Journal of Structural Engineering*, 130, 1954-1963, 2004.
- [20] Silvestre N, Dinis PB, Camotim D, Batista EM "DSM design of lipped channel columns undergoing local/distortional/global mode interaction", *Proceedings of the stability and ductility of steel structures*, 2010.

On the numerical optimization of multi-load spatial Michell trusses using a new adaptive ground structure approach

Tomasz Sokół¹ and George I. N. Rozvany²

¹ Warsaw University of Technology, FCE, Poland, t.sokol@il.pw.edu.pl

² Budapest University of Technology and Economics, DSM, Hungary, .rozvany@t-online.hu

1. Abstract

In this paper a new method of solving large-scale linear programming problems related to Michell trusses, generalized to multiple load conditions and three-dimensional domains, is proposed. The method can be regarded as an extension of the adaptive ground structure methods developed recently by the first author. In the present version both bars and nodes can be switched between active and inactive states in subsequent iterations allowing significant reduction of the problem size. Thus, the numerical results can be attained for denser ground structures giving better approximation of exact solutions to be found. The examples of such exact solutions (new 3D Michell structures), motivated by the layouts predicted numerically, are also presented and can serve as benchmark tests for future methods of numerical optimization of structural topology in 3D space.

2. Keywords: 3D Michell structures, multiple load cases, adaptive ground structure method, linear programming, active set and interior point methods, new exact solutions for structural topology optimization.

3. Introduction

In spite of some inherent limitations (e.g. neglecting stability requirements for compression bars), the classical theory of Michell structures plays an important role in structural topology optimization, by enabling the derivation of exact analytical solutions for the least-weight trusses capable of transmitting the applied loads to the given supports within limits on stresses in tension and compression. Thus the exact solutions derived by means of this theory may serve as valuable benchmarks for any structural topology optimization method.

In general, the exact solutions are very hard to obtain since they require in advance a good prediction of the optimal layouts. Fortunately, this difficult task of predicting the optimal layout can effectively be carried out numerically using the adaptive *ground structure* method developed recently by the first author. In this method the solution is achieved iteratively using a small number of properly chosen active bars from the huge set of possible connections. The problem of enormous number of potential bars becomes particularly hard for space trusses subjected to multiple load conditions because the optimization problem grows very rapidly and becomes too large even for supercomputers.

In this paper a new and more advanced solution method for large-scale optimization problems is proposed. It is based on adaptive activating of new bars in the ground structure and eliminating large number of unnecessary bars. Moreover, in this new method the nodes can also be switched between active and inactive states. This is particularly important for 3D problems because the optimal 3D trusses tend to assume forms of lattice surfaces (shell-like structures) while most of design space becomes empty. As a result, the size of the problem can be significantly reduced. The method makes it possible to obtain new numerical solutions for deriving new optimal topologies for 3D Michell structures. A class of new 3D exact solution inspired by numerical results is also presented. The method proposed in the present paper is a natural extension of the adaptive ground structure methods developed by Gilbert and Tyas [1], Pritchard et al. [3] and Sokół [5-7].

Concluding, the aim of this paper is two-fold: a) to develop a reliable and efficient optimization method based on the adaptive ground structure approach, and b) to obtain substantially new exact solutions of spatial Michell trusses subjected to multiple load cases.

4. Primal and dual forms of the optimization problems of multi-load plastic design

Any optimization problem can be written in different forms which are mathematically equivalent but can lead to significantly different calculation times using the given optimization method (see [7]). In other words, the formulation of the optimization problem should be matched to the method applied.

According to well-known duality principles, the plastic design optimization problem can be written in either primal or in dual form. Both of them play an important role in the proposed method and should be considered together.

The most concise formulation of plastic design optimization problem for multi-load cases can be written as follows:

$$\begin{aligned}
& \min_{\mathbf{A}, \mathbf{S}_{(l)} \in \mathbf{R}^M} V = \mathbf{L}^T \mathbf{A} \\
& \text{s.t.} \quad \mathbf{B}^T \mathbf{S}_{(l)} = \mathbf{P}_{(l)} \quad \text{for all load cases} \\
& \quad \quad -\mathbf{A} \sigma_C \leq \mathbf{S}_{(l)} \leq \mathbf{A} \sigma_T \quad l = 1, 2, \dots, K
\end{aligned} \tag{1}$$

where V is the total volume of the structural material in the truss of M potential bars; \mathbf{L} is the vector of lengths of bars; \mathbf{B} is the geometric matrix; vectors $\mathbf{P}_{(l)}$ define nodal forces for the given load cases $l = 1, 2, \dots, K$, where K is the number of load cases; $\mathbf{S}_{(l)}$ is the vector of member forces for load case l ; \mathbf{A} is the vector of cross-section areas (the main design variables); σ_T and σ_C denote the permissible stresses in tension and compression, respectively. The primal form (1) is not convenient for direct application of *simplex* or *interior point method* and it is recommended to convert it to a more applicable form (see [7] for details). The inequalities (1)₃ can be converted to equality constraints using properly adjusted slack variables $\mathbf{c}_{(l)}$ and $\mathbf{t}_{(l)}$,

$$\begin{aligned}
\sigma_T \mathbf{A} - \mathbf{S}_{(l)} - \frac{\sigma_T + \sigma_C}{\sigma_C} \mathbf{c}_{(l)} &= \mathbf{0}, \quad \mathbf{c}_{(l)} \geq \mathbf{0} \\
\sigma_C \mathbf{A} + \mathbf{S}_{(l)} - \frac{\sigma_T + \sigma_C}{\sigma_T} \mathbf{t}_{(l)} &= \mathbf{0}, \quad \mathbf{t}_{(l)} \geq \mathbf{0}
\end{aligned} \tag{2}$$

which then allow elimination of original design variables \mathbf{A} and $\mathbf{S}_{(l)}$

$$\mathbf{A} = \frac{\mathbf{t}_{(l)}}{\sigma_T} + \frac{\mathbf{c}_{(l)}}{\sigma_C} \quad \text{and} \quad \mathbf{S}_{(l)} = \mathbf{t}_{(l)} - \mathbf{c}_{(l)} \tag{3}$$

Note that $\mathbf{c}_{(l)}$ and $\mathbf{t}_{(l)}$ are the vectors of slack variables which can be interpreted as the additional forces which can be added without violating the restrictions of permissible stresses (1)₃ (i.e. they denote not forces itself but unused reserves of internal forces).

Using (3) the original problem (1) can be converted to the standard linear programming problem with the following primal form:

$$\begin{aligned}
& \min_{\mathbf{t}_{(l)}, \mathbf{c}_{(l)} \in \mathbf{R}^M} V = \sum_l \mathbf{L}^T \left(\frac{\mathbf{t}_{(l)}}{\sigma_T} + \frac{\mathbf{c}_{(l)}}{\sigma_C} \right) \\
& \text{s.t.} \quad \mathbf{B}^T (\mathbf{t}_{(l)} - \mathbf{c}_{(l)}) = \mathbf{P}_{(l)} \quad \text{for } l = 1 : K \\
& \quad \quad \frac{\mathbf{t}_{(l+1)}}{\sigma_T} + \frac{\mathbf{c}_{(l+1)}}{\sigma_C} = \frac{\mathbf{t}_{(l)}}{\sigma_T} + \frac{\mathbf{c}_{(l)}}{\sigma_C} \quad \text{for } l = 1 : K - 1 \\
& \quad \quad \mathbf{t}_{(l)} \geq \mathbf{0}, \mathbf{c}_{(l)} \geq \mathbf{0} \quad \text{for } l = 1 : K
\end{aligned} \tag{4}$$

The problem (4) looks for the first time as much more complicated than problem (1), but contrary to (1), all the design variables are non-negative and all constraints are equalities, so after comparison of the standard form of (1) with (4), one can easily deduce that the size of the problem is reduced more than twice. Note that the form (4) is new in the literature and more economical than the formulations proposed in [3] or [7]. Moreover, for $K = 1$ it automatically reduces to a well-known form used for one-load case problem (see [1] or [5]) thus no additional separate code is needed for this special case.

Note that (4) is written directly in the standard linear programming formulation

$$\begin{aligned}
& \min_{\mathbf{x}} \quad \mathbf{c}^T \mathbf{x} \\
& \text{s.t.} \quad \mathbf{H} \mathbf{x} = \mathbf{b} \\
& \quad \quad \mathbf{x} \geq \mathbf{0}
\end{aligned} \tag{5}$$

but the order of the design variables $\mathbf{t}_{(l)}$ and $\mathbf{c}_{(l)}$ is very important because it influences the bandwidth of the coefficient matrix \mathbf{H} and consequently the computational time. The best choice is grouping the variables by subsequent load cases:

$$\mathbf{x}_{2KM} = \{\mathbf{t}_{(1)}, \mathbf{c}_{(1)}, \mathbf{t}_{(2)}, \mathbf{c}_{(2)}, \dots, \mathbf{t}_{(K)}, \mathbf{c}_{(K)}\} \tag{6}$$

so the appropriate cost vector \mathbf{c} and right hand side vector \mathbf{b} can be defined as

$$\begin{aligned}
\mathbf{c}_{2KM} &= \{\mathbf{L} / \sigma_T, \mathbf{L} / \sigma_C, \mathbf{0}, \dots, \mathbf{0}\} \\
\mathbf{b}_{KN+(K-1)M} &= \{\mathbf{P}_{(1)}, \mathbf{0}, \mathbf{P}_{(2)}, \mathbf{0}, \dots, \mathbf{P}_{(K)}\}
\end{aligned} \tag{7}$$

The coefficient matrix of problem (23) under ordering (25) has a possibly small bandwidth (almost block-diagonal) and as before (c.f. (7)) is regular, repetitive, very sparse; and can be written as

$$\mathbf{H}_{(KN+(K-1)M) \times 2KM} = \begin{bmatrix} \mathbf{F} & \mathbf{0} & \mathbf{0} & & \mathbf{0} \\ \mathbf{G} & -\mathbf{G} & \mathbf{0} & & \mathbf{0} \\ \mathbf{0} & \mathbf{F} & \mathbf{0} & \dots & \mathbf{0} \\ \mathbf{0} & \mathbf{G} & -\mathbf{G} & & \mathbf{0} \\ \mathbf{0} & \mathbf{0} & \mathbf{F} & & \mathbf{0} \\ & \vdots & \ddots & \ddots & \vdots \\ & \vdots & & \ddots & \vdots \\ \mathbf{0} & \mathbf{0} & \mathbf{0} & \mathbf{G} & -\mathbf{G} \\ \mathbf{0} & \mathbf{0} & \mathbf{0} & \mathbf{0} & \mathbf{F} \end{bmatrix} \quad (8)$$

where sub-matrices \mathbf{F} and \mathbf{G} are defined as follows

$$\mathbf{F}_{N \times 2M} = [\mathbf{B}^T \quad -\mathbf{B}^T] \quad \text{and} \quad \mathbf{G}_{M \times 2M} = [\mathbf{I}/\sigma_T \quad \mathbf{I}/\sigma_C] \quad (9)$$

The evident advantage of the formulation (4) can be recognized after comparing the sizes of coefficient matrices \mathbf{H} in (1) and (4) and one can easily check that the size (both number of rows and columns) of matrix \mathbf{H} in (4) is more than two times smaller. Moreover, the new matrix \mathbf{H} is more efficient for computation due to its almost block-diagonal form, and for rather special case with only one load condition $\mathbf{H} = \mathbf{F}$ which means that it is as efficient as casual formulation for one-load case problem (c.f. Sokół [5]).

For activating new bars in the adaptive ground structure method we need also dual variables but using the *primal-dual version of the interior point method* they are calculated automatically and for free. The convenient for next treatment dual form of multi-load case problem was derived in [7] and is given by

$$\begin{aligned} \max_{\mathbf{u}_{(l)} \in \mathbf{R}^N, \mathbf{e}_{(l)}^+, \mathbf{e}_{(l)}^- \in \mathbf{R}^M} W &= \sum_l \mathbf{P}_{(l)}^T \mathbf{u}_{(l)} \\ \text{s.t.} \quad \sum_l (\sigma_T \mathbf{e}_{(l)}^+ + \sigma_C \mathbf{e}_{(l)}^-) &\leq \mathbf{L} \\ \mathbf{B} \mathbf{u}_{(l)} - \mathbf{e}_{(l)}^+ &\leq \mathbf{0} \\ -\mathbf{B} \mathbf{u}_{(l)} - \mathbf{e}_{(l)}^- &\leq \mathbf{0} \\ \mathbf{e}_{(l)}^+ \geq \mathbf{0}, \quad \mathbf{e}_{(l)}^- &\geq \mathbf{0} \\ \text{for } l &= 1, 2, \dots, K \end{aligned} \quad (10)$$

where \mathbf{u} , \mathbf{e}^+ , \mathbf{e}^- are Lagrange multipliers, called *adjoint nodal displacements* and *adjoint member elongations* for tension and compression, respectively. They are independent variables for every load condition (l) but constrained together by (10)₂ which enables deriving the generalized optimality criteria for multi-load trusses. These criteria can be formulated as follows (see [7] for details).

Theorem

In the stress-based multi-load truss optimization problem the optimal solution has to satisfy the following conditions:

1) for every bar of the truss the "total adjoint multi-load strain $\hat{\varepsilon}_i$ " is restricted by 1

$$\forall i = 1, 2, \dots, M \quad \hat{\varepsilon}_i \leq 1 \quad (11)$$

where

$$\hat{\varepsilon}_i = \sum_l (\sigma_T \varepsilon_{(l),i}^+ + \sigma_C \varepsilon_{(l),i}^-) \quad (12)$$

$$\varepsilon_{(l),i}^+ = \max(\varepsilon_{(l),i}, 0) \quad (13)$$

$$\varepsilon_{(l),i}^- = \max(-\varepsilon_{(l),i}, 0)$$

$$\varepsilon_{(l),i} = \mathbf{B}_i \mathbf{u}_{(l)} / L_i \quad (14)$$

2) moreover, the non-zero cross-section area A_i is needed only for ‘fully strained’ bar:

$$\begin{aligned} \text{if } A_i > 0 \text{ then } \hat{\varepsilon}_i &= 1 \\ \text{if } \hat{\varepsilon}_i < 1 \text{ then } A_i &= 0 \end{aligned} \quad (15)$$

The term “fully strained” corresponds to the total and normalized adjoint strain defined in (12) but from the other point of view every bar in the truss is also fully stressed for some load case but not necessarily for other ones. It is a subtle and different situation from one-load case problem for which all bars are fully stressed together. Here, for multi-load case, some bars can be fully stressed only for chosen load conditions and can even be inactive for other ones.

The conditions (11,12) define the domain of feasible adjoint strain fields and can be utilized in the adaptive ground structure method discussed in the next section. They are used to filter the set of new active bars and also as a stop criterion.

5. The adaptive ground structure method with selective subsets of active bars and nodes

Due to limited space of the paper we can describe the new method only briefly. The main idea of activating new bars is the same as before [7] but now after each iteration the nodes are split into two subsets: active and inactive nodes. Then, in the subsequent iteration the adjoint displacements are updated only for active nodes. Inactive nodes appear in empty regions where no material is needed. Thus before starting the next iteration all bars connected with inactive nodes can also be eliminated (temporary for the current iteration). Consequently, the size of the coefficient matrix of the problem (3) is much smaller in terms of the number of rows and columns. It should be noted that inactive nodes are not removed forever from the ground structure and can be activated if necessary. Moreover, the adjoint displacements of these nodes have to be preserved for subsequent iterations for checking the optimality criteria. Of course this complicates the code but is necessary and crucial to assure convergence to a globally optimal solution. The step by step procedure for the proposed method can be described as follows:

First iteration:

1. Set $iter = 1$, $d = 1$ and generate the initial ground structure $N_x \times N_y \times N_z: 1 \times 1 \times 1$ with bars connecting only the neighbouring nodes. Contrary to the previous versions these bars can also be deactivated in subsequent iterations.
2. Solve the problem (4) for this initial ground structure and get the dual variables $\mathbf{u}_{(l)}^{(1)}$.

Next iterations:

3. Increment the number of iteration $++iter$.
4. Increment the distance of connections $d := \max(d_{max}, d+1)$, together with d_x, d_y, d_z .
5. Select the new set of active bars in the ground structure $N_x \times N_y \times N_z: d_x \times d_y \times d_z$:
 - for every bar compute normalized strain using the displacement fields from the previous iteration:

$$\mathbf{u}_{(l)}^{(iter-1)} \Rightarrow \hat{\varepsilon}_i = \sum_l (\sigma_T \varepsilon_{(l),i}^+ + \sigma_C \varepsilon_{(l),i}^-) \quad (\text{see (12)-(13)}),$$
 - if $\hat{\varepsilon}_i \geq 1 - tol$, then activate (add) i -th bar,
 - otherwise, if $\hat{\varepsilon}_i < 0.3$ and $d < d_{max}$ then deactivate (remove) bar,
 - if $d < d_{max}$ and the number of added bars is too small then go to step 4.
6. Check the stopping criterion:
 - if $d = d_{max}$ and there are no new bars added then finish (we approach the optimum solution because for all potential bars $i = 1:M$ the constraints $(10)_2$ are satisfied and the solution cannot be further improved)
7. Calculate the volumes of material connected to nodes; if the volume of a chosen node is equal or close to zero and, moreover, no any new bar is added to this node, then deactivate it together with all connecting bars; then remove the appropriate degrees of freedom from the system but keep adjoint displacements of inactive nodes ‘frozen’ for the next iteration.
8. Solve primal problem (4) for reduced system of active bars and nodes and get dual variables $\mathbf{u}_{(l)}^{(iter)}$ (combine the updated adjoint displacements of active nodes with frozen displacements of inactive nodes).
9. Repeat from step 3.

The program implementing the above algorithm has been written in Mathematica using parallel computing.

6. Examples of two-load case problems with spatial Michell trusses

In both examples presented in this section we assume: a) equal permissible stresses in tension and compression $\sigma_T = \sigma_C = \sigma_0$, b) and equal magnitudes of applied point forces $\|\mathbf{P}_{(1)}\| = \|\mathbf{P}_{(2)}\| = P$.

As the first example, consider the two-load case problem presented in Fig. 1 in which the two independent point loads are applied in the centre of the upper square of the bounding cuboidal domain $d/\sqrt{2} \times d/\sqrt{2} \times 3d$ and

directed along x and y axes, while the continuous full support is applied on the whole bottom square. In Fig. 1a we present the exact optimal solution obtained using the superposition principles and the concept of component loads [4]. The optimal structure is composed of two orthogonal long cantilevers lying in diagonal planes. The exact volume of the structure can be calculated using the formulae derived by Lewiński et al. [2]. The numerical confirmation of this analytical prediction is presented in Fig. 1b and was performed for the ground structure with $20 \times 20 \times 60$ cells, 26901 nodes and more than 300mln potential bars. The solution was obtained in less than 2 hours using classical computer with Intel i7 processor which clearly indicates a good efficiency of the proposed method. Note that ‘numerical’ volume is only 0.3% worse than the exact analytical solution.

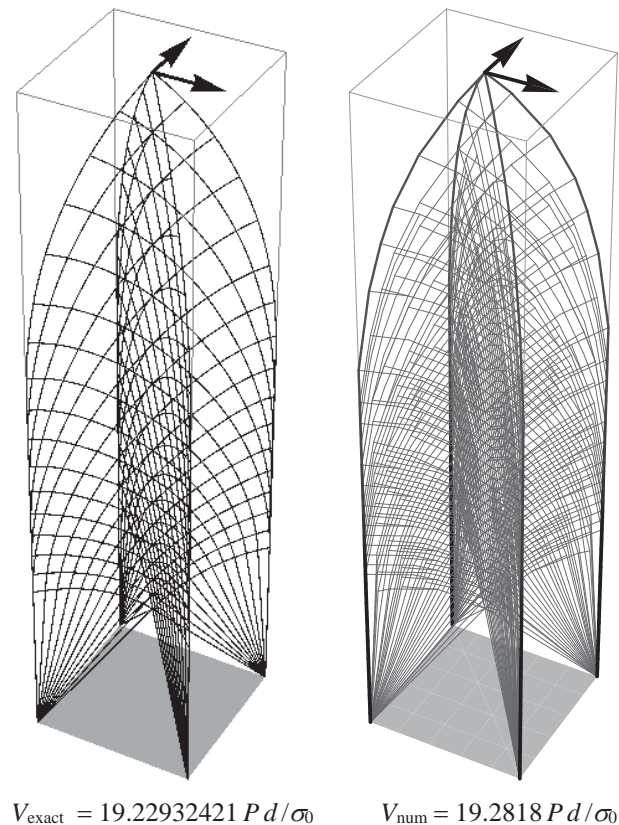


Figure 1: Example of a 3D Michell structure for two loading conditions:
a) an exact analytical prediction using the concept of component loads,
b) numerical confirmation using the ground structure with 300mln potential bars

The second example is presented in Fig. 2 and is a subtle modification of the previous problem. Now the independent point loads are directed along the diagonals of the upper square of the bounding cuboidal domain $d \times d \times 3d$. Moreover, these loads have to be optimally transmitted to four fixed supports in the corners of bottom square. The exact analytical solution of this modified problem is harder to predict even using the concept of component loads. Hence in this example we firstly discovered the optimal layout numerically using the same density of the ground structure as before (i.e. more than 300mln bars). The numerical result presented in Fig. 2a suggests that the exact solution consists of four plane long cantilevers forming a specific hip roof (it is not clearly visible just from Fig. 2a but is evident after rotating this structure in 3D space). Then, employing the layout predicted numerically, the new exact analytical solution was obtained and presented in Fig. 2b. As before, the exact volume of this complex structure can be calculated using the formulae derived in [2], and is about 0.3% better than the volume obtained numerically. At the end, both numerical and analytical solutions of Fig. 2ab were also verified by using the superposition of two trusses corresponding to appropriate component loads, see Fig. 3c.

7. Concluding Remarks

Note that the optimal solutions presented in Figs 1 and 2 form shell-like structures composed of lattice surfaces with Michell trusses inside. Hence most of design space is empty and it was the main motivation for developing a new improved method in which both bars and nodes can be eliminated if unnecessary. As before, despite the iterative nature of the method the convergence to a global optimum as guaranteed.

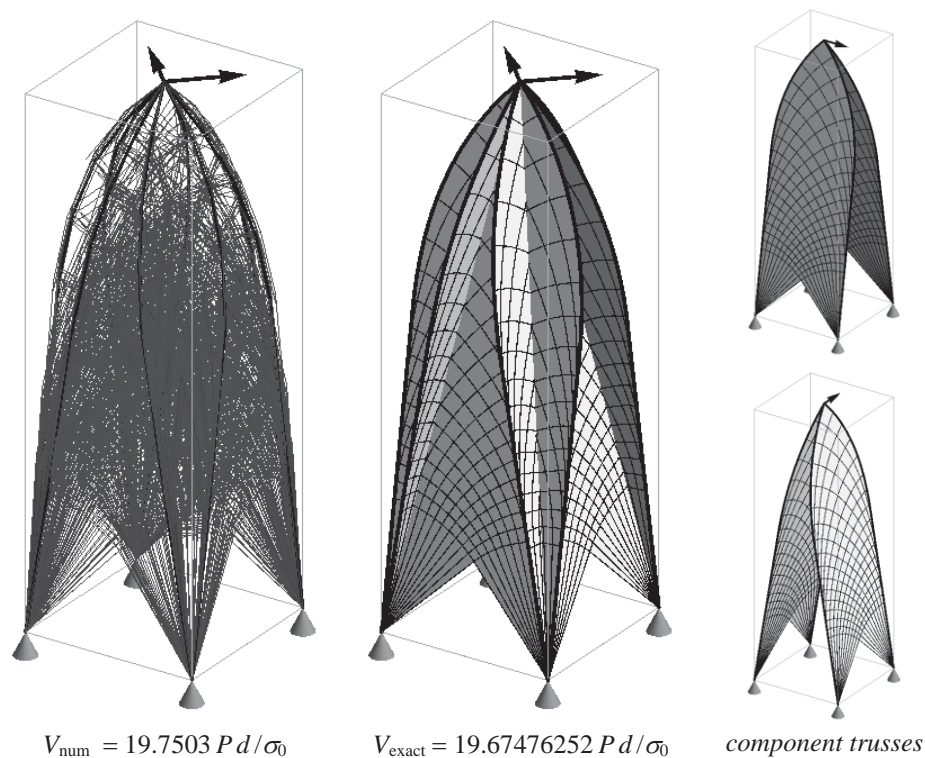


Figure 2: Example of 3D Michell truss for two independent load cases: a) numerical recognition of the optimal layout; b) exact analytical solution; c) optimal trusses for two component loads

8. Acknowledgements

The paper was prepared within the Research Grant no 2013/11/B/ST8/04436 financed by the National Science Centre, entitled: *Topology optimization of engineering structures. An approach synthesizing the methods of: free material design, composite design and Michell-like trusses.*

9. References

- [1] Gilbert M. and Tyas A., Layout optimization of large-scale pin-jointed frames, *Eng. Comput.*, 20, pp. 1044-1064, 2003.
- [2] Lewiński T., Zhou M. and Rozvany G.I.N., Extended exact solutions for least-weight truss layouts—part I: cantilever with a horizontal axis of symmetry, *Int. J. Mech. Sci.*, 36, pp. 375–398, 1994.
- [3] Pritchard T.J., Gilbert M. and Tyas A., Plastic layout optimization of large-scale frameworks subject to multiple load cases, member self-weight and with joint length penalties, *WCSMO-6*, Rio de Janeiro, Brazil, 30May–03June, 2005.
- [4] Rozvany G.I.N. and Hill R.H., Optimal plastic design: superposition principles and bounds on the minimum cost. *Comp. Meth. Appl. Mech. Eng.*, 13, pp. 151-173, 1978.
- [5] Sokół T., A 99 line code for discretized Michell truss optimization written in Mathematica. *Struct. Multidisc. Optim.*, 43, pp. 181-190, 2011.
- [6] Sokół T., Numerical approximations of exact Michell solutions using the adaptive ground structure approach, in S. Jemioło and M.Lutomirska, *Mechanics and materials*, Ch.6, pp. 87-98, Warsaw University of Technology, 2013.
- [7] Sokół T., Multi-load truss topology optimization using the adaptive ground structure approach, in T. Łodygowski, J. Rakowski, P. Litewka, *Recent Advances in Computational Mechanics*, Ch. 2, pp. 9-16, CRC Press, London, 2014.

Topology Optimization of Members of Dynamically Loaded Flexible Multibody Systems using Integral Type Objective Functions and Exact Gradients

Alexander Held¹, Sven Knüfer², Robert Seifried¹

¹ Hamburg University of Technology, Germany, {alexander.held,robert.seifried}@tuhh.de

² University of Stuttgart, Germany, knuefer@gmx.de

1. Abstract

In this work a procedure is presented to perform topology optimization of components of flexible multibody systems, which are modeled with the floating frame of reference formulation. For the topology optimization, the solid isotropic material with penalization (SIMP) method is used. In order to capture the actual loads on the flexible components in the optimization, integral type objective functions are employed and exact gradients are provided. The latter are computed by the adjoint variable method to handle the large number of design variables.

2. Keywords: Topology Optimization, Flexible Multibody Systems, Integral Type Objective Function, Sensitivity Analysis, Adjoint Variable Method

3. Introduction

For topology optimization of components of dynamically loaded flexible multibody systems the equivalent static load method is often employed, see [5, 7]. Thereby, the actual loads on the flexible components are first imitated by a finite set of equivalent static loads. These loads are derived from the results of a dynamic multibody system simulation and are assumed to be static and design independent. Then a static response optimization is carried out with regard to the equivalent static loads. Finally, the next optimization loop is started performing another multibody system simulation using the optimized design. By this procedure the computation of the objective function and its gradient is significantly eased. However, the gradient is only an approximation of the actual dynamic problem.

Depending on the origin of the loads, e.g. whether they are caused by external forces or due to the inertia of their self-weight, the simplifications made in the equivalent static load method can lead to severe differences in the gradients. These might cause the optimization algorithm to search in the wrong direction and converge to undesired solutions. Therefore, a topology optimization procedure is presented, which relies on integral type objective functions and exact gradients, which are computed using the adjoint variable method, see [3]. In this way the actual dynamical loads can be captured in the objective function and the gradient.

The paper is organized in the following way. Section 4 addresses the topology optimization of flexible multibody system. Some basics of the floating frame of reference formulation and the SIMP method are given and the optimization procedure is described. In Section 5 the gradient computation of functional type objective functions using the adjoint variable method is explained. Then, in Section 6 the procedure is tested performing a topology optimization of a piston rod of a flexible slider-crank mechanism, which is only loaded by its own inertia forces. Finally, Section 7 concludes with a brief summary and discussion.

4. Topology Optimization of Flexible Multibody Systems

The method of flexible multibody systems is a well established approach to model and analyze compliant mechanisms, which perform large rigid body motions. These systems are assembled from rigid and flexible bodies, spring and damper elements, and actuators, which are connected via joints and bearings, see Fig. 1(a). If the deformations are comparatively small the floating frame of reference formulation can be used to efficiently incorporate flexible bodies into the multibody system. In the following the basic ideas of the floating frame of reference formulation are briefly reviewed, for a detailed description see [10, 11]. In addition, the SIMP approach and the optimization procedure are described, which are used to perform topology optimization of components of flexible multibody systems.

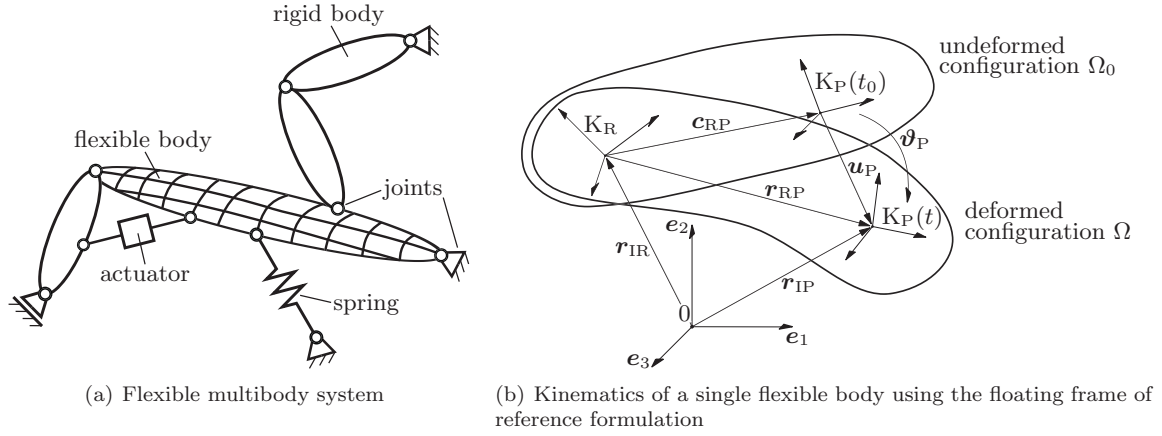


Figure 1: Flexible multibody systems modeled with the floating frame of reference formulation

4.1 The Floating Frame of Reference Formulation

In the floating frame of reference formulation the flexible body motion is defined using two sets of coordinates, see Fig. 1(b). One set gives the position and orientation of a body-related reference frame K_R and describes the large nonlinear motion. The second set describes the deformation of the body with respect to K_R using a Ritz approach. That is, the displacement \mathbf{u}_P at the point P and the rotation ϑ_P of the coordinate system K_P fixed in P are approximated by

$$\mathbf{u}_P(\mathbf{c}_{RP}, t) = \Phi(\mathbf{c}_{RP})\mathbf{q}(t) \quad \text{and} \quad \vartheta_P = \Psi(\mathbf{c}_{RP})\mathbf{q}(t) \quad (1)$$

as products of global shape functions Φ and Ψ and time-dependent elastic coordinates \mathbf{q} . The global shape functions are often obtained from finite element (FE) models of the flexible bodies. More precisely, the equations of motion of a linear FE model of the flexible body

$$\mathbf{M}_e \ddot{\mathbf{q}}_e + \mathbf{K}_e \mathbf{q}_e = \mathbf{f}_e, \quad (2)$$

with the mass matrix \mathbf{M}_e , the stiffness matrix \mathbf{K}_e , the vector of applied loads \mathbf{f}_e and the nodal degrees of freedom $\mathbf{q}_e \in \mathbb{R}^n$ have to be set up. Then, the global shape functions Φ and Ψ are obtained from a model reduction of (2) using, for instance, modal truncation or component mode synthesis, see [4].

After the kinematics of the bodies is derived the equations of motion of the flexible multibody system can be obtained in minimal coordinates by applying a principle of mechanics, such as d'Alembert's principle, and it yields

$$\mathbf{M}(t, \mathbf{y})\ddot{\mathbf{y}} = \mathbf{f}(t, \mathbf{y}, \dot{\mathbf{y}}). \quad (3)$$

Thereby, \mathbf{M} is the global mass matrix and $\mathbf{y} \in \mathbb{R}^f$ are the generalized coordinates, which comprise both the rigid body degrees of freedom \mathbf{y}_r and the elastic degrees of freedom \mathbf{q} . The right-hand-side vector \mathbf{f} contains the applied forces, inner forces from elastic deformations as well as centrifugal, Coriolis, and gyroscopic forces.

4.2 The SIMP Approach

One way to perform topology optimization is to distribute a limited amount of mass in a discretized design domain such that an objective function, for instance the compliance, becomes minimal under certain loading conditions. A common method to relax and treat this kind of hard to solve mass/no mass integer optimization problem is the SIMP approach, see [1, 2]. Thereby, continuous density-like design variables $x_i \in [0, 1]$, $i = 1 \dots m$, are introduced and used to parameterize the material properties of the m subdomains. Following the penalization strategy in [9], the density and stiffness of an element i is computed as

$$\rho_i = \begin{cases} cx_i^q \rho_0, & \text{for } x_{\min} = 0.01 \leq x_i < 0.1, \\ x_i \rho_0, & \text{for } 0.1 \leq x_i \leq 1, \end{cases} \quad (4)$$

$$E_i = x_i^p E_0.$$

Thereby, ρ_0 and E_0 are the density and the stiffness of the solid material, while c , p and q are scalar parameters. In the topology optimization, the FE model (2), which is used to determine the global shape

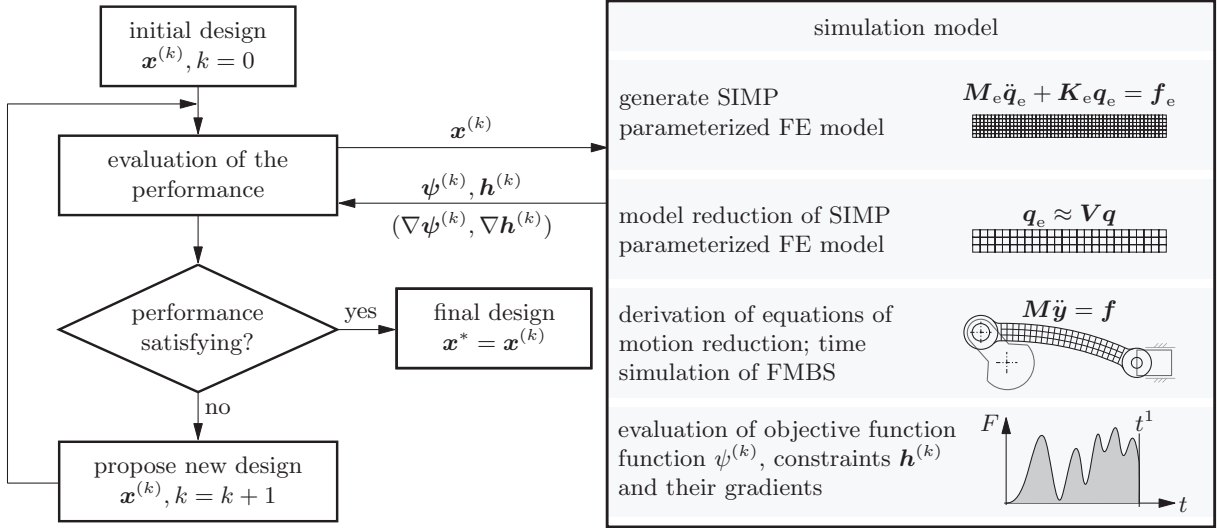


Figure 2: Schematic representation of the optimization procedure

functions Φ and Ψ , is parameterized by this SIMP approach, whereby each element is a subdomain.

4.3 Optimization Procedure

The established topology optimization procedure including a detailed description of the simulation model is shown in Fig. 2. Starting from the initial design $\mathbf{x}^{(0)}$, at first the performance of $\mathbf{x}^{(0)}$ is evaluated by a numerical simulation of the flexible multibody system. The simulation model contains the following steps.

At first, a SIMP parameterized FE model is generated in a reference domain. Then, a model reduction of the SIMP parameterized FE model is performed to reduce the number of elastic degrees of freedom and to determine the global shape functions. In the next step, the flexible multibody system is assembled from rigid and flexible bodies, i.e. the equations of motion (3) are derived in minimal coordinates, and thereafter the time simulation can be performed. In the last step of the simulation model the objective function and, if present, the constraint equations and their gradients are evaluated.

Continuing the iterative optimization procedure, it is checked whether the performance of the design $\mathbf{x}^{(k)}$ satisfies given criteria. If this is the case $\mathbf{x}^* = \mathbf{x}^{(k)}$ is accepted as the solution of the optimization problem and the optimization procedure is terminated. If the performance is not satisfying yet, an improved design $\mathbf{x}^{(k+1)}$ is proposed by the optimization algorithm and the next optimization loop is started. As optimization algorithm an elementary version of the Method of Moving Asymptotes [12] is used.

The whole optimization procedure from the generation of the FE model, the model reduction, the modeling of the flexible multibody system, the time simulation to the optimizer is established in MATLAB.

5. Sensitivity Analysis of Functional Type Objective Functions

For a successful application of the optimization procedure presented in the previous section, the efficient gradient computation is of major importance. Due to the large number of design variables the usage of the finite difference method would result in excessively high computation times. Therefore, the gradients are computed using the adjoint variable method instead. It is derived in [3] for the sensitivity analysis of rigid multibody systems and can be transferred to flexible multibody systems as described in [6].

Given a parameterized flexible multibody system in minimal coordinates as initial value problem

$$\begin{aligned}
 \text{equations of motion (ODE): } & \mathbf{M}(t, \mathbf{y}, \mathbf{x}) \ddot{\mathbf{y}} - \mathbf{f}(t, \mathbf{y}, \dot{\mathbf{y}}, \mathbf{x}) = \mathbf{0}, \\
 \text{initial positions and velocities: } & \Phi^0(t^0, \mathbf{y}^0, \mathbf{x}) = \mathbf{0}, \quad \dot{\Phi}^0(t^0, \mathbf{y}^0, \dot{\mathbf{y}}^0, \mathbf{x}) = \mathbf{0}, \\
 \text{implicit final condition: } & H^1(t^1, \mathbf{y}^1, \dot{\mathbf{y}}^1, \mathbf{x}) = 0,
 \end{aligned} \tag{5}$$

then the gradient of functional type objective functions in form of

$$\psi(\mathbf{x}) = \int_{t^0}^{t^1} F(t, \mathbf{y}, \dot{\mathbf{y}}, \ddot{\mathbf{y}}, \mathbf{x}) dt \quad (6)$$

can be computed with the adjoint variable method as follows. At first, the adjoint variables, which are also referred to as Lagrange multipliers, $\tau \in \mathbb{R}$, $\boldsymbol{\mu} \in \mathbb{R}^f$ and $\boldsymbol{\nu} \in \mathbb{R}^f$ have to be determined at the final time t^1 from the equations

$$\tau^1 = \frac{F^1}{\dot{H}^1}, \quad \boldsymbol{\mu}^1 = -\tau^1 \frac{\partial H^1}{\partial \mathbf{y}^1} \quad \text{and} \quad \mathbf{M}^1 \boldsymbol{\nu}^1 = -\tau^1 \frac{\partial H^1}{\partial \dot{\mathbf{y}}^1}. \quad (7)$$

Thereafter, the adjoint differential equations for $\boldsymbol{\mu}$ and $\boldsymbol{\nu}$, which read

$$\begin{aligned} \dot{\boldsymbol{\mu}} &= \left(\frac{\partial \text{ODE}}{\partial \mathbf{y}} \right)^T (\boldsymbol{\nu} + \boldsymbol{\xi}) - \frac{\partial F}{\partial \mathbf{y}}, \\ \mathbf{M} \dot{\boldsymbol{\nu}} &= -\boldsymbol{\mu} - \dot{\mathbf{M}} \boldsymbol{\nu} + \left(\frac{\partial \text{ODE}}{\partial \dot{\mathbf{y}}} \right)^T (\boldsymbol{\nu} + \boldsymbol{\xi}) - \frac{\partial F}{\partial \dot{\mathbf{y}}}, \end{aligned} \quad (8)$$

are derived and solved by a backward time integration from the final time t^1 to the initial time t^0 . The auxiliary variables $\boldsymbol{\xi} \in \mathbb{R}^f$ are computed from the algebraic equation $\mathbf{M} \boldsymbol{\xi} = \partial F / \partial \dot{\mathbf{y}}$. It should be mentioned that the adjoint differential equations and, hence, the effort to solve them do not depend on the design variables \mathbf{x} . However, the partial derivatives of the equations of motion with respect to the generalized positions \mathbf{y} and velocities $\dot{\mathbf{y}}$ have to be provided.

After the backward time integration of Eq. (8) the adjoint variables $\boldsymbol{\eta}^0 \in \mathbb{R}^f$ and $\boldsymbol{\zeta}^0 \in \mathbb{R}^f$ are determined from the equations

$$\left(\frac{\partial \dot{\boldsymbol{\Phi}}^0}{\partial \dot{\mathbf{y}}^0} \right)^T \boldsymbol{\eta}^0 = \mathbf{M}^0 \boldsymbol{\nu}^0 \quad \text{and} \quad \left(\frac{\partial \boldsymbol{\Phi}^0}{\partial \mathbf{y}^0} \right)^T \boldsymbol{\zeta}^0 = \boldsymbol{\mu}^0 - \left(\frac{\partial \dot{\boldsymbol{\Phi}}^0}{\partial \mathbf{y}^0} \right)^T \boldsymbol{\eta}^0. \quad (9)$$

Finally, the gradient can be computed as

$$\nabla \psi = -\tau^1 \frac{\partial H^1}{\partial \mathbf{x}} - \left(\frac{\partial \boldsymbol{\Phi}^0}{\partial \mathbf{x}} \right)^T \boldsymbol{\zeta}^0 - \left(\frac{\partial \dot{\boldsymbol{\Phi}}^0}{\partial \mathbf{x}} \right)^T \boldsymbol{\eta}^0 + \int_{t^0}^{t^1} \left[\frac{\partial F}{\partial \mathbf{x}} - \left(\frac{\partial \text{ODE}}{\partial \mathbf{x}} \right)^T (\boldsymbol{\nu} + \boldsymbol{\xi}) \right] dt, \quad (10)$$

whereby the adjoint variables and the partial derivatives of the equations of motion with respect to the design variables \mathbf{x} are needed. For the computation of $\partial \text{ODE} / \partial \mathbf{x}$ the global shape functions, used to approximate the deformations of the flexible bodies, have to be differentiated with regard to the design variables. To compute these derivatives efficiently Nelson's method is used, see [8].

6. Application Example

In order to test the proposed optimization procedure, the topology of a flexible piston rod of a slider-crank mechanism is optimized, see Fig. 3(a). The results are compared with those of a second optimization, in which the equivalent static load method is used. In the modeling of the slider-crank mechanism the slider block is omitted. Therefore, the piston rod is only loaded by its own inertia forces, which occur during the motion of the system.

The motion is composed of two stages. In the first one, the crank is accelerated within two seconds from a resting position until a constant angular velocity is reached. In the second stage, the angular velocity is kept constant for another second.

The design domain, in which the optimal topology of the piston rod shall emerge, possesses the dimensions $(1.0 \times 0.06 \times 0.01)$ m and is discretized using 200×12 finite elements, see Fig. 3(b). Thereby, the interface elements, which include the elements of the first and the last column in the mesh, are solid. The inner 2376 elements are parameterized by the SIMP law (4) using the parameters $c = 10^5$, $p = 3$, $q = 6$, $E_0 = 0.5 \cdot 10^{11}$ N/m² and $\rho_0 = 8750$ kg/m³.

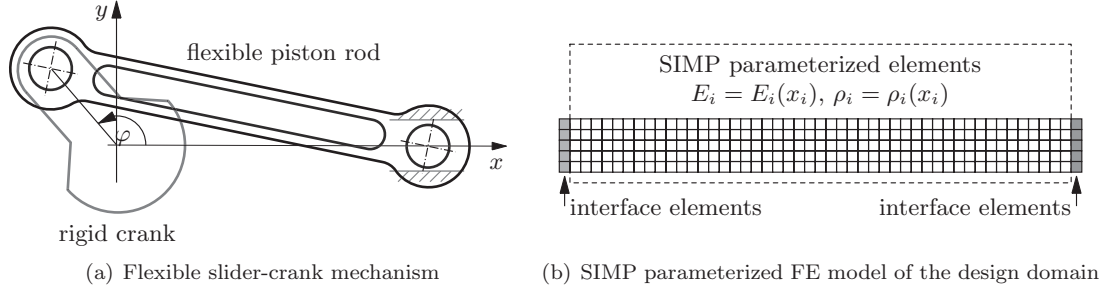


Figure 3: Flexible slider-crank mechanism

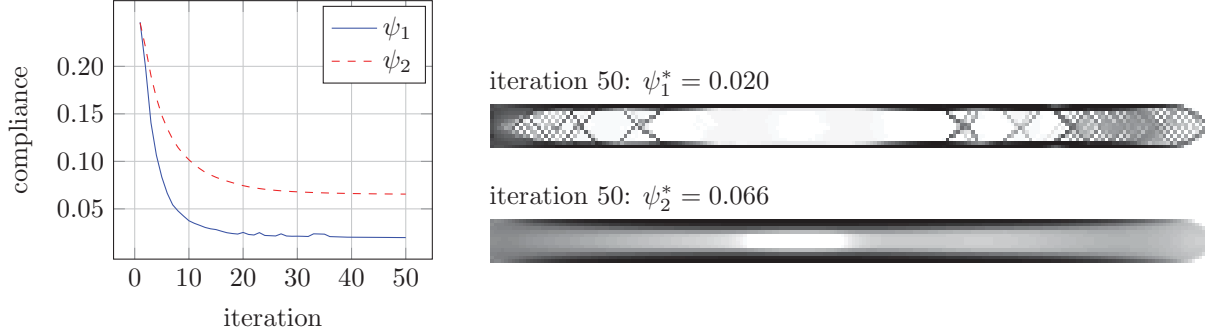


Figure 4: Optimization results comparing integral type objective functions and equivalent static loads

The optimization problem is formulated as minimal compliance problem with a volume restriction $V(\mathbf{x})/V_0 \leq 0.5$ and reads

$$\begin{aligned} \min_{\mathbf{x} \in \mathbf{R}^h} \quad & \psi_i(\mathbf{x}) \\ \text{subject to} \quad & \mathbf{h}(\mathbf{x}) = V(\mathbf{x}) - \frac{1}{2}V_0 \leq 0, \\ & 0.01 \leq x_i \leq 1, \quad i = 1 \dots h, \end{aligned} \quad (11)$$

whereby two different objective functions $\psi_i(\mathbf{x}), i = 1, 2$ are defined. On the one hand, being an example of functional type objective functions, the integral compliance

$$\psi_1(\mathbf{x}) = \int_{t^0}^{t^1} \mathbf{q}_e^T \mathbf{K}_e \mathbf{q}_e dt \quad (12)$$

shall be minimized. On the other hand, employing the equivalent static load method [5, 7] the compliance is evaluated and summed up at $n_{\text{esl}} = 100$ time points t_j , which are uniformly distributed in $[t^0, t^1]$. Here, the objective function $\psi_2(\mathbf{x})$ is computed as follows

$$\psi_2(\mathbf{x}) = \frac{t^1}{n_{\text{esl}}} \sum_{j=1}^{n_{\text{esl}}} \mathbf{q}_{e,j}^T \mathbf{K}_e \mathbf{q}_{e,j}, \quad (13)$$

whereby the scaling t^1/n_{esl} is not necessarily needed but introduced to ease the comparison of ψ_1 and ψ_2 . The elastic coordinates $\mathbf{q}_{e,j} = \mathbf{q}_e(t_j)$ are recovered after the time simulation and are assumed to be constant in the gradient computation of the static response optimization.

Two optimizations are carried out, in which ψ_1 and ψ_2 are minimized. The resulting compliance histories and material distributions after 50 iterations are given in Fig. 4. It can be seen that in both optimizations, the evolving designs are stiffened with regard to bending loads. However, while the optimization of ψ_2 gets stuck in an intermediate layout with a majority of gray elements, a design emerges in the optimization of ψ_1 , where most of the elements are either white or black and even checkerboard patterns are formed. This clear difference can also be observed in the compliance which is reduced from $\psi_1(\mathbf{x}^{(0)}) = \psi_2(\mathbf{x}^{(0)}) = 0.246$ to $\phi_1^* = 0.02$ and $\phi_2^* = 0.066$, respectively.

It can therefore be concluded that for the application example the simplifications made in the equivalent static load method do not apply and as a consequence the optimization yields an unsatisfying design. In contrast, the presented optimization procedure, which relies on an integral type objective function and exact gradients, is able to solve the problem. However, this ability comes with a price. While the optimization of ψ_2 takes only about 1.5 h, the optimization of ψ_1 needs roughly two days due to the increased effort in the gradient computation.

7. Summary and Conclusion

An optimization procedure is presented to perform topology optimization of flexible multibody systems, modeled with the floating frame of reference formulation. The flexible bodies are parameterized using the SIMP approach. In contrast to previous approaches, functional type objective functions are employed and exact gradients are provided. In the gradient computation the adjoint variable method is used to handle the large number of design variables. As testing and comparing example, a topology optimization is performed for a flexible piston rod of a slider-crank mechanism. The results show that it is possible with the presented method to optimize multibody systems, which do not meet the necessary requirements to use the equivalent static load method. However, even though an appropriate method is used to evaluate the gradients efficiently the total optimization time is comparatively high.

Acknowledgements

The authors thank the German Research Foundation (DFG) for financial support of the project within the Cluster of Excellence in Simulation Technology (EXC 310/2) at the University of Stuttgart.

References

- [1] Bendsøe, M. 1989: Optimal Shape Design as a Material Distribution Problem. *Structural and Multidisciplinary Optimization* **1**(4), 193–202.
- [2] Bendsøe M.; Sigmund, O. 2003: *Topology Optimization - Theory, Methods and Applications*. Springer-Verlag, Berlin.
- [3] Bestle, D.; Eberhard, P. 1992: Analyzing and Optimizing Multibody System. *Journal of Structural Mechanics*, **20**(1), 67-92.
- [4] Fehr, J. 2011: Automated and Error-Controlled Model Reduction in Elastic Multibody Systems, *Dissertation, Schriften aus dem Institut für Technische und Numerische Mechanik der Universität Stuttgart*, vol. 21. Shaker Verlag, Aachen.
- [5] Häußler, P.; Emmrich, D.; Müller, O.; Ilzhöfer, B.; Nowicki, L.; Albers, A. 2001: Automated Topology Optimization of Flexible Components in Hybrid Finite Element Multibody Systems using ADAMS/Flex and MSC. Construct. In ADAMS European User's Conference, Berchtesgaden, Germany, 14th-15th November.
- [6] Held, A. 2014: On Structural Optimization of Flexible Multibody Systems, *Dissertation, Schriften aus dem Institut für Technische und Numerische Mechanik der Universität Stuttgart*, vol. 33. Shaker Verlag, Aachen.
- [7] Kang, B.; Park, G. 2005: Optimization of Flexible Multibody Dynamic Systems Using the Equivalent Static Load Method. *AIAA Journal* **43**(4), 846–852.
- [8] Nelson, R.B. 1976: Simplified Calculation of Eigenvector Derivatives. *AIAA Journal* **14**(9) , 1201–1205.
- [9] Olhoff, N.; Du, J. 2005: Topological Design of Continuum Structures Subjected to Forced Vibration. In: 6th World Congresses of Structural and Multidisciplinary Optimization.
- [10] Schwertassek, R.; Wallrapp, O. 1999: *Dynamik flexibler Mehrkörpersysteme (in German)* Vieweg, Braunschweig.
- [11] Shabana, A.A. 2005: *Dynamics of Multibody Systems*, Cambridge University Press, New York.
- [12] Svanberg, K. 1987: The Method of Moving Asymptotes - A New Method for Structural Optimization. *International Journal for Numerical Methods in Engineering* **24**, 359–373.

High-fidelity Structural optimization of a tow-steered composite wing

Timothy R. Brooks¹, John T. Hwang², Graeme J. Kennedy³, Joaquim R. R. A. Martins⁴

¹ University of Michigan, Ann Arbor, Michigan, USA, timryanb@umich.edu

² University of Michigan, Ann Arbor, Michigan, USA, hwangjt@umich.edu

³ Georgia Institute of Technology, Atlanta, Georgia, USA, graeme.kennedy@aerospace.gatech.edu

⁴ University of Michigan, Ann Arbor, Michigan, USA, jrrom@umich.edu

1. Abstract

Composite materials are now making their way into the primary structures of large transport aircraft and have contributed to more efficient airframes. However, the composites used so far consist in conventional plies with fixed angles. The introduction of the capability to manufacture tow-steered composites opens the door to more efficient airframes by enabling more tailored structures. This paper will propose a general method for setting up tow-steered composite structural optimization problems. This method also features a method for mapping potentially thousands of discrete ply angles to a complex structure of interest. This mapping is amenable to adjoint gradient computation, which would otherwise be prohibitively expensive for any problem with a high enough fidelity to be of use. While the motivation of this method is to parameterize and optimize composite tow angles, it can handle both spatially varying tow angle and thickness variables separately and together. Several structural problems are proposed and their results presented. From these results we show that this method offers a robust design parameterization while being general enough to be applicable to a large number of structures. While purely structural, the presented methodology can be extended to aerostructural design optimization.

2. Keywords: Structural optimization, tow-steered composites, composites, fuel burn, flexible wing

3. Introduction

Tow steering is a relatively new composite manufacturing technique in which a machine is used to distribute composite fibers with a continuously varying direction on a surface, as opposed to the typical uni-directional laminae. This effectively gives the designer control over the local stiffness properties of their structures and enables the tailoring of the deflected shape for a prescribed load. This allows the structure to deform in ways that reduce stress concentrations, or result in passive load alleviation. With such unprecedented control over the behavior of the structure, a natural question to ask is: How can we find the optimal fiber distribution to maximize the performance of our structure? This question can be answered with multidisciplinary design optimization (MDO). Examples of these problems would include designing a wing to defect in flight to optimally reduce fuel burn, such as in Kenway and Martins [8], or designing structure that can withstand complex load distributions while minimizing weight. Spatially varying composite ply distribution optimization has been studied by Kennedy and Martins [6] and Hvejsel et al. [1] among others. However in these cases the fiber angles were forced to take discrete values due to manufacturing constraints. In the present paper we now relax that constraint and allow all angles to take continuous values. Continuous tow steered optimization has been investigated by groups such as Jegley et al. [4] and Jutte et al. [5]. The difference is the paper proposes a new method for tow parametrization and optimization over a full 3D model using gradient based optimization techniques.

4. Method

In this section, we describe the method for performing tow-steering via numerical optimization. The high-level approach is to use a shell-element structural solver with the shell stiffness computed from the local tow angle through first-order shear deformation theory (FSDT). The shell stiffness matrices are permitted to vary within each element, reusing the element shape functions. The tow angle distribution across a structural component is smoothly parametrized using B-spline surfaces, so the design variables for optimization are the B-spline control points of this parameterization. A necessary intermediate step between the B-spline parameterization and computation of the stiffness matrices is to perform a local tow angle transformation to reverse the effect of each quadrilateral elements orientation because we use unstructured quad meshes, in general. We use a gradient-based optimizer with adjoint-based derivative computation to enable optimization with a large number of design variables. Figure 1 illustrates the steps involved in mapping the design variables to the objective and constraint functions using an extended design structure matrix (XDSM) [9] diagram.

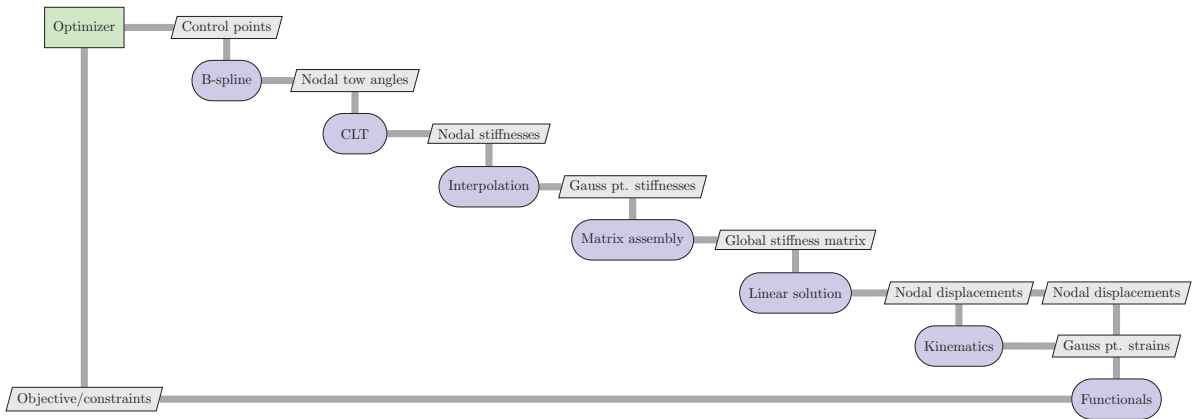


Figure 1: Extended design structure matrix (XDSM) diagram showing the steps in the tow-steering optimization.

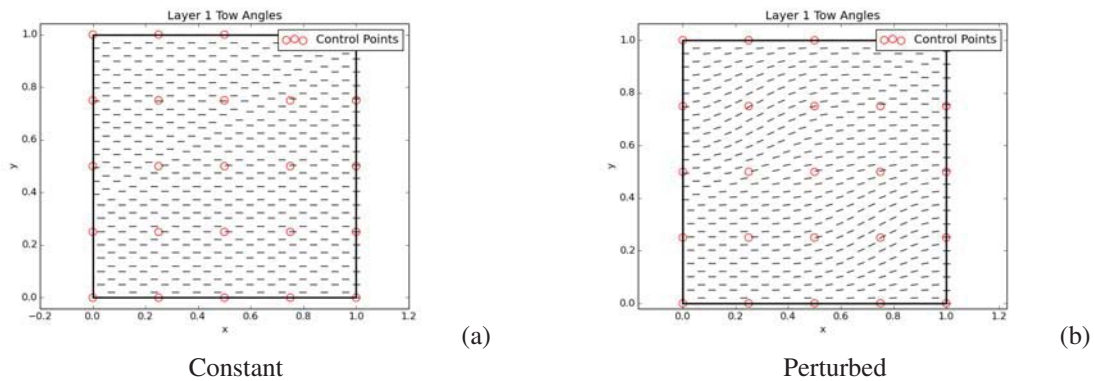


Figure 2: B-spline control points and the resulting tow angle distributions.

Section 4.1 describes the B-spline parameterization and Sec. 4.2 discusses the FSDT formulation and the aforementioned local angle transformation. Section 4.3 provides brief descriptions of the structural solver and optimizer used in this work.

4.1 B-spline parameterization

A unique requirement of the tow-steering problem is a parameterization that ensures that the tow paths on each structural component are smooth, while maintaining freedom for the optimizer. We achieved such a parameterization by using B-spline surfaces to define a continuous and smooth tow angle distribution within each structural component. Additional smoothness of the fiber paths can be assured by applying a constraint on the minimum radius of curvature of the path. The tow angle distributions are controlled by the B-spline control points, which can be considered the inputs for the parameterization, and the outputs are the tow angle values at the nodes. For this work, we use shell elements whose stiffness matrices vary using the same shape functions as the displacements.

We use B-splines because of their many favorable properties—they have compact support, the number of control points and order can be arbitrarily controlled, and they have a constant Jacobian since they are linear with respect to the control point values. A B-spline surface is simply a tensor-product generalization of a B-spline curve and is mathematically defined as

$$P(u, v) = \sum_{i=1}^m \sum_{j=1}^n B_i(u) B_j(v) C_{ij},$$

where P is the output of the B-spline surface, C_{ij} are the control point values, u, v are the parametric coordinates, and B_k are the piecewise-polynomial basis functions. In this context, $P(u, v)$ would be the tow angle evaluated at a parametric location (u, v) in the structural component, which are assumed to be topologically 4-sided, and C_{ij} are the tow angle control points. Figure 2 shows the B-spline control point locations overlaid on a constant and a perturbed tow angle distribution.

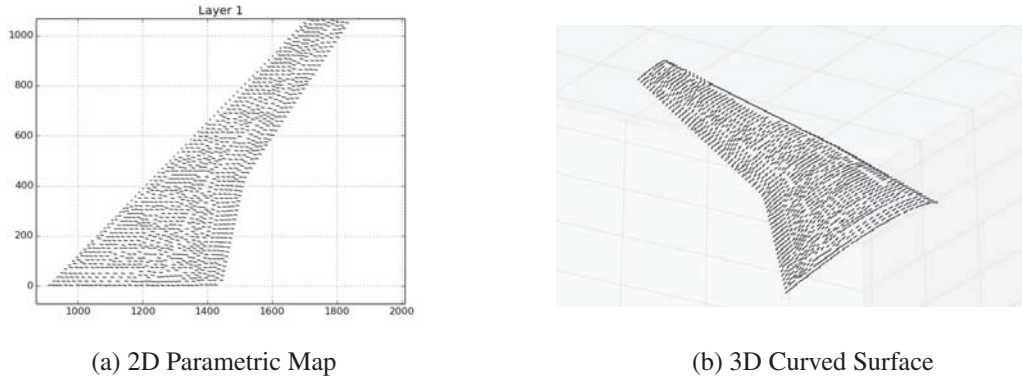


Figure 3: Illustration of the local tow angle transformation.

4.2 Computation of the stiffness matrices

Given the tow angle at each node, the shell stiffness properties are calculated using FSDT; that is, we obtain the A , B , D , and A^* matrices. Prior to this, however, the nodal tow angles given by the B-spline parameterization must be transformed to obtain the equivalent angle in the elements frame that would produce the same effective angle. This transformation is pre-computed as an initialization step; starting with one of the elements, the algorithm marches out to neighboring elements, computing the rotation of each neighboring element relative to the current one. In each element, the pre-computed rotation is added to the tow angle from the global frame to obtain the correct angle in the local frame. This effectively guarantees a continuous fiber distribution so long as the surface can be transformed into the 2D mapping with at most one cut, so an example where this would not work would be a cube. This method can be generalized for any number of control points or laminae layers. A special case of this mapping is the case in which tow angle control points are all set to the same value, which in 3D corresponds to wrapping parallel lines around the curvature of the surface. The parametric warping process can be seen in Fig. 3.

4.3 Structural solver and optimizer

The structural solver used in this work is the toolkit for the analysis of composite structures (TACS) [7]. TACS is a general finite-element package that enables the implementation of custom elements and material models, but in this work, we use shell elements with a mixed interpolation of tensorial components (MITC) formulation and FSDT. TACS has been developed specifically for gradient-based optimization, so it provides the necessary routines to implement the adjoint method. The adjoint method enables the computation of a gradient at a cost roughly equal to running a single structural analysis, and this cost is independent of the number of design variables. For a detailed explanation of the adjoint method, the reader is referred to Martins and Hwang [10].

The optimizer we use in this work is SNOPT [2], an active-set reduced Hessian Sequential Quadratic Programming (SQP) algorithm. SNOPT is effective in solving large-scale nonlinear optimization problems with sparse constraints. We interface to SNOPT from Python via the pyOpt package [11]; pyOpt is an optimization suite that enables simple access to many optimizers with a common optimization problem definition.

5. Results

5.1 Optimization problem

Several compliance minimization problems will be considered, each of which takes the form .

$$\begin{aligned} & \text{minimize} && \frac{1}{2} u^T K u \\ & \text{with respect to} && \theta_{cp} \end{aligned}$$

The compliance is minimized subject to each of the control point tow angles parameterizing the design. For every case only a single ply optimization was considered, however multi-ply optimization is possible as well. The composite properties used for each problem are listed below in Tab. 1.

5.2. Verification of B-spline parameterization

To assess the robustness of the B-spline parameterization, we solved the optimization case originally proposed by Hvejsel et al. [1] . In this case, a 1 m x 1 m x 0.05 m plate is clamped on all edges and subjected to a uniform pressure loading on the top. The objective of this optimization is to minimize the compliance of the plate with

Table 1: Material Properties

Property	Value
E_1	54 GPa
E_2, E_3	18 GPa
G_{12}, G_{13}, G_{23}	9 GPa
ν_{12}	0.25

respect to the ply angles. In the case of Hvejsel et al. [1], the angles were forced to take discrete values. In our case, we relax that requirement and allow a continuous fiber distribution. The discrete case was used as a benchmark and the result can be seen in Fig. 4. The continuous optimization case was run with 25, 100, and 200 control points uniformly distributed throughout the plate, and in each case, we started with all the fibers in the x -direction. The optimization results are shown in Fig. 5. It can be seen that the optimal designs for the discrete and continuous cases are similar in pattern: the fibers point radially towards the edges and form a diamond toward the center. Due to their smooth nature the bi-splines have a more difficult time modeling the sharp angle changes seen in the boundary between the inner and outer square regions. The final compliance for the 25, 100, and 400 control point designs was 10.19 J, 9.18 J and 8.89 J, respectively. For reference, the discrete case yields a compliance of 8.83 J, while the initial zero degree case yields. It is not surprising to see that as the number of control point is increased, the minimum compliance decreases. While it is surprising that the continuous cases did not outperform the discrete case, it is important to note that due to the symmetry of the problem this case features local minima as is explored in the following section. Using different initial distributions, the solution will converge to a slightly better optimum.

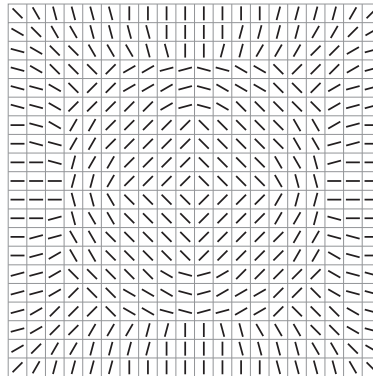
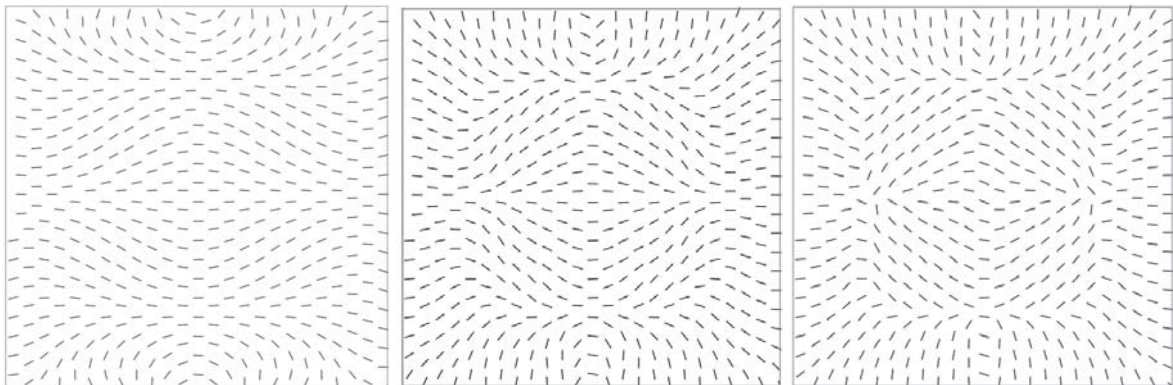


Figure 4: Solution to the discrete case (8.83 J).



(a) 25 Control point case (10.19 J). (b) 100 Control point case (9.18 J). (c) 400 Control point case (8.89 J).

Figure 5: Clamped plate solutions for variable tow angles

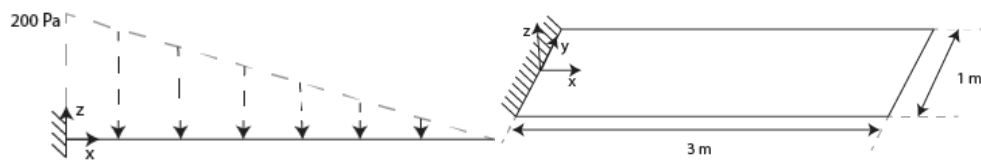


Figure 6: Cantilevered plate problem.

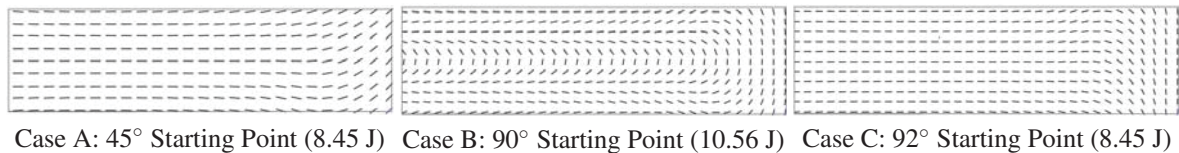


Figure 7: Cantilevered plate solutions.

5.2. Exploration of Local Minima

The next problem that was looked at was a simple cantilevered 3 m x 1 m x 0.01 m plate under a triangular distributed load shown in Fig. 6. The objective function was again compliance, which was minimized with respect to 40 control point ply angles. The global minimum to this problem is when all fibers point along the axis of bending, in this case the x -axis or 0° . This problem was run with three different initial uniform tow distributions, of 45° , 90° , and 92° , corresponding to cases A, B, and C, respectively. The model contained 9801 elements with 60,000 degrees of freedom. The results for each case are shown in in Fig. 7. As was expected, in all three cases the optimizer tries to re-orientate the tow angles to 0° . The fibers furthest away from the clamped end change the least since the compliance is very insensitive to these values. What is interesting to note is that while case A and C converged to a compliance of 8.45 J case B only converged to 10.56 J, a difference of 25%. We can see from the pattern that while most of the fibers point along the x -axis there is a 'U' shaped pattern going down the center, preventing it from achieving the same value as cases A and C. The fact that the solution for case B and C differ so much despite only differing slightly in initial values seems to suggest that there is a local minimum to the problem due to the symmetry of the problem.

5.3. Structural Wing Box Optimization

The final problem that was considered was a full wing box modeled from the NASA Common Research Model (CRM). This wing box structure is created using GeoMACH [3], an open-source parametric modeler for aircraft geometries and structures. We first create the wing box geometry in GeoMACH, and once we specify the desired locations of the ribs, spars, and stringers, GeoMACH automatically generates a parametric unstructured quadrilateral mesh of the structure. In this work, we do not change the geometry of the wing.

For this problem the structure was loaded with a uniform suction pressure on the upper surface and an equal in magnitude positive pressure on the lower surface such that the net resultant force on the wing is upward. The magnitude of the pressure on both surfaces was 3.6 kPa. The model contains 16,659 elements with just under 100,000 degrees of freedom. The optimization was again a compliance minimization of the entire structure. The design variables consist of 80 tow angle control points, 40 on both the upper and lower skins of the wing box. This problem was run from two initial designs: one with the fibers pointing along the span of the wing and the other with the fibers pointed along the chord. The initial compliance was 28.7 MJ for the spanwise case, and 50.1 MJ for the chordwise case. Both cases converge to the solution seen in Fig8 (b) with a final compliance value of 25 MJ. This is a 50% and 13% improvement for the chordwise and spanwise cases respectively. The figures show the upper surface only, however the lower surface shares similar features in fiber distribution. While this is an impressive improvement for the chordwise distribution, clearly this case would represent one of the poorest engineering choices in practice. It is more informative to compare the optimum with the spanwise case, since this represents a more intuitive design choice. We can see that for the optimized wing, most of the fibers still point in the spanwise direction. The differences exist toward the trailing edge, where the fibers change direction sharply to point in the chordwise direction. The span-wise fibers on the main part of of the wing act to reduce the bending stresses, since this is where the load is carried. The reason for the sharp transition at the aft of the wing is that this juncture is where the ribs end the model, so the optimizer places the fibers in the chord-wise direction to make up for the loss of rigidity in the aft region.

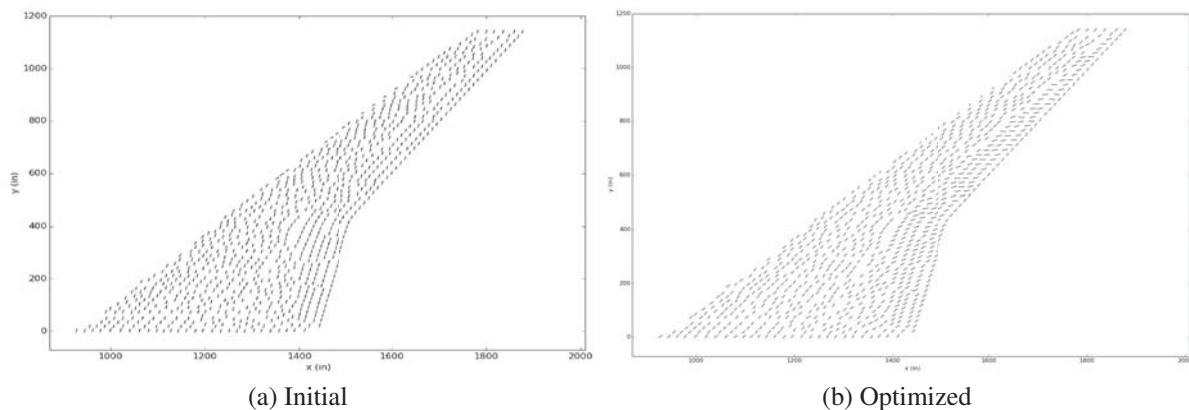


Figure 8: Initial and optimized tow angle distributions.

6. Conclusion

We presented a method for parameterizing and optimizing tow steered composite structures. We presented two 2D optimization problems to benchmark the performance of the parameterization, and included a third, more sophisticated, problem in three dimensions to demonstrate its utility. From our study we conclude that the method is indeed robust, however is limited in the sense that sharp tow angle changes are difficult to achieve. It has also been shown that certain problems may be subject to local minima due to the parameterization. While the optimization cases presented in this paper focused on compliance minimization it can be easily extended to more general optimization problems with multiple laminae layers.

7. Acknowledgments

The authors gratefully acknowledge support from NASA towards the provided in this paper.

8. References

- [1] E. L. C. Hvejsel and M. Stolpe. Optimization strategies for discrete multi-material stiffness optimization. *Structural and Multidisciplinary Optimization*, (44):149–163, 2006.
- [2] P. E. Gill, W. Murray, and M. A. Saunders. An SQP algorithm for large-scale constrained optimization. *Society for Industrial and Applied Mathematics*, 47(1), 2005.
- [3] J. T. Hwang, G. K. W. Kenway, and J. R. R. A. Martins. Geometry and structural modeling for high-fidelity aircraft conceptual design optimization. In *Proceedings of the 15th AIAA/ISSMO Multidisciplinary Analysis and Optimization Conference*, Atlanta, GA, June 2014. AIAA 2014-2041.
- [4] D. Jegley, B. Tatting, and Z. Gurdal. *Optimization of Elastically Tailored Tow-Placed Plates with Holes*. American Institute of Aeronautics and Astronautics, 2014/05/31 2003.
- [5] C. V. Jutte, B. K. Stanford, C. D. Wieseman, and J. B. Moore. Aeroelastic tailoring of the nasa common research model via novel material and structural configurations. In *Proceedings of the AIAA 52nd Aerospace Sciences Meeting*, January 2014.
- [6] G. J. Kennedy and J. R. R. A. Martins. A laminate parametrization technique for discrete ply angle problems with manufacturing constraints. *Structural and Multidisciplinary Optimization*, 48(2):379–393, August 2013.
- [7] G. J. Kennedy and J. R. R. A. Martins. A parallel finite-element framework for large-scale gradient-based design optimization of high-performance structures. *Finite Elements in Analysis and Design*, 87:56–73, September 2014.
- [8] G. K. W. Kenway and J. R. R. A. Martins. Multipoint high-fidelity aerostructural optimization of a transport aircraft configuration. *Journal of Aircraft*, 51(1):144–160, January 2014.
- [9] A. B. Lambe and J. R. R. A. Martins. Extensions to the design structure matrix for the description of multidisciplinary design, analysis, and optimization processes. *Structural and Multidisciplinary Optimization*, 46:273–284, August 2012.
- [10] J. R. R. A. Martins and J. T. Hwang. Review and unification of methods for computing derivatives of multidisciplinary computational models. *AIAA Journal*, 51(11):2582–2599, November 2013.
- [11] R. E. Perez, P. W. Jansen, and J. R. R. A. Martins. pyOpt: a Python-based object-oriented framework for nonlinear constrained optimization. *Structural and Multidisciplinary Optimization*, 45(1):101–118, January 2012.

Design optimization of multi-point constraints in structures

Daniel N. Wilke¹, Schalk Kok²

¹ Department of Mechanical and Aeronautical Engineering, University of Pretoria, South Africa, nico.wilke@up.ac.za

² Department of Mechanical and Aeronautical Engineering, University of Pretoria, South Africa, schalk.kok@up.ac.za

1. Abstract

Multi-point constraints have been used in analysis of structures, since the early 1970's. However, limited research regarding the sensitivity analysis and design optimization of multi-point constraints have been done. We recently showed for the master-slave elimination approach that for the analysis using Newton's method, the exact consistent tangent contribution requires the second derivative contribution of the multi-point constraint relations. However, the second-order contribution is often omitted when conducting the analysis resulting in an inexact consistent tangent contribution.

In this study, we investigate whether the exact consistent tangent contribution is essential when designing multi-point constraints for structural applications. The multi-point constraint design problem is to design a frictionless roller guide for a center loaded simply supported beam. The unconstrained design problem aims to find the geometry of a frictionless roller guide such that the centroid of the beam follows a prescribed load path. We compute the exact analytical gradients of the objective function using the exact consistent tangent contribution of the multi-point constraints. In addition, we also compute the approximate analytical gradients of the objective function, where the only approximation in the sensitivity analysis is the inexact consistent tangent contribution of the multi-point constraints.

We then investigate the difference in design optimization performance when supplying the exact and approximate analytical gradients. We compare the ability and performance of steepest descent and BFGS conjugate gradient algorithms with a cubic line search strategy to design the multi-point constraints when both the exact and inexact gradients are supplied.

2. Keywords: Multi-point constraint, exact consistent tangent, inexact consistent tangent, design optimization, analytical sensitivities.

3. Introduction

Finite element based multi-point constraint (MPC) research was introduced in the middle seventies by the well known Gallagher textbook [2]. This textbook was supplemented by a number of papers from the late seventies [3, 4] to early eighties [5, 6, 7]. These papers mainly included discussions on the analysis of linear and nonlinear MPCs for the master-slave elimination and Lagrangian approaches. The discussion on MPCs got rekindled in the nineties and early 2000s, with papers that mainly focussed on linear MPCs [8, 9, 10, 11, 12]. These papers touched on implementation approaches [9, 10, 11], programming abstractions that are well suited to implement MPCs [8] or specific applications [12].

Unfortunately, not much work has been conducted on the sensitivity analysis or the use of sensitivities in the design of nonlinear MPCs. We recently showed [1] that for the analysis of MPCs using Newton's method in the master-slave elimination approach the exact consistent tangent contribution requires the second derivative contribution of the multi-point constraint relations. However, the second-order contribution is often omitted when conducting the analysis resulting in an inexact consistent tangent contribution that are often employed with inexact Newton strategies. The inexact consistent tangent contribution is sufficient to efficiently analyze nonlinear MPCs. It however remains unclear whether they are sufficient to approximate design sensitivities for the efficient design of MPCs.

In this paper, we investigate whether the design sensitivities requires the exact consistent tangent or whether the inexact consistent tangent is sufficient to design MPCs efficiently or at all using conventional gradient based algorithms. Instead of using the master-slave elimination approach we conduct all analyses using the Lagrangian approach to enforce MPCs. To the best of our knowledge this is the first time that the design sensitivities computed using the exact consistent tangent from the primary analysis for MPCs is investigated.

In this study, we indicate vectors by $\{\cdot\}$ and matrices using $[\cdot]$.

4. Sensitivity Analysis

Consider the partitioning of the nonlinear system of equations into free (f), prescribed (p) and MPC (c) degrees of

freedom,

$$\{\mathcal{R}_f\} = \{\mathcal{F}_f^{\text{int}}\} - \{\mathcal{F}_f^{\text{ext}}\} = \{0\} \quad (1)$$

$$\{\mathcal{R}_c\} = \{\mathcal{F}_c^{\text{int}}\} - \{\mathcal{F}_c^{\text{ext}}\} = \{0\} \quad (2)$$

$$\{\mathcal{R}_p\} = \{\mathcal{F}_p^{\text{int}}\} - \{\mathcal{F}_p^{\text{ext}}\} = \{0\}, \quad (3)$$

which we solve using Newton's algorithm. The MPC (c) degrees of freedom are all the degrees of freedom that are associated with the MPC equations. The prescribed displacements are applied at the start of the iterative process, which leaves only the free and MPC degrees of freedom to solve

$$\{\mathcal{R}_f\} = \{\mathcal{F}_f^{\text{int}}\} - \{\mathcal{F}_f^{\text{ext}}\} = \{0\}, \quad (4)$$

$$\{\mathcal{R}_c\} = \{\mathcal{F}_c^{\text{int}}\} - \{\mathcal{F}_c^{\text{ext}}\} = \{0\}, \quad (5)$$

in addition, to the nonlinear MPC equations that are written in residual form

$$\{\mathcal{R}_c^{\text{mpc}}\} = \{0\}. \quad (6)$$

The Lagrangian approach allows us to formulate the problem using the potential energy approach [2]. The potential energy for elastic media is given by the sum of the strain energy or equivalently the work conducted by the external loads, and the work potential of the external loads [13],

$$\Pi(U_f, U_c) = \int \{\mathcal{F}_f^{\text{int}}\}^T d\{U_f\} + \int \{\mathcal{F}_c^{\text{int}}\}^T d\{U_c\} - \{\mathcal{F}_f^{\text{ext}}\}^T \{U_f\} - \{\mathcal{F}_c^{\text{ext}}\}^T \{U_c\}, \quad (7)$$

which we can augment with the nonlinear MPC equations to obtain the Lagrangian functional

$$\mathcal{L}(U_f, U_c, \lambda) = \int \{\mathcal{F}_f^{\text{int}}\}^T d\{U_f\} + \int \{\mathcal{F}_c^{\text{int}}\}^T d\{U_c\} - \{\mathcal{F}_f^{\text{ext}}\}^T \{U_f\} - \{\mathcal{F}_c^{\text{ext}}\}^T \{U_c\} + \{\lambda\}^T \{\mathcal{R}_c^{\text{mpc}}(U_c)\}. \quad (8)$$

Note the presence of the additional unknowns $\{\lambda\}$, the Lagrange multipliers. The stationary point of (8) is given by the first order optimality conditions

$$\begin{cases} \frac{d\mathcal{L}(U_f, U_c, \lambda)}{d\{U_f\}} \\ \frac{d\mathcal{L}(U_f, U_c, \lambda)}{d\{U_c\}} \\ \frac{d\mathcal{L}(U_f, U_c, \lambda)}{d\{\lambda\}} \end{cases} = \begin{cases} \{\mathcal{F}_f^{\text{int}}\} - \{\mathcal{F}_f^{\text{ext}}\} = \{0\}, \\ \{\mathcal{F}_c^{\text{int}}\} - \{\mathcal{F}_c^{\text{ext}}\} + \{\lambda\}^T \frac{d\{\mathcal{R}_c^{\text{mpc}}\}}{d\{U_c\}} = \{0\}, \\ \{\mathcal{R}_c^{\text{mpc}}\} = \{0\}. \end{cases} \quad (9)$$

The resulting system of equations (9), can then be solved using Newton's method to obtain the following update formula

$$\begin{bmatrix} \frac{d\{\mathcal{F}_f^{\text{int}}\}}{d\{U_f\}} & \frac{d\{\mathcal{F}_f^{\text{int}}\}}{d\{U_c\}} & \{0\} \\ \frac{d\{\mathcal{F}_c^{\text{int}}\}}{d\{U_f\}} & \frac{d\{\mathcal{F}_c^{\text{int}}\}}{d\{U_c\}} + \{\lambda\}^T \frac{d^2\{\mathcal{R}_c^{\text{mpc}}\}}{d\{U_c\}^2} & \left(\frac{d\{\mathcal{R}_c^{\text{mpc}}\}}{d\{U_c\}}\right)^T \\ \{0\} & \frac{d\{\mathcal{R}_c^{\text{mpc}}\}}{d\{U_c\}} & \{0\} \end{bmatrix} \begin{Bmatrix} \Delta\{U_f\} \\ \Delta\{U_c\} \\ \Delta\{\lambda\} \end{Bmatrix} = - \begin{Bmatrix} \{\mathcal{R}_f\} \\ \{\mathcal{R}_c\} + \{\lambda\}^T \frac{d\{\mathcal{R}_c^{\text{mpc}}\}}{d\{U_c\}} \\ \{\mathcal{R}_c^{\text{mpc}}\} \end{Bmatrix}, \quad (10)$$

which needs to be solved at each iterate until convergence.

Note the presence of the second derivative $\frac{d^2\{\mathcal{R}_c^{\text{mpc}}\}}{d\{U_c\}^2}$ of the MPC relations in (10). Similarly, we can compute the second derivative of the i^{th} constraint equation w.r.t. all $\{U_c\}$ and multiply the result by the i^{th} Lagrange multiplier. This process is then repeated for all the constraint equations to finally obtain the symmetric matrix $\left[\{\lambda\}^T \frac{d^2\{\mathcal{R}_c^{\text{mpc}}\}}{d\{U_c\}^2}\right]$.

However, the second derivative is ofte omitted in the consistent tangent contribution that results in an inexact consistent tangent. In this study inexact consistent tangent is taken to imply the omission of $\left[\{\lambda\}^T \frac{d^2\{\mathcal{R}_c^{\text{mpc}}\}}{d\{U_c\}^2}\right]$ in the consistent tangent, whereas the exact consistent tangent includes this term.

The sensitivity analysis for the design of an MPC can be computed using the direct sensitivity or adjoint sensitivity approach. Consider the sensitivity analysis for the unconstrained objective function $f(\{U\}(\{x\}))$

$$\left\{ \frac{df}{d\{x\}} \right\} = \left\{ \frac{df}{d\{U\}} \right\} \left[\frac{d\{U\}}{d\{x\}} \right]. \quad (11)$$

As usual in implicit sensitivity calculations, $\left[\frac{d\{U\}}{d\{x\}}\right]$ can be computed from the consistent tangent computed during the Newton step of the primary analysis and the explicit dependency of the non-linear equations w.r.t. the design variables $\{x\}$. For the design of MPCs, only the MPC equations depend explicitly on $\{x\}$. Hence, right-hand side vectors of the explicit dependency of the residual equations with respect to $\{x\}$ is then given by multiple right-hand sides stored in a right-hand side matrix

$$- \begin{bmatrix} [0] \\ \left[\{\lambda\}^T \frac{d}{dx} \left(\frac{d\{\mathcal{R}_c^{mpc}\}}{d\{U_c\}} \right) \right] \\ \left[\frac{d\{\mathcal{R}_c^{mpc}\}}{d\{x\}} \right] \end{bmatrix}, \quad (12)$$

with each column associated with a design variable.

In computing these sensitivities we consider the exact and inexact consistent tangent from the primary analysis to compute the exact and inexact gradients used in the design optimization of the MPCs.

5. Numerical example

We demonstrate the optimal design of MPCs on a slender beam with a nonlinear tip path that is modelled using a MPC, as depicted in Figure 1. The left edge is clamped. The aim is to find the required frictionless tip path defined by a MPC constraint that best predicts a prescribed load path of the centroid at which the load is applied.

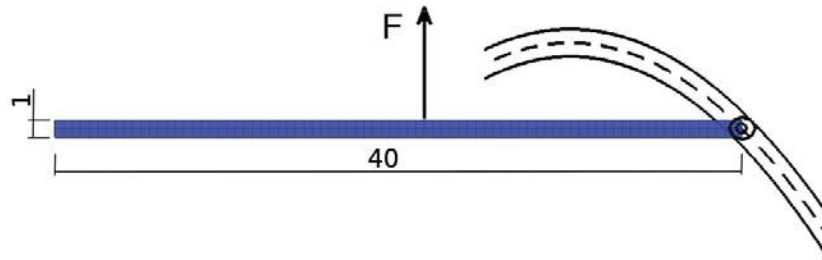


Figure 1: A slender beam with a predefined nonlinear tip path parameterized by a quadratic MPC relation.

The slender beam has a length of 40 mm, height of 1mm and a thickness of 10 mm. The slender beam is modeled using non-linear elastic finite elements in plane strain, with an applied vertical load at the centroid of the beam. The load depicted in Figure 1 indicates the positive direction. The plane strain linear elastic material properties are Young's modulus of 200 GPa and Poisson's ration of 0.3. The load path is specified by the centroid position for five load cases. The five load cases are $-1, \dots, -5$ kN and the required centroid positions tabulated in Table 2. The non-linear geometrical problem is solved using load control. The x- and y-displacements are respectively indicated under the column headings ($\{U\}_{xc}$ and $\{U\}_{yc}$). The optimal MPC solution is depicted in Figure 2. Also depicted is the deformed structure under the five load cases, in addition to the requested centroid positions for each load case.

The nonlinear tip path modeled by a MPC is parameterised by the following simple quadratic relation

$$y = a(x - b)^2 - c, \quad (13)$$

with a , b and c the design variables for the MPC design optimisation problem.

To allow us to assess the quality of the MPC design optimization solutions, we choose the parameters $a = 0.05$, $b = 30$ and $c = 5$ to compute the desired tip displacements for the five load cases given in Table 2. Hence, the optimal solution for this simple problem is known. We formulate the MPC design optimization problem as a least squares minimization problem of the error between the desired and actual centroid displacements. To ensure the points weighted properly, we normalize the centroid displacements by the solution given in Table 2 when computing the least squares error.

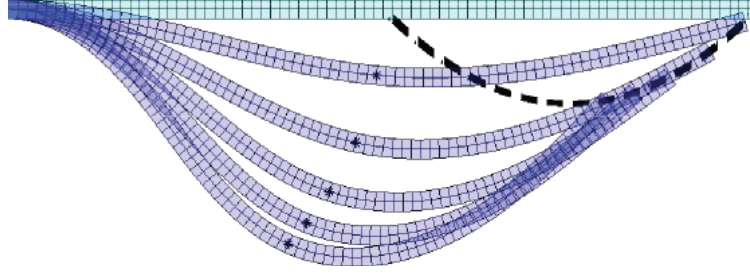


Figure 2: The optimal MPC design indicated by the dashed line. The desired centroid positions for each load case is indicated by the star markers together with the deformed structure for each load case. The undeformed structure is depicted in cyan.

Table 1: Desired tip displacement for five prescribed loadings.

Loading (kN)	$\{U\}_{xc}$ (mm)	$\{U\}_{yc}$ (mm)
-1	-0.352054942516627	-3.498394714046134
-2	-1.474966653993082	-7.072093243279817
-3	-2.868280374657851	-9.677838609719000
-4	-4.086135653307218	-11.353803264917335
-5	-5.051015315558891	-12.449137211538474

We consider two optimization algorithms that employ a cubic line search strategy. Firstly, the steepest descent (SD) algorithm and secondly the well-known Quasi-Newton Broyden-Fletcher-Goldfarb-Shanno (BFGS) algorithm. For each algorithm we supply the exact analytical gradient using the exact consistent tangent indicated by SD-EG and BFGS-EG. In addition we also have the algorithms indicated by SD-IG and BFGS-IG for which the inexact gradients are supplied. The inaccuracies result solely from using the incomplete consistent tangent from the primary analysis in the sensitivity analysis. Lastly, to quantify the effective computational savings we indicate the SD-FD and BFGS-FD algorithms to only use numerically computed finite difference gradients.

All algorithms start from the initial guess $\{x_0\} = [0.1, 25, 10]$. The four convergence criteria used in this study are

1. $\|\{\Delta x\}\| \leq 10^{-6}$,
2. $\Delta f \leq 10^{-6}$,
3. $\|\{\nabla f\}\| \leq 10^{-6}$,
4. the maximum number of function evaluations is 300.

As an initial investigation we compute the exact ∇f_{exact} and inexact $\nabla f_{inexact}$ gradients at the starting point for the objective function, as well as the complex-step ∇f_{cs} computed sensitivities using a complex step size of 10^{-20} [14]. For this problem, the inexact consistent tangent contribution is surprisingly inaccurate when compared to the exact and complex-step computed sensitivities. Since our MPC relation is quadratic, the second order consistent tangent contribution that is neglected is $2a$ multiplied by the Lagrange multiplier. The Lagrange multiplier scales with the reaction force required to enforce the MPC, and consequently amplifies this neglected contribution.

Table 2: Desired tip displacement for five prescribed loadings.

∇f	∇f_{exact}	$\nabla f_{inexact}$	∇f_{cs}
$\frac{\partial f}{\partial x_1}$	20.020650821600508	29.629165450470268	20.020650813878873
$\frac{\partial f}{\partial x_2}$	-0.220751984034818	-0.399390566601492	-0.220751983922336
$\frac{\partial f}{\partial x_3}$	0.096695873252482	0.060859843096620	0.096695873297742

The results for all six algorithms are summarized in Table 3. The steepest descent algorithms all terminated prematurely before reaching a stationary point. The SD-EG and SD-FD terminated due to the maximum number of function values being reached. The SD-IG terminated the computed descent direction failed to indicate descent. We note that convergence is very slow for steepest descent directions. Although not explored in this study, this indicates that appropriate scaling might play a significant role to improve the results. However, both the SD-EG and SD-FD is continuously improving the solution as opposed to terminating like SD-IG. Here, it is clear that the inexact gradient is insufficient to solve this problem using conventional gradient based algorithms. The BFGS algorithms using exact gradients be it analytical (BFGS-EG) or numerical (BFGS-FD) converged to the optimum. In turn, BFGS-IG terminated since the computed descent direction failed to indicate descent. The computational benefit of using analytical gradients as opposed to numerically computed finite differences is also evident, even if the problem has only three design variables.

Table 3: Optimization results.

Parameter	SD-EG	SD-IG	SD-FD	BFGS-EG	BFGS-IG	BFGS-FD
Iterations	75	4	19	41	3	41
Function Evaluations	300	39	300	46	19	184
$\ \{x\}^* - \{x\}^{\text{target}}\ $	7.063	7.070	7.067	3.557×10^{-7}	7.070	1.685×10^{-6}
$\ \nabla f(\{x\}^*)\ $	0.254	4.473	0.255	2.902×10^{-8}	1.508	2.173×10^{-6}
f^*	0.331	0.334	0.332	9.184×10^{-16}	0.336	3.029×10^{-13}

The convergence histories for the steepest descent algorithms are depicted in Figures 3 (a)-(c), and the BFGS algorithms in Figures 4 (a)-(c). Figures 3 (a) and 4(a) indicate the function value histories. Figures 3 (b) and 4 (b) indicate the step size norm at the various iterations. Figures 3(c) and 4 (c) indicate the gradient norm history.

From Figure 3(a), the steady improvement by the steepest descent algorithms and dramatic improvement by the BFGS algorithms is evident in Figure 4(a), when the exact gradient is made available.

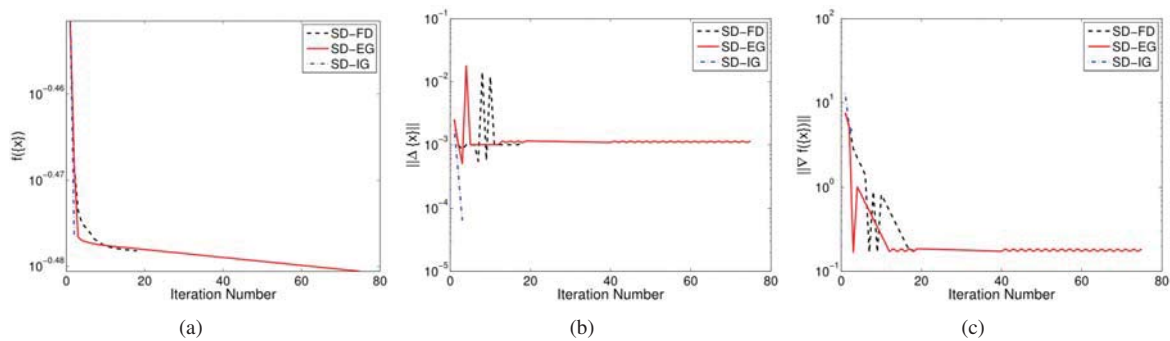


Figure 3: (a) Function value, (b) step size norm and (c) gradient norm history for the SD-FD, SD-IG and SD-EG algorithms.

5. Conclusions

We demonstrated that the inexact consistent tangent contribution from the primary analysis is not reliable to compute design sensitivities for MPC design. The inexact gradients were not able to compute descent directions and consequently the conventional gradient based algorithms terminated. The second order contribution often omitted for the primary analysis cannot be omitted when using the consistent tangent from the primary analysis for the sensitivity analysis to design MPCs. It is essential that the exact consistent tangent contribution be used to compute reliable design sensitivities, which requires the second derivative of the MPC constraint relation to be computed.

6. References

- [1] S. Kok and D.N. Wilke, Understanding linear and non-linear multi-point constraints in finite element analysis, *9th South African Conference on Computational and Applied Mechanics*, Somerset West, 14 - 16 January 2014.
- [2] R. Gallagher, *Finite element analysis: Fundamentals*, John Wiley & Sons, Ltd, 1975.

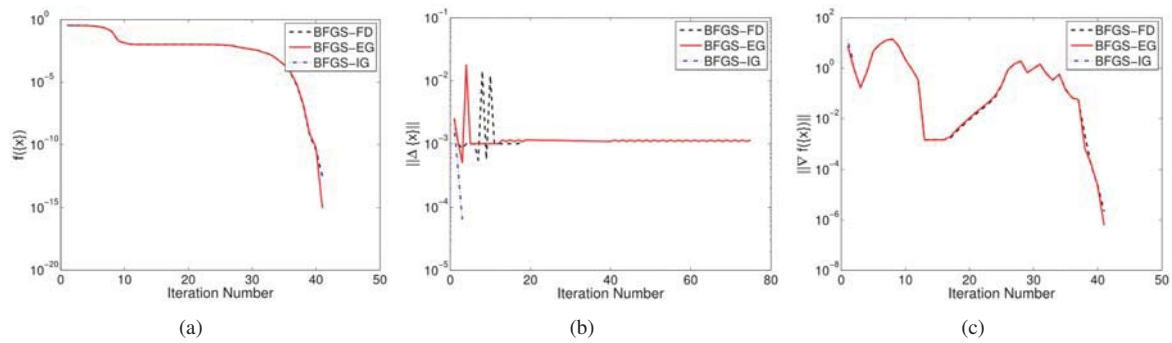


Figure 4: (a) Function value, (b) step size norm and (c) gradient norm history for the BFGS-FD, BFGS-IG and BFGS-EG algorithms.

- [3] J. Curiskis and S. Valliappan, A solution algorithm for linear constraint equations in finite element analysis, *Computers & Structures*, 8, 117 - 124, 1978.
- [4] J. F. Abel and M. S. Shephard, An algorithm for multipoint constraints in finite element analysis, *International Journal for Numerical Methods in Engineering*, 14, 464- 467, 1979.
- [5] J. Barlow, Constraint relationships in linear and nonlinear finite element analyses, *International Journal for Numerical Methods in Engineering*, 18, 521 - 533, 1982.
- [6] M. S. Shephard, Linear multipoint constraints applied via transformation as part of a direct stiffness assembly process, *International Journal for Numerical Methods in Engineering*, 20, 2107 - 2112, 1984.
- [7] O. S. Narayanaswamy, Processing nonlinear multipoint constraints in the finite element method, *International Journal for Numerical Methods in Engineering* 21, 1283 - 1288, 1985.
- [8] Y. Dubois-Pélerin and P. Pegon, Linear constraints in object-oriented finite element programming, *Computer Methods in Applied Mechanics and Engineering*, 154, 31 - 39, 1998.
- [9] R.-P. Mechnik, Consideration of constraints within the finite element method by means of matrix operators, *International Journal for Numerical Methods in Engineering*, 31, 909 - 926, 1991.
- [10] H. L. Schreyer and D. A. Parsons, Direct application of constraints to symmetric algebraic systems, *Communications in Numerical Methods in Engineering*, 11, 563 - 573, 1995.
- [11] E. Chow, T. A. Manteuffel, C. Tong and B. K. Wallin, Algebraic elimination of slide surface constraints in implicit structural analysis, *International Journal for Numerical Methods in Engineering*, 57, 1129 - 1144, 2003.
- [12] L. Jendele and J. Cervenka, On the solution of multi-point constraints: application to FE analysis of reinforced concrete structures, *Computers & Structures* 87, 970 - 980, 2009.
- [13] M. Silhavy, *The Mechanics and Thermodynamics of Continuous Media*, Springer, 1997.
- [14] J. Martins, P. Sturdza, J.J. Alonso, The Complex-Step Derivative Approximation, *ACM Transactions on Mathematical Software*, 29, 245-262, 2003.

Distributed NSGA-II for seismic retrofitting optimization with multi-core PC cluster

Keunhyoung Park¹, Hyo Seon Park²

¹ Yonsei University, Seoul, South Korea, tugurun@yonsei.ac.kr

² Yonsei University, Seoul, South Korea, hspark@yonsei.ac.kr

1. Abstract

The distributed Genetic Algorithm (GA) for PC cluster with multi-core-CPU is proposed as a time reducing method for determining the schemes of retrofitting existing buildings with Buckling restrained Brace (BRB). Non-dominated Sorting Genetic Algorithm-II (NSGA-II), one of the derivative evolutionary algorithm in heuristic method, was applied since the optimization problem have a multi-objective function. Two problem case was selected for validating performance of the distributed GA. The first case is seismic retrofitting of a two-dimensional steel frame structure with nonlinear static analysis, and the other one is seismic retrofitting of a three-dimensional reinforced concrete frame structure with nonlinear dynamic analysis. The objectives in both problems are minimization of cost for retrofitting and damage of retrofitted frame structure. To reduce the time for searching optimal solutions, the cluster computer consists of off-the-shelf Personal Computer (PC) with central processing unit (CPU) of quad-core processor was used. The PCs of the cluster were connected to local area network (LAN) through network switch have gigabits bandwidth. As a result, this study confirmed the possibility of using the cluster computer composed with multi-core-CPU as High Performance Computing (HPC) for seismic retrofitting optimization.

2. Keywords: seismic retrofitting, buckling restrained braces (BRBs), design optimization, genetic algorithms (GA), personal computer cluster, multi-core-CPU

3. Introduction

Buckling restrained braces (BRB), a kind of Hysteretic dampers (HD), is one of effective method for preventing the damage of main frame structure [1]. There are many research and application cases for using BRB for improving seismic capacity of the target building [2-6]. Conventional optimization algorithms are not suitable for BRB retrofitting design optimization since the relation between changing of design variables and structural performance of the retrofitted building is discontinuous and nondifferentiable [7].

Although Genetic Algorithm (GA) can overcome the limits of conventional optimization algorithms, development of BRB retrofitting design optimization using GA have to manage the possible excessive computation time of repeated nonlinear structural analysis in iteration process of GA. For this reason, many researchers has try to apply personal computer (PC) cluster to structural optimization [8-15].

In this study, to improve the efficiency of existing retrofitting methods using BRB, the distributed GA-based optimal seismic retrofit design using BRBs for conjugating cluster of commercial PCs with multi-core CPU is suggested. The PC with i7-2600 quad-core processor [16] are connected to local area network (LAN) through switching network [17] have communication speed of Gbits per second.

The distributed GA is considering the communication configuration of PC cluster with multi-core-CPU. Performance of The distributed GA was evaluated by applying to 2-dimensional retrofitting design optimization with nonlinear static structural analysis and 3-dimensional retrofitting design optimization with nonlinear dynamic structural analysis.

4. Formulation of retrofit design optimization problem

4.1 Design variables

In this study, circular hollow sections [18, 19] and rectangular section contained cross shaped steel core [18] are considered as BRB section. Material of the BRB are same as of Sarno and Elanshai's case. The section configuration of BRB installed at spans in target building is determined by width, depth, and thickness of steel core.

4.2 Objective functions

4.2.1 Objective function for 2D frames with nonlinear static analysis

Section area of steel core in BRB is dominant factor of total retrofitting cost while the area determine the capacity of BRB. Thus, first objective function f_1 , which is minimizing total volume of steel core in the installed BRBs, is calculated in Equation 1 as presented below.

$$\text{Minimize Objective } f_1(\mathbf{x}) = \sum_{i=1}^B 2A_i l_i \quad \text{Equation 1}$$

A_i and l_i are cross-sectional area and length of BRB installed at i th span. B is available spans to installed BRB. The volume is doubled because the BRB is installed as X shape at a span. Second objective function f_{2D-2} suggested Wen and Kang [20] is minimizing expecting lifetime seismic damage cost, and calculated in Equation 2 as below.

$$\text{Minimize Objective } f_{2D-2}(\mathbf{x}) = \frac{U}{\lambda} (1 - e^{-\lambda t}) \sum_{i=1}^k C_i P_i \quad \text{Equation 2}$$

U is annual occurrence probability. λ is lognormal distribution parameters in the seismic hazard distribution, t is expected lifetime of retrofitted building. k is the number of limit states as seismic damage. C_i and P_i are life-cycle cost and probability of a single hazard of i th damage state. P_i is calculated based on the interstory drift ratio Δ , as defined in Equations 3 and 4.

$$P_i = P(\Delta > \Delta_i) - P(\Delta > \Delta_{i+1}) \quad \text{Equation 3}$$

$$P(\Delta > \Delta_i) = -\frac{1}{U \times t} \left\{ \ln \left[1 - P_i(\Delta > \Delta_i) \right] \right\} \quad \text{Equation 4}$$

Δ_i is interstory drift ratio, $P_i(\Delta > \Delta_i)$ is occurrence probability of i th damage state through a period (0, t). In this study, seismic level have occurrence probability of 50%, 10%, 2% during 50 years is considered for $P_i(\Delta > \Delta_i)$ [21].

4.2.2 Objective function for 3D frames with nonlinear dynamic analysis

In 3D frame optimization case, objective function for minimizing total volume of BRB is same as the Equation 1. On the other hand, to avoid excessive computation time, second objective function f_{3D-2} is the form of minimizing dissipated seismic energy at the main frame structure retrofitted by BRB [7, 22], as defined in Equation 5.

$$\begin{aligned} f_{3D-2}(\mathbf{X}) &= \sum_{i=1}^M \int (V_i d_i + M_i \theta_i) dt \\ \text{Minimize} \quad &= \sum_{i=1}^M \sum_{t=1}^N \left[\frac{(V_i(t) + V_i(t+1))}{2} \times (d_i(t+1) - d_i(t)) + \frac{(M_i(t+1) + M_i(t))}{2} \times (\theta_i(t+1) + \theta_i(t)) \right] \end{aligned} \quad \text{Equation 5}$$

$V_i(t)$ and $M_i(t)$ are shear force and moment of j th element at time step t . $d_i(t)$ and $\theta_i(t)$ are deformation and rotation of j th element at time step t . M is the number of element of the main frame, N is the number of points of inputted ground motion data.

4.3. Constrained conditions

To secure structural performance capacity of the retrofitted building, maximum interstory drift is regulated to be limited in allowable interstory drift ratio [21, 23, 24]. The condition about inter story-drift ratio is represented in Equation 7.

$$c = \Delta_{\max} / \Delta_a \leq 1.0 \quad \text{Equation 6}$$

Δ_{\max} is maximum interstory drift ratio in analysis, Δ_a is allowable interstory drift ratio. The allowable interstory drift ratio 2% is meaning structural performance level of life safety of braced steel frames and concrete frame in Table C1-3 FEMA-356 [25], and is middle value of heavy damage state range [26].

4.4. Distributed GA on multi-core PC cluster

The CPU of PC in the PC cluster is Intel Core i7 2600K which have 4 core processor of 3.4GHz clock rate [16]. The PC cluster consists of 16 of PC, which is meaning 16 of quad-core CPUs, 64 of core processor. The scheduler for parallelizaion of retrofitting design optimization algorithm is function of toolbox of MATLAB Distributed Computing Server (MDCS) [27]. The core processor as a master node, is also switched to a slave node, communicate with other core processor which is slave node through a network switch. It means that core processors in a PC have to share a LAN card of the PC, because the LAN card is only communication route of the PC. As a result, more frequent communication between master node and slave nodes casue more serious bottle-neck effect in the algorithm. In this study, considering the configuration of the PC cluster and GA which is containg nonlinear struatural analysis, the distributed GA is parallelized as candidate solutions level to minimize the number of communication times.

5. Performance of Distributed NSGA-II

Performance of the distributed NSGA-II was evaluated by the standard of global convergnace, computation time efficiency, and quality of optimal solutions while enlarging the number of core processors in the PC cluster as 1, 2, 4, 8, 16, 32, 64 (1/4, 1/2, 1, 2, 4, 8, 16 of quad-core CPUs). The optimization was repeated at each cases of the number of core processors because GA has probability.

Pareto-front lines from the repeated optimization trials were assessment to evaluate global convergence test. Computation time efficiency was mesearured by the speedup of elapsed computation time of generation part in GA. Ideal speedup Sideal was calculated by Amdahl’s Law [28]. Improvement in structural quality was assessed by comparing the objective function values of candidate solutions to the values of not optimized case.

5.1. 2-dimensional steel frame structure case with nonlinear static analysis

The BRBs retrofitting design for existing steel moment resisting frames suggested by Sarno and Elnashai was selected as target building of 2-dimensional frame structure case [19].

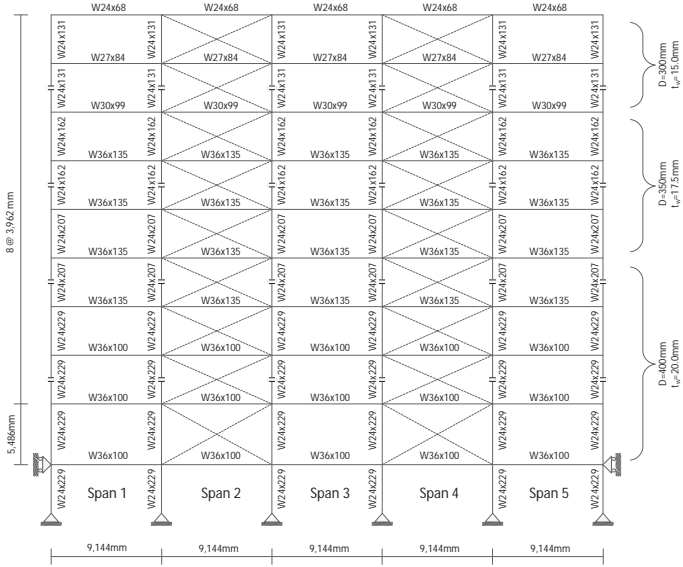


Figure 1: Scheme of 2D braced frame of Sarno and Elnashai

In this study, for considering most severe optimization case while securing the symmetry of the retrofitted building, the section area of BRB can be varied independently of the location of span, or story. Pushover analysis performed at seismic level of occurance propability 2% during 50 year. The analysis followed analysis procedure of FEMA 356.

Global convergence was confirmed by comparing all of Pareto-front solutions from repeated optimization trials to objective function value of Sarno and Elnashai’s retrofitting case. At the same time, improvement of seismic capacity of the candidate solutions also evaluated by the Pareto-front solutions.

When using 64 of core processor (16 of quad-core CPUs), the distributed NSGA-II is 27.55 times faster than serial version. The efficiency of actual speedup related to ideal speedup are better than 83% except the case of using 32 of core processors (8 of quad-core CPUs), the efficiency of 79.07%. Actual speedup was decreased while used computation resources was increased. However, the tendency of the ratio of actual speedup to ideal speedup is not according size of computation recources.

5.2. 3-dimensional irregular reinforced concrete frame structure with nonlinear dynamic analysis case BRB retrofitting optimization of SPEAR building was performed. The SPEAR building is 3-story reinforced concrete frame building has irregular plane, presented in figure as bellow.

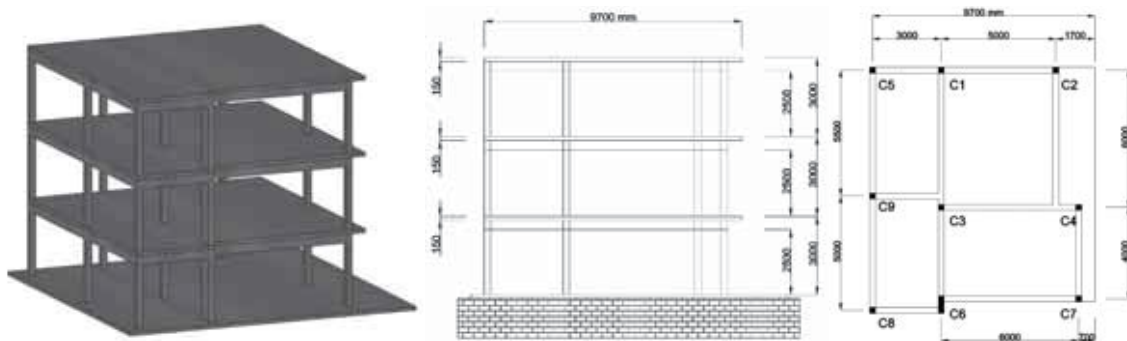


Figure 2: Configuration of SPEAR building before being optimized

The SPEAR building represents older construction in Greece and elsewhere in the Mediterranean region without engineered earthquake resistance since the SPEAR building was designed considering only gravity load only [29, 30].

In this study, the post-test model modified by Strantan and Fajfar was employed as analysis modeling of SPEAR building in BRB retrofitting design optimization. More specific information about the SPEAR building can be found in research of Fajfar [30, 31]. Nonlinear dynamic analysis is performed by using seismic input signal used in the research of Dolšek and Fajfar [32], presented in Figure 11.

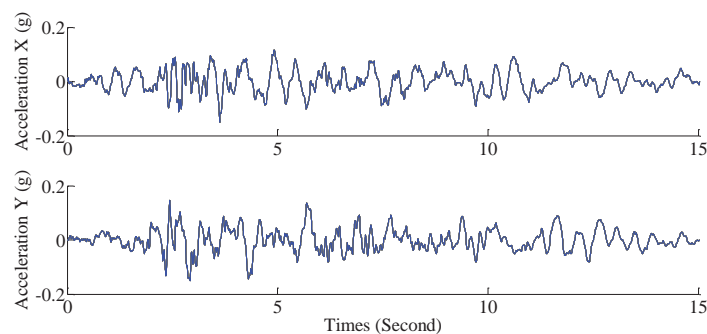


Figure 3: The time-history graph of bi-directional ground motion data normalized to PGA=0.15g

Global convergence was confirmed by comparing all of Pareto-front solutions from repeated optimization trials. Improvement of seismic capacity of the candidate solutions also evaluated by the Pareto-front solutions. Actual speedup was decreased while the size of computation resources was increased. However, the tendency of the ratio of actual speedup to ideal speedup is not according size of computation resources.

Elapsed time of parallelized part of 3-d irregular reinforced concrete frame structure case is increased from 98.52% to 99.85% since structural analysis of the case took 6 times as longer as computation time of 2-D case. The enlarged the ratio of parallelized part results improved parallelization efficiency. When using 64 of core processor (16 of quad-core CPUs), the distributed NSGA-II is 48.36 times faster than serial version. The efficiency of actual speedup related to ideal speedup are better than 80%. The tendency of the ratio of actual speedup to ideal speedup is not according size of computation resources as the tendency of 2-D case.

6. Conclusion

In this study, the distributed NSGA-II for multi-core PC cluster to overcome excessive computation time for BRB retrofitting design optimization was suggested and assessed the performance by applying to optimization problems. The distributed NSGA-II employed master-slave parallel model and performed on the PC cluster with 16 of quad-core CPUs. Performance of the algorithm assessed by the standard of global convergence, computation time efficiency, and quality of optimal solutions while applying the optimization problems.

Global convergence and improved quality of optimal solutions are confirmed by Pareto-front solutions from

repeated optimization trials of retrofitting problems. The fluctuation of actual speedup ratio have no certain relation with the number of core processors, but appeared similar tendency at the both of optimization cases. The ratio of actual speedup to ideal speedup of all optimization trials have minimum efficiency of 79.07%. Maximum actual speedups are 27.55 in 2-D and 48.36 in 3-D optimization case. The decrease of the ration of actual speedup was diminished in 3-D optimization case than 2-D optimization case. Moreover, there was phenomenon that the ratio of actual speedup to the ideal speedup is increased while using more core processors. In conclusion, the results of optimization trials show that stable and effective performance of the distributed NSGA-II with multi-core PC cluster

7. Acknowledgements

This work was supported by the National Research Foundation of Korea (NRF) grant funded by the Korea government (Ministry of Education, Science and Technology, MEST) (No. 2011-0018360).

8. References

- [1] Huang, Y., et al., Seismic performance of moment resistant steel frame with hysteretic damper. Behaviour of Steel Structures in Seismic Areas: STESSA: p. 403-409.2000.
- [2] Kim, J. and H. Choi, Behavior and design of structures with buckling-restrained braces. Engineering Structures, 26(6): p. 693-706.2004.
- [3] Xie, Q., State of the art of buckling-restrained braces in Asia. Journal of Constructional Steel Research, 61(6): p. 727-748.2005.
- [4] Fahnestock, L.A., J.M. Ricles, and R. Sause, Experimental evaluation of a large-scale buckling-restrained braced frame. Journal of Structural Engineering, 133(9): p. 1205-1214.2007.
- [5] Sabelli, R., S. Mahin, and C. Chang, Seismic demands on steel braced frame buildings with buckling-restrained braces. Engineering Structures, 25(5): p. 655-666.2003.
- [6] Tremblay, R., et al., Seismic testing and performance of buckling-restrained bracing systems. Canadian Journal of Civil Engineering, 33(2): p. 183-198.2006.
- [7] Farhat, F., S. Nakamura, and K. Takahashi, Application of genetic algorithm to optimization of buckling restrained braces for seismic upgrading of existing structures. Computers and Structures, 87(1-2): p. 110-119.2009.
- [8] Dixon, M. and M. Zubair. Calibration of stochastic volatility models on a multi-core CPU cluster. in 6th Workshop on High Performance Computational Finance, WHPCF 2013 - Held in Conjunction with the International Conference for High Performance Computing, Networking, Storage and Analysis, SC 2013. of Conference. Denver, CO. Year.
- [9] Park, H.S., et al., Distributed hybrid genetic algorithms for structural optimization on a PC cluster. Journal of Structural Engineering, 132(12): p. 1890-1897.2006.
- [10] Park, H.S. and C.W. Sung, Distributed structural analysis of large-scale structures on a cluster of personal computers. Computer-Aided Civil and Infrastructure Engineering, 17(6): p. 409-422.2002.
- [11] Park, H.S. and C.W. Sung, Optimization of steel structures using distributed simulated annealing algorithm on a cluster of personal computers. Computers and Structures, 80(14-15): p. 1305-1316.2002.
- [12] Kennedy, G.J. and J.R.R.A. Martins, A parallel aerostructural optimization framework for aircraft design studies. Structural and Multidisciplinary Optimization.2014.
- [13] Okamoto, Y., et al., Topology optimization of rotor core combined with identification of current phase angle in IPM motor using multistep genetic algorithm. IEEE Transactions on Magnetics, 50(2).2014.
- [14] Adeli, H. and S. Kumar, Distributed genetic algorithm for structural optimization. Journal of Aerospace Engineering, 8(3): p. 156-163.1995.
- [15] Munir, S., R.R. Hussain, and A.B.M.S. Islam, Parallel framework for earthquake induced response computation of the SDOF structure. Journal of Civil Engineering and Management, 20(4): p. 477-484.2014.
- [16] Intel, Intel® 64 and IA-32 Architectures Optimization Reference Manual. 2014.
- [17] NETGEAR, ProSafe® 24- and 48-port GSM72xxPS Stackable Gigabit PoE L2+ Managed Switches Data Sheet, NETGEAR, Editor., NETGEAR: San Jose. p. Manual. 2015.
- [18] Güneş, E.M., Seismic reliability of steel moment resisting framed buildings retrofitted with buckling restrained braces. Earthquake Engineering and Structural Dynamics, 41(5): p. 853-874.2012.
- [19] Di Sarno, L. and A.S. Elnashai, Bracing systems for seismic retrofitting of steel frames. Journal of Constructional Steel Research, 65(2): p. 452-465.2009.
- [20] Wen, Y.K. and Y.J. Kang, Minimum building life-cycle cost design criteria. II: Applications. Journal of structural engineering New York, N.Y., 127(3): p. 338-346.2001.
- [21] Liu, M., S.A. Burns, and Y.K. Wen, Optimal seismic design of steel frame buildings based on life cycle cost considerations. Earthquake Engineering and Structural Dynamics, 32(9): p. 1313-1332.2003.
- [22] Choi, H. and J. Kim, Energy-based seismic design of buckling-restrained braced frames using hysteretic

- energy spectrum. *Engineering Structures*, 28(2): p. 304-311.2006.
- [23] Fragiadakis, M. and M. Papadrakakis, Performance-based optimum seismic design of reinforced concrete structures. *Earthquake Engineering and Structural Dynamics*, 37(6): p. 825-844.2008.
- [24] Zou, X.K. and C.M. Chan, Optimal seismic performance-based design of reinforced concrete buildings using nonlinear pushover analysis. *Engineering Structures*, 27(8): p. 1289-1302.2005.
- [25] FEMA 356, Prestandard and Commentary for The Seismic Rehabilitation of Buildings, F.E.M. Agency, Editor., The American Society of Civil Engineers: Washington, DC. 2000.
- [26] Park, Y.-J., A.H.S. Ang, and Y.K. Wen, SEISMIC DAMAGE ANALYSIS OF REINFORCED CONCRETE BUILDINGS. *Journal of Structural Engineering*, 111(4): p. 740-757.1985.
- [27] MATHWORKS. MATLAB Distributed Computing Server. [cited 2015 2015-1-13]; Available from: <http://kr.mathworks.com/products/distriben/?refresh=true>.2015.
- [28] Amdahl, G.M., Validity of the single processor approach to achieving large scale computing capabilities, in Proceedings of the April 18-20, 1967, spring joint computer conference. ACM: Atlantic City, New Jersey. p. 483-485. 1967.
- [29] Dolek, M. and P. Fajfar, Mathematical modelling of an infilled RC frame structure based on the results of pseudo-dynamic tests. *Earthquake Engineering and Structural Dynamics*, 31(6): p. 1215-1230.2002.
- [30] Stratan, A. and P. Fajfar, Influence of modelling assumptions and analysis procedure on the seismic evaluation of reinforced concrete GLD frames, in IKPIR Report. Institute of Structural Engineering, Earthquake Engineering and Construction IT: Ljubljana. 2002.
- [31] Fajfar, P.D., M.; Marušić, D.; Stratan, A., Pre- and post-test mathematical modelling of a plan-asymmetric reinforced concrete frame building. *Earthquake Engineering and Structural Dynamics*, 35(11): p. 1359-1379.2006.
- [32] Dolšek, M. and P. Fajfar, Post-test analyses of the SPEAR test building, in University of Ljubljana, www.ikpir.com/projects/spear. 2005.

Enhanced second-order reliability method and stochastic sensitivity analysis using importance sampling

Jongmin Lim¹, Byungchai Lee¹, Ikjin Lee^{1*}

¹ Korea Advanced Institute of Science and Technology, Daejeon, Korea, ikjin.lee@kaist.ac.kr

1. Abstract

The enhanced second-order reliability method (eSORM) is proposed in this study in order to improve accuracy in estimating a probability of failure. Conventional SORM additionally approximates an already approximated quadratic performance function to a parabolic surface, indicating that those methods are based on an incomplete second-order Taylor expansion of the performance function. This additional approximation means a loss of accuracy in estimating the probability of failure. The proposed SORM utilizes the importance sampling to calculate the probability of failure of a complete second-order Taylor expansion of the performance function without the parabolic approximation, so it shows better accuracy compared to the conventional SORM methods. The proposed SORM method also utilizes an approximated Hessian of the performance function by using the symmetric rank-one update in Quasi-Newton method, which means that additional function calls are not required except the computation used for MPP search. In addition to the improvement of the accuracy, stochastic sensitivity analysis is performed in the proposed method by applying the importance sampling to the quadratically approximated performance function. Therefore, the second-order sensitivity of the probability of failure as well as the first-order one can be easily computed in the proposed method without additional function calls.

2. Keywords: Reliability analysis, Second-order reliability method, Stochastic sensitivity analysis, Importance sampling, Approximated Hessian

3. Introduction

In a reliability analysis, it is quite difficult to estimate the probability of failure defined as a multi-dimensional integration over a nonlinear domain in a real engineering problem especially including finite element analysis. Hence, reliability methods based on function approximation are commonly used such as first-order reliability method (FORM) [1], second-order reliability method (SORM) [2-5], and dimension reduction method (DRM) [6-8]. Those methods approximate the performance function at the most probable point (MPP) which has the highest probability density on a limit-state surface and can be obtained by searching the minimum distance from the origin to the limit-state surface in the standard normal space (U-space). FORM which linearizes the performance function at MPP is the most commonly used reliability method due to its numerical efficiency. FORM shows reasonable accuracy when the performance function is almost linear or mildly nonlinear. However, FORM might give erroneous reliability estimation if the performance function is highly nonlinear. More accurate reliability estimation can be performed using SORM even for a highly nonlinear system since curvature of the performance function near MPP is considered in SORM by calculating second-order derivatives of the performance function. In spite of the fact that SORM is obviously more accurate than FORM, SORM is limitedly used in engineering problems due to the calculation of the second-order derivatives of the performance function, which might require huge computational cost.

After the second-order Taylor series of the performance function is constructed at MPP using the first and second-order derivatives of the performance function, the approximated function is once more approximated to a parabolic surface, indicating that the incomplete Taylor series is used in conventional SORM methods [9]. Furthermore, to obtain analytical formulation to calculate the probability of failure, an additional approximation such as an asymptotic approximation is introduced in the conventional SORM method. These two approximations mean a loss of accuracy in estimating the probability of failure.

To calculate the probability of failure more accurately without approximations additional to the quadratic approximation, the enhanced SORM (eSORM) method is proposed in this study. The proposed eSORM utilizes the importance sampling to calculate the probability of failure of the complete second-order Taylor expansion of the performance function without the parabolic approximation. Thus, it shows better accuracy compared to the conventional SORM methods. Sampling methods [10-12] such as the Monte Carlo Simulation (MCS) and the importance sampling estimate readily the probability of failure using the stochastic sampling because the complex analytical formulation is not required in the sampling method. In addition to the calculation of the probability of failure, stochastic sensitivity analysis is also readily performed without additional function calls in the sampling method [13]. However, the computational demand for the sampling method is generally prohibitive if an

engineering problem including virtual simulation such as finite element analysis is considered. Since the proposed eSORM applies the importance sampling not to the original performance function but to quadratically approximated function, the required computational cost except for the Hessian calculation is negligible. The proposed eSORM method also utilizes an approximated Hessian of the performance function by using the symmetric rank-one update in Quasi-Newton method, which means that additional function calls are not required except the computation used for MPP search [14]. In addition to the improvement of the accuracy, the stochastic sensitivity analysis is performed in the proposed method by applying the stochastic sensitivity analysis of the sampling method to the quadratically approximated performance function. The second-order sensitivity of the probability of failure as well as the first-order one can be easily computed in the proposed method without additional functional calls.

4. Enhanced second-order reliability method (eSORM)

4.1. FORM and SORM

The probability of failure can be defined as a multi-dimensional integral as [15]

$$P_f = P[G(\mathbf{X}) > 0] = \int_{G(\mathbf{X}) > 0} f_{\mathbf{X}}(\mathbf{x}) d\mathbf{x} \quad (1)$$

where $P[\cdot]$ is a probability function, X_i is a random variable and x_i is a realization of X_i . $f_{\mathbf{X}}(\mathbf{x})$ is a joint probability density function of \mathbf{X} , and $G(\mathbf{X})$ is a performance function such that $G(\mathbf{X}) > 0$ is defined as failure and $G(\mathbf{X}) = 0$ is defined as a limit-state equation. Due to difficulties in computing the multi-dimensional integral in Eq. (1), FORM linearizes the performance function $G(\mathbf{X})$ at a most probable point (MPP) \mathbf{u}^* in U-space obtained by the transformation [16] as

$$G(\mathbf{X}) = g(\mathbf{U}) \cong g(\mathbf{u}^*) + \nabla g^T(\mathbf{U} - \mathbf{u}^*) \quad (2)$$

FORM is the most commonly used reliability analysis method due to the computational efficiency, and it shows reasonable accuracy in calculating the probability of failure for linear and mildly nonlinear performance functions. However, the error incurred by the linearization becomes considerable when the performance function is highly nonlinear. For this reason, SORM approximates the performance function quadratically given as [9]

$$g_Q(\mathbf{U}) = g(\mathbf{u}^*) + \nabla g^T(\mathbf{U} - \mathbf{u}^*) + \frac{1}{2}(\mathbf{U} - \mathbf{u}^*)^T \mathbf{H}(\mathbf{U} - \mathbf{u}^*) \quad (3)$$

where \mathbf{H} is the Hessian matrix evaluated at MPP in U-space. Equation (3) is transformed to V-space and is rewritten as

$$\frac{\tilde{g}_Q(\mathbf{V})}{\|\nabla g\|} = V_N - \beta + \tilde{\mathbf{V}}^T \tilde{\mathbf{A}} \tilde{\mathbf{V}} + \frac{\beta^2}{2} \boldsymbol{\alpha} \frac{\mathbf{H}}{\|\nabla g\|} \boldsymbol{\alpha} - \beta \boldsymbol{\alpha}^T \frac{\mathbf{H}}{\|\nabla g\|} \mathbf{R} \mathbf{V} + 2V_N \mathbf{A}_{N1} \tilde{\mathbf{V}} + A_{NN} V_N^2 \quad (4)$$

where $\tilde{\mathbf{V}} = \{V_1, V_2, \dots, V_{N-1}\}^T$, $\mathbf{A} = \frac{\mathbf{R}^T \mathbf{H} \mathbf{R}}{2\|\nabla g\|} = \begin{bmatrix} \tilde{\mathbf{A}} & \mathbf{A}_{1N} \\ \mathbf{A}_{N1} & A_{NN} \end{bmatrix}$ and V-space is transformed using the orthogonal

transformation $\mathbf{u} = \mathbf{R} \mathbf{v}$. \mathbf{R} is an $N \times N$ orthogonal rotation matrix whose N^{th} column is $\boldsymbol{\alpha} = \frac{\nabla g}{\|\nabla g\|}$, and computed

using Gram-Schmidt orthogonalization such that \mathbf{R} is written as $\mathbf{R} = [\mathbf{R}_1 | \boldsymbol{\alpha}]$ where $\boldsymbol{\alpha}^T \mathbf{R}_1 = \mathbf{0}$. In order to obtain the closed-form formula of the probability of failure, second-order approximated function in Eq. (4) is further approximated to a parabolic surface by neglecting all cross terms between $\tilde{\mathbf{V}}$ and V_N as follows

$$\frac{\tilde{g}_Q(\mathbf{V})}{\|\nabla g\|} = V_N - \beta + \tilde{\mathbf{V}}^T \tilde{\mathbf{A}} \tilde{\mathbf{V}} \quad (5)$$

Based on the parabolic approximation in Eq. (5), Breitung [3] proposed a simple formula for the probability of

failure with additional approximations such as an asymptotic approximation, which is given by

$$P_f^{SORM} \cong \Phi(-\beta) \left\| \mathbf{I}_{N-1} - 2\beta\tilde{\mathbf{A}} \right\|^{-\frac{1}{2}} \quad (6)$$

In SORM, errors due to the approximations can be categorized as follows [9]

Type 1: Error due to approximating the performance function by the second-order Taylor expansion.

Type 2: Error due to further approximating the second-order approximated function to the parabolic surface.

Type 3: Error due to the additional approximations to obtain the closed-form formula for the probability of failure.

The error of type 1 cannot be eliminated unless higher-order Taylor expansion is constructed. The parabolic approximation in the error of type 2 means that the conventional SORM methods have been based on an incomplete second-order Taylor expansion, and the approximation in type 3 leads to the additional loss of accuracy in estimating the probability of failure.

4.2 The proposed eSORM

In order to improve accuracy in estimating probability of failure in SORM, the enhanced second-order reliability method (eSORM) is proposed in this study by utilizing the stochastic sampling method. Since eSORM calculates the probability of failure based on the complete second-order Taylor expansion of a performance function, its accuracy is considerably improved compared to the conventional SORM methods. The approximated Hessian of the performance function is used in this study, indicating that additional function calls are not required except the computation used for MPP search [14]. Furthermore, the second-order sensitivity of the probability of failure as well as the first-order sensitivity can be readily computed in the proposed eSORM.

By introducing an indicator function for failure region, the probability of failure in Eq. (1) can be rewritten as its expectation as [17]

$$P_f = \int_{\mathbf{R}^{nrv}} I_{\Omega_f}(\mathbf{x}) f_{\mathbf{x}}(\mathbf{x}) d\mathbf{x} = E \left[I_{\Omega_f}(\mathbf{X}) \right] \quad (7)$$

where nrv means the number of random variables and $I_{\Omega_f}(\mathbf{x})$ is the indicator function which is defined as

$$I_{\Omega_f}(\mathbf{x}) \equiv \begin{cases} 1, & \mathbf{x} \in \Omega_f \\ 0, & \text{otherwise} \end{cases} \quad (8)$$

where Ω_f is the failure region which is defined as $G(\mathbf{X}) > 0$. In order to calculate the probability of failure in Eq. (7) using the stochastic sampling method, numerous function calls are required which is computationally very expensive and almost impossible if the computer simulation is included. Hence, instead of the original performance function, the quadratically approximated performance function defines the failure region in Eq. (8) in the proposed method as follows

$$I_{\hat{\Omega}_f}(\mathbf{x}) \equiv \begin{cases} 1, & \mathbf{x} \in \hat{\Omega}_f \\ 0, & \text{otherwise} \end{cases} \quad (9)$$

In Eq. (9), the failure region $\hat{\Omega}_f$ is defined using the second-order Taylor expansion of the performance function as

$$\hat{\Omega}_f \equiv \{ \mathbf{x} : G_Q(\mathbf{x}) > 0 \} \quad (10)$$

where $G_Q(\mathbf{x})$ is the quadratic performance function approximated in the original space (X-space) at MPP. Since a

reference point of the second-order Taylor expansion is MPP in SORM, the approximation is accurate near MPP and is the most accurate at MPP. Hence, the importance sampling method selecting MPP as a sampling center is performed to calculate the probability of failure about the quadratic performance function $G_Q(\mathbf{x})$ in this study as

$$P_f = \int_{\mathbf{R}^{nrv}} I_{\hat{\Omega}_f}(\mathbf{x}) \frac{f_{\mathbf{X}}(\mathbf{x})}{h(\mathbf{x})} h(\mathbf{x}) d\mathbf{x} = E \left[I_{\hat{\Omega}_f}(\mathbf{X}) \frac{f_{\mathbf{X}}(\mathbf{X})}{h(\mathbf{X})} \right] \quad (11)$$

where $h(\mathbf{x})$ is an instrumental density function for the importance sampling.

The proposed eSORM is based on the complete second-order Taylor expansion without the parabolic approximation, indicating that the type 2 error can be readily eliminated. The importance sampling is performed using the approximated performance function, not the original one in eSORM. Therefore, the computational cost to calculate the probability of failure after constructing the approximated function is negligible even though sufficient number of samples are evaluated. Considering that accurate calculation of probability of failure is possible in the sampling method with sufficient samples, the type 3 error incurred during obtaining the closed-form formula for the probability of failure in the conventional SORM is also easily removed. In this way, the proposed eSORM contains only the type 1 error and its accuracy is thus significantly improved even though the total computational cost of eSORM is the same as one of the conventional SORM.

Even though SORM usually shows great accuracy in estimating probability of failure, the calculation of the Hessian of a performance function aggravates the numerical burden of SORM. When SORM is used within RBDO, this problem intensifies due to the repeated reliability assessment. Hence, the proposed eSORM utilize approximated SORM [14] recently proposed in order to resolve the heavy computational burden in SORM by using the quasi-Newton approach to approximate the Hessian. Since the approximated Hessian is used instead of calculating the true Hessian, the additional function evaluation except for the MPP search is not required in order to construct the second-order Taylor expansion of the performance function.

4.3. The proposed stochastic sensitivity analysis

This study presents the sensitivity analysis of eSORM, so that eSORM is readily utilized to obtain the accurate reliability-based optimum in RBDO. Since the proposed eSORM is based on the stochastic sampling method, the stochastic sensitivity analysis using eSORM can be performed efficiently and simply using the stochastic sensitivity analysis of the stochastic sampling method. In the stochastic sampling method, the sensitivity of the probability of failure with respect to the mean of random variables is given by [17]

$$\frac{\partial P_f}{\partial \mu_j} = \int_{\mathbf{R}^{nrv}} I_{\hat{\Omega}_f}(\mathbf{x}) \frac{\partial \ln f_{\mathbf{X}}(\mathbf{x})}{\partial \mu_j} f_{\mathbf{X}}(\mathbf{x}) d\mathbf{x} = E \left[I_{\hat{\Omega}_f}(\mathbf{X}) \frac{\partial \ln f_{\mathbf{X}}(\mathbf{X})}{\partial \mu_j} \right] \quad (12)$$

where $\frac{\partial \ln f_{\mathbf{X}}(\mathbf{x})}{\partial \mu_j}$ is known as the first-order score function which can be analytically obtained. If the random

variables are correlated, the score function can be evaluated using a copula function. In a similar fashion with Eq. (11), Eq. (12) can be re-written using the instrumental density function and the failure region defined using the second-order Taylor expansion of the performance function in Eq. (10) as

$$\frac{\partial P_f}{\partial \mu_j} = \int_{\mathbf{R}^{nrv}} I_{\hat{\Omega}_f}(\mathbf{x}) \frac{\partial \ln f_{\mathbf{X}}(\mathbf{x})}{\partial \mu_j} \frac{f_{\mathbf{X}}(\mathbf{x})}{h(\mathbf{x})} h(\mathbf{x}) d\mathbf{x} = E \left[I_{\hat{\Omega}_f}(\mathbf{X}) \frac{\partial \ln f_{\mathbf{X}}(\mathbf{X})}{\partial \mu_j} \frac{f_{\mathbf{X}}(\mathbf{X})}{h(\mathbf{X})} \right] \quad (13)$$

In Eq. (13), the instrumental density function $h(\mathbf{x})$ is independent with the design variable μ_j .

The second-order sensitivity of the probability of failure in eSORM can be readily calculated in a similar way as

$$\begin{aligned} \frac{\partial^2 P_f}{\partial \mu_i \partial \mu_j} &= \int_{\mathbf{R}^{nrv}} I_{\hat{\Omega}_f}(\mathbf{x}) \left[\frac{\partial^2 \ln f_{\mathbf{X}}(\mathbf{x})}{\partial \mu_i \partial \mu_j} + \frac{\partial \ln f_{\mathbf{X}}(\mathbf{x})}{\partial \mu_j} \frac{\partial \ln f_{\mathbf{X}}(\mathbf{x})}{\partial \mu_i} \right] \frac{f_{\mathbf{X}}(\mathbf{x})}{h(\mathbf{x})} h(\mathbf{x}) d\mathbf{x} \\ &= E \left[I_{\hat{\Omega}_f}(\mathbf{X}) \left[\frac{\partial^2 \ln f_{\mathbf{X}}(\mathbf{X})}{\partial \mu_i \partial \mu_j} + \frac{\partial \ln f_{\mathbf{X}}(\mathbf{X})}{\partial \mu_j} \frac{\partial \ln f_{\mathbf{X}}(\mathbf{X})}{\partial \mu_i} \right] \frac{f_{\mathbf{X}}(\mathbf{X})}{h(\mathbf{X})} \right] \end{aligned} \quad (14)$$

where $\frac{\partial^2 \ln f_{\mathbf{X}}(\mathbf{x})}{\partial \mu_i \partial \mu_j}$ is the second-order score function which can be also analytically computed. Since the joint probability density function is known, calculation of the higher-order score function is very straightforward even for other parameters such as variance of the random variables [18]. The first and second-order sensitivity of the probability of failure in Eqs. (13) and (14) can be efficiently computed since the failure region $\hat{\Omega}_f$ is defined as the approximated performance function.

4.4. Numerical example - Reliability analysis for two dimensional performance function
Let's consider a two dimensional mathematical example given by [19]

$$g(\mathbf{X}) = [\exp(0.8X_1 - 1.2) + \exp(0.7X_2 - 0.6) - 5] / 10 \quad (15)$$

where $X_1 \sim N(4, 0.8^2)$ and $X_2 \sim N(4, 0.8^2)$.

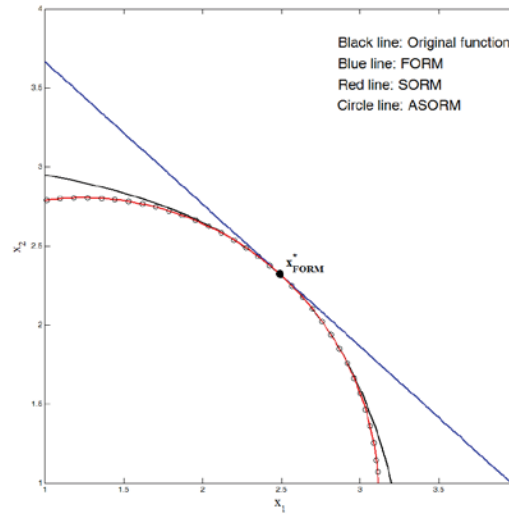


Figure 1: Limit-state equations in FORM, SORM and ASORM

Table 1: The results of reliability analysis and stochastic sensitivity analysis in the 2-D example

	FORM	SORM (Breitung [3])	Proposed SORM	MCS
P_f	0.240%	0.162%	0.153%	0.158%
$\partial P_f / \partial \mu_1$	-0.00627	-	-0.00410	-0.00424
$\partial P_f / \partial \mu_2$	-0.00695	-	-0.00455	-0.00466
$\partial^2 P_f / \partial \mu_1 \partial \mu_1$	-	-	0.00916	0.00960
$\partial^2 P_f / \partial \mu_1 \partial \mu_2$	-	-	0.0118	0.0121
$\partial^2 P_f / \partial \mu_2 \partial \mu_2$	-	-	0.0116	0.0119
F.E.	8 ^a	8 ^a + Hessian	8 ^a	10 ⁷

^a The number of function evaluation and sensitivity analysis for MPP search

Figure 1 illustrates the original and approximated performance functions at MPP in X-space. The approximated performance function of ASORM is obtained using the Hessian approximated by SR1 update. Since the original performance function has a large curvature near MPP, the linearly approximated function does not sufficiently describe the nonlinearity of the original function. As illustrated in Fig. 1, since the functions in SORM and ASORM locally approximate the original function near MPP quite well, the accurate reliability can be estimated by applying the importance sample selecting MPP as a sampling center to the quadratically approximated function. Table 1 shows results of the reliability analysis. In order to obtain the reference solution, Monte Carlo simulation (MCS) with sample size of 10^7 is performed. Due to the high nonlinearity as illustrated in Fig. 1, FORM shows significant error in estimating the probability of failure as well as the stochastic sensitivity. While SORM proposed

by Breitung reduces the error of the probability of failure by calculating the Hessian of the performance function, it is quite difficult to calculate the stochastic sensitivity due to the absence of research on the stochastic sensitivity in SORM. The proposed eSORM evaluates accurate probability of failure by using the approximated Hessian. Furthermore, second-order sensitivity as well as first-order one is accurately calculated. In spite of the improvement in terms of accuracy, additional function calls are not required after MPP search since the proposed method uses the approximated Hessian utilizing the previous derivative information.

5. Conclusions

An accurate and efficient reliability analysis method is proposed in this paper. By utilizing the importance sampling to estimate the probability of failure and its sensitivities, the proposed eSORM can achieve better accuracy than conventional SORM methods since the complete second-order Taylor expansion of a performance function is used. In the proposed eSORM, SR1 update is also utilized using derivatives data obtained during MPP search in order to approximate the Hessian of the performance function. In this way, eSORM requires computation only used in MPP search, indicating that the proposed method shows the same efficiency with FORM.

6. References

- [1] A. M. Hasofer, and N. C. Lind, Exact and invariant second-moment code format, *ASCE Journal of the Engineering Mechanics Division*, 100 (1), 111-121, 1974.
- [2] M. Hohenbichler, and R. Rackwitz, Improvement of second-order reliability estimates by importance sampling, *Journal of Engineering Mechanics*, 114 (12), 2195-2199, 1988.
- [3] K. Breitung, and M. Hohenbichler, Asymptotic approximations for multivariate integrals with an application to multinormal probabilities, *Journal of Multivariate Analysis*, 30 (1), 80-97, 1989.
- [4] L. Tvedt, Distribution of quadratic forms in normal space-application to structural reliability, *Journal of Engineering Mechanics*, 116 (6), 1183-1197, 1990.
- [5] I. Lee, Y. Noh, and D. Yoo, A Novel Second-Order Reliability Method (SORM) Using Noncentral or Generalized Chi-Squared Distributions, *Journal of Mechanical Design*, 134 (10), 100912, 2012.
- [6] S. Rahman, and D. Wei, A univariate approximation at most probable point for higher-order reliability analysis, *International journal of solids and structures*, 43 (9), 2820-2839, 2006.
- [7] I. Lee, K. K. Choi, L. Du *et al.*, Inverse analysis method using MPP-based dimension reduction for reliability-based design optimization of nonlinear and multi-dimensional systems, *Computer Methods in Applied Mechanics and Engineering*, 198 (1), 14-27, 2008.
- [8] I. Lee, K. K. Choi, and D. Gorsich, Sensitivity analyses of FORM-based and DRM-based performance measure approach (PMA) for reliability-based design optimization (RBDO), *International Journal for Numerical Methods in Engineering*, 82 (1), 26-46, 2010.
- [9] S. Adhikari, Reliability analysis using parabolic failure surface approximation, *Journal of engineering mechanics*, 130 (12), 1407-1427, 2004.
- [10] J. C. Helton, J. D. Johnson, C. J. Sallaberry *et al.*, Survey of sampling-based methods for uncertainty and sensitivity analysis, *Reliability Engineering & System Safety*, 91 (10), 1175-1209, 2006.
- [11] R. Y. Rubinstein, and D. P. Kroese, *Simulation and the Monte Carlo method*, John Wiley & Sons, New Jersey, 2011.
- [12] I. Lee, J. Shin, and K. K. Choi, Equivalent target probability of failure to convert high-reliability model to low-reliability model for efficiency of sampling-based RBDO, *Structural and Multidisciplinary Optimization*, 48 (2), 235-248, 2013.
- [13] I. Lee, K. K. Choi, and L. Zhao, Sampling-based RBDO using the stochastic sensitivity analysis and Dynamic Kriging method, *Structural and Multidisciplinary Optimization*, 44 (3), 299-317, 2011.
- [14] J. Lim, B. Lee, and I. Lee, Second-order reliability method-based inverse reliability analysis using Hessian update for accurate and efficient reliability-based design optimization, *International Journal for Numerical Methods in Engineering*, 100 (10), 773-792, 2014.
- [15] H. O. Madsen, S. Krenk, and N. C. Lind, *Methods of structural safety*, Prentice Hall, Englewood Cliffs, NJ, 2006.
- [16] M. Rosenblatt, Remarks on a multivariate transformation, *The annals of mathematical statistics*, 470-472, 1952.
- [17] S. Rahman, Stochastic sensitivity analysis by dimensional decomposition and score functions, *Probabilistic Engineering Mechanics*, 24 (3), 278-287, 2009.
- [18] R. Y. Rubinstein, The score function approach for sensitivity analysis of computer simulation models, *Mathematics and Computers in Simulation*, 28 (5), 351-379, 1986.
- [19] B. D. Youn, K. K. Choi, and Y. H. Park, Hybrid analysis method for reliability-based design optimization, *Journal of Mechanical Design*, 125 (2), 221-232, 2003.

TV packaging optimization of the frontal drop impact using equivalent static loads

Insik Han¹, Youngmyung Lee ², and Gyung-Jin Park³

¹ LG Electronics, Pyeongtaek, Republic of Korea, insik.han@lge.com

² Hanyang University, Seoul, Republic of Korea, lymkd@hanyang.ac.kr

³ Hanyang University, Ansan, Republic of Korea, gjpark@hanyang.ac.kr

1. Abstract

In electronic industries, packaging designs for protection are very important because electronic products are easily damaged in distribution. While distributing products, drop impacts are mainly issues. To protect electronic products, buffer materials like Expandable Poly-Styrene (EPS), and Expandable Poly-Propylene (EPP) are used in packaging. Therefore, packaging designers are effort to develop packaging design for improvement of product protection as well as reduction of the packaging size, and weight. These conditions should be considered as an objective functions or design constraints when optimizing a packaging design. However, it is difficult to apply gradient-based optimization methods to impact optimization problems because of the large nonlinearity of the problems which should be considered in the time domain. Although the capability of the computer has been developed and numerical algorithms have been advanced, drop impact optimization is still quite difficult owing to high non-linearity and numerical cost. The equivalent static loads method for non-linear static response structural optimization (ESLSO) has been developed for such nonlinear dynamic response structural optimization. equivalent static loads (ESLs) are linear static loads which generate the same displacement in the linear static analysis as those of the nonlinear dynamic analysis at a certain time step. Nonlinear analysis and linear static response optimization using ESLs are carried out sequentially until the convergence criteria are satisfied. A new ESLSO method is proposed for TV packaging shape optimization and is verified using a practical example. Design optimization of TV packaging is carried out to minimize weight packaging. The glass panel in TV is the most important part and design constraints are composed with it. The shape and size of EPS packaging are optimized. The weight is minimized and the size is optimized while the glass panel is protected in drop impact. The drop test of a TV packaging is analysed by LS-DYNA, and NASTRAN is used for optimization.

2. Keywords: Structural optimization, equivalent static loads (ESLs), Shape optimization

3. Introduction

Fragile electronic products, especially television have to be designed to operate reliably enough after shipping to consumer. Therefore, the research and evaluation is performed by the actual product to experiment in order to reduce the risk of product damage [1]. Also, researches considering the stress of the impact acceleration and the cushion of the product are performed using a high cost of computational simulation-based experimental design [2]. Recently, the development cycle of new products is becoming shorter. And prototype products design should be verified faster. However, making prototype products for performing experiments are very cost burden. Because this trends, computer simulations are used instead of direct experiment. Nevertheless, the simulation also requires both considerable time and effort to simulate the instability of the product. Therefore, it is necessary to shorten the overall time required for development by shortening the time required for the simulation. The products are packed in packaging material to prevent damage like deformation and crack during transporting to consumer. The shape and form of the packing material varies widely depending on the type of product. Most of TV packaging design is a typical area for performing design engineers rely on the know-how and intuition. To verify the TV packaging design, it should be performed the standard tests. The drop test is a typical standard test. TV drop simulation is performed based on the nonlinear dynamic response analysis. And time required for a nonlinear dynamic response analysis is very long. Design of Experiments also commonly used when performing an optimal design through a non-linear dynamic response analysis. For optimal design problem of a large number of design variables using a Design of Experiments is a necessary nonlinear dynamic response analysis and increases the number of very large and inefficient. Therefore, the development of new techniques is required in order to reduce optimal packaging design time. In this research, optimization of TV-packing is performed using ESLSO. The finite element model of an actual TV-set from LG Electronics Inc. is utilized as a reference. Nonlinear dynamic analysis is carried out using LS-DYNA 971 [3], linear static response structural optimization is conducted by using NASTRAN [4]. The final design is compared with the reference model and verified by testing prototype.

4. TV packaging and drop test

4.1. TV packaging

The TV package is consist of cushion and paper box to protect the product. The cushion is usually made with EPS or EPP that materials are good in the efficiency for the compression. However, it is hard to simulate accurately because there is a severe non-linearity by its density and compression strain rate of the material. So, accurate physical properties should be obtained through experiments. In this research, the stress strain curves of the EPS material are obtained by material experiment for accurate computer simulation.

The Universal Transverse Machine (UTM) in Figure 1 a) is difficult to test in fast compression strain. So, dynamic drop tester in Figure 1 b) is performed to obtain stress-strain curve in high strain rate.

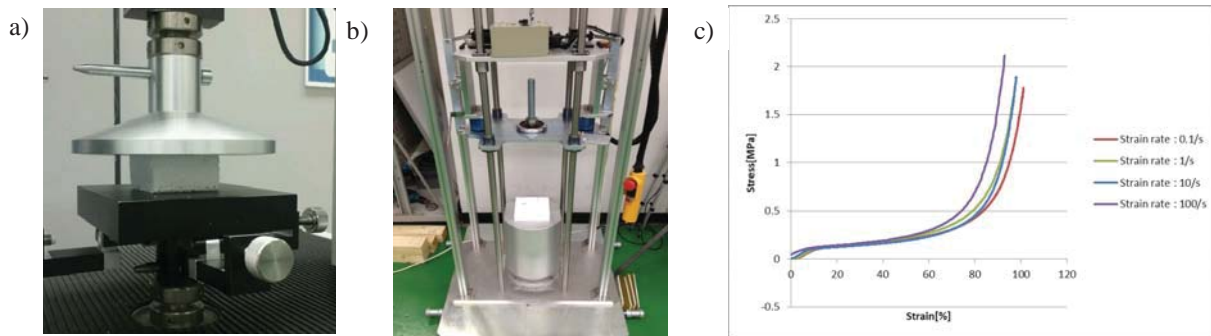


Figure 1: Material experiments: a) static UTM, b) dynamic drop tester, c) strain-stress curve for EPS

4.2. Drop test

There are various standard tests for verifying the distribution of TV products. Serious damage to the product in the distribution is derived mainly from the impact on the front of the product. Front drop test is performed to verify

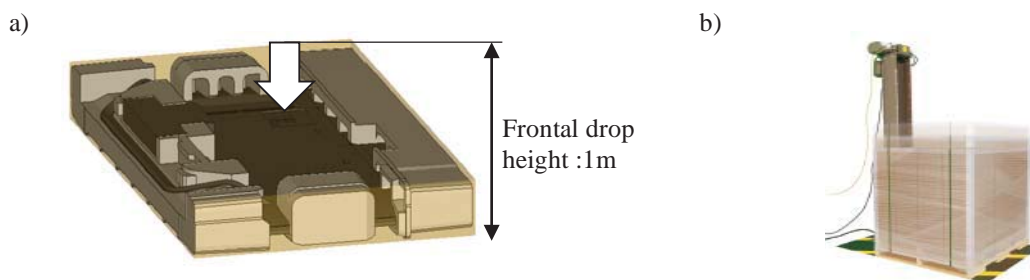


Figure 2: Frontal drop test: a) drop height, b) drop test machine

the design of packaging and to determine proper operation. The height of the drop varies by weight of the product. In this research, the front drop height of TV is 1 meter.

5. Equivalent static loads method for nonlinear dynamic response structural optimization

The process of calculating ESLs is described in detail. Eq.(1) is the governing equation of nonlinear dynamic response analysis.

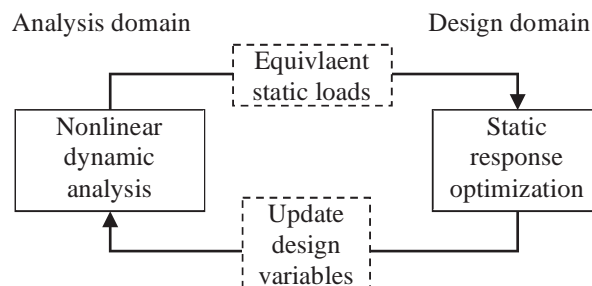


Figure. 3 Schematic flow of equivalent static loads method

$$\mathbf{M}(\mathbf{b}, \mathbf{z}(t))\mathbf{z}_N(t) + \mathbf{K}_N(\mathbf{b}, \mathbf{z}(t))\mathbf{z}_N(t) = \mathbf{f}(t) \quad (t = 0, \dots, l) \quad (1)$$

where $\mathbf{b} \in R^n$ is the design variable vector, n is the number of design variables, \mathbf{M} is the mass matrix, $\mathbf{z}_N(t)$ is

the acceleration vector, \mathbf{K} is the stiffness matrix, $\mathbf{z}_N(t)$ is the displacement vector, and $\mathbf{f}(t)$ the is dynamic load vector, subscript N means that it is from nonlinear analysis, t is time and l is the number of time steps. The ESLs vector $\mathbf{f}_{eq}(s)$ is calculated as the product of linear stiffness matrix $\mathbf{K}_L(\mathbf{b})$ and the displacement vector $\mathbf{z}_N(t)$.

$$\mathbf{f}_{eq}(s) = \mathbf{K}_L(\mathbf{b})\mathbf{z}_N(t); \quad s = 1, \dots, l \quad (2)$$

The overall process is as follows:

- Step 1. Set the initial design variables (cycle number: $k = 0$, design variables: $\mathbf{b}^{(k)} = \mathbf{b}^{(0)}$).
- Step 2. Perform nonlinear dynamic response analysis with $\mathbf{b}^{(k)}$.
- Step 3. Calculate the ESLs using Eq.(2).
- Step 4. Solve the linear static response structural optimization problem with ESLs.
- Step 5. When $k = 0$, go to Step 6. When $k > 0$, if the convergence criterion is satisfied then terminate the process. Otherwise, go to Step 6.
- Step 6. Update the design variables, set $k = k + 1$ and go to Step 2.

6. TV Packaging optimization using equivalent static loads

6.1. The finite element model of TV

In this research, we use commercially available finite element model of the television from LG and perform the optimal design. For optimal efficiency of the design, we modify the front packing in the form of a rectangular shape. From now on, we call the modified model to the 'reference model'. This reference model Figure. 3 is composed of 504,438 elements and 471,079 nodes. The four types of packaging materials protect the TV, and the outside is packaged in a box. Non-linear dynamic response analysis using the LS-DYNA performed the front drop simulation. NASTRAN was used as the structural optimization solver. The algorithm used in structural optimization is a method of feasible directions (MFD).

6.2. Shape optimization of TV packaging

Figure 34 shows the 6 design variables and displacement constraints. The objective function is the mass of the packing, and shape optimization is carried out. The displacement constraints are defined using the distance from the fixer A to the fixer B. The fixer A and B are structures for holding TV panel from set. The detachment of the panel is defined as the relative distance between the two structures. Using the displacement constraints, the detachment of the panel is constrained. The lower bound for the constraint is 0 mm.

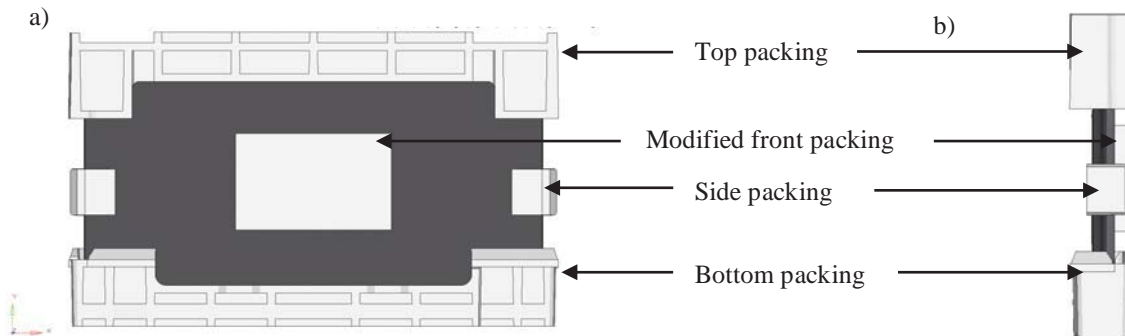


Figure 2: The finite element model of TV : a) Front view, b) Side view

Design formulation is as follows:

$$\begin{aligned} \text{Find} \quad & b_i \quad (i = 1, 2, \dots, 6) & (2) \\ \text{to minimize} \quad & \text{mass of the packing} & (3) \\ \text{subject to} \quad & \delta_k > 0 \text{mm} \quad (k = 1, 2, \dots, 28) & (4) \end{aligned}$$

where b_i is the i th design variable that is perturbation vector of the packing shape, and δ_k are the relative displacements of the fixer A and B. On the upper panel, there are 12 attached points between the panel and the set. And on the side panel there are 16 attached points. Total attached points are 28.

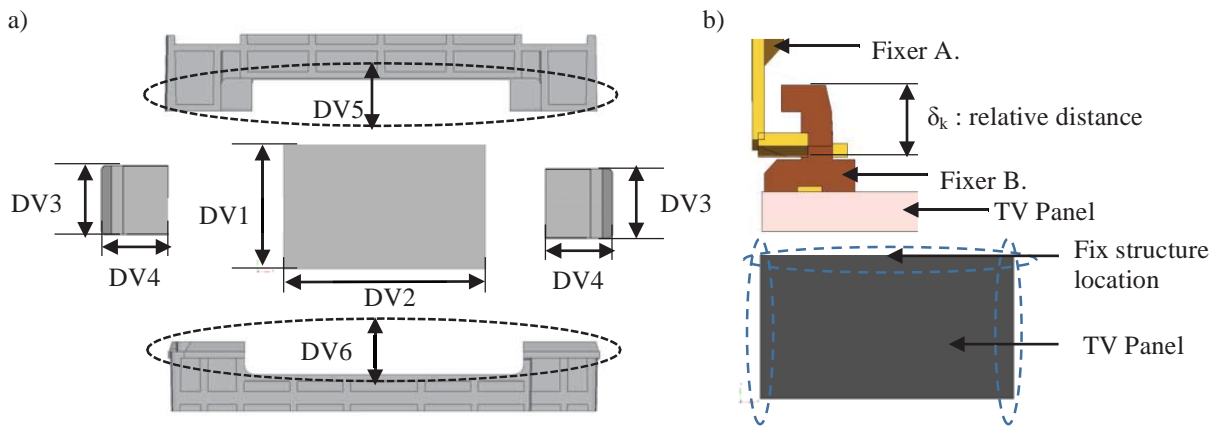


Figure 4: Design variables and constraints :
a) Perturbation vectors of shape optimization. b) Displacement constraints

Figure shows the history of optimization. The process converges to the optimum solution in the 6th cycle. The mass is reduced by 11% from 617g to 553g while the displacement constraints are satisfied.

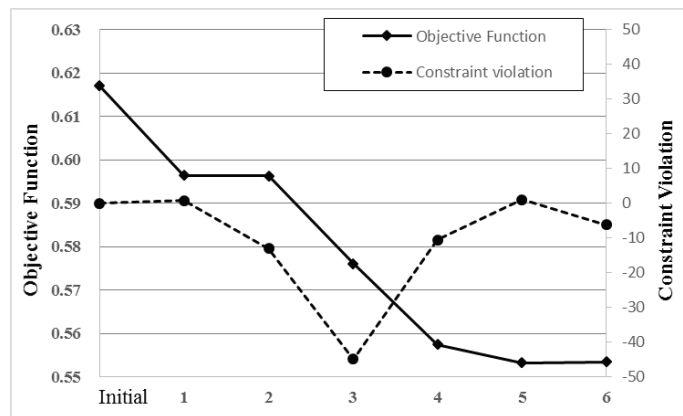


Figure 5: History of objective function and constraint violation of drop test

6.3. Verification test of the results

In order to verify the optimum design results, drop test was performed by pilot sample. As a result of the test, the pilot sample was working properly without damage.



Figure 6: Verification test of the results : a) Pilot package, b) Drop test

7. Conclusions

Nonlinear dynamic response structural optimization of high-fidelity finite element model seems to be almost impossible in conventional gradient based optimization due to high nonlinearity and time-dependent behavior. In this research, TV package optimization with the frontal drop test is carried out using ESLM. Practical examples are solved by the proposed method.

TV package optimization is carried out to determine 6 design variables. The optimum shape is derived by

performing 6 nonlinear dynamic analyses. The displacement constraint is satisfied and the mass is reduced by 11%. Verification test by pilot samples is performed and the pilot sample is working properly. As a result of verification test, using ESLM for optimizing design of TV package is efficient.

Table 1: Comparison of packing shape of the initial and the optimum

Cycle No.	DV1	DV2	DV3	DV4	DV5	DV6
Initial	257.5	418.0	122.2	120.0	233.0	210.0
Optimum	220.55	370.3	99.11	108.5	220.4	191.1

8. References

- [1] Kim, C. S., Bae, B. K., and Sung, Do. Y., 2010, "Drop Analysis of a Package and Cushion Performance of Drum Washing Machine," *Trans. Korean Soc. Mech. Eng. A*, Vol. 34, No. 11, pp. 1733~1740.
- X. Liao, Q. Li, X. Yang, W. Zhang and W. Li, Multiobjective optimization for crash safety design of automobiles using stepwise regression model, *Structural and Multidisciplinary Optimization*, 35 (6), 561-569, 2008.
- [2] Kum, D. H., Kim, Won. Jin., Kim, S. D., and Park, S. H., 2004, "Optimal Design for Cushioning Package of a Heavy Electronic Product Using Mechanical Drop Analysis," *Korean Soc. for Noise and Vibration Eng.*, Vol. 14, No. 2, pp.128~135.
- [3] LS-DYNA 971 version user's manual, *Livermore Software Technology Co.*, CA, 2007.
- [4] NASTRAN user's guide, *MSC Software Co.*, Santa Ana, CA, 2013.

Sensitivity Analysis of Structural Response to External Load Position

D. Wang

Northwestern Polytechnical University, Xi'an, Shaanxi, P.R. China, dwang@nwpu.edu.cn

Abstract

Procedures for sensitivity analysis of the static responses of a plate or shell structure, i.e., the nodal displacement and mean compliance, with respect to the position of an external applied load are developed in this work mainly because these responses are highly affected by the application point of the load imposed. Based on the essential ideas of the finite element analysis, an external concentrated load is first transformed into the equivalent nodal forces such that the influence of its move or shift is represented completely by the value variation of the associated nodal forces. As a result, the first-order derivatives of an external load to its location change can be performed appropriately by the aid of the shape functions of a plate element. Subsequently, the relevant sensitivities of the structural responses are formulated readily with the discrete methodology upon the finite element formulation. Finally, a numerical example is provided to demonstrate the validity of the sensitivity formulations presented, and the numerical results show the high accuracy of the response sensitivity calculations.

Keywords: sensitivity analysis; external applied load location; nodal displacement; compliance;

1. Introduction

In the preliminary design stage of an engineering structure, there always exist some uncertainties associated not only with the structural design parameters, but also with a part or all of the external loads. That is, the loads imposed to the structure may often experience modifications in their values, directions and/or positions during the design process in order to testify the resulting design to comply with some strict regulations in various circumstances [1]. Over the past several decades, the mechanical analysis and optimization of a plate- or shell-type structure with design dependent or independent loadings were undertaken extensively in many aspects. Most commonly, the application position of an external load is fixed in [2, 3]. However, it is also noticed that even a small move or shift of external load may bring about a significant influence on both the performance of the structure and then the structure final design. This fact makes it highly desirable for developing an efficient technique capable of estimating variations of the structural performances due to a small motion of an applied load, and such a sensitivity analysis can quantitatively afford an explicit and quick solution to the problem.

As is widely known, the sensitivity analysis is extremely useful in the scope of design optimization processes, especially in the gradient-based optimization algorithms, where the design sensitivity can be used as a guide to implement the structural modification. In effect, the design sensitivity analysis has become a major computational cost in most structural optimization solutions [4]. As a result, a simple and precise formulation for an adequate sensitivity calculation has always been an active topic in the fields of the structural optimization design.

This paper is aimed to extend the previous study by the present author [5] for the related sensitivity analysis of the structural responses into the plate/shell flexural situation. In this work, the sensitivity formulations of the structural displacement and mean compliance are conducted, respectively, with respect to the position variations of an external concentrated load. The sensitivity analysis is still carried out with use of the finite element (FE) analysis mainly because the corresponding responses are usually obtained on the same strategy. First, the equivalent nodal forces of the external applied load are constructed by the adequate interpolation functions of the plate element. Due primarily to this direct transformation, the effect of the external load shift is fully represented by the value variation of the equivalent nodal forces. Next, the explicit formulations of the first-order derivatives of the nodal force vector to change of the application point of the external load are derived fairly with the aid of the essential features of the plate element. Later, with the above derivations the explicit formulations of the sensitivity derivatives of the nodal displacements and the compliance are developed immediately to the movement of the external load. As the structural analysis resorts most regularly to the numerical execution with FE methodology, such a derivation of the design sensitivity has an advantage of compatibility with the numerical estimations of the structural responses upon the same discrete model, and most importantly, can be applied in conjunction with an existing commercial FE analysis package. Finally, the sensitivity calculations of the responses will be

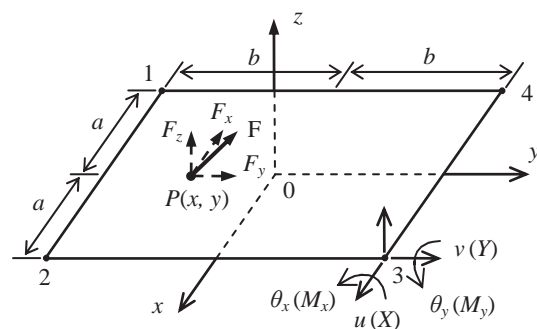


Figure 1: A rectangular plate element subject, at point $P(x, y)$, to a concentrated force \mathbf{F} of the components F_x , F_y and F_z

illustrated and the resultant accuracy be demonstrated with a typical numerical example.

2. Derivative of an External Load

Consider an isotropic, thin rectangular plate (or shallow shell) element of thickness h subjected to a concentrated or point load \mathbf{F} at an interior point $P(x, y)$ in the element region. Figure 1 shows a typical rectangular plate element with 5 degrees of freedom (DOFs) at each of the corners, and the corresponding nodal forces are shown in the parentheses. The element or local coordinate system is chosen such that the x - y plane coincides with the midplane of the plate. The external applied force may have three components F_x , F_y and F_z parallel, respectively, to each of the coordinate axes. Herein, the classical Kirchhoff hypothesis for thin plates applies for describing the transverse deflection. Based on the FE theory, the midplane displacements inside the element can be approximated as explicit functions of the element nodal displacements:

$$\begin{Bmatrix} u \\ v \\ w \end{Bmatrix} = [N] \{d\}^e \quad (1)$$

where u and v are the in-plane displacement components in the x - y coordinate system, respectively, and w is the lateral displacement component along the z -axis at any point on the plate element midplane (i.e., $z=0$). $\{d\}^e$ is a vector of 20 entries denoting the generalized element nodal displacements:

$$\{d\}^e = [\{d_1\}^T \quad \{d_2\}^T \quad \{d_3\}^T \quad \{d_4\}^T]^T \quad (2)$$

in which, the superscript T denotes matrix transpose. $\{d_i\}$ represents the DOFs at each corner node i ($i=1, 2, 3, 4$), see Figure 1,

$$\{d_i\} = \begin{Bmatrix} u_i \\ v_i \\ w_i \\ \theta_{xi} \\ \theta_{yi} \end{Bmatrix} = \left[u_i \quad v_i \quad w_i \quad \left(\frac{\partial w}{\partial y} \right)_i \quad - \left(\frac{\partial w}{\partial x} \right)_i \right]^T \quad (3)$$

where u_i , v_i and w_i are the nodal displacements along each of the local axes at a node. θ_{xi} and θ_{yi} denote the associated rotations about the x - and y -axis, respectively. In the small deflection theory of thin plates, the transverse displacement w is uncoupled from the in-plane displacements u and v . Consequently, these displacements can be interpolated separately as is already known [6]. The matrix of shape functions of the plate element in Eq. (1) is

$$[N] = [[N_1] \quad [N_2] \quad [N_3] \quad [N_4]] \quad (4a)$$

in which

$$[N_i] = \begin{bmatrix} N_i & 0 & 0 & 0 & 0 \\ 0 & N_i & 0 & 0 & 0 \\ 0 & 0 & \bar{N}_i & \bar{N}_{xi} & \bar{N}_{yi} \end{bmatrix} \quad (i=1, 2, 3, 4) \quad (4b)$$

is the matrix of shape functions to each of the four nodes. The usual shape functions read commonly as [7]:

$$N_i = (1 + \xi_i \xi)(1 + \eta_i \eta) / 4 \quad (5)$$

For the in-plane components u_i and v_i identically, and

$$\begin{cases} \bar{N}_i = (1 + \xi_i \xi)(1 + \eta_i \eta)(2 + \xi_i \xi + \eta_i \eta - \xi^2 - \eta^2) / 8 \\ \bar{N}_{xi} = -b \eta_i (1 + \xi_i \xi)(1 + \eta_i \eta)(1 - \eta^2) / 8 \\ \bar{N}_{yi} = a \xi_i (1 + \xi_i \xi)(1 + \eta_i \eta)(1 - \xi^2) / 8 \end{cases} \quad (6a)$$

for the transverse components w_i , θ_{xi} and θ_{yi} , respectively. In the above expressions,

$$\begin{cases} \xi = \frac{x}{a} \in [-1, 1], & \xi_i = \frac{x_i}{a} \\ \eta = \frac{y}{b} \in [-1, 1], & \eta_i = \frac{y_i}{b} \end{cases} \quad (6b)$$

For a concentrated force \mathbf{F} acting at a point $P(x, y)$ within an element, the equivalent nodal forces acting on the same element is defined by the virtual work principle of the external load [6],

$$\{f\}^e = [N]_{(x,y)}^T \begin{Bmatrix} F_x \\ F_y \\ F_z \end{Bmatrix} \quad (7)$$

Upon this simple mathematical transformation, a concentrated or point force \mathbf{F} , positioned at $P(x, y)$, is now replaced entirely by the equivalent nodal force vector $\{f\}^e$ of size 20, of which the component values depend only upon the coordinates of the application point P . In other words, the outcomes induced by continuous movement of the external force \mathbf{F} can now be represented completely by those resulting from the magnitude variation of the equivalent coupled nodal forces $\{f\}^e$. Therefore, the derivative research of the structural responses to the motion of the external force \mathbf{F} itself turns, from now on, into the derivative analyses with respect to the relevant changes of the equivalent nodal force vector $\{f\}^e$. Moreover, the derivative of the equivalent nodal force due primarily to modification of the acting point of the external load can be performed with ease,

$$\frac{\partial \{f\}^e}{\partial x} = \frac{\partial [N]^T}{\partial x} \begin{Bmatrix} F_x \\ F_y \\ F_z \end{Bmatrix}, \quad \frac{\partial \{f\}^e}{\partial y} = \frac{\partial [N]^T}{\partial y} \begin{Bmatrix} F_x \\ F_y \\ F_z \end{Bmatrix} \quad (8)$$

3. Derivatives of Nodal Displacements of a Structure

Suppose a general plate structure is modeled with an adequate FE mesh, the overall equations of the force equilibrium in terms of the nodal displacements are represented as follows:

$$[K]\{u\} = \{P\} + \{F(s)\} \quad (9)$$

where $[K]$ is the system stiffness matrix, $\{u\}$ is a vector of the unknown nodal displacements, which is dependent on both the magnitude and position of the external loads. On the right hand of the equation, the external loads applied on the structure are separated into two parts: $\{P\}$ is the load invariable during the design process, whereas $\{F(s)\}$ is a vector of the nodal forces which is a function of the application position variable s . Taking partial derivatives of Eq. (9) with respect to a location variable s of the external applied load yields:

$$[K] \frac{\partial \{u\}}{\partial s} = \frac{\partial \{F(s)\}}{\partial s} \quad (10)$$

here it has been supposed that the plate structure itself is essentially independent of the external applied loads. Notably, the procedure for the displacement sensitivity solution $\partial \{u\} / \partial s$ can be carried out by solving Eq. (10) caused by $\partial \{F(s)\} / \partial s$, which is rather similar to the solution of the displacement $\{u\}$ under the external loads, see Eq. (3). In view of this similarity, $\partial \{F(s)\} / \partial s$ is generally considered as a pseudo or fictitious load for each of the position variables [5]. With the relevant result attained in Eq. (8), by assembly of the related element results, it is then a trivial task to computed the first-order sensitivity of the nodal displacement vector of a plate structure,

$$\frac{\partial \{u\}}{\partial s} = [K]^{-1} \frac{\partial \{F(s)\}}{\partial s} \quad (11)$$

4. Compliance Sensitivity Formulation

In the past years, the topology optimization problems of a plate structure with consideration of the overall stiffness have been investigated exhaustively, where the structure is generally designed to be stiff enough to carry a given set of the external loads properly [2, 3, 8]. Usually the mean compliance, i.e., the total work done by the external loads under a particular configuration, is posed as the objective function. Thus, it is recognized that the compliance is actually a highly load-dependent measurement of the structural stiffness in this capacity. Consequently, the sensitivity analysis of the compliance to the external applied force is of particular interest in practical cases since a small movement of the external load may remarkably alter the system compliance obtained.

The mean compliance C of a plate structure is defined as half the scalar product of the applied forces and the corresponding displacements at equilibrium, and is given in the FE format:

$$C = \frac{1}{2} (\{P\} + \{F(s)\})^T \{u\} = \frac{1}{2} (\{P\} + \{F(s)\})^T [K]^{-1} (\{P\} + \{F(s)\}) \quad (12)$$

Differentiating the above expression with respect to the location variable s yields

$$\frac{\partial C}{\partial s} = (\{P\} + \{F(s)\})^T [K]^{-1} \frac{\partial \{F(s)\}}{\partial s} = \{u\}^T \frac{\partial \{F(s)\}}{\partial s} = \sum_{e=1}^{n_e} (\{d\}^e)^T \frac{\partial \{f\}^e}{\partial s} \quad (13)$$

Obviously, the compliance sensitivity can be computed as long as the displacements and the derivative of the external applied load, or the pseudo load, are obtainable. With this sensitivity result, it is capable to make a primary estimate of the structural compliance value after variation of the load position by the linear Taylor series expansion,

$$\bar{C} \approx C + \frac{\partial C}{\partial s} \Delta s \quad (14)$$

5. Illustrative Example

In this section, the numerical results of the structural responses are solved using the FE analyzer ANSYS program. Then, the corresponding sensitivities are evaluated with the program coded in Matlab providing several digits of accuracy to verify the reliability and accuracy of the sensitivity formulation presented.

A quarter cylinder shell of the thickness $h=2$ mm is simply supported at its four corners while it bears a concentrated vertical point force $F=3$ kN at the structural center. Figure 2 displays the geometry, dimensions and external load. The structural projection onto the x - y plane is a square. At the same time, the gravity load is also involved in the analysis (the gravitational constant $g=9.8$ m/s²). The cylinder is discretized with a sufficiently fine mesh of the finite elements 18×18 . Assume the Young's modulus is $E=210$ GPa, Poisson ratio $\nu=0.3$ and the mass density $\rho=2800$ kg/m³. First, the displacement values and the related sensitivities at the center points of the free edges, Point A and B, are computed to the position move of the vertical load in the x - and y -axis, respectively, and indicated in Table 1.

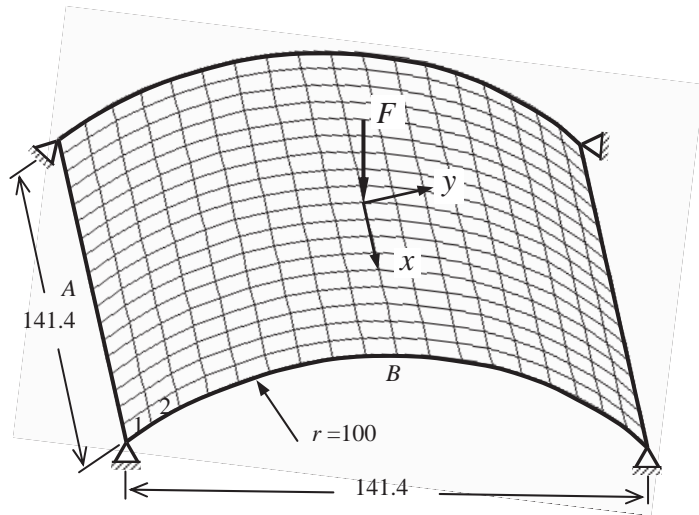


Figure 2: A quarter cylinder simply supported at corners is subject to a vertical concentrated force F at the center point

Table 1: Displacements at points A and B and the corresponding sensitivities to the position of the external vertical forces applied at the center of the cylinder shell

Point	Displacements		Sensitivity to position of the vertical force in the axis	
	component	value	x	y
A	u (mm)	0	4.87261E-5	0
	v (mm)	-4.67423E-1	7.38329E-7	-1.09879E-2
	w (mm)	5.68054E-1	-1.25806E-6	1.47863E-2
	θ_x (rad)	-1.36695E-2	1.54653E-5	4.77687E-1
	θ_y (rad)	0	-9.91461E-2	0
	θ_z (rad)	0	-9.08507E-2	0
B	u (mm)	-9.19519E-3	1.03708E-3	-1.07670E-6
	v (mm)	0	0	-1.64534E-2
	w (mm)	-3.69736E-1	-8.65907E-3	3.24734E-6
	θ_x (rad)	0	0	-1.15354
	θ_y (rad)	2.60914E-4	1.22743E-1	-1.70148E-4
	θ_z (rad)	0	0	-3.95777E-3

First of all, it can be seen that the displacement terms u , θ_y and θ_z at Point A and the corresponding sensitivities to the y -motion of the concentrated load are all zeroes. So are the terms v , θ_x and θ_z at Point B to its x -motion. This is true due essentially to the symmetry of the structure. It is therefore understood that these displacements are very blunt to the position disturbances of the applied force in the related directions. However, it is found that the sensitivity to the companion axial move is not null, and the results are comparatively very notable. Secondly, the

related sensitivities are much smaller for the major displacement terms v , w and θ_x at Point A (in gray) to the x -motion of the concentrated load than to its y -motion. A similar observation can also be made about the sensitivities of the displacement terms u , w and θ_y at Point B (in gray) to the y -motion of the vertical load than to its x -motion. This is just the case as is expected.

Table 2: Displacements at points A and B before and after an imaginary move of the external vertical force individually in the x - or y -directions by an element size

Point	component	Displacements with the external force moved by an element size in the positive direction of different axes			
		linear estimation		solution by FEM	
		x	y	x	y
A	u (mm)	3.82829E-4	0	3.47619E-4	0
	v (mm)	-4.67417E-1	-5.63189E-1	-4.64374E-1	-5.43768E-1
	w (mm)	5.68044E-1	6.96925E-1	5.62859E-1	6.68839E-1
	θ_x (rad)	-1.36694E-2	-9.50617E-3	-1.36056E-2	-9.30330E-3
	θ_y (rad)	-7.78966E-4	0	-7.72402E-4	0
	θ_z (rad)	-7.13790E-4	0	-7.07776E-4	0
	B	u (mm)	-1.04714E-3	-9.20457E-3	-7.93013E-4
v (mm)		0	-1.43401E-1	0	-1.41692E-1
w (mm)		-4.37768E-1	-3.69708E-1	-4.41272E-1	-3.49618E-1
θ_x (rad)		0	-1.00539E-2	0	-9.91328E-3
θ_y (rad)		1.22528E-3	2.59431E-4	1.30799E-3	3.99758E-4
θ_z (rad)		0	-3.44943E-5	0	-3.38898E-5

Based on the displacement sensitivities shown in Table 1, it is quite simple to predict the nodal displacement terms with a conceived motion of the concentrated force F in x - or y -direction. The new displacements $\{\bar{d}\}$ after a position perturbation of the concentrated load by a small step can be estimated in the linear Taylor series

$$\{\bar{d}\} = \{d\} + \frac{\partial\{d\}}{\partial s} \Delta s \quad (15)$$

Table 2 lists the deflections at Point A and B with the position of the vertical concentrated force disturbed by an element size individually along the axes. In contrast, the corresponding solutions with the FE method are given simultaneously for comparison. By a close examination, it is found that the displacements estimated linearly on the sensitivity analysis are in good agreement with the FE solution for the major displacement terms.

Table 3: Structural mean compliances and the related sensitivities to the position of the external vertical load applied at the center of the cylinder shell

Compliance (J)	First-order sensitivity in different directions		Compliance with the concentrated load moved by an element size in the positive direction	
	axis	value	estimation	by FEM
1.06775	x	4.92985E-2	1.06814	1.07465
	y	1.94058E-1	1.06944	1.10675

The structural mean compliance and the associated first-order sensitivities to the position of the vertical load are illustrated in Table 3. It is shown evidently from the sensitivities that the structural compliance will increase if the vertical force moves away from the center. Therefore, it can be known explicitly that the center of the cylinder in the present example is the most appropriate location for the vertical load under the particular consideration of the structural stiffness. Moreover, it is observable from Table 3 that the compliance is much more sensible to the y -direction move than to its x -direction move of the vertical load. This is very important for the analysis of the

uncertain external forces in practice.

6. Conclusions

In the preliminary design of a practical structure, the external applied loads may change their application locations in order to testify that the structural design is appropriate to support or withstand the loads in various conditions. The ability to quickly evaluate the response changes of a structure to the location variation of an external load is of great importance to the structural designers/analysts. This paper is really an extension of the previous work by the author for 2D plane stress conditions [5]. By means of the discrete method in combination with the features of the plate/shell element, the derivative of an external load is first obtained. Then, the sensitivity expressions of the structural responses, such as the nodal displacement and mean compliance, are developed readily for a bending plate structure. Subsequently, a typical example is presented to validate the sensitivity formulations, and the numerical results show that the proposed process can provide the response sensitivities with an excellent accuracy.

Acknowledgements

This work is supported by the Aerospace Technology Support Foundation, China (2014-HT-XGD).

References

- [1] S. McWilliam, Anti-optimisation of uncertain structures using interval analysis. *Computers and Structures*, 79, 421–430, 2001.
- [2] L.H. Tenek and I. Hagiwara, Optimal rectangular plate and shallow shell topologies using thickness distribution or homogenization, *Computer Methods in Applied Mechanics and Engineering*, 115, 111-124, 1994.
- [3] C.S. Long, P.W. Loveday and A.A. Groenwold, Effects of finite element formulation on optimal plate and shell structural topologies, *Finite Elements in Analysis and Design*, 45, 817-825, 2009.
- [4] R.J. Yang and C.J. Chen, Stress-based topology optimization, *Structural Optimization*, 12, 98–105, 1996.
- [5] D. Wang, Sensitivity analysis of structural response to position of external applied load in plane stress condition, *Structural and Multidisciplinary Optimization*, 50(4), 605-622, 2014.
- [6] K.J. Bathe, *Finite Element Procedures*, Prentice-Hall, New Jersey, 1996.
- [7] B.F. Zhu, *Principle and applications of finite element method*, Waterpower Publisher, Beijing, 1998, (in Chinese).
- [8] B. Zheng, C.J. Chang and H.C. Gea. Topology optimization with design-dependent pressure loading, *Structural and Multidisciplinary Optimization*, 38, 535-543, 2009.

Topology and sizing optimisation of integral bus chassis with the use of a cooperative coevolutionary genetic algorithm with independent ground structures

Wei Zhong¹, Ruiyi Su², Liangjin Gui¹, Zijie Fan¹

¹ State Key Laboratory of Automotive Safety and Energy, Department of Automotive Engineering, Tsinghua University, Beijing, China, zhongw10@mails.tsinghua.edu.cn

² Beijing System Design Institute of Electromechanical Engineering, Beijing, China, sry@mails.tsinghua.edu.cn

1. Abstract

It is an attractive field to apply structural optimisation on bus body to enhance its performances. Since chassis is the most complex part of the bus body and bears most of loads, this paper focuses on the simultaneous topology and sizing optimisation of an integral bus chassis by treating it as a discrete variable optimisation problem. The objective is to reduce the mass. The torsional stiffness, the foundational frequency and the max Von Mises stress under full-loaded bending case are constrained. Meanwhile, some essential functional and manufacturing requirements are considered. Firstly, the finite element analysis models of the original bus were created and validated by experiments. Then, a special architecture of cooperative coevolutionary genetic algorithm with independent ground structures (CCGA-IGS) is proposed to improve the flexibility of the solution method and decrease the complexity of the optimisation problem: two different ground structures are defined for topology optimisation and sizing optimisation, and then the topological variables and sizing variables are divided into two subpopulations which evolve in two different GA systems but interact with each other in each iteration. Moreover, a strategy is presented to automatically reload the uniformly distributed loads when the topology of the chassis is changed. The weight of the optimal design is decreased as much as 246.45 kg with all the constraints satisfied.

2. Keywords: integral bus chassis; topology optimisation; sizing optimisation; cooperative coevolutionary genetic algorithm; independent ground structures

3. Introduction

Significant progress has been made in theoretical research on structural optimisation of discrete structures, in which application of the theory mostly focuses on ideal simple structures [1, 2]. Theoretical research shows that performances of discrete structures can be improved remarkably with the use of structural optimisation. Recently, much attention has been paid to the application of structural optimisation on practical engineering products, but practical research is still much slower than theoretical research [3]. Typically, structural optimisation consists of topology optimisation, sizing optimisation and shape optimisation, among which sizing optimisation is the most widely employed technique in optimisation of bus body frames. Gauchia, et al. [4] conducted sizing optimisation on a real bus structure for lightweight without spoiling vehicle safety. Su, et al. [2] performed the multi-objective sizing optimisation on an integrated bus body frame to minimize the weight and maximize the torsional stiffness with the constraints of strength and rollover safety.

This paper concentrates on simultaneous topology and sizing optimisation of an integral bus chassis. It is a complex problem to solve. The challenges of solving the problem come from several reasons. First, large number of discrete variables are involved which would deteriorate the performance of the optimisation algorithm [5]. Second, design constraints are diverse including performance constraints, manufacturing constraints, functional constraints and so on. Third, since a bus undergoes various loadings during lifetime, multiple conditions need to be handled, such as linear static analysis, eigenvalue extraction, etc.

Decomposing a complex problem into smaller sub-problems is an effective way to solve problem with large number of variables [6]. A cooperative coevolutionary genetic algorithm (CCGA) proposed by Potter and De Jong [7] is introduced in this paper. In CCGA, variables are assigned into subpopulations that evolve concurrently. Meanwhile, individuals in different subpopulations collaborate with one another for evaluations in each iteration. Cooperative coevolutionary evolutionary algorithms (CCEAs) have achieved successful application in many fields [8, 9], but there is no one versatile architecture suitable for all problems so far. This paper aims to propose a CCGA architecture for simultaneous topology and sizing optimisation of bus body frame chassis.

Due to the stochastic nature of GA, structures that cannot be easily manufactured or cannot satisfy functional requirements are easily generated in structural optimisation. Therefore, it is quite necessary to include manufacturing and functional constraints. However, those constraints are usually difficult to be expressed in rigorous mathematical equations. In order to handle those constraints, actions are taken before the optimisation by appropriately defining the design spaces and grouping variables. In order to define design spaces and constraints more flexibly for topology and sizing optimisation, a strategy called independent ground structures (IGS) is

presented, where different ground structures are constructed for topology optimisation and sizing optimisation independently. IGS strategy is integrated into the CCGA architecture, and a method named CCGA-IGS is presented, which was implemented on the bus chassis frame.

4. Original Finite Element Model and Validation

The integral bus used in this paper is a 12-meter-long intercity bus with luggage compartments and toilet, and has a maximum 47-passenger capacity. The performances of the bus are implicit functions of design variables, and finite element analysis method is adopted.

4.1. Original Finite Element Models

The FE model of the original bus body frame is created with beam elements as shown in Figure 1(a), which is used for modal and torsional stiffness analyses. For strength analysis, the FE models of the suspension system, the wheels and full loads are created and assembled with the FE model of the bus body frame, as shown in Figure 1(b).

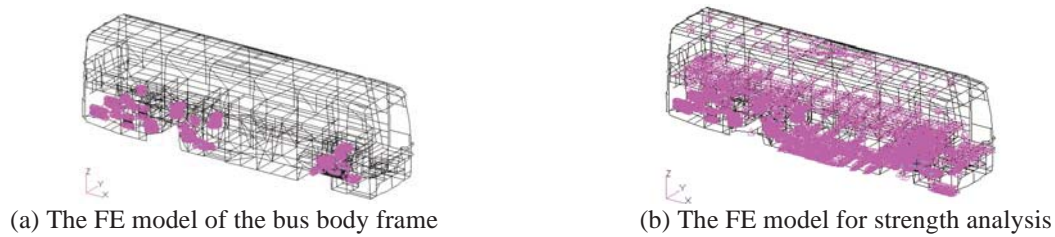


Figure 1: The FE models

Because free vibration of the bus body frame is concerned in this paper, the free-free boundary is used for modal analysis. In the analysis of the torsional stiffness, the boundary constraints are defined as follows: the nodes in the centers of front-right and front-left air spring supports are forced to move 5 mm in opposite z-direction while the rear axle is fixed. The result of finite element analysis provides the reaction forces of the nodes with enforced displacement, and then the torsional stiffness is obtained according to Eq. (1)

$$K_{\psi} = \frac{FL}{\frac{180}{\pi} \left(\frac{2d}{L} \right)} = \frac{\pi FL^2}{360d} \quad (1)$$

Where K_{ψ} is the torsional stiffness of the bus body frame, F is the reaction force, L is the distance between the nodes with enforced displacement, and d is the enforced displacement. Here, $L=1266$ mm and $d=5$ mm. In the strength analysis, the max Von Mises stress under full-loaded case is taken into consideration. The boundary condition for strength analysis is that all rigid body displacements of the bus are removed via fixing the translational degrees of freedom of the nodes of the wheels which are connected with the ground. The material of the bus body frame is Q345C whose Elasticity modulus is 206 GPA, Poisson ratio is 0.3, density is 7.86×10^3 kg·m⁻³ and Yield limit is 510 MPA.

4.2. Validation

Modal test and static bending test were carried out to validate the accuracy of the FE models. In the modal test, the bus body frame was supported by inner tubes whose natural frequency is less than 2 Hz. The comparison of the first seven natural frequencies between the test and the simulation is listed in Table 1, which shows that the difference between the test and the simulation is small. The maximum difference occurs at the second natural frequency, with a difference of 9.60%.

Table 1: Comparison of the natural frequencies between the test and the simulation

Mode No.	Test / Hz	Simulation / Hz	error	Mode No.	Test / Hz	Simulation / Hz	error
1-first torsion	8.38	7.73	-7.76%	2	9.25	10.14	9.60%
3	11.88	12.37	4.16%	4	14.25	13.64	-4.31%
5	15.75	15.27	-3.07%	6	17.00	16.81	-1.11%
7-first bend	17.94	17.74	-1.08%				

In static bending experiment, the front and rear axles were supported and sand pails that totally weigh 1320kg and 840 kg were evenly put on the passenger floors and compartment floors respectively. It should be noted that the

loading case in the test was different from the case used in the optimisation mentioned in Section 4.1. The Von Mises stress of four points on the bus body frame were obtained. For comparison, the loading case used in the test is also loaded on the FE model. The comparison is offered in Table 2. The maximum difference between the test and the simulation is 11.75% at the second point.

In conclusion, the FE models created above is adequate for the optimisation.

Table 2: Comparison of the stress between the test and the simulation

Test Point	1#	2#	3#	4#
Test / MPA	45.24	27.83	30.49	31.31
Simulation / MPA	44.85	31.1	27.9	32.45
error	-0.86%	11.75%	-8.49%	3.65%

5. CCGA-IGS architecture

5.1. Independent ground structures (IGS)

The chassis frame is a very complex structure on which multiple loads are applied, including the power system, the transmission system, the steering system, and the passenger seats etc. As an engineering product, the layout of the chassis frame is required to satisfy the predefined functions. For example, beams should be arranged suitably for the installation of the aforementioned loads, and specific spaces should be reserved for the luggage compartments and toilet. Consequently, the chassis frame should be designed not only to improve the performances of the bus but also to meet the functional requirements.

Ground structure approach is widely employed in simultaneous topology and sizing optimisation of discrete structure. The ground structure determines the design space of the optimisation. Therefore, defining proper ground structure is a key point to satisfy the functional requirements. Generally, topology optimisation and sizing optimisation share one ground structure. Nevertheless, in order to satisfy the functional requirements on engineering products, not all beams should engage in the topology optimisation. Likewise, sizing optimisation should not be performed on these beams given specially shaped cross-sections for installation. Hence, an independent ground structures strategy is presented, where different ground structures are defined for topology and sizing optimisation.

First of all, based on the original chassis, 88 diagonal beams are added to the area of passenger seat floor and luggage compartment floor to form a whole structure as shown in Figure 2 (a). To be specific, in the whole structure, it must be guaranteed that no beams go across the spaces for luggage compartment etc.

Then, part of beams in the whole structure participate in the topology or sizing optimisation. Topology optimisation changes the layout of the structure significantly. In order to avoid the change of the overall architecture of the chassis frame, 90 diagonal beams, 41 longitudinal beams, 42 cross beams and 7 vertical beams are selected from the region of the passenger seat floor and luggage compartment floor to form the topological ground structure (TGS) as shown in Figure 2(b), in which beams in the TGS are in red color. Besides those beams with specially shaped cross-sections, all beams in the whole structure are chosen to compose the sizing ground structure (SGS) which are outlined in red in Figure 2(c).

Essential functional constraints are satisfied via constructing proper whole structure and ground structures before the optimisation. With the introduction of IGS, it is more flexible to choose suitable design spaces for topology optimisation and sizing optimisation.

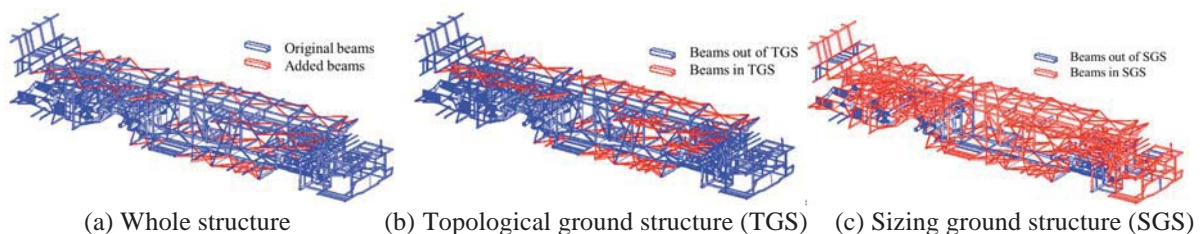


Figure 2: Whole structure and ground structures of the chassis frame

5.2. CCGA

The FE model of the chassis frame is created with thousands of beam elements. Each beam in the TGS has a topological variable, and each beam in the SGS has a sizing variable. The number of design variables in the simultaneous topology and sizing optimisation is very large. Therefore, a cooperative coevolutionary genetic

algorithm (CCGA) is introduced to divide the complex search space into smaller spaces.

Decomposition and collaboration are two key features for CCGA architecture. Decomposition describes how to divide the variables into subpopulations. The design variables in this research are decomposed in a natural way, in which the topological variables and sizing variables are assigned into two subpopulations which evolve independently and concurrently. Meanwhile, the interaction between the two subpopulations happens during iterations, which is the process of collaboration. In order to evaluate an individual in one subpopulation, it is necessary to select a representative from the other subpopulations to form a complete solution. The best individual in the other subpopulation is chosen as the representative in this paper.

With CCGA, topological variables and sizing variables evolve in two different GA systems. Hence, it is possible to choose different optimisation parameters according to the features of topology optimisation and sizing optimisation.

IGS is employed in the preparation stage, while CCGA is utilized in the process of optimisation. Both provide topology optimisation and sizing optimisation with independence. Therefore, it is natural to integrated IGS and CCGA together.

6. Implementation

6.1. Formulation

The objective is to minimize the mass of the bus body frame. The performances of the bus body frame including the torsional stiffness, the foundational frequency and the max Von Mises stress under full-loaded bending case are constrained to be no worse than the original bus body frame. Symmetry and consistency constraints are two types of manufacturing constraints included in this research. Symmetry constraint, which requires the topology/cross-section of beam elements in the TGS/SGS to be symmetric about a line or a plane, is helpful to reduce the number of variables, lower the manufacturing cost and improve the aesthetic feature. Consistency constraint divides the beam elements in the TGS/SGS into groups, and the topological/sizing variables of those beam elements in a group are supposed to have the same value. Consistency constraint is taken into consideration for two reasons: first, during FE modelling, a beam is usually modelled with several elements, so consistency constraint is applied on these elements to make sure that the beam is deleted or retained entirely and the cross-section is consistent along the beam; second, relative beams in the structure are required to be consistent for the same purpose as the symmetry constraint. The formulation of simultaneous topology and sizing optimisation of the bus chassis is as follows:

$$\begin{cases} \min m \\ \text{s.t. } K_{\Psi} / K_{\Psi}^0 - 1 \geq 0 \\ f_1 / f_1^0 - 1 \geq 0 \\ \sigma_{\max} / \sigma_{\max}^0 - 1 \leq 0 \\ t_i = t_j, (i, j) \in \text{Sym}T \cup \text{Con}T \\ x_i = x_j, (i, j) \in \text{Sym}S \cup \text{Con}S \\ t_i \in \{0, 1\}, i \in T \\ x_i \in X, i \in S \end{cases} \quad (2)$$

Where m , K_{Ψ} and f_1 are the mass, the torsional stiffness and the fundamental frequency of the bus body frame with the new chassis frame respectively, and K_{Ψ}^0 and f_1^0 are the torsional stiffness and the fundamental frequency of the original bus body frame; σ_{\max} and σ_{\max}^0 are the max Von Mises stress under full-loaded bending case of new and original bus body frame respectively; t_i and x_i are the topological variable and the sizing variable of the i^{th} beam respectively; $\text{Sym}T$ and $\text{Sym}S$ represent the sets of members required to be symmetric in the TGS and the SGS respectively. $\text{Con}T$ and $\text{Con}S$ represent the sets of members required to be consistent in the TGS and the SGS respectively; T and S correspond to the sets of members in the TGS and the SGS respectively; the cross-sections of the beams must be selected from an available set, and X is the set of property IDs corresponding to the available cross-sections. Table 3 shows the available square and rectangular cross-sections in this research.

Table 3: The set of available cross-sections

Property IDs (PID)	1	2	3	4	5	6	7	8	9	10
Width (W) / mm	20	20	20	30	30	30	40	40	40	50
Height (H) / mm	20	30	40	30	40	50	40	50	60	50
Thickness (T) / mm	2	2	2	2	2	2	2	2	2	2

6.2. Optimisation parameters

After grouping, there are 112 topological variables and 70 sizing variables. A topological variable can be 1 or 0, and a sizing variable can be 1 to 10. Therefore, the design spaces for topology optimisation and sizing optimisation are 5.19×10^{33} and 1×10^{70} , respectively. Due to the great distinction between the design spaces, the population sizes for topological subpopulation and sizing subpopulation are set differently, which are 150 and 250 respectively. The probabilities of the crossover and the mutation are 0.8 and 0.05 respectively. The tournament selection is utilized, and the tournament size is 2. The optimisation is terminated when the generation reaches 250.

6.3. Automatic reloading

Many beams of the chassis frame bear uniformly distributed loads such as passenger seats, luggage and so on. Generally, beams with loads cannot be deleted during optimisation. However, the design space of topology optimisation would be very limited if those beams are kept mandatorily. In order to tackle this conflict, the uniformly distributed loads are reloaded according to the new topology of the chassis frame. Unlike concentrated load applied on a specific node, the uniformly distributed loads are beared by a region of beams. When some beams in the region are removed, the loads are reloaded automatically on the retained beams so that the removed beams do not bear any loads and the total loads applied uniformly on the retained beams remain unchanged.

7. Results

The performances of the original bus and the optimal bus are listed in Table 4; compared with the original bus, the mass reduces by 246.45 kg (8.42% of the original bus), while other performances are not worse. Figure 3 depicts the topology of the optimal chassis, in which retained beams in the TGS are marked in red including 25 diagonal beams, 5 longitudinal beams, 22 cross beams and 7 vertical beams. For comparison, the topologies of the region F1 and F2 (see Figure 3) in the optimal chassis and the original chassis are given in Figure 4(a) - (d) respectively. Compared with the original chassis with 2 diagonal beams, 41 longitudinal beams, 40 cross beams and 7 vertical beams in the TGS, diagonal beams are preferred, longitudinal beams are reduced significantly and close to half of the cross beams are removed from the TGS of the optimal chassis.

Figure 5(a) - (i) illustrate the cross-sections selected by the beams, in which the beams with the cross-sections indicated in the captions are marked in red. Referring to the figures, relatively small cross-sections (PID 1-3) are mainly employed in the diagonal beams in perpendicular direction and the longitudinal beams; medium-sized cross-sections (PID 4-6) are principally selected by the small span diagonal beams in the region of floors and the vertical beams; large cross-sections (PID 7-9) are less adopted, which are chiefly used in long span diagonal beams in the region of floors and reinforced beams in the installation area of the rear axle.

Table 4: The performances of the original bus and the optimal bus

Model	Mass / kg	Torsional stiffness / $\text{kNm} \cdot (\text{°})^{-1}$	Fundamental frequency / Hz	Max Von Mises stress / MPA
Original bus	2926.34	39.88	7.67	158
Optimal bus	2679.89	39.89	7.70	158

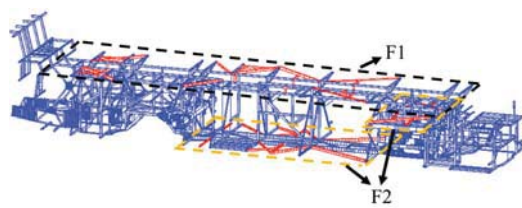


Figure 3: Topology of the optimal chassis

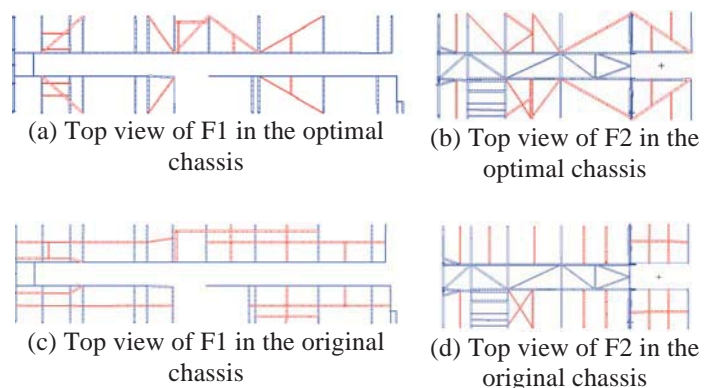


Figure 4: Topologies of F1 and F2

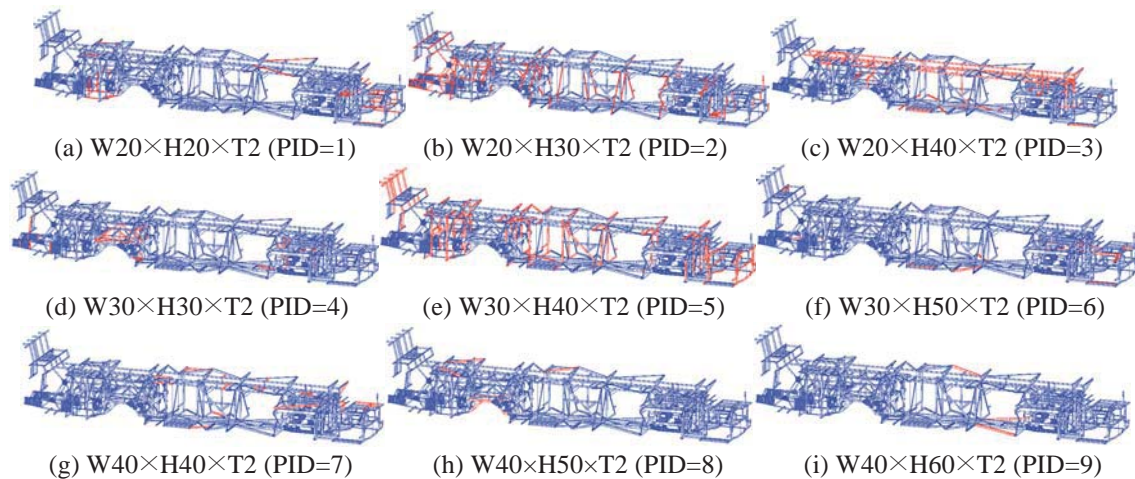


Figure 5: Cross-sections of the optimal chassis

8. Conclusion

An architecture of CCGA-IGS was put forward for simultaneous topology and sizing optimisation of an integral bus chassis. In the preparation stage, additional beams were added to the original chassis to form a whole structure, and then different set of beams were chosen from the whole structure to construct ground structures for topology optimisation and sizing optimisation respectively, namely the process of the IGS strategy. The pre-defined functional requirements are guaranteed in this stage. Variables were grouped according to symmetry and consistency constraints to decrease the number of variables and satisfy the manufacturing constraints. Then, in order to overcome the hindrance of large number of design variables, CCGA was introduced to solve the problem, in which topological variables and sizing variables were divided into two subpopulations that evolved in two different GA systems. During the optimisation, the uniformly distributed loads on the chassis frame were reloaded in accordance with the topology of the newly generated chassis.

The bus body frame with the optimal chassis is significantly lighter than the original bus body frame, while the torsional stiffness, the foundational frequency and the max Von Mises stress are not worse. Meanwhile, the optimal chassis satisfies the functional and manufacturing requirements considered in this paper.

9. Acknowledgements

This work was supported by the National Natural Science Foundation of China under Grant No. 51175285. The authors are grateful to the support.

10. References

- [1] X. F. Liu, G. D. Cheng, J. Yan *et al.*, Singular optimum topology of skeletal structures with frequency constraints by AGGA, *Structural and Multidisciplinary Optimization*, 45 (3), 451-466, 2012.
- [2] R. Y. Su, X. Wang, L. J. Gui *et al.*, Multi-objective topology and sizing optimization of truss structures based on adaptive multi-island search strategy, *Structural and Multidisciplinary Optimization*, 43 (2), 275-286, 2011.
- [3] A. Arzhang, M. F. Christopher, and P. Shahram, Benchmark Problems in Structural Design and Performance Optimization: Past, Present, and Future—Part I, *19th Analysis and Computation Specialty Conference*, Orlando, Florida, USA, 455-466, 2010.
- [4] A. Gauchia, V. Diaz, M. J. L. Boada *et al.*, Torsional Stiffness and Weight Optimization of a Real Bus Structure, *International Journal of Automotive Technology*, 11 (1), 41-47, 2010.
- [5] F. Van Den Bergh, and A. P. Engelbrecht, A cooperative approach to particle swarm optimization, *Ieee Transactions on Evolutionary Computation*, 8 (3), 225-239, 2004.
- [6] H. F. Teng, Y. Chen, W. Zeng *et al.*, A Dual-System Variable-Grain Cooperative Coevolutionary Algorithm: Satellite-Module Layout Design, *IEEE Transactions on Evolution Computation* 14 (3), 438-455, 2010.
- [7] M. A. Potter, and K. A. De Jong, A cooperative coevolutionary approach to function optimization, *The Third Conference on Parallel Problem Solving from Nature*, Jerusalem, Israel, 249--257, 1994.
- [8] A. A. Chaaoui, and F. Florez-Revuelta, Optimizing human action recognition based on a cooperative coevolutionary algorithm, *Engineering Applications of Artificial Intelligence*, 31, 116-125, 2014.
- [9] P. B. Nair, and A. J. Keane, Coevolutionary architecture for distributed optimization of complex coupled systems, *AIAA Journal*, 40 (7), 1434-1443, 2002.

Reliability-Based Design Optimization of Wind Turbine Blades for Fatigue Life under Wind Load Uncertainty

Weifei Hu¹, K.K. Choi¹, Hyunkyoo Cho¹, Nicholas J. Gaul¹, Olesya I. Zhupanska¹

¹ The University of Iowa, Iowa City, Iowa, USA, kyung-choi@uiowa.edu

1. Abstract

Conventional wind turbine blades have been designed using fatigue life predictions based on a fixed wind load distribution that does not fully capture uncertainty of the wind load. This could result in early fatigue failure of blades and eventually increase the maintenance cost of wind turbines. To produce reliable as well as economical wind turbine blades, this paper studies reliability-based design optimization (RBDO) of a wind turbine blade using a novel wind load uncertainty model. In the wind load uncertainty model, annual wind load variation has been extended over a large spatiotemporal range using 249 groups of wind data. The probability of fatigue failure during 20-year service life is estimated using the uncertainty model in the RBDO process and is reduced to meet a desired target probability of failure. Meanwhile, the cost of composite materials used in the blade is minimized by optimizing the composite laminate thicknesses of the blade. In order to obtain the RBDO optimum design efficiently, deterministic design optimization (DDO) of a 5-MW wind turbine blade is first carried out using the mean wind load obtained from the uncertainty model. At the DDO optimum design, fatigue hotspots for RBDO are identified among the laminate section points. For efficient sampling-based RBDO process to handle dynamic wind load uncertainty, instead of generating surrogate models of the overall output performance measure, which is 20-year fatigue life, a number of surrogate models of the 10-minute fatigue damages D_{10} at the hotspots are accurately created using the dynamic Kriging (DKG) method. Using these surrogate models and the wind load uncertainty model, probability of failure of 20-year fatigue life at these hotspots and their design sensitivities are calculated at given design points. Using the sampling-based method, RBDO of the 5-MW wind turbine blade is carried out starting at the DDO optimum design to meet the target probability of failure of 2.275%.

2. Keywords: Wind Turbine Blade, Reliability-Based Design Optimization, Fatigue Life, Wind Load Uncertainty

3. Introduction

As an expensive component in large wind turbine systems, designing reliable wind turbine blades for 20-year fatigue life is one of the most important factor in wind turbine design. A cost-effective design of the blades reduces the initial investment, and a reliable design reduces maintenance cost of the wind turbine systems. This paper proposes reliability-based design optimization (RBDO) process and methods for optimizing reliable wind turbine blades considering dynamic wind load uncertainty.

It is challenging to accurately predict the fatigue damage/life of wind turbine blades due to various uncertainties from material properties, manufacturing process, and external loads. Among those uncertainties, dynamic wind load uncertainty is the most significant source of uncertainty affecting the fatigue reliability of wind turbine blades. Hence, better understanding of the dynamic wind load uncertainty is critical for the reliable optimum design of wind turbine blades.

Reliability analysis of wind turbine blades considering wind load uncertainty has been studied [1-6]. Probabilistic models for mean wind speed have been applied to characterize the annual wind load variation [1-10]. Measured fatigue loadings, e.g., stress and bending moment, were applied to wind turbine fatigue and reliability analysis [3,4]. Traditional reliability analysis of wind turbines involves a specific distribution, e.g., Weibull distribution or Rayleigh distribution, of mean wind speed to account for the frequency of fatigue damage under different wind loads. However, by applying a fixed Weibull distribution, only deterministic fatigue life can be obtained because the assumed Weibull distribution is invariant in different years. The fixed Weibull distribution based either on wind turbine standards [11,12] or measured wind data over one year at a specific location cannot truly render the wind load uncertainty over a larger spatiotemporal range, for instance at different locations and in different years. Tarp-Johansen [5] has studied the statistical uncertainty of two parameters of the Weibull distribution for mean wind speed based on one-year measurements over a period of 52 years.

Besides the mean wind speed, the fluctuations in the wind speed about the short-term mean naturally have a significant impact on the design loadings, as they are the source of extreme gust loads and a large part of the blade fatigue loading [13,14]. The distribution of turbulence intensity has been involved in the reliability analysis of wind turbine blades [1,6]. Another simple way to consider the wind load uncertainty is by using partial safety factors [11,12,15-17]. However, the spatial and temporal wind load variation cannot be represented accurately

using partial safety factors. In this paper, the reliability analysis of wind turbine blades applies a wind load uncertainty model, which considers both annual wind load variation and wind load variation in a large spatiotemporal range.

Reliability-based design of wind turbine blades against fatigue failure has been studied by Ronold et al. [1], whose probabilistic model was applied to reliability analysis of a site-specific wind turbine of a prescribed make. Toft and Sørensen [18] presented a probabilistic framework for design of wind turbine blades, which requires tests with the basic composite materials and full-scale blades during the design process. Reliability-based design of wind turbines against failure under extreme condition has also been studied [19,20]. However, very few research has well addressed RBDO of wind turbine blades for fatigue life under wind load uncertainty. This paper presents RBDO of wind turbine blades for fatigue life using the developed wind load uncertainty model, by which the obtained RBDO optimum design satisfies a reliability requirement considering realistic uncertain wind load during the designed 20-year lifespan.

4. Fatigue Analysis of Composite Wind Turbine Blades

4.1. Parametric blade modelling

A parametric composite wind turbine blade model has been developed for fatigue analysis, deterministic design optimization (DDO), reliability analysis and RBDO. The aerodynamic properties of the blade model, e.g., airfoil type, chord length, and twist angle, are the same with the 5-MW NREL reference wind turbine blade [21]. However, material properties and laminate schedules are different from the NREL blade. The current blade is composed of seven parts, which are the root, forward shear web, aft shear web, leading edge, spar cap, trailing edge, and tip, as shown in Fig. 1. Each part consists of a different number of panels. In total, there are 71 panels in the seven parts. The forward shear web, aft shear web, leading edge, and trailing edge consist of sandwich panels, in which composite laminates are laid at both the top and bottom surfaces and a foam core is laid in the middle. Other parts are made of composite laminates. Composite laminates QQ1 and P2B are selected from the SNL/MSU/DOE Composite Material Fatigue Database [22]. The laminate thicknesses of QQ1 and P2B in panels are changing in DDO and RBDO because they are connected to the design variables for DDO and RBDO.

4.2. Fatigue analysis procedure

A comprehensive fatigue analysis procedure has been developed to calculate 10-minute fatigue damage D_{10} given blade design variable vector \mathbf{d} , 10-minute mean wind speed V_{10} , and 10-minute turbulence intensity I_{10} . The design variable vector \mathbf{d} controls the thicknesses of composite laminates used in the wind turbine blade. The fatigue analysis procedure is briefly explained as follows.

Given the V_{10} and I_{10} at hub height, a 10-minute wind field realization is first simulated using TurbSim [23]. The simulated wind field is then used to calculate resultant aerodynamic lift force, drag force, and moment force at the aerodynamic centre of each blade section by AeroDyn [24]. In order to avoid stress concentration using resultant aerodynamic forces, detailed wind pressure obtained from XFOIL [25] is modified to match the aerodynamic forces calculated by AeroDyn. Then, the modified wind pressure could be applied on the blade surface to carry out FEA using Abaqus [26]. Detailed explanation of obtaining the modified wind pressure is provided in the previous work [27]. At the same time, gravity load and centrifugal load have been considered in the stress analysis. The non-proportional multi-axial complex stresses at section points, which indicate locations through laminate thickness in the wind turbine blade, is extracted out for fatigue damage calculation. A multi-axial fatigue damage index [28] is used to calculate the fatigue damage considering longitudinal stress σ_{11} , transverse stress σ_{22} , and shear stress σ_{12} in principal material coordinates. The 95% lower bounds of the probabilistic S-N curves and constant life diagrams (CLDs) are applied when calculating the number of allowable cycles at a certain stress level. Finally, the 10-minute fatigue damage at a section point is accumulated by Miner's rule.

In summary, the 10-minute fatigue damage D_{10} at a section point in the blade can be determined by design variable vector \mathbf{d} , 10-minute mean wind speed V_{10} , and 10-minute turbulence intensity I_{10} as

$$D_{10} = D_{10}(\mathbf{d}, V_{10}, I_{10}) \quad (1)$$

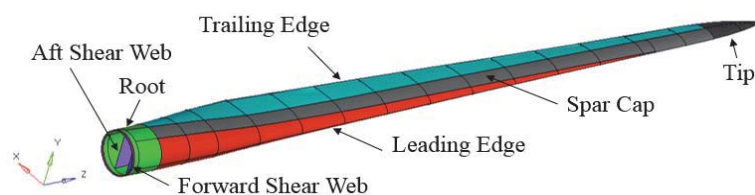


Figure 1: Seven Parts of the Composite Wind Turbine Blade

5. Dynamic Wind Load Uncertainty Model

The developed wind load uncertainty model involves both the annual wind load variation and the wind load variation in a large spatiotemporal range. The annual wind load variation represents variation of 10-minute mean wind speed V_{10} and 10-minute turbulence intensity I_{10} in a year using a joint probability density function (PDF) of V_{10} and I_{10} . However, it is not appropriate to obtain the joint PDF of V_{10} and I_{10} directly from their marginal PDFs due to the correlation between V_{10} and I_{10} . It is found that V_{10} and I_{10} have statistical correlation. Moreover, there is also a mathematical correlation between V_{10} and I_{10} because I_{10} is calculated by Σ_{10}/V_{10} , where Σ_{10} is 10-minute standard deviation of wind speed. To exclude the mathematical correlation in the joint PDF, the joint PDF of V_{10} and Σ_{10} is obtained first and then transferred to the joint PDF of V_{10} and I_{10} .

Based on the 249 groups of wind data, the marginal PDFs of V_{10} and Σ_{10} have been identified to be Weibull distribution and Gamma distribution, respectively, using the Maximum Likelihood Estimate (MLE) method [29]. The statistical correlation between V_{10} and Σ_{10} is represented using Gumbel copula, which is also the maximum likely copula type [30]. Because the transformation from the random vector (V_{10}, Σ_{10}) to the random vector (V_{10}, I_{10}) is a one-to-one transformation with the Jacobian of the transformation $J = v_{10}$, the joint PDF of V_{10} and I_{10} could be derived using the joint PDF of V_{10} and Σ_{10} as

$$f_{VI}(v_{10}, i_{10}) = f_{V\Sigma}(v_{10}, \sigma_{10}) |J| = f_{V\Sigma}(v_{10}, v_{10} \cdot i_{10}) v_{10} \quad (2)$$

where f_{VI} and $f_{V\Sigma}$ are the joint PDFs for (V_{10}, I_{10}) and (V_{10}, Σ_{10}) , respectively; v_{10} , i_{10} and σ_{10} are realizations of V_{10} , I_{10} , and Σ_{10} , respectively; and $\sigma_{10} = v_{10} \cdot i_{10}$. Using the identified copula for V_{10} and Σ_{10} , the joint PDF of V_{10} and Σ_{10} can be expressed as [30]

$$f_{V\Sigma}(v_{10}, \sigma_{10}) = c_{V\Sigma}(v_{10}, \sigma_{10}) f_{V10}(v_{10}) f_{\Sigma10}(\sigma_{10}) \quad (3)$$

where $c_{V\Sigma}$ is the copula density function for V_{10} and Σ_{10} , and f_{V10} and $f_{\Sigma10}$ are the marginal PDFs of V_{10} and Σ_{10} , respectively. Using Eqs. (2) and (3), the joint PDF of V_{10} and I_{10} can be expressed as

$$f_{VI}(v_{10}, i_{10}) = c_{V\Sigma}(v_{10}, v_{10} \cdot i_{10}) f_{V10}(v_{10}) f_{\Sigma10}(v_{10} \cdot i_{10}) v_{10} \quad (4)$$

The marginal PDFs of Weibull distribution for V_{10} and Gamma distribution for Σ_{10} take the forms

$$f_{V10}(v_{10}; C, k) = \frac{k}{C} \left(\frac{v_{10}}{C} \right)^{k-1} \exp \left[- \left(\frac{v_{10}}{C} \right)^k \right] \quad (5)$$

$$f_{\Sigma10}(\sigma_{10}; a, b) = \frac{1}{b^a \Gamma(a)} \sigma_{10}^{a-1} \exp \left(- \frac{\sigma_{10}}{b} \right) \quad (6)$$

respectively, where C and k are the scale parameter and shape parameter for the Weibull distribution, respectively; a and b are the shape parameter and scale parameter for the Gamma distribution, respectively; and $\Gamma(a)$ is the gamma function of a . The Gumbel copula density function $c_{V\Sigma}$ for V_{10} and Σ_{10} is expressed as [30]

$$c_{V\Sigma}(u, v; \theta) = \frac{(-\ln u)^{\theta-1} (-\ln v)^{\theta-1} (\theta + w^{1/\theta} - 1) w^{1/\theta-2} \exp(-w^{1/\theta})}{uv} \quad (7)$$

where u and v are marginal cumulative distribution functions (CDFs) of V_{10} and Σ_{10} , respectively; w is equal to $(-\ln u)^\theta + (-\ln v)^\theta$; and θ is the copula parameter, which can be calculated from Kendall's tau τ as [30]

$$\theta = 1/(1-\tau) \quad (8)$$

Based on Eqs. (4) - (8), the derived joint PDF of V_{10} and I_{10} is determined by parameters C , k , a , b , and τ . Using the 249 groups of wind data, 249 different sets of (C, k, a, b, τ) have been calculated. Each set of (C, k, a, b, τ) contains annual wind load variation. The calculated 249 sets of (C, k, a, b, τ) indicate that there is a wind load variation in the large spatiotemporal range, i.e., in different years and at different locations. Therefore, the dynamic wind load variation in the large spatiotemporal range can be represented by providing the distributions of (C, k, a, b, τ) . These distributions are identified by the MLE method using the 249 sets of (C, k, a, b, τ) . The identified distribution types of C , k , a , b , and τ are log-logistic, normal, generalized extreme value, Weibull, and extreme value distributions, respectively. The specific parameters for PDFs of C , k , a , b , and τ are obtained as well from the 249 sets, assuming that C , k , a , b , and τ are statistically independent. Due to space limitations, these PDFs are omitted from presentation here.

6. Reliability Analysis under Dynamic Wind Load Uncertainty

6.1. Twenty-year Fatigue Damage Calculation

Applying the 10-minute fatigue damage D_{10} in Eq. (1) and the derived joint PDF of V_{10} and I_{10} in Eq. (4), the one-year fatigue damage D_{1year} can be calculated as

$$D_{1year}(\mathbf{d}, C, k, a, b, \tau) = 52560 \int_{V_{low}}^{V_{upp}} \int_{I_{low}}^{I_{upp}} f_{VI}(v_{10}, i_{10}; C, k, a, b, \tau) D_{10}(\mathbf{d}, v_{10}, i_{10}) dv_{10} di_{10} \quad (9)$$

where “52560” indicates the number of 10-minute periods in one year; V_{low} and V_{upp} are the lower and upper bounds of V_{10} , respectively; and I_{low} and I_{upp} are the lower and upper bounds of I_{10} , respectively. The one-year fatigue damage in Eq. (9) cannot be explicitly expressed as a function of \mathbf{d} , C , k , a , b , and τ , due to the complexity of the joint PDF and 10-minute fatigue damage calculation. Thus, in practical damage calculation, the double integration in Eq. (9) is numerically calculated using the Riemann integral as

$$D_{1year}(\mathbf{d}, C, k, a, b, \tau) \approx 52560 \sum_{i=1}^m \sum_{j=1}^n P_{VI}^{i,j}(v_{10}^i, i_{10}^j; C, k, a, b, \tau) D_{10}^{i,j}(\mathbf{d}, v_{10}^i, i_{10}^j) \quad (10)$$

where m and n are the number of selected V_{10} and I_{10} , respectively. The probability of the V_{10} and I_{10} in (i, j) cell can be calculated as

$$P_{VI}^{i,j}(v_{10}^i, i_{10}^j; C, k, a, b, \tau) = f_{VI}(v_{10}^i, i_{10}^j; C, k, a, b, \tau) \Delta v_{10} \Delta i_{10} \quad (11)$$

where Δv_{10} and Δi_{10} are the size of the (i, j) cell in directions of V_{10} and I_{10} , respectively. (v_{10}^i, i_{10}^j) is the center point of the (i, j) cell. In this paper, a large range of V_{10} and I_{10} has been considered to examine the fatigue damage considering all possible wind conditions, i.e., combination of V_{10} and I_{10} . The lower bound and upper bound of V_{10} are set to be the cut-in wind speed of 3 m/s and cut-out wind speed of 25 m/s, respectively [21]. The lower bound and upper bound of I_{10} are set to be 0.02 and 1, respectively. The 10-minute fatigue analyses are run over the range of V_{10} between 3 m/s and 25 m/s in 2 m/s increments, and the range of I_{10} between 0.02 and 1 in 0.02 increments. Therefore, the number of realizations of V_{10} and I_{10} are $m = 12$ ($i = 1, \dots, 12$) and $n = 50$ ($j = 1, \dots, 50$), respectively, in Eq. (10). At each wind condition, a wind load probability $P_{VI}^{i,j}$ is calculated using Eq. (11), and a 10-minute fatigue damage $D_{10}^{i,j}$ is calculated using the developed fatigue analysis procedure in Section 4.2. In this way, a 12-by-50 wind load probability table for $P_{VI}^{i,j}$ and a 12-by-50 10-minute fatigue damage table for $D_{10}^{i,j}$ can be constructed.

Considering the wind load variation in a 20-year range, a 20-year fatigue damage at a given design \mathbf{d} can be calculated as

$$\begin{aligned} D_{20year}(\mathbf{d}, \mathbf{C}, \mathbf{k}, \mathbf{a}, \mathbf{b}, \boldsymbol{\tau}) &= \sum_{t=1}^{20} D_{1year}^t(\mathbf{d}, C^t, k^t, a^t, b^t, \tau^t) \\ &= 52560 \sum_{t=1}^{20} \sum_{i=1}^{12} \sum_{j=1}^{50} P_{VI}^{i,j}(v_{10}^i, i_{10}^j; C^t, k^t, a^t, b^t, \tau^t) D_{10}^{i,j}(\mathbf{d}, v_{10}^i, i_{10}^j) \end{aligned} \quad (12)$$

where random vectors \mathbf{C} , \mathbf{k} , \mathbf{a} , \mathbf{b} , and $\boldsymbol{\tau}$ contain 20 sets of (C, k, a, b, τ) as $\mathbf{C} = [C^1, C^2, \dots, C^{20}]$, $\mathbf{k} = [k^1, k^2, \dots, k^{20}]$, $\mathbf{a} = [a^1, a^2, \dots, a^{20}]$, $\mathbf{b} = [b^1, b^2, \dots, b^{20}]$, and $\boldsymbol{\tau} = [\tau^1, \tau^2, \dots, \tau^{20}]$. The realizations of random vectors can be randomly drawn from the obtained PDFs of C , k , a , b , and τ in Section 5.

6.2. Reliability Analysis Using Monte Carlo Simulation

In this paper, the probability of fatigue failure is calculated using a sampling-based reliability method that uses Monte Carlo simulation (MCS). Using Eq. (12) and MCS, the probability of fatigue failure is calculated as

$$\begin{aligned} P(\text{Fatigue Life} < 20 \text{ years}) &= P(D_{20year}(\mathbf{Y}) > 1) = \int_{D_{20year}(\mathbf{Y}) > 1} f_{\mathbf{Y}}(\mathbf{y}) d\mathbf{y} \\ &= \int_{\Omega_F} I_{\Omega_F}(\mathbf{y}) f_{\mathbf{Y}}(\mathbf{y}) d\mathbf{y} \cong \frac{1}{NMCS} \sum_{i=1}^{NMCS} I_{\Omega_F}[\mathbf{y}^{(i)}] \end{aligned} \quad (13)$$

where $\mathbf{Y} = [\mathbf{X}, \mathbf{C}, \mathbf{k}, \mathbf{a}, \mathbf{b}, \boldsymbol{\tau}]$, and $\mathbf{y}^{(i)}$ is the i^{th} realization of \mathbf{Y} . It is worth noting that the realization $\mathbf{y}^{(i)}$ is randomly generated based on the PDF of a random design vector \mathbf{X} and the PDFs of random parameters (C, k, a, b, τ) in the wind load uncertainty model. In reliability analysis, the realizations of \mathbf{X} replace the design variable vector \mathbf{d} in order to consider the design uncertainty. The mean of the random design vector \mathbf{X} is the design variable vector \mathbf{d} in RBDO. Each realization $\mathbf{y}^{(i)}$ includes 20 sets of (C, k, a, b, τ) , which represent the wind load variation in 20 years. $NMCS$ is the number of realizations for MCS. Ω_F is the failure domain such that $D_{20year}(\mathbf{Y}) > 1$, and I_{Ω_F} is an

indicator function defined as

$$I_{\Omega_f}(\mathbf{y}) = \begin{cases} 1, & \text{for } \mathbf{y} \in \Omega_f \\ 0, & \text{otherwise} \end{cases} \quad (14)$$

7. Reliability-Based Design Optimization under Dynamic Wind Load Uncertainty

7.1. Random Design Variables

In RBDO, the uncertainty of composite laminate thickness due to the manufacturing process has been considered. The coefficient of variation (CoV) of thicknesses of QQ1 and P2B laminate are referred from the SNL/MSU/DOE Composite Material Fatigue Database [22]. There are seven random design variables that control laminate thicknesses in seven parts accordingly. A linear relationship is used to link an RBDO design variable to laminate thicknesses in panels of a part. The linear relationship between each RBDO design variable and the linked laminate thicknesses is based on the DDO optimum design, as the normalized DDO optimum design variables are used as the initial design variables of RBDO. Due to space limitations, the DDO procedure and results are omitted in this paper. The properties of random design variables for RBDO are listed in Table 1, where \mathbf{d}^L , \mathbf{d}^O , and \mathbf{d}^U are the normalized lower bound, mean, and upper bound of the random design variables, respectively. The CoV of a random design variable is equal to that of thickness of the corresponding composite laminate and is fixed in the RBDO process.

Table 1: Properties of Random Design Variables

Random Design Variable	Distribution	\mathbf{d}^L	\mathbf{d}^O	\mathbf{d}^U	CoV	Corresponding Part	Composite Laminate
d_1	Normal	0.7811	1	3.1243	0.0323	Root	QQ1
d_2	Normal	0.6820	1	2.2741	0.0323	Forward Shear Web	QQ1
d_3	Normal	1.0000	1	1.9133	0.0323	Aft Shear Web	QQ1
d_4	Normal	0.6014	1	2.4057	0.0323	Tip	QQ1
d_5	Normal	0.8974	1	3.5897	0.0323	Leading Edge	QQ1
d_6	Normal	0.4823	1	1.9291	0.0323	Trailing Edge	QQ1
d_7	Normal	0.4626	1	1.3878	0.0203	Spar Cap	P2B

7.2. Objective Function

The normalized total cost of composite materials that are used in the blade is set as the objective function, which is expressed as

$$C(\mathbf{d}) = \left(4.18 \times 1000 \times \sum_i^6 m_i^0 \frac{d_i}{d_i^0} + 11.70 \times 1000 \times m_7^0 \frac{d_7}{d_7^0} \right) / Cost^0 \quad (15)$$

where m_i^0 (unit: ton) is the initial mass of the i^{th} part; d_i^0 is the normalized initial design variable corresponding to the i^{th} part; normalized d_i is the current design corresponding to the i^{th} part; $i = 1, 2, \dots, 7$; and $Cost^0$ is the initial cost. According to TPI Composites, the material costs of QQ1 and P2B are taken to be \$4.18/kg and \$11.70/kg, respectively [31]. It is worth noting that the cost of the carbon/glass-hybrid-fiber-reinforced laminate P2B is 2.799 times more expensive than that of QQ1, which is a glass-fiber-reinforced laminate. The objective function in Eq. (15) is minimized in the RBDO process.

7.3. Probabilistic Constraints

The probabilistic constraint is that the probability of fatigue failure in Eq. (13) at a hotspot should be smaller than a target probability of failure $P_F^{\text{tar}} = 2.275\%$. Hotspots are the section points in seven parts (corresponding to seven design variables) that show maximum fatigue damage at the RBDO initial design. For the current RBDO problem, there are seven probabilistic constraints corresponding to seven hotspots, which are identified at the DDO optimum design. The probabilistic constraints are expressed as

$$P(D_{20\text{year}}^j(\mathbf{Y}) > 1) \leq P_{F_j}^{\text{tar}} = 2.275\%, \quad j = 1, \dots, 7 \quad (16)$$

In order to efficiently calculate 20-year fatigue damage in Eq. (12), accurate global surrogate models for 10-minute fatigue damage D_{10} with respect to design variables have been created using the dynamic Kriging (DKG) method [32]. Because each RBDO constraint requires 600 D_{10} 's corresponding to 12-by-50 different wind conditions (see Section 6.1), there are 4,200 D_{10} surrogate models for seven RBDO constraints. The design of

experiments (DoE) samples for creating surrogate models are sequentially sampled. In total, 1,000 DoE samples are used for creating all 4,200 D_{10} surrogate models. After the accurate surrogate models are created, the design sensitivities of the probabilistic constraints are calculated using MCS and score function [33].

The ratio between true 20-year fatigue damage using the 10-minute fatigue analysis procedure and predicted 20-year fatigue damage using D_{10} surrogate models is calculated. The same MCS of 20 sets of (C, k, a, b, τ) are used for the two types of 20-year fatigue damage. The ratios are calculated at another 1000 design points randomly drawn in the design domain. Table 2 shows the minimum ratio, mean ratio, maximum ratio, standard deviation of ratios, and number of ratios between 0.99 and 1.01 among 1000 ratios for each RBDO constraint. Because the numbers of ratios between 0.99 and 1.01 are larger than 950 (95%), the surrogate models are treated as accurate surrogate models for RBDO.

Table 2: Accuracy Check for Surrogate Models

RBDO Constraint	Minimum Ratio	Mean Ratio	Maximum Ratio	Standard Deviation of Ratios	Number of Ratios Between 0.99 and 1.01
1	0.9939	1.0001	1.0099	0.0013	1000
2	0.9850	1.0002	1.0137	0.0030	990
3	0.9617	1.0001	1.0480	0.0051	963
4	0.9929	0.9998	1.0083	0.0019	1000
5	0.9851	0.9999	1.0260	0.0048	957
6	0.9771	0.9998	1.0347	0.0049	957
7	0.9638	1.0002	1.0276	0.0030	994

7.4. RBDO Formulation and Procedure

The RBDO problem can be formulated as

$$\begin{aligned}
 & \text{minimize} && \text{Cost}(\mathbf{d}) \\
 & \text{subject to} && P(D_{20\text{year}}^j(\mathbf{Y}) > 1) \leq P_{F_j}^{\text{tar}} = 2.275\%, \quad j = 1, \dots, 7 \\
 & && \mathbf{d}^L \leq \mathbf{d} \leq \mathbf{d}^U, \quad \mathbf{d} \in \mathbb{R}^7 \text{ and } \mathbf{X} \in \mathbb{R}^{107}
 \end{aligned} \tag{17}$$

where \mathbf{Y} is the 107-dimensional random vector including seven random design variables and 20 sets of (C, k, a, b, τ) ; \mathbf{d} is the 7-dimensional design variable vector; $\text{Cost}(\mathbf{d})$ is the normalized cost as shown in Eq. (15); and $D_{20\text{year}}^j$ is the 20-year fatigue damage for the j^{th} probabilistic constraint $P(D_{20\text{year}}^j(\mathbf{Y}) > 1) \leq P_{F_j}^{\text{tar}}$. The flowchart of the RBDO procedure including global surrogate model generation is given in Fig. 2.

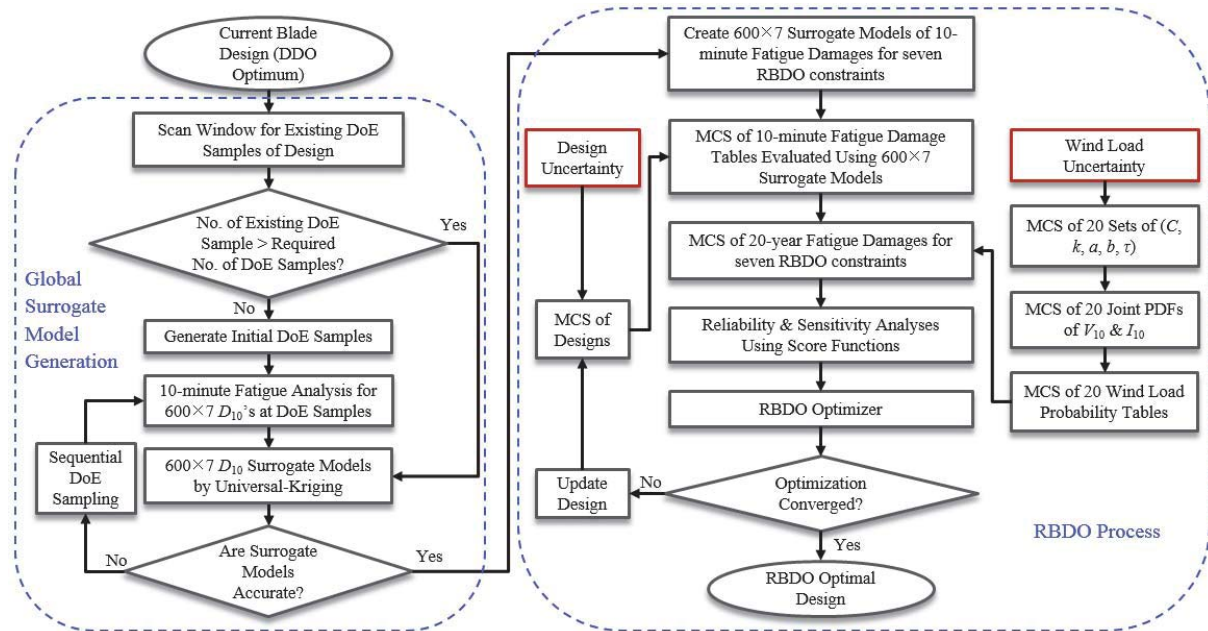


Figure 2: Flowchart of the RBDO Procedure Including Global Surrogate Model Generation

8. Results and Discussion

The RBDO procedure is successfully converged using 13 iterations. At each iteration, 200,000 MCS of 20 sets of (C, k, a, b, τ) are used to calculate the probabilities of failure and design sensitivities of the probabilistic constraints. The probability of failure was reduced from 56.902% at the RBDO initial design (DDO optimum design) to 2.369% at the RBDO optimum design. The histories of the normalized cost and maximum probability of failure among seven RBDO constraints are shown in Figure 3. Table 3 compares the RBDO initial design, RBDO optimum design, true cost, and weight. It is observed that through the RBDO process the cost is reduced by 8% while the weight is increased by 13.3%. The reason is that more cheap but heavy composite material, QQ1, is applied at the RBDO optimum design than that applied at the RBDO initial design. Meanwhile, a less expensive composite material, P2B, is chosen at the RBDO optimum design.

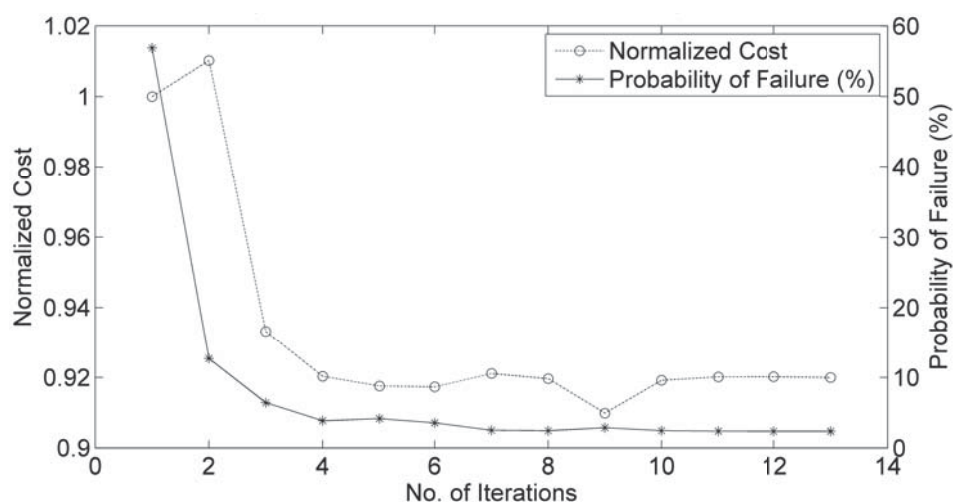


Figure 3: Histories of the Normalized Cost and Maximum Probability of Failure among Seven RBDO Constraints

Table 3: Comparison of the RBDO Initial Design and RBDO Optimum Design

	d_1	d_2	d_3	d_4	d_5	d_6	d_7	Cost (\$)	Weight (ton)
RBDO Initial Design	1	1	1	1	1	1	1	101331	17.7473
RBDO Optimum Design	1.1885	2.1922	1.9132	0.6987	0.9968	1.3262	0.5413	93224	20.1080

9. Conclusions

The RBDO of wind turbine blades for fatigue life under wind load uncertainty is investigated in this paper. The wind load uncertainty model could provide realistic uncertain wind load through the designed 20-year lifespan. A reliability analysis method for wind turbine blades under the wind load uncertainty model has been developed. Based on the reliability analysis method, RBDO has been carried out to obtain fatigue reliable design for a 20-year lifespan considering wind load uncertainty. The obtained RBDO optimum design minimizes the material cost and reduces the probability of failure to 2.369% based on the current surrogate models. This research demonstrates that applying RBDO methods to wind turbine blades could provide safer and more economical designs considering wind load uncertainty.

10. Acknowledgements

This research is primarily supported by the Iowa Alliance Wind Innovation and Novel Development (IAWIND) 09-IPF-15 and NSF EPSCoR project EPS-1101284. These supports are greatly appreciated.

11. References

- [1] K.O. Ronold, W.H. Jakob and C.J. Christensen, Reliability-based fatigue design of wind-turbine rotor blades, *Engineering Structures*, 21 (12), 1101-1114, 1999.
- [2] K.O. Ronold and C.J. Christensen, Optimization of a design code for wind-turbine rotor blades in fatigue, *Engineering Structures*, 23 (8), 993-1004, 2001.
- [3] P.S. Veers and S.R. Winterstein, Application of measured loads to wind turbine fatigue and reliability

- analysis, *Proceedings of 1997 ASME Wind Energy Symposium, 35th AIAA Aerospace Science Meeting & Exhibit*, Reno, NV, 1997.
- [4] J.H. Sutherland and P.S. Veers, Fatigue Case Study and Reliability analyses for Wind Turbines, *ASME/JSME/JSES International Solar Energy Conference*, Sandia National Laboratory, Albuquerque, 1995.
 - [5] N.J. Tarp-Johansen, Examples of Fatigue Lifetime and Reliability Evaluation of Larger Wind Turbine Components, Report No.: Risø-R-1418(EN), Risø National Laboratory, Denmark, 2003.
 - [6] W. Hu, K.K. Choi, N.J. Gaul, H. Cho and O. Zhupanska, Reliability Analysis of Wind Turbine Blades for Fatigue Life Under Wind Load Uncertainty, *14th AIAA/ISSMO Multidisciplinary Analysis and Optimization Conference*, Indianapolis, Indiana, September 17-19, 2012.
 - [7] D.T. Griffith and T.D. Ashwill, The Sandia 100-meter All-glass Baseline Wind Turbine Blade: SNL 100-00, SANDIA REPORT SAND2011-3779, Sandia National Laboratories, USA, 2011.
 - [8] J.A. Carta, P. Ramirez and S. Velazquez, A Review of Wind Speed Probability Distributions Used in Wind Energy Analysis Case Studies in the Canary Islands, *Renewable and Sustainable Energy Reviews*, 13 (5), 933-955, 2009.
 - [9] M.M. Shokrieh and R. Rafiee, Simulation of Fatigue Failure in A Full Composite Wind Turbine Blade, *Composite Structures*, 74, 332-342, 2006.
 - [10] L. Manuel, P.S. Veers and S.R. Winterstein, Parametric Models for Estimating Wind Turbine Fatigue Loads for Design, *Proceedings of 2001 ASME Wind Energy Symposium, 39th AIAA Aerospace Sciences Meeting & Exhibit*, Reno, NV, 2001.
 - [11] IEC 61400-1, Wind Turbines – Part I: Design Requirements, 3rd Ed., International Electrotechnical Commission, 2005.
 - [12] Germanischer Lloyd, Guideline for the Certification of Wind Turbines Edition 2010, Hamburg, Germany, 2010.
 - [13] T. Burton, N. Jenkins, D. Sharpe and E. Bossanyi, *Wind Energy Handbook, 2nd Ed.*, John Wiley & Sons, Ltd., West Sussex, UK, 2011.
 - [14] J.F. Manwell, J.G. Mcgowan and A. L. Rogers, *Wind Energy Explained: Theory, Design and Application 2nd Ed.*, John Wiley & Sons, Ltd., West Sussex, UK, 2009.
 - [15] C. Kong, J. Bang and Y. Sugiyama, Structural Investigation of Composite Wind Turbine Blade Considering Various Load Cases and Fatigue Life, *Energy*, 30, 2101-2114, 2005.
 - [16] C. Kong, T. Kim, D. Han and Y. Sugiyama, Investigation of Fatigue Life for A Medium Scale Composite Wind Turbine Blade, *International Journal of Fatigue*, 28, 1382-1388, 2006.
 - [17] D. Veldkamp, A Probabilistic Evaluation of Wind Turbine Fatigue Design Rules, *Wind Energy*, 11, 655-672, 2008.
 - [18] H.S. Toft and J.D. Sørensen, Reliability-based design of wind turbine blades, *Structural Safety*, 33 (6), 333-342, 2011.
 - [19] K.O. Ronold and G.C. Larsen, Reliability-based design of wind-turbine rotor blades against failure in ultimate loading, *Engineering Structures*, 22 (6), 565-574, 2000.
 - [20] P.W. Cheng, A Reliability Based Design Methodology for Extreme Responses of Offshore Wind Turbines, Ph.D. dissertation, Wind Energy Research Institute, Delft University of Technology, Netherlands, 2002.
 - [21] J. Jonkman, S. Butterfield, W. Musial and G. Scott, Definition of a 5-MW Reference Wind Turbine for Offshore System Development, NREL/TP-500-38060, Golden, CO, National Renewable Energy Laboratory, 2009.
 - [22] J.F. Mandell and D.D. Samborsky, SNL/MSU/DOE Composite Material Fatigue Database Mechanical Properties of Composite Materials for Wind Turbine Blades Version 23.0, Montana State University – Bozeman, 2014.
 - [23] B.J. Jonkman, TurbSim User's Guide: Version 1.50, NREL/TP-500-46198, Golden, CO, National Renewable Energy Laboratory, 2009.
 - [24] P. J. Moriarty and A.C. Hansen, AeroDyn Theory Manual, NREL/EL-500-3881, Golden, CO, National Renewable Energy Laboratory, 2005.
 - [25] M. Drela and H. Youngren, XFOIL 6.9 User Guide, Massachusetts Institute of Technology, Cambridge, MA, 2001.
 - [26] ABAQUS/CAE Version 6.11, Abaqus User Documentations, Dassault Systems, 2011.
 - [27] W. Hu, K.K. Choi, O. Zhupanska and J.H.J. Buchholz, A New Fatigue Analysis Procedure for Composite Wind Turbine Blades, *32nd ASME Wind Energy Symposium*, National Harbor, Maryland, 2014.
 - [28] Y. Liu and S. Mahadevan, Probabilistic fatigue life prediction of multidirectional composite laminates, *Composite Structures*, 69 (1), 11-19, 2005.
 - [29] R.V. Hoog, J.W. McKean and A.T. Craig, *Introduction to Mathematical Statistics, 6th Ed.*, Pearson Prentice Hall, Upper Saddle River, NJ, 2005.
 - [30] Y. Noh, K.K. Choi and I. Lee, Identification of marginal and joint CDFs using Bayesian method for RBDO,

- Structural and Multidisciplinary Optimization*, 40 (1), 35-51, 2010.
- [31] TPI Composites Inc., Innovative Design Approaches for Large Wind Turbine Blades, Sandia Report SAND2003-0723, 2003.
- [32] L. Zhao, K.K. Choi, I. Lee, Metamodeling Method Using Dynamic Kriging for Design Optimization, *AIAA Journal*, 49 (9), 2034-2046, 2011.
- [33] I. Lee, K.K. Choi, Y. Noh, L. Zhao and D. Gorsich, Sampling-Based Stochastic Sensitivity Analysis using Score Functions for RBDO Problems with Correlated Random Variables, *Journal of Mechanical Design*, 133 (2), 021003, 2011.

Multidisciplinary optimization of auto-body lightweight design using modified particle swarm optimizer

Zhao Liu¹, Ping Zhu², Wei Chen³, Ren-Jye Yang⁴

¹ *The State key laboratory of Mechanical System and Vibration, School of Mechanical Engineering, Shanghai Jiao Tong University, Shanghai P.R. China, kakalz@163.com*

² *The State key laboratory of Mechanical System and Vibration, School of Mechanical Engineering, Shanghai Jiao Tong University, Shanghai P.R. China, pzhu@sjtu.edu.cn*

³ *Department of Mechanical Engineering, Northwestern University, USA, weichen@northwestern.edu*

⁴ *Research and advanced Engineering, Ford Motor Company, USA, yangrenjye@gmail.com.*

1. Abstract

Rising complexity of the automotive industry results in enormously increasing of disciplines. It becomes highly important to find the best compromise among these disciplines in the automotive design process. The coupling strategy among different disciplines and the algorithms employed to solve optimization problems are two core aspects defined by the architecture of multidisciplinary design optimization (MDO). In this paper, a MDO architecture is investigated to decide the best compromise among multiple working conditions (frontal impact, frontal offset impact, lateral impact, rear impact, auto-body stiffness and mode cases) with respect to auto-body lightweight design. Since the selection of optimization algorithms has a significant influence on the optimization time and the final solution, particle swarm optimization (PSO) algorithm is modified and promoted to accommodate different load cases. The established MDO architecture is applied to a lightweight design application of an auto-body, and the results verify its effectiveness and validity.

2. Keywords: Multidisciplinary design optimization; Particle swarm optimization; Collaborative optimization; Auto-body lightweight design; Kriging modeling technique.

3. Introduction

Because of rising complexity of industrial development, the number of disciplines to be concerned in automotive design has been increased enormously. The different disciplines, such as multiple crash cases, NVH and so on, often have conflicting objectives. So appropriate design strategies which provide an opportunity to integrate each discipline and conduct compromise searching process are required instead of solving each discipline separately [1]. Hence, multidisciplinary design optimization (MDO) has been investigated and introduced to achieve the best compromise solution.

MDO aims to utilize the couplings among different disciplines to search the global optimal design [2], and has been applied in many engineering systems, such as bridges [3], buildings [4,5], automobiles [6,7], ships [8,9] and so on. The coupling strategy of different disciplines and the algorithms employed to solve an optimization problem are two core aspects defined by the MDO architecture which significantly influence the solution time and optimal searching efficiency [10]. With respect to the auto-body design process, the traditional gradient-based methods or local search strategies are unsuitable for solving multidisciplinary optimization due to the multimodal character of the objective and the numerical noise encountered in the crash cases [1]. So global optimization algorithms should be introduced into the MDO optimization procedure. Particle swarm optimization (PSO), proposed by Kennedy and Eberhart [11], is a global optimization algorithm. Its principle is derived from the cooperative behavior appeared among species like birds, fishes etc. Because of its simplicity of implementation and strong capacity to quickly find a reasonably satisfactory solution, the PSO algorithm is becoming very popular and has been widely used. However, PSO suffers from premature convergence problem because of the quick loss of diversity in the solution search. In this research, the basic PSO is modified by OLHD technique and a reset operator to enhance the diversity among particles.

In this paper, multiple working conditions (frontal impact, frontal offset impact, lateral impact, rear impact, auto-body stiffness and mode cases) are taken into consideration. Kriging modeling technique is employed to surrogate the time consuming finite element simulation. A MDO architecture based on Collaborative Optimization (CO) method is established so that each sub-system can control its own design variables and is only bounded by its own corresponding constraints. Then, with the purpose of improving the efficiency and accuracy of the optimization problem, PSO optimizer is applied and modified according to the property of each discipline. The rest of this paper is organized as follows: in Section 4, the technical base is described. In Section 5, the MDO architecture for the auto-body design is presented in detail. The lightweight design process of a car model is depicted in Section 6 and Section 7 is the conclusions of our work.

4. Technical base

4.1. Collaborative Optimization

Collaborative optimization (CO), initially developed by Braun [12], is a discipline feasible constraint method whose architecture is designed to improve disciplinary autonomy while satisfying interdisciplinary compatibility. The problem is decomposed into disciplinary sub problems sketched in Figure 1. Each sub-discipline controls its own design variables and is bounded by its own specific constraints. Interdisciplinary compatibility is the objective of each sub-discipline optimizer. At the system-level, an optimizer is employed to coordinate the whole process and optimizes the overall objective.

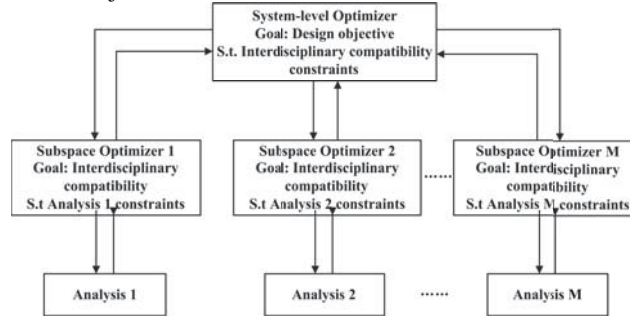


Figure 1: Collaborative optimization

4.2. Particle swarm optimization

The PSO method maintains a population of candidate solutions located in the design space of the fitness/cost function. Each potential solution is called particle and the entire population of candidate solutions is called swarm. Fitness function values of all the particles are computed in the current positions. Each particle abides two rules, trying to return to its previous best location as well as pursuing the best position of its group. The positions of particles are updated iteratively based on the algorithm. Based on the rules, the particle swarm moves like a group. The overall behavior prompts all particles to go forward the optimal solutions of the fitness/cost function.

In the standard Particle swarm optimization, consuming a problem with D-dimensions, a potential solution is expressed as the velocity and position of a particle. Vector x_k^i stands for the position of the i^{th} particle while vector v_k^i is the velocity. p_k^i represents the best previously visited position of each particle and p_k^g is the global best position found by particle swarm. The whole swarm is controlled by equations (1) and (2).

$$v_{k+1}^i = \omega v_k^i + c_1 \cdot r_1 \cdot (p_k^i - x_k^i) + c_2 \cdot r_2 \cdot (p_k^g - x_k^i) \quad (1)$$

$$x_{k+1}^i = x_k^i + v_{k+1}^i \quad (2)$$

$$\omega(ite) = \frac{(ite_{max} - ite)}{ite_{max}} \times (\omega_{max} - \omega_{min}) + \omega_{min} \quad (3)$$

Equation (1) is the velocity update equation. Its first part is the initial velocity with inertia factor ω which provides momentum for particles to move across the design space [13]. Shi and Eberhart have proposed a linearly varying inertia weight which had a significant improvement in the performance of standard PSO [14], shown as equation (3), in which ite represents the current generation and ite_{max} is the maximum generation. The second part of equation (1) is the cognition component represents the personal behavior of a particle and encourages each particle to move toward its own best previous position. The third part is called the social component which stands for cooperation behavior among particles [15]. The social component always pulls the particles moving forward the global best position. c_1 is named as cognitive scaling parameter and c_2 is the social scaling parameter [16]. r_1 and r_2 are two uniformly distributed random numbers within the range [0,1].

4.3. Metamodels construction

Metamodeling techniques are widely used to construct surrogate models, since simulation of automotive finite element models are computationally expensive [17,18]. The Kriging model [19] is employed in this research. The stochastic process is used in Kriging model for predicting the values of unknown points. Sample points are interpolated to estimate the trend of the stochastic process by Gaussian random function. The model has been proved applicable to represent the multimodal and nonlinear functions. The accuracy of the metamodels with respect to finite element models is essential for response prediction. The generally used R^2 is verified in this research. The objective-oriented sequential sampling method is implemented to improve the precision of the constructed metamodels [20].

5. MDO architecture for the auto-body lightweight design

In this research, six load cases are employed (frontal impact, frontal offset impact, lateral impact, rear impact, auto-body stiffness and auto-body mode conditions shown in Figure 2) to conduct lightweight design of autobody. This Section has two parts. The first describes the modified PSO algorithm and the established MDO architecture is presented in the second part.

5.1. Modified PSO algorithm

In order to ensure a full coverage of the design space, the OLHD technique [21] is used to generate the first generation of particle swarm instead of the uniformly random distributed method (labeled as PSO optimizer version 2). In order to make a distinct comparison, particles are generated in two-dimensional space by the traditional method and OLHD technique, shown in Figure 3. It is clearly found that the distribution of particles generated by OLHD technique in Figure 3(b) is more reasonable than the random method in Figure 3(a).

From the observation of the mathematical experiments, the convergence rate of the PSO optimizer version 2 is slightly lower than the basic PSO in the beginning of the optimization procedure because of the scattering distribution of initial particles, but the former always finds a better solution at last. So the optimization ability of the basic PSO is successfully improved by OLHD technique.

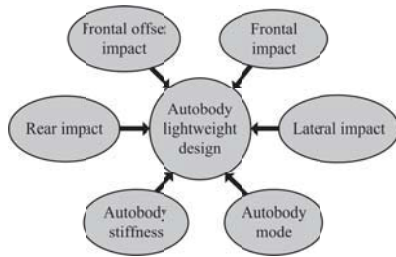
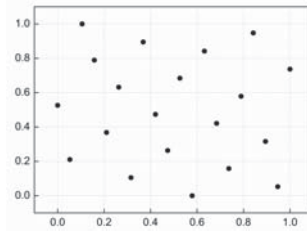
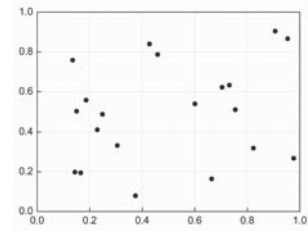


Figure 2: Load cases considered in MDO



(a) OLHD Samples



(b) Random Samples

Figure 3 Comparison of initial particles in two-dimension

Through experiments with numerical benchmarks, it has been observed that PSO quickly finds a relatively good local solution but sometimes stagnates in the local optimum for a considerable number of generations without any improvement. An adaptive reset operator worked on velocity is employed to enhance the global optimization ability of PSO (labeled as PSO optimizer version 1). When the optimization procedure is trapped into stagnation for several generations, the velocity of particles will be reset equation (5)

$$V_{reset} = \mu \cdot rw \cdot V_{rand}, \quad \mu = \frac{(iter_{max} - iter_{current})}{iter_{max}}, \quad rw = (rw_{max} - rw_{min}) * \frac{(iter_{max} - iter_{current})}{iter_{max}} + rw_{min} \quad (4)$$

V_{rand} is randomly generated velocity matrix of particles under predefined range $[-V_{max}, V_{max}]$. μ is a generation correlation coefficient which is linearly decreased along with generation. $iter_{max}$ is the max generation and $iter_{current}$ is the current generation. rw is a velocity correlation coefficient, and its concept is derived from the inertia weight factor ω of the standard PSO. Its boundary is the predefined $[rw_{min}, rw_{max}]$. Following the searching process, the left generation number ($iter_{max} - iter_{current}$) is decreased and the value of μ is diminished, so that the algorithm convergence property can be guaranteed by shrinking the amplitude of V_{reset} , while rw improves the distribution of reset particles in consideration of the global and local search ability. The particles are scattered away from the stagnation position by equation (5) after the adaptive reset operator activated.

$$P_p = P_{stagnation} + V_{reset} \quad (5)$$

From the history of mathematical experiments, the reset operator will be activated when the stagnation judgment criterion and the predefined probability satisfied. It is obvious that the reset operator is active during the middle of the optimization history when the standard versions are fallen into stagnation. So the reset operator effectively assists the algorithm jumping out from stagnation and finding a better optimization solution. The amplitude of the reset process is decreased following the left generation diminished observed at the later stage of the optimization program, so that the convergence of the optimization program can be guaranteed. Compared with the modified PSO version 2, the convergence rate of this version is relatively lower, but it is more suitable for high-nonlinear and multimodal optimization problems benefitted from the diversity enhanced mechanism.

5.2. The MDO architecture

The flowchart of the auto-body optimization process is presented in Figure 4.

- (1) The high-fidelity finite element models are established at the first step.

- (2) Based on design of experiment methodology [21], implement a certain number of finite element analyses to provide data basis for metamodel technique.
- (3) Construct metamodels by Krging technique and validate the precision of each surrogate model
- (4) Sequential sampling method based on the expected improvement criterion[20] is applied to improve the accuracy of each metamodel.
- (5) MDO procedure is launched after all the surrogate models have been prepared. The architecture of MDO is illustrated in Figure 5. In system-level, the objective is mass. The optimization constraints are derived from the interdisciplinary compatibility constraints and auto-body stiffness and mode cases. In consideration of the computational efficiency, the basic version of PSO is employed to search the optimal solution. There exist three sub-systems, frontal, lateral and rear impact. The frontal and frontal offset impact crash cases are included in the frontal impact system. According to the high non-linear property of the crash cases [1], the PSO optimizer version 1 abovementioned is adopted to search the optimum. The second sub-system solves the lateral impact case and the PSO optimizer version 2 mentioned in part one is used to conduct the optimization process. The third discipline is the rear impact case and the PSO optimizer version 2 is employed as the optimization algorithm.
- (6) Validate the optimization solution using finite element analysis and output the verified results.

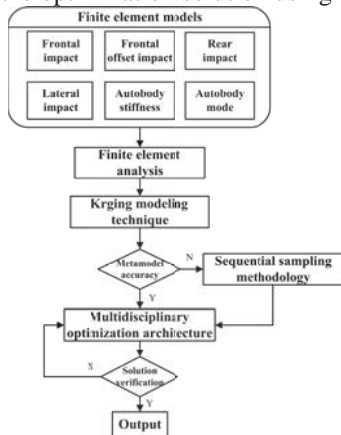


Figure 4: The flowchart of auto-body design

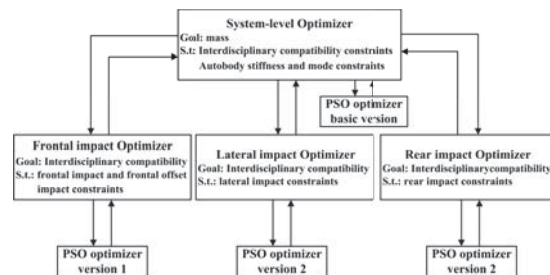


Figure 5: The MDO architecture

6. The Lightweight design of an auto-body

A B-class vehicle model is introduced in this paper illustrated in Figure 6. Strict meshing criteria are used to achieve the quality requirements so that the simulation accuracy can be promoted. The average mesh size is 10mm, while 1005019 shell elements and 22575 solid elements are contained in the full-size model. The finite element model has been verified and is available for further study [22,23]. The auto-body frame FE model are presented in Figure 7 and crash cases simulation in Figure 8.

Multi-load cases and constraints are presented in Table 1. The variable is the thickness of each component. Due to limited space, the detailed variables list is not included in this paper. For auto-body stiffness and mode cases, 90 variables are considered. Its performance indicators are served as the constraints in system optimizer so that the coupling variables can be significantly decreased to ensure the searching convergence. Because of the similar performance indicators, the frontal and frontal offset crash cases are integrated in one sub-system. The objective is the interdisciplinary compatibility and the PSO optimizer version 1 is conducted for optimal searching. 500 generations are preseted for sufficiently optimal searching. The lateral impact contains 15 variables and the PSO optimizer version 2 is employed. 300 generations are used for the optimization process. There are 8 variables in rear impact case, so the optimization searching is relatively simpler than the other two sub-systems. 100 generations are predefined with the PSO optimizer version 2. In the system-level, the basic PSO optimizer is employed and 100 generations are preseted for improving computational efficiency. The particle number is set to 20 for all the problems.



Figure 6: Full size FE model

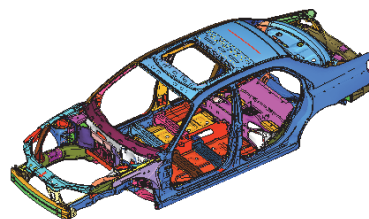


Figure 7: Auto-body frame FE model

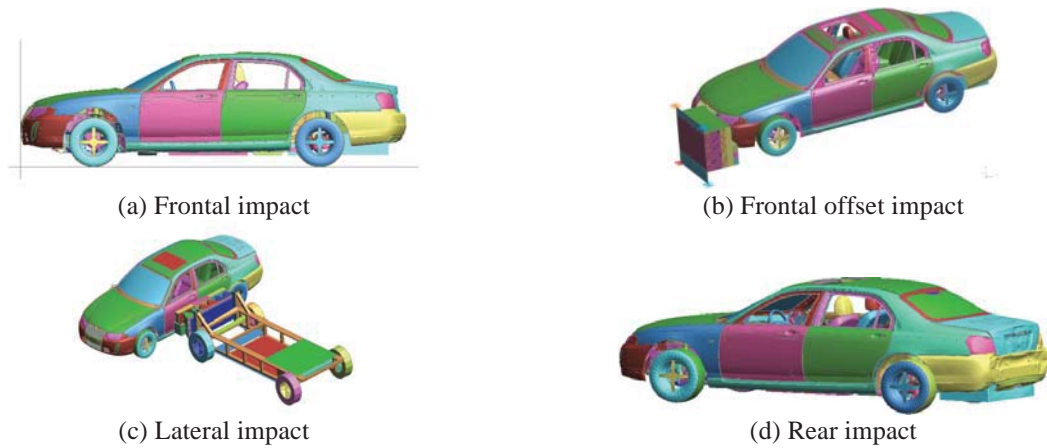


Figure 8 Crash cases simulation

In order to verify the efficiency and effectiveness of the modified PSO optimizer, a comparison MDO case is built with all the sub-systems optimized by basic PSO version. The predefined parameters are invariable. Because of the randomness of the results achieved by PSO, 30 repeated trials are conducted in these two MDO architecture. The best optimization result of the MDO with the modified PSO optimizer is 418.36kg, while the comparison case is 435.17kg. It is obvious that the modified PSO optimizer is efficient and effective to achieve a better optimization solution.

The original mass of the auto-body structure is 450kg. Round the thickness values of all the variables acquired from the MDO optimization procedure, and verify the feasibility by finite element analysis. The structure mass of the auto-body is 423.86kg after the lightweight design process and all the performance indicators are satisfied. So the auto-body lightweight design program based on MDO architecture and the modified PSO optimizer successfully achieve an outcome of 5.80% mass reduction.

Table 1 Load cases description

Load cases	Design variables	Performance indicators	Constraints	
Auto-body stiffness	90	Bending stiffness	$\geq 11000\text{N/mm}$	
		Torsion stiffness	$\geq 12000\text{Nm}/^\circ$	
Auto-body mode		First-order torsion mode	$\geq 34\text{Hz}$	
Crash cases	Frontal impact	12	Left B-Pillar acceleration	$\leq 40\text{g}$
			Left Toe-board intrusion	$\leq 80\text{mm}$
			Right Toe-board intrusion	$\leq 80\text{mm}$
	Frontal offset impact	21	Left B-Pillar acceleration	$\leq 40\text{g}$
			A-Pillar deformation	$\leq 80\text{mm}$
			Left Toe-board intrusion	$\leq 80\text{mm}$
	Lateral impact	15	Right Toe-board intrusion	$\leq 80\text{mm}$
			Lower rib deflection	$\leq 32\text{mm}$
			B-Pillar intrusion velocity	$\leq 9\text{m/s}$
			Door deformation velocity	$\leq 9\text{m/s}$
			Abdomen load	$\leq 1.5\text{kN}$
	Rear impact	8	Pubic symphysis force	$\leq 4\text{kN}$
Left contact force of Hydrogen bottle			$\leq 50\text{kN}$	
Middle contact force of Hydrogen bottle			$\leq 50\text{kN}$	
		Right contact force of Hydrogen bottle	$\leq 50\text{kN}$	

7. Conclusions

In this paper, MDO architecture for auto-body lightweight design is established and the modified PSO optimizer is incorporated into the optimization procedure. From the experimental results, the following conclusions can be summarized:

(1) The MDO architecture based on Collaborative Optimization guarantees the disciplinary autonomy while satisfying interdisciplinary compatibility, so that the sub-system can be operated flexibly. For the auto-body lightweight design problem, different optimization algorithms can be chosen according to the character of each sub-system

(2) The optimization ability of basic PSO is successfully improved by OLHD technique and the velocity reset operator. The MDO comparison results demonstrate that the modified PSO version is more suitable for the auto-body lightweight design.

In the future work, more load cases will be considered to incorporate into the MDO architecture while the problem convergence property is assured. More efficient PSO versions will be investigated to accommodate different requirements from multiple load cases.

8. References

- [1] Fabian Duddeck, Multidisciplinary optimization of car bodies, *Structural and Multidisciplinary Optimization*, 35:375-389, 2008
- [2] Sobieski I., Multidisciplinary design optimization: attempt at definition. In: *Industry university workshop on multidisciplinary aircraft design*, 23-48, 1993.
- [3] Balling, R., and Rawlings, M. R., Collaborative Optimization with Disciplinary Conceptual Design, *Structural and Multidisciplinary Optimization*, 20(3), 232-241, 2000.
- [4] Choudhary, R., Malkawi, A., and Papalambros, P. Y., Analytic Target Cascading in Simulation- Based Building Design, *Automation in Construction*, 14(4), 551-568, 2005.
- [5] Geyer, P., Component-Oriented Decomposition for Multidisciplinary Design Optimization in Building Design, *Advanced Engineering Informatics*, 23(1), 12-31, 2009.
- [6] McAllister, C. D., and Simpson, T. W., Multidisciplinary Robust Design Optimization of an Internal Combustion Engine, *Journal of Mechanical Design*, 125(1), 124-130, 2003.
- [7] Kokkolaras, M., Louca, L. S., Delagrammatikas, G. J., Michelena, N. F., Filipi, Z. S., Papalambros, P. Y., Stein, J. L., and Assanis, D. N., Simulation-Based Optimal Design of Heavy Trucks by Model- Based Decomposition: An Extensive Analytical Target Cascading Case Study, *International Journal of Heavy Vehicle Systems*, 11(3/4), 403-433, 2004.
- [8] Peri, D., and Campana, E. F., Multidisciplinary Design Optimization of a Naval Surface Combatant, *Journal of Ship Research*, 47(1), 1-12, 2003,.
- [9] Kalavalapally, R., Penmetsa, R., and Grandhi, R., Multidisciplinary Optimization of a Lightweight Torpedo Structure Subjected to an Underwater Explosion, *Finite Elements in Analysis and Design*, 43(2), 103-111, 2006.
- [10] Joaquim R.R.A. Martins, Andrew B. Lambe, Multidisciplinary Design Optimization: A Survey of Architectures, *AIAA Journal*, 51(9), 2049-2075, 2013.
- [11] R. Eberhart, J. Kennedy, A new optimizer using particle swarm theory. In: *Proceedings of the Sixth International Symposium on Micro Machine and Human Science*, 39-43, 1995.
- [12] Braun R, Kroo I, Development and application of the collaborative optimization architecture in a multidisciplinary design environment. In: *Multidisciplinary design optimization: state of the art*. SIAM, Philadelphia, 98-116, 1995.
- [13] Y. H. Shi and R. C. Eberhart, A Modified Particle Swarm Optimizer, *IEEE International Conference on Evolutionary Computation*, ANCHORAGE, AK, 69-73,1998.
- [14] Y. H. Shi and R. C. Eberhart, Empirical study of particle swarm optimization, *IEEE International Conference on Evolutionary Computation*, Washington, DC, USA, 3, 101-106, 1999.
- [15] J. Kennedy, The Particle Swarm: Social Adaptation of Knowledge, *IEEE International Conference on Evolutionary Computation*, Indianapolis, Indiana, 303-308,1997.
- [16] R. C. Eberhart and Y. Shi, Particle Swarm Optimization: developments, Applications and Resources, *IEEE International Conference on Evolutionary Computation*, Seoul, South Korea, 1, 81-86, 2001.
- [17] Youn BD, Choi KK, Yang RJ, Gu L, Reliability-based design optimization of crashworthiness of vehicle side impact. *Structural and Multidisciplinary Optimization*, 26, 272-283, 2004.
- [18] Zhang Y, Zhu P, Chen GL, Lightweight design of automotive front side rail based on robust design. *Thin Wall Struct*, 45, 670-676, 2007.
- [19] Timothy, W. S., Timothy M. M., John, J. K., and Farrokh, M., Comparison of Response Surface and Kriging Models for Multidisciplinary Design Optimization, *AIAA Paper*, 98-4755, 1998.
- [20] Jones D.R., Schonlau, M. and Welch, W.J., Efficient global optimization of expensive black-box functions. *Journal of Global optimization*, 13(4), 455-462,1998.
- [21] Jin R, Chen W, and Sudjianto A., An Efficient Algorithm for Constructing Optimal Design of Computer Experiments. *Journal of Statistical Planning and Inference*, 134, 268-287, 2005.
- [22] Siliang Zhang, Ping Zhu and Wei Chen, Crashworthiness-based lightweight design problem via new robust design method considering two sources of uncertainties., *Journal of Mechanical Engineering Science*, 0(0), 1-11, 2012.
- [23] Siliang Zhang, Ping Zhu, Wei Chen and Paul Arendt, Concurrent treatment of parametric uncertainty and metamodeling uncertainty in robust design, 2013, *Structural and Multidisciplinary Optimization*, 47, 63-76, 2013.

Elastic Moduli Identification Method for Orthotropic Structures based on Vibration Data

Akira Saito¹, Yasunari Nishikawa², Shintaro Yamasaki², Kikuo Fujita²,
Atsushi Kawamoto¹, Masakatsu Kuroishi¹, Hideo Nakai¹

¹ Toyota Central R&D Labs., Inc. Nagakute, Japan, akira-saito@mosk.tytlabs.co.jp

² Department of Mechanical Engineering, Osaka University, Suita, Japan, yamasaki@mech.eng.osaka-u.ac.jp

1. Abstract

A novel numerical-experimental methodology for the identification of elastic moduli of orthotropic structures is proposed. Special attention is given to the elastic moduli of laminated electrical steel sheets, which are widely used for the magnetic cores of electric motors and generators. The elastic moduli are determined specifically for use with finite element vibration analyses, such that the dynamic characteristics of such structures can properly be predicted by using the identified elastic moduli. The identification problem is formulated as an inverse problem with nonlinear least squares fit between the measured and computed modal frequencies. The problem is sequentially solved with increasing number of modes that are carefully yet automatically selected based on the analytic sensitivity of the modal frequencies on the elastic moduli. Using the results of numerical experiments, it is shown that the optimal solution obtained by the proposed method converges to the accurate elastic moduli as the number of modes increases. Furthermore, it is also shown that the method not only converges faster but also is numerically more stable than conventional methods. Finally, the method is applied to the experimentally-obtained modal frequencies of the laminated electrical steel sheets, and successfully identifies the elastic moduli where the finite element modal analysis can reproduce accurate modal frequencies.

2. Keywords: Inverse problem, Nonlinear least squares, Orthotropic material, Electrical steel sheets, Laminated plates.

3. Introduction

There is a growing demand to model and predict the dynamic characteristics of the electric machines, as electrified vehicles such as hybrid-electric vehicles and electric vehicles become prevalent. One of the most important yet challenging tasks is the accurate modeling of the modal characteristics of the electric machines. Without the accurate modal characteristics, even if the magnetic force excitation is accurately predicted, it is impossible to accurately capture the forced response of the electric machines [1]. In particular, we shall pay special attention to the modal characteristics of the laminated electrical steel sheets, which are widely used as the magnetic cores of the electric machines. The elastic behavior of the laminated electrical steel is represented by orthotropic constitutive relationship between stress and strain. In this paper, a novel elastic moduli identification method for orthotropic structures is proposed, which is based on the nonlinear least squares (LS) parameter identification procedure using measured mode shapes and frequencies, in conjunction with finite element (FE) model updating technique. The proposed method incorporates the LS procedure with successive increments of the number of modal frequencies and initial condition updates, which enables fast and accurate convergence of the identification procedure.

This paper is organized as follows. Mathematical formulation of the nonlinear LS problem is described in Section 4. In Section 5, the validity of the proposed approach is confirmed by numerical experiments. In Section 6, the methods are applied to the measured mode shapes and frequencies of the laminated electrical steel sheets, and the effectiveness of the proposed methods is discussed. Conclusions are provided in Section 7.

4. Mathematical formulation

4.1 Nonlinear least squares minimization

Let us suppose that the space occupied by the vibrating body of interest is denoted as $\Omega \subset \mathbb{R}^3$, and the body of interest consists of a material with orthotropic constitutive relationship. Assuming that a set of n modal frequencies of the body has been extracted from the results of modal testing, they are denoted as \tilde{f}_k , $k = 1, \dots, n$. With the measured modal frequencies, we try to identify the set of nine independent engineering elastic moduli of the orthotropic material, which is denoted here as $\mathbf{p} = [E_1, E_2, E_3, G_{12}, G_{23}, G_{13}, \nu_{12}, \nu_{23}, \nu_{13}]^T$. Denoting numerically-obtained modal frequencies with \mathbf{p} as $f_k(\mathbf{p})$, $k = 1, \dots, n$, we solve the following minimization problem:

$$\underset{\mathbf{p}}{\text{minimize}} \mathcal{L}_n(\mathbf{p}) := \frac{1}{2} \|\mathbf{r}_n(\mathbf{p})\|^2, \quad (1)$$

where $\|\cdot\|$ denotes the 2-norm of a vector, $\mathbf{r}_n(\mathbf{p}) = \mathbf{f}_n(\mathbf{p}) - \tilde{\mathbf{f}}_n(\mathbf{p})$, $\mathbf{f}_n(\mathbf{p}) = [f_1(\mathbf{p}), f_2(\mathbf{p}), \dots, f_n(\mathbf{p})]^T$, and $\tilde{\mathbf{f}}_n = [\tilde{f}_1, \tilde{f}_2, \dots, \tilde{f}_n]^T$. For the minimization algorithm, we assume general-purpose, gradient-based nonlinear minimization algorithm, such as Gauss-Newton methods and quasi-Newton methods. Fundamentally, we seek the stationary point of the function where the first order derivative of $\mathcal{L}_n(\mathbf{p})$ with respect to \mathbf{p} vanishes, i.e.,

$$\nabla_{\mathbf{p}} \mathcal{L}_n(\mathbf{p}) = \mathbf{0}, \quad (2)$$

where $\nabla_{\mathbf{p}}$ denotes the vector differential operator with respect to \mathbf{p} . It means that the derivative of the eigenfrequencies with respect to \mathbf{p} needs to be evaluated because

$$\nabla_{\mathbf{p}} \mathcal{L}_n(\mathbf{p}) = \mathbf{J}_n^T(\mathbf{p}) \mathbf{r}_n(\mathbf{p}), \quad (3)$$

where $\mathbf{J}_n(\mathbf{p})$ is the Jacobian matrix whose i th row and j th column element is denoted as

$$[\mathbf{J}_n(\mathbf{p})]_{ij} = \frac{\partial f_i(\mathbf{p})}{\partial p_j}, \quad i = 1, \dots, n, \quad j = 1, \dots, 9. \quad (4)$$

The $i - j$ component of the Jacobian matrix can be written as:

$$[\mathbf{J}_n(\mathbf{p})]_{ij} = -\frac{1}{8\pi^2 f_i(\mathbf{p})} \int_{\Omega} \tilde{\boldsymbol{\varepsilon}}(\phi_i) \cdot \tilde{\mathbf{C}} \cdot \left(\frac{\partial \tilde{\mathbf{S}}}{\partial p_j} \right) \cdot \tilde{\mathbf{C}} \cdot \tilde{\boldsymbol{\varepsilon}}(\phi_i) d\Omega. \quad (5)$$

$$\tilde{\mathbf{C}} = \tilde{\mathbf{S}}^{-1} = \begin{bmatrix} 1/E_1 & -\nu_{21}/E_2 & -\nu_{31}/E_3 & 0 & 0 & 0 \\ -\nu_{12}/E_1 & 1/E_2 & -\nu_{32}/E_3 & 0 & 0 & 0 \\ -\nu_{13}/E_1 & -\nu_{23}/E_2 & 1/E_3 & 0 & 0 & 0 \\ 0 & 0 & 0 & 1/G_{12} & 0 & 0 \\ 0 & 0 & 0 & 0 & 1/G_{23} & 0 \\ 0 & 0 & 0 & 0 & 0 & 1/G_{13} \end{bmatrix}^{-1}, \quad (6)$$

where ϕ_i denotes the i th mode shape, $\tilde{\boldsymbol{\varepsilon}}$ denotes the Voigt notation of the Cauchy's strain tensor, $\tilde{\mathbf{C}}$ and $\tilde{\mathbf{S}}$ denote the stiffness and the compliance matrices, respectively.

4.2 Successive augmentation of the least squares problem and initial condition updates

There are three key factors that greatly affect the results of the minimization problem: the number of modes, the initial conditions, and the types of modes used in the objective function. In this paper, we propose guidelines to deal with these factors to improve the accuracy of the solutions of the LS problem.

- Number of modes and initial conditions

In general, it is possible to improve the solution of the LS problem by using more measurement data than the number of parameters to be determined. In our case, if the number of modes exceeds the number of the elastic moduli, it becomes an over-determined problem, and the LS solution is expected to be improved. Namely, we augment the LS problem by adding more residuals to be minimized.

The initial condition for the minimization problem is another important factor, considering that this minimization problem is an ill-posed problem [2]. That is, a "good" initial condition that is close enough to the optimal solution should be selected a priori, before starting the minimization. Even though it is not always possible to choose a good initial condition, a simple alteration to the algorithm would alleviate this difficulty. Namely, during the successive augmentations of the LS problem, the initial values \mathbf{p}_0 for the minimization of $\mathcal{L}_k(\mathbf{p})$ are updated to the converged solution of $\mathcal{L}_{k-1}(\mathbf{p})$.

- Mode selection algorithm

When forming Eq. (1), it is not obvious which vibration modes should be used for the accurate determination of the elastic moduli. Therefore, we try to construct the mode selection criteria for Eq. (1) based on the following arguments. The Taylor expansion of the function $\mathcal{L}_k(\mathbf{p})$ around a specific point $\bar{\mathbf{p}}$ up to second order gives the following quadratic function:

$$\tilde{\mathcal{L}}_k(\mathbf{p}) := \mathcal{L}_k(\bar{\mathbf{p}}) + [\nabla_{\mathbf{p}} \mathcal{L}_k(\bar{\mathbf{p}})]^T [\mathbf{p} - \bar{\mathbf{p}}] + \frac{1}{2} [\mathbf{p} - \bar{\mathbf{p}}]^T \nabla_{\mathbf{p}}^2 \mathcal{L}_k(\bar{\mathbf{p}}) [\mathbf{p} - \bar{\mathbf{p}}]. \quad (7)$$

where $\nabla_{\mathbf{p}}^2 \mathcal{L}_k(\bar{\mathbf{p}})$ is the Hessian matrix that can also be written as

$$\nabla_{\mathbf{p}}^2 \mathcal{L}_k(\bar{\mathbf{p}}) = \mathbf{J}_k^T \mathbf{J}_k + (\nabla_{\mathbf{p}}^2 \mathbf{f}_k)^T \mathbf{r}_k. \quad (8)$$

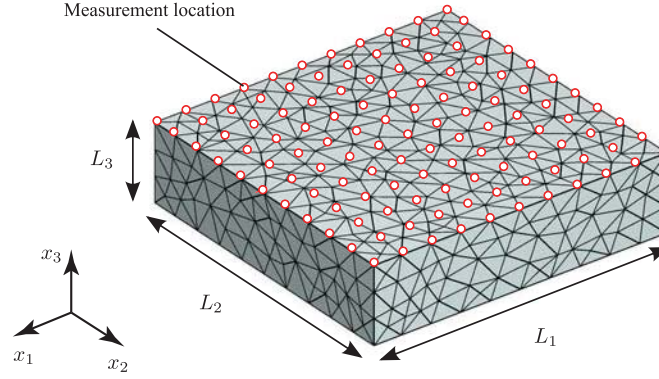


Figure 1: Numerical model with orthotropic material model

If we employed the exact Newton method, the algorithm would attempt to solve the minimization of Eq. (1) by successively finding the stationary point of the quadratic function $\tilde{\mathcal{L}}_k(\mathbf{p})$ at each iteration, i.e., $\nabla_{\mathbf{p}}\tilde{\mathcal{L}}_k(\mathbf{p}) = \mathbf{0}$. It means that the increment $\Delta\mathbf{p}$ at each iteration would be determined by solving the following linear equations:

$$\left[\mathbf{J}_k^T \mathbf{J}_k + (\nabla_{\mathbf{p}}^2 f_k)^T \mathbf{r}_k \right] \Delta\mathbf{p} = -\nabla_{\mathbf{p}}\tilde{\mathcal{L}}_k(\mathbf{p}). \quad (9)$$

When the iteration reaches near the stationary point, $\mathbf{r}_k \approx \mathbf{0}$ and $\nabla_{\mathbf{p}}^2 f_k$ can also be assumed to be very small. Therefore, if $\|\mathbf{r}_k\|_2$ is very small, or $\tilde{\mathcal{L}}_k(\mathbf{p})$ is evaluated near the stationary point, the Eq. (9) reduces to the following relationship:

$$(\mathbf{J}_k^T \mathbf{J}_k) \Delta\mathbf{p} \approx -\nabla_{\mathbf{p}}\tilde{\mathcal{L}}_k(\mathbf{p}). \quad (10)$$

One may notice that Eq. (10) implies that the accuracy of the increment $\Delta\mathbf{p}$ is influenced by the nature of the matrix $\mathbf{J}_k^T \mathbf{J}_k$. That is, if the *condition number* of the matrix $\mathbf{J}_k^T \mathbf{J}_k$, or equivalently that of $\mathbf{J}_k(\mathbf{p})$ is large, then the solution we obtain by solving Eq. (10) can be inaccurate. It means that it is important to keep the condition number of $\mathbf{J}_k^T \mathbf{J}_k$ as small as possible, for the accurate and stable determination of the increment $\Delta\mathbf{p}$. Therefore, we propose that the mode sequence at each minimization be selected, such that the condition number of \mathbf{J}_k is the smallest among the possible set of modes. Denoting the minimizer of $\mathcal{L}_k(\mathbf{p})$ as $\hat{\mathbf{p}}_k$, $\mathcal{L}_{k+1}(\mathbf{p})$ is updated such that:

$$\mathcal{L}_{k+1}(\mathbf{p}) = \mathcal{L}_k(\mathbf{p}) + \frac{1}{2} (f_\ell(\mathbf{p}) - \tilde{f}_\ell)^2, \quad (11)$$

where the mode index ℓ is found such that:

$$\kappa([\mathbf{J}_k(\hat{\mathbf{p}}_k), \nabla_{\mathbf{p}} f_\ell(\hat{\mathbf{p}}_k)]) = \text{minimum}, \quad (12)$$

where κ denotes the condition number, or the ratio between the maximum and the minimum singular values of the matrix. A more qualitative statement of this argument is that the algorithm chooses the modes so that the columns of \mathbf{J}_k become as linearly-independent as possible.

5. Numerical validation: rectangular thick plate with orthotropic material model

In this section, the nonlinear LS problem presented in the previous section is examined using a numerical example. For the FE modal analyses as well as the evaluation of the eigenvalue sensitivity, COMSOL Multiphysics® was used. The BFGS algorithm [3] was employed for the minimization of Eq. (1), and implemented in the Matlab® environment. The numerical model is presented in Fig. 1, where $L_1 = 0.2[\text{m}]$, $L_2 = 0.2[\text{m}]$, and $L_3 = 0.05[\text{m}]$. The material model is an artificial orthotropic material with $E_1=150\text{GPa}$, $E_2=180\text{GPa}$, $E_3=100\text{GPa}$, $G_{12}=60\text{GPa}$, $G_{23}=70\text{GPa}$, $G_{13}=80\text{GPa}$, $\nu_{12}=0.1$, $\nu_{23}=0.2$, and $\nu_{13}=0.3$. The analysis procedure is stated as follows. First, the modal analysis was conducted by an FEA, and the eigenvalues and the associated eigenvectors were extracted. These eigenfrequencies are herein treated as the "measured" modal frequencies from a (numerical) experiment, and used as $\tilde{f}_k, k = 1, \dots, 20$. Second, the eigenvectors were sampled at the evenly-spaced points on the top surface of the model as shown in Fig. 1. This simulates the vibration measurement of the mode shapes with a limited number of measurement locations. The Eq. (1) was then minimized using the "measured" data.

To demonstrate the advantage of the proposed algorithm, the minimization without the initial condition updates and the mode selection was also conducted, and the results are compared with those obtained by the proposed

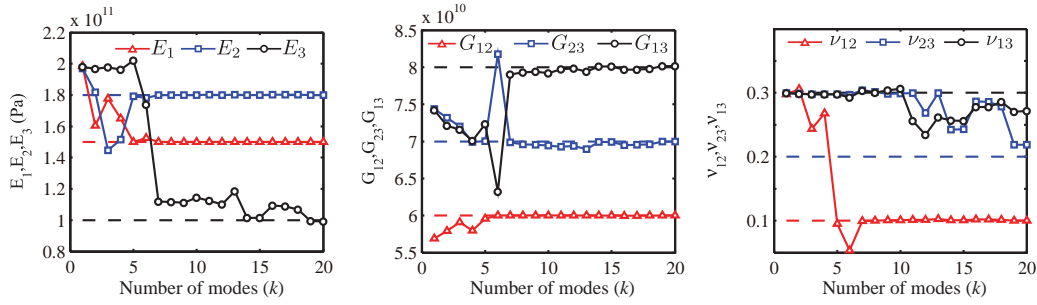


Figure 2: Convergence histories of the parameters (without initial condition updates and mode selection)

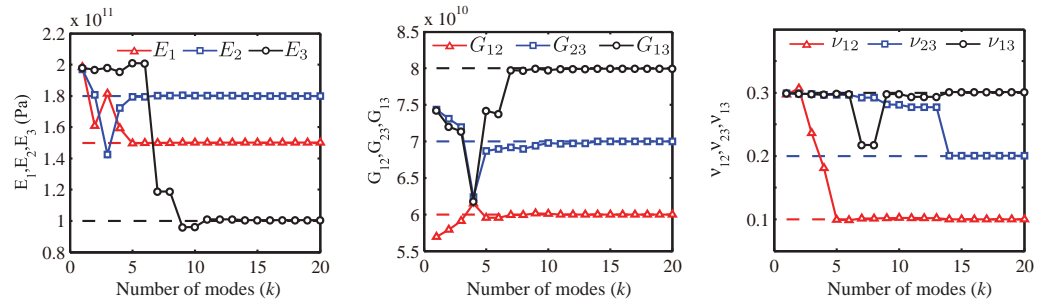


Figure 3: Convergence histories of the parameters (with initial condition updates and mode selection)

algorithm. The initial values of \boldsymbol{p} for both algorithms were assumed to be the elastic moduli for an isotropic material, where $E_1=200\text{GPa}$, $E_2=200\text{GPa}$, $E_3=200\text{GPa}$, $G_{12}=76.9\text{GPa}$, $G_{23}=76.9\text{GPa}$, $G_{13}=76.9\text{GPa}$, $\nu_{12}=0.3$, $\nu_{23}=0.3$, and $\nu_{13}=0.3$. The convergence histories of the elastic moduli without and with the initial condition updates and mode selection algorithm are shown respectively in Figs. 2 and 3. The dashed-lines in the figures show the target values for each modulus. As can be seen in Figs. 2 and 3, the converged solutions are improved as the number of modes increases for both cases. However, as seen in Fig. 2, the convergence histories fluctuates as the number of modes changes, and the algorithm even fails to identify the target values for ν_{23} , and ν_{13} . On the contrary, the proposed method successfully determines all the elastic moduli with only 14 modes. Another advantage of the proposed approach with the mode selection is that the convergence histories of the parameters are smoother than those without the initial condition updates and the mode selection. Thus, we can almost be sure that the converged solutions we obtain from the minimizations can be improved by adding more modes.

6. Application to laminated electrical steel sheets

In this section, we discuss the application of the proposed method to the identification of the elastic moduli of the laminated electrical steel sheets. The photograph of the test specimen is shown in Fig. 4. The test specimen consists of electrical steel sheets with nominal thickness of 0.35mm, which are bonded together by adhesive layers, where $L_1 = 0.199\text{m}$, $L_2 = 0.199\text{m}$, and $L_3 = 0.0518\text{m}$. The total number of the sheets is 146, and the total mass of the test specimen is 15.8kg. Using the specimen, modal testing was conducted. The mode shapes with the associated mode frequencies are shown in Fig. 5. For the first five modes, the mode shapes show typical out-of-plane bending vibration modes of plates. The 6th and the 7th modes, however, show slightly distorted higher-order vibration shapes that do not typically appear in low frequency ranges of the vibration modes of plates. This appears to be caused by the inhomogeneity of the microscopic adhesive layers between the electrical steel sheets. The 8th through the 12th modes are the typical in-plane bending vibration modes of plates.

Using the modes obtained by the experimental modal analysis, the proposed elastic moduli identification method was applied, and the elastic moduli of the test specimen were determined. The initial values of the elastic moduli were $E_1=180\text{GPa}$, $E_2=180\text{GPa}$, $E_3=100\text{GPa}$, $G_{12}=76.9\text{GPa}$, $G_{23}=7.69\text{GPa}$, $G_{13}=7.69\text{GPa}$, $\nu_{12}=0.3$, $\nu_{23}=0.3$, and $\nu_{13}=0.3$. It is noted that preliminary studies revealed that starting the algorithm with the initial values that were used in the numerical validation would result in very slow convergence. Therefore, the initial values were chosen such that the model is “softer” in the direction of lamination (x_3), i.e., $E_3 < \{E_1, E_2\}$ and $\{G_{23}, G_{13}\} < G_{12}$. The Poisson’s ratios were simply set to the typical values used for isotropic steel.

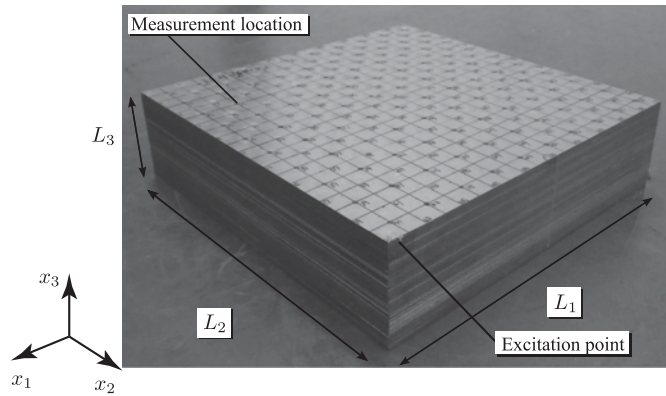


Figure 4: Photograph of the test specimen: laminated electrical steel sheets

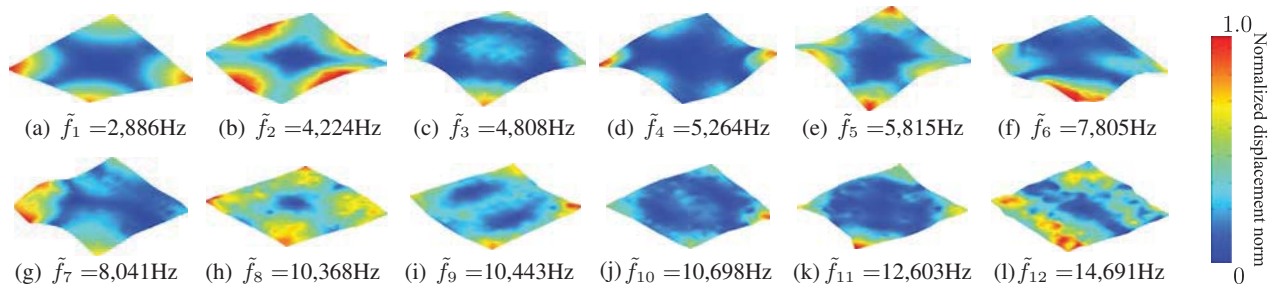


Figure 5: Measured mode shapes and associated modal frequencies

The minimization histories of the elastic moduli with respect to the number of modes are shown in Fig. 6. The converged elastic moduli with $n = 12$ were $E_1=204\text{GPa}$, $E_2=198\text{GPa}$, $E_3=99.8\text{GPa}$, $G_{12}=81.2\text{GPa}$, $G_{23}=11.7\text{GPa}$, $G_{13}=13.6\text{GPa}$, $\nu_{12}=0.30$, $\nu_{23}=0.29$, and $\nu_{13}=0.31$. The errors between the measured frequencies and those computed with the initial values \mathbf{p}_0 , and the converged solution with the proposed method are shown in Fig. 7. As we can see in Fig. 7, all frequency errors decrease when the converged solution is used. Indeed, the average error computed with the initial value \mathbf{p}_0 is 11.75%, whereas that computed with the converged solution by the proposed method decreases down to 1.72%. This shows the validity of the proposed method.

Conclusions

In this paper, we proposed an elastic moduli identification method for orthotropic media based on nonlinear LS fit between the measured and the computed modal frequencies, with accelerated convergence and improved accuracy. In Section 4, the nonlinear LS problem was formulated, and a novel analysis procedure has been proposed, which

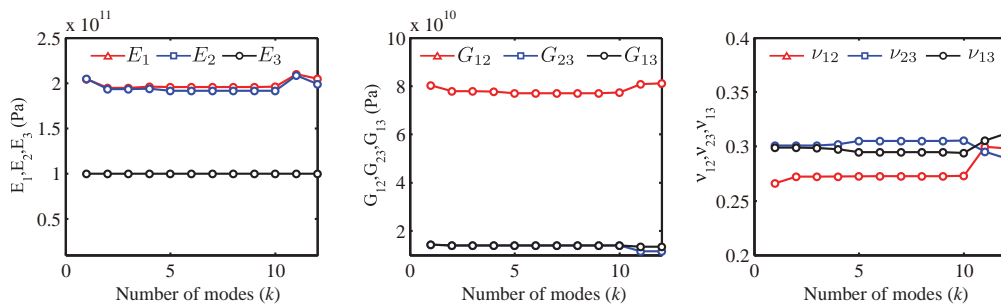


Figure 6: Convergence histories of the parameters for laminated electrical steel sheets

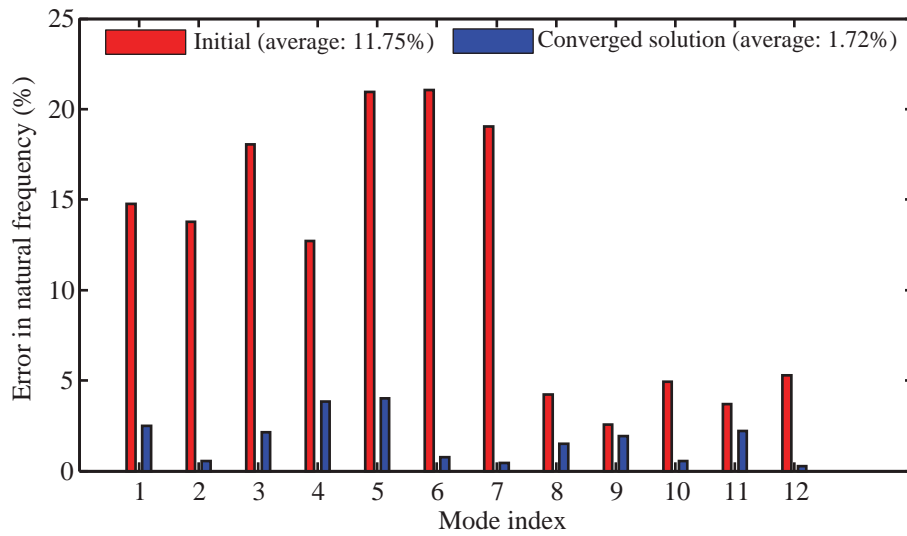


Figure 7: Errors in the predicted natural frequencies

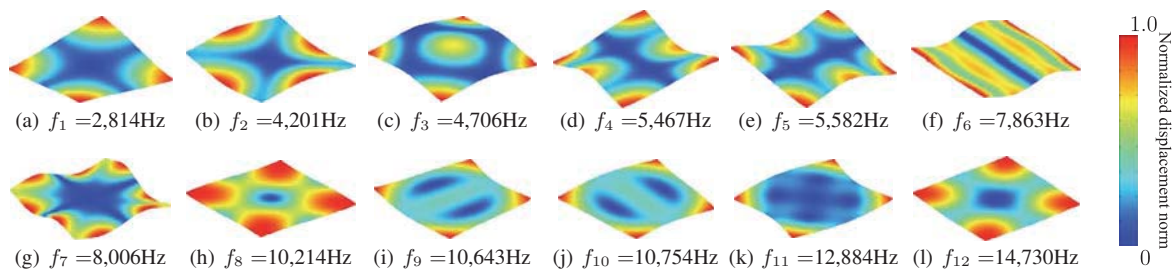


Figure 8: Computed mode shapes and associated modal frequencies

improves the LS solutions by successive increments of the number of modal frequencies and initial condition updates. In Section 5, the minimization method was applied to a numerical example, and its validity was confirmed. In Section 6, the method was applied to the identification of the elastic moduli of the laminated electrical steel sheets, and it successfully determined the elastic moduli where the average frequency error is minimized.

References

- [1] A. Saito, H. Suzuki, M. Kuroishi, and H. Nakai. Efficient forced vibration reanalysis method for rotating electric machines. *Journal of Sound and Vibration*, 334 (2015) pp.388–403.
- [2] G.M.L. Gladwell. Matrix Inverse Eigenvalue Problems. *Dynamical Inverse Problems: Theory and Application*. G.M.L Gladwell and A. Morassi (Eds.), Springer Wien New York, 2011, pp.1–28.
- [3] D. G. Luenberger. *Linear and Nonlinear Programming, second edition*. Addison Wiley, 1989.

Accuracy Improvement of MPP-Based Dimension Reduction Method Using the Eigenvectors of the Hessian Matrix

Seongbin Kang¹, Ikjin Lee¹, Jongmin Lim¹

¹ Korea Advanced Institute of Science and Technology, Daejeon, Korea, kangsb@kaist.ac.kr

1. Abstract

The main purpose of this study is to develop an accurate methodology for the most probable point (MPP)-based dimension reduction method (DRM) by proposing a proper orthogonal transformation to calculate a probability of failure more accurately. In this study, dependency of an axis direction is shown in the univariate DRM, indicating that the probability of failure can be differently calculated according to a different orthogonal transformation. In order to obtain a proper axis direction for DRM, the Hessian of a performance function is utilized in this study. By performing orthogonal transformation using eigenvectors of the Hessian matrix, axes of Gaussian quadrature points for numerical integration are selected along the principal eigenvector directions of the Hessian. In this way, the error incurred by the univariate dimension reduction is minimized, so the probability of failure can be calculated more accurately. Numerical examples verify the accuracy of the proposed method by comparing with existing MPP-based DRM.

2. Keywords: Dimension Reduction Method (DRM), Most Probable Point (MPP), First-Order Reliability Method (FORM), Hessian Matrix, Eigenvector

3. Introduction

Nowadays engineers are facing new and emerging challenges which include intensive use of computational simulations and application of new technologies into complex systems. Due to this, the requirements of high quality and reliability, and the reliable decision-making under uncertainty are essential. To overcome these things, reliability analysis has been advanced gradually. As a result, reliability analysis has been widely and successfully applied to various engineering applications.

There are various reliability analysis methods and the most popular methods are analytical methods and sampling methods. Analytical methods are called most probable point(MPP)-based methods which include First-Order Reliability Method(FORM) [1,2], Second-Order Reliability Method(SORM) [3-5] and Dimension Reduction Method(DRM) [6-10]. When calculating the probability of failure by FORM and SORM, a performance function is approximated by the first or second-order Taylor series expansion at MPP. Through a linear approximation, the probability of failure could be simply calculated in FORM. However, if the performance function is highly nonlinear and/or multidimensional, the result of FORM could be erroneous. SORM is definitely more accurate than FORM because it approximates the performance function in a quadratic form. But SORM also includes errors [5] caused by a few approximations. MPP-based DRM [8-10] has been recently proposed to approximate a multidimensional function using the sum of lower dimensional functions. MPP-based DRM is much more accurate than FORM and users can control its accuracy by changing the number of quadrature (or integration) points. In the MPP-based DRM, probability of failure calculation is related to axis directions because the quadrature points are located along the axes.

The main objective of this study is to improve the accuracy of the MPP-based DRM using eigenvectors of the Hessian matrix. The probability of failure calculation in the MPP-based DRM changes according to the axes because locations of quadrature points depend on the axes. To obtain more accurate calculation, the quadrature points should be located in proper position. In other words, the proper axes should be obtained through an appropriate transformation from the original space. Therefore it is a main issue to find an orthonormal rotation matrix which arranges axes in the proper position in the proposed method. To apply the proposed method, an MPP should be found first after transforming all random variables in the original \mathbf{X} -space to the standard normal \mathbf{U} -space through the Rosenblatt transformation [12]. After finding MPP, the existing method (i.e., MPP-based DRM) uses Gram-Schmidt orthogonalization to obtain the rotation matrix but the proposed method has additional process which uses eigenvectors of the Hessian matrix at MPP in \mathbf{U} -space. With the rotation matrix which is obtained by using eigenvectors of the Hessian matrix, the quadrature points are arranged in proper position and the probability of failure calculation becomes more accurate.

The paper is organized as follows. Section 4 covers basic concepts of reliability analysis. Section 5 covers the detail process of the proposed method. In Section 6, numerical examples are tested to demonstrate that the proposed MPP-based DRM can calculate the probability of failure of a performance function more accurately than the existing MPP-based DRM.

4. Basic concepts and review for previous method

4.1 FORM and SORM

FORM has been extensively used for a reliability analysis which includes calculation of probability of failure, denoted as P_f which is defined using a multidimensional integral [1, 11]

$$P_f \equiv P[G(\mathbf{X}) > 0] = \int_{G(\mathbf{x}) > 0} f_{\mathbf{x}}(\mathbf{x}) d\mathbf{x} \quad (1)$$

where $G(\mathbf{X})$ is the performance function such that $G(\mathbf{X}) > 0$ is defined as failure. $\mathbf{X} = \{X_1, X_2, \dots, X_N\}^T$ is an N-dimensional random vector where the upper case X_i means that they are random variables, and $f_{\mathbf{x}}(\mathbf{x})$ is a joint PDF of \mathbf{X} .

For calculation of the probability of failure in Eq. (1), FORM linearizes $G(\mathbf{X})$ at MPP in \mathbf{U} -space obtained by the Rosenblatt transformation [12] and first-order Taylor approximation such that

$$G(\mathbf{X}) = g(\mathbf{U}) \equiv g_L(\mathbf{U}) = g(\mathbf{u}^*) + \nabla g^T (\mathbf{U} - \mathbf{u}^*) \quad (2)$$

where \mathbf{u}^* is the MPP in \mathbf{U} -space which means the minimum distance point on the limit state function from the origin. MPP can be found by solving the following optimization problem to

$$\begin{aligned} & \text{minimize} && \|\mathbf{u}\| \\ & \text{subject to} && g(\mathbf{u}) = 0 \end{aligned} \quad (3)$$

∇g is the gradient vector of the performance function calculated at the MPP in \mathbf{U} -space. A reliability index, denoted as β , is defined as the distance from the origin to \mathbf{u}^* [2]. With a linearized performance function and the reliability index β , FORM approximates the probability of failure in Eq. (1) as

$$P_f^{\text{FORM}} \equiv \Phi(-\beta) \quad (4)$$

where $\Phi(\bullet)$ is the standard normal cumulative distribution function (CDF).

Using a normalized MPP vector $\boldsymbol{\alpha}$, quadratic approximation of the performance function in \mathbf{U} -space and rotational transformation, the probability of failure can be approximated by SORM as [3, 4, 9]

$$P_f^{\text{SORM}} \equiv \Phi(-\beta) \left| \mathbf{I}_{N-1} - 2 \frac{\phi(\beta)}{\Phi(-\beta)} \mathbf{A}_{N-1} \right|^{-\frac{1}{2}} \quad (5)$$

where $\mathbf{A} = \begin{bmatrix} \mathbf{A} & \mathbf{A}_{1N} \\ \mathbf{A}_{N1} & \mathbf{A}_{NN} \end{bmatrix} = \frac{\mathbf{R}^T \mathbf{H} \mathbf{R}}{2 \|\nabla g\|}$, \mathbf{H} is the Hessian matrix of the performance function at MPP, and \mathbf{R} is the orthonormal rotation matrix used in $\mathbf{U} = \mathbf{R} \mathbf{V}$.

4.2 MPP-based DRM

DRM is a method to approximate the multi-dimensional integration of the performance function using a function with reduced dimension. There are several types of DRM according to the level of dimension reduction. In MPP-based DRM which uses a univariate DRM, any N-dimensional performance function $G(\mathbf{X})$ can be reduced to summation of one-dimensional functions as [8, 9]

$$G(\mathbf{X}) \equiv \hat{G}(\mathbf{X}) \equiv \sum_{i=1}^N G(x_1^*, \dots, x_{i-1}^*, X_i, x_{i+1}^*, \dots, x_N^*) - (N-1)G(\mathbf{x}^*) \quad (6)$$

where $\mathbf{x}^* = \{x_1^*, x_2^*, \dots, x_N^*\}^T$ is the MPP obtained by Eq. (3). To calculate the probability of failure using the MPP-based DRM, transformation to rotated standard normal \mathbf{V} -space is required. To rotate \mathbf{U} -space into \mathbf{V} -space,

it is necessary to construct an $\mathbf{N} \times \mathbf{N}$ orthonormal matrix \mathbf{R} whose N^{th} column is the normalized MPP vector $\boldsymbol{\alpha}$, i.e., $\mathbf{R} = [\mathbf{R}_1 | \boldsymbol{\alpha}]$ where $\mathbf{N} \times (\mathbf{N}-1)$ matrix \mathbf{R}_1 satisfies $\boldsymbol{\alpha}^T \mathbf{R}_1 = \mathbf{0}$ and N is the number of random variables. In \mathbf{V} -space, the probability of failure can be expressed as

$$P_F \equiv P[G(\mathbf{V}) > 0] = \int_{G(\mathbf{V}) > 0} f_{\mathbf{V}}(\mathbf{v}) d\mathbf{v} \quad (7)$$

where $G(\mathbf{V}) = G(\mathbf{X}(\mathbf{V}))$ is obtained from the Rosenblatt transformation and rotational transformation. The probability of failure is calculated using the constrain shift such that [10]

$$G^S(\mathbf{v}) \equiv G(\mathbf{v}) - G(\mathbf{v}^*) \quad (8)$$

where $G^S(\mathbf{v})$ is a shifted performance function and $\mathbf{v}^* = \{0, \dots, 0, \beta\}^T$ is the MPP in \mathbf{V} -space. In a general N -dimensional space, $G^S(\mathbf{v})$ is expressed as [10]

$$\begin{aligned} G^S(\mathbf{v}) &\equiv \hat{G}^S(\mathbf{v}) \equiv \sum_{i=1}^N G_i^S(v_i) - (N-1)G^S(\mathbf{v}^*) \\ &= G^S(v_1, v_2^*, \dots, v_N^*) + G^S(v_1^*, v_2, \dots, v_N^*) + \dots + G^S(v_1^*, v_2^*, \dots, v_N) \\ &= G^S(v_1, 0, \dots, \beta) + G^S(0, v_2, \dots, \beta) + \dots + G^S(0, 0, \dots, v_N) \end{aligned} \quad (9)$$

Using the first-order Taylor series expansion at the MPP, the last univariate component in Eq. (9) is linearly approximated as

$$G^S(0, \dots, v_N) \equiv \left. \frac{\partial G(\mathbf{v})}{\partial v_N} \right|_{\mathbf{v}=\mathbf{v}^*} (v_N - \beta) = b_1 (v_N - \beta), \quad b_1 = \left. \frac{\partial G(\mathbf{v})}{\partial v_N} \right|_{\mathbf{v}=\mathbf{v}^*} \quad (10)$$

This linear approximation along v_N -axis is also used for the probability of failure calculation in SORM [3, 4]. Using the above equations and the linear approximation, the probability of failure in the MPP-based DRM is calculated as [9, 10, 13, 14]

$$P_F^{\text{DRM}} \equiv \frac{\prod_{i=1}^{N-1} \sum_{j=1}^n w_j \Phi\left(-\beta + \frac{G_i^S(v_i^j)}{b_1}\right)}{\Phi(-\beta)^{N-2}} \quad (11)$$

where v_i^j are quadrature points, w_j are weights, and n is the number of quadrature points and weights. Table 1 shows values of the quadrature points and weights.

Table 1. Gaussian quadrature points and weights

n	Quadrature points	Weights
1	0.0	1.0
3	$\pm\sqrt{3}$	0.166667
	0.0	0.666667
5	± 2.856970	0.011257
	± 1.355626	0.222076
	0.0	0.533333

5. MPP-based DRM using the eigenvectors of the Hessian matrix

The objective of the MPP-based DRM using eigenvectors of the Hessian matrix is to improve the accuracy of DRM. Dependency of an axis direction is shown in the univariate DRM, indicating that the probability of failure would be calculated differently according to a different orthogonal transformation. In order to obtain a proper axis direction for DRM, eigenvectors of the Hessian matrix of a performance function at MPP is used when transforming \mathbf{U} -space to \mathbf{V} -space. This method consists of 2 steps to obtain the rotation matrix that has the Hessian information before calculating the probability of failure by the MPP-based DRM

Step 1. Transforming \mathbf{U} -space to \mathbf{H} -space using eigenvectors of the Hessian

First, it is required to find eigenvectors of the Hessian matrix of a performance function $g(\mathbf{U})$ at MPP. Eigenvectors are arranged in column vectors of the first rotation matrix \mathbf{R}_1 . Using the orthonormal transformation $\mathbf{U} = \mathbf{R}_1\mathbf{H}$, \mathbf{U} -space is transformed to the standard normal \mathbf{H} -space. Through this process, all axes are arranged in eigenvector directions of the Hessian of $g(\mathbf{U})$ and thus cross-term effects can be minimized.

Step 2. Transforming \mathbf{H} -space to \mathbf{V} -space

To apply the MPP-based DRM, N^{th} axis direction should be aligned to the α -direction which is the normalized MPP vector in \mathbf{U} -space. To obtain this axis, it is necessary to obtain an $N \times N$ orthonormal matrix \mathbf{R}_2 whose N^{th} column is the normalized MPP vector in \mathbf{H} -space given by

$$\tilde{\alpha} \equiv \mathbf{R}_1^{-1}\alpha \tag{12}$$

i.e., $\mathbf{R}_2 = [\mathbf{R}_3 | \tilde{\alpha}]$ where $N \times (N - 1)$ matrix \mathbf{R}_3 satisfies $\tilde{\alpha}^T \mathbf{R}_3 = \mathbf{0}$ and N is the number of random variables. \mathbf{R}_3 is determined by the Gram-Schmidt orthogonalization. The Gram-Schmidt process takes linearly independent set $S = \{s_1, \dots, s_N\}$ which consists of the normalized MPP vector ($s_1 = \tilde{\alpha}$) and standard basis vector (s_2, \dots, s_N) and it generates an orthogonal set $S' = \{s'_1, \dots, s'_N\}$. Normalized S' vector set comprises an orthonormal matrix \mathbf{R}_2 . Using the orthonormal transformation $\mathbf{H} = \mathbf{R}_2\mathbf{V}$, \mathbf{H} -space is rotated to the standard normal \mathbf{V} -space. Figure 1 shows 3-D limit state function contours in each space obtained from the proposed method.

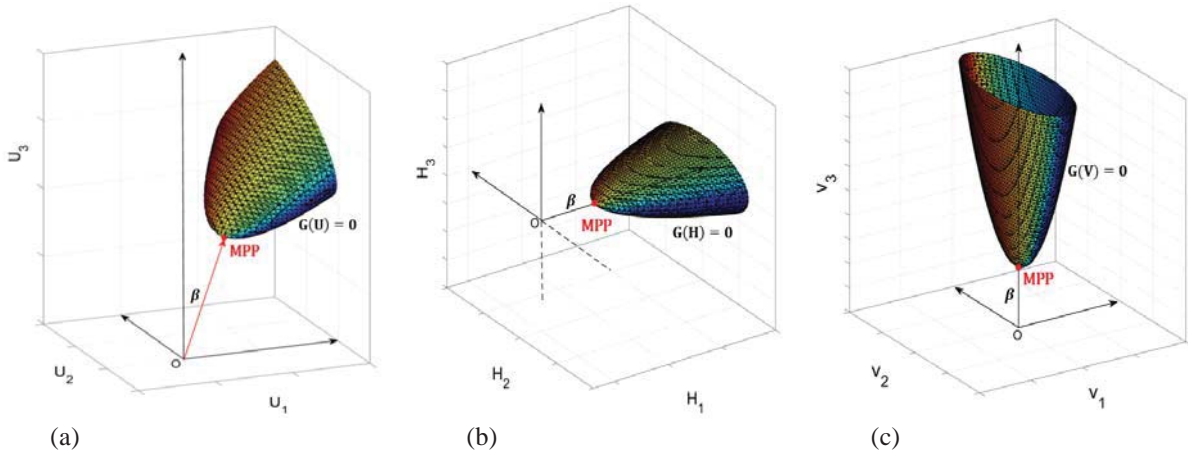


Fig. 1. 3-D limit-state function contour in (a) \mathbf{U} -space; (b) \mathbf{H} -space; (c) \mathbf{V} -space

Through these 2 steps, 2 orthonormal transformations are combined into $\mathbf{U} = \mathbf{R}_1\mathbf{R}_2\mathbf{V}$. Substituting $\mathbf{R}_1\mathbf{R}_2$ with \mathbf{R}_H , \mathbf{U} -space is rotated(transformed) to \mathbf{V} -space by \mathbf{R}_H . Finally, the orthonormal rotation matrix \mathbf{R}_H is obtained which has the Hessian information of $g(\mathbf{U})$ and the N^{th} column of \mathbf{R}_H is the normalized MPP vector α . Using \mathbf{R}_H , \mathbf{V} -space axes have the Hessian information and quadrature points required to calculate the probability of failure are aligned in the \mathbf{V} -space axes direction. For this reason, accuracy of the proposed MPP-based DRM is further improved. Figure 2 shows the position of the quadrature points of the limit state function contour in $V_1 - V_2$ plane depending on whether the eigenvector direction is used or not.

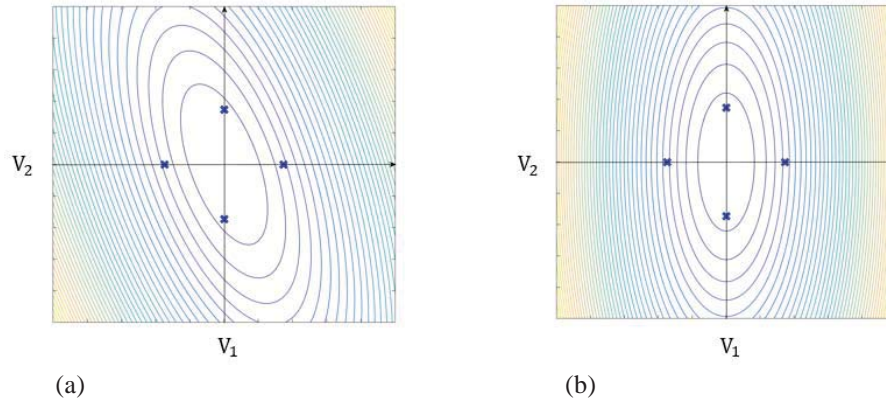


Fig. 2. $V_1 - V_2$ plane contour : (a) MPP-based DRM; (b) Proposed DRM

6. Numerical example

Accuracy improvement of the MPP-based DRM using eigenvectors of the Hessian matrix is verified by comparing it with the existing MPP-based DRM. To compare 2 methods, consider a 3-dimensional high-order function given by

$$G_1(\mathbf{X}) = X_1^4 + X_2^3 + X_3 + X_1X_2^2 + X_2X_3 - 12 \quad (11)$$

where the random variable X_i ($i = 1, 2, 3$) follows the standard normal distribution. For the comparison, Monte Carlo Simulation (MCS) [15] result is considered as the true value of the probability of failure. To calculate the probability of failure, 3 quadrature points along each axis are used. The calculation of the probability of failure in the proposed DRM has less error compared to MCS result than existing DRM as shown in Table 2. The effect of the proposed method is shown visibly in Fig. 3 which includes the location of quadrature points and the contours of the performance function in $V_1 - V_2$ plane which are obtained by the proposed method and existing method, respectively. The contours show that the proposed DRM minimizes the cross-term effect of the performance function.

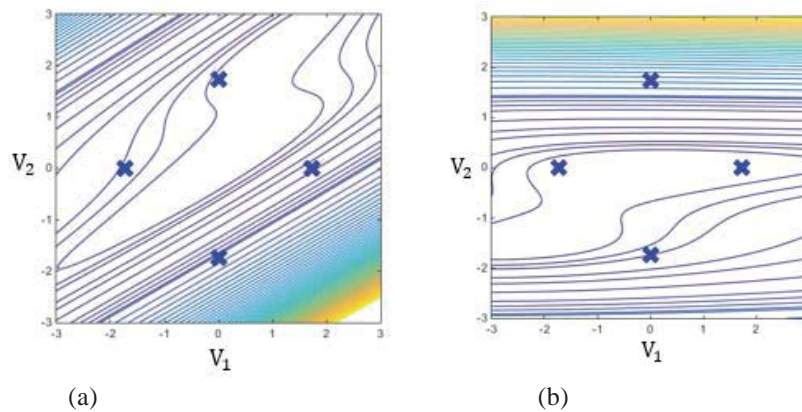


Fig. 3. $V_1 - V_2$ plane contour in 3-D example : (a) MPP-based DRM; (b) Proposed DRM

Table 2. Probability of failure calculation by two methods for 3-D example

	MPP-based DRM (3pts)	Proposed DRM (3pts)	MCS (10^7 samples)
P_F (%)	4.14	6.50	7.90
Error (%)	47.59	17.7	-

7. Conclusion

To improve the accuracy of the existing MPP-based DRM, it is proposed to use eigenvectors of the Hessian matrix when transforming to the rotated standard normal V -space. To verify the accuracy improvement in calculation of the probability of failure, a 3-D example with high order is tested and the results show that using the proposed MPP-based DRM is more accurate than the existing method. More research on the proposed MPP-based DRM and application to Reliability Based Design Optimization (RBDO) problems are ongoing.

8. Acknowledgements

This work was supported by the Industrial Innovation Technology Development Program in Plant Engineering Area (10048341) funded by the Ministry of Trade, Industry & Energy (MOTIE, Korea).

9. References

- [1] Haldar, and S. Mahadevan, Reliability and Statistical Methods in Engineering Design, *John Wiley & Sons*, New York, NU, 2000.
- [2] A.M. Hasofer, and N.C. Lind, An exact and invariant first order reliability format, *ASCE Journal of the Engineering Mechanics Division*, 100 (1), 111-121, 1974.
- [3] M. Hohenbichler, and R. Rackwitz, Improvement of second-order reliability estimates by importance sampling, *ASCE Journal of Engineering Mechanics*, 114(12), 2195-2199, 1988.
- [4] K. Breitung, Asymptotic approximations for multinormal integrals, *ASCE Journal of Engineering Mechanics*, 110 (3), 357-366, 1984.
- [5] S. Adhikari, Reliability Analysis Using Parabolic Failure Surface Approximation, *ASCE J. Eng. Mech.*, 130 (12), 1407–1427, 2004.
- [6] S. Rahman, and H. Xu, A univariate dimension–reduction method for multidimensional integration in stochastic mechanics, *Probabilistic Engineering Mechanics*, 19, 393–408, 2004.
- [7] H. Xu, and S. Rahman, A generalized dimension–reduction method for multidimensional integration in stochastic mechanics, *International Journal for Numerical Methods in Engineering*, 61 (12), 1992–2019, 2004.
- [8] S. Rahman, D. Wei, A univariate approximation at most probable point for higher-order reliability analysis, *International Journal of Solids and Structures*, 43, 2820–2839, 2006.
- [9] D. Wei, A univariate decomposition method for higher-order reliability analysis and design optimization, Ph.D. Thesis, University of Iowa, 2006.
- [10] Lee, K. K. Choi, L. Du, and D. Gorsich, Inverse Analysis Method Using MPP-Based Dimension Reduction for Reliability-Based Design Optimization of Nonlinear and Multi-Dimensional Systems, *Comput. Methods Appl. Mech. Eng.*, 198 (1), 14–27, 2008.
- [11] H. O. Madsen, S. Krenk, and N. C. Lind, Methods of Structural Safety, *Prentice-Hall, Englewood Cliffs*, NJ, 1986.
- [12] M. Rosenblatt, Remarks on a Multivariate Transformation, *Ann. Math. Stat.*, 23, 470–472, 1952.
- [13] H. Xu, and S. Rahman, A moment-based stochastic method for response moment and reliability analysis, *Proceedings of 2nd MIT Conference on Computational Fluid and Solid Mechanics*, Cambridge, MA, 2003.
- [14] K.E. Atkinson, An Introduction to Numerical Analysis, *John Wiley & Sons*, New York, NY, Chapter 5, 1989.
- [15] C.Y. Lin, W.H. Huang, M.C. Jeng, J.L. Doong, Study of an assembly tolerance allocation model based on Monte Carlo simulation, *Journal of Materials Processing Technology*, 70, 9–16, 1997.

Utilization of Gaussian Kernel Reliability Analyses in the Gradient-based Transformed Space for Design Optimization with Arbitrarily Distributed Design Uncertainties

Po Ting Lin¹

¹ Department of Mechanical Engineering, Chung Yuan Christian University, Chungli, Taoyuan, Taiwan, potinglin@cycu.edu.tw

1. Abstract

Several Reliability-Based Design Optimization (RBDO) algorithms have been developed to solve engineering optimization problems under design uncertainties. Some existing methods transform the random design space to standard normal design space to estimate the reliability assessment for the evaluation of the failure probability. When the random variable is arbitrarily distributed and cannot be properly fitted to any known form of probability density function, the existing RBDO methods, however, cannot perform reliability analysis either in the original design space or in the standard normal space. This paper proposes a novel method, Ensemble of Gradient-based Transformed Reliability Analyses (EGTRA), to evaluate the failure probability of arbitrarily distributed random variables in the original design space. The arbitrary distribution of the random variable is approximated by a merger of multiple Gaussian kernel functions. Each Gaussian kernel function is transformed to a single-variate coordinate that is directed toward the gradient of the constraint function. The failure probability is then estimated by the ensemble of each kernel reliability analysis. This paper further derives a linearly approximated probabilistic constraint at the design point with allowable reliability level in the original design space using the aforementioned fundamentals and techniques. Numerical examples with generated random distributions show EGTRA is capable of solving the RBDO problems with arbitrarily distributed uncertainties in the original design space.

2. Keywords: gradient-based transformation; Gaussian kernel density estimation; reliability-based design optimization; arbitrarily distributed design uncertainty.

3. Introduction

In engineering design, traditional deterministic optimization has been successfully applied to improve quality, processes and reduced costs. However, uncertainties have to be considered to make designs more confident and reliable. These traditional deterministic approaches for optimization of components, products and systems are slowly being replaced in the past decades of approaches that integrate probabilistic considerations. These probabilistic considerations were investigated and have been known to be material property deviation [1], allowable failure probabilities from standards [2], production condition [3], reported incidences of failures or satisfactions [4] and operating conditions [5], to mention a few. The basic concept behind Reliability-Based Design Optimization (RBDO) methods is to integrate and consider these probabilistic factors in the optimization process and many approaches have been developed in the past.

Reliability Index Approach (RIA) [6-9] formulated the probabilistic constraints based on the evaluations of reliability indices. Lin et al. [10] resolved the convergence problems of RIA [11] by modifying the reliability index to correctly evaluate the failure probability for both feasible and infeasible design points. Performance Measure Approach (PMA) [11-15], on the other hand, implements an inverse reliability analysis, which determines the performance measure of a target design point. Probabilistic constraints are then formulated from these performance measures. Observations of the strengths and weaknesses of both RIA and PMA has led to the development of Hybrid Reliability Approach (HRA) [16, 17]. HRA uses a selection factor to determine whether PMA or MRIA would be efficient to use. Derivations of a Unified Reliability Formulation (URF) [18] had revealed how various RBDO algorithms can be reformulated into one general equation based on the reliability analyses in the standard normal design space and the fundamental aspect of linear expansions with allowable reliabilities.

Recently, the design optimization problems with arbitrarily distributed uncertainties have drawn high attentions [19-21] because they cannot be properly solved by RBDO algorithms that require transformation of the original design space to the standard normal design space. Therefore, the situations such as unknown random distribution type, undeterminable transformation to the standard normal design space, and insufficient information about the random distribution, are difficult for most RBDO algorithms. Thus, a new method that is capable of efficiently solving the RBDO problem with arbitrarily distributed uncertainties in the original design space is desirable.

In this paper, a novel method called Ensemble of Gradient-based Transformed Reliability Analyses (EGTRA) is derived based on estimation of arbitrary distribution in the original design space using Kernel Density Estimation

(KDE) [22, 23] and reliability analyses along the gradient-based transformed direction [24]. A linearly approximated probabilistic constraint is formulated at the design point determined at the allowable reliability level. The aforementioned derivations and technologies are conducted in the original space; therefore, EGTRA is expected to be capable of solving RBDO problems with arbitrarily distributed uncertainties. Two numerical examples are solved in order to investigate the numerical performances of the proposed method.

4. Derivation of Ensemble of Gradient-based Transformed Reliability Analyses (EGTRA)

A typical RBDO problem is formulated as follows:

$$\text{Min } f(\mathbf{d}) \quad \text{s.t.} \quad P[g_i(\mathbf{X}) > 0] \leq P_{f,i} \quad i = 1 \dots M \quad (1)$$

where \mathbf{X} is the randomly distributed design variable; \mathbf{d} is the mean of \mathbf{X} and is commonly used as the design variable; f is the objective (or cost) function; g_i is the i^{th} constraint function and $g_i \leq 0$ represents the i^{th} safe region; $P_{f,i}$ is i^{th} allowable failure probability. There are M constraints and L variables. Several RBDO algorithms have been investigate the failure probability in Eq. (1) during the optimization process to reach the optimality, feasibility and reliability simultaneously. However, some existing methods cannot perform the reliability analysis properly when the following conditions occur: (1) Distribution type of \mathbf{X} is unknown. (2) Transformation of \mathbf{X} to the i^{th} standard normal design space \mathbf{U}_i is difficult to determine or does not exist. (3) Data about the random distribution is insufficient.

This paper assumes the relative positions between the sampling points and the design point remain constant and are independent from the location of the design point. The following gradient-based transformation [24] is first considered to transform the original coordinate to the single variate design space y_i toward the direction of the i^{th} constraint gradient $\mathbf{v}_i = \nabla_{\mathbf{x}} g_i(\mathbf{d}) / \|\nabla_{\mathbf{x}} g_i(\mathbf{d})\|^{-1}$:

$$y_{i,p} = (\mathbf{s}_p - \mathbf{d}) \cdot \mathbf{v}_i \quad (2)$$

where the design point \mathbf{d} is the origin of the i^{th} gradient-based transformed design space, denoted by Ω_i ; the value of $y_{i,p}$ is the projection of the p^{th} sampling point in Ω_i . Figure 1 (a) illustrates the transformation to the constraint gradient direction and the mapping of the sampling points to Ω_i .

A Most Probable Target Point (MPTP) in Ω_i , denoted by $y_i^\#$, is defined such that the summation of the cumulative probability of each kernel function from the MPTP to infinity is equal to the allowable failure probability, as illustrated in Figure 1 (b). Therefore, $y_i^\#$ is determined by solving the following equation:

$$N^{-1} \sum_{p=1}^N \Phi_p(y_i^\#) = P_{f,i} \quad (3)$$

In Eq. (3), Φ_p is the p^{th} Gaussian Cumulative Distribution Function (CDF) and is defined as below:

$$\Phi_p(y_0) = \int_{y_0}^{\infty} \sigma^{-1} (\sqrt{2\pi})^{-1} \exp[-0.5(y_i - y_{i,p})^2 \sigma^{-2}] dy_i \quad (4)$$

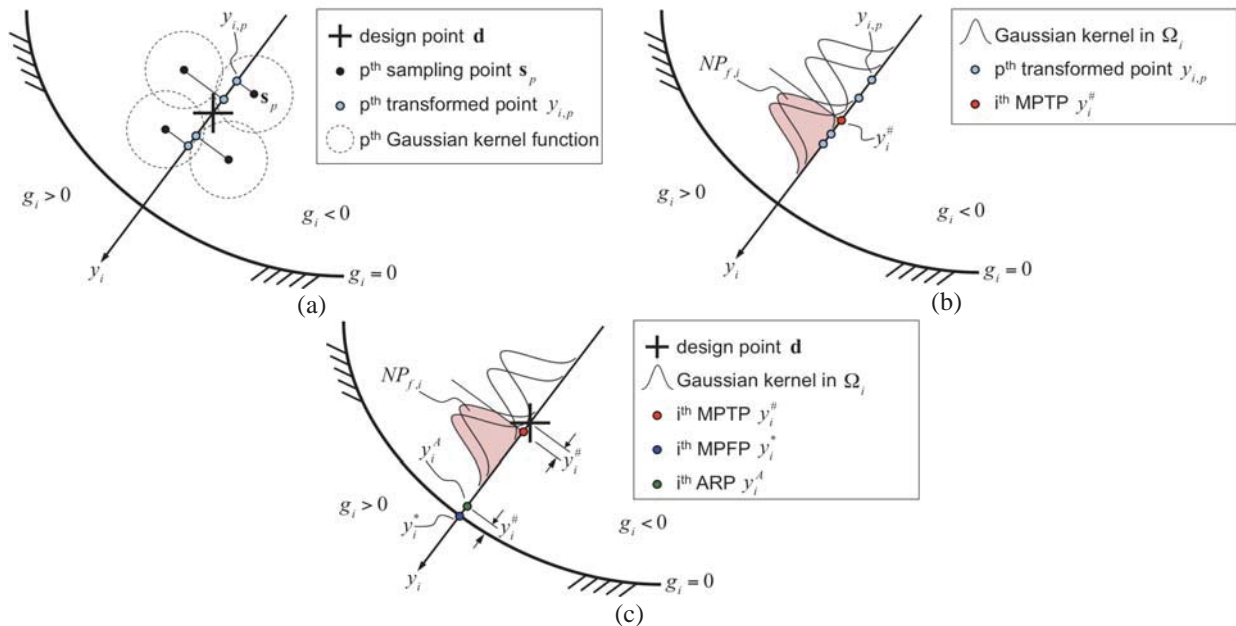


Figure 1. Illustration of the proposed method in Ω_i : (a) Transformation of sampling points to Ω_i ; (b) Determination of Most Probable Target Point; (c) Determination of Allowable Reliability Point.

where σ is a shape parameter in KDE [22, 23]. The size of σ is critical for the accuracy of the estimation of the

arbitrarily distributed PDF. The location of MPTP is essential for the estimation of the design point with allowable reliability and the further formulation of probabilistic constraint.

The RBDO process in Ω_i is expected to move the MPTP to the limit state; therefore, the value of $y_i^\#$ also represents the allowable tolerance near the limit state, as illustrated in Figure 1 (c). The i^{th} Allowable Reliability Point (ARP) y_i^A is then determined by

$$y_i^A = y_i^* - y_i^\# = -g_i(\mathbf{d}) \|\nabla_{\mathbf{x}} g_i(\mathbf{d})\|^{-1} - y_i^\# \quad (5)$$

where y_i^* is the Most Probable Failure Point (MPFP) in Ω_i . In the end, the RBDO procedure is expected to move the design point to the location of the ARP. Thus, the failure probability of the new design point is expected to reach the allowable level.

Using URF [18], the linearly approximated probabilistic constraint is formulated below:

$$(\mathbf{d} - \mathbf{x}_i^A) \cdot \mathbf{v}_i \leq 0 \quad (6)$$

where \mathbf{x}_i^A is the i^{th} Allowable Reliability Point (ARP) in the original design space. Therefore, a final formulation of the i^{th} probabilistic constraint using the EGTRA is given as follows:

$$\{\mathbf{d} - \mathbf{d}^{(k)} + [g_i(\mathbf{d}^{(k)}) \|\nabla_{\mathbf{x}} g_i(\mathbf{d}^{(k)})\|^{-1} + y_i^\#] \mathbf{v}_i^{(k)}\} \cdot \mathbf{v}_i^{(k)} \leq 0 \quad (7)$$

From the derived Eq. (7), it is noted that $y_i^\#$ is not only a most probable allowable tolerance but also a newly defined reliability assessment in the original design space for the proposed EGTRA method.

5. Numerical Examples

This section first introduces the procedure of random distribution generation that is used in this paper. Two mathematical problems are then solved by the proposed EGTRA.

5.1 Generations of Arbitrarily Distributed Random Variables

This paper considers the design point at the mean value of the generated random distribution. All problems are solved in the two-dimensional design space, i.e. $L = 2$, for better illustration of the results. The following distributions are artificially generated by specified procedures for research purpose and may not be seen in real world. This paper intentionally generates some distributions that are ‘‘concavely’’ ranged and are difficult for conventional reliability analyses.

Figure 2 (a) shows the generated heart-shaped distribution with its mean point at the origin of the coordinate. If it is improperly considered as a Gaussian distribution, as shown by the dashed contour, the standard deviations along the x and y directions will be computed as [0.3896, 0.1648], respectively. Figure 2 (b) to (d) show the generated ‘‘like’’-shaped, star-shaped and corona-shaped distributions, respectively. If these distributions are improperly considered as Gaussian distributions, the standard deviations along the x and y directions are computed as [0.2493, 0.3045], [0.3596, 0.3606] and [0.4329, 0.4337] for the ‘‘like’’-shaped, star-shaped and corona-shaped distributions, respectively.

The heart-shaped distribution shows a concave distribution supported in the entire design space. The ‘‘like’’-shaped distribution shows a combined distribution that is partially supported in in the entire domain and partially supported in a semi-interval. The star-shaped distribution shows a uniform distribution in a concave region. The corona-shaped distribution shows a distribution supported in the entire design space with a void region at the center.

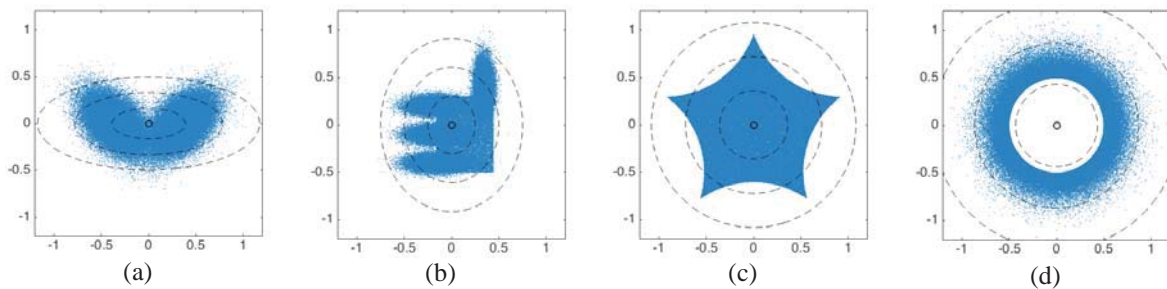


Figure 2. Generated (a) heart-shaped, (b) ‘‘like’’-shaped, (c) star-shaped and (d) corona-shaped distributions.

5.2 Example 1: A Linear Math Problem

The first example is a linear mathematical problem [10, 11], which is shown in Eq. (8).

$$\begin{aligned} \text{Min}_d \quad & d_1 + d_2 \\ \text{s.t.} \quad & P[g_1 = -X_1 - 2X_2 + 10 > 0] \leq P_f; \quad P[g_2 = -2X_1 - X_2 + 10 > 0] \leq P_f; \quad 0.1 \leq d_1, d_2 \leq 10 \end{aligned} \quad (8)$$

In this paper, two various levels of allowable failure probabilities are investigated: $P_f = 1\%$ and 30% . The initial

design point is located at [5, 5]. Figure 3 shows the optimal solutions using EGTRA with $N = 50000$ to solve the problem in Eq. (8) in the generated random distributions. The subfigures (a) to (d) are the results for $P_f = 1\%$ while the subfigures (e) to (h) are for $P_f = 30\%$. The red lines represent the limit states of the original constraints and the black lines are the linearly approximated probabilistic constraints, which are determined using the Eq. (7).

Because each kernel reliability analysis in EGTRA is completed along the same gradient direction, the required function evaluation of each constraint per iteration is only 3. Monte Carlo Simulations (MCS) with 10^5 sampling points were used to evaluate the true failure probabilities. The numerical results showed the proposed method is capable of solving the problems with the generated design uncertainties with accurate estimations of reliabilities in the original design space, i.e. errors were less than 1%.

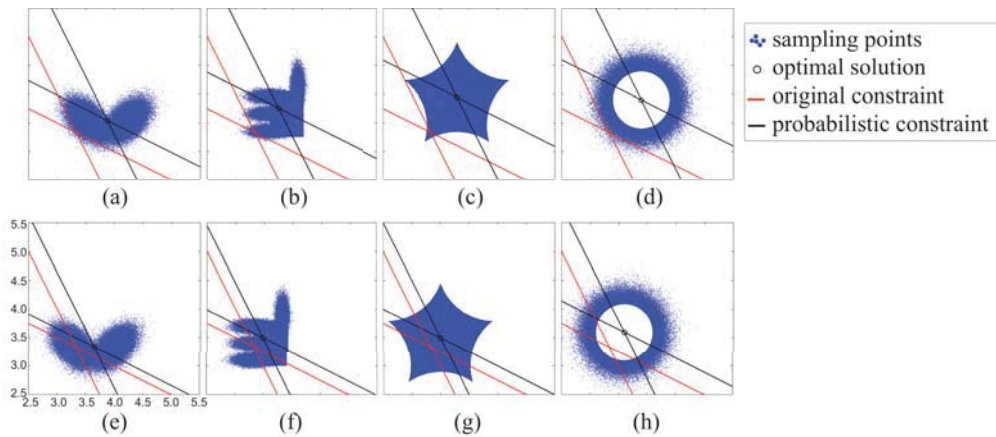


Figure 3. Solutions of example 1 in various distributions and allowable failure probabilities: (a) heart, 1% ; (b) “like”, 1% ; (c) star, 1% ; (d) corona, 1% ; (e) heart, 30% ; (f) “like”, 30% ; (g) star, 30% ; (h) corona, 30% .

5.3 Example 2: A Nonlinear Benchmark Problem

The second example is a well-known benchmark mathematical problem [10, 11, 25, 26] that contains three nonlinear constraints. Because the third constraint is inactive, it is removed and the following problem formulation is considered in this paper.

$$\begin{aligned} \text{Min}_{d_1, d_2} \quad & d_1 + d_2 \\ \text{s.t.} \quad & P[g_1 = 1 - (X_1^2 X_2)/20 > 0] \leq P_f; \quad P[g_2 = 1 - (X_1 + X_2 - 5)^2/30 - (X_1 - X_2 - 12)^2/120 > 0] \leq P_f; \quad 0.1 \leq d_1, d_2 \leq 10 \end{aligned} \quad (9)$$

In this problem, two various levels of allowable failure probabilities, i.e. $P_f = 1\%$ and 30% , are studied. EGTRA is used to solve the problem with $N = 50000$. The initial design point is located at [5, 5]. The rest of the problem setting is the same as the first example. Figure 4 (a) to (d) show the optimal solutions for $P_f = 1\%$ while the subfigures (e) to (h) show the ones for $P_f = 30\%$. EGTRA was capable of solving the given problems with only $3M$ function evaluations per iteration. However, the accuracy of EGTRA slightly dropped because linear approximations were utilized for the nonlinear constraints in Eq. (9), i.e. error increased up to around 6%.

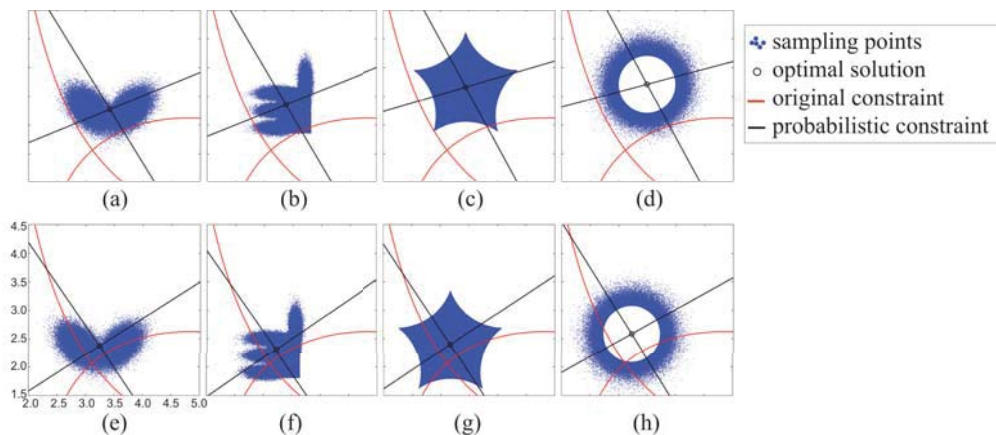


Figure 4. Solutions of example 2 in various distributions and allowable failure probabilities: (a) heart, 1% ; (b) “like”, 1% ; (c) star, 1% ; (d) corona, 1% ; (e) heart, 30% ; (f) “like”, 30% ; (g) star, 30% ; (h) corona, 30% .

6. Conclusions

Some existing RBDO algorithms transformed the original random design space to the standard normal design space in order to perform the reliability analyses for the evaluation of failure probabilities. However, these reliability analyses cannot be properly executed when the transformation to the standard normal design space cannot be determined. A new RBDO algorithm, Ensemble of Gradient-based Transformed Reliability Analyses (EGTRA), was developed to solve design optimization problems with arbitrarily distributed uncertainties in the original design space. The arbitrarily distributed PDF was approximated by KDE and then transformed to a single-variate coordinate toward the constraint gradient direction. The entire reliability analysis is decomposed to multiple kernel reliability analyses in the gradient-based transformed design space and the results are merged together for the formulation of a linearly approximated probabilistic constraint function. Because each kernel reliability analysis is completed along the same gradient direction, the required function evaluation of each constraint per iteration is only 3. The numerical results showed the proposed method is capable of solving the problems with the generated design uncertainties with accurate estimations of reliabilities in the original design space.

The newly developed method does not need transformation to the standard normal design space and reliability analyses that require additional function evaluations. EGTRA is able to perform very accurate reliability analysis for linear RBDO problems and the accuracy reduces when the constraints are nonlinear. EGTRA is a method that requires information about the sampling points of the arbitrarily distributed random variables. Insufficient sampling points may lead to inaccurate estimations of PDF and failure probabilities. The performance of EGTRA will reduce when the sampling at the tail of the distribution is insufficient. This may happen when the amount of sampling points and the level of allowable failure probability are both very low.

7. Acknowledgments

The supports from Ministry of Science and Technology, Taiwan (grant number MOST 103-2221-E-033-015), Research and Development Center for Microsystem Reliability, and Center for Robotics Research at Chung Yuan Christian University, Taiwan are greatly appreciated.

8. References

- [1] H.-S. Jung and S. Cho, "Reliability-based topology optimization of geometrically nonlinear structures with loading and material uncertainties," *Finite elements in analysis and design*, vol. 41, pp. 311-331, 2004.
- [2] B. Ellingwood, *Development of a probability based load criterion for American National Standard A58: Building code requirements for minimum design loads in buildings and other structures*, 577, US Department of Commerce, National Bureau of Standards, 1980.
- [3] R. D. Pope and R. A. Kramer, "Production uncertainty and factor demands for the competitive firm," *Southern Economic Journal*, pp. 489-501, 1979.
- [4] S. S. Hasan, J. M. Leith, B. Campbell, K. L. Smith, and F. A. Matsen III, "Characteristics of unsatisfactory shoulder arthroplasties," *Journal of shoulder and elbow surgery*, vol. 11, pp. 431-441, 2002.
- [5] M. Karamouz and H. V. Vasiliadis, "Bayesian stochastic optimization of reservoir operation using uncertain forecasts," *Water Resources Research*, vol. 28, pp. 1221-1232, 1992.
- [6] E. Nikolaidis and R. Burdisso, "Reliability Based Optimization: A Safety Index Approach," *Computers & Structures*, vol. 28, pp. 781-788, 1988.
- [7] I. Enevoldsen, "Reliability-Based Optimization as an Information Tool," *Mechanics of Structures and Machines*, vol. 22, pp. 117-135, 1994.
- [8] I. Enevoldsen and J. D. Sorensen, "Reliability-Based Optimization in Structural Engineering," *Structural Safety*, vol. 15, pp. 169-196, 1994.
- [9] S. V. L. Chandu and R. V. Grandhi, "General Purpose Procedure for Reliability Based Structural Optimization under Parametric Uncertainties," *Advances in Engineering Software*, vol. 23, pp. 7-14, 1995.
- [10] P. T. Lin, H. C. Gea, and Y. Jaluria, "A Modified Reliability Index Approach for Reliability-Based Design Optimization," *Journal of Mechanical Design*, vol. 133, 044501, 2011.
- [11] J. Tu, K. K. Choi, and Y. H. Park, "A New Study on Reliability Based Design Optimization," *Journal of Mechanical Design*, vol. 121, pp. 557-564, 1999.
- [12] B. D. Youn and K. K. Choi, "An Investigation of Nonlinearity of Reliability-Based Design Optimization Approaches," *Journal of Mechanical Design*, vol. 126, pp. 403-411, 2004.
- [13] B. D. Youn and K. K. Choi, "Selecting Probabilistic Approaches for Reliability-Based Design Optimization," *AIAA Journal*, vol. 42, pp. 124-131, 2004.
- [14] B. D. Youn, K. K. Choi, and L. Du, "Adaptive Probability Analysis Using an Enhanced Hybrid Mean Value Method," *Structural and Multidisciplinary Optimization*, vol. 29, pp. 134-148, 2005.
- [15] B. D. Youn, K. K. Choi, and L. Du, "Enriched Performance Measure Approach for Reliability-Based Design Optimization," *AIAA Journal*, vol. 43, pp. 874-884, 2005.
- [16] P. T. Lin, Y. Jaluria, and H. C. Gea, "A Hybrid Reliability Approach for Reliability-Based Design

- Optimization," in *ASME 2010 International Design Engineering Technical Conferences & Computers and Information in Engineering Conference, IDETC/CIE 2010*, Montreal, Quebec, Canada, DETC2010-28871, 2010.
- [17] P. T. Lin, M. C. E. Manuel, Y.-H. Liu, Y.-C. Chou, Y. Ting, S.-S. Shyu, C.-K. Chen, and C.-L. Lee, "A Multifaceted Approach for Safety and Reliability-Based Design Optimization," *Mathematical Problems in Engineering*, 817820, 2014.
- [18] P. T. Lin, "Ensemble of Unified Reliability Formulations (EURF)," in *10th World Congress on Structural and Multidisciplinary Optimization, WCSMO10*, Orlando, FL, USA, 5476, 2013.
- [19] X. Lai, "A modified method to compute the reliability with arbitrary independent random variables," *Proceedings of the Institution of Mechanical Engineers, Part E: Journal of Process Mechanical Engineering*, vol. 228, pp. 320-331, 2014.
- [20] P. T. Lin and S.-P. Lin, "Ensemble of Gaussian-based Reliability Analyses (EoGRA) in the Original Design Space for Design Optimization Under Arbitrarily Distributed Design Uncertainties," in *The 8th China-Japan-Korea Joint Symposium on Optimization of Structural and Mechanical Systems, CJK-OSM8*, Gyeongju, Korea, 2014.
- [21] P. T. Lin and S.-P. Lin, "Reliability-Based Design Optimization in X-Space Using Ensemble of Gaussian Reliability Analyses (EoGRA)," in *ASME 2015 International Design and Engineering Technical Conferences & Computers and Information in Engineering Conference, IDETC/CIE 2015*, Boston, MA, USA, DETC2015-46130, 2015.
- [22] M. Rosenblatt, "Remarks on some nonparametric estimates of a density function," *The Annals of Mathematical Statistics*, vol. 27, pp. 832-837, 1956.
- [23] E. Parzen, "On estimation of a probability density function and mode," *The annals of mathematical statistics*, pp. 1065-1076, 1962.
- [24] P. T. Lin and H. C. Gea, "A Gradient-Based Transformation Method in Multidisciplinary Design Optimization," *Structural and Multidisciplinary Optimization*, vol. 47, pp. 715-733, 2013.
- [25] R. J. Yang and L. Gu, "Experience with Approximate Reliability-Based Optimization Methods," *Structural and Multidisciplinary Optimization*, vol. 26, pp. 152-159, 2004.
- [26] H. C. Gea and K. Oza, "Two-Level Approximation Method for Reliability-Based Design Optimisation," *International Journal of Materials and Product Technology*, vol. 25, pp. 99-111, 2006.

Robust Design and Optimisation of a Radial Turbine Within a Supercritical CO₂ Solar Brayton Cycle

Rodney Persky¹, Emilie Sauret², Andrew Beath³

¹ Queensland University of Technology, QLD, Australia, rodney.persky@hdr.qut.edu.au

² Queensland University of Technology, QLD, Australia, emilie.sauret@qut.edu.au

³ CSIRO Energy, NSW, Australia, andrew.beath@csiro.au

1. Abstract

The generation of solar thermal power is dependent upon the amount of sunlight exposure, as influenced by the day-night cycle and seasonal variations. In this paper, robust optimisation is applied to the design of a power block and turbine, which is generating 30MWe from a concentrated solar resource of 560°C. The robust approach is important to attain a high average performance (minimum efficiency change) over the expected operating ranges of temperature, speed and mass flow. The final objective function combines the turbine performance and efficiency weighted by the off-design performance. The resulting robust optimisation methodology as presented in the paper gives further information that greatly aids in the design of non-classical power blocks through considering off-design conditions and resultant performance.

2. Keywords: Radial Turbine, Off-design, Supercritical CO₂, Robust Optimisation.

3. Introduction

The power block is sensitive to operational parameters including inlet temperature, mass flow, which is reflected by the efficiency of the turbine [1]. Robust optimisation is an approach to solve optimisation problems under uncertainty in the knowledge of the underlying parameters. The application of this approach is necessary to determine the parametric factors for the optimisation of turbo machinery within a solar thermal power system. Optimisation of the mean performance is achieved by minimising its variation, through optimising the product and process design to make the performance minimally sensitive to the various causes of variation.

Literature covers many methods to perform robust optimisation and concentrates on the probability distribution near the mean values [2]. These parameters may include the variation of efficiency (η) in response to temperature, pressure, mass flow, rotational speed and turbine load. There are many approaches to consider off-design performance as demonstrated by Bonaiuti [3] who applied a multipoint approach applied to the inverse design method for the design of radial turbomachinery.

Studies of the off-design performance for turbomachinery has been done by authors at different levels from the analytical turbine model such as that by Fiaschi [4], to a full three-dimensional computational fluid dynamics analysis by Sauret [1]. These studies considered the variations of total-to-total pressure ratio (Π_{tt}), total temperature at inlet ($T_{T,in}$), rotational speed (ω) as well as some operational and design variables including blade-to-jet speed ratio. Many authors have applied full robust optimisation starting from a response surface approximation [5], the application of robust optimisation within evolutionary algorithms [6], to the extension to decision trade-offs [7].

This paper is part of the ongoing discussion on the gaps between the design of the thermodynamic cycle and the turbine design, addressing the robust optimisation approach useful to the analysis of both systems. The aim of this paper is to analyse the design of a radial turbine in a supercritical CO₂ cycle to determine which parameters the design is sensitive to when considering the variability of the solar-thermal resource.

4. System and Geometry Description

Radial turbomachinery are often used for low power systems, and are incredibly robust – there are many ongoing studies to determine their applicability to the current system and similar systems such as that by Sandia Lab [8]. Both supercritical CO₂ and radial turbomachinery have been identified based on their better overall plant economics due to the high power conversion efficiency given a moderate inlet temperature, compact size, and use of more common materials for construction [8]. The power block design for turbomachinery is a well-studied area, and the modelling using analytical heuristic models is well understood within literature [9].

The present work is considering the application of robust optimisation to a single turbine, fluid and working cycle configuration with operational parameters given in Table 1. Uncertainty is applied to the turbine speed, inlet temperature and mass flow to determine the response of the turbine similar to Sauret [1]. Each variable is studied at a range wide enough to capture the trend of the measured variables; the variation is indicated alongside the operating parameters (Table 1).

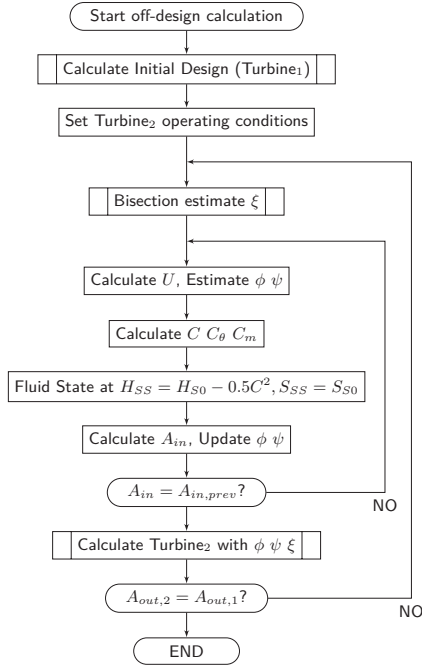


Figure 1: Off-design calculation process

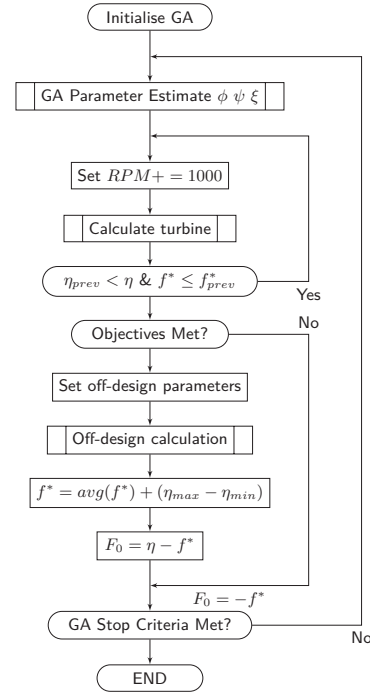


Figure 2: Robust optimisation process

The current power block design method was developed using the REFPROP library for thermodynamics [10] incorporating the real gas functions within the sizing and performance calculations [11]. The method primarily draws from that by Baines [9] with some modifications from Aungier [12] and Erbas [13] for the incidence and loss models respectively. There are numerous constraints on the design of radial inflow turbines by many authors as tabulated in Table 2 [9, 12, 13] in Section 6.1. The combined effect of the number of constraints is significant, and there is great difficulty when considering off-design performance being able to satisfy all of them especially the relative inflow angle ($\beta_{b,in}$). Constraint handling in the present work is implemented as an objective function with a penalty (f^*) value that is progressively reduced through the optimisation approach to zero (representing no deviation from expected value A_i to the present value F_i for objective i).

$$f^* = \sum_{i=1}^n f_i^*, \text{ where } f_i^* = e^{|\delta_{\text{objective},i}|} \quad (1)$$

$$\delta_{\text{objective},i} = \begin{cases} \frac{A_i - F_i}{A_i} & \text{for single bound} \\ \frac{A_i - F_i}{A_{\text{max},i} - A_{\text{min},i}} & \text{for range bound} \end{cases} \quad (2)$$

5. Problem Definition and Optimisation Approach

5.1. Single Objective Optimisation

The present work uses a combined single objective approach built from two separate approaches; firstly, a heuristic single objective optimisation algorithm PGAPACK [14] sets the non-dimensional geometric parameters (flow, stage and size coefficients). Secondly, a goal seeking method determines the ideal operation speed of the turbine that maximises efficiency without compromising the design as measured by a number of equality constraints (given in Table 1). The ideal operating speed is found through redesigning the turbine at different turbine speeds (RPM) within the optimisation loop, where the ideal RPM is determined as when:

- The efficiency is at a maximum value, and
- The penalty function does not deteriorate

The objective function is set based on the following conditions:

1. No deviation from expected parameter constraints and ranges given in Table 1, and

2. Minimum efficiency is met and does not exceed physical limits

If one of these should be violated the objective function is set to a negative value which is calculated as the exponential sum of constraint violations (see Section 4). Otherwise, the objective function is the turbine efficiency or a composition as described in Section 5.3.

Table 1: Parameter values and design range

Parameter	Nominal Value	Off-design range
Mass flow \dot{m} [kg/s]	422.3	+ - 100 kg/s
Temperature $T_{t,in}$ [C]	560	+ - 10%
Pressure $P_{t,in}$ [MPa]	20	-
Turbine Speed [RPM]	-	+ - 20 %

Initial optimisation was done with PGAPACK to determine the absolute best possible design given the inlet conditions and is presented in Table 3 (Section 6). A design that achieve approximately 95% total-to-static efficiency was developed which meets the design criteria at the nominal conditions. The high efficiency is to be expected from the heuristic approach given that there are a number of simplifications to a realistic design [12]. Similarly performing designs have been presented by many authors which then using computational fluid dynamics have an efficiency reduction such as that by Sauret [1].

5.2. Off-Design method

The design of radial turbomachinery is based on the fluid change in velocity (Euler turbine equations), which are expected to change when operating at different conditions (e.g different speed). The method presented below follows the design point calculation method from Baines [9] which is then rearranged to determine the three non-dimensional design parameters flow coefficient (ϕ), loading coefficient (ψ) and sizing coefficient (ϵ). Additional parameters in the design include the turbine power, speed ratio (ξ), mass flow (\dot{m}), pitch speed (U), area (A) and the derived parameters are absolute flow vector ($\vec{C} = [C_m, C_\theta]$).

$$\Delta H_0 = \frac{\text{power}}{\dot{m}}, \quad \psi = \Delta H_0 / U_{in}^2, \quad \phi = \frac{\dot{m}}{A \rho \xi U_{in}} \quad (3)$$

$$\begin{aligned} U_{in} &= r \times \omega \\ C_\theta &= U_{in} \psi, \quad C_m = \xi \psi U_{in}, \quad C = \sqrt{C_\theta^2 + C_m^2} \\ A &= \dot{m} / \rho C_m \end{aligned} \quad (4)$$

The method is effective at matching exiting turbine parameters, however the value of ξ in Equation (4) is unable to be derived through a simple numerical approach and is calculated through the bisection method iterating the full turbine calculation the outlet sizing is matched. The resulting off-design process is shown in Figure 1.

5.3. Robust Optimisation

Design optimisation is a decision-making problem and involves the selection of the optimum design based on a certain criteria with a progressively refined design evolving from information about the turbine fitness and performance. The primary goal of the turbine optimisation is to determine not only the best design, but also the design that is most unaffected by variations in how the turbine is used. Variations are often minor as the turbines and the use of robust optimisation as described by [15] is formulated based on:

1. The data are uncertain / inexact,
2. The optimal solution, even if computed very accurately, may be difficult to implement accurately,
3. The constraints must remain feasible for all meaningful realisations of the data,
4. 'Bad' optimal solutions which are very sensitive to operating conditions are not uncommon

The present work adopts the same approach as [16], and integrates it into the genetic algorithm as described earlier. Here $x \in \mathbb{R}^n$ is a vector of design variables, f_0, f_i are constraint values, $u_i \in \mathbb{R}^k$ are disturbance vectors or parameter uncertainties. $U_i \subseteq \mathbb{R}^k$ is the uncertainty sets, will be a vector of known quantities with respect to the nominal case (See Table 1).

$$\begin{aligned} &\text{maximise} && f_0(x) \\ &\text{subject to} && f_i(x, u_i) \leq 0, \forall u_i \in U_i, i = 1 \dots m. \end{aligned} \quad (5)$$

Robust optimisation as implemented in the present code considers the optimality to be a function of the overall change (difference between minimum and maximum) of the decision variable over the range of parameter values tested. The present method is similar to Deb [17] (although only applied to a single objective) and considers the off-design efficiency response (η^*) to varied parameters:

$$\begin{aligned} & \text{minimise} && \eta_{max}^* - \eta_{max}^*(x) \\ & \text{subject to} && F_0^*(x, u_i) > 0, \forall u_i \in U_i, i = 1 \dots m. \end{aligned} \quad (6)$$

The method is subject to a single objective function (F_0) which captures the response of η and f^* . In the present work we are only concerned when the efficiency is lower than the current efficiency – it is observed from Figure 3 and Figure 4 that the turbine is sensitive to turbine speed and mass flow. The final objective therefore includes a composition between the design point efficiency, the off-design efficiency change (η^*). Finally, the constraint violation for the off-design method was included into the F_0 reduction where the average value of the cost function (Section 4) across the variation was subtracted from the objective function.

$$F_0 = \eta_{ts} - (\eta_{max}^* - \eta_{min}) - f_{avg}^* \quad (7)$$

The method for robust optimisation is captured in Figure 2 showing the inclusion of the robust objective F_0 into the initial optimisation routine.

6. Results

Preliminary variation study was performed to determine which parameters had the greatest effect on turbine performance. It is seen in Figure 3 that the turbine speed (RPM) has the greatest and most predictable effect on the performance. Proceeding the preliminary study, a parametric analysis was performed that explored how efficiency changed with RPM over the maximum range of flow and stage loading coefficients as illustrated in Figure 4. The parametric study shows regions where the designs are available and regions where those designs have high sensitivity of efficiency with respect to RPM ($\partial^2\eta/\partial RPM^2$). Figure 4 highlights regions of low sensitivity in yellow and higher sensitivities are deeper colours. The off-design method as detailed in Section 5.2 was then integrated into the optimisation routine to find a design with the least sensitivity to changes in RPM.

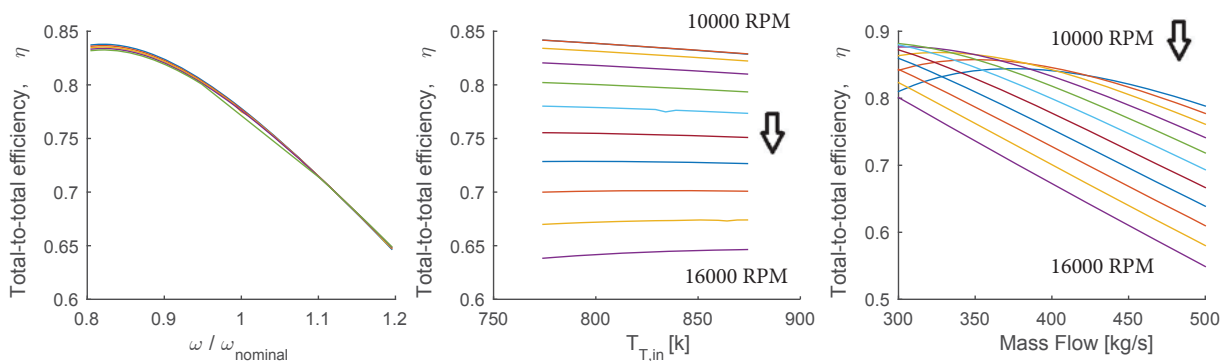


Figure 3: Results from initial off-design study

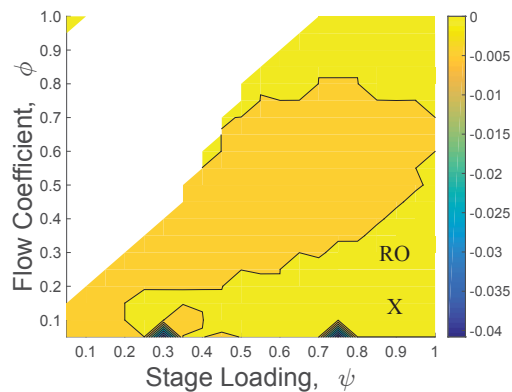


Figure 4: $\partial^2\eta/\partial RPM^2$ at design conditions

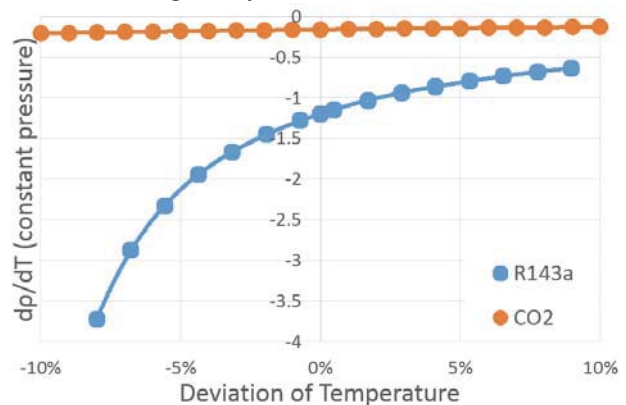


Figure 5: dp/dT for CO_2 and R143a [10]

Table 2: Design constraints for nominal case

Design Variables	Minimum	Maximum
Velocity Constraints		
C_{in} [Mach]	-	0.9
C_{out} [Mach]	-	0.9
W_{in} [Mach]	-	0.9
Angle Constraints		
β_{in} [deg]	-44	-18
α_{in} [deg]	30	80
α_{exit} [deg]	-30	30
Size Constraints		
$r_{in}/r_{out,tip}$ [-]	1.2	-
$r_{out,hub}/r_{out,tip}$ [-]	0.4	-
$r_{in,hub}$ [mm]	10.1	-
b_{in} [mm]	5	50
Z_r (even) [-]	14	20
Non-Dimensional Constraints		
ϕ [-]	0.1	0.4
ψ [-]	-	1.2
ξ [-]	0.75	-
ϵ [-]	-	1.0

Table 3: Initial and robust optimisation results

Rotor Variables	Initial optimisation	Robust optimisation
Design Variables		
ϕ [-]	0.1765	0.2957
ψ [-]	0.9385	0.7146
ξ [-]	1	1
ϵ [-]	0.32847	0.3246
Ω [RPM]	13000	20000
Turbine Information		
r_4 [mm]	248.62	185.199
b_4 [mm]	47.771	32.183
r_6^h [mm]	81.667	60.118
C_4 [m/s]	338.47	299.995
Z_r	18	14
Π_{ts} [-]	2.109	2.204
η_{tt} [%]	95.75	90.89
η_{ts} [%]	94.25	86.10
f^* Information		
	(-10%, +10%)	(-10%, +10%)
β_{in} [deg]	66.09, -59.16	19.53, -60.81
α_{in} [deg]	82.03, -	- , -
C_{in} [Mach]	0.932, -	- , -

6.1. Preliminary variation study

The preliminary variation study considered the off-design ranges and parameters based on work by Sauret [1] to determine which variables most affect performance. It was seen in Figure 1 that the off-design performance follows a similar trend for turbine speed; however the variation of the operational temperature does not affect the performance in contrast to the study by Sauret [1] which showed significant variation on this metric. A plot of density vs temperature is given in Figure 5 over the same temperature deviation (range) CO_2 behaves much closer to an ideal gas compared to R143a, and the change in density with respect to pressure is minimal. The plot suggests that the behaviour of CO_2 is much simpler compared to R143a explaining the reduced sensitivity of the present turbine to temperature variations.

6.2. Robust optimisation

Robust optimisation was then performed observing the change of efficiency over the range of expected rotational speeds. It was found that the efficiency would change by approximately 10% from the nominal case to the extreme cases. However, the constraints were typically difficult to meet fully and dictated the form of the objective function given in Section 5.3 with the final robust design generating 90% total-to-total and 86% total-to-static efficiency as given in Table 3.

6.3. Comparison Robust to Initial Optimisation

There is minimal differences between the robust optimisation and initial single objective optimisation given the minimal variance of CO_2 in the current operation range with geometric design shown in Table 3. However, when including the robust optimisation the efficiency (total-to-static) does reduce as the flow coefficient raised to ensure minimal deviation from constraints. The robust optimisation was unable to find a turbine that was able to completely satisfy all constraints at $\pm 10\%$ variation of turbine speed, Table 3 shows the constraints that were not satisfied at these turbine speeds. The robust optimisation case had a deviation from expected for the relative inflow angle (β_{in}) of 37° (at 16000 RPM) and 16° (at 24000 RPM); this clearly indicates that the new turbine performs poorly at the extreme ends of the off-design range. In comparison, the robust turbine is significantly better than the original design which had deviations from the expected inlet Mach number (C_{in}), inlet relative flow angle and inlet absolute flow angle (α_{in}).

The location of the robust design (RO) is marked alongside the location of the initial design (X) on Figure 4 where the flow coefficient is higher for the robust design. It is interesting to note that the robust design is closer to a region where there is significant sensitivity of the design conditions on the efficiency at different turbine speeds on design conditions.

7. Conclusions

A robust optimisation method has been developed including an off-design performance to the initial optimisation of radial-inflow turbines and successfully applied. It was found that for the present design using supercritical CO₂ (a near ideal gas) as a working fluid, the off-design performance varies little with wide variations in operating parameters. The method used is a fast, heuristic approach for turbomachinery design and has great potential in the initial design of turbomachinery when considering the computational cost of higher order methods such as coupled computational fluid dynamics and inverse design. Future work building from this will include the analysis of working fluids such as R143a as presented by Sauret [1] which are useful in quite a number novel designs. Furthermore the analysis will be extended to consider Axial turbomachinery and components of the cycle in order to develop a model that is able to help deliver the best Levelised Cost of Electricity.

8. Acknowledgements

This research is part of the Australian Solar Thermal Research Initiative (ASTRI), a project supported by the Australian Government, through the Australian Renewable Energy Agency (ARENA).

9. References

- [1] Sauret, E., and Gu, Y., 2014. “Three-dimensional off-design numerical analysis of an organic rankine cycle radial-inflow turbine”. *Applied Energy*, **135**, pp. 202–211.
- [2] Zang, C., Friswell, M., and Mottershead, J., 2005. “A review of robust optimal design and its application in dynamics”. *Computers & Structures*, **83**(4), pp. 315–326.
- [3] Bonaiuti, D., and Zangeneh, M., 2009. “On the Coupling of Inverse Design and Optimization Techniques for the Multiobjective, Multipoint Design of Turbomachinery Blades”. *Journal of Turbomachinery*, **131**(2), p. 021014.
- [4] Fiaschi, D., Manfrida, G., and Maraschiello, F., 2015. “Design and performance prediction of radial ORC turboexpanders”. *Applied Energy*, **138**, pp. 517–532.
- [5] Shimoyama, K., Lim, J. N., Jeong, S., Obayashi, S., and Koishi, M., 2009. Practical Implementation of Robust Design Assisted by Response Surface Approximation and Visual Data-Mining.
- [6] Saha, A., and Ray, T., 2011. “Practical robust design optimization using evolutionary algorithms”. *Journal of Mechanical Design*, **133**(10), p. 101012.
- [7] Kalsi, M., Hacker, K., and Lewis, K., 2001. “A comprehensive robust design approach for decision trade-offs in complex systems design”. *Journal of Mechanical Design*, **123**(1), pp. 1–10.
- [8] Conboy, T., Wright, S., Pasch, J., Fleming, D., Rochau, G., and Fuller, R., 2012. “Performance Characteristics of an Operating Supercritical CO₂ Brayton Cycle”. *Journal of Engineering for Gas Turbines and Power*, **134**(11), p. 111703.
- [9] Baines, N. C., 2003. “Radial Turbine Design”. In *Axial and Radial Turbines*, H. Moustapha, ed. Concepts NREC, White River Junction, Vt, pp. 199–327.
- [10] Lemmon, E., Huber, M., and McLinden, M., 2013. NIST Standard Reference Database 23: Reference Fluid Thermodynamic and Transport Properties-REFPROP, Version 9.1.
- [11] Persky, R., Sauret, E., and Ma, L., 2014. “Optimisation methods for coupled thermodynamic and 1D design of radial-inflow turbines”. In Fluids Engineering Division Summer Meeting, ASME.
- [12] Aungier, R. H., 2005. *Turbine Aerodynamics*. ASME, New York.
- [13] Erbas, M., Sofuoglu, M. A., Biyikoglu, A., and Uslan, I., 2013. “Design and Optimization of a Low Temperature Organic Rankine Cycle and Turbine”. In Proceedings of the ASME International Mechanical Engineering Congress and Exposition, ASME.
- [14] Levine, D., 1996. “Users guide to the pgapack parallel genetic algorithm library”. *Argonne National Laboratory*.
- [15] Ben-Tal, A., and Nemirovski, A., 2002. “Robust optimization—methodology and applications”. *Mathematical Programming*, **92**(3), pp. 453–480.
- [16] Bertsimas, D., Brown, D. B., and Caramanis, C., 2011. “Theory and applications of robust optimization”. *SIAM review*, **53**(3), pp. 464–501.
- [17] Deb, K., and Gupta, H., 2006. “Introducing robustness in multi-objective optimization”. *Evolutionary Computation*, **14**(4), pp. 463–494.

Topology and Size Optimization of Modular Ribs in Aircraft Wings

A.Rinku¹, G K Ananthasuresh²

¹PhD Student, Department of Mechanical Engineering, Indian Institute of Science & Principal Scientist, National Aerospace Laboratories, Bengaluru, India, rinku@ccadd.cmmacs.ernet.in

²Professor, Department of Mechanical Engineering, Indian Institute of Science, Bengaluru, India, suresh@mecheng.iisc.ernet.in

1. Abstract

Semi-monocoque construction currently followed for ribs with full-depth web in aircraft wings requires extensive elastic analysis to ensure adequate stiffness, strength, and stability against local buckling while reducing the weight. In this work, we address this problem by developing a modular design enabled by fewer components as compared to current design. As a result, the cost and complexity of manufacturing the components as well as the overall assembly reduce. Furthermore, the design process of the overall wing becomes computationally efficient. Optimality is achieved by topology and size optimization techniques. A systematic three-stage procedure for rib design for any given aircraft wing is developed and is demonstrated using the wing of a light transport aircraft.

Keywords

Design optimization, Topology-Optimization, Wing ribs, Modular design.

2. Introduction

There are several successful examples of application of topology optimization in optimal aircraft structural design. Balabanov and Haftka [1] represented the internal structure of a wing as a truss and optimized the cross-sectional area of the ground structure of the interconnected truss elements. In the A380 project of Airbus Industries, topology optimization was used to obtain new and lighter component designs such as the inboard outer fixed leading-edge ribs and the fuselage door intercostals. This has contributed weight savings on the order of 1000 kg per aircraft [2]. The successful engineering practices of the topology optimization are due to intense research in this field [3-10]. Locatelli et al. [11] proposed a new design concept in wing-box design called “Sparibs” by using topology and sizing optimization techniques, instead of using the classic design concept of straight spars and ribs. Wang et al. [12] proposed a topology optimization method which is based on the subset simulation method used in reliability analysis on improving the computational efficiency. They demonstrated this technique in optimizing the wing leading edge ribs and were able reduce the weight of the rib by 18.4%.

In this work, we propose a modular design of wing-ribs with fewer components than conventional semi-monocoque design (web reinforced with stiffeners), which is likely to lower the cost of manufacturing and assembly. Furthermore, the design process of the overall wing becomes computationally efficient. Optimality is achieved by topology and size optimisation techniques. A systematic three-stage procedure is developed and demonstrated on a typical light transport aircraft wing ribs.

3. Optimization of wing ribs

A typical Light transport aircraft (LTA) wing under consideration is of two-spar construction, with 23 rib stations per side of the wing. At each rib station, the rib is divided into three portions, viz., Nose rib, Inter spar (I/S) rib, and trailing edge rib. This paper deals with optimization of I/S ribs. A typical LTA wing is shown in Fig.1a and conventional semi-monocoque rib design is shown in Fig. 1b, in which the web is reinforced with vertical stiffeners to resist the loads acting on the rib and to avoid buckling. The optimization procedure is explained next.

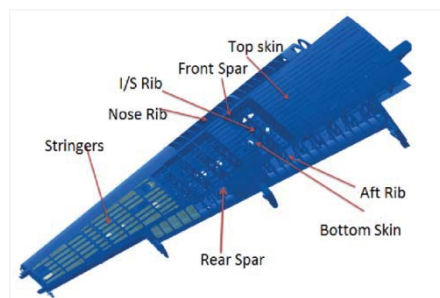


Figure 1a: Typical Light Transport Aircraft wing

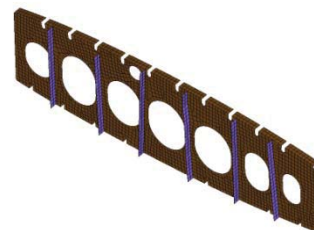


Figure 1b: Typical conventional semi-monocoque rib

4. Optimization Framework

The three stages in the proposed design procedure include two stages of optimization followed by modular design of the rib as shown in Fig. 2. Step 1 involves topology optimization of a few selected ribs where mean compliance is minimized subject to the volume constraint. As the loads and lengths of the ribs are proportional to the chord, the pattern repeatability of the internal structure was achieved by maintaining the same area-ratio between design and non-design areas for all the ribs. The non-design material region exist all along the periphery of the I/S ribs.

Step 2 involves size optimization of the ribs obtained through topology optimization done in the first step. The objective here is to minimize the mass subject to stress and buckling constraints. Each topology-optimized rib is thus improved by determining the cross-section dimensions of the beam segments in the rib.

Step 3 is the modular design of the intermediate ribs. As the pattern repeatability is achieved through topology optimization, the internal members of the rib can be located proportionally as per the chord-length using non-dimensional analysis. Non-dimensional stiffness, stress, and other parameters [13] help design any intermediate rib with standard available beam segments by maintaining the area and the moment of inertia.

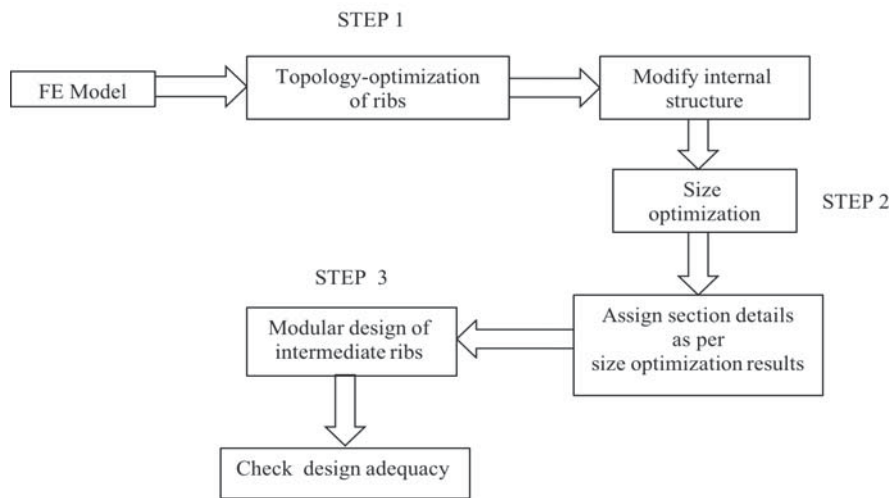


Figure 2: Three-step optimization framework for rib design aircraft wings

4.1 Topology optimization of wing ribs

Topology optimization was carried out on a few arbitrarily selected I/S ribs; Rib no. 8,12, 16 and 19 as shown in Fig. 3. The objective function is to minimize the strain energy (SE) with the constraint on volume. This can be stated in the discretized finite element framework as follows:

$$\min_{\mathbf{x}} SE = \frac{1}{2} \mathbf{u}^T \mathbf{k} \mathbf{u} = \frac{1}{2} \sum_{i=1}^n x_i^p u_i^T k_i u_i$$

$$\mathbf{k} \mathbf{u} = \mathbf{f}$$

$$\frac{V}{V_0} = 0.3$$

$$\mathbf{x} = \{x_1, x_2, \dots, x_n\}^T$$

$$0 < x_{min} \leq x_i \leq 1 \quad (i = 1, \dots, n) \quad (1)$$

where \mathbf{u} is the global displacement vector of size $n \times 1$, \mathbf{k} the global stiffness matrix, \mathbf{f} the external load vector, V_0 the initial volume, V the final volume, and x_i the i^{th} element's density that indicates the presence or absence of the material in the corresponding element..

Topology optimization was carried out using commercial software Altair Optistruct. The ribs were analyzed as continuum structure using 2D finite elements CQUAD4 and CTRIA3. The aim of this step is to obtain optimum distribution of material and to achieve pattern repeatability in the rib geometry. The chord-wise load distribution was computed using *panel code* by the aerodynamic group at the National Aerospace Laboratories, Bengaluru [14] on the top and bottom wing surfaces for V_D (Dive Speed) case at the selected rib locations shown in Fig. 4. As can be seen in the figure, the loads are proportional to the local chord. Portions of the rib at the top, bottom and sides are defined as non-design space to accommodate the stringer cut-outs and attachments to spars.

With the rib loads and lengths being proportional to the local chord and by maintaining the same ratio between design space area (A_{DS}) and total rib area (A_{Tot}) for all the ribs as shown in Fig. 5, the topology optimization results are shown in Fig. 6. In this, the red colour indicates presence of the material and blue colour the void regions. It is evident that there is pattern repeatability in the rib structure which points to generalized rib

geometry shown in Fig. 7. The general rib geometry shown in Fig. 7 also indicates the dimensions required to construct any intermediate rib in the wing. In Fig. 7, “11, 12, 13, 14, 15, 16” indicates the lengths of the inclined members and “a, b, c, d, e, f, g, h” indicates the intersection points of the inclined members with top flange, bottom flange, front spar and rear spar, which are measured from front spar top (Ft). These dimensions can be mentioned in terms of % chord in relation to the rib location (% span) as shown in Fig. 8. With this non-dimensional graph, it is possible to define geometry of any intermediate rib.

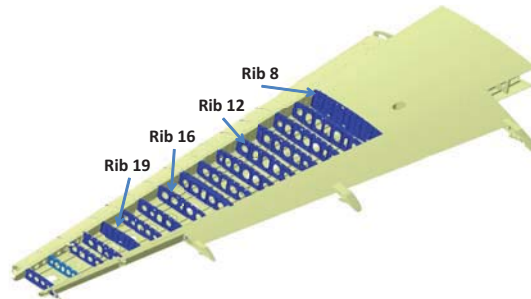


Figure 3. Typical LTA wing with conventional Rib design

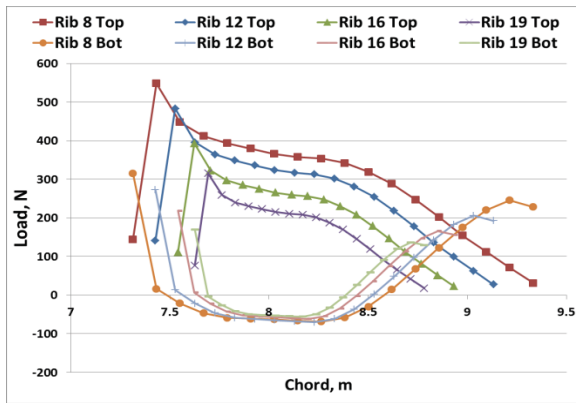


Figure 4: Chord wise load distribution

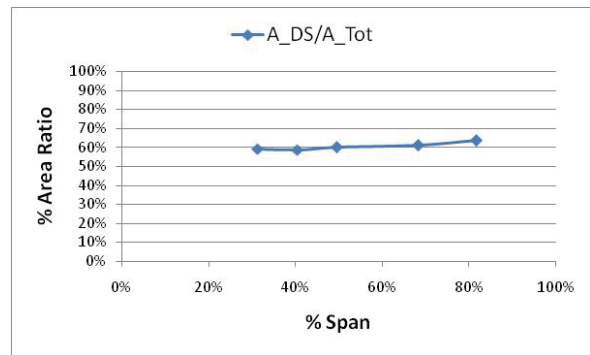


Figure 5: Area Ratio

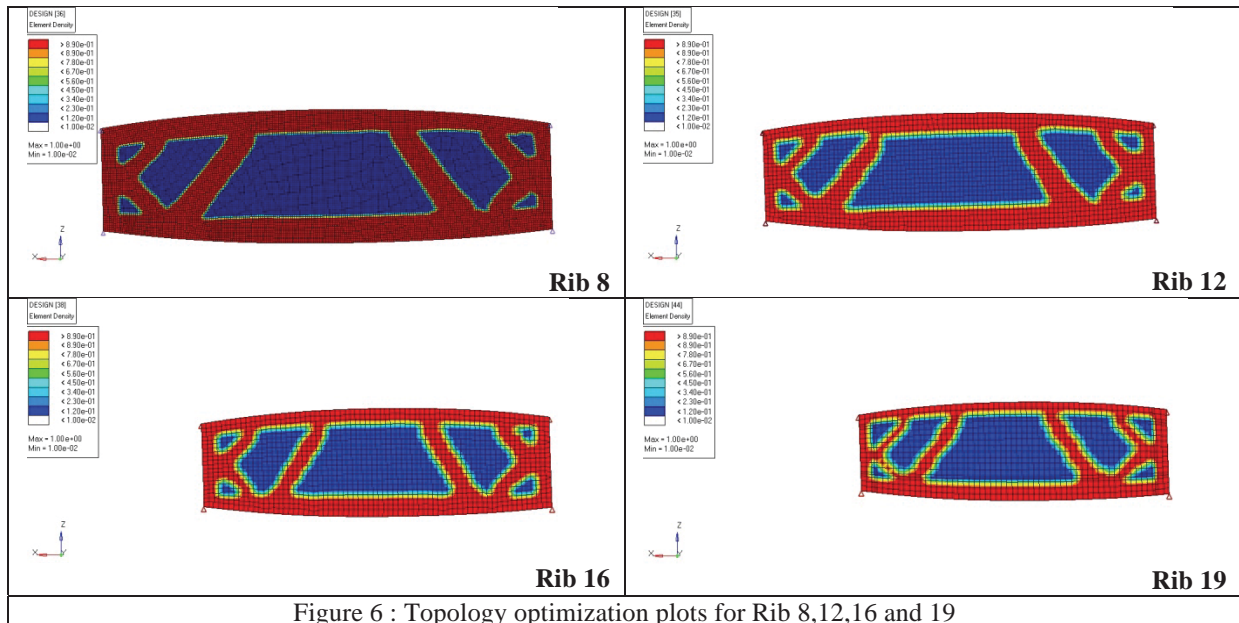


Figure 6 : Topology optimization plots for Rib 8,12,16 and 19

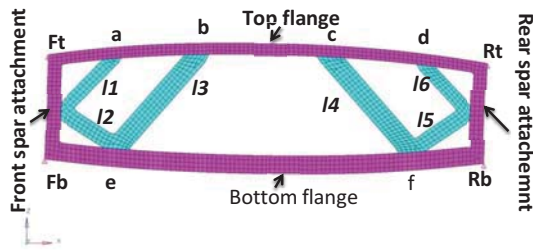


Figure 7: Generalized Rib geometry

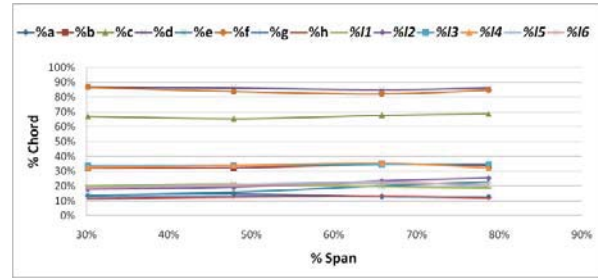


Figure 8: Non dimensional plot of Rib geometry

4.2. Size optimization of the wing ribs

Step 2 involves size optimization of the topology optimized ribs for minimizing the mass (M) with stress (σ_{max}) and buckling constraints (Buckling factor, BF). A typical buckling constraint is a lower bound of 1.0 indicating that the structure is not to buckle under the given static load. Each topology optimized rib was subjected to size optimization to get thicknesses of various internal elements of the rib. This problem can be formulated as follows:

$$\begin{aligned}
 & \min M \\
 & \sigma_{max} << 265 \text{ MPa} \\
 & 1 - BF \leq 1 \\
 & 0.8 \leq T \leq 5
 \end{aligned}
 \quad (2)$$

Size optimization was carried out on ribs 8, 12, 16, and 19 using Altair Optistruct. With the optimum thickness values and corresponding widths of the various elements of the rib, area (A) and Moment of inertia (MI) values were computed for each element and plotted with respect to % span. Typical graphs are shown Figs. 9 and 10 for the bottom flange. By using these graphs, cross section of any intermediate rib can be defined, as explained next.

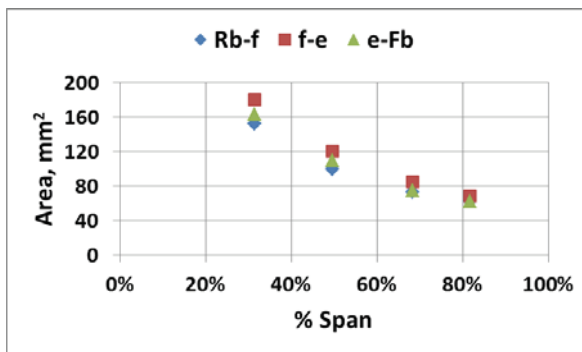


Figure 9: Cross sectional area graph for bottom flange

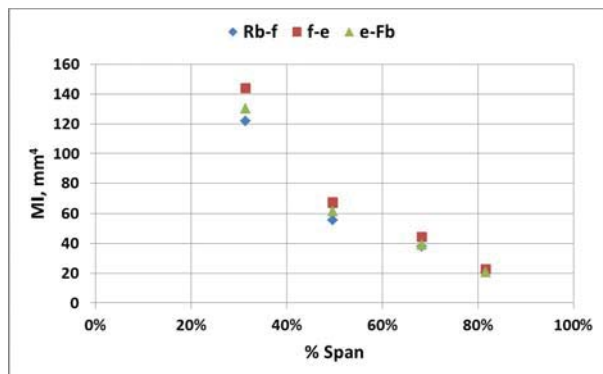


Figure 10: Moment of inertia graph for bottom flange

4.3. Modular design of intermediate ribs

Step 3 is modular design of the intermediate ribs. As the pattern repeatability is achieved through topology optimization, internal structure of any intermediate rib can be obtained by using non-dimensional plot of rib geometry shown in Fig. 8. Cross sectional details obtained from the topology and size optimization process, it is possible to decide the cross section detail of any intermediate rib by selecting the standard available section by maintaining the area and moment of inertia values obtained from the optimization (Figs. 9, 10).

To demonstrate this process an intermediate rib 10 is considered. Its internal structures can be obtained from the Fig. 8 by locating the rib at its span wise location (39%). Once the rib internal structure is obtained, its cross sectional area can be decided by using Area and MI graphs. We can choose a suitable standard section which meets cross sectional requirements and local crippling criteria. In this case, we have selected a channel section to check the design adequacy. Linear static and buckling analysis were carried out using Altair Optistruct and the results are shown in Table 1. The geometry of rib 10 with modular design concept is shown Figs. 11 and 12. Fig. 12 shows the geometry of the rib with stringer cut-outs as per the practical design requirement.

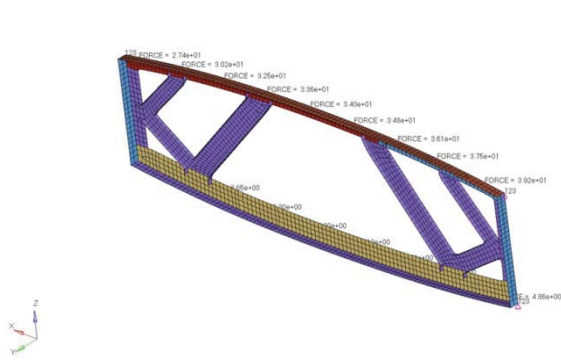


Figure 11: Modular design of rib 10 (without stringer cut-out)

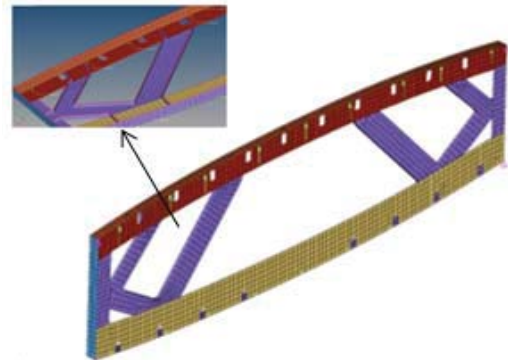


Figure 12: Modular design of rib 10 (with stringer cut-out)

To prove the efficiency of the modular design procedure, we have compared the results of modular design with the two-step optimization procedure and conventional rib design. The conventional rib design is shown in Fig.13, which contains full depth web, with lightening holes and stiffeners at regular interval to meet the buckling requirements. Size optimization was carried out on this rib with stress and buckling constraints and the results are shown in Table 1.

The rib was optimized using two-step optimization procedure comprising topology optimization followed by size optimization. The topology optimization result is shown in Fig. 14, where it can be seen that it is very much similar to the modular design obtained using Fig. 8. Next, size optimization was carried out to meet buckling and stress requirements whose results are shown in Table 1.

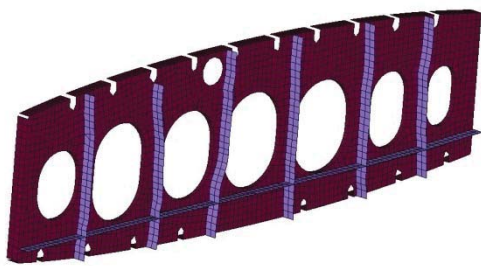


Figure 13 : Conventional design of Rib 10



Figure 14 : Topology optimization plot for Rib 10

Table 1: Results of Rib 10 Optimization

Rib 10		Weight(Kg)	Max Deflection (mm)	Stress (MPa)	Buckling factor
Modular design	Without stringer cut-out	0.7	0.4	60	4
	With stringer cut-out	0.76	0.39	70.6	3.23
Conventional rib design		0.974	0.42	45	1
Two-step optimization (Without stringer cut-out)		0.68	0.35	63	1

4.4. Discussion

Results of modular design, two-step optimization procedure, and conventional design are shown in Table 1. A rib designed with two-step optimization procedure is 30% lighter as compared to the conventional rib design for the same buckling factor. The modular rib design is 22% lighter as compared to conventional design with three times more buckling factor. The two step optimization process and the modular design concept proposed in this paper results in much lighter structure as compared to conventional design. Even though von Mises stress is more in the proposed modular design as compared to conventional design, the absolute value is much less than the maximum allowable stress of 265 MPa. The complete wing with modular rib design is shown in Fig. 15.

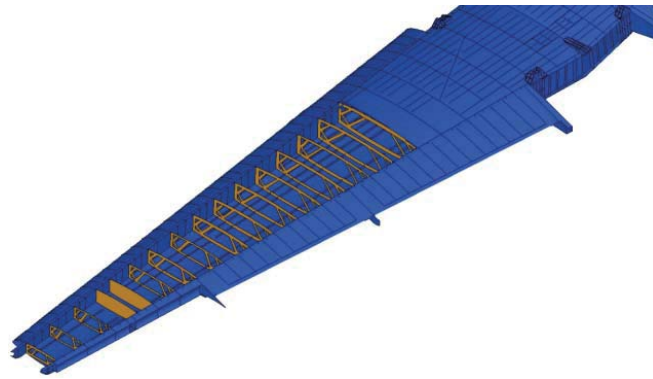


Figure 15. Typical Light transport aircraft wing with modular Ribs

5. Conclusion

The modular rib design is “satisficing” in nature in that it satisfies all the design and manufacturing requirements but is only nearly optimal. However, the unique feature of this procedure is the modular design wherein the internal members of all the ribs are decided as per their position in the wing. As a result, the design is amenable for economical manufacturing. Through an example, it is proved that the new design procedure is more efficient as compared to current practices in terms of weight and performance.

6. Acknowledgments

Authors thank Dr. Vidyadhar Mudkavi, Head, CTFD, CSIR-NAL, for his support and encouragement. Also thank Director, CSIR-NAL and Head, C-CADD, CSIR-NAL for granting permission to carry out the work.

7. References

1. Balabanov V O, Haftka R T, Topology optimization of transport wing internal structure, *Journal of Aircraft*, 33(1), 232-233, 1996.
2. Krog L, Tucker A, Kamp M, Boyd R., "Topology Optimization of Aircraft Wing Box Ribs," *The Altair Technology Conference 2004*, Vol. 6, Altair Engineering, Troy, MI, 2004, pp. 1-16.
3. Bendsøe M P, Kikuchi N, "Generating Optimal Topologies in Structural Design Using Homogenization," *Computer Methods in Applied Mechanics and Engineering*, Vol. 71, 1988, pp. 197-224.
4. Bendsøe M P, "Optimal Shape Design as a Material Distribution Problem," *Structural and Multidisciplinary Optimization*, Vol. 1, No. 4, 1989, pp. 193-202.
5. Zhou M, Rozvany G I N, "The Coc Algorithm, Part II: Topological, Geometry and Generalized Shape Optimization," *Computer Methods in Applied Mechanics and Engineering*, Vol. 89, Nos. 1-3, 1991, pp. 309-336.
6. Sigmund O, "A 99 Line Topology Optimization Code Written in Matlab," *Structural and Multidisciplinary Optimization*, Vol. 21, No. 2, 2001, pp. 120-127.
7. Svanberg K, "The Method of Moving Asymptotes: A New Method for Structural Optimization," *International Journal for Numerical Methods in Engineering*, Vol. 24, 1987, pp. 359-373.
8. Bruggi M, Duysinx P, Topology optimization for minimum weight with compliance and stress constraints. *Structural and Multidisciplinary Optimization* (2012).
9. Kočvara M, Stingl M, Solving stress constrained problems in topology and material optimization, *Structural and Multidisciplinary Optimization*, January 2012.
10. Sigmund O, Maute K, Topology optimization approaches .A comparative review, *Structural and Multidisciplinary Optimization* (2013) 48:1031–1055.
11. Locatelli D, Mulani S B, Kapania R K, Wing-Box Weight Optimization Using Curvilinear Spars and Ribs (SpaRibs), *Journal of Aircraft*, Vol. 48, No. 5, September-October 2011.
12. Wang Q, Lu Z, Zhou C, New Topology Optimization Method for Wing Leading-Edge Rib, *Journal of Aircraft*, Vol. 48, No. 5, September-October 2011.
13. Bhargav S. D. B., Varma H. I., and Ananthasuresh G. K., Non-dimensional Kinetoelastostatic Maps for Compliant Mechanisms, *Proc. ASME 2013 International Design Engineering Technical Conferences*, August 4-7, 2013, Portland, Oregon, USA, Paper no. DETC2013-12178.
14. Internal report, C-CADD, National Aerospace Laboratories, Bengaluru, India.

Design and optimization of a variable stiffness composite laminate

Yan Zhang¹, Fenfen Xiong²

¹ Qian Xuesen Laboratory of Space Technology, Beijing, China, zyande@hotmail.com

² Beijing Institute of Technology, Beijing, China, fenfenx@bit.edu.cn

1. Abstract

With the wide use of fiber-reinforced composite laminates in aerospace industry, structural instability is one of the most key aspects for flight vehicles. Hence, the research on structural instability mechanisms of composite laminates, especially buckling characteristics, is of great significance. In this paper, the buckling characteristics analysis and design optimization of the variable stiffness composite (VSC) panel with given geometry and material properties are studied. Pagano's three layer constant stiffness laminate is investigated as the baseline case. The method of layered modeling and numerical structural analysis of VSC panel in the commercial package ABAQUS is described. The design optimization of the VSC panel aims to maximize the critical buckling load with the fiber orientation angles at the center and end as design variables, which is solved by the sequential quadratic programming method. It is found that with the same weight, the optimal critical buckling load of the designed VSC panel is increased up to 67.9% compared to the baseline laminate. To further verify the accuracy of the optimal design solution, based on the first von Karman equation, critical buckling load differential equation of a rectangular laminate is deduced, and the fiber orientation angle corresponding to the optimal critical buckling load is derived by theoretical analysis, which is compared with the optimal critical fiber angle by optimization. It is noticed that the two critical fiber angles show great agreement to each other. Therefore, the finite element analysis in conjunct with optimization method is proved to be accurate for solving buckling issues of VSC laminates, which thus could be used in further study of the performance of VSC laminates. It is concluded that, compared to the traditional fiber-reinforced composite laminates, the VSC laminates can be designed with more flexibility to achieve better load redistribution, resulting in great improvements of the structural performance.

2. Key words: variable stiffness composites; buckling analysis; design optimization; finite element analysis.

3. Introduction

Research on application of new material with superior performance is always a hot topic in aircraft structural design due to the high demand for lightweight structures. Fiber reinforced composite material has many advantages, such as high specific strength and modulus, designable performance and excellent integral forming capability, etc, which almost determines the structure performances of aircraft. Application of fiber reinforced composite material to aircraft structure can significantly reduce the weight, meanwhile improve the aerodynamic and flight performances [1].

In order to improve the structural performances and lower the cost during the life cycle, it is necessary to carry out design of composite material, of which one focus is to fully explore the directionality of composites and the designable capability of the structural performance. It is possible to take full advantage of the directionality by using variable stiffness composites (VSC)[2], in which the fiber can be steered in plane with the fiber angle as a function of space. The continuously changed fiber orientation results in the variation of stiffness at different locations, based on which the designers can adjust the distribution of internal load to improve the structural performance or reduce weight [3].

Gurdal and Olmedo [4,5] proposed a fiber placement method by changing the fiber orientation angle along the coordinate axis. They analyzed the in-plane and buckling response of variable stiffness composite panels by closed analytical and numerical methods. The VSC showed considerable improvements in load-carrying capabilities compared to traditional composite laminates. Gurdal and Tatting [6] studied the effects of stiffness variation on the in-plane and buckling response for variable stiffness composite panels. The curvilinear fiber paths for fiber-steered variable stiffness laminates were designed and optimized based on lamination parameters distribution by Setoodeh [7]. Tatting and Gurdal carried out the design and manufacture of tailored tow placed plates, in which the buckling characteristics were studied by both finite element analysis and experimental method [8,9]. Analysis and optimization of variable angle tow composite plates for pre-buckling [10], buckling [11] and post-buckling behavior [12] have been done with differential quadrature method by Raju and Wu.

The structural instability is one of the important issues that impact the structural performance in the application of composite materials, causing structural deformation, decreased load-carrying capacity and even structural damage. Therefore, it is necessary to study the structural instability of composite laminates, such as buckling characteristics. In this paper, the buckling characteristics are designed and optimized for variable stiffness composite laminates, in which the fiber orientation angle linearly varies along the direction of the load. Structural analysis is done in the finite element software ABAQUS. Sequential quadratic programming algorithm (SQP) is

used to optimize the design. In the following, firstly the process of FEA modeling is described. Then theoretical analysis method for the fiber orientation angle corresponding to the critical buckling load is given. Furthermore the design problem for variable stiffness composite laminate is defined. Finally the results of optimization are presented.

4. FEA modeling of variable stiffness composite laminate

Fibers in every single ply are straight for conventional composite laminates, which therefore can be designed only by changing the stacking sequence. However, fibers can be steered in plane to make the fiber orientation angle continuously vary with spacial location for variable stiffness composite laminates, which makes its stiffness as a function of spacial location.

The scheme of the reference path of steered fiber proposed by Gurdal [2] is used in this paper. The fiber orientation angle linearly varies along the direction of loading, and function of fiber orientation angle of the reference path is as follows:

$$q(x) = \frac{2(T_1 - T_0)}{a}|x| + T_0 \quad (1)$$

Eq.(1) is written as $q(x) = k|x| + b$ for convenience, where $k = 2(T_1 - T_0)/a$ and $b = T_0$. Then the reference path of curve fiber can be defined as:

$$y = \begin{cases} \frac{1}{k} \{ \ln \cos(kx + b) - \ln \cos(b) \} & -\frac{a}{2} \leq x < 0 \\ \frac{1}{k} \{ \ln \cos(kx + b) - \ln \cos(b) \} & 0 < x \leq \frac{a}{2} \end{cases} \quad (2)$$

Pagano's three layer case [13] is studied as the reference case. The panel is square with cross-ply [0/90/0] stacking sequence. Its side length is $a = 50\text{mm}$ and thickness is $h = 1\text{mm}$. The variable stiffness cases studied in this paper are also stacked in a cross-ply $[(T_0 - 90)|(T_1 - 90)]/[(T_0 | T_1)]/[(T_0 - 90)|(T_1 - 90)]$ sequence, where the function of fiber orientation angle is $q(x) = k|x| + b$ in the middle ply, and $q(x) = k|x| + b - 90$ in the top and bottom ply. The ABAQUS user subroutine ORIENT is employed to implement the different orientation to fibers within the plane of each ply in variable stiffness composite laminate. 8-nodded elements C3D8I with incompatible modes are used to establish FEA model for each single ply of laminates, respectively. The panel is simply supported at all the four sides, and it carries unidirectional compression load. The same carbon fiber/epoxy resin material with the reference case is used, and its performance parameters are listed in Table 1. The subscripts 1, 2 and 3 represent fiber direction, transverse direction and thickness direction respectively.

Table 1: Performance parameters of carbon fiber/epoxy resin material

E_{11} [GPa]	E_{22} [GPa]	E_{33} [GPa]	G_{12} [GPa]	G_{13} [GPa]	G_{23} [GPa]	ν_{12}	ν_{13}	ν_{23}
25	1.0	1.0	0.5	0.5	0.2	0.25	0.25	0.25

5. Theoretical analysis of the critical buckling load

The first von Karman equation for large deflections is as follows [16]:

$$D_{11} \frac{\partial^4 w}{\partial x^4} + 2(D_{12} + 2D_{66}) \frac{\partial^4 w}{\partial x^2 \partial y^2} + D_{22} \frac{\partial^4 w}{\partial y^4} = N_x \frac{\partial^2 w}{\partial x^2} + 2N_{xy} \frac{\partial^2 w}{\partial x \partial y} + N_y \frac{\partial^2 w}{\partial y^2} - p_x \frac{\partial w}{\partial x} - p_y \frac{\partial w}{\partial y} + p_z \quad (3)$$

For laminate under unidirectional in-plane loading, the governing equation is obtained by setting $N_{xy} = N_y = p_x = p_y = p_z = 0$:

$$D_{11} \frac{\partial^4 w}{\partial x^4} + 2(D_{12} + 2D_{66}) \frac{\partial^4 w}{\partial x^2 \partial y^2} + D_{22} \frac{\partial^4 w}{\partial y^4} = N_x \frac{\partial^2 w}{\partial x^2} \quad (4)$$

where w is the out-of-plane displacement of the laminate.

The laminate is assumed to be simply supported all around its boundary and the only load is N_x . Then the boundary conditions are:

$$w = M_x = -D_{11} \frac{\partial^2 w}{\partial x^2} - D_{12} \frac{\partial^2 w}{\partial y^2} = 0 \text{ at } x=0 \text{ and } x=a; \quad w = M_y = -D_{12} \frac{\partial^2 w}{\partial x^2} - D_{22} \frac{\partial^2 w}{\partial y^2} = 0 \text{ at } y=0 \text{ and } y=a.$$

where a is the length of the square laminate. In order to satisfy all of the boundary conditions, the expression for w is assumed as:

$$w = \hat{A} \hat{A} A_{mn} \sin \frac{m\pi x}{a} \sin \frac{n\pi y}{a} \quad (5)$$

Substituting Eq.(5) into Eq.(4), one has

$$p^2 A_{mn} \ddot{D}_{11} m^4 + 2(D_{12} + 2D_{66})m^2 n^2 + D_{22} n^4 = - A_{mn} a^2 N_x m^2 \quad (6)$$

The out-of-plane displacement w is nonzero when buckling occurs, indicating that the coefficient A_{mn} is nonzero thus can be neglected in Eq.(6),

$$p^2 \ddot{D}_{11} m^4 + 2(D_{12} + 2D_{66})m^2 n^2 + D_{22} n^4 = - a^2 N_x m^2 \quad (7)$$

For convenience, the buckling load is denoted by $N_o = - N_x$, where the minus sign indicates compression. Then we get the buckling load as:

$$N_o = \frac{p^2 \ddot{D}_{11} m^4 + 2(D_{12} + 2D_{66})m^2 n^2 + D_{22} n^4}{a^2 m^2} \quad (8)$$

where m is the number of half-waves in the x direction and n is the number of half-waves in the y direction, which define the buckling mode. The buckling load N_o is a function of m and n , and changes with m and n . The critical buckling load is the lowest value of Eq.(8), so it is necessary to minimize the right hand side of Eq.(8) with respect to m and n . Obviously, this minimum is achieved when $n=1$, which means that there is only one half-wave in the transverse direction of the applied loading. Substituting $n=1$ into Eq.(8), one obtains,

$$N_o = \frac{p^2 \ddot{D}_{11} m^2 + 2(D_{12} + 2D_{66}) + \frac{D_{22}}{m^2}}{a^2} \quad (9)$$

The buckling load of a simply supported square composite laminate under unidirectional compression load can be obtained through minimizing Eq.(9) with respect to m . The partial derivative with respect to m is

$$\frac{\partial N_o}{\partial m} = \frac{2p^2 \ddot{D}_{11} m}{a^2} - \frac{D_{22}}{m^3} = 0 \quad (10)$$

Since $\frac{p^2}{a^2} \pi > 0$, the buckling load is obtained when $D_{11} m - \frac{D_{22}}{m^3} = 0$. The bending stiffness matrix [D] is

$$D = \frac{h^3}{12} (G_0 + G_1 V_{1D} + G_2 V_{2D} + G_3 V_{3D} + G_4 V_{4D}) \quad (11)$$

and the corresponding laminate parameters are

$$(V_{1D}, V_{2D}, V_{3D}, V_{4D}) = 12 \int_{-\frac{1}{2}}^{\frac{1}{2}} \bar{z}^2 (\cos 2q(x), \sin 2q(x), \cos 4q(x), \sin 4q(x)) d\bar{z} \quad (12)$$

Then the laminate parameters of the three layer cross-ply laminates in this paper are expressed as:

$$V_{1D} = 12 \int_{-\frac{1}{2}}^{\frac{1}{2}} \bar{z}^2 \cos 2q(x) d\bar{z} + \int_{-\frac{1}{6}}^{\frac{1}{6}} \bar{z}^2 \cos 2(q(x) + 90) d\bar{z} + \int_{-\frac{1}{6}}^{\frac{1}{6}} \bar{z}^2 \cos 2q(x) d\bar{z} = \frac{25}{27} \cos 2q(x) \quad (13)$$

$$V_{2D} = 12 \int_{-\frac{1}{2}}^{\frac{1}{2}} \bar{z}^2 \sin 2q(x) d\bar{z} + \int_{-\frac{1}{6}}^{\frac{1}{6}} \bar{z}^2 \sin 2(q(x) + 90) d\bar{z} + \int_{-\frac{1}{6}}^{\frac{1}{6}} \bar{z}^2 \sin 2q(x) d\bar{z} = \frac{25}{27} \sin 2q(x) \quad (14)$$

$$V_{3D} = 12 \int_{-\frac{1}{2}}^{\frac{1}{2}} \bar{z}^2 \cos 4q(x) d\bar{z} + \int_{-\frac{1}{6}}^{\frac{1}{6}} \bar{z}^2 \cos 4(q(x) + 90) d\bar{z} + \int_{-\frac{1}{6}}^{\frac{1}{6}} \bar{z}^2 \cos 4q(x) d\bar{z} = \cos 4q(x) \quad (15)$$

$$V_{4D} = 12 \int_{-\frac{1}{2}}^{\frac{1}{2}} \bar{z}^2 \sin 4q(x) d\bar{z} + \int_{-\frac{1}{6}}^{\frac{1}{6}} \bar{z}^2 \sin 4(q(x) + 90) d\bar{z} + \int_{-\frac{1}{6}}^{\frac{1}{6}} \bar{z}^2 \sin 4q(x) d\bar{z} = \sin 4q(x) \quad (16)$$

Substituting these laminate parameters into Eq.(11), the coefficients of bending stiffness matrix are obtained as follows:

$$D_{11} = \frac{h^3}{12} \left[U_1 + \frac{25}{27} U_2 \cos 2q(x) + U_3 \cos 4q(x) \right] \quad (17)$$

$$D_{22} = \frac{h^3}{12} \left[U_1 - \frac{25}{27} U_2 \cos 2q(x) + U_3 \cos 4q(x) \right] \quad (18)$$

Substituting D_{11} and D_{22} into Eq.(10), one has,

$$m \left[U_1 + \frac{25}{27} U_2 \cos 2q(x) + U_3 \cos 4q(x) \right] - \frac{1}{m^3} \left[U_1 - \frac{25}{27} U_2 \cos 2q(x) + U_3 \cos 4q(x) \right] = 0 \quad (19)$$

Substituting m (the number of half-waves in the x direction) into Eq.(19), the fiber orientation angle

$q(x)$ corresponding to the critical buckling state can be obtained.

6. Design and optimization of variable stiffness composite laminate

6.1 Optimization model and method

The slope and initial value of the function of fiber orientation angle are considered as the design object in the optimization model for the variable stiffness composite laminates, and the objective is to achieve the maximum buckling load. Because both the slope and initial value are determined by the fiber angle at the center point of the panel denoted as T_0 and the fiber angle at the end of the panel denoted as T_1 , T_0 and T_1 are treated as design variables. The mathematical model of the optimization of variable stiffness composite laminate is defined as:

$$\begin{aligned} \max \quad & f(X) \\ \text{s.t.} \quad & -90 \leq X_1 \leq 90 \\ & -90 \leq X_2 \leq 90 \end{aligned} \quad (20)$$

where design variables X_1 and X_2 are T_0 and T_1 , respectively. The objective function $f(X)$ presents the eigenvalues of linear buckling analysis for the variable stiffness composite laminate. The constraint conditions are the ranges of the value of T_0 and T_1 .

Since the design variables are continuous, the gradient-based sequential quadratic programming (SQP) is used in this optimization. Because SQP is inclined to converge to local minima near the initial value, optimization from multiple initial points are made in this paper in order to increase the possibility to get the optimal design.

User subroutines are used to define the fiber orientation angle of the variable stiffness composite laminate. Thus it is necessary to simultaneously parameterize the FEA model and the user subroutines. For each iteration during the optimization process, the design variables are firstly transferred to the user subroutine, in which relevant parameters are modified, a new user subroutine is generated and then implements different fiber orientation angles to the FEA model to complete the buckling analysis.

6.2 Optimization results

A variable stiffness composite laminate is optimized using SQP in this paper. Table 2 shows the critical buckling load of constant stiffness composite (CSC) laminate, the initial and optimal variable stiffness composite (VSC) laminate respectively. Since fiber orientation angle of each single layer in CSC laminate is constant, the CSC laminate with the stacking sequence [0|0|90] is obtained by setting $T_0 = T_1 = 0$. It can be seen from Table 2 that there are two optimal design points as $X_1^* < 35.1 | 50.6 >$ and $X_2^* < -35.1 | -50.6 >$ in this optimization, with the same critical buckling load as 58.291MPa, which is improved up to 67.9% and 182.5% compared with that of the CSC reference case (34.717MPa) and the initial VSC baseline (20.632MPa). And the reason is that the functions of fiber orientation angles corresponding to these design points are as:

$$X_1^* : q_1(x) = k_1x + b_1 = \frac{50.6 - 35.1}{25}x + 35.1 = 0.62x + 35.1 \quad (21)$$

$$X_2^* : q_2(x) = k_2x + b_2 = \frac{-50.6 + 35.1}{25}x - 35.1 = -0.62x - 35.1 \quad (22)$$

It is obvious that $q_2(x) = -q_1(x)$, which means fiber orientation angles at all points in the fiber paths defined by these two functions will have the same magnitude but opposite direction, if their coordinate value at x -direction are the same. The VSC panel is square, so its structure is symmetric with respect to the x -axis. The structural performance are the same when fiber orientation angles have the same magnitude and opposite direction. Thus there definitely exist two optimal solutions with equal magnitude but opposite directions.

Table 1: Optimization results of VSC laminate

	CSC	VSC initial	Optimum X_1^*	Optimum X_2^*
X_1	0	0	35.1	-35.1
X_2	0	15	50.6	-50.6
$f(X)$	34.717	20.632	58.291	58.291

The variation of critical buckling load of VSC laminates with the slope and initial value of the function of fiber orientation angle are further studied in the optimization process, shown in Figure 1. There are two maximum peaks and two second largest peaks with the double-saddle distribution.

It can be seen from the projected contour that both these two pairs of peaks are symmetric with respect to the Point (0, 0), which demonstrates that the critical buckling load is a binary function of the slope of the initial value, and

also confirms the results of the above analysis that there are two optimal solutions with equal magnitude and opposite directions. When the initial value is kept constant, the critical buckling load varies with the slope similar to an M shape, and the maximum value in each group increases substantially with the increase of the absolute value of the initial value and achieves maximum when the initial value is in the vicinity of $\pm 45^\circ$. Meanwhile, when the slope is kept constant, the critical buckling load also varies with the initial value similar to an M shape, and the maximum value in each group increases substantially with the decrease of the absolute value of the slope and achieves maximum when the slope is in the vicinity of ± 0.5 .

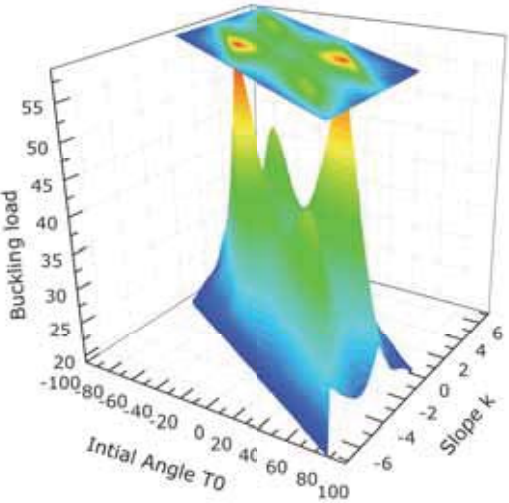


Figure 1: Variation of critical buckling load of VSC laminates with the slope and initial value of the function of fiber orientation angle

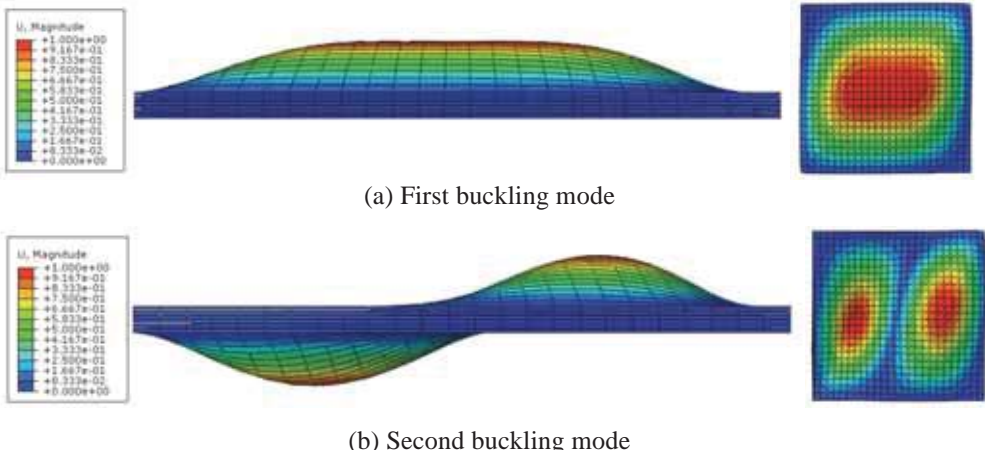


Figure 2: The buckling modes and displacement distribution of the optimal design

Figure 2 shows the X-Y and X-Z views of the first and second buckling modes and displacement distribution of the optimal design $X_1^* < 35.1 | 50.6 >$, which are significantly different from each order.

It is noticed from Figure 2(a) that there is one half-wave in the x -direction in the first mode, which means $m=1$, and the maximum displacement occurs at the center area of the panel. Substituting $m=1$ into Eq.(19), one has,

$$\frac{\ddot{U}_1}{\ddot{U}_1} + \frac{25}{27} U_2 \cos 2q(x) + U_3 \cos 4q(x) - \frac{\ddot{U}_1}{\ddot{U}_1} - \frac{25}{27} U_2 \cos 2q(x) + U_3 \cos 4q(x) = \frac{50}{27} U_2 \cos 2q(x) = 0 \quad (23)$$

Since U_2 is invariant determined by material characteristics and is a non-zero constant, it can be neglected from Eq.(23), then

$$\cos 2q(x) = 0 \quad (24)$$

Then the theoretical fiber angle corresponding to the critical buckling load is obtained as $q(x) = \pm 45^\circ$. The functions of the fiber orientation angle corresponding to the two optimal design points are respectively $q_1(x) = 0.62x + 35.1$ and $q_2(x) = -0.62x - 35.1$. The maximum stresses of the first mode occurs in the central

region of the panel, and the corresponding range for fiber angle is $q \in [39^\circ, 46.8^\circ]$ approximately. Clearly, the result of the theoretical model locates within this range. It indicates that the finite element analysis method and design methodology used in this paper are reasonable and accurate.

7. Conclusions

A variable stiffness composite laminate was optimized for maximum buckling load carrying capability. Its buckling characteristics were analyzed by both theoretical derivation and finite element analysis method. The optimal design under unidirectional compression loading was obtained, with the improvement up to 67.9% compared with the reference constant stiffness case.

The buckling characteristics of variable stiffness composite laminates have close relationship with the initial value and the slope of the function of fiber orientation angle, with which the value of critical buckling load, the shape of buckling modes and the distribution of displacement have great variation.

The fiber orientation angle of the optimal design shows great agreement with that of the theoretical model. It verifies the reasonability and accuracy of the combined solution of the finite element analysis method and design methodology, which can be used in future research of variable stiffness composite materials.

Compared with constant stiffness composite laminates, variable stiffness composite materials with steered fibers have the advantage of high design flexibility. The reference fiber path can be designed according to specific mission requirements, in order to achieve redistribution of loads and thus improve the performance of whole structure.

8. References

- [1] W.J. Li, B.F. Song, X.S. Sun and Y. Zhang, *Aircraft Structure Optimization*, National Defense Industry Press, Beijing, 2005.
- [2] Z. Gurdal and R. Olmedo, Composite Laminates with Spatially Varying Fiber Orientation: Variable Stiffness Panel Concept, *Proceedings of the 33rd AIAA/ASME/AHS/ASC Structures, Structural Dynamics, and Materials Conference*, AIAA, 798-808, 1992.
- [3] A.W. Blow, *Structural Performance of Fiber-Placed, Variable-Stiffness Composite Conical and Cylindrical Shells*, Delft: Delft University of Technology, 2010.
- [4] Z. Gurdal and R. Olmedo, In-Plane Response of Laminates with Spatially Varying Fiber Orientations: Variable Stiffness Concept, *AIAA Journal*, 31(4), 751-758, 1993.
- [5] R. Olmedo and Z. Gurdal, Buckling Response of Laminates with Spatially Varying Fiber Orientations. *AIAA-93-1567*, 1993.
- [6] Z. Gurdal, B.F. Tatting and C.K. Wu, Variable Stiffness Composite Panels: Effects of Stiffness Variation on the In-plane and Buckling Response, *Composites: Part A*, 39, 911-922, 2008.
- [7] S. Setoodeh, M.M. Abdalla and Z. Gurdal, Design of Variable-Stiffness Laminates Using Lamination Parameters, *Composites: Part B*, 37, 301-309, 2006.
- [8] Tatting B F, Gurdal Z. Automated Finite Element Analysis of Elastically-Tailored Plates. *NASA/CR-2003-212679*, 2003.
- [9] B.F. Tatting and Z. Gurdal, Design and Manufacture of Elastically Tailored Tow Placed Plates. *NASA/CR-2002-11919*, 2002.
- [10] G. Raju, Z. Wu, B.C. Kim and P.M. Weaver, Prebuckling and Buckling Analysis of Variable Angle Tow Plates with General Boundary Conditions, *Composite Structures*, 94, 2961-2970, 2012.
- [11] Z. Wu, P.M. Weaver, G. Raju and B.C. Kim, Buckling Analysis and Optimization of Variable Angle Tow Composite Plates, *Thin-Walled Structures*, 60, 163-172, 2012.
- [12] Z. Wu and P.M. Weaver, Post Buckling Analysis of Variable Angle Tow Composite Plates, *International Journal of Solids and Structures*, 50, 1770-1780, 2013.
- [13] N.J. Pagano, Exact Solutions for Rectangular Bidirectional Composites and Sandwich Plates, *Journal of Composite Materials*, 4, 20-34, 1970.
- [14] Dassault Systemes Simulia Corporation, *ABAQUS/CAE User's Manual Version 6.11*. Dassault Systemes Simulia Corporation, Providence, RI, 2011.
- [15] Dassault Systemes Simulia Corporation, *ABAQUS Analysis User's Manual Version 6.11*. Dassault Systemes Simulia Corporation, Providence, RI; 2011.
- [16] C. Kassapoglou, *Design and Analysis of Composite Structures*, West Sussex: John Wiley & Sons Ltd, 2010.

Parameter Estimation Method Using Bayesian Statistics Considering Uncertainty of Information for RBDO

Makoto Ito¹, Nozomu Kogiso²

¹ Osaka Prefecture University, Osaka, Japan, st102005@edu.osakafu-u.ac.jp

² Osaka Prefecture University, Osaka, Japan, kogiso@aero.osakafu-u.ac.jp

1. Abstract

Reliability-based design optimization (RBDO) is one of the methods considering the effect of uncertainties on the design optimization. However, the probabilistic parameters of the random variables also have uncertainties due to lack of sufficient information under actual situation, for example in case that the number of experiments is limited. This study considers the uncertainty of the probabilistic parameter of the random variables for the RBDO. On this proposed method, the distribution parameters are also considered random variables. Based on Bayesian statistics, the confidence intervals of the parameters are estimated with high accuracy. Then, the confidence interval of the reliability-based optimum design is also evaluated. That is, the accuracy of the obtained reliability-based optimum design is evaluated through the interval estimation, when sufficient information is not available. Through numerical examples, the validity of the proposed method is demonstrated.

2. Keywords: Parameter estimation, Bayesian statistics, Uncertainty, Reliability, Optimization

3. Introduction

Recently, the importance of the reliability is growing in the structural design requirements. The reliability-based design optimization (RBDO) has been adopted to evaluate the design under the reliability constraints in terms of random variables [1]. RBDO generally requires the probabilistic distribution parameters of random values for the reliability evaluation. For example, the first order reliability method (FORM) converts the probabilistic distribution of random variables into the standardized normal distribution.

However, for the actual design problem, the probabilistic parameters of random parameters are sometimes obtained with insufficient accuracy due to the limited number of experiments. In that case, the distribution parameters such as mean and the standard deviation also have uncertainties.

This study addresses to investigate the effect of the parameter uncertainties on the reliability-based optimization. For the purpose, this study proposes the distribution parameter estimation method considering uncertainties due to the lack of information. Then, the effect of the uncertainties on the RBDO is clarified as the confidence interval of the reliability-based optimum design.

The probabilistic distribution parameter is estimated based on Bayesian statistics. Bayesian statistics is the subset of the field of statistics and related to conditional probability [2]. This statistics is well known to be suited to estimating statistical model and employed for calculating distribution of failure probability. Gunawan *et al.* [2] proposed the method considering incomplete information uncertainties, which RBDO problem is converted to the multiobjective problem whose Pareto solutions reflect to the trade-off between performance and confidences. Wang *et al.* [3] presented the paradigm of the reliability prediction using evolving, insufficient information applying Bayes' theory. They showed that Bayesian statistics is useful tool for the distribution parameter estimation and that Bayesian updating method, the tool of Bayes' theory, makes the probabilistic distribution or the estimated reliability sufficient accuracy. However, under the lack of the number of the sample data or information of the random values, Bayesian updating does not bring the sufficient accuracy.

First in this study, the parameter estimation method is proposed under the cases of the lack of the information. In the next section, the reliability-based design optimization is reviewed. Then, Bayesian statistics is reviewed in Section 5.. The proposed method is described in Section 6.. The validity of the proposed method is illustrated through simple numerical examples in Section 7.. Finally, the conclusions are remarked.

4. Reliability-based design optimization

The RBDO is generally formulated as follows:

$$\begin{aligned} & \text{Minimize : } f(\mathbf{d}) \\ & \text{subject to : } P[g_j(\mathbf{d}, \mathbf{X}) \leq 0] \leq \Phi(-\beta_j) \quad (j = 1, \dots, NC) \end{aligned} \quad (1)$$

where $\mathbf{d} = (d_1, \dots, d_{ND})$ and $\mathbf{X} = (x_1, \dots, x_{NR})$ indicate the design variables and the random variables, respectively. The random variable is assumed to have an independent Gaussian distribution for simplicity. The reliability constraints indicate that the failure probabilities are lower than the upper limit, where $g_j(\mathbf{d}, \mathbf{X})$ is the j -th limit state function and β_j is the target reliability index value corresponding failure mode. ND , NR and NC are the number of the design variables, the random variables, and the reliability constraints, respectively.

As the RBDO algorithm, this study adopts the Modified-SLSV (Single-Loop-Single-Vector) method [4]. The original SLSV method [5] converts the double-loop optimization loop of the RBDO into the single loop approach by approximating the MPP (most probable point). The modified-SLSV method improves the convergence by eliminating zigzagging iteration that will yield divergence of the optimum design searching.

At first, the MPP (most probable point) is described in \mathbf{X} -space as follows:

$$\mathbf{x}_j^* = \boldsymbol{\mu} - \beta_j \boldsymbol{\sigma} \boldsymbol{\alpha}_j^* \quad (j = 1, \dots, NC) \quad (2)$$

$$\boldsymbol{\alpha}_j^* = \frac{\boldsymbol{\sigma}_j \nabla g_j(\boldsymbol{\mu}, \mathbf{x}_j^*)}{|\boldsymbol{\sigma} \nabla g_j(\boldsymbol{\mu}, \mathbf{x}_j^*)|} \quad (j = 1, \dots, NC) \quad (3)$$

where $\boldsymbol{\mu}$ is the mean value of the random vector that is allocated as the design variables and $\boldsymbol{\sigma}$ is a diagonal matrix whose diagonal element consists of the standard deviation of each random variable. $\boldsymbol{\alpha}_j^*$ denotes the normalized gradient vector of the j -th limit state function evaluated at the MPP \mathbf{x}_j^* .

The reliability constraint is replaced into the deterministic constraints using Eq. (2) as follows:

$$g_j(\boldsymbol{\mu}, \boldsymbol{\mu} - \beta_j \boldsymbol{\sigma} \boldsymbol{\alpha}_j^*) \geq 0 \quad (4)$$

where $\boldsymbol{\alpha}_j^*$ should be evaluated after obtaining the MPP \mathbf{x}_j^* .

On the SLSV method, the normalized gradient vector $\boldsymbol{\alpha}_j^*$ is approximated by the vector obtained at the previous iteration as follows:

$$\mathbf{x}^{(k+1)} = \boldsymbol{\mu}^{(k+1)} - \beta_j \boldsymbol{\sigma} \boldsymbol{\alpha}_j^{*(k)} \quad (5)$$

where the superscript (k) indicates the number of iteration. This strategy makes the RBDO computationally efficient.

However, the searching sometimes fails to converge or lead to an inaccurate solution. In the Modified-SLSV method, the sensitivity is replaced to improve the convergence by using the previous values as follows:

$$\boldsymbol{\alpha}^{(k)} = \boldsymbol{\alpha}^{(k-2)} + \boldsymbol{\alpha}^{(k-1)} \quad (k > 2) \quad (6)$$

5. Bayesian statistics

On Bayes' theory, the following conditional probability formulation is used.

$$P(A|B) = \frac{P(B|A)P(A)}{P(B)} \quad (7)$$

where event A is considered as a cause of a result B . $P(A)$ is called a prior probability that the cause A happens, and $P(B|A)$ is called a likelihood that the result B happens under the condition that the cause A happens. On the other hand, $P(A|B)$ is called a posterior probability that indicates the cause A happens under the condition that the result B happens.

In employing for parameter estimation, event A convert to the distribution parameter θ , this is, the random variable X is assumed to have distribution parameter θ . $P(A)$ convert to $\pi(\theta)$ because θ is defined as a distributed continuous function. Then, Eq. (7) is described as follows:

$$\pi(\theta|B) \propto f(B|\theta)\pi(\theta) \quad (8)$$

Eq. (8) indicates that the product of prior distribution $\pi(\theta)$ and likelihood $f(B|\theta)$ is directly proportional to the posterior distribution $\pi(\theta|B)$. However, it is difficult to evaluate the product, because it is usually defined as a multiple integral form. Usually, a natural conjugate prior distribution or Markov chain Monte Carlo (MCMC) methods are used to evaluate the product efficiently. This study adopts the natural conjugate prior distribution.

Then, Bayesian confidence interval is evaluated by the posterior distribution to use for interval estimation, that is, θ fall in this interval with the probability of α . (α is defined as $3\sigma=99.6\%$ in this research.)

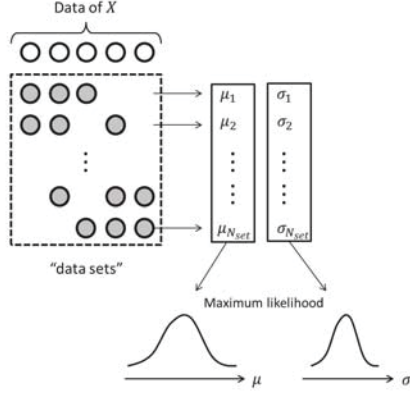


Figure 1: Estimation of prior distribution

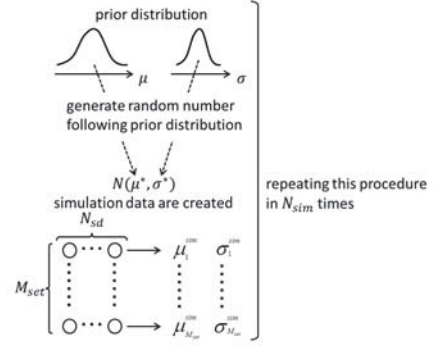


Figure 2: Procedure of creating simulation data

6. Proposed method

6.1 Estimate prior distribution

This study assumes that we have N_D data of the normally distributed random variable X , where the parameters μ_X and σ_X are unknown. In order to estimate the unknown parameter, M_D data of X are chosen among N_D data without repetition at first. This combination is called “data set” and the number of “data set” is denoted as $N_{set}(= N_D C_{M_D})$. Each “data set” has its own estimated mean value and standard deviation, $(\mu_1, \dots, \mu_{N_{set}})$ and $(\sigma_1, \dots, \sigma_{N_{set}})$. From N_{set} mean values and standard deviations, the prior estimation of the parameters are performed by using the maximum likelihood method. This procedure is shown in Fig. 1.

Under the assumption that the mean value and the standard deviation are also normally distributed, their distribution parameters are evaluated as follows:

$$\mu_{\mu}^{pri} = \frac{1}{N_{set}} \sum_{j=1}^{N_{set}} \mu_j, \quad \sigma_{\mu}^{pri2} = \frac{1}{N_{set}} \sum_{j=1}^{N_{set}} (\mu_j - \mu_{\mu})^2 \quad (9)$$

$$\mu_{\sigma}^{pri} = \frac{1}{N_{set}} \sum_{j=1}^{N_{set}} \sigma_j, \quad \sigma_{\sigma}^{pri2} = \frac{1}{N_{set}} \sum_{j=1}^{N_{set}} (\sigma_j - \mu_{\sigma})^2 \quad (10)$$

where $\mu_{(\cdot)}^{pri}$ and $\sigma_{(\cdot)}^{pri2}$ are the estimated mean value and the variance of the distribution parameters.

6.2 Create simulation data

To estimate the distribution parameter of X , simulation data is created from the estimated prior distributions as follows.

1. The distribution parameters μ^* and σ^* are generated from their estimated prior distribution.
2. The N_{sd} simulation data are created by Gaussian distribution $N(\mu^*, \sigma^*)$ and their mean value and standard deviation are evaluated.
3. The procedure of 2. repeats M_{set} times. Then, we have M_{set} number of the mean value and the standard deviation, which sets are called “simulation data set”.
4. The “simulation data sets” are prepared N_{sim} sets.

This procedure is shown in Fig. 2.

6.3 Bayesian updating

Bayesian updating is formulated as follow:

$$\mu_{\mu}^{post} = \frac{A\mu_{\mu}^{pri} + B\bar{\mu}^{sim}}{A + B}, \quad \sigma_{\mu}^{post} = \sqrt{\frac{1}{A + B}} \quad (11)$$

$$\mu_{\sigma}^{post} = \frac{C\mu_{\sigma}^{pri} + D\bar{\sigma}^{sim}}{C + D}, \quad \sigma_{\sigma}^{post} = \sqrt{\frac{1}{C + D}} \quad (12)$$

where

$$A = \frac{1}{(\sigma_{\mu}^{pri})^2}, \quad B = \frac{M_{set}}{(\sigma_{\mu}^{sim})^2}, \quad C = \frac{1}{(\sigma_{\sigma}^{pri})^2}, \quad D = \frac{M_{set}}{(\sigma_{\sigma}^{sim})^2} \quad (13)$$

The posterior distribution parameters are evaluated from M_{set} data set.

It is important to confirm the estimated parameter for initial data of X . In this study, the log likelihood is evaluated for each estimated parameter. When the random value X is assumed to follow Gaussian distribution, its log likelihood is obtained as follows:

$$L = \sum_{j=1}^{M_{set}} \left(-\frac{(x_j^{sim} - \mu^{post})^2}{2(\sigma^{post})^2} - \frac{1}{2} \log(2\pi(\sigma^{post})^2) \right) \quad (14)$$

The estimated parameter with the maximum log likelihood is considered as fit for the initial data and substituted for the prior distribution parameter to iterate this process. If the parameters are considered as converged, the estimation value and the confidence interval of distribution parameters are evaluated by their distribution parameters. Using a constant α , the interval is evaluated as $(\mu - \alpha\sigma, \mu + \alpha\sigma)$ for the normal distribution.

The proposed method is summarized as follows.

Step1 M_D data of X are chosen among N_D data without repetition. (Making N_{set} number of “ data set ”)

Step2 N_{set} mean values and standard deviations, the prior estimation of the parameters are estimated by using the maximum likelihood method.

Step3 Simulation data are created from the estimated prior distributions and N_{sim} “ simulation data set ” are prepared. (see Fig. 2)

Step4 The posterior distribution parameters are evaluated by using Bayesian updating and the estimated parameter with the maximum log likelihood is considered as fit for the initial data.

Step5 The posterior distribution parameter is substituted for the prior distribution parameter.

Step6 If the parameters are considered as converged, the estimation value and the confidence interval of distribution parameters are evaluated by their distribution parameters. Otherwise, go back to step 3 with increase N_{sd} .

7. Numerical example

In this research, the property $N_D, M_D, N_{sim}, M_{set}$ is fixed as 5, 3, 1000 and 5. N_{sd} is arithmetical progression as 5, 10, 15 \cdots each repetition. Due to the importance of the standard deviation in Modified-SLSV method, if the estimated standard deviation is considered as converged, the iteration of parameter estimation is finished.

7.1 Mathematical problem

As the first example, the following two-dimensional mathematical RBDO problem [6] is considered:

$$\begin{aligned} \text{Minimize : } & f(\mathbf{d}) = d_1 + d_2 & (15) \\ \text{subject to : } & P(g_j(\mathbf{x}) \leq 0) \leq \Phi(-\beta_j^T) \quad (j = 1, 2) \\ \text{where : } & g_1(\mathbf{x}) = \frac{x_1^2 x_2}{20} - 1 \leq 0 \\ & g_2(\mathbf{x}) = \frac{(x_1 + x_2 - 5)^2}{30} + \frac{(x_1 - x_2 - 12)^2}{120} - 1 \leq 0 \\ & 0 \leq d_1 \leq 10, 0 \leq d_2 \leq 10 \end{aligned}$$

where the design variables are set as the mean value of the random variable, $\mathbf{d} = \boldsymbol{\mu} = (\mu_1, \mu_2)^T$, and the target reliability is set as $\beta_j = 3$.

The random variables \mathbf{x} follow normal distribution and the standard deviation of x_2 is known as $\sigma_2 = 0.3$. Here, the standard deviation of x_1 is unknown and should be estimated from a limited number of the experimental data shown in Table 1, where the data is made from the normal distributed random number $N(0.0, 0.3)$ because the original problem uses $\sigma_1 = 0.3$ in [6]. The distribution parameters of x_1 are evaluated by the proposed method at first. Table 2 shows the sample values, the estimated value and the confidence interval of the estimated parameters. In this problem, the number of iteration is 6 times.

Table 1: Initial experimental data of x_1 in problem 7.1

x_1	0.1952	-0.02904	-0.3141	0.09188	0.6509
-------	--------	----------	---------	---------	--------

Table 2: Estimated parameter values in problem 7.1

	Sample value	Estimated mean value	Estimated standard deviation	Confidence interval(3σ)
μ	0.1190	0.1189	0.0101	0.0885 to 0.1494
σ	0.3232	0.3063	0.03672	0.2781 to 0.3539

Table 3: Formulation of crashworthiness problem

(a) Design variables, side constraints, and cov in random variables

Name	Variable	Lower bound	Upper bound	σ
Thickness of B-pillar inner (mm)	d_1	0.5	1.5	0.03
Thickness of B-pillar reinforcement (mm)	d_2	0.5	1.5	0.03
Thickness of floor side inner (mm)	d_3	0.5	1.5	0.03
Thickness of cross members (mm)	d_4	0.5	1.5	0.03
Thickness of door beam (mm)	d_5	0.5	1.5	0.03
Thickness of door belt line reinforcement (mm)	d_6	0.5	1.5	unknown
Thickness of roof rail (mm)	d_7	0.5	1.5	0.03
Material yield stress for B-pillar inner (GPa)	d_8	0.192	0.750	unknown
Material yield stress for floor side inner (GPa)	d_9	0.192	0.750	0.006

(b) Objective function and ten constraints

Name	Upper limit	Formulation
Weight (kg)	f	—
Abdomen load (kN)	g_1	1.0
VC upper (m/s)	g_2	0.32
VC middle (m/s)	g_3	0.32
VC lower (m/s)	g_4	0.32
Rib deflection upper (mm)	g_5	32.0
Rib deflection middle (mm)	g_6	32.0
Rib deflection lower (mm)	g_7	32.0
Public symphysis force (kN)	g_8	4.0
B-Pillar velocity (m/s)	g_9	9.9
Door velocity	g_{10}	0.35

(c) Initial experimental data of x_6 and x_8 in problem 7.2

x_6	0.9773	1.038	1.015	0.9737	0.9603
x_8	0.2954	0.3076	0.3031	0.2947	0.2921

Then, the optimum design is obtained using the estimated parameters. The optimum solution consisting the confidence interval of σ_1 is shown in Fig. 3. The “real solution” indicates the optimal solution using $\sigma_1 = 0.3$, that is included in the confidence interval. The distribution and the confidence interval indicate the effect of the uncertainty of σ_1 from estimated from the proposed method on the optimal solution. It is also found that this result has an sufficient estimation accuracy regardless that it is estimated only from five sample data.

7.2 Crashworthiness problem for side impact

As the second numerical example, the following crashworthiness problem for side impact [7] is adopted. The formulation is summarized in Table 3 (a) and (b). In this paper, the mean value of each random variable is treated as design variable $d = \mu$ and the target reliability is set as $\beta_j = 3$. The random variable x have independent normal distributions.

To simulate the lack of information, the standard deviations of x_6 and x_8 are set as unknown. Instead, it is determined from the simulation data from the random numbers following $N(\mu_6, \sigma_6) = N(1.0, 0.03)$ and $N(\mu_8, \sigma_8) = N(0.3, 0.006)$, where the standard deviations are selected from the original problem [7]. The simulation data are listed in Table 3 (c).

The estimated distribution parameters of x_6 and x_8 are listed in Table 4. The confidence interval of the optimal solution obtained with the confidence interval of σ_6 and σ_8 are shown Fig. 4. In this problem, the number of iteration for estimated σ_6 and σ_8 are 4 times and 5 times respectively. It is found that the estimated parameters

Table 4: The estimated distribution parameter of X_6 and X_8

	mean(estimated value)	s. d.	Confidence interval(3σ)
μ_6	0.9929	0.0045	0.9794 to 1.0064
σ_6	0.0290	0.0023	0.021 to 0.0359
μ_8	0.2986	0.0016	0.2938 to 0.3034
σ_8	0.0058	0.0008	0.0034 to 0.0082

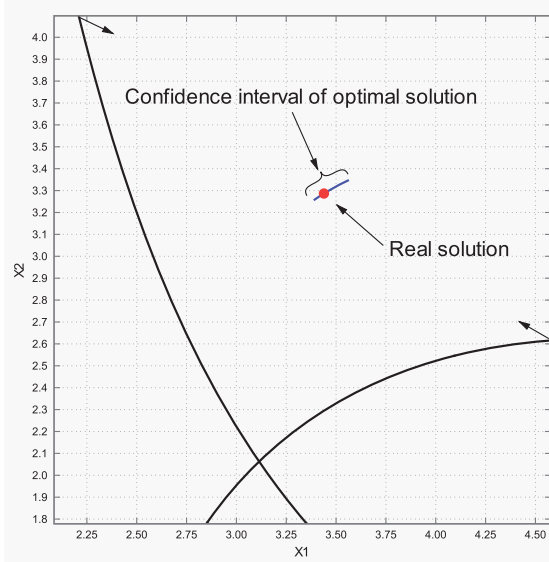


Figure 3: Confidence interval of optimal solution in problem 7.1

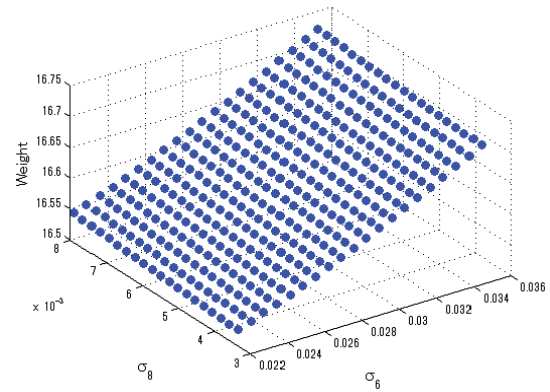


Figure 4: Confidence interval of optimal solution in problem 7.2

have almost linear effect on the optimum design.

8. Conclusion

This paper proposes a parameter estimation method with lack of information and investigates the effect of the information uncertainty on the optimum design of RBDO using the confidence interval.

The prior distribution are estimated using 'data set' which are created by an initial experimental data. To evaluate the lack of information, the simulation data by the prior distribution is used in this study. Then, using Bayesian updating method, the accuracy of estimated value is improved. Through numerical examples, it is demonstrated the validity of proposed method.

In the future, the proposed method will be used on actual design e.g., space structural system under the lack of information to estimate the distribution parameters.

References

- [1] Aoues, Y. , and Chateauneuf, A. , Benchmark Study of Numerical Methods for Reliability-Based Design Optimization, *Structural and Multidisciplinary Optimization*, Vol. 41, (2010), pp. 277-294.
- [2] Gunawan, S. and Papalambros, P. Y. , A Bayesian Approach to Reliability-Based Optimization With Incomplete Information, *Journal of Mechanical Design*, Vol. 128, (2006), pp. 909-918.
- [3] Wang, P. Youn, B. , Xi, Z. and Kloess, A. , Bayesian Reliability Analysis With Evolving, Insufficient, and Subjective Data Sets, *Journal of Mechanical Design*, Vol. 131, (2009), pp. 111008.
- [4] Kogiso, N., Young, Y. S., KIM, B. J., and LEE, J. O., Modified Single-Loop-Single-Vector Method for Efficient Reliability-Based Design Optimization, *Journal of Advanced Mechanical Design, Systems, and Manufacturing*, Vol. 6, No. 7, (2012), pp. 1-16.
- [5] Chen X., Hasselman T. K., Neill, D. J., Reliability Based Structural Design Optimization for Practical Applications, *38th AIAA/ASME/ASCE/AHS/ASC Structures, Structural Dynamics, and Materials Conference* (1997), AIAA-97-1403.
- [6] Youn, B. D., and Choi, K. K., Selecting Probabilistic Approaches for Reliability-Based Design Optimization, *AIAA Journal*, Vol. 24, No. 1 (2004), pp. 124-131.
- [7] Youn, B. D. Choi, K. K. Yang, R.-J. Gu, L. , Reliability-based Design Optimization for Crashworthiness of Vehicle Side Impact, *Structural and Multidisciplinary Optimization*, Vol. 26, (2004), pp. 272-283.

A Sequential Optimization and Mixed Uncertainty Analysis Method Based on Taylor Series Approximation

Xiaoqian Chen, Wen Yao, Yiyong Huang, Yi Zhang

College of Aerospace Science and Engineering, National University of Defense Technology, Changsha, 410073, Hunan Province, P. R. China, chenxiaoqian@nudt.edu.cn

1. Abstract

In this paper reliability-based optimization (RBO) under both aleatory and epistemic uncertainties is studied based on combined probability and evidence theory. Traditionally the mixed uncertainty analysis is directly nested in optimization which is computationally prohibitive. To solve this problem, an effective way is to decompose the RBO problem into separate deterministic optimization and mixed uncertainty analysis sub-problems by sequential optimization and mixed uncertainty analysis (SOMUA) method, which are solved sequentially and alternately till convergence. SOMUA transforms the RBO problem into its quasi-equivalent deterministic formulation based on the inverse Most Probable Point (iMPP) of objective and constraint functions in each focal element. As the iMPP identification calculation is complex, the computational cost grows rapidly with the increase of focal elements. To improve the efficiency of SOMUA, in this paper it is proposed to use Taylor approximation to transform deterministic optimization. The efficacy of the proposed method is demonstrated with two test problems. It shows that the computational cost can be greatly reduced. However, the optimum may be very close to but not as good as that of SOMUA, which needs further research.

2. Keywords: Reliability-based optimization, Aleatory uncertainty, Epistemic uncertainty, Sequential optimization, Taylor series approximation

3. Introduction

Due the existence of uncertainties in engineering, reliability-based optimization (RBO) is widely studied and applied to enhance the system reliability. Generally uncertainties include two categories: the aleatory type arising from the inherent system randomness and the epistemic type due to subjective lack of knowledge [1]. In this paper, combined probability and evidence theory is used to deal with the mixed uncertainties. Based on probability and evidence theory, the RBO problem under mixed uncertainties is formulated as

$$\left\{ \begin{array}{l} \text{find } \boldsymbol{\mu}_x \\ \text{min } \tilde{f} \\ \text{s.t. } \text{Pl}\{f(\mathbf{x}, \mathbf{p}, \mathbf{z}) > \tilde{f}\} \leq P_{f_obj} = 1 - R_{obj} \\ \text{Pl}\{g(\mathbf{x}, \mathbf{p}, \mathbf{z}) < c\} \leq P_{f_con} = 1 - R_{con} \\ \mathbf{x}^L \leq \boldsymbol{\mu}_x \leq \mathbf{x}^U \end{array} \right. \quad (1)$$

where P_{f_obj} and P_{f_con} are the target failure plausibility of the objective and constraint respectively. The design variable vector \mathbf{x} is subject to random uncertainties and its mean value is optimized. The parameter vector \mathbf{p} and \mathbf{z} are random and epistemic uncertainty vectors respectively. From this formulation it is clear that at each search point the failure plausibility of the objective and constraint must be analysed which needs conduct the expensive mixed uncertainty analysis. Thus if the mixed uncertainty analysis is directly nested in the optimization, the computational cost would be unaffordable. To alleviate this problem, Yao proposed a sequential optimization and mixed uncertainty analysis (SOMUA) method to decompose the RBO problem into separate deterministic optimization and mixed uncertainty analysis sub-problems, which are solved sequentially and alternately until convergence is achieved [2]. SOMUA firstly decomposes the total reliability target into each focal element of the epistemic uncertainties. Then in each focal element the uncertain objective and constraint are transformed into the quasi-equivalent deterministic formulations by calculating the inverse Most Probable Point (iMPP) corresponding to the target reliability target in this focal element. The iMPP search is based on optimization, which induces extra calculation and gets worse when the number of focal elements grows big. To solve this problem, it is proposed to use Taylor approximation to transform deterministic optimization. In each cycle, uncertainty analysis is conducted at the deterministic optimum to obtain its MPP in each focal element. Then the epistemic uncertainties are assigned the values of MPP under the assumption that the worst case will happen with these values. Since the epistemic uncertainties are fixed, only random uncertainties are left. Thus the uncertain distributions of the objective and

constraint functions are also random, which can be approximated by Taylor series approximation methods. As this method has the same structure as SOMUA to conduct the optimization and mixed uncertainty analysis sequentially, it is named as Taylor-SOMUA indicating that the deterministic transformation is based on Taylor series. The original SOMUA method in is denoted as iMPP-SOMUA emphasizing the iMPP based deterministic transformation. The rest of the paper is structured as follows. First, the preliminaries of RBO and the SOMUA method are introduced. Then the proposed method Taylor-SOMUA is developed, followed by two test demonstrations. Finally some conclusion remarks are presented.

4. Preliminaries

4.1. Reliability analysis under mixed uncertainties

The probability space of a random uncertain vector $\mathbf{x} = [x_1 \ x_2 \ \dots \ x_{N_x}]$ is described by a triple (X, Υ, \Pr) , where X is the universal set of all possible values of \mathbf{x} , Υ is a σ -algebra over X , and \Pr is a probability measure indicating the probability that the elements of Υ occur. The evidence space of an epistemic uncertain vector $\mathbf{z} = (z_1 \ z_2 \ \dots \ z_{N_z})$ is also described by a triple (C, Υ, m) , where C contains all the possible distinct value set of \mathbf{z} , m is the basic probability assignment (BPA) function which maps C to $[0,1]$ satisfying the following axioms: 1) $\forall A \in C, m(A) \geq 0$; 2) for the empty set \emptyset , $m(\emptyset) = 0$; 3) for all the $A \in C$, $\sum m(A) = 1$. The set A which satisfies $m(A) > 0$ is called a focal element. Υ is the set of all the focal elements [3, 4].

For a system response function $g(\mathbf{x}, \mathbf{z})$, its input includes both the aleatory uncertain vector \mathbf{x} defined by $(\Omega, \mathcal{A}, \Pr)$ and the epistemic uncertain vector \mathbf{z} described by (C, Υ, m) with N_c focal elements. Denote the failure region as $F = \{(\mathbf{x}, \mathbf{z}) \mid g(\mathbf{x}, \mathbf{z}) < a\}$. The precise probability of failure is bounded by its lower limit called belief (Bel) and its up limit called plausibility (Pl) defined as [2, 5, 6]

$$\text{Bel}\{(\mathbf{x}, \mathbf{z}) \in F\} = \sum_{k=1}^{N_c} (m(c_k) \cdot \text{Bel}_k\{(\mathbf{x}, \mathbf{z}) \in F\}); \quad \text{Bel}_k\{(\mathbf{x}, \mathbf{z}) \in F\} = \Pr\{\mathbf{x} \mid \forall \mathbf{z} \in c_k, g(\mathbf{x}, \mathbf{z}) < a\} \quad (2)$$

$$\text{Pl}\{(\mathbf{x}, \mathbf{z}) \in F\} = \sum_{k=1}^{N_c} (m(c_k) \cdot \text{Pl}_k\{(\mathbf{x}, \mathbf{z}) \in F\}); \quad \text{Pl}_k\{(\mathbf{x}, \mathbf{z}) \in F\} = \Pr\{\mathbf{x} \mid \exists \mathbf{z} \in c_k, g(\mathbf{x}, \mathbf{z}) < a\} \quad (3)$$

$\text{Bel}_k\{(\mathbf{x}, \mathbf{z}) \in F\}$ and $\text{Pl}_k\{(\mathbf{x}, \mathbf{z}) \in F\}$ are called the sub-belief and sub-plausibility of the focal element c_k ($1 \leq k \leq N_c$). The methods to calculate $\text{Bel}_k\{(\mathbf{x}, \mathbf{z}) \in F\}$ and $\text{Pl}_k\{(\mathbf{x}, \mathbf{z}) \in F\}$ are referred to [7] and [5].

4.2. The SOMUA method

Denote the cycle number as $i = 1$. Directly ignore all the uncertainties (the uncertain variables are assigned with fixed values) and run the deterministic optimization. Denote the optimum as $\mu_{\mathbf{x}}^{(i)*}$ and its objective response as $\tilde{f}^{(i)*}$. Analyze the plausibility of the objective failure and the constraint failure at the optimum $\mu_{\mathbf{x}}^{(i)*}$ under mixed uncertainties with the mixed uncertainty analysis method SLO-FORM-UUA [5]. For each focal element c_k ($1 \leq k \leq N_c$), the sub-plausibility $\text{Pl}_k^{(i)}(F_{\text{obj}})$ and $\text{Pl}_k^{(i)}(F_{\text{con}})$ can be first calculated with the MPP $[\mathbf{x}_{k_MPP_obj}^{(i)*}, \mathbf{p}_{k_MPP_obj}^{(i)*}, \mathbf{z}_{k_MPP_obj}^{(i)*}]$ and $[\mathbf{x}_{k_MPP_con}^{(i)*}, \mathbf{p}_{k_MPP_con}^{(i)*}, \mathbf{z}_{k_MPP_con}^{(i)*}]$. Then the total failure plausibility $\text{Pl}^{(i)}(F_{\text{obj}})$ and $\text{Pl}^{(i)}(F_{\text{con}})$ can be calculated with (3). Calculate the target sub-plausibility $\text{Pl}_{k_T}^{(i+1)}(F_{\text{obj}})$ and $\text{Pl}_{k_T}^{(i+1)}(F_{\text{con}})$ of the objective failure and the constraint failure for each focal element c_k ($1 \leq k \leq N_c$) by $\text{Pl}_{k_T}^{(i+1)}(F_{\text{obj}}) = \text{Pl}_k^{(i)}(F_{\text{obj}}) - \Delta \text{Pl}_{\text{obj}}^{(i)}$ and $\text{Pl}_{k_T}^{(i+1)}(F_{\text{con}}) = \text{Pl}_k^{(i)}(F_{\text{con}}) - \Delta \text{Pl}_{\text{con}}^{(i)}$ where $\Delta \text{Pl}_{\text{obj}}^{(i)} = \text{Pl}^{(i)}(F_{\text{obj}}) - P_{f_obj}$ and $\Delta \text{Pl}_{\text{con}}^{(i)} = \text{Pl}^{(i)}(F_{\text{con}}) - P_{f_con}$. Identify the corresponding inverse MPP of $\mu_{\mathbf{x}}^{(i)*}$, which are denoted as $[\mathbf{x}_{k_iMPP_obj}^{(i)*}, \mathbf{p}_{k_iMPP_obj}^{(i)*}, \mathbf{z}_{k_iMPP_obj}^{(i)*}]$ and $[\mathbf{x}_{k_iMPP_con}^{(i)*}, \mathbf{p}_{k_iMPP_con}^{(i)*}, \mathbf{z}_{k_iMPP_con}^{(i)*}]$ for the objective and constraint in k th focal element respectively. Then the deterministic optimization problem for the $i + 1$ th cycle can be formulated as

$$\left\{ \begin{array}{l} \text{find } \mu_{\mathbf{x}}^{(i+1)} \\ \text{min } \tilde{f}^{(i+1)} = \max_{1 \leq k \leq N_c} f_k^{(i+1)}(\mu_{\mathbf{x}}^{(i+1)}), \quad f_k^{(i+1)}(\mu_{\mathbf{x}}^{(i+1)}) = f(\mu_{\mathbf{x}}^{(i+1)} - \mathbf{s}_{k_obj}^{(i+1)}, \mathbf{p}_{k_iMPP_obj}^{(i)*}, \mathbf{z}_{k_iMPP_obj}^{(i)*}) \\ \text{s.t. } g_k^{(i+1)}(\mu_{\mathbf{x}}^{(i+1)}) \geq c, \quad 1 \leq k \leq N_c \\ g_k^{(i+1)}(\mu_{\mathbf{x}}^{(i+1)}) = g(\mu_{\mathbf{x}}^{(i+1)} - \mathbf{s}_{k_con}^{(i+1)}, \mathbf{p}_{k_iMPP_con}^{(i)*}, \mathbf{z}_{k_iMPP_con}^{(i)*}) \\ \mathbf{s}_{k_obj}^{(i+1)} = \mu_{\mathbf{x}}^{(i)*} - \mathbf{x}_{k_iMPP_obj}^{(i)*}, \quad \mathbf{s}_{k_con}^{(i+1)} = \mu_{\mathbf{x}}^{(i)*} - \mathbf{x}_{k_iMPP_con}^{(i)*} \\ \mathbf{x}^L \leq \mu_{\mathbf{x}}^{(i+1)} \leq \mathbf{x}^U \end{array} \right. \quad (4)$$

Increase the cycle number $i = i + 1$ and conduct the deterministic optimization of the next cycle. Repeat the preceding steps until convergence is achieved. For more detailed introduction of SOMUA, please refer to [2].

5. Taylor-SOMUA

5.1. The transformation of deterministic objective and constraint

At the optimum of the i th deterministic optimization, conduct the mixed uncertainty analysis and obtain the MPP $[\mathbf{x}_{k_MPP_con}^{(i)*}, \mathbf{p}_{k_MPP_con}^{(i)*}, \mathbf{z}_{k_MPP_con}^{(i)*}]$. Assign the fixed value $\mathbf{z}_{k_MPP_con}^{(i)*}$ to the epistemic uncertainty vector \mathbf{z} under assumption that the failure will occur with bigger probability when the epistemic uncertainty vector is at this value. Then only random uncertain vectors \mathbf{x} and \mathbf{p} are left. Accordingly the constraint function response $g(\mathbf{x}, \mathbf{p}, \mathbf{z}_{k_MPP_con}^{(i)*})$ is also random. Denote $g_{k_rand}(\mathbf{x}, \mathbf{p}) = g(\mathbf{x}, \mathbf{p}, \mathbf{z}_{k_MPP_con}^{(i)*})$. Assume the distribution of g_{k_rand} follows the normal distribution, then its mean and standard deviation can be approximated based on the first order Taylor series expansion as follows:

$$\begin{aligned} \mu(g_{k_rand}) &= g_{k_rand}(\boldsymbol{\mu}_x, \boldsymbol{\mu}_p) \\ \sigma(g_{k_rand}) &= \sqrt{\sum_{i=1}^{n_x} \left(\frac{\partial g_{k_rand}(\mathbf{x}, \mathbf{p})}{\partial x_i} \right)^2 \sigma_{x_i}^2 + \sum_{i=1}^{n_p} \left(\frac{\partial g_{k_rand}(\mathbf{x}, \mathbf{p})}{\partial p_i} \right)^2 \sigma_{p_i}^2} \end{aligned} \quad (5)$$

According to the target failure plausibility $\beta_{k_T_con}^{(i+1)} = \Phi^{-1}(\text{Pl}_{k_T}^{(i+1)}(F_{con}))$, where Φ is standard normal cumulative distribution function and generally $\beta_{k_T_con}^{(i+1)} < 0$ as $\text{Pl}_{k_T}^{(i+1)}(F_{con}) < 0.5$, reliability constraint can be formulated as

$$\mu(g_{k_rand}(\mathbf{x}, \mathbf{p})) + \beta_{k_T_con}^{(i+1)} \cdot \sigma(g_{k_rand}(\mathbf{x}, \mathbf{p})) > c \quad (6)$$

Actually $g_{k_rand}(\mathbf{x}, \mathbf{p})$ may not be normally distributed, thus it should be verified whether the normal distribution assumption is rational and the accuracy of approximation formulation (6) is within acceptable level. Denote $\beta_{k_con}^{(i)} = \Phi^{-1}(\text{Pl}_k^{(i)}(F_{con}))$. Substitute $[\mathbf{x}_{k_MPP_con}^{(i)*}, \mathbf{p}_{k_MPP_con}^{(i)*}]$ into (5) and obtain $\mu_{k_con}^{(i)*}(g_{k_rand})$ and $\sigma_{k_con}^{(i)*}(g_{k_rand})$.

If g_{k_rand} follows normal distribution, then the equation $\mu_{k_con}^{(i)*}(g_{k_rand}) + \beta_{k_con}^{(i)} \sigma_{k_con}^{(i)*}(g_{k_rand}) = c$ should exist.

Thus denote $\varepsilon = \left| \mu_{k_con}^{(i)*}(g_{k_rand}) + \beta_{k_con}^{(i)} \sigma_{k_con}^{(i)*}(g_{k_rand}) - c \right|$. If ε is smaller than the predefined threshold, then the normal distribution assumption is rational. Otherwise it is suggested to revise the standard deviation as

$$\sigma_{k_con}^{(i+1)}(g_{k_rand}) = \left(c - \mu_{k_con}^{(i)*}(g_{k_rand}) \right) / \beta_{k_con}^{(i)} \quad (7)$$

And use this value instead of the one estimated in (5) for constraint transformation in (6). The transformation of the objective function is the same as the aforementioned procedure, and the deterministic objective is formulated as

$$\min \tilde{f} = \max_{1 \leq k \leq N_C} \left[\begin{aligned} & f(\boldsymbol{\mu}_x, \boldsymbol{\mu}_p, \mathbf{z}_{k_MPP_obj}^{(i)*}) \\ & - \Phi^{-1}(\text{Pl}_{k_T}^{(i+1)}(F_{obj})) \cdot \sqrt{\sum_{i=1}^{n_x} \left(\frac{\partial f(\mathbf{x}, \mathbf{p}, \mathbf{z}_{k_MPP_obj}^{(i)*})}{\partial x_i} \right)^2 \sigma_{x_i}^2 + \sum_{i=1}^{n_p} \left(\frac{\partial f(\mathbf{x}, \mathbf{p}, \mathbf{z}_{k_MPP_obj}^{(i)*})}{\partial p_i} \right)^2 \sigma_{p_i}^2} \end{aligned} \right] \quad (8)$$

5.2. The Taylor-SOMUA algorithm

To sum up, the detailed procedure of the Taylor-SOMUA algorithm is as follows:

Step 1: Denote $i = 1$. Directly ignore all the uncertainties and run the deterministic optimization.

Step 2: For the i th cycle solve the deterministic optimization problem. Denote the optimum as $\boldsymbol{\mu}_x^{(i)*}$ and the objective value as $\tilde{f}^{(i)*}$.

Step 3: Conduct uncertainty analysis at $\boldsymbol{\mu}_x^{(i)*}$ with SLO-FORM-UUA method [5]. For each focal element $c_k (1 \leq k \leq N_C)$, calculate the sub-plausibility $\text{Pl}_k^{(i)}(F_{obj})$ and $\text{Pl}_k^{(i)}(F_{con})$ with the MPP $[\mathbf{x}_{k_MPP_obj}^{(i)*}, \mathbf{p}_{k_MPP_obj}^{(i)*}, \mathbf{z}_{k_MPP_obj}^{(i)*}]$ and $[\mathbf{x}_{k_MPP_con}^{(i)*}, \mathbf{p}_{k_MPP_con}^{(i)*}, \mathbf{z}_{k_MPP_con}^{(i)*}]$. Denote the objective failure plausibility as $\text{Pl}^{(i)}(F_{obj})$ and constraint failure plausibility as $\text{Pl}^{(i)}(F_{con})$. If all the failure plausibility satisfies the reliability requirement, go to Step 5. Otherwise go to next step.

Step 4: Fix the value of epistemic uncertainty vector as $\mathbf{z}_{k_MPP_con}^{(i)*}$ or $\mathbf{z}_{k_MPP_obj}^{(i)*}$ and substitute it into the constraint and objective function. Denote $g_{k_rand}(\mathbf{x}, \mathbf{p}) = g(\mathbf{x}, \mathbf{p}, \mathbf{z}_{k_MPP_con}^{(i)*})$ and $f_{k_rand}(\mathbf{x}, \mathbf{p}) = f(\mathbf{x}, \mathbf{p}, \mathbf{z}_{k_MPP_obj}^{(i)*})$. Denote $\beta_{k_con}^{(i)} = \Phi^{-1}(\text{Pl}_k^{(i)}(F_{con}))$ and $\beta_{k_obj}^{(i)} = \Phi^{-1}(\text{Pl}_k^{(i)}(F_{obj}))$. Denote $\varepsilon_{k_con}^{(i)} = \left| \mu_{k_con}^{(i)*}(g_{k_rand}) + \beta_{k_con}^{(i)} \sigma_{k_con}^{(i)*}(g_{k_rand}) - c \right|$

and $\varepsilon_{k_obj}^{(i)} = \left| \mu_{k_obj}^{(i)*}(f_{k_rand}) - \beta_{k_obj}^{(i)} \sigma_{k_obj}^{(i)*}(f_{k_rand}) - \tilde{f}^{(i)*} \right|$. Then the deterministic optimization problem of $i+1$ th cycle is formulated as

$$\left\{ \begin{array}{l} \text{find } \boldsymbol{\mu}_x^{(i+1)} \quad (\mathbf{x}^L \leq \tilde{\boldsymbol{\mu}}_x^{(i+1)} \leq \mathbf{x}^U) \\ \text{min } \tilde{f}^{(i+1)} = \max_{1 \leq k \leq N_C} f_k^{(i+1)}(\boldsymbol{\mu}_x^{(i+1)}) \\ \\ f_k^{(i+1)}(\boldsymbol{\mu}_x^{(i+1)}) = f(\boldsymbol{\mu}_x^{(i+1)}, \boldsymbol{\mu}_p, \mathbf{z}_{k_MPP_obj}^{(i)*}) - \Phi^{-1}(\text{Pl}_{k_T}^{(i+1)}(F_{obj})) \cdot \sigma_{k_obj}^{(i+1)}(f_{k_rand}) \\ \text{if } \varepsilon_{k_obj}^{(i)} > \varepsilon_0, \quad \sigma_{k_obj}^{(i+1)}(f_{k_rand}) = (c - \mu_{k_obj}^{(i)*}(f_J)) / \beta_{k_obj}^{(i)} \\ \\ \text{if } \varepsilon_{k_obj}^{(i)} \leq \varepsilon_0, \quad \sigma_{k_obj}^{(i+1)}(f_{k_rand}) = \sqrt{\sum_{i=1}^{n_x} \left(\frac{\partial f(\mathbf{x}, \mathbf{p}, \mathbf{z}_{k_MPP_obj}^{(i)*})}{\partial X_i} \right)^2 \sigma_{x_i}^2 + \sum_{i=1}^{n_p} \left(\frac{\partial f(\mathbf{x}, \mathbf{p}, \mathbf{z}_{k_MPP_obj}^{(i)*})}{\partial P_i} \right)^2 \sigma_{P_i}^2} \\ \\ \text{s.t. } g_k^{(i+1)}(\boldsymbol{\mu}_x^{(i+1)}) \geq c, \quad 1 \leq k \leq N_C \\ g_k^{(i+1)}(\boldsymbol{\mu}_x^{(i+1)}) = g(\boldsymbol{\mu}_x^{(i+1)}, \boldsymbol{\mu}_p, \mathbf{z}_{k_MPP_con}^{(i)*}) + \Phi^{-1}(\text{Pl}_{k_T}^{(i+1)}(F_{con})) \cdot \sigma_{k_con}^{(i+1)}(g_{k_rand}) \\ \text{if } \varepsilon_{k_con}^{(i)} > \varepsilon_0, \quad \sigma_{k_con}^{(i+1)}(g_{k_rand}) = (c - \mu_{k_con}^{(i)*}(g_{k_rand})) / \beta_{k_con}^{(i)} \\ \\ \text{if } \varepsilon_{k_con}^{(i)} \leq \varepsilon_0, \quad \sigma_{k_con}^{(i+1)}(g_{k_rand}) = \sqrt{\sum_{i=1}^{n_x} \left(\frac{\partial g(\mathbf{x}, \mathbf{p}, \mathbf{z}_{k_MPP_con}^{(i)*})}{\partial X_i} \right)^2 \sigma_{x_i}^2 + \sum_{i=1}^{n_p} \left(\frac{\partial g(\mathbf{x}, \mathbf{p}, \mathbf{z}_{k_MPP_con}^{(i)*})}{\partial P_i} \right)^2 \sigma_{P_i}^2} \end{array} \right. \quad (9)$$

where the symbol k in the subscript represents the focal element index. Denote $i = i+1$ and go to Step 2.
 Step 5: Check convergence. If the relative change between the optimums of two consecutive cycles is smaller than the threshold, end the algorithm. Otherwise go to Step 4.

6. Tests

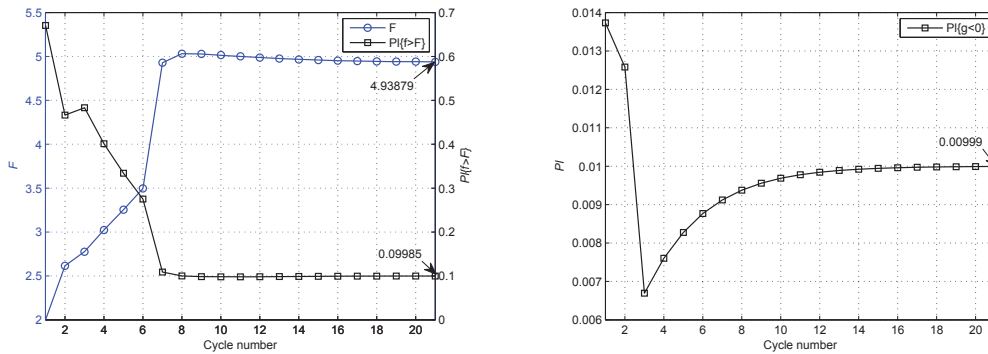
6.1. Test 1: a numerical problem

$$\left\{ \begin{array}{l} \text{find } \mu_x \\ \text{min } \tilde{f} \\ \\ \text{s.t. } \text{Pl}\{f(x, p, z) > \tilde{f}\} \leq 0.1, \quad f(x, p, z) = (x+2.5)^2 + p + z \\ \text{Pl}\{g(x, p, z) < 0\} \leq 0.01, \quad g(x, p, z) = -x + (z-0.7) + p, \quad -3 \leq \mu_x \leq 2 \end{array} \right. \quad (10)$$

The optimization variable x is subject to normal distribution $N(\mu_x, 1.0)$. The uncertain parameter p follows normal distribution $N(2.0, 1.0)$. The BPA of the epistemic uncertainty z is as follows:

$$c_1 = [-1, 0), \quad m(c_1) = 0.5; \quad c_2 = [0, 1], \quad m(c_2) = 0.5 \quad (11)$$

The optimization result of Taylor-SOMUA is compared with that of iMPP-SOMUA and the traditional nested method, which are presented in Table 1. The convergence history is depicted in Figure 1. All of the three methods obtain optimization designs which satisfy reliability requirements. It can be observed that the optimum of Taylor-SOMUA is slightly bigger than that of other two methods, but its computational cost is the smallest, which proves its efficacy in balancing the computation cost and optimization effect.



(a) The convergence history of the objective and its failure plausibility (b) The convergence history of the constraint failure plausibility

Figure 1: The optimization convergence history of Test 1

Table 1: The optimization results of Test 1

	iMPP-SOMUA	Taylor-SOMUA	Traditional nested method
x	-2.60076	-2.70490	-2.60073
$PI(F_{con})$	0.00998	0.00956	0.01001
F	4.93895	5.02799	4.93891
$PI(F_{obj})$	0.09994	0.09856	0.09997
Cycle number	9	9	1
Total number of function calls	8262	7985	169724
Number of function calls used for deterministic transformation	780	268	--

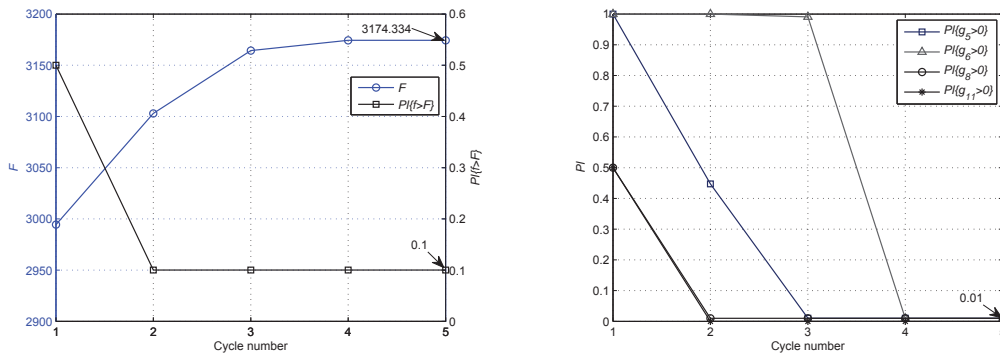
6.2. Test 2: The Golinski's speed reducer design optimization problem

$$\begin{cases}
 \text{find: } \mu_x = [\mu_{x_1} \ \mu_{x_2} \ x_3 \ \mu_{x_4} \ \mu_{x_5} \ \mu_{x_6} \ \mu_{x_7}]^T \\
 \text{min: } \tilde{f} \\
 \text{s.t. } PI\{f > \tilde{f}\} \leq 10\%, \quad PI\{g_i > 0\} \leq 1\%, \quad 1 \leq i \leq 11 \\
 f(\mathbf{x}) = 0.7854x_1x_2^2(3.3333x_3^2 + 14.9334x_3 - 43.0934) \\
 \quad - 1.5079x_1(x_6^2 + x_7^2) + 7.477(x_6^3 + x_7^3) + 0.7854(x_4x_6^2 + x_5x_7^2) \\
 g_1 : 27.0 / (x_1x_2^2x_3) - 1 \leq 0, \quad g_2 : 397.5 / (x_1x_2^2x_3^2) - 1 \leq 0, \quad g_3 : 1.93x_4^3 / (x_2x_3x_6^4) - 1 \leq 0 \\
 g_4 : 1.93x_5^3 / (x_2x_3x_7^4) - 1 \leq 0, \quad g_5 : A_1 / B_1 - 1100 \leq 0, \quad g_6 : A_2 / B_2 - 850 \leq 0 \\
 g_7 : x_2x_3 - 40.0 \leq 0, \quad g_8 : 5.0 \leq x_1 / x_2, \quad g_9 : x_1 / x_2 \leq 12.0 \\
 g_{10} : (1.5x_6 + 1.9) / x_4 - 1 \leq 0, \quad g_{11} : (1.1x_7 + 1.9) / x_5 - 1 \leq 0 \\
 A_1 = \left[\left(\frac{a_1x_4}{x_2x_3} \right)^2 + a_2 \times 10^6 \right]^{0.5}, \quad B_1 = a_3x_6^3, \quad A_2 = \left[\left(\frac{a_1x_5}{x_2x_3} \right)^2 + a_4 \times 10^6 \right]^{0.5}, \quad B_2 = a_3x_7^3 \\
 2.6 \leq \mu_{x_1} \leq 3.6, 0.7 \leq \mu_{x_2} \leq 0.8, 17 \leq x_3 \leq 28, 7.3 \leq \mu_{x_4} \leq 8.3 \\
 7.3 \leq \mu_{x_5} \leq 8.3, 2.9 \leq \mu_{x_6} \leq 3.9, 5.0 \leq \mu_{x_7} \leq 5.5
 \end{cases} \quad (12)$$

The optimization variables except x_3 are random. The mean values are optimized and the standard deviations are [21um, 1um, 30um, 30um, 21um, 30um] for $[x_1 \ x_2 \ x_4 \ x_5 \ x_6 \ x_7]$ respectively. For the four epistemic uncertainties $a_1, a_2, a_3,$ and a_4 , one interval is considered for each uncertainty as follows:

$$a_1 \in [740.0, 750.0], a_2 \in [16.5, 17.5], a_3 \in [0.09, 0.11], a_4 \in [157, 158] \quad (13)$$

The optimization results of Taylor-SOMUA and iMPP-SOMUA are presented in Table 2. The convergence history of Taylor-SOMUA is depicted in Figure 2. The optimum of Taylor-SOMUA is slightly bigger than that of iMPP-SOMUA, but its computational cost is much less than iMPP-SOMUA, which proves its efficiency.



(a) The convergence history of the objective and its failure plausibility (b) The convergence history of the failure plausibility of the hard constraints

Figure 2: The optimization convergence history of Test 2

Table 2: The optimization results of Test 2

	Deterministic optimum	Taylor-SOMUA optimum	iMPP-SOMUA optimum
Design variables	3.5, 0.7, 17, 7.3, 7.7153, 3.3502, 5.2867	3.50502, 0.7, 7.3, 7.94452, 3.49492, 5.48559	3.5050, 0.7, 17, 7.3, 7.9348, 3.4949, 5.4856
Objective	2994.355	3174.334	3174.108
Constraints	$Pl\{f > F\}$	0.5	0.1
	$Pl\{g_5 > 0\}$	1	0.01
	$Pl\{g_6 > 0\}$	1	0.01
	$Pl\{g_8 > 0\}$	0.5	0.01
	$Pl\{g_{11} > 0\}$	0.5	0
Cycle number	--	6	5
Total number of function calls	--	875	3290

7. Acknowledgements

This work was supported in part by National Natural Science Foundation of China under Grant No. 50975280 and 51205403.

8. Conclusions

In this paper, the RBO method under mixed uncertainties is studied based on sequential optimization and mixed uncertainty analysis method. To alleviate the computational problem of the original SOMUA method which needs iMPP to transform the deterministic optimization formulation, it is proposed to use Taylor approximation to transform the deterministic objective and constraint in this paper. The efficacy of the proposed method is demonstrated with two test problems. It shows that the computational cost can be greatly reduced. However, the optimum may be very close to but not as good as that of iMPP-SOMUA, which proves the efficacy of the proposed method in balancing the computational efficiency and optimization effect. However, the applicability of this method in highly nonlinear optimization problems still needs further studies.

9. References

- [1] J.C. Helton, J.D. Johnson, Quantification of margins and uncertainties: alternative representations of epistemic uncertainty, *Reliability Engineering and System Safety*, 96(9), 1034-1052, 2011.
- [2] W. Yao, X.Q. Chen, Y.Y. Huang, Z. Gurdal, M. van Tooren, A sequential optimization and mixed uncertainty analysis method for reliability-based optimization, *AIAA Journal*, 51(9), 2266-2277, 2013.
- [3] G. Shafer. *A mathematical theory of evidence*. Princeton University Press, Princeton, 1976.
- [4] W.L. Oberkampf, J.C. Helton, Investigation of evidence theory for engineering applications, *4th Non-Deterministic Approaches Forum*, Denver, Colorado, 2002(AIAA-2002-1569).
- [5] W. Yao, X.Q. Chen, Y.Y. Huang, M. van Tooren, An enhanced unified uncertainty analysis approach based on first order reliability method with single-level optimization. *Reliability Engineering and System Safety*, 116(August), 28-37, 2013.
- [6] X. Du, Uncertainty analysis with probability and evidence theories. *The 2006 ASME International Design Engineering Technical Conferences & Computers and Information in Engineering Conference*, PA, 2006.
- [7] X. Du, Unified uncertainty analysis by the first order reliability method, *Journal of Mechanical Design*, 130(9): 91401, 2008.

Zooming in Surrogate Optimization Using Convolute RBF

Masao Arakawa¹

¹ Kagawa University, Takamatsu, JAPAN, arakawa@eng.kagawa-u.ac.jp

1. Abstract

There are a lot of efficient methods in surrogate optimization. Convolute RBF is the one of them, and we have examined its effectiveness for years. However, in most case, if the number of design variables raise and/or the searching range extended, they have some problems in approximating functions both in local accuracy and global trends. They have the same reason of sparseness of given data with respect to its searching range, and which happens by the nature of large scale optimization. In this study, zooming technique in approximation is proposed. When we have a certain amount of data, we can divide given datum into some parts and restrict its searching range to some small area. Then in each part, we can achieve more accuracy for local approximation. Moreover, if we can restrict searching range smaller, we have more possibilities to achieve global solution within given searching range. Besides, we can have local optima for each part, which can be candidates for true global solution in the future. In this paper, we examined effectiveness of the method through numerical example.

2. Keywords: Surrogate Optimization, Convolute RBF, Data Distribution

3. Introduction

There are a lot of excellent studies on Surrogate Optimization. Kashiwamura, Shiratori and Yu had published response surface method by experimental design [1], in 1998. Todoroki and Ishikawa used D-Optimality in data distributions [2]. And Myers, Montgomery and Aderson-Cook's book[3] was one of the most contributions in this area. They are all based on quadratic form. Well distribution of initial data for its approximation form. As for Meta-Modeling, Spline[4], Kriking[5], RBF network[6] and SVR[7] have been widely used to have a better approximations rather than quadratic form. Among all these studies, EGO[8] is one of the best contribution that it add strategy for global optimization especially in sampling of new data points.

I have proposed parameter optimization in setting RBF[9], recommendation function for new data points[10], convolution of RBF[11,12], data distribution method, basis distribution method [13] and so on to have better efficiency in the past.

In surrogate optimization, we already have amount of datum. Which means we can scope approximation around some data points; most likely the best solution data. When we can zoom the searching range, we may have the following advantages: 1) as the searching range shrinks, it makes easier to find make better approximation, 2) it makes easier to optimize surrogate function, and so on.

In this paper, we are going to propose the method and examined its effectiveness through numerical example.

4. Convolute RBF

4.1. RBF networks

When we think about approximation of function $y(\mathbf{x})$ by linear summation of basis functions $h_i(\mathbf{x})$, approximate function $f(\mathbf{x})$ can be expressed as follow.

$$f(\mathbf{x}) = \sum_{i=1}^m w_i h_i(\mathbf{x}) \quad (1)$$

In Eq.(1) we assume that we have m basis functions. When we have p teaching data, we can calculate energy of RBF as follow

$$E = \sum_{j=1}^p \left(y(\mathbf{x}_j) - f(\mathbf{x}_j) \right)^2 + \sum_{i=1}^m \lambda_i w_i^2 \quad (2)$$

Learning for RBF means trying to minimize energy in Eq.(2) with respect to weights of w_j . Thus, we can have final solutions as follows.

$$\mathbf{w} = A^{-1} H^T \mathbf{y} \quad (3)$$

Where

$$A = (H^T H + \Lambda)$$

$$H = \begin{bmatrix} h_1(\mathbf{x}_1) & h_2(\mathbf{x}_1) & \cdots & h_m(\mathbf{x}_1) \\ h_1(\mathbf{x}_2) & h_2(\mathbf{x}_2) & \cdots & h_m(\mathbf{x}_2) \\ \vdots & \cdots & \ddots & \vdots \\ h_1(\mathbf{x}_p) & h_2(\mathbf{x}_p) & \cdots & h_m(\mathbf{x}_p) \end{bmatrix}$$

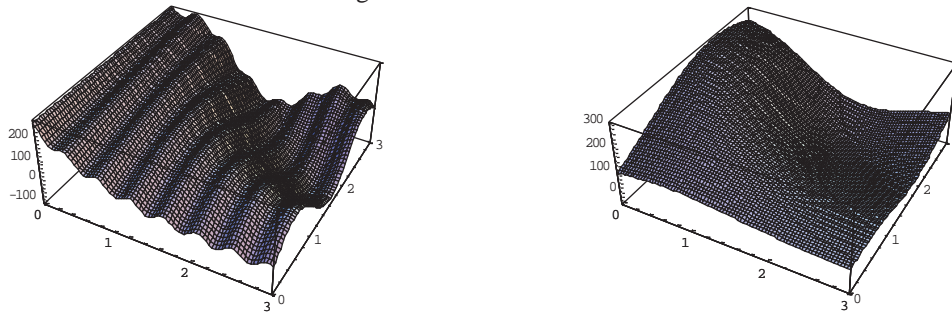
$$\Lambda = \begin{bmatrix} \lambda_1 & 0 & \cdots & 0 \\ 0 & \lambda_2 & & \vdots \\ \vdots & & \ddots & 0 \\ 0 & \cdots & 0 & \lambda_m \end{bmatrix}$$

4.2. Convolute RBF

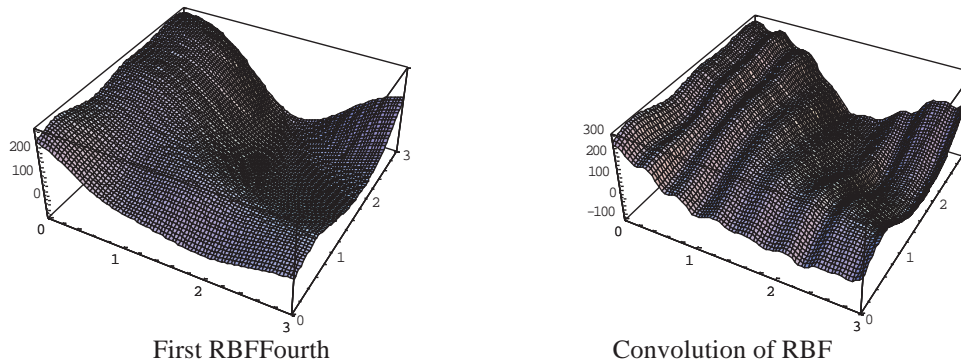
As a nature of RBF, it does not go through teaching data of $y(\mathbf{x}_i)$. However, average of error that is given from $y(\mathbf{x})$ and $y_{app}(\mathbf{x})$ is almost always close to zero. Thus, we can approximate these errors again and again until we satisfy with the error. Thus convolute RBF (Arakawa 2007) can be expressed as follow

$$y_{app}(\mathbf{x}) = b(\mathbf{x}) + \sum_{l=1}^m f_l(\mathbf{x}) \quad (6)$$

Example of convolute RBF can be seen in Fig.1.



Real function: we distribute 200 teaching data randomly Second order of polynomial as basic function



First RBF

Convolution of RBF

Fig. 1 Convolute RBF

4.3. Data Distribution

For better approximation for over all region, we would like to distribute initial data as equal as possible. For that purpose, we use 2-norm as following steps. Assume we would like to have m data.

- 1) Distribute m x M candidate data randomly.
- 2) Choose data #1 which is close to average of all m x M data.
- 3) Choose data #2 that has maximum distance from data #1. (Currently, we have 2 decided data)
- 4) Find candidate that has maximum 2-norm.

2-norm=minimum distance + second minimum distance

But, if minimum distance=0 then, 2-norm=0.

Figure 2 shows illustration of this method. At the beginning, we choose #1 as closest one to average. Then, we choose #2, that has maximum distance from #1. Then, #3 is chosen by calculating maximizing 2-norm between #1 and #2.

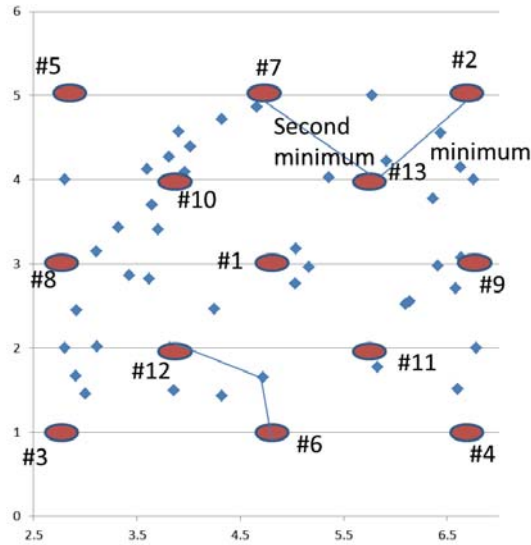


Fig. 2 Illustration of 2-norm distribution

4.4 Selection of Basis Center

For i th convolution, estimate errors at teaching data points for $i-1$ th results. We are going to approximate these errors.

- 1) Find teaching data point that has maximum absolute error. (\mathbf{x}_{max}) Archive sign of error at this point as $sign_{max}$.
- 2) Find closest candidate of basis function to \mathbf{x}_{max} . (\mathbf{c}_{clo})
- 3) Center of basis function is given by following

$$\mathbf{c}_j = \alpha \mathbf{x}_{max} + (1 - \alpha) \mathbf{c}_{clo} \quad (7)$$

Where, α is 0 at the first convolution and 1 at the final convolution.

- 4) Give radius according to the following

$$r_{ij} = ratio_k \times (\max_i - \min_i) / 10 \quad (8)$$

- 5) Count data points within the radius. If there are more than minimum request go to 6), Otherwise enlarge radius by following
- 6) Count the number of data that has same sign with $sign_{max}$. If its ratio is higher than given ratio then learn RBF and estimate errors and go to 1) until it becomes number of basis function for accuracy. Otherwise go to 7)
- 7) Find data that has opposite sign and farther distance from center of basis function \mathbf{c}_j , as \mathbf{x}_{far} . Calculate maximum value of the following

$$t_{max} = \max_i |x_{far,i} - c_{ji}| / (\max_i - \min_i)$$

If t_{max} is given by i_{max} variable, then change radius of i_{max} to

$$r_{i_{max}} = |x_{far,i_{max}} - c_{ji_{max}}|$$

Then go to 6). If we cannot satisfy both condition simultaneously for several times, we will quit there and learn RBF and go to next one.

4.6 Flow of Surrogate Optimization

Figure 3 shows the flow chart of the surrogate Optimization.

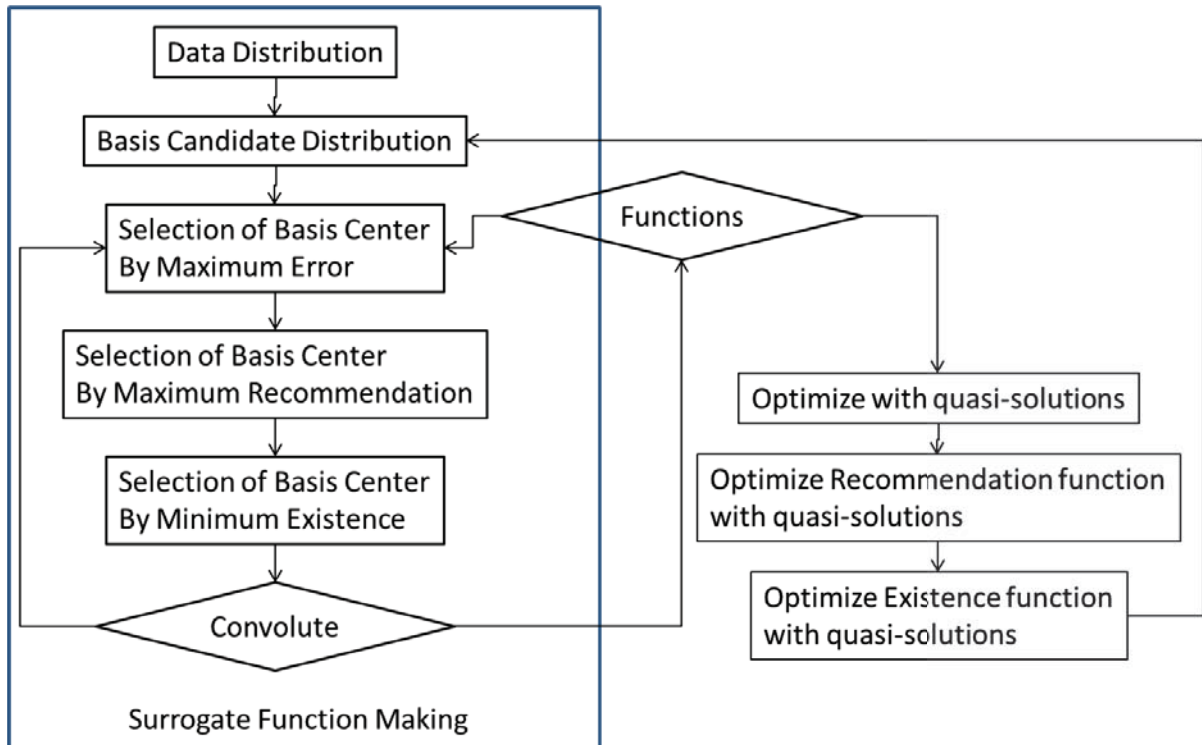


Fig. 3 Flow Chart of Surrogate Optimization

5. Proposed Method

When the number of design variables increase and/or searching range for each design variables expanded, it is sometimes difficult to obtain global optimization within a small number of function calls. Even in those cases, as a nature of surrogate optimization, we can get close to global optimization relatively in a small number of function calls. From there on, we need to repeat a number of iterations to find the solutions. One of the ways to get rid of these situations is to zoom the searching range with existence information. In this study, we propose to shrink the searching range close to the best data when it gets some amount of datum. Figure 4 shows the flow of the proposed method.

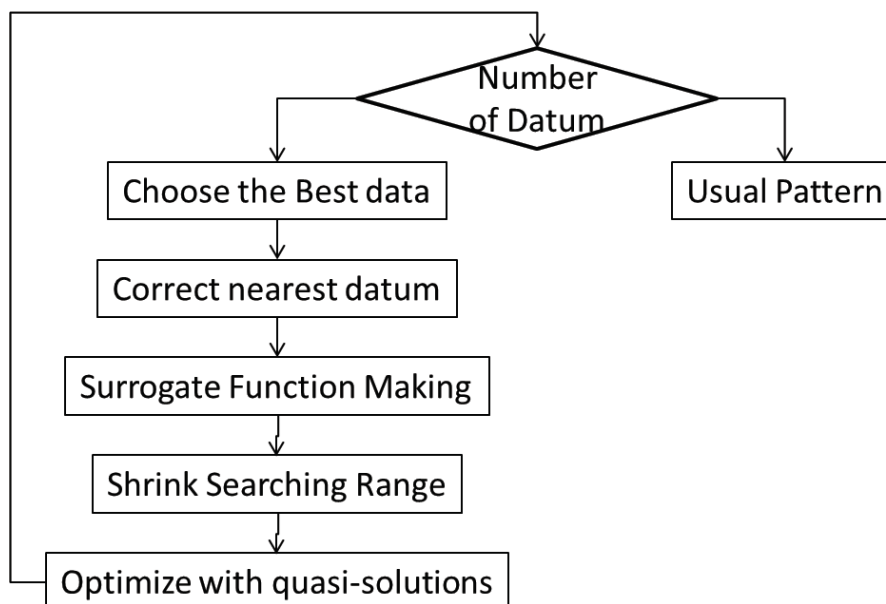


Fig.4 Flow Chart of the proposed method

6. Numerical Example

We use a famous pressure vessel problem as an example. Table 1 shows comparison of the results in some methods.

As this problem is mixed variable problem, so it is very complicated problem. In GRGAs, it needs more than 10,000 function calls to obtain final results, and also it needs more than 6000 function calls to get close to global optima.

Table 1 Comparison of the results of Pressure Vessel Problem

	Sandgren Penalty 1990	Qian GA 1993	Kannan ALM 1994	Lin SA 1992	Hsu GA 1995	Lewis RS+NLP 1996	Arakawa ARGA 1997
R m	1.212	1.481	1.481	N/A	1.316	0.985	0.986
L m	2.990	1.132	1.198	N/A	2.587	5.672	5.626
Ts cm	2.858	2.858	2.858	N/A	2.540	1.905	1.905
Th cm	1.588	1.588	1.588	N/A	1.270	0.953	0.953
g1	0.840	1.000	1.000	N/A	1.000	0.997	1.000
g2	0.747	0.890	0.890	N/A	0.989	0.986	1.000
g3	0.445	0.186	0.182	N/A	0.424	0.938	0.922
g4	1.000	1.000	1.000	N/A	0.831	0.930	1.000
f \$	8129.80	7238.83	7198.20	7197.70	7021.67	5980.95	5850.38

Table 2 was the results that we had in the previous study[12]. Correlation means that we have added 10 new data after “Cut 5900”, and it is the average of correlation of actual value and RBF outputs for all functions. Indeed, if we add only one optimum solution, we need more than 300~500 function calls to cut 5900 and still keep constraints. Thus, we can safely say that recommendation function and multi-adding points really works better. Table 3 shows the results that we have obtained by using the proposed method. In each case, starting from 50 data, and they are the same compared with the results in Table 2.[13]

Table 2 Results of the previous method

Case	1	2	3
C base to G loba l	80	80	80
Inside C onstraints	100	100	110
Cut 5900	120	120	120
Its Cost	5859.34	5870.29	5865.91
C orrelations	0.995	0.994	0.996

We start from the same Initial data with Table 2. However, we add 3 datum for optimization in each case, and add 3 for recommendation function and add 3 for minimization of existence. And we zoomed after we had more than 40 datum at least. Which means, we zoomed after we had more than 80, 120. Table 3 shows the results of the proposed method. In this case, zooming started after we came close to global solutions, so that we could not see the effect of zooming to find global solutions. However, we can still see effectiveness in the number of function calls, and also its accuracy.

Table 3 Results of the proposed method

Case	1	2	3
C base to G loba l	77	77	77
Inside C onstraints	98	98	98
Cut 5900	110	110	122
Its Cost	5854.29	5851.03	5853.92
C orrelations	0.996	0.997	0.996

7. Conclusion

In this paper, we propose zooming of searching range for surrogate optimization. As surrogate optimization has a number of datum before we are going to approximate functions. Thus, we can select the best data, and also we can gather nearest datum around the best data. With these datum, we can zoom searching range. It makes approximation of global optima much easier to approximate precisely, and also it makes optimization much easier to find the global solution. In this paper, we have shown the effectiveness of the method through numerical example.

8. References

- [1] Kashiwamura, T., Shiratori, M., Yu, K., Optimization of Nonlinear Problem by Using Experimental Design, 1998, Asakura Publishing, In Japanese.

- [2] Akira Todoroki, Tetsuya Ishikawa, Design of Experiments for Stacking Sequence Optimizations with Genetic Algorithm using Response Surface Approximation, Composite Structures, 64(3-4),(2004),pp.349-357.
- [3] Myers, R.H., Montgomery, D.C., Anderson-Cook, C.M., Response Surface Methodology: Process and Product Optimization Using Designed Experiments, Wiley, 2011.
- [4] Arai, H., Suzuki, T., Kaseda, C., Ohyama, K. and Takayama, K., "Bootstrap Re-sampling Technique to Evaluate the Optimal Formulation of Theophylline Tablets Predicted by Non-linear Response Surface Method Incorporating Multivariate Spline Interpolation", Chem. Pharm. Bull., 55-4, 2007, p.586-593.
- [5] Simpson, T., Korte, J., Mauery, T. and Mistree, F., Comparison of Response Surface and Kriking Models for Multidisciplinary Optimization, NASA, 1998
- [6] Arakawa, M., Nakayama, H., Ishikawa, H., "Optimum Design Using Radial Basis Function Network and Adaptive Range Genetic Algorithms", Proc Design Engineering Technical Conference'99, (in CD-ROM), ASME, Las Vegas, 1999, 9
- [7] Nakayama, H., Yun, Y., Asada, T., Yoon, Min, "Goal Programming Approaches to Support Vector Machines", Knowledge-Based Intelligent Information and Engineering Systems, Vol. 2773, (2003), 356-363
- [8] Jones, D.R., Schonlau, M., Welch, W.J., Efficient global optimization of expensive black-box functions, Journal of Global Optimization, 13, (1998), 455-492.
- [9] Arakawa, M., Nakayama, H., Yun, Y.B., Ishikawa, H., Optimum Design Using Radial Basis Function Networks by Adaptive Range Genetic Algorithms (Determination of Radius in Radial Basis Function Networks), Proceedings of 2000 IEEE International Conference on Industrial Electronics, Control and Instrumentation; 21st Century Technology and Industrial Opportunities, in CD-ROM, IEEE, Nagoya, 2000.10
- [10] Arakawa, M., Nakayama, H., Ishikawa, H., "Approximate Optimization Using RBF Network and Genetic Range Genetic Algorithms: Proposal of Base Function and Basic Consideration", Trans. JSME, 70-697, 2004, 112-119, (In Japanese)
- [11] Arakawa, M., Andatsu, A., Development of Convolute Approximation of Radial Basis Network for Sequential Approximation Optimization, The 7th International Conference on Optimization: Techniques and Application, Kobe, Japan, 2007.12
- [12] Arakawa, M., Kitayama, S., Scheme for positions of radial basis functions and radius considering supports for accuracy of approximation in convolute RBF, 10th World Congress of Structural and Multidisciplinary Optimization, Orlando, USA, 2013.5
- [13] Arakawa, M., Kitayama, S., "Scheme in Setting Position and Radius of RBF in Convolute RBF for Surrogate Optimization", Proc. Of ENGOPT 2014, Lisbon, 2014.9

Surrogate Models for Data-inspired Reliability Design

Norio Takeda¹, Tatsuya Kameyama²

¹ Hitachi Research Laboratory, Hitachi, Ltd., Hitachinaka, Japan, norio.takeda.uf@hitachi.com

² Central Research Laboratory, Hitachi, Ltd., Kokubunji, Japan, tatsuya.kameyama.sd@hitachi.com

1. Abstract

A design concept is proposed called 'Data-inspired Reliability Design', where measured data are aggressively used to improve the accuracy of structural reliability design, and surrogate models suitable for this design concept are investigated. Since the amount of measured data is limited due to the cost of sensors, the structural responses that are not measured should be predicted using the measured data. To best use the measured data, the hybrid surrogate models generated using both the measured data and simulation results are applied to predict structural responses in this study. For the hybrid models, the discrepancy between the measured data and simulation results is approximated using response surface methodology. The Gauss process model and an artificial neural network were used as the response surface, and the suitability of the response surfaces were checked for use as virtual sensors. To validate the hybrid surrogate models, the structural responses of a welded structure were predicted using both the measured responses and those analyzed using a simulation. As a result, the predicted responses agreed well with the measured ones. It can therefore be concluded that using the hybrid surrogate models is one way to predict structural responses instead of using sensors in the proposed design concept.

2. Keywords: Virtual sensor, Surrogate model, Gauss process model, Neural networks, Data-inspired design

3. Introduction

Today, pieces of infrastructure include many sensors for collecting operational and environmental data. The collected data are then used, for example, to control infrastructure machinery more efficiently, to determine the maintenance interval of parts appropriately, and to design more reliable machinery. As the number of sensors increases, we can gain more benefits from the collected data, because the amount of information obtained from the data increases. On the other hand, the increase in the number of sensors raises the initial cost of machinery. It is therefore better to obtain much information about operational condition and environment with the fewest sensors. To increase the amount of information without increasing the number of sensors, the surrogate model that predicts responses to be measured can be used as a virtual sensor.

Although the surrogate model should be accurate enough to be used as a virtual sensor, an accurate surrogate model is difficult to generate with few sensor outputs. To overcome this difficulty, we can employ the method for generating a surrogate model by using both measured outputs and simulation results. According to this hybrid modelling method, the discrepancy between real output and simulated output is explicitly included in the model of target output [1][2][3], so accordingly the target out is predicted by adding the discrepancy to the simulation result. The discrepancy is usually approximated with the Gauss process (GP) model [4], which is a response surface model, hence the parameters in the GP model, called hyper-parameters, are determined with known discrepancies. Since the GP model is based on a stochastic framework, the hyper-parameters can be determined by using the Markov chain Monte Carlo method (MCMC). The estimation of an unknown response with the GP model is, however, computationally demanding; hence, this high computational cost limits the usage of the GP model. In addition to the GP model, an artificial neural network is therefore applied to the approximation of the discrepancy in this study. Once an artificial neural network has been learned, a target response can be estimated quickly by using the learned neural network.

In the following sections, first, the design concept is introduced where the collected data can be effectively employed, and then a procedure is described for generating the GP model and estimating unmeasured responses with a hybrid modelling method. Furthermore, we propose a procedure for using an artificial neural network to interpolate the discrepancy instead of the GP model. These procedures are applied to predict the strains occurring on a typical welded structure, and the approximation accuracy is investigated for three validation scenarios.

4. Data-inspired Reliability Design

When developing a product, the structural reliability of the product is usually designed in accordance with a design standard for the product. The design standard provides the safety margin for structural reliability, such as the safety margin for fatigue resistance; hence, the structure of the product is designed so that the product is within the safety margin. If operational and environmental conditions, for example, applied loads, are uncertain for the product to be designed, the safety margin for structural reliability is set to a large value. As a result, the developed product will

be inappropriate for a sustainable society because it is too heavy, and heavy products need a large amount of material and energy for manufacturing and operating them. A decrease in the uncertainty of the conditions therefore leads to the development of products that are appropriate for a sustainable society. A better way to decrease the uncertainty is to clarify the uncertain conditions with the data collected during the bench test, test operation, and field operation. By repeating the data collection and improving the design standard for structural reliability, the reliability of products can be improved continuously as shown in Figure 1. We call this design concept "data-inspired reliability design".

The data-inspired reliability design can be applied to the reliability design of the products (such as wind turbines, construction machinery and trains) for which operational and environmental data are monitored. Figure 2 shows an example of the data analytics performed to confirm the safety margin for fatigue resistance of a wind turbine. The fatigue damage of the welded joints in the tower of the wind turbine was estimated with measured strain data, and then the estimated damage was compared with the damage that had been evaluated in accordance with a design standard. Since strain sensors are mounted on the tower at two different heights, the structural reliability of the tower was evaluated there. If the number of sensors is increased, the structural reliability can be evaluated at other positions. The number of sensors, however, increases the cost of products; hence, the number of sensors used for a product has to be limited. To overcome this limitation, virtual sensor technology, namely, surrogate models, can be used for collecting data to supplement real sensors.

5. Surrogate models

5.1. Bias-corrected model

The hybrid surrogate model using both measured data and simulation results is applied to predict unknown responses. There is generally a discrepancy between the output of computer simulation and measured output because simulation models approximate the target physical phenomenon and the measured output includes measurement noise. When formulating the prediction model of a target phenomenon, the measurement noise is usually modelled as a Gaussian noise with zero mean. On the other hand, for the discrepancy caused by model

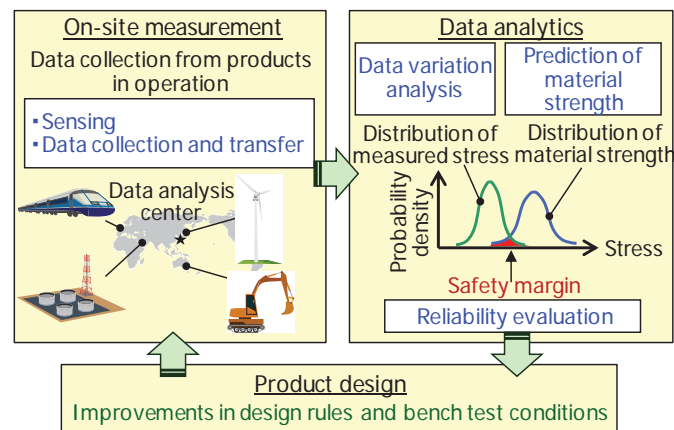


Figure 1: Data-inspired reliability design

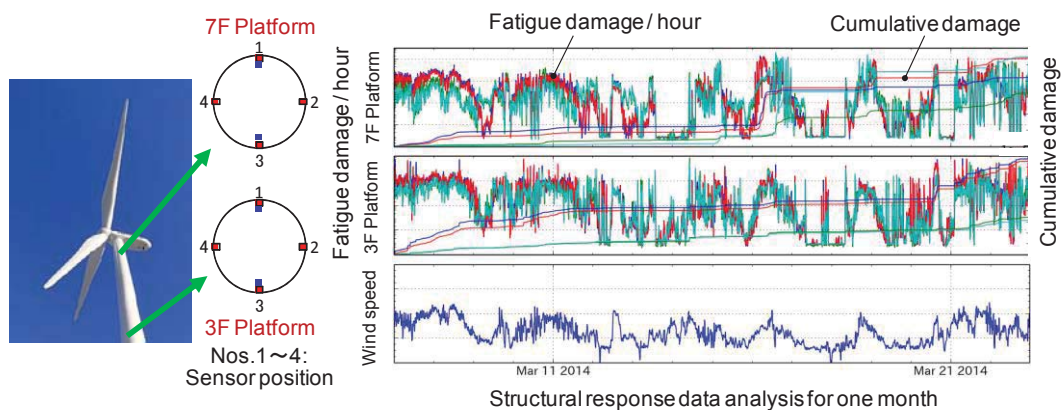


Figure 2: Fatigue damage estimated with the collected data for wind turbine

approximation, methods for modelling the discrepancy as a bias have been proposed in the last decade. In accordance with these methods, the real output of the target phenomenon that does not include measurement noise is formulated as

$$y^R = y^M + \delta \quad (1)$$

where y^R and y^M are the real and simulation outputs, respectively, and δ is the bias between the two outputs. When the outputs are strains that have to be evaluated at some positions and for some applied loads, Eq. (1) could be rewritten as follows.

$$y^R(\mathbf{x}, \mathbf{F}) = y^M(\mathbf{x}, \mathbf{F}) + \delta(\mathbf{x}, \mathbf{F}) \quad (2)$$

where \mathbf{x} and \mathbf{F} are respectively the vectors of positions and applied loads.

5.2. Output prediction using Gauss process model

To estimate the real output $y^R(\mathbf{x}, \mathbf{F})$, two response surfaces for simulated outputs $y^M(\mathbf{x}, \mathbf{F})$ and bias $\delta(\mathbf{x}, \mathbf{F})$ were constructed by using the GP model. The mean and covariance of the applied GP model are

$$m(\mathbf{x}) = \beta \quad (3)$$

$$k(\mathbf{x}, \mathbf{x}') = \sigma^2 \exp\left\{-\sum_{j=1}^q \omega_j (x_j - x'_j)^2\right\} \quad (4)$$

where β , σ , and ω_j are the hyper-parameters. In this study, these parameters were adjusted by using the MCMC method. Bayesian analysis was also applied to predict the expected mean of real output because the uncertainty of the hyper-parameters should be considered for the prediction. The whole prediction process proposed in this study is as follows.

- 1) Generate the GP response surface for interpolating simulated outputs $y^M(\mathbf{x}, \mathbf{F})$
- 2) Generate the GP response surface for interpolating bias $\delta(\mathbf{x}, \mathbf{F})$
- 3) Obtain posterior distributions for the hyper-parameters of the bias response surface by using Bayesian analysis
- 4) Obtain the expected mean of real output from the posterior distributions of the hyper-parameters and the bias

If the computational cost of the simulation is not expensive, we can skip prediction process step 1. The expected mean of real output was calculated with

$$\hat{y}^R(\mathbf{x}, \mathbf{F}) = \frac{1}{N} \sum_{i=1}^N [y^M(\mathbf{x}, \mathbf{F}) + \delta^{(i)}(\mathbf{x}, \mathbf{F})] = \frac{1}{N} \sum_{i=1}^N y^{R(i)}(\mathbf{x}, \mathbf{F}) \quad (5)$$

where $\delta^{(i)}(\mathbf{x})$ is a sample of the bias drawn by using Bayesian analysis in step 4, and N is the number of samples. The same as the expected mean of the real output, the expected mean of the bias can be estimated with

$$\hat{\delta}(\mathbf{x}) = \frac{1}{N} \sum_{i=1}^N \delta^{(i)}(\mathbf{x}) \quad (7)$$

5.3. Output prediction using artificial neural network

Artificial neural networks can be also used to predict the real response in accordance with the model bias correction; that is, the response surfaces of the simulated output and the bias can be generated using artificial neural networks as well as the GP model. However, conventional neural networks sometimes fit only teacher data, hence the generated response surface does not become smooth enough to use it, especially for the interpolation of the bias. The Bayesian framework for learning neural networks [5][6] is therefore applied when generating the response surfaces by the neural networks in this study. On the basis of the Bayesian framework, the objective function to be minimized for the learning of neural networks is formulated as follows.

$$M = \alpha E_w + \beta E_D \quad (8)$$

where E_D is error sum of squares and E_w is a generalization term that expresses the prior information for the weighing coefficients of the neural network to be learned. The prior information introduced here means that the response surface should be smooth; therefore, the weighing coefficients should preferably be small values. α and β in Eq. (8) are hyper-parameters that are determined by maximizing the likelihood of the hyper-parameters.

After the development of a formula, the equations for maximizing the likelihood are

$$\alpha = \frac{\gamma}{2E_w}, \quad \beta = \frac{N-\gamma}{2E_D} \quad (9)$$

where γ is the effective number of the weighing coefficients and means how many coefficients are accurately determined with teacher data. Given that the eigenvalues of matrix $\beta \nabla \nabla E_D$ are λ_a ($a = 1 \sim k$), γ can be calculated by

$$\gamma = \sum_{a=1}^k \frac{\lambda_a}{\lambda_a + \alpha}. \quad (10)$$

By repeating the learning of the neural network and the update of the hyper-parameters sequentially, the smooth response surface of the bias was generated in this study.

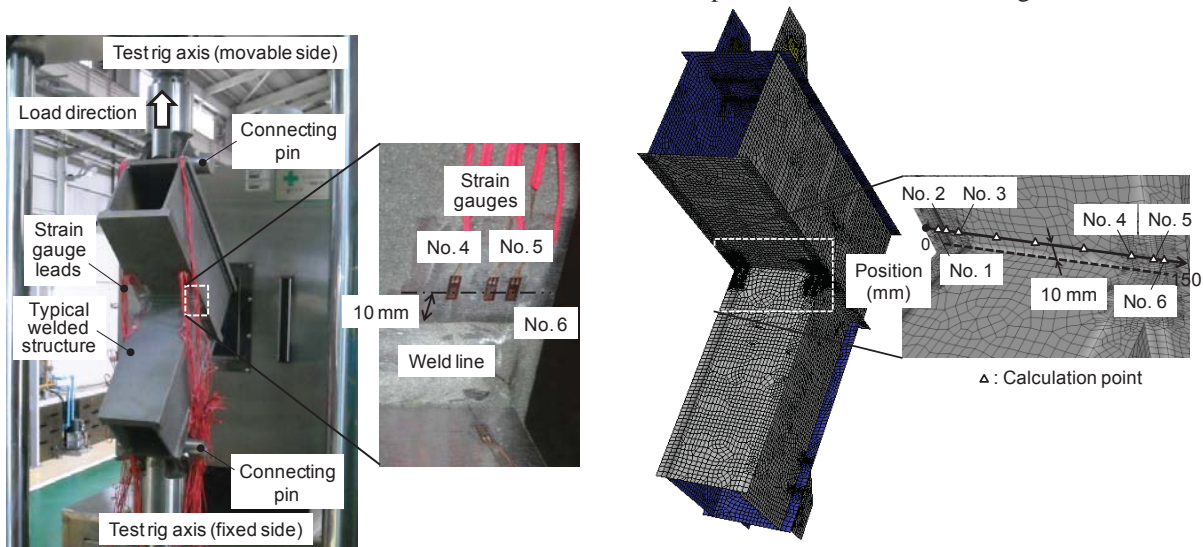
6. Example

6.1. Measurement and simulation of typical welded structure

A welded structure that includes the weld joints typically used in construction machinery was designed and experimentally produced. A load of 100 kN was applied to the produced welded structure, and strains were measured with strain gauges near a weld line as shown in Figure 3(a). This static load test was performed twice, and the strains were accordingly measured twice. Although the strains were measured at a static load of 100 kN, the strains measured at the other applied loads were needed to investigate the prediction accuracy of the bias correction model in Eq. (2). A virtual load history shown in Figure 4 was therefore assumed, and then the measured strain histories caused by the load history were generated by using the linear relationship between the applied load and the strains. In addition, the finite element model of the typical structure was also prepared to calculate strains at the points where the strain gauges were placed. The finite element model shown in Figure 3(b) was composed of shell elements, each of which was rectangular and had four nodes. Numbers 1 to 6 in Figure 3 show the points where strains were measured on the produced structure. The measured and simulated strains were then utilized to predict real strains $y^R(\mathbf{x}, \mathbf{F})$ at the points where strains were not measured by using the procedure described in section 5. The measured and simulated strain values for this prediction are shown in Figure 5. Since the measured strains in Figure 5 were generated using the two test results, two measured values are shown at a position and a load. Notice that there is obviously a model bias caused by incomplete modeling because the simulated strains are larger than the measured ones except for one point. Despite this discrepancy, the finite element model shown in Figure 3(b) was generated in accordance with the International Institute of Welding recommendations.

6.2. Prediction of real strain and bias with GP model

In the case of the GP model, the two strains measured at the same position and load were averaged, and



(a) Experimentally produced structure

(b) Finite element model

Figure 3: Illustrative welded structure

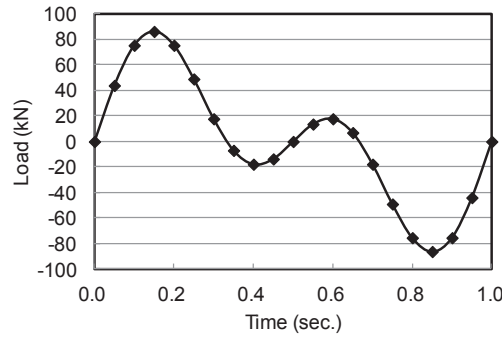


Figure 4: Applied load history

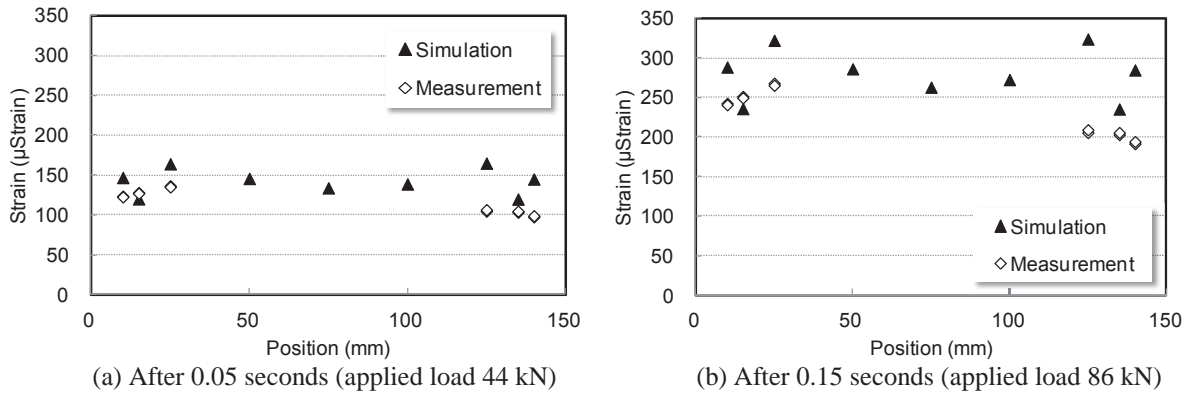


Figure 5: Simulated and measured strains

the averaged value is regarded as a measured strain to predict real strain $y^R(\mathbf{x}, \mathbf{F})$. To validate the prediction accuracy of the bias-corrected model in Eq. (2), not all the measurement points were used to predict the real strains. That is, four out of the six points were selected and used to model the real strain, and then the other two points were used to validate the generated model. Figure 6 shows the expected mean of bias $\delta(\mathbf{x}, \mathbf{F})$ defined in Eq. (7) and the predicted real strain $y^R(\mathbf{x}, \mathbf{F})$ when selecting Nos. 2, 3, 4, and 5 for the modeling. Note that the expected mean of the bias is smooth, hence the predicted real strain represents the feature of the simulated strains, especially for the positions where strains are not measured. By comparing the predicted and measured strains at the points for validation, the predicted strains are respectively 118 % and 119 % of the measured strains for positions Nos. 1 and 6. On the other hand, the simulated strains are respectively 120 % and 148 % of the measured strains for positions Nos. 1 and 6 as shown in Figure 7. It is therefore clear that the bias-corrected model with the GP model works well for predicting the real strains.

6.3. Prediction of real strain and bias with neural network

In the case of the artificial neural network, all the measured values were used to generate the response surface of bias $\delta(\mathbf{x}, \mathbf{F})$. Figure 8 shows the resulting response surfaces of bias $\delta(\mathbf{x}, \mathbf{F})$ and the predicted real strain $y^R(\mathbf{x}, \mathbf{F})$. It can be seen that the response surface of the bias obtained using the neural network is smooth and so is the expected

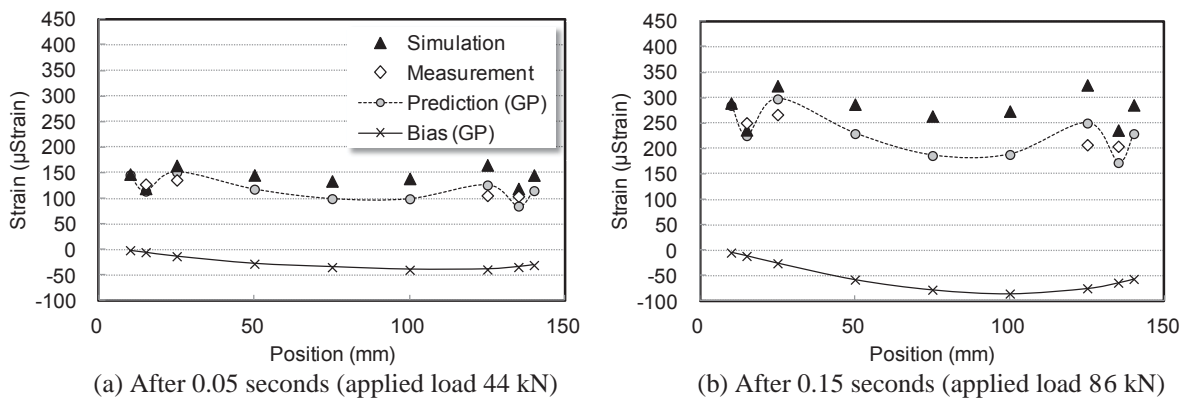


Figure 6: Strain and bias predicted with GP model

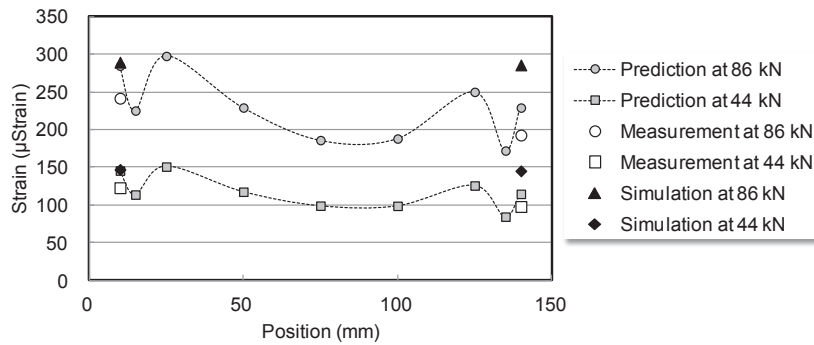


Figure 7: Verification of predicted strains

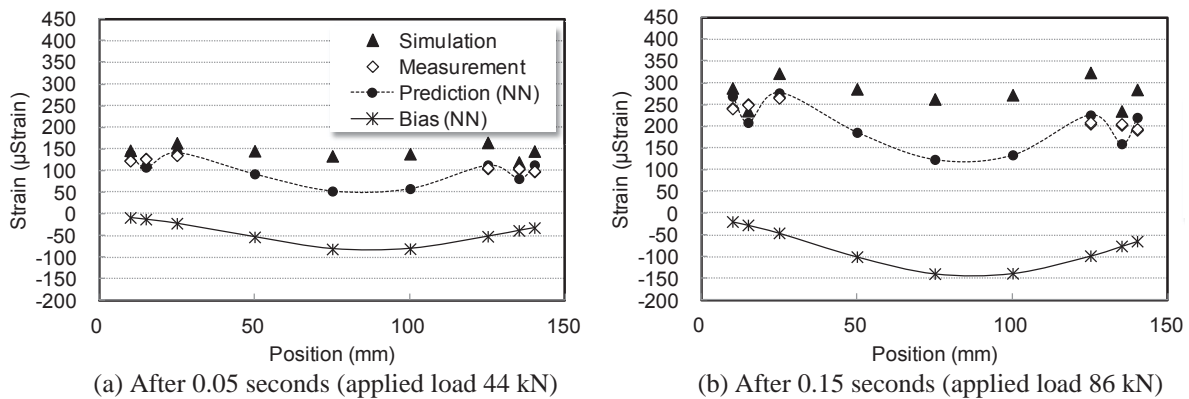


Figure 8: Strain and bias predicted with neural network

mean of the bias obtained using the GP model. While the absolute value of the bias when using the neural network is larger than that when using the GP model at 50mm to 100mm positions, both response surface models generate almost the same bias near the measurement positions.

7. Conclusion

Surrogate models can be used as virtual sensors for monitoring the operation condition of infrastructures. Methods for generating a surrogate model using measured data and simulation results have been applied to several engineering examples in the last decade. This hybrid surrogate model is accurate enough to be used as virtual sensors and therefore was used to predict structural responses, namely strains, in this study. To investigate the accuracy of prediction in unmeasured strains, a typical welded structure was experimentally produced to obtain the measured strains, and the numerical analysis of the welded structure was also conducted to obtain the simulated strains. When predicting the strains, the discrepancy between the measured and simulated strains was approximated with the response surfaces, namely the GP model and the neural network. In the results of this investigation, the predicted strains agreed well with the measured ones. It can therefore be concluded that the hybrid surrogate model can work as virtual sensors.

8. References

- [1] Bayarri, M. J., Berger, J. O., Sacks, J., Cafeo, J. A., Cavendish, C. H., Lin, C. H., and Tu, J., A Framework for Validation of Computer Models, *National Institute of Statistical Science Technical Report*, 162, 2005.
- [2] Xiong, Y., Chen, W., Tsui, K. and Apley, D. W., A Better Understanding of Model Updating Strategies in Validating Engineering Models, *Computer methods in applied mechanics and engineering*, 198, 1327-1337, 2009.
- [3] Kennedy, M. C. and O'Hagan, A., Bayesian Calibration of Computer Models, *Journal of the Royal Statistical Society, Series B* 63(3), 425-464, 2001.
- [4] Rasmussen, C. E. & Williams, C. K. I., *Gaussian Processes for Machine Learning*, The MIT Press, Cambridge, 2006.
- [5] Mackay, D. J. C., A Practical Bayesian Framework for Backpropagation Networks, *Neural Computation*, 4, 448-472, 1992.
- [6] Takeda, N., Response Surfaces of Neural Networks Learned Using Bayesian Framework and Its Application to Optimization Problem, *Journal of Computational Science and Technology*, 3(1), 315-326, 2009.

Optimal Design of a Parallel Beam System with Elastic Supports to Minimize Flexural Response to Harmonic Loading

Bret R. Hauser¹, Bo P. Wang²

¹ University of Texas at Arlington, Arlington, TX, USA, bret.hauser@tx.rr.com

² University of Texas at Arlington, Arlington, TX, USA, bpwang@uta.edu

1. Abstract

Mechanical systems subject to vibration are prevalent across many industries. Although potentially different in application, they sometimes share the need to minimize aspects of flexural deformation given harmonic loading and the need to consider a variety of design variable and response-based constraints in the process. Practical design efforts also sometimes include the need for consideration of the optimal response of a platform-style product, including responses of multiple design variants supported by a common base structure. Harmonic problems can be especially challenging to optimize due to the likelihood that the response will be multi-modal; influenced by system natural frequencies throughout the design space. Further, analysis of these systems often involves large and complex computer models which require significant resources to execute. A harmonically loaded, platform-style parallel beam system with multiple family variants is used as an example in this work to demonstrate a proposed method for identifying an optimum in a constrained, multi-modal response environment with consideration for Expensive Black Box Functions (EBBF).

The presented method leverages benefits of a combined approach where the domain is first surveyed for potential areas of optimal response using a method of Steepest Feasible Descent (SFD), followed by a search in the optimal region using direct search methods. The method of SFD is a modification of the classical method of Steepest Descent, made useful for constrained models by a penalty system including both deterministic and programmatic methods. A sensitivity-based search vector method also helps to manage situations where significant difference in magnitude exists among the design variables. Evidentiary support for these key program elements is provided using standardized test functions. The effectiveness of the method is demonstrated by seeking a minimum flexural response for a parallel beam system subject to elastic support and response constraints.

2. Keywords: harmonic optimization, parallel beam, elastic supports

3. Introduction

Figure 1 illustrates the problem under study; a harmonically loaded parallel beam system with elastic supports and three (3) family variants, subject to harmonic loading through a range of frequencies. The objective of the study is to minimize flexural deformation of the tip mass 'm' subject to location constraints of the elastic supports as well as a maximum allowable static deformation of the tip masses 'm'. A total of ten (10) design variables are considered.

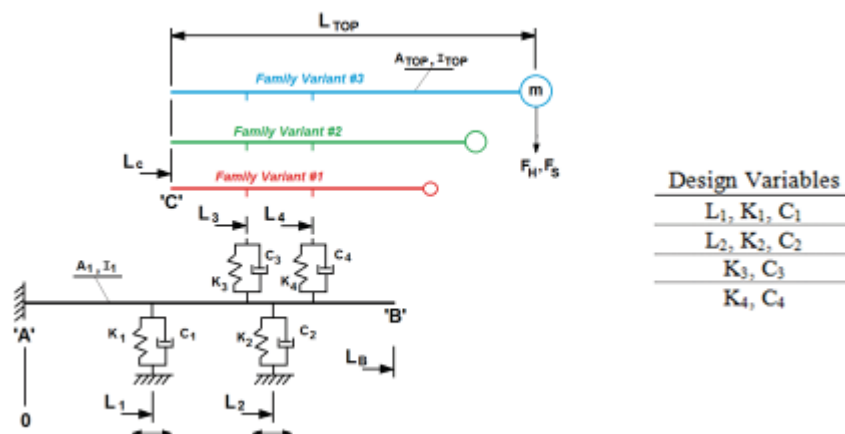


Figure 1: Elastically supported parallel beam structure with 3 family variants

The family variants differ in upper-beam definition only, each constrained with a specified and differing length, tip

mass and cross-sectional geometry. As shown, the location of intermediate supports (L_3 and L_4) are fixed and represent a design constraint often encountered in platform-style products; the need for common interface design. The objective function (flexural response) is multi-objective; being comprised of the summed effect of all family variants (upper beams) upon the integrated response across the prescribed frequency range as well as the maximum range of response across the frequency range.

A common approach in the design of vibrating systems is to stiffen the structure such that the fundamental natural frequency is higher than the operating range. As is demonstrated later with this example, such a philosophy is not always possible given the design constraints and an alternate method is needed. In his text on the subject, Den Hartog [1] discusses the use of a damped dynamic vibration absorber (DDVA) as a means to reduce the magnitude of the response near to the natural frequencies. The DDVA is illustrated in Figure 2 and the Equation of Motion given in Eq.(1) below.

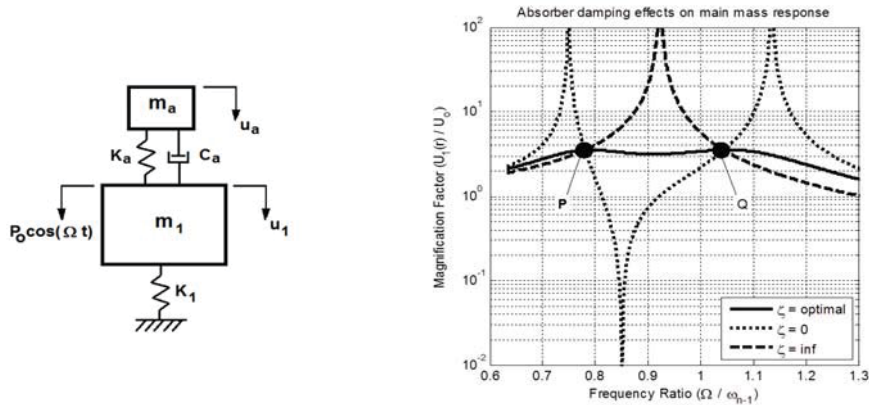


Figure 2: Damped dynamic vibration absorber

$$\begin{bmatrix} m_1 & 0 \\ 0 & m_a \end{bmatrix} \begin{Bmatrix} \ddot{u}_1 \\ \ddot{u}_a \end{Bmatrix} + \begin{bmatrix} c & -c \\ -c & c \end{bmatrix} \begin{Bmatrix} \dot{u}_1 \\ \dot{u}_a \end{Bmatrix} + \begin{bmatrix} k_1 + k_a & -k_a \\ -k_a & k_a \end{bmatrix} \begin{Bmatrix} u_1 \\ u_a \end{Bmatrix} = \begin{Bmatrix} p_0 \\ 0 \end{Bmatrix} \cos(\Omega t) \quad (1)$$

Also illustrated in Figure 2 is the frequency response plot for the DDVA, illustrating the effect of damping coefficient upon the system. As described by Den Hartog [1], an optimal response exists for some finite value of damping coefficient whereby the response is minimized; the slope of which becomes horizontal at frequency points 'P' and 'Q'. It is this type of system behaviour that is sought for the parallel beam system in order to minimize flexural response among the family variants given that some resonant conditions may exist within the frequency range of interest. Since the parallel beam system is complex relative to the DDVA of Figure 2, a numerical optimization approach is needed to identify the optimal values.

Multiple strategies exist for optimization of such a system. Among the simplest are 'First-Order' methods, including the method of Steep Descent (SD) [2]. These gradient-based methods are known to be initially productive, but overall inefficient as the solution nears the optimal result. In addition, they are useful for single objective and unconstrained searches; neither of which applies to the parallel beam problem at hand. Fliege and Svaiter [3] however, propose using the method of SD for multicriteria optimization as well as adaptation of Zoutendijk's [4] method of feasible directions for use in constrained cases. They conclude though that since the result is a first-order method, it should be considered only as a 'first step' toward an overall efficient method rather than an efficient method unto itself. 'Second-Order' methods improve upon first-order methods by incorporating Hessian matrix information and result in a more efficient process [2]. This information however is not readily available for Black Box methods [5]. Since a goal of this effort is to find a method suitable to Expensive Black Box Functions (EBBF's), second-order methods are not considered further.

Direct methods including Genetic Algorithm (GA) [6], Particle Swarm Optimization (PSO) [5] and Sequential Quadratic Programming (SQP) [2] are advantageous in that they are suitable for constrained functions, but are known to potentially require a high number of function evaluations, particularly for multi-modal responses [2], making them undesirable for EBBF's. In addition, although SQP, is known as a more efficient method than first-order methods, it is primarily a 'local' search tool with respect to multimodal response in that it has the potential to be 'constrained' by local maxima.[2] Laskari et al. [5], compare the use of PSO as a means of optimizing minimax problems to SQP. They conclude that for Black Box functions where gradient information is not available (as with EBBF's) that PSO may be a good alternative as an initial search tool with continued optimization performed by more efficient methods such as SQP.

Laskari et al.'s conclusion [5], together with Fliege and Svaiter's similar conclusion regarding SD [3] is the basis for the proposed method here. That is, that the best overall method may be to initially investigate the design space using a first-order method and then, from the region of most promising minimum response, continue the search using SQP. A first order method, when limited to a few jumps and modified for use with constraints, is theorized to be more efficient for the initial search than direct methods. In addition, the use of a polynomial approximation during the steepest descent's 1-D search is theorized to be effective in identifying 'global' minima in a multi-modal environment.

4. Development and validation of proposed optimization method

The proposed optimization method uses a derivative of the first-order method of SD as the initial search method in order to make it effective for constrained searches. The derivative, termed Steepest Feasible Descent (SFD), features a deterministic penalty system as well as programmatic considerations to assure feasibility of the result from the 1-D line search. Also, consideration is given to orientation of the search vector to assure that only feasible space is searched. Finally, weighting is given to the search vector with respect to differences in order of magnitude among the design variables in order to improve effectiveness of the search.

4.1. Steepest Feasible Descent as a constrained search tool

Feasibility is considered during the execution of the 1-D line search in multiple ways. First, the length of the line search is limited by design variable constraint bounds (both side bounds and other). Secondly, as proposed by Vanderplaats [2], an external penalty term is combined with the function value to form a penalized function value to be used in the objective function. This is shown in Eq.(2) below.

$$f(x)_{pen} = f(x) + \alpha_p \sum_{j=1}^n (\max[0, g_j(x)]^2) \quad (2)$$

By Eq.(2), a penalty is assessed to the function value only if constraints are violated (and scaled by the multiplier α_p), which is intended to aid the 1-D line search in identifying only those minima that are in feasible space. However, as illustrated in Figure 3 below, it remains possible that a local minimum of the penalized function value could be infeasible; particularly with a multi-modal response. This is due to the effect of the squared term in Eq.(2) which minimizes the penalty near the constraint bounds.

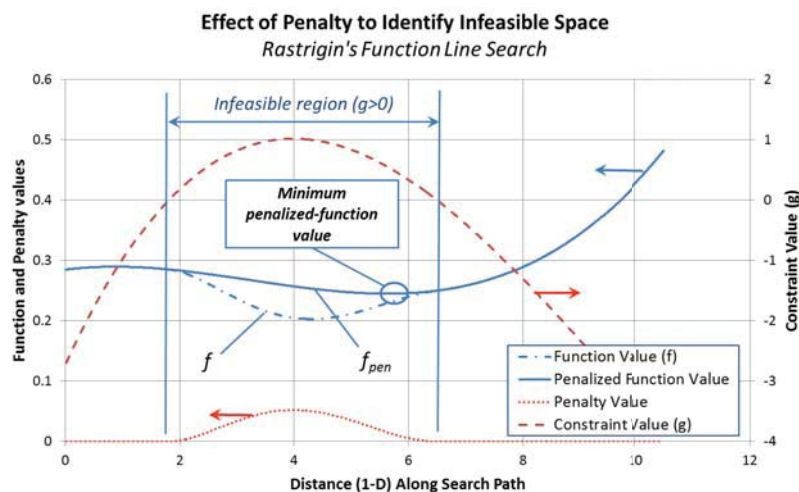


Figure 3: Identification of constraint boundaries

It is recognized that this effect could be limited by converting the penalty term in Eq.(2) to a linear function. However that would potentially cause a more abrupt transition in the resulting penalized function value at the transition from feasible to infeasible space, leading to numeric difficulties in the optimization which could be problematic. Therefore, a programmatic element is incorporated in the event that a minimum (f_{pen}) is identified within infeasible space to search the 1-D vector for a minimum penalized function value that is feasible.

In addition to considerations during the 1-D line search, feasibility is considered in the determination of the descent vector by a programmatic implementation of the Method of Feasible Directions (MFD) [2]. One common implementation of MFD is to incorporate an offset or 'push-off factor' [2] to the search vector in order to avoid a

constraint bound. In the case of a nonlinear constraint bound however, an additional ‘optimization exercise’ is needed within the larger optimization effort [2] to avoid infeasible space. Given consideration to use of this tool for cases where multiple, highly non-linear constraints may exist; a programmatic implementation of the method of feasible directions is selected to avoid a potentially large subproblem. A minimum length for the 1-D search vector is established (as a percentage of the bounded design space). If the distance from starting point of the search vector (X0) to the nearest constraint bound (along the search vector) is measured to be below this limit, then the vector direction is programmatically modified by eliminating the coordinate term which points most directly to the nearby bound. In so doing, the resulting search vector is redirected to a trajectory ‘approximately parallel’ to the subject constraint bound. In this way, the new descent vector is guaranteed to provide at least a minimum search length within feasible space.

4.2. Sensitivity-based search vector

As experienced with the parallel beam problem, design variables may have significantly different orders of magnitude (length vs. spring stiffness vs. damping coefficient). If the gradient for the search vector is determined via a finite difference approach, as may be typical for Black Box functions, then an error in vector sensitivity could occur. That is, if a common step size were used for the finite difference calculation that is appropriate to the smaller variable, then it could be so small as to have an insignificant effect upon a larger variable’s effect. By scaling the finite difference step size (in the direction of each given design variable) to the magnitude of the given variable, then the likelihood is increased that the descent vector will be sensitive to the impact of each variable. Eq.(3) below illustrates one method of determining such a scale effect upon the finite difference step size in a given design variable direction.

$$\Delta_x = \alpha_a \left(\frac{x_{Upper\ Bound} - x_{Lower\ Bound}}{2} \right), \quad \alpha_a = 0.5\% \quad (2)$$

4.3. Confirmation of optimization method

It is proposed that a ‘combined’ search methodology of SFD followed by SQP is an efficient overall search tool by leveraging the strengths of each individual method. To challenge this theory and determine if the combined method is truly better than either of the methods used individually, a test was conducted using four (4) standard test functions [7] where theoretical global optimums are known; De Jong, Rosenbrock, Rastrigin and Schwefel. For each test function, the proposed ‘combined’ search methodology as well as each of the component methods were run from an array of 75 starting points across the 2-dimensional design space, determined using MATLAB’s ‘haltonset’ quasi-random method. For each case, the coordinate location of the global optimum, optimal function value and number of function evaluations was recorded. Results are shown in Table 1 below.

Table 1: Unconstrained test results

	De Jong’s	Rosenbrock’s	Rastrigin’s	Schwefel’s
Coordinate Location of Overall Minimum				
Theoretical	(0,0)	(1,1)	(0,0)	(420.969,420.969)
SFD	(4.2e-4, -4.5e-4)	(1.0067, 1.0135)	(-0.0070, 0.0117)	(421.109, 419.456)
SQP	(7.4e-6, 1.0e-3)	(0.9793, 0.9597)	(4.7e-5, 1.0e-3)	(-296.88, 438.27)
Combined	(3.9e-4, -1.4e-3)	(1.0065, 1.0135)	(6.3e-4, 7.7e-4)	(421.109, 419.458)
Function Value of Overall Minimum				
Theoretical	0	0	0	0
Steep Descent	0	0	4.6e-4	2.0e-4
Direct (SQP)	2.03e-8	1.55e-7	2.7e-6	0.107
Combined	4.3e-8	1.7e-8	2.5e-6	1.9e-4
Number of Function Evaluations				
Steep Descent	1131	1190	2233	1869
Direct (SQP)	1344	4863	2118	450

Combined	1137	1194	2250	1875
----------	------	------	------	------

With consideration for EBBF's, a minimum Design Variable step size was established as a stopping criterion, the order of magnitude of which might be considered meaningful with respect to practical design (0.001% of design variable magnitude). The error of the individual SQP solution for the Schwefel function is attributed to this fact, proof of which is not presented here due to brevity. However, a reduced value resulted in a result of similar accuracy to SFD or the Combined, but at the expense of significantly greater function evaluations.

For the multi-modal responses of Rosenbrock and Schwefel then, the proposed 'combined' search method yielded the most accurate result of either of the two (2) individual methods, while also utilizing approximately the fewest of the function evaluations of the individual methods. No practical benefit is demonstrated for De Jong's unimodal function and the proposed method is slightly less efficient (5.8%) for Rastrigin. Together, these results confirm that the combined method leverages the 'best' qualities of either of the individual methods for some multi-modal responses (with consideration for use with EBBF's), without significant consequence for the other functions.

Constrained response of the proposed method was evaluated similarly using the same test functions [7], with the addition of a circular region of infeasibility centered at the location of theoretical global optimum. Results for De Jong's and Rosenbrock's functions are shown in Figure 4 below. For each test, the location of the (same) 75 start points is identified as are the optimization path and optimum solution for each start point's search. The location of the global optimum is also identified. As shown, the modifications incorporated to the SFD approach, as well as use of the follow-on SQP method successfully prevent solutions from being identified in the infeasible region.

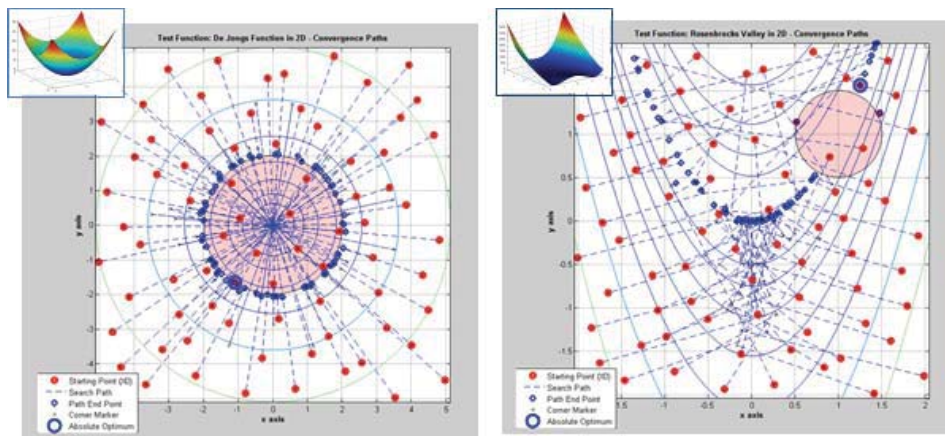


Figure 4: Constrained test results

5. Parallel beam optimization

The parallel beam problem was solved using the proposed 'combined' method with multiple start points. A 'single' objective function was defined for multi-objective use by summing combined responses of tip deflection across frequencies and for each family variant as well as the range across both frequency and model. In addition to side-bound constraints, location constraints were established for each of the supports to address the practical need that a minimum spacing must be allowed for the physical attachment structures. A response-based constraint was also considered for the static deflection of the upper beam in order to assure a minimum stiffness to the structure; to prevent the optimal harmonic design from being so flexible as to be impractical.

As indicated previously, the global SFD search was conducted from multiple start points, resulting in many areas of potential optimum throughout the design space. The best result from the among these multiple SFD results was used as the start point for the subsequent SQP search, resulting in an optimal design with relative positioning of the supports as shown in Figure 1. That is, $L_1 < L_3$ and $L_3 < L_2 < L_4$. For purposes of comparison, frequency response plots for the 'worst' of the global SFD searches as well as the global optimal result are shown in Figure 5. Note that these data include response for each of the family variants.

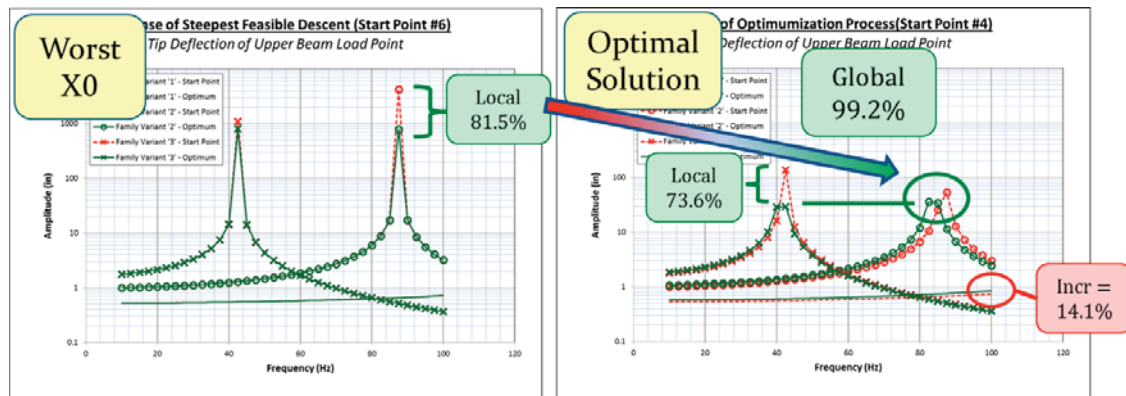


Figure 5: Parallel Beam Results

As shown, the global optimal solution results in an approximate 99.2% reduction in peak amplitude as compared to the ‘worst’ starting point. However, natural frequencies remain within the range of interest for two (2) of the family variants. Although not shown for brevity, these resonant responses are the fundamental frequency of the upper beam(s). Given the design constraints on upper beam specification, these frequencies could not be significantly altered. However, the resonant responses were significantly modified as predicted by Den Hartog’s [1] explanation of the DDVA in Figure 2. The optimal solution is also shown to be a ‘compromise’ in that, although significant reductions were made in the resonant responses, the third (stiffest) family variant worsened slightly in the process. This highlights an important aspect of platform-style design, that ‘compromise’ solutions must be considered and managed in the optimization process.

6. Conclusions

A proposed ‘combined’ optimization method utilizing the method of Steepest Feasible Descent as an initial search tool, followed by a use of the more efficient SQP method for ‘local’ refinement was demonstrated to be effective on both classical test functions and a parallel beam problem. Key conclusions are as follows:

- The combined method is shown to leverage the ‘best’ of the component methods for an improved result on some multi-modal responses, without consequence to other test surfaces used.
- The proposed method of SFD is shown to be effective as a constrained search tool, incorporating both deterministic and programmatic feasibility elements as well as a sensitivity-based search vector.
- The proposed method is shown to be more tolerant of a coarse design variable step size as a stopping criterion than SQP implemented individually. This is an important benefit with respect to use with EBBF’s.
- The platform-style parallel beam structure was successfully optimized for harmonic loading, with significant improvements to peak response amplitudes, even though natural frequencies remained in the frequency range of interest due to design constraints of the system.

8. References

- [1] J.P. Den Hartog, *Mechanical Vibrations*, 4th Edition, Dover Publication, 1985.
- [2] G. Vanderplaats, *Multidiscipline Design Optimization*, 1st Edition, Vanderplaats Research and Development Inc., 2007.
- [3] J. Fliege, B. Svaiter, Steepest descent methods for multicriteria optimization, *Mathematical Methods of Operations Research*, Vol. 51, No. 3, 479-494, 2000.
- [4] G. Zoutendijk, *Methods of feasible directions*, Elsevier, Amsterdam, 1960.
- [5] E. Laskari, K. Parsopoulos, M. Vrahatis, Particle swarm optimization for minimax problems, *Evolutionary Computing CEC2002*, Vol. 2, 1980-1987, 2004.
- [6] B. Wang, J. Chen, Application of genetic algorithm for the support location optimization of beams, *Computers and Structures*, Vol. 58, No. 4, 797-800, 1996.
- [7] M. Molga, C. Smutnicki, *Test Functions for Optimization Needs*, 2005.

Damage process sensitivity analysis using an XFEM-Level Set framework.

L. Noël¹, P. Duysinx², K. Maute³

¹ University of Liege, Liege, Belgium, lise.noel@ulg.ac.be

² University of Liege, Liege, Belgium, p.duysinx@ulg.ac.be

³ University of Colorado, Boulder, USA, kurt.maute@Colorado.EDU

1. Abstract

Designing efficient and lightweight structures is a key objective for many industrial applications such as in aerospace or the automotive industry. To this end, composite materials are appealing as they combine high stiffness and light weight. The main challenge slowing down the integration of such materials in real structures is their damage behavior. The latter should be considered in the design process of the structures. This work focuses on developing a systematic approach to designing structures that can sustain an acceptable amount of degradation or exhibit a low sensitivity to damage. An optimization approach is chosen to achieve this goal. To deal with complex geometries and to allow for large shape modifications in the optimization process, the extended finite element method (XFEM) is advantageously combined with a level set description of geometry. The degradation of materials is modeled by using a non-local damage model, motivated by the work of James and Waisman [1] on a density approach to topology optimization. To solve design problems with damage constraints by gradient-based optimization method, a sensitivity analysis of the damage process is developed. Damage propagation and growth is an irreversible process. Therefore, the path dependence of the structural response needs to be accounted for in the sensitivity analysis. In this paper, we present an analytical approach for efficiently and accurately evaluating the design sensitivities, considering both direct and adjoint formulations. Finally, the sensitivity analysis approach is studied with simple benchmark problems and compared with the results obtained by finite differences.

2. Keywords: damage, sensitivity analysis, XFEM, level set.

3. Introduction

This research work focuses on introducing the effect of degradation in the design process of structures. Taking into account the potential degradation of materials at the design stage allows creating structures that can sustain an acceptable amount of degradation and exhibit a low sensitivity to damage. To achieve this goal, a shape optimization approach is chosen. The work aims at developing systematic tools to evaluate the influence of damage on the optimal design of structures. First, a sensitivity analysis of the non-linear damage process is developed and is the key objective of this study. The analysis of the structures is performed exploiting both a level set description of the geometry, which enables dealing with moving boundaries and complex structures, and the extended finite element method (XFEM), which allows working on fixed non-conforming meshes. The degradation of materials is represented using a non-local damage model, which reduces the material stiffness by a scalar damage value D . To perform the sensitivity analysis, an analytical approach is proposed. As damage is an irreversible process, the history of the structural response has to be accounted for in the sensitivity computation. Finally, the proposed analytical approach is validated and compared against finite differences for a simple benchmark example: a bimaterial bar in tension. Ongoing work is devoted to apply the approach to academic examples.

4. Framework

This research work aims at accounting for the damage behavior of materials in the design process. To this end, damage constraints are introduced in the optimization problem. These constraints include either bounds on the maximum damage value or a global restriction on the percentage of damage tolerated in the structures for a given load level.

To predict the structural response, the XFEM is combined with a level set description of the geometry. The XFEM allows working with non-conforming mesh and avoids costly remeshing operations required in classical shape optimization. The level set description enables an easy handling of moving boundaries and certain topological modifications as geometric entities can merge or disappear. The basics of these methods, necessary for further developments, are outlined in the following sections.

4.1. Level set description of the geometry

The level set method was introduced in 1988 by Osher and Sethian [5] to describe propagating fronts. In a n dimensional space, the method represents the boundaries implicitly resorting to a level set function ϕ of dimension $n + 1$. An iso-level of this function ϕ , generally the iso-zero level, is selected to represent the boundaries and so the distribution of the materials on a given domain. The level set function ϕ can be expressed as a function of the spatial coordinates \mathbf{x} and some design parameters \mathbf{s} as:

$$\begin{cases} \phi(\mathbf{x}, \mathbf{s}) > 0, & \forall \mathbf{x} \in \Omega_A \\ \phi(\mathbf{x}, \mathbf{s}) = 0, & \forall \mathbf{x} \in \Gamma_{AB} \\ \phi(\mathbf{x}, \mathbf{s}) < 0, & \forall \mathbf{x} \in \Omega_B \end{cases}, \quad (1)$$

where Ω_A is the domain filled with material A, Ω_B the domain filled with material B, and Γ_{AB} the interface between materials A and B.

Working on a discrete mesh, the level set function ϕ is typically represented through its nodal values ϕ_i that are interpolated using classical finite element shape functions $N_i(\mathbf{x})$ to capture the singular behavior:

$$\phi^h(\mathbf{x}, \mathbf{s}) = \sum_i N_i(\mathbf{x}) \phi_i. \quad (2)$$

4.2. The extended finite element method

The XFEM offers a convenient way to represent discontinuities and singularities within the elements by adding particular shape functions to the approximation field:

$$u^h = \sum_{i \in I} N_i(\mathbf{x}) u_i + \sum_{i \in I^*} N_i^*(\mathbf{x}) a_i, \quad (3)$$

where I is the set of all the mesh nodes, $N_i(\mathbf{x})$ the classical finite element shape functions, u_i the degrees of freedom related to $N_i(\mathbf{x})$, I^* the set of enriched nodes, $N_i^*(\mathbf{x})$ the enriched shape functions, a_i the additional degrees of freedom related to $N_i^*(\mathbf{x})$.

There exists different types of enrichment functions ψ depending on the type of discontinuity across material interfaces. This work focuses on materials exhibiting different properties. This kind of interface are characterized by a continuous displacement field, but a discontinuous strain field. A commonly used enrichment function for material interface is the ridge function proposed by Moës [3]:

$$\psi(\mathbf{x}) = \sum_i N_i(\mathbf{x}) |\phi_i| - \left| \sum_i N_i(\mathbf{x}) \phi_i \right|. \quad (4)$$

The enriched shape functions are obtained multiplying the enrichment function ψ and the classical finite element shape functions $N_i(\mathbf{x})$:

$$N_i^*(\mathbf{x}) = N_i(\mathbf{x}) \psi(\mathbf{x}). \quad (5)$$

5. Non-linear damage analysis

The degradation of materials is accounted for using a non-local damage model, motivated by the work of James and Waisman [1], who implemented a non-local approach to perform topology optimization. The non-local damage model and the computational scheme for predicting the structural response are summarized in the following subsections.

5.1. Non-local damage model

The damage is represented by a scalar value D . The degradation of the structure is described by the evolution of this scalar value from $D = 0$, corresponding to the undamaged state of the material to $D = 1$, where the material is fully degraded and unable to sustain any higher load. In a finite element model, the damage parameter D is evaluated at each Gauss point. The evolution law governing the growth of material degradation is given as a function of the displacements:

$$\mathbf{D} = g(\mathbf{u}). \quad (6)$$

Typically, damage laws provide the evolution of damage as a function of the stresses or the strains. Degradation is generally initiated at a prescribed stress or strain threshold leading to an abrupt change in the damage values and a non-smooth dependence in stresses or strains. To avoid these problems degrading the convergence, the damage law is smoothed using some regularization function f^S :

$$\mathbf{D}^S = f^S(\mathbf{D}). \quad (7)$$

The damage is considered non-local to avoid the localisation of damage in a thin strip of mesh elements. The damage value at each Gauss point is then influenced by the damage values at neighboring Gauss points, i.e. Gauss point located within a given distance l_c to the considered Gauss point. The value of the damage at a given Gauss point is then computed as:

$$D_i^{NL} = \frac{\sum_{j \in N} W(d_{ij}) D_j^S}{\sum_{i \in N} W(d_{ij})}, \quad (8)$$

where the subscript i accounts for the treated Gauss point, N is the set of Gauss points in the neighborhood of the treated one, W a given weighting function depending on the distance d_{ij} between the treated Gauss point i and its neighbor j .

5.2. Analysis of the damage process

The damage process is non-linear and exhibits a limit point in its force-displacement curve, as shown in Figure 1. The evaluation of the structural response of the system is conducted using a path-following procedure. This form of structural response can not be analyzed by classical solvers as Newton-Raphson, unless working with low damage values. As a first step, a Newton-Raphson solver is used. Later, a displacement control or a Riks-Crisfield solver will be used to follow the force-displacement curve further than the limit point.

The procedure followed by the iterative solver to evaluate the structural response of the system is illustrated in Figure 1. The problem is solved simultaneously for the displacement variables \mathbf{u} and the damage variables \mathbf{D} , collected in the vector \mathbf{y} . The residuals are also collected in a vector \mathbf{R} given as:

$$\mathbf{R}^{(k)} = \begin{bmatrix} \mathbf{R}_u^{(k)} \\ \mathbf{R}_D^{(k)} \end{bmatrix} = \begin{bmatrix} \mathbf{K}^{(k)} \mathbf{u}^{(k)} - \mathbf{f}^{(k)} \\ \mathbf{D}^{(k)} - g(\mathbf{u}^{(*)}) \end{bmatrix}, \quad (9)$$

where $\mathbf{K}^{(k)}$ is the stiffness matrix, $\mathbf{u}^{(k)}$ the displacements variables, $\mathbf{f}^{(k)}$ the external forces, $\mathbf{D}^{(k)}$ the damage variables at iteration k and $\mathbf{u}^{(*)}$ the displacement variables at an iteration \star where the maximum damage was reached so far.

As showed in (9), the residuals can depend on several or all the prior iterations and can be expressed in the most general way as:

$$\mathbf{R}^{(k)} = \mathbf{R}^{(k)}(\mathbf{s}, \mathbf{y}^{(k)}, \mathbf{y}^{(k-1)}, \dots, \mathbf{y}^{(1)}) \quad (10)$$

6. Sensitivity analysis

To solve optimization problems with damage constraints, a sensitivity analysis has to be developed. An important feature of the degradation process is that the damage propagation is irreversible. Therefore, the path dependence of the structural response has to be taken in account in the sensitivity analysis. An analytical approach to the sensitivity analysis, based on the work by Michaleris et al. [2], is proposed and explained in the following sections.

6.1. Derivative of an objective/constraint function

Let us consider an objective or constraint function \mathcal{F} given as follow:

$$\mathcal{F} = \mathcal{F}(\mathbf{s}, \mathbf{y}^{(k)}) \quad (11)$$

where \mathbf{s} are the design parameters and $\mathbf{y}^{(k)}$ are the discrete state variables at iteration k , i.e. the displacements \mathbf{u} and the damage \mathbf{D} .

The derivative of this function with respect to a particular design parameter s_i can be expressed as:

$$\frac{d\mathcal{F}}{ds_i} = \frac{\partial \mathcal{F}}{\partial s_i} + \frac{\partial \mathcal{F}}{\partial \mathbf{y}^{(k)}} \frac{d\mathbf{y}^{(k)}}{ds_i} \quad (12)$$

where $\frac{d}{ds_i}$ and $\frac{\partial}{\partial s_i}$ are the total and the partial derivative with respect to the design parameter s_i .

To evaluate this expression, the total derivative of the state variables $\mathbf{y}^{(k)}$ with respect to the design variable s_i is computed through the derivatives of the residuals $\mathbf{R}^{(k)}$. Taking the derivative of (10) with respect to a particular design parameter s_i , one gets:

$$\frac{d\mathbf{R}^{(k)}}{ds_i} = \frac{\partial \mathbf{R}^{(k)}}{\partial s_i} + \frac{\partial \mathbf{R}^{(k)}}{\partial \mathbf{y}^{(k)}} \frac{d\mathbf{y}^{(k)}}{ds_i} + \frac{\partial \mathbf{R}^{(k)}}{\partial \mathbf{y}^{(k-1)}} \frac{d\mathbf{y}^{(k-1)}}{ds_i} + \dots + \frac{\partial \mathbf{R}^{(k)}}{\partial \mathbf{y}^{(1)}} \frac{d\mathbf{y}^{(1)}}{ds_i} \quad (13)$$

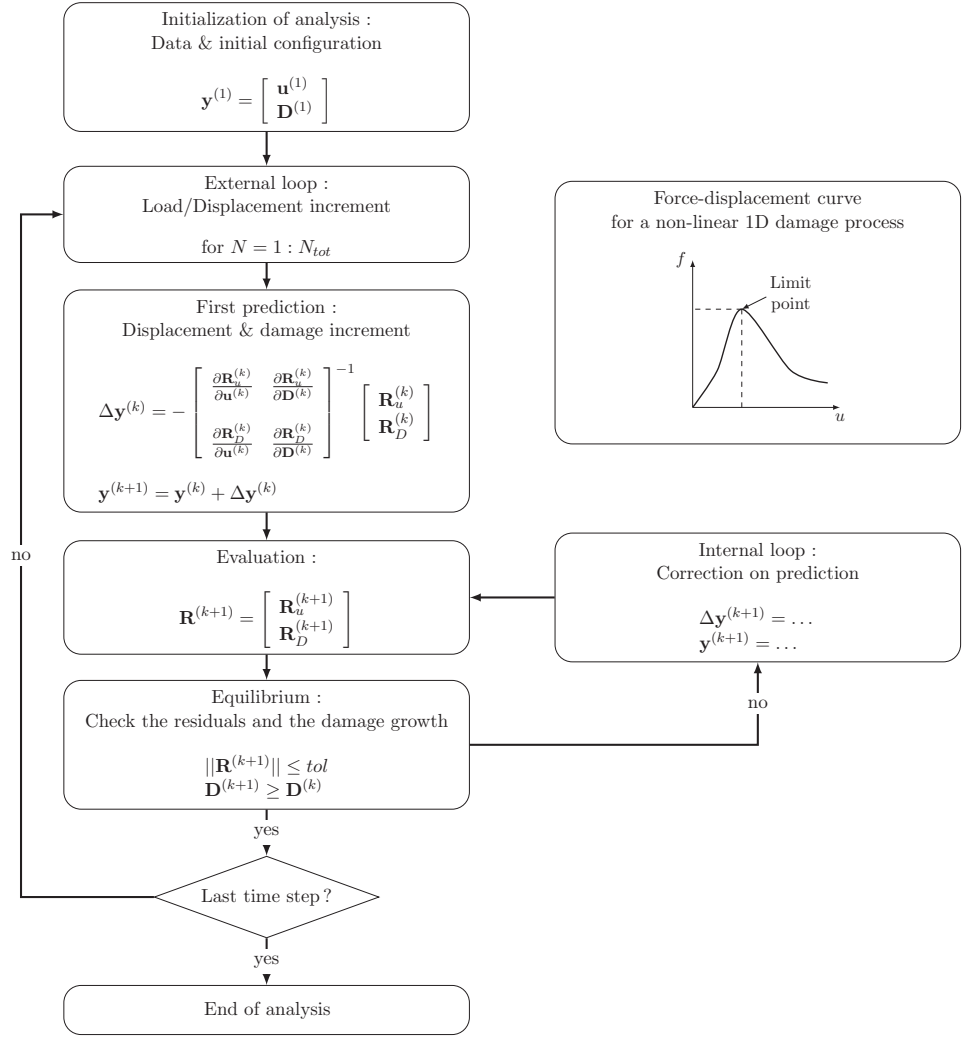


Figure 1: Procedure of the non-linear damage analysis.

Starting from (13) evaluated at the first iteration and proceeding to the last iteration, the derivatives of the problem variables \mathbf{y} can be successively evaluated at each iteration provided that the derivatives of the residuals $\frac{\partial \mathbf{R}^{(k)}}{\partial s_i}$ and $\frac{\partial \mathbf{R}^{(k)}}{\partial \mathbf{y}^{(l)}}$, $l = 1, \dots, k$ are known.

The derivative of the residuals $\mathbf{R}^{(k)}$ at iteration k with respect to a particular design parameter s_i can be expressed as:

$$\frac{\partial \mathbf{R}^{(k)}}{\partial s_i} = \begin{bmatrix} \frac{\partial \mathbf{R}_u^{(k)}}{\partial s_i} \\ \frac{\partial \mathbf{R}_D^{(k)}}{\partial s_i} \end{bmatrix}, \text{ where} \quad \frac{\partial \mathbf{R}_u^{(k)}}{\partial s_i} = \frac{\partial \mathbf{K}^{(k)}}{\partial s_i} \mathbf{u}^{(k)} - \frac{\partial \mathbf{f}^{(k)}}{\partial s_i}, \quad (14)$$

$$\frac{\partial \mathbf{R}_D^{(k)}}{\partial s_i} = -\frac{\partial g(\mathbf{u}^{(k)})}{\partial s_i}.$$

The derivative of the residuals $\mathbf{R}^{(k)}$ at iteration k with respect to the state variable $\mathbf{y}^{(l)}$ at any iteration $l = 1, \dots, k$ can be expressed as:

$$\frac{\partial \mathbf{R}^{(k)}}{\partial \mathbf{y}^{(l)}} = \begin{bmatrix} \frac{\partial \mathbf{R}_u^{(k)}}{\partial \mathbf{u}^{(l)}} & \frac{\partial \mathbf{R}_u^{(k)}}{\partial \mathbf{D}^{(l)}} \\ \frac{\partial \mathbf{R}_D^{(k)}}{\partial \mathbf{u}^{(l)}} & \frac{\partial \mathbf{R}_D^{(k)}}{\partial \mathbf{D}^{(l)}} \end{bmatrix}, \text{ where} \quad \frac{\partial \mathbf{R}_u^{(k)}}{\partial \mathbf{u}^{(l)}} = \begin{cases} \mathbf{K}^{(k)} & \text{if } k = l \\ 0 & \text{if } k \neq l \end{cases}, \quad \frac{\partial \mathbf{R}_u^{(k)}}{\partial \mathbf{D}^{(l)}} = \frac{\partial \mathbf{K}^{(k)}}{\partial \mathbf{D}^{(l)}} \mathbf{u}^{(k)}, \quad (15)$$

$$\frac{\partial \mathbf{R}_D^{(k)}}{\partial \mathbf{u}^{(l)}} = -\frac{\partial g(\mathbf{u}^{(k)})}{\partial \mathbf{u}^{(l)}}, \quad \frac{\partial \mathbf{R}_D^{(k)}}{\partial \mathbf{D}^{(l)}} = \begin{cases} 1 & \text{if } k = l \\ 0 & \text{if } k \neq l \end{cases}.$$

All the derivatives are evaluated analytically starting from the discretized governing equations and taking their derivatives with respect to the design parameters s . The procedure to compute the analytical derivatives, within an XFEM-level set framework for shape optimization of bimaterial structures, is detailed in [4].

7. Application

The sensitivity analysis method described above is illustrated and validated with a simple benchmark example: a bimaterial bar in tension. The bar is loaded with a force F that increases monotonously at each iteration of the path-following procedure. The setting of the problem is illustrated in Figure 2, where a single mesh element is used to model the bar. The location of the interface, given by s , is used as design variable. All the parameters of the problem are summarized in Table 1. The damage law used to evaluate the propagation of the degradation is given as:

$$D_{gp} = 1 - \exp\left(1 - \frac{\varepsilon_{gp}}{\varepsilon_{th}}\right), \quad (16)$$

where ε_{gp} is the strain at the considered Gauss point and ε_{th} the strain threshold from which the material degradation is initiated. The damage law is then smoothed using a Kreisselmeier-Steinhauser function:

$$D_{gp}^S = \frac{1}{\eta_S} \ln(1 + \exp(\eta_S D_{gp})), \quad (17)$$

where η_S is a smoothing parameter.

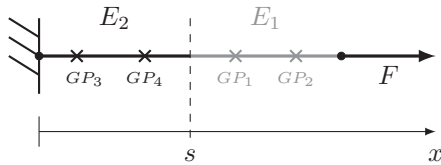


Figure 2: First benchmark - bar in tension.

Table 1: Bimaterial bar in tension - parameters

Dimensions	[m]	$L = 2$
Elastic moduli	[N/m ²]	$E_1 = 1, E_2 = 5$
Load	[N]	$F = 10^{-4}$
Level set function		$\phi(x, s) = x - s$
Gauss points per subelement		$n_{gp} = 2$
Strain threshold		$\varepsilon_{th} = 10^{-4}$
Smoothing parameter		$\eta_S = 7$

The structural response of the bar is computed by a Newton-Raphson solver, as damage is kept small. The design sensitivities are computed by the analytical approach (A) and validated against finite differences (FD).

Figure 3 depicts the evolution of the displacements and its derivatives. Figure 3(a) shows the displacements at the interface and at the bar tip. Figures 3(b) gives the evolution of the free degrees of freedom of the structure u_2 and a_2 . Figure 3(c) shows the evolution of the derivatives of these degrees of freedom with respect to the design parameter s . As can be seen, both sensitivity analysis approaches are in good agreement.

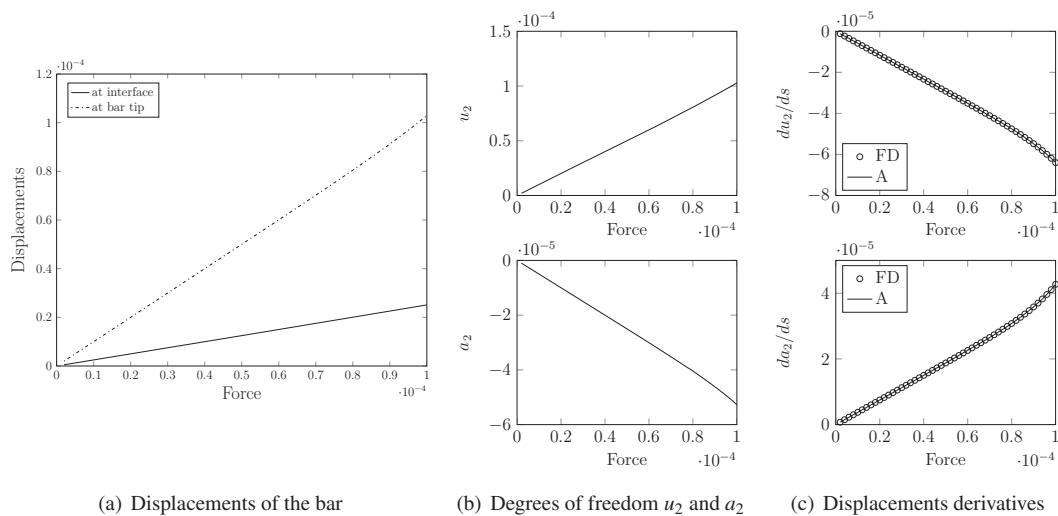


Figure 3: Structural response and sensitivity analysis of the displacement variables \mathbf{u} .

Figure 4 presents the results of the damage variables. Figures 4(a) shows the evolution of the damage parameter at each Gauss point of the structure; Figure 4(b) shows the evolution of the derivatives of these damage parameters with respect to the design parameter s . Once again, the sensitivity results are in excellent agreement.

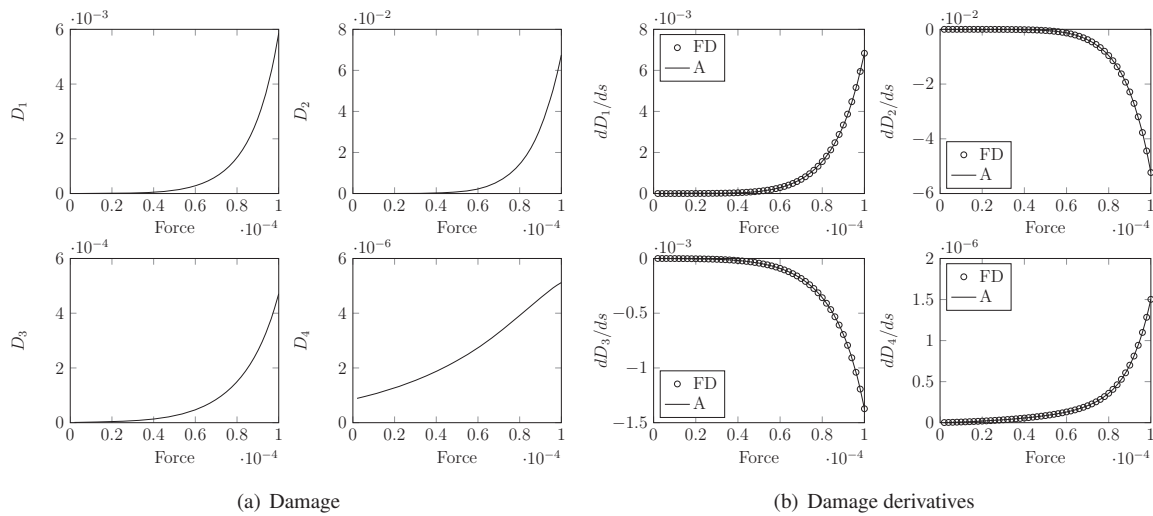


Figure 4: Structural response and sensitivity analysis of the damage variables \mathbf{D} .

8. Conclusion

An analytical approach to the sensitivity analysis of damaged structures for shape optimization has been developed. The approach combines the extended finite element method and a level set description of the geometry. The level set function is given as a function of some design parameters. The degradation of materials is described by a non-local damage model, which reduces the material stiffness by scalar damage value D . The sensitivity analysis is performed analytically, starting from the discretized governing equations and taking their derivatives with respect to the design parameters. The proposed analytical approach is validated and compared against finite differences for a simple benchmark: a bimaterial bar in tension. The sensitivity results obtained with the proposed analytical approach are in good agreement with finite differences results. In further work, the sensitivity approach is extended to two dimensional structures and optimization problems including damage constraints are solved.

9. Acknowledgements

The first author, Lise Noël, is supported by a grant from the Belgian National Fund for Scientific Research (F.R.S.-FNRS) which is gratefully acknowledged.

10. References

- [1] K. A. James and K. Waisman, Failure mitigation in optimal topology design using a coupled nonlinear continuum damage model, *Computer Methods in Applied Mechanics and Engineering*, 268, 614-631, 2014.
- [2] P. Michaleris, D. Tortorelli and C. A. Vidal, Tangent operators and design sensitivity formulations for transient non-linear coupled problems with applications to elastoplasticity, *International Journal for Numerical Methods in Engineering*, 37 (14), 2471-2499, 1994.
- [3] N. Moës, M. Cloirec, P. Cartraud and J. F. Remacle, A computational approach to handle complex microstructures geometries, *Computer Methods in Applied Mechanics and Engineering*, 192, 3163-3177, 2003.
- [4] L. Noël, L. Van Mieghroet and P. Duysinx, Analytical sensitivity analysis using the eXtended Finite Element Method in shape optimization of bimaterial structures, *submitted*.
- [5] S. Osher and J. A. Sethian, Fronts propagating with curvature-dependent speed: Algorithms based on the Hamilton-Jacobi formulation, *Journal of Computational Physics*, 79, 12-49, 1988.

A RBF Neural Network Modeling Method based on Sensitivity Analysis and Pareto Law

Zongyu Wu, Yong Chen, Wen Yao, Xiaoqian Chen

National University of Defense Technology, Changsha, China, vjzwzy@outlook.com

1. Abstract

Radial basis function neural network (RBFNN) has been widely used in nonlinear function approximation. In this paper, two limits of RBFNN have been handled which are network complexity and large-scale calculation respectively. Firstly, network complexity, which results from problems of numerous width parameters optimization, is solved by a method of space decomposition based on sensitivity analysis. If a dimension is more sensitive to approximation error, the design space along this dimension is decomposed into several subspaces and the width parameter in each subspace is regarded as an independent variable and optimized respectively. In this way, the number of width parameters to be optimized can be reduced while the flexibility of parameter settings is maintained, so that the approximation accuracy and modeling efficiency can be balanced. Secondly, large-scale calculations, which come from leave-one-out method for cross validation error estimation, are improved by adopting the Pareto law in economic science. According to the Pareto law, referred as “majority is decided by the minority”, we propose to choose only those sample points, which play dominant roles on the global errors, as cross validation points. Then large-scale calculations can be greatly reduced as the cross validation need not be conducted at those samples which have minor effects on the global errors. Combining the space decomposition and leave-one-out methods, the improved RBFNN modeling method based on sensitivity analysis and Pareto principle can effectively reduce the calculation costs and improves the accurate. Finally, several mathematical examples are tested to verify the efficacy of this method.

2. Keywords: RBFNN, sensitivity analysis, Pareto law

3. Introduction

With the development of computer technology, numerical simulation has been playing an increasingly important role in modern engineering design, but the huge amount of calculation is always a barrier. In recent years, metamodel, also called response surface method, is found to be a valuable tool in simulation areas. A metamodel is an approximation to system response constructed from its value at a limited number of selected input values [1]. Because of its simplicity and accurate results, it is used to instead of complex and computationally expensive systems.

The commonly used metamodels include Kriging, polynomial response surface model, support vector machine, radial basis function, neural network model et al. As the combination of radial basis function and neural network, radial basis function neural network is not only simple but also accurate. It is one of the most suitable approximation methods in approximating high nonlinear systems [2]. Especially in modeling the deterministic computer experiment response data which are identical each time the simulation is repeated, the interpolation modeling feature of RBFNN is very feasible and applicable. In the classical interpolation form of RBFNN, the RBF centers of neurons in network hidden layer are the training sample data. The accuracy of the model directly depends on the selected basis functions and the training samples [3].

With an unknown system, an efficient method to improve the approximation quality is to increase the number of sample data, which is also the neuron number in hidden layer of the network. If the number is big, the network would be extremely complicated and the calculation efficiency would be influenced. Besides, every sample data needs to run the high fidelity model to obtain the system response. If the sample set is too large, the calculation burden may be unacceptable. In recent years, the commonly used method to improve the approximation quality is shape parameter optimization instead of increasing the number of sample data. The present research on the shape parameter optimization mainly includes two categories:

- a) The shape parameters of all the RBF neurons are fixed to the same value with optimization methods.
- b) The shape parameters of all the RBF neurons are designed respectively with optimization methods.

In the first category, the shape parameters of all the RBF neurons are set to be the same. It is much easier to design and optimize this single parameter, but this simplification may greatly limit the capability of RBFNN in complex highly nonlinear approximation problems. The second category designs and optimizes the shape parameter of each neuron respectively. Theoretically this method can find the best approximation model, but the giant calculation cost of each neuron optimization respectively may be unacceptable.

In this paper, two limits of RBFNN have been handled which are network complexity and large-scale calculation respectively. Actually, network complexity is also the problem of large-scale calculation. Firstly, we propose a

new method of space decomposition based on sensitivity analysis to solve the problem of network complexity, which results from problems of numerous width parameters optimization. In this way, the number of width parameters to be optimized can be reduced while the flexibility of parameter settings is maintained, so that the approximation accuracy and modeling efficiency can be balanced. Secondly, we improved the traditional leave-one-out method for cross validation error estimation by adopting the Pareto law, to solve the problem of large-scale calculations. In this way, large-scale calculations can be greatly reduced. Combining the space decomposition and leave-one-out methods, the improved RBFNN modeling method based on sensitivity analysis and Pareto principle can effectively reduce the calculation costs and improves the accurate. Finally, several mathematical examples are taken to verify the proposed method, and the results are discussed.

4. RBFNN based on sensitivity analysis and Pareto law

4.1. RBF neural network

Radial basis function neural network is essentially an interpolation method. In classical RBFNN model, the approximation response is defined as a linear combination of radial functions. The approximation response expression is as follows,

$$\hat{y} = \sum_{i=1}^{N_s} w_i \phi_i(\|x - x_i\|) \quad (1)$$

N_s is the number of hidden layer neurons, which is also the number of sample points. x_i is the sample point, and w_i is the output layer weight. ϕ_i is the radial basis function of the Euclidean distance $\|x - x_i\|$. \hat{y} is the approximation response at the unknown point x .

The output weighs constitute a vector $W = [w_1, w_2, \dots, w_{N_s}]^T$, and the radial basis functions constitute a vector $\varphi(x) = [\phi_1(\|x - x_1\|), \phi_2(\|x - x_2\|), \dots, \phi_{N_s}(\|x - x_{N_s}\|)]^T$. Eq.(1) can be written as

$$\hat{y} = W^T \cdot \varphi(x) \quad (2)$$

The weight vector W can be obtained from

$$W = \Phi^{-1} Y \quad (3)$$

The accurate responses of sample points constitute the vector $Y = [y_1, y_2, \dots, y_{N_s}]^T$. The expression of matrix Φ can be written as

$$\Phi = \begin{bmatrix} \phi_1(x_1, x_1) & \phi_2(x_1, x_2) & \phi_{N_s}(x_1, x_{N_s}) \\ \phi_1(x_2, x_1) & \phi_2(x_2, x_2) & \phi_{N_s}(x_2, x_{N_s}) \\ \phi_1(x_{N_s}, x_1) & \phi_2(x_{N_s}, x_2) & \phi_{N_s}(x_{N_s}, x_{N_s}) \end{bmatrix} \quad (4)$$

The radial basis function $\phi_i(\cdot)$ has many forms such as the Gaussian function, the thin-plate-spline function, the multi-quadric function, etc.[4, 5]. As the theoretical investigation and practical results suggest that multi-quadric function has a high rate of convergence [6, 7], in this paper we choose multi-quadric function as basis function. We use r_i substituting the Euclidean distance $\|x - x_i\|$, then the radial basis function can be written as

$$\phi_i = \sqrt{r_i^2 + c_i^2} \quad (5)$$

c_i is constant number of each neuron. Because the shape characteristic of basis function is decided by c_i , we call c_i the shape parameter.

4.2. Space decomposition base on sensitivity analysis

To obtain the high approximation accuracy, we usually choose the second category of shape parameter optimization stated in section 3, but the expensive computational cost is a barrier. To improve the computational efficiency in solving the shape parameter optimization problem, a method of space decomposition is proposed based on sensitivity analysis. We decompose the whole design space into several sub-spaces, and the shape parameter in each subspace is regarded as an independent variable and optimized respectively. In this way, the number of shape parameters to be optimized can be reduced. Therefore, the large-scale optimization problem is decomposed into several sub-problems, each of which has less optimization variables and smaller matrix to

manipulate.

For a n -dimensional design space, a simple method to decompose the space is: if each dimension is divided into m parts equally, we can obtain m^n sub-spaces. This method is simple and easy to operate, but it may encounter a problem, dimension disaster. For a 20-dimensional design space, we divide each dimension into 2 parts, then the design space is decomposed into 2^{20} sub-spaces. The big number of sub-spaces makes it difficult to complete the computation.

Sensitivity analysis is the study of how the change in the output of a mathematical model or system can be apportioned to different sources of change in its inputs. It is an important method to solve the complex problem in MDO. In this section, a practical approach of space decomposition is proposed based on sensitivity analysis. The basic idea of this method includes three parts:

- a) Analyze the sensitivity of each dimension respectively, and arrange these dimensions according to the impact on system in an order from largest to smallest.
- b) If a dimension is more sensitive to approximation error, we insist that change in this dimension has larger influence to system. Select k dimensions which have largest impact on the system, and divide these dimensions into m parts respectively. Then the design space is decomposed into m^k sub-spaces and the shape parameter in each subspace is regarded as an independent variable and optimized respectively.
- c) If a dimension is less sensitive to approximation error, we insist that change in this dimension has little influence to system. Therefore, measures are not taken to this dimension.

For a 20-dimensional design space, we divide each dimension into 2 parts, then the design space is decomposed into 220 sub-spaces. The big number of sub-spaces makes it difficult to complete the computation.

4.3. Leave-one-out method based on Pareto law

Leave-one-out method is a cross validation method of estimating the approximation model prediction error. The basic ideas of this method are as follows:

- a) For a sample set $X=[x_1, x_2, \dots, x_{Ns}]^T$, leave out one sample point $x_i (1 \leq i \leq N_s)$, and construct metamodel based on the rest of the sample points $X_{-i}=[x_1, x_2, \dots, x_{i-1}, x_{i+1}, \dots, x_{Ns}]^T$.
- b) Use this metamodel to predict the response on the leave-out point \hat{y}_i .
- c) Calculate the difference e_i between the prediction \hat{y}_i and the accurate response y_i .

Generally speaking, we use RMSE (root of mean square errors) to estimate the global error of metamodel. The RMSE is calculated by the following equation:

$$\text{RMSE} = \sqrt{\left(\sum_{i=1}^{N_s} (y_i - \hat{y}_i)^2 \right) / N_s} \quad (6)$$

Where N_s is the number of sample points, \hat{y}_i and y_i are the predicted response and accurate response. The smaller the value of RMSE, the better accurate the metamodel will be.

By optimizing Eq.(6), the smallest value of RMSE can be found. But the drawback of this optimization based on leave-one-out is large-scale calculations. It will take much time to build the leave one out metamodel for cross validation of every point in the sample set, especially for RBFNN which needs large matrix calculation. To save cross validation time and calculation cost, we improve the leave-one-out method by Pareto law, which only use part of the sample data as the key points to conduct cross validation and build the global error prediction metamodel.

The Pareto law (also known as the law of vital few) states that, for many events, roughly 80% of the effects come from 20% of the causes. Therefore, many businesses have an easy access to dramatic improvements by focusing on the most effective areas and eliminating, ignoring the rest, as appropriate.

According to the Pareto law, referred as “majority is decided by the minority”, we propose to choose only those sample points, which play dominant roles on the global errors, as cross validation points. Then large-scale calculations can be greatly reduced as the cross validation need not be conducted at those samples which have minor effects on the global errors.

The leave-one-out method is improved by the Pareto law, and the main idea of this method is as follows:

- a) Calculate the square errors $e_i^2 (1 \leq i \leq N_s)$ based on the traditional leave-one-out method by the following equation,

$$e_i^2 = |y_i - \hat{y}_i|^2 \quad (7)$$

- b) Rearrange the sample set $X=[x_1, x_2, \dots, x_{Ns}]^T$, according to the value of $e_i^2 (1 \leq i \leq N_s)$ in an order from largest to smallest. Then, we obtain the new sample set $X'=[x'_1, x'_2, \dots, x'_{Ns}]^T$.

c) It is obvious that, those points with larger square error have larger influence on the global error. Choose k points with larger square error as Pareto points from the new sample set X' by the following program:

```

E' = 0;
m = 0;
for i = 1: Ns
    E' = E' + e_i'^2;
    m = m + 1;
    if (E' ≥ μE)
        break;
    end
end
return(m);
    
```

(8)

Where $\mu(0 < \mu \leq 1)$ is a constant, we call it Pareto coefficient. We set it to 0.8.

d) After determining the Pareto points, the RMSE is calculated by the following equation:

$$\text{RMSE} = \sqrt{\left(\sum_{i=1}^k (y_i' - \hat{y}_i')^2\right) / k} \quad (9)$$

Where \hat{y}_i' and y_i' are the predicted value and accurate value on the point x_i' .

4.4. The method of SAPRBFNN

Combining the space decomposition and leave-one-out methods, the RBFNN modeling method based on sensitivity analysis and Pareto principle (SAPRBFNN) is proposed. The flowchart of SAPRBFNN is shown in Fig.1.

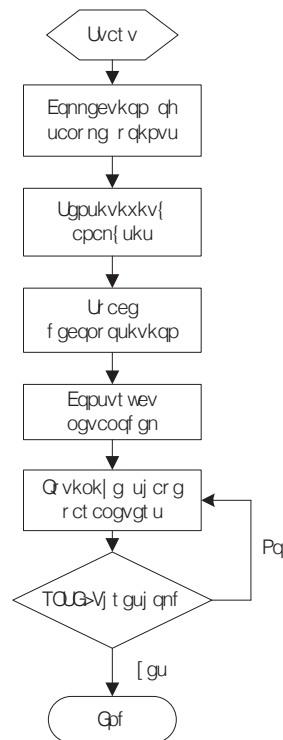


Figure 1: SAPRBFNN modeling flowchart

The proposed method mainly includes the following parts:

a) Collection of sample points. In this paper, an optimum Latin hypercube design method is utilized to construct the uniformly distributed sample points filling the design space.

- b) Sensitivity analysis. Analyze the sensitivity of each dimension respectively, and arrange these dimensions according to the impact on system in an order from largest to smallest.
- c) Space decomposition. Select k dimensions which have largest impact on the system, and divide these dimensions into m parts respectively. Then the design space is decomposed into m^k sub-spaces and the shape parameter in each subspace is regarded as an independent variable and optimized respectively.
- d) Construct metamodel in each sub-space respectively.
- e) Optimize shape parameters based on Pareto law. Determine the Pareto points of each sub-space, and then calculate RMSE by Eq.(9). The shape parameter in each subspace is regarded as an independent variable and optimized respectively.
- f) Judge the convergence of the optimization. When RMSE reaches the required accuracy threshold, the optimization process terminates.

5. Tests of SAPRBFNN

Now we will test SAPRBFNN using Camelback function and a 7-dimensional function. All the two functions are constructed through optimum Latin hypercube design sampling strategy.

5.1. Camelback function

$$f(x_1, x_2) = (4 - 2.1x_1^2 + x_1^4/3)x_1^2 + x_1x_2 + (4x_2^2 - 4)x_2^2, \quad x_1 \in [-1, 1], x_2 \in [-1, 1] \quad (10)$$

The sample set is composed of 100 uniformly distributed points in the design space designed by optimum Latin hypercube design method. Comparing the traditional RBFNN and SAPRBFNN, and the results are shown in Fig. 2 and Table 1.

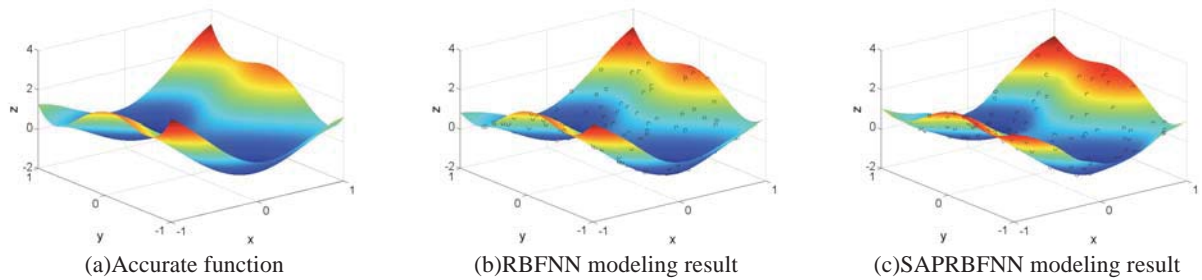


Figure 2: Test result of Camelback function

Table 1: Test result of Camelback function

Method	Shape parameter	Percentage of validation points	RMSE
RBFNN			0.0451
SAPRBFNN	Subspace 1	0.3189	17%
	Subspace 2	0.1046	8%
	Subspace 3	0.3305	11%
	Subspace 4	0.0098	16%

5.2. 7-dimensional function

$$f(x) = 0.7854x_1x_2^2(3.3333x_3^2 + 14.9334x_3 - 43.0934) - 1.5079x_1(x_6^2 + x_7^2) + 7.477(x_6^3 + x_7^3) + 0.7854(x_4x_6^2 + x_5x_7^2), \quad 1 \leq x_i \leq 5 \quad (11)$$

The sample set is composed of 300 uniformly distributed points in the design space designed by optimum Latin hypercube design method. Firstly, analyzing the sensitivity of this function. After the normalization process, the results of sensitivity analysis is depicted in Fig. 3. It is obvious that x_2 and x_3 are more sensitive than other variables. Therefore, these two dimensions is divided into 2 parts respectively. Then the design space is decomposed into 4 sub-spaces. Comparing the traditional RBFNN and SAPRBFNN, and the results are shown in Table 2.

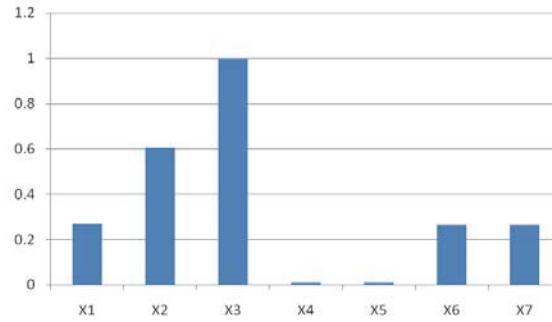


Figure 3: Sensitivity analysis

Table 2: Test result of 7-dimensional function

Method	Shape parameter	Percentage of validation points	RMSE
RBFNN			93.7760
SAPRBFNN	Subspace 1	0.2886	18%
	Subspace 2	0.5836	20%
	Subspace 3	1.0060	19%
	Subspace 4	0.0198	19%

6. Discussions and conclusions

From Camelback function, the number of shape parameters is decreased from 100 to 4, and the percentage of validation points (Pareto points) in all sample points is less than 20%. As the Fig. 3 shows, the accuracy remains almost the same with the traditional RBFNN. The RMSE test also supports the judgment. For 7-dimensional function, we can draw the same conclusion.

In this paper, two limits of RBFNN have been handled which are network complexity and large-scale calculation. Firstly, a method of space decomposition based on sensitivity analysis is proposed to solve network complexity, which results from problems of numerous width parameters optimization. In this way, the number of width parameters to be optimized can be reduced while the flexibility of parameter settings is maintained, so that the approximation accuracy and modeling efficiency can be balanced. Secondly, the leave-one-out is improved by Pareto law to solve the problem of large-scale calculations, which come from cross validation error estimation. Then large-scale calculations can be greatly reduced as the cross validation need not be conducted at those samples which have minor effects on the global errors. The results of the benchmark functions show that, the proposed SAPRBFNN which combining the space decomposition based on sensitivity analysis and leave-one-out based on Pareto law can effectively reduce the calculation costs. Most importantly, the accuracy remains almost the same with the traditional RBFNN. Further research of this method should be conducted in high dimensional problems and engineering application problems.

7. Acknowledgements

This work is supported by the National Natural Science Foundation of China (No. 11404405)

8. References

- [1] X. Wei, Y.Z. Wu and L.P. Chen, A new sequential optimal sampling method for radial basis functions, *Applied Mathematics and Computation*, 218, 9635-9646, 2012.
- [2] J. Park and W. Sandberg, Universal approximation using radial basis function networks, *Neural Computation*, 3, 246-257, 1991.
- [3] H.B. Fang and H.F. Mark, Metamodeling with radial basis functions, *The 46th AIAA/ASME/ASCE/ AHS/ASC Structures, Structural Dynamics and Materials Conference*, Austin, Texas, AIAA2005-2059, 2005.
- [4] M.J.D. Powell, Radial basis functions for multivariable interpolation: A review, *Algorithms for Approximation*, Clarendon Press, New York, 143-167, 1987.
- [5] M.J.D. Powell, Radial basis function approximations to polynomials, *12th Biennial Numerical Analysis Conference*, Dundee, 223-241, 1987.
- [6] L.P. Wang, X.Y. Wang and H.R. Zhan, The error analysis of element-free method based on radial basis function used in mechanical problems, *Mechanics in Engineering*, 35 (2), 67-72, 2013.
- [7] V. Bayona, M. Moscoso and M. Kindelan, Optimal variable shape parameter for multiquadric based RBF-FD method, *Journal of Computational Physics*, 231(6), 2466-2481, 2012.

A Novative Optimal Shape Design Based on an Isogeometric Approach: Application to Optimization of Surface Shapes With Discontinuous Curvature.

Sarah Julisson^{1,2,3}, Christian Fourcade², Paul de Nazelle³, Laurent Dumas¹

¹ University of Versailles Saint-Quentin-en-Yvelines, Versailles, France, laurent.dumas@uvsq.fr

² Renault S.A.S, Guyancourt, France, christian.fourcade@renault.com

³ IRT SystemX, Palaiseau, France, sarah.julisson@irt-systemx.fr, paul.denazelle@irt-systemx.fr

1. Abstract

When designing complex structures, optimization can play a major role. The most common procedure uses finite element analysis conducted on a mesh of the shape. Since the mesh is an approximation of the structure geometry, the quality of the simulations and consequently the optimization results are often downgraded. In this paper, we propose a computation method using the exact shape geometry for multi-shells structures. This method is based on isogeometric approach and allows to get better computation and optimization results.

2. Keywords: Isogeometry, Thin Shell, Shell Junctions, Shape Optimization.

3. Introduction

In order to conceive better products, industrial projects use more and more optimization methods during the numerical design process. The common work-flow relies on different steps. Each of these steps requires a particular expertise. In the case of automotive industry, designers create a parameterized shape, known as the CAD model, then engineers mesh it and run simulations using finite elements analysis to carry out the shape optimization [12]. This standard process raises several limitations such as: the design time, the computational cost and one of the most important, the return to a CAD model from a mesh after computation, which can corrupt the optimization expectations. To offset these limitations, some methods like the isogeometric approach have been proposed. The isogeometric consists on running computations directly on the shape by using the exact geometry of the shape to perform the finite elements analysis[6], [7]. Thereby, the difficulty of the CAD return disappears since the optimization is conducted on the geometry described by the CAD model. In this paper, we propose a method based on the isogeometric approach for surface shape using deep shell models. As they enable high curvature variations, deep shells represent a great interest in the automotive industry and for shape optimization. The technique we present uses shape functions based on Bézier's patches of the CAD model. Since complex structures are designed with the help of multiple CAD patches, we consider each patch as a Koiter's shell and we ensure the connections between patches with shell junctions. This process enables to carry out optimization on shape with discontinuous curvature. In the first part of this paper, we recall the Koiter's shell model, deal with shell junctions in the next and finally we present the results of an optimization test case.

4. Koiter's shell linear model

Thin shells are used as components in many industrial structures and thus are a real concern in numerical simulation. In this paper, we will use the Einstein's summation convention. Both Greek indices or exponents take their values in {1,2} while Roman are in {1,2,3}.

4.1. Description of a thin shell geometry

Let Ω be a open subset in a plane \mathcal{E}^2 , the euclidean space, with a boundary noted Γ . The middle surface \mathcal{S} of a shell is defined as the image in \mathcal{E}^3 of $\bar{\Omega}$ by a mapping $\vec{\phi} \in (\mathcal{C}^3(\bar{\Omega}))^3$:

$$\vec{\phi} : (\xi^1, \xi^2) \in \Omega \subset \mathcal{E}^2 \rightarrow \vec{\phi}(\xi^1, \xi^2) \in \mathcal{S} \subset \mathcal{E}^3 \quad (1)$$

ϕ is called the shape function and Ω the reference domain, which is independent from the shape. The mechanical equations are formulated on the reference domain in curvilinear coordinates. In the interest of formulating the mechanical equations, we recall some differential geometry entities. We define the two linearly independent vectors $\vec{a}_\alpha = \vec{\phi}_{,\alpha} = \partial\phi/\partial\xi^\alpha$, $\alpha = 1, 2$ for all points $\xi = (\xi^1, \xi^2) \in \bar{\Omega}$. The (a_α) vectors define the tangent plane to the middle surface. With the unit normal vector $\vec{a}_3 = \vec{a}_1 \wedge \vec{a}_2 / |\vec{a}_1 \wedge \vec{a}_2|$, they constitute the covariant basis. Associated to the covariant basis, the contravariant basis is defined through the relation $\vec{a}^\alpha \cdot \vec{a}_\beta = \delta_\beta^\alpha$ where

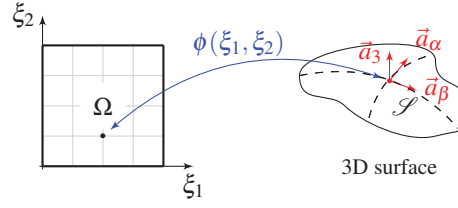


Figure 1: Definition of the middle surface

δ_{β}^{α} is the Kronecker's symbol. The first fundamental covariant form is given by $a_{\alpha\beta} = a_{\beta\alpha} = \vec{a}_{\alpha} \cdot \vec{a}_{\beta}$ and the second by $b_{\alpha\beta} = b_{\beta\alpha} = -\vec{a}_{\alpha} \cdot \vec{a}_{3,\beta} = \vec{a}_{3,\alpha} \cdot \vec{a}_{\beta}$. The mixed components of the second fundamental form are defined by $b_{\alpha}^{\beta} = a^{\beta\lambda} b_{\lambda\alpha}$ with $a^{\alpha\beta} = \vec{a}^{\alpha} \cdot \vec{a}^{\beta}$. Finally, in order to compute the basis vector derivative, $\vec{a}_{\alpha,\beta} = \Gamma_{\alpha\beta}^{\gamma} \vec{a}_{\gamma} + b_{\alpha\beta} \vec{a}_3$; $\vec{a}_{,\beta}^{\alpha} = -\Gamma_{\beta\lambda}^{\alpha} + b_{\beta}^{\alpha} \vec{a}_3$; $\vec{a}_{3,\alpha} = \vec{a}_{,\alpha}^3 = -b_{\alpha}^{\gamma} \vec{a}_{\gamma}$. Christoffel's symbols are also used to compute the covariant derivative of surface tensors: $T_{\alpha|\gamma} = T_{\alpha,\gamma} - \Gamma_{\alpha\gamma}^{\lambda} T^{\lambda}$; $T^{\alpha}{}_{|\gamma} = T^{\alpha}_{,\gamma} + \Gamma_{\lambda\gamma}^{\alpha} T^{\lambda}$. The origin and the relations between all these entities are detailed in [6].

4.2. Koiter's shell model

The Koiter's thin shell model was introduced by W. T. Koiter in 1966. The linear model relies on the Kirchhoff-Love assumptions: straight lines normal to the middle surface remain normal to the middle surface after deformation and the stresses remain plane and parallel to the tangent plane of the middle surface. We assume that the shell is clamped along a part Γ_0 of its boundary and that it is loaded on its complementary part Γ_1 by a distributed force \vec{N} and a distributed moment \vec{M} . We also suppose that \vec{p} is the external loads referred to the middle surface and $\vec{\psi}(\vec{v})$ is the infinitesimal rotation vector such as $\vec{\psi}(\vec{v}) = \varepsilon^{\lambda\beta} (v_{3,\beta} + b_{\beta}^{\alpha} v_{\alpha}) \vec{a}_{\lambda} + \frac{1}{2} \varepsilon^{\lambda\beta} v_{\beta|\lambda} \vec{a}_3$. The variational formulation of Koiter's linear model is

$$\text{Find } \vec{u} \in \vec{V} \text{ such as } a(\vec{u}, \vec{v}) = f(\vec{v}), \quad \forall \vec{v} \in \vec{V} \quad (2)$$

where

$$a(\vec{u}, \vec{v}) = \int_{\Omega} e E^{\alpha\beta\lambda\mu} \left[\gamma_{\alpha\beta}(\vec{u}) \gamma_{\lambda\mu}(\vec{v}) + \frac{e^2}{12} \rho_{\alpha\beta}(\vec{u}) \rho_{\lambda\mu}(\vec{v}) \right] \sqrt{a} d\xi^1 d\xi^2 \quad (3)$$

$$f(\vec{v}) = \int_{\Omega} \vec{p} \vec{v} \sqrt{a} d\xi^1 d\xi^2 + \int_{\Gamma_1} \vec{N} \vec{v} + \vec{M} \vec{\psi}(\vec{v}) ds \quad (4)$$

and

$$\vec{V} = \left\{ \vec{v} = (v_{\alpha}, v_3) \in ((H^1(\Omega))^2 \times H^2(\Omega)); \vec{v}|_{\Gamma_0} = \vec{0}, \frac{\partial v_3}{\partial n} \Big|_{\Gamma_0} = 0 \right\} \quad (5)$$

with $\vec{u} = (u_1, u_2, u_3)$ the displacement of the middle surface, e the shell thickness, $\sqrt{a} = |\vec{a}_1 \wedge \vec{a}_2|$, $E^{\alpha\beta\lambda\gamma}$ the elastic modulus tensor for plane stresses, $\gamma_{\alpha\beta}(\vec{u})$ the middle surface strain tensor, and $\rho_{\alpha\beta}(\vec{u})$ the modified change of curvature tensor. The expression of these tensors are given by: $E^{\alpha\beta\lambda\mu} = \frac{E}{2(1+\nu)} \left[a^{\lambda\mu} a^{\beta\mu} + a^{\alpha\mu} a^{\beta\lambda} + \frac{2\nu}{1-\nu} a^{\alpha\beta} a^{\lambda\mu} \right]$, $\gamma_{\alpha\beta}(\vec{u}) = \frac{1}{2} (u_{\alpha|\beta} + u_{\beta|\alpha}) - b_{\alpha\beta} u_3$, and $\rho_{\alpha\beta}(\vec{u}) = -(u_{3|\alpha\beta} - b_{\alpha}^{\lambda} b_{\lambda\beta} u_3 + b_{\alpha|\beta}^{\lambda} u_{\lambda} + b_{\alpha}^{\lambda} u_{\lambda|\beta} + b_{\beta}^{\lambda} u_{\lambda|\alpha})$ where E is Young's modulus and ν is Poisson's ratio.

Complex structures are made of multiple shells. To conduct satisfying simulations, each shell must have a good approximation as well as the description of their junctions.

5. Shells junction

5.1. Description of the shells junction problem

In the case of a structure composed of shells connected with \mathcal{C}^1 geometric continuity, the equality of the displacement from either side of a junction may be a sufficient condition to ensure the quality of the simulation. However, some constructions like the body frame of a car body are assemblies of several shells with \mathcal{C}^0 geometric continuity. In order to treat these parts, we propose to implement the Koiter's shells junction equation described in [2] and [3]. Let \mathcal{S} and $\tilde{\mathcal{S}}$ be two middle surfaces of two shells sharing a common boundary, known as the hinge Γ . \mathcal{S} and $\tilde{\mathcal{S}}$ are the images of reference domains Ω and $\tilde{\Omega}$ by the mappings $\vec{\phi}$ and $\vec{\tilde{\phi}}$. We suppose that \mathcal{S} , respectively $\tilde{\mathcal{S}}$, is clamped along a part $\partial\mathcal{S}_0$, respectively $\partial\tilde{\mathcal{S}}_0$, and loaded along a part $\partial\mathcal{S}_1$, respectively $\partial\tilde{\mathcal{S}}_1$. Let \vec{p} , respectively $\vec{\tilde{p}}$, be the external load to the middle surface \mathcal{S} , respectively $\tilde{\mathcal{S}}$, \vec{N} (respectively $\vec{\tilde{N}}$), the distributed force

on $\partial\mathcal{S}_1$, respectively $\partial\tilde{\mathcal{S}}_1$, and \vec{M} respectively $\vec{\tilde{M}}$ the distributed moment. We note $\gamma = \phi^{-1}(\Gamma)$ and $\tilde{\gamma} = \tilde{\phi}^{-1}(\tilde{\Gamma})$. The figure 2 shows the problem configuration. The action-reaction principle enforces the transmission of stresses.

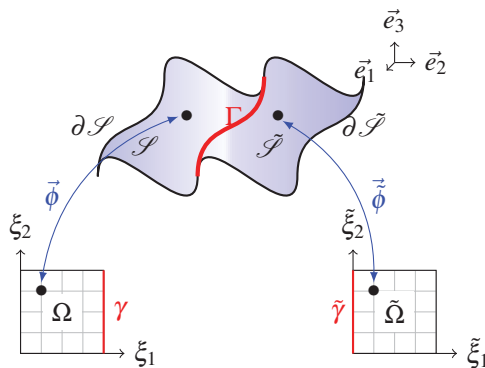


Figure 2: Junction between two shells

Therefore, $\vec{N}(P) = \vec{\tilde{N}}(P)$ and $\vec{M}(P) = \vec{\tilde{M}}(P)$. In [2] and [3], two types of hinge behaviour are considered:

- the rigid behaviour for which the continuity of the displacements and the continuity of the tangential rotations along the hinge Γ are ensured: $\vec{u}(P) = \vec{\tilde{u}}(P) \quad (\vec{\psi} \cdot \vec{t})(P) = (\vec{\tilde{\psi}} \cdot \vec{t})(P) = (\vec{t} \cdot \vec{t})(\vec{\tilde{\psi}} \cdot \vec{t})(P) \quad \forall P \in \Gamma$
- the elastic behaviour for which only the continuity of the displacements is ensured:
 $\vec{u}(P) = \vec{\tilde{u}}(P) \quad M_n(P) = k[(\vec{\psi} - \vec{\tilde{\psi}}) \cdot \vec{t}](P), \quad \forall P \in \Gamma$. The tangential component of moment is proportional to the jump of the tangential components of the rotations along the hinge. The coefficient k represents the elastic stiffness along the hinge.

$\vec{\psi}$ being the infinitesimal rotation vector and \vec{t} , respectively $\vec{\tilde{t}}$, the tangent vector to Γ in the tangent plane to \mathcal{S} , respectively $\tilde{\mathcal{S}}$. We also introduce the normal vector \vec{n} , respectively $\vec{\tilde{n}}$, to the boundary Γ in the tangent plane to \mathcal{S} , respectively $\tilde{\mathcal{S}}$.

The variational formulations of the junction problems are determined by summing the Koiter's formulation on each shell and applying the relations expressed above.

5.2. Variational formulations

The variational formulation for a junction problem with an elastic hinge is:

$$\text{Find } (\vec{u}, \vec{\tilde{u}}) \in W_{elas} \text{ such as } a[(\vec{u}, \vec{\tilde{u}}), (\vec{v}, \vec{\tilde{v}})] + kb[(\vec{u}, \vec{\tilde{u}}), (\vec{v}, \vec{\tilde{v}})] = l(\vec{v}, \vec{\tilde{v}}) \quad \forall (\vec{v}, \vec{\tilde{v}}) \in W_{elas} \quad (6)$$

where

$$W_{elas} = \{(\vec{v}, \vec{\tilde{v}}) \in \vec{V} \times \vec{\tilde{V}}, \vec{v} = \vec{\tilde{v}} \text{ on } \gamma\} \quad (7)$$

and

$$\left\{ \begin{aligned} a[(\vec{u}, \vec{\tilde{u}}), (\vec{v}, \vec{\tilde{v}})] &= \int_{\Omega} eE^{\alpha\beta\lambda\mu} \left[\gamma_{\alpha\beta}(\vec{u}) \gamma_{\lambda\mu}(\vec{v}) + \frac{e^2}{12} \rho_{\alpha\beta}(\vec{u}) \rho_{\lambda\mu}(\vec{v}) \right] \sqrt{ad} \xi^1 d\xi^2 + \\ & \int_{\tilde{\Omega}} \tilde{e}\tilde{E}^{\alpha\beta\lambda\mu} \left[\tilde{\gamma}_{\alpha\beta}(\vec{\tilde{u}}) \tilde{\gamma}_{\lambda\mu}(\vec{\tilde{v}}) + \frac{\tilde{e}^2}{12} \tilde{\rho}_{\alpha\beta}(\vec{\tilde{u}}) \tilde{\rho}_{\lambda\mu}(\vec{\tilde{v}}) \right] \sqrt{\tilde{a}\tilde{d}} \tilde{\xi}^1 d\tilde{\xi}^2 \end{aligned} \right. \quad (8)$$

$$b[(\vec{u}, \vec{\tilde{u}}), (\vec{v}, \vec{\tilde{v}})] = \int_{\gamma} [n^{\beta}(u_{3,\beta} + b_{\beta}^{\alpha} u_{\alpha}) - \tilde{n}^{\beta}(\vec{t} \cdot \vec{t})(\tilde{u}_{3,\beta} + \tilde{b}_{\beta}^{\alpha} \tilde{u}_{\alpha})] [n^{\beta}(v_{3,\beta} + b_{\beta}^{\alpha} v_{\alpha}) - \tilde{n}^{\beta}(\vec{t} \cdot \vec{t})(\tilde{v}_{3,\beta} + \tilde{b}_{\beta}^{\alpha} \tilde{v}_{\alpha})] d\gamma \quad (9)$$

$$l(\vec{v}, \vec{\tilde{v}}) = \int_{\Omega} \bar{p}\vec{v} \sqrt{ad} \xi^1 d\xi^2 + \int_{\partial\Omega_1} \vec{N}\vec{v} + \vec{M}\vec{\psi}(\vec{v}) ds + \int_{\tilde{\Omega}} \tilde{\bar{p}}\vec{\tilde{v}} \sqrt{\tilde{a}\tilde{d}} \tilde{\xi}^1 d\tilde{\xi}^2 + \int_{\partial\tilde{\Omega}_1} \vec{\tilde{N}}\vec{\tilde{v}} + \vec{\tilde{M}}\vec{\tilde{\psi}}(\vec{\tilde{v}}) d\tilde{s} \quad (10)$$

The variational formulation for a junction problem with a rigid hinge is given by:

$$\text{Find } (\vec{u}, \vec{\tilde{u}}) \in W_{rig} \text{ such as } a[(\vec{u}, \vec{\tilde{u}}), (\vec{v}, \vec{\tilde{v}})] = l(\vec{v}, \vec{\tilde{v}}) \quad \forall (\vec{v}, \vec{\tilde{v}}) \in W_{rig} \quad (11)$$

where:

$$W_{rig} = \{(\vec{v}, \vec{\tilde{v}}) \in \vec{V} \times \vec{\tilde{V}}, \vec{v} = \vec{\tilde{v}} \text{ on } \gamma; n_{\beta}(v_{3,\beta} + b_{\beta}^{\alpha} v_{\alpha}) - (\vec{t} \cdot \vec{t}) \tilde{n}_{\beta}(\tilde{v}_{3,\beta} + \tilde{b}_{\beta}^{\alpha} \tilde{v}_{\alpha}) = 0 \text{ on } \gamma\} \quad (12)$$

and a and l correspond to (8) and (10).

The proofs of these results are presented in [3]. Each of these problems admits a unique solution. What is more, the solution of elastic hinge problem converges strongly to the solution of the rigid hinge problem when k tends to infinity.

6. Application of the method in an optimization process

As explained previously, the interest in using an isogeometric approach is the idea of working on the exact geometry of the shape. This approach can be useful in a shape optimization work-flow when at the end of the optimization the return to a CAD model is immediate. Some optimization results using the same method for one patch are presented in [10]. In this paragraph, we will combine our method with an optimization problem and present the first results.

6.1. The shape function

The shape function $\vec{\phi}$ is the link between the reference domain in dimension 2, Ω , and the surface in dimension 3. In order to describe an exact geometric model, CAD model patches are used to define the shape functions. Several types of patches can be used in CAD modelling. Bézier's surfaces, B-Spline surfaces or NURBS constitute some of them. The definition and properties of these surfaces are detailed in [11]. In our case, Bézier's surfaces are the components of the shape functions. A Bézier's surface is defined as a tensor product of two Bézier's curves. The expression of a Bézier's curve of degree n is given by:

$$\mathcal{C}(u) = \sum_{i=0}^n B_{i,n}(u)P_i \quad 0 \leq u \leq 1 \quad (13)$$

where the basis functions $\{B_{i,n}(u)\} = \frac{n!}{i!(n-i)!}u^i(1-u)^{n-i}$ are Bernstein polynomials of degree n . The coefficient P_i are called the control points or poles and are the geometric coefficient that tune the curve. Thus, a Bézier's surface of degree n and m can be expressed by:

$$\mathcal{B}(u,v) = \sum_{i=0}^n \sum_{j=0}^m B_{i,n}(u)B_{j,m}(v)P_{i,j} \quad 0 \leq u,v \leq 1 \quad (14)$$

CAD models are composed of multiple patches. In our approach, we consider each patch as a shell and ensure the

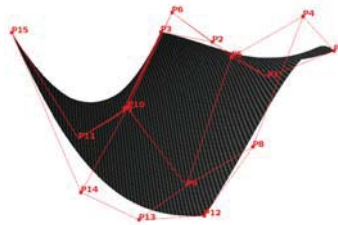


Figure 3: Example of a Bézier surface of degree 3

connection between them with shells junction conditions. As Bézier's surfaces are defined by their control points, these poles will be the optimization's variables. In comparison, for a classical industrial optimization problem, the number optimization variables matches the number of the shape's nodes mesh, which can be significant. By choosing the control points as variables, the dimension of the optimization problem substantially decreases.

6.2. The optimization problem

As a test case, we considered the optimization of the plate shape presented in Figure 4 under a compliance criteria. We supposed that the structure, modeled by two Bézier's patches of degree 5, is supported on its curved edges and subjected to self weight. A shape optimization problem is composed of an objective function $J(\vec{\phi})$ to minimize and a state equation depending on the shape function ϕ , and a space of admissible shapes \mathcal{G}_{ad} . In this application, the state equation is given by the equations (6) or (11). The space of admissible shapes is described by the constraints on the control points of the surfaces. The studied optimization problem is:

$$\begin{cases} \min_{\phi \in \mathcal{G}_{ad}} J(\vec{\phi}, \vec{u}_p) \\ \text{subject to } \{ \text{Find } \vec{u}_p \in W \text{ such as } a_p(\vec{\phi}, \vec{u}_p, \vec{v}_p) = f_p(\vec{\phi}, \vec{v}_p) \quad \forall \vec{u}_p \in W \} \end{cases} \quad (15)$$

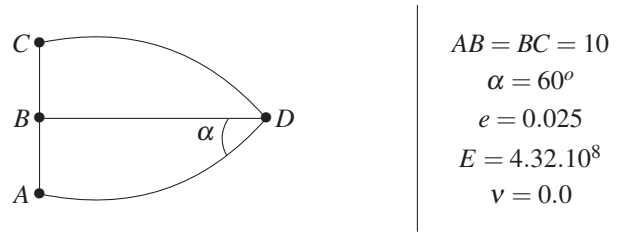


Figure 4: Description of the shape of the test case

where $\vec{u}_p = (\vec{u}, \vec{u})$ and $\vec{v}_p = (\vec{v}, \vec{v})$. The state equation depends on the type of junction. For an elastic hinge $W = W_{elas}$ from (7) and $a_p(\vec{\phi}, \vec{u}_p, \vec{v}_p) = a[(\vec{u}, \vec{u}), (\vec{v}, \vec{v})] + kb[(\vec{u}, \vec{u}), (\vec{v}, \vec{v})]$ from (8) and (9). For a rigid hinge $W = W_{rig}$ from (12) and $a_p(\vec{\phi}, \vec{u}_p, \vec{v}_p) = a[(\vec{u}, \vec{u}), (\vec{v}, \vec{v})]$ from (8). In both configurations, $f_p(\vec{\phi}, \vec{v}_p) = l(\vec{v}, \vec{v})$ with l from (10). Since the optimization criteria is the compliance $J(\vec{\phi}, \vec{u}_p) = \frac{1}{2}a_p(\vec{\phi}, \vec{u}_p, \vec{u}_p)$, the space of admissible shapes \mathcal{G}_{ad} depends on the constraints imposed to the shape. Its definition is crucial as it has a direct impact on the existence of a solution to the optimization problem. We have chosen as optimization variables only the z coordinates of the control net. Regarding the constraints, we imposed the equality of the poles located on the hinge and that the area of the optimal shape must be around $\pm 15\%$ of the area of the original surface. The problem (15) admits at least one solution with these conditions. The algorithm used for the optimization is the Powell's free-derivative algorithm COBYLA.

6.3. Results

The result provided by the algorithm is the shape displayed on Figure 5(b). The compliance has dropped by 24% and the area has increased of 12% approximately. The new shape presents more curvatures and thus is more subjected to membrane deformations than bending deformations that stiffen the structure. It has been observed that discontinuous curvature appeared during the optimization especially at the point (D). The implementation of the shell junction allows to carry on computations even with this discontinuity. Those results are encouraging and corroborate the efficiency of the method. The next step in this work will consist in comparing the results with other examples in the literature [5],[8],[13].

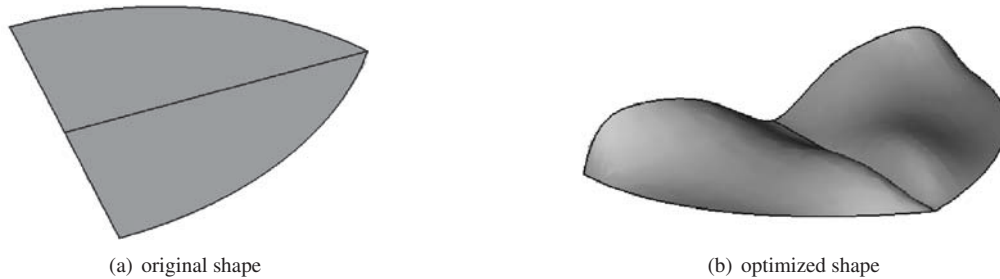


Figure 5: Original shape and optimization result

7. Conclusion

The application showed that the proposed method can be integrated in a shape optimization process with a result given in the form of a CAD model. On the other hand, several shapes could be considered, even shapes with discontinuous curvature. However, as mentioned previously, the definition of the optimization problem can raise some difficulties. Indeed, as in every shape optimization problem, the space of admissible solution must be carefully chosen in order to ensure the existence of a solution. Besides, in the application case, as the optimization variables are control points, the shape constraints must be expressed on the control points, which can be difficult in some cases.

8. Acknowledgements

This research work has been carried out in the framework of the Technological Research Institute SystemX in collaboration with Renault S.A.S and the University of Versailles Saint-Quentin-Yvelines. It is therefore partially granted with public funds within the scope of the French Program "Investissements d'Avenir".

9. References

- [1] G. Allaire, *Conception optimale des structures*, Springer-Verlag, Berlin, 2007.
- [2] M. Bernadou, *Méthodes des Éléments Finis Pour les Problèmes de Coques Minces*, Masson, Paris, 1994.
- [3] M. Bernadou and A. Cubier, *Numerical Analysis of Junctions Between Thin Shell, Part 1: Continuous Problems*, Research report, INRIA, 1996.
- [4] M. Bernadou and A. Cubier, *Numerical Analysis of Junctions Between Thin Shell, Part 2: Approximation by Finite Elements Methods*, Research report, INRIA, 1996.
- [5] K. Bletzinger, M. Firl, J. Linhard, and R. Wuchner, Optimal shapes of mechanically motivated surfaces, *Computer Methods in Applied Mechanics and Engineering*, 199(5-8):324–333, 2010. ISSN 0045-7825.
- [6] P. G. Ciarlet, *An Introduction to Differential Geometry With Applications to Elasticity*, Springer-Verlag, New York Inc, 2006.
- [7] T. J. R. Hughes, J. A. Cottrell and, Y. Bazilevs, *Isogeometric analysis: Toward Integration of CAD and FEA*, Wiley-Blackwell, 2009.
- [8] M. C. Delfour and J.-P. Zolésio, *Shapes and Geometries: Metrics, Analysis, Differential Calculus, and Optimization*, SIAM, 2010. ISBN 978-0-898714-89-0.
- [9] J. M. Kiendl, *Isogeometric Analysis and Shape Optimal Design of Shell Structures*, Ph.D Thesis, Technische Universität München, 2011.
- [10] P. de Nazelle, *Paramétrage de formes surfaciques pour l'optimisation*, Ph.D Thesis, Ecole Centrale de Lyon, 2013.
- [11] L. Piegl and W. Tiller, *The NURBS Book, Second Edition*, Springer-Verlag, Berlin, 1997.
- [12] K. Saitou, K. Izui, S. Nishiwaki and P. Papalambros, A Survey of Structural Optimization in Mechanical Product Development, *Journal of Computing and Information Science in Engineering*, vol. 5, no. 3, pages 214-226, 2005.
- [13] J. Sokolowski, *Displacement derivatives in shape optimization of thin shells* Research report, INRIA, 1996.

Optimization of structural topology using unstructured Cellular Automata

Bogdan Bochenek¹, Katarzyna Tajs-Zielińska²

¹ Cracow University of Technology, Cracow, Poland, Bogdan.Bochenek@pk.edu.pl

² Cracow University of Technology, Cracow, Poland, Katarzyna.Tajs-Zielinska@pk.edu.pl

1. Abstract

For a few decades topology optimization has been one of the most important aspects of structural design. One of the most important issues stimulating permanent development of this research area is implementation of efficient and versatile methods for generation of optimal topologies. Many modern computational techniques are nowadays invented so as to perform similarly to biological systems. They have gained widespread popularity among researchers because they are easy for numerical implementation, do not require gradient information, and one can easily combine this type of algorithms with any finite element structural analysis code. Among biologically inspired methods, which have recently aroused interest of designers one can find also Cellular Automata (CA). The idea of Cellular Automata is to replace a complex problem by a sequence of relatively simple decision making steps. In engineering implementation of Cellular Automaton the design domain is decomposed into a lattice of cells, and a particular cell together with cells to which it is connected form neighborhood. It is assumed that the interaction between cells takes place only within the neighborhood, and the states of cells are updated synchronously in subsequent time steps according to some local rules. In recent years the Cellular Automata concept has been successfully applied to structural topology optimization problems. The majority of results that have been obtained so far were based on regular lattices of cells. Practical engineering analysis and design require however using, in many cases, highly irregular meshes for complicated geometries and/or stress concentration regions. The aim of the present paper is to extend the concept of Cellular Automata towards implementation of unstructured grid of cells related to non-regular mesh of finite elements. Introducing irregular lattice of cells allows to reduce number of design variables without losing accuracy of results and without excessive increase of number of elements caused by using fine mesh for a whole structure. It is worth noting that the non-uniform density of finite elements can be, but not necessary is, directly related to design variables which are related to cells of Cellular Automaton. The implementation of non-uniform cells of Cellular Automaton requires a reformulation of standard local rules, for which the influence of neighborhood on current cell is independent of sizes of neighboring cells.

2. Keywords: topology optimization, Cellular Automata, unstructured mesh.

3. Introduction

Topology optimization of structures is a permanently developing research area. Since the early paper by Bendsoe and Kikuchi [1] one can find in the literature numerous approaches to generating optimal topologies based both on optimality criteria and evolutionary methods. A general overview as well as a broad discussion on topology optimization concepts are provided by many survey papers e.g. [10], [12]. At the same time hundreds of papers present numerous solutions including classic Michell examples as well as complicated spatial engineering structures, implementing specific methods ranging from gradient based approaches to evolutionary structural optimization, biologically inspired algorithms, material cloud method, spline based topology optimization and level set method. It is a permanently developing area and one of the most important issues stimulating this progress nowadays is implementation of efficient and versatile methods to generation of optimal topologies for engineering structural elements. In recent years the Cellular Automata paradigm has been successfully applied to topology optimization problems. In engineering implementation of Cellular Automaton the design domain is decomposed into a lattice of cells, and a particular cell together with cells to which it is connected form neighborhood. It is assumed that the interaction between cells takes place only within the neighborhood, and the states of cells are updated synchronously according to some local rules. The first application of CA to optimal structural design, and to topology optimization in particular, was proposed by Inou et al. [5]. The idea of implementation of CA to optimal design was described also by Kita and Toyoda [6]. During the last two decades implementation of CA in structural design has been under permanent development, and numerous papers related to application of CA to topology optimization, see e.g. [2], [3], [4], [8], [11] or [14], have been published.

The majority of structural topology optimization results that have been obtained so far were based on regular lattices of cells, among which the most common choice is a rectangular grid. One can find only isolated examples of implementation of triangular or hexagonal lattices. Practical engineering analysis and design require however

using, in many cases, highly irregular meshes for complicated geometries and/or stress concentration regions. The aim of the present paper is to extend the concept of Cellular Automata lattice towards irregular grid of cells related to non-regular mesh of finite elements. The strategy which consists of resizing of traditional uniform grid of cells allows to obtain more flexible solutions. The advantage of using of non-uniform lattice of cells is the most evident, when the design domain is extremely irregular and it is even impossible to cover design domain with uniform e.g. rectangular cells. On the other hand, it is well known, that holes and sharp edges indicate stress concentration, and the regions of such intensity should be covered with a more fine mesh, what is not necessary for structure as a whole. In other words, a non-uniform density of cells is used in order to achieve a more accurate solution without excessive increase of number of elements caused by using fine mesh for a whole structure. It is worth noting that the non-uniform density of finite elements can be, but not necessary is, directly related to density of cells of Cellular Automaton. The implementation of non-uniform cells of Cellular Automaton requires a reformulation of standard local rules, for which the influence of neighborhood on current cell is independent of sizes of neighboring cells and neglects for example the length of mutual boundaries. This paper proposes therefore new local update rules dedicated to implemented irregular lattices of cells. The novel concept is discussed in detail and the performance of the numerical algorithm based on the introduced idea is presented.

4. Unstructured Cellular Automata

Most of to date applications of Cellular Automata in structural optimization are conventionally based on regularly spaced, structured meshes. On the other hand using unstructured computational meshes provides more flexibility for fitting complicated geometries and allows local mesh refinement. Some attempts to implement unstructured Cellular Automata have been already reported in the literature e.g. [7], [9], but application to topology optimization is rather incidental (see [13]).

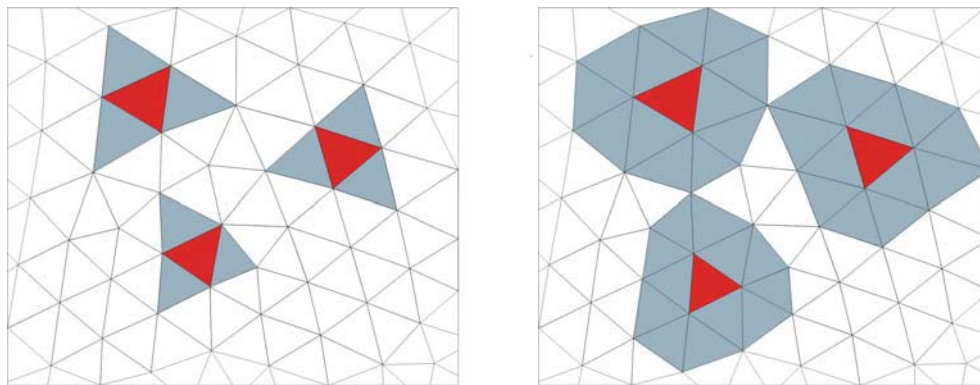


Figure 1: Unstructured triangular mesh. The von Neuman type neighborhood (left) and the Moore type neighborhood (right)

In this paper the concept of topology generator based on Cellular Automata rules is extended to unstructured meshes. Similar to structured (regular) Cellular Automata, several neighborhood schemes can be identified. The two most common ones are the von Neumann type and the Moore type. As can be seen in the Fig.1 in case of the von Neumann configuration only three immediate neighbors are taken into account. These neighboring cells share common edges with the central cell. In the Moore type neighborhood any triangle that has common edges or common vertices with the central cell can be considered as a neighbor of the central triangle. It is worth noting that this type of neighborhood involves more neighbors around the central cell, and the number of neighbors can vary since it depends on particular unstructured mesh arrangement.

5. The algorithm

The performance of Cellular Automata algorithms, reported in literature, is often based on heuristic local rules. Similarly, in the present paper the efficient heuristic algorithm, being extension of the one introduced by Bochenek and Tajs-Zielińska [2], [3], has been implemented. The power law approach defining solid isotropic material with penalization (SIMP) with design variables being relative densities of a material has been utilized. The elastic modulus of each cell element is modelled as a function of relative density d_i using power law, according to Eq.(1). This power p penalizes intermediate densities and drives design to a solid/void structure.

$$E_i = d_i^p E_0, \quad d_{min} \leq d_i \leq 1 \quad (1)$$

The local update rule applied to design variables d_i associated with central cells is now constructed based on the information gathered from adjacent cells forming the Moore or von Neumann type neighborhood. It is set up as linear combination of design variables corrections with coefficients, the values of which are influenced by the states of the neighborhood surrounding each cell, as presented in Eq.(2):

$$d_i^{(t+1)} = d_i^{(t)} + \delta d_i, \quad \delta d_i = (\alpha_0 + \sum_{k=1}^N \alpha_k)m = \tilde{\alpha}m \quad (2)$$

The compliance values calculated for central cell U_i and N neighboring cells U_{ik} are compared to a selected threshold value U^* . The quantities A_i and A_{ik} stand for areas of central and neighboring cells, respectively. Based on relations Eq.(3) and Eq.(4) specially selected positive or negative coefficients C_{α_0} for central cell and C_α for surrounding cells are transferred to the design variable update.

$$\alpha_0 = \begin{cases} -C_{\alpha_0} & \text{if } U_i \leq U^* \\ C_{\alpha_0} & \text{if } U_i > U^* \end{cases} \quad (3)$$

$$\alpha_k = \begin{cases} -C_\alpha & \text{if } U_{ik} \frac{A_{ik}}{A_i} \leq U^* \\ C_\alpha & \text{if } U_{ik} \frac{A_{ik}}{A_i} > U^* \end{cases} \quad (4)$$

The move limit m implemented in the above algorithm controls the allowable changes of the design variables values. The numerical algorithm has been build in order to implement the above proposed design rule. As to the optimization procedure the sequential approach, has been adapted, meaning that for each iteration, the structural analysis performed for the optimized element is followed by the local updating process. Simultaneously a global volume constraint can be applied for specified volume fraction. If so the generated optimal topology preserves a specified volume fraction of a solid material.

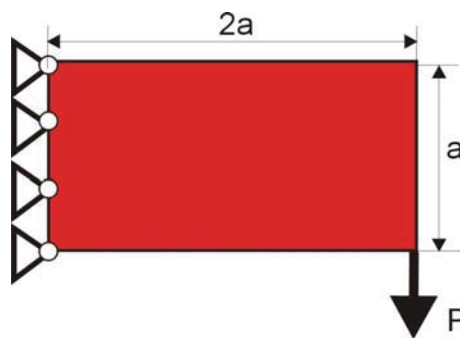


Figure 2: The rectangular Michell-type structure

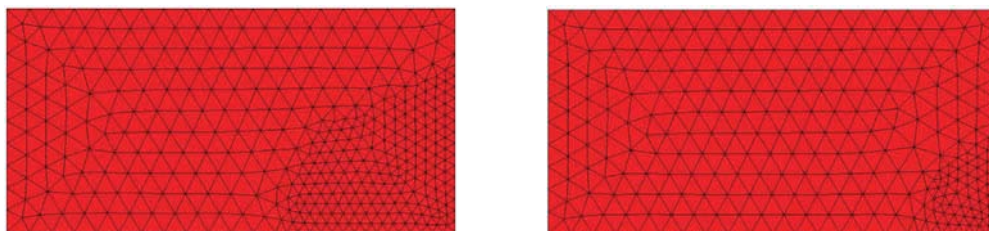


Figure 3: The rectangular Michell-type structure. Irregular meshing

6. Generation of optimal topologies

Selected examples of compliance-based topologies generated using the approach presented in this article are discussed in this section. The first one it is a rectangular Michell-type structure , clamped at the left edge and loaded

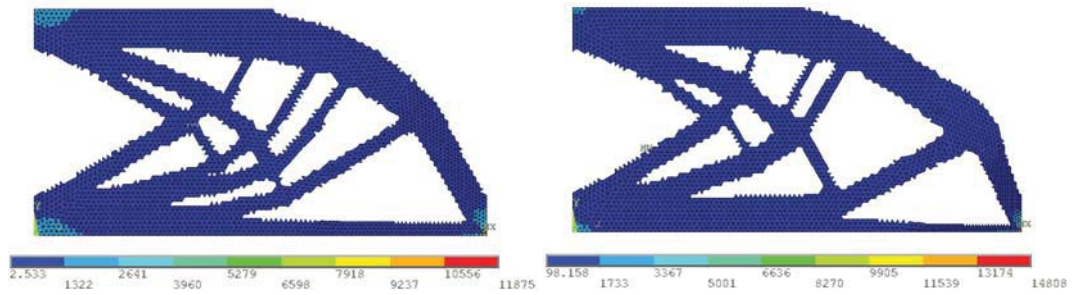


Figure 4: The rectangular Michell-type structure, force $P=500$ N, $a=5$ m, material data $E=200$ GPa, $\nu=0.3$. Final compliance: $8.58 \cdot 10^{-5}$ Nm (left) and $8.62 \cdot 10^{-5}$ Nm (right).

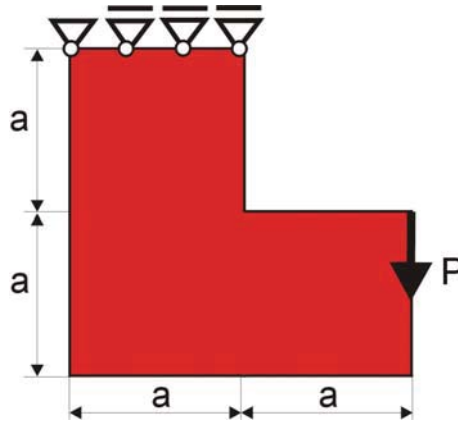


Figure 5: The L-shaped structure

by a vertical force applied at the bottom right corner, see Fig.2. The irregular mesh that consists of triangular elements/cells has been applied. The more dense mesh surrounds right bottom corner of the rectangle, as shown in the Fig.3. The two cases are considered, namely larger and smaller area of mesh concentration. The topology optimization has been performed and the obtained results are presented in the Fig.4, with final compliance $8.58 \cdot 10^{-5}$ Nm for total number of cells 10594 and $8.62 \cdot 10^{-5}$ Nm for 10439 cells, respectively. The latter case represents more dense mesh surrounding stress concentration region. Calculating von Mises stress gives maximal values of 11.9 kPa for less concentrated and 14.8 kPa for more concentrated mesh. It is worth noting that in order to reflect such stress values with regular meshes it is necessary to use 28056 and 42230 cells, respectively.



Figure 6: The L-shaped structure. Irregular (left) and regular (right) lattice of cells

The next example it is the L-shaped structure shown in the Fig.5. The unstructured mesh that consists of triangular elements/cells has been applied. The more dense mesh surrounds two corners within stress concentration

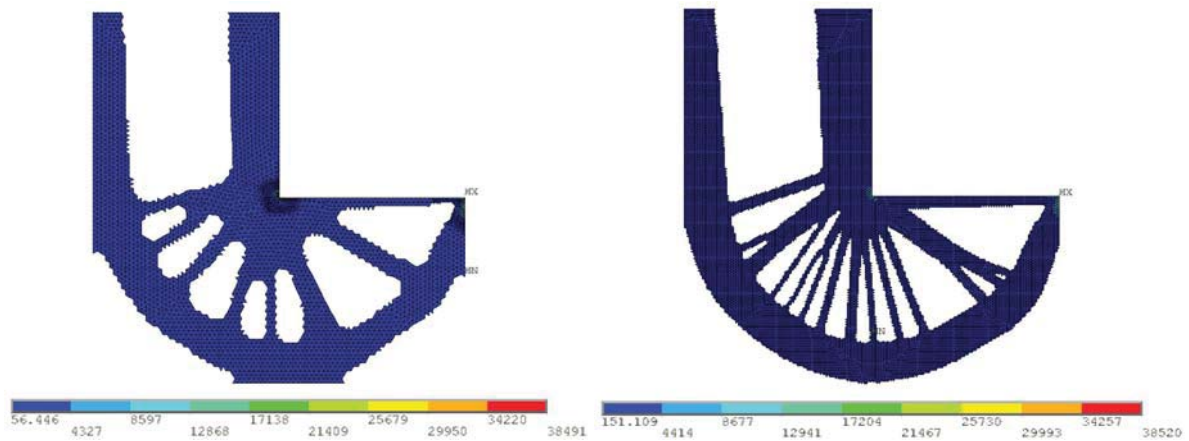


Figure 7: The L-shaped structure, force $P=100$ N, $a=0.8$ m, material data $E=200$ GPa, $\nu=0.3$. Final compliance: Irregular lattice of 11396 cells $4.1 \cdot 10^{-6}$ Nm (left) and regular lattice of 36490 cells $4.0 \cdot 10^{-6}$ Nm (right), volume fraction 0.5

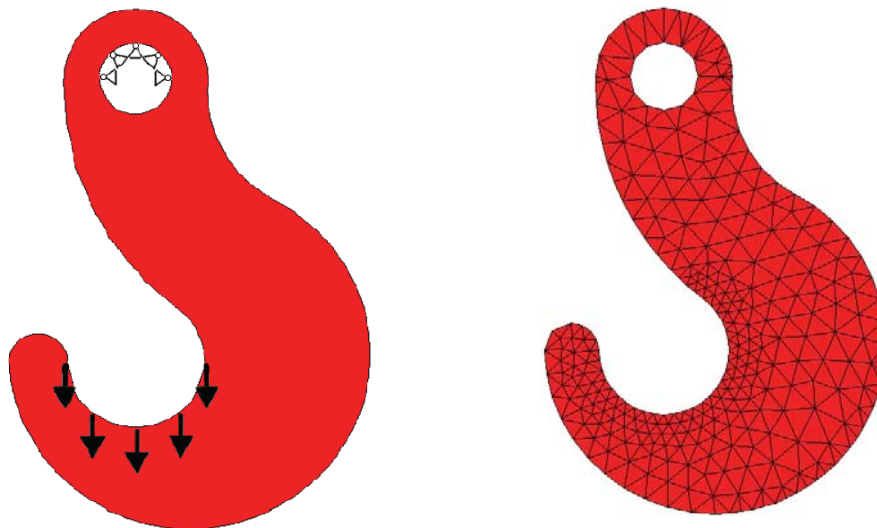


Figure 8: The Hook structure. Loading and support (left), irregular lattice (right)

regions as shown in the Fig.6. The exemplary regular mesh is presented as well. The topology optimization has been performed and the obtained results are presented in the Fig.7, with final compliance $4.1 \cdot 10^{-6}$ Nm for irregular lattice of 11396 cells and $4.0 \cdot 10^{-6}$ Nm for regular lattice of 36490 cells, respectively. Calculating von Mises stress gives maximal value of 38.5 kPa for both unstructured and regular mesh. It is worth noting that in order to obtain comparable results more than 3 times more cells for regular mesh were required.

The final example it is the Hook structure shown in the Fig.8. As for the previous cases, the irregular/unstructured mesh that consists of triangular elements/cells has been applied. The more dense mesh surrounds region of loading application. The minimal compliance topologies have been found for the considered structure and the obtained results are presented in the Fig.9 for two cases of volume fraction.

7. Concluding remark

The proposal of extension of Cellular Automata concept towards unstructured/irregular grid of cells related to non-regular mesh of finite elements has been presented. The subject is still under development but it seems that the approach presented in this paper demonstrates a significant potential of application to problems which cannot be adequately represented by regular grids. The use of unstructured meshes may be helpful while modelling a domain geometry, accurately specify design loads or supports and compute structure response.

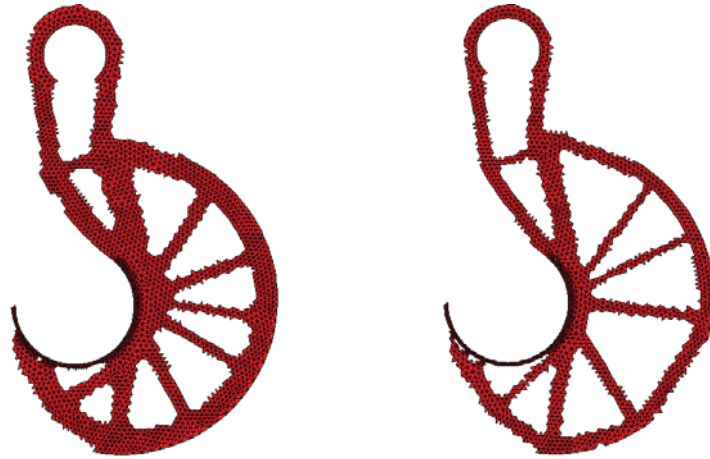


Figure 9: The Hook structure, loading $q=1.67$ N/mm, material data $E=200$ GPa, $\nu=0.25$. Final topology, volume fracture 0.5 (left), volume fracture 0.35 (right)

8. References

- [1] M.P. Bendsoe and N. Kikuchi, Generating optimal topologies in optimal design using a homogenization method, *Computational Methods and Applications in Mechanical Engineering*, 71, 197-224, 1988.
- [2] B. Bochenek and K. Tajs-Zielińska, Novel local rules of Cellular Automata applied to topology and size optimization, *Engineering Optimization*, 44, 1, 23-35, 2012.
- [3] B. Bochenek and K. Tajs-Zielińska, Topology optimization with efficient rules of cellular automata, *Engineering Computations*, 30, 8, 1086-1106, 2013.
- [4] Y. Du, D. Chen, X. Xiang, Q. Tian and Y. Zhang, Topological design of structures using a cellular automata method, *Computer Modeling in Engineering and Sciences*, 94, 1, 53-75, 2013.
- [5] N. Inou, N. Shimotai and T. Uesugi, A cellular automaton generating topological structures, *Proceedings of the 2nd European Conference on Smart Structures and Materials*, 2361, 47-50, 1994.
- [6] E. Kita and T. Toyoda, Structural design using cellular automata, *Structural and Multidisciplinary Optimization*, 19, 64-73, 2000.
- [7] Y. Lin, A.E. Mynett and H. Li, Unstructured Cellular Automata for modelling macrophyte dynamics, *Journal of River Basin Management*, 9, 3-4, 205-220, 2011.
- [8] S. Missoum, Z. Gurdal and S. Setoodeh, Study of a new local update scheme for cellular automata in structural design. *Structural and Multidisciplinary Optimization*, 29, 103-112, 2005.
- [9] D. O Sullivan, Exploring spatial process dynamics using irregular cellular automaton models, *Geographical Analysis*, 33, 1, 1-18, 2001.
- [10] G.I.N. Rozvany, A critical review of established methods of structural topology optimization, *Structural and Multidisciplinary Optimization*, 37, 217-237, 2008.
- [11] E. Sanaei and M. Babaei, Cellular Automata in topology optimization of continuum structures, *International Journal of Engineering Science and Technology*, 3, 4, 27-41, 2011.
- [12] O. Sigmund and K. Maute, Topology optimization approaches, *Structural and Multidisciplinary Optimization*, 48, 1031-1055, 2013.
- [13] C. Talischi, G.H. Paulino, A. Pereira and I.F.M. Menezes, PolyTop: a Matlab implementation of a general topology optimization framework using unstructured polygonal finite element meshes, *Structural and Multidisciplinary Optimization*, 45, 329-357, 2012.
- [14] A. Tovar, N.M. Patel, G.L. Niebur, M. Sen and J.E. Renaud, Topology optimization using a hybrid cellular automaton method with local control rules, *Journal of Mechanical Design*, 128, 1205-1216, 2006.

Topology optimisation of passive coolers for light-emitting diode lamps

Joe Alexandersen¹, Ole Sigmund, Niels Aage

Department of Mechanical Engineering, Technical University of Denmark

¹ joealex@mek.dtu.dk

1. Abstract

This work applies topology optimisation to the design of passive coolers for light-emitting diode (LED) lamps. The heat sinks are cooled by the natural convection currents arising from the temperature difference between the LED lamp and the surrounding air. A large scale parallel computational framework is used to perform topology optimisation for minimising the temperature of the LED package subjected to highly convection-dominated heat transfer.

The governing equations are the steady-state incompressible Navier-Stokes equations coupled to the thermal convection-diffusion equation through the Boussinesq approximation. The fully coupled non-linear multiphysics system is discretised using stabilised trilinear equal-order finite elements and solved using Newton's method and a multigrid-preconditioned iterative method. Topology optimisation is carried out using the density-based approach.

The optimisation results show interesting features that are currently being incorporated into industrial designs for enhanced passive cooling abilities.

2. Keywords: topology optimisation, passive cooler, LED lamp, heat sink design, natural convection.

3. Introduction and motivation

The motivation for this work is the design of efficient and visually-pleasing passive coolers for LED lamps. LED lamps are a highly energy-efficient light source, however, it remains a problem to adequately cool them. This is a problem since around 70% of the energy supplied to an LED is converted to heat, which severely affects their lifespan unless effectively cooled. From an industrial design perspective, LEDs offer a large degree of design freedom since LED units are generally quite small and the passive cooling elements have the opportunity to make up the majority of the full lamp design as illustrated by figure 1.

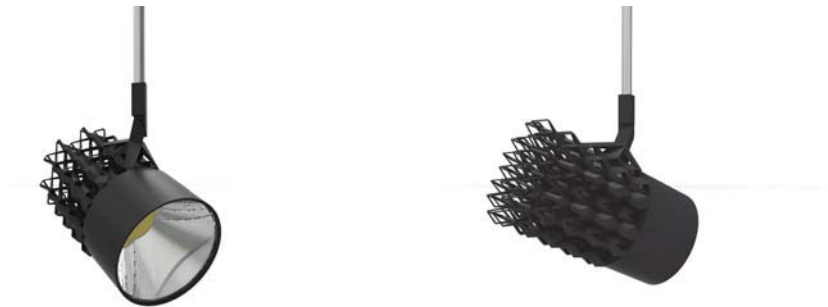


Figure 1: Design concept of a high-power LED spot with a 3D printed aluminium heat sink for passive cooling. Pictures are courtesy of AT Lightning Aps.

In order to fully utilise the design freedom and to allow for the appearance of non-intuitive designs, topology optimisation [1] is used. This is done using the density-based approach as detailed in [2] for two-dimensional natural convection problems. Despite the methodology being the same, the extension to three-dimensions has been far from trivial in the sense of the vast growth in computational workload. Topology optimisation for fluid systems began with the treatment of Stokes flow [3] and has since been applied to Navier-Stokes, as well as scalar transport problems. However, to the authors knowledge, this work is the first to treat a real-life application using a correct and coupled physical model.

4. Theory

4.1. Governing equations

The incompressible Navier-Stokes equations are coupled to the convection-diffusion equation through the Boussinesq assumption. The dimensionless equations are:

$$u_j \frac{\partial u_i}{\partial x_j} - Pr \frac{\partial}{\partial x_j} \left(\frac{\partial u_i}{\partial x_j} + \frac{\partial u_j}{\partial x_i} \right) + \frac{\partial p}{\partial x_i} = -\alpha(\mathbf{x})u_i - GrPr^2 e_i^g T \quad (1)$$

$$\frac{\partial u_j}{\partial x_j} = 0 \quad (2)$$

$$u_j \frac{\partial T}{\partial x_j} - \frac{\partial}{\partial x_j} \left(K(\mathbf{x}) \frac{\partial T}{\partial x_j} \right) = s(\mathbf{x}) \quad (3)$$

where u_i is the velocity field, p is the pressure field, T is the temperature field, x_i denotes the spatial coordinates, e_i^g is the unit vector in the gravitational direction, $\alpha(\mathbf{x})$ is the spatially-varying effective impermeability, $K(\mathbf{x})$ is the spatially-varying effective thermal conductivity, $s(\mathbf{x})$ is the spatially-varying volumetric heat source term, Pr is the Prandtl number, and Gr is the Grashof number.

The effective impermeability is set to 0 in the fluid subdomain and α_{max} in the solid subdomain. Likewise, the effective thermal conductivity is set to 1 in the fluid subdomain and $\frac{1}{C_k} = \frac{k_s}{k_f}$ in the solid subdomain. The volumetric heat source is only active within a specified subdomain, within which it has a constant value.

4.2. Optimisation problem

In order to perform topology optimisation, continuous variables, γ_e , varying between 0 and 1 are introduced in each finite element, e , of the discrete system. Fluid is represented by $\gamma_e = 1$ and solid by $\gamma_e = 0$. For values between 0 and 1, the effective material properties, impermeability and conductivity, are interpolated as described in [2].

$$\begin{aligned} & \underset{\gamma \in \mathbb{R}^n}{\text{minimise:}} f(\gamma, \mathbf{s}) = \mathbf{f}_t^T \mathbf{t} \\ & \text{subject to: } g(\gamma) = \frac{\sum_{e \in \mathbb{E}_d} (1 - \gamma_e) v_e}{v_f \sum_{e \in \mathbb{E}_d} v_e} - 1 \leq 0 \\ & \mathcal{R}(\gamma, \mathbf{s}) = \mathbf{0} \\ & 0 \leq \gamma_i \leq 1 \quad \text{for } i = 1, \dots, n \end{aligned} \quad (4)$$

where γ is a vector of n design variables, $\mathbf{s} = \{\mathbf{u}, \mathbf{p}, \mathbf{t}\}^T$ is the vector of state field variables, f is the objective functional, g is the volume constraint functional and $\mathcal{R}(\gamma, \mathbf{s}) = \mathbf{M}(\gamma, \mathbf{s})\mathbf{s} - \mathbf{b}(\gamma, \mathbf{s})$ is the residual of the discretised system of equations.

The objective functional, f , is chosen as the thermal compliance, where \mathbf{f}_t is the vector arising from the discretised volumetric flux and \mathbf{t} is the vector of nodal temperatures. Since the flux load is constant, the optimisation problem essentially becomes to minimise the temperature of the heat source. The constraint functional, g , is a volume constraint on the solid material usage, where \mathbb{E}_d is the set of elements belonging to the design domain and v_e is the volume of element e . Although not always necessary for convection-dominated problems, the volume constraint helps the design to converge to well-defined topologies.

The optimisation problem is solved using the nested formulation, where the discretised system of equations for the state field is solved separately from the design problem. The design sensitivities are found using the adjoint method.

5. Numerical implementation

The governing equations are discretised using stabilised trilinear finite elements as described in [2] and have been implemented in a large scale parallel topology optimisation framework based on PETSc [4, 5].

The resulting fully-coupled non-linear system of equations is solved using a damped Newton method. For the initial design iteration, a slow ramping strategy on the heat flux is applied in order to reach convergence from a zero initial vector. For subsequent design iterations, the state solution from the previous design iteration is used as the initial vector.

The linearised systems of equations is solved using an iterative solver, more specifically F-GMRES with a Galerkin-projection geometric multigrid (GMG) preconditioner. For the GMG smoother and coarse grid solver,

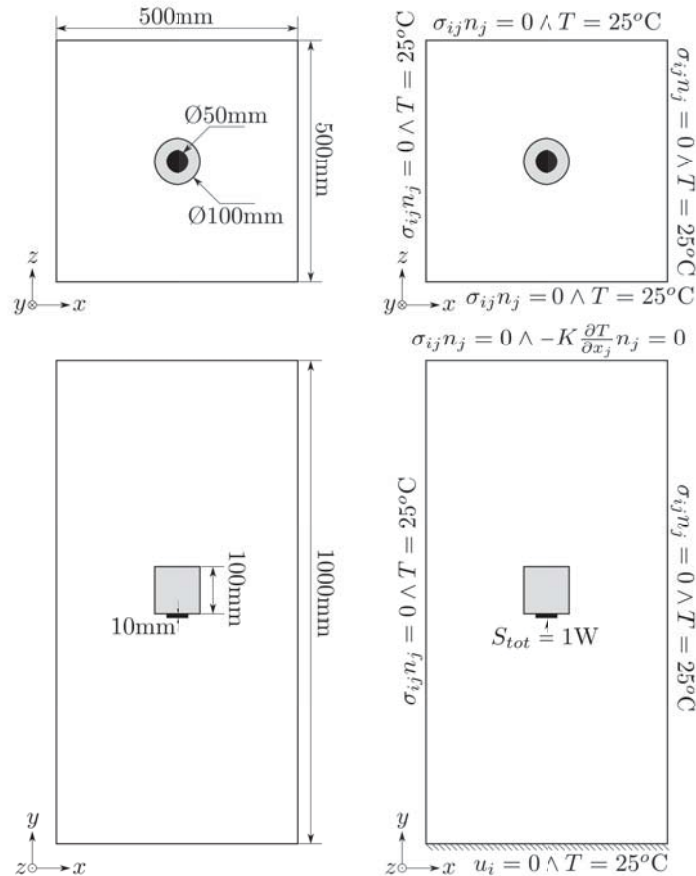


Figure 2: Illustrations of the problem setup showing the dimensions and the prescribed boundary conditions.

GMRES with a Jacobi preconditioner is used. Although multigrid is known not to be an optimal solver for non-elliptic systems of equations, the performance is very good and allows for the optimisation of the presented problem in a reasonable time.

The design field is regularised using the partial differential equation (PDE) filter [6] and the optimisation problem is solved using the method of moving asymptotes (MMA) [4, 7].

6. Problem setup

The problem setup is presented in figure 2. As an initial investigation, the lamp is oriented vertically downwards allowing for quarter symmetry to be imposed. The lamp is sought modelled suspended in free space, so all boundaries should ideally be left as open, that is $\sigma_{ij}n_j = 0$. However, as all rooms are finite, a floor (no-slip condition) is added at the bottom of the domain. This has the added advantage of stabilising the solution process and to ensure the Newton solver converges to a correct physical solution. The temperature field is imposed to be equal to the reference room temperature at all boundaries except the top-most boundary which acts as an outflow.

The reference temperature is assumed to be 25°C and properties of air and aluminium for this reference temperature have been used. The resulting dimensionless numbers for the presented problem are:

$$\begin{aligned}
 Pr &= 0.74 \\
 Gr &= 1.60 \times 10^5 \\
 C_k &= 1.08 \times 10^{-4}
 \end{aligned} \tag{5}$$

where the Grashof number, Gr , is defined using the diameter of the LED package as the reference length.

The computational domain is truncated around the lamp to a rectangle $10 \times 20 \times 10$ times larger than the diameter of the LED package. Based on initial investigations of the flow field, this is assumed to be large enough for the open boundary conditions not to affect the solution around the lamp significantly. The LED package is modelled as a solid slab of aluminium with a uniform volumetric heat source totalling a power of $S_{tot} = 1\text{W}$. This

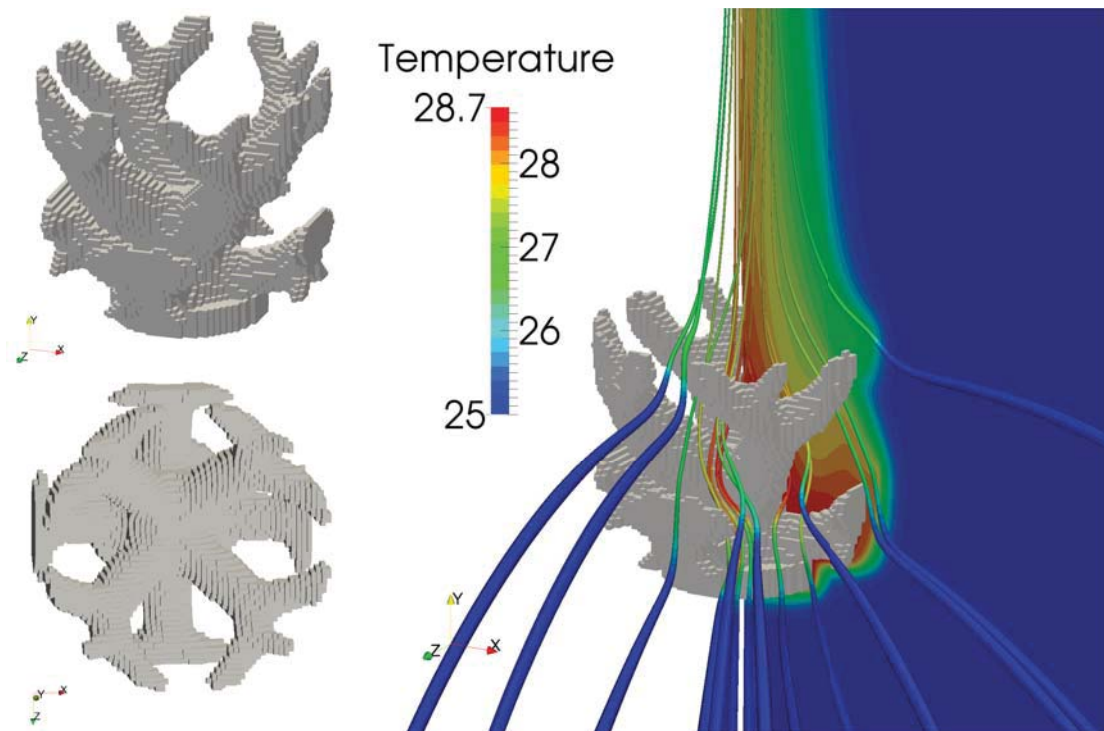


Figure 3: Optimised design from various angles and shown with a slice of the temperature field and streamtubes.

is at the lower end of the intended application range, but is chosen for numerical stability and to demonstrate a proof-of-concept.

Initial investigations using the full domain showed that the flow, temperature and design fields remained quarter-symmetric throughout the optimisation and the computational domain has thus been reduced to a quarter with symmetry boundary conditions. The computational mesh used is $160 \times 640 \times 160$ elements yielding a total number of 16,384,000 elements and 83,076,805 degrees of freedom (velocity, pressure and temperature). The design domain consists of 51,776 elements and the filter radius is set to 4mm.

7. Optimisation results

Figure 3 shows the optimised design from various angles and also with a slice of the temperature field and streamtubes. The design exhibits tree-like branches extending out from the centre of the LED package. This intuitively makes sense as the thermal hotspot is located in the centre of the LED package. The branches conduct the heat away from the LED package and transfer it to the moving air by allowing the flow to move between the members. It can clearly be seen that the offset of the members enables the flow to zig-zag through the cooler in the vertical direction.

Figure 4 shows the optimised design together with slices showing the global velocity and temperature fields. It can be seen that the highest velocity is found some distance above the lamp, as expected and observed from experiments. The air is generally moving slowly far from the lamp and is accelerated above it, when it has been drawn in from the surroundings. The temperature field shows that globally the heat transfer is highly convection-dominated. The ambient temperature is observed in the entire computational domain, except for close to the lamp where a plume forms above it.

The computations have been performed using 2560 cores (128 nodes with two Intel Xeon e5-2680v2 10-core 2.8GHz processors) and the total computational time was approximately 8.5 hours for 200 design iterations. After the first design iteration, the number of Newton steps is around 2-4 and the number of F-GMRES iterations per linear solve is 20-30 for the state problem and 30-40 for the adjoint problem.

8. Conclusions and future work

Initial results for the application of topology optimisation to the design of passive coolers for LED lamps have been presented. A computational model problem has been set up to model the natural convection flow around a freely hanging LED lamp. Topology optimisation has been successfully applied to the highly convection-dominated heat transfer problem using a large scale parallel computational framework. The initial optimisation

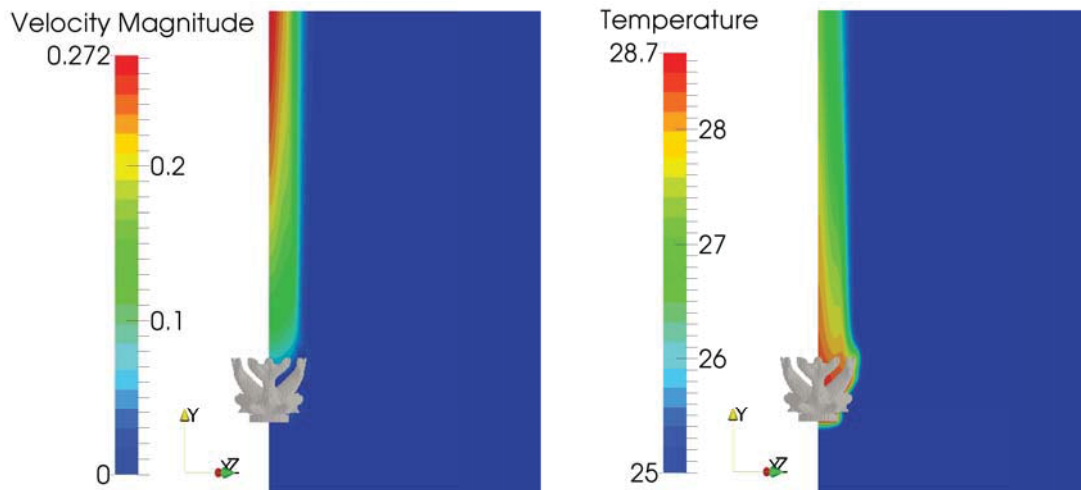


Figure 4: Optimised design with slices showing the global velocity and temperature fields. Please note that the bottom of the domain is not shown due to lack of interesting details.

results show interesting features, such as organic tree-like structures with offset members, that are currently being incorporated into industrial designs for enhanced passive cooling abilities.

Further developments will be presented in a journal paper in the near future. This includes comparison of the numerical model to experimental results in order to validate modelling assumptions and design performance. Initial results show promise and that the modelling assumptions are satisfied at the settings of interest. However, in order to treat higher power LED packages, it may be necessary to extend the analysis and optimisation to handle time-dependent flows. Also, investigations into the modelling accuracy of the fluid and thermal boundary layers is necessary to ensure physically accurate optimisation.

9. Acknowledgements

The research work by all authors was funded by Villum Fonden through the NextTop project, as well as by Innovation Fund Denmark through the HyperCool project.

10. References

- [1] M.P. Bendsoe and O. Sigmund, *Topology Optimization: Theory, Methods and Applications*, Springer-Verlag, Berlin, 2003.
- [2] J. Alexandersen, N. Aage, C.S. Andreasen and O. Sigmund, Topology optimisation for natural convection problems, *International Journal for Numerical Methods in Fluids*, 76 (10), 699-721, 2014.
- [3] T. Borrvall and J. Petersson, Topology optimization of fluids in Stokes flow, *International Journal for Numerical Methods in Fluids*, 41 (1), 77-107, 2003.
- [4] N. Aage, E. Andreassen and B.S. Lazarov, Topology optimization using PETSc: An easy-to-use, fully parallel, open source topology optimization framework, *Structural and Multidisciplinary Optimization*, available online, 2014.
- [5] S. Balay, S. Abhyankar, M.F. Adams, J. Brown, P. Brune, K. Buschelman, V. Eijkhout, W.D. Gropp, D. Kaushik, M.G. Knepley, L.C. McInnes, K. Rupp, B.F. Smith and Hong Zhang, *PETSc Users Manual*, Argonne National Laboratory, ANL-95/11 - Revision 3.5, <http://www.mcs.anl.gov/petsc>, 2014.
- [6] B.S. Lazarov and O. Sigmund, Filters in topology optimization based on Helmholtz-type differential equations, *International Journal for Numerical Methods in Engineering*, 86 (6), 765-781, 2011.
- [7] K. Svanberg, The method of moving asymptotes - a new method for structural optimization, *International Journal for Numerical Methods in Engineering*, 24 (2), 359-373, 1987.

Topology Optimization considering design-dependent Stokes flow loads

Renato Picelli¹, William Martins Vicente¹, Renato Pavanello¹, Fred van Keulen²

¹ University of Campinas, Campinas, Brazil, picelli@fem.unicamp.br

² Delft University of Technology, Delft, The Netherlands

1. Abstract

This article presents an evolutionary topology optimization method for mean compliance minimization of structures under design-dependent viscous fluid flow loads. The structural domain is governed by the elasticity equation and the fluid by the incompressible Stokes flow equations. When the modelling of a system consists in the interaction of multiple domains, the classic density-based topology optimization methods become arduous within the framework of dealing with the moving multi-physics loads and interfaces, due to the considerable volume of intermediate density elements. Herein it is suggested an alternative methodology to handle this type of loading problems. With an extended Bi-directional Evolutionary Structural Optimization (BESO) method, design-dependent Stokes flow loads are modelled straightforward during the optimization procedure. The discrete nature of the method allows both fluid and structural domains to be modelled separately in each step of the optimization. In order to validate the methodology, only small structural displacements and a simple staggered fluid-structure interaction algorithm are considered in this paper. Primary results are shown for a 2D flexible structure immersed in an incompressible viscous flow channel.

2. Keywords: Topology Optimization; BESO Method; Design-dependent loads; Fluid-structure interaction; Stokes flow.

3. Introduction

In order to improve the structural design in the field of engineering, Structural Topology Optimization [1,2] has been developed. The idea is to find optimal structural topologies inside predefined design domains concerning objective functions and constraints.

Through the last years, topology optimization has been under some strong scientific effort to be extended for different classes of engineering systems [3-5]. Some of them include fluid flow or even multiphysical effects, such as fluid-structure interaction problems [6,7,8].

Only a few authors have studied the topology optimization of FSI coupled systems. The classic element density-based topological optimization methods become arduous when dealing with FSI problems within the framework of separated domains with explicit boundaries. That is because this kind of analysis methods requires predefined explicit interfacing boundary descriptions for the coupling boundary conditions. Thus, it is necessary to devise new computational techniques to overcome this limitation [8].

In this context, the presented work proposes the extension of the Bi-directional Evolutionary Structural Optimization (BESO) [9] method for FSI systems design. The discrete nature of the evolutionary methods imply that no intermediate density elements are allowed during the optimization procedures. Thus, fluid-structural boundaries are always explicit and the coupling boundary conditions evaluation is straightforward. To the best of the authors' knowledge, fluid-structure interaction problems still have not been treated with the evolutionary topology optimization methods..

4. Governing equations and finite element model

4.1. Fluid domain

In this work we shall consider fluids with the following properties:

- The medium is incompressible.
- The medium has a Newtonian character.
- The medium properties are temperature independent and uniform.
- The flow is laminar and at steady-state.
- Inertia forces are not considered.

- There are no body forces.

For the above restrictions, the governing partial differential equations for the motion of the fluid can be expressed as the incompressible Stokes flow equations

$$\begin{cases} -P_{,i}{}^f + \mu v_{i,jj} = 0 \\ v_{j,j} = 0 \end{cases} \quad (1)$$

where μ is the dynamic viscosity and P and v are the pressure and velocities on the fluid domain, respectively. The boundary conditions applied in this work are

- No-slip condition: $v_j = 0$ at fluid flow walls.
- Velocity profile given at inflow: $v_j = v_j^0$
- Pressure value given: $P^f = P_0$

4.2. Solid domain

Herein we shall consider linear elasticity for the solid domain under fluid flow loads. Neglecting body forces and any acceleration, the linear structural analysis is governed by

$$\sigma_{ij,j}^s(u) = -(-P_{,i}{}^f + \mu v_{i,jj})^{fsi} \quad (2)$$

where σ_s is the Cauchy stress tensor, u is the displacement field and the superscript *fsi* denotes the vector with the loads from the fluid flow. Equation (2) is also given as the fluid-structure interface boundary condition. For the solid domain, the following Dirichlet boundary condition is applied:

$$u_i = 0 \quad (3)$$

4.3. Finite element model

A mixed finite element is chosen to model Stokes flow equations, in which velocities and pressures from the fluid domain are interpolated in the same finite element. With the correct shape functions these elements are stable and satisfy compatibility conditions [10]. Although they are too costly for large-scale problems, they showed to be effective for the cases explored in this work. The finite element used herein is known as Q2P1, in which velocities are interpolated with quadratic shape functions and pressures with bilinear shape functions in isoparametric axes.

The finite element matrices for solving (1) are

$$\begin{bmatrix} \mathbf{K}_f & -\mathbf{Q} \\ -\mathbf{Q} & \mathbf{0} \end{bmatrix} \begin{Bmatrix} \mathbf{v}_f \\ \mathbf{P}_f \end{Bmatrix} = \begin{Bmatrix} \mathbf{0} \\ \mathbf{0} \end{Bmatrix} \quad (4)$$

where \mathbf{P}_f and \mathbf{v}_f are the pressure and velocities vector, respectively. The fluid stiffness matrix \mathbf{K}_f and the incompressibility matrix \mathbf{Q} are evaluated as follows:

$$\mathbf{K}_f = \mu \int_{\Omega_e} \mathbf{B}^T \mathbf{I}_0 \mathbf{B} d\Omega_e \quad (5)$$

$$\mathbf{Q} = \int_{\Omega_e} \nabla \mathbf{N}_v^T \mathbf{N}_p d\Omega_e \quad (6)$$

where the matrices \mathbf{N} contain the shape functions for velocities and pressures with the correspondent v and P subscripts, respectively. The matrix \mathbf{B} contains the partial derivatives of the shape functions and, for 2D cases,

$$\mathbf{I}_0 = \begin{bmatrix} 2 & 0 & 0 \\ 0 & 1 & 0 \\ 0 & 0 & 1 \end{bmatrix} \quad (7)$$

Considering only Stokes flow loads, the finite element model for the structure is expressed as

$$\mathbf{K}_s \mathbf{u}_s = -(\mathbf{K}_f \mathbf{v}_f - \mathbf{Q} \mathbf{P}_f)^{fsi} \quad (8)$$

where \mathbf{K}_s is the finite element matrix for the structure and \mathbf{u}_s is the displacements vector. The fluid loads $(\mathbf{K}_f \mathbf{v}_f - \mathbf{Q} \mathbf{P}_f)^{fsi}$ are evaluated at the fluid-structure interfaces.

In order to model the fluid-structure interaction, some assumptions were made:

- Incompressible fluid and structure are at steady state.
- The control volumes of a fluid domain before and after structural deformation shall be distinguishable.
- Small structural displacements are considered. However, fluid-induced forces in the linear elasticity equation are dependent on the structural displacements.

5. Optimization problem and sensitivity analysis

The examples considered in this work concern compliance minimization with volume constraints of structures under fluid flow loading. The fluid model considered is the Stokes flow. The objective is to find the distribution of a given amount of solid material to obtain a structure with maximum stiffness (or minimum compliance C). The evolutionary topology optimization problem for this case can be stated as:

$$\begin{aligned}
\min_{x_i}: \quad & C(x_i) = \frac{1}{2} \mathbf{u}_s^T \mathbf{K}_s \mathbf{u}_s \\
\text{subject to:} \quad & h = V(x_i) / V_0 = V_s \\
& \mathbf{K}_s \mathbf{u}_s = -(\mathbf{K}_f \mathbf{v}_f - \mathbf{Q} \mathbf{P}_f)^{f,si} \\
& x_i = [0, 1]
\end{aligned} \tag{9}$$

where C is the structural compliance, V_0 is the full design domain volume, V_s is the prescribed final solid volume, nel is the number of elements inside the design domain and x_i represents the discrete design variables, in which 1 is a solid element and 0 is void or fluid.

The sensitivity of the structural compliance due to an element removal can be obtained by its derivative:

$$\frac{\partial C}{\partial x_i} = -\mathbf{u}_s^T \frac{\partial \mathbf{K}_f}{\partial x_i} \mathbf{v}_f + \mathbf{u}_s^T \frac{\partial \mathbf{Q}}{\partial x_i} \mathbf{P}_f - \frac{1}{2} \mathbf{u}_s^T \frac{\partial \mathbf{K}_s}{\partial x_i} \mathbf{u}_s \tag{10}$$

We assume that the first term from the sensitivity expressed in (10) is zero at the element level, since there are no-slip boundary conditions at the walls ($\mathbf{v}_f = \mathbf{0}$). For the second term, the derivatives of the incompressibility matrix is expressed as

$$\frac{\partial \mathbf{Q}}{\partial x_i} = \mathbf{Q}^i \tag{11}$$

where \mathbf{Q}^i is the fluid elemental incompressibility matrix. It represents an addition of a fluid matrix in the problem, once the solid element is removed. The variation of the stiffness is defined by the derivatives of the material as

$$\frac{\partial \mathbf{K}_s}{\partial x_i} = \mathbf{K}_s^i \tag{12}$$

when $x_i = 1$ and null when $x_i = 0$ (fluid or void elements). \mathbf{K}_s^i is the i th element stiffness matrix.

Thus, the sensitivity numbers for stiffness maximization of structures under Stokes fluid flow loads are

$$\alpha_i = -\frac{\partial C}{\partial x_i} = \begin{cases} \frac{1}{2} \mathbf{u}_i^T \mathbf{K}_s^i \mathbf{u}_i - \mathbf{u}_i^T \mathbf{Q}^i \mathbf{P}_i & \text{if } x_i = 1 \\ 0 & \text{if } x_i = 0 \end{cases} \tag{13}$$

where the subscript i indicates the values of \mathbf{u}_s and \mathbf{P}_f at the element level.

6. The extended BESO method for fluid-structure interaction problems

The following algorithm lists the steps of extended the BESO method for steady state and small displacements fluid-structure interaction problems.

1. Define design domain, loads and boundary conditions.

2. Define BESO parameters.
3. Discretize the design domain using a FE mesh for the given fluid and structure domains.
4. Apply the fluid boundary conditions and solve fluid flow FE Equations (4).
5. Identify the fluid flow loads considering the fluid-structure boundary conditions, apply the solid boundary condition and solve structural FE Equation (8).
6. Calculate the sensitivity numbers according to Equation (13).
7. Apply a filter scheme. Project the nodal sensitivity numbers on the finite element mesh and smooth the sensitivity numbers for all (fluid, void and solid) elements in the design domain.
8. Average the sensitivity numbers with their previous iteration ($n - 1$) numbers and save the resulting sensitivity numbers for the next iteration.
9. Determine the target structural volume V_{n+1} for the next iteration.
10. Construct a new fluid-structure design by switching design variables x_i from 1 to 0 and from 0 to 1, tracking the advance of the fluid-void regions. Details of the material update scheme can be found in [7,9].
11. Assemble the global matrices according to the change of the current design.
12. Repeat steps 2-12 until the following stop criterion is satisfied:

$$error = \frac{|\sum_{k=1}^5 C_{n-k+1} - \sum_{k=1}^5 C_{n-5-k+1}|}{\sum_{i=1}^5 C_{n-k+1}} \leq \tau \quad (14)$$

7. Numerical results

The studied example considers a fluid channel with a flexible structure obstructing the flow. The physical model is shown in Figure 1. The fluid flows through the channel with an inlet velocity $v_j = 0.0001$ m/s. The pressure boundary condition is imposed at the outlet as $P^f = 0$ and no-slip conditions are imposed at the fluid flow walls. The fluid density is chosen to be $\rho_f = 1000$ kg/m³ and its viscosity as $\mu = 0.001$ kg m⁻¹ s⁻¹. The structural design domain is represented by a flexible structure of 60×60 μ m, including a rectangular area of 50×10 μ m considered as a solid box in order to avoid trivial solutions or a void structure. The elasticity modulus of the structure is chosen to be as $E = 3 \times 10^9$ N/m² and the Poisson's ratio $\nu = 0.3$. This example is similar to the one presented by [8] for compliance minimization considering design-dependent fluid flow loads.

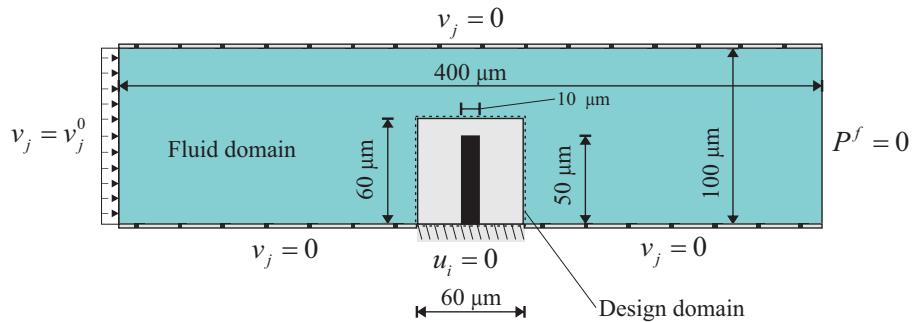


Figure 1: Structural design problem for a fluid flow channel.

The model was discretized with 25600 finite elements in total, being 2304 solid elements and the other 23296 ones modeling the fluid flow. The BESO method started from the initial full design domain with an evolutionary ratio $ER = 2\%$, i.e., removing 2% of the initial structural volume each iteration until the prescribed volume fraction, taken as $V_s = 30\%$ from the design domain. The other BESO parameters are chosen to be the maximum admission ratio $AR_{max} = 1\%$, filter radius $r_{min} = 7.5 \times 10^{-6}$ m and the convergence error tolerance $\tau = 0.001$. Figure 2

shows the structural topology solution, as well as streamlines, velocity and pressure fields of the fluid domain after the structural optimization process. Figure 3 presents the evolutionary history of the structural mean compliance (objective function) along the optimization. The final solution presents a structural topology with mean compliance $C = 2.0800 \times 10^{-20}$.

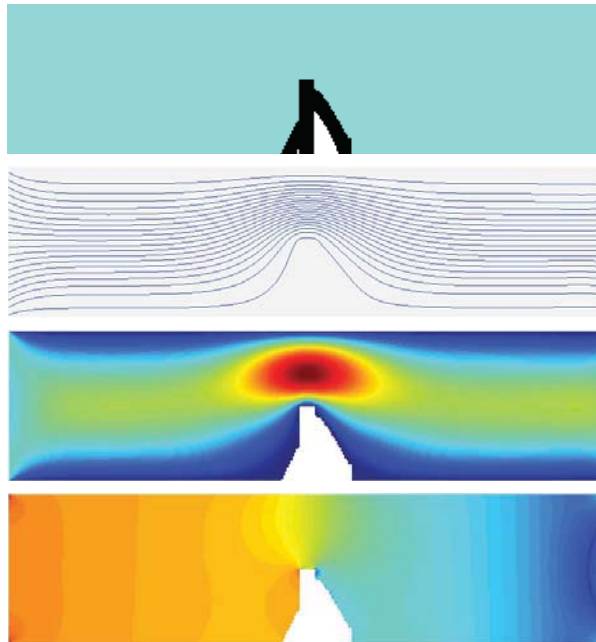


Figure 2: Final topology solution for the structure after the optimization and fluid streamlines, velocity and pressure fields.

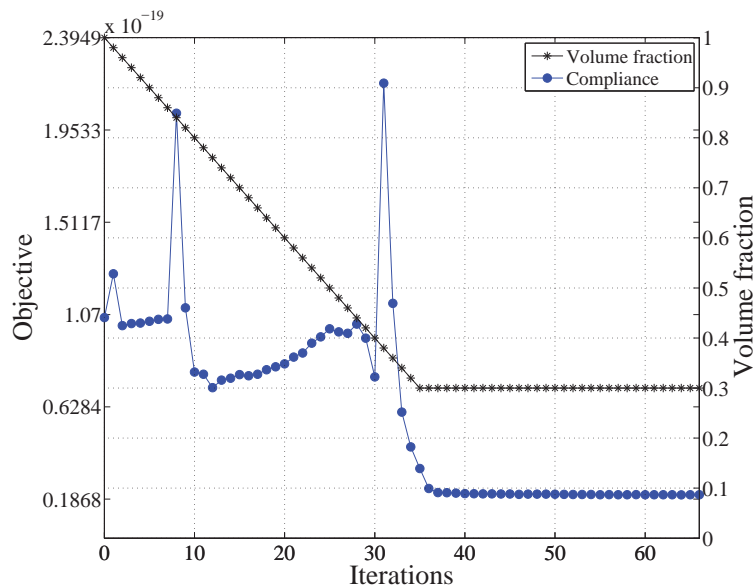


Figure 3: Evolutionary history of the structural mean compliance during the optimization.

The evolutionary procedures showed to be effective in dealing with the moving fluid-structure interfaces. Solid elements were replaced by fluid ones and the fluid flow advanced into the structural design domain. This represents a great potential for design problems considering design-dependent FSI loads and topology optimization. The new term $\mathbf{u}_i^T \mathbf{Q}^i \mathbf{P}_i$ on the sensitivity showed similar behavior as the pressure loading sensitivities from design-dependent pressure loading problems presented in [7]. A greater portion from the regions with low strain energy were first

removed due to the subtraction of this new term on the sensitivity.

10. Conclusions

This paper described a topology optimization problem of structures under viscous fluid flow loading. A new sensitivity analysis is presented. The features of the evolutionary methods allow the switch between fluid and solid elements, which address the main challenge of dealing with moving fluid-structural boundaries during the optimization procedures. This presents some potential use for the area of fluid-structure interaction systems design and it might be of some impact in the research of structural topology optimization. The results considered a flexible structure in contact with stokes fluid flow. The structural topology was designed considering compliance minimization and design-dependent FSI loads. The ongoing research expects to explore new results and bring further discussions on fluid-structure interaction problems considering topology optimization.

9. Acknowledgements

This work was supported by the São Paulo Research Foundation (FAPESP) [grant number 2011/09730-6], [grant number 2013/08293-7].

10. References

- [1] M.P. Bendsoe and N. Kikuchi, Generating optimal topologies in structural design using a homogenization method, *Computer Methods in Applied Mechanics and Engineering*, 71 (2), 197-224, 1998.
- [2] M.P. Bendsoe and O. Sigmund, *Topology Optimization: Theory, Methods and Applications*, Springer-Verlag, Berlin, 2003.
- [3] T. Borrvall and J. Petersson, Topology optimization of fluids in Stokes flow, *International Journal for Numerical Methods In Fluids*, 41 (1), 77-107, 2003.
- [4] G.H. Yoon, J.S. Jensen and O. Sigmund, Topology optimization of acoustic-structure problems using a mixed finite element formulation, *International Journal for Numerical Methods In Engineering*, 70 (9), 1049-1075, 2007.
- [5] F.I. Silva and R. Pavanello, Synthesis of porous-acoustic absorbing systems by an evolutionary optimization method, *Engineering Optimization*, 42 (10), 887-905, 2010.
- [6] S. Kreissl, G. Pingen, A. Evgrafov and K. Maute, Topology optimization of flexible micro-fluidic devices, *Structural and Multidisciplinary Optimization*, 42 (4), 494-516, 2010.
- [7] R. Picelli, W.M. Vicente and R. Pavanello, Bi-directional evolutionary structural optimization for design-dependent fluid pressure loading problems, *Engineering Optimization*, 10.1080/0305215X.2014.963069, 2014.
- [8] G.H. Yoon, Topology optimization for stationary fluid-structure interaction problems using a new monolithic formulation, *International Journal for Numerical Methods In Engineering*, 82 (5), 591-616, 2010.
- [9] Y.M. Xie and X. Huang, *Evolutionary topology optimization of continuum structures: methods and applications*, Wiley, Chichester, 2010.
- [10] P.M. Gresho and R.L. Sani, *Incompressible Flow and the Finite Element Method, Volume 2, Isothermal Laminar Flow*, John Wiley & Sons, Inc. West Sussex, 1998.

Blended Composite Optimization combining Stacking Sequence Tables and a Modified Shepard's Method

Yasser M. Meddaikar¹, François-Xavier Irisarri², Mostafa M. Abdalla³

¹ DLR - Institute of Aeroelasticity, Göttingen, Germany, muhammad.meddaikar@dlr.de

² ONERA, Châtillon, France, francois-xavier.irisarri@onera.fr

³ Aerospace Structures - Delft University of Technology, Delft, The Netherlands, m.m.abdalla@tudelft.nl

1. Abstract

This article presents a computationally-efficient optimization tool for stacking sequence design of blended composite structures. In this tool, blended laminates are designed using stacking sequence tables (SST), coupled with a suitable genetic algorithm (GA). The SST approach guarantees complete-blending, ensuring manufacturability of the optimized design. The concept of successive structural approximations is implemented to improve computational efficiency. Optimizations are carried out on the approximations of responses rather than actual responses themselves, thus reducing the number of expensive design analyses. A recently-proposed modified Shepard's interpolation enriches the quality of the approximations used, by constructing multi-point approximations using the elite designs of the previous iterations. The generality and efficiency of the algorithm is further improved by directly approximating panel loads, thus enabling implementation of a wide range of stress-based design criteria.

An analytical multi-panel blended composite problem is presented as an application. The results show that completely blended and feasible stacking sequence designs can be obtained, having its structural performance close to the theoretical continuous optimum itself.

2. Keywords: stacking sequence optimization, blended composites, structural approximations.

3. Introduction

The use of composite materials in today's aerospace industry is experiencing a strongly increasing trend. The superior mechanical properties of composites and the ability to tailor their properties efficiently has been a major reason for this increased focus on its research and application. For practical design purposes, the ply angles and thickness of composites are usually restricted to a discrete set. The vast design space, coupled with the discrete nature of the design variables poses a tricky task of optimally designing composites.

The focus of this article is toward the design of efficient and manufacturable composite structures with varying stacking sequences in different regions. Spatially varying ply layups are necessary to efficiently tackle local load requirements. However, unless these individual zones or panels are designed correctly, abrupt ply-angle changes or ply-drops may occur, degrading the structural integrity of the component.

In order to overcome this, the concept of laminate blending [1] was introduced. Blending accounts for continuity of material and fibre content between adjacent panels having different stacking sequences. A blended design hence increases manufacturability and structural integrity. The optimization of blended composite designs has been well-studied and presented in [2–6].

Irisarri et al. [7] present a technique for achieving fully-blended designs by optimizing stacking sequence tables (SST) using a genetic algorithm (GA). In addition to guaranteeing fully-blended designs, optimizing using SST provides a detailed manufacturing insight of the ply-drop and transition region between adjacent panels. Furthermore, the GA takes into account several composite effects such as resin accumulation, free-edge delamination and transverse matrix cracking, by implementing industry-standard guidelines as part of the optimization.

In the design of composite structures on a practical-scale using GAs, an important challenge pertaining to computational costs arises from the large number of designs that need to be analysed. The concept of successive structural approximations [8] helps to reduce the computational costs by optimizing on approximations of the responses rather than on expensive responses themselves. Using response approximations in GAs to optimize for stacking sequence have been presented in [4, 9–12].

Irisarri et al. [13] present an effective approach in improving the quality of the approximations used. This is achieved by constructing multi-point structural approximations using a modified Shepard's

method. As a result of the improved quality, the number of FE analyses required in the optimization is shown to be significantly reduced.

The stacking sequence design tool presented here uses the GA for SST [7] as the optimization algorithm. The GA was extended to account for load re-distribution using the optimization strategy presented in [13] for improved computational efficiency. In this work, panel loads are directly used as the responses to be approximated using which, structural responses like buckling and strain are obtained analytically. This novel approach provides the potential of including a wide range of stress-based responses in the optimization using in-house strength prediction tools.

Results from the weight-optimization of a multi-panel stiffened composite plate demonstrate the efficiency of the developed framework. Fully-blended designs having its performance reasonably close to the theoretical optimum were achieved, while requiring a low number of design FE analyses.

4. Optimization Framework

In a successive approximation technique as implemented here, optimizations are carried out on approximations of structural responses, followed by a design update with an FE analysis. This iterative optimization and update helps to reduce the number of required FE analyses.

The structural approximations used in this work are based on the generic formulation presented in [4] as

$$\tilde{f} = \sum_{i=1}^n (\Psi_i^m : A_i + \Psi_i^b : D_i + \Phi_i^m : A_i^{-1} + \Phi_i^b : D_i^{-1} + \alpha_i h_i) + c \quad (1)$$

where \tilde{f} is the approximated response, A_i and D_i are the in-plane and bending stiffness matrices of the i^{th} design region or panel and n is the total number of design regions in the structure. The terms Ψ_i^m , Ψ_i^b , Φ_i^m , Φ_i^b are the sensitivities of the response with respect to the membrane, flexural stiffness matrices and their inverses and α_i is the sensitivity with respect to the laminate thickness h_i . The $:$ operation is the matrix contraction or dot product and is defined as the trace of the product of two square matrices.

4.1 Stacking sequence tables

The optimizer uses a GA for SST [7] as the optimization algorithm. An SST is an intuitive method to represent and design a blended composite structure. For efficient use with a GA, the entire SST is encoded using just three chromosomes

1. SST_{lam} : stacking sequence of the thickest laminate in the SST.
2. SST_{ins} : order of insertion of the plies from the thinner laminate to subsequent thicker ones.
3. N_{str} : number of plies in each of the R panels or regions in the structure.

By optimizing the three chromosomes, an optimal stacking sequence distribution in the blended panels and a safe ply-drop distribution between them are simultaneously obtained.

The GA for SST was extended in the present work to handle multiple independent skins. The term skin hereby denotes a region of the structure locally blended within the panels in that region. For designs of a practical-scale like aircraft wings, the structure is usually manufactured in segments before being joined together. Ensuring complete blending over the entire structure is unnecessary and only restricts the design space. In a multiple-skin optimization, each skin is characterized by its own genotype, subjected independently to the various GA operators. Such a blended scheme is more appealing from an industrial perspective, while also enlarging the available design space.

4.2 Modified Shepard's method - evaluation of panel loads

The present tool uses load approximations to approximate only the panel loads. Vanderplaats et al. [14] present a similar approach in their optimization of isotropic plates. The motive behind such an approach is that once the panel loads in the structure are known, in-house analytical tools can be efficiently used to evaluate a multitude of structural responses, e.g., local buckling, strength at ply-level etc.

The approximated panel load in the k^{th} panel, constructed at a point i can be formulated similar to Eq. 1 as,

$$\tilde{N}_{i_k} = \sum_{j=1}^n (\Psi_{j,k}^m | i : A_j + \Psi_{j,k}^b | i : D_j + \Phi_{j,k}^m | i : A_j^{-1} + \Phi_{j,k}^b | i : D_j^{-1} + \alpha_{j,k} | i h_j) + c_{i_k} \quad (2)$$

where $\Psi_{j,k}^m$, $\Psi_{j,k}^b$, $\Phi_{j,k}^m$, $\Phi_{j,k}^b$ and $\alpha_{j,k}$ are the sensitivities of the panel loads in the k^{th} panel to the respective laminate properties of the j^{th} panel and n is the total number of panels in the structure.

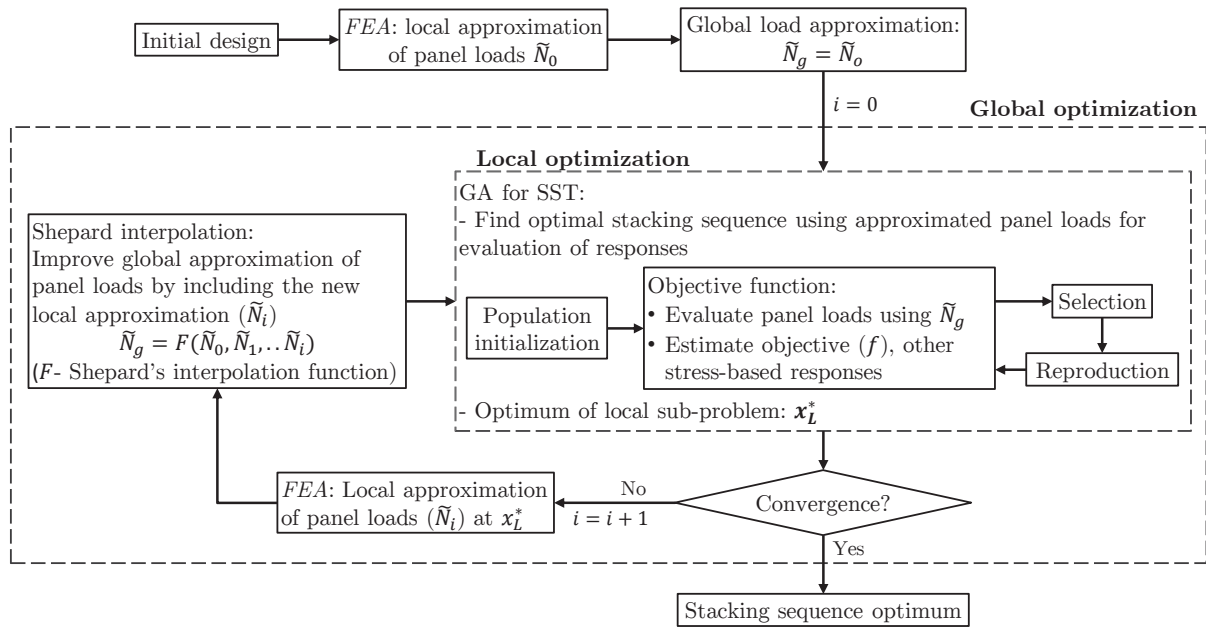


Figure 1: The optimization tool for the discrete optimization step - using GA for SST as the optimization method, Shepard's interpolation for approximation-improvement - assembled within a successive approximation framework.

The approximation in Eq. 2 is a single-point approximation and as such, is accurate in value and derivative only at the point i where it is constructed. The modified Shepard's method presented in [13] improves the quality of the approximation by constructing a multi-point global interpolant using information from several previous points. The actual panel loads \tilde{N} are then evaluated using the multi-point Shepard's approximation constructed from all previous local approximations as

$$\tilde{N} = \frac{\sum_{i=1}^{n_i} w_i \tilde{N}_i}{\sum_{i=1}^{n_i} w_i} \quad (3)$$

where \tilde{N}_i is the local approximation constructed at the i^{th} Shepard point (Eq. 2), n_i is the total number of previous design points and w_i is the interpolation weight [13].

In effect, the modified Shepard's interpolation ensures that as more points are added to the global approximation, the accuracy of the response surface increases over the entire spectrum of previous points leading to a much faster convergence.

4.3 Optimization process

The optimization tool thus combines two core constructs: a GA for SST and a modified Shepard's interpolation. The GA for SST utilizes a multi-point approximation for the evaluation of the panel loads. The GA itself is positioned within a successive approximation framework to account for load re-distribution, whereby new single-point local approximations, Eq. 2, are added after each subsequent global loop to the multi-point Shepard approximation, Eq. 3. The entire optimization procedure can hence be summarized from Fig. 1 as follows:

1. Perform FE analysis at a starting design to obtain first single-point approximation of the panel loads.
2. *Local optimization* - obtain the optimal stacking sequence design of the local problem using the approximated loads to evaluate the structural responses. The GA for SST is utilized for this step.
3. If the design has not converged, construct a new single-point approximation at the optimal design obtained from the sub-problem in Step 2, with an FE analysis. Convergence here occurs when there is no change in the objective of the optimal GA design obtained from two successive global loops.

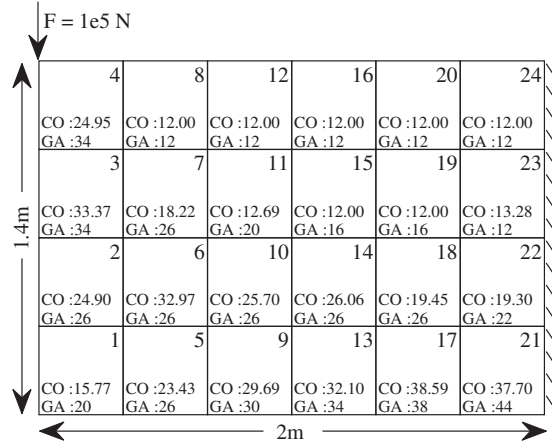


Figure 2: Problem definition and comparison of thickness distribution in the panels for the continuous optimum (CO) and GA optimum (GA).

4. Formulate the multi-point load approximation (Eq. 3) using previous single-point approximations (Eq. 2). Repeat Step 2.

A converged design in Step 3 corresponds then to the optimal stacking sequence design.

5. Results and discussions

A 4X6 multi-panel analytical problem (Fig. 2) was chosen to study the performance of the proposed tool. The objective of the optimization was weight-minimization of the blended composite structure, subjecting the individual panels to buckling, laminate strength and laminate robustness [15] constraints. The stacking sequence of the individual panels were optimized while the properties of the stiffeners were kept a constant; $E = E_1$, $A = 10^{-3}m^2$. The material properties of the Carbon/Epoxy listed in Table 1 with a ply thickness of $0.121mm$ were used. Ply orientations were restricted to steps of 15° . Additionally the following guidelines [7] from the SST were also enforced: laminate balance and symmetry, ply contiguity with a maximum of 4 contiguous plies, ply-disorientation and outer ± 45 plies for damage tolerance.

A two dimensional membrane FE-routine was used to solve for the panel loads and their sensitivities. The separable approximations were constructed using only sensitivities with respect to the in-plane stiffness matrix Ψ_i^m . The local approximation from Eq. 2 is hence reduced to

$$\tilde{N}_{i_k} = \sum_{j=1}^n \Psi_{j,k}^m |i : A_j + c_{i_k} \quad (4)$$

For the sake of comparison, the mass of the designs presented have been normalized with respect to the optimal mass obtained independently using a lamination-parameter based optimizer [16] - $11.351kg$. The design obtained from this continuous optimization can be conveniently termed the continuous optimum. As such, the continuous optimum represents the theoretical upper-bound in performance that can be achieved, since a lamination parameter-based continuous optimization assumes both ply-angles and thickness as continuous variables, while also not including the required constraint on blending. It is hence a convenient measure of comparison for the discrete designs obtained.

5.1 Optimal stacking sequence design

The optimal, fully-blended and feasible design obtained from the proposed tool was found to have a normalized mass of 1.097 , after just 14 global iterations. This increase in weight of $\sim 10\%$ over the continuous optimum is reasonable considering: the discrete stacking sequence design is fully blended, includes practical design guidelines and is limited by the discrete nature of the ply angles and thickness. The stacking sequence of this GA optimum can be obtained from its genotype and corresponding SST, presented in Table 3.

5.2 Optimization with multiple skins

Of particular interest to large-scale problems is the ability to design blended structures, where the blending

Table 1: Material properties: AS4/3501-6 [17]

E_{11} (GPa)	E_{22} (GPa)	G_{12} (GPa)	ν_{12}	ρ (kg/m ³)
142	10.3	7.2	0.27	1570
X_t (MPa)	X_c (MPa)	Y_t (MPa)	Y_c (MPa)	S (MPa)
2280	1440	57	228	71

Table 2: Mass optimization with multiple blended skins - normalized objective and critical constraint failure (the set of panels within each pair of braces constitute an independent skin)

Independently-blended skins	Objective	Critical constraint failure
1 - {1-24}	1.097	1.010
2 - {1-12}, {13-24}	1.079	1.004
2 - {1,2,5,6,9,10,13,14,17,18,21,22}, {3,4,7,8,11,12,15,16,19,20,23,24}	1.056	1.005
3 - {1-8}, {9-16}, {17-24}	1.062	1.001

is enforced in segments. The results in Table 2 show the optimal designs when the 24-panel structure is comprised of 1, 2 and 3 independently-blended skins.

As can be expected, an increase in the number of skins leads to a weakening on the requirement of blending, since blending is now enforced over a smaller number of panels. The resultant increase in design space leads to a reduction in mass as the number of skins increases. The term critical constraint failure here denotes the lowest factor of safety among all constraints. A value greater than 1 would hence imply a feasible design.

6. Conclusions

This article proposes an efficient optimization tool for blended composite design. The proposed approach combines two techniques: a GA using stacking sequence tables and multi-point approximations using a modified Shepard's interpolation method. A novel approach of directly approximating the structural loads is presented in this work. Working with panel loads directly is consistent with an industrial quick-sizing approach, providing the potential to include a large range of stress-based criteria in the optimization using in-house tools.

The performance of the tool is studied on a 24-panel composite blending problem. The results show that fully blended, feasible and guidelines-adhering stacking sequence designs can be obtained having its performance comparable to the theoretical optimum itself. Of equal importance, a low number of FE analyses required to reach the optimal design also show the computational efficiency of the proposed method.

7. References

- [1] Z. Zabinsky. Global optimization for composite structural design. In *Proceedings of the 35th AIAA/ASME/ASCE/AHS/ASC Structures, Structural Dynamics, and Material Conference*, 1994.
- [2] B. Liu and R. T. Haftka. Composite wing structural design optimization with continuity constraints. In *Proceedings of 42nd AIAA/ASME/ASCE/AHS/ASC Structures, Structural Dynamics, and Materials Conference, AIAA Paper*, volume 1205, 2001.
- [3] D. B. Adams, L. T. Watson, Z. Gürdal, and C. M. Anderson-Cook. Genetic algorithm optimization and blending of composite laminates by locally reducing laminate thickness. *Advances in Engineering Software*, 35(1):35–43, 2004.
- [4] S. IJsselmuiden, O. Seresta, M. Abdalla, and Z. Gürdal. Multi-step stacking sequence design and blending of composite structures. In *7th World Congress on Structural and Multidisciplinary Optimization*, pages 795–803, 2007.
- [5] J. Van Campen, O. Seresta, M. M. Abdalla, and Z. Gürdal. General blending definitions for stacking sequence design of composite laminate structure. In *Proceedings of 49th AIAA/ASME/ASCE/AHS/ASC structures, structural dynamics, and materials conference, Schaumburg, IL, USA*, pages 7–10, 2008.
- [6] O. Seresta, M. M. Abdalla, and Z. Gürdal. A genetic algorithm based blending scheme for design of multiple composite laminates. In *50th AIAA/ASME/ASCE/AHS/ASC Structures, Structural Dynamics, and Materials Conference*, 2009.

Parallel Particle Swarm Optimization on GPU with Application to Trajectory Optimization

Qi Wu¹, Fenfen Xiong²

¹ Beijing Institute of Technology, School of Aerospace Engineering, Beijing, wuqi_55@163.com

² Beijing Institute of Technology, School of Aerospace Engineering, Beijing, fenfenx@bit.edu.cn. Corresponding author

Abstract

In simulation-based design optimization, one of the greatest challenges is the intensive computing burden. In order to reduce the computational time, a parallel implementation of the particle swarm optimization (PSO) algorithm on graphic processing unit (GPU) is presented in this paper. Instead of executed on the central processing unit (CPU) in a serial manner, the PSO algorithm is executed in parallel taking advantage of the general-purpose computing ability of GPU in the platform of compute unified device architecture (CUDA). The processes of the fitness evaluation, the updating of velocity and position of all the particles of PSO are parallelized and respectively introduced in detail. Comparative studies on optimization of three benchmark test functions are conducted by running the PSO algorithm on GPU (GPU-PSO) as well as CPU (CPU- PSO), respectively. The impact of design dimension, as well as the number of particles and optimization iteration in PSO on the computational time is investigated. From test results, it is observed that the computational time of GPU-PSO is much shorter compared to that of CPU- PSO, which demonstrates the remarkable speedup capability of GPU-PSO. Finally, GPU-PSO is applied to a practical gliding trajectory optimization problem to reduce the computing time, which further demonstrates the effectiveness of GPU-PSO.

Keywords: PSO; GPU; CUDA; Trajectory Optimization

1. Introduction

Particle swarm optimization (PSO) developed by Kennedy *et. al.* in 1995 is an intelligent random global optimization algorithm inspired by the social behaviour of bird flocking or fish schooling [1]. In PSO, each particle in the swarm adjusts its position in the search space based on the best position it has found so far as well as the position of the known best-fit particle of the entire swarm, and finally converges to the global best point in the whole search space. Due to its easy implementation and competitive performances, the PSO algorithm has been extensively applied to optimization of very complex functions in a wide range of applications [2]. However, since the optimizing process of PSO requires a large number of fitness evaluations in the whole search space, it takes a long time for PSO to find optimal solutions especially for problems with high dimension or that needs a large swarm population for search. This becomes more serious when the performance functions are highly computational expensive. Traditionally, the fitness evaluations in PSO are done in a sequential way on the central processing unit (CPU). Thus, the computing speed of PSO may be quite slow for practical applications.

At present, it is difficult to improve the computing speed of PSO from the viewpoint of algorithm. Meanwhile, it may reduce the computing accuracy. As a traditional graphics-centric workshop, the graphics processing unit (GPU) shows faster float-point operation and higher memory bandwidth in scientific computing fields compared to CPU [3]. Through integrating CPU and GPU and taking advantages of both, the heterogeneous computing technique has become a research focus for computational speedup in recent years. The compute unified device architecture (CUDA) developed by NVIDIA corporation is a famous platform for heterogeneous computing, which has greatly simplified programming on GPU and been applied to lots of general computing [4]. In order to reduce the computational time of PSO, a parallel implementation of the PSO algorithm based on GPU in CUDA is developed, named as GPU-PSO for short in this paper, which greatly speeds up the computing.

2. Review of PSO

PSO is a stochastic global optimization technique inspired by the social behaviour of bird flocking or fish schooling. With PSO, each particle in the swarm adjusts its position in the search space based on its best position found so far as well as the position of the known best-fit particle of the entire swarm, and finally converges to the global best point. The search of the whole design space is done by a swarm with a specific number of particles. During each of the optimization iteration, the position and velocity of each particle are both updated according to its current best position ($P_{gDb}(t)$) and best position of the entire swarm ($P_{pDb}(t)$). The position X_{ij} and velocity V_{ij} of each particle on one dimension are updated as follows:

$$V_{ij}(t+1) = wV_{ij}(t) + c_1r_1(P_{pDb}(t) - X_{ij}(t)) + c_2r_2(P_{gDb}(t) - X_{id}(t)),$$

$$X_{ij}(t+1) = X_{ij}(t) + V_{ij}(t), \quad i = 1, 2, \dots, n; j = 1, 2, \dots, d.$$
(1)

where n is the number of particles in the swarm; d is the optimization dimension; c_1 and c_2 are learning factors, which are non-negative constants; r_1 and r_2 are random numbers uniformly located in the interval $[0, 1]$; w is the inertia weight used to balance the global and local search abilities of PSO, which is a constant lies between 0 and 1; $V_{ij} \in [-V_{max}, V_{max}]$ is the velocity on the j^{th} dimension of the i^{th} particle with V_{max} as a constant pre-specified according to the objective function. If $|V_{ij}| \geq V_{max}$, it will be set as $V_{ij} = V_{max}$ or $V_{ij} = -V_{max}$. The convergence rate is impacted by V_{max} , which can avoid premature of PSO. The general procedure of the PSO algorithm is described step by step in Figure 1 as below.

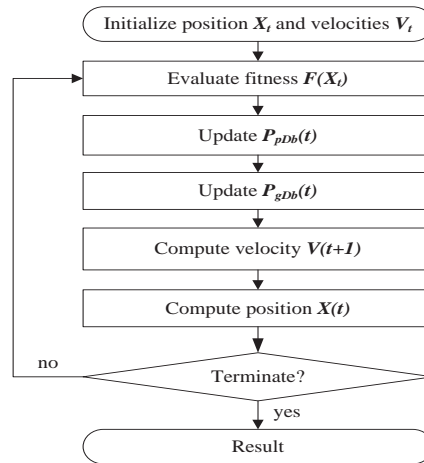


Figure 1: Flowchart of the particle swarm optimization algorithm

3. Introduction of GPU based parallel computing

GPU was originally designed especially for the purpose of image and graphic processing on computers, where computational intensive and highly parallel computing is required. It has been reported that the floating-point computation speed is 10 times of CPU, and the memory bandwidth is 5 times of the general memory compared to the cotemporary CPU [3]. Therefore, the GPU has been widely applied to general-purpose computing, such as scientific computation, fluid mechanics simulation, molecular mechanics computation etc. [5-6].

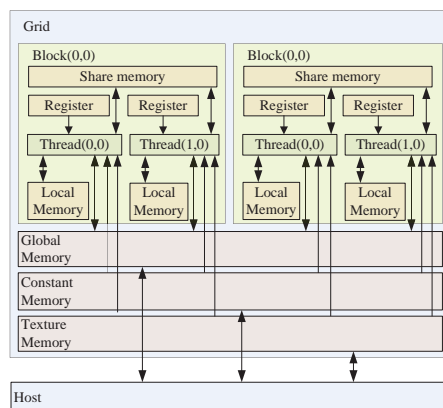


Figure 2: Memory Model of CUDA [7]

CUDA is a parallel computing platform based on the SIMD (Single Instruction, Multiple Data) [4]. The memory model of CUDA is depicted in Figure 2, in which threads are divided into three levels: thread, block and grid. Each thread and block has its unique index. Each thread has a small and fast private register, while each block has a faster shared memory. The operation of memory read and write can be done by all threads in the same block. Both global memory and constant memory existing in grid are visible to all threads.

As an extended library in the environment of C/C++, CUDA C/C++ greatly facilitates the fast coding of kernel function running on GPU of NVIDIA for developers. Through calling the kernel function by CPU, the program can be run on the GPU parallelly. The program execution process of CUDA is divided into three steps: copy data to

GPU, execute kernel function and copy data to CPU.

4. GPU-Based PSO

Clearly, the evaluation of fitness function and updating of each particle in PSO is independent to each other. Therefore, PSO has the basic architecture of parallel computing. The whole process of parallel computing can be achieved through the one-one correspondence between each particle in PSO and the thread of GPU. The detailed procedure is: (1) thread is set on GPU with the same number as that of particles; (2) storage space is set up for each particle to store its velocity, position and other related data; (3) fitness evaluation and updating for all the particles are done simultaneously using GPU. Here, the execution model for position updating of particle in Figure 3 is used as a demonstration to show the parallel computing procedure of PSO. For the parallel computing of velocity updating and fitness evaluation, the procedure is the basically same.

In Figure 3, each block contains (N_b+1) thread. The smallest unit in CUDA is half-warp (16 threads). Therefore, (N_b+1) is generally set as the integer multiple of 16. Pid is the index number of thread, *i.e.* the serial number of each particle in PSO. n is the total number of particles, d is the optimization dimension. N_t is the total number of thread block, which is determined by $N_t = (n + N_b - 1) / N_b$.

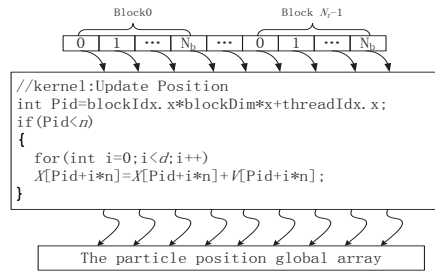


Figure 3: The execution model based on CUDA

Based on the procedure of PSO and the parallel scenario introduced above, GPU-PSO is established, of which the flowchart is illustrated in Figure 4. Clearly, the processes of initiation, updating and fitness evaluation are all paralleled, of which the fitness evaluation is the prime component for parallelization.

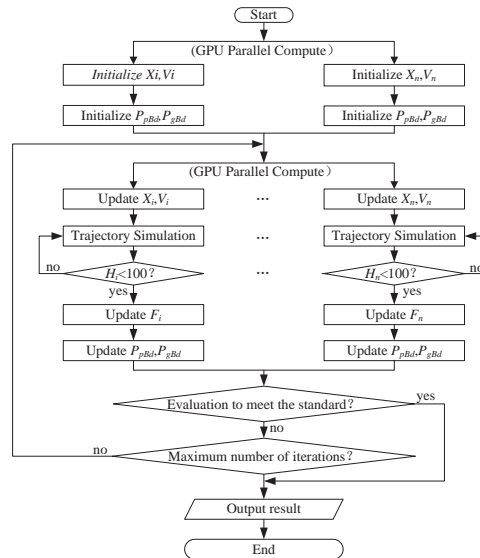


Figure 4: Flowchart of GPU-PSO

5. Comparative studies

In this section, four commonly used functions listed in Table 1 are used to verify the effectiveness of the developed PSO-GPU. The PSO algorithm without parallel computing (CPU-PSO) is also employed to optimize these functions. The speedup ratio s_p of GPU-PSO is calculated by taking the ratio of the computational time t_{cpu} of CPU-PSO and t_{gpu} of GPU-PSO.

All the parameters in PSO are set as follows as is commonly done in practice: the inertia weight $w = 0.7298$, learning factor $c_1 = c_2 = 2.05$, velocity of updating particle is the right bound of each function. In order to

effectively investigate the speedup capability of GPU-PSO over CPU-PSO, the convergent criterion is set as that when the number of optimization iterations reaches 5000, the optimization is stopped. The design dimension is set as $d=50$ for all the four functions, and different number of particles n are tested to investigate its impact on the speed-up ratio. The computational environment employed in this work is shown as Table 2.

Table 1: Test functions

Names	Functions
Sphere	$f_1 = \sum_{i=1}^d x_i^2, \quad -100 \leq x_i \leq 100$
Rosenbrock	$f_2 = \sum_{i=1}^d [x_i^2 - 10 \cos(2\pi x_i + 100)], \quad -10 \leq x_i \leq 10$
Griewank	$f_3 = \frac{1}{4000} \sum_{i=1}^d x_i^2 - \prod_{k=1}^d \cos(x_i / \sqrt{i}) + 1, \quad -600 \leq x_i \leq 600$
Ackley	$f_4 = -20 * \exp\left(-0.2 * \text{sqrt}\left((1/d) * \left(\sum_{i=1}^d x_i^2\right)\right)\right) - \exp\left((1/d) * \left(\sum_{i=1}^d \cos(2\pi x_i)\right)\right) + \exp(1) + 20, \quad -8 \leq x_i \leq 8$

Table 2: The computational environment

CPU	Intel i7-4770k
GPU	NVIDIA GTX TITAN BLACK
Memory	16G
OS	Windows 7 X64
Platform	Visual Studio 2013, CUDA6.5

Table 3: The results of Sphere function ($d=50$)

n	f^*		t/s		s_p
	CPU	GPU	CPU	GPU	
1600	0.775	0.000	11.342	1.638	6.924
2500	0.000	0.000	18.235	1.703	10.708
3600	0.000	0.000	24.820	1.841	13.482
4900	0.000	0.000	40.404	1.888	21.400
6400	0.000	0.000	59.657	1.950	30.593

Table 4: The results of Rosenbrock function ($d=50$)

n	f^*		t/s		s_p
	CPU	GPU	CPU	GPU	
1600	1.636	11.851	11.996	1.638	7.324
2500	33.599	5.272	21.606	1.716	12.591
3600	48.648	3.988	26.645	1.825	14.600
4900	30.998	2.679	42.295	1.918	22.052
6400	32.283	0.080	61.261	1.966	31.460

Table 5: The results of Griewank function ($d=50$)

n	f^*		t/s		s_p
	CPU	GPU	CPU	GPU	
1600	0.693	0.000	42.323	1.935	21.872
2500	0.000	0.000	66.628	1.747	38.139
3600	0.000	0.000	98.093	1.872	52.400
4900	0.000	0.000	141.198	1.950	72.409
6400	0.000	0.000	193.207	1.950	99.081

Table 6: The results of Ackley function ($d=50$)

n	f^*		t/s		s_p
	CPU	GPU	CPU	GPU	
1600	0.031	0.000	43.025	1.310	32.844
2500	0.000	0.000	75.536	1.342	56.281
3600	0.000	0.000	98.186	1.389	70.688
4900	0.000	0.000	143.191	1.435	99.7429
6400	0.000	0.000	198.465	1.435	138.303

Table 7: The results of Griewank function ($d=100$)

n	f^*		t/s		s_p
	CPU	GPU	CPU	GPU	
1600	0.000	0.000	99.391	3.454	28.776
2500	0.001	0.000	173.736	3.624	47.940
3600	0.000	0.000	250.893	3.770	66.550
4900	0.000	0.000	315.421	3.913	80.681
6400	0.000	0.000	464.017	4.013	115.628

Table 8: The results of Ackley function ($d=100$)

n	f^*		t/s		s_p
	CPU	GPU	CPU	GPU	
1600	0.018	0.000	86.429	2.449	35.292
2500	0.003	0.000	168.461	2.538	66.376
3600	0.000	0.000	221.264	2.620	84.566
4900	0.000	0.000	341.765	2.701	126.533
6400	0.000	0.000	434.846	2.767	157.154

The optimal objective function values (f^*), the computing time (t) and the speedup ratio (s_p) are listed in Tables 3-8, from which it is clearly observed that the GPU-PSO runs much faster than CPU-PSO with very high speed-up

ratio. Meanwhile, the optimal solutions of GPU-PSO and CPU-PSO are basically the same, which show great agreements to the real optimal solutions ($f=0$), indicating the good convergence property of GPU-PSO. It is also noticed that the complexity of test functions has large impact on the speed-up ratio, which can be derived from the results in Tables 3-6. Clearly, from the Sphere to Ackley functions, the complexity is basically increasing, and the corresponding speed-up ratio is increasing as well. Meanwhile, the speed-up ratio is also increased with the increase of the number of particles n . This is self-evident since the evaluation of all particles are executed serially in CPU-PSO, thus more particles yields more computational time, while this is done all at once in GPU-PSO. However, once n reaches to a certain value, the speedup ratio is increased very slowly. The reason is that GPU only contains 2880 CUDA CORE.

To further study the impact of design dimension on the speed-up ratio, $d=100$ are also tested. Considering the space limit, only results of the last two functions are shown (see Tables 7 and 8). It is found that for all the functions, the speed-up ratio with $d=100$ is larger than that with $d=50$, indicating that the speed-up ratio is improved with the increase of optimization dimension. It can be concluded that generally the higher of the dimension and the more of the particles, the larger of the speed-up ratio obtained by GPU-PSO. All these results demonstrate the effectiveness and good speed-up capability of GPU-PSO.

6. Application of GPU-PSO to trajectory optimization

6.1. Description of trajectory optimization

Trajectory optimization of aircraft is actually an optimal control problem, which is generally solved by the direct method [8]. As a traditional direct method, the direct shooting method is frequently used for solving practical trajectory optimization due to its simplicity and convenience. With this method, the optimal control is transcribed into a nonlinear programming problem (NLP) through parameterizing the control on certain time nodes and treated as design variables. For engineering applications, it is necessary to generate trajectory as fast as possible. However, oftentimes, a large number of discreted nodes are required to parameterize the control variable in order to ensure high accuracy especially for complex and long-time flight mission, which may increase the time of optimal trajectory generation. Therefore, GPU-PSO is applied to the glide trajectory optimization to save computational time. The optimal control of the glide trajectory optimal problem is formulated as [9]:

$$\begin{aligned}
 & \text{Find } \alpha(t), \quad 0^\circ \leq \alpha \leq 10^\circ \\
 & \text{Max } J = L(\tau_f) \\
 & \text{s.t. } h(\tau_f) \leq 100 \\
 & \begin{cases} m \frac{dV}{dt} = -C_x q S - mg \sin \theta \\ mV \frac{d\theta}{dt} = C_y q S - mg \cos \theta \\ \frac{dL}{dt} = V \cos \theta, \quad \frac{dh}{dt} = V \sin \theta \end{cases} \quad (2)
 \end{aligned}$$

where V, θ, L, h are respectively velocity, trajectory angle and height, with initial values as $V_0=542.725\text{m/s}$, $\theta_0 = 10^\circ$, $L_0=0.0\text{m}$ and $H_0=28541\text{m}$; q, C_x, C_y are the dynamic pressure, drag coefficient and lift coefficient, respectively; $S=0.126\text{m}^2$ is the reference area; $g = 9.8\text{m/s}^2$ is the acceleration of gravity; $m=210\text{kg}$ is the mass of vehicle. C_x and C_y are calculated using linear interpolation with respect to h, Ma and α .

The design variable of the problem is the law of the angle of attack $\alpha(t)$, which is constrained during flight due to the structural and control requirements. The objective function is to maximize the range of the vehicle $L(\tau_f)$ without any power by control as much as possible. The terminal boundary constraint is $h(\tau_f) \leq 100\text{m}$, i.e. the flight task is completed when the flight height is less than 100m. The direct shooting method is employed to solve the gliding trajectory optimization in Eq. (2) and GPU-PSO is employed to solve the transcribed NLP. The flight time $[\tau_0, \tau_f]$ is divided into N sub-intervals as $\tau_0 < \tau_1 < \dots < \tau_{N-1} < \tau_N = \tau_f$. Correspondingly, the angle of attack $\alpha(t)$ is discreted at the $N+1$ discreted time nodes as $\alpha_0, \alpha_1, \dots, \alpha_i, \dots, \alpha_{N-1}, \alpha_N$. The control variable $\alpha(t)$ at anytime point is predicted by the spine interpolation over the $N+1$ discreted time nodes and the corresponding angle of attack. Clearly, the flight time τ_f is unknown. In this work, it is not considered as a design variable, and is only used for the calculation of trajectory and interpolation of angle of attack. If the flight time $\tau > \tau_f$, then $\alpha(\tau) = \alpha_{\tau_f}$.

6.2. Results

For this problem, the optimization process is terminated when the variation of the maximum flight range is less than $0.01m$. The number of particles is set as $n=10000$ and $d=51$ ($N=50$). The parameters in PSO are set as the same as those in the above four mathematical examples. The optimal angle of attack is shown in Figure 5. It is found that both methods yield almost the same optimal solutions, while GPU-PSO (1464.146s) needs much shorter time than CPU-PSO (9.064s), with about 161X speedup. The optimal angle of attack and range of GPU-PSO are slightly different from those of CPU-PSO, which is caused by the difference of the floating point computing method between CPU and GPU. This can be reduced and even eliminated by screwing up the code [10].

Although, the speed-up capability is remarkable, it is necessary to verify the accuracy of GPU-PSO. From the theory of lift-to-drag ratio, the maximum range can be approximately obtained when gliding with maximum lift-to-drag ratio [11]. Therefore, the trajectory with maximum lift-to-drag ratio is calculated by plugging different angle of attack $\alpha(\tau)=1^\circ, \dots, 10^\circ$ into the dynamic model in Eq. (2) and Rung-Kutta numerical integration is used to obtain the lift-to-drag ratio and range. It is found that $\alpha(\tau)=10^\circ$ yields the largest lift-to-drag ratio, so as the range. Clearly, the optimal angle of attack by GPU-PSO is equal to 10° during almost the whole flight mission, which is basically the same as that derived from the lift-to-drag theory. The trajectories of $\alpha(\tau)=10^\circ$, GPU-PSO and CPU-PSO are shown in Figure 6. It is noticed that the three trajectories are almost the same, yielding very similar range (129.02, 129.06 and 129.70km). These results demonstrate the effectiveness of GPU-PSO.

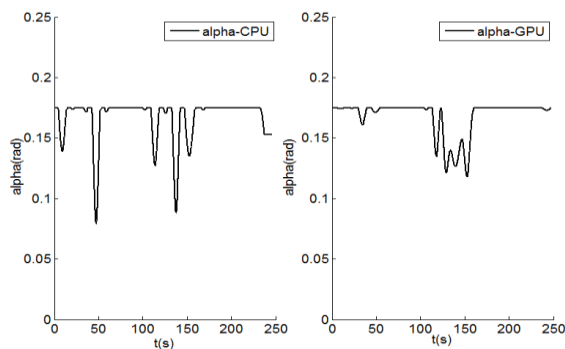


Figure 5: The optimal $\alpha(\tau)$ of both methods

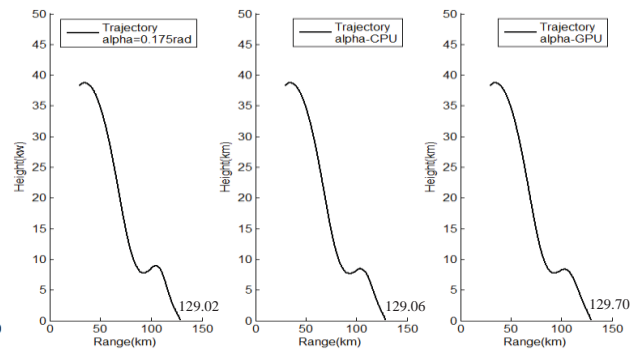


Figure 6: Optimal trajectories

7. Conclusions

In this paper, based on the standard PSO algorithm, the parallel computing of PSO is developed using the GPU technique in the CUDA platform. Through the comparison of GPU-PSO and CPU-PSO by four mathematical functions, it is observed that the developed GPU-PSO can greatly save computational time, while yields good accuracy and convergence properties. The application of GPU-PSO to a glide trajectory optimization problem further demonstrates the effectiveness and advantage of GPU-PSO, as well as its great potential to practical engineering optimization.

References

- [1] J. Kennedy, R C.Eberhart, Particle Swarm Optimization, *Proc of IEEE International Joint Conference on Neural Networks*, Washington DC : IEEE Computer Society, 1995: 1942 - 1948.
- [2] F. Bergh, A. P. Engelbrecht, Cooperative Learning in Neural Net Works Using Particle Swarm Optimizers, *South African Computer Journal*, 200 (011): 84 – 90.
- [3] Y. Zhou, Y. Tan, et al, GPU-based Parallel Particle Swarm Optimization, *2009 IEEE Congress on Evolutionary Computation* (CEC 2009).
- [4] NVIDIA, *NVIDIA CUDA C Programming Guide 6.5*, 2014.
- [5] J. D. Owens, M. Houston, D. S. Luebke, et al, *GPU Computing*, IEEE, 2008, 96(5): 879 – 899.
- [6] J. D. Owens, D. Luebke, N. Govindaraju, et al, A Survey of General-purpose Computation on Graphics Hardware, *Computer Graphics Forum*, 2007, 26(1): 80 – 113.
- [7] J. Sanders and E. Kandrot, *CUDA by Example: An Introduction to General-Purpose GPU Programming*, Addison-Wesley Professional, 2010
- [8] E. Yong, L. Chen, G. Tang, A Survey of Numerical Methods for Trajectory Optimization of Spacecraft, *Journal Of Astronautics*, 2008, 29(2): 398-406.
- [9] X. F. Qian, R. X. Lin, and Y. N. Zhao, *Flight Dynamics of Missile*, Beijing: Beijing Institute of Press, 2000. (in Chinese)
- [10] D. B. Kirk, W. Hu, *Programming Massively Parallel Processors*, Elsevier Science Ltd, 2010.
- [11] J. Shi, Z. Wang, X. Cao, W. Liu, K. Yang, Design of glide trajectory for gliding range-extended projectile, *Journal of Nanjing university of Science and Technology*, 2007, 31(2): 147 – 153.

Method of Variable Transformation for Topology Optimization with Clear Boundary Shape

Vladimir M. Uskov¹, Kirill A. Balunov¹

¹ Central Aerohydrodynamic Institute, Zhukovsky, Moscow region, Russia, vladimiruskov@tsagi.ru

1. Abstract

The problem of topology optimization based on the density-based approach using gradient optimization methods is considered in the paper. The filtering procedure is used to avoid local minima and to control the topology design. Commonly this procedure is applied to the sensitivity field, since filtering of the design variables leads to strong blur solutions. To overcome these blurring an additional procedure is required. In this paper both sensitivity filter and density filter are used. But for the density filter the following new approach is applied. Transformation of variables with values from 0 to 1 to new design variables with values from $-\infty$ to $+\infty$ is performed. Then simple Gauss filtering is applied and reverse transformation to the original variables is fulfilled. The transformation function has the following features: for the “grey values” it is nearly linear, and at $-\infty$ and $+\infty$ it approaches asymptotically to the value 0 and 1, respectively. Variation statement of the problem of finding this transformation function is proposed. Also, the change of the properties of transformation function allows controlling topology layout. This approach is demonstrated on the problems of topology optimization for minimization of structural compliance at a given volume. The advantages of proposed approach and the obtained solutions are discussed.

2. Keywords: Topology optimization, Conservative filtering, Design variable transformation, Clear boundaries

3. Introduction

Topology optimization is a modern tool of structural design. In this method, the distribution of the structural material is described by design variables taking the discrete values 0 and 1. For the efficient use of gradient optimization methods it is required to switch from integer to real design variables. The general approach is the addition of intermediate values between 0 and 1. However, this leads to “gray” solutions that are difficult to interpret by designer, and besides, they may significantly differ from the optimal “clear” solutions. In common methods of topology optimization with penalization [1] the proportion of “gray” is regulated by penalization parameter p . The increase in parameter p enhances the sharpness of the design shape boundaries, but it can also increase the risk of sub-optimal design, so this parameter should be limited. One of the ways to avoid the risk of stopping the algorithm in a local minimum is to use filtering procedure. On the other hand, filtering also increases the proportion of “gray”. It is necessary to find a compromise between the increase in penalization parameter and the degree of filtering. There are some methods of filtering, which reduce the side effect of blurring. Firstly, it is due to the filtering of the derivative of the objective function with respect to the design variables (sensitivity) instead of filtering of design variable values. Secondly, the filtering result is subjected to further processing, for example, by application of projection method [2]. This projection filtering method requires additional computations and significantly increases computational costs. There is also the problem to satisfy the specified constraints. To overcome this difficulty related procedure has become quite complicated [3]. An alternative approach is shown in [4]. This approach is accomplished by a transition to an infinitely large penalization parameter and by an introduction of new design variables which belong to the range $(-\infty, \infty)$. Filtering procedure in this method is carried out on these new variables. This method allows getting closer to the optimal design with clear boundary shape at low computational cost. The problem of finding the best transformation function to the new design variables is considered in the paper.

4. Conservative filtering

We introduce a new design variables z of the computational domain $(-\infty, \infty)$, which are associated with the design variables y of the physical domain $[0, 1]$ as follows:

$$y = \frac{1}{2}(1 + f(2z)), \quad (1)$$

$$z = \frac{1}{2}f^{-1}(2y - 1) \quad (2)$$

In paper [4] function $f(z)=\tanh(z)$ is used. Not formally speaking, this transformation does not change the “gray”

values because the mapping is close to the identity, while the “white” and “black” values vary significantly. Filtration of the y values is performed in three stages. First, turn to the computational domain, according to Eq.(2), then carry out Gaussian filtering of distribution of values z , and return to the physical domain, according to Eq.(1). Let us demonstrate the result of filtering in the one-dimensional and two-dimensional cases. Figure 1 shows the result of one-dimensional filtering case with the initial stepwise distribution:

$$y(t) = \begin{cases} \varepsilon_{\min} & , t < 0 \\ 1 - \varepsilon_{\max} & , t \geq 0 \end{cases}$$

With the same Gaussian filter radius r_s , three sets of values ε_{\min} and ε_{\max} is considered: 1) $\varepsilon_{\min} = \varepsilon_{\max} = \varepsilon_2$, 2) $\varepsilon_{\min} = \varepsilon_2$, $\varepsilon_{\max} = \varepsilon_1$, 3) $\varepsilon_{\min} = \varepsilon_{\max} = \varepsilon_1$. Values ε_1 and ε_2 satisfy the inequalities $0 < \varepsilon_1 < \varepsilon_2 < 1$. These examples demonstrate that the closer to the boundary values, the less blur. We also call attention to the possibility of shifting the position of step without significant blurring (Figure 1b).

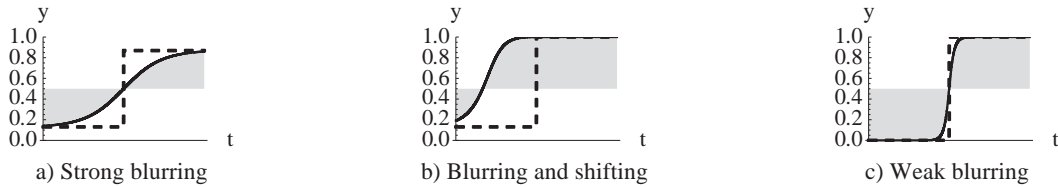


Figure 1: Filtering of stepwise distribution in new design variables

Figure 2 shows the result of filtering in two dimensions with different radii r_s . The initial distribution contains three sets of values ε , 0.5 , $1 - \varepsilon$, $\varepsilon \ll 1$ submitted by the shades of gray. The boundaries between these values vary significantly in various ways. The boundary between the black and gray, as well as the boundary between gray and white is not preserved, it is blurred and shifted so that the gray area is significantly reduced when large radii filtration. On the contrary, the boundary between black and white is still the same, it is not blurred and does not move. The dashed line is applied for clarity, to emphasize this effect.

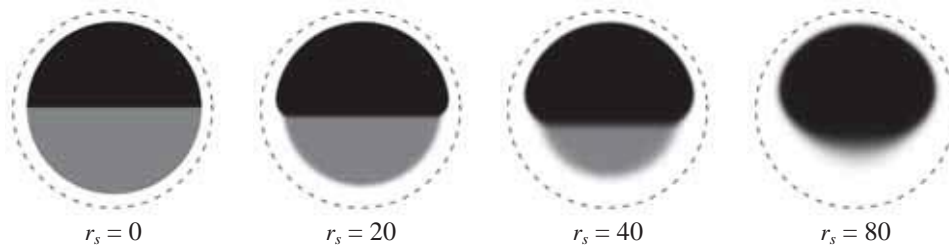


Figure 2: Conservative filtering with different radii r_s

Since this filter keeps formed boundaries of the structure, it can be called conservative filtering.

5. The choice of transformation function

The transformation function f , used in the Eq.(1) and Eq.(2), must have the following properties. For simplicity, we consider only the antisymmetric functions and therefore we consider the range from 0 to ∞ , and for negative values of z we redefine the function as follows $f(z) = -f(-z)$. The function must be monotonically increasing, have a linear region near zero, asymptotically fast enough approaches the limit values -1 and 1 , it is necessary for conservative filtering effect. From heuristic reasons, we assume that the best function is the least different from linear in all computational domain. A measure of the difference can be written as functional. These requirements lead us to the variation formulation of finding the optimum transformation function

$$\begin{cases} F(f, m, \alpha) = \int_0^{\infty} \frac{f^{(m)}(x)^2}{f'(x)^\alpha}, & \alpha \geq 0 \\ f'(x) \geq 0, f'(0) = 1, f(\infty) = 1, f^{(2k)}(0) = 0, k = \overline{0, [(m-1)/2]} \end{cases} \quad (3)$$

Meaning of the parameter α is that it allows us to control the speed of the asymptotic approaching, and at the same time the value of $\alpha > 0$ guarantees a monotonic increase function. Two cases $m=2$ and $m=3$ for $\alpha=1$ are considered. In the case $m=2$ the functional Eq.(3) attains its minimum on the extremal

$$f(z) = 1 - e^{-z} \quad (4)$$

This function has a non-zero second derivative; therefore, the redefined function has a discontinuous second derivative at zero and is not smooth enough. In examples discussed in [4], it was found that the results of the function Eq.(4) are close to $f(z)=\tanh(z)$.

Smoother solutions are obtained in the case $m=3$, the functional Eq.(3) attains its minimum on the extremal

$$f(z) = \frac{7 + 4\sqrt{3} - e^{-\sqrt{3}z}}{(2 + \sqrt{3} + e^{-\sqrt{3}z})^2} (1 - e^{-\sqrt{3}z}) \quad (5)$$

For computational efficiency it is required to calculate quickly the derivative of the function f , but for Eq.(5) the derivative is rather cumbersome. It turned out that there is a good approximation with a simple derivative, yielding on some test cases indistinguishable results. Five variants of transformation functions are presented in Table 1 with their asymptotic rate and values of the functional. The value of the functional on the extremal is a measure of the accuracy of approximation for other functions. The function f_3 is the best approximation function for both extremal f_4 and f_5 with last it is almost identical: $F(f_3,2,1) - F(f_5,2,1) = 0.2337$, $\max(f_3(z) - f_4(z)) = 0.1094$ $F(f_3,3,1) - F(f_5,3,1) = 0.04403$, $\max(f_3(z) - f_5(z)) = 0.005752$.

Table 1: Transformation functions and their properties

i	1	2	3	4	5
$f_i(z)$	$\operatorname{erf}\left(\frac{\sqrt{\pi}}{2} z\right)$	$\tanh(z)$	$\frac{2}{\pi} \operatorname{gd}\left(\frac{\pi}{2} z\right)$	$1 - e^{-z}$	$\frac{7 + 4\sqrt{3} - e^{-\sqrt{3}z}}{(2 + \sqrt{3} + e^{-\sqrt{3}z})^2} (1 - e^{-\sqrt{3}z})$
$\frac{df_i}{dz}$	$e^{-\frac{\pi}{4}z^2}$	$\operatorname{sech}(z)^2$	$\operatorname{sech}\left(\frac{\pi}{2} z\right)$	e^{-z}	$\frac{9 \cosh(\sqrt{3}z) + 6\sqrt{3} \sinh(\sqrt{3}z)}{(1 + 2 \cosh(\sqrt{3}z) + \sqrt{3} \sinh(\sqrt{3}z))^2}$
$\lim_{z \rightarrow \infty} (1 - f_i(z))$	$O\left(z^{-1} e^{-\frac{\pi}{4}z^2}\right)$	$O(e^{-2z})$	$O\left(e^{-\frac{\pi}{2}z}\right)$	$O(e^{-z})$	$O(e^{-\sqrt{3}z})$
$F(f_i,2,1)$	1.5708	1.33333	1.2337	1	1.23594
$F(f_i,3,1)$	4.9348	3.2	3.04403	-	3

In the future, all the calculations are carried out for $f = f_3$, unless otherwise is specified. Then the expressions Eq.(1) and Eq.(2) take the form

$$y = \frac{2}{\pi} \arctan(e^{\pi z}),$$

$$z = \frac{1}{\pi} \ln\left(\tan\left(\frac{\pi}{2} y\right)\right)$$

6. The problem of topology optimization

Simple and proven method of topology optimization of structure is based on the minimum compliance problem of the structure

$$\min C(x_1, x_2, \dots, x_n) = \mathbf{f}^T \mathbf{u}$$

subjected to

$$\mathbf{K} \mathbf{u} = \mathbf{f}$$

$$V(x) = \sum_{i=1}^n x_i = V_0$$

where C – the potential strain energy (compliance), $x_i = 0$ or 1 – the design variables, $i = 1, \dots, n$, n – the number of finite elements, V_0 – the given volume, \mathbf{u} – the vector of displacements, \mathbf{K} – the global stiffness matrix and \mathbf{f} – the vector of forces. In common method SIMP [1] an artificial power law is used (penalization) with parameter penalization $p > 1$ of the elastic properties of the material from the design variables $E_i(x_i) = x_i^p E_0$, where E_0 is Young modulus. In this case $C(y_1, y_2, \dots, y_n)$ is minimized and is identical with the initial goal. However, now the constraint on the volume is nonlinear function of design variables

$$V(y) = \sum_{i=1}^n y_i^{1/p} = V_0$$

As for intermediate values y_i the inequality $\sum_{i=1}^n y_i < V_0$ is valid, one can choose a reduced value for the volume optimization step, which will lead to the same result as for the optimization step in the initial formulation. Thus, the solution obtained with $p > 1$, coincides with the solution for $p = 1$ (without penalization), but with the reduced value of volume. The idea of using a reduced value of the volume lies in the fact that the gradual removal of an important element for the structure comes a moment when the sensitivity of properties of the structure sharply increases (a derivative of compliance) with respect to the design variable corresponding to this element. The presence or absence of growth of sensitivity is the criterion that this element must be left or removed. The problem of minimum compliance with the constraint on the volume is solved by conventional way. The Lagrange function is used $L=C-\lambda(V-V_0)$, where λ is the Lagrange multiplier. Initial data is specified for design variables and then they are changed on the step h

$$y^{new} = y - h \frac{\partial L}{\partial y}. \quad (6)$$

The sensitivity with respect to the element is

$$\frac{\partial C}{\partial y} = 2\mathbf{u}^T \frac{\partial \mathbf{f}}{\partial y} - \mathbf{u}^T \frac{\partial \mathbf{K}}{\partial y} \mathbf{u}.$$

The derivative of volume constraint is

$$\frac{\partial V}{\partial y} = \frac{1}{p} y^{\frac{1}{p}-1}.$$

Thus

$$\frac{\partial L}{\partial y} = \frac{\partial C}{\partial y} - \lambda \frac{1}{p} y^{\frac{1}{p}-1}.$$

This expression can proceed to the $p \rightarrow \infty$. Dependence on y is simplified to

$$\frac{\partial L}{\partial y} = \frac{\partial C}{\partial y} - \frac{\lambda}{y}, \quad (7)$$

where instead of λ/p is written simply λ because its value is still required to determine. By multiplying by y the speed of design variable change is slowed when approaching to $y=0$ so that instead of Eq.(7) the following expression is used

$$\left. \frac{\partial L}{\partial y} \right|_{delay} = y \frac{\partial C}{\partial y} - \lambda \quad (8)$$

Transfer to computational domain z is performed with agreement to Eq.(1) and Eq.(2). Control parameters *scale* and *shift* of linear transformation of argument of derivative.

$$\left. \frac{dy}{dz} \right|_{control} = \left. \frac{dy}{dz} \right|_{z \leftarrow scale \cdot z + shift}$$

Instead of Eq.(6) we obtain the following expression:

$$z^{new} = z - h \left. \frac{\partial L}{\partial y} \right|_{delay} \left. \frac{dy}{dz} \right|_{control} \quad (9)$$

Control parameters influence on speed of change for design variables on bounds $y=0$ and $y=1$. Taking Eq.(8) instead of Eq.(9) we use expression, including filtering both sensitivity and design variables:

$$z^{new} = \langle z \rangle - h \left\langle \left(y \frac{\partial C}{\partial y} - \lambda \right) \left. \frac{dy}{dz} \right|_{control} \right\rangle \left(\langle z \rangle \right),$$

where $\langle \rangle$ means application of Gaussian filtering. Computational costs are sufficiently reduced, because 100

steps of renewing of design variables are performed for one step of renewing of sensitivity values. The Lagrange multiplier λ is determined for new values of z^{new} . Since the constrain $V(y)=V_0$ is degenerated at $p \rightarrow \infty$, then the value of λ can be found from heuristic considerations $z_{n_0}^s + z_{n_0+1}^s = 2z_0$. Here $z^s = sort(z^{new})$ is sorted list of new values for design variables z^{new} , the index n_0 is equal to the number of removing elements and $z_0 = y^{-1}(y_0)$, where y_0 is predetermined value (Figure 3).

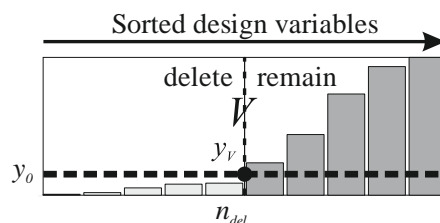


Figure 3: The criteria for determination of the Lagrange multiplier from the constraints on given

7. Numerical optimization results

Two-dimensional problem is considered, in which the initial structure is modeled by quadrilateral isoparametric finite elements of 2D theory of elasticity. All elements have constant thicknesses and equal 1. Initial domain is rectangle. All physical values are specified in non-dimensional manner. Poisson's ratio is 0.3, given volume $V_0=0.5$ and nominal Young's modulus $E_0=1$. The design domains are given below with boundary conditions and loads together with optimization results for typical examples. In first two examples the concentrated force is applied. In the third one the distributed structural weight loads are considered. It was shown that it is possible to control the topology layout complexity by using parameters $y_0, r_s, scale, shift$. The results are presented in ascending order of compliance value C . Number of iterations $Niter$ differs significantly for these cases. Note that the last structure in each example does not have holes. So, structural topology optimization is equivalent to shape optimization. The results for MBB beam for different values of control parameters are given in Table 2.

Table 2: MBB beam results

C	94.2125	95.1154	101.275	117.588	285.886
$Niter$	436	87	247	122	82
y_0	0.5	0.3	0.5	0.5	0.1
r_s	1.	1.	1.	1.	1.
$scale$	0.5	0.8	0.5	0.5	0.5
$shift$	0.75	0.5	0.78	0.8	1.3

The results for cantilever for different values of control parameters are given in Table 3. Note that the nonsymmetrical solutions can be obtained for symmetrical formulation (third structure). Also here it is possible to control optimization result, if the non-uniform initial distribution of design variables is specified. This is shown in the low row for third and last structure. The number of iterations significantly depends on the initial values, e.g. only 42 iterations are needed for the last structure, on contrary for the last but one it is needed 765 iterations.

Table 3: Cantilever results

C	180.223	183.432	186.639	187.067	195.328	201.315	207.835	254.127	635.884
$Niter$	57	84	470	232	377	289	664	765	42
y_0	0.3	0.3	0.0025	0.3	0.3	0.04	0.02	0.02	0.3
r_s	0.25	0.5	0.25	0.6	0.6	0.5	0.3	0.3	0.25
$scale$	1.	0.9	0.7	0.7	0.7	0.7	0.5	0.5	0.5
$shift$	0.03	0.5	0.7	0.98	1.05	1.4	2.	2.1	1.

The values of compliance in the considered examples are lower than the obtained ones in [4]. The results for beam

with hinged movable support (Figure 4a) and hinged immovable support (Figure 4b) under gravity forces for different control parameters.

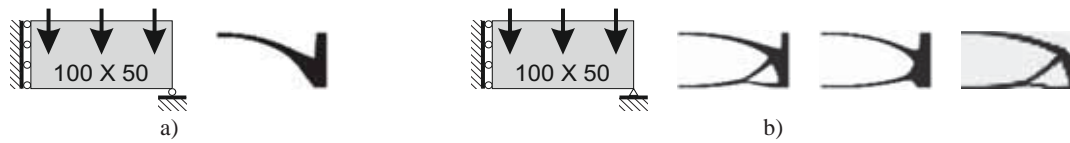


Figure 4: Beam under self-weight

This example brightly demonstrates a necessity of obtaining clear boundary shape. Here we got significantly different structure if compared with the result from paper [5]. It is last picture in Figure 4b.

7. Conclusion

New method of variable transformation for topology optimization for obtaining clear boundary shape of structures has been proposed. This method was demonstrated on the problems of topology optimization for minimization of structural compliance at a given volume. The advantages of proposed approach and the obtained solutions are discussed. All obtained solutions have clear boundary shape. Another advantage of the method is its computational efficiency in comparison with known SIMP methods with continuation and Heaviside projection filter.

6. References

- [1] M.P. Bendsoe and O. Sigmund, *Topology Optimization: Theory, Methods and Applications*, Springer-Verlag, Berlin, 2003.
- [2] J.K. Guest, J.H. Prévost, T. Belytschko, Achieving minimum length scale in topology optimization using nodal design variables and projection functions, *International Journal for Numerical Methods in Engineering*, 61(2), 238–254, 2004
- [3] J. K. Guest, A. Asadpoure, S.-H. Ha, Eliminating beta-continuation from Heaviside projection and density filter algorithms, *Structural and Multidisciplinary Optimization*, 44, 443–453, 2011
- [4] V.M. Uskov, K.A. Balunov, Method for topology optimization with clear boundary shape of structure, *International Conference on Engineering and Applied Sciences Optimization (OPT-i)*, Kos, Greece, 2014 (ISBN:978-960-99994-5-8).
- [5] M. Bruyneel and P. Duysinx, Note on topology optimization of continuum structures including self-weight, *Structural and Multidisciplinary Optimization*, 29, 245–256, 2005.

Gradient-based Optimization of Parameterized CAD Geometries

Timothée Leblond^{1,2}, Pierre Froment¹, Paul de Nazelle¹, Reda Sellakh², Philippe Serré², Gaël Chevallier³

¹ Technological Research Institute SYSTEMX, F-91120 Palaiseau, France,
{timothee.leblond,pierre.froment,paul.denazelle}@irt-systemx.fr

² LISMMA – EA-2336, Supméca, F-93407 Saint-Ouen, France,
{reda.sellakh,philippe.serre}@supmeca.fr

³ FEMTO-ST Institute – UMR 6174, CNRS-UFC-ENSMM-UTBM, F-25000 Besançon, France,
gael.chevallier@univ-fcomte.fr

1. Abstract

This paper presents a novative method for gradient-based optimization with regard to CAD parameters. This method allows to respect manufacturing, design and surface quality rules, particularly required in computational fluid dynamics (CFD). It can be used with any objective function available in adjoint solvers (both in structural and CFD). To prove the efficiency of the method, the workflow schedule was apply on an air-conditionning duct so as to maximize the eigen frequency and then to minimize the pressure drop.

2. Keywords: CAD parameters, sensitivity, optimization, CFD, adjoint solvers.

3. Introduction

Thanks to HPC, numerical optimization methods are more and more used to determine an optimal shape at a lower cost in faster.

Among these methods, both design of experiments and surrogate modeling methods allow to work directly on CAD parameters with the exception that the design space, i.e. the number of parameters, should be confined enough in order to be explored within a reasonable computational time. Other methods are based on the gradients provided by adjoint solvers, that is to say on the sensitivity of a cost function with respect to the displacement boundaries. The sensitivity is used to know how to change the shape at any node of the mesh to obtain better performance. They naturally get over the number of degrees of freedom but they are computed with respect to the coordinates of the vertices of the surface mesh. However, since manufacturing constraints are difficult to express mathematically, they are not taken into account during the mesh morphing. This drawback can be avoid by using a CAD model that implicitly includes these manufacturing constraints.

To take advantage of both approaches, this method proposes to extend these gradients to CAD parameters. This paper presents the developments of this method and its integration into an optimization loop. Applications on structural and CFD problems will be presented to prove the feasibility of this approach and the possible gains about the number of resolutions.

4. Shape Sensitivity with regard to CAD Parameters

During an optimization, the shape of the geometry is modified in order to improve its performance regarding an objective function. Here, it can only be modified thanks to CAD parameters. So, it is necessary to determine the shape sensitivity of the objective function with regard to CAD parameters ($d_{\alpha}J$) given by Eq.(1).

$$d_{\alpha}J = \partial_x J \times \partial_{\alpha} x \quad (1)$$

$\partial_x J$ represents the shape sensitivity of the objective function J with regard to node displacements. It is given by adjoint solvers and indicates how to move the nodes of the mesh to improve the objective function. In that scheme, any objective function available in adjoint solvers can be applied in this equation. The term $\partial_{\alpha} x$ represents the shape sensitivity with regard to CAD parameters and indicates how the shape is impacted by a CAD parameter perturbation.

4.1. State of the Art

The bibliography have pesented three ways to compute the sensitivity of the shape with regard to CAD parameters. The first one is an analytic way that suggests to derivate the CAD surface equations. Yu et al. [10] present the main advantage of this method, i.e. the accuracy of the results. However, it is necessary to know the explicite definition of the shape in order to derivate these equations. Mostly, these formal expressions are not available in the CAD

systems that are often proprietary software and that use implicate geometric solvers. It is therefore difficult to compute shape derivation.

The numerical approach consists in evaluating the gradient by finite differences as proposed by Armstrong et al. [1]. It compares the initial and perturbed geometries prior to generate the meshes. This approach requires the disponibility of the geometric representation of CAD models [3] so as to be able to work with u, v coordinates. Moreover, a parameter variation may result in additionnal patches and different naming [4]. These changes makes surface identification difficult [6].

Another numerical approach is based on the discretization of the CAD geometry. The evaluation of the gradient is done by finite differences between both the meshes of the initial shape and the perturbed shape. The main difficulty is to determine the deformation field that projects one mesh on the other and that limits the distortion of cells. The deformation of the initial mesh is presented in many methods and Toivanen et al. [9] present one of them but the cell distortion is hardly mastered. Robinson et al. [6] propose to project the nodes of the initial mesh on the deformed one along the normal but it causes difficulties on the process and requires adjustments.

4.2. Proposed Method

When meshes are used to compute the gradient, one of the main problems is the absence of isoconnectivity between both the mesh of the initial shape and the mesh of the geometry after the variation of a parameter. The evaluation of the displacement of any node of the mesh is used to compute the sensitivity. To determine this displacement, the mesh of the initial shape is morphed on the mesh of the perturbed shape. During this operation, it is easy to follow each node and create an isoconnectivity between the mesh of both geometries. The harmonic projection [2, 5] is used to project 3D geometries on a 2D parametric domain, it corresponds to a reparameterization in 2D space. The latter is considered as a reference space for both shapes.

The theoretical process is detailed with a geometry Ω_α with one frontier. At each iteration of the optimization, α_0 represents the set of CAD parameters for the initial shape Ω_{α_0} , considered as the reference geometry. The perturbed geometry Ω_{α_i} is obtained after the variation of i^{th} parameter. The respective meshes of the initial and the perturbed shapes are noted $\tilde{\Omega}_{\alpha_0}$ and $\tilde{\Omega}_{\alpha_i}$.

Each mesh is projected by a harmonic transformation on a unit disk, respectively noted $\tilde{\mathcal{D}}_{\alpha_0}$ and $\tilde{\mathcal{D}}_{\alpha_i}$. Given \mathcal{U}_{α_0} and \mathcal{U}_{α_i} the functions used to obtain respectively these disks and $\mathcal{U}_{\alpha_0}^{-1}$ and $\mathcal{U}_{\alpha_i}^{-1}$ the inverse functions:

$$\mathcal{U}_\chi : \tilde{\Omega}_\chi \subset \mathbb{R}^3 \longrightarrow \tilde{\mathcal{D}}_\chi(0, 1) \quad (2)$$

$$(x, y, z) \longmapsto \begin{cases} u_\chi(x, y, z) \\ v_\chi(x, y, z) \end{cases} \quad \chi \in \{\alpha_0, \alpha_1, \dots, \alpha_i, \dots, \alpha_p\}$$

The figure 1 gives an illustration of the previous step. For example, a cube, opened on the lower face, is considered as the reference shape Ω_{α_0} . The variation of the parameter controlling the height of an edge provides the perturbed shape Ω_{α_i} . The respective meshes $\tilde{\Omega}_{\alpha_0}$ and $\tilde{\Omega}_{\alpha_i}$, done separately, are projected onto the disks $\tilde{\mathcal{D}}_{\alpha_0}$ and $\tilde{\mathcal{D}}_{\alpha_i}$.

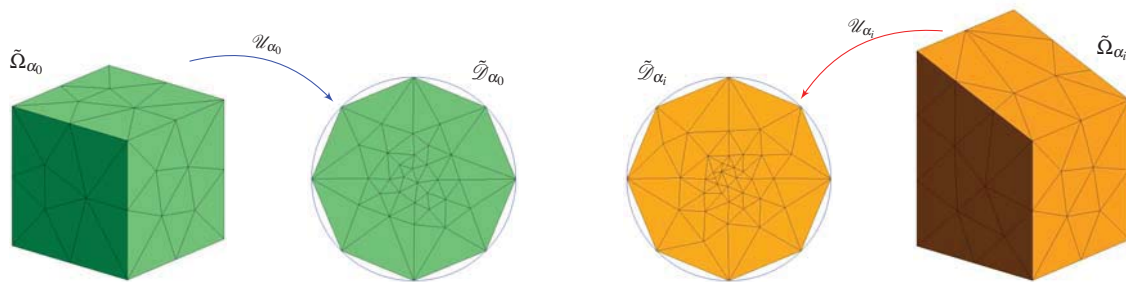


Figure 1: Projection of the mesh of the initial and perturbed shapes

The harmonic function is one-to-one, so it is possible to apply $\mathcal{U}_{\alpha_i}^{-1}$ on the disk $\tilde{\mathcal{D}}_{\alpha_0}$. The nodes of $\tilde{\mathcal{D}}_{\alpha_0}$ are interpolated with ones of $\tilde{\mathcal{D}}_{\alpha_i}$. So, the initial mesh $\tilde{\Omega}_{\alpha_0}$ is fitted on the perturbed mesh $\tilde{\Omega}_{\alpha_i}$. Thus, the new values of the coordinates of $\tilde{\Omega}_{\alpha_0}$ are known. The evaluation of the perturbation is given by the finite differences of the old and new coordinates of each node, as given by Eq.(3).

$$\partial_{\alpha_i} \Omega \simeq \frac{\mathcal{U}_{\alpha_i}^{-1}(\tilde{\mathcal{D}}_{\alpha_0}(0, 1)) - \tilde{\Omega}_{\alpha_0}}{\delta \alpha_i} \quad i = 1 \dots p \quad (3)$$

It is now possible to compute the Eq.(1). Nevertheless, the presented method requires that the 3D surface and the parametric domain are homeomorphic. In this paper, we handle CAD geometries so has to make them be home-

omorphous to a disk $\tilde{\mathcal{D}}_\chi$. Indeed, the surface is cut to obtain a homeomorphic surface to a disk. This solution was used to verify the feasibility of the proposed approach in an optimization loop.

5. Applications in structure and CFD

The optimization loop uses the result of the Eq.(1) into a gradient descent algorithm. The optimization loop can be used in structural and CFD domains. In direct optimization, even if the computation time is limited, it is possible with the gradient to directly improve the solution, particularly in CFD where the computational cost can be very expensive. This method, breaking away from the usual industrial process, was applied on different academic test cases. Two of them are detailed after and a summary of specific ones is done in the table 1.

As presented by the figure 2, the initial values of the parameters α_0 are given to the CAD software. The outputs are the initial geometry Ω_{α_0} and every geometries Ω_{α_i} corresponding to the variation of each parameter α_i . In this case, the variation of each parameters are chosen arbitrarily at 5% of the initial value. All these geometries are meshed and the mesh of the initial one is given directly to the primary and the adjoint solvers. During the resolution, every meshes, corresponding to each perturbed geometries, are compared to the initial mesh by the processus presented in 4.2. Both information given by the adjoint solver and the sensitivity computation is used in an optimizer to determine the new values of α_0 for the next iterations.

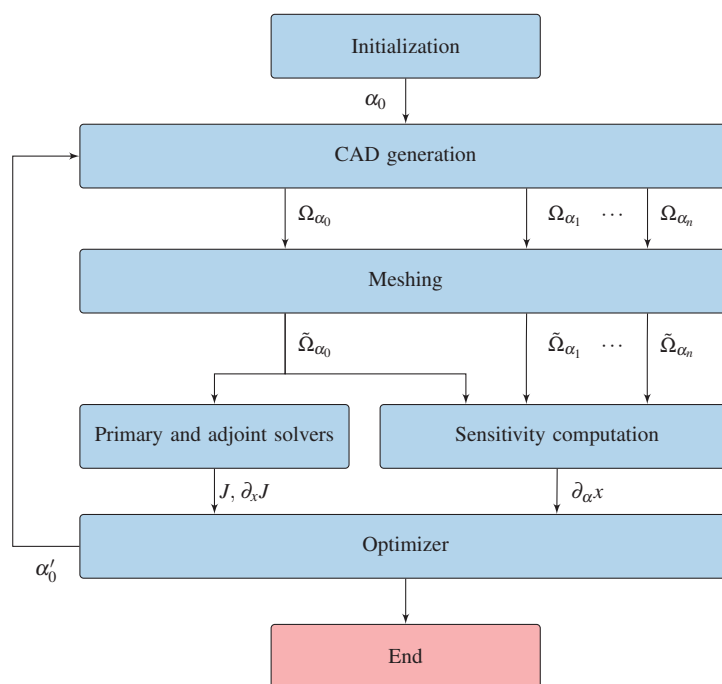


Figure 2: Scheme of the optimization loop

First, gradients from Nastran (available since 1995) were used to prove the efficiency of the method. The optimization problem was to maximize the eigen frequency of an air-conditionning duct. The CAD geometry (figure 3(a)) is a multi-section surface defined by 7 sections. The parameters and the boundary conditions, applied to the first and the last section, give 13 parameters and a frequency of 300 Hz. After about 40 iterations, the frequency was more than 1000 Hz. So, the optimization improve significantly the shape regarding this objective function only by modifying CAD parameters.

Second, the optimization problem was to minimize the pressure drop of the air-conditionning duct. The Star-CCM+ adjoint solver was used to compute the sensitivity of the objective function. The CAD geometry (figure 3(b)) has a S-bend profile defined by a multi-section surface with 7 sections. The parameters of each section and the boundary conditions give a model with 25 parameters and an initial pressure drop of 530 Pa. After 14 iterations, the gain was around 40 percent only by modifying CAD parameters.

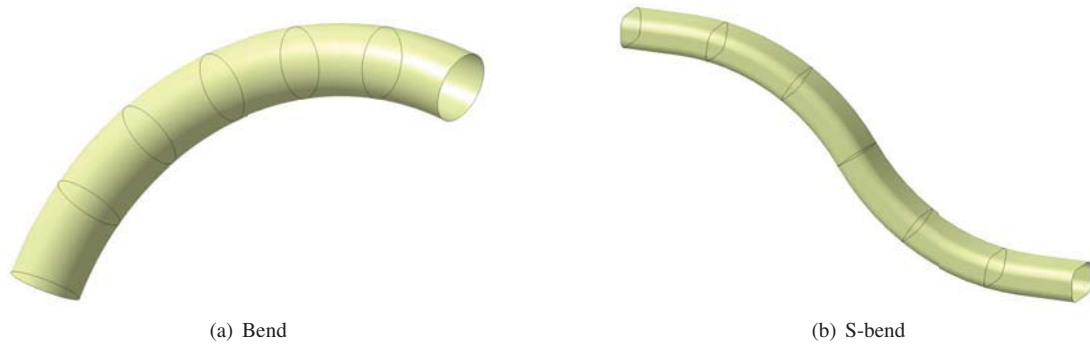


Figure 3: CAD geometries used in optimization loops

Table 1: Summary of results obtained with the optimization loop in structure and CFD – *Structure¹*: maximizing the eigen frequency – *Structure²*: minimizing this displacement due to a force – *CFD*: minimizing the pressure drop

Physic involved	Profile of duct	Number of parameters	Number of iterations	Objective function		Gain [%]
				initial	final	
Structure ¹	Bend	13	36	306.2 Hz	1007.6 Hz	229
Structure ¹	Bend	14	52	217.6 Hz	673.9 Hz	210
Structure ²	Bend	11	45	9.05 mm	1.21 mm	86.6
Structure ²	Bend	30	66	5.68 mm	0.55 mm	90.3
CFD	Bend	10	23	4.86 Pa	2.44 Pa	49.8
CFD	Bend	25	15	4.32 Pa	1.75 Pa	59.5
CFD	S-bend	25	14	532 Pa	302 Pa	43.2

6. Conclusion

Current results are obtained by cutting the CAD geometries in order to make the 3D surface be homeomorphic to a disk. However, this requires an extra step to the designer to find a cutting surface valid whatever the value of parameters. Further developments will avoid this extra step and project multi-boundary surface on the disk.

Results prove the feasibility of the presented method with significant gain regarding the number of resolutions. It would be interesting to use these gradients in more complex algorithms such as conjugate gradient or quasi-Newton or in response surface modeling.

In this paper, structural and CFD domains are separately treated. Further developments will allow to apply this loop on multiphysic cases.

7. Acknowledgements

This research work has been carried out under the leadership of the Technological Research Institute SystemX, and therefore granted with public funds within the scope of the French Program "Investissements d'Avenir".

We thanks CD-Adapco France for providing us the Star-CCM+ licenses.

8. References

- [1] C.G. Armstrong, T.T. Robinson, H. Ou and C. Othmer. *Linking adjoint sensitivity maps with CAD parameters*, Evolutionary methods for design, optimization and control, pages 234-239, 2007.
- [2] X.D. Gu and S.T. Yau. *Computational conformal geometry*, volume 3 of Advanced lectures in mathematics, International Press, 2008.
- [3] E. Hardee, K.H. Chang, J. Tu, K.K. Choi, I. Grindeanu and X. Yu. *A CAD-based design parameterization for shape optimization of elastic solids*, Advances in Engineering Software, vol. 30, no. 3, pages 185-199, 1999.

- [4] J. Kripac. *A mechanism for persistently naming topological entities in history-based parametric solid models*, Computer-Aided Design, vol. 29, no. 2, pages 113-122, 1997.
- [5] J.F. Remacle, C. Geuzaine, G. Compère and E. Marchandise. *High-quality surface remeshing using harmonic maps*, International Journal for Numerical Methods in Engineering, vol. 83, pages 403-425, 2010.
- [6] T.T. Robinson, C.G. Armstrong, H.S. Chua, C. Othmer and T. Grahs. *Sensitivity-based optimization of parameterized CAD geometries*, In Proceedings of 8th World Congress on Structural and Multidisciplinary Optimization. ISSMO, 2009.
- [7] T.T. Robinson, C.G. Armstrong, H.S. Chua, C. Othmer and T. Grahs. *Optimizing parameterized CAD geometries using sensitivities-based on adjoint functions*, Computer-Aided Design and Applications, pages 253-268, 2012.
- [8] D. Thévenin and G. Janiga. *Optimization and computational fluid dynamics*, Springer, 2008.
- [9] J.I. Toivanen and J. Martikainen. *A new method for creating sparse design velocity fields*, Computer Methods in Applied Mechanics and Engineering, vol. 196, no. 1-3, pages 528-537, 2006.
- [10] G. Yu, J.D. Müller, D. Jones and F. Christakopoulos. *CAD-based shape optimisation using adjoint sensitivities*, Computers & Fluids, vol. 46, no. 1, pages 512-516, 2011. 10th ICFD Conference Series on Numerical Methods for Fluid Dynamics.

Multidisciplinary Design Optimization of Sound Radiation from Underwater Double Cylindrical Shell Structure

Deqing Yang¹, Guilian Yi², Jiapeng Cheng³

¹ Shanghai Jiao Tong University, Shanghai, China, yangdq@sjtu.edu.cn

² Seoul National University, Seoul, Republic of Korea, flybirdyi@126.com

³ Shanghai Jiao Tong University, Shanghai, China, c.j.p.1990@sjtu.edu.cn

1. Abstract

Underwater acoustic radiation analysis for the shell structure mainly yields to the coupling of structural vibration analysis and acoustic analysis. For example, a weak coupling relay analysis is usually performed by combining an ANSYS software-based structural vibration analysis and a SYSNOISE software-based acoustic analysis, and a strong coupling analysis for vibration and acoustic is normally based on VAONE software, which is an integrated analysis tool. However, it is much easier to use ABAQUS software for the integrated analysis of structural vibration and acoustic. On the other hand, constructing surrogate models for the acoustic analysis is the best way to simplify the acoustic analysis procedures and formula accuracy and efficient structural acoustic design optimization model, where an explicit analytical formulation of the acoustic radiation characteristics regards to the structural sizes is provided. Therefore, this paper utilizes the Latin Hypercube Sampling method to select sampling points, and considers three types of surrogate models, polynomial response surface approximation, Kriging, and radial basis neural network, to approximate the acoustic radiation of a double cylindrical shell structure. Through comparison of the approximation accuracy of three types of surrogate models, the appropriate surrogate models are chosen to construct the optimization model, and the optimization model is solved by using Matlab optimization toolbox. This research provides references for predicting the acoustic radiation of underwater structures and performing acoustic design.

2. Keywords: underwater cylindrical shell, acoustic radiation, acoustic design, surrogate model, structural optimization

3. Introduction

The probing for underwater structures is mostly about the water sound. How to reduce the sound radiation of underwater structures becomes the key point of improving the invisibility of underwater objectives. It is also significant for the acoustic optimization design of the naval structures. Reducing the underwater sound radiation of naval structures cannot only improve the invisibility, but also increase the reaction distance of their sound navigation and ranging (SONAR) system. The sound-solid interaction characteristic of underwater structures is currently the main consideration regarding to the coupling of structural vibration and sound radiation. Because of the complexity of underwater structures, analysing approaches for structural vibration and sound radiation include analytical method and numerical method. The numerical method can be used to solve sound radiation problems of relative complex structures and structures with complex boundary conditions. However, it is impossible to obtain the characteristics of structural vibration and sound radiation for complex structures by using the analytical method. Transfer matrix method (TMM), finite element method (FEM), boundary element method (BEM), FEM combined with BEM (FEM/BEM), and FEM combined with infinite element method et al. [1] are numerical methods often used. With the developments of computing techniques and large calculation softwares, FEM/BEM is the most popular method. For example, a weak coupling relay analysis is usually performed by combining an ANSYS software-based structural vibration analysis and a SYSNOISE or Virtual. Lab software-based acoustic analysis, and a strong coupling analysis for vibration and acoustic is normally based on VAONE software, which is an integrated analysis based on FEM/BEM.

The sound radiation characteristic of an underwater double cylindrical shell structure is studied in this paper. Although the double cylindrical shell structure is used widely in naval engineering, such as submarine, oil platform, the sound radiation caused by the internal vibration is hardly predicted precisely, and normally underestimated in the process of noise control. In order to simplify the computing procedure and improving calculating efficiency, this paper utilizes a large commercial software ABAQUS for the coupling analysis of structural vibration and acoustic. The acoustic medium is adopted to describe the fluid. The boundary impedance technology is used to simulate sound wave spreading in the infinite water and to provide underwater sound radiation results of the double cylindrical shell structure.

The factors that infect the structural sound radiation of double cylindrical shell structure are complicated, such as structural shaping, inner and outer shell thicknesses, and number of ribs et al. [2]. Calculation for the

relationship between structural design parameters and sound radiation is complicated and time-consuming. If this numerical calculation is performed directly in optimization design, it is impossible to be carried out smoothly due to numerous calculations. An effective solution for this issue is to use surrogate models [3]. The thicknesses of inner and outer shells of the double cylindrical shell structure significantly effect on structural vibration models and underwater radiation noise. In this paper, the effects of the shell thicknesses on the structural sound radiation are studied by utilizing surrogate modeling method. Three surrogate models, Polynomial Response Surface approximation (PRS), Kriging, and Radial Basis Neural Network (RBNN), are employed to approximate the function expression of the sound pressure level in near field regarding to the inner and outer shell thicknesses. The optimization model of minimizing structural mass with the near field sound pressure level constraint is constructed at the end. The “fmincon” function in MATLAB is utilized to solve the optimization model, and the optimal shell thicknesses are obtained.

4. ABAQUS-based integrated analysis for acoustic-solid interaction of double cylindrical shell structure

4.1. Finite element model of double cylindrical shell structure

The double cylindrical shell structure is 10m long along the axial direction. It has ribs between the inner and outer shells, and the distance between two ribs is 1m. The ribs are round with constant sections, height of 0.06m, and thickness of 0.01m. The diameters of the inner and outer shells are, respectively, 1.0m and 1.12m. The excitation force is 50N and applied at the centre point of the outer shell along the circumferential direction. As shown in Figure 1, both the inner and outer shells have round ribs, and both ends have seal plates.

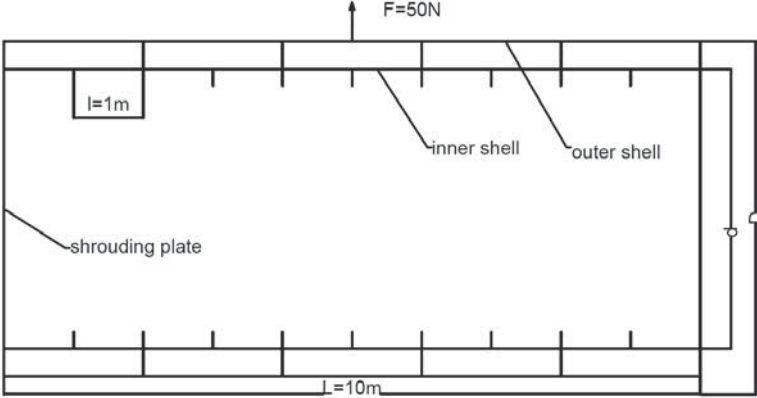


Figure 1: Intersection of the double cylindrical shell structure

For the material properties of the cylindrical shell structure, Young’s modulus is $2.05 \times 10^{11} \text{Pa}$, the Poisson’s ratio is 0.3, and the density is 7800kg/m^3 . The initial design of the cylindrical shell structure is that, the thickness of inner shell is 0.015m, and the thickness of outer shell is 0.01m. For the material properties of the fluid, the speed of the sound is 1460m/s, the density of water is 1000kg/m^3 , and the volume modulus is $2.1204 \times 10^9 \text{N/m}^2$.

According to paper [4], when the space distance for mesh, Δx , is $\Delta x / \lambda < 1/6$, where λ is the wave length, the discrete meshes would satisfy the requirement of accuracy. It means that, in the fluid, there are at least 6 nodes in a wave length. The S4R elements are used for meshing the structure, which is shown in Figure 2.



Figure 2: Finite element model of the double cylindrical shell structure

ABAQUS software has special acoustic elements for the acoustic-solid interaction model. In order to assure the computing accuracy, the second order tetrahedron acoustic element, AC3D10, is used for meshing fluid. Zero

impedance is set along the boundaries of the outside fluid to achieve the no-reflecting boundary condition. Therefore, the infinite fluid field can be simulated, and the sound waves can be absorbed by the fluid boundaries in distance field. In order to get a better result, the outside boundaries should be far from the structure as much as possible. Generally, it requires a distance that is larger than 1/3 of a sound wave length. A fluid area that is 10 times of the structural overall dimensions is built for the fluid field, which is shown in Figure 3.



Figure 3: Finite element model of the fluid field

4.2. Average Sound Pressure Level

The acoustic module in ABAQUS is utilized for structural sound radiation analysis. The node that is 1m far from the outer shell under the initial design, Node 7078, is selected as the designated point, and the sound pressure frequency response curve at this node from 0 to 350Hz is obtained and shown in Figure 4.

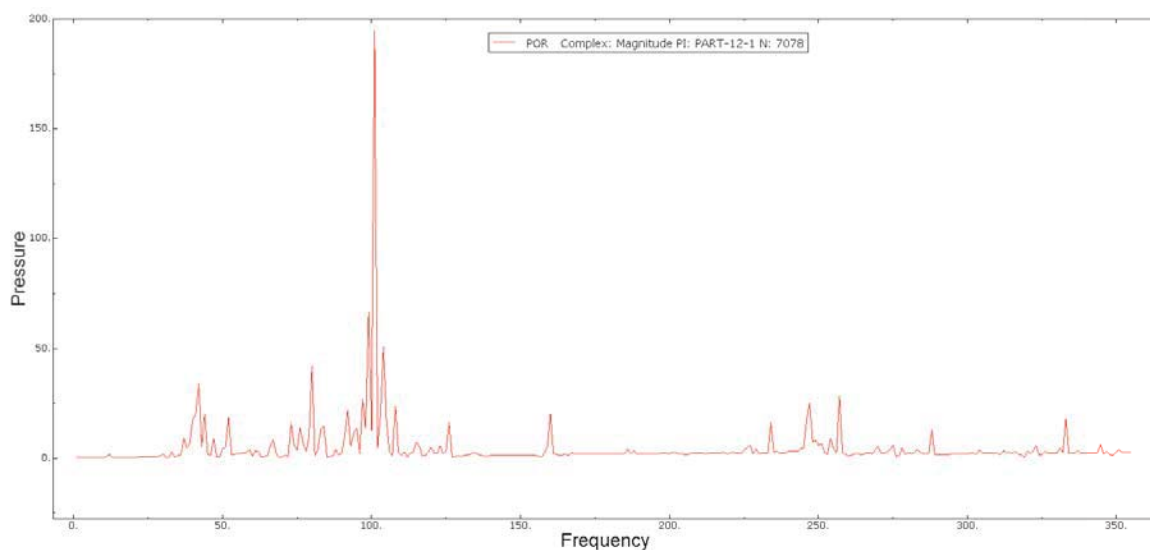


Figure 4: Sound pressure frequency response curve at Node 7078

The sound pressures (SP) of the designated point at the center frequencies of 1/3 oct frequency band within 300Hz are observed in this paper. The sound pressure level (SPL) can be obtained according to the following formula

$$L_p = 20 \lg \frac{p}{p_0} \quad (1)$$

where L_p is the sound pressure level (SPL) (unit: dB), p is the sound pressure, and p_0 is the standard sound pressure, which equals to 10^{-6} Pa in the water. Table 1 shows SP and SPL values at Node 7078.

Table 1: Sound pressure and sound pressure level values at middle frequencies of 1/3 octave

Frequency/Hz	SP/Pa	SPL/dB
--------------	-------	--------

16	0.295	89.406
20	0.166	84.417
25	0.486	93.738
31.5	0.836	98.446
40	17.659	124.939
50	4.201	112.467
63	0.434	92.747
80	41.944	132.453
100	12.341	121.827
125	3.135	109.925
160	20.180	126.098
200	2.125	106.547
250	5.815	115.291
315	2.311	107.275

Then, the average sound pressure level (APL) at Node 7078 is calculated based on the following formula

$$L_{AP} = 10 \lg \sum_{k=1}^N 10^{0.1L_{pk}} \quad (2)$$

where L_{AP} is the APL value, which is also called the structural synthetic sound pressure level. “ k ” is the number of the sound pressure, and N is the total number of sound pressures that are observed, which equals to 14 according to Table 1. L_{pk} is the k -th sound pressure. Therefore, the APL value for the structure under the initial design is 134.32dB.

Since different thicknesses of inner and outer shells will yield different underwater sound radiation characteristics, the APL value at the designated point is considered as a designated indicator, and it should be no more than 125dB. Based on this constraint, optimization design for the cylindrical shell structure will be performed in the following sections to seek the lightest structure and a lower sound radiation pressure at the same time.

5. Optimization model

The thicknesses of the inner and outer shells are considered as the design variables, and t_1 and t_2 are for the thicknesses of the inner and outer shells separately. They range from 0.01m to 0.05m. The mass of the shell structure is the objective, and the APL value at the designated point is the constraint. Therefore, the optimization model for sound radiation of the cylindrical shell structure is formulated as below

$$\begin{aligned} & \min Mass \\ & \text{s.t. } L_{AP} \leq 125 \\ & \quad 0.01 \leq t_1 \leq 0.05 \\ & \quad 0.01 \leq t_2 \leq 0.05 \end{aligned} \quad (3)$$

where $Mass$ is the structural mass, and it is expressed as below

$$Mass = 98195.76\pi_1 + 78000\pi_2 \quad (4)$$

Because the expression of L_{AP} regarding to the design variables is unknown, a well-established method, the surrogate modeling method is employed to construct an explicit expression of L_{AP} . Then, the optimization model in Eq. (3) can be solve smoothly based on the surrogate model of L_{AP} .

6. Surrogate modeling for APL

6.1. Design of experiment

The Latin Hypercube Sampling (LHS) method is an effective way to select sampling points in the process of design of experiment (DOE). Compared to the random sampling method, LHS can make sure the range of each design variable is completely covered, and sampling points are distributed at each level as much as possible. So the LHS method is used here to select sampling and test points.

In order to decrease the approximation error, 4 corner points in the design area are firstly selected as sampling points. Then, another 16 points are selected from the design area by using the LHS method. A total of 20 sampling

points are selected for approximating surrogate model and their distribution in the design area is shown in Figure 5.

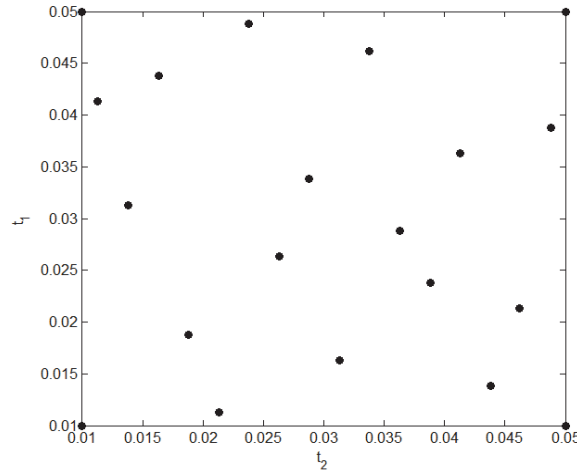


Figure 5: Distribution of 20 sampling points

Based on the finite element analysis in Section 3, the responses at each sampling point are obtained from ABAQUS, where the script language Python is used for pre- and post-process of the FE model. Programming is coded to change the thicknesses of inner and outer shells, submit FEA job for calculation, and read results from result files. Therefore, 20 APL values of sampling points are obtained automatically and quickly.

Because of the large differences between the values of design variables and APL, it is necessary to normalize the data. All variables are normalized such that ‘0’ corresponds to the minimum value and ‘1’ corresponds to the maximum value of the variable. The normalization is carried out with the following formulations

$$x_i = \frac{t_i - t_{i\min}}{t_{i\max} - t_{i\min}} \quad (i=1, 2) \quad (5)$$

$$y = \frac{L_{AP} - L_{AP\min}}{L_{AP\max} - L_{AP\min}} \quad (6)$$

where “ i ” is the number of design variable. t_i and x_i are, respectively, the design variables before and after normalization. $t_{i\min}$ and $t_{i\max}$ denote, respectively, the minimum and maximum values of design variables among 20 sampling points. L_{AP} and y are, respectively, the APL values before and after normalization. $L_{AP\min}$ and $L_{AP\max}$ denote, respectively, the minimum and maximum values among 20 APL values.

In order to test the accuracy of surrogate models, 9 more points are selected as testing points by using the LHS method, and they are used to calculate the error of the approximation. The Root Mean Square Error (RMSE) is used to test the approximate accuracy, and it is expressed by the following formula

$$\text{RMSE} = \sqrt{\frac{1}{n} \sum_{j=1}^n (y_j - \hat{y}_j)^2} \quad (7)$$

where “ j ” is the number of test points. n is the total number of test points and $n = 9$. y_j and \hat{y}_j represent, respectively, the approximated and true values of normalized APL. A lower RMSE value indicates a surrogate model with a higher accuracy.

6.2. Surrogate modeling

Three types of surrogate models, polynomial response surface (PRS), Kriging, and radial basis neural network (RBNN), are utilized in this paper to approximate the APL function. The best surrogate models from each type will be used as the constraint function in Eq. (3).

All of three types of surrogate models are obtained by using the “SurrogateToolbox” integrated within MATLAB, which was developed by Haftka and Viana. The tool box includes several types of surrogate models, and it can be used for regression analysis of surrogate models, multiple errors calculation, and figure plotting [5-6]. It is easily to be used and conducted.

In this paper, 2nd order, 3rd order and 4th order polynomials (represented by order2, order3, and order4 separately) are considered for PRS approximation; zero order, 1st order, and 2nd order polynomial regression

functions (represented by regpoly0, regpoly1, and regpoly2 separately) with Gaussian correlation function are considered for Kriging approximation; three values of the spread constant, 0.2, 0.5, and 1.0 for the radial basis function (represented by spread_0.2, spread_0.5, and spread_1.0 separately) are considered for RBNN approximation. RMSE values for each observed surrogate models are shown in Table 2.

Table 2: Comparison of surrogate models in RMSE

PRS	RMSE	KRG	RMSE	RBNN	RMSE
order2	0.309	regpoly0	0.342	spread_0.2	0.386
order3	0.307	regpoly1	0.347	spread_0.5	0.427
order4	0.530	regpoly2	0.343	spread_1.0	0.524

The RMSE values in Table 2 indicate that the 3rd order PRS, “regpoly0” Kriging, and “spread_0.2” RBNN are three nominations of the APL function. Therefore, three optimization models based on three approximations of APL functions are constructed, and the solutions are carried out in MATLAB with “fmincon” function.

6.3. Optimization results

Based on the 3rd order PRS, the optimal point is $[t_1^*, t_2^*] = [0.01, 0.01]$ (m), and structural total mass is $Mass = 5.535 \times 10^3$ kg. At the optimal point, the APL value from surrogate model is $L_{AP} = 124.83$ dB, and the true value of APL is $L_{AP}^* = 129.80$ dB. The relative error between them is 3.83%.

Based on the “regpoly0” Kriging, the final results are $[t_1^*, t_2^*] = [0.0348, 0.0240]$ (m), $Mass = 1.661 \times 10^4$ kg, and $L_{AP} = 125.00$ dB. The true value of APL is $L_{AP}^* = 122.43$ dB. The relative error between them is 2.10%.

Based on the “spread_0.2” RBNN, the final results are $[t_1^*, t_2^*] = [0.0349, 0.0231]$ (m), $Mass = 1.661 \times 10^4$ kg, and $L_{AP} = 125.00$ dB. The true value of APL is $L_{AP}^* = 122.31$ dB. The relative error between them is 2.20%.

The results indicate that, the relative errors between the approximated and surrogated APL at the optimal points are less than 5%, and the “regpoly0” Kriging and “spread_0.2” RBNN yield better results than the 3rd order PRS. Therefore, both Kriging and RBNN can approximate the APL function very well. Their results demonstrate the validity and effectiveness of the employed methods in the optimization design for structural sound radiation.

7. Conclusions

This paper uses the ABAQUS-based integrated analysis method for acoustic-solid interaction problems to compute sound radiation of the underwater double cylindrical shell structure. The surrogate modeling method is employed successfully to obtain the approximation of average sound pressure level at the designated point. Fine results are achieved in the multidisciplinary design optimization of structural sound radiation. This research provides references for predicting the acoustic radiation of underwater structures and performing acoustic design.

8. Acknowledgements

The authors acknowledge the supports of National Natural Science Foundation under grant No. 51479115, and Specialized Research Fund for the Doctoral Program of Higher Education under grant No. 20100073110011.

9. References

- [1] M.X. Chen, D.P. Luo and X.N. Chen, et al., Analytical solution of radiation sound pressure of double cylindrical shells in fluid medium, *Applied Mathematics and Mechanics*, 23 (4), 463-470, 2002.
- [2] A. Zhang, D. Qian and X. Yao, Effect of structure types on underwater sound radiation from double cylindrical shell, *Chinese Journal of Ship Research*, 2 (3), 1-6, 2007.
- [3] T.W. Simpson, J.D. Peplinski, and P.N. Koch, et al., Metamodels for computer-based engineering design: survey and recommendations, *Engineering with Computers*, 17 (2), 129-150, 2001.
- [4] D. Shang and Z. He, The numerical analysis of sound and vibration from a ring-stiffened cylindrical double-shell by FEM and BEM, *Acta Acoustica*, 26 (3), 193-201, 2001.
- [5] F.A.C. Viana, R.T. Haftka and L.T. Watson, Efficient global optimization algorithm assisted by multiple surrogate techniques, *Journal of Global Optimization*, 56 (2), 669-689, 2013.
- [6] F.A.C. Viana, R.T. Haftka and L.T. Watson, Sequential sampling for contour estimation with concurrent function evaluations, *Structural and Multidisciplinary Optimization*, 45 (4), 615-618, 2012.

An explicit feature control approach in structural topology optimization

Weisheng Zhang¹, Xu Guo¹ Wenliang Zhong¹

¹ State Key Laboratory of Structural Analysis for Industrial Equipment,
Department of Engineering Mechanics,
Dalian University of Technology, Dalian, 116023, P.R. China

1. Abstract

The present paper aims to address a long-standing and challenging problem in structural topology optimization: explicit feature control of the optimal topology. The basic idea is to introduce feature control constraints which are closely related to structural skeleton, which is a key concept in mathematical morphology and a powerful tool for describing structural topologies. Benefit from the ability of structural skeleton in geometrical and topological properties of the shape, the feature control constraints can be represented as local and explicit scheme without any post-processing. To illustrate the effectiveness of the proposed approach, the feature control problem is solved under level set and SIMP framework, respectively. Numerical examples show that the proposed approach does have the capability to give a complete control of the feature size of an optimal structure in an explicit and local way.

2. Keywords: Topology optimization; Feature control; Level-set; SIMP; Structural skeleton.

3. Introduction

Topology optimization of continuum structures, which is, in its mathematical nature, a discrete optimal control problem of the coefficients of partial differential equations in infinite dimensional space, is the most challenging structural optimization problem [1].

One long standing problem in structural topology optimization, which is closely related to regularization, is feature control of optimal structural topology [2-6]. More recently, Guo and Zhang et al.[7,8] proposed two explicit and local approaches for feature control in optimal topology designs.

In the present paper, we intend to discuss how to carry out local and explicit feature control in structural topology optimization under level-set and SIMP-based computational framework, respectively.

4. Mathematical foundation

In order to give a precise feature control of a structure, it is necessary to define the minimum/maximum length scale in a mathematical rigorous way. In the following, this will be achieved by introducing the concept of structural skeleton of a given structure.

Definition 1. The minimum/maximum length scale of a structure under level set framework

In the present paper, the minimum length scale of a domain Ω is defined as

$$d^{\min-ls}(\Omega) = \min_{x \in \mathcal{MS}(\Omega)} \min_{\substack{y, z \in \mathcal{CP}(x) \\ yz \cap \mathcal{MS}(\Omega) \neq \emptyset}} \|y - z\|, \quad (1)$$

where $\mathcal{CP}(x) = \{y | y \in \text{Arg min}_{z \in \partial\Omega} \|z - x\|\}$ is the set of closest points of $x \in \mathcal{MS}(\Omega)$ on $\partial\Omega$ and yz denotes the line segment with two end points y and z , respectively. $\mathcal{MS}(\Omega)$ is the medial surface of a closed and bounded domain Ω . Accordingly, the maximum length scale of a domain Ω is defined as

$$d^{\max-ls}(\Omega) = \max_{x \in \mathcal{MS}(\Omega)} \max_{y, z \in \mathcal{CP}(x)} \|y - z\|, \quad (2)$$

Under level set framework and based on the above definitions, we have the following propositions which constitute the mathematical foundation of the proposed approach.

Proposition 1. If $\min_{x \in \mathcal{MS}(\Omega)} \phi^{\text{SDF}}(x) \geq \underline{d}$, then $d^{\min-ls}(\Omega) \geq 2\underline{d}$.

Proposition 2. If $\max_{x \in \mathcal{MS}(\Omega)} \phi^{\text{SDF}}(x) \leq \bar{d}$, then $d^{\max-ls}(\Omega) \leq 2\bar{d}$.

Here, $\phi^{\text{SDF}}(x)$ is the so-called signed distance level set function.

Based on the above definitions and propositions, it becomes clear that the minimum and maximum length scale of a domain Ω can be completely controlled by imposing lower and upper bounds on the values of its signed distance function associated with the points in $\mathcal{MS}(\Omega)$.

Definition 2. The minimum/maximum length scale of a structure under SIMP framework

In order to differentiate between level set and SIMP description, the structural skeleton is defined as $\mathcal{SS}(\Omega)$ under

SIMP framework. Then the minimum length scale $d^{\min}(\Omega)$ and maximum length scale $d^{\max}(\Omega)$ of Ω can be defined as

$$d^{\min-s}(\Omega) = \inf_{\mathbf{x} \in \mathcal{SS}(\Omega)} D(\mathbf{x}) \quad (3)$$

and

$$d^{\max-s}(\Omega) = \sup_{\mathbf{x} \in \mathcal{SS}(\Omega)} D(\mathbf{x}), \quad (4)$$

respectively, where $D(\mathbf{x})$ is defined as

$$D(\mathbf{x}) = \sup_{r \geq 0} \{2r | \mathcal{B}(\mathbf{x}, r) \subseteq \Omega\}, \quad \text{for } \forall \mathbf{x} \in \mathcal{SS}(\Omega). \quad (5)$$

In Eq.(3), $\mathcal{B}(\mathbf{x}, r)$ denotes a closed ball centered at \mathbf{x} with radius r .

If the topology of a structure can be represented by a binary bitmap, numerous well established image processing techniques can be employed to extract its skeleton.

5. Problem formulation with feature control

Armed with above facts, the following problem formulation is proposed for topology optimization of continuum structures with feature control under level set-based framework:

$$\begin{aligned} & \text{Find } \phi^{\text{SDF}}(\mathbf{x}), \mathbf{u}(\mathbf{x}) \\ & \text{Min } I = I(\phi^{\text{SDF}}, \mathbf{u}) \\ \text{s.t.} & \\ & \int_D H(\phi^{\text{SDF}}) \mathbb{E} : \boldsymbol{\varepsilon}(\mathbf{u}) : \boldsymbol{\varepsilon}(\mathbf{v}) dV = \int_D H(\phi^{\text{SDF}}) \mathbf{f} \cdot \mathbf{v} dV + \int_{\Gamma_t} \mathbf{t} \cdot \mathbf{v} dS, \quad \forall \mathbf{v} \in \mathcal{U}_{\text{ad}}, \\ & \int_D H(\phi^{\text{SDF}}) dV \leq \bar{V}, \\ & \phi^{\text{SDF}}(\mathbf{x}) \geq \underline{d}, \quad \forall \mathbf{x} \in \mathcal{MS}(\Omega), \\ & \phi^{\text{SDF}}(\mathbf{x}) \leq \bar{d}, \quad \forall \mathbf{x} \in \mathcal{MS}(\Omega), \\ & \mathbf{u} = \bar{\mathbf{u}}, \quad \text{on } \Gamma_{\text{u}}. \end{aligned} \quad (6)$$

In Eq. (6), D is a prescribed design domain in which optimal material distribution is sought for. \mathbf{f} and \mathbf{t} denote the body force density in D and the traction force on Neumann boundary Γ_t , respectively. $\bar{\mathbf{u}}$ is the prescribed displacement on Dirichlet boundary Γ_{u} . The symbol $\boldsymbol{\varepsilon}$ denotes the second order linear strain tensor. $\mathbb{E}^k = \mathbb{E}^s / (1 + (\nu^s)^2) [\mathbb{I} + \nu^s / (1 - 2\nu^s) \delta \otimes \delta]$ (\mathbb{I} and δ denote the fourth and second order identity tensor, respectively) is the fourth order isotropic elasticity tensor of the solid material with \mathbb{E}^s and ν^s denoting the corresponding Young's modulus and Poisson's ratio, respectively. \mathbf{u} and \mathbf{v} are the displacement field and the corresponding test function defined on D with $\mathcal{U}_{\text{ad}} = \{\mathbf{v} | \mathbf{v} \in \mathbf{H}^1(D), \mathbf{v} = \mathbf{0} \text{ on } \Gamma_{\text{u}}\}$. The function H is such that $H(x) = 1$, if $x \geq 0$; $H(x) = 1.0e - 06$, otherwise. I and \bar{V} are the objective functional and prescribed upper bound of the solid material. They are all functional of ϕ^{SDF} and \mathbf{u} . As discussed in the previous section, the constraints imposed on the signed distance ϕ^{SDF} play the role of feature control. With use of these constraints, the minimum and maximum length scales of the obtained structure will be greater than $2\underline{d}$ and less than $2\bar{d}$, respectively.

In the SIMP framework, the optimization problem can be formulated as follows:

$$\begin{aligned} & \text{Find } \boldsymbol{\rho} = (\rho_1, \rho_2, \dots, \rho_n)^T, \mathbf{u} \\ \text{Min } & C = \mathbf{u}^T \mathbf{K}(\boldsymbol{\rho}) \mathbf{u} \\ \text{s.t.} & \\ & \mathbf{K}(\boldsymbol{\rho}) \mathbf{u} = \mathbf{f}, \\ & V(\boldsymbol{\rho}) = \sum_{i=1}^n \rho_i v_i \leq \bar{V}, \\ & g_1(\boldsymbol{\rho}) = \sum_{j \in I_{\text{min}}} (\rho_j - 1)^2 \leq \epsilon_1, \\ & g_2(\boldsymbol{\rho}) = \sum_{k \in I_{\text{max}}} (\rho_k - \rho_{\text{min}})^2 \leq \epsilon_2, \\ & \rho_{\text{min}} \leq \rho_i \leq 1, \quad \forall i = 1, \dots, n. \end{aligned} \quad (7)$$

In Eq. (7), $\boldsymbol{\rho}$ is the vector of the design variables with ρ_i and v_i denoting the density and volume of the i -th element. The symbol n denotes the total number of finite element used for discretizing the prescribed design domain D . $\mathbf{K} = \sum_{i=1}^n \rho_i^p \mathbf{K}_0$ (p is the penalization index and $p = 3$ is adopted in the present study) is the global

stiffness matrix with \mathbf{K}_0 representing the element stiffness matrix corresponding to $\rho_i = 1$. ρ_{\min} is the lower bound of the element density. $g_1 \leq \epsilon_1$ and $g_2 \leq \epsilon_2$ are the minimum and maximum length scale constraint, respectively. \mathbf{f} and \mathbf{u} are the external load and the displacement field, respectively. In Eq. (3.1), I_{\min} and I_{\max} are two index sets such that

$$I_{\min} = \left\{ j \mid j \in \{1, \dots, n\}, \Omega_j \in \bigcup_{\mathbf{x} \in \mathcal{SS}(\Omega)} \mathcal{B}(\mathbf{x}, \underline{d}) \right\} \quad (8)$$

and

$$I_{\max} = \left\{ k \mid k \in \{1, \dots, n\}, \Omega_k \notin \bigcup_{\mathbf{x} \in \mathcal{SS}(\Omega)} \mathcal{B}(\mathbf{x}, \bar{d}) \right\}, \quad (9)$$

respectively.

6. Numerical solution aspects

In this section, numerical solution aspects of the proposed method will be discussed in detail.

4.1. The Identification of $\mathcal{MS}(\Omega)$ and $\mathcal{SS}(\Omega)$

From the above discussions, it is obvious that the key point for solving the optimization problem in Eq. (6) and (7) is to identify the medial surface of Ω , i.e., $\mathcal{MS}(\Omega)$ and $\mathcal{SS}(\Omega)$. In the present work, as suggested in [9], the following approximated Laplacian and then a line sweeping algorithm are applied to ϕ^{SDF} sequentially to identify the points in $\mathcal{MS}(\Omega)$ approximately as

$$\mathcal{MS}(\Omega) \cong \{\mathbf{x} \mid \phi^{\text{SDF}}(\mathbf{x}) > 0, |\nabla^2 \phi^{\text{SDF}}(\mathbf{x})| > 0\}, \quad (10)$$

with

$$\nabla^2 \phi_{ij}^{\text{SDF}} \cong \phi_{i+1,j}^{\text{SDF}} + \phi_{i-1,j}^{\text{SDF}} + \phi_{i,j+1}^{\text{SDF}} + \phi_{i,j-1}^{\text{SDF}} - 4\phi_{i,j}^{\text{SDF}}. \quad (11)$$

Taking the possible numerical error into consideration, $\mathcal{MS}^\epsilon(\Omega)$ defined as

$$\mathcal{MS}^\epsilon(\Omega) \cong \left\{ \mathbf{x} \mid \phi^{\text{SDF}}(\mathbf{x}) > 0, \left| \nabla^2 \phi^{\text{SDF}}(\mathbf{x}) / \max_{\mathbf{x} \in \Omega} |\nabla^2 \phi^{\text{SDF}}(\mathbf{x})| \right| > \epsilon \right\}, \quad (12)$$

where ϵ is a small positive number, is used in numerical implementation to guarantee the robustness of the solution process. In fact, $\mathcal{MS}^\epsilon(\Omega)$ constitutes a narrow band around $\mathcal{MS}(\Omega)$.

In SIMP framework, we propose to introduce the following projection operator to transform the gray-valued density field (i.e., $\rho(\mathbf{x})$) into a pure black-and-white density field (i.e., $\hat{\rho}(\mathbf{x})$) used for extracting the structural skeleton:

$$\hat{\rho}(\mathbf{x}) = \begin{cases} 1, & \text{if } \rho(\mathbf{x}) \geq \bar{\rho}, \\ 0, & \text{otherwise,} \end{cases} \quad (13)$$

where $\bar{\rho}$ is a threshold value for density projection. In the present work, we will make use of Otsu method [10] to determine $\bar{\rho}$ in every optimization step adaptively in order to avoid misrecognition. Once the binary density field is identified, the iterative skeleton algorithm [11] can be adopted to identify the structural skeleton.

4.1. The sensitivity analysis

In Eq.(6), the existence of a large number of point-wise feature control constraints makes the direct solution approaches computationally intractable. In the present paper, the technique proposed in [12] is employed to transfer the local feature control constraints into a global one in a mathematically equivalent way. This can be achieved as follows. By defining

$$g^\epsilon = \int_{\mathcal{MS}^\epsilon(\Omega)} \mathcal{H}(\phi^{\text{SDF}}(\mathbf{x}), \underline{d}, \bar{d}) dV, \quad (14)$$

with

$$\mathcal{H}(\phi^{\text{SDF}}(\mathbf{x}), \underline{d}, \bar{d}) = \begin{cases} (\phi^{\text{SDF}} - \bar{d})^2, & \text{if } \phi^{\text{SDF}} > \bar{d}, \\ (\phi^{\text{SDF}} - \underline{d})^2, & \text{if } \phi^{\text{SDF}} < \underline{d}, \\ 0, & \text{otherwise.} \end{cases} \quad (15)$$

The basic assumptions behind shape sensitivity analysis are such that both \mathbb{E} and \mathbf{t} are spatial invariant, i.e., $(\mathbb{E})' = \mathbb{O}$ and $(\mathbf{t})' = \mathbf{0}$. It is also assumed that $\bar{\mathbf{u}} = \mathbf{0}$ on Γ_{I} as well as the part of the Neumann boundary Γ_{t} where $\mathbf{t} \neq 0$ are non-designable. For g^ϵ , we have

$$\begin{aligned}
(\dot{g}^\epsilon) = & \int_{\mathcal{MS}^\epsilon(\Omega)} \frac{\partial \mathcal{H}(\phi^{\text{SDF}}(\mathbf{x}), \underline{d}, \bar{d})}{\partial t} dS + \int_{\mathcal{MS}^\epsilon(\Omega)} (-v_n^{\mathcal{MS}}) \mathbf{n}^{\mathcal{MS}} \cdot \nabla \mathcal{H}(\phi^{\text{SDF}}(\mathbf{x}), \underline{d}, \bar{d}) dS \\
& + \int_{\mathcal{MS}^\epsilon(\Omega)} (-v_n^{\mathcal{MS}}) \kappa^{\mathcal{MS}} \mathcal{H}(\phi^{\text{SDF}}(\mathbf{x}), \underline{d}, \bar{d}) dS, \tag{16}
\end{aligned}$$

where $\mathbf{n}^{\mathcal{MS}}$ and $\kappa^{\mathcal{MS}}$ are the outward normal vector and curvature of $\mathcal{MS}(\Omega)$, respectively. In Eq. (18), $v_n^{\mathcal{MS}}$ is the outward normal velocity of $\mathcal{MS}(\Omega)$.

Since

$$\frac{\partial \mathcal{H}(\phi^{\text{SDF}}(\mathbf{x}), \underline{d}, \bar{d})}{\partial t} = \mathcal{H}'(\phi^{\text{SDF}}(\mathbf{x}), \underline{d}, \bar{d}) \frac{\partial \phi^{\text{SDF}}(\mathbf{x})}{\partial t}, \tag{17}$$

$$\nabla \mathcal{H}(\phi^{\text{SDF}}(\mathbf{x}), \underline{d}, \bar{d}) = \mathcal{H}(\phi^{\text{SDF}}(\mathbf{x}), \underline{d}, \bar{d}) \nabla \phi^{\text{SDF}}(\mathbf{x}), \tag{18}$$

where

$$\mathcal{H}'(\phi^{\text{SDF}}(\mathbf{x}), \underline{d}, \bar{d}) = \begin{cases} 2(\phi^{\text{SDF}} - \bar{d}), & \text{if } \phi^{\text{SDF}} > \bar{d}, \\ 2(\phi^{\text{SDF}} - \underline{d}), & \text{if } \phi^{\text{SDF}} < \underline{d}, \\ 0, & \text{otherwise.} \end{cases} \tag{19}$$

Since $\partial \phi^{\text{SDF}} / \partial t = -v_n^{\phi^{\text{SDF}}} |\nabla \phi^{\text{SDF}}|$ and $|\nabla \phi^{\text{SDF}}| = 1$, we finally arrive at the result that

$$\begin{aligned}
(\dot{g}^\epsilon) = & \int_{\mathcal{MS}^\epsilon(\Omega)} \frac{\partial \mathcal{H}(\phi^{\text{SDF}}(\mathbf{x}), \underline{d}, \bar{d})}{\partial t} dV \\
& + \int_{\partial \mathcal{MS}^\epsilon(\Omega)} (-v_n^{\mathcal{MS}^\epsilon}) \mathcal{H}(\phi^{\text{SDF}}(\mathbf{x}), \underline{d}, \bar{d}) dS = \int_{\mathcal{MS}^\epsilon(\Omega)} \mathcal{H}'(\phi^{\text{SDF}}(\mathbf{x}), \underline{d}, \bar{d}) (-v_n^{\phi^{\text{SDF}}}) dV \\
& + \int_{\partial \mathcal{MS}^\epsilon(\Omega)} (-v_n^{\mathcal{MS}^\epsilon}) \mathcal{H}(\phi^{\text{SDF}}(\mathbf{x}), \underline{d}, \bar{d}) dS \tag{20}
\end{aligned}$$

At this position, it is worthy of noting that $v_n^{\mathcal{MS}^\epsilon}$ is not an independent quantity that can be chosen freely. In fact, it is dependent on $v_n^{\phi^{\text{SDF}}}$ in an implicit way. Therefore, it is somewhat difficult to determine the descent ensuring velocity field of g_1 or g_1^ϵ in the same way as in traditional level set methods. In our numerical implementation, g^ϵ is employed to control the minimum structural feature length scale. Under this circumstance, by neglecting the second term in Eq.(20). Numerical experiments showed that the above treatment is effective to deal with the feature control constraints.

The velocity fields associated with g^ϵ is only defined on $\mathcal{MS}^\epsilon(\Omega)$, which is only a subset of D (i.e., $\mathcal{MS}^\epsilon(\Omega) \subset \Omega \subset D$). The evolution of ϕ^{SDF} , however, requires the velocity field on all points in D. In the present study, the PDE-based velocity extension method proposed is employed to extend the velocity fields associated with g^ϵ defined primarily on $\mathcal{MS}^\epsilon(\Omega)$ to D.

Under SIMP framework, by assuming that the index sets I_{\min} and I_{\max} , do not change before and after the perturbations of design variables, it holds that $\partial g_1 / \partial \rho_j = 2(\rho_j - 1), \forall j \in I_{\min}, \partial g_1 / \partial \rho_j = 0, \forall j \notin I_{\min}$ and $\partial g_2 / \partial \rho_k = 2(\rho_k - \rho_{\min}), \forall k \in I_{\max}, \partial g_2 / \partial \rho_k = 0, \forall k \notin I_{\max}$, respectively.

7. Numerical examples

In this section, the proposed approach is applied to several benchmark examples of topology optimization to illustrate its effectiveness for feature control. In the following tested examples, the Young's modulus and Poisson's ratio of the solid material are taken as $E^s = 1$ and $\nu^s = 0.3$, respectively unless otherwise stated. Under SIMP framework, the lower bound of the density variable is $\rho_{\min} = 10^{-2}$ in numerical implementation. Unless otherwise stated, the relaxation parameters ϵ_1 and ϵ_2 are set to be 10^2 initially and reduced to 1 within 20 iterative steps.

First, we test the feature control capability of Eq.(6) under level set framework. As shown in Fig. 1, the design domain is 2×1 rectangular sheet with its left side clamped. A unit vertical load is applied at the middle point of the right side of the sheet. The design domain is discretized by an 120×60 FEM mesh.

The structure is optimized to minimize the mean compliance of the structure under the available solid material constraint $V_s \leq 0.5|D|$. The parameters for the feature controlled optimization are $\underline{d} = 0.5 \times \min(\Delta x, \Delta y)$, $\bar{d} = 1.5 \times \min(\Delta x, \Delta y)$ and $\epsilon = 0.6$, respectively. Fig. 2 shows the optimal topologies without and with feature control constraints. The obtained numerical results indicate that the proposed approach does have the capability of complete feature size control and the optimal solution obtained with feature size constraints may be quite different from that obtained without considering feature size constraints. The value of the objective functional of the feature controlled optimal design is $I = 85.12$ with solid volume $V_s = 0.5|D|$ while the corresponding values of the no

controlled design are $I = 62.41$ and $V_s = 0.5|D|$, respectively.

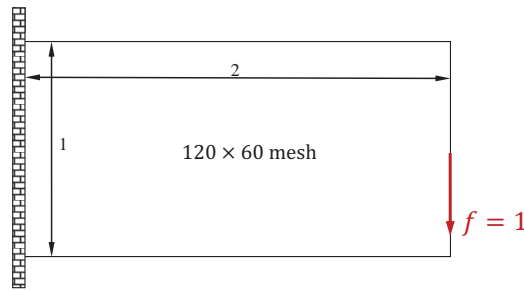


Fig. 1 The design domain of the short beam example

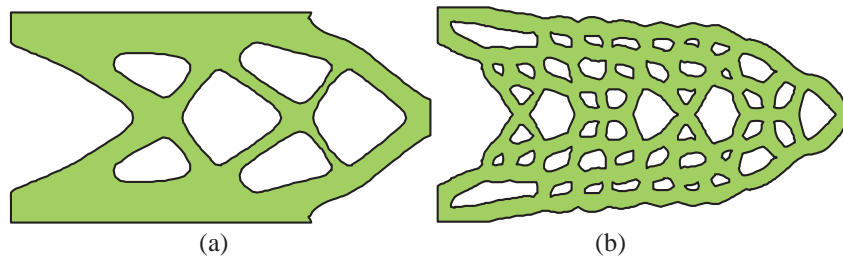


Fig.2. The optimal design of the short beam example:
 (a) without feature control (b) with feature control

Under SIMP framework, the heat conduction problem shown in Fig. 3, where the objective is to maximize the heat transfer capacity, is examined under minimum length scale control constraint. The design domain where distributed unit thermal loading uniformly applied is discretized with a 100×100 FEM mesh and the temperature of left-middle side is set to 0, as shown in Fig. 3. When the upper bound of the available solid material volume is $\bar{V} = 0.5$, the optimized structure without length scale constraints is shown in Fig. 4a. It can be seen that this optimal design is unfavorable for manufacturing due to the existence of a large number of fins with small thickness. Next, the same problem is reconsidered with length scale constraint being taken into consideration. It is required that the minimum length scale of the thermal fins should be greater than $\underline{d} = 7 \times \min(\Delta x, \Delta y)$. The optimized design and the corresponding structural skeleton are shown in Fig. 4b. From Fig. 4b, it can be seen that compared with the design shown in Fig. 4a, several main heat transfer paths are still retained in the optimal design subjected to length scale constraint. However, the fins with small widths have been eliminated. The optimal design shown in Fig. 4b is more reasonable from manufacturability point of view. Accordingly, the value of the objective function has been decreased from 186.63 to 133.35, due to the existence of length scale constraint.

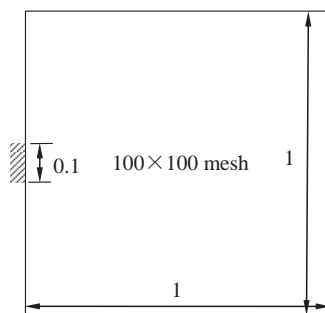


Fig. 3 The design domain of the heat conduction example.

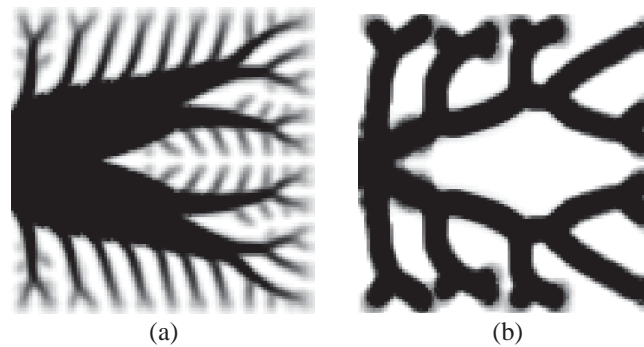


Fig. 4 The optimized design of the heat conduction problem:
(a) without feature control (b) with with control

8. Concluding remarks

In the present paper, two problem formulations and the corresponding numerical solution algorithm for feature control in optimal topology designs are proposed under level set framework and SIMP framework, respectively. Our methods are established based on the concept of structural skeleton, which has been well addressed in the field of image processing. Compared with the existing feature control approaches, the advantages of the proposed methods are such that they are local and explicit feature control schemes without resorting to any post-processing or continuation treatment. Numerical examples show that the proposed methods can give a complete (i.e., minimum and maximum length scales) control of the feature sizes in the optimized structures.

9. Acknowledgements

The financial supports from the National Natural Science Foundation (10925209, 91216201, 11372004, 11402048), 973 Project of China (2010CB832703), Program for Changjiang Scholars, Innovative Research Team in University (PCSIRT) and 111 Project (B14013) are also gratefully acknowledged.

10. References

- [1] M.P. Bendsoe and O. Sigmund, *Topology Optimization: Theory, Methods and Applications*, Springer-Verlag, Berlin, 2003.
- [2] J. Petersson, O. Sigmund, Slope constrained topology optimization, *International Journal for Numerical Methods in Engineering*, 41, 1417–1434, 1998.
- [3] T.A. Poulsen, A new scheme for imposing minimum length scale in topology optimization, *International Journal for Numerical Methods in Engineering*, 57,741–760, 2003.
- [4] J.K. Guest, Achieving minimum length scale in topology optimization using nodal design variables and projection functions, *International Journal for Numerical Methods in Engineering*, 61, 238-254, 2004.
- [5] J.K. Guest, Imposing maximum length scale in topology optimization, *Structural and Multidisciplinary Optimization*, 37, 463-473, 2009.
- [6] S.K. Chen, M.Y. Wang, A.Q. Liu, Shape feature control in structural topology optimization, *Computer Aided Design*, 40, 951-962, 2008.
- [7] W.S. Zhang, X. Guo, W.L. Zhong. An explicit length scale control approach in SIMP-based topology optimization, *Computer Methods in Applied Mechanics and Engineering*, 282, 71-86, 2014.
- [8] X. Guo, W.S. Zhang, W.L. Zhong. Explicit feature control in structural topology optimization via level set method, *Computer Methods in Applied Mechanics and Engineering*, 272, 354-378,2014.
- [9] A.A. Eftekharian, H.T. Llies, Distance functions and skeletal representations of rigid and non-rigid planar shapes, *Computer Aided Design*, 41, 856-876,2009.
- [10] N. Otsu, A threshold selection method from gray-level histograms, *IEEE Transactions on Systems, Man, and Cybernetics*, 9, 62-66,1979.
- [11] A. Rosenfeld, L.S. Davis, A note on thinning, *IEEE Transactions on Systems, Man, and Cybernetics*, 25,226-228,1976.
- [12] W.S. Zhang, X. Guo, M.Y. Wang, P. Wei, Optimal topology design of continuum structures with stress concentration alleviation via level set method, *International Journal for Numerical Methods in Engineering*. 93, 942–959, 2013.

Structural Dynamic Topology Optimisation of a Direct-Drive Single Bearing Wind Turbine Generator

M. Kirschneck¹, H. Polinder¹, R.A.J. van Ostayen¹, F.C.M. van Kempen¹, D.J. Rixen²

¹ Delft University of Technology, Delft, The Netherlands, m.kirschneck@tudelft.nl

² Technische Universität München, Munich, Germany

1. Abstract

Reducing weight of off-shore wind turbine nacelles is currently a key driver of innovation within the wind turbine industry. Weight reduction will not only lead to smaller loads and thus smaller towers of the turbine, but also reduce logistic costs during the turbine's installation. This holds even more so for off-shore turbines, the costs related to installing a turbine is a substantial investment compared to the operational cost. A reduced nacelle weight will, subsequently, lead to reduced cost of wind energy.

For direct-drive turbines, the generator is one of the heaviest parts of the wind turbine nacelle. Due to the low rotational speed of the generator, the loads are especially high in this type of turbine, which increases the necessary structural mass of the rotor. Recently, designed flexibility has been identified as one approach to achieve weight reduction. However, reducing the weight of the support structure has proven difficult, due to the complex pattern of dynamic excitation forces.

Until now, density based topology optimisation has hardly been employed for the design of wind turbine parts. This publication investigates the possible weight reduction which results from applying this method to the support structure of the generator rotor. As a first step, crucial excitation frequencies and spatial force distributions that are generated by the magnetic field are presented. Then the topology optimisation is executed using a modal and a harmonic approach, applying the identified force distributions.

Keywords: density based structural topology optimisation, direct-drive wind turbine generators, modal participation factors

2. Introduction

In multi-megawatt direct-drive wind turbines the operating conditions of the generator are influenced by the design choice to omit the gear box between hub and generator rotor. The rotational speed of the hub, and hence of the generator rotor, is determined by the tip speed ratio and thus by the length of the blades. The huge nominal power that is generated in such a machine leads to a large torque that needs to be transformed into electrical power in the generator. The torque is proportional to the squared of the magnetic flux density, which is limited to a certain magnitude in radial flux electric machines. An increased air gap surface least and increased total flux in the machine and thus also to an increased total torque. This leads to large generator diameters, which requires heavy structures to transfer the electro magnetic forces to the bearing of the rotor. In the past optimisation of the structural elements of a wind turbine with the goal of weight reduction has been at the focus of several publications. [1, 2] investigate direct-drive wind turbine generators and how their weight can be optimised. [3] explores designed flexibility as a solution for weight reduction for this type of generator. [4] optimises a slip ring permanent magnet generator.

Topology optimisation was identified as one technique to compute the optimal topology for the rotor structure that supports the electro-magnetic active parts of the generator. The technique has been used before in combination with forces originating from magnetic fields. [5] uses the technique to minimise vibrations generated by magnetic harmonic forces. [6] uses topology optimisation in a magneto-mechanical coupled system to minimise compliance of the yoke structure.

All of the above studies lack either the focus on electric machines, or the focus on structural dynamical behaviour of the system. This paper will investigate the optimal distribution of material to minimise dynamic resonance for the rotor of a permanent magnet direct-drive wind turbine generator. The forces considered include static as well as dynamic forces that are generated by the magnetic field in the air gap.

The paper follows two approaches for the optimisation process. The first approach uses an harmonic analysis to calculate the dynamic energy within the structure at certain frequencies. The second approach calculates the vibration modes and uses mode sensitivities to optimise the mode shapes to minimise participation factors of modes in a certain frequency range. In both approaches the 'Method of Moving Asymptotes' [7] was used.

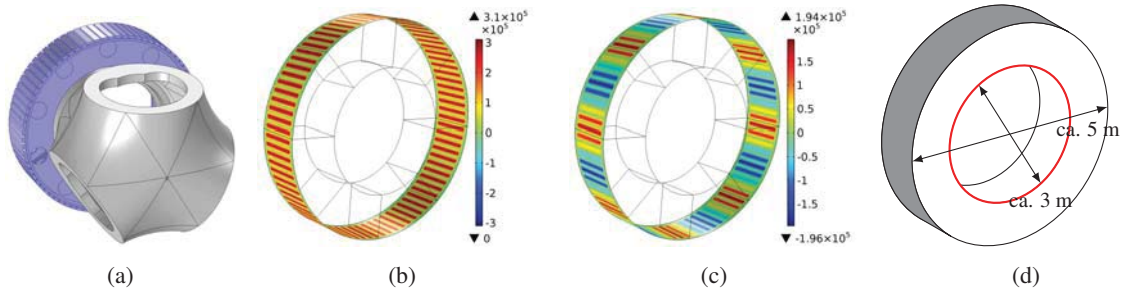


Figure 1: The XD-115 feature a direct-drive generator (a). The force distribution is depicted in (b) for the static case and in (c) for the dynamic case in $\frac{N}{m^2}$. The domain for the topology optimisation can be described by a hollow cylinder (d). The red line indicates the edge that is clamped in three directions. The grey surface indicates the barrel surface of the cylinder where the magnetic forces are applied.

3. The XD-115 – The System to Optimise

The XD-115 is a 5MW wind turbine by XEMC-Darwind [8]. It incorporates a direct-drive topology that is commonly found in off-shore wind turbines, and a permanent magnet generator. The diameter of the generator is about 5 m and its axial length is about 1 m. The single bearing supporting the rotor has a diameter of about 2 m less than the diameter of the air gap. The bearing is located between the generator and the hub of the rotor. That location reduces bearing torques and leads thus to small bearing loads. Fig. 1 a shows the current structure. The rotor part that is of interest for this study is highlighted in blue.

3.1. The force distribution

In electric machines the main source of dynamic excitation is the torque ripple, which is created by the interaction of the permanent magnets with the stator slots and the space harmonics which are caused by the distribution of the winding. The force distribution encountered in the air gap only depends on the number of poles and the winding distribution. These parameters do not change during the operation of the machine. The force distribution is, thus, constant for any operating point of the machine. Contrary to this, the magnitude and the frequency of the excitation forces depend on the relative position of the rotor to the stator and does thus depend on the rotation frequency. This is especially important for variable speed wind turbines where the operation rotational speed depends on the wind speed and thus changes significantly during operation. Therefore, the generator should be designed in such a way that the amplitude of the dynamic response does not depend on the frequency of the exciting force.

The magnitude of the dynamic and static forces can be estimated from the rotational speed and the nominal power of the turbine. The rotational speed of the turbine is at maximum power about 18 rpm. The torque that needs to be transmitted from the hub to the electro-magnetic active parts in the generator is thus 2.6 MNm. The force is distributed around the circumference of the rotor. Due to the design of the generator, the force distribution is fixed and rather well known. It can be described by

$$\mathbf{f}_{mag,stat}(\mathbf{x}_{mag}) = \hat{f}_{mag} \begin{bmatrix} 50(1 - \sin(n_{poles}\theta)) \\ (1 - \sin(n_{poles}\theta + \frac{\pi}{2})) \\ 0 \end{bmatrix} \quad (1)$$

in cylindrical coordinates, where θ denotes the circumferential coordinate in cylindrical coordinates, n_{poles} the number of poles of the machine and \hat{f}_{mag} the amplitude of the force distribution. At full load, the force in radial direction is about 50 times higher than the tangential force.

Additionally, there is a much smaller dynamic force that excites the structure dynamically. This force acts at the same location as the static force. It can be described by

$$\mathbf{f}_{mag,dyn}(\mathbf{x}_{mag}) = \frac{\hat{f}_{mag}}{50} \begin{bmatrix} (1 - \sin(n_{poles}\theta)) e^{j\theta_{shift}} \\ (1 - \sin(n_{poles}\theta + \frac{\pi}{2})) e^{j\theta_{shift}} \\ 0 \end{bmatrix} e^{j\frac{n_{poles}}{2}\omega_{mech}t} \quad (2)$$

with $\theta_{shift} = \theta n_{sym}$

where j is the imaginary unit. Previous research showed that the dynamic force in radial direction was about 50 times smaller than the static force. The same was assumed for the dynamic forces in tangential direction. θ_{shift} denotes the phase shift of the magnetic force. This is caused by the cyclic symmetry within the machine. The value depends on n_{sym} , the number of symmetric sections of the electro-magnetic active part of the generator. The

$\frac{\pi}{2}$ originates from the fact that the radial force peak has a phase shift with respect to the tangential force peak of a quarter of a pole. \mathbf{x}_{mag} is the subset of \mathbf{x} that includes all points, where the magnetic force \mathbf{f}_{mag} is applied. To make sure that the total torque is equivalent to the 2.6 MNm

$$\iint_{\Omega_{mag}} \mathbf{e}_\theta \cdot \mathbf{f}_{mag,stat} d\Omega_{mag} = 2.6 \text{ MNm} \quad (3)$$

where Ω_{mag} denotes the surface of the cylinder barrel, where the magnetic force is applied and \mathbf{e}_θ a vector pointing in tangential direction. Solving Eq. 3 for \hat{f}_{mag} yields the amplitude of the magnetic force distribution.

3.2. The Optimisation Approach

The goal of the topology optimisation is to find a design that shows the smallest displacement of the structure at the air gap und the excitation of the dynamic magnetic forces described in Eq. 2. The excitation frequencies are determined by the operating speed of the turbine. As a result, the optimisation can be restricted to a certain frequency range.

To make the design magnetically feasible, a magnetically conducting connection needs to be established between the magnets. This is usually accomplished by placing the magnets on a magnetically conducting hollow cylinder. To ensure that the solution of the optimisation problem satisfies this, a constraint is introduced that limits the minimal mass of the outer surface of the optimisation domain. Further, it is necessary to ensure that the solution of the optimisation limits the maximal displacement for the statically applied forces described in Eq. 1. This is done by introducing a constraint that limits the strain energy at the barrel surface of the design domain.

Fig. 1d shows the design domain that is defined for the topology optimisation. At the red edge the degrees of freedoms are clamped in all directions. The grey surface indicates the barrel surface of the domain at which the electro magnetic forces defined by Eq. 1 and Eq. 2 are applied.

A penalty function was introduced for the stiffness and density of the structure to ensure regions with full or zero density are more beneficial. Further, the density of the structure was lowered to avoid unphysical local modes with low resonance frequencies. A solid isotropic material with penalisation model is used [9]. Using this model, the young modulus and density of the material can be described by

$$E = 200 \cdot 10^9 (0.1 + 0.9 \rho_f^3) \quad (4)$$

$$\rho = \begin{cases} \rho_f & \text{for } \rho_f > 0.1 \\ \rho_f^{10} & \text{for } \rho_f < 0.1 \end{cases} \quad (5)$$

Two approaches are followed in this paper to minimise the displacement in the air gap of the generator due to dynamic excitation. The harmonic approach solves the system of equations in the frequency domain at certain predefined frequencies. The modal approach uses a modal analysis of the system to calculate the participation factors for the modes within the frequency range of interest.

The selection of which method to use is based on the size of the numerical system and the frequency range that is relevant for the optimisation. Larger frequency ranges should be optimised by the 'modal' approach while smaller frequency ranges should be optimised using the 'harmonic' approach. In this paper both methods are used separately.

3.2.1. Harmonic Approach

For the Harmonic approach a set of frequencies ω_{freq} has been chosen for which the displacements of the system as a result of the dynamic forces are calculated. In order to do this, the system of equations is transformed to the frequency domain. The result can be written as

$$(-\mathbf{M}\omega^2 + j\omega\mathbf{C} + \mathbf{K})\mathbf{u} = \mathbf{f}_{mag} \quad (6)$$

For this approach, the optimisation problem can be described by

$$\begin{aligned} & \min_{\rho_f(\mathbf{x})} \sum_{\omega_{freq}} \mathbf{f}_{mag}(\mathbf{x}_{mag}) \cdot \mathbf{u}(\mathbf{x}_{mag}, \omega_{freq}) \\ \text{subject to } & \int_{\Omega} \rho_f(\mathbf{x}) d\Omega < m_{max} \quad ; \quad \int_{\Omega_{mag}} \rho_f(\mathbf{x}) d\Omega > m_{mag,min} \\ & \mathbf{u}(\mathbf{x}_{mag}) \cdot \mathbf{f}_{mag}(\mathbf{x}_{mag}) < w_{max} \\ & 10^{-2} \leq \rho_f \leq 1 \end{aligned} \quad (7)$$

where m_{max} denotes a maximal mass of the rotor structure, $\mathbf{f}_{mag}(\mathbf{u}_{mag})$ the force distribution originating from the magnetic field in the air gap and ρ the density of the structure. Ω_{mag} denotes the barrel surface of the domain where the magnetic forces are applied and w_{mag} the maximal strain energy associated with the displacement at the barrel surface. To make sure that mass is placed at the barrel surface to create a ring that connects the magnets, a constraint is introduced that limits the minimal mass at the barrel surface. $m_{mag,min}$ denotes this minimal mass.

This approach has the disadvantage that the number of frequencies ω_{freq} has a direct influence on the calculation cost of this method. The more frequencies are included the more often Eq. 6 needs to be solved. The frequencies in ω_{freq} should not be too close to each other, because this increases the computational costs. Choosing the distance between them too large could entail that a resonance frequency is not captured by the algorithm and is thus not included in the optimisation function.

The harmonic optimisation was conducted with 8 frequencies within the frequency range of interest. The distance between the frequencies was about 20 Hz. The model consists of approximately 318000 degrees of freedom it contains 106000 design variables for the topology optimisation, one for each node of the finite element model.

3.2.2. Modal Approach

The modal approach minimises the displacement caused by the harmonic excitation forces by minimising the participation factors of the mode within the frequency range of interest. To do that, it solves the eigenvalue problem to calculate the mode shapes

$$(\mathbf{K} - \omega_r^2 \mathbf{M})\Phi_r = 0 \quad (8)$$

where ω_r denotes the r^{th} eigenvalue of the system and Φ_r the corresponding eigenvector. The optimisation problem can then be written

$$\begin{aligned} & \min_{\rho_f(\mathbf{x})} \sum_k (\mathbf{f}_{mag}(\mathbf{x}_{mag}) \cdot \Phi_k(\mathbf{x}_{mag})) (\mathbf{f}_{mag}^*(\mathbf{x}_{mag}) \cdot \Phi_k(\mathbf{x}_{mag})) \\ \text{subject to } & \int_{\Omega} \rho_f(\mathbf{x}) \, d\Omega < m_{max} \\ & \int_{\Omega_{mag}} \rho_f(\mathbf{x}) \, d\Omega > m_{mag,min} \\ & \mathbf{u}(\mathbf{x}_{mag}) \cdot \mathbf{f}_{mag}(\mathbf{x}_{mag}) < w_{max} \\ & 0 > \rho_f > 1 \end{aligned} \quad (9)$$

where the asterix denotes the complex conjugate of the load vector and Φ_k denotes a set of eigenvectors that is chosen from all solutions of Eq. 8 by choosing the eigenvectors with the highest values within a certain frequency range. This means that the objective function can change abruptly when a the eigenfrequency of a vibration mode changes and the mode is no longer considered in the objective function. This approach harbours the danger that the optimisation algorithm does not converge but instead is caught in a loop of evaluating the same sets of design parameters. This can happen when a mode is no longer considered for the objective function due to an eigenfrequency that is too low or too high and the optimisation subsequently change the set of design parameters, so that the mode is considered again.

The 'modal method' has the advantage that the system has to be solved less often than for the harmonic method. The eigenvalue solver will identify the resonance frequencies which are not specifically calculated in the harmonic method. The drawback is that the optimisation function is not self adjoint. The adjoint variables need to be calculated for every mode that is included in the objective function. For that a linear system of equations of the size of Eq. 8 is solved.

The model for the modal method consists of about 154000 degrees of freedoms. The density field was described per element, leading to a total number of 44352 design variables.

4. Results

To be able to compare the optimised design with the original design the maximal strain energy resulting from the static forces and the maximal weight of the structure were set to the same values that the original design has. This way the optimisation yields results that exhibit the same displacement and weight as the original design. The participation factors indicate to what extend the new design is better or worse than the old design.

4.1. Harmonic Optimisation Approach

Fig. 2 shows the results of the harmonic approach. The participation factors associated with this design are listed in Tab. 1. It is apparent that the resulting participation factors are higher than the ones of the original design. The

Mode Type	harmonic approach		modal approach		original analysis	
	norm freq	part factor	norm freq	part factor	norm freq	part factor
tilting	$0.83 + 0.01i$	$0.54 + 0.1i$	0.58	$-0.07 + 0.01i$	0.68	$0.13 - 0.02i$
	$0.82 + 0.01i$	$0.09 + 0.2i$	0.6	$0.01 - 0.07i$	0.68	$0.01 - 0.18i$
1 st bending	$1.61 + 0.02i$	$-0.38 - 0.43i$	1.17	$0.05 - 0.04i$	1.2	$0.02 - 0.04i$
	$1.61 + 0.02i$	$0.54 - 0.11i$	1.19	$0.07 - 0.04i$	1.2	$-0.02 - 0i$
axial	$1.15 + 0.014i$	$-0.04 - 0i$	1.27	$-0.07 - 0.02i$	1.29	$0.01 + 0.01i$
2 nd bending	-	-	1.83	$0.03 + 0.04i$	3.18	$-0.8 + 1.55i$
	-	-	1.85	$0.04 - 0.03i$	3.2	$2.33 + 0.74i$
torsional	$2.3 + 0.03i$	$0.04 - 0.12i$	1.47	$0.06 + 0.06i$	3.24	$-0.04 + 0.02i$
shear	$1.91 + 0.02i$	$0.71 + 0.23i$	1.61	$-0.04 + 0.06i$	-	-
	$1.91 + 0.02i$	$-0.05 + 0.17i$	1.66	$0.03 + 0.02i$	-	-

Table 1: The participation factors for selected modes and the two approaches. The participation factor for the current design are stated as reference

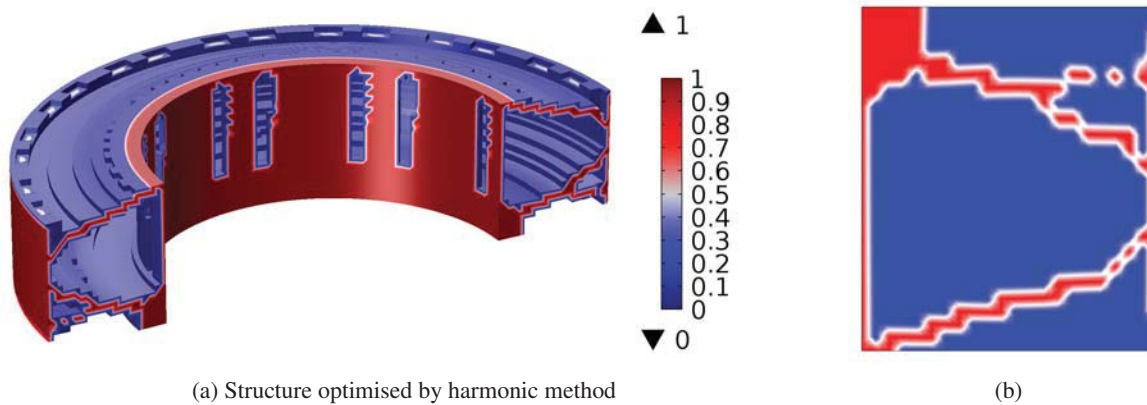


Figure 2: The result of the harmonic approach. On the left the, half of the optimised structure in 3D is depicted. On the right, a cut through the structure optimised by harmonic method is depicted. The magnetic force is applied at the right hand side. The fixed constraint is located in the bottom left corner

here presented design, does violate the maximal mass constraint and the maximal strain energy constraint slightly. The structure is thus slightly heavier and slightly less stiff in the static case than the original design.

4.2. Modal Optimisation Approach

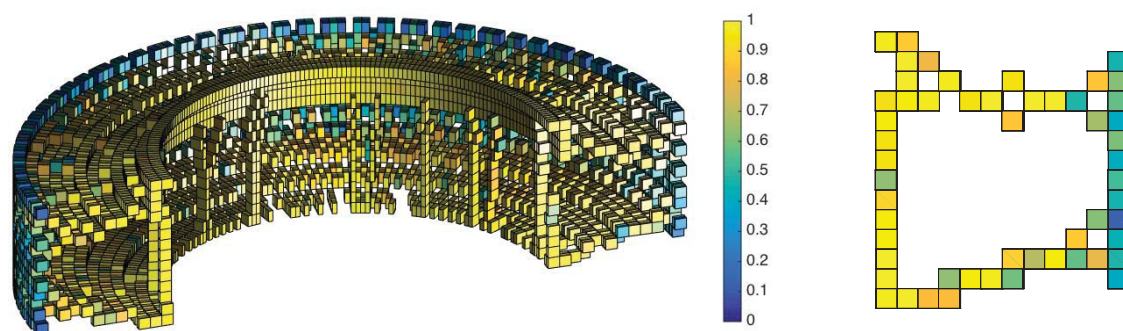


Figure 3: The result of the modal approach. On the left, half of the optimised structure is depicted. On the right, a cut through the structure. The magnetic force is applied at the right hand side. The fixed constraint is located in the bottom left corner

The results of the modal method are depicted in Fig 3. The participation factors are given by Tab. 1. The participation factors are for most of the relevant modes lower than for the original design. However it should be noted that the constraint limiting the static compliance is violated for this result. Fig. 3 also shows that the density

at the barrel surface is not high enough to satisfy the second constraint. The high participation factors and the not satisfied boundary conditions for the modal approach result can be explained by the coarse mesh. The density is described element wise. One element has a side length of 10 cm. This yields a minimal wall thickness of 10 cm. The static compliance constraint cannot be satisfied with this coarse mesh. Likewise the constraint that the outer ring is solid and filled with elements of full density cannot be satisfied without violating the maximum mass constraint for the whole structure.

5. Discussion

Topology optimisation of such a large structure that requires a high resolution for the density field is difficult. The results are thus at the lower resolution limit that is barely able to describe the structure and the modes. The results have to be used with caution as the finite element approximation for the stiffness of thin walled structures might not be accurate when the structure is only one element wide. This is the case at several location in the solution. A shape optimisation, whose topology is based on the results of this study could increase the confidence in the results that are presented here.

Methods to overcome the problem, that the limit of degrees of freedom imposes on the model, include the application of a cycle symmetric eigenvalue solver, employing flopped theory [10]. This approach requires further research to what extend the flopped theory can be included in the optimisation algorithm.

The result of the harmonic method also show higher participation factors than the one of the original solution. This might be caused by a gap that is too large between consecutive frequencies at which the displacement was calculated. Better results are expected when a finer frequency resolution is chosen.

6. Conclusion

Topology optimisation was used to analyse and improve the design of a direct drive wind turbine generator. Special emphasis was given to the dynamic behaviour of the structure, that is excited by the magnetic force in the air gap. Various methods resulted in similar topologies. However, the optimised results did not perform better than the original design. Further research is necessary to identify why the performance could not be improved.

Acknowledgements

The authors would like to thank XEMC-Darwind for the providing access to the XD-115 and its design data. Further, the authors would like to thank Prof. Krister Svanberg for the possibility to use his MMA code.

References

- [1] A. Zavvos, A. McDonald, and M. Mueller, "Optimisation tools for large permanent magnet generators for direct drive wind turbines," *IET Renew. Power Gener.*, pp. 163–171, 2013.
- [2] A. Zavvos, "Structural Optimisation of Permanent Magnet Direct Drive Generators for 5MW Wind Turbines," Ph.D. dissertation, The University of Edinburgh, 2013.
- [3] G. Shrestha, "Structural flexibility of large direct drive generators for wind turbines," Ph.D. dissertation, Tu Delft, 2013.
- [4] J. H. J. Potgieter, "Optimal topology and critical evaluation of slip synchronous permanent magnet wind generator," Ph.D. dissertation, Stellenbosch University, Apr. 2014.
- [5] N. Kikuchi, "Topology optimization for reduction of vibration caused by magnetic harmonic excitation," *IEEE Transactions on Magnetics*, vol. 38, no. 6, pp. 3643–3649, Nov. 2002.
- [6] K. Hameyer, "Topology Optimization for Compliance Reduction of Magnetomechanical Systems," *IEEE Transactions on Magnetics*, vol. 44, no. 3, pp. 346–351, Mar. 2008.
- [7] K. Svanberg, "The method of moving asymptotes – a new method for structural optimization," *International Journal for Numerical Methods in Engineering*, vol. 24, no. 2, pp. 359–373, Feb. 1987.
- [8] XEMC-Darwind, "XEMC-Darwind Web Page." <http://www.darwind.nl/Wind-turbines/XD115-5MW>. Retrieved 09/04/2015
- [9] D. Tcherniak, "Topology optimization of resonating structures using SIMP method," *International Journal for Numerical Methods in Engineering*, vol. 54, no. 11, pp. 1605–1622, Aug. 2002.
- [10] B. Lalanne and M. Touratiere, "Aeroelastic Vibrations and Stability in Cyclic Symmetric Domains," *International Journal of Rotating Machinery*, vol. 6, no. 6, pp. 445–452, 2000.

Topology Optimization of Cellular Materials for Properties Governed by Nonlinear Mechanics

Josephine V. Carstensen¹, Reza Lotfi¹, James K. Guest¹

¹ Civil Engineering Department, Johns Hopkins University, Maryland, USA, jvcarstensen@jhu.edu, reza.lotfi@gmail.com and jkguest@jhu.edu

1. Abstract

Topology optimization offers a means to leverage the advancement in manufacturing technologies that in recent years have made it possible to fabricate cellular materials with complex but prescribed topologies. Topology optimization has previously been used for unit cell design of materials with elastic properties and herein we look to extend these approaches to design materials with properties that are governed by nonlinear mechanics, such as energy absorption. One of the primary challenges in this setting is the lack of unit cell upscaling techniques for nonlinear behaviour, including both material and geometric nonlinearities. In its absence, we turn instead to the assumption of finite periodicity. The proposed formulation uses existing nonlinear sensitivity analysis schemes as the backbone of the design algorithm. Two new topologies optimized for energy absorption are presented and experimental results of actual fabricated samples are discussed.

2. Keywords: Topology optimization, nonlinear mechanics, cellular materials.

3. Introduction

In recent years manufacturing techniques and controls have improved significantly, making it possible to fabricate cellular materials with increasingly complex topologies. Cellular materials herein refers to materials that are periodic and porous. This technological advancement makes two questions relevant: (1) how does the topology influence the bulk material properties (the forward problem); and (2) what is the unit cell topology that optimizes these effective properties? (the inverse problem). The focus of this work is to use topology optimization to solve the inverse problem and hence to design cellular materials with optimized effective properties. Specifically we seek to design an effective material of Bulk Metallic Glass with a maximized energy absorption. This is a nonlinear property and will therefore require both geometric and material nonlinearities to be included in the problem formulation.

Several researchers have used topology optimization to design materials with optimized effective (homogenized) properties, including elastic properties such as negative Poisson's ratio [1], thermoelastic [2], fluid permeability [3, 4], and stiffness-thermal conductivity [5]. These works, however, all consider linear properties, enabling analysis (and design) of a single unit cell to estimate effective bulk properties through homogenization.

In this paper we will discuss elastic cellular material design and how the design problem changes when designing for nonlinear mechanical properties. This is all done using a density based topology optimization approach with the well-known SIMP [6, 7] penalization scheme to give preference to 0-1 solutions and the Method of Moving Asymptotes [8] as the gradient-based optimizer.

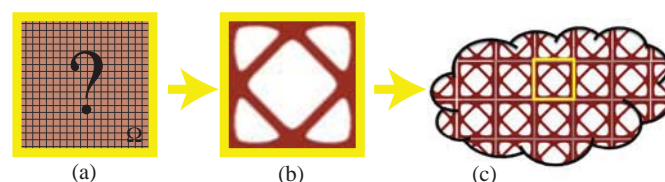


Figure 1: (a) discretized unit cell, (b) optimized unit cell topology and (c) unit cells in cellular material.

4. Design of Cellular Materials with Elastic Properties

Topology optimization for design of cellular materials can be illustrated by the schematic in Fig. 1, where Fig. 1a shows how the characteristic unit cell is defined as the design domain Ω . The problem is posed formally as an optimization problem whose solution gives the optimized unit cell topology, as seen in Fig. 1b. Finally, Fig. 1c illustrates the periodic arrangement of the unit cell to form a cellular material, and underscores the need to estimate

effective material properties from analysis of the unit cell structure. When designing for linear elastic properties, the topology optimization problem is often posed as:

$$\begin{aligned}
& \underset{\phi}{\text{minimize}} && f(\phi, \mathbf{C}^H) \\
& \text{subject to} && \mathbf{K}(\phi) \mathbf{d}^{(i)} = \mathbf{f}^{(i)} \quad \forall \quad i \\
& && g(\mathbf{C}^H(\phi, \mathbf{d}^{(i)})) \geq g_{min} \\
& && V_{min} \leq \sum_{e \in \Omega} \rho^e(\phi) v^e \leq V_{max} \\
& && \phi_{min} \leq \phi_n \leq \phi_{max} \quad \forall \quad n \in \Omega \\
& && \mathbf{d}^{(i)} \text{ is } \Omega\text{-periodic}
\end{aligned} \tag{1}$$

Here f is the objective function that can be chosen as some (negative if maximizing) effective property such as Young's-, shear or bulk modulus or Poisson's ratio. Further, ϕ is the design variables and stress and strain are denoted by σ and ϵ under the small strain assumption. $\mathbf{K}(\phi)$ is the global stiffness matrix and constraints are defined by g with allowable magnitude g_{min} . A typical constraint, for example, is elastic symmetry, which is usually chosen as either square symmetric or isotropic. The bounds on the volume fraction or relative density are defined by V_{min} and V_{max} and ϕ_{max} and ϕ_{min} describes the design variable bounds that in this work are taken as 0 and 1. The element volume is denoted v^e and $\rho^e(\phi)$ is the element density of element e . \mathbf{C}^H is the homogenized constitutive matrix computed using numerical homogenization and hence by applying test strain fields $\epsilon^{0(i)}$ to the unit cell. In Eq.(1), $\mathbf{d}^{(i)}$ and $\mathbf{f}^{(i)}$ are the displacements and force vectors for the test strain field i . The homogenization follows the description in [9]:

$$\mathbf{C}_{ij}^H = \frac{1}{|\Omega|} \sum_{e \in \Omega} (\mathbf{d}_0^{e(i)} - \mathbf{d}^{e(i)})^T \mathbf{K}^e(\phi) (\mathbf{d}_0^{e(j)} - \mathbf{d}^{e(j)}) \tag{2}$$

Here $\mathbf{d}_0^{e(i)}$ is the vector of nodal displacements for element e corresponding to the test strain field $\epsilon^{0(i)}$ and $\mathbf{K}^e(\phi)$ is the element stiffness matrix.

4.1. Penalization of intermediate values

The element stiffnesses are related to the topology using the Solid Isotropic Material with Penalization (SIMP) method [6, 7] and the Young's modulus of the element therefore expressed as

$$E^e(\phi) = ((\rho^e)^\eta + \rho_{min}^e) E_0^e \tag{3}$$

where $\eta \geq 1$ is the exponent penalty term, E_0^e is the Young's modulus of a pure solid element and ρ_{min}^e is a small positive number to maintain positive definiteness of the global stiffness matrix.

4.2. Heaviside Projection Method

To improve the manufacturability of the topology-optimized designs we herein control the minimum length scale of the topological features. The length scale is generally defined as the minimum radius or diameter of the material phase of concern, here the solid phase. It is well established that controlling the length scale has the additional advantage that it circumvents numerical instabilities, such as checkerboard patterns and mesh dependency.

Several methods for controlling the length scale of a topology optimization design exist. Herein, the Heaviside Projection Method (HPM) [10] is used, since the operator of this method is capable of yielding 0-1 designs in which the minimum length scale is fulfilled without adding constraints to the problem. In HPM, the design variables are associated with a material phase and projected onto the finite elements by a Heaviside function. The problem is thus separated into two spaces; a design variable space, where the optimization is performed, and a finite element space, where the physical equilibrium is solved. The connection between the two spaces is the projection which typically is done radially. Therefore, the projection radius can easily be chosen as the prescribed minimum length scale r_{min} . Computationally a neighborhood N^e that records the design variables within the distance r_{min} is set up for each element. The design variables are mapped onto the elements by computing a weighted average $\mu^e(\phi)$, often called linear filtering, and to obtain binary solutions, the average design variables $\mu^e(\phi)$ are passed through a Heaviside function to obtain the element volume fraction ρ^e .

$$\rho^e = 1 - e^{-\beta \mu^e(\phi)} + \frac{\mu^e(\phi)}{\phi_{max}} e^{-\beta \phi_{max}} \tag{4}$$

Here $\beta \geq 0$ dictates the curvature of the regularization which approaches the Heaviside function as β approaches infinity. For full algorithmic details please see [10].

4.3. Sensitivities

The sensitivities of the objective function are calculated as follows:

$$\frac{\partial f}{\partial \phi_i} = \sum_{e \in \Omega} \frac{\partial f}{\partial \rho^e} \frac{\partial \rho^e}{\partial \phi_i} \quad (5)$$

The partial derivative of the objective function f with respect to the element volume fraction ρ^e is problem dependent and calculated using the adjoint method. The partial derivative of the element volume fraction with respect to the design variables follows the chain rule. By differentiating Eq.(4) the following expression is found:

$$\frac{\partial \rho^e}{\partial \phi_i} = \left(\beta e^{-\beta \mu^e(\phi)} + \frac{1}{\phi_{max}} e^{-\beta \phi_{max}} \right) \frac{\partial \mu^e}{\partial \phi_i} \quad (6)$$

5. Design of Cellular Materials with Nonlinear Properties

Topology optimization for energy absorption requires considering the fully nonlinear response of the designed structure. This thus includes material nonlinearities and geometric nonlinearities. In this research we optimize for both types of nonlinearities by combining the existing sensitivity formulations for material and geometric nonlinearities under displacement controlled loading from [13] and [12], respectively. This means that finite deformations are included and that we describe the nonlinear material behavior by Von Mises yield function with isotropic hardening. An elasto-plastic material model is used and we assume linear hardening. The SIMP approach is extended as in [12], however, we have used the same SIMP exponent for all the material parameters.

Topology optimization for nonlinear effective properties is a far more challenging task than for linear properties. Homogenization of nonlinear mechanics from unit cell analysis is not yet established, and thus we perform the optimization of a sample with finite periodicity. Effective elastic properties and symmetries are estimated using elastic homogenization as dictated by the problem formulation, leading to a unit cell topology optimization problem with analysis conducted over two different domains: the unit cell for elastic properties and structure with finite periodicity for the nonlinear properties. The problem formulation used herein is as follows:

$$\begin{aligned} & \underset{\phi}{\text{minimize}} && f(\phi, \mathbf{C}^H, \mathbf{S}, \mathbf{E}) \\ & \text{subject to} && \mathbf{K}_E(\phi) \mathbf{d}_E^{(i)} - \mathbf{f}_E^{(i)}(\phi) \quad \forall \quad i \\ & && \mathbf{R}^t(\phi, \mathbf{d}) = \mathbf{K}^t(\phi, \mathbf{d}) \mathbf{d}^t - \mathbf{f}^t(\phi) = 0 \quad \forall \quad t \\ & && g_E(\mathbf{C}^H(\phi, \mathbf{d}_E^{(i)})) \geq g_{E,min} \\ & && g_{NL}(\boldsymbol{\sigma}(\phi, \mathbf{d}), \boldsymbol{\varepsilon}(\phi, \mathbf{d})) \geq g_{NL,min} \\ & && V_{min} \leq \sum_{e \in \Omega} \rho^e(\phi) v^e \leq V_{max} \\ & && \phi_{min} \leq \phi_n \leq \phi_{max} \quad \forall \quad n \in \Omega \\ & && \mathbf{d}_E^{(i)} \text{ is } \Omega\text{-periodic} \end{aligned} \quad (7)$$

where the subscript E refers to the elastic and NL to the nonlinear parts. The superscript t refers to the current load step and \mathbf{d}^t is hence the displacement vector at the current load step and \mathbf{d} the displacement vector unto t . The elastic unit cell equilibrium is given by the first constraint, and constraints g_E include the effective elastic property constraints such as the symmetry conditions. The nonlinear equilibrium constraints are given in the second set of constraints, and constraints g_{NL} comprise nonlinear property constraints as needed. In Eq.(7) the equilibrium condition is described in terms of $\mathbf{R}(\phi, \mathbf{d})$ which is the residual force vector. This equilibrium condition must be solved using an iterative nonlinear FE solver. For the designs presented in the following we have taken total absorbed energy as given by as the objective:

$$f = - \int_{\Omega} \int \boldsymbol{\sigma}^T d\boldsymbol{\varepsilon} d\Omega \quad (8)$$

5.1. Solids-Only Modeling in the Physical Space

It is well established that the modelling of void elements required by the density based topology optimization approach introduces numerical instabilities such as excessive distortions under finite deformations. In addition

the elements of negligible volume fraction are quite detrimental to analysis as they maximize the system to be solved and thus computational expense. They are, however, needed in the optimization process for reintroduction of material as the design evolves. It can therefore be said that they are necessary for the design portion of the optimization process, not the analysis.

Different methods for circumventing these instabilities such as re-meshing [14], modified nonlinear convergence criteria [13], and stabilizing the stiffness matrix following Gaussian elimination [15] have been proposed. These methods require a threshold ρ_t to be set below which element stiffness is considered negligible. In this work, we simply introduce artificial boundary conditions to degrees of freedom that are surrounded completely by void elements. This is achieved by marking the nodes of elements whose stiffness is to be modeled ($\rho^e > \rho_t$). Nodes that are unmarked receive a temporary boundary condition. Equation numbering and finite element assembly proceed in the standard manner, although it is noted the assembly routine need not check the equation numbers of void elements (including along the structural interface). This process is performed at each design iteration where the solids-topology changes.

It should be noted that the solids only finite element modeling makes the ρ_{min} parameter in Eq.(3) unnecessary. Herein we have therefore used $\rho_{min} = 0$.

6. Design of a Cellular Bulk Metallic Glass

The cellular material topology optimization design problem stated in Eq. (7) for maximizing the absorbed energy considering both geometric and material nonlinearities has been used to design a cellular bulk metallic glass material. Bulk metallic glasses (BMGs) are a class of amorphous structural materials with high strength and elasticity. However, they typically exhibit a brittle failure mode in bulk form. It is therefore desirable to design a cellular material that introduces ductility to BMG material systems.

We have considered a number of maximum volume fractions, and report on solutions found using $V_{max} = 10\%$ and $V_{max} = 12.5\%$ herein. An elasto-plastic uniaxial behavior (based on a small strain formulation) is assumed for the solid phase and the following material properties are assumed: $E = 86.9$ GPa, $\nu = 0.375$, $\sigma_{y0} = 1.475$ GPa and $H_0 = 0.84$ GPa. Square symmetry conditions were applied and the minimum length scale of the topological features specified herein was $1.2h$ where h is the side length of the finite element mesh. The results presented herein have $h = 0.005$ mm.

As mentioned above, finite periodicity has been used in the lack of a recognized upscaling method for nonlinear mechanical properties. The finite sample is considered fixed horizontally and vertically at its bottom and at the top a downward displacement is applied vertically while horizontal movement is restricted. The presented unit cell designs were arrived at using a 5×5 unit cell sample. The effect of the sample size on the response has been investigated and 5×5 was found to have a reasonably converged response without an excessive computational effort.

The stopping criterion for the topology optimization problem is collapse initiation of a unit cell and contact is hence not considered.

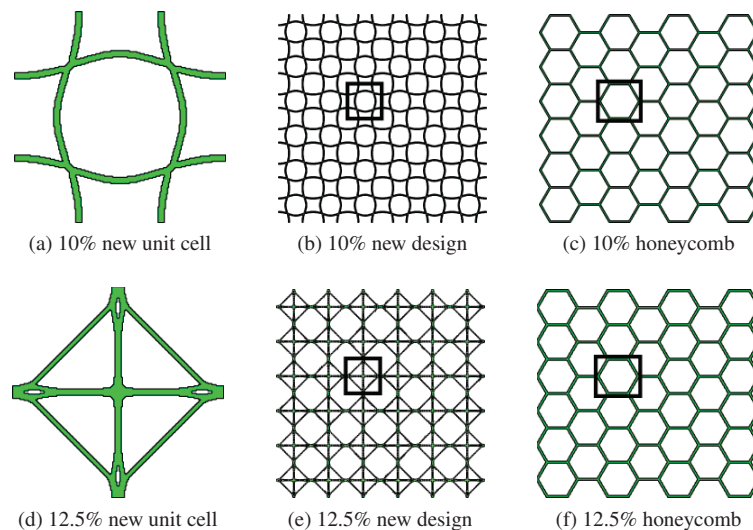


Figure 2: (a,d) unit cell and (b,e) 6×6 periodic samples of cellular materials optimized for energy absorption. (c,f) are 6×6 samples of honeycomb topologies.

In the proceeding, the numerical and experimental analyses are conducted on 6×6 samples. The design solu-

tions are shown in Fig. 2 where both unit cells (a,e) and periodic samples of 6x6 unit cells (b,f) are given for the two considered volume fractions.

6.1. Numerical Analysis of the Stress-Strain Behavior

Samples of 6x6 unit cells are FE analyzed and compared to analyses of samples with the same volume fractions of $V_{max} = 10\%$ and $V_{max} = 12.5\%$, respectively, and a more traditional honeycomb topology (Fig. 2c,f). Figure 3 contains the stress-strain responses of these analyses and the absorbed energies are indicated in the plots. We clearly see from the plots that the unit cell topology has a large effect on the response and absorbed energy of the effective bulk material. As expected, it is seen that the topology optimized designs has a higher level of energy absorption when measuring until instability that causes unit cell collapse is seen. These instabilities are found at different strains for all four considered samples. If comparing to the typical honeycomb topology the energy absorption is seen to be about 66% and 2% higher for the 10% and the 12.5% designs, respectively. It is interesting to note the difference in the deformation mechanisms used by two optimized the designs to achieve this improved energy absorbance. For the 10% volume fraction a soft material that can undergo large deformations before unit cell failure occurs is designed, whereas the 12.5% design has both higher strength and stiffness than the conventional honeycomb topology although this was not an objective of the optimization.

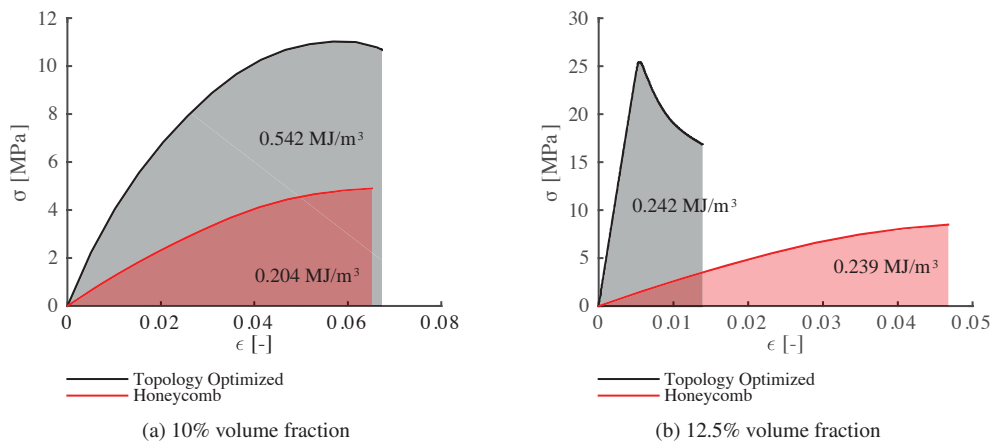


Figure 3: Stress-strain responses obtained from the FE-analyses of the considered sample topologies. The energy absorbed by each of the samples is indicated on the plot.

6.2. Experimental Results

A 6x6 unit cell sample of the designed topology with $V_{max} = 12.5\%$ was fabricated in BMG and tested. A honeycomb sample with the same volume fraction was also fabricated and tested for comparison. The performed tests were uniaxial in-plane compression tests with quasi-static displacement control and the samples were tested till full densification. This is well beyond the stopping criterion of the optimization, but will enable the test to identify deformation mechanisms that would be beneficial to include in future optimization formulations.

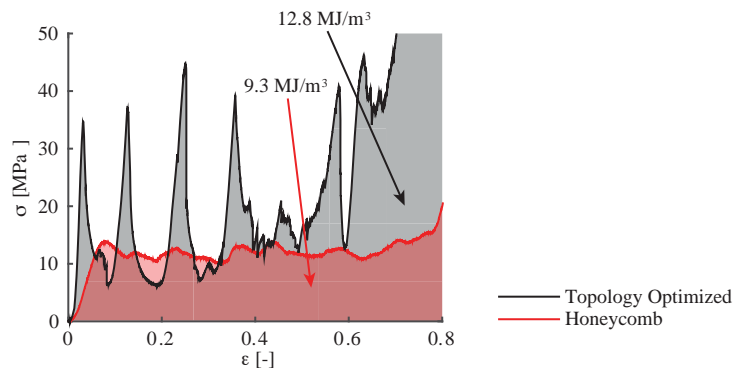


Figure 4: Stress-strain response from the experimental analysis of 6x6 samples with $V_{max} = 12.5\%$.

In the plot in Fig. 4 the experimental results are given and the amounts of energy absorbed by each of the two tested topologies are indicated. As expected, the energy absorption is significantly higher for the new de-

sign; an increase of about 38% is seen. This is higher than the improvement found by the numerical analysis, however a difference was expected as the two stopping criteria are not the same. Further, as in the numerical analysis the new design is seen to have a much higher initial stiffness and strength than the honeycomb topology. However, for both the honeycomb and the newly proposed topology the post initial peak behavior is seen to fluctuate and hence contain a series of peaks and drops. The amplitude of this cyclic behavior is most severe for the topology-optimized unit cell design. A future research focus is to alleviate this cyclic effect in the response.

7. Conclusion

The rapid improvement of manufacturing technologies presents a significant opportunity going forward in topology optimization for cellular material design. The design for elastic effective material properties is well understood, including optimization considering manufacturing constraints. Topology optimization-based design for nonlinear response properties of cellular material topologies, however, is significantly more challenging. As demonstrated, however, it also offers tremendous opportunities in designing materials with new capabilities.

8. Acknowledgements

Wen Chen and Jan Schroers from the Department of Mechanical Engineering and Material Science at Yale University, New Haven, Connecticut, are gratefully acknowledged for the experimental results in this paper. The work was supported by DARPA under the MCMA Program Award Number 60700-EG-DRP.

9. References

- [1] O. Sigmund, Materials with Prescribed Constitutive Parameters: An Inverse Homogenization Problem, *Struct. Multidisc. Optim.*, 31 (17), 2313-2329, 1994.
- [2] O. Sigmund and S. Torquato, Composites with extremal thermal expansion coefficients, *Applied Physics Letters*, 69 (21), 3203-3205, 1996.
- [3] J.K. Guest and J.H. Prévost, Design of maximum permeability material structures, *Int. J. Solids Structures*, 43 (22), 7028-7047, 2006.
- [4] V.J. Challis, J.K. Guest, J.F. Grotowski and A.P. Roberts, Computationally generated cross-property bounds for stiffness and fluid permeability using topology optimization, *Int. J. Solids Structures*, 49 (23), 3397-3408, 2012.
- [5] V.J. Challis, A.P. Roberts and A.H. Wilkins, Design of Three Dimensional Isotropic Microstructures for Maximized Stiffness and Conductivity, *Int. J. Solids Structures*, 45 (14), 4130-4146, 2008.
- [6] M.P. Bendsøe, Optimal shape design as a material distribution problem, *Structural Optimization*, 1 (4), 193-202, 1989.
- [7] G.I.N. Rozvany, M. Zhou and T. Birker, Generalized shape optimization without homogenization, *Structural Optimization*, 4 (3-4), 250-252, 1992.
- [8] K. Svanberg, The method of moving asymptotes: A new method for structural optimization, *Int. J. Numer. Meth. Engng.*, 24 (2), 359-373, 1987.
- [9] J. Guedes and N. Kikuchi, Preprocessing and postprocessing for materials based on the homogenization method with adaptive finite element methods, *Comput. Methods Appl. Mech. Engrg.*, 83 (2), 143-198, 1990.
- [10] J.K. Guest, J.H. Prévost and T. Belytschko, Achieving minimum length scale in topology optimization using nodal design variables and projection functions, *Int. J. Numer. Meth. Engng.*, 61 (2), 238-254, 2004.
- [11] T.E. Bruns and D.A. Tortorelli, Topology optimization of non-linear elastic structures and compliant mechanisms, *Comput. Methods Appl. Mech. Engrg.*, 190 (26), 3443-3459, 2001.
- [12] K. Maute, S. Schwarz and E. Ramm, Adaptive topology optimization of elastoplastic structures, *Structural Optimization*, 15 (2), 81-91, 1998.
- [13] T. Buhl, C.B.W. Pedersen and O. Sigmund, Stiffness design of geometrically nonlinear structures using topology optimization, *Struct. Multidisc. Optim.*, 19 (2), 93-104, 2000.
- [14] K. Maute and E. Ramm, Adaptive topology optimization, *Structural Optimization*, 10 (2), 100-112, 1995.
- [15] T.E. Bruns and D.A. Tortorelli, An element removal and reintroduction strategy for the topology optimization of structures and compliant mechanisms, *Int. J. Numer. Meth. Engng.*, 57 (10), 1413-1430, 2003.

Applications of a Consistent Grayscale-free Topology Optimization Method to Industrial Design Problems

Shintaro Yamasaki¹, Atsushi Kawamoto², Tsuyoshi Nomura³, Kikuo Fujita⁴

¹ Osaka University, Suita, Japan, yamasaki@mech.eng.osaka-u.ac.jp

² Toyota Central R&D Labs., Inc., Nagakute, Japan, atskmt@mosk.tytlabs.co.jp

³ Toyota Central R&D Labs., Inc., Nagakute, Japan, nomu2@mosk.tytlabs.co.jp

⁴ Osaka University, Suita, Japan, fujita@mech.eng.osaka-u.ac.jp

1. Abstract

In a previous research, we proposed a consistent grayscale-free topology optimization method using the level-set method and zero-level boundary tracking mesh. In this method, the shape and topology of the design target are represented using the level-set method and the state variables are computed using a mesh tracking the zero iso-contour of the level-set function, which we call the zero-level boundary. Because of the characteristics of the level-set method and zero-level boundary tracking mesh, essentially grayscale-free representation is achieved. Furthermore, a double-well potential based regularization technique is employed in the proposed method to regularize the structural optimization problem. Because of these enhancements, we realize essentially grayscale-free topology optimization where the design variables are updated on the basis of the standard framework of mathematical programming. In the present research, we apply the proposed grayscale-free topology optimization method to several structural optimization problems in industry, such as the minimum compliance and invehicle reactor design problems. Through the application to these design problems, we investigate the potential of the proposed grayscale-free topology optimization method.

2. Keywords: Topology optimization, Level-set method, Grayscale-free method, Design problem

3. Introduction

Topology optimization is a design approach for yielding superior structural designs while considering the shape and topology. There are two basic ideas in topology optimization: one is replacing the original structural design problem with a material distribution problem in a given design domain, and the other is updating the design variables representing material distribution by using mathematical programming. Because of mathematical programming, it is expected that the optimal solution, i.e., the optimal structure, is obtained.

While homogenization or density based topology optimization [1, 2] has achieved great success, topology optimization based on the level-set method has recently gained attention from many researchers. The level-set method [3] is a shape representation method for different two phases; the distribution of these two phases is represented by the sign of a scalar function called the level-set function. On the basis of this shape representation method, the material distribution of the target structure is represented using the level-set function in level-set based topology optimization [4, 5, 6].

Because the structural boundary is always clearly represented by the level-set method, grayscale elements seems to be suppressed in level-set based topology optimization. This is a great advantage when comparing with homogenization or density based topology optimization. However, grayscale elements cannot be completely suppressed even in level-set based topology optimization when the state variables are computed using a fixed mesh such as the Eulerian mesh for maintaining the level-set function. To realize completely grayscale-free topology optimization, we have proposed a level-set based topology optimization method [7]. In the proposed method, the shape and topology of the design target are represented using the level-set function, and the state variables are computed using a mesh that conforms to the structural boundary, i.e., the zero iso-contour of the level-set function.

In this paper, we further investigate the usefulness of the proposed method by applying it to several design problems, concretely, the minimum compliance problem and an invehicle reactor design problem. In Section 4, we briefly explain the grayscale-free topology optimization method that we previously proposed. In Section 5, we discuss how apply the proposed method to the two design problems. In Section 6, we provide several numerical examples to confirm the validity of the applications. Finally, we conclude the discussion in Section 7.

4. Proposed Grayscale-free Topology Optimization Method

In this section, we briefly explain the grayscale-free topology optimization method proposed in Reference [7].

4.1. Shape Representation Based on the Level-set Method

In the proposed method, the shape and topology of the target structure are represented using the level-set function $\phi(\mathbf{x})$, which is defined as

$$\begin{aligned} \phi(\mathbf{x}) &> 0 && \text{for } \forall \mathbf{x} \in \Omega \setminus \partial\Omega \setminus \partial D, \\ \phi(\mathbf{x}) &= 0 && \text{for } \forall \mathbf{x} \in \partial\Omega \setminus \partial D, \\ \phi(\mathbf{x}) &< 0 && \text{for } \forall \mathbf{x} \in D \setminus \Omega, \end{aligned} \quad (1)$$

where D is the design domain, Ω is the material domain, ∂D and $\partial\Omega$ are, respectively, the boundaries of D and Ω , and \mathbf{x} is a position in D . Furthermore, the smoothness of ϕ is ensured by solving the following equation [8]:

$$-R^2 \nabla^2 \phi = \psi \quad \text{in } D, \quad \frac{\partial \phi}{\partial \mathbf{n}} = 0 \quad \text{on } \partial D, \quad (2)$$

where ψ is a function that governs ϕ , and R is the length scale parameter.

In the implementation, ϕ and ψ are discretized using the Eulerian mesh, and the discretized ϕ and ψ are represented by the respective nodal value vectors Φ and Ψ . Ψ are the design variables in the proposed method, and these are bounded as follows:

$$-1 \leq \Psi_i \leq 1 \quad \text{for } i = 1, \dots, n_{\text{psi}} \quad (3)$$

where Ψ_i is the i th component of Ψ and n_{psi} is the component number of Ψ .

4.2. State Variable Computation Using the Zero-level Boundary Tracking Mesh

As explained in Section 4.1, the material domain Ω is represented by Φ in the discrete system. Then, the Eulerian mesh that maintains Φ does not conform to the zero iso-contour of the level-set function (hereafter, we call it the zero-level boundary) in usual cases. Therefore, grayscale elements are yielded around the zero-level boundary when the state variables are computed using the Eulerian mesh. To completely suppress such grayscale elements, a mesh that accurately tracks the zero-level boundary is generated at every optimization iteration in the proposed method. This zero-level boundary tracking mesh is generated by moving the nodes of the Eulerian mesh, and used to compute the state variables. For the details of the mesh generation procedure, see Reference [7].

4.3. Sensitivity Analysis

In the proposed method, it is assumed that the objective and constraint functions are computed using the zero-level boundary tracking mesh. On the other hand, the nodal level-set functions Φ are maintained at each node of the Eulerian mesh. Therefore, the relationship of sensitivities between the Eulerian and zero-level boundary tracking meshes should be known to derive the sensitivities with respect to Φ . Fortunately, this relationship has been clearly given in Reference [7], therefore, the sensitivities with respect to Φ can be successfully derived if the sensitivities with respect to the nodal coordinates of the zero-level boundary tracking mesh. Furthermore, the sensitivities with respect to the design variables, i.e., Ψ can be clearly derived using the sensitivities with respect to Φ as shown in Reference [7].

As a result, the sensitivities with respect to the design variables are derived using the framework proposed in Reference [7], if the sensitivities with respect to the nodal coordinates of the zero-level boundary tracking mesh are derived.

4.4. Double-well Potential Based Regularization

In the proposed method, a double-well potential based regularization technique is used to regularize the structural optimization problem. That is, the structural optimization problem is formulated as follows:

$$\begin{aligned} &\underset{\Psi}{\text{minimize}} && f_0 + w f_{\text{reg}}, \\ &\text{subject to} && f_i \leq f_{i \text{ max}}, \quad \text{for } i = 1, \dots, n_{\text{cns}}, \end{aligned} \quad (4)$$

where f_0 is the original objective function, f_i and $f_{i \text{ max}}$ are, respectively, the i th constraint function and the corresponding allowable upper limit, n_{cns} is the number of constraints, and w is the weighting coefficient. f_{reg} is the double-well potential based regularization term that is computed with the Eulerian mesh as follows:

$$f_{\text{reg}} = \bigcup_{e=1}^{n_D} \int_{V^e} (\phi^*{}^2 - 1)^2 \, dv, \quad (5)$$

where $\int_{V^e} dv$ represents the volume integral in an element, ϕ^* is the level-set function in that element, and $\bigcup_{e=1}^{n_D}$ represents the union set of the elements in D . Because of the regularization term f_{reg} , the level-set function tends

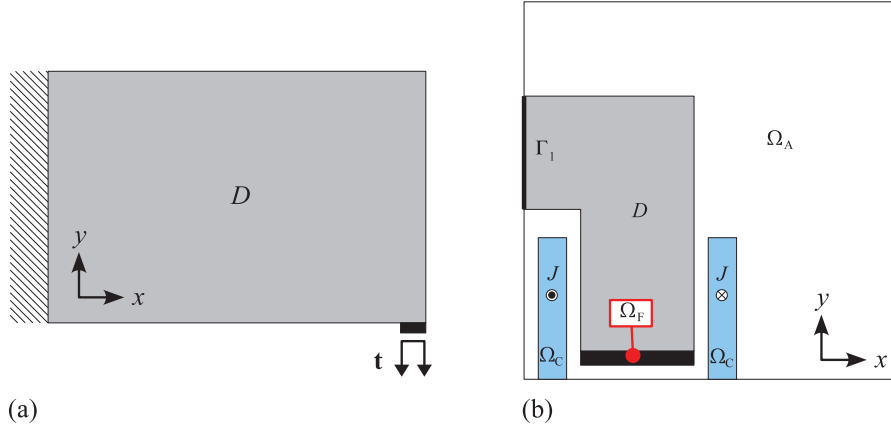


Figure 1: Analysis models: (a) minimum compliance problem; and (b) invehicle reactor design problem.

to move 1 or -1 except around the zero-level boundary.

4.5. Optimization Flow

On the basis of the discussions in Sections 4.1, 4.2, 4.3, and 4.4, the optimization flow of the proposed method is described as follows:

- (i) Provide an Eulerian mesh and initialize the design variables Ψ .
- (ii) Compute the nodal level-set functions, i.e., Φ , by solving Equation (2) in the discrete system.
- (iii) Generate the zero-level boundary tracking mesh as explained in Section 4.2.
- (iv) Compute f_i with the zero-level boundary tracking mesh while computing f_{reg} with the Eulerian mesh.
- (v) Terminate the optimization successfully if the termination condition is satisfied.
- (vi) Compute the sensitivities with respect to Φ and Ψ as explained in Section 4.3.
- (vii) Update the design variables using nonlinear programming to solve the optimization problem formulated in Equation (4), and return to (ii).

Note that, the proposed method assumes the Eulerian mesh consisting of linear triangular elements because of the mesh generation procedure.

As explained in Section 4.3, the sensitivities with respect to the nodal coordinates of the zero-level boundary tracking mesh must be derived for applying the proposed method to respective structural design problems. We derive them in the next section.

5. Applications to Several Design Problems

5.1. Minimum Compliance Problem

In the minimum compliance problem, we assume a two-dimensional analysis model shown in Figure 1(a). As shown in this figure, the design domain D is displayed in gray, a surface load \mathbf{t} is applied in a part of the boundary, and the displacement is fixed on a part of the boundary. Then, our objective is minimizing the mean compliance while constraining the volume of the structure. That is, f_0 and f_1 in Equation (4) are computed with the zero-level boundary tracking mesh as follows:

$$f_0 = \mathbf{U}^T \mathbf{T}, \quad (6)$$

$$f_1 = \bigcup_{e=1}^{n_\Omega} \int_{V^e} dv, \quad (7)$$

where $\bigcup_{e=1}^{n_\Omega}$ represents the union set of the elements in Ω , \mathbf{U} and \mathbf{T} are, respectively, the discretized displacement field and surface load. Furthermore, \mathbf{U} is computed by solving the following equation:

$$\mathbf{T} - \mathbf{K}\mathbf{U} = \mathbf{0}, \quad (8)$$

where \mathbf{K} is the total stiffness matrix.

From Equations (6) and (8), we obtain

$$f_0 = \mathbf{U}^\top \mathbf{T} - \mathbf{V}^\top \{\mathbf{T} - \mathbf{K}\mathbf{U}\}, \quad (9)$$

where \mathbf{V} is the adjoint variable vector. Therefore, the sensitivities of f_0 with respect to the nodal coordinates of the zero-level boundary tracking mesh are derived as follows:

$$\frac{\partial f_0}{\partial X_i} = \left\{ \frac{\partial \mathbf{U}}{\partial X_i} \right\}^\top \mathbf{T} - \mathbf{V}^\top \left\{ -\frac{\partial \mathbf{K}}{\partial X_i} \mathbf{U} - \mathbf{K} \frac{\partial \mathbf{U}}{\partial X_i} \right\} - \mathbf{V}^\top \frac{\partial \mathbf{K}}{\partial X_i} \mathbf{U}, \quad (10)$$

where X_i is the x coordinate of the i th node of the zero-level boundary tracking mesh, and \mathbf{V} is the solution of the following adjoint equation:

$$\mathbf{T} - \mathbf{K}^\top \mathbf{V} = \mathbf{0}. \quad (11)$$

By denoting the y coordinate of the i th node as Y_i , the corresponding sensitivity is similarly derived as

$$\frac{\partial f_0}{\partial Y_i} = -\mathbf{V}^\top \frac{\partial \mathbf{K}}{\partial Y_i} \mathbf{U}. \quad (12)$$

The sensitivities of f_1 with respect to the nodal coordinates of the zero-level boundary tracking mesh are simply derived as

$$\frac{\partial f_1}{\partial X_i} = \frac{\partial}{\partial X_i} \left\{ \bigcup_e^{n_\Omega} \int_{V_e} dv \right\}, \quad \frac{\partial f_1}{\partial Y_i} = \frac{\partial}{\partial Y_i} \left\{ \bigcup_e^{n_\Omega} \int_{V_e} dv \right\}. \quad (13)$$

By incorporating Equations (10), (12), and (13) into the topology optimization method explained in Section 4, we can obtain the optimized structure that minimizes the mean compliance.

5.2. Invehicle Reactor Design Problem

Invehicle reactor is a component of the DC-DC converter, which is used in hybrid and electric vehicles. Because the invehicle reactor contributes to performances of those vehicles, it is important to design superior invehicle reactors. In this paper, we assume a two-dimensional analysis model shown in Figure 1(b). This analysis model is a quarter model where the left and bottom edges are the symmetric boundaries. Ω_A is the domain filled with air, Ω_F is the domain filled with ferrite, Ω_C represents coils, and D is the design domain where ferrite and air are distributed. Electric current density J is imposed in the coil domains Ω_C .

Here, our objective is minimizing the eddy-current loss in the coils while maintaining sufficient inductance. Then, f_0 and f_1 in Equation (4) are given as follows:

$$f_0 = \mathbf{A}^\top \mathbf{F} \mathbf{A}, \quad (14)$$

$$f_1 = \mathbf{A}^\top \mathbf{G}, \quad (15)$$

where \mathbf{A} is the discretized magnetic potential for computing the magnetic flux density B_x, B_y , \mathbf{F} is the matrix for integrating $B_x^2 - B_y^2$ in Ω_C , and \mathbf{G} is the vector for integrating B_y on Γ_1 . \mathbf{A} is computed by solving the following equation:

$$\mathbf{H} \mathbf{A} = \mathbf{L}, \quad (16)$$

where \mathbf{H} is the magnetic stiffness matrix and \mathbf{L} is the vector representing the imposed current. From Equations (14) and (16), the sensitivity of f_0 with respect to X_i is derived as

$$\begin{aligned} \frac{\partial f_0}{\partial X_i} &= \left\{ \frac{\partial \mathbf{A}}{\partial X_i} \right\}^\top \mathbf{F} \mathbf{A} - \mathbf{A}^\top \mathbf{F} \frac{\partial \mathbf{A}}{\partial X_i} - \mathbf{V}_1^\top \left\{ \mathbf{H} \frac{\partial \mathbf{A}}{\partial X_i} - \frac{\partial \mathbf{H}}{\partial X_i} \mathbf{A} \right\} \\ &\quad - \left\{ \frac{\partial \mathbf{A}}{\partial X_i} \right\}^\top \left\{ \mathbf{F} \mathbf{A} - \mathbf{F}^\top \mathbf{A} - \mathbf{H}^\top \mathbf{V}_1 \right\} - \mathbf{V}_1^\top \frac{\partial \mathbf{H}}{\partial X_i} \mathbf{A} \\ &\quad - \mathbf{V}_1^\top \frac{\partial \mathbf{H}}{\partial X_i} \mathbf{A}, \end{aligned} \quad (17)$$

where the adjoint variable vector \mathbf{V}_1 is obtained by solving the following adjoint equation:

$$\mathbf{F} \mathbf{A} - \mathbf{F}^\top \mathbf{A} - \mathbf{H}^\top \mathbf{V}_1 = \mathbf{0}. \quad (18)$$

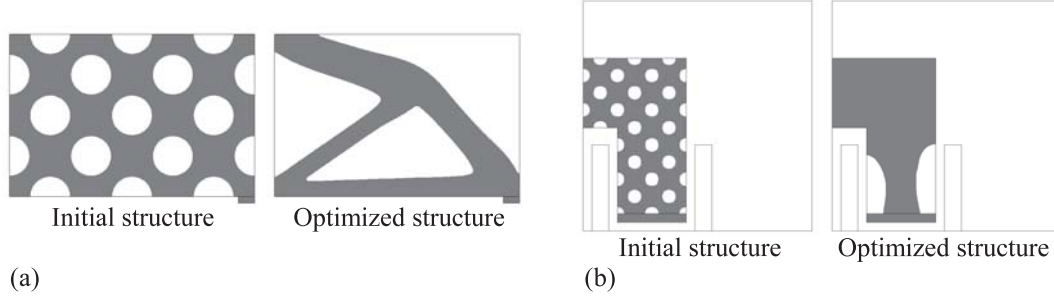


Figure 2: Initial and Optimized structures: (a) minimum compliance problem; and (b) invehicle reactor design problem.

Similarly, the sensitivity of f_0 with respect to Y_i is derived as

$$\frac{\partial f_0}{\partial Y_i} = \mathbf{V}_1^\top \frac{\partial \mathbf{H}}{\partial Y_i} \mathbf{A}. \quad (19)$$

From Equations (15) and (16), the sensitivities of f_1 with respect to X_i and Y_i are derived as

$$\frac{\partial f_1}{\partial X_i} = \mathbf{V}_2^\top \frac{\partial \mathbf{H}}{\partial X_i} \mathbf{A}, \quad \frac{\partial f_1}{\partial Y_i} = \mathbf{V}_2^\top \frac{\partial \mathbf{H}}{\partial Y_i} \mathbf{A}, \quad (20)$$

where the adjoint variable vector \mathbf{V}_2 is obtained by solving the following adjoint equation:

$$\mathbf{G} - \mathbf{H}^\top \mathbf{V}_2 = \mathbf{0}. \quad (21)$$

In the same manner as the minimum compliance problem, we can obtain optimized invehicle reactors by incorporating Equations (17), (19), and (20) into the topology optimization method explained in Section 4.

6. Numerical Examples

In this section, we provide two numerical examples for the minimum compliance and invehicle reactor design problems. First, we consider the analysis domain shown in Figure 1(a) for the minimum compliance problem. Its total size is 0.75×0.5 and it is discretized with triangular elements whose maximum length is 0.005. The young's modulus and poisson's ratio of the structural material are set to 1 and 0.3, respectively. The surface load \mathbf{t} is set to $(0, -0.01)$. The parameter R in Equation (2) is set to 0.01. The maximum allowable volume, i.e., $f_{1 \max}$, is set to 0.15. The optimizer is sequential linear programming (SLP) and its move limit is set to 0.05. On the above problem settings, we provide the initial structure shown in Figure 2(a), and as a result of optimization, we obtain the optimized structure shown in Figure 2(a) at iteration 493. Because the obtained optimized structure is very similar to optimized structures obtained in many relevant studies, we consider that the application to the minimum compliance problem is successfully achieved.

Next, we consider the analysis domain shown in Figure 1(b) for the invehicle reactor design problem. Its total size is $0.08\text{m} \times 0.08\text{m}$ and it is discretized with triangular elements whose maximum length is 0.001m. The relative permeability of ferrite is set to 150. The electric current density in the coils, i.e., J , is set to $3 \times 10^6 \frac{\text{A}}{\text{m}^2}$. The parameter R in Equation (2) is set to 0.002m. $f_{1 \max}$ is set to $-0.058\text{T} \cdot \text{m}$, that is, the minimum allowable magnetic flux through Γ_1 is set to $0.058\text{T} \cdot \text{m}$. The optimizer is SLP and its move limit is set to 0.05. On the above problem settings, we provide the initial structure shown in Figure 2(b), and as a result of optimization, we obtain the optimized structure shown in Figure 2(b) at iteration 109. Note that, ferrite distribution is displayed in gray in Figure 2(b). As shown in Figure 2(b), left and right bottom parts are clipped in the optimized structure. By eliminating ferrite in neighborhood of the coil domains Ω_C , leakage flux in Ω_C can be effectively decreased. Furthermore, such elimination does not deteriorate the inductance so much. Because physically appropriate ferrite distribution is obtained, we consider that the application to the invehicle reactor design problem is also successfully achieved.

7. Conclusion

In this paper, we applied our previously proposed method to the minimum compliance and invehicle reactor design problems. Our previously proposed method is a consistent grayscale-free topology optimization method and it is

promising because of its grayscale-free property. Furthermore, because the optimization framework has already been established, only the nodal coordinate sensitivities of the objective and constraint functions are required when applying our previously proposed method to design problems in industry. To demonstrate the potential of our previously proposed method, we investigated two applications, i.e., the applications to the minimum compliance and invehicle reactor design problems. Especially, the invehicle reactor design problem is important in an industrial view point because it is a great objective in industry to realize high performance hybrid and electric vehicles. As shown in the numerical examples, physically valid optimized structures were obtained in both two design problems, therefore, we consider that the applications to these design problems are successfully achieved. In future works, we will investigate applications to further design problems in industry and propose functional structures which have superior performances.

8. References

- [1] M. P. Bendsøe and N. Kikuchi. Generating optimal topologies in structural design using a homogenization method. *Computer Methods in Applied Mechanics and Engineering*, 71(2):197–224, November 1988.
- [2] M. P. Bendsøe. Optimal shape design as a material distribution problem. *Structural Optimization*, 1(4):193–202, 1989.
- [3] S. Osher and J. A. Sethian. Fronts propagating with curvature-dependent speed: Algorithms based on Hamilton-Jacobi formulations. *Journal of Computational Physics*, 78(1):12–49, November 1988.
- [4] J. A. Sethian and A. Wiegmann. Structural boundary design via level-set and immersed interface methods. *Journal of Computational Physics*, 163(2):489–528, September 2000.
- [5] M. Y. Wang, X. Wang, and D. Guo. A level set method for structural topology optimization. *Computer Methods in Applied Mechanics and Engineering*, 192(1–2):227–246, 2003.
- [6] G. Allaire, F. Jouve, and A. M. Toader. Structural optimization using sensitivity analysis and a level-set method. *Journal of Computational Physics*, 194(1):363–393, February 2004.
- [7] S. Yamasaki, A. Kawamoto, T. Nomura, and K. Fujita. A consistent grayscale-free topology optimization method using the level-set method and zero-level boundary tracking mesh. *International Journal for Numerical Methods in Engineering*, 101(10):744–773, March 2015.
- [8] A. Kawamoto, T. Matsumori, S. Yamasaki, T. Nomura, T. Kondoh, and S. Nishiwaki. Heaviside projection based topology optimization by a PDE-filtered scalar function. *Structural and Multidisciplinary Optimization*, 44(1):19–24, July 2011.

Solving Multiple Tour Multiple Traveling Salesman Problem with Evolutionary Programming

László Kota¹, Károly Jármai²

¹ University of Miskolc, Institute of Logistics, Hungary, altkota@uni-miskolc.hu

² University of Miskolc, Institute of Logistics, Hungary, altjar@uni-miskolc.hu

1. Abstract

Nowadays in the field of globalized production and service industry the significance of the tightly integrated logistic systems are increasing. In the service industry the technical inspection and maintenance systems has a great importance, because they provide safety and reliable operation of production and service facilities. The reliable, accident free, and economic operation require periodic technical inspections and maintenances. In these systems the inspection generally require specialized knowledge, sometimes it even requires special certificate. At elevators, which inspection and maintenance are very important from the aspect of life protection, there are governmental regulations available.

The paper describes a single phase algorithm for the fixed destination multi-depot multiple traveling salesman problem with multiple tours (mmTSP). This problem widely appears in the field of logistics mostly in connection with maintenance networks. In the first part we show the general model of the technical inspection and maintenance systems, where this problem usually emerges. We propose a mathematical model of the system's object expert assignment with the constraints like experts minimum and maximum capacity, constraints on experts' maximum and daily tours. In the second part we describe the developed evolutionary programming algorithm which solves the assignment, regarding the constraints introducing penalty functions in the algorithm. In the last part of the paper the convergence of the algorithm and the run times are presented.

2. Keywords: heuristics, optimization, evolutionary programming.

3. Introduction

The significance of the technical inspection and maintenance systems are increasing in the field of globalized service industry. These systems ensure the safe and reliable operation of the production and service systems and they are important in the field of residential services like communal services, water, sewage, electricity, telecommunication services, monitoring and measuring devices, critical network control device or even elevator maintenance systems. The reliable, accident free and economical operation of these types of systems requires periodical inspections and maintenance requirements on site. The technical inspection tasks and maintenance in most cases require special knowledge and specially trained people. For example of the elevator inspection and maintenance systems where the technical inspection and maintenance are vital, and the proper operation can save lives; thus there are governmental regulations available [1].

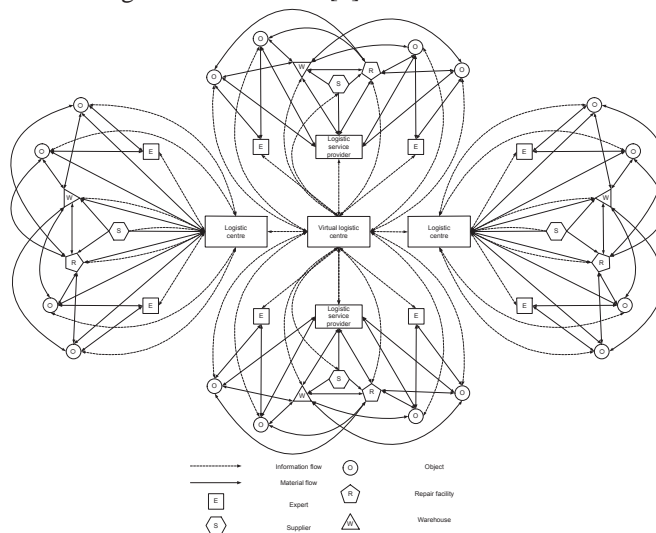


Figure 1: General structure of a technical inspection and maintenance system

The network like technical inspection and maintenance systems (Figure 1) can extend a city, a region, a country, continent wide, or even worldwide. The duties of these systems are a regular supervision of the objects in a defined time period and maintenance and/or repair the parts of the objects [2]. The effective realizations of the maintenance tasks is ensure by one or more scattered raw material and tool warehouses and repair facilities.

The role of the logistic system is to ensure the availability of the resources - experts, raw materials, tools- required by the technical inspection and maintenance tasks.

The system is controlled by a virtual logistic center [3] (Fig. 1.), but in smaller scale – regional or country wide systems – the core of the system, the controller facility could be a logistic center where the information processing and the material flow is simultaneously present. The virtual logistic center which controls the system uses complex mathematical models and optimization processes, where it minds the operational requirements, governmental regulations and many other conditions as constrains [4].

4. Mathematical model and the optimization problem

The main optimization problem in these systems is the assignment of the object have to be supervised and the experts who is doing the supervision. The system main parameter is the path matrix L, which shows the distances between the system elements. In our case the path matrix is an integrated matrix, built up from several sub-matrixes, the sub-matrices defined by the number of elements in the system.

$$L = [l_{ij}], \quad (1)$$

The assignment matrix Y is one of the main output parameter of the model. The assignment matrix:

$$Y = [y_{ij}] \quad (2)$$

where

- $y = \begin{cases} 1 \\ 0 \end{cases}$ according to the system elements are assigned together (1) or not (0),

Defining the y_{ij} is the assignment task which has to be solved in this complex system.

4.1 Objects

The main parameters of the objects are:

- p : is the number of the objects, it is constant in this model,
- L matrix defines the location of the objects, and the distance from the other system elements,
- $\kappa_i (i=1..p)$ is the mandatory inspection number per object,

The number of the technical inspections and maintenances could be prescribed by the maintenance plan or even law or governmental regulations in some cases where human life is endangered, like at elevators. The maintenances can't happen in an arbitrary period, there is a time period which has to be defined to every object when the next maintenance task could perform.

$$\tau^m = [\tau_i^m]_{i=1..p} \quad (3)$$

The interval of the inspections fulfil the constraint

$$\tau_i^m * (\varepsilon_i - 1) \leq \vartheta, \quad (4)$$

where:

ε_i : is the number of the maintenance tasks of object i , and ϑ : is the examination period.

In real life of these systems the inspection and maintenance tasks are performed usually by the same expert so the special knowledge collected at the previous inspections is well utilized, so the maintenance times could be shortened.

3.1 Experts

The parameters for the mathematical description of the experts are the following:

- s : is the number of the experts, this is constant in most cases and in this model we modelled as constant,

The time required to travel between object i and j :

$$\tau_{i,j} = \frac{l_{i,j}}{v}; \quad \begin{matrix} i = 1..p \\ j = 1..p' \end{matrix} \quad (5)$$

where:

- $l_{i,j}$: is the distance between the object i and j ,
- p : is the number of the objects,

- \bar{v} is the average speed of the expert.
- P : is the performance of the experts, it shows how much maintenance task is performed by the expert.

Constraints:

The performance of the expert has to be between the defined minimum and maximum values:

$$P_{i \min} < P_i < P_{i \max}, \quad (6)$$

where:

$$P_i = \sum_{j=1}^p (Y_{12,i,j} * \varepsilon_j) \quad (7)$$

The cycle time (τ_{\max}) - generally one day - is also a constraint, in one cycle the expert visit the objects do the inspection and return to his base location:

$$\tau^t = \tau_{0,1}^f + \tau_1^k + \sum_{i=2}^{c^t} (\tau_i^k + \tau_{i-1,i}) + \tau_{q,0}^f < \tau_{\max}, \quad (8)$$

where:

τ^t : is the interval when the expert start from his base location, visits the objects and return, it is generally one day at the regional or countrywide maintenance systems and:

$$\sum_{i=1}^T \tau_i^t = \vartheta,, \quad (9)$$

where:

- T : is the number of cycles in the ϑ interval,
- τ_{\max} : time interval of a cycle,
- c^t :: the number of objects has to visit in the cycle t ,
- $\tau_{0,1}^f$: the travel time to the first object from the start location,
- $\tau_{q,0}^f$: the travel time from the last object (q) to the experts base location,
- τ_i^k : the average inspection time of the object i .

The set of objects can be defined which have to inspect by the expert c :

$$O_c := \{o_i \mid Y_{12,s,i} = 1; i = 1..p\}, \quad (10)$$

$$|O_c| = P_c, \quad (11)$$

and the subsets, the objects have to be inspected in one cycle:

$$O_c^t \subseteq O_s, \quad (12)$$

where:

O_s : is an ordered set, the objects assigned to the given expert, the ordering function is:

$$o_p \in O_i; o_q \in O_i; o_p < o_q \text{ where } t_{o_p} < t_{o_q}, \quad (13)$$

where:

- t_{o_p} is the inspection time of o_p , and t_{o_q} is the inspection time of o_q ,
- so the set is ordered by the visiting time.

$$|O_c^t| = c^t \leq P_c, \quad (14)$$

$$\cup_{t=1}^T O_c^t = O_s, \quad (15)$$

and

$$\cup_{s=1}^p O_s^t = O. \quad (16)$$

However the expert performs more than one inspection on an object so the object is counted in the sets defined at (12) as many times as the number of inspection has to be performed.

To determine the interval of the inspections the following distance functions can be applied:

$$d(o_i; o_j \mid o_i \in O_p^t; o_j \in O_q^t) = p - q, \quad (17)$$

so based on the constraint in eq. (4):

$$\min\{d(o_i; o_j \mid o_i \in O_p^t; o_j \in O_q^t)\} \geq \tau_i^m. \quad (18)$$

So the path travelled by the expert i in a cycle t can be describe as:

$$l_i^t = l_{0,o_i^t(1)} + \sum_{c=1}^{|O_i^t|-1} (l_{o_i^t(c),o_i^t(c+1)} + l_{o_i^t(|O_i^t|),0}), \quad (19)$$

and the total path travelled by the expert i can be described as:

$$l_i^T = \sum_{t=1}^T \left[l_{0,o_i^t(1)} + \sum_{c=1}^{|o_i^t|-1} \left(l_{o_i^t(c),o_i^t(c+1)} \right) + l_{o_i^t(|o_i^t|),0} \right] = \sum_{t=1}^T l_p^t. \quad (20)$$

The expenditures (C) of the experts (S) in a given period (T) can be described as:

$$C^S = \left[\sum_{j=1}^S \left(\sum_{t=1}^T l_j^t \right) \right] * c_u + \left[\sum_{j=1}^S P_j \right] * c_v \quad (21)$$

where:

- c_u : is the specific cost for one kilometer,
- c_v : the specific cost for an object.

Further in the article the specific cost is calculated with the multiplier 1, so only the distance is considered.

The target of the optimization is:

$$C^S \rightarrow \min,, \quad (22)$$

the expenditures has to be minimal.

4. The evolutionary algorithm

The algorithm we developed solves the fixed destination multiple depot multiple route multiple travelling salesman problem and optimize the number of salesman in one phase and can be used for large or very large problems. The one phase algorithms not common in this area, there are only two phase algorithms were presented since then [5, 6], most of them using clustering [7] or partitioning [8] as one phase. As there are multiple salesmen: the experts, multiple depot: all the experts have different locations, fixed destination: all the expert start and return to their initial location, and all the experts do the travel (generally) in one day cycles.

The developed solution method based on a multi chromosome technique [9] which is not widely used in genetic algorithm but it could simply implement in the evolutionary programming. The data structure of the optimization is built as a cascaded structure. The biggest container is the population which consists of defined constant number of individuals, which is an input parameter of the optimization.

The algorithm is an evolutionary programming algorithm which has the following pseudo code:

1. generate the first population, in most cases it is random generated,
2. calculate the population fitness values,
3. while not done
 - 3.1. copy the population into a temporary population,
 - 3.2. run the mutation operators on the temporary population,
 - 3.3. select the survivors for the next population,
4. end while.

In the computer solution first initialize the data, random generator, etc. Then initialize the first population. In heavily constrained problems there are two cases:

- the randomly generated population individual is invalid: it violates the constraints,
- the individual is in the feasible region: but this is a very rare case.

There are several methods to get valid individual from simply dispose invalid individuals to create special operators which retain the individual's integrity. But the simplest solution is using penalty function. In the penalty function one can regulate the algorithm which solutions are preferred.

After the creation of the initial population it has to be copied into a temporary population then the mutation operators run on the temporary population. In most cases the high impact mutations have less chance to run and the low impact operators have a bigger chance. After the mutation we have to compute the mutated individuals' fitness value and then choose the survivor individuals to the descendant population which happens with a tournament. One simple way to perform the tournament is choose two random individuals one from the original and one from the mutated population and that will survive which has less (or bigger if the fitness not normalized) fitness value, we have to repeat this until the new population not filled.

4.1. Penalty functions

The penalty function is one of the simplest and fastest way to rate the individual, so the goodness of the actual solution. In this algorithm there are two different levels of penalty functions as it follows the multichromosome paradigm:

- local: the penalty function is applied to the expert,
- global: the penalty function is applied to the whole individual.

4.2 Local penalties

There are three different local penalty functions:

- Number of cycles penalty: when the expert do more route cycles than allowed,

- Few penalty : the expert has to get a minimal number of maintenance events,
- More penalty: the expert cannot get more maintenance events than his maximum capacity,

4.4 Global penalties

There are three different global penalty functions, which calculated after the local penalties:

- Near penalty: the maintenance events of one object cannot be arbitrarily close to each other.
- Scatter penalty: This applied when maintenance events of an object are scattered among several experts.
- Number of expert penalty: The employment of the expert has a fixed cost in this model. The algorithm tries to minimize the number of employed experts due to these penalty functions [10].

5. Results

We present the convergence of the algorithm on two test instances as the paper limits us. In these instances there are three experts and the objects are around them in a perfect circle. This instance can be easily solved by a human but it is hard to solve perfectly with a computer algorithm.

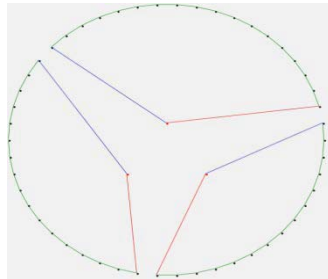


Figure 2: Test instance with 3 experts

Table 1: Running times of the optimization

Iteration number	35457
Run time	48 min 33 sec
Penalty	0
Cost	4484,47
Iteration number	35457

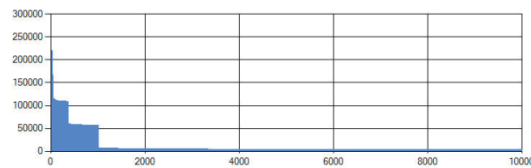


Figure 3: Convergence of the solution

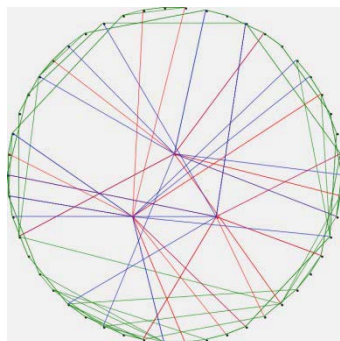


Figure 4: Test instance with 3 experts

Table 2: Running times of the optimization

Iteration number	50000
Run time	1 h 11 min 9 sec
Penalty	5
Cost	760731,64
Iteration number	50000

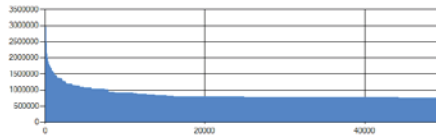


Figure 5: Convergence of the solution

6. Conclusion

The algorithm we designed and presented in this paper is great to solve this kind of problems, like the scheduled inspection and maintenance of any equipment or machines and it is even usable at waste collection systems. The algorithm can take the constraints of these types of systems into consideration and give result even if there are no optimal solution according to the constraints, it will give the least bad solution. The convergence of the algorithm is good and it performed well on large scale instances but at large scale a very high computing capacity computer or computer cloud needed.

7. Acknowledgements

The research was supported by the TÁMOP-4.2.4B/2-11/1-2012-0001 project entitled ‘Campus Hungary’, supported by the European Union, co-financed by the European Social Fund. The research was supported also by the Hungarian Scientific Research Fund OTKA T 109860 projects and was partially carried out in the framework of the Center of Excellence of Innovative Engineering Design and Technologies at the University of Miskolc.

8. References

- [1] J. Levitt, The handbook of maintenance management, Industrial Press Inc, ISBN 978-0-8311-3389-4, p. 477, 2004
- [2] D. Achermann, Modeling, Simulation and Optimization of Maintenance Strategies under Consideration of Logistic Processes, PhD. thesis, Swiss Federal Institute of Technology, Zurich, Diss. ETH No. 18152, 2008
- [3] L. Cser, J. Cselényi, M. Geiger, M. Mäntylä, A.S. Korhonen, Logistics from IMS towards virtual factory, Journal of Materials Processing Technology, Vol. 103, No. 1, pp.: 6-13, ISSN 0924-0136, 2000 [http://dx.doi.org/10.1016/S0924-0136\(00\)00412-X](http://dx.doi.org/10.1016/S0924-0136(00)00412-X).
- [4] Á. Bányai, Das virtuelle Logistikzentrum als Koordinator der logistischen Aufgaben. In: Modelling and optimization of logistic systems – Theory and practice, Bányai, T. & Cselényi, J. (Eds.), pp. 42-50, ISBN 963 661 402 4, Published by the University Miskolc, 1999.
- [5] M. Lam M., J. Mittenthal, Capacitated hierarchical clustering heuristic for multi depot location routing problems, International Journal of Logistics Research and Applications: A Leading Journal of Supply Chain Management, 2013, DOI: 10.1080/13675567.2013.820272
- [6] P.C. Pop, I. Kara, A.H. Marc, New mathematical models of the generalized vehicle routing problem and extensions, Applied Mathematical Modelling 36, (1), 97–107, 2012, <http://dx.doi.org/10.1016/j.apm.2011.05.037>
- [7] D. Chao, C. Ye, H. Miao, Two-Level Genetic Algorithm for Clustered Traveling Salesman Problem with Application in Large-Scale TSPs, Tsinghua Science and Technology, Vol. 12, No. 4, 2007, pp459-465, ISSN 1007-0214 15/20
- [8] G. Mosheiov, Vehicle routing with pick up and delivery: Tour Partitioning heuristics, Computers and Industrial Engineering, Vol. 34, No. 3, pp. 669-684, 1998, doi:10.1016/S0360-8352(97)00275-1
- [9] A. Király, J. Abonyi, Optimization of Multiple Traveling Salesmen Problem by a Novel Representation based Genetic Algorithm, Studies in Computational Intelligence, Vol. 313, pp. 141-151, 2010, doi: 10.1007/978-3-642-15220-7_12
- [10.] L. Kota, K. Jármai, Mathematical modelling of multiple tour multiple traveling salesman problem using evolutionary programming, Applied Mathematical Modelling, Vol. 39, No. 12, 2015, pp 3410-3433. doi: 10.1016/j.apm.2014.11.043.

Level Set-Based Topology Optimization Using the Lattice Boltzmann Method Considering Two-Phase Fluid Flows

Kentaro Yaji¹, Takayuki Yamada², Masato Yoshino³,
Toshiro Matsumoto⁴, Kazuhiro Izui⁵, Shinji Nishiwaki⁶

¹ Kyoto University, Kyoto, Japan, yaji.kentarou.74v@kyoto-u.ac.jp

² Kyoto University, Kyoto, Japan, takayuki@me.kyoto-u.ac.jp

³ Shinshu University, Nagano, Japan, masato@shinshu-u.ac.jp

⁴ Nagoya University, Nagoya, Japan, t.matsumoto@nuem.nagoya-u.ac.jp

⁵ Kyoto University, Kyoto, Japan, izui@me.kyoto-u.ac.jp

⁶ Kyoto University, Kyoto, Japan, shinji@prec.kyoto-u.ac.jp

1. Abstract

This paper presents a topology optimization method using the lattice Boltzmann method for the design of a flow channel considering two-phase fluid flows. This approach enables the design of fluidic devices such as two-phase microchannels that achieve a desired flow with maximal performances such as mixing and reaction, and extraction efficiencies. The optimization problems are formulated using the continuous Boltzmann equation, and the design sensitivities are derived based on the adjoint lattice Boltzmann method. In the adjoint lattice Boltzmann method, based on a novel discretization strategy similar to that of the lattice Boltzmann method, the adjoint equations can be implemented as simple time evolution equations. Based on the above formulations, we construct a topology optimization method incorporating level set boundary expressions for the design of a two-phase microchannel that aims to maximize extraction efficiency while minimizing the pressure drop. A numerical example is provided to confirm the utility of the proposed method.

2. Keywords: Topology Optimization, Lattice Boltzmann Method, Two-Phase Flow, Level Set Method

3. Introduction

The aim of this research is to construct a topology optimization method for the design of a flow channel considering two-phase fluid flows. Using this approach, fluidic devices such as two-phase microchannels can be designed so that they achieve a desired flow and accomplish maximal mixing and reaction, or extraction efficiencies.

These performances strongly depend on the design of the channel configuration, so that each process, such as mixing, reaction, or extraction, is finished as quickly as possible (Fig. 1). In addition, to prevent damage to the microchannels, minimizing the pressure drop in the microchannel system is an important factor. Thus, to meet the most important design requirements of a two-phase microchannel, the maximization of the above efficiencies and the minimization of the pressure drop must be simultaneously considered. Designer intuition alone, however, seldom yields an optimal channel configuration that sufficiently satisfies these requirements.

To overcome this problem, topology optimization [1] is a particularly powerful approach for obtaining useful designs for the channel configuration of the devices under consideration here. The basic concept of topology optimization is the introduction of an extended design domain, the so-called fixed design domain, and the replacement of the optimization problem with a material distribution problem, using the characteristic function. Borrvall and Petersson [2] pioneered a topology optimization method for a dissipation energy minimization problem under Stokes flow, in which the material distribution in the fixed design domain is represented as consisting of either fluid or solid domains.

Based on this methodology, Okkels and Bruus [3] proposed a topology optimization method for the design of a micro reactor in which the reaction effect is mathematically modeled, and the aim was to achieve maximal reaction efficiency in the microchannel system given a uniform concentration of reactants. Andreasen et al. [4] proposed a topology optimization method for the design of a micro mixer in which maximization of mixing performance was the aim. And Makhija et al. [5] applied the lattice Boltzmann method (LBM) [6] in mixing performance maximization problem and investigated the relationship between the mixing performance and the pressure drop.

The basic idea of the above optimization methodologies for multi-component fluid flows is the introduction of concentration, governed by a convective-diffusion equation, into the formulation of the optimization problem. That is, since the fluid flow is not affected by concentration (one-way coupling), the above research cannot treat fluid flows of immiscible liquids in which the interface effect between the two phases must be considered. In particular, since the extraction process strongly depends on the difference between molecular diffusive coefficients

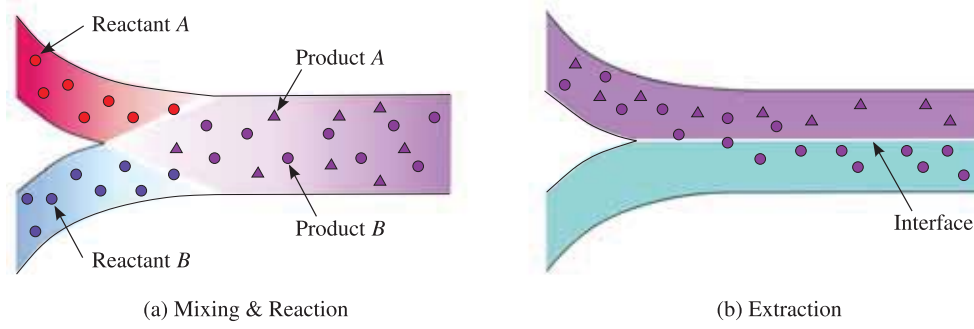


Figure 1: Schematic diagram of typical experiments in microchannel device.

in two-phase fluid flows [7], the conventional approach must be extended so that flows can be treated in extraction efficiency maximization problems.

Here, we construct a new topology optimization method for an extraction efficiency maximization problem, in which two-phase fluid flows are analyzed based on the two-phase LBM proposed by Inamuro et al. [8]. Since special treatments for tracking an interface are unnecessary in this method, the LBM is suitable for the computation of multi-phase fluid flows. In addition, since the LBM is an explicit scheme based on a simple time evolution equation, the adjoint equation can be formulated with this equation that is discretized using the LBM [9]. Previously, we investigated the applicability of this *adjoint lattice Boltzmann method* to topology optimization problems, and verified that this approach enables the design sensitivity to be quickly obtained at each optimization step [10].

In the following section, the basic concept of the two-phase LBM is discussed and the topology optimization problem is formulated for the extraction efficiency maximization problem. The numerical implementations and optimization algorithms are then explained and, finally, we provide a numerical example to validate the utility of the proposed method.

4. Formulation

4.1. Two-Phase Lattice Boltzmann Method

We now discuss the concept of the two-phase LBM [8] that will be applied here to incompressible fluids while considering two-phase fluid flows under identical density conditions. In the following, we use non-dimensional variables, as used as in [8]. In the LBM, a modeled fluid, composed of identical particles whose velocities are restricted to a finite set of N vectors \mathbf{c}_i , is considered. We use the two-dimensional nine-velocity model ($N = 9$)[6] and three particle velocity distribution functions, f_{Ai} , f_{Bi} , and f_{Ci} . The function f_{Ai} is used as an index function for computation of the interface profile in phase X and phase Y , f_{Bi} is used for computation of the pressure and velocity of the two-phase fluid flows, and f_{Ci} is used for computation of the concentration.

The evolution of the particle distribution functions $f_{\sigma i}(\mathbf{x}, t)$ ($\sigma = A, B, C$) with velocity \mathbf{c}_i at point \mathbf{x} and at time t are computed with the following equation:

$$f_{\sigma i}(\mathbf{x} + \mathbf{c}_i \Delta x) - f_{\sigma i}(\mathbf{x}, t) = \frac{1}{\tau_{\sigma}} \{f_{\sigma i}(\mathbf{x}, t) - f_{\sigma i}^{\text{eq}}(\mathbf{x}, t)\}, \quad (1)$$

where $f_{\sigma i}^{\text{eq}}$ are equilibrium distribution functions, τ_{σ} represents non-dimensional single relaxation times, Δx is the spacing of the grid, and Δt is the time step.

The index function $\psi(\mathbf{x}, t)$, pressure $p(\mathbf{x}, t)$, velocity $\mathbf{u}(\mathbf{x}, t)$, and concentration $T(\mathbf{x}, t)$ are defined as follows:

$$\psi = \sum_{i=1}^9 f_{Ai}, \quad p = \frac{1}{3} \sum_{i=1}^9 f_{Bi}, \quad \mathbf{u} = \sum_{i=1}^9 f_{Bi} \mathbf{c}_i, \quad T = \sum_{i=1}^9 f_{Ci}. \quad (2)$$

The equilibrium distribution functions $f_{\sigma i}^{\text{eq}}(\mathbf{x}, t)$ are given by

$$f_{Ai}^{\text{eq}} = H_i \psi + F_i (p_0 - \kappa_f \psi \nabla^2 \psi) + 3E_i \psi \mathbf{c}_i \cdot \mathbf{u} + E_i \kappa_f \mathbf{G} : (\mathbf{c}_i \otimes \mathbf{c}_i), \quad (3)$$

$$f_{Bi}^{\text{eq}} = E_i \left\{ 3p + 3\mathbf{c}_i \cdot \mathbf{u} - \frac{3}{2} |\mathbf{u}|^2 + \frac{9}{2} (\mathbf{c}_i \cdot \mathbf{u})^2 \right\} + E_i \kappa_g \mathbf{G} : (\mathbf{c}_i \otimes \mathbf{c}_i), \quad (4)$$

$$f_{Ci}^{\text{eq}} = E_i T (1 + 3\mathbf{c}_i \cdot \mathbf{u}), \quad (5)$$

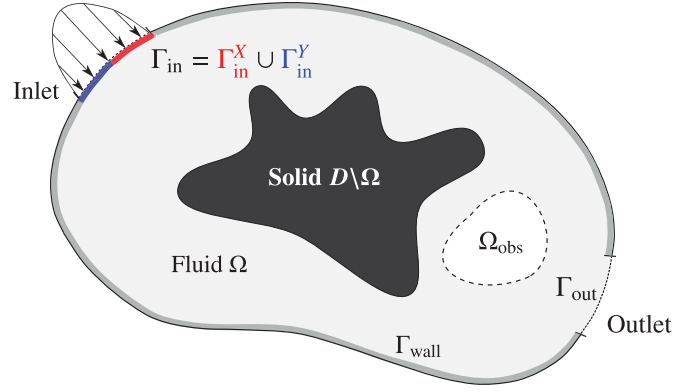


Figure 2: Schematic figure of fixed design domain D in the extraction efficiency maximization problem.

where parameters E_i , H_i , and F_i are defined so that $E_1 = 4/9$, $E_2 = E_3 = E_4 = E_5 = 1/9$, $E_6 = E_8 = E_9 = 1/36$, $H_1 = 1$, $H_2 = H_3 = \dots = H_9 = 0$, $F_1 = -7/3$, and $F_i = 3E_i$ ($i = 2, 3, \dots, 9$). κ_f and κ_g are parameters with constant values that determine the width of the interface and the strength of the interfacial tension, respectively. The tensor $\mathbf{G}(\mathbf{x}, t)$ is defined as follows:

$$\mathbf{G} = \frac{9}{2} \nabla \psi \otimes \nabla \psi - \frac{3}{2} |\nabla \psi|^2 \boldsymbol{\delta}, \quad (6)$$

where $\boldsymbol{\delta}$ represents the Kronecker delta. In addition, $p_0(\mathbf{x}, t)$ is given by

$$p_0 = \psi \bar{T} \frac{1}{1 - b\psi} - a\psi^2, \quad (7)$$

where a , b , and \bar{T} are parameters for determining the profile of index function ψ .

Applying the asymptotic theory to Eqs. (1)–(7), we find that the macroscopic variables, p and \mathbf{u} , satisfy the Navier-Stokes equations with relative errors of $O(\Delta x^2)$. Note that the pressure is given by $p + (2/3)\kappa_g \nabla |\psi|^2$ in the interface [8]. In addition, the concentration T satisfies the convective-diffusion equation, and the extraction process is represented based on the values of T . The details of the extraction process will be described in the next.

4.2. Topology Optimization Problem

We now formulate the topology optimization problem for the design of a flow channel considering two-phase fluid flows. A schematic diagram of this problem is shown in Fig. 2, with fixed domain D composed of fluid domain Ω and solid domain $D \setminus \Omega$. The inlet boundary condition includes a prescribed velocity, $\mathbf{u} = \mathbf{u}_{in}$ at Γ_{in} , and the outlet boundary condition includes a prescribed pressure, $p = p_{out}$ at Γ_{out} . At the inlet boundary Γ_{in} , the order parameters ψ and concentrations T are respectively set to $\psi = \psi_{in}^X$ at Γ_{in}^X , $\psi = \psi_{in}^Y$ at Γ_{in}^Y , $T = T_{in}^X$ at Γ_{in}^X , and $T = T_{in}^Y$ at Γ_{in}^Y , where $\Gamma_{in} = \Gamma_{in}^X \cup \Gamma_{in}^Y$ and $\Gamma_{in}^X \cap \Gamma_{in}^Y = \emptyset$. In addition, the boundary condition for ψ and T at $\Gamma_{out} \cup \Gamma_{wall}$ is set to a Neumann condition, with $\partial \psi / \partial \mathbf{n} = \mathbf{0}$ and $\partial T / \partial \mathbf{n} = \mathbf{0}$.

To simultaneously evaluate the extraction efficiency and pressure drop, we define an objective functional, J , based on the weighted sum method, as follows:

$$J = w_1 \int_{t_0}^{t_1} \int_{\Gamma} -\mathbf{n} \cdot \mathbf{u} \left(p + \frac{1}{2} \rho |\mathbf{u}|^2 \right) d\Gamma dt + w_2 \int_{t_0}^{t_1} \int_{\Omega_{obs}} \frac{(T - \langle T \rangle_{in})^2}{2 \langle T \rangle_{in}^2} d\Omega dt, \quad (8)$$

where t_0 and t_1 represent the time step of the LBM calculation, w_1 and w_2 are the weighting parameters, ρ is the fluid density given by $3p$ due to the characteristic of the LBM, and $\langle T \rangle_{in}$ is the average value of T at the inlet boundary. In the above equation, the second term represents the relative error of T with respect to $\langle T \rangle_{in}$ in the observation domain, $\Omega_{obs} \subset D$. The phase X and phase Y concentrations are set to different values, i.e., $T_{in}^X \neq T_{in}^Y$. Thus, the second term in Eq. (8) seldom becomes equal to zero during the optimization process. Here, we assume that the extraction process is completely finished when the value of this term does become equal to zero. In addition, since the molecular diffusive coefficient, $k = 1/3 \tau_C \Delta x$, is depend on the kind of fluid, the relaxation time τ_C is defined as follows:

$$\tau_C(\psi) = \frac{\psi_{in}^Y - \psi}{\psi_{in}^Y - \psi_{in}^X} \tau_C^X + \frac{\psi - \psi_{in}^X}{\psi_{in}^Y - \psi_{in}^X} \tau_C^Y, \quad (9)$$

where τ_C^X and τ_C^Y represent the relaxation time in phase X and phase Y , respectively.

Based on the above objective functional in Eq. (8), we formulate a topology optimization problem based on our previous research [10], in which the Boltzmann equation is employed when applying a continuous adjoint sensitivity analysis, as follows:

$$\begin{aligned} & \inf_{\gamma \in \mathcal{A}} J[f_{\sigma i}; \gamma], & (10) \\ & \text{subject to } \begin{cases} Sh \frac{\partial f_{\sigma i}}{\partial t} + \mathbf{c}_i \cdot \nabla f_{\sigma i} = -\frac{1}{\tau_{\sigma i}} (f_{\sigma i} - f_{\sigma i}^{\text{eq}}) + 3E_i \mathbf{c}_i \cdot \mathbf{F}_\gamma \delta_{\sigma B} & \text{(Boltzmann equation),} \\ f_{\sigma i}(\mathbf{x}, t_0) = f_{\sigma i}^0 & \text{(initial condition),} \\ f_{\sigma i}(\mathbf{x}, t) = f_{\sigma i}^{\text{bc}}(\mathbf{x}, t) & \text{(boundary condition),} \end{cases} & (11) \end{aligned}$$

where $\gamma(\mathbf{x})$ represents the design variable belonging to the function space $\mathcal{A} = \{\gamma \in L^\infty(D) \mid 0 \leq \gamma \leq 1 \text{ in } D, V_\gamma \leq 0\}$, where $V_\gamma (= \int_D \gamma d\Omega - V_{\max})$ is the volume constraint that restricts the maximum fluid volume to V_{\max} . We let γ vary between zero and unity, with $\gamma = 0$ corresponding to a solid domain and $\gamma = 1$ to a fluid domain. In Eq. (11), Sh is the Strouhal number, and $f_{\sigma i}^0$ and $f_{\sigma i}^{\text{bc}}$ represent the initial and boundary values for the Boltzmann equation, respectively. We note that the above Boltzmann equation is the so-called *discrete Boltzmann equation* that is not the original equation, since the discrete particle velocities \mathbf{c}_i are used. The reason why we use this equation to formulate the optimization problem is that the boundary conditions for adjoint equations can be easily derived based on the adjoint sensitivity analysis.

In addition, \mathbf{F}_γ is an artificial force, based on the design variable γ , defined as

$$\mathbf{F}_\gamma = -\alpha(\gamma)\mathbf{u}, \text{ where } \alpha(\gamma) = \alpha_{\min} + (\alpha_{\max} - \alpha_{\min})\hat{H}(\gamma). \quad (12)$$

In this equation, $\alpha(\mathbf{x})$ is the local inverse permeability based on Darcy's law [2], and α_{\min} and α_{\max} are parameters constant value that determine the profile of α . In this study, these parameters are set to $\alpha_{\min} = 0$ and $\alpha_{\max} = 1.0$, respectively. The profile of \hat{H} is defined as a convex interpolation whose formulation will be described later.

4.3. Level Set-Based Topology Optimization Method

Based on the previous study [11], we use the level set function, $\phi(\mathbf{x})$, to express the boundary, $\partial\Omega$, between fluid and solid domains, as follows:

$$\begin{cases} 0 < \phi(\mathbf{x}) \leq 1 & \text{for } \mathbf{x} \in \Omega \setminus \partial\Omega, \\ \phi(\mathbf{x}) = 0 & \text{for } \mathbf{x} \in \partial\Omega, \\ -1 \leq \phi(\mathbf{x}) < 0 & \text{for } \mathbf{x} \in D \setminus \Omega. \end{cases} \quad (13)$$

The level set function has upper and lower limits imposed for the regularization term used to regularize the optimization problem. In addition, \hat{H} is replaced by a smoothed Heaviside function $\hat{H}_\phi(\phi)$ that is defined so that $0 \leq \hat{H}_\phi \leq 1$, as used in the previous study [11].

In a level set-based approach, the optimization problem is replaced with a problem to find an optimal distribution of the level set function. We explore the optimal distribution of ϕ using a time evolution equation, as follows:

$$\frac{\partial \phi(\mathbf{x}, \zeta)}{\partial \zeta} = -K \{J'(\mathbf{x}, \zeta) - \tau \nabla^2 \phi(\mathbf{x}, \zeta)\}, \quad (14)$$

where $K > 0$ is a constant parameter, $\tau > 0$ is the regularization coefficient that is set to an appropriate value so that the smoothness of ϕ is maintained during the optimization process, and ζ is a fictitious time corresponding to a time step in the optimization. The design sensitivity J' is defined based on the Fréchet derivative.

5. Optimization Algorithm

The optimization algorithm of the proposed method is the following.

Step 1. aThe initial level set function is set.

Step 2. bThe two-phase lattice Boltzmann equations are calculated until a steady-state condition is satisfied.

Step 3. cIf the criteria of the objective functional and inequality constraint are satisfied, an optimal configuration is obtained and the optimization is finished, otherwise the design sensitivity is calculated based on the adjoint sensitivity analysis [10].

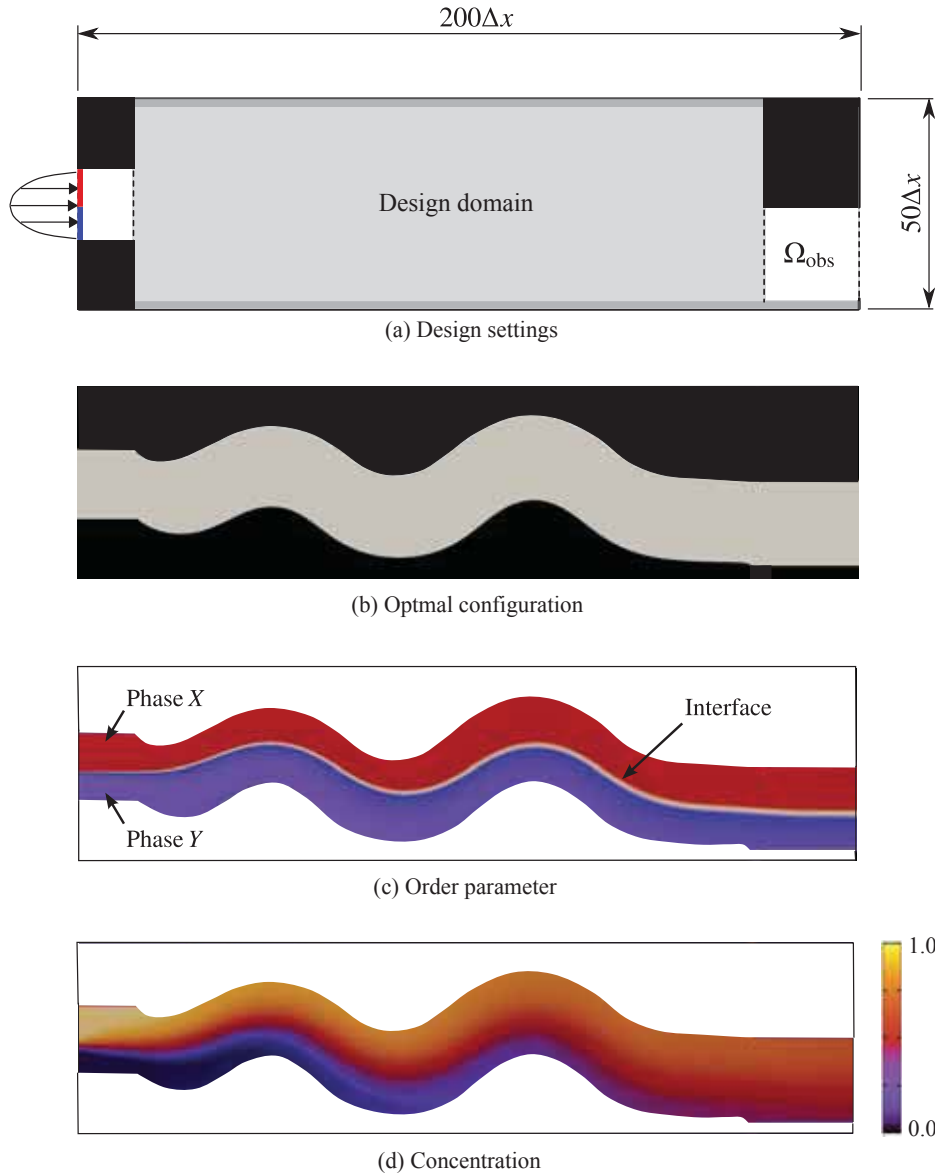


Figure 3: Design settings, optimal configuration, and the distributions of order parameter and concentration.

Step 4. The level set function is updated using the finite element method, after which the optimization procedure returns to Step 2 of the iterative loop.

6. Numerical Example

Here, we provide a numerical example using the proposed method. Figure 3(a) shows the design settings in the extraction maximization problem. The analysis domain is discretized using $200\Delta x \times 50\Delta x$ grids, and the volume constraint is set with $V_{\max} = 0.5$. The optimization parameters are set so that $K = 1$, $\tau = 8.0 \times 10^{-3}$, $\Delta\zeta = 0.5$, $w_1 = 1.0$, and $w_2 = 0.01$. The initial distribution of the level set function is set to $\phi(\mathbf{x}, 0) = \sin(6\pi x/200\Delta x) \sin(2\pi y/50\Delta x)$, so that several holes are present in D at the initial optimization step, $\zeta = 0$. The Reynolds number is set as $Re = 10$, with the reference length using the inlet width and the reference velocity using the inlet velocity. The kinematic viscosity is given by $\nu = 1/3(\tau_B - 1/2)\Delta x$. The parameters for the two-phase LBM are set so that $\kappa_f = \kappa_g = 1.0 \times 10^{-2}$, $a = 9/49$, $b = 2/21$, $\bar{T} = 0.55$, $T_{\text{in}}^X = 1.0$, $T_{\text{in}}^Y = 0.0$, $\psi_{\text{in}}^X = 1.0$, $\tau_C^X = 0.503$, $\tau_C^Y = 0.553$, and $\psi_{\text{in}}^Y = 0.5$. Thus, the Schmidt number and the Péclet number are given by $Sc = 10$ and $Pe = 100$, respectively.

As shown in Fig. 3(b), a sinuous channel is obtained as an optimal configuration, a suitable form that sufficiently diffuses the concentration of the two phases, whose distribution is shown in Fig. 3(d). In addition, we can confirm that the interface between phase X and phase Y is expressed by the order parameter value, whose

distribution is shown in Fig. 3(c). We note that the obtained optimal configuration is similar to the results of previous studies [5,12], in which the interface effect is not treated while the concentration is calculated based on the convective-diffusion equation.

7. Conclusion

This paper proposed a new topology optimization method using a two-phase LBM for the design of the channel configuration in a microchannel device. In this research, the extraction process was modeled using concentration values that are governed by a convective-diffusion equation. The presented method was applied to an extraction maximization problem and a numerical example demonstrated the validity of the proposed method.

8. Acknowledgments

This work was supported in part by a grant for JSPS KAKENHI, Grant Number 26820032.

9. References

- [1] O. Sigmund and K. Maute, Topology optimization approaches, *Structural and Multidisciplinary Optimization*, 48 (6), 1031-1055, 2013.
- [2] T. Borrvall and J. Petersson, Topology optimization of fluids in Stokes flow, *International Journal for Numerical Methods in Fluids*, 41 (1), 77-107, 2003.
- [3] F. Okkels and H. Bruus, Scaling behavior of optimally structured catalytic microfluidic reactors, *Physical Review E*, 75 (1), 016301, 2006.
- [4] C.S. Andreasen, A.R. Gersborg and O. Sigmund, Topology optimization of microfluidic mixers, *International Journal for Numerical Methods in Fluids*, 61 (5), 498-513, 2009.
- [5] D. Makhija, G. Pinggen, R. Yang and K. Maute, Topology optimization of multi-component flows using a multi-relaxation time lattice Boltzmann method, *Computers and Fluids*, 67, 104-114, 2012.
- [6] S. Succi, *Lattice Boltzmann Equation for Fluid Dynamics and Beyond*, Oxford University Press, New York, 2001.
- [7] P. Znidarsic-Plazl and I. Plazl, Steroid extraction in a microchannel system—mathematical modeling and experiments, *Lab on a Chip*, 7, 883-889, 2007.
- [8] T. Inamuro, R. Tomita and F. Ogino, Lattice Boltzmann simulations of drop deformation and breakup in shear flows, *International Journal of Modern Physics B*, 17 (1,2), 21-26, 2003.
- [9] M.M. Tekitek, M. Bouzidi, F. Dubois and P. Lallemand, Adjoint lattice Boltzmann equation for parameter identification, *Computers and Fluids*, 35 (8,9), 805-813, 2006.
- [10] K. Yaji, T. Yamada, M. Yoshino, T. Matsumoto, K. Izui and S. Nishiwaki, Topology optimization using the lattice Boltzmann method incorporating level set boundary expressions, *Journal of Computational Physics*, 274, 158-181, 2014.
- [11] T. Yamada, K. Izui, S. Nishiwaki and A. Takezawa, A topology optimization method based on the level set method incorporating fictitious interface energy, *Computer Methods in Applied Mechanics and Engineering*, 199 (45-48), 2876-2891, 2010.
- [12] D. Makhija and K. Maute, Level set topology optimization of scalar transport problems, *Structural and Multidisciplinary Optimization*, 51 (2), 267-285, 2014.

Simultaneous Optimization of Topology and Orientation of Anisotropic Material using Isoparametric Projection Method

Tsuyoshi Nomura¹, Ercan M. Dede², Tadayoshi Matsumori¹ and Atushi Kawamoto¹

¹Toyota Central R&D Labs., Inc. Aihchi, Japan, nomu2@mosk.tytlabs.co.jp

²Toyota Research Institute of North America, MI, USA,
eric.dede@tema.toyota.com

1. Abstract

New fiber reinforced composite fabrication technologies, such as tailored fiber placement or continuous fiber printing technology, enables realization of arbitrary orientation distribution of reinforcement fiber in a structure. Thus, building structures with optimal shape, topology and fiber orientation is now possible with aid of these technologies. In order to design such optimal structures, we propose a general topology optimization method, which is capable of simultaneous design of topology and orientation of anisotropic material, by introducing orientation design variables in addition to the density design variable. The proposed method supports not only discrete fiber orientation but also continuous fiber orientation design by using a Cartesian style orientation vector as the design variable combined with a projection method using isoparametric shape functions. The proposed method is less likely to be trapped at unwanted local optima when compared with classic continuous fiber angle optimizations, CFAOs, which directly uses orientation angle as the design variables; this is because vector representation offers more paths from one design solution to another, including an orientation vector with smaller norm, which represents weaker orientation. Another advantage of the proposed method is that it is compatible with filtering methods, especially design variable filtering, so that designers can control the complexity of the orientation angle distribution. The proposed method is built upon modern topology optimization technique, thus, it is versatile and flexible enough to solve multiload problems or even multiphysics problems.

2. Keywords: Topology optimization, Orientation design, Isoparametric projection, Tailored fiber placement, 3D printing

3. Introduction

Fiber orientation is the most important factor for demanding the mechanical properties of fiber reinforced composites such as carbon fiber reinforced plastics, CFRPs. In the past, fiber orientation design for such materials was rather limited. The composite is either unidirectional or woven fabric and the designers have to choose one option and can only determine the combination of given composites. These days, there are several new fabrication technologies that have become reality such as tailored fiber placement, TFP [1, 2], based on automated stitching machines, or continuous fiber printing systems [3] based on 3D printing technology. These technologies drastically expand the degree of freedom in orientation design of anisotropic composites, however, the design methodology to elicit maximum performance out of these technologies is not well established, yet. Topology optimization [4] looks to be the most forward thinking option to support this goal. Topology optimization was originally developed under consideration of anisotropy in material properties in the intermediate state by the homogenization design method with anisotropic microstructure, and there still has been enormous effort made for solving anisotropy topology optimization problems [5, 6, 7, 8]. In fact, solution of this anisotropic material layout problem has been demanded by the aerospace industry for a long time, and a large amount of effort has been made using a variety of numerical strategies [9, 10]. However, due to the difficulty in avoiding local optima [7, 11], a general optimization method has not been established yet, especially for the simultaneous optimization of topology and material orientation.

In this study, we propose a general topology optimization method, which is capable of simultaneous design of topology and orientation of anisotropic material, by introducing orientation design variables in addition to the density design variable by expanding the idea of design variable projection methods.

4. Formulation

In this paper, the formulation of the design variable is briefly summarized to focus the discussion. Readers are referred to the complete formulation as provided in a journal paper by the authors [12].

4.1. Topology design representation

Assume that a fixed design domain, D , is given, and inside of D , the following characteristic function is defined to indicate the object domain to be designed, Ω_d ;

$$\chi(\mathbf{x}) = \begin{cases} 0 & \text{for } \forall \mathbf{x} \in D \setminus \Omega_d, \\ 1 & \text{for } \forall \mathbf{x} \in \Omega_d. \end{cases} \quad (1)$$

Here, $\chi(\mathbf{x})$ is defined by an implicit function, ϕ , and Heaviside function such that

$$\chi(\mathbf{x}) = H(\phi(\mathbf{x})) = \begin{cases} 0 & \text{for } \forall \mathbf{x} \in D \setminus \Omega_d, \\ 1 & \text{for } \forall \mathbf{x} \in \Omega_d. \end{cases} \quad (2)$$

For regularization of the function space, a Helmholtz filter is used[13, 14],

$$-R_\phi^2 \nabla^2 \tilde{\phi} + \tilde{\phi} = \phi, \quad (3)$$

where R_ϕ is the filter radius and $\tilde{\phi}$ is a filtered field. The regularized Heaviside function is introduced to relax $\chi(\mathbf{x})$ to the material density field $\rho(\mathbf{x})$

$$\rho(\tilde{\phi}) = \tilde{H}(\tilde{\phi}), \quad (4)$$

where $\tilde{H}(\tilde{\phi})$ is a regularized Heaviside function.

The constitutive tensor, e.g. the stiffness tensor for a structural problem, is interpolated between void and solid state using ρ

$$\mathbf{C}_\rho = \mathbf{C}_v + \rho^p (\mathbf{C}_s - \mathbf{C}_v), \quad (5)$$

where \mathbf{C}_ρ , \mathbf{C}_v , \mathbf{C}_s are the interpolated tensor, void tensor, and solid material tensor, respectively, and p is the density penalty parameter. In the following discussion, \mathbf{C}_s is extended to anisotropic materials with a material physical parameter orientation design variable.

4.2. Orientation design representation with Isoparametric projection

For simplicity, this discussion is focused on a two-dimensional case, hereafter. A Cartesian representation is chosen for the design variable, and the orientation field in a given fixed design domain is declared as follows;

$$\vartheta(\mathbf{x}) = \begin{bmatrix} \xi(\mathbf{x}) \\ \zeta(\mathbf{x}) \end{bmatrix}, \quad (6)$$

where

$$|\vartheta(\mathbf{x})| \leq 1 \quad \text{for } \forall \mathbf{x} \in D. \quad (7)$$

Let the $v(\mathbf{x})$ be the precursor design vector field having natural coordinate values, ξ and η , as its elements

$$v(\mathbf{x}) = \begin{bmatrix} \xi(\mathbf{x}) \\ \eta(\mathbf{x}) \end{bmatrix}, \quad (8)$$

where

$$\xi \in [-1, 1] \quad \text{and} \quad \eta \in [-1, 1]. \quad (9)$$

We then define the orientation vector field as follows;

$$\vartheta(\mathbf{x}) = \mathbf{N}(v(\mathbf{x})) = \begin{bmatrix} N_x(\xi(\mathbf{x}), \eta(\mathbf{x})) \\ N_y(\xi(\mathbf{x}), \eta(\mathbf{x})) \end{bmatrix}, \quad (10)$$

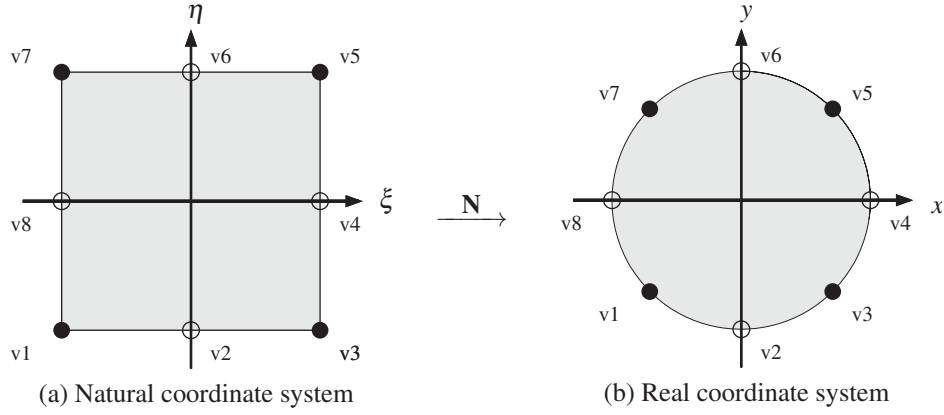


Figure 1: The eight node bi-quadratic serendipity element. Left: natural coordinates. Right: real coordinates.

where \mathbf{N} is an appropriate shape function whose boundary forms a unit circle. If the element is in the unit circle, then $\|\vartheta\| \leq 1$ is naturally fulfilled. There are various options in choosing an isoparametric shape function, \mathbf{N} , and the eight node bi-quadratic quadrilateral element [15, 16], namely the “serendipity” element, is used and defined as follows;

$$\begin{cases} N_x(\xi, \eta) = \sum_{i=1}^8 u_i N_i(\xi, \eta) \\ N_y(\xi, \eta) = \sum_{i=1}^8 v_i N_i(\xi, \eta), \end{cases} \quad (11)$$

where $\mathbf{v}_i = \{u_i, v_i\}^T$ is the coordinate of the i -th node in the real coordinate system, as shown in right side image of Figure 1. The function $N_i(\xi, \eta)$ is defined as follows;

$$\begin{cases} N_1(\xi, \eta) = - (1 - \xi)(1 - \eta)(1 + \xi + \eta) / 4 \\ N_2(\xi, \eta) = (1 - \xi)(1 - \eta)(1 + \xi) / 2 \\ N_3(\xi, \eta) = - (1 + \xi)(1 - \eta)(1 - \xi + \eta) / 4 \\ N_4(\xi, \eta) = (1 + \xi)(1 - \eta)(1 + \eta) / 2 \\ N_5(\xi, \eta) = - (1 + \xi)(1 + \eta)(1 - \xi - \eta) / 4 \\ N_6(\xi, \eta) = (1 - \xi)(1 + \eta)(1 + \xi) / 2 \\ N_7(\xi, \eta) = - (1 + \xi)(1 + \eta)(1 + \xi - \eta) / 4 \\ N_8(\xi, \eta) = (1 - \xi)(1 - \eta)(1 + \eta) / 2. \end{cases} \quad (12)$$

The relationship between ϑ and \mathbf{v} is analogous to the relationship between $\rho(\mathbf{x})$ and $\phi(\mathbf{x})$. Similarly, a Helmholtz filter is used to regularize \mathbf{v} , which resides in L^∞ space projected to H^1 space. However, this time, the regularized field is a vector field

$$\tilde{\mathbf{v}}(\mathbf{x}) = \begin{bmatrix} \tilde{\xi}(\mathbf{x}) \\ \tilde{\eta}(\mathbf{x}) \end{bmatrix}, \quad (13)$$

where \mathbf{v} has a box bound, but $\tilde{\mathbf{v}}$ does not have explicit bounds.

The regularization is enforced with the following equation

$$-\mathbf{R}_v \nabla^2 \begin{bmatrix} \tilde{\xi} \\ \tilde{\eta} \end{bmatrix} + \begin{bmatrix} \tilde{\xi} \\ \tilde{\eta} \end{bmatrix} = \begin{bmatrix} \xi \\ \eta \end{bmatrix}, \quad (14)$$

where $\mathbf{R}_v = R_v^2 \mathbf{I}$ and R_v is the filter radius for the vector field, and \mathbf{I} is the identity matrix. Then, unbounded $\tilde{\mathbf{v}}$ is projected into $-1 \leq \tilde{\xi} \leq 1$, $-1 \leq \tilde{\eta} \leq 1$ in a manner similar to the $\tilde{\phi}$ to ρ projection.

$$\bar{\mathbf{v}} = \begin{bmatrix} \tilde{\xi}(\mathbf{x}) \\ \tilde{\eta}(\mathbf{x}) \end{bmatrix} = \begin{bmatrix} 2\tilde{H}(\tilde{\xi}(\mathbf{x})-1) \\ 2\tilde{H}(\tilde{\eta}(\mathbf{x})-1) \end{bmatrix}. \quad (15)$$

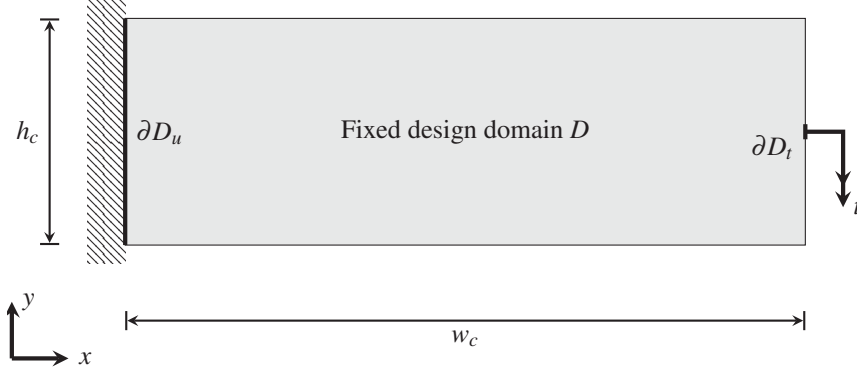


Figure 2: Geometry settings for the short cantilever problem.

In concert with equation (10), the regularized orientation field $\tilde{\vartheta}$ is obtained as follows;

$$\tilde{\vartheta}(\mathbf{x}) = \mathbf{N}(\tilde{\mathbf{v}}(\mathbf{x})) = \begin{bmatrix} N_x(\tilde{\xi}(\mathbf{x}), \tilde{\eta}(\mathbf{x})) \\ N_y(\tilde{\xi}(\mathbf{x}), \tilde{\eta}(\mathbf{x})) \end{bmatrix} \quad \text{for } \forall \mathbf{x} \in D. \quad (16)$$

Finally, the constitutive tensor is transformed according to $\tilde{\vartheta}$

$$\mathbf{C}_a = \mathbf{C}_i + \hat{\mathbf{T}}^{-1}(\tilde{\vartheta}) \cdot (\mathbf{C}_u - \mathbf{C}_i) \cdot \hat{\mathbf{T}}'(\tilde{\vartheta}), \quad (17)$$

where \mathbf{C}_a is an interpolated tensor in terms of anisotropy, \mathbf{C}_u is a given unrotated anisotropic tensor, \mathbf{C}_i is an isotropic component subtracted from \mathbf{C}_u , and $\hat{\mathbf{T}}$ and $\hat{\mathbf{T}}'$ are transformations to rotate a tensor to a direction given by ϑ ; refer to the detailed description in a paper[12].

With this formulation, the following three states are continuously interpolated. When $\|\tilde{\vartheta}\| = 1$, this equation is equivalent to simple rotation of given \mathbf{C}_u , that is,

$$\mathbf{C}_a = \mathbf{T}^{-1}(\theta) \cdot \mathbf{C}_u \cdot \mathbf{T}'(\theta), \quad (18)$$

where $\theta = \angle \hat{\vartheta}$, and $\mathbf{T}(\theta)$ and $\mathbf{T}'(\theta)$ are rotation tensor for the stress tensor and strain tensor, respectively. This relationship holds owing to distributive property of tensor algebra and the isotropic nature of \mathbf{C}_i , that is, $\mathbf{C}_i = \mathbf{T}^{-1}(\theta) \cdot \mathbf{C}_i \cdot \mathbf{T}'(\theta)$. Therefore, if the design is converged to $\|\tilde{\vartheta}\| = 1$, it provides a purely orientation design result. When $0 < \|\tilde{\vartheta}\| < 1$, this allows the change of magnitude of anisotropy according to $\|\tilde{\vartheta}\|$, in addition to rotation according to $\angle \tilde{\vartheta}$. This provides a solution with orientation with various magnitude of anisotropy, that extends flexibility in change of design to help dynamic change during the optimization procedure to avoid local optima.

One major advantage is that this interpolation accepts the design variable $\mathbf{v} = \{0, 0\}^T$ that represents isotropic state. Therefore, the optimization procedure can be started from almost isotropic state to avoid influence of initial design orientation. Another important advantage of this approach is its bijective nature. This guarantees that design variables can be continuous if actual orientation distribution is continuous. Therefore, it works well with projection schemes without unphysical smear.

Substituting \mathbf{C}_s from (5) into the previous expression, the complete material interpolation function is finally defined as

$$\mathbf{C}(\rho, \vartheta) = \mathbf{C}_v + \rho^p (\mathbf{C}_i + \hat{\mathbf{T}}^{-1}(\tilde{\vartheta}) \cdot (\mathbf{C}_u - \mathbf{C}_i) \cdot \hat{\mathbf{T}}'(\tilde{\vartheta}) - \mathbf{C}_v). \quad (19)$$

5. Numerical example

A short cantilever benchmark problem where the left side is fixed and the middle of the right side is subjected to a surface loading is solved. The analysis geometry and boundary condition settings are as shown in Figure 2. The $w_c \times h_c$ rectangular domain is given as the analysis domain and the entire area is designated as a fixed design domain, D . The geometric parameters w_c and h_c are 3 and 1, respectively. The entire left side is fixed as ∂D_u , and ∂D_t is defined at the middle of the right side. The $-y$ directional surface load, t , on ∂D_t is set to unity and the length of ∂D_t is $h_c/10$. A square grid mesh with a side length of $d = 0.02$ is used in combination with Lagrange linear quadrilateral elements. The upper bound of volume fraction is set to 0.5.

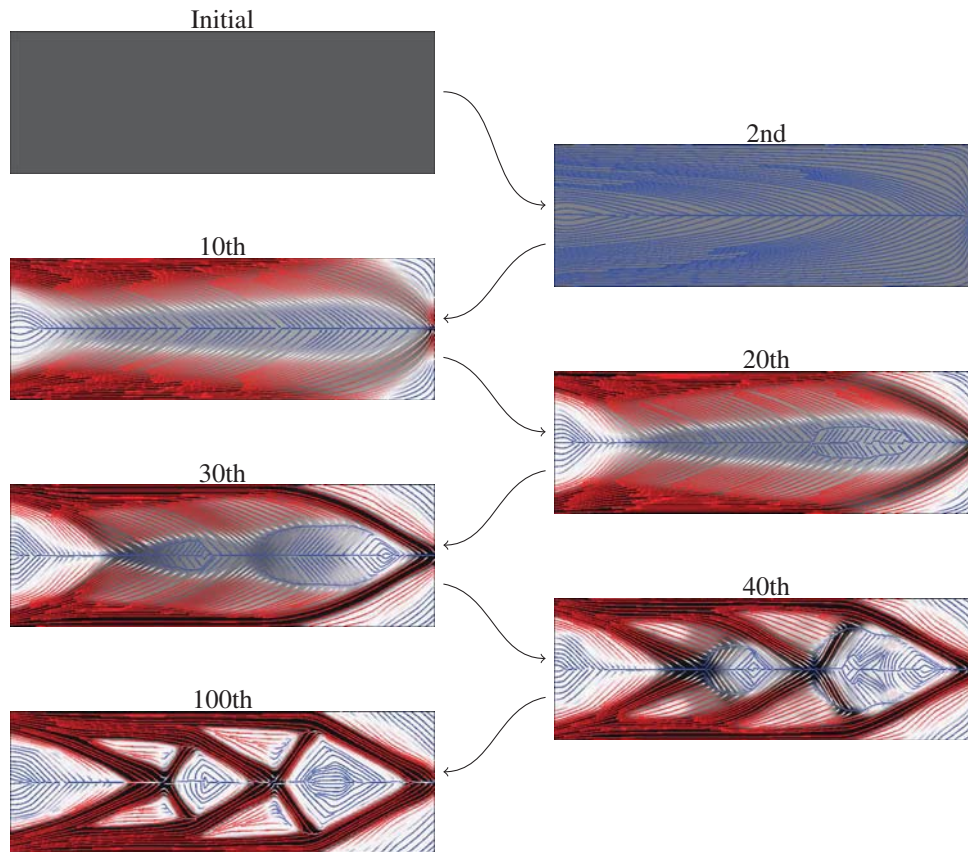


Figure 3: Optimization results for short cantilever problem with volume fraction 0.5. Configurations at various iteration steps are shown to describe evolution of the design. Gray scale image, stream line and color of the streamline indicate density, orientation direction and norm of orientation vector (blue: weak orientation, red: strong orientation), respectively

Figure 3 shows the obtained design solution. The figure shows eight configurations with various iteration steps to depict evolution of the topology and orientation distribution by the proposed method. The gray scale image on the background shows topology density, the stream line shows direction of orientation vector and the color of the stream line shows the norm of the orientation vector. Blue stream line shows that the orientation vector has small norm so that it has weak orientation, while red stream line shows that the orientation is strongly defined to a line direction. At the beginning, indicated as “initial” in the figure, the orientation vector design variable is uniform so that there is no stream line. At the second iteration, the stream lines appear and it is along with the principal stress direction of rectangular cantilever. At 10th step, non-uniform distribution of the density and orientation vector norm is recognized, but, it is still smooth except for the middle line and there is no large change in topology. At the 20th iteration, a site with different orientation direction is generated at the middle beam region with smallest density. At the 30th iteration, the number of discontinuous angle sites increases with and a hole is initiated at the tip of the cantilever. At the 40th iteration, the topology evolves to double cross configuration and the orientation distribution shows more complexity. Finally, at iteration 100, the topology becomes clear and the fiber reinforcement orientation angle is aligned with the small bars comprising the cantilever structure. Since it is single load problem, the obtained topology is almost identical to the one obtained by isotropic material optimization supporting empirical knowledge that the optimal orientation should coincide with the principal stress direction. Note that the orientation vector smoothly rotates as the topology progresses, and sometimes the change of the fiber orientation angle occurs prior to the topological change.

6. Conclusion

A topology optimization method which is capable of simultaneous design of topology and orientation vector using isoparametric projection method was reviewed. The method is based on density filter topology optimization

methods and an orientation vector is used for orientation representation along with a projection method using isoparametric shape functions. A benchmark example is provided and it shows a reasonable result.

7. Reference

- [1] P. Mattheij, K. Gliesche, and D. Feltin, "Tailored fiber placement-mechanical properties and applications," *Journal of Reinforced Plastics and Composites*, vol. 17, no. 9, pp. 774–786, 1998.
- [2] K. Uhlig, A. Spickenheuer, L. Bittrich, and G. Heinrich, "Development of a highly stressed bladed rotor made of a cfrp using the tailored fiber placement technology," *Mechanics of Composite Materials*, vol. 49, no. 2, pp. 201–210, 2013.
- [3] M. Namiki, M. Ueda, A. Todoroki, Y. Hirano, and R. Matsuzaki, "3D printing of continuous fiber reinforced plastic," in *Society for the Advancement of Material and Process Engineering 2014*, (Seattle), p. 6, SAMPE, jun 2014.
- [4] M. P. Bendsøe and N. Kikuchi, "Generating optimal topologies in structural design using a homogenization method," *Computer Methods In Applied Mechanics And Engineering*, vol. 71, pp. 197–224, 1988.
- [5] P. Pedersen, "Examples of density, orientation, and shape-optimal 2D-design for stiffness and/or strength with orthotropic materials," *Structural and Multidisciplinary Optimization*, vol. 26, no. 1-2, pp. 37–49, 2004.
- [6] K. Zhou and X. Li, "Topology optimization for minimum compliance under multiple loads based on continuous distribution of members," *Structural and Multidisciplinary Optimization*, vol. 37, no. 1, pp. 49–56, 2008.
- [7] J. Stegmann and E. Lund, "Discrete material optimization of general composite shell structures," *International Journal for Numerical Methods in Engineering*, vol. 62, no. 14, pp. 2009–2027, 2005.
- [8] T. Gao, W. Zhang, and P. Duysinx, "A bi-value coding parameterization scheme for the discrete optimal orientation design of the composite laminate," *International Journal for Numerical Methods in Engineering*, vol. 91, no. 1, pp. 98–114, 2012.
- [9] G. N. Vanderplaats, "Structural optimization-past, present, and future," *AIAA Journal*, vol. 20, pp. 992–1000, Jul 1982. doi: 10.2514/3.51158.
- [10] C. E. Harris, J. H. Starnes, and M. J. Shuart, "Design and manufacturing of aerospace composite structures, state-of-the-art assessment," *Journal of Aircraft*, vol. 39, pp. 545–560, Jul 2002. doi: 10.2514/2.2992.
- [11] R. Ansola, J. Canales, J. Tarrago, and J. Rasmussen, "On simultaneous shape and material layout optimization of shell structures," *Structural and Multidisciplinary Optimization*, vol. 24, no. 3, pp. 175–184, 2002.
- [12] T. Nomura, E. M. Dede, J. Lee, S. Yamasaki, T. Matsumori, A. Kawamoto, and N. Kikuchi, "General topology optimization method with continuous and discrete orientation design using isoparametric projection," *International Journal for Numerical Methods in Engineering*, 2014.
- [13] A. Kawamoto, T. Matsumori, S. Yamasaki, T. Nomura, T. Kondoh, and S. Nishiwaki, "Heaviside projection based topology optimization by a PDE-filtered scalar function," *Structural and Multidisciplinary Optimization*, vol. 44, no. 1, pp. 19–24, 2011.
- [14] B. S. Lazarov and O. Sigmund, "Filters in topology optimization based on helmholtz-type differential equations," *International Journal for Numerical Methods in Engineering*, vol. 86, no. 6, pp. 765–781, 2011.
- [15] I. Ergatoudis, B. Irons, and O. Zienkiewicz, "Curved, isoparametric, "quadrilateral" elements for finite element analysis," *International Journal of Solids and Structures*, vol. 4, no. 1, pp. 31 – 42, 1968.
- [16] D. Arnold and G. Awanou, "The serendipity family of finite elements," *Foundations of Computational Mathematics*, vol. 11, no. 3, pp. 337–344, 2011.

An efficient parallel coordination method for decomposition-based optimization using two duality theorems

Meng Xu¹, Georges Fadel¹, Margaret M. Wiecek², Paolo Guarneri³

¹ Clemson University, Department of Mechanical Engineering, Clemson, SC, USA, {xu7, fgeorge}@clemson.edu

² Clemson University, Department of Mathematical Science, Clemson, SC, USA, wmalgor@clemson.edu

³ Technical University of Cluj-Napoca, Department of Electrical Machines and Drives, Cluj-Napoca, Romania, paolo.guarneri@emd.utcluj.ro

Abstract

In decomposition-based optimization, coordination of sub-problems always plays an important role because it eliminates the inconsistencies between the decomposed sub-problems and drives their solutions towards the optimal solution of the original problem. Coordination is often carried out in an iterative manner and efficiency becomes a critical issue during this process as the complexity of engineering problems continues to grow rapidly. This growing complexity increases the computational cost of iterations and thus parallel coordination methods are preferred over non-parallel methods in many cases. In this paper, based on the Alternating Direction Method of Multipliers (ADMM), a new parallel coordination method with a high efficiency is proposed. Unlike other popular coordination methods in the literature which use duality theorems just once, the proposed method uses duality theorems twice. Specifically, the ordinary duality theorem is applied initially to the original problem to generate a dual problem and then the ADMM is applied to the dual problem. The resulting method requires fewer copies of shared variables for the decomposition, which decreases the coordination effort necessary for the optimization to converge. Numerical tests are conducted on one mathematical and one engineering problem and the results show an increase in efficiency and accuracy for the new method when compared to the centralized Augmented Lagrangian Coordination (ALC), which is one of the most popular parallel coordination methods. Additionally, this increase in performance is consistently displayed by the new method when solving a multimodal structural optimization problem repeatedly starting from different random initial designs, while the centralized ALC fails to show similar robustness.

Keywords: Decomposition-based optimization, ADMM, ALC, duality theorem

1. Introduction

The optimization task applied to modern complex systems normally involves several different disciplines and many components. This multiplicity makes it impossible and undesirable for the optimization to be conducted by one design person or one disciplinary group. As a result, the original optimization problem is usually decomposed into multiple smaller sub-problems according to certain rules (component, disciplines, model-based or hybrid) [1]–[4]. A coordination strategy is then established to deal with the couplings between these sub-problems and drive the solutions of all the sub-problems towards a consistent optimal solution for the original problem. This partition and coordination process is called decomposition-based optimization.

Some theoretical studies in mathematical optimization have been applied to the decomposition-based optimization process and the Alternating Direction Method of Multipliers (ADMM) is one result of these studies [3]. ADMM [5] is a powerful algorithm developed in the field of convex optimization. The algorithm solves problems of the form:

$$\begin{aligned} & \text{minimize} && f_1(\mathbf{v}) + f_2(\mathbf{z}) \\ & \text{subject to} && \mathbf{A}\mathbf{v} + \mathbf{B}\mathbf{z} = \mathbf{e} \end{aligned} \quad (1)$$

The augmented Lagrangian function of this problem is

$$L_\rho(\mathbf{v}, \mathbf{z}, \mathbf{p}) = f_1(\mathbf{v}) + f_2(\mathbf{z}) + \mathbf{p}^T(\mathbf{A}\mathbf{v} + \mathbf{B}\mathbf{z} - \mathbf{e}) + (\rho/2) \|\mathbf{A}\mathbf{v} + \mathbf{B}\mathbf{z} - \mathbf{e}\|_2^2 \quad (2)$$

ADMM solves the problem in Eq. (1) through the following iterations

$$\mathbf{v}^{(k+1)} := \arg \min_{\mathbf{v}} L_\rho(\mathbf{v}, \mathbf{z}^{(k)}, \mathbf{p}^{(k)}) \quad (3)$$

$$\mathbf{z}^{(k+1)} := \arg \min_{\mathbf{z}} L_\rho(\mathbf{v}^{(k+1)}, \mathbf{z}, \mathbf{p}^{(k)}) \quad (4)$$

$$\mathbf{p}^{(k+1)} := \mathbf{p}^{(k)} + \rho(\mathbf{A}\mathbf{v}^{(k+1)} + \mathbf{B}\mathbf{z}^{(k+1)} - \mathbf{e}) \quad (5)$$

In decomposed-based optimization, the Augmented Lagrangian Coordination (ALC) adopts ADMM and the resulting algorithm has become one of the most popular coordination methods in recent years [3][6]. ADMM

enables ALC to decouple the sub-problems using the augmented Lagrangian relaxation and to update the dual multipliers through the method of multipliers [3]. There are three types of ALC algorithms which either include an inner loop or not: Exact (ENMOM) inner loop, inexact (INMOM) inner loop, and alternating direction (ADMOM) without inner loop. At each iteration, ENMOM and INMOM first use the Block Coordinate Descent (BCD) [7] method to iterate, solving each sub-problem with fixed dual multipliers and penalty weights until they reach a consistent solution, which represents the termination of the inner loop. Then the dual multipliers and penalty weights are updated in the outer loop to prepare the whole optimization process for the next iteration. The difference between the two inner loop methods is that ENMOM uses a small fixed convergence tolerance for the inner loop whereas in INMOM, the inner loop tolerance is relatively large at the beginning and decreases as the optimization process proceeds. ADMOM however, contains no inner loop since it uses ADMM and all sub-problems are solved only once at each iteration. Many tests have proven that ADMOM is the most robust and efficient algorithm among the three ALC algorithms since it does not require the expensive computational efforts of the inner loops when the current solution is far from the optimal solution [3]. Furthermore, the ADMOM algorithm is shown to perform better than other popular coordination methods such as the Analytical Target Cascading (ATC) which is based on a quadratic penalty method and the Lagrangian duality-based coordination [6][8][9] which is based on the ordinary Lagrangian duality theorem.

Similar to ALC-ADMOM, Consensus Optimization via the Alternating Direction Method of Multipliers (CADMM) is another application of ADMM to decomposition-based optimization. At each iteration of CADMM, all sub-problems are solved only once and their solutions are collected together and used to calculate the consensus values for the shared variables, which are then used as targets for sub-problems in the next iteration. The efficacy of CADMM has been verified through several test problems [4][10][11].

In either ALC or CADMM, the ADMM is applied directly to the primal problem. In this study, inspired by the research in convex optimization [12], the ADMM is applied to the dual of the primal problem. Specifically, we first introduce copies of shared variables to the original optimization problem to get a primal problem set up for decomposition-based optimization, then apply the ordinary duality theorem to that primal problem to generate a dual problem, after which we apply ADMM to the dual problem. In the resulting algorithm, all sub-problems are independent from each other and thus can be solved in parallel. The derivations of the algorithm are presented in Section 2. Section 3 tests the proposed algorithm using both mathematical and engineering problems and compares its performance with that of the parallel ALC-ADMOM. Section 4 summarizes this study and proposes possible futures research directions.

2. Derivation

Depending on the ways an optimization problem is partitioned, the resulting partition can have either a hierarchical or a network structure. The hierarchical partition can be considered a special case of the network partition, which is in great demand since in many cases partitions in the engineering area are non-hierarchical. Multi-disciplinary optimization exemplifies network structures, and several nonhierarchical coordination methods have been proposed in this area [4][11][13][14][15][16]. This study deals with decomposed sub-problems with a network structure.

Assuming a quasi-separable problem with M potential sub-systems with a network partition structure, the optimization problem is written as:

$$\begin{aligned} \min_{\mathbf{y}, \mathbf{x}_1, \dots, \mathbf{x}_M} \quad & \sum_{j=1}^M f_j(\mathbf{y}, \mathbf{x}_j) \\ \text{subject to} \quad & \mathbf{g}_j(\mathbf{y}, \mathbf{x}_j) \leq \mathbf{0} \\ & \mathbf{h}_j(\mathbf{y}, \mathbf{x}_j) = \mathbf{0} \end{aligned} \quad (6)$$

where $\mathbf{y} \in R^N$ is the vector of shared variables, which can either be the linking design variables between two sub-problems or the analysis output of one sub-system which is required as input for another sub-system. $\mathbf{x}_j \in R^K$ is the vector of local design variables which appears only in the sub-problem j .

2.1. Applying the ordinary duality theorem to the primal problem

To decompose the problem in Eq. ((6) into M sub-problems, $M-1$ copies of \mathbf{y} are first introduced into the problem:

$$\begin{aligned} \min_{\mathbf{y}_1, \dots, \mathbf{y}_M, \mathbf{x}_1, \dots, \mathbf{x}_M} \quad & \sum_{j=1}^M f_j(\mathbf{y}_j, \mathbf{x}_j) \\ \text{subject to} \quad & \mathbf{g}_j(\mathbf{y}_j, \mathbf{x}_j) \leq \mathbf{0} \\ & \mathbf{h}_j(\mathbf{y}_j, \mathbf{x}_j) = \mathbf{0} \\ & \mathbf{S}_1 \mathbf{y}_1 + \dots + \mathbf{S}_M \mathbf{y}_M = \mathbf{0} \\ & j = 1, \dots, M \end{aligned} \quad (7)$$

where \mathbf{y} is renamed as \mathbf{y}_M and $\mathbf{y}_1, \dots, \mathbf{y}_{M-1}$ are the $M-1$ copies newly created.

The new equality constraints $\mathbf{S}_1\mathbf{y}_1 + \dots + \mathbf{S}_M\mathbf{y}_M = \mathbf{0}$ are called primal consistency constraints, and are added to the formulation to ensure that all the copies of the shared variables have the same value. Since elements in \mathbf{y}_j do not necessarily appear in every row of the consistency constraints, thus a selection matrix, $\mathbf{S}_j \in R^{P \times N}$, which is similar to those introduced by Michalek and Papalambros [17] for ATC and by Tosserams [3] for ALC, is adopted. The elements of \mathbf{S}_j can be 0, 1 or -1 and each row of \mathbf{S}_j must only contain one "1" or one "-1". For example, assume a partition in Figure 1 with three sub-problems in a network structure coupled through three shared variables:

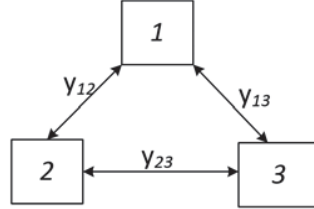


Figure 1: A partition with a three-node network structure for the illustration of selection matrix

The vector of shared variables in this partition is $\mathbf{y} = [y_{12}, y_{13}, y_{23}]^T$. After creating two copies of the shared variables $\mathbf{y}_1 = [y_{12}^1, y_{13}^1, y_{23}^1]^T$ and $\mathbf{y}_2 = [y_{12}^2, y_{13}^2, y_{23}^2]^T$, renaming \mathbf{y} as $\mathbf{y}_3 = [y_{12}^3, y_{13}^3, y_{23}^3]^T$, and assigning $\mathbf{y}_1, \mathbf{y}_2, \mathbf{y}_3$ to the sub-problems 1, 2 and 3 respectively, the resulting consistency constraints for the shared variables are $y_{12}^1 - y_{12}^2 = 0, y_{13}^1 - y_{13}^3 = 0$, and $y_{23}^2 - y_{23}^3 = 0$. Then the selection matrices for the three sub-problems should be $\mathbf{S}_1 = [1 \ 0 \ 0; 0 \ 1 \ 0; 0 \ 0 \ 0]$, $\mathbf{S}_2 = [-1 \ 0 \ 0; 0 \ 0 \ 0; 0 \ 0 \ 1]$ and $\mathbf{S}_3 = [0 \ 0 \ 0; 0 \ -1 \ 0; 0 \ 0 \ -1]$, thus $\mathbf{S}_1\mathbf{y}_1 + \mathbf{S}_2\mathbf{y}_2 + \mathbf{S}_3\mathbf{y}_3 = \mathbf{0}$ would generate the above consistency constraints. It can be seen that some elements in \mathbf{y}_j are not used in sub-problem j at all, so in the practical implementation, \mathbf{y}_j may only contain the shared variables relevant to sub-problem j instead of all shared variables.

Given the vector of Lagrangian multipliers $\mathbf{v} \in R^P$, the Lagrangian function L [7] is:

$$\begin{aligned} L(\mathbf{y}_1, \dots, \mathbf{y}_M, \mathbf{x}_1, \dots, \mathbf{x}_M, \mathbf{v}) &= \sum_{j=1}^M f_j(\mathbf{y}_j, \mathbf{x}_j) + \mathbf{v}^T (\mathbf{S}_1\mathbf{y}_1 + \dots + \mathbf{S}_M\mathbf{y}_M) \\ &= \sum_{j=1}^M (f_j(\mathbf{y}_j, \mathbf{x}_j) + \mathbf{v}^T \mathbf{S}_j \mathbf{y}_j) \end{aligned} \quad (8)$$

The Lagrangian dual problem can be written as

$$\begin{aligned} &\underset{\mathbf{v}}{\text{maximize}} \quad d(\mathbf{v}) \\ &\text{where } d(\mathbf{v}) = \inf_{\substack{\mathbf{y}_1, \dots, \mathbf{y}_M, \mathbf{x}_1, \dots, \mathbf{x}_M \\ \mathbf{g}_1 \leq 0, \dots, \mathbf{g}_M \leq 0, \mathbf{h}_1 = 0, \dots, \mathbf{h}_M = 0}} L(\mathbf{y}_1, \dots, \mathbf{y}_M, \mathbf{x}_1, \dots, \mathbf{x}_M, \mathbf{v}) \end{aligned} \quad (9)$$

Since the Lagrangian function in Eq. (8) is separable, the dual problem can be rewritten as:

$$\begin{aligned} &\underset{\mathbf{v}}{\text{maximize}} \quad \sum_{j=1}^M d_j(\mathbf{v}) \\ &\text{where } d_j(\mathbf{v}) = \inf_{\mathbf{y}_j, \mathbf{x}_j, \mathbf{g}_j \leq 0, \mathbf{h}_j = 0} (f_j(\mathbf{y}_j, \mathbf{x}_j) + \mathbf{v}^T \mathbf{S}_j \mathbf{y}_j) \\ &\quad j = 1, \dots, M \end{aligned} \quad (10)$$

2.2. Applying the ADMM duality theorem to the dual problem

At this step we apply ADMM to the dual problem in Eq. (10). M Copies of the Lagrangian multipliers \mathbf{v} are introduced to the dual problem to decouple the objective, and new consistency constraints for the multipliers are added to the formulation. We obtain

$$\begin{aligned} &\underset{\mathbf{v}}{\text{maximize}} \quad \sum_{j=1}^M d_j(\mathbf{z}_j) \\ &\text{subject to } \mathbf{v} - \mathbf{z}_j = \mathbf{0} \\ &\text{where } d_j(\mathbf{z}_j) = \inf_{\mathbf{y}_j, \mathbf{x}_j, \mathbf{g}_j \leq 0, \mathbf{h}_j = 0} (f_j(\mathbf{y}_j, \mathbf{x}_j) + \mathbf{z}_j^T \mathbf{S}_j \mathbf{y}_j) \\ &\quad j = 1, \dots, M \end{aligned} \quad (11)$$

where \mathbf{z}_j is the copy of \mathbf{v} at the sub-problem j .

Dual consistency constraints $\mathbf{v} - \mathbf{z}_j = \mathbf{0}$ are added to Eq. (11) to guarantee \mathbf{v} and its M copies share the same value. Relaxing the dual consistency constraints for the multipliers using Augmented Lagrangian Relaxation and applying ADMM in Eqs. (3) – (5) to the problem result in the following procedures to solve the problem in Eq. (11).

$$\mathbf{v}^{(k+1)} = \arg \min_{\mathbf{v}} \left\{ \sum_{j=1}^M ((\mathbf{p}_j^{(k)})^T \mathbf{v}) + \frac{\rho}{2} \sum_{j=1}^M \|\mathbf{v} - \mathbf{z}_j^{(k)}\|_2^2 \right\} \quad (12)$$

$$\mathbf{z}_j^{(k+1)} = \arg \max_{\mathbf{z}_j} \left\{ d_j(\mathbf{z}_j) + (\mathbf{p}_j^{(k)})^T \mathbf{z}_j - \frac{\rho}{2} \|\mathbf{v}^{(k+1)} - \mathbf{z}_j\|_2^2 \right\} \quad (13)$$

$$\mathbf{p}_j^{(k+1)} = \mathbf{p}_j^{(k)} + \rho(\mathbf{v}^{(k+1)} - \mathbf{z}_j^{(k+1)}) \quad (14)$$

where \mathbf{p}_j is the vector of multipliers of the dual consistency constraints. The superscript in $(\cdot)^{(k+1)}$ is used to indicate the value of a term at the iteration $(k+1)$. It should be noted that since the terms $(\mathbf{p}_j^{(k)})^T \mathbf{z}^{(k)}$ and $(\mathbf{p}_j^{(k)})^T \mathbf{v}^{(k+1)}$ are constant and are simply added to the objectives, they are dropped from Eq. (12) and Eq. (13) respectively. Eq. (12) is a quadratic optimization problem with respect to \mathbf{v} , thus it has an analytical solution:

$$\mathbf{v}^{(k+1)} = \frac{1}{M} \sum_{j=1}^M (\mathbf{z}_j) - \frac{1}{M\rho} \sum_{j=1}^M \mathbf{p}_j^{(k)} \quad (15)$$

Substituting $d_j(\mathbf{z}_j)$ from Eq. (11) into Eq. (13), we obtain

$$\begin{aligned} \mathbf{z}_j^{(k+1)} &= \arg \max_{\mathbf{z}_j} \left\{ \inf_{\mathbf{y}_j, \mathbf{x}_j, \mathbf{g}_j \leq \mathbf{0}, \mathbf{h}_j = \mathbf{0}} [f_j(\mathbf{y}_j, \mathbf{x}_j) + \mathbf{z}_j^T \mathbf{S}_j \mathbf{y}_j] + (\mathbf{p}_j^{(k)})^T \mathbf{z}_j - \frac{\rho}{2} \|\mathbf{v}^{(k+1)} - \mathbf{z}_j\|_2^2 \right\} \\ &= \arg \max_{\mathbf{z}_j} \left\{ \inf_{\mathbf{y}_j, \mathbf{x}_j, \mathbf{g}_j \leq \mathbf{0}, \mathbf{h}_j = \mathbf{0}} [f_j(\mathbf{y}_j, \mathbf{x}_j) + \mathbf{z}_j^T (\mathbf{S}_j \mathbf{y}_j + \mathbf{p}_j^{(k)})] - \frac{\rho}{2} \|\mathbf{v}^{(k+1)} - \mathbf{z}_j\|_2^2 \right\} \end{aligned} \quad (16)$$

Let $L(\mathbf{y}_j, \mathbf{x}_j, \mathbf{z}_j)$ represent the objective function in Eq. (16)

$$L(\mathbf{y}_j, \mathbf{x}_j, \mathbf{z}_j) = f_j(\mathbf{y}_j, \mathbf{x}_j) + \mathbf{z}_j^T (\mathbf{S}_j \mathbf{y}_j + \mathbf{p}_j^{(k)}) - \frac{\rho}{2} \|\mathbf{v}^{(k+1)} - \mathbf{z}_j\|_2^2 \quad (17)$$

According to Theorem 37.3 and 37.6 in [18], if $L(\mathbf{y}_j, \mathbf{x}_j, \cdot)$ and $L(\cdot, \cdot, \mathbf{z}_j)$ are convex functions, $L(\mathbf{y}_j, \mathbf{x}_j, \mathbf{z}_j)$ has a saddle point and satisfies

$$\max_{\mathbf{z}_j} \left\{ \min_{\mathbf{y}_j, \mathbf{x}_j, \mathbf{g}_j \leq \mathbf{0}, \mathbf{h}_j = \mathbf{0}} [L(\mathbf{y}_j, \mathbf{x}_j, \mathbf{z}_j)] \right\} = \min_{\mathbf{y}_j, \mathbf{x}_j, \mathbf{g}_j \leq \mathbf{0}, \mathbf{h}_j = \mathbf{0}} \left\{ \max_{\mathbf{z}_j} [L(\mathbf{y}_j, \mathbf{x}_j, \mathbf{z}_j)] \right\} \quad (18)$$

Thus, the optimization problem in Eq. (16) becomes

$$\begin{aligned} &\min_{\mathbf{y}_j, \mathbf{x}_j, \mathbf{g}_j \leq \mathbf{0}, \mathbf{h}_j = \mathbf{0}} \left\{ \max_{\mathbf{z}_j} [L(\mathbf{y}_j, \mathbf{x}_j, \mathbf{z}_j)] \right\} \\ &= \min_{\mathbf{y}_j, \mathbf{x}_j, \mathbf{g}_j \leq \mathbf{0}, \mathbf{h}_j = \mathbf{0}} \left\{ \max_{\mathbf{z}_j} [f_j(\mathbf{y}_j, \mathbf{x}_j) + \mathbf{z}_j^T (\mathbf{S}_j \mathbf{y}_j + \mathbf{p}_j^{(k)})] - \frac{\rho}{2} \|\mathbf{v}^{(k+1)} - \mathbf{z}_j\|_2^2 \right\} \end{aligned} \quad (19)$$

Since $L(\mathbf{y}_j, \mathbf{x}_j, \mathbf{z}_j)$ is a quadratic function with respect to \mathbf{z}_j , the solution to $\max[L(\mathbf{y}_j, \mathbf{x}_j, \mathbf{z}_j)]$ in vector form is

$$\mathbf{z}_j^{(k+1)} = \mathbf{v}^{(k+1)} + \frac{1}{\rho} (\mathbf{p}_j^{(k)} + \mathbf{S}_j \mathbf{y}_j^{(k+1)}) \quad (20)$$

or

$$z_{ij}^{(k+1)} = v_i^{(k+1)} + \frac{1}{\rho} (p_{ij}^{(k)} + (\mathbf{S}_j \mathbf{y}_j^{(k+1)})_i) \quad (21)$$

in scalar form, where $\mathbf{z}_j^{(k+1)} = [z_{1j}^{(k+1)}, \dots, z_{ij}^{(k+1)}, \dots, z_{Nj}^{(k+1)}]^T$.

Substituting Eq. (20) into Eq. (19) we have

$$\begin{aligned} &\min_{\mathbf{y}_j, \mathbf{x}_j, \mathbf{g}_j \leq \mathbf{0}, \mathbf{h}_j = \mathbf{0}} \left\{ f_j(\mathbf{y}_j, \mathbf{x}_j) + [\mathbf{v}^{(k+1)} + \frac{1}{\rho} (\mathbf{p}_j^{(k)} + \mathbf{S}_j \mathbf{y}_j^{(k+1)})]^T (\mathbf{p}_j^{(k)} + \mathbf{S}_j \mathbf{y}_j^{(k+1)}) - \frac{\rho}{2} \left\| \frac{1}{\rho} (\mathbf{p}_j^{(k)} + \mathbf{S}_j \mathbf{y}_j^{(k+1)}) \right\|_2^2 \right\} \\ &= \min_{\mathbf{y}_j, \mathbf{x}_j, \mathbf{g}_j \leq \mathbf{0}, \mathbf{h}_j = \mathbf{0}} \left\{ f_j(\mathbf{y}_j, \mathbf{x}_j) + \sum_{i=1}^N v_i^{(k+1)} [p_{ij}^{(k)} + (\mathbf{S}_j \mathbf{y}_j^{(k+1)})_i] + \frac{1}{\rho} \sum_{i=1}^N [p_{ij}^{(k)} + (\mathbf{S}_j \mathbf{y}_j^{(k+1)})_i]^2 - \frac{1}{2\rho} \sum_{i=1}^N [p_{ij}^{(k)} + (\mathbf{S}_j \mathbf{y}_j^{(k+1)})_i]^2 \right\} \\ &= \min_{\mathbf{y}_j, \mathbf{x}_j, \mathbf{g}_j \leq \mathbf{0}, \mathbf{h}_j = \mathbf{0}} \left\{ f_j(\mathbf{y}_j, \mathbf{x}_j) + \frac{1}{2\rho} \sum_{i=1}^N [p_{ij}^{(k)} + (\mathbf{S}_j \mathbf{y}_j^{(k+1)})_i]^2 + \sum_{i=1}^N v_i^{(k+1)} [p_{ij}^{(k)} + (\mathbf{S}_j \mathbf{y}_j^{(k+1)})_i] + \frac{\rho}{2} \sum_{i=1}^N (v_i^{(k+1)})^2 - \frac{\rho}{2} \sum_{i=1}^N (v_i^{(k+1)})^2 \right\} \\ &= \min_{\mathbf{y}_j, \mathbf{x}_j, \mathbf{g}_j \leq \mathbf{0}, \mathbf{h}_j = \mathbf{0}} \left\{ f_j(\mathbf{y}_j, \mathbf{x}_j) + \frac{\rho}{2} \sum_{i=1}^N [v_i^{(k+1)} + \frac{1}{\rho} (p_{ij}^{(k)} + (\mathbf{S}_j \mathbf{y}_j^{(k+1)})_i)]^2 - \frac{\rho}{2} \sum_{i=1}^N (v_i^{(k+1)})^2 \right\} \end{aligned} \quad (22)$$

where ρ and $v_i^{(k+1)}$ are constants and thus the last term in Eq. (22) can be dropped. The optimization problem in Eq. (13) is then simplified as

$$\min_{\mathbf{y}_j, \mathbf{x}_j, \mathbf{g}_j \leq \mathbf{0}, \mathbf{h}_j = \mathbf{0}} f_j(\mathbf{y}_j, \mathbf{x}_j) + \frac{\rho}{2} \sum_{i=1}^N [v_i^{(k+1)} + \frac{1}{\rho} (p_{ij}^{(k)} + (\mathbf{S}_j \mathbf{y}_j^{(k+1)})_i)]^2 \quad (23)$$

with Eq. (20) as the solution for $\mathbf{z}_j^{(k+1)}$.

2.3. A new parallel coordination algorithm

In summary, the problem in Eq. (6) can be solved through the following steps. The flowchart of this new algorithm is shown in Figure 2.

Step 1: Initialization

Step 2: Compute the master copy of multipliers: $\mathbf{v}^{(k+1)} = \frac{1}{M} \sum_{j=1}^M (\mathbf{z}_j) - \frac{1}{M\rho} \sum_{j=1}^M \mathbf{p}_j^{(k)}$ (24)

Step 3: For $j = 1, \dots, M$, optimize the sub-problem j :

$$\text{minimize}_{\mathbf{y}_j, \mathbf{x}_j} f_j(\mathbf{y}_j, \mathbf{x}_j) + \frac{\rho}{2} \sum_{i=1}^p \left(v_i^{(k+1)} + \frac{1}{\rho} (p_{ij}^{(k)} + (\mathbf{S}_j \mathbf{y}_j)_i) \right)^2 \quad (25)$$

$$\text{subject to } \mathbf{g}_j(\mathbf{y}_j, \mathbf{x}_j) \leq \mathbf{0}$$

$$\mathbf{h}_j(\mathbf{y}_j, \mathbf{x}_j) = \mathbf{0}$$

$\mathbf{z}_j^{(k+1)} = (z_{1j}^{(k+1)}, \dots, z_{n_y j}^{(k+1)})$ can be determined by the solution $\mathbf{y}_j^{(k+1)}$:

$$z_{ij}^{(k+1)} = v_i^{(k+1)} + \frac{1}{\rho} (p_{ij}^{(k)} + (\mathbf{S}_j \mathbf{y}_j^{(k+1)})_i) \quad (26)$$

Step 4: check if the optimization converges, if not, compute the Lagrangian multipliers for multipliers and go to step 2

$$\mathbf{p}_j^{(k+1)} = \mathbf{p}_j^{(k)} + \rho(\mathbf{v}^{(k+1)} - \mathbf{z}_j^{(k+1)}) \quad (27)$$

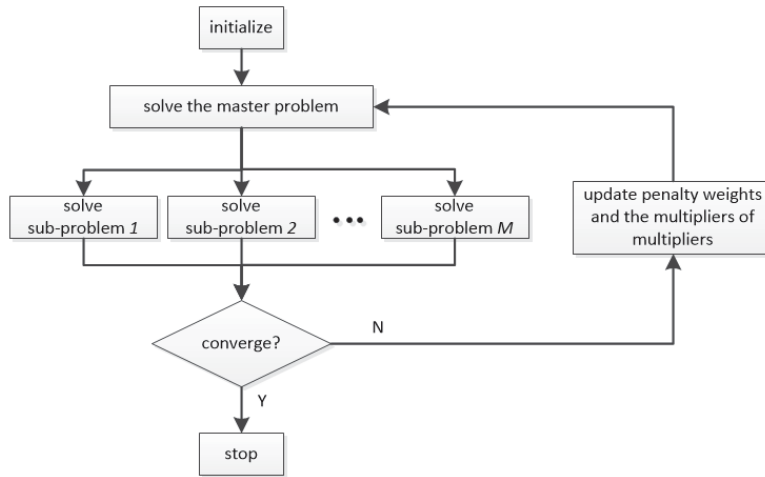


Figure 2: The flowchart of the proposed method

During this process, since copies of shared variables and Lagrangian dual multipliers are generated, consistency constraints are introduced to ensure these copies share the same values. There are two kinds of consistency constraints at iteration k : the primal consistency constraints \mathbf{c}_p and the dual consistency constraints \mathbf{c}_d .

$$\mathbf{c}_p^{(k)} = \mathbf{S}_1 \mathbf{y}_1^{(k)} + \dots + \mathbf{S}_M \mathbf{y}_M^{(k)} = \mathbf{0} \quad (28)$$

$$\mathbf{c}_d^{(k)} = \mathbf{v}^{(k)} - \mathbf{z}_j^{(k)} = \mathbf{0}$$

$\mathbf{y}_1, \dots, \mathbf{y}_M$ are shared variables and their copies and \mathbf{c}_p are used to ensure they have the same values at the end of optimization for the primal problem in Eq. (7). $\mathbf{v}, \mathbf{z}_1, \dots, \mathbf{z}_M$ are dual multipliers and their copies and \mathbf{c}_d are used to ensure they have the same values at the end of optimization for the dual problem in Eq. (11).

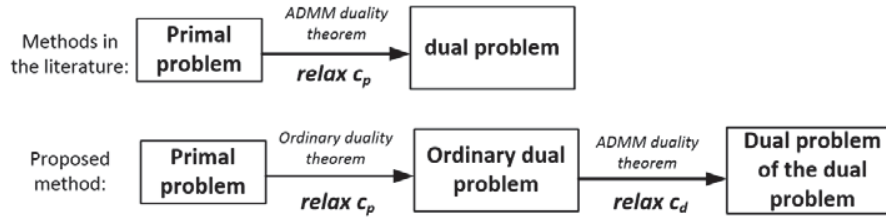


Figure 3 : Dual transformations in the proposed method and other methods in the literature

Figure 3 shows how the duality theorems are applied to the methods in literature and the proposed method. Most developed methods apply ADMM directly to the primal problem, relax \mathbf{c}_p into the objective and solve the resulting dual problem instead of solving the original problem. In contrast, in the proposed method two kinds of duality theorems are employed. First the ordinary duality theorem is used to relax \mathbf{c}_p and an ordinary dual problem is generated, to which ADMM is then applied to relax \mathbf{c}_d and a dual problem of the first dual problem is formulated. Instead of solving the original problem, the proposed method is solving this dual problem of the dual problem to achieve the optimal solution for the original problem. Since the ordinary duality is applied initially, the sub-problems in the proposed method are independent from each other and therefore can be solved in parallel. It should be noted that in mathematical programming, the dual problem of the dual problem is supposed to be the primal problem. However, this is not the case here since the two different duality theorems are used in this transformation.

The ultimate goal of the developed algorithm is to solve the primal problem which is difficult to handle directly thus we turn to solving the dual of its dual problem. In view of this, as the convergence criteria of the optimization process only the primal consistency constraints \mathbf{c}_p are checked and \mathbf{c}_d is not used. As long as the primal consistency constraints \mathbf{c}_p satisfy certain conditions and are very close to zero, the current solutions can be considered as consistent and feasible for the primal problem, which is the original problem we want to solve. Thus the convergence criterion for the proposed method are set as

$$\|\mathbf{c}_p^{(k)} - \mathbf{c}_p^{(k-1)}\|_\infty < \varepsilon \quad \text{and} \quad \|\mathbf{c}_p^{(k)}\|_\infty < \varepsilon \quad (29)$$

where ε is a convergence tolerance, which normally is set to be very small.

The centralized ALC needs M copies of shared variables while the proposed method only needs $M-1$. As a result, the number of elements in \mathbf{c}_p in the proposed method is less than that in the centralized ALC. This is expected to bring certain benefits to the proposed method and is explored in the next section.

3. Numerical tests and results analysis

One mathematical problem and one engineering problem are used to test the efficacy of the proposed method. The number of function evaluations is recorded to represent the computational resources consumed. Errors of the design variables and the objective of each problem during the optimization process are also collected. The errors are defined as the relative errors of the decomposition-based optimization results with respect to the reference solution from the All-in-One formulation. All the sub-problem optimizations are solved using “*fmincon*” in Matlab. The centralized ALC-ADMOM is also applied to these test problems for comparison. Through the introduction of an artificial master problem, the centralized ALC-ADMOM allows parallel computation for all decomposed sub-problems and has been proven to be more efficient than other coordination methods [3]. In the following part of this research it is referred to as the centralized ALC for convenience.

3.1. Problem 1 – Geometric optimization problem

The first test problem is a simple geometric optimization problem which has been widely used in the literature [6] [19]. Here the problem is partitioned into two sub-problems and both the centralized ALC and the proposed method need a master problem to coordinate the two sub-problems, as shown in Figure 4. For the centralized ALC, the linking variables between the master problem and the sub-problems are the shared design variables. In the proposed method, the linking variables are the dual multipliers associated with the shared design variables and their copies. In both methods the master problems are simple quadratic programming problems thus their analytical solutions can be easily calculated. The solution process of the master problem is merely a parameter update procedure based on the results of the sub-problems.

$$\begin{aligned}
& \min_{z_1, \dots, z_7} f = z_1^2 + z_2^2 \\
& \text{subject to} \quad g_1 = (z_3^{-2} + z_4^2)z_5^{-2} - 1 \leq 0, \\
& \quad \quad \quad g_2 = (z_5^2 + z_6^{-2})z_7^{-2} - 1 \leq 0, \\
& \quad \quad \quad h_1 = (z_3^2 + z_4^{-2} + z_5^2)z_1^{-2} - 1 = 0, \\
& \quad \quad \quad h_2 = (z_5^2 + z_6^2 + z_7^2)z_2^{-2} - 1 = 0,
\end{aligned} \tag{30}$$

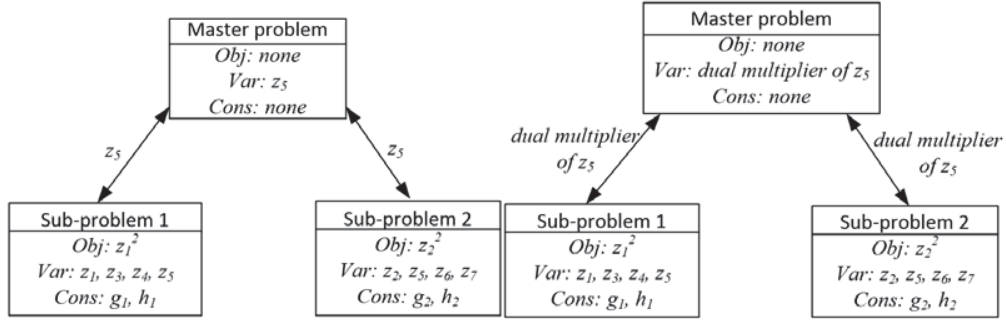


Figure 4 : The decompositions of the centralized ALC (left) and the proposed method (right) when solving the geometric optimization problem

To explore the effects of the penalty weight ρ on the primal and dual consistency constraints, different values of ρ , 10, 1, 0.1, and 0.01, are considered. The biggest violations of \mathbf{c}_p and \mathbf{c}_d during the optimization process are plotted in Figure 5 for different ρ . Here the starting points for the design variables in all cases are set to one and the convergence tolerance ε in Eq. (29) is set to 0.001

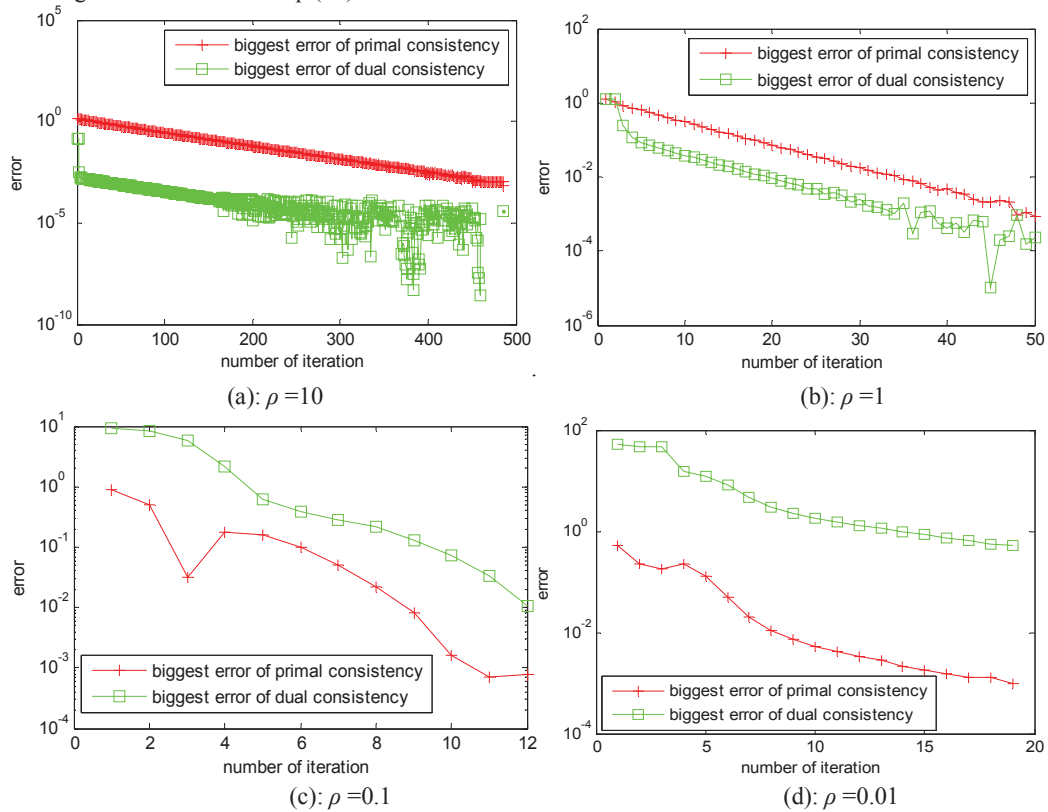


Figure 5 : The curves of the biggest primal and dual consistency errors under different ρ

Figure 5 clearly indicates that a large ρ can effectively reduce the dual consistency error, which is reasonable because a large ρ places a high penalty on the differences between the copies of dual multipliers. For $\rho=10$, the dual

consistency error reaches around $1e-3$ just after a few iteration while it takes the primal consistency error 487 iterations to reach $1e-3$. As the value of ρ decreases, the primal consistency error drops faster and the dual consistency error drops more slowly. For $\rho=0.01$, the dual consistency error is around 0.5 when the primal consistency error reaches $1e-3$.

Inspired by the above observation, we propose to decrease the value of ρ throughout the optimization process, instead of fixing it to a constant. Eq. (31) is the proposed update scheme for ρ . We want to keep ρ relatively big at the beginning to quickly reduce the dual consistency error, and then we decrease ρ to reduce the primal consistency error faster thus to accelerate the convergence speed of optimization.

$$\rho^{(k+1)} = \beta\rho^{(k)}, \quad 0 < \beta < 1 \quad (31)$$

By adjusting the convergence tolerance in Eq. (29), we can control the solution error of decomposition-based optimization. Here, the tolerance ε is set to $1e-2$, $1e-3$, $1e-4$ and $1e-5$ for both the centralized ALC and the proposed method. Their performances are collected in Figure 6. The initial ρ in the proposed method and the initial w in centralized ALC are all set to one. The update parameter β for ρ in Eq. (13) is 0.8. For the centralized ALC, we use the weight update scheme in [3] and set $\beta = 1.1$ and $\Upsilon = 0.9$, as suggested in [3]. The initial Lagrangian multipliers are set to zero, and the initial design variables are set to one. Figure 6 shows the proposed method is more efficient than the centralized ALC in terms of function evaluation numbers.

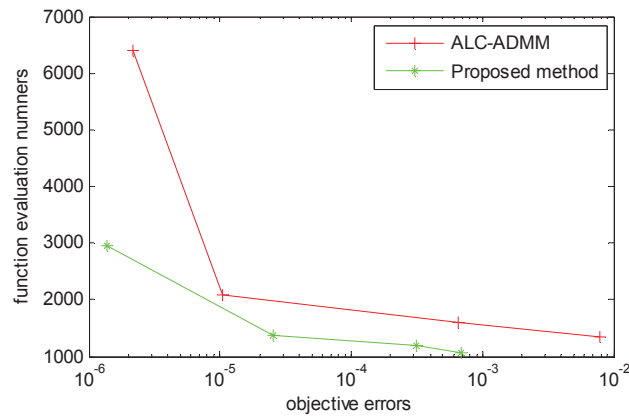


Figure 6: The test results of the centralized ALC and the proposed method on the geometric optimization problem (From right to left: $\varepsilon = 1e-2$, $1e-3$, $1e-4$ and $1e-5$)

3.2. Problem 2 – Portal frame design problem

The second test problem is a structural optimization problem – the portal frame design problem. The optimization objective is to minimize the volume of the whole structure by changing the dimensions of cross sectional areas. Since a horizontal force and a concentrated moment are applied on the structure, normal and shear stresses are incurred. The design constraints are to satisfy all stress limits and geometry requirements. Readers may find more details about this problem in [20].

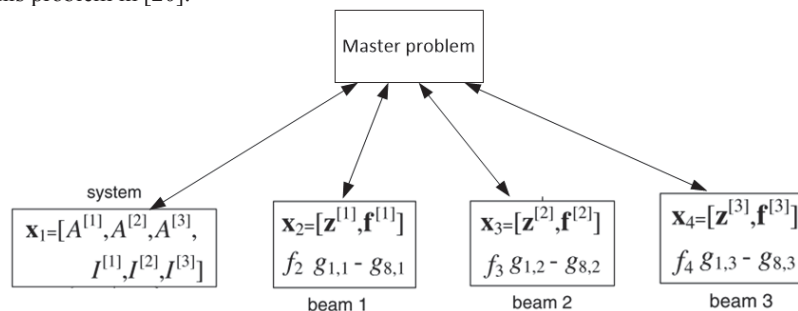


Figure 7: The decompositions of the proposed method and the centralized ALC when solving the portal frame design problem

Due to the uncertainty of one set of the geometry constraints in this problem (which requires that either the top flange area is twice as large as the bottom one or vice versa), this problem has many local optimal solutions and one global optimal solution. Previous research has found that ALC with a hierarchical structure could reach the global solution 54 times out of 100 tries [20]. However the ALC in [20] cannot solve the sub-problems in parallel. For this problem, the centralized ALC in [13] is adopted and compared to the proposed method. Both methods use

the structure shown in Figure 7.

20 tests are performed for the two methods, starting from random points between the lower bounds and upper bounds of the design variables. The objective errors of these test results are collected in Figure 8. The convergence tolerance ϵ is set to $1e-3$ for both the centralized ALC and the proposed method. For the proposed method, the initial ρ is 1 and β is 0.96. For the centralized ALC, a large initial w such as 1 or 0.1 does not work and always causes the optimization to converge prematurely, so the initial w is set to 0.01 and the update parameters are set as $\beta = 1.05$ and $\Upsilon = 0.9$. All initial Lagrangian multipliers are set to 0. The AIO optimal objective value is 0.1661, which is used as the global optimal objective value to calibrate the objective error for decomposition-based optimization.

For the centralized ALC, the objective errors for the 20 tests in Figure 8 range from 0.53% to 9.95% with an average value of 3.5%. While for the proposed method, all 20 tests in Figure 8 have reached the same objective value, 0.1660, with the objective error as low as 0.1%, which means the proposed method has greatly improved the solution accuracy and has high robustness. On the efficiency side, the average function evaluation number of the proposed method is 181,421 while that number for the centralized ALC is 368,028.

In a summary, for this multi-modal engineering problem, starting from random design variables, the proposed method consumes only half of the computation resources of the centralized ALC while it reaches a much better solution than the centralized ALC does. Also, the results of the centralized ALC vary a lot as the starting points change while the proposed method can consistently reach an accurate solution.

The numerical tests in this study have proven the high efficiency and accuracy of the proposed method over the centralized ALC. These advantages might from the major fact that the proposed method creates one less set of copies of all shared variables than the centralized ALC, which makes it easier for the algorithm to coordinate and reach a consistent solution. While in the proposed method copies of dual multipliers are introduced, these copies do not necessarily need to be equal to each other for the algorithm to generate the optimal solution for the original problem. For example, the portal frame design problem originally has 24 shared variables. In the proposed method, 24 duplicated shared variables are introduced and thus 24 primal consistency constraints are added to the decomposition formulation. In the centralized ALC, the number of duplicated shared variables is 48 because each original shared variable requires two copies. As a result, the number of primal consistency constraint increases to 48. The convergence criterion for both methods is the closeness of the primal consistency error to zero, and it is apparently much easier to satisfy this condition with 24 rather than 48 primal consistency constraints.

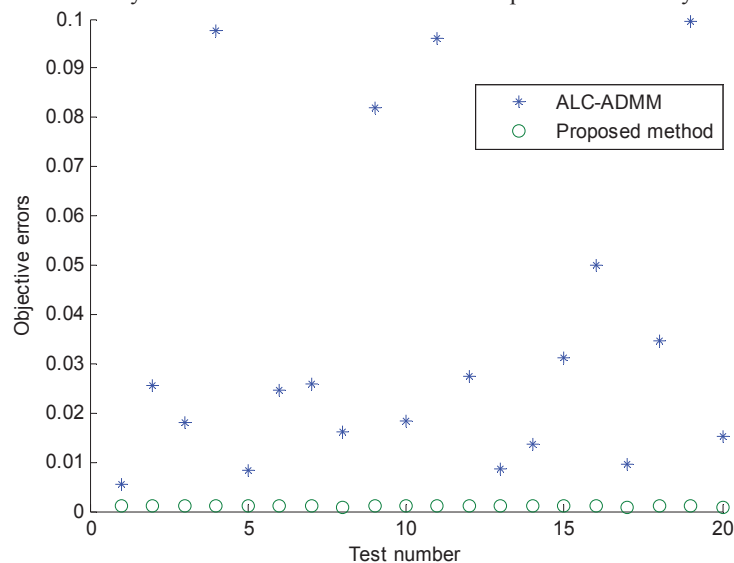


Figure 8: The objective errors of ALC-ADMM and the proposed method for 20 tests of the portal frame problem

4. Conclusions

A new parallel coordination method for decomposition-based optimization is proposed in this paper. Instead of applying ADMM directly to the primal problem, we first employ the ordinary duality theorem to generate an ordinary dual problem, and then apply ADMM to the dual problem. The resulting formulation is the dual problem of the dual problem, in which all sub-problems are independent from each other thus they can be solved in parallel. The mathematical derivations of the method are presented in the paper along with its final computation procedures. One mathematical and one engineering example are used to test the proposed method and the results are compared to those of another popular parallel coordination method: the centralized ALC. The results show that for the

mathematical problem, the proposed method consumes less function evaluations than the centralized ALC does while reaching the same objective accuracy. For the complex multi-modal structural optimization problem, the proposed method is more accurate (with an average objective error as 0.1% compared to 3.5% for the centralized ALC), efficient (needs only half of the function evaluation number of the centralized ALC), and robust (consistently reaches the same accurate solution while the solutions of the centralized ALC vary when starting from random initial points).

In the future, more numerical tests need to be conducted to compare the proposed method with other parallel coordination methods. It is also worthwhile to investigate how the penalty weight ρ affects the optimization process, and come up with an improved update scheme for ρ .

5. Acknowledgements

This research was partially supported by the National Science Foundation under grant # CMMI-1129969 entitled "Network Target Coordination for Complex System Optimization". The views presented here do not necessarily reflect those of our sponsor whose support is gratefully acknowledged.

6. References

- [1] H. Kim, "Target Cascading in Optimal System Design," Ph.D. thesis, University of Michigan, 2001.
- [2] N. Michelena, H. M. Kim, and P. Papalambros, "A System Partitioning and Optimization Approach to Target Cascading", Proceedings of the 12th International Conference on Engineering Design. Vol. 2. 1999.
- [3] S. Tosserams, "Distributed Optimization for Systems Design An Augmented Lagrangian Coordination Method," Ph. D. thesis, Eindhoven University of Technology, 2008.
- [4] M. Xu, W. Wang, P. Guarneri, and G. Fadel, "CADMM applied to hybrid network decomposition," 10th World Congress on Structural and Multidisciplinary Optimization, Orlando, Florida, May 19-24, 2013.
- [5] S. Boyd, N. Parikh, E. Chu, B. Peleato, and J. Eckstein, "Distributed optimization and statistical learning via the alternating direction method of multipliers," Foundations and Trends® in Machine Learning 3, no. 1: 1-122, 2011.
- [6] Y. Li, Z. Lu, and J. J. Michalek, "Diagonal Quadratic Approximation for Parallelization of Analytical Target Cascading," Journal of Mechanical Design, 130(5), 051402, 2008.
- [7] D. P. Bertsekas, Nonlinear Programming, 2nd ed., Athena Scientific, Belmont, MA, 1999.
- [8] H. M. Kim, D. G. Rideout, P. Y. Papalambros, and J. L. Stein, "Analytical Target Cascading in Automotive Vehicle Design," Journal of Mechanical Design, 125(3), 481-489, 2003.
- [9] J. B. Lassiter, M. M. Wiecek, and K. R. Andrighetti, "Lagrangian coordination and Analytical Target Cascading: solving ATC-decomposed problems with Lagrangian duality," Optimization and Engineering, 6(3), 361-381, 2005.
- [10] W. Wang, M. Xu, P. Guarneri, G. Fadel, and V. Blouin, "A Consensus Optimization via Alternating Direction Method of Multipliers for Network Target Coordination." In 12th AIAA Aviation Technology, Integration, and Operations (ATIO) Conference and 14th AIAA/ISSMO Multidisciplinary Analysis and Optimization Conference. 2012.
- [11] W. Wang, "Network Target Coordination for Design Optimization of Decomposed Systems," Ph.D. thesis, Clemson University, 2012.
- [12] M. Fukushima, "Application of the alternating direction method of multipliers to separable convex programming problems," Computational Optimization and Applications, vol. 1, pp. 93-111, 1992.
- [13] S. Tosserams, M. Kokkolaras, L. F. P. Etman, and J. E. Rooda, "A Nonhierarchical Formulation of Analytical Target Cascading," Journal of Mechanical Design, 132(5), p. 051002, 2010.
- [14] P. Guarneri, J. T. Leverenz, M. M. Wiecek, and G. Fadel, "Optimization of nonhierarchically decomposed problems," Journal of Computational and Applied Mathematics, vol. 246, pp. 312-319, 2013.
- [15] M. Xu, G. Fadel, and M. M. Wiecek, "Solving structure for network-decomposed problems optimized with Augmented Lagrangian Coordination," In ASME-IDETC 2014, Buffalo, NY, USA, 2014.
- [16] M. Xu, G. Fadel, and M. M. Wiecek, "Dual Residual for Centralized Augmented Lagrangian Coordination Based on Optimality Conditions," Journal of Mechanical Design, 137(6), 2015.
- [17] J. J. Michalek and P. Y. Papalambros, "Weights, Norms, and Notation in Analytical Target Cascading," Journal of Mechanical Design, vol. 127, no. 3, p. 499, 2005.
- [18] R. T. Rockafellar, Convex Analysis. No. 28. Princeton university press, 1970.
- [19] S. Tosserams, L. F. P. Etman, P. Y. Papalambros, and J. E. Rooda, "An augmented Lagrangian relaxation for analytical target cascading using the alternating direction method of multipliers," Structural and Multidisciplinary Optimization, vol. 31, no. 3, pp. 176-189, 2006.
- [20] S. Tosserams, L. F. P. Etman, and J. E. Rooda, "Multi-modality in augmented Lagrangian coordination for distributed optimal design," Structural and Multidisciplinary Optimization, vol. 40, no. 1-6, pp. 329-352, 2009.

Electromagnetic levitation coil design using gradient-based optimization

Suzanne Roberts¹, Schalk Kok², Johan Zietsman³, Helen Inglis⁴

¹ University of Pretoria, Pretoria, South Africa, suzanne.elize.roberts@gmail.com

² University of Pretoria, Pretoria, South Africa, schalk.kok@up.ac.za

³ University of Pretoria, Pretoria, South Africa, johan.zietsman@up.ac.za

⁴ University of Pretoria, Pretoria, South Africa, helen.inglis@up.ac.za

1. Abstract

Electromagnetic levitation melting is a containerless technique to obtain material properties of reactive, electrically conductive materials that would otherwise result in sample contamination when in contact with a container at high temperatures. The levitation coil geometry, and the magnitude and frequency of the alternating current determine the sample sizes of a specific material that can be levitated as well as the temperature of the levitated sample.

The levitation cell is modelled using a one-dimensional analytical approach. This model requires the material properties of the sample and surrounding atmosphere as input variables. Since there is a large amount of uncertainty in measuring these properties they are regularized using experimental data from a known coil design and current. The levitation cell model with regularized material properties is then used in a gradient-based optimization scheme to design a coil for the levitation melting of specified sample size and material.

The consequences of using a multistart, gradient-based optimization scheme are reported. Coils are designed to minimize the temperature of the levitated sample or maximize the stability of the sample during levitation.

2. Keywords: gradient-based, multistart, electromagnetic levitation

3. Introduction

Measuring the physical properties of metals at high temperatures present some challenges especially for containing the sample, since many materials have a corrosive nature at high temperatures. Experiments often result in the container being destroyed or the sample being contaminated by container material while in contact with the container at high temperatures. Electromagnetic levitation melting is an alternative non-contact experimental approach to measure physical properties including viscosity and surface tension.

Trial and error methods are common practice for levitation coil design [1], [2]. However, this often results in levitation cell experiments being complicated by coil designs that are very sensitive to sample position in the coil and/or small changes in coil geometry. There also exists a need to use levitation melting for an increased variety of materials while accessing a larger range of temperatures with more precise control [2].

The sample sizes of a specific material that can be levitated and the temperature of the levitated sample are determined by the levitation coil geometry, and the magnitude and frequency of the alternating current. Royer et al. [2] use a genetic-like algorithm to design a levitation coil that would minimize the temperature of the levitated sample for a large range of currents. In this paper we use a gradient-based, multistart optimization algorithm to design similar coils. We specifically investigate formulating levitation coil design as an optimization problem to develop a design tool based on a levitation cell model that would allow the design of robust and reliable coils for the levitation melting of specified sample materials and sizes. In the process we also use optimization to regularize the material properties in the Royer et al. [2] model and to minimize the difference between two functions. In all three instances the constrained optimization function (`fmincon`) in Matlab's optimization toolbox is utilized.

4. Electromagnetic levitation melting process description

An electromagnetic levitation cell basically consists of a water-cooled coil supplied with high frequency alternating current. The coil has an associated high frequency alternating magnetic field around it since a magnetic field is generated around any current-carrying conductor. Faraday's law states that a changing magnetic field induces an electric field [3]. Therefore the alternating magnetic field will induce eddy currents in any electrically conductive body placed inside the coil.

The magnetic field of the induced eddy currents opposes that of the coil [2]. The interaction of the magnetic field of these eddy currents with the magnetic field of the coil current results in a Lorentz force [1], [2], [4]. If a position exists inside the coil where the Lorentz force is equal and opposite to the weight of the body, the body will be levitated in that position inside the coil. Additionally, the induced eddy currents in the body will cause resistive

heating (Ohmic / Joule heating) [1], [4]. If this causes the body to melt, the Lorentz force will cause flow inside the molten droplet [1], [5].

In order to create a region inside the coil where stable levitation is possible, the current in a part of the coil has to flow in the opposite direction to the current in the rest of the coil [1]. This can be achieved by adding a stabilizing part to the coil that is connected in series to the main coil and wound in the opposite direction.

5. Levitation cell model

The analytical one dimensional levitation cell model proposed by Fromm and Jehn [6] and used by Royer et al. [2] has been implemented. The current induced in the sample is modelled using the concept of mutual inductances. This results in a nonlinear expression for the Lorentz force on a sample in terms of the sample position. The sample levitation position is found where the Lorentz force is equal and opposite to the weight of the sample. The temperature of the sample is solved from another nonlinear equation resulting from the energy balance of the induced heating of the sample and the convection and radiation heat losses to the environment. The electromagnetic and thermal parts of the problem are coupled because the heat induced in the sample is a function of its levitated position.

The model approximates the helical coil as a set of axisymmetric circular loops (Fig.1). It is further based on the assumptions that the sample size is small relative to the coil, the sample is spherical, the coil is operating at high frequencies and the alternating magnetic field over the sample position is uniform in space.

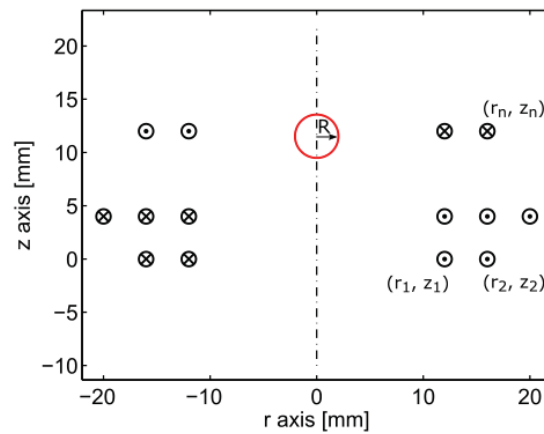


Figure 1: Axisymmetric approximation of a levitation cell coil with the sense of the current in the loop and the sample levitation position indicated. Crosses and dots indicate opposite alternating current senses.

The magnetic field predicted by the Fromm and Jehn model [6] is highly nonlinear around the sample. To compensate for this and the spatial distribution of the sample mass within the coil, Royer et al. [2] suggests discretizing the sample into a number of disks, computing the induced heat in each disk using the method of Fromm and Jehn [6] and then using a volume weighted average to find the total heat induced in the sample. Fromm and Jehn [6] compute the induced heat as

$$\dot{q}_L = 3 \left(\frac{\pi^3 \mu f}{\gamma} \right) R^2 H^2 \quad (1)$$

where H is the originally assumed uniform magnetic field strength. In our implementation of the model we replace H with a volume average \tilde{H} , computed numerically from the non-uniform magnetic field strength $H(z)$ as

$$\tilde{H} = \frac{1}{V} \int H(z) dV. \quad (2)$$

6. Regularization

Royer et al. [2] report uncertainty in the sample emissivity and temperature dependent material properties (the sample conductivity and the properties of the fluid surrounding the sample) as possible sources of error in their model.

We attempt to address this problem with regularization. The experimental results from a known coil design and electrical current is used to adjust the uncertain material properties in such a way that the difference between

the model predictions and experimental results are minimized while penalizing large variations in the material properties. The experimental results reported by Royer et al. [2] for their seed coil geometry is used for regularization. An equality constraint requires the Lorentz force to be equal to the sample weight to ensure levitation takes place and the inequality constraint $dF/dz < 0$ ensures that the levitation position is stable. Analytical gradients are supplied to the optimization algorithm to reduce the computational time requirement.

The regularized material properties are given in the table below.

Table 1: Regularization results

Material property	Original value	Regularized value	% change
Sample emissivity, ε	0.1	0.0934	-6.5
Sample electrical conductivity, γ	4252890	4252890	0.0
Fluid thermal conductivity, k_f	0.0177	0.0287	61.8
Fluid density, ρ_f	0.1625	0.1797	10.6
Fluid kinematic viscosity, η	1.9900×10^{-5}	1.9089×10^{-5}	-4.0
Fluid specific heat, C_p	520.3	520.3	0.0

In Fig.2 sample temperature predictions at various currents given by the model with and without the regularized material properties are compared to the experimental results reported by Royer et al. [2]. It can be seen that the model is improved by including the regularized material properties but the model still has difficulty predicting the gradient of the experimental results.

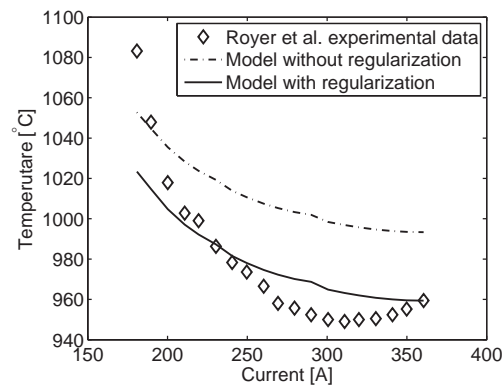


Figure 2: Model results with and without regularization compared to experimental results reported by Royer et al. [2].

7. Coil design using gradient-based optimization

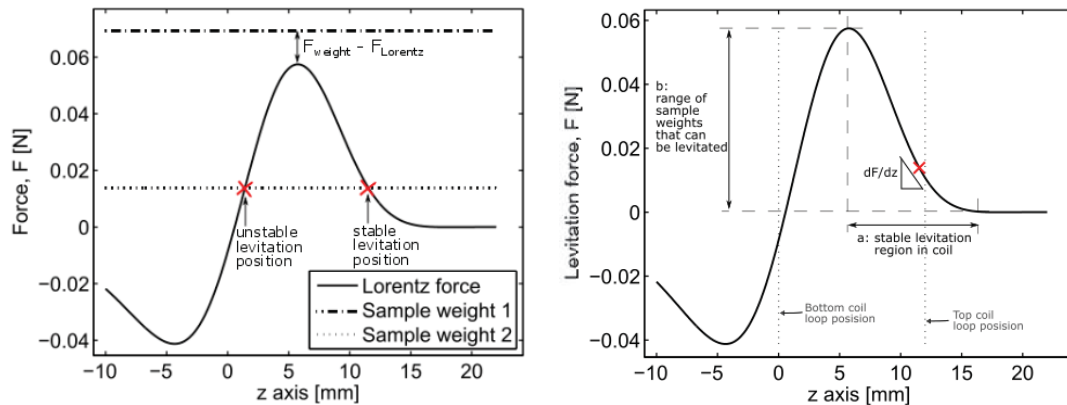
A gradient-based multistart optimization formulation with a Sequential Quadratic Programming (SQP) algorithm is used to design coils for various experimental requirements. The variables used as design variables are: the total number of loops in the coil, the number of loops in the stabilizing part of the coil, the magnitude and frequency of the current supplied to the coil and the radial and axial positions of each of the coil loops.

The total number of loops in the coil and the number of loops in the stabilizing part of the coil are discrete variables. The optimization algorithm is therefore repeated for every possible permutation of these two variables and the permutation that obtains the lowest value of the objective function at its optimum is selected.

All the design variables are bounded. The number of coil loops are between five and seven of which either two or three loops have the opposite current sense to form the stabilizing part of the coil. Current magnitude can vary between 150 A and 400 A and current frequency is in the range 100 – 200 kHz. The maximum radius of the coil is 95 mm and the minimum radius of any coil loop is 10 mm to allow enough space for the sample inside the coil. The axial position of the coil loops can be anywhere between 0 mm and 20 mm. Constraints are applied to prevent any of the 3mm tubes that form the coil loops from overlapping. Further constraints ensure that the Lorentz force is equal to the sample weight for levitation and that the levitation position is stable, $dF/dz < 0$. Fig.3 illustrates the last two constraints. The constraints applied to the coil design optimization is kept at a minimum to allow us

to investigate which coil design properties produce specific levitation cell characteristics. This could result in coil designs that are difficult to manufacture and it might later be necessary to add manufacturing constraints to the coil design optimization formulation.

The shape of the Lorentz force curve in Fig.3 is determined by the coil geometry and the electrical current in the coil. Since these are design variables, some combinations will not satisfy the equality constraint that requires the Lorentz force to be equal to the sample weight (e.g. Sample weight 1 in Fig.3a). If this is the case the analysis will minimize the square of the difference between the sample weight and the Lorentz force within the coil and return the corresponding sample position to the optimization algorithm. In this way the optimization algorithm still receives information that will allow it to determine in which direction to search for a solution which would satisfy the equality constraint.



(a) Possibilities of stable, unstable and no levitation. (b) Effect of dF/dz on stability and the range of sample weights that can be levitated.

Figure 3: Typical variation of the Lorentz force along the z-axis of a coil.

7.1. Minimizing the temperature of the levitated sample

For some comparison with the results obtained by Royer et al. [2] who minimize the temperature of the levitated sample for a large range of currents, the first objective function that is investigated, is to minimize the temperature of the sample during stable levitation.

It is found that the minimum value obtained with this objective function varies significantly depending on the initial design vector supplied to the algorithm. A multistart optimization formulation with ten starts for each of the six discrete variable permutations is therefore used. The initial design vector for each start is a random value within the lower and upper bounds. Fig.4 shows the sorted objective function values obtained at the optima of the various starting points that yielded feasible coil designs.

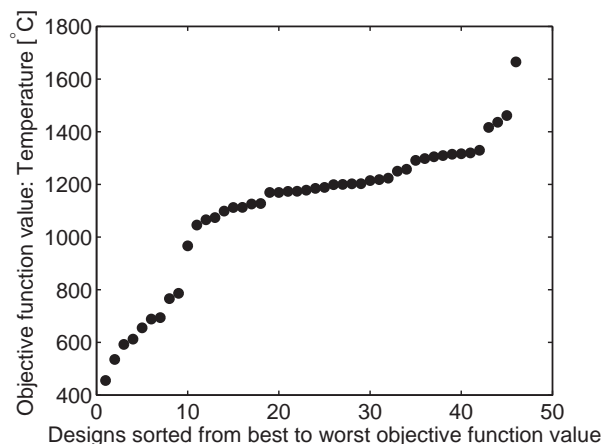


Figure 4: Sorted objective function values for multi-start coil design optimization to minimize temperature.

It can be seen from Fig.4 that there are nine designs that are significantly better than the rest. The three coil designs that yield the lowest sample temperatures as well as the design proposed by Royer et al. [2] for minimizing the sample temperature for a wide range of currents are given in Fig.5.

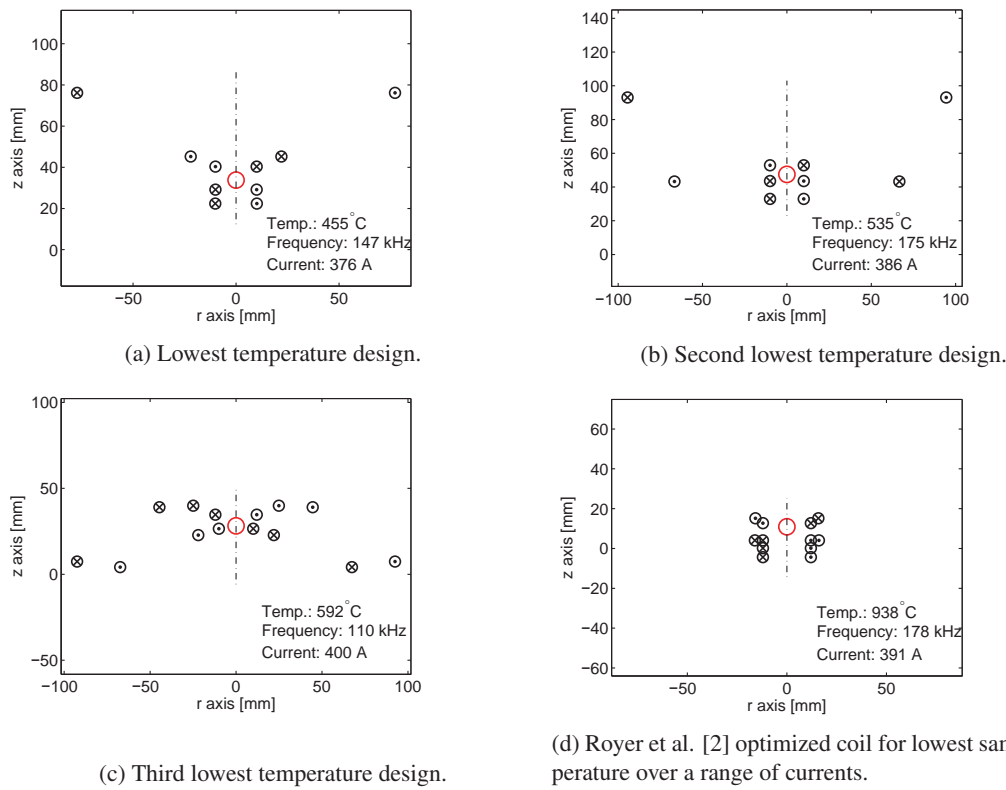


Figure 5: Sorted objective function values for multi-start coil design optimization to minimize temperature.

These results cannot be directly compared to that of Royer et al. [2], since we include current magnitude and frequency as design variables, which Royer et al. [2] does not, and we are minimizing the sample temperature at any specific current while Royer et al. [2] minimize the sample temperature over a range of currents. However, some similarities can be observed between the first two designs obtained and the design obtained by Royer et al. [2]. In all three cases the bottom three coil loops have a very small equal radius while the top two loops form a conical shape. An interesting difference is that we get a result where the sense of coil current changes twice from the bottom to the top of the coil as opposed to most coils in literature that report only one change in the sense of the current. We also obtain larger maximum coil radii than Royer et al. [2]. These might be trends in the coil designs, but a larger number of different starting points is required to show this definitively.

7.2. Maximizing the stability of the sample position

We are interested in designing levitation cell coils with which experimental work would be as easy, reliable and repeatable as possible. One factor that determines this is the stability of the sample levitation position. Therefore the objective function in the optimization problem is now changed to make the slope of the Lorentz force-position curve, which has to be negative for stability, as steep as possible

$$\max \left| \frac{dF}{dz} \right|. \quad (3)$$

Once again a multistart optimization formulation with ten starts for each permutation of the discrete design variables is used. Of all the results that are obtained, the four designs given in Fig.6 have significantly larger values for $|dF/dz|$ than the rest. These four designs all have a loop with a small radius directly below the sample levitation position. All except the third coil have at least three closely spaced small radius loops around the sample position and two or three large radius loops. The first two coil designs both have small overall heights.

Fig.7 shows the variation of the Lorentz force along the z-axis of the four coils designed for maximum stability. It is evident from this figure that a consequence of maximizing $|dF/dz|$ is that the part of the coil where stable

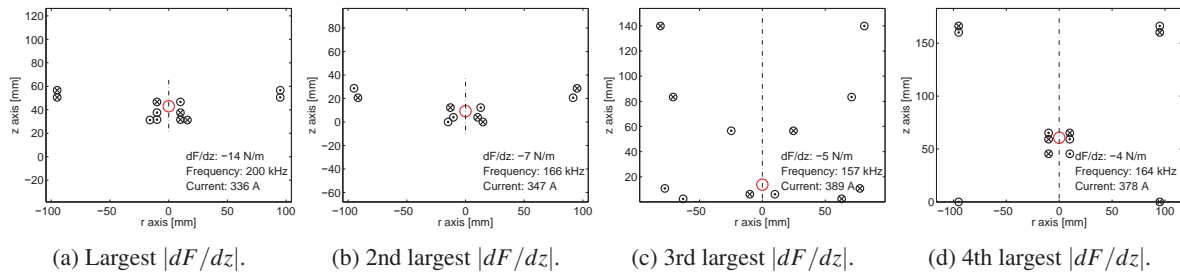


Figure 6: Multistart coil design optimization to maximize stability. Coil designs sorted according to objective function value.

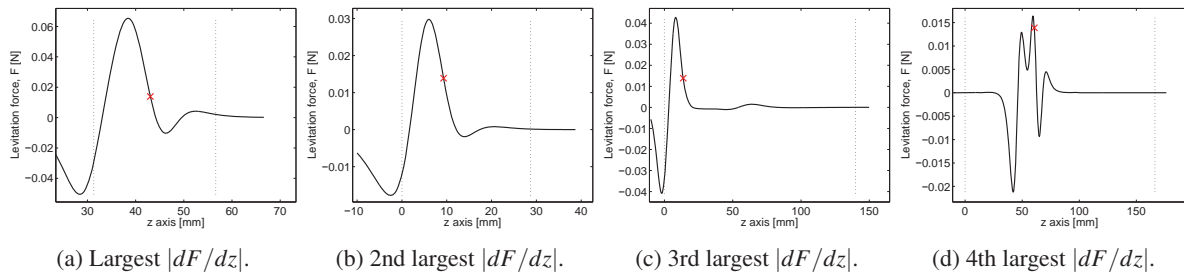


Figure 7: Multi-start coil design optimization to maximize stability. Variation of the Lorentz force along the z-axis of the coil.

levitation is possible becomes small - around 5 mm for these four designs. The fourth design also shows multiple peaks in the force curve which is not desirable. Fig.3b shows that by maximizing $|dF/dz|$ we are increasing the range of sample weights that can be levitated, while the part of the coil where stable levitation is possible becomes smaller. It can therefore be recommended to add a constraint to specify the minimum size of the part of the coil where stable levitation is possible.

8. Conclusion

We show that a multistart, gradient-based optimization algorithm can be used to design levitation cell coils for different experimental applications.

We are learning how to develop a design tool for repeatable and reliable levitation cell experiments through experimentation with different formulations of the optimization problem. Future work will include replacing the one dimensional levitation cell model with a more accurate one and experimentally validating the optimized levitation cell designs.

9. References

- [1] A. Kermanpur, M. Jafari, and M. Vaghayenegar. Electromagnetic-thermal coupled simulation of levitation melting of metals. *Journal of Materials Processing Technology*, 211:222-229, 2011.
- [2] Z. L. Royer, C. Tackes, R. LeSar, and R. E. Napolitano. Coil optimization for electromagnetic levitation using a genetic like algorithm. *Journal of Applied Physics*, 113:214901-1 - 214901-9, 2013.
- [3] David J. Griffiths. *Introduction to Electrodynamics*. Prentice Hall, 1999.
- [4] ZA Moghimi, M Halali, and M Nusheh. An investigation on the temperature and stability behavior in the levitation melting of nickel. *Metallurgical and Materials Transactions B*, 37(6):997-1005, 2006.
- [5] N El-Kaddah and J Szekely. The electromagnetic force field, fluid flow field, and temperature profiles in levitated metal droplets. *Metallurgical Transactions B*, 14(3):401-410, 1983.
- [6] E. Fromm and H. Jehn. Electromagnetic forces and power absorption in levitation melting. *British Journal of Applied Physics*, 16:653 - 659, 1965.

Reliability-based Design Optimization of Nonlinear Energy Sinks

Ethan Boroson¹ and Samy Missoum²

¹ University of Arizona, Tucson, USA, ethanboroson@email.arizona.edu

² University of Arizona, Tucson, USA, smissoum@email.arizona.edu

1. Abstract

Nonlinear Energy Sinks (NESs) are a promising technique for passively reducing the amplitude of vibrations, especially for use as energy pumping devices for buildings under seismic loading. Through nonlinear stiffness properties, a NES is able to passively and irreversibly absorb energy. Unlike the traditional Tuned Mass Damper (TMD), the NES has no inherent natural frequency, allowing the NES to absorb energy over a wide range of frequencies. The efficiency of the NES, however, is extremely sensitive to small perturbations in design parameters or initial conditions. In many cases, it has been observed that the most efficient NES designs are in fact very close to low efficiency regions in the design space.

This work will present an optimization technique for NESs. In order to optimize NES devices, the high sensitivity of NES to uncertainty, with almost discontinuous behaviors, requires specific reliability-based design optimization (RBDO) techniques. In this work, a support vector machine classifier, insensitive to discontinuities, is used to construct the boundaries of the failure domain (low efficiency regions) through adaptive sampling and clustering. Several RBDO results for various NES configurations will be provided. In particular, NES configurations in parallel will be investigated.

2. Keywords: Nonlinear Energy Sinks, RBDO, SVM, Clustering.

3. Introduction

Nonlinear Energy Sinks (NESs) are an emerging technique for passive and irreversible reduction of amplitude of vibration [3]. NESs have a wide variety of applications, such as energy pumping away from a building under seismic loading [8, 9] or in aeroelasticity [4]. NESs rely on a nonlinear, typically cubic, stiffness property which is at the origin of the irreversible transfer of energy. Two NES configurations are typically used in the literature: Configuration I—NES coupled to a vibrating system through a weak linear spring, and connected to the ground via a nonlinear spring—and Configuration II—NES with small mass directly coupled to linear system through nonlinear spring [7]. The effectiveness of a NES with small mass makes the configuration II NES ideal for use in a building under seismic loading [9].

NESs are often proposed as an alternative to Tuned Mass Dampers (TMDs) that are widely used to absorb and dissipate energy from a vibrating main system. NESs act passively, like TMDs, but unlike TMDs, they do not have to be tuned to a specific natural frequency to effectively dissipate energy from the vibrating main system. Instead, NESs absorb energy over a wide range of natural frequencies, which is particularly attractive in designing a system with a changing natural frequency.

It has been observed that NESs are very sensitive to perturbations in design parameters or loading conditions, leading to a near discontinuous behavior of performance metrics such as the amount of absorbed energy. This discontinuous behavior allows one to identify two distinct regions: one where energy pumping occurs and another one where it does not [7, 2].

4. Configuration II NES

The Configuration II NES consists of a small mass directly coupled to a linear system through a nonlinear spring. A simple two DOF system can be used to illustrate the principles of NES behavior and is depicted in figure 1a. It is composed of a main system 1 (with angular eigen-frequency ω_1 , damping λ_1) and a sub-system 2 (the NES) with nonlinear stiffness α , damping λ_2 and mass ratio (NES mass divided by main system mass) ϵ . The system is excited through an initial velocity (\dot{x}_0) applied to the main system. The full system behavior is calculated through equation 1. The efficiency of the NES is quantified by the percentage of initial energy that the NES dissipates ($E_{NES_{inf}}$), expressed in equation 2 [7].

$$\begin{cases} \ddot{x} + \lambda_1 \dot{x} + \lambda_2 (\dot{x} - \dot{y}) + \omega_1^2 x + \alpha (x - y)^3 = 0 \\ \epsilon \ddot{y} + \lambda_2 (\dot{y} - \dot{x}) + \alpha (y - x)^3 = 0 \end{cases} \quad (1)$$

$$E_{NES_{inf}} = \lim_{t \rightarrow \infty} \frac{\lambda_2 \int_0^t (\dot{y}(\tau) - \dot{x}(\tau))^2 d\tau}{\frac{1}{2} v_1^2} \quad (2)$$

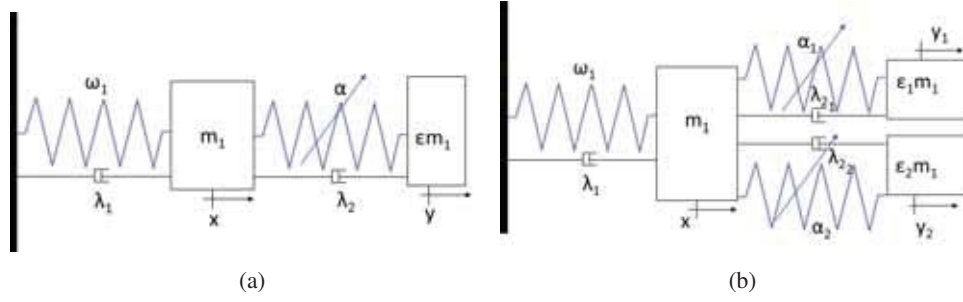


Figure 1: One (a) and Two (b) Configuration II NES systems

This article also details a 3 DOF case where two NESs in parallel are coupled to a main system as in figure 1b. The equations of motion in this case are given in equation 3 [6]. The efficiency of the two NES system is measured as the combined percentage of energy dissipated by the two NESs.

$$\begin{cases} \ddot{x} + \lambda_1 \dot{x} + \lambda_{2_1}(\dot{x} - \dot{y}_1) + \lambda_{2_2}(\dot{x} - \dot{y}_2) + \omega_1^2 x + \alpha_1(x - y_1)^3 + \alpha_2(x - y_2)^3 = 0 \\ \varepsilon_1 \ddot{y}_1 + \lambda_{2_1}(\dot{y}_1 - \dot{x}) + \alpha_1(y_1 - x)^3 = 0 \\ \varepsilon_2 \ddot{y}_2 + \lambda_{2_2}(\dot{y}_2 - \dot{x}) + \alpha_2(y_2 - x)^3 = 0 \end{cases} \quad (3)$$

5. Discontinuities and activation thresholds

The sensitivity of the efficiency of the NES to small perturbations can be very marked [7], [2]. Figure 2a provides an example where $E_{NES_{inf}}$ is plotted as a function of \dot{x}_0 . A discontinuity occurs at $\dot{x}_0 = 0.15$ m/s, but there is also a relatively steep decay of $E_{NES_{inf}}$ as \dot{x}_0 is further increased. These jumps can be seen as activation energy necessary for energy pumping to occur [6]. At the threshold of the activation energy, the NES performance will be extremely efficient, but beyond the threshold the performance deteriorates. Each NES has a relatively narrow range of initial energies where energy dissipation is high. Similar marked changes in behavior appear when studying $E_{NES_{inf}}$ as a function of design parameters α and ε (figure 2b). Once again a discontinuity appears between the regions of energy pumping and no energy pumping. Due to this high sensitivity to design and excitation perturbations, techniques for the design optimization of NESs must be tailored to stay away from the inefficient regions (non energy pumping as well as low $E_{NES_{inf}}$ values).

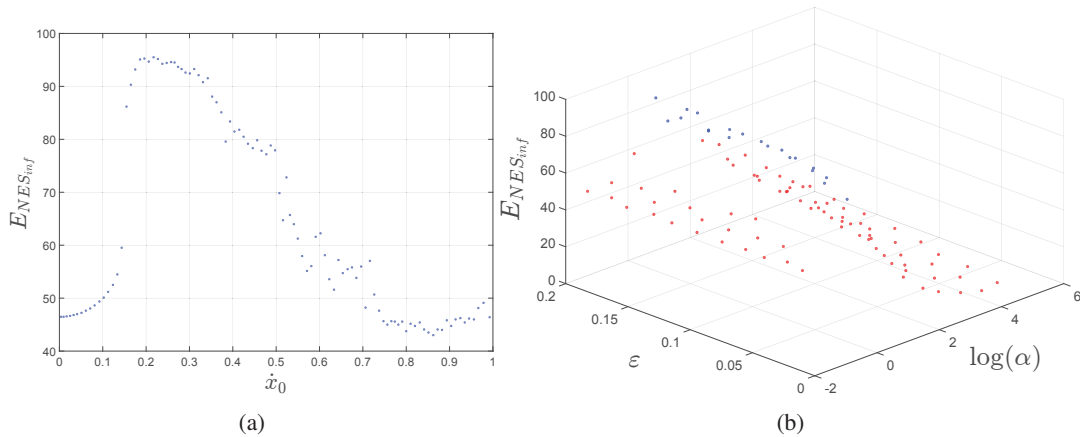


Figure 2: Discontinuities in $E_{NES_{inf}}$ metric. (a) $E_{NES_{inf}}$ response to variations in \dot{x}_0 , with $\varepsilon=0.1$, $\alpha=1$, $\lambda_1=0.004$, $\lambda_2=0.008$, $\omega_1=1$. (b) $E_{NES_{inf}}$ response to variations in α and ε , $\lambda_1=0.01$, $\lambda_2=0.01$, $\omega_1=5$ and $\dot{x}_0=5$ with clustering on $E_{NES_{inf}}$ values.

6. Identification of failure regions

6.1. Clustering

The first step in reliability based design optimization is to segregate efficient and inefficient NES behaviors. The discontinuity illustrated in the previous section enables such a classification, however the location of the discontinuities is often difficult to obtain, especially in high dimensional space. For this reason, a clustering technique such as K-means constructed from a design of experiments can be used without any *a priori* knowledge

of the location of the discontinuities. However, the clustering technique does not always identify properly the clusters as there can be a wide range of energy values over the design space. In order to help the clustering algorithm, samples corresponding to “low” energy levels are removed. This low level energy is found by setting α to its minimum value while maintaining the other parameters at their mean value. Although this approach is rather heuristic, it was shown for the problems treated to provide a proper clustering. An example of clustering in the ε and α space using the proposed technique is depicted in figure 2b.

6.2. SVM

Beyond clustering of the system’s responses, we would like to identify the region of the parameter space where the efficiency of the NES is “acceptable”. In other words, we would like to find the region of the space corresponding to the cluster of better efficiency, using the $E_{NES_{inf}}$ metric. For this purpose, we will use a technique referred to as explicit design space decomposition (EDSD) [1]. The basic idea is to construct the boundary separating two classes of samples (e.g., belonging to the two clusters) in terms of chosen parameters. This is achieved using a Support Vector Machine (SVM) which provides an explicit expression of the boundary in terms of the parameters. The SVM boundary is trained using a design of experiments.

6.3. Refinement of the SVM boundary. Adaptive sampling.

Because the approximated SVM boundary might not be accurate, an adaptive sampling scheme is used to refine the boundary. The sampling algorithm is described in detail in [1]. A fundamental aspect of the algorithm is the selection of samples in the sparse regions of the space (i.e., as far away as possible from existing samples) and also in the regions of highest probability of misclassification by the SVM. The latter criterion is obtained by locating the samples on the SVM. These samples are found by solving the following global optimization problem (side constraints omitted):

$$\begin{aligned} \max_{\mathbf{x}} \quad & \|\mathbf{x} - \mathbf{x}_{nearest}\| \\ \text{s.t.} \quad & s(\mathbf{x}) = 0 \end{aligned} \quad (4)$$

The results section will provide examples of two and three dimensional boundaries constructed using both design and aleatory variables.

7. Reliability Based Design Optimization

The efficient calculation of probabilities with SVM using Monte-Carlo simulations can be used towards the solution of a reliability-based design optimization (RBDO) problem [5], which in the case of a NES, could be formulated as follows:

$$\begin{aligned} \max_{\boldsymbol{\mu}^d} \quad & \mathbb{E}(E_{NES_{inf}}(\mathbf{X}^d, \mathbf{X}^a)) \\ \text{s.t.} \quad & \mathbb{P}((\mathbf{X}^d, \mathbf{X}^a) \in \Omega) \leq P_T \\ & \boldsymbol{\mu}_{\min}^d \leq \boldsymbol{\mu}^d \leq \boldsymbol{\mu}_{\max}^d \end{aligned} \quad (5)$$

where \mathbb{E} is the expected value, $\boldsymbol{\mu}^d$ is the vector of means of the distributions of the random design variables \mathbf{X}^d . \mathbf{X}^a are aleatory random variables which contribute to the expected value of the objective function as well as the probabilistic constraints, but whose hyper-parameters are not to be optimized. Ω is the failure region as defined by the SVM boundary, P_T is a target probability.

Note that the probabilistic constraint in the previous problem cannot be used as such because of the noise introduced by the Monte-Carlo simulations which would make the constraint non-differentiable. For this reason, this constraint is typically approximated using a response surface or a metamodel such as Kriging. To regularize the problem further, the reliability index β is approximated instead of the probability P_f itself [5]. β can be defined using the standard cumulative distribution function Φ :

$$\beta = -\Phi^{-1}(P_f) \quad (6)$$

To further reduce computational time and make this RBDO problem tractable, the objective function (i.e., the expected value) as well as the energy are both approximated using a Kriging metamodel.

8. Results

The first two RBDO problems solved use NES parameters as random design variables and main system initial velocity \dot{x}_0 as an aleatory variable. The parameters of the main system (ω_1 , and λ_1) are fixed. In the first problem, only α and ε are random design variables while λ_2 is fixed. In the second problem all three NES design parameters are random design variables. These problems focus on optimally tuning a NES for a given main system so that the expected value of the efficiency is maximized for a range of initial main system velocities. In both cases the failure

domain Ω is defined by the SVM constructed using the clustering technique described in Section 6.1. In all cases 10^6 Monte-Carlo samples are used.

8.1. 1 NES. 3D RBDO with α, \dot{x}_0 , and ε

$$\begin{aligned} \max_{\mu_\alpha, \mu_\varepsilon} \quad & \mathbb{E}(E_{NES_{inf}}(\mu_\alpha, \mu_\varepsilon, \dot{x}_0)) \\ \text{s.t.} \quad & \mathbb{P}((\alpha, \varepsilon, \dot{x}_0) \in \Omega) \leq 0.15 \\ & -2 \leq \log(\mu_\alpha) \leq 5 \\ & 0.01 \leq \mu_\varepsilon \leq 0.2 \qquad 1 \leq \dot{x}_0 \leq 10 \end{aligned} \tag{7}$$

where $\log(\alpha)$ and ε follow normal distributions: $\log(\alpha) \sim N(\mu_{\log(\alpha)}, 0.07^2)$ and $\varepsilon \sim N(\mu_\varepsilon, 0.0019^2)$. The standard deviations correspond to 1% of the range of $\log(\alpha)$ and ε respectively. The excitation follows a uniform distribution $\dot{x}_0 \sim U(1, 10)$. The fixed parameters are $\lambda_1 = \lambda_2 = 0.01$ and $\omega_1 = 5$.

The failure region Ω (i.e., the SVM) is presented in Figure 3. The Kriging approximations $\tilde{\mathbb{E}}(\tilde{E}_{NES_{inf}})$ and β as well as the training points are depicted in Figures 4a and 4b. It is noteworthy that the approximation of the energy is built using the cluster with highest values only. Approximation error metrics are provided in Table 2.

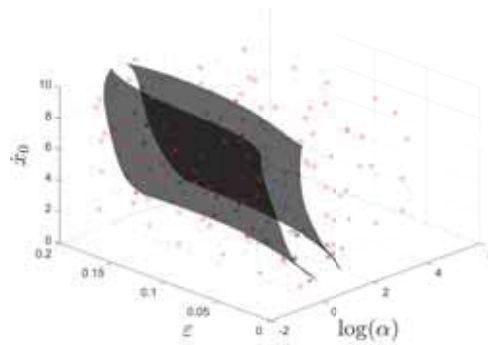


Figure 3: SVM separating the two levels of NES efficiency identified through clustering of $E_{NES_{inf}}$ for α , ε , and \dot{x}_0 .

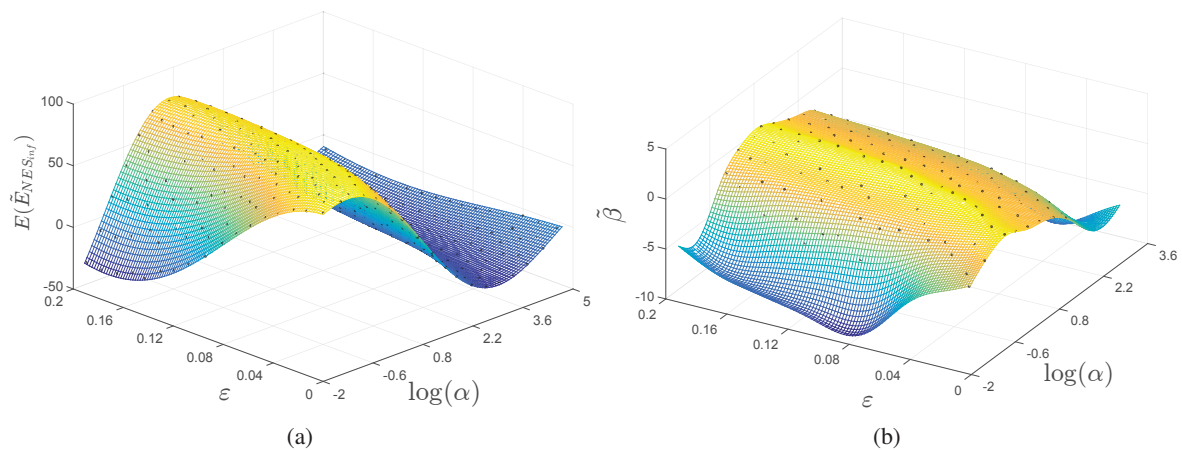


Figure 4: Training and approximations of (a) $\mathbb{E}(\tilde{E}_{NES_{inf}})$ and (b) β for RBDO problem varying α , ε , and \dot{x}_0 .

The RBDO results are given in Figure 5 and summarized in Table 1. The actual probability of failure (as opposed to the approximated one) calculated based on the SVM is also provided in the table.

Table 1: Results table for 1 NES RBDO problem varying α , ε , and \dot{x}_0 .

Probabilistic Optimum	
α	1.32
ε	0.099
P_f from $\tilde{\beta}$	0.15
P_f from SVM	0.19
$\tilde{\mathbb{E}}(\tilde{E}_{NES_{inf}})$	84.9 %
$\mathbb{E}(E_{NES_{inf}})$	77.6 %

Table 2: Error metrics table for 1 NES RBDO problem varying α , ε , and \dot{x}_0 .

Approximation	RMAE	R^2
$\tilde{E}_{NES_{inf}}$	1.11	0.91
$\tilde{\beta}$	0.171	0.99

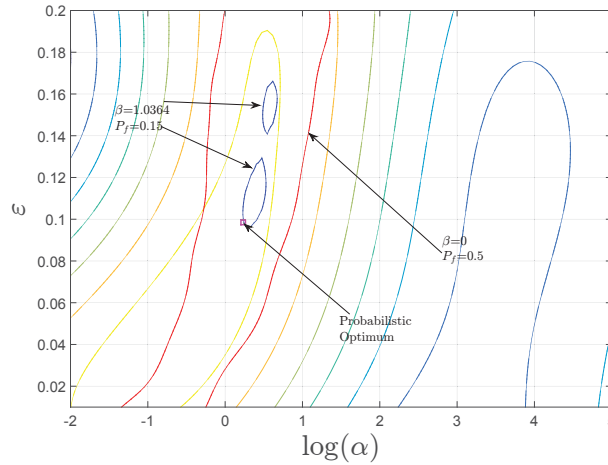


Figure 5: Results plot for 1 NES RBDO problem varying α , ε , and \dot{x}_0 .

8.2. 1 NES 4D RBDO ($\alpha, \dot{x}_0, \lambda_2$, and ε)

This RBDO problem adds λ_2 as a random design variable with a normal distribution. In this problem all three NES parameters are treated as random design variables, while \dot{x}_0 is still treated as an aleatory variable.

$$\begin{aligned}
 & \max_{\mu_\alpha, \mu_\varepsilon, \mu_{\lambda_2}} \mathbb{E}(E_{NES_{inf}}(\mu_\alpha, \mu_\varepsilon, \mu_{\lambda_2}, \dot{x}_0)) & (8) \\
 & s.t. \quad \mathbb{P}((\alpha, \varepsilon, \lambda_2, \dot{x}_0) \in \Omega) \leq 0.2 \\
 & \quad \quad -2 \leq \log(\mu_\alpha) \leq 5 \quad \quad \quad 0.01 \leq \mu_\varepsilon \leq 0.2 \\
 & \quad \quad 0.001 \leq \mu_{\lambda_2} \leq 0.1 \quad \quad \quad 1 \leq \dot{x}_0 \leq 10
 \end{aligned}$$

where $\log(\alpha)$, ε , and λ_2 follow normal distributions: $\log(\alpha) \sim N(\mu_{\log(\alpha)}, 0.07^2)$, $\varepsilon \sim N(\mu_\varepsilon, 0.0019^2)$, and $\lambda_2 \sim N(\mu_{\lambda_2}, 0.00099^2)$.

Error metrics for this four dimensional problem are used to check the quality of the Kriging approximations (Table 4).

Table 3: Results of 1 NES 4D RBDO problem with α , ε , λ_2 , and \dot{x}_0 varied.

Approximation	RMAE	R^2
$\tilde{E}_{NES_{inf}}$	1.61	0.76
$\tilde{\beta}$	1.61	0.97

Table 4: Error metrics of 1 NES 4D RBDO problem with α , ε , λ_2 , and \dot{x}_0 varied.

Probabilistic Optimum	
α	2.76
ε	0.16
λ_2	0.09
P_f from $\tilde{\beta}$	0.00
P_f from SVM	0.00
$\tilde{\mathbb{E}}(\tilde{E}_{NES_{inf}})$	95.7 %
$\mathbb{E}(E_{NES_{inf}})$	96.1 %

8.3. 2 NES RBDO (α_1, α_2 , and \dot{x}_0). Comparison to 1 NES.

The final RBDO problem demonstrates the efficiency of a two NES system as compared to a single NES system. For the single NES problem, the nonlinear stiffness α of the NES and the initial velocity \dot{x}_0 are varied and the corresponding optimization problem is:

$$\begin{aligned} \max_{\mu_\alpha} \quad & \mathbb{E}(E_{NES_{inf}}(\mu_\alpha, \dot{x}_0)) \\ \text{s.t.} \quad & \mathbb{P}((\alpha, \dot{x}_0) \in \Omega) \leq 10^{-3} \\ & -2 \leq \log(\mu_\alpha) \leq 5 \quad 1 \leq \dot{x}_0 \leq 10 \end{aligned} \quad (9)$$

where $\log(\alpha)$ follows a normal distribution: $\log(\alpha) \sim N(\mu_{\log(\alpha)}, 0.21^2)$. The standard deviations correspond to 3% of the range of $\log(\alpha)$. $\dot{x}_0 \sim U(1, 10)$ and $\lambda_1 = \lambda_2 = 0.01$, $\varepsilon = 0.1$, and $\omega_1 = 5$. The two dimensional SVM is given in Figure 7a. The problem does not have a feasible solution with one NES. In fact, the minimum probability of failure is over 20%. The approximated $\mathbb{E}(\tilde{E}_{NES_{inf}})$ value at this point is 82.4%. The error metrics for the Kriging fits for this problem are given in table 5.

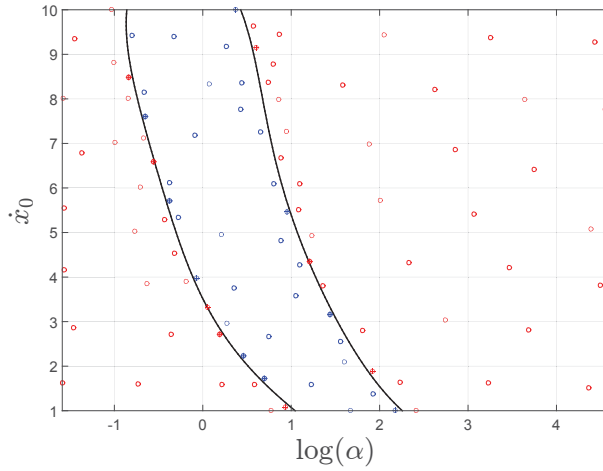


Figure 6: SVM for 1 NES problem varying α and \dot{x}_0 .

Table 5: One NES problem error metrics.

Approximation	RMAE	R^2
$\tilde{E}_{NES_{inf}}$	0.42	0.96
$\tilde{\beta}$	0.047	0.99

For the 2 NES case, the optimization problem becomes:

$$\begin{aligned} \max_{\mu_{\alpha_1}, \mu_{\alpha_2}} \quad & \mathbb{E}(E_{NES_{inf}}(\mu_{\alpha_1}, \mu_{\alpha_2}, \dot{x}_0)) \\ \text{s.t.} \quad & \mathbb{P}((\alpha_1, \alpha_2, \dot{x}_0) \in \Omega) \leq 10^{-3} \\ & -2 \leq \log(\mu_{\alpha_1}) \leq 5 \quad -2 \leq \log(\mu_{\alpha_2}) \leq 5 \quad 1 \leq \dot{x}_0 \leq 10 \end{aligned} \quad (10)$$

where $\log(\alpha_1)$ and $\log(\alpha_2)$ follow normal distributions: $\log(\alpha_1) \sim N(\mu_{\log(\alpha_1)}, 0.21^2)$ $\log(\alpha_2) \sim N(\mu_{\log(\alpha_2)}, 0.21^2)$. The standard deviations correspond to 3% of the range of $\log(\alpha)$, $\dot{x}_0 \sim U(1, 10)$, $\lambda_1 = \lambda_2 = \lambda_{21} = \lambda_{22} = 0.01$, and $\omega_1 = 5$. In addition, the mass of each NES is 5% (i.e., $\varepsilon_1 = \varepsilon_2 = 0.05$) of the main system total mass, adding to a total NES mass of 10%, which is the value used in the one NES problem. The three dimensional SVM approximation of the failure domain is depicted in Figure 7a. The SVM appears symmetric because the fixed NES parameters are identical for the two NESs. The approximation $\mathbb{E}(\tilde{E}_{NES_{inf}})$ and the training points are given in figure 7b. The error metrics for all Kriging approximations are given in Table 7. The $\tilde{\beta}$ approximation is given in Figure 8a. Finally, the RBDO results are given in Figure 8b and Table 6. The actual value of the probability of failure as calculated from the SVM is given in Table 6.

The two NES system gives a more robust optimum, successfully achieving a probability of failure of 10^{-3} . The $\mathbb{E}(\tilde{E}_{NES_{inf}})$ value is also larger in the two NES case. The distributions of $E_{NES_{inf}}$ over the \dot{x}_0 space for the optimal

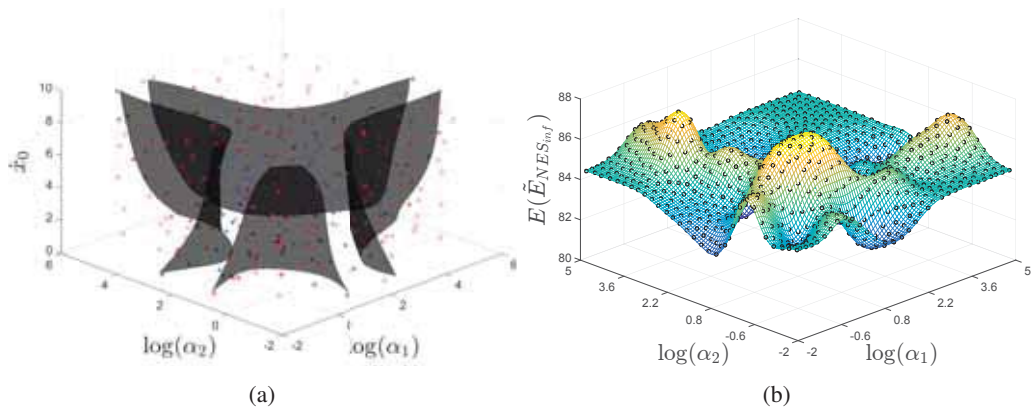


Figure 7: (a) Three dimensional SVM and (b) $\mathbb{E}(\tilde{E}_{NES_{mf}})$ approximation for two NES RBDO varying α_1 , α_2 , and \dot{x}_0 .

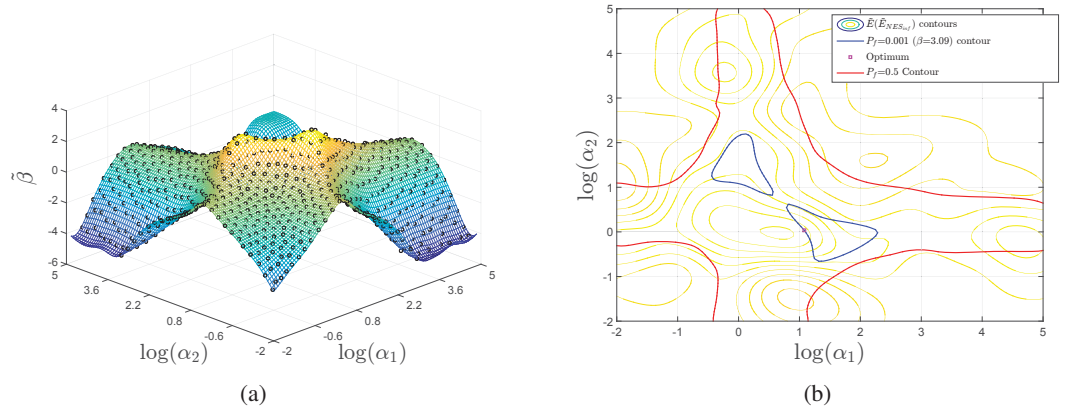


Figure 8: (a) β approximation and (b) RBDO results for two NES RBDO varying α_1 , α_2 , and \dot{x}_0

Table 6: Results table for 2 NES RBDO problem varying α_1 , α_2 , and \dot{x}_0 .

	Probabilistic Optimum
α_1	11.9
α_2	1.08
P_f from $\tilde{\beta}$	$1.00 * 10^{-3}$
P_f from SVM	$9.0 * 10^{-4}$
$\tilde{\mathbb{E}}(\tilde{E}_{NES_{mf}})$	90.3 %
$\mathbb{E}(E_{NES_{mf}})$	90.6 %

Table 7: Error metrics table for 2 NES RBDO problem varying α_1 , α_2 , and \dot{x}_0 .

Approximation	RMAE	R^2
$\tilde{E}_{NES_{mf}}$	0.00	0.99
$\tilde{\beta}$	0.080	0.99

NESs are given in figure 9. The two NES system has a higher $E_{NES_{mf}}$ value for most of the excitation range. The two NES system is more robust and the decline in $E_{NES_{mf}}$ is slower as \dot{x}_0 increases.

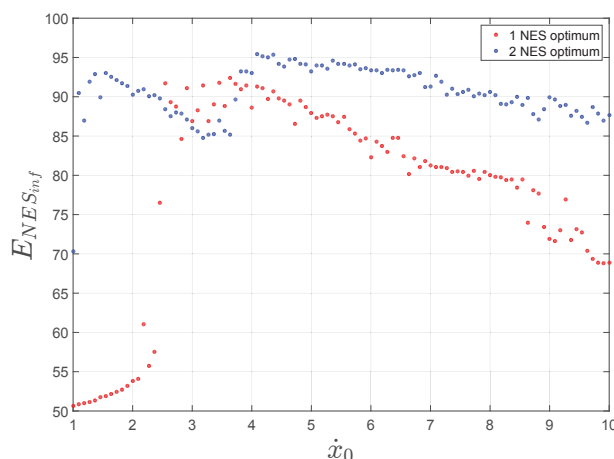


Figure 9: Variation of $E_{NES_{inf}}$ with respect to \dot{x}_0 for the optima found through RBDO of one and two NESs varying α and \dot{x}_0 .

9. Conclusion

This paper introduces a new methodology for the optimization under uncertainty of a Configuration II NES. The methodology stems from the realization that the efficiency of a NES might be discontinuous and highly sensitive to uncertainty. For this reason, specific tools such as SVM and clustering are used to perform the optimization and propagate uncertainty. In addition a one NES and a two NES system were compared. The two NES system is more robust and gives a higher expected performance than the one NES system with an equal total NES mass. The next steps of this research will continue to increase the dimensionality for both the single NES and the multi NES systems. A transition towards more realistic simulations will be explored, particularly through the use of finite element modeling.

10. References

- [1] A. Basudhar and S. Missoum. An improved adaptive sampling scheme for the construction of explicit boundaries. *Structural and Multidisciplinary Optimization*, pages 1–13, 2010.
- [2] E. Boroson, S. Missoum, P.-O. Mattei, and C. Vergez. Optimization under uncertainty of nonlinear energy sinks. In *ASME 2014 International Design Engineering Technical Conferences and Computers and Information in Engineering Conference*. American Society of Mechanical Engineers, 2014.
- [3] O. Gendelman, L. Manevitch, A. F. Vakakis, and R. M'closkey. Energy pumping in nonlinear mechanical oscillators: Part i: Dynamics of the underlying hamiltonian systems. *Journal of Applied Mechanics*, 68(1):34–41, 2001.
- [4] Y. S. Lee, A. F. Vakakis, L. A. Bergman, D. M. McFarland, and G. Kerschen. Enhancing the robustness of aeroelastic instability suppression using multi-degree-of-freedom nonlinear energy sinks. *AIAA journal*, 46(6):1371–1394, 2008.
- [5] S. Missoum, C. Dribusch, and P. Beran. Reliability-based design optimization of nonlinear aeroelasticity problems. *Journal of Aircraft*, 47(3):992–998, 2010.
- [6] T. A. Nguyen and S. Pernot. Design criteria for optimally tuned nonlinear energy sinkspart 1: transient regime. *Nonlinear Dynamics*, 69(1-2):1–19, 2012.
- [7] A. F. Vakakis. *Nonlinear targeted energy transfer in mechanical and structural systems*, volume 156. Springer Science & Business Media, 2008.
- [8] A. F. Vakakis, A. N. Kounadis, and I. G. Raftoyiannis. Use of non-linear localization for isolating structures from earthquake-induced motions. *Earthquake engineering & structural dynamics*, 28(1):21–36, 1999.
- [9] N. Wierschem, B. Spencer Jr, L. Bergman, and A. Vakakis. Numerical study of nonlinear energy sinks for seismic response reduction. In *Proceedings of the 6th International Workshop on Advanced Smart Materials and Smart Structures Technology (ANCRiSST 2011)*, pages 25–26, 2011.

Multi-Objective Topology Optimization of Composite Structures Considering Resin Filling Time

Yuqing Zhou¹, Kazuhiro Saitou²

¹ University of Michigan, Ann Arbor, USA, yuqingz@umich.edu

² University of Michigan, Ann Arbor, USA, kazu@umich.edu

1. Abstract

This paper presents multi-objective topology optimization of composite structures manufactured by resin transfer molding. The problem is formulated as minimizing both structural compliance and resin filling time. The empirical model of resin filling process is constructed by mining the results of numerical process simulations of massively sampled structural topologies within a fixed bounding box, using Random Forest statistical learning. Thanks to the abstract topology features inspired by underlying physics of the filling process, the resulting process model is far more generalizable than the traditional surrogate models based on, *e.g.*, bitmap and local feature representation, with no penalty in computation time. In particular, the model can reasonably be applied to the situations with the different inlet gate locations and initial bounding boxes from the training samples, while the traditional surrogate models completely fail in such situations.

Three case studies for composite structure topology optimization are discussed with different inlet gate locations and initial bounding boxes in order to demonstrate the robustness of the developed process model. The multi-objective topology optimization problem is solved by the Kriging-interpolated level-set approach and multi-objective genetic algorithm (MOGA). The resulting Pareto frontiers offer opportunities to select the designs with little sacrifice in structure performance, yet dramatically reduced resin filling time as compared to the structurally optimized design.

2. Keywords: Topology Optimization, Manufacturing Constraint, Composite Structure, Resin Transfer Molding (RTM), Resin Filling Time

3. Introduction

The gap between the output of computer-based structure topology optimization and the final component ready for manufacturing is still considered as a barrier for further adoption of topology optimization in industries. Practically, some modifications are applied to the component generated by topology optimization to improve its manufacturability, which usually requires empirical expert knowledge. Such practice, however, is likely to yield suboptimal solutions with respect to either structure performance (*e.g.* stiffness) or component manufacturability, due to the nonlinearity of both responses to the change of component topologies. To resolve this problem, the process simulation (*e.g.* sheet metal stamping [1], injection molding [2] and casting [3]) can be incorporated to topology optimization as a tool of evaluating component manufacturability during optimization. Since the finite element based process simulation is usually computationally expensive, surrogate models of sampled process simulations are usually used as a means for approximate evaluation of component manufacturability. Nevertheless, the lack of generalizability of the traditional surrogate models to samples not similar to the training set has severely limited their applicability in topology optimization, where component geometries can undergo dramatic changes during optimization process. To overcome this limitation, this paper presents the application of a new class of surrogate models of manufacturing processes for evaluating component manufacturability during topology optimization. The model for resin filling process in resin transfer molding of composites is built using the data-driven manufacturing constraint modeling (MCM) [4] we previously developed. The model is trained with resin filling simulations of massive sampled topologies and statistical learning regression model. Thanks to the abstract topology features inspired by underlying physics of the filling process, the resulting process model is far more generalizable than the traditional surrogate models.

Resin transfer molding (RTM) is a closed mold manufacturing process of fiber reinforced composite materials. Due to the requirement of lightweight structures in automotive and aerospace industries, it has become a promising economic solution for components made of polymer composite materials. The mass production of BMW i3 (2013) whose body structures are made of carbon fiber composite with RTM process, is an example of its recent application in automotive industry. The design of RTM component is currently a challenge due to the lack of empirical experience and design for manufacturing (DFM) guidelines which are available to the components made by traditional manufacturing processes such as sheet metal stamping. The potential manufacturability issues of RTM process could be preform deformation due to compaction [5] and draping [6], racetracking [7], void formation [8], etc. In the early exploration of composite structure topologies, the resin filling time is a critical manufacturability concern which affects the product lead time, especially for mass production automotive applications. Figure 1 shows an example of two composite structures with the identical volume, material properties

and process parameters, but a large difference in resin filling time, due to the topology difference.,

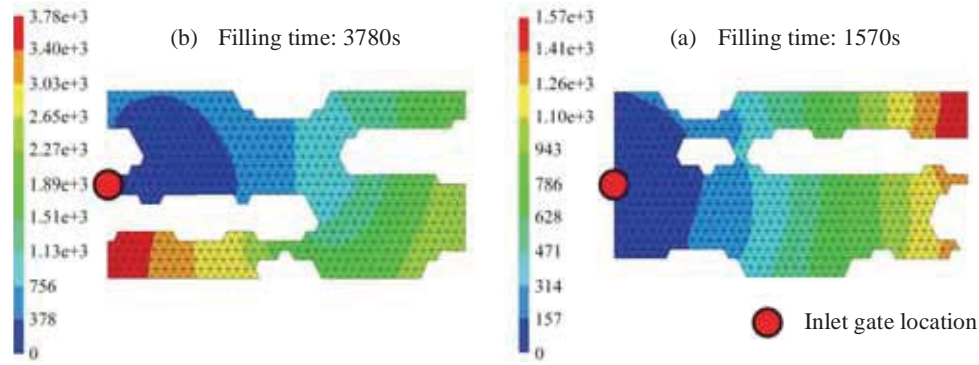


Figure 1 Examples of the non-efficient filling topology (a: 3780s) and the efficient filling topology (b: 1570s).

The rest of the paper is organized as following. Section 4 reviewed the related works on manufacturing constraint in computer-based structure optimization. Section 5 presented the data-driven predictive modeling of composite resin filling time. Section 6 discussed the result of three topology optimization case studies with the trained process model. Finally, section 7 summarized the current study and opportunities for future works.

4. Related Works

In order to improve the manufacturability of components generated by the computer-based structure optimization, many types of manufacturing constraints have been incorporated into the structure optimization loop. Several researchers proposed the algorithms to control minimum member size [9-11] and maximum length scale [12] in topology optimization. As a result, the designer gained control over member sizes which could influence the component manufacturability and cost. As for manufacturing constraints tailored for specific manufacturing processes, Harzheim *et al.* [13] developed the program TopShape to enforce casting manufacturing constraint for structure topology optimization. Zhou *et al.* [14] added the empirical sheet metal stamping manufacturing cost objective to the multi-component topology optimization. Nadir *et al.* [15] considered the manufacturing cost model of abrasive water jet process for the shape optimization. Zuo *et al.* [16] added the machining constraints to generate manufacturable topologies. Edke *et al.* [17] incorporated virtual machining simulation into the shape optimization of heavy load carrying components to ensure the manufacturability of the structurally optimized result.

As for the composite structure, Boccard *et al.* [18] proposed a semi-analytic model to determine the resin filling time of the preforms with isotropic permeability. In addition, Park *et al.* [19] applied the model to the composite structure optimization problem with both mechanical performance and manufacturing cost objectives. Kaufmann *et al.* [20] and Lee *et al.* [21] used the software SEER-MFG to estimate the manufacturing cost of resin transfer molding component and added it to the composite structure design process. Gantois *et al.* [22] combined the manufacturing cost with the initial multidisciplinary design optimization framework of minimum weight and maximum aerodynamic efficiency for the civil aircraft application.

However, the manufacturing process models used in these works are usually overly-simplified and tend to be conservative, in order to keep the model generalizability. We resolve it by using more accurate process simulations to evaluate structure manufacturability, and data driven predictive models to generalize the knowledge.

5. Data-Driven Composite Resin Filling Time Predictive Modeling

This section briefly summarizes the composite resin filling time predictive modeling process. The model is trained with massive process simulations and data mining of topology abstract feature representation inspired by underlying physics of the filling process. For detailed explanation, please refer to our previous work on predictive modeling of resin filling time of composite molding process [23].

5.1 Data Generation

Within the initial $2m \times 1m$ bounding box (see Figure 2), 50000 random topologies are generated by Kriging level-set method [24] and labeled by their resin filling time, simulated by PAM-RTM (ESI Group). The material fraction volume, the fraction of the volume of structural materials to that of the whole bounding box is set as 0.7. The preform permeability is assumed isotropic and set as $1.0e - 9 m^2$, the thickness as $1.0e - 3 m$ and the porosity as 0.5. The inlet pressure is $1.0e5 Pa$. As a result, the training set D_0 can be summarized as Eq.(1) below:

$$D_0 = \{x_i, y_i | i = 1, 2, \dots, n\}, \quad (1)$$

where:

x_i : binary bitmap representation of topology i ;
 $x_{ij} = 0$ if void and $x_{ij} = 1$ if filled (j : number of element in the bounding box);
 y_i : resin filling time simulation result of topology i ;
 n : number of training samples (= 50000 in this case).

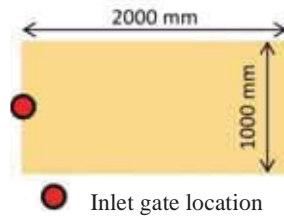
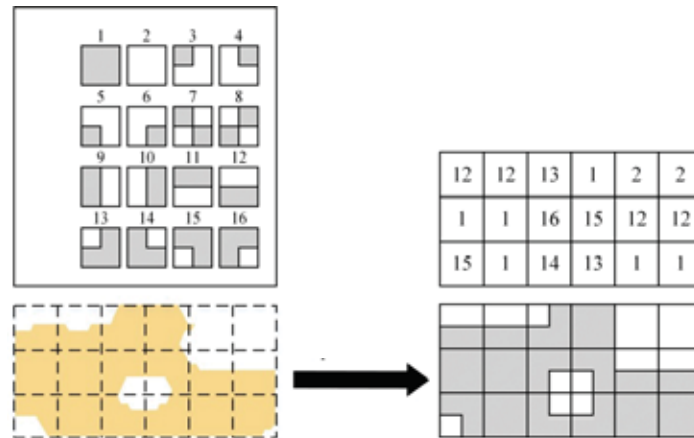


Figure 2 Bounding box for process simulation data generation.

5.2 Knowledge-Inspired Feature Representation

The performance of the predictive model depends on the quality of input features. The generalizability of the model also depends on how the topologies are represented. It is straightforward that the process model can be trained on the topology bitmap representation shown in Eq.(1). However, since the dimension of feature input is fixed as the number of elements in the initial bounding box, it is not scalable to problems with different number of element. In addition, the number of element is usually large which also poses challenges to the predictive model training process.

To resolve the scalability issue, the topology local feature representation is proposed. Figure 3 shows an example of topology local feature representation. The bounding box is divided into pieces of squared patches, each of which is matched with a member of the pre-defined feature basis by calculating the minimum Euclidean distance. As a result, the topology is represented as a vector of 18 elements. To transform the bitmap representation to local feature representation, the dimension of the input attribute reduces dramatically and no longer sensitive to the element size. However, the topology local feature representation is still not generalizable to test samples with different initial bounding box (therefore different number of patches) and different inlet gate location.



To further resolve the generalizability issue, the knowledge-inspired feature representation is proposed, which is inspired by the underlying physics of filling. An example of topology knowledge-inspired feature representation is shown in Figure 4, which consists of three major steps described below:

- 1) The flow through porous medium is governed by the Darcy's law which states that the flow rate per unit area is proportional to the pressure gradient. The relatively small preform area, especially at the beginning of the flow, leads to dramatically reduction of resin pressure. Therefore, to capture this phenomenon, the material fraction volume (M) in each segment along the major flow route is calculated (upper right of Figure 4);
- 2) The length of the overall flow route also has great influence on the composite resin filling time. To capture that information, the skeleton of the initial topology is extracted using image processing thinning algorithm [25]. Then run the flood filling [26] simulation over the topology skeleton, starting at the point closest to the inlet gate location, and calculate the step count to finish the filling, defined as N (lower left of Figure 4);
- 3) The initial topology bitmap is then transformed to the local feature representation. Based on a pre-defined critical patch pool, the search of critical patch with different sliding window size results in a sparse vector C , explained in Eq.(2) below:

$$C = [c_1, c_2, \dots, c_q], \quad (2)$$

where:

- $c_i = 0$, if critical patch i not in topology;
- $c_i = 1$, otherwise;
- q : number of selected critical patches.

The critical patch pool is selected according to the filter-based feature selection criterion, Fisher score [27], inspired by the physics of flow that the resin filling time is effected by undesired local geometric patterns (lower right of Figure 4).

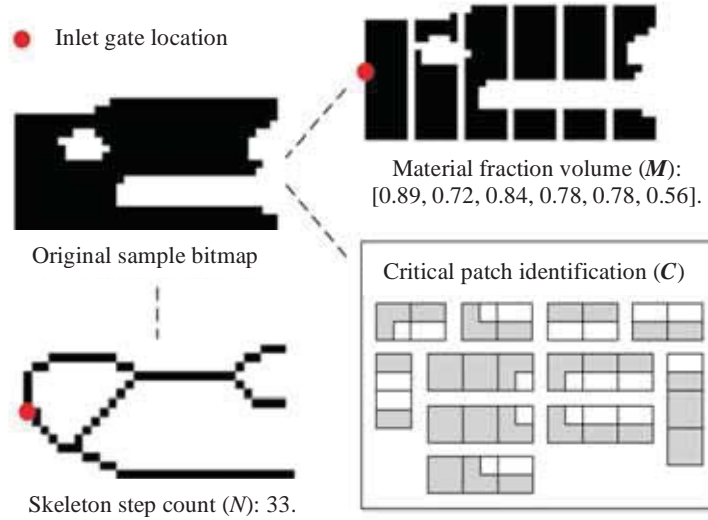


Figure 4 An example of knowledge-inspired topology feature representation.

The proposed knowledge-inspired feature representation is a more general topology representation for mold flow applications. Different from the bitmap and local feature representation, it is not sensitive to the number of element or the number of patch segment in the bounding box. In addition, it provides valuable information when the inlet gate location changes. Therefore, the trained predictive model is expected to be more generalizable to topologies not similar to the training set. Three topology optimization cases will be discussed in section 6 to test the process model robustness.

5.3 Random Forest Regression Model

After data generation and topology knowledge-inspired feature representation, the resulting transformed training set $D^{(t)}$ is summarized as Eq. (3) below:

$$D^{(t)} = \{ \mathbf{x}_i^{(t)}, y_i | i = 1, 2, \dots, n \}, \quad (3)$$

where:

- $\mathbf{x}_i^{(t)}$: knowledge-inspired feature representation of topology i , $\mathbf{x}_i^{(t)} = [\mathbf{M}, \mathbf{C}, N]$;
- y_i : resin filling time simulation result of topology i ;
- n : number of training samples (= 50000 in this case).

Since the input feature set is a mixture of continuous and discrete variables, the Random Forest [28] regression model is applied to the training set $D^{(t)}$ to build the resin filling time predictive model. The current model uses 50 trees with the minimum leaf size of 20 as the tuning parameters. In our previous study [23], the trained regression model was tested to be generalizable to testing samples with different inlet gate locations and initial bounding box, while the other two surrogate models trained on bitmap and local feature representations failed.

6. Topology Optimization considering Composite Resin Filling Time

The resulting manufacturing process model from section 5 is applied to the compliance minimization topology optimization problem. The multi-objective optimization problem is formulated as minimizing both structure compliance and resin filling time, summarized in Eq. (4) below:

$$\begin{aligned} \min: & f_1(\mathbf{x}), f_2(\mathbf{x}) \\ \text{s. t.} & V(\mathbf{x}) = V_0, \end{aligned} \quad (4)$$

where:

- $f_1(\mathbf{x})$: structure compliance, obtained by finite element calculation;

$f_2(\mathbf{x})$: resin filling time, predicted by the trained manufacturing process model from section 5;

$V(\mathbf{x})$: material fraction volume, set as $V_0 = 0.7$.

Since there is no known analytical sensitivity information for the random forest decision tree model, multi-objective genetic algorithm (MOGA) and Kriging level-set (KLS) [24] are used to alleviate the need for objective gradients and dramatically reduce the number of design variables. The dimension of the design variable vector \mathbf{x} depends on the number of knot points which is independent from the mesh size. The Pareto frontier results of three test cases are generated (GA settings: 500 generations, 1000 populations per generation). The plotted objective values are normalized by the minimum value of each objective respectively. The selected non-dominated Pareto results' resin filling time responses are validated by process simulations to demonstrate the accuracy and robustness of the trained manufacturing process model.

6.1 Test Case 1: Short Cantilever

Test 1 has the identical bounding box and inlet gate location setting as the manufacturing process model training data generation, known as the *in-the-bag* test. Figure 5 below shows the support and load conditions of the short cantilever problem and its Pareto frontier result. The normalized compliance and resin filling time objective values for five selected non-dominated Pareto frontier points (green dots in Figure 5) are summarized in Table 1. The result shows a clear trade-off between the structure compliance and resin filling efficiency.

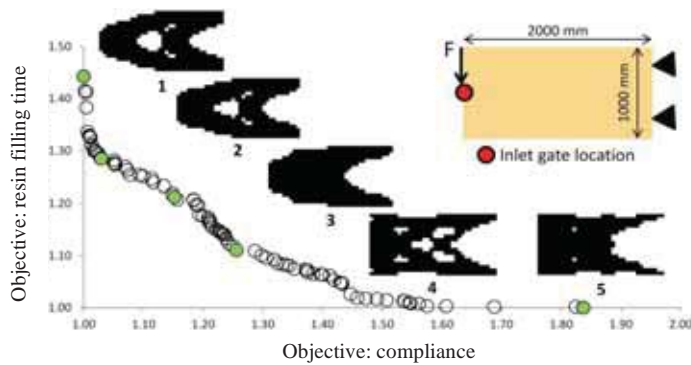


Table 1 Objective values of selected Pareto frontier points in test case 1.

Topology	Compliance	Filling Time
1	1.00	1.44
2	1.03	1.28
3	1.15	1.21
4	1.26	1.11
5	1.84	1.00

Figure 5 Pareto frontier result for test case 1.

While traditional surrogate models would produce high quality approximations for such *in-the-bag* tests, the proposed data-driven model also performs excellently. To validate the manufacturing process model output, the five selected topologies' resin filling time simulation results are shown in Figure 6. The simulation validation results are consistent with the predictive model outputs. As a result, if topology 2 is selected as the optimized result with both compliance and resin filling time as objectives, compared with the structurally optimized result (topology 1), it reduces the resin filling time of 4.8% (1499.75s to 1427.79s) and sacrifices the structure compliance of 2.9% (49.66 to 48.25).



6.2 Test Case 2: Bridge

The same resin filling time manufacturing process model is also applied to another topology optimization problem with different inlet gate location as the process model training set, known as the *out-of-bag* test. It is a “bridge” problem with two-point support and mid-span load. The inlet gate location is set in the center of the structure. The resulting Pareto frontier is shown in Figure 7. The objective values for selected non-dominated points (green dots in Figure 7) are summarized in Table 2.

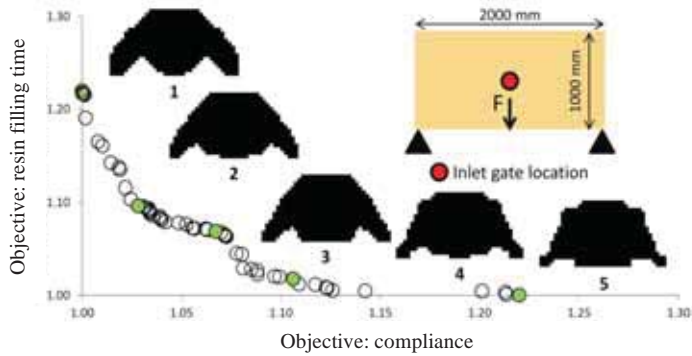
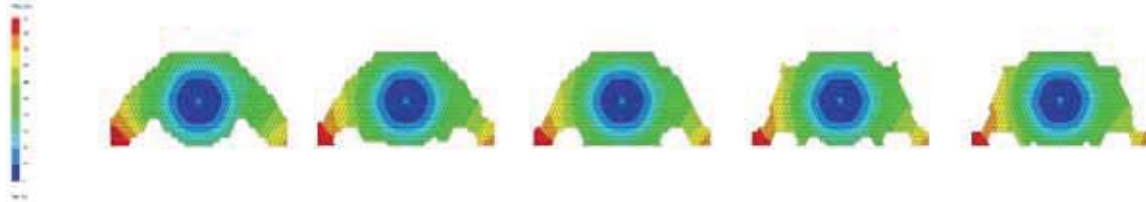


Table 2 Objective values of selected Pareto frontier points in test case 2.

Topology	Compliance	Filling Time
1	1.00	1.22
2	1.03	1.10
3	1.07	1.07
4	1.11	1.02
5	1.22	1.00

Figure 7 Pareto frontier result for test case 2.

The filling simulation result of selected Pareto points is shown in Figure 8. Though the predictive performance of out-of-bag topologies in case 2 is not as accurate as that of in-the-bag topologies in case 1, the simulation result is still consistent in terms of ranking as the process model output. It should be noted that traditional surrogate models would fail to provide reasonable approximations in this case since the gate location is different from that of the training set. As a result, if topology 2 is selected as the multi-objective optimized structure, compared with the structurally optimized result (topology 1), it reduces the resin filling time of 6.7% (410.53s to 382.85s) and sacrifices the structure compliance of 2.9% (6.93 to 7.13).



6.3 Test Case 3: Long Cantilever

Similarly, another out-of-bag test with different initial bounding box is conducted to further demonstrate the process model robustness. As discussed in section 5, while the traditional surrogate models cannot be applied due the change of input feature dimension, the proposed process model trained by more general features is still valid. The Pareto frontier result for test case 3 is presented in Figure 9. The objective values for selected non-dominated points (green dots in Figure 9) are summarized in Table 3.

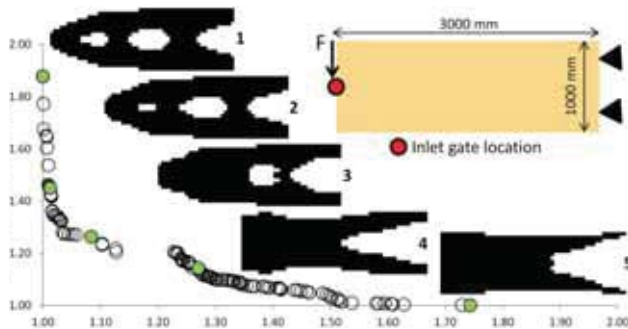


Table 3 Objective values of selected Pareto frontier points in test case 3.

Topology	Compliance	Filling Time
1	1.00	1.88
2	1.01	1.45
3	1.08	1.26
4	1.27	1.14
5	1.74	1.00

The filling simulation result of selected Pareto points for test case 3 is shown in Figure 10. The simulation result is consistent in terms of ranking as the process model output. As a result, compared with the structurally optimized topology (topology 1), if topology 2 is selected as the multi-objective optimized result, it reduces the resin filling time of 6.0% (3466.09s to 3258.48s) and sacrifices the structure compliance of 1.3% (141.29 to 143.09).

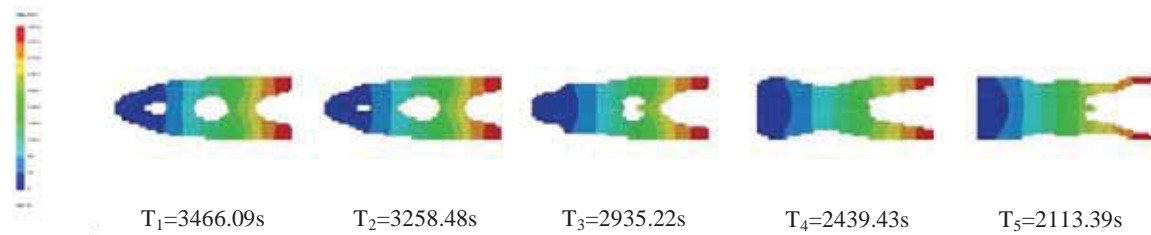


Figure 10 Resin transfer molding simulation validation result for selected Pareto frontier points in case 3.

According to the result of three multi-objective topology optimization test cases above, the resin filling time process model trained on features inspired by underlying physics of filling provides consistent topology filling efficiency approximation for both in-the-bag and out-of-bag tests. The model applicability to testing samples not similar to the training set demonstrates its better generalizability than traditional surrogate models which usually struggle in out-of-bag tests.

7. Discussion

This paper applies the resin filling time manufacturing process model to the compliance minimization topology optimization problem to identify topologies with improved manufacturability, yet minimum structure performance sacrifice, compared with the structurally optimized result. The scalability and generalizability of the data-driven process model is validated by three topology optimization test cases. The model applicability to samples not similar to the training set resolves the key limitation of traditional surrogate models. As of the future works, other topology representations can be studied to further improve the model predictive accuracy and generalizability. Several current assumptions should be relaxed including fixed material fraction volume and isotropic permeability of the preform. In addition, the data-driven manufacturing constraint modeling (MCM) can also be applied to other manufacturing processes (see, for example, sheet metal stamping application in reference [4]) to improve the manufacturability of components generated by computer-based structure optimization.

8. Acknowledgements

This work was supported by the U.S. Department of Energy (DOE) under Award Number DE-PI0000012, through the Clean Energy Research Center - Clean Vehicle Consortium.

9. References

- [1] Tekkaya, A. E., 2000, "State-of-the-Art of Simulation of Sheet Metal Forming," *Journal of Materials Processing Technology*, **103**(1), pp. 14-22.
- [2] Chang, R. Y., and Yang, W. H., 2001, "Numerical Simulation of Mold Filling in Injection Molding Using a Three-Dimensional Finite Volume Approach," *International Journal for Numerical Methods in Fluids*, **37**(2), pp. 125-148.
- [3] Vijayaram, T. R., Sulaiman, S., Hamouda, A. M. S., and Ahmad, M. H. M., 2006, "Numerical Simulation of Casting Solidification in Permanent Metallic Molds," *Journal of Materials Processing Technology*, **178**(1-3), pp. 29-33.
- [4] Zhou, Y., and Saitou, K., 2014, "Identification of Manufacturability Constraints through Process Simulation and Data Mining," *ASME 2014 International Design Engineering Technical Conferences and Computers and Information in Engineering Conference*.
- [5] Chen, B. X., Lang, E. J., and Chou, T. W., 2001, "Experimental and Theoretical Studies of Fabric Compaction Behavior in Resin Transfer Molding," *Materials Science and Engineering a-Structural Materials Properties Microstructure and Processing*, **317**(1-2), pp. 188-196.
- [6] Bickerton, S., Simacek, P., Guglielmi, S. E., and Advani, S. G., 1997, "Investigation of Draping and Its Effects on the Mold Filling Process During Manufacturing of a Compound Curved Composite Part," *Composites Part a-Applied Science and Manufacturing*, **28**(9-10), pp. 801-816.
- [7] Bickerton, S., and Advani, S. G., 1999, "Characterization and Modeling of Race-Tracking in Liquid Composite Molding Processes," *Composites Science and Technology*, **59**(15), pp. 2215-2229.
- [8] Kang, M. K., Lee, W. I., and Hahn, H. T., 2000, "Formation of Microvoids During Resin-Transfer Molding Process," *Composites Science and Technology*, **60**(12-13), pp. 2427-2434.
- [9] Zhou, M., Shyy, Y. K., and Thomas, H. L., 2001, "Checkerboard and Minimum Member Size Control in Topology Optimization," *Structural and Multidisciplinary Optimization*, **21**(2), pp. 152-158.
- [10] Poulsen, T. A., 2003, "A New Scheme for Imposing a Minimum Length Scale in Topology Optimization," *International Journal for Numerical Methods in Engineering*, **57**(6), pp. 741-760.
- [11] Guest, J. K., Prevost, J. H., and Belytschko, T., 2004, "Achieving Minimum Length Scale in Topology Optimization Using Nodal Design Variables and Projection Functions," *International Journal for Numerical*

Methods in Engineering, **61**(2), pp. 238-254.

[12] Guest, J., 2009, "Imposing Maximum Length Scale in Topology Optimization," *Structural and Multidisciplinary Optimization*, **37**(5), pp. 463-473.

[13] Harzheim, L., and Graf, G., 2006, "A Review of Optimization of Cast Parts Using Topology Optimization - Ii - Topology Optimization with Manufacturing Constraints," *Structural and Multidisciplinary Optimization*, **31**(5), pp. 388-399.

[14] Zhou, Z. B., Hamza, K., and Saitou, K., 2014, "Decomposition Templates and Joint Morphing Operators for Genetic Algorithm Optimization of Multicomponent Structural Topology," *Journal of Mechanical Design*, **136**(2).

[15] Nadir, W., Kim, I. Y., and De Weck, O. L., 2004, "Structural Shape Optimization Considering Both Performance and Manufacturing Cost," 10th AIAA/ISSMO Multidisciplinary Analysis and Optimization Conference, Albany, NY, **30**.

[16] Zuo, K. T., Chen, L. P., Zhang, Y. Q., and Yang, J. Z., 2006, "Manufacturing- and Machining-Based Topology Optimization," *International Journal of Advanced Manufacturing Technology*, **27**(5-6), pp. 531-536.

[17] Edke, M. S., and Chang, K. H., 2006, "Shape Optimization of Heavy Load Carrying Components for Structural Performance and Manufacturing Cost," *Structural and Multidisciplinary Optimization*, **31**(5), pp. 344-354.

[18] Boccard, A., Lee, W. I., and Springer, G. S., 1995, "Model for Determining the Vent Locations and the Fill Time of Resin Transfer Molds," *Journal of Composite Materials*, **29**(3), pp. 306-333.

[19] Park, C. H., Lee, W. I., Han, W. S., and Vautrin, A., 2004, "Simultaneous Optimization of Composite Structures Considering Mechanical Performance and Manufacturing Cost," *Composite Structures*, **65**(1), pp. 117-127.

[20] Kaufmann, M., Zenkert, D., and Wennhage, P., 2010, "Integrated Cost/Weight Optimization of Aircraft Structures," *Structural and Multidisciplinary Optimization*, **41**(2), pp. 325-334.

[21] Lee, M., Ceisel, J., Liu, Z., and Mavris, D., 2012, "A Parametric, Preliminary Structural Analysis and Optimization Approach with Manufacturing Cost Considerations," 53rd Structures, Structural Dynamics, and Materials and Co-located Conferences, Honolulu, HI.

[22] Gantois, K., and Morris, A. J., 2004, "The Multi-Disciplinary Design of a Large-Scale Civil Aircraft Wing Taking Account of Manufacturing Costs," *Structural and Multidisciplinary Optimization*, **28**(1), pp. 31-46.

[23] Zhou, Y., and Saitou, K., 2015, "Data-Driven Predictive Model of Resin Filling Time of Composite Molding Process," ASME 2015 International Design Engineering Technical Conferences and Computers and Information in Engineering Conference, Boston, MA.

[24] Hamza, K., Aly, M., and Hegazi, H., 2014, "A Kriging-Interpolated Level-Set Approach for Structural Topology Optimization," *Journal of Mechanical Design*, **136**(1).

[25] Lam, L., Lee, S. W., and Suen, C. Y., 1992, "Thinning Methodologies - a Comprehensive Survey," *Ieee Transactions on Pattern Analysis and Machine Intelligence*, **14**(9), pp. 869-885.

[26] Soille, P., 1999, *Morphological Image Analysis : Principles and Applications*, Springer, Berlin ; New York.

[27] Duda, R. O., Hart, P. E., and Stork, D. G., 2001, *Pattern Classification*, Wiley, New York.

[28] Breiman, L., 2001, "Random Forests," *Machine Learning*, **45**(1), pp. 5-32.

Future challenges for topology optimization for the usage in automotive lightweight design technologies

**Sierk Fiebig¹, Jürgen Sellschopp², Holger Manz³, Thomas Vietor⁴,
Joachim K. Axmann⁵, Axel Schumacher⁶**

¹ Volkswagen AG, Braunschweig, Germany, sierk.fiebig@volkswagen.de

² Volkswagen AG, Braunschweig, Germany, juergen.sellschopp@volkswagen.de

³ Volkswagen AG, Braunschweig, Germany, holger.manz@volkswagen.de

⁴ Institute for Engineering Design, Technische Universität Braunschweig, Braunschweig, Germany,
t.vietor@tu-braunschweig.de

⁵ Institute for Engineering Design, Technische Universität Braunschweig, Braunschweig, Germany,
j.axmann@tu-braunschweig.de

⁶ Chair for Optimization of Mechanical Structures, University of Wuppertal, Germany,
schumacher@uni-wuppertal.de

1. Abstract

Nowadays the development of mechanical components is driven by ambitious targets. Engineers have to fulfill technical requirements simultaneously under the restrictions of minimized costs and reduced weight for mechanical components. Accordingly in the last years newly developed and tested optimization methods have been integrated in the development processes of industrial companies. Today, especially topology optimization methods are gaining in importance and are often used for the first design proposal of casting parts.

However, these design proposals must be interpreted and transferred to CAD-models by design engineers and in later development phases manufacturing aspects must be considered. Both steps need more development time and normally material must be added to the design ideas. Beside castings parts, topology optimization is only a little help for the design of sheet structures, because framework structures are the result. Also crash and acoustic requirements cannot be completely supported by optimization methods.

Beginning with the current situation four challenges for further work can be formulated. First the technical aspects like crashworthiness and acoustic requirements should be implemented into the topology optimization. The second future path focus on sheet structures and hybrid parts. With new manufacturing rules, the result of the topology optimization should only consist of thin and plane orientated material. As an extension, structures with more than one sheet should be possible in the future. The costs of needed welding seams must be considered. The third challenge is the integration of manufacturing simulation. By including a casting simulation for example, each iteration of a topology optimization can be analyzed to the castability. By modifications of the design, beside the mechanical needs also casting aspects will be recognized.

The last future path treats a continuous and integrated development process. For this target, the CAE description of the topology results must be smoothed and automatically transferred to CAD models, which fulfills the design methodology in order to allow easy modifications.

2. Keywords: Topology optimization, integrated casting simulation, multimaterial optimization, sheet structures, CAE2CAD process

3. Introduction

Today several approaches are in use for topology optimizations. The starting point for FEM based topology optimization can be found in literature in [1]. Bendsøe introduced his homogenization method first [2]. Parallel to the homogenization method, Bendsøe presented the SIMP approach (Solid Isotropic Microstructure with Penalization) [3]. This method gained popularity because other researchers applied it to their work [4]. Today the SIMP approach is a standard method for topology optimizations. For example, the commercial tool Tosca[®] from FE-Design [5] is based on SIMP. SIMP uses the element densities as continuous design variables. The coupled stiffness values of the elements transfer the modifications of the optimization to the structure results. At the end of each topology optimization run, a discrete distribution of material for the interpretation of the results is needed. For this reason, the SIMP approach penalizes intermediate density values using a penalization factor to assign lower stiffness values to these elements [13]. SIMP is combined with gradient algorithms, e.g. the method of moving asymptotes [7].

Since 1992 two other important approaches have been developed and published: ESO/BESO and the SKO method. The Evolutionary Structural Optimization (ESO) is focused to remove unnecessary material from too conservatively designed parts [8]. For ESO, it is only possible to remove material. A binary element modeling is in

use in comparison to SIMP [9]. To enable material growth, Querin introduced the Additive Evolutionary Structural Optimization method (AESO) [10]. AESO adds material to areas in order to improve the structure. The combination of ESO and AESO leads to the Bidirectional Evolutionary Structural Optimization [BESO] method [8, 9, 12]. The main idea behind ESO, AESO and BESO is to remove lowly stressed elements and adding material to higher stressed regions. To designate these elements, a so called “reference level” is defined. Elements below the reference level are removed from the structure. In the surrounding of elements with higher stresses then the reference level, material is added. During the optimization this level is adapted to the optimization progress. BESO uses here - depending on the individual approaches - direct, gradient or interpolated information about material properties to change the structure [9]. Due to these facts, for ESO/BESO the compliance-volume product can be assumed as an objective function [6].

The Soft Kill Option method (SKO method) was introduced by Mattheck, Baumgartner and Hartzheim in [13]. Inspired by the growth of trees and bones, the biological growth rule was formulated. In highly stressed areas material can be added and in lowly stressed areas material will be removed. Homogeneous and constant stresses should be generated especially at the surface of the structure. To change the structure, the SKO method modifies the Young Modulus of the FEM-elements as a function of the temperature. High temperature indicates high Young Modulus and low temperature causes low Young Modulus [11, 13, 14, 15].

The SIMP method in combination with gradient algorithms achieved a widely-used application in industry. The main reason for the success of the approach is the integration of manufacturing restrictions [16, 17, 18]. Without manufacturing restrictions, it is impossible in most cases to get a feasible design for real life problems. Today nearly no suggestions for the integration of manufacturing restriction for BESO and the SKO method have been published. Only for SKO a further development, called Topshape[®], which offers manufacturing restrictions, has been published [19].

4. The basic approach of the topology optimization

The new approach for topology optimization is designed for industrial purposes. Taking into consideration, for engineering and daily work, the optimization focus is on the improvements of existing results instead of searching for global optima. The main targets are costs and weights of the parts. In the development of casting parts, a reduction of weight is coupled with a reduction of material costs. So it is consequent to use the weight as target function. Additional important aspects are the necessary time and costs in the development process. To achieve this and to improve the general usage, linear and nonlinear FEM analysis should be combined with the new topology optimization method. Nonlinear effects can be found for example in plastic material behavior as well as by bushings and by contact problems. Finally the last point, manufacturing requirements need to be fulfilled [20, 21].

The flow chart in figure 1 illustrates the main steps of this new topology optimization method. A step size controller calculates first a basic rate. Depending on this basic rate, the numbers of removing and adding elements are defined for the modification of structural elements. According to the added element, hotspot areas are corrected. After this correction process, the lowest stress elements depending on the reduction rate are removed. After adding and removing elements, the structure will be checked to insure it is connected: all force transmission points must be connected to the support elements. If this check fails, the controller modifies the correction and reduction rate in order to produce a feasible structure. During the heuristic steps, non-connecting elements are removed from the structure. The interface routines for the FEM solver are integrated in the optimization software. After finishing all changes and checks, the optimizer writes the solver specific input decks with all active elements and coupled nodes. After the FEM analysis, the post-processing evaluates all target functions and constraints. An interface transfers this information to the controller.

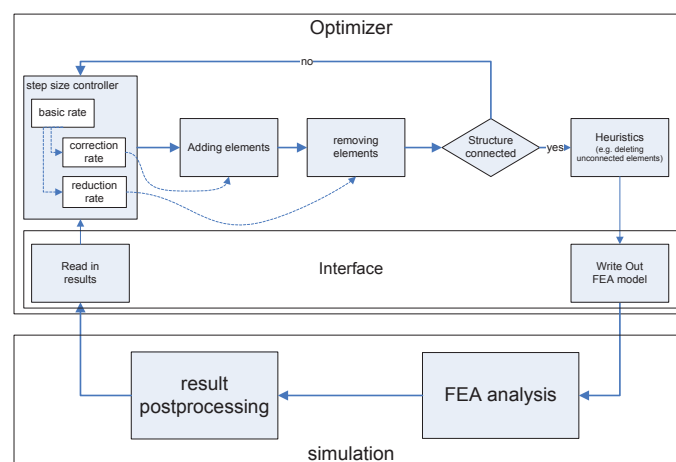


Figure 1: Flow chart of basic Topology Optimization Method

The step size controller is an important element of this new method. The main idea is to control the target function “weight” by using the progress of the constraints during the optimization. In the first step, the basic rate is modified. In a second step the reduction and correction rate are calculated depending on the basic rate to vary the structure.

The basic principle is simple. A smooth increase or decrease of the constraint function allows the removal of more elements up to the allowed maximum. In the other case, when the constraint increases, the step size is reduced, allowing only a limited number of elements to be removed but more hotspots have to be fixed. When a structure violates the maximum allowed constraint limit two times one after another interaction, the step size has to be reduced significantly: no elements are removed. In such a situation it is only allowed to add new elements to the structure. This is based on a simple heuristic from an engineer’s knowledge.

Figure 2 describes the change of the basic rates dependent on the possible events and the coupling between basic rate, correction and reduction rate. High basic rates allow high reductions and less corrections will be necessary. For basic rates from 0.1 to 0, fewer reductions should be carried out. When the basic rate tends to zero, more corrections are needed. Only corrections will be done in case of a basic rate lower than zero [20].

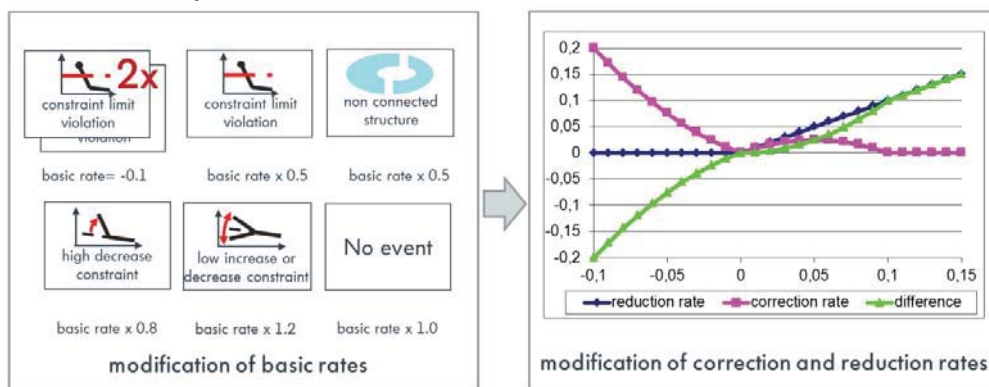


Figure 2: Step size controller modifications on the basic rates cause variations on correction and reduction rates

After the calculation of the step sizes for corrections and reductions, the structure will be modified. To avoid problems in the FEM-simulation only binary states of the material are allowed: material is solid or not available. This binary material modeling allows only a switch between both states. Similar to ESO/BESO and the biological growth rule, material will be added at the highest stress values and removed at the lowest stressed regions. In figure 3 the process is illustrated. Instead of any calculated derivations of properties to generate gradients, the stress values of the structure will be sorted in descending order. Using the step size for corrections, the neighbor elements next to the highest stress values will be added to the structure and the elements with the lowest stress values according to the reduction rate will be directly removed from the structure.

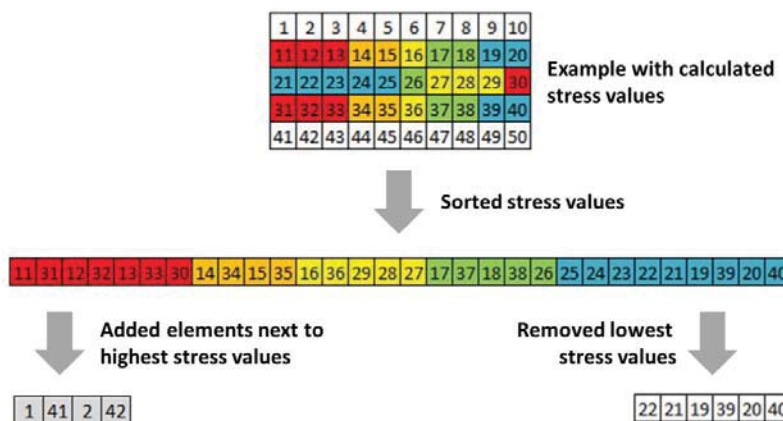


Figure 3: Modifications of an example structure by adding and removing elements by calculated stress values

The integration and implementation of the FEM simulation can be done very easily. No special material model without mayor modifications and programming work must be integrated into the code. The input deck for the FEM simulation is identical to an input deck for single simulation of a design. The interface of the optimizer writes a standard input deck of all existing elements. No removed elements will be written out. Due to this fact all FEM solvers can be used. For the simulation of the examples in this paper, Abaqus® has been used [22]. Linear,

nonlinear and explicit simulations can be performed with Abaqus® [23, 24] based on the theory of the FEM [25, 26]. Using the integrated scripting procedures the stress values and constraints will be extracted to files. The optimizer starts the next optimization loop based on the information from these files.

5. Necessary additional technical requirements

The topology optimization presented in chapter 4 gives the possibility to fulfill all requirements for stress constraints and misuse requirements. However the design for crashworthiness of vehicles has additional specific requirements: geometry (e.g. large displacements and rotations), boundary condition (e.g. contact) and material (e.g. plasticity, failure and strain rate dependency) [27]. Usually crash simulations are performed with Finite Element Method codes which can handle the nonlinearities by using explicit time integration. These explicit simulations are right now integrated in the topology optimization presented in chapter 4 [28]. For the further development of the approach, the optimization algorithm must be extended to handle the specific crash requirements like the existence of bifurcation points, the usage of special structural responses like energy absorption and injury criteria. The huge number of local optima make the optimization of crashworthiness structures even more complex. The conflicting goals of stiffness for structural integrity and compliance for a smooth and controlled energy absorption are important parts of the crashworthiness of vehicles.

Also acoustic requirements are not yet implemented in the current optimization tool. With regard to acoustics the research code *elementary Parallel Solver – ePaSo* developed at the *Institute for Engineering Design, Technische Universität Braunschweig* can be used to predict the acoustical parameters. The code ePaSo can run in parallel on distributed systems on multiple platforms and in multiple architectures. It is based on the Finite Element Method, the Boundary Element Method, the Scaled Boundary Finite Element Method, and hybrid numerical approaches [29, 30, 31]. The code is able to simulate a wide range of acoustical applications, from vibroacoustical sound paths to sound insulation and to the radiation of sound. Special models for viscous, viscoelastic, and poroelastic materials are already implemented just as models that describe e.g. flow-induced sound in structures.

6. New type of components and structures

At the moment, topology optimization is very popular for casting parts. If the target design should contain sheet structure or more than one material, additional extensions must be implemented. Here an improved optimization method is a topology optimization based on solid finite elements with an included manufacturing constraint for flat structures. The developed manufacturing constraint ensures that the structure does not exceed a given thickness and that the optimized sheet metal has no undercuts in order to deep draw the structure in one step. Figure 4 shows optimized structures for the same design space and load case with and without the manufacturing constraint for deep drawable sheet metals. Further information is provided by the contribution *Topology optimization considering the requirements of deep-drawn sheet metals* by Dienemann, Schumacher and Fiebig [35].

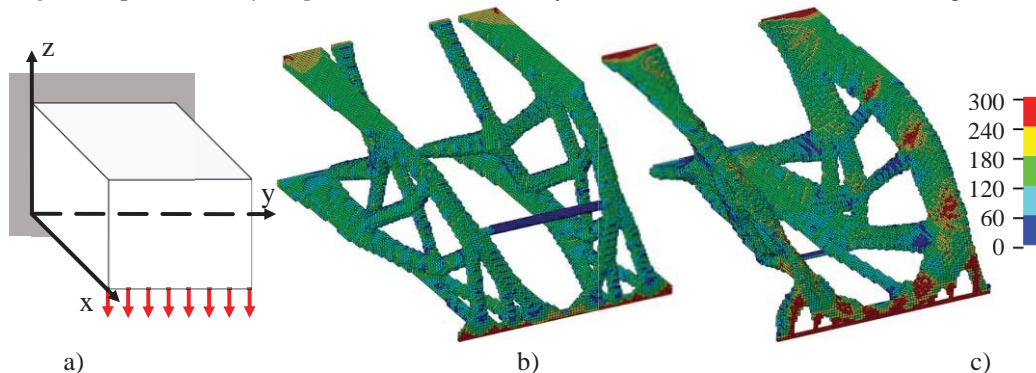


Figure 4: a) Design space and loadcase b) framework structure c) flat structure without undercuts in punch direction z

To achieve even more ambitious targets in terms of weight reduction and cost savings in the development of mechanical components, new strategies are required. Hybrid components are success-promising because of the large possibilities the use of two or more material offers. Nowadays the development methods are just at the beginning and no universal process is available. To offer a first idea of the ideal distribution of the two materials, the new topology optimization is capable of handling multi-material-structures. Therefore the binary material model is expanded by distinguishing two different materials, one strong material with a high density and a weaker material with a lower density. The step size controller also differentiates between the two materials, thus the correction and reduction rates are separate for both materials. Furthermore, a new intermediate step for the modification of structural elements is introduced. Before an element of the strong material is deleted, it is converted to an element of the weaker material. If the stress value in this element is still low, it is deleted in the next

iteration. A transformation from the weaker material to the stronger material is also possible, but on stress hot spots the same material is always added. The new optimization process is shown in figure 5.

An important factor on the final design of a multi-material-component is the type of joining, as an adhesive bonding leads to a different design of the joint than an interlocking structure. Both joining types are implemented in the new topology optimization.

To simulate an adhesive bond in the FE analysis, cohesive elements are added to the structure before the FE input deck is written. An algorithm searches for joints in the structure between the two elements. If a joint was found, the nodes are duplicated and a cohesive element is added. For cohesive elements with a geometric thickness the nodes are displaced by an offset, which is limited by the distortion of the connected elements. If a zero-thickness modelling is used, the coordinates for the duplicated nodes are coincident. The cohesive elements return stress values which represent the stress distribution in the adhesive layer. Hence an active design of the joint by the optimizer is possible, as the size of contact areas could be increased and load directions could be changed.

For interlocking structures, contact conditions between both materials are defined. To improve the load-bearing capacity of the joint, the structure of the contact surface could be modified or enclosing structures could be formed. In contrast to a single material casting part, the component cost is also directly influenced by the costs of the joining process. Therefore an expansion of the cost model is suitable, which could then be used as a target function for the multi-material-optimization.

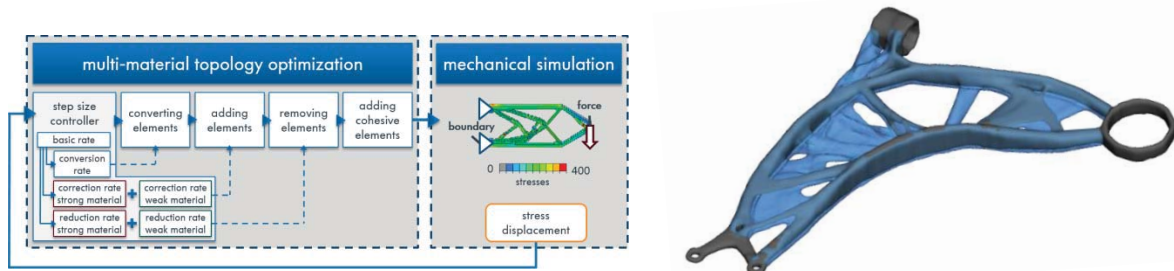


Figure 5: Topology optimization for multi-material, flowchart and exemplary optimization of a control arm

7. Integration of manufacturing simulation

Currently the topology optimization considers only the mechanical simulation results to modify the structure. Only basic rules for manufacturing restrictions, like the casting direction are integrated. Therefore, much work is necessary to optimize the castability after the first design proposals. This work can be saved and the quality of the first concept can be massively increased by the integration of a two-step-approach. First the optimization procedure is extended by more detailed manufacturing rules such as a draft angle and minimum hole and pocket sizes. Secondly a casting simulation is integrated in the topology optimization to determine the castability of the design. Figure 6 shows the new workflow of the optimization process. In each optimization loop, a casting simulation runs parallel.

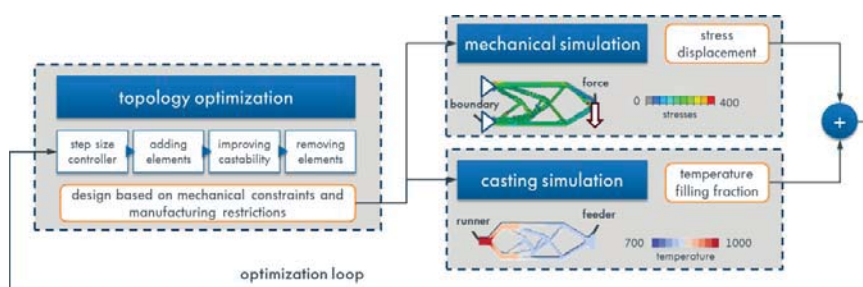


Figure 6: Topology optimization with integrated casting simulation

The results of the casting simulation are used in the optimization to improve the castability after the adding of material due to high stresses. Elements which aren't filled completely are grouped. It is assumed, that these regions are too thin or inappropriately placed to be filled properly. Depending on the visibility the elements are removed or reinforced. Figure 7 shows the compact result of this procedure. To prevent deep cuts in the structure a maximum depth mechanism is used. This whole procedure causes a violation of the structure every time elements are removed with high stresses. Because only few elements are changed in each iteration, the optimization can repair the structure in the next step and a feasible design is ensured.

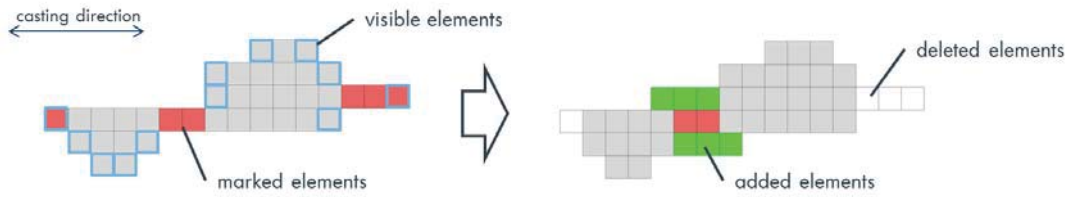


Figure 7: Changing of the structure due to not filled elements

This approach is discussed in a simple example. The target is the weight reduction. A stress restriction is used; the material of the part is an aluminium alloy. Two symmetric load cases are defined. Figure 8 shows two optimization results. The first design was generated with the basic optimization. The weight is reduced to 35.5% of the start design. The structure contains a lot of small beams and is complicated to produce. Parallel the optimization was done with an integrated casting simulation. The small beams are deleted every time they become too small to be filled. The result is a clear structure with few beams. In this case the weight is reduced to 35.3%. This is even lighter than the result of the basic optimization. Although more restrictions are used and the result is clearly different in topology and shape, a higher weight reduction can be reached.

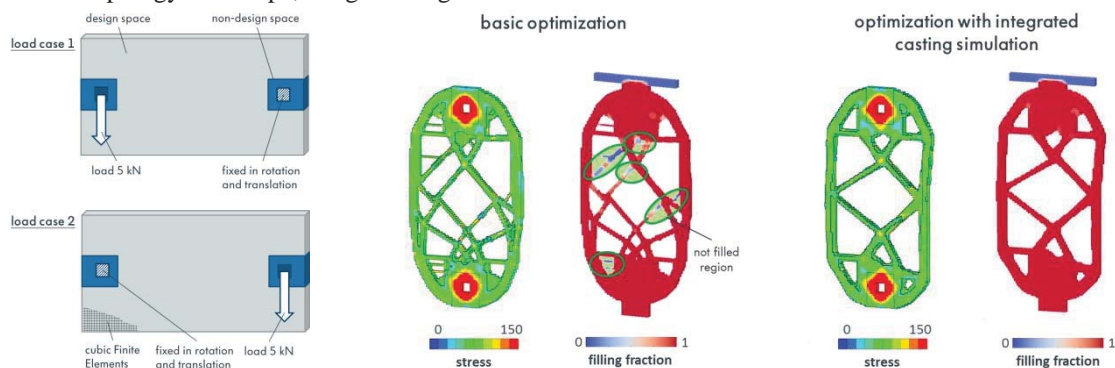


Figure 8: Modelling and result of a basic optimization and one with integrated casting simulation

8. Improved development process

One of the biggest challenges around the topology optimization for the next years is the conversion of the final optimized meshes in CAD geometries. Nowadays, the designers have to create a new part design with a smoothed result structure as design proposal. This step is very time consuming and some features of the optimization result get lost.

To improve this procedure, at least two steps are necessary as a minimum. First the result must be smoothed and secondly the smoothed structure must be described with CAD geometry elements to achieve a CAD design, which fulfills necessary design rules and can be modified.

The current smoothing algorithms do not allow transferring all the geometry information achieved by topology optimization to the CAD program. Surface mesh smoothing is a field studied for decades, however algorithms such as Laplace iterative smoothing, marching cube algorithm and the smoothing algorithm proposed by Wang and Wu still do not solve one of the biggest problems in the mesh smoothing of topology optimization results [32, 33, 34]. This problem is schematically represented in figure 9 on the left side. The left picture illustrates that the part corners are always rounded and the correct information in these specific zones is always lost. Even the new developed smoothing methods that are focused in not shrinking the final volume, don't allow to solve this problem.

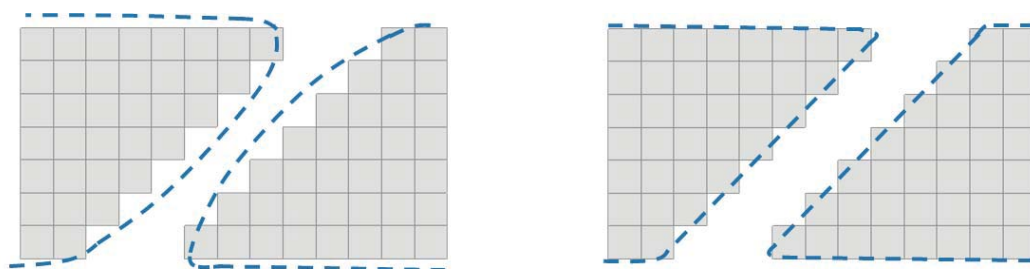


Figure 9: current smoothing result on the left side and needed result on the right side

The needed smoothing algorithms must be able to transfer the shape features, defined in the optimization results, to the final CAD geometry, without the loss of geometrical information. The target design should be changed to the characteristic of a part designed by engineers with clear feature lines. As a possible intermediate step, geometry elements can be written in dead geometry formats like IGES and STEP. The benefits are a strong reduction of the size of the files and resulting handling advantages, the distance between lines can be measured and they can be used for sketches. In the final step, the feature lines and surfaces must be transferred inside the CAD programs.

9. Conclusion

The presented paper describes four future challenges for structural optimization in order to extend the advantages of the topology optimization to fields, where today manual development loops must be accepted. If an optimization algorithm can handle acoustic and crash requirement, it will be possible to use it for more parts and applications, especially if also sheet structures or hybrid parts should be the result. The quality of the first design proposal will increase strongly and due to this, new possibilities of weight and cost reductions are offered. By saving weight, fuel consumption and CO₂-emissions can be additionally reduced. Beside these effects, also development time at the beginning of a project can be saved.

With the integration of the manufacturing process, the resulting part design follows not only mechanical aspects. As first step, the casting parts are the main focus. In each optimization loop, an additional casting simulation will be executed. Due to this, the castability gets a strong increase and weight and material costs stay on the same level in current projects. On the one hand, manual development loops for improving the quality of the casting process can be reduced and on the other hand also in the manufacturing process costs will be saved.

The fourth and last future challenge takes care of the process after the end of the optimization and the next steps of the part design. Today, a lot of design work must be invested to find a first CAD-design of the part. The today used smoothing algorithm changes the surface of the optimization result with possible influences to the mechanical behavior. Unnecessary weight could be added and feature lines get lost. With a new smoothing algorithm these negative effects can be avoided. After finding a way to generate CAD design automatically more development time and costs can be reduced.

With all four future challenges, the development of mechanical components can fulfill in the next years the ambitious targets inside the automotive industry.

10. References

- [1] **Rozvany, G.I.N.:** *Aims, scope, methods, history and unified terminology of computer-aided topology optimization in structural mechanics*, Struct Multidisc Optim 21, 90–108, Springer-Verlag, Berlin, 2001
- [2] **Bendsøe, M.P.:** *Optimal shape design as a material distribution problem*, Struct. Optim. 1: 193-202, 1989
- [3] **Bendsøe, M.P., Sigmund, O.:** *Topology Optimization: Theory, Methods and Applications*, Springer-Verlag, Berlin, 2003
- [4] **Rozvany, G.I.N., Zhou, M., Birker, T.:** *Generalized shape optimization without homogenization*. Struct. Optim. 4, 250–254, 1992
- [5] www.fe-design.de
- [6] **Edwards, C. S., Kim, H. A., Budd, C. J.:** *An evaluative study on ESO and SIMP for optimising a cantilever tie-beam*, Struct Multidisc Optim 34: 403-414, Springer-Verlag, Berlin, 2007
- [7] **Svanberg, K.:** *The method of moving asymptotes-a new method for structural optimization*, Int J Numer Methods Eng 24:359–373, 1987
- [8] **Xie, Y.M., Steven, G.P.:** *A simple evolutionary procedure for structural optimization*, Elsevier Science, 1992
- [9] **Huang, X. Xie, Y.M.:** *Evolutionary Topology Optimization of Continuum Structures*, Wiley, Chichester, 2010
- [10] **Querín, Q.M., Steven, G.P., Xie, Y.M.:** *Evolutionary structural optimisation using an additive algorithm*, Finite Elements in Analysis and Design 34: 291-308, ELSEVIER, 2000
- [11] **Mattheck, C.:** *Design in der Natur*, Rombach Verlag, Freiburg im Breisgau, 1997
- [12] **Querín, Q.M., Young, V., Steven, G.P., Xie, Y.M.:** *Computational efficiency and validation of bi-directional evolutionary structural optimization*, Comput. Methods Appl. Mech. Eng. 189: 559-573, ELSEVIER, 2000
- [13] **Baumgartner, A., Harzheim, H., Mattheck, C.:** *SKO (soft kill option): the biological way to find an optimum structure topology*, Int. Journey Fatigue, 1992
- [14] **Harzheim, L., Graf G.:** *Optimization of Engineering Components with the SKO Method*, International Conference On Vehicle Structural Mechanics & Cae, 1995
- [15] **Mattheck, C., Tesari, I.:** *Konstruieren wie die Natur- Bauteile wachsen wie Bäume und Knochen*, VDWF im Dialog 1/2005, Schwendi, 2005

- [16] **Guest, J.K.:** Multiphase Length Scale Control in Topology Optimization, 8th World Congress on Structural and Multidisciplinary Optimization, June 1-5, Lisbon, 2009
- [17] **Gersborg, A.R., Andreasen, C.S.:** *An explicit parameterization for casting constraints in gradient driven topology optimization*, DCAMM Report No. 745, DTU, Aalborg, 2010
- [18] **Pedersen, C.B.W, Allinger, A.:** *Industrial Implementation and application of topology optimization and future needs*, Springer Verlag, 2006
- [19] **Harzheim, L., Graf, G.:** TopShape: *An attempt to create design proposals including manufacturing constraints*, Int. J. Vehicle Design, Vol. 28, no 4, pp. 389-409, 2002
- [20] **Fiebig, S., Axmann, J.K.:** *Combining nonlinear FEA simulations and manufacturing restrictions in a new discrete Topology Optimization method*, 9th World Congress on Structural and Multidisciplinary Optimization, June 13 -17, , Shizuoka, Japan, 2011
- [21] **Fiebig, S., Axmann, J.K.:** *Intelligenter Leichtbau durch neue Topologieoptimierung für Betriebsspannungen und plastisches Materialverhalten*, 16. Kongress SIMVEC – Berechnung, Simulation und Erprobung im Fahrzeugbau 2012, VDI-Berichte 2169, S. 695-712, 20-21 November, Baden-Baden, 2012
- [22] www.3ds.com/de/products/simulia/
- [23] **Abaqus Theory Manuel**
- [24] **Abaqus Getting Started Manuel**
- [25] **Zienkiewicz, O.C., Taylor, R.L., Zhu, J.Z.:** *The Finite Element Method: Its Basis and Fundamentals, Sixth edition*, Elsevier Butterworth Heinemann, Amsterdam, 2000
- [26] **Matthies, H., Strang G.:** *The Solution of Nonlinear Finite Element Equations*, International Journal for Numerical Methods in Engineering, vol. 14, pp. 1613–1626, 1979
- [27] **Ortmann, C.; Schumacher, A.:** *Graph and heuristic based topology optimization of crash loaded structures*, Journal of Structural and Multidisciplinary Optimization (2013) 47:839-854, Springer, Berlin, 2013
- [28] **Fiebig, S., Axmann, J.K.:** *Using a binary material model for stress constraints and nonlinearities up to crash in topology optimization*, 10th World Congress on Structural and Multidisciplinary Optimization, June 13 -17, , Orlando, USA, 2013
- [29] **Sisámon, A.E.; Beck, S.C.; Langer, S.C.; Cisilino, A.P.:** *Inverse scattering analysis in acoustics via the BEM and the topological-shape sensitivity method*, Journal of Computational Mechanics. DOI 10.1007/s00466-014-1051-z, 2014
- [30] **Beck, S. C.; Langer S.:** *Flow-Induced sound of structures with porous layer*, International Journal of Numerical Methods in Engineering, DOI: 10.1002/nme.4622
- [31] **Schauer, M.; Roman, J.E.; Quintana-Ortí, E.S.; Langer, S.:** *Parallel Computation of 3-D Soil-Structure Interaction in Time Domain with a Coupled FEM/SBFEM Approach*, DOI: 10.1007/s10915-011-9551-x Journal of Scientific Computing, 52, (2), 446-467, 2012
- [32] **Wang, J., Yu, Z.:** *A Novel Method for Surface Mesh Smoothing: Applications in Biomedical Modeling*, Proceedings of the 18th International Meshing Roundtable, pp. 195-210 (2009)
- [33] **Field, D.:** *Laplacian smoothing and Delaunay triangulations*, Communications in Applied Numerical Methods 4, 709–712 (1988)
- [34] **Lorensen, W., Cline, H.:** *Marching cubes: A high resolution 3d surface construction algorithm*, ACM Computer Graphics 21 (4): 163–169(1987)
- [35] **Dienemann, R., Schumacher, A., Fiebig, S.:** *Topology optimization considering the requirements of deep-drawn sheet metals*, 11th World Congress on Structural and Multidisciplinary Optimization, June 7 -12, Sydney, Australia, 2015

Tailored natural components – functional geometry and topology optimization of technical grown plants

Anna-Lena Beger¹, Manuel Löwer¹, Jörg Feldhusen¹, Jürgen Prell², Alexandra Wormit², Björn Usadel², Christoph Kämpfer³, Thomas-Benjamin Seiler³, Henner Hollert³, Franziska Moser⁴, Martin Trautz⁴

¹Chair and Institute for Engineering Design (ikt), RWTH Aachen University, Germany, beger@ikt.rwth-aachen.de

²Institute for Biology I, RWTH Aachen University, Germany, jprell@bio1.rwth-aachen.de

³Institute for Environmental Research, RWTH Aachen University, Germany, christoph.kaempfer@bio5.rwth-aachen.de

⁴Structures and Structural Design, RWTH Aachen University, Germany, fmoser@trako.arch.rwth-aachen.de

1. Abstract

The prominence of ecologically produced and sustainably operable goods is constantly increasing and society's acceptance is rising. For ecological reasons and for society's demand sustainable materials are thus also of increasing importance in the manufacturing industries. Substituting conventional substances such as metals or plastics is therefore an important issue in the field of product development. Until now, most of the eco-design approaches are limited to the selection of the right material but the industrial processing to manufacture the desired design is done in a conventional way. Consequently a better eco balance can only be expected for material extraction, recycling and disposal while manufacturing is not considered in a way it should be.

The authors of this contribution are scientists from the areas of cell-biology, eco-toxicology, structural-, engineering- and industrial-design. They teamed up to analyse the potential and the behaviour of bio-materials being influenced during their growth period into predefined shapes, which can be produced on an industrial scale and which are used as semi-finished products. The aim is to minimize conventional production steps and thus decrease the amount of resources needed for manufacturing. To find out which products and plants offer promising potential, in the first step possible plants are categorized and analysed in general and on a structural cell level. In addition, requirements and main elementary functions for different sorts of products are defined, and matching parts of both databases are identified. For a systematic approach, engineering methodology e.g. according to Pahl and Beitz is taken as a basis.

It is expected that plants being influenced during their growth will go through a natural topology optimization compared to a plant being reformed and shaped during a manufacturing process after the plant has been cut. A higher grade of mechanical stability can therefore be predicted if the plant is absorbing the same strain while it is growing as it will during usage as a technical product. The aim of this project is to investigate these structural differences in mechanical testing, on a cell level in the laboratory as well as in simulations using Finite Element Analysis (FEA). Bamboo is taken as a first exemplary plant for its high pace of growth.

For a holistic view the potentials of the renewable materials will be evaluated by a comparison to conventional materials considering mechanical properties. Moreover, the assessment of the eco balance of the entire life cycle of a product, the Life Cycle Assessment (LCA), is employed to compare the impact of conventional and renewable materials. The outcome will be a data base with mechanical, ecological and economic information to help the developer to decide which material to choose for which technical product and what ecologic impact is implicated.

2. Keywords: Eco Manufacturing, Grown Components, Technical Product Harvesting, Natural Topology Optimization

3. Introduction

The demand for sustainably produced goods is constantly growing, considering societal as well as political calls. An ongoing process has therefore been to substitute conventional material like plastic or metal by natural, renewable materials. But until now products have mainly been copied using a "new" material without taking advantage of the materials' characteristics and natural topology. The approach in this project is not to concentrate on the topology of the conventional product but to break the product down into its elementary functions. A product with the same function which is made of a different material can therefore look totally different depending on the material's characteristics. The goal is to produce structurally well designed, sustainable products that can be reproducibly manufactured on an industrial scale. The natural topology of a plant is influenced during its growth; thus the plant can grow into a certain shape which can be used as a semi-finished product. In addition to the already better eco balance compared to conventional materials even manufacturing steps can be saved that way.

Additionally it is expected that plants go through a natural topology optimization if the same loadcase is applied during their growth as it will be when the plant is used as a technical product or part. Structural advantages are very likely. The potential of possible structurally gained strength is investigated experimentally and in simulations. The

aim is to formulate design guidelines for different biomaterials with which the potential of these materials can be utilized up to a high capacity. To achieve this, a consortium of scientist from the areas of cell-biology, eco-toxicology, structural-, engineering- and industrial-design has teamed up to work on the task of Technical Product Harvesting (TEPHA). All gathered data about technical requirements and functions and material properties of biomaterial will be summarized and linked in a data base.

In addition to the mainly functional and structural analysis the ecological impact of the whole lifecycle of products is being analysed. The Life Cycle Assessment (LCA) of different products considering their life from cradle to grave is looked at. Also economic data that arises from the manufacturing process until the recycling is considered in the database.

With help of the database the developer, engineer, architect or designer, should be able to choose the right sustainable material considering the function of the product, the ecological impact as well as economic issues. For each case he can decide on his own whether the structural function, the ecologic or economic issues are most important. Approaches and first results of this fresh cooperative research are presented in this contribution.

4. Approach and state of the art

4.1. Approach

The goal is to fully exploit the natural given mechanical und topological properties of sustainable materials. To make sure not to only copy an existing part and substitute the material, the functions of certain representative products are broken down to their elementary functions and requirements. Additionally the goal is to find new applications for natural materials without being prejudiced by already existing products made of those materials. To achieve this, on the one hand technical functions will be systematically analysed and classified according to the engineering design methodology of e.g. Pahl and Beitz [1], see also 6.1. On the other hand biological data is summarized and clustered considering structural material parameters such as Young's modulus, Poisson ratio as well as biological data as growth rate and required growing conditions. All data will be stored in a database to eventually find matching partners for fulfilling a certain technical function with a certain natural material. Additionally but independent from the functional parameters the database will include information on ecological data considering the whole LCA of certain products or functions as well as data about economic figures for the use of each material (see 4.3).

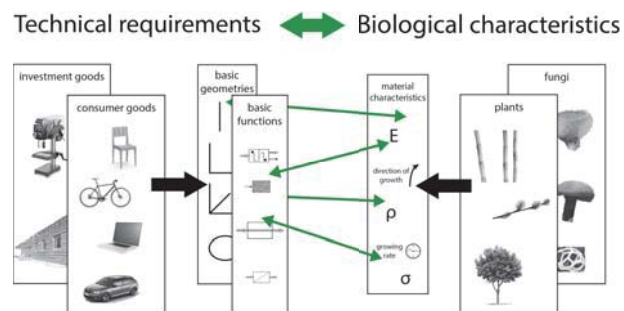


Figure 1: Systematically finding matching technical requirements and biological characteristics

Eventually the database will also contain design guidelines of how to design with the given material. This information is varying for the different bio-material since the natural topology needs to be considered. Information will therefore include growing dimensions, e.g. bamboo is only growing one directional with no branches and is always made of a hollow stem with a certain radius and nodes. When bending a bamboo a certain bending radius cannot be exceeded. Whereas a fungus, growing 3-dimensionally, has hardly any restrictions in topology and its structure is usually foam-like with hollow lightweight cells.

To fully exploit the plants properties it is also necessary to analyse to what extend the plant can be manipulated in its growths and what effect the manipulation causes considering structural behaviour. For its rapid growth this scenario is exemplarily tested on bamboo. The experimental and simulative procedures are displayed in section 6.2. The way the plant is presented in this work is to be seen exemplarily. The aim of the project is to investigate numerous species of plants and fungi in a similar way.

4.2. Current use of sustainable material for technical purposes

Current products made of sustainable material that fulfil a technical function and that are produced on an industrial scale do not or hardly take advantage of the natural topology of the plant. To achieve the required shape of a product either external connection pieces are needed or they consist of laminates that require complex manufacturing processes as well as chemical additives. Changing the shape of a whole e.g. bamboo cane takes

place under heat and pressure. Structural damage is expected here. (See Figure 2)

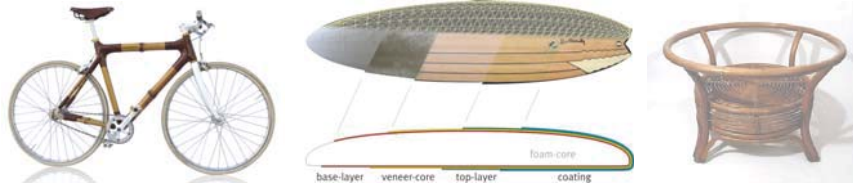


Figure 2: (a) Bicycle made of bamboo [2], (b) Surfboard made of bamboo laminate [3], (c) framework of table

Natural materials grown into certain shapes as design objects have been presented by several artists. The so called “chair farm” by Werner Aisslinger is one of the most famous artefacts. With his installation (Figure 3a) Aisslinger wants to indicate the change in consumer behaviour to a more regional and sustainable demand.

But so far, growing plants and the use of their characteristic shapes have mainly been used as unique artefacts or design objects. The “Pooktre Living Chair” is a well known example. The chair in Figure 3b was planted in 1998 and has been growing since. The new field of botanical construction or “living architecture” is an approach to use the natural topology for technical functions. In German it is referred to as “Baubotanik” and it was established in 2007 by Prof. Dr. Gerd de Bruyn in Stuttgart (Figure 3c,d). But despite its technical function they are unique solutions that cannot be manufactured or reproduced on a large scale.



Figure 3: (a) “Chair Farm” by Aisslinger [4], (b) Chair made of a living tree [5]
(c), (d) Natural fixation for a handrail of a bridge [6]

Biomimetic is another current research area. Imitating the topology and its functionality of natural systems is the main aspect. The material employed can be either sustainable or conventional.



Figure 4: (a) Technical/architectural structures inspired by natural growth [7]
(b) Technical Plant Stem as fibrous compound material, inspired by biological templates [8]

Only very little research could be identified where the shape of a living plant is modified and used for technical purposes. The Industrial Design faculty at Monash University, Melbourne, Australia concentrated on a rickshaw-vehicle design made of bamboo grown into the shape of the vehicle frame. So far the possibility of manipulating the shape with a certain bending radius and influencing the cross section of the cane could be shown.



Figure 5: Bamboo shape modification over substructures [9]

But until now it is hardly known that the growth itself has been influenced to produce near net shaped structures

that are reproducible. Achieving reproducibility on an industrial scale is the major aim to achieve in this project.

4.3 Ecological impact

One of the project goals is to establish a comprehensive life cycle assessment of the near net shape grown components as well as for their conventional equivalents. This allows to evaluate if the bio-based components can be produced more environmental friendly. The LCA of a product covers the whole process from the raw material extraction and acquisition, through energy and material production and manufacturing, to its use and end of life treatment up to the final disposal [10], Figure 6.

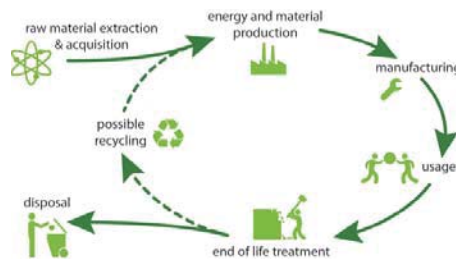


Figure 6: Life Cycle Assessment (LCA)

5. Exemplary plant: Bamboo. Biological background

Bamboo is a tribe (Bambuseae) within the plant family of true grasses (Poacea) which comprises more than 1400 species [11]. Bamboos grow mainly in the tropical and subtropical regions around the globe and are of significant cultural and economic importance in Southeast Asia. Bamboo is used in building, construction, as raw material for plywood or composites and even as bamboo viscose for clothing. A great advantage of bamboo is that some species belong to the fastest-growing plants in the world [12] The culms of *Dendrocallamus giganteus* can grow within one growth period of a few months to full height (up to 35m) with impressive diameters (up to 30cm). The culms then lignify, harden and incorporate silica to extraordinary strong material [1313131313]. Bamboos produce wooden stems with a higher compressive-strength than tree wood, brick or concrete, a tensile strength that rivals steel and a surface with extraordinary hardness [14]. Lignin is responsible for the high compressive-strength of bamboo wood and cellulose for its unusual tensile- and break-strength [15]. The special organization of the wood in a hollow stem with longitudinal fibers, intersections and the hardest material on the stem-surface produces extraordinary properties. This is why bamboo has received a lot of attention in material sciences.

Hence, to ensure the success of bamboo cultivation under North Rhine-Westphalian conditions, bamboo species were selected based on their frost-resistance. *Phyllostachys vivax* and *Phyllostachys bissettii* as two possible bamboo species for the production of near net shape components can tolerate temperatures down to -20°C , resp. -23°C . Moreover *Phyllostachys vivax* is a very dry resistant species possibly tackling the irrigation issue [16].

6. Procedure

6.1 Methodical approach

According to Pahl and Beitz, in the conceptual state, all technical systems can be described as a combination of several principal solutions. These in turn consist of three elements: “physical effect”, “effect carrier” (material) and the “qualitative embodiment parameters of the working location” [1]. It is obvious that even in this early stage of product development not every physical effect for a given function can be realized with every sort of material or any geometrical shape.

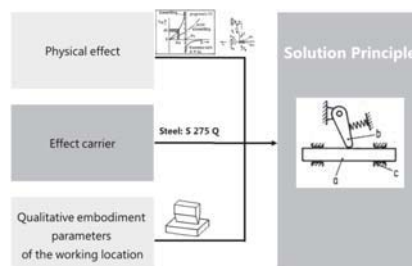


Figure 7. Elements of Principle Solutions [1]

In order to address the technical functions, on the one hand the authors use the Koller approach of elementary functions, which cannot be subdivided to a lower hierarchical level and can directly be implemented with at least one corresponding physical effect [17]. A set of different elementary functions has been defined for the material,

energy and signal flow, which can potentially be covered by naturally near netshape grown materials. At the same time, a systematic analysis of a wide range of products from consumer goods to machine tools and plant engineering as well as architecture/civil engineering is carried out to cluster different product characteristics and identify archetypal application patterns for the material substitution. The results are implemented in the product-function database including amongst other parameters information about the three mentioned aspects of the principle solution. The database will thus contain classifications of products which lead to basic functions and required material properties. At the same time the database includes data about growing organisms such as mechanical properties as well as geometric limitations during growth. Besides it will also contain quantitative data on the LCA (Figure 6) and economic data.

Hence with help of the database it will be possible to identify the basic functions of a product. In the second step it will lead the user to the material requirements needed to fulfil these functions. To match the technological requirements and the biological characteristics the requirements are then compared to the material data of the possible natural effect carriers (Figure 7). Along with the evaluation of the fulfilment of the technical functions, ecological and economical criteria will be displayed. Ideally the user will then have the choice of different materials and can weigh which aspect next to the functionality is most important for his case. Based on this he may choose a natural substitute for the conventional material.

Since a detailed product not only consists of structural elements or elements which are directly involved in the fulfilment of a technical function, but is also composed of material volumes which do not contribute functionally [17], the embodiment design and styling of these parts need to be considered as well. Particularly it is obvious that not every contour or outline can be realized without additional technological processing.

Currently the availability of adequate material data for the TEPHA approach is very limited, not only in terms of the number of different plant species but also concerning guidelines for controlled and guided growth respectively the alteration of physical material characteristics caused by the manipulation. To overcome this lack of information the consortium has set up different plantings and tests material from the same species conventionally grown as well as according to the outlined method. For the first stage the authors concentrate mainly on structural functions of products.

6.2. Experimental approach

The procedure to analyse the behaviour of plants being manipulated while they are growing consists of different approaches. Bamboo will be manipulated while it is growing. Because the lignification until the bamboo reaches its full hardness takes up to three years, structural testing cannot be done on the manipulated plants. But structural testing can be done on bamboo canes that have grown normally, yet under the same nutritional conditions as the manipulated plants. To estimate the gain of structural strength of naturally grown structures compared to canes with the same topology that have lignified and then modified under pressure and heat, a simulation model is set up.

Experimental growing procedure

For the mentioned advantages in section 5 the first stage of the experiments deals with different species of bamboo. It is systematically tested to what extent bamboo can be influenced in its natural growth.

Different parameters such as bending angles and radii as well as the cross section will be gradually changed to get to know the limits. A variation of tools will lead to the optimal way to create reproducible elements.

Knowing what basic geometric elements are producible, it will be possible to predict what kind of whole products or semi-finished products are contrivable. So far it could be shown that it is possible that the bamboo is manipulable in its shape. The tested plant is growing in a loop of approximately 20 cm (Figure 8). In further experiments different species of bamboo and other plants and fungi will be tested.

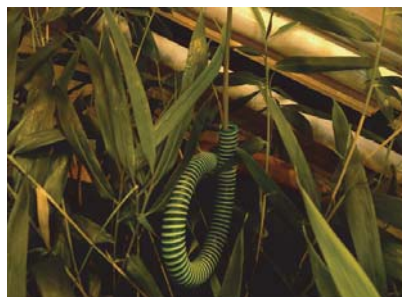


Figure 8. Bamboo growing in a loop trough a tube

Structural evaluation

Regarding the topology of naturally grown structures such as e.g. trees it is noticeable that these structures develop exactly the topology needed for the loadcase which is applied by wind, rain etc. [18]. The aim of this project is to make use of this characteristic for technical purposes and to quantify the gained advantage compared to plants that have been manipulated after their growth was finished.

Since the lignification of the bamboo needs approximately three years, no structural testing can be done during the two-year-project. But the potential of the manipulated plants can be estimated by setting up a simulative FE-model for straight bamboo. That model can be expanded to simulate the behaviour of bamboo that has been grown into a certain shape since it can be assumed that for both growing scenarios no cells have been injured. Comparing this to the results of structural testing from bamboo that was bent after its lignification, a quantitative prediction can be made about the structural advantage of grown structures.

The goal is to find out to what extent natural growing into a wanted shape has structural advantages to structures that have been bent afterwards.

7. Discussion and Outlook

In the project TEPHA the potential of substituting conventional materials with sustainable bio-material for products that are manufactured on an industrial scale is investigated. By creating a database with which it is possible to evaluate products according to their function and not to their topology it will be possible to find matching natural materials that fulfil the requirements needed for that certain function. The goal is to fully exploit the material properties. To do so design-guidelines for each material will be developed.

For the guideline and to estimate the potential of manipulated grown structures, the structural behaviour is going to be evaluated. In particular for the chosen example bamboo it is analysed how much the grown structure is stronger than the one bent after lignification. This contribution only provides the approach for further research and first supposable qualitative results of this project. It is expected that there will be quantitative results of first exemplary plants soon after the first growing phase when results of simulations and of real grown plants can be verified.

But even if the structural strength will be worse or equal, the eco balance of the grown material is still of better value because of the way the raw material is extracted and because of less manufacturing steps. The authors therefore see great potential ecological wise. Economically the growing time and needed space have to be kept in mind as well as possible tolerances for the produced products. It is obvious that still it remains a natural material that can only be manipulated in a certain range. High production tolerances can therefore not be predicted which limits the selection of possible products.

The presented methodology in which elementary functions are used to choose a certain material could also be introduced for other material groups to ensure best exploitation for certain materials.

6. Acknowledgements

The presented research is funded through means of the German Excellence Initiative.

7. References

- [1] G. Pahl, W. Beitz, J. Feldhusen, K.-H. Grote. Konstruktionslehre. 8th Edition Berlin: Springer 2013.
- [2] Bambooride OG, <http://www.bambooride.com/>, 2015.
- [3] L. Schürg, <http://pointtwenty.com>, 2015.
- [4] W. Aisslinger, Chair Farm. www.aisslinger.de, 2012.
- [5] P. Cook, <http://pooktre.com/>, 2014.
- [6] G. de Bruyn, F. Ludwig, H. Schwertfeger, <http://www.baubotanik.de/>, 2015.
- [7] J. Burgee, <http://www.sacredarchitecture.org/>, 2015.
- [8] O. Speck, Kompetenznetz Biomimetik, <http://www.bionik-bw.de/>, 2014.
- [9] A. Vittouris, M. Richardson, Australasian Transport Research Forum 2011 Proceedings. Adelaide, Australia
- [10] Environmental management Life cycle assessment – Principles and framework (ISO 14040:2006). 2006
- [11] S.A. Kelchner, Bamboo Phylogeny Group. Higher level phylogenetic relationships within the bamboos (Poaceae: Bambusoideae) based on five plastid markers. *Mol Phylogenet Evol.* 67(2):404-13. 2013
- [12] D. Farrelly, *The Book of Bamboo*. Sierra Club Books 1984.
- [13] J.J.A. Janssen. *Mechanical properties of bamboo*. University of Eindhoven, NL. 1991
- [14] E. Rottke, *Mechanical Properties of Bamboo*. RWTH Aachen University. Faculty of Architecture. Aachen, Sect. 3, page 11; Sect. 4, page 11. 2002.
- [15] W. Liese, *The anatomy of bamboo culms*. International Network of Bamboo and Rattan. 1998.
- [16] D. Lewis, C. Miles, *Farming Bamboo*. 1 ed. Raleigh: Lulu Press; 2007.
- [17] R. Koller, *Konstruktionslehre für den Maschinenbau: Grundlagen zur Neu- und Weiterentwicklung technischer Produkte mit Beispielen*. Berlin: Springer 1998
- [18] C. Mattheck, I. Tesari, *Konstruieren wie die Natur. Bauteile wachsen wie Bäume und Knochen, Konstruieren und Giessen*, Vol. 27, p. 4-10, 2002

Topology Optimization of a Jacket Structure for an Offshore Wind Turbine with a Genetic Algorithm

Johan Henrik Martens^{1,2}, Daniel Zwick³, Michael Muskulus⁴

¹ Norconsult AS, Oslo, Norway, johan.henrik.martens@norconsult.com

² Norwegian University of Science and Technology, NTNU, Trondheim, Norway

³ Norwegian University of Science and Technology, NTNU, Trondheim, Norway, daniel.zwick@ntnu.no

⁴ Norwegian University of Science and Technology, NTNU, Trondheim, Norway, michael.muskulus@ntnu.no

1. Abstract

Structural optimization of support structures for wind turbines is complicated by the need to assess fatigue damage. Due to nonlinearities in the rotor loads, this situation calls for transient time-domain simulations, with combined wind and wave action. The structural model considered here is a jacket consisting only of beam elements that is subject to one 90 second operational loadcase from which the fatigue constraint is evaluated. Since no optimality theory exists for such a case, the optimization was performed with a genetic algorithm using a small population of designs. Under a ground structure approach, the structure was initially modeled with a large set of beams. By storing favorable design traits and discarding bad traits, the beams were sized in an iterative manner. Beams under a certain minimum size were removed. The objective function includes a term for the cost of welding and painting the beams, and thereby favors less structural elements. Results show that it is possible to obtain reasonable structures with this approach, similar to what would be obtained by straightforward manual optimization, but often with a lower weight. Due to the many simplifications the final designs are not completely realistic, but this study highlights the important issues that do arise and is a first step toward more comprehensive automatic design optimization.

2. Keywords: Wind Turbine, Jacket, Optimization, Genetic Algorithm

3. Introduction

The construction of offshore wind farms for electricity production has shown great promise. Both as a contributing element in mitigating the ongoing climate changes, and in lessening the global oil dependency. Wind power is in terms of cost of energy the second cheapest of all renewable energy sources, after hydro-power. Still, construction and operation cost is a limiting factor in utilization of offshore wind energy on a significant scale. For an onshore installation, the cost of the turbine and tower itself will typically be 64-84% of total capital costs, while for offshore wind farms it will only make up 30-50% [1]. To realize cost efficient offshore wind farms, minimization of the support structure cost is essential. For water depths between 30 and 60 m, tubular steel lattice towers, i.e. jackets, are a favored solution. Environmental factors that need consideration when designing offshore wind turbines include high wind speeds, turbulence, wave loading, ice, currents, tides, marine growth and corrosion [2]. Not only are all these factors hard to predict and design for individually, but their coupled effects are also important to consider.

Structural optimization is a design scheme for finding optimal solutions. The goal of the process is structures that are stiff, economical and easily producible while satisfying mechanical constraints like displacements, stress levels, fatigue damage, buckling and eigenfrequencies. Several methods can be employed to arrive at an optimized design. However, most existing methods are based on maximizing stiffness, using one or more static loadcases, whereas the problem here has to take fatigue constraints into account. This is difficult with gradient-based algorithms [3], especially for a system that is subject to such a complex dynamics as a wind turbine. The current state of the art of support structure optimization is therefore the use of heuristics [4, 5].

One such method is the genetic algorithm (GA), which mimics the evolutionary process known as "survival of the fittest". By continuously passing on good design traits and discarding unfavorable traits, the design will improve over generations. Evolutionary optimization schemes are powerful because they can find innovative solutions to complex problems in an enormous search space. The solution adapts to changing environments and one can easily take advantage of parallel processing. Compared to more traditional, gradient-based, optimization methods it is also relatively straightforward to implement. Weaknesses of GA are among others difficulties relating to premature convergence of the solution and in defining a suitable fitness function, which defines the goal of the optimization process.

4. Methodology

The optimization process is based on an interaction between Fedem Windpower (Ver. R7.1- α 2, Fedem Technology AS, Trondheim) and a MATLAB script. Fedem Windpower is a flexible multibody software specialized in dynamic simulation of wind turbine systems. It offers tools for designing realistic rotors and support structures, and for modeling wind and sea conditions. The topology is optimized by reducing the task to an equivalent sizing problem of a ground structure of varying complexity. The ground structure includes all possible beam connections between predefined nodes in the jacket. The inner and outer diameter of the beams are sized by the script and beams that have a diameter which is smaller than a certain limit will be removed. To limit the size of the search space, a maximum outer diameter, as well as upper and lower bounds for the ratio between the inner and outer diameter are inputs to the optimization script.

As the goal of this research is to optimize a jacket structure, an existing model of the transition piece, tower and rotor nacelle assembly (RNA) was utilized. Namely, a model from the OC4 project [6], illustrated in Fig. 1. Data about the wind and sea conditions the wind turbine was subjected to during analysis were gathered from a reference site in the Dutch North Sea [7]. The wind file was generated by TurbSim, a tool developed by NREL (National Renewable Energy Laboratory, Boulder). Wave loading was applied using a JONSWAP sea wave spectrum. Total analysis time was set at 90 seconds and data was recorded in every time step (size 0.05 s) of the last 30 seconds of the analysis. The first 60 seconds are devoted to accelerating the turbine, i.e., to reach steady state conditions. An overview of the entire design optimization process utilized is illustrated in the flowchart in Fig. 2.



Figure 1: Wind turbine model from the OC4 project

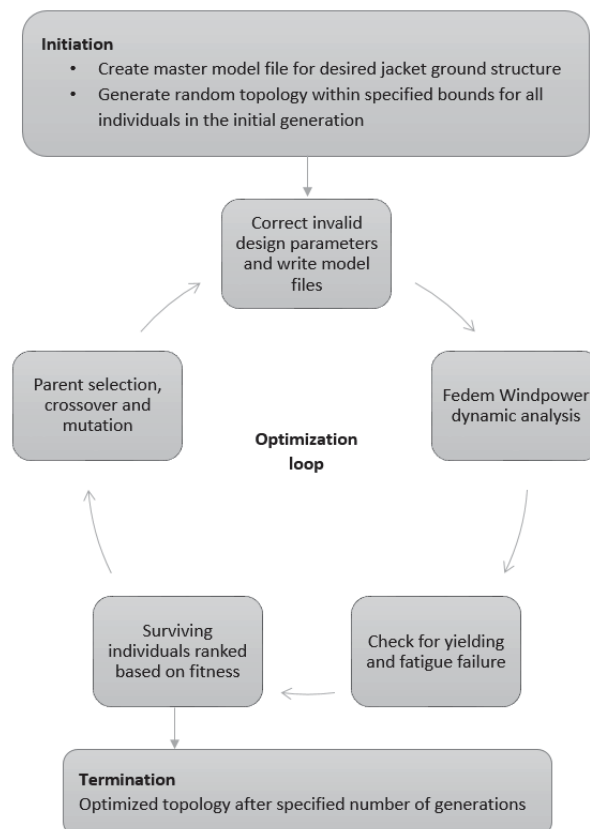


Figure 2: Flowchart of optimization process

The genetic algorithm was carried out by a MATLAB-script. The first generation of jackets were generated with a random topology, the only limitations being the ground structure definition and the diameter bounds. The script also ensured that all four faces of the jacket were symmetric. Fedem input-files were written for all individuals, i.e. jackets, in the generation and were analyzed in parallel. Data exported from Fedem were axial force and moment about the Y and Z axis for both ends of all active beams in the model. The forces were converted to a stress time series which was checked for yielding and fatigue failure. Working by the DNV guidelines [8], all beams were evaluated for fatigue damage in eight hot spots at both ends. Extraction of stress ranges from the stress time series was done by rainflow counting following standard procedure [9]. The 30 second loadcase from the analysis was

scaled in order to predict fatigue damage through a 20 year lifespan.

After testing the yield criterion and the fatigue limit state, all surviving individuals were evaluated for fitness. Casualties, either by fatigue, yielding or by the Fedem solver module crashing, were discarded. Fitness was calculated as an arbitrary constant minus the objective function. The objective function to be minimized represents a rough estimate of the total cost of the jacket and includes both a fixed cost per member, as well as material cost. This ensures that jackets with less members are favored by the algorithm. In order to track the evolution and determine which individuals will pass on their genome to the next generation, a leader table/mating pool is updated and stored for each generation. The number of individuals in the mating pool equalled the population size. For all generations except the first, the result of the current generation was added to the mating pool. This list was then sorted from best to worst fitness, mixing new results with the old leaders. Hence, an individual in the mating pool will not leave the mating pool unless replaced by an individual with better fitness. Next, individuals in the mating pool bred children for the following generation. Two parent individuals were selected by means of a weighted roulette wheel, ensuring that individuals with the highest fitness have the highest probability of being chosen as parents. All inner and outer beam diameters in a parent, i.e. chromosomes, were converted to binary numbers where each bit represents a gene. A crossover was performed by mixing chunks of genes from both parents in each child chromosome. A mutation was implemented by randomly switching genes from 1 to 0 and vice versa. The probability of such a mutation adapts to the diversity in the mating pool in an effort to avoid premature convergence. A low diversity among the leading designs calls for a higher mutation probability. The diameters of the beams in the children were checked to be inside the user-specified bounds and new Fedem input-files were written. This iterative optimization loop was carried out for a specified number of generations. The winning design is the individual with the highest fitness upon termination. More details can be found in [10].

5. Results

In the following, examples of two optimization runs are presented. First, an unrealistically low cubic jacket with 3 nodes along its width, i.e. nodes in all corner legs and one additional node in between, was optimized. Second, a more realistic 32 m tall jacket with 2 nodes along its width, i.e. only nodes along the four legs, was analysed. Satisfactory results with a 32 m tall jacket with 3 nodes along its width could not be obtained with the available processing power. Having 2 nodes along its width implies that X-braces are not connected, i.e. welded together, at their intersection.

5.1. Optimization of a cubic jacket

Figure 3 shows a plot of the evolution throughout the optimization process. The plot shows the fitness on the left abscissa, and the generation number on the ordinate. The maximum fitness is 50, which would correspond to a structural cost of 0. The optimization was set to run for 50 generations and each generation had a population of 16 individuals. The thick blue line indicates the fitness of the best design so far in the optimization process, while the thin green line shows the fitness of the best individual in each generation. The dotted line illustrates the mean fitness in the mating pool. If the distance between the mating pool mean and the leading design is small, the diversity in the mating pool is low.

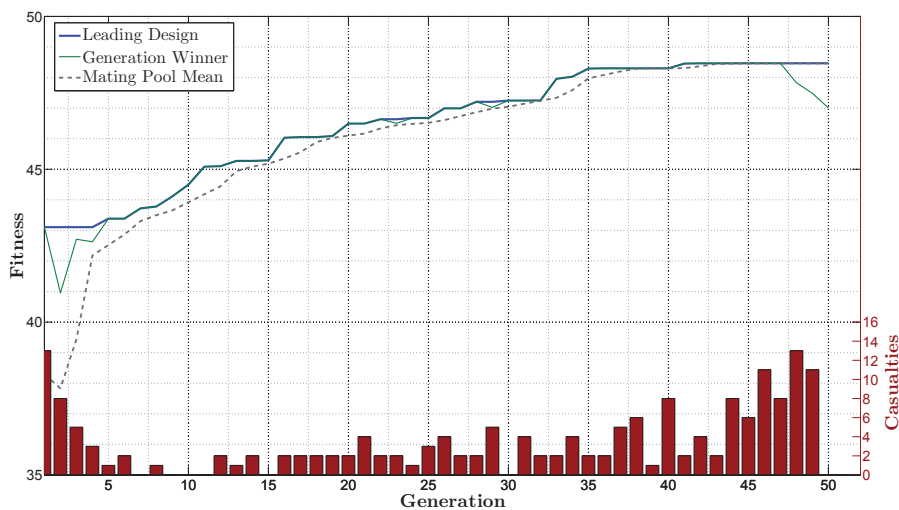


Figure 3: Optimization of a cubic jacket

As one would expect, the diversity is high in the initial generations and lower as the design converges towards a solution. The red bars with the corresponding right abscissa illustrate the number of casualties, i.e. failures, within each generation. The effect of the adaptive mutation probability can be seen at the very end of the optimization evolution. As the diversity in the mating pool decreases, the mutation probability increases, as illustrated by lower fitness of the generation winners and more casualties.

Fig. 4a illustrates a random topology from the initial generation. By the 15th generation, Fig. 4b, the structure is lighter and somewhat more purposefully designed. The winning design is produced in the 46th generation, as seen in Fig. 4c. Its fitness increased from 43.1 in the initial generation to 48.5 in the 46th generation. A classic X-brace has been formed in parallel with a horizontal support. The small dimensions of the X-brace have probably made the horizontal support mandatory in controlling wave induced oscillations of the braces. Although the topology of the winning design can be found within the leading design of generation 15, there are many other possibilities that have been discarded in the optimization process.

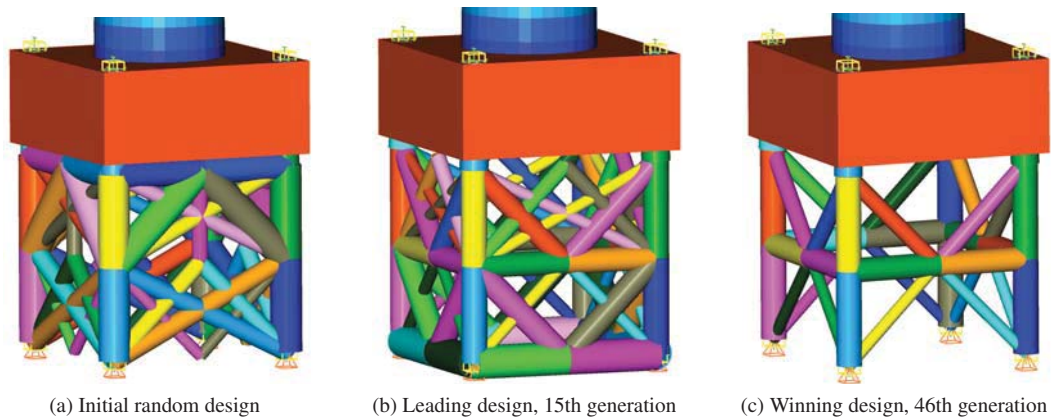


Figure 4: Cubic jacket at different optimization stages

5.2. Optimization of a tall jacket

The jacket with two nodes along its width was optimized over 100 generations with 16 individuals in each generation. The maximum fitness in this example is 100. The entire optimization took roughly 24 hours in a completely automatic process on a regular workstation, and was subdivided into 12 hours of Fedem analyses, 10 hours of stress and fatigue analyses and 2 hours of writing model files. As seen in Fig. 5, most of the increase in fitness is done before the 25th generation. The second half of the optimization, from generation 50 to 100, displays traits of many bad designs through the fluctuating fitness of the generation winners and a high number of casualties.

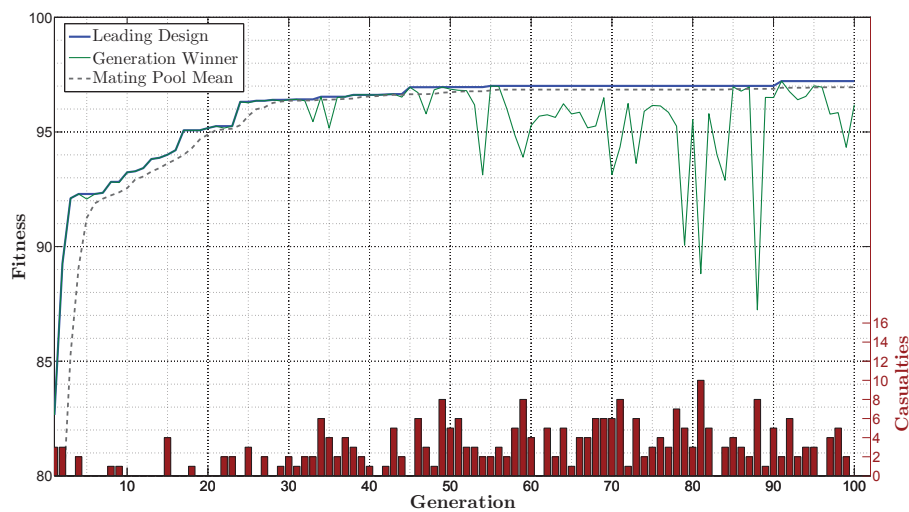


Figure 5: Optimization of a tall jacket

The evolution of the topology is illustrated in Fig. 6a-6c and exhibits how structural cost is being minimized by the optimization script. A lot of the initial weight has been cut already by the 5th generation, as shown in Fig. 6b. From generation 5 and onwards the only non-sizing changes are the removal of two horizontal beams and two X-braces on each face. The winning design in Fig. 6c looks inexpensive and reasonable for the given loading, which was the goal of the objective function. It has a thin stabilizing X-brace in the middle of each face and large legs with an outer diameter of 1.537 m and a thickness of 25 mm. It is impressive that the single brace formed exactly halfway up the jacket, where there is need for support, considering that there is no enforced symmetry about the horizontal middle line. However, the design seems prone to buckling failure, which was not evaluated by the script.

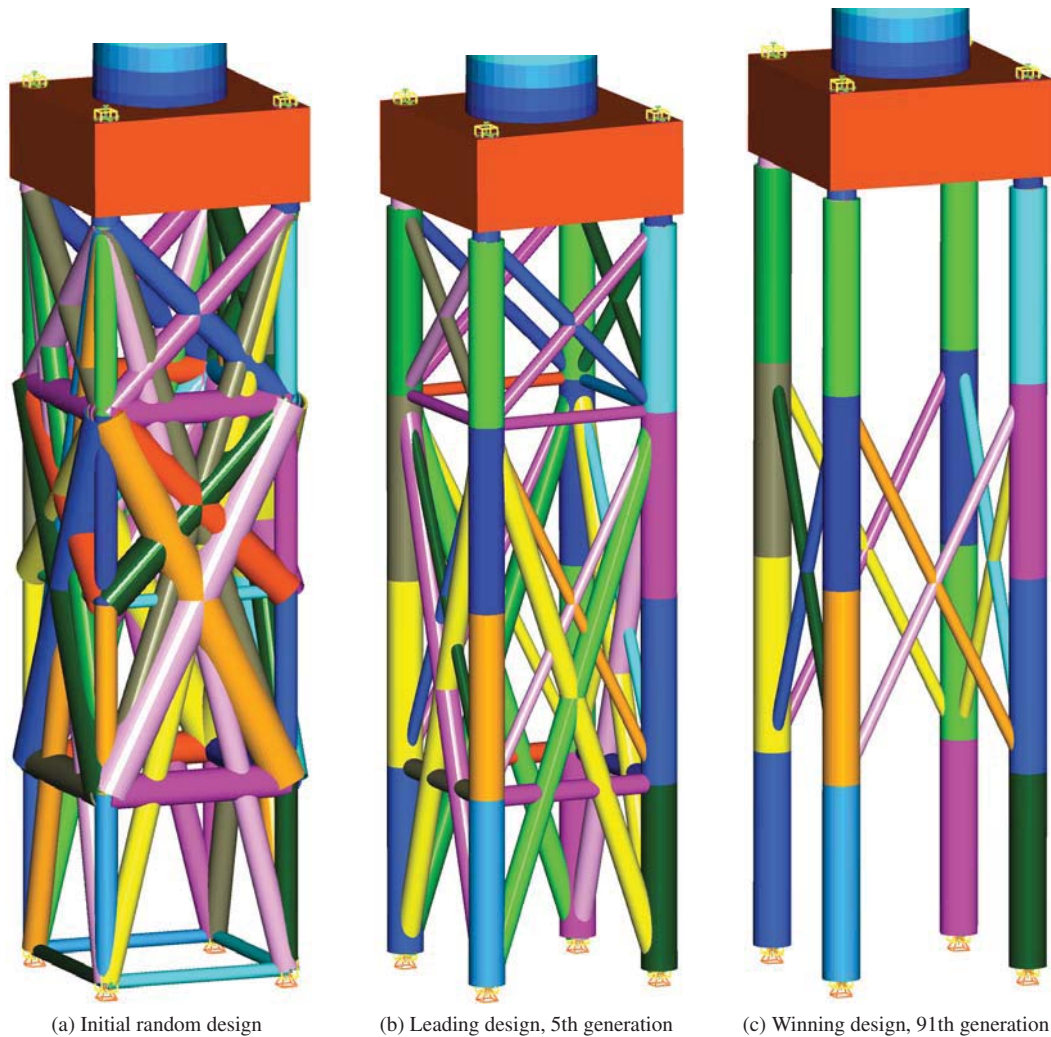


Figure 6: Tall jacket at different optimization stages

5.3. Comparison with manual optimization

In order to have a basis of comparison for the automatically optimized designs, a simple manual optimization was carried out. A classic topology with one X-brace on each face as well as four legs was assumed as the optimal design for the cubic jacket. The tall jacket was modeled with four such X-braces throughout its height as a basis for the manual optimization. The initial cross sections of the legs and braces were set equal to the inner and outer diameters of the legs and braces from the jacket model used in the OC4 project [11].

To minimize the cost of the structure manually, the outer diameter was kept constant while a sizing optimization was carried out for the inner diameters. In other words, the manual optimization process had two design variables, the inner diameter of the braces and the inner diameter of the legs. The jacket was subjected to the same loading and stress assessment as with the automatic optimization. If a brace or leg failed, either by yielding or fatigue, the inner diameter was decreased and vice versa if no failures occurred. This iterative process was carried out until an increase of 1 cm of the inner diameter of either the legs or the braces would cause a failure. To compare this result with the jackets that were optimized by GA, the fitness score of the manually optimized jacket was calculated by

Table 1: Comparison of automatic and manual optimization process

	Maximum fitness	Automatic	Manual
Cubic jacket	50	48.4658	47.9314
Tall jacket	100	97.2175	97.7768

the same rules as in the automatic optimizations. The automatic optimization was superior for a cubic jacket, but not for the tall jacket. Fitness results are given in Table 1.

6. Conclusion

The jacket topologies generated by means of evolutionary optimization showed a complexity-dependent quality. The automatic optimization of a simple cubic jacket beat the quick manual optimization of the same ground structure. The taller and more complex jacket topology had a marginally better fitness by manual optimization. The employed optimization process is by no means without fault and there is much room for improvement. Some of the weaknesses of the implementation include that no ultimate limit state load case was checked, buckling of members was not assessed and the ground structure did not allow for inclined legs. Still, important aspects regarding the use of evolutionary optimization on a jacket have been explored. The results have shown that structural cost can be minimized in a reasonable manner under fatigue constraints using genetic algorithms. Reasonable and innovative designs were generated in a very large search space of possible solutions. The method shows great promise because it is powerful and at the same time easy to implement. If a more general ground structure were to be optimized on a supercomputer by use of a combination of GA and manual optimization, it is likely that more cost-efficient designs could be constructed.

7. References

- [1] International Renewable Energy Agency (IRENA), *Renewable power generation costs in 2012: an overview*, Technical Report, Abu Dhabi, United Arab Emirates, 2013.
- [2] F. Vorphal, H. Schwarze, T. Fischer, M. Seidel and J. Jonkman, *Offshore wind turbine environment, loads, simulation, and design*, WIREs Energy Environ, 2, 548-570, 2013.
- [3] E. Holmberg, B. Torstenfelt and A. Klarbring, *Fatigue constrained topology optimization*, Structural and Multidisciplinary Optimization, 50, 207-219, 2014.
- [4] M. Muskulus and S. Schafhirt, *Design optimization of wind turbine support structures — a review*, Journal of Ocean and Wind Energy, 1, 12-22, 2014.
- [5] L.B. Pasamontes, F.G. Torres, D. Zwick, S. Schafhirt and M. Muskulus, Support structure optimization for offshore wind turbines with a genetic algorithm, *ASMS 2014 33rd International Conference on Ocean, Offshore and Arctic Engineering*, OMAE2014, San Francisco, USA, 2014 (ISBN: 978-0-7918-4554-7).
- [6] W. Popko, F. Vorphal, et al, Offshore Code Comparison Collaboration Continuation (OC4, phase I — results of coupled simulations of an offshore wind turbine with jacket support structure, *22nd International Society of Offshore and Polar Engineers Conference*, ISOPE2012, Rhodes, Greece, 2012 (ISBN: 978-1-880653-94-4).
- [7] T. Fischer, W. de Vries and B. Schmidt, *Upwind design basis (WP4: Offshore foundations and support structures)*, Technical Report, Endowed Chair of Wind Energy (SWE), Institute of Aircraft Design, Universität Stuttgart, Germany, 2010.
- [8] Det Norske Veritas AS, *Fatigue design of offshore steel structures*, Recommended practice DNV-RP-C203, Høvik, Norway, 2012.
- [9] C. Amzallag, J.P. Gerey, J.L. Robert and J. Bahuadl, *Standardization of the rainflow counting method for fatigue analysis*, International Journal of Fatigue, 16, 287-293, 1994.
- [10] J.H. Martens, *Topology optimization of a jacket for an offshore wind turbine by utilization of genetic algorithm*, Master thesis, Department of Civil and Transport Engineering, Norwegian University of Science and Technology, Trondheim, Norway, 2014.
- [11] F. Vorphal, W. Popko and D. Kaufer, *Description of a basic model of the UpWind reference jacket for code comparison in the OC4 project under IEA Wind Annex 30*, Technical Report, Fraunhofer IWES, Bremerhaven, Germany, 2013.

Surrogate-based Particle Swarm Optimization for Large-scale Wind Farm Layout Design

Ali Mehmani¹, Weiyang Tong², Souma Chowdhury³, Achille Messac⁴

¹ Syracuse University, Syracuse, NY, USA, amehmani@syr.edu

² Syracuse University, Syracuse, NY, USA, wtong@syr.edu

³ Mississippi State University, Mississippi State, MS, USA, chowdhury@bagley.msstate.edu

⁴ Mississippi State University, Mississippi State, MS, USA, messac@ae.msstate.edu

1. Abstract

Wind farm layout optimization (WFLO) is the process of optimizing the location of turbines in a wind farm site, with the possible objective of maximizing the energy production or minimizing the average cost of energy. Conventional WFLO methods not only limit themselves to prescribing the site boundaries, they are also generally applicable to designing only small-to-medium scale wind farms (<100 turbines). Large-scale wind farms entail greater wake-induced turbine interactions, thereby increasing the computational complexity and expense by orders of magnitude. In this paper, we further advance the Unrestricted WFLO framework by designing the layout of large-scale wind farms with 500 turbines (where energy production is maximized). First, the high-dimensional layout optimization problem (involving $2N$ variables for a N turbine wind farm) is reduced to a 6-variable problem through a novel mapping strategy, which allows for both global siting (overall land configuration) and local exploration (turbine micro-siting). Secondly, a surrogate model is used to substitute the expensive analytical WF energy production model; the high computational expense of the latter is attributed to the factorial increase in the number of calls to the wake model for evaluating every candidate wind farm layout that involves a large number of turbines. The powerful *Concurrent Surrogate Model Selection (COSMOS)* framework is applied to identify the best surrogate model to represent the wind farm energy production as a function of the reduced variable vector. To accomplish a reliable optimum solution, the surrogate-based optimization (SBO) is performed by implementing the Adaptive Model Refinement (AMR) technique within Particle Swarm Optimization (PSO). In AMR, both local exploitation and global exploration aspects are considered within a single optimization run of PSO, unlike other SBO methods that often either require multiple (potentially misleading) optimizations or are model-dependent. By using the AMR approach in conjunction with PSO and COSMOS, the computational cost of designing very large wind farms is reduced by a remarkable factor of 26, while preserving the reliability of this WFLO within 0.05% of the WFLO performed using the original energy production model.

2. Keywords: Large-scale wind farm; Layout optimization; Surrogate-based optimization; Concurrent surrogate model selection; Predictive estimation of model fidelity; Particle Swarm Optimization

3. Introduction

The wind energy harvested through large utility-scale wind farms can compete with conventional energy resources. A large utility-scale wind farm generally has a 500 MW installed capacity (can consist hundreds of wind turbines). Planning such a large scale wind farm is a complex process and extremely time-consuming. It includes various mutually correlated factors and large-scale effects, especially the energy losses due to the wake effects caused by a large number of turbines. The wind farm layout optimization (WFLO) for large-scale wind farms is desired, however, performing the WFLO of a large scale wind farm is computationally expensive. Surrogate-based optimization approaches can be applied to alleviate the computational burden in this complex design problem.

3.1 Surrogate-base Optimization

Surrogate models are purely mathematical models (i.e., not derived from the system physics) that are used to provide a tractable and inexpensive approximation of the actual system behavior. They are commonly used as an alternative to expensive computational simulations or to the lack of a physical model in the case of experiment-derived data. Major surrogate modeling methods include Polynomial Response Surfaces, Kriging, Moving Least Square, Radial Basis Functions (RBF), Support Vector Regression (SVR), and Neural Networks [1]. These methods have been applied to a wide range of disciplines, from aerospace design and automotive design to chemistry and material science [2].

The major pitfall in using surrogate models in optimization is that they can often mislead the search process, leading to suboptimal or infeasible solutions. To address this issue and provide optimum designs with high fidelity system evaluations, “*Surrogate-Based Optimization*” strategy can be applied. In these approaches, the accuracy and robustness of the surrogate model is improved by adding points where additional evaluations of the high fidelity model / experiment are desired to be performed. Infill points are generally added in (i) the region where the optimum is located (local exploitation); and/or (ii) the entire design space to improve the global accuracy of the surrogate (global exploration)[3, 4]. Infill points can be added in a fully sequential (one-at-a-time), or can be added in a batch sequential manner. There exist various criteria for determining the locations of the infill points including (i) Index-based criteria (e.g., Mean Square Error and Maximum Entropy criteria) and (ii) Distance-based criteria (e.g., Euclidean distance, Mahalanobis distance, and Weighted distance criteria) [5].

Over the last two decades, different Surrogate-Based Optimization strategies have been developed [6, 7]. Trosset and Torczon in 1997 [8] proposed an approach where the balance between exploitation and exploration was considered using the aggregate *merit function*, $\hat{f}(x) - \rho d_{min}(x)$, where, $d_{min}(x) = \text{Min}_x \|x - x^i\|$, $\rho > 0$. It is important to note that, this technique is independent of the type of surrogate modeling technique being considered. Jones et al. in 1998 [6] developed a well-known model management strategy that is based on an *Expected Improvement (EI)* criterion, and is called *Efficient Global Optimization (EGO)*. This powerful approach is however generally limited to surrogate models based on Gaussian processes. The surrogate-based optimization presented in this paper has the following characteristics: (i) It is independent of the type of model, (ii) It uses a reliable surrogate model (with a desired level of fidelity) at any given iteration of SBO, and (iii) It determines the optimal batch size for the infill points for the upcoming iteration of SBO.

3.2 Layout Optimization of Large Scale Wind Farms

The current research on solving the large layout optimization problem is mostly limited to quantify the layout using the streamwise and the spanwise spacings between turbines, and assumes that a specified number of turbines are uniformly distributed in pre-defined boundaries. As a result, the optimization is incompletely performed due to the prescribed conditions. Fuglsang et al. [9] defined the wind farm layout as a function of the spacings between rows and columns for a specified number of turbines. Perez et al. [10] used the numbers of rows and columns, the streamwise spacing and the spanwise spacing between neighboring turbines, the turbine rotor diameter, and a specified rectangular boundary to determine the wind farm layout. Wagner et al. [11] developed a framework that can solve the WFLO for up to 1000 turbines. In this framework, the initial location of turbines is restricted to an array-like layout. However, a radial displacement around each turbine is allowed. The approach presented in this paper is capable of optimizing the location of turbines for large wind farms, i.e., 500-turbine scale wind farms, without prescribing the farm boundaries.

4. Mapping of the Layout for a Large Scale Wind Farm

In this section, we present a mapping approach to quantify the layout of a very large wind farm using six mapping factors: (i) the maximum allowable *streamwise* and *spanwise* spacings between neighboring turbines (s_{max} and r_{max}), (ii) the average spacings of rows and columns (d_r and d_c), (iii) the normalized local radial displacement, (iv) the turbine rotor diameter (D), (v) Number of turbines (N_{turb}), (vi) the farm site orientation (ϕ), and (v) the maximum number of rows and/or the maximum side length of the wind farm. The maximum allowable *streamwise* and *spanwise* spacings between neighboring turbines are determined based on the size of turbine rotor diameter. the average spacings of rows and columns are variable for difference rows and columns, and given by

$$\begin{aligned} d_r &= (r_{max} - r_{min}) \times \left\{ A\pi \frac{j}{N_{row}} - \lfloor \frac{1}{2} + (A\pi \frac{j}{N_{row}}) \rfloor + 1 \right\} + r_{min} \\ d_c &= (s_{max} - s_{min}) \times \left\{ B\pi \frac{i}{N_{column}} - \lfloor \frac{1}{2} + (B\pi \frac{i}{N_{column}}) \rfloor + 1 \right\} + s_{min} \end{aligned} \quad (1)$$

where s_{min} and r_{min} are the minimum *streamwise* and *spanwise*, respectively; A and B are design factors in mapping function; i and j are respectively the row and column indexes; N_{row} and N_{column} are number of rows and column, respectively. By this definition, non-uniform spacings between rows and columns are allowed.

In this paper, the normalized local radial displacement is expressed as the Gaussian distribution with zero mean ($\mu = 0$) and the variable standard deviation (σ) [11]. The actual radial displacement is

obtained by multiplying the minimum *streamwise/spanwise* between turbines. This allows the turbines not to be restricted to be in the grid form. The side length of the wind farm can be provided based on the average land usage of US commercial wind farms. Therefore, the coordinates of the turbine at the I^{th} row and the J^{th} column are given by

$$\begin{aligned} X_I &= \sum_{j=1}^J \left[(r_{max} - r_{min}) \times \left\{ A\pi \frac{j}{N_{row}} - \left\lfloor \frac{1}{2} + \left(A\pi \frac{j}{N_{row}} \right) \right\rfloor + 1 \right\} + r_{min} \right] + r_{min} \hat{r}(0, \sigma) \\ Y_J &= \sum_{i=1}^I \left[(s_{max} - s_{min}) \times \left\{ B\pi \frac{i}{N_{column}} - \left\lfloor \frac{1}{2} + \left(B\pi \frac{i}{N_{column}} \right) \right\rfloor + 1 \right\} + s_{min} \right] + s_{min} \hat{r}(0, \sigma) \end{aligned} \quad (2)$$

5. Surrogate model selection using COSMOS

In Section 4, the dimensionality reduction is performed. In this section, the *Concurrent Surrogate Model Selection (COSMOS)* framework (developed by Chowdhury et al. [12]) is applied to select the best surrogate model to represent the *average annual energy production of a large-scale wind farm* as a function of the mapping factors and the farm site orientation (ϕ), illustrated in Table 2. In this paper, this automated model selection is based on the error measure given by the Predictive Estimation of Model Fidelity (PEMF) [13] and Mixed Integer Nonlinear Programming (MINLP). Unlike most other model selection methods, the COSMOS framework coherently operates at all the three levels necessary to facilitate optimal selection, i.e., (i) selecting the model type (e.g., RBF or SVR), (ii) selecting the kernel function type (e.g., cubic or multiquadric kernel in RBF), and (iii) determining the optimal values of the typically user-prescribed parameters (e.g., shape parameter in RBF) – thereby allowing selection of globally competitive models. COSMOS offers five different criteria for selection of optimal surrogates. In the current implementation, three of them are selected including: (i) the median error (E_{med}^{mo}), (ii) the maximum error (E_{max}^{mo}), and (iii) the variance of the median error ($E_{med}^{\sigma^2}$).

Next, the proposed approach is implemented in a 500-turbine wind farm. In this problem, the number of sample points for training the surrogate models considered in the COSMOS framework is $N(\{X\}) = 200$ and the average annual energy production in these sample points is estimated using the model incorporated in the Unrestricted Wind Farm Layout Optimization framework [14]. The surrogate models identified using COSMOS for the average annual energy production of a large-scale wind farm under the mentioned three criteria, are listed in Table 1. In this problem, the selected surrogate model will be

Table 1: The set of surrogate models given by COSMOS for the wind farm energy production problem

COSMOS TEST	Pareto Surrogate Model Selected
Test I: $\min[E_{med}^{mo}, E_{max}^{mo}]$	Kriging with Linear correlation, SVR with Sigmoid kernel
Test II: $\min[E_{med}^{mo}, E_{med}^{\sigma^2}]$	Kriging with Linear & Exponential correlation, SVR with Sigmoid kernel

used as an initial model in the surrogate-based optimization process. In the surrogate-based optimization process, the fidelity of surrogate model iteratively should be improved by adding infill points in the optimization process. Therefore, Kriging model with Linear correlation function that is selected in Test I and Test II could be the best choice. The dimensionality reduction and the implementation of the surrogate model reduce the computational cost on a very large wind farm layout optimization more than 95%.

4. Adaptive Model Refinement (AMR)

The major challenge of using surrogate models in optimization is that they can often mislead the search process due to underestimation or overestimation of system behavior and leading to suboptimal or infeasible solutions. To address this issue, surrogate-based optimization with adaptive model refinement (AMR) [15] is applied in this paper. In AMR, reconstruction (or refinement) of the model is performed by sequentially adding a batch of new samples at any given iteration (of surrogate-based optimization (SBO)) when a switching metric is met. The major components of the surrogate-based optimization using AMR method include:

- (i) The model switch metric [16]: This metric is perceived as a decision-making tool for the timing of surrogate model refinement. Performing model refinement (by adding infill points) too early in the optimization process can be computationally expensive while wasting resources to explore undesirable regions of the design domain. On the other hand, updating surrogate model too late might mislead the search process early on to suboptimal regions of the design domain, i.e., leading to scenarios

where the global optimum is outside of the region spanned by the population of candidate solutions in later iterations. This metric is formulated by comparing (1) the uncertainty associated with the outputs of the current model, and (2) the distribution of the latest fitness function improvement over the population of candidate designs. Whenever the model switching metric is met, the history of the fitness function improvement is used to determine the desired fidelity for the upcoming iterations of SBO.

- (ii) The Predictive Estimation of Model Fidelity [13]: In AMR, the PEMF method with certain implementation is used to quantify the surrogate model fidelity, and identify the optimal batch size (e.g., size of infill points). The inputs and outputs of PEMF (in the AMR method) are expressed as:

$$[\mathbb{P}_{(\mu_\varepsilon, \sigma_\varepsilon)}, \Gamma^{Infill}] = f_{PEMF}(X, \varepsilon^*) \quad (3)$$

where the vector X represents the sample data (input and output) used for training the surrogate model; and ε^* is the desired fidelity in the model refinement process. In Eq. 3, $\mathbb{P}_{(\mu_\varepsilon, \sigma_\varepsilon)}$, and Γ^{Infill} respectively represent the distribution of the error in the surrogate model, and the batch size for the infill points to achieve a desired level of fidelity in the AMR method.

- (iii) Optimization algorithm: Mixed-Discrete PSO (MDPSO): In the presented surrogate-based optimization methodology, optimization is performed using an advanced implementation of the Particle Swarm Optimization (PSO). In this paper, we use one particular advanced implementation of the PSO algorithm called Mixed-Discrete PSO (MDPSO), which was developed by Chowdhury et al [17].

6. Numerical Experiments

In this section the proposed approach is implemented to design a 500-turbine wind farm for measured site data, in order to illustrate the effectiveness of this unique wind farm layout optimization approach. The objective is to maximize the average annual energy production of the farm through layout optimization ($P_{farm} = \text{annual energy production}/365 \times 24$). In this problem, the farm layout optimization is started using the best surrogate model selected in Sec. 4 (Kriging with Linear correlation function). To reach a reliable optimum solution, a refinement of the surrogate is then performed by sequentially adding batches of new samples using the adaptive model refinement approach. The optimization problem is defined as

$$\begin{aligned} \max_V : \quad & f = P_{farm} \\ & V = \{v_1, v_2, \dots, v_6\} \\ \text{subject to} \quad & \\ & g_1(v) \leq 0 \\ & g_2(v) \leq 0 \\ & V^{Lower} \leq v_i \leq V^{Upper} \end{aligned}$$

The upper and lower bounds of design variables ($v_i = 1, 2, \dots, 6$) are listed in Table 2. These variables include the mapping factors (that defines the coordinates of the wind turbines in the farm), and the farm site orientation (ϕ). In Eq. 4, $g_1(v) = \|A_{MW} - 45(\text{hectare}/MW)\|$ is the land area constraints. This constraint is defined based on the average land usage of US commercial wind farms in 2009. In this equation, $g_2(v) = \sum_{i,j=1, i \neq j}^{N=500} \max\{4D - d_{ij}\}$ is the minimum inter-turbine spacing constraints. In this paper, the GE-1.5MW-XLE turbine is chosen as the specified turbine-type [18]; the minimum *streamwise* (s_{min}) and *spanwise* (r_{min}) are set to the same value: $4D$; and the wind data is obtained from the North Dakota Agricultural Weather Network (NDAWN)[19].

Table 2: Upper and lower bounds of design variables

Design variables	Lower bound	Upper bound
r_{max}	5D	15D
s_{max}	5D	15D
A	-20	20
B	-20	20
σ	0	1
ϕ	0	90

7 Results and Discussion

In this optimization problem, the AMR is applied at every iteration of PSO. The population size of PSO is pre-specified to $N_{pop} = 300$, and the PSO algorithm converges by satisfying the predefined function

tolerance, $\delta f = 1e - 6$. In this problem the model refinement will be implemented if the current size of data set is less than $N(\{X\}) = 500$. In this optimization problem, the initial population of particles is generated using the Kriging with Linear correlation function. The AMR approach adaptively improve the fidelity of the surrogate model fifteen times during the optimization process (over a total of 110 iterations), resulting in an optimum design with a reasonable level of fidelity.

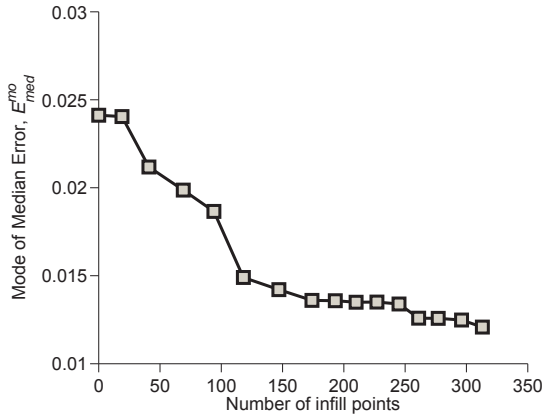


Figure 1: The improvement of the surrogate model fidelity through sequential model refinement process with AMR

set ($N(\{X\}) = N^{Current}(\{X\}) + \Gamma^{Infill}$) used to refine (update) the active surrogate model in the AMR approach, and (iii) the iteration that the model refinement is performed (the AMR metric is met). It is observed that, from the first iteration till the 8th iteration the initial surrogate model with $N(\{X\}) = 200$ is active, before refining the model using additional 19 sample data through the AMR approach. The final switching event, from the surrogate model constructed using $N(\{X\}) = 496$ training points to the surrogate model constructed using $N(\{X\}) = 513$, occurs at the 96th iteration. The optimization progresses using the surrogate model constructed using $N(\{X\}) = 513$ training points for another 14 iterations before reaching convergence. In this case, the algorithm converges by satisfying the predefined function tolerance, $\delta f = 1e - 6$.

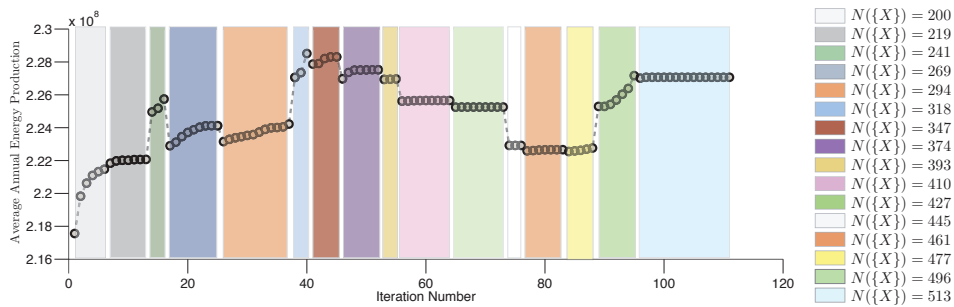


Figure 2: Convergence history of the surrogate-based optimization using AMR

Next, we investigate how the AMR method performs better than simply using the single stage sampling strategy for SBO. The result yielded by the AMR method are therefore compared with the results yielded by running MDPSO using the surrogate model constructed in the one-step method (using all 500 sample points). The optimum results are thus obtained, and the total number of function evaluations in each case are reported in Table 3. The final column of this table shows the actual function estimate for the optimum design obtained under each optimization run. It is observed that the PSO-AMR not only requires 26 times less computing time compared to PSO-HF, it also provides the optimum value that is 14.9 MWh better than simply using the single stage sampling strategy for SBO. It is also observed that, in the PSO-AMR approach, the optimum is located in the region where the SM model has 0.63% error.

Table 3: Optimization results using different optimization approaches

Approach	v_1^* $\times D$	v_2^* $\times D$	v_3^*	v_4^*	v_5^*	v_6^* (degree)	Optimum function P_{farm} ($f^* \times 10^8$)	Model in last iteration	No. of HF function evaluations	HF response at optimum ($f_{HF}(v^*) \times 10^8$)	A_{MW}
PSO-SM	14.03	13.40	15.68	4.72	0.05	70.73	2.3013	SM	500	2.1248	29.7085
PSO-HF	13.70	13.54	16.27	4.92	0.08	69.69	2.2760	HF	300×45	2.2760	43.80
PSO-AMR	12.65	12.57	9.99	-2.53	0.03	72.17	2.2892	SM	513	2.2748	44.74

PSO-SM: optimization performed by MDPSO solely using the surrogate model with all 500 sample points

PSO-HF: optimization performed by MDPSO solely using the high fidelity model

PSO-AMR: optimization performed by MDPSO using AMR approach (surrogate-based optimization using AMR)

8 Conclusion

This paper presented a new approach for layout optimization of very large scale wind farms. A mapping of the wind farm layout to the detailed turbine coordinates was created, allowing the wind farm layout to be represented by a set of 6 parameters. As a result, the design variable space for optimizing the layout of a large scale wind farm is significantly reduced. The COSMOS framework was then applied to select the globally-best surrogate model to represent the energy production of the wind farm as a function of the reduced set of layout variables. Surrogate-based optimization was then performed using the Adaptive Model Refinement approach, implemented through Particle Swarm Optimization. The objective of wind farm layout optimization was to maximize the average annual energy production of a 500-turbine wind farm. The results indicated that AMR along with Mixed Discrete PSO improved the efficiency of the optimization process by a factor of 26 when compared to optimization using the standard energy production model, while retaining an accuracy of within 0.05% of the latter.

References

- [1] A. Messac. *Optimization in Practice with MATLAB: For Engineering Students and Professionals*. Cambridge University Press, 2015.
- [2] J Zhang, S. Chowdhury, A. Mehmani, and A. Messac. Characterizing uncertainty attributable to surrogate models. *Journal of Mechanical Design*, 136(3), 2014.
- [3] A. J. Keane and P. B. Nair. *Computational Approaches for Aerospace Design: The Pursuit of Excellence*. Wiley, New York, 2005.
- [4] A. I. J. Forrester, A. Sóbester, and A. J. Keane. *Engineering Design via Surrogate Modelling: A Practical Guide*. Wiley, New York, 2008.
- [5] B. Williams, J. L. Loepky, L. M. Moore, and M. S. Macklem. Batch sequential design to achieve predictive maturity with calibrated computer models. *Reliability Engineering and System Safety*, 96(9):1208–1219, 2011.
- [6] D. Jones, M. Schonlau, and W. Welch. Efficient global optimization of expensive black-box functions. *Journal of Global Optimization*, 13(4):455–492, 1998.
- [7] J. P. Kleijnen, W. Van Beers, and I. Van Nieuwenhuysse. Expected improvement in efficient global optimization through bootstrapped kriging. *Journal of global optimization*, 54(1):59–73, 2012.
- [8] M. W. Trosset and V. Torczon. Numerical optimization using computer experiments. Technical report, DTIC Document, 1997.
- [9] P. Fuglsang and T. Kenneth. Cost optimization of wind turbines for large-scale offshore wind farms. Technical report, Risoe National Lab, Roskilde (Denmark), 1998.
- [10] G. Perez, L. M. Joseba, L. Val, A. Sumper, F. Schuon, de Prada M, M. Aragues, H. Lopes, H. Ergun, and D. van Hertem. Deep offshore wind farm planning and cost calculation tools. In *Wind Energy Association Off-shore*, 2013.
- [11] M. Wagner, K. Veeramachaneni, F. Neumann, and U O’Reilly. Optimizing the layout of 1000 wind turbines. In *European Wind Energy Association Annual Event*, pages 205–209, 2011.
- [12] S. Chowdhury, A. Mehmani, and A. Messac. Concurrent surrogate model selection (cosmos) based on predictive estimation of model fidelity. In *ASME 2014 International Design Engineering Technical Conferences (IDETC)*, Buffalo, NY, August 2014.
- [13] A. Mehmani, S. Chowdhury, and A. Messac. Predictive quantification of surrogate model fidelity based on modal variations with sample density. *Structural and Multidisciplinary Optimization*, 2015.
- [14] Souma Chowdhury, Jie Zhang, Achille Messac, and Luciano Castillo. Optimizing the arrangement and the selection of turbines for wind farms subject to varying wind conditions. *Renewable Energy*, 52:273–282, 2013.
- [15] A. Mehmani, S. Chowdhury, and A. Messac. Variable-fidelity optimization with in-situ surrogate model refinement. In *ASME 2015 International Design Engineering Technical Conferences (IDETC)*, Boston, MA, August 2015.
- [16] A. Mehmani, S. Chowdhury, W. Tong, and A. Messac. Adaptive switching of variable-fidelity models in population-based optimization algorithm. *Engineering and Applied Sciences Optimization*, 1(1), 2015.
- [17] S. Chowdhury, W. Tong, A. Messac, and J. Zhang. A mixed-discrete particle swarm optimization algorithm with explicit diversity-preservation. *Structural and Multidisciplinary Optimization*, 47(3):367–388, 2013.
- [18] GE Energy. GE 1.5MW wind turbine series, 2009. Accessed: January 2015.
- [19] NDSU. The north dakota agricultural weather network. <http://ndawn.ndsu.nodak.edu>, [Accessed: January 2012].

One-dimensional Function Extrapolation Using Surrogates

Yiming Zhang¹, Nam-Ho Kim², Chan-Young Park³, Raphael T. Haftka⁴

¹ University of Florida, Gainesville, FL, USA, yimingzhang521@ufl.edu

² University of Florida, Gainesville, FL, USA, nkim@ufl.edu

³ University of Florida, Gainesville, FL, USA, cy.park@ufl.edu

⁴ University of Florida, Gainesville, FL, USA, haftka@ufl.edu

1. Abstract

Surrogate modeling is commonly used to estimate function values efficiently and accurately at unsampled points. The estimation procedure is called interpolation when target points are inside the convex hull of sampled points while extrapolation otherwise. This paper explores one-dimensional deterministic function extrapolation using surrogates. We first define a new error metric, relative average error, for quantifying overall performance of extrapolation technique. Ordinary Kriging and Linear Sheppard surrogates proved to be safer on several challenging functions than polynomial response surfaces, support vector regression or radial basis neural functions. This reflected that prediction of these surrogates converge to mean value of samples at points far from samples.

It's commonly recognized that long-range extrapolation is likely to be less accurate than short-range extrapolation. Two kinds of effective extrapolation distance are defined to indicate how far we can extrapolate test functions. We propose using the correlation between the nearest sample and the prediction point given by Ordinary Kriging as indicator of effective extrapolation distance. The relationship between effective extrapolation distance and corresponding correlation over the distance is examined by several test functions. A large value of correlation is associated with effective extrapolation distance.

2. Keywords: One-dimensional extrapolation, Extrapolation distance, Kriging, Error metric

3. Introduction

In surrogate modeling, it is common to sample a function f at several points and fit them with an explicit function in order to estimate the function at other points[1]. This is often required for optimization or reliability analysis in which thousands of function evaluations are common, and each sample often means expensive simulation or costly or time-consuming experiment.

Function estimation is defined as interpolation when target points are inside the convex hull of sampled data points and extrapolation otherwise. For one-dimensional samples, convex hull is the smallest interval containing the samples. Although many research results have been reported on the accuracy of surrogate modeling, most focused on the prediction accuracy in interpolation. Extrapolation is usually associated with large estimation errors [2] and commonly encountered in three situations:

- 1) Sampling pattern such as Latin Hypercube sampling is adopted, which typically does not sample at or near the boundaries of sampling region.
- 2) For function estimation in high-dimensional space, we usually cannot afford enough points to avoid extrapolation. For example, in twenty-dimensional box, more than million points (2^{20}) are required.
- 3) Region of interest changes after samples are collected[3].

Besides the above conditions, extrapolation may be useful when the target points cannot be sampled via simulation or experiment due to the need to know future events, inadequacy of simulation software or high cost to perform experiments[4]. As a first step to explore effective extrapolation scheme in engineering problems, attention is limited here to one-dimensional (1D) function extrapolation.

This paper investigates general issues on extrapolation using surrogates. Section 4 illustrates possible behavior of surrogates for extrapolation and potentials of extrapolation using surrogates. Section 5 proposes an error metric designed for extrapolation. Extrapolation of a few examples using five surrogates are compared in Section 6. Section 7 discusses the possibility of estimating extrapolation distance using surrogates.

4. Possible behaviours of extrapolation using surrogates

Estimation of several analytical functions using ordinary kriging is presented to illustrate possible behavior in the extrapolation region, which is assumed here to be inaccessible. Figure1 presents three 1D functions which have different function behavior between the accessible and inaccessible domains. These three functions are estimated

using Ordinary Kriging in Fig.2. It is seen extrapolation results approximate the true function value surprisingly well. Since extrapolation in Kriging is based on correlation between function values based on distance, we evaluate first the correlation between inaccessible domain and accessible domain.

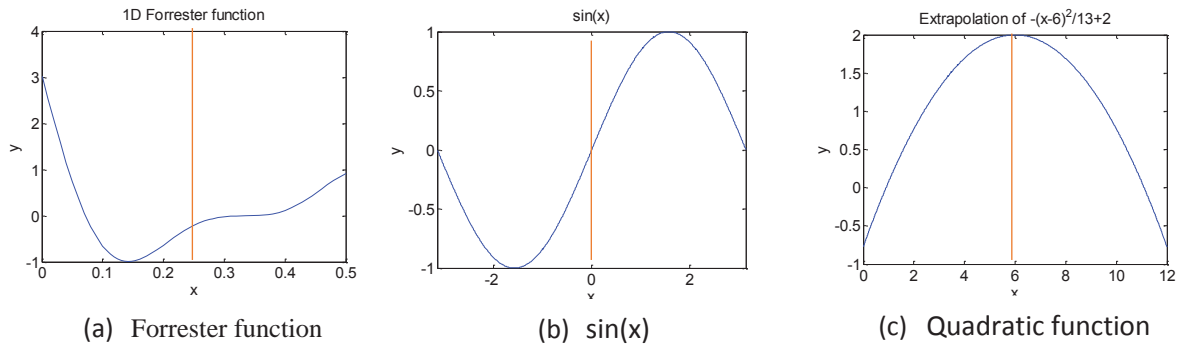


Figure 1: (a) Forrester function, (b) $f(x) = \sin(x)$ and (c) $f(x) = -(x-6)^2/13+2$. Vertical line denotes border of inaccessible domain which is on the left and accessible domain which is on the right

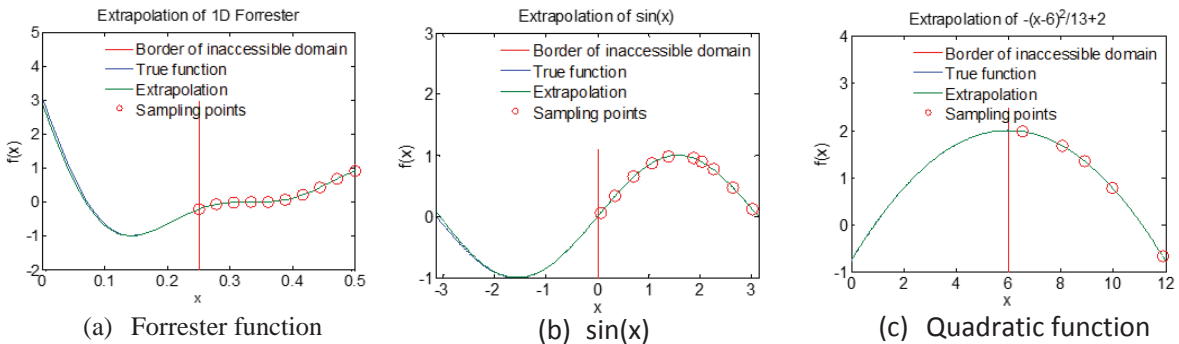


Figure 2: Extrapolation of (a) Forrester function, (b) $f(x) = \sin(x)$ and (c) $f(x) = -(x-6)^2/13+2$. Vertical line denotes border of inaccessible domain which is on the left and accessible domain which is on the right

Denote by r the ratio of length of extrapolation distance to that of accessible domain. As expected, extrapolation error increases with r as shown in Fig. 3 for the log function. In this paper, the length of inaccessible domain and accessible domain are set to be equal, which would typically be considered as long range extrapolation.

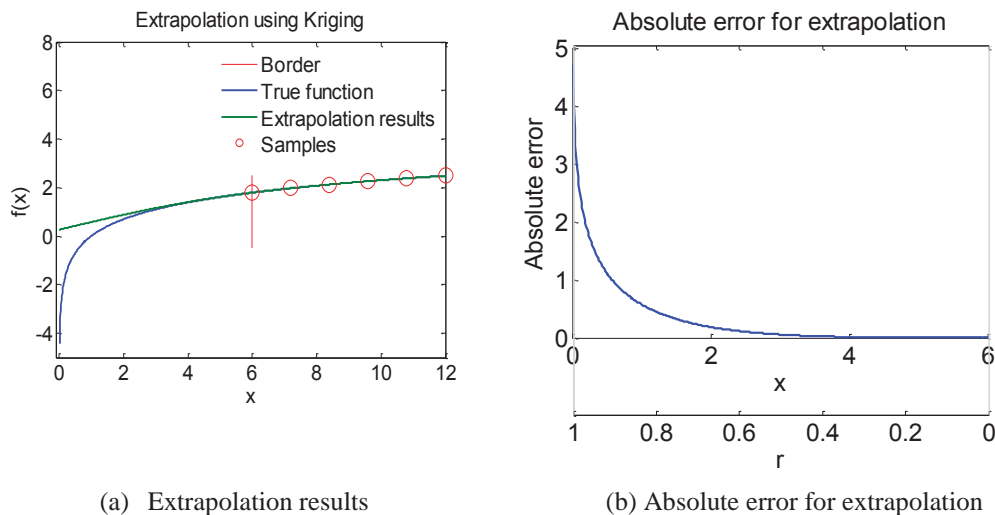


Figure 3: Extrapolation of $f(x) = \log(x)$

Another factor determining the extrapolation accuracy is how close the samples to the boundary are. Figure 4 illustrates that by using samples close to the boundary. Extrapolation accuracy improves obviously after shifting

samples close to inaccessible domain.

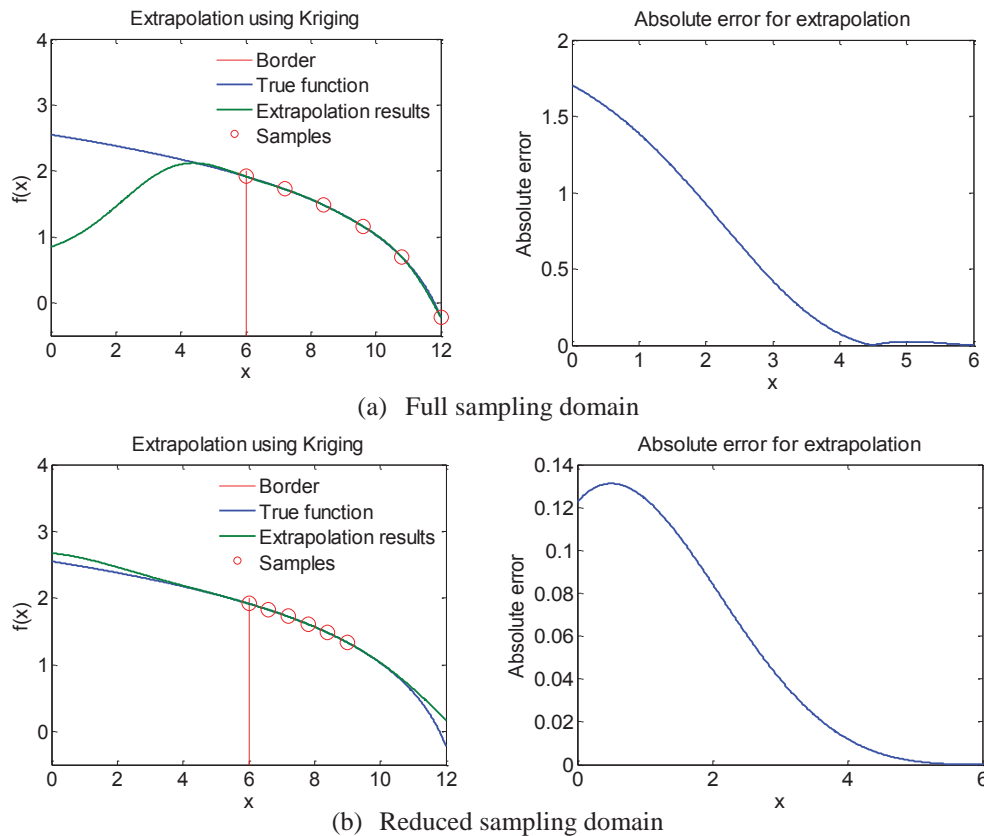


Figure 4: Extrapolation of $f(x) = \log(12.8 - x)$ from (a) Full sampling domain and (b) Reduced sampling domain

The examples and discussion above identified three issues, which are correlation between inaccessible domain and accessible domain, relative extrapolation distance and absolute extrapolation distance, which are important for extrapolation research.

5. An error metric for 1D extrapolation

We denote extrapolation result by $\hat{f}(x)$. The performance of one-dimensional extrapolation technique may be quantified by various error measures. Relative error $e_{cr}(x)$ is

$$e_{cr}(x) = \left| \frac{\hat{f}(x) - f(x)}{f(x)} \right| \quad (1)$$

$e_{cr}(x)$ may be misleading when the function changes sign. So one often uses the range of the function instead of the function value for normalization. In addition, for extrapolation, we are often interested in the error in predicting change from a boundary point x_b . This error, $e_{ec}(x)$ is:

$$e_{ec}(x) = \left| 1 - \frac{\hat{f}(x) - f(x_b)}{f(x) - f(x_b)} \right| \quad (2)$$

For example, if based on this year's record we predict that gas prices will rise from \$4/gallon today to \$5/gallon a year from now, and they rise only to \$4.50, we may consider $e_{ec}(x) = 100\%$ this as rather than $e_{cr}(x) = 11\%$ error. Of course, this error measure will fail if the change in the function is near zero, and for this case an alternate relative error is defined as $e_r(x)$. Denoting $range(f)$ as the range of true function in the extrapolation domain, $e_r(x)$ is:

$$e_r(x) = \left| \frac{\hat{f}(x) - f(x)}{range(f)} \right| \quad (3)$$

$e_r(x)$ is used in the following for extrapolation comparisons. We may also use $range(f(x)) = \max(f_1) - \min(f_1)$, where f_1 denotes function value in the range between extrapolation point x and the closest sample. In order to evaluate the overall performance of extrapolation, we use the average error AE in extrapolation domain:

$$AE = \frac{\int_{x_i}^{x_b} e_r(x) dx}{x_b - x_i} \quad (4)$$

6. Surrogate comparison for extrapolation

Surrogates have different performance for interpolation and extrapolation. We test the performance of five popular surrogates: Ordinary Kriging, Polynomial response surface (PRS), Radial basis neural network (RBNN), Linear Shepard (moving least squares), and Support vector regression (SVR). Four test functions were extracted from well-known multidimensional functions taken from [5] and shown in Fig. 5.

The number of sampling points along each line is 6. Sampling points are generated using Latin hypercube sampling with 5 iterations, which introduces randomness in the position of the samples. To average out the effect of the positions of the sampling points, 30 sets of samples are generated for each test function, and the mean value of AE for all the sample sets are computed. The extrapolation results of test functions are listed in Table 1. All the surrogates except Ordinary Kriging and Linear Shepard can generate huge errors. Kriging and Linear Shepard do not extrapolate well, but do not incur huge errors. This is because function estimation using Ordinary Kriging and Linear Shepard are weighted sum of samples and they eventually revert to the mean of the samples. Ordinary Kriging was then selected for further testing in the next section.

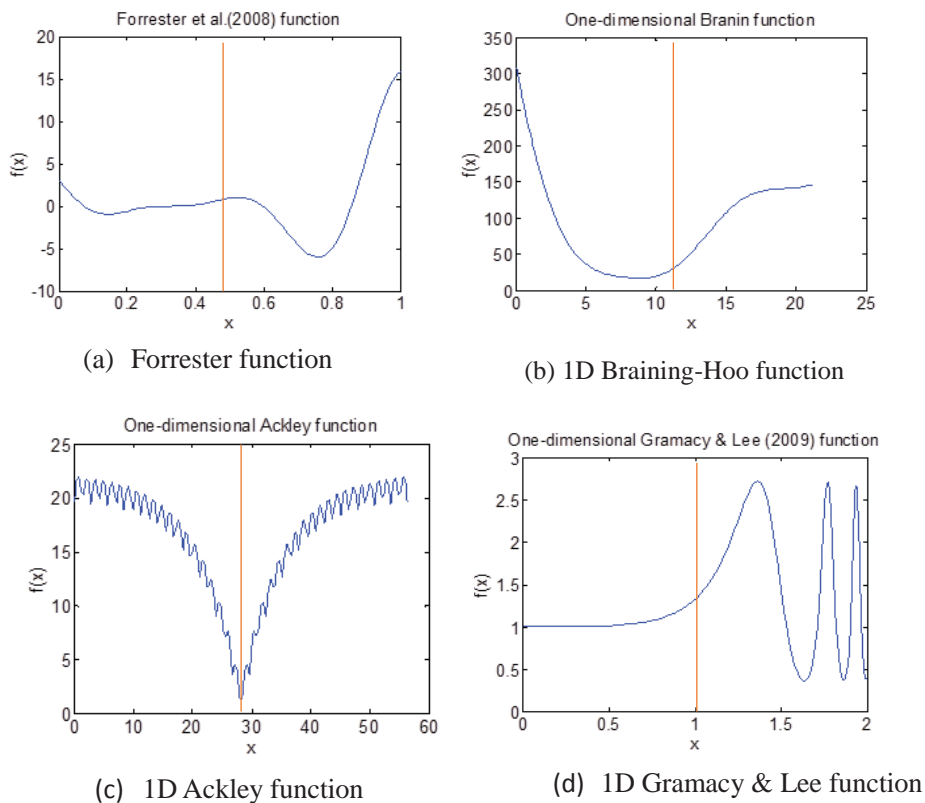


Figure 5: Four test functions for surrogate selection. Domains close to origin are inaccessible domain.

Table 1: Average AE for extrapolation of test functions using 30 sets of samples

Surrogate models	Test functions			
	Average AE of Forrester et al.(2008) function	Average AE of one-dimensional Branin-Hoo function	Average AE of one-dimensional Ackley function	Average AE of one-dimensional Gramacy & Lee (2009) function

Kriging	0.80	0.13	0.31	1.44
Quadratic PRS	13.36	0.97	2.01	6.13
Cubic PRS	7.54	0.53	4.02	60.22
Quartic PRS	93.62	3.18	8.67	442.14
RBNN	2322.5	0.2	0.54	25612
Linear Shepard	0.44	0.19	0.56	1.85
SVR	20.7	0.26	0.76	188.08

7. Estimating extrapolation distance

Kriging is based on a correlation structure between points based on their distance. Large correlation between extrapolation points to closest sample may indicate reliable extrapolation. We defined two types of effective extrapolation distance and tried to find the relation between extrapolation distances of test functions and corresponding correlation over that extrapolation distance.

7.1. Effective extrapolation distance

Ordinary Kriging assumes that the error at a point is normally distributed with a mean of zero and a given standard deviation. Error bounds here are set by 95% confidence interval of this normal distribution. The conservative extrapolation distance d is defined for measuring how far the error bounds of the surrogate bound the true function.

The second extrapolation distance is denoted as accuracy distance. Accurate distance is inside conservative distance and in which estimated error bounds of the points are less than 30% of $range(f)$. We make an exception to the requirement of being within the error bounds when they are very tight, allowing error bounds to be off by 1% of $range(f)$. Two types of effective extrapolation distance are illustrated in Fig. 6.

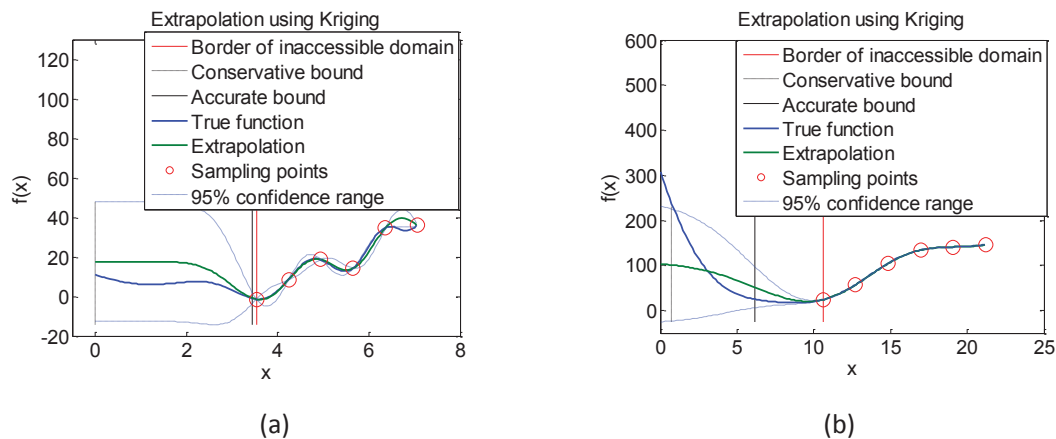


Figure 6. Conservative and accurate distances for extrapolation

7.2 Identification of effective extrapolation distance using correlation

The error estimates get less dependable as we go deeper into the extrapolation domain. We tried to find certain indicators of effective extrapolation distance based on Kriging. Prediction of Ordinary Kriging is based on the assumption that correlation between function values decay with distance at a rate controlled by θ , with the correlation r between two points at a distance l being equal to

$$r(l) = \exp(-\theta \times l^2) \quad (5)$$

θ is usually found by maximizing likelihood of observing that the samples come from Gaussian process. Large θ means short wavelength, large curvature, fast changing function, and reverse for small θ . It is reasonable to expect that as the correlation between function values in the sampling domain and extrapolation domain diminishes, the reliability of the error estimates deteriorates. Distance corresponds to given small correlation as possible measure of how far we can go.

We have performed a test to figure out the relation between effective extrapolation distance and corresponding correlation value. 10 multi-dimensional functions: Branin-Hoo function, Ackley function, Gramacy & Lee (2009) function, Hartmann 3-D Function, Hartmann 6-D Function, Sasena Function, Friedman Function, Zhou (1998) Function, Franke's Function, Dette & Pepelyshev (2010) curved Function.

These functions are commonly used for testing algorithm performance and can be found from [5]. 3 lines are

extracted towards one random vertex from each function. We use 6 uniformly spaced samples to train Kriging. In Fig.7, we present corresponding correlation value between effective extrapolation bounds and closest sample. Accurate bounds are associated with large correlation value. The third quartiles of correlation values corresponding to accurate bounds and conservative bounds are both 0.99. The box plots of distance ratios are dispersed and imply extrapolation accuracy vary with functions.

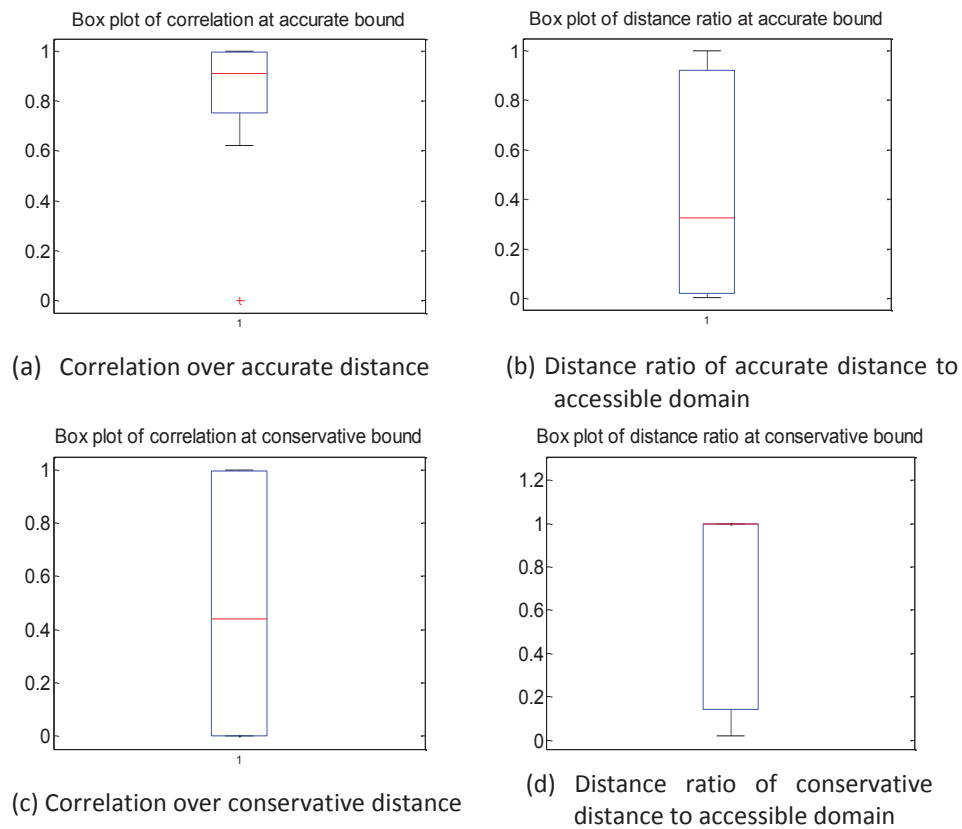


Figure 7: Correlation and distance ratio over effective distance while extrapolating 30 1D functions

8. Summary

This paper first illustrated the possibility of extrapolating 1D function using surrogates and proposed an average error metric designed for quantifying the performance of extrapolation technique. Testing extrapolation on several challenging functions indicated that Kriging and Linear Shepard were safer than other surrogates. We defined two types of effective extrapolation distance and correlation of Ordinary Kriging has been demonstrated as a possible indicator for effective extrapolation distance based on the tests of 30 one-dimensional functions.

9. Acknowledgement

This work is supported by the U.S. Department of Energy, National Nuclear Security Administration, Advanced Simulation and Computing Program, as a Cooperative Agreement under the Predictive Science Academic Alliance Program, under Contract No. DE-NA0002378.

10. References

- [1] N. V. Queipo, R. T. Haftka, W. Shyy, T. Goel, R. Vaidyanathan, and P. Kevin Tucker, "Surrogate-based analysis and optimization," *Progress in aerospace sciences*, vol. 41, pp. 1-28, 2005.
- [2] A. Chaudhuri and R. T. Haftka, "Optimistic Bias in Surrogate Prediction near Surrogate Optima."
- [3] V. Balabanov, O. Weckner, and J. Wu, "Reducing Error of Polynomial Approximation Outside of Designated Design Space for Practical Problems," 2014.
- [4] D. An, J.-H. Choi, N. H. Kim, and S. Pattabhiraman, "Fatigue life prediction based on Bayesian approach to incorporate field data into probability model," *Structural engineering & mechanics*, vol. 37, p. 427, 2011.
- [5] "Virtual Library of Simulation Experiments: Test Functions and Datasets", [Online] Available: <http://www.sfu.ca/~ssurjano/optimization.html>

Fatigue Sensitivity Analysis of Offshore Wind Turbine Structures

Kok-Hon Chew¹, Michael Muskulus², Srikanth Narasimalu³, Kang Tai⁴, E.Y.K. Ng⁵

¹School of Mechanical and Aerospace Engineering, Nanyang Technological University, Singapore, chew0272@e.ntu.edu.sg

²Department of Civil and Transport Engineering, Norwegian University of Science and Technology, Trondheim, Norway, michael.muskulus@ntnu.no

³Energy Research Institute @ NTU, Nanyang Technological University, Singapore, nsrikanth@ntu.edu.sg

⁴School of Mechanical and Aerospace Engineering, Nanyang Technological University, Singapore, mktai@ntu.edu.sg

⁵School of Mechanical and Aerospace Engineering, Nanyang Technological University, Singapore, mykng@ntu.edu.sg

1. Abstract

Design optimization of offshore wind turbine structures is generally fatigue driven, yet the fatigue sensitivities with respect to design variables are commonly approximated using finite differences, leading to inefficiency and unreliable information. This paper presents analytical methods to calculate the gradients of fatigue damage and equivalent fatigue loads in both time and frequency domains, focusing on their use with the rainflow counting and Dirlik's methods, respectively, for implementation in the optimization of offshore wind turbine structures. Comparison studies against finite difference schemes, for simulated stress data experienced by the OC4 jacket substructure, show that the fatigue damage gradients were very sensitive to response sensitivities, while highlighting several key suggestions which could improve the numerical fatigue sensitivity analysis.

2. Keywords: Fatigue; sensitivity analysis; structural optimization; gradient-based; offshore wind.

3. Introduction

Fatigue assessment is critical in the design of offshore wind turbine structures, as the structures experience vibrations during operation, while subject to time-varying wind and wave loads [1]. When performing structural optimization, the gradients of fatigue damage with respect to design variables are valuable for an optimizer to determine the best direction for improvement [2]. A finite difference method is commonly employed to approximate the sensitivity information, since the method is easy to implement while the dynamic analysis of a wind turbine system generally requires specialized software which often cannot be modified or extended [2,3]. Nevertheless, the method can be inefficient and unreliable when it is used for design sensitivity analysis [4]. On the other hand, the analytical formulae for fatigue damage sensitivities cannot be evaluated readily. Various fatigue assessment techniques (e.g. in the time domain and by spectral methods) are available and the process to calculate stress range histograms or stress range probability density functions (PDF) requires one to go through the cycle counting or the Fourier transform, respectively. In this paper, methods to calculate the analytical fatigue damage gradients for both time and frequency domains are presented. Further studies are carried out to compare them against the finite difference schemes under consideration of various parameters, such as step sizes, time steps, joint configurations and stress concentration effects; and discuss their implications on the fatigue gradients estimation.

4. Fatigue assessment of offshore wind turbine structures

The general approach for fatigue assessment of offshore wind turbine structures is documented in [5,6,7]. Fig. 1 illustrates the procedure. Internal nominal stresses, in the form of time series which are recovered from system responses, are pre-multiplied with Stress Concentration Factors (SCF) and superimposed to obtain the Hot Spot Stresses (HSS). The SCF can be computed using empirical formulae as prescribed by Det Norske Veritas, given the joint class, geometry and dimensions [5]. As for the HSS, they are evaluated at eight different spots around the circumference of joint intersections, at both brace and leg sides.

The HSS output is variable in amplitudes; therefore post-processing is required to estimate the stress ranges before one can proceed to calculate the fatigue damage. This can be achieved either by using cycle counting or spectral techniques. ASTM's rainflow counting algorithm is a commonly used cycle counting method which identifies the stress ranges and associated number of cycles (half or full cycles) for the HSS time series by pairing the peaks and valleys in analogy with rain flowing down a pagoda roof [8]. Alternatively, the Dirlik's method obtains the stress range PDF from a spectrum. It assumes that the stress range PDF is a weighted combination of an exponential and two Rayleigh distributions; and is intended for both wide- and narrow-band processes [9]. The Dirlik's method is frequently used in conjunction with dynamic analysis performed in the frequency domain, where the power spectral density (PSD) of HSS is calculated using transfer functions. The individual stress ranges of the histogram or PDF are then compared against the S-N curves to determine the fatigue damage. By applying the Palmgren-Miner's rule, the damage for each stress range is summed up linearly, which gives the total accumulated damage.

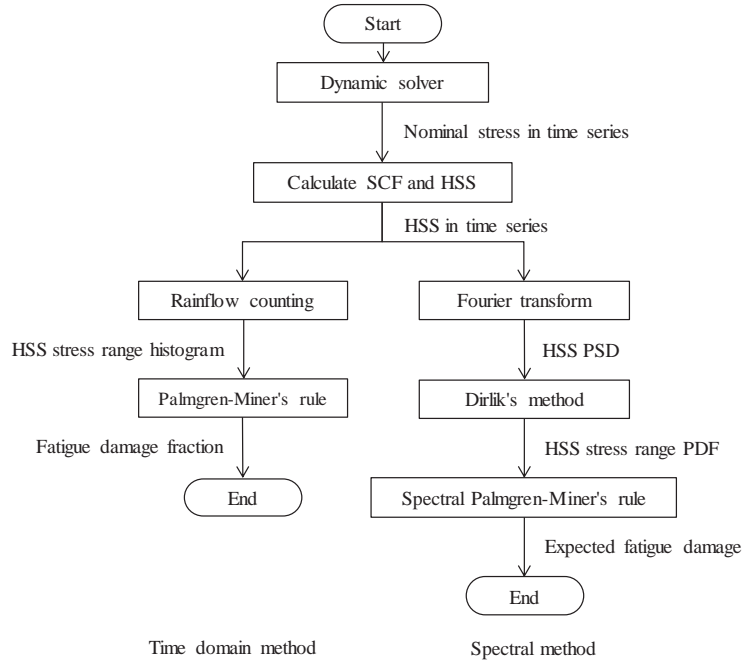


Figure 1: Procedure to calculate fatigue damage, either using time domain or spectral method

5. Methodology to calculate analytical fatigue gradients

The gradients of fatigue damage with respect to design variables were obtained analytically using the Direct Differentiation Method (DDM) [10]. The term ‘fatigue damage’ refers to the fraction of accumulated fatigue damage, with 0 meaning fatigue free and 1 signifying failure. This is also called fatigue utilization factors.

5.1 Time domain method

The gradients of fatigue damage D and equivalent fatigue loads EFL , using DDM, were given by Eqs. (1) and (2), respectively:

$$\nabla D = \sum_{i=1}^l \left[\frac{mn_i}{\bar{a}} \cdot (S_i)^{m-1} \cdot \frac{dS_i}{d\mathbf{b}} \right] \quad (1)$$

$$\nabla EFL = \frac{1}{mD} \cdot \left(\frac{\bar{a}D}{N} \right)^{\frac{1}{m}} \cdot \nabla D \quad (2)$$

where \bar{a} = intercept of S-N curve with log N axis; m = negative inverse slope of the S-N curves; S_i = stress range of HSS [MPa]; n_i = number of stress cycles corresponding to S_i ; and \mathbf{b} = design variable vector. The S_i here referred to the individual stress ranges without binning, while n_i corresponded to either a half or full cycle. As such, the $dn_i/d\mathbf{b}$ term could be neglected in Eq. (1).

The derivative of stress range $dS_i/d\mathbf{b}$ was calculated by taking the difference of stress (in this case HSS) sensitivities $d\sigma(t)/d\mathbf{b}$ at $t = t_{i,1}$ and $t = t_{i,2}$, where $t_{i,1}$ and $t_{i,2}$ are the times of initial and reversal points for S_i , respectively, see Eq. (3). The $t_{i,1}$ and $t_{i,2}$ could be identified during the rainflow counting process.

$$\frac{dS_i}{d\mathbf{b}} = \begin{cases} \left. \frac{d\sigma(t)}{d\mathbf{b}} \right|_{t=t_{i,1}} - \left. \frac{d\sigma(t)}{d\mathbf{b}} \right|_{t=t_{i,2}} & \text{for } \sigma(t_{i,1}) > \sigma(t_{i,2}) \\ \left. \frac{d\sigma(t)}{d\mathbf{b}} \right|_{t=t_{i,2}} - \left. \frac{d\sigma(t)}{d\mathbf{b}} \right|_{t=t_{i,1}} & \text{for } \sigma(t_{i,2}) > \sigma(t_{i,1}) \end{cases} \quad (3)$$

3.2 Spectral method

The gradient of expected fatigue damage $E[D]$, by using DDM, could be written as Eq. (4):

$$\nabla E[D] = \frac{T}{\bar{a}} \cdot \left\{ \sum_{k=1}^K [S_k^m \cdot p(S_k) \cdot \Delta S_k] \cdot \frac{d}{d\mathbf{b}} E[P] + E[P] \cdot \sum_{k=1}^K \frac{d}{d\mathbf{b}} [S_k^m \cdot p(S_k) \cdot \Delta S_k] \right\} \quad (4)$$

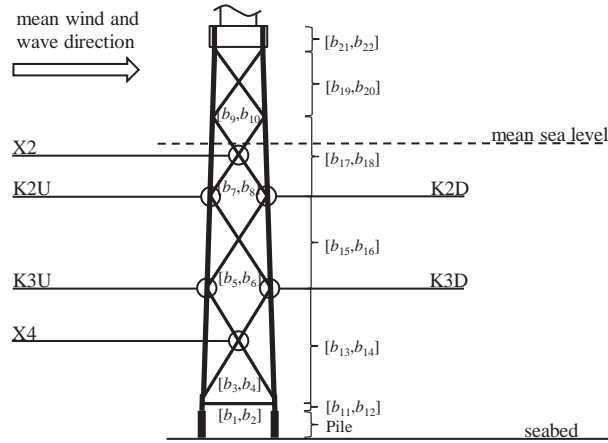


Figure 2: OC4 Jacket substructure model and locations identified for simulated HSS data output

where $p(S)$ = Dirlik's stress range PDF; T = total time [s]; and $E[P]$ = expected number of peaks per unit time [s^{-1}]. The empirical distribution weight factors of $p(S)$ and $E[P]$ are governed by spectral moments m_n :

$$m_n = \sum_{l=1}^L [f_l^n \cdot P_s(f_l) \cdot \Delta f_l] \quad (5)$$

The PSD $P_s(f)$ was obtained by the Fourier transform of $\sigma(t)$. The Welch method (modified periodogram) with Hamming windows and overlaps was used in this study, as the taper reduces leakage from the spectral density near the large peaks in the spectrum [11]. The sensitivity of Welch's method was derived as:

$$\frac{d}{db} P_s(f) = \frac{4}{QJUF_s} \sum_{q=1}^Q [\text{Re}(A_q(f)) \cdot \text{Re}(A_q'(f)) + \text{Im}(A_q(f)) \cdot \text{Im}(A_q'(f))]$$

$$\text{where } A_q(f) = \sum_{j=0}^{J-1} [\sigma_q(j) \cdot W(j) \cdot \exp(-2\pi i j f / J)] \quad (6)$$

$$A_q'(f) = \sum_{j=0}^{J-1} \left\{ \frac{d}{db} [\sigma_q(j)] \cdot W(j) \cdot \exp(-2\pi i j f / J) \right\}$$

$$U = \frac{1}{J} \sum_{j=0}^{J-1} W^2(j)$$

where Q = number of window segments; J = number of samples within the window; W = windowing function (e.g. Hamming); F_s = sampling frequency; and $i = \sqrt{-1}$. Note: Scaling factor of $1/J$ to be used for samples at zero frequency and Nyquist frequency. Comparably, the gradient of EFL for the spectral method was derived as:

$$\nabla EFL = \frac{1}{m} \cdot \left(\frac{\bar{a} \cdot E[D]}{E[N]} \right)^{\frac{1}{m}} \cdot \left(\frac{\nabla E[D]}{E[D]} - \frac{\nabla E[N]}{E[N]} \right) \quad (7)$$

The $E[N]$ in Eq. (7), unlike $N = \sum n_i$ in Eq. (2), is a function of m_n and therefore varies with respect to \mathbf{b} .

6. Comparison of fatigue damage sensitivities

A comparison between analytical and numerical fatigue damage sensitivities was carried out on simulated stress data obtained from the numerical wind turbine model used within the Offshore Code Comparison Collaboration Continuation (OC4) Project. The model consists of the 5 MW wind turbine model developed by National Renewable Energy Laboratory, mounted on a support structure system that includes a tubular tower, a concrete transition piece and a jacket substructure [12,13]. The HSS were evaluated at six distinct locations. They are the middle K-joints facing upwind (K2U) and downwind (K2D), the bottom K-joints facing upwind (K3U) and downwind (K3D), the X-joints at 2nd bay (X2) and 4th bay (X4) from top (Fig. 2). The vector \mathbf{b} consists of 22 design variables, i.e. $b_1 - b_{22}$, where the odd and even numbered variables represent the member diameters and thicknesses, respectively. The fatigue damage sensitivities were evaluated at initial jacket dimensions against the 4th bay brace diameter b_3 , 4th bay brace thickness b_4 , 4th bay leg diameter b_{13} , 4th bay leg thickness b_{14} , 2nd bay brace diameter b_7 , 2nd bay brace thickness b_8 , 2nd bay leg diameter b_{17} and 2nd bay leg thickness b_{18} .

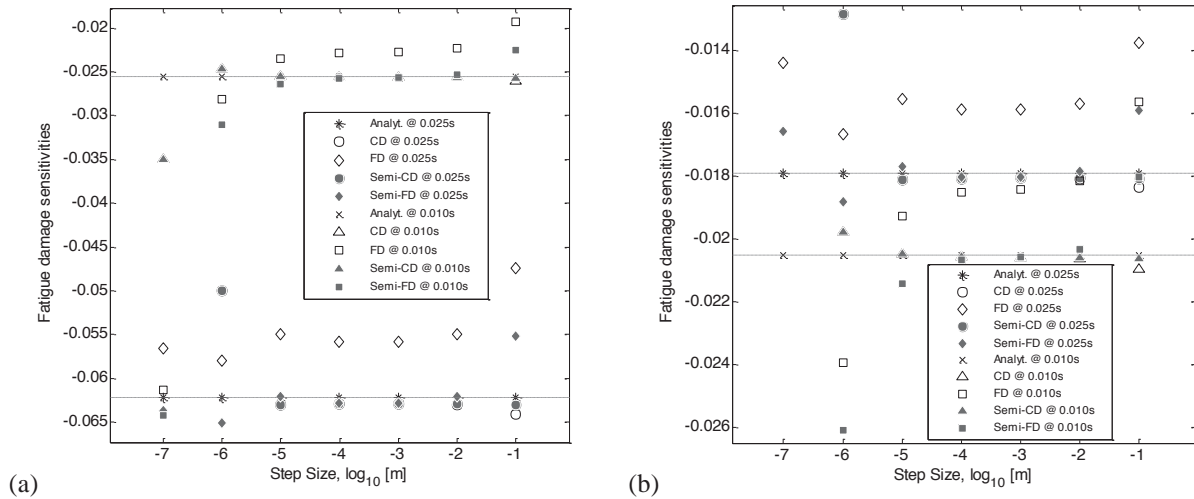


Figure 3: Comparison of fatigue damage sensitivities varying against design variable step sizes and time steps in the numerical sensitivity analysis, for (a) spectral and (b) time domain methods. Sensitivities were calculated against b_{13} at hot spot location 1 of K3U (leg side) joint.

6.1 Step sizes and time steps

Fig. 3 depicts the variation of fatigue damage sensitivities with respect to step sizes and time steps used in the sensitivity analysis. The design variables were perturbed in steps of tenfold increments from 10^{-7} to 10^{-1} , while two different time steps, 0.025 s and 0.010 s, were used. Both central difference (CD) and forward difference (FD) schemes followed different patterns, with each attaining minimum numerical errors at different step sizes. The ‘optimal’ step sizes also varied for different joint and hot spot locations (not shown here), resulting in difficulties to determine a ‘good’ step size to be used in the overall design sensitivity analysis. The numerical errors consist of truncation and condition errors, which are positively and inversely proportional to the step sizes, respectively. The CD generally yielded smaller numerical errors as compared with the FD due to a higher order of approximation. However, in some cases, the CD could be more erroneous (Fig. 4). Similarly, the finite difference approximations improved when smaller time steps were used. The analytical solutions for fatigue damage sensitivities between the time domain and spectral methods came closer when a smaller time step was implemented. The spectral method was more sensitive to the time step change, since the method is based on the Fourier transform which is more susceptible to the quality of input signals. Besides, the semi-finite difference methods could help to enhance the numerical sensitivity analysis. In this method, the HSS sensitivities were estimated numerically using finite difference schemes while the final fatigue sensitivity analysis was performed using analytical formulations. The results of this approach matched well with the finite difference methods (Fig. 4). However, in some cases, they could avoid numerical artefacts, as shown for the FD in Fig. 3. The above mentioned findings have demonstrated the subtle characteristics of fatigue sensitivity analysis with regard to the response sensitivities. Therefore, it is imperative to make sure that the quality of response sensitivities is sufficient when calculating the numerical gradients for fatigue damage. Often the analytical solutions are not available for the response sensitivities due to software constraints. In such case, the semi-finite difference approach is suggested.

6.2 Joint locations and hot spot locations

Fig. 4 summarizes the fatigue damage sensitivities calculated using the analytical, finite difference and semi-finite difference methods at various joint and hot spot locations. The last two were taken at step sizes which resulted in the smallest numerical errors. The percentage errors of numerical sensitivities against the analytical solutions (1st bars) were listed above and below the respective bars, for the time domain and spectral methods.

In Fig. 4(a), the fatigue damage sensitivities at specific joint locations are shown to be localized, i.e. to be influenced most by the design variables which the joint was directly connected to. The finite difference schemes also gave smaller errors when evaluating fatigue sensitivities at locations where the design variable was directly connected to. On the contrary, the associated errors at joint locations where the design variables were not in connection with could reach values as high as 1700 percent or could be wrong in sign. Whereas Fig. 4(b) indicates that the fatigue damage sensitivities were distinct at various hot spot locations. Although the time domain and spectral methods differ in estimating the damage sensitivities (of which the accuracy depends on the quality of response sensitivities), the percentage errors of their finite difference counterparts were generally similar in scale.

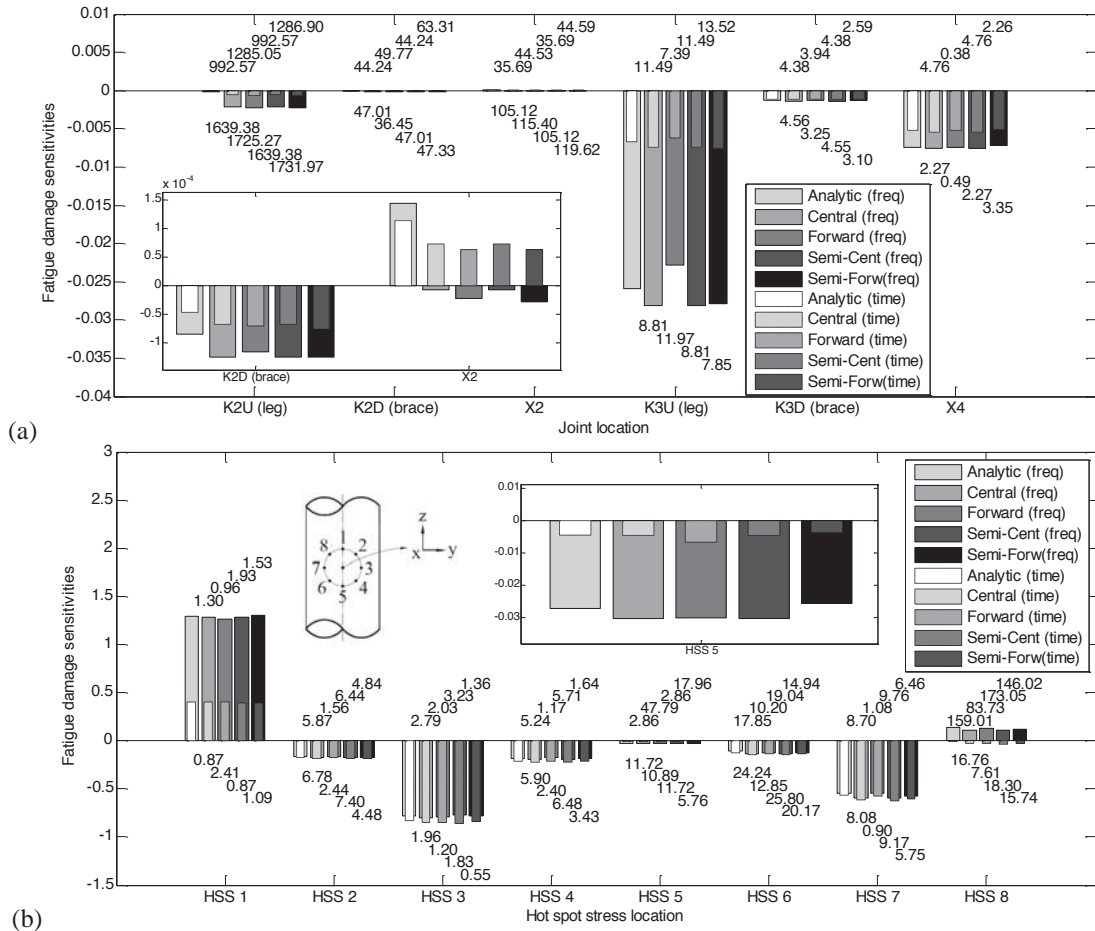


Figure 4: Comparison of fatigue damage sensitivities at various (a) joint locations and (b) hot spot locations. (a) Sensitivities were calculated against b_3 at hot spot location 1 for various joints and (b) Sensitivities were calculated against b_8 at K2U (leg side) for 8 hot spot locations using time domain ('time') and spectral ('freq') methods.

6.3 Stress concentration effects

So far all the fatigue damage sensitivities discussed earlier have considered the SCF variations against the design variables. However, since the empirical formulae to estimate the SCF are laborious to use, it raised the interest to investigate the contributions of SCF derivatives in the overall fatigue sensitivity analysis. HSS are geometric stresses that account for stress concentration effects occurring at the joint regions. The sensitivities depend on both the sensitivities of nominal stress as well as the sensitivities of SCF with respect to design variables. Fig. 5 shows the analytical fatigue damage sensitivities, performed with and without consideration of the SCF derivatives. The SCF were treated as constants in the latter case. Results indicate that the SCF derivatives exerted significant influences in the calculation, for all joint types. In some cases, the sensitivities could be inverted in sign. Therefore, it is important to include the SCF variations in the gradient assessment of fatigue damage, when HSS are used.

7. Conclusions

This paper presented analytical formulations to calculate the gradients of fatigue damage and equivalent fatigue loads, for both time domain and spectral methods. Detailed comparison studies using the stress data obtained from the numerical OC4 wind turbine model revealed that:

- Fatigue sensitivity analysis was very susceptible to the quality of response sensitivities. Several recommendations which could help improve the overall quality of numerical sensitivities include using sufficiently small step sizes when perturbing the design variables; implementing more robust time domain methods when evaluating the fatigue damage; or adopting the semi-finite difference methods.
- The fatigue damage sensitivities were localized, as they were affected most by the design variables in close proximity with the joints. The errors associated with fatigue damage sensitivities for joints which the design variables were not directly connected to, could be very high for the finite difference approximations.
- The derivatives of SCF exerted significant influences in determining the fatigue damage sensitivities. This should always be considered when the hot spot stress methodology is used for the fatigue assessment.

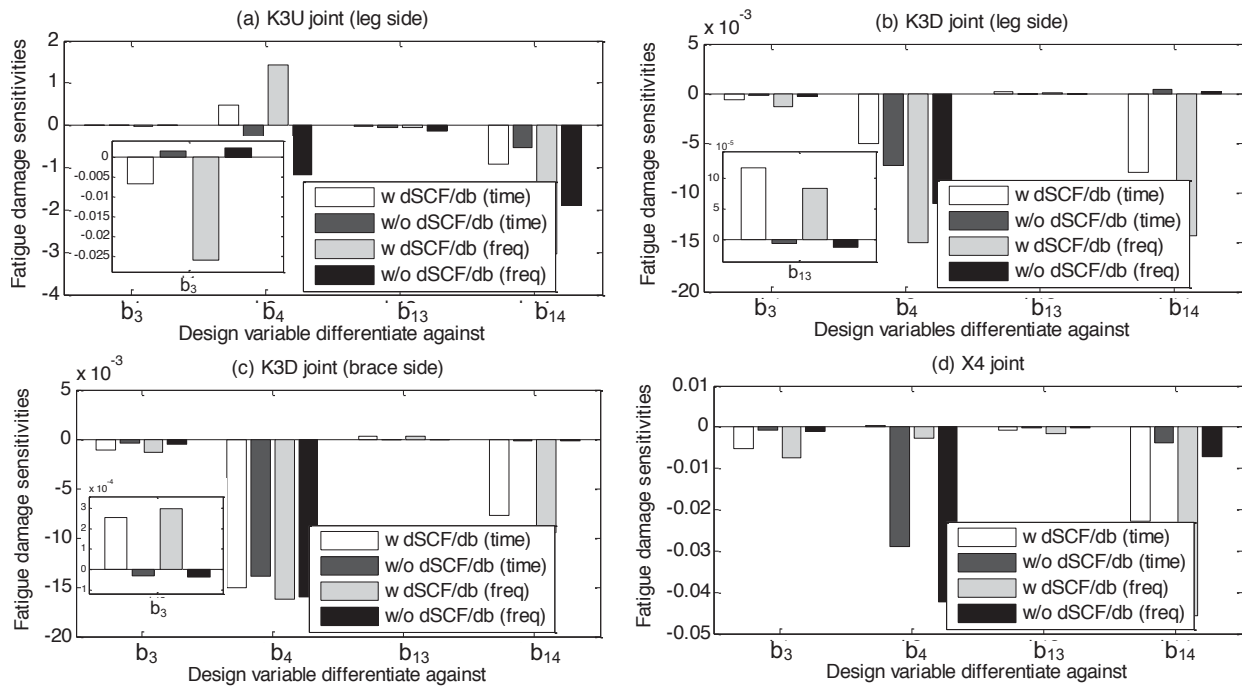


Figure 5: Comparison of analytical fatigue damage sensitivities with and without consideration of SCF derivative. Sensitivities are calculated against b_i at hot spot location 1 for various joints using time domain ('time') and spectral ('freq') methods.

8. Acknowledgements

The authors would like to thank the Singapore Economic Development Board (EDB) – DNVGL – Energy Research Institute @ NTU (ERI@N) Joint Industry PhD Program. Support from Norwegian Research Centre for Offshore Wind Technology (NOWITECH FME, Research Council of Norway, grant 193923) is acknowledged.

9. References

- [1] F. Vorpahl, H. Schwarze, T. Fischer, M. Seidel and J. Jonkman, Offshore Wind Turbine Environment, Loads, Simulation, and Design, *WIREs Energy Environ*, 2, 548-570, 2013.
- [2] M. Muskulus and S. Schafhirt, Design Optimization of Wind Turbine Support Structures – A Review, *Journal of Ocean and Wind Energy*, 1 (1), 12-22, 2014.
- [3] D.A. Tortorelli and M. Panagiotis, Design Sensitivity Analysis: Overview and Review, *Inverse Problems in Engineering*, 1, 71-105, 1994.
- [4] KH. Chew, K. Tai, E.Y.K. Ng, M. Muskulus, *Optimization of Offshore Wind Turbine Support Structures Using Analytical Gradient-Based Method*, Technical Report BAT/MB/OW-R01/2015, Norwegian University of Science and Technology, Trondheim, Norway, 23 pp, 2015.
- [5] DNV, Fatigue Design of Offshore Steel Structures, Recommended Practice DNV-RP-C203, Det Norske Veritas AS, Høvik, Norway, 178 pp, 2012.
- [6] IEC, *Wind Turbines – Part 1: Design Requirements*, International Standard IEC 61400:1, International Electrotechnical Commission, Geneva, Switzerland, 85 pp, 2005.
- [7] IEC, *Wind Turbines – Part 3: Design Requirements for Offshore Wind Turbines*, International Standard IEC 61400:3, International Electrotechnical Commission, Geneva, Switzerland, 263 pp, 2009.
- [8] ASTM, *Standard Practices for Cycle Counting in Fatigue Analysis*, ASTM E1049-85, American Society of Testing Materials, West Conshohocken, USA, 10 pp, 2011.
- [9] T. Dirlik, *Application of Computers in Fatigue Analysis*, PhD Thesis, Univ of Warwick, UK, 234 pp, 1985.
- [10] G.J. Park, *Analytic Methods for Design Practice*, Springer, Berlin, 627 pp, 2007.
- [11] P. Ragan and L. Manuel, Comparing Estimates of Wind Turbine Fatigue Loads using Time-Domain and Spectral Methods, *Wind Engineering*, 31 (2), 83-99, 2007.
- [12] J. Jonkman, S. Butterfield, W. Musial and G. Scott, *Definition of a 5MW Reference Wind Turbine for Offshore System Development*, Technical Report NREL/TP-500-38060, National Renewable Energy Laboratory, Golden, CO, 63 pp, 2009.
- [13] F. Vorpahl, W. Popko and D. Kaufer, *Description of a Basic Model of the "UpWind Reference Jacket" for Code Comparison in the OC4 Project under IEA Wind Annex*, Technical Report, Fraunhofer IWES, Bremerhaven, 14 pp, 2011.

Optimization of laminated structures considering manufacturing efforts

Markus Schatz¹, Horst Baier²

¹ Technische Universität München, Lehrstuhl für Leichtbau, Germany, schatz@lb.mw.tum.de

² Technische Universität München, Lehrstuhl für Leichtbau, Germany, baier@lb.mw.tum.de

1. Abstract

In many cases, structural design optimization highlights great weight saving potentials, but yet, engineers may face difficulties unlocking these potentials, since further economical and technical constraints need to be obeyed. This especially holds for the optimization of composites, because manufacturing techniques often not only imprint limits onto realizable parameter configurations for a given design, but furthermore differ considerably in the associated manufacturing effort level for different parameter configurations. This work mitigates this issue of inchoate designs, by introducing a method capable of quantifying expert knowledge regarding manufacturing effort at early design phases and, thereby, leveraging the optimization's significance by introducing technical aspects into the optimization responses. The method will be introduced and displayed at length and thereafter be presented for a structural design optimization task.

2. Keywords: Composite design optimization, quantification of manufacturing effort, considering efforts associated with the prepreg lamination technology, ply waste algorithm.

3. Introduction and literature review

It is evident, that structural optimization can solely bring forth designs comprising aspects, which are explicitly modeled and being incorporated into the optimization process. In this regard, the designs derived via structural optimization, are only as relevant as the underlying optimization models are holistic. This especially holds for structural design optimization of composites, where given manufacturing processes impinge not only on whether or not derived optima are technically realizable, but further determine associated levels of manufacturing effort and, in that consequence, also the products final manufacturing cost. This marks the importance of capturing manufacturing aspects - specifically those leading to efforts - in tandem with structural mechanics, when optimizing composite structures, designated to actually be build with moderate or even low manufacturing effort. For this sake, a method facilitating the modeling of verbal expert knowledge for any given knowledge domain - herein apparently manufacturing effort - will be introduced and displayed for an exemplary optimization task. The introduction of this method will be given in chapter 5, followed by chapter 6, where the simultaneous mass and effort optimization will be displayed. Prior, to that, the general formulation of a vector optimization task is being introduced. The paper will be topped off by summarizing the conducted work, discussing the key results and sketching prospective research work. Next, a brief overview of literature addressing the demand for holistic structural design optimization models, i.e. optimization models including further aspects beside those stemming from structural mechanics, will be given.

Wang and Costin [1] used analytical manufacturing constraints for capturing restrictions associated with the hand prepreg lay-up process. By doing so, they were able to show the importance of these technical aspects within the structural optimization. Similar to this research work, many researchers incorporated technical aspects via sharp bound based on analytical equations such as Henderson et al. [2] and many more. Pillai, Beris and Dhurijati [3] used soft computing approaches so as to model the operating of an autoclave. The knowledge-based system they derived is able to predict the curing of thick composite laminates and served as a source of inspiration for the approach displayed in this paper.

4. General definition of the optimization task

With Eq.(1) the optimization task is stated in its general form, where f , \mathbf{g} , \mathbf{x} and \mathcal{X} are the objective, vector of inequality constraints, vector of design variables and design space respectively. More information regarding optimization can be found in [4].

$$\min_{\mathbf{x} \in \mathcal{X}} \{f(\mathbf{x}) \mid \mathbf{g}(\mathbf{x}) \leq \mathbf{0}\} \quad (1)$$

In the later solved optimization problem, the manufacturing effort e will be defined as one objective beside mass m . Thus, this leads to a multi-objective problem - or also referred to as vector optimization task. Since mass and manufacturing effort are conflicting goals, a so-called pareto frontier will emerge, as being exemplary displayed in sub-figure 1a. In this work gradient-based algorithms will be used, for which reason, both objectives need to be condensed to one single objective for obtaining one pareto optimal solution, i.e. one point on the pareto frontier. For that purpose, the following general norm as a distance to a fictitious design point, being composed of extremal pareto optimal values is being defined and given with Eq.(2). It is further displayed in sub-figure 1b.

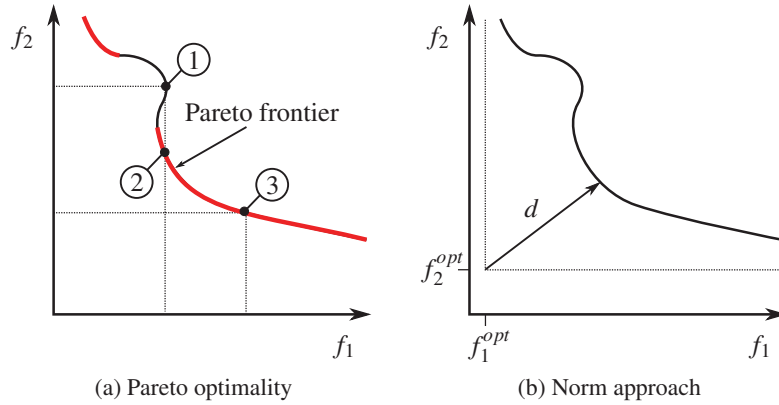


Figure 1: Pareto frontier and vector norm definition for gradient-based optimization

$$f = d(f_1, \dots, f_{n_f}) = \|f_i - f_i^{\text{opt}}\|_q \quad i \in \{1, \dots, n_f\} \quad (2)$$

Inserting the two objectives - mass m and manufacturing effort e - into the euclidean norm, i.e. $q = 2$ in Eq.(2), leads to the objective definition as used herein. Note that ξ_i represent the weight factor for mass ($i = m$) and effort ($i = e$).

$$f = \sqrt{\xi_m(m - m^{\text{opt}})^2 + \xi_e(e - e^{\text{opt}})^2} \quad (3)$$

5. Modeling manufacturing effort based on verbal expert knowledge

This chapter aims to give a brief outline on how expert knowledge is modeled. Obviously, the challenge in hand, is the quantification of verbal information; or more precisely, the transformation of verbal expert knowledge into a knowledge domain expressed in algorithm-close rule networks.

5.1. Quantification of verbal expert knowledge

At first, the knowledge domain of the manufacturing effort model needs to be acquired. A knowledge domain can be comprehended as a gathering of information for a given field and is most commonly expressible in a sequence of inference logic rules. Because verbal knowledge, and in that consequence inherently qualitative information, needs to be gathered, evaluated and processed, the so called fuzzy logic will be used. This theory is founded by Zadeh [5] and, among other features, enables the handling of imprecise and qualitative information. It is owed to this qualitative modeling approach, why it is also referred to as soft computing [6]. Herein, the knowledge domain is defined by human expertise concerning manufacturing effort associated to the prepreg technology. In [7], the authors discuss the process of how a knowledge domain can be derived at length. The demonstration technology therein is braiding. This also highlights the general nature of the proposed approach.

5.2. Generating the rule network

With figure 2 an overview of the derived fuzzy inference system (FIS) is given. As depicted, the input parameters are the curvature, ply number, wastage, ply-drop-offs, continuity and radii. These inputs do not have to be passed by the user; instead they are fetched from the finite element analysis (FEA) input deck automatically. So, for instance, the continuity requirement is evaluated based on a neighborhood search for each ply and the check whether or not plies do continue into their neighbors. The rule network computes, based on these input parameters, the effort

level for that given design configuration. This is done by evaluating each implemented rule of the knowledge domain by checking, which verbal variable is active (antecedent) thereafter the degree of fulfillment for each rule (implication). The final output is then obtained by summing up active rules (aggregation).

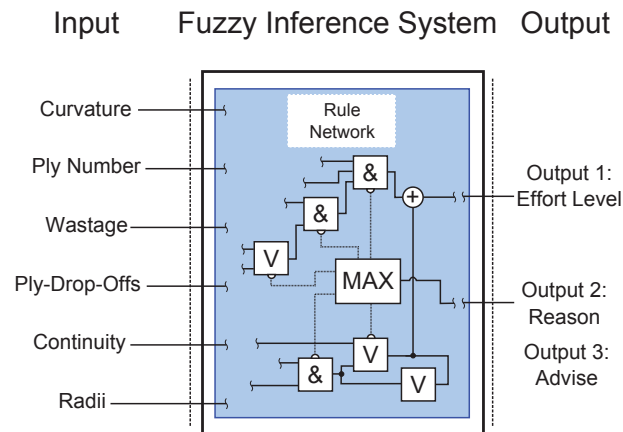


Figure 2: The prepreg manufacturing effort model based on the fuzzy inference system

The output can be expanded, when each implication value is being cross-checked with the knowledge domain, since this reveals the reason for the output. This reason supports the optimizer in verifying one specific output by making it plausible within the post-processing or by re-consulting an expert. Another feature of the knowledge domain can be unlocked, when the implication and antecedent values are inspected. This combination provides insight on how the design can further be improved, because one gets insight on which rule was active and moreover which verbal variable did trigger it the most. This latter can be understood as an elaboration advise and is highlighted as the output number three in figure 2.

5.3. Modeling ply wastage

As can be seen in figure 2 one input parameter for the manufacturing effort model is the play wastage. This ply wastage is determined by the ply's geometry, thus width and length for square patches, the orientation of the ply and available rolls, i.e. orientation and width of the prepreg roll from which the ply will be cut. For that purpose a wastage algorithm has been developed in python. An exemplary results of this algorithm is shown next. One can

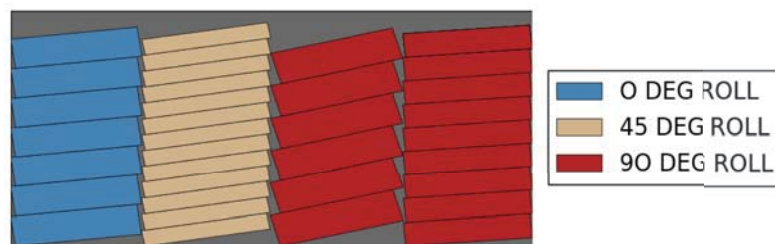


Figure 3: Ply wastage for given lay-up illustrated in gray

see in figure 3 how the wastage (depicted in gray) is computed for four different ply bundles. These bundles are of orientation 7° , 35° , 75° and 85° and are therefore cut from the rolls of 0° , 45° and both latter ones from 90° orientation.

5.4. Preparing the rule network for the subsequent optimization

Prior to the optimization on responses from both models - hence, finite element and manufacturing effort model - the effort model's condition needs to be leveraged to a higher level, by introducing relaxation schemes, e.g. interpolation or meta-modeling for discrete variables and parameters such as ply number or continuity. This guarantees efficient and robust gradient-based optimization runs resulting in fast convergence. Figure 4 provides an example, where the continuity check is relaxed for two neighboring plies (θ and 0°). The plot displays the regular check for angle difference $\Delta\theta = \theta - 0^\circ$ as a red singleton and the relaxed one in blue. The relaxation in this case has been realized via $C = 1 - \frac{\Delta\theta}{90}^{0.2}$ and clearly improves the models behavior in terms of differentiability and continuity in

the derivatives in light of gradient-based optimization.

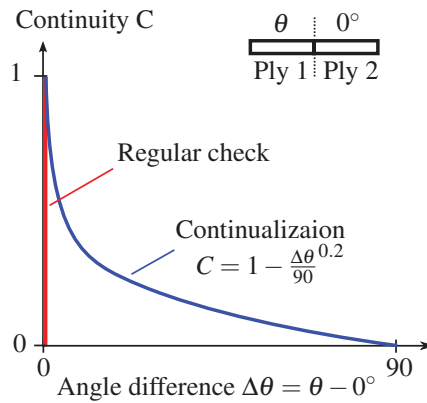


Figure 4: Demonstration of the continualization for two given plies

6. Optimizing an automotive A pillar considering manufacturing efforts

For the purpose of demonstrating the derived approach, the following example of an automotive A pillar of the convertible *Roding Roadster R1* is defined and optimized. The load cases are derived from a roof crush test according to FMVSS 216a and driving dynamics requirements addressing the structure's stiffness. They are illustrated in figure 5. Along the lengthwise extrusion axis, the A pillar has been fully parametrized in its geometry, so as to allow the optimization algorithm to vary not only curvature and length properties of the extrusion axis but also all profile dimensions.

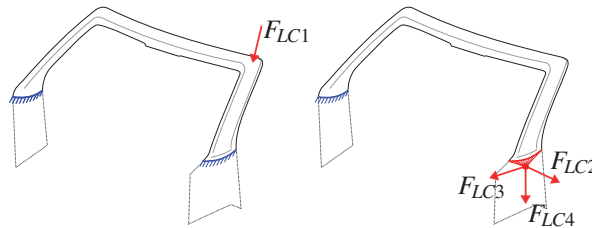


Figure 5: Illustration of the load cases for the A pillar structure [7]

The optimization task can be stated as follows,

$$\min_{\mathbf{x} \in \mathcal{X}} \{f(\mathbf{x}) \mid \mathbf{g}(\mathbf{x}) \leq \mathbf{0}\} \quad (4)$$

where

$$\begin{aligned} f(\mathbf{x}) &= d(m, e) \\ \mathbf{g}(\mathbf{x}) &= \begin{aligned} &g_i = \frac{F_{LCi}}{0.9} - 1 && \forall i \in \{1, \dots, n_{\text{Secs}}\} \\ &g_{1+n_{\text{Secs}}} = \frac{u_{LC1}}{u_{\text{Intrusion}}} - 1 \\ &g_{2+n_{\text{Secs}}} = \frac{K_{LC2}}{K_{\text{min},1}} - 1 \\ &g_{3+n_{\text{Secs}}} = \frac{K_{LC3}}{K_{\text{min},2}} - 1 \\ &g_{4+n_{\text{Secs}}} = \frac{K_{LC4}}{K_{\text{min},3}} - 1 \end{aligned} \\ \mathbf{x} &= [\mathbf{x}_{\text{Profile}}, \mathbf{x}_{\text{Extrusion}}, \mathbf{x}_{\text{Orientations}}, \mathbf{x}_{\text{Thicknesses}}]^T \end{aligned}$$

define the objective and constraint functions. As stated, the objective is set to d as defined with Eq.(2) and displayed in sub-figure 1b.

Prior to directly solving the optimization task given with Eq.(4), the two extremal solutions, i.e. minimal mass m^{opt} and minimal effort e^{opt} , need to be found by minimizing $f = m$ and $f = e$ respectively. Obviously, the constraints as defined in Eq.(4) are imposed throughout the individual minimization of mass and effort as well.

With the following two sub-figures the two extrema of the pareto frontier are given. In sub-figure 6a the thickness distribution for the minimal mass solution is given, whereas the sub-figure 6b depicts the one of the minimal effort design. Both designs can be made plausible, considering that the left design is characterized by maximizing bending stiffness resulting into a blown up A pillar design and on the contrary, that the left, thus minimal effort, is showing neat patch geometries, and therefore rectangularly shaped, for minimizing the ply wastage.

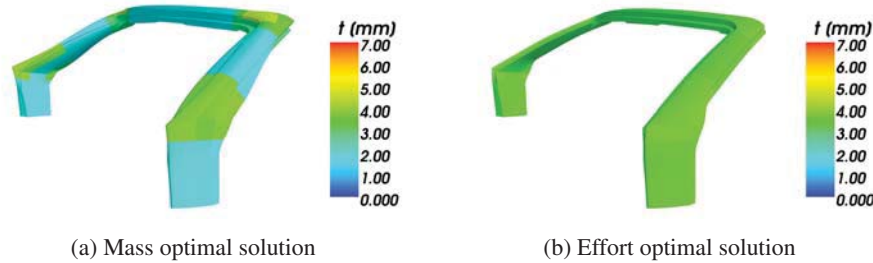


Figure 6: Thickness plotted for both extremal solutions, thus mass and effort minima

In addition to the thickness distribution, one can also visualize the associate manufacturing effort level and its origin. This is achieved by plotting the manufacturing effort density, which is being computed for each ply region, leading to the final effort level via an integration scheme. Figure 7 depicts again both extremal solutions, but now the manufacturing effort density is plotted for minimal mass (sub-figure 7a) and minimal effort (sub-figure 7b)

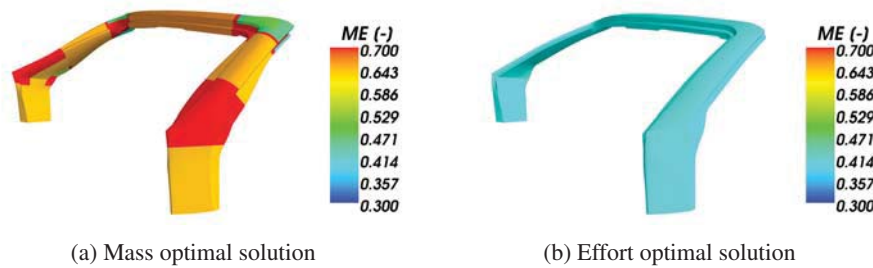


Figure 7: Manufacturing effort density plotted for both extremal solutions, thus mass and effort minima

As the objective in the defined optimization task Eq.(4) is set as the distance to the fictitious combination of both extremal optima of the pareto frontier the solution represents a compromise. The engineer could define different weights ξ_i for shifting the compromise in favour of mass ($i = m$) or effort ($i = e$). Here, both weights have been set to one. With figure 8 the compromise solution is illustrated. Due to its relative position within the minimal mass and effort design it can be stated, that this solutions indeed strikes a compromise.

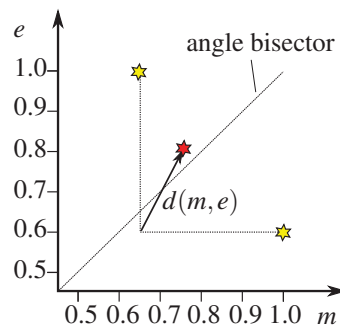


Figure 8: Optimal compromise (red start) struck in-between the two mass and effort (yellow stars are individual optima)

7. Summary and outlook

It has been shown, that the integration of technical aspects via soft computing has been proven to be a viable approach. By doing so, the optimization process can be enriched through information regarding manufacturing effort, thereby increasing the optimization's significance. The optimization evinces a greater significance, since derived optima not only satisfy structural requirements, but also honor technical constraints arising from the chosen manufacturing process. Moreover, the modeling of manufacturing effort enabled the optimization to meet an optimal compromise by simultaneously maximizing structural efficiency and minimizing effort.

Because of the fact, that in [7] the presented approach has been applied for braiding and herein for the prepreg lay-up process, it can be concluded that this technique is of general nature and can in that consequence be applied for various manufacturing processes.

It also has been shown, that the manufacturing effort model not only computes the effort level for a given design, but also provides reasoning about the determined effort level. This supports the engineer in the post-processing of the optimization in a manner, that effort levels can be verified.

8. Acknowledgements

This work is based on studies within the MAI-Design project, which is financed by the German Federal Ministry of Education and Research (BMBF).

9. References

- [1] B.P. Wang and D.P. Costin, Optimum Design of a Composite Structure with Three Types of Manufacturing Constraints, *AIAA Journal*, 30, 1991.
- [2] J.L. Henderson, Z. Gürdal and A.C. Loos, Combined Structural and Manufacturing Optimization of Stiffened Composite Panels, *Journal of Aircraft*, 36, 246-254, 1999.
- [3] V. Pillai, A.N. Beris and P. Dhurjati, Intelligent Curing of Thick Composites Using a Knowledge-Based System, *Journal of Composite Materials*, 1997.
- [4] G.N. Vanderplaats, *Multidiscipline Design Optimization*, Vanderplaats Research & Development Inc., 2007.
- [5] L.A. Zadeh, Fuzzy Sets *Information and control*, 338-353, 1965.
- [6] P. Hajela, Soft computing in multidisciplinary aerospace design - new directions for research *Aerospace Sciences*, 38, 1-21, 2002.
- [7] M. Schatz and H. Baier, An approach toward the incorporation of soft aspects such as manufacturing efforts into structural design optimization *Journal of Mechanics Engineering and Automation*, 4 (11), 2014.

A Visually-Informed Decision-Making Platform for Wind Farm Layout Optimization

Souma Chowdhury¹, Weiyang Tong², Ali Mehmani³, Achille Messac⁴

¹ Aerospace Engineering, Mississippi State University, Mississippi State, USA, chowdhury@bagley.msstate.edu

² Mechanical and Aerospace Engineering, Syracuse University, Syracuse, USA, wtong@syr.edu

³ Mechanical and Aerospace Engineering, Syracuse University, Syracuse, USA, amehmani@syr.edu

⁴ Aerospace Engineering, Mississippi State University, Mississippi State, USA, messac@ae.msstate.edu

1. Abstract

Wind Farm Layout Optimization (WFLO) is a typical model-based complex system design process, where the popular use of low-medium fidelity models is one of the primary sources of uncertainties propagating into the estimated optimum cost of energy (COE). Therefore, the (currently lacking) understanding of the degree of uncertainty inherited and introduced by different models is absolutely critical (i) for making informed modeling decisions, and (ii) for being cognizant of the reliability of the obtained results. A framework called the Visually-Informed Decision-Making Platform (VIDMAP) was recently introduced to quantify and visualize the inter-model sensitivities and the model inherited/induced uncertainties in WFLO. Originally, VIDMAP quantified the uncertainties and sensitivities upstream of the energy production model. This paper advances VIDMAP to provide quantification/visualization of the uncertainties propagating through the entire optimization process, where optimization is performed to determine the micro-siting of 100 turbines with a minimum COE objective. Specifically, we determine (i) the sensitivity of the minimum COE to the top-level system model (energy production model), (ii) the uncertainty introduced by the heuristic optimization algorithm (PSO), and (iii) the net uncertainty in the minimum COE estimate. In VIDMAP, the eFAST method is used for sensitivity analysis, and the model uncertainties are quantified through a combination of Monte Carlo simulation and probabilistic modeling. Based on the estimated sensitivity and uncertainty measures, a color-coded model-block flowchart is then created using the MATLAB GUI.

2. Keywords: Model-based systems design, Particle Swarm Optimization, Sensitivity analysis, Uncertainty quantification, Wind farm layout optimization.

3. Introduction:

3.1 Model-based Systems Design

Computational approximation models are crucial building blocks of most design processes in the 21st century. This includes both physics-based models (e.g., FEA and FVM) and statistical models (e.g., surrogate models and empirical models). An informed application of such computational models demands the knowledge of how uncertainties, both inherited and introduced by such models, propagate through the model-based design process. In a broader sense, the complexity of a system and/or the inability to fully understand and address it can also be perceived as uncertainty.

There exists very few quantitative design frameworks that determine the uncertainty in the information flowing along a design optimization process, and even fewer in the arena of visualizing information attributes in the model-based design process. Allaire et al. [1] presented a new definition of system complexity and a quantitative measure of that complexity based on information theory. They performed sensitivity analysis to indicate key contributors to system complexity. This method created opportunities to use the complexity information, to make better modeling decisions, towards increasing the reliability of the resulting designs. While making a uniquely important contribution towards model-based complex system design, in its current form (that does not involve visualization), this method does not provide a strategy to actually integrate *design automation* and *human decision-making*.

In a recent paper, Chowdhury et al. [2] explored the hypothesis that, "such integration could be accomplished by a visualization platform that will enable the user/designer to be cognizant of the *criticality*, *fidelity*, and *expense* of information at any stage or model-level of the design process". In other words, such a visual platform will allow the designer to make informed modeling decisions in a model-based complex system design (MB-CSD) process. In that paper, a new framework concept was proposed to quantify and visualize the inter-model sensitivities (*information criticality*) and the uncertainty (*information fidelity*) introduced by each model in the process of designing wind farm layouts – this framework was called a Visually-Informed Decision-Making Platform or VIDMAP. Wind farm layout design is a complex process, which involves multiple layers of highly non-linear models and highly uncertain input parameters. In this initial implementation of VIDMAP, Chowdhury et al. [2] demonstrated

a quantification and visualization of the inter-model sensitivities and model-induced uncertainties leading up to the estimation of the energy production of a 100 turbine wind farm. The VIDMAP visualization obtained thereof provided a unique illustration of which models and input parameters (in this case, turbine power response and wake width estimation models, and turbine features) have the strongest impact on the energy production estimations.

3.2 Impact of VIDMAP

The end goal of understanding (and analyzing) the inter-model sensitivities and the model-induced uncertainties along a MB-CSD process is to *accomplish a desirable level of reliability in the final solutions (or designs) at an acceptable expense and within a reasonable time-frame*. To this end, the user is required to make modeling decisions, such as: (i) *model selection*, (ii) *specification of prescribed model parameters and/or kernel functions*, (iii) *sampling or design of experiments*, (iv) *model improvement*, (v) *grid refinement*, and (vi) *computational resource allocation*. These modeling decisions can be partly automated and partly user-guided (through informed decision-making), only if measure(s) of pertinent information attributes are available to guide quantitative decision-making. With VIDMAP, we are exploring the potential of constructing and using a novel platform that quantifies and provides a visual representation of these information attributes.

In this paper, we are presenting a significant advancement to the development and implementation of VIDMAP, with the following research objectives:

1. Develop a computationally-efficient approach to exploit the previously quantified uncertainty in the top-level system evaluation model in estimating the sensitivities and uncertainty of the final optimum design, where the system evaluation model itself comprises several uncertain downstream models.
2. Quantify the uncertainty introduced by a heuristic optimization algorithm into the final optimum design.
3. Apply the new VIDMAP to the entire wind farm layout optimization (WFLO) process, thereby extending the visualization platform from the "energy production model" (demonstrated in [2]) to the optimum Cost of Energy (COE) obtained by WFLO.

A brief discussion of the wind farm layout optimization (WFLO) process and existing methods in this arena is provided in Section 4.1. Sections 4.2 and 4.3 respectively provide an overview of VIDMAP and the advancement of VIDMAP (undertaken in this paper) in order to apply it to the entire WFLO process. Illustration and discussion of the results obtained from the application of the advanced VIDMAP to WFLO is provided in Section 5.

4. An Informed Approach to Model-based Design of Wind Farm Layouts

4.1 Wind Farm Layout Optimization

The energy losses in a wind farm due to wake effects can be reduced by optimizing the selection and the arrangement of turbines over the site, a process commonly known as *wind farm layout optimization* (WFLO). Two primary classes of turbine arrangement (or layout optimization) methods exist in the literature: (i) methods that divide the wind farm into a discrete grid in order to search for the optimum grid locations of turbines [3, 4, 5, 6], (ii) more recent methods that define the turbine location coordinates as continuous variables, thereby allowing turbines to take up any feasible location within the farm [7, 8, 9]. A few of the above methods also allow optimal selection of commercial turbines along with optimal turbine arrangement [9, 10]. A majority of these *wind farm layout optimization* methods seek to either maximize energy production or minimize the cost of energy (COE).

In this paper, we use the Unrestricted Wind Farm Layout Optimization framework [9], as it is one of the most comprehensive WFLO frameworks in terms of the variety of design and natural factors that it incorporates in the process of searching for the most optimal wind farm layouts. More specifically, the energy production model [9], the land usage model [11], and the optimization methodology [9] used in demonstrating VIDMAP are all adopted from the UWFLO framework. In UWFLO, the COE (in \$/kWh) of a wind farm is expressed as

$$COE = C_{farm}/E_{farm} \quad (1)$$

where C_{farm} and the E_{farm} are respectively the average annual cost (in \$) of the wind farm and the average annual energy production (in kWh) of the wind farm. There are several wind farm cost models in the literature [12, 13, 14], which are generally empirical in nature, and represent cost in terms of different sets of parameters such as turbine features, nameplate capacity, and labor costs. The *energy production model* in the UWFLO framework is a complex model that represents the wind farm energy production as a function of the turbine features, turbine locations, and the incoming wind conditions over a given period of time.

The energy production model is a collection of several models: (i) the *wind distribution model* that estimates the frequency of wind speeds based on the measured site data; (ii) the *wind shear model* that determines the wind

speed at a given height above the ground (generally the hub height) based on measured/reference wind speed at a different height; (iii) the *wake model* that estimates the wake width and the wind speed in the wake downstream from each turbine within the farm; and (iv) the *turbine power response model* that yields the power generated by each turbine with respect to the wind speed directly encountered by the turbine. The energy production of the wind farm (E_{farm}) is estimated as a numerical integration of the wind farm power generation over a distribution of wind conditions, which can be expressed as:

$$E_{farm} = (365 \times 24) \sum_{i=1}^{N_p} P_{farm}(U^i, \theta^i) p(U^i, \theta^i) \Delta U \Delta \theta, \quad \text{where } \Delta U \Delta \theta = U_{max} \times 360^\circ / N_p \quad (2)$$

where $P_{farm}(U^i, \theta^i)$ represents the power generated by the farm (in kW) for the i^{th} sample wind speed (U^i) and direction θ^i – estimated using the wind shear model, the turbine power response model, and the wake model. In Eq. 2, $p(U^i, \theta^i)$ represents the probability of the occurrence of the i^{th} sample wind condition, which is given by the wind distribution model. The parameters U_{max} and N_p are respectively the reference maximum wind speed at a site (e.g., 15 m/s) and the number of sample wind conditions considered (20 in this paper).

Wind farm layout optimization (WFLO) can be readily perceived as a complex system design process. The energy production of a wind farm depends on several compound factors, such as (i) atmospheric boundary layer (ABL) variations, (ii) local topography, (iii) turbine geometry, (iv) turbine power characteristics, (v) arrangement of turbines over the site. These factors themselves comprise of multiple sub-factors or characteristics; e.g., the ABL, even in its simplest representation, consists of (i) mean wind speed and direction, (ii) turbulence intensity, (iii) wind shear, and (iv) air density, all of which vary with time and space. Several of these factors are highly uncertain, and the implicit functional relationships are highly nonlinear. In addition, high-fidelity estimations of some of these functional relationships have extensive computational footprint, making them practically prohibitive in the context of designing utility-scale wind farms – e.g., with current high-fidelity LES wake models (e.g., NREL SOFWA), one will require approximately 600 million CPU-hours for optimizing a 25-turbine wind farm [15, 9].

WFLO thus comprises a series of interdependent/interconnected models. A information flow perspective to WFLO can therefore enable significant advancements in informed decision-making compared to the state of the art. VIDMAP provides such an information flow visualization for WFLO through a synergistic implementation of *sensitivity analysis*, *uncertainty quantification*, and a novel *visual interface*. In its complete form, VIDMAP could provide a major leap forward not only in addressing issues of “wind farm underperformance” and “concept-to-installation delays”, but also in effective “risk mitigation” in wind energy projects. The following section describes the major components of VIDMAP in the context of WFLO.

4.2 Visually-Informed Decision-Making Platform (VIDMAP)

The Visually-Informed Decision-Making Platform (VIDMAP) for WFLO comprises the following 3 components:

1. *Uncertainty Quantification*: Uncertainty quantification (UQ) is in general performed in VIDMAP to gauge the fidelity or quality of information at any stage in the design process; in other words, UQ techniques are applied to estimate the uncertainty in the *originating information* (i.e., inputs to the most upstream models), and to subsequently estimate the uncertainty generated by the models (themselves) along the design process.
2. *Sensitivity Analysis*: Sensitivity analysis is performed for each constitutive model (in the design process) to gauge the relative impact of different inputs (incoming information) on the model output (outgoing information). It essentially illustrates the inter-model dependency/sensitivities within the design process.
3. *Informed Graphical Representation*: A graphical user interface (GUI) is created to illustrate the *uncertainty in the information generated by each model* and the *inter-model sensitivities*.

The VIDMAP GUI is therefore intended to be an important step towards integrating *design automation*, *evolving heuristics*, and *human decision-making* in the context of model-based design. The VIDMAP GUI is developed using the MATLAB GUI toolbox, and associated built-in functions. The initial VIDMAP GUI constructed in [2], which shows the entire WFLO framework and specifically illustrates the estimated inter-model sensitivities and model uncertainties up to the energy production model stage, is shown in Fig. 1.

In Fig. 1, the color bar shows a qualitative representation (e.g, high/low) of the uncertainty and sensitivity. Variance is used as the measure of uncertainty, and is normalized w.r.t. reference values to allow ready comparison across different models. The measure of sensitivity used in this case is the variance-based first-order index, which can take any positive real value less than or equal to 1. These sensitivity indices are estimated using the Extended Fourier Amplitude Sensitivity Test (eFAST), developed by Saltelli and Bolado [16].

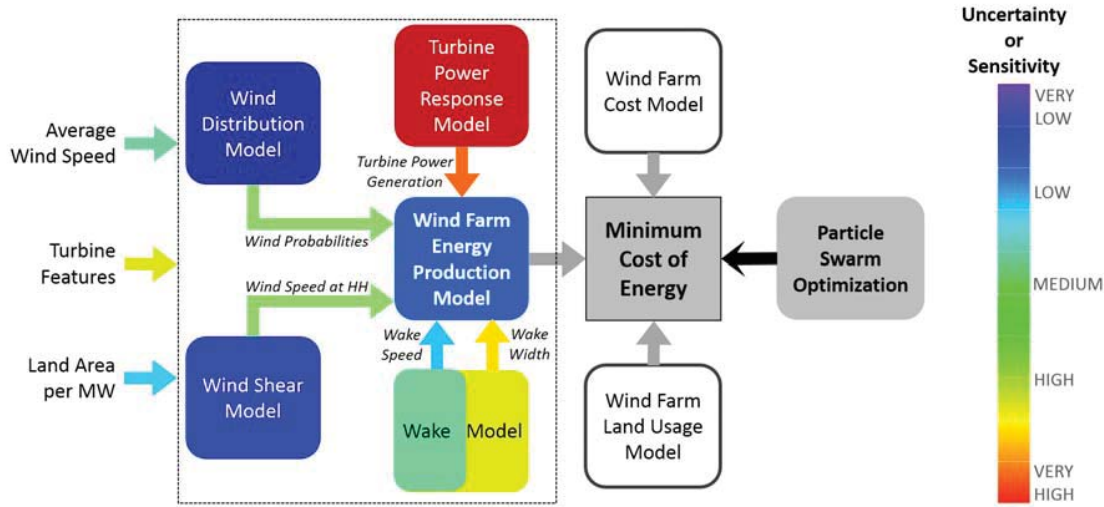


Figure 1: The VIDMAP graphical interface for WFLO, where (i) the color of a model block depicts the uncertainty in the corresponding model output;(ii) the color of a connector depicts the sensitivity of the corresponding downstream model output to the upstream information-source; and (iii) a gray-colored block or connector indicates that the corresponding sensibility or uncertainty values have not yet been computed

The approaches used to quantify the uncertainty in the upstream models, and propagate the uncertainty downstream, is further described in [2] In this paper, we particularly extend the VIDMAP for WFLO to estimate the uncertainty introduced by the PSO algorithm, the sensitivity of the minimum COE (associated with the optimized layout) to the uncertainties in the “energy production model”, and the resulting uncertainty in the minimum COE. The WFLO problem definition and the VIDMAP advancements are discussed in the next Section.

4.3 Advancing VIDMAP for WFLO

The objective of wind farm layout optimization here is to minimize the cost of energy (COE) of a 100-turbine wind farm, for given (i) turbine type(s), (ii) maximum allowed land area per MW installed (LAMI), (iii) land aspect ratio, and (iv) wind distribution. A Rayleigh distribution of wind speed is considered, where the single-parameter Rayleigh distribution is estimated from the given *average incoming wind speed* (U_{av}). The variables in the optimization problem are the locations of each turbine (X_j, Y_j) – a total of 200 design variables. The optimization problem is defined as

$$\begin{aligned}
 & \text{Min}_V f = COE(V, T) \\
 & \text{subject to} \\
 & \quad g_1(V) \leq 0 \\
 & \quad g_2(V) \leq 0 \\
 & \quad V = \{X_1, X_2, \dots, X_{100}, Y_1, Y_2, \dots, Y_{100}\}
 \end{aligned} \tag{3}$$

where the COE is estimated from Eq. 1; T represents the turbine type (a vector of features for a given commercial turbine); the inequality constraint g_1 represents the minimum clearance required between any two turbines, which is set at “ $2 \times$ rotor diameter” of the installed turbines; and the inequality constraint g_2 represents the maximum allowed LAMI (A_{MW}). Since a land aspect ratio of $7/3$ is assumed, the farm dimensions can be estimated from the maximum allowed LAMI as: $L = \sqrt{7/3} \times 100A_{MW}$ and $B = \sqrt{3/7} \times 100A_{MW}$.

In order to decouple the variance of the *energy production model* from that of the independent parameters, the deviation in the output (E_{farm} , given by Eq. 2) of the energy production model is represented by a stochastic parameter (ϵ_E) that follows the probability distribution determined via uncertainty propagation in [2] – where E_{farm} had an estimated variance of 0.0063. Thus, the return value from the energy production model (the top-level system evaluation model) whenever it is called by the optimization algorithm is given by $f_E = E_{farm} (1 + \epsilon_E)$. The effective set of input parameters for the sensitivity analysis and uncertainty quantification of the minimized COE is provided in Table 1; this table also shows the upper and lower bounds of the input parameters, and the sampling strategy for these parameters. The first three inputs are the independent inputs, and the last input represents the stochastic deviation in the energy production estimates.

Table 1: Continuous Design variables

Input Parameter	Lower Bound	Upper Bound	Sampling Strategy
Average Wind Speed (U_{av})	3.5 m/s	10.0 m/s	Normal Distribution with mean= 5.6m/s and $\sigma = 1.3$ m/s [17]
Turbine Feature Vector (T_i)	$i = 1$	$i = 24$	Uniform
Land Area per MW (A_{MW})	10 ha/MW	50 ha/MW	Uniform Pseudorandom (LHS) [2]
Deviation in WF Energy Production (ϵ_E)	$-\infty$	∞	Normal Distribution with zero mean and $\sigma = 0.079$ [2]

Based on the information provided in Table 1, a mixture of 50 samples is created with the following three parameters: Average Wind Speed (U_{av}), Land Area per MW (A_{MW}), and Deviation in WF Energy Production (ϵ_E). WFLO is then performed for each sample w.r.t. each turbine type (turbine feature vector). For the sake of computational efficiency, a small set of 24 different turbine types are chosen from the comprehensive list of 131 commercial turbines considered in [2]. Therefore, WFLO is performed for a total set of $50 \times 24 = 1200$ samples.

Heuristic optimization algorithms such as particle swarm optimization (PSO) and genetic algorithms (GA) involve random operators, and are also initiated with randomly generated population of candidate designs. As a result, the optimum solution obtained by such heuristic optimization algorithms could vary from one run to another. Hence, these algorithms are generally run multiple times to gauge their robustness during benchmark testing or practical application. In this paper, WFLO is performed using the mixed-discrete PSO adopted from the UWFO framework [18]. The uncertainty introduced by the PSO algorithm (due to its random operators) is estimated by running WFLO with this algorithm 5 times for each of the 1200 samples. The number of optimization runs per sample although small is considered practically adequate, since the observed variance in the PSO results was small, and it also helped in retaining desirable computational efficiency of the overall VIDMAP framework. The uncertainty in the estimated minimum (σ_f^{PSO}) due to the PSO algorithm is then determined by

$$\sigma_f^{PSO} = \frac{stddev(f_1^{PSO}, \dots, f_5^{PSO})}{\min(f_1^{PSO}, \dots, f_5^{PSO})} \quad (4)$$

where the generic f_k^{PSO} represents the optimum value of the objective function obtained in the k^{th} run of PSO for a given sample. The resulting VIDMAP GUI for the overall WFLO framework is illustrated next.

5. VIDMAP for WFLO: Results

It is observed from Fig. 2 that the optimization algorithm is significantly robust with an average estimated vari-

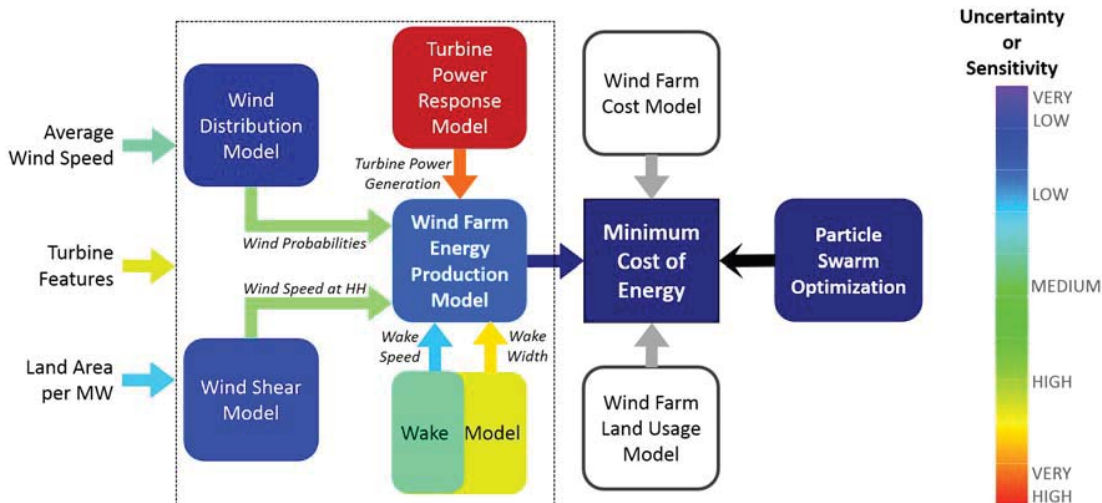


Figure 2: The final VIDMAP graphical interface for WFLO; gray colored blocks represent deterministic models; otherwise the color of a block represents the corresponding model uncertainty

ation in the obtained minimum over 5 runs (for each sample) of only 0.12%. This observation further establishes the use the PSO as a suitable algorithm for WFLO. The sensitivity of the computed minimum COE to the energy production model appears to be small (from Fig. 2) due to the first order index of 0.00118. However, it is to be

noted that the total order index of the deviation in the output of the energy production model is estimated to be 0.87. This observation indicates that the impact of the uncertainties in the energy production model is highly coupled with the variation in the wind resource, allowed land usage, and selected turbine features. Hence, the uncertainty in the energy production model is likely to influence decision-making when multiple wind farm sites, multiple turbine configuration, and different land plot availability is being considered in the planning stage of wind farm development. Moreover, it indicates that VIDMAP needs to be further advanced to illustrate both the first and total order indices with respect to inter-model sensitivities.

6. Concluding Remarks

In this paper, we advanced the Visually-Informed Decision-Making Platform to understand and analyze the impact of the uncertainties in the system model and the heuristic optimization algorithm on the uncertainties in the minimum Cost of Energy (COE) obtained through wind farm layout optimization. VIDMAP was applied in the layout optimization of a 100 turbine wind farm, where 1200 different samples of allowed land usage, wind resource strengths, turbine configurations, and (previously quantified) deviations in the energy production estimates are used to perform the sensitivity and uncertainty analysis. The uncertainty due to the random operators in the optimization algorithm (Particle Swarm Optimization) was determined by running the algorithm 5 times for each sample. It was observed that the Particle Swarm Optimization algorithm is remarkably robust, whereas the total order sensitivity of the minimum COE with respect to the deviations in the energy production estimates and the input parameters was noticeable.

7. Acknowledgement: Support from the NSF Award CMMI-1437746 is gratefully acknowledged. Any opinions, findings, and conclusions or recommendations expressed in this paper are those of the authors and do not necessarily reflect the views of the NSF.

References

- [1] Allaire, D., He, Q., Deyst, J., and Willcox, K., 2012. "An information-theoretic metric of system complexity with application to engineering system design". *ASME Journal of Mechanical Design*, **134**, October, pp. 100906–1.
- [2] Chowdhury, S., Tong, W., Mehmani, A., and Messac, A., 2014. "A visually-informed decision-making platform for model-based design of wind farms". In The AIAA Aviation and Aeronautics Forum and Exposition, AIAA.
- [3] Beyer, H. G., Lange, B., and Waldl, H. P., 1996. "Modelling tools for wind farm upgrading". In European Union Wind Energy Conference, AIAA.
- [4] Grady, S. A., Hussaini, M. Y., and Abdullah, M. M., 2005. "Placement of wind turbines using genetic algorithms". *Renewable Energy*, **30**(2), February, pp. 259–270.
- [5] Sisbot, S., Turgut, O., Tunc, M., and Camdali, U., 2009. "Optimal positioning of wind turbines on gkceada using multi-objective genetic algorithm". *Wind Energy*, **13**(4), pp. 297–306.
- [6] Gonzalez, J. S., Rodriguezb, A. G. G., Morac, J. C., Santos, J. R., and Payan, M. B., 2010. "Optimization of wind farm turbines layout using an evolutive algorithm". *Renewable Energy*, **35**(8), August, pp. 1671–1681.
- [7] Kusiak, A., and Song, Z., 2010. "Design of wind farm layout for maximum wind energy capture". *Renewable Energy*, **35**, pp. 685–694.
- [8] Chowdhury, S., Zhang, J., Messac, A., and Castillo, L., 2012. "Unrestricted wind farm layout optimization (uwflo): Investigating key factors influencing the maximum power generation". *Renewable Energy*, **38**(1), February, pp. 16–30.
- [9] Chowdhury, S., Zhang, J., Messac, A., and Castillo, L., 2013. "Optimizing the arrangement and the selection of turbines for a wind farm subject to varying wind conditions". *Renewable Energy*, **52**, April, pp. 273–282.
- [10] Mustakerov, I., and Borissova, D., 2010. "Wind turbines type and number choice using combinatorial optimization". *Renewable Energy*, **35**(9), September, p. 18871894.
- [11] Tong, W., Chowdhury, S., and Messac, A., 2014. "A consolidated visualization of wind farm energy production potential and optimal land shapes under different land area and nameplate capacity decisions". In AIAA Science and Technology Forum and Exposition, no. AIAA 2014-0998, AIAA.
- [12] Herman, S., 1983. Probabilistic cost model for analysis of offshore wind energy costs and potential. Tech. rep., Energy Research Center, May.
- [13] NREL, 2009. Jobs and economic development impact (jedi) model. Tech. rep., Golden, Colorado, USA, October.
- [14] Zhang, J., Chowdhury, S., Messac, A., and Castillo, L., 2012. "A response surface-based cost model for wind farm design". *Energy Policy*, **42**, pp. 538–550.
- [15] Annoni, J., Seiler, P., Johnson, K., Fleming, P., and Gebraad, P., 2014. "Evaluating wake models for wind farm control". American Control Conference.
- [16] Saltelli, A., and Bolado, R., 1998. "An alternative way to compute fourier amplitude sensitivity test (fast)". *Computational Statistics & Data Analysis*, **26**(4), pp. 445–460.
- [17] Chowdhury, S., Zhang, J., Catalano, M., Mehmani, A., Notaro, S. J., Messac, A., and Castillo, L., 2012. "Exploring the best performing commercial wind turbines for different wind regimes in a target market". In 53rd AIAA/ASME/ASCE/AHS/ASC Structures, Structural Dynamics, and Materials Conference, no. AIAA 2012-1352, AIAA.
- [18] Chowdhury, S., Tong, W., Messac, A., and Zhang, J., 2013. "A mixed-discrete particle swarm optimization with explicit diversity-preservation". *Structural and Multidisciplinary Optimization*, **47**(3), March, pp. 367–388.

Shape Optimisation of a Gas Injector

Ruber Arley Ruiz-Mesa¹, Manuel Julio García²

¹ EAFIT University, Medellín, Colombia, rruizme@eafit.edu.co

² EAFIT University, Medellín, Colombia, mgarcia@eafit.edu.co

1. Abstract

One of the main functions of a gas injector in a domestic oven combustion system is to improve the air-fuel ratio in the burner in order to increase the efficiency in the reaction process (combustion). For such a case, it would be necessary to maximise the primary air that enters into the combustion system and this could be done by redesigning the internal geometry of the injector. By improving this design, it is expected that the chemical reaction process between the fuel and the air becomes cleaner since the mixture inside the burner would be closer to its stoichiometric value and therefore the flame would have a smaller diffusive component. Currently, experimentation is the most used methodology to find the most appropriate shape of the injector. This paper presents an alternative way of finding the injector's geometry by using shape optimisation. Navier Stokes equations written in variational formulation were used to model the flow in the injector/mixer system. The aim was to maximise the primary air entrainment. A shape optimisation method based on Hadamard boundary variation using differentiation with respect to the domain was applied. Results showed improvements of 19.5% in the amount of air dragged into the burner for the optimised injector when compared to the original geometry. The geometry found by the optimisation procedure presents a manufacturability advantage as it requires less tooling to manufacture and allows greater dimensional accuracy. Finally, the method presented is automatic and can be used over any injector-mixer combination, provided that they are axisymmetric. This approach has significant advantages over other experimental or computational methodologies due to its reduced time and cost of development.

2. Keywords: CDF, shape optimisation, Navier-Stokes, gas injector.

3. Introduction

In any combustion system operating with a premixed atmospheric burner, the gas injector (nozzle) is the device responsible for controlling the thermal power and accelerate the fuel gas to generate a low region pressure at the outlet of the nozzle and thus induce the entrainment of the primary air required for the combustion process. Namkhat and Jugjai [1], theoretically established that the primary aeration is a function of fuel flow rate, gas type, nozzle geometry, mixing tube geometry and the burner ports geometry. Therefore, the design of the injector together with the burner is of great importance, as the system must bring a better air-fuel ratio to achieve higher use of the fuel thermal energy and generate lower emissions.

Most conventional domestic burners have high energy losses due to their open flame system which has a relatively low thermal efficiency, less than 30% according to [2, 3]. The traditional design of the nozzles has mainly been based on trial and error tests, where the designer's experience is crucial in selecting the most appropriate form factor. Modern techniques includes the use of experimental setups and computational fluids mechanics. For example, Zhang et al. [4] conducted studies using CFD to improve the gas-air mixture in a premixed burner through the inclusion of an orifice plate in the mixing chamber, resulting in improved uniformity of the velocity at the burner output ports by 234.2 % and fuel-gas mixing by 2.2 %. The results were validated experimentally, showing a reduction of pollutant emissions in the combustion process. They define the objective function as the uniformity of the velocity at the different output ports and use an iterative correction in order to achieve the minimum.

In atmospheric burners, efficient combustion depends largely on the amount of primary air entrained by the jet issuing from a nozzle or orifice [5]. Furthermore, the gas injector shape play an important role in improving air entrainment and the degree of mixing between the fuel jet and the primary air into the mixing tube. For this reason Singh et al. conducted a pilot study with nozzles of circular and non-circular shape to investigate the characteristics of air entrainment from the environment into the mixing tube cross sections [5]. They found that the entrainment ratio increases to a maximum value for small mixing pipe diameters and little separation between the injector and mixer. However, for a larger mixing tube or shifted jet locations, the noncircular jets entrain more of ambient fluid. The results were verified with theoretical approximations made by Pritchard et al. [6] and also with the similarity solution proposed by Becker et al. for circular nozzles [7].

Another important factor to consider in the design of burners, particularly when measuring the primary air entrainment, is the preheating of the air around the burner when it is operating. Namkhat and Jugjai [1] performed

experiments on a self-aspirating burner using both hot and cold tests. They found that the hot test gives about 37% lower primary aeration value than that of the cold test because of the preheating effect caused by combustion. The optimisation in fluid dynamics has been studied from different points of view and multiple approaches have been developed. The first applications can be seen on minimising the drag on wing profiles [8, 9, 10]. More recently, general optimisation procedures have been applied to the optimisation of problems involving fluids. In [11] Mohammadi and Pironneau present a short survey of optimal shape design (OSD) for fluids. Lohner et al. [12] show developments on shape optimisation for aeronautical applications based on the adjoint method. A gathering of different methods and specific applications is presented on [13] with an engineering emphasis. Shape and topology optimisation for Navier–Stokes problem using variational level set method is presented in [14]. In this paper a shape optimisation method for internal geometry of a gas injector of a premixed atmospheric burner is applied. The objective is to maximise the primary air entrainment. Due to its cylindrical symmetry, the flow is modelled with the Navier Stokes equations in cylindrical coordinates and the optimisation model is based on the Hadamard boundary variation, using differentiation with respect to the domain.

4. Optimisation problem

4.1. Model description

The equivalence ratio, ϕ , is the ratio between the quantities of air and fuel used in a stoichiometric reaction $(A/C)_s$, relative to that used in the actual process $((A/C)_a$, that is

$$\phi = \frac{(A/C)_s}{(A/C)_a} \quad (1)$$

This paper presents a shape optimisation methodology, of the internal shape of the fuel injector, for the minimisation of the equivalence ratio Eq.(1) of a combustion system that uses a premixed atmospheric burner, see Figure 1. The fuel used by the burner is natural gas, for which, according to [15], its stoichiometric air to fuel ratio is equal to $(A/C)_s = 9.52 \text{ m}_{\text{air}}^3 / \text{m}_{\text{fuel}}^3$. Assuming a constant gas flow (k) through the injector, Eq.(1) can be expressed as:

$$\phi = \frac{9.52}{(A/k)_a} \quad (2)$$

Therefore, in order to minimise the equivalence ratio, the amount of air entrainment (A) induced into the burner should be increased. Due to its geometry, a cylindrical coordinate system is used (r, z, θ) , with r the radial coordinate, z the coordinate along the axis of the injector/mixer, and θ the angular coordinate along which the properties are assumed constant in this study. The global geometry of the injector-mixer set is described in Figure 1. The assumed working conditions are also shown in the figure. They consist of a developed fuel flow at the entrance of the injector, Γ_{D1} , no slip conditions in the internal walls, Γ_{D2} , radial velocity equal to zero over the axis of symmetry, open boundary conditions at the entrainment zone of the mixer, and open boundary conditions at the exit of the mixer, Γ_N .

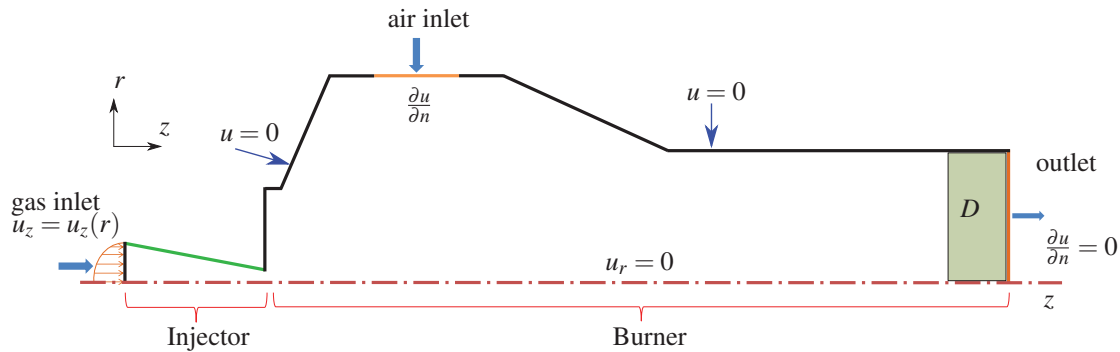


Figure 1: Axisymmetric model of the injector-mixer system used in the optimisation problem

4.2. Mathematical model

Given the fact that minimising the equivalence rate requires the increase in the amount of primary air entering the burner as shown in Eq.(1), and the fuel flow in the injector remains constant, minimising the equivalent rate is identical to increased flow at the output of mixer. Therefore, that can be expressed in terms of a minimisation function by defining a target velocity v_d , whose value is greater that it could be expected at the exit, and minimising the distance of the actual velocity to the target velocity, that is

$$\text{minimise } J(\Omega, u(\Omega)), \quad \text{with } J(\Omega, u(\Omega)) = \int_D |u - v_d|^2 d\Omega \quad (3)$$

where \mathcal{O} is the space of all admissible domains Ω and $D \in \Omega$ is a part of the domain at the exit region where the velocity needs to be maximised. The Cea's method, developed by Jean Cea [16] is proposed to obtain the shape derivative. It is based on the formulation of the Lagrange operator and the solution of the adjoint state equation to find the objective function derivative.

The original problem involves the mixture of two different gasses and the entrainment of air due to the fuel jet. However, in terms of shape optimisation, the problem is equivalent to minimise an air entrainment due to air jet. That is an air-to air problem. This assumption greatly simplifies the physics of the problem and allow us to concentrate on the optimisation algorithm. The complete optimisation problem can be written as

$$\begin{aligned} & \underset{\Omega \in \mathcal{O}}{\text{minimise}} \quad J(\Omega, u(\Omega)) = \int_D |u_i - u_d|^2 d\Omega & (4) \\ & \text{subject to} \quad \begin{cases} R_i(\Omega, u_i, p) : & -\nu \Delta u_i + (u_i \cdot \nabla) u_i + \nabla p = 0 & \text{in } \Omega \\ C(\Omega, u_i) : & \text{div } u_i = 0 & \text{in } \Omega \\ & u_i = u_i^D & \text{on } \Gamma_{D_1} \\ & \frac{\partial u_i}{\partial n} = 0 & \text{on } \Gamma_N \\ & u_r = 0 & \text{on } \Gamma_A \\ & u_i = 0 & \text{on } \Gamma_{D_2} \end{cases} & (5) \end{aligned}$$

The constraints of the problem correspond to the state equation, Eq.(4), plus boundary conditions, Eq.(5). This is an implicit (or nested) formulation of the optimisation problem as the objective function depends on the design variables, which in this case is the domain Ω , and the state variable, the velocity u is also a function of the design variable $u = u(\Omega)$. As the flow can be consider stationary and incompressible, the state equations in Eq.(5) represent the momentum and mass conservation equations. The rest of the constraint correspond to the boundary conditions

As it is a constrained problem, the Lagrangian is defined as

$$\mathcal{L}(\Omega, u_i, p, v_i, q) = J(\Omega, u_i) + \int_{\Omega} v_i R_i(\Omega, u_i, p) d\Omega + \int_{\Omega} q C(\Omega, u_i) d\Omega \quad (6)$$

where the state equations (R_i) and (C) are incorporated into the Lagrangian function by using the Lagrange multipliers v and q .

Using the first Green identity and taking into account that the momentum and mass conservation equations are written in cylindrical coordinates the weak form of the Eq.(5), can be found as [17]:

$$\begin{cases} a(u_i, v_i) + d(u_i, u_i, v_i) + b(v_i, p) = \int_{\Omega} f \cdot v_i r dx \\ b(u_i, q) = 0 \end{cases} \quad (7)$$

where:

$$a(u_i, v_i) = \nu \int_{\Omega} (\nabla u_i : \nabla v_i) r dx + \nu \int_{\Omega} u_r v_r \frac{1}{r} dx \quad (8)$$

$$d(w_i, u_i, v_i) = \int_{\Omega} ((w_i \cdot \nabla) u_i) \cdot v r dx \quad (9)$$

$$b(v_i, p) = - \int_{\Omega} (\text{div } v_i) p r dx - \int_{\Omega} v_r p dx \quad (10)$$

$$b(u_i, q) = - \int_{\Omega} (\text{div } u_i) q r dx - \int_{\Omega} u_r q dx \quad (11)$$

The nonlinear convective term, Eq.(9), is linearised using a fixed point like iteration [18, 19]. Therefore, substituting Eq.(8) and Eq.(11) in Eq.(7), the Lagrangian, Eq.(6), is defined as:

$$\begin{aligned} \mathcal{L}(\Omega, u_i, p, v_i, q) = & \int_D |u_i - u_d|^2 d\Omega + \nu \int_{\Omega} (\nabla u_i : \nabla v_i) r d\Omega + \nu \int_{\Omega} u_r v_r \frac{1}{r} d\Omega + \int_{\Omega} (u_o \cdot \nabla u_i) \cdot v_i r d\Omega \\ & - \int_{\Omega} (\text{div } v_i) p r d\Omega - \int_{\Omega} v_r p d\Omega - \int_{\Omega} f \cdot v_i r d\Omega + \int_{\Omega} (\text{div } u_i) q r d\Omega + \int_{\Omega} u_r q d\Omega \end{aligned} \quad (12)$$

The variables v_i and q appear as Lagrange multipliers and act as a test function to obtain the variational formulation

of the state equations R_i and C into \mathcal{L} as shown on Eq.(12). Then, the last two terms of Eq.(6) define the weak form of the state equation. Here u_o is the velocity in the previous iteration.

Finding u_i and p as the solution to the state equation, Eq.(5), one can define the objective function as:

$$J(\Omega) = \mathcal{L}(\Omega, u_i, p, v_i, q) \quad \forall v_i, q \quad (13)$$

According to [20], a variation in the shape of the domain (without topological changes) can be defined with displacement field θ over the initial domain Ω_0 . Assuming θ small, a deformed domain Ω is represented as $\Omega = (I + \theta)(\Omega_0)$. Details of the mathematical model are presented in [21] and [22]. Taking into account that definition, the derivative of the function \mathcal{L} with respect to a domain variation in the θ direction is obtained:

$$\begin{aligned} \mathcal{L}'(\Omega, u_i, p, v_i, q)(\theta) &= \frac{\partial \mathcal{L}}{\partial \Omega}(\Omega, u_i, p, v_i, q)(\theta) + \frac{\partial \mathcal{L}}{\partial u_i}(\Omega, u_i, p, v_i, q)(\dot{u}_i(\theta)) \\ &+ \frac{\partial \mathcal{L}}{\partial p}(\Omega, u_i, p, v_i, q)(\dot{p}(\theta)) + \frac{\partial \mathcal{L}}{\partial v_i}(\Omega, u_i, p, v_i, q)(\dot{v}_i(\theta)) \\ &+ \frac{\partial \mathcal{L}}{\partial q}(\Omega, u_i, p, v_i, q)(\dot{q}(\theta)) \end{aligned} \quad (14)$$

This result is obtained taking advantage of the non dependency of the variables (u_i, p, v_i, q) on the domain. The partial derivatives with respect to these variables, that are different from the domain, are calculated as follows:

$$\begin{aligned} \frac{\partial \mathcal{L}}{\partial u_i}(\Omega, u_i, p, v_i, q)(\dot{u}_i(\theta)) &\rightarrow \\ \partial_\lambda \mathcal{L}(\Omega, u_i + \lambda \hat{u}_i, p, v_i, q)|_{\lambda=0} &= J'(u_i, \hat{u}_i) + v \int_{\Omega} (\nabla \hat{u}_i : \nabla v_i) r \, d\Omega + v \int_{\Omega} \hat{u}_r v_r \frac{1}{r} \, d\Omega \\ &+ \int_{\Omega} (u_o \cdot \nabla \hat{u}_i) \cdot v_i \, r \, d\Omega + \int_{\Omega} (\text{div} \hat{u}_i) q \, r \, d\Omega + \int_{\Omega} \hat{u}_r \, q \, d\Omega \end{aligned} \quad (15)$$

$$\frac{\partial \mathcal{L}}{\partial p}(\Omega, u_i, p, v_i, q)(\dot{p}(\theta)) \rightarrow \partial_\lambda \mathcal{L}(\Omega, u_i, p + \lambda \hat{p}, v_i, q)|_{\lambda=0} = - \int_{\Omega} (\text{div} v_i) \hat{p} \, r \, d\Omega - \int_{\Omega} v_r \, \hat{p} \, d\Omega \quad (16)$$

$$\begin{aligned} \frac{\partial \mathcal{L}}{\partial v_i}(\Omega, u_i, p, v_i, q)(\dot{v}_i(\theta)) &\rightarrow \\ \partial_\lambda \mathcal{L}(\Omega, u_i, p, v_i + \lambda \hat{v}_i, q)|_{\lambda=0} &= v \int_{\Omega} (\nabla u_i : \nabla \hat{v}_i) r \, d\Omega + v \int_{\Omega} u_r \hat{v}_r \frac{1}{r} \, d\Omega \\ &+ \int_{\Omega} (u_o \cdot \nabla u_i) \cdot \hat{v}_i \, r \, d\Omega - \int_{\Omega} (\text{div} \hat{v}_i) p \, r \, d\Omega - \int_{\Omega} \hat{v}_r \, p \, d\Omega \end{aligned} \quad (17)$$

$$\frac{\partial \mathcal{L}}{\partial q}(\Omega, u_i, p, v_i, q)(\dot{q}(\theta)) \rightarrow \partial_\lambda \mathcal{L}(\Omega, u_i, p, v_i, q + \lambda \hat{q})|_{\lambda=0} = \int_{\Omega} (\text{div} u_i) \hat{q} \, r \, d\Omega + \int_{\Omega} u_r \, \hat{q} \, d\Omega \quad (18)$$

The derivative of the objective function, $J'(u)$, is calculated as:

$$J'(u_i, \hat{u}_i) = \int_D 2(u_i - u_d) \hat{u}_i \, d\Omega \quad (19)$$

Equations Eq.(17) and Eq.(18) correspond to the weak form of the momentum and continuity equations and they solve for u_i and p), for any arbitrary \hat{v}_i and \hat{q} test functions. on the other hand, equations Eq.(15) and Eq.(16) correspond to the adjoint system. Eq.(15) has the same form of the state equation with a source term defined by the derivative of the objective function J' . In this case, one solves the state equation for the variables (u_i, p) and then they are used to compute the source term J' and them the adjoint system is solve for the variables (v_i, q) . Finally, after making all these terms null, the shape derivative, Eq.(14), reads:

$$\mathcal{L}'(\Omega, u_i, p, v_i, q)(\theta) = \frac{\partial \mathcal{L}}{\partial \Omega}(\Omega, u_i, p, v_i, q)(\theta) \quad (20)$$

The partial derivative $\partial \mathcal{L} / \partial \Omega$ is computed using the Structure Theorem, see [16], [23, theorem 3.6 p. 479] and [22, theorem 2.2.2] for a detail explanation.

$$\begin{aligned} \frac{\partial \mathcal{L}}{\partial \Omega}(\Omega, u_i, p, v_i, q)(\theta) &= \int_{\partial \Omega_0} \theta \cdot \hat{n}_i (|u_i - u_d|^2 + v (\nabla u_i : \nabla v_i) r + v u_r v_r \frac{1}{r} + (u_i \cdot \nabla u_i) \cdot v_i \, r \\ &- (\text{div} v_i) p \, r - v_r \, p - f \cdot v_i \, r + (\text{div} u_i) q \, r + u_r \, q) \, ds, \end{aligned} \quad (21)$$

where \hat{n}_i is the unitary vector that defines the normal direction of $\partial\Omega_0$. The terms (v_i, q) are the solution to the adjoint system defined by Eq.(15) and Eq.(16). The shape derivative can be defined as the sensitivity of the objective function $J(\Omega)$ with respect to a variation of the domain shape defined by the boundary displacement field of magnitude θ on the normal direction \hat{n}_i .

This model was implemented using FreeFem++ [24] using the initial geometry shown in 1. The visualisation of the results is accomplished exporting the results into VTK format and visualising into ParaView.

5. Results

The minimum diameter of the injector defines the thermic power of the burner. Therefore, in order to preserve the thermic power of the system an additional restriction was set to ensure that the smallest dimension in the radial direction was not less than a given value.

The optimisation problem defined by Eq.(4) and Eq.(5) was implemented with a initial geometry as shown in figure 1. Although the sensitivity was calculated for any point in Ω only the shape of the injector was allowed to evolve. The variation on the boundary was accomplished according to the shape derivative defined in Eq.(21). Each iteration involves the computation of the shape sensitivity, a correction in the injector shape, remeshing of the injector domain and computation of the new objective function

Figure 2 presents the initial and optimised injector geometries, the evolution of the optimisation function and the variation of air entrainment. It can be observed that, as expected, the objective function decreases and the amount of primary air drawn into the burner increases. Only eight iterations were required until the minimum diameter of the injector reached its minimum limit, so it can guaranty the required thermic power of the burner.

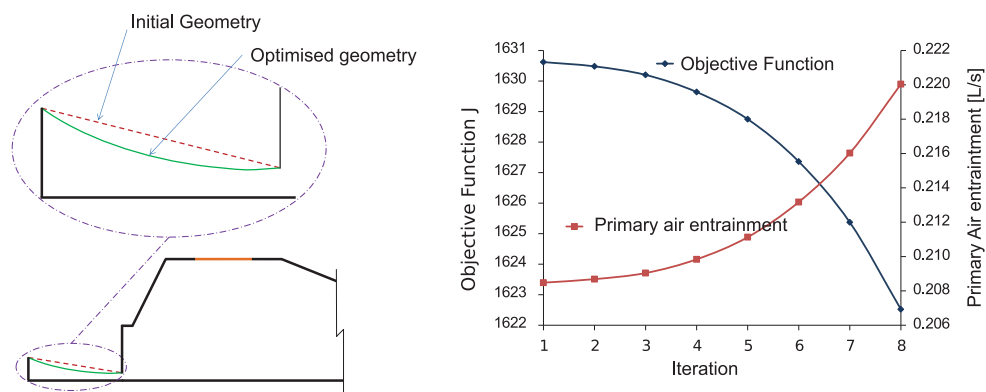
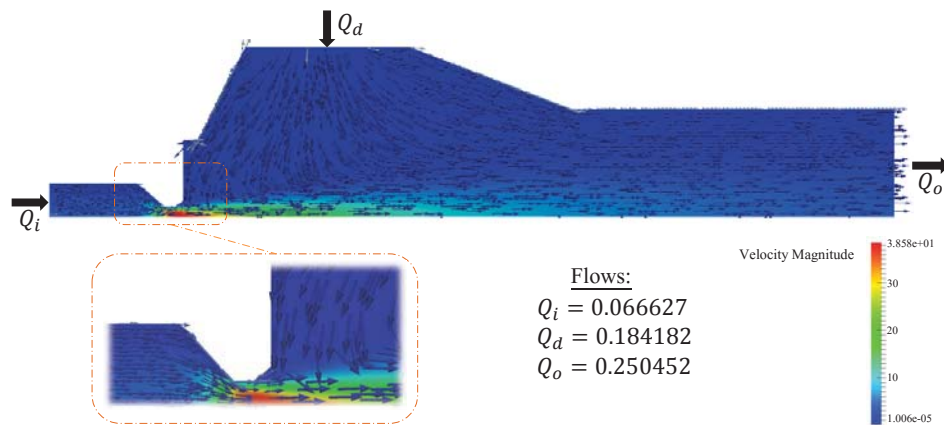


Figure 2: Left: Initial geometry and its final shape after running the optimisation algorithm. Right: behaviour of the objective function and the air flow entrainment at each iteration

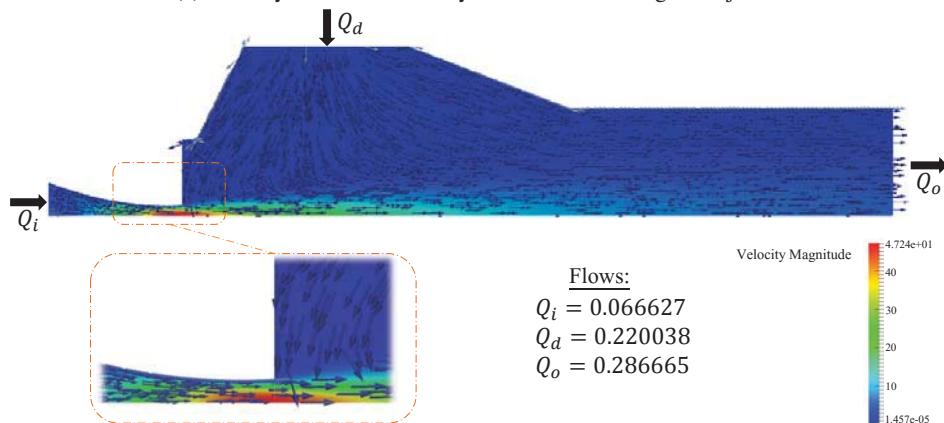
In Figure 3 the geometries of both, the original injector and the found by the optimisation procedure are compared. The original geometry refers to the current design of the injector that has led to the study in this paper. A comparison of the flow field in the original and the optimised injector is shown. Figure 3a presents the velocity field on the original injector, a balance of the flows and a scale showing the magnitude of the velocity. Likewise, Figure 3b presents the same information for the optimised injector. The fields were calculated solving Eq.(5) for each of the geometries. It can be appreciated that the velocity at the output is larger for the optimised model. Also the primary air entrainment is increased from $Q_d = 0.184182$ L/s for the original one to $Q_d = 0.220038$ L/s to the optimised one. That is equivalent to an increment of the 19.5% and maintaining the same level of flow at the injector input. From the manufacturability point of view, it can be observed that the construction of the optimised shape is easy compared with the current design as it requires less tooling and manufacturing processes.

5. Conclusions

The shape optimisation method using shape derivatives, has been successfully applied to optimise the equivalence rate on a gas injector of an atmospheric burner. The objective function was written in terms of minimising the distance of the velocity to a target velocity at the outlet. A shape optimisation method based on Hadamard boundary variation using differentiation with respect to the domain was applied. The results showed improvements of 19.5% in the primary air entrainment when compared to the previous geometry. This implies a combustion system with higher thermal efficiency and lower emissions. Additionally, the geometry found by the optimisation procedure



(a) Velocity field and summary of flows for the original injector



(b) Velocity field and summary of flows for the optimised injector

Figure 3: Comparison of the flow fields in the original and optimised injector.

presents a manufacturability advantage as it requires less tooling to manufacture and allows greater dimensional accuracy. Finally, the method presented is automatic and can be used over any injector-mixer combination, provided that they are axisymmetric. This approach has significant advantages over other experimental or computational methodologies due to its reduced time and cost of development.

6. Acknowledgements

This work was supported by EAFIT University, Industrias HACEB and COLCIENCIAS (Colombia) under research grant No 1216-562-37637.

7. References

- [1] A. Namkhat and S. Jugjai. Primary air entrainment characteristics for a self-aspirating burner: Model and experiments. *Energy*, 35(4):1701–1708, April 2010.
- [2] S Jugjai, S Tia, and N Rungsimuntuchart. Experimental Study on Efficiency Heat -recirculating Gas Burners Based on the Porous Medium Technology. *Asian J. Energy Environ*, 2:169–198, 2001.
- [3] Sumrerng Jugjai and Natthawut Rungsimuntuchart. High efficiency heat-recirculating domestic gas burners. *Experimental Thermal and Fluid Science*, 26(5):581–592, July 2002.
- [4] Tian Hu Zhang, Feng Guo Liu, and Xue Yi You. Optimization of gas mixing system of premixed burner based on CFD analysis. *Energy Conversion and Management*, 85:131–139, 2014.
- [5] Ghanshyam Singh, T. Sundararajan, and K. a. Bhaskaran. Mixing and Entrainment Characteristics of Circular and Noncircular Confined Jets. *Journal of Fluids Engineering*, 125(September 2003):835, 2003.

- [6] Robert Prichard, J.J. Guy, and N.E. Connor. *Handbook of Industrial Gas Utilization*. Van Nostrand Reinhold Co., New Providence, NJ., 1997.
- [7] H. A. Becker, H. C. Hottel, and G. C. Williams. Mixing And Flow in Ducted Turbulent Jets. In *9th Int. Symp. Combustion, The Combustion Institute*, pages 7–20, Pittsburgh, 1963. Academic Press.
- [8] Juan J. Alonso, Juan J. Alonso, Ilan M. Kroo, Ilan M. Kroo, Antony Jameson, and Antony Jameson. Advanced algorithms for design and optimization of quiet supersonic platforms. *of*, 14, 2002.
- [9] F. Bauer, P. Garabedian, D. Korn, and A. Jameson. *Supercritical Wing Sections*. Springer, Berlin, 1977.
- [10] O. Pironneau. On optimum design in fluid mechanics. *Journal of Fluid Mechanics*, 64:97–110, 6 1974.
- [11] B. Mohammadi and O. Pironneau. Applied optimal shape design. *Journal of Computational and Applied Mathematics*, 149(1):193 – 205, 2002. Scientific and Engineering Computations for the 21st Century - Methodologies and Applications Proceedings of the 15th Toyota Conference.
- [12] R Löhner, O Soto, and C Yang. An adjoint-based design methodology for CFD optimization problems. *School of computational science*, 2003.
- [13] Dominique Thvenin and Gbor Janiga. *Optimization and Computational Fluid Dynamics*. Springer Publishing Company, Incorporated, 1st edition, 2008.
- [14] Xian-Bao Duan, Yi-Chen Ma, and Rui Zhang. Shape-topology optimization for navier–stokes problem using variational level set method. *Journal of Computational and Applied Mathematics*, 222(2):487 – 499, 2008.
- [15] Andrés Amell Arrieta. Estimación de las propiedades de combustión de combustibles gaseosos. Technical report, Universidad de Antioquia, Medellín, 2002.
- [16] Jean C ea. Conception optimale ou identification de formes: calcul rapide de la d eriv e directionnelle de la fonction co ut. *Mod elisation math ematique et analyse num erique*, 20:371–402, 1986.
- [17] Simone Deparis. *Numerical Analysis of Axisymmetric Flows and Methods for Fluid-Structure Interaction Arising in Blood Flow Simulation*. PhD thesis,  cole polytechnique f d erale de Lausanne, 2004.
- [18] Wolfgang A. Wall. *Fluid-Struktur-Interaktion mit stabilisierten Finiten Elementen*. PhD thesis, University Stuttgart, 1999.
- [19] Volker Gravemeier. *The Variational Multiscale Method for Laminar and Turbulent Incompressible Flow* Volker Gravemeier. PhD thesis, Stuttgart University, 2003.
- [20] Jacques Hadamard. *M emoire sur le probl eme d’analyse relatif   l’ quilibre des plaques  lastiques encastr ees*. M emoires pr esent es par divers savants l’Acad emie des sciences de l’Institut de France:  xtrait. Imprimerie nationale, Paris, 1908.
- [21] Gr egoire Allaire. *Conception optimale de structures: Majeure Sciences de l’ing nieur, simulation et mod elisation*.  cole polytechnique, D epartement de Math ematiques appliqu ees, 2006.
- [22] Charles Dapogny. *Shape optimization, level set methods on unstructured meshes and mesh evolution*. PhD thesis,  cole Doctorale Paris Centre, 2013.
- [23] M. C. Delfour and J.-P. Zol esio. *Shapes and Geometries: Metrics, Analysis, Differential Calculus and Optimization*. SIAM, 2nd edition, 2011.
- [24] F Hecht. New development in FreeFem++. *J. Numer. Math.*, 20(3-4):251–265, 2012.

Simultaneous Optimization of Initial Blank Shape and Blank Holder Force Trajectory for Square Cup Deep Drawing Using Sequential Approximate Optimization

Satoshi Kitayama¹, Marina Saikyo², Kiichiro Kawamoto³, Ken Yamamichi⁴

¹ Kanazawa University, Kanazawa, Japan, kitayama-s@se.kanazawa-u.ac.jp

² Graduate School of Natural Science & Technology, Kanazawa University, Kanazawa, Japan, saikyo@stu.kanazawa-u.ac.jp

³ Komatsu Industry Corp., Komatsu, Japan, kiichirou_kawamoto@komatsu.co.jp

⁴ Komatsu Industry Corp., Komatsu, Japan, ken_yamamichi@komatsu.co.jp

1. Abstract

Optimal blank shape minimizing earing in deep drawing has a direct influence on material saving as well as product quality. This paper proposes a method for determining the optimal blank shape design in square cup deep drawing using sequential approximate optimization (SAO) with a radial basis function (RBF) network. The earing is minimized under tearing and wrinkling constraints with a variable blank holder force (VBHF), which varies through the punch stroke. Through numerical and experimental results, the validity of the proposed approach is examined.

2. Keywords: Deep Drawing Blank Shape Design, Variable Blank Holder Force, Sequential Approximate Optimization

3. Introduction

Sheet metal forming processes involve a complicated deformation that is affected by process parameters such as material properties, blank holder force (BHF), die geometry, blank shape, friction, and lubrication condition. Among these, the blank shape has a direct influence on the product quality. The desired product cannot be obtained with a small initial blank shape, while a large initial blank shape produces a large flange part that is trimmed off as waste. Furthermore, a small BHF can lead to wrinkling while a large BHF results in tearing. Thus, it is important to find a suitable blank shape with an optimal BHF for the material saving and product quality. A number of different approaches have been proposed to determine the optimal blank shape in deep drawing, and these are mainly classified into two categories: the use of a closed-loop type algorithm, or those based on the response surface method (RSM).

Sheet forming simulation is currently so numerically intensive that the use of RSM is a valid option. Hino et al. used the RSM for obtaining the optimal blank shape in deep drawing [1], in which earing, as defined by the amount of trimmed material, was minimized under two design constraints. Naceur et al. used a moving least square approximation to determine the optimal blank shape [2], for which the risk of tearing/wrinkling was approximated using a quadratic polynomial, and 7 control points (nodes of the blank) were taken as the design variables.

This paper proposes a method for determining the optimal blank shape with the VBHF in deep drawing. The objective is to find out the optimal blank shape minimizing the earing under tearing/wrinkling constraints with the VBHF approach. In this paper, two objective functions are developed to evaluate the earing. The tearing/wrinkling is evaluated using the forming limit diagram (FLD) and are regarded as the design constraints. In order to identify a set of pareto-optimal solutions with a small number of simulation runs, a sequential approximate optimization using the RBF network has been adopted. The validity of the proposed approach is examined through the experiment using a servo press.

4. Blank Shape Optimization with Variable Blank Holder Force

4.1. Finite element analysis model

The FEA model used in this paper is shown in Fig.1, in which the blank holder force is applied in the positive z -direction. The counter punch and die drop to the negative z -direction with a total stroke of 62 mm. The element type and the number of finite elements are shown in Table 1. The friction coefficient μ of the interfaces (blank/blank holder, blank/punch, blank/die, and blank/counter punch) is set to 0.10. Considering the symmetry, one-quarter model is used for the numerical simulation as shown in Fig. 1. An initial blank size of 92.5 mm \times 92.5 mm is actually used. A Belyschko-Tsay shell element with seven integration points along the thickness direction is used for the shell mesh of the blank. The penalty coefficient for contact (blank/blank holder, blank/punch, blank/die, and blank/counter punch) is set to 0.10. The element types and the number of finite elements are listed in Table 1. In addition, Steel Plate Formability Cold (SPFC) 440 is selected as the test material. The material properties are listed in Table 2.

The quarter-model deformation of the initial blank is shown in Fig. 2, in which the dashed line represents the target (trimmed) contour and the area above this contour is defined as earing. As shown in Fig. 2, the earing in this square cup deep drawing is generated in the x - y plane. Ideally, the target contour should be set to the exact shape of the product denoted by the bold line. However, it is very difficult to set the exact shape as the ideal target contour in this deep drawing. The tolerance of 5 mm from the exact shape is then considered and is set as the target contour.

Table 1 Element type and number of finite elements

	Element type	Number of finite elements
Counter punch	Rigid	120
Die	Rigid	924
Blank	Shell (Belytschko-Tsay)	2116
Blank holder	Rigid	432
Punch	Rigid	962

Table 2 Material properties of SPFC440

Density: ρ [kg/mm^3]	7.84×10^{-6}
Young's Modulus: E [MPa]	2.06×10^5
Poisson's Ratio: ν	0.3
Yield Stress: σ_y [MPa]	353
Tensile Strength: σ_T [MPa]	479
Normal Anisotropy Coefficient: r	0.98
Strain Hardening Coefficient: n	0.189

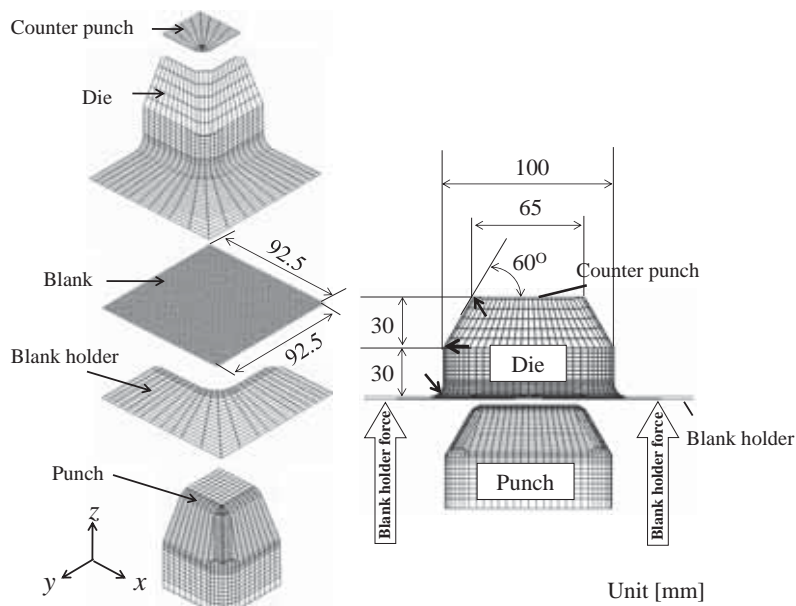


Fig.1 Finite element analysis model

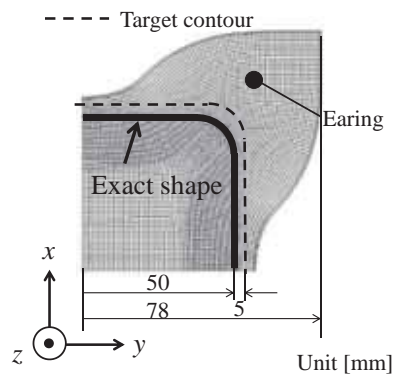


Fig.2 Deformation of initial blank (quarter model)

4.2. Design Variables

The blank shape is determined using the four design variables shown in Fig.3, where one-quarter model of the formed product is depicted. The three nodes denoted by black squares are taken as the design variables for determining the blank shape. Nodes 1 and 3 move along the vertical and 45 degree line, respectively, while the movement of Node 2 depends on x_4 . These nodes are connected by straight line as shown in Fig. 3, and the initial blank shape is then determined. VBHF is also taken into consideration to control the material flow into the die. For the VBHF, total stroke L_{max} is partitioned into n sub-stroke steps and the BHF of each sub-stroke is taken as the design variables. An illustrative example of these design variables is shown in Fig.4, where it should be noted that the design variable for VBHF starts from x_5 .

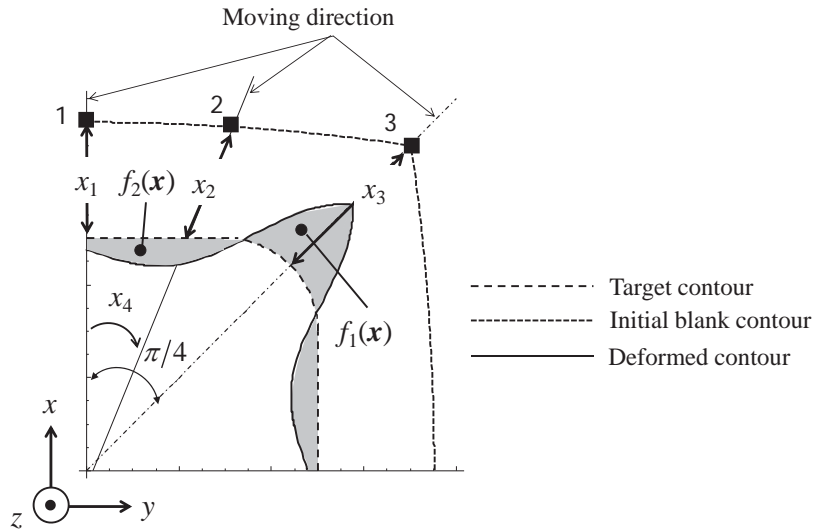


Fig.3 Illustrative example for evaluating earing and design variables for blank shape

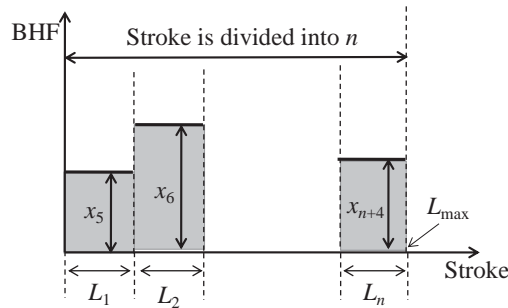


Fig.4 Design variables for variable blank holder force

4.3. Objective functions

Let us explain how to evaluate the earing with Fig.3, in which the dashed line represents the target (trimmed) contour. First, the area above the target contour is evaluated as the first objective function $f_1(x)$, as shown in Fig.3. Unfortunately, in this method, the area below the target contour cannot also be evaluated. Consequently, this area below the target contour is evaluated as the second objective function $f_2(x)$. As $f_1(x)$ will be large with a large blank shape, while $f_2(x)$ will be large with a small blank shape, a trade-off between these objectives can thus be observed.

4.4. Constraints

The forming limit diagram (FLD) is used to evaluate the tearing and wrinkling. In order to evaluate the degree of tearing and wrinkling, the strains in the formed element are analyzed and compared against the forming limit curve (FLC, as shown in Fig.5). The following FLC was defined in the principal plane of logarithmic strains proposed by Hillman and Kubli [5].

$$\varepsilon_1 = \varphi_T(\varepsilon_2) \quad \varepsilon_1 = \varphi_W(\varepsilon_2) \quad (1)$$

where φ_T is the FLC that controls tearing, and φ_W is the FLC that controls wrinkling. The following safety FLC

is defined:

$$\left. \begin{aligned} \theta_T(\varepsilon_2) &= (1-s)\varphi_T(\varepsilon_2) \\ \theta_W(\varepsilon_2) &= (1+s)\varphi_W(\varepsilon_2) \end{aligned} \right\} \quad (2)$$

where s represents the safety tolerance, and is defined by the engineers (in this paper, s is set to 0.2). If an element comes to or lies above FLC, it is expected that a risk of tearing can be observed. Similarly, a risk of wrinkling can be assumed if an element lies in the wrinkling region. The risk of both wrinkling and tearing were evaluated as follows:

For tearing:

$$g_1(\mathbf{x}) = \left(\sum_{j=1}^{nelm} T_j \right)^{1/p} \quad (3)$$

where

$$\left. \begin{aligned} T_j &= (\varepsilon_1^j - \theta_T(\varepsilon_2^j))^p & \varepsilon_1^j > \theta_T(\varepsilon_2^j) \\ T_j &= 0 & \text{otherwise} \end{aligned} \right\} \quad (4)$$

For wrinkling:

$$g_2(\mathbf{x}) = \left(\sum_{j=1}^{nelm} W_j \right)^{1/p} \quad (5)$$

where

$$\left. \begin{aligned} W_j &= (\theta_W(\varepsilon_2^j) - \varepsilon_1^j)^p & \varepsilon_1^j < \theta_W(\varepsilon_2^j) \\ W_j &= 0 & \text{otherwise} \end{aligned} \right\} \quad (6)$$

p is set to 4, and $nelm$ represents the number of finite elements of the blank.

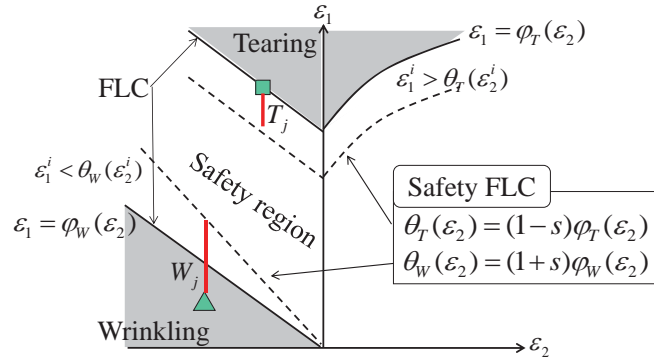


Fig.5 Forming limit diagram for evaluating tearing and wrinkling

5. Flow of Sequential Approximate Optimizatoion

The flow can be summarized as follows:

(STEP1) Initial sampling points are generated by the LHD.

(STEP2) Numerical simulation is carried out, in which objective functions ($f_1(\mathbf{x})$ and $f_2(\mathbf{x})$) and constraints ($g_1(\mathbf{x})$ and $g_2(\mathbf{x})$) are numerically evaluated at all sampling points.

(STEP3) All functions are approximated by the RBF network; wherein the approximated objective functions are denoted as $\tilde{f}_i(\mathbf{x})$ ($i=1,2,\dots,K$), and the approximated constraint functions are denoted as $\tilde{g}_j(\mathbf{x})$ ($j=1,2,\dots,m$).

(STEP4) A pareto-optimal solution for the response surface is found using the weighted l_p norm method:

$$\left\{ \begin{aligned} \left[\sum_{i=1}^K (\alpha_i \tilde{f}_i(\mathbf{x}))^p \right]^{1/p} &\rightarrow \min \\ \tilde{g}_j(\mathbf{x}) &\leq 0 \quad j=1,2,\dots,m \end{aligned} \right\} \quad (7)$$

where α_i ($i=1,2,\dots,K$) represents the weight of the i -th objective function, and p is the parameter (set to 4 in this paper). In order to obtain a set of pareto-optimal solutions, various weights are assigned.

(STEP5) The density function is constructed and minimized, and the optimal solution of the density function is added as a new sampling point [4]. This step is repeated till a terminal criterion is satisfied.

(STEP6) If terminal criterion is satisfied, the SAO algorithm will be terminated. Otherwise, return to STEP 2.

5. Numerical and Experimental Results

Numerical simulation was carried out to obtain the optimal blank shape and VBHF. For the VBHF, the total stroke was divided into 3 (L_1 , L_2 , and L_3). Then, the total number of design variables is 7. The lower and upper bounds of the design variables are defined as follows:

$$\left. \begin{aligned} 38 \leq x_1 \leq 42.5[mm] \quad 33 \leq x_2 \leq 40[mm] \quad 23 \leq x_3 \leq 62[mm] \\ \pi/12 \leq x_4 \leq \pi/6[rad] \\ 20 \leq x_5 \leq 120[kN] \quad \text{for } 0 \leq L_1 \leq 20[mm] \\ 20 \leq x_6 \leq 120[kN] \quad \text{for } 20 \leq L_2 \leq 40[mm] \\ 20 \leq x_7 \leq 120[kN] \quad \text{for } 40 \leq L_3 \leq 62[mm] \end{aligned} \right\} \quad (7)$$

Fifteen initial sampling points are first generated with the LHD, and the pareto-frontier is identified. The error in the pareto-optimal solutions is adopted as the terminal criterion, which is set to 5.0 %. Various weights are assigned to the each objective function, and a total of 56 sampling points (simulation runs) are required to identify the pareto-frontier. All feasible sampling points in the objective space are shown in Fig.6. It can be seen that the pareto-frontier is disconnected. Furthermore, we can also see that the optimal blank shape and the deformed shape are not qualitatively different, but the same is not true in the case of the optimal VBHF.

At point A, the initial BHF is low but gradually increases. This implies that the material readily flows into the die with the low BHF, but becomes hardened as the BHF increases. On the other hand, at point B, the material is hardened at the initial stage by the high BHF; with the lower BHF needing to be applied during the middle stage in order to prevent tearing. Finally, the material is again hardened by the high BHF at the final stage.

Based on the numerical results, the experiments using a servo press (H1F200, Komatsu Industry Corp.) are carried out. The photos of punch and blank holder are shown in Fig. 7. Points A and B shown in Fig.6 is used for the experiments. An expert commented that the blank holder will be injured if the optimal blank obtained the numerical result is directly used in the experiment. Based on his suggestion, the blank shape considering the tolerance of 5 mm is used, which is shown in Fig. 7. The VBHF trajectory and the product through the experiments are shown in Figs. 8 and 9, respectively. It is found from the experimental results that no tearing/wrinkling can be observed. The validity of the proposed approach is confirmed through the numerical and experimental results.

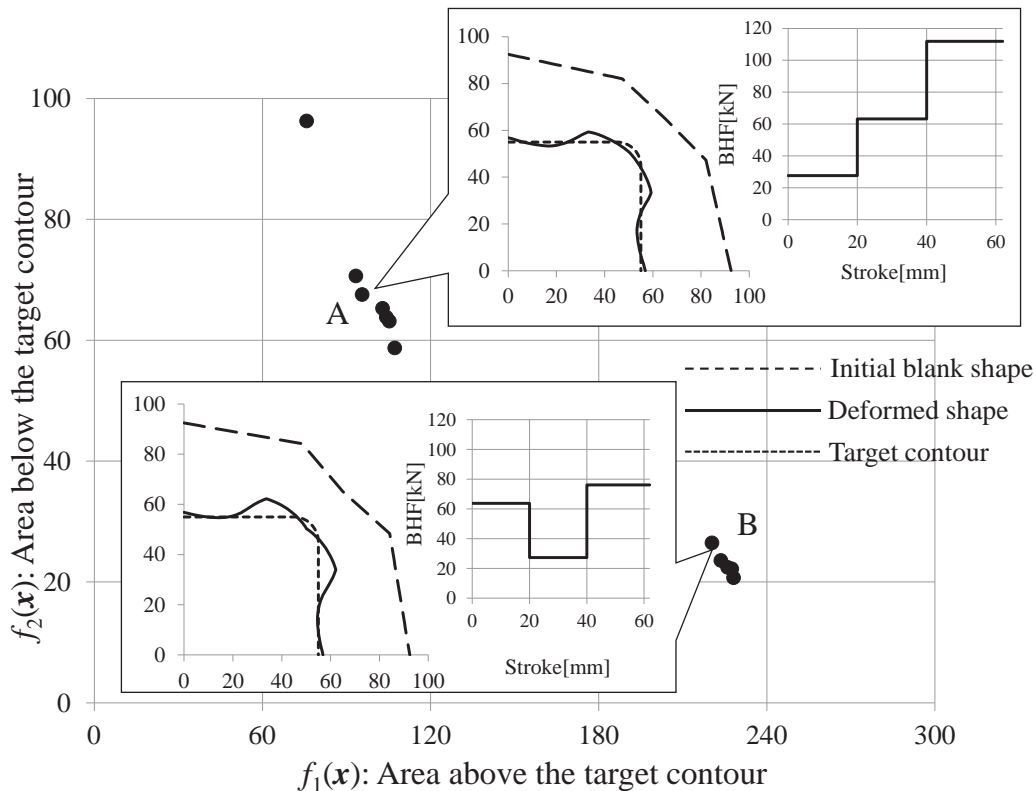


Fig.6 Pareto-frontier with an optimal blank shape and VBHF

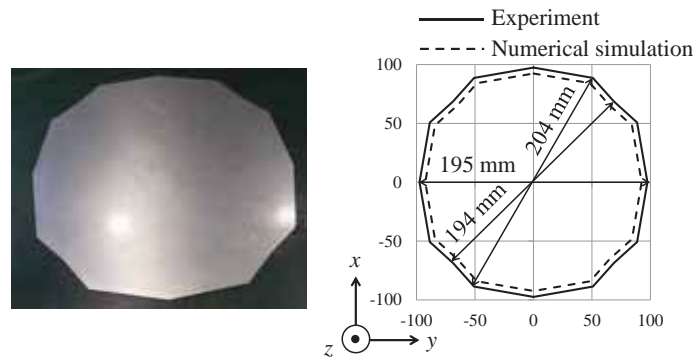


Fig. 7 Blank shape used in the experiment

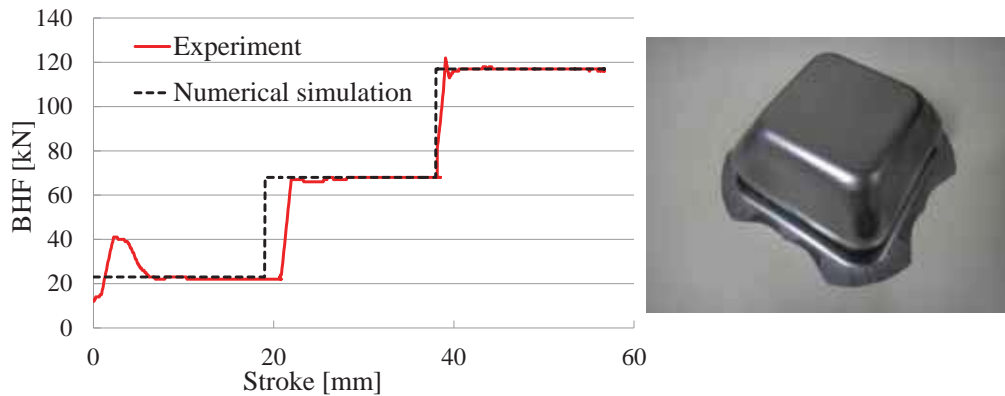


Fig. 8 VBHF trajectory and product at point A

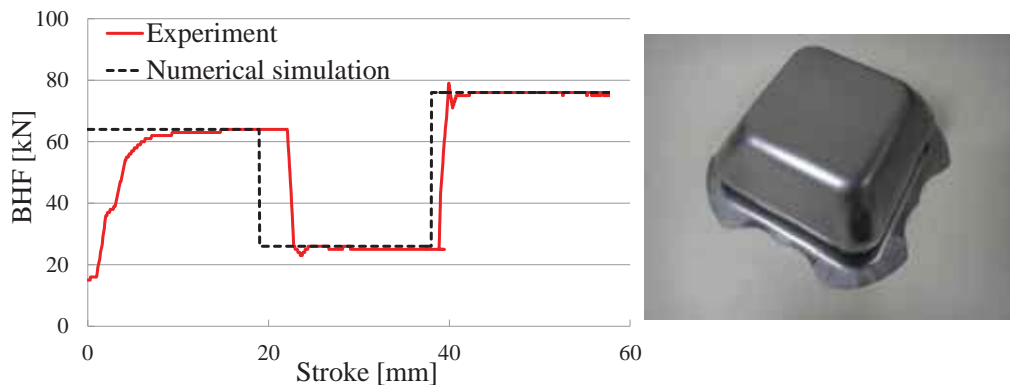


Fig. 9 VBHF trajectory and product at point B

6. Concluding Remarks

This paper proposes a method to determine the optimal blank shape minimizing the earing and the optimal VBHF trajectory. The numerical result indicates that there are two kinds of VBHF trajectories for the successful sheet forming whereas the optimal blank is qualitatively same. Based on the numerical results, the experiments using servo press is carried out. No tearing/wrinkling can be observed through the experiments, and the validity of the proposed approach is then confirmed.

References

- [1] Hino, R., Yoshida, F., Toropov, V.V., (2006), Optimum blank design for sheet metal forming based on the interaction of high- and low-fidelity FE models, *Archive of Applied Mechanics*, 75(10): 679-691.
- [2] Naceur, H., Ben-Elechi, S., Batoz, J.L., Knopf-Lenoir, C., (2008), Response surface methodology for the rapid design of aluminum sheet metal forming parameters, *Materials and Design*, 29: 781-790.
- [3] Hillmann, M., Kubli, W., (1999), Optimization of sheet metal forming processes using simulation programs, in : *Numisheet '99*, Beasnc, France, 1: 287-292.
- [4] Kitayama, S., Arakawa, M., Yamazaki, K., (2011), Sequential approximate optimization using radial basis function network for engineering optimization, *Optimization and Engineering*, 12(4): 535-557.

Robust shape optimization under vibroacoustic criteria and uncertain parameters

Frédéric Gillot¹, Renata Troain¹, Koji Shimoyama², Sébastien Besset¹

¹ DySCo/LTDS, Ecole Centrale de Lyon, Lyon, France, frederic.gillot@ec-lyon.fr

² Institute of Fluid Science, Tohoku University, Sendai, Japan

1. Abstract

Our paper addresses the noise reduction level in acoustic cavities subject to uncertain parameters. Such issue is nowadays of paramount importance when treating inflight conditions of commercial planes or boats. The noise level is represented by an energy density in the cavity. This objective function is provided through an energy method called Simplified Energy Method. We use a transformation function mapping a given 3D cavity surface on a 2D domain. The optimization process directly relies on this function and thus avoids remeshing of the initial geometry. We consider geometrical and material uncertainties during the shape optimization process. Such uncertainties are usually generated by involved manufacturing processes. Robust optimization is performed using the non-dominated sorting genetic algorithm (NSGA-II) together with the Kriging surrogate model. We will show in our presentation the influence of geometrical and material characteristics on the optimal solution.

2. Keywords: Shape optimization, Simplified energy method, Robust optimization, Kriging, Genetic algorithm .

3. Introduction

Reducing noise level in cavities enable human transport means to increase their attractively and wellness. From a research point of view the noise level can be considered as a design objective, when proceeding with robust shape optimization of such cavities. This noise level can be described with the Simplified Energy Method (here and after referred as MES). This method has been fully validated for transient and stationary cases [1, 2], and for various elastic media such as membranes and plates [3].

We already demonstrated that such method can be efficiently used in an iso-geometric like description of a cavity, enabling efficient optimization loop scheme [4] We focus here on the robust shape optimization with regards to geometrical and material uncertainties.

4. MES in curvilinear coordinates

4.1. Short description of the MES

Detailed description of the MES can be found in [5, 6, 7].

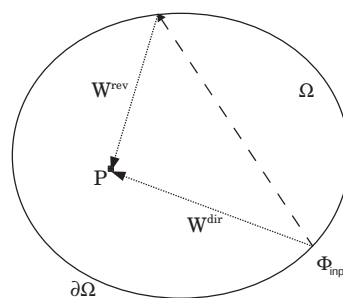


Figure 1: MES formulation: direct and reverberated fields

Since W is a quadratic variable made of partial energy quantities corresponding to both direct and reverberated fields (see Fig. 1), the superposition principle can be applied:

$$W = W_{dir} + W_{rev}. \quad (1)$$

The energy density inside the cavity can then be expressed as a function of the primary sources and fictitious sources (reverberated field sources) located on the boundaries:

$$W(P) = \int_{\partial\Omega} \Phi(M) \bar{\mathbf{u}}_{PM} \cdot \bar{\mathbf{n}}(M) G(M) d\partial\Omega + \int_{\partial\Omega} \sigma(M) \bar{\mathbf{u}}_{PM} \cdot \bar{\mathbf{n}}(M) G(M) d\partial\Omega, \quad (2)$$

where P is a point inside the cavity where W is measured, M is a point of integration on the cavity surface, $G(r) = 1/(4r^2\Pi c)$, $\bar{\mathbf{u}}_{PM} = \mathbf{PM}/\|\mathbf{PM}\|$, $\bar{\mathbf{n}}(M)$ the unit normal at the point M , $\Phi(M)$ are the acoustic boundary sources and $\sigma(M)$ are the fictitious boundary sources. We will use the term “boundary source” to denote the sources located on the cavity boundary (which may be due, for example, to external excitations).

For every point M_0 of the boundary $\partial\Omega$, $\sigma(M_0)$ depends on the absorption coefficient α , acoustic boundary sources of the system Φ and fictitious boundary sources in all other points of $\partial\Omega$:

$$\begin{aligned} \sigma(M_0) &= (1 - \alpha) \int_{\partial\Omega} \sigma(M) \bar{\mathbf{u}}_{M_0M} \cdot \bar{\mathbf{n}}(M) G(M) d\partial\Omega \\ &+ (1 - \alpha) \int_{\partial\Omega} \Phi(M) \bar{\mathbf{u}}_{M_0M} \cdot \bar{\mathbf{n}}(M) G(M) d\partial\Omega. \end{aligned} \quad (3)$$

Energy variables are given as a solution of a Fredholm equation, corresponding to an energy balance at the boundary of the domain.

4.2. Curvilinear coordinates

We choose to describe 3D cavity by parametrized functions of two variables. This approach is fully described in [11]. Such approach enable the used of complex geometries to describe the cavity, such as Bezier curves, Splines, NURBS and so on. Moreover the discretization is conducted on a 2D domain, while design variables are coefficient of transformation function thus avoiding the remitting during the optimization procedure. The matrix formulation of our proposed approach is then

$$\bar{W} = [S] \bar{\sigma} + [R] \bar{\Phi}, \quad (4)$$

where $[S]$ and $[R]$ are matrices corresponding to the discretization of the integral formulations of MES. $\bar{\sigma}$ is expressed as follows:

$$\bar{\sigma} = ([Id] - [\alpha]) [T] \bar{\sigma} + ([Id] - [\alpha]) [Q] \bar{\Phi}, \quad (5)$$

where $[Id]$ is the identity matrix and $[\alpha]$ the diagonal matrix of the absorption coefficients. Expressing σ as a function of Φ gives:

$$\bar{\sigma} = ([Id] - [T] + [\alpha][T])^{-1} ([Id] - [\alpha]) [Q] \bar{\Phi}. \quad (6)$$

Using (4) and (6) we obtain:

$$\bar{W} = ([R] + [S] ([Id] - [T] + [\alpha][T])^{-1} ([Id] - [\alpha]) [Q]) \bar{\Phi} = [M] \bar{\Phi}. \quad (7)$$

Such matrix formulation gives an advantage when computing the robustness towards material absorption coefficients. These coefficients are given in matrix $[\alpha]$, while other matrices depend only on geometrical properties of the cavity. That is why calculation of W distribution for given geometry and α following normal law doesn't demand high computational cost. We have to obtain geometry matrices once and after calculate W for every α changing just the values of $[\alpha]$ matrix.

6. Robustness problem

The quantity f to be minimized can be formulated as follows:

$$f = \|\bar{W}(x_i, \alpha)\|. \quad (8)$$

After specifying the geometry of the cavity Ω with bounding surface $\partial\Omega$ and the function of transformation $\bar{F}(\xi_1, \xi_2) = [x(\xi_1, \xi_2), y(\xi_1, \xi_2), z(\xi_1, \xi_2)]$ the geometrical design variables x_i can be defined as characteristics of the transformation function, *i.e.* the parameters of the functions $x(\xi)$, $y(\xi)$ and/or $z(\xi)$. Absorption coefficients α are chosen to be material design variables. Geometric uncertainties due to cavity manufacturing process are modeled by considering normally distributed design variables with the standard deviation σ_1 around its nominal value μ_1 , *i.e.*, it is represented as a normal random variable $N(\mu_1, \sigma_1^2)$. Absorption coefficients are assigned to each panel, and these values are assumed to be independent, represented as a normal random variables $N(\mu_2, \sigma_2^2)$

6.1. Optimization method

The first step samples values of objective function at several different values of design variables, and approximates a response of objective function using the Kriging surrogate model [8]. It enables an optimizer to promptly *estimate* objective function values at other points where the values of objective function are not given.

The next step performs robust optimization using the non-dominated sorting genetic algorithm (NSGA)-II [9] directly on the Kriging surrogate model. The present robust optimization considers minimizing both the mean and standard deviation of objective function against uncertainties.

6.2. Application exemple

We applied the robust optimization scheme to a parallelepiped acoustic cavity. It takes an area $\Omega = \{x \in [0;4]; y \in [0;2]; z \in [0;2]\}$ (Fig. 2). The cavity surface is considered to be assembled with six patches of Bezier surfaces. Every patch is determined by (4×4) control vertices as presented in Fig. 2.

An acoustic source is applied on the surface (Fig. 2, marked with cross); the test point inside the cavity with

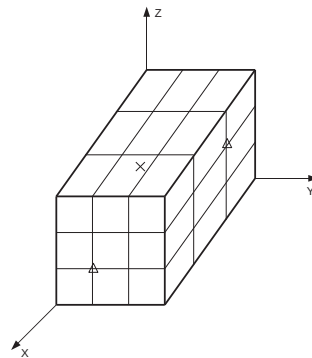


Figure 2: Cavity shape characteristics: control vertices distribution for the Bezier surface definition; position of acoustic source (cross); control points chosen to be optimization variables (triangles)

coordinates $(1.33; 0.6; 0.6)$ was chosen to compute energy density vector. Two control vertices were chosen to be design parameters (Fig. 2, marked with triangles). The coordinate of these vertices perpendicular to the patch plane are under consideration, so the optimization problem depends on two design variable x_1 and x_2 .

6.3. Results and discussion

Results of the optimization process performed by the NSGA-II algorithm are given in Fig. 3. In Fig. (3, a), we can see these non-dominated solutions only appear for a few ranges of the criterion corresponding to the mean of W , which shows the importance of the design: for example, two points are near from .0004 in term of standard deviation of W ; nevertheless, the first one leads to $W = 7 \text{ dB}$ and the second one leads to $W = 7.25 \text{ dB}$. If we want to obtain this kind of value for the standard deviation, it is obvious that the first point should be chosen. Hence, the optimization problem under geometric uncertainties appears to lead to several optimal solutions, and the choice of the design should be done carefully to favor one criterion or the other. Fig. (3, b) is radically different since the optimal solutions are the same for both W and its standard deviation. This means that the two considered criteria are changing in the same direction: thus, it is not useful to consider the material uncertainties for this kind of problem.

In

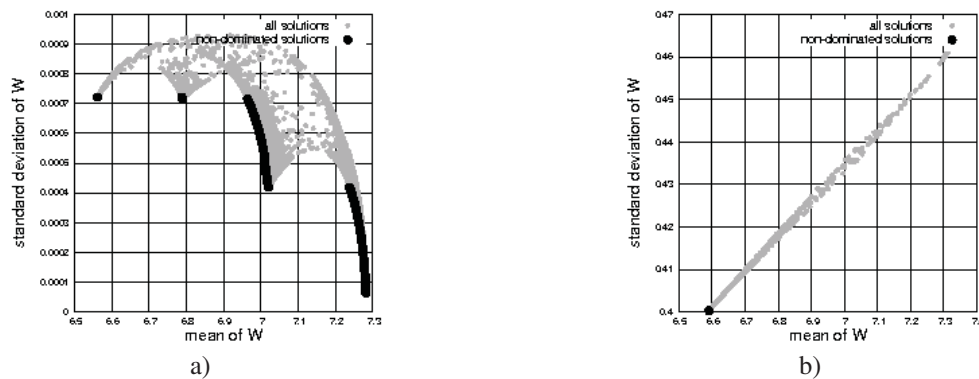


Figure 3: Solutions searched by the robust optimization of cavity shape a) under geometric uncertainties b) under material uncertainties

In Fig. 4 an optimal cavity shape for the non dominated solution is presented, where $\mu(F) = 7.02 \text{ dB}$; $\sigma(F) = 0.00041$; $x_1 = 10 \text{ m}$; $x_2 = 2.58 \text{ m}$. Changing of the color reflects the change in the coordinate normal to the parallelepiped side. This solution corresponds to the compromise between mean and standard deviation of the objective function toward geometrical uncertainties.

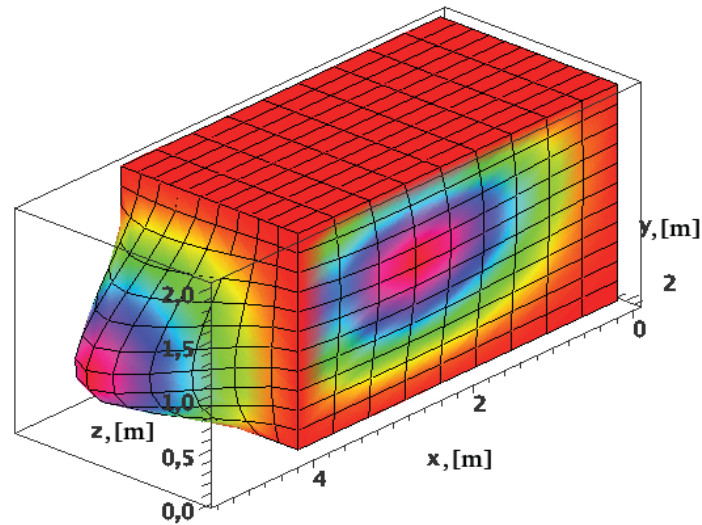


Figure 4: The resulting shape of the cavity after the optimization process. Compromise solution. $\mu(F) = 7.02 \text{ dB}$; $\sigma(F) = 0.00041$; $x_1 = 10 \text{ m}$; $x_2 = 2.58 \text{ m}$.

7. Conclusion

In this paper we introduced a robust shape optimization of cavities under vibroacoustic criteria and uncertain parameters. We used MES approach combined with a projection function to reach, for any cavity described by parametric functions, the energy density value W . We investigated the effect of geometrical as well as material parameters uncertainties on such genetic algorithm (NSGA II) based optimization loop on a Kriging meta model representing the first and second moment order of W with regard to uncertain parameters variation. We applied our approach on an exemple and conclude that material uncertainties can be ignored in such optimization scheme, but not geometrical uncertainties which lead to antagonist behavior of the average and standard deviation of the objective function W .

6. Acknowledgements

The authors would like to thank the financial support provided by the French National Research Agency through the framework of its project ANR-12-JS09-0009. This work was also partly supported by the JSPS Core-to-Core Program, A. Advanced Research Networks, "International research core on smart layered materials and structures for energy saving".

7. References

- [1] F. Sui, "Prediction of Vibroacoustics Energy Using a Discretized Transient Local Energy Approach and Comparison with Tsea," *J. Sound Vibr.* **251**, 163–180 (2002).
- [2] A. Wang, N. Vlahopoulos, and K. Wu, "Development of an energy boundary element formulation for computing high-frequency sound radiation from incoherent intensity boundary conditions," *J. Sound and Vibr.* **278**(1–2), 413 – 436 (2004).
- [3] O. Bouthier and R. Bernhard, "Simple models of energy flow in vibrating membranes," *Journal of Sound and Vibration* **182**(1), 129 – 147 (1995).

- [4] R. Troian, S. Besset, and F. Gillot, "Shape optimization under vibroacoustic criteria in the mid-high frequency range," *Journal of Computational Acoustics* **22**(02), 1450003 (2014).
- [5] S. Beset, M. N. Ichchou, and L. Jezequel, "A coupled BEM and energy flow method for mid-high frequency internal acoustic," *J. Comp. Acoust.* **18**(01), 69–85 (2010).
- [6] S. Besset and M. Ichchou, "Acoustic absorption material optimisation in the mid-high frequency range," *Appl. Acoust.* **72**(9), 632 – 638 (2011).
- [7] J. Sacks, W. J. Welch, T. J. Mitchell, and H. P. Wynn, "Design and analysis of computer experiments," *Stat. Science* **4**(4), 409–435 (1989).
- [8] K. Deb, A. Pratap, S. Agarwal, and T. Meyarivan, "A fast and elitist multi-objective genetic algorithm: NSGA-II," *IEEE Transac. on Evolut. Comput.* **6**(2), 182–197 (2002).

Optimal Design of Wind Farm Layout and Control Strategy

Longyan Wang*, Md Rifat Shahriar*, Andy Tan* and Yuantong Gu*

*Queensland University of Technology, Brisbane, QLD, Australia, longyan.wang@student.qut.edu.au

1. Abstract

Wind energy as one of the alternative energy sources is growing at a rapid rate for its property of renewability and abundance in the current society. However, high power losses have been witnessed due to the intervention of air flow induced by the upstream wind turbines in the wind farm. Though researches show that the great power losses can be reduced through the optimal design of wind farm layout and control strategy, up to now only separate optimization of wind farm layout or control strategy, i.e., either the wind farm layout optimization with the constant wind turbine operations or the control optimization with the fixed wind turbine positions is reported in literatures. Meanwhile, even though it is convinced that the unrestricted coordinate method is superior to the grid based method for the wind farm layout optimization due to its flexibility to place wind turbines, the comparison between these two wind farm design methods is not made by considering the control optimization. Therefore, this paper aims to fill these research gaps. The combined wind farm layout plus control optimization is conducted in this paper for the first time, and the results of which are compared with the separate wind farm layout optimization and control optimization to demonstrate its effectiveness using both wind farm design methods. The comparative results show that the layout optimization is most inefficient in the optimal wind farm design. The control optimization has most stable performance almost without deviations for repeated calculations, and it is able to attain the best optimization results under 45 degree constant wind direction condition using the unrestricted coordinate method. Even though the combined layout plus control optimization is theoretically superior to the other optimizations which obtains the better results, it is apt to be stuck into the local optima while the global optima cannot be guaranteed with single calculation.

2. Keywords:

Layout optimization; Control optimization; Combined layout plus control optimization; Grid based method; Unrestricted coordinate method

3. Introduction

The exploitation of wind energy transformed into the electric power is accomplished by wind turbines placed in clusters to take full advantage of the local wind resources. Compared to the single-placed wind turbine, the dense placement of wind turbines in close proximity results in the problem of the wind shadowing from the upstream turbines to the nearby downstream ones, which is known as the wake effects or wake interventions [1]. With the reduced wind power output of the downstream wind turbines, the total wind farm power production is decreased affecting the cost competitiveness of the wind power. To alleviate the wake effects in the wind farm, great efforts have been made to the wind farm optimization study. And the wind farm layout optimization, i.e., changing the wind turbine positions is one approach to achieve this, while the optimization of wind farm control strategy, i.e., changing the wind turbine operations is another approach.

The study of wind farm layout optimization begins with Mosetti et al. [2], who applied the Genetic Algorithm (GA) to optimize the wind turbine positions for a square-shape wind farm in which the wind farm area is subdivided into 10×10 identical small square grids. The results indicate it has a great improvement for both total wind farm power production and the cost per unit power with the optimized wind farm layouts under all three tested wind conditions compare to the random wind farm layouts. Since then, large number of researches have been reported regarding the wind farm layout optimization problem through the employment of the other optimization algorithms or the improved wind farm models [3]. Nevertheless, it is found that they all share one same setting for the wind farm layout optimization studies in literatures, that is the uniform operation is applied for all wind turbines enabling every single wind turbine produces the maximum power for itself. However, researches show that the self-optimum wind farm control strategy is not the optimum choice for the total wind farm power output when taking the wake effect into account.

The improvement of the wind farm performance achieved by the wind farm control optimization has also been witnessed by researches. A wind tunnel test with 8 rows of 3 turbines was done by Corten [4] under constant wind speed condition. With the optimized control strategy by pitching the first row of wind turbines to the maximum angle, the total wind farm power output increase of 4.6% is identified. The Energy Research Centre of the Netherlands (ECN) conducted a full scale field test which consists of five variable speed, pitch

controlled turbines of 2.5 MW and 80 m diameter in a row at a spacing of 3.8 RD. It was reported that the optimized WF power output can increase up to over 0.5% containing all wind directions [5]. And the big discrepancy of the power increase percentage between the wind tunnel test and the field test was claimed to be because the realistic wind conditions is quite different from the constant wind condition in the wind tunnel. Reference [6] was one of the few researches that computationally study the optimization of wind farm control strategy. In the research, four different wind farm cases were tested in the research and the performance increase was about 4% to 6% depending on the cases. However, all the above mentioned control optimization studies are proceed based on the fixed wind turbine positions while no combined optimization study of the wind farm layout plus control strategy is reported.

Therefore, this paper aims to fill the research gaps. The combined layout plus control optimization is performed for the first time and the results are compared with other two optimizations which included the layout optimization and control optimization using the two wind farm design methods. The comparative results are able to shed light on the effectiveness of the different types of optimization studies as well as the two design methods.

4. Description of the wind farm optimization problem

For the study of the optimal design of wind farm, the main objective is to reduce the wake power losses caused by the wake interventions between wind turbines. To incorporate the wind farm wake interference into optimization study, one of the critical procedures is to establish the wind turbine wake model using the explicit mathematical expressions. Among all the applied wake models, PARK model [7] is most widely used for the wind farm optimization due to its cost-effective property and accuracy compared to the real wind farm data.

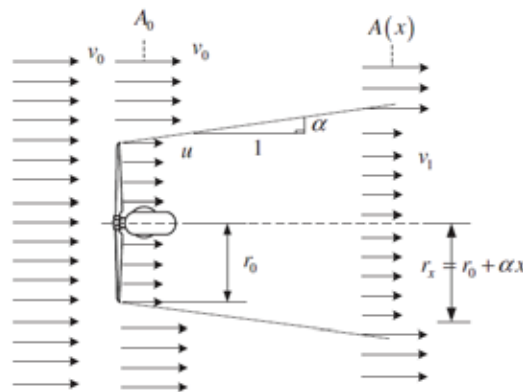


Fig. 1 Diagram of PARK wake model [8]

The PARK model assumes a linear expansion of the wake (see Fig. 1). Based on the theory of momentum conservation, the velocity in the wake of an upstream wind turbine at a distance of x towards the wind direction can be given by:

$$v_x = v_0 \left[1 - 2a \left(\frac{r_0}{r_0 + \alpha x} \right)^2 \right] \quad (1)$$

where r_0 is downstream rotor radius, α is the wake spreading coefficient, x is the proximity of the two wind turbines parallel to the wind direction, and a is axial induction denoting the percentage of wind speed decreasing from the free stream air to the air at the rotor place which is given by:

$$a = \frac{v_0 - u}{v_0} \quad (2)$$

According to the actuator disk theory [9], the single wind turbine power efficiency C_p and thrust efficiency C_T are related to the axial induction as follows:

$$C_p = \frac{P_{\text{turbine}}}{P_{\text{wind}}} = 4a(1-a)^2 \quad (3)$$

$$C_T = \frac{\text{Thrust Force}}{\text{Dynamic Force}} = 4a(1-a)$$

According to the Eq (3), the theoretic maximum power efficiency can be achieved when the a is equal to $1/3$, which is known as the Betz limit (C_p equals $16/27$). Therefore, for only one wind turbine it should be operated at the self-optimum point to produce the maximum wind power. For multiple wind turbines in a wind farm, the traditional control strategy is to ensure every single wind turbine produces the maximum wind power of its own with a equaling $1/3$. However, the self-optimum control strategy is proved to be sub-optimum when considering the wake effect, which is explained numerically in reference [6]. For the situation of more than two wind turbines in a wind farm, the total power output increase achieved by adjusting the individual control strategy for different wind turbines has been witnessed through the numerical simulation and optimization [10, 11]. However, these wind farm control optimization studies are all conducted based on the fixed wind turbine positions. And no study of the combined wind farm layout plus control optimizations has been reported in literatures, which is theoretically convinced to be able to find better results since both optimization variables are free to change.

Based on the design method that is applied for the wind farm layout optimization studies, they can be divided into two categories: the grid based method and unrestricted coordinate method. For the grid based method, first the wind farm area is divided into a large number of identical grids and only fixed position within the cell is allowed to place the wind turbine. By employing the grid based method for wind farm layout optimization, both the placement and the number of wind turbines can be optimized during the process. For the unrestricted coordinate method, the location of each wind turbine is represented by the X - Y Cartesian coordinates for the two dimension region. Compared to the counterpart method, the advantage of the unrestricted coordinate method is that it helps to find better optimization results with more flexible wind turbine placements. Even though the unrestricted coordinate method is reported to be more superior to the grid based method in literatures [12, 13], from the authors' point of view the conclusion lacks the powerful evidence due to two reasons. Firstly, the coarse grid density of 10×10 is applied for the grid based method when making comparison, while researches indicate that the better results can be obtained with finer grids [14]. Secondly, the comparison is made with fixed self-optimal control strategies for all wind turbines, and the results maybe different when incorporating the control optimization. Therefore, it is necessary to conduct the comparative study of the two wind farm design methods in a more comprehensive manner for both wind farm layout and control optimizations.

The wind farm optimization problem studied in this paper is mathematically described in Fig. 2. The objective function of this study is the cost of per unit wind power and a traditional wind farm cost which is applied in reference [2] is employed, and the total wind farm power production is calculated as the summation of the individual wind turbine power output P_i . For the layout optimization study, the individual wind turbine power is simply related to the incoming wind speed which is calculated based on the wake deficit model described above. For the control optimization as well as the combined optimization, however, it is dependent on both the incoming wind speed and selection of axial induction value a . The optimization is carried out under the proximity constraint which ensures the minimum distance (chosen to be 5 wind turbine diameters in the study) between any two wind turbines to prevent from the damage. And the expressions of the proximity constraint for the two wind farm design methods are different. The wind turbine position using the grid based method is represented by the row number (m) and column number (n), while it is represented by the x and y coordinates for the unrestricted coordinate method.

Objective function:

$$\text{CoE} = N \times \left(\frac{2}{3} + \frac{1}{3} e^{-0.00174N^2} \right) / \sum_{i=1}^N P_i$$

$$\text{where, } \begin{cases} P_i = 0.3v_i^3 & \text{(for layout optimization)} \\ P_i = 2.032a(1-a)^2 v_i^3 & \text{(for control optimization and the combined optimization)} \end{cases}$$

Constrained by:

$$\sum_{i=1}^{N-1} \sum_{j=i+1}^N \sqrt{[2.5D((m(j) - m(i)))^2 + [2.5D((n(j) - n(i)))]^2} < 5D \quad \text{(for grid based method)}$$

$$\sum_{i=1}^{N-1} \sum_{j=i+1}^N \sqrt{((x(j) - x(i))^2 + ((y(j) - y(i))^2} < 5D \quad \text{(for unrestricted coordinate method)}$$

Fig. 2 Mathematical description of the wind farm optimization problem for different kinds of optimizations and different wind farm design methods

5. Results and Discussion

In order to investigate the relationship between different optimizations using the two wind farm design methods, C++ codes tailored for the different optimization studies implementing the Genetic Algorithm (GA) tool are developed for the two cases. They share the same wind farm square shape of $2 \text{ km} \times 2 \text{ km}$ dimensions with flat terrain, and the wind conditions for the two cases are shown as follows:

- 1) The constant wind speed of 12 m/s and constant wind direction of 0 degree (from the east to the west).
- 2) The constant wind speed of 12 m/s and constant wind direction of 45 degree (anticlockwise rotation).

5.1 0 degree wind direction case

The three different types of wind farm optimization study are performed under the 0 degree constant wind condition in the first place. Fig. 3 (a) reports the optimization fitness values using the grid based wind farm design method while the deviations of the repeated optimization results are indicated in the bar chart. It is apparent that the wind farm layout optimization yields the worst fitness value, and the combined wind farm layout plus control optimization yields the best results. For both of the two optimizations, large deviations of the repeated optimization results are detected implying that the results are highly dependent on the repeated calculations and the best optimization results cannot be ensured with single run. For the control optimization, however, even though the results are sub-optimal, they are extremely stable for different calculations with approximately no deviations. The fitness results of the three different optimizations using the unrestricted coordinate method are reported in Fig. 3 (b). It should be noted that the optimal number of turbines obtained from the grid based method optimization is used as the midpoint value of the X axis (number of wind turbines) in the plotting of the unrestricted coordinate method optimization results. Same as the grid based method result, it can be seen that the layout optimization yields the worst results as well for the unrestricted coordinate method. And the best results are obtained for the combined layout plus control optimization. For both the two optimizations, large deviations are witnessed while the deviation of the control optimization is negligible. By comparing the fitness value results of the two design methods, it is obvious that the better results are attained for the unrestricted coordinate method (approx. 1.36×10^{-3}) in comparison to the grid based method (approx. 1.38×10^{-3}).

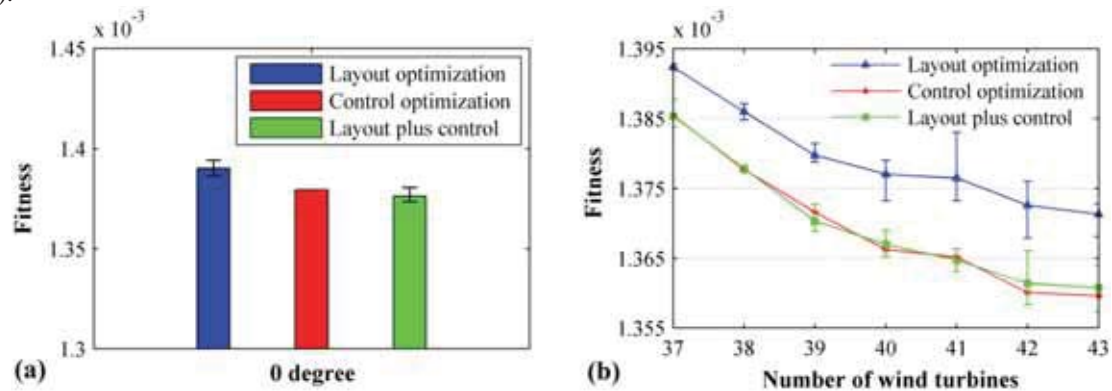


Fig. 3 Fitness value results for Layout optimization, control optimization and layout plus control optimization with (a) the grid based method and (b) the unrestricted coordinate method under 0 degree wind direction

Fig. 4 (a) reports the distribution of the wind turbine axial induction values according to the optimization results using the grid based method, and Fig. 4 (b) reports the distribution of the wind turbine axial induction values according to the optimization results using the unrestricted coordinate method. For both figures, the optimal wind farm layout is also indicated with circles denoting the wind turbines. As can be seen, most of the wind turbines are distributed along the wind farm two sides perpendicular to the wind direction. As a result, the wake interventions between wind turbines can be alleviated with enlarged distances. The leeward (downstream) wind turbines have the largest axial induction values of Betz limit $1/3$, since there are no other turbines affected by them and they adopt the self-optimum control strategy to produce the maximum wind power of their own. The windward (upstream) turbines have smaller axial induction values ranging from 0.28 to 0.31 according to the optimization results using the grid based method, and ranging from 0.29 to 0.32 according to the optimization results using the unrestricted coordinate method. For the two design methods, the axial induction values of the windward turbines for the optimization using the unrestricted coordinate method are relatively bigger than that using the grid based method.

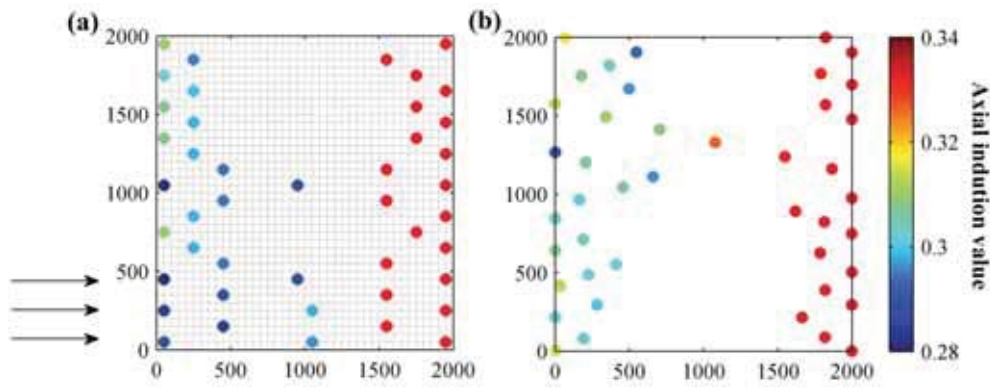


Fig. 4 Optimal wind turbine position and the optimized axial induction values with (a) the grid based method and (b) the unrestricted coordinate method under 0 degree wind direction. And the wind turbines are denoted with painted circles.

5.2 45 degree wind direction case

In this section, the different types of wind farm optimization study are performed under the constant 45 degree wind direction condition. Fig. 5 (a) reports the fitness results using the grid based wind farm design method while the deviations of the repeated optimization results are indicated. Like the results of the 0 degree wind direction case, the wind farm layout optimization yields the worst fitness value as well in this case, and the combined wind farm layout plus control optimization yields the best results. For both of the two optimizations, large deviations of the repeated optimization results are detected. For the control optimization, however, the deviations of the fitness are negligible indicating the stable optimization results for the repeated calculations. Then, the fitness results of the three different optimizations using the unrestricted coordinate method are reported in Fig. 5 (b). Like the above 0 degree wind direction case, the optimal number of turbines obtained from the grid based method optimizations is used as the midpoint value of the X axis (number of wind turbines) in the plotting of the unrestricted coordinate method optimization results. It can be seen that the layout optimization yields the worst results using the unrestricted coordinate method which has the same conclusion as the above case. Nonetheless, for all different number of wind turbines the control optimization achieves much better results than the combined layout plus control optimization in the 45 degree wind direction case, and it is because the combined optimization is stuck into the local minima.

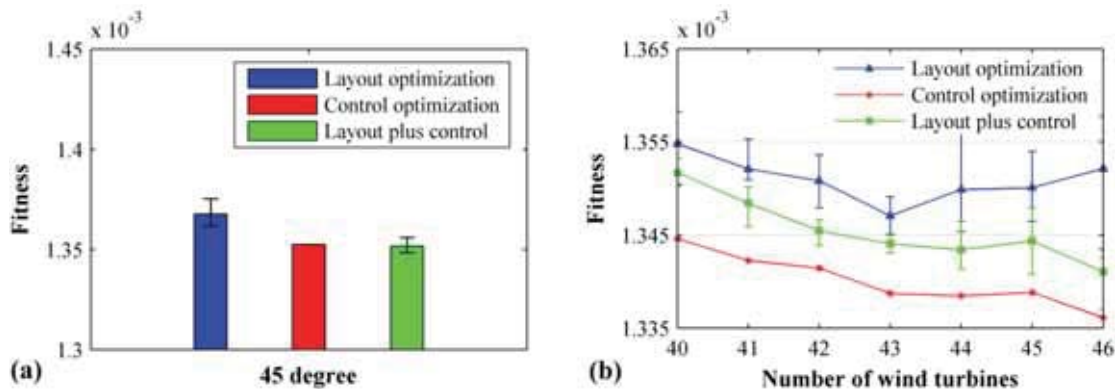


Fig. 5 Fitness value results for Layout optimization, control optimization and layout plus control optimization with (a) the grid based method and (b) the unrestricted coordinate method under 45 degree wind direction

In the same manner as above case, the optimization results of the axial induction distribution under 45 degree wind direction are reported as well using both the grid based and unrestricted wind farm design methods (see Fig. 6 (a) and (b)). Unlike optimal wind farm layout under 0 degree wind direction, most of the wind turbine are scattered along all four sides of the wind farm under 45 degree wind direction. The leeward wind turbines are operated at the self-optimum point with 1/3 axial induction value while the windward turbines are operated with the axial induction value ranging from 0.29 to 0.31 for the optimization using both wind farm design methods.

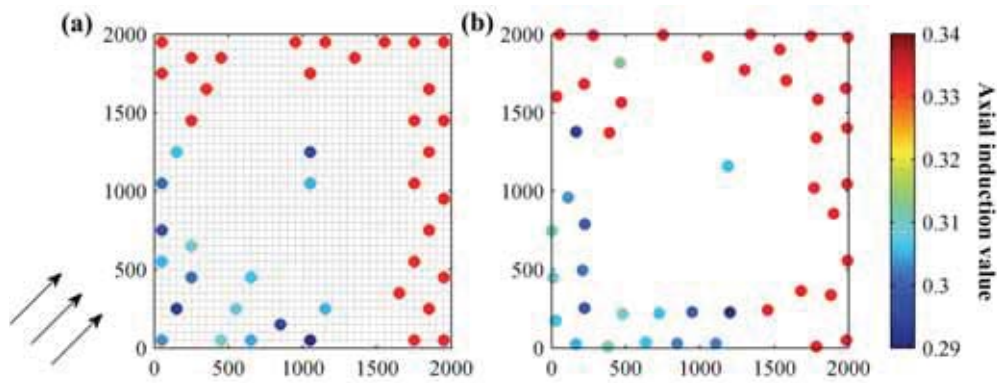


Fig. 6 Optimal wind turbine position and the optimized axial induction values with (a) the grid based method and (b) the unrestricted coordinate method under 45 degree wind direction. And the wind turbines are denoted with painted circles.

6. Conclusions

The topic of the optimal wind farm design considering both the wind turbine placements and controls is investigated in the current paper. Among which, the combined wind farm layout plus control optimization study is carried out for the first time. The comparative results show that the layout optimization is most inefficient in the optimal design of the wind farm obtaining the worst optimization results with large deviations for repeated calculations. The control optimization has most stable performance and it finds the best optimization results under 45 degree wind direction condition using the unrestricted coordinate method. In comparison, even though the combined layout plus control optimization is theoretically superior to the others, it is dependent on the studied wind conditions which tends to be stuck into the local minima.

7. Acknowledgements

The High performance computer (HPC) system provided by the Queensland University of Technology (QUT) is gratefully acknowledged which is the main tool of the optimization work.

References

1. VerHulst, C. and C. Meneveau, *Altering Kinetic Energy Entrainment in Large Eddy Simulations of Large Wind Farms Using Unconventional Wind Turbine Actuator Forcing*. *Energies*, 2015. **8**(1): p. 370-386.
2. Mosetti, G., C. Poloni, and B. Diviacco, *Optimization of wind turbine positioning in large windfarms by means of a genetic algorithm*. *Journal of Wind Engineering and Industrial Aerodynamics*, 1994. **51**(1): p. 105-116.
3. González, J.S., et al., *Overall design optimization of wind farms*. *Renewable Energy*, 2011. **36**(7): p. 1973-1982.
4. Corten, G. and P. Schaak, *Heat and Flux: Increase of Wind Farm Production by Reduction of the Axial Induction*. *Wind Energy*, 2013. **2012**: p. 2011.
5. Machiels, L., et al., *Evaluation of "Heat and Flux" Farm Control*.
6. Scholbrock, A.K., *Optimizing Wind Farm Control Strategies to Minimize Wake Loss Effects*, 2011, University of Colorado at Boulder: Ann Arbor. p. 101.
7. Jensen, N.O., *A note on wind generator interaction*. 1983.
8. *Engineering Model (OffWindEng)*. Available from: <http://offwind.eu/Help/EngWindSim>.
9. *Froudes' Momentum Theory: (Actuator Disk Theory)*. Available from: <http://www.public.iastate.edu/~aero442/unit2.pdf>.
10. Bitar, E. and P. Seiler. *Coordinated control of a wind turbine array for power maximization*. in *American Control Conference (ACC), 2013*. 2013. IEEE.
11. Mikkelsen, R., et al. *Analysis of power enhancement for a row of wind turbines using the actuator line technique*. in *Journal of Physics: Conference Series*. 2007. IOP Publishing.
12. Wan, C., et al. *Optimal siting of wind turbines using real-coded genetic algorithms*. in *Proceedings of European Wind Energy Association Conference and Exhibition*. 2009.
13. Wan, C., et al., *Optimal micro-siting of wind farms by particle swarm optimization*, in *Advances in swarm intelligence*. 2010, Springer. p. 198-205.
14. Wang, F., D. Liu, and L. Zeng. *Study on computational grids in placement of wind turbines using genetic algorithm*. in *World Non-Grid-Connected Wind Power and Energy Conference, 2009. WNWEC 2009*. 2009. IEEE.

Reduced Order Simulation Surrogate for Wind Turbine Component Design

Robert T. Rudolf

Flensburg University of Applied Sciences: Wind Energy Technology Institute, Schleswig-Holstein, Germany,
robert.rudolf@fh-flensburg.de

1. Abstract

Small changes in the structural dynamic properties of wind turbine components can have a large influence on the ultimate and fatigue loads they experience. This is due to strong coupling between the aerodynamic (aero), control-system (servo) and structural (elastic) behaviours of the wind turbine system. Therefore attempts to design these structures using algorithm-driven numerical parameter studies are more likely to lead to feasible designs when the load calculation is integrated into the optimization problem formulation. Industry-standard aero-servo-elastic (ASE) simulation codes are, however, too computationally expensive to iterate in the constraint evaluation of a highly-dimensional design optimization problem. More efficient load simulation methods are needed to make optimization algorithms practical for the structural design of major wind turbine components.

A reduced-fidelity ultimate and fatigue load approximation method is proposed as a means to conduct sizing optimization for lightweight structures. The new method, termed ROSS for reduced orders simulation surrogate, leverages FEM substructuring operations and surrogate modelling to reduce the degrees of freedom in the load simulation. This speeds computation and reduces the dimensionality of the design space (to select terms in the condensed mass and stiffness matrices). In the first step, all design load cases are simulated for each sample point in a design of experiments (DOE) on the reduced design space. Then ultimate loads and damage equivalent fatigue loads (DEL) are calculated and a metamodel is calibrated to approximate the DEL for arbitrary mass and stiffness matrices. Finally, the constraints can be analysed for the original set of design variables by a sequence of substructuring, metamodel evaluation and static FEM analysis using the approximated ultimate loads and DEL.

The additional FEM calculations and metamodel evaluations are orders of magnitude faster than the many ASE time series simulations which they replace. This enables optimization algorithms to design lightweight (flexible) turbine structures with a highly dimensional design space exhibiting a large range of natural frequencies. Uses for ROSS extend beyond constraint evaluation for frame optimization problems; the method can also be utilized to replace the static load assumption in topology optimization schemes.

2. Keywords: approximation, sizing, frame design, reduced order simulation surrogate (ROSS)

3. Introduction

The Intergovernmental Panel on Climate Change recently ranked onshore wind as having the lowest lifecycle equivalent CO₂ emissions per kWh of all commercially-available electricity generation technologies. In many scenarios, it also has the lowest cost per kWh [1]. Structural optimization research is a priority for the wind industry since lightweight structures improve both the numerator and denominator of these key selling points which have driven the growth of wind power. The steel and concrete mass in the tower and foundation are the primary sources of emissions [2] and costs related to wind energy. Lighter structures enable more cost-effective manufacturing, logistics and erection of taller towers supporting larger rotors (which increase energy production and amortize fixed costs) [3]. A 2014 review of optimization methods applied to wind turbine structures references 130 scientific papers, 90 % of them published since the year 2000, demonstrating the emergence and rapid development in this research niche [4]. The authors identify computationally-expensive simulations as the main obstacle preventing search algorithms and automated design of experiments from replacing “manual optimization” in selecting the design parameters of wind turbine structures.

3.1 Load Calculation

The structural finite element models used in wind turbine simulation models are generally very simple. Coarsely discretized beam models with as few as 28 degrees of freedom (DOF) are used in industry to model the entire rotor-nacelle-tower-foundation system [5]. The computational expense involved in load simulation is driven by the need to increment the states of the aerodynamic and controller models together with the structural response in small time steps. This co-simulation of the entire turbine system operating state in the time domain is necessary to account for the significant non-linear coupling effects between the wind field, rotor aerodynamics, structural kinematics and control systems (e.g. active blade pitch, generator torque, nacelle yaw control, etc.). This requires numerous ASE time series with different initial conditions and simulated events (including emergency stops and system failures). In this way, all possible scenarios which could generate an ultimate load are simulated.

Additionally, accurate calculation of the fatigue load necessitates that all normal operating conditions are also included in the simulation. Thus any change in a wind turbine's structural design that affects its dynamic response (i.e. changes in stiffness, mass and damping matrices) will have a unique influence on each time series history and an unpredictable influence on the ultimate and fatigue loads [6]. This necessitates that new structural designs can only be analysed in conjunction with new ASE simulations (typically using proprietary ASE codes which contain aerodynamic and controller parameters closely guarded by wind turbine manufacturers). A notable consequence is that wind turbine structures must be designed together with the wind turbine system. It is therefore very difficult to change the rotor, tower or foundation design for an existing turbine without working together with a manufacturer to simulate the loads; accommodating modifications to other components or systems are usually needed (especially controller modifications).

3.2 Existing Methods to Accelerate Load Simulation

As it is impractical to iterate an expensive simulation for each point sampled in a design space, all previous efforts to apply optimization algorithms to wind turbine structures have sought to avoid or limit the number of ASE time series used to evaluate structural design candidates. The most common approach is to assume fixed ultimate and fatigue loads if the natural frequency for the candidate design remains within a given tolerance from the design used to calculate the applied loads. This engineering assumption is permissible under some wind turbine design certification codes. (A natural frequency calculation tolerance of 5 % is allowed in the GL certification guideline for towers [7].) This method, depicted in Fig.(1), has been applied by Yoshida at Fuji Heavy Industries in 2006 [8] and the wind turbine design consultancy Windrad in 2014 [9] to optimize the thickness and diameter distributions of tubular steel towers. The computational savings of this technique are, however, limited to applications where the design variables have a small effect on the natural frequency and mode shapes (i.e. fine-tuning of a design using a small range of inputs).

Alternatively, Long, Moe and Fischer recently demonstrated in 2012 that a frequency domain analysis technique can be applied to estimate the ultimate and fatigue loads for design spaces with a wide range of structural dynamic responses [10]. This method cannot, however, model time history-dependant ASE effects which have a large influence on ultimate and fatigue loads, such as controller response to gust disturbances. Other published methods include the use of readily-computable proxy data to steer search algorithms toward designs with favourable structural dynamic response. A recent example is the use of tower top deflection under static load as a measure of fatigue damage in the sizing optimization of a tower and foundation by Nicholson in 2013 [11].

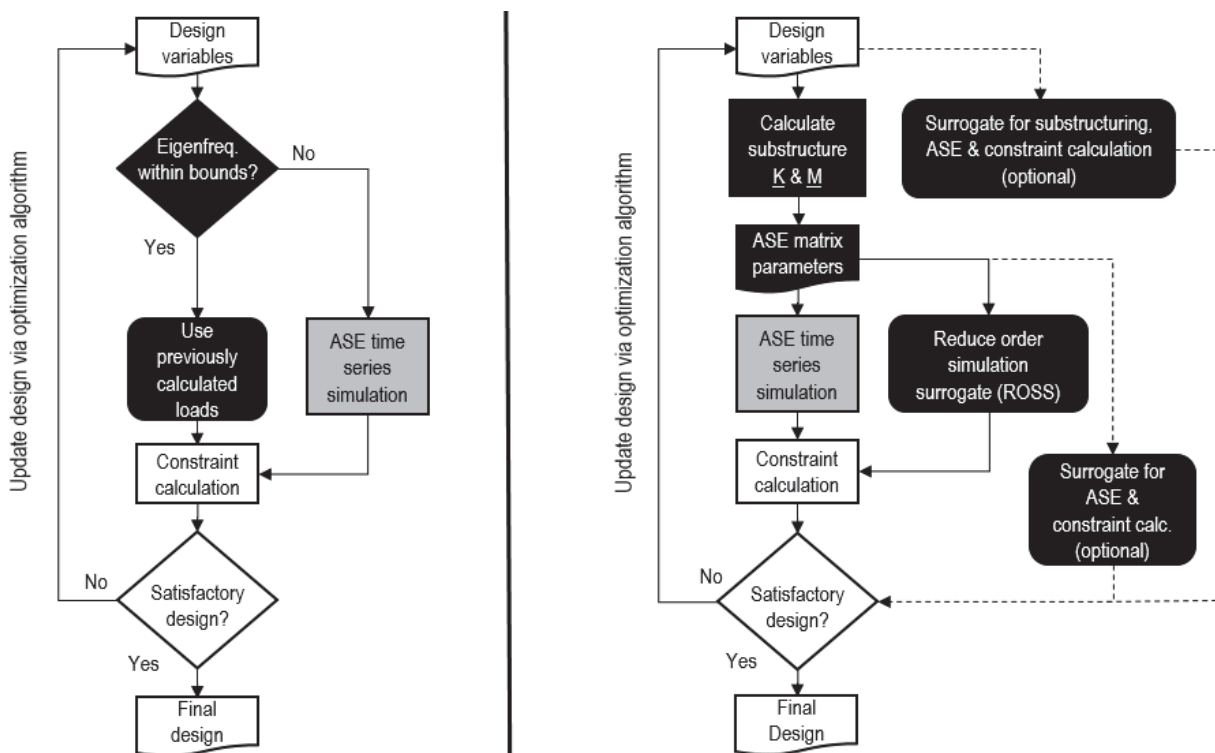


Figure 1: (left)
Figure 2: (right)

Optimization via static loads assumption for structural constraint analysis
Proposed reduced order simulation surrogate (ROSS) method

4. Proposed Aero-Servo-Elastic Surrogate Optimization Method

The present work introduces a new approach that models loads independently for each design point using a surrogate model. The metamodel is calibrated from a DOE of industry-standard aero-servo-elastic time series simulations. The ultimate and fatigue load responses are approximated for select parameters in the generalized mass and stiffness matrices, which are linked to the original design variables using an intermediate substructuring operation.

4.1 Process Flow

The general process flow for using ROSS to accelerate constraint calculations for structural component design is depicted in Fig.(2). To initialize the ROSS approximation the following procedure is proposed:

- (0) Perform “SubDOE” using the design variables (and their bounds) as inputs and the reduced stiffness and mass matrices as outputs. (Optional.) A 2-level fractional-factorial experiment such as an orthogonal array is recommended if the number of parameters is very large.
- (1) Perform “SimDOE” using select terms in the mass and stiffness matrices as inputs for the aero-servo-elastic time series simulation and the post-processed ultimate and fatigue loads as outputs. Use results from (0), if available, to eliminate unnecessary factors and establish bounds for the intermediate variables.
- (2) Fit “ROSS” approximation to the SimDOE.
- (3) Integrate load simulation approximation into the constraint evaluation of the design optimization process.

The dotted lines shown in the process flow represent alternative pathways that may further accelerate a ROSS optimization. Depending upon the computational expense involved in the substructuring and constraint evaluation, it may be beneficial to calibrate additional approximations for these processes. Particularly, the SubDOE data from step (0) can be leveraged to build an approximation without any additional (sampling) computation, provided the error is acceptable.

4.2 Reduced Order Structural Model

Modal condensation is commonly applied to reduce the degrees of freedom in ASE wind turbine simulation codes, which are based on the general equation of motion for linear dynamic systems, Eq.(1),

$$\underline{M} \cdot \ddot{\underline{x}} + \underline{D} \cdot \dot{\underline{x}} + \underline{K} \cdot \underline{x} = \underline{f} \quad (1)$$

where

- \underline{M} , \underline{K} , \underline{D} : are reduced mass, stiffness and damping matrices of the structure,
 \underline{f} : is a vector of external time- and position dependent forces acting on the reduced structure and
 \underline{x} : is a time-dependant displacement vector of the nodal positions of the reduced structure.

A practical example of this so-called substructuring process is the common practice of using static condensation and Guyan reduction to generate reduced mass and stiffness matrices for an offshore foundation [5, 12]. Although the designer may have a very large set of design variables to select (e.g. cross section dimensions, frame element endpoints, etc.), the detailed FEM model might be reduced to a single node with 6 degrees of freedom (or less) so that the loads can be calculated with the ASE code. If off-diagonal terms of the reduced mass and stiffness are sufficiently small, orthogonality conditions can be assumed and the mass and stiffness matrices can be further reduced to 6 terms each. Thus regardless of the number of design parameters and their values, only 12 parameters must be passed to the industry-standard ASE simulation in order to evaluate a design alternative for this example. (The damping matrix can be calculated from the mass and stiffness matrices using the Rayleigh method [13]). In fact, it is sometimes possible to reduce this number of “ASE matrix parameters” to 8 due to symmetry (as is the case for a rotationally-symmetric foundation or a tripod structure) or even less if the range of values for a specific term in the reduced mass and stiffness terms is small and therefore has a negligible influence on the ASE load calculation.

The proposed ROSS method simply exploits this existing reduction method built into the ASE by performing the SimDOE on the few significant and unique degrees of freedom in the ASE simulation, rather than the larger set of design variables. This saves computational expense when the structural design parameter count is large, as the dimensionality of the SimDOE is comparatively smaller.

4.3 Parameter Bounds for ASE Simulation

The minimum and maximum values for the studied terms in the reduced mass and stiffness matrices have a strong influence on the performance of the ROSS method. Ideally, these limits are calibrated to the most extreme possible output values for the substructuring process considering the given bounds of the structural design variables. If the bounds are too wide, the density of sample points in the design space is reduced (costing surrogate accuracy) and the computational expense must be increased to compensate. If the bounds are chosen too narrow, the ASE loads approximation will be invalid and the optimization is likely to perform poorly and suggest many infeasible designs.

4.4 Constraint Calculation using ASE-calibrated Surrogate

The ultimate and fatigue loads estimated by the ASE surrogate require post-processing in order to calculate the constraints included in the design optimization. The structural constraints typically include verification of strength, stability, extreme deformation and fatigue. These analyses are possible by statically applying the ultimate loads and fatigue DEL using nonlinear static FEM. Although such FEM calculations are orders of magnitude faster than the ASE, it is likely that FEM is still too slow to search the design space unless the number of parameters is very low. Therefore metamodel optimization methods are likely necessary.

Examples of surrogate-based structural optimization using static load under stress constraints can be referenced from Rudolf et al. [14] and the aforementioned work by Nicholson [11]. Some structures, such as tubular towers, can be verified against all constraints using simple engineering equations in place of FEM. This negates the need to use a surrogate (other than the ASE) to search the design space (and avoids the error associated with the additional approximation).

4.5 Limitations and Assumptions of ROSS Method

The modal reduction schemes used by most ASE turbine simulation codes assume linear-elastic behaviour of the substructure elements. Effects such as the catenary sag in guyed supported structures and nonlinear soil stiffness cannot be modelled within (single node) condensed matrices and require additional degrees of freedom. As the number of active ASE matrix parameters increases, the computational expense associated with the use of these terms for the SimDOE rapidly increases. In these cases it may be more beneficial to perform a surrogate model optimization using the original structural design variables for the SimDOE rather than a potentially larger set of ASE matrix parameters, especially if this will reduce the dimensionality of the ASE experiment.

Additional limitations are associated with the excitement and damping of higher-order modes in the reduced structure. The higher-order mode shapes and frequencies of the substructure are omitted from the ASE model. Therefore the resonance of individual members (if any) in the substructure is not accounted for in the load calculations. This should be considered if applying ROSS to study a truss structure. Similarly, geometry-specific external forces (such as aerodynamic damping, hydrodynamic loading and wind loading) are held constant under the ROSS method despite them being a function of the structural design. Regardless of these shortcomings it is important to remember that ROSS is a design tool – not a verification tool – and the method is an improvement versus optimization under a static load assumption.

5. Conclusion, Recommendations and Future Work

This work addresses a major obstacle to the widespread adoption of computer-aided structural design optimization in the wind industry by introducing a faster alternative to time series simulation that is also more accurate than assuming static loads. The proposed decoupling of the design variables and load simulation suggested by the ROSS method takes advantage of the existing substructuring operations used in modal ASE codes. This enables the loads for a very large number of design variables to be approximated from a dataset calibrated from a reduced set of parameters. In addition, the same ROSS model can be reused to study new design problems with unrelated variables. For example, only one ASE matrix parameter DOE could be used in the design optimization of both an offshore tripod foundation and a jacket foundation. Main limitations of the ROSS method are associated with having too few nodes in the AES simulation (i.e. the excitement and damping of higher-order modes, modelling of structural nonlinearities and modelling of external forces). Attempting to resolve these issues by using larger substructures defeats the purpose of ROSS if the number of ASE matrix parameters exceeds the number of design variables.

Applications for the ROSS method extend beyond sizing optimization and frame design. Cast components such as slab foundations, rotor hubs and some nacelle structures might use ROSS within topology optimization schemes to update their boundary conditions and penalizations functions between iterations. In this way the changing mass and stiffness matrix terms of the lighter and more flexible structures are accounted for in the loads and beneficial dynamic characteristics can be used to arrive at lighter designs. The published method remains in development and is currently being applied to optimize the design of a cable-truss tower for a 2.5 MW commercial wind turbine prototype with 140 m hub height.

6. Acknowledgements

This research is conducted as part of the project “Prototype Design of an Energy-efficient Guyed Steel Tower Concept for 50 % Material Savings and CO₂ Emissions” at the Wind Energy Technology Institute in Flensburg, Germany. It is funded by the Gesellschaft für Energie und Klimaschutz Schleswig-Holstein GmbH (translated “Organization for Energy and Climate Protection in Schleswig-Holstein”) and Aerodyn Energiesysteme GmbH, who is also a technical partner in the project and designer of various wind turbines amounting to over 30 GW of installed wind power capacity.

7. References

- [1] S. Schlömer, T. Bruckner et al., Annex III: Technology-specific cost and performance parameters, *Climate Change 2014: Migration of Climate Change. Contribution of Working Group III to the Fifth Assessment Report of the Intergovernmental Panel on Climate Change*, Cambridge University Press, Cambridge, United Kingdom and New York, USA, 2014.
- [2] M. Lenzen and J. Munksgaard, Energy and CO₂ life-cycle analyses of wind turbines – review and applications, *Renewable Energy*, 26, 2001.
- [3] R.T. Rudolf, Taller Towers for Lager Wind Turbines: a Market Study of Support Structure Technology for Onshore Wind Turbines, University of Applied Sciences Flensburg, 2013.
- [4] M. Muskulus and S. Schafhirt, Design Optimization of Wind Turbine Support Structures – A Review, *Journal of Ocean and Wind Energy*, 1 (1), 12-22, Trondheim, Norway, 2014.
- [5] C. Böker, Load simulation and local dynamics of support structures for offshore wind turbines, Institute for Steel Construction, Leibniz University Hannover, 2009.
- [6] M. Seidel, G. Foss, Impact of different substructures on turbine loading and dynamic behaviour for the DOWNVInD Project in 45m water depth, Conference Proceedings EWEC, EWEA Athens, Greece, 2006.
- [7] Germanischer Lloyd, Guideline for the Certification of Wind Turbines, Edition 2010.
- [8] S. Yoshida, Wind Turbine Tower Optimization Method Using Genetic Algorithm, Japan, Fuji Heavy Industries Ltd, Wind Turbine Project, Yonan Utsunomiya, Japan, 2006.
- [9] M. Hänler and T. Bauer, Cost-optimized design of tubular steel support structures, Windrad Engineering GmbH, PO.ID 183, EWEA Barcelona, Spain, 2014.
- [10] H. Long, G. Moe and T. Fischer, Lattice Towers for Bottom-Fixed Offshore Wind Turbines in the Ultimate Limit State: Variation of Some Geometric Parameters, *J Offshore Mech Arct Eng*, 134, 1-13, 2012.
- [11] J.C. Nicholson, J.S. Arora, D. Goyal and J.M. Tinjum, Multi-Objective Structural Optimization of Wind Turbine Tower and Foundation Systems using Isight: A Process Automation and Design Exploration Software, 10th World Congress on Structural and Multidisciplinary Optimization, Florida, USA, 2013.
- [12] M. Seidel, M. v. Mutius and D. Steudel, Design and load calculations for offshore foundations of a 5MW turbine, Conference Proceedings DEWEK, DEWI Wilhelmshaven, Germany, 2004.
- [13] K.-J. Bathe, Finite-Elemente-Methoden, Springer-Verlag, Berlin, 1990.
- [14] R.T. Rudolf, F. Roscheck, Y. Aono and T. Faber, Mass-optimized Design of Guyed Wind Turbine Tower Struts, Key Engineering Materials, Vols. 577-578, pp 277-280, Wind Energy Technology Institute Flensburg, Kurume National College of Japan, 2014.

Adjoint Methods of Sensitivity Analysis for Lyapunov Equation

Boping Wang¹, Kun Yan²

¹ Department of Mechanical and Aerospace Engineering, University of Texas at Arlington, P.O. Box 19023, Arlington, TX 76019, USA, bpwang@uta.edu

² State Key Laboratory of Structural Analysis for Industrial Equipment, Faculty of Vehicle Engineering and Mechanics, Dalian University of Technology, Dalian 116023, P. R. China

1. Abstract

The existing direct sensitivity analysis of optimal structural vibration control based on Lyapunov's second method is computationally expensive when applied to finite element models with a large number of degree-of-freedom and design variables. A new adjoint sensitivity analysis method is proposed in this paper. Using the new method the sensitivity of the performance index, a time integral of a quadratic function of state variables, with respect to all design variables is calculated by solving two Lyapunov matrix equations. Two numerical examples demonstrate the accuracy and efficiency of the proposed method. Finally, we use the adjoint sensitivity analysis scheme to solve a topology optimization problem.

2. Keywords: Adjoint method, sensitivity analysis, topology optimization

3. Introduction

In time domain, there is a classic problem formulation of passive structural vibration control that deals with the dynamic system disturbed by initial conditions. The objective is to find design parameters of the damped vibration system that minimize the performance index in the form of time integral of the quadratic function of state variables (displacement and velocities, e.g. see Eq.(5)). This performance index can be evaluated by Lyapunov's second method [1].

Based on the Lyapunov equation, the evaluation of performance indices are simplified into matrix quadratic forms and do not require the time domain integration. Parameter optimization problems with a quadratic performance index have been solved by this method [2~8]. Wang et al. [9] applied the Lyapunov equation to solve the transient response optimization problem of linear vibrating systems excited by initial conditions. In their work, the Lyapunov equation was expanded to a set of linear equation and direct sensitivity was carried out by use of the same system of linear equation. The computational effectiveness of the method is illustrated by applying it to the classical vibration absorber and to a cantilever beam carrying an absorber at its midpoint. Du [10] applied the Lyapunov equation to obtain the optimum configuration of dynamic vibration absorber (i.e., DVA) attached to an undamped or damped primary structure. The Lyapunov equation is also used in other fields of optimal design.

In this paper, we consider one case of passive control optimization problem, that is, to minimize an integrated quadratic performance measure for damped vibrating structures subjected to initial conditions. The goal of this paper is to present an adjoint sensitivity analysis method considering the above mentioned objective function based on Lyapunov's second function. The results indicate the potential of application of the proposed method to topology optimization under the special time domain criterion.

4. Application of Lyapunov's second method to optimize transient response of mechanical systems

Consider a viscously damped linear vibration system governed by the equation:

$$\mathbf{M}\ddot{\mathbf{u}} + \mathbf{C}\dot{\mathbf{u}} + \mathbf{K}\mathbf{u} = \mathbf{0} \quad (1)$$

where $\mathbf{M}(N \times N)$ is the mass matrix, $\mathbf{C}(N \times N)$ is the damping matrix, $\mathbf{K}(N \times N)$ is the stiffness matrix, and $\mathbf{u}(N \times 1)$ is displacement vector. N is the structural degree of freedoms.

Assume the system is excited by initial displacements or velocities. The design problem is to find in \mathbf{M} , \mathbf{K} and \mathbf{C} matrices to minimize a performance matrix in the form

$$J = \int_0^T q(\mathbf{u}, \dot{\mathbf{u}}) dt \quad (2)$$

where, $q(\mathbf{u}, \dot{\mathbf{u}}) = \mathbf{u}^T \mathbf{Q}_u \mathbf{u} + \dot{\mathbf{u}}^T \mathbf{Q}_v \dot{\mathbf{u}}$ is a quadratic function of \mathbf{u} and $\dot{\mathbf{u}}$. Transient dynamic responses have to be performed to evaluate the objective function. Direct or adjoint methods can be applied to evaluate the response sensitivity required for evaluation sensitivity of the performance. Alternative, if we replace the upper bound of integration to infinite, we can use Lyapunov's second method to evaluate the performance without performing transient dynamic response analysis.

To apply Lyapunov's second method to this system, it is necessary to rewrite Eq.(1) in the state space form

$$\dot{\mathbf{X}} = \mathbf{A}\mathbf{X} \quad (3)$$

Where

$$\mathbf{A} = \begin{bmatrix} \mathbf{O} & \mathbf{I} \\ -\mathbf{M}^{-1}\mathbf{K} & -\mathbf{M}^{-1}\mathbf{C} \end{bmatrix} \quad \mathbf{X} = \begin{bmatrix} \mathbf{u} \\ \dot{\mathbf{u}} \end{bmatrix} \quad (4)$$

The matrix \mathbf{A} is $(2N \times 2N)$. The vector \mathbf{X} is $(2N \times 1)$. Structural design parameters such as mass density, damping ratio and spring stiffness are contained in the matrix \mathbf{A} . The optimization problem is to choose these parameters to minimize the performance measure J defined by

$$J = \int_0^{\infty} \mathbf{X}^T \mathbf{Q} \mathbf{X} dt \quad (5)$$

for a given initial excitation $\mathbf{X}(0)$. In Eq.(5), \mathbf{Q} ($2N \times 2N$) is a positive semi-definite symmetric weighting matrix and t denotes time. According to Lyapunov theory of stability, for an asymptotically stable system, there exist a symmetric positive semi-definite matrix \mathbf{P} ($2N \times 2N$) satisfying

$$\mathbf{A}^T \mathbf{P} + \mathbf{P} \mathbf{A} = -\mathbf{Q} \quad (6)$$

Eq.(6) is the well-known Lyapunov equation. Based on the Lyapunov's second equation, the Eq.(5) can be further simplified as

$$J = \mathbf{X}(0)^T \mathbf{P} \mathbf{X}(0) \quad (7)$$

That is to say, to minimize J in Eq.(5) is equivalent to minimize $\mathbf{X}(0)^T \mathbf{P} \mathbf{X}(0)$, where $\mathbf{X}(0)$ is the initial state vector and the unknown symmetric matrix \mathbf{P} can be obtained by solving Eq.(6).

5. Sensitivity analysis scheme

To apply gradient-based optimization method to solve the above optimization problem, sensitivity (gradient) of the objective functions with respect to the design variables is needed. The adjoint method will be developed in this paper. The new method just needs to solve the Lyapunov function twice to obtain the sensitivities with respect to all the design variables.

For ease of presentation of the new sensitivity analysis scheme, we adopt Du's approach of using Kronecker product and column expansion to expand the Lyapunov equation as a system of linear equation. The column expansion of matrix \mathbf{V} is defined as a vector that stacks all columns of this \mathbf{V} matrix. For example, for the 3×3 matrix \mathbf{V}

$$\mathbf{V} = \begin{bmatrix} V_{11} & V_{12} & V_{13} \\ V_{21} & V_{22} & V_{23} \\ V_{31} & V_{32} & V_{33} \end{bmatrix} \quad (8)$$

the column expansion $cs(\mathbf{V})$ of \mathbf{V} is

$$\bar{\mathbf{V}} = cs(\mathbf{V}) = [V_{11} \ V_{12} \ V_{13} \ V_{21} \ V_{22} \ V_{23} \ V_{31} \ V_{32} \ V_{33}]^T \quad (9)$$

Note that $cs(\mathbf{V})$ is a 9×1 vector. The operator $cs(*)$ refers to the expansion operation. For an N -dof system, using the Kronecker product, (6) can be written as

$$\mathbf{G} \bar{\mathbf{P}} = -\bar{\mathbf{Q}} \quad (10)$$

where $\bar{\mathbf{P}} = cs(\mathbf{P})$, $\bar{\mathbf{Q}} = cs(\mathbf{Q})$ and the matrix \mathbf{G} can be obtained from the matrix \mathbf{A} by Kronecker product. That is

$$\mathbf{G} = (\mathbf{A}^T \otimes \mathbf{E} + \mathbf{E} \otimes \mathbf{A}^T) \quad (11)$$

and \mathbf{E} ($2N \times 2N$) is an identity matrix with the same size of \mathbf{A} . Now, by direct calculation, the objective function in Eq.(7) can be written as

$$J = \bar{\mathbf{S}}^T \bar{\mathbf{P}} \quad (12)$$

where

$$\bar{\mathbf{S}} = cs(\mathbf{S}), \quad \mathbf{S} = \mathbf{X}(0)\mathbf{X}(0)^T \quad (13)$$

\mathbf{S} also is a positive semi-definite symmetric matrix as matrix \mathbf{Q} . From the Eq.(10), the term $\frac{\partial \bar{\mathbf{P}}}{\partial d_k}$ can be obtained

by

$$\frac{\partial \bar{\mathbf{P}}}{\partial d_k} = -\mathbf{G}^{-1} \left(\frac{\partial \mathbf{G}}{\partial d_k} \bar{\mathbf{P}} + \frac{\partial \bar{\mathbf{Q}}}{\partial d_k} \right) \quad (14)$$

Thus sensitivity can be expressed as

$$\frac{\partial J}{\partial d_k} = \mathbf{X}(0)^T \frac{\partial \mathbf{P}}{\partial d_k} \mathbf{X}(0) = -\bar{\mathbf{S}}^T \mathbf{G}^{-1} \left(\frac{\partial \mathbf{G}}{\partial d_k} \bar{\mathbf{P}} + \frac{\partial \bar{\mathbf{Q}}}{\partial d_k} \right) \quad (15)$$

The right hand of Eq.(15) can be rewritten as

$$\frac{\partial J}{\partial d_k} = \mathbf{X}(0)^T \frac{\partial \mathbf{P}}{\partial d_k} \mathbf{X}(0) = \bar{\boldsymbol{\lambda}}^T \bar{\mathbf{D}}^k \quad (16)$$

where

$$\bar{\boldsymbol{\lambda}}^T = -\bar{\mathbf{S}}^T \mathbf{G}^{-1} \quad (17)$$

$$\bar{\mathbf{D}}^k = \left(\frac{\partial \bar{\mathbf{Q}}}{\partial d_k} + \frac{\partial \mathbf{G}}{\partial d_k} \bar{\mathbf{P}} \right) \quad (18)$$

Note that $\bar{\boldsymbol{\lambda}}$ and $\bar{\mathbf{D}}^k$ are the column expansion of matrices $\boldsymbol{\lambda}$ and \mathbf{D}^k , respectively.

$$\mathbf{A}\boldsymbol{\lambda} + \boldsymbol{\lambda}\mathbf{A}^T + \mathbf{S} = 0 \quad (19)$$

$\boldsymbol{\lambda}$, the adjoint matrix, can be obtained by solving the above Lyapunov matrix equation. \mathbf{D}^k can be also computed by

$$\mathbf{D}^k = \frac{\partial \mathbf{Q}}{\partial d_k} + \frac{\partial \mathbf{A}^T}{\partial d_k} \mathbf{P} + \mathbf{P} \frac{\partial \mathbf{A}}{\partial d_k} \quad (20)$$

Finally, the sensitivity of the objective function with respect to the design variable can be expressed as

$$\frac{\partial J}{\partial d_k} = \frac{\partial \mathbf{X}(0)^T}{\partial d_k} \mathbf{P} \mathbf{X}(0) + \mathbf{X}(0)^T \mathbf{P} \frac{\partial \mathbf{X}(0)}{\partial d_k} + \sum_{i=1}^{2N} \sum_{j=1}^{2N} \lambda_{ij} D_{ij}^k \quad (21)$$

For the case $\mathbf{X}(0)$ independent of design variables, the Eq.(21) can be simplified as

$$\frac{\partial J}{\partial d_k} = \sum_{i=1}^{2N} \sum_{j=1}^{2N} \lambda_{ij} D_{ij}^k \quad (22)$$

6. Numerical example

Two examples are presented in this section. The first example is used to demonstrate the accuracy and efficiency of the proposed methods. The optimal support location is solved as a topology optimization problem in the second example.

6.1. Example 1

In this example, we consider a clamped-free beam (3m×0.02m×0.02m) attached with several identical damped springs (along Y direction). The beam material is linear elastic with the elastic modulus 2.1×10^{11} Pa and mass density 7850Kg/m³. The spring stiffness k_s is to be determined (N/m), and the damping coefficient is 10^3 N·s/m. Figure 1 shows the beam model used in this example. Specially, the beam is uniformly meshed into 50 2-node beam elements. Each node has 2 DOFs (lateral displacement and rotation about Z-axis). Five equally spaced damped spring supports are considered. The initial displacements and velocities of all nodes are zero and 10m/s respectively. The stiffness k of each spring is chosen as the design variable. Thus, there are 5 design variables. Firstly, we compare the sensitivity results from three methods, central difference method, adjoint method and direct method to validate the proposed adjoint method.

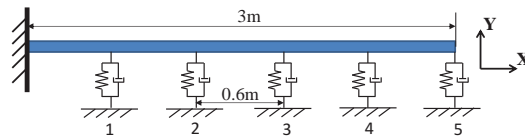


Figure 1: The beam model with 5 damped springs

The objective function is

$$J = \sum_{i=1}^R \int_0^{\infty} y_i^2 dt \quad (23)$$

where y_i is the Y-direction displacement of the i th node of the beam, R is the total number of the free nodes of the beam.

To study the effect of step size in central difference analysis, we calculate the approximation of sensitivity of spring stiffness of the spring at right hand of beam at $k_s=10^5\text{N/m}$ for three different step sizes. The results are shown in table 1. We choose $\Delta k_s=100\text{N/m}$ for further study in this example.

Table 1: Sensitivity results at $k_s=1.0 \times 10^5\text{N/m}$ from different step sizes

Step size	10^4	10^3	10^2
Sensitivity result	-2.4858×10^{-11}	-2.4715×10^{-11}	-2.4714×10^{-11}

The sensitivity results of the objective function with respect to k_s of each spring at $k_s=1.0 \times 10^5\text{N/m}$ from central difference method, adjoint method and direct method are shown in figure 2 and are represented by the black crosses, red squares and blue rounds, respectively. The results show that the adjoint method obtains identical results with the central difference method and direct method.

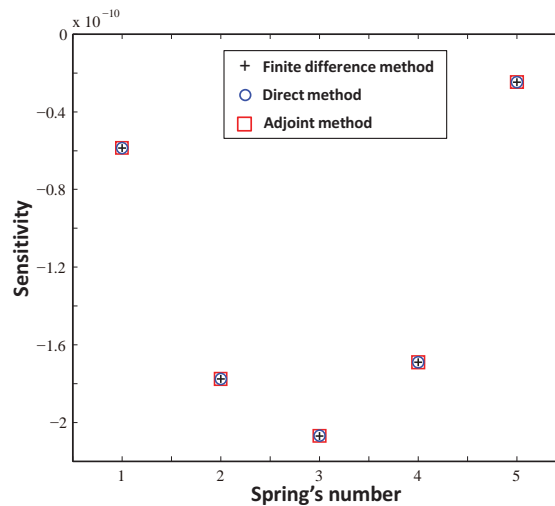


Figure 2: Sensitivity results of the stiffness k of each spring from three methods

In this paper, the CPU time results are the average values of CPU time of 10 repeated analyses. The computer used in this paper is i7-3770 3.4GHz, Windows 7.

Now, we compare the CPU time of direct method and adjoint method. The CPU time results of these two methods are summarized in table 2. The results show that total CPU time of the sensitivity analysis process of adjoint method is less than direct method, especially when the problem has large number of DOFs. T_A is the CPU time of the sensitivity analysis process of adjoint method, and T_D is the CPU time of the sensitivity analysis process of direct method.

Table 2: CPU time of two methods vs. number of DOFs in the model

Number of DOFs	CPU time (s)		T_A/T_D
	T_A (adjoint)	T_D (direct)	
100	0.091	0.232	39.34%
600	22.095	61.802	35.75%

6.2. Example 2

Topology optimization problems always have large numbers of design parameters. We construct a topology optimization problem to test the new sensitivity analysis methods. In this example, we consider a $1\text{m} \times 1\text{m} \times 0.01\text{m}$ plate attached with several identical damped springs ($k_s=10^6\text{N/m}$, $c_s=100\text{N}\cdot\text{s/m}$). One edge of the plate is clamped

and other three edges are free. The material of the plate is linear elastic with elastic modulus 2.1×10^{11} Pa, Poisson ratio 0.3, and mass density 7850 Kg/m^3 . The initial velocity of Z direction of all the free nodes of plate is 10 m/s . The design problem is to decide the optimized location of H damped springs to minimize a criterion defined below. We formulate this problem as a topology optimization problem. This is achieved by introducing an artificial density variable to describe the spatial distribution of the damped springs and use interpolation model of SIMP to obtain 0-1 design. Specifically, an identical potential damped spring (along Z direction) is placed between every free nodes and the ground.

Set a virtual density ρ_i to every spring as the design variable. ρ_i is a continuous variable, and $\rho_i \in [\rho_{\min}, 1]$.

We introduce an artificial relation between density (ρ_i) and the parameters of the damped springs.

$$K_i = \rho_i^l K_0, C_i = \rho_i^l C_0 \quad (24)$$

where l is the penalty parameter. In this example, l is chosen as 1.2. The analysis model is shown in Figure 3, where the purple lines are the damped springs and the blue square elements are the 4-node square plate elements (shell63 in Ansys). Each node of the element has 3 DOFs, u_z , θ_x and θ_y . The element size of the plate is 0.1 m (there are 110 free nodes). The analysis model has 330 DOFs and 110 design parameters. The topology optimization problem can be expressed as

$$\begin{aligned} \min \quad & J = \sum_{i=1}^{110} \int_0^{\infty} z_i^2 dt \\ \text{const.} \quad & \sum_{i=1}^M \rho_i = H \\ & 0 < \rho_{\min} \leq \rho_i \leq 1 \end{aligned} \quad (25)$$

where H specifies the material volume available for the damped springs. Here we assume each spring, if any, uses material volume 1, H will be the number of damped springs in the final optimum design. z_i is the Z-direction displacement of the i th node of the plate. The model has 110 free nodes, so the objective function concerns the displacements of all the free nodes. It should be noted this example mainly serves to compare different methods of sensitivity analysis through solving the topology optimization problem described by Eq.(25).

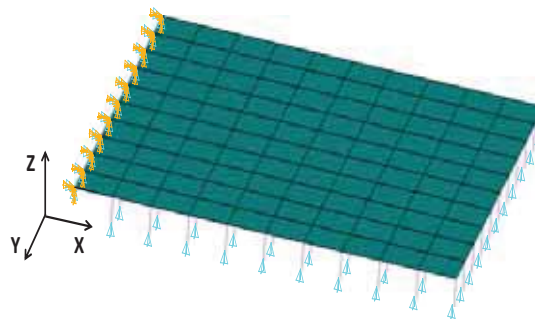


Figure 3: The analysis model in topology optimization

The CPU time of solving processes of adjoint method and direct method is summarized in table 3. The computing time of adjoint method is much shorter than the computing time of direct method.

Table 3: CPU time of sensitivity analysis of two methods

	Adjoint	Direct
CPU time (s)	10.575	181.130

Finally, we use above mentioned four sensitivity analysis schemes to solve the topology optimization described in Eq.(25). H is set to 2. Figure 4 shows that optimization using different sensitivity analysis methods have identical iteration histories and obtain same optimized designs. The CPU time of solving processes of topology optimization problem using different sensitivity analysis methods is summarized in table 4. The optimization process using adjoint method just takes about 10 minutes which is far less than the CPU time of other one.

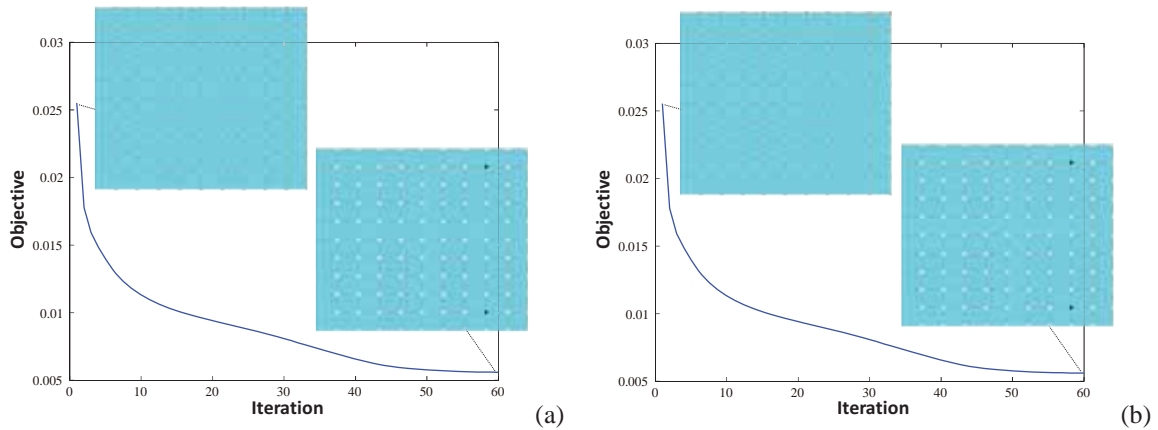


Figure 4: Iteration histories of the objective function of optimization process: (a) Ajoint method; (b) Direct method

Table 4: CPU time of optimization processes using different sensitivity analysis methods

	AVMF	DVMF
CPU time (s)	636.852	10886.824

7. Conclusion

A new adjoint sensitivity analysis method for the integral square performance index is proposed in this paper. The new approach requires the solutions of two Lyapunov equations only, one for the performance index and one for the adjoint vector. In contrast, direct sensitivity analysis requires the solution of a Lyapunov equation for each design variable. This improvement in computational efficiency makes the approach applicable to optimal design problem with a large number design variable. The accuracy and efficiency of the proposed method are demonstrated by two numerical examples.

8. Acknowledgement

The first author is grateful to the support of this work from State Key Laboratory of Structural Analysis for Industrial Equipment (Project No. GZ1301)

9. References

- [1] Kalman RE, Bertram, JE, Control System Analysis and Design Via the “Second Method” of Lyapunov: I—Continuous-Time Systems. *Journal of Fluids Engineering*, 82(2), 371-393, 1960.
- [2] Ogata K, Yang Y, *Modern control engineering*, 1970.
- [3] Truhar N, Veselic K. An efficient method for estimating the optimal dampers' viscosity for linear vibrating systems using Lyapunov equation. *SIAM Journal on Matrix Analysis and Applications*, 31(1): 18-39, 2009.
- [4] Kuzmanović I, Tomljanović Z, Truhar N. Optimization of material with modal damping. *Applied mathematics and computation*, 218(13): 7326-7338, 2012.
- [5] Cox S J, Nakić I, Rittmann A, et al. Lyapunov optimization of a damped system. *Systems & control letters*, 53(3): 187-194, 2004.
- [6] Marano GC, Greco R, Chiaia B, A comparison between different optimization criteria for tuned mass dampers design. *Journal of Sound and Vibration*, 329(23), 4880-4890, 2010.
- [7] Marano GC, Greco R, Trentadue F, Chiaia B, Constrained reliability-based optimization of linear tuned mass dampers for seismic control. *International Journal of Solids and Structures*, 44(22), 7370-7388, 2007.
- [8] Chang W, Gopinathan S V, Varadan V V, et al. Design of robust vibration controller for a smart panel using finite element model. *Journal of vibration and acoustics*, 124(2): 265-276, 2002.
- [9] Wang BP, Kitis L, Pilkey WD, Transient Response Optimization of Vibrating Structures by Liapunov’s Second Method. *J. Sound Vib.*, 96, pp. 505–512, 1984.
- [10] Du D, Analytical solutions for DVA optimization based on the Lyapunov equation. *Journal of Vibration and Acoustics*, 130(5), 054501, 2008.

Structural Damage Identification by Means of Neural Network (Evaluation of Identification Capability)

Kazuyuki Hanahara¹, Yukio Tada²

¹ Kobe University, Kobe, Japan, hanahara@cs.kobe-u.ac.jp

² Kobe University, Kobe, Japan, tada@cs.kobe-u.ac.jp

1. Abstract

Damage identification of structural system can be dealt with by means of an inverse problem approach; that is, the location as well as the magnitude of damage is determined by inversely solving the relationship between the damage and the corresponding change in structural characteristics. In this study, we adopt a definite number of natural frequencies as such structural characteristics. A multi-layered neural network approach based on an alternative error back-propagation with fixed connection weights is used to solve the inverse problem. The damage identification based on change in natural frequencies inherently has ill-posed nature. We carry out a comprehensive simulation study and discuss the capability of the proposed damage identification approach.

2. Keywords: structural health monitoring, inverse problem, neural network, natural frequencies, truss.

3. Introduction

Damage of a structural system has to be identified in order to repair or replace the damaged parts or members to maintain its original system performance. This research field is referred to as non-destructive testing, structural damage identification, or structural health monitoring. There are several approaches for the purpose. For example, the eddy current approach[1] and the ultrasonic approach[2] are typical examples of non-destructing testing. Giurgiutiu et al.[3] use piezoelectric devices to detect crack or defect. Approaches based on change in dynamic characteristics such as the natural frequencies of the target structure have also been studied [4]-[6].

We deal with the damage identification based on the change in dynamic characteristics of the entire structure caused by the damage on its constituent parts; the natural frequencies of the target structure are also adopted in this study. The relation between the local damage and the change in natural frequencies is implemented as a multi-layered neural network[7]. The error back-propagation technique with fixed connection weight [8][9] is adopted to solve the inverse problem of determining the location and magnitude of the damage corresponding to the given change in natural frequencies.

The inverse problem to be solved for the damage identification is a typical ill-posed problem in such a case, since it is fundamentally impossible to identify all of the patterns of the damaged parts based only on a limited number of natural frequencies[4]. The damage identification approach based on neural network, however, works fairly well[10]; it has been demonstrated with examples that damaged members of truss structure are successfully identified based only on its limited number of natural frequencies, in the case that the number of damaged members is small.

In the current study, we carry out comprehensive simulations in order to examine the capability of this damage identification approach based on multi-layered neural network. On the basis of the numerical experiments with truss structures, we investigate the characteristics of availability of the approach. We take into account the following: such as the size of the neural network, the constituents of the learning data set, and so on.

4. Inverse Problem Formulation of Damage Identification

There are two types of damage identification approaches. One is to identify directly the location as well as the magnitude of the damage by means of installed sensing devices or scanning equipments. The other is the indirect approach, which deduces or estimates the location and magnitude of the damage based on the observed change in some characteristics of the entire target structure. We deal with the latter approach from the inverse problem point of view.

4.1. Basic Idea

Let \mathbf{x} be the state variable vector corresponding to the condition of parts or members of the target structure, such as thickness of structural elements or stiffness of truss members. Let \mathbf{y} be the characteristics vector of the entire structure affected by the structural damage, which is expected to be obtained by means of some measurement

devices. The relationship between the two variables can be expressed in the following general form:

$$\mathbf{y} = \mathbf{y}(\mathbf{x}) \quad (1)$$

In the case that we have a structural characteristic value \mathbf{y}^* which is obtained by means of the measurement, the corresponding damaged structural condition \mathbf{x}^* can be determined by solving the following problem:

$$\text{Find } \mathbf{x}^* \text{ such that } \mathbf{y}(\mathbf{x}^*) = \mathbf{y}^*, \quad (2)$$

which is a typical inverse problem based on Eq.(1). This is the basic idea of our damage identification approach.

4.2 Adopting Natural Frequencies as Key Structural Characteristics

This damage identification approach significantly depends on the type of the structural characteristics \mathbf{y} in Eq.(1). We adopt the change in natural frequencies of the entire structure due to damage as such structural characteristics, in this study. There are following reasons for this selection:

- the values can be numerically calculated for various damage patterns taken into consideration
- damage of any structural elements can affect these characteristics of the entire structure, to some extent
- the values are obtained by means of a non-invasive measurement in general; application to existing structures can be possible

One of the issues in the case of adopting the natural frequencies for this purpose is that the inverse problem (2) becomes inherently ill-posed since the order of natural frequencies to be measured is less than the number of structural elements for damage identification in general. The aim of the current study is to investigate the feasibility of the following neural network approach based on the natural frequencies.

5. A Multi-Layered Neural Network Approach

A multi-layered neural network has the ability to acquire its input-output relationship by the error back-propagation learning[7]. The alternative error back-propagation with fixed connection-weights[8] is adopted to solve the inverse problem based on the acquired relationship. In order to make the article self-contained, we summarize this approach to solve an inverse problem by means of multi-layered neural network.

5.1 Multi-Layered Neural Network and Error Back-Propagation Learning

Figure 1(a) shows a conceptual illustration of multi-layered neural network. Neurons are depicted as circles and connected in a layered manner. The input and output layers placed at leftmost and rightmost sides are the 0th and N th layers; the so-called hidden neurons are placed between them and make up the 1st \dots $N-1$ th layers. The behavior of the i th neuron of the k th layer is modeled as follows:

$$v_i^k = f(u_i^k), \quad u_i^k = \sum_j w_{ij}^k v_j^{k-1}, \quad f(u_i^k) = \frac{2}{1 + \exp(-2u_i^k)} - 1, \quad (3)$$

where u_i^k and v_i^k are the internal state and the output value of the neuron and w_{ij}^k is the connection weight between the i th neuron of the k th layer and the j th neuron of the $k-1$ th layer. The characteristic function of a neuron

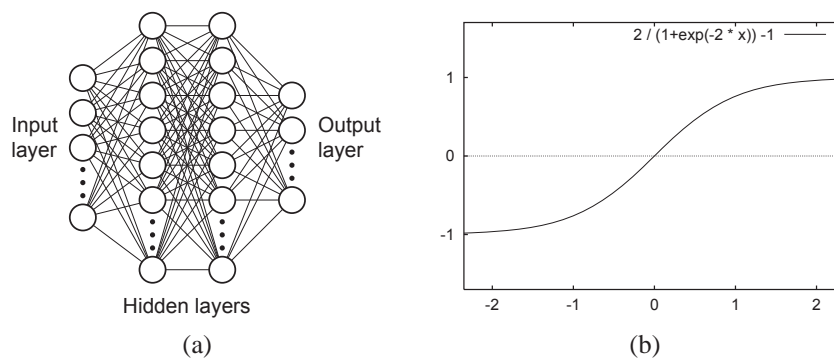


Figure 1: Multi-layered neural network

is expressed as f , which is shown in Fig.1(b). The input-output relation as the entire neural network can be represented in the following form:

$$\mathbf{v}^N = \mathbf{v}^0 + \mathbf{w} \quad (4)$$

where \mathbf{v}^0 and \mathbf{v}^N are the input and output vectors. The connection weights \mathbf{w} determines the input-output relation.

On the basis of the error function to the desired output value \underline{v}^N expressed as

$$E = \frac{1}{2} (\mathbf{v}^N - \underline{\mathbf{v}}^N)^T (\mathbf{v}^N - \underline{\mathbf{v}}^N) = \frac{1}{2} \sum_i (v_i^N - \underline{v}_i^N)^2, \quad (5)$$

the following iterative modification of the connection weights are conducted for various input values and their corresponding desired output values:

$$w_{ij}^k \leftarrow w_{ij}^k - \Delta w_{ij}^k, \quad \Delta w_{ij}^k = \varepsilon \frac{\partial E}{\partial w_{ij}^k} \quad (6)$$

where ε is an adequate small coefficient. The modification Δw_{ij}^k is obtained in the following manner:

$$\Delta w_{ij}^k = \Delta v_i^k \cdot f' (u_j^{k-1}) \cdot v_j^{k-1}, \quad (7)$$

$$\Delta v_i^k = \varepsilon \frac{\partial E}{\partial v_i^k} = \sum_j \Delta v_j^{k-1} \cdot f' (u_j^{k-1}) \cdot w_{ji}^{k-1}, \quad (8)$$

$$\Delta v_i^N = \varepsilon \frac{\partial E}{\partial v_i^N} = \varepsilon (v_i^N - \underline{v}_i^N). \quad (9)$$

Equation (8) denotes the error back-propagation process from the $(k-1)$ th layer to the k th layer.

5.2 Solving Inverse Problem by Means of Alternative Error Back-Propagation

We deal with the inverse problem (2) in terms of the following error minimization problem:

$$\text{Minimize } E = \frac{1}{2} (\mathbf{y} - \mathbf{x})^T (\mathbf{y} - \mathbf{x}^*) \quad \text{with respect to } \mathbf{x}. \quad (10)$$

The solution can be obtained by means of an iterative gradient procedure as

$$\mathbf{x} \leftarrow \mathbf{x} - \Delta \mathbf{x}, \quad \Delta \mathbf{x} = \varepsilon \frac{\partial E}{\partial \mathbf{x}} \quad (11)$$

based on an adequate initial value of \mathbf{x} . After the input-output relationship (4) of the neural network has been trained to represent the intended relationship (1), the gradient $\Delta \mathbf{x} = \varepsilon \frac{\partial E}{\partial \mathbf{x}}$ can be obtained as the modification to the input layer at the neural network, $\Delta \mathbf{v}^0 = \varepsilon \frac{\partial E}{\partial \mathbf{v}^0}$, in terms of Eq.(8) as the result of the error back-propagation process, since the error function (5) for the learning and the error in the minimization problem (10) to solve the inverse problem are essentially the same at this point. This enables us to solve the inverse problem (2) in terms of the minimization problem (10) by means of the neural network. Note that the connection weights of the neural network are fixed in the case of the solving process of the inverse problem, so that the implemented input-output relation should not be changed.

5.3 Damage Identification Based on Natural Frequencies by Means of Neural Network

The damage identification approach based on the change in natural frequencies by means of a multi-layered neural network is performed as follows. First, the learning data set of various damages on the target structure and the corresponding change in natural frequencies has to be prepared. This can be performed by means of numerical calculation. Second, an adequate neural network is prepared and trained to represent the intended relationship with the learning data set. After the learning process of the neural network is completed, it can be used to identify the damage of the target structure based on the measured change in natural frequencies by means of the alternative error back-propagation.

6. Comprehensive Simulation Study with Truss Structures

A number of numerical experiments are carried out in order to evaluate the capability of the proposed damage identification approach.

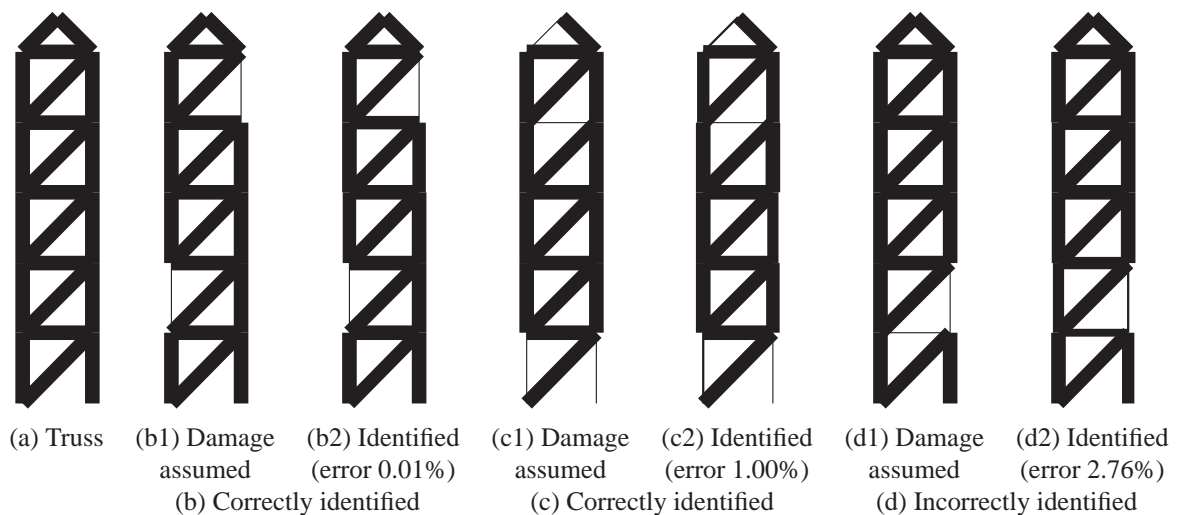


Figure 2: Example damage identification results based on 5-unit truss (magnitude of damage exaggerated)

6.1 Simulation Condition

Figure 2(a) shows the 2D truss structure adopted in this simulation study. The square truss units are $1\text{m} \times 1\text{m}$; all the truss members are steel rod of 10mm diameter; a mass of 1kg is attached to the top node of the truss. Damage is given in the form of degradation of stiffness of truss members; the maximum magnitude of the damage is assumed to be 10% of the stiffness. Learning data sets for the neural networks are prepared by means of numerical calculation of natural frequencies based on randomly generated various damage conditions. In the current study, the number of back-propagation learning is 500 million for all of the cases, which is considered to be enough for the convergence. The damage identification capability of the approach is examined based on all of the 5% stiffness damage combinations of 1 to 4 truss members: that is, ${}_{22}C_1 = 22$ single-member-damage patterns, ${}_{22}C_2 = 231$ two-member-damage patterns, ${}_{22}C_3 = 1540$ three-member-damage patterns, ${}_{22}C_4 = 7315$ four-member-damage patterns and 9108 patterns as the total. In these numerical experiments, an obtained damage identification result is judged adequate in the case that the maximum error in the estimated member stiffness is less than 1%, that is, the member stiffness is 94% to 96% of the original stiffness for the damaged members and 99% to 100% for the non-damaged members.

6.2 Evaluation of Damage Identification Capability

Table 1 summarizes the damage identification results based on the approach with various neural networks. On the basis of the results shown in Table 1, it is clear that the number of modes of natural frequencies has significant influence on the damage identification capability. The results based on 5 natural frequencies show that even in the case of single member damage, it is only 40% to 55% of the patterns (9 to 12 within 22 members) that are adequately identified. In the case of 8 natural frequencies, the damage identification results are significantly improved and 86% to 95% of the patterns (19 to 21 within 22 members) are adequately identified in the case of single member damage; about half are adequately identified even in the case of two member damage patterns based on the neural network having learned the data set consisting of 50,000 patterns of two member damage. In the case of 10 natural frequencies, all of the single member damage patterns are adequately identified; more than 80% of two member damage patterns and about 60% of three member damage patterns are adequately identified based on the neural networks having learned the data set consisting of two or three member damage patterns.

Composition of the learning data set should also be taken into consideration. In the case of neural networks having only learned the data set of single member damage patterns, it is shown that the identification capability is significantly limited even in the case of neural network based on 10 natural frequencies. This is considered to be because such data set does not reflect the interrelation between the damages on different truss members. The neural networks having learned two or three member damage patterns exhibit comparable identification capabilities. It is interesting that the neural networks based on three member damage patterns show marginally lower performance than those based on two member damage patterns in any case, regardless that the three member patterns are fundamentally extensions of the two member patterns.

The simulation studies are carried out based on neural networks of various sizes, that is, neural networks consisting of different numbers of neurons of hidden layers. On the basis of the results, it is demonstrated that larger neural networks have superior capabilities than smaller networks as a matter of course; however, this improvement

Table 1: Damage identification results

learning data set			neurons of hidden layers	adequately identified patterns (%)				
natural frequencies	damaged members	number of patterns		total 1-4	case of damaged number			
			1		2	3	4	
5	1	1,000	25, 25	0.4	50.0	7.8	0.5	0.0
5	1	1,000	50, 50	0.4	54.5	10.0	0.3	0.0
5	2	50,000	10, 10	0.7	40.9	9.1	1.4	0.2
5	2	50,000	25, 25	0.7	40.9	8.7	1.2	0.2
5	2	50,000	50, 50	0.7	40.9	9.1	1.4	0.2
5	2	50,000	80, 80	0.7	40.9	9.1	1.4	0.2
5	3	100,000	50, 50	0.7	40.9	7.8	1.2	0.2
5	3	100,000	100, 100	0.7	40.9	8.2	1.3	0.2
8	1	1,000	50, 50	1.5	95.5	38.1	1.6	0.0
8	2	50,000	50, 50	10.6	90.9	50.6	21.4	6.8
8	2	50,000	100, 100	11.5	90.9	51.9	22.5	7.7
8	3	100,000	50, 50	9.2	86.4	44.2	18.0	6.0
8	3	100,000	100, 100	9.6	90.9	46.8	18.7	6.2
10	1	1,000	50, 50	0.9	100.0	26.0	0.0	0.0
10	2	50,000	10, 10	26.2	100.0	81.0	45.8	20.1
10	2	50,000	25, 25	36.4	100.0	86.1	57.9	30.1
10	2	50,000	50, 50	38.7	100.0	86.1	59.3	32.7
10	2	50,000	80, 80	40.1	100.0	86.6	60.7	34.1
10	3	100,000	50, 50	36.0	100.0	83.1	55.5	30.2
10	3	100,000	80, 80	35.8	100.0	83.5	55.2	30.0
10	3	100,000	100, 100	37.0	100.0	83.5	56.3	31.3

converges at certain sizes. This indicates that the size of the neural network is not insignificant but the data set to be learned is definitely significant in this damage identification approach.

Figures 2(b)-(d) show typical examples of damage identification results based on the neural network consisting of two hidden layers of 50 neurons having learned the data set composed of patterns of 10 natural frequencies corresponding to two damaged members. The member stiffness damage assumed for these examples is 5%; the magnitude of damage in the figures is exaggerated based on this values. Figure 2(b) shows an accurate result. Figure 2(c) is a result judged marginally adequate; in the damage identification result of Fig.2(c2), slight degradation of stiffness is observed also in some of the non-damaged truss members such as the vertical members of the uppermost square unit. Figure 2(d) is a damage identification result judged inadequate; the assumed damaged members are two as shown in Fig.2(d1), but we can observe other degraded members around the two members as shown in Fig.2(d2).

7. Concluding Remarks

In this article, structural damage identification was dealt with from an inverse problem point of view. The natural frequencies of the entire structure are adopted as the key structural characteristics for the damage identification; the multi-layered neural network is used to represent the required relationship and to solve the inverse problem based on the relation, by means of the alternative error back-propagation with fixed connection weights. The approach is applied to a damage identification problem of a truss structure and simulation studies are carried out in order to evaluate its damage identification capability.

On the basis of the numerical experiment results with the 5-unit truss, the followings are concluded. It is theoretically impossible to identify *all* of the damage patterns of 22 truss members based only on 10 natural frequencies; however, it has been demonstrated that the neural network approach has the capability to identify quite significant part of the combination patterns in the case that the number of damaged members is limited. The damage identification capability significantly depends on the number of adopted natural frequencies. The learning data set for the neural network should include some patterns that represent the interrelation between the damaged parts.

It is obvious that the natural frequencies are not applicable to the case of identifying damage on symmetrical parts of a symmetrical structure. Some additional structural characteristics in order to cope with this limitation are the issue to be dealt with. From the viewpoint of practical application, sensing devices and signal processing methodologies should also be taken into consideration. These are the future works.

8. References

- [1] J. Mercklé et al., Intelligent Sensing for Non-Destructive Testing Using Eddy Currents, *NDT International*, 23 (6), 335-344, 1990.
- [2] M. Saka and Y. Fukuda, NDT of Closed Cracks by Ultrasonic Propagation along the Crack Surface, *NDT & E International*, 24 (4), 191-194, 1991.
- [3] V. Giurgiutiu, A. Zagrai and J. J. Bao, Piezoelectric Wafer Embedded Active Sensors for Aging Aircraft Structural Health Monitoring. *Structural Health Monitoring*, 1 (1), 41-61, 2002.
- [4] O. S. Salawu, Detection of Structural Damage through Changes in Frequency: A Review, *Engineering Structures*, 19 (9), 718-723, 1997.
- [5] M. Mehrjoo, N. Khaji, H. Moharrami and A. Bahreininejad, Damage Detection of Truss Bridge Joints using Artificial Neural Networks, *Expert Systems with Applications*, 35 (3), 1122-1131, 2008.
- [6] Z. Yang and L. Wang, Structural Damage Detection by Changes in Natural Frequencies, *Journal of Intelligent Material Systems and Structures*, 21 (3), 309-319, 2010.
- [7] D. E. Rumelhart, J. L. McClelland and PDP Research Group, *Parallel Distributed Processing (Explorations in the Microstructure of Cognition)*, The MIT Press, 1989.
- [8] M. Tanaka, K. Hanahara and Y. Seguchi, Configuration Control of the Truss-type Parallel Manipulator by the Modular Neural Network Model, *JSME International Journal Series III*, 35 (1), 89-95, 1992.
- [9] Y. Ootao, R. Kawamura, Y. Tanigawa and T. Nakamura, Neural Network Optimization of Material Composition of a Functionally Graded Material Plate at Arbitrary Temperature Range and Temperature Rise, *Archive of Applied Mechanics*, 68 (10), 662-676, 1998.
- [10] K. Hanahara and Y. Tada, Structural Health Monitoring by Means of Neural Network (Consideration on Modeling Errors), *Proceedings of the JSASS / JSME / JAXA Structures Conference*, 197-199, 2014. (in Japanese)

Multiscale structural topology optimization

Liang Xia, Piotr Breitkopf

Sorbonne universités, Université de technologie de Compiègne, CNRS, Laboratoire Roberval, Centre de Recherches de Royallieu, CS 60319, 60203, Compiègne Cedex, France, liang.xia@utc.fr

1. Abstract

This work develops firstly a nonlinear framework for concurrent topology optimization of material and structure. It has been shown that though linear models are assumed at both scales, the structural equilibrium is in general nonlinear due to the adaptation of local material microstructures. Secondly, the new regime of nonlinearity due to material optimization is approximated by a precomputed database model. As a result of this off-line step, the effective strain-energy and stress-strain relations required for the concurrent design are provided in a numerically explicit manner, which significantly reduces computational cost and enables design of larger-scale problems.

2. Keywords: Model reduction, Homogenization, Multiscale analysis, Topology optimization

3. Introduction

Existing researches of topology optimization focus mainly on monoscale designs, either designing homogeneous structures [1], or designing materials for expected effective performance [2]. A usual strategy applied to bridge the two scales is designing an universal material microstructure either for a fixed [3] or concurrently changed [4] structure at the macroscopic scale. In fact, earlier attempt traces back to [5], where simultaneous optimal designs are performed for both structure and elementwisely varying cellular materials following a decomposed design procedure [6]. Concerning multiscale design, cellular materials are designed in response to the displacement solution at the structural scale while their variations in turn modify the structural constitutive behavior. The equilibrium problem at the structural scale is therefore in general nonlinear. Such nonlinearity has been neglected in the early works (e.g., [4, 5]) where both scale design variables were updated simultaneously and the equilibrium at the structural scale was not enforced.

Unlike the previous models, in [7] we revisited concurrent topology optimization of material and structure while using a nonlinear iterative solution scheme, FE² [8], to address the nonlinearity due to the optimization or the adaptation of material microstructures. In addition, we have defined cellular material models pointwisely that in the context of finite element analysis they were assigned at the Gauss integration points. A schematic illustration of concurrent topological design of material and structure is shown in Fig. 1. Bi-directional Evolutionary Structural Optimization (BESO) method [9] was applied for the designs at both scales. Note that, this concurrent design framework requires intensive computational cost due to large number of repetitive material optimizations.

In our successive work [10], in viewing the material optimization process as a generalized constitutive behavior, we made a step further and adapt the Numerically EXplicit Potentials (NEXP) model [11] to approximated this new regime of nonlinearity. By this model, we constructed firstly a database from a set of numerical experiments so as to describe the effective strain energy density in a test space of macroscopic strain tensor. By tensor decomposition, a continuous representation of the strain energy density function is built as a sum of products of one-dimensional interpolation functions. As a result of this *a priori* off-line step, the effective strain-energy and stress-strain relations required for macroscopic structural evaluation and optimization are provided in a numerically explicit manner. The explicit material behavior representation given by the reduced database model is then used to serve the concurrent design [7] at a negligible computational cost.

4. Multiscale structural topology optimization [7]

Let $\rho(x)$ and $\eta(x, y)$ denote the design variables at the two scales, respectively. \mathcal{A} defines an integral admissible set consisting of two subsets \mathcal{A}_ρ and \mathcal{A}_η for $\rho(x)$ and $\eta(x, y)$, respectively. Both variables take binary values: 0 or 1, indicating void and solid materials, respectively. Volume fraction constraints are considered. Using the principle of minimum potential energy, the minimum compliance problem in a displacement-based formulation is [12]

$$\max_{(\rho, \eta) \in \mathcal{A}} \min_{u \in \mathcal{U}} \left\{ \frac{1}{2} \int_{\Omega} C_{ijkl}(x, \rho, \eta) \frac{\partial u_i}{\partial x_j} \frac{\partial u_k}{\partial x_l} d\Omega - l(u) \right\}, \quad (1)$$

where $C_{ijkl}(x, \rho, \eta)$ is the fourth-order elastic stiffness tensor at point x depending on $\rho(x)$ and $\eta(x, y)$. \mathcal{U} denotes the space of kinematically admissible displacement fields and $l(u)$ is the loading potential term. Since $\rho(x)$ and

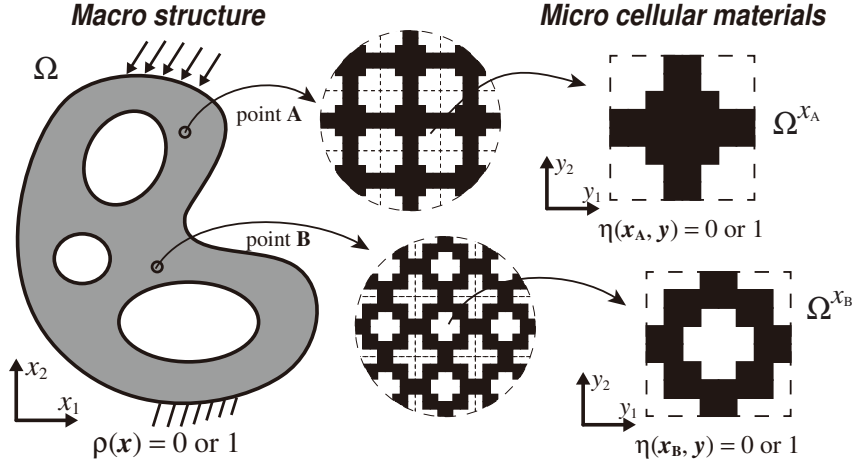


Figure 1: Illustration of concurrent topology optimization of material and structure [7, 10].

$\eta(x, y)$ are defined independently at two scales, Eq. (1) can be reformulated to

$$\max_{\rho \in \mathcal{A}_\rho} \min_{u \in \mathcal{U}} \left\{ \int_{\Omega} \left\{ \max_{\eta \in \mathcal{A}_\eta} \frac{1}{2} C_{ijkl}(x, \rho, \eta) \frac{\partial u_i}{\partial x_j} \frac{\partial u_k}{\partial x_l} \right\} d\Omega - l(u) \right\}, \quad (2)$$

where the pointwise maximization of strain energy density is treated as a subproblem. Note that, because materials defined at the microscopic scale are optimized according to the current strain loading statuses and the optimized materials in turn update the constitutive behavior at the macroscopic scale, the interface equilibrium is therefore in general nonlinear even though linear models are assumed at both scales.

To address this interface nonlinearity, we employ a nonlinear iterative solution scheme, so named FE² according to [8]. In general nonlinear case, it asserts that each point of the macroscopic discretization is associated with a Representative Volume Element (RVE). Then for each macroscopic equilibrium iteration, a nonlinear load increment has to be computed for each of the (many) RVEs. In return the average stress across the RVE is then used as the macroscopic stress tensor without the need of effective constitutive relations at hand. Therefore, the macroscopic stress $\Sigma(x)$ is computed as a function of the microscopic stress state by means of volume averaging (or via surface integrals) according to

$$\Sigma(x) = \langle \sigma(x, y) \rangle = \frac{1}{|\Omega^x|} \int_{\Omega^x} \sigma(x, y) dV = \frac{1}{|\Omega^x|} \int_{\partial\Omega^x} t \otimes x dA. \quad (3)$$

Similarly, the macroscopic strain $E(x)$ defines the mean of the microscopic strain via

$$E(x) = \langle e(x, y) \rangle = \frac{1}{|\Omega^x|} \int_{\Omega^x} e(x, y) dV = \frac{1}{|\Omega^x|} \int_{\partial\Omega^x} \text{sym}(u \otimes n) dA, \quad (4)$$

where n is the normal vector on the boundary of the microstructure. The interface equilibrium is solved iteratively using the Newton-Raphson method

$$\mathcal{R}(u, \rho, \eta) = f_{\text{ext}} - \int_{\Omega} B^T \langle \sigma(x, y) \rangle d\Omega = 0, \quad (5)$$

where $\mathcal{R}(u, \rho, \eta)$ and f_{ext} are the residual and external force at the macroscopic scale, respectively, and B is the linear strain-displacement matrix. It is important to emphasize that $\sigma(x, y)$ is evaluated on the optimized material, which is obtained using the BESO method [9] according to the imposed macroscopic strain $\langle e(x, y) \rangle = E(x)$.

4.1. Material design for a two-scale bridge-type structure

In order to illustrate the equilibrium nonlinearity due to the material optimizations, a simple two-scale bridge-type structure (Fig. 2(a)) is considered, where the cellular materials are optimized so as to maximize the global structural stiffness. The bridge-type structure is discretized into quadratic 8-node elements. Four Gauss integration points are defined for each finite element and each integration point is attributed with a cellular material model discretized into 80×80 bilinear 4-node elements. Young's modulus and Poisson's ratio of solid material at the microscopic scale are set to be 1 and 0.3, respectively. Volume fraction constraint for each cellular material model is set to 60%.

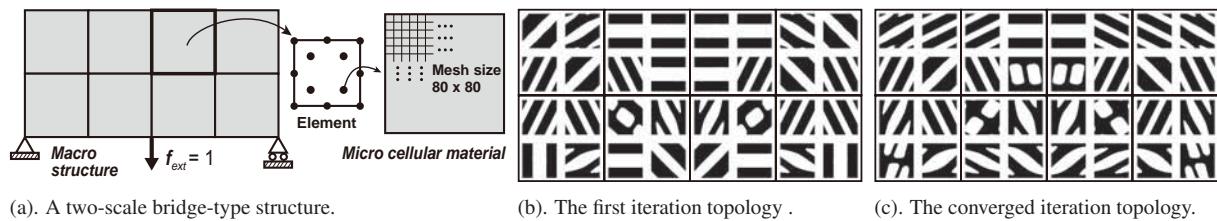


Figure 2: Illustration of the equilibrium nonlinearity: material design for a bridge-type structure [7].

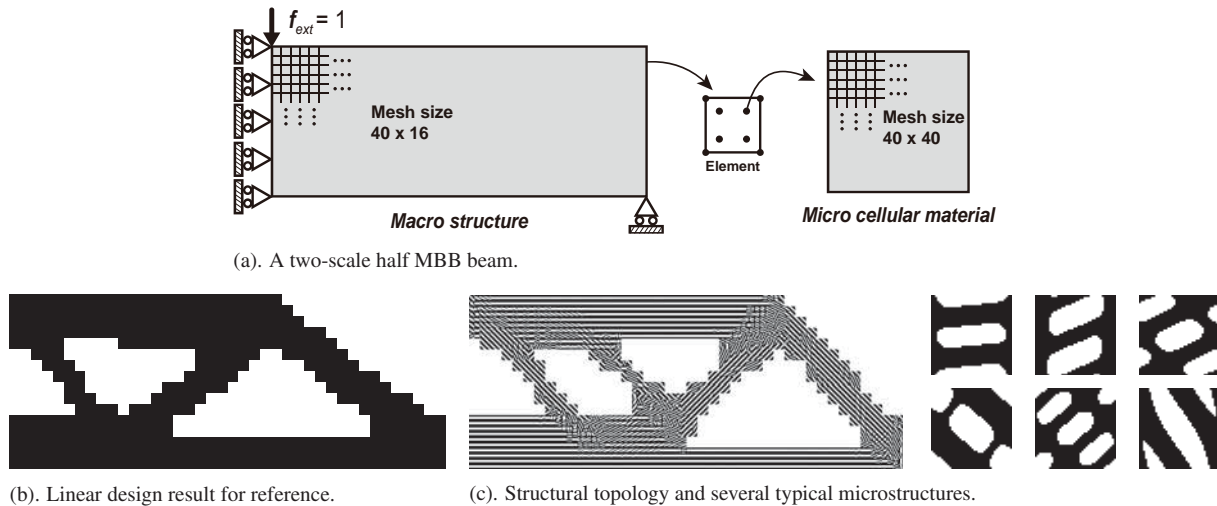


Figure 3: Concurrent topological design of a two-scale half MBB beam [7].

The evolution rate in the BESO is set to 0.02, which determines the percentage of removed material at each design iteration. Sensitivity filtering is used to avoid checkerboard pattern and mesh-dependency.

The topologies of the first and the converged (6th) iterations are shown in Figs. 2(b) and (c), respectively. The difference between Figs. 2(b) and (c) demonstrates the necessity of considering the nonlinearity of the interface equilibrium. Note that, in Figs. 2(b) and (c) the optimized cellular materials on the Gauss points are enlarged for a clear visualization. Upon the homogenization theory, the optimized cellular material only represents the optimal design at the microscopic scale for that material point, i.e., Gauss integration point. Therefore, the optimized cellular materials in the neighboring points represent only the tendency of the topological variations while are not necessarily continuous.

4.2. Concurrent material and structure design for a two-scale MBB beam

In this example, the so-called MBB beam [12] is considered and optimal designs are carried out concurrently at both structural and material scales. Due to the symmetry of the problem, only half MBB beam is considered as shown in Fig. 3(a). The macroscopic structure is discretized into 40×16 bilinear 4-node elements, which means in total $N_{gp} = 4 \times 40 \times 16$, 2560 cellular material models are considered concurrently at the microscopic scale. At the macroscopic structure, $N = 40 \times 16$, 640 design variables are accordingly defined. Microscopic cellular material model is discretized into 40×40 bilinear 4-node elements with $M = 40 \times 40$ design variables. Volume constraints of solid material are set to 60% at both scales. The evolution rate in the BESO is set to 0.02 and sensitivity filtering is applied as in the previous example.

It takes around 6 solution iterations to reach the macroscopic equilibrium for each design iteration. The final topologies of both cellular materials and structure are shown in Fig. 3(c). The standard monoscale design within the regime of linear elasticity is given in Fig. 3(b) for the purpose of comparison. Some typical microstructures obtained in the nonlinear two-scale design is also given in Fig. 3(c). Similarly, the optimized cellular material only represents the optimal design at the microscopic scale for that material point satisfying the assumptions of scale-separation and periodicity. The optimized cellular materials in neighboring points represent only the tendency of the topological variations. As can be observed in Fig. 3(c), uniaxial materials may be sufficient at the main branches of the structure; while in order to have a higher structural performance, anisotropic materials have to be used at the joints of the main branches due to the more complex loading status.

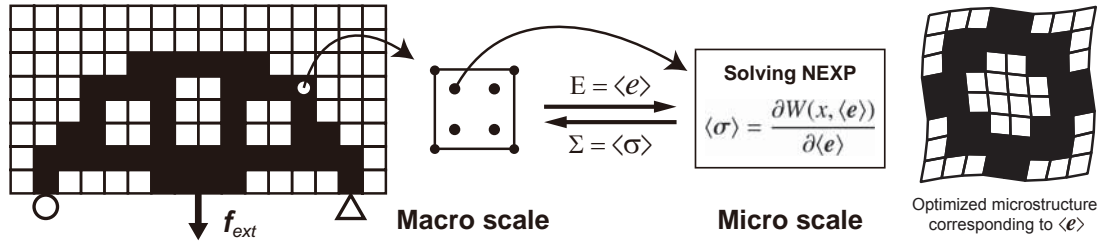


Figure 4: Illustration of the monoscale structural design with the NEXP model [10].

5. Reduced multiscale structural topology optimization [10]

In viewing the local material optimization process as a particular regime of material nonlinearity, the main objective of this part of work is to construct an explicit representation of the strain energy density $W(\langle e \rangle)$ in terms of $\langle e \rangle$ such that the concurrent design can be performed with an effective stress-strain relationship provided at an extremely reduced computational cost. For such reason, following the NEXP strategy [11], we construct an approximate expression of $W(\langle e \rangle)$ using a precomputed database. An illustrative scheme is shown in Fig. 4.

The NEXP model aims to construct an explicit approximation $\tilde{W}(\langle e \rangle)$ over the tensor space using a precomputed database and interpolation schemes, expecting $\tilde{W}(\langle e \rangle)$ close enough to $W(\langle e \rangle)$

$$W(\langle e \rangle) \approx \tilde{W}(\langle e \rangle) = \sum N_q(\langle e \rangle) W_q, \quad (6)$$

where N_q are the interpolation functions and W_q are the strain energy density values stored in the database, which are evaluated by means of a set of numerical experiments over the test tensor space. It is important to emphasize that W_q corresponds to the energy density of an optimized material for a given $\langle e \rangle_q$. Once the database model is built, the effective stress-strain relationship is obtained as

$$\langle \sigma \rangle \approx \sum \frac{\partial N_q(\langle e \rangle)}{\partial \langle e \rangle} W_q, \quad (7)$$

provided the interpolation functions N_q are continuously differentiable.

Still following [11], the precomputed full database is further approximated by a sum of products of one-dimensional interpolation functions via higher-order tensor decomposition. The Voigt notation is applied such that $\{\langle e \rangle_1, \langle e \rangle_2, \langle e \rangle_3, \langle e \rangle_4, \langle e \rangle_5, \langle e \rangle_6\}$ corresponds to $\{\langle e \rangle_{11}, \langle e \rangle_{22}, \langle e \rangle_{33}, \langle e \rangle_{23}, \langle e \rangle_{13}, \langle e \rangle_{12}\}$. Let \mathbb{W} denote the hypermatrix which stores the database. It can be approximated in a tensor decomposed representation

$$\mathbb{W} \approx \sum_{r=1}^R \phi_1^r \otimes \phi_2^r \otimes \cdots \otimes \phi_6^r, \quad (8)$$

where ϕ_j^r are real-valued vectors corresponding to the effective strain tensor components $\langle e \rangle_j$ and R is the number of expanded terms. The vectors ϕ_j^r involved in (8) are determined by solving the following least square problem for a given value of R

$$\inf_{\phi_j^r} \left\| \mathbb{W} - \sum_{r=1}^R \phi_1^r \otimes \phi_2^r \otimes \cdots \otimes \phi_6^r \right\|^2, \quad (9)$$

where $\|\cdot\|$ is the Frobenius norm. Once the decomposed vectors in (8) are obtained, the continuous representation of $W(\langle e \rangle)$ written in terms of separated components can be constructed by interpolation

$$W(\langle e \rangle_1, \langle e \rangle_2, \dots, \langle e \rangle_6) \approx \sum_{r=1}^R \tilde{\phi}_1^r(\langle e \rangle_1) \tilde{\phi}_2^r(\langle e \rangle_2) \cdots \tilde{\phi}_6^r(\langle e \rangle_6), \quad (10)$$

where $\tilde{\phi}_j^r(\langle e \rangle_j)$ are the interpolated values of ϕ_j^r . The tensor decomposed database requires only one-dimensional interpolations for effective stress evaluation, which further reduces computing time.

5.1. Validation of the NEXP model

Consider the same cellular material model setting as in the previous section. The NEXP model is built over the strain domain. Each dimension of the strain space is discretized into $p = 21$ uniformly distributed points, which means in total 21^3 local material optimizations are carried out at the off-line phase. With a relative reconstruction

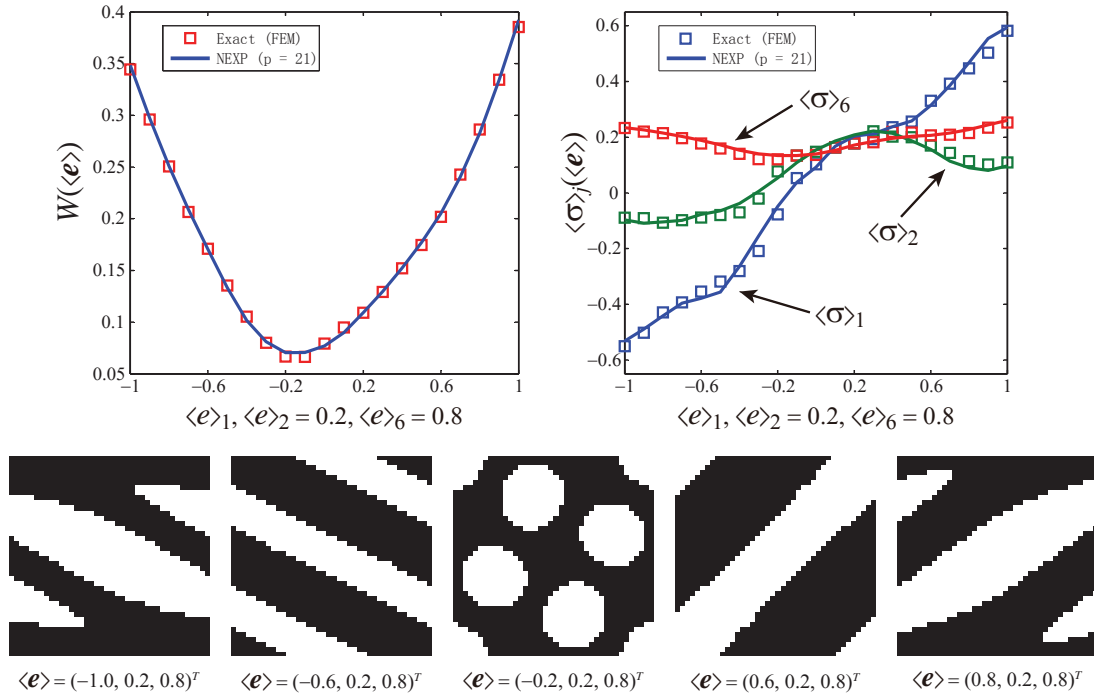


Figure 5: Comparison of the exact and approximate values evaluated using FEM and NEXP [10].

error chosen as 0.01, we obtain $R = 9$ truncated modes in each dimension for the reduced approximation \tilde{W} . To validate the performance, we compare the values evaluated using the NEXP model and the exact computations. A first comparison is given in Fig. 5, where $\langle e \rangle_2 = 0.2$, $\langle e \rangle_6 = 0.8$ are fixed and $\langle e \rangle_1$ varies from -1 to 1 . Several observations can be found from Fig. 5. Firstly, the approximate values given by the NEXP model are in very good agreement with the exact solutions. Secondly, the strain energy density is a convex function over the effective strain space. Thirdly, the selected optimal material microstructures show the tendency of topological variation along $\langle e \rangle_1$, which introduces nonlinearity to the interface equilibrium.

5.2. Design of a two-scale half MBB beam with fine discretization

With the constructed NEXP model, we are now capable of designing a much larger scale or finely discretized two-scale MBB beam with 120×60 bilinear 4-node elements. Volume constraint at the macroscopic structure is set to 60%. The evolution rate in the BESO is set to 0.02 and sensitivity filtering is applied. Fig. 6 gives the optimized structure topology together with the retrieved optimal cellular material topologies. Three local zones are selected and zoomed for a better visualization of microscopic material topologies. This test takes around 6 hours for all 35 design iterations on the used personal computer. Retrieving microscopic material topologies at the final design requires one additional hour computing. Assuming 6 substeps required in average for each structural design iteration and one hour computing for each substep of each design iteration, then the concurrent design strategy [7] would require in total more than 200 hours computing time for solving this problem on the used personal computer. In the contrast, using the constructed NEXP material model, it requires only 7 hours computing to reach the final design. Note that this time can still be further reduced with parallel computing.

6. Conclusion

This work develops a FE^2 -based multiscale structural topology optimization framework and adapts the NEXP strategy into this framework to limit the computational cost. This framework is independent with the type of design variables, other parameters such as geometrical or even manufacturing process parameters can be considered for the design. Future works will focus on considering more realistic multiscale structures constituted by 3D knitted or woven composites with more complex nonlinear constitutive behaviors.

7. Acknowledgements

This work was carried out in the framework of the Labex MS2T, which was funded by the French Government, through the program ‘‘Investments for the future’’ managed by the National Agency for Research (Reference ANR-11-IDEX-0004-02).

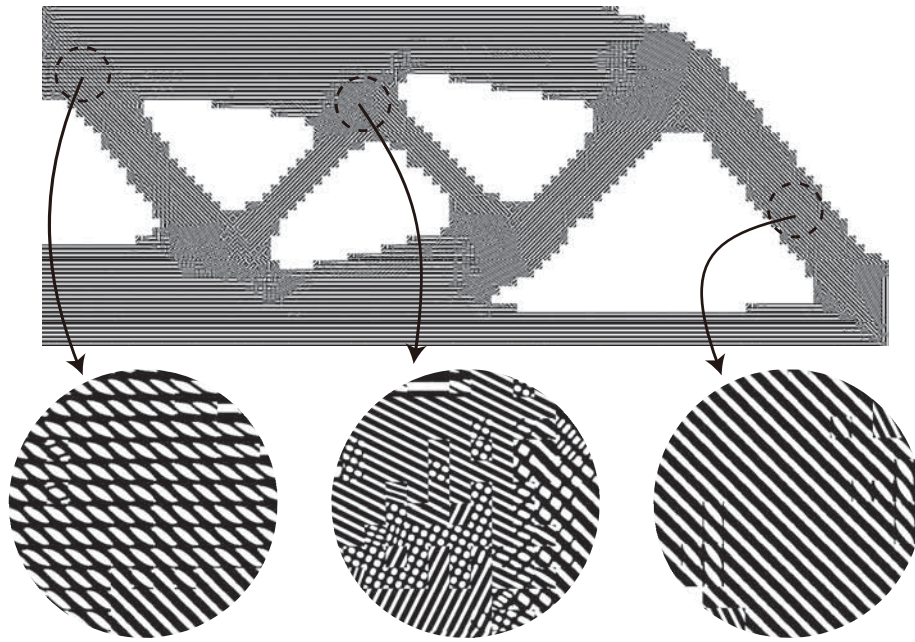


Figure 6: Two-scale design of half MBB beam with retrieved local optimal material topologies [10].

8. References

- [1] J.D. Deaton, R.V. Grandhi, A survey of structural and multidisciplinary continuum topology optimization: post 2000, *Structural and Multidisciplinary Optimization*, 49, 1-38, 2014.
- [2] J. Cadman, S. Zhou, Y. Chen, Q. Li, On design of multi-functional microstructural materials, *Journal of Materials Science*, 48, 51-66, 2013.
- [3] X. Huang, S. Zhou, Y.M. Xie, Q. Li, Topology optimization of microstructures of cellular materials and composites for macrostructures. *Computational Materials Science*, 67, 397-407, 2013.
- [4] X. Yan, X. Huang, Y. Zha, Y.M. Xie, Concurrent topology optimization of structures and their composite microstructures, *Computers and Structures*, 133, 103-110, 2014.
- [5] H. Rodrigues, J.M. Guedes, M.P. Bendsøe, Hierarchical optimization of material and structure, *Structural and Multidisciplinary Optimization*, 24(1):1-10, 2002.
- [6] M.P. Bendsøe, A.R. Diaz, R. Lipton, J.E. Taylor, Optimal design of material properties and material distribution for multiple loading conditions, *International Journal for Numerical Methods in Engineering*, 38(7):1149-1170, 1995.
- [7] L. Xia, P. Breitkopf, Concurrent topology optimization design of material and structure within FE^2 nonlinear multiscale analysis framework, *Computer Methods in Applied Mechanics and Engineering*, 278, 524-542, 2014.
- [8] F. Feyel, J. Chaboche, FE^2 multiscale approach for modelling the elastoviscoplastic behaviour of long fibre sic/ti composite materials, *Computer Methods in Applied Mechanics and Engineering*, 183, 309-330, 2000.
- [9] X. Huang, Y. M. Xie, *Topology Optimization of Continuum Structures: Methods and Applications*, John Wiley & Sons, Chichester, 2010.
- [10] L. Xia, P. Breitkopf, Multiscale structural topology optimization with an approximate constitutive model for local material microstructure, *Computer Methods in Applied Mechanics and Engineering*, 286, 147-167, 2015.
- [11] J. Yvonnet, D. Gonzalez, Q. C. He, Numerically explicit potentials for the homogenization of nonlinear elastic heterogeneous materials, *Computer Methods in Applied Mechanics and Engineering*, 198, 2723-2737, 2009.
- [12] M. P. Bendsøe, O. Sigmund, *Topology optimization: theory, methods and applications*, Springer-Verlag, Berlin, 2003.

Optimization of Elastic Plastic Plates of Piecewise Constant Thickness

Jaanellep¹, Julia Polikarpus², Boriss Vlassov³

¹ University of Tartu, Tartu, Estonia, jaan.lellep@ut.ee

² University of Tartu, Tartu, Estonia, julia.polikarpus@ut.ee

³ University of Tartu, Tartu, Estonia, boriss.vlassov@ut.ee

1. Abstract

Numerical and analytical methods of analysis and optimization of elastic plastic plates are developed. The cases of linear and non-linear yield surfaces are studied. Necessary optimality conditions are derived with the aid of variational methods. The obtained system of equations is solved numerically. The effectivity of the design established is assessed in the cases of one- and multi-stepped plates made of Tresca or Mises materials.

2. Keywords: plate, optimization, elastic plastic material, minimum weight.

3. Introduction

Evidently, there exists the need for new computer-aided techniques for calculation and optimization of elastic plastic plates. Optimization of axisymmetric plates operating in the range of elastic plastic deformations was studied by Lellep and Polikarpus [2, 3] in the case of the material obeying Tresca's yield condition and by Lellep and Vlassov [4, 5] in the case of von Mises material.

New analytical and numerical techniques of optimization of axisymmetric plates are developed in the present paper. The material of plates is an ideal elastic plastic material obeying a linear or non-linear yield condition and the associated flow law.

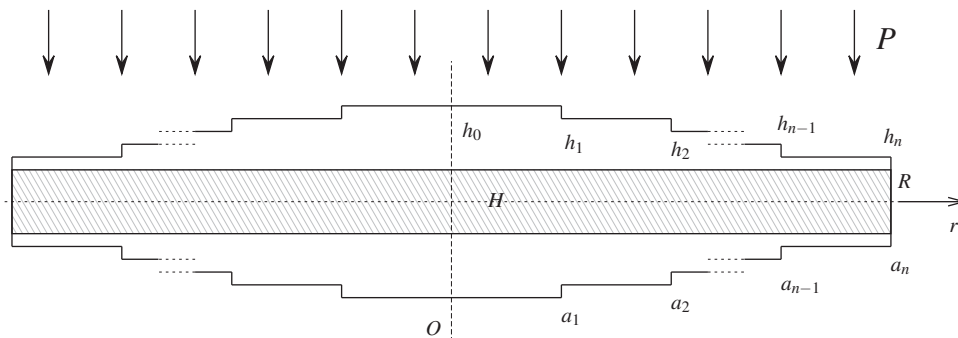


Figure 1: Stepped plate.

4. The cost function

Circular and annular plates with radii R (outer radius) and a (inner one) will be considered. Let us assume that an axisymmetric plate is subjected to the axisymmetric transverse pressure of intensity $p = p(r)$, where r is the current radius. The analysis will be carried out under the assumption that the hypotheses of Kirchhoff hold good in the regimes of elastic and plastic deformations. The plates with sandwich cross section will be considered. A sandwich plate is a structure which consists of two carrying layers of thickness h and of a layer of a core material between the rims. Let the thickness of carrying layers be piecewise constant, e. g.

$$h = h_j, \quad r \in S_j \quad (1)$$

where $S_j = (a_j, a_{j+1})$; $j = 0, \dots, n$.

Evidently, the plate can be subdivided into elastic and plastic regions in the case of a sandwich plate. Let us denote the elastic region by S_e and the plastic region by S_p . In principle, both of these may consist of several regions S_{e_j} and S_{p_j} , respectively. Here $S_{e_j} = S_j$ if the region S_j is a pure elastic one, e. g. if $j \in K_e$. Similarly, $S_{p_j} = S_j$,

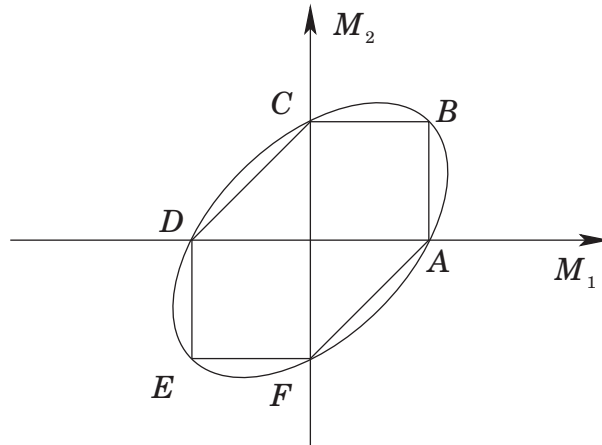


Figure 2: Yield conditions.

if $j \in K_p$. These intervals where both, the elastic and plastic deformations take place are denoted by S_{ep} whereas $S_{ep} = S_j$ for $j \in K_{ep}$. Evidently,

$$K_e \cup K_p \cup K_{ep} = \{0, 1, \dots, n\}. \quad (2)$$

The thickness of the rim is much smaller than the thickness of the core material H . Note that the quantities h_0 , h_j and a_j ($j = 1, \dots, n$) are preliminarily unknown constant design parameters when solving a problem of optimization.

As regards the formulation of an optimization problem, one can find in literature a lot of different particular problems (see Lellep [1]).

In the general case the cost function can be presented as

$$J = \sum_{j=0}^n \left(G_j + \int_{S_j} F_j dr \right) \quad (3)$$

where G_j and F_j are given functions of design parameters. For the sake of simplicity it is assumed that the functions F_j and G_j are continuous and continuously differentiable with respect to their variables.

The optimal design to be established must satisfy the constraints imposed on the stress-strain state of the plate. Let the additional constraints be presented as integral constraints

$$\sum_{j=0}^n \int_{S_j} F_{ij}^0 dr \leq K_i \quad (4)$$

for $i = 1, \dots, k$. The functions F_{ij}^0 in Eq. (4) are given continuous functions of design parameters and K_i – given constants.

In particular cases the optimization problem consists in the determination of design parameters so that the cost function (total weight, for instance) attains its minimum value and the constraints imposed on the stress strain state of the plate are satisfied. For instance, the cost of carrying layers can be presented in the form

$$V = \sum_{j=0}^n h_j (a_{j+1}^2 - a_j^2) \quad (5)$$

where $a_0 = a$ and $a_{n+1} = R$.

5. Basic equations

Making use of the classical plate theory the principal moments M_1 , M_2 and the shear force Q are connected as

$$\begin{aligned} \frac{d}{dr}(rM_1) - M_2 - rQ &= 0, \\ \frac{d}{dr}(rQ) + Pr &= 0. \end{aligned} \quad (6)$$

Equations (6) hold good equally in elastic and plastic regions of a plate. In an elastic region of the plate the Hooke's law holds good. According to the generalized Hooke's law

$$\begin{aligned} M_1 &= D_j(\kappa_1 + \nu\kappa_2), \\ M_2 &= D_j(\kappa_2 + \nu\kappa_1) \end{aligned} \quad (7)$$

where ν is the Poisson ratio. In Eq. (7) and henceforth

$$D_j = \frac{EH^2h_j}{2(1-\nu^2)} \quad (8)$$

where E stands for the Young modulus. Here κ_1 and κ_2 stand for the curvatures (W is the transverse deflection)

$$\begin{aligned} \kappa_1 &= -\frac{d^2W}{dr^2}, \\ \kappa_2 &= -\frac{1}{r} \frac{dW}{dr}. \end{aligned} \quad (9)$$

It can be shown that the system of governing equations in an elastic region for $r \in S_{ej}$ can be presented as (see Lellep, Vlassov [4, 5])

$$\begin{aligned} \frac{dW}{dr} &= Z, \\ \frac{dZ}{dr} &= -\frac{M_1}{D_j} - \frac{\nu Z}{r}, \\ \frac{dM_1}{dr} &= -\frac{(1-\nu^2)D_j Z}{r^2} - \frac{(1-\nu)M_1}{r} + Q \end{aligned} \quad (10)$$

whereas the following equation

$$M_2 - \nu M_1 + \frac{D_j(1-\nu^2)Z}{r} = 0 \quad (11)$$

must be satisfied for each $r \in S_{ej}$. Note that here $j \in K_e$ and $j \in K_{ep}$ and Z can be treated as an auxiliary variable. In plastic regions of the plate the stress profile lies on a yield surface $\Phi = 0$. It is assumed that the material of the plate obeys a yield condition

$$\Phi_j(M_1, M_2, M_0) \leq 0 \quad (12)$$

for $r \in S_{pj}$, $j \in K_p$.

It can be shown that in the case of a von Mises material one can take

$$\Phi_j = M_1^2 - M_1 M_2 + M_2^2 - M_{0j}^2. \quad (13)$$

In the case of a Tresca plate one has to check the suitability of each side of the hexagon $ABCDEF$ (Fig. 2) separately. However, if it is clear previously that, for instance, $M_1 \geq 0$, $M_2 \geq 0$ for each $r \in S_p$ one can concentrate at the flow regime BC (AB is not suitable for most cases). Thus now

$$\Phi_j = M_2 - M_{0j} \quad (14)$$

for $r \in S_{pj}$, $j \in K_p$. The associated flow law states that

$$\begin{aligned} \kappa_1 &= \frac{\lambda \partial \Phi_j}{\partial M_1}, \\ \kappa_2 &= \frac{\lambda \partial \Phi_j}{\partial M_2} \end{aligned} \quad (15)$$

for $r \in S_{pj}$, $j \in K_p$. Here λ is a non-negative scalar multiplier. Thus combining Eq. (12), (15) with Eq. (6) one has

$$\begin{aligned} \frac{dW}{dr} &= Z, \\ \frac{dZ}{dr} &= \frac{Z \frac{\partial \Phi_j}{\partial M_1}}{r \frac{\partial \Phi_j}{\partial M_2}}, \\ \frac{dM_1}{dr} &= \frac{M_2}{r} - \frac{M_1}{r} + Q, \end{aligned} \quad (16)$$

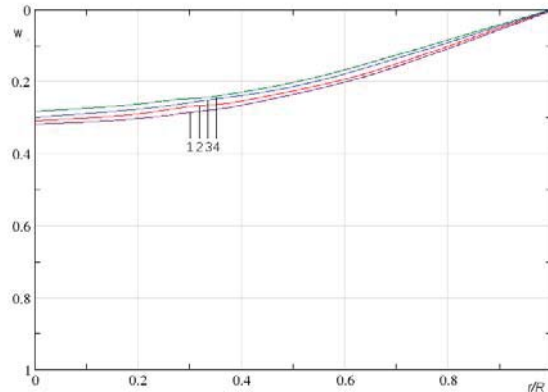


Figure 3: Transverse deflection.

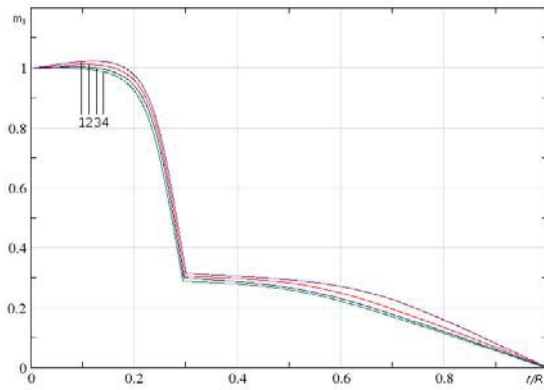


Figure 4: Bending moment.

where the quantity Q can be handled as a given function. Indeed it follows from the equilibrium equations that

$$Q = -\frac{1}{r} \int_a^r P(r) r dr. \quad (17)$$

6. Necessary optimality conditions

In order to derive optimality conditions let us introduce an extended functional

$$\begin{aligned} J_* = & \sum_{j=0}^n G_j + \sum_{j \in K_{e_j}} \int_{S_{e_j}} \left\{ \psi_1 \left(\frac{dW}{dr} - Z \right) + \psi_2 \left(\frac{dW}{dr} + \frac{M_1}{D_j} + \frac{\nu Z}{r} \right) \right. \\ & + \left. \psi_3 \left(\frac{dM_1}{dr} + (1 - \nu^2) D_j + \frac{(1 - \nu) M_1}{r} - Q \right) + \nu_{0j} \left(M_2 + \frac{D_j (1 - \nu^2) Z}{r} - \nu M_1 \right) \right\} dr \\ & + \sum_{j \in K_{p_j}} \int_{S_{p_j}} \left\{ \psi_1 \left(\frac{dW}{dr} - Z \right) + \psi_2 \left(\frac{dZ}{dr} - \frac{Z}{r} \frac{\partial \Phi_j}{\partial M_1} \right) + \psi_3 \left(\frac{dM_1}{dr} - \frac{M_2}{r} + \frac{M_1}{r} - Q \right) \right\} dr \\ & + \sum_{j=0}^n \int_{a_j}^{a_{j+1}} [\phi_{0j} (\phi_j + \Theta_j^2) + F_j + \nu_i F_{ij}^0] dr \end{aligned} \quad (18)$$

where Θ_j are new control functions and $\psi_1 - \psi_3$ – the adjoint variables. The boundary conditions are not presented

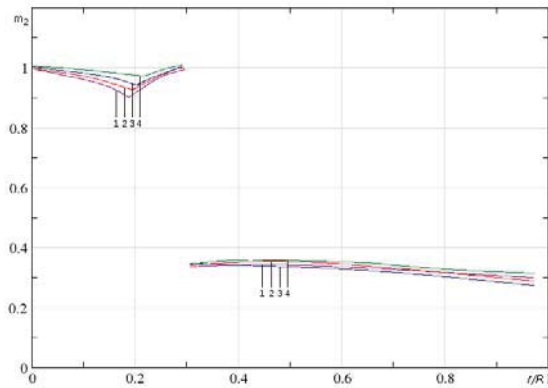


Figure 5: Circumferential moment.

in Eq. (18); these must be taken into account when solving the equation $\Delta J_* = 0$. Calculating the total variation of Eq. (18) and equalizing it to zero leads to the set of optimality conditions. The procedure of the variation of Eq. (18) is similar to that performed in [4, 5].

7. Numerical results

In the case of a non-linear materials the problem is solved numerically making use of finite elements and the method of wavelets. The results of calculations are presented in Fig. 3–5 in the case when the number of steps $n = 1$.

The distributions of transverse deflections, radial and circumferential bending moments are presented in Fig. 3, 4 and Fig. 5, respectively. Different curves in Fig. 3–5 correspond to the plates made of a Hill material and subjected to the uniform transverse pressure. Here the labels of curves correspond to $p = 3.15$; $p = 3.25$; $p = 3.45$ and $p = 3.65$, respectively, and

$$p = \frac{PM_{00}}{R^2}, \quad \alpha_i = \frac{a_i}{R}, \quad m_i = \frac{M_i}{M_{00}}. \quad (19)$$

The results depicted in Fig. 3–5 correspond to the case when $h_1 = 0.6h_0$; $a_1 = 0.35R$. The region of plastic deformations reaches to $r = 0.304$ for $p = 3.15$ and to $r = 0.385$ for $p = 3.65$.

The distributions of M_1 and M_2 are depicted in Fig. 6–7 in the case of the Tresca material. It can be seen from Fig. 6, 7 that the hoop moment is discontinuous and the radial moment is a continuous non-smooth, as might be expected.

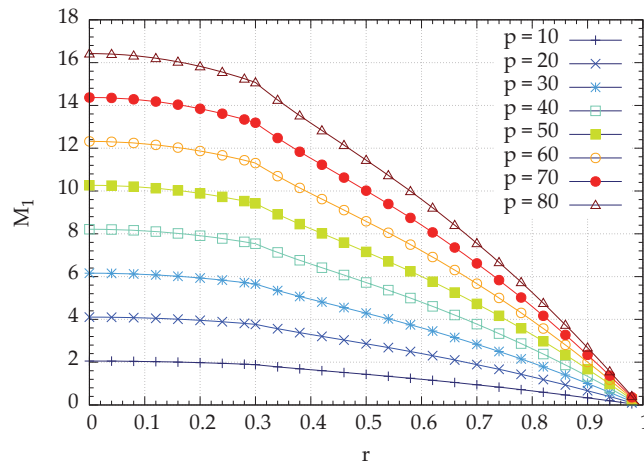


Figure 6: Bending moment.

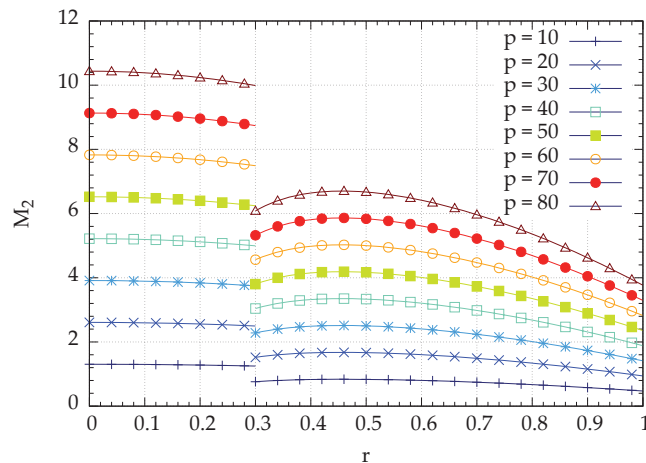


Figure 7: Circumferential moment.

8. Concluding remarks

Methods of optimal design of axisymmetric plates are developed under the assumption that the plates are operating in the elastic plastic stage of deflection. Necessary conditions of optimality are derived making use of variational methods. Numerical results are obtained for plates obeying the Mises or Tsai-Wu criterion with the aid of Haar wavelets. Calculations carried out showed remarkable material saving can be achieved when using the design of stepped plate.

9. Acknowledgements

This research was supported by the Grant No 9110 of the Estonian Science Foundation and by the institutional research funding IUT20-57 of the Estonian Ministry of Education and Research.

10. References

- [1] J. Lellep, *Optimization of Plastic Structures*, UT Press, Tartu, 1991.
- [2] J. Lellep, J. Polikarpus, Optimization of anisotropic circular plates, *Recent Advances in Mechanical Engineering*, M. Shitikova et al (Eds.), WSEAS, 40-45, 2014.
- [3] J. Lellep, J. Polikarpus, Optimization of elastic-plastic circular plates under axisymmetric loading, *Continuous Optimization and Knowledge-Based Technologies, EUROPT'2008*, Sakalauskas, L.; Weber, G. W.; Zavadskas, E.K. (Eds.), Vilnius Gediminas Technical University Press "Technika", 291-295, 2008.
- [4] J. Lellep, B. Vlassov, Optimization of axisymmetric plates, *Advances in Circuits, Systems, Automation and Mechanics*, WSEAS, Montreux, 148-153, 2012.
- [5] J. Lellep, B. Vlassov, Optimization of stepped elastic plastic plates, *Advanced Materials Research*, Trans Tech Publicatons Ltd, 209-214, 2013.

Form finding by shape optimization with the Vertex Morphing Method – About the equivalence of sensitivity filtering and standard spline models

Kai-Uwe Bletzinger, Majid Hojjat, Electra Stavropoulou

Technische Universität München, Germany, kub@tum.de

1. Abstract

The proper parameterization of structural shape which is suitable for creating structural form and shape optimal design is a great challenge. The demand for large design spaces with large and very large numbers of design parameters is in conflict with the robustness of the numerical model. There is a need for regularization. The currently most successful techniques which overcome those burdens and, simultaneously, are most intuitive and easy to be used are so-called filter techniques. They directly use the coordinates of the discretization nodes as design parameters. Filters are applied to smooth the shape sensitivity fields as the generator of the design update towards the optimum. However, the filters are much more than mathematical means to prevent numerical problems such as mesh distortion or checker board patterns. Even more important, from the point of view of shape design they deal as a design tool to controlling the local and global shape properties. The actual presentation will show that filtering is equivalent to the implicit definition of standard spline models. Impressive applications in the fields of CSD and CFD with problem sizes up to 3.5 million design parameters can easily be handled by this technique.

2. Keywords: Shape optimization, sensitivity filtering, morphing, structural optimization, CFD optimization

3. Introduction

Sensitivity filtering is a well-established and very successful procedure in discrete topology and shape optimization. It is used to regularize the optimization problem by introducing an additional filter length scale which is independent of the discretization. The filter is both, a design tool controlling local shape or density distribution and a mean to prevent numerical problems such as mesh distortion or checker board patterns. Together with adjoint sensitivity analysis to determine the discretized shape gradient, the filter technique is a most powerful optimization procedure and successively applied to the largest optimization problems known. Filtering is the key technology for using the vertices of even the finest discretization mesh directly as design handles for discrete shape optimization. In contrast to standard shape morphing techniques and CAD methodologies no other design handles are used.

Among those techniques which do not use CAD parameters to parameterize shape there are meshfree and node-based or parameter-free methods which means “free of CAGD parameters” (Le et al. 2011; Scherer et al. 2010; Hojjat et al. 2014), the traction method (Azegami and Takeuchi 2006), for CFD problems (Pironneau 1984; Jameson 1995, 2000, 2003; Mohammadi and Pironneau 2000, 2004; Stück and Rung 2011).

4. Continuous Shape control by using filters

We start by introducing an additional field p . This serves as the control which steers the evolution of shape. In analogy to splines the control field can be identified as the continuous equivalent to the convex hull which is discretized by control nodes. As with splines where the coordinates of the control nodes are the design variables, now, the control field represents the design degrees of freedom which drive the shape.

The considered shape optimization problem states as:

$$\begin{aligned} & \min_p f(x, z(x, p), u(x, z(x, p))) \\ \text{s.t.: } & \mathbf{R}(x, z(x, p), u(x, z(x, p))) = 0 \\ & g_j(x, z(x, p), u(x, z(x, p))) \leq 0; \quad j = 1, \dots, m \end{aligned} \quad (1)$$

where f and g_j are the objective function and constraints and \mathbf{R} are the state equations which may be non-linear. There are four fields describing the state u , the surface coordinate x , the geometry z as well as the design control field p , Fig. 1. For the sake of simplicity, (1) is formulated in 1D geometric space. As a consequence, the geometry z is a function of the one spatial surface coordinate x and the design control p . Extended to 3D, (1) represents the classical view at a surface controlled shape optimization problem following the ideas of Hadamard. Then, the shape relevant modifications of geometry z are identified as in the normal direction to the surface spanned by

surface coordinates x_1 and x_2 .

The geometry z at x_0 is generated from the design control field $p(x)$ by a filter operation as integration over the surface Γ with filter function F_0 of radius r and center at x_0 :

$$z(x_0) = \int_{\Gamma} F_0 p d\Gamma = \int_{x_0-r}^{x_0+r} F(x, x_0, r) p(x) dx; \quad \left. \frac{dz}{dp} \right|_{x_1} = F(x_1, x_0, r) \quad (2)$$

where $\int_{x_0-r}^{x_0+r} F_0 dx = 1$ and $F_0 = 0$ if $x < x_0 - r$ or $x > x_0 + r$

Applying the chain rule of differentiation the derivative of a response function f with respect to the design control p at x_1 is given as

$$\left. \frac{df}{dp} \right|_{x=x_1} = \int_{\Gamma} \frac{df}{dz} \frac{dz}{dp} d\Gamma = \int_{\Gamma} \frac{df}{dz} F(x_1, x, r) d\Gamma = \int_{\Gamma} \frac{df}{dz} A_1 d\Gamma \quad (3)$$

The geometry gradient df/dz is filtered by the adjoint filter function A_1 where the center coordinate x_1 and the free coordinate x are exchanged compared to F_1 .

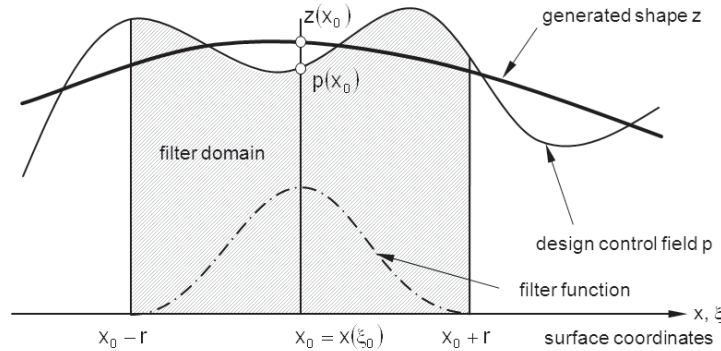


Figure 1: Filtering of design control field to generate shape

5. Shape discretization and discrete sensitivity filtering

The design control field and the geometry derivative are discretized using shape functions N_j related to design and geometry parameters p_j and z_i , respectively:

$$p = N_j p_j = N_j(x) p_j$$

$$\frac{df}{dz} = N_i \frac{df}{dz_i} \quad (4)$$

The discrete versions of (2) and (3) are:

$$z_i = \int_{\Gamma} F_i N_j p_j d\Gamma = B_{ij} p_j \quad (5)$$

$$\frac{df}{dp_j} = \int_{\Gamma} \frac{df}{dz_i} N_i A_j d\Gamma = \int_{\Gamma} F_i N_j \frac{df}{dz_i} d\Gamma = B_{ij} \frac{df}{dz_i}$$

On regular grids together with symmetric filter functions $F_i = A_i$ the filter operator matrix B_{ij} is symmetric as well.

6. Choice of filters and shape functions, relations to splines

Linear hat functions are the simplest choice for filter and shape functions F and N . Filtering a linear shape function by a linear filter results in a cubic geometry. As a matter of fact the control field is the continuous equivalent of spline control polygons. For the special case of regular grids and linear hat functions for $F = N$, a cubic B-spline geometry is derived from a piecewise linear control field, Figs. 2 and 3, [3]. The filter technique is equivalent with the subdivision spline technique sharing important properties with general splines. The technique is straight forward extended to 3D [1].

As the filter modifies the gradient vector the filtering effect can be exploited best by first order gradient methods. Those methods converge to that local minimum which is characterized by a shape mode wave length that is not

smaller than the filter radius or the variance in case of Gaussian filters. The filter shape is not important at all. That allows to using any kind of filter for the sensitivity filtering as long as B_{ij} remains non-singular. In turn, we can conclude that every simple gradient method with sensitivity filtering will converge to a solution of the original, unmodified problem. For non-convex problems, the choice of filter will affect which local optimum will finally be found. This is the intended effect which helps to efficiently explore the design space.

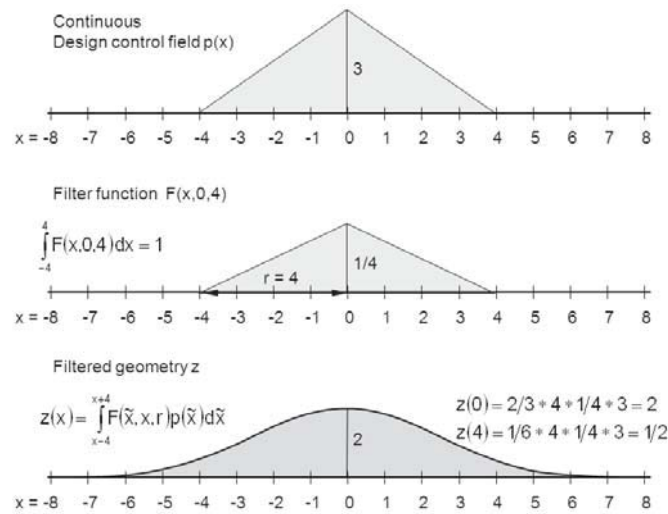


Figure 2: Cubic B-Spline by applying a linear hat-filter to a linear hat-shape design control field.

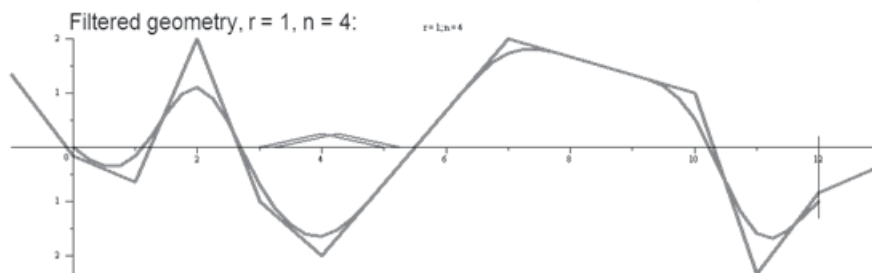


Figure 3: Convex hull and approximation property of a piecewise linear design control field.

7. Selected Example

7.1. Staggered optimization of a fiber reinforced composite shell

The shape of a bend cantilever is determined, assuming a composite shell with two layers of fiber reinforcement, Fig. 4. The filter technique has been applied to regularize the optimization of fiber orientation as well. The objective is maximum stiffness; altogether there are about 80,000 shape and fiber angle variables.

7.2. VW-Passat side mirrors.

The technique is successfully applied to all kind of structural and fluid shape optimization problems. As a representative example the shape optimization of the VW Passat side mirrors is presented which was done in close cooperation with Volkswagen and others partners of the EU-project FLOWHEAD, Figs. 5-6. The goal was to reduce the drag of the complete car by shape modifications of the mirrors only. That gives 32,000 design parameters for each mirror, i.e. 64,000 in total. A complete model of the car had to be simulated in an appropriate numerical wind tunnel using OpenFoam for CFD simulation, an adjoint solver provided by project partners, and CARAT++ for optimization which is the own optimization and structural simulation code. In further applications, the complete car body had been optimized which comes together with up to 3.5 Mio shape parameters.

5. Acknowledgements

The authors gratefully acknowledge the support of the Deutsche Forschungsgemeinschaft (DFG) under various grants as well as the support of the European Commission under THEME SST.2007-RTD-1: Competitive product development, as part of the project FLOWHEAD.

8. References

- [1] M. Hojjat, E. Stavropoulou and K.-U. Bletzinger, The vertex morphing method for node-based shape optimization, *Computer Methods in Applied Mechanics and Engineering*, 268, 494-513, 2014.
- [2] E. Stavropoulou, M. Hojjat and K.-U. Bletzinger, In-plane mesh regularization for parameter-free shape optimization problems, *Computer Methods in Applied Mechanics and Engineering*, 275, 39-54, 2014.
- [3] K.-U. Bletzinger, A consistent frame for sensitivity filtering and the vertex assigned morphing of optimal shape, *Structural and Multidisciplinary Optimization*, 49, 873-895, 2014.
- [4] M. Firl, R. Wüchner and K.-U. Bletzinger, Regularization of shape optimization problems using FE-based Parameterization, *Structural and Multidisciplinary Optimization*, 47, 507-521, 2013.
- [5] M. Firl and K.-U. Bletzinger, Shape optimization of thin walled structures governed by geometrically nonlinear mechanics, *Computer Methods in Applied Mechanics and Engineering*, 237, 107-117, 2012.

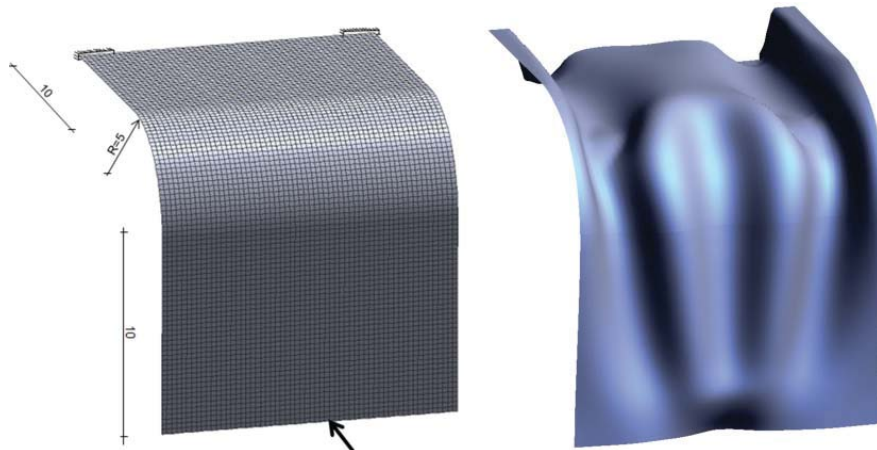


Figure 4: Staggered shape and fiber optimization of a bend cantilever. Initial shape and loading (left), optimal shape equivalent to a B-spline surface, filter size relates to the visible bead width (right).

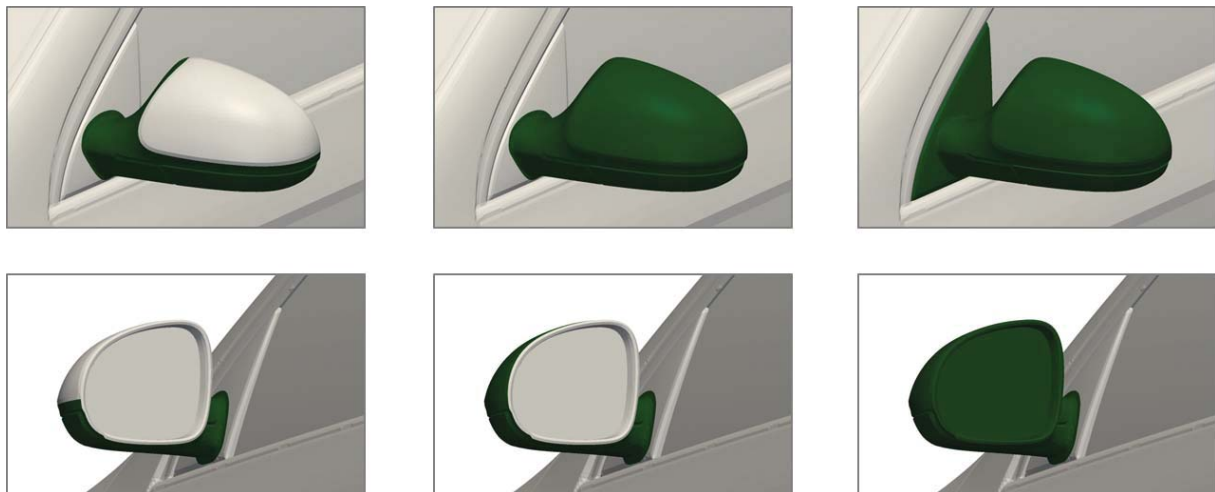


Figure 5: Selected design scenarios for the VW-Passat side mirror. The dark parts are allowed to be modified by shape optimization.

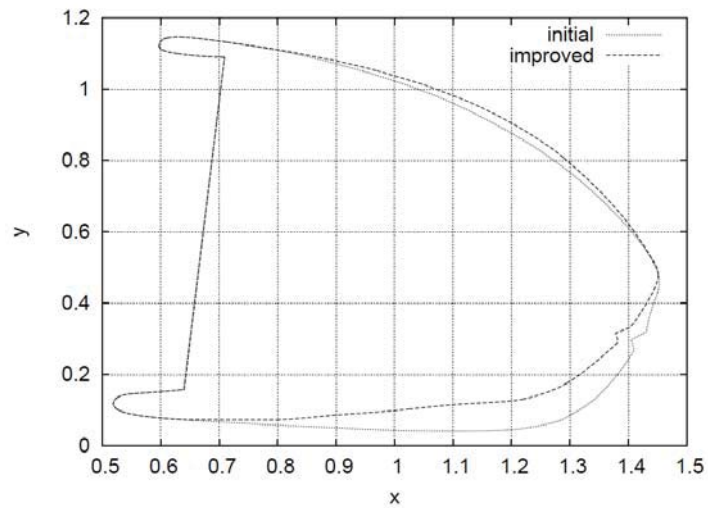


Figure 6: Shape optimization of the side mirrors for drag reduction of the complete car referring to the center column of Fig. 5. Longitudinal section of the mirror body. The shape is morphed whilst the displayed feature lines are maintained. The shape of the mirror itself (left straight line) has been constrained to guarantee the usability. Therefore, the optimizer was prevented to simply remove the mirrors to reduce drag.

Stability-ensured topology optimization of boom structures with stress constraints

Wenjun Li¹, Qicai Zhou¹, Zhen Jiang², Wei Chen²

¹ Tongji University, Shanghai, China, wenjun.li.nu@gmail.com, qczhou@tongji.edu.cn

² Northwestern University, Evanston, USA, ZhenJiang2015@u.northwestern.edu, weichen@northwestern.edu

1. Abstract

The use of giant boom cranes has gained an ever-increasing popularity due to their superior handling abilities. Lightweight design of a giant boom structure, which is usually achieved by topology optimization, becomes critical in reducing the energy consumption of the whole crane. In topology optimization of giant boom structures, geometrically nonlinear analysis has been adopted to capture the accurate structural response. A common issue is that the stiffness of some members keeps decreasing during the optimization process, which is often a generator of some slender struts leading to buckling issue. Therefore, a stability-ensured topology optimization algorithm for structural design is needed to maintain sufficient stability of boom structures while reducing the weight.

The stability performance is studied either as a constraint or as an objective in topology optimization problems [1]. The evolutionary structural optimization (ESO) method was extended to linear buckling problems, and a simple method not involving variational calculus or Lagrangian multipliers was presented for the optimum design of columns and frames [2]. Kemmler et al. [3] considered the lowest critical load level as an inequality constraint and conducted topology optimization of structures including kinematics. The design problem of maximizing the buckling load factor of laminated composite shell structures was investigated using the discrete material optimization approach [4-6]. Lindgaard and Dahl [7] investigated a range of different compliance and buckling objective functions for maximizing the buckling resistance of a snap-through beam structure. The gradient-based optimization methods have been widely applied in many stability constrained problems, but they are not appropriate for topology optimization problems with large number of local stability constraints due to difficulties in calculating the sensitivities of numerous constraints with respect to each of the design variables.

In the presence of aforementioned drawbacks of gradient-based methods, non-gradient-based methods are put forward to provide a convenient way for topology optimization of geometrically nonlinear boom structures. Although non-gradient nature-inspired methods are not viable alternatives for the vast majority of topology optimization problems, they actually solve discrete topology optimization problems with surprisingly high efficiency [8]. For example, the Soft Kill Option (SKO) method is a heuristic topology optimization method based on the simulation of the biological growth rule of biological growth carriers like bones [9]. It reduces human error to a minimum, and even in really complex cases makes it possible for the first time to find a draft design that is already close to the optimum [10]. Even though sensitivity analysis is not used, the results obtained with the SKO method are very similar to those by gradient-based methods using OptiStruct [11, 12]. Our previous work [13] extended the SKO method into topology optimization of bars structures and sets the foundation for this research.

A couple of member buckling judgment methods for bars structures have been presented in recent years. Shen et al. [14] proposed a middle plastic hinge model of the member, assuming that the member is in a completely elastic deformation condition before buckling. Fan et al. [15] adopted the curve of axial force-relative deflection of the member and the energy method to judge the member buckling. To better monitor the stability of the structure, global stability index (GSI) and compression member stability index (MSI) are defined in this paper. The global stability constraint can be easily formulated by GSI, while member buckling of any compression member can be detected by MSI. Apart from stability, the volume and stress should also be taken into consideration in topology optimization of boom structures so that the topology design is close to industrial application. However, it is very difficult to find optimization algorithms for discrete problems that can treat multiple non-trivial constraints [8]. The traditional volume constraint always conflicts with global stability and stress constraints, thus the predetermined target volume fraction may not be achieved. Adaptive volume constraint algorithm is proposed by Lin and Sheu [16] so that the maximum stress in the optimal structural configuration is guaranteed to be below the predefined stress limit.

The stability indices are utilized as a part of a novel Stability-Ensured Soft Kill Option (SSKO) algorithm, which is a heuristic topology optimization approach proposed in this work on the basis of the existing SKO method. The objective is to minimize the discrepancy between structural volume and predetermined target volume, while the global stability, member stability and stress are regarded as constraints. To demonstrate the effectiveness of the proposed approach, the SSKO algorithm with different scenarios is applied to topology optimization of a ring crane boom, and stable topologies are achieved with high efficiency and consistency.

2. Keywords: boom structures, topology optimization, stability index, Stability-Ensured Soft Kill Option, geometric nonlinearity

3. Stability indices

3.1. Global stability index

For a static structure, the overall stiffness can be defined as the slope of load-displacement curve of a certain position at the last convergence incremental step, represented by S_g . A positive S_g infers a stable structure, while S_g decreases to zero or a negative number when the structure becomes global buckling. In the process of topology optimization, we need to quantitatively express the global stability status for monitoring the global stability constraint, and the global stability index (GSI) is defined as

$$GSI^{(k)} = S_g^{(k)} / S_g^{(0)}, \quad k = 0, 1, \dots, k_{\max} \quad (1)$$

where k is the indicator of iteration number, $k=0$ means the initial analysis of the structure, and k_{\max} is the maximum number of iterations. $GSI^{(k)}$ is the global stability index in the k -th iteration, and $S_g^{(k)}$ denotes the overall stiffness of the structure in the k -th iteration. $GSI^{(0)}$ is equal to 1 if the whole structure is stable in the initial analysis. Similar to the overall stiffness, a positive GSI infers a stable structure, while it decreases to zero or a negative number when the structure becomes global buckling.

3.2. Compression member stability index

Fig.1 shows the deformation of a compression member in the global coordinate system O - XYZ . AB is the initial configuration before deformation and $A'B'$ is the configuration after deformation. All the non-end loads have been converted to the end loads, such as gravity load and wind load. Two local coordinate systems, the member coordinate system A' - xyz and the member end coordinate system B' - $x_o y_o z_o$, are defined as follows. In the member coordinate system: the direction of vector $\overline{A'B'}$ (pointing from A' to B') is defined as $+x$ direction, $+y$ direction is parallel to plane XY and its angle with $+Y$ is smaller than or equal to 90° ; in the case when axial x is parallel to axial Z , axial y is defined to be parallel to axial Y . In the member end coordinate system, the outward tangential direction at B' is defined as $+x_o$ direction, $+y_o$ direction is parallel to plane XY and its angle with $+Y$ is smaller than or equal to 90° ; similarly to the member coordinate system, when axial x_o is parallel to axial Z , axial y_o is defined to be parallel to axial Y . Both local coordinate systems are right-handed and depend on the configuration after deformation. The loading condition at the end B' is expressed in the member end coordinate system (Fig.1). They are three force components $F_{x_o}, F_{y_o}, F_{z_o}$ and three bending moments $M_{x_o}, M_{y_o}, M_{z_o}$.

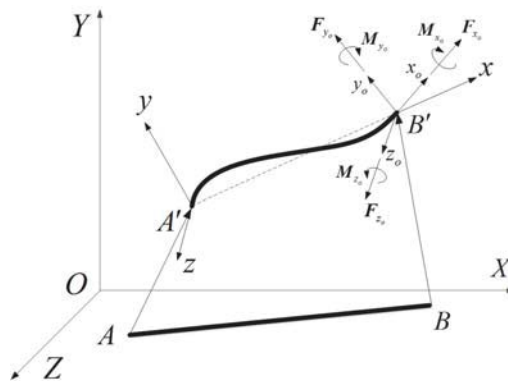


Figure 1: Deformation of a compression member

The axial vector of member AB after deformation is

$$\mathbf{a} = \overline{A'B'} \quad (2)$$

The three force components $F_{x_o}, F_{y_o}, F_{z_o}$ are projected onto the axial vector, and the projection sum is the axial force of member AB after deformation

$$F_a = (\mathbf{F}_{x_o} + \mathbf{F}_{y_o} + \mathbf{F}_{z_o}) \cdot \mathbf{a} / \|\mathbf{a}\| \quad (3)$$

where $\| \cdot \|$ denotes the module of a vector, similarly hereinafter; a positive value of F_a means tension while a negative value means compression.

The relative axial displacement between the ends of member AB is written as

$$\Delta u = \|a\| - \|AB\| \quad (4)$$

A positive value of Δu means elongation while a negative value means shortening.

For any member AB in a frame structure, its axial stiffness at time t can be defined as

$${}^t S_a = ({}^t F_a - {}^{t-\Delta t} F_a) / ({}^t \Delta u - {}^{t-\Delta t} \Delta u) \quad (5)$$

Here $t - \Delta t$ is the time with a tiny time period Δt difference prior to time t .

According to the definition of stability of compression members, when the axial compression force begins to decline and the absolute value of the relative axial displacement is still increasing, this member is buckling. In other words, a compression member is buckling when its ${}^t S_a$ value changes from a positive number to a negative number. Hence, capturing the changes of axial stiffness can help judge whether a compression member is unstable. This judgment method is applicable to the elastic or elastoplastic, limit point, flexural or flexural-torsional buckling of compression member considering only the end forces.

In the optimization process, we can quantitatively evaluate the compression member stability status by the MSI defined as

$$MSI_{(j)}^{(k)} = S_{a(j)}^{(k)} / S_{a(j)}^{(0)}, \quad k = 0, 1, \dots, k_{\max} \quad (6)$$

where $MSI_{(j)}^{(k)}$ is the stability index of member j in the k -th iteration. $S_{a(j)}^{(k)}$ denotes the axial stiffness of member j in the k -th iteration, which is determined in Eq. (5). It is equal to 1 if member j is stable in the initial analysis. When $MSI_{(j)}^{(k)}$ decreases to zero or a negative value, the compression member j buckles.

4. Optimization procedure

4.1. Formulation of the optimization problem

The stability-ensured topology optimization of boom structures with volume and stress considerations can be formulated as follows:

$$\begin{aligned} & \text{find} && \mathbf{E} = (E_1, E_2, \dots, E_n)^T \\ & \text{min} && \left| \sum_{j=1}^n (v_{oj} E_j / E_{\max}) - V_o \times v_{\text{target}}^f \right| \quad (j = 1, 2, \dots, n) \\ & \text{s.t.} && GSI > 0 \\ & && MSI_{(j)} > 0 \quad (j = 1, 2, \dots, n) \\ & && \sigma_{\max} \leq [\sigma] \\ & && E_{\min} \leq E_j \leq E_{\max} \quad (j = 1, 2, \dots, n) \end{aligned} \quad (7)$$

Where E_j is the Young's modulus of member j ($j = 1, 2, \dots, n$), v_{oj} is the initial volume of member j , $\sum_{j=1}^n (v_{oj} E_j / E_{\max})$ denotes the total volume of design domain, V_o is the total volume of initial structure in a design domain and v_{target}^f is the predetermined target volume fraction. GSI is the global stability index defined in Eq. (1), σ_{\max} is the maximum stress, and $[\sigma]$ is the allowable stress. E_{\min} and E_{\max} are the lower and upper bounds of Young's modulus, respectively.

4.2. SKO method for bars structures

The SKO method has been used to obtain the optimal design of linear bars structures [13]. Using this method, once the maximum stress and reference stress of bars are obtained after finite element analysis, the temperature index of each bar is calculated by Eqs.(8)-(10) [9, 13]. The temperature index has no definite physical meaning, which is an intermediate variable bridging the stress to the Young's modulus.

$$T_j^{(k)} = T_j^{(k-1)} - s_j^{(k)} (\sigma_j^{(k-1)} - \sigma_{\text{ref}(j)}^{(k)}) \quad (8)$$

$$T_j^{(k-1)} = \begin{cases} 100 & T_j^{(k-1)} \geq 100 \\ 0 & T_j^{(k-1)} \leq 0 \\ T_j^{(k-1)} & \text{otherwise} \end{cases} \quad (9)$$

$$s_j^{(k)} = T_0 / \sigma_{ref(j)}^{(k)} \quad (10)$$

where $\sigma_j^{(k-1)}$ is the maximum stress of member j in the $(k-1)$ -th iteration, and $\sigma_{ref(j)}^{(k)}$ is the reference stress of member j in the k -th iteration. The reference stress equals either the average stress of all bars or the average stress of member j and its adjacent bars in a design domain. In general, the optimization process convergences faster by using the latter one as the reference stress, which is thus applied in this paper. $s_j^{(k)}$ is the step factor of member j in the k -th iteration. $T_j^{(k)}$ denotes the temperature index of member j in the k -th iteration, which has a linear relationship with the Young's modulus. $T_j^{(0)} = 0$ and $T_0 = 100$. According to Eqs.(8)-(10), if $\sigma_j^{(k-1)}$ is higher than $\sigma_{ref(j)}^{(k)}$, the temperature index of member j will be reduced and its Young's modulus will be increased; otherwise, the Young's modulus of member j will be reduced. When $T_j^{(k-1)} \leq 0$, $E = E_{max}$ is the real material Young's modulus. When $T_j^{(k-1)} \geq 100$, $E = E_{min} = E_{max} / 1000$ [9].

4.3. Proposed Stability-Ensured Soft Kill Option (SSKO) algorithm

This paper proposes a novel SSKO algorithm based on the SKO method for bars structures and stability indices. The SSKO algorithm is divided into three stages: initial analysis, preliminary optimization, and stability-ensured optimization, shown in Fig.2. Superior to other algorithms, SSKO detects the buckling chord members through MSI and subsequently freezes them and their relative web members during the stability-ensured optimization stage. The relative bracing system [17] is the most common bracing system applied in large scale three-dimensional frame structures, especially in boom structures. Fig.3 shows the initial structure of a typical standard section of boom structures, which is composed of chord members and web members. The exterior web members are located at the six outer surfaces of a standard section, and the other web members are interior web members. In order to reinforce the buckling chord members identified though MSI, we present a technique of “freeze”, which means that Young's modulus is set to the true value of the real material and cannot be modified. When a chord member is judged to be buckling we will first freeze itself and its exterior relative members (Fig.4(a)), then in the following iteration if the chord member is judged to be buckling again we will freeze its interior relative members (Fig.4(b)). A growth factor of the reference stress is introduced as a step function with respect to the iteration number to optimize the structure to have a volume close to the predefined target. All details will be explained in the following.

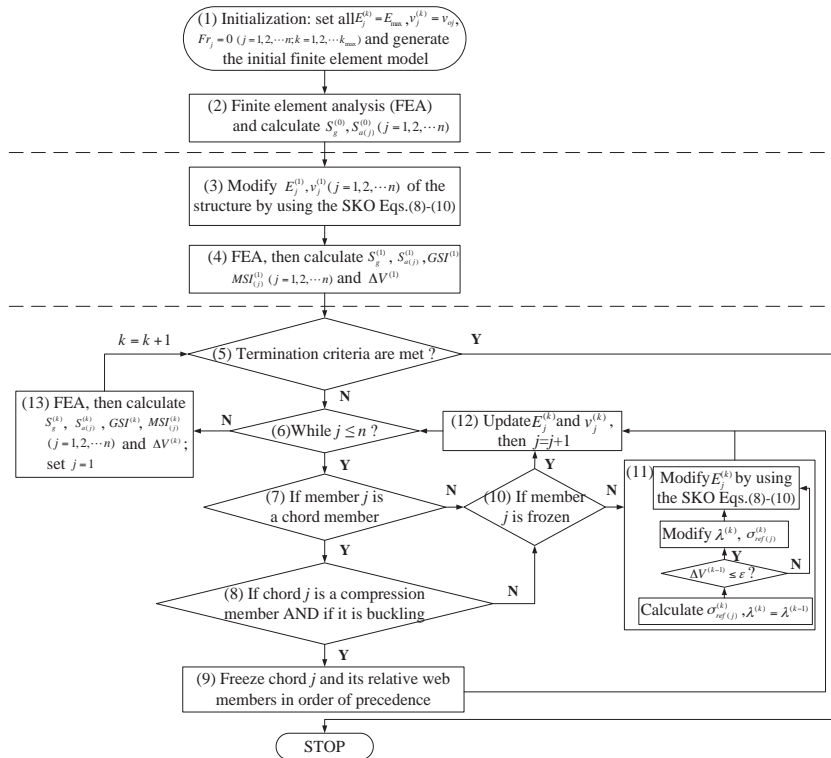


Figure 2: Flow chart of the SSKO algorithm

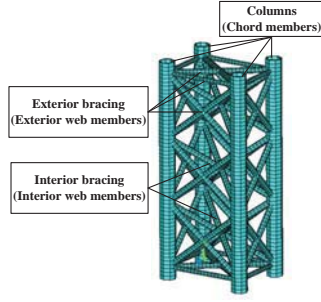


Figure 3: Initial structure of a standard section

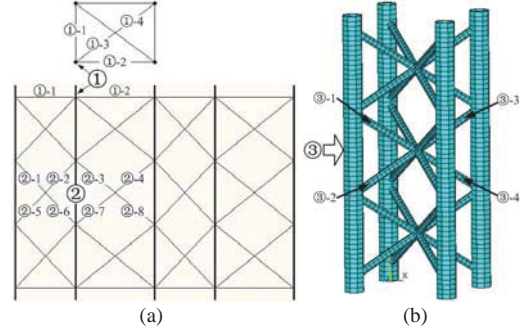


Figure 4: The relative members of a chord member

In the initial analysis stage (STEPS 1-2), this algorithm defines an initial finite element model and conducts geometrically nonlinear analysis, then calculates the overall stiffness $S_g^{(0)}$ and the axial stiffness of each compression member (Eq. (5)). $F_{r_j} = 0$ means that member j is not frozen, and $F_{r_j} = 1$ means member j is frozen.

In the preliminary optimization stage (STEPS 3-4), the Young's modulus of each member is modified by the SKO Eqs. (8)-(10) directly, then the finite element analysis of the structure is carried out. Afterwards, the overall stiffness, the axial stiffness of compression members, GSI, MSI and the total volume change are calculated as the references of subsequent iterations. The stability-ensured optimization stage (STEPS 5-13) is the key part.

STEP 5: If any of the following criteria (Eqs. (11)-(14)) is met, stop the procedure. Otherwise, move to STEP 6.

$$\Delta V^{(k-1)} = |V^{(k-1)} - V^{(k-2)}| \leq \varepsilon \quad \text{and} \quad \Delta V^{(k-2)} = |V^{(k-2)} - V^{(k-3)}| \leq \varepsilon \quad (11)$$

$$v_f^{(k-1)} \leq v_f^{\text{target}} \quad \text{and} \quad \Delta V^{(k-1)} \leq \varepsilon \quad (12)$$

$$\sigma_{\max}^{(k-1)} \geq [\sigma] \quad (13)$$

$$k > k_{\max} \quad (14)$$

In Eq. (11), the tolerance of total volume change ε is a sufficiently small positive real number. The total volume change among the last three iterations should be lower than ε . The volume fraction in the last iteration reaches the target volume fraction and the total volume change in the last iteration is lower than the tolerance, as shown in Eq. (12). Generally, the total volume change is required to be equal to zero in order to get a topology with the steady distribution of Young's modulus. The maximum stress in the last iteration is greater than the allowable stress (Eq. (13)). The maximum iteration number k_{\max} is a sufficiently large positive integer. If the iteration number k becomes larger than k_{\max} , the procedure terminates.

STEP 6-STEP12: Check all members in a design domain one by one, and update the Young's modulus of each member. STEP 8 is to judge whether chord j is buckling by Eq. (6), and STEP 9 is to freeze chord j and its relative web members. If member j is not frozen, its Young's modulus can be modified by the SKO Eqs. (8)-(10). The reference stress $\sigma_{ref(j)}^{(k)}$ in the SKO equations should be raised by Eqs. (15)-(17) to make the structure to be close to the target volume fraction if the total volume change in the last iteration is lower than ε .

$$\sigma_{ref(j)}^{(k)} = \sigma_{ref(j)}^{(k-1)} \lambda^{(k)} \quad (15)$$

$$\lambda^{(k)} = \lambda^{(k-1)} + \Delta \lambda^{(k)} \quad (16)$$

$$\Delta \lambda^{(k)} = \frac{1 - v_f^{(k-1)}}{1 - v_f^{\text{target}}} \Delta \lambda_{\max} \quad (17)$$

Here, $\lambda^{(k)}$ denotes the growth factor of the reference stress, and $\lambda^{(0)} = 1$. $\Delta \lambda^{(k)}$ means the increment of the growth factor, and $\Delta \lambda_{\max}$ is the maximum increment of the growth factor in each iteration, such as $\Delta \lambda_{\max} = 0.15$. When the volume fraction of the structure becomes closer to the target volume fraction, the increment of the growth factor gets larger.

The modified reference stress may be larger than the allowable stress sometimes, so this procedure records the original reference stress $\sigma_{ref}^{\text{origin}} = \sigma_{ref(j)}^{(k)}$, then adjusts the reference stress and the growth factor by Eqs. (18)-(19).

$$\sigma_{ref(j)}^{(k)} = [\sigma] \quad (18)$$

$$\lambda^{(k)} = [\sigma] / \sigma_{ref}^{\text{origin}} \quad (19)$$

STEP 13: Execute FEA, then calculate $S_g^{(k)}$, $S_{a(j)}^{(k)}$, $GSI^{(k)}$, $MSI_{(j)}^{(k)}$ ($j = 1, 2, \dots, n$) and $\Delta V^{(k)}$. Reset $j = 1$, go back to STEP 5.

5. An illustrative example

A 45.5m-long combined boom of 2500-tonne ring crane (see Fig.5) is studied as an illustrative example. All the twelve standard sections are replaced by typical standard sections (Fig.3 and Fig.6). Considering the symmetry of the combined boom, only half structure is analyzed. Fig.7 shows the finite element model of the half-boom. The left part of Fig.7 is the view of the luffing plane (XY plane), and the right part is the view of the swing plane (YZ plane). The range of the boom is 10m (“range” refers to the horizontal distance between the center of boom foot pins and boom tip pins), a lifting load $F_Q=14320000\text{N}$ is applied at the lifting point, and a +X direction wind load $F_W=26778\text{N}$ is uniformly distributed on end points of chord members of standard sections.

To improve the calculation efficiency, the plate structures at the ends of the boom are simplified as rigid bars, which belong to non-design domain. At the top of boom, only the Z-axis rotational and Y-axis translational degrees of freedom are released. At the bottom of boom, only the Z-axis rotational degree of freedom is released. At the symmetry plane of the whole combined boom, the Z-axis translational degree of freedom is constrained.

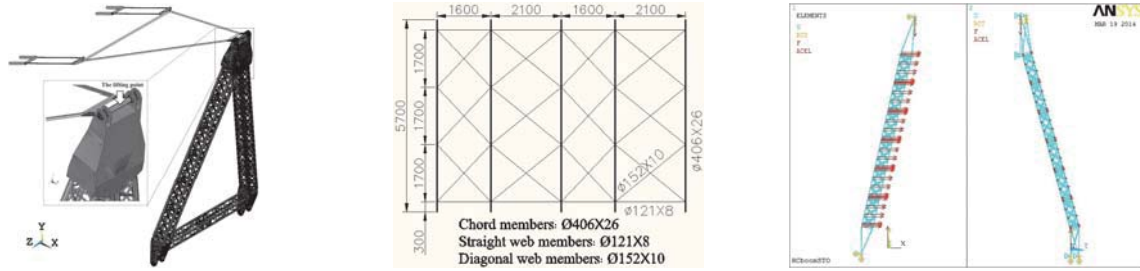


Figure 5: A 45.5m boom structure Figure 6: Dimensions of standard section Figure 7: FE model of half-boom

Three scenarios are applied in the topology optimization of this boom structure, and their performances are listed in Table 2. We make $\Delta\lambda_{\max}$ equal a large number in scenario 2-1, intentionally to get a fast convergence speed, but it turns out not to be the case. Fig.8 is the optimization results using scenario 2-1 (The layout of Fig.8(a) and Fig.9 is the same as Fig.7). It is obvious that this topology is not the optimal solution because the stress of most retained members is lower than 380MPa and the maximum stress which is above 500MPa happens at a local connection area (see Fig.8(a)). Fig.8(b) shows that the maximum stress begins to fluctuate divergently from the 40th iteration and goes beyond the allowable stress in the 141st iteration resulting in termination of optimization process. The GSI decreases to a minimum of 0.5465 in the 139th iteration but the structure still keeps in a stable state. The volume fraction also begins to fluctuate divergently from the 40th iteration as a result of the growth factor of the reference stress λ exceeding 2.5. When the growth factor becomes large, the reference stress gets an enormous growth at each step that leads to a sharp decrease of the volume fraction (Eq. (8)). It means that a considerable portion of material is removed which usually causes the occurrence of stress concentration (see Fig.8(a)). The maximum stresses of many members become higher than the reference stress in the subsequent iterations, so the volume fraction increases after its significant decrease. It has also been demonstrated by other case studies we conducted that under most circumstances λ should not be larger than 2.5 in order to ensure the stability of optimization.

Table 1: The performances of SSKO algorithm in boom structure problem

Scenario	v_{target}^f	$\Delta\lambda_{\max}$	$[\sigma]$	GSI	Volume fraction	Max. stress	No. of Iterations
2-1	0.5	0.90	500	0.8969	0.8163	571.14	141
2-2	0.5	0.30	500	0.9860	0.7823	173.68	84
2-3	0.5	0.15	500	0.9860	0.7823	173.68	129

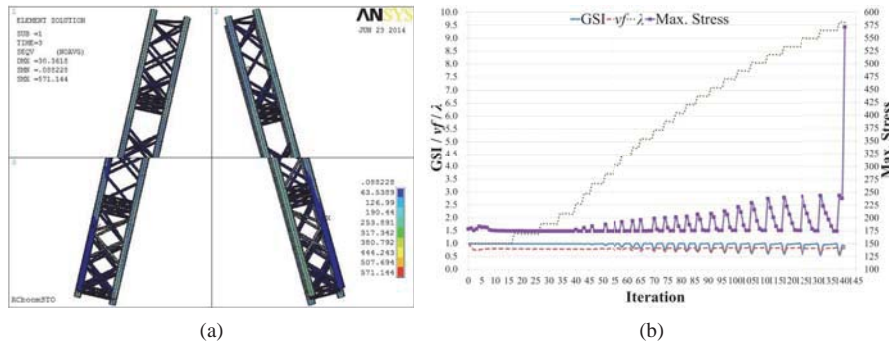


Figure 8: Optimization results by scenario 2-1 (a) von Mises stress (b) Convergence history

The maximum increment of the growth factor is reduced in scenarios 2-2 and 2-3 to make the optimization process more stable. The optimization results (see Fig.9) are the same by either scenario 2-2 or 2-3, which justifies the proposed SSKO algorithm. Fig.10 shows the convergence histories of the SSKO algorithm in boom structure problem by strategies 2-2 and 2-3 respectively. The procedures converge after several step growths of λ , and the scenario 2-2 has a higher optimization efficiency than the scenario 2-3. The anti-buckling mechanism works well since the GSI keeps at around 1. The volume fraction decreases to 0.7823 and the maximum stress becomes 173.68MPa eventually.

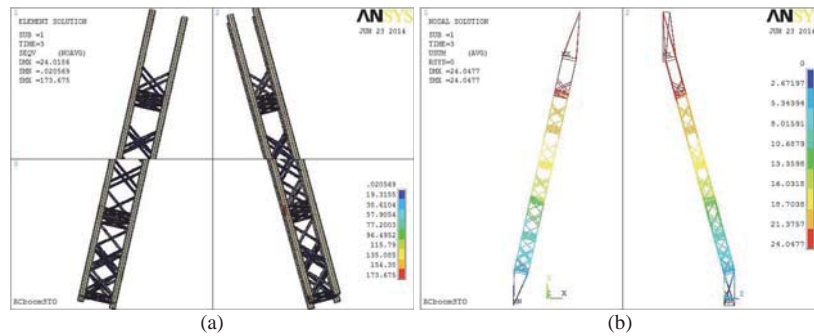


Figure 9: Optimization results by either scenario 2-2 or 2-3 (a) von Mises stress (b) displacement

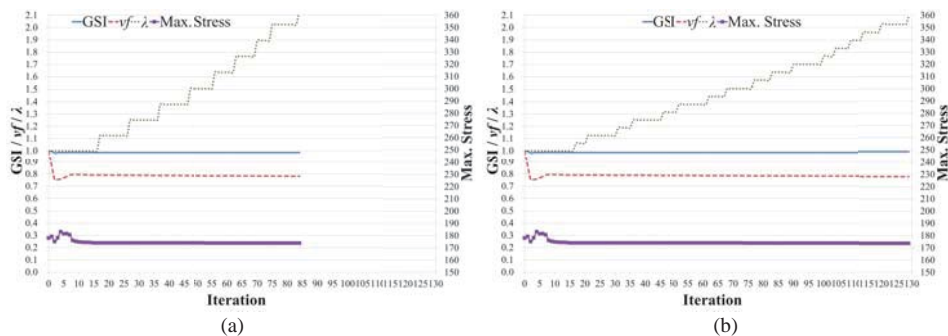


Figure 10: Convergence histories of SSKO algorithm by scenarios (a)2-2 (b)2-3, respectively

The SSKO algorithm reduces the total volume significantly and gives a stable optimal design with the maximum stress being lower than the predetermined stress limit as long as we select an appropriate maximum increment of the growth factor. This example also demonstrates the high efficiency since it convergences to the same result through only a few dozens of iterations.

6. Conclusions

This paper presents a Stability-Ensured Soft Kill Option (SSKO) algorithm for structural topology design of geometrically nonlinear boom structures including stress constraints. This algorithm is developed for bars structures with large number of constraints by employing the proposed global stability index (GSI), compression member stability index (MSI) and the knowledge of bracing systems for resisting buckling of columns. The MSI can be used to distinguish the buckling of almost any kinds of compression members in boom structures. The results of the boom structure problem indicates that an appropriate maximum increment of the growth factor plays a crucial role in converging to the optimal design. The consistent optimization results using different scenarios

demonstrate the applicability of the SSKO algorithm. The proposed algorithm can be applied to optimize other boom structures with different layout of web members as long as we develop a proper freezing strategy for the specific initial structure.

7. Acknowledgements

Funding for this research was provided by the National Natural Science Foundation of China (NSFC) under award number 51375345. Financial support for the first author, Wenjun Li, was provided in part by the China Scholarship Council.

8. References

- [1] O. Makoto and I. Kiyohiro, *Stability and optimization of structures generalized sensitivity analysis*, Springer, New York, 2007.
- [2] D. Manickarajah, Y. M. Xie and G. P. Steven, Optimisation of columns and frames against buckling, *Computers & Structures*, 75(1), 45-54, 2000.
- [3] R. Kemmler, A. Lipka and E. Ramm, Large deformations and stability in topology optimization, *Structural and Multidisciplinary Optimization*, 30(6), 459-476, 2005.
- [4] E. Lund, Buckling topology optimization of laminated multi-material composite shell structures, *Composite Structures*, 91(2), 158-167, 2009.
- [5] E. Lindgaard and E. Lund, Nonlinear buckling optimization of composite structures, *Computer Methods in Applied Mechanics and Engineering*, 199(37-40), 2319-2330, 2010.
- [6] E. Lindgaard and E. Lund, A unified approach to nonlinear buckling optimization of composite structures, *Computers & Structures*, 89(3-4), 357-370, 2011.
- [7] E. Lindgaard and J. Dahl, On compliance and buckling objective functions in topology optimization of snap-through problems, *Structural and Multidisciplinary Optimization*, 47(3), 409-421, 2013.
- [8] O. Sigmund and K. Maute, Topology optimization approaches A comparative review, *Structural and Multidisciplinary Optimization*, 48(6), 1031-1055, 2013.
- [9] A. Baumgartner, L. Harzheim and C. Mattheck, SKO (Soft Kill Option) - The biological way to find an optimum structure topology, *International Journal of Fatigue*, 14(6), 387-393, 1992.
- [10] C. Mattheck, *Design in nature: learning from trees*, Springer-Verlag, Berlin, New York, 1998.
- [11] L. Harzheim and G. Graf, A review of optimization of cast parts using topology optimization - I - Topology optimization without manufacturing constraints, *Structural and Multidisciplinary Optimization*, 30(6), 491-497, 2005.
- [12] L. Harzheim and G. Graf, A review of optimization of cast parts using topology optimization - II - Topology optimization with manufacturing constraints, *Structural and Multidisciplinary Optimization*, 31(5), 388-399, 2006.
- [13] W. Li, Q. Zhou, X. Zhang et al., Topology optimization design of bars structure based on SKO method, *Applied Mechanics and Materials*, 394(1), 515-520, 2013.
- [14] Z. Shen, C. Su and Y. Luo, Application of Strut Model on Steel Spatial Structure, *Building Structure*, 37(1), 8-11, 2007. [In Chinese]
- [15] F. Fan, J. Yan and Z. Cao, Stability of reticulated shells considering member buckling, *Journal of Constructional Steel Research*, 77, 32-42, 2012.
- [16] C. Y. Lin and F. M. Sheu, Adaptive volume constraint algorithm for stress limit-based topology optimization, *Computer-Aided Design*, 41(9), 685-694, 2009.
- [17] American Institute of Steel Construction (AISC), *Specification for Structural Steel Buildings* ANSI/AISC 360-10, Chicago, AISC, 2010.

Elimination of void element influence on optimization for nonlinear compliance with a buckling constraint using moving iso-surface threshold method

Liyong Tong¹, Quantian Luo²

¹ School of Aerospace, Mechanical and Mechatronic Engineering, The University of Sydney, Sydney, NSW 2006, Australia, liyong.tong@sydney.edu.au

² School of Aerospace, Mechanical and Mechatronic Engineering, The University of Sydney, Sydney, NSW 2006, Australia, quantian.luo@sydney.edu.au

Abstract

This article presents an algorithm that eliminates some of the adverse influences of the void elements used in nonlinear structural topology optimization with a buckling constraint by using moving iso-surface threshold (MIST) method. The basic idea of this algorithm is to conduct the finite element analysis in a sub design domain with solid and grey elements and to construct each updated response function in the full design domain. In this algorithm, void elements are excluded in all the finite element analyses but included in design variable update. In doing so in MIST, the material removed with void elements can reappear. In the present study, the strain energy density at the final state in a nonlinear finite element analysis is selected as the response function in MIST to minimize the nonlinear compliance, and the iso-surface threshold value is determined by using a prescribed volume constraint and then used to define optimal topology containing solid materials only. Exclusion of void elements in all the finite element analyses allows avoidance of several numerical issues, such as material reappearance, discontinuous design and numerical instability encountered in topology optimization for structures, in particular, with large displacements. In the present algorithm, a buckling constraint is also introduced to consider the influence of load level on nonlinear topology optimization.

Keywords: optimization, nonlinearity, void element, numerical stability, buckling constraint

1. Introduction

It is known that the inclusion of large displacements in topology optimizations, for example, to minimize the structural compliance, can significantly affect the final designs and serious numerical issues were encountered in nonlinear topology optimizations owing to the use of void elements [1-6]. These issues include: 1) the geometrically nonlinear finite element analysis (FEA) is hardly convergent to the full level of an applied loading state due to excessively large displacements caused by rather low stiffness of the void elements; 2) the convergence is poor as the excessively large displacements cause mesh distortions which in turn deteriorate the displacement fields; and 3) numerical instabilities can occur in a localized region with a cluster of void elements so that the obtained topology may not be well defined and practical. Therefore, an adequate treatment of the void elements is essential in order to effectively conduct topology optimization for geometrically nonlinear structures.

A number of methods have been proposed to attempt to circumvent the influences of void elements in topology optimization problem to minimize nonlinear compliance. One direct approach to completely solve the issues is to remove all void elements. However, this creates other issues, e.g. material reappearance, disconnected or disjointed structure and design domain re-meshing. This study aims to develop an effective algorithm that resolves these issues by excluding all void elements in FEA and including all of them in design updates.

As the optimum topology obtained via minimizing the nonlinear compliance can be highly dependent on the level of the applied loads, in this paper, we propose a novel algorithm by introducing a buckling constraint in which the applied load varied with iteration is constrained by the critical buckling factor. This is because buckling is one of the most serious structural failure mechanisms, particularly for the optimized structures as they are often thin-walled, therefore the introduction of the buckling constraint in general form is also important in topology optimization.

For topology optimization problems involving buckling, there also exist severe numerical difficulties due to the adverse effects of low density and void elements [7-13]. In the present novel algorithm, these adverse influences can also be eliminated effectively via the exclusion and inclusion of all void elements in FEA and design updates.

2. Problem statement

Let us consider the minimum mean compliance problem for nonlinear structures. To use MIST [14], the nonlinear compliance needs to be expressed in an integral form. When the external loads are expressed as a

function of time t_n and the total Lagrangian formulation is used to describe the equilibrium equations in $(t_n + \Delta t_n)$, the nonlinear compliance can be expressed as:

$$C = \lim_{n \rightarrow \infty} \sum_{i=1}^n (\mathbf{F}_i^T + \mathbf{F}_{i-1}^T) \Delta \mathbf{u}_{i-1} = 2 \int_0^{t_L} \mathbf{F}^T d\mathbf{u} = 2 \lim_{n \rightarrow \infty} \sum_{i=0}^{n-1} \int_{\Omega_1}^{(t_n + \Delta t_n)} S_{ij} \delta \varepsilon_{ij} d\Omega = 2 \int_{\Omega_1} \left(\int_0^{t_L} S_{ij} d\varepsilon_{ij} \right) d\Omega \quad (1a)$$

where $\{\mathbf{F}_i\}$ denotes the stress resultant vector in the state of time t_i ; \mathbf{u} is the displacement vector; t_L denotes a final equilibrium state with full loads; Ω_1 denotes design domain 1 that contains solid and grey elements only; S_{ij} and ε_{ij} are the Piola-Kirchhoff stress and the Green-Lagrange strain. For linearly elastic material, ${}^t_n S_{ij} = {}^t_n C_{ijkl} \varepsilon_{kl}$ and ${}^t_n C_{ijkl}$ is the constant tensor. Thus the nonlinear compliance can be defined as:

$$C = 2 \int_{\Omega_1} \frac{1}{2} {}^t_L S_{ij} {}^t_L \varepsilon_{ij} d\Omega \quad (1b)$$

We now define the MIST formulation for the problem of minimizing nonlinear compliance with a buckling constraint as follows:

$$\text{Minimize: } C \quad (2a)$$

$$\text{Subject to: } \begin{cases} \{\mathbf{R}(\mathbf{u}, \mathbf{x}_e)\} = 0 & \text{in } \Omega_1 \\ \sum_{e=1}^{N_s} (x_e V_e) \leq V_f V \\ \bar{\lambda}_1 \geq 1 \\ \text{Load path continuity in } \Omega_1 \\ 0 \leq x_e \leq 1 \end{cases} \quad (2b)$$

$$\Phi \text{ function: } \Phi = \begin{cases} \frac{1}{2} {}^t_L S_{ij} {}^t_L \varepsilon_{ij} & \varepsilon < x_e \leq 1 \quad \text{in } \Omega_1 \\ 0 & 0 \leq x_e \leq \varepsilon \quad \text{in } \Omega_2 \end{cases} \quad (2c)$$

where \mathbf{x}_e denotes the design variables, e.g. representing solid ($x_e = 1$), grey ($\varepsilon < x_e < 1$) and void ($0 \leq x_e \leq \varepsilon$) elements; ε is the small parameter (e.g., $\varepsilon = 10^{-3}$); V_e and V represent volumes of element e and the design domain (Ω); V_f is the prescribed volume fraction; N_s is the number of solid and grey elements in domain 1 (Ω_1); Ω_2 is domain 2 with void elements only; N_e is the total element number; Φ denotes the response function; ${}^t_L S_{ij}$ and ${}^t_L \varepsilon_{ij}$ are the Piola-Kirchhoff stress and the Green-Lagrange strain in a final state with the full load; $\{\mathbf{R}\}$ is the residual force; $\bar{\lambda}_1$ is the buckling factor of mode 1.

The residual force $\{\mathbf{R}\}$ in the equilibrium equations and the buckling factor $\bar{\lambda}_1$ are defined as:

$$\{\mathbf{R}\} = \{\mathbf{F}\} - \{\mathbf{F}_r\} \quad (3)$$

$$\bar{\lambda}_1 P_n = P_{n-1} + \lambda_{n1} \Delta P_n \quad (4)$$

where $\{\mathbf{F}\}$ is the external force vector; $\{\mathbf{F}_r\}$ denotes the stress resultant vector in the final state; F^k and u^k are the external force component and the corresponding displacement; N_F and N_L are numbers of force components and load increments; P_n represents the final state of load increments; P_{n-1} is the last 2nd load step; and λ_{n1} is the buckling factor of mode 1 due to load increment ΔP_n .

It is worth noting that equation (2b) shows that all FEA are conducted in Ω_1 and equation (2c) reveals that the response function Φ is constructed in Ω which enables design updates in full design domain.

3. An efficient MIST algorithm

The MIST involves finding and updating an iso-surface threshold value for the chosen response function subjected to a prescribed constraint. The objective function in MIST can be expressed as [14]:

$$J = \int_{\Omega} \Phi(x) H(t, \Phi(x)) d\Omega \quad (5)$$

where $\Phi(x)$ is the response function; $H(t, \Phi(x))$ is the Heaviside function: $H(t, \Phi(x)) = 1$ for every x in the set of $\Phi(x) \geq t$, and $H(t, \Phi(x)) = 0$ for x in the set of $\Phi(x) < t$; Ω represents the full design domain. When the threshold level t is determined, the design variable x is defined by:

$$\begin{cases} \Phi(x) \geq t & \Leftrightarrow x = 1 \\ \Phi(x) < t & \Leftrightarrow x = 0 \end{cases} \quad (6)$$

where $x = 1$ and $x = 0$ represent solid and void at location x .

In the finite element based optimization, the response function is constructed using the nodal physical quantities and the material density x_e ($e = 1, 2 \dots N_e$) defined by the fraction of the solid material in element e are used as the design variables. At iteration k , $(x_e)_k^{(1)} = 1$ if $\Phi_k \geq t_k$ at all nodes of element e ; $(x_e)_k^{(1)} = 0$ if $\Phi_k < t_k$ at all nodes and $(x_e)_k^{(1)} = A_{epj} / A_e$ when $\Phi_k \geq t_k$ at some nodes, where A_{epj} is the project area of the $\Phi(t_k)$ ($\geq t_k$) within the element. The design variables are updated by:

$$\{\mathbf{x}_e\}_k^{(2)} = \{\mathbf{x}_e\}_{(k-1)} + k_{mv} (\{\mathbf{x}_e\}_k^{(1)} - \{\mathbf{x}_e\}_{k-1}) \quad (7)$$

$$(x_e)_k^{(3)} = \begin{cases} (x_e)_k^{(2)} & (x_e)_k^{(2)} > \varepsilon \\ 0 & (x_e)_k^{(2)} \leq \varepsilon \end{cases} \quad (e = 1, 2, \dots, N_e) \quad (8)$$

where k_{mv} is the move limit and $0 \leq k_{mv} \leq 1$.

A distinctive feature of the present MIST algorithm is the use of two meshes that facilitate element removal and reappearance easily. One mesh is fixed for the full design domain Ω used for constructing the Φ function and determining design variable updates, and the other is dynamic denoted Ω_1 with solid and grey elements only for conducting all FEA. As all void elements are excluded in the FEA, thus the associated adverse effects are completely eradicated. The re-meshing issue can be solved by renumbering the elements in Ω_1 and the material reappearance is automatically realized by using equations (2c), (7) and (8). Another feature of the MIST algorithm is that it can be easily interfaced with any commercially available FEA software. In this study, the MIST algorithm is interfaced with NASTRAN.

4. A MIST algorithm for including a buckling constraint

It is known that the topology optimization of geometrically nonlinear structures can rely on the magnitude of an applied load. This raises an issue which one is the optimal topology in a topology design optimization. We propose that the topology obtained by the maximum load without causing buckling be the optimum one. This can be defined by applying the buckling constraint as given in Eq. (2b).

By using the MIST, the optimization can be conducted by applying load:

$$P_k = \bar{\lambda}_1^{k-1} P_{k-1} \quad (9)$$

where P_{k-1} and P_k are the applied loads at iteration $(k-1)$ and k ; $\bar{\lambda}_1^{k-1}$ is the buckling factor in equation (4) at iteration $(k-1)$.

As discussed in [9, 15], an accurate calculation of a linear buckling factor can be very difficult in topology optimization due to the impact of low density and void elements. It is even more difficult to accurately calculate the nonlinear buckling factor, as indicated by equation (4). Hence it is evident that the removal of all void elements is of paramount importance in solving design optimization problem, such as to minimize nonlinear structural compliance. An approach for the removal of void elements and material reappearance in MIST has been developed to minimize the nonlinear compliance of a structure with material and geometric nonlinearities [16]. This method is extended in this study to the topology optimization for minimum nonlinear compliance with the buckling constraint as the optimal design depends on the magnitude of the applied load.

When the material nonlinearity is not considered, the linear buckling factor may be used to reduce the computational cost as it is usually slightly larger than the nonlinear buckling factor, and hence it is used in this study for simplicity. When there is no buckling mode in an optimal structure, the maximum stress constraint may be introduced to obtain the optimal topology for the nonlinear compliance. In the early iterations, the buckling factor may be sharply altered due to the effects of low density elements. In practical computations, the buckling constraint can be introduced after certain number of iteration. In all the present computation, the buckling constraint is applied when the removal of void elements commences.

3. Numerical results and discussion

Numerical results are presented for the two samples shown in Figure 1 to illustrate the effectiveness of the present MIST algorithm for topology optimization of geometrically nonlinear structures.

3.1 Optimization for a specific load

Sample 1 of Figure 1(a) was studied in [17-19]. The data given in Figure 1(a) are the same as those in [19]. When $F = 2$ MN, the optimal topologies obtained by using the present algorithm are illustrated in Figure 2(a) and 2(b), which are similar to those in [19]. However, the linear and nonlinear compliances predicted by the present

computation are 24.5% and 9.64% lower than those (C^* in Figure 2(a) and (b)) in [19]. Variations of the nonlinear compliance (C), the buckling factor (Eig_1) and the numbers of void (N_void) and solid (N_solid) elements are illustrated in Figure 2(c).

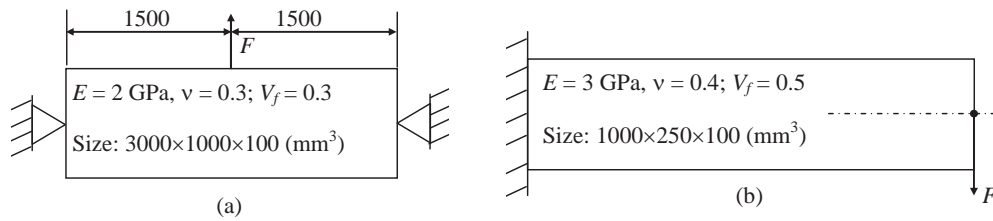


Figure 1 Design domains of samples 1 (mesh: 120×40) and 2 (mesh: 160×40)

Sample 2 in Figure 1(b) was investigated by many researchers [1, 2, 6, 19, 20]. When $F = 144$ kN, the optimal topologies obtained in the present computation are plotted in Figure 3, which collate well with those in [1]. The present linear and nonlinear compliances are 8.74% and 9.03% lower than those (C^* in Figure 3) in [1].

Figures 2 and 3 show that the present nonlinear compliances are around 9% lower than those in the literature even though the topologies were similar; this could be due to the effects of the void elements on the accurate estimation of the nonlinear compliances. Figure 2(c) also indicates that the all the quantities converge almost within 30 iterations. Material distributions or densities at iterations 1, 5, 10 and 30 are given in Figure 4. It can be seen that the removal of void elements and material reappearance can be realized in the present computation. At iteration 30, $C = 432.7$ kJ, $\lambda_1 = 6.402$, $N_void = 3214$ and 1296; and at iteration 100, these data are 430.5 kJ, 6.418, 3234 and 1308, respectively. Figures 2(c) and 4 reveal a fast convergence rate of the present algorithm.

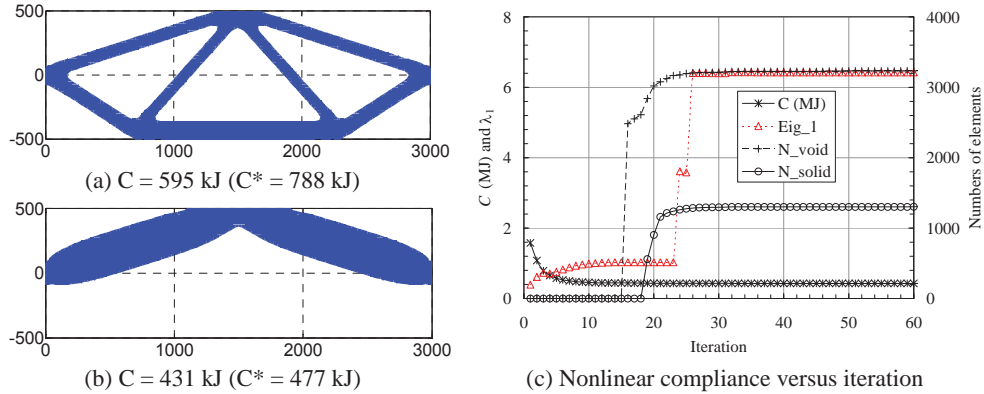


Figure 2 Optimization for sample 1: (a) optimal topology for linear analysis; (b) optimal design for nonlinear analysis; (c) nonlinear compliance and removal of void elements

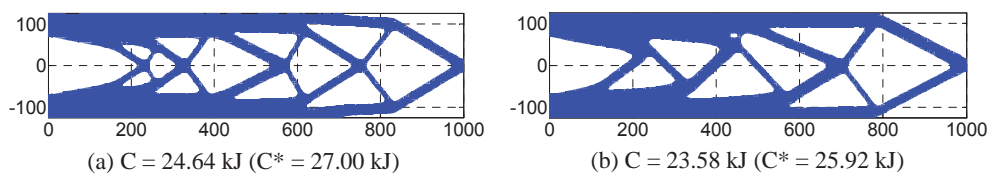


Figure 3 Optimization for sample 2: (a) topology for linear analysis; (b) optimal design for nonlinear analysis

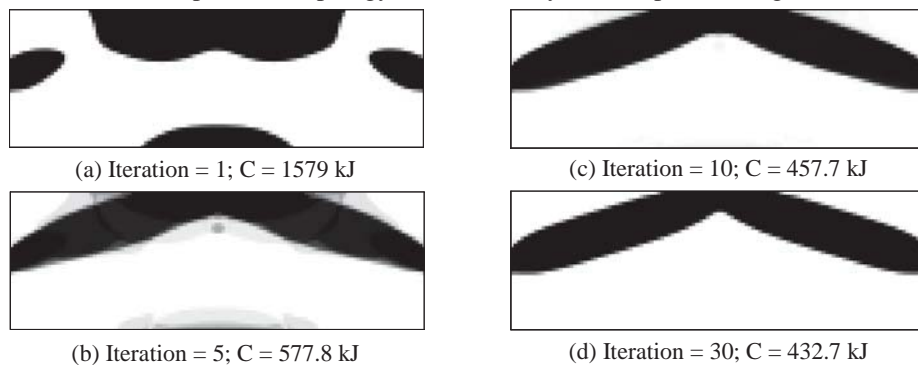


Figure 4 Material distributions at iterations 1, 5, 10 and 30

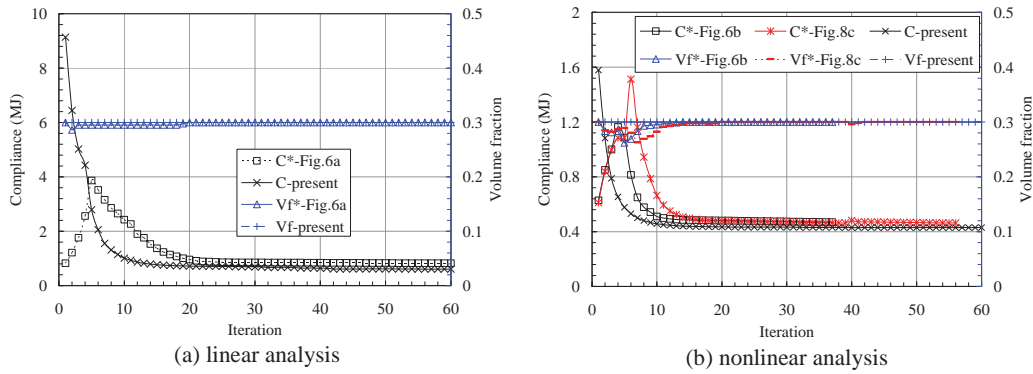


Figure 5 A comparison of the compliances predicted by the MIST and SIMP [19](quantities with asterisks)

A comparison of the compliance versus iteration curves for linear and nonlinear cases computed by the present algorithm and in [19] is illustrated in Figure 5. It is evident that the numerical stability, convergence performance and the minimum compliances of the present computation appear better than those in [19] where the SIMP was used by combining a meshless method with a density interpolation to treat void elements.

For the cases of $F = -10$ kN and $F = -1$ MN, the present optimal designs are plotted in Figure 6. It is obvious that the two designs are different. Different designs were also observed for different load levels in [1] for sample 2. That is, topologies can be dependent on the load levels in optimization for nonlinear compliance. In the present algorithm, the buckling constraint is used to find the optimal designs.

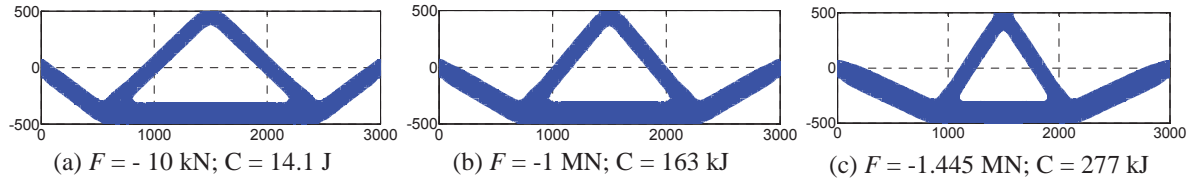


Figure 6 Optimization for nonlinear compliance of sample 1

3.2 Optimal design with buckling constraint

In the present iteration process, equation (9) is applied when the removal of void elements starts. The optimal topology to minimize the nonlinear compliance for sample 2 predicted by the present algorithm is shown in Figure 6(c), which is different from those in Figure 6(a) or 6(b). Figure 7(a) illustrates the variations of C , λ_1 , load level, the numbers of void and solid elements with iteration number. In the iteration process, F is chosen as -1 MN initially. It can be seen that: 1) $\lambda_1 \rightarrow 1$ after iteration 33; 2) the maximum load level is $F = -1.445$ MN; 3) good convergences are achieved for these quantities in Figure 7(a). Figures 6 and 7(a) indicate the importance of introducing the buckling constraint in the optimization of geometrically nonlinear structures. Figure 7(b) illustrates the convergence histories of the iso-surface level (t) and compliance (C) in linear and nonlinear analyses. It is interesting to note that the fluctuation in t in the linear analysis is larger than that in the nonlinear analysis. After iteration 60, t and C are converged for linear and nonlinear cases.

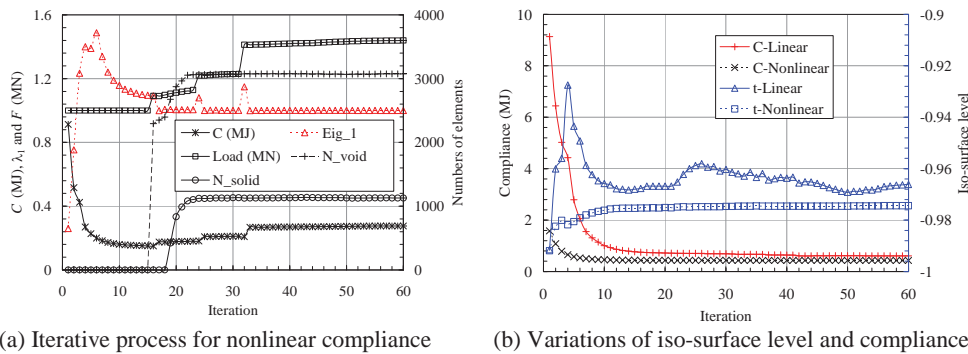


Figure 7 (a) optimization for nonlinear compliance with the maximum load of -1.445 MN; (b) variations of t and C

4. Concluding remarks

Topology optimization for geometrically nonlinear compliance is re-defined as new formulation by removing void elements in FEA and introducing the buckling constraint. Numerical results show that the

numerical issues in topology optimization for geometrically nonlinear structures can be resolved by excluding void elements in all nonlinear FEA and including them in the design variable update allowing reappearance of the material removed in previous iteration in the present MIST algorithm. By introducing a buckling constraint, optimal design can be obtained for geometrically nonlinear structures and the maximum load level without buckling can also be determined.

Acknowledgements

The authors are grateful for the support of the Australian Research Council via Discovery-Project Grants (DP140104408).

References:

- [1] T. Buhl, C. B. W. Pedersen and O. Sigmund, Stiffness design of geometrically nonlinear structures using topology optimization, *Structural and Multidisciplinary Optimization*, **19** (2): 93-104, 2000.
- [2] G. H. Yoon and Y. Y. Kim, Element connectivity parameterization for topology optimization of geometrically nonlinear structures, *International Journal of Solids and Structures*, **42** (7): 1983-2009, 2005.
- [3] X. Huang and Y. M. Xie, Topology optimization of nonlinear structures under displacement loading, *Engineering Structures*, **30** (7): 2057-2068, 2008.
- [4] T. E. Bruns and D. A. Tortorelli, An element removal and reintroduction strategy for the topology optimization of structures and compliant mechanisms, *International Journal for Numerical Methods in Engineering*, **57** (10): 1413-1430, 2003.
- [5] R. Kemmler, A. Lipka and E. Ramm, Large deformations and stability in topology optimization, *Structural and Multidisciplinary Optimization*, **30** (6): 459-476, 2005.
- [6] F. Wang, B. S. Lazarov, O. Sigmund and J. S. Jensen, Interpolation scheme for fictitious domain techniques and topology optimization of finite strain elastic problems, *Computer Methods in Applied Mechanics and Engineering*, **276** 453-472, 2014.
- [7] G. I. N. Rozvany, Difficulties in truss topology optimization with stress, local buckling and system stability constraints, *Structural optimization*, **11** (3-4): 213-217, 1996.
- [8] M. Zhou, "Topology optimization for shell structures with linear buckling responses," presented at the Computational Mechanics, WCCM VI, Beijing, China, 2004.
- [9] M. Bruyneel, B. Colson and A. Remouchamps, Discussion on some convergence problems in buckling optimisation, *Structural and Multidisciplinary Optimization*, **35** (2): 181-186, 2008.
- [10] E. Lindgaard and J. Dahl, On compliance and buckling objective functions in topology optimization of snap-through problems, *Structural and Multidisciplinary Optimization*, **47** (3): 409-421, 2013.
- [11] P. A. Browne, C. Budd, N. I. M. Gould, H. A. Kim and J. A. Scott, A fast method for binary programming using first-order derivatives, with application to topology optimization with buckling constraints, *International Journal for Numerical Methods in Engineering*, **92** (12): 1026-1043, 2012.
- [12] S. Uwe, Z. Ming, T. Poh-Soong and H. Cathal, "Topology Layout of Structural Designs and Buckling," in *10th AIAA/ISSMO Multidisciplinary Analysis and Optimization Conference*, ed: American Institute of Aeronautics and Astronautics, 2004.
- [13] D. Manickarajah, Y. M. Xie and G. P. Steven, Optimisation of columns and frames against buckling, *Computers & Structures*, **75** (1): 45-54, 2000.
- [14] L. Tong and J. Lin, Structural topology optimization with implicit design variable-optimality and algorithm, *Finite Elements in Analysis and Design*, **47** (8): 922-932, 2011.
- [15] Q. Luo and L. Tong, Elimination of effects of low density elements on optimization for buckling structures, (**under review**), 2014.
- [16] Q. Luo and L. Tong, Eradication of effects of void elements on optimization for nonlinear compliance, (**under review**), 2015.
- [17] H. C. Gea and J. Luo, Topology optimization of structures with geometrical nonlinearities, *Computers & Structures*, **79** (20-21): 1977-1985, 2001.
- [18] F. A. M. Gomes and T. A. Senne, An algorithm for the topology optimization of geometrically nonlinear structures, *International Journal for Numerical Methods in Engineering*, **99** (6): 391-409, 2014.
- [19] Q. He, Z. Kang and Y. Wang, A topology optimization method for geometrically nonlinear structures with meshless analysis and independent density field interpolation, *Computational Mechanics*, **54** 629-644, 2014.
- [20] R. D. Lahuerta, E. T. Simões, E. M. B. Campello, P. M. Pimenta and E. C. N. Silva, Towards the stabilization of the low density elements in topology optimization with large deformation, *Computational Mechanics*, **52** (4): 779-797, 2013.

Optimization of Pulsating Blank Holder Force for Deep Drawing of Cylindrical Cups

Jing Han¹, Shinji Natsume², Satoshi Kitayama², Koetsu Yamazaki², Hiroaki Uchida¹

¹ Universal Can Corporation, Sunto, Japan, hanjing@mmc.co.jp

² Kanazawa University, Kanazawa, Japan

1. Abstract

A further improvement in the drawability may lead to a further light-weight cylindrical drawn cup, hence to a more environment-friendly and sustainable industrial product such as an aluminium beverage can & bottle. A pulsating blank holder force (BHF) with a frequency ranged from ultra-high to ultra-low values, is reported that can improve the drawability, as compared with a static constant BHF. However, it still needs a lot of efforts before applying the pulsating BHF industrially, for example, investigation into the optimum property of vibration added to the blank holder during deep drawing of cylindrical cups.

This study implemented an optimization on the properties of the vibration such as the oscillation amplitude, frequency and phase, by applying the structure optimization technique, based on numerical simulations of the cup drawing process. Parameters used to determine a sinusoidal vibration wave are taken as design variables. Wrinkling and tearing are major defects in deep drawing, therefore are considered as design constraints. The limit drawing ratio (LDR) is one of indicators to evaluate the drawability, therefore LDR is maximized through maximizing the limiting drawing depth that could be achieved for a specified drawing ratio. A sequential approximate optimization method is successfully applied to perform design optimization, which leading to a satisfied improvement in the drawability.

2. Keywords: Deep drawing process, Formability, Cylindrical cup, Pulsating blank holder force, Optimum design.

3. Introduction

As shown in [Figure 1](#), during deep drawing of a cylindrical cup, the circular punch forces the blank through the draw die and forms into a cup. The blank holder is used to prevent it from wrinkling due to the tangential compressive strain in the forming zone. The limit drawing ratio (LDR), defined as the ratio of the maximum blank diameter which is successfully drawn to the punch diameter, is one of indicators to evaluate the drawability. Factors causing wrinkling, tearing and earring during deep drawing, such as material properties and shape dimensions of the blank / tools, lubrication condition between the blank and tools, temperature and forming speed, have been extensively studied experimentally, theoretically and numerically [1-10].

A further improvement in the sheet formability may lead to a further light-weight cylindrical drawn cup, hence to a more environment-friendly and sustainable industrial product, for example, an aluminium beverage can & bottle ([Figure 2](#)) [11]. To improve formability and forming quality, a lot of techniques have been investigated, for example, groove pressing the blank, coating the tools, shaping the surfaces of the blank holder, adding lubrication holes on the die shoulder, applying an adaptive blank holder force (BHF) varying with the punch stroke, and applying a circumferentially segmented BHF [12-18]. Moreover, forming processes with hydraulic pressure [19-21], with high-pressured water jet [22], with a radial inward force in the flange region [23], are also being developed.

Recently, a pulsating BHF with a frequency ranged from ultra-high to ultra-low values is reported that can reduce friction and deformation resistance, hence can increase LDR, as compared with a static constant BHF [24-27]. With industrial technology fast developing, practicality of the pulsating BHF may be expected. However, it still needs a lot of efforts before applying the pulsating BHF industrially, for example, investigation into the optimum property of vibration added to the blank holder during deep drawing of cylindrical cups.

On the other hand, research and development of the structural optimization technique and its applications on the metal sheet forming process have been going on. The response surface approximation method is one of practical optimization methods, therefore is applied widely in industry. To efficiently obtain accurate response surfaces, the orthogonal array in the design-of-experiment technique is used [28]. Recently, several new techniques have been proposed and applied to improve accuracy of the approximation. The sequential approximate optimization (SAO) method using radial basis function (RBF) network has been applied to

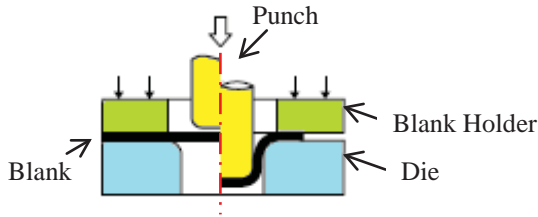


Figure 1: Deep drawing of cylindrical cups



Figure 2: An aluminium beverage bottle

optimize a series of sheet metal forming processes, for efficiently searching a highly accurate global optimal solution [29-31].

This study optimizes the properties of the vibration such as the amplitude, frequency and phase, based on deep drawing simulations. Parameters used to determine a sinusoidal vibration wave are taken as design variables. Wrinkling and tearing are considered as design constraints. LDR is maximized through maximizing the limiting drawing depth that could be achieved for a specified larger drawing ratio. The SAO method using RBF network is applied to perform design optimization.

4. Deep drawing process simulation

A three-dimensional finite element analysis model is established to simulate deep drawing process of the cylindrical cup with the static constant BHF and with various pulsating BHF.

4.1. Finite element model

Figure 3 shows the deep drawing analysis model used in this study [18]. The flat circular blank is clamped by the circular die ring and the blank holder with smooth surfaces. In order to save calculating cost, one-fourth finite element model is adopted due to symmetry. The explicit finite element code, LS-DYNA is utilized to perform the deep drawing simulation.

The blank with 83.44mm diameter and 0.208mm initial uniform thickness t_0 , is divided by four-node shell elements. The aluminium blank is defined as an elasto-plastic body, and the material properties are assumed as Young's modulus: 68.9GPa, Poisson's ratio: 0.33.

The diameter of the punch is 45.72 mm; hence, the draw ratio comes to be 1.8, which is larger than usual. The punch moves at a constant speed of $v_0 = 350$ mm/s. The diameter of the die is 46.74 mm. Both the die and blank holder are defined as rigid bodies. The friction coefficient between tools and the blank is assumed as 0.05.

The pulsating BHF used in this study is defined in Eq. (1),

$$PBHF = F_0 + aF_0 \sin(2\pi ft + \phi) \quad (1)$$

Where, F_0 is a primary BHF, f denotes the pulsating frequency, ϕ denotes the phase, and aF_0 represents the amplitude, a is a scalar ranged from 0 to 1, t is punch moving time. Figure 4 shows example sine curves for calculating the pulsating BHF defined by the same parameters of F_0 , a , f but different ϕ .

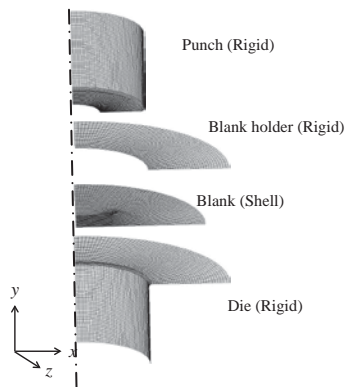


Figure 3 : Numerical analysis model

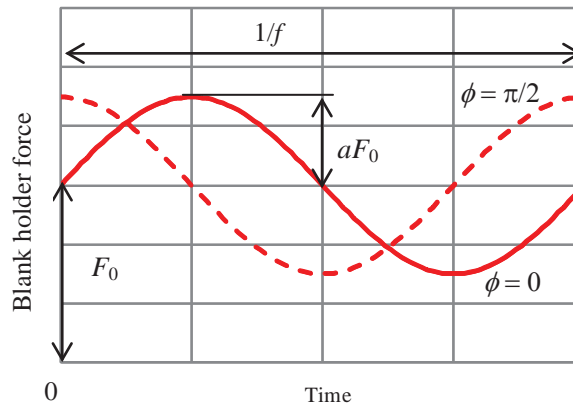


Figure 4: Example curves of pulsating BHF

4.2. Simulation results

In deep drawing process, excessive material flow causes wrinkling at the flange (Figure 5(a)) while insufficient material flow leads to thinning and tearing of the cup (Figure 5(b)). For convenient, the ratio ($r_w = D_{max}/t_0$) of the maximum axial distance D_{max} between the blank holder and the die during the deep drawing process to the initial blank thickness t_0 , is used to predict the risk of wrinkling. The ratio ($r_t = t_{min}/t_0$) of the minimum thickness t_{min} of the cup to the initial blank thickness t_0 , is used to predict the risk of tearing. In this study, defects of the drawn cup are determined when r_w is more than 1.2 or r_t is less than 0.8.

To a given relatively large draw ratio, the limiting drawing depth L_a that can be achieved before wrinkling or tearing occurs, during the deep drawing process, is used as an indicator to compare the drawability.

In order to observe the influences of the parameters of the pulsating BHF on the drawability, deep drawing simulations were carried out for several models with the static constant BHF as well as with various pulsating blank holder force, as shown in Table 1 and Figure 6. Model 1 and Model 2 were applied by the static constant BHF, while else models were applied by the pulsating BHF of various vibration properties defined by Eq.(1) in terms of four parameters. The points at where wrinkling or tearing occurred, are marked with symbols for each model in the same figure, respectively.

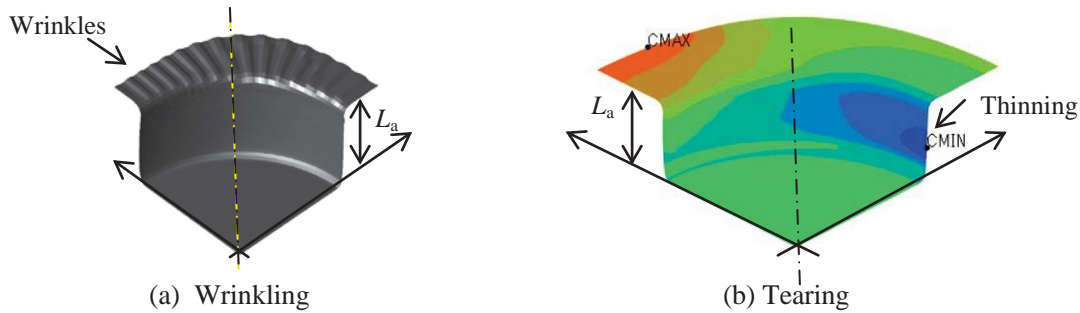


Figure 5: Defects in deep drawing process

Table 1 Finite element analysis results

Model	F_0 / kN	a	f / Hz	ϕ	L_a / mm	Results
1	1.000	N/A	N/A	N/A	12.20	Wrinkling
2	2.000	N/A	N/A	N/A	9.10	Tearing
3	4.786	0.815	5.536	3.899	13.7	Wrinkling
4	2.264	0.332	14.062	4.866	9.45	Tearing
5	0.539	0.768	15.815	3.421	2.45	Wrinkling
6	3.835	0.624	1.249	2.497	4.20	Tearing

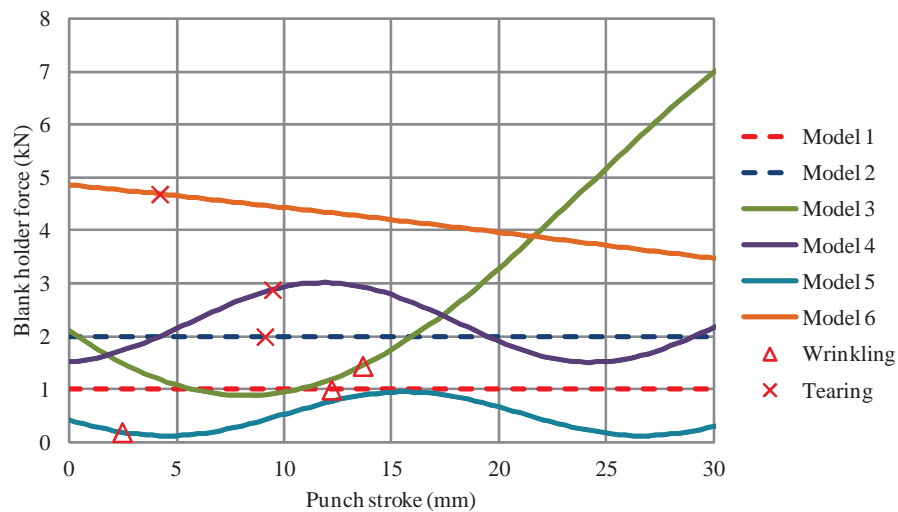


Figure 6: Simulation results of models applied by various BHF

Simulation results, for example, results of Model 1 and Model 2 show that the given blank cannot be drawn successfully into a cup with the given tooling systems. Wrinkling occurs if BHF is too small as that in Model 1, and tearing occurs if BHF is too large as that in Model 2.

Simulation results of Model 3 and Model 4 show that, by applying the pulsating BHF, the limiting drawing depth L_a can be extended, in other words, failure can be delayed, and a deeper cup may be obtained.

However, simulation results of Model 5 and Model 6 show that, by applying the pulsating BHF, the limiting drawing depth L_a also may be shortened, which is not expected.

On the basis of numerical simulation results, it is confirmed that the parameters of the pulsating BHF do influence the deep drawing process, and that need to be investigated and optimized to obtain a drawn cup of a deeper depth, hence, to achieve a larger drawing ratio.

5. Optimization of pulsating BHF

5.1. Formulation of the optimization problem

The parameters of the pulsating BHF are selected as design variables. The objective of the optimization is to maximize the limiting drawing depth L_a for a specific larger drawing ratio. The ratios r_w and r_t are defined as design constraints to avoid wrinkling and tearing. The optimization problem is then posted as

$$\text{Find design variables: } X = \{x_i\}, \quad i = 1, \dots, n \quad (n: \text{the number of design variables}) \quad (2)$$

$$\text{Maximize } f(X) = L_a(X), \quad (3)$$

Subject to

$$g_1 = r_w / r_{w\max} - 1 \leq 0, \quad (4)$$

$$g_2 = r_{t\min} / r_t - 1 \leq 0, \quad (5)$$

$$x_i^L \leq x_i \leq x_i^U, \quad i = 1, \dots, n \quad (6)$$

where $r_{w\max}$ is the allowable upper bound of the ratio r_w , and $r_{t\min}$ is the allowable lower bound of the ratio r_t . x_i^L and x_i^U are the upper and lower bounds of design variables i , respectively. It is noted that if the given blank is successfully drawn into the cups without defects determined by Eq.(4) and Eq.(5), the values of the design variables are considered as optimal values, though L_a may not be the deepest one. Therefore, the optimal solution for the pulsating BPF may not be only one.

5.2. Optimization results

The SAO method using RBF network is adopted to perform design optimization. In the optimizing process, at first, the response surface of the objective and constraint functions in terms of design variables, is constructed and optimized based on the numerical simulation results of a number of sampling design points. The optimal solution of the response surface is then added as a new sampling design point to improve the local approximation accuracy, and several new sampling points around the unexplored region in the design space are also added to improve global approximation accuracy. At last, the response surface is reconstructed and optimized to get a better optimal solution. This process is repeated until the prescribed terminal criterion is satisfied.

The pulsating BHF applied in the deep drawing process described in this study is optimized. Four parameters of pulsating BHF, F_0 , a , f and ϕ are selected as design variables. The upper and lower bounds of the design variables are given as [0.10, 5.00] for design variable F_0 , [0, 1] for a , [1, 20] for f , and [0, 2π] for ϕ . The $r_{w\max}$ and $r_{t\min}$ are considered as 1.2 and 0.8, respectively.

The optimal values of the design variables are obtained as $F_0 = 4.78$ kN, $a = 0.826$, $f = 4.177$, $\phi = 4.637$, and the optimal pulsating BHF is then calculated by substituting the above four optimal values into Eq.(1), as shown in Figure 7. It is clear that the optimal pulsating BHF curve bypassed both of the wrinkling zone and the tearing zone. The objective value is 29.75 mm, and it is observed that the given blank is drawn successfully into a cup without wrinkling and tearing, as shown in Figure 8. Consequently, it is also may concluded that, a specified larger LDR may be achieved by applying an optimal pulsating BHF during the deep drawing process.

6. Conclusions

This paper proposed a technique to optimize the pulsating BHF to maximize the limiting drawing depth, consequently, to achieve a specified lager LDR. The finite element analysis model was built to simulate deep drawing process of the cylindrical cup using the pulsating BHF, and effects of the pulsating BHF on the drawability were investigated. It's found that the drawability may be improved by applying a proper pulsating BHF. The sequential approximate optimization method was then applied to efficiently search for the optimal pulsating BHF. The proposed optimization technique also can be applied to other optimization

problems of the pulsating BHF under different conditions.

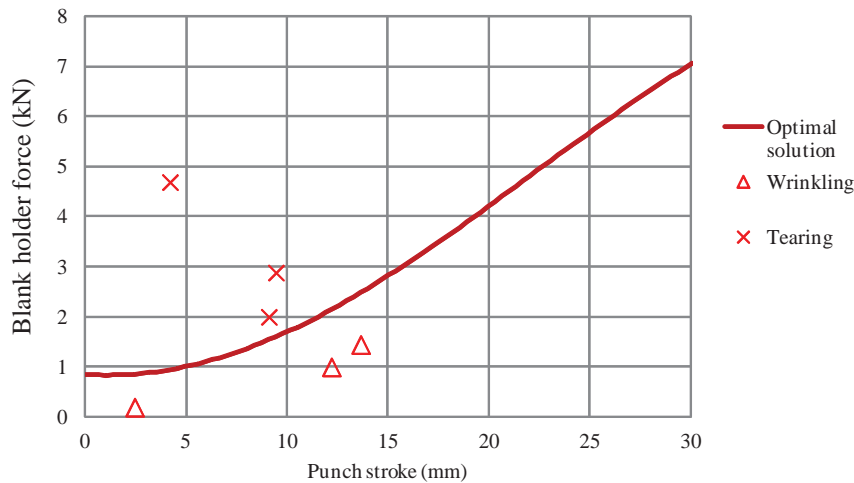


Figure 7: Optimized pulsating BHF

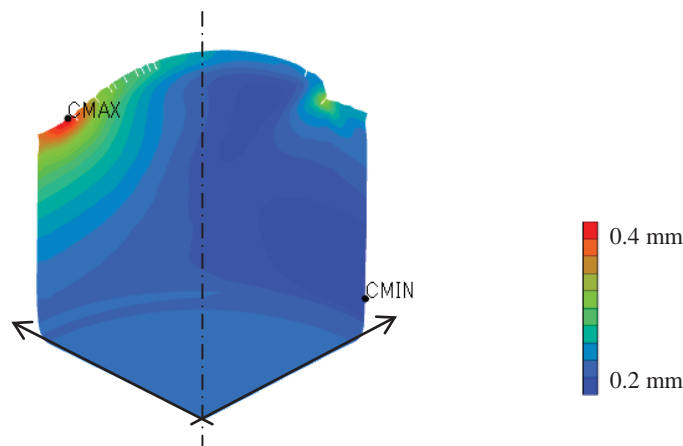


Figure 8: Drawn cup using optimized pulsating BHF

7. References

- [1] S. Y. Chung and H. W. Swift, Cup-drawing from a Flat Blank: Part I. Experimental Investigation, *Proceedings of the Institution of Mechanical Engineers*, 165(1), 199-211, June 1951.
- [2] M.G. El-Sebaie, P.B. Mellor, Plastic instability conditions in the deep-drawing of a circular blank of sheet metal, *International Journal of Mechanical Sciences*, 14(9), Pages 535-540, 1972.
- [3] M. Schünemann, M. A. Ahmetoglu and T. Altan, Prediction of process conditions in drawing and ironing of cans, *Journal of Materials Processing Technology*, 59(1-2), 1-9, 1996.
- [4] A.M Zaky, A.B Nassr, M.G El-Sebaie, Optimum blank shape of cylindrical cups in deep drawing of anisotropic sheet metals, *Journal of Materials Processing Technology*, 76(1-3), 203-211, 1998.
- [5] Cebeli Özek, Muhammet Bal, The effect of die/blank holder and punch radiuses on limit drawing ratio in angular deep-drawing dies, *The International Journal of Advanced Manufacturing Technology*, 40(11-12), 1077-1083, 2009.
- [6] S. M. Mahdavian and Tui Mei Yen Fion, Effect of Punch Geometry in the Deep Drawing Process of Aluminium, *Materials and Manufacturing Processes*, 22(7-8), 2007.
- [7] S. Sezek, V. Savas and B. Aksakal, Effect of Die Radius on Blank Holder Force and Drawing Ratio: A Model and Experimental Investigation, *Materials and Manufacturing Processes*, 25(7), 557-564, 2010.
- [8] I. Dejmaj, J. Tirosh, A. Shirizly and L. Rubinsky, On the optimal die curvature in deep drawing processes, *International Journal of Mechanical Sciences*, 44(6), 1245-1258, 2002.
- [9] T. Naka, F. Yoshida, Deep drawability of type 5083 aluminium–magnesium alloy sheet under various

- conditions of temperature and forming speed, *Journal of Materials Processing Technology*, 89–90, 9-23, 1999.
- [10] M.M Moshksar and A. Zamanian, Optimization of the tool geometry in the deep drawing of aluminium, *Journal of Materials Processing Technology*, 72(3), 363-370, 1997.
- [11] J. Han, R. Itoh, S. Nishiyama and K. Yamazaki, Application of structure optimization technique to aluminum beverage bottle design, *Structural and Multidisciplinary Optimization*, 29(4), 304-311, 2005.
- [12] G. Niranjana and U. Chakkingal, Deep drawability of commercial purity aluminum sheets processed by groove pressing, *Journal of Materials Processing Technology*, 210, 1511-1516, 2010.
- [13] K.H.W. Seah and K.S. Lee, The benefits of coating the tools with titanium nitride in the deep drawing of mild steel cups, *Journal of Materials Processing Technology*, 37(1–4), 125-135, 1993.
- [14] M. Y. Demeri, Drawbeads in sheet metal forming, *Journal of Materials Engineering and Performance*, 2(6), 863-866, 1993.
- [15] Y. Q. Shi, Experimental Study of the Small Lubrication Holes on the Die Shoulder on the Formability in Cylindrical Cup Deep-Drawing, *Applied Mechanics and Materials* (Volumes 37-38), 428-431, 2010.
- [16] S. Thiruvardhulan and N.H. Loh, Deep drawing of cylindrical cups with friction-actuated blank holding, *Journal of Materials Processing Technology*, Volume 40, Issues 3–4, January 1994, Pages 343-358
- [17] S. Tommerup and B. Endelt, Experimental verification of a deep drawing tool system for adaptive blank holder pressure distribution, *Journal of Materials Processing Technology*, 212(11), 2529-2540, 2012.
- [18] K. Yamazaki, S. Makino, J. Han and H. Uchida, Earing Minimization with Segmented and Variable Blank Holder Force during Deep Drawing Process for Circular Cup Forming, *11th World Congress on Structural and Multidisciplinary Optimization*, Sydney, Australia, 2015.
- [19] J. Tirosh and P. Konvalina, On the hydrodynamic deep-drawing process, *International Journal of Mechanical Sciences*, Volume 27, Issue 9, 1985, Pages 595-607
- [20] F. Djavanroodi, D. S. Abbasnejad and E. H. Nezami, Deep Drawing of Aluminum Alloys Using a Novel Hydroforming Tooling, *Materials and Manufacturing Processes*, Volume 26, Issue 5, May 2011, pages 796-801
- [21] S.H Zhang, M.R Jensen, J Danckert, K.B Nielsen, D.C Kang and L.H Lang, Analysis of the hydromechanical deep drawing of cylindrical cups, *Journal of Materials Processing Technology*, 103(3), 367-373, 2000.
- [22] Y. Horikoshi, T. Kuboki, M. Murata, K. Matsui and M. Tsubokura, Die design for deep drawing with high-pressured water jet utilizing computer fluid dynamics based on Reynolds' equation, *Journal of Materials Processing Technology*, 218, 99-106, 2015.
- [23] Z. Lai, Quanliang Cao, Bo Zhang, Xiaotao Han, Zhongyu Zhou, Qi Xiong, Xiao Zhang, Qi Chen and Liang Li, Radial Lorentz force augmented deep drawing for large drawing ratio using a novel dual-coil electromagnetic forming system, *Journal of Materials Processing Technology*, In Press, Available online 28 February 2015.
- [24] A. Mostafapur, S. Ahangar and R. Dadkhah, Numerical and experimental investigation of pulsating blankholder effect on drawing of cylindrical part of aluminum alloy in deep drawing process, *The International Journal of Advanced Manufacturing Technology*, 69(5-8), 1113-1121, 2013.
- [25] S. Ali, S. Hinduja, J. Atkinson, P. Ilt and R. Werkhoven, Effect of ultra-low frequency pulsations on tearing during deep drawing of cylindrical cups, *International Journal of Machine Tools and Manufacture*, 48, 558-564, 2008.
- [26] T. Jimma, Y. Kasuga, N. Iwaki, O. Miyazawa, E. Mori, K. Ito and H. Hatano, An application of ultrasonic vibration to the deep drawing process, *Journal of Materials Processing Technology*, 80(81), 406-412, 1998.
- [27] A. Pasierb and A. Wojnar, An experimental investigation of deep drawing and drawing processes of thin walled products with utilization of ultrasonic vibrations, *Journal of Materials Processing Technology*, 34, 489-494, 1992.
- [28] J. Han, K. Yamazaki, R. Itoh and S. Nishiyama, Multi-Objective Optimization of a Two-Piece Aluminum Beverage Bottle Considering Tactile Sensation of Heat and Embossing Formability, *Structural and Multidisciplinary Optimization*, 32(2), 141-151, 2006.
- [29] S. Kitayama, M. Arakawa and K. Yamazaki, Sequential Approximate Optimization using Radial Basis Function network for engineering optimization, *Optimization and Engineering*, 12(4), 535-557, 2011.
- [30] S. Kitayama, K. Kita and K. Yamazaki, Optimization of variable blank holder force trajectory by sequential approximate optimization with RBF network, *Journal of Advanced Manufacturing Technology*, 61(9-12): 1067-1083, 2012.
- [31] S. Kitayama, S. Huang and K. Yamazaki, Optimization of variable blank holder force trajectory for spring back reduction via sequential approximate optimization with radial basis function network, *Structural and Multidisciplinary Optimization*, 47(2): 289-300, 2013.

Acoustic radiation and sensitivity analysis of a randomly excited structure based on FEM/IBEM combined with PEM

Baoshan Liu¹, Liyong Tong²

¹ Department of Engineering Mechanics, College of Pipeline and Civil Engineering, China University of Petroleum, QingDao, Shandong, P.R. China, liubs@upc.edu.cn

² School of Aerospace, Mechanical and Mechatronics Engineering, The University of Sydney, Sydney, Australia, liyong.tong@sydney.edu.au

Abstract

The objective of this study is to develop a computational method for calculating the acoustic radiation and sensitivity analysis of a structure subjected to a stochastic excitation, based on the finite element method (FEM), the indirect boundary element method (IBEM) and the pseudo excitation method (PEM). In this work, FEM and IBEM are used respectively to calculate the dynamic and acoustic responses of a structure, and PEM is used to determine the acoustic stochastic responses for the acoustic radiation problems via transforming the random responses into the structural-acoustic harmonic ones. Using the PEM, the acoustic radiation sensitivities of the structure are developed in the context of the transformed harmonic sensitivity analyses, and they are validated by comparing with the results predicted using the finite difference method. Numerical example is given to demonstrate the effectiveness of the methods proposed in this paper.

Keywords: Sensitivity analysis, Stochastic Excitation, FEM, IBEM, PEM

1. Introduction

The sensitivity analysis and design optimization have become an effective means of reducing vibration and noise in many areas of practical engineering in recent years. Wang and Lee [1] developed a global design sensitivity analysis of exterior noise with respect to structural sizing design variables. Allen et al. [2] presented a study on the stochastic acoustic radiation and sensitivity analysis. Liu et al. [3] proposed a new effective method for computing the acoustic radiation and its sensitivity analysis of a structure subject to a stochastic excitation.

The aim of the present work is to determine the acoustic power spectral density (PSD) and its sensitivity on a structural-acoustic system subjected to a stochastic excitation. FEM and IBEM are combined with an accurate and highly effective algorithm for stationary/non-stationary random structural response analysis, named as PEM, to solve the acoustic random radiation problem. PEM and FEM are used to calculate the pseudo responses of the structural vibration when the stochastic excitations are applied on the structure. IBEM is used to calculate the random acoustic radiation analysis, in which the structural pseudo response constitutes the boundary condition in acoustic indirect boundary element analysis. Thus, the acoustic PSD analysis could be obtained by means of harmonic analysis, and this method will make the calculation procedure of random acoustic analysis highly simple and efficient.

2. Structural random response analysis

A brief introduction of the structural random response analysis is given based on the PEM in this section [4], and that constitutes the boundary condition of the subsequent acoustic random response analysis. The finite element system equation for a structure subjected to a single random excitation can be expressed as follows:

$$[M]\{\ddot{y}\} + [C]\{\dot{y}\} + [K]\{y\} = \{R_x\}x(t) \quad (1)$$

where $x(t)$ is a stationary random process with a specified PSD $S_{xx}(\omega)$ for which the transformation between them is not considered, and $\{R_x\}$ is a given constant vector represents the distribution of the random excitation.

According to the PEM, substituting $\tilde{x}(t) = \sqrt{S_{xx}(\omega)}e^{i\omega t}$, as a pseudo excitation ($\tilde{\#}$ represents the pseudo variable of the random variable #), into Eq.(1), it leads to the following traditional harmonic equation:

$$[M]\{\ddot{y}\} + [C]\{\dot{y}\} + [K]\{y\} = \{R_x\}\sqrt{S_{xx}(\omega)}e^{i\omega t} \quad (2)$$

The solution of Eq.(2) can be easily obtained, such as $\{\tilde{y}(t)\} = \{Y(\omega)\}e^{i\omega t}$, by using mode-superposition method or other methods, the PSD matrix of $\{y\}$ can be computed as follows:

$$[S_{yy}(\omega)] = \{\tilde{y}\}^* \{\tilde{y}\}^T = \{Y(\omega)\}^* \{Y(\omega)\}^T \quad (3)$$

where the superscripts * and T represent the complex conjugate and transpose respectively, and a detailed

description of the PEM for the structural random response analysis can be found in Ref. [4].

3. Acoustic random radiation analysis

Considering a structural velocity boundary condition for simplicity, the acoustic system equation in IBEM can be expressed as follows [5]:

$$[A]\{q\} = \{f\} \quad (4)$$

where $[A]$ is the acoustic system matrix, $\{q\}$ is the vector of unknown primary variables on the surface of the boundary element model, $\{f\}$ is the vector of the excitation derived linearly from the velocity boundary condition.

$$\{f\} = [T_1]\{v_n\} = [T_1][T_2]\{y\} = [T_1][T_2]\{y\} \quad (5)$$

where $[T_1]$ is the transformation matrix to convert element normal velocities $\{v_n\}$ into the exciting vector $\{f\}$, and $[T_2]$ in which a factor $(i\omega)$ has been included is the transformation matrix to convert nodal displacements $\{y\}$ into element normal velocities $\{v_n\}$.

Once Eq.(4) has been solved, the pressures at several field points (e.g., m) within the acoustic domain can be written as

$$\{p_f\} = [A_f]\{q\} \quad (6)$$

where $[A_f]$ is the matrix with m row vectors depending on the frequency, the structural surface and the locations of m field points.

Substituting Eqs.(4) and (5) into Eq.(6) results in

$$\{p_f\} = [A_f][A]^{-1}\{f\} = [A_f][A]^{-1}[T_1][T_2]\{y\} = [T]\{y\} \quad (7)$$

where $[T] = [A_f][A]^{-1}[T_1][T_2]$ is for simplicity.

After the PEM is applied to the structural random response analysis, the PSD matrix $[S_{yy}(\omega)]$ of $\{y\}$ is already decomposed in Eq.(3). By using Eq.(5), the pseudo response of $\{f\}$ can be easily obtained, $\tilde{f}(t) = \{F(\omega)\}e^{i\omega t} = [T_1][T_2]\{Y(\omega)\}e^{i\omega t}$, and that constitutes the pseudo excitation on the right-hand side of Eq.(4). Then, the pseudo response of $\{q\}$ can be computed when the PEM is used in the IBEM, and the responding acoustic PSD matrix $[S_{qq}(\omega)]$ can be computed as follows:

$$[S_{qq}(\omega)] = \{Q(\omega)\}^* \{Q(\omega)\}^T \quad (8)$$

Similarly, the responding acoustic PSD matrix of the acoustic pressures at m field points can be computed as follows:

$$[S_{p_f p_f}(\omega)] = \{P_f(\omega)\}^* \{P_f(\omega)\}^T \quad (9)$$

The output auto-PSD of the acoustic pressure response at field point n can be represented as a sound pressure level (SPL) in decibel via

$$SPL_n = 10 \log \left(\frac{|S_{p_n p_n}|}{P_{ref}^2} \right) \quad (10)$$

where $P_{ref} = 2 \times 10^{-5}$ Pa is the reference acoustic pressure.

4. Acoustic pressure PSD sensitivity analysis

The sensitivity of the acoustic field pressure PSD with respect to a given structural design variable can be obtained through the differentiation of the acoustic field pressure PSD, Eq.(9), with respect to a structural sizing design variable d_i

$$\frac{\partial [S_{p_f p_f}(\omega)]}{\partial d_i} = \frac{\partial \{P_f(\omega)\}^*}{\partial d_i} \{P_f(\omega)\}^T + \{P_f(\omega)\}^* \frac{\partial \{P_f(\omega)\}^T}{\partial d_i} = 2 \{P_f(\omega)\}^* \frac{\partial \{P_f(\omega)\}^T}{\partial d_i} \quad (11)$$

$$\frac{\partial \{P_f(\omega)\}^T}{\partial d_i} = \frac{\partial [T]}{\partial d_i} \{Y(\omega)\} + [T] \frac{\partial \{Y(\omega)\}}{\partial d_i} \quad (12)$$

where $\{Y(\omega)\}$ is the structural harmonic displacement response derived from the finite element analysis. The change in sizing design variable is very small compared to the wavelength in our problem, so the sensitivities of the matrix $[T]$ with respect to sizing design variable are assumed to be equal to zero, that is, they are independent of the sizing design variable. Hence Eq.(12) is simplified as follows:

$$\frac{\partial\{P_f(\omega)\}}{\partial d_i} = [T] \frac{\partial\{Y(\omega)\}}{\partial d_i} \quad (13)$$

From the above equation, it can be seen that the sensitivity of the pseudo acoustic pressure response is transformed into structural harmonic sensitivity analysis based on the PEM.

5. Numerical results and discussion

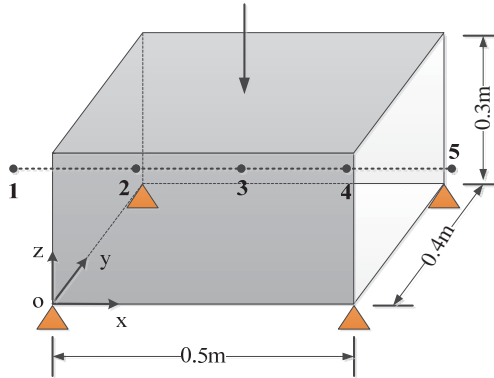


Figure 1: Structure used in the numerical simulations

In this section, as an illustrative example, the numerical results of an open box are presented to demonstrate the effectiveness of the present method in calculating the acoustic pressure PSD and its sensitivity with respect to the thickness of the open box. The open box is comprised of 4 aluminum plates: top, bottom, front and back as shown in Fig.1. The aluminum plate has a thickness of 2×10^{-3} m, Poisson's ratio 0.33, Young's modulus 6.9×10^{10} Pa, and density 2.7×10^3 kg/m³. The open box is fixed at four bottom corners. The finite element model of the box consists of 308 nodes and 506 3-node plate/shell elements. The analysis of this structural-acoustic system is conducted over the frequency range of 10-200 Hz, and the damping is not considered in the structural response analysis of this example. The length of the large element side satisfies the inquiry of the six-element-per-wavelength rule in the BEM model.

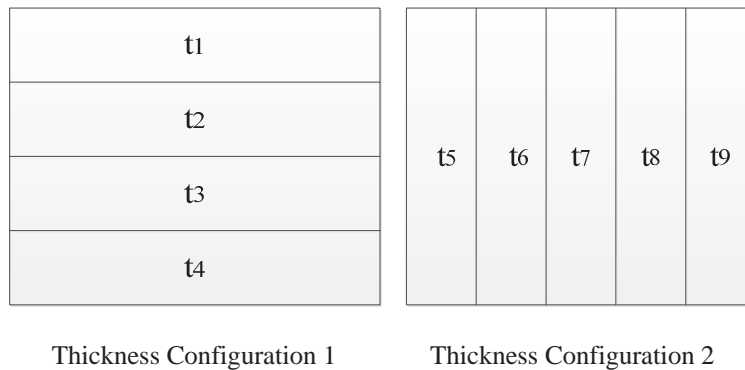


Figure 2: Thickness configurations for the top plate of the open box

A single stochastic excitations is applied on the open box's top plate. The PSD of the excitation is constant unity throughout the band frequency. The thickness of the top plate is used as the structural design variable. There are two kinds of configurations as shown in Fig.2. The first configuration consists of four strips positioned longitudinally. The thickness of the top plate at each strip is considered as an independent design variable. The second configuration consists of five strips running transversely along the top plate, and the corresponding plate thicknesses of the strip constitute the design variables. A uniform thickness 0.003m is considered as the initial thickness for all sensitivity computations. There are five field points considered, which are shown in Fig.2. All the five field points 1-5 are located at (-0.25, 0.20, 0.15) m, (0, 0.20, 0.15) m, (0.25, 0.20, 0.15) m, (0.50, 0.20, 0.15) m and (0.75, 0.20, 0.15) m respectively.

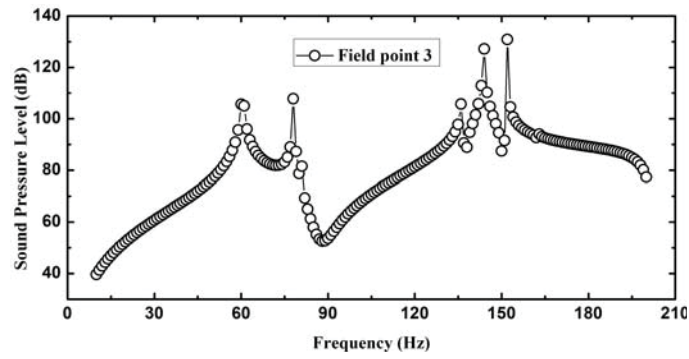


Figure 3: SPL response of the open box at field point 3 for the mid-point excitation

An acoustic pressure spectral density curve is obtained in Fig. 3 that shows the results of the analyzed frequency band. In Fig. 3, the acoustic pressure spectral density is the equivalent decibel value calculated from Eq.(10). Not all the natural frequencies of the open box are observed in the results of the analyzed frequency band from the curve. This is mainly due to the fact that the point at which the response is sought corresponds to a nodal point of the corresponding mode, Such as, the first system resonance (40Hz) is not stirred from the swinging back and forth mode, while the following two system resonances occur at 60 Hz and 78 Hz, and these frequencies coincide with the second and the third mode of the open box.

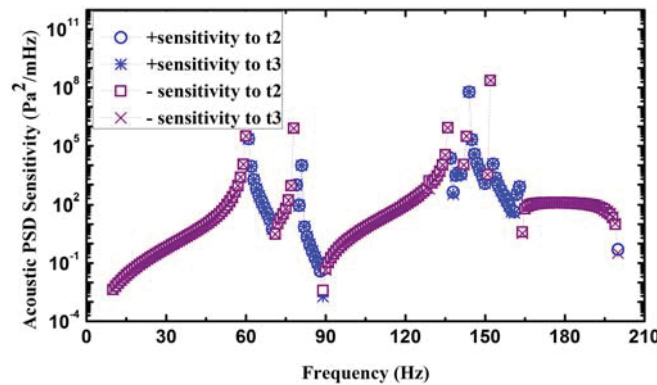


Figure 4: Acoustic PSD sensitivity values of field point 3 with respect to design variables in configuration 1

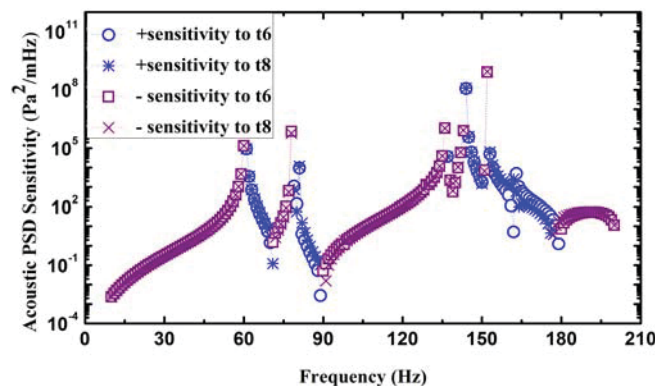


Figure 5: Acoustic PSD sensitivity values of field point 3 with respect to design variables in configuration 2

It should be pointed out firstly that the blue symbols represent positive sensitivities and the purple symbols represent negative sensitivities in all the following Figures. The acoustic PSD sensitivity values for field point 3 with respect to t2 and t3 are shown in Fig. 4, because of the symmetry of the box and that the excitation applied at the centre of the top plate, the acoustic PSD sensitivity values for field point 3 with respect to design variables t2 and t3 are expected to be the same. The acoustic PSD sensitivity values of field point 3 with respect to t6 and t8 are shown in Fig. 5, similar results can be seen and they are considered reasonable.

To further validate the sensitivity computation, the numerical results of the acoustic pressure PSD computed using the present method are compared with those calculated by using the finite difference method (FDM). The finite difference method applied here is the central difference procedure

$$p_i = \frac{p_i(\alpha + \Delta\alpha) - p_i(\alpha - \Delta\alpha)}{2\Delta\alpha} \quad (14)$$

and the step length $\Delta\alpha$ is chosen as 0.01 in Ref. [6].

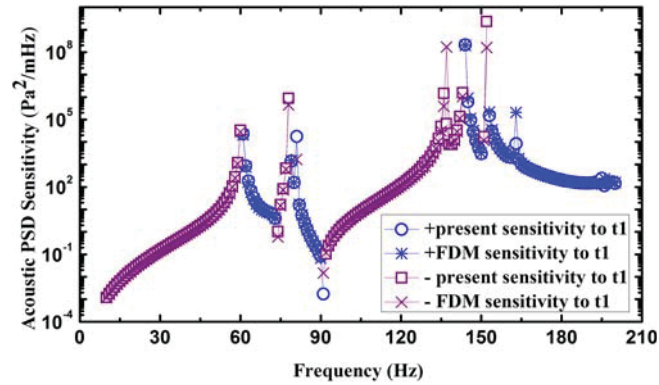


Figure 6: Acoustic PSD sensitivity values of field point 3 with respect to design variable t_1

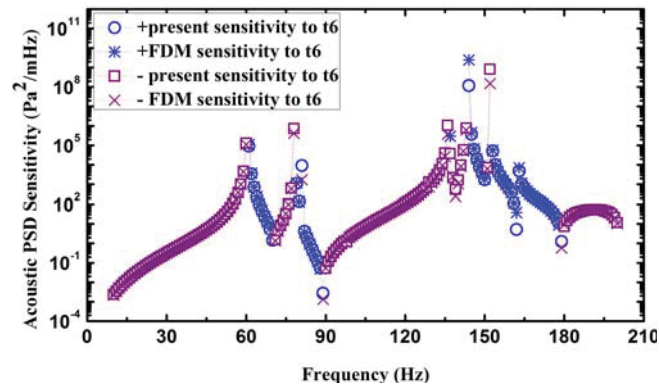


Figure 7: Acoustic PSD sensitivity values of field point 3 with respect to design variable t_6

Figures 6 and 7 show the comparisons of the acoustic PSD sensitivities with respect to the design variables t_1 and t_6 in configurations 1 and 2, respectively, predicted using the present method and the finite difference method. As shown in both figures, overall there exists a very good correlation between the predictions by these two methods in several broad frequency bands except for some natural frequencies (This is perhaps mainly due to the neglect of the damping in the structural response analysis). As the exciting frequency increases, the modal density of the structure increases too. Hence the structure would be excited more strongly in the associated modal frequency. The differences in the computed sensitivities at some natural frequencies between these two methods represent a response shift into the very sharp acoustic resonance at these frequencies. This reflects the difficulty in capturing accurately the changes when moving in an extremely narrow resonance peak. These differences were also observed in the results for other design variables.

6. Conclusions

In this paper, a new method is developed to solve random acoustic radiation problems. The acoustic pressure PSD and its sensitivity of a randomly excited structure are investigated based on FEM and IBEM combined with PEM. When the PEM is applied to random acoustic radiation problems, the random response is transformed into the harmonic response, and the sensitivity analysis of the random response is transformed into that of the harmonic response. The formula for computing the sensitivity for a structural acoustic radiation random response is derived. The sensitivities of acoustic response with respect to structural design variables are calculated for one example and validated by comparing with the results using the finite difference method. The present integrated FEM/IBEM combined with PEM procedure provides an efficient and convenient method for engineers to solve acoustic radiation problems under stationary stochastic excitations.

Acknowledgements

The authors would like to acknowledge the support by the Fundamental Research Funds for the Central Universities (Grant No.12CX04071A) and the Australian Research Council (Grant No. DP140104408).

References

- [1] S. Wang, J. Lee, Acoustic design sensitivity analysis and optimization for reduced exterior noise, *AIAA Journal*, 39 (4), 574-580, 2001.
- [2] M. J. Allen, R. Sbragio, N. Vlahopoulos, Structural/acoustic sensitivity analysis of a structure subjected to stochastic excitation, *AIAA Journal*, 39 (7), 1270-1279, 2001.
- [3] B. S. Liu, G. Z. Zhao, A. Li, PEM based sensitivity analysis for acoustic radiation problems of random responses, *Journal of Vibration and Acoustics*, 132 (2), 021012, 2010.
- [4] J. H. Lin, Y. Zhao, Y. H. Zhang, Accurate and highly efficient algorithms for structural stationary/non-stationary random responses, *Computer Methods in Applied Mechanics and Engineering*, 191 (1-2), 103-111, 2001.
- [5] Z. Z. Zhang, N. Vlahopoulos, S. Raveendra, T. Allen, K. Y. Zhang, A computational acoustic field reconstruction process based on an indirect boundary element formulation, *The Journal of the Acoustical Society of America*, 108 (5), 2167-2178, 2000.
- [6] J. H. Luo, H. C. Gea, Modal sensitivity analysis of coupled acoustic-structural systems, *Journal of Vibration and Acoustics*, 1997, 119 (4) 545-550, 1997.

An Immersed Boundary Approach for Sensitivity Analysis of Fluid-structure Interactions

Ramana V. Grandhi¹, Koorosh Gopal²

¹ Wright State University, Dayton, Ohio, ramana.grandhi@wright.edu

² Wright State University, Dayton, Ohio, gopal.2@wright.edu

1. Abstract

Gradient-based optimization algorithms are highly advantageous for computer intensive simulations such as fluid-structure interaction (FSI) problems. Typical simulation involves solution of the Navier-Stokes equations and their response sensitivities. Due to the use of body conformal meshes, mesh topology modification is required in structural shape optimization; however, this can be time consuming for complex structural boundaries. In this research, we introduce a method based on adding force terms to the Navier-Stokes equations to decouple the solid boundary definition from the mesh. Therefore, the governing equations can be solved on a Cartesian grid with efficient solvers. Decoupling the solid boundary from the mesh enables us to deform the solid domain without mesh modification allowing a significant reduction in computational costs. To calculate the sensitivity response of the system, the continuum sensitivity method is developed. Force terms are used to represent the solid boundaries and convective terms are removed in boundary conditions sensitivity equations because the boundaries do not depend on domain configuration. The methodology is verified using the sensitivity of laminar flow over a Joukowski airfoil with respect to change in camber radius. The force terms are applied using the regularized Heaviside function to satisfy the no-slip condition in the solid domain.

2. Keywords: Fluid-solid interaction, Sensitivity analysis, Immersed boundary method.

3. Introduction

The analytical methods for calculating the design sensitivities can be divided into discrete and continuum methods. In the discrete method, the continuous governing equations are discretized and then differentiated resulting in equations that govern the sensitivity of responses [1]. However, discrete methods require the modification of the source-code of the black-box CFD/FEA solvers. This might not be possible due to the unavailability and complexity of the solver [2].

Continuum sensitivity analysis (CSA) involves solving a set of partial differential equations called the continuum sensitivity equations (CSEs). Choi and Kim developed the CSA formulation extensively for structural optimization [3]. Pelletier and Etienne have applied CSA to fluid-structure interaction (FSI) problems [4]. Liu and Canfield [5] used the finite element method to solve the potential flow around an airfoil and applied CSA to find the sensitivity of the solution to the airfoil's maximum camber. These works are built around using body-conformal meshes to discretize the domain. Since the shape of the immersed structure can change, mesh deformation algorithms are required to generate a new mesh that can be utilized to calculate the new response of the system. Mesh deformation and boundary movement are also reflected in the definition of boundary conditions for the CSEs [5].

Mesh deformation schemes are separated into algebraic and elasticity-based methods. Algebraic mesh movement methods are efficient but limited to small changes in shape [6]. Elasticity methods, including the spring analogy, are based on continuum mechanics. The use of spring analogy can result in tangled meshes and negative cell volumes, particularly for large deformations. To enhance the robustness of the scheme, nonlinear torsional stiffness has been introduced to mesh nodes; however, this increases the required computational cost.

Body conformal meshes require the computational mesh to contact all the boundaries, resulting in the dependence of mesh topology on the shape of the immersed body. By decoupling the boundary definition from the mesh topology, the mesh deformation step can be removed from the solution scheme. Moreover, the boundary conditions for the CSEs will be greatly simplified. This can be achieved by using the body-force terms in the Navier-Stokes equations in such a way that the effect of immersed bodies can be captured within the governing equation. Since the immersed boundary effect is included in the governing equation, its shape can be modified without changing the topology of the computational mesh. The effect of certain boundary conditions can be modeled with an external force field rather than with specification of boundary parameter values. The immersed boundary method uses this technique to decouple the solid and fluid domains. The term immersed boundary (IB) method refers to techniques that simulate viscous flows with immersed boundaries on grids that do not conform to the shape of the immersed boundaries [7].

In this research, we use the idea of IB method to add force terms to the governing equations. The force term is responsible for generating the pressure drop which represents the existence of solid boundaries in the domain. This approach is in contrast to the usual IB method that uses the velocity data to calculate the required force terms. Moreover, the force terms are linearly related to the flow parameters and no extra effort is needed to calculate them. The force terms are added to the governing equations using a regularized Heaviside function [8] which defines the boundary contour of the solid region. This is similar to a smooth representation of a step function. Regularized Heaviside functions are widely used in the topology optimization community as filters to eliminate checkerboards and mesh-dependencies. This is in contrast to their application in this paper, where they are functions of space [9].

4. Numerical Method

The Navier-Stokes equations permit the presence of an externally imposed body force that may vary in space and time. The force term is used to introduce the pressure drop that is proportional to the velocity of each point. The Navier-Stokes equation with body force S_i is defined as

$$\frac{\partial}{\partial t}(\rho u_i) + u_j \frac{\partial}{\partial x_j}(\rho u_i) = -\frac{\partial p}{\partial x_i} + \mu \frac{\partial \tau_{ij}}{\partial x_j} + S_i \quad (1)$$

with the force term

$$S_i = -\mu D u_i \cdot H[\mathcal{C}(\mathbf{x})] \quad (2)$$

where \mathcal{C} is the contour representation of the boundary of the solid region. The regularized Heaviside function, H , is used to assign the force term, S_i , to the regions within the contour represented by \mathcal{C} . Using this method, the shape of the solid domain is modified through changing the location of force terms which does not change the mesh topology.

In this formulation, the zero velocity (no-slip condition) is satisfied both inside and also on the surface of the solid boundary contour. The force terms are defined with no extra interpolation from the the velocity field. This also adds to the simplicity of the method compared to the IB techniques where a further interpolation is usually required for calculating the force terms. It is also noteworthy to mention that the force terms are calculated at the same time as the velocity components; therefore, no extra cost is introduced in the solution of the discretized governing equations.

For a two-dimensional case, curve \mathcal{C} , is a non-self-intersecting continuous loop that defines the boundary of the solid region. The technique used for assigning the force term to mesh cells needs to be differentiable since the governing equation (1) is differentiated for deriving the CSEs. To satisfy these requirements, the regularized Heaviside function is used to assign the force terms. Different regularized Heaviside functions used in the literature are shown in Figure 1.

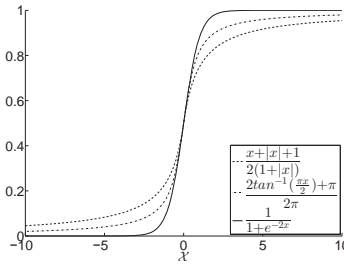


Figure 1: Comparison between different regularized Heaviside functions.

In this work, the regularized Heaviside function shown below is used due to its fast transition from zero to one.

$$H(\mathcal{X}) = \frac{1}{1 + e^{-\kappa \mathcal{X}}} \quad (3)$$

As shown in Figure 1, the regularized Heaviside function, $H(\mathcal{X})$, gives one for positive values of \mathcal{X} and zero otherwise. The positive and negative values of \mathcal{X} correspond to cells outside and inside the solid boundary curve. It should be noted that near the boundary, there is a transition region where the value of the regularized Heaviside function is between zero and one. Therefore, it introduces error in the simulation result by generating unrealistic

pressure drop in the domain. These cells are known as *gray cells* in the topology optimization community. One way to alleviate this problem is to force the transition region to occur within one cell. This is done by modifying the Heaviside function as shown in Figure 2.

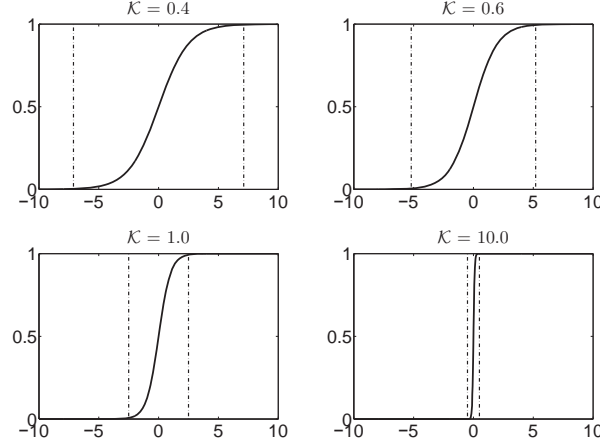


Figure 2: Effect of modifying the regularized Heaviside function in the transition region.

It should be noted that the center of each cell defines its location with respect to the solid boundary curve. Because the force terms are assigned to each volume, it is not possible to capture the exact boundary curve on a coarser mesh. However, by refining the mesh near the boundary curve, the effect of curvature can be captured almost completely on the solution of the problem.

Consider the following general, nonlinear boundary value system defined in a domain Ω with a boundary Γ

$$\mathcal{A}(u, L(u)) = f(x, t; b) \quad (4)$$

with boundary conditions defined as

$$\mathcal{B}(u, L(u)) = g(x, t; b) \quad \text{on } \Gamma \quad (5)$$

for which we seek a solution $u(x, t; b)$. In the above equation, $u = u(x, t; b)$ is dependent on design variable b implicitly and L is a linear differential operator, such as $\frac{\partial}{\partial x_i}$, that appears in the governing differential equations or boundary conditions. \mathcal{A} and \mathcal{B} are vectors of algebraic functions of u and $L(u)$. $\mathcal{B}(u, L(u))$ can be a simple function of u , such as a prescribed boundary condition for Dirichlet boundary conditions, or involve a differential operator for Neumann boundary conditions.

The CSE is formulated by directly differentiating the governing equations of Equation (4) as shown below where $u' = \frac{\partial u}{\partial b}$.

$$\frac{\partial \mathcal{A}}{\partial u} u' + \frac{\partial \mathcal{A}}{\partial L} L(u') = \frac{\partial f(x, t; b)}{\partial b} \quad (6)$$

For a problem with moving boundaries, the boundary conditions for Equation (6) can be derived by taking the total derivative of boundary condition Equation (5). The total derivative is needed here because the shape of boundaries can change [5]. This arises mostly when calculating the sensitivities due to change in shape of the domain. The total derivative is written as

$$\frac{Du}{Db} = \frac{\partial u}{\partial b} + \frac{\partial u}{\partial x} \frac{\partial x}{\partial b} \quad (7)$$

where $\frac{\partial x}{\partial b}$ is the geometric sensitivity or design velocity, which is dependent on domain parameterization. After taking the total derivative of Equation (5), the CSE boundary conditions are written as

$$\frac{\partial \mathcal{B}}{\partial u} u' + \frac{\partial \mathcal{B}}{\partial L} L(u') = \dot{g}(x, t; b) - \frac{\partial x}{\partial b} \cdot \left(\frac{\partial \mathcal{B}}{\partial u} \frac{\partial u}{\partial x} + \frac{\partial \mathcal{B}}{\partial L} L \left(\frac{\partial u}{\partial x} \right) \right) \quad (8)$$

where $\dot{g}(x,t;b)$ is the material derivative of the boundary condition. Within the scope of this paper, the boundary conditions are only applied at the outer part of the computational domain. It is assumed that these boundaries are independent of the domain configuration and their locations are not affected by the design variables. This is a valid assumption because the outer boundary conditions are typically defined as *far-field* values for flow-field variables (i.e. velocity and pressure, or their gradients). Their locations do not change and the design sensitivity is equal to zero at the boundaries; therefore, the material and local derivatives are equal on the boundaries. Equation (8) can be simplified as

$$\frac{\partial \mathcal{B}}{\partial u} u' + \frac{\partial \mathcal{B}}{\partial L} L(u') = g'(x,t;b) \quad (9)$$

The CSE of Equation (6) with the boundary conditions given in Equation (9) is a well posed system of equations in terms of sensitivity variable u' that can be solved using same numerical method used for solving the analysis problem. The spatial gradient of u in Equation (9) can be found from the solution of governing equation (4).

5. Demonstration Results

Laminar flow over a Joukowski airfoil is selected to verify the methodology. The fluid-solid interaction is defined by mounting the airfoil on an elastic sting. The load and moment from the aerodynamic loads are transferred to the structure through the mounting point. The sting is 4 m in length, with a cross-sectional area of 0.002 m², and modulus of elasticity of 200 GPa. The initial angle of attack is selected at 8 degrees with a freestream velocity of 26 m/s. This gives the Reynolds number of 2600 for this simulation.

The airfoil is defined using the Joukowski transformation shown in Equation (10), it is possible to map a circle passing through $z_1 = 1$ and containing the point $z_2 = -1$ to a curve shaped like the cross section of an airplane wing. The Joukowski transformation is done in a complex plane.

$$J(z) = z + \frac{1}{z} \quad (10)$$

By changing the location of the original circle, it is possible to change the airfoil camber. More importantly, the airfoils have analytical definition that will be used in imposition of the force terms to the mesh cells. The effect of change in the location of original circle to the camber of the airfoil is shown in Figure 3. It should be noted that after generation, the airfoils are normalized such that the chord length is always equal to one.

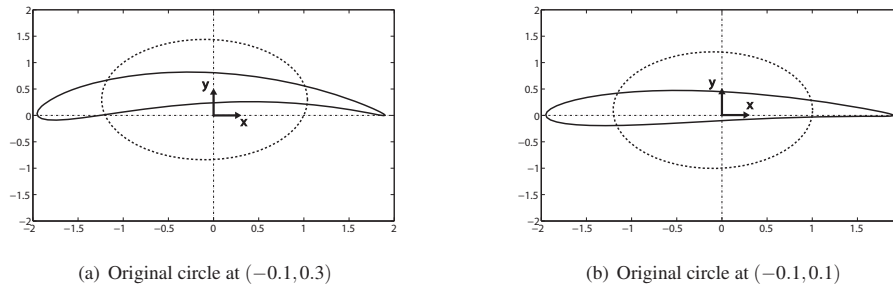


Figure 3: Airfoil definition by Joukowski transformation (not normalized).

The governing equations, along with the boundary conditions, are differentiated to derive the CSEs. The resulting system of equations is solved to get the sensitivity response of the system. As shown in Figure 3, the y coordinate of the center of the original circle defines the camber. Thus, the sensitivity of the pressure field to airfoil's camber can be calculated by differentiating the governing equation by the y coordinate of the center of the original circle (design variable, b).

The differentiated governing equations can be written as

$$u \frac{\partial \mathcal{U}}{\partial x} + v \frac{\partial \mathcal{U}}{\partial y} = -\frac{\partial \mathcal{P}}{\partial x} + \mu \left[\frac{\partial^2 \mathcal{U}}{\partial x^2} + \frac{\partial^2 \mathcal{U}}{\partial y^2} \right] + \frac{\partial S_x}{\partial b} - \mathcal{U} \frac{\partial u}{\partial x} - \mathcal{V} \frac{\partial u}{\partial y} \quad (11a)$$

$$u \frac{\partial \mathcal{V}}{\partial x} + v \frac{\partial \mathcal{V}}{\partial y} = -\frac{\partial \mathcal{P}}{\partial y} + \mu \left[\frac{\partial^2 \mathcal{V}}{\partial x^2} + \frac{\partial^2 \mathcal{V}}{\partial y^2} \right] + \frac{\partial S_y}{\partial b} - \mathcal{U} \frac{\partial v}{\partial x} - \mathcal{V} \frac{\partial v}{\partial y} \quad (11b)$$

$$\frac{\partial \mathcal{U}}{\partial x} + \frac{\partial \mathcal{V}}{\partial y} = 0 \quad (11c)$$

where $\mathcal{U} = \frac{\partial u}{\partial b}$, $\mathcal{V} = \frac{\partial v}{\partial b}$, and $\mathcal{P} = \frac{\partial p}{\partial b}$. The values for u and v (velocity components in x and y direction) are known from the solution of governing equations. Furthermore, the spatial gradients of u and v are calculated via the QUICK scheme using the surrounding cell data. This is the same method that is used for discretizing the spatial gradients in the governing equations. The QUICK scheme is based on a quadratic function and has third order accuracy on a uniform mesh.

The derivative of the force terms on the right hand side of Equation (11) has the following form.

$$\frac{\partial S_x}{\partial b} = -\mu \mathcal{U} DH(\mathcal{X}, b) - \mu u D \frac{\partial H(\mathcal{X}, b)}{\partial b} \quad (12a)$$

$$\frac{\partial S_y}{\partial b} = -\mu \mathcal{V} DH(\mathcal{X}, b) - \mu v D \frac{\partial H(\mathcal{X}, b)}{\partial b} \quad (12b)$$

In the above equations, the derivative of the regularized Heaviside function introduces the effect of shape change in the solution of the sensitivity equations. In previous works [5], this was included in the boundary condition definition through convective terms. Boundary conditions are selected independently from the configuration of the domain. Therefore, the specified values for the CSE boundary condition are assigned as zero values. It should be noted that the derivative of shape boundaries to design variable, b , is buried in the derivative of the Heaviside function. This can be calculated analytically by using the chain rule on Equations (10) and (3).

Comparing Equations (11) and (1), it is evident that the same solver can be used for solving both systems of governing equations; the difference is in adding additional source terms to Equation (1). It should be noted that this does not affect the numerical method used to solve the problem as these terms can be incorporated in the body force terms. The solution of Equation (1) is used for initializing the convective terms, i.e. u and v , in Equation (11). This results in faster convergence of the sensitivity solution compared to the governing equations. The sensitivity of pressure around an airfoil based on original circle location at $(-0.1, 0.1)$ is shown in Figure 5.

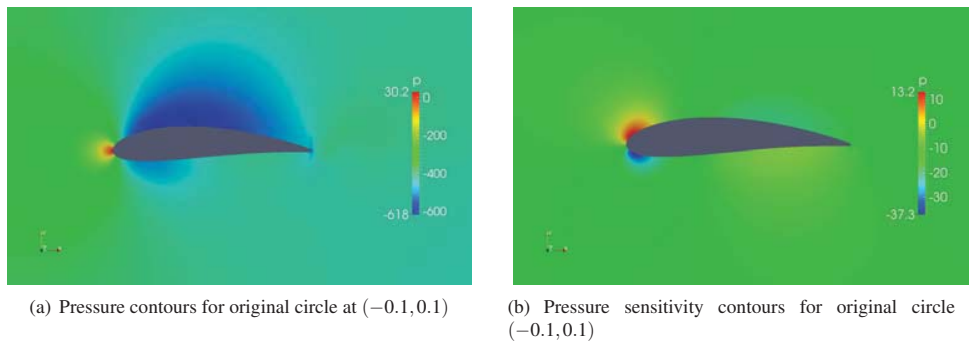


Figure 4: Sensitivity of pressure field around airfoil to camber line variation.

The sensitivity of pressure field on top and bottom surfaces of the airfoil to camber line variation is shown in Figure 5. It should be noted that the method of moving average with 4 points is used to further smoothen the data over the boundaries.

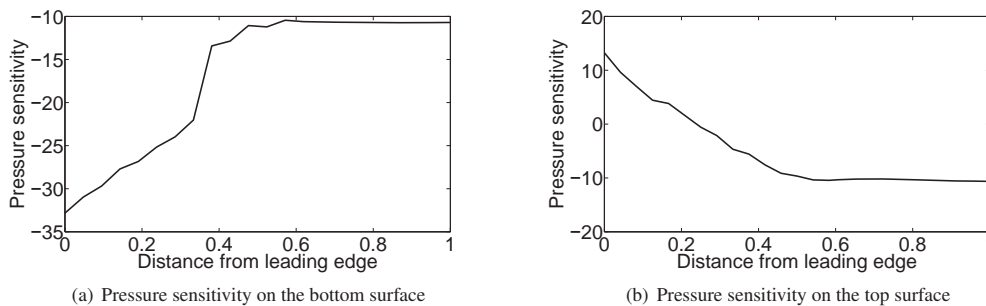


Figure 5: Sensitivity of pressure field on airfoil surface to camber line variation.

6. Conclusions

In this work, force terms are added to the Navier-Stokes equations to represent the solid boundaries inside the domain. The force terms act as a high pressure drop that results in satisfying the no-slip boundary condition in the solid domain. Using this method, it is possible to decouple the definition of solid boundary from the computational mesh; therefore, it is not required to deform the mesh topology when the solid boundary shape changes. Moreover, using this method, the governing equations are solved on a Cartesian structured grid where efficient solvers can be utilized. This reduces the computational time and memory requirements for the simulations.

The regularized Heaviside function is used to apply the force terms on the mesh volumes. Several regularized Heaviside functions are introduced and a model with the fastest transition is selected. One of the problems of using the regularized Heaviside function is the gray region within the domain and the numerical error associated with it. To remove the gray-cells from the computational domain, the regularized Heaviside function is forced to have a transition region within one cell. Using this approach, errors from the existence of gray-cells are minimized within the domain. The noise is further reduced by using the method of moving average when reporting the results on immersed boundary surfaces.

The continuum sensitivity equations are derived by differentiating the governing equations and their corresponding boundary conditions. In this approach, the interface boundary conditions are removed from the simulation by introducing the force terms. The outer boundary conditions usually do not depend on the domain configuration. Therefore, in most cases, the boundary conditions will be zero for sensitivity analysis using this approach. On the other hand, the effect of shape change is introduced to the domain through the derivative of the regularized Heaviside function. This acts as an additional force term in the governing equations. These equations have the same structure as the original governing equations and they can be solved using the same solver.

The applicability of this method is investigated by solving the flow and the sensitivity response of the laminar flow over a Joukowski airfoil. The requirement of mesh deformation and use of body conformal mesh are removed from the simulation, which can save a significant amount of computational time and resources for conducting optimization.

6. References

- [1] Martins, J. R. and Hwang, J. T., Review and unification of methods for computing derivatives of multidisciplinary computational models, *AIAA Journal*, Vol. 51, No. 11, 2013, pp. 2582-2599.
- [2] Peter, J. E. and Dwight, R. P., Numerical sensitivity analysis for aerodynamic optimization: A survey of approaches, *Computers & Fluids*, Vol. 39, No. 3, 2010, pp. 373-391.
- [3] Choi, K. and Kim, N., Structural Sensitivity Analysis and Optimization, Vol. 1, *Springer Science + Business Media*, 2005.
- [4] Etienne, S. and Pelletier, D., A general approach to sensitivity analysis of fluid-structure interactions, *Journal of fluids and structures*, Vol. 21, No. 2, 2005, pp. 169-186.
- [5] Liu, S. and Canfield, R. A., Boundary velocity method for continuum shape sensitivity of nonlinear fluidstructure interaction problems, *Journal of Fluids and Structures*, Vol. 40, No. 0, 2013, pp. 284-301.
- [6] Hicken, J. E. and Zingg, D. W., Aerodynamic optimization algorithm with integrated geometry parameterization and mesh movement, *AIAA Journal*, Vol. 48, No. 2, 2010, pp. 400-413.
- [7] Mittal, R. and Iaccarino, G., Immersed boundary methods, *Annu. Rev. Fluid Mech.*, Vol. 37, 2005, pp. 239-261.
- [8] Gopal, K., Grandhi, R. V., and Kolonay, R. M., Continuum Sensitivity Analysis for Structural Shape Design Variables Using Finite-Volume Method, *AIAA Journal*, Vol. 53, No. 2, 2015, pp. 347-355.
- [9] Deaton, J. D. and Grandhi, R. V., A survey of structural and multidisciplinary continuum topology optimization: post 2000, *Structural and Multidisciplinary Optimization*, Vol. 49, No. 1, 2014, pp. 1-38.

MIST Topology Optimization for Bending Plates under Static Loading

Mahmoud Alfouneh¹, Liyong Tong²

¹ School of Aerospace, Mechanical and Mechatronic Engineering, The University of Sydney, NSW, Australia,
Mahmoud.alfouneh@usyd.edu.au

² School of Aerospace, Mechanical and Mechatronic Engineering, The University of Sydney, NSW, Australia,
liyong.tong@usyd.edu.au

Abstract

This article extends the moving iso-surface threshold (MIST) method to solve the topology optimization problem of bending plates under static loading. In the extended MIST, multiple layer-wise objective functions and volume constraints are employed in the optimization formulation of multiple-layered bending plates. Considered are three types of objective functions: minimum mean compliance, maximum mutual strain energy and fully-stressed design. The associated response functions chosen are, respectively, the strain energy density, mutual strain energy density and the Von Mises stress for each layer. The nodal values of these response functions in a fixed FE mesh are smoothed using a modified filter. Numerical examples are presented to validate the extended MIST in application to topology optimizations of single- and multi-layered plates under static loading.

Keywords: MIST topology optimization, multi-layer plate, minimum mean compliance, compliance mechanism, fully-stressed design.

1. Introduction

Topology optimization of bending plates is about finding the optimum material distribution to achieve optimum or better performance. Bending plates can come in the form of a single-layer or multiple-layers and its topology optimization is conducted for one or multiple layers. Topology optimization of bending plates and shells under static loading has attempted by a number of researchers using different optimization methods [1-10]. In this study, we extend the MIST method [11-12] to the case of topology optimization with multiple layer-wise objective functions and volume constraints. MIST method has applied for solving some 2D plane stress or strain or 3D problems, but has not been used to study the topology optimization of bending plates, in particular multiple layered plates, under static loading. The article is organized as follows. Section 2 presents the problem statement with multiple layer-wise objective functions and volume constraints. Section 3 presents some implementation details of the MIST method. Section 4 presents several numerical examples including single-layered or multiple-layered bending plates under static loadings. A brief summary is provided in Section 5.

2. Problem statement

For a single- or multiple layered bending plates under static loading, we define its topology optimization problem as follows:

$$\begin{aligned} & \min \text{ or } \max f_i \quad (i = 1, 2, \dots, n) \\ & \text{subject to: } \mathbf{K}\mathbf{U}_{(j)} = \mathbf{F}_{(j)} \quad (j = 1, 2) \\ & \sum_{k=1}^{N_E} (x_{ki} A_k) = \alpha_i \sum_{k=1}^{N_E} A_k \quad (\varepsilon \leq x_{ki} \leq 1; \quad i = 1, 2, \dots, n) \end{aligned} \quad (1)$$

where f_i and α_i are the objective function and the material volume fraction for the i^{th} layer, n is the total number of layers in a multiple-layered plate, \mathbf{K} is the global stiffness matrix of the plate structure, \mathbf{U}_j and \mathbf{F}_j are the nodal displacement and load vectors for the j^{th} load case (where $j=1$ refers to the real load case, whereas $j=2$ represents the dummy load case with an applied unit load at chosen degree of freedom, x_{ki} is the weighting factor or density of the k^{th} element for the i^{th} layer and varies from 0 to 1 ($x_{ki} = 0$ means void and $x_{ki} = 1$ indicates solid), A_k is the volume or area of the k^{th} element, and N_E represents the total number of elements for each layer (In this study same N_E is used for the numerical examples). In the literature, $\varepsilon = 0.001$ is typically chosen in numerical computations to avoid stiffness matrix singularity.

Three types of objective functions are considered in this study and the corresponding statements are:

(a) to minimize the mean compliance i.e.

$$\min f_i = \int_{\Omega_i} \frac{1}{2} \boldsymbol{\sigma}_i^T \boldsymbol{\varepsilon}_i d\Omega \quad (2a)$$

(b) to maximize the deflection in the direction of a chosen degree of freedom, i.e.

$$\max f_i = u_{out} = \int_{\Omega} \boldsymbol{\sigma}_{(2)}^T \boldsymbol{\varepsilon}_{(1)} d\Omega, \text{ or } \min f_i = -u_{out} = -\int_{\Omega} \boldsymbol{\sigma}_{(2)}^T \boldsymbol{\varepsilon}_{(1)} d\Omega \quad (2b)$$

and

(c) to minimize the maximum Von Mises stress, i.e.

$$\min f_i = \sum_{k=1}^{N_{node}} \sigma_{vmk}^{(i)} \quad (2c)$$

Where $\sigma_{vmk}^{(i)}$ denotes the Von Mises stress at the k^{th} node for the i^{th} layer and N_{node} denotes the total number of nodes for each layer.

3. MIST algorithm and implementation

The MIST algorithm can be schematically depicted in the flowchart in Figure 1.

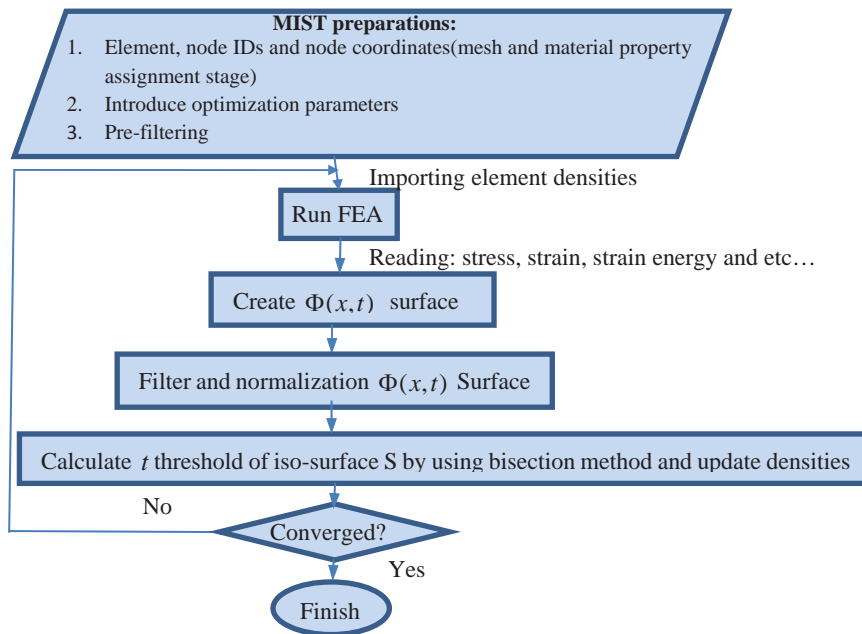


Figure 1: MIST algorithm flowchart

The MIST method is interfaced with ANSYS to solve all the FEM problems. In each iteration after each FEA run, selected FEA results, such as strain energy density, strain and stress are imported from the ANSYS output files and then used to construct the response function Φ for the design domain. For the three types of problems given in equations (1) and (2), the Φ function for the i^{th} iteration is, respectively, given by:

$$\Phi_i(x, t) = \frac{1}{2} \boldsymbol{\sigma}_i^T \boldsymbol{\varepsilon}_i \quad (3a)$$

$$\Phi_i(x, t) = -\frac{1}{2} \boldsymbol{\sigma}_{i(2)}^T \boldsymbol{\varepsilon}_{i(1)} \quad (3b)$$

$$\Phi_i(x, t) = \sigma_{vmi} \quad (3c)$$

where $\boldsymbol{\varepsilon}_{i(1)}$ and $\boldsymbol{\sigma}_{i(2)}$ represent the strain and stress vectors for load case 1 and 2 respectively. Nodal values of Φ function can be either output from ANSYS or calculated by using relevant stress or strain values at Gaussian or nodal points.

In MIST, a filtering scheme is applied to the nodal values of Φ function. Consider node j , the filtered value of Φ_j , denoted by $\hat{\Phi}_j$, can be determined by

$$\hat{\Phi}_j = \frac{\Phi_{qj}}{c_{uj}} \quad (4a)$$

where

$$c_{ij} = \sum_{q=1}^{N_q} c_{jq} \quad (4b)$$

$$\Phi_{ij} = \sum_{q=1}^{N_q} c_{jq} \Phi_q \quad (4c)$$

and

$$c_{jq} = \pi (r_{\min} - R_{jq})^2 \quad (4d)$$

where r_{\min} is the spatial radius (typically of the value of approximately 3 times of element length), N_q denotes the number of nodes that lie within the circle with a radius of r_{\min} , R_{jq} is the distance between node j and q . Φ_q is the Φ value at node q which lies within the circle.

The elastic modulus of an element in a structure is updated using:

$$E(x_k)_i = (x_k^p)_i E_{(solid)_i} \quad (5)$$

Where x_k represents the fraction of solid area to the total one of the k^{th} element and p is the penalty factor.

4. Numerical results and discussion

4.1 Minimum mean compliance

The problem considered in this section is the minimum mean compliance problem or the problem of minimizing the total strain energy of the structure. Firstly, for single-layer plate, we study the effects of spatial radius and the volume fraction on the selected results of topology design optimization using MIST, e.g. the objective function versus iteration histories and the final topologies; Secondly, we investigate the topology optimization of multiple layers in multi-layered plates. In all the calculations for this problem, the Φ function defined in equation (3a) is adopted. For the case of multiple-layered plates, the Φ function given in equation (3a) is used to construct the relevant response function for every design layer.

4.1.1 Effect of spatial radius r_{\min}

Consider the topology optimization of a four-side clamped square plate with side length of 60mm and thickness of 0.5mm subject to a point load $F_z = -5\text{N}$ at its centre and a volume fraction of 0.5. Assume $E = 70000\text{ MPa}$ and $\nu = 0.3$. The square plate is meshed with 3600 (60 elements by 60 elements) solid181 elements in ANSYS. As in MIST, we use the following parameters: move limit=0.1, penalty factor=3. Figure 2 depicts the curve of the total strain energy versus iteration for $r_{\min} = 7\text{mm}$. It is evident that the objective function converges rapidly and smoothly.

Figure 3 depicts the final optimum topologies for various values of spatial radius r_{\min} e.g., 1, 3, 6 and 7 mm or 1, 3, 6 and 7 element lengths. As shown in Figure 3, for small spatial radius hinges exist in the optimum topologies, whereas for large spatial radius these hinges disappear, which makes the topology more practical in the sense of load diffusion.

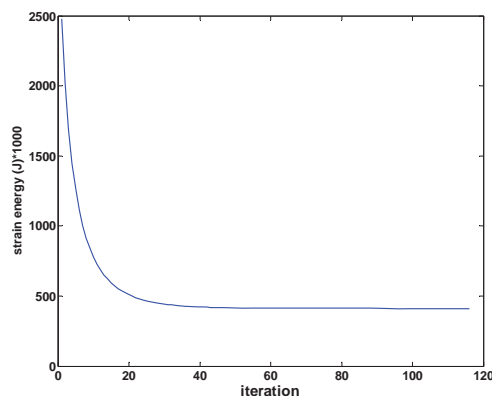


Figure 2: The objective function- iteration history

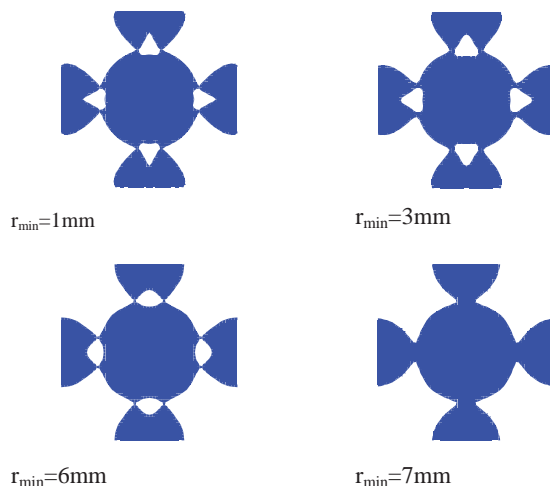


Figure 3: The effects of filtering radius on the optimal topology

4.1.2 Influence of volume fractions

Consider the same plate as used in example 4.1.1 except for the four-side clamped boundary condition being replaced by four-side simply supported one. This example is to illustrate the effect of the volume fraction on the convergence history of the objective function and the final optimum topologies. Figure 4 depicts the curves of the objective function versus iteration number for four different volume fractions, e.g. 20%, 40%, 60% and 80%. It is noted that the objective function converges with 50 iterations for 20% and 40% volume fractions and with 30 for the cases of 60% and 80% volume fractions. Figure 5 depicts the final topologies for the four volume fraction cases. It can be seen that the topologies for the 20% and 40% or the 60% and 80% volume fractions resembles to certain extent, the difference between the topologies for the 20% and 40% volume fractions are quite different from the other two topologies with 60% and 80% volume fractions. There appears a topological shape change when the volume fraction varies from 40% to 60%.

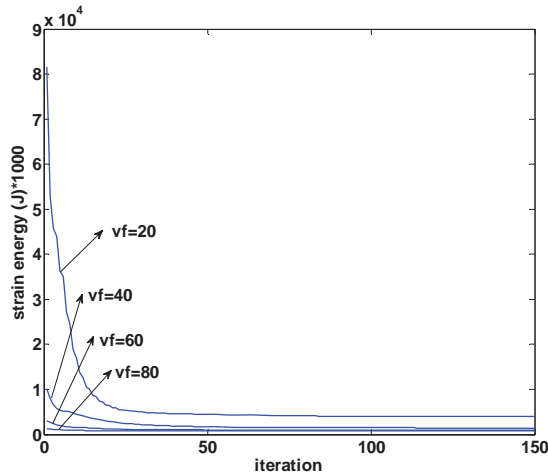


Figure 4: Variations of strain energy versus iteration for different v_f

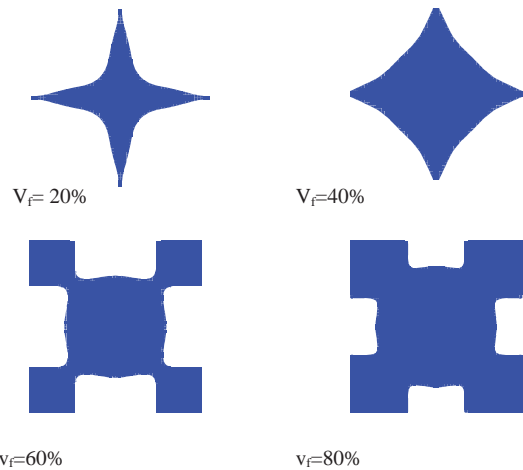


Figure 5: Different optimal shapes with different v_f

4.1.3 Multiple-layered plate

Consider a four-side clamped four-layer square plate. The side length is 300 mm, and the thickness of each layer is 1 mm ($t_1=t_2=t_3=t_4=1\text{mm}$). The material properties for all four layers are: $E_1=E_4=69\text{ GPa}$, $E_2=E_3=220\text{ MPa}$, $\nu_1=\nu_3=\nu_4=0.3$, $\nu_2=0.49$. At the centre of the square plate a vertical point load $F_z=-200\text{N}$ is applied. A total number of 3600 (ANSYS Solid185) elements are used to uniformly mesh each layer. In all the MIST calculations, the following parameters are used: dynamic move limit of minimum=0.1, spatial radius=0.0125mm in filtering, and penalty factor = 3. Layers 2 and 4 are the design layers with $v_{f2} = v_{f4} = 50\%$. Figure 6 depicts the convergence histories of the total strain energies calculated for the second layer, the fourth layer and all layers. Evidently, the total strain energies for the second, fourth and all layers converge within 100 iterations.

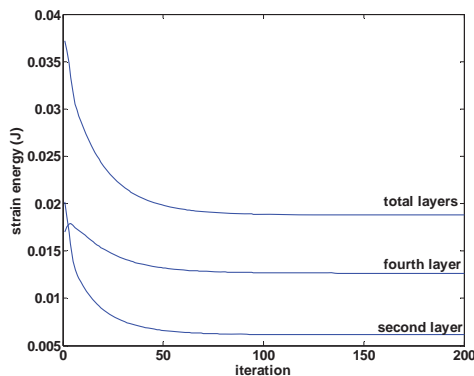


Figure 6: Iteration histories for different layers

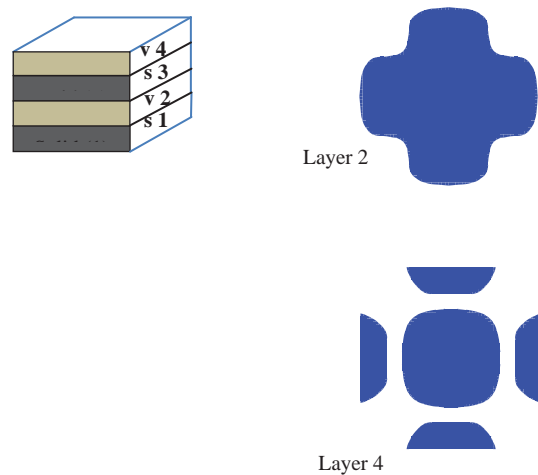


Figure 7: Optimum shapes of layers 2 and 4

Figure 7 depicts the sketch of the four-layer plate and the optimum topologies of layers 2 and 4. The material distribution of layer 4 is discontinuous whereas that for layer 2 has a continuous load diffusion path with the layer.

4.2 Compliance mechanism

The objective function for this example is to maximize deflection under dummy load based on Φ function introduced in equation (3b). A three layer plate which layer 3 (top layer) is under design layer with volume fraction $v_{f3}=50\%$, is considered. Two other layers are non-design layers (figure 9). The plate dimensions and material properties are the same as example 4.1.3 except at this example there is not layer 4. The elements, meshing scheme and solver used are also the same as example 4.1.3. The plate is clamped at left edge. Two load cases are applied. Load case 1, $FR = -200 N$ is real load and applied vertically at the centre of plate and load case 2 is dummy load $FU = -1 N$ applied in z direction same as direction of real load at the centre of opposite edge.

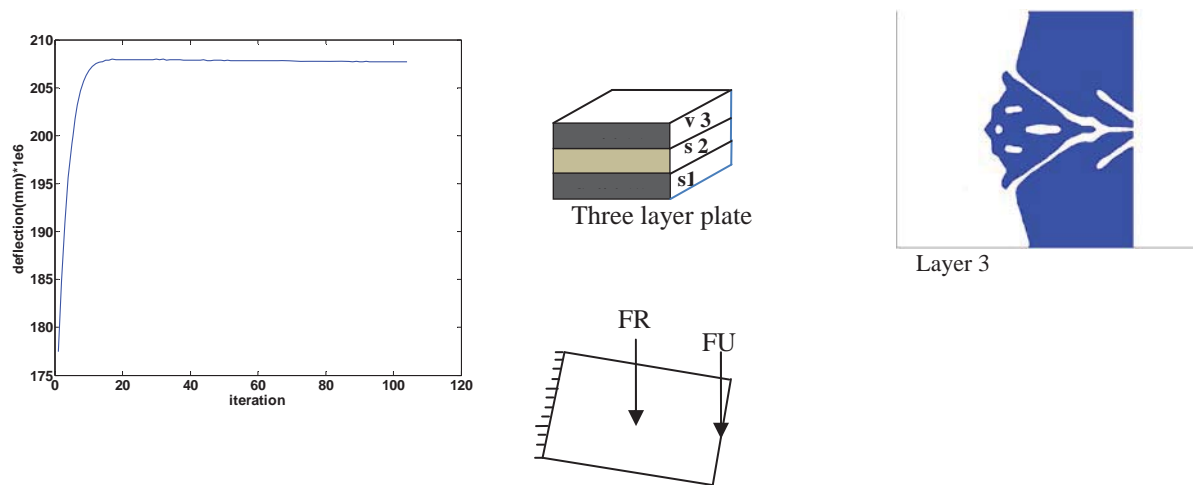


Figure 8: iteration histories versus deflection under dummy load Figure 9: optimal shape

As can be seen from figure 8, deflection under dummy load is maximised alongside of optimization increment and finally it is stable. The initial value for objective function is approximately $177e-6$ mm which reaches to a stable value around $207e-6$ mm in just 20 iterations. It is a considerable maximization about 1.169 times of initial value. Small fluctuations as seen in iteration history curve can be removed by considering low values of move limit say lower than 0.1. Corresponding optimal shape is demonstrated in figure 9 and it is shown that material distributed in the right half side of design layer.

4.3 Fully-stressed design

The aim of this example is to use the Φ function given in equation (3c) to develop fully stressed designs for selected layers. The plate is clamped at four sides and a force of $Fz=-200 N$ is applied at the center. The plate dimensions and material properties are the same as example 4.1.3. The elements, meshing scheme and solver used are also the same as example 4.1.3. As shown in Figure 11, the inner two layers are non-design layers whereas the outer two layers are the design layers with different volume fractions, e.g. $v_{f1}=70\%$ and $v_{f4}=20\%$. Figure 10 shows the iteration histories of the total von Mises stress in layer 1, layer 4 and all layers. Once again, all three quantities converge within 60 iterations. As shown in this figure, minimizing total Von Mises stress happens as expected for all the design layers. It is seen that for layer 4 the reduction happens visibly although these values are so small since its volume fraction is much lower than layer 1. Figure 11 depicts the corresponding topologies of layer 1 and layer 4. It is noted that the topology in layer 4 resembles to that in layer 4 in example 4.1.3 as both layers are in compression in the bending plate.

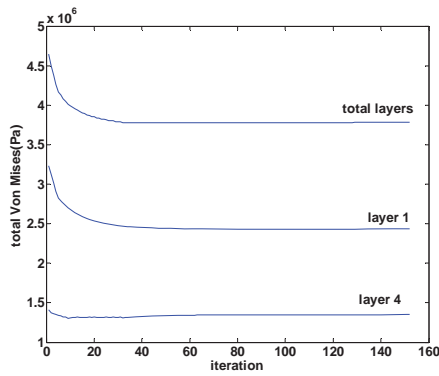


Figure 10: Iteration histories for fully stressed design

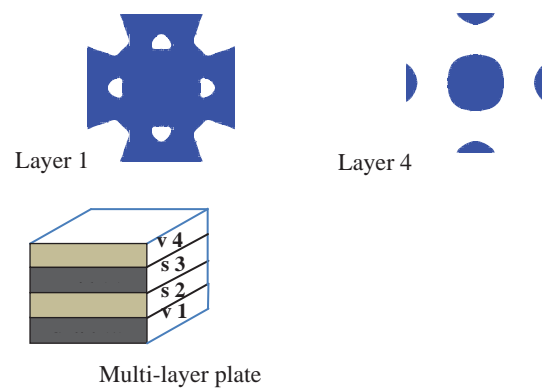


Figure 11: optimal shapes for top and bottom layers

5. Concluding remarks

The salient points of the present study can be summarized as follows: (a) an extended MIST formulation is presented for topology optimization of multiple-layered plate structures with multiple volume fractions; (b) three problems with different objective functions are considered and then solved by using three different response functions; and (c) the present numerical results illustrate the effects of the spatial radius in the filter used and the volume fraction on the optimum topologies as well as the stable convergence history observed.

Acknowledgements

The authors would like to acknowledge the support of the Australian Research Council via Discovery-Project Grants (DP140104408).

References

1. Liang, Q.Q., Y.M. Xie, and G.P. Steven, A performance index for topology and shape optimization of plate bending problems with displacement constraints. *Structural and Multidisciplinary Optimization*, 2001. **21**(5): p. 393-399.
2. Zhao, C., G. Steven, and Y. Xie, Evolutionary natural frequency optimization of thin plate bending vibration problems. *Structural optimization*, 1996. **11**(3-4): p. 244-251.
3. Kang, Z. and X. Wang, Topology optimization of bending actuators with multilayer piezoelectric material. *Smart Materials and Structures*, 2010. **19**(7): p. 075018.
4. Belblidia, F., J. Lee, and S. Rechak, Topology optimization of plate structures using a single-or three-layered artificial material model. *Advances in Engineering Software*, 2001. **32**(2): p. 159-168.
5. Mukherjee, A. and S. Joshi, Piezoelectric sensor and actuator spatial design for shape control of piezolaminated plates. *AIAA journal*, 2002. **40**(6): p. 1204-1210.
6. Halkjær, S., O. Sigmund, and J.S. Jensen, Maximizing band gaps in plate structures. *Structural and Multidisciplinary Optimization*, 2006. **32**(4): p. 263-275.
7. Pedersen, N.L., On topology optimization of plates with prestress. *International Journal for Numerical Methods in Engineering*, 2001. **51**(2): p. 225-239.
8. Stegmann, J. and E. Lund, Nonlinear topology optimization of layered shell structures. *Structural and Multidisciplinary Optimization*, 2005. **29**(5): p. 349-360.
9. Kögl, M. and E.C. Silva, Topology optimization of smart structures: design of piezoelectric plate and shell actuators. *Smart materials and Structures*, 2005. **14**(2): p. 387.
10. Hansel, W. and W. Becker, Layerwise adaptive topology optimization of laminate structures. *Engineering Computations*, 1999. **16**(7): p. 841-851.
11. Tong, L. and J. Lin, Structural topology optimization with implicit design variable—optimality and algorithm. *Finite Elements in Analysis and Design*, 2011. **47**(8): p. 922-932.
12. Vasista, S. and L. Tong, Design and testing of pressurized cellular planar morphing structures. *AIAA journal*, 2012. **50**(6): p. 1328-1338.

Structural Optimization under Complementarity Constraints

Sawekchai Tangaramvong¹, Francis Tin-Loi²

¹ Centre for Infrastructure Engineering and Safety, School of Civil and Environmental Engineering, The University of New South Wales, Sydney, NSW 2052, Australia, sawekchai@unsw.edu.au (corresponding author)

² Centre for Infrastructure Engineering and Safety, School of Civil and Environmental Engineering, The University of New South Wales, Sydney, NSW 2052, Australia, f.tinloi@unsw.edu.au

1. Abstract

This paper provides an overview of the challenging class of structural optimization problems with complementarity conditions, generally known as a “mathematical program with equilibrium constraints” (MPEC). Complementarity, mathematically defined by the perpendicularity of two sign constrained vectors, describes such common mechanical behaviour as elastoplasticity and contact conditions. The MPEC is in effect the inverse counterpart of a state problem formulated as a “mixed complementarity problem” (MCP), and is moreover far more challenging to process since an MPEC is in general nonsmooth and nonconvex. We briefly describe a promising class of solution methods, all based on some regularization technique, to convert the MPEC into a standard nonlinear programming (NLP) problem, and illustrate its application for the optimal design of engineering structures.

2. Keywords: complementarity, nonconvex and nonsmooth mathematical program, structural optimization.

3. Introduction

Complementarity (the requirement that two nonnegative vectors are orthogonal) is a typical and recurrent mathematical feature in the nonlinear analysis of structures, e.g. to represent elastoplasticity and contact-like conditions. The resulting state problems lead to instances of mathematical programs known generally as “mixed complementarity problems” (MCPs) [1] for which, under certain conditions (e.g. definiteness of some key matrices), can be efficiently solved. However, the inverse problem that for example arises in structural optimization under complementarity conditions is far more challenging to process since the underlying mathematical programming problem, known as a “mathematical program with equilibrium constraints” (MPEC) [2], is nonsmooth and/or nonconvex.

We introduce the concept of complementarity, and review the state problem and its solution before presenting the generic formulation for structural optimization under complementarity constraints [3-7]. We then provide an overview of a promising class of solution methods that can be used to solve the resulting MPECs [2]. These all involve application of some regularizing technique followed by conversion of the MPEC into a standard nonlinear programming (NLP) problem. Finally, we give two illustrative examples to illustrate this approach.

4. Complementarity Conditions in Engineering Mechanics

Various engineering state problems can be formulated as a standard MCP [1] which, in general, consists of three pieces of basic information, namely lower bounds $\mathbf{z}_l \in \mathfrak{R}^l$, upper bounds $\mathbf{z}_u \in \mathfrak{R}^l$ and functions $\mathbf{Y}(\mathbf{z}) \in \mathfrak{R}^l$. The aim is to

$$\begin{aligned}
 &\text{find} && \mathbf{z}, \mathbf{v}, \mathbf{k} \in \mathfrak{R}^l \\
 &\text{subject to} && \mathbf{Y}(\mathbf{z}) - \mathbf{v} + \mathbf{k} = \mathbf{0} \\
 &&& \mathbf{z}_l \leq \mathbf{z} \leq \mathbf{z}_u \\
 &&& \mathbf{v}^T (\mathbf{z} - \mathbf{z}_l) = \mathbf{0}, \mathbf{v} \geq \mathbf{0} \\
 &&& \mathbf{k}^T (\mathbf{z}_u - \mathbf{z}) = \mathbf{0}, \mathbf{k} \geq \mathbf{0}
 \end{aligned} \tag{1}$$

where $-\infty \leq \mathbf{z}_l \leq \mathbf{z}_u \leq \infty$ and $\mathbf{Y}(\mathbf{z})$ are continuously differentiable. As an illustration, we briefly review in the following two engineering mechanics problems (see e.g. [7]) formulated as MCP (1); one involves elastoplasticity, the other contact conditions with complementarity conditions schematically shown in Fig. 1.

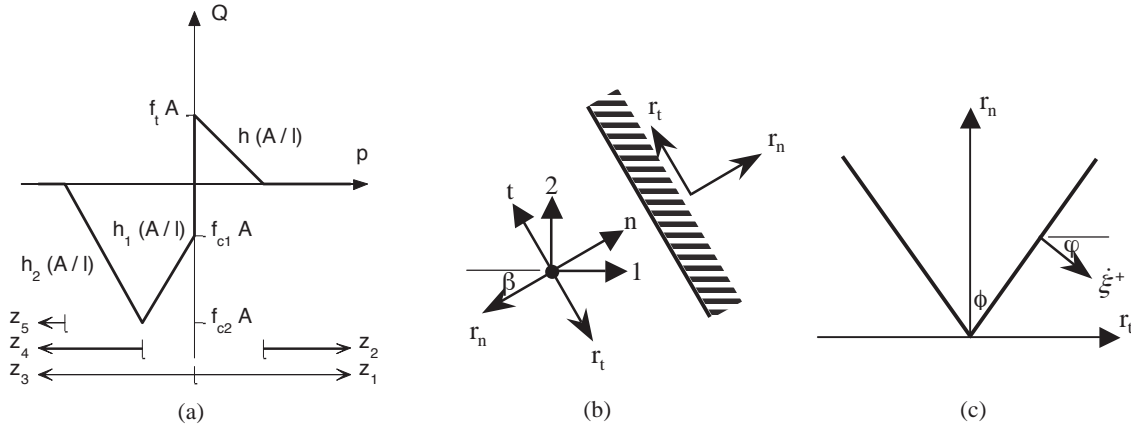


Figure 1: Complementarity conditions (a) softening material, (b) contact forces, (c) friction law.

4.1 Analysis of Elastoplastic Structures

The governing state problem for the holonomic (path-independent) analysis of structures (suitably discretised into n number of elements, d degree of freedoms, m generalized stresses/strains and y yield functions) with inelastic material properties can be cast as an MCP in variables $(\mathbf{Q}, \mathbf{u}, \mathbf{z})$ as follows [4]:

$$\begin{aligned}
 -\alpha \mathbf{f} + \mathbf{C}^T \mathbf{Q} &= \mathbf{0} \\
 \mathbf{Q} - \mathbf{S} \mathbf{C} \mathbf{u} + \mathbf{S} \mathbf{N} \mathbf{z} &= \mathbf{0} \\
 \mathbf{w} = -\mathbf{N}^T \mathbf{Q} + \mathbf{H} \mathbf{z} + \mathbf{r} &\geq \mathbf{0}, \quad \mathbf{z} \geq \mathbf{0}, \quad \mathbf{w}^T \mathbf{z} = 0
 \end{aligned} \tag{2}$$

Clearly problem (2) is an instance of MCP (1), where the first two relations in Eq.(2) correspond to the first condition in Eq.(1) with $\mathbf{0} \leq \mathbf{z} \leq \infty$, $\mathbf{v} = \mathbf{w} \geq \mathbf{0}$ and $\mathbf{k} = \mathbf{0}$.

Physically, the first equation in MCP (2) describes linear equilibrium between the externally applied forces $\alpha \mathbf{f} \in \mathcal{R}^d$ and the generalized stresses $\mathbf{Q} \in \mathcal{R}^m$ through a constant compatibility matrix $\mathbf{C} \in \mathcal{R}^{m \times d}$, where α and $\mathbf{f} \in \mathcal{R}^d$ denote a positive load scalar and a basic force vector, respectively. The second equation expresses the relationship between stresses \mathbf{Q} and the elastic strains defined as $\mathbf{q} - \mathbf{p} \in \mathcal{R}^m$, where $\mathbf{S} \in \mathcal{R}^{m \times m}$, $\mathbf{q} \in \mathcal{R}^m$ and $\mathbf{p} \in \mathcal{R}^m$ are, respectively, the conventional (unassembled) elastic stiffness matrix, generalized strains written in terms of nodal displacements $\mathbf{u} \in \mathcal{R}^d$, and generalized plastic strains. In the third and final relation, an associative flow rule prescribes the plastic strains \mathbf{p} as functions of plastic multipliers $\mathbf{z} \in \mathcal{R}^y$, where $\mathbf{N} \in \mathcal{R}^{m \times y}$ collects the normal directions to all piecewise linear (PWL) yield hyperplanes [8] in Fig. 1a. The yield functions $\mathbf{w} \in \mathcal{R}^y$ mathematically describe the PWL yield model of this Fig. 1a in terms of \mathbf{Q} and \mathbf{z} , where $\mathbf{H} \in \mathcal{R}^{y \times y}$ and $\mathbf{r} \in \mathcal{R}^y$ denote a hardening/softening matrix and a plastic limit vector, respectively. Finally, the complementarity condition $\mathbf{w}^T \mathbf{z} = 0$ (describing a componentwise relationship $w_j \geq 0$, $z_j \geq 0$ and $w_j z_j = 0$ for $j = 1$ to y) between the two positive sign constrained vectors $\mathbf{w} \geq \mathbf{0}$ and $\mathbf{z} \geq \mathbf{0}$ implies either elastic ($w_j > 0$ and $z_j = 0$) or plastic ($w_j = 0$ and $z_j > 0$) behaviour, and also allows reversal (holonomy) of plastic strains

An elastoplastic analysis maps out the complete load versus displacement responses of the inelastic structure by collecting the resulting variables \mathbf{Q} , \mathbf{u} and \mathbf{z} obtained from a series of MCP (2) solves under specified increasing values of load multiplier α . MCP (2) can be processed directly using, for instance, the industry standard complementarity solver PATH [1]. For computational and modelling convenience PATH is often called from within some mathematical programming environment such as GAMS (an acronym for “general algebraic modelling system”) [9].

4.2 Analysis of Structures with Frictional Contacts

We consider rigid perfectly plastic structures with c unilateral frictional contacts as shown in Figs. 1b-c. The state problem can be formulated as the following MCP in variables $(\alpha, \mathbf{Q}, \dot{\mathbf{u}}, \dot{\mathbf{z}}, \mathbf{r}_n, \mathbf{r}_t, \xi)$ [7]:

$$\begin{aligned}
& \mathbf{f}^T \dot{\mathbf{u}} = 1 \\
& -\alpha \mathbf{f} + \mathbf{C}^T \mathbf{Q} + \mathbf{C}_n^T \mathbf{r}_n + \mathbf{C}_t^T \mathbf{r}_t = \mathbf{0} \\
& -\mathbf{C} \dot{\mathbf{u}} + \mathbf{N} \dot{\mathbf{z}} = \mathbf{0} \\
& -\mathbf{C}_t \dot{\mathbf{u}} + \mathbf{V}_t \dot{\boldsymbol{\xi}} = \mathbf{0} \\
& \mathbf{w} = -\mathbf{N}^T \mathbf{Q} + \mathbf{r} \geq \mathbf{0}, \quad \dot{\mathbf{z}} \geq \mathbf{0}, \quad \mathbf{w}^T \dot{\mathbf{z}} = 0 \\
& \boldsymbol{\pi}_c = \mathbf{N}_n^T \mathbf{r}_n - \mathbf{N}_t^T \mathbf{r}_t \geq \mathbf{0}, \quad \dot{\boldsymbol{\xi}} \geq \mathbf{0}, \quad \boldsymbol{\pi}_c^T \dot{\boldsymbol{\xi}} = 0 \\
& \boldsymbol{\pi}_n = -\mathbf{C}_n \dot{\mathbf{u}} + \mathbf{V}_n \dot{\boldsymbol{\xi}} \geq \mathbf{0}, \quad \mathbf{r}_n \geq \mathbf{0}, \quad \boldsymbol{\pi}_n^T \mathbf{r}_n = 0
\end{aligned} \tag{3}$$

Solution of this MCP (3) provides one set of response variables $\alpha, \mathbf{Q}, \dot{\mathbf{u}}, \dot{\mathbf{z}}, \mathbf{r}_n, \mathbf{r}_t, \dot{\boldsymbol{\xi}}$ for the structural system considering rigid perfectly plastic material properties and nonassociative frictional contact conditions.

The first relation represents a (normalised) positive dissipation produced by \mathbf{f} and displacement rates $\dot{\mathbf{u}} \in \mathfrak{R}^d$. Linear equilibrium between $\alpha \mathbf{f}$, \mathbf{Q} and the two contact forces in the normal $\mathbf{r}_n \in \mathfrak{R}^c$ and tangential $\mathbf{r}_t \in \mathfrak{R}^c$ directions is given in the second relation, where $\mathbf{C}_n, \mathbf{C}_t \in \mathfrak{R}^{c \times d}$ are the corresponding compatibility matrices at the contacts. Compatibility between $\dot{\mathbf{u}}$ and the plastic multiplier rates $\dot{\mathbf{z}} \in \mathfrak{R}^y$ is described by the third relation. The fourth relation indicates the compatibility between tangential displacement rates $\mathbf{C}_t \dot{\mathbf{u}}$ along the contact interface and the sliding rates $\mathbf{V}_t \dot{\boldsymbol{\xi}}$, where $\dot{\boldsymbol{\xi}} \in \mathfrak{R}^{2c}$ and $\mathbf{V}_t \in \mathfrak{R}^{c \times 2c}$ are sliding multiplier rates and a constant matrix, respectively. Finally, the three complementarity conditions between (i) \mathbf{w} and $\dot{\mathbf{z}}$, (ii) $\boldsymbol{\pi}_c \in \mathfrak{R}^{2c}$ and $\dot{\boldsymbol{\xi}}$, and (iii) $\boldsymbol{\pi}_n \in \mathfrak{R}^c$ and \mathbf{r}_n enforce a perfectly plastic material law, the assumed frictional contact model (shown in Figs. 1b-c) and nonpenetration at contact interfaces, respectively [7]. $\mathbf{V}_n \in \mathfrak{R}^{c \times 2c}$, $\mathbf{N}_n \in \mathfrak{R}^{c \times 2c}$ and $\mathbf{N}_t \in \mathfrak{R}^{c \times 2c}$ are appropriate transformation matrices.

5. Optimization with Complementarity Conditions

We now consider the inverse problems corresponding to MCPs (2) and (3) that arise in the optimal design of structures with inelastic material properties and/or frictional contact conditions. The aim of such a design is to automatically determine the minimum and safe material distribution (i.e. typically represented by unknown cross-sectional areas \mathbf{A}) of the structural members such that the predefined physical and material requirements are simultaneously satisfied. This involves the formulations and solutions of “nonstandard” optimization problems, known as MPECs [2], where the so-called “equilibrium constraints” are, in our case, complementarity constraints expressing certain intrinsic structural behaviors, such as the ones in MCPs (2) and (3).

5.1 Optimization of Elastoplastic Structures

The MPEC in variables $(\mathbf{A}, \mathbf{Q}, \mathbf{u}, \mathbf{z})$ that describes the optimal design of elastoplastic (softening) structures is [4]

$$\begin{aligned}
& \text{Minimize } V(\mathbf{A}) \\
& \text{Subject to } -\alpha \mathbf{f} + \mathbf{C}^T \mathbf{Q} = \mathbf{0} \\
& \quad \mathbf{Q} - \mathbf{S}(\mathbf{A}) \mathbf{C} \mathbf{u} + \mathbf{S}(\mathbf{A}) \mathbf{N} \mathbf{z} = \mathbf{0} \\
& \quad \mathbf{w} = -\mathbf{N}(\mathbf{A})^T \mathbf{Q} + \mathbf{H}(\mathbf{A}) \mathbf{z} + \mathbf{r}(\mathbf{A}) \geq \mathbf{0}, \quad \mathbf{z} \geq \mathbf{0}, \quad \mathbf{w}^T \mathbf{z} = 0 \\
& \quad \mathbf{A}_{lo} \leq \mathbf{A} \leq \mathbf{A}_{up} \\
& \quad \text{Technological and displacement constraints}
\end{aligned} \tag{4}$$

MPEC (4) minimizes the total weight/volume $V(\mathbf{A})$ of the structure (directly related to the total cost) subject to the constraints given by the state problem in MCP (2), where the stiffness matrix \mathbf{S} , the normality matrix \mathbf{N} , the softening/hardening matrix \mathbf{H} and the vector of yield limits \mathbf{r} are written in terms of the unknown cross sectional areas \mathbf{A} that are bounded within available lower \mathbf{A}_{lo} and upper \mathbf{A}_{up} size limits. Technological and displacement constraints [3,4] impose specific conditions to accommodate, for instance, the requirement of identical member sizes for certain groups of structural members and displacement limits at some specified locations, respectively.

5.2 Optimization of Structures with Frictional Contacts

The inverse or optimal design problem to MCP (3) aims to obtain a minimum volume solution for rigid perfectly plastic structures with frictional contacts. The governing MPEC formulation in variables $(\mathbf{A}, \mathbf{Q}, \dot{\mathbf{u}}, \dot{\mathbf{z}}, \mathbf{r}_n, \mathbf{r}_t, \dot{\boldsymbol{\xi}})$ [3] is

$$\begin{aligned}
& \text{Minimize } V(\mathbf{A}) \\
& \text{Subject to } \mathbf{f}^T \dot{\mathbf{u}} = 1 \\
& \quad -\alpha \mathbf{f} + \mathbf{C}^T \mathbf{Q} + \mathbf{C}_n^T \mathbf{r}_n + \mathbf{C}_t^T \mathbf{r}_t = \mathbf{0} \\
& \quad -\mathbf{C} \dot{\mathbf{u}} + \mathbf{N} \dot{\mathbf{z}} = \mathbf{0} \\
& \quad -\mathbf{C}_t \dot{\mathbf{u}} + \mathbf{V}_t \dot{\xi} = \mathbf{0} \\
& \quad \mathbf{w} = -\mathbf{N}(\mathbf{A})^T \mathbf{Q} + \mathbf{r}(\mathbf{A}) \geq \mathbf{0}, \dot{\mathbf{z}} \geq \mathbf{0}, \mathbf{w}^T \dot{\mathbf{z}} = 0 \\
& \quad \boldsymbol{\pi}_c = \mathbf{N}_n^T \mathbf{r}_n - \mathbf{N}_t^T \mathbf{r}_t \geq \mathbf{0}, \dot{\xi} \geq \mathbf{0}, \boldsymbol{\pi}_c^T \dot{\xi} = 0 \\
& \quad \boldsymbol{\pi}_n = -\mathbf{C}_n \dot{\mathbf{u}} + \mathbf{V}_n \dot{\xi} \geq \mathbf{0}, \mathbf{r}_n \geq \mathbf{0}, \boldsymbol{\pi}_n^T \mathbf{r}_n = 0 \\
& \quad \mathbf{A}_{lo} \leq \mathbf{A} \leq \mathbf{A}_{up} \\
& \quad \text{Technological constraints}
\end{aligned} \tag{5}$$

in which matrix \mathbf{N} and vector \mathbf{r} are functions of the area variables \mathbf{A} .

5.3 MPECs – An Overview

The systematic study of MPECs has increasingly attracted research interest due to the fact that, in addition to being theoretically difficult and computationally challenging, MPECs find numerous applications in economic and engineering problems involving equilibrium systems [10]. An MPEC is an optimization problem, in which some or all constraints are defined by a parametric variational inequality or complementarity system [2]. The most prominent feature of an MPEC, and one that distinguishes it from a standard nonlinear programming (NLP) problem, is the presence of complementarity constraints. These constraints classify the MPEC as a nonlinear disjunctive (or piecewise) program. Consequently, besides the common issues associated with general NLP problems, the MPEC carries with it a “combinatorial curse” – a standard feature of all disjunctive problems.

There are three main reasons why an MPEC is difficult to solve [2]. First, the complementarity constraints are disjunctive. As is well-known from the integer programming literature, disjunctive constraints such those embodied by the complementarity condition (e.g. either $w_j = 0$ or $z_j = 0$) are very difficult to handle. This, as a result, makes the MPEC disjunctive. There is no feasible point for which all inequalities are strictly satisfied. Even under restrictions, this makes the feasible region a union of finitely many closed sets. Second, the feasible region of an MPEC may not be convex. Third, the feasible region of an MPEC may not be connected.

Any subset of these three difficulties may (and frequently) occur making the problem hard to handle and is often expected to show up as a severe numerical instability. To date, no algorithm has yet been proposed to guarantee solution of general MPECs.

6. Regularization Approaches

A direct attempt to solve the MPEC given in Eq. (4) or (5) is likely to suffer from numerical difficulties. A far better approach is to reformulate it as a standard NLP problem by suitably “treating” the complementarity constraints by some regularization technique. The idea is to solve a series of NLP subproblems such that the original complementarity condition is increasingly enforced, as some (positive) scalar parameter μ is increased or decreased. We outline three such NLP-based algorithms in the following.

Penalization: The complementarity term is transferred to the objective function and penalized (e.g. [3,4]). In particular, this involves modifying the objective function by adding the term $\mu \mathbf{w}^T \mathbf{z}$ in MPEC (4) and $\mu(\mathbf{w}^T \dot{\mathbf{z}} + \boldsymbol{\pi}_c^T \dot{\xi} + \boldsymbol{\pi}_n^T \mathbf{r}_n)$ in MPEC (5). The algorithm then simply increases parameter μ at each NLP iterate, with the intention of driving the complementarity term to zero.

Smoothing: The complementarity conditions are replaced by a set of smooth functions $\psi_\mu(w_j, z_j) = 0$ for all j in MPEC (4), and by $\psi_\mu(w_j, \dot{z}_j) = 0$, $\psi_\mu(\boldsymbol{\pi}_{c,j} \dot{\xi}_{c,j}) = 0$ and $\psi_\mu(\boldsymbol{\pi}_{n,j} r_{n,j}) = 0$ for all j in MPEC (5). A common function φ_μ used is the Fischer-Burmeister function [11] written as

$$\psi_\mu(w_j, z_j) = \sqrt{w_j^2 + z_j^2 + 2\mu} - (w_j + z_j) \tag{6}$$

This function ψ_μ has the property that $\psi_\mu(w_j, z_j) = 0$ if and only if $w_j \geq 0$, $z_j \geq 0$ and $w_j z_j = 0$. The algorithm then iteratively decreases parameter μ in order to drive the complementarity term to zero (e.g. [7]).

Relaxation: The original complementarity constraints are replaced by their relaxed version $\mathbf{w}^T \mathbf{z} \leq \mu$ in MPEC (4) and by $\mathbf{w}^T \dot{\mathbf{z}} + \boldsymbol{\pi}_c^T \dot{\xi} + \boldsymbol{\pi}_n^T \mathbf{r}_n \leq \mu$ in MPEC (5). The relaxed problem is solved for successively smaller values of μ to

force the complementarity term, which is nonnegative at feasible points, to approach zero (e.g. [7]).

- (a) The success of which algorithm to use can be problem dependent, but we have found that all three regularizations performed robustly for our optimal design problems. The attraction of these schemes is that each subproblem is a standard NLP problem, for which the standard solvers, such as CONOPT [12], can be used.

7. Illustrative Examples

Two examples are provided: one concerns an optimal synthesis involving elastic softening materials (Fig. 1a) [4] and the other rigid perfectly plastic materials with frictional contacts (Figs. 1b-c) [3]. All examples can be solved efficiently by any of the three regularization techniques mentioned above.

The first example considers the simultaneous topology and size design of a 3D cantilever beam (Fig. 2a) subjected to two points loads of 100α and 50α kN ($\alpha = 1$), where v_1 and v_2 denote the corresponding displacements (m). The beam was translationally restrained in all directions at the four corner nodes at its supported end. The displacement limits imposed were $-0.02 \leq v_1, v_2 \leq 0.02$ m. The design adopted a ground structure (shown in Fig. 2b) consisting of truss members. The PWL elastic softening material properties (kN, m units with $E = 28000 \times 10^3$, $f_t = f_{c1} = 14 \times 10^3$, $f_{c2} = 28 \times 10^3$, $h_1 = 16800 \times 10^3$, and $h = h_2 = -2800 \times 10^3$) in Fig. 1a were used throughout, where l defines the member length. Area bounds for all members were set to $0 \leq A \leq \infty$.

The discrete truss model in Fig. 2b contains 99 nodes, 710 members, 285 degrees of freedom and 3550 yield functions.

An optimal design with total volume $V = 0.2305 \text{ m}^3$ was successfully obtained by solving MPEC (4). The designed member distribution is as drawn in Fig. 2c.

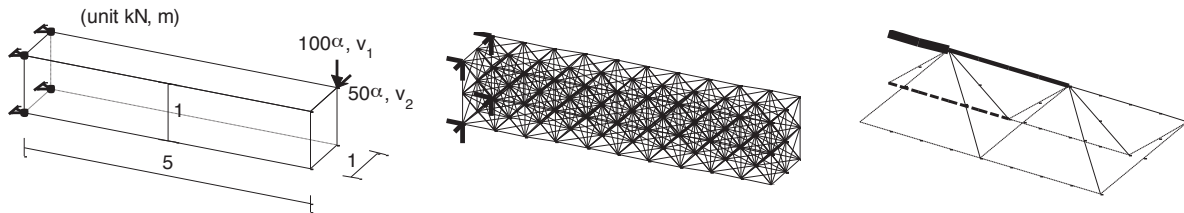


Figure 2: 3D cantilever beam (a) geometry and loads, (b) ground structure, (c) optimal designed structure (solid line denotes tension member and dashed line compression member) [4].

The second example is the 3D double layer roof truss (16 m \times 16 m in plan size and 2.828 m in height) shown in Fig. 3a. The structure was restrained only at some bottom layer nodes, in the y-axis direction along its perimeter and in all directions at four corners. At these bottom layer nodes 2, 3, 5, 8, 9, 12, 14 and 15, unilateral (along the x-axis) Coulomb frictional (Fig. 1c with $\tan\phi = 0.3$ and $\varphi = 0$) supports were installed along the perimeter.

The roof truss was designed for $\alpha = 20$ applied at top layer nodes, namely $F(x:y:z) = (16\alpha:4\alpha:-16\alpha)$ at each node shown by \circ in Fig. 3a, and $0.5F$ and $0.25F$ at the nodes indicated by \bullet and \otimes , respectively. Standard CHS sections with a yield stress of $f_y = 250 \times 10^3 \text{ kNm}^{-2}$ were adopted. All bottom layer members had the same area A_1 , all top layer members area A_2 , and diagonal members area A_3 , with all areas bounded as $820 \times 10^{-6} \leq A \leq 2710 \times 10^{-6} \text{ m}^2$.

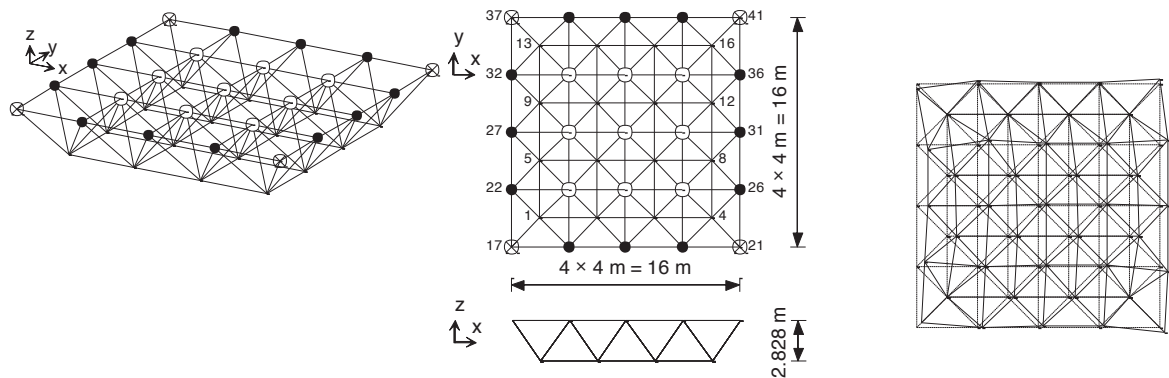


Figure 3: 3D double layer roof truss (a) geometry and loads and (b) collapse mechanism (\circ , \bullet and \otimes denote applied forces F , $0.5F$ and $0.25F$, respectively) [3].

The discrete truss model consists of 128 members, 41 nodes and 103 degrees of freedom.

The MPEC (5) was successfully solved to provide the optimal design in Fig. 3b, with $V = 0.8899 \text{ m}^3$, $A_1 = 2044 \times 10^{-6} \text{ m}^2$, $A_2 = 1093 \times 10^{-6} \text{ m}^2$ and $A_3 = 2027 \times 10^{-6} \text{ m}^2$. The corresponding collapse mechanism in Fig. 3b involves translation at 6 contacts (namely supports 2, 3, 5, 8, 9 and 12) and no translation at 2 contacts (supports 14 and 15).

8. Concluding Remarks

Various state problems in engineering mechanics can be formulated as mathematical programs with complementarity constraints or more specifically as MCPs. The inverse or synthesis problems to such MCPs lead naturally to a challenging problem class known as MPECs. This short review is intended to provide an overview of the formulations and solution approaches to certain MPECs that arise in the context of structural optimization. The complementarity conditions describe naturally and elegantly elastoplasticity and contact conditions.

While MCPs that arise in the structural mechanics context are eminently solvable since most possess key matrices with “nice” properties (e.g. positive definiteness), MPECs, on the other hand, are far more difficult to solve since they can be disjunctive, nonconvex and/or nonsmooth. Such properties are invariably associated with severe computational difficulties, similar to those in integer programming.

In spite of these difficulties, we have had considerable success in solving structural optimization problems formulated as MPECs. The key idea is to regularize the complementarity conditions and transform the MPEC into a standard NLP problem, the iterative solution of which increasingly enforces complementarity. Three such techniques are penalization, smoothing and relaxation. All perform equally well with the structural optimization described. Numerous examples, two of which are provided herein, attest to their robustness and efficiency.

9. Acknowledgement

This research was supported by the Australian Research Council.

10. References

- [1] M.C. Ferris and T.S. Munson, Complementarity problems in GAMS and the PATH solver, *Journal of Economic Dynamics and Control*, 24, 165-188, 2000.
- [2] Z.Q. Luo, J.S. Pang and D. Ralph, *Mathematical Programs with Equilibrium Constraints*, Cambridge University Press, Cambridge, 1996.
- [3] S. Tangaramvong and F. Tin-Loi, Optimal plastic synthesis of structures with unilateral supports involving frictional contact, *CMES-Computer Modeling in Engineering and Sciences*, 49, 269-296, 2009.
- [4] S. Tangaramvong and F. Tin-Loi, Topology optimization of softening structures under displacement constraints as an MPEC, *Structural and Multidisciplinary Optimization*, 49, 299-314, 2014.
- [5] M. Kočvara and J.V. Outrata, Optimization problems with equilibrium constraints and their numerical solution, *Mathematical Programming*, 101, 119-149, 2004.
- [6] M. Kočvara and J. Outrata, Effective reformulations of the truss topology design problem, *Optimization and Engineering*, 7, 201-219, 2006.
- [7] S. Tangaramvong and F. Tin-Loi, Collapse load evaluation of structures with frictional contact supports under combined stresses, *Computers & Structures*, 89, 1050-1058, 2011.
- [8] G. Maier, A matrix structural theory of piecewise linear elastoplasticity with interacting yield planes, *Meccanica*, 5, 54-66, 1970.
- [9] A. Brooke, D. Kendrick, A. Meeraus, R. Raman, *GAMS: A User's Guide*, GAMS Development Corporation, Washington, DC, 2014.
- [10] M.C. Ferris, J.S. Pang, Engineering and economic applications of complementarity problems, *SIAM Review*, 39, 669-713, 1997.
- [11] C. Kanzow, Some noninterior continuation methods for linear complementarity problems, *SIAM Journal on Matrix Analysis and Applications*, 17, 851-868, 1996.
- [12] A.S. Drud, CONOPT—a large-scale GRG code, *ORSA Journal on Computing*, 6, 207-216, 1994.

Conceptual Design of Box Girder Based on Three-dimensional Topology Optimization

Dongchen Qin¹, Peng Du¹, Qiang Zhu¹, Junjie Yang¹

¹Zhengzhou University, Zhengzhou, China, dcqin@zzu.edu.cn

1 Abstract

The box girder is widely used in mechanical equipments. Since the design of box girder mainly relies on traditional experience, the structure is very heavy. This paper applies the topology optimization to the design of box girder to reduce weight. First, an optimization model for the three-dimensional box girder, in which the compliance is minimized and volume is constrained, is established based on SIMP method, and different filter functions are used to avoid numerical instabilities that will occur in the optimization process. By loading the box girder in three different positions respectively and using the Optimality Criteria to solve each of load conditions, three kinds of structures are obtained. Finally, an optimal topology configuration is obtained by combining the three structures, and its validity is tested by FEM. In this paper, by using three-dimensional model, the internal structure of box girder can be obtained, which is useful for the layout of the ribs. The results provide a reference for the conceptual design of box girder, and lay some foundation for the multi-load cases problem.

2 Keywords: Topology Optimization; Box girder; Conceptual Design

3 Introduction

To industrial equipments, the box girder, one kind of the fundamental pieces of manufacturing, is not only very common but also very important. Many parts that can be found in the factories, such as the girder of bridge crane, the bed of machine tool, belong to the box girder. The weight of box girder is usually accounted for a large proportion of the total weight of the device. The box girder directly or indirectly determines the precision, carrying capacity and other basic performance of equipment. And of course, the internal structure of box girder is more complex and difficult to reach a rational design.

Currently, when designing box girder structure, traditional design methods include experience design and analogy design are used, and the results is particularly heavy. Bulky parts use more material in the manufacturing process, expend more energy during transport and adversely affect the device performance due to its excessive inertia. Therefore, the design by reducing weight of box-beams is urgent. In structural optimization, topology optimization that is innovative in design is a hot research field. With the method of topology optimization, Huayang Xu^[1] has optimized the arm of flight simulator under inertial load, Lunjie Xie^[2] has obtained a rational load bearing structure of electric car body in conceptual design phase, Bret^[3] has designed a structure for flapping mechanism under multiple load cases, etc.

This paper focuses on applying topology optimization to the box girder design. First, the box girder is abstracted as a simply supported beam, and an optimization model is established of which the objective function is compliance and the constraint is the volume, then, problems in the model solution process are studied and the method to solve them is found. Second, this model and method is used to design some kinds of new structures for the bridge crane girder with the loads position changed. Based on those structures, a new structure that can be applied to different load conditions is designed.

4 topology optimization theory

4.1 SIMP method

SIMP method is widely used among the topology optimization methods. It has been proposed by Mlejnek^[4] in 1993, which builds the relationship between the material density and elastic modulus by the following formula:

$$E_i(x_i) = x_i^p E_0, \quad x_i \in [0, 1] \quad (1)$$

where E_0 is the elastic modulus of material, x_i is the i th element's density, and p is the penalization power ($p > 1$). When using this method to the simply supported beam, the Eq. above is changed to the following in order to prevent stiffness matrix singular which will happen when the number of material density equal to 0:

$$E(x_i) = E_{\min} + x_i^p (E_0 - E_{\min}), \quad x_i \in [0, 1] \quad (2)$$

where E_{\min} is the elastic modulus which is very little.

4.2 The penalization power

Material density varies continuously between 0 and 1 in SIMP method. Thus, the structure after optimization

exists middle density areas which can not be manufactured in reality and are need to be suppressed as much as possible. The utility of penalization power is to penalize those areas. Supposed the elastic modulus of material $E_0 = 2.0 \times 10^5 \text{ MPa}$, according to Eq.(1), the Figure 1 is gotten, which shows the penalization power's influence on the elastic modulus. From this picture, when the value of penalization power increases, the middle density closers to the two ends of the interval of the elastic modulus, which achieves the desired effect of penalization power.

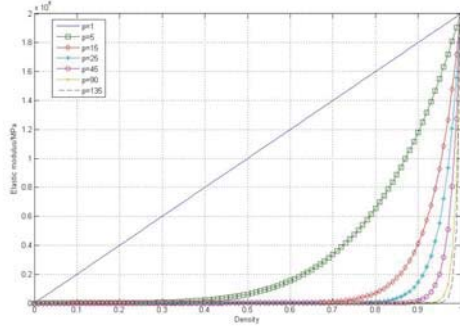


Figure 1: The penalization power's influence on the elastic modulus

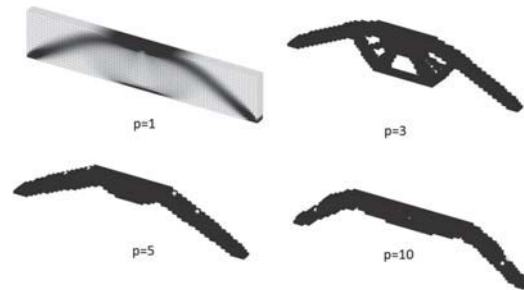


Figure 2: The impact of different penalization power on simply supported beam's optimization results

Note that the results of topology optimization change as the penalization power is changed, and once the value is bigger than a certain value, the results of topology optimization may be wrong^[5]. The Figure 2 show this phenomenon. When $p=1$, there is no any effect of the penalization power and the result is not clear; when $p=3$, the structure is clear and can be used; when $p=5$ and $p=10$, the simply supported beam becomes a structure with some rods, which does not meet the engineering requirements. From this comparison, to get a right result for the simply supported beam, the penalization power's value at 3 is better, which is used in this paper.

4.3 Optimization Model

When building an optimization model, the simply supported beam is discretized by the finite element method. And each element has a density x_i , which together forms a design space \mathbf{X} :

$$\mathbf{X} = [x_1, x_2, \dots, x_i, \dots, x_n]^T \quad (3)$$

where n is the number of element after discretized. For the simply supported beam, we build a optimization model of which the objective function is to minimize compliance and the constraint is the volume as following:

$$\begin{aligned} \min \quad & c(\mathbf{X}) = \mathbf{F}^T \mathbf{U}(\mathbf{X}) \\ \text{s.t.} \quad & \begin{cases} v(\mathbf{X}) = \mathbf{X}^T \mathbf{V} - \bar{v} \leq 0 \\ \mathbf{0} \leq \mathbf{X} \leq \mathbf{1} \end{cases} \end{aligned} \quad (4)$$

where \mathbf{F} is the load applied in the model, which is determined on the size of the load, direction and acting position; $\mathbf{V} = [v_1, \dots, v_n]^T$ is the vector of element volume; \bar{v} is the volume that is wanted to reach. $\mathbf{U}(\mathbf{X})$ is the displacement of each node, which can be get from the Eq.(5):

$$\mathbf{K}(\mathbf{X})\mathbf{U}(\mathbf{X}) = \mathbf{F} \quad (5)$$

4.4 Sensitivity Analysis

Since the design variable is nothing to do with the load \mathbf{F} , the following Eq. can be gotten:

$$\frac{\partial \mathbf{F}}{\partial x_i} = 0 \quad (6)$$

The partial derivative of Eq. (5) is:

$$\frac{\partial \mathbf{K}}{\partial x_i} \mathbf{U} + \mathbf{K} \frac{\partial \mathbf{U}}{\partial x_i} = 0 \quad (7)$$

The partial derivative of volume constraint is:

$$\frac{\partial v(\mathbf{X})}{\partial x_i} = \frac{\partial (\mathbf{X}^T \mathbf{V} - \bar{v})}{\partial x_i} = v_i \quad (8)$$

where v_i is the volume of the i th element.

The partial derivative of objective function is:

$$\frac{\partial c}{\partial x_i} = \frac{\partial \mathbf{U}^T}{\partial x_i} \mathbf{K} \mathbf{U} + \mathbf{U}^T \frac{\partial \mathbf{K}}{\partial x_i} \mathbf{U} + \mathbf{U}^T \mathbf{K} \frac{\partial \mathbf{U}}{\partial x_i} \quad (9)$$

Using Eq.(7):

$$\frac{\partial c}{\partial x_i} = -\mathbf{U}^T \frac{\partial \mathbf{K}}{\partial x_i} \mathbf{U} \quad (10)$$

According to FEM theory, in each element ,there is:

$$\mathbf{D}_i^0(x_i) = E_i(x_i) \mathbf{D}_i^0 \quad (11)$$

where \mathbf{D}_i^0 is the elasticity matrix of each element, which is a constant matrix.

The element stiffness matrix is based on isoparametric element theory, the element stiffness matrix is:

$$\mathbf{k}_i(x_i) = \int_{-1}^1 \int_{-1}^1 \int_{-1}^1 \mathbf{B}^T \mathbf{D}_i \mathbf{B} |\mathbf{J}| d\xi d\eta d\zeta \quad (12)$$

where \mathbf{B} is the strain-displacement matrix, $|\mathbf{J}|$ is the determinant of Jacobian matrix. Using(11):

$$\mathbf{k}_i(x_i) = E_i(x_i) \mathbf{k}_i^0 \quad (13)$$

Last, the sensitivity of the objective function is:

$$\frac{\partial c}{\partial x_i} = -\mathbf{u}_i^T \left[p x_i^{p-1} (E_0 - E_{\min}) \mathbf{k}_i^0 \right] \mathbf{u}_i \quad (14)$$

4.5 Optimality criteria

The optimization model of simply supported beam is nonlinear, which can be solved by the Optimality Criteria (OC) method. This method which is based on K-T condition is used in topology optimization due to it's simply and efficient. Supposed $\mathbf{0} \leq \mathbf{X} \leq \mathbf{1}$ is satisfies, namely it is inactive, the design variables are updated using the following :

$$x_i^{new} = \begin{cases} \max(0, x_i - m), & \text{when } x_i B_i^\eta \leq \max(0, x_i - m) \\ \min(1, x_i + m), & \text{when } x_i B_i^\eta \geq \min(1, x_i + m) \\ x_i B_i^\eta, & \text{otherwise} \end{cases} \quad (15)$$

where

$$B_i = \frac{\mathbf{u}_i^T \left[p x_i^{p-1} (E_0 - E_{\min}) \mathbf{k}_i^0 \right] \mathbf{u}_i}{\lambda v_i} \quad (16)$$

To this problem, $m=0.2$ and $\eta =0.5$ is recommended^[6]. Then, there is only one unknown number λ in the Eq.(15), which can be get by following the steps below:

- 1) Let $\lambda_{\min}^{(1)} = 0$, and $\lambda_{\max}^{(1)}$ is a large number, such as 1×10^9 ;
- 2) Calculate $\lambda^{(k)} = (\lambda_{\min}^{(k)} + \lambda_{\max}^{(k)}) / 2$
- 3) Get \mathbf{X}^{new} by Eq.(15), then ,calculate $v(\mathbf{X}^{new})$, when $v(\mathbf{X}^{new}) < 0$, let $\lambda^{(k+1)} = \lambda_{\max}^{(k)}$; and when $v(\mathbf{X}^{new}) > 0$, let $\lambda^{(k+1)} = \lambda_{\min}^{(k)}$;
- 4) Repeat steps 2 and 3 until to $v(\mathbf{X}^{new}) = 0$.

4.6 Filter function

Among the optimization process of simply supported beam, there may be numerical instabilities, such as checkerboard problem and mesh-dependency. Generally , those problems appear simultaneously, thus, the method that can inhibit the checkerboard problem also can inhibit the mesh-dependence. One common approach to suppress these problems is using the density filter function^[7], which is defined as:

$$x_i = \frac{\sum_{j \in N_i} H_{ij} v_j x_j}{\sum_{j \in N_i} H_{ij} v_j} \quad (17)$$

Another commonly used method is the gray scale filter^[8], which is a nonlinear method. This method is an update of OC method:

$$x_i^{new} = \begin{cases} \max(0, x_i - m), & \text{if } x_i B_i^n \leq \max(0, x_i - m) \\ \min(1, x_i + m), & \text{if } x_i B_i^n \geq \min(1, x_i - m) \\ (x_i B_i^n)^q, & \text{otherwise} \end{cases} \quad (18)$$

The value of q is a key. For this optimization model, q=2 is recommended^[9]. And it is just the OC method when q=1.

Different filter functions have different impact on the topology optimization results. In Figure 3, (a) is the result without any filter function, (b) is the result using the density filter function, (c) is the result using the gray scale filter function, (d) is the result using density filter and gray scale filter. Compared with no filter function, the structure is more clear and less checkerboard phenomenon when using filter function. When using two filter functions alone, the density filter is better than gray scale filter from (b) and (c), because (c) appears checkerboard problem. That is to say the gray scale filter shouldn't be used alone. Compared (b) with (d), there are some differences in the structure. Based on this study, in order to get the most reasonable structure of simply supported beam, the density filter method and another method that uses density filter and gray scale filter together are applied to the optimization model respectively.

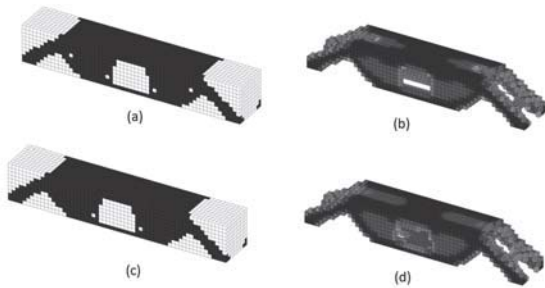


Figure 3: Different filter function's impact on optimization results

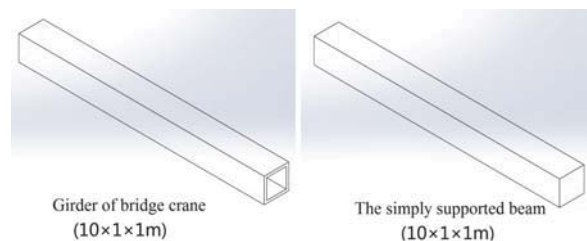


Figure 4: The girder and its Simply supported beam

5 Topologies under different conditions

Box girders are widely used in machines. In order to use the topology theory above to get a new structure of box girder, the girder of bridge crane is selected as the research object, which can be simplified as a simply supported beam.

The size of bridge crane girder is 10×1×1m, which is showed in Figure 4, and the maximum lifting capacity of it is 50 tons. The material of girder is Q345, of which the elastic modulus is 2.0e5MPa, and the Poisson's ratio is 0.3. Since the safety factor of this material is 1.4, the allowable stress is 246MPa. According to the girder's length and stiffness, the allowable deflection of girder is 12.5mm. This girder is abstracted as a simply supported beam, which is showed in Figure 4.

In terms of the model loads, they are given by the lifting trolley through four wheels, and the loads are uncertain, whose size and acting position vary from time to time. However, in the optimization model, the loads are certain, and are known constants. Thus, the uncertain loads need to be simplified to certainty in this paper. When the lifting trolley is in the middle of girder, the structure is under the most dangerous condition, and when the lifting trolley is at both sides of girder, the structural deformation is least. Considering these, there are 4 kinds of lifting conditions to the girder, which the loads are the maximum lifting capacity: (a) the lifting trolley position is at the upper middle of the simply supported beam; (b) the lifting trolley position is 1/4 away from the left side of the simply supported beam; (c) the lifting trolley position is 1/4 away from the right side of the simply supported beam; (d) the lifting trolley position is at the three position above at the same time(it does not exist in reality).

According to the filter function analysis above, different results can be gotten by using different filter function, and the results to the simply supported beam is in the Figure 5. The results using density filter is on the left, and the results using density filter and gray scale filter is on the right. The letters in the pictures correspond to the respective lifting conditions above.

There are many common grounds in the results using two kinds of filter functions. All the structures show a trapezoidal shape, which can be divided into two parts: the main structure on the middle and the support structure on left and right sides. Middle part of the structure is wider at the top, which is hollow, and on the front and rear web position, there are big trapezoidal holes, whose position are just below the loads. The hole does not appear on the Cover on the four kinds of lifting conditions. The support structure is the two trapezoidal sides., and the upper and lower materials on each side are removed. In the results, dark black units represent the main unit, which can be enhanced by adding an appropriate amount of ribs in these place.

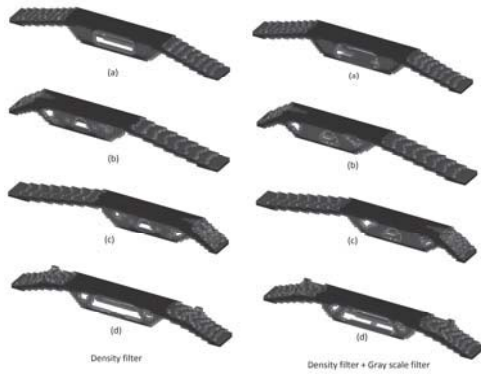


Figure 5: The results of the simply supported beam using different filters

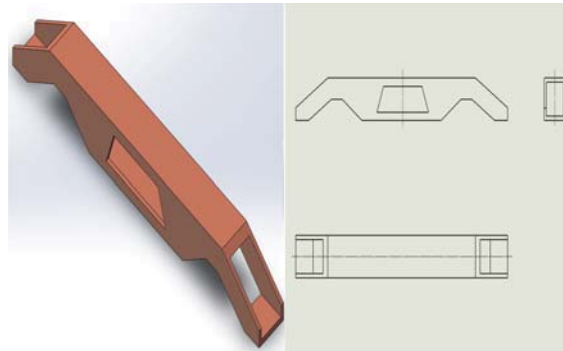


Figure 6: Bridge crane girder conceptual structure

In addition to the same points, there are differences between two results. The most obvious point is on the Under Cover. After using density filter, the Under Cover is gone, thus, the cross section is a inverted U. However, when using the other filter function, the Under Cover still exists, thus, the cross section is a rectangle. Theoretically, the loads is straight down , then these two cross-sectional structures have the same stabilities . However, the loads are uncertain in direction on actual working conditions, then the rectangle cross section is better than the other one. Therefore, the exists of Under Cover is necessary.

6 Structure synthesis and verification

According to the analysis of different results above, a conceptual structure for the bridge crane girder is gotten by removing materials on some parts of girder. The conceptual structure is showed in Figure 6.

In order to validate the conceptual structure , finite element model is built. When the lifting trolley is in the middle of girder , the structure is under the most dangerous condition. To this condition, the results is in Figure 7, Figure 8 and Table 1. In the figures, (1) represents the simply supported beam; (2) represents the bridge crane girder; (3) represents the conceptual structure. According to the results, the displacement of three models increase successively, and the conceptual structure one is 4.85mm which is the largest one, but it is still less than the allowable deflection which is 12.5mm yet. The maximum stress of three models increase successively too, and the largest one is the conceptual structure's stress which is 103MPa, but it is still less than the allowable stress which is 246MPa yet. Most importantly, stress region is more uniform in the conceptual structure , which represents material is efficiently used. In conclusion , when the trolley is in the middle of girder, the conceptual structure's displacement meet the requirements and stress is better than the others.

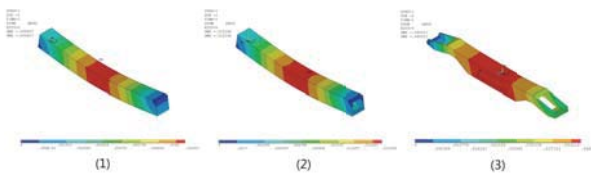


Figure 7: Displacement contour plot when trolley in the middle

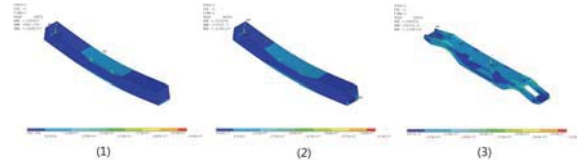


Figure 8: Von Mises stress contour plot when trolley in the middle

Table 1: Displacement and stress when trolley in the middle

	Simply supported beam	Bridge crane girder	Conceptual structure
Displacement/mm	0.86	1.53	4.85
Maximum stress/MPa	56.60	81.90	103.00

When the lifting trolley is 1/4 away from the left side , the results is in Figure 9, Figure 10 and Table 2. From the results, the displacement and stress of conceptual structure are the largest ones, but still in the allowable range, and stress region is uniform too. Due to the symmetry of the structure , the results to the condition trolley 1/4 away from the right is just the same as this results. The last condition in the four lifting conditions does not exist in reality ,thus there is no need to verify the structure in this condition.

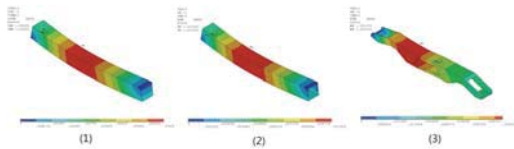


Figure 9: Displacement contour plot when trolley 1/4 away from the left

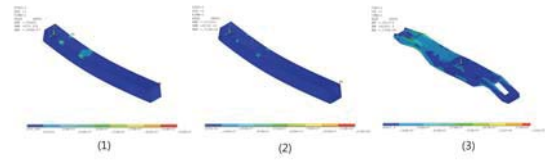


Figure 10: Von Mises stress contour plot when trolley 1/4 away from the left

Table 2: Displacement and stress when trolley 1/4 away from the left

	Simply supported beam	Bridge crane girder	Conceptual structure
Displacement /mm	0.63	1.10	5.11
Maximum stress /MPa	56.60	115	130.00

Table 3: Volumes to different models

	Volume/m ³	percentage
Simply supported beam	10.00	22.5%
Bridge crane girder	3.60	62.5%
Conceptual structure	2.25	100%

From the Table 3, compared with the other structures, the conceptual structure is more light since they all have the same density and the volume of conceptual structure is least. In conclusion, the conceptual structure meets the requirements, and is a new weight light structure for the bridge crane girder.

7 Conclusions

This paper applies topology optimization method to the box girder's concept design stage. For simply supported beam, SIMP method is briefly introduced. The filter function that density filter combined with gray scale filter is better for simply supported beam when using SIMP method. Topology optimization is used on girder of bridge crane, getting a new conceptual structure which is verified by finite element analysis in two conditions. The conceptual structure is light and efficient in material using. However, the optimization model does not consider the stress, which is the future research direction.

8 References

- [1] Huayang Xu, Liwen Guan; and Liping Wang, Topology Optimization for the Arm of Flight Simulator under Inertial Loads, *Journal of Mechanical Engineering*, 9:14-23, 2014.
- [2] Lunjie Xie, Weigang Zhang, and Weibo Chang, Multi-objective Topology Optimization for Electric Car Body Based on SIMP Theory, *Automotive Engineering*, 35(7):583-587, 2013
- [3] S. Bret, and B. Philip, Optimal compliant flapping mechanism topologies with multiple load cases. *J Mech Des*, 134(5), 2012.
- [4] H. P. Mlejnek and R. Schirmacher, An engineer's approach to optimal material distribution and shape finding, *Computer Methods in Applied Mechanics and Engineering*, 106:1-26, 1993.
- [5] Xiang CHEN and Xinjun LIU, Solving Topology Optimization Problems Based on RAMP Method Combined with Guide-weight Method, *Journal of Mechanical Engineering*, 48(1): 135-140, 2012.
- [6] O. Sigmund, A 99 line topology optimization code written in matlab, *Struct Multidiscip Optim*, 21(2):120-127, 2001.
- [7] Kong tian ZUO, Shu ting WANG and Li ping CHEN etc., Research on Algorithms to Eliminate Numerical Instabilities in Topology Optimization, *Mechanical Science and Technology*, 24(1):86-93, 2005.
- [8] A. A. Groenwold and L. F. P. Ertman, A simple heuristic for gray-scale suppression in optimality criterion-based topology optimization. *Struct Multidiscip Optim*, 39(2):217-225, 2009.
- [9] Kai Liu and A. Tovar, An efficient 3D topology optimization code written in Matlab, *Struct Multidiscip Optim*, 2014

Production-based Multi-criteria Design Optimisation of an Unconventional Composite Fuselage Side Panel by Evolutionary Strategies and a Surrogate Model of Manufacturability Analysis

Onur Deniz¹, Peter Horst¹, Carsten Schmidt²

¹ Tech. Universität Braunschweig, Institute of Aircraft Design and Lightweight Structures (IFL), Braunschweig, Germany, o.deniz@tu-braunschweig.de

² Leibniz Universität Hannover, Institute of Production Engineering and Machine Tools (IFW), Garbsen, Germany

1. Abstract

This paper introduces a novel multi-criteria optimisation framework that efficiently combines manufacturing analysis of composite structures with respect to various production criteria such as manufacturability and limitation of process-based material deviations. These criteria include gaps induced by fibre placement systems as well as structural constraints regarding material failure, stability and damage tolerance. Within this optimisation framework, evolutionary algorithms are coupled with an in-house parametric FE-Model generation tool, which exhibits an extensive design scope comprising various unconventional stiffener topologies, evaluates buckling modes and obtains composite specific failure criteria according to multiple load cases. This work focuses on multi-criteria optimisation of a lattice-stiffened fuselage panel with novel double-curved stiffeners aiming for minimum weight. The final design is compared to a conventional aircraft stiffener topology with respect to weight and window size.

2. Keywords: Design Optimisation of Composite Panel, Evolutionary Algorithms, Response Surface Models, Automated Fibre Placement, Estimation of Prepreg Tow Gaps

3. Introduction

Increased utilisation of composite materials due to their specific properties such as strength-to-weight ratio, damage tolerance, reduced maintenance costs and flexibility has led to advanced production technologies such as Automated Fibre Placement (AFP) systems. Despite of high positioning accuracy these systems induce manufacturing deviations mainly provoked by geometric complexity of composite structures and restrictions in the structural design space by the dimensions and flexibility of the layup head [1]. Furthermore, unconventional designs adapted to loading conditions can significantly improve efficiency of the stiffened thin-walled structures in terms of weight savings compared to current composite applications in commercial aircrafts. However, increased geometric complexity of composite structure can lead to redesign necessities due to manufacturability requirements and significant production deviations, such as gaps between tows and deviations in fibre orientations by AFP. If not considered, consequently a reduced structural performance would be obtained [2]. Regarding manufacturing deviations of AFP systems, tow gaps have a vital role on mechanical performance of the prepreg laminated composite structures which is precisely presented by [3]. However, AFP induced gaps are most commonly analysed separately after completion structural designs. This may lead to recurring design phases or expansive manufacturing strategies to overcome this issue. Hence, as a solution methodology, especially for unconventional stiffeners, structural optimisation can be coupled with production analysis so that the structure adapts its topology to defined production technology unlikely to process adaptation to the final design to avoid significant material deviations. Thus, a novel optimisation approach is presented that associates structural optimisation with manufacturability of components and restriction of deviations regarding a newly developed AFP system.

4. Panel Concept and Production Phases

Initial concept of the aircraft side panel is based on evolution in biology such as bones or branches that have risen from various loading conditions in their environment. A detailed global topology optimisation of a fuselage barrel presented by [4] exhibits slanted, lattice and intersecting material densities around the window sections. Nevertheless, slanted stiffeners offer increased performance under fuselage regions loaded with shear forces [5] which lead to efficient material usage in terms of weight savings. Stiffener topology of the panel concept consists of a pure grid stiffened region with local stabilisers, so-called stiffener peaks around the windows and conventional stringer frame distribution in upper and lower regions where the slanted grid topology ends. This combination also

allows an efficient assembly process in circumferential directions of the fuselage. Advantageous of the machining technologies on foam structures are utilised for serial production of complex sandwich stiffener topologies [6] (see Figure 1).

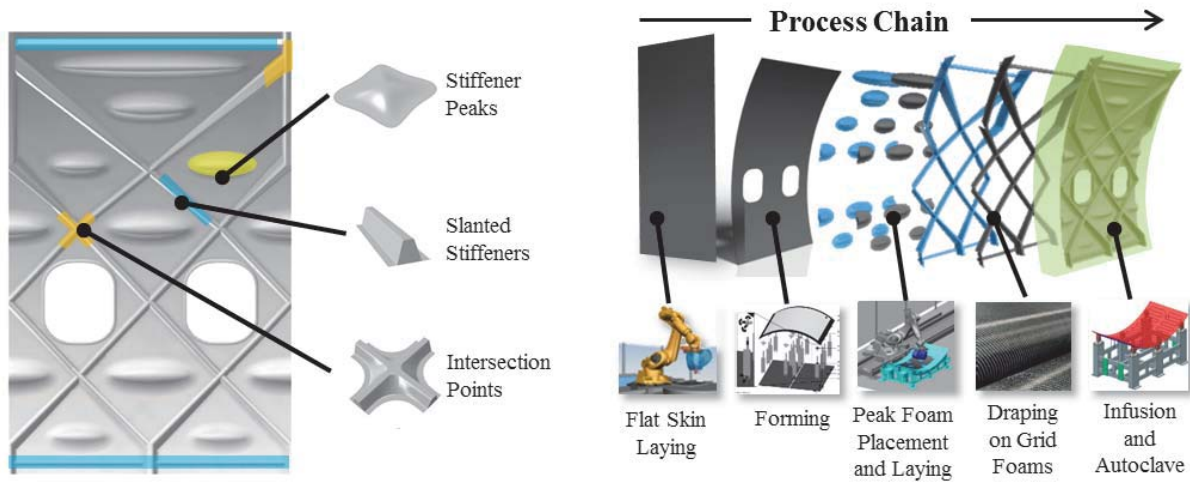


Figure 1: Illustration of concept panel components (left) and the process chain (right)

The manufacturing process starts with the prepreg-skin being placed on a 2D surface by AFP and then being transformed into 3D by a flexible forming process. Foam of stiffener peaks are placed and processed as well in AFP followed by the placement of the more complex grid-stiffeners. Draping process on lattice stiffeners and intersection points using innovative textile-concept is carried out and afterwards slanted stiffeners are infused and bonded to prepreg skin via co-curing process in autoclave. The production concept yields a significant reduction in manufacturing costs due to a single bonding of all panel components.

5. Automated Fibre Placement System

Main advantages of the in-house system are increased laying velocity around 3 m/s and form flexible compaction device with a decreased minimal tape length compared to state of the art. Hence, the layup head design not only allows for manufacturing geometric complex structures but also for placing slit tapes on plane fuselage skin with high productivity. To adapt to different surface conditions like stiff metal moulds or the more elastic foams, the compaction device is separated in four force-controlled compaction segments, allowing an additional radial displacement. The geometric characteristics are presented in Figure 2, and as well as the most important criteria for design optimisation regarding restrictions of the compaction device.

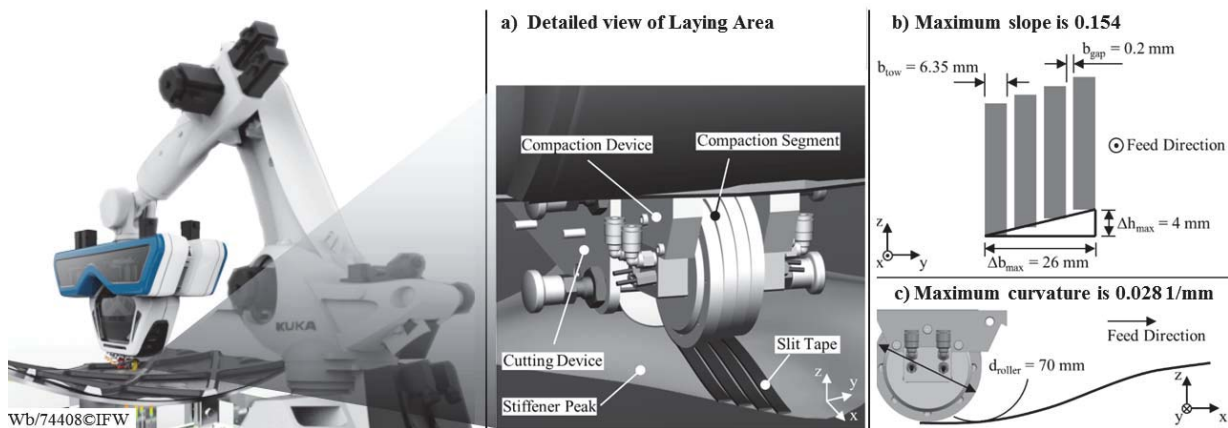


Figure 2: Illustration of newly developed modular layup head at left and manufacturability criteria at right

The newly developed layup head processes 1/4" (6.35 mm) slit tape. Between each tow and compaction segment a gap of 0.2 mm exists because of tow guidance. Each segment is able to perform a radial displacement to adapt curved surfaces of up to 4 mm. With an overall width of 26 mm the resulting maximum slope of the compaction device is 0.154 across feed direction (b). Another criterion derived from the compaction device is the curvature (c). The segment diameter of 70 mm allows a maximum curvature of 0.028 1/mm for concave arched surfaces. These

three criteria, the gap, the maximum slope and the maximum curvature are taken into account within the optimisation procedure.

6. Estimation of Manufacturability

The manufacturability analyses focus on the production of the double curved stiffener peaks presented in Figure 1. Due to geometric complexity, during the optimisation, manufacturability analysis has to be carried out in order to adapt the structural surface to machine restrictions shown in Figure 2. This analysis is automatically performed with an AFP-interface-algorithm within the in-house parametric simulation tool. Computations of surface slopes and curvatures are performed by projecting partitioning lines on the stiffener peak according to the global fibre placement direction. Distances between lines are set to two tow widths including segmentation spacing of the compaction roller. By this means, the neutral fibre lines can be obtained between two partitioning lines representing projected fibre path borders. Ascending surface slopes are computed along the vertical direction of neutral fibre paths (Figure 3 left). Allowable curvature and minimum radius are iteratively computed regarding the neutral fibre line information.

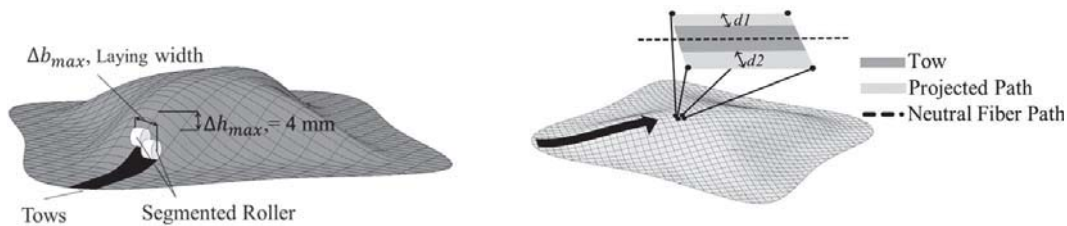


Figure 3: Computation of allowable surface slopes in layup direction (left), geometric gap analysis (right)

Based on the same methodology, partial geometric gaps, $d1$, $d2$ (in Figure 3 right) are analysed at the points that are lying on the intersection of vertical partitioning lines and projected borders of tows with assumption of infinitesimal material strains vertical to fibre direction. The maximum gap value is calculated iteratively on each cell with summation of partial gap values of neighbour cells as follows:

$$\max(d1_i + d2_{i-1}, d1_{i+1} + d2_i), i = \text{number of the parallel neighbour cells} \tag{1}$$

The estimation of the gaps will be larger than experimental values due to missing material behaviour during the compaction. However, this assumption will affect the mechanical performance in a positive way since the gaps are also minimized more than expected values which lead to increased fibre volume fraction in gap regions.

7. Surrogate Models of Manufacturability Outputs

In order to increase optimisation efficiency in terms of computation time, a response surface generation of the manufacturability output of stiffener peaks is carried out using radial basis function, artificial neural networks (RBF-ANN) that are based on biological process of neurons [7]. This methodology offers a faster approximation method by creating an output of linear combinations of weighted radial basis functions, in this case Gaussian functions, to get sufficient non-linear approximation models.

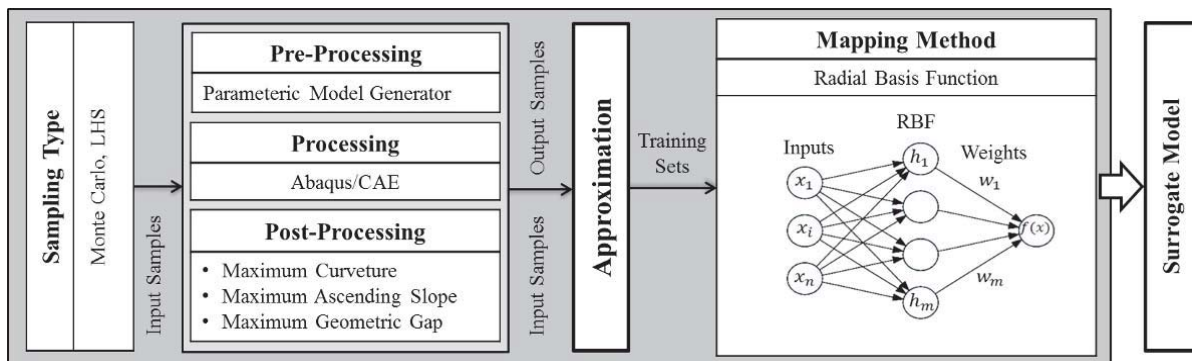


Figure 4: Response surface generation of manufacturability output of stiffener peaks

The Latin hypercube sampling method is chosen to generate input samples. The surrogate model generation represented in Figure 4 is carried out according to training data sets that contain input samples regarding

optimisation parameters of the FE panel model and corresponding output sets containing maximum tow gaps, ascending slope, and curvature information of peak topology. Since the lay-up orientations are restricted to 0° , $+45^\circ$, -45° , 90° , other orientations are not necessary to be included during computation of maximum gap, slope and curvature information.

8. Multi-criteria Optimisation

The objective of the multi-criteria optimisation is formulated to reach minimum weight goal based on a conventional reference panel, under structural and manufacturability constraints of stiffener peaks. Evolutionary strategies based on selection, recombination and mutation operators are used to minimise fitness value consisting of approximated manufacturing outputs, structural responses and weight of the panel. The optimisation framework combines manufacturability outputs from surrogate models with FE analysis by adding and weighting mapping functions of objective C^{opt} and mapping functions of constraints $C_l^{=<}$. Summation is the fitness evaluation, C , of each individual represented in equation (2) where X presents the system parameters, also $F(X_i)$ and $f(X_i)$ are representing respectively, the weight objective and the constraints.

$$\text{minimise } \left\{ C(F(X_i), f(X_i)) = w_0 C^{opt}(F(X_i)) + \sum_{l=1}^{n+n_c} w_l C_l^{=<}(f_l(X_i)) \right\} \quad \begin{array}{l} i = \text{number of design variables} \\ l = \text{number of constraints} \end{array} \quad (2)$$

8.1 Design Variables and loading conditions

As presented in Figure 5, an optimisation model is automatically generated by an in-house parametric panel generation tool which is written in Python. Window cut out topology can also be varied during the optimisation and can be changed from oval to lozenge shape. The object oriented structure of the panel generation tool automatically enables FE models of different kind of stiffener topologies and profiles to expand the design scope with large number of design parameters.

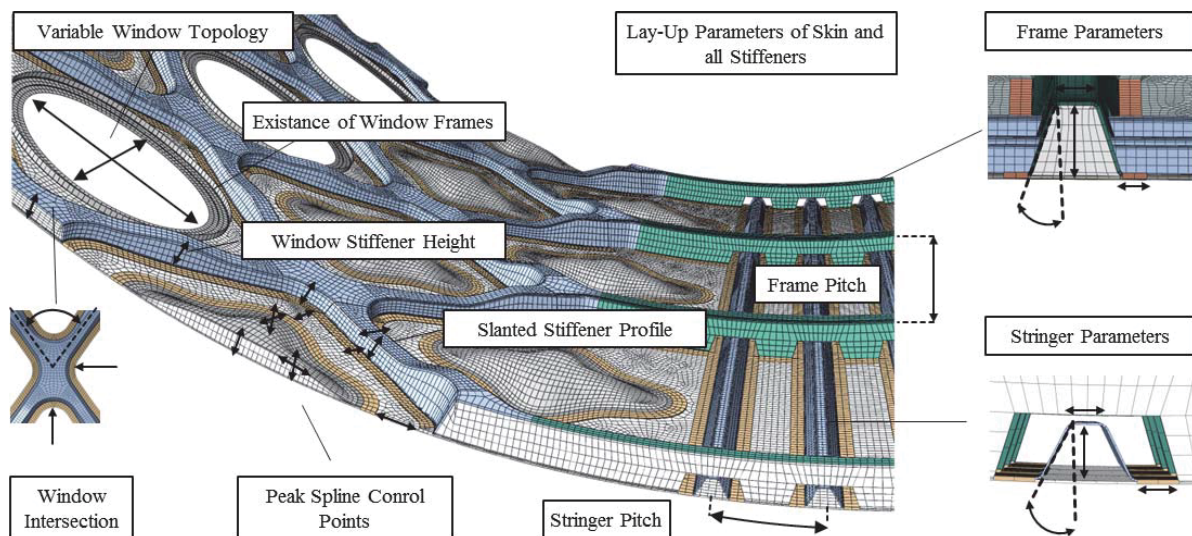


Figure 5: Design variables of newly developed fuselage side panel

Automated design of producible lay-ups and thickness adjustments on overlapping zones or sections of different textile topologies are handled with composite module and production module (AFP and draping) within the panel generation tool. The layup parameters are optimised with an interface to the table of allowable layups consisting of combinations of all possible stacking sequences based on number of layers, orientations ($+45^\circ$, -45° , 90° , 0°) and production requirements in [8], such as symmetry and balance condition where at least 8 % of fibres have same orientation, not more than four plies having the same direction could be stacked in a sequence and orientation of the outermost layers are restraint to $+45^\circ$ or -45° in order to minimise impact effects. Within this strategy all layup parameters such as number and orientations of the layups are reduced to only one index variable of the allowable layup table.

In order to realise aircraft fuselage deformations on the panel level, periodic boundary conditions are applied at the edges of the FE model. Different loading scenarios stated in Table 1 and corresponding failure analyses are automatically performed during the optimisation.

Table 1: Load cases and origins of loading conditions with corresponding analysis type in optimisation process

Load Case	Loading Type	Analysis Type	Cabin Pressure [mbar]	Axial Loading, $n_{x,x}$ [N/mm]	Shear Loading, $n_{x,\theta}$ [N/mm]
1	Cabin Pressure	Static	1200	120.0	-
2	Manoeuvre	Static	600	60.0	-86
3	Lateral Gust	Static	600	197.0	-1.0
4	Lateral Gust	Static, Buckle	-	-	-86
5	Manoeuvre	Static, Buckle	-	-137.0	-67.0

8.2 Structural and Mechanical Constraints

The damage tolerance requirement of the panel is satisfied by the maximum strain condition ϵ_{max} in each load case (see Table 1). Due to the positive effect of the cabin pressure, only load cases 4 and 5 are considered for buckling. Furthermore, out of plane deformations are not allowed around the windows in order to prevent faster delamination in weak regions and sustain damage tolerance. Manufacturability constraints (5, 6 and 7 in Table 2) are assigned according to the requirements illustrated in Figure 2 and approximated by the response surface method. Manufacturability of the stiffener peaks is handled as upper restriction and the outputs under upper limit constraints are ranked equally since secondary influences such as machine speed in terms of laying rate are not considered.

Table 2: Structural Constraints 1–4 and manufacturability constraints 5–7 with source of computations

No	Constraint Type	Constraints	Source
1	Allowable Strain in each Load Case, ϵ	$\epsilon < \epsilon_{max}$	FEM – Abaqus®
2	No Buckling Forms Around Windows, Load Cases 2, 4, 5	$U_r < U_{min}$	FEM – Abaqus®
3	Reserve Factor Load Case 4, RF_1	$RF_1 > 1$	FEM – Abaqus®
4	Reserve Factor Load Case 5, RF_2	$RF_2 > 1$	FEM – Abaqus®
5	Maximum Ascending Slope, m	$m < 0.154$	Response Surface
6	Maximum Curvature, k	$k < 0.028$ 1/mm	Response Surface
7	Maximum Tow Gaps, d	$d \leq 0.55$ mm	Response Surface

9. Results and conclusions

The evolution parameters of the panel are set to 30 populations with 80 offspring per generation and infinite lifespan in the optimisation environment. Convergence of the multi-criteria problem is observed at 27th generation after approx. 2600 structural evaluations, with static and buckling analysis in conjunction with response surface approximation of AFP manufacturability analysis. Lozenge shape of window cut-outs adapted to stiffener layout around the window is one of the significant outcomes of the optimisation. Even though the objective is to reach minimum weight based on reference value, panel offers 12 % larger windows compared to optimised reference composite panel under same loading conditions and constraints (Figure 6). Oval shapes of the windows are restricting the intersection angles to lower degrees in order to satisfy allowable window sizes. Significantly increased stability is observed on pure shear loading ($RF1$) due to lattice topology and adaptation of intersection angles and material properties to the dominant loading condition ($RF2$, combined shear and compression loading).

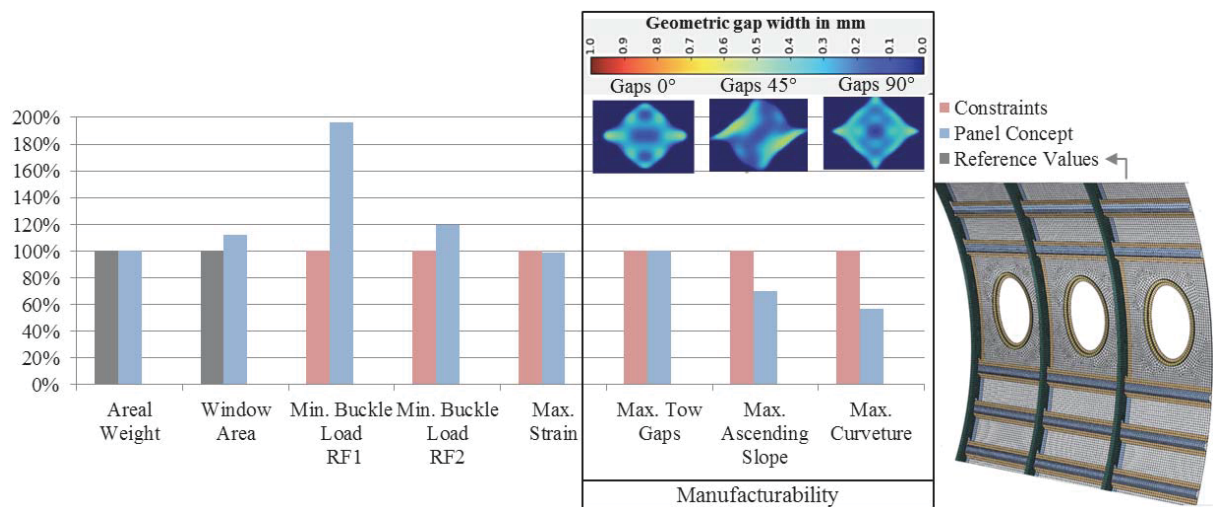


Figure 6: Optimisation result with constraints and reference panel (right) and true geometric gap fields on peaks

Therefore, buckling values in load case 5 (compression and shear loading) are significantly reduced in all parameter combinations of oval shapes. Besides, configurations offering smaller window size than the reference panel are not included and ranked in the structural evolution. Additionally as presented in Figure 7, an efficient convergence is obtained for the layout index parameters of the allowable layup array, which comprises thousands of allowable stacking sequences sorted by ascending layer numbers.

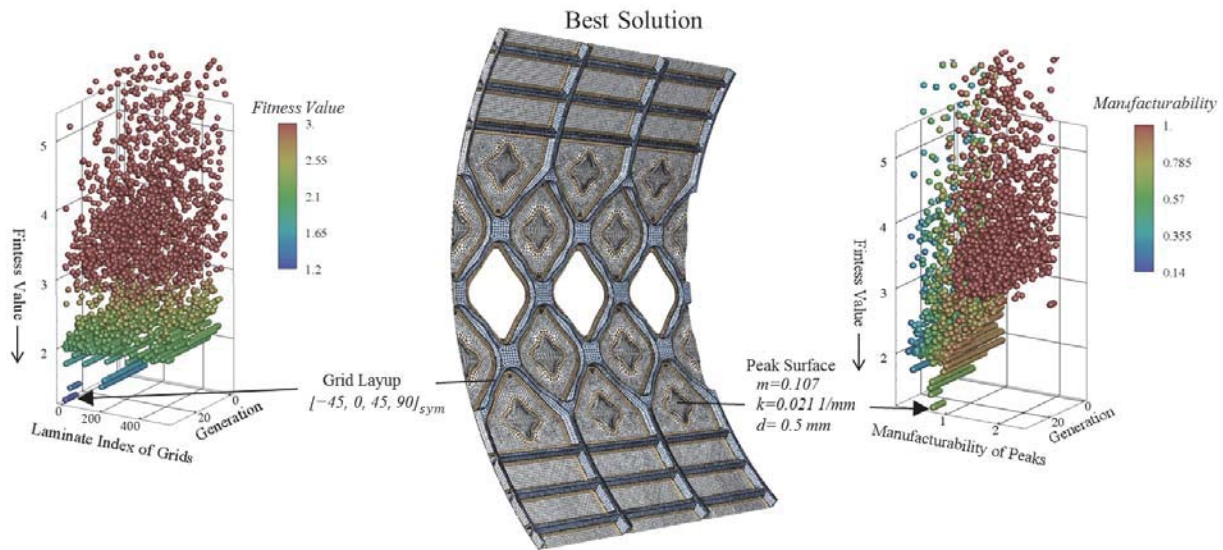


Figure 7: Best stiffener and window topology, convergence of grid laminate and manufacturability parameters

The obtained peak configuration satisfies all requirements regarding production quality. Within this methodology, an automated structural evolution together with production quality can be obtained simultaneously without any requirements such as complex path programming to avoid large gaps between tows. To effectively improve manufacturing quality, gap information will in future be used to monitor the layup process continuously and to feedback data about real material behaviour in the optimisation framework. The alternative design and methodology can be improved even further by integrating influences of the draping process and other loading conditions in the structural evolution.

10. Acknowledgements

The authors would like to thank the federal state of Lower Saxony and the European Regional Development Fund (ERDF) for financial and organisational support of the project “High Performance Production of CFRP-Structures” (HP CFK).

11. References

- [1] G. H. Clementine. Multiple-use Robots for Composite Part Manufacturing, *JEC Composites*, volume (62):28-29, 2011
- [2] O. Deniz, A. Biel, P. Horst, G. Ziegmann, C. Schmidt. Simulation Based Design Optimization of a Cfrp Fuselage Panel According to Draping Process of Carbon Fibre Textiles using Evolutionary Algorithms and Response Surface Methods. In *Sampe 2013 Long Beach*, pages 1110-1124, 2013
- [3] K. Fayazbakhsh, M.A. Nik, D. Pasini. Defect layer method to capture effect of gaps and overlaps in variable stiffness laminates made by Automated Fiber Placement. *Composite Structures*, volume 97 : 245-251, 2013
- [4] O. M. Querin, V. V. Toporov, D. Liu, L. H. Busch, C. Hühne, S. Niemann, B. Kolesnikov, Topology And Parametric Optimisation Of A Lattice Composite Fuselage Structure, <http://www.altairuniversity.com/2014/04/01/fuselage-topology-optimisation-paper/>, 2014
- [5] A. Klinzmann, *Optimierung von nicht konventionellen Strukturen als Flugzeugrumpfversteifung*, P.hD. Thesis, Cuvillier Verlag Göttingen, Braunschweig, 2011
- [6] Evonik Industries. ROHACELL® 71 RIMA
- [7] M. J. Orr, *Introduction to Radial Basis Function Networks Technical Report*, Institute for Adaptive and Neural Computation, Division of Informatics, Edinburgh University, www.anc.ed.ac.uk/mjo/papers/intro.ps, 1996
- [8] E. Barkanov, S. Gluhik, O. Ozoliņš, E. Eglītis, F. Almeida, M. C. Bowering, G. Watson. Optimal Weight Design of Laminated Composite Panels with Different Stiffeners under Buckling Loads. *27th International Congress of the Aeronautical Sciences*, pages 2030-2038, 2010

Structural Optimization for Stabilized and Stiffened Structural System by Tension Members

Yohei Yokosuka¹, Toshio Honma²

¹ Assist. Prof., Dept. of Architecture and Architectural Engineering, Graduate School of Science and Engineering,
Kagoshima University, Japan, yokosuka@ae.kagoshima-u.ac.jp

² Prof., Dept. of Architecture and Architectural Engineering, Graduate School of Science and Engineering,
Kagoshima University, Japan

1. Abstract

This paper presents a numerical method for stabilized and stiffened structural system by tension members. In these structures, it is generally difficult to control a shape and prestress because of high dependency between them. Our proposal model has similar features of these systems, and we find the resisting structural form efficiently for compression occurred by prestressing.

Our analytical approach is to divide a structure into two groups which are instable system and statically indeterminate system. We formulated equations of stabilizing process in each group. These shapes of structures become a unique shape under the specified prestress. In previous research [1], we analyzed two-dimensional models and verified the proposed method. In this paper, we analyzed three-dimensional models and show some results which would be available to apply for spatial structures. Next, we present the optimization method for these structures. In this method, we define the strain energy as an objective function, and magnitude of prestress as design variables. It is difficult to apply linear analysis of stress and displacement in these structural models, because it would be instable without prestress. Therefore, we apply the geometrically nonlinear analysis with prestress by FEM. We focus a form-finding analysis and optimization for these structures in this paper.

2. Keywords: Structural optimization, Stabilized and Stiffened Structural System, Genetic Algorithm

3. Introduction

This paper presents a numerical method for a structural system stiffened by tension members, such as tensegrity structures and cable domes. These structures are utilized for a spatial structure with light weight and attractive appearance. However, in engineering process, it is generally difficult to control a shape and prestress. Therefore, we have to apply the form-finding analysis for an equilibrium shape. Many numerical analysis methods of such structures have been proposed and it would be successful methods. On the other hand, similar types of these structures have been investigated and constructed. These are called “tension-stabilizing truss”, and “tensegric dome” [2]. A different feature from tensegrity is that these systems are utilized for comparatively low stiffness structures, or instable structures. These systems are useful to stiffen the single-layered truss shell. We focus a form-finding analysis and optimization for these structures in this paper.

4. Isotonic Soap Films Stretched on the Polyhedron

Isotonic soap film stretched on the polyhedron is a conceptual model of our proposed structural one. J. Plateau, a Belgian physicist in the 19th Century, formulated Plateau’s law which describes the structure of bubble soap films from his experimental observation (Fig.1). It shows that isotonic soap films are stretched on the polyhedron wire frame. It also can be assumed that the equilibrium shape by self-stress exists in the member arrangement which is a state of tension members covered with compression members. That is to say, in the case of low stiffness shell, it can be stiffened by only tension members. Besides, this structural system is not necessary to be rigid at the compression member’s joint, it would become light weight and high stiffness structure with prestressing.

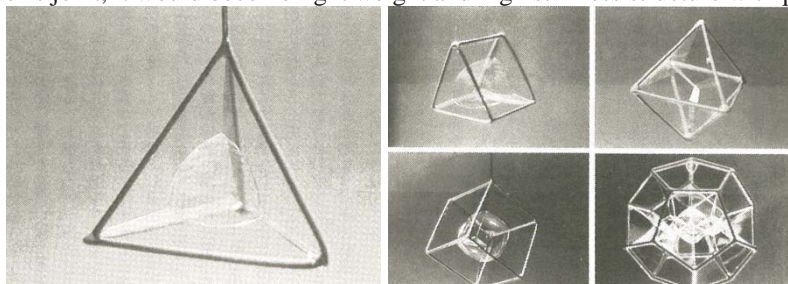


Fig.1 Isotonic soap films stretched on polyhedron formed wire frame (Reprinted from [3])

5. Numerical Analysis

5.1 Analytical Model

It is shown the initial shape consist of truss, cable members and pin joints in Fig.2. Variables of p_1 and p_2 are acting in the cable members. This model is a simple one of stabilized and stiffened structural system.

We explain the outline of form-finding analysis. Our approach is to divide a structure into two groups. The first (g_1) is a group of instable system in which some rigid body displacements modes exist. This group consists of compression truss members shown in left side of Fig.4. Compression members could be rotated at the node, and bending moment doesn't occur inside of members. The second (g_2) is a group of statically indeterminate system in which some self-equilibrating stress modes exist. This group consists of tension members shown in right side of Fig.4. In order to form these assumed systems, we must modify boundary conditions. To analyze these systems, we must set forcible deformations as initial values (p_1, p_2). And then, we control the shape of the structure by displacements toward the stable state. The g_2 will be change the shape of the structure with specified deformations of members forcibly, and the g_1 will be change the shape of the structure as rigid body displacement by acting reversed force of the g_2 's self-stress. In this way, we can obtain the stabilizing shape at the convergence. At last, forcible deformation as the initial values take the place of prestress values. The flow of analysis is shown in Fig.5.

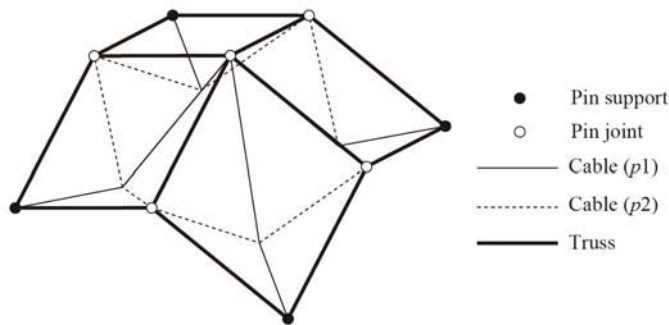


Fig.2 Initial shape and members

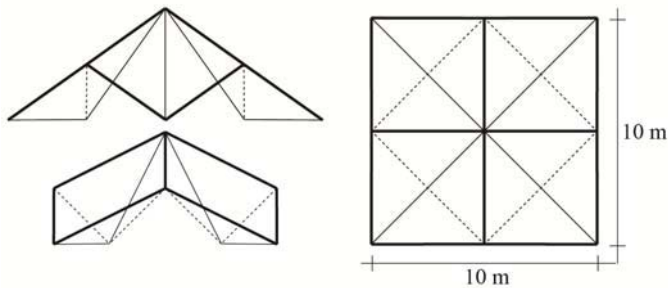


Fig.3 elevation (left side) and plan view (right side)

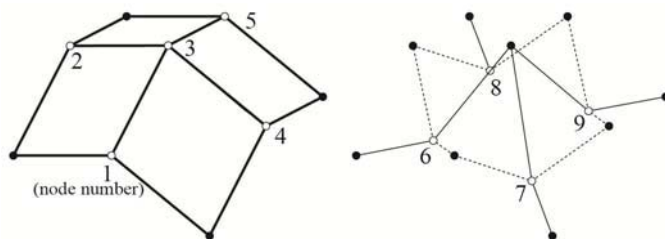


Fig.4 compression group (g_1) and tension group (g_2)

We investigate whether the structure has stiffness by the method of geometrically nonlinear analysis with prestress. It is assumed that the external force is acting as vertical load. The model could be applied linear analysis by FEM, but we have to avoid acting compression force into tension members. It appears that this stiffened system of structure would be useful.

5.2 Formulation of form-finding

The discretized static equilibrium equation of truss structures can be written as

$$An = f \quad (1)$$

A : equilibrium matrix, n : axial force vector, f : external force vector

The deformation–displacement relation can be written as

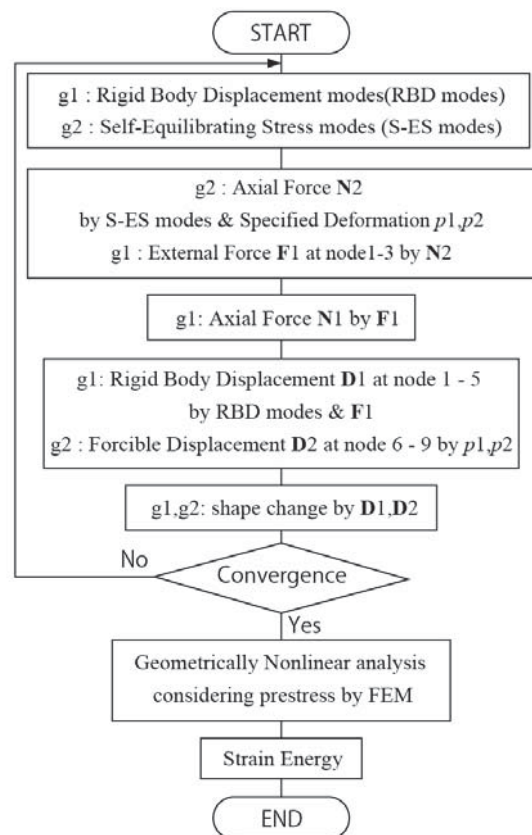


Fig.5 Analytical flow of form-finding

$$Bd = \Delta l \quad (2)$$

B : deformation – displacement matrix, d : displacement vector, Δl : deformation vector

Now, we consider two groups of structural system. Rigid body displacement occurs by acting the External force in g1. Under the assumption of rigid body displacement, Eq. (2) becomes

$$Bd = \mathbf{0} \quad (\text{in g1}) \quad (3)$$

$\mathbf{0}$: null vector

The Moore–Penrose generalized inverse matrix gives the displacement vector d as

$$d = [I_n - B^+ B] \alpha \equiv H \alpha \quad (4)$$

I_n : unit matrix(n, n), B^+ : Moore – Penrose generalized inverse matrix, α : arbitrary column vector
 H : matrix of rigid body displacement modes

To consider the convergence of the external potential energy, d can be written as

$$d = \alpha H f \quad (5)$$

α : incrementation parameter

The axial force vector n in g1 can be written as

$$n = -(B^+)^T f \quad (6)$$

Obtained n in this way become least-square solutions.

Next, we formulate the displacement of g2. Acting the specified deformation causes the forcible displacement in g2. This specified deformation takes the place of prestress at the convergence of stabilizing process.

Under the assumption of self-equilibrium state, Eq. (1) becomes

$$An = \mathbf{0} \quad (\text{in g2}) \quad (7)$$

The Moore–Penrose generalized inverse matrix gives the displacement vector n as

$$n = [I_m - BB^+] \beta \equiv G \beta \quad (8)$$

I_m : unit matrix(m, m), B^+ : Moore – Penrose generalized inverse matrix, β : arbitrary column vector
 G : matrix of self – equibrating stress modes

To consider the convergence of the complementary energy, n can be written as

$$n = -G \Delta l \quad (9)$$

Δl is known value as specified deformation in g2. And, it is negative value. The external force of g1 can be obtained to calculate n of Eq. (9) such as Fig. 6.

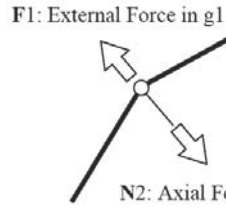


Fig.6 Relation of force in g1 and g2

The displacement of g2 can be written as

$$d = \alpha B^+ \Delta l \quad (10)$$

Obtained d become least-square solutions, and we regard d as the forcible displacement. To use d of Eq. (5), and (10), the shape of structure is changing. The convergence condition is in below.

$$\begin{aligned} e_1 &= d^T f \quad (\text{in g1}) \\ e_2 &= (-\Delta l - n)^T (-\Delta l - n) \quad (\text{in g2}) \\ e &= e_1 + e_2 < \varepsilon \end{aligned} \quad (11)$$

$-\Delta l$ becomes prestress when Eq. (11) is established. Therefore, the structure would be stabilized.

5.3 Geometrically Nonlinear Analysis with Prestress

In this paper, we show the geometrically nonlinear analysis with prestress by FEM. This analytical model stiffened by prestress, and it is important to include the geometric stiffness. This method is described as incremental analysis and updated Lagrange method. We apply the Newton-Raphson method as the solution of nonlinear equations.

In the incremental interval, equilibrium equation can be written as

$$K \Delta d = \Delta f \quad (12)$$

K : tangent stiffness matrix, Δd : incremental displacement vector, Δf : incremental force vector

Eq. (12) is expressed as below.

$$K = K_E + K_G \quad (13)$$

K_E : elastic stiffness matrix, K_G : geometric stiffness matrix

$$\Delta f = r = f - q \quad (14)$$

r : residual force vector, q : internal force vector

The prestress n_0 is including in K_G and q . n_0 can be calculated by using Eq. (6), (8).

To determine deformation, axial force, and internal force, we use B matrix of the structure.

$$\Delta l = B \Delta d \quad (15)$$

$$n_k = \frac{E_k A_k}{l_k} \Delta l_k \quad (16)$$

$$\mathbf{q} = \mathbf{B}^T (\mathbf{n}_0 + \mathbf{n}) \quad (17)$$

E : elastic modulus, A : sectional area of member

n_k is the axial force in the process of deformation by external force acting. According to the Newton-Raphson method, $\Delta \mathbf{d}$ can be calculated as

$$\Delta \mathbf{d} = \mathbf{K}^{-1} \mathbf{r} \quad (18)$$

To quantify the stiffness of the structure, we define the strain energy U as below. Considering the effect of prestress, it is expressed by using strain energy including prestress.

$$U = \sum_{k=1}^m (n_{0k} \Delta l_{0k} + n_k \Delta l_k) \quad (19)$$

5.4 Result of Form-finding Analysis

We show the analysis for a fundamental type of structure (Fig.3). This model has 12 compression members and 16 tension members. These are truss members and cable members. We assume that cable members are symmetrically prestressing. Thus, we set a limit to the number of parameters, and we can draw a strain energy surface of various shape structures. Two results (A,B) of numerical analysis and physical property for FEM are shown as below.

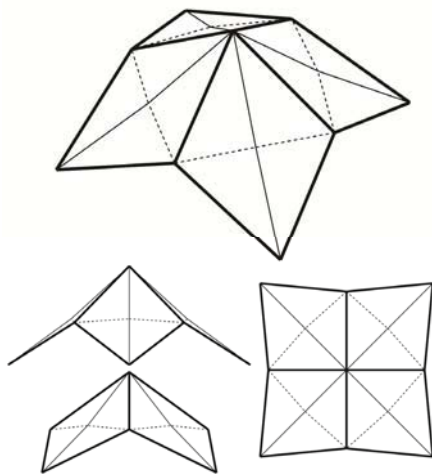


Fig.7 Analysis result-A ($p_1=1.80, p_2=1.10$)

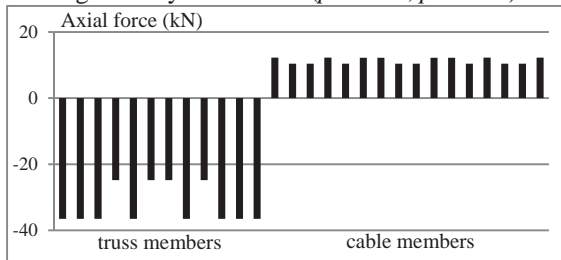


Fig.9 Axial force in result-A

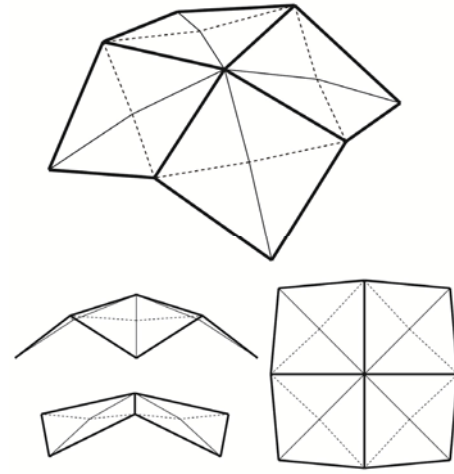


Fig.8 Analysis result-B ($p_1=1.15, p_2=1.40$)

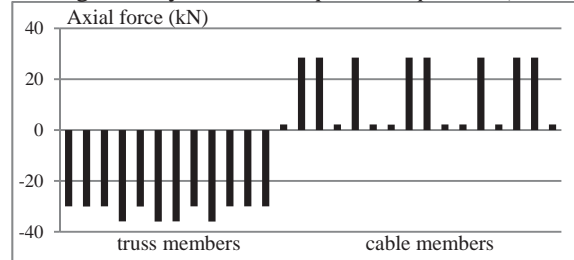


Fig.10 Axial force in result-B

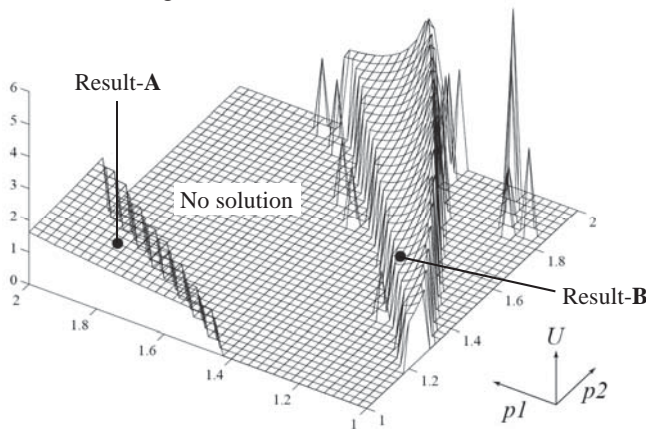


Fig.11 Strain energy surface

Tab.1 Physical property and analysis condition

Vertical load	1.0 kN/m ²
Young's modulus (truss)	2.1×10 ⁸ kN/m ²
Young's modulus (cable)	1.4×10 ⁸ kN/m ²
Section area (truss)	9.8×10 ⁻⁴ m ²
Section area (cable)	9.5×10 ⁻⁵ m ²
Coefficient for prestress	10

Form of analysis result of form-finding in section 5.2 is shown in Fig.7,8. Changing the variables $p1, p2$, various forms can be obtained. The physical property and analysis condition for geometrically nonlinear analysis with prestress are shown in Tab.1. The truss members are assumed the steel pipes of $D = 101.6$ mm. The cable members are assumed the strand cables of $D = 14.0$ mm. Coefficient for prestress is weight factor of prestress. n_0 of Eq.(17) include the coefficient for prestress in formulation.

Axial force in geometrically nonlinear analysis is shown in Fig.9, 10. It appears that compression members are acted negative axial force, and tension members are acted positive axial force. This result means that it is effective to apply prestress for this model. If this model have solved by using linear analysis in FEM, tension members would be acted negative axial force.

Strain energy surface in Fig. 11 show that this analysis is difficult to converge for optimization. Two cases of problem exist, the first is cable members cannot have almost same value of $p1$ and $p2$, it occurs vibration in form-finding. The second in FEM is the Coefficient for prestress is comparatively low value, tension members are acted negative axial force. Moreover, if the coefficient for prestress increase, compression force also increase in truss members. Thus, structural optimization is difficult to solve stably in this strain energy field.

6. Structural Optimization by Genetic Algorithm

In this paper, we apply Genetic Algorithm (GA) for structural optimization. GA is useful for an optimization problem such as finding global optimal solution without the gradient of objective function. In our proposed model, it is difficult to define the relationship between variables $p1, p2$ and strain energy, the gradient of energy cannot be obtained. Therefore, we chose GA for this problem. However, if we execute GA in this problem, many of individuals are fall in “No solution” region in Fig.11. It would not be efficient to converge. Therefore, we propose to change the variable space like Fig.12. This method is useful to avoid the region in which algorithm search. The formulation of optimization is shown in below.

$$\begin{aligned}
 & \text{Find} && p1, p2 \\
 & \text{to minimize} && f(p1, p2) \\
 & \text{subject to} && p^{L1} < p1 < p^{U1} \\
 & && p^{L2} < p2 < p^{U2} \\
 & && f(p1, p2) : \text{Strain energy in Eq. (19)} \\
 & && p^{L1}, p^{U1}, p^{L2}, p^{U2} : \text{Upper and lower constrain} \\
 & && p^{L1} = 1.0, p^{U1} = 1.4, p^{L2} = 1.375 p1 + 0.025, p^{U2} = 2.0
 \end{aligned}$$

These formulation search the hill in which the Result-A exist in Fig. 11. The parameter of GA is shown in Tab. 2. We executed the GA optimization three times. Thus, we show the result of optimization in Fig. 13-15. The relationship between strain energy and Iteration number is shown in Fig.13. The relationship between entropy Dp and Iteration number is shown in Fig.14. Entropy Dp is the value of assessment for convergence. It appears that these GA optimizations are in the state of convergence and finished in all trials.

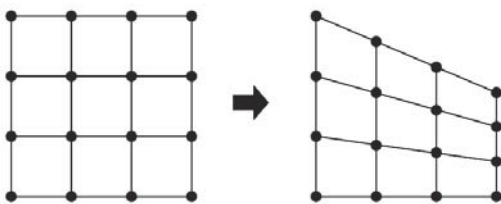


Fig.12 Mapping of variable space

Individual number	100	Generation number	50
Mutation ratio	0.06	selection	tournament elite
Crossover ratio	0.7	string	16bit

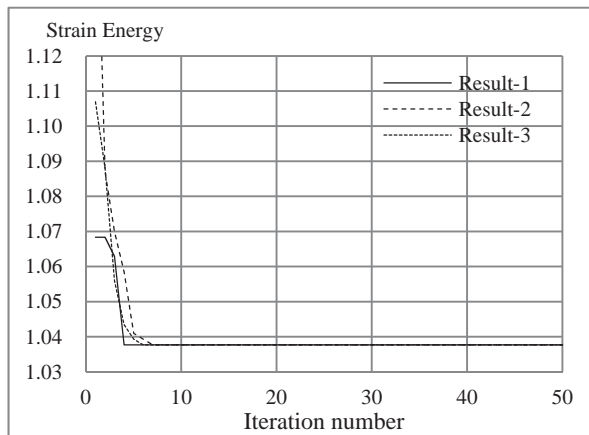


Fig.13 Strain energy – Iteration number

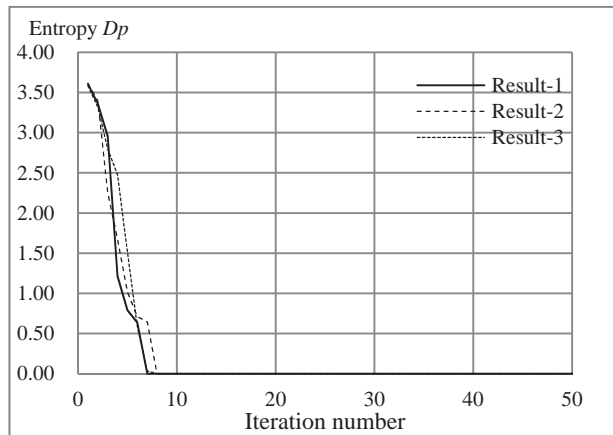


Fig.14 Entropy Dp – Iteration number

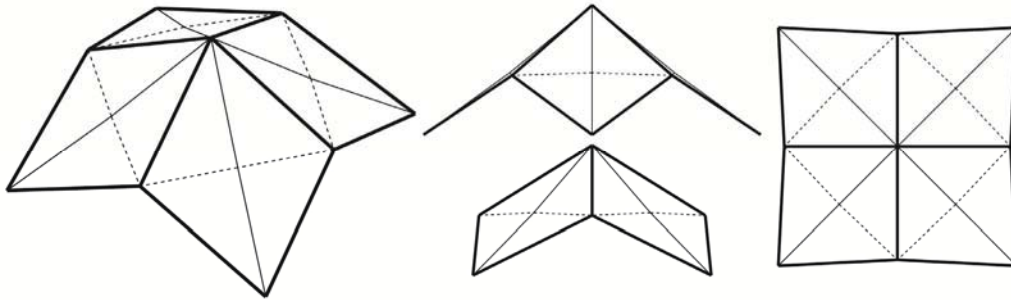


Fig.14 Form of GA optimization result ($p_1 = 1.433, p_2 = 1.000, f(p_1, p_2) = 1.038$)

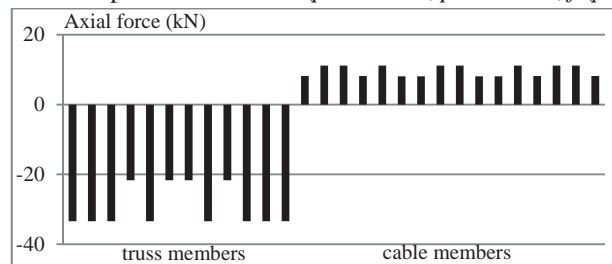


Fig.15 Axial force in GA optimization result

The form of GA optimization result is shown in Fig. 14. Axial force is shown in Fig. 15. Comparing with strain energy surface, the point of variables obtained by optimization is an optimal solution in the set region. Although axial force tends to be in the state of result-A in form-finding, the values of axial force are totally low.

7. Conclusion

This paper presents a numerical method for a structural system stiffened by tension members. The form-finding analysis can obtain the form in equilibrium state with prestress. The geometrically nonlinear analysis allows to apply the structure with prestress. The strain energy surface show that this model is difficult to converge for optimization, but mapping of variable space is useful for the case including the “No solution” region. The structural optimization by GA is available to find optimal solution for a high stiffened structure.

This model is simple and static structure in the view of relation of member connection. This proposed method is useful for more complicated model such as instable structure with more tension members. The next step is to arrange these stabilized and stiffened structural models from every direction.

8. References

- [1] Yohei Yokosuka, Toshio Honma, Form-finding Analysis for Structural System Stiffened by Tension Members, The Eighth China-Japan-Korea Joint Symposium on Optimization of Structural and Mechanical Systems (CJK-OSM8), Gyeongju, Korea, No.182, pp.1-6, 2014
- [2] Masao Saito, Story of Space and Structure-Structural Design's Future (in Japanese), SHOKOKUSHA, 2003
- [3] Philip Ball (translator: Masaru Hayashi), Shapes : Nature's Pattern (in Japanese), Hayakawa Shobo, 2011
- [4] Yohei Yokosuka, Shape-finding Analysis for Variable Geometry Structures Formed by a Multilink Spherical Joint and Fluid Analysis Based on Generalized Inverse Matrix (in Japanese), JAIST Theses, 2013
- [5] Yasuhiko Hangai, and Ken'ichi Kawaguchi, Shape Analysis - Generalized Inverses and Applications (in Japanese), Baifukan Press, 1991
- [6] Ken'ichi Kawaguchi, Generalized Inverse and its Applications to Structural Engineering (in Japanese), CORONA PUBLISHING CO., Ltd, 2011
- [7] Toshiaki Hisada, and Hirohisa Noguchi, The foundations and applications of nonlinear finite element method (in Japanese), Maruzen, 1995.
- [8] Eiki Magara, Jiro Kunita, Shigeya Kawamata, Analysis of Cable Nets in Mixed Formulation Part2-Rigorous Solution of the Geometrically Nonlinear Problems, Transactions of the Architectural Institute of Japan (220), 35-45, 64, 1974
- [9] Kazuo Mitsui, Makoto Ohsaki, Hiroshi Ohmori, Hiroshi Tagawa, Toshio Honma, Heuristic Methods for Optimization of structural Systems (in Japanese), CORONA PUBLISHING CO., Ltd, 2004

Sizing Optimization for Industrial Applications

Miguel A.A.S. Matos¹, Peter M. Clausen², Claus B.W. Pedersen³

Dassault Systèmes Deutschland GmbH, Albert-Nestler-Str. 17, 76131 Karlsruhe, Germany,

¹miguel.matos@3ds.com; ²peter.clausen@3ds.com; ³claus.pedersen@3ds.com

1. Abstract

The current work presents the use of sizing optimization for large scale industrial applications with multiphysics phenomena. Presented are some examples which include either structural-acoustic or thermal-structural coupling. Moreover, these incorporate advanced simulation features such as contact modelling and efficient equation solvers dedicated to handle such large models.

This is achieved using the optimization system SIMULIA Tosca Structure as a direct add-on module for Abaqus. This module targets the thickness layout of the different structural sheet components for optimizing the static or dynamic responses of the structure computed using the users' existing Abaqus workflows.

Traditional design responses such as static stiffness, mass, internal and reaction forces and modal eigenfrequencies can be selected for both the objective function and constraints allowing the optimization of typical engineering setups where the shell thicknesses are the primary design variables.

Sizing optimization is a powerful tool for efficient structural design, being already employed across several industries to systematically achieve structure configurations with competitive performance and reduced design times.

The potential of this technology is here illustrated using some large applications from different industries, including a full automotive model from the transportation and mobility sector and a jacket offshore structure for wind turbines from the renewable energy sector. These represent some typical engineering sizing optimization setups of multiphysics and multidisciplinary problems like fully coupled acoustic structural interaction for NVH (Noise, Vibration and Harshness) design or thermo-structural coupling for designing high temperature components. Furthermore, the work demonstrates how sizing optimization benefits from advanced finite element modelling capabilities such as the support for contact inside or outside the design elements and approaches to handle large models with increased numerical efficiency, for instance the automatic multi-level substructuring eigenfrequency solver (AMS) introduced in Abaqus.

2. Keywords: Industrial applications, sizing optimization, structural optimization software

3. Introduction

Structural optimization has shown to be a powerful automatic tool to fulfil the growing industry requirement for efficient resource usage [1, 2, 3]. Frequently, after defining the overall layout of sheet metal structures, there is a need to find the optimal thickness distribution that meets the functional requirements. While trial and error modifications represent a tedious and slow process, the use of sizing optimization tools represents a systematic procedure to automatically obtain optimized sheet thicknesses.

The optimization system SIMULIA Tosca Structure [4] integrates optimization technologies in practical engineering environments as an add-on module easily integrated into the existing Abaqus [5] workflows as shown in Figure 1. After creating the finite element (FE) model of the structure, an optimization task can be defined by selecting the objective function to be minimized or maximized, the respective constraints and elements defined as design elements. All setups and definitions can be done in Abaqus CAE environment for pre-processing. Afterwards, the optimization task is completed by an iterative procedure where the model is automatically updated and modified using a robust non-linear constrained optimizer [8] based on sensitivities derived using the semi-analytical adjoint method [1]. Both the FE equilibrium and adjoint equations are solved by the Abaqus solver. At the end of the optimization job, the final model with optimized thicknesses is readily available for the typical CAE post-processing.

The current paper presents the advantages and possibilities that such a tool is able to bring to engineering design tasks addressing several typical industrial optimization setups. The first example addresses the maximization of the lowest eigenfrequencies for an offshore wind turbine jacket structure. The second example addresses a coupled structural-acoustic problem where the sound pressure generated by a structural excitation is minimized at a certain location. This mimics applications in Noise, Vibration and Harshness (NVH) related to the driving user comfort. To conclude, a full automotive model will be subjected to a mass minimization task with stiffness constraints, underlining the capabilities and ease of use of these optimization tools.

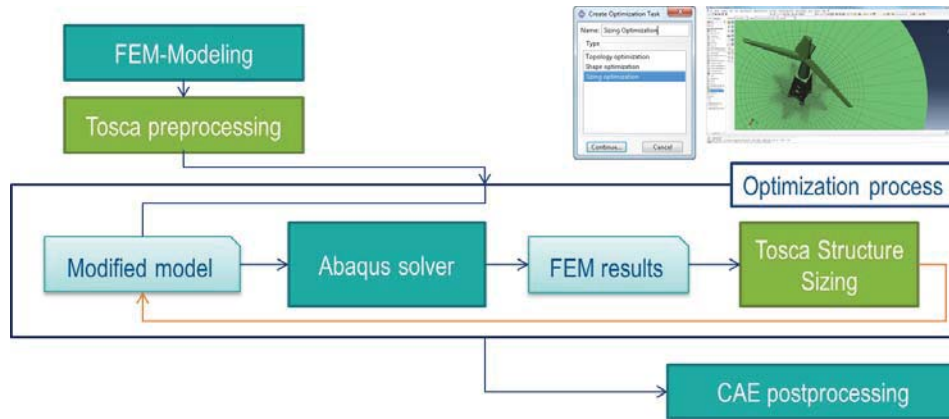


Figure 1 – Tosca Sizing process workflow

4. Offshore wind turbine jacket structure

The first example will consider the modal dynamic behaviour of a jacket structure that supports a 5MW offshore wind turbine, presented in Figure 2a. We optimize the thickness configuration of the truss jacket structure for maximizing its lowest eigenfrequencies. The structure is shown in Figure 2b, modelled with S4R (4 node reduced integration) 3D shell elements. The remaining components of the wind turbine are modelled using continuum elements, membrane elements and rigid bodies, accounting for their correct inertial distribution and the foundations are represented by four piles which are fixed in the ground. The total finite element model has 155300 elements and 612807 degrees of freedom (DOF) and the eigenfrequency analysis is performed using Abaqus AMS (Automatic Multi-level Substructuring) eigenvalue solver [5]. This allows for significant overall analysis runtime reduction in large-scale simulations [6]. The present case requires the evaluation of the first 10 modes and the analyses are performed using 24 CPU cores. The total CPU time is reduced by 60% when compared to the traditional Lanczos eigenvalue solver. This reduction is severely increased when the number of requested modes is increased: 75% for 50 modes and 90% for 100 modes considering the current example. This reveals a good scalability when considering larger models.

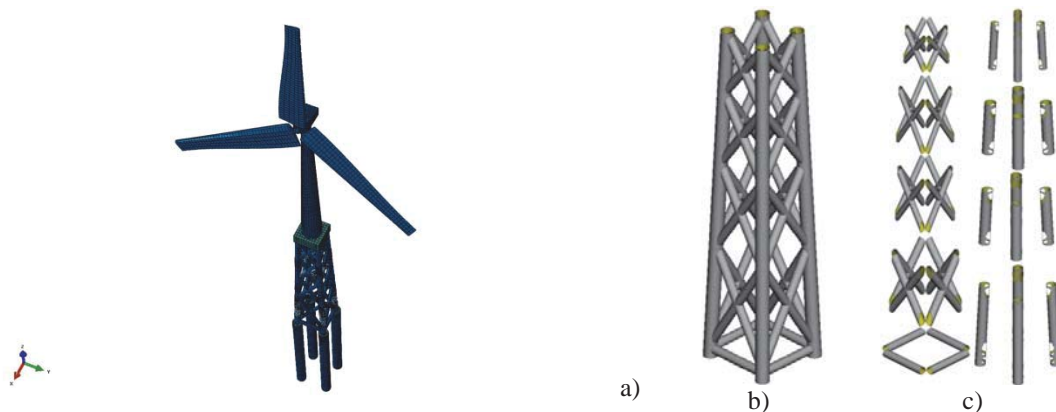


Figure 2 – Offshore wind turbine: a) FEM model, b) shell jacket structure to be optimized and c) defined groups for clustering the thicknesses

The objective of the current optimization task is to maximize the lowest eigenfrequencies of the structure with a mass constraint. The objective function (ϕ) is defined using the Kreisselmaier-Steinhauser [4] formulation described in equation (1) and will consider the first 4 ($J = 4$) eigenmodes:

$$\phi = -\frac{1}{k} \ln \sum_{j=1}^J e^{-k f_j}, \quad k = \frac{30}{f_{\min}} \quad (1)$$

The design domain is meshed by 83020 shell elements modelling the truss structure. Each of the respective shell thicknesses represents one design variable – also called free sizing. As a consequence, the thickness of the shell

elements varies freely. This will tell how to subdivide the optimized into various constant thicknesses profiles. Alternatively, these elements can be clustered into groups that have the same thickness, therefore reproducible by assembling different parts together. In the present case we consider 9 independent groups represented in Figure 2c, thus reducing the 83020 thickness design variables to 9.

The free optimization result is shown in Figure 3a and the respective optimization iterative process in Figure 4, showing an increase in the objective function of 41% without increasing the weight of the structure. For the clustered optimization the results are presented in Figure 3b and Figure 5. The additional constraint of grouping the design variables still allows an increase for the objective function of 15% for the same initial mass.

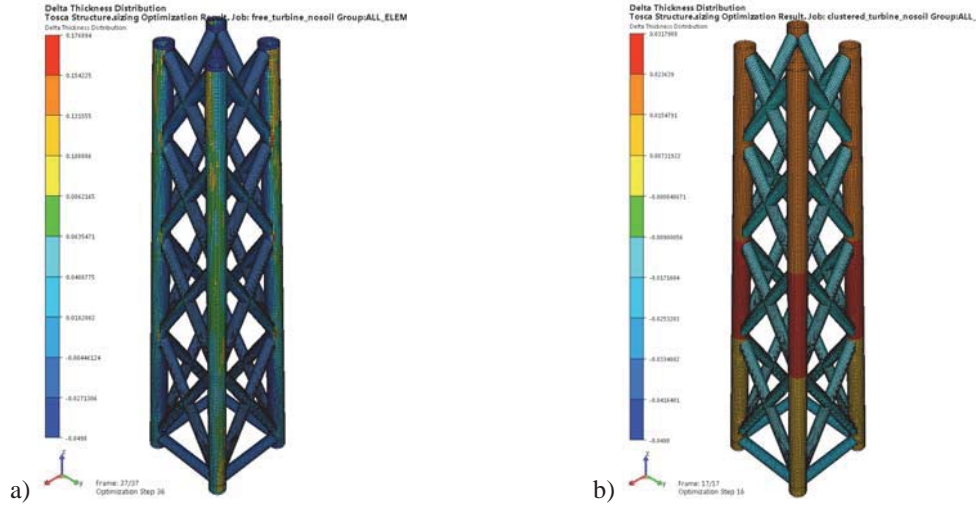


Figure 3 – Change of thickness of the optimized structure: a) with free sizing and b) with clustered sizing

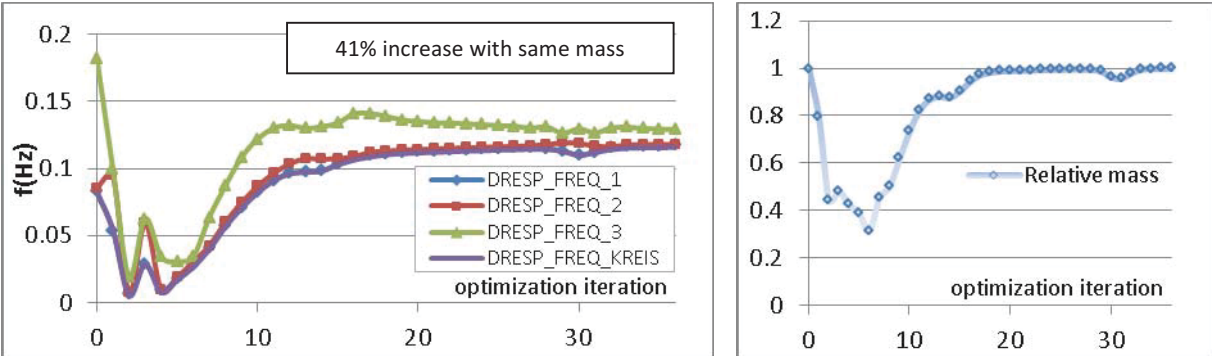


Figure 4 – Optimization iteration history for the free sizing optimization for the objective function, lowest eigenfrequencies and normalized mass

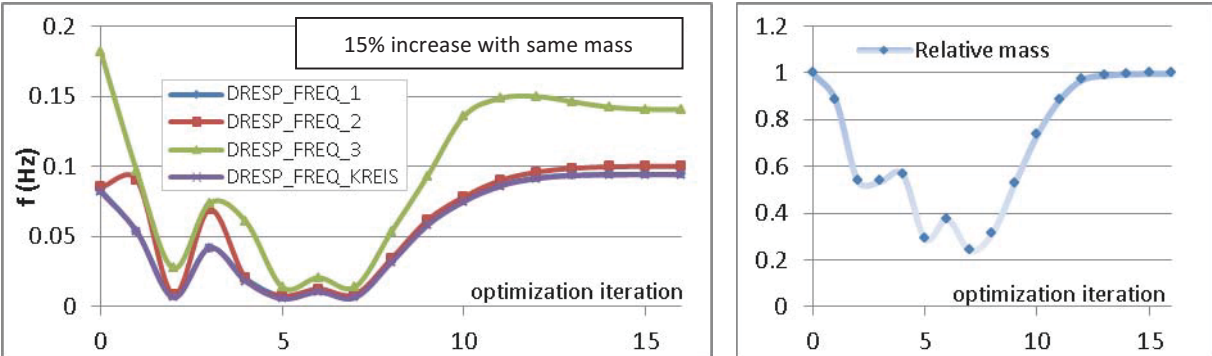


Figure 5 – Optimization iteration history for the clustered sizing optimization

5. Fully coupled structural-acoustic sizing optimization

The current application reveals the optimization of a structural shell plate coupled with an air cavity in order to minimize the pressure measured at a nodal location inside the acoustic domain when the structural component is subjected to a harmonic loading as illustrated in Figure 6a. The plate is simply supported at its boundaries and loaded at its central point.

The governing finite element equilibrium equation for a structure with structural and acoustic domains subjected to harmonic loading and assuming a steady-state time-harmonic response can be described by equation (2) [7]:

$$-\Omega^2 \begin{bmatrix} M_s & 0 \\ A^T & M_a \end{bmatrix} \begin{Bmatrix} u_A \\ p_A \end{Bmatrix} + i\Omega \begin{bmatrix} C_s & 0 \\ 0 & C_a \end{bmatrix} \begin{Bmatrix} u_A \\ p_A \end{Bmatrix} + \begin{bmatrix} K_s & -A \\ 0 & K_a \end{bmatrix} \begin{Bmatrix} u_A \\ p_A \end{Bmatrix} = \begin{Bmatrix} P_s \\ P_a \end{Bmatrix} \quad (2)$$

where Ω is the excitation frequency of the applied load and resulting response. M , C and K are the mass, damping and stiffness matrices. P is the load amplitude for the structural or acoustic domain, according to the respective suffix s and a . The interaction between both domains is quantified by the coupling matrix A and the response amplitudes given by u_A and p_A for the structural and acoustic degrees of freedom, respectively.

The objective is to minimize the resulting pressure amplitude at the centre of the cavity considering an exciting frequency from 500 to 1000 Hz while keeping its weight below the initial value. In order to consider the frequency response across the defined spectrum with N discrete excitation frequencies, we introduce the Q-mean norm formulation for the objective function as explained in [7] and defined in equation (3):

$$\min_{\{t\}} \left(\frac{1}{N} \sum_{n=1}^N (p_A(\Omega_n))^Q \right)^{1/Q} \quad (3)$$

subject to: equilibrium – represented by equation (2) and mass constraint – $m(\{t\}) \leq m_{init}$

where p_A represents the amplitude of the pressure at the node(s) of interest, m the total mass of the structure and m_{init} its initial value and $\{t\}$ the vector of the thickness design variables. Q is set to 6 as it reveals to be numerically stable and to cause only a small error when compared to the min-max formulation [7].

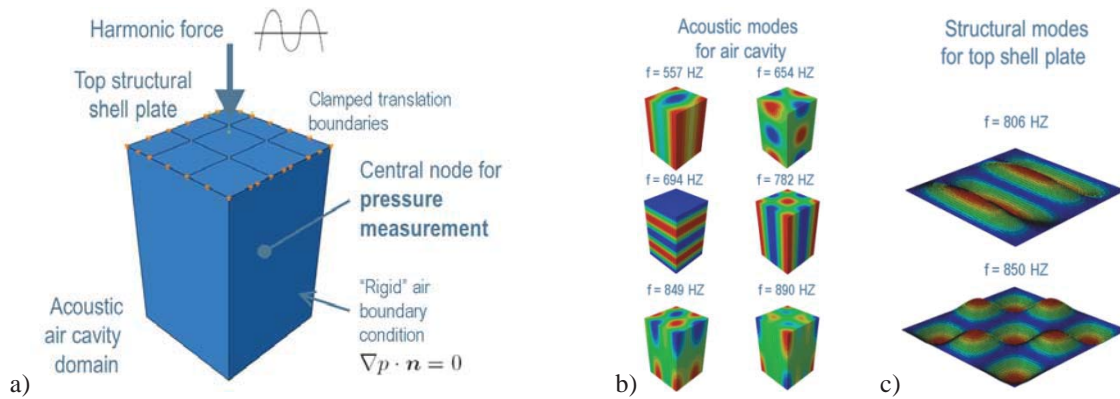


Figure 6 – a) Coupled structural-acoustic model, b) acoustic modes for air cavity and c) shell plate initial modes

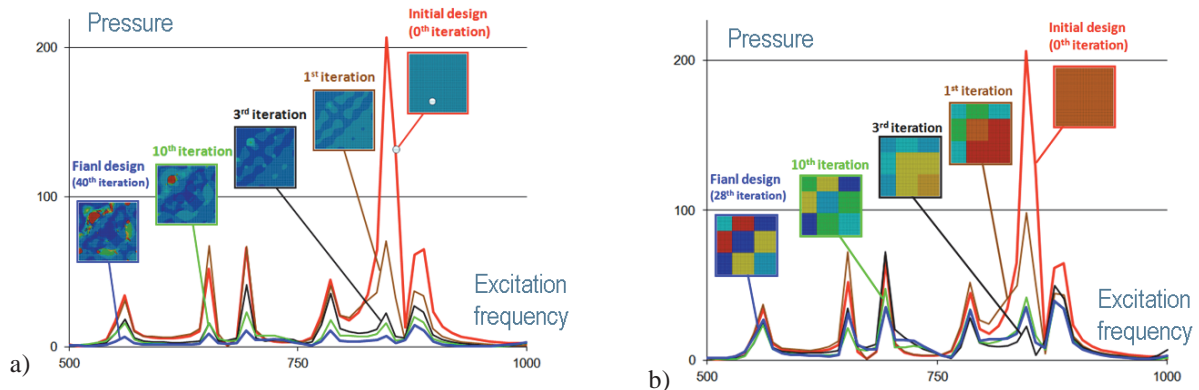


Figure 7 – Optimization iteration history of the pressure frequency response amplitude at the centre of the air cavity for the a) free sizing and b) clustered sizing optimization, respectively

The initial structure modes and eigenfrequencies are represented in Figure 6b and Figure 6c for the uncoupled domains.

The results for free and clustered sizing optimizations are shown in Figure 7a and Figure 7b, respectively, where we can observe a significant reduction of nodal acoustic pressure during the optimization iterations.

6. Automotive sizing optimization

The current application of sizing optimization considers a full automotive model available as an Abaqus example model [5], shown in Figure 8. The vehicle is modelled considering 331578 S4 (4 node shell elements with full integration) and 17443 S3R (3 node shell elements having reduced integration) shell elements, totalling approximately 2 million of degrees of freedom.

The objective of the optimization is to minimize the mass of the structure subject to stiffness constraints. Both free and clustered optimization will be considered. The clustered thickness optimization groups the thicknesses into 198 section groups color-coded in Figure 8.



Figure 8 – Automotive finite element model considered for sizing optimization

We will require that the all bending, torsional and axial stiffness remain above the initial values. The structure is submitted to 3 representative different load cases defined in Figure 9 being clamped at the rear and loaded at the front wheel knuckles. The resulting displacement at the load locations is used to represent the stiffness of the car in these scenarios and combined as represented in equation (4) where the first subscript of the displacement u represents its orientation and the second the nodal location. In order to compute the sensitivities of these displacement constraints, the respective adjoint equations are solved for each required DOF and iteration using Abaqus solver.

<p>Bending stiffness:</p> $\frac{u_{z,2} + u_{z,1}}{2} \leq u_{\text{bending}}^{\text{target}}$	<p>Torsional stiffness:</p> $\frac{u_{z,2} - u_{z,1}}{2} \leq u_{\text{torsional}}^{\text{target}}$	<p>Axial stiffness:</p> $\frac{u_{x,2} + u_{x,1}}{2} \leq u_{\text{axial}}^{\text{target}} \tag{4}$
<p>Bending stiffness</p>	<p>Torsional stiffness</p>	<p>Axial stiffness</p>

Figure 9 – Illustration of the stiffness constraints for the mass minimization optimization

The shell thicknesses are constrained to vary between -20% and 20% of the initial value and the optimization convergence curves are presented in Figure 10 and Figure 11 for the free and clustered options, respectively. In both cases, a significant mass reduction of 19% and 15% can be achieved with the same axial and bending initial stiffness measures and even with a significant increase in torsional stiffness.

7. Conclusion

The use of sizing optimization with SIMULIA Tosca Structure is capable of bringing major improvements to the design of shell structures. As here demonstrated with several applications we were able to maximize the structural eigenfrequencies or to reduce the acoustic pressure without increasing the weight of the structures. Additionally, we have also minimized the structural mass while also keeping or improving its stiffness. Being able to easily integrate these optimizations into existing workflows, it is a valuable tool for the design of structural shell components.

At the conference, additional examples will be presented illustrating the use of sizing optimization to applications that involve thermo-structural coupling and include contact modelling.

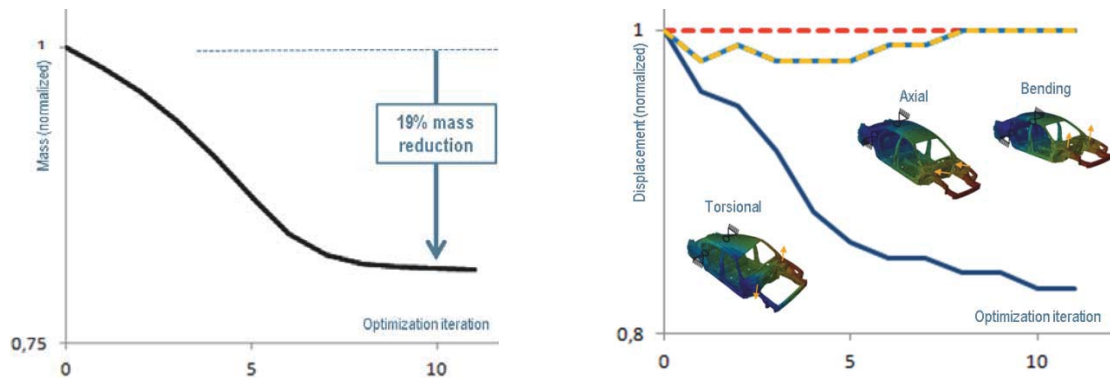


Figure 10 – Mass and stiffness constraints optimization iteration history for the free sizing optimization process

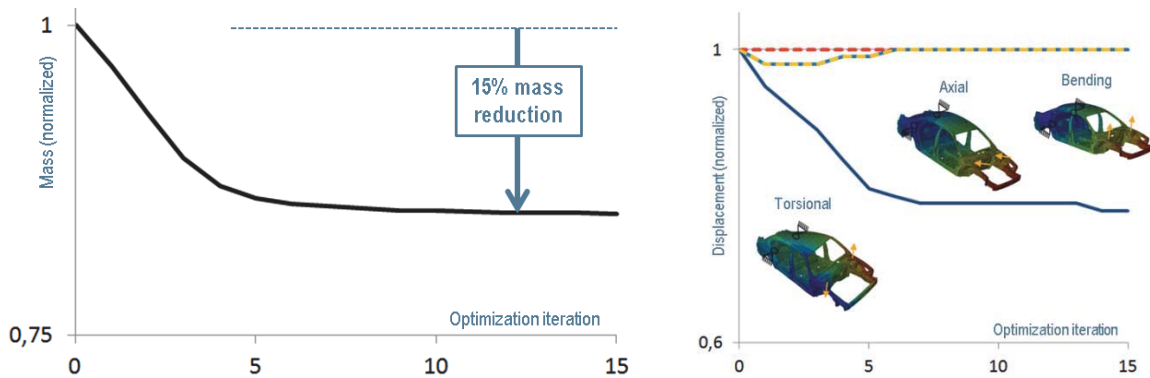


Figure 11 – Mass and stiffness constraints optimization iteration history for the clustered sizing optimization process

8. Acknowledgements

The current work has been supported by the European Commission under the 7th Framework Programme through the Marie Curie Action: “Industry-Academia Partnerships and Pathways” of the “Capacities” Programme. Project: “LaSciSO”, Grant number 285782.

9. References

- [1] M.P. Bendsoe and O. Sigmund, *Topology Optimization: Theory, Methods and Applications*, Springer-Verlag, Berlin, 2003.
- [2] P.M. Clausen, C.B.W. Pedersen, Non-parametric NVH optimization of industrial designs, *Proceedings of the 8th World Congress on Structural and Multidisciplinary Optimization*, Lisbon, Portugal, 2009.
- [3] C.B.W. Pedersen, P. Allinger, Industrial Implementation and Applications of Topology Optimization and Future Needs, *IUTAM Symposium on Topological Design Optimization of Structures, Machines and Materials (Solid Mechanics and Its Applications)*, M.P. Bendsoe, N. Olhoff, O. Sigmund (Eds.), vol. 137, 229–238, 2006, Springer Netherlands (ISBN 978–1–4020–4729–9).
- [4] Dassault Systèmes – Simulia, *SIMULIA Tosca Structure Documentation*, Version 8.1.0, 2014.
- [5] Dassault Systèmes – Simulia, *Abaqus Documentation*, Version 6.14, 2014.
- [6] M. Belyi, V. Belsky, A. Bajer, M. Kim and C. Ianculescu, Advanced linear dynamics and substructuring capabilities in Abaqus with applications in noise and vibration analysis, *Proceedings of ISMA2012*, Leuven, Belgium, 2012.
- [7] M.B. Søndergaard, C.B.W. Pedersen, Applied topology optimization of vibro-acoustic hearing instrument models, *Journal of Sound and Vibration*, 333 (3), 683–692, 2014 (ISSN 0022-460X).
- [8] K. Svanberg, The method of moving asymptotes—a new method for structural optimization, *International Journal for Numerical Methods in Engineering*, 24 (2), 359–373, 1987.

A New Method for Maximum Dynamic Response Topology Optimization in the Time Domain

Junpeng Zhao¹, Chunjie Wang²

¹ School of Mechanical Engineering and Automation, Beihang University, Beijing, China, zhaojunpeng@buaa.edu.cn

² State Key Laboratory of Virtual Reality Technology and System, Beihang University, Beijing, China, wangcj@buaa.edu.cn

1. Abstract

The widely used static topology optimization methods try to find optimal design of structures under loads that are static or vary slowly. However, when the loads change rapidly, their time-dependent characteristic and the inertia effect must be taken into consideration, and therefore dynamic response topology optimization methods should be employed. Two difficulties in solving such problems are the treatment of time-dependent responses and sensitivity analysis. This paper proposes a one-parameter functional to approximate the extreme value of time-dependent response. The accuracy of the approximation can be controlled by the parameter and some of its important properties are discussed. The proposed functional is incorporated into topology optimization problem to minimize the maximum value of time-dependent response at prescribed material volume. The displacement of a specific point of the structure is considered. The density-based approach is used to solve the topology optimization problems and the adjoint variable method is employed to perform sensitivity analysis. The design variables are updated by the Method of Moving Asymptotes. Two numerical examples are conducted to demonstrate the effectiveness of the proposed method and the time-dependent characteristic of the dynamic loads and inertia effect on the topology optimization results.

2. Keywords: Time-dependent response Topology Optimization One-parameter functional Adjoint variable method.

3. Introduction

The widely used static topology optimization methods try to find optimal design of structures under loads that are static or vary slowly[1]. However, when the loads change rapidly, the time-dependent characteristic and inertia effect must be taken into consideration, and therefore dynamic response topology optimization methods should be employed[2]. This work tries to minimize the maximum dynamic response of structure at prescribed material volume. Two difficulties in solving such problems are the treatment of maximum operator in the objective function and sensitivity analysis. This work proposes a one-parameter functional to approximate the maximum value of time-dependent response and incorporated it into topology optimization problem. The density-based approach is used to solve the topology optimization problems and the adjoint variable method is employed to perform sensitivity analysis. The design variables are updated by the Method of Moving Asymptotes. Two numerical examples are conducted to demonstrate the effectiveness of the proposed method and the time-dependent characteristic of the dynamic loads and inertia effect on the topology optimization results.

4. One-parameter Functional to Approximate the Extreme Value of Time-dependent Response

Let $f(t)$ be a continuous function defined on the interval $[0, T]$, M and m respectively its maximum and minimum values. Zhuang and Xiong[3] proposed a functional $\psi(f, \alpha)$ to approximate M based on the discrete form of V_a -approximation[4]

$$\psi(f, \alpha) = \frac{\int_0^T f(t) \alpha^{f(t)} dt}{\int_0^T \alpha^{f(t)} dt} \quad (1)$$

where α is a positive constant and when it tends to positive infinity, $\psi(f, \alpha)$ tends to M .

This work makes a simple transformation $p = \ln \alpha$ and obtains the following one-parameter functional.

$$\varphi(f, p) = \frac{\int_0^T f(t) e^{pf(t)} dt}{\int_0^T e^{pf(t)} dt} \quad (2)$$

The functional has the following properties:

- (i) $m \leq \varphi(f, p) \leq M$.
- (ii) $\lim_{p \rightarrow -\infty} \varphi(f, p) = m$, $\lim_{p \rightarrow \infty} \varphi(f, p) = M$.
- (iii) $\varphi(f, p)$ is nondecreasing.

The proof of (i) and (ii) is easy and will be omitted here. To prove (iii), we note that

$$\frac{d\varphi}{dp} = \frac{\int_0^T f^2 t e^{pf t} dt \int_0^T e^{pf t} dt - \int_0^T f t e^{pf t} dt^2}{\int_0^T e^{pf t} dt^2} \quad (3)$$

Thanks to the Cauchy-Schwarz inequality, we have

$$\int_0^T f^2 t e^{pf t} dt \int_0^T e^{pf t} dt \geq \int_0^T f t e^{pf t} dt^2 \quad (4)$$

so $d\varphi/dp \geq 0$, which implies (iii). It also can be proved that $d\varphi/dp = 0$ iff $f t$ is a constant function.

According to the properties listed above, $\varphi(f, p)$ can be a good approximation to the maximum or minimum value of the function $f t$ when the value of p is sufficiently large or small. More importantly, the accuracy of this approximation can be controlled by adjusting the parameter p . When increasing the value of p , $\varphi(f, p)$ approximates the maximum value of the function better; on the contrary, if the value of p is decreased, $\varphi(f, p)$ approximates the minimum value of the function better.

5. Maximum Dynamic Response Topology Optimization

5.1. Maximum Dynamic Response Topology Optimization Formulation

In order to solve the dynamic response topology optimization problem, the popular density-based approach is employed. The density-based topology optimization approach assigns each element e a density variable η_e and then links its Young's modulus E_e and structural density (mass density) ρ_e with η_e by appropriate interpolation schemes. To prevent the appearance of the localized modes in dynamics analysis, the polynomial interpolation model proposed in [5] will be used.

$$E_e = E_0 15\eta_e^3 \quad \eta_e / 16 \quad (5)$$

$$\rho_e = \rho_0 \eta_e \quad (6)$$

where E_0 and ρ_0 respectively are the Young's modulus and structural density of the solid material.

By using the density-based approach, the dynamic response topology optimization problem in the time domain can be formulated as (7). The objective is to minimize the maximum dynamic response of the structures during the loading phase.

$$\begin{aligned} \min_{\eta} \quad & \max_{0 \leq t \leq T} f(\mathbf{u}, t, \eta) \\ \text{s.t.} \quad & \mathbf{M}\ddot{\mathbf{u}} + \mathbf{C}\dot{\mathbf{u}} + \mathbf{K}\mathbf{u} = \mathbf{f}(t) \\ & g(\eta) = \mathbf{V}(\eta) - V_{\max} = \sum_{e=1}^N \eta_e v_e - V_{\max} \leq 0 \\ & \mathbf{0} < \eta_{\min} \leq \eta \leq \mathbf{1} \end{aligned} \quad (7)$$

where $f(\mathbf{u}, t, \eta)$ is the dynamic response of the structure at time t . \mathbf{M} , \mathbf{C} and \mathbf{K} are respectively the global mass, damping and stiffness matrices. N is the number of elements, v_e is the volume of element e and V_{\max} is the prescribed volume of total material. η_{\min} is a positive lower bound vector assigned to η to avoid singularity of the stiffness matrix during topology optimization process. Given the value of the design variable vector η and the initial condition of the structure $\mathbf{u}(0) = \mathbf{u}_0, \dot{\mathbf{u}}(0) = \dot{\mathbf{u}}_0$, the displacement vector $\mathbf{u}(t)$, velocity vector $\dot{\mathbf{u}}(t)$ and acceleration vector $\ddot{\mathbf{u}}(t)$ can be obtained by solving the dynamic equilibrium equations.

It is difficult to solve this problem directly, here we replace the objective function by the one-parameter functional (2) and formulate the following topology optimization problem.

$$\begin{aligned} \min_{\eta} \quad & \varphi(f, p) \\ \text{s.t.} \quad & \mathbf{M}\ddot{\mathbf{u}} + \mathbf{C}\dot{\mathbf{u}} + \mathbf{K}\mathbf{u} = \mathbf{f}(t) \\ & g(\eta) = \mathbf{V}(\eta) - V_{\max} = \sum_{e=1}^N \eta_e v_e - V_{\max} \leq 0 \\ & \mathbf{0} < \eta_{\min} \leq \eta \leq \mathbf{1} \end{aligned} \quad (8)$$

5.2. Sensitivity Analysis

As we wish to apply a gradient-based optimization algorithm to find the optimal material distribution of the design, the sensitivity of the objective function with respect to the design variables must be evaluated. Considering that the number of design variables is larger than the number of constraints in topology optimization problems, the adjoint variable method [6] is preferred.

We assume that the loads and the initial conditions are independent of the design, that is $\partial \mathbf{f} / \partial \eta_e = \mathbf{0}, \partial \mathbf{u}_0 / \partial \eta_e = \mathbf{0}, \partial \dot{\mathbf{u}}_0 / \partial \eta_e = \mathbf{0}$. Then according to the adjoint variable method, when seeking the derivative $\partial J / \partial \eta_e$, it can be

augmented with the product of a Lagrangian multipliers λ^T and the derivative of the residual(which is zero at equilibria)

$$\begin{aligned} \frac{\partial \varphi}{\partial \eta_e} &= \frac{\partial \varphi}{\partial \eta_e} \int_0^T \lambda^T \frac{\partial}{\partial \eta_e} \mathbf{M}\ddot{\mathbf{u}} - \mathbf{C}\dot{\mathbf{u}} - \mathbf{K}\mathbf{u} - \mathbf{f} dt \\ &= C_p \int_0^T 1 - p f - p \varphi e^{p f} \frac{\partial f}{\partial \eta_e} \frac{\partial f}{\partial \mathbf{u}} \frac{\partial \mathbf{u}}{\partial \eta_e} dt + \int_0^T \lambda^T \frac{\partial}{\partial \eta_e} \mathbf{M}\ddot{\mathbf{u}} - \mathbf{C}\dot{\mathbf{u}} - \mathbf{K}\mathbf{u} dt \\ &= C_p \int_0^T 1 - p f - p \varphi e^{p f} \frac{\partial f}{\partial \eta_e} dt + \int_0^T \lambda^T \frac{\partial \mathbf{M}}{\partial \eta_e} \ddot{\mathbf{u}} - \frac{\partial \mathbf{C}}{\partial \eta_e} \dot{\mathbf{u}} - \frac{\partial \mathbf{K}}{\partial \eta_e} \mathbf{u} dt \\ &= C_p \int_0^T 1 - p f - p \varphi e^{p f} \frac{\partial f}{\partial \mathbf{u}} \frac{\partial \mathbf{u}}{\partial \eta_e} dt + \int_0^T \lambda^T \mathbf{M} \frac{\partial \ddot{\mathbf{u}}}{\partial \eta_e} - \mathbf{C} \frac{\partial \dot{\mathbf{u}}}{\partial \eta_e} - \mathbf{K} \frac{\partial \mathbf{u}}{\partial \eta_e} dt \end{aligned} \quad (9)$$

where $C_p = 1/\int_0^T e^{p f} dt$.

Twice integrating-by-parts the last term and rearranging yields

$$\begin{aligned} \frac{\partial \varphi}{\partial \eta_e} &= C_p \int_0^T 1 - p f - p \varphi e^{p f} \frac{\partial f}{\partial \eta_e} dt + \int_0^T \lambda^T \frac{\partial \mathbf{M}}{\partial \eta_e} \ddot{\mathbf{u}} - \frac{\partial \mathbf{C}}{\partial \eta_e} \dot{\mathbf{u}} - \frac{\partial \mathbf{K}}{\partial \eta_e} \mathbf{u} dt \\ &= \int_0^T \frac{\partial \mathbf{u}}{\partial \eta_e}^T \mathbf{M} \ddot{\lambda} - \mathbf{C} \dot{\lambda} - \mathbf{K} \lambda - C_p 1 - p f - p \varphi e^{p f} \frac{\partial f}{\partial \mathbf{u}}^T dt + \left. \frac{\partial \mathbf{u}}{\partial \eta_e}^T - \mathbf{M} \dot{\lambda} - \mathbf{C} \lambda - \frac{\partial \dot{\mathbf{u}}}{\partial \eta_e}^T \mathbf{M} \lambda \right|_t^T \end{aligned} \quad (10)$$

Since (10) holds for arbitrary λ^T , the Lagrangian multipliers can be chosen to eliminate the last two terms of the right-hand side of (10)

$$\begin{aligned} \mathbf{M} \ddot{\lambda} - \mathbf{C} \dot{\lambda} - \mathbf{K} \lambda &= -C_p 1 - p f - p \varphi e^{p f} \frac{\partial f}{\partial \mathbf{u}}^T, t \in 0, T \\ \lambda^T &= \mathbf{0}, \dot{\lambda}^T = \mathbf{0} \end{aligned} \quad (11)$$

And the derivative $\partial \varphi / \partial \eta_e$ can now be simply given as

$$\frac{\partial \varphi}{\partial \eta_e} = C_p \int_0^T 1 - p f - p \varphi e^{p f} \frac{\partial f}{\partial \eta_e} dt + \int_0^T \lambda^T \frac{\partial \mathbf{M}}{\partial \eta_e} \ddot{\mathbf{u}} - \frac{\partial \mathbf{C}}{\partial \eta_e} \dot{\mathbf{u}} - \frac{\partial \mathbf{K}}{\partial \eta_e} \mathbf{u} dt \quad (12)$$

In order to obtain λ^T , we apply the transformation $\mathbf{\Lambda}^T s = \lambda^T T - s$, then Eq. (11) becomes

$$\begin{aligned} \mathbf{M} \ddot{\mathbf{\Lambda}}^T s - \mathbf{C} \dot{\mathbf{\Lambda}}^T s - \mathbf{K} \mathbf{\Lambda}^T s &= \mathbf{P}^T s, s \in 0, T \\ \mathbf{\Lambda}^T &= \mathbf{0}, \dot{\mathbf{\Lambda}}^T = \mathbf{0} \end{aligned} \quad (13)$$

where $\mathbf{P}^T s$ is given as

$$\mathbf{P}^T s = -C_p 1 - p f - p \varphi e^{p f} \frac{\partial f}{\partial \mathbf{u}}^T \Big|_t^{T-s} \quad (14)$$

When $\mathbf{\Lambda}^T s$ is obtained by numerical methods, λ^T can be obtained by $\lambda^T = \mathbf{\Lambda}^T T - t$.

In particular, when the displacement response is considered, $f = \mathbf{L}^T \mathbf{u}$, $\partial f / \partial \mathbf{u} = \mathbf{L}^T$, $\partial f / \partial \eta_e = 0$, where \mathbf{L} is a unit length vector with zeros at all degrees of freedom except at the point where the displacement is considered.

When \mathbf{u}^T , $\dot{\mathbf{u}}^T$, $\ddot{\mathbf{u}}^T$ and λ^T have all been obtained, the objective function and the sensitivities can be evaluated by (2) (12) and the trapezoidal summation[7]

$$\int_0^T h(t) dt \approx \sum_{n=0}^{N_s} h(t_n) w_n \quad (15)$$

where N_s is the number of steps used to discrete the time domain, t_n are time points and the weights are

$$2w_0 = w_1 = \dots = w_{N_s-1} = 2w_{N_s} = T/N_s \quad (16)$$

6. Numerical Examples

This section presents two numerical examples which minimize the maximum displacement of the loading point of the structure. In both examples, the International System of Units(SI) is adopted and Young's modulus $E_0 = 2.0E11$, Poisson's ration $\nu = 0.3$ and structural density $\rho_0 = 7800$ for fully solid material is assumed. The Rayleigh damping $\mathbf{C} = \alpha_r \mathbf{M} + \beta_r \mathbf{K}$ is assumed and the coefficients α_r and β_r are considered to be design-independent and

are chosen as $\alpha_r = 10$ and $\beta_r = 10^{-5}$. The sensitivity filter[8] is employed to avoid the checkerboards and mesh-dependencies phenomena. The radius of the sensitivity filter is set to be three times the size of the elements used to discretize the design domain. The standard settings are used for the MMA optimizer[9]. The Newmark method is used to solve the dynamics equilibrium equation. The value of the parameter in the functional is set to be $5/f_{max}$, where f_{max} is the maximum value of the displacement during the loading phase. For comparison, a corresponding static design problem is also set up for each example, where the magnitude of the static load is the same as the maximum value of the dynamic load over loading phase.

6.1. Cantilever Beam under Sinusoidal Loading

This example uses a cantilever beam design problem as shown in Fig. 1(a) to demonstrate the effectiveness of the proposed method. The design domain is a 8×4 rectangular area with thickness 0.01. A dynamic load is vertically applied at the bottom right of the structure. The prescribed volume fraction of material is set to 0.5. The dynamic loading is assumed as the sinusoidal function, and two different integration time $T = 0.02, 0.2$ are considered.

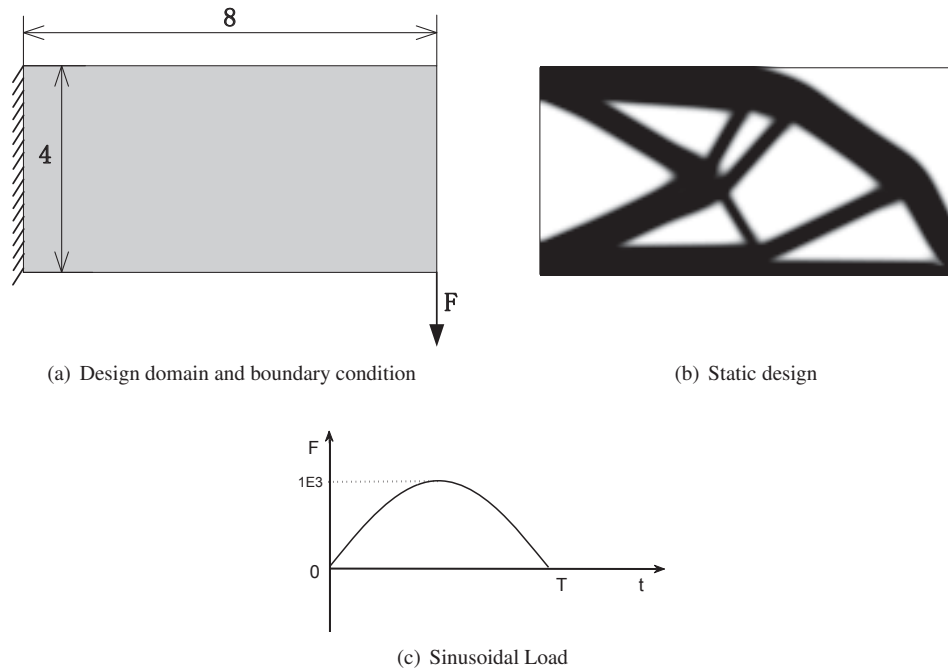


Figure 1: Topology optimization problem of cantilever beam under sinusoidal loading

In order to solve the topology optimization problem, the design domain is discretized by square bilinear plane stress elements whose size is 0.05. The corresponding static design is shown in Fig. 1(b). The optimal designs under dynamic loading are shown in Fig. 2. They clearly show that the change rate of the dynamic load have great influence on the design result. When the load changes slowly, the dynamic design is similar to the static design. When the load changes rapidly, the dynamic design is obviously different from its static counterpart. The data listed in Table 1 show that, the dynamic design is better than the static design when the time-dependent characteristic of the load and the inertia effect are considered.

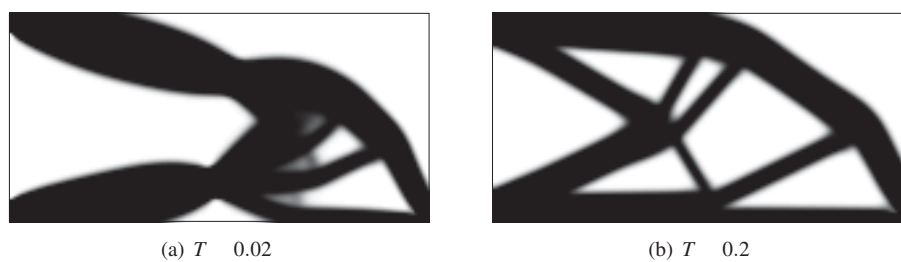


Figure 2: Topology optimization results of cantilever beam under sinusoidal loading

Table 1: Maximum displacement of the design for cantilever beam under sinusoidal loading

	Integration time	Dynamic design	Static design
T	0.02	$4.37e-5$	$5.35e-5$
T	0.2	$3.72e-5$	$3.73e-5$

6.2. Clamped Beam under Cosine Loading

The topology optimization problem is shown in Fig. 3(a). The design domain is a 12×2 clamped rectangular area with thickness 0.01. A dynamic load is vertically applied at the centerline of the bottom of the structure. The prescribed volume fraction of material is set to 0.4. The dynamic loading is assumed as the cosine function, and four different integration time $T = 0.02, 0.05, 0.1$ and 2.0 are considered.

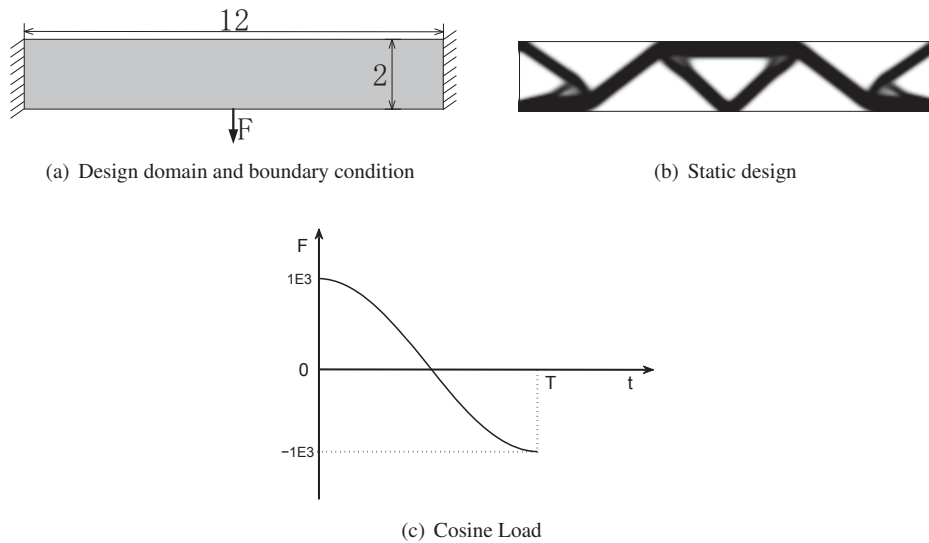


Figure 3: Topology optimization problem of clamped beam under cosine loading

In order to solve the topology optimization problem, the design domain is discretized by square bilinear plane stress elements whose size is 0.05. The corresponding static design is shown in Fig. 3(b). The optimal designs under dynamic loading are shown in Fig. 4. They clearly show that the change rate of the dynamic load have great influence on the design result. When the load changes slowly, the dynamic design is similar to the static design. When the load changes rapidly, the dynamic designs are obviously different from their static counterpart. The dynamic design corresponding to different integration time are also different from each other. The data listed in Table 2 show that, the dynamic design are better than their static counterpart when the structure subjected to the given dynamic loading. This example again demonstrate the effectiveness of the proposed method.

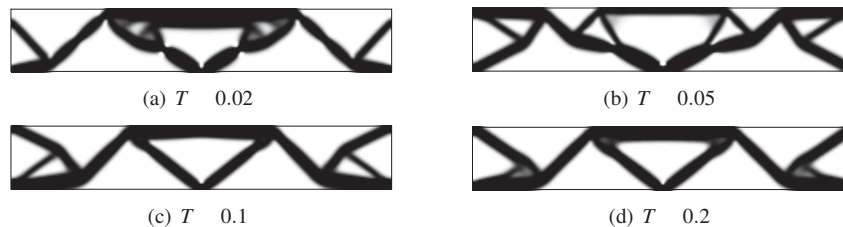


Figure 4: Topology optimization results of clamped beam under cosine loading

7. Acknowledgements

Table 2: Maximum displacement of the design for clamped beam under cosine loading

	Integration time	Dynamic design	Static design
T	0.02	2.20e-5	3.14e-5
T	0.05	3.02e-5	4.02e-5
T	0.1	3.39e-5	4.21e-5
T	2.0	4.08e-5	4.25e-5

The authors would like to thank Krister Svanberg for providing the matlab code of MMA optimizer. This paper is supported by the Innovation Foundation of BUAA for PhD Graduates.

8. References

- [1] M.P. Bendsoe and O. Sigmund, *Topology Optimization: Theory, Methods and Applications*, Springer-Verlag, Berlin, 2003.
- [2] H. Jang, H. Lee, J. Lee and G. Park, Dynamic Response Topology Optimization in the Time Domain Using Equivalent Static Loads, *AIAA Journal*, 50 (1), 226-234, 2012.
- [3] C. Zhuang and Z. Xiong, A Global Heat Compliance Measure Based Topology Optimization for the Transient Heat Conduction Problem, *Numerical Heat Transfer, Part B: Fundamentals*, 65 (5), 445-471, 2014.
- [4] X. Wen, A New Algorithm for Unconstrained Min-max Optimization, *Journal of Xidian University*, 16, 166-174, 1989(in Chinese).
- [5] J. Zhu, W. Zhang and P. Beckers, Integrated Layout Design of Multi-component System, *International Journal for Numerical Methods in Engineering*, 78 (6), 631-651, 2009.
- [6] B. Kang, G. Part and J. Arora, A review of optimization of structures subjected to transient loads, *Structural and Multidisciplinary Optimization*, 31, 81-95, 2006.
- [7] J. Jensen, P. Nakshatrala and D. Tortorelli, On the consistency of adjoint sensitivity analysis for structural optimization of linear dynamic problems, *Structural and Multidisciplinary Optimization*, 49 (5), 831-837, 2014.
- [8] O. Sigmund, On the design of compliant mechanisms using topology optimization, *Journal of Structural Mechanics*, 25 (4), 493-524, 1997.
- [9] K. Svanberg, The method of moving asymptotes—a new method for structural optimization, *International Journal for Numerical Methods in Engineering*, 24 (2), 359-373, 1987.

Convergence analysis of full elastic tensors to homogenization predictions in periodic composite material design

P.G. Coelho¹, L.D. Amiano², J.M. Guedes³, H.C. Rodrigues³

¹ UNIDEMI, DEMI, Faculty of Sciences and Technology, Universidade Nova de Lisboa, Portugal, pgc@fct.unl.pt

² DEMI, Faculty of Sciences and Technology, Universidade Nova de Lisboa, Portugal

³ IDMEC, Universidade de Lisboa, Portugal

1. Abstract

Periodic homogenization models are often used to compute the elastic properties of periodic composite materials based on the shape and periodicity of a given material microstructure. This paper extends previous work to 3-D analysis and anisotropic design cases investigating how rapidly the mean compliance and the 21 independent elastic coefficients from the apparent stiffness tensor converge to the corresponding values of the homogenized tensor. The outcome indicates that it is sufficient to have a low scale factor to replace the non-homogeneous composite by the equivalent homogeneous material with the moduli computed by homogenization.

2. Keywords: Homogenization, Optimization, Topology, Scale, Cellular

3. Introduction

The optimal design of periodic composites has been an area of intense research [1]. The so-called "unit-cell" is the microstructure representative of the smallest periodic heterogeneity of the material domain. The resulting macroscopic material is then defined assembling unit-cells. The use of continuum finite elements, homogenization and the SIMP (Solid Isotropic Material with Penalization) parameterization constitutes the traditional approach to obtain optimized porous materials through topology optimization. Topology optimization, in the frame of continuum elasticity, is an iterative design method that optimizes a material distribution in a given design domain with respect to a specified objective function and a set of constraints [2]. Topology optimization can be used to design materials by inverse homogenization. In this case the microstructure does not exist a priori but one seek to come up with a microstructure (interior topology of a unit-cell) using objective functions that consider prescribed or extreme homogenized properties [3].

In this work one uses the inverse homogenization method to extremize the energy density based objective function subjected to volume or permeability constraints. For instance, ensuring permeability isotropy while prescribing a preferential stiffness direction is of practical interest concerning bone implants (scaffolds). Bio-transport properties in the scaffold region is fundamental because cells, nutrients and waste products are supposedly to migrate easily inside the scaffold microstructure for tissue regeneration. At the same time the scaffold is a bearing load device which demands for increased mechanical stiffness. An appropriate trade-off between the conflicting properties of permeability and stiffness can be achieved by performing topology optimization [4-9].

The inverse homogenization method assumes that the scale of a unit-cell is indeterminate (infinitely small) as well as periodic Boundary Conditions (BC's) [10-13]. This makes uncertain whether the obtained topology can be translated into real composites of macroscale. In practice, one has a finite number of measurable unit-cells assembled together to define the composite material. Moreover, the stress or strain fields are in general arbitrary (not periodic) near the boundary of the composite.

Therefore one important contribution here is to investigate scale-size effects on the mechanical response of periodic materials with finite periodicity applying standard testing procedures and compare them with the predictions from the homogenization method. This study follows similar studies already reported in the literature which investigated scale-size effects although involving only two-dimensional bi-material unit-cells with prescribed material symmetry, see [14-17]. This work extends the analysis of the scale-size effects to solid-void three-dimensional periodic composites, anisotropic design cases and investigates how rapidly the mean compliance and the 21 independent elastic coefficients from the apparent fourth-order stiffness tensor converge to the corresponding values of the homogenized stiffness tensor.

4. Material model

The material model here is a 3-D porous composite material generated by the repetition of a unit-cell in all directions of the space. The unit-cell represents the smallest periodic heterogeneity of the composite domain Ψ . Periodic repetition of a unit-cell made up of a given parent material will yield a porous macroscopic material whose constitutive properties may differ substantially from the parent one. This macroscopic behavior can be

evaluated using homogenization theory. This theory assumes periodic boundary conditions (BC's) applied to the unit-cell domain Y and infinite periodicity of the unit-cell (Y -periodic), i.e. its feature size d is much smaller than the cellular material global size D ($d/D \rightarrow 0$), see Fig. 1a. These assumptions make uncertain whether the obtained topology can be translated into real composites of macroscale. In practice, the composite material comprises a finite number of measurable unit-cells and the stress or strain fields are not periodic near the structure boundary. The optimal material microstructure topology is found here using the topology optimization method applied to the unit-cell design domain Y . This domain is considered cubic and unitary, $|Y| = 1$. For a numerical problem solution, this domain is discretized using 8-node isoparametric hexahedral finite elements such that the resulting mesh is $20 \times 20 \times 20$ elements, see Fig. 1b. The effective material properties (homogenized properties) can be found using a numerical homogenization procedure described in [13]. The relative density μ of material in each finite element is the problem design variable and it is assumed constant inside the element volume. Solid and void corresponds to $\mu = 1$ and 0, respectively. The topology optimization problem may consist in finding the distribution of density μ in Y that extremizes the elastic energy density given a stress field as detailed in the next section.

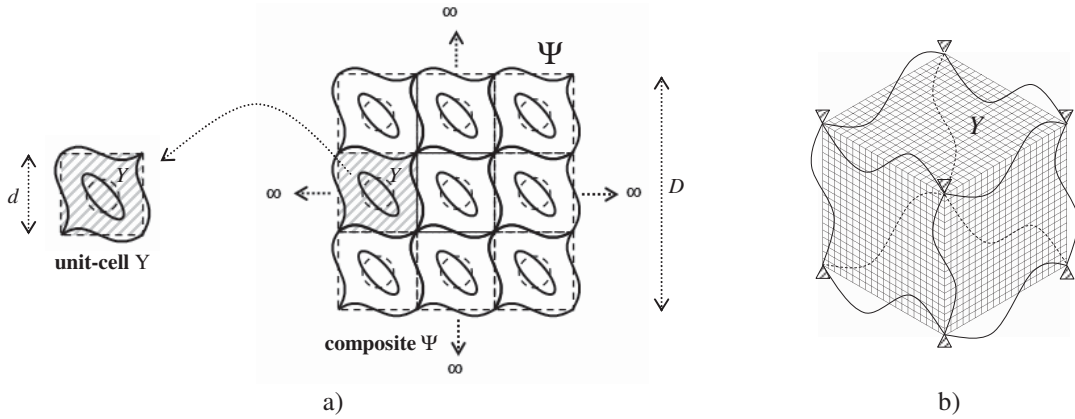


Figure 1: a) Material model to be interpreted in the light of the homogenization theory. Array of $n \times n \times n$ unit-cells of global size D and one unit-cell of size d . Periodic boundary conditions are illustrated; b) Material numerical model with schematic periodic boundary conditions.

5. Optimization problem

The local anisotropy problem of finding the optimal lay-out of a unit-cell for minimum compliance and requiring at least orthotropic permeability or prescribed volume fraction can be stated as,

$$\begin{aligned} \min_{\mu} \frac{1}{2} C_{mnlk}^H(\mu) \bar{\sigma}_{mn} \bar{\sigma}_{kl} \\ K_{ij}^H(\mu) \geq k^* ; i=j=1, \dots, 3 \wedge K_{ij}^H(\mu) = 0 ; i \neq j \text{ and } i, j = 1, \dots, 3 \\ \text{or} \\ \int_Y \mu(\mathbf{y}) dY \leq V^* \end{aligned} \quad (1)$$

In Eq. (1) μ is the local density varying between 0 (void) and 1 (material) which depends on the spatial variable \mathbf{y} in the unit-cell design domain Y . The stress tensor is $\bar{\sigma}$ and characterizes an averaged macroscopic stress field applied to the composite. The homogenized compliance tensor is \mathbf{C}^H , i.e. the inverse of the homogenized stiffness tensor \mathbf{E}^H . The stiffness tensor at each point of Y is related to the tensor \mathbf{E}^0 of the base material properties through the SIMP interpolation scheme [18]. Regarding the permeability constraints, one enforces the permeability tensor to be diagonal and each diagonal coefficient has to be "equal" or "greater than" a threshold, k^* . This way one gets an interconnected pore network on the periodic material satisfying a critical (minimum) permeability in all direction of the space. The permeability measure of porous media is given by the homogenized tensor \mathbf{K}^H . This tensor is obtained homogenizing a potential flow problem in periodical porous media characterized by the Darcy law (Darcy flow is assumed) [10,12]. Here one considers the interpolation between permeability and local density μ given by a power-law (see e.g. [19,20]). The permeability tensor for the base material, \mathbf{K}^0 , is here considered to be unitary, diagonal and isotropic. This way the interpolation scheme means that void and solid have high (100%) and low (0%) permeability, respectively. Consequently, the homogenized permeability tensor \mathbf{K}^H characterizing the periodic material medium becomes normalized, i.e. its coefficients take values between 0 and 1 (0% and

100%), and thus the threshold k^* in Eq. (1) can also be fixed between these bounds.

6. Numerical testing procedures

Recall that the homogenized elastic properties in Eq. (1) are calculated when $n \rightarrow \infty$. Consequently, they are n independent and there is no size of the unit-cell ($d \rightarrow 0$). That is why, it is critical to investigate how accurate homogenization predictions are compared to the actual properties of a composite with the unit-cell scaled n times. In this work the scale factor n , defined as D/d with $D = 1$, varies from 1 to 6 as illustrated in Fig. 2.

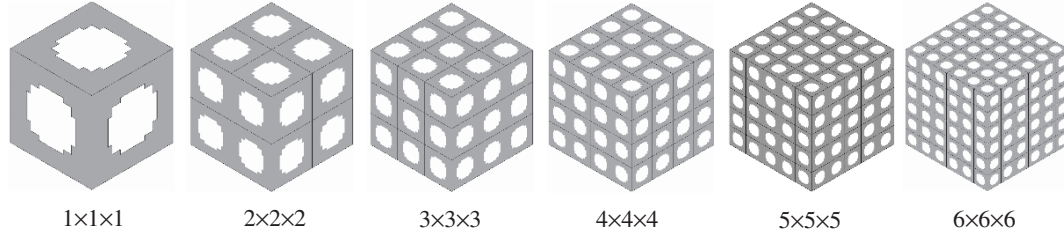


Figure 2: Unitary arrays containing $n \times n \times n$ unit-cells (n varies from 1 to 6).

In order to estimate apparent elastic properties, this work follows a standard numerical testing procedure described in [21] and summarized as follows. For instance, let's consider the Dirichlet-type displacement boundary conditions,

$$\mathbf{u}(\mathbf{x})|_{\partial\Psi} = \Theta^{(i)} \cdot \mathbf{x}|_{\partial\Psi} \quad i = 1 \text{ to } 6 \quad (2)$$

as well as the Neumann-type traction boundary conditions:

$$\boldsymbol{\sigma}(\mathbf{x}) \cdot \mathbf{n}|_{\partial\Psi} = \Theta^{(i)} \cdot \mathbf{n}|_{\partial\Psi} \quad i = 1 \text{ to } 6 \quad (3)$$

where

$$\Theta^i = \begin{bmatrix} \beta & 0 & 0 \\ 0 & 0 & 0 \\ 0 & 0 & 0 \end{bmatrix}, \begin{bmatrix} 0 & 0 & 0 \\ 0 & \beta & 0 \\ 0 & 0 & 0 \end{bmatrix}, \begin{bmatrix} 0 & 0 & 0 \\ 0 & 0 & 0 \\ 0 & 0 & \beta \end{bmatrix}, \begin{bmatrix} 0 & \beta & 0 \\ \beta & 0 & 0 \\ 0 & 0 & 0 \end{bmatrix}, \begin{bmatrix} 0 & 0 & 0 \\ 0 & 0 & \beta \\ 0 & \beta & 0 \end{bmatrix}, \begin{bmatrix} 0 & 0 & \beta \\ 0 & 0 & 0 \\ \beta & 0 & 0 \end{bmatrix} \quad (4)$$

and $\partial\Psi$ is the boundary of the composite sample Ψ , \mathbf{u} is the displacement vector, \mathbf{x} is the spatial position vector, $\boldsymbol{\sigma}$ is the Cauchy stress tensor, \mathbf{n} is the outward normal unit vector and β is a constant. The upper script index i on tensor Θ means the application of six fundamental tests (three normal and three shear mechanical tests shown in Eq. 4). In the case of Dirichlet-type conditions, where the applied displacement field is x linearly dependent, the sample Ψ is tested at a uniform strain β . In case of Neumann's, the test is carried out on Ψ at a uniform stress β . The specific nature of the Dirichlet and Neumann-type conditions allow direct estimation of the stiffness and compliance tensors, referred to as Dirichlet \mathbf{E}^D and Neumann \mathbf{C}^N tensors, respectively. In both cases, average stress $\langle \boldsymbol{\sigma} \rangle$ and strain $\langle \boldsymbol{\varepsilon} \rangle$ fields are computed in the volume $|\Psi|$ and then,

$$\langle \boldsymbol{\sigma} \rangle = \mathbf{E}^D \langle \boldsymbol{\varepsilon} \rangle \quad \text{and} \quad \langle \boldsymbol{\varepsilon} \rangle = \mathbf{C}^N \langle \boldsymbol{\sigma} \rangle \quad (5)$$

In turn, defining $\mathbf{E}^N = (\mathbf{C}^N)^{-1}$ as the Neumann stiffness tensor, yields

$$\langle \boldsymbol{\sigma} \rangle = \mathbf{E}^N \langle \boldsymbol{\varepsilon} \rangle \quad (6)$$

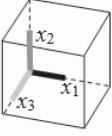
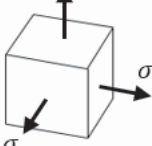
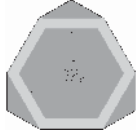
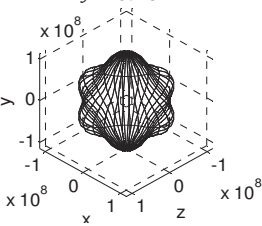
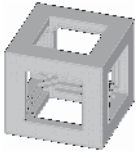
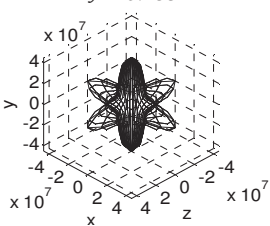
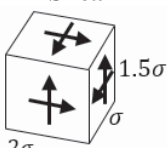
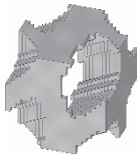
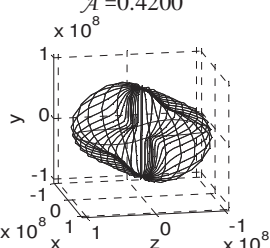
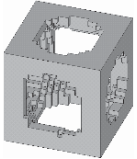
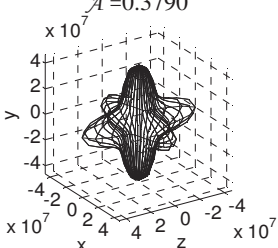
One considers here two additional types of BC's because Neumann-type conditions underestimate too much the apparent properties of porous materials due to the larger compliance of the void phase near the boundary.

On the one hand, one pursues a battery of fundamental tests applying the constant pressure, either normal or shear, only on the solid phase. On the other hand, one applies mixed BC's, i.e. a uniform pressure upon a rigid plate that in turn transfers the normal load to the top surface of the "solid" and "void" elements. Using rigid plates for shear tests here is cumbersome. For shear, one applies instead displacement-based BC's as given by Eq. (2), $i = 4$ to 6. However, the displacements are only applied to two sets of opposite facets and only the displacements that are \mathbf{x} -dependent are applied (this is less restrictive than Dirichlet's). The application of these additional BC's is restricted here to orthotropic designs for the sake of getting tensor symmetry and static equilibrium.

7. Results

Two macroscopic stress fields are selected for demonstration purposes, *hydrostatic* and three different *shear* forces as indicated in Table 1. The corresponding optimal microstructures are shown considering either volume or permeability as design constraints in Eq. (1). The hydrostatic optimal solution with volume constraint is a closed-wall unit-cell (cut section view is shown) whereas the remaining cases show an open-cell microstructure as optimal. The anisotropy plots along with parameter \mathcal{A} shown in Table 1 are also used and explained in [22,23].

Table 1: Macroscopic stress fields and corresponding optimal designs (solid part only) for volume and permeability constraints. Graphical representation of anisotropy and parameter \mathcal{A} .

Macroscopic stresses	Volume constraint $V^* = 50\%$		Permeability constraint $k^* = 50\%$	
 $(\sigma_{11}; \sigma_{22}; \sigma_{33}; \sigma_{12}; \sigma_{23}; \sigma_{13})$	Topology	Anisotropy	Topology	Anisotropy
Hydrostatic  $(\sigma; \sigma; \sigma; 0; 0; 0)$		$\mathcal{A} = 0.1644$ 		$\mathcal{A} = 0.4351$ 
Shear  $(0; 0; 0; \sigma; 2\sigma; 1.5\sigma)$		$\mathcal{A} = 0.4200$ 		$\mathcal{A} = 0.3790$ 

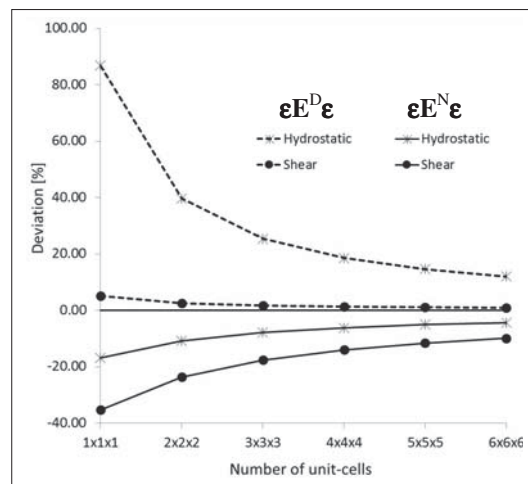


Figure 3: Strain energy density convergence for Dirichlet-type BC's and Neumann-type BC's.

The convergence of the strain energy density and the independent coefficients of the stiffness tensor to the homogenization values for the hydrostatic (with permeability) and shear (with volume constraint) cases are shown in Fig. 3 to 5, respectively. For the highest scale factor studied here ($n = 6$), Fig. 3 shows a rapid rate of convergence of energy (deviations $< 10\%$) and the longitudinal coefficient estimates E_{iii}^D and E_{iii}^N are below 7%

of deviation with respect to homogenization (see Fig 4a, 4b and 5). However, estimates of E_{iii}^N are based on a moderate contrast ratio $E^{\text{solid}}/E^{\text{void}} = 10$ rather than $E^{\text{solid}}/E^{\text{void}} = 10^{12}$ used in the remaining cases. This avoids excessive compliance of the void phase making the Neumann BC's effective only for non-porous composites. To test porous materials, Neumann conditions can be slightly changed such that the uniform pressure is only applied on the solid phase or mixed BC's can be used also as explained in section 6. Having the analyses restricted to orthotropic cases, the resulting estimates deviate from homogenization less than 20%, as seen in Fig. 4c and 4d. In general, while the convergence of longitudinal coefficients is quite exceptional, the rate of convergence is not so good for some non-longitudinal coefficients. Enlarging the number of targeted tensor coefficients up to 21 with the shear case, one sees actually a pretty convergence in Fig. 5a with most deviations less than 10% for $n = 6$. Larger deviations are obtained in Fig. 5b.

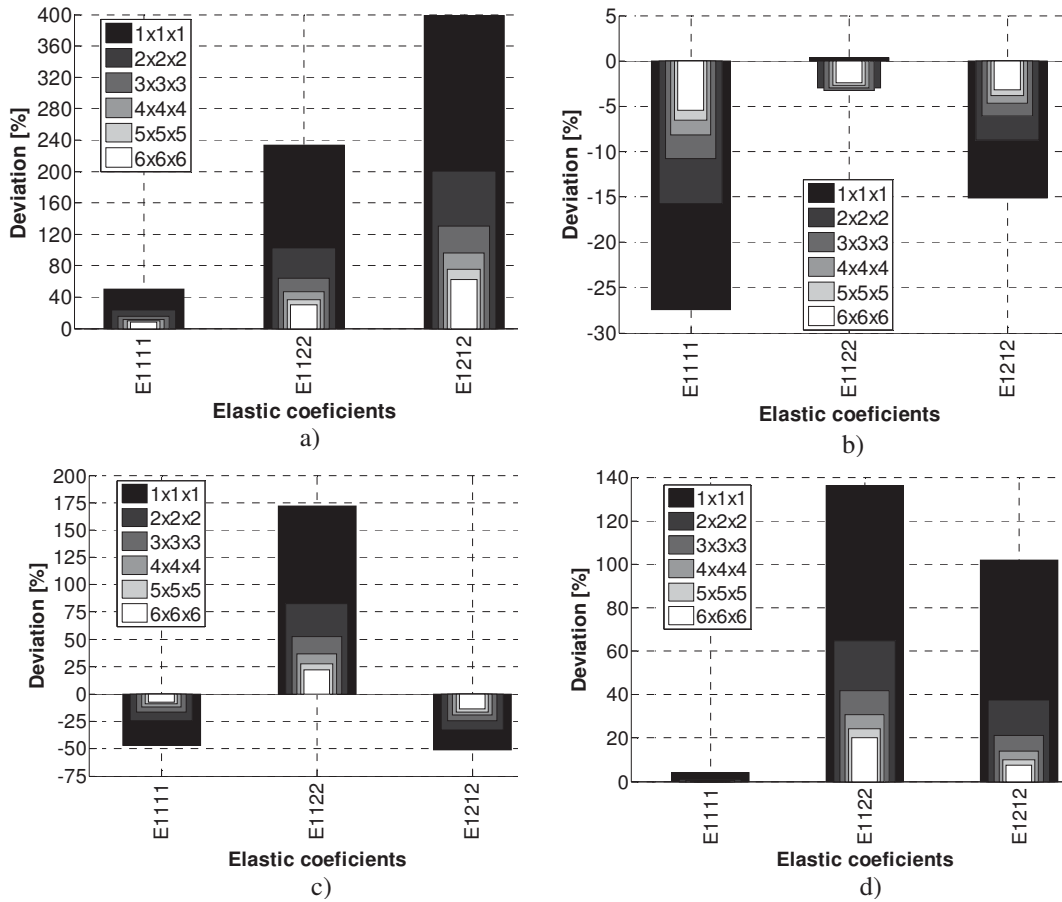


Figure 4: Scale-size effects analysis for the *hydrostatic* case. a) Dirichlet-type BC's; b) Neumann-type BC's with $E^{\text{solid}}/E^{\text{void}} = 10$; c) Constant stress on solid; d) Mixed BC's.

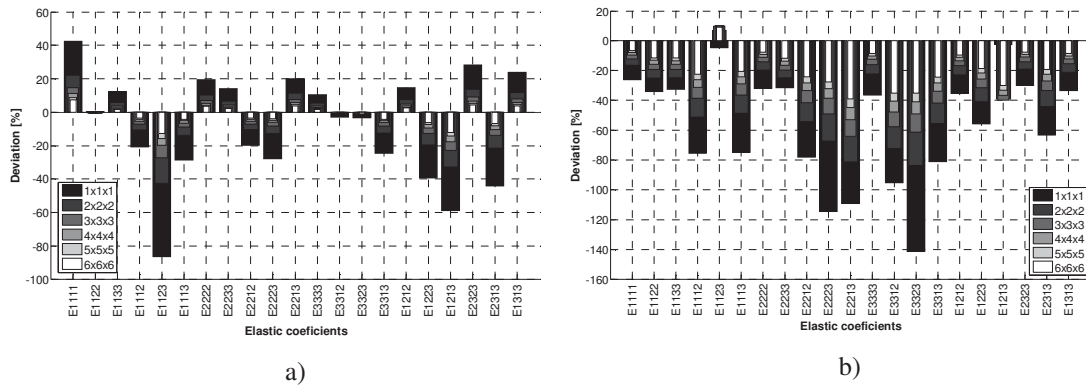


Figure 5: Scale-size effects analysis for the *Shear* case. a) Dirichlet-type BC's; b) Neumann-type BC's with $E^{\text{solid}}/E^{\text{void}} = 10$.

8. Conclusions

Homogenization assumes the unit-cell infinitely small and with periodic BC's. However, in practice, the composite material comprises a finite number of measurable unit-cells and the stress or strain fields are not periodic near the structure boundary. It is thus critical to investigate whether the obtained topologies are affected when applied in the context of real composites. This is done here by scaling the unit-cell an increasing number n of times. For each n one accesses the apparent properties of the resulting composite by means of numerical experiments applying *e.g.* Dirichlet and Neumann-type BC's. Alternative stress-based BC's are investigated to test porous materials overcoming excessive compliance of the void phase. Convergence to the homogenized properties can then be checked. The present work indicates that for practical purposes, even for microstructures with low scale factor ($n = 6$), it is mechanically admissible to use the equivalent moduli given by the periodic homogenization theory.

9. References

- [1] J.E. Cadman, S. Zhou and Y. Chen, On design of multi-functional microstructural materials, *J Mater Sci*, 48:51-66, 2013.
- [2] M.P. Bendsøe and O. Sigmund, *Optimization. Theory, Methods and Applications*, Springer, 2003.
- [3] O. Sigmund, Materials with prescribed constitutive parameters: an inverse homogenization problem, *Int J Solid and Struct*, 31(7), 2313-2329, 1994.
- [4] P.G. Coelho, P.R. Fernandes and H.C. Rodrigues, Multiscale modeling of bone tissue with surface and permeability control, *Journal of Biomechanics*, 44(2), 321-329, 2011.
- [5] R.D. Marta, J.M. Guedes, C.L. Fanagan, S.J. Hollister and P.R. Fernandes, Optimization of scaffold design for bone tissue engineering: a computational and experimental study, *Journal Medical Engineering & Physics*, 36, 448-457, 2014.
- [6] J.K. Guest and J.H. Prévost, Optimizing multifunctional materials: design of microstructures for maximized stiffness and fluid permeability, *Int J of Solids and Struct*, 43, 7028-7047, 2006.
- [7] S.J. Hollister and Y.L. Cheng, Computational design of tissue engineering scaffolds, *Comput Methods Appl Mech Engrg*, 196, 2991-2998, 2007.
- [8] S. Xu and G. Cheng, Optimum material design of minimum structural compliance under seepage constraint, *Struct Multidisc Optim*, 41, 575-587, 2010.
- [9] H. Kang, C-Y. Lin and S.J. Hollister, Topology optimization of three-dimensional tissue engineering scaffold architectures for prescribed bulk modulus and diffusivity, *Struct Multidisc Optim*, 42, 633-644, 2010.
- [10] J.F. Bourgat, Numerical experiments of the homogenization method for operators with periodic coefficients, *Lecture Notes in Mathematics*, 704, 330-356, 1977.
- [11] A. Bensoussan, J.L. Lions and G. Papanicolaou, *Asymptotic analysis for periodic structures*, North-Holland, 1978.
- [12] E. Sanchez-Palencia, *Lecture Notes in Physics*, Vol 127, Springer-Verlag; 1980.
- [13] J.M. Guedes and N. Kikuchi, Preprocessing and postprocessing for materials based on the homogenization method with adaptive finite element method, *Comput Meth Appl Mech Eng*, 83, 143-198, 1990.
- [14] W. Zhang and S. Sun, Scale-related topology optimization of cellular materials and structures, *International Journal for Numerical Methods in Engineering*, 68, 993-1011, 2006.
- [15] G. Dai and W. Zhang, Cell size effects for vibration analysis and design of sandwich beams, *Acta Mech Sin*, 25, 353-365, 2009.
- [16] S. Pecullan, L.V. Gibiansky and S. Torquato, Scale effects on the elastic behavior of periodic and hierarchical two-dimensional composites, *Journal of the Mechanics and Physics of Solids*, 47, 1509-1542, 1999.
- [17] S.J. Hollister and N. Kikuchi, A comparison of homogenization and standard mechanics analyses for periodic porous composites, *Computational Mechanics*, 10, 73-95, 1992.
- [18] M.P. Bendsøe, Optimal shape design as a material distribution problem, *Structural Optimization*, 1, 193-202, 1989.
- [19] M.R. Dias, J.M. Guedes, C.L. Flanagan, S.J. Hollister and P.R. Fernandes, Optimization of scaffold design for bone tissue engineering: A computational and experimental study, *Med Eng Phys*, 36(4), 448-57, 2014.
- [20] P.G. Coelho, P.R. Fernandes and H.C. Rodrigues, Multiscale modeling of bone tissue with surface and permeability control, *Journal of Biomechanics*, 44(2), 321-329, 2011.
- [21] T.I. Zohdi and P. Wriggers, *Introduction to computational micromechanics*, Springer, 2004.
- [22] T. Böhlke and C. Brüggemann, Graphical representation of the generalized Hooke's Law, *Technische Mechanik*, 21, 145-158, 2001.
- [23] V.J. Challis, A.P. Roberts and A.H. Wilkins, Design of three dimensional isotropic microstructures for maximized stiffness and conductivity, *Int J Solids and Structures*, 45, 4130-4146, 2008.

Common Automotive and Aerospace Requirements for Commercial Structural Optimization Software

Steve Georgiadis¹, Vladimir Balabanov², Rodney Dreisbach², David Trop², Moritz Frenzel³, Daniel Heiserer³, David Keller³, Markus Schemat³.

¹The Boeing Company, VIC, Australia; steve.georgiadis@boeing.com

²The Boeing Company, Seattle, WA, USA; vladimir.balabanov@boeing.com

³BMW Group, Munich, Germany; moritz.frenzel@bmw.de`

1. Abstract

To widen the scope of structural optimization applications at the enterprise level in the automotive and aerospace industries, and to increase the community of engineers using integrated structural optimization software effectively, certain industrial needs have to be met by such software a priori. These needs, which are yet to be met, are discussed in this paper. Satisfying these needs includes establishing a new form of collaboration between software developers and industry and will bring applications of the integrated structural optimization software in the automotive and aerospace industries to new heights. The subject needs are not limited to commercial structural optimization software, but should be viewed as desired features in any integrated structural optimization software.

2. Keywords

Structural Optimization, Commercial Software, Integrated Software, Intelligent Software, Industrial Application, Computer Aided Engineering CAE, Collaboration

3. Introduction

Over the past decade there has been a significant growth in industrial structural optimization applications. Capabilities of Commercial Structural Optimization Software (CSOS) have increased considerably, now allowing for incorporating analysis results ranging from stiffness and strength, to crashworthiness, and durability. Some of these analyses are performed inside the CSOS. More importantly, CSOS allows for linking with the analyses performed outside of CSOS. This is a reflection of the current situation in the automotive and aerospace industries where no structural part is designed without performing a vast number of different numerical analyses. Analysts and designers need to account for an ever-increasing number of requirements to produce realistic industrial designs. The fact that structural optimization can now be applied to total vehicles with the number of influential parameters increasing from tens to thousands has only added to the complexity of the tasks to be performed by the CSOS.

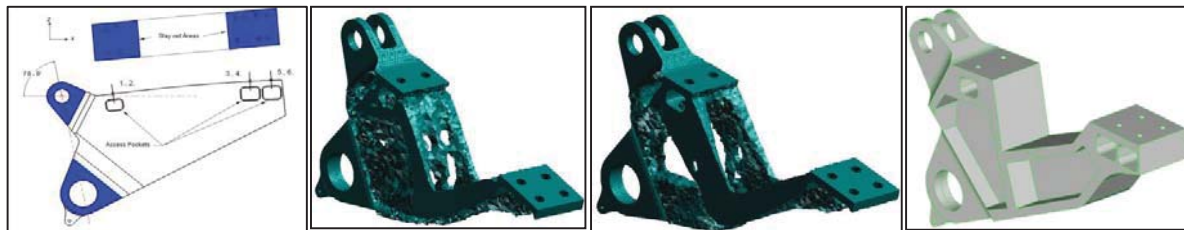
From an enterprise perspective it is often advantageous to utilize CSOS as opposed to Process Integration and Design Optimization (PIDO) tools: PIDO tools typically require their own sub-processes to be created. PIDO tools also often impose additional requirements on the analysis programs and sub-processes to be included in PIDO. Thus, the designers and analysts have to master the challenges arising from the complexity of the new enhancements and extra processes. This approach can be contrasted with using CSOS, which typically result in simpler final processes that are easier to maintain.

In spite of the analyst's efforts, even when a specific optimization process is effective, it is often not suitable for wide applications from an enterprise standpoint. One of the main reasons being the requirement to convince the approving/certification authorities that the obtained solution is a viable one.

To improve the current CSOS capabilities and to increase the community of engineers using structural optimization effectively, CSOS must adapt to the realities of the industrial design processes. Several broad categories where improvements should be made in CSOS are presented below. The listed needs are not limited to CSOS, but should be viewed as desired features in any integrated structural optimization software.

4. Ease of use and flexibility

CSOS must be robust and easy to use by people with limited or no optimization background. Example of what can happen with the current CSOS usability is presented in Figure 1. Figure 1(a) shows the design space for a highly loaded fitting. The fitting was optimized using several CSOS tools. Figure 1(b) shows two of many solutions obtained via topology optimization. All of the CSOS vendors struggled when using their own tools to arrive at a valid solution. As shown in Figure 1(c), valid solution was eventually found after an exhaustive combination of topology and shape optimizations requiring high levels of analysis and interpretation skills.



(a) Design space

(b) Topology optimization possibilities

(c) Valid solution

Figure 1. Stages of a typical topology optimization problem

In addition to the expertise required to operate CSOS, effective debugging also presents a problem. Two examples of error messages that have been encountered when solving structural optimization problems are presented in Figure 2. In both cases, the software developers could not easily determine the cause of these errors and how to fix them. It is obvious that these messages are not interpretable by the most end users of the software.

```
-- BEGIN ITERATION NUMBER 2
*** USER FATAL MESSAGE 1126 (GNFIST)
MODULE      IS ATTEMPTING TO OUTPUT DATABLOCK  210 NAME = PROPO , WHICH ALREADY EXISTS.
USER ACTION: DELETE THE DATABLOCK, OR USE FILE PROPO=OVRWRT
0FATAL ERROR
1          *** END OF JOB ***

*** ERROR # 1898 ***
Approximated constraint 308 does not match with response 182130 at the
first iteration.
Approximated constraint = -1.938295e+00
Approximated response   =  1.334531e+00.

*** INTERNAL PROGRAMMING ERROR ***
in file "conapp.F", at location # 4037.
```

Figure 2. Example of non-interpretable error messages from CSOS

Easy access to clear step-by step “How-to” tutorials on various aspects of using the specific features of the software is mandatory. These tutorials should not refer to other tutorials; they should not require additional reading to accomplish the tasks described in the tutorial. The majority of the finite element (FE) structural optimization software on the market lacks such tutorials.

CSOS must provide enough controls to expert users to access the solution details, the details of the optimization algorithms, and allow re-adjusting considerably the optimization procedural steps. For example, most of the FE CSOS has a limited control over how many times the gradients of the external response should be evaluated during a design cycle. In case of thousands of variables and computationally expensive external responses, the external finite difference gradient calculations may take a significant amount of time. Allowing users to control how many times the response gradients are calculated can significantly reduce the computational time required for optimization.

5. Integration with legacy tools and flexibility of internal equations

CSOS vendors often strive to bring more and more analysis capabilities inside of their software. Although helpful in some cases, such an approach is not always acceptable. Both automotive and aerospace industries have legacy tools that are required to be used, regardless of how easy to use, accurate, and effective CSOS might be. Such tools are trusted by the experienced designers. Such tools have been verified and validated as required for product certification. Intuitive and easy interfaces to such legacy tools with minimum or no programming experience are essential. The ideal CSOS should allow external tools to calculate not only the responses, but also the element and material properties, as well as variable values – everything that currently can be computed inside of Finite Element Analysis (FEA) codes. In addition, it is essential to allow for handling not only scalar inputs and outputs from external codes, as it is done now, but also arrays of inputs and outputs via a single call to external programs. Current capabilities to link to external programs often require extensive knowledge of computer systems, access to very specific versions of compilers, and having administrative privileges on the computer. Analysts don't have any of that. Struggling with linking external codes into CSOS often eliminates any desire to use structural optimization. Efficient and easy-to-use linking to external analyses is an essential part of establishing CSOS processes at the enterprise level.

To prevent calculating many characteristics outside of CSOS codes, increasing the flexibility of the internal equations could be very helpful, as well as allowing the use of some programming language syntax in the equations. Alternatively, an ability to translate from a programming language into the equations would be very useful to the analyst. The current equations provided by CSOS have similarities to the Fortran function syntax; however, these equations don't allow any loops of "if" statements. This makes them very limited and restrictive, as it requires tedious and error-prone translations of existing routines from programming languages into the CSOS equations.

It is not uncommon for the equations to reach hundreds of lines in length. Difficulties with handling the equations combined with the error-prone strict requirements for the way of compiling external analyses for CSOS often forces finite element codes to be used for analysis only. In this case FEA is coupled with PIDO optimization engines due to flexible internal equations and easier and more flexible interfaces to legacy codes.

This problem will get worse as the automotive and aerospace industries increase exploiting applications of non-metallic materials. Specifically, CSOS make use of failure criteria which are of little use for practical structural design and which are not recognized by the product certification authorities.

6. Intelligence and guidance

CSOS should support and guide users during all phases of the optimization process: during problem setup, execution of the optimization procedure, and when reviewing the results. The tool intelligence should be derived from the intermediate solution results and from efficient incorporation within the tool the knowledge and expertise of existing in-house tools, processes, best practices, and design criteria.

6.1 Intelligence and guidance during optimization problem setup

CSOS developments have already gone through great lengths of making it easier for end users to set up all aspects of a design problem in a graphical way. Often, even the order in which menu items are presented, suggests the most reasonable way for the sequence of operations to be set up for a specific optimization problem. One of the inconveniences that users experience in the current problem setup procedure is too many mouse clicks required to select various sub-options to define the problem correctly. By the time the user starts setting up the optimization problem, CSOS already has the information about the associated FE model. Thus, the choices the user makes in setting up the problem are not entirely arbitrary. An example of code-embedded intelligent guidance would be to allow the user to define the type of optimization problem first (topology, sizing, etc.), then - what specific part should be optimized, and some general parameters of the problem. Based on this information the software may be able to automatically define a majority of the parameters and relations between design variables and responses, leaving the user merely to check and adjust what was not correctly identified by the default setup.

6.2 Intelligence and guidance during execution of the optimization

The current CSOS approach to running optimization problems is to have the user set up the problem and then let the optimizer arrive to a better solution point without interruption. However, user intervention, user decision, and appropriate visualization technique are essential during the solution phase of complex problems. Especially when the optimizer encounters problems in finding a good solution and/or when the model and/or the objectives and constraints are not well defined. Possible techniques allowing analysts to target specific region of exploration are illustrated conceptually in Figure 3.

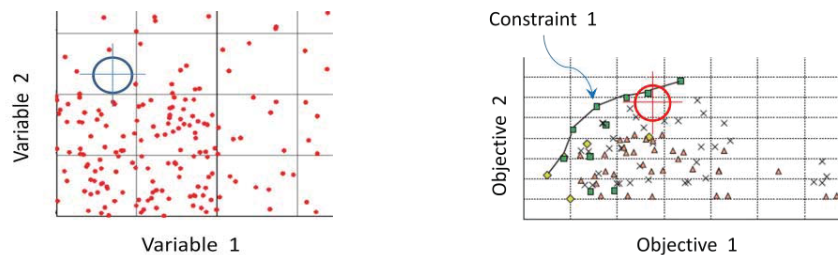


Figure 3. Conceptual examples of visually indicating the target (preferred) region of exploration where optimization should be concentrating its efforts

Note that such kind of visualization should be dynamic and accessible while an optimization procedure is being executed, thereby allowing a user to influence the direction (path) of optimizing if so desired. Using such visualization techniques allows the analyst to decide whether to tighten or to remove certain constraints on the fly during an optimization solution.

Tightly connected with flexibility of exploration is the robustness of the code. Currently, if the code encounters an error, the optimization procedure stops, asking the user to fix the error. A much more robust approach would be for the code to continue the optimization/exploration process regardless of the error. CSOS has the information about all the previous, successfully analyzed solution points; therefore nothing should prevent the software to go to one of the previously visited points, adjust the search direction, and continue the optimization, while keeping detailed textual and graphical logs of what has happened and what has caused the setback.

6.3 Intelligence and guidance during optimization post-processing

Visualization is essential after a candidate (optimum) solution is obtained. It is not enough to arrive to a good solution. It is essential to convince the approving and certification authorities that the obtained solution is viable. The analyst is required to clearly, visually, and without much effort, explain *why* the specific solution was obtained, *how* it was obtained, and *what happens if* some parameters of the solution were to be changed.

To answer these questions, specialized optimization-oriented visualization capabilities need to be created. Currently, most CSOS visualization tools create contour plots of responses superimposed on the structural model. These types of plots are analysis oriented. This means that for the analyst to visualize the optimization *process* he or she must go through a number of analysis result plots (e.g., stresses for several load cases), determine which ones contain critical results for the most important load cases, and then try to create the combined plot for several important iterations.

Automating and easing up this process would help to answer the “how” questions. Dynamically showing how the locations of the critical regions change from one iteration to another would also assist in managing the critical regions in the structure. Such dynamic and static contour plots on the structural model should also identify the specific load cases which caused the critical regions to appear.

Another example is the ability to immediately and easily visually compare analysis results of different iterations. All the required information for this is readily available inside the CSOS, but it is not currently presented to the analyst in a convenient form.

Readily available 2D plots of the objective function, constraint violations, and design variables with respect to the iteration number are useful from the conceptual standpoint. However such plots don't provide insight into the optimization procedure, and are not able to answer the above-mentioned "how, why, and what if" questions. To help answer the "why" questions, advanced multidimensional visualization techniques may be required.

Figure 4 illustrates an approach suggested in Ref. [1] when 2D alpha plots were used to study the tradeoffs between three airplane planform configurations. The objective values, as well as the constraints, were represented in a single plot to illustrate where the designs were located with respect to constraints. Many other multidimensional visualization techniques of this type are already available.

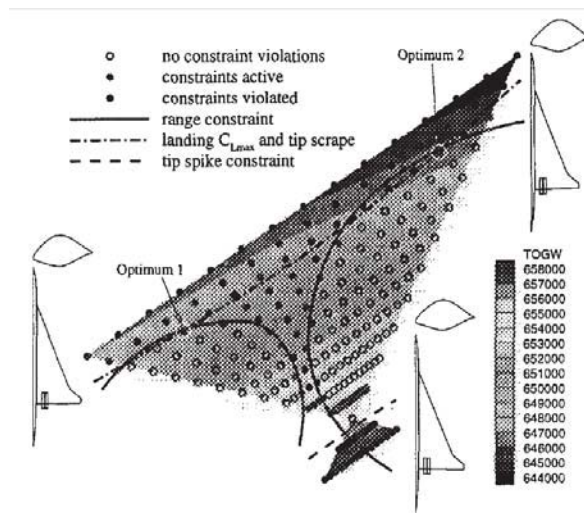


Figure 4. Illustration of a multidimensional visualization technique for a non-convex design space from Ref. [1].

Another feature desired by many analysts is the ability to visualize the response sensitivities, as well as the sensitivities of the objective and constraints superimposed on the structural components, much like the contour plots for stresses. The conceptual example of such a plot is presented in Figure 5. Such types of plots help the analyst to answer potential "what if" questions. It is even more desirable to make such plot interactive, so that the user can actually change some parameters on the plot, and observe changes in the results.

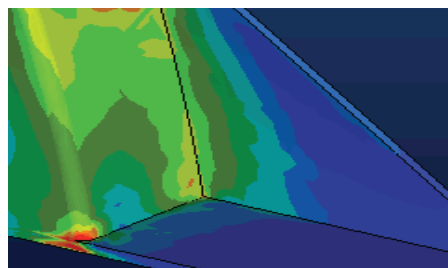


Figure 5. Conceptual example of a contour plot showing sensitivities of a structural response

Along with displaying sensitivity information comes the CSOS ability to identify the most influential variables and to suggest which variables could be eliminated or made constant. As the optimization problems are at the point

11th World Congress on Structural and Multidisciplinary Optimisation

07th -12th, June 2015, Sydney Australia

when having thousands of variables is not an unusual setup, a capability to filter out important and non-important variables automatically and represent these choices graphically will be a big help to analysts.

A CSOS with enhanced intelligence may suggest users how to improve/augment design variables during (or after) optimization. For example, if a stiffness response is sensitive to thickness design variables and the loading is dominated by a bending behavior, it is reasonable to assume that introducing shape or topology variables will result in more improvements compared to the thickness variables. Thus the software may suggest possible improvements/augmentations to the existing design variables as well as the location on the part where such new variables could be defined. The software could also define these new variables automatically using default settings if a user wants that.

Extremely desirable is the ability to calculate approximate results on the fly as a response to changes in some design parameters, without performing complete FEA solutions to answer “what if” questions. Such a capability would be especially useful for large models, when FEA takes considerable amounts of time.

7. Optimization-related capabilities

It is common in the automotive and aerospace industries to consider dozens, hundreds, and sometimes thousands of load cases. Some of these load cases are not relevant for finding an optimal design as they don't result in active constraints. For such cases, the CSOS should have an option to automatically and robustly handle a multitude of load cases, neglect the non-critical ones, and consider only the relevant load cases and constraints in solving the optimization problem. This procedure of load case screening should be dynamic, where the active load cases should be adjusted as the optimization process progresses.

Optimization is not the only approach to design space exploration and finding a better solution. Design of Experiments (DOE) and trade/sensitivity studies are quite popular in the aerospace and automotive industries. Currently, even if FEA must be used in such studies, the studies themselves are performed outside of CSOS with the problem setup being started from scratch. Whereas after the design optimization problem is setup in CSOS, everything is ready for both DOE and sensitivity studies. Yet these studies, which are often a part of the internal optimization algorithms, are not exposed to the user and appropriate visualization is not being created for them.

CSOS codes always proudly and rightfully claim to utilize the high quality next-generation internal approximations. CSOS could more extensively use these approximations. Such techniques as approximate Pareto optimization, global optimization, probabilistic optimization, and user-guided optimization, could all use these high quality internal approximations. The acquired data could be used by CSOS to provide analysts with a large variety of options for efficient and fast design space exploration and to arrive at a solution that is valuable from the analysts' standpoint, and not only from the optimization algorithm's standpoint. This is best illustrated by the fitting example in Figure 1, where the optimization algorithm continued to return a solution which was not practical for manufacturing and required the analyst to intervene several times prior to arriving at a valid design.

8. Collaboration between industry and CAE vendors

In the past, Computer Aided Engineering (CAE) software vendors have been co-located with industry on design projects for the wrong reason: too often, the software has been difficult to use and required vendors to be co-located with the company's engineering team to interpret the solution results from the CSOS. An important issue in accepting CSOS in aerospace and automotive industries at the enterprise level is the early interaction between the software vendors and customers (industry) regarding the features that are planned for implementation in CSOS. Up to this point, the CAE vendors often have developed new features that the vendors thought would be important. These features were then implemented in the CSOS in a way that the vendors thought would be convenient for their customers. As a result, industry often received the newly-developed software that was not doing exactly what was needed. The specialized intermediate fixes and updates issued by vendors to bring software closer to exact industry needs were hard to install due to computer security in industry. As a result, the needed capabilities were often

11th World Congress on Structural and Multidisciplinary Optimisation

07th -12th, June 2015, Sydney Australia

obtained by industry a year or two after the features were officially first released. This situation would change if software vendors were to discuss the new features (analytical requirements) with customers before starting development of the features. Not only functionality, but also appearance, performance, ease of use, and future extendibility of the new software enhancements should be discussed through ongoing technical dialogs between industry users and CAE vendors.

9. Conclusions

The analytical software requirements discussed in this paper would allow CSOS to gain more industrial support and a faster increase in its user-base across multiple industries. The reason for such requirements to surface at this time is that 10 years ago the CSOS were not mature enough to be seriously considered for use in the enterprise product design processes. Now, with improved CSOS capabilities and robustness, the possibility of exploiting CSOS tools more extensively in the enterprise design processes is real; however, such an opportunity comes with new and stricter requirements. Without fulfilling the proposed requirements, including advanced problem-solving techniques in addition to embedding decision-making algorithms through predictive analytics, the CSOS user-base in the aerospace and automotive industries will most likely remain static or grow slowly. This is primarily because there would be significant difficulties in persuading program management to attempt utilizing the current optimization tools more extensively in the enterprise-wide detailed-design processes. Although CSOS is the primary target of the subject needs, they are not limited to CSOS but should be viewed as desired features in any integrated structural optimization software.

References

- [1] D. L. Knill, A. A. Giunta, C. A. Baker, B. Grossman, W. H. Mason, R. T. Haftka, and L. T. Watson, "HSCT Configuration Design Using Response Surface Approximations of Supersonic Euler Aerodynamics", 36th AIAA Aerospace Sciences Meeting and Exhibit, 1998, DOI: 10.2514/6.1998-905.

Multidisciplinary optimization and integration requirements for large-scale automotive and aerospace design work

Moritz Frenzel¹, Daniel Heiserer¹, David Keller¹, Markus Schemat¹, Vladimir Balabanov², Rodney Dreisbach², Steve Georgiadis³, David Trop²

¹ BMW Group, Munich, Germany, moritz.frenzel@bmw.de

² The Boeing Company, Seattle, WA, USA, vladimir.balabanov@boeing.com

³ The Boeing Company, VIC, Australia; steve.georgiadis@boeing.com

1. Abstract

Automotive and aero industries are rapidly increasing applications of numerical simulations for structural, structure-interfacing, and multi-field analyses ranging from structural stiffness and strength, to crashworthiness and durability. Simulation applications and tool chains are cast into sophisticated, but strict, processes to ensure reliability, design integration, and interaction between partners, departments and suppliers.

Commercial and in-house optimization frameworks, i.e., process integration and design optimization (PIDO) tools, have evolved considerably, allowing for coupling of processes, tools, and individual design parameters. Thus, the designer/CAE specialist is required to master the challenges arising from the complexity of such processes. Although originally intended for this specific purpose, even efficient PIDO implementations may not be suitable for general applications from an enterprise standpoint. Especially for multi-disciplinary optimization when analyses from various disciplines compete and their influences need to be balanced.

This paper presents the background and rationale why PIDO implementations may not be suitable from an enterprise aerospace/automotive perspective. A view of the bottlenecks is also presented, along with proposed approaches to resolve them.

Specifically, to increase the efficient use of commercial PIDO tools in the automotive and aerospace industries, these integration and optimization frameworks should provide:

- Friendlier ways of integrating existing third-party and legacy tools
- Interactive human control of the optimization process, i.e., “on-the-fly” adjustments of the design variables, targets, constraints, and optimization methods
- Intuitive and robust support of heterogeneous computing systems
- Ease of maintaining and modifying the created processes that should be available both in GUI and batch modes.

The PIDO approach demands high flexibility, with strong end-user interaction and interfacing.

2. Keywords: Process Integration and Design Optimization (PIDO), MDO, Complex Engineered Systems, Enterprise Optimization Framework, Big Data, Preliminary Design

3. Motivation

Recent years have seen an enormous growth in computer aided engineering (CAE). In the coming years, the available computing power will increase even faster. Any item and part with structural requirements within complex products such as automotive vehicles or airplanes is designed using high fidelity structural simulations including finite element analyses. Usage of high fidelity, fast computational structural mechanics (CSM), computational fluid dynamics (CFD), and multidisciplinary optimization (MDO) tools and processes has significantly improved product performance and greatly reduced product development costs. By taking advantage of advanced computational analysis tools and coupling analyses to multidisciplinary optimization tasks, designers can simultaneously improve the product design, and reduce the time and cost incurred during every design cycle. There is a widespread virtualization strategy in industry to reduce the number of experimental validations required to “certify by analysis” [1]. The objective is to further reduce product development costs for the aero-industry, and for “development on demand” for the automotive industry with its massive unit numbers and customer drive for superior performance and individualization.

Today’s approach within large enterprise CAE development organizations is to cast each and every tool and development step into a clearly defined process. Interaction of the design disciplines, development partners, and

suppliers, together with strict project schedules, necessitate strict responsibilities. Such responsibilities are reflected in reasonably strict CAE process chains. To accommodate this CAE development environment, software tools are required to provide very effective and efficient interfaces. There has been a flurry of merger and acquisition activities taking place in the software industry, with the objective of providing the “one and only” software suite that is the best “integrator” around. However, no single application or system is capable of handling all of the product design issues, spread out to all companies and all departments, and to resolve the necessary interactions between the tools and data. Product data management (PDM) systems are mostly in place but have not truly penetrated the CAE simulation world yet. Mastering the entirety of simulation data generated within an enterprise, even within a period of only one year, constitutes a big burden of resources and development cost.

Optimization, specifically in the sense of PIDO, shifts these challenges into another dimension. Commercial software tools such as Optimus [2], Isight [3], Dakota [4], ModeFrontier [5], among others, are offering a reasonable coverage of system integration from CAD and CAE software to optimization, visualization, statistical analysis, and full product data management (PDM) integration. The underlying approach has always been to introduce a so-called “master flow” which determines the optimization process that includes analyses, iteration loops, along with computing resource and job management.

From an enterprise standpoint, this master flow approach is not reasonable. It inevitably brings out several issues which are presented below. The current design work in industry is already so complex that no single tool, or vendor, or process is capable of adequately adjusting to all of the demands of high fidelity design work. In this paper, this issue is elaborated, along with a vision of how to overcome this trap. Our vision is driven by the belief in computational design, data affinity, and future design processes.

The issues of a master-slave context are presented in the following section with respect to computing resources by considering a specific type of genetic algorithm (GA) as an example. Next, the basis of a vision for a next generation computing and numerical optimization environment is presented by reassembling the building blocks of a (potentially automated) design process. Finally, the requirements for this transition presented, along with a discussion via several open questions.

4. GA with respect to computing resources: Synchronous Master-Slave versus an Asynchronous Approach

Genetic algorithms (GAs) are an attractive class of techniques for solving a variety of complex search and optimization problems. Although they are not the only possible approach even for discontinuous problems, GAs are an integral part of most PIDO tools. GAs offer a global optimization strategy at the cost of heavy computing resources for state evaluation in every generation. Classical GA starts by evaluating responses at a predefined number of points. This set of points is called a generation. For a large number of points, the evaluations are usually performed in parallel. For large-scale problems of practical importance, distributed computing techniques are typically implemented. However, classical GA also requires synchronization; it requires correlation of the results of all the points in a single generation after all the points in the generation are evaluated. This synchronization point becomes a road block for a heterogeneous computing environment when the process to evaluate a single point in the generation is significantly slower than for the others. The overall process is determined by a so-called master process which consists of generation synchronization (environmental selections) and offspring generations. Multiple, parallel point evaluations constitute the slave jobs. Such types of algorithms are called synchronous distributed master-slave GA (SDGA).

The speedup lost in synchronizing a point may be considerable in networked, heterogeneous computing environments [6]. Asynchronous (also called generation-less) GAs have been proposed to overcome this drawback via alternative implementations of the individual’s life-cycle dissolving a strict generational evaluation. The reader is referred to [7] for details regarding modelling of an individual’s life-cycle and mating strategies. In computing terminology, an asynchronous distributed GA (ADGA) is obtained by “unrolling” the loop of generation, crossover, and mutation until convergence is achieved.

In heterogeneous network environments, one single slow processor may impede the overall progress in executing SDGA. Significant speedup can be obtained by implementing the idea of ADGA [6]. Moreover, complete resource management and scheduling could be decoupled. Implementation of such ADGA may achieve partitioning of GA schemes into pieces of work which can be processed in parallel. An optimal partitioning in terms of runtime speedup should allow for a full utilization of all available resources.

5. PIDO approach and the eternal resource bottleneck in enterprise design work

Transferring the idea of asynchronous versus synchronous genetic algorithms to the whole optimization process reveals significant issues within current PIDO tools and their proposed integration into enterprise design work. For

this case, the PIDO tool assumes the role of the master, with the slave-jobs being plugged in via numerous interfaces. The master thus controls the overall optimization process; however, in every enterprise, the resources required to fulfill design work are always limited. This includes the required computing power in the form of the number of computer cores, computing time, disk space, and computer memory; they are referred to as hardware cost. The PIDO tool also assumes the role of a scheduler to distribute slave jobs to any computing environment by controlling all of the associated resources. Moreover, when evaluating sophisticated functions by CSM, CFD, or MDO tools, computation of the state evaluations presents a resource issue on its own, e.g., with respect to software licensing. One should not underestimate the challenge for an enterprise to decide whether a number of licenses is provided for multiple design tasks instead of using the same number of licenses for one sophisticated multi-job task. Smart decisions must be based on the expected payoff for the engineering design problem, but should also include estimation of computing and license resource consumption. Today, PIDO tools lack transparent visualization and tracking of such resources. Furthermore, clear insight into multi-job status, job scheduling, and solution convergence and robustness are essential.

Last but not least, for enterprise design work, the limited resource *time to solution* represents not just computing wall clock time, but also engineering decision time. Typically the analyst is faced with the dilemma of setting up one fast single job for a specific design versus a multi-job design exploration or optimization process. Intelligence and guidance for optimization post-processing to understand why a particular design is superior to another is a key to fast decisions in the time-pressured enterprise project work environment.

From an enterprise standpoint, it is believed that the current master-slave PIDO approaches will never be able to fulfill all of these requirements. Instead, it is proposed that a different approach is followed in the future for reassembling the typical PIDO modules as described in the following.

6. Vision of Optimization Data Management Engine for Resource-optimal Enterprise Design Work

To resolve the issues described above, it is proposed that the classical master-slave approach be decomposed and moved to what is called an Optimization Data Management Engine (ODME). By analogy with the genetic algorithms presented above, any synchronization points within the complete CAE design process can be avoided. To illustrate, consider the multidisciplinary optimization tasks of airplane or car design where CFD and structural analyses such as crash and noise, vibration, and harshness (NVH) are involved. Suppose that the CFD or crash analysis takes more time and resources than for the structural analysis. For a typical master-slave PIDO, all analysis results are synchronized only after all of the analyses are completed. Thus, a quick structural analysis will typically need to wait for the CFD or crash analysis to be completed. This bottle-neck is inherent to master-slave approaches.

Our vision for a multidisciplinary multi-job optimization environment is to break up the master-slave components into process modules. A conceptual draft of the *reassembled* modules is depicted in Fig. 1 which consists of evaluation modules (CSM/CFD/MDO tools), post-processing and visualization modules, resource controller modules (computing load share, licensing control, job scheduling), and driver modules (DOE, RSM, single analysis request, Data Mining, Optimization algorithms, etc.). The core around which those modules are arranged is a high-performance database storing all relevant analysis models and results: CAD/CAE model properties, design variables, dedicated response values, as well as job Meta data such as job run time, resource consumption, submission status, etc. Based on today's technical standards, open or standard protocol (SQL) database concepts can be utilized to implement such a database.

Let us refer again to the MDO optimization example illustrated above and show how it would look within the ODME. The optimization algorithm is initiated from some driver module and sent to a Resource Controller in the database; this is identified by a "to evaluate" marker for the corresponding CFD, Crash and NVH analyses being scheduled by the Resource Controller according to the available software licenses and high-performance computing (HPC) load sharing. As soon as the license and HPC load share are available, every particular Evaluation Module starts its analysis. Thus, a prioritized single job evaluation may "overtake" an optimization evaluation for a period of time, but not prevent the rest of the evaluations in the running generation. Meanwhile, quick and cheap evaluation results, if present, are already fed back to the Database Resource Controller and could be visualized by a selected Visualization Module. Based on the current solution information, the user might want to change the optimization parameters or variables, or to set up a completely new Driver Module. At some point, all of the required evaluations are completed, with the initial optimization task being completed and the results being stored in the Database.

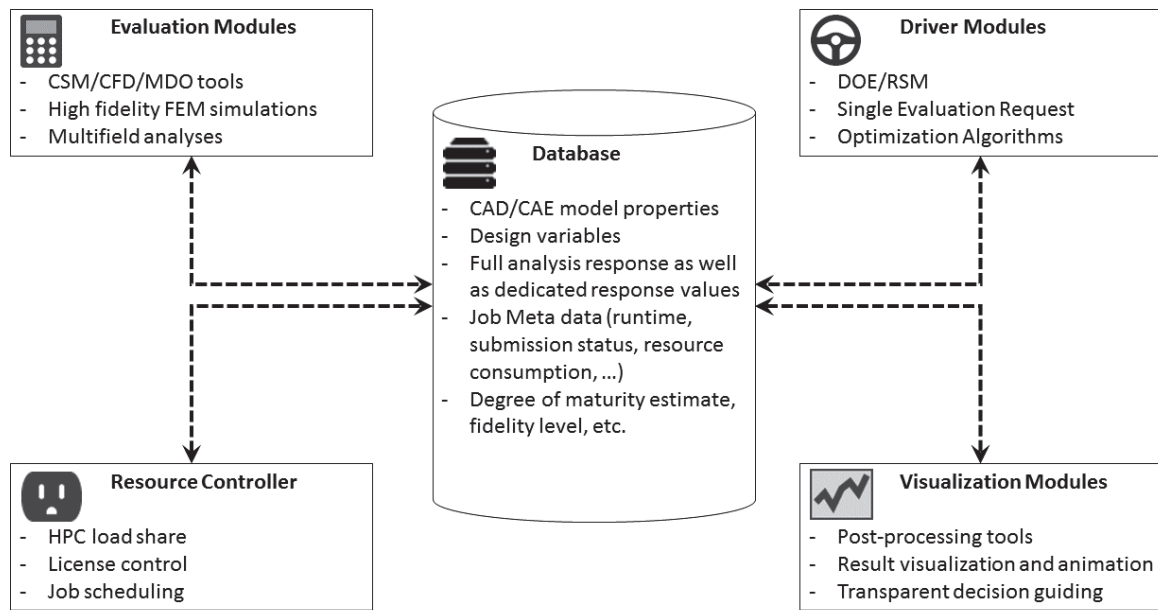


Figure 1: Optimization Data Management Engine as a reassembly of PIDO master-slave approach: Database interacts with Resource Controller, Driver, Evaluation, and Visualization modules

Within the proposed environment, more features could be implemented successively. Eventually, a classification of the maturity of the analysis results is envisioned to account for different levels of fidelity. Such a classification would allow for efficient data usage in different design stages, from predesign and design exploration up to detailed design, life cycle analysis, and certification. More practical features could easily be implemented such as multiple user and client access, web-based interfaces, etc.

7. Conclusions

The classic PIDO-based numerical optimization approach is presented in this paper, along with its conceptual drawbacks in the context of the enterprise design work requirements from the automotive and aerospace perspectives. To overcome the underlying issues of this approach, numerous changes are proposed for the standard master-slave approach being implemented in today's PIDO tools. An enterprise computing environment based on an optimization data management engine (ODME) is envisioned by reassembling the existing PIDO modules around a central analysis evaluation and storage database with a resource controller.

It is expected that when the proposed new paradigm is implemented, multidisciplinary and large-scale optimization capabilities will be easier to adapt to existing design processes in the automotive and aerospace industries. Furthermore, it is expected that the PIDO-based approach and other approaches to optimization will gain more industrial support and enterprise-wide implementation. As a result of implementing the new proposed PIDO concept, it is anticipated that a new phase of growth of numerical optimization and associated numerical simulation in enterprise design work will ensue.

8. References

- [1] Somanath Nagendra et. al., Industry Perspectives on Integrated System Optimization and MDO, *10th World Congress on Structural and Multidisciplinary Optimization*, In: Proceedings of World Congress on Structural and Multidisciplinary Optimization WCSMO-10, 19.-24.05.2013, Orlando, FL (USA)
- [2] Optimus Software Package, Release 10.15, 2015, Noesis Solutions, Gaston Geenslaan, 11 B4, 3001 Leuven | Belgium, <http://www.noesisolutions.com/Noesis>
- [3] Isight/Simulia Execution Engine (SEE) Software package, Release 5.9, 2015, Simulia, Simulia World Headquarters, 166 Valley Street, Providence, RI 02909 USA, <http://www.3ds.com/products-services/simulia/products/isight-simulia-execution-engine>
- [4] Dakota Software Package, Release 6.1, November 15, 2014, Sandia National Laboratories, 1515 Eubank SE, Albuquerque, NM 87123, <https://dakota.sandia.gov>
- [5] modeFRONTIER Software Package, Release 2014, Esteco, Padriciano 99, 34149 Trieste Italy, Building L2, <http://www.esteco.com/modelfrontier>

- [6] John W. Baugh and Sujay V. Kumar, Asynchronous genetic algorithms for heterogeneous networks using coarse-grained dataflow, *Genetic and Evolutionary Computation - GECCO 2003*, 2003.
- [7] David C. Keller, Evolutionary Design of Laminated Composite Structures, available from <http://dx.doi.org/10.3929/ethz-a-006082073>, ETH Zürich, Zürich, Switzerland, 2010.

Topology Optimization of a Transient Thermo-Mechanical Problem using Material Penalization

Emiel van de Ven^{1,2}, Evert Hooijkamp², Matthijs Langelaar², Fred van Keulen²

¹ National Aerospace Laboratory, Amsterdam, the Netherlands, emiel.van.de.ven@nlr.nl

² Delft University of Technology, Delft, the Netherlands, m.langelaar@tudelft.nl, a.vankeulen@tudelft.nl

1. Abstract

Designing transient thermal mechanical systems is a challenging task. Material can have many different functions: it can provide heat capacity, heat conduction, mechanical stiffness or even function as an actuator. Topology optimization can provide the engineer with valuable insight on such a problem. One of the most popular topology optimization approaches is the density method. This method is applied to a transient thermal mechanical problem. In order to ensure manufacturability, penalization is applied to suppress intermediate densities in the final design. However, for transient thermal mechanical optimization problems, conventional penalization does not work for most objective functions. A new penalization method, material penalization, is presented that does suppress intermediate densities in the transient thermal mechanical domain. Each element is given its own unique set of penalization parameters which are optimized to maximize the objective function for a minimization problem. By reusing sensitivity information from the density variables, the additional computational cost is limited.

2. Keywords: Topology optimization, Penalization, Manufacturability, Transient thermo-mechanical.

3. Introduction

In the density method, the usually discrete material placement problem is relaxed, allowing for intermediate element densities. The material properties of the elements are scaled with these densities. To ensure manufacturability and to allow for interpretation, however, the final design of a topology optimization (TO) should not contain intermediate densities. In order to achieve an intermediate density free, or black-and-white, design with the density method, the intermediate material is penalized. SIMP (Simplified Isotropic Material with Penalization) is a common approach, but in this paper RAMP (Rational Approximation of Material Properties) [1] is used because of its reported superior performance on thermo-elastic problems [2]. For stiffness optimizations, SIMP and RAMP penalization are able to result in a black-and-white design. However, for transient thermal mechanical (TM) problems, SIMP or RAMP penalization is often not sufficient to result in a black-and-white design. Because of the complex relationship between element density and objective in transient TM problems, intermediate densities are in some places more optimal than a void or completely filled element, even in absence of a volume constraint. SIMP and RAMP are not able to change this, which is also apparent in literature. Most transient TM topology optimizations that utilize the density approach contain intermediate densities ([3], [4]). This is also the case for steady-state TM optimization problems ([5], [6]).

Besides penalization, there are other methods to suppress intermediate densities. Grey penalization is a widely applied method. The objective function is augmented with a term, that increases when intermediate densities are present. However, determining the scaling of this grey penalization term w.r.t. the original objective is cumbersome. By choosing it too high, the design will end up in an inferior local minimum. Too low, and final design will still contain intermediate densities. Grey penalization has been used in, for example, in [6]. Nonetheless, it was not able to produce a black-and-white design for every design case. Other methods that are available are projection methods. This has been used in [4] as a post-processing step, where a threshold was set at 0.5. However, the thresholded design had a much lower performance, because there is no guarantee that a post processed design is still an optimum. Projection during the optimization, as proposed in [7] has, by the author's best knowledge, not yet been applied to transient TM problems. This might create an intermediate density free design without deteriorating the performance, however, in this study a different approach has been chosen.

In this paper an extension to the conventional penalization method is presented that is able to create a black-and-white design for transient TM problems. This is done by assigning individual penalization parameters to every element, which are included in the optimization with very limited extra computational cost. In the following section, Section 4, background on penalization in transient TM systems is given. In Section 5 the new penalization method is presented and the resulting topology optimization problem is stated in Section 6. Finally, the new penalization method is applied to a transient TM problem in Section 7.

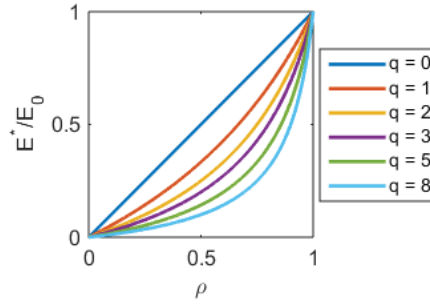


Figure 1: Standard RAMP penalization for different penalization parameters.

4. Background on penalization in TM systems

In density-based topology optimization involving solid mechanics, the Young's modulus is interpolated with the element densities. With RAMP penalization, the interpolated Young's modulus of an element is defined as:

$$E^*(\rho) = E_{min} + \frac{\rho}{1 + q(1 - \rho)}(E_0 - E_{min}), \quad (1)$$

where E^* indicates the interpolated Young's modulus, E_0 the Young's modulus of the original material and E_{min} denotes a lower bound added for numerical reasons, chosen a factor 10^{-6} lower than E_0 . ρ is the virtual element density and q the penalization parameter. The effect of q on the interpolation can be observed in Figure 1. It is apparent that if an intermediate value of the Young's modulus is optimal, penalization will not prevent the optimizer from utilizing this intermediate density since all the intermediate values of the Young's modulus are still available after penalization, only with different corresponding density values.

In transient TM problems, four material properties can be penalized: the Young's modulus E , the coefficient of thermal expansion (CTE) α , the heat capacity c and the heat conductivity k . In this study, instead of the CTE, the thermal stress coefficient (TSC) β is penalized, defined as $\beta = E\alpha$, as advised in [2]. Little research has been conducted on how to penalize the material properties, often they are all penalized with the same penalization factor. By the author's knowledge, the possibility of penalizing the material properties by different factors for TM problems is first mentioned in [8]: "In principle, the power p [the penalization parameter] could take different values for each physical property. However, for simplicity and to avoid having to choose multiple parameters, the same power is selected for all material interpolations." The latter is common practice in TM optimizations. Gao and Zhang [2] explored the effect of different penalizations, but only on an optimization of a mechanical system with a given temperature rise. Outside of the TM field, some research has been done on the effect of different penalization parameters. For piezoelectric systems, [9] pose a set of rules for different penalization parameters. In [9], different penalization rules are found for different types of piezoelectric systems. The effect of different penalization parameters on a piezoelectric energy harvesting device under static and dynamic loading is investigated in [10]. They find that different sets of penalization parameters produce different layouts. Because these papers employ the electro-mechanical domain it is hard to draw quantitative conclusions for the TM domain. However, as in the electro-mechanical domain, it is likely that different penalization parameters have an influence on the final layout of TM optimization problems.

5. Material penalization

When all the material properties are penalized by the same factor, the material behavior at intermediate densities will be similar to the original material, except it will behave as if there is less material (for example, a less thick plate in 2D). However, when the penalization parameters are changed relative to each other, the material behavior at intermediate densities will change. Let q_c , q_k , q_E and q_β be the penalization parameters for the heat capacity, heat conduction, Young's modulus and TSC respectively. An element with, for example, $q_c = 0$, $q_k = 5$, $q_E = 0$ and $q_\beta = 0$, will have a much lower heat conduction in relation to the change of the other material properties at intermediate densities, because the conduction is penalized more. This intermediate material can be related to concrete, which is stiff but has a low heat conduction. On the other hand, an element with $q_c = 0$, $q_k = 0$, $q_E = 5$ and $q_\beta = 0$ has a much lower stiffness in relation to the other material properties. The intermediate material could represent a type of copper wire connection. Thus, by changing the penalization parameters relative to each other, a range of material behaviors can be generated.

The basic idea of the new penalization method, material penalization, is: find a set of penalization parameters, that gives the material at intermediate densities adverse behavior for the optimization problem. This will prevent the optimizer from using intermediate densities as design elements. For example, when high conduction is optimal,

the intermediate material should behave insulating. However, the adverse behavior is often not easily selected and depends on different aspects. At first, different objectives benefit from other sets of penalization parameters, as shown in [9]. It is, therefore, not possible to find a single set of penalization parameters that gives a black-and-white design for all transient TM TO problems. Secondly, within one problem, intermediate material that is adverse at one location can have favorable behavior at other locations. Thus, in order to ensure a black-and-white design, each element needs its *individual set of penalization parameters* that creates intermediate material that behaves adversely. Thirdly, as the design evolves during optimization, the function of an element may also evolve and therefore, the penalization parameters need to be altered. Concluding, because the adverse behavior depends on the design problem, element location and function, the penalization parameters of each element are included as design variables.

The penalization parameters are optimized simultaneously with the density variables, but the penalization parameters are optimized to maximize the objective function, whereas the density variables minimize the objective function. Maximizing will provide the set of penalization parameters for each element that gives intermediate material adverse behavior. Keep in mind that these parameters will not change the material properties of the final design, as it should consist of only black or white elements, which are not affected by the material penalization. The new optimization problem can be stated as a continuous min-max problem.

6. Topology optimization

6.1 Problem formulation

As stated, the focus of this study is on TM problems. Mechanical coupling to the thermal domain is neglected, and therefore a one-way coupled system of equations has to be solved to get the system response. Furthermore, the mechanical behavior is considered to be quasi-static compared to the thermal dynamics. The finite element method (FEM) is used to discretize the thermal and mechanical equilibrium equations in space. This gives the following initial value problem:

$$\mathbf{C}_T \dot{\mathbf{T}}(t) + \mathbf{K}_T \mathbf{T}(t) = \mathbf{Q}(t), \quad (2)$$

$$\mathbf{K}_U \mathbf{u}(t) = \mathbf{A} \mathbf{T}(t), \quad (3)$$

$$\mathbf{T}(0) = \mathbf{T}_{ambient}, \quad (4)$$

where \mathbf{C}_T and \mathbf{K}_T denote the heat capacitance- and conduction-matrix, respectively, \mathbf{T} and \mathbf{Q} indicate the nodal temperature- and the thermal loading-vector, \mathbf{K}_U denotes the mechanical stiffness matrix, \mathbf{A} denotes the thermal-mechanical coupling matrix and \mathbf{u} indicates the nodal displacement vector. These equations are solved by Euler backward time integration with an initial temperature field which is given in Equation 4. For the example in this study, the objective is only a function of displacements and time. The optimization problem can thus be written as:

$$\min_{\rho_i} \max_{s_{i,j}} \left(f = \int_0^{t_f} p(\mathbf{u}(t), t) dt \right), \quad (5)$$

$$\text{subject to: } \mathbf{C}(\rho_i, s_{i,j}) \dot{\mathbf{T}} + \mathbf{K}_T(\rho_i, s_{i,j}) \mathbf{T} = \mathbf{Q}, \quad (6)$$

$$\mathbf{K}_U(\rho_i, s_{i,j}) \mathbf{u} = \mathbf{A}(\rho_i, s_{i,j}) \mathbf{T}, \quad (7)$$

$$0 \leq \rho_i \leq 1, \quad (8)$$

$$-1 \leq s_{i,j} \leq 1, \quad i \in [1, N], \quad j \in [1, 4], \quad (9)$$

where f is the objective, p a chosen function of the displacements and time, N the total number of elements and t_f the end time. ρ_i is the virtual density of element i , and $s_{i,j}$ is the penalization parameter design variable of property j and element i . Since there are four penalized material properties per element, there are $4N$ penalization parameters in total. Note that all the system matrices are dependent on the element densities ρ , as well as on the penalization parameters design variables s .

In order to normalize the penalization parameters and to smoothen the variation of the RAMP curve over the domain of s , a mapping has been applied that maps the domain of the design variables s onto the domain of the actual penalization parameters q which are input to the RAMP equation (Equation 1):

$$s^* = c_1 s^3 + c_2 s, \quad (10)$$

$$q = \begin{cases} s^* & s^* \geq 0 \\ \frac{s^*}{1-s^*} & s^* < 0 \end{cases}, \quad (11)$$

where the constants c_1 and c_2 are chosen as 13 and 2 respectively. Now, the design variables range from -1 to 1, which is handled better by the optimizer than the penalization parameters which range from $-15/16$ to 15. The

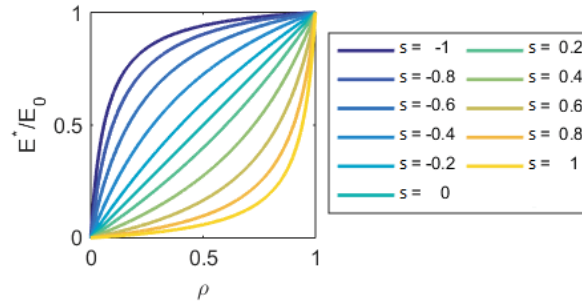


Figure 2: RAMP extended to also promote besides of penalizing properties. Design variable s varies from -1 to 1 and the RAMP curve changes roughly at the same rate over the complete range of s .

course of the RAMP curve for different values of the design variables s can be seen in Figure 2.

6.2 Sensitivity analysis

Since the topology optimization contains many design variables and few constraints, adjoint sensitivities are used to calculate the sensitivities in order to save computational time compared to direct sensitivities [11]. By augmenting the objective with the governing equations (Equation 2 and 3), each multiplied with an adjoint variable, the following equations for the sensitivities can be derived [12]:

$$\frac{df}{dv_i} = \int_0^{t_f} \left[\boldsymbol{\lambda}^T(t) \left(\frac{d\mathbf{K}_U}{dv_i} \mathbf{u}(t) - \frac{d\mathbf{A}}{dv_i} \boldsymbol{\Gamma}(t) \right) + \boldsymbol{\mu}^T(t) \left(\frac{d\mathbf{C}_T}{dv_i} \dot{\boldsymbol{\Gamma}}(t) + \frac{d\mathbf{K}_T}{dv_i} \boldsymbol{\Gamma}(t) - \frac{d\mathbf{Q}(t)}{dv_i} \right) \right] dt \quad (12)$$

$$\boldsymbol{\lambda}^T(t) \mathbf{K}_U = \frac{dp(t)}{d\mathbf{u}} \quad (13)$$

$$-\dot{\boldsymbol{\mu}}^T \mathbf{C}_T + \boldsymbol{\mu}^T(t) \mathbf{K}_T = \boldsymbol{\lambda}^T(t) \mathbf{A} \quad (14)$$

$$\boldsymbol{\mu}(t = t_f) = 0 \quad (15)$$

where $\boldsymbol{\lambda}$ and $\boldsymbol{\mu}$ denote the adjoint vectors, independent of the design variables to which the objective is derived. Note that the numerator-layout notation has been used. The adjoint (Equation 14) is discretized in time using an Euler forward interpolation scheme. Since the adjoint problem is a terminal value problem (Equation 15), integration is done backwards in time, causing the Euler forward scheme to become implicit. In equation 12, the objective function is derived w.r.t. a yet to be defined parameter v_i . This can be both the element density as well as one of its penalization parameters. Note that for both cases the same adjoint variables can be used since no definition of v_i is needed in their calculation. This implies that the sensitivity information of the penalization parameters comes at little extra cost once the density sensitivities have been determined. Only the derivatives of the system matrices, which are known exactly, differ between the densities and the penalization parameters. The interpolated material property needs to be derived to either the density or the penalization parameter.

6.3 Optimization procedure

Linear programming with adaptive move limits is used as optimization algorithm. Every iteration the density variables are moved in the direction in which their derivatives w.r.t. the objective function is negative. Simultaneously, the penalization variables are moved in the direction in which their derivatives are positive, in order to maximize the objective function. The move limits determine the step size. The ratio between the size of the move limits of the density and penalization variables determines how fast the one can change with respect to the other. This has a large influence on the result. It was observed that when the density variables have much larger move limits than the penalization variables, the chance of ending up in an inferior local minimum is the lowest. However this also increases the number of iterations because the penalization variables change slowly due to their small move limits. Equal move limits for the penalization and density variables have been used as this already gave satisfactory results.

7. Transient TM demonstrator

In this section, the material penalization method presented in the previous sections will be applied on a transient TM case, as depicted in Figure 3. On the left and right side the domain is fixed, and ambient temperature is prescribed, which is also the initial temperature for the whole domain. The top and bottom side are thermally isolated. On the red elements a heat load is applied from $t = 0$. The objective is to minimize the thermal error from $t = 30\text{s}$ to $t = 60\text{s}$. The thermal error is defined as: $|u_{obj} - 1.5 \cdot 10^{-3}|$, which means that a displacement of 1.5mm

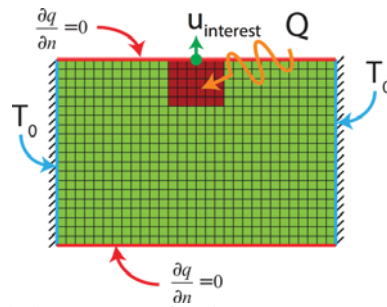
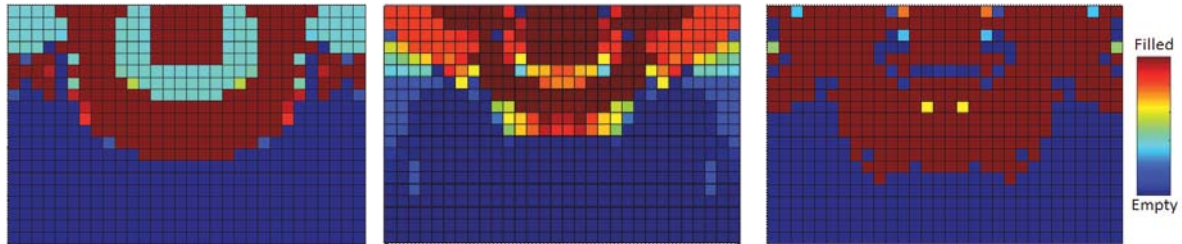


Figure 3: Transient TM test case. Red elements are fixed, green elements are design variables. The heat load is applied equally on the red elements.



(a) Final design without penalization. (b) Final design with conventional penalization. (c) Final design with material penalization.

Figure 4: TO results for the transient TM case for different penalization settings.

is desired over the time frame of interest.

The solution without penalization is displayed in Figure 4a. The design shows a mechanism that pushes the area on which the heat load is applied upward, to reach the target displacement. Around the fixed domain there is a ring that provides heat capacity and slightly decreases the objective displacement when it expands. This complex design gives a clue for the engineer in what direction the final design can be made, but it leaves a lot undecided. No design for the suspension of the domain on which the heat load is applied can be deduced because it is suspended in intermediate densities. Adding conventional penalization does not improve the situation, as can be seen in Figure 4b. When material penalization is applied, it becomes much clearer what the final design should look like. This is displayed in Figure 4c. Now there are hardly any intermediate densities left. The remaining intermediate densities are in areas where for example a certain stiffness is required: around hinge points. These are areas to which the engineer should pay special attention, for example, when determining the exact required thickness.

This also shows that a black-and-white design is only achieved when there are competing material properties. On the hinge points, where intermediate densities are present, only the stiffness of the elements is dominant (and desires an intermediate value). When this is the case, material penalization will not be able to result into a black-and-white design.

8. Conclusion

In this research TO is applied to a transient TM problem. A new penalization method, material penalization, is presented for transient TM TO problems. Every element is given its unique set of penalization parameters which are optimized to maximize the objective function, where the overall goal is to minimize the objective function. Material penalization will not always be able to create a black-and-white design, as it needs counteracting material properties. However, when this is the case, it is shown that material penalization, unlike conventional penalization, is able to result in a manufacturable, intermediate density free, design for a complex transient TM problem.

Further investigation into the relative optimization speeds of the density and penalization variables and how this compares to the total number of iterations will be relevant in order to reduce the total number of iterations. Furthermore, when minimizing the penalization parameters instead of maximizing them, this method might be used to investigate which material properties (and thus material) are favourable at different locations of the design.

9. Acknowledgements The author would like to thank ASML for enabling this research and providing financial support.

10. References

- [1] M. Stolpe and K. Svanberg. "An alternative interpolation scheme for minimum compliance topology optimization". English. In: *Structural and Multidisciplinary Optimization* 22.2 (2001), pp. 116–124.

- [2] T. Gao and W. Zhang. “Topology optimization involving thermo-elastic stress loads”. English. In: *Structural and Multidisciplinary Optimization* 42.5 (2010), pp. 725–738.
- [3] Y. Li et al. “Topology optimization of thermally actuated compliant mechanisms considering time-transient effect”. In: *Finite Elements in Analysis and Design* 40.11 (2004), pp. 1317–1331.
- [4] L. A. M. Mello et al. “On response time reduction of electrothermomechanical MEMS using topology optimization”. In: *Computer Methods in Applied Mechanics and Engineering* 247–248.0 (2012), pp. 93–102.
- [5] S. Cho and J.-Y. Choi. “Efficient topology optimization of thermo-elasticity problems using coupled field adjoint sensitivity analysis method”. In: *Finite Elements in Analysis and Design* 41.15 (2005), pp. 1481–1495.
- [6] L. Yin and G. Ananthasuresh. “A novel topology design scheme for the multi-physics problems of electrothermally actuated compliant micromechanisms”. In: *Sensors and Actuators A: Physical* 97–98.0 (2002), pp. 599–609.
- [7] J. K. Guest et al. “Achieving minimum length scale in topology optimization using nodal design variables and projection functions”. In: *International Journal for Numerical Methods in Engineering* 61.2 (2004), pp. 238–254.
- [8] O. Sigmund. “Design of multiphysics actuators using topology optimization – Part I: One-material structures”. In: *Computer Methods in Applied Mechanics and Engineering* 190.49–50 (2001), pp. 6577–6604.
- [9] J. E. Kim et al. “Multi-physics interpolation for the topology optimization of piezoelectric systems”. In: *Computer Methods in Applied Mechanics and Engineering* 199.49–52 (2010), pp. 3153–3168.
- [10] J. Y. Noh and G. H. Yoon. “Topology optimization of piezoelectric energy harvesting devices considering static and harmonic dynamic loads”. In: *Advances in Engineering Software* 53.0 (2012), pp. 45–60.
- [11] G. N. Vanderplaats. “Comment on” Methods of Design Sensitivity Analysis in Structural Optimization”. In: *AIAA Journal* 18.11 (1980), pp. 1406–1407.
- [12] R. T. Haftka. “Techniques for thermal sensitivity analysis”. In: *International Journal for Numerical Methods in Engineering* 17.1 (1981), pp. 71–80.

Robust shape optimization method for shell structures with unknown loadings

Tomohiro Nagano¹, Masatoshi Shimoda²

¹ Graduate School of Engineering, Toyota Technological Institute, Aichi, Japan, sd14417@toyota-ti.ac.jp

² Toyota Technological Institute, Aichi, japan, shimoda@toyota-ti.ac.jp

1. Abstract

In this paper, we propose a robust shape optimization method for a shell structure with unknown loadings. The concept of the principal compliance minimization for minimizing the maximal compliance is applied to the shape optimization design of a shell structure. The principal compliance minimization problem can be transformed to the equivalent maximization problem of the fundamental eigenvalue of the stiffness term, and this problem is formulated as the distributed-parameter optimization problem based on the variational method. The derived shape gradient function is applied to the H^1 gradient method for shells to determine the optimal shape variation, or the optimal free-form. With this method, the optimal smooth curvature distribution of a shell structure can be determined without shape parameterization. The calculated results show the effectiveness of the proposed method for robust shape optimization of a shell with unknown loadings.

2. Keywords: Robust shape optimization, shell structure, loading uncertainties, principal compliance, H^1 gradient Method,

3. Introduction

Structural optimization techniques are widely utilized in many structural design fields. In general optimum design problems, the boundary condition is treated deterministically, although the condition such as loading condition frequently contains uncertainties. A design problem we often encounter loading conditions from all directions or multiple loading conditions by sharing of parts in actual design problems, which is one of the design problems with unknown or uncertain loadings. As the optimal design is generally vulnerable to the variation of loading because the structural performances such as stiffness or strength are strongly influenced by loading, the reliability design is often introduced to the formulation of optimal design problems. Safety factor or probabilistic approach is a method of reliability design problems. However, too large factor often causes excessive performances, redundant structure and weight gain.

Another approach to avoid the vulnerability of the optimally designed structure to variations of loading has been proposed by Cherkaev et al. [1], in which the concept of the principal compliance minimization is introduced, which is defined as the minimization of the maximal compliance under the worst possible loading. They formulated it as a min-max compliance problem, and showed that the principal compliance minimization problem can be transformed to the equivalent maximization problem of the fundamental eigenvalue of the stiffness term. They applied this idea to a simple size optimization problem. Takezawa et al. [2] applied the concept of the principle compliance to a topology optimization problem under the assumption that the loading domain is limited in a small sub-domain of the linear elastic domain to solve the full size linear elastic system efficiently.

In this paper, we newly propose a robust shape optimization method for shell structures by employing this concept to the free-form optimization method for shells. This method is a parameter-free shape optimization method based on the variational method, which was proposed by one of the authors [3]. In this method, a shape optimization problem is formulated in the continuous system, and the optimal smooth curvature distribution of a shell structure is determined without any shape parameterization, although almost all shape optimization methods need shape parameterization. The principal compliance minimization problem is transformed to the equivalent maximization problem of the fundamental eigenvalue of the stiffness term based on this concept. The transformed objective functional is maximized under the volume constraint, and the shape gradient function is theoretically derived using the material derivative method and the adjoint variable method. The derived shape gradient function is applied to the H^1 gradient method for shells to determine the optimal shape variation, or the optimal free-form. We carried out a numerical example to verify the effectiveness of the proposed robust shape optimization method.

4. Governing equation for a shell as a set of infinitesimal flat surfaces

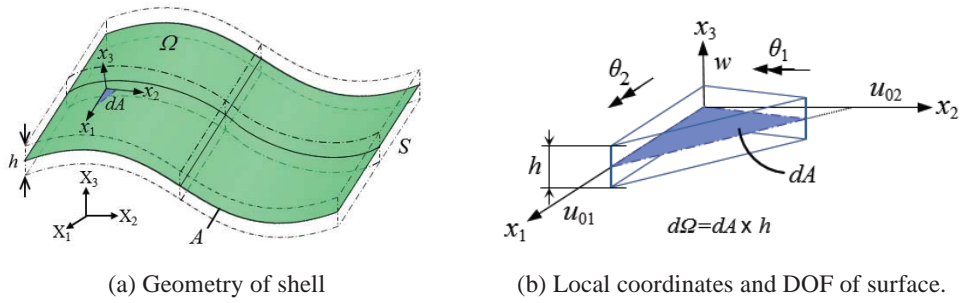


Fig.1 Shell consisting of infinitesimal flat surfaces.

As shown in Fig.1 and Eq.(1), consider a linear elastic shell having an initial bounded domain $\Omega \subset \mathbb{R}^3$, mid-area A with the boundary of ∂A , side surface S and thickness h . It is assumed that a shell structure occupying a bounded domain is a set of infinitesimal flat surfaces as shown in Fig.1, and stress and strain of the shell are expressed by superposing the membrane and bending components based on the Reissner-Mindlin theory.

$$W = \int_{\Omega} \left\{ (x_1, x_2, x_3) \in \mathbb{R}^3 \mid (x_1, x_2) \in A, \tilde{\alpha} \in \mathbb{R}^2, x_3 \in \left[-\frac{h}{2}, \frac{h}{2} \right] \right\} d\Omega, \quad W = A \times \left(-\frac{h}{2}, \frac{h}{2} \right), \quad S = \partial A \times \left(-\frac{h}{2}, \frac{h}{2} \right) \quad (1)$$

As shown in Fig.1(b), Eq.(2) and Eq.(3), the displacement vector expressed by the displacements in local coordinate $\mathbf{u} = \{u_i\}_{i=1,2,3}$ is considered by dividing into the in-plane direction $\{u_a\}_{a=1,2}$ and the out-of-plane direction u_3 . In this paper, the subscripts of the Greek letters are expressed as $\alpha = 1, 2$ and the tensor subscript notation uses Einstein's summation convention and a partial differential notation.

$$u_a(x_1, x_2, x_3) = u_{0a}(x_1, x_2) - x_3 q_a(x_1, x_2) \quad (2)$$

$$u_3(x_1, x_2, x_3) = w(x_1, x_2) \quad (3)$$

where $\mathbf{u}_0 = \{u_{0a}\}_{a=1,2}$, w and $\mathbf{q} = \{q_a\}_{a=1,2}$ express the in-plane displacements, out-of-plane displacement and rotational angles of the mid-area of the shell, respectively. Then, the weak form state equation relative to $\mathbf{u} = (\mathbf{u}_0, w, \boldsymbol{\theta}) \in U$ can be expressed as Eq.(4). An in-plane load $\{f_\alpha\}_{\alpha=1,2}$, an out-of-plane load $\{f_3\}$ are considered as the external forces.

$$a((\mathbf{u}_0, w, \boldsymbol{\theta}), (\bar{\mathbf{u}}_0, \bar{w}, \bar{\boldsymbol{\theta}})) = l((\bar{\mathbf{u}}_0, \bar{w}, \bar{\boldsymbol{\theta}})), \quad \forall (\bar{\mathbf{u}}_0, \bar{w}, \bar{\boldsymbol{\theta}}) \in U, \quad (\mathbf{u}_0, w, \boldsymbol{\theta}) \in U \quad (4)$$

where $(\bar{\cdot})$ expresses a variation. In addition, the bilinear form $a(\cdot, \cdot)$ and the linear form $l(\cdot)$ are defined.

$$a((\mathbf{u}_0, w, \boldsymbol{\theta}), (\bar{\mathbf{u}}_0, \bar{w}, \bar{\boldsymbol{\theta}})) = \int_{\Omega} \left\{ C_{\alpha\beta\gamma\delta} (u_{0\alpha,\beta} - x_3 \theta_{\alpha,\beta}) (\bar{u}_{0\gamma,\delta} - x_3 \bar{\theta}_{\gamma,\delta}) + C_{\alpha\beta}^s (w_{,\alpha} - \theta_\alpha) (\bar{w}_{,\alpha} - \bar{\theta}_\alpha) \right\} d\Omega \quad (5)$$

$$l((\bar{\mathbf{u}}_0, \bar{w}, \bar{\boldsymbol{\theta}})) = \int_{\Omega} \bar{f}_i \bar{u}_i d\Omega = \int_{\Omega} \left\{ f_1 (\bar{u}_{01} - x_3 \bar{\theta}_1) + f_2 (\bar{u}_{02} - x_3 \bar{\theta}_2) + f_3 \bar{w} \right\} d\Omega \quad (6)$$

where $\{C_{\alpha\beta\gamma\delta}\}_{\alpha,\beta,\gamma,\delta=1,2}$ and $\{C_{\alpha\beta}^s\}_{\alpha,\beta=1,2}$ express an elastic tensor with respect to the membrane stress and an elastic tensor with respect to the shearing stress, respectively. It will be noted that U in Eq.(4) is given by the following equation.

$$U = \left\{ (u_{0,1}^{(1)}, u_{0,2}^{(1)}, w^{(1)}, \theta_1^{(1)}, \theta_2^{(1)}) \in (H^1(A))^5 \mid \text{satisfy the given Dirichlet condition on each sub-boundary} \right\} \quad (7)$$

where H^1 is the Sobolev space of order 1.

5. Robust shape optimization of shell structure

5.1. Domain variation

We consider that a linear elastic shell structure having an initial domain Ω , mid-area A , boundary ∂A and side surface S undergoes domain variation \mathbf{V} (i.e., design velocity field) in the out-of-plane direction such that its

domain, mid-area, boundary and side surface become Ω_s , A_s , ∂A_s , and S_s as shown in Fig.2, respectively. It is assumed that the thickness h remains constant under the domain variation. The subscript s expresses the iteration history of the domain variation.

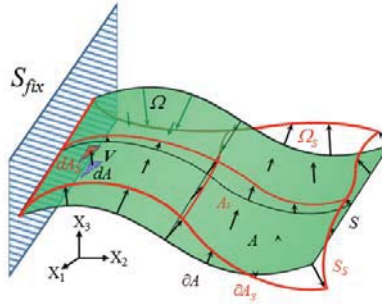


Fig.2 Out-of-plane shape variation by V .

5.2. Principal compliance

In a domain Ω , the principal compliance l_p of a structure is defined as the maximal compliance under all admissible unknown loadings [1].

$$l_p = \max(l) = \max \left\{ \int_A f_i u_i dA \right\} \quad (8)$$

where the unknown loadings satisfy following normalizing condition as shown in Eq.(9).

$$\frac{1}{2} \int_{\Omega} A_{ij}^{-1} f_i f_j dx = 1 \quad (9)$$

where f is the force vector, and $\{A_{ij}\}_{i,j=1,2,3}$ is a diagonal tensor which expresses the loading positions and their magnitude. The component of A_{ij} is proportional to the magnitude of the force corresponding, and has an infinitesimal δ at the point without loading. Then, the inverse tensor of A_{ij} expresses the weight factor to describe the set of admissible loadings. The principal compliance minimization problem can be transformed to the equivalent maximization problem of the fundamental eigenvalue $\lambda^{(1)}$, because the maximal compliance can be expressed as the inverse of the fundamental eigenvalue of the stiffness tensor [1].

$$l_p \propto 1/\lambda^{(1)} \quad (10)$$

$$a((\mathbf{u}_0^{(1)}, w^{(1)}, \boldsymbol{\theta}^{(1)}), (\bar{\mathbf{u}}_0, \bar{w}, \bar{\boldsymbol{\theta}})) = \lambda^{(1)} b((\mathbf{u}_0^{(1)}, w^{(1)}, \boldsymbol{\theta}^{(1)}), (\bar{\mathbf{u}}_0, \bar{w}, \bar{\boldsymbol{\theta}})), \quad (\mathbf{u}_0^{(1)}, w^{(1)}, \boldsymbol{\theta}^{(1)}) \in U, \forall (\bar{\mathbf{u}}_0, \bar{w}, \bar{\boldsymbol{\theta}}) \in U \quad (11)$$

where the bilinear form $b(\cdot, \cdot)$ is defined as

$$b((\mathbf{u}_0, w, \boldsymbol{\theta}), (\bar{\mathbf{u}}_0, \bar{w}, \bar{\boldsymbol{\theta}})) = \int_{\Omega} A_{ij} u_i \bar{u}_j dx = \int_{\Omega} \left\{ A_{\alpha\beta} (u_{0\alpha} - x_3 \theta_{\alpha}) (\bar{u}_{0\beta} - x_3 \bar{\theta}_{\beta}) + A_{33} w \bar{w} \right\} dx \quad (12)$$

5.3. Problem formulation

Let us consider a free-form optimization problem for minimizing the principal compliance of a shell structure. Letting the state equations in Eq.(11) and the volume be the constraint conditions, and the fundamental eigenvalue be the objective functional to be minimized, a distributed parameter shape optimization problem for determining the optimal design velocity field V can be formulated based on the variational method as

$$\text{Given } A, \hat{M} \quad (13)$$

$$\text{Find } V \quad (14)$$

$$\text{that minimize } -\lambda^{(1)} \quad (15)$$

$$\text{subject to } \text{Eq.(11) and } M (= \int_A h dA) \leq \hat{M} \quad (16)$$

where M and \hat{M} denote the volume and its constraint value, respectively.

5.4. Derivation of shape gradient function and optimality conditions

The Lagrange multiplier method is used to transform this constrained shape optimization problem to the unconstrained one. Letting $(\bar{\mathbf{u}}_0, \bar{w}, \bar{\boldsymbol{\theta}})$ and Λ denote the Lagrange multipliers for the state equation and volume constraints, respectively, the Lagrange functional L associated with this problem can be expressed as

$$L((\mathbf{u}_0^{(1)}, w^{(1)}, \boldsymbol{\theta}^{(1)}), (\bar{\mathbf{u}}_0, \bar{w}, \bar{\boldsymbol{\theta}}), \Lambda) = -\lambda^{(1)} + \lambda^{(1)} b((\mathbf{u}_0^{(1)}, w^{(1)}, \boldsymbol{\theta}^{(1)}), (\bar{\mathbf{u}}_0, \bar{w}, \bar{\boldsymbol{\theta}})) - a((\mathbf{u}_0^{(1)}, w^{(1)}, \boldsymbol{\theta}^{(1)}), (\bar{\mathbf{u}}_0, \bar{w}, \bar{\boldsymbol{\theta}})) + \Lambda(M - \hat{M}) \quad (17)$$

The material derivative of the Lagrange functional L can be derived as shown in Eq.(18) using the design velocity field \mathbf{V} .

$$\begin{aligned} \dot{L} = & -a((\mathbf{u}_0^{(1)\Phi}, w^{(1)\Phi}, \boldsymbol{\theta}^{(1)\Phi}), (\bar{\mathbf{u}}_0, \bar{w}, \bar{\boldsymbol{\theta}})) + \lambda^{(1)} b((\mathbf{u}_0^{(1)\Phi}, w^{(1)\Phi}, \boldsymbol{\theta}^{(1)\Phi}), (\bar{\mathbf{u}}_0, \bar{w}, \bar{\boldsymbol{\theta}})) - a((\mathbf{u}_0^{(1)}, w^{(1)}, \boldsymbol{\theta}^{(1)}), (\bar{\mathbf{u}}_0, \bar{w}, \bar{\boldsymbol{\theta}})) \\ & + \lambda^{(1)} b((\mathbf{u}_0^{(1)}, w^{(1)}, \boldsymbol{\theta}^{(1)}), (\bar{\mathbf{u}}_0, \bar{w}, \bar{\boldsymbol{\theta}})) + \dot{\lambda}^{(1)} \{b((\mathbf{u}_0^{(1)}, w^{(1)}, \boldsymbol{\theta}^{(1)}), (\bar{\mathbf{u}}_0, \bar{w}, \bar{\boldsymbol{\theta}})) - 1\} + \Lambda(M - \hat{M}) \\ & + \langle \mathbf{Gn}, \mathbf{V} \rangle, \quad \mathbf{V} \in \mathcal{C}_Q \end{aligned} \quad (18)$$

$$\langle \mathbf{Gn}, \mathbf{V} \rangle = \int_A \mathbf{Gn} \cdot \mathbf{V} dA = \int_A (G^{(1)} + G_M) \mathbf{V}_n dA \quad (19)$$

where $\mathbf{Gn}(= \mathbf{G})$ expresses the shape gradient function. \mathcal{C}_ϕ is the suitably smooth function space that satisfies the constraints of the domain variation. H is twice the mean curvature of mid-area A . The notations \mathbf{n}^{top} and \mathbf{n}^{bm} denote unit outward normal vectors at the top surface and the bottom surface, respectively, and a unit normal vector at the mid-area $\mathbf{n}^{mid}(= \mathbf{n}) = \mathbf{n}^{top} = -\mathbf{n}^{bm}$ is assumed by Shimoda et al. [3]. The coefficient function of the shape gradient function G consist of $G^{(1)}$ and G_M corresponding to 1st eigenvalue and volume constraint, respectively. The optimality conditions of the Lagrange functional L with respect to $(\mathbf{u}_0, w, \boldsymbol{\theta})$, $(\bar{\mathbf{u}}_0, \bar{w}, \bar{\boldsymbol{\theta}})$ and Λ are expressed as

$$a((\mathbf{u}_0^{(1)}, w^{(1)}, \boldsymbol{\theta}^{(1)}), (\bar{\mathbf{u}}_0, \bar{w}, \bar{\boldsymbol{\theta}})) = l^{(1)} b((\mathbf{u}_0^{(1)}, w^{(1)}, \boldsymbol{\theta}^{(1)}), (\bar{\mathbf{u}}_0, \bar{w}, \bar{\boldsymbol{\theta}})), \quad (\mathbf{u}_0^{(1)}, w^{(1)}, \boldsymbol{\theta}^{(1)}) \in \mathcal{U}, \quad (\bar{\mathbf{u}}_0, \bar{w}, \bar{\boldsymbol{\theta}}) \in \mathcal{U} \quad (20)$$

$$a((\mathbf{u}_0^{(1)\Phi}, w^{(1)\Phi}, \boldsymbol{\theta}^{(1)\Phi}), (\bar{\mathbf{u}}_0, \bar{w}, \bar{\boldsymbol{\theta}})) = \lambda^{(1)} b((\mathbf{u}_0^{(1)\Phi}, w^{(1)\Phi}, \boldsymbol{\theta}^{(1)\Phi}), (\bar{\mathbf{u}}_0, \bar{w}, \bar{\boldsymbol{\theta}})), \quad (\bar{\mathbf{u}}_0, \bar{w}, \bar{\boldsymbol{\theta}}) \in \mathcal{U}, \quad (\mathbf{u}_0^{(1)\Phi}, w^{(1)\Phi}, \boldsymbol{\theta}^{(1)\Phi}) \in \mathcal{U}, \quad (21)$$

$$\lambda^{(1)} \{b((\mathbf{u}_0^{(1)}, w^{(1)}, \boldsymbol{\theta}^{(1)}), (\bar{\mathbf{u}}_0, \bar{w}, \bar{\boldsymbol{\theta}})) - 1\} = 0 \quad (22)$$

$$A(M - \hat{M}) = 0, \quad A \geq 0, \quad M - \hat{M} \leq 0 \quad (23)$$

When the optimality conditions are satisfied, L becomes

$$L = \langle \mathbf{Gn}, \mathbf{V} \rangle \quad (24)$$

Considering the self-adjoint relationship $(\mathbf{u}_0^{(1)}, w^{(1)}, \boldsymbol{\theta}^{(1)}) = (\bar{\mathbf{u}}_0, \bar{w}, \bar{\boldsymbol{\theta}})$, which is obtained from comparing Eq.(20) and Eq.(21), the shape gradient functions $G^{(1)}, G_M$ are derived as

$$\begin{aligned} G = & - \{C_{abcd}(u_{0a,b}^{(1)} + \frac{h}{2}q_{a,b}^{(1)})(u_{0g,d}^{(1)} + \frac{h}{2}q_{g,d}^{(1)}) - C_{abcd}(u_{0a,b}^{(1)} - \frac{h}{2}q_{a,b}^{(1)})(u_{0g,d}^{(1)} - \frac{h}{2}q_{g,d}^{(1)})\} \\ & + l^{(1)} \{A_{ab}(u_{0a}^{(1)} + \frac{h}{2}q_a^{(1)})(u_{0b}^{(1)} + \frac{h}{2}q_b^{(1)}) + A_{33}w^{(1)}w^{(1)}\} - l^{(1)} \{A_{ab}(u_{0a}^{(1)} - \frac{h}{2}q_a^{(1)})(u_{0b}^{(1)} - \frac{h}{2}q_b^{(1)}) + A_{33}w^{(1)}w^{(1)}\} + hH\Lambda \end{aligned} \quad (25)$$

$$G_M = hH\Lambda \quad (26)$$

6. H¹ Gradient method for shells

The free-form optimization method for shell was proposed by Shimoda [3], which consists of main three processes; (1) Derivation of shape gradient function (2) Numerical calculation of shape gradient function (3) The H¹ gradient method for determining the optimal shape variation. The H¹ gradient method is a gradient method in a Hilbert space. The original H¹ gradient method was proposed by Azegami in 1994 [4] and also called the traction method. Shimoda modified the original method for free-form shell optimization. In the present paper, we employ the H¹ gradient method for shells to determine the optimal shape variation for the robust shape optimization problem. It is a node-based shape optimization method that can treat all nodes as design variables and does not require any design variable parameterization.

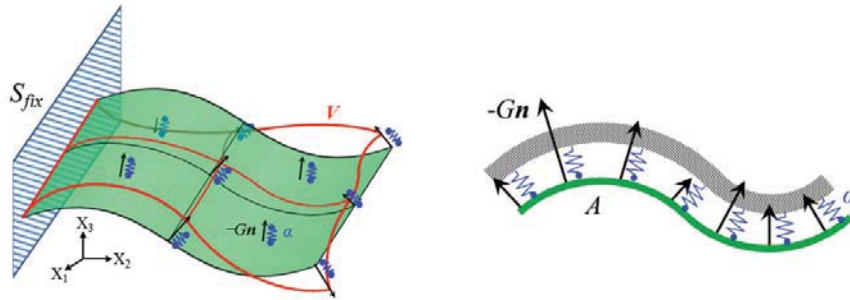


Fig.3 H¹ gradient method for shells.

This minimax problem may encounter the repeated eigenvalue problem of the objective functional. When this problem occurs, we change the objective and constraint functions as shown in Eq.(27). $r(\geq 2)$ denotes the number of repeating. The repeated eigenvalue is judged by introducing the range δ . In this paper we use $\delta_{-0}^{+0.02\lambda^{(1)}}$.

$$L((\mathbf{u}_0^{(1)}, w^{(1)}, \boldsymbol{\theta}^{(1)}), (\mathbf{u}_0^{(r)}, w^{(r)}, \boldsymbol{\theta}^{(r)}), (\bar{\mathbf{u}}_0, \bar{w}, \bar{\boldsymbol{\theta}}), \Lambda) = \sum_{k=1}^r \left\{ -\lambda^{(k)} + \lambda^{(k)} b((\mathbf{u}_0^{(k)}, w^{(k)}, \boldsymbol{\theta}^{(k)}), (\bar{\mathbf{u}}_0, \bar{w}, \bar{\boldsymbol{\theta}})) - a((\mathbf{u}_0^{(k)}, w^{(k)}, \boldsymbol{\theta}^{(k)}), (\bar{\mathbf{u}}_0, \bar{w}, \bar{\boldsymbol{\theta}})) \right\} + \Lambda(M - \hat{M}) \quad (27)$$

In an analogous way, the shape gradient function becomes

$$G = \sum_{k=1}^r (G^{(k)}) + G_M \quad (28)$$

$$G = - \{ C_{abgd}(u_{0a,b}^{(k)} + \frac{h}{2}q_{a,b}^{(k)})(u_{0g,d}^{(k)} + \frac{h}{2}q_{g,d}^{(k)}) - C_{abgd}(u_{0a,b}^{(k)} - \frac{h}{2}q_{a,b}^{(k)})(u_{0g,d}^{(k)} - \frac{h}{2}q_{g,d}^{(k)}) \} + l^{(k)} \{ A_{ab}(u_{0a}^{(k)} + \frac{h}{2}q_a^{(k)})(u_{0b}^{(k)} + \frac{h}{2}q_b^{(k)}) + A_{33}w^{(k)}w^{(k)} \} - l^{(k)} \{ A_{ab}(u_{0a}^{(k)} - \frac{h}{2}q_a^{(k)})(u_{0b}^{(k)} - \frac{h}{2}q_b^{(k)}) + A_{33}w^{(k)}w^{(k)} \} + hHA \quad (29)$$

5. Results of numerical calculation

The proposing method is applied to a simple problem to confirm the validity of the proposed method. Fig.4 shows the shape optimization problem definition of a box-shaped cantilever shell structure. As shown in Fig.4(b), an unknown loading is applied to the center of the free end face. The volume constraint is set as the same as the initial value.

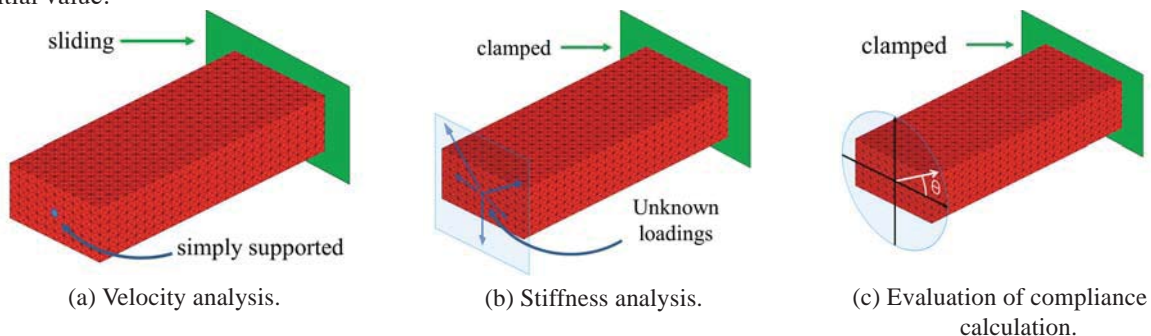
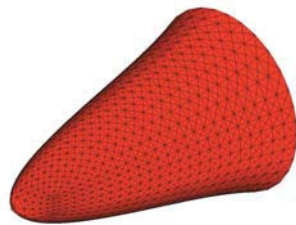
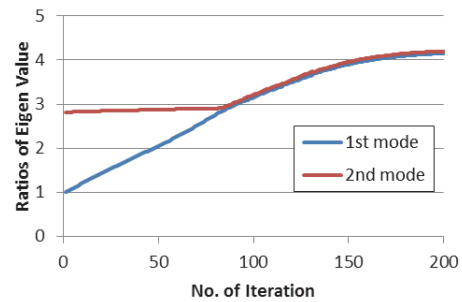


Fig.4 Boundary conditions.

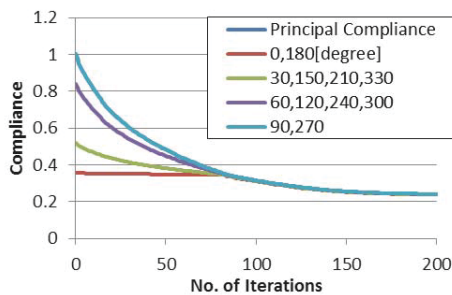
Fig.5(a) shows the obtained optimal shape. The clamped end expands while the area of free end narrows toward the loading point. The iteration convergence histories of the 1st and 2nd eigenvalues are shown in Fig.5(b). To confirm the robustness of the result, we use the polar coordinate in which the origin is the point of the loading, and measure the compliance of every 30 degree in the circumferential direction. The convergence history of the principal and the evaluation compliance of every 30 degree in the circumferential direction is shown in Fig.5(c), and comparison of compliances of each loading direction is shown in Fig.5(d). It is confirmed that the 1st eigenvalue is maximized as shown in Fig.5(b). The compliance is reduced by approximately 76% as shown in Fig.5(c)(d). We confirm that the optimal robust shape with high stiffness and independence of loading direction can be obtained with this method.



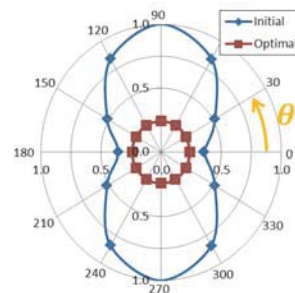
(a) Obtained shape



(b) Iteration histories of ratios of eigenvalue.



(c) Convergence history of principal and evaluation compliance.



(d) Comparison of compliances for loading directions.

Fig.5 Results of robust shape optimization.

5. Conclusions

In this paper, a robust shape optimization method for a shell structure with unknown loadings was constructed based on the concept of the principal compliance minimization which was transformed to the equivalent maximization problem of the fundamental eigenvalue of the stiffness term. A principal compliance maximization problem subject to both constraints of the volume and the state equation of shell structure was formulated as a distributed-parameter shape optimization problem, and the sensitivity function for this problem was theoretically derived. The derived shape gradient function was applied to the H^1 gradient method for shell structures to determine the robust optimal shape. The calculated result showed the effectiveness of the proposed method for robust shape optimization of a shell structure with unknown loading, or for creating the smooth optimal shell structure with high stiffness and independence of loading directions.

6. References

- [1] E. Cherkaev, A. Cherkaev, "Minimax optimization problem of structural design", *Computers and Structures*, Vol. 86 (2008), pp.1426-1435.
- [2] T. Takezawa, S. Nii, M. Kitamura and N. Kogiso, "Topology optimization for worst load conditions based on the eigenvalue analysis of an aggregated linear system" *Comput. Methods Appl. Mech. Engrg.* Vol. 200 (2011), pp.2268–2281.
- [3] Shimoda, M, Yang, L, A non-parametric free-form optimization method for shell structures, *Struct Multidisc Optim*, 50, 409-423, 2014.
- [4] Azegami, H, A Solution to Domain Optimization Problems, *Trans. of Jpn. Soc. of Mech. Eng.*, Ser. A, 60, 1479-1486, 1994.

Optimal Design of a Wheelchair Suspension Based on a Compliant Mechanism

Masakazu Kobayashi¹

¹ Toyota Technological Institute, Nagoya, Japan, kobayashi@toyota-ti.ac.jp

1. Abstract

In recent years, a compliant mechanism has been paid to attention as a new mechanism to replace a traditional rigid link mechanism and the use of compliant mechanisms in mechanical products, medical instruments and MEMS can be expected to increase. In our previous research, we focused on a vehicle suspension as a promising application target of a compliant mechanism and proposed an optimal design method for a vehicle suspension based on a compliant mechanism or a compliant suspension. In this research, we now apply a compliant suspension to a wheelchair and design a compliant suspension for a wheelchair using the method developed in the previous research. Most wheelchairs except some expensive ones don't have a suspension and only rely on tires for absorbing vibration and shock from a road. Since a compliant suspension consists of fewer parts than a traditional suspension and can be potentially integrated into a frame of a wheelchair, a compliant suspension can be added to a wheelchair at low cost. We design and manufacture a compliant suspension, retrofit an existing wheelchair with it and test ride quality of a wheelchair with a compliant suspension.

2. Keywords: Wheelchair, Suspension, Compliant mechanism, Topology optimization, Shape optimization.

3. Introduction

In mechanical design, mechanisms consisting of rigid parts linked to moveable joints are often used, and in such mechanisms, the relative motion of the links is constrained by the joints. On the other hand, compliant mechanisms [1] utilize a structure's flexibility to achieve a specified motion, by deforming the structure elastically instead of relying on joint movements. Such compliant mechanisms often consist of fewer parts than rigid link mechanisms, or can even be monolithic, and, compared to rigid link mechanisms, they have several merits [1] [2], such as reduced wear and operation noise, zero backlash, freedom from lubrication requirements, weight savings, manufacturing advantages, and ease of miniaturization. Therefore, the use of compliant mechanisms in mechanical products such as mechanical products, medical instruments and MEMS (Micro-Electro Mechanical Systems) [1] [3] can be expected to increase. In our previous research [4] [5], we focused on a vehicle suspension as a promising application target of a compliant mechanism and developed an optimal design method for a vehicle suspension based on a compliant mechanism or a compliant vehicle suspension.

In this research, we now apply a compliant suspension to a wheelchair and design a compliant suspension for a wheelchair using the method developed in the previous research. Most wheelchairs except some expensive ones don't have a suspension and only rely on tires for absorbing vibration and shock from a road. Figure 1 shows examples of wheelchairs without and with suspensions. Since a compliant suspension consists of fewer parts than a traditional suspension and can be potentially integrated into a frame of a wheelchair, a compliant suspension can be added to a wheelchair at low cost.



Figure 1: Wheelchairs without a suspension [6] (Left) and with a suspension [7] (Right)

4. Two stage design method of a compliant mechanism

Two stage design method [8] is the method for designing a compliant mechanism, consisting of topology and shape optimization. In this method, topology optimization first creates an initial outline of a compliant mechanism by considering only linear analysis. The optimal configuration of topology optimization is converted to an initial shape optimization model. At this point, design domains not considered during topology optimization can be added. Shape optimization then yields the detailed shape of a compliant mechanism by considering non-linear

analysis, stress constraints and making accurate quantitative performance evaluations. Using this method, a designer can more easily and efficiently create a practical compliant mechanism. In a series of our previous researches, two stage design method was extended to apply a design of a vehicle suspension based on a compliant mechanism. From many design requirements for a practical vehicle suspension, 5 essential requirements i.e. stroke, camber angle, roll centre height, lateral rigidity and natural frequency of a suspension system were selected and used as an objective function and constraints conditions of topology and shape optimization. See the references [4] [5] for their details. In this research, this method is applied to a design of a wheelchair suspension based on a compliant mechanism.

5. Design of a compliant wheelchair suspension

5.1 Design concept and conditions of a wheelchair suspension

Figure 2 shows the concept of a wheelchair suspension designed in this paper. A suspension is an independent part and attached to an existing wheelchair by an aluminium plate. Design domain of a suspension is 0.40m width and 0.25m height. Material of a suspension is ABS with Young's modulus of 2600MPa, Poisson's ratio of 0.32 and density of 1050kg/m³. Allowable stress is 58MPa. Thickness of a suspension is 0.02m. As for load, a wheelchair has 2 front small wheels and 2 rear large wheels and they share the weight of people and a wheelchair itself. After consideration of total weight, position of the centre of gravity and shock load, it is assumed that maximum load of a suspension is 500N. As for design requirements specific to a suspension, only stroke is considered. Target length of stroke is 0.02m when maximum load is applied.

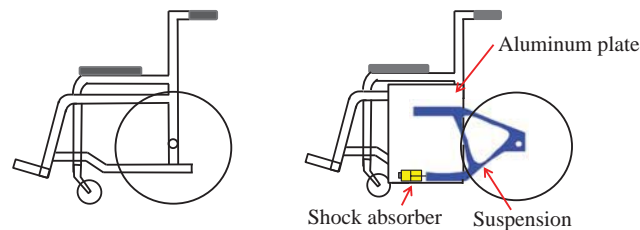


Figure 2: Existing wheelchair (Left) and concept of installation of a suspension (Right)

5.2 Topology optimization

By changing positions of input, output and constraints, the most promising initial outline of a suspension is explored. The volume constraint is set at 15%. Figure 3 and 4 show the design conditions and optimal configuration that are finally adopted respectively.

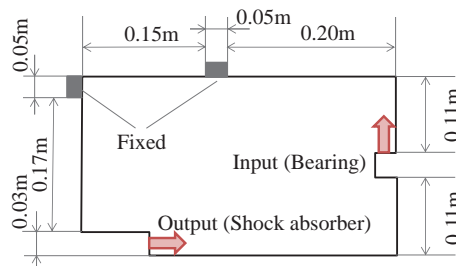


Figure 3: Design conditions

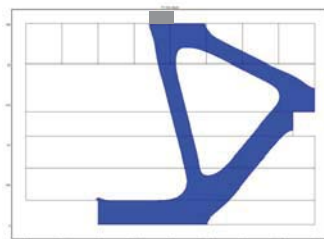


Figure 4: Optimal configuration

5.3 Shape optimization

The optimal configuration shown in Figure 4 is converted to an initial shape optimization model. In addition, connecting and bearing area is added to the model. Figure 5 shows the initial shape optimization model. Arrows shown in Figure 5 indicates control points whose coordinates are used as design variables of shape optimization. Table 1 summarizes initial, target and optimized values of stroke, maximum stress and weight. Figure 6 shows the optimal structure of a wheelchair suspension.

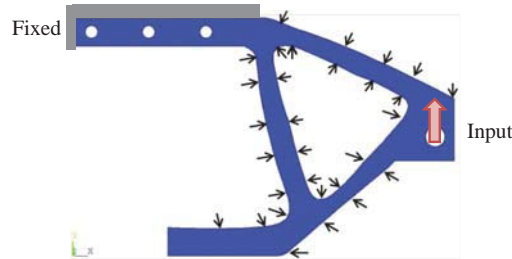


Figure 5: Initial shape optimization model

Table 1: Initial, target and optimized values of stroke, maximum stress and weight

	Initial	Target	Optimized
Stroke (m)	0.0056	0.02	0.02
Maximum stress (MPa)	22.9	<58.0	47.5
Weight (kg)	0.743	-	0.630

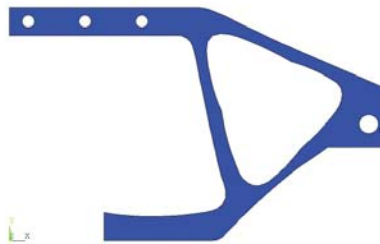


Figure 6: Optimal structure

6. Manufacturing and riding test of a wheelchair compliant suspension

The optimal structure of a suspension designed in the previous section is converted to a CAD model of SolidWorks. A suspension is made from an ABS plate by using a milling machine Roland D.G. MDX-540. Figure 7 shows the finished product. The suspension is attached to a wheelchair by an aluminium plate. Figure 8 shows a wheelchair with compliant suspensions. Since adequate shock absorbers cannot be bought due to time limitation, shock absorbers are not installed at this time. This is one of future subjects. The stroke length of a suspension when people ride on a wheelchair under stationary condition is 0.0085m.



Figure 7: Suspension manufactured by a milling machine



Figure 8: Wheelchair in which a suspension is installed

To test the effectiveness of a suspension, a riding test is conducted. 10 undergraduates participate the test as subjects. For comparison, they ride on wheelchairs with and without suspensions. A subject rides on a wheelchair and another person pushes a wheelchair to pass the obstacle shown in Figure 9. The obstacle is 0.45m width and 0.03m height. Ride quality of a wheelchair without suspensions when passing the obstacle is set at 3 and a subject relatively evaluates ride quality of a wheelchair with suspensions on a scale of 0.5 to 5. Figure 10 shows evaluation results and indicates that a suspension contributes the improvement of ride quality of a wheelchair.



Figure 9: Obstacle used for a riding test

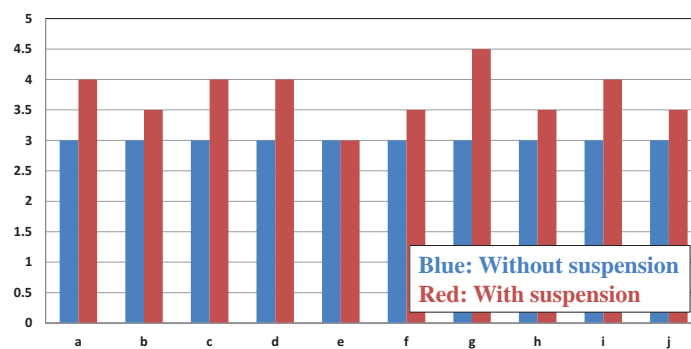


Figure 10: Evaluation of ride quality

7. Conclusion

In order to improve ride quality of a wheelchair with limited weight and cost, this paper proposes a wheelchair suspension based on a compliant mechanism. A suspension is designed by using two stage design method consisting of topology and shape optimization. To indicate the effectiveness of a suspension, it is designed, manufactured and attached to an existing wheelchair and a riding test is conducted.

As for future works, (1) installation of shock absorbers and measurement using accelerometer and (2) design of a suspension integrated into a frame of a wheelchair are planned.

8. Acknowledgements

This study was supported in part by a grant of Strategic Research Foundation Grant-aided Project for Private Universities from Ministry of Education, Culture, Sport, Science, and Technology, Japan (MEXT), 2013-2018 (S1311034).

9. References

- [1] L. L. Howell, *Compliant Mechanisms*, John Wiley & Sons, Inc., New York, 2001.
- [2] G. K. Ananthasuresh, and S. Kota, Designing compliant mechanisms, *ASME Mechanical Engineering*, 1995, 93-96.
- [3] U. D. Larsen, O. Sigmund and S. Bouswstra, Design and fabrication of compliant micromechanisms and structures with negative Poisson's ratio, *Journal of Microelectromechanical Systems*, 6 (2), 1997, 99-106.
- [4] M. Kobayashi and M. Higashi, Design method for a compliant vehicle suspension based on a combination of topology and shape optimizations, *Proceeding of 8th World Congress on Structural and Multidisciplinary Optimization*, June 1 - 5, 2009, Lisbon, Portugal.
- [5] M. Kobayashi, S. Omoto and M. Higashi, Optimal Design Method for a Vehicle Suspension Using a Compliant Mechanism Considering Static and Dynamic Characteristics, *The Seventh China-Japan-Korea Joint Symposium on Optimization of Structural and Mechanical Systems*, June, 18-21, 2012, Huangshan, China.
- [6] KV22-SB40, Kawamura Cycle Co. Ltd., <http://www.kawamura-cycle.co.jp/>
- [7] ZZR, OX ENGINEERING Co. Ltd., <http://www.oxgroup.co.jp/>
- [8] M. Kobayashi, S. Nishiwaki, K. Izui and M. Yoshimura, An innovative design method for compliant mechanisms combining structural optimisations and designer creativity, *Journal of Engineering Design*, 20 (2), 2009, 125-154.

Reliability-based design optimization of vehicle front-end structure for pedestrian lower extremity protection

Guangyong Sun¹, Xiaojiang Lv^{1,2}, Jianguang Fang³, Xianguang Gu¹, Qing Li³

1 State Key Laboratory of Advanced Design and Manufacturing for Vehicle Body, Hunan University, Changsha, 410082, China, sgy800@126.com;

2 Zhejiang Key Laboratory of Automobile Safety Technology, Geely Automobile Research Institute, Hangzhou, 311228, China;

3 School of Aerospace, Mechanical and Mechatronic Engineering, The University of Sydney, Sydney, NSW 2006, Australia

Abstract

Injuries to the lower extremities are one of the major issues in vehicle to pedestrian collisions. To minimize injury risks of pedestrian lower extremity, this paper presents the design optimization of a typical vehicle front-end structure subjected to two different impact cases of TRL-PLI and Flex-PLI. Several approaches involving sampling techniques, surrogate model, multiobjective optimization algorithm and reliability analysis are introduced and applied. In order to take into account the effect of design variables uncertainty, the reliability-based design optimization (RBDO) is conducted, and a Monte Carlo Simulation (MCS) is adopted to generate random distributions of the constraint functions for each design. The differences of the different Pareto fronts of the deterministic optimization and RBDO are compared and analyzed in this study. Finally, the reliability-based optimum design result is verified by using test validation. It is shown that the pedestrian lower extremity injury can be substantially improved for meeting product development requirements through the proposed approach.

Keywords: Reliability optimization; Vehicle front-end structure; Pedestrian protection; Multiple impact cases

1. Introduction

According to World Health Organization (WHO) statistical data, 22% of deaths on the world roads are pedestrians, and this proportion is as high as two thirds in some countries^[1]. Meanwhile, the frequency of lower extremity injuries is higher in vehicle to pedestrian collisions. For example, serious lower extremity injuries from bumper contact occurred in 43% of seriously injured pedestrian cases in US, 35% in German and 43% in Japan^[2-3]. So, researches on protection of pedestrian lower extremity have become a very important part in both the academe and automotive industry.

To evaluate the performance of lower extremity protection, two different subsystem legform tests have been used in the extensive government regulations and standards. One is Transport Research Laboratory Pedestrian Legform Impactor (TRL-PLI) in the European Union (EU) regulation, the other is Flexible Pedestrian Legform Impactor (Flex-PLI) in European New Car Assessment Program (EuroNCAP)^[4-5]. For instance, Shin et al.^[6] performed bumper size optimization and the result could meet requirements of TRL-PLI impact. Lee et al.^[7] researched the front-end structure for Flex-PLI impact. However, the above investigations on design optimization in the existing literature mainly focus on the single legform impactor. Matsui^[8] investigated the characteristics of safety assessment results of different vehicle types using the TRL-PLI and the Flex-PLI. The results showed that the tibia injury assessment was different between the TRL-PLI and the Flex-PLI owing to their different sensor types. So, the vehicle front-end structure is subjected to multiple legform impactor cases which should be verified for the required regulation and standard. However, the traditional approach is to tune the design manually for each test mode separately. It is therefore hardly to find a design that is work properly for all test modes.

All optimization problems cannot neglect the uncertainty, which exists in material properties, geometries and manufacturing precision etc. In order to take into account various uncertainty, Reliability-based design optimization (RBDO) is introduced and aims at finding a reliable optimum solution by converting the deterministic constraints into probabilistic ones. Many researchers have focused on this field^[9-12]. Nevertheless, vehicle front-end structural optimization for minimizing injury risks of TRL-PLI and Flex-PLI impact considering the uncertainty has received limited attention in the literature. To address the issue, The paper presents a comprehensive study approach of how different non-deterministic optimization schemes are performed in the design of vehicle front-end structure under multiple impact cases.

2 Performance assessment and experimental validation

2.1 TRL-PLI and Flex-PLI

According to EU regulation, the fracture risk of the tibia is evaluated from the upper tibia acceleration (a_{UT}) and the knee ligament damage risk is evaluated from the knee bending angle (a_{KB}) and knee shear displacement

(D_{KS}) as shown in Figure 1(a). The fracture risk of the tibia is evaluated from the tibia bending moment measured at multiple locations, and the knee ligament damage risk is evaluated from knee ligament elongations of Anterior Cruciate Ligament (ACL), Posterior Cruciate Ligament (PCL), and Medial Collateral Ligament (MCL) according to EuroNCAP as shown in Figure 1(b).

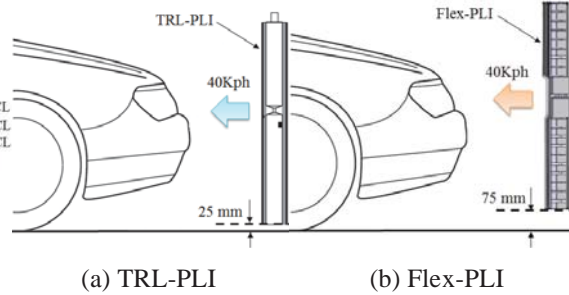
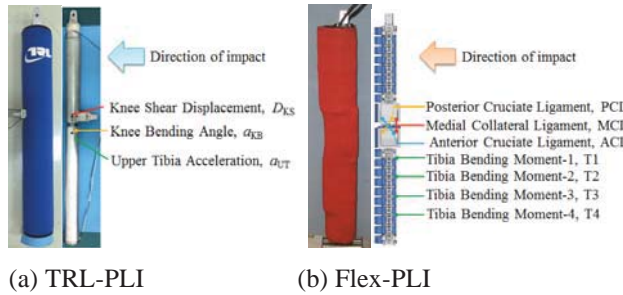


Figure 1: Injury criteria

Figure 2: The test condition of legform-to-bumper

2.2 Assessment of TRL-PLI and Flex-PLI

Tibia and knee injuries are assessed after completion of the legform-to-bumper test under the conditions shown in Figure 2. The initial velocity of two impact cases is 40 kph. In this study, the impact location is selected as the center of the bumper. The test results of the TRL-PLI and Flex-PLI injury is shown in Table 1. According to Table 1, the a_{UT} of the TRL-PLI (197.2g) is higher than the EU regulation limit value (170g). It is found that the ACL (11.2mm) is more than 10mm, which cannot meet the Euro-NCAP assessment rating requirements.

Table 1 The assessment of the TRL-PLI and Flex-PLI test results

		TRL-PLI				Flex-PLI			
	Injury	Requirement	Test	Assessment	Injury	Requirement	Test	Assessment	
Tibia injuries	a_{UT} (g)	≤ 170	197.2	Violated	T1 (Nm)	≤ 282	209.1	Satisfied	
					T2 (Nm)	≤ 282	264.5	Satisfied	
					T3 (Nm)	≤ 282	278.3	Satisfied	
					T4 (Nm)	≤ 282	161.5	Satisfied	
Knee injuries	α_{KB} (°)	≤ 19	13.1	Satisfied	MCL (mm)	≤ 19	16.4	Satisfied	
	D_{KS} (mm)	≤ 6	2.3	Satisfied	ACL (mm)	≤ 10	11.2	Violated	
	/	/	/	/	PCL (mm)	≤ 10	5.0	Satisfied	

To meet the design requirement, the multiobjective reliability-based optimization design is introduced to design the front-end structure for minimize injury values of TRL-PLI and Flex-PLI. This procedure is shown in Figure 3. The Optimal Latin Hypercube Sampling (OLHS) technique adopted for constructing the surrogate models. The RBF model is constructed based on the response results of sampling points. The MOPSO is applied to search the optimal solution set. The Monte Carlo Simulation (MCS) is applied to perform a reliable analysis.

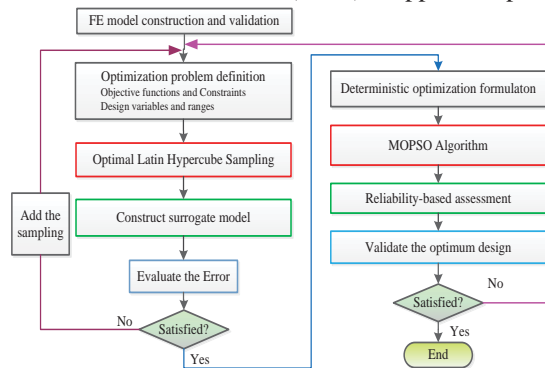


Figure 3: Flowchart of the reliability design optimization process

2.3 Numerical model and validation

To assess the protection performance of various vehicle front-end structures, the finite element (FE) model need be constructed. The baseline model, as shown in Figure 4, consists of the following groups of components: bumper, hood, front rail, lamp, energy absorbing plate, spoiler support plate et al. In this study, the validity of CAE model is conducted by comparing the simulation results with the corresponding physical test results with these

curves of a_{UT} and ACL elongation as plotted in Figure 5. From which, the simulation curves of the a_{UT} and ACL elongation all well agree with the corresponding results obtained from the physical test. The maximum difference between simulation and test is less than 5% and the total area and trend of curves are rather alike. As shown in Figure 6, each legform campaign gesture agrees well with the physical test. Therefore, the CAE model is accurate and effective for the vehicle front-end structure design optimization in the subsequent study.

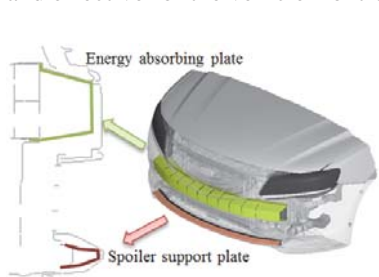


Figure 4: The FE model

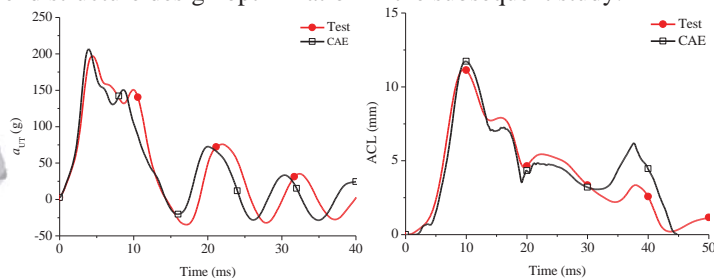


Figure 5: Comparison of the curves between simulation and physical test

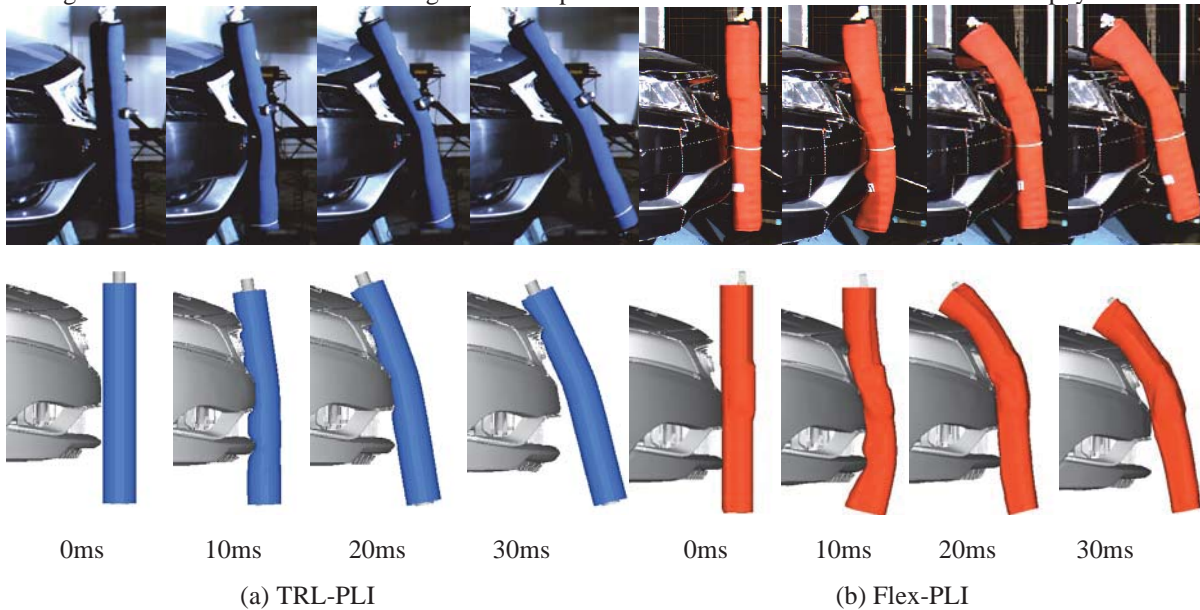


Figure 6: Different time steps of TRL-PLI and Flex-PLI impact between the simulation and physical test

3 Vehicle front-end structure design optimization

3.1 Design responses and variables

From engineering experience, the rigidity of energy absorbing plate and spoiler support plate have important effect on pedestrian legform injury, thereby making the best possible combination of these components under each legform impact conditions. The thickness of energy absorbing plate (x_1), the X-direction distance of energy absorbing plate (x_2), the thickness of spoiler support plate (x_3), the X-direction distance of spoiler support plate (x_4), have significant influences on front-end structure rigidity. Thus, these parameters are taken as design variables, as show in Figure 7. Table 2 provides the list of the design variables, the baseline design values, as well as the corresponding lower and upper bounds. In order to take into account the uncertainties, the design variables are assumed to distribute normally in this study, whose coefficient of variation is given as 5% from typical manufacturing and assembly tolerance. The variations of design parameters are selected in terms of possible design changes allowed.

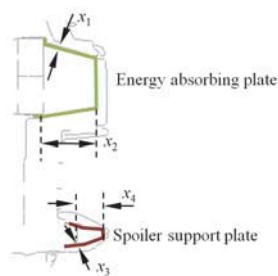


Figure 7: Design variables

According to Table 1, the upper tibia acceleration of TRL-PLI and ACL of Flex-PLI could not meet the design requirements. For this reason, they are chosen as the design objectives in Table 3. Considering that the design variables have an influence on other eight injury values of TRL-PLI and Flex-PLI, and eight of them are chosen as the constraints. Table 3 lists the responses of baseline design and the allowance of each constraint.

Table 2 The value of the design variables

Design variations	Distribution	COV(σ/μ)	Initial value	Boundary value	
				Lower	Upper
x_1	Normal	5%	1.0mm	0.6mm	1.4mm
x_2	Normal	5%	80mm	20mm	100mm
x_3	Normal	5%	1.0mm	0.6mm	1.4mm
x_4	Normal	5%	80mm	20mm	100mm

Table 3 The baseline design and design optimization target

Responses	Objectives					Constraints				
	a_{UT}	ACL	a_{KB}	D_{KS}	T1	T2	T3	T4	MCL	PCL
	$f_1(x)$	$f_2(x)$	$g_1(x)$	$g_2(x)$	$g_3(x)$	$g_4(x)$	$g_5(x)$	$g_6(x)$	$g_7(x)$	$g_8(x)$
Baseline	206.71	11.70	13.60	2.23	218.78	263.24	290.80	162.81	16.92	5.21
Target	Min	Min	≤ 18.05	≤ 5.7	≤ 267.9	≤ 267.9	≤ 267.9	≤ 267.9	≤ 18.05	≤ 9.5

3.2 Constructed metamodel

For four continuous variables $\mathbf{x} = (x_1, x_2, x_3, x_4)$, the number of levels for each variable can be selected to be 5 and a total of 25 sampling points are generated in the design space by the OLHS method. The objective and constraint values of each sampling point are obtained by using LS-DYNA version 971. Four typical basis functions of RBF including thin-plate spline, Gaussian, multiquadric and inverse multiquadric are used and their accuracies are compared. In this study, additional 10 validation points are selected to assess the accuracy of these surrogates. Based on these validation points, the accuracies of basis function of RBF model can be assessed by using estimators of R^2 and RAAE. Validation results of selected error metrics for different functions of RBF metamodel are shown in Table 4. The fitting results of multiquadric function of RBF model are very good with high values of $R^2 \geq 0.9$ and low $RAAE \leq 0.3$. Therefore, the Multiquadric function of RBF model is considered most suitable and are selected to perform the design optimization below.

Table 4 Error assessment for different functions of RBF metamodel

	Thin-plate spline		Gaussian		Multiquadric		Inverse multiquadric	
	R^2	RAAE	R^2	RAAE	R^2	RAAE	R^2	RAAE
a_{UT}	0.9092	0.574	0.8412	0.273	0.9532	0.252	0.9462	0.331
ACL	0.8721	0.413	0.8651	0.440	0.9123	0.231	0.9354	0.332
a_{KB}	0.8126	0.388	0.8135	0.255	0.934	0.218	0.8936	0.327
D_{KS}	0.8215	0.554	0.8341	0.465	0.9616	0.222	0.9321	0.251
T1	0.8934	0.257	0.815	0.367	0.9251	0.159	0.8955	0.359
T2	0.8232	0.452	0.8189	0.279	0.9294	0.212	0.9094	0.453
T3	0.8971	0.630	0.9063	0.312	0.9571	0.203	0.9013	0.370
T4	0.9136	0.471	0.933	0.307	0.9072	0.291	0.9036	0.271
MCL	0.8752	0.484	0.8653	0.491	0.9136	0.289	0.9022	0.284
PCL	0.8751	0.352	0.8852	0.342	0.9203	0.291	0.8713	0.451

3.3 Reliability-based design optimization

In the reliability-based design optimization, the desired reliability of eight design constraints (R_j) are set as 95% and 99%. And the minimize value of mean value is set for the two objectives, respectively. The reliability-based design is formulated as:

$$\begin{aligned}
 & \min \quad \mu(f_1(\mathbf{x})) \\
 & \quad \mu(f_2(\mathbf{x})) \\
 \text{s.t.} \quad & P(g_1(\mathbf{x}) \leq 18.05^\circ) \geq R_j \\
 & P(g_2(\mathbf{x}) \leq 5.7\text{mm}) \geq R_j \\
 & P(g_3(\mathbf{x}) \leq 267.9\text{Nm}) \geq R_j \\
 & P(g_4(\mathbf{x}) \leq 267.9\text{Nm}) \geq R_j \\
 & P(g_5(\mathbf{x}) \leq 267.9\text{Nm}) \geq R_j \\
 & P(g_6(\mathbf{x}) \leq 267.9\text{Nm}) \geq R_j \\
 & P(g_7(\mathbf{x}) \leq 18.05\text{mm}) \geq R_j \\
 & P(g_8(\mathbf{x}) \leq 9.5\text{mm}) \geq R_j \\
 & \mathbf{x}^L \leq \mathbf{x} \leq \mathbf{x}^U, \quad \mathbf{x} = (x_1, x_2, x_3, x_4)^T
 \end{aligned} \tag{1}$$

The four design variables according to the probability distribution defined previously are incorporated, and reliability-based optimization is performed. The Pareto fronts are obtained using the MOPSO algorithm with the population size (50) and number of generations (100). The MCS is consisted with 10,000 descriptive sampling points using given distribution in this study. Performing the Monte Carlo analysis using RBF to the functions instead of CAE function evaluations allows a significant reduction in the cost of the procedure. Figure 8 presents the Pareto fronts for multiobjective deterministic and reliable designs.

In three Pareto fronts, each point represents one solution in different cases, which indicates the trade-off between upper tibia acceleration and ACL elongation. Obviously, these two objectives strongly compete with each other: the lower upper tibia acceleration, the higher ACL elongation. It is noted that the Pareto front of the 95% reliable design is farther away from the deterministic counterpart and the 99% reliable design is farthest away from the 95% reliable design in Figure 8.

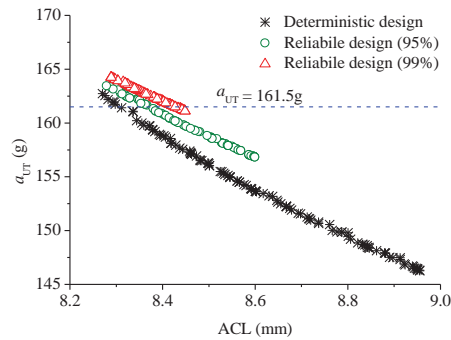


Figure 8: Pareto fronts of the deterministic and reliable design optimization

3.4 Comparison and validation of optimization results

Figure 9 shows the optimal Flex-PLI response results of physical test at different times. It is noted that the optimal is obtained by the minimum distance selection method (TMDSM). Compared with Figure 6, the third image shows that the knee bending degree is obviously abated at 20ms. The kinetic energy can be adequately absorbed by the front-end structure in the optimum design.

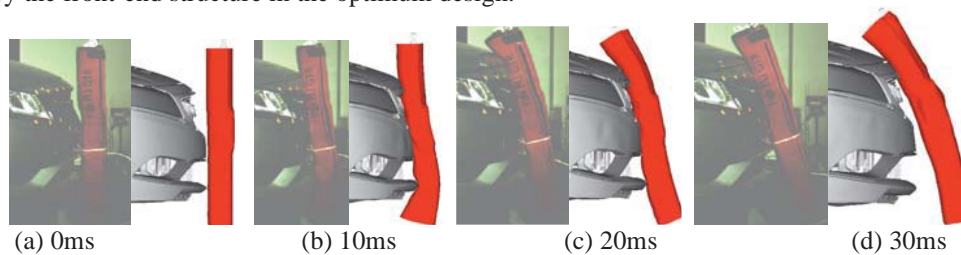


Figure 9: Animation after the optimization design

Table 5 The test results between the baseline and optimal design

Description		Baseline (Test)	Optimal result (Test)	Reduction (%)
Objectives	$f_1(x)$	197.2	156.71	20.53
	$f_2(x)$	11.2	8.09	27.77
Constraints	$g_1(x)$	13.1	11.51	
	$g_2(x)$	2.3	2.38	
	$g_3(x)$	209.1	186.26	
	$g_4(x)$	264.5	252.34	

	$g_5(x)$	278.3	263.87
	$g_6(x)$	161.5	149.12
	$g_7(x)$	16.4	14.59
	$g_8(x)$	5.0	5.46
Variables	x_1	1.0mm	0.62mm
	x_2	80mm	45.02mm
	x_3	1.0mm	0.81mm
	x_4	80mm	84.98mm

According to the response values of tests, the results between the baseline and optimal is compared in Table 5. The injury values of a_{UT} and ACL elongation are reduced to 20.53% and 27.77% relative to the initial design, respectively. Thus, the optimization result satisfies the design requirements. In summary, the presented method is effective for the front-end structure design, and these results show that the optimal design has improved the pedestrian safety significantly.

4 Conclusions

A system approach has been developed to design and optimize the vehicle front-end structure for minimizing injury risks of pedestrian lower extremity based on TRL-PLI and Flex-PLI in this study. The numerical model of TRL-PLI and Flex-PLI impact vehicle was constructed first and validated with physical test. Then, the optimal Latin hypercube sampling (OLHS) method was adopted for design of experiment (DOE) and the surrogate model was constructed through Radial basis function (RBF). The optimal problems involving in a number of objectives were solved by the multiobjective particle swarm optimization (MOPSO) algorithm in this study. In order to take into account the uncertainties of design variables, the Monte Carlo simulation (MCS) is used as reliability analysis. It was found that the result of reliability-based design was more conservative than the results of deterministic optimization as expected. As the variation of performance constraint functions raised by the uncertainties of design variables was considered, the reliability of the front-end structure design for the vehicle safety was greatly improved in the real engineering application.

Acknowledgments

This work is supported jointly by National Natural Science Foundation of China (51405123, 11202072) and the Open Fund of Zhejiang Key Laboratory of Automobile Safety Technology (No. 2009E10013).

References

- [1] The World Health Organization (WHO), Global status report on road safety 2013: supporting a decade of action, *WHO Report*, 2013
- [2] Mallory A, Rikard F, Erik R, Bruce D, Pedestrian Injuries By Source: Serious and Disabling Injuries in US and European Cases, *Association for the Advancement of Automotive Medicine*, 56: 13-24, 2012
- [3] Matsui Y, Possibility of installing a data acquisition system in a pedestrian headform impactor, *Int J Crashworthiness*, 19(2): 115-125, 2014
- [4] Regulation (EC) No78/2009 of the European Parliament and of the Council of 14 January 2009, *Official J of the European Union*, 2009
- [5] Euro NCAP, Pedestrian Protection Assessment Protocol, version 8.0, <http://www.euroncap.com/files/>, 2014
- [6] M Shin, S Yi, O Kwon, G Park, Structural optimization of the automobile frontal structure for pedestrian protection and the low-speed impact test, *Proceedings of the Institution of Mechanical Engineers*, 222 (D12): 2373-2387, 2008
- [7] Lee Y, Joo Y, Park J, Kim Y, Yim H, Robust design optimization of frontal structures for minimizing injury risks of flex pedestrian legform impactor, *Int J Auto Tech*, 15(5): 757-764, 2014
- [8] Matsui Y, Safety assessment characteristics of pedestrian legform impactors in vehicle-front impact tests, *Accid Anal Prev*, 73: 65-72, 2014
- [9] Shi L, Zhu P, Yang R, Lin S, Adaptive sampling-based RBDO method for vehicle crashworthiness design using Bayesian metric and stochastic sensitivity analysis with independent random variables, *Int J Crashworthiness*, 18(4): 331-342, 2013
- [10] Gu XG, Lu JW, Wang HZ, Reliability-based design optimization for vehicle occupant protection system based on ensemble of metamodels, *Struct Multidisc Optim*, DOI 10.1007/s00158-014-1150-7, 2014
- [11] Sinha K, Reliability-based multiobjective optimization for auto-motive crashworthiness and occupant safety, *Struct Multidisc Optim*, 33(3): 255-268, 2007
- [12] Huang T, Wu J, Hsiao C, Wang M, Lee K, Design of a bumper system for pedestrian lower-leg protection using the Taguchi method, *J Auto Eng*, 225: 1578-1586, 2011
- [13] Sun GY, Li GY, Hou SJ, Zhou SW, Li W, Li Q, Crashworthiness design for functionally graded foam-filled thin-walled structures, *Mat Sci Eng A*, 527(7-8):1911-1919, 2010

Optimization of bone tissue scaffolds fabricated by robocasting technique

Ali Entezari¹, Zhongpu Zhang², Junning Chen³, Qing Li⁴

¹School of Aerospace, Mechanical and Mechatronic Engineering, University of Sydney, NSW, Australia, aent9923@uni.sydney.edu.au

²School of Aerospace, Mechanical and Mechatronic Engineering, University of Sydney, NSW, Australia, leo.zhang@sydney.edu.au

³School of Aerospace, Mechanical and Mechatronic Engineering, University of Sydney, NSW, Australia, jche8767@uni.sydney.edu.au

⁴School of Aerospace, Mechanical and Mechatronic Engineering, University of Sydney, NSW, Australia, qing.li@sydney.edu.au

1. Abstract

While excellent biological and mechanical properties of ceramic scaffolds place them amongst the main candidates for applications of bone and cartilage repair, an optimum trade-off between critical biological and mechanical functions remains challenging during design process. These ceramic scaffolds should not only enhance tissue regeneration function, but also be of adequate mechanical strength particularly in load-bearing applications. One of the techniques used for the fabrication of ceramic scaffolds is robocasting which has so far received little attention in the currently available optimization analyses related to the design of these scaffolds. In this study a vigorous optimization analysis based on finite element (FE) method is performed to maximize compressive strengths of such scaffolds while maintaining the minimum biological functions required for tissue ingrowth. The results demonstrate that an optimized functionality of ceramic scaffolds fabricated by robocasting needs a careful design of critical geometrical features.

2. Keywords: Robocasting, bone tissue engineering, ceramic scaffolds, optimization

3. Introduction

Today, there is an increasing need for the treatment of bone defects caused by trauma, infection, or injuries. Current treatments for bone defects include autografts, allografts and other synthetic substitutes such as metals and bio-ceramics [1] which all have their own problems and limitations. As a result, recent research has been devoted to bone tissue engineering (BTE) which emerged in the early 1990s to address limitations of tissue grafting [2]. In the scaffold tissue engineering strategy, a 3D scaffold populated with cells and signaling molecules is used to provide temporary biomechanical environment for tissue regeneration for promoting cell attachment and growth of neo-tissue. Despite remarkable progress in BTE, many challenges and limitations still exist on the way of such scaffolds to be marketed and replace current conventional treatments of bone defects. One of the most important challenges associated with BTE scaffolds is to optimize their mechanical and biological functionality so that they can provide adequate mechanical support and enhance tissue regeneration. These two functions often result in conflicting design goals, because improved mechanical support function needs a dense scaffold while enhanced tissue regeneration function requires a porous scaffold. Therefore, an optimum trade-off between biological and mechanical criteria is necessary in the design of bone scaffolds.

A number of different optimization studies based on numerical methods have been established in literature [3, 4]. Hollister and colleagues [5] were amongst the first who applied the finite element based homogenization theory to relate periodic orthogonal pore diameters of a scaffold to its effective stiffness and porosity. They used topology optimization approach to matching the effective moduli of minipig mandibular cancellous bone to ceramic material. In other studies, the direct homogenization [6] and inverse homogenization approaches [7] were implemented to maximize the effective modulus of BTE scaffolds. Further studies were performed by Chen et al. [8] and Adachi et al. [9], in which the interaction process of scaffold degradation and tissue regeneration were also taken into account in the optimization process.

While significant advances have been made in available optimization studies on tissue engineering scaffolds, almost none of these studies have considered fabrication limitations induced by the so-called robocasting technique. Another concern associated with currently available optimization studies is that they do not take account of scaffold's strength as a design criterion in the optimization process because stress is a non-differentiable quantity [10, 11] which could have significantly limited the reliability of such optimization approaches. Therefore consideration of fracture strength is critical to develop more trustworthy optimization methods, particularly for ceramic scaffolds whose application in load-bearing scenarios is often limited due to the inherent brittleness and relatively low fracture strength. Numerical methods have shown their capability to effectively predict fracture strength of such scaffolds based on the stress fields obtained by FE simulations [12].

In this study, FE method will be used to conduct a design optimization analysis of Hydroxyapatite (HA) scaffolds fabricated by robocasting technique to maximize their strength for load-bearing applications.

4. Method

Different parameters such as porosity, pore size, and interconnectivity of scaffolds affect the quality of tissue regeneration, among which porosity is the main design variable known to influence tissue regeneration [13], which has often been considered as a biological design criterion in different optimization studies. Here, while a constraint is imposed on the porosity of scaffolds in order to satisfy biological functions, the effect of different geometrical features will be investigated on strength and effective modulus of the scaffolds. Since the scaffolds are assumed to be fabricated by the robocasting technique, fabrication limitations related to this technique should be taken into account. Robocasting or direct ink writing (DIW) technique is a solid free form (SFF) fabrication method in which a filament of ink is extruded from a nozzle in a layer-wise fashion and ultimately forms a 3-D mesh of interpenetrating struts whose structure can have different patterns depending on design requirements [14]. Figure 1 shows three of most common patterns fabricated by this technique.

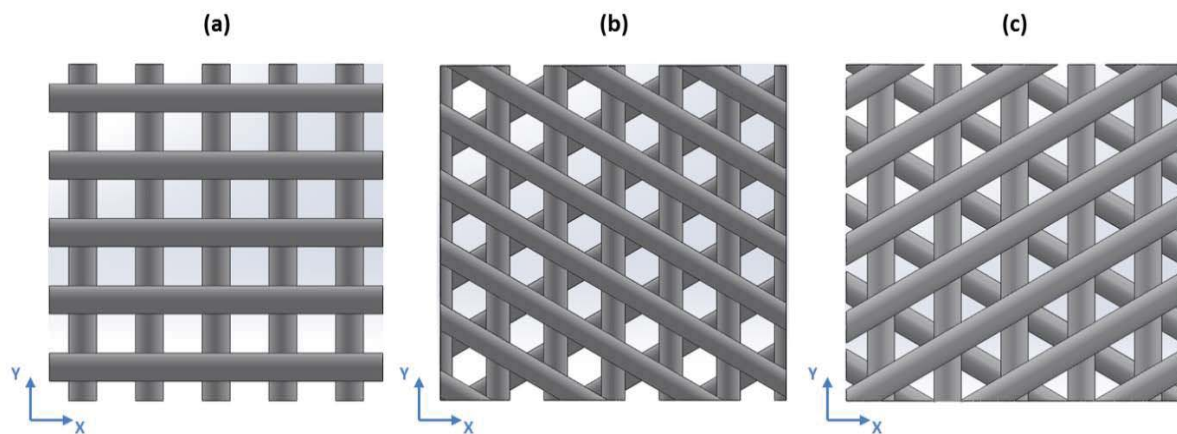


Figure 1 : Three of most common patterns fabricated by robocasting technique; (a) square pattern; (b) honey comb pattern; (c) triangle pattern

In the first step, a comparison will be made between the fracture strengths related to each of the above patterns. For this purpose, three different scaffolds based on these patterns are created in SolidWorks software. All three scaffolds have similar porosity, strut and pore size. Then FE simulations are carried out using ABAQUS/CAE software in which the scaffolds are placed in between two parallel analytical rigid plates. One of the rigid plates is fixed while the other can move under the action of a linearly increasing applied force. The force is applied perpendicular to the printing plane (x-y plane) simulating a compression test in the z direction. Fracture strength for each test is predicted based on a critical stress criterion by assuming an opening fracture mode (mode I), which is the most commonly activated in brittle materials [15]. This fracture mode is known to induce cracking perpendicular to the rod axes over the entire structure at the points experiencing the highest tensile stress (σ_t) [12]. Hence, in the current analyses, fracture is presumed to occur when the maximum of σ_t in the structure equals the inert fracture strength (σ_f) of the rods reported in [12]. For instance, Figure 2 represents FE stress contours corresponding to the highest range of tensile stress in the square pattern. Since an applied compressive stress of 39 (MPa) on the top surface leads to the maximum tensile stress equivalent to σ_f in the structure, it will be taken as the compressive strength of the scaffold. For the determination of the maximum of tensile stress, stress at near-contact regions and singularities are ignored. Intrinsic mechanical properties of HA [12] used in current numerical simulations have been given in Table 1.

Table 1 : Intrinsic mechanical properties of HA

	E (GPa)	ν	σ_f (MPa)
Hydroxyapatite (HA)	85	0.28	80

Table 2 represents the mechanical properties related to the three different configurations of tissue scaffolds obtained by FE analysis.

Table 2 : Mechanical properties for the three different configurations of scaffolds

	Square pattern	Honey comb pattern	Triangle pattern
Compressive strength (MPa)	39	6.5	33.8
Compressive effective modulus (GPa)	11.7	4.08	11.7

The results show that square pattern offers the highest compressive strength compared with the other two topologies. Another fact that can be concluded from the above results is that effective modulus of scaffolds may not be correlated to their strength, because as it can be observed, while square and triangle patterns have similar effective modulus, their strengths are not the same. Moreover, honey comb pattern offers an effective modulus which is almost three times less than the one related to square pattern, nevertheless, its strength is more than 6 times smaller than the one for square array. All these results signify the importance of considering strength as an optimization criterion for the design of bone tissue engineering scaffolds.

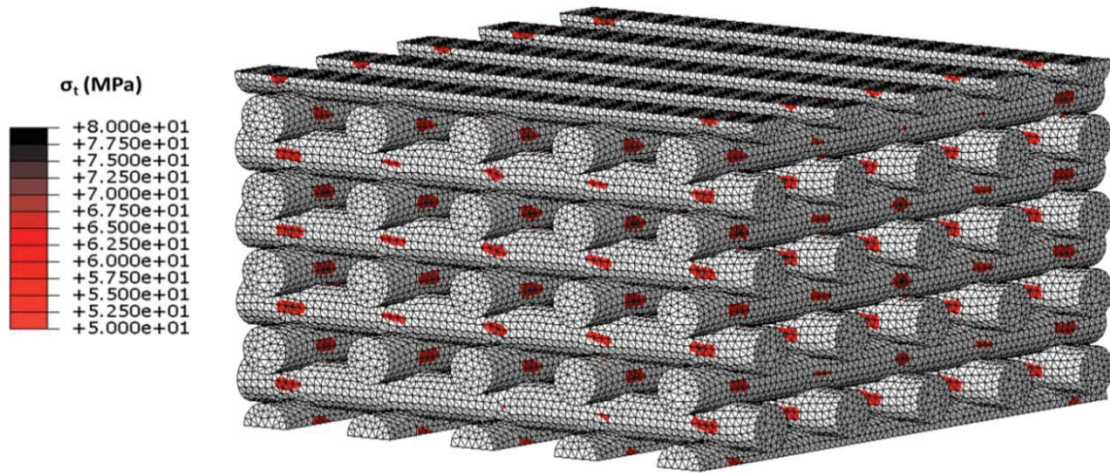


Figure 2 : FE stress contours corresponding to the highest range of tensile stress in the square pattern when a compressive stress of 39 MPa is applied perpendicular to the top surface (note that the stress contour shows only the top range of tensile stresses and the rest in grey indicates the lower stress)

Since it was observed that the square pattern offers better mechanical properties, the geometry of this pattern will be optimized as follows. In order to define controllable geometrical features, a representative volume element (RVE) whose repetition forms the entire scaffold needs to be defined. A RVE can often be found within scaffolds fabricated by the robocasting technique. Figure 3a clearly shows how the repetition of a RVE forms a scaffold with a square pattern.

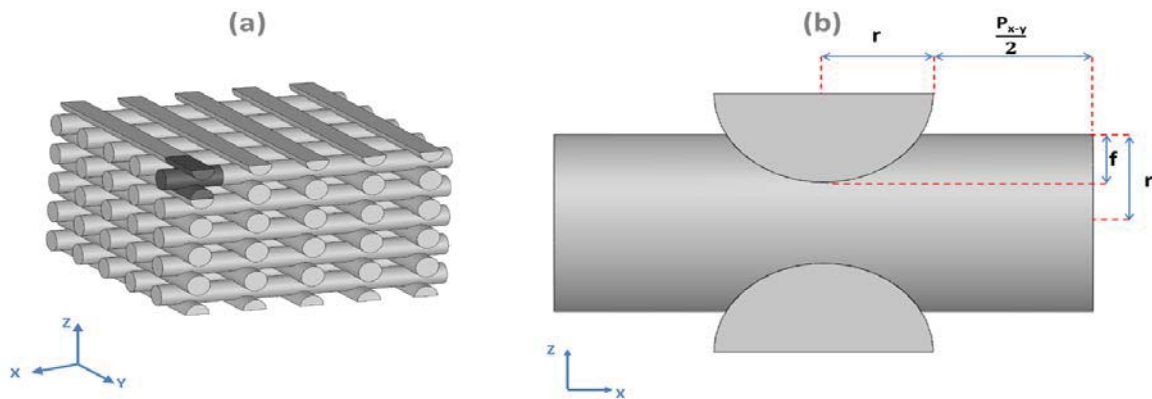


Figure 3 : A scaffold with square array fabricated by the robocasting technique; (a) the scaffold and a section displayed in black color represents a RVE within the scaffold; (b) controllable geometrical features in a RVE

Once a RVE is extracted from the scaffold, its geometrical features can be defined in terms of three controllable parameters as shown in Figure 3b. These parameters include scaffold's pore size in the printing plane (P_{x-y}), radius of each strut's cross section (r), and overlapping depth of two struts at top of one another (f). Given that the RVE is used to represent the entire scaffold, the porosity of scaffold can be expressed as:

$$Porosity = 100 \times \left[1 - \frac{2\pi r^2 (p_{x-y} + 2r) - 2V_f}{(4r - 2f)(p_{x-y} + 2r)^2} \right] \quad (1)$$

where V_f represents the intersection volume of two overlapping struts at top of one another, expressed as:

$$V_f = 4 \int_{r-f}^r \int_0^{\sqrt{r^2-x^2}} \int_0^{\sqrt{r^2-(2r-f-x)^2}} dz dy dx \quad (2)$$

Given that a desirable minimum value is required for porosity in order to satisfy tissue ingrowth function, the effect of other geometrical features on the strength and effective modulus of scaffolds can be investigated. It is obvious that at least two of the aforementioned geometrical features must change simultaneously, in order to maintain a constant desirable porosity of the scaffold. In this study a constraint is imposed on the porosity of scaffold (porosity = 60%), and 8 scaffolds with similar strut's radius (r) but different pore size (P_{x-y}) and overlapping depth (f) will be compared. Ratio of overlapping depth to radius (f/r), which can be easily adjusted during fabrication process by changing layer spacing, has a range from 10% to 80% in this study [16, 17]. The details of geometrical features related to these 8 scaffolds are given in Table 3.

Table 3 : Details of geometrical features related to 8 different scaffolds

	f/r	P_{x-y} (μm)	f (μm)	Porosity
Scaffold 1	0.1	1140	30	60%
Scaffold 2	0.2	1080	60	60%
Scaffold 3	0.3	1020	90	60%
Scaffold 4	0.4	960	120	60%
Scaffold 5	0.5	900	150	60%
Scaffold 6	0.6	840	180	60%
Scaffold 7	0.7	780	210	60%
Scaffold 8	0.8	720	250	60%

5. Results and discussion

Figure 4 draws a comparison between compressive strengths related to these 8 different scaffolds with varying pore sizes (P_{x-y}) and overlapping depths (f) listed in Table 3. While a constant porosity is maintained for all scaffolds, a change in their controllable geometrical features can result in significant improvement of their compressive strength. It was observed that the optimum ratio of f/r for the geometry of such scaffolds is around 0.4. In fact, this optimized geometry could enhance the compressive strength by 32% and 17% compared with the cases in which f/r was 0.1 and 0.8 respectively.

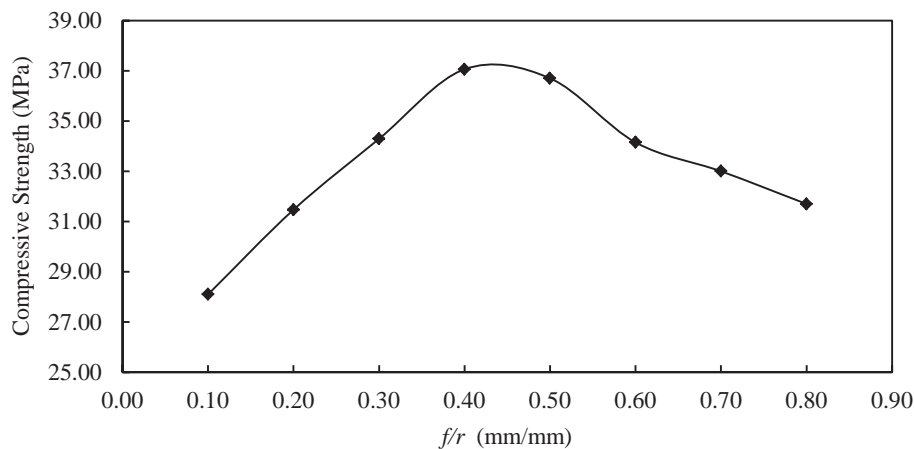


Figure 4 : Comparison between compressive strengths related to scaffolds with different f/r ratio

Since effective modulus of bone tissue engineering scaffolds plays an important role on their biomechanical functions, a comparison is also drawn between the compressive effective modulus related to these 8 scaffolds, which is presented in Figure 5. The results demonstrate that the optimized geometry will possess a greater effective modulus as well. Interestingly, it was observed that effective modulus for the optimized geometry ($f/r = 0.4$) was enhanced by 52% compared with the worst case ($f/r = 0.1$), whereas this improvement was only 32% for the compressive strength, a fact that shows it is important to take into the account the mechanical strength of scaffolds in the design optimization of bone tissue engineering scaffolds.

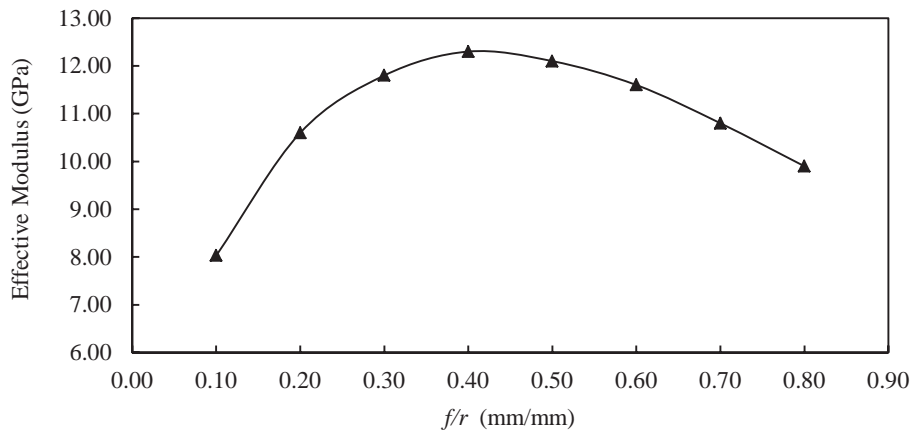


Figure 5 : Comparison between effective modulus related to scaffolds with different f/r ratio

6. Conclusion

This article could provide valuable insight into the optimization of ceramic scaffolds for bone tissue engineering applications fabricated by the robocasting technique. The results demonstrated that an optimized functionality of such scaffolds needs a careful control over particular geometrical features during design process. The square patterns showed better mechanical properties in terms of compressive strength compared with honey comb and triangular patterns. Moreover, for a square pattern, the results confirmed that an optimum relationship exists between its geometrical features which would significantly increase the compressive strength of such scaffolds while a constraint is imposed on its total porosity. It was also observed that effective modulus of scaffolds may not always represent their strength, a fact that signifies the importance of fracture strength to be considered as a design criterion in optimizations analyses of scaffolds.

7. References

- [1] Goldberg, V.M., *Natural history of autografts and allografts*, in *Bone implant grafting*. 1992, Springer. p. 9-12.
- [2] Moore, W.R., S.E. Graves, and G.I. Bain, *Synthetic bone graft substitutes*. ANZ journal of surgery, 2001. **71**(6): p. 354-361.
- [3] Chan, K.S., et al., *A multiscale modeling approach to scaffold design and property prediction*. Journal of the Mechanical Behavior of Biomedical Materials, 2010. **3**(8): p. 584-593.
- [4] van Cleynenbreugel, T., et al., *Trabecular bone scaffolding using a biomimetic approach*. Journal of Materials Science: Materials in Medicine, 2002. **13**(12): p. 1245-1249.
- [5] Hollister, S., R. Maddox, and J. Taboas, *Optimal design and fabrication of scaffolds to mimic tissue properties and satisfy biological constraints*. Biomaterials, 2002. **23**(20): p. 4095-4103.
- [6] Lin, C.Y., N. Kikuchi, and S.J. Hollister, *A novel method for biomaterial scaffold internal architecture design to match bone elastic properties with desired porosity*. Journal of Biomechanics, 2004. **37**(5): p. 623-636.
- [7] Hollister, S.J. and C.Y. Lin, *Computational design of tissue engineering scaffolds*. Computer Methods in Applied Mechanics and Engineering, 2007. **196**(31-32): p. 2991-2998.
- [8] Chen, Y., S. Zhou, and Q. Li, *Microstructure design of biodegradable scaffold and its effect on tissue regeneration*. Biomaterials, 2011. **32**(22): p. 5003-5014.
- [9] Cahill, S., S. Lohfeld, and P. McHugh, *Finite element predictions compared to experimental results for the effective modulus of bone tissue engineering scaffolds fabricated by selective laser sintering*. Journal of Materials Science: Materials in Medicine, 2009. **20**(6): p. 1255-1262.

- [10] Steven, G.P., Q. Li, and Y.M. Xie, *Multicriteria optimization that minimizes maximum stress and maximizes stiffness*. Computers & Structures, 2002. **80**(27–30): p. 2433-2448.
- [11] Li, Q., G.P. Steven, and Y. Xie, *Evolutionary structural optimization for stress minimization problems by discrete thickness design*. Computers & Structures, 2000. **78**(6): p. 769-780.
- [12] Miranda, P., A. Pajares, and F. Guiberteau, *Finite element modeling as a tool for predicting the fracture behavior of robocast scaffolds*. Acta biomaterialia, 2008. **4**(6): p. 1715-1724.
- [13] Mikos, A.G., et al., *Prevascularization of porous biodegradable polymers*. Biotechnology and Bioengineering, 1993. **42**(6): p. 716-723.
- [14] Stuecker, J.N., et al., *Advanced support structures for enhanced catalytic activity*. Industrial & engineering chemistry research, 2004. **43**(1): p. 51-55.
- [15] Lawn, B.R., *Fracture of brittle solids*. 1993: Cambridge university press.
- [16] Maazouz, Y., et al., *Robocasting of biomimetic hydroxyapatite scaffolds using self-setting inks*. Journal of Materials Chemistry B, 2014. **2**(33): p. 5378-5386.
- [17] Miranda, P., et al., *Mechanical properties of calcium phosphate scaffolds fabricated by robocasting*. Journal of Biomedical Materials Research Part A, 2008. **85A**(1): p. 218-227.